

Proceedings of ICoEV 2015 International Conference on Engineering Vibration

Ljubljana, 7 - 10. September

CIP
National and University Library of Slovenia

621.8.034(082)(0.034.2)

INTERNATIONAL Conference on Engineering Vibration (2015 ; Ljubljana)
Proceedings of ICoEV 2015 [Electronic source] / International Conference on Engineering Vibration, Ljubljana, 7 - 10. September ; [editors Miha Boltežar, Janko Slavič, Marian Wiercigroch]. - EBook. - Ljubljana : Faculty for Mechanical Engineering, 2015

ISBN 978-961-6536-97-4 (pdf)
1. Boltežar, Miha
281005824

FOREWORD

Welcome to ICoEV 2015 - an IFTOMM conference in Ljubljana, at the heart of Slovenia. Like with previous editions, this conference brings together a broad spectrum of scientists and researchers, who are focusing on Engineering Vibrations in a very broad sense.

The International Conference of Engineering Vibration (ICoEV) originated from a long-running series of events called the International Conference of Vibrational Problems (ICoVP), which was founded in India over 20 years ago. The last two conferences ICoVP were organised in Prague (2011) and Lisbon (2013), where the chair of the ICoVP event was heavily involved, and were very successful, attracting over 250 and 400 participants, respectively, from around the world.

This Ljubljana conference has attracted 200 participants from 31 countries; they include senior scientists, as well as master and PhD students.

The Steering and Organising Committees of the conference have made great efforts to maintain the high scientific standard of the papers. The conference is based on three and half days of technical presentations, structured into four parallel sessions. On each day of the conference there will be an invited lecture in the morning. The oral presentations are organized into 17 mini-symposia and eight other general topics.

The social programme includes a reception at Ljubljana Castle on Monday, which is free for everybody, a Tuesday afternoon trip to Bled and the conference dinner on Wednesday for the registered participants. We are confident that Ljubljana will provide interesting experiences for all participants, as it is well placed for reaching a wide variety of different attractions in a short time.

We express our gratitude to the Secretary of the Organizing Committee, Assoc. Prof. Janko Slavič, who has done an excellent job in making this conference a reality. Further thanks also go to the members of both the Scientific and Steering Committees, to our four invited speakers, to the organisers of the mini-symposia, to our sponsors and to all the contributing authors.

On behalf of the Steering and Organizing Committees we sincerely hope that you will all enjoy your time in Ljubljana during our conference.

Prof. Miha Boltežar
Chair of the Organizing Committee
University of Ljubljana, Slovenia

Prof. Marian Wiercigroch
Chair of the Steering Committee
University of Aberdeen, UK

ORGANISING COMMITTEE

Miha Boltežar,
University of Ljubljana,
Faculty of Mechanical Engineering

Janko Slavič,
University of Ljubljana,
Faculty of Mechanical Engineering

STEERING COMMITTEE

Marian Wiercigroch, University of Aberdeen, Scotland, United Kingdom
Miha Boltežar, University of Ljubljana, Slovenia
Zuzana Dimitrovová Universidade Nova de Lisboa, Faculdade de Ciência e Technologia, Caparica, Portugal
Tomasz Kapitaniak Technical University Of Lodz, Poland
Edwin Kreuzer Hamburg University of Technology, Hamburg, Germany
S. Narayanan Indian Institute of Technology Madras, Chennai, India
Giuseppe Rega University of Rome "La Sapienza", Rome, Italy
Jian Xu Tongji University, Shanghai, China

SCIENTIFIC COMMITTEE

Marco Amabilli, MacGill University, Canada
Jerome Antoni, Insa Lyon, France
Bala Balachandran, University of Maryland, US
Miha Boltežar, University of Ljubljana, Slovenia
Qingjie Cao, Harbin Institute of Technology, China
Joseph Paez Chavez, Dresden University of Technology, Germany
Anindya Chatterjee, Indian Institute of Technology - Kanpur, India
Zuzana Dimitrovová, Universidade Nova de Lisboa, Portugal
Takashi Hikihara, University of Kyoto, Japan
John Hogan, University of Bristol, UK
Haiyan Hu, Beijing University of Technology, China
Gengkai Hu, Beijing Institute of Technology, China
Tomasz Kapitaniak, Technical University Of Lodz, Poland
Piotr Koziol, Cracow University of Technology, Poland
Edwin Kreuzer, Hamburg University of Technology, Germany
Stefano Lenci, University of Marche, Italy
Caishan Liu, Peking University, Beijing, China
Qishao Lu, Beijing University of Aeronautics and of Astronautics, China
Nuno M.M. Maia, Technical University of Lisbon, Portugal
John E. Mottershead, University of Liverpool, UK
Sri Nachmachivaya, University of Illinois Urbana Champaign, US
S. Narayanan, Indian Institute of Technology Madras, India
Giuseppe Rega, University of Rome "La Sapienza", Italy
Daniel Rixen, Technical University of Munich, Germany
Marcelo Savi, Federal University of Rio de of Janeiro, Brazil
Janko Slavič, University of Ljubljana, Slovenia
Pol Spanos, Rice University, US
Andrzej Stefanski, Lodz Universty of Technology, Poland
Yoshisuke Ueda, University of Aberdeen, UK
Hans Webber, Pontifical Catholic University of University Janeiro, Brazil
Marian Wiercigroch, University of Aberdeen, UK

Contents

Foreword . . . 2

Organising committee . . . 3

Steering Committee . . . 4

Scientific Committee . . . 4

Mathematical Modelling (TP01) . . . 16

89 - ENERGY HARVESTING FROM TRANSVERSE GALLOPING USING A FLEXIBLE CRANK-ROD . . . 17

109 - MODELLING OF HEAVY VEHICLE TRANSMISSION SYNCHRONIZER USING CONSTRAINED LAGRANGIAN FORMALISM . . . 28

147 - MATHEMATICAL MODELING OF THE MECHANICAL SYSTEM OF THE VIBRATING TABLE WITH ORTHOGONAL MOVEMENT AND HYDRAULIC TURBINE WITH INCLINED BLADES . . . 38

215 - MODELLING AND AUTOMATIC CONTROL FOR A SCAN EAGLE SIMULATOR . . . 48

258 - RESPONSE STATISTICS AND BIFURCATION ANALYSIS IN STOCHASTIC VIBRO-IMPACT SYSTEM . . . 61

307 - FORCE FIELD SEPARATION OF VIBROFLUIDIZED GRANULAR MATERIALS, MATHEMATICAL MODEL AND PRACTICAL APPLICATIONS . . . 71

Experimental Techniques (TP02) . . . 78

114 - VIBRATION OF AEROSOLS IN THE TUBES . . . 79

136 - INTRODUCING SHAPER-BASED FILTERS FOR THE IMPROVEMENT OF THE LOAD CELL RESPONSE IN DYNAMIC WEIGHING SYSTEMS . . . 89

138 - INFLUENCES OF EXTERNAL VIBRATION ON PRECISION MACHINES - THEORETICAL AND EXPERIMENTAL INVESTIGATIONS . . . 99

165 - AXIAL BEHAVIOR OF SELF-COMPACTING, SELF-STRESSING AND HIGH-STRENGTH CONCRETE FILLED STEEL TUBE . . . 109

199 - EFFECTS OF CENTER DISTANCE AND MICROGEOMETRY ON THE DYNAMIC BEHAVIOUR OF A SPUR GEAR PAIR . . . 119

281 - A BENCHMARK FOR TIP TIMING MEASUREMENTS OF FORCED RESPONSE IN ROTATING BLADED DISKS . . . 131

283 - EXPERIMENTAL RESEARCH OF THE KINEMATICS AND CONTACT CONDITIONS OF THE BRUSH AND SLIP-RING . . . 144

305 - INVESTIGATING THE APPLICATION OF GUIDED WAVE PROPAGATION FOR ICE DETECTION ON COMPOSITE MATERIALS . . . 152

Computational Methods (TP03) . . . 162

106 - APPLICATION OF THE WAVE BASED METHOD TO STEADY-STATE VIBRATIONS OF THICK PLATES . . . 163

183 - THE HELMHOLTZ EQUATIONS BY THE NULL-FIELD AND THE INTERIOR FIELD METHODS ON CIRCULAR DOMAINS . . . 173

323 - CONTACT SITUATIONS IN RIGID BODY DYNAMICS . . . 185

Structural Dynamics (TP05) . . . 186

108 - MASING RULE MOTIVATED LOCAL DISCRETE MODELLING OF CONTACT INTERFACES TO PREDICT DYNAMICAL BEHAVIOUR OF JOINTED STRUCTURES . . . 187

155 - RISK ASSESSMENT OF SAFETY ANALYSIS OF NPP STRUCTURES DUE TO EARTHQUAKE EVENS . . . 197

157 - DETERMINISTIC AND PROBABILISTIC ANALYSIS OF THE ACCIDENTAL TORSION EFFECT TO SEISMIC RESISTANCE OF MULTI-STOREY BUILDINGS . . . 207

170 - DESIGN AND OPTIMIZATION OF A COMPACT HIGH-FREQUENCY ELECTROMAGNETIC SHAKER . . . 217

207 - REDUCED THIN-LAYER ELEMENT MODEL FOR JOINT DAMPING . . . 226

209 - NUMERICAL AND EXPERIMENTAL INVESTIGATIONS INTO MASS, STIFFNESS AND DAMPING MATRIX UPDATING THROUGH A TWO-STAGE FRAMEWORK . . . 234

245 - A PARAMETRIC ANALYSIS OF THE NONLINEAR RESPONSE OF STEEL FRAMES UNDER BASE EXCITATION IN FREQUENCY DOMAIN . . . 268

260 - DIRECT DAMPING IDENTIFICATION METHODS IN FREQUENCY DOMAIN . . . 278

264 - DAMAGE IDENTIFICATION IN BEAM STRUCTURE USING MODE SHAPE DATA: FROM SPATIAL CONTINUOUS WAVELET TRANSFORM TO MODE SHAPE CURVATURE METHODS . . . 288

266 - BIODYNAMIC BASED EXPERIMENTAL VALIDATION OF A HUMAN FINGER MODEL 298

362 - STRUCTURAL MODEL UPDATING BASED ON MEASURED RESPONSE . . . 308

265 - STOCHASTIC MODEL FOR THERMORHEOLOGICALLY SIMPLE MATERIALS USING FRACTIONAL DERIVATIVE OPERATORS . . . 318

Fluid-Structure Interactions (TP09) . . . 319

19 - INVESTIGATION ON CAVITATION BUBBLE NEAR AN ELASTIC SPHERE . . . 320

80 - STABILIZATION CONTROL OF SELF-EXCITED VIBRATIONS IN A FLEXIBLE FLUID-CONVEYING PIPE . . . 325

113 - INVESTIGATION OF TYPICAL SECTION AERODYNAMIC TRANSFER FUNCTIONS USING A VISCOUS CFD FORMULATION . . . 326

128 - TRANSVERSE SEISMIC RESPONSE ANALYSIS OF SUBMERGED FLOATING TUNNEL CONSIDERING BOUNDARY SOIL PROPERTY . . . 336

261 - CFD CALIBRATED WAKE OSCILLATOR MODEL FOR VORTEX-INDUCED VIBRATIONS . . . 346

Identification and Modal Analysis (TP10) . . . 347

15 - APPLICATION OF EQUIVALENT MATERIAL PROPERTIES IN FREE VIBRATION ANALYSIS OF A PARTIALLY PERFORATED PLATE WITH TRIANGULAR PENETRATION PATTERN . . . 348

21 - HIGH-FREQUENCY CONTROL OF THE THE SLOW MOTIONS . . . 358

115 - STRATEGY FOR IDENTIFICATION OF DAMPING RATIO USING MORLET WAVE DAMPING IDENTIFICATION METHOD . . . 359

166 - BIOMECHANICAL MODEL OF A SMART MIDDLE EAR PROSTHESIS . . . 373

177 - NUMERICAL TRANSFER PATH ANALYSIS FOR THE ASSESSMENT OF AIR-BORNE NOISE IN INTERNAL COMBUSTION ENGINES . . . 383

181 - FAST ONLINE MONITORING AND SYSTEM IDENTIFICATION FOR THE APPLICATION IN THE FIELD OF AEROELASTICITY . . . 393

228 - INDUSTRIAL USE OF METHODS FOR MODAL ANALYSIS OF SMALL AND LIGHT STRUCTURES . . . 403

233 - FDD MODAL IDENTIFICATION FROM EARTHQUAKE RESPONSE DATA WITH EVALUATION OF SOIL-STRUCTURE INTERACTION EFFECTS . . . 412

288 - ASSESSMENT OF DAMPING PROPERTIES OF LARGE 2-STROKE MARINE DIESEL ENGINES . . . 422

303 - DYNAMIC TESTS AND DESIGN OF A VIBRATION-BASED SHM SYSTEM FOR PROMPT POST-EARTHQUAKE ASSESSMENT OF AN ITALIAN HOSPITAL . . . 432

Dynamics of Rotating Systems (TP12) . . . 444

17 - EVALUATION OF THE DYNAMIC CHARACTERISTICS OF THE THREE-LOBE JOURNAL BEARING WITH FINITE LENGTH USING ANALYTICAL METHODS . . . 445

18 - EVALUATION OF THE FLOATING RING BEARING CHARACTERISTICS USING ANALYTICAL METHODS . . . 457

102 - INFLUENCE OF THE OIL TEMPERATURE OF THRUST BEARINGS ON THE VIBRATORY BEHAVIOR OF SMALL TURBOCHARGERS . . . 469

149 - ROTOR UNBALANCE ESTIMATION USING A SINGLE MACHINE RUNDOWN WITH REDUCED NUMBER OF SENSORS . . . 479

151 - DYNAMICS OF A ROTATING HUB-BLADE STRUCTURE WITH NONIDEAL ENERGY SOURCE . . . 489

163 - ANALIZING THE STIFFNESS OF A ROTOR WITH TRIANGULAR CROSS FRACTURE 499

172 - DYNAMICS OF THE ROTOR WITH FOIL BEARINGS AT AN ELEVATED TEMPERATURE . . . 509

206 - VIBRATION OF A TWO DEGREE OF FREEDOM AIR BEARING-ROTOR SYSTEM WITH ASYMMETRIC SUPPLY PRESSURE . . . 519

210 - EFFECTS OF A JOURNAL BEARING CLEARANCE ON ROTORDYNAMICS OF TURBOCHARGER . . . 529

235 - A NUMERICAL INVESTIGATION INTO THE EFFECT OF THE SUPPORTS ON THE VIBRATION OF ROTATING SHAFTS . . . 539

238 - STRUCTURAL DYNAMICS OF A WIND TURBINE DRIVE TRAIN HIGH SPEED SUBSYSTEM: MATHEMATICAL MODELING AND VALIDATION . . . 553

304 - MODELLING OF MAGNETORHEOLOGICAL OILS IN ROTORDYNAMIC DAMPING DEVICES BY BILINEAR MATERIAL . . . 563

327 - INVESTIGATION OF HIGH VIBRATION ON LARGE FAN MOTOR . . . 571

355 - EVALUATION OF THE DYNAMIC RESPONSE OF HIGH-SPEED SYSTEMS USING AN ANALYTICAL MODEL FOR THE FLOATING RING BEARINGS OF FINITE LENGTH . 578

Vibration Control and Isolation (TP14) . . . 590

94 - ON THE REMOVAL OF BREAK SQUEAL BY TUNED MASS DAMPERS . . . 591

104 - TECHNIQUE TO OVERCOME PIEZO STACK ACTUATOR SATURATION USING PARALLEL STIFFNESS COMBINATION FOR AN ACTIVE SUSPENDED HANDLE . . . 592

144 - A CONTRIBUTION TO THE REDUCTION OF SELF-EXCITED VIBRATIONS OF DYNAMICAL SYSTEMS BY IMPULSIVE PARAMETRIC EXCITATION . . . 601

145 - ACTIVE SUSPENSION LQ CONTROL FOR IMPROVING RIDING COMFORT . . . 611

164 - FRACTIONAL PID CONTROLLER TO AN ACTIVE IMAGE STABILIZATION SYSTEM . 621

227 - VIBRATION PROTECTION OF OBJECT WITH HELP OF THIN-LAYERED RUBBER-METAL ELEMENTS . . . 631

232 - EFFECTIVENESS OF SEISMIC-TUNED PASSIVE TUNED MASS DAMPERS ACCOUNTING FOR SOIL-STRUCTURE INTERACTION . . . 641

247 - A METHODOLOGY TO DECOUPLE THE TONAL NOISE SOURCES OF A COMPRESSOR SYSTEM . . . 651

Non-linear Dynamics and Dynamic Stability (MS01) . . . 661

85 - QUASI-PERIODIC RESPONSE TYPES OF A SINGLE NON-LINEAR DYNAMIC SYSTEM IN RESONANCE AND OUT OF RESONANCE DOMAINS . . . 662

97 - INTERACTION OF FRICTIONAL AND REGENERATIVE MECHANISM OF CHATTER VIBRATIONS . . . 672

116 - INFLUENCE OF SHEAR DEFORMABILITY AND AXIAL/ROTATIONAL INERTIA IN THE NONLINEAR FREE VIBRATIONS OF BEAMS WITH DIFFERENT BOUNDARY CONDITIONS . . . 680

205 - MULTI-MODE SOLUTIONS IN A PERIODIC ARRAY OF COUPLED NONLINEAR PENDULUMS UNDER PRIMARY RESONANCE . . . 681

225 - A PARAMETRIC STUDY OF THE NON-LINEAR RESPONSE OF PLANE FRAME STRUCTURES UNDER SEISMIC LOADS IN FREQUENCY DOMAIN . . . 690

272 - NUMERICAL AND EXPERIMENTAL INVESTIGATION OF AN UNDERPLATFORM DAMPER TEST RIG . . . 691

293 - A ROTATING PENDULUM WITH IRRATIONAL NONLINEARITY . . . 704

308 - DISCONTINUITY INDUCED BIFURCATIONS IN HIGHER DIMENSION FILIPPOV SYSTEMS . . . 714

Frequency-based spectral methods for vibration random fatigue (MS02) . . . 724

10 - DERIVATION OF EQUIVALENT POWER SPECTRAL DENSITY SPECIFICATIONS FOR SWEPT SINE-ON-RANDOM ENVIRONMENTS VIA FATIGUE DAMAGE SPECTRA . . . 725

12 - FATIGUE ASSESSMENT OF NON GAUSSIAN RANDOM VIBRATIONS BY USING DECOMPOSITION IN GAUSSIAN PORTIONS . . . 733

90 - AN ANALYTICAL APPROACH TO MEASURE THE ACCURACY OF VARIOUS DEFINITIONS OF THE "EQUIVALENT VON MISES STRESS" IN VIBRATION MULTIAXIAL FATIGUE . . . 743

120 - SIMULATION OF THE WHOLE WIND-INDUCED FATIGUE LIFE OF A SLENDER STEEL STRUCTURE . . . 753

167 - SHAKER TESTING SIMULATION OF NON-GAUSSIAN RANDOM EXCITATIONS WITH THE FATIGUE DAMAGE SPECTRUM AS A CRITERION OF MISSION SIGNAL SYNTHESIS . . . 763

193 - FULL FIELD EXPERIMENTAL MODELLING IN SPECTRAL APPROACHES TO FATIGUE PREDICTIONS . . . 773

282 - EXPERIMENTAL COMPARISON OF MULTI-AXIAL CRITERIA IN FREQUENCY-DOMAIN . . . 783

318 - A REVIEW AND COMPARISON OF CYCLE IDENTIFICATION METHODS FOR FATIGUE AND FRACTURE ANALYSIS . . . 792

Vibration Problems in the Solids Systems With Dry Friction (MS03) . . . 793

271 - ON VIBRATIONAL SMOOTHING OF DRY FRICTION AND ITS APPLICATION TO REVOLUTE JOINTS . . . 794

289 - IDENTIFICATION STRATEGIES FOR FRICTION LAWS: A NUMERICAL STUDY 802

298 - INFLUENCE OF CONTACT CHARACTERISTICS ON THE DYNAMIC BEHAVIOR OF RUBBING STRUCTURES. 809

335 - ON THE DYNAMICS OF THE SYMMETRICAL SOLIDS ON A VIBRATION RUBBED HORIZONTAL PLANE 819

344 - FALLING MOTION OF A CIRCULAR CYLINDER INTERACTING DYNAMICALLY WITH A POINT VORTEX 827

348 - EXPERIMENTAL INVESTIGATION ON SQUEAL-NOISE OF DISK-BRAKES FOR RAILWAY APPLICATIONS 843

Optimization on Vibration Control of Seismic Structures (MS04) 851

22 - OPTIMIZATION OF TMDS FOR SEISMIC STRUCTURES CONSIDERING NEAR FIELD GROUND MOTION SETS 852

23 - A ROBUST OPTIMUM DESIGN APPROACH OF TMDS CONSIDERING STRUCTURAL UNCERTANITY 860

118 - EFFECT OF ECCENTRICITY ON ACTIVE CONTROL OF SEISMIC STRUCTURES . . . 868

169 - MULTI OBJCETIVE OPTIMIZATION OF DOUBLE TUNED MASS DAMPERS CONSIDERING MAXIMUM STROKE CAPACITY 878

230 - CONTROLLING OF THE FULL VEHICLE MODEL USING SLIDING MODEL CONTROL OPTIMIZED BY GENETIC ALGORITHM 886

231 - SUPPRESSION OF STRUCTURAL VIBRATIONS USING DYNAMIC ABSORBER 897

351 - SEISIMC ANALYSIS ON MULTI-LEVEL SUPPORTED PRESSURE RETAINING COMPONENTS IN NPPS BY USING RESPONSE SPECTRUM METHOD 908

361 - ADAPTIVE INERTIAL SHOCK-ABSORBER FOR VIBRATION DAMPING 916

Vibration Analysis of Steel and Steel-Concrete Composite Structures (MS05) 924

73 - VIBRATION ANALYSIS OF STEEL-CONCRETE COMPOSITE MULTI-STOREY BUILDINGS 925

101 - HUMAN COMFORT ANALYSIS OF CONCRETE PEDESTRIAN FOOTBRIDGES USING BIODYNAMIC MODELS 935

112 - VIBRATION CONTROL AND HUMAN COMFORT EVALUATION OF STEEL-CONCRETE COMPOSITE FLOORS UNDER AEROBICS 945

Vibration of Solids and Structures Under Moving Loads: Modelling and Analysis (MS06) 955

72 - MULTIPOINT CONTACT MODEL FOR DYNAMIC INTERACTION ANALYSIS OF HIGH-SPEED TRAIN AND RAILWAY STRUCTURE AFTER DERAILMENT DURING AN EARTHQUAKE . . . 956

126 - AN ABAQUS NUMERICAL METHOD TO PREDICT GROUND VIBRATIONS INDUCED BY HIGH-SPEED RAILWAY LINES . . . 966

137 - ENERGY HARVESTING FROM MOVING LOADS ON A BEAM WITH ELASTIC FOUNDATION . . . 974

273 - ANALYTICAL MODELLING OF RAILWAY TRACK DYNAMICS . . . 985

332 - UNIFORMLY MOVING LOAD ON A BEAM SUPPORTED BY A FOUNDATION WITH FINITE DEPTH . . . 994

Nonlinear Dynamic Interactions and Phenomena: Emergent Methods... (MS07) . . . 1004

11 - FORCED NONLINEAR VIBRATION ANALYSIS OF CYLINDRICAL PANELS . . . 1005

14 - INCREASING PRACTICAL SAFETY OF VON MISES TRUSS VIA CONTROL OF DYNAMIC ESCAPE . . . 1015

75 - CUBIC SOFTENING NONLINEAR ELASTICITY MEASUREMENT OF MAGNETIC ATTRACTION MODEL USING SELF-EXCITED OSCILLATION . . . 1025

83 - PARAMETRIC STUDY OF A MACRO-SCALE TUNING FORK GYROSCOPE . . . 1026

98 - ON ENERGY TRANSFER BETWEEN VIBRATION MODES AND FREQUENCY-VARYING EXCITATIONS FOR ENERGY HARVESTING . . . 1036

111 - DYNAMICAL VIBRATION ABSORBER BY USING SHAPE MEMORY MATERIALS . . . 1046

154 - NONLINEAR DISCONTINOUS PHENOMENA IN ATOMIC FORCE MICROSCOPY . . . 1056

180 - DYNAMICS OF BEAMS AND PLATES UNDER COUPLED THERMO-MECHANICAL LOADING . . . 1057

Influencing Vibrations by Dissipative Effects (MS08) . . . 1067

77 - EXCITATION TECHNIQUES FOR THE SOUND ANALYSIS OF ELECTRIC GUITARS . . . 1068

92 - PRELIMINARY STUDY INVESTIGATING THE CAPABILITY OF EULERIAN- AND LAGRANGIAN-ACOUSTIC ELEMENTS TO DESCRIBE THE COCHLEAR FLUID-STRUCTURE INTERACTIONS . . . 1069

100 - NUMERICAL AND EXPERIMENTAL INVESTIGATION OF THE EFFECT OF A FLUID PIPE ON SYSTEMS SUBJECTED TO FORCED VIBRATIONS . . . 1079

107 - ON THE INFLUENCE OF DAMPING IN BRAKE VIBRATIONS . . . 1088

208 - ON THE EFFECT OF THE DISTRIBUTED FRICTION IN THE ARC SPRING ON THE DYNAMIC BEHAVIOR OF THE AUTOMOTIVE TRANSMISSION . . . 1099

279 - A MECHANICAL MODEL FOR THE DYNAMICAL CONTACT OF ELASTIC ROUGH BODIES WITH VISCOELASTIC PROPERTIES . . . 1109

301 - SYNCHRONIZATION VIA DISCONTINUOUS COUPLING 1118

Dynamics Drilling Deep Boreholes - Drillstring and Drillbit Vibrations (MS09) 1128
5 - AXIAL EXCITATION TOOL STRING MODELLING 1129

284 - LOCALIZING THE EXCITATION SOURCE OF HIGH FREQUENCY TORSIONAL OSCILLATIONS 1145

320 - PROPAGATION OF TORSIONAL VIBRATIONS IN DRILLSTRINGS: HOW BOREHOLE GEOMETRY AFFECTS TRANSMISSION AND IMPLICATIONS ON MITIGATION TECHNIQUES 1155

Inverse Problems and Uncertainty Quantification (MS10) 1163
74 - IDENTIFICATION OF UNCERTAIN BOUNDARY CONDITION OF A BEAM MODEL USING THE BAYESIAN APPROACH AND EXPERIMENTAL DATA 1164

125 - ROBUST OPTIMIZATION OF HORIZONTAL DRILLSTRING RATE OF PENETRATION THROUGH A NONLINEAR STOCHASTIC DYNAMIC MODEL 1173

146 - STABILITY OF TRANSVERSE VIBRATIONS OF A ROTATING UNIFORM WIND TURBINE BLADE USING THE FLOQUET THEORY 1184

194 - PARTIAL EIGENSTRUCTURE ASSIGNMENT IN VIBRATING SYSTEMS THROUGH HOMOTOPY OPTIMIZATION 1192

214 - COMPARISON BETWEEN MULTI-OBJECTIVE GENETIC ALGORITHM AND BAYESIAN INFERENCE ON IDENTIFICATION OF ROTATING MACHINERY PARAMETERS. . . .1202

216 - DAMAGE IDENTIFICATION UNDER MODELLING UNCERTAINTIES 1212

221 - DETERIORATION OF TENSILE STRENGTH AND STIFFNESS OF ELASTIC STRUCTURAL ADHESIVE JOINTS DUE TO ENVIRONMENTAL FACTORS 1218

Substructuring Techniques in Structural Dynamics (MS11) 1224
150 - SELECTION OF INTERNAL DOFS TO REPLACE HARD-TO-MEASURE COUPLING DOFS IN SUBSTRUCTURE DECOUPLING 1225

218 - ADAPTIVE FEEDFORWARD CANCELLATION FOR REALTIME HYBRID TESTING WITH HARMONIC EXCITATION. 1235

270 - COMPARISON BETWEEN PRIMAL AND DUAL CRAIG-BAMPTON SUBSTRUCTURE REDUCTION TECHNIQUES 1245

286 - A COMPARISON ON MODEL ORDER REDUCTION TECHNIQUES FOR GEOMETRICALLY NONLINEAR SYSTEMS BASED ON A MODAL DERIVATIVE APPROACH USING SUBSPACE ANGLES 1255

302 - AN INTERFACE FORCE MEASUREMENTS-BASED SUBSTRUCTURE IDENTIFICATION 1265

325 - EFFECTS OF INTERFACE LOADING IN DYNAMIC SUBSTRUCTURING 1275

Gresimo (MS12) 1286
79 - DYNAMIC RESPONSE OF LAMINATED STRUCTURES USING A REFINED ZIGZAG THEORY (RZT) SHELL ELEMENT 1287

197 - SURFACE IMPEDANCE PREDICTION USING PHASED GEOMETRICAL ACOUSTICS, A SMALL REVERBERANT CHAMBER AND OPTIMIZATION 1297

204 - ON THE EFFECTS OF DAMPING ON WAVE PROPAGATION IN PERIODIC VIBRO-ACOUSTIC META-MATERIALS 1306

269 - NVH PERFORMANCES OF AUTOMOTIVE CAR BODIES WITH DIFFERENT STRUCTURAL CONTRASTS 1318

321 - ON VARIABLE SCREENING AND OPTIMIZATION OF CAR BODY STRUCTURES SUBJECT TO MULTIDISCIPLINARY CONSTRAINTS 1331

322 - THE IMPACT OF THE STRUCTURAL NON-LINEARITY ON THE VIBRATION FATIGUE DAMAGE ACCUMULATION 1332

324 - EQUIVALENT MATERIAL MODELLING OF SANDWICH BEAM ASSEMBLIES: PROPAGATING AND EVANESCENT WAVE CONSIDERATIONS 1342

326 - AN INVERSE METHODOLOGY FOR LOW-FREQUENCY TRANSMISSION LOSS CHARACTERIZATION OF A LIGHTWEIGHT PANEL IN A SMALL REVERBERANT TRANSMISSION SUITE 1352

336 - THE FINITE ELEMENT ANALYSIS ASSESSMENT OF STRUCTURE PROPERTIES FOR A L7E CLASS VEHICLE UNDER THE BENDING, TORSION STATIC AND CRASH LOADS 1362

337 - A SAMPLING CRITERION FOR ACOUSTIC RADIATION PROBLEMS: PRACTICAL APPLICATIONS 1374

338 - DETERMINING VIBRATION SOURCES IN SOLID MEDIA USING TIME REVERSAL TECHNIQUE 1384

400 - SIMULTANEOUS OPTIMIZATION OF COMPOSITE STRUCTURES WITH SHUNTED PIEZOCERAMICS 1392

Power-transformer noise (MS13) 1393
243 - THE INFLUENCE OF MAGNETIC ANISOTROPY ON MAGNETOSTRICTION FORCES AND VIBRATION IN POWER TRANSFORMERS 1394

278 - A COMPARISON BETWEEN NUMERICAL AND EXPERIMENTAL MODAL PARAMETERS OF TRANSFORMER CORE 1404

329 - MEASUREMENT AND ANALYSIS OF NOISE AND VIBRATION OF 800KV CONVERTER TRANSFORMERS 1412

340 - SPATIAL DISTRIBUTION OF MAGNETOSTRICTION, STRAIN, DISPLACEMENTS AND NOISE GENERATION OF MODEL TRANSFORMER CORES 1421

341 - NUMERICAL MACC-MODELLING OF LOCAL PEAK-TO-PEAK MAGNETOSTRICTION DISTRIBUTIONS IN A 3-PHASE TRANSFORMER CORE PACKAGE 1431

342 - DEVELOPMENT OF NUMERICAL MODEL FOR COMPUTATION OF POWER TRANSFORMER NOISE 1441

346 - ACOUSTIC FIELD INSIDE THE OIL-FILLED TRANSFORMER TANK MODEL AND ITS CONSEQUENCE IN THE OVERALL NOISE RADIATION 1451

347 - VIBROACOUSTIC BEHAVIOR OF 120 MVA POWER TRANSFORMER 1459

363 - THE BEHAVIOUR OF VIBRATION, NEAR- AND FAR-FIELD NOISE OF ULTRAHIGH VOLTAGE (1000KV) POWER TRANSFORMERS - A FIELD TEST INVESTIGATION . . 1466

The dynamics of an axially moving continuum (MS14) 1476

20 - MODELLING THE BELTS - ENVELOPE INTERACTIONS DURING THE POSTAL MAIL CONVEYING BY A SORTING MACHINE 1477

76 - EXPERIMENTAL ANALYSIS OF NONLINEAR RESPONSE IN SIMPLY SUPPORTED BEAM SUBJECTED TO PARAMETRIC EXCITATION 1487

168 - THE NATURAL FREQUENCIES OF AN AXIALLY MOVING BEAM SUPPORTED BY AN INTERMEDIATE SPRING 1488

343 - ROTATIONAL RESPONSE AND SLIP PREDICTION OF SERPENTINE BELT DRIVES USING ABSOLUTE NODAL COORDINATE FORMULATION 1498

Engineering solutions for damping vibrations (MS15) 1507

9 - TUNED MASS DAMPER USE FOR STRUCTURAL IMPROVEMENT BEHAVIOUR IN SOME REPRESENTATIVE ITALIAN CONSTRUCTIONS 1508

87 - STIFFNESS AND LOSS FACTOR OF UNBONDED, MULTI-STRAND BEAMS UNDER FLEXURAL DEFORMATION 1518

121 - NONLINEAR DYNAMIC ABSORBER TO REDUCE VIBRATION IN HAND HELD IMPACT MACHINES 1530

143 - EHRLICH-ABERTH ITERATION FOR VIBRATIONAL SYSTEMS 1540

330 - STRUCTURAL OPTIMIZATION OF A MATERIAL EXHIBITING NEGATIVE STIFFNESS 1549

Full Field Measurements for Advanced Structural Dynamics (MS18) 1558

191 - COMPARATIVE STUDIES ON FULL FIELD FRFS ESTIMATION FROM COMPETING OPTICAL INSTRUMENTS 1559

192 - ACCURATE FRF ESTIMATION OF DERIVATIVE QUANTITIES FROM DIFFERENT FULL FIELD MEASURING TECHNOLOGIES 1569

196 - MODEL UPDATING FROM FULL FIELD OPTICAL EXPERIMENTAL DATASETS 1579

251 - DETERMINING SUBPIXEL FULL-FIELD DISPLACEMENTS FROM VIDEOS BY USING OPTICAL FLOW 1589

Non-smooth Dynamical Systems (MS19) 1604

248 - HIDDEN DYNAMICS OF DRY-FRICTION OSCILLATORS 1605

259 - MODELLING THE NON-SMOOTH DYNAMICS OF WINDSCREEN WIPERS 1615

292 - THE STICK-SLIP CHAOTIC MOTIONS OF AN ARCHETYPE SELF-EXCITED SD OSCILLATOR WITH DRY FRICTION 1623

300 - MULTIPLE BUCKLING AND HIGH CO-DIMENSION ANALYSIS OF A NOVEL SMOOTH AND DISCONTINUOUS OSCILLATOR 1632

Posters 1642

99 - THERMAL BUCKLING OF FUNCTIONALLY GRADED PANELS BASED ON PHYSICAL NEUTRAL SURFACE 1643

142 - MODAL PROPERTIES AND SIMULATION OF SELF-SUPPORTING SANDWICH FACADE PANELS 1650

161 - INTERACTING ACOUSTIC WAVES WITH STATIONARY STRATIFIED MEDIUM COMPRISING A LAYER OF BUBBLY LIQUID 1658

176 - DMA ANALYSIS AND VISCOELASTIC MODEL OF POLYURETHANE BASED ADHESIVE UNDER VARIOUS CONDITIONS 1665

299 - LAMB WAVE GENERATION USING LASER ABLATION 1674

315 - ELASTIC WAVE PROPAGATION IN PLANE ROD SYSTEM 1682

317 - SIMULATION OF LIQUID OSCILLATIONS IN ROAD TANK AT ITS BRAKING 1692

349 - OVERVIEW OF THE SOURCE AND ADDITIONAL FACTORS WHICH INFLUENCE THE POWER TRANSFORMER NOISE 1702

Index of authors 1708

Mathematical Modelling (TP01)

11th International Conference on Engineering Vibration
Ljubljana, Slovenia, 7–10 September 2015

ENERGY HARVESTING FROM TRANSVERSE GALLOPING USING A FLEXIBLE CRANK-ROD

Sorribes-Palmer, F., Sanz-Andres, A. and Alonso, G.

IDR/UPM, E.T.S.I. Aeronáuticos
Universidad Politécnica de Madrid
Pza. Cardenal Cisneros, 3
28040 Madrid, Spain
{felix.sorribes, angel.sanz.andres, gustavo.alonso}@upm.es

Keywords: Transverse galloping, energy extraction, flexible crack-rod.

Abstract. *In this paper a coupled fluid-structure model of a flexible crank-rod connected to an electrical generator is analyzed and compared with other ways to extract energy from transverse galloping [13]. One of the problems of energy harvesting is the conversion of linear oscillatory motion to a type of motion more compatible with an energy conversion device. One possibility is to transform the linear motion into a rotational one. The model considers a two degree-of-freedom galloping oscillator where fluid forces are described resorting to a quasi-steady condition by using a quasi-steady aerodynamics model. Transverse galloping is a dynamic instability in which IDR/UPM (Instituto de Microgravedad Ignacio Da Riva, Universidad Politécnica de Madrid) has a large interest [12, 3, 4]. This instability can be used for energy extraction. One possible application could be as a damping system for pressure waves in high speed railway tunnels. The wind speed induced by a pressure waves generated by a high speed train during its transit through a railway tunnel can surpass 5 m/s, and the train wake can induce speeds over 25 m/s. Due to the nature of the excitation and with a proper location for the device in the tunnel, these can be an optimal emplacement for devices based on aeroelastic instabilities such as transverse galloping.*

1 INTRODUCTION

The interest on energy harvesting in slow flows by aeroeslastic instabilities has recently increased [3, 12, 2, 5, 6, 8, 9, 11]. One of the key factors to extract energy from a variable amplitude oscillations, as it can be the case of transverse galloping, is the conversion of this kinetic energy into electrical energy which could be accumulated in batteries for later use. This mechanical energy can be converted by piezoelectric, electrostatic, or electromagnetic means.

Transverse galloping is caused by a coupling between the aerodynamic forces and the across-wind oscillations induced in the structure, this changes the angle of attack, which in turn varies the aerodynamic forces modifying the dynamical response of the structure. The structure, which usually has low stiffness and low damping, moves in the direction normal to the average wind speed. This motion is characterized by oscillations of large amplitude and low frequency. The most important parameters which influence galloping (considered here as a one-degree-of-freedom oscillator subjected to aerodynamic forces) are: the geometric shape, the angle of incidence, the free stream flow speed, the density and viscosity of the fluid, the turbulence intensity of the flow, and the system's mechanical properties (mass, stiffness and damping).

The optimization of energy extraction from transverse galloping using electromagnetic generator is studied in [13]. A electro-fluid-elastic model is introduced to describe the coupling between the galloping body and the linear motion electromagnetic generator. The maximum efficiency of the proposed mechanism is achieved when the speed of the flow is twice the speed to trigger transverse galloping. Also an expression for the optimal electrical load resistance as a function of the reduced velocity is presented.

In [14] a dual mass system as a method to enhance energy extraction from transverse galloping is discussed. Three different configurations are analyzed. The importance of parasitic damping to improve energy harvested in a broader band of incident flow velocities is shown.

Geometry restrictions or flow conditions (as gust flows, wakes of array devices, high turbulent flows, etc.) that could lead to aeroelastic problems on a wind turbine can be an opportunity for transverse galloping devices.

Another example are the ducted wind turbines with shrouded inlets used in energy harvesting at low flow speeds. Some are used for to deliver power to wireless sensors as shown in [7]. The concepts of wind turbines with double diffusers are studied in [10]. Turbines need a constant flow to be efficient and also a big air volume around them.

A possible location for transverse galloping devices could be in railway tunnels for high speed trains. The flow induced by the pressure waves generated during the passing train through the tunnel is enough to trigger galloping.

When a train approaches a tunnel entrance portal, the air inside the tunnel begins to be compressed due to the open-air local field preceding the train nose. Once the train head reaches the tunnel entrance, the pressure increases faster until the nose is completely inside the tunnel. This interaction between the tunnel entrance hood and the train nose determines the shape of the compression wave generated, but the total pressure gauge Δp_N remains constant. The pressure continues to increase slowly due to the viscous effects on the tunnel wall and the train surface Δp_{fr}, until the end of the train reaches the tunnel entrance portal, and a rarefaction wave is then generated with a pressure decrease Δp_T. The pressure decreases suddenly Δp_{HP} when the train nose passes the measurement point. These pressure variations are known as the train reference signature, and is defined in the standard [1] (see Figure 1).

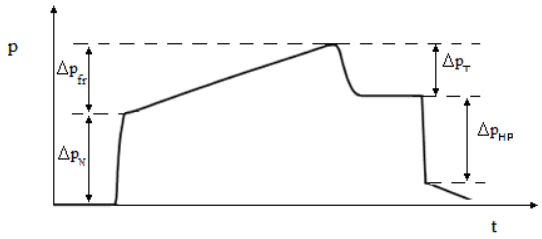


Figure 1: Train reference signature defined by the standard [1].

As a rough estimation of the amount of available energy inside a railway tunnel for transverse galloping devices, lets consider a train of 200 m length entering at 300 km/h. The characteristic time of the pressure wave generated is 2.4 s, the pressure gauge of the wave generated by a tunnel-train combination is around 1-3 kPa, this depends on the blockage and of the altitude of the tunnel entrance. Idealizing the pressure wave as a squared pulse of 2 kPa, the speed induced by the wave will be close to 5 m/s. The average energy density per unit area of a plane wave is 15 N/m^2. Assuming that each device has a frontal area of 0.2 m^2 and the efficiency of conversion is 10 % the extractable energy by each device would be 1.5 W. When using the flow speed induced by the wake of the train (speed can rise up to 20 m/s depending on train speed and blockage ratio) this extractable energy can rise till 100 W per galloping device. Assuming a logarithmic decrement of 0.01 with oscillation frequency of 2 Hz, the time to reduce the oscillation to a 10 % of the maximum amplitude would be approximately 10 seconds. In long enough tunnels, this time could be used to extract energy before the next reflection reaches the device again. In this moment the speed induced by the wave would be in the opposite direction. If the body shape used in the device had a symmetric behavior, the energy extracted or damped would be of the same order in both directions. A matrix configuration could be distributed around different sections in the tunnel and optimally separated with higher flow speeds. These devices could be also used as remote sensors for tunnel illumination.

In this paper a flexible crank-rod mechanism to transform the oscillations of variable amplitude of transverse galloping into a rotary motion of an electric generator is presented.

2 MATHEMATICAL MODEL

Let us consider a galloping body of mass M_1 attached to another mass M_2 through a spring of stiffness K. The mass M_2 is attached to a system crank-rod to an electric generator with moment of inertia I and a rotation angle θ. The scheme of the mechanism is shown in Figure 2.

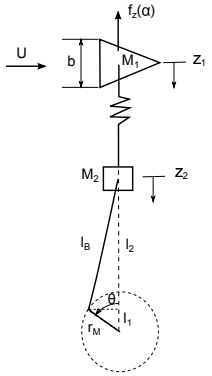


Figure 2: Scheme of a flexible crank-rod galloping mechanism.

The kinetic and potential energy of the mechanism are

$$\begin{aligned} T &= \frac{1}{2}M_1\dot{z}_1^2 + \frac{1}{2}M_2\dot{z}_2^2 + \quad \frac{1}{2}I\dot{\theta}^2 \\ U &= \frac{1}{2}K\left(z_2 - z_1\right)^2 \qquad , \end{aligned} \tag{1}$$

where z_1 denotes the position of the galloping body and z_2 the position of mass M_2. The parameters z_2 and θ are related through the expression

$$\begin{aligned} l_1 + l_2 &= r_M\cos\theta + \sqrt{l_B^2 - r_M^2\sin^2\theta} = r_M\cos\theta + l_B\sqrt{1 - \tfrac{r_M^2}{l_B^2}\sin^2\theta} \\ &\simeq r_M\cos\theta + l_B\left(1 - \tfrac{1}{2}\tfrac{r_M^2}{l_B^2}\sin^2\theta\right) = r_M\cos\theta + l_B\left(1 - \tfrac{1}{2}\tfrac{r_M^2}{l_B^2}\tfrac{1-\cos^2 2\theta}{2}\right) \\ &= r_M\cos\theta + l_B\left(1 - \tfrac{1}{4}\tfrac{r_M^2}{l_B^2} + \tfrac{1}{4}\tfrac{r_M^2}{l_B^2}\cos 2\theta\right) \\ &= r_M\cos\theta + \tfrac{r_M}{4}\left(\tfrac{r_M}{l_B}\right)\cos 2\theta - l_B\left(1 - \tfrac{1}{4}\tfrac{r_M^2}{l_B^2}\right) , \end{aligned} \tag{2}$$

considering $r_M \ll l_B$, so then the displacement of the mass M_2 is $z_2 \simeq -r_M\cos\theta$ and its speed $\dot{z}_2 = r_M\,\theta\sin\theta$. The kinetic energy can be written as

$$T = \frac{1}{2}M_1\dot{z}_1^2 + \frac{1}{2}M_2 r_M^2\dot{\theta}^2\sin^2\theta + \frac{1}{2}I\dot{\theta}^2. \tag{3}$$

Applying Lagrange equations

$$M_1\ddot{z}_1 + K\left(z_1 - z_2\right) = f_z\left(\alpha\right) \tag{4}$$

$$M_2 r_M^2[\sin 2\theta\dot{\theta}^2 + \sin^2\theta\ddot{\theta}] + I\ddot{\theta} - M_2 r_M^2\dot{\theta}^2\sin\theta\cos\theta - K\left(z_1 - z_2\right)r_M\,\sin\theta = M(\dot{\theta}) \tag{5}$$

where $f_z(\alpha)$ is the aerodynamic transverse force applied to the mass M_1 immersed in the incoming flow and $M(\dot{\theta})$ is the torque applied by the electric generator. The relationship $\frac{\mathrm{d}}{\mathrm{d}t}\left[\sin\theta\dot{\theta}\right] = 2\sin\theta\cos\theta\dot{\theta}^2 + \sin^2\theta\ddot{\theta}$ has been used.

2.1 Simplified case $M_2 = 0$

In the case that $M_2 = 0$ the Eqs. 4 and 5 can be simplified as follows

$$M_1\ddot{z}_1 + K\left(z_1 - z_2\right) = f_z\left(\alpha\right) \tag{6}$$

$$I\ddot{\theta} - K\left(z_1 - z_2\right)r_M\,\sin\theta = M(\dot{\theta})\,. \tag{7}$$

A quasi-steady solution can be obtained under the assumption that if the moment of inertia I is large enough then the speed of the electric generator is almost constant $\dot{\theta} \simeq \Omega_0$, and then $\theta = \Omega_0 t + \varepsilon\theta_1$. The equations can be rewritten

$$M_1\ddot{z}_1 + K\left(z_1 + r_M\,\cos\theta\right) = f_z\left(\alpha\right) \tag{8}$$

$$I\varepsilon\ddot{\theta}_1 - K\left(z_1 + r_M\cos\Omega_0 t\right) r_M \sin\theta = M(\dot{\theta})\,, \tag{9}$$

if the mass M_1 is oscillating due to galloping at the resonance frequency of the system $\omega_0 = \sqrt{K/M_1}$ and the crankshaft of the electric generator turns at the same angular frequency $\Omega_0 = \omega_0$. Then Eq. 6 can be rewritten

$$M_1\ddot{z}_1 + Kz_1 = f_z\left(\alpha\right) - Kr_M\cos\Omega_0 t = F\,, \tag{10}$$

which is the equation of the forced oscillator, under the action of a force F. The aerodynamic force in the direction transverse to the flow $f_z(\alpha)$, is

$$f_z(\alpha) = \frac{1}{2}\rho b U^2 C_z(\alpha)\,, \tag{11}$$

where $\tan\alpha = (1/U)\dfrac{\mathrm{d}z_1}{\mathrm{d}t}$, U the velocity of the incident flow, ρ the fluid density, b the characteristic dimension of the body in the direction transverse to the flow, and $C_z(\alpha)$ is the dimensionless coefficient of the instantaneous aerodynamic force on the galloping body in the transverse direction to the incident flow

$$C_z(\alpha) = -\frac{C_l(\alpha) + C_d\tan\alpha}{\cos\alpha} = \sum a_n\tan^n\alpha\,. \tag{12}$$

This expression refers to the study of the transverse oscillatory motion at a given pitch angle of the body θ_p considered as reference, with $\theta_p = 0$ as origin. If the lift $c_l(\theta_p)$ and drag $c_d(\theta_p)$ coefficients determined in static conditions ($\theta_p = \alpha$) are defined as a function of the pitch angle of the body θ_p, and the reference point of study is $\theta_{p0} \neq 0$, doing the change of variable $\alpha = \theta_p - \theta_{p0}$, the functions $c_l(\alpha)$ and $c_d(\alpha)$ can be generated for each θ_{p0}. The quasi-steady hypothesis is assumed, in which the timescale of the oscillating body is much larger than the residence timescale of the flow particles. The critical speed for transverse galloping is

$$U_{cr} = 4m\omega\zeta/(\rho b H)\,, \tag{13}$$

where $H = \dfrac{\partial c_l}{\partial\alpha} + c_d$ and ζ is the damping coefficient. In this model, the damping or energy extraction is produced by the torque of the electric generator.

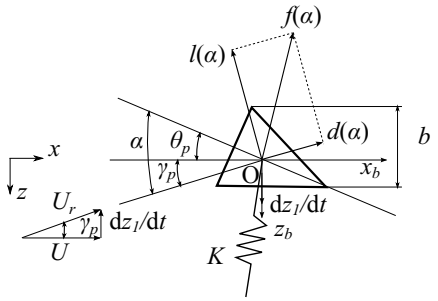


Figure 3: Schematic representation of aerodynamic forces and the angle of attack, α, pitch angle of the velocity, γ_p, pitch angle of the body, θ_p; z, x is the inertial reference frame and z_b, x_b is the reference frame attached to the body.

There must exist a phase delay φ between the displacement z_1 and the position angle of the crank-rod, for the transmitted power by the spring averaged in a cycle not being zero. So then

$$z_1 = A\cos(\omega_0 t - \varphi) \qquad \dot{z}_1 = -A\omega_0 \sin(\omega_0 t - \varphi)\,. \tag{14}$$

The extracted power averaged per cycle is

$$P_e = \frac{1}{T}\int_0^T f_z \frac{\mathrm{d}z_1}{\mathrm{d}t}\mathrm{d}t = \frac{\rho U^2 b}{2T}\int_0^T C_z \frac{\mathrm{d}z_1}{\mathrm{d}t}\mathrm{d}t\,, \tag{15}$$

and the transmitted power averaged per cycle is

$$\begin{aligned} P_t = \tfrac{1}{T}\textstyle\int_0^T (-Kr_M\cos\omega_0 t)\,\frac{\mathrm{d}z_1}{\mathrm{d}t}\mathrm{d}t = \tfrac{1}{T}Kr_M\omega_0 A\textstyle\int_0^T \cos(\omega_0 t)\sin(\omega_0 t-\varphi)\mathrm{d}t \\ = -\frac{1}{2}Kr_M\omega_0 A\sin\varphi\,. \end{aligned} \tag{16}$$

The equilibrium of the oscillator of Eq. 10 is reached when $P_e + P_t = 0$. Analyzing the rotational motion, integrating Eq. 9 multiplied by $\dot{\theta}$

$$\varepsilon I\int_0^T \ddot{\theta}_1\dot{\theta}\mathrm{d}t + K\int_0^T (z_1 + r_M\cos\omega_0 t)\,r_M\sin\omega_0\dot{\theta}\mathrm{d}t = \int_0^T M(\omega_0)\dot{\theta}\mathrm{d}t \tag{17}$$

as we are assuming periodic motion, the first part of the integral is zero. And as $\dot{\theta} \simeq \omega_0$

$$K\int_0^T \left[\left(A\cos(\omega_0 t-\varphi)r_M\sin\omega_0 + r_M^2\sin\omega_0\cos\omega_0 t\right)\omega_0\right]\mathrm{d}t = \int_0^T M(\omega_0)\omega_0\mathrm{d}t \equiv P_t T\,. \tag{18}$$

The first term is the transmitted power

$$P_t T = -\frac{T}{2}Kr_M\omega_0 A\sin\varphi\,. \tag{19}$$

The dimensionless extracted power averaged per cycle is

$$\begin{aligned} p_e = \frac{P_e}{\frac{1}{2}\rho b U^3} = \tfrac{1}{UT}\textstyle\int_0^T C_z\frac{\mathrm{d}z_1}{\mathrm{d}t}\mathrm{d}t = \tfrac{1}{UT}\textstyle\int_0^T \sum a_n\tan^n(\alpha)\frac{\mathrm{d}z_1}{\mathrm{d}t}\mathrm{d}t \\ = \frac{1}{2}\left[a_1\left(\frac{A^*}{U^*}\right)^2 + \frac{3}{4}a_3\left(\frac{A^*}{U^*}\right)^4 + ...\right]\,. \end{aligned} \tag{20}$$

A typical dimensionless extracted power curve, as a function of the amplitude A^*/U^* is shown in Figure 2.1. There is a maximum extracted power point p_{emax} which is attained at $(A^*/U^*)_{max}$. The dimensionless transmitted power is defined as

$$p_t = \frac{P_t}{\frac{1}{2}\rho b U^3} = \frac{A\Omega_0 Kr_M\sin\varphi}{\frac{1}{2}\rho b U^3} = \frac{A\Omega_0^3 M_1 r_M\sin\varphi}{\frac{1}{2}\rho b U^3} = \frac{2m^*\sin\varphi}{U^*}\left(\frac{A^*}{U^*}\right)^2\frac{r_M^*}{A^*}\,, \tag{21}$$

where the amplitude of the oscillations has been divided by the characteristic dimension of the body in the direction transverse to the flow b, $A^* = \dfrac{A}{b}$, $r_M^* = r_M/b$, the mass of the body by the characteristic mass of the surrounding fluid, $m^* = M_1/(\rho b^2)$; the spring stiffness is $K = \Omega_0^2 M_1$ and the dimensionless velocity $U^* = U/(\omega_0 b)$. Comparing the Eq. 21 with the classic of the dissipated power [12]

$$p_d = \frac{2m^*\xi}{U^*}\left(\frac{A^*}{U^*}\right)^2 , \tag{22}$$

the $\sin\varphi$ is taking the role of the damping coefficient ξ, and r_M^*/A^* is replacing A^{*2}.

On one side the expression for the dimensionless dissipated power in the electric generator is

$$p_d = \frac{1}{T}\frac{1}{\frac{1}{2}\rho b U^3}\int_0^T M(\omega)\omega \mathrm{d}t = \frac{M(\omega_0)\omega_0}{\frac{1}{2}\rho b U^3} , \tag{23}$$

where it has been assumed that $\omega = \omega_0$ is a constant. Under the assumption of a electric generator with linear behavior, $M(\omega_0) = k_M\omega_0$ from Eq. 23 is

$$p_d = \frac{k_M\omega_0^2}{\frac{1}{2}\rho b U^3} = \frac{k_M}{\frac{1}{2}\rho b^4\omega_0}\frac{1}{U^{*3}} = \frac{C_M}{U^{*3}} , \tag{24}$$

where $C_M = 2k_M/(\omega_0\rho b^4)$. The balance of power transmitted Eq. 16 and dissipated Eq. 24 at the electric generator leads to

$$\frac{1}{2}M_1\omega_0 A r_M \sin\varphi \;\; = k_M . \tag{25}$$

From this equation the relation between φ and A is obtained

$$\sin\varphi = \frac{2k_M}{M_1\omega_0 A r_M} \tag{26}$$

On the other hand, imposing that $p_e = p_d$ from Eq. 20 and Eq. 24

$$p_e = \frac{1}{2}\left[a_1\left(\frac{A^*}{U^*}\right)^3 + \frac{3}{4}a_3\left(\frac{A^*}{U^*}\right)^4 + ...\right] = \frac{C_M}{U^{*3}} = p_d , \tag{27}$$

so p_d can be expressed as a function of A^*/U^*

$$p_d = \frac{C_M}{A^{*3}}\left(\frac{A^*}{U^*}\right)^3 . \tag{28}$$

In this way it is easy to find the condition for maximum extractable power (see Figure 2.1). The process to obtain the maximum power is the following, as the extractable power can be calculated directly from the test data as a function of A^*/U^* and at the same time it is $p_e = p_{emax} = C_M/U^{*3}$, the dimensionless speed can be calculated $U^{*3} = p_{emax}/C_M$. As $(A^*/U^*)_{max}$is known by using $A^*/U^* = (A^*/U^*)_{max}$, hence

$$A^* = U^*\left(\frac{A^*}{U^*}\right)_{max} = \sqrt[3]{\frac{p_{emax}}{C_M}}\left(\frac{A^*}{U^*}\right)_{max} . \tag{29}$$

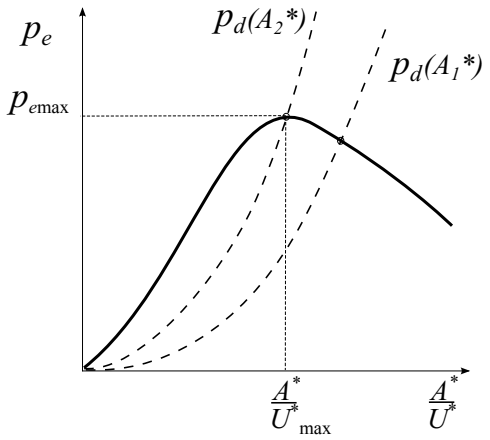


Figure 4: Determination of the maximum dimensionless extracted power $p_{e\max}$. Variation of dimensionless extracted power, p_e , as a function of relative amplitude, $\frac{A^*}{U^*}$, for two values of the dimensionless amplitude oscillations A^*.

3 EXTRACTABLE ENERGY FROM DIFFERENT GALLOPING BODIES

From the experimental data in [12] where different bodies shapes were tested in the wind tunnel we obtain $f_z(\alpha)$, and using a characteristic $M(\omega)$ of a common electric electric generator, we can calculate the extractable energy from the flow by using a device based on transverse galloping and using a linear to rotatory energy conversion mechanism. The parameters used for the evaluation of the relative amplitude of the oscillations summarized in Table 1 have been selected based on [13].

Characteristic transverse dimension of the body, b [m]	0.1
Mass per unit length, m [kg/m]	0.612
Crank-shaft dimension, r_M [m]	0.05
Density of the fluid, ρ [kg/m^3]	1.225

Table 1: Values of the parameters used to estimate the dimensionless dissipated power, p_d.

In Table 2 is presented the maximum extractable power per averaged per cycle, made dimensionless by using the maximum relative amplitude $A^*/U^*|_{p_{emax}}$ in a cycle (or specific power) for different galloping body shapes,

$$\tilde{p}_{emax} = \frac{p_{emax}}{\left.\frac{A^*}{U^*}\right|_{p_{emax}}} , \tag{30}$$

and the pitch angle of the body at which this energy is extracted.

In Figure 5 is shown the specific extracted power $\tilde{p}_{e\max}$ for the body shapes indicated in Table 2, and the specific dissipated power $\tilde{p}_d$

$$\tilde{p}_d = \frac{C_M}{A^{*3}} \left(\frac{A^*}{U^*}\right)^2 . \tag{31}$$

Body shape	$\frac{A^*}{U^*}\Big\vert_{\tilde{p}_{emax}}$	$\tilde{p}_{emax}$	θ_p [rad]
D-shape	0.33	0.19	1.42
Triangle $\beta = 30^o$	0.33	0.11	3.16
Triangle $\beta = 40^o$	0.47	0.13	3.18
Triangle $\beta = 60^o$	0.77	0.14	3.14

Table 2: Efficiency of galloping body to convert energy through linear to rotatory mechanism.

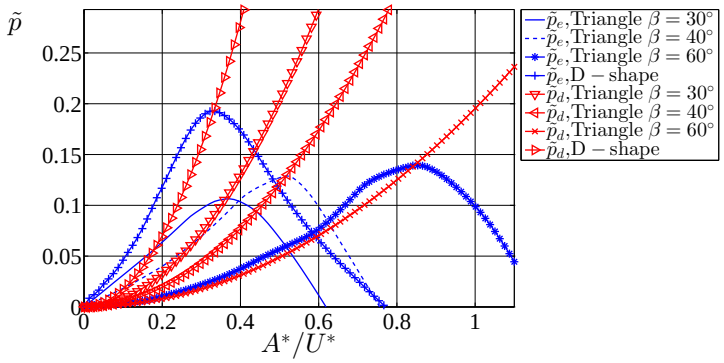


Figure 5: Determination of the maximum dimensionless extracted power $\tilde{p}_{e\max}$. Variation of dimensionless extracted power, $\tilde{p}_e$, as a function of relative amplitude, $\frac{A^*}{U^*}$.

The stiffness of the spring would be selected depending on the body shape chosen. The phase delay can be modified as the flow speed conditions vary by modifying the torque of the electric generator (a multiplication system) in order assure maximum power extraction. In Table 3 are indicated the reduced amplitude of the oscillations, reduced speed, the phase delay, the angular frequencies for the stiffness of the different strings selected and with $k_M = 10^{-3}$.

Body shape	K [N/m]	C_M	A^*	U^*	φ [rad]	ω [rad/s]
Triangle $\beta = 30^o$	10	4.04	1.59	4.89	0.076	4.04
Triangle $\beta = 40^o$	95	1.31	1.3	2.79	0.051	12.45
Triangle $\beta = 60^o$	50	1.81	1.97	2.56	0.033	9.04
D-shape	60	1.65	0.98	2.87	0.067	9.90

Table 3: Mechanism parameters selected for transverse galloping energy harvesting.

In case of selecting $k_M = 10^{-2}\mathrm{Nm/(rad/s)}$ and $k = 6$ N/m and keeping the rest of the parameters the angular frequency will be $\omega = 3.13$ [rad/s]. The relative amplitude and reduced speed of oscillations at the equilibrium are presented in Table 4.

Body shape	A^*	U^*	φ [rad]
Triangle $\beta = 30^o$	3.74	11.46	0.58
Triangle $\beta = 40^o$	4.45	9.53	0.49
Triangle $\beta = 60^o$	6.04	7.87	0.35
D-shape	3.07	9.38	0.75

Table 4: Relative amplitude A^*, reduced speed $U^*$and phase delay φ of oscillations at the equilibrium.

A gearbox (a speed multiplication of approximately 20) should be used to make the electric generator work in an efficient point. In order to compare this results with other devices the mechanical efficiency of the mechanism η_M, and the efficiency of the electric generator η_E, must be taken into account. Assuming $\eta_M = 0.9$ and $\eta_E = 0.9$ the electric power extracted per unit area would be close to 0.16 mW/cm^{2}which is close to results presented in [7].

4 CONCLUSIONS

- The extractable power from oscillations of transverse galloping by using a linear to rotary conversion mechanism has been analyzed.
- The maximum extractable energy by using transverse galloping for different body shapes is presented.
- A method to design the energy harvesting mechanism, using an expression for the relative oscillation amplitude that maximizes the efficiency, is proposed.

REFERENCES

[1] [en 14067-5:2006:08] - railway applications - aerodynamics - part 5: Requirements and test procedures for aerodynamics in tunnels, 2006.

[2] G. Alonso, A. Sanz-Lobera, and J. Meseguer. Hysteresis phenomena in transverse galloping of triangular cross-section bodies. *Journal of Fluids and Structures*, 33:243–251, August 2012.

[3] A. Barrero-Gil, G. Alonso, and A. Sanz-Andres. Energy harvesting from transverse galloping. *Journal of Sound and Vibration*, 329(14):2873–2883, July 2010.

[4] A. Barrero-Gil, A. Sanz-Andrés, and M. Roura. Transverse galloping at low Reynolds numbers. *Journal of Fluids and Structures*, 25(7):1236–1242, October 2009.

[5] Antonio Barrero-Gil, Santiago Pindado, and Sergio Avila. Extracting energy from Vortex-Induced Vibrations: A parametric study. *Applied Mathematical Modelling*, 36(7):3153–3160, July 2012.

[6] M. Gomez, I.and Chavez, G. Alonso, and E. Valero. Numerical Investigation of Galloping Instabilities in Z-Shaped Profiles. *The Scientific World Journal*, 2014(1):14, January 2014.

[7] D. Howey, A. Bansal, and S. Holmes. Design and performance of a centimetre-scale shrouded wind turbine for energy harvesting. *Smart Materials and Structures*, 20(8):085021, 2011.

[8] Hyung-Jo Jung and Seung-Woo Lee. The experimental validation of a new energy harvesting system based on the wake galloping phenomenon. *Smart Materials and Structures*, 20(5):055022, May 2011.

[9] Hyung-Jo Jung, Seung-Woo Lee, and Dong-Doo Jang. Feasibility study on a new energy harvestin electromagnetic device using aerodynamic instability. *IEEE Transactions on Magnetics*, 45(10), 2009.

[10] T Saravana Kannan, Saad A Mutasher, and Y H Kenny Lau. Design and low velocity simulation of diffuser augmented wind turbine using CFD. *Journal of Engineering Science and Technology*, 8(4):372–384, 2013.

[11] J. Meseguer, A. Sanz-Andrés, and G. Alonso. Determination of maximum mechanical energy efficiency in energy galloping systems. *Journal of Engineering Mechanics*, 141(1):04014101, 2015.

[12] F. Sorribes-Palmer and A. Sanz-Andres. Optimization of energy extraction in transverse galloping. *Journal of Fluids and Structures*, 43:124–144, November 2013.

[13] D. Vicente-Ludlam, A.. Barrero-Gil, and A. Velazquez. Optimal electromagnetic energy extraction from transverse galloping. *Journal of Fluids and Structures*, 51:281–291, November 2014.

[14] D. Vicente-Ludlam, A. Barrero-Gil, and A. Velazquez. Enhanced mechanical energy extraction from transverse galloping using a dual mass system. *Journal of Sound and Vibration*, 339:290–303, 2015.

International Conference on Engineering Vibration
Ljubljana, Slovenia, 7-10 September 2015

Modelling of Heavy Vehicle Transmission Synchronizer using Constrained Lagrangian Formalism

Muhammad Irfan*, Viktor Berbyuk, Håkan Johansson

Department of Applied Mechanics
Chalmers University of Technology
SE - 412 96 Göteborg, Sweden
{irfan.muhammad, viktor.berbyuk, hakan.johansson}@chalmers.se

Keywords: Constrained Lagrangian Formalism, Generic Synchronizer, Synchronizer Performance, Sensitivity Analysis, Synchronization Time.

Abstract. *Robust and efficient synchronizers are keys elements to ensure good gear shift in heavy vehicles. In order to improve existing as well as develop new synchronizers, efficient simulation tools are needed.*

In this contribution, a mechanical system with 5 degrees of freedom modelling a generic synchronizer consisting of engaging sleeve, synchronizer ring and gearwheel are considered. Due to the design of the different components and their interactions the synchronizing process is described in terms of different steps or phases; presynchronization, main synchronization, blocker transition and engagement. The four main phases are further divided into sub-phases. To study the whole process in a unified manner, Constrained Lagrangian Formalism (CLF) turns out to be a suitable method in which the interactions between components (sleeve, synchronizer ring and gearwheel) are described by unilateral or/and bilateral constraints imposed on generalized coordinates of the system during different phases.

Using CLF a mathematical model of a generic synchronizer is developed and represented by the system of differential-algebraic equations. Kinematics and kinetics of the generic synchronizer are modelled for each sub-phase. The sleeve is considered as a master and the gearwheel is considered as a slave. The statement of the dynamics problem for a generic synchronizer is given and the numerical algorithm is implemented in Matlab for solving the differential-algebric equations resulting from CLF. The generic synchronizer computational model is adapted to available experimental setup and validated using obtained measurement data. Sensitivity of the synchronization time is studied varying the cone angle, coefficient of dry friction and sleeve force. Effect of driveline vibrations on synchronization performance is also studied.

1 INTRODUCTION

The demands for decreasing vehicle emissions, particularly for heavy vehicles, have led to higher demands on drive train components; by lower engine speed the gearbox must sustain higher torque, more torque vibrations and more frequent and faster shifts to keep engine running as close as possible to optimal speed. In order to design new synchronizers meeting these demands, simulation tools to study gearbox synchronizer performance are needed. The transmission system is a key element in motorized vehicles to transfer mechanical power from the engine to the wheels. It has great impact on the vehicle fuel consumption, power efficiency, noise and shift comfort. For manual transmission, synchronizer mechanisms were developed in the 1920s to allow smooth gear changing both for the durability of the transmission and the comfort for the users [1].

The gear synchronizer mechanism in its traditional design has the purpose that during released clutch, a new gearwheel is engaged by reducing the speed difference between outgoing shaft and the gearwheel to be engaged using a sleeve. This involves frictional contact between conical surfaces, and a design such that the sleeve is not engaged until the speed difference between sleeve and gearwheel is sufficiently small.

Lovas [2] explained the dynamics of the synchronizer and validate the numerical simulation results with the test bench measurements. Hoshino [3] simulated the synchronization mechanism by using ADAMS and studied the abnormal shift reaction force.

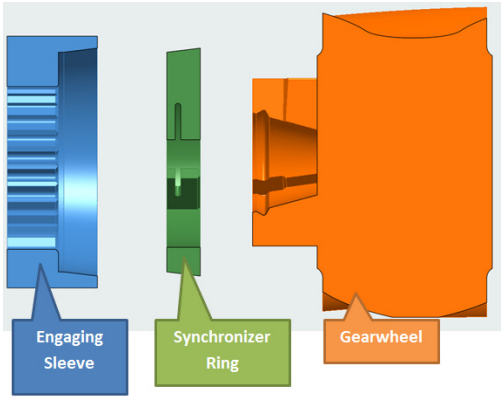


Figure 1: A common layout of a synchronizer.

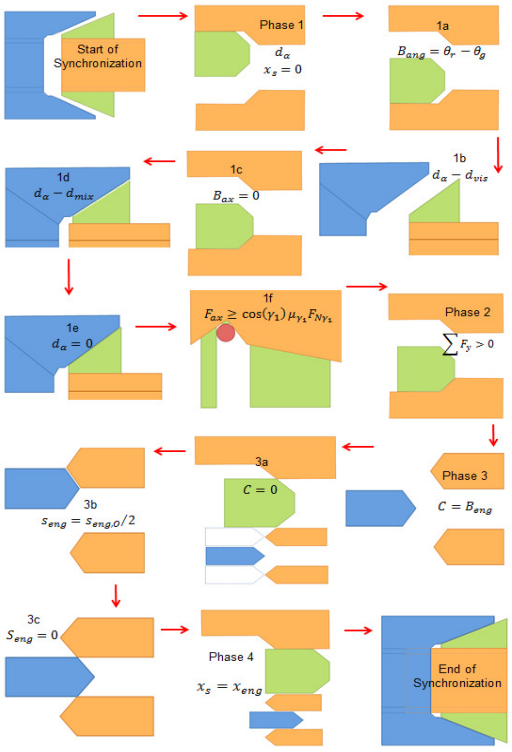


Figure 2: Division of synchronization in different phase events.

Kelly and Kent [4] developed a dynamic model to depict the entire selector system and correlated against the test data. Häggström and Nordlander developed a Matlab program for

the synchronization of transmission [5]. Transmission gear shifting improvement with respect to smooth, quick and energy efficient synchronizer performance is still one of the major concern areas for automotive industry and academia, see e.g [6-10].

Design optimization of synchronizer requires an efficient mathematical model. In this paper, a generic synchronizer is studied as a representative for common synchronizer designs used in manual and semi-automatic gearboxes. The considered synchronizer consists of an engaging sleeve, a synchronizer ring (also called blocker ring or baulk ring) and gearwheel. The engaging sleeve is attached to the gearbox output shaft (operated by gear selector) and the gearwheel is connected to the gearbox input shaft (clutch disengaged from motor). Constrained Lagrangian formalism is introduced in this paper to predict the dynamics of a generic synchronizer with emphasis on the different kind of interaction between bodies. Sensitivity of the synchronization time is analysed by varying the cone angle, coefficient of friction, rate of shift force, maximum allowable shift force and driveline vibrations with varying frequency and amplitude.

2 MODELLING OF A GENERIC SYNCHRONIZER MECHANISM

Here the equations of motion for a generic synchronizer are presented based on CLF. The kinematics of a generic synchronizer mechanism is determined from detailed description of the phases of the synchronization process.

2.1 Equations of motion

The generic synchronizer, as depicted in Figure 2 is considered as a multibody system (MBS) consisting of 3 rigid bodies

$$MBS = \{Engaging\ Sleeve, Synchronizer\ Ring, Gearwheel\} \tag{1}$$

The components are assembled on a shaft, on which the engaging sleeve and synchronizer ring may slide axially. The vector of generalized coordinates for the considered MBS is

$$\boldsymbol{q} = \left[x_s, \theta_s, x_r, \theta_r, \theta_g\right]^T \tag{2}$$

Here in θ_s, θ_r and θ_g are angular coordinates of the sleeve, ring and gearwheel, respectively; x_s and x_r are translational coordinates of the sleeve and ring, respectively. Following Lagrangian mechanics [12, 13], the Lagrangian L of the system is defined as

$$L = T(\boldsymbol{q}, \dot{\boldsymbol{q}}) - U(\boldsymbol{q}) \tag{3}$$

where $T(\boldsymbol{q}, \dot{\boldsymbol{q}})$ is a kinetic energy, $U(\boldsymbol{q})$ is a potential energy. Due to the design of synchronizer, the motion of the system is restricted by a set of holonomic kinematic constraints $\boldsymbol{\Phi}(\boldsymbol{q}, \boldsymbol{t}) = \boldsymbol{0}$. By introducing $\boldsymbol{\lambda}$ as the Lagrange multiplier vector, the motion of the system is described by a set of differential-algebraic equations (DAE)

$$\begin{cases} \left[\frac{d}{dt}\left(\frac{\partial L}{\partial \dot{\boldsymbol{q}}}\right)\right] - \left[\frac{\partial L}{\partial \boldsymbol{q}}\right] + \left[\frac{\partial \boldsymbol{\Phi}}{\partial \boldsymbol{q}}\right]^T \boldsymbol{\lambda} = \boldsymbol{Q}^A \\ \boldsymbol{\Phi}(\boldsymbol{q}, \boldsymbol{t}) = \boldsymbol{0} \end{cases} \tag{4}$$

where $\boldsymbol{Q}^A$ is a vector of generalized forces due to non-conservative applied loads. The vector of non-conservative forces $\boldsymbol{Q}^A$ is further divided into $\boldsymbol{Q}^A = \boldsymbol{Q}^A_{app} + \boldsymbol{Q}^A_{fric}$ where $\boldsymbol{Q}^A_{fric}$ are forces arising due to friction between bodies and other losses and $\boldsymbol{Q}^A_{app}$ are applied forces arising from external stimuli. For the generic synchronizer under consideration, Eq. (4) is written as follows

$$\begin{cases} \begin{bmatrix} m_s & 0 & 0 & 0 & 0 \\ 0 & I_s & 0 & 0 & 0 \\ 0 & 0 & m_r & 0 & 0 \\ 0 & 0 & 0 & I_r & 0 \\ 0 & 0 & 0 & 0 & I_g \end{bmatrix} \begin{bmatrix} \ddot{x}_s \\ \ddot{\theta}_s \\ \ddot{x}_r \\ \ddot{\theta}_r \\ \ddot{\theta}_g \end{bmatrix} + \left[\frac{\partial \boldsymbol{\Phi}}{\partial \boldsymbol{q}}\right]^T \boldsymbol{\lambda} = \begin{bmatrix} F_s \\ 0 \\ 0 \\ 0 \\ 0 \end{bmatrix}^{app} - \begin{bmatrix} F_{sf} \\ M_{sf} \\ F_{rf} \\ M_{rf} \\ M_{gf} \end{bmatrix}^{fric} + \begin{bmatrix} C_{s\alpha}\, sign(\dot{x}_s) \\ C_s \dot{\theta}_s \\ C_{r\beta}\, sign(\dot{x}_r) \\ C_r\, \dot{\theta}_r \\ C_g\, \dot{\theta}_g \end{bmatrix}^{oil,losses} \\ \boldsymbol{\Phi} = \begin{bmatrix} \boldsymbol{\Phi}^{imposed} \\ \boldsymbol{\Phi}^{internal} \end{bmatrix} = \mathbf{0} \text{ where } \boldsymbol{\Phi}(\boldsymbol{q}, \boldsymbol{t})^{imposed} = \theta_s - \omega_s t \end{cases} \quad (5)$$

where F_s is the applied shift force and $F_{rf} = -F_{sf}$, $M_{rf} = M_{gf} = -M_{sf}$. The set of internal constraints and parameters values is detailed in Table 1.

2.2 Different phases of a synchronization process

In the process of synchronization of the gear shift, different parts interact with each other to ensure the engagement or disengagement without clashing of the teeth. In this study, the division of the synchronization is not only based on relative position of the parts but also on interaction of the parts to capture the forces arising during synchronization. Each phase will be described in detail below. Pertinent constraints are given in Table 1 and the different events are shown in Figure 2.

Phase 1-Presynchronization. The phase 1 has the purpose of indexing. It starts from neutral position and ends where the axial force overcomes the axial resistance of the detent after contact of the synchronizer ring's chamfer with the gear's chamfer.

Here the phase 1 is further divided into different sub-phases based on the relative movement of the sleeve, the synchronizer ring and the gearwheel and varying oil film thickness between cone surfaces leading to identify the viscous, mixed and solid friction states.

Phase 1a-Angular indexing of the ring. Splines of the ring and the gear will be in contact at top as shown in Figure 2. At start of the phase 1a torque transfers from the sleeve to the ring through oil film and the ring will get angular rotation. After a while splines of the ring and the gear will come in contact at bottom at end of the phase 1a. The axial clearance between the cones is d_α.

Phase 1b-Free flight. The sleeve continues to move axially and oil film thickness decreases. The phase 1b ends when viscous friction must be taken into account at particular oil film thickness.

Phase 1c-Axial indexing of the ring. Chamfers of the gearwheel and the ring are at an axial clearance B_{ax}. The sleeve and the ring with oil film thickness d_{vis} move axially together until the chamfers come in contact.

Phase 1d-Viscous friction. The phase 1d is viscous friction phase when the oil between cones is squeezed out until the conditions between cones are shifted to mixed friction.

Phase 1e-Mixed friction. Axial clearance between the cones at start of the event is $d_\alpha - d_{vis}$ and at end is $d_\alpha - d_{mix}$. The phase 1e corresponds to mixed friction condition between cones.

Phase 1f-Force buildup. In this phase the amount of shift force further exceeds the detent axial resistance offered by the spring stiffness. The sub-phase will end when the condition will meet $\sum F_{ax} = F_s \geq \cos(\gamma_1)\, \mu_{\gamma_1} F_{N\gamma_1}$ where γ_1 is the detent angle and $F_{N\gamma_1}$ is the normal force at contact between detent and spring.

Phase 2-Main synchronization. Here the shift force increases while there is no axial movement of the sleeve and the transferred torque from cone friction will cause the rotation speed of the slave system (gearwheel) to adjust to the master system (sleeve). The phase 2 will end when the sleeve again starts to move axially and blocking torque at chamfers contact increases the cone torque or when the condition meets $\sum F_y > 0$.

Phase 3-Blocker transition. During the phase 3 the speed difference further decreases and reaches zero. The shift force is also needed to move the sleeve and the ring axially but the shift force will drop down from start of the phase 3. A detailed description for feasible and unfeasible synchronization is given in [11]. "Double bump" due to squeezing of oil between chamfers, turning of gear and cone sticking occurs during this phase.

Phase 3a-synchronized. Clearance c between the engaging teeth decreases to zero and the engaging teeth chamfers come in contact with a zero rpm difference. $B_{eng} = c = 0$ where B_{eng} is chamfers axial length.

Phase 3b-synchronized. Before the phase 3b the engaging teeth chamfers are at clearance S_{eng} and after the phase the chamfers come in full contact as shown in Figure 2. Relative rotational speed of the gear will be determined from the axial speed of the sleeve $\omega_g = \frac{v_s}{r_\beta} \tan\beta$ where r_β is mean radius at chamfers contact and β is angle of chamfers.

Phase 3c-synchronized. The phase 3c ends when the engaging teeth chamfers come out of contact and $S_{eng} = 0$.

Phase 4-Engagement. This is last phase of the synchronization where the engaging teeth get the engagement for transmission of the torque. The shift force is just needed to translate the sleeve and the ring for engagement of the teeth. The sleeve covered displacement x_{eng}.

Phase	Constraint: $\boldsymbol{\Phi(q,t)^{internal}}$	Phase	Constraint: $\boldsymbol{\Phi(q,t)^{internal}}$
1a	$[x_r]$=0	2	$\begin{bmatrix} x_r - d_\alpha \\ \theta_r - \theta_g - B_{ang} \end{bmatrix}$=**0**
1b	$\begin{bmatrix} x_r \\ \theta_r - \theta_g - B_{ang} \end{bmatrix}$=**0**	3a	$\begin{bmatrix} x_s - x_r - d_\alpha \\ \theta_r - \theta_g - B_{ang} - \frac{x_r - B_{ax}}{r_\beta}\tan\beta \end{bmatrix}$=**0**
1c	$\begin{bmatrix} x_s - x_r - d_{vis} \\ \theta_r - \theta_g - B_{ang} \end{bmatrix}$=**0**	3b	$\begin{bmatrix} x_s - x_r - d_\alpha \\ \theta_r - \theta_g - B_{ang} - \frac{x_r - B_{ax}}{r_\beta}\tan\beta \end{bmatrix}$=**0**
1d	$\begin{bmatrix} x_s - x_r - d_{mix} \\ \theta_r - \theta_g - B_{ang} \end{bmatrix}$=**0**	3c	$\begin{bmatrix} x_s - x_r - d_\alpha \\ \theta_r - \theta_g - B_{ang} - \frac{x_r - B_{ax}}{r_\beta}\tan\beta \end{bmatrix}$=**0**
1e	$\begin{bmatrix} x_s - x_r - d_\alpha \\ \theta_r - \theta_g - B_{ang} \end{bmatrix}$=**0**	4	$\begin{bmatrix} x_s - x_r - d_\alpha \\ \theta_r - \theta_s + \theta_{r_s} \\ \theta_r - \theta_g - B_{ang} + \theta_{g_s} \end{bmatrix}$=**0**
1f	$\begin{bmatrix} x_s - x_r - d_\alpha \\ \theta_r - \theta_g - B_{ang} \end{bmatrix}$=**0**		

Table 1: Internal constraints during subphases of the synchronization.

Here in Table 1 θ_{r_s} is difference in angular displacement between the ring and the gearwheel and θ_{g_s} is difference in angular displacement between the sleeve and the gearwheel before the phase 4.

3 DYNAMICS OF A GENERIC SYNCHRONIZER MECHANISM

In this section, the statement of the dynamics problem for a generic synchronizer mechanism is given and simulation results for a main gear downshift case are shown. The sleeve is taken as master and the gearwheel as slave. Downshift implies that the sleeve has high constant (prescribed) rotational speed and gearwheel has initially a lower speed that is to be synchronized to the sleeve speed. Sensitivity analysis of the synchronization time with respect to cone angle and coefficient of friction is also presented.

3.1 Problem formulation and synchronizer performance diagram

Problem A. Given the axial force acting on the sleeve, $F_s(t)$ (shift force), and the sleeve rotational speed $\dot{\theta}_s(t)$ during the synchronization process, i.e. for all $t \in [0, t_s]$.

It is required to determine motion of the sleeve, the ring and the gearwheel as well as contact forces between the sleeve and the ring and between the gearwheel and the ring that all together satisfy the differential-algebraic equations of motion, Eqs. (5), the initial conditions

$$\begin{cases} x_s(0) = x_s^0 & \dot{x}_s(0) = 0 & x_r(0) = x_r^0 & \dot{x}_r(0) = 0 \\ \theta_s(0) = \theta_s^0 & \dot{\theta}_s(0) = \dot{\theta}_s^0 & \theta_r(0) = \theta_r^0 & \dot{\theta}_r(0) = \dot{\theta}_r^0 \end{cases} \quad \theta_g(0) = \theta_g^0 \quad \dot{\theta}_g(0) = \dot{\theta}_g^0 \tag{6}$$

and the final conditions

$$\begin{cases} x_s(t_s) = x_s^s & \dot{x}_s(t_s) = \dot{x}_s^s & x_r(t_s) = x_r^s & \dot{x}_r(t_s) = \dot{x}_r^s \\ \theta_s(t_s) = \theta_s^s & \dot{\theta}_s(t_s) = \dot{\theta}_s^s & \theta_r(t_s) = \theta_r^s & \dot{\theta}_r(t_s) = \dot{\theta}_r^s \end{cases} \quad \theta_g(t_s) = \theta_g^s \quad \dot{\theta}_g(t_s) = \dot{\theta}_g^s$$
$$\dot{\theta}_s(t_s) = \dot{\theta}_r(t_s) = \dot{\theta}_g(t_s) = \omega \tag{7}$$

Here in Eqs. (6) and (7): x_s^0, θ_s^0, θ_r^0, $\dot{\theta}_s^0$, $\dot{\theta}_r^0$, θ_g^0 and $\dot{\theta}_g^0$ are arbitrary prescribed parameters; the synchronization time t_s to be determined; x_s^s, $\dot{x}_s^s$, x_r^s, $\dot{x}_r^s$, θ_r^s and θ_g^s are determined at the end of the synchronization process. The Eqs. (7) expresses the synchronization conditions.

To solve the Problem A, a computational model of the dynamics of the synchronizer mechanism in question was developed in MATLAB. The core of the computational model is implementation of predictor-corrector type algorithm [12, 13] to solve the system of DAE Eqs. (5) with initial and boundary conditions given by Eqs. (6) and (7).

3.2 Numerical solution of Problem A

For simulation of the dynamics of the generic synchronizer mechanism the particular input data is used as shown in Table 2.

$$F_s(t) = \begin{cases} \dot{F}_s t & t_0 \le t_{F_{s,max}} \\ F_{s,max} & t_{F_{s,max}} \le t_{phase,2} \\ 300 + \dot{F}_{s,3} t & t_{phase,2} \le t_{phase,3a} \\ F_{bumb} + \dot{F}_{s,3} t & t_{phase,3a} \le t_{end} \end{cases}$$

where $\dot{F}_{s,3}$ is decreasing force rate and F_{bumb} is double bump force.

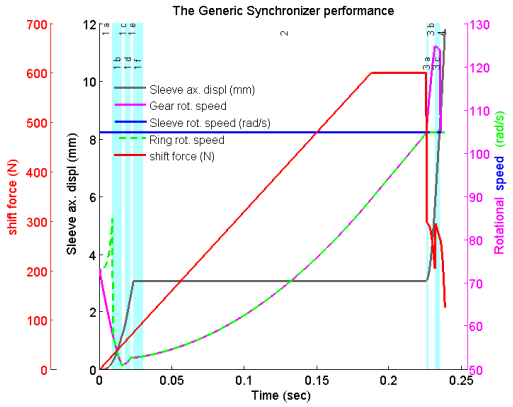


Figure 3: Synchronizer performance diagram.

As an example of the solution of the Problem A the axial position of sleeve and synchronizer ring, as well as sleeve force and rotational speeds of sleeve, ring and gearwheel

are collected in the diagram as shown in Figure 3, where also duration of sub-phases are shown.

As it follows from Figure 2 when the sleeve moves during the phase 1a and phase 1b the rotational speed of gearwheel and ring will decrease because of the oil splash losses. During the phase 1c the oil thickness between the cones is also not sufficient to transfer the torque from the sleeve to the gear. From the phase 1d to start of the phase 2 the gear almost retain its speed but the shift force increases to break the oil film thickness between the cones. From the phase 2 increment in the shift force is the main cause to increase gear speed while during phase 3, speed difference is because of turning of the gearwheel by the sleeve indirectly.

Variable	Name	Variable	Name
$m_s = 1.5$ kg	Sleeve mass	$m_r = 0.5$ kg	Ring mass
$m_{spr} = 0.2$ kg	Spring ring mass	$I_s = 0.01$ kgm^2	Sleeve moment of inertia
$I_r = 0.004$ kgm^2	Ring moment of inertia	$I_g = 0.2$ kgm^2	Gear moment of inertia
$r_\alpha = 0.1$ m	Cones mean radius	$r_\beta = 0.07$ m	Chamfers mean radius
$r_{spr} = 0.04$ m	Spring mean radius	$F_{spr} = 50$ N	Spring force
$b = 5$ mm	Cones contact length	$d_\alpha = 2$ mm	Cones Initial clearance
$d_{vis} = 1$ mm	Viscous friction clearance	$h_{min} = 0.1$ mm	Mixed friction clearance
$T_{oil} = 90^o$ C	Temperature at start	$\Delta T_{oil} = 20^o$ C	Temperature change
$\alpha = 7^o$	Cone angle	$B_{ang} = 5^o$	Angular clearance
$\beta = 60^o$	Chamfer angle	$\gamma = 5^o$	Detent angle
$\rho = 15$ mm^2/s	Oil viscosity [2]	$\mu_\alpha = 0.17$	Cones friction coefficient
$C_g = 5$	Gear oil splash losses	$C_s = 1$	Sleeve oil splash losses
$C_r = 0.003$	Ring sliding friction	$C_{s\alpha} = 0.02$	Sleeve sliding friction
$\omega_{s_o} = 1000$ rpm	Sleeve rotational speed	$\omega_{g_o} = 700$ rpm	Initial gear rotational speed
$\mu_{spr} = 0.12$	Spring friction coefficient	$\mu_\beta = 0.09$	Chamfers friction coefficient
$C_{r\alpha} = 0.002$	Ring sliding friction	$T_c = \lambda_{cons}\,\mu_\alpha F_s$	Cone Torque [2]
$F_{sf} = 16\pi\rho\dot{x}_s \sin(\alpha)\; r_c \left(\frac{b}{h}\right)^3$		Axial force transferred during viscous friction [2]	
$M_{sf} = 4\pi\rho\dot{x}_s r_c^3\; \omega_s \frac{b}{h}\left(1 - \frac{\omega_g}{\omega_s}\right)$		Torque transfer in viscous friction [2]	
$F_{s,max}$		Maximum acceptable applied shift force	

Table 2: Input parameters for the generic synchronization process.

4 SENSITIVITY ANALYSIS

A sensitivity analysis is done in order to see how cone angle, coefficient of friction and how the sleeve force affect the predicted synchronization time. In Figure 4 the synchronization time decreases with decreasing cone angle α and with increasing coefficient of friction μ. In Figure 5 the synchronization time decreases with increasing $F_{s,max}$ and $\dot{F}_s$. For higher values of the $F_{s,max}$ and $\dot{F}_s$ the synchronization time decreases rapidly than at lower values.

One problem of synchronizer design is its sensitivity to driveline vibrations. Here, the prescribed output shaft speed is modelled as $\omega_s = A\sin(2\pi f t + \vartheta)$ with frequency f and amplitude A. The sensitivity of synchronization time with respect to amplitude and frequency is shown in Figure 6 and 7. Since the phase shift is a random parameter $\vartheta \in [0, 2\pi]$, the mean synchronization time for 200 different values of ϑ is depicted.

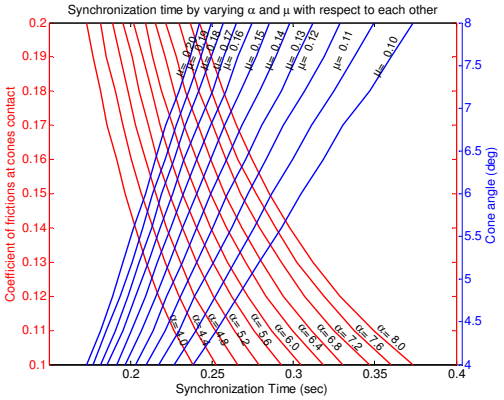


Figure 4: Synchronization time at varying cone angle α and coefficient of friction μ.

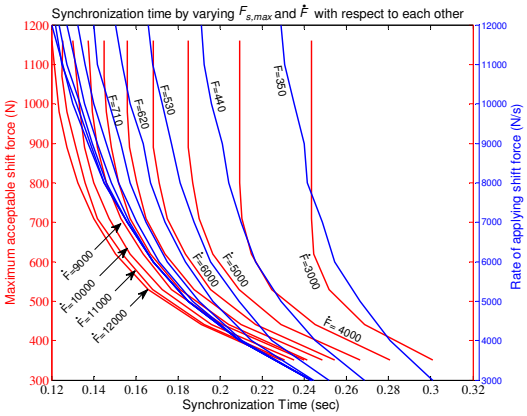


Figure 5: Synchronization time at varying $F_{s,max}$ and $\dot{F}_s$.

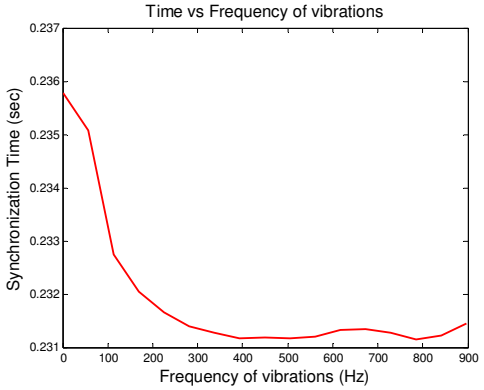


Figure 6: Variation of synchronization time with varying frequency of vibrations.

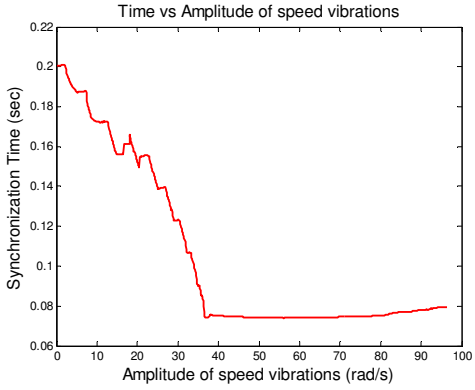


Figure 7 : Variation of synchronization time with varying amplitude of vibrations.

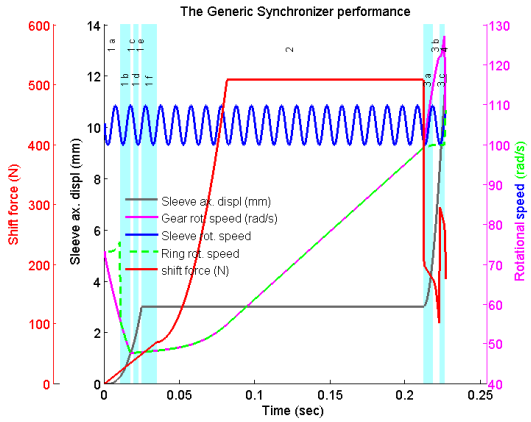


Figure 8: Synchronizer performance diagram with driveline vibrations.

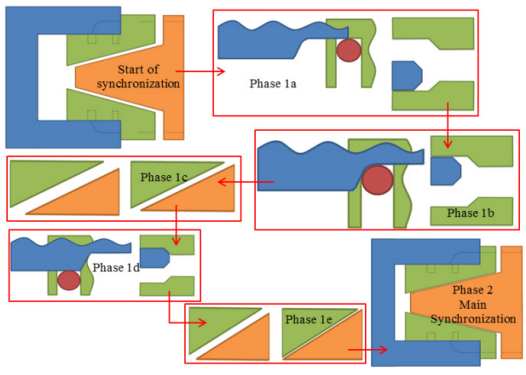


Figure 9: The modified generic synchronizer.

The synchronization time decreases with increasing frequency and amplitude of the vibrations at average values of the phase shift as shown in Figure 6 and 7. Before about 38 rad/s amplitude the decrease in time is sharp with small variations and after not only the time variation is small but also time increases. This kind of behaviour shows that at particular

values of other variables, effects of increase in amplitude upon the synchronization time are limited to a certain value. Figure 8 shows the generic synchronizer performance diagram at 100 Hz frequency of the vibrations and 5 rad/s amplitude of the speed vibrations.

5 MODEL VALIDATION

The generic synchronizer is modified according to the available experimental set-up as shown in Figure 9. Positions of cone and chamfer of the synchronizer ring are exchanged. The sleeve is blocked by the chamfers contact between the sleeve and the ring. The gearwheel and the ring have cones contact. Sub-phase of the spring happen before sub-phase of the viscous friction. Sub-phases of the axial indexing and angular indexing of the ring are also exchange their order. The detailed description is given in [11]. The measured shift force is taken as applied sleeve force in the model and time and speed difference are computed. The performance diagram is shown in Figure 10. From the experimental set-up 9 measurements are taken and the results are agreed closely, see Figure 11.

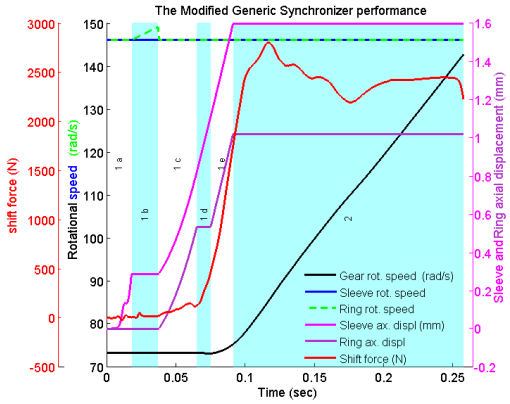


Figure 10: The modified generic synchronization process.

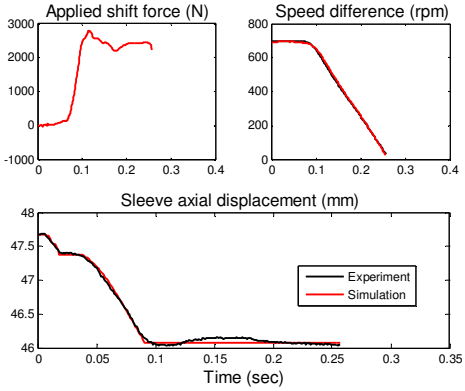


Figure 11: Applied shift force and speed difference during the generic synchronization.

6 CONCLUSIONS AND OUTLOOK

In this paper, the dynamics of a generic synchronizer was modelled using Constrained Lagrangian Formalism with constraints to describe each sub-phase of the synchronization process. The sensitivity analysis for cone angle, coefficient of friction, maximum acceptable shift force and rate of applied shift force and validation against test rig data show that the developed mathematical model using CLF predicts motion and internal forces in the system during the synchronization process reasonably well. Synchronization performance diagram is obtained by also introducing the vibrations to the generic synchronizer. Next, the model will be used to get further insight into synchronizer design with aid of global sensitivity analysis and Pareto optimization.

ACKNOWLEDGMENTS

Scania CV AB, Volvo GTT and the Sweden's Innovation Agency, VINNOVA are gratefully acknowledged for financially supporting the presented research, (project No: 2012-04619). The authors wish to thank Magnus Andersson for suggesting the generic synchronizer and Daniel Häggström and Kenth Hellström for experimental data and fruitful discussions.

REFERENCES

[1] A. Bedmar, *Synchronization processes and synchronizer mechanisms*. Diploma work no. 2013:20 Department of Applied Mechanics, Chalmers University of Technology, Göteborg, Sweden 2013.

[2] L. Lovas, *Etude des relations entre le comportment et la fabrication des synchronisateurs des.* National Institute of Applied Sciences, Lyon, PhD Thesis, 2004.

[3] H. Hoshino, Analysis on Synchronization Mechanism of Transmission. *International Congress and Exposition,* Detroit, Michigan, March 1-4, 1999.

[4] D. Kelly and C. Kent, Gear Shift Quality Improvement In Manual Transmissions Using Dynamic Modelling. *FISITA World Automotive Congress*, Seoul, Korea, June 12-15, 2000.

[5] D. Häggström and M. Nordlander, *Development of a program for calculating gearbox synchronization.* Master thesis, Department of Engineering Sciences and Mathematics, Luleå University of Technology, Luleå, 2011.

[6] P.D. Walker and N. Zhang, Parameter study of synchronizer mechanisms applied to Dual Clutch Transmissions. *Int. J. Powertrains,* vol. 1(2), pp. 198-220, 2011.

[7] A. Sandoza, Double synchronizer to amplify the synchronizer capacity. *SAE technical paper series,* 2012-2003, 2012.

[8] M.K. Sharma and J. Salva, Shift system inertia mass optimization techniques to minimize double bump for manual transmission. *SAE technical paper series,* 2012-01-1999, 2012.

[9] D. Häggström, U. Sellgren and S. Björklund, Robust pre-synchronization in heavy truck transmissions. *In Proc. Of the Int. gear conference*, Lion, 2014.

[10] V. Berbyuk, Towards pareto optimization of performance of a generic synchronizer of transmission systems. In *Proc. of IDETC/CIE ASME 2015*, Boston, USA, 2015 August 2-5, paper DETC 2015-46773.

[11] M. Irfan, V. Berbyuk and H. Johansson, *Constrained Lagrangian Formulation for modelling and analysis of transmission synchronizers.* 2015:05 Department of Applied Mechanics, Chalmers University of Technology, Gothenburg, 2015.

[12] E. J. Haug, *Intermediate Dynamics*, Prentice Hall Englewood Cliffs, New Jersey, 1992.

[13] A. A. Shabana, *Dynamics of multibody system*, Cambridge University Press, Cambridge, 1998 Second edition.

11th International Conference on Engineering Vibration
Ljubljana, Slovenia, 7–10 September 2015

MATHEMATICAL MODELING OF THE MECHANICAL SYSTEM OF THE VIBRATING TABLE WITH ORTOGONAL MOVEMENT AND HYDRAULIC TURBINE WITH INCLINED BLADES

Kuatbay Bissembayev[1], **Zharilkassin Iskakov***[2]

[1]The laboratory for mathematical modelling of vibration protection systems, the Institute of Mechanics and Machine Science Kurmangazy 29, Almaty, Kazakhstan
kuat_06@mail.ru

[2]The laboratory of vibratory mechanisms and machinery, the Institute of Mechanics and Machine Science Kurmangazy 29, Almaty, Kazakhstan
iskakov53@mail.ru

Keywords: Dynamic Interaction, Vibrating table, Orthogonal Movement, Hydraulic Turbine, Nonlinear Equation.

Abstract. *Functioning of many important and crucial vibrating machines and mechanisms is based on the use of different energy sources. If the energy source has an ideal excitation, i.e. it has an unlimited power; the inverse effect of oscillatory system upon excitation source of oscillations is neglected. However, on practice, there are frequent situations, when power consumed of the oscillating load is comparable on value with power of exciter oscillations. In such cases, using of the "ideal" mathematical models can lead to gross errors in dynamics description both the oscillatory system, so and excitation source of oscillations. The present work is devoted to the research of interaction of link mechanism of vibrating table with orthogonal movement and stimulating element of its oscillation with damless hydraulic turbine with inclined blades and a limited power. Relatedness of processes of the link mechanism with orthogonal movement and energy source, i.e. hydraulic turbine leads to the qualitatively new effects in their dynamics, which cannot be detected by investigating the problem in the formulation of ideal excitation. The special attention is paid to the research of influence of parameters of the link mechanism with orthogonal movement to movement modes of the hydraulic turbine. It is established that a equation of system movement is significantly non-linear and has a big parameter of non-linearity under the first derivative, the angular speed of the hydraulic turbine (driving member) is oscillated about its average value, the coefficient of movement non-uniformity of the hydraulic turbine (driving member) depends on parameters of link mechanism and hydraulic turbine. The patterns of change of angular speed amplitude of the driving member were determined depending on parameters of the link mechanism with orthogonal movement and hydraulic turbine. The results of research can be successfully used by projecting of the vibrating table on the basis of the link mechanism with orthogonal movement with non-ideal energy source, i.e. with the damless hydraulic turbine.*

1 INTRODUCTION

Vibratory machines and technological processes are used in almost all the branches of industry. In some cases, the specific technological processes may be performed only by virtue of using the vibration, and in other cases, using of the vibration leads to a significant enhancement of the processes and increasing of qualitative indicators.

Construction diagrams of vibratory machines, as a rule, are not complicated, however for successful work one needs to determine their parameters accurately, and that may be performed only based on study of the dynamics of vibration machines and the technological processes performed by them.

K. Bissembayev and Zh. Iskakov [1] have studied the oscillation motion of the vibratory table of automatic molding machine in flat leverage mechanisms. A mathematic model has been developed for the automatic molding machine vibratory table with orthogonal motion.

The ideas on the properties of oscillation systems interacting with energy source have been further developed in the works [2, 3]. Analysis of self-oscillating systems dynamics that interact with energy sources under existence of non-linear elastic linkages, periodic, parametric effects and delay is given herein.

The objective of this work is to perform a study of the dynamics of link mechanism of vibratory table with orthogonal motion, with drive damless hydro-turbine with fixed load (consideration of load) on the operating link.

2 MOTION EQUATION

Analytical model of link mechanism with orthogonal motion is shown in the Figure 1. We place the origin OXY of coordinate system in the crank rotation axis. Here, through X and Y, we mark the coordinates of articulated link C (Figure 1).

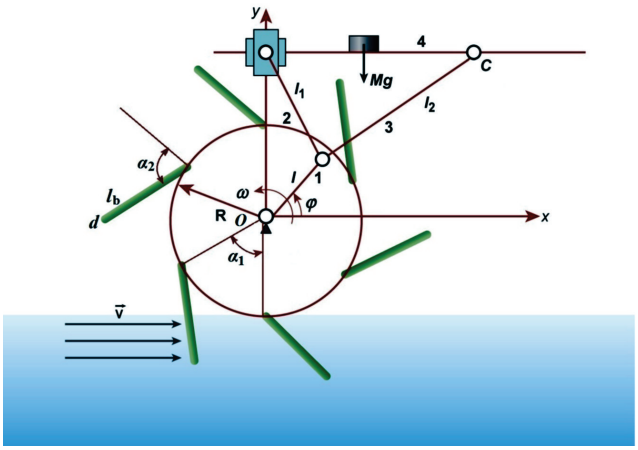


Figure 1: Diagram of vibratory table orthogonal mechanism with damless hydro-turbine drive.

From the closeness equations of the vector contours in projections to the coordinate axes we can write the following kinematic relations

$$\xi = X - X_{av} = l\cos\varphi - l_2\left[\sqrt{1-\frac{l_1^2}{l_2^2}+\frac{l^2}{l_2^2}} - \sqrt{1-\frac{l_1^2}{l_2^2}+\frac{l^2}{l_2^2}\cos^2\varphi}\right], \tag{1}$$

$$\eta = Y - Y_{av} = l\sin\varphi - l_1\left[\sqrt{1-\frac{l^2}{l_2^2}} - \sqrt{1-\frac{l^2}{l_1^2}\cos^2\varphi}\right],$$

where ξ, η are deviations of coordinates X and Y of the hinge C from their average value X_{av} and Y_{av}; l, l_1, l_2 are lengths of links 1, 2, 3 accordingly, φ is an angle of rotation axis of a crank (Figure 1).

A motion equation of the link mechanism with orthogonal motion is discussed in the work [1] and considering characteristics of driving torque of hydro-turbine with six flat blades [4] and using the certain trigonometric relations and substitution $d\tau = \omega_0 dt$ it may be transformed into the following non-dimensional form

$$\frac{d^2\varphi}{d\tau^2} + \frac{b}{\omega_0 A_0}\frac{d\varphi}{d\tau} + \varepsilon\left(\cos\varphi - 4\sin 2\varphi + 3\cos 3\varphi\right)\left(\frac{d\varphi}{d\tau}\right)^2 + \cos\varphi = \frac{a}{\omega_0^2 A_0}. \tag{2}$$

Here

$$\omega_0^2 = \frac{P}{A_0}, \quad \varepsilon = \frac{A_3}{A_0}, \quad A_0 = M\left(1+\frac{m_3}{M}\right)l^2 + J,$$

$$a = \frac{\rho_w Q^2}{h}\left(3W - T_1\mu_{11} + D_1\mu_{21}\right), \quad b = \frac{\rho_w Q^2}{h}\left(E_1\lambda_{11} + K_1\lambda_{21}\right),$$

where

$$A_3 = 2Ml^2\frac{l}{l_1}; \quad P = M\left[1+\frac{m_1}{M}+\frac{m_2}{M}+\frac{m}{2M}\right]gl; \quad J = \frac{1}{3}ml^2,$$

M - load mass, m, m_1, m_2 and m_3 - masses of links 1, 2, 3 and 4; J - momentum of inertia of link 1;

$$T_1 = \frac{1}{2}\frac{R}{l_b}\left[\sin\alpha_2 + \sin\left(2\alpha_1+\alpha_2\right) + \sin\left(4\alpha_1+\alpha_2\right)\right] +$$
$$+\frac{1}{4}\left[\sin 2\alpha_2 + \sin 2\left(\alpha_1+\alpha_2\right) + \sin 2\left(2\alpha_1+\alpha_2\right)\right];$$

$$D_1 = \frac{1}{2}\frac{R}{l_b}\left[\cos\alpha_2 + \cos\left(2\alpha_1+\alpha_2\right) + \cos\left(4\alpha_1+\alpha_2\right)\right] +$$
$$+\frac{1}{4}\left[\cos 2\alpha_2 + \cos 2\left(\alpha_1+\alpha_2\right) + \cos 2\left(2\alpha_1+\alpha_2\right)\right];$$

$$E_1 = \frac{J_h C}{\vartheta}\left[\cos\alpha_2 + \cos\left(\alpha_1+\alpha_2\right) + \cos\left(2\alpha_1+\alpha_2\right)\right];$$

$$W = \frac{1}{2}\frac{R}{l_b}\cos\alpha_2 + \frac{1}{4}; \quad C = \frac{R^2}{l_b^2} + \frac{R}{l_b}\cos\alpha_2 + \frac{1}{3}; \quad Q = \vartheta h l_b;$$

$$K_1 = \frac{J_h C}{\vartheta} \left[\sin\alpha_2 + \sin\left(\alpha_1 + \alpha_2\right) + \sin\left(2\alpha_1 + \alpha_2\right)\right];$$

$$J_h = \frac{1}{2} M_r R^2 + 6\rho_b h l_b d \left(R^2 + \frac{1}{3} l_b^2 + R l_b \cos\alpha_2\right);$$

$$\mu_{11} = \frac{1}{\pi - 2\alpha_1 - \alpha_2} \int_0^{\pi - 2\alpha_1 - \alpha_2} \sin 2\varphi d\varphi, \quad \mu_{21} = \frac{1}{\pi - 2\alpha_1 - \alpha_2} \int_0^{\pi - 2\alpha_1 - \alpha_2} \cos 2\varphi d\varphi,$$

$$\lambda_{11} = \frac{1}{\pi - 2\alpha_1 - \alpha_2} \int_0^{\pi - 2\alpha_1 - \alpha_2} \sin \varphi d\varphi, \quad \lambda_{21} = \frac{1}{\pi - 2\alpha_1 - \alpha_2} \int_0^{\pi - 2\alpha_1 - \alpha_2} \cos \varphi d\varphi,$$

ρ_w - liquid density, ϑ - liquid velocity, Q - fluid flow rate in the blade pressure side, α_1 - angle between blades, α_2 - angle of inclination of blades, R and M_r - radius and mass of hydro-turbine driving wheel, h, l_b and d - width, length and thickness of hydro-turbine blade, respectively, ρ_b - density of the blade's material.

The damless hydro-turbine refers to the slow-speed drives and for that reason a value of speed of rotational motion of damless hydro-turbine is equal to few units and condition $b < \omega_0 A_0$ is imposed.

The equation Eq. 4 turns out to be essentially nonlinear since the nonlinear term enters the equation without small parameter.

3 SOLUTION OF MOTION EQUATION BY ASYMPTOTIC METHOD

Now let's get down to the solution of motion equation Eq. 2 by asymptotic method Eq. 5. The static equilibrium of the mechanism is determined by the equation

$$\cos\varphi = \frac{a}{\omega_0^2 A_0}. \tag{3}$$

We find from here a condition of excitation of the rotational motion as

$$\frac{a}{\omega_0^2 A_0} < 1. \tag{4}$$

Substitution

$$\varphi = z, \quad \dot{z} = \Omega + x \tag{5}$$

will transform the equation Eq. 2 into the form

$$\dot{x} = -\frac{b}{\omega_0 A_0} x - \varepsilon \left(\cos z - 4\sin 2z + 3\cos 3z\right)\left(\Omega + x\right)^2 - \cos z, \tag{6}$$
$$\dot{z} = \Omega + x,$$

where

$$\Omega = \frac{a}{\omega_0 b}$$

Suppose that $\tau = \mu^2 s$, where $\mu = \dfrac{\omega_0 A_0}{b}$. Then the system of equations Eq. 6 will transform into the form:

$$x' = -\mu x - \mu^2 \varepsilon \left(\cos z - 4\sin 2z + 3\cos 3z\right)\left(\Omega + x\right)^2 - \mu^2 \cos z, \qquad (7)$$
$$z' = \mu^2 \Omega + \mu^2 x,$$

where the denotation is accepted $x' = \dfrac{dx}{ds}$.

For the system Eq. 7, let's agree solve the following Cauchy problem.

At

$$s = 0, \quad z = 0, \quad z' = 0, \quad x = \bar{x}. \qquad (8)$$

Following to the work [5], we suppose that

$$x = \bar{x} + \mu u_1(\bar{x}, \bar{z}) + \mu^2 u_2(\bar{x}, \bar{z}) + \mu^3 u_3(\bar{x}, \bar{z}) + ..., \qquad (9)$$
$$z = \bar{z} + \mu \upsilon_1(\bar{x}, \bar{z}) + \mu^2 \upsilon_2(\bar{x}, \bar{z}) + \mu^3 \upsilon_3(\bar{x}, \bar{z}) + ...,$$

where the functions $\bar{x}$ and $\bar{z}$ meet the following equations:

$$\bar{x}' = \mu_1(\bar{x}) + \mu_2^2(\bar{x}) + \mu_3^3(\bar{x}) + ..., \qquad (10)$$
$$\bar{z}' = \mu^2 \Omega + \mu_1(\bar{x}) + \mu_2^2(\bar{x}) + \mu_3^3(\bar{x}) + ...$$

Assume that the functions u_i, υ_i, $\dfrac{\partial u_i}{\partial \bar{x}}$ and $\dfrac{\partial \upsilon_i}{\partial \bar{x}}$ are limited. Now, in order to meet the condition Eq. 6, let's accept

$$u_i\left(\bar{x}, 0\right) = \upsilon_i\left(\bar{x}, 0\right) = 0; \quad \frac{\partial u_i\left(\bar{x}, 0\right)}{\partial \bar{x}} = \frac{\partial \upsilon_i\left(\bar{x}, 0\right)}{\partial \bar{x}} = 0. \qquad (11)$$

Equations for determining the functions u_i, υ_i, A_i and B_i will be as follows:

$$1.\, A_1 = -\bar{x};\ 2.\, B_1 = 0;\ 3.\, \bar{x}\frac{\partial u_1}{\partial \bar{x}} - u_1 = A_2 + \cos\bar{z} + \varepsilon\left(\Omega + \bar{x}\right)^2\left(\cos\bar{z} - 4\varepsilon\sin 2z + 3\cos 3\bar{z}\right); \qquad (12)$$
$$4.\, \bar{x}\frac{\partial \upsilon_1}{\partial \bar{x}} = B_2 - \bar{x}; \quad 5.\, \bar{x}\frac{\partial u_2}{\partial \bar{x}} - u_2 = A_3 + \frac{\partial u_1}{\partial \bar{x}}A_2 + \left(\Omega + B_2\right)\frac{\partial u_1}{\partial \bar{z}} - \varepsilon\upsilon_1\left(\Omega + \bar{x}\right)^2 \times$$
$$\times\left(\sin\bar{z} + 8\cos 2\bar{z} + 9\sin 3\bar{z}\right) + 2\varepsilon u_1\left(\Omega + \bar{x}\right)\left(\cos\bar{z} - 4\sin 2\bar{z} + 3\cos 3\bar{z}\right) - \upsilon_1;$$
$$6.\, \bar{x}\frac{\partial \upsilon_2}{\partial \bar{x}} = B_3 + \frac{\partial \upsilon_1}{\partial \bar{x}}A_2 + \left(\Omega + B_2\right)\frac{\partial \upsilon_1}{\partial \bar{z}} - u_1.$$

Consider the third equation of the system Eq. 12. From conditions Eq. 11 we will find

$$A_2 = -\left[1 + 4\varepsilon\left(\Omega + \bar{x}\right)^2\right]. \qquad (13)$$

The substitution $u_1 = \bar{x} \cdot \psi$ will transform the equation Eq. 12 into the form of

$$\frac{\partial \psi}{\partial \bar{x}} = -\frac{1}{\bar{x}^2} - 4\varepsilon\left(\frac{\Omega^2}{\bar{x}^2} + \frac{2\Omega}{\bar{x}} + 1\right) + \varepsilon\left(\cos\bar{z} - 4\sin 2\bar{z} + 3\cos 3\bar{z}\right) \times$$
$$\times\left(\frac{\Omega^2}{\bar{x}^2} + \frac{2\Omega}{\bar{x}} + 1\right) + \frac{1}{\bar{x}^2}\cos\bar{z}.$$

Therefore, solution of the equation Eq. 12 will take the form of

$$u_1(\bar{x},\bar{z}) = 1-\cos\bar{z}+\varepsilon(\Omega^2-2\Omega\bar{x}\ln\bar{x}-\bar{x}^2)\times \\ \times(4-\cos z+4\sin 2\bar{z}-3\cos 3\bar{z})+C_1(\bar{z})\cdot\bar{x}, \tag{14}$$

where $C_1(\bar{z})$ is the arbitrary function $\bar{z}$. However, the condition Eq. 11 gives us immediately $C_1(\bar{z})=0$. Repeating the reasoning for fourth, fifth and sixth equation of the system Eq. 12, we obtain

$$B_2=\bar{x},\quad \upsilon_1=0,\quad A_3=-8\varepsilon(\Omega+\bar{x})\left(\Omega^2+2\Omega\bar{x}\ln\bar{x}-\bar{x}^2\right),$$
$$u_2(\bar{x},\bar{z})=(\bar{x}\ln\bar{x}-\Omega)\sin\bar{z}+\varepsilon(8-\beta)\left(\Omega^3-\Omega\bar{x}^2+\frac{1}{2}\bar{x}^3+\Omega\bar{x}\ln^2\bar{x}-\right.$$
$$\left.-\Omega^2\bar{x}\ln\bar{x}+2\Omega\bar{x}^2\ln\bar{x}\right)+2\varepsilon\gamma\left[\Omega\ln\bar{x}-\bar{x}\ln\bar{x}+4\varepsilon\left(\Omega^2\bar{x}\ln\bar{x}+\Omega^3\ln\bar{x}-\right.\right.$$
$$\left.\left.-\Omega^2\bar{x}\ln^2\bar{x}-\Omega\bar{x}^2\ln\bar{x}-\frac{1}{2}\bar{x}^3\right)\right],$$
$$B_3=0,\quad \upsilon_2(\bar{x},\bar{z})=\ln x\cdot(\cos\bar{z}-1)-\varepsilon\gamma\left[\Omega^2\ln\bar{x}-2\Omega\bar{x}(\ln\bar{x}-1)-\frac{1}{2}\bar{x}^2\right],$$

where

$$\gamma=4-\cos\bar{z}+4\sin 2\bar{z}-3\cos 3\bar{z},$$
$$\beta=\sin\bar{z}+8\cos 2\bar{z}+9\sin 3\bar{z}.$$

Having continued this procedure, we can easy to get A_4 etc. Being limited in our computations by the terms of the order of (μ^2), let's give the equations Eq. 9 and Eq. 10 the following form

$$x=\bar{x}+\mu(1-\cos\bar{z})+\mu\varepsilon\gamma\left(\Omega^2-2\Omega\bar{x}\ln\bar{x}-\bar{x}^2\right)+\mu^2\left(\bar{x}\ln\bar{E}-\Omega\right)\sin\bar{z}+ \\ +\mu^2\varepsilon(8-\beta)\left(\Omega^3-\Omega\bar{x}^2+\frac{1}{2}\bar{x}^3+\Omega\bar{x}\ln^2\bar{x}-\Omega^2\bar{x}\ln\bar{x}+2\Omega\bar{x}^2\ln\bar{x}\right)+ \\ +2\mu^2\varepsilon\gamma\left[\Omega\ln\bar{x}-\bar{x}\ln\bar{x}+4\varepsilon\left(\Omega^2\bar{x}\ln\bar{x}+\Omega^3\ln\bar{x}-\Omega^2\bar{x}\ln^2\bar{x}-\Omega\bar{x}^2\ln\bar{x}-\frac{1}{2}\bar{x}^3\right)\right], \\ z=\bar{z}+\mu^2\ln\bar{x}(\cos\bar{z}-1)-\mu^2\varepsilon\gamma\left[\Omega^2\ln\bar{x}-2\Omega\bar{x}(\ln\bar{x}-1)-\frac{1}{2}\bar{x}^2\right], \tag{15}$$

$$\bar{x'}=-\mu\bar{x}-\mu^2\left[1+4\varepsilon(\Omega+\bar{x})^2\right], \\ \bar{z}'=\mu^2(\Omega+\bar{x}). \tag{16}$$

Integrating the third and fourth ones of the equations Eq. 16 and considering the initial conditions Eq. 8, we obtain

$$\bar{x}=D\cdot\frac{1+Ae^{-\mu\alpha s}}{1-Ae^{-\mu\alpha s}}-B, \\ \bar{z}=\mu^2(\Omega-\sigma)\cdot s+k\ln(1-Ae^{-\mu\alpha s})-k\ln(1-A), \tag{17}$$

where

$$\alpha=\sqrt{(1+8\mu\varepsilon\Omega)^2-16\mu^2\varepsilon(1+4\mu\varepsilon\Omega^2)},\quad D=\frac{\alpha}{8\varepsilon\mu},$$
$$B=\frac{1+8\mu\varepsilon\Omega}{8\mu\varepsilon},\quad \sigma=\frac{(1+8\mu\varepsilon\Omega)-\alpha}{8\mu\varepsilon},\quad k=\frac{1}{4\varepsilon},\quad A=\frac{1-\alpha}{1+\alpha}.$$

4 MOTION STABILITY

Let's consider the stability of stationary modes of the orthogonal mechanism rotational motion, which are determined by expressions Eq. 17. For this purpose, let's make up the variational equations for Eq. 15 and Eq. 16 system. Suppose that

$$\begin{aligned} \bar{x} &= \bar{x}^* + q, \\ \bar{z} &= \bar{z}^* + p. \end{aligned} \tag{18}$$

where $\bar{x}^*$ and $\bar{z}^*$ are the stationary solutions of equations Eq. 15 and Eq. 16, which at the initial conditions $s = 0$, $\bar{z} = 0$, $\bar{z}' = 0$, have the form of

$$\bar{x}^* = D\frac{1 + Ae^{-\mu\alpha s}}{1 - Ae^{-\mu\alpha s}} - B,$$

$$\bar{z}^* = \mu^2 (\Omega - \sigma) \cdot s + k \ln\left(1 - Ae^{-\mu\alpha s}\right) - k \ln(1 - A).$$

Substituting the expressions Eq. 18 to Eq. 15 and Eq. 16 and after linearization by respect to variations q and p, we get

$$\begin{aligned} q' &= -\mu \left[1 + 8\mu\varepsilon \left(\Omega + \bar{x}^*\right)\right] q, \\ p' &= \mu^2 q. \end{aligned} \tag{19}$$

Integrals of equation system Eq. 19 will take the form

$$\begin{aligned} q &= \frac{Ce^{-\mu\alpha s}}{(1 - Ae^{-\mu\alpha s})^2}, \\ p &= -\frac{\mu C}{\alpha A}\frac{1}{(1 - Ae^{-\mu\alpha s})}. \end{aligned} \tag{20}$$

Stability condition is of the form of inequality

$$F = 1 + 16\mu\varepsilon (\Omega - \mu) > 0. \tag{21}$$

5 RESULTS AND ANALYSIS

Coming back to variables $t = \dfrac{\mu^2}{\omega_0} s$ and $\varphi = z$, and based on formulas Eq. 7, Eq. 15 and Eq. 17, the graphs of dependence of angular speed from an angle of rotation of the hydroturbine at various values of radius of the driving wheel, water flow speed, load mass at the operating link and length of the driving link have been plotted (Figure 2 and Figure 3).

Computations have been performed with the following values of parameters:

$$\begin{gathered} \vartheta = 1m/s, \quad \rho_w = 10^3 kg/m^3, \quad l_b = 1m, \quad h = 1m, \quad d = 2 \cdot 10^{-3} m, \quad \alpha_1 = \pi/3, \quad \alpha_2 = \pi/6, \\ R = 13 \cdot 10^{-2} m, \quad M_r = 28kg, \quad \rho_b = 2.7 \cdot 10^3 kg/m^3, \quad m = 2kg, \quad m_1 = 2.5kg, \quad m_2 = 3kg, \\ m_3 = 3.5kg, \quad M = 70kg, \quad l = 0.1m, \quad l_1 = 1m, \quad l_2 = 2m. \end{gathered}$$

In the Figure 2 (a) the lines 1, 2 and 3 have been plotted upon the results of analytical solutions, and line 4 - upon the results of numeric solutions of the system of equations Eq. 6. Similarity of curves 2 and 4 provides a rough idea of closeness of results of analytical and

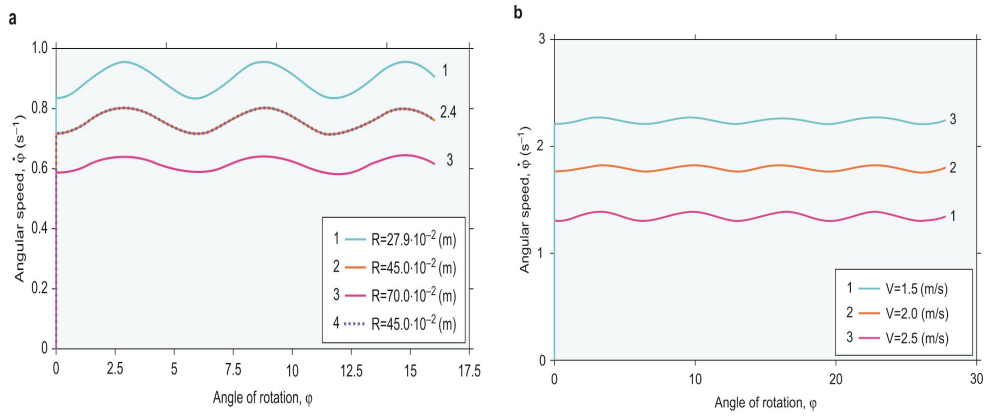


Figure 2: Graphs of dependence of angular speed from an angle of rotation of the hydro-turbine at various values of radius of the driving wheel (a) and of water flow speed (b).

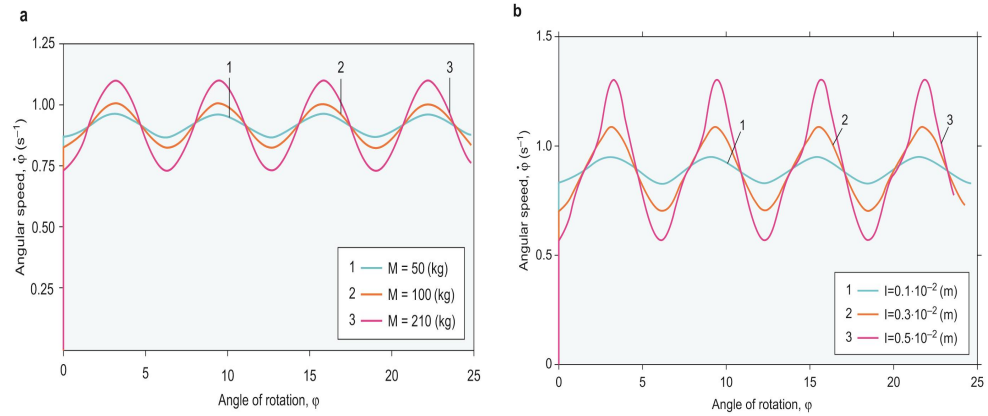


Figure 3: Graphs of dependence of angular speed from an angle of rotation of the hydro-turbine at various values of the mass of cargo on the working link (a) and of the length of the driving member the link mechanism (b).

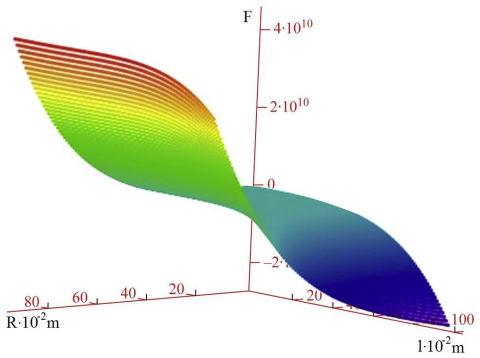


Figure 4: The stable and unstable zones.

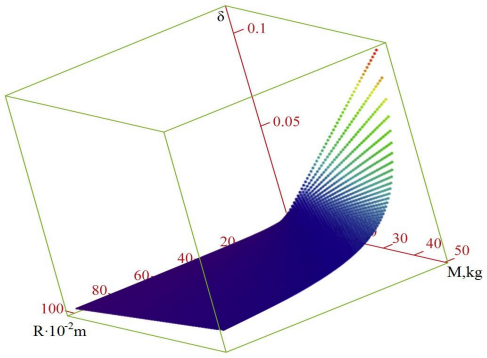


Figure 5: Graphs of dependence of the coefficient of movement non-uniformity from radius of the driving wheel of the hydro-turbine and the load mass on the

numerical solutions. From graphs in the Figure 2 and Figure 3 is shown in the first instance that angular speed of the damless hydro-turbine oscillates about its average value. In its turn, this value of the hydro-turbine angular speed depends on the radius of the driving wheel (Figure 2 (a)) and of water flow speed (Figure 2 (b)), i.e., on the hydro-turbine parameters and does not depend on the parameters of link mechanism (Figure 3 (a)) and (Figure 3 (b)). Both hydro-turbine parameters (Figure 2), and parameters of the link mechanism with orthogonal motion (Figure 3) have an effect on deviation amplitude of this angular speed from its average value.

The Figure 4 represents geometrically a function F depending on the hydro-turbine driving wheel radius and length of the link mechanism driving member, from where the stability area and non-stability area, and transition between them are seen distinctly.

At steady-state condition the speed $\dot{\varphi}$ of driving member remains although at the average constant, but it changes within the cycle, going through the maximum $\dot{\varphi}_{max}$ and minimum $\dot{\varphi}_{min}$ values. Irregularity in rotation speed is estimated by the irregularity coefficient

$$\delta = \left(\dot{\varphi}_{max} - \dot{\varphi}_{min}\right) / \dot{\varphi}_a, \tag{22}$$

where $\dot{\varphi}_a$ - average speed per cycle. Coefficient δ characterizes a range of speed fluctuation with regard to its average value.

Therefore, the irregularity coefficient depends on parameters of the link mechanism with orthogonal motion and hydro-turbine. The graphs of dependence of the irregularity coefficient δ from the radius R of hydro-turbine driving wheel and load mass M are given in the Figure 5. Based on analysis of these graphs we can say that selecting parameters of hydro-turbine and link mechanism with orthogonal motion is possible to obtain the reasonably small value of the irregularity coefficient δ.

6 CONCLUSIONS

- Dynamics of link mechanism with orthogonal motion, with drive damless hydro-turbine with fixed load in the vibration table has been studied.
- It has been found that angular speed of the damless hydro-turbine oscillates near its average value, and this value depends on the hydro-turbine driving wheel radius and water flow speed.
- Dependencies of deviation amplitude of this angular speed from its average value depending on hydro-turbine driving wheel radius, water flow speed, load mass at the operating link and length of the driving member are given.
- Dependence of driving member rotation irregularity coefficient from parameters of link mechanism with orthogonal motion and hydro-turbine has been determined, according that, selecting these parameters it is possible to obtain a reasonable value of the irregularity coefficient, which is need for optimal designing of link mechanism with orthogonal motion with drive damless hydro-turbine.

REFERENCES

[1] . Bissembayev and Zh. Iskakov, Mathematic model of the orthogonal mechanism of the press machine vibrating table. *Bulletin of the Kazakh National Teachers Training University named after Abai*, **3 (39)**, 32–38, 2012.

[2] A.A. Alifov and K.V Frolov, *Interaction of non-linear oscillation systems with sources of energy*. Science, Moscow, 1985.

[3] V.O. Kononenko, *Oscillation systems with restricted excitation*. Science, Moscow, 1964.

[4] A.K. Tuleshov, . Bissembayev and E.K. Zhamenkeev, The force moment and capacity of hydro-turbine at the beginning of blade immersion. *The Bulletin of the Moscow City Pedagogical University, Series computer science and informatization of education*, **4 (14)**, 154–161, 2008.

[5] N.N. Moyseyev, *Asymptotic methods of non-linear mechanics*. Science, Moscow, 1969.

11th International Conference on Engineering Vibration
Ljubljana, Slovenia, 7–10 September 2015

MODELLING AND AUTOMATIC CONTROL FOR A SCAN EAGLE SIMULATOR

Juan C. Rivera Medina*[1], Diego Hernandez[1], Fernando C. Pinto[2], William Hernandez[2], Daniel Castello[2], Diego Godoy [2]

[1]CODALTEC
jrivera@vertial.codaltec.com, dhernandez@codaltec.com
[2]UFRJ
fcpinto@ufrj.br, castello@mecanica.coppe.ufrj.br, wpinto@ufrj.br, dgodoy@ufrj.br

Keywords: Dynamic modelling, Simulator, Automatic Control, Scan Eagle

Abstract. *Unmanned aircrafts are very useful nowadays because of their great performance and the ability to perform different kind of tasks without the direct presence of humans. The Scan Eagle is one of the most versatile aircrafts available on the market, therefore it is necessary to train pilots to accomplish the different missions assigned. A simulator was then developed to train those pilots to fly these kind of aircrafts. The simulator allows the pilots to be trained in different situations close to the reality of the flight. To achieve a real flight description, a dynamic model of the Scan Eagle and an automatic control were developed and will be presented in this document. The Scan eagle has a special configuration, that doesn't use a tail to achieve stability, instead it uses two elevons placed on the wings to regulate the total lift force of the plane, also has two winglets on the outside tip of the wings on vertical position with elevons that make a variation of the thrust allowing the rotation of the aircraft along its Z axis. This paper will first describe the development of the equations of motion, establishing different frames to describe the movements, as a second step the model of forces and torques is developed, finally the deduction of the aerodynamic forces and coefficients using specialized software for airfoil design and analysis as XFLR5 is discussed. Having the complete dynamic model an automatic control is developed that allows the system to be on a stable state over the whole flight. The automatic control will allow the control tracking of the of the controlled states t o make smooth filghts and follow predetermined trajectories. Some test were made, implementing the model on Matlab-Simulink, to verify the correct behavior of the model and controller.*

1 INTRODUCTION

The Scan Eagle has been a very useful aircraft in the Colombian territory for surveillance and rescue missions. This kind of aircrafts is used all over the country, so its necessary to train several pilots to control and execute the missions. A simulator of the whole system was designed and developed to train the pilots to deal with different situations on flight. Further to create an enviroment so the pilots can feel the real mission, it is necessary to have an accurate model of the airplane so it can behave as in real flight.

The present document was devided in 5 parts, the first part will describe the dynamic model of the aircraft, where it will be shown the equations of motion of the aircraft and the analisys of forces and torques considering the aircraft configuration, the second part will describe the aerodynamic equations of lift and drag with each of its parameters and how they are calculated, the second part will show the considerations taken for the controller design and the linear model, the fourth part of the document shows a simulation demostrating the right behavior of the aircraft over some conditions like tracking and stabilization to disturbance, at the end of the document are shown the conclusions of the present work.

2 DYNAMIC MODEL

The development of a dynamic model of the aircraft for the simulator is a very important task, because with a correct behavior the pilot will ”feel” how to react to different situations, improving the pilots performance and avoiding damages to the aircraft.

The procedure to develop the mathematical model was devided into 3 main parts, the first part related to the frames used to describe each of the equations of motion, the second part will describe the different forces and torques that are interacting with the airplane and finally the third part will describe the aerodynamic equations and some simulations to stablish the different parameters.

To the develop the model some considerations were made [1] [5]

1. The aircraft is considered as a rigid body.
2. The curvature of the earth i neglected.

2.1 EQUATIONS OF MOTION

A fixed wing aircraft as an airplane, base all its motions in its forward velocity, this because the lift forces depend quadraticly on the velocity of displacement as it will be shown later. This characteristic will influence in the whole motion of the aircraft, stablishing conditions for the wind that impact with the aircraft increasing the effect of the drag. The first step will be to define the frames where the equations are going to be evaluated.

2.1.1 Frames defintinion

Four frames are defined to describe the kinematic equations.

1. Earth Frame (*EF*): This frame is defined fixed on the center of the earth and pointing the *x* vector pointing *North* and the *y* vector pointing to the *East*.
2. Spatial Frame (*SF*): The spatial frame is fixed on the center of gravity (*COG*) of the airplane, and will be oriented as the *EF*.

3. Body Frame (*BF*): The body frame is fixed on the *COG* of the aircraft, but its orientation will change with the motion of the aircraft, as in figure 1.

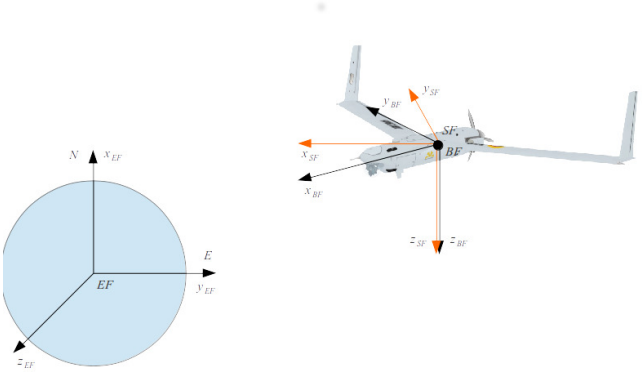


Figure 1: Earth, Spatial and Body Frame definition

4. Wind Frame (*WF*): The wind frame is fixed to the *COG* of the aircraft,but its orientation will depend on two angles. The angle of attack due to pitch movement, and the angle of attack due to yaw, as shown in figure 2.

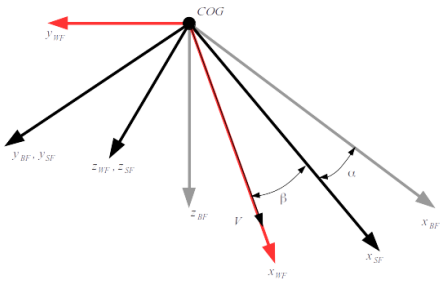


Figure 2: Wind Frame definition

2.2 Wind Equations

To describe the relationship between the influence of the wind and the displacement of the airplane, the V_w is decomposed on the *BF* and the linear velocities (u^{BF},v^{BF},w^{BF}) are defined using the reference shown on figure 2.[1] [9].

$$u^{BF} = V_w * cos(\alpha) * cos(\beta) \tag{1}$$

$$v^{BF} = V_w * sin(\beta) \tag{2}$$

$$w^{BF} = V_w * sin(\alpha) * cos(\beta) \tag{3}$$

Then to calculate the angles of attack, using some trigonometric relation the following equations can be use:

$$\alpha = \arctan(\frac{w^{BF}}{u^{BF}}) \tag{4}$$

$$\beta = \arcsin(\frac{u^{BF}}{v^{BF}}) \tag{5}$$

$$|V_w| = \sqrt{(u^{BF})^2 + (v^{BF})^2 + (w^{BF})^2} \tag{6}$$

2.3 Translational Equations

Having defined the wind equations it is possible to develop the translational equations. Using Newtons second law, the displacement of the ***BF*** can be described as:

$$\dot{V}^{BF} = \frac{1}{m} * F^{BF} + \Omega \times V^{BF} \tag{7}$$

because of the relationship between the V_w and the ***BF***, the transalational velocity will be written as follows:

$$\dot{V}^{BF} = \frac{1}{m} * F^{BF} + \begin{pmatrix} q * V * sin(\alpha) * cos(\beta) - r * V * sin(\beta) \\ r * V * cos(\alpha) * cos(\beta) - p * V * sin(\alpha) * cos(\beta) \\ p * V * sin(\beta) - V * q * cos(\alpha) * cos(\beta) \end{pmatrix} \tag{8}$$

where $\Omega = [p, q, r]^T$, are the rotational velocities descibed in the ***BF*** and $\dot{V}^{BF} = [u, v, w]^T$. The translation movement influenced by the orientation of the aircraft, the Velocity and angle of attack, so it is necessary to define the equations that describe the orientation. [4], [1].

2.4 Orientation Equations

The orientation model, is based on the Euler angles using a ZYX orientation order, this will describe the orientation of the ***BF*** with respect to the ***SF*** using matrix R_{zxy} 9

$$R_{ZXY}(\varphi, \theta, \psi) = \begin{pmatrix} c\theta c\psi & c\theta s\psi & -s\theta \\ s\varphi s\theta c\psi - c\varphi s\psi & s\varphi s\theta s\psi + c\varphi c\psi & s\varphi c\theta \\ c\varphi s\theta c\psi + s\varphi s\psi & c\varphi s\theta s\psi - s\varphi c\psi & s\varphi c\theta \end{pmatrix} \tag{9}$$

Where $c = cos$, $s = sin$ and φ, θ and ψ are the rotation of the Z, Y, X frames respectively.

2.4.1 Euler angles rate definition

On the orientation model there are two types of velocities that must be described, the first is the angular velocity described by the $(p, q, r)^T$ variables, the second one is the euler angles rates of change $(\dot{\varphi}, \dot{\theta}, \dot{\psi})^T$. This definitions are important since the order of the rotation of the body is not commutative and will give some restrictions to the model, then the relationship between this two velocities will give as result the equation 10:

$$\begin{pmatrix} p \\ q \\ r \end{pmatrix} = \begin{pmatrix} 1 & s\varphi t\theta & c\varphi t\theta \\ 0 & c\varphi & -s\varphi \\ 0 & \frac{-s\varphi}{c\theta} & \frac{c\varphi}{c\theta} \end{pmatrix} \begin{pmatrix} \dot{\varphi} \\ \dot{\theta} \\ \dot{\psi} \end{pmatrix} \tag{10}$$

With $t = tan$. The fractional item on the matrix have a $cos(\theta)$ on the denominator, this means that the pitch will have a restriction between $\pi/2 < \theta$ and $\theta > -\pi/2$. There are some representations of the angular position like the quaternions, that avoid this type of restrictions, but because the configuration of the ScanEagle the airplane can not reach this position unless it gets out of the control surface, there where not used. [1],[3]

2.4.2 Angular accelerations

The angular accelerations equations will decribe the motion of the aircraft due to the torques and forces effects. This accelerations are defined on the ***BF*** of the aircraft and will depend on the angular velocities (p, q, r). All the torques are defined with respect to the COG, the inertial matrix ***I*** can be considered as a diagonal matrix, and the equuation 11 can be wirten as :

$$\tau = \dot{\omega} I + \omega \times (I\omega) \tag{11}$$

manipulating the equation 11, the angular accelerations can be written as 12:

$$\dot{\omega} = I^{-1}(\tau - \omega \times (I\omega)) \tag{12}$$

then the angular accelerations of the aircraft, will be described by the equation 13.

$$\begin{pmatrix} \dot{p} \\ \dot{q} \\ \dot{r} \end{pmatrix} = \begin{pmatrix} \frac{q(I_{yy}-I_{zz})r+L^{BF}}{I_{xx}} \\ \frac{-p(I_{xx}-I_{zz})r+M^{BF}}{I_{yy}} \\ \frac{p(I_{xx}-I_{yy})qN^{BF}}{I_{zz}} \end{pmatrix} \tag{13}$$

where the $(L^{BF}, M^{BF}, N^{BF})^T$, are the torque defined on the COG of the aircraft, and I_{xx}, I_{yy}, I_{zz} are the moments of inertia. [1] [7]

3 FORCES AND TORQUES MODEL

After describing the equations of motion, it is necessary to define the forces and torques that influence the movements of the aircraft. Because the Scan Eagle is a fixed wing aircraft, the total force will depend on the Velocity of its displacemt V_{BF}, this velocity will affect the drag and lift forces of the entire aircraft.[4], [1].

3.1 Forces

As mentioned before the lift and drag forces will depend on the V_{BF} velocity of the aircaft. To extract a model that describes this behavior some considerations are made.

- Each of the wings will generate a constant lift force, and its variation will depend on the angle of attack, the variations on the dimensions of the wing and the total velocity V of the aircraft.
- The propeller generates a constant thrust that dependent, only from the revolutions per minute on the definition of the equation.
- The density of the air is constant at all flight conditions, and the atmospherical variations like change on temperature, presion or others are neglected.

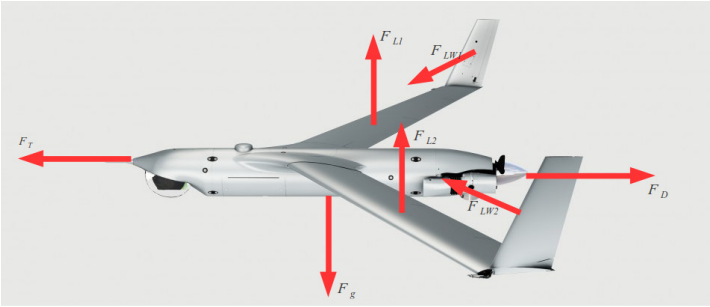


Figure 3: Scan Eagle Forces

Figure 3.1, shows the definition of the forces and where they react over the aircraft.

Fg : Gravity force

F_L : Force due to the lift of each wing.

F_{LW} : Force due to the winglets.

F_D : Drag force.

F_T : Thrust force.

Adding each of this forces it is possible to define the total force F_T.

$$F_T = F_{L1} + F_{L2} + F_{LW1} + F_{LW2} + F_g + F_D + F_T \tag{14}$$

Each of these forces where define in the COG of the aircraft having as reference frame de *BF*, then the components of each force will be, as in equation 15,

$$\begin{pmatrix} F_{xT} \\ F_{yT} \\ F_{zT} \end{pmatrix} = \begin{pmatrix} 0 \\ 0 \\ -F_{L1} \end{pmatrix} + \begin{pmatrix} 0 \\ 0 \\ -F_{L2} \end{pmatrix} + \begin{pmatrix} 0 \\ -F_{L1W} \\ 0 \end{pmatrix} + \begin{pmatrix} 0 \\ F_{L2W} \\ 0 \end{pmatrix} + \begin{pmatrix} m*g*s(\theta) \\ -m*g*s(\phi)c(\theta) \\ m*g*c(\phi)c(\theta) \end{pmatrix} + \begin{pmatrix} T_M \\ 0 \\ 0 \end{pmatrix} + \begin{pmatrix} -F_D \\ 0 \\ 0 \end{pmatrix}$$

3.2 Torques

Having defined the forces over the entire aircraft, each of these forces will generate a respective torque because of its magnitud and direction over the frame. Four torques are identify:

τ_{L1} : Torque due to F_{L1}

τ_{L2} : Torque due to F_{L2}

τ_{LW1} : Torque due to F_{LW1}

τ_{LW2} : Torque due to F_{LW2}

Motion over the θ and ϕ are influenced by the τ_{L1} and τ_{L2} torques. This is a very importan characteristic, becuse knowing that this type of aircraft has no tail to control the pitch angle, the configuration and variation of its wings allows the movement over ϕ to be compensated with the variations of the elevons. To define the components of each of the torques, general variables of length are used, and the total the total torque is:

$$\begin{pmatrix} L \\ M \\ N \end{pmatrix} = \begin{pmatrix} F_{L1W}Z_{L1W} - F_{L2w}Z_{L2w} - F_{L1}Y_{L1} - F_{L2}Y_{L2} \\ F_{L1}X_{L1} + F_{L2}X_{L2} \\ -F_{L1W}X_{L1W} + F_{L2W}X_{L2W} \end{pmatrix} \tag{15}$$

As described before, because of the tailess of the aircraft it was necessary to make some considerations in the model. One of the considerations is the change on the lift vector F_L because of the variation of the elevons on the wing, changing its point of action over the X label forward and backwards. To describe this behavior it was assume that the movement was like a pendulum, that will depend on the angles of the elevons and will make that X_{L1} and X_{L2} move in to the negative and positive direction over the X label, having as reference the ***COG***, then generating a momentum M over the aircraft.

4 AERODYNAMIC MODEL

The charactacteristics of the aerodynamic model will depend on the construction of the aircraft, to calculate each of the components it is necessary to use specialized software to know the behavior of the fluid like the air, and how this influence on the movements. [11]

4.1 Lift

The model of lift will depend on three objects, the Velocity of the air V_W, the lift coefficient, and the geometry of the wing. Equation 16, describes the total lift of the two wings.

$$F_L = \frac{1}{2}\rho V^2 A c_L \tag{16}$$

where ρ will be the density of the air, V the relative velocity of the aircraft, A the total area of the wings, and c_L the lift coefficient. To calculate these parameters it is necessary to know the geometry and configuration of the wing used for this aircraft. Because in most of the cases this type information is not available in the data sheets, it was necessary to use some empirical tests to find the correct wing geometry.

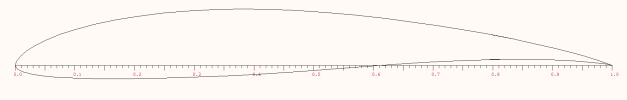


Figure 4: Airfoil

To define the geometry of the airfoil the NACA airfoils data was used, defining the E214, because of its configuration and its lift characteristics. Figure 4.1 shows the form of the E214 implemented on the XFLR5 simulator.

Another important characteristic is that this airfoil has some small elevons that will affect the roll, and pitch angles, these elevons can move differentially and in the same direction, affecting the geometry of the wing and therefore the distance X where the total lift is generated.

To calculate the parameters of the airfoil using the XFLR5, the airfoil was created with its inner and outer elevons, and was simulated to calculate the behavior of the C_L and C_D coefficients. Each of these values will depend on the angle of attack α, and will give the limits of maximum and minimum lift of the airplane. [11], [2]

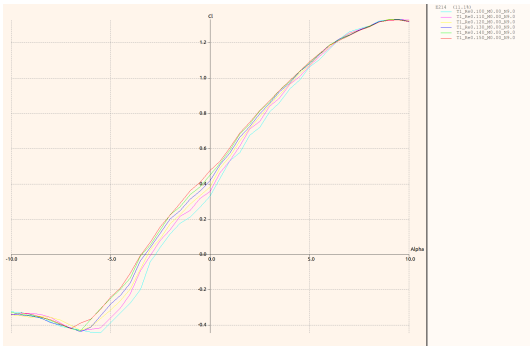


Figure 5: C_L vs α

On Figures 4.1, are shown the behavior of the C_L considering an approximation to a linear behavior between $-5 < \alpha < 10$. Because of the configuration of the elevons over the wing, the C_L will have some variations, this depends on the angles of the elevons that will cause the geometry of the wing change.

The Scan Eagle has another special characteristic,its wings have an angle of almost 60 degrees from the center of the airplane, the position of the total lift vector is therefore at the end of the fuselage. Because of the position of the total lift vector different from the *COG*, this generates a momentum that generates variation over the pitch as shown on Figure 4.1. [2]

4.2 Drag

The drag model, describes the effect of the wind in the opposite direction of motion. Equation 17 shows the dependence on the relative velocity of the airplane, and the C_D coeficient.

$$F_D = \frac{1}{2}\rho V^2 A c_D \tag{17}$$

On Figure 4.2, the behavior of the C_D is shown changing the angle of attack α, for a constant lift, having a parabolic behavior, that depends directly from the relative velocity of the plane.

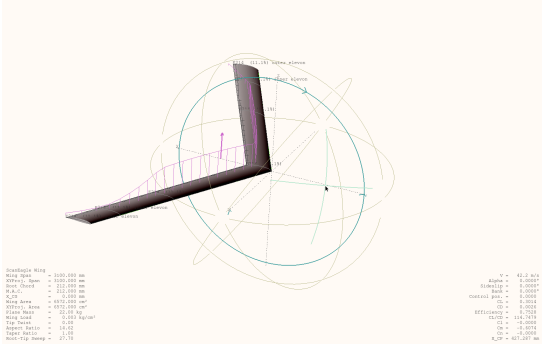


Figure 6: Lift and momentum

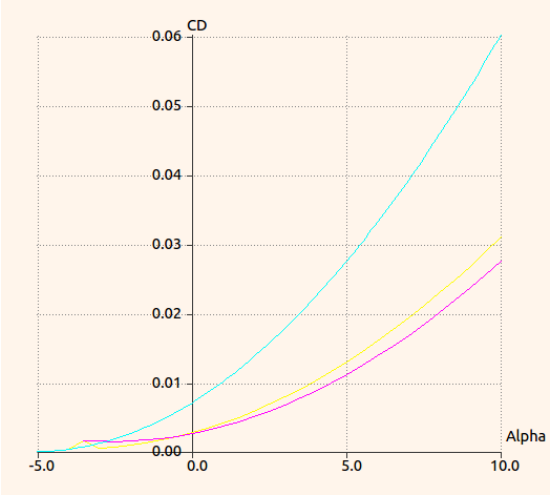


Figure 7: C_D vs α

During this investigation a linearization was made to simplify the equations realted to the c_L and c_D, this was necessary to simplify the process of the no linear model.

5 CONTROLLER DESIGN

After the determination of all the equations and parameters as the c_L and c_D, the data sheet of the airplane is used to determine the *COG* over the X, Y and Z. Another parameters defined are the distance from the torques to complete each of the L,M and N equations.

Because a linear controller is considered to be design, the linearization of the model is necessary. For this, some consideration are followed, first each of the wings will give one half of the total lift, second the point of linearization is considered as the initiation when the lift force will be equal to the maximum weight of the aircraft, and third the θ, ϕ and φ positions will be equal to zero.

Following these considerations, the linerazation was made using the Taylor series approximation and small angle considerations, with the translational and angular variables, having as result a state vector as in equation 18. [5]

$$\dot{x} = \begin{bmatrix} V & u & v & w & p & q & r & \varphi & \theta & \phi \end{bmatrix}^T \tag{18}$$

To implement a linear controller as the LQR, it is necessary to evaluate the controllability of the model, for this Matlab was used with the *ctrb* command, and it is possible to find that the total state vector is not controllable, but only 7 of its states. To identify wich states are controllable it is necessary to make some tests of the model, verifying the restrictions. Finally after some tests, a new state vector x_c was defined as in equation 19

$$\dot{x_c} = \begin{bmatrix} p & q & r & \varphi & \theta & \phi & w \end{bmatrix}^T \tag{19}$$

Then, the state space model can be defined as

$$\dot{x_c}(t) = \begin{pmatrix} 0 & 0 & 0 & 0 & 0 & 0 & 0 \\ 0 & 0 & 0 & 0 & 0 & 0 & 0 \\ 0 & 0 & 0 & 0 & 0 & 0 & 0 \\ 1 & 0 & 0 & 0 & 0 & 0 & 0 \\ 0 & 1 & 0 & 0 & 0 & 0 & 0 \\ 0 & 0 & 1 & 0 & 0 & 0 & 0 \\ 0 & 0 & 0 & 0 & 0 & 0 & 0 \end{pmatrix} x_c(t) + \begin{pmatrix} 304.5455 & -304.5455 & 1.2148 & -1.2148 \\ 4.3118 & 4.3118 & 0 & 0 \\ 0 & 0 & -2.7597 & 2.7597 \\ 0 & 0 & 0 & 0 \\ 0 & 0 & 0 & 0 \\ 0 & 0 & 0 & 0 \\ 10.0000 & 10.0000 & 0 & 0 \end{pmatrix} u(t) \tag{20}$$

Using this state space model, a LQR constroller is designed to stabilize the aircraft. To calculated correctly the gain of the controller it is necessary to tune the *Q* and *R* matrices , to control the states and the inputs. The main objective of the controller is to leave all the poles of the system into the left side of the imaginary plane, so after some tests an stabilization controller is found letting all the poles as shown in figure 8.[5]

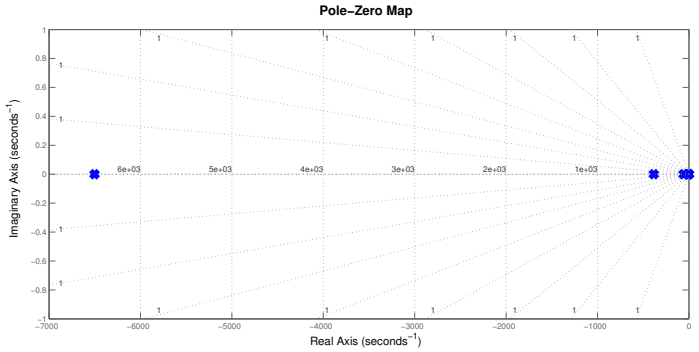


Figure 8: Pole and Zeros Map of the Model and Controller

The blue signs are the poles at the left side of the plane. It is possible to see that one of the poles is very far from the 0 label, and the others are more closer, this will affect the system having some times a slow respond but without not to much overshoots.

This controller will allow the aircraft to have a smooth flight, whats gives a really good approach to the real aircraft, this comparation is necessary because of the objective is to recreate the behavior of the real aircraft, so that the pilots can be trained as in a real envirorment. [7].

6 SIMULATIONS

After the design of the controller some test are made, using the no linear model, this is necessary because in most of the times, the values of the controller must be retuned because of some small considerations made at the moment of the linearization. Figure 6 shows the total no linear model implemented on Simulink.

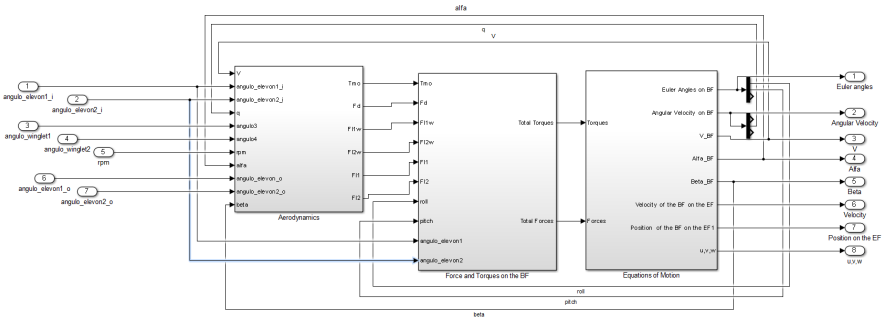


Figure 9: Total no linear model

The model is devided in three parts, the first block called *Aerodynamics* will have the equations due to the lift, drag, and thrust forces, this will gives the results of the magnitudes , the *Forces and Torques* block, will generate the vectors of the total forces and torques calculated on the model, giving as a result two total vectors to introduce on the kinematic equations of the third block of *Equations of motion*.

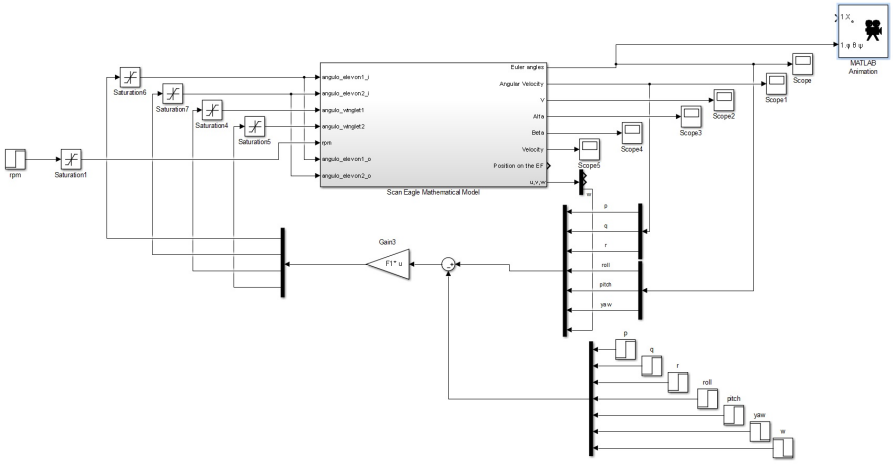


Figure 10: Scan Eagle dynamic model

Figure 6, shows the total model of the Scan Eagle, and in the lower part is the controller, it has some input parameters that allow to track the controlled variables. Using this model some test are made to show the stabilization of the system.

A complete test of stabilization and tracking is made where the aircraft was put through some movements over the yaw angle as shown on Figure 6.

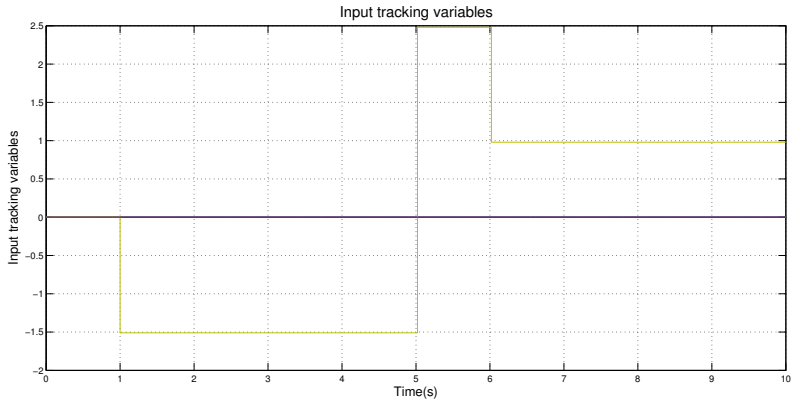


Figure 11: Inputs to the aircraft, variation on yaw orientation

Figure 6 shows the behavior of each of the states of the controllable dynamic model, the yellow line shows how the input of the yaw angle (ϕ) changes until approximatly -1.5 rads, because of this movement and the coupled variables, the r state is affected generating a negative desaceleration, but when the yaw reach a stable state it is compensated getting to zero again.

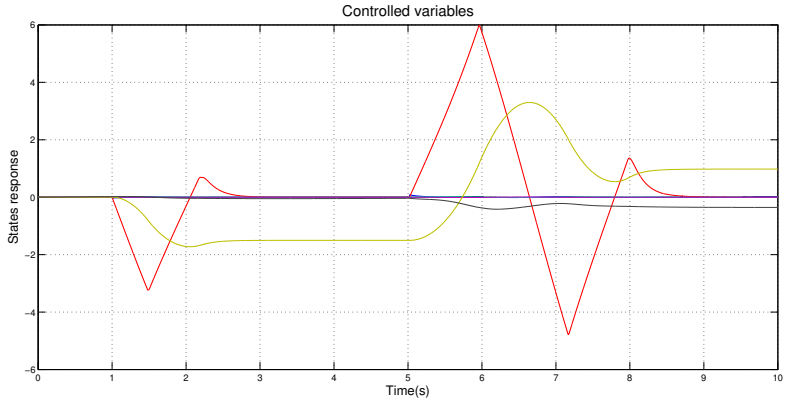


Figure 12: States vector response to tracking

At five seconds the yaw angle varied again, one more time the r state is affected generating a positive acceleration when the aircraft is moving, and then a negative desaceleration is generated to get into the stable state. Another variable that is affected by these movements is the w state, generating a desaceleration on the aircraft.

This test shows how the non linear dynamic model can be controlled using an LQR controller and is able to follow angular positions to orientate the aircraft. Another important characteristic, because of the tunnig of the controller it gives smooth movements to the aircraft, staying at the limits of instability or singularities of the model.

7 CONCLUSIONS

The development of the present work shows the begining of a research on the modelling and control of the Scan Eagle. To design the model it is necessary to use of different software tools to determine the parameters and reactions of the plane to the flight conditions.

Using this model it was possible to find a close approximation to the behavior of the Scan Eagle aircraft, that will be implemented on the simulator to be tested for the pilots. The next step to this project is to start to consider the weather conditions and how this conditions affect the behavior of the aircraft and the limits of the controller.

REFERENCES

[1] Eugene L. Duke, Robert F. Antoniewicz and Keith D. Krambeer, *Derivation and definition of a linear aircraft model*. Nasa Reference publication 1207, August 1988.

[2] Derric Yeo, Ella M. Atkins, Luis P. Bernal, *Aerodynamic sensing for a fixed wing UAS operating at high angles of attack*. AIAA Atmospheric Flight Mechanics Conference, 13 - 16 August 2012, Minneapolis, Minnesota.

[3] Duane McRuer, Irving Ashkenas, Dunsain Graham, *Aircraft dynamics and automatic control*. Technical report No 129-1, Systems technology Inc, Hawthrone California.

[4] Jhon H. Blakelock, *Automatic control for Aircraft and Misseles, Second Edition*. Airforce institute of technology.

[5] Donald McLean, *Automatic flight control systems*. University of Southampton, United Kingdom, 1990.

[6] Grzegorz Kowaleczko, Michal Wachlaczenko, *Aircraft dynamics during flight in icing conditions*, Airforce Institute of Technology, Warsaw, Poland. Journal of Theorycal and Applied Mechanics Warsaw 2012.

[7] Bernard Etkin, Lloyd Duff Reid, *Dynamics of flight, Stability and Control*. Institute for Aerospace Studies, University of Toronto.

[8] Pasquale M. Sforza, *Commercial airplane design principles*. University of Florida, First Edition 2014.

[9] Usaf Test Pilot Schoool, Edwards AFB CA, *Flying Qualities Phase, Volume II, Chapter 4, Equations of Motion*. October 1988.

[10] Karl Johan Astrom, Richard M. Murray,*Feedback Systems: An Introduction for Scientists and Engineers*, 16 of September 2006.

[11] A. Deperrois, *About Stability Analysis using XFLR5*. Technical presentation,November 2010.

11th International Conference on Engineering Vibration
Ljubljana, Slovenia, 7–10 September 2015

RESPONSE STATISTICS AND BIFURCATION ANALYSIS IN STOCHASTIC VIBRO-IMPACT SYSTEM

Pankaj Kumar[1], **S. Narayanan**[1], **Sayan Gupta**[2]

[1]Department of Mechanical Engineering, Indian Institute of Technology Madras, Chennai, India
pankajiit1@yahoo.co.in, narayans@iitm.ac.in

[2]Department of Applied Mechanics, Indian Institute of Technology Madras, Chennai, India
gupta.sayan@gmail.com

Keywords: Vibro Impact, Bifurcation, Fokker-Planck equation, Finite element, Zhuravlev transformation, Nordmark Mapping

Abstract. *This paper investigates the stationary response probability density function (pdf), bifurcation, and stability analysis of Duffing Van der Pol (DVDP) oscillator with impact under additive and multiplicative Gaussian white noise excitations. The original discontinuous vibro impact system is mapped on to a continuous phase plane by the Zhuravlev non-smooth coordinate transformation. The mod, and Dirac-delta functions which are discontinuous and which appear in the resultant equation of motion are approximated using suitable arc tangent and Gaussian distribution functions respectively. The Fokker-Planck (FP) equation corresponding to the transformed and approximate equation of motion of the nonlinear oscillator is solved using the finite element(FE) method. Damping coefficient and coefficient of restitution are considered as the bifurcation (control) parameters. The FE solutions are validated with Monte Carlo simulation (MCS) results with good agreement between the two. Stochastic bifurcation and stability analyses are carried out in terms of the largest Lyapunov exponent (LLE) which is computed using the Wedig algorithm and the Nordmark construction of the local Poincare' map. From the results it is observed that P-bifurcation and D-bifurcation need not occur in same parameter regimes.*

1 INTRODUCTION

The analysis of the dynamics of systems with vibro-impacts such as that occur in turbine blade vibration, motion limiting stops, meshing gears, is complex because of the discontinuous nonlinearities present in such impacting systems [1]. The vibro impact system exhibits rich phenomena such as grazing bifurcation, torus bifurcation, chatter and sticking motions [2, 3]. Recently, there has been a lot of research interest evinced in the study of the dynamics of vibro-impact systems subjected to random excitations. The stochastic excitation further complicates the analysis and dynamics of the already complex vibro-impact system.

Nonlinear systems subjected to random excitation exhibit mainly two types of bifurcations, the P-bifurcation and the D-bifurcation . The phenomenological P-bifurcation is characterized by topological changes in the stochastic attractors with parametric variations and is characterized by a fundamental change in the nature of the steady-state probability density function(pdf) of the response .The D-bifurcation is associated more with the stability of the system and is characterized by a sign change in the largest Lyapunov exponent(LLE) as a parameter is varied.

In the analysis of vibro-impact system Zhuravlev [4] introduced a mirror image transformation to take care of the discontinuity in the equation of motion introduced by the impact. This transformation has also been used in the analysis of vibro-impact systems subjected to random excitation. An extension of the stochastic averaging method [5] along with the Zhuravlev variable transformation was used to study the response of vibro-impact systems subjected to stochastic excitations. Dimentberg and Lourtchenko [6] have presented an extensive review of the research on the response of vibro-impact systems to stochastic excitation and covered topics such as impact energy losses, response pdfs and chaotic response. Davies [7] used the equivalent linearazation method for the random vibration analysis of a beam impact. The method of multiple scales was used by Rong et al.[8] for the response analysis of vibro-impact system to a combination of harmonic and random excitation. The above mentioned approximate methods are mainly suitable to handle vibro-impact problems when the impact losses are very small, when the impact process is very nearly elastic when the coefficient of restitution e is very nearly equal to 1. Recently, Zhu [9] used the exponential polynomial closure method and Dimentberg et al.[10] used the path integration method for the solution of the FP equation to obtain the response pdfs of vibro-impact systems to random excitations. The methods are applicable even for high impact energy losses unlike the approximate methods like the stochastic averaging or equivalent linearization as they are directed towards solving the FP equation and not just the response statistics.

The joint pdf of the response obtained by the solution of the FP equation not only enables the computation of the response statistics but also helps in the study of the P-bifurcation as one can observe any qualitative change in the pdf as a system parameter is varied. In this paper a finite element method developed by the authors [11] is used to solve the FP equation corresponding to a single degree of freedom Duffing-Van der Pol vibro-impact oscillator subjected to random external and parametric excitations. The Zhuravlev transformation is used to transform the impact condition. The computed joint pdf enables the study of the P-bifurcations of the vibro-impact system.

The dynamic or D-bifurcation of the stochastic vibro-impact system can be identified by a sign change in the LLE. Oseledec[12] has presented the theory of the uniqueness and existence of the Lyapunov exponents of nonlinear dynamical systems. The Lyapunov exponents(LE) are measures of exponential convergence or divergence of neighboring trajectories of a nonlinear dynamical system. All LEs being negative correspond to convergence and the LLE becoming

positive corresponds to divergence. The calculation of the LEs and the subsequent bifurcation analysis of smooth nonlinear dynamical systems are straight forward [13, 14]. However for nonlinear systems with discontinuities such as in the vibro-impact nonlinear oscillator the calculation of the LLE poses difficulties because of the evaluation of the Jacobian matrix at the discontinuities. The Wolf's [13] and the Wedig's [14] methods cannot be directly applied in these cases for the LE computation. Recently, based on local mapping procedures Muller[15] and De Souza and Caldas[16] calculated the LLE using respectively transitional conditions of the linearized equations and a transcendental mapping technique at the discontinuities for the vibro-impact systems.

Nordmark [17] proposed a discontinuity mapping scheme providing a local decomposition of Poincare's mapping into a sequence of four classes to distinguish between the contribution from the flow and those from the discontinuity for calculation of the LEs. Recently Jin et.al [18] proposed a general calculation method of the spectrum of LEs for deterministic non smooth systems based on the Nordmark local mapping[17] . Feng et. al [19] computed the LLE for a vibro-impact system subjected to stochastic excitation using a combination of Nordmark mapping and Wedig's [14] algorithm.

This paper investigates the P-bifurcation and D-bifurcation of a Duffing-Van der Pol vibro-impact oscillator with both parametric and external Gaussian white noise excitations. The Zhuravlev transformation is applied to the original equation of motion transforming the impact condition and embedding the same into the equation of motion through signum and delta functions.These functions are approximated by suitable arc tangent and Gaussian functions and the corresponding FP equation of the smooth system is solved by the FE method for obtaining the joint pdf. From the joint pdf the marginal pdfs are also obtained. The variation in the nature of the pdfs are studied with respect to the coefficient of restitution and damping coefficient to investigate the P-bifurcations. The results show that P-bifurcations of the vibro-impact system occur with respect to variations in the coefficient of restitution and the damping coefficient. The D-bifurcations are investigated by computing the LLE using the Nordmark point mapping combined with the Wedig's algorithm. It should be noted here that for the LLE calculation using the Nordmark transformation, the equation of motion is retained in the original form and only the Jacobian corresponding to the linearized system assumes different forms depending on the states of the system whether corresponding to the flow or to the discontinuity point at impact. The results obtained by the FE method agree closely with the MCS results.

2 Problem Statement

Consider the DVDP vibro-impact system with an unilateral zero offset barrier (Fig. 1), under additive and multiplicative Gaussian white noise excitations

$$\ddot{X} - (\alpha + \sigma_1 W_1(t))X - \beta_1 \dot{X} + \beta_2 X^2 \dot{X} + \beta_3 X^3 = \sigma_2 W_2(t), X > 0, \tag{1}$$

subject to the condition of classical impact of instantaneous velocity jumps

$$\dot{X}^+ = -e\dot{X}^-, \quad X = 0, \quad 0 < e \leq 1, \tag{2}$$

where, α and $\beta_i(t)$ $\{i = 1, 2, 3\}$ are system parameters, $W_i(t)$ $\{i = 1, 2\}$ are stationary zero mean unit Gaussian white noise processes, σ_i $\{i = 1, 2\}$ represent their intensities, e is the restitution coefficient and X is the displacement from equilibrium. The number of over dots represents the order of differentiation with respect to the time parameter t. Eq.(2) relates the velocities before ($\dot{X}^- = \dot{X}(t^* - 0)$) and after ($\dot{X}^+ = \dot{X}(t^* + 0)$) impact in terms of

the coefficient of restitution e. $e = 1$ corresponds to elastic impact without any losses which increase with decrease in the value of e. In the absence of damping and for a value of e very nearly equal to 1 the system can be treated as quasi-conservative and approximate methods like equivalent linearization and stochastic averaging have been used in the analysis of the vibro-impact system to random excitation.

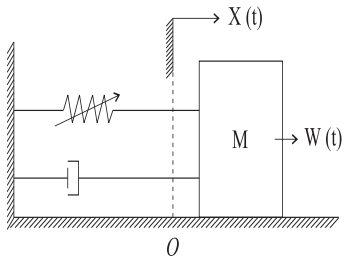


Figure 1: Schematic of the vibro-impact system with a unilateral zero offset barrier.

Equations (1-2) represent a set of coupled equations with discontinuity at $X = 0$. This singularity at the grazing condition presents analytical and computational difficulties in subsequent numerical analysis. The discontinuity can be removed by invoking the mirror image transformation of state variables as proposed by Zhuravlev [4]. This involves defining a set of new state variables, given by

$$X = X_1 = |Y| = Y sgn(Y), \qquad \dot{X} = X_2 = \dot{Y} sgn Y, \qquad \ddot{X} = \ddot{Y} sgn Y \tag{3}$$

where

$$\mathrm{sgn}(Y) \ = \begin{cases} 1 & \text{if } Y > 0; \\ -1 & \text{if } Y < 0. \end{cases} \tag{4}$$

The Zhuravlev transformation [4] maps the domain $X > 0$ of original phase plane $(X, \dot{X})$ onto the new phase plane $(Y, \dot{Y})$. The transformed equation of motion in $Y, \dot{Y}$ can be expressed as

$$\ddot{Y} - (\alpha + \sigma_1 sgn(Y) W_1(t))Y - \beta_1 \dot{Y} + \beta_2 Y^2 \dot{Y} + \beta_3 Y^3 = \sigma_2 sgn(Y) W_2(t), t \neq t^*, \tag{5}$$

$$\dot{Y^+} = e\dot{Y^-}, t = t^*, \tag{6}$$

Using Eq. (6) one can write

$$(\dot{Y}^- - \dot{Y}^+)\delta(t - t^*) = (1 - e)\dot{Y}\delta(t - t^*), \tag{7}$$

provided $| \dot{Y}^+ | \leq | \dot{Y} | \leq | \dot{Y}^- |$. By setting $\delta(t - t^*) = \delta(Y(t)/\dot{Y}(t))$ Eq. (7) can be written as

$$(1 - e)\dot{Y}\delta(t - t^*) = (1 - e)\dot{Y}|\dot{Y}|\delta(Y) \tag{8}$$

Now it is possible to incorporate the residual velocity jump into the transformed SDEs using the Dirac-delta function as a multiplier. Using Eq. (8), Eqs. (5) and (6) are combined into one equation by adding the impulsive damping term

$$\ddot{Y} - (\alpha + \sigma_1 sgn(Y) W_1(t))Y - \beta_1 \dot{Y} + \beta_2 Y^2 \dot{Y} + \beta_3 Y^3 + (1 - e)\dot{Y}|\dot{Y}|\delta(Y) = \sigma_2 sgn(Y) W_2(t) \tag{9}$$

The term $(1-e)\dot{Y}|\dot{Y}|\delta(Y)$ represents the impact losses of the system which can be considered as an impulsive damping term. Thus by the Zhuravlev transformation Eqs. (1-2) representing the original vibro-impact oscillator are reduced to a single Eq. (9).

Eq. (9) still contains discontinuous functions such as $sgn(Y), |\dot{Y}|$ and $\delta(Y)$ which poses problems in further numerical analysis. For the P-bifurcation analysis which involves the computation of the joint pdf of the transformed response $Y, \dot{Y}$ using the FP equation corresponding to Eq.(9). $|\dot{Y}|$ is expressed as $\dot{Y}sgn\dot{Y}$. The signum function is approximated by [20]

$$sgn(\dot{Y}) = \frac{2}{\pi}atan(\gamma\dot{Y}) \qquad \gamma >> 1 \tag{10}$$

where γ is a large number. $\gamma = 10^4$ seems to be an adequately large number for the problem considered in this paper.

The Dirac delta function $\delta(Y)$ is approximated by the Gaussian distribution with a very small variance. For variance $\approx 10^{-3}$ a good approximation of Dirac-delta function has been obtained with good convergence.

3 P-bifurcation analysis

P-bifurcation analysis is based on the qualitative changes in the probabilistic structure of the stationary joint-pdf of the state variables at different parameter regimes. Using the state space approach, Eq. (9) can be expressed in terms of the Itô stochastic differential equations (SDE) as

$$\mathrm{d}Y_1 = Y_2\mathrm{d}t, \tag{11}$$

$$\mathrm{d}Y_2 = (\alpha Y_1+\beta_1 Y_2-\beta_2 {Y_1}^2 Y_2-\beta_3 {Y_1}^3-(1-e)Y_2|Y_2|\delta(Y_1))\mathrm{d}t+\sigma_1 sgn(Y_1)Y_1 dB_1(t)+\sigma_2 sgn(Y_1)dB_2(t) \tag{12}$$

where $dB(t)$ is Brownian motion increment. The state vector $\mathbf{Y} = [Y_1\ Y_2]^T$ constitutes a Markov process in $\Re^2$. The transitional joint pdf $p(\mathbf{Y}, t|\mathbf{Y}_0, t_0)$, is governed by the FP equation

$$\frac{\partial p}{\partial t} = -Y_2\frac{\partial p}{\partial Y_1} - \frac{\partial(\alpha Y_1 + \beta_1 Y_2 - \beta_3 {Y_1}^3 - \beta_2 {Y_1}^2 Y_2 - (1-e)Y_2|Y_2|\delta(Y_1))p}{\partial Y_2} + \frac{1}{2}\frac{\partial^2(Q)p}{\partial {Y_2}^2} \tag{13}$$

where $Q = {\sigma_1}^2{Y_1}^2 + {\sigma_2}^2$. The stationary solution of the FP equation can be obtained by letting $\partial p(\mathbf{Y}, t|\mathbf{Y}_0, t_0)/\partial t = 0$.

Following the weak form of the FE method proposed in [11] and using the Galerkin projection, the time varying discretized FP equation governing the transition $p(Y, t)$ joint pdf is expressed as [11]

$$\mathbf{M}\dot{\mathbf{p}} + \mathbf{K}\mathbf{p} = \mathbf{0}, \tag{14}$$

where the elements of matrix $\mathbf{M}$ and $\mathbf{K}$ are given by

$$M_{rs} = \int_\Omega \psi_r(\mathbf{Y})\psi_s(\mathbf{Y})\mathrm{d}\mathbf{Y} \tag{15}$$

$$\begin{aligned} K_{rs} \;=\; & \int_\Omega \Big[-Y_2\psi_r\frac{\partial[\psi_s]}{\partial Y_1} - \psi_r\frac{\partial[(\alpha Y_1 + \beta_1 Y_2 - \beta_3 {Y_1}^3 - \beta_2 {Y_1}^2 Y_2 - (1-e)Y_2|Y_2|\delta(Y_1))\psi_s]}{\partial Y_2} \\ & -\frac{1}{2}\frac{\partial[\psi_r]}{\partial Y_2}\frac{\partial[Q\psi_s]}{\partial Y_2}\Big]\mathrm{d}\mathbf{Y} \end{aligned} \tag{16}$$

where ψ_i is the shape function corresponding to node i.

Once the stationary joint-pdf $p_{Y_1,Y_2}(y_1, y_2)$ is obtained for the transformed variables Y_1, Y_2, the stationary joint-pdf $p_{X_1,X_2}(x_1, x_2)$, can be obtained by using the inverse transformation of Eq.(3). Considering the symmetry property of the transformed stationary joint-pdf $p_{Y_1,Y_2}(y_1, y_2)$, joint-pdf of the variable X_1 and X_2 can be obtained as;

$$p_{X_1,X_2}(x_1, x_2) = p_{Y_1,Y_2}(x_1, x_2) + p_{Y_1,Y_2}(-x_1, -x_2) = 2p_{Y_1,Y_2}(x_1, x_2) \tag{17}$$

3.1 Numerical results

The joint pdf of X and $\dot{X}$ are obtained by solving the FP equation using the FE method. The parameters $\alpha = -1; \beta_2 = \beta_3 = 0.01$ are kept at fixed values in all the cases. The space domain is chosen as $[-10, 10] \times [-10, 10]$ with a grid size of 400×400 for the FE mesh. The parameters e, β_1 are varied in the numerical calculations.

Fig. 2 shows the joint pdf of response for three values of the coefficients of restitution e namely $e = 1, 0.98, 0.96$. The values of β_1, σ_1 and σ_2 are taken as $\beta_1 = 0.01, \sigma_1 = \sigma_2 = 0.1$. The contour plots corresponding to Fig. 2 are shown in Fig. 3.From the figures it is clearly observed the the joint pdf changes from a crater like behaviour to a unimodal nature as the value of e is decreased from the value of 1. Fig. 2b ($e = 0.98$) shows clearly the transition when the depth of the crater reduces to almost nothing with a flat top before the joint pdf has sharp uni-modal peak in Fig. 2c ($e = 0.96$). The change in the nature of the joint pdf as e is varied clearly indicates a P-bifurcation. The marginal pdfs corresponding to Fig. 2 are shown in Fig. 4 along with MCS results with good agreement between the two. The P- bifurcation behaviour is also clearly observed in the marginal pdfs. The value of e for which the crater like pdf transits to unimodal character is 0.985. Reduction of e from 1 implies more energy losses due to impact and hence the response has a higher probability of staying near the boundary of the impact barrier.

Fig. 5 shows the joint pdf of the response for three different values of $\beta_1 = 0.008, 0.015$ and 0.02. The value of e is taken as 0.98 and the value of σ_1 and σ_2 are taken as 0.1. In this case as the value of β_1 is increased the joint pdf changes from a uni-modal type to crater like characteristic. The value of β_1 represents negative linear damping of the Van der Pol term and as its value is increased more of the limit cycle behaviour of the Van der Pol oscillator is revealed. In this case also the P-bifurcation occurs.

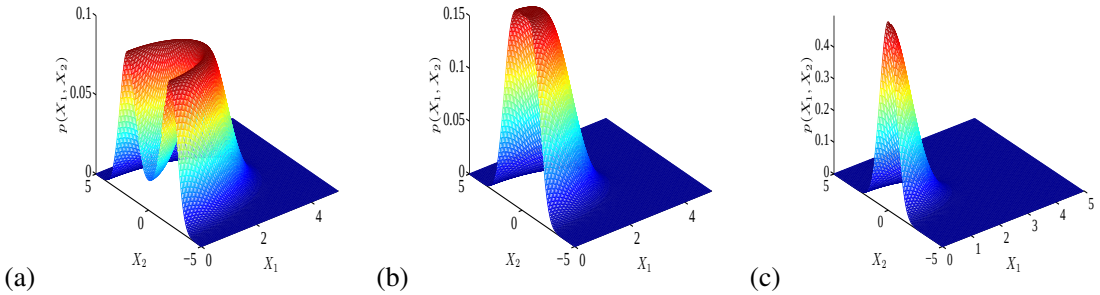


Figure 2: Joint pdf of the DVDP vibro-impact oscillator (a) $e = 1$, (b) $e = 0.98$,(c) $e = 0.96$

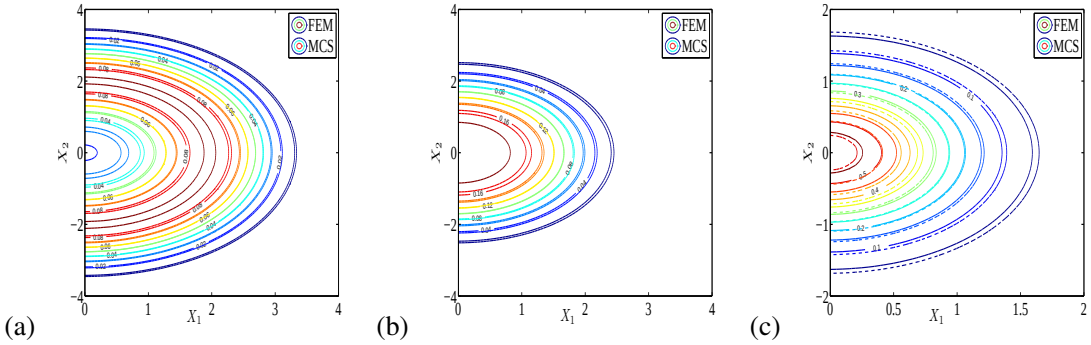


Figure 3: Contour plot corresponding to Fig.2

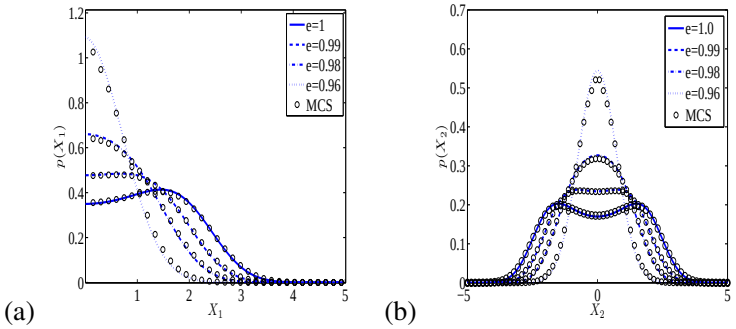


Figure 4: Marginal pdf of displacement and Velocity for the DVDP vibro-impact oscillator

4 D-BIFURCATION

For performing a D-bifurcation analysis the LLE is calculated by a combination of the Wedig's algorithm and the Nordmark point mapping scheme. When the LLE changes from a negative value to a positive value it represents a loss of stability of the dynamical system and a D-bifurcation. Because of the presence of discontinuities in the vibro-impact oscillator the calculation of the LLE poses difficulties as the Jacobian matrix becomes discontinuous at the discontinuity point. Nordmark [17] proposed a discontinuous mapping scheme which is a synthesized Poincare map which is piece-wise smooth and defined locally near the grazing point at which a trajectory interacts with a discontinuity boundary. This procedure combined with the conventional methods of calculating the LEs of continuous systems such as the Wolf et al.[13] or Wedig [14] algorithm can be used to calculate the LLE.

The Nordmark mapping and the calculation of the LLE for the DVDP oscillator is described briefly. For $X > 0$, when the flow trajectory is continuous, a small perturbation $\mathbf{v}$ to the trajectory $X_0(t)$ of Eq.(1) is governed by the linearized equation

$$\dot{\mathbf{v}} = \Big[\frac{\partial F}{\partial \mathbf{X}}\Big]_{X_0(t)} \mathbf{v} = \mathbf{J(t)v} \qquad \mathbf{X} > \mathbf{0} \tag{18}$$

where, $\mathbf{J}$ is the Jacobian matrix corresponding to Eq.(1).

$$\mathbf{J} = \left\{ \begin{array}{cc} 0 & 1 \\ \alpha + \sigma_1 W_1(t) - 2\beta_2 X_1 X_2 - 3\beta_3 X_1^2 & \beta_1 - \beta_2 X_1^2 \end{array} \right\} \tag{19}$$

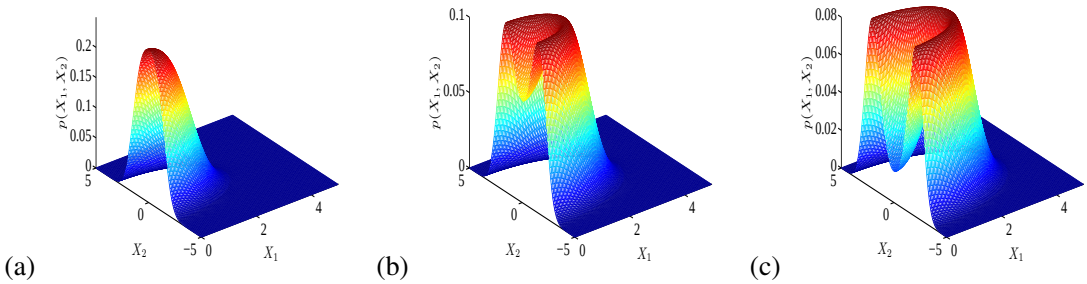


Figure 5: Joint pdf of the DVDP vibro-impact oscillator (a)$\beta_1 = 0.008$ (b)$\beta_1 = 0.015$ (c) $\beta_1 = 0.02$.

The approximate discrete map, for the perturbation $\mathbf{v}$ at time of impact, i.e $X_1 = 0$ can be constructed using Nordmark [17] local map

$$\mathbf{v_k^+} = \Big[\mathbf{DP}_c\Big]_{\mathbf{X}_0(t)} \mathbf{v_k^-}, \qquad \mathbf{X_1 = 0} \tag{20}$$

where $\mathbf{DP}_c$ is a compound map which describes the impact process through the Jacobian matrix

$$\mathbf{DP}_c = \begin{Bmatrix} -e & 0 \\ \frac{(1+e)((\alpha+\sigma_1 W_1(t))X_1+\beta_3 X_1^3+\sigma_2 W(t))}{X_2} & -e \end{Bmatrix} \tag{21}$$

The resultant discrete map eliminates the necessity for the Jacobian matrix calculations at the singularity and simplifies the computations. Subsequently, Wedig's algorithm can be applied for estimating the LLE which is defined as

$$\lambda_m = \lim_{t \to \infty} \frac{1}{t} \log \| \mathbf{v(t)} \| = \lim_{t \to \infty} \frac{1}{t} \log \Big[\| \mathbf{v(t)} \| \Big]_{t \neq t_k} + \lim_{n \to \infty} \frac{1}{n} \sum_{k=1}^{n} \log \Big[\| \mathbf{DP}_c S_k^- \| \Big]_{t=t_k} \tag{22}$$

For stochastic case presence of noise may cause a small fluctuation of the LLE, hence an average LLE $\hat{\lambda}_i$ is used in this work. The trivial solution of Eq.22 will be stable with probability one, if the largest LE is negative and unstable, if it is positive. A large but, negative LE is associated with the fast convergence of a strongly stable attractor. On the other had, a small negative LE indicates a stable system, but which can become unstable in the presence of excitation.

4.1 Numerical Results

The LLE computed using a combination of the Wedig algorithm and the arc tangent approximation as well as that is computed by the Nordmark mapping as a function of β_1 and for two different values of the coefficients of restitution are shown in Fig. 6. The LLEs calculated by the two methods show the same trend of variation but show a slight difference in the values for the lower values of β_1. In the entire region of β_1 the LLE is positive showing that the system is dynamically unstable. The intensities of Gaussian white noise are taken to be $\sigma_1 = \sigma_2 = 0.1$. The value of the LLE for an impact free system is also shown in the figure. In this case the LLE remains negative for lower values of β_1 and becomes positive for $\beta_1 \approx 0.025$ indicating a D-bifurcation. The presence of the barrier at $X = 0$ which is also a stable fixed point for the oscillator, prevents the trajectories from converging to it, and results in the system losing stability with the impact. This is a discontinuity induced stochastic instability.

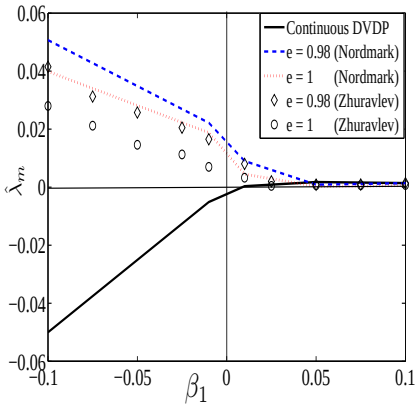


Figure 6: Estimates of LLE with β_1 as bifurcation parameter

5 CONCLUSIONS

The dynamics of a vibro-impact DVDP oscillator under parametric and external white noise excitations is investigated by the solution of the FP equation using the FE method. The Zhuvarlev transformation of variables is used to embed the impact velocity condition into the equation of motion itself enabling the formulation of the FP equation and its solution. The discontinuities in the resultant equations of motion that poses numerical difficulties are bypassed by adopting appropriate continuous approximations. P-bifurcations occur with respect to variations of the coefficient of restitution e and the damping parameter β_1. As e is decreased from 1 corresponding to perfect elastic impact the joint pdf changes from a crater like appearance corresponding to the Van der Pol limit cycle behaviour to unimodal character. As β_1 is increased for a particular value of e the joint pdf changes from unimodal character to a crater like appearance indicative again of a P-bifurcation but in the reverse direction. The LLE calculated using the Nordmark point mapping technique as well the conventional method by suitable continuous approximations of the discontinuous vibro-impact system show that the vibro-impact system is essentially dynamically unstable as LLE remains positive for the values of β_1 considered in the paper. For the impact free system a D-bifurcation occurs for a particular value of β_1. The impact free system is dynamically stable for most of lower values of β_1 and becomes dynamically unstable after a critical value of β_1.

REFERENCES

[1] Ibrahim RA. Vibro-Impact Dynamics Modeling, Mapping and Applications, Springer,2009.

[2] Di Bernardo M, Nordmark A, Olivar G. Discontinuity-induced bifurcations of equilibria in piecewise smooth and impacting dynamical systems. Physica D. 2008;119:136.

[3] Wagg DJ, Bishop SR. Chatter, sticking and chaotic impacting motion in a two degree of freedom impact oscillator.Int. Jr. of Bifurcation and Chaos,2001;11(1):57-71.

[4] Zhuravlev VF. A method for analyzing vibro-impact systems by means of special functions, Mechanics of Solids,1976;11:23-27.

[5] Feng JQ,Xu W,Wang R. Stochastic response of vibro impact Duffing oscillator excited by additive Gaussian Noise. Journal of Sound and Vibration,2008;309(3-5):730-738.

[6] Dimentberg MF, Iourtchenko DV. Random vibrations with impacts:A review. Nonlinear Dynamics. 2004;36(2-4):229-254.

[7] Davies HG. Random vibrations of a beam impacting stops. Journal of Sound and Vibration,1980;68(4):479-487.

[8] Rong H, Wang X, Xu W, Feng T. Resonant response of a non-linear vibro impact system to combined deterministic harmonic and random excitations. International Jr. of Non-Linear Mechanics,2010;45:474-481.

[9] Zhu HT. Stochastic response of Vibro-impact Duffing oscillator under external and parametric Gaussian white noises. Journal of Sound and Vibration,2014;333:954-061.

[10] Dimentberg MF, Gaidai O, Naess A. Random vibration with strongly inelastic impacts: Response PDF by the path integration method. International Jr. of Non-Linear Mechanics,2009;44:791-796.

[11] Pankaj Kumar, Narayanan S, Gupta S. Finite element solution of Fokker-Planck equation of nonlinear oscillators subjected to colored non-Gaussian noise. Probabilistic Engineering Mechanics. 2014;38:143-155

[12] Oseledec VI. A multiplicative ergodic theorem: Lyapunov characteristic exponents for dynamical systems. Trans.Moscow Math.Soc.1968;19:197-231.

[13] Wolf A, Swift JB, Swinney HL, Vastano JA. Determining Lyapunov exponents from a time series. Physica D 1985;16:285-317.

[14] Wedig W. Dynamic stability of beams under axial forces-Lyapunov exponents for general fluctuating loads.InW.B.Kr-ig,et al.,(Eds), Proceedings Eurodyn'90,Conference on Structural Dynamics, 1990;1:57-64.

[15] Muller P. Calculation of Lyapunov exponent for dynamics system with discontinuities. Chaos, Solution Fractals.1995;5:1671-1681.

[16] Souza SLT De, Caldas IL. Calculation of Lyapunov exponent in systems with impacts. Chaos, Solution Fractals.2004;19:569-579.

[17] Nordmark AB. Non-periodic motion cause by grazing incidence in an impact oscillator. Journal of Sound and Vibration.1991;145:279-297.

[18] Jin L, Lu QS, Twizell EH. A method for calculating the spectrum of Lyapunov exponents by local maps in non-smooth impact vibrating systems. Journal of Sound and Vibration. 2006;298:1019-1033.

[19] Feng J, Xu W. Analysis of bifurcation for nonlinear stochastic non-smooth vibro impact systems via top Lyapunov exponent. Applied Mathematics and Computation. 2009;213:577-586.

[20] Narayanan S, and Jayaraman K. Chaotic vibration in a non-linear oscillator with Coulomb damping. Journal of Sound and Vibration. 1991;146:17-31.

11th International Conference on Engineering Vibration
Ljubljana, Slovenia, 7–10 September 2015

FORCE FIELD SEPARATION OF VIBROFLUIDIZED GRANULAR MATERIALS, MATHEMATICAL MODEL AND PRACTICAL APPLICATIONS

Kirill S. Ivanov[1], Ivan V. Demidov[1], Leonid A. Vaisberg[1], Anton J. Mezenin[1], Sergey V. Dmitriev[1], Andrey S. Murachev*[1]

[1]REC "Mekhanobr-tekhnika"
ivanov_ks@npk-mt.spb.ru

Keywords: Dry Separation, Mathematical Modelling, Granular Gas, Vibration.

Abstract. *Water is a resource of rapidly growing importance. Rational use of water in minerals processing presents both environmental and economic benefits. Water is often used as the disperse media for granular materials. In some cases, the dispergation effect could be obtained by using vibration instead of watering. Thus, minerals are being treated in the so-called state of vibrofluidization.*

This work presents a technology for force field (electrostatic and electromagnetic) separation of granular materials in vibrofluidized layers and also a mathematical model for the process. The model is developed in assumption of low content of the extracted minerals thuswise allowing considering separately the dynamics of the vibrofluidized layer and individual particles of the extracted minerals within the layer.

1 INTRODUCTION

Studies of the effects of vibration on granular materials are very complex. The specific nature of the problem consists in the fact that, when subjected to vibration, a granular material may occur in different aggregate states, such as a granular gas, liquid or solid [1]. A separate description is required for each of the states. Therefore, the main theoretical approaches to the description of granular systems are applied in this area, such as microscopic models and simulation by molecular dynamics methods, statistical mechanics and kinetic theory, phenomenological models and continuum models [2]. It should also be noted that so far no adequate descriptions have been developed for granular fluids and gases consisting of highly inelastic particles, which forces current models to widely use the assumption of almost elastic particles.

2 SYSTEM LAYOUT

A plane layer of particulate material is studied under vibration. As is known, different types of material behavior are possible, depending on vibration intensity. In particular, if the layer thickness is small [3], the particulate material behaves like a gas. At higher layer thicknesses, convection currents may occur [3, 4]. Theoretical simulations of magnetic separation differ greatly for the two extreme cases: when the concentration of ferromagnetic particles is negligible and their movement may be regarded as independent of each other, and when their concentration is comparable to the concentration of the ¡main¿ medium. In the case of a low concentration of the target product, the equation of motion for a single ferromagnetic particle in the laboratory frame of reference may be used as the initial, most basic model, as it is done in this paper.

3 GRANULAR GAS

If the thickness of a particulate material layer is small, the particulate material behaves under vibration like a gas (granular gas) consisting of inelastically colliding particles. This behavior of the material may be well described by hydrodynamic models [3-5]. In these studies, it is assumed that the granular medium consists of almost elastic balls of equal size, while the air resistance is completely ignored (since the particles are sufficiently large). Consequently, the below calculation of the thickness of the fluidized bed should be regarded as an estimate used to determine the characteristic size of the layer and its dependence on environmental parameters and vibration. It is also assumed that the typical layer thickness is significantly smaller than the characteristic lengths in the xy plane; therefore, the problem may be regarded as a one-dimensional problem along axis z. The equation for the state of the granular gas is as follows:

$$p = nT \tag{1}$$

where p is the pressure; $n = N/V$ is the concentration of particles (number of particles per unit volume); T is the granular temperature determined as the average kinetic energy of the random motion of particles, i.e. $T = m\langle v^2\rangle/2$ ($k_B = 1$).

Balance of forces equation:

$$\frac{dp}{dz} = -mgn \tag{2}$$

where m is the weight of a single particle; g is the acceleration of gravity. Energy balance equation:

$$k\frac{d}{dz}\left(T^{\frac{1}{2}}\frac{d}{dz}T\right) = Dn^2T^{3/2} \tag{3}$$

where $k = 2\pi^{-1/2}m/d$, $D = 2\pi^{1/2}md(1-R)$.

The system of equations (1) - (3) should be supplemented by boundary conditions. The granular temperature of the oscillating plane surface is constant:

$$T(0) = T_0 = \text{const} \tag{4}$$

The number of particles in the system remains unchanged:

$$\int_0^\infty n(z)dz = Kn_cd \tag{5}$$

where K is the number of particle layers; n_c is the particle concentration in the rest state. Disappearance of the energy flow at large distances from the plane:

$$\lim_{z\to\infty}\frac{dT}{dz} = 0 \tag{6}$$

By solving this system of equations, distribution of particle concentration over the height of the layer may be plotted, and the layer height may be determined. With the layer height and the law of motion of ferromagnetic particles determined, the maximum particle ascension time may be obtained. Subsequently, it is possible to select the parameters of the system so as to ensure that there is enough time for particles to be captured by the magnetic field.

The maximum possible height of the layer is achieved at T = const. This means that the system has no energy losses and that the granular gas is not "cooled" due to collisions. The entire energy exerted by the vibrating plane is used to overcome the force of gravity. By solving the respective system of equations at T = const, the following is obtained:

$$n(z) = \frac{mgdKn_c}{T}\exp\left(-\frac{mgz}{T}\right) \tag{7}$$

The result is quite predictable: the gas formed consists of elastic particles and represents an ideal gas, which follows the Boltzmann distribution law in a gravitational field. Since the temperature is constant, it is equal both in the medium and near the vibrating plane, i.e. $T(0) = mA^2\omega^2$. As a result, the following is obtained:

$$n(z) = \frac{gdKn_c}{A^2\omega^2}\exp\left(-\frac{gz}{A^2\omega^2}\right) \tag{8}$$

The characteristic scale at which the particle concentration decreases by e times is $\tilde{z} = A^2\omega^2/g$.

4 MAGNETIC FORCE CALCULATION

. If a magnetic substance is placed in a magnetic field, the energy per unit volume of the body is determined as

$$u = -\int \mathbf{B}\cdot d\mathbf{J} = -\chi_\mu\int \mathbf{B}\cdot\mathbf{B} = -\frac{1}{2}\chi_\mu B^2 \tag{9}$$

The magnetization formula was used here (for the magnetic moment per unit volume of material) of $J = \chi\mu B$, which is a strong assumption for ferromagnetic materials due to the presence of hysteresis. It may be used for moderate fields provided that the initial magnetization of the material is equal to zero.

The energy of the system is expressed as an integral over the volume of the body

Hence, the force acting on the particle is as follows:

$$U = \int u d\upsilon = -\frac{1}{2}\chi_\mu \int B^2 d\upsilon \tag{10}$$

$$\mathbf{F} = \frac{1}{2}\chi_\mu \int d\upsilon \nabla B^2 \tag{11}$$

Assuming the particles are small, $\bigtriangledown B$ may be taken out of the integral, rendering the following:

$$\mathbf{F} = \frac{1}{2}\chi_\mu \upsilon \nabla B^2 \tag{12}$$

Since only the projection of the magnetic force on axis z is of interest, the following is finally obtained:

$$F_\mu = \frac{1}{2}\chi_\mu \upsilon \frac{\partial B^2}{\partial z} = \chi_\mu \upsilon B \frac{\partial B}{\partial z} \tag{13}$$

The force will therefore act on the particle only if the magnetic field is not uniform in the vicinity of the particle.

In the case of an electric field, the following is true:

$$\mathbf{F}_e = q\mathbf{E} \tag{14}$$

where q is the full charge of the particle; and E is the electric field. Fields E and B should be determined by solving Maxwell's equations. For complex systems, various software packages may be used, such as COMSOL Multiphysics, or ANSYS.

Consider a specific example. It is known that magnetic induction in the operating area of an electromagnetic separator changes exponentially [6]:

$$B = B_m e^{-\frac{r}{\alpha}} \tag{15}$$

where B_m is the maximum value of the magnetic field; r is the distance from the point of measurement of magnetic induction to the active pole; and α is the empirical coefficient. In the case of particle location under the pole, the following is true:

$$F_\mu = -\frac{1}{2}\chi_\mu \upsilon B_m^2 e^{\frac{2z}{\alpha}} \tag{16}$$

5 MOTION EQUATION

The motion equation for a ferromagnetic particle in a granular gas in the projection on axis z is as follows:

$$m\ddot{z} = -mg + \xi(z,t) + F_\mu(z) - \gamma\dot{z} \tag{17}$$

where m is the weight of the particle; $m\ddot{z} = d^2z/dt^2$ is the particle acceleration; g is the acceleration of gravity; $\xi(z,t)$ is the random force exerted by other particles; $F\mu$ is the magnetic force acting on the particle and exerted by the magnetic field; and γ is the coefficient of resistance to motion from the ambient air (since the particles are small, the Stokes' formula may be applied, and $\gamma = 6\pi \mathrm{d}\eta$ may be assumed, where η is the viscosity of air).

Since the particle collisions are random, it may be assumed that $\xi(t)$ satisfies the following conditions:

$$\langle \xi(t) \rangle = 0, \langle \xi(t)\xi(t-\tau) \rangle = b\delta(\tau) \tag{18}$$

where the angle brackets denote averaging over all possible manifestations of the random force. This averaging, however, only applies to such manifestations for which the condition $z'(0) = v_0$ is true at $t = 0$. Equation (17), therefore, is a stochastic differential equation, often referred to as the Langevin equation. In our problem, it is valid at distances of $\tilde{z}$; at $z > \tilde{z}$, collisions are rare and therefore the random force has different properties.

Note that this does not take into account friction with other particles, i.e. it is assumed that the particles are smooth, while $\xi(z,t)$ comprises the effects of particles moving at an angle to the considered plane (in addition to those moving head-on).

It is also assumed that the process of collisions of ferromagnetic particles with particles of the ¡primary medium¿ is a Gaussian process. It should be explained that the correlation function $(\xi(t)\xi(t-\tau))$ is equal to the delta function, which indicates the availability of correlations of the random force concentrated in the shortest time interval of the characteristic time intervals of the problem.

The amplitude of the random force may be evaluated as the average change in the particle momentum caused by collisions. The average for the collisions maximum momentum change (i.e. at direct ¡head on¿ impacts) is $\triangle p = -R\mu(v1-v2)$, where $\mu = m1m2/(m1+m2) = m/2$ is the reduced mass of the colliding particles, and $v1$, $v2$ is the velocity of the colliding particles.

By definition, the collision rate represents the number of collisions of the particle with particles of the medium per unit time

$$\nu = nvs(v) \tag{19}$$

where n is the concentration of particles; v is the relative velocity; $s(v)$ is the total scattering cross-section.

After estimation of the cross section as d (in two dimensions), the following expression is obtained for the amplitude of the random force

$$\xi_{\max} = |\Delta \mathbf{p}|\, \nu = \frac{mR}{2}|\mathbf{v}_1 - \mathbf{v}_2|(v_1 - v_2)n(z)\pi d \tag{20}$$

If $v1 - v2$ is estimated as $A\omega$, i.e. as the maximum thermal velocity, then

$$\xi_{\max}(z) = \frac{mR}{2}A^2\omega^2 n(z)d \tag{21}$$

Then, using (8), the following is obtained

$$\xi_{\max}(z) = \frac{mgRd^2Kn_c}{2}\exp\left(-\frac{gz}{A^2\omega^2}\right) \tag{22}$$

Assuming that in the rest state the granular material formed a dense hexagonal packing, $n_c = 2/(\sqrt{3}rmd2)$. Therefore, finally

$$\xi_{\max}(z) = \frac{mgRK}{\sqrt{3}} \exp\left(-\frac{gz}{A^2\omega^2}\right) \tag{23}$$

For the sake of completeness, the plane motion equation should be added, and variations in the velocity of particles upon contact with the plane should be described. If the magnetic force is sufficiently high to make particles move up on the average, the interaction of particles with the plane may be disregarded. The vibration is expressed in the fact that the equation of motion contains the random force characterizing the collision of the ferromagnetic particle with other particles.

Standard actions shall be then taken, namely, the problem of the bouncing particle on the vibrating plane must be solved, with the only difference consisting in the fact that the motion of the particle on the plane is not a free fall (due to interference with other particles, and the influence of the magnetic field).

If the plane is in motion harmonically, its speed is determined as $u = u0\cos\omega t$.

The velocity of particle v' immediately after impact (at time $t = t0$) in the laboratory frame of reference has the following form:

$$v'_n = R(v_n + u_n) + u_n \tag{24}$$

where u_n is the plate velocity at impact; and R is the recovery rate (equal to 1 in the perfectly elastic case).

The particle velocity and coordinate are determined by the equation of its motion. If $v = v(t)$ and $z = z(t)$, and the plane coordinate in the laboratory frame of reference is determined as $Asin\omega t$, the exact time of the next impact may be determined by solving the following equation:

$$z(t - t_0) = A\sin\omega t \tag{25}$$

Obviously, if the magnetic force is high, this equation does not have real roots, since the particle never reaches the plane and is drawn out from the layer by the magnetic field. Therefore, in the case of a strong magnetic field, the problem is solved at the first 'iteration'. Further, if the particle manages to reach the plane, this equation may have (several) roots. In this case, the root of $t = t1$ should be selected as the closest to $t0$. With t1, the plane velocity at this time may be calculated. Then formula (24) may be used to calculate the velocity after impact, after which the Langevin equation must be solved, etc.

6 PARTICLE SIZE

In order to simplify the calculations, it was assumed that all particles are spherical. However, usually granular media are polydisperse in nature. Assuming the size of the particles is a one-dimensional random variable, its distribution may be established using $D(\delta)$, where $D(\delta)$ is the ratio of the mass or number of particles that are smaller than δ to the total weight or number of particles [7]. The particle size means the average 'diameter of the projected surface', determined as the area of the circle having the same area as the projection of the particle.

In the calculations, the particle diameter is the result of averaging of the diameter of the projected surface over the distribution function. If averaged over all particles, then

$$d = \int_0^1 \delta dD \tag{26}$$

Due to its simplicity, the Rosin-Rammler-Sperling-Bonnet approximate function is widely used:

$$D(\delta) = 1 - \exp\left(-\left(\frac{\delta}{\delta_e}\right)^a\right) \tag{27}$$

where a and δe are empirical constants. Then, the integral of the following form is obtained:

$$d = \frac{a}{\delta_e^a} \int_0^1 \delta^a \exp\left(-\left(\frac{\delta}{\delta_e}\right)^a\right) d\delta \tag{28}$$

Upon calculation, the following is obtained:

$$d = \frac{\delta_e}{a}\left[\Gamma\left(\frac{1}{a}\right) - a\Gamma\left(\frac{1}{a}+1, \left(\frac{1}{\delta_e}\right)^a\right)\right] \tag{29}$$

where

$$\Gamma(a,z) = \int_z^\infty t^{a-1}\exp(-t)dt \tag{30}$$

is the upper incomplete gamma function.

Determination of geometrical parameter d does not solve the problem. Due to the fact that the particles are not spherical, their energy may be redistributed along the rotational degrees of freedom, which must be taken into account in the future.

As follows from the experiment, the particle packing density must be known, and their complex geometry must be taken into account, which represents a rather complex mathematical problem.

REFERENCES

[1] H. Jaeger, S.R. Nagel. Granular Solids, Liquids, and Gases.*Rev. Mod. Phys. 68, 1259*, 1996.

[2] I. S. Aranson, L. S. Tsimring. Patterns and Collective Behavior in Granular Media: Theoretical Concepts. *Rev. Mod. Phys. . 78, 641*, 2006.

[3] P. Eshius. *Collective Phenomena in Vertically Shaken Granular Matter.//ISBN 978-90-365-2616-6*. 2008.

[4] P. Eshius, M. Devaraj, A. Meheboob, Onset of Convection in Strongly Shaken Granular Matter *Phys. Rev. Lett. 104, 038001*. 2010.

[5] J. Eggers. Sand as Maxwell's Demon. *Phys. Rev. Lett. 83, 5322*, 2014.

[6] V.S. Zuev, V.I. Charykov.*Electromagnetic Separators: Theory, Structure (In Russian)*, 2002.

[7] G.M. Ostrovsky. *Applied mechanics of heterogeneous media. // St.Petersburg: Nauka*,2002.

Experimental Techniques (TP02)

International Conference on Engineering Vibration
Ljubljana, Slovenia, 7-10 September 2015

VIBRATION OF AEROSOLS IN THE TUBES

Damir A. Gubaidullin*[1,2], Rinat G. Zaripov[1,2], Liudmila A. Tkachenko[1,2]

[1]Institute of Mechanics and Engineering, Kazan Science Center,
Russian Academy of Sciences, Kazan, Russia
[2]Kazan (Volga Region) Federal University, Kazan, Russia
damirgubaidullin@gmail.com, zaripov@mail.knc.ru, ludatkachenko1977@gmail.com

Keywords: Aerosol, Coagulation, Deposition, Oscillations, Experiment.

Abstract. *In the present work, longitudinal oscillations of a small-dispersed aerosol in tubes are considered. Experimental investigations oscillations of an aerosol were carried out for different length of tubes with various geometry on the end in the shock-wave and the shock-free modes in the vicinity of the resonance frequencies equal to the first eigenfrequency and the frequency that is twice lower than the first eigenfrequency (subharmonic resonance). Di-ethyl-hexyl-sebacate is used as the working fluid to generate aerosol. Numerical concentration of aerosol droplets for all experiments monotonously decreases with time. In the case of a closed tube, this process is defined by the coagulation of aerosol and deposition of droplets on the tube walls. In a half-open tube, the discharge of aerosol to the environment is observed in addition to the coagulation of aerosol and deposition of droplets on the tube walls. The dependence of the time scale of the coagulation and deposition of aerosol and the time scale of the clearing of aerosol on the excitation frequency likewise exhibits a nonmonotonic pattern. With increase of intensity of the oscillations, the caused increase of excitation amplitude, and decrease of the tube length these times decreases. Nonlinear dependence of the time scale of coagulation of droplets is established at nonlinear oscillations of an aerosol in a tube from initial number concentration of an aerosol. It is established, that presence of a flange slows down process of the clearing of aerosol. Reduction of internal diameter of a flange results in increase in the time scale of the clearing of aerosol. In so doing, the time scale of the clearing of aerosol in the case of a half-open tube is reduced by a factor of 1.5 and more compared to the time scale of the coagulation and deposition of aerosol in a closed tube. The time scale of the coagulation and deposition of aerosol in the closed tube by 2-4 times and time scale of the clearing of aerosol in a half-open tube by 6-12 times lower than at natural depositing.*

1 INTRODUCTION

In modern equipment, diverse inhomogeneous and multiphase media serve as the main working media. In so doing, numerous phenomena exhibit a wave and unsteady-state pattern. The investigation of wave processes in such media is an urgent problem in the dynamics and thermophysics of multiphase systems. Of the diversity of heterogeneous media, disperse flows may be identified which are relatively regular and represent a mixture of several phases, of which one consists of various inclusions (such as droplets, bubbles, solid particles), i.e., aerosols, fogs, bubble liquids, suspensions, and the like. Basic models of wave dynamics of multiphase media and some related results are given in monograph [1]. The oscillation processes in two-phase bounded media are treated in detail in [2, 3]. The dynamics of traveling waves in gas-droplet systems are dealt with in [4, 5]. Of special importance is the study of oscillation with highly nonlinear fronts of waves and coagulation of aerosols, because both are of interest from the standpoint of practical applications (intensification of the atomization of liquids with a view to cleaning waste gases in harmful production processes, deposition of aerosol in various technical devices, intensification of stirring and combustion, and the like). The acoustic coagulation of aerosols, which is accompanied by agglomeration of small particles or droplets under the effect of acoustic waves, is a well-known phenomenon treated in detail in the monographs [6-11] and papers [12-14] and in other publications. Widely employed is a system of the type of resonance tube, in which the excitation of the medium in the vicinity of resonance causes the emergence of highly nonlinear pressure waves up to periodic shock waves at resonance. The investigations of nonlinear resonance oscillation of a homogeneous gas in tubes with different conditions at the ends are reviewed in [15]. It is noted that the resonant modes of oscillation are accompanied by a number of nonlinear effects such as the turbulization of flow, emergence of secondary flows and acoustothermal processes, generation of higher harmonics, formation of a pulsating jet in the external wave field in the vicinity of the open end, and so on. Some investigations involving aerosols in large volumes were performed for conditions of intense harmonic excitation outside of the resonance frequencies of oscillation in work [7]. Most interesting is the case of nonlinear resonance oscillation of aerosols in tubes; however, only several studies were devoted to experimental study of this phenomenon [16-23]. The behavior of the aerosol with its nonlinear oscillations in a closed tube near the first eigenfrequency was studied in experimental works [16-18, 20-23]. Some results are given in [19] of an experimental investigation of oscillations in closed and half-open tubes near the subharmonic resonance, the frequency of which is two times lower than the first eigenfrequency. The main nonlinear effect was accelerated coagulation and deposition of the droplets of machine oil and tobacco smoke [16], oleic acid droplets [17], smoke particles produced by the combustion of an incense stick [18], and droplets obtained from liquid Di-ethyl-hexyl-sebacate (DEHS) [19-23] on the tube walls. The geometric diameter of the aerosol droplets and particles was 1–10 μm [16, 17], 0.3 μm [18], and 0.83 μm [19-23].

This paper deals with studies of nonlinear oscillation of small-dispersed aerosol (with a droplet diameter of less than 1 μm) in tubes of different lengths with various geometry on the end in a wide range of excitation frequencies including half of the first eigenfrequency of the medium (subharmonic resonance). Also, this work is aimed at experimental study of the features of coagulation and deposition of the vibrating aerosol near the first eigenfrequency in the closed and the half-open tubes in the shock-free mode.

2 NONLINEAR OSCILLATIONS OF AEROSOL IN THE TUBES IN THE VICINITY OF SUBHARMONIC RESONANCES

2.1 Experimental conditions

An experimental facility including a resonance tube, a system of excitation of oscillation, and a system for recording the process parameters was used to investigate the nonlinear oscillation of aerosol in a tube. A standard compressor with the amplitude of piston travel $l_0 = 0.043$ m and inside diameter of the cylinder $2R = 0.077$ m was used for the excitation of aerosol oscillation. The crankshaft of the crank mechanism was connected to the rotor of a 3.2-kW P-42 dc electric motor. The voltage was applied to the electric motor in a special electric circuit via autotransformer; this enabled one to smoothly vary the rotor r.p.m. and accordingly, the piston oscillation frequency. The compressor cylinder was connected to the resonance tube via tapering adapter of height $h = 0.22$ m. The tube consisted of identical sections with a length of 0.5 m and inside diameter $2R_0 = 0.048$ m. One section made of quartz glass was 1.2 m long. For all experiments in the closed tube, this latter section was installed in the middle of the tube; in the case of an open end, it was located at a distance of 1.87 m from the tapering adapter.

The piston oscillation frequency $\nu = \omega/2\pi$, where ω is the cyclic frequency, was measured using a photoelectric sensor the signals from which were applied to the frequency meter of an F-4372 combined instrument. The frequency was measured within 0.1 Hz and varied from 0 to 18 Hz. A transparency sensor installed on the quartz section of the tube was used to measure the concentration of aerosol in the process of its oscillation. A directed light beam passed through the aerosol normally to the tube and fell on a photoresistor. Then the signal from the photoresistor through an amplifier was transformed to voltage which was recorded by a digital voltmeter. Di-ethyl-hexyl-sebacate $C_{26}H_{50}O_4$ was used as the working fluid to generate aerosol. The experiments involved the use of generator of aerosols ATM 225 (TOPAS). The distribution by the geometric diameter of aerosol droplets was determined by an LAP-320 laser spectrometer (TOPAS). The aerosol droplets range in size from 0.839 to 1.06 μm. The majority of droplets have the geometric diameter $D = 0.863$ μm.

The measurements were performed for different values of tube length L_0 in the range of frequencies containing subharmonic resonance. The oscillation frequency of aerosol in closed and half-open tubes at resonance was determined by the formulas $\nu_{1/2} = c_0/4L$ and $\nu_{1/2} = c_0/8L$, where $\nu_{1/2} = \nu_1/2$, c_0 is the equilibrium velocity of sound in the aerosol [15], and $L = L_0 + l + (m^2 + m + 1)h/3$ is the reduced tube length, where $l = m^2 l_0$, $m = R/R_0$. In the case of an open end, the reduced length additionally contains the Rayleigh correction σR_0 with $\sigma = 0.6133$.

In the experiments, the aerosol filled the tube uniformly without excess pressure. The time of filling with aerosol was selected such that the initial numerical concentration of aerosol droplets for different values of the tube length would remain constant ($N_0 = 2.75\times10^6$ cm^{-3}) and be 80, 110, 140, and 200 s for tubes of length $L_0 = 2.7$, 3.7, 4.7, and 6.7 m, respectively. After filling the tube with aerosol, the voltmeter reading was registered and the electric motor started. At the same time, the time reading was started using a stopwatch. A variation of the aerosol transparency occurred in the experiments, which caused the voltmeter readings to vary throughout the process being investigated. It was assumed that the correlation between the voltage and numerical concentration of aerosol droplets in the tube is linear and, consequently, the relation $N = N_0 U/U_0$ cm^{-3} may be used for the calculation of numerical concentration of aerosol droplets, where U_0 is the voltmeter reading at the initial instant of time. After each experiment, the tube was taken apart and thoroughly cleaned of the layer of aerosol droplets deposited on the walls.

2.2 Experimental results

As experiments have shown the concentration of droplets monotonically decreases with time. In the closed tube this process includes the coagulation of aerosol droplets upon their coalescence and deposition on the tube walls. The time of variation of concentration is the time scale of coagulation and deposition of aerosol. In the half-open tube the monotonic process of the decrease in concentration with time includes mainly the coagulation of aerosol droplets, their deposition on the tube walls, and the unsteady discharge of aerosol from the open end of the tube in the form of a pulsating jet. Therefore, we will refer to the characteristic time of this process as the time scale of clearing of the aerosol [7] rather than the time scale of coagulation and deposition as in the case of a closed tube. The obtained dates were used to determine the time scale of coagulation and deposition of aerosol and the time scale of clearing of aerosol as a function of frequency for different values of the tube length. Figure 1 gives appropriate plots for the closed and the half-open tubes, where each point corresponds to a separate experiment. One can see in Figure 1(a) that, for tubes of length L_0 = 2.7, 3.7, 4.7 m, an increase in frequency in the pre-resonance mode of oscillation causes a decrease in the time scale of coagulation and deposition of droplets. This is due to the fact that, on approaching the resonance, the amplitude of aerosol oscillation increases. For a tube 6.7 m long, a minimum of the time scale of coagulation and deposition of aerosol at resonance frequency is observed. After this minimum the time starts increasing, with the oscillation amplitude exhibiting a maximum at this frequency. Therefore, the dependence of the time scale of coagulation and deposition of aerosol on the excitation frequency exhibits a nonmonotonic pattern. For tubes of smaller length, the resonance frequencies lie above 18 Hz; therefore, they were not attained in our experiment. Note that in the case of a half-open tube (Figure 1(b)), the curve for a tube of length L_0 = 4.7 m also exhibits a nonmonotonic pattern, has a minimum at resonance frequency and a maximum behind resonance, where the time scale of clearing of aerosol somewhat increases after which its further decrease is observed. This pattern of the dependence is attributed to the fact that the amplitude of forced oscillation of aerosol increases when resonance is approached, as in the case of a closed tube, and this leads to a decrease in the time scale of clearing. At resonance, the amplitude reaches its maximal value; accordingly, the time scale of clearing is minimal. Behind resonance, the amplitude decreases; as a result, the time scale of clearing of aerosol increases to a certain value. A further increase in the excitation frequency causes an abrupt decrease in the time scale of clearing. This is associated with the effect of the discharge of aerosol from the open end of the tube increasing with frequency. In experiments involving other values of tube length, a similar decrease of the time scale of clearing of aerosol is observed with increasing excitation frequency in the pre-resonance mode of oscillation. However, no resonant behavior of dependences is observed, because the relevant subharmonic resonances are outside of the investigated range of aerosol excitation frequencies. Also the influence of the flanges at the passive end of the tube on the process of the coagulation and deposition of aerosol and process of the clearing of aerosol are studied. In Figure 2 is given the dependence the time scale of the coagulation and deposition of aerosol and the time scale of clearing of aerosol on the excitation frequency for the closed and half-open tubes without flange, as well as a half-open tube with flanges of different internal diameters. Figure 2 shows that the decrease in the internal diameter of the flange $2R_{\text{in.f}}$ results in an increase the time scale of clearing of aerosol which reaches a maximum value in the case of the closed tube. This is due, firstly, to the significant influence of the unsteady discharge of aerosol from the open end of the tube, and secondly, with the approach of the investigated excitation frequencies of aerosol in a half-open tube to its resonance frequency [24, 25]. Note that the time scale of clearing of aerosol in a half-open tube with the flange is longer than in a half-open tube

without a flange. This is due to the fact that a half-open tube with a flange which is in connection with the tube forms a right angle, the consumption on the formation of vortices near the outlet section is greater than in the tube with the rounded open end [26].

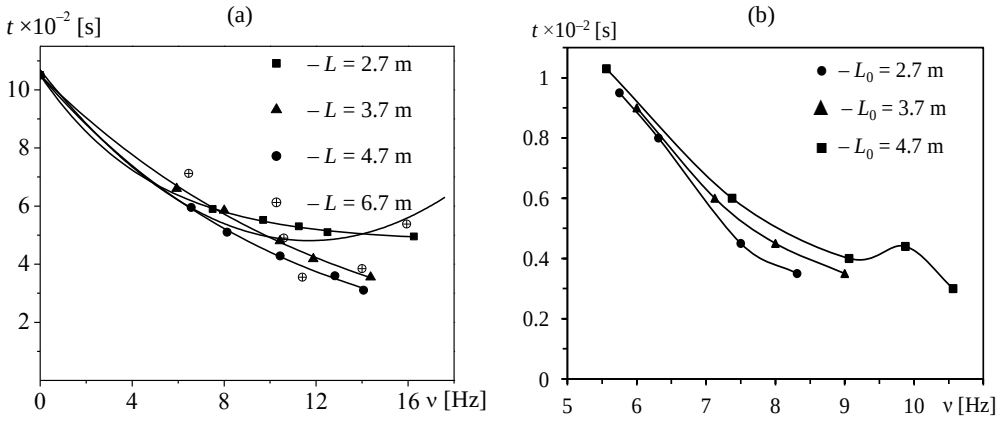


Figure 1: The time scale of coagulation and deposition of aerosol (a) and the time scale of clearing of aerosol (b) as a function of frequency for different values of length of a closed tube. The points indicate the experimental data, and the solid lines indicate the polynomial approximation.

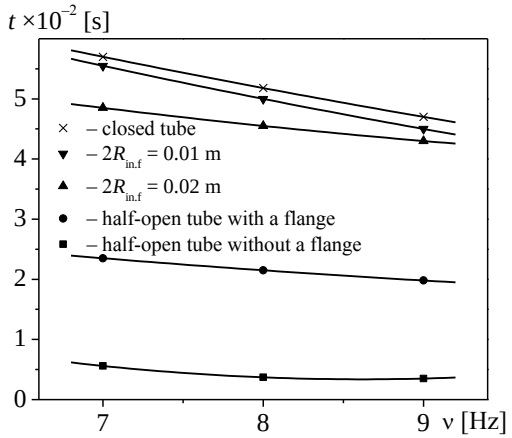


Figure 2: Dependence of the time scale of coagulation and deposition of aerosol and the time scale of clearing of aerosol from frequency in to-resonance regime for tube length L_0= 2.7 m with flanges of different internal diameters. The points indicate the experimental data, and the solid lines indicate the polynomial approximation.

We will examine the data on the dependence of the time scale of coagulation and deposition of aerosol on the intensity of aerosol oscillation. Because the mass content of droplets in the aerosol being treated was very low, the velocity of sound in the gas-droplet mixture [1, 4] differed little from the velocity of sound in pure gas: this explains the absence of the resonance frequency shift with respect to pure gas. As a result, the intensity of aerosol oscillation was calculated by the theory for homogeneous gas [27], $I = c_0 \rho_0 V^2/2$, where ρ_0 is the density of unperturbed gas, and V is the gas velocity. Figure 3 gives the dependence of the time scale of coagulation and deposition of aerosol on the dimensionless intensity of oscillation $\bar{I} = I/I_m = V_m^2$ for different values of tube length, where I_m corresponds to the intensity at $V = c_0$. The maximal oscillation amplitude of aerosol velocity in a closed tube has the form

$V_m = M_p\left(\cos^2 kL\,\mathrm{sh}^2 kL\beta' + \sin^2 kL\,\mathrm{ch}^2 kL\beta'\right)^{-1/2}$ [28]. Here, $M_p = \omega l/c_0$, $k = \omega/c_0$ is the wave number, $\beta' = 0{,}5\left[1+(\gamma-1)/\sqrt{\mathrm{Pr}}\right]\left(R_0\sqrt{\omega\rho_0/2\mu}\right)^{-1}$, μ is the dynamic viscosity, Pr is the Prandtl number, and γ is the adiabatic exponent. One can see in Figure 3 that the time scale of coagulation and deposition of aerosol decreases monotonically with increasing intensity of aerosol oscillation for all values of the tube length.

It is known that, in a tube, the amplitude of pressure oscillation of the medium at resonance is proportional to ε^a, where $\varepsilon = l/L$ and $a > 0$ [15]. Therefore, a decrease in the tube length causes an increase in the amplitude of pressure oscillation and, accordingly, of intensity of oscillation. Figure 4 gives the time scale of clearing of aerosol as a function of the parameter ε for the excitation frequency ν = 6, 7, and 8 Hz. These results indicate that an increase in ε causes a decrease in the time scale of clearing of aerosol. As the excitation frequency increases, the slope of the curves becomes steeper. This is expressed quantitatively in an increase in the ratio of the maximal value of the time scale of clearing to the minimal value for each frequency.

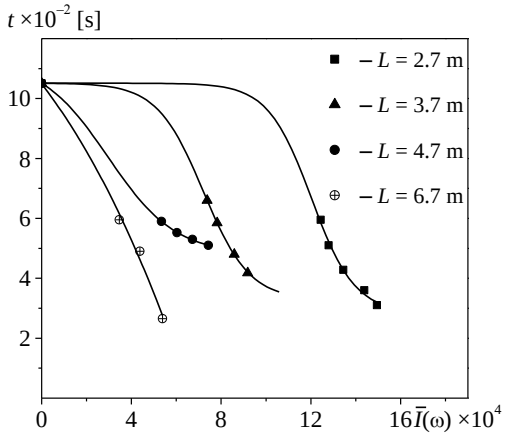


Figure 3: The time scale of coagulation and deposition of droplets as a function of oscillation intensity for different values of length of a closed tube. The points indicate the experimental data, the solid line indicates the Boltzmann approximation.

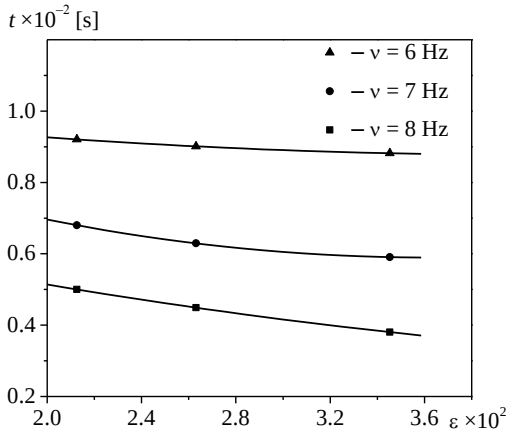


Figure 4: The time scale of clearing of aerosol as a function of the parameter ε in a half-open tube for different values of frequency. The points indicate the experimental data, the solid lines indicate the polynomial approximation.

3 COAGULATION AND DEPOSITION OF OSCILLATING AEROSOL IN A TUBES IN THE SHOCK-FREE MODE NEAR THE FIRST EIGENFREQUENCIES

3.1 Experimental conditions

The longitudinal oscillations of an aerosol in a vertical quartz tube of length $L = 1.06$ m and internal diameter $2R_0 = 0.0365$ m are created by a planar piston. It is put into motion on a vibrostand with a power amplifier TV51075 (TIRA). On the passive end of the tube is covered by the cap for studies in a closed tube and cap with an orifice coinciding with diameter of the tube for research in a half-open tube. The measurements and control of the sinusoidal oscillations are performed in real time with the help of program module SineVIEW, installed in a computer, by means of a piezoelectric IEPE accelerometer 4513-001(Bruel & Kjaer) and a

controller VR8500-1 (Vibration Research Corporation). The values of the frequency ν and amplitude of the piston travel l are set with an accuracy of up to 10^{-6} Hz and 10^{-7} m, respectively. The system of the pressure measurement of the medium consists of a pressure sensor 8530C-15 (Bruel & Kjaer) with a diameter of 3 mm placed near the piston, a three-channel bridge voltage amplifier ENDEVCO-136 (Bruel & Kjaer), and a digital oscilloscope DSO 3062A (Agilent Technologies). Oscilloscope control and recording of the shape and values of the output signal with an accuracy of up to 0.3 mV also performs from a computer using the software DSO3000. To determine the transparency of the aerosol is used a measuring complex, consisting of the light source, which is a laser with the wavelength of 630 nm and power 0.16 W with a remote control and an ATT-1505 digital luxmeter (Aktakom). The aerosol is created by an aerosol generator ATM 225 (TOPAS) from di-ethyl-hexyl-sebacate $C_{26}H_{50}O_4$.

The measurements are performed for different values of the amplitude of piston travel in the range of frequencies containing resonance. The observed resonant frequencies of the presence of the near-wall losses $\nu^* = 160.7$ Hz for a closed tube and $\nu^* = 78.6$ Hz for a half-open tube different from the resonant frequencies $\nu_1 = 161.8$ Hz and $\nu_1 = 80.1$ Hz calculated by the linear theory of acoustics. The experiments are conducted in two stages. At the first stage, the pressure oscillations of media are measured. The oscillations of a given frequency and amplitude are run, and the output signal with the pressure sensor is recorded. At the second stage, the transparency of an oscillating aerosol is measured. The light source and the light sensor of luxmeter are mounted on the racks so that the light beam passed perpendicular to the tube axis through its medium and fell into the center of the sensor. The initial luxmeter reading Φ_0 for the air filling tube is recorded. The tube is filled aerosol without excess pressure with the help of the aerosol generator. Time to fill the tube aerosol is selected so that its initial concentration for all experiments was constant and equal to 3.5×10^6 см$^{-3}$. The luxmeter reading Φ_1 is recorded and oscillations are run. A variation of the aerosol transparency occurs in the experiments, which cause the luxmeter readings Φ_t to vary throughout the process being investigated. It is assumed that the correlation between the illuminance and numerical concentration of aerosol droplets in the tube is linear and, consequently, the relation $N = 3.5\times10^6 (\Phi_t - \Phi_0)/(\Phi_1 - \Phi_0)$ cm^{-3} may be used for the calculation of numerical concentration of aerosol.

3.2 Experimental results

As well as in case of oscillations near a subharmonic resonance the numerical concentration of the droplets monotonically decreases with time. And under natural deposition a slower decrease in the aerosol concentration with time takes place. The obtained dates are used to determine the time scale of coagulation and deposition of aerosol for the closed tube and the time scale of clearing of aerosol for the half-open tube as functions of the frequency oscillations and amplitude of piston travel.

The dependences of the time scale of coagulation and deposition of aerosol and the time scale of clearing of aerosol on the parameter ε at the frequencies of the observed resonance are given in Figure 5. It is seen that the increase in ε leads to nonlinear reduction of the time scale of coagulation and deposition of aerosol in the closed tube (Figure 5(a)) and almost linear decrease in the time scale of clearing of the aerosol in the half-open tube (figure 5(b)). It is possible to note that the time scale of the coagulation and deposition of aerosol is 2-4 times, and the time scale of clearing of aerosol is 6-12 times less than time scale of natural deposition in the absence of oscillations. Observed effective coagulation of aerosol droplets and their deposition in the tube due to the secondary flow in the manner of two toroid vortices [15], formed as a result of the nonlinearity of the resonant oscillations. At the small amplitude of the medium obeys the harmonic law in the closed and in the half-open tubes: the shape of

the pressure wave is continuous and symmetrical. The amplitude of the pressure oscillations increases with increasing amplitude of piston travel. In the closed tube the wave shape is distorted and in the half-open tube the shape of the pressure wave is is nearly harmonic form.

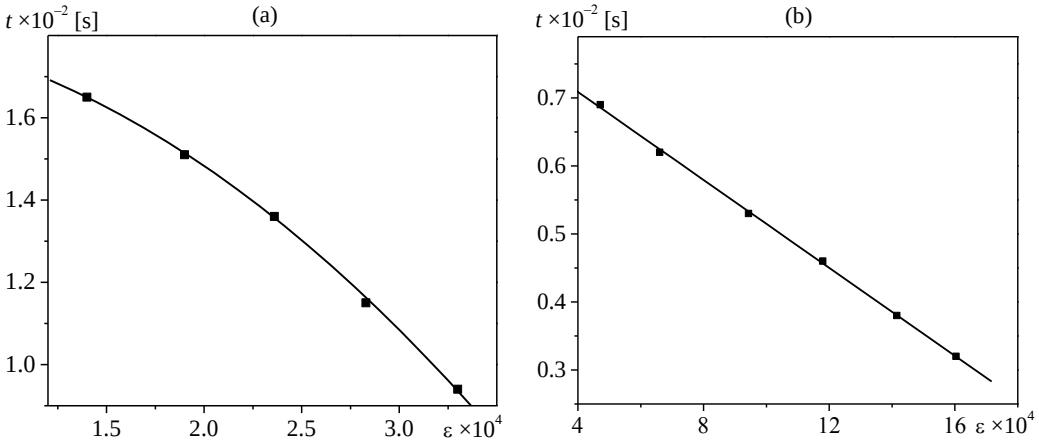


Figure 5: Dependence of the time scale of coagulation and deposition of aerosol (a) and the time scale of clearing of aerosol (b) on the parameter ε at observed resonant frequency: the line is the polynomial approximation.

Figure 6 gives dependence of time scale of coagulation and deposition and time scale of clearing of aerosol on the excitation frequency for the amplitude of piston travel l = 0.3 mm, where each point corresponds to a separate experiment. The dependence exhibits a nonmonotonic pattern with a minimum value at resonance frequency. This is due to the fact that, on approaching the resonance, the amplitude of aerosol oscillation increases. Such dependence is explained by the fact that the resonance is approached the amplitude of the forced oscillations of aerosol increases, which reduces the process time. At resonance, the amplitude reaches the maximum value, respectively, the process time is minimum. Over the resonance amplitude decreases again, leading to an increase in the process time. It may be noted that the time scale of clearing of aerosol droplets in the half-open tube about 1.5 times less than the time scale of coagulation and deposition of aerosol droplets in a closed tube. This is connected to the fact that in a half-open tube portion aerosol is released into the environment.

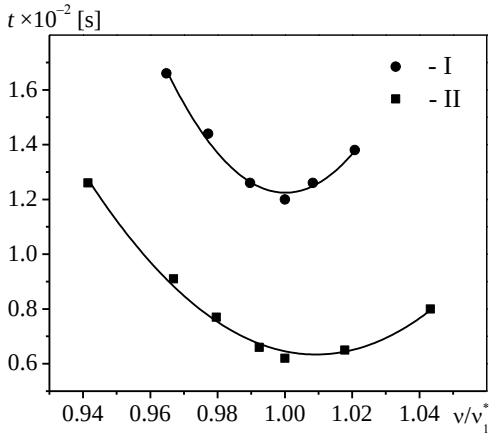


Figure 7: Dependence of the time scale of coagulation and deposition (I) and the time scale of clearing (II) of the aerosol on the excitation frequency for the amplitude of piston travel l = 0.3 mm: the line is the polynomial approximation.

4 CONCLUSIONS

- It is shown that the presence of oscillations leads to acceleration of coagulation and deposition of aerosol. The increase in intensity of the oscillations, caused by increase in amplitude of piston travel or a decrease in the tube length, leads to reduction of process time. The time scale of coagulation and deposition aerosol in a closed tube by 2-4 times, in a half-open tube is 6-12 times lower, than at natural deposition.
- It is established, that presence of a flange slows down process of the clearing of aerosol. Reduction of internal diameter of a flange results in increase in the time scale of clearing of aerosol. In so doing, the time scale of clearing of aerosol in the case of a half-open tube in a shock-wave mode is reduced by a factor of 1.5 and more compared to the time scale of coagulation and deposition in a closed tube.
- The nonmonotonic pattern of the dependence of the time scale of coagulation of aerosol in a closed tube and the time scale of clearing of aerosol in a half-open tube on the frequency of excitation with a minimal value at resonance frequencies has been found.

ACKNOWLEDGMENTS

The study was performed by a grant from the Russian Science Foundation (project No. 15-11-10016).

REFERENCES

[1] R. I. Nigmatulin, *Dynamics of Multiphase Media*, Hemisphere, New York, 1990.

[2] R. F. Ganie, and L. E. Ukrainskii, *Dynamics of Particles under the Effect of Vibration*, Naukova Dumka, Kiev, 1975.

[3] R. F. Ganiev, N. I. Kobasko et al., *Oscillation Phenomena in Multiphase Media and Their Uses in Technology*, Tekhnika, Kiev, 1980.

[4] D. A. Gubaidullin, *Dynamics of Two-Phase Gas-Vapor-Droplet Media*, Kazan Mathematical Society, Kazan, 1998.

[5] D. A. Gubaidullin and R. I. Nigmatulin, On Theory of Acoustic Waves in Polydispersed Gas-Vapor-Droplet Suspension. *Int. J. Multiphase Flow*, **26**, 207–228, 2000.

[6] L. Bergmann, *Ultrasonics*, Bell, London, 1938.

[7] E. P. Mednikov, *Acoustic Coagulation and Precipitation of Aerosols*, Consultant Bureau, New York, 1965.

[8] N. A. Fuks, *Aerosol Mechanics*, USSR Acad. Sci., Moscow, 1955.

[9] V. M. Voloshchuk and Yu. S. Sedunov, *Coagulation Processes in a Dispersed System*, Gidrometeoizdat, Leningrad, 1975.

[10] V. M. Voloshchuk, *Kinetic Theory of Coagulation*, Gidrometeoizdat, Leningrad, 1984.

[11] S. Temkin, *Suspension Acoustics: an Introduction to the Physics of Suspensions*, Cambridge University Press, New York, 2005.

[12] D. T. Shaw, *Acoustic Agglomeration of Aerosols, in Recent Developments in Aerosol Sciences*, Wiley Interscience, New York, Chap. 13, 279–319, 1978.

[13] T. L. Hoffmann and G. H. Koopmann, Visualization of Acoustic Particle Interaction and Agglomeration: Theory and Experiments. *JASA*, **99**(4), 2130–2141, 1996.

[14] T. L. Hoffmann and G. H. Koopmann, Visualization of Acoustic Particle Interaction and Agglomeration: Theory Evoluation. *JASA*, **101**(6), 3421–3429, 1997.

[15] M. A. Ilgamov, R. G. Zaripov, R. G. Galiullin and V. B. Repin, Nonlinear oscillations of a gas in a tube. *Appl. Mech. Rev.*, **49(**3), 137–154, 1996.

[16] A. I. Gulyaev and V. M. Kuznetsov, Aerosol Coagulation under Periodic Shock Waves. *Sov. Phys. Acoust.*, **8**(4), 236–238, 1963.

[17] S. Temkin, Droplet Agglomeration Induced by Weak Shock Waves. *Phys. Fluids*, **13**, 1639–1641, 1970.

[18] K. Shuster, M. Fichman, A. Goldshtein and C. Gutfinger, Agglomeration of Submicrometer Particles in Weak Periodic Shock Waves. *Phys. Fluids*, **14**(5), 1802–1805, 2002.

[19] D. A. Gubaidullin, R. G. Zaripov, R. G. Galiullin, E. R. Galiullina and L. A. Tkachenko, An Experimental Investigation of the Coagulation of Aerosol in a Tube in the Vicinity of Subharmonic Resonance. *High Temperature*, **42**(5), 794–802, 2004.

[20] D. A. Gubaidullin, R. G. Zaripov, and L. A. Tkachenko, Experimental Study of Coagulation and Sedimentation of Aerosols in a Closed Tube in the Shock-Free Mode. *High Temperature*, **50**(4), 564–566, 2012.

[21] D. A. Gubaidullin, R. G. Zaripov, and L. A. Tkachenko, Experimental Study of Oscillations of Aerosols in an Open Tube in the Shock-Free Mode. *High Temperature*, **51**(6), 955–957, 2013.

[22] D. A. Gubaidullin, R. G. Zaripov, and L. A. Tkachenko, Experimental Study of Nonlinear Oscillations of Aerosols in Tubes in the Shock-Free Mode near Resonance. *Doklady Physics*, **58**(9), 392–395, 2013.

[23] D. A. Gubaidullin, R. G. Zaripov, and L. A. Tkachenko, Nonlinear Oscillations of Finely Dispersed Aerosol in a Flanged Pipe. *J. of Engin. Physics and Thermophysics*, **85**(2), 259–264, 2012.

[24] J. Jimenez, Nonlinear gas oscillations in pines. Pt.1. Theory. *Fluid Mech.* **59**. 23–46, 1973.

[25] B. B. Sturtevant, Nonlinear gas oscillations in pines. Pt. 2. Experiment. *J. Fluid Mech.*, **63**, 97–120, 1974.

[26] B. B. Sturtevant and J. J. Keller, Subharmonic non-linear acoustic resonances in open tubes. Pt. 2: Experimental investigation of the open-end boundary condition. *Z. Angew. Math. Physics*, **29**(3), 473–485, 1978.

[27] V. A. Krasil'nikov and V. V. Krylov, *Introduction to Physical Acoustics*, Nauka, Moscow, 1984.

[28] R. G. Galiullin, E. R. Galiullina and E. I. Permyakov, Influence of Absorption on Nonlinear Vibrations of Gas. *J. of Engin. Physics and Thermophysics*, **68**(3), 346–353, 1995.

International Conference on Engineering Vibration
Ljubljana, Slovenia, 7-10 September 2015

INTRODUCING SHAPER-BASED FILTERS FOR THE IMPROVEMENT OF THE LOAD CELL RESPONSE IN DYNAMIC WEIGHING SYSTEMS

Dario Richiedei*, Alberto Trevisani
[1] Università degli Studi di Padova
Stradella San Nicola 3,
36100, Vicenza
dario.richiedei@unipd.it, alberto.trevisani@unipd.it

Keywords: Load Cells, Dynamic Weighing, Automatic weighing, Shaper Based Filters, Signal processing.

Abstract. *A novel model-based signal filtering technique is proposed in this work to compute accurately and rapidly the value of the measurand by taking advantage of the idea of the Input Shaping (IS), which has been developed for the optimal planning of command position references in flexible systems. The typical IS application is the manoeuvring of overhead cranes. The literature on IS has shown that less residual vibrations of crane suspended loads are obtained whenever IS is adopted to synthesize the motion reference.*

Following such a theory, this paper proposes an effective technique for performing high-speed filtering of load cell measurements, capable of reducing the time the filtered signal requires to settle down (i.e. to get and remain within a specified standstill range). The digital filters obtained, referred to as Shaper-Based Filters (SBF), are based on the convolution of the load cell signal with a sequence of a few impulses (typically from 2 to 5). The amplitudes and the instants of application of such impulses are computed through the system dynamic model by imposing the level of admissible residual oscillation in the steady-state filtered signal and by requiring the desired sensitivity of such an outcome. The inclusion of robustness specifications also allows effectively tackling uncertainty and variability on the load cell dynamic model parameters, i.e. frequency and damping.

The effectiveness of the SBFs is proved experimentally by applying them to industrial load cells and by comparing their performances with those provided by other filters most widely employed both in industries and in literature.

1 INTRODUCTION

Load cells are sensors widely employed for performing dynamic weighing, i.e. to compute accurately and rapidly the value of the measurand while the sensor output is still in oscillation and before stable equilibrium is achieved. In order to cope with the underdamped oscillatory response of load cells, which is forced by impulsive and step-like excitations, effective signal filtering is essential to trade off between bandwidth and settling time. Besides the general purpose filters developed in the field of signal processing (e.g. Bessel or Butterworth filters), some filtering techniques have been specifically addressed to load cell response correction. Model-based filtering schemes have been often synthesized. Adaptive schemes have been proposed in [1] and [2] to perform pole-zero cancellation, or to optimally trade off between bandwidth and settling time [3]. The use of a Kalman-filter has been exploited in [4] for objects moving on a weighing table with known speed. A filtering technique based on an array of accelerometers has been proposed in [5] to remove those low frequency components in load cell signals that are due to the frame flexibility. A different type of approach is the synthesis of non-model based filters, such as those using neural network [6], recursive least square procedures [7] or model-free discrete nonstationary filter [8].

Effective filters are usually required to ensure short settling time with no steady-state error (i.e. unitary steady-state gain), to grant adequate robustness with respect to uncertainty and variability of the system physical parameters, and finally to ensure ease of implementation and small computational effort. The latter requirement is necessary whenever filters are to be implemented in industrial hardware. In the light of these performance specifications, this paper proposes a novel model-based filtering technique which is devoted to weighing processes through load cells. The proposed method takes advantage of the idea of the Input Shaping (IS) open-loop (feedforward) control, which has been developed for the optimal planning of command position references in flexible systems (see e.g. [11]-[13]). The typical application of IS is the manoeuvring of overhead cranes, where it is applied to ensure no residual load oscillations after the end of the crane motion by physically modifying the actuator exerted force or the crane displacement. The literature on IS has shown that less residual vibrations of crane suspended loads are obtained whenever IS is adopted to synthesize the motion reference. Indeed, IS outperforms most of the other feedforward control techniques proposed in literature, even when relevant modelling errors are present. In practice, motion planning with IS relies on the convolution of the actuator force or of the position reference of the crane with a sequence of a few impulses (typically from 2 to 5 impulses), referred to as the shaper, to modify the crane trajectory in time.

The shapers, which are adopted to avoid load oscillation in flexible systems, are here reinterpreted as the transfer function of a filter to be convolved with the load cell measured output signals, rather than being employed to perform a physical modification of the crane motion. Indeed, the dynamic behaviour of a load cell can be modelled as a second-order resonant system, whose frequency and damping coefficient can be easily identified through simple and well-established experimental procedures. The obtained filters fit well with the specifications of short settling time, low computational effort, small memory required and robustness, that are usually posed in weighing applications. To the best of the Author's knowledge, no application of the IS theory in the field of signal processing can be found in literature.

2 THE LOAD CELL MODEL

The dynamic behavior of load cells commonly used in weighing devices, such as for instance strain-gauge load cells, can be effectively modelled through a single degree-of-freedom lumped model, whenever they are fixed on a rigid frame. In particular, if the sensor transverse

sensitivity is neglected and the elastic behaviour is linear, as it is common in practice, the second-order spring-damper-mass system model can be assumed (see e.g. [5]):

$$\ddot{\varepsilon}(t)+2\xi\omega_N\dot{\varepsilon}(t)+\omega_N{}^2\varepsilon(t)=\gamma\omega_N{}^2M(t) \tag{1}$$

where $\varepsilon(t)$ is the load cell response (i.e. the measured signal), γ is the load cell static gain, and $M(t)$ is the measurand mass. By assuming a lumped parameter model the natural frequency ω_N, and the damping ratio ξ are defined as:

$$\omega_N(t)=\sqrt{\frac{k}{M_c+M(t)}},\quad \xi(t)=\frac{c}{2\sqrt{k\left(M_c+M(t)\right)}} \tag{2}$$

In Eq. (1), k and c are, respectively, the constant load cell equivalent linear stiffness and damping coefficient in the measuring direction. M_c is the empty load cell equivalent mass, which comprises the contribution of the uniformly distributed mass M_s of the sensor and the mass M_b of the bucket. For instance, in the case of a cantilever load cell $M_c = 0.23M_s+M_b$ [5].

3 BASIC THEORY OF THE SHAPER-BASED FILTERS

3.1 Theoretical development of the Zero Vibration SBF

Let us consider the unitary step response of load cell represented through Eq. (1):

$$\varepsilon(t)=\begin{cases}0 & t<0\\ \gamma\left(1-e^{-\xi\omega_N t}\left(\dfrac{\xi}{\sqrt{1-\xi^2}}\sin\left(\omega_D t\right)+\cos\left(\omega_D t\right)\right)\right) & t\geq 0\end{cases} \tag{3}$$

where $\omega_D=\omega_N\sqrt{1-\xi^2}$ is the damped frequency. With no lack of generality, it is assumed that the step is applied at t=0.

The idea of the SBFs is to convolve the sensed signal with the filter impulse response $F(t)$, the so called shaper, which is made by the sequence of N>1 Dirac impulses $\delta(t-t_i)$ exerted at time t_i and whose amplitude is A_i:

$$F(t)=\sum_{i=1}^{N}A_i\,\delta(t-t_i) \tag{4}$$

The filter transfer function $\mathrm{F}(s)$ can be therefore expressed in the Laplace domain as follows:

$$\mathrm{F}(s)=\sum_{i=1}^{N}A_i e^{-sT_i} \tag{5}$$

Let us first assume N=2, for clarity of explanation. The extension and the implications on assuming more than two impulses are discussed in Section 4. The convolution of the sensed signal with the filter in Eq. (4) leads to the following response for any $t\geq t_2$ (i.e. after the last impulse of the shaper):

$$\begin{aligned}\varepsilon_F(t)=&\gamma\left(A_1+A_2\right)-\gamma A_1 e^{-\xi\omega_N(t-t_1)}\left(\frac{\xi}{\sqrt{1-\xi^2}}\sin\left(\omega_D(t-t_1)\right)+\cos\left(\omega_D(t-t_1)\right)\right)\\ &-\gamma A_2 e^{-\xi\omega_N(t-t_2)}\left(\frac{\xi}{\sqrt{1-\xi^2}}\sin\left(\omega_D(t-t_2)\right)+\cos\left(\omega_D(t-t_2)\right)\right)\end{aligned} \tag{6}$$

Equation (6) can be expressed in a more compact form as

$$\varepsilon_F(t) = \gamma(A_1 + A_2) - \gamma\sin(\omega_D t)\Phi - \gamma\cos(\omega_D t)\Theta \tag{7}$$

where the two term $\Phi(t)$ and $\Theta(t)$ are defined as follows:

$$\begin{aligned}\Phi(t) = &\frac{\xi}{\sqrt{1-\xi^2}} A_1 e^{-\xi\omega_N(t-t_1)}\cos(\omega_D t_1) + A_1 e^{-\xi\omega_N(t-t_1)}\sin(\omega_D t_1) \\ &+ \frac{\xi}{\sqrt{1-\xi^2}} A_2 e^{-\xi\omega_N(t-t_2)}\cos(\omega_D t_2) + A_2 e^{-\xi\omega_N(t-t_2)}\sin(\omega_D t_2)\end{aligned} \tag{8}$$

$$\begin{aligned}\Theta(t) = &-\frac{\xi}{\sqrt{1-\xi^2}} A_1 e^{-\xi\omega_N(t-t_1)}\sin(\omega_D t_1) \;\; A_1 e^{-\xi\omega_N(t-t_1)}\sin(\omega_D t_1) \\ &+ \frac{\xi}{\sqrt{1-\xi^2}} A_2 e^{-\xi\omega_N(t-t_2)}\sin(\omega_D t_2) + A_2 e^{-\xi\omega_N(t-t_2)}\sin(\omega_D t_2)\end{aligned} \tag{9}$$

The values of the suitable impulse amplitudes (A_1, A_2) and time (t_1, t_2) can be calculated by requiring the residual vibration to be zero after the last impulse, i.e. $\varepsilon_F(t) = \gamma$ for any $t \geq t_2$, which holds if and only if

$$\Phi = 0 \quad \text{and} \quad \Theta = 0 \tag{10}$$

Additionally, the unitary steady-state gain condition is posed:

$$\lim_{s\to 0} \mathrm{F}(s) = \sum_{i=1}^{N} A_i = 1 \tag{11}$$

The solution of Eq. (10) in the presence of constraint in Eq. (11) leads to the following results:

$$\begin{aligned} A_1 &= \frac{1}{1 + e^{\frac{-\pi\xi}{\sqrt{1-\xi^2}}}} \qquad t_1 = 0 \\ A_2 &= 1 - A_1 \qquad t_2 = \frac{\pi}{\omega_N\sqrt{1-\xi^2}} \end{aligned} \tag{12}$$

In solving the nonlinear Eq. (10) for t_2, which admits more solution, it has been selected the minimum solution, which is the earliest time at which the second input impulse should be added. Such a time instant results at one half of the damped natural period of the load cell, $2\pi/\omega_D$. In accordance with the usual name adopted in the IS motion planning, this kind of shaper, with two impulses leading to null residual vibration, is referred to as Zero Vibration (ZV) filter. This kind of SBF involves the smallest number of impulses and therefore ensures the shortest time to filter all the signal oscillating in the ideal case (i.e. exact knowledge of the load cell frequency and damping ratio, and absence of disturbances or neglected dynamics)
The graphical explanation of the ZV SBF filter is represented in Figure 1. In particular, Figure 1.a shows the load cell response (in the sketch it has been assumed γ=1, $\omega_N = 2\pi$ *rad/s* and $\xi = 0.05$) to a unitary step, i.e. the unfiltered signal. Figure 1.b shows the filtered signal (green line). The two components, due to the convolution with the two impulses (referred to as A_1 and A_2 responses in Figure 1), will add destructively to yield zero residual vibration. The capability of SBFs to cancel the load cell signal oscillation can be therefore interpreted as the destructive interference of damped sinusoidal waves.

The result here obtained agrees with the one usually proposed in the motion planning of flexible systems [11], where optimal values of *t* and *A* are calculated for impulse excitation, whose response, in the case of unitary impulse applied at time t_i, is

$$\varepsilon(t)=\gamma\frac{\xi}{\sqrt{1-\xi^2}}e^{-\xi\omega_N t}\sin\left(\omega_D\left(t-t_i\right)\right) \tag{13}$$

Similarly, it can be easily proved that the baseline of impulses shown in Eq. (12) ensures zero residual vibration in the presence of any arbitrary excitation.

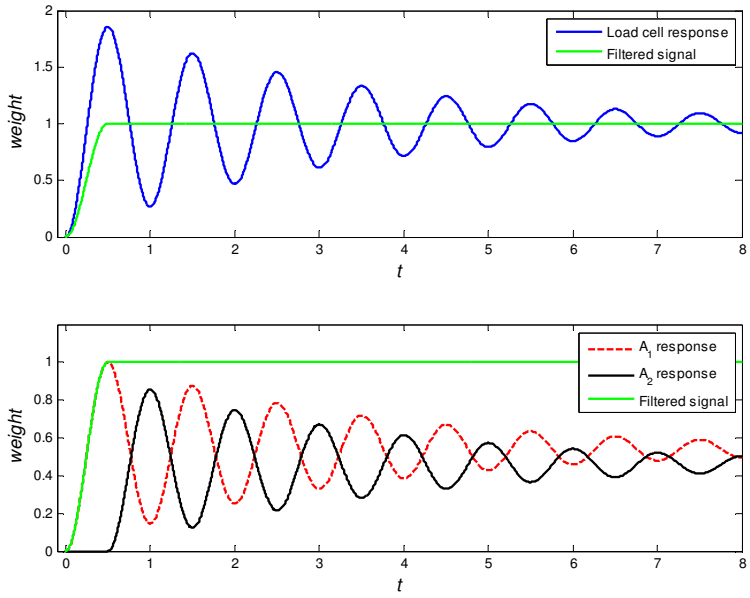


Figure 1: Principle of the ZV SBF.

3.2 Sensitivity to model parameter uncertainty

If the actual natural frequency of the load cell deviates from the nominal one, e.g. because of the product drop or uncertainty and errors in system model identification, the effectiveness of the ZV decreases. In practice, the destructive interference is only partially obtained and signal oscillation cancellation is performed. This results in large settling time of the load cell filtered signal.

By taking into consideration an arbitrary shaper, with arbitrary N, and on the basis of Eq. (3), the absolute residual oscillation after the last impulse of the shaper (exerted at time t_n) can be written in the following form:

$$\varepsilon_F(t)-\gamma=\frac{-\gamma e^{-\xi\omega_N t}}{\sqrt{1-\xi^2}}\sin\left(\omega_D t+\operatorname{acos}(\xi)\right)\sqrt{\left(\sum_{i=1}^{N}A_i e^{\xi\omega_N t_i}\sin\left(\omega_D t_i\right)\right)^2+\left(\sum_{i=1}^{N}A_i e^{\xi\omega_N t_i}\cos\left(\omega_D t_i\right)\right)^2} \tag{14}$$

Dividing $\left(\varepsilon_F(t)-\gamma\right)$ by the amplitude of the residual unfiltered oscillation from a unitary step applied at t=0, $-\gamma/\sqrt{1-\xi^2}$, it is obtained the time-varying amplitude of the percentage residual oscillation:

$$V\left(t,\xi,\omega_N\right)=e^{-\xi\omega_N t}\sqrt{\left(\sum_{i=1}^{N}A_i e^{\xi\omega_N t_i}\sin\left(\omega_D t_i\right)\right)^2+\left(\sum_{i=1}^{N}A_i e^{\xi\omega_N t_i}\cos\left(\omega_D t_i\right)\right)^2} \tag{15}$$

4 ROBUST SBFS

The value of V here computed for the step response of a load cell is the same of the one proposed in [13] for the impulse responses adopted in IS. The theory proposed in such papers for the synthesis of robust motion planning techniques for overhead cranes with uncertain dynamics [13] can therefore be adapted for synthesizing robust SBFs, capable of effectively tackling uncertainty and variability in the model parameters. Insensitivity, or robustness, constraints are set by imposing the percentage residual vibration $V\left(t=t_n,\xi,\omega_N\right)$ to be flat or smaller than a prescribed threshold in a neighbor of the modeling (nominal) frequency.

The first type of robustness constraints is obtained by requiring V to be flat in a neighborhood of the nominal model, i.e. by imposing the additional constraints

$$\frac{\partial V\left(t_n,\xi,\omega_N\right)}{\partial \omega_N}=0 \tag{16}$$

To solve this additional requirement, together with the zero-oscillation specification, three impulses should be included in the shaper. The solution of the problem for the case of the load cell filtering is the same of the IS [13] and is reported in Table 1, where it has been defined, for brevity of notation, the coefficient λ:

$$\lambda=e^{\frac{-\pi\xi}{\sqrt{1-\xi^2}}} \tag{17}$$

Higher robustness, i.e. flatter sensitivity curves in a neighborhood of the nominal model, can be obtained by requiring also the second or the third derivatives of $V\left(t_n,\xi,\omega_N\right)$ with respect to ω_N, to be zero. This additional requirements lead to, respectively, four and five impulses, and the related shaper are referred to as ZVDD (zero vibration and double derivative) and ZVDDD shaper (zero vibration and triple derivative) [13]. The time and the amplitude of the impulses are those reported in Table 1. The increase in the number of impulses causes an increase in the filter settling time in the ideal case.

Impulse i	t_i	***ZVD***	***ZVDD***	***ZVDDD***
1	0	$\frac{1}{1+\lambda+\lambda^2}$	$\frac{1}{1+3\lambda+3\lambda^2+\lambda^3}$	$\frac{1}{1+4\lambda+6\lambda^2+4\lambda^3+\lambda^4}$
2	π/ω_D	$\frac{\lambda}{1+\lambda+\lambda^2}$	$\frac{3\lambda}{1+3\lambda+3\lambda^2+\lambda^3}$	$\frac{4\lambda}{1+4\lambda+6\lambda^2+4\lambda^3+\lambda^4}$
3	$2\pi/\omega_D$	$\frac{\lambda^2}{1+\lambda+\lambda^2}$	$\frac{3\lambda^2}{1+3\lambda+3\lambda^2+\lambda^3}$	$\frac{6\lambda^2}{1+4\lambda+6\lambda^2+4\lambda^3+\lambda^4}$
4	$3\pi/\omega_D$	-	$\frac{\lambda^3}{1+3\lambda+3\lambda^2+\lambda^3}$	$\frac{4\lambda^3}{1+4\lambda+6\lambda^2+4\lambda^3+\lambda^4}$
5	$4\pi/\omega_D$	-	-	$\frac{\lambda^4}{1+4\lambda+6\lambda^2+4\lambda^3+\lambda^4}$

Table 1: Robust SBFs.

5 EXPERIMENTAL RESULTS

The experimental assessment of the method effectiveness is provided through an industrial load cell, and by comparing the settling time obtained with those of other state-of-the-art filters, which are often recognized as among the most effective in this kind of applications. The load cell is fixed on a quasi-rigid frame and is a strain-gauge single-point industrial load cell,

with range $\pm$ 15 kg and accuracy $\pm$0.2% of the full scale output. The load cell signal is conditioned and acquired through a 32 bit National Instrument board, recording the measured signal with a 2000 Hz sampling rate. A sample mass of 100 grams has been weighed and, in order assess the filter repeatability, the same test has been repeated 10 times to show both the mean values of the settling time and their standard deviations. A thorough investigation with different masses will be performed in future works.

A picture of the setup is provided in Figure 2 (some parts are masked with a gray square to hide some components of the commercial device). It is an industrial weigher, usually employed in multi-head weighing machines [5]. Besides the load cell, the device comprises a bucket rigidly coupled with the load cell itself, which collects the product to be weighed falling from above. The bucket, in turn, includes some leverages for opening and closing it, once the correct weight has been computed. The presence of such a mechanism, made through some kinematic pairs with clearance, introduces an interesting non-linear behavior in the weighing device that allows testing the SBF effectiveness and reliability in a severe test where the actual system deviates from the nominal model assumed for the filter synthesis.

Figure 3 shows the recorded load cell response in one of the tests, assumed as a sample. It clearly highlights the underdamped behavior (a value of ξ=0.05 has been estimated) and the large peak in the sensor measurement, due to the product impact with the weigher.

The results of just the three robust SBFs are discussed because the ZV is, in practice, ineffective. Indeed it does not tackle the frequency and damping uncertainty and shift due to the product drop. The ZVD, ZVDD and ZVDDD filters have been tuned by assuming the frequency of the empty load cell (i.e. ω_N=21.8 Hz) , to test the most severe case for these filters. An additional low-pass filter (2nd order Bessel filter with 45 Hz bandwidth) is also applied after the SBFs, just to remove quantization and electrical noise. The results obtained in a sample test are shown in Figure 4 for the three SBFs. It clearly proves that these novel filters provide a very effective and quick settling of the estimated weight within the accuracy threshold (which is for instance assumed in Figure 4 as $\pm$3 grams threshold about the exact weight).

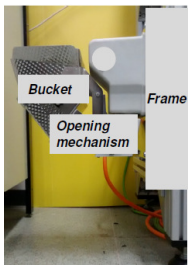


Figure 2: Picture of the experimental setup

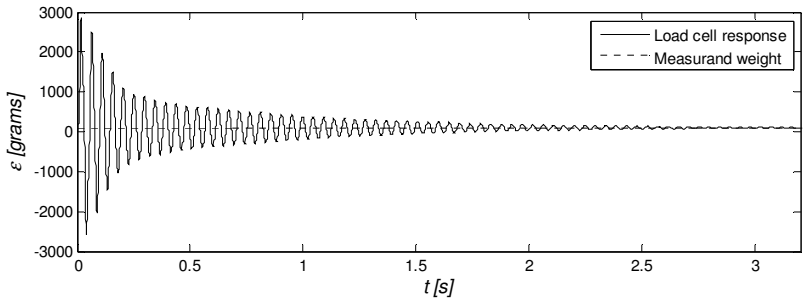


Figure 3: Load cell response to 100 grams to be weighed.

In order to evaluate more clearly the results, the comparison with other benchmark filters is proposed in Figure 5 and in Tables 2 and 3. Figure 5 shows the application of four different Bessel low-pass filters, which are often employed for load cell filtering because of their effectiveness to the same sample test shown in Figure 4. Different combination of filter order (2^{nd}, 4^{th} and 6^{th}) and bandwidth ω_B (which is parameterized with respect of the cell natural frequency ω_N) have been investigated, and a representative selection is shown.

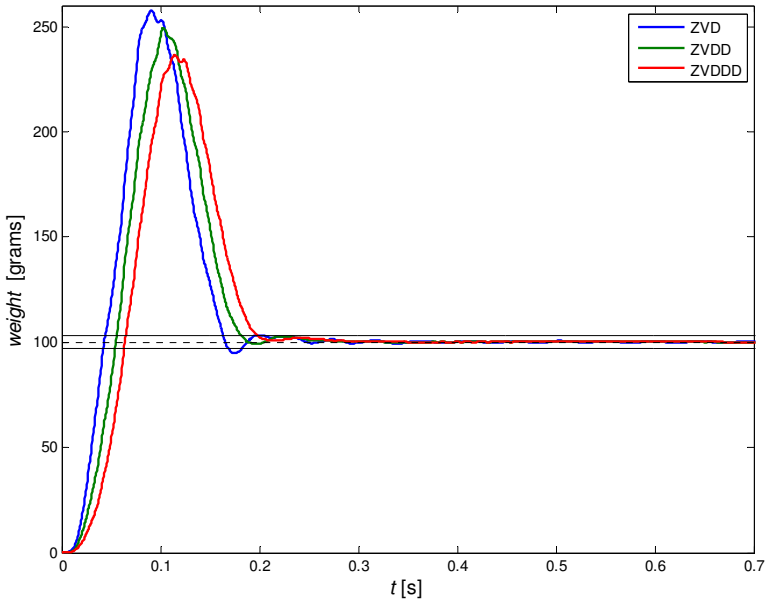


Figure 4: Filtered signals with three SBFs.

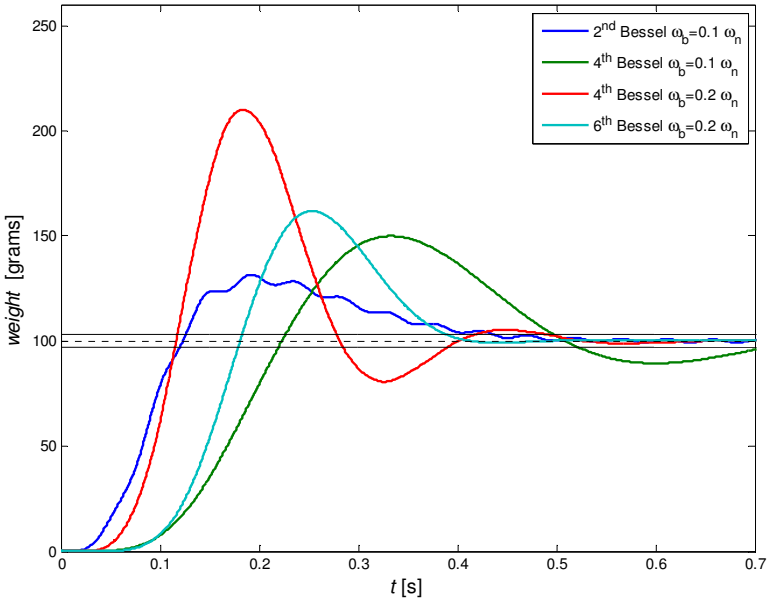


Figure 5: Filtered signals with four example of Bessel low-pass filters.

The mean value and the standard deviation (σ) of the settling time t_s in ten repetitions of the test are instead stated in Table 2 and in Table 3 in the cases of, respectively, $\pm$3 grams and $\pm$1 gram thresholds, for both the three SBFs and the four Bessel filters. The comparison of Figure 4 and 5 and the results in Tables 2 and 3, clearly highlight that SBFs allows settling the signal in a much shorter time, as a consequence of its very short rise time (leading to a significant filter overshoot) and its capability to compensate for the load cell natural frequency. This improvement is even greater if the smaller $\pm$1 gram threshold is required.

Settling time t_s	ZVD	ZVDD	ZVDDD	Bessel 4th $\omega_b=\omega_N*0.1$	Bessel 4th $\omega_b=\omega_N*0.2$	Bessel 6th $\omega_b=\omega_N*0.2$	Bessel 2nd $\omega_b=\omega_N*0.1$
Mean [s]	0.2750	0.2857	0.2978	0.5648	0.4755	0.4005	0.4475
σ [s]	0.0406	0.0424	0.0417	0.0145	0.0133	0.0360	0.0186

Table 2: 3-gram settling time: summary of the results.

Settling time t_s	ZVD	ZVDD	ZVDDD	Bessel 4th $\omega_b=\omega_N*0.1$	Bessel 4th $\omega_b=\omega_N*0.2$	Bessel 6th $\omega_b=\omega_N*0.2$	Bessel 2nd $\omega_b=\omega_N*0.1$
Mean [s]	0.3304	0.3179	0.3324	0.6151	0.5716	0.4779	0.5738
σ [s]	0.0376	0.0401	0.0373	0.0142	0.0394	0.0560	0.0319

Table 3: 1-gram settling time: summary of the results.

6 CONCLUSIONS

A novel model-based filtering technique for load cells is proposed in this work. The technique takes advantage of the idea of the Input Shaping (IS), which has been developed for the optimal planning of command position references in flexible systems (e.g. manoeuvring of overhead cranes). The shapers, which are adopted to avoid load oscillation in flexible systems, are here re-interpreted as filters to be convolved with the load cell measured output signals, rather than being employed to perform a physical modification of the crane motion in term of trajectory or exerted force (i.e. of the input exciting the system).

The filters obtained, referred to as Shaper-Based Filters (SBF), are based on the convolution of the load cell signal with a sequence of a few impulses (typically from 2 to 5 impulses). The amplitudes and the instants of application of such impulses are computed, on the basis of the system dynamic model, of the level of admissible residual oscillation in the steady-state filtered signal, and of the desired robustness. This filter structure also ensures ease of implementation, which makes SBFs well suited for industrial applications.

The effectiveness of the SBFs has been proved experimentally, by applying them to an industrial load cell and by comparing their performances with those provided by some low-pass filters most typically employed. The analysis of the settling time shows that SBFs outperform the other benchmark filters, by requiring shorter settling time. Indeed, their synthesis just relies on a few design specifications expressed in the time domain which allow a short rise time and an effective compensation of the load cell underdamped dynamics.

Among the three different robust SBF techniques experimentally tested, similar performances are obtained, by demonstrating that also the ZVD has adequate degree of robustness.

Besides being effective and requiring a small computational effort, the proposed SBFs are easy to be tuned. Indeed, just the load cell frequency and damping factor should be estimated with a reasonable degree of accuracy by taking advantage of some straightforward state-of-

the-art techniques based on the impulse or step response analysis. Therefore, no time-consuming trial-and-error tuning should be performed, as it is often the case for other filters.

ACKNOWLEDGNMENT

The authors wish to acknowledge the technical support of PFM Packaging Machinery S.p.A.

REFERENCES

[1] M. Jafaripanah and B.M. Al-Hashimi, Application of analog adaptive filters for dynamic sensor compensation. *IEEE Transactions on Instrumentation and Measurement* **54**, 245-251, 2005.

[2] W.J. Shi, N.M. White and J.E. Brignell, Adaptive filters in load cell response correction. *Sensors and Actuators A:Physical*, **37-38**, 280-285, 1993.

[3] J. Piskorowski and T. Barcinski, Dynamic compensation of load cell response: a time-varying approach. *Mechanical Systems and Signal Processing*. 22, 1694-1704, 2008.

[4] M. Halimic and W. Balachandran, Kalman filter for dynamic weighing system. *Proceedings of the IEEE International Symposium on Industrial Electronics*, Athens, 787-791, 1995.

[5] G. Boschetti, R. Caracciolo, D. Richiedei and A. Trevisani, Model-based dynamic compensation of load cell response in weighing machines affected by environmental vibrations. *Mechanical Systems and Signal Processing*, **34 (1)**, 116-130, 2013.

[6] S.M.T. Alhoseyni, A. Yasin and N.M. White, The application of artificial neural network to intelligent weighing systems. *Science, Measurement and Technology, IEE Proceedings*, **146**, 265-269, 1999.

[7] W. Hernandez, Improving the response of a load cell by using optimal filtering recursive least-squares (RLS) lattice algorithm to perform adaptive filtering. *Sensors*, **6**, 697-711, 2006.

[8] P. Pietrzak, Fast filtration method for static automatic catchweighing instruments using a nonstationary filter. *Metrology and Measurement System*, **16**, 669-676, 2009.

[9] R. Kaszynski and J. Piskorowski, Selected structures of filters with time-varying parameters. *IEEE Transaction Instrumentation and Measurement*, **56 (6)**, 2338–2345, 2007.

[10] P.Pietrzak, M. Meller and M. Niedźwiecki, Dynamic mass measurement in checkweighers using a discrete time-variant low-pass filter. *Mechanical Systems and Signal Processing*, **48 (1)**, 67-76, 2014.

[11] N.C. Singer and W.P. Seering, Preshaping Command Inputs to Reduce System Vibration, *ASME Journal of Dynamic Systems, Measurement, and Control*, **112,** 76-82, 1990.

[12] N.C. Singer and W.P. Seering, Design and Comparison of Command Shaping Methods for Controlling Residual Vibration, *Proceedings of the IEEE International Conference on Robotics and Automation*, Scottsdale, 888-893, 1989.

[13] J. Vaughan, A. Yano and W. Singhose, Comparison of robust input shapers. *Journal of Sound and Vibration*, **315 (4)**, 797-815, 2008.

11th International Conference on Engineering Vibration
Ljubljana, Slovenia, 7–10 September 2015

INFLUENCES OF EXTERNAL VIBRATION ON PRECISION MACHINES - THEORETICAL AND EXPERIMENTAL INVESTIGATIONS

Isabel Husung[1], **Bernd Fiedler**[1], **Erik Gerlach**[1], **Klaus Zimmermann**[1]

[1]Technische Universität Ilmenau, Department of Mechanical Engineering
isabel.husung@tu-ilmenau.de
{bernd.fiedler,erik.gerlach,klaus.zimmermann}@tu-ilmenau.de

Keywords: precision machines, external vibration, vibration isolation, vibration measurement, machine hook-up.

Abstract. *The investigations in the paper concern the optimal setup of high precision machines, working in nanometer dimensions. The objective is the optimization of the complete system in terms of dynamical behavior, especially in the case of external vibrations. Methods of multi-body system dynamics may be used for parameter estimation and for the analysis of the dynamics of the machine and their modules, respectively. To guarantee optimal working conditions, environmental influences (e.g. vibrations, airflow, temperature variations) acting on the machines need to be minimized. Therefore the analysis of the problems of active and passive vibration isolation is necessary. As the occurring vibrations, induced from the environment to the machine, are in the focus of investigations, the results of measurements (machines at different locations) of the vibration velocity are introduced for selected measuring points from the ground to the top of the machine. The identified amplitudes of the vibration velocity at the laboratory floor are mostly larger than permitted by the vibration criteria for nanotechnology facilities, defined in NIST A (U.S. National Institute of Standards and Technology), which makes additional vibration isolation indispensable. The design of most devices to mount a machine (machine feet, vibration isolators, dampers) focuses on the vertical-direction and neglects the effects of vibrations in the horizontal plane, while ponderable vibrations in this plane are traceable. To fulfill the requirements for high dynamic positioning and measuring machines, the conditions at the place of installation need to be considered.*

1 INTRODUCTION

Current and future high technologies demand increasing ranges of motion, extreme precision and high positioning velocities. Machines, fulfilling this extreme requirements, are highly sensitive against disturbances, such as vibration, noise, airflow and fluctuation of temperature. This disturbances originate from either external or internal influences. To assure the aimed accuracy of precision machines they need to be protected from this disturbances, or - at least - the influence of the disturbances has to be reduced. Besides design measures, carried out at the machine itself, the valid dimensioning of the hook-up of the machine is important at this point.

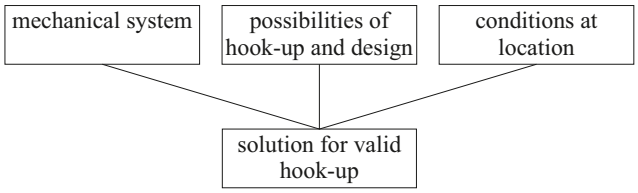


Figure 1: Aspects for an optimal hook up.

The protection from airflow or fluctuations of temperature may be achieved by placing the machine within a appropriate cabin. Concentrating on the protection of precision machines from external vibrations, several aspects have to be regarded (Figure 1):

- The dynamical behavior of the machine as mechanical system
- The conditions at the location, where the machine is placed
- The possibilities, which are available to reduce the effects from external vibrations on the machine or to protect the machine from external vibrations (damp and / or isolate)

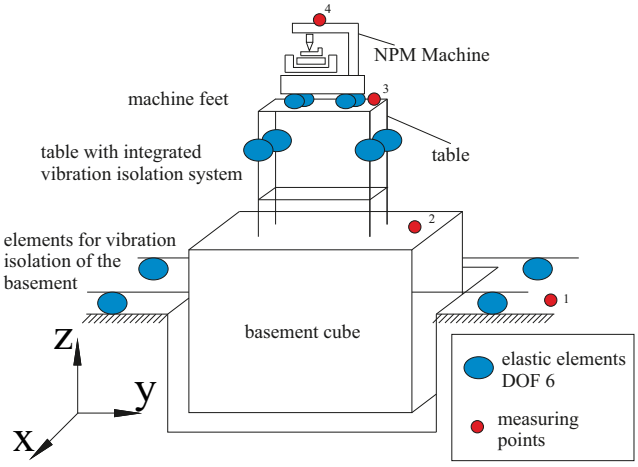


Figure 2: Hook up - system with three arrays of elastic elements.

Typical measures of vibration isolation are damper-spring-feet to mount the machine, tables with integrated active or passive vibration isolation systems or specially isolated - self-nivelling basements. Options of the design of machine hook up with respect to vibration control and matters of vibration analysis themselves are discussed in literature, like [1] and [2]. Figure 2 shows a sketch of a possible hook up system for a machine, assuming all named measures are realised. In this case, three additional arrays of elastic elements are implemented.

2 CONSIDERATION OF ACCEPTABLE DISTURBANCES

Research on the matter of optimal conditions for precision machines led to the formulation of vibration criteria for precision machines in NIST-A (U.S. National Institute of Standards and Technology, Figure 3). The criteria limit the allowed amplitudes of vibration velocity vs. frequency in vertical direction at the laboratory floor. This criteria are very tough and not satisfied at all laboratory. Therefore additional vibration isolation measures need to be taken.

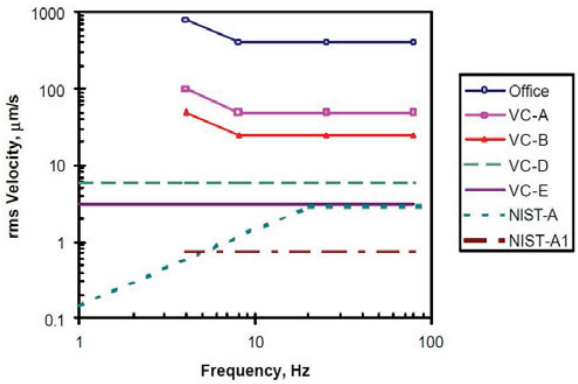


Figure 3: Vibration criteria defined in [3].

Presuming, precision machines being put up only at locations with a minimum dynamical load, for the process of dimensioning the vibration isolation systems, the identification of relevant vibrations is essential. Relevant vibrations course disturbances at the working point of the machine, such as displacements or fluctuations of contact-forces, which lead to insufficient working results. To narrow down acceptable displacements, simple geometric analysis are sufficing. To identify relevant vibrations, several methods may be used [4]. For the detection of critical frequencies FEM-models of single parts or modules should be used, running modal- and transient-analysis as well as simulations with defined vibration stimulation. MBS-models serve well considering the dynamical behavior of the whole system [5, 9], including the hook-up of the machine, which may add up to three arrays of elastic elements as introduced.

3 NPM MACHINES AS AN EXAMPLE OF PRECISION MACHINES

During the detailed discussion of necessary investigations for the selection of a valid set-up, the Nanopositioning and Nanomeasuring Machine (NPM Machine) serves as an example of precision machines. The NPM Machine allows the measurement of micro- and nanostructures with sub nanometre resolution in a measuring range of 25 x 25 x 5 mm^3. The concept of the NPM Machine bases on fibre coupled laser interferometers, fixed on a metrological frame. The

interferometers are arranged, allowing Abbe error free measurements in all measuring axes (Figure 4). The test objects are placed upon a 3D-precision stage, which is positioned in the three axis through translational movement. Besides the minimization of the length offset between the measuring axis and the normal axis, an additional angular measurement allows detection of angular deviations of the three guiding axis of the stage. [6, 7]

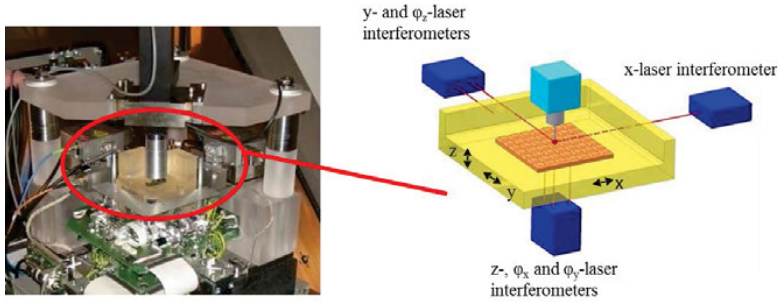


Figure 4: Working principle of the NPM Machine.

4 THEORETICAL CONSIDERATIONS FOR NPM MACHINES

In case of the example NPM Machine, considering the working principle of the machine, vibration stimulation coursing any relative movement of the three laser interferometers and the 3D-precision stage would lessen the accuracy of the machine. After defining a maximum acceptable vertical deviation of the laser beam at the measuring point, the determination of permissible displacements and angular deviations of the laser interferometers is possible, following the sketch in Figure 5. Assuming the laser interferometers as rigid bodys for this consideration.

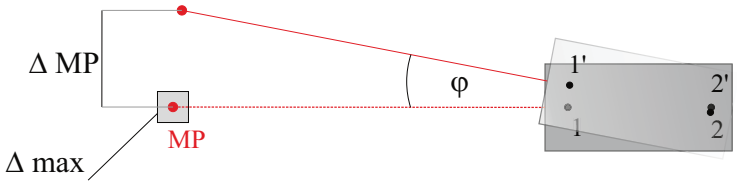


Figure 5: Displacement and angular deviation of Laser Interferometer. [8]

The thus gained information about the allowed range of position deviations of the laser interferometers may afterwords be used, interpreting the analysis of a FEM-model of the metrological frame. As the laser interferometers are fixed upon the metrological frame, the evaluation of the position of certain knots of the FEM-Model, after running modal and transient analysis, may provide information about critical frequencies for vibration stimulation at the bearings of the metrological frame. Data for the simulation of defined vibration stimulation of the FEM-model are gained from measurements at the location, where the machine is placed, or from results of other dynamical analysis. Analysis of MBS-models of the hook up provide information of the dynamical load at the bearing of the metrological frame, caused by vibration stimulation at the

basement. They also offer the possibility of evaluating the influence of parametervariations of the hook up-elements, seeking an optimization of the hook up.

5 INTRODUCTION OF EXEMPLARY EXPERIMENTAL RESULTS

In addition to the introduced theoretical considerations, experimental studies of vibrations provide information of the existing dynamic load at the location as well as information of the dynamic behavior of the whole system. Measuring points and measuriung equipment are chosen, depending on the seeked information. Concentrating on external vibration stimulation of precision machines, following the vibration criteria in Figure 3, the measurement of vibration velocity is indicated, paying attention especially to the lower frequencies. The following results of vibration velocity measurements were obtained by use of geophones as sensors (Figure 6). The measurements were run for NPM Machines, at different locations with varying hook up designs. The chosen measuring points are marked red in Figure 2 - depending on the layout of the hook up MP 2 not always existed. MP 1 at the ground provides information of occurring external vibrations, while MP 2 to 4 provide information of how the vibration pursue through the system.

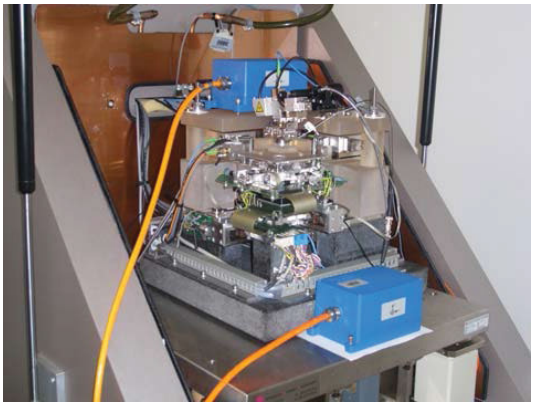


Figure 6: Geophones at MP 3 and MP 4.

Figure 7 shows exemplary the spectrum of the velocity in vertical direction, gained from measurements run at MP 1 at three locations. Regarding the criteria introduced in Figure 3 only location 2 is fulfilling the requirements. At locations 1 and 3 additional measures for the protection from external vibration excitation are necessary, while at location 2 the implementation of vibration isolation systems may concentrate on the reduction of self-induced vibrations.

To investigate, how vibration pursue through complex hook up structures, the following results were obtained from measurements, run at a NPM Machine with a hook up containing three arrays of elastic elements. The tested NPM Machine was mounted by the use of elastomer-feet upon a table top with an integrated, pneumatic vibration isolation system, which was placed upon a pneumatic isolated basement block.

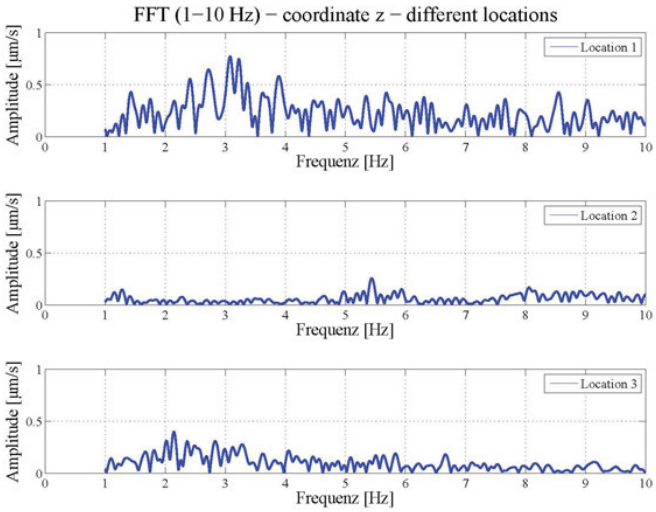


Figure 7: FFT of velocity vs. time in z-direction at three locations.

5.1 MEASUREMENTS AT STATIONARY NPM-MACHINE

First measurements were run, on an activated, stationary NPM Machine (Position of 3D-precision stage held actively by controlled driving elements), to avoid self induced vibration during the positioning process. To assure the working accuracy of the NPM Machine, vibration phenomenon close to the working point are of interest.

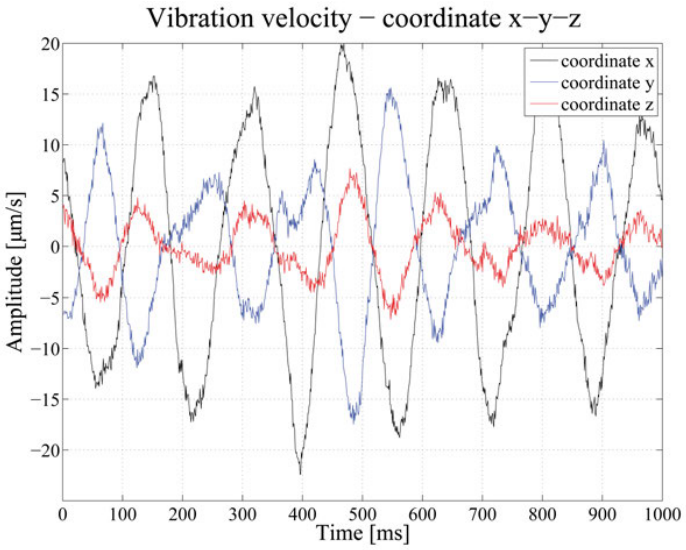


Figure 8: Vibration velocity vs. time at MP 4 in all directions.

The vibration velocity vs. time at the metrological frame (MP 4) is shown in Figure 8. As expected, with approximately 6 Hz, a lower frequency is dominating the excited vibrations. The amplitudes of the vibration velocity are bigger in x- and y- direction, than in z- direction. Geometric reasons (vertical distances of MP 4 and center of mass) and vibration isolation tools, concentrating on the vertical direction, may lead to this effect.

As the biggest amplitudes at MP 4 arose for the x- direction, the following diagrams concentrate on vibration velocities in this direction. Figure 9 presents the vibration velocity vs. time in x- direction at the four measuring points. The amplitudes becoming larger from ground to metrological frame. The biggest change in amplitudes can be observed from MP 3 to MP 4. Esteeming the low stiffness of the elastomer-feet to be the reason for this amplification, this feet were replaced by steel-blocks. A comparison of the vibration velocity vs. time in x- direction for the different machine feet at MP 3 and MP 4 is presented in Figure 10 The effect on the amplitudes at MP 4 is quite obvious, while at MP 3 no ponderable effects arise.

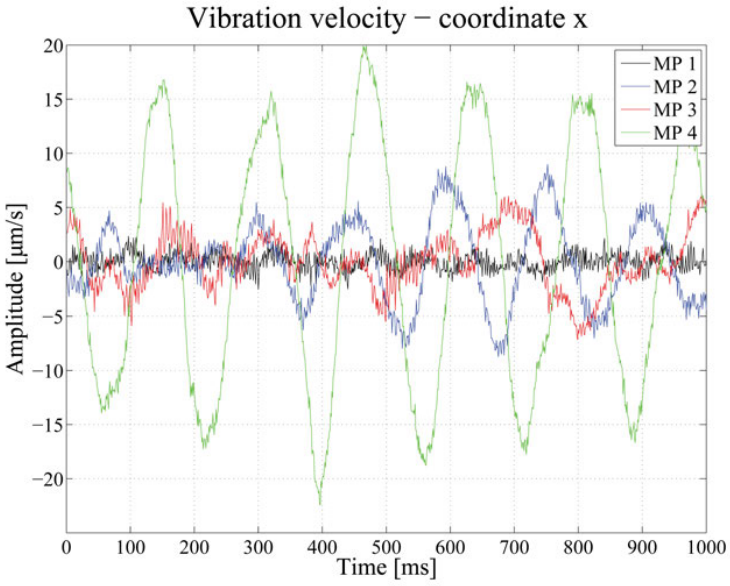


Figure 9: Vibration velocity vs. time in x-direction for MP 1 to MP 4.

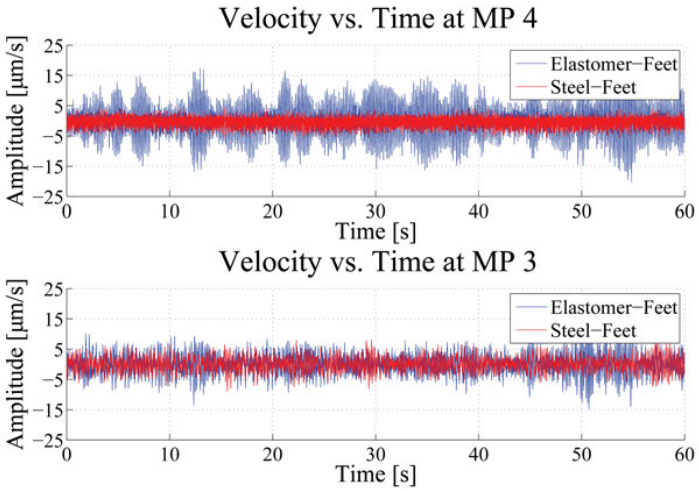


Figure 10: Comparison of vibration velocity vs. time at MP 3 and MP 4 for steel- and elastomerfeet, x-direction.

5.2 MEASUREMENTS AT NPM-MACHINE DURING POSITIONING PROCESS

The effects of self induced vibrations of course cant be neglected. To obtain information of the dynamical behavior of the whole system, containing machine and hook up, through experimental analysis, a simple positioning routine was created. The 3D-precision stage was to follow a meandering path as shown in Figure 11, with a velocity of 2,5 mm/s - stopping at the turning points.

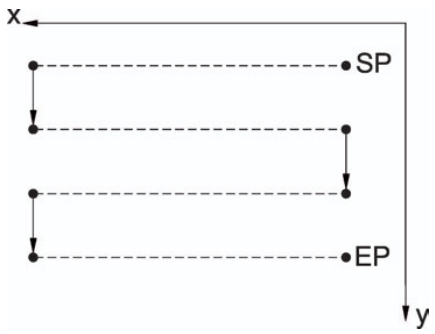


Figure 11: Scetch of the programmed movement of the 3D-precision stage.

Figure 12 again shows the comparison of vibration velocity vs. time for elastomer-feet and steel-feet at MP 4. Once, pictured in the upper diagram, for the stationary NPM Machine an once, pictured in the lower diagram, for the machine, following the introduced meandering path. It can be detected, that the positive effects of the steel-feet for the stationary NPM Machine, dont

become true for the moving machine. The damping properties of the elastomer-feet are much more effective, to reduce excitations during the positioning process.

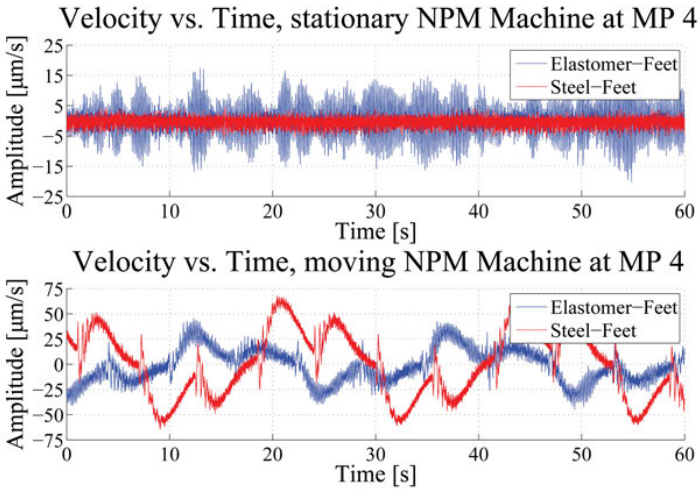


Figure 12: Comparison of vibration velocity vs. time, stationary - moving machine, MP 4, x-direction.

6 CONCLUSIONS AND OUTLOOK

To investigate the influence of external vibration excitation on precision machines both, theoretical and experimental methods, may be used. Theoretical investigations can be done analytically and numerically, where FEM and MBS are valid methods. The NPM Machines served as an example of precision machines, to discuss necessary investigations. Some results of experimental analysis were introduced. Amongst the most important conclusions of the results is the finding, that concentrating only on vibrations in vertical direction is not sufficient. While vibration criteria are formulated only for the vertical direction, the biggest amplitudes may be observed in the horizontal plane. As most available vibration isolation systems also concentrate on the vertical direction, often problems occure. One of the most challanging tasks is to find hook up solutions, protecting from external excitation as well as from internal excitation.

ACKNOWLEDGEMENTS The project was supported by the collaborative research center 622 Nanopositionier- und Nanomessmaschinen, forwarded by the German Research Foundation (DFG).

REFERENCES

[1] Dresig, H.; Holzweiszig, F. *Maschinendynamik*, Springer-Verlag 2005, 6. Auflage, ISBN 3-540-22546-3

[2] Beltran-Carbajal, F. *Vibration Analysis and Control - New Trends and Developments*, InTech 2011, ISBN 978-953-307-433-7

[3] Amick, H.; Gordon, C. *Buildings for Advanced Technologies.*, Workshop II, Mesa Arizona, 2004

[4] Fiedler, B.; Gerlach, E.; Husung, I.; Zeidis, I.; Zimmermann, K.; Füssl, R.; Manske, E.; Hausotte, T.; Theska, R. *Positioning with nanometre precision requires a high tech Nanopositioning and Nanomeasuring Machine and an optimal machine setup*, 58th ILMENAU SCIENTIFIC COLLOQUIUM, Ilmenau, 2014, urn:nbn:de:gbv:ilm1-2014iwk-029:6

[5] Gerlach, E.; Zimmermann, K; Oberthür, S.; Tröbs, A. *Simulating the dynamics of Nanopositioning and Nanomeasuring Machines using methods of multi-body system dynamics*, 6th EUROSIM Congress on Modelling and Simulation, Ljubljana, 2007

[6] Jäger, G.; Manske, E.; Hausotte, T.; Büchner, H.-J. *The metrological basis and operation of nanopositioning and nanomeasuring machine NMM-1*, Technisches Messen, 5, 2009, pp. 227 234.

[7] Manske, E.; Jäger, G.; Hausotte, T.; Fül, R. *Recent developments and challenges of nanopositioning and nanomeasuring technology.* , Measurement Science and Technology, Vol. 23, 2012.

[8] Petryanina, A. *FEM-Betrachtung des dynamischen Verhaltens des metrologischen Rahmens der Nanopositionier und Nanomessmaschine*, Master-Thesis, Technisches Universität Ilmenau, 2014

[9] Tröbs, A. *Ein Beitrag zur Mehrkörperdynamik-Simulation von Nanopositionier- und Nanomessmaschinen mittels spezifischer Modellelemente*, PhD-Thesis, Technisches Universität Ilmenau, 2010

International Conference on Engineering Vibration
Ljubljana, Slovenia, 7-10 September 2015

AXIAL BEHAVIOR OF SELF-COMPACTING, SELF-STRESSING AND HIGH STRENGTH CONCRETE FILLED STEEL TUBE

Lihua Xu[1], Yushan Gu*[1], Yin Chi[1]

[1]School of Civil Engineering, Wuhan University, WuChang, 430072, China
xulihua@whu.edu.cnA
yushanjoanna@hotmail.com
yin.chi@whu.edu.cn

Keywords: Concrete Filled Steel Tube, Self-stress, Short Columns, Axial Behavior

Abstract. *The concrete filled steel tube (CFST) components are gaining increasing applications in practical engineering. However, the difficulties in tamping after pouring, and the decrease of straining force caused by concrete creep and shrinkage are needed to be solved. The proposed composite structure of self-compacting, self-stressing and high strength CFST is aimed at this problem. This paper attempts to explore the mechanical performance of self-stressing CFST short columns under axial compression. The expanding agent was added to form the self-compacting, self-stressing and high strength CFST columns. The influence of the self-stress on the axial behavior of CFST short columns was addressed. The main variables considered were the self-stress value, the strength of concrete as well as the thickness of steel tube. The results showed that the ultimate strengths of all the CFST columns were invariably improved due to the contribution of self-stress, high strength of concrete and thick steel tube. The ductility of self-compacting, self-stressing and high strength CFST short columns can also be enhanced by high confining factor. Subsequently, predictive equations for ultimate bearing capacity of self-compacting, self-stressing and high strength CFST short columns were developed, which can serve as a reference for further analytical study of CFST and provide a foundation for real practical applications.*

1 INTRODUCTION

With the advantages of high bearing capacity, good plasticity， good ductility and low cost, concrete filled steel tubes(CFSTs) have been widely used in the construction. CFST columns combine the best characteristics of both concrete and steel tube. What's more, the straining force provided by steel tube makes the core concrete in three-dimensional pressure, which helps improve the mechanical performance of the columns. However, the difficulty in tamping after pouring exists, especially in large-scale structures. So as to guarantee the quality of concrete, self-compacting concrete was adopted in the CFST structures. The previous research showed that the self-compacting concrete is especially suitable for the position that difficult to placing, and the comprehensive economic benefits are remarkable[1]. Zhang et al.[2] conducted tests on self-compacting high performance concrete, and found that the mechanical performance of self-compacting concrete is fairly stable, and the aggregates were evenly distributed.

When the CFST column is subject to small axial load, the confinement can be ignored because of the different poison ratio of the core concrete and steel tube[3–6]. As the load increases, the core concrete expands faster than the steel tube. Only when the deformation of core concrete catches up with that of steel tube, the confinement appeared. In order to make full use of the confinement provided by steel tube, the self-stressing CFST was proposed, in which the expansive core concrete was adopted to compensate for the concrete shrinkage and creep. Wang et al.[11] did research on the creep of expansion concrete in CFST, and it was observed that the concrete curing conditions in steel tube was in favor of concrete hydration, which restrained the creep of concrete. Shang[12] compared the hydrated products cured in three constraints and free maintenance, and found that the cement structure was denser in three constraints conditions. Dai et al.[13] proposed a finite element analysis model considering concrete creep and all kinds of boundary conditions. The proposal is based on the relationship of deformation compatibility and equilibrium condition according to the experimental results, and it is a good means to analysis self-stressing concrete creep.

In the past, there were a large number of studies on compressive behavior of CFST columns and beams[14–18], but the studies on self-compacting and self-stressing CFST were not much. Wang et al.[19] conducted the short-term and long-term mechanical performance experiments on self-stressing CFST fabricated by two different means. The results showed that long-term mechanical performance is quite different from the short-term one, and tended to be unstable in the end. Xu[20] studied the initial stress effect on CFST short and long columns, and the results showed that the relationship of improvement of ultimate bearing capacity to initial stress ratio (initial stress value/ strength of concrete) can be expressed as quadratic parabola. Chang[21] proposed a constitutive relationship for the core concrete of self-stressing CFST column under axial load by analysis-separation method, which provided a foundation for real practical applications.

However, all the previous work focused on the ordinary strength CFST columns. In order to combine the advantages of self-compacting concrete, self-stressing concrete and the requirements for high strength concrete, the research on axial behavior of CFST short columns with self-compacting, self-stressing and high strength is studied in this paper.

2 EXPERIMENTAL PROGRAM

2.1 Materials and Mix Proportions

In this experimental research, 7 branches of concrete were adopted. I and II represent the target self-stress is about 2 MPa and 3 MPa, respectively. Ordinary Portland cement (P.O 52.5)

was used as the binder for the mixtures, and the broken stones with size < 20mm were adopted as the coarse aggregate. In order to produce the self-compacting concrete, I fly ash and mineral powder were added in the mix, which contribute to improve the flowability of the concrete. A high efficient expansion agent manufactured in China Academy of Building Research was used in the mix design. The specific mix proportion is shown in Table 1. The slump of fresh concrete was 24cm, the slump flow approximated to 60mm, and the segregation phenomenon was not observed.

All circular steel tubes used in this test have an outside diameter (D) of 159mm and the length (l) of all the short columns are 477mm. Three kinds of thickness (t) of steel tube are selected, including 3.14mm, 3.92mm and 4.68mm. The parameters were measured by tensile test on the method by Steel and Steel Products-Location and Preparation of Test Pieces for Mechanical Testing (GB/T2975-1998) [23], and three samples were tested on each kind of thickness. The mechanical performance of steel tubes is shown in Table 2.

Sample ID	52.5MPa concrete	I Fly ash	Silica fume	Tiny beads	Mineral powder	Expanding agent	River sands	Broken stones	Water	Water reducer/ %
C50	336	84	--	56	84	--	750	950	150	2.0
C50 I	336	28	--	56	84	56	750	950	150	2.0
C50 II	336	30	--	56	60	78	750	950	146	2.0
C60 I	380	86	40	--	34	60	750	950	138	2.3
C60 II	380	86	40	--	22	72	750	950	138	2.3
C70 I	410	100	48	--	10	62	750	950	135	2.8
C70 II	410	100	46	--	--	74	750	950	135	2.8

Table 1:The proportions of concrete mix.

Sample ID	Steel ratio	Yield strength f_y/MPa	Ultimate strength f_u/MPa	Elasticity modulus E_s/MPa	Poisson ratio	Ductility
159×3.14	0.084	345.54	464.31	1.99×10^5	0.271	24.5%
159×3.92	0.106	367.35	484.96	2.03×10^5	0.275	24.7%
159×4.68	0.129	346.79	455.27	2.05×10^5	0.286	24.2%

Table 2: The mechanical performance of steel tube

2.2 Specimens

In this experiment, 7 sets of 21 specimens were fabricated. The main variables considered were the strength of concrete, the self-stress value as well as the thickness of steel tube. The strengths of concrete include 50 MPa, 60 MPa and 70 MPa, and the self-stress of core concrete ranges from 1.83 to 3.24Mpa. Three kinds of thickness (t) of steel tube are selected, including 3.14mm, 3.92mm and 4.68mm.

The steel plates of 5mm were welded at the bottom of the steel tube to contain the concrete during casting, as well as two steel handles in the upper part of the tube. The handles were set for easy lifting. The concrete was mixed by double-horizontal-shaft forced type concrete mixer, and was poured into the steel tube with the help of funnel. After the initial curdle of concrete, the tubes were sealed by the epoxy resin to prevent the moisture loss. The specimens were cured for 28 days before testing could be conducted. In order to obtain the self-stress value, the strain of the steel tube was measured after pouring, and lasted for the whole curing of 28 days. The specific parameters and bearing capacity measurements are shown in Table 3.

Sample ID	$D\times t\times l$	Self-stress value	confining factor	f_y /*MPa*	f_c /*MPa*	Experimental results/ *kN*	The standard value/ *kN*	Ratio
T2L1C1S1-1	159×3.92×477	1.98	0.737	367.35	52.88	2376	1988	1.20
T2L1C1S2-2	159×3.92×477	3.24	0.737	367.35	53.20	2424	2000	1.21
T2L1C2S1-3	159×3.92×477	1.88	0.614	367.35	63.64	2506	2164	1.16
T2L1C3S1-4	159×3.92×477	1.83	0.542	367.35	72.08	2613	2300	1.14
T1L1C1S1-5	159×3.14×477	2.13	0.547	345.54	52.88	2055	1730	1.19
T3L1C1S1-6	159×4.68×477	2.32	0.844	346.79	52.88	2476	2109	1.17
T2L1C1-7	159×3.92×477	0.00	0.584	367.35	54.59	1825	1809	1.01

Table.3: The specific parameters of specimens and the bearing capacity measurements.

Note: *D* is the outside diameter of the steel tube, *t*, *l* represent the thickness and length of the tube. f_c is the compressive strength of cube concrete, f_y is the yield strength of steel tube.

2.3 Testing scheme

The axial compression test was performed under the 500t universal testing machine in Wuhan University. In these tests, monotone cascade loading method was adopted. At the initial stage, the load was divided into 1/12 of the estimated ultimate load as a grade load. When the load accumulated to 1/2 of the estimated ultimate load, each load division was reduced to 1/25 of the estimated ultimate load. Every grade load was lasted for 2 minutes to fully develop the deformation of the specimen. When the deformation of the specimen was too large so that it could not load further, the test would be stopped (normally, 300mm for axial displacement).

An extra steel plate was put on the top of the short columns to avoid the marginal local buckling caused by inconsistent stiffness. Two displacement transducers were placed to monitor the axial displacement of the specimens (shown in Figure 1). In order to get the exact strain of the columns, 8 strain gauges with size of 3×2mm were attached on the surface of the steel tubes at axial and circumferential directions respectively. The sampling frequency of Data acquisition system for the measuring device was set to 1Hz to ensure the

synchronization of data collection.

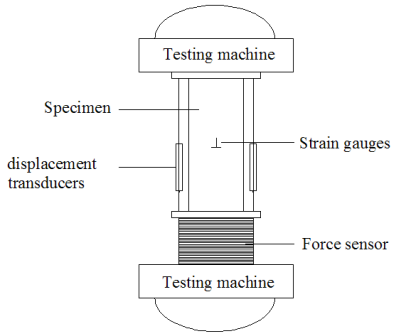


Figure 1: Testing setup.

3 TESTING RESULTS AND ANALYSIS

3.1 Experimental phenomenon and failure patterns

In the beginning 75% part of the loading no obvious deflection was observed. At that time, the maximum strain of the tube was about $1000\sim2000\times10^{-6}$ which meant the specimens were still in the elastic phase. With the loading increasing, the strain of core concrete increases. The average strain of the tube at the ultimate strength was about $2000\sim4000\times10^{-6}$, which represented the specimens were at the elastic-plastic phase. After the ultimate load, the local bucklings were observed. The load droped quickly at first, then tended to be stable in the end.

As shown in Figure 2, there were two kinds of failure patterns appeared in the test. The first one is shear failure (shown in Figure (a)), two local bucklings were observed and situated in the middle part of the specimen. The reason for this phenomenon is that the core concrete is damaged in shear manner. In the initial stage, the straining force provided by steel tube contributes to restrain the deformation. As the load increasing, the deformation developed and presented the shear failure pattern. However, the other kind of failure pattern appeared is the local buckling on the top part of the columns, as shown in Figure 2. (b). This phenomenon can be explained by marginal effect. The specimen in marginal part is more likely to deform when subject to axial load. In addition, it is hard to avoid the inconsistency of stiffness of the short columns, which leads to the uneven transfer of force.





(a) Shear Failure (b)Marginal local buckling

Figure 2: Failure mode.

3.2 Effect of self-stress

The experimental results of specimens 1, 2 and 5 are presented in Figure 3. From this figure, it can be observed that load-deformation curve of CFST with self-stressing, self-compacting and high strength is similar to the plain CFST, including three stages: elastic stage, elastic-plastic stage and plastic stage. The self-stress of core concrete is shown in Table 3, and the corresponding calculation method can be found in literature[21].

This figure shows us the results of specimens with different self-stress value, and it can be found that the self-stress helps enlarge the elastic phase, which improves the ultimate bearing capacity. The effect of self-stress is presented in the elastic stage mainly. Both the axial and hoop strain of steel tube are in tension state because of the initial self-stress. When subjected to the axial load, the stress turned from tension to compression state, which helps prolong the elastic phase. The other reason for this phenomenon is that the self-stress contributes to make the core concrete pressed in three dimensions, which improves the bearing capacity of the concrete. In addition, the reinforcing force contributed by steel tube helps to restrain and restrict the crack extension and propagation of the concrete in a certain degree.

However, it can also be concluded that the self-stress weakens the displacement ductility. Wang et al.[24] employed the formula $\mu_\Delta = \frac{\Delta_u}{\Delta_y}$, where Δ_u represented the nominal yield displacement and Δ_y was the displacement when load decreased to 85% of the ultimate load. According to this formula, the displacement ductility of self-stressing CFSTs is worse than the plain ones. The explanation is that the brittleness of self-stress concrete is enhanced due to the initial stress, which leads to rapid drop in bearing capacity.

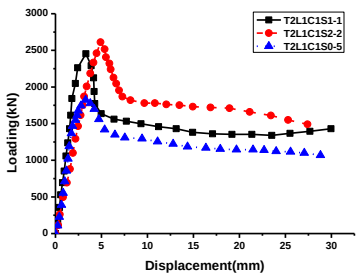


Figure 3: Effect of self-stress on specimens.

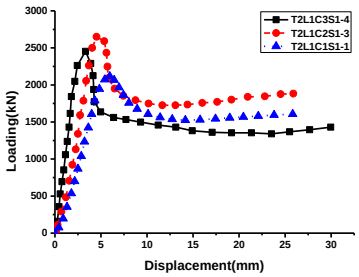


Figure 4: Effect of concrete strength on specimens.

3.3 Effect of concrete strength

Figure 4 presents the comparisons of specimens with different strength of concrete. According to this figure, it can be concluded that the strength of concrete plays an important role in the ultimate bearing capacity. With the strength of concrete increasing, the bearing capacity of the specimens is enhanced. Specimens 1, 3, 4 in this figure shares the similar self-stress value, but the bearing capacity is still affected by the concrete strength.

However, the ductility for high strength CFST is worse than the plain ones, which can be explained by the brittleness of the high-strength concrete. For specimen T2L1C3S1-4, the final bearing capacity drops to about 60% of the ultimate load. The shearing mechanism for self-compacting, self-stressing and high strength CFSTs are different[21] from the plain ones. For plain CFST, the coarse aggregate was not damaged, which provide a high friction force to bear the loading, while the coarse aggregate in high strength CFST was crushed in the end. What's more, the proportion of coarse aggregate is relatively small for self-compacting concrete. All of these factors lead to the degradation of ductility.

3.4 Effect of steel tube thickness

The same as the strength of concrete, the confining factor is also an important effect factor both on bearing capacity and ductility. The experimental results of specimens 1, 5, and 6 are shown in Figure 5 and the confining factor of which are 0.737, 0.547 and 0.844, respectively. According to the loading-deformation curve of specimen 6, the bearing capacity is enhanced due to the thicker steel tube. After the ultimate load, the bearing capacity tends to rise again in a certain degree, which is not observed in specimen 5. Therefore, the thicker steel tube can provide more straining force for core concrete to bear the loading. For specimen 5, the deformation ductility is about 1.65, while it is 2.26 for specimen 6. It can be inferred that the confining factor plays a positive role in improving the ductility.

Figure 6 shows the curve of load and strain in the middle section of the columns. The axial strain is presented on the left side, and the circumferential one is on the right. It is obviously shown that both the axial and circumferential ultimate strain is enhanced due to the increase of the thickness of steel tube. What's more, for specimen 6, the poison ratio is about 0.403, much larger than 0.286 (measured on steel tube samples, shown in Table 2). It can be concluded that the thicker steel tube provides more confining factor for short columns.

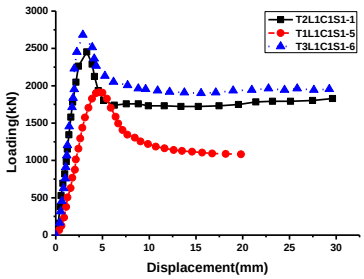


Figure 5: Effect of the thickness of steel tube on specimens.

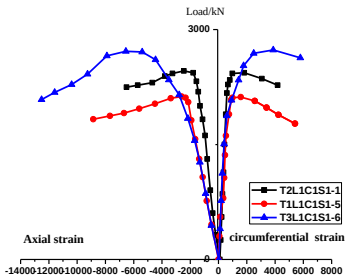


Figure 6: Load-strain curve of specimens with different thickness of steel tube.

4 AXIAL COMPRESSION BEARING CAPACITY CALCULATION

There are two common axial bearing capacity calculation equations mentioned in Technical specification for concrete-filled steel tubular structures (CECS 28:2012). One is proposed based on the limit analysis theory, and the other is founded on unification theory.

However, these two equations are both applied for the plain CFSTs. The bearing capacity calculation of self-stressing CFSTs has not been proposed in design specifications. Based on the limit analysis theory, a modified axial bearing capacity calculation of self-compacting, self-stressing and high strength CFSTs is proposed in this paper.

The axial bearing capacity of CFSTs can be described as:

$$N_0 = 0.9A_c f_c(1 + \alpha\theta) \tag{1}$$

$$\theta = \frac{A_s f_s}{A_c f_c} \tag{2}$$

where A_c, A_s represent the area of core concrete and steel tube. f_c, f_s is the axial compressive strength of core concrete and steel tube, respectively. α is selected as 1.8, which is related to the strength of concrete.

The comparison of experimental results and the calculated ones from specification are shown in Table 3. In order to take self-stress into account, the coefficient φ_s considering the function of self-stress will be included in the bearing capacity calculation equation. Self-stress level was come up with in literature[20], which represented the ratio of self-stress value and strength of concrete. Regression analysis was made on the experimental results (shown in Figure 7), and the equation including self-stress and the ratio of experimental results and standard calculated results can be described as:

$$N_{us} = \varphi_s N_0 \tag{3}$$

$$\varphi_s = 1.69 - 18.25\eta + 163.94\eta^2 \tag{4}$$

Where η represents the ratio of self-stress value and strength of concrete. The fitting results agree well with the experimental data, with the average value of 1.03 and standard deviation of 0.04.

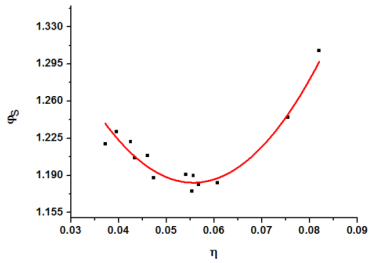


Figure 7:The Regression result of φ_s and η.

5 CONCLUSION

Based on the experimental results of 21 self-compacting, self-stressing, and high CFST short columns, the conclusions can be described as follows:

(1)The failure patterns of CFSTs with self-compacting, self-stressing and high strength are similar to the plain CFSTs. Two failure patterns appeared in the tests are shear failure and local buckling in the marginal part.

(2)The self-stress helps improve the bearing capacity of short columns, but weakens the ductility. The elastic phase can be enlarged to 80%-90% of the whole curve, which leads to the enhancement of bearing capacity. However, the brittleness of self-stress concrete is enhanced due to the initial stress, which leads to rapid drop in bearing capacity.

(3)The strength of concrete is the main factor that determines the axial behavior of self-compacting, self-stressing and high strength CFST short columns. However, the brittleness of concrete is still the reason that leads to the decrease in ductility.

(4) The thickness of steel tube is an important effect factor both on bearing capacity and ductility. The confining factor can improve the weakness in ductility in a certain degree, and the bearing capacity as well.

(4)In order to modify the axial bearing capacity calculation of CFSTs, the parameter φ_s considering self-stress and ratio of experimental results and standard calculated results is proposed. The modified calculation equation can serve as a reference for further analytical study of self-stress CFST and provide a foundation for real practical applications.

REFERENCES:

[1] Okamura H. Self-compacting High-Performance Concrete[J]. Concrete International, 1997,19(7):50-54.

[2] Zhang qing, Lian huizhen, Wang Ping. The evaluation method on construction performance of self-compacting hgih performance concrete. Application of high strength and high performance of concrete. (Proceedings of the third academic seminars.) 1998，10.

[3] Susantha KAS, Ge HB, Usami T. A capacity prediction procedure for concrete filled steel columns. J Earthquake Eng 2001;5(4):483-520.

[4] Shanmugam NE, Lakshmi B. State of the art report on steel-concrete composite columns. J Constr Steel Res 2001;57:1041-80.

[5] Johansson M. The efficienty of passive confinement in CFT columns. Steel Comp Struct 2002;2(5):37996.

[6] Sakino K, Nakahara H, Morino S, Nishiyama A. Behavior of centrally loaded concrete-filled steel-tube short columns. J Struct Eng 2004;130(2):180-8.

[7] Wang zhan, The creep of expansion concrete steel tube. Journal of Harbin engineering college. 1994,(6), 14-17.

[8] Shang Zuoqing. Research on mechanical behavior of self-stressing and self-compacting concrete filled steel tube columns. Ph.D thesis, Dalian, PR China,Dalian University of Technology; 2007.

[9] Experimental study on mechanical performance of steel fiber self-stressing concrete. Journal of building materials. 2001; 1-4(1):70-74.

[10] Elremaily A, Azizinamini A. Behavior and strength of circular concrete-filled tube columns. Journal of Constructional Steel Research 2002;58(12):1567 91.

[11] Ge HB, Usami T. Strength of concrete-filled thin-walled steel box columns. Journal of Constructional Steel Research 1994;30:607 12.

[12] Ge HB, Usami T. Cyclic tests of concrete filled steel box columns. Journal of Structural Engineering, ASCE 1996;122(8):1169 77.

[13] Kato B. Column curves of steel concrete composite members. Journal of Constructional Steel Research 1996;39(2):121 35.

[14] Amit H Varma, James M Ricles, Richard Sause, Le Wu Lu. Seismic behavior and modeling of high-strength composite concrete-filled steel tube (CFT) beam columns. Journal of Constructional Steel Research 2002;58:725 58.

[15] Wang Fangli, Wang Jiaquan, Xu Hewen, Li Jianzhi. Study on self-stressing CFST. Beijing: Journal of Beijing university of technology. 1998, June, 24(2).

[16] Xu Lei. Research on the design theory for self-stressing and self-compacting concrete filled steel tube column under axial load. Ph.D. thesis, Dalian, PR China, Dalian University of Technology, 2005.

[17] Chang Xu. Research on mechanical behavior of self-stressing and self-compacting concrete filled steel tube columns. Ph.D thesis, Dalian, PR China, Dalian University of Technology; 2008.

[18] Jiang Decheng. Research on mechanical behavior of Self-stressing and self-compacting Concrete Filled Steel Tube. Master thesis, Dalian, PR China, Dalian University of Technology; 2007.

[19] National Standard of the People's Republic of China. Location and Preparation of Test Pieces for Mechanical Test of Steel and Steel Products (GBT2975-1998). Beijing: China Standard Press, 1998 (in Chinese)

[20] Wang Qingxiang, Zhao Guofan, Lin Liyan, Experimental study on ductility of high strength concrte columns. Journal of building structures. 1995, 16(4): 22-31

International Conference on Engineering Vibration
Ljubljana, Slovenia, 7-10 September 2015

EFFECTS OF CENTER DISTANCE AND MICROGEOMETRY ON THE DYNAMIC BEHAVIOUR OF A SPUR GEAR PAIR

S. Shweiki[1,2], **A. Palermo**[1,2,3], **A. Toso**[1], **D. Mundo**[2], **W. Desmet**[3]

[1] Siemens Industry Software NV,
Interleuvenlaan 68, 3001 Leuven, BELGIUM

[2] University of Calabria, Department of Mechanical, Energy and Management Engineering (DIMEG), Ponte Pietro Bucci, 87036 Rende, ITALY

[3] KU Leuven, Department of Mechanical Engineering
Celestijnenlaan 300 B, B-3001, Heverlee, BELGIUM

Keywords: Gear dynamics, Transmission Error, Gear Profile Micro-modifications, Experimental Analysis.

Abstract. *Quietness and reliability, together with efficiency and lightweight design, are key requirements to compete in current mechanical industry. Within the latter, gearboxes play an important role as the usual choice to transmit mechanical power with high power density, especially when using cylindrical involute gears. Noise and vibration performance are strongly dominated by tooth microgeometry modifications. Typical modifications are applied along the profile and at the lead of the teeth. Profile modifications mainly compensate for tooth deflections, while lead modifications mainly compensate for angular misalignments. Both modification types yield optimal performance at a given operating condition (e.g. nominal transmitted torque under ideal alignment), minimizing the meshing excitation. One key operating condition for the gear pair is represented by the instantaneous center distance between the gears. Center distance variations affect mainly the pressure angle for the transmitted contact force, the total contact ratio and the active tooth height. Furthermore after a change in center distance, the contacting surfaces on the tooth flanks shift with respect to each other, which yields a mismatch with respect to the theoretical start for the tooth profile modifications.*

A precision gear test rig, where operating conditions can be varied and tightly controlled, is used in this paper to evaluate the effects of center distance variations on the dynamic behaviour of a spur pair of identical spur gears. The dynamic behaviour is analysed by measuring the Static Transmission Error (STE). Spectral analysis of the STE provides an indication of the internal excitation generated by gear meshing.

1 INTRODUCTION

In the field of geared transmission the dynamic behaviour of gears plays a central role in determining the quality of the transmission itself. Meshing gears are a dynamic excitation source for the transmission and for the structure in which the transmission is mounted [1]. Vibrations generated and transmitted to the structure cause noise and dynamic loads that propagate from the meshing teeth to the whole structure through the mechanical connections, affecting in this way the reliability of the transmission. Among the different dynamic excitations generated during gear meshing the Transmission Error (TE) is considered by the designer as the main excitation source for a transmission. Understanding the factors that affect it is crucial to enable a reliable design of the full transmission. The TE is defined as the difference between the angular position that the driven gear would assume if the meshing process would involve only perfect involute teeth and the actual position. Several factors such as tooth geometry, manufacturing and assembly errors [2] and effective working conditions defined in terms of transmitted load [3] and relative positions between the gears [4][5] influence the TE. Applied torque causes gear teeth to bend under load resulting in a kinematically non-conjugate tooth-profile contact. Deliberate tooth-profile microgeometry modifications influence the magnitude of the TE [6] as well, by partially compensating for teeth deflection under load. The torque transmitted by the gears generates also forces that deform the supporting shafts and the bearing housing, thus causing a relative displacement between the gears. If the case in which the two gear axes remain parallel is considered, the relative misalignment is intended as a variation in the center distance of the two gears. In this paper the effects of center distance variations and microgeometry modifications on the TE curve for a pair of identical spur gears are investigated. By using a precision gear test rig, TE curves are measured for different transmitted loads and for different center distance values. TE is measured at low speed and will be named Static Transmission Error (STE).
The outline of the paper is the following: section 2 describes the test rig used to test the gear in the different conditions. Section 3 provides a theoretical analysis of the effects of the center distance variation. Section 4 focuses on the experimental results. Conclusions are reported in the last section.

2 TEST RIG AND TEST GEAR PAIR SPECIFICATIONS

For the measurement campaign described in this paper a precision test rig, instrumented as to enable the experimental analysis of the dynamic behaviour of a pair cylindrical gears, has been used [7]. The CAD model of the test rig is shown in figure 1.
The test rig allows to measure different physical quantities related to the gear meshing under different and tightly controlled working conditions for the tested gears. The test rig, which has a power recirculation arrangement, consists of the two different parts shown in Figure 1. On the reaction side, a pair of helical gears, which are not intended to be tested, applies a reaction torque to the system. The test side hosts the gear pair to be tested. Both the reaction side and the test side are mounted on the same concrete base which provides a stable alignment reference for the two sides, and isolates the test side from the external vibrations while excitations coming from the reaction side are isolated by flywheels, long connecting shafts and elastomeric couplings.
Thanks to the possibility to install a large number of sensors, different physical quantities can be measured, both in dynamic and static conditions depending on the rotational speed.
All the measurements can be performed in a wide range of operating conditions, according to the specifications reported in table 1.

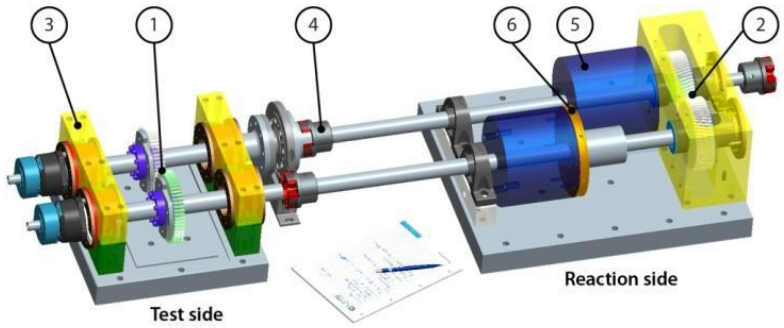


Figure 1: Three-dimensional representation of the test rig. 1. Test gears; 2. Reaction Gears; 3. Bearings support plates; 4. Flexible couplings; 5. Flywheels; 6. Clutch flange for preload.

Parameter	Range	Uncertainty
Speed	0 to 4500 rpm (0 to 75Hz)	Measured
Torque	0 to 500 Nm	± 0.05 %
Angular misalignments	0 to 2 mrad	0.1 mrad
Parallel misalignments	0 to 0.3 mm	0.020 mm

Table 1: Test rig specifications.

The gears are driven by an electric motor, of which the speed can be set by a frequency inverter. The torque transmitted by the gears can be changed by using calibrated weights that allow to apply an elastic rotational preload of the shafts, thus entrapping the desired torque value in the system. The relative position between the gears can be modified by rotating the eccentric bearing housing. In-phase rotation of the housing of the same shaft causes the gears to move in a parallel direction, while out-of-phase rotations impose an angular misalignment between the gears. Combined configurations are also possible within the allowed ranges.
The experimental TE curves are derived by directly measuring the angular displacements of the two shafts using digital encoders.
The design specifications for the test gears and for the reaction gears are reported in Table 2.

	Test Gears
Number of teeth	57
Normal module	2.60 mm
Normal pressure angle	20 deg
Tip diameter	154.50 mm
Root diameter	141.70 mm
Facewidth	23 mm
Normal circular tooth thickness at theoretical pitch circle	3.780 mm
Contact Ratio	1.456

Table 2: Gear specifications.

A grinding process according to ISO 1328 Quality 3 standard and an additional superfinishing process are performed on the teeth surface in order to reduce the broadband excitation due to surface finishing. The meshing stiffness is tuned by choosing adequate gear macro-geometry parameters.
Two different combinations of spur gears, with different amount of micro-geometry modifications applied on the teeth flanks are tested. The first pair consists of two unmodified gears where the tooth profile is the theoretical one with the exception of the manufacturing tolerances. The second gear pair consists of two gears with a global parabolic profile modification of 15 µm.

3 EFFECTS OF CENTER DISTANCE VARIATIONS

As discussed above several causes, such as elastic deformations of the supporting elements or manufacturing tolerances, concur to vary the nominal center distance between two gears.
The center distance variation brings the gears to operate in a different position from the nominal one, affecting in this way the amplitude of the STE. The teeth stiffness defined as the load needed to cause a certain displacement along the line of action of two gears varies substantially along the tooth height, with a non-linear dependency on the tooth shape.
The stiffness variation along the active flank of a tooth depends highly on the gear geometry. For the spur gears examined in this paper, FEM analysis performed along the tooth flank (figure. 2) shows a stiffness reduction up to 70% moving from the tooth root to the tip (figure. 3).

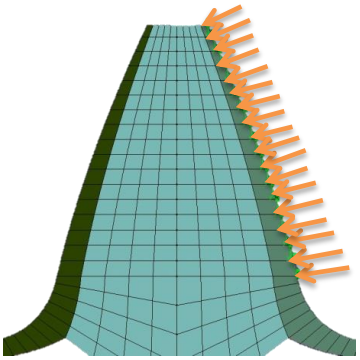


Figure 2: FE model used to compute tooth stiffness.

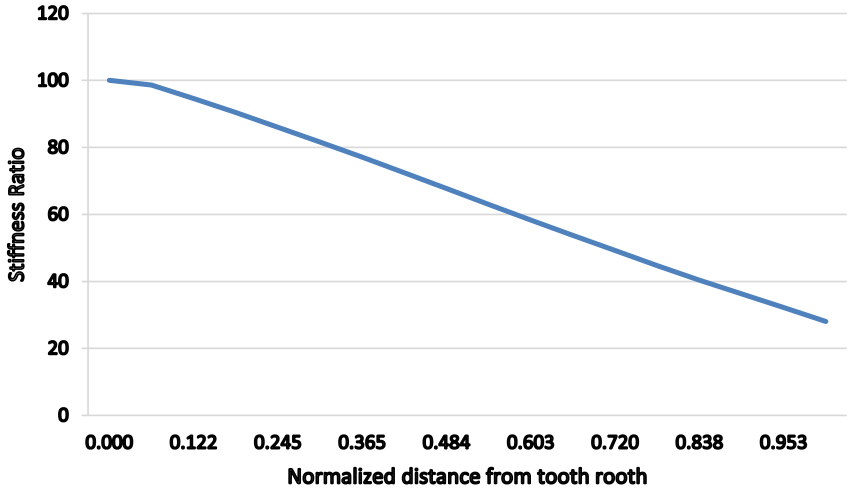


Figure 3: Tooth stiffness variation (100% at the stiffer point).

The effect due to the center distance variations is the pressure angle variation that in turn causes a change of the magnitude of the load acting on the teeth and of the ratio between its radial component F_r and its tangential component F_t (figure 4). The latter is responsible for the tooth deflection. Assuming a defined tooth stiffness, this leads to a change in the TE.

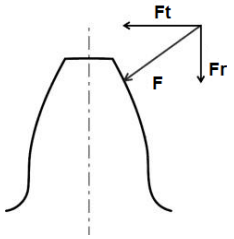


Figure 4: Tooth load components.

The center distance influences also the contact ratio, defined as the average number of teeth pairs in contact during one mesh cycle.

4 EXPERIMENTAL RESULTS

Two different gear pairs, one with involute tooth profiles (*unmodified gears*), another with modified tooth profiles, have been tested for different values of applied torque. Three steps of center distance variations have been applied, by properly orienting the bearing caps. A check on the contact patterns has been performed, in order to have a visual confirmation of the correct alignment of the gears. The evolution of the painted pattern for an increasing number of meshing cycles at a constant load of 200 Nm is shown in figure 5. The removed paint from the tooth surface confirms that the gears are properly aligned.

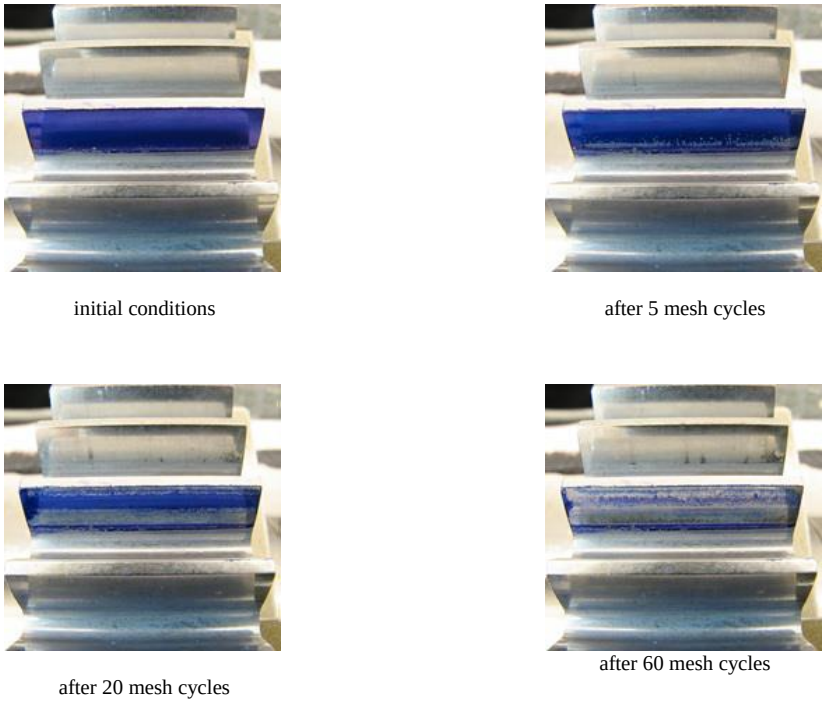


Figure 5: Contact path evolution with the meshing cycles.

An additional check has been performed by placing an analog length gauge normal to the surface of a gear. Given the tight planar tolerance on both gear surfaces, such a setup can be used to derive the tilting angle of the rotating gear. An angular misalignment of 6.7E-5 radians has been measured, which has a negligible effect on the STE measurements.

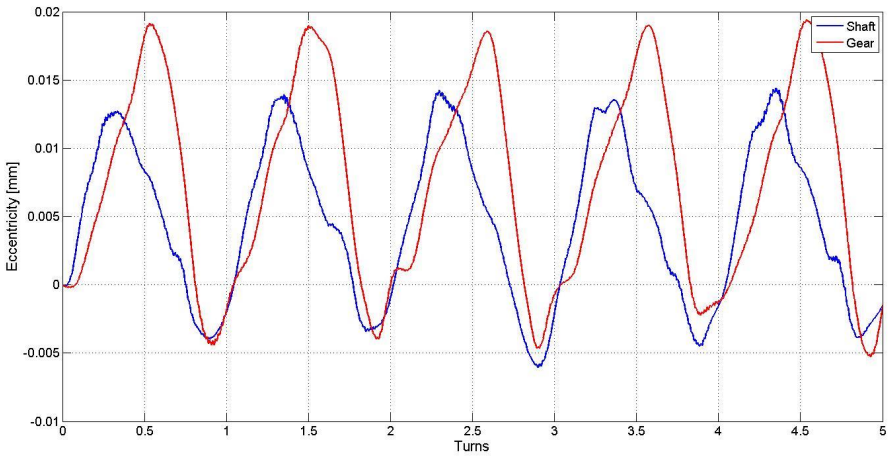


Figure 6: Measured eccentricity on the shaft (blue) and on the gear (red)

The eccentricity of the gears with respect to the rotating shafts is responsible for the low-frequency content of the measured TE. Such components of the excitation should be as low as possible in order to ensure a proper repeatability of TE measurements along different meshing

cycles. For this reason, an additional check on the mounting eccentricity of the gears has been performed (figure 6) by measuring the eccentricity on the shaft (blue curve) and on the gear collar (red curve). Eccentricity values of the order of 20 μm have been detected for both the shafts and the gear collars, which proves that the gear clamping elements cause only small additional eccentricity to the gears, in the order of 7 μm.
Due to the bending flexibility of the shafts, the operational CD is affected by the applied torque. In order to allow a proper compensation of the load-dependent CD variations, shaft deflection has been measured for different values of applied torque. The results are shown in figure 7, where a maximum CD of about 0.05 mm can be noticed for a single gear.

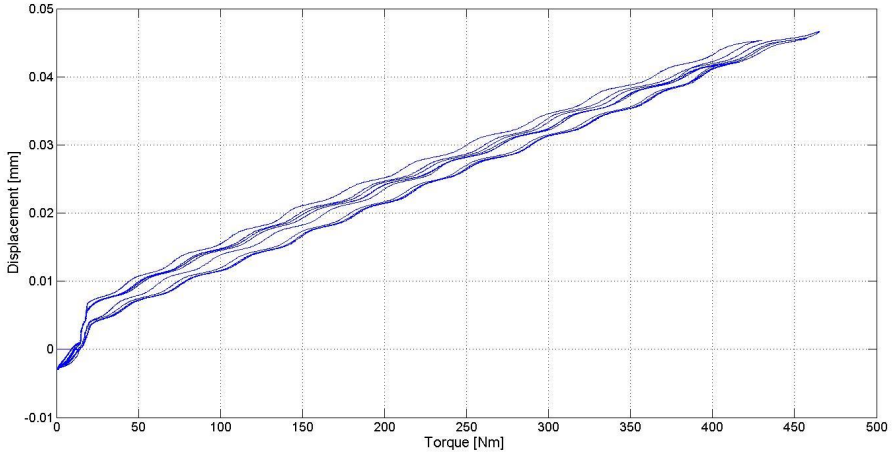


Figure 7: Measured shaft deflection as a function of the applied torque

Based on the measured deflection-torque curves shown in figure 7, a proper compensation of the CD variation due to shaft flexibility is done as a preparation step before starting each measurement.
The experimental TE curves were generated by rotating the shafts at a low speed of circa 10 rpm and by measuring the angular displacements of the two shafts at a sampling frequency of 51.2 kHz. Measured data were post-processed performing the following operations:

- derive TE data from measured angular displacements of the two gears [1] in time domain;
- convert the time domain TE data in angle domain TE data;
- calculate an angle-domain FFT of the TE;
- separate and filter out the runout contribution to the TE in the frequency domain;
- reconstruct the decomposed signal in angle domain by inverse FFT.

A measurement campaign was performed for values of transmitted torque increasing from 50 Nm to 350 Nm in steps of 50 Nm. For each value of transmitted torque, the TE curves have been measured for both the unmodified and the micro-modified gears for the following different values of the CD:

- CD1: 149.85 mm, -0.1% of the nominal CD;
- CD2: 150.00 mm, nominal value of the CD;
- CD3: 150.15 mm, +0.1% of the nominal CD;

- CD4: 150.30 mm, +0.2% of the nominal CD.

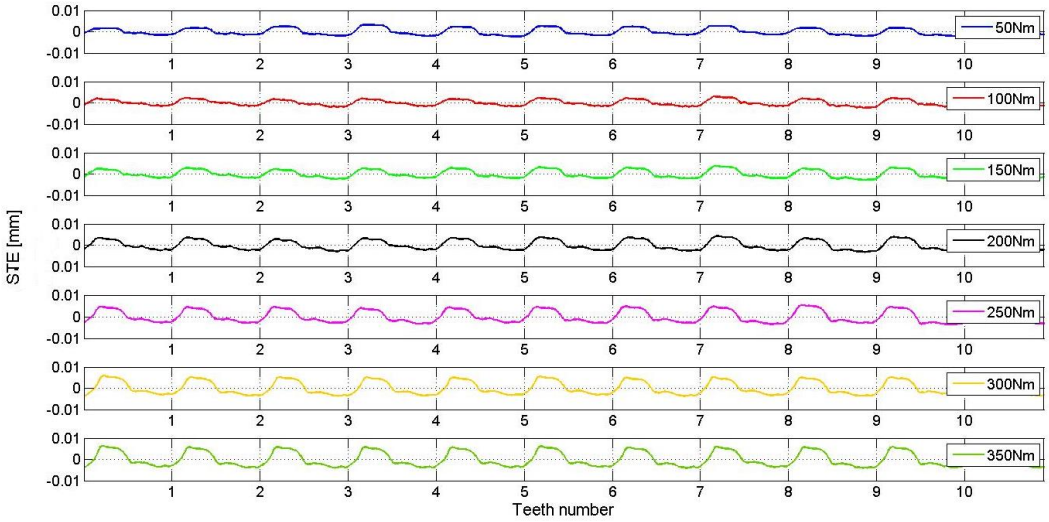


Figure 8: STE curves at different loads for unmodified gears for the CD4 case.

The results for CD4 and CD1 cases and for different values of the transmitted load are shown in figure 8 and 10 respectively.
Figure 9 shows STE curves measured for the unmodified gears, at a constant torque of 350 Nm for the four different CD values. A transition between lower STE-value zones and higher STE-value zones in each meshing cycle can be noticed. Such a fluctuation is linked to the gear contact ratio, which has a nominal value of 1.45 for the tested gears.

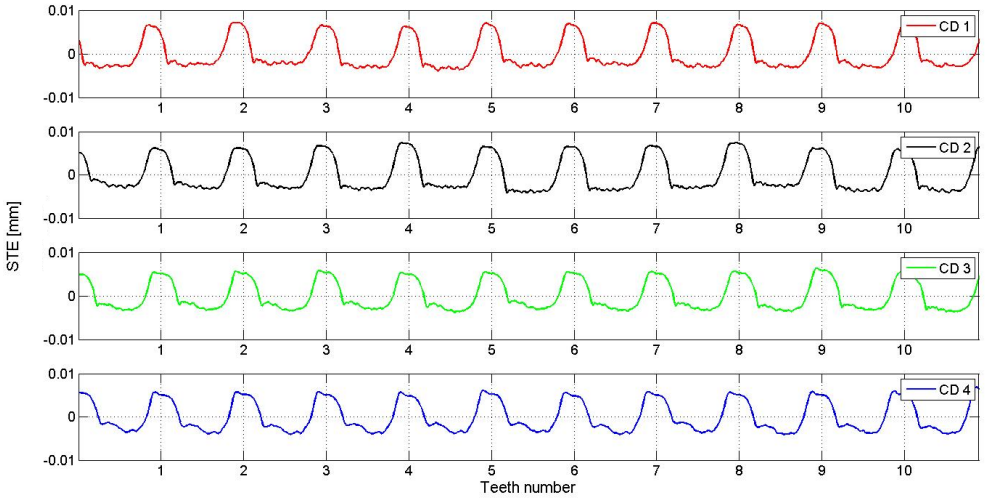


Figure 9: STE curves at 350Nm for unmodified gears for different CDs.

Considering that higher values of the STE are expected when one tooth pair is in contact, an estimate of the gear contact ratio can be achieved by comparing the durations of the lower STE-value and of the higher STE-value phases during one meshing cycle. From the STE curves shown in figures 9, it can be pointed out that a higher value of the contact ratio is achieved in CD1 case, confirming the theoretical dependency of the contact ratio on the CD.

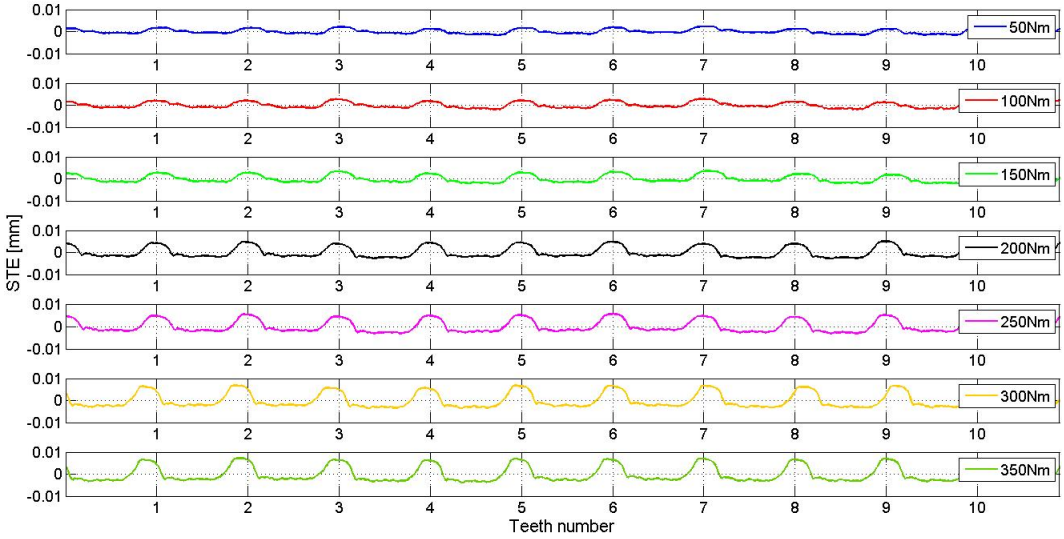


Figure 10: STE curves at different loads for unmodified gears for the CD1 case.

Figure 11 shows the comparison between the amplitude of the meshing order of the TE for the different values of transmitted loads and at different CD values for the unmodified gears. From this figure, a substantially linear load-dependence of such amplitude can be noticed, while CD variations do not affect such a trend significantly.

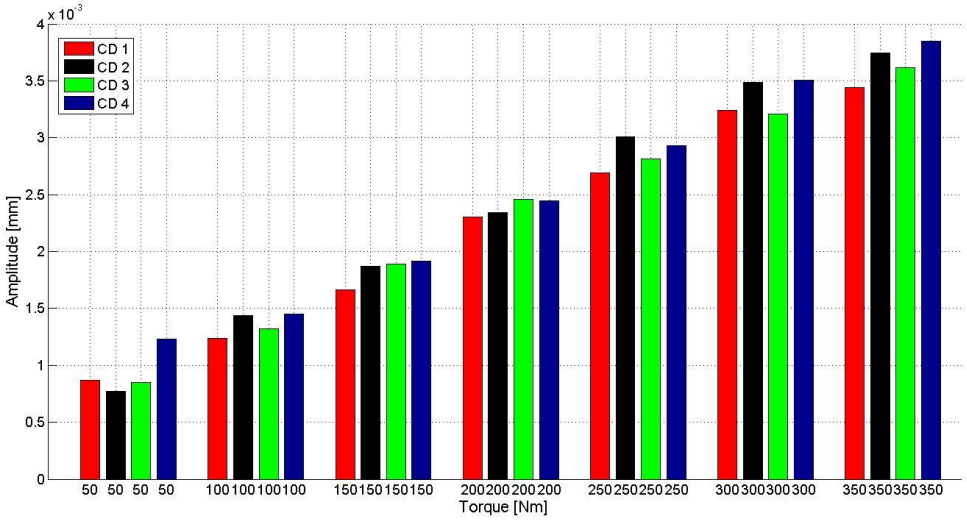


Figure 11: Meshing order amplitude at different CDs for the unmodified gear pair.

The same TE measurements have been performed by testing a micro-modified gear pair with a total modification of 15µm parabolic profile crowning.
As shown in figure 12, the measured STE curves show a significantly different shape compared to the unmodified gears, due to the different microgeometry of the teeth.

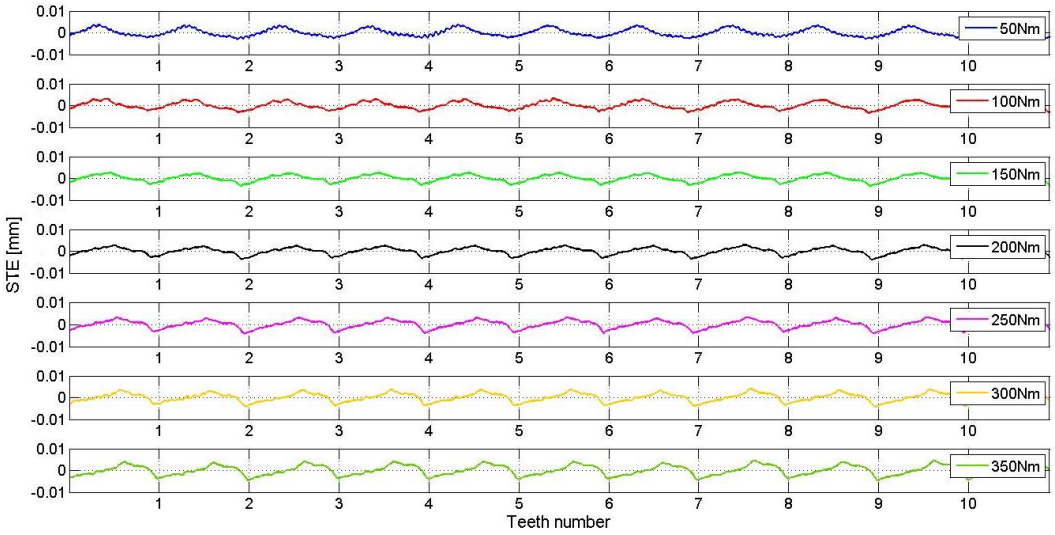


Figure 12: STE curves at different loads for the profile-modified gear pair. CD=150mm.

By comparing the measured STE in terms of meshing order amplitude at different CD values (figures 13 and 14), it is clear that the amplitude is not a monotonically increasing function of the applied load as in the case of unmodified gears. A convex trend can be noticed, with an optimal value of the applied torque, that is the torque value for which the STE amplitude is minimal, which varies with the CD. Such experimental evidence can be explained by considering that in the optimal torque region, tooth deflection values are close to the profile micro-modifications, from which a compensation effect of the latter on the STE derives.

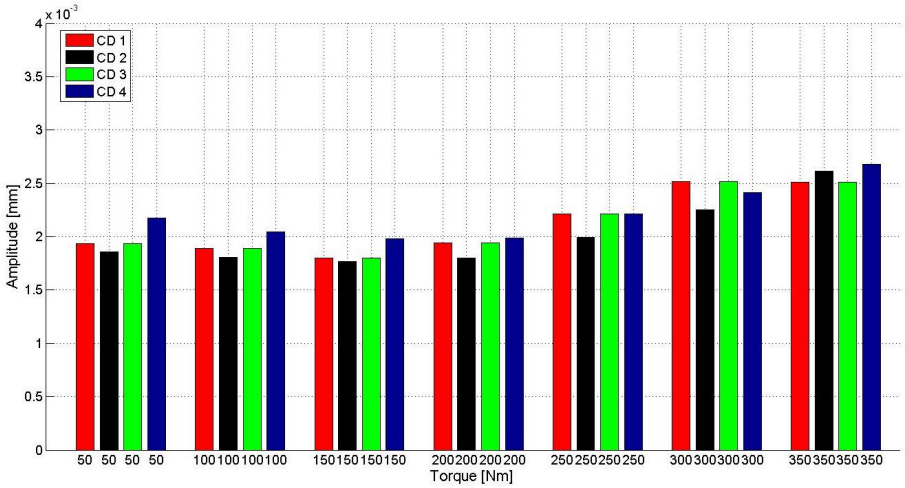


Figure 13: Meshing order amplitude at different CDs for the profile-modified gear pair.

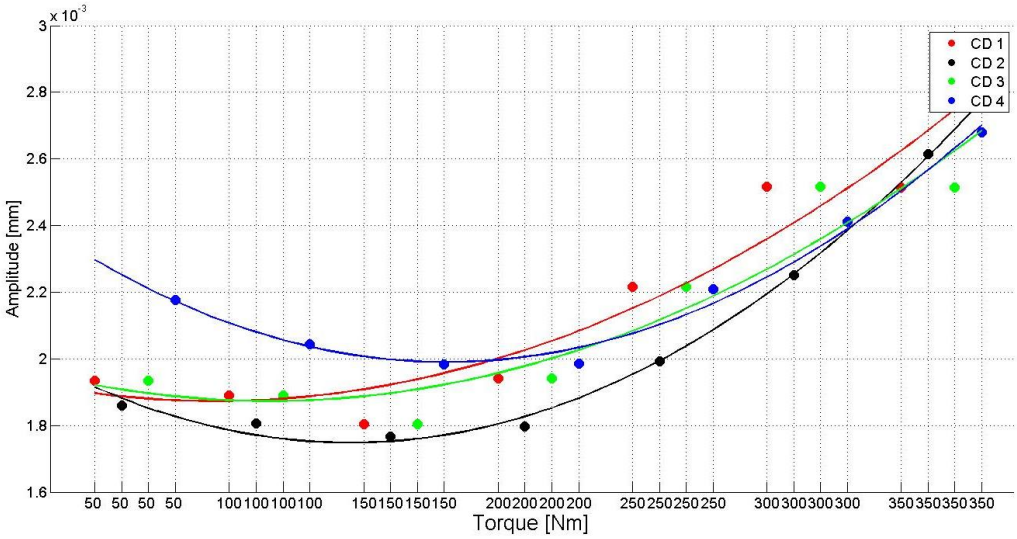


Figure 14: Parabolic fitting of the meshing order amplitude for the profile-modified gear pair.

5 CONCLUSIONS

The measurement of the STE in a high precision gears proves to be challenging. However, accurate and repeatable measurements have been obtained and guidelines have been provided in the paper.

Measurements have been performed to investigate the influence of the center distance on the STE. Such investigation shows that STE is sensitive to small changes in center distance (in the order of 0.1% of the nominal value). This sensitivity is limited in case of unmodified teeth.

A different trend can be noticed if the modified tooth is considered. A minimum in the peak-to-peak value shows that the profile modifications are optimal for a certain torque value. The effect of the CD variation on the modified gear pair is to shift the optimal torque considered as the torque value where the peak-to-peak amplitude of the STE has its minimum.

ACKNOWLEDGEMENTS

The results described in this paper have been obtained through research activities funded by the People Programme (Marie Curie Actions) of the 7th Framework Programme of the European Union FP7/2007-2013, under the contract with the Research Executive Agency (REA) n. 324336 and the related research project DEMETRA – "Design of Mechanical Transmissions: Efficiency, Noise and Durability Optimization" (www.fp7demetra.eu).

The Belgian partners want to also gratefully acknowledge the support from the IWT Flanders within the MODRIO and OptiWind project, as well as the support of ITEA2 through the MODRIO project. KU Leuven also acknowledges the Belgian Programme on Interuniversity Attraction Poles, initiated by the Belgian Federal Science Policy Office (DYSCO).

REFERENCES

[1] J. D. Smith, *Gear noise and vibration*, Marcel Dekker, Cambridge, 2003.

[2] S. Li, *Effects of machining errors, assembly errors and tooth modifications on loading capacity, load-sharing ratio and transmission error of a pair of spur gears*, Mech. Mach. Theo., 42, 698-726 (2007).

[3] S. L. Harris, *Dynamic loads on the teeth of spur gears*, Proc. IMechE, 172, 87-112 (1957).

[4] T. Koide, S. Oda, S. Matsuura, A. Kubo, *Equivalent misalignment of gears due to deformation of shafts, bearings and gears*, JSME Int J., 46, 1563-1571 (2003).

[5] W. Kim, J. Y. Lee, J. Chung, *Dynamic analysis for a planetary gear with time-varying pressure angles and contact ratios*, J. Sound Vib., 331, 883-901 (2012).

[6] A. Palermo, J. Anthonis, D. Mundo, W. Desmet, *A novel gear test rig with adjustable shaft compliance and misalignments*. *Part I: Design*, CMMNO (2013).

[7] J. Haigh, J. N. Fawcett, *Effects of misalignment on load distribution in large face-width helical gears*, Proc. IMechE, Part K, 217, 93-98 (2003).

[8] R. G. Munro, *A review of the theory and measurement of gear transmission error*, Proc. IMechE Int. Conf. Gearbox Noise and Vibration, 3-10 (1990).

[9] R. White, V. Palan, *Measurement of Transmission Error Using Rotational Laser Vibrometers*, Proc. ASME IDETC/CIE 2007, paper DETC2007-34430.

11th International Conference on Engineering Vibration
Ljubljana, Slovenia, 7–10 September 2015

A BENCHMARK FOR TIP TIMING MEASUREMENT OF FORCED RESPONSE IN ROTATING BLADED DISKS

Giuseppe Battiato*[1], Christian M. Firrone[2],Teresa M. Berruti[2]

[1]Dep. of Mechanical Engineering
Politecnico di Torino
Corso Duca degli Abruzzi, 24
10129 - Turin, Italy
giuseppe.battiato@polito.it

[2]Dep. of Mechanical Engineering
Politecnico di Torino
Corso Duca degli Abruzzi, 24
10129 - Turin, Italy
{christian.firrone,teresa.berruti}@polito.it

Keywords: Blade Tip Timing, Strain Gauges, Beam Shutter Configuration, Synchronous Vibrations.

Abstract. *The Blade Tip-Timing is a well known non-contact measurement technique for the identification of the dynamic properties of rotating bladed disks. Even if it is an industry-standard technique its reliability has to be proved for the different operation conditions by comparison with other well established measurement techniques. Typically a strain gauges system in conjunction with radio telemetry is used as reference.*

This paper aims at evaluating the accuracy of a last generation Tip-Timing system on two bladed dummy disks characterized by different geometrical, structural and dynamical properties. Both the disks were tested into a spinning rig where a fixed number of permanent magnets, equally spaced around the casing, excites a synchronous resonance vibration with respect to the rotor speed.

The so called beam shutter method was adopted for the Tip-Timing system. Due to the presence of shrouds a particularly set up of the probes was chosen in order to avoid that the probes look radially inward at the blade tips as in the most common configurations.

The probes are optical laser sensors pointing at leading and trailing edges locations where the blade experiences the greatest magnitude of displacement. The Blade Tip-Timing measured data are post-processed by two different methods, the Single Degree of Freedom Fit (SDOF) and the Circumferential Fourier Fit (CFF). The amplitude and frequency values at resonance obtained by the Tip-Timing system are compared with those obtained by the strain gauge measurements.

1 INTRODUCTION

Vibrations of turbomachinery blades in service could reduce their fatigue life by increasing the risk of crack formation. In this frame the blade health monitoring is an important challenge in order to prevent unexpected blade failures. Traditionally, the rotor blade vibrations have been detected using strain gauges which still represent nowadays the most reliable measurement system. The strain gauges have the disadvantage that, since they need to be stuck on the blade airfoil, they cannot be used in the engine in service. For this reason in the last years for the blades monitoring, the non-contact measurement technique Blade Tip-Timing (BTT) has gained ground.

The BTT technique is based on the analysis of arrival times related to the blade passages under a set of stationary sensors [1, 2]. In the standard cases the BTT sensors are mounted on the casing, oriented radially in order to detect the blade displacements at the tip [3]. One of the main advantages of the BTT is that, besides being non contact and usable on a working engine, all the blades are monitored during the rotation, giving the possibility to identify if one blade vibrates more than the others (for typical mistuning problems).

The last generation industry-standard BTT systems process the arrival times by using indirect [4, 5, 6, 7] or direct [5, 8, 9, 10] identification methods in order to determine the modal parameters characterizing the vibrating blade. A verification on the correctness of the obtained parameters represents a due step in order to consider a BTT system as reliable. Different authors have demonstrated a good correlation between measurements from BTT and strain gauges for both real [3] and controlled [11] operation conditions, in the case where the displacements are measured at the blades tip using the standard radial sensors positioning.

This paper presents results and validation of a new way of using optical sensors in the BTT, the so called *beam shutter* or *beam interrupted* configuration. This configuration is adopted for the identification of the modal parameters of a disk by measuring the displacements at the mid leading or trailing edge of the blades. Instead of the standard configuration for optical probes, where the laser beam is reflected by the measured blades, in the beam shutter configuration the laser beam is interrupted by the blade passage. The technique is here tested on two different dummy disks that experience synchronous vibration patterns when excited by means of a fixed set of permanent magnets. The first dummy disk has the simple geometry of a flat plate and it is characterized by blade bending vibration modes along the axial direction. The second dummy disk was designed to simulate a dynamic behavior closer to a real turbine disk where the blades are connected each other at the tip by an outer ring. The test campaign was performed such that the blade vibrations could be detected simultaneously by using the BTT and strain gauges measurement systems.

2 THE SPINNING TEST RIG

The dummy disks were tested in a laboratory spinning rig under vacuum conditions [12]. As shown in Figure 1-a the test rig has vertical axis with two cylindrical protection structures (1) and (2) which are mounted coaxial to the rotating shaft which is positioned under the floor. On the top of the shaft a flange allows the disk accommodation (3). The cylinder (1) also supports two static rings (Figure 1-b) aimed at keeping in a fixed position a set of permanent magnets (ring 1), which are used to excite the rotating disk, and the Tip-Timing laser sensors (ring 2).

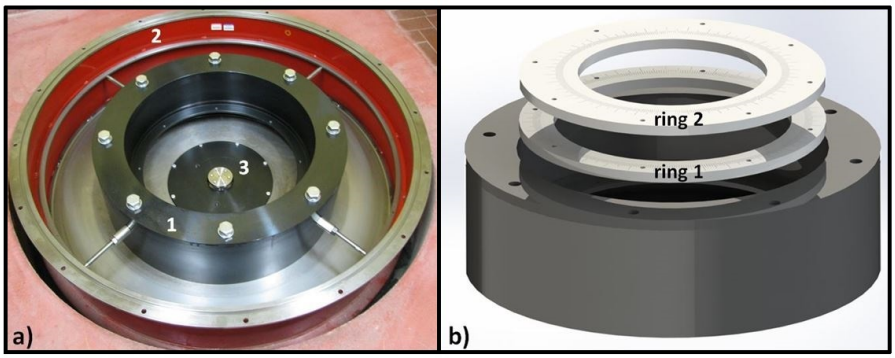


Figure 1: a) The spinning rig, b) static rings for magnets and laser sensors.

2.1 The dummy disks

The dummy disk 1 (Figure 2-a) is an aluminum disk with a simple geometry of a flat plate where each blade has the shape of a cantilever beam. The disk 1 has 12 blades whose length and width are 150 mm and 25 mm respectively. The axial height and the outer diameter of the disk are 5mm and 400 mm. A cylindrical magnet (5 mm diameter, 5 mm height) is glued in a special housing machined at each blade's tip.

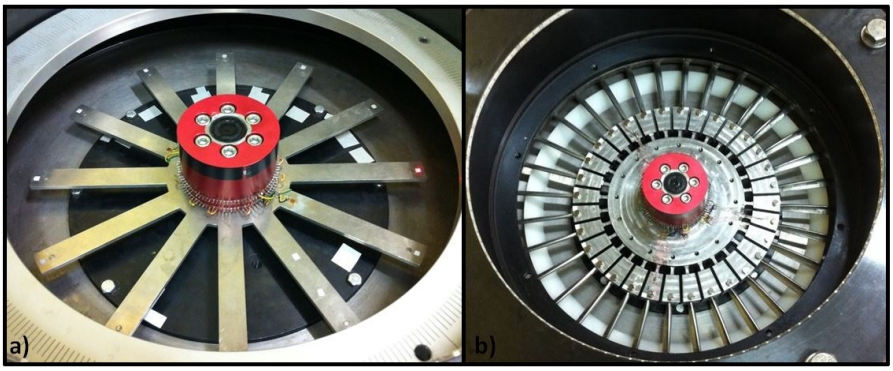


Figure 2: a) The dummy disk 1, b) the dummy disk 2.

The dummy disk 2 (Figure 2-b) was designed to be closer in the dynamic behavior to a real turbine disk where the blades are connected each other at the tips by an outer ring as in the case of shrouded blades. It is a single piece made of ferromagnetic steel AISI 460 in order to allow the magnetic interaction between the permanent magnets and the blade airfoils. The dummy disk 2 has 32 real profiled blade whose length and aspect ratio are respectively 100 mm and 7,31. Its outer diameter and axial height are 630 mm and 20 mm.

2.2 The excitation system

The excitation system in the spinning test rig uses cylindrical permanent magnets (diameter 18 mm, height 10 mm, magnetization N52). The magnets are mounted in equally spaced posi-

tions on the static ring facing the rotating test article (ring 1 in Figure 1-a). A graduated scale impressed on the ring upper surface is used to fix the magnets at the right angular positions [12].

Different supporting rings with different inner diameter are available in order to guarantee the correct radial positioning of the permanent magnets. Each magnet is glued on the tip of a screw which allows the regulation of the axial gap with respect to the test article blades. Six of the magnets are instrumented with force transducers which measure the force in axial direction during the tests [12].

The number of magnets used in a specific test must be equal to the main engine order (EO) characterizing the excitation force that should be simulated. The main engine order EO_m^1 can be defined as the fist not-null harmonic index resulting from the Fourier transform of the excitation force. In general for m equally spaced magnets, the EO pattern exciting the disk is defined as follows:

$$EO_m^i = i \cdot m, \qquad \forall\, i = 1, 2, 3, \ldots \tag{1}$$

A modal shape corresponding to a certain number of nodal diameter (ND) can be excited by different EO according to the following relationship:

$$EO = jN_b \pm ND, \qquad \forall\, j = 0, 1, 2, 3, \ldots \tag{2}$$

Where N_b is the number of blades characterizing the disk. The excitation frequency is related both to the EO and to the rotational speed n by the following equation:

$$f_{exc} = \frac{EO \cdot n}{60} \tag{3}$$

Where n is expressed in rpm and f_{exc} in Hz.

From the Eq. 3 it can be stated that higher EO values can correspond to the same f_{exc} for lower rotational speeds.

2.3 The strain measurement system

The two dummy disks were instrumented by means of strain gauges. For both the disks the identification of the strain gauge positions came out from their FE modal analyses in cyclic symmetry conditions. Areas of high strains and low strain gradients were identified as best locations for strain gauges. The strain gauges signals are acquired through a telemetry system.

For the dummy disk 1 the strain gauges where attached at the two sides of the blade root (Figure 3-a). This position was chosen in order to measure the out-of-plane bending (1F) mode belonging to the first modal family. Each strain gauge is composed by a single grid (1.52 mm $\times$ 3.05 mm, grid resistance 350 Ω). The two grids at the two sides of the blade were connected together as a half bridge. For the dummy disk 2 the strain gauge was attached on the back of the blade airfoil (Figure 3-b). The selected area is not affected by strain gradients for both the flap-restricted (1FR) and torsional (1T) mode shapes belonging to the second and third modal family respectively. The strain gauge is a tee rosette (grid resistance 350 Ω) composed by two separate grids (1.52 mm $\times$ 1.78 mm) with perpendicular axes. The two grids were connected together as a half bridge.

The strain gauges measurement chain was verified by means of a static test on the dummy disk 1. The static test on the instrumented blade consists in measuring the bending strain at the blade root due to calibrated masses positioned on its free end.

Three static tests corresponding to three different dead masses were performed. The measured

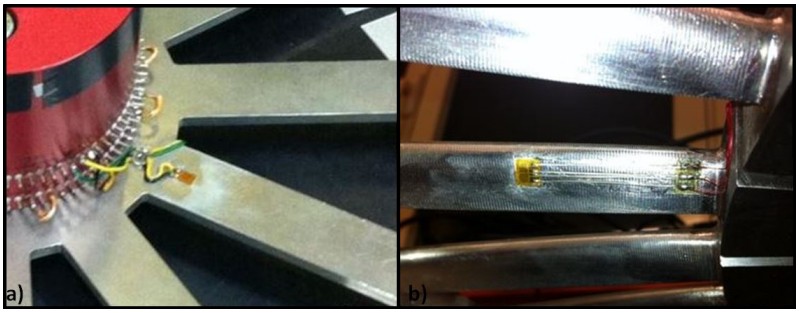


Figure 3: a) Strain gauge at the blade root of the dummy disk 1, b) strain gauge at the back of the airfoil for the dummy disk 2.

Mass	*Strain Gauge*	*FE model*
kg	$\mu\epsilon$	$\mu\epsilon$
0,76	130,23	130,19
1	169,30	169,27
1,99	342,32	342,25

Table 1: Experimental and numerical strains for static tests on dummy disk 1.

strains were compared to the corresponding numerical strains determined by means of the static FE analysis.
The results listed in Table 1 show the reliability of the strain gauges which can be used as a reference measurement system for the validation of the BTT technique.

3 THE BLADE TIP TIMING SYSTEM

The Blade Tip Timing technique uses a set of non contact sensors constrained to the casing and facing the rotating disk [1, 2, 3]. This technique is based on the measurement of the Times-of-Arrival (ToA) of each blade under each of the stationary sensor. From the analysis of the ToA the dynamic properties of each blade, i.e. the resonance frequency, the vibration amplitude and the damping, can be determined. The BTT has two main advantages over the strain gauges:

- it is a non-contact measurement system that does not affect the dynamic behavior of the blade;
- it allows the measurement of all the blades of the disk, while the strain gauges are usually attached only to some blades.

The BTT system used in this activity is a last generation system with laser optical probes. For the dummy disks 1 and 2 all the tests were performed by employing 5 optical laser sensors for detecting the blades vibrations. An additional sensor (1/rev sensor) which measures the rotational speed was used a reference for the other sensors.

The BTT software which post-processes the measured blades displacements uses two different approach to extract the vibration data:

- *Single Degree of Freedom Fit* (SDOF): it is based on the analysis of data collected during an rpm sweep. The data coming from only a single sensor can provide the resonance

parameters. The curve measured by sensor for one blade has one of the shapes shown in Figure 4. The peak-to-peak values are equal to each other and represent the zero-peak value of the actual response in resonance condition [4].

- *Circumferential Fourier Fit* (CFF): it uses a different mathematical approach to determine the resonance parameter that the SDOF. This method requires 3 or more sensors installed on the same chord-wise position. Assuming a certain response order, corresponding to the selected EO, for each averaged rpm a least mean squares fitting of the data with a sinusoidal wave is performed [5, 8, 9, 10].

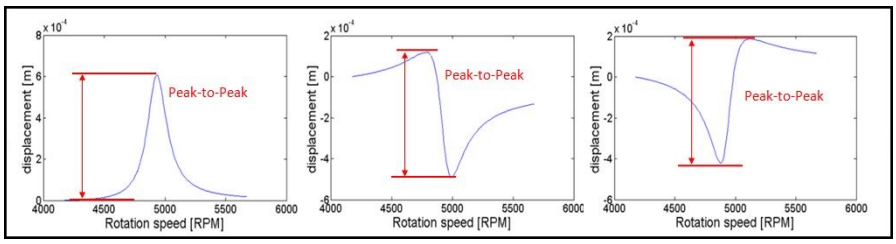


Figure 4: Curves for one blade measured by three sensors placed at $0°$ $120°$ and $240°$ respectively.

3.1 The beam shutter method and sensor positioning

The standard BTT measurement approach is based on sensors which are positioned in radial direction in order to measure the blade displacement at the tip. In this activity a new sensor configuration called *beam shutter* or *beam interrupted* has been tested. The beam shutter configurations employed in the spinning test rig for the dummy disks 1 and 2 are shown in Figure 5.

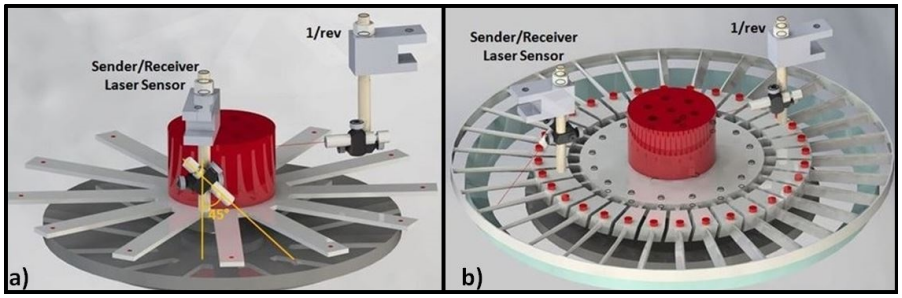


Figure 5: Beam shutter configuration implemented for the dummy disk 1 a) and the dummy disk 2 b).

A set of sender/receiver optical laser sensors with lenses was used for both the disks. Each sensor is mounted above the disk and produces a laser beam which is collimated on a reflective tape stuck on a stationary surface placed under the disk. When the disk rotates the passing blade acts as a shutter, blocking the returning light towards the sender/receiver sensor. The system is set up in order to detect the ToA of the leading or the trailing edge of the blade.

The sensors were installed at the same distance from the disk center. The relative circumferential position of the sensors was chosen in both cases by means of an optimization tool which allows to avoid the aliasing effect in the measurement of the traveling wave characterizing the vibrating disk. The optimization tool requires as input the number of sensors, the engine order of the travelling wave of and the number of blades.

4 THE RESULTS COMPARISON METHOD

The vibration parameters detected by the BTT system have to be compared to the same parameters coming from the strain gauges connected to the telemetry system. Simultaneous measurements with BTT and strain gauges were performed for a certain set of vibrating modes characterizing the dummy disks.

The comparison in terms of resonance frequencies is straightforward and requires a fast data processing. The comparison in terms of vibration amplitudes is a more demanding task. It requires a finite element (FE) modal analysis of the disks, since the strain gauges system measures strains (ϵ_{SG}), while the BTT measures displacements (u_{BTT}).

By the FE model the parameter $K_{mod} = u_{mod}/\epsilon_{mod}$ can be calculated, where:

- u_{mod} is the modal displacement of the node corresponding to the laser position on the blade in the same direction of the displacement detected by the BTT;
- ϵ_{mod} is the modal strain in the area corresponding to the strain gauges position in the same direction of the strain detected by the strain gauges.

The same parameters can be defined for the physical measured quantities u (displacement of the blade at the BTT laser position) and ϵ (strain at the strain gauges position) $K_{phy} = u/\epsilon$. Since the two disks can be considered linear and their responses give well separated modes, the following relationship should be satisfied:

$$K_{phy} = K_{mod} \quad \Rightarrow \quad \frac{u}{\epsilon} = K_{mod} \tag{4}$$

The displacement of the blade corresponding to the strain measurement from Eq. 4 can be determined as:

$$u_{SG} = K_{mod} \cdot \epsilon_{SG} \tag{5}$$

Since the FE model was tuned previously by the strain gage measurements (see Table 1) the obtained parameter u_{SG} is considered as reference for the displacement value measured by the BTT system u_{BTT}.

5 RESULTS ON DUMMY DISK 1

In order to predict the natural frequencies and the modal shapes a FE dynamic calculation in cyclic symmetry conditions was performed. In Figure 6-a the natural frequencies of the disk are plotted against the nodal diameters. The modal family plotted in Figure 6-a is the family $1F_{oop}$ where each blade vibrates according to a bending out-of-plane mode shape for each ND. The calculated numerical Campbell diagram is shown in Figure 6-b. From this plot the rotational speeds at which the resonances occur can be estimated. The modes corresponding to 5 and 6 ND were chosen to be tested. The mode at ND6 is excited with E0 6, while, in order to avoid high operation speed, it was chosen to excite the mode at ND5 not by EO 5 but by EO 7 according to Eq. 2.

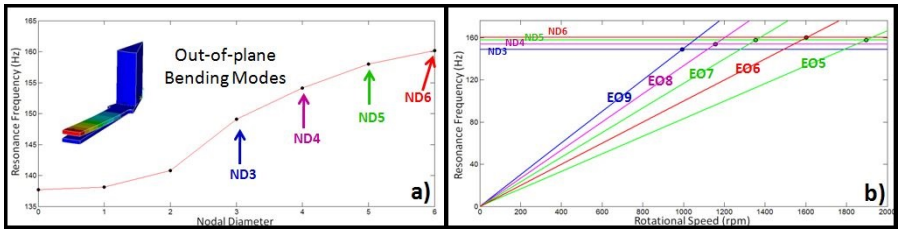


Figure 6: a) numerical ND-resonance frequency diagram for the dummy disk 1, b) numerical Campbell diagram for the dummy disk 1.

5.1 Displacement measurement with the Tip-Timing

The vibration modes of the dummy disk 1 are out-of-plane (axial direction). In order to obtain a configuration where the optical beam is interrupted by the blade during an out of plane vibration, the sensors must be positioned with an angle with respect to the disk plane as shown in Figure 5-a. Each sensor was then tilted by an angle which is $45°$ with respect the plane containing the undeformed disk. This particular angle of the sensors allows the BTT system to see an axial displacement as it was tangential as shown by the scheme of the blade interrupting the laser beam in Figure 7-a. The detected ToA corresponds to the apparent tangential displacement which is equal to the axial displacement.

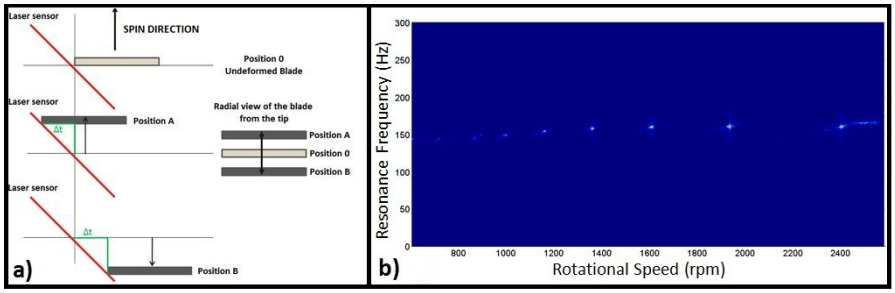


Figure 7: a) Beam shutter working principle adopted for detecting out-of-plane vibration mode for the dummy disk 1, b) experimental Campbell diagram for the dummy disk 1.

5.2 Preliminary test

A preliminary rotating test was performed to identify the real resonance frequencies. A single magnet was mounted on the test rig so that the disk could be excited simultaneously by means of an infinite number of harmonic excitations. The test was planned in order to investigate the speed range 600 rpm - 2600 rpm with an acceleration of 1.6 s/Hz.

From the strain gauges time signal the *experimental* Campbell diagram (Figure 7-b) was processed using Matlab. The natural frequencies for ND 5 and 6 which were determined by reading the y-axis values of the white points are listed in Table 2.

EO	*ND*	n_{res}	f_{res}
-	-	rpm	Hz
7	5	1356	158,2
6	6	1591	159,1

Table 2: Preliminary test results obtained for a 10 mm gap between the fixed magnet and the rotating blade.

5.3 Test campaign

The test campaign was performed for the selected nodal diameters which can be excited by the EO determined from Eq. 2 for j = 1. A single permanent magnet was adopted for the excitation. A gap of 7 mm between the permanent magnet and those glued on the blades was set for all the tests. Strain and displacement were acquired simultaneously for 2 speed ranges including the values of n_{res} at which the resonances occur.

The main tests parameters are listed in Table 3. The test campaign was repeated 3 times.

EO	*ND*	n-range
-	-	rpm
7	5	1300 - 1400
6	6	1550 - 1650

Table 3: Test campaign for the dummy disk 1.

For each test a linear speed sweep with acceleration of 3.2 s/Hz was performed.

5.4 The test results

The strain gauges and BTT data were processed for each of the studied modes. For the strain gauges data processing the same procedure employed for the preliminary test was used. Both the SDOF identification and the CFF methods were adopted for BTT data processing. Since the two identification method gave very close results, only the results produced by the SDOF are here reported. The measured displacement amplitude values in resonance condition and the correspondence resonance frequencies were averaged over three acquisitions. The measured values showed high repeatability (standard deviation $\bar{\sigma} < 0.13\%$).

In Table 4 the displacement amplitude values and the natural frequencies detected both by stran gauges (SG) and by the BTT system are listed. The parameters e_f, e_u are the percentage differences between the resonance frequencies and vibration amplitudes values detected by the strain gauges and BTT, that is:

$$e_f = \frac{\bar{f}_{SG} - \bar{f}_{BTT}}{\bar{f}_{SG}} \cdot 100 \qquad (6)$$
$$e_u = \frac{\bar{u}_{SG} - \bar{u}_{BTT}}{\bar{u}_{SG}} \cdot 100$$

From Table 4 it can be noted that the difference in terms of resonance frequency is negligible (e_f is lower than 0.5%). The difference in terms of resonance amplitude is also very low, the paramer e_u is less than 2%.

ND	f_{SG}	f_{BTT}	e_f	$\bar{u}_{SG}$	$\bar{u}_{BTT}$	e_u
-	Hz	Hz	%	μm	μm	%
5	158,0	158,0	0	1662,23	1631,48	1,88
6	159,3	160,2	0,44	2298,75	2275,60	1,02

Table 4: BTT - strain gauges comparison for the dummy disk 1.

6 RESULTS ON DUMMY DISK 2

The dummy disk 2 shows a dynamic more similar to real turbine disk. Measurements on this disk allow testing the capability of the BTT system to give accurate results even on a disk with a more complex dynamics. The FE dynamic calculation of the dummy disk 2 showed that the first three modal families are the flap (1F), flap restricted (1FR) and torsional (1T) modes. The plot of the calculated frequencies-nodal diameters for these three modal families is shown in Figure 8-a. In the selected position chosen for the strain gauges (middle on the blade airfoils, Figure 3-b), the FE model showed that the highest strains are given by the 1FR and 1T modes. It was then decided to excite in the tests these two modes for a certain nodal diameter in order to compare BTT and strain gauges measurements.

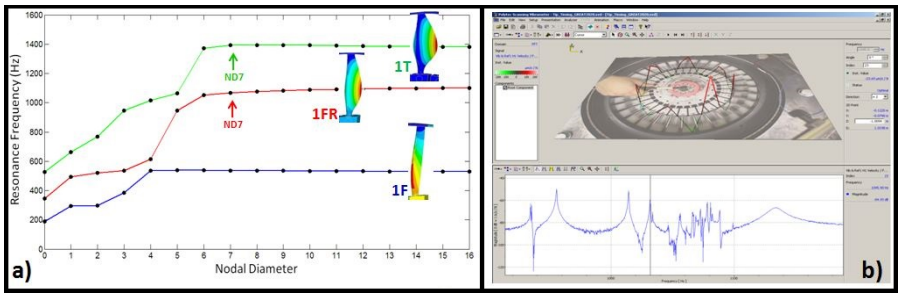


Figure 8: a) numerical ND-resonance frequency diagram for the dummy disk 2, b) hammer test on dummy disk 2: 1FR mode identification.

6.1 Preliminary test - Hammer test

A preliminary hammer test was performed to detect the modal parameters of the disk in static conditions (not rotating). In order to have the same constraints with the shaft as during the rotation, the disk was kept mounted on the spinning rig during the hammer test. The response of each blade was measured by a laser scanner. It was observed that the cleanest disk responses for both the 1FR and 1T modes occur at nodal diameter ND = 7 that is at 1029 Hz and 1402 Hz respectively. In Figure 8-b an example of the response detected by the laser scanner is shown. Considering this preliminary results, it was chosen to compare the BTT and SG measurements during rotation for the 1FR and 1T family modes at ND = 7.

6.2 Test campaign

According to Eq. 2 considering that the number of blades is N_b = 32, and assuming j = 2, it can be deduced that the ND = 7 can be excited by an engine order EO = 57. Moreover from Eq. 1 it can be derived that assuming i = 3 a number of equally spaced magnets m = 19 posi-

tioned in front of the rotating disk can produce an excitation force at EO = 57 in the disk. A test campaign was then performed with 19 permanent magnets (Figure 9) at a gap of 5 mm from the blade leading edges in order to produce in the disk a travelling excitation force with EO^1_{19} = 57 which in a given speed range excites the modes at ND = 7.

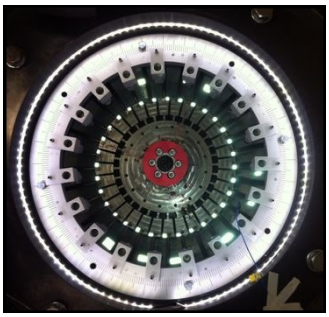


Figure 9: Spinning test rig with 19 permanent magnets.

The main tests parameters are listed in Table 5. Strain and displacement were acquired simultaneously for the 2 speed ranges (Table 5), including the values of n_{res} at which the resonances occur. For each test a linear speed sweep with an acceleration of 3.2 s/Hz was performed. The test campaign was repeated 3 times.

EO	*ND*	n-range
-	-	rpm
57	7	1000 - 1150
57	7	1350 - 1500

Table 5: Test campaign for the dummy disk 2.

6.3 The test results

The same procedure used for the previous disk was used to process the strain gauges signals. In the BTT data processing both the SDOF and CFF post processing methods were adopted. The displacement amplitudes in resonance obtained by the BTT were averaged over three acquisitions. Even for this disk the measured values showed high repeatability (standard deviation $\bar{\sigma} < 0.21\%$).

Tables 6 and 7 report the displacement amplitude values and the natural frequencies detected both by stran gauges (SG) and by the BTT system. In Table 6 the BTT data come from SDOF post-processing, while in Table 7 the BTT data come from the CFF post-processing method.
From the comparison of the e_f and e_u values (defined in Eq. 6) of Table 6 and Table 7 it can be noticed that they are both higher in Table 6 where the SDOF method is used than in Table 7 where the CFF method is used. It can be then be observed that with the dummy dusk 2 the acceptable method to post-process the BTT data is only the CFF where for the frequency $e_f < 2,5\%$ for the and vibration amplitudes $e_u < 5\%$. This differences between the two methods was explained considering the low vibration amplitude values of the dummy disk 2 which leads to measured points detected by the BTT probes more affected by the noise. The

Mode	*ND*	f_{SG}	f_{BTT}	e_f	$\bar{u}_{SG}$	$\bar{u}_{BTT}$	e_u
-	-	Hz	Hz	%	μm	μm	%
1FR	7	$1029,40$	$1144,00$	$11,13$	$136,43$	$173,30$	$27,02$
1T	7	$1402,20$	$1496,84$	$6,75$	$155,48$	$230,90$	$48,51$

Table 6: BTT-strain gauges comparison for the dummy disk 2 when the SDOF method is adopted.

Mode	*ND*	$\bar{f}_{SG}$	$\bar{f}_{BTT}$	e_f	$\bar{u}_{SG}$	$\bar{u}_{BTT}$	e_u
-	-	Hz	Hz	%	μm	μm	%
1FR	7	$1029,40$	$1022,75$	$0,65$	$136,43$	$131,37$	$3,70$
1T	7	$1402,20$	$1368,05$	$2,43$	$155,48$	$162,54$	$4,54$

Table 7: BTT-strain gauges comparison for the dummy disk 2 when the CFF method is adopted.

CFF method proved to be more robust for these noisy initial data since it uses the measurement coming from all the probes in one fitting procedure, while the SDOF method uses the data coming only from one probe.

7 CONCLUSIONS

A new measurement configuration for a BTT system usable with optical probes, the so called beam shutter or beam interrupted configuration, was tested by comparing the BTT results with the strain gauges results. The comparison was performed on two different dummy disks.

The beam shutter configuration proved to work properly since it gives the expected collection of measured data from the time of arrivals of each blade under each probe. These data has to be post processed to obtain frequency and amplitude in resonance condition.

The dummy disk 1 has a simple geometry and in resonance for the selected modes high blades displacement amplitudes (1600 - 2300 μm) were obtained. In this case the BTT system gave accurate values of frequency and amplitude in resonance using indifferently the two methots (SDOF or the CFF) for BTT data post-processing.

The dummy disk 2 is more similar to a real disk, it presents family of modes close to each others. Using a high EO value it was possible to excite two isolated modes at ND = 7 for two different modal families. The comparison between BTT and SG measurement was performed for these two modes. The amplitude of the displacements for both modes at the measured point was in this case smaller (130-150 μm) than in the previous disk. The low amplitude values leads to a set of data collected by the tip timing probes more noisy. In this case the final values of the dynamic parameters coming from the post-processing of the measured data proved to be more affected by the method selected for the post-processing. The CFF method which uses the signal of all probes in one fitting procedure, gave more accurate results.

8 ACKNOWLEDGEMENTS

The work described in this paper has been developed within the GREAT 2020-2 project funded by the Italian Government.

REFERENCES

[1] Zielinski, M., and Ziller, G.: *Noncontact vibration measurements on compressor rotor blades*. Meas. Sci. Technol., 11: 847-856, 2000.

[2] Zablotsky, I.Ye., and Korostelev, Yu.A.: *Measurement of Resonance Vibrations of Turbine Blades with the ELURA device*. Energomashinostroneniye, 2: 36-39, 1970.

[3] Zielinski M. and Ziller G.: *Noncontact Blade Vibration Measurement System for Aero Engine Application*. ISABE, 2005-1220, 2005.

[4] Heath, S., and Imregun, M.: *An improved single-parameter Tip-Timing method for turbomachinery blade vibration measurements using optical laser probes*. Int. J. Mech. Sci., 38 (10): 1047-1058, 1996.

[5] Dimitriadis, G., Carrington, I.B., Wright, J.R., and Cooper, J.E.: *Blade-Tip Timing measurement of synchronous vibrations of rotating blade assemblies*. Mechanical Systems and Signal Processing, 16 (4): 599-622, 2002.

[6] Heath, S., and Imregun, M.: *A Survey of Blade Tip-Timing Measurement Techniques for Turbomachinery Vibration*. Journal of Engineering for Gas Turbines and Power ASME, 120: 784-791, 1998.

[7] Heath, S.: *A New Technique for Identifying Synchronous Resonances Using Tip-Timing*. Journal of Engineering for Gas Turbines and Power ASME, 122: 219-224, 2000.

[8] Carrington, B., Wright, J.R., Cooper, J.E., and Dimitridas, G.: *A comparison of blade tip timing data analysis methods*. Proc. Instn. Mech. Engrs., 215 (G): 301-312, 2001.

[9] Gallego-Garrido, J., Dimitriadis, G., and Wright, J.R.: *A Class of Methods for the Analysis of Blade Tip Timing Data from Bladed Assemblies Undergoing Simultaneous Resonances* Part I: Theoretical Development. International Journal of Rotating Machinery, 27247: 1-11, 2007.

[10] Gallego-Garrido, J., Dimitriadis, G., Carrington, I.B., and Wright, J.R.: *A Class of Methods for the Analysis of Blade Tip Timing Data from Bladed Assemblies Undergoing Simultaneous Resonances* Part II: Experimental Validation. International Journal of Rotating Machinery, 73624: 1-10, 2007.

[11] Knappett D. and Garcia J.: *Blade tip timing and strain gauges correlation on compressor blades*. DOI: 10.1243/09544100JAERO257.

[12] Berruti T., Maschio V., Calza P.: *Experimental Investigation on the Forced Response of a Dummy Counter Rotating Turbine Stage with Friction Damping*. GT2012-69059, Proceedings of ASME Turbo Expo 2012, June 11-18, 2011, Copenhagen, Denmark.

11th International Conference on Engineering Vibration
Ljubljana, Slovenia, 7–10 September 2015

EXPERIMENTAL RESEARCH OF THE KINEMATICS AND CONTACT CONDITIONS OF THE BRUSH AND SLIP-RING

Aleš Turel[1], Janko Slavič[2], Miha Boltežar*[2]

[1]MAHLE Letrika d.o.o., Polje 15, 5290 Šempeter pri Gorici, Slovenia
ales.turel@si.mahle.com

[2]University of Ljubljana, Faculty of Mechanical Engineering, Aškerčeva 6, 1000 Ljubljana, Slovenia
janko.slavic@fs.uni-lj.si
miha.boltezar@fs.uni-lj.si

Keywords: Brush, Slip-ring, Sliding contact, Temperature, Experimental dynamics research.

Abstract. *To increase the reliability and to extend the lifetime of alternators the dynamics of the brush and the slip-ring are essential. The dynamics of the brush and the slip-ring is highly dependent on the contact situations between the slip-ring with the brush, the brush with the brush-holder, and the brush with the spring.*
For validated numerical and experimental modelling it is required to have good experimental insight into the dynamics and contact situations of the researched system. For this reason, the electrical, thermal, and kinematical details of the contact between the slip-rings with the brush were experimentally researched. A special test bench, where individual parameters (e.g.: rotational speed, temperature, electrical current) can be researched with regards to the kinematics and contact conditions.
Besides the newly introduced experimental approach, the results of this study are also the experimentally identified influences of the rotational speed and electrical current on the dynamics, contact conditions and consequently to wear. The presented experimental approach can also be used for model validation and updating.

1 INTRODUCTION

Despite the fact that for decades, the alternators operate on internal combustion engines with development of engines, the demands and lifetime limits of the alternators are increasing. One of essential components that affect the lifetime of classic alternators is the contact between slip-ring and brush. The contact is complex because of its interactions and influence of several parameters. These parameters are: rotational speed of slip-ring, the density of electric current, current orientation, spring force, coefficient of friction and temperature.

During the lifetime of the brush the contact situations are changing because of different operating conditions and wear (brush length, spring force,...) resulting in substantially changed dynamic as properties of the studied system.

Contacts between the slip ring—brush or commutator—brush can also be found in other electric machines. That is why, many researches were researching similar cases. In the next paragraphs we will take a brief look at some of the research work.

Slavič et al. have done a lot of numerical and experimental work on the contact between commutator and brush of electro motor. Their researches where they studied the influence of surface roughness, temperature and electrical current with relation to the material properties and local contact dynamics were published in [1, 2, 3, 4, 5]. Most of this work with theory and numerical verifications were collected in his doctoral dissertation [6]. In [6] a general approach of modeling the dynamics of planar rigid bodies of arbitrary shape was presented.

Milković and Ban [7] studied the influence of the pulsating current supply of the commutator machine on the size of contact area. Experimentally, they found that an increase of amplitude of the pulsating current leads to a decrease in the coefficient of friction.

Senouci et al. studied the wear mechanism of a electric sliding contact between graphite-copper [8]. They found that the orientation of graphite and applied normal load affects on the wear which increase the mechanical wear but decrease the electrical wear. Furthermore, they observed the decrease of coefficient of friction and small difference of wear between anode and cathode brush.

Recently Argibay et al. researched [9] the irregular wear between the anode and the cathode brush. They observed differences between brushes in the coefficient of friction, contact resistance and temperature.

The influence of the current, sliding speed and normal load on the coefficient of friction and wear of a carbon-graphite material were studied by Zhao et al. [10]. They found, the wear rate to follow Archard's law [10] when the contact was without electrical current. When the electrical current was applied the friction and wear behaviours changed significantly [10].

Zhonglinag et al. [11] studied the impact factor, consisting of the contact pressure and peripheral speed, on the wear of carbon brushes. The wear of the brushes was found to depend on the power density. Up to 0,5MW/m^2, the contact film was good and dominated mechanical wear. If the power density was greater than 0,5MW/m^2 then it begins to dominate the electrical wear, which increases exponentially. The increased wear was induced by changing the state of the surface film (high temperature on brushes).

The effect of temperature on the wear of the brush was studied by Hsing-Pang et al. [12]. They found out that the brush wear rate dropped steeply as the brush temperature increased from $80°$C to $103°$C at 10m/s sliding speed. When the sliding speed was 40m/s, they found that the brush wear rate suddenly increased by several times as brush temperature approached $149°$C. With this results they indicated that the brush wear rate generally increased with increasing brush temperature.

The influence of humidity and current density abrasion were studied by Hu et al. [13]. They found that by increasing the current density increases the thickness of the oxide film on the surface, which increases the resistance and consequently on the wear of brushes. However, the oxide film acts as a lubricant and it is in need to compensate for the air humidity, which influences the formation of the oxide film. They found that at 10% humidity a sufficient film thickness can not be formed, therefore the wear rate compared with 50% humidity was higher.

The aim of our work was to study the essential parameters which effects on the wear of the electric brushes. The previous research only rarely emphasizes the effect of changes in the voltage drop and temperature as a function of speed, and at constant electric current to the brush wear rate. The focus of this paper is to experimentally research the influence of rotational speed and electrical current on the contact situations.

2 EXPERIMENTAL SETUP

A scheme of the test machine which is a kind of pin-on-slip ring design, is shown in Figure 1.

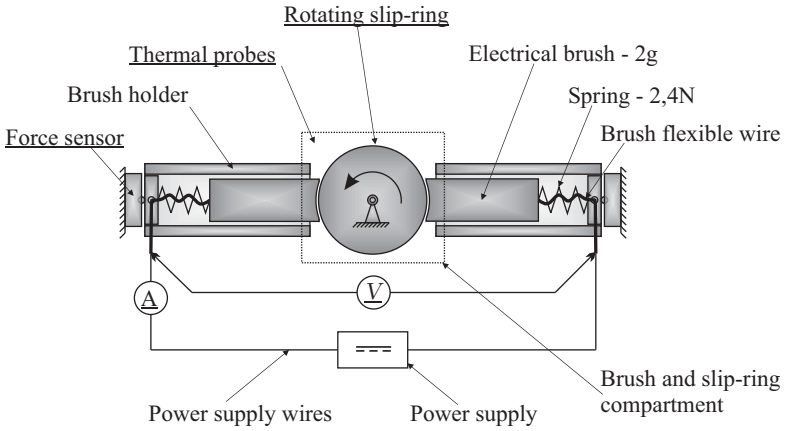


Figure 1: Schematic test bench. Measured and controlled parameters are underlined.

The shaft with the slip-rings is driven by servo motor (Unimotor fm, 115) via belt. This allow us to rotate slip-rings up to 15000 revolutions per minute (RPM). Because the shaft is driven with the pulleys, the rotational speed of the shaft is measured with an encoder and a Hall sensor (HallD).

The slip-rings were mounted on the shaft and short-circuited (surfaces connected between with short copper wire). They are connected in electrical circuit through the contacts with brushes. The nominal contact area between the brush tip and slip-ring is approximately 6,4mm $\times$ 4,6mm through which flows up to 5A of DC electrical current, generated by power supply (TDK Lambda, HWS600-2). The current is controlled with Mosfet (ST, BDX53C) by National Instruments - Analog output card (NI 9269) and measured with Lem (LEM, HX 10-P/SP2). For better understanding what is happening in the contacts, we are measuring the voltage drop between left brush, slip-rings and right brush with NI 9239, as shown in Figure 1.

The contact between 2g electrical brush and slip-ring is provided by the spring. The spring is mounted between the end of the brush and adapter to the force sensor. Inside of the spring a flexible wire slightly increases the force on the contact with its stiffness. With the force sensor

(HONEYWELL, FSS1500NSB), the contact pressure is measured.

The brush and slip-ring compartment on the test bench is the same size as in the alternator. To simulate different operating thermal loads on the test bench, we can apply thermal loads with the heat-gun. The temperature is measured at the slip-ring compartment and on the brushes with a K type thermal probes (ambient, slip-ring compartment, brush holder, brushes).

3 IDENTIFICATION OF TEMPERATURE AND VOLTAGE DROP AT THE BRUSHES

The slip-rings with outer copper ring (from SE-Cu material with 1,65mm wall thickness) molded in plastic (for insulation between slip-ring and shaft) were mounted on the shaft. Before the test, slip-rings were machined with finished assembly of the shaft on the 16,4mm other diameter, to ensure correct roundness and roughness on slip-rings surfaces.

The tested brushes were metal-graphite. They were made by sintering process and contain approximately 36% of copper and 64% of carbon with small percentage of other materials. Because the deviations of proportions of materials in brush have insignificant impact on brush wear and on our results, all the tests below were done on this type of brush and on the brushes from the same batch.

During the tests presented below we ensure constant ambient temperature at 23°C and in tolerance $\pm$ 2°C. Also the load on brushes were constant and in tolerances 2,8 $\pm$ 0,2 N.

The research were done at different electrical loads and rotating speeds. Simulated loads were defined by experiences and by alternator operating profile. Therefore rotating speed varied from 1000 to 12000 RPM and electrical loads from 1 A to 3 A.

The voltage drop at the brush according to rotating speed and current versus time are presented in Figures 2, 3 and 4. As can be seen in Fig. 2 the voltage drop decreased with the increase of rotating speed. The same can be seen in Figure 3 for 2A electrical load and in Figure 4 for 1A electrical load.

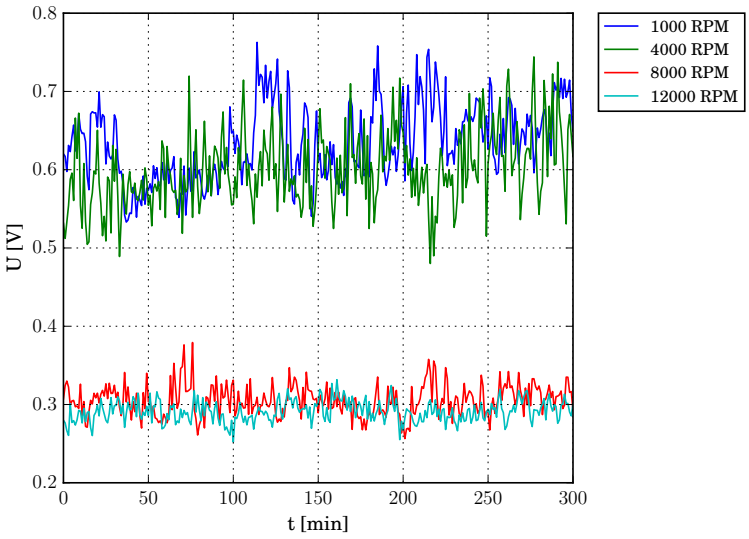


Figure 2: Effect of rotating speed on voltage drop at constant 3A current.

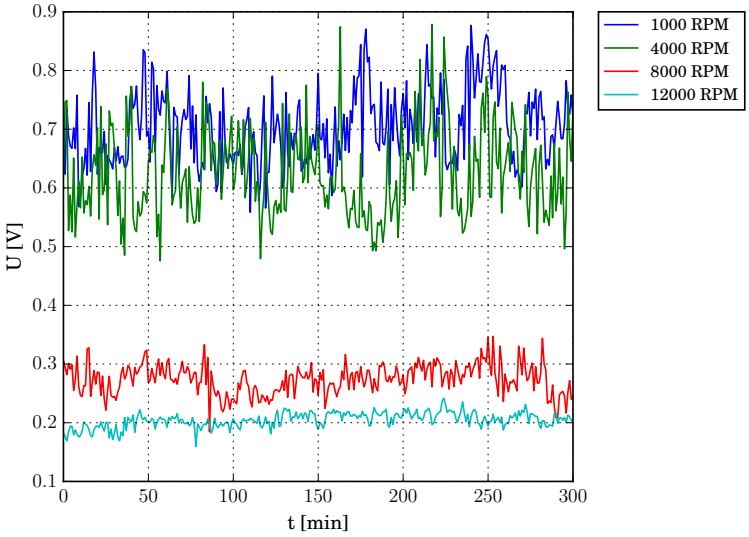


Figure 3: Effect of rotating speed on voltage drop at constant 2A current.

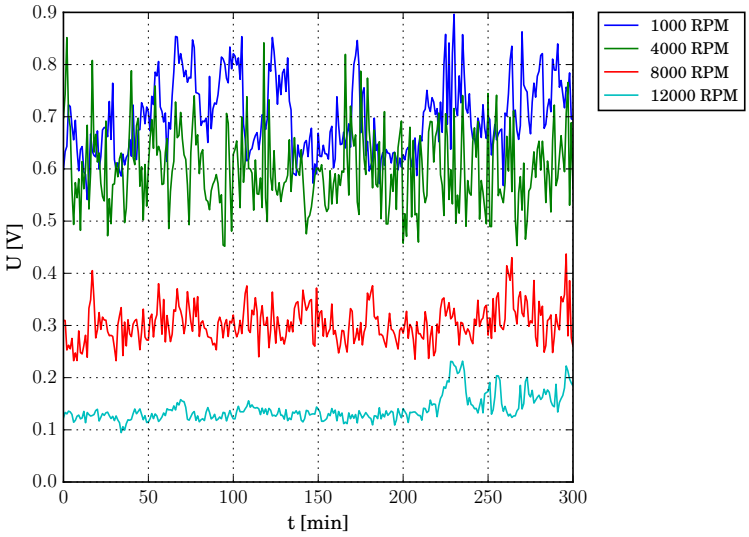


Figure 4: Effect of rotating speed on voltage drop at constant 1A current.

The response of temperature as a function of rotating speed and electrical current versus time is presented in Figure 5. As can be seen, the temperature increase, if the rotating speed increase. On the other side with the increase of the electrical load, there was no significant influence on change of temperature. One reason for this is the small difference between electrical load and

the second, the temperature represents the slip-rings compartment temperature.

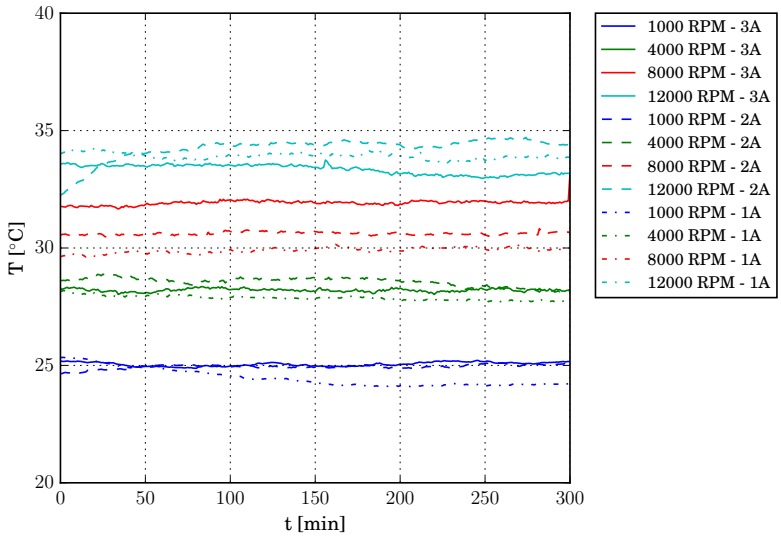


Figure 5: Effect of rotating speed and current on temperature.

4 RESULTS AND DISCUSSION

The variable rotating speed of the slip-ring and different electrical loads, leads the brushes to different contact situations and speed of wear.

Before comparing the results, it is important to point the effect of voltage drop and temperature at the beginning of the tests. If the test specimen was inactive for more than 2 hours it is necessary to run-in the slip-rings and brushes for more than 1 hour at constant conditions (rotating speed and current). In this run-in time, the temperature was rising sharply to maximum temperature. At that point the temperature start decreasing slowly to constant temperature when it stabilized. On the length of run-in time depends rotating speed and electrical current. When the system become stable, the measurements were taken for 300 minutes.

A comparison of Fig. 2 with Fig. 3 and Fig. 4 showed the effect of voltage drop versus electrical current at different rotating speeds. In all figures are the same effect, when the rotating speed increases the voltage drop in whole system (brush, slip-rings, brush) decreases. At higher rotating speeds there were also less deviations of voltage drop.

At 3A current the voltage drop versus different rotating speeds there were smaller deviations compared to the 2A or 1A electrical load. At lower electrical loads there was also wider range of voltage drop at constant rotating speed.

In Fig. 5 where are all temperatures for different loads, we can conclude that the rotating speed of the slip-ring have major effect on temperature rise. These correlations were also presented on the wear process.

5 CONCLUSIONS

A test machine with the capacity of 15000RPM and 5A current was developed. The temperature, voltage drop and wear behaviours of metal graphite brushes in combinations of rotating speed and electrical current were studied.

The rotating speed of the slip-rings have the main influence on the contact formulation which responses on voltage drop and on temperature. These combinations have also influence on the wear of brushes which reflected on different speeds of wear.

REFERENCES

[1] Slavič J., Nastran M. and Boltežar M., Modeling and analyzing the dynamics of an electric-motor brush. *Journal of Mechanical Engineering*, **52**, 126–137, 2006.

[2] Slavič J. and Boltežar M., Non-linearity and non-smoothness in multi-body dynamics: application to woodpecker toy. *Proceedings of the Institution of Mechanical Engineers, Part C: Journal of Mechanical Engineering Science*, **220**, 285–296, 2005.

[3] Slavič J. and Boltežar M., Simulating Multibody Dynamics With Rough Contact Surfaces and Run-in Wear. *Nonlinear Dynamics*, **45**, 353–365, 2006.

[4] Slavič J. and Boltežar M., Measuring the dynamic forces to identify the friction of a graphite-cooper contact for variable temperature and current. *Wear*, **260**, 1136–1144, 2006.

[5] Slavič J., Bryant M. and Boltežar M., A new approach to roughness-induced vibrations on a slider. *Journal of Sound and Vibration*, **306**, 732–750, 2007.

[6] Slavič J., Nonlinear and nonsmooth dynamics of discretely defined system of rigid bodies with unilateral contacts. *Doctoral dissertation, University of Ljubljana, Faculty of Mechanical Engineering*, 2005.

[7] Milković M. and Ban D., Influence of the pulsating current amplitude on the dynamic friction coefficient of electrographite brushes. *Carbon*, **34**, 1207–1214, 1996.

[8] A. Senouci, J. Frene and H. Zaidi, Wear mechanism in graphite-copper electrical sliding contact. *Wear*, **225-229**, 949–953, 1999.

[9] N. Argibay, J.A. Bares and W.G. Sawyer, Asymmetric wear behavior of self-mated copper fiber brush and slip-ring sliding electrical contacts in a humid carbon dioxide environment. *Wear*, **268**, 455–463, 2009.

[10] H. Zhao, G.C. Barber and J. Liu, Friction and wear in high speed sliding with and without electrical current. *Wear*, **249**, 409–414, 2001.

[11] Hu Zhongliang, Chen Zhenhua, Xia Jintong and Ding Guoyun, Effect of PV factor on the wear of carbon brushes for micromotors. *Wear*, **265**, 336–340, 2007.

[12] Liu Hsing-Pang, Robert W. Carnes and John H. Gully, Effect of temperature on wear rate of homopolar pulse consolidated electrical brushes. *Wear*, **167**, 41–47, 1993.

[13] Z.L. Hu, Z.H. Chen and J.T. Xia, Study on surface film in the wear of electrographite brushes against copper commutators for variable current and humidity. *Wear*, **264**, 11–17, 2007.

International Conference on Engineering Vibration
Ljubljana, Slovenia, 7-10 September 2015

INVESTIGATING THE APPLICATION OF GUIDED WAVE PROPAGATION FOR ICE DETECTION ON COMPOSITE MATERIALS

Siavash Shoja*, Viktor Berbyuk, Anders Boström

Applied Mechanics, Chalmers University of Technology, SE-412 96, Gothenburg, Sweden
{siavash.shoja,viktor.berbyuk,anders.bostrom}@chalmers.se

Keywords: Guided Waves, Composite, Ice Detection, Wind Turbines, Multi-layered Material.

Abstract. *Wind turbines operating in cold regions face icing problems. At the same time these regions are one of the best places to install the wind turbines. To minimize this problem and optimize the de-icing system it is very important to have an efficient ice detection system. Application of guided wave propagation has been previously considered in aircraft industries. To study this application for wind turbines, guided wave propagation should be investigated in composite materials. In the current work, first the guided wave propagation in multi-layered anisotropic materials is mathematically modelled and dispersion curves were obtained. Moreover the composite plate was homogenized to an anisotropic plate in order to simplify the calculations. Comparison of dispersion curves shows changes in group velocity when a second layer as ice is added on top of the first layer. Next, a finite element model was made to observe the effects of ice accretion on top of a composite plate. An experimental set-up was also developed at a cold climate lab on a composite test object used in wind turbine industry. The guided wave propagation was studied experimentally to see the effect of temperature and ice on the material and measurement data was obtained to validate the computational model. Both numerical and experimental results show that a patch of ice on top of a composite plate reflects the propagated guided waves with an amplitude that raises by increasing the thickness of the ice layer. Furthermore, ice accumulation affects the group velocity of the guided waves and it proves that the use of guided waves is a promising method to detect ice on turbine blades.*

1 INTRODUCTION

Some of the best sites to install wind turbines are located at higher altitudes or in cold regions. Wind speed increases approximately by 0.1 m/s each 100 m of altitude for the first 1000 m [1]. Moreover, wind turbines operating in cold regions have higher potential of wind power due to higher air density and consequently higher wind kinetic energy [2].

One of the biggest obstacles which prevents the wind farms to be set up in these regions is icing problems. Previous studies show that ice accumulation on wind turbine blades influences the power production [3, 4]. Accretion of ice on the blades reshape the blade airfoil. Virk *at al.* [5] found a significant change in the flow behavior and aerodynamic characteristics of the blades which leads to considerable power loss. Additionally, increasing ice accretion on the blades causes mechanical failure due to higher load on the blades, electrical failure, measurement error and safety hazard due to ice throw [1, 6]. In order to optimize the de-icing system of the wind turbines it is important to know the location of ice, amount of it and type of it. This information can be gained using an efficient ice detection method.

Homola *et al.* [7] and Parent *et al.* [1] made comprehensive reviews on the available methods of ice detection. Generally the methods can be divided into two groups of in-direct and direct methods. The direct methods detect some parameter which changes by accretion of ice such as mass, wave velocity, reflective properties etc. In the in-direct methods, the measurement is based on either the weather conditions which lead to icing problems or measuring the effect of icing such as reductions in power production. The above reviews show that all of the available ice detection methods have pronounced disadvantages and are not highly efficient. However, using ultrasonic guided wave approach is one of the most promising ones applicable to wind turbines [7].

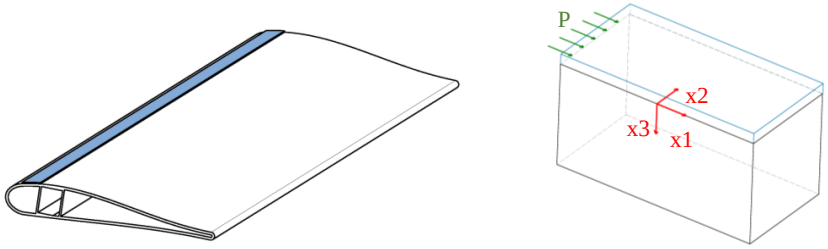
Application of guided wave propagation for ice detection on aircraft wings has been previously introduced. Chamuel [8] has proposed and designed a detection system by monitoring variations in flexural waves transmitted through the outer surface of an aircraft airfoil. A somewhat similar system was proposed by Luukkala [9]. In his work a device was designed and used to collect the water on the wing and continuously examine it using ultrasonic waves to find out if ice is built. Liu *et al.* [10] used two types of ultrasonic transducers on the inner part of an aircraft wing skin to monitor the ice build-up by measuring the thickness. Using this technique they could measure the thickness of ice in the range of 1 mm to 1.5 mm on a 3 mm aluminum plate. Gao and Rose [11] proposed a new model based on the analysis of guided-wave propagation in multi-layered structures to detect the ice. Using the model they could detect thickness and type of ice accumulated on an aluminum plate. They also evaluated the method using a sample experiment.

More studies have been done on de-icing models using ultrasonic waves in which it has been tried to use the shear force due to wave propagation to remove the ice from the surface of the plates [12-14, 6].

The current work is focused on using guided waves in order to detect the ice on a composite plate which has applications on wind turbines. First a mathematical model is proposed to analyze the guided wave propagation in multi-layers. The multi-layer structure consists of two layers where the first one is an anisotropic material representing the composite plate and the second layer is an isotropic material representing the ice. Next, the composite plate is simplified by a homogenization model in order to be able to build a FE model and the numerical results are presented. Finally an experimental set-up was developed and changes in the output signal are presented in different scenarios.

2 THEORY

The skin of wind turbine blades is mainly made of composite materials and its thickness varies depending on size and type of the turbine. The surface has an airfoil shape and has curvature, however, in a selected region along the blade it can be considered as a flat plate. Since in our model the wavelength of the guided wave is much larger than the thickness of the plies, the composite plate is considered as a homogenous and anisotropic material. At the beginning of ice accretion on the blade, it follows the shape of the blade. In this case, ice can also be modelled as a flat plate and by neglecting its microstructure, it can be modeled as a homogenous and isotropic material.



(a) (b)

Figure 1: (a) Schematic view of a piece of turbine blade and accumulated ice; (b) 3D view of a 2-layered model.

2.1 Wave mechanics

Wave propagation in multilayers has been investigated by the transfer matrix method [15, 16]. In this method propagation equations are built in a matrix form for an arbitrary number of layers. The solution of each layer is connected to the next one by applying the continuity conditions. This method is used for multilayered anisotropic materials by Nayfeh [17, 18] and different scenarios were considered later on for different combinations of isotropic and anisotropic layers [19]. The problem is solved here for this specific case.

The displacement of the wave field in each layer can be obtained by applying Hooke's law and deriving the equation of motion:

$$\rho^{(n)}\ddot{u}_i = C_{ijkl}^{(n)} \frac{\partial^2 u_l}{\partial x_j \, \partial x_k} \qquad n = (1,2) \tag{1}$$

Here n is the number of each layer, ρ is the density and C is the stiffness matrix. To solve the equation, the displacement is assumed in the form

$$u_i^{(n)} = U_i e^{i(k_m x_m - \omega t)} \tag{2}$$

where k_m is the wave number and ω is the angular frequency. Since the material changes in the vertical direction from the first material to the second one, k_3 becomes a function of thickness. By using Eq. (2) and Eq. (1) the following Christofel equation is obtained

$$\left(\Gamma_{im}^{(n)} - \rho^{(n)}\omega^2 \delta_{im}\right)\{U_m\} = 0 \tag{3}$$

Here

$$\Gamma_{im} = C_{iklm} k_k k_l \tag{4}$$

For a nontrivial solution, the determinant of the coefficient matrix in Eq. (3) has to be set equal to zero:

$$\left|\Gamma_{im}^{(n)} - \rho^{(n)}\omega^2 \delta_{im}\right| = 0 \tag{5}$$

Since the problem is going to be solved in 2D, U_2, x_2 and k_2 are removed from the equations. By solving Eq. (5) for k_3, four solutions will be obtained in each layer where each solution is a function of k_1 (wave-number in the direction of propagation) and ω. By rewriting Eq. (3) based

on the obtained results for k_3 it is possible to make the equation only depending on k_1 and ω. Eqs. (6) to (9) are obtained for displacement and stress by summing up all the results.

$$U_1^{(n)} = \sum_{j=1}^{4} B_{1j}^{(n)} U_{1j}^{(n)} e^{i(k_1 x_1 + k_{3j}^{(n)} x_3 - \omega t)} \tag{6}$$

$$U_3^{(n)} = \sum_{j=1}^{4} B_{3j}^{(n)} U_{3j}^{(n)} e^{i(k_1 x_1 + k_{3j}^{(n)} x_3 - \omega t)} \tag{7}$$

$$\sigma_{33}^{(n)} = \sum_{j=1}^{4} i k_1 D_{1j} U_{1j} e^{i(k_1 x_1 + k_{3j}^{(n)} x_3 - \omega t)} \tag{8}$$

$$\sigma_{13}^{(n)} = \sum_{j=1}^{4} i k_1 D_{3j} U_{1j} e^{i(k_1 x_1 + k_{3j}^{(n)} x_3 - \omega t)} \tag{9}$$

Here B_1, B_3, D_1 and D_3 are constants which should be found later. Next, by applying the boundary conditions (BCs) it is possible to create the transformation matrix in the Eq. (10). The BCs are continuity of stress and displacement between the two layers and zero stress and traction in top and bottom free surfaces (Figure 2).

$$\begin{bmatrix} A_{11} & \cdots & A_{18} \\ \vdots & \ddots & \vdots \\ A_{81} & \cdots & A_{88} \end{bmatrix} \begin{Bmatrix} B_1^{(1)} \\ \vdots \\ D_3^{(2)} \end{Bmatrix} = 0 \tag{10}$$

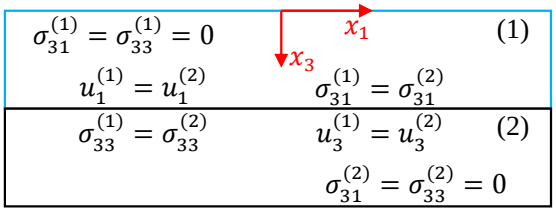


Figure 2: 2D model of the layers with appropriate BCs.

The matrix A is a function of k_1 and ω and for nontrivial solution, the determinant of the coefficients has to set equal to zero which makes the dispersion relation.

$$|A(k_1, \omega)| = 0 \tag{11}$$

Solving the dispersion equation includes numerical difficulties. Garcia *et al* [20] introduced a new method to create the dispersion curves using Floquet-Bloch theory in a unite cell and solve it by finite elements. In this study, their method is first evaluated in one case and then used to create the dispersion curves in other scenarios.

2.2 Homogenization of material

One method to investigate the propagation of guided waves in composite structures is to calculate equivalent stiffness properties for the structure and consider it as one layer of anisotropic material. Here a plate theory can be used. Classical laminate plate theory neglects shear deformations. To include the shear forces, other theories such as first order shear deformation theory (FSDT) or higher order shear deformation theory have been introduced. It has been shown that FSDT gives good accuracy in wave propagation problems, however, the results depends on shear correction factor and plate thickness [21].

The material used in this study is a 20 mm thick composite plate with 62 layups. To investigate the validity of using FSDT to homogenize the material, first the equations for dispersion curves were solved for a multilayered geometry with 62 layers and the results have been compared with the dispersion curves in a homogenized plate with the same thickness. Figure 3 shows that reasonable results are obtained for the frequencies lower than 0.7 kHz m for the first 3 modes (the green zone) which means it is possible to use this method for further calculations.

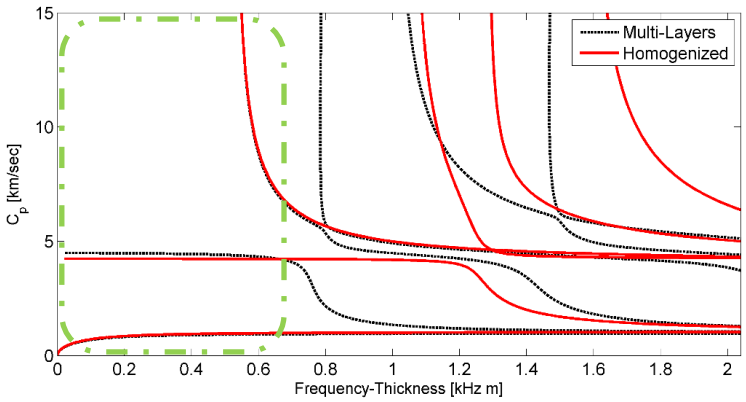
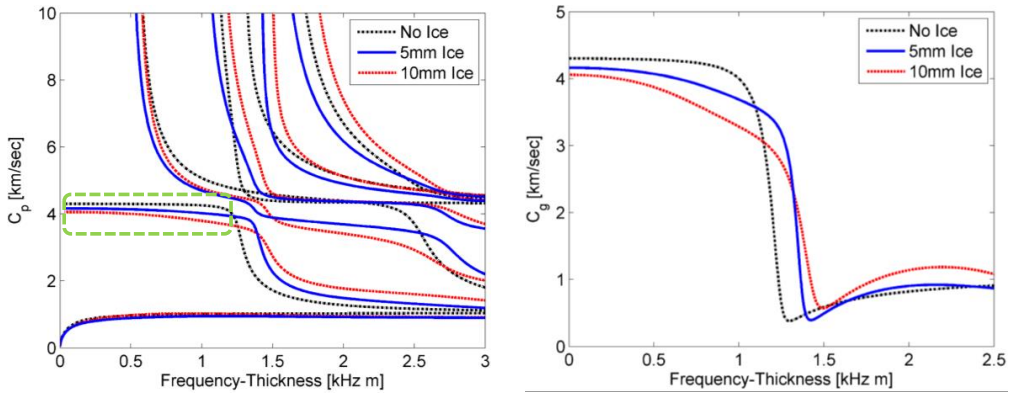


Figure 3: Comparison of dispersion curves obtained for multilayered structure versus a homogenized plate.

2.3 Effect of ice layer on dispersion curves

To make a rough estimation about the possibility of ice detection using guided waves, dispersion curves were obtained for two layers of homogenized composite plate and a layer of ice. As mentioned, ice is modeled as an isotropic material and properties are taken from the literature [22]. Figure 4 shows the results for a 20 mm composite plate in 3 scenarios of no-ice, 5mm ice and 10mm ice.



(a) (b)

Figure 4: Comparison of dispersion curves for no ice on the plate, 5mm ice and 10mm ice on the plate (a) Phase velocity versus frequency (b) group velocity versus frequency for symmetric modes.

Changes due to accretion of ice is negligible in the first mode, but it is significant in the second and higher modes. The green zone in Figure 4 shows the best possible frequencies which make significant change in phase velocity during ice accumulation.

3 NUMERICAL MODEL

The numerical study is performed by creating a 2D FE model and applying the excitation on one side. The geometry is a 20 mm by 8 m rectangle as the composite plate and a rectangle as ice with 1m length and different sizes for the thickness. The second layer is located between 4 m and 5 m length from the excitation side of the plate. Wave is applied as a windowed sinus wave with 5 kHz center frequency and it is detected at 2 m and 6 m from the excitation side. Figure 5 shows the schematic view of the FE model.

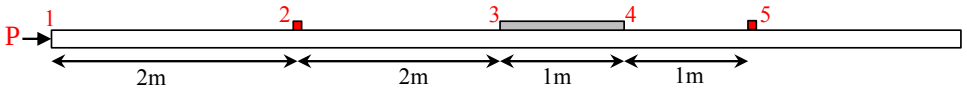


Figure 5: Schematic view of FE model.

Since the excitation is in the longitudinal direction, waves propagate as symmetric modes. However, when the wave reaches the second layer it creates reflections in both symmetric and asymmetric modes. The effect of reflection is visible in Figure 6 (Region I). The amplitude of reflections rises proportionally by increasing thickness of ice layer (Figure 7-a).

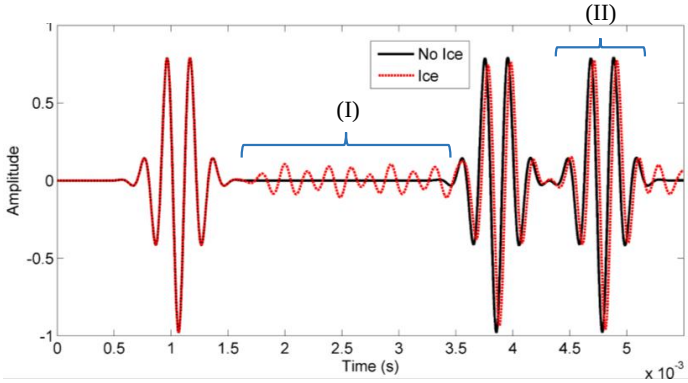


Figure 6: Comparison of the signal at the first detection point for a plate with and without ice.

The amplitude of the signal decreases after the wave propagates two times through the material when a layer of ice is added on the plate. Furthermore, a phase shift can be observed in the signal which is due to change in group velocity. Figure 7-b shows a comparison in this region for different thickness of the ice layer.

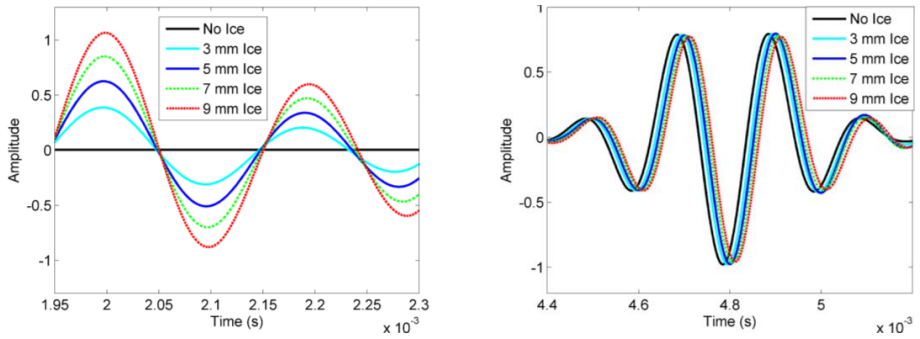


Figure 7: Comparison of the signal for different thickness of ice layer in (a) region I and (b) region II.

4 EXPERIMENTAL STUDY

The experimental setup was made in a cold climate lab on a composite plate with the dimensions of 0.02 × 0.2 × 8 m (Figure 8). The test object contains 62 layups of glass fiber and Vinylester which is a common material used in the wind turbine industry. The plate was excited from one side using a transducer in the longitudinal direction. The signal was detected at two points 2 m and 6 m from the excitation side using two accelerometers. The excitation signals are windowed sinus waves at the three frequencies 3, 5 and 7 kHz. More details about the experimental setup has been explained in previous work [23]. The effect of temperature and ice is investigated in this experimental work.

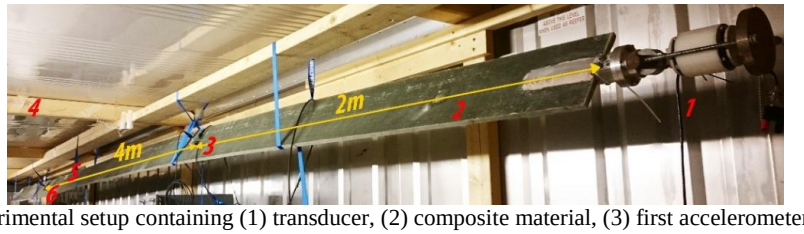
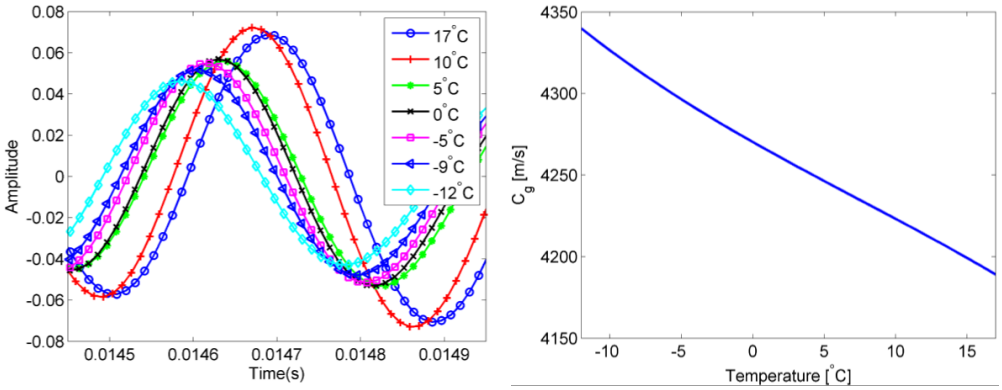


Figure 8: Experimental setup containing (1) transducer, (2) composite material, (3) first accelerometer, (4) thermometer for surrounding temperature, (5) thermometer for material temperature, (6) second accelerometer.

4.1 Effect of temperature

It is important to know how the behavior of the material changes at low temperatures when a wave is propagating through it. To investigate this characteristic the material was cooled down from the room temperature to -12 ºC and the signal was detected continuously.



(a) (b)

Figure 9: (a) Comparison of signal for different temperatures and (b) group velocity versus temperature

Results show that by decreasing the temperature, the amplitude of the signal is decreasing but the group velocity is increasing (Figure 9). These changes can be observed even between -9 ºC and -12 ºC. This is because Young's modulus of the resin is highly depended on temperature and lowering the temperature makes the composite more rigid.

4.2 Effect of ice accretion

The effects of ice accration was investigated by building ice on the plate. The method of manufacturing ice has been explained in previous work [23]. Here ice was built at -12 ºC and it is a mixture of glaze and rime ice and located between 4 m and 5 m from the excitation side.

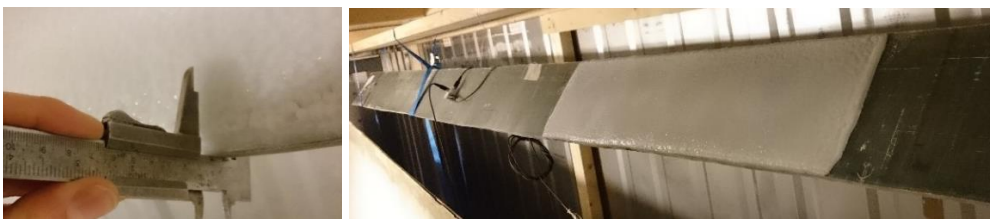


Figure 10: manufactured ice on the plate.

Changes of the signal due to icing conditions can be observed in two different regions (Figure 11), first when the signal reflects back to the first sensor from the ice layer which makes

larger amplitude (I) and second when wave travels two times through the plate which lowers the amplitude and group velocity (II).

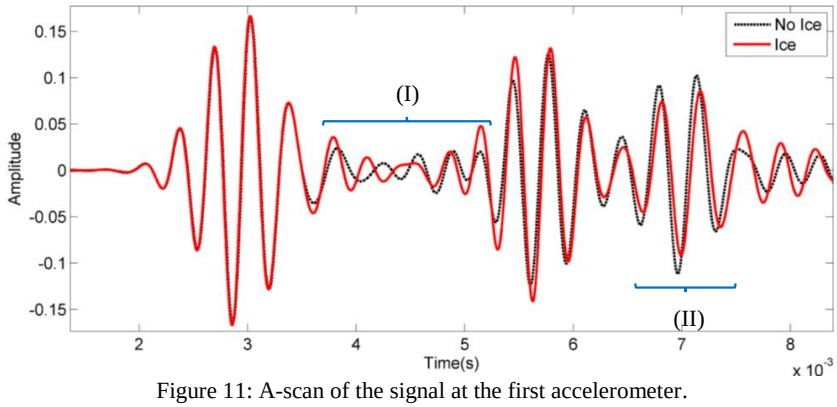
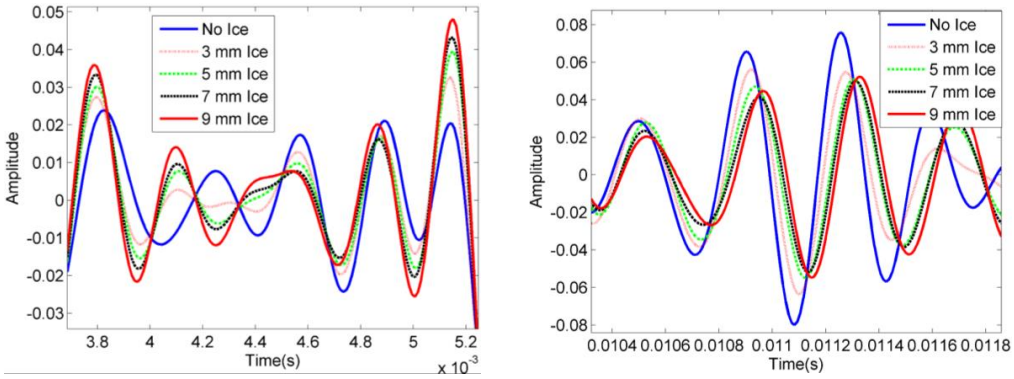


Figure 11: A-scan of the signal at the first accelerometer.

The changes of the signal can be observed further in Figure 12 for different ice thicknesses. Comparisons show that increasing the thickness of ice creates larger reflections (a) and lowers the amplitude and group velocity (b).



(a) (b)

Figure 12: A-scan of the signal for different thicknesses of ice in (a) region I and (b) region II.

Finally by calculating the group velocity for different ice thicknesses, it is possible to see the changes due to icing on the material. Group velocity was calculated for three different excitation frequencies. The decrease in group velocity because of ice accretion is significant.

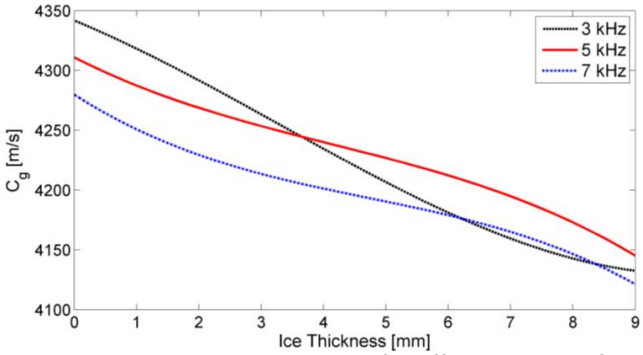


Figure 13: Group velocity versus ice thickness for different excitation frequencies.

5 CONCLUSIONS

Propagation of guided wave in composite materials has been investigated in this study in order to be able to detect a layer of ice on the plate. Studying the dispersion curves shows that FSDT can be used to approximate the composite plate with a homogeneous material for frequencies lower than 1.2 kHz m. Moreover, adding a second layer (ice) on top of the composite layer makes significant changes in phase and group velocity of symmetric modes in a specific frequency range.

A numerical model was also made to predict the results due to ice accretion and it shows that adding a second layer as ice on top of the first layer creates reflections, for which the amplitude raises by increasing the thickness of the ice layer. After the wave propagates two times through the material it is possible to see a decrease in amplitude and group velocity of the wave.

Significant dependency of the properties of the material on temperature was observed in the experimental work. It showed that group velocity of the wave raises by lowering the temperature. Ice was manufactured on top of the composite plate and the plate was excited at three different frequencies. It is possible to see that accretion of ice creates reflections and the amplitude of the reflected wave raises by increasing the ice thickness. Moreover, increasing the thickness of ice creates lower amplitude and lower group velocity of the wave. The group velocity decreases about 200 m/s when 10 mm ice is accumulated on the plate.

6 ACKNOWLEDGEMENTS

This project is part of a PhD project “Ice detection for smart de-icing of wind turbines” and it funded by Swedish Energy Agency (Dnr 2013-001475, project 37286-1). The authors would like to thank Mr. Jan Möller for all the technical support in the experimental tests.

REFERENCES

[1] Parent, O. and A. Ilinca, *Anti-icing and de-icing techniques for wind turbines: Critical review*. Cold Regions Science and Technology, 2011. **65**(1): p. 88-96.

[2] Fortin, G., J. Perron, and A. Ilinca, A Study of Icing Events at Murdochville: Conclusions for the Wind Power Industry, in International Conference of Wind energy and remote regions. 2005: Magdalen Islands.

[3] Homola, M.C., et al., Performance losses due to ice accretion for a 5 MW wind turbine. Wind Energy, 2012. **15**(3): p. 379-389.

[4] Lacroix, A. and J.F. Manwell, *Wind Energy: Cold Weather Issues*, in *Renewable Energy Research Laboratory*. 2000, University of Massachusetts at Amherst: Amherst.

[5] Virk, M., M. Homola, and P. Nicklasson, Effect of Rime Ice Accretion on Aerodynamic Characteristics of Wind Turbine Blade Profiles. Wind Engineering, 2010. **34**(2): p. 207-218.

[6] Shajiee, S., L. Pao, and R. McLeod, *Monitoring Ice Accumulation and Active De-icing Control of Wind Turbine Blades*, in *Wind Turbine Control and Monitoring*, N. Luo, Y. Vidal, and L. Acho, Editors. 2014, Springer International Publishing. p. 193-230.

[7] Homola, M.C., P.J. Nicklasson, and P.A. Sundsbø, *Ice sensors for wind turbines.* Cold Regions Science and Technology, 2006. **46**(2): p. 125-131.

[8] Chamuel, J.R., Ultrasonic aircraft ice detector using flexural waves. 1984, Google Patents.

[9] Luukkala, M., Detector for indicating ice formation on the wing of an aircraft. 1995, Google Patents.

[10] Liu, Q., et al., In situ ice and structure thickness monitoring using integrated and flexible ultrasonic transducers. Smart Materials and Structures, 2008. **17**(4).

[11] Gao, H. and J.L. Rose, *Ice detection and classification on an aircraft wing with ultrasonic shear horizontal guided waves.* Ultrasonics, Ferroelectrics, and Frequency Control, IEEE Transactions on, 2009. **56**(2): p. 334-344.

[12] Venna, S., Y.-J. Lin, and G. Botura, Piezoelectric Transducer Actuated Leading Edge De-Icing with Simultaneous Shear and Impulse Forces. Journal of Aircraft, 2007. **44**(2): p. 509-515.

[13] Zhu, Y., Structural tailoring and actuation studies for low power ultrasonic de-icing of aluminum and composite plates. 2010, The Pennsylvania State University: Ann Arbor. p. 196.

[14] Overmeyer, A., J. Palacios, and E. Smith, *Ultrasonic De-Icing Bondline Design and Rotor Ice Testing.* AIAA Journal, 2013. **51**(12): p. 2965-2976.

[15] Thomson, W.T., *Transmission of Elastic Waves through a Stratified Solid Medium.* Journal of Applied Physics, 1950. **21**(2): p. 89-93.

[16] Haskell, N.A., *The dispersion of surface waves on multilayered media.* Bulletin of the Seismological Society of America, 1953. **43**(1): p. 17-34.

[17] Nayfeh, A.H., *The general problem of elastic wave propagation in multilayered anisotropic media.* The Journal of the Acoustical Society of America, 1991. **89**(4): p. 1521-1531.

[18] Nayfeh, A.H., Wave propagation in layered anisotropic media : with Applications to Composites. 1st ed. 1995: North Holland. 332.

[19] Maghsoodi, A., A. Ohadi, and M. Sadighi, *Calculation of Wave Dispersion Curves in Multilayered Composite-Metal Plates.* Shock and Vibration, 2014: p. 6.

[20] García, P.G. and J.-P. Fernández-Álvarez, *Floquet-Bloch Theory and Its Application to the Dispersion Curves of Nonperiodic Layered Systems.* Mathematical Problems in Engineering, 2015. **2015**: p. 12.

[21] Maio, L., et al., Ultrasonic wave propagation in composite laminates by numerical simulation. Composite Structures, 2015. **121**(0): p. 64-74.

[22] Carney, K.S., et al., *A phenomenological high strain rate model with failure for ice.* International Journal of Solids and Structures, 2006. **43**(25–26): p. 7820-7839.

[23] Berbyuk, V., Peterson, B., Möller, J., Towards early ice detection on wind turbine blades using acoustic waves. *Proc. of SPIE, Nondestructive Characterization for Composite Materials, Aerospace Engineering, Civil Infrastructure, and Homeland Security, San Diego, California, USA, March 09, 2014*, 9063 pp. 90630F-1 - 90630F-11.

Computational Methods (TP03)

11th International Conference on Engineering Vibration
Ljubljana, Slovenia, 7–10 September 2015

APPLICATION OF THE WAVE BASED METHOD TO STEADY-STATE VIBRATIONS OF THICK PLATES

M. Klanner*[1], K. Ellermann[2]

[1]Graz University of Technology, Institute of Mechanics, Kopernikusgasse 24/IV, 8010 Graz, Austria
michael.klanner@tugraz.at

[2]Graz University of Technology, Institute of Mechanics, Kopernikusgasse 24/IV, 8010 Graz, Austria
ellermann@tugraz.at

Keywords: Structural dynamics, Wave Based Method, Indirect Trefftz method, Mindlin plate theory, Plate bending vibrations.

Abstract. *The numerical simulation of low frequency harmonic responses of plates is usually carried out with deterministic methods, especially with the Finite Element Method (FEM), while for high frequencies statistical methods are used like the Statistical Energy Analysis (SEA). In the so-called mid-frequency region, the computational load of FEM is generally too high for practical simulations, while the assumptions of SEA are not meet. The applicability of a deterministic method called Wave Based Method (WBM) can be extended to the mid-frequency range due to a higher computational efficiency. The WBM is an indirect Trefftz method and uses exact solutions of the governing equations to approximate the unknown field variables. The method has already been developed for thin plates using the Kirchhoff plate theory, which neglects the shear deformation and rotatory inertia. A first order shear deformation theory, the Mindlin plate theory, accounts for the shear deformation and rotatory inertia and is used to extend the applicability of the WBM to thick plates. A numerical example is shown for a non-convex plate domain under point force excitation, which requires the decomposition into convex subdomains to ensure convergence. The convergence rate and computational efficiency of the WBM is compared to the FEM.*

1 INTRODUCTION

Due to government regulations and costumer requirements, the enhanced importance of noise and vibration characteristics of newly developed products needs to be taken into account in the early design phases. Therefore, efficient and accurate calculation methods are required, since virtual prototyping is commonly used in the early stages of product development.

Depending on the viewed frequency range, different kinds of methods are commonly used for the calculations. In the low frequency range, the Finite Element Method (FEM) [1] is commonly applied for the calculation of the structural vibrations, while the Boundary Element Method (BEM) [2] is used for the acoustic simulations. The efficiency of these two methods decreases with higher frequencies, since a certain number of elements per wavelength is needed to get accurate results [3].

In the high frequency range, statistical methods like the Statistical Energy Analysis (SEA) [4] become suitable for the calculation of vibration and noise. The accuracy of SEA depends on certain assumptions like high modal overlap and equipartition of energy, which are usually only fulfilled at high frequencies.

There is a gap between the low and high frequency range, for which neither the commonly used deterministic methods like FEM and BEM nor the SEA is practically suited. Many researchers developed new methods for this so-called mid-frequency gap to overcome the limitations of the classical deterministic and statistical methods. Some of these methods extend the applicability of deterministic methods to higher frequencies due to a higher calculation efficiency like the Complex Envelope Vectorization (CEV) [5] or the Variational Theory of Complex Rays (VTCR) [6]. Other methods try to reduce the assumptions of statistical methods and apply them to lower frequencies, for example the Statistical modal Energy distribution Analysis (SmEdA) [7] or the Energy Distribution Analysis (EDA) [8]. Also, hybrid methods like the Hybrid FE/SEA [9] have been developed to benefit from both types of methods.

Another deterministic method for the low and mid-frequency range is the Wave Based Method (WBM), which was developed by Desmet [10]. The WBM is an indirect Trefftz approach and has been used to calculate the harmonic response of structures and acoustic cavities. It has been applied for the interior and exterior acoustic simulation [11] and structural simulation like membrane problems and bending of thin plates [12, 13]. A complete overview of the WBM is shown in [14].

In a previous work, the authors of this paper extended the applicability of the WBM to thick plates [15]. In this paper, the results found in [15] are extended to non-convex problems and the convergence and efficiency compared to the FEM is shown. The outline of this paper is as follows: First the Mindlin theory is presented shortly, then the Wave Based Method for thick plates is described and the needed extension for non-convex problems is given. Next, a non-convex validation example is shown and the convergence and efficiency is compared to a FEM model. Finally, a conclusion is given.

2 THE MINDLIN PLATE THEORY

The Mindlin plate theory is a so-called first order shear deformation theory, which takes shear deformation and rotatory inertia into account [16]. Compared to the Kirchhoff theory, which neglects these two effects, the Mindlin plate theory is suitable for thicker plates. In [17] it is shown that the theory is quite accurate for wavelengths down to the plate thickness. The theory is described in many textbooks like [18] and a short summery is given here.

2.1 Governing Equations

In the Mindlin plate theory it is assumed that a straight line, which is normal to the middle plane in the undeformed plate, remains straight but not necessary normal to the middle surface in the deformed state. Therefore, the plate model has three degrees of freedom, the displacement of the middle surface in z-direction and the rotations about the x-axis and y-axis denoted with ψ_x and ψ_y. In Figure 1 the degrees of freedom of the plate are shown.

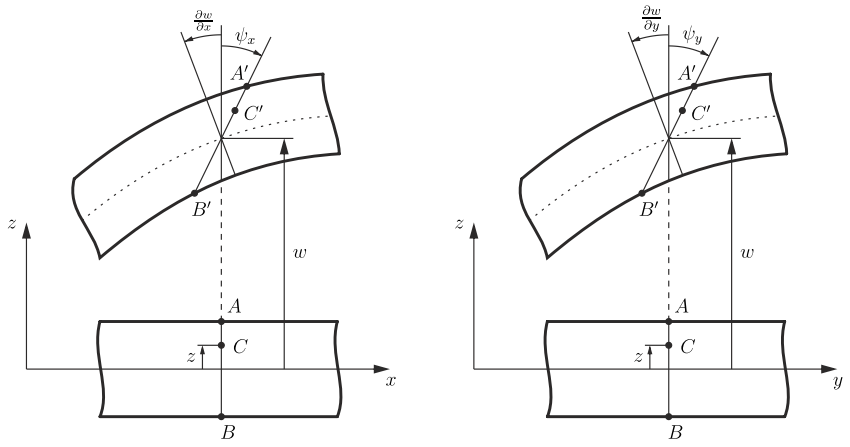


Figure 1: Degrees of freedom of the plate.

It is apparent that ψ_x is the positive rotation about the y-axis and ψ_y the negative rotation about the x-axis. Using the linear strain-displacement relations and Hook's law, the equilibrium of forces in z-direction and the equilibrium of moments about the x- and y-axis lead to the governing equations of the Mindlin plate in Cartesian coordinates

$$k^2\,G\,h\,\left(\frac{\partial^2 w}{\partial x^2}+\frac{\partial^2 w}{\partial y^2}+\Phi\right)+f=\rho\,h\,\frac{\partial^2 w}{\partial t^2}, \tag{1}$$

$$\frac{D}{2}\left[(1-\nu)\nabla^2\psi_x+(1+\nu)\frac{\partial \Phi}{\partial x}\right]-k^2\,G\,h\,\left(\psi_x+\frac{\partial w}{\partial x}\right)=\frac{\rho\,h^3}{12}\,\frac{\partial^2\psi_x}{\partial t^2}, \tag{2}$$

$$\frac{D}{2}\left[(1-\nu)\nabla^2\psi_y+(1+\nu)\frac{\partial \Phi}{\partial y}\right]-k^2\,G\,h\,\left(\psi_y+\frac{\partial w}{\partial y}\right)=\frac{\rho\,h^3}{12}\,\frac{\partial^2\psi_y}{\partial t^2}, \tag{3}$$

with $\nabla^2=\partial^2/\partial x^2+\partial^2/\partial y^2$ and $\Phi=\partial\psi_x/\partial x+\partial\psi_y/\partial y$. In Eqs. (1 - 3) G is the shear modulus, ν is the Poisson ration, h is the plate thickness, ρ is the density, $D=E\,h^3\,/\,(12\,(1-\nu^2))$ is the plate modulus, E is the elastic modulus and k^2 is the shear correction factor (Reissner $5/6$, Mindlin $\pi^2/12$) to account for the actual shear stress distribution in z-direction. An external vertical load in z-direction is denoted with f.

2.2 Decoupling of the Governing Equations

In the case of free harmonic vibrations ($f = 0$) at angular frequency ω a decoupling of the three governing equations is shown in [16]. The decoupling leads to three Helmholtz equations

$$\nabla^2 w_1 + \delta_1^2 \, w_1 = 0, \tag{4}$$

$$\nabla^2 w_2 + \delta_2^2 \, w_2 = 0, \tag{5}$$

$$\nabla^2 H + \delta_3^2 \, H = 0 \tag{6}$$

and the vertical displacement and rotations are given by

$$\psi_x = (\mu_1 - 1) \, \frac{\partial w_1}{\partial x} + (\mu_2 - 1) \, \frac{\partial w_2}{\partial x} + \frac{\partial H}{\partial y}, \tag{7}$$

$$\psi_y = (\mu_1 - 1) \, \frac{\partial w_1}{\partial y} + (\mu_2 - 1) \, \frac{\partial w_2}{\partial y} - \frac{\partial H}{\partial x}, \tag{8}$$

$$w = w_1 + w_2. \tag{9}$$

The used constants in Eqs. (4 - 9) can be found in [16].

2.3 Boundary and Interface Conditions

The Mindlin plate theory requires three boundary conditions at the plate edges to give an unique solution. The most common boundary conditions are

- kinematic boundary conditions $\boldsymbol{x} \in \tau_u$:

$$\boldsymbol{R}_u(\boldsymbol{x}) = \boldsymbol{u}(\boldsymbol{x}) - \overline{\boldsymbol{u}}(\boldsymbol{x}) = 0, \tag{10}$$

- mechanical boundary conditions $\boldsymbol{x} \in \tau_t$:

$$\boldsymbol{R}_t(\boldsymbol{x}) = \boldsymbol{t}(\boldsymbol{x}) - \overline{\boldsymbol{t}}(\boldsymbol{x}) = 0, \tag{11}$$

- mixed boundary conditions $\boldsymbol{x} \in \tau_{ut}$:

$$\begin{aligned} \boldsymbol{R}_{ut1}(\boldsymbol{x}) &= \boldsymbol{u}_i(\boldsymbol{x}) - \overline{\boldsymbol{u}}_i(\boldsymbol{x}) = 0, \\ \boldsymbol{R}_{ut2}(\boldsymbol{x}) &= \boldsymbol{t}_k(\boldsymbol{x}) - \overline{\boldsymbol{t}}_k(\boldsymbol{x}) = 0, \end{aligned} \tag{12}$$

with $\boldsymbol{u} = [w, \psi_n, \psi_s]^T$, $\boldsymbol{t} = [Q_n, M_n, M_{ns}]^T$ and $\boldsymbol{u}_i$, $\boldsymbol{t}_k$ as the ith or kth components of $\boldsymbol{u}$ and $\boldsymbol{t}$ respectively. The plate boundary τ is divided into three non-overlapping parts τ_u, τ_t and τ_{ut} to define the three types of boundary conditions and $\boldsymbol{x}$ is the position vector at the boundaries. Q_n is the transverse shear force and M_n, M_{ns} are the bending and twisting moments, which can be defined by the displacement variables and their deviations [15]. The subscripts n and s stand for the normal and tangential direction of the plate boundary. The boundary residuals $\boldsymbol{R}_u$, $\boldsymbol{R}_t$, $\boldsymbol{R}_{ut1}$ and $\boldsymbol{R}_{ut2}$ become zero if the prescribed boundary values $\overline{\boldsymbol{u}}$ and $\overline{\boldsymbol{t}}$ are perfectly matched.

3 THE WAVE BASED METHOD

The Wave Based Method uses exact solutions of the governing equations as basic functions to describe the displacement field of the plate. Therefore, errors only occur at the boundaries of the plate and also at the interfaces in case the plate domain has to be divided into subdomains. The boundary and interface residuals are minimized in an integral sense, using a weighted residual formulation.

3.1 Field Variable Expansion

The decoupling of the governing equations in Helmholtz equations simplifies the definition of exact solutions and the variables w_1, w_2 and H are approximated with

$$w_1(x,y) \approx \tilde{w}_1(x,y) = \sum_{i_{w1}=0}^{n_{w1}} a_{i_{w1}}\, \Psi_{i_{w1}}(x,y) + \hat{w}_{1p}, \tag{13}$$

$$w_2(x,y) \approx \tilde{w}_2(x,y) = \sum_{i_{w2}=0}^{n_{w2}} a_{i_{w2}}\, \Psi_{i_{w2}}(x,y) + \hat{w}_{2p}, \tag{14}$$

$$H(x,y) \approx \tilde{H}(x,y) = \sum_{i_H=0}^{n_H} a_{i_H}\, \Psi_{i_H}(x,y) + \hat{H}_p, \tag{15}$$

with $\Psi_{i_{w1}}$, $\Psi_{i_{w2}}$ and Ψ_{i_H} as solutions of the governing equations Eqs. (4 - 6) and $\hat{w}_{1p}$, $\hat{w}_{2p}$ and $\hat{H}_p$ as particular solution functions, which satisfy the inhomogeneous part of the Eqs. (1 - 3). The used basic functions $\Psi_{i_{w1}}$, $\Psi_{i_{w2}}$ and Ψ_{i_H} are listed in Table 1 and have been derived in [15]. The dimensions of the smallest rectangular bounding box of a considered convex domain are denoted with L_x and L_y. The particular solution functions for a point force excitation are given by

$$\hat{w}_{1p} = \frac{1}{\mu_1 - 1}\, \frac{-\mathrm{H}_0^{(1)}(\delta_1\, r)}{D\,\sqrt{k_B^8\,(R-S)^2 + 4\,k_B^4}}\, \frac{j}{4}, \tag{16}$$

$$\hat{w}_{2p} = \frac{1}{\mu_2 - 1}\, \frac{\mathrm{H}_0^{(1)}(\delta_2\, r)}{D\,\sqrt{k_B^8\,(R-S)^2 + 4\,k_B^4}}\, \frac{j}{4}, \tag{17}$$

$$\hat{H}_p = 0, \tag{18}$$

with $\mathrm{H}_0^{(1)}$ the zero order Hankel function of the first kind and the distance to the excitation point r. The solutions in Eqs. (16 - 18) are the response of an infinite plate to a point force excitation [19]. The given basic functions ensure convergence for a rectangular plate domain [15], which equally ensures the convergence for a convex domain [10]. In the case of a non-convex plate domain, the domain needs to be subdivided into convex subdomains and interface conditions have to be applied.

3.2 Weighted Residual Formulation

The wave functions in Table 1 satisfy the governing equations of the Mindlin plate independently of the weighting factors $a_{i_{w1}}$, $a_{i_{w2}}$ and a_{i_H}. The weighting factors are determined by the boundary conditions and interface conditions, using a minimization of the approximation error of the boundary and interface residuals through a weighted residual formulation. The boundary residuals for a convex subdomain α of the plate are defined in Eqs. (10 - 12). The interface conditions between two connected convex plate domains α and β are defined as

$$\boldsymbol{R}_{I_u}^{(\alpha,\beta)}(\boldsymbol{x}) = \boldsymbol{u}^{(\alpha)}(\boldsymbol{x}) - \boldsymbol{u}^{(\beta)}(\boldsymbol{x}), \tag{19}$$

$$\boldsymbol{R}_{I_t}^{(\alpha,\beta)}(\boldsymbol{x}) = \boldsymbol{t}^{(\alpha)}(\boldsymbol{x}) + \boldsymbol{t}^{(\beta)}(\boldsymbol{x}). \tag{20}$$

The residuals are orthogonalized with respect to weighting functions $\hat{w}_1$, $\hat{w}_2$ and $\hat{H}$ and like in the Galerkin procedure these weighting functions are chosen as an expansion of the same basic

Table 1: Wave function sets.

	wave functions for w_1		
set 1	$\Psi_{i_{w1}} = \cos(k_{i_{w1},x}\, x)\, \exp(-j\, k_{i_{w1},y}\, y)$	$k_{i_{w1},x} = \frac{i_{w1}\,\pi}{L_x}$	$k_{i_{w1},y} = \pm\sqrt{\delta_1^2 - k_{i_{w1},x}^2}$
	$\Psi_{j_{w1}} = \exp(-j\, k_{j_{w1},x}\, x)\, \cos(k_{j_{w1},y}\, y)$	$k_{j_{w1},y} = \frac{j_{w1}\,\pi}{L_y}$	$k_{j_{w1},x} = \pm\sqrt{\delta_1^2 - k_{j_{w1},y}^2}$
set 2	$\Psi_{i_{w1}} = \sin(k_{i_{w1},x}\, x)\, \exp(-j\, k_{i_{w1},y}\, y)$	$k_{i_{w1},x} = \frac{i_{w1}\,\pi}{L_x}$	$k_{i_{w1},y} = \pm\sqrt{\delta_1^2 - k_{i_{w1},x}^2}$
	$\Psi_{j_{w1}} = \exp(-j\, k_{j_{w1},x}\, x)\, \sin(k_{j_{w1},y}\, y)$	$k_{j_{w1},y} = \frac{j_{w1}\,\pi}{L_y}$	$k_{j_{w1},x} = \pm\sqrt{\delta_1^2 - k_{j_{w1},y}^2}$
	wave functions for w_2		
set 1	$\Psi_{i_{w2}} = \cos(k_{i_{w2},x}\, x)\, \exp(-j\, k_{i_{w2},y}\, y)$	$k_{i_{w2},x} = \frac{i_{w2}\,\pi}{L_x}$	$k_{i_{w2},y} = \pm\sqrt{\delta_2^2 - k_{i_{w2},x}^2}$
	$\Psi_{j_{w2}} = \exp(-j\, k_{j_{w2},x}\, x)\, \cos(k_{j_{w2},y}\, y)$	$k_{j_{w2},y} = \frac{j_{w2}\,\pi}{L_y}$	$k_{j_{w2},x} = \pm\sqrt{\delta_2^2 - k_{j_{w1},y}^2}$
set 2	$\Psi_{i_{w2}} = \sin(k_{i_{w2},x}\, x)\, \exp(-j\, k_{i_{w2},y}\, y)$	$k_{i_{w2},x} = \frac{i_{w2}\,\pi}{L_x}$	$k_{i_{w2},y} = \pm\sqrt{\delta_2^2 - k_{i_{w2},x}^2}$
	$\Psi_{j_{w2}} = \exp(-j\, k_{j_{w2},x}\, x)\, \sin(k_{j_{w2},y}\, y)$	$k_{j_{w2},y} = \frac{j_{w2}\,\pi}{L_y}$	$k_{j_{w2},x} = \pm\sqrt{\delta_2^2 - k_{j_{w2},y}^2}$
	wave functions for H		
set 1	$\Psi_{i_H} = \sin(k_{i_H,x}\, x)\, \exp(-j\, k_{i_H,y}\, y)$	$k_{i_H,x} = \frac{i_H\,\pi}{L_x}$	$k_{i_H,y} = \pm\sqrt{\delta_3^2 - k_{i_H,x}^2}$
	$\Psi_{j_H} = \exp(-j\, k_{j_H,x}\, x)\, \sin(k_{j_H,y}\, y)$	$k_{j_H,y} = \frac{j_H\,\pi}{L_y}$	$k_{j_H,x} = \pm\sqrt{\delta_3^2 - k_{j_H,y}^2}$
set 2	$\Psi_{i_H} = \cos(k_{i_H,x}\, x)\, \exp(-j\, k_{i_H,y}\, y)$	$k_{i_H,x} = \frac{i_H\,\pi}{L_x}$	$k_{i_H,y} = \pm\sqrt{\delta_3^2 - k_{i_H,x}^2}$
	$\Psi_{j_H} = \exp(-j\, k_{j_H,x}\, x)\, \cos(k_{j_H,y}\, y)$	$k_{j_H,y} = \frac{j_H\,\pi}{L_y}$	$k_{j_H,x} = \pm\sqrt{\delta_3^2 - k_{j_H,y}^2}$

functions used for the field variable approximation. This leads to

$$\int_{\tau_u} \hat{\boldsymbol{t}}^{(\alpha)^{\boldsymbol{T}}}\, \boldsymbol{R}_u^{(\alpha)}\, \mathrm{d}\tau - \int_{\tau_t} \hat{\boldsymbol{u}}^{(\alpha)^{\boldsymbol{T}}}\, \boldsymbol{R}_t^{(\alpha)}\, \mathrm{d}\tau + \int_{\tau_{tv}} \hat{\boldsymbol{t}}^{(\alpha)^{\boldsymbol{T}}}\, \boldsymbol{R}_{tu1}^{(\alpha)}\, \mathrm{d}\tau - \tag{21}$$
$$\int_{\tau_{tv}} \hat{\boldsymbol{u}}^{(\alpha)^{\boldsymbol{T}}}\, \boldsymbol{R}_{tu2}^{(\alpha)}\, \mathrm{d}\tau + \sum_{\beta,\beta\neq\alpha} \int_{\tau_{I_u}} \hat{\boldsymbol{t}}^{(\alpha)^{\boldsymbol{T}}}\, \boldsymbol{R}_{I_u}^{(\alpha,\beta)}\, \mathrm{d}\tau - \sum_{\beta,\beta\neq\alpha} \int_{\tau_{I_t}} \hat{\boldsymbol{u}}^{(\alpha)^{\boldsymbol{T}}}\, \boldsymbol{R}_{I_t}^{(\alpha,\beta)}\, \mathrm{d}\tau = 0$$

for each convex subdomain. If Eq. (21) is evaluated for each subdomain, a system of linear equations results, which can be solved for the unknown contribution factors.

4 VALIDATION EXAMPLE

The WBM is used to calculate the displacement field of a clamped U-shaped plate and the results are compared to a reference model. The convergence rate of the WBM is compared to a FEM model built in *ANSYS*® 16.0, to show its effectiveness.

4.1 Plate configuration

The U-shaped plate is shown in Figure 2 and has a thickness h of $0.05\,m$. The plate is made of aluminium with an elasticity modulus $E = 70 \times 10^9\,N/m^2$, a Poisson ratio $\nu = 0.3$ and a density $\rho = 2790\,kg/m^3$. The shear correction factor k^2 is set to $5/6$.

A normal load $f = 1000\,N$ is acting at the point F_1 with an excitation frequency of $10000\,Hz$. The validation points P_1 - P_5, listed in Table 2, are used to compare the displacements of the WBM and the FEM. Since the plate is non-convex, it is divided into three convex subdomains Ω_1, Ω_2 and Ω_3, which is indicated by the dashed lines in Fig. 2. All edges of the plate are clamped ($\overline{\boldsymbol{u}} = 0$).

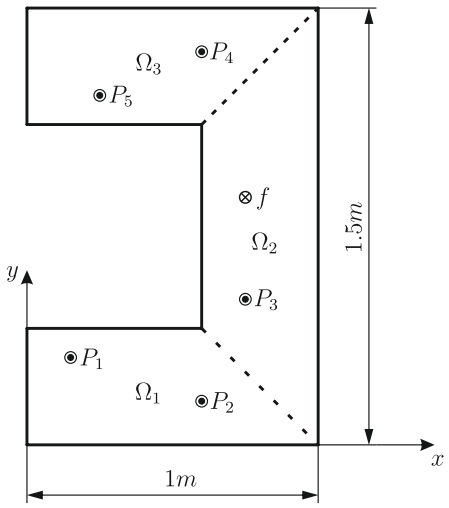


Figure 2: Geometry of the validation example.

Points	x [m]	y [m]
P_1	$0.15\,m$	$0.30\,m$
P_2	$0.60\,m$	$0.15\,m$
P_3	$0.75\,m$	$0.50\,m$
P_4	$0.60\,m$	$1.35\,m$
P_5	$0.25\,m$	$1.20\,m$
F_1	$0.75\,m$	$0.85\,m$

Table 2: Coordinates of the validation points.

The FEM reference model is meshed with the quadric 8-noded quadrilateral Shell281 element and the element size is set to $1.667\,10^{-3}\,m$. The occurring wavelength in the example is $0.165\,m$ and therefore, 100 elements per wavelength are used for the reference model. According to [20] only three quadric elements would be necessary to get accurate results.

The wave based model is built in *MATLAB*® $R2014b$. The integrals in Eqs. (21) are evaluated, using the Gauss-Legendre quadrature and the resulting system of linear equations is solved with the singular value decomposition (SVD).

4.2 Displacement results

A wave based model with 1980 wave function is used to calculate the displacements and rotations of the plate, shown in Figure 3. It is apparent that the applied boundary conditions and the interface conditions between the subdomains are well fulfilled. Therefore, the error inside the domain is small, as it will become apparent from the convergence calculations, since errors are only introduced at the boundary and interface conditions.

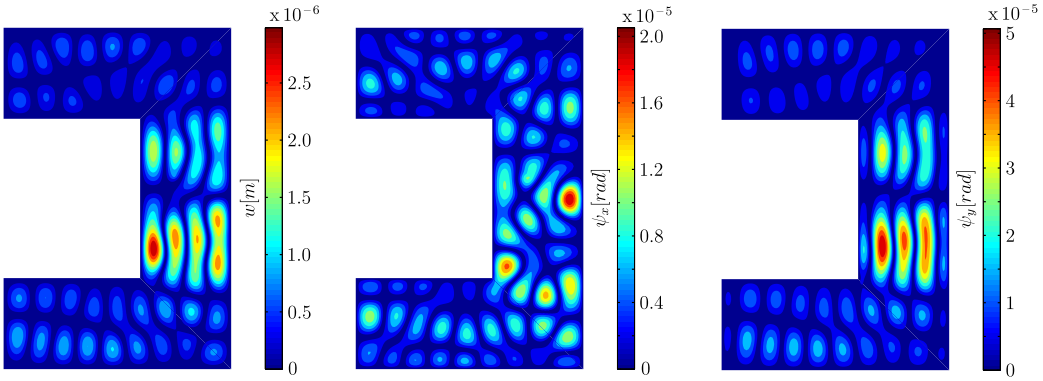


Figure 3: Displacements and rotations of the plate at 10000 Hz excitation.

The definition of the relative predicted error

$$\langle \epsilon \rangle = \frac{1}{n_P} \sum_{j=1}^{n_P} \epsilon_{Pj} \tag{22}$$

with

$$\epsilon_{Pj} = \frac{||w(\boldsymbol{x_{Pj}}) - w^{ref}(\boldsymbol{x_{Pj}})||}{||w^{ref}(\boldsymbol{x_{Pj}})||} \tag{23}$$

is used to investigate the convergence of the WBM compared to FEM. Therefore, five different numbers of wave functions (780, 900, 1380, 1740, 1980) and six different element sizes ($0.025\,m$, $0.02083\,m$, $0.0166\,m$, $0.0125\,m$, $0.01042\,m$, $0.0083\,m$) are used to calculate the displacement field. The results are shown in Figure 4.

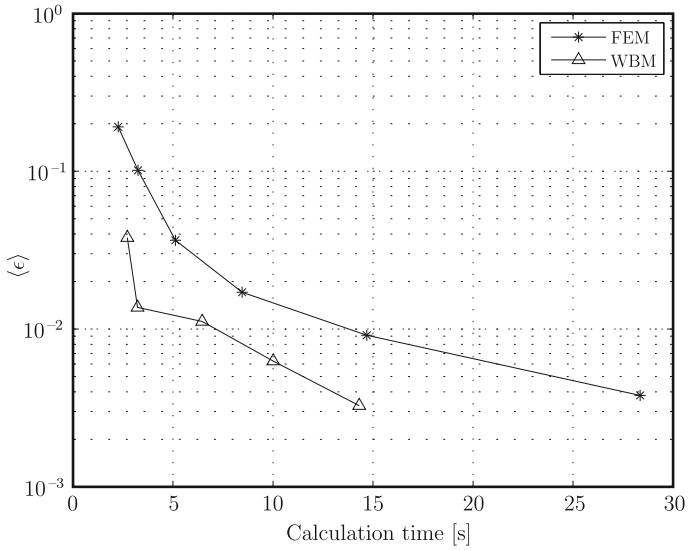


Figure 4: Convergence rate of the WBM.

The WBM has a higher computational efficiency for the given problem compared to FEM. The calculation time of the WBM could be further reduced if an optimized implementation of the WBM is used. It needs to be mentioned that for the geometry of the example plate and the chosen boundary conditions, singularities of the transverse shear force and moments occur in the two corners with obtuse angles. This has a bad influence on the convergence rate of the WBM and can be resolved by introducing special purpose functions, which account for the singularities [13]. The special purpose functions are not available for the Mindlin plate theory yet.

5 CONCLUSION

The Mindlin plate theory, which includes shear deformation and rotatory inertia, has been used to calculate the displacement field of a clamped non-convex plate. The governing equations have been solved by using the Wave Based Method, which required the decomposition of the non-convex plate into convex subdomains and the definition of interface conditions. The convergence rate of the WBM has been compared to the FEM and it has been shown that the WBM outperforms the FEM, although the WBM is implemented in *MATLAB*® $R2014b$ and is not optimized.

REFERENCES

[1] K. Bathe, *Finite Element Procedures*. Prentice-Hall, New Jersey, 2006.

[2] L. Wrobel and H. Aliabadi, *The Boundary Element Method*. Wiley, Chichester, 2002.

[3] S. Marburg, Six boundary elements per wavelength: Is that enough? *Journal of Computational Acoustics*, **10 (1)**, 25–51, 2002.

[4] R. Lyon and R. DeJong, *Theory and Application of Statistical Energy Analysis*. Butterworth-Heinemann, Newtown, 1995.

[5] O. Giannini, A. Carcaterra and A. Sestieri, High frequency vibrations analysis by the complex envelope vectorization. *The Journal of the Acoustical Society of America*, **6**, 3472–3483, 2007.

[6] P. Ladevèze, L. Arnaud, P. Rouch and C. Blanzè, The variational theory of complex rays for the calculation of medium-frequency vibrations. *Engineering Computations*, **18 (1)**, 193–214, 2001.

[7] L. Maxit and J. L. Guyader, Extension of sea model to subsystems with non-uniform modal energy distribution. *Journal of Sound and Vibration*, **265 (2)**, 337–358, 2003.

[8] G. Tanner, Dynamical energy analysis - determining wave energy distribution in vibro-acoustical structures in the high-frequency regime. *Journal of Sound and Vibration*, **320**, 1023–1038, 2009.

[9] P. J. Shorter and R. Langley, Vibro-acoustic analysis of complex systems. *Journal of Sound and Vibration*, **288 (3)**, 669–699, 2005.

[10] W. Desmet, *A wave based prediction technique for coupled vibroacoustic analysis*. Phd thesis, KU Leuven, 1998.

[11] B. Pluymers, W. Desmet, D. Vandepitte and P. Sas, Application of an efficient wave-based prediction technique for the analysis of vibro-acoustic radiation problems. *Journal of Computational and Applied Mathematics*, **168**, 353–364, 2004.

[12] C. Vanmaele, D. Vandepitte and W. Desmet, An efficient wave based prediction technique for plate bending vibrations. *Computer Methods in Applied Mechanics and Engineering*, **196**, 3178–3189, 2007.

[13] C. Vanmaele, *Development of a wave based prediction technique for the efficient analysis of low- and mid-frequency structural vibrations*. Phd thesis, KU Leuven, 2007.

[14] E. Deckers, O. Atak, L. Coox, R. D'Amico, H. Devriendt, S. Jonckheere, K. Koo, B. Pluymers, D. Vandepitte and W. Desmet, The wave based method: An overview of 15 years of research. *Wave Motion*, **51 (4)**, 550–565, 2014.

[15] M. Klanner and K. Ellermann, Wave Based Method for the Steady-State Vibrations of Thick Plates. *Journal of Sound and Vibration*, **345**, 146–161, 2015.

[16] R. D. Mindlin, Influence of rotatory inertia and shear on flexural motions of isotropic, elastic plates. *Journal of Applied Mechanics*, **18**, 31–38, 1951.

[17] L. R. F. Rose and C. H. Wang, Mindlin plate theory for damage detection: source solution. *The Journal of the Acoustical Society of America*, **116 (1)**, 154–171, 2004.

[18] S. Rao, *Vibration of Continuous Systems*. Wiley, New Jersey, 2007.

[19] L. Palermo Jr., On the fundamental solution to perform the dynamic analysis of reissner-mindlin's plates. *Boundary Element Technology*, **XV**, 2003.

[20] L. L. Thompson and P. M. Pinsky, Complex wavenumber Fourier analysis of the p-version finite element method. *Computational Mechanics*, **13 (4)**, 255–275, 1994

11th International Conference on Engineering Vibration
Ljubljana, Slovenia, 7–10 September 2015

THE HELMHOLTZ EQUATIONS BY THE NULL-FIELD AND THE INTERIOR FIELD METHODS ON CIRCULAR DOMAINS

M.G. Lee*[1], Z.C. Li*[2], H.T. Huang*[3] , Kun-Ming Yu*[4]

[1]Department of Leisure and Recreation Management/ Ph.D. Program in Engineering Science,
Chung Hua University, Hsin-Chu, Taiwan 30012.
mglee1990@gmail.com

[2]Department of Applied Mathematics, National Sun Yat-sen University, Kaohsiung, Taiwan 80424.
zicaili1@gmail.com

[3]Department of Applied Mathematics, I-Shou University, Kaohsiung, Taiwan 84001.
huanght@isu.edu.tw.

[4]Department of Computer Science and Information Engineering,
Chung Hua University, Hsinchu, Taiwan 30012.
yu@chu.edu.tw

Keywords: Null-field method, interior field method, spurious eigenvalues, Helmholtz equations, eigenvalue problems.

Abstract. *The null-field method (NFM) is applied to the Helmholtz equation $\Delta u + k^2 u = 0$, and the explicit algebraic equations are derived. The field nodes may be pushed to the domain boundary, to give the interior field method (NFM). There must exist the unique solutions when $k^2 \neq \lambda$, where λ is the eigenvalue of $\Delta u + \lambda u = 0$. However, the NFM and the IFM fail to solve the the Helmholtz equation when k^2 being the spurious eigenvalues. On the other hand, for eigenvalue problems the NFM and the IFM will produce those extra-spurious eigenvalues, which need to identify from numerical solutions and to recover the real approximate eigenvalues. Although a great deal of efforts have been paid to this kind of identification by many researchers, the NFM and the IFM are still inefficient in real application, because the spurious eigenvalues are so many, and because the computational work of identification is exhausted, which is unnecessary if other methods are chosen. New modification of the IFM is explored in this paper, to bypass all spurious eigenvalues, but it falls into the Trefftz methods in [10, 15, 14]. Hence, the collocation Trefftz methods are strongly recommended for both Helmholtz and eigenvalue problems.*

1 Introduction

For circular domains with circular holes, the null-field method (NFM) was proposed and developed by Chen's group with numerous publications, such that [8, 7] for Laplace's equation, and [4, 5, 6, 9] for Helmholtz and eigenvalue problems. The algorithmic analysis is explored in Li et al. [12], where the explicit algebraic equations are derived, and a simple stability analysis is made. The field nodes may be pushed to the domain boundary if the solutions are smooth enough. Numerical experiments and stability analysis display that the field nodes should be located on the domain boundary, to support the numerical results in Chen's publications.

In this paper, the null-field method (NFM) is applied to the Helmholtz equation $\Delta u + k^2 u = 0$, and the explicit algebraic equations are derived. The field nodes may be pushed to the domain boundary, to give the interior field method (IFM). There must exist the unique solutions when $k^2 \neq \lambda$, where λ is the eigenvalue of $\Delta u + \lambda u = 0$. However, the NFM and the IFM fail to solve the the Helmholtz equation when k^2 being the spurious eigenvalues. On the other hand, for eigenvalue problems the NFM and the IFM will produce those extra-spurious eigenvalues, which need to identify from numerical solutions and to recover the real approximate eigenvalues. Although a great deal of effort has been paid in many research, the NFM and the IFM are still inefficient in real application, because the spurious eigenvalues are so many, and because the computational work of identification is exhausted, which is unnecessary if other methods are chosen. New modification of the IFM is explored in this paper, to bypass all spurious eigenvalues, but it falls into the Trefftz methods in [10, 15, 14]. Hence, the collocation Trefftz methods are strongly recommended for both Helmholtz and eigenvalue problems.

This paper is organized as follows. In the next section, the explicit discrete equations and the analytic solutions of the NFM are derived. In Section 3, the field nodes Q may be pushed to the domain boundary ∂S with a strict proof, and the new interior method is proposed, which is equivalent to the NFM by $Q \in \partial S$. A modification of the IFM solution leads to the Trefftz solutions is given at Section 4.

2 Explicit Algorithms of Null Field Methods

2.1 Basic Algorithms

The series expansions of fundamental solutions (FS) are important to the error analysis of the method of fundamental solutions, and the null-field method (NFM), which is developed by Chen and his colleagues for Laplace' equation in circular domain with circular holes [7, 8]. The NFM and the IFM are efficient for Laplace's equation, but not for the Helmholtz equation and eigenvalue problems, because so many spurious eigenvalue exist.

Denote the disks S_R and S_{R_1} with radii R and R_1, respectively. Then $S_{R_1} \subset S_R$, and the eccentric circular domains S_R and S_{R_1} may have different origins. Let $2R_1 < R$. The annular solution domain $S = S_R \backslash S_{R_1}$ with the exterior and the interior boundaries ∂S_R and ∂S_{R_1}, respectively. In [8], $R = 2.5$ and $R_1 = 1$ and the origins of S_R and S_{R_1} are located at $(0, 0)$ and $(-R_1, 0)$, respectively. The following Helmholtz problem is discussed

$$\Delta u + k^2 u = \frac{\partial^2 u}{\partial x^2} + \frac{\partial^2 u}{\partial y^2} + k^2 u = 0 \ \ in \ \ S, \tag{1}$$

$$u = 1 \ \ on \ \ \partial S_R, \ \ u = 0 \ \ on \ \ \partial S_{R_1}. \tag{2}$$

where (ρ, ϕ) are the polar coordinates of S_{R_1} with the origin $(0, 0)$. Eqs. (1) – (2) are called Model problem in this paper.

On the exterior boundary ∂S_R, suppose that there exist the approximations of Fourier expansions,

$$u = u_0 := a_0 + \sum_{m=1}^{M} \{a_m \cos k\theta + b_m \sin m\theta\} \ \ on \ \ \partial S_R, \tag{3}$$

$$\frac{\partial u}{\partial \nu} = q_0 := p_0 + \sum_{k=m}^{M} \{p_m \cos m\theta + q_m \sin m\theta\} \ \ on \ \ \partial S_R, \tag{4}$$

where a_k, b_k, p_k and q_k are coefficients. On the interior boundary ∂S_{R_1}, similarly

$$\bar{u} = \bar{u}_0 := \bar{a}_0 + \sum_{m=1}^{N} \{\bar{a}_m \cos m\bar{\theta} + \bar{b}_m \sin m, \bar{\theta}\} \ \ on \ \ \partial S_{R_1}, \tag{5}$$

$$\frac{\partial \bar{u}}{\partial \bar{\nu}} = -\frac{\partial \bar{u}}{\partial \bar{r}} = \bar{q}_0 := \bar{p}_0 + \sum_{m=1}^{N} \{\bar{p}_m \cos m\bar{\theta} + \bar{q}_m \sin m\bar{\theta}\} \ \ on \ \ \partial S_{R_1}, \tag{6}$$

where $\bar{a}_k, \bar{b}_k, \bar{p}_k$ and $\bar{q}_k$ are coefficients. In (3) – (6), θ and $\bar{\theta}$ are two polar coordinates of S_R and S_{R_1} with the origins $(0,0)$ and $(-R_1, 0)$, respectively, and ν and $\bar{\nu}$ are the outer normal of ∂S_R and ∂S_{R_1} respectively. For the Dirichlet, the Neumann conditions, and their mixed types on ∂S_R are given with the known coefficients.

For solving (1) we need a special function, the Hankel function of the first kind of order n is given by Watson [16]

$$H_n^{(1)}(z) \ \ = \ \ J_n(z) + iY_n(z), \tag{7}$$

where $J_n(z)$ and $Y_n(z)$ are the Bessel and the Neumann functions of order n, respectively, defined by

$$J_\mu(r) \ \ = \ \ \sum_{i=0}^{\infty} \frac{(-1)^i}{\Gamma(i+1)\Gamma(i+\mu+1)} (\frac{r}{2})^{2i+\mu}, \tag{8}$$

$$Y_\mu(r) \ \ = \ \ \frac{J_\mu(r)\cos(\mu\pi) - J_{-\mu}(r)}{\sin(\mu\pi)}. \tag{9}$$

When ν is integer, the Neumann functions are given by the limit of (9) for a noninteger ν. The Hankel function $H_0^{(1)}(z)$ of the first kind and zero order satisfies the Sommerfeld radiation condition, see [2], p. 122. We are interested in only real solutions, to choose the real part $Y_0(z)$ of $iH_0^{(1)}(z)$ as the FS.

In S, denote two nodes $\mathbf{x} = Q = (x, y) = (\rho, \theta)$, and $\mathbf{y} = P = (\xi, \eta) = (r, \phi)$, where $x = \rho\cos\theta, y = \rho\sin\theta, \xi = r\cos\phi$,and $\eta = r\sin\phi$. Then $\rho = \sqrt{x^2+y^2}$ and $r = \sqrt{\xi^2+\eta^2}$. The real FS of Helmholtz's equation is given by

$$U(\mathbf{x}, \mathbf{y}) = \frac{\pi}{2} Y_0(k\overline{PQ}) = \frac{\pi}{2} Y_0(k\sqrt{\rho^2 - 2\rho r\cos(\theta-\phi) + r^2}). \tag{10}$$

From the BEM theory in [2, 3], for the smooth boundary ∂S we have different formulas for different locations of the field nodes $Q(\mathbf{x})$:

$$\int_{\partial S} \{U(\mathbf{x}, \mathbf{y}) \frac{\partial u(\mathbf{y})}{\partial \nu} - u(\mathbf{y}) \frac{\partial U(\mathbf{x}, \mathbf{y})}{\partial \nu}\} d\sigma_{\mathbf{y}} = \begin{cases} -2\pi u(Q), & Q \in S, \\ -\pi u(Q), & Q \in \partial S, \\ 0, & otherwise, \end{cases} \tag{11}$$

where $P(\mathbf{y}) \in (S \cup \partial S)$, and the series expansions of the FS are given by (see [1, 16])

$$U(\mathbf{x},\mathbf{y}) = \frac{\pi}{2} Y_0(k|PQ|) = \frac{\pi}{2} Y_0(k\sqrt{\rho^2 - 2\rho r\cos(\theta-\phi) + r^2})$$
$$= \begin{cases} U^i(\mathbf{x},\mathbf{y}) = \frac{\pi}{2}\sum_{n=0}^{\infty} \epsilon_n Y_n(kr) J_n(k\rho)\cos n(\theta-\phi), & \rho < r, \\ U^e(\mathbf{x},\mathbf{y}) = \frac{\pi}{2}\sum_{n=0}^{\infty} \epsilon_n Y_n(k\rho) J_n(kr)\cos n(\theta-\phi), & \rho > r, \end{cases} \tag{12}$$

where $\epsilon_0 = 1$, $\epsilon_n = 2$ for $n \geq 1$, $\mathbf{x} = (\rho,\theta)$ and $\mathbf{y} = (r,\phi)$. Then we have two kinds of derivative expansions of FS,

$$\frac{\partial U^i(\mathbf{x},\mathbf{y})}{\partial r} = \frac{\pi}{2}\sum_{n=0}^{\infty} k\epsilon_n Y_n'(kr) J_n(k\rho)\cos n(\theta-\phi), \quad \rho < r, \tag{13}$$

$$\frac{\partial U^e(\mathbf{x},\mathbf{y})}{\partial r} = \frac{\pi}{2}\sum_{n=0}^{\infty} k\epsilon_n Y_n(k\rho) J_n'(kr)\cos n(\theta-\phi), \quad \rho > r, \tag{14}$$

where the superscripts "e" and "i" designate the exterior and interior field nodes $\mathbf{x}$, respectively.

To distinguish the boundary element method (BEM) which is based on the second equation of the Green formula (11), the NFM is based on the third equation by using the FS expansions, we have

$$\int_{\partial S_R \cup \partial S_{R_1}} U(\mathbf{x},\mathbf{y}) \frac{\partial u(\mathbf{y})}{\partial \nu} d\sigma_{\mathbf{y}} = \int_{\partial S_R \cup \partial S_{R_1}} u(\mathbf{y}) \frac{\partial U(\mathbf{x},\mathbf{y})}{\partial \nu} d\sigma_{\mathbf{y}}, \quad \mathbf{x} \in \bar{S}^c, \tag{15}$$

where $\bar{S}^c$ is the complementary domain of $S \cup \partial S$. Substituting the Fourier expansions (12) –(14) into (15) yields the basic algorithms of NFM, where the exterior normal of ∂S_{R_1} is given by $\frac{\partial U(\mathbf{x},\mathbf{y})}{\partial \nu} = -\frac{\partial U(\mathbf{x},\mathbf{y})}{\partial r}$. Although the basic descriptions above have been used in Chen's many papers, there exist no explicit equations reported so far. The explicit equations are important not only to understand the intrinsic nature of the NFM, but also to extend their applications. The first goal of this paper is to develop the explicit algebraic equations of the NFM.

2.2 Explicit Algebraic Equations

First, consider the exterior field nodes $\mathbf{x} = (\rho,\theta)$ with $\rho > r = R$. On ∂S_R, by substituting (3) - (4) and (12) – (14) into (15), we have from orthogonality of Fourier series,

$$\int_{\partial S_R} u(\mathbf{y}) \frac{\partial U^e(\mathbf{x},\mathbf{y})}{\partial \nu} d\sigma_{\mathbf{y}} = \int_0^{2\pi} \{a_0 + \sum_{m=1}^{M} [a_m \cos m\phi + b_m \sin m\phi]\} \tag{16}$$
$$\times \{\frac{\pi}{2}\sum_{n=0}^{\infty} k\epsilon_n Y_n(k\rho) J_n'(kR)\cos n(\theta-\phi)\} R d\phi$$
$$= R\pi^2 k\{Y_0(k\rho) J_0'(kR) a_0 + \sum_{n=1}^{M} Y_n(k\rho) J_n'(kR)(a_n \cos n\theta + b_n \sin n\theta)\},$$

$$\int_{\partial S_R} \frac{\partial u(\mathbf{y})}{\partial \nu} U^e(\mathbf{x},\mathbf{y}) d\sigma_{\mathbf{y}} = \int_0^{2\pi} \{p_0 + \sum_{m=1}^{M} [p_m \cos m\phi + q_m \sin m\phi]\} \tag{17}$$
$$\times \{\frac{\pi}{2}\sum_{n=0}^{\infty} \epsilon_n Y_n(k\rho) J_n(kR)\cos n(\theta-\phi)\} R d\phi$$
$$= R\pi^2 \{Y_0(k\rho) J_0(kR) p_0 + \sum_{k=1}^{M} Y_n(k\rho) J_n(kR)(p_n \cos n\theta + q_n \sin n\theta)\}.$$

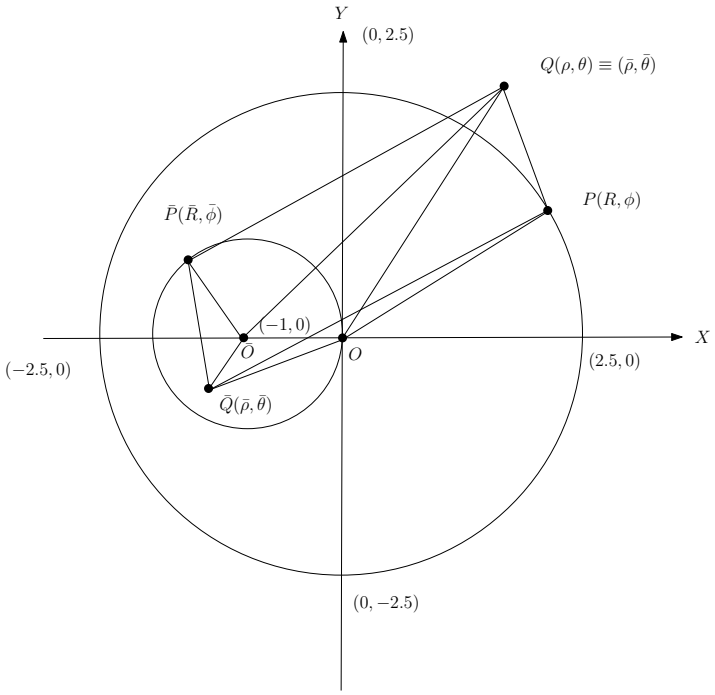


Figure 1: The polar coordinate systems with $\mathbf{x} = Q(\rho, \theta)$ (or $\mathbf{x} = \bar{Q}(\bar{\rho}, \bar{\theta})$), $\mathbf{y} = P(r, \phi)$ (or $\mathbf{y} = \bar{P}(\bar{r}, \bar{\phi})$)

Denote two systems of polar coordinates by (ρ, θ) and $(\bar{\rho}, \bar{\theta})$ with the origins $(0, 0)$ and (x_1, y_1) for S_R and S_{R_1}, respectively, see Figure 1. There exist the following conversion relations,

$$\rho = \sqrt{(\bar{\rho}\cos\bar{\theta} + x_1)^2 + (\bar{\rho}\sin\bar{\theta} + y_1)^2}, \quad \tan\theta = \frac{\bar{\rho}\sin\bar{\theta} + y_1}{\bar{\rho}\cos\bar{\theta} + x_1}, \tag{18}$$

$$\bar{\rho} = \sqrt{(\rho\cos\theta - x_1)^2 + (\rho\sin\theta - y_1)^2}, \quad \tan\bar{\theta} = \frac{\rho\sin\theta - y_1}{\rho\cos\theta - x_1}. \tag{19}$$

Since the exterior field nodes (ρ, θ) with $\rho > R$ to ∂S_R is also the exterior field node to ∂S_{R_1}, by noting $\frac{\partial}{\partial\nu} = -\frac{\partial}{\partial\bar{r}}$ we may obtain similarly from (16) and (17)

$$\int_{\partial S_{R_1}} \bar{u}(\mathbf{y}) \frac{\partial U^e(\mathbf{x}, \mathbf{y})}{\partial\bar{\nu}} d\sigma_{\mathbf{y}} = -\int_{\partial S_{R_1}} \bar{u}(\mathbf{y}) \frac{\partial U^e(\mathbf{x}, \mathbf{y})}{\partial\bar{r}} d\sigma_{\mathbf{y}} \tag{20}$$

$$= -\int_0^{2\pi} \{\bar{a}_0 + \sum_{m=1}^{N} [\bar{a}_m \cos m\bar{\phi} + \bar{b}_m \sin m\bar{\phi}]\}$$

$$\times \{\frac{\pi}{2} \sum_{n=0}^{\infty} k\epsilon_n Y_n(k\bar{\rho}) J_n'(kR_1) \cos n(\bar{\theta} - \bar{\phi})\} R_1 d\bar{\phi}$$

$$= -kR_1\pi^2 \{Y_0(k\bar{\rho}) J_0'(kR_1)\bar{a}_0 + \sum_{n=1}^{N} Y_n(k\bar{\rho}) J_n'(kR_1)(\bar{a}_n \cos n\bar{\theta} + \bar{b}_n \sin n\bar{\theta})\},$$

$$\int_{\partial S_{R_1}} \frac{\partial\bar{u}(\mathbf{y})}{\partial\bar{\nu}} U^e(\mathbf{x}, \mathbf{y}) d\sigma_{\mathbf{y}} = \int_0^{2\pi} \{\bar{p}_0 + \sum_{m=1}^{N} [\bar{p}_m \cos m\bar{\phi} + \bar{q}_m \sin m\bar{\phi}]\} \tag{21}$$

$$\times\{\sum_{n=0}^{\infty}\epsilon_n Y_n(k\bar{\rho})J_n(kR_1)\cos n(\bar{\theta}-\bar{\phi})\}R_1 d\bar{\phi}$$
$$= R_1\pi^2\{Y_0(k\bar{\rho})J_0(kR_1)\bar{p}_0 + \sum_{n=1}^{N} Y_n(k\bar{\rho})J_n(kR_1)(\bar{p}_n\cos n\bar{\theta} + \bar{q}_n\sin n\bar{\theta})\}.$$

Combining (15) and (16) – (21) gives the first NFM equation for the exterior field nodes,

$$\mathcal{L}_{ext}(\rho,\theta;\bar{\rho},\bar{\theta}) := \tag{22}$$
$$kR\pi^2\{Y_0(k\rho)J_0'(kR)a_0 + \sum_{n=1}^{M} Y_n(k\rho)J_n'(kR)(a_n\cos n\theta + b_n\sin n\theta)\}$$
$$-R\pi^2\{Y_0(k\rho)J_0(kR)p_0 + \sum_{k=1}^{M} Y_n(k\rho)J_n(kR)(p_n\cos n\theta + q_n\sin n\theta)\}$$
$$-kR_1\pi^2\{Y_0(k\bar{\rho})J_0'(kR_1)\bar{a}_0 + \sum_{n=1}^{N} Y_n(k\bar{\rho})J_n'(kR_1)(\bar{a}_n\cos n\bar{\theta} + \bar{b}_n\sin n\bar{\theta})\}$$
$$-R_1\pi^2\{Y_0(k\bar{\rho})J_0(kR_1)\bar{p}_0 + \sum_{n=1}^{N} Y_n(k\bar{\rho})J_n(kR_1)(\bar{p}_n\cos n\bar{\theta} + \bar{q}_n\sin n\bar{\theta})\} = 0.$$

Similarly, by considering the interior field nodes $\mathbf{x} = (\bar{\rho},\bar{\theta})$ with $\bar{\rho} < \bar{r} = R_1$. For ∂S_{R_1}, by noting $\frac{\partial}{\partial\nu} = -\frac{\partial}{\partial\bar{r}}$, after some manipulation, we can have the second NFM method for interior field nodes as,

$$\mathcal{L}_{int}(\rho,\theta;\bar{\rho},\bar{\theta}) := \tag{23}$$
$$\{\ k\pi^2 R\{Y_0'(kR)J_0(k\rho)a_0 + \sum_{n=1}^{M} Y_n'(kR)J_n(k\rho)(a_n\cos n\theta + b_n\sin n\theta)\},$$
$$-\pi^2 R\{Y_0(kR)J_0(k\rho)p_0 + \sum_{n=1}^{M} Y_n(kR)J_n(k\rho)(p_n\cos n\theta + q_n\sin n\theta)$$
$$-k\pi^2 R_1\{Y_0'(kR_1)J_0(k\bar{\rho})\bar{a}_0 + \sum_{n=1}^{N} Y_n'(kR_1)J_n(k\bar{\rho})(\bar{a}_n\cos n\bar{\theta} + \bar{b}_n\sin n\bar{\theta})\}$$
$$-\pi^2 R_1\{Y_0(kR_1)J_0(k\bar{\rho})\bar{p}_0 + \sum_{n=1}^{N} Y_n(kR_1)J_n(k\bar{\rho})(\bar{p}_n\cos n\bar{\theta} + \bar{q}_n\sin n\bar{\theta})\}\ \} = 0.$$

Eqs. (22) and (23) are called the *explicit* algebraic equations of the NFM in this paper.

2.3 Explicit Solutions

Since one of the Dirichlet and the Neumann conditions is given on ∂S_R and ∂S_{R_1}, only $2(M+N)+2$ coefficients in (3) – (6) are unknown. We choose $2M+1$ and $2N+1$ field nodes on $\bar{S}^c$, which may be located uniformly on the exterior and the interior circles (see Figure 2):

$$(\rho,\theta) = (R+\epsilon, i\Delta\theta),\ \ i = 0,1,...,2M, \tag{24}$$
$$(\bar{\rho},\bar{\theta}) = (R_1-\bar{\epsilon}, i\Delta\bar{\theta}),\ \ i = 0,1,...,2N, \tag{25}$$

where $\epsilon \geq 0$, $0 \leq \bar{\epsilon} < R_1$, $\Delta\theta = \frac{2\pi}{2M+1}$ and $\Delta\bar{\theta} = \frac{2\pi}{2N+1}$. Denote the explicit equations (22) and (23) by

$$\mathcal{L}_{ext}(\rho,\theta;\bar{\rho},\bar{\theta}) = 0,\ \ \mathcal{L}_{int}(\rho,\theta;\bar{\rho},\bar{\theta}) = 0. \tag{26}$$

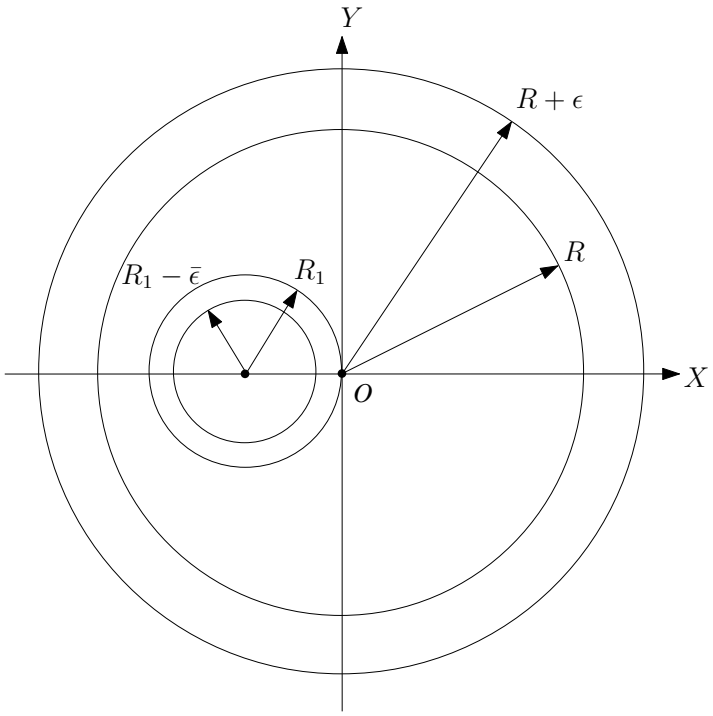


Figure 2: The polar coordinate systems with $\mathbf{x} = Q(\rho, \theta)$ (or $\mathbf{x} = \bar{Q}(\bar{\rho}, \bar{\theta})$), $\mathbf{y} = P(r, \theta)$ (or $\mathbf{y} = \bar{P}(\bar{r}, \bar{\phi})$)

We obtain $2(M + N) + 2$ discrete equations from (26)

$$\mathcal{L}_{ext}(R + \epsilon, i\Delta\theta; \bar{\rho}_i, \bar{\theta}_i) = 0, \quad i = 0, 1, ..., 2M, \tag{27}$$

$$\mathcal{L}_{int}(\rho_i, \theta_i; R_1 - \bar{\epsilon}, i\Delta\bar{\theta}) = 0, \quad i = 0, 1, ..., 2N, \tag{28}$$

where the corresponding coordinates (ρ_i, θ_i) and $(\bar{\rho}_i, \bar{\theta}_i)$ are obtained from $(R + \epsilon, i\Delta\theta)$ and $(R_1 - \bar{\epsilon}, i\Delta\bar{\theta})$, respectively, based on (18) and (19). Hence from (27) and (28) we obtain the following linear equations

$$\mathbf{A}\mathbf{z} = \mathbf{b}, \tag{29}$$

where the matrices $\mathbf{A} \in R^{n\times n}$, the vector $\mathbf{z}(\in R^n) = [a_i, b_i, p_i, q_i, \bar{a}_i, \bar{b}_i, \bar{p}_i, \bar{q}_i]^T$, the right-hand side vector $\mathbf{b}(\in R^n)$ and $n = 2(M + N) + 2$. The unknown coefficients $\mathbf{z}$ can be obtained from (29) if $\mathbf{A}$ is nonsingular.

Once all the coefficients are known, based on the first equation of the Green formula (11) as given in the BEM theory, the solution at the interior nodes: $\mathbf{x} = (\rho, \theta) \in S$ is expressed by

$$u(\mathbf{x}) = u(\rho, \theta) = -\frac{1}{2\pi}\int_{\partial S_R \cup \partial S_{R_1}} \{U(\mathbf{x}, \mathbf{y})\frac{\partial u(\mathbf{y})}{\partial \nu} - u(\mathbf{y})\frac{\partial U(\mathbf{x}, \mathbf{y})}{\partial r}\} d\sigma_{\mathbf{y}} \tag{30}$$

$$= -\frac{1}{2\pi}\{\int_{\partial S_R} \{U^i(\mathbf{x}, \mathbf{y})\frac{\partial u(\mathbf{y})}{\partial \nu} - u(\mathbf{y})\frac{\partial U^i(\mathbf{x}, \mathbf{y})}{\partial r}\} d\sigma_\xi$$

$$+ \int_{\partial S_{R_1}} \{U^e(\mathbf{x}, \mathbf{y})\frac{\partial u(\mathbf{y})}{\partial \bar{\nu}} + u(\mathbf{y})\frac{\partial U^e(\mathbf{x}, \mathbf{y})}{\partial \bar{r}}\} d\sigma_{\mathbf{y}}\}, \quad \mathbf{x} \in S.$$

For $(\rho,\theta)\in S$, from (3) – (6) and (12) – (14), after some manipulation, Eq. (30) can lead to an *explicit solution* as,

$$
\begin{aligned}
&u_{M-N}=u_{M-N}(\rho,\theta;\bar{\rho},\bar{\theta})= \qquad (31)\\
&-\frac{\pi}{2}\{-kRY_0'(kR)J_0(k\rho)a_0-kR\sum_{n=1}^{M}Y_n'(kR)J_n(k\rho)(a_n\cos n\theta+b_n\sin n\theta)\\
&+RY_0(kR)J_0(k\rho)p_0+R\sum_{n=1}^{M}Y_n(kR)J_n(k\rho)(p_n\cos n\theta+q_n\sin n\theta)\\
&+.kR_1Y_0(k\bar{\rho})J_0'(kR_1)\bar{a}_0+kR_1\sum_{n=1}^{N}Y_n(k\bar{\rho})J_n'(kR_1)(\bar{a}_n\cos n\bar{\theta}+\bar{b}_n\sin n\bar{\theta})\\
&+R_1Y_0(k\bar{\rho})J_0(kR_1)\bar{p}_0+R_1\sum_{n=1}^{N}Y_n(k\bar{\rho})J_n(kR_1)(\bar{p}_n\cos n\bar{\theta}+\bar{q}_n\sin n\bar{\theta})\}, \quad (r,\theta)\in S,
\end{aligned}
$$

where $(\bar{\rho},\bar{\theta})$ are also given from (19).

Note that the explicit algebraic equations (22) and (22) and the explicit solutions (31) are, in the first time, derived in a research article, although some preliminary orthogonality formulas and semi-analytic formulas are provided in Chen et al. [5].

3 The Interior Field Method

3.1 Validity for the NFM as $\epsilon,\bar{\epsilon}\to 0$

In the Green formula (15), the field node $\mathbf{x}=(\rho,\theta)$ is supposed to locate outside of the solution domain $S\cup\partial S$ only; this is why the algorithms of Chen is called the null-field method (NFM). The first question arises: Can we locate the field nodes just on the domain boundary: $\mathbf{x}\in\partial S$?

In this subsection, for the NFM we will show that when the solution $u\in H^p(\partial S), u_\nu\in H^{p-1}(\partial S)(p\geq 2)$, Eqs. (22) and (23) hold for $\rho\to R$ and $\bar{\rho}\to R_1$.

We cite a few lemmas from Li et al. [12].

Lemma 3.1 *Let $u\in H^p(\partial S_R), u_\nu\in H^{p-1}(\partial S_R)(p\geq 2)$ be given, the true coefficients have the following asymptotes*

$$a_n,b_n=O(n^{-p}),\ \ p_n,q_n=O(n^{-(p-1)}). \qquad (32)$$

Lemma 3.2 *Let $u\in H^p(\partial S_R), u_\nu\in H^{p-1}(\partial S_R)(p\geq 2)$ be given. There exist the bounds for large M*

$$|R_M(\rho)|,|R_M^*(\rho)|=O(M^{-(p-1)}),\ \ R\leq\rho. \qquad (33)$$

Lemma 3.3 *Let $u\in H^p(\partial S_{R_1}), u_\nu\in H^{p-1}(\partial S_{R_1})(p\geq 2)$ be given. There exist the bounds for large M*

$$|\bar{R}_N(\bar{\rho})|,|\bar{R}_N^*(\bar{\rho})|=O(N^{-(p-1)}),\ \ \rho\leq R_1. \qquad (34)$$

Based on Lemmas 3.2 and 3.3, we can easily prove the following theorem.

Theorem 3.1 *Let $u\in H^p(\partial S)\cup u_\nu\in H^{p-1}(\partial S)(p\geq 2)$ be given. Eqs. (22) and (23) hold for $\rho\to R$ and $\bar{\rho}\to R_1$, respectively.*

Last, consider the explicit solutions (31). We have the following theory.

Theorem 3.2 *Let $u \in H^p(\partial S) \cup u_\nu \in H^{p-1}(\partial S)(p \geq 2)$ be given. Eq. (31) holds for $\rho \to R$ and $\bar{\rho} \to R_1$.*

Theorem 3.2 implies the solutions (31) are valid in both solution domain and boundary $\partial S_R \cup \partial S_{R_1}$. This is distinct from the BEM, where the numerical solutions resulting from the first equation of the Green formula (11) can not approach to the boundary. Hence the errors of the BEM near the boundary ∂S are much larger than those inside the solution domain.

3.2 Algorithms and Relation to the NFM

We may simply use the explicit solution (31) only, and call it the interior field method (IFM), by comparing to the derivation of NFM using many formulas, such as, (22) and (23). Consider the Dirichlet conditions

$$u_{M-N}\Big|_{\rho=R} = u_{M-N}(R, \theta; \bar{\rho}, \bar{\theta}) = a_0 + \sum_{n=1}^{M}(a_n \cos n\theta + b_n \sin n\theta), \tag{35}$$

$$u_{M-N}\Big|_{\bar{\rho}=R_1} = u_{M-N}(\rho, \theta; R_1, \bar{\theta}) = \bar{a}_0 + \sum_{n=1}^{N}(\bar{a}_n \cos n\bar{\theta} + \bar{b}_n \sin k\bar{\theta}), \tag{36}$$

where u_{M-N} is given in (31). The relation between the IFM and the NFM is given in the following theorem.

Theorem 3.3 *Let $u \in H^3(\partial S_R \cup \partial S_{R_1})$ and $u_\nu \in H^2(\partial S_R \cup \partial S_{R_1})$. Equations (35) and (36) are identical to (22) at $\rho = R$, and (23) at $\bar{\rho} = R_1$, respectively.*

The advantage of this approach is that only one formula u_{M-N} in (31) is used, while two more formulas in (22) and (23) are needed in the NFM with $\epsilon = \bar{\epsilon} = 0$. More importantly, the error analysis can be easily proceeded by following [10, 15, 14].

4 Numerical Experiments

4.1 Failure with Spurious Eigenvalues

Consider the eigenvalue problem

$$\Delta u + \lambda u = \frac{\partial^2 u}{\partial x^2} + \frac{\partial^2 u}{\partial y^2} + \lambda u = 0 \ \ in \ \ S, \tag{37}$$

$$u = 1 \ \ on \ \ \partial S_R, \ \ u = 0 \ \ on \ \ \partial S_{R_1}, \tag{38}$$

where (λ, u) with $u \neq 0$ are the eigenpair. When $k^2 \neq \lambda$ the solutions of the Helmohltz problem in (1) and (2) are existent and unique, and they may be sought by effective numerical methods, such as the collocation Trefftz method (CTM) in [10, 14] and the method of fundamental method (MFS) in [13, 15]. When $k^2 \to \lambda$, the singularity of the discrete matrices may lead to the eigenvalue solutions, see [10, 15] and [14], Chapters 9 and 10. For the IFM and the NFM, there exists many spurious (i.e., the fictitious) eigenvalues λ^+, then the Helmholtz problem can be only found if $k^2 \neq \lambda \cup k^2 \neq \lambda^+$. For the eigenvalue problems (37) and (38) by the IFM, one has paid a great effort to identify the spurious eigenvalues λ^+, see Chen's many papers. No doubt, spurious eigenvalues are the intrinsic drawbacks of the NFM and the IFM.

4.2 Modified IFM

In this paper, we provide a modified IFM for the solution of aforementioned eigenvalues problem as,

$$
\begin{aligned}
&u^*_{M-N} = u^*_{M-N}(\rho,\theta;\bar{\rho},\bar{\theta}) = \\
&t_0 J_0(k\rho)p^*_0 + \sum_{n=1}^{M} t_n J_n(k\rho)(p^*_n \cos n\theta + q^*_n \sin n\theta) \\
&+Y_0(k\rho)\tau_0 \bar{p}^*_0 + \sum_{n=1}^{N} Y_n(k\rho)\tau_n(\bar{p}^*_n \cos n\bar{\theta} + \bar{q}^*_n \sin n\bar{\theta}) \\
&-\frac{\pi}{2}\{ -kRY'_0(kR)J_0(k\rho)a_0 - kR\sum_{n=1}^{M} Y'_n(kR)J_n(k\rho)(a_n \cos n\theta + b_n \sin n\theta) \\
&+kR_1 Y_0(k\bar{\rho})J'_0(kR_1)\bar{a}_0 + kR_1 \sum_{n=1}^{N} Y_n(k\bar{\rho})J'_n(kR_1)(\bar{a}_n \cos n\bar{\theta} + \bar{b}_n \sin n\bar{\theta})\}, \quad (r,\theta) \in S,
\end{aligned}
\tag{39}
$$

For (1) and (2), choose $k = 2$, and assume that $k^2 = 4$ is not an eigenvalue of (37) and (38). Based on symmetry, the solutions (39) are simplified by

$$
\begin{aligned}
&u^*_{M-N} = u^*_{M-N}(\rho,\theta;\bar{\rho},\bar{\theta}) = \\
&t_0 J_0(k\rho)p^*_0 + \sum_{n=1}^{M} t_n J_n(k\rho)p^*_n \cos n\theta + Y_0(k\rho)\tau_0 \bar{p}^*_0 + \sum_{n=1}^{N} Y_n(k\rho)\tau_n \bar{p}^*_n \cos n\bar{\theta} \\
&-\frac{\pi}{2}\{ -kRY'_0(kR)J_0(k\rho)a_0 + kR_1 Y_0(k\bar{\rho})J'_0(kR_1)\bar{a}_0 \}, \quad (r,\theta) \in S,
\end{aligned}
\tag{40}
$$

to give

$$
u^*_{M-N}\Big|_{\rho=R} = u_{M-N}(R,\theta;\bar{\rho},\bar{\theta}) = a_0 = 1\}, \tag{41}
$$

$$
u^*_{M-N}\Big|_{\bar{\rho}=R_1} = u_{M-N}(\rho,\theta;R_1,\bar{\theta}) = \bar{a}_0 = 0\}. \tag{42}
$$

By following Subsection 2.2, we may choose the number of collocation equations $m \geq n = M + N + 2$, to form an over-determined system,

$$
\mathbf{F}\mathbf{x} = \mathbf{b}, \tag{43}
$$

where $\mathbf{F} \in R^{m\times n}(m \geq n)$, $\mathbf{x} \in R^n$ and $\mathbf{b} \in R^m$. The condition number is given by

$$
\text{Cond} = \frac{\sigma_{max}}{\sigma_{min}}, \tag{44}
$$

where σ_{max} and σ_{min} are the maximal and the minimal singular values, respectively. The effective condition number is defined in [11] by

$$
\text{Cond_eff} = \frac{\|\mathbf{b}\|}{\sigma_{min}\|\mathbf{x}\|}, \tag{45}
$$

where $\|\mathbf{x}\|$ is the Euclidean norm.

On the other hand, we may choose the simple CT solutions (40)

$$u^{CT}_{M-N}(\rho,\theta) = J_0(k\rho)a_0 + \sum_{n=1}^{M} J_n(k\rho)a_n \cos n\theta \tag{46}$$
$$+Y_0(k\rho)\bar{a}_0 + R_1 \sum_{n=1}^{N} Y_n(k\rho)\bar{a}_n \cos n\theta, \quad (r,\theta) \in S,$$

Choosing the particular solutions (46) satisfying (41) and (42) also provides the over-determined system, (43). Evidently, the CTM is simpler than the modified IFM.

REFERENCES

[1] M. Abramowitz and I. A. Stegun, **Handbook of Mathematical Functions with Formulas, Graphs and Mathematical Tables**, Dover Publications, Inc. New York, 1964.

[2] C. A. Brebbia, J.C.F. Telles and L.C. Wrobel, **Boundary Element Techniques, Theory and Applications in Engineering** Springer-Verlag, Berlin Heidelberg, New York, 1984.

[3] G. Chen and J. Zhou, **Boundary Element Methods**, Academic Press, Chapter 9, New York, 1992.

[4] J. T. Chen, C. T. Chen, and I. L. Chen, *Null-field integral equation approach for eigenproblems with circular boundaries*, J. of Comp. Acoustics, Vol. 15, pp. 401–428, 2007.

[5] J. T. Chen, C. T. Chen, P.Y. Chen and I. L. Chen, *A semi-analytical approach for radiation and scattering problem with circular boundaries*, Computer Methods in Applied Mechanics and Engineering, Vol. 196, pp. 2751 – 2764, 2007.

[6] J. T. Chen, S. K. Kao, W.M. Lee and Y. T. Lee, *Eigenproblems of a multiply-connected domain with circular boundaries using the multipole Trefftz method*, Engineering Analysis with Boundary Elements, Vol. 34, No. 5 pp. 463–475, 2010.

[7] J. T. Chen, C. F. Lee. J. L. Chen and J. H. Lin, *An alternative method for degenerate scale problem in boundary element methods for two-dimensional Laplace equation*, Engineering Analysis with Boundary Elements, Vol. 26, pp. 559 – 569, 2002.

[8] J. T. Chen and W. C. Shen, *Null-field approach for Laplace problems with circular boundaries using degenerate kernels*, Numer. Meth. PDE., vol. 25, pp. 63 – 86, 2009.

[9] S. R. Kuo, J. T. Chen, and C.X. Huang, *Analytical study and numerical experiments for a circular cavity using the real-part dual BEM*, Int. J. Numer Meth. Engng, vol. 48, pp. 1401–1422, 2000.

[10] Z. C. Li, *The Trefftz method for the Helmholtz equation with degeneracy*, Applied Numer. Math., vol. 58, pp. 131–159, 2008.

[11] Z. C. Li, C. S. Chien and H. T. Huang, Effective Condition number for finite difference method, *J. Computational and Applied Mathematics*, Vol. 198, 208-235, 2007.

[12] Z.C. Li, H. T. Huaug, C. P. Liaw, and M. G. Lee, *The null-field method of Dirichlet problems of Laplace's equation on circular domains with circular holes*, Analysis with Boundary Elements, vol. 36, pp. 477-491, 2012.

[13] Z. C. Li and T. T. Lu, *The method of fundamental solution for Helmholtz equations*, Technical report, 2012.

[14] Z.C. Li, T.T. Lu, H.Y. Hu and A.H.D. Cheng, **Trefftz and Collocation Methods**, WIT Press, Southampton, 2008.

[15] Z. C. Li, T. T. Lu, H. S. Tsai, and A. H.-D. Cheng(2006), *The Trefftz method for solving eigenvalue problems*, Engineering Analysis with Boundary Elements[SCI](IF:0.883), Vol. 39, pp. 292-308, 2006.

[16] G. N. Watson, **A treatise on the Bessel Functions** (Sec. Ed.), Cambridge University Press, Cambridge, London, 1980.

11th International Conference on Engineering Vibration
Ljubljana, Slovenia, 7–10 September 2015

CONTACT SITUATIONS IN RIGID BODY DYNAMICS

Luka Skrinjar[1], Janko Slavič[2], Miha Boltežar*[2]

[1]ETI Elektroelement d.d., Obrezija 5, 1411 Izlake, SI, Slovenia
luka.skrinjar@eti.si

[2]University of Ljubljana, Faculty of Mechanical Engineering, Aškerčeva 6, 1000 Ljubljana, SI, Slovenia
janko.slavic@fs.uni-lj.si
miha.boltezar@fs.uni-lj.si

Keywords: Computational methods, Time integrators, Rigid body dynamics, Imperfect kinematic constraints

Abstract. *Rigid body dynamics highly depends on the contact situations. The goal of this research is to simulate the dynamics of a system of rigid bodies with kinematic joints and contact situations, which correspond to the imperfections that can be observed at experiment. The basic theory of dynamics describes kinematic joints and impacts as ideal, but in reality, there are always imperfections present, such as clearance of the kinematic joints, surface roughness, friction, lubricated contact and surface wear. In this approach, the numerical simulation of dynamics of multibody system is based on the theory of Absolute Nodal Coordinate Formulation (ANCF) and for contact evaluation a elastic contact force model is used, while numerical integration is done with Runge-Kutta method. Real conditions like clearance and dry friction are included in a revolute joint with a goal to evaluate the effect on the dynamics of multibody system. The approach is presented with a test case of a subassembly in mechanism of a circuit breaker. A custom designed measurement rig was built to evaluate the applied force on a subassembly component and to evaluate contact parameters. The presented experimental and numerical approach showed as appropriate for research of rigid body dynamics of kinematic joints and contact situations with imperfections.*

Structural Dynamics (TP05)

11th International Conference on Engineering Vibration
Ljubljana, Slovenia, 7–10 September 2015

MASING RULE MOTIVATED LOCAL DISCRETE MODELLING OF CONTACT INTERFACES TO PREDICT DYNAMICAL BEHAVIOUR OF JOINTED STRUCTURES

A. Sharma*[1], W. Mueller-Hirsch[1], S. Herold[2], T. Melz[2]

[1]Robert Bosch GmbH, Division of Automotive Electronics - AE/EDE3, Robert Bosch Strasse 2, 71701, Schwieberdingen, Germany
{anuj.sharma2, wolfgang.mueller-hirsch}@de.bosch.com

[2]Fraunhofer Institute for Structural Durability and System Reliability LBF, Bartning Strasse 47, 64289, Darmstadt, Germany
{sven.herold,tobias.melz}@lbf.fraunhofer.de

Keywords: Contact stiffness, Contact damping, friction, Vibration

Abstract. *Assembled structure use various joints to fasten different sub-parts. Due to these joints, assembled structure experience local non-linearity near the regions of the jointed sections. Although the joints are sources of local non-linearity, they do influence the global dynamical properties - like the resonance frequency and damping of the assembled structure. This paper presents an equivalent quasi-linearised contact model with use of local discrete elements at the contact interface. The discrete elements are characterized through the Kelvin-Voigt elements. The normal contact behaviour is formulated based on the modified Greenwood-Williamson surface roughness model. The tangential contact behaviour is formulated based on the Hyperbolic constitutive laws in conjecture with Masing rules for visco-elastic systems. The non-linear contact forces are disintegrated into equivalent contact stiffness and damping, which are explicitly defined based on the modifications of the governing normal and tangential contact constitutive laws. The conventional time domain method or the family of harmonic balance methods are computationally time in-efficient for large systems, with difficulties in obtaining convergent solutions. The proposed new model utilizes local linearisation to retain the advantages of linear systems, while the non-homogeneous description over contact interface accounts for the non-linear behaviour. A double layered beam structure fastened using four bolted joints is used for the validation of the proposed model. A random-force controlled white noise excitation with varying excitation level is used to obtain the FRF-mobility curve and utilized for the comparison with simulation model. A very good match between the experiment and simulation results confirms the robustness of the proposed model, to capture the effects from the bolted joints for moderately non-linear systems.*

1 INTRODUCTION

Assembled structures under dynamic excitation require numerical models to capture the effects of the non-linearity from contacts on the global dynamic behaviour. The conventional methods describe the contact behaviour based on the formulation of frictional constitutive laws like Coulomb model in the transient domain description. However, large models under broad band excitation cannot be solved using transient domain calculations. A frequency domain calculation based on the harmonic balance methods provides an alternate to transient domain calculations, but their implementation is restricted to periodic excitation and not feasible for random excitations. This paper proposes a methodology to capture the predominant effects of contact interfaces on dynamic response of structures under random excitations.

The influence of joints on the damping of the structures was first studied by GOODMAN AND KLUMPP (1956) [1], wherein it was observed that for specific optimal pressure maximum dissipation can be achieved. Successive studies performed by authors like UNGAR(1973)[2] characterized the dissipation from the contacts as a form of equivalent structural damping. Later GAUL ET.AL[3] developed experimental models to study the isolated joints and obtain the parameters required for the simulation models. Based on the experimental and analytical models, constitutive laws for contact friction models were developed. The HERTZ(1881) and MINDLIN(1949)[4] model described the normal and tangential contact models, while GREENWOOD AND WILLIAMSON(1966)[5] extended the scope for including surfaces roughness effects. The discrete modelling approach of contact interfaces was presented by MASING(1926) [6] to describe the hysteresis formulation between the stress-strain behaviour for materials for load reversals. This also forms the foundation for describing the hysteresis models of frictional contacts based on the relative displacement and velocity between the interfaces.

The proposed method defines an equivalent contact stiffness and damping of the non-linear contact forces based on the general constitutive laws. The contact stiffness are defined for the normal and tangential direction. The normal contact behaviour is defined based on the extension of Hertz and Greenwood-Williamson model. The material models for describing soil dynamical behaviour based on the HARDIN AND DRNEVICH(1972) model [7] is taken as the motivation to describe the tangential dry frictional contact behaviour. The paper is divided into four sections-first section describes the formulation fo the equivalent contact stiffness, the second describes the formulations for the equivalent contact damping, third section describes the implementation of the proposed model in finite element and the last section shows the comparison between the simulation and the experimental results to validate the applicability of the model in predicting the dynamic behaviour of the test structure.

2 Equivalent Contact Stiffness

The contact stiffness is determined based on the constitutive relations between the contact forces and the relative displacements. This section describes the steps of formulating the constitutive relations for the normal and the tangential contact problems based on the conventional governing laws of dry frictional contacts.

2.1 Normal Contact

The contact formulation is always initiated with a normal contact problem, wherein two bodies under normal load approach each other. With initiation of the contacts, increase in the normal loading increase the deformation of the mating interfaces. One of the first analytical representation of the normal contact behaviour of two elastic spheres in contact was presented by

HERTZ (1881). The normal contact force (F_{N}) is calculated based on the integration of Hertzian pressure distribution over the contact area and expressed in terms of the normal displacement (δ_{N}) as

$$F_{\mathrm{N}} = \frac{4}{3} E^* R^{*1/2} \delta_{\mathrm{N}}^{3/2} \tag{1}$$

where, E^* and R^* are the composite elastic modulus and radius of spheres in contact respectively. The normal contact stiffness is calculated as the derivative of the normal force with respect to the relative displacement as,

$$k_{\mathrm{N}} = 2E^* R^{1/2} {\delta_{\mathrm{N}}}^{1/2} \tag{2}$$

The contact stiffness is dependent on the radius of the spheres in contact (indenter spheres). The radius of indenter sphere can be associated with the radius of asperities for the rough surfaces in contact. The radius of the asperities cannot be distinctly determined for each asperity and also a numerical implementation of almost infinite asperity contact spots is very difficult. To overcome these issues, GREENWOOD AND WILLIAMSON (1966) [5] formulated the constitutive equations for modelling nominal flat surfaces with inclusion of the surfaces roughness by approximating the distribution of the peaks by a Gaussian normal distribution. However, later the distribution was modified to an exponential distribution [8, 9] to give closed form solution and have an approximate match to the Gaussian distribution. Motivated from the surface roughness based model, an exponential pressure-penetration law [10, 11, 12] is used for characterising the normal contact behaviour.

$$P_{\mathrm{N}} = P_{\mathrm{N0}}\, e^{\lambda(\delta_{\mathrm{N}} - \delta_{\mathrm{N0}})} \tag{3}$$

where, P_{N} refers to the contact pressure. The pressure-penetration relation has two constants P_{N0} and δ_{N0}, as shown in above Eq.(3). The pressure existing under no loading is refereed as the initial pressure P_{N0}, which has a non-zero value to give physical description of pressure-penetration relation. Similarly, the initial penetration δ_{N0} is understood as the penetration experienced at zero contact pressure. The important parameter used is λ, which is ideally the inverse of the standard deviation of the roughness of the surface in contact. As the pressure-penetration relation is an exponential function, there will be very large magnitude of pressure for very small increment in penetration after certain values of the penetration. These very large magnitudes of pressure leads to problems in numerical convergence. To circumvent this issue, defined is a saturation pressure (P_{N1}), after which the pressure-penetration relation is transformed to a linear relation.

The stiffness density K_{N} is calculated as the derivative of the pressure with respective to the penetration. There exists a linear relation between the stiffness density and pressure, with slope as curvature parameter λ. However, as the pressure-penetration formulation is modified into regions of non-linear and linear, the stiffness density exhibits two states - linear and constant stiffness.

$$K_{\mathrm{N}} = \frac{dP_{\mathrm{N}}}{d\delta_{\mathrm{N}}} = \begin{cases} \lambda P_{\mathrm{N}} & P_{\mathrm{N}} \leq P_{\mathrm{N1}} \qquad \text{Non-linear region} \\ \\ \lambda P_{\mathrm{N1}} & P_{\mathrm{N}} > P_{\mathrm{N1}} \qquad \text{Linear region} \end{cases} \tag{4}$$

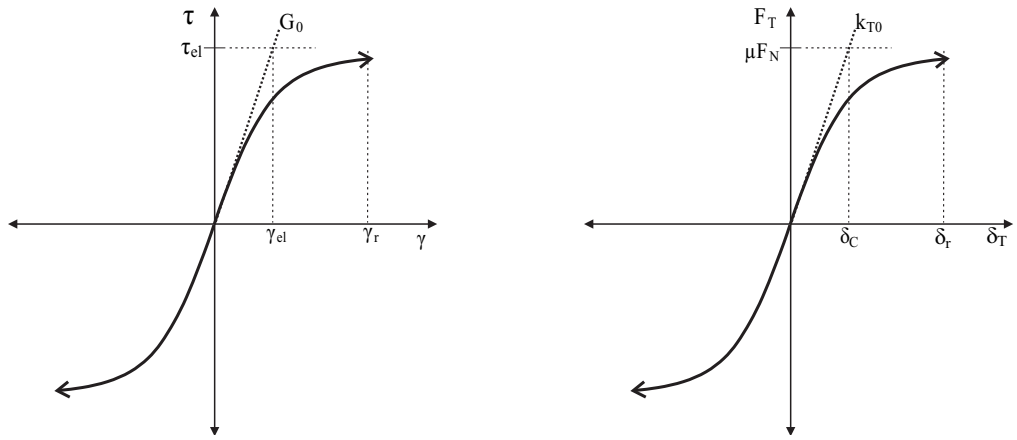
The stiffness density is directly related to the normal contact stiffness density. The contact stiffness density is hence dependent on the curvature parameter λ and transition pressure P_{N1}. These parameters are optimized to match the eigen-frequency of the structures, as the stiffness controls the resonance frequency of the structure.

2.2 Tangential Contact

The tangential contact is characterized as under- stick state or sliding state. For complete sliding the contact stiffness is zero, while for the stick state the tangential contact stiffness can be defined based on the results of the MINDLIN model (1949) [4]. The stick state tangential contact stiffness is defined by scaling the normal contact stiffness with use of the coupling constant (β_0) as shown in below equation,

$$K_{\mathrm{T0}} = \beta_0 K_{\mathrm{N}} \qquad \beta_0 = \frac{4G^*}{E^*} \tag{5}$$

here, G^* is the composite shear modulus of bodies in contact.



(a) Shear stress vs shear strain

(b) Skeleton curve of tangential contact

Figure 1: Co-relation between the stress-strain skeleton curve behaviour with the non-linear dry contacts behaviour between the tangential force and the relative displacement.

MINDLIN(1949) [4] described the partial slip state- wherein a region of the body undergoes sliding and the rest of the interface is under stick state. This lead to defining the contact stiffness as a smooth transition from stick to slip state with a non-linear behaviour between the tangential force and the relative displacement. HARDIN AND DRNEVICH(1972) [7] proposed an approximation for the evaluation of shear modulus of the soil for given strain state [13], or to say the skeleton curve defining the stress-strain behaviour. An analogy is formed between the shear stress-strain relation to define the non-linear relation between the tangential force and the relative displacement to characterize the tangential contact behaviour.

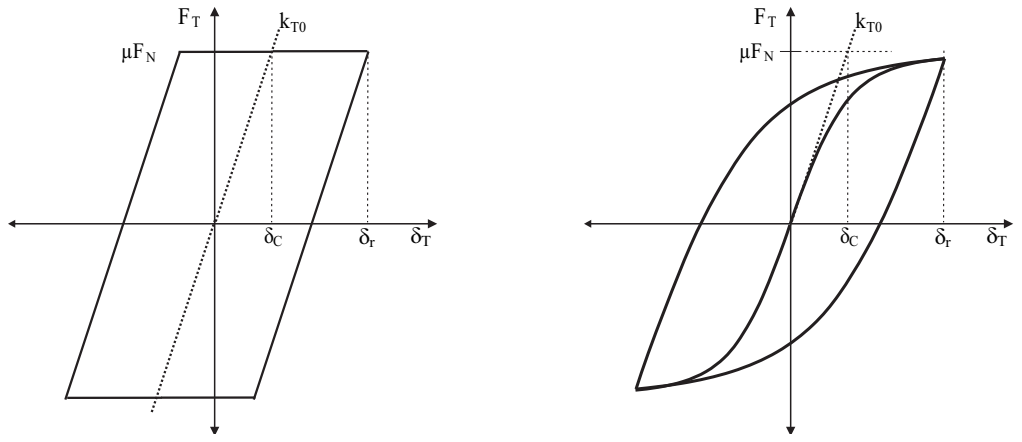
Figure 1 shows the stress-strain relation and the analogy to the tangential force - relative displacement. The γ_{el} is the elastic strain or the reference strain, which is associated to δ_{C} defined as the relative displacement reached for the coulomb friction force. The maximum shear modulus G_0 is directly associated with the initial contact tangential stiffness K_{T0}. The non-linear varying shear modulus is given by,

$$G = \frac{G_0}{\left(1 + \dfrac{\gamma_{\mathrm{r}}}{\gamma_{\mathrm{el}}}\right)} \qquad \longrightarrow \qquad K_{\mathrm{T}} = \frac{K_{\mathrm{T0}}}{\left(1 + \dfrac{\delta_{\mathrm{r}}}{\delta_{\mathrm{C}}}\right)} \tag{6}$$

In Eq.(6), δ_r is the maximum relative displacement achieved for external loading, or to say in the hyperbolic constitutive laws the point at which the load reversal takes place. With normal contact stiffness and tangential contact stiffness definition, required is also the estimation of the contact damping to solve the dynamic problems, which is

3 Equivalent Contact Damping

The shear stress-strain relation is ideally a hyperbolic constitutive law, wherein at the load reversal the curve get mirrored and lead to generation of hysteresis based on the MASING rule [6, 14]. The hysteresis generated for stress-strain relation can be attributed directly to the hysteresis generated for the dry frictional contacts. The hysteresis is dependent on the skeleton curve of the tangential force- relative displacement relation following Masing rule at the load reversals. Two forms of the hysteresis can be obtained for the contact dissipation with respect to the state of sliding contact. In case of considering a sudden transition from stick to slide state, a parallelogram type hysteresis is formed. However, when considering the micro-slip state as the intermediate state form stick to slide state, a smooth transition from stick to slide state with hyperbolic hysteresis is obtained. The two hysteresis shape are shown in figure 2.



(a) Parallelogram Hysteresis (b) Hyperbolic hysteresis

Figure 2: Hysteresis behaviour having parallelogram and hyperbolic shapes for only stick-slip and stick-microslip-complete slip states respectively

The area under the hysteresis is ideally the damping. The conventional form of the estimation of the damping from the hysteresis is done through the calculation of the loss factor. The loss factor in turn is equated to the form of lehr's damping ratio to be used in the vibration equation. The loss factor (η) is defined as the ratio of the dissipated energy (the area under the hysteresis ΔE) to the elastic stored energy ($U_{\max}$) for a period of oscillation,

$$\eta = \frac{\Delta E}{4\pi U_{\max}} \tag{7}$$

The corresponding loss factor for the hysteresis defined for only stick-slip states is [15]

$$\eta = \frac{2}{\pi}\left(\frac{1-\frac{\delta_C}{\delta_r}}{2-\frac{\delta_C}{\delta_r}}\right) \tag{8}$$

The corresponding loss factor for the Masing hysteresis based on the hyperbolic constitutive law is [16]

$$\eta = \frac{4}{\pi}\left(1+\frac{\delta_{\mathrm{r}}}{\delta_{\mathrm{C}}}\right)\left[1-\frac{\delta_{\mathrm{r}}}{\delta_{\mathrm{C}}}\ln\left(1+\frac{\delta_{\mathrm{C}}}{\delta_{\mathrm{r}}}\right)\right]-\frac{2}{\pi} \tag{9}$$

The hysteresis generated by the contact dissipation for the dry contacts is independent of the velocity but dependent on the relative displacement and the reversal points. Hence, the contact damping is independent of the frequency of the excitation and can be defined in terms of the equivalent structural damping based on loss factor.

4 Implementation

The implementation of the proposed constitutive contact stiffness and contact damping equations is done through the use of the discrete point-to-point coupling elements. The point-to-point coupling elements are characterized by the use of 3-D kelvin-voigt elements having three springs constituting to the contact stiffness behaviour and two damper elements in tangential directions constituting to the contact damping behaviour. A flow work of the description of the point-to-point coupling is shown in the figure 3.

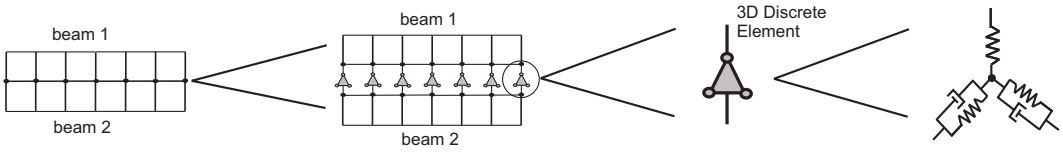


Figure 3: Implementation in FE

The implementation of the proposed model for dynamic excitations can be done directly in the time domain with implicit calculations predicting the relative displacement. However, for broad band random excitations it is not feasible to implement the model in the time domain with equivalent contact stiffness and damping based on the unknown relative displacement. The equivalent contact stiffness and damping can be characterized with a new parameter to determine the relative displacement in terms of the maximum relative displacement that is achieved at the coulomb friction limit (δ_{Tmax}). The parameter defines the ratio between the actual relative displacement to the maximum relative displacement at macro-slip state

$$\delta_{\mathrm{T}} = \alpha\delta_{\mathrm{Tmax}} \tag{10}$$

here , $\delta_{\mathrm{Tmax}} = \dfrac{\mu E^*}{4G^*}\delta_{\mathrm{N}}$. The normal displacement is obtained from the normal contact problem and the α can be optimized to match the experimental results. Although this provides a method to define the model in an equivalent linear basis, it is to be realized that this proposed description in frequency domian is possible for systems which are slightly non-linear and not highly non-linear.

The implementation of the combined normal and tangential contact problem is done into two phases- first the quasi-static loading of the bolting process through the pressure-penetration normal contact law and second phase of the dynamic excitation based on the modal superposition analysis. To solve damped modal superposition random PSD analysis, the equivalent modal

damping ratio of each mode is estimated based on the modal strain energy method. The modal damping ratio ξ^m as defined as the ratio of the damped modal strain energy to the un-damped modal strain energy,

$$\xi^m = \frac{\sum_{r=1}^{n} \phi_m \eta^r K \phi_m^T}{\sum_{n=1}^{r} \phi_m K \phi_m^T}. \tag{11}$$

here, ϕ represents the mode shape from the modal analysis. Hence, the modal damping ratio for each mode is dependent on the stiffness, damping and the modal deformation.

5 Model Validation

The test structure used is a double layered beam fastened using four bolted joints. The two beams are identical in dimensions and are made of structural steel. The beams are fastened using M6 bolts. The dimension of the individual beam is 500mm x 20mm x 10mm. The beam test structure is used to study the influences of the contact on the dynamical behaviour of the test structure. The comparison of the Frequency Response Function (FRF) spectrum between the experiment and simulation is performed to match the resonance frequency and damping. For the mode superposition analysis, the results for the modal-frequencies and the damping ratios from damped modal analysis form the fundamental building block for following harmonic or random-PSD analysis. The emphasis of this paper is to propose a model to capture the effects from non-linear contact for the non-deterministic types of excitation like random-PSD excitations.

Prior to the model validation with determining the contact parameters, the material properties of the test structure are to be given as an input (the intrinsic property independent of contacts) in the simulation model. The material properties of single beam are determined by the conventional method of model updating, with having good match of the modal frequencies between the Experimental modal analysis and simulation for the freely hanging single beam. The resulting elastic properties of the stainless steel material used for test structure are shown in table 1.

Elastic Properties		Damping	
Young's modulus (E)	192 GPa	Mass factor (α_r)	0.3
Poisons ratio (ν)	0.3	Stiffness factor (β_r)	4.85e-08
Mass density (ρ)	7845 kg/m^3		

Table 1: Elastic properties of the stainless steel beam used in Double beam test structure

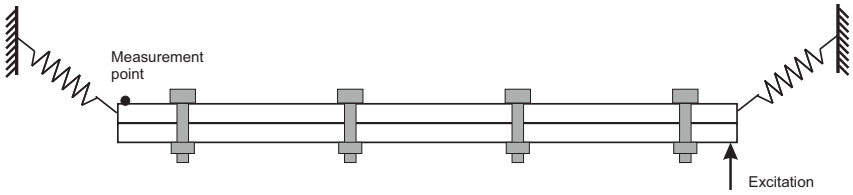
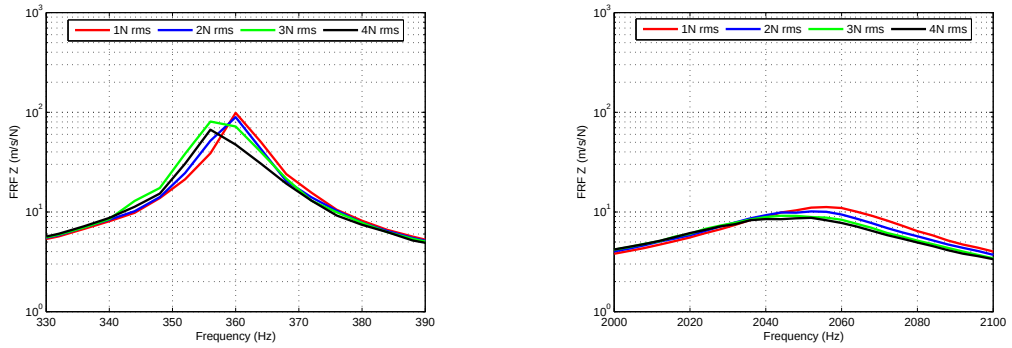


Figure 4: Experimental set-up of double layered beam with 4 bolted joints excited with a shaker stinger.

5.1 Random Excitation

The experimental set-up of the test structure is shown in figure 4, wherein the one end of test structure is excited and the measurement is done at the other end of test structure. The measurement of velocity is done using a laser vibrometer. A stinger is used to couple the test structure and modal electro-dynamic shaker, to excite the structure with force controlled PSD signal. The forced controlled PSD point excitation is done in the normal direction to excite the out-of plane modes, as the in-plane modes do not influence the contact status [12]. The frequency range for the excitation is 200-2200 Hz, with root mean square (rms) value of the force as 1N, 2N ,3N and 4N used. The effect of excitation is studied with the bolting torque of 3Nm. The shaker stinger experiment induces undesirable peaks due to the resonances of the stinger and other coupled effects on the FRF [17, 18]. With use of least square complex exponential modal fit algorithms, the result of mobility-FRF from measurements are obtained with good accuracy, especially at the resonance regions. The comparison between the experiment and simulation is done with the modal fit synthesized mobility-FRF.

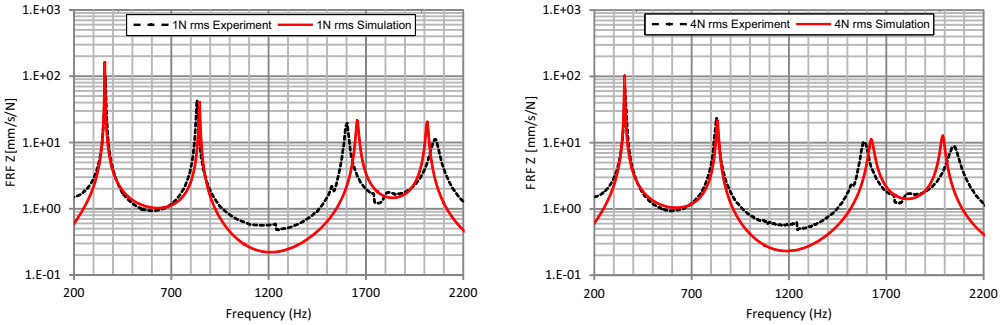


(a) Mode 1 (b) Mode 4

Figure 5: Effect of rms Force-PSD controlled excitation amplitudes on the mobility FRF of test structure with 3Nm of bolting torque

Figure 5 shows the effect on the mobility-FRF of the test structure with varying excitation amplitudes for 3Nm bolting torque. It can be seen that with increase in the excitation amplitude, the resonance frequency decreases and the damping increases. This confirms the non-linear behaviour of the test structure. In the simulation, the pre-stress modal analysis is further extended to the random PSD analysis. The modification done to the test structure in the simulations are : adding an extra 30 gms mass at the point of excitation, which accounts to the mass of the force sensor. From the experiment observation, due to increase in the excitation amplitude the resonance frequency is decreased while the damping is increased. The decrease in resonance frequency is due to the decrease in the tangential contact stiffness. Also, with increase in the excitation amplitude, the dissipation area too increases leading to increase in the damping.

The comparison between the experimental results and simulation results of the mobility FRF are concentrated in the resonance regions. The mobility-FRF shapes are in generality are symmetric for the random excitations and hence a comparison with modal superposition frequency analysis is possible. Figure 6 shows the comparisons for 3Nm bolting torque test structure for different excitation amplitudes. There is a very good match between the experiment and simulation.



(a) 1N rms Excitation
$\lambda = 4000$, $\lambda P_{\mathrm{N1}} = 25000$, β_0 = 0.83
$\mu = 0.3$, α=0.5

(b) 4N rms Excitation
$\lambda = 4000$, $\lambda P_{\mathrm{N1}} = 25000$, β_0 = 0.83
$\mu = 0.3$, α=0.45

Figure 6: Comparison between shaker stinger experiment and D-PDJ simulation results of mobility-FRF of the double layered beam test structure with 3Nm bolting torque

The contact parameters λ and P_{N1} are optimized to match the resonance frequency for the test structure for the lower excitation amplitudes. The coupling factor β_0 is evaluated based on the elastic and shear modulus of the structural steel. To estimate the damping, α is optimized and updated with increase in the excitation amplitudes. This parameter not only increase the damping but also reduces the tangential contacts stiffness to bring the effects on the resonance frequency and the peak amplitudes. The used parameters are mentioned in the figure 6, leading to a conservative good match between the experiment and simulation with deviations observed in higher frequency regime.

6 Conclusion

The proposed model characterizes the contact interfaces as an assimilation of discrete point to point coupling, where each contact pair describes the contact between the two asperities. Each contact pair is characterised with equivalent contact stiffness and damping. This defines a non-homogeneous contribution over the global contact interface with linearisation at the local contact pair. The local linearisation retains the advantages of linear system while the non-homogeneous definition contributes to capturing the non-linear effects from contacts. Implementation of proposed discrete model in frequency domain hence allows to simulate the non-deterministic excitation cases using modal superposition random-PSD vibration analysis. A very good match between the experiment and simulation motivates the use of the model for large complex structures used in industries.

REFERENCES

[1] L. E. Goodman, J.H. Klumpp, Analysis of slip damping with reference to turbine blade vibration, *Journal of Applied Mechanics*. **23**, 421, 1956.

[2] E. E. Ungar, The Status of Engineering Knowledge Concerning the Damping of Built-Up Structures, *Journal of Sound and Vibration*. **26**(1), 141–154, 1973.

[3] L. Gaul, J. Lenz, Nonlinear dynamics of structures assembled by bolted joints, ACTA MECHANICA. **125**, 169–181, 1997.

[4] R. D. Mindlin, Compliance of Elastic Bodies in Contact, *Journal of Applied Mechanics*, **16**, 259–268, 1949.

[5] J. A. Greenwood, J. B. P. Williamson, Contact of Nominally Flat Surfaces, Proceedings of Royal Society of London. **295**, 300–319, 1966.

[6] G. Masing, Eigenspannungen un verfestigung beim messing, In: *Second International Congress for Applied Mechanics*, Zurich, 332–335, 1926.

[7] B.O. Hardin and V. P. Drnevich, Shear modulus and damping in soils; design equations and curves, *Journal of the Soil Mechanics and Foundations Divison, ASCE*, **89**, 667–692, 1972.

[8] J. A. Greenwood, J. B. P. Williamson, Developments in the Theory of Surface Roughness, *In Proceedings of 4th Leeds-Lyon Symposium on Tribology, 1977.*

[9] A. A. Polycarpou, I. Etsion, Analytical Approximations in Modeling Contacting Rough Surfaces, *Journal of Tribology*, **121**, 471–493, 1999.

[10] M. Mayer, Zum Einfluss von Fuegestellen auf das dynamische Verhalten zusammengesetzter Strukturen, PhD thesis, University Stuttgart, Germany, 2007.

[11] U. Bittner, Strukturakustische Optimierung von Axialkolbeneinheiten, PhD thesis, Karlsruhe Institute of Technology, Germany, 2013.

[12] A. Sharma, W. Mueller-Hirsch, S. Herold, T. Melz (2014), Non-homogeneous localized Kelvin-Voigt model for estimation of dynamical behaviour of structures with bolted joints, *Proc. of 11th World congress on computational mechanics*, Barcelona, Spain.

[13] Surendra K. Saxena, Krishna R. Reddy, Dynamic moduli and damping ratios for monterey no.0 sand by resonant column tests, *Soils and Foundations*, **29**(2), 37–51, 1989.

[14] K. Smith, P. Watson, T. Topper, A stress-strain function for the fatigue of metals, *Journal of Matter*, **5**(4), 767–778, 1970.

[15] M. Groper, Microslip and macroslip in bolted joints, *Experimental Mechanics*, **25**, 171–174, 1985.

[16] H. G. Schmidt, Lecture notes on Soil dynamics, Institute Bodenmechanik, Bauhaus-University Weimar.

[17] K. G. McConnell, P. Cappa, Transducer inertia and stinger stiffness effects on frf measurements, *Mechanical Systems and Signal Processing*, **14**(4), 625–636, 2000.

[18] D. Cloutier, P. Avitabile, R. W. Bono, M. A. Peres, Transducer inertia and stinger stiffness effects on frf measurements, *Proceedings of the Twenty-Seveth International Modal Analysis Conference*, 197–203, 2009.

International Conference on Engineering Vibration
Ljubljana, Slovenia, 7-10 September 2015

RISK ASSESSMENT OF SAFETY ANALYSIS OF NPP STRUCTURES DUE TO EARTHQUAKE EVENS

J. Králik*[1]

[1]Department of structural mechanics, Faculty of Civil Engineering, SUT Bratislava, Radlinského 11, Bratislava 813 68, Slovakia
juraj.kralik@stuba.sk

Keywords: Earthquake, NPP, Risk, Probability, Safety, ANSYS.

Abstract. *This paper gives the results of the risk-based safety analysis of the seismic resistance of the NPP (Nuclear Power Plants) in Slovakia. The probabilistic assessment of NPP safety analysis is presented. On the base of the geophysical and seismological monitoring of locality the peak ground acceleration and the uniform hazard spectrum of the acceleration was defined for the return period 10 000 years using the Monte Carlo simulations. There is showed summary of calculation models and calculation methods for the probability analysis of the structural safety considering load, material and model uncertainties. The numerical simulations were realized in the system ANSYS. The results from the reliability analysis of the NPP structures are presented.*

.

1 INTRODUCTION

The IAEA (International Atomic Energy Agency) set up a program [3] to give guidance to its member states on the many aspects of the safety of nuclear power reactors. The risk of the NPP performance from the point of the safety must be calculated by consideration of the impact of the all effects during plant operation. The PSA (Probabilistic Safety Analysis) is one from the effective methods to analyze the safety and reliability of the NPP. The international standard NUREG [13] defines the principal steps for the calculation of the risk of the NPP performance by LHS probabilistic method

- Accident frequency (systems) analysis
- Accident progression analysis
- Radioactive material transport (source term) analysis
- Offsite consequence analysis
- Risk integration.

The accidents caused by the earthquake even are the critical emergencies from the point of the NPP performance. This paper gives the experiences from the seismic analysis of the operated NPP in Slovakia [4 - 11]. The earthquake resistance analysis of NPP buildings in Slovakia were based on the recommends of international organization IAEA in Vienna to get international safety level of the nuclear power plants [3]. Seismic safety evaluation programs of the NPP structures should contain three important parts [8]

- The assessment of the seismic hazard as an external event, specific to the seismic-tectonic and soil conditions of the site, and of the associated input motion;
- The safety analysis of the NPP resulting in an identification of the selected structures, systems and components appropriate for dealing with a seismic event with the objective of a safe shutdown;
- The evaluation of the plant specific seismic capacity to withstand the loads generated by such an event, possibly resulting in upgrading.

2 SEISMIC SAFETY METHODOLOGY

On the base of the experience from the re-evaluation programs in the membership countries IAEA in Vienna the seismic safety standard No.28 was established at 2003 [3]. Seismic safety evaluation programs should contain three important parts

- The assessment of the seismic hazard as an external event, specific to the seismic-tectonic and soil conditions of the site, and of the associated input motion;
- The safety analysis of the NPP resulting in an identification of the SSSCs (Selected Structures, Systems and Components) appropriate for dealing with a seismic event with the objective of a safe shutdown;
- The evaluation of the plant specific seismic capacity to withstand the loads generated by such an event, possibly resulting in upgrading.

2.1 Seismic hazards

The assessment of the seismic hazards specific to the seismic-tectonic conditions at a site is performed on the following bases:

- IAEA Safety Guides [4-6],
- Use of current internationally recognized methods and criteria [8, 12, 13 and 14],
- New data [10 and 11].

Two levels of the seismic load are defined in the standards [3]. SL-1 (First level) is coincident with the design earthquake and SL-2 (second level) corresponds to the maximum design

earthquake. On the base of the IAEA requirements the NPP structures of the first category have been resistance due to seismic level SL-2. This seismic level [3] should be updated in accordance with the above bases in the event that a reason for this has appeared since the evaluation of the SL-2 design level and should be used in the evaluation. In particular, the PGA (Peak Ground Acceleration) of the RLE (Review Level of Earthquake) should not be less than 0.1g. The level of the seismic risk is characterized by the probability level (return period) and the peak ground accelerations values, which are the typical free field zero period acceleration values at the ground surface. The comparison of the ground motion input level for new plants is presented in the Table 1.

		Probability/ Return Period	Peak Ground Acceleration*
Bulgaria		10^{-4}	0,20g
Canada		10^{-3} to 10^{-4}	
Czech Republic		10^{-4}	0,10g
Germany		10^{-4} to 10^{-5}	0,10g - 0,20g
Japan	S1	10^{-4}	0,20g - 0,45g
	S2		0,38g - 0,60g
Korea		10^{-3} to 10^{-4}	
Slovak Republic		10^{-4}	0,14g - 0,34g
Sweden		10^{-3}	
Schwitzerland		10^{-4}	
UK		10^{-4}	
US	Design		0,30g
	Margin		0,50g

Table 1: Comparison of the PGA in various countries

3 SEISMIC RE-EVALUATION PROGRAM IN SR

A re-assessment of the seismic hazard specific to the seismic-tectonic conditions at the site was considered by the SAV (Slovak Academy of Sciences) based on IAEA NUSS SO-SG-S1 and S8; US NRC-RG 1.60 and NUREG/CR-0098 [12]. IAEA is providing technical assistance to the Slovak regulatory authorities for reviewing the work results. Therefore the RLE (Review Level Earthquake) should correspond to the SL-2 level (Second Seismic Level), directly related to ultimate safety requirements. This is a level of extreme ground motion that shall have a very low probability of being exceeded during the plant lifetime and represents the maximum level of ground motion to be used for design and re-evaluation purposes. For the probability of occurrence a typical value of 10^{-4}/yr is usually used and for the ground response spectra an elastic one is selected.

As formulated by the Slovak authorities, the main objective of the seismic re-evaluation programs of NPP is to enhance the seismic safety of the plant to the level generally accepted by the international community and in compliance with the valid standards and recognized practice. These programs should have three important components:

(i) the re-assessment of the seismic hazard as an external event, specific to the site seismic-tectonic conditions;

(ii) the evaluation of the plant specific seismic capacity to withstand the loads generated by such event;

(iii) upgrading if necessary.

Regarding the first component (i), the geological stability and the ground motion parameters should be assessed according to specific site conditions and in compliance with criteria and methods valid for new facilities. In relation to the second component of the programs (ii) and considering that the plant has been originally designed for an earthquake level lower than the one would preliminarily be established for the site in compliance with IAFA NUSS 50-SG-S1. On the base of the results of the seismic analysis of the structure capacity the upgrade concept (iii) will be designed.

3.1 Safety aspects

The decision should be made early on whether either the SPSA (Seismic Probabilistic Safety Assessment), SMA (Seismic Margin Assessment), or EPRI (Electric Power Research Institute) seismic safety evaluation methods are to be used [8, 12, 13 and 14]. These methods have an advantage in that the entire plant may be evaluated as an integrated unit, including system and spatial interactions, common cause failure, human actions, non-seismic failures and operating procedures. The seismic resistance of the existing building structures as well as the technological equipment can be executed by the SMA method, especially its variant known as CDFM (Conservative Deterministic Failure Margin) depending on HCLPF (High Confidence Low Probability of Failure) determination of the seismic margin values. The CDFM method is based on an assumption that all the building structures and all the technological equipment components were designed properly for any non-seismic loads and conditions.

The HCLPF approach or an equivalent method may be used to verify the seismic capacity of NPP. The general criteria for CDFM approach is contained in [1].

The value of the HCLPF parameter depends on the equipment structure or component resistance (R) and the corresponding effect of action (E) using elastic or inelastic behavior.
The resistance factor are calculated as follows:

$$(FS)_{ep} = (R - E_{NS}) / (E_{Si} / k_D)^2 + (E_{Sa} \cdot k_D)^2]^{1/2} \quad (1)$$

where E_{Si}, or E_{Sa} is the seismic response to RLE (SL-2) inertial actions, or corresponding different seismic support movement, k_D is ductility coefficient ($k_D \geq 1.0$).
Generally the HCLPF parameter is

$$\text{HCLPF (CDFM)} = (\text{FS})\text{ep} \cdot \text{PGA}_{\text{RLE}}=\text{SL-2} \quad (2)$$

and this value must always be *HCLPF > PGA*.

The HCLPF seismic margin value can also be determined via a non-linear elastic-plastic calculation (e.g. limit analysis defined in the ASME BPVC Section III (ed. 92) – Mandatory Appendix XIII).

3.2 Seismic input data

Please, The seismic response can be calculated in the frequency (spectrum response analysis) or time domain (transient analysis) [8].

Also, hence the earthquake input must be specified in terms of free-field ground motion accelerograms for time-history dynamic analyses [1]. The foundation of the reactor building NPP can be embedded into the subsoil. This embedment has generally two effects on the dynamic analysis of the building:

- In comparison to a surface foundation the dynamic behavior of the foundation is different. In the case of rock these differences are minimal. The impedance analysis results in

stiffness parameters and damping ratios for the foundation soil system, which are higher than those for a surface foundation.

- The second effect is that the acceleration time histories at foundation level are different from the control motions specified at the surface of the free field.

In the case where structure and soil are idealized in only one Finite Element System or a consistent sub-structuring analysis the control motion is specified at the top of the surface and the effect of the embedment on both impedance and free field motion are automatically taken into account.

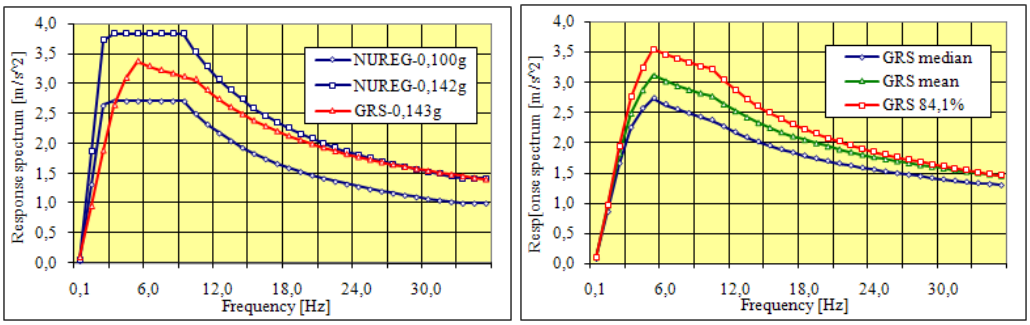


Figure 1: Comparison of the horizontal acceleration response spectrum NUREG, GRS

3.3 Response spectrum compatible accelerogram

To provide input excitations to structural models for sites with no strong ground motion data, it is necessary to generate the synthetic accelerogram. It has long been established that due to parameters such as geological conditions of the site, distance from the source, fault mechanism, etc. different earthquake records show different characteristics. Based on Kanai's investigation regarding the frequency content of different earthquake records, Tajimi proposed the following relation for the spectral density function of the strong ground motion with a distinct dominant frequency [8]:

$$S(\omega)=\frac{\left[1+4\xi_g^2\left(\omega/\omega_g\right)^2\right]}{\left[1-\left(\omega/\omega_g\right)^2\right]+4\xi_g^2\left(\omega/\omega_g\right)^2}S_0 \tag{3}$$

Here ξ_g and ωg are the site dominant damping coefficient and frequency, and S_0 is the constant power spectral intensity of the bed rock excitation. The generalized no stationary Kanai-Tajimi's model is represented by the following equation:

$$\ddot{u}_f+2\xi_g\omega_g\dot{u}_f+\omega_g^2u_f=y(t)\quad,\qquad \ddot{u}_g=-(2\xi_g\omega_g\dot{u}_f+\omega_g^2u_f).e(t) \tag{4}$$

where u_f is the filtered response, ω_g is dominant ground frequency, ξ_g is the effective ground damping coefficient, $\ddot{u}_g$ is the output ground damping acceleration, and *e(t)* is the amplitude envelope function. After numerical integration of eq. (4) can be evaluate the ground damping acceleration $\ddot{u}_g$.

The FORTRAN program "COMPACEL" has been developed by Králik [8] for generate synthetic ground motion accelerogram assuming the site effect and requirement of standard.

The requirements for the synthetic ground motion accelerogram according to standard ASCE 4/98 [1] are following:

1. The mean of the zero-period acceleration (ZPA) values shell equal or exceed the design ground acceleration,

2. In the frequency range 0,5 to 33 Hz, the average of the ratios of the mean spectrum to the design spectrum, where the ratios are calculated frequency by frequency, shall be equal to or greater than 1.
3. No one point of the mean spectrum (from the time histories) shall be more than 10% below the design spectrum.
4. The three components of motion in the orthogonal directions shall be statistically independent (with mean correlation smaller than 0,3), and the time histories shall be different.

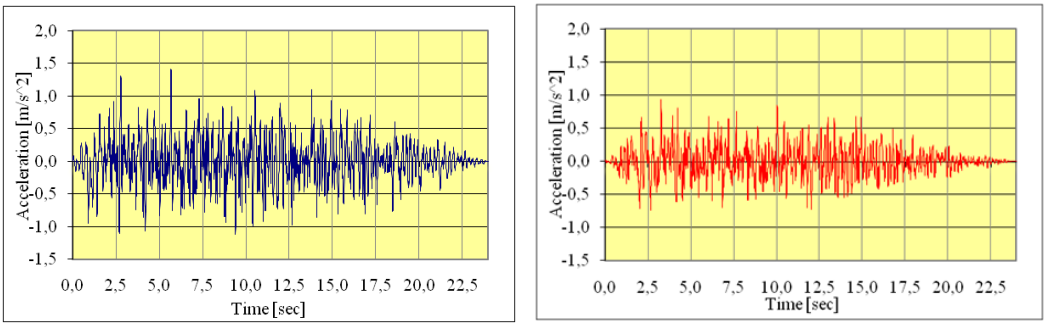


Figure 2: The spectrum compatible design horizontal and vertical accelerograms.

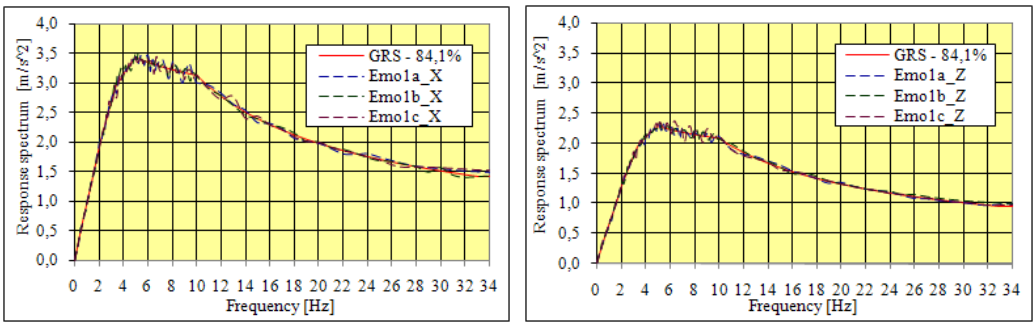


Figure 3: Comparison of the synthetic acceleration spectrum and GRS spectrum.

The program COMPACEL was created by J.Kralik to generate synthetic accelerograms. The comparison of the synthetic acceleration spectrum and GRS spectrum in the case of three and one accelerograms is showed in Figure 3.

Using three accelerograms for the calculation of spectrum response the calculation results is less conservative than for one accelerogram.

3.4 Calculation model of NPP structure

The NPP WWER 440 building consists of six objects - reactor building, bubbler tower, air-conditioning centre, turbine building, and lengthwise side electrical building and cross side electrical building [12]. The foundation plate (75,0/43,0m) under building on part V-D/10-22 is on two levels -8.5m. The foundation plate (39,5m/27,0m) under bubbler tower on part D-E/10-17 is on level -8.5m too. The foundation strip and foot under columns are in the cross side electrical building and turbine building. The global geometry of the NPP structures in Jaslovské Bohunice and Mochovce is identical, but the bracing system and the section area of the steel elements are different. The NPP building was discredited [12] by the 3D finite elements model to obtain realistic behavior of structure.

The model (VUT Brno and STU Bratislava) consists of 161 856 elements with 440 531 degrees of freedom. The drawbars are modeled by bilinear elements and contact between bubbler tower and air-conditioning center by gap elements.

The seismic loading was considered by spectrum compatible 3D accelerograms at foundation level to response. The material damping occurring in the soil and the structure mainly involves a frictional loss of energy [17].

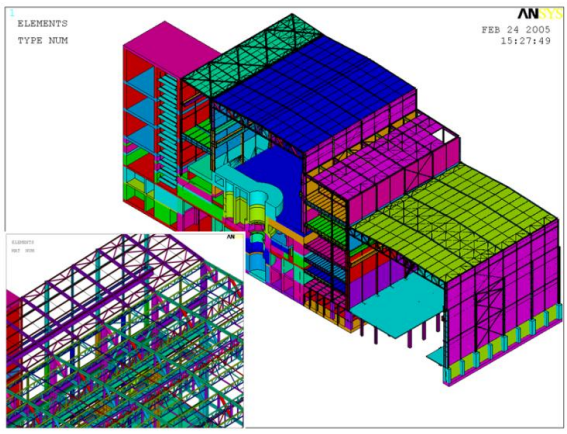


Figure 4: Calculation model of NPP.

3.5 Seismic response analysis

The differential equation of motion of finite element system under seismic motion of ground can be written [3] in the well-know matrix form

$$[M].(\{\ddot{u}_r\} + \{\ddot{u}_b\}) + [C].\{\dot{u}_r\} + [K].\{u_r\} = \{0\}, \tag{5}$$

where **[*M*], [*C*], [*K*]** are mass, damping and stiffness matrices respectively; $\{u_r\}, \{\dot{u}_r\}, \{\ddot{u}_r\}$ are relative vector of nodal displacements, velocities and accelerations; $\{\ddot{u}_b\}$ is absolute vector of base accelerations (earthquake excitation).

The transient analysis was realized by direct integration in time of dynamic equations (5) by Newmark. This method is move convenient for problem solution with necessity to wave character of action.

4 SEISMIC RESISTANCE OF NPP BUILDINGS

On the base of SMA methodology the seismic resistance of the NPP structures in Slovakia was calculated. The locality of J. Bohunice and Mochovce are in the different tectonic and seismic site. Also, hence the seismic risk level and the geological condition are different too.

The original design seismic load was defined in accordance with the contemporary Soviet standards VSN - 15 - 78 and SNIP-2-7-81.

The following values were defined at that time for the seismic design of seismic category I buildings:

- Design Earthquake-DE, with an intensity 5 in MSK-64 scale;
- Maximal Calculation Earthquake - MCE, with an intensity 6 in MSK-64 scale, and PGA= 0,05g (e.g. PGA= 0,1g) for Mochovce (e.g. J.Bohunice).

During the last 30 years the seismic monitoring of these localities were realized under the supervision of the Slovak Academy of Sciences [10 and 11].

In the actual time the new values of the peak ground accelerations were defined – PGA_{RLE}=0,35g in J.Bohunice and PGA_{RLE}=0,14g in Mochovce site for the re-evaluation of the seismic resistance of the NPP structures. The seismic resistance of the origin structures in J. Bohunice was not convenience from the point of new IAEA requirements and new seismic load. During the years 2001-2003 the NPP structures in J. Bohunice were upgraded. The seismic upgrading concept was created in cooperation the STU Bratislava and Stevenson &

Associate, subsequently it was developed in cooperation the STU Bratislava and Framatome ANP GmbH [8]. The principal conception included the jointed of steel structure of reactor hall to the concrete structure of bubbler condenser tower at roof level of the ventilating building (module G-D/10-22) using the new horizontal bracing system (Figure 5). The bracing systems of the vertical wall in turbine hall, reactor hall longitude and transversal galleries were strengthened. The anchorage of steel structures of gallery floors to the concrete structure of the reactor building was strengthened.

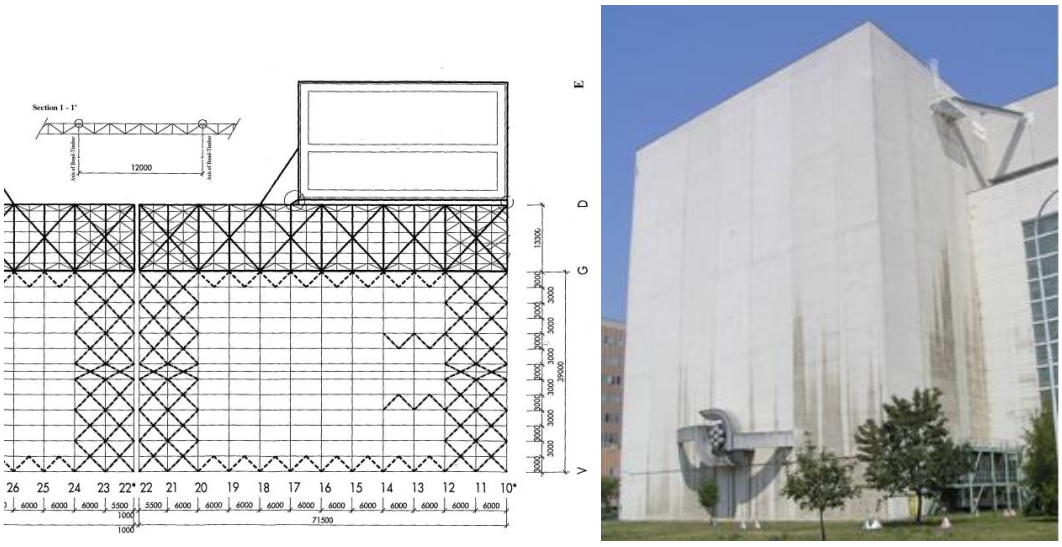


Figure 5: View and scheme of jointed of steel structure of reactor hall and concrete structure of bubbler tower.

The seismic safety of NPP building, after strengthening of the steel structures of gallery building floors to the concrete structure of the reactor building, is determined by the seismic resistance of the gallery anchors and secondary columns of the ventilating hall.

5 FLOOR RESPONSE SPECTRUM

The equipment and interior structures of NPP are designed using FRS (Floor Response Spectrum) as seismic loads. This spectrum is calculated from the time-history motions resulting from the dynamic analysis of the supporting structures in accordance of requirements of nuclear guide RG 1.122 [14].

The FRS can be calculated from the in-structure spectra on the base of deterministic and semi probabilistic methods [8]. The results from the calculation of FRS in all NPP buildings show, that in the case of the floor with the higher variability of distributed masses and slab stiffness, the FRS values are more conservative as the envelope of maximum spectrum values in various points of floor [8].

- **Deterministic method** to generate FRS is defined in NUREG 0800 [13] and IAEA rep.No28 [3]. The response spectrum in the points of floor is calculated using the transient analysis of the structure from synthetic 3D accelerograms (median+sigma). One or three 3D accelerograms can be used as input loads. The material properties are calculated with median values (best estimation). The damping values are requirement in ASCE 4/98 [1] (max.7% for steel and 10% for concrete structures and rock soil). The floor response spectrum may be calculated as envelope of maximum of mean spectrum values in each typical point (minimum 5 points are recommended).

- **Probabilistic method** to generate FRS is based on the statistical methods considering the uncertainties as a seismic risk, soil structure interaction, material properties, calculation model and other... The response spectrum in the points of floor is calculated using the transient analysis of the structure from group of synthetic 3D accelerograms [8]. In the case of the rock soil the median and variation of the input accelerograms must be equivalent to values of seismic risk for this locality. The FRS may be calculated as statistical envelope (median+sigma) of the spectrum values in all typical point. The statistical characteristic of input and output parameters are investigated for lognormal distribution.
- **Semi-probabilistic method** to generate FRS is based on the combination of deterministic and probabilistic methods. The total variation is calculated from the variation of the input loads, material properties and response in various typical points on the floor.

The uncertainties of the soil-structure interaction effects and calculation model can be considered by broadening and lowering of in-structure time history motion n accordance of requirements of standard ASCE 4/98 [1].

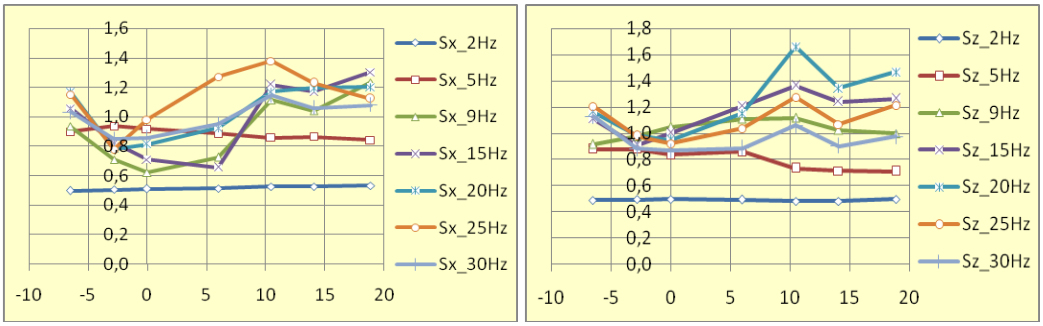


Figure 6: Comparison of ratio GRS/RLE floor response X and Z-spectrum GRS/RLE in the Box PG NPP.

The results from the calculation of FRS in all NPP buildings show, that in the case of the floor with the higher variability of distributed masses and slab stiffness, the FRS values are more conservative as the envelope of maximum spectrum values in various points of floor.

6 CONCLUSIONS

This paper presented the deterministic and probabilistic methodology to analysis the seismic resistance of NPP in Slovakia. There were summarized the works performed by the IAEA in the areas of safety review. There were summarized the works performed by the IAEA in the areas of safety review. The generation of the seismic loads on the base of probabilistic seismic risk analysis was described. The calculation models and methods for generation FRS in the NPP buildings in accordance with international standard were presented. The synthetic spectrum compatible accelerograms generated in program COMPACEL (created by Kralik) were presented in comparison with requirements ASCE4/98 standard. The results from this analysis present the international level of the seismic resistance of the NPP structures in Slovakia.

Acknowledgments

The project was realized with the financial support of the Grant Agency of the Slovak Republic (VEGA). The project registration number is VEGA 1/1039/12.

REFERENCES

[1] ASCE 4-98, *Seismic Analysis of Safety Related Nuclear Structures*, ASCE Standard, New York, 1999.

[2] R.W. Clough, and J. Penzien,J., *Dynamics of Structures*, Mc Graw-Hill, Inc. 1993.

[3] IAEA, *Safety Guide No. 28, Seismic Evaluation of Existing Nuclear Power Plants*, IAEA, Vienna, 2003.

[4] J. Králik and M. Šimonovič, Earthquake response analysis of nuclear power plant buildings with soil-structural interaction. *Mathematics and Computers in Simulation* 50. IMACS/Elsevier Science B.V. 1999, Pp. 227-236.

[5] J. Králik, Comparison of Probabilistic and Deterministic Assessments for Evaluation of Seismic Safety of Nuclear Power Plants in Slovakia. In: *First European Conference on Earthquake Engineering and Seismology*. 3-8 September, Geneve, Switzerland. Pp 422, 2006.

[6] J. Králik, Probability Seismic Hazard Analysis of Nuclear Power Plant Buildings in Mochovce. In: 6th *European Solid Mechanics Conference*. Budapest, 28. august – 1. september 2006, CD.

[7] J. Králik, Comparison of Deterministic and Probabilistic Methods to Determine Floor Response Spectrum. In proc. *Engineering Mechanics 2008*, National Conference with International Participation, May 12-15, 2008. ITAM AS CR Prague, pp. 126-128, ISBN: 978-80-87012-11-6.

[8] J. Králik, *Safety and Reliability of Nuclear Power Buildings in Slovakia. Earthquake-Impact-Explosion*. Ed. STU Bratislava, 307pp, 2009.

[9] J. Králik and J. Králik, jr., Seismic Analysis of Reinforced Concrete Frame-Wall Systems Considering Ductility Effects in Accordance to Eurocode. *Engineering Structures*. Elsevier 2009, ISSN 0141-0296, Vol.31, Issue 12, pp. 2865 - 2872, December 2009.

[10] P. Labák, A. Bystrická, P. Moczo, & L. Rosenberg, *Probabilistic seismic hazard computation for the Bohunice Nuclear Power Plant site*. Manuscript, Geophys. Inst. Slov. Acad. Sci., Bratislava, 3–20, 1997.

[11] P. Moczo, et al. Seismological and integrated geophysical research in Slovakia 2007-2010, In Report to IASPEI, Slovak National Report to IUGG 2007-2010. *Contr. Geophys. Geod.* 41, 83-111. ISSN 1335-2806, 2011.

[12] N. M. Newmark and W. J. Hall, *Development of Criteria for Seismic Review of Selected Nuclear Power Plants*. Report NUREG/CR-0098. NRC, Washington, 1975.

[13] NUREG 0800, *Standard Review Plan for the Review of Safety Analysis Reports for Nuclear Power Plants*. US NRC, 2007.

[14] NUREG/CR-6926, *Evaluation of the Seismic Design Criteria in ASCE/SEI Standard 43-05 for Application to Nuclear Power Plants*, BNL-NUREG-77569-2007, U.S. Nuclear Regulatory Commission Washington, DC 20555-0001, Job Code N6112, 2007.

[15] Z. Plocek, P. Štěpánek, V. Salajka, J. Kala and V. Kanický, Design of Earthquake Resistance Enhancements of the Dukovany Nuclear Power Plant Building Structures, In Proc. *Second International Symposium on Nuclear Power Plant Life Management*, 15–18 October, Shanghai, 2007.

International Conference on Engineering Vibration
Ljubljana, Slovenia, 7-10 September 2015

DETERMINISTIC AND PROBABILISTIC ANALYSIS OF THE ACCIDENTAL TORSION EFFECT TO SEISMIC RESISTANCE OF MULTI-STOREY BUILDINGS

J. Králik *[1] and J. Králik, jr. [2]

[1]Faculty of Civil Engineering, SUT Bratislava, Radlinského 11, Bratislava 813 68, Slovakia
juraj.kralik@stuba.sk

[2]Faculty of Architecture, SUT Bratislava, Námestie slobody 19, 812 45 Bratislava, Slovakia
kralik@fa.stuba.sk

Keywords: Probability, Seismicity, High rise building, Eurocode, FEM, LHS, ANSYS.

Abstract. *This paper presents the results from the deterministic and probabilistic seismic analysis of the influence of centre mass eccentricity to symmetric high rise building. During the structural design process, the problems of the safety, reliability and durability of a single structural element as well as the entire structure from the point of view of its planned life cycle must be considered. The methodology of the seismic analysis of the reinforced concrete high rise building structures on the base of deterministic and probabilistic assessment are presented. The methodology of the seismic analysis of the symmetrical structures in Eurocode and JCSS is discussed. The possibilities of the utilization the LHS method to analyze the extensive and robust tasks in FEM is presented in the case of high rise buildings with central core and columns system. The influence of the various input parameters (material, geometry, soil, masses,…) is considered. The deterministic and probability analysis of the seismic resistance of the structure was calculated in the ANSYS program.*

1 INTRODUCTION

During the structural design process, an engineer has to consider problems of the safety, reliability and durability of a single structural element as well as the entire structure from the point of view of its planned life cycle. Randomness in the loading and the environmental effects, the variability of the material and geometric characteristics of structures and many other "uncertainties" affecting errors in the computing model lead to a situation where the actual behavior of a structure is different from the modeled one [7]. Recent advances and the general accessibility of information technologies and computing techniques give rise to assumptions concerning the wider use of the probabilistic assessment of the reliability of structures through the use of simulation methods [1, 4, 6, 7, 8, 9, 10, 11, 12, 13 and 14] .

Most problems concerning the reliability of building structures [12] are defined today as a comparison of two stochastic values, loading effects E and the resistance R, depending on the variable material and geometric characteristics of the structural element.

The deterministic definition of the reliability condition has the form

$$R_d \geq E_d \tag{1}$$

and in the case of the probabilistic approach, it has the form

$$RF = R - E \geq 0 \tag{2}$$

where RF is the reliability function, which can be expressed generally as a function of the stochastic parameters X_1, X_2 to X_n, used in the calculation of R and E.

$$RF = g(X_1, X_2, ..., X_n) \tag{3}$$

The failure function $g(\boldsymbol{X})$ represents the condition (reserve) of the reliability, which can either be an explicit or implicit function of the stochastic parameters and can be single (defined on one cross-section) or complex (defined on several cross-sections, e.g., on a complex finite element model).

The most general form of the probabilistic reliability condition is given as follows:

$$p_f = P(R - E < 0) \equiv P(RF < 0) < p_d \tag{4}$$

where p_d is the so-called design ("acceptable") value of the probability of failure [2].

2 RELIABILITY ANALYSIS

From the point of view of one's approach to the values considered, structural reliability analyses can be classified in two categories, i.e., deterministic analyses and stochastic analyses [6]. In the case of the stochastic approach, various forms of analyses (statistical analysis, sensitivity analysis, probabilistic analysis) can be performed. Considering the probabilistic procedures, Eurocode 1 recommends a 3-level reliability analysis. The reliability assessment criteria according to the reliability index are defined here.

Most of these methods are based on the integration of Monte Carlo (MC) simulations [11]. The advantages and disadvantages of these methods are described in detail in the paper [7]. The ANSYS Program belongs among the complex programs for solving potential problems [7]. It contains a postprocessor, which enables the execution of the probabilistic analysis of structures. The probabilistic calculation procedures are based on Monte Carlo simulations (DS, LHS, user-defined sampling) and "Response Surface Analysis Methods (RSM)" (CCD, BBM, user-defined sampling). The sensibility post-processor processes the data numerically and graphically and provides information about the sensitivity of the variables and about the correlation matrices.

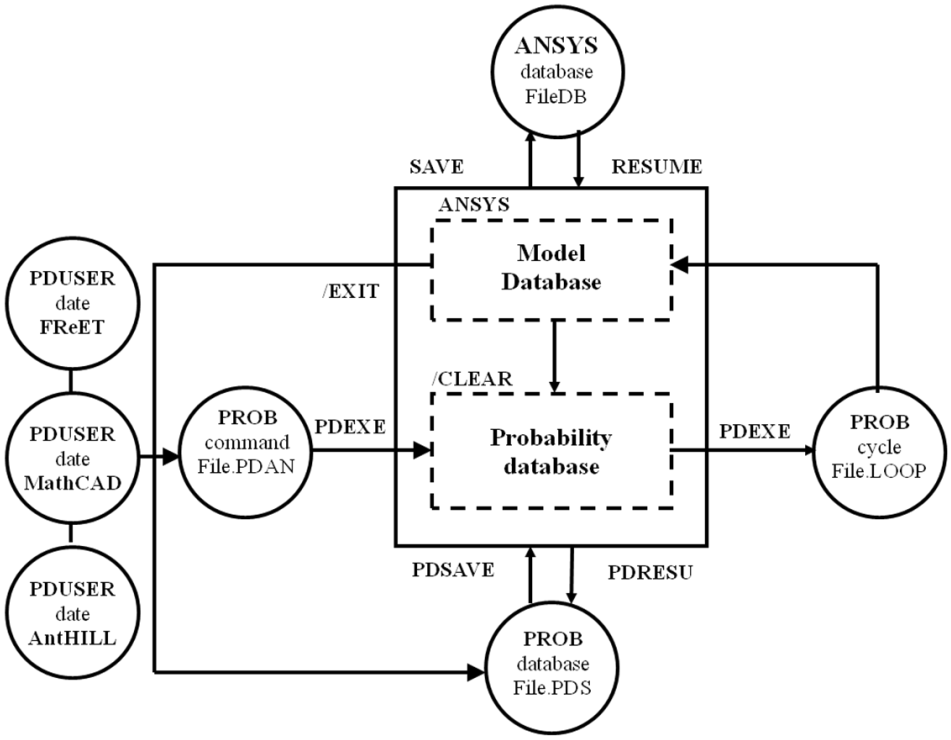


Figure 1: Procedural diagram of probabilistic calculations using the ANSYS software system

3 SEISMIC ANALYSIS

The seismic resistance of the core-column structural system was investigated using the deterministic and probabilistic analysis. The ENV 1998 [3] requires, that the seismic resistance of structures must be checked to the accidental torsional effects. In order to cover uncertainties in the location of masses and in the spatial variation of the seismic motion, the calculated centre of mass at each floor *i* shall be considered displaced from its nominal location in each direction by an accidental eccentricity due to the requirements of ENV 1998.

The accidental torsional effect is defined as follow

$$e_{ai} = \pm 0{,}05 . L_{\mathrm{i}} \tag{5}$$

where e_{ai} is an accidental eccentricity of storey mass *i* from its nominal location, applied in the same direction at all floors, L_i is a floor-dimension perpendicular to the direction of the seismic action.

The influence of accidental torsional effect will be considered using the accidental eccentricity of storey mass (5) for deterministic analysis. In the case of probabilistic analysis this effect should be considered as variable nonsymmetrical distribution of masses. The neglecting of the random eccentricities of the mass distribution or seismic excitation in the calculation of the seismic response of the symmetric buildings could be the reason of the structure failure in the reality.

The seismic analysis of the nonsymmetrical masses distribution is considered on two types of tall building – one is the biaxial symmetric structures with one central core and columns and second is the symmetrical structures with two cores and columns. A 15 storey buildings

with the prismatic, square cross-section and constant storey height of 3m, shown in Fig. 1 are considered.

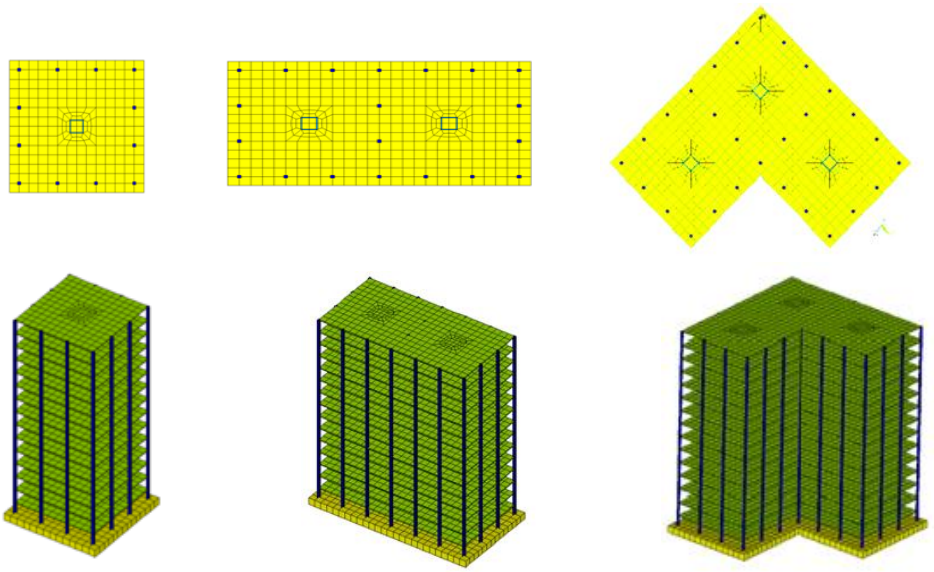


Figure 2: Model VSB1-bisymmetrical, VSB2 -one symmetrical and VSB3 - L symmetrical

All columns in these buildings are 500/500mm in cross-section. The outer dimensions of the cores are 2x2m with the wall thickness of 150mm. A reinforced concrete foundation plate with thickness 1m has 21x21m and 21x39m in horizontal plane. The thickness of floor reinforced concrete plate is 220mm. All floor slabs have a permanent load of 1,5kN/m^2 and variable load of 3,0kN/m^2. The material properties of this concrete building are Young's modulus, E=30000MPa and Poisson's ratio μ = 0,2.

4 LOADING AND LOAD COMBINATION

The loading and load combination in the case of the deterministic as well as the probability calculation is different due to requirements of ENV 1990 [2] and JCSS 2000 [5], too.

The seismic load was taken in accordance with ENV 1998 [3] as a design acceleration response spectrum for B type of soil and design acceleration a_g = 1,0ms^{-2}.

In the case of **deterministic calculation** and the ultimate limit state of the structure the load combination is considered according to ENV 1990 [2] as follows:

➲ ***Seismic design situation – deterministic method***

$$E_d = G_k + \psi_{2.Q} Q_k \pm A_{Ed} \tag{6}$$

where G_k is the characteristic value of the permanent loads, Q_k - the characteristic value of the variable loading, A_{Ed} (=$\gamma_1 A_{Ed.k}$) - the design value of the seismic loading, $A_{Ed.k}$ - the characteristic design value of the seismic loading, γ_1 – importance factor (of the building structure), $\psi_{2.Q}$ - the combination factor according to ENV 1990 ($\psi_{2.Q}$ = 0,3).

In the case of **probabilistic calculation** and the ultimate limit state of the structure the load combination we take following:

➲ ***Seismic design situation– probability method***

$$E = G + Q + A_E = g_{\text{var}} G_k + q_{\text{var}} Q_k + a_{\text{var}} A_{E.k} \tag{7}$$

where gvar, qvar, avar are the variable parameters defined in the form of the histogram calibrated to the load combination in compliance with Eurocode [2].

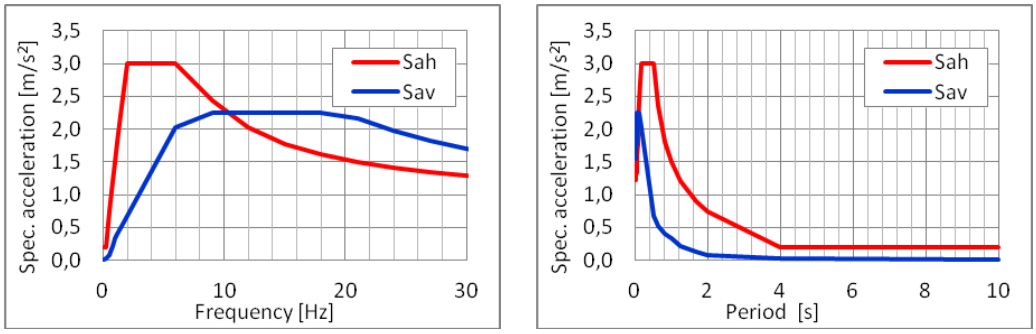


Figure.3: Response spectrum acceleration in horizontal and vertical direction

5 SPECTRUM ANALYSIS

The seismic analysis of the tall building structure was realized using the linearized response spectrum method [7]. This method allows an approximate determination of the maximum response of an MDOF system without performing a time history analysis. The response spectrum method is based on the solution of dynamic equation by modal superposition method in time.

The dynamic equation for MDOF system with n-DOF due to support excitation is defined in the form

$$\mathbf{M}(\ddot{\mathbf{u}}+\ddot{\mathbf{u}}_s)+\mathbf{C}\dot{\mathbf{u}}+\mathbf{K}\mathbf{u}=\mathbf{0}, \tag{8}$$

where **M**, **C**, **K** are matrix (*n x n*) of the mass, damping and stiffness, $\mathbf{u}, \dot{\mathbf{u}}, \ddot{\mathbf{u}}$ are vectors (*n x 1*) of relative displacements, velocities and accelerations, $\ddot{\mathbf{u}}_s$ is vector (*n x 1*) of support accelerations (seismic excitation). After transformation the equations (8) to the modal coordinate system by next substitution

$$\mathbf{u}=\sum_{i=1}^{m}\boldsymbol{\Phi}_i.\mathbf{Y}_i, \tag{9}$$

we obtain the m-independent equations of motion in the form

$$\ddot{\mathbf{Y}}_i+2.\xi_i.\omega_i.\dot{\mathbf{Y}}_i+\omega_i^2.\mathbf{Y}_i=-\boldsymbol{\Gamma}_i.\ddot{\mathbf{u}}_s \tag{10}$$

where $\boldsymbol{\Phi}_i$ is an eigenvector (*m x 1*) for mode *i* after normalization of mass matrix $\boldsymbol{\Phi}_i^T\mathbf{M}\boldsymbol{\Phi}_i = 1$, $\mathbf{Y}_i$ is a modal coordinate vector (*m x 1*), ξ_i is relative damping for mode *i*, ω_i angular frequency mode *i*, $\boldsymbol{\Gamma}_i$ is participation factor for mode *i* in the form

$$\boldsymbol{\Gamma}_i=\frac{\boldsymbol{\Phi}_i^T.\mathbf{M}.\mathbf{1}}{\boldsymbol{\Phi}_i^T.\mathbf{M}.\boldsymbol{\Phi}_i}, \tag{11}$$

Response spectrum analysis consists of three steps [7]:

1. Modal analysis, i.e., determination of the natural modes of vibration and the associated frequencies

2. Determination of the maximum response in each mode, "modal response," included in the analysis; this involves determination of maximum value of the modal coordinate, $Y_{i.max}$, over the duration of the earthquake loading for each mode
3. Combination of the modal responses to obtain approximate maximum response
4. The maximum modal response for mode i, $Y_{i.max}$, can be expressed in terms of the acceleration response spectrum, $S_a(\omega_i)$:

The response spectrum of the displacements and forces from the excitation in direction $a=1, 2, 3$ is calculated from the modal response by method square root of sum of squares mode (SRSS) in the form

$$R_a = \left[\sum_{i=1}^{N} \left(R_i \right)^2 \right]^{\frac{1}{2}} \tag{12}$$

The total response spectrum is calculated from three base acceleration spectra (in space) alternatively from the combination SRSS or standard combination rule

$$R_{tot}=R_1+0,3R_2+0,3R_3 \quad \text{or} \quad R_{tot}=0,3R_1+0,3R_2+R_3 \quad \text{or} \quad R_{tot}=0,3R_1+R_2+0,3R_3 \tag{13}$$

where R_i (i=1,2,3) are response values from the acceleration excitation in the direction 1, 2, 3.

The modal analysis of these two models of buildings was realized on the software ANSYS using Lanczos method. The first mode of the model with one core is 0,361547Hz with 50% of effective masses and in the case of two cores it is 0,365143Hz with 53% effective masses.

6 UNCERTAINTIES OF INPUT VARIABLES

The effect of soil-structure interaction can be investigated in the case of probabilistic assessment by sensitivity analysis of the influence of variable properties of soil. A soil stiffness variability in the vertical direction is defined by the characteristic stiffness value k_z from the geological measurement and the variable factor k_z_var. The stiffness of the structure is determined with the characteristic value of Young's modulus E_k and variable factor e_var. A load is taken with characteristic values G_k, Q_k, $A_{E,k}$ and variable factors g_var, q_var and a_var. The uncertainties of the calculation model are considered by variable model factor θ_R and variable load factor θ_E for Gauss's normal distribution.

$$q(x,y) = \left\{ q_{z,\text{var}} + 2\frac{(x-x_o)}{l_x} q_{yy.\text{var}} + 2\frac{(y-y_o)}{l_y} q_{xx.\text{var}} \right\} q_k \,, \tag{14}$$

where q_k is characteristic value of live load (q_k = 1kN/m^2), x_o, y_o are coordinates of building slab gravity centre, L_x and L_y are the plane dimensions of the slabs in directions x and y.

The random live load is considered in two alternatives – model VSB1p takes the variable live load on the plane only and model VSB1pm takes the variable live load both on the plane and height of building. The variability of the stiffness and masses parameters of the building has the significant influence on the modal characteristic of the building.

The results of the probability analysis of the model VSB1 present that the principal frequencies in the direction X (resp. Z) are in the interval from 0,320HZ to 0,475Hz (resp. from 3,961Hz to 6,003Hz). In the case of model VSB2de the principal frequencies in the direction X (resp. Z) are in the interval from 0,353HZ to 0,422Hz (resp. from 2,776Hz to 3,181Hz). In the case of model VSB3 the principal frequencies in the direction X (resp. Z) are in the interval from 0,353HZ to 0,422Hz (resp. from 2,776Hz to 3,181Hz). This frequency interval has

the important influence to intensity value of seismic excitation on the part of the response spectrum acceleration about of frequency 2Hz (resp. 7Hz).

Name	Quantity	Charact. value	Variable paramet.	Histogram	Mean	Stand. deviation	Min. value	Max. value
Soil	Stiffness	$k_{z,k}$	k_z_var	Normal	1	0,200	0,451	1,490
Material	Young's modulus	E_k	e_var	Normal	1	0,120	0,645	1,293
Load	Dead	G_k	g_var	Normal	1	0,010	0,755	1,282
	Live	Q_{k1}	q_z_var	Uniform	0,5	0,290	0	1
			q_{xx}_var	Uniform	0	0,580	-1	1
			q_{yy}_var	Uniform	0	0,580	-1	1
	Seismic	$A_{Ed,k}$	a_var	Beta (T. I)	0,67	0,142	0,419	1,032
Resistance	Shear	Vu_k	Vu_var	Lognormal	1	0,100	0,726	1,325
Model	Action uncertaint	θ_E	Te_var	Normal	1	0,100	0,875	1,135
	Resistance uncert	θ_R	Tr_var	Normal	1	0,100	0,875	1,135

Table 1: Probabilistic model of input parameters

7 RELIABILITY CRITERIA

Reliability of the structures is designed in accordance of standard requirements STN 731201 and ENV 1998 [3] for ultimate and serviceability limit state. Horizontal reinforced plane structures are designed on the bending and shear loads for ultimate limit state function (3) in the next form

$$g(M) = 1 - M_E / M_R \geq 0, \qquad g(V) = 1 - V_E / V_R \geq 0 \tag{15}$$

where M_E, V_E are design bending moment and design shear force of the action and M_R, V_R are resistance bending moment and resistance shear force of the structure element. Vertical plane reinforced concrete structures are designed to the tension or compression and shear resistance for function of failure [7] in the form

$$g(N) = 1 - N_E / N_R \geq 0, \qquad g(V) = 1 - V_E / V_R \geq 0 \tag{16}$$

where N_E, V_E are normal and shear design forces of action and N_R, V_R are resistance normal and shear forces to unit length.

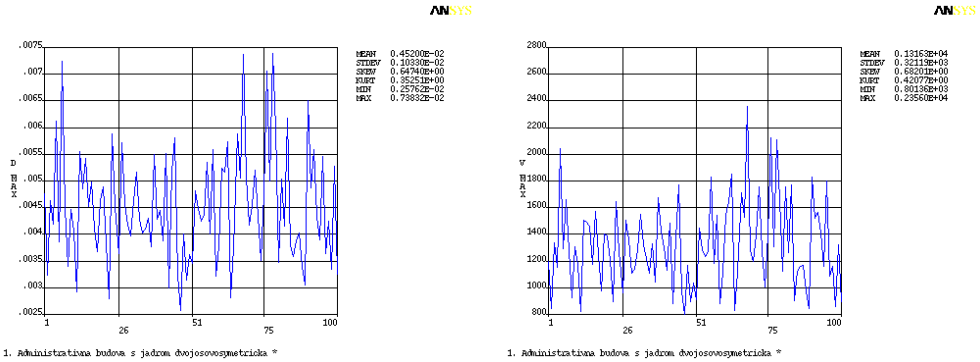


Figure 4: LHS simulation of interstorey drift D_{max} and shear force V_{max} in model VSB1

Damage limitation of the reinforced concrete structures depend on the criterion of the maximum interstorey drifts. The standard ENV 1998 [3] define the function of failure in the form

$$g(d) = 1 - d_E / d_R \geq 0 \tag{17}$$

where d_E is interstorey horizontal displacement, d_R ($d_R = 0,005.h/\nu$) is limit value of interstorey horizontal displacement defined (for non-structural elements of brittle materials attached to the structure), h is storey height (h = 3m) and ν is reduction factor to take into account the lower return period of the seismic action associated with the damage limitation requirement (ν = 0,4).

8 SENSITIVITY ANALYSIS

Sensitivity analysis of the influence of the variable input parameters to the reliability of the structures depends on the statistical independency between input and output parameters. Matrix of correlation coefficients of the input and output parameters is defined by Spearman

$$r_s = \frac{\sum_i^n \left(R_i - \bar{R}\right)\left(S_i - \bar{S}\right)}{\sqrt{\sum_i^n \left(R_i - \bar{R}\right)^2}\sqrt{\sum_i^n \left(S_i - \bar{S}\right)^2}}, \tag{18}$$

where R_i is rank of input parameters within the set of observations $[x_i]^T$, S_i is rank of output parameters within the set of observations $[y_i]^T$, $\bar{R}, \bar{S}$ are average ranks of the parameters R_i and S_i respectively.

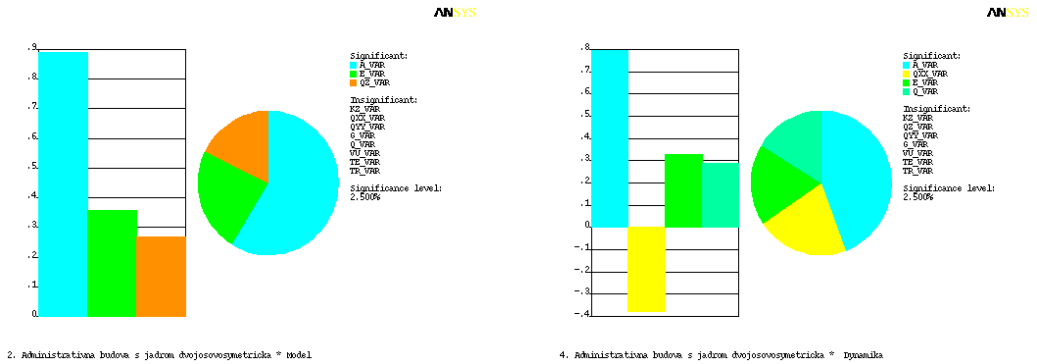


Figure 5: Sensitivity analysis for the shears resistance in the model VSB1p and VSB3p

The results of the sensitivity analysis of the interstorey drift present, that the variability of seismic load has the most significant influence on the interstorey drift in the model VSB1p, VSB1pm and VSB3p too. A variability of the live load is second important parameter in the model VSB3p.

The variability of dead load and concrete stiffness (e.g. live load and dead load) are significant for first mode in model VSB1p (e.g. VSB3p). In the case of the shear resistance sensitivity analysis of the building, the most important variable parameters in the model VSB1p are the seismic load, concrete stiffness, live load in the vertical direction. Otherwise the seismic load and live load on the model VSB3p are the variables with significant effect. The sensitivity analysis gives the valuable information about the influence of uncertainties of input variables (load, material, model,) to engineer for optimal design of the structures.

9 COMPARISON OF ANALYSES

Deterministic calculation of the seismic resistance of the tall building was taken on the model VSB1d, VSB1de, VSB2d, VSB2de and VSB3d, VSB3de. The probabilistic calculation was carried out on the model VSB1p, VSB2p and VSB3p. The influence of the eccentricity of masses centre was considered on the models with index "e". The comparison of deterministic and probabilistic analyses is presented in table 1. The influence of the torsional excentricity to the interstorey drift in deterministic (or probabilistic) analysis is equal to 66% (or 41%) in VSB1d (or VSB1p) model, 74% (or 59%) in VSB2d (or VSB2p) model and 276% (or 54%) in VSB3d (or VSB3p) model. The lower differences are in the extreme shear forces.

Method	Model	Extreme interstorey drift [mm] d_r=37,5mm				Extreme shear force[kN] V_R=1990kN/m			
		Min	Max	Mean	St.dev	Min	Max	Mean	St.dev
Model of tall building with one reinforced concrete core – VSB1									
Deterministic	VSB1d	-	15,72	-	-	-	1009,5	-	-
	VSB1de	-	26,11	-	-	-	1349,2	-	-
Probabilistic	VSB1p	7,73	22,15	13,56	3,99	710,15	2356,0	1316,3	321,2
Model of tall building with two reinforced concrete cores – VSB2									
Deterministic	VSB2d	-	18,19	-	-	-	841,2	-	-
	VSB2de	-	31,72	-	-	-	1416,7	-	-
Probabilistic	VSB2p	8,34	28,84	15,21	3,72	712,36	2481,6	1364,8	339,5
Model of tall building with three reinforced concrete cores – VSB3									
Deterministic	VSB3d	-	9,39	-	-	-	517,2	-	-
	VSB3de	-	35,37	-	-	-	1537,8	-	-
Probabilistic	VSB3p	4,16	14,45	7,49	1,98	429,4	1514,0	758,3	211,8

Table 2: Comparison of deterministic and probabilistic analyses

10 CONCLUSIONS

The influence of the accidental torsional effect to the seismic resistance of the reinforced concrete tall buildings with the core-columns system was investigated in this paper in accordance with the Eurocode requirements. This effect represents the uncertainties in the location of masses and in the spatial variation of the seismic motion. The methodology of the seismic analysis of the reinforced concrete tall building structures on the base of deterministic and probabilistic assessment was considered. This analysis was realized on the example of the one, biaxial and L symmetrical tall building structures. A 15 storey reinforced concrete building with one central square core and three cores with the system of columns around it was considered. In the case of deterministic seismic analysis the accidental eccentricity of masses is defined in the Eurocode. The random distribution of mass eccentricity on the building slab was considered as the linear approximation of the distribution of live load on all the floors (VSB1p, VSB2p, VSB3p). From the summary of the results it follows that the unequal distribution of the masses has the significant influence on the structure seismic resistance. The maximum difference in the interstorey drift was obtained in the building L symmetrically with 3 cores (model VSB3). The deterministic analysis with the eccentricity of masses give us more conservative results as probabilistic analysis.

Acknowledgement

The project was realized with the financial support of the Grant Agency of the Slovak Republic (VEGA). The project registration number is VEGA 1/1039/12.

REFERENCES

[1] Ellingwood, B., Galambos, T.B., MacGregor, J.C., and Cornell, C.A., *Development of a probability Based Load Criterion for American National Standard A58*, NBS Special Publication SP577, National Bureau of Standards, Washington, D.C., 1980.

[2] ENV 1990, *Eurocode - Basis of structural design*, CEN Brussels 2002.

[3] ENV 1998, *Eurocode-Design of structures for earthquake resistance, Part 1: General rules, seismic actions and rules for buildings*, CEN Brussels 2003.

[4] Janas, P., Krejsa, M., Krejsa, V., Structural Reliability Assessment Using Direct Determined Probabilistic Calculation. In *Proceedings of the Twelfth International Conference on Civil, Structural and Environmental Engineering Computing*, paper 72, Topping, Costa Neves & Barros (eds), Funchal, Madeira, Portugal. Civil-Comp Press, 2009. ISBN 978-1-905088-31-7.

[5] JCSS-OSTL/DIA/VROU-10-11-2000, *Probabilistic Model Code, Part 1, Basis of Design*, Working material, http://www.jcss.ethz.ch/, 2001.

[6] Konečný, P., Brožovský, J., Křivý, V., Towards Parallel Computing using the Simulation-based Reliability Assessment Method. *Proceedings of the First International Conference on Parallel, Distributed and Grid Computing for Engineering*, Civil Comp Press, 2009, s. 542-549. 978-1-905088-29-4.

[7] Králik, J., *Reliability Analysis of Structures Using Stochastic Finite Element Method*, Published by STU Bratislava, 2009, 143pp. ISBN 978-80-227-3130-0.

[8] Králik, J., Králik, J.,jr., Seismic Analysis of Reinforced Concrete Frame-Wall Systems Considering Ductility Effects in Accordance to Eurocode. *Engineering Structures*. Elsevier 2009, ISSN 0141-0296, Vol.31, Issue 12, pp. 2865 - 2872, December 2009.

[9] Králik, J., Králik, J.,jr., Deterministic and Probabilistic Analysis of Nonsymmetrical Wind Effects to Symmetrical High Rise Buildings. In proc. *European Safety and Reliability Conference, ESREL 2009, Reliability, Risk and Safety, Theory and Applications*, CRC Press/A.Balkema Book, Prague, Czech Republic, 7-10 September, Vol.2, p.1393-1396, ISBN 978-0-415-55509-8, Full text in CD.

[10] Králik,J., Králik,J.jr:: Probability Assessment of Analysis of High-Rise Buildings Seismic Resistance, In: Advanced Materials Research, Vols 712 – 715 (2013), pp. 929-936, © (2013) Trans Tech Publications, Switzerland, DOI 10.4028/www.scientific.net/ AMR.712-715.929, ISSN 1662-8985.

[11] Rosovsky, D.V., *Structural Reliability*. Part of publication W. Chen, *The Civil Engineering Handbook*, CRC Press, W.F. Chen Ed. 1995, Clemson University, SC.

[12] Saito, T. et al. Seismic damage analysis of reinforced concrete buildings based on statistics of structural lateral resistance. *Structural Safety*, Vol.19, No.1, pp.141-151, 1997.

[13] Soares, R.C. et al., Reliability analysis of non-linear reinforced concrete frames using the response surface method. *Journal of Reliability Engineering &System Safety*, vol. 75, pp. 1-16, 2002.

[14] M. Sýkora and M. Holický, Assessment of Uncertainties in Mechanical Models, Applied Mechanics and Materials Vol. 378 (2013) pp 13-18, © (2013) Trans Tech Publications, Switzerland, doi:10.4028/www.scientific.net/AMM.378.13.

11th International Conference on Engineering Vibration
Ljubljana, Slovenia, 7–10 September 2015

DESIGN AND OPTIMIZATION OF A COMPACT HIGH-FREQUENCY ELECTROMAGNETIC SHAKER

Leonardo Bertini[1], **Paolo Neri***[1], **Ciro Santus**[1]

[1]University of Pisa, Department of Civil and Industrial Engineering - DICI.
Largo L. Lazzarino 2, 56122 Pisa, Italy
leonardo.bertini@ing.unipi.it paolo.neri@for.unipi.it ciro.santus@ing.unipi.it

Keywords: Electromagnetic shaker, Stinger, Bladed wheels, Modal analysis, Harmonic response analysis.

Abstract. *Dynamic characterization and resonances prediction of mechanical structures is a crucial issue in industry. Performing experimental modal analysis and harmonic response requires an excitation source able to operate in a wide frequency range, depending on the analyzed structure. In the present paper, the optimization and the design of an electromagnetic shaker is presented. This device has been engineered for a test bench to investigate the vibrational dynamics of centrifugal compressor bladed wheels. A really compact solution is needed since the final test bench provides up to* 20 *shakers on the circumference hoop, one for each blade, and the excitation frequency ranges from* 1 *to* 10 *kHz. Different stinger solutions are proposed and compared in the paper, in order to monitor the stinger effects on the dynamic response of the analyzed structure. The investigated solutions are: a beam stinger (diameter* 1 *mm), a wire stinger (diameter* 0.2 *mm), and a ball stinger (diameter* 3 *mm) which was tested with two different contact solutions. Experimental tests were performed on a shaker prototype to verify the vibrational loads applied by the device and to compare the different stinger solutions.*

1 INTRODUCTION

Experimental Modal Analysis (EMA) and Harmonic Response Analysis (HRA) are crucial for structure dynamic characterization. Any time that a component is excited by a cyclic load, a deep knowledge of its vibrational response is needed in order to avoid resonance excitations that could imply efficiency drop or even induce fatigue fracture failures. High rotational speed bladed wheels, such as turbines and compressors, are remarkable examples of mechanical structures that experience vibrations with high frequency harmonics. The blades interact with the fluid coming from stator vanes [1, 2, 3], so that high frequency excitation happens at the rotational speed regimes of the machine. Indeed, EMA tests have been proposed for this kind of components [4, 5] with single or double shaker configurations. On the other hand, HRA needs a more complex setup because a high number of excitation sources is needed to properly reproduce the operational conditions, in principle one exciter is required for each blade. Since the number of blades can be considerable, the exciter lateral dimension issue implies a really critical constraint for this application. Contact-less solutions are available in literature, however they are limited to low load intensity and low maximum frequency [6], while for the present investigation the frequency values are in the range $1 - 10$ kHz, therefore electromagnetic shakers were considered. Several commercial solutions are available, but they do not guarantee to cover the whole frequency range or they do not satisfy the dimensional limitations, for this reason a custom electromagnetic shaker was designed. A static copper coil was wired and axially aligned with a moving permanent magnet, which was then connected to the target structure. Analytical and numerical models were implemented for the geometry optimization, in order to achieve relevant force values, still within the dimensional limitations and the required frequency range. The main drawback of this solution is the connection between the blades and the exciters, which can influence the dynamic component response. In order to prevent any inertia effect caused by the exciter moving part (i.e. the permanent magnet and the load cell) several stinger configurations were analyzed. The aim was to select a stinger transferring the force along the exciter direction only, filtering out all the other forces and torques, and minimizing the difference between the force, as measured by the load cell, and the actual force (and torque) acting on the tested structure. Four different configurations were compared: rigid connection, beam stinger, wire stinger, and ball stinger. A test bench was developed to study the effect of each stinger kind, with respect to the measured vibration, by comparing the Frequency Response Functions (FRFs).

2 ELECTROMAGNETIC SHAKER DESIGN

The required severe design specifications for the electromagnetic exciter are summarized in Table 1.

Quantity	Value
Frequency range	$1 - 10$ kHz
Maximum radius	17 mm
Peak force (at 10 kHz)	0.1 N

Table 1: Specifications for the electromagnetic excitation device.

The basic design configuration was chosen, with a coil wired on a support (fixed part) which is axially aligned with a floating permanent magnet (moving part). The permanent magnet al-

lowed to have a high force density just with a limited volume of the moving part. Neodymium magnets were chosen for this application, since they can be found in a great variety of dimensions and at reasonable costs. The use of permanent magnets also allowed to build simple analytical/numerical models of the device, which made possible an optimization of the geometry sizes. All the structural parts of the device were manufactured in aluminum alloy, being non-ferromagnetic, to have the generated magnetic field not influenced. Other non-ferromagnetic and non-metal materials, such as plexiglass, were also considered in order to limit the eddy current losses. However, the machining of those materials would have introduced some limitations on the possible manufacturing geometries, thus they were not chosen at the present research stage. As a consequence, the eddy current issue implies a higher power supply and then some overheating to be monitored. The connection between the fixed and the moving parts was finally designed. As reported below, the specification was to provide an almost free (or largely compliant) support along the axial direction while a quite stiffer support along the radial direction.

2.1 Analytical and numerical models

Several different approaches are available in literature for solenoid-permanent magnet interaction modeling [7]; among them two analytical models have been focused in this research. The first, and simpler, uses the Biot-Savart law which is aimed at the determination of the flux density $\vec{B}$ on the axes of a current loop. The solenoid was modeled as a cylinder, having the coil winded between r_1 and r_2 (inner and outer solenoid radii). A cylindrical portion of the coil was initially considered, having a radial extension of dr and z as axial coordinate. Each dz segment was supposed to contain a number of coils equal to $N/(L(r_2-r_1))\mathrm{d}z\mathrm{d}r$, being N the total number of coils and L the total solenoid length. The intensity of $\vec{B}$ at any coordinate z can then be computed by integrating the contribution of each portion $\mathrm{d}A = \mathrm{d}z\,\mathrm{d}r$, from $-L/2$ to $L/2$ and from r_1 to r_2, being the origin of the reference system positioned at the center of the solenoid. The value of $|\vec{B}|$ was computed along the solenoid axes, assuming that it remains constant along the radius with a variation along the z coordinate only. This hypothesis introduces an error which decreases as the solenoid length L increases with respect to its radius. The permanent magnet was modeled as a cylinder having an height h and a radius R_m and a constant magnetization M. Thus, it was possible to compute the magnetic field in the solenoid [8] and then obtain the force acting on the magnet [7]:

$$
\begin{aligned}
B_1 &= (z+L/2)\ln\left(\frac{r_2+\sqrt{r_2^2+(z+L/2)^2}}{r_1+\sqrt{r_1^2+(z+L/2)^2}}\right) \\
B_2 &= (z-L/2)\ln\left(\frac{r_2+\sqrt{r_2^2+(z-L/2)^2}}{r_1+\sqrt{r_1^2+(z-L/2)^2}}\right) \\
B_z(z) &= |\vec{B}(z)| = \frac{\mu_0 IN}{2L(r_2-r_1)}(B_1-B_2) \\
F(Z) &= \frac{\pi R_\mathrm{m}^2 M}{\mu_0}(B_z(Z+h/2)-B_z(Z-h/2))
\end{aligned}
\tag{1}
$$

where μ_0 is the vacuum permeability, Z represents the distance between the center of the solenoid and the center of the permanent magnet and I is the current circulating in the solenoid.

The second considered model was the so called "shell method". The solenoid was modeled as a series of thin cylinders in which the current density is I/N_r, where N_r is the number of radial windings. Also the permanent magnet was modeled as a thin cylindrical surface. The current density circulating on this surface was related to the value of M. The total force acting on the permanent magnet could then be obtained by summing the contributions of all the thin solenoid surfaces F_s:

$$F(Z) = \frac{1}{N_\mathrm{r}} \sum_{n=1}^{N_\mathrm{r}} F_s(R_\mathrm{m}, r_n, h, L, Z) \tag{2}$$

where r_n represents the radial distance between the axes of the permanent magnet and the $n-$th thin surface. F_s formulation can be found in [9, 10] and it involves complete elliptic integrals of the first, second and third kinds.
These two models were implemented on an electronic sheet and very similar results were obtained in terms of force estimation, Figure 1. An experimental validation (described below) has been performed and the results are also reported in the figure.

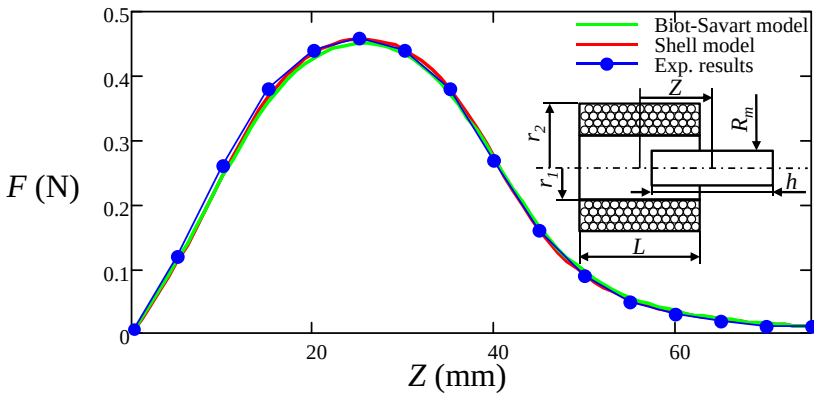


Figure 1: Analytical models comparison with $L/r_1 = 5$ and successful experimental validation.

The models were then used for identifying the geometrical parameters of the solenoid and optimize the force intensity. Since some dimensions were fixed (see Table 1), the models were really useful to choose the total length L of the solenoid along with the permanent magnet dimensions. The optimized chosen parameter values are reported in Table 2.

2.2 Moving part support

The support of the moving part is a crucial issue in the design. Depending on the chosen stinger, the exciter should work with no axial preload (beam stinger), tensile preload (wire stinger) or compression preload (ball stinger). The connection between the fixed and the moving parts of the shaker needs to carry the desired static preload, and it should be almost insensitive to high frequency excitation. In order to achieve this result, an elastic membrane was chosen. During the assembly, a rubber membrane disk was glued to the outer diameter of the fixed body so that the shaker moving part was supported as (almost) free-free [11] along the axial direction. The radial stiffness was significantly higher then axial stiffness providing ad adequate static support to the moving part of the shaker for any mounting orientation. Nevertheless,

Quantity	Value
r_1	10 mm
r_2	15 mm
L	50 mm
Wire diam.	1.2 mm
N	150
h	30 mm
R_m	5 mm

Table 2: Electromagnetic shaker dimensions.

this setup introduced a new constraint on the shaker sizing. Since the support stiffness highly depends on the unglued portion of the membrane, the clearance between the inner diameter of the coil and the outer diameter of the permanent magnet can not be too small. Figure 2 shows a schematic section view of the elastic support. The permanent magnet was implemented as separate cylinders, which are attached to each other (and to the membrane) by means of the reciprocal magnetic forces. A very simple and reliable connection between the moving part and the elastic support was therefore obtained without any fastener that would be difficult to include in such a compact design. In addition, this elastic support solution allowed for the application of the static preload both tensile or compression.

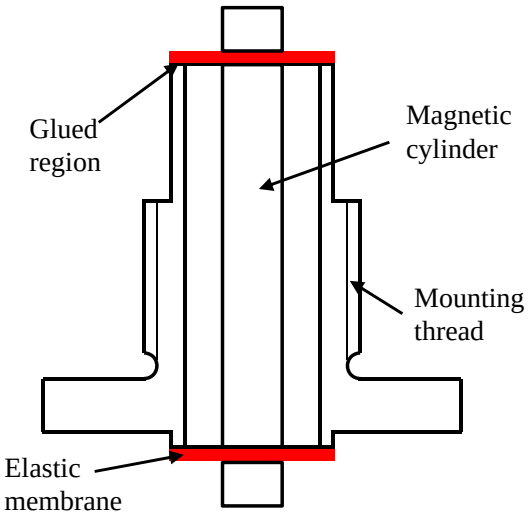
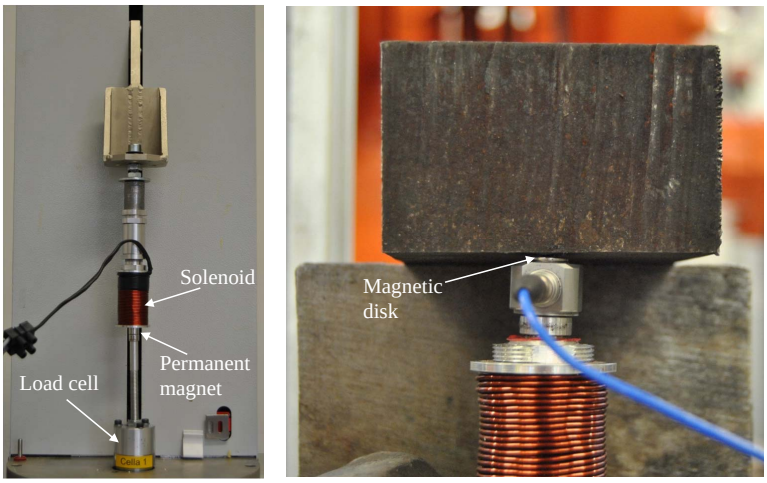


Figure 2: Elastic support section view.

3 SHAKER TESTS

The described models allowed to determine the device dimensions to satisfy the Table 1 specifications. The force as calculated with the proposed models is the interaction between the permanent magnet and the external coil and this is equal to the actual force acting on the structure only under static conditions. A static test was performed on a shaker prototype, Figure 3 (a), and a successful validation of the analytical models, described above, is reported in Fig-

ure 1. When the shaker is powered with a time varying signal, the difference between the force acting on the structure and that applied to the permanent magnet equals the product between mass and acceleration of the shaker moving part. This is the reason why dynamic tests were initially performed on a shaker prototype, to check if the peak force specification was satisfied at the highest operational frequency of 10 kHz, which implies the highest acceleration. A simplified test setup was arranged with a fixed support to hold the shaker and a rigid structure as constraint, indeed, a high stiffness target reduces the moving mass acceleration. The target object was a steel beam having a cross section of 60×100 mm held in fixed conditions, obviously remarkably stiffer than the parts of the shaker. The moving part was then connected to the beam through a piezoelectric load cell using a magnetic disk, Figure 3 (b). In order to decouple the shaker behavior from other effects, no stinger was introduced. The device was controlled through a LMS SCADAS function generator in terms of excitation amplitude and frequency. A Behringer EP2000 amplifier was used as a power supply for the device. The shaker voltage and current values were measured along with the obtained force, to check both electric and mechanical device properties. The supply current was limited to 10 A, since the copper wire used for the coil had a diameter of 1.2 mm, thus it could not undertake such high current levels for more then few minutes. Anyway, this limit was reached only at higher frequency (about 10 A were needed to produce 0.14 N at 10 kHz), so that the overheating of the device was found to be a potential warning only for long tests at very high frequency. Since the actual test conditions do not require long time excitation, the result was considered acceptable.



(a) (b)

Figure 3: Shaker tests: (a) static test and (b) dynamic test.

4 STINGERS COMPARISON

After the achievement of the design specifications, the attention was focused to the characterization of the different stinger solutions. An ideal stinger should transmit just the load component along the chosen direction, filtering out all the other five components (i.e. 2 forces and 3 torques). A specific test bench was prepared to prove the effectiveness of the different stingers, Figure 4. Two shakers were mounted on a cantilever beam along the two transver-

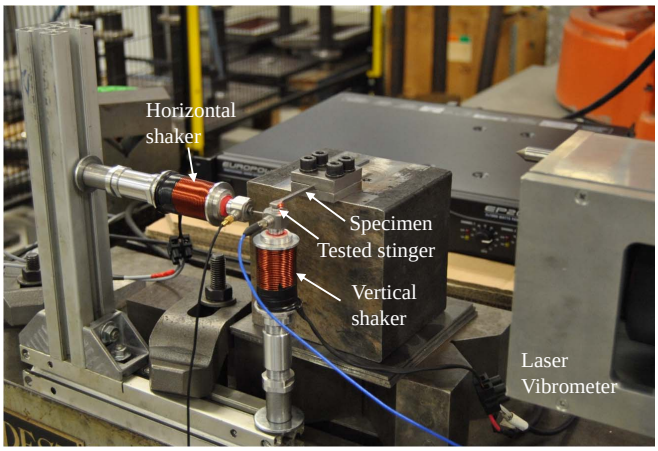


Figure 4: Test bench setup for stinger characterization.

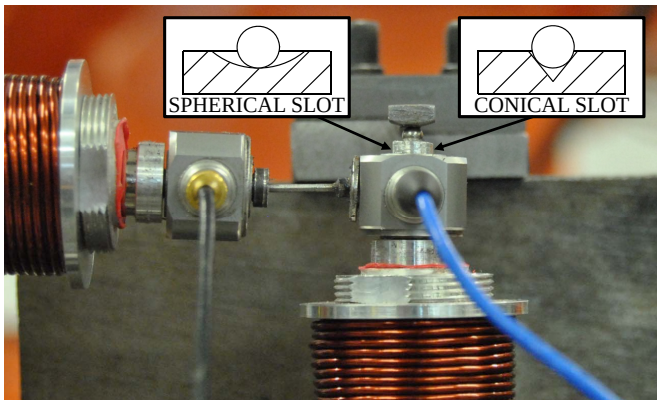


Figure 5: Ball stinger setup.

sal orthogonal directions. A load cell was mounted at the end of the vertical shaker, and one among the investigated stingers was used to connect this load cell with the beam along the vertical direction. The moving part of the other shaker was then attached to the vertical load cell, along the horizontal direction, through another load cell and a beam stinger. A laser Doppler vibrometer was used to measure the oscillation velocity of the cantilever beam (horizontal direction). Four different connection systems were compared in this study. Since some of them needed a compressive or a tensile preload, the vertical shaker was used as a support to provide this preload. Only the horizontal stinger was then excited during the test and the FRF between the force and the horizontal velocity was calculated. Stiffer stingers would lead the FRF to be not-zero while more compliant stingers should guarantee a good filtering of the horizontal force component, giving a really low FRF. Firstly, the vertical load cell was glued to the specimen using no stinger, then the tests were performed with: a beam stinger (no preload, $\phi = 1$ mm, $l = 10$ mm), a ball stinger (compression preload, $\phi = 3$ mm) and a wire stinger (tensile preload, $\phi = 0.2$ mm, $l = 7$ mm). Two different supports were considered for keeping the ball in its

stable equilibrium, either with a conical or with a spherical slot. Figure 5 shows a picture of the ball stinger mounting. All the stingers were screwed on the load cell and glued to the specimen. On the contrary, the ball stinger does not involve any gluing to connect the exciter to the structure, and this implies higher reliability and also reduces the mounting time. Figure 6 shows the comparison between the obtained FRFs. As can be seen, all the FRFs show a peak around 5500 Hz, which is a resonance frequency of the excited specimen. The glue, the beam stinger, the wire stinger and the ball stinger with the conical slot also show one or more other peaks at frequencies lower then 4000 Hz. On the other hand, the ball stinger with the spherical slot provided the lowest FRF in the whole studied frequency range, showing just one peak in proximity of 5500 Hz. For this reason the ball with the spherical slot was chosen as the best stinger solution at least in this range of load level and frequency.

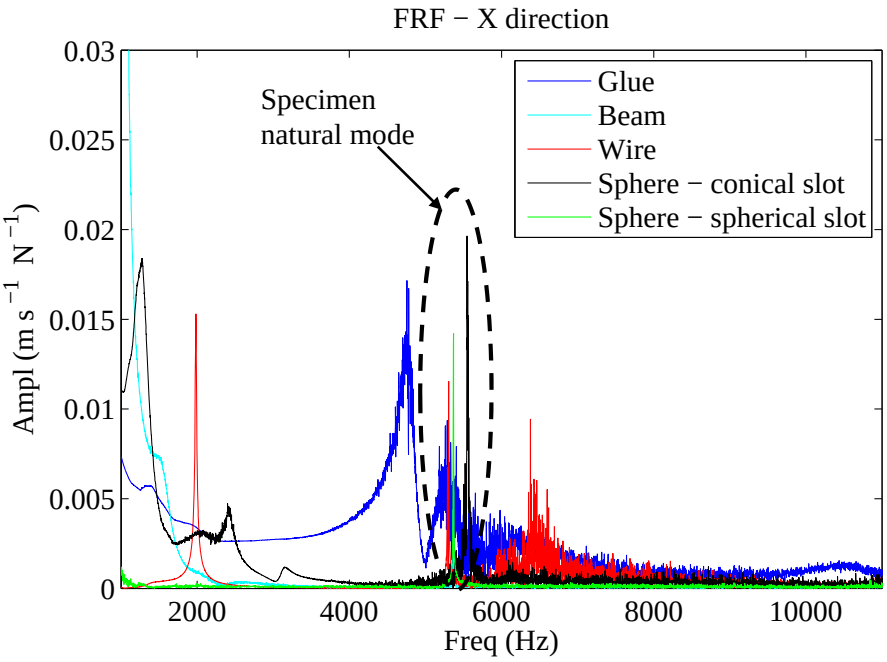


Figure 6: Test results, FRF along the *X* direction.

5 CONCLUSIONS

The paper presents the design and the optimization of a customized electromagnetic shaker. This device should operate in a wide frequency range, with very small lateral dimensions. A solenoid with permanent magnet configuration was chosen, proving to meet all the design specification prescribed. Several different stinger configurations were also compared: glue, beam, wire, and ball using two different mounting interfaces about the latter. The ball stinger with spherical slot support was found to be the more effective by means of transverse load filtering, and also the more convenient in terms of mounting time and reliability.

REFERENCES

[1] N. Mukhopadhyay, S.G. Chowdhury, G. Das, I. Chattoraj, S. Das, D. Bhattacharya, An investigation of the failure of low pressure steam turbine blades. *Engineering Failure Analysis*, **3**, 181–193, 1998.

[2] A. Kammerer, R. Abhari, Experimental study on impeller blade vibration during resonance. Part I. Blade vibration due to inlet flow distortion. *Journal of Engineering for Gas-Turbines and Power*, **2**, 2009.

[3] L. Bertini, P. Neri, C. Santus, A. Guglielmo, G. Mariotti, Analytical expression of the safe diagram for bladed wheels, numerical and experimental validation. *Journal of Sound and Vibration*, **333**, 4771–4788, 2014.

[4] Y. Bidaut and U. Baumann, Identification of eigenmodes and determination of the dynamical behavior of open impellers. *Proceedings of ASME Turbo Expo, Parts A and B*, Copenhagen, Denmark, 1063–1073, 2012.

[5] L. Bertini, B. Monelli, P. Neri, C. Santus, A. Guglielmo, Robot assisted modal analysis on a stationary bladed wheel. *ASME 2014 12th Biennial Conference on Engineering Systems Design and Analysis*, ESDA, Copenhagen, Denmark, 1–8, 2014.

[6] T. Berruti, C. Firrone, M. Gola, A test rig for non contact traveling wave excitation of a bladed disk with underplatform dampers. *Journal of Engineering for Gas Turbines and Power*, **133**, 032502, 2011.

[7] E.P. Furlani, *Permanent Magnet and Electromechanical Devices*. Academic Press - Elsevier, London, England, 2001.

[8] D.E. Mapother, J.N. Snyder, *The Axial Variation of the Magnetic Field in Solenoids of Finite Thickness*. University of Illinois Bulletin, Urbana, Illinois, 1955.

[9] W. Robertson, B. Cazzolato, A. Zander, A Simplified Force Equation for Coaxial Cylindrical Magnets and Thin Coils. *IEEE TRANSACTIONS ON MAGNETICS,*, **47**, 2045–2049, 2011.

[10] W. Robertson, B. Cazzolato, A. Zander, Axial Force Between a Thick Coil and a Cylindrical Permanent Magnet: Optimizing the Geometry of an Electromagnetic Actuator. *IEEE TRANSACTIONS ON MAGNETICS,*, **48**, 2479–2487, 2012.

[11] D.J. Ewins, *Modal Testing, theory, practice and application, 2nd Edition*. Research Studies Press Ltd - Wiley, Hertfordshire, England, 2000.

11th International Conference on Engineering Vibration
Ljubljana, Slovenia, 7–10 September 2015

REDUCED THIN-LAYER ELEMENT MODEL FOR JOINT DAMPING

Christian Ehrlich*[1], André Schmidt[2], Lothar Gaul[1]

[1]Institute for Nonlinear Mechanics, Research Group Prof. Gaul, University of Stuttgart
{ehrlich, gaul}@inm.uni-stuttgart.de

[2]Institute for Nonlinear Mechanics, University of Stuttgart
schmidt@inm.uni-stuttgart.de

Keywords: Joints, Damping, Thin-Layer Elements, FEM.

Abstract. *Damping properties of assembled structures are largely influenced by frictional damping between joint interfaces. Therefore, these effects must be considered during the modelling process. Applying thin-layer elements (TLEs) with a linear, orthotropic material model on mechanical interfaces to incorporate joint damping has shown good agreement with experimental modal analysis in previous work. In the TLE model, constant hysteretic damping is assumed. The damping and stiffness parameters for the TLEs are experimentally identified on an isolated lap joint. Imprecisions caused by model simplifications and parameter uncertainty are addressed by model updating or uncertainty analysis. This requires multiple evaluations of systems that are equivalent besides their TLE parametrization. In this work, a model reduction technique for the thin-layer element modelling approach is presented which significantly reduces computational cost for the re-calculation of eigenvalues after joint parameters are changed. The reduction is based on an eigensensitivity analysis and results in a single, linear equation for each eigenvalue. The presented approach is applied to a model updating example. Here, the model reduction allows for a larger number of design variables. Therefore, experimental results can be reproduced more accurately.*

1 INTRODUCTION

While eigenfrequencies and mode shapes of assembled structures can be predicted reliably with the Finite Element Method, the incorporation of damping is subject to ongoing research. The key to valid damping predictions of assembled structures is accurate representation of joint damping caused by friction on mechanical interfaces. A proposed modelling technique for joint damping is the thin-layer element (TLE) approach which has shown promising results in previous work [1, 2]. Thereby, a thin layer of finite elements is placed on the joint interface. These TLEs contain a linear, phenomenological model of the joint behaviour. The major advantage of this approach is that the main contributions to energy dissipation in assembled structures are incorporated spatially correct while efficient evaluation of the model through eigenvalue analysis is still possible. Additionally, the linear approach facilitates comparison with data from experimental modal analysis. On the other hand, experimental investigations clearly show the non-linear behaviour of bolted joints [3]. Thus, the accuracy of the linear TLE approach is limited. The main source of inaccuracy is parameter and model uncertainty connected to the joint loss factor. To mitigate the effects of these inaccuracies, model updating [4] or uncertainty analysis [5] are employed. That, however, requires a large number of model evaluations with varying loss factors.

In this work, a model reduction technique for the TLE modelling approach and an application to model updating are presented. The reduction is based on an eigensensitivity analysis and takes advantage of the particularly simple formulation of joint damping in the form of constant hysteretic damping. The result is a single, linear equation for each eigenvalue.

2 THIN-LAYER ELEMENT JOINT MODEL

This section covers the basic approach of joint modelling using TLEs. Further details can be found in [2, 6]. As mentioned above, the basic idea of the TLE modelling approach is to place a layer of elements with a linear, orthotropic material model on all joint interfaces (Fig. 1). The

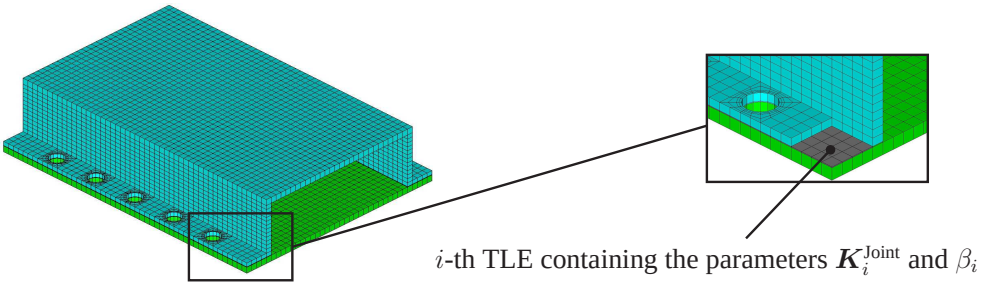


Figure 1: FE model of the test structure with exposed thin-layer elements.

TLEs reproduce the localized occurrence of joint damping in assembled structures in contrast to e.g. Rayleigh Damping where the energy dissipation is distributed over the entire structure. The TLEs are implemented as hexahedral elements with a height to width ratio of up to 1:100. As joints have distinct behaviour in normal and tangential direction with respect to the interface, an orthotropic material is model employed. Stiffness and damping parameters of the joint are experimentally identified on a specialized experimental setup [6].

Joint damping shows only weak dependence on frequency. Therefore, the model of constant hysteretic damping is applied [7]. The starting point for the implementation of constant

hysteretic damping is the discrete equation of motion of a free, undamped system

$$\boldsymbol{M}\ddot{\boldsymbol{u}} + \boldsymbol{K}\boldsymbol{u} = \boldsymbol{0}\,. \tag{1}$$

Here, $\boldsymbol{M}$ is the mass matrix, $\boldsymbol{K}$ the real-valued stiffness matrix and $\boldsymbol{u}$ the displacement vector. Constant hysteretic damping can now be incorporated by replacing the real-valued stiffness matrix $\boldsymbol{K}$ with a complex-valued stiffness matrix $\boldsymbol{K}^*$ with

$$\boldsymbol{K}^* = \boldsymbol{K} + \mathrm{j}\sum_{i=1}^{n}\alpha_i\boldsymbol{K}_i^{(\text{Material})} + \mathrm{j}\sum_{i=1}^{m}\beta_i\boldsymbol{K}_i^{(\text{Joint})}\,, \tag{2}$$

where $\boldsymbol{K}_i^{(\text{Material})}$ are the regular element stiffness matrices, $\boldsymbol{K}^{(\text{Joint})}$ are the TLE stiffness matrices and j is the complex unit. The material loss factor is represented by α_i and the joint loss factor by β_i. While material and joint damping are accounted for by this approach, joint damping is decisive for accurate damping predictions. Thus, further elaboration is limited to the joint loss factor β_i.

Replacing $\boldsymbol{K}$ in Eq. (1) by $\boldsymbol{K}^*$ from Eq. (2), the eigenvalue problem can be formulated

$$(\lambda_k^2\boldsymbol{M} + \boldsymbol{K}^*)\boldsymbol{\psi}_k = \boldsymbol{0}, \tag{3}$$

with eigenvalues λ_k and eigenvectors $\boldsymbol{\psi}_k$.

3 THIN-LAYER ELEMENT MODEL REDUCTION

3.1 Derivation

As mentioned above, models with TLEs often require multiple evaluations of Eq. (3) for systems that are equivalent in all respects but the joint loss factors β_i. In this chapter, a more efficient way to calculate the resulting eigenvalues in the sense of a model reduction is presented. For the sake of brevity, all derivations will be shown for λ_k^2. Modal damping is presented in terms of $\mathrm{Im}(\lambda_k^2)$. Expansion to λ_k is possible at each step.

First, two systems are introduced. The base system with the system matrices $\boldsymbol{M}$ and $\boldsymbol{K}$, and an augmented system represented by $\hat{\boldsymbol{M}}$ and $\hat{\boldsymbol{K}}$ (henceforth $\hat{\bullet}$ denotes affiliation to the augmented system). The two systems differ only in joint damping which means

$$\hat{\boldsymbol{M}} = \boldsymbol{M} \quad \text{and} \tag{4}$$

$$\hat{\boldsymbol{K}}^* = \boldsymbol{K}^* + \mathrm{j}\sum_{i=1}^{m}\Delta\beta_i\boldsymbol{K}_i^{(\text{Joint})}\,. \tag{5}$$

$\Delta\beta_i$ denotes the difference of the loss factor between the augmented system and the base system

$$\Delta\beta_i = \hat{\beta}_i - \beta_i\,. \tag{6}$$

Eigensensitivity analysis is now employed to find a relation between the change of the i-th loss factor $\Delta\beta_i$ and the k-th squared eigenvalue $\hat{\lambda}_k^2$ of the augmented system.

Rearranging Eq. (3) into its Rayleigh Quotient [8] form and scaling $\boldsymbol{\psi}_k$ such that

$$\boldsymbol{\psi}_k^T\boldsymbol{M}\boldsymbol{\psi}_k = 1\,, \tag{7}$$

one obtains

$$\lambda_k^2 = -\boldsymbol{\psi}_k^T\boldsymbol{K}^*\boldsymbol{\psi}_k\,. \tag{8}$$

Using the definition of the complex-valued stiffness matrix $\boldsymbol{K}^*$ in Eq. (2), the partial derivative of Eq. (8) with respect to β_i yields

$$\frac{\partial \lambda_k^2}{\partial \beta_i} = -\boldsymbol{\psi}_k^T (\mathrm{j}\boldsymbol{K}_i^{(\mathrm{Joint})}) \boldsymbol{\psi}_k = J_{ik} \,. \tag{9}$$

A more detailed derivation of this result can be found in [9, 10, 11]. Equation (9) reveals that the derivative of λ_k^2 with respect to a joint loss factor β_i only depends on the corresponding (constant) stiffness matrix $\boldsymbol{K}_i^{\mathrm{Joint}}$ and eigenvector $\boldsymbol{\psi}_k$. In typical applications, the TLEs have negligible influence on the mode shape since they constitute only a small fraction of the overall structure. Hence it is feasible to assume

$$\frac{\partial \boldsymbol{\psi}_k}{\partial \beta_i} \approx \mathbf{0} \,. \tag{10}$$

Therefore, J_{ik} is independent of β_i and Eq. (9) can be used to formulate a reduced model:

$$\hat{\lambda}_k^2 = \lambda_k^2 + \sum_{i=1}^{m} J_{ik} \Delta\beta_i \,. \tag{11}$$

With Eq. (11), eigenvalues of the augmented system can be calculated from a single, linear equation. One evaluation of the full base model is necessary to calculate λ_k^2 and $\boldsymbol{\psi_k}$. During this evaluation, all TLE stiffness matrices $\boldsymbol{K}_i^{\mathrm{Joint}}$ are assembled as well and can be stored for the calculation of $\boldsymbol{J}_{ik}$.

As long as Eq. (10) is a sufficiently exact approximation, Eq. (11) is valid for all reasonable values of $\Delta\beta_i$. One can further assume that the eigenvectors, though in reality complex, are approximately real-valued. Therefore, J_{ik} is purely imaginary and Eq. (11) reveals that a change of the loss factor β_i only affects the imaginary part of $\hat{\lambda}_k^2$. This is equivalent with the intuitive assumption, that a variation of the loss factor mainly affects modal damping ratios without significantly altering eigenfrequencies.

3.2 Validation

The reduced model is validated by examining the first eight eigenvalues of the test structure depicted in Fig. 1. To that end, the eigenvalues of the system are calculated for different loss factors by evaluating the full model (Eq. (3)) and by using the reduced model (Eq. (11)). It is important to note that here, in contrast to the model updating example in Section 4, all TLEs have identical loss factors β_i. Figure 2 shows the modal damping (in terms of $\mathrm{Im}(\lambda_k^2)$) for the first eight modes for loss factors ranging between 0 and 1. The solid line depicts the simulation with the reduced model and the dots represent values from full model evaluations. The base system used for the model reduction has a loss factor of $\beta_i = 0.05$ which is close to the lower limit of the parameter range. Nonetheless, all deviations from values calculated with the full model are smaller than 0.15 $\%$.

4 MODEL UPDATING WITH REDUCED MODEL

The TLE modelling approach was introduced as an efficient way to predict damping in assembled structures before a physical prototype exists. The original approach [2] employs an uniform loss factor parametrization across the joint surface. While this approach is effective for damping predictions, it is not well suited for model updating because only a single design parameter exists.

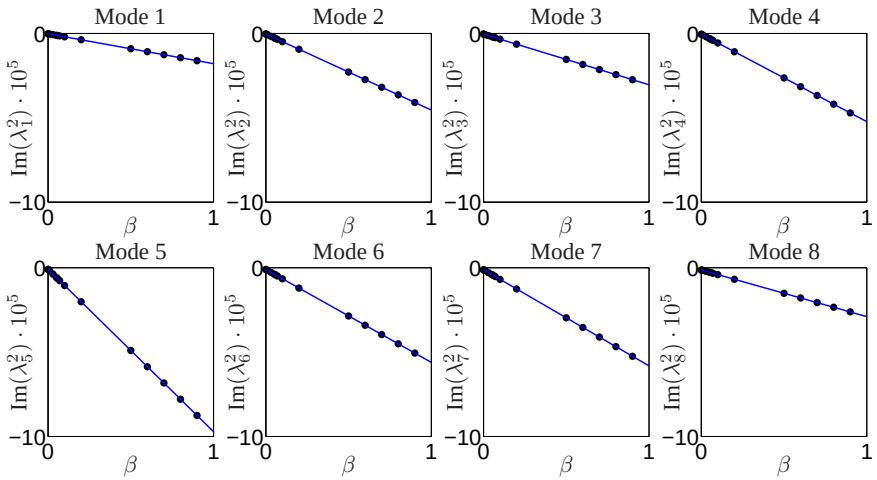


Figure 2: Validation of the reduced model by comparison of $\mathrm{Im}(\lambda_k^2)$ calculated by full model evaluations (dots) and reduced model evaluations (solid line).

With the reduced model, a more numerically compliant TLE approach can be devised. Instead of a single parameter for the entire joint interface, each element can be allocated an independent loss factor parameter. This increases the number of design variables for the optimization from one in the original approach, to several hundred (880 in the presented example). An optimization with such a high number of variables requires a large number of iterations which is only feasible under the utilization of the reduced model.

In the presented example, parameters for 880 TLEs are to be found such that the experimentally determined modal damping ratios for the first eight modes are reproduced in an optimal way. Due to the large number of design variables, this problem has various solutions with most of them being physically not feasible. Therefore, a set of boundary conditions has to be defined which reduces the set of solutions to physically reasonable ones.

As first boundary condition, the maximum difference of the loss factor of neighbouring elements $\Delta\beta_{\text{max}}$ is limited. The loss factor depends on normal and tangential loads [12]. As these loads change gradually, the loss factor must follow accordingly. This is implemented as an inequality boundary condition. For two elements, i and j, which have at least one common node, the following inequalities are enforced:

$$|\beta_i - \beta_j| < \Delta\beta_{\text{max}} \tag{12}$$

With the second boundary condition, symmetry is enforced. As stated before, the loss factor is determined by tangential and normal loads. Therefore, a geometrically symmetric assembly under symmetric loads must also have a symmetric joint parameter distribution. The example structure has two planes of symmetry. Figure 3 shows four elements, k, l, m, n which are assigned identical parameters.

As a final condition, the mean loss factor β_{mean} is kept constant. This condition is implemented as an equality constraint

$$\sum_i^n \frac{\beta_i}{n} = \beta_{\text{mean}}\,. \tag{13}$$

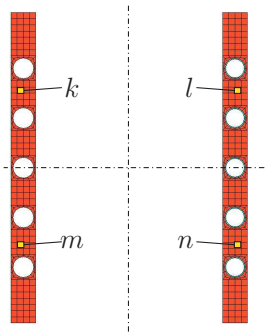


Figure 3: Joint interface of the example structure with four elements k, l, m, n that must be allocated identical loss factors.

It ensures that the optimization is not achieved by uniformly adapting the loss factor. Comparability of different models is maintained this way, too.

With these boundary conditions, the loss factor parameters are optimized such that the first eight experimentally determined modal damping ratios of the test structure are reproduced optimally in a least-squares sense. The algorithm converges after 1330 iterations in 58 seconds. At approximately 20 seconds per full model evaluation and numerous model evaluations per iteration, the cost advantage of the reduced model is significant. As base line, model updating with uniform parametrization is performed. This optimization with a single degree of freedom is representative of the performance of the original TLE modelling approach. In Figure 5, the relative error

$$\delta \operatorname{Im}(\lambda_k^2) = \left| \frac{\operatorname{Im}(\lambda_k^2) - \operatorname{Im}(\lambda_{k,\mathrm{exp}}^2)}{\operatorname{Im}(\lambda_{k,\mathrm{exp}}^2)} \right| \tag{14}$$

of the resulting modal damping values with respect to experimentally determined reference values $\operatorname{Im}(\lambda_{k,\mathrm{exp}}^2)$ is depicted. While it is evident that the original approach already yields good results, especially for lower order modes, the new approach improves the performance. Higher order modes have geometrically more complex mode shapes. The original, uniform parametrization approach cannot depict these conditions as accurately as the element-wise independent parametrization employed in the new approach. Comparing the loss factor parameter

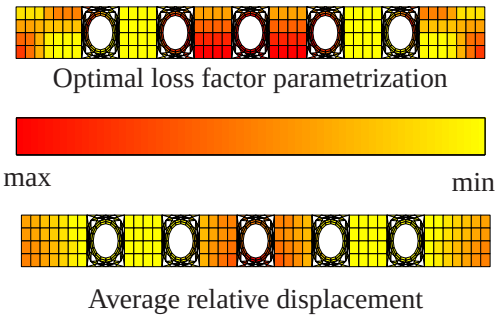


Figure 4: Comparison of the loss factor parametrization after model updating and the average relative displacement for the first eight modes.

distribution resulting from the new model updating approach with the average relative displacement over all relevant modes, a strong similarity is evident (Fig. 4). High relative displacement

in the joint causes high energy dissipation [12]. Thus, Fig. 4 indicates that the optimization under the derived boundary conditions arrives at a physically meaningful solution.

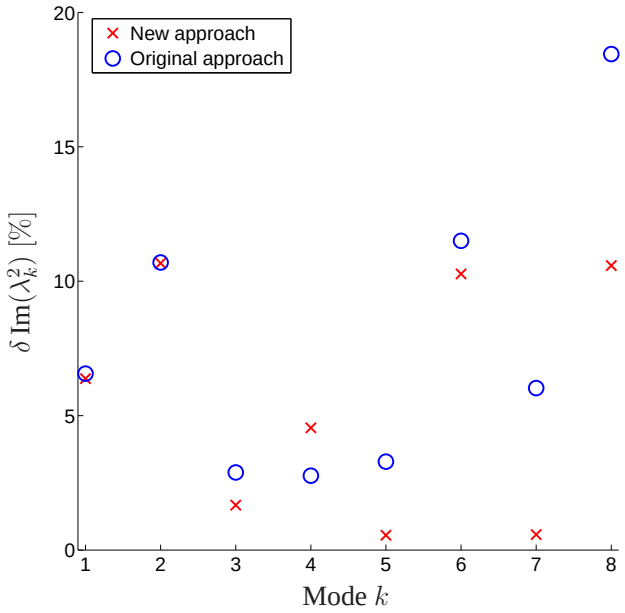


Figure 5: Relative error of the modal damping after model updating with the new and original approach.

5 CONCLUSIONS

The existing thin-layer element modelling approach is extended by a model reduction. The reduced model is derived through an eigensensitivity analysis and provides a single, linear equation for each eigenvalue. A prerequisite for the applicability of the presented technique is a negligible influence of the TLE parametrization on the eigenvectors.

Through the model reduction, the TLE modelling approach can be augmented for better performance in model updating applications. This approach reproduces experimental data more accurately by providing a very large number of design variables to the optimization algorithm. Several boundary conditions are defined in order to generate physically meaningful results. While the original TLE approach localizes joint damping at mechanical interfaces but does not consider variations over the area of the interface, the new model updating approach identifies areas of high and low energy dissipation on the interface.

REFERENCES

[1] C. S. Desai, M. M. Zaman, J. G. Lightner, and H. J. Siriwardane. Thin-layer element for interfaces and joints. *International Journal for Numerical and Analytical Methods in Geomechanics*, 8(1):19–43, 1984.

[2] S. Bograd, P. Reuss, A. Schmidt, L. Gaul, and M. Mayer. Modeling the dynamics of mechanical joints. *Mechanical Systems and Signal Processing*, 25(8):2801 – 2826, 2011.

[3] L. Gaul and J. Lenz. Nonlinear dynamics of structures assembled by bolted joints. *Acta Mechanica*, 125(1-4):169–181, 1997.

[4] M. Friswell and J. E. Mottershead. *Finite element model updating in structural dynamics*, volume 38. Springer Science & Business Media, 1995.

[5] M. Hanss. The transformation method for the simulation and analysis of systems with uncertain parameters. *Fuzzy Sets and Systems*, 130(3):277–289, 2002.

[6] C. Ehrlich, A. Schmidt, and L. Gaul. Microslip joint damping prediction using thin-layer elements. In *Dynamics of Coupled Structures, Volume 1*, pages 239–244. Springer, 2014.

[7] B. J. Lazan. *Damping of materials and members in structural mechanics*, volume 214. Pergamon press Oxford, 1968.

[8] K.-J. Bathe. *Finite element procedures*. Klaus-Jurgen Bathe, 2006.

[9] R. Fox and M. Kapoor. Rates of change of eigenvalues and eigenvectors. *AIAA journal*, 6(12):2426–2429, 1968.

[10] H. M. Adelman and R. T. Haftka. Sensitivity analysis of discrete structural systems. *AIAA journal*, 24(5):823–832, 1986.

[11] S. Adhikari. Rates of change of eigenvalues and eigenvectors in damped dynamic system. *AIAA journal*, 37(11):1452–1458, 1999.

[12] M. Clappier, C. Ehrlich, and L. Gaul. Linearized joint damping model for assembled structures with inhomogeneous contact pressure using thin-layer elements. In *Proceedings of ICSV 22, Florence, Italy*. 2015.

International Conference on Engineering Vibration
Ljubljana, Slovenia, 7-10 September 2015

NUMERICAL AND EXPERIMENTAL INVESTIGATIONS INTO MASS, STIFFNESS AND DAMPING MATRIX UPDATING THROUGH A TWO-STAGE FRAMEWORK

Sharad Pradhan*[1], S.V. Modak[2]

[1]Department of Mechanical Engineering, NITTTR, Bhopal – 462002, India
spradhan@nitttrbpl.ac.in

[2] Dept of Mechanical Engg, Indian Institute of Technology, Delhi – 110016, India
svmodak@mech.iitd.ac.in

Keywords: Model updating; complex FRFs; Normal FRFs; Frequency response function; damping matrix.

Abstract. *Finite element model updating techniques are used to update a structural dynamic FE model so as to obtain an accurate representation of a structure in terms of mass, stiffness and damping matrix. Some of the existing updating methods update all the three matrices simultaneously using either complex FRF or modal data. These methods, however, are faced with numerical problems in practical implementation due to large difference in the magnitude of stiffness and mass matrix elements and damping matrix elements. Two novel approaches, one for updating mass and stiffness matrix and the other for updating damping matrix have been developed. These two approaches provide a theoretically consistent formulation for updating mass and stiffness matrix and damping matrix respectively. These two approaches have been independently validated through numerical studies. However, for updating all the three matrices, these two approaches need to be used in a sequential manner in a two-stage framework. Updating in a sequential manner couples the performance of the damping matrix updating in the second stage to mass/stiffness matrix updating in the first stage. Inaccuracies in the updated matrices in first stage may have an adverse impact on the performance of the second stage and this coupling of the performances needs to be investigated. The incompleteness of the reference or measured data and any noise in it also plays a role in making the second stage performance dependent on the first stage. The performance of the two-stage updating framework in the presence of actual experimental data also needs to be assessed. These are the issues, related to mass, stiffness and damping matrix updating through a two-stage framework, which form the subject matter of this paper. The paper undertakes numerical and experimental studies with the objective of analyzing above issues. A numerical study of a fixed-fixed beam structure is first presented followed by an experimental study of an F shape structure. A new method called 'hybrid' method to deal with data incompleteness in the context of two-stage updating is suggested. Effect of equivalent updating parameters on performance of two-stage updating is studied. The results of the investigations carried out in this paper would be helpful in proper implementation and application of two stage updating method in practice.*

1 INTRODUCTION

Accurate mathematical models of engineering structures are needed in order to predict their dynamic characteristics accurately. In this context finite element model updating is considered as an invaluable tool for obtaining updated dynamic finite element (FE) model of a structure that accurately represents its dynamics.

Updating of the structural dynamic FE models has been an active area of research for the last three decades and several approaches have been proposed as shown in the surveys by Imregun and Visser [1], Mottershead and Friswell [2] and in the text by Friswell and Mottershead [3]. Model updating is essentially an inverse problem as it attempts to identify certain unknown or uncertain model parameters from the knowledge of the test data (Mottershead and Datta [4]). Model updating methods can be broadly classified into direct methods, which are essentially non-iterative ones, and the iterative methods. The direct methods are based on experimental modal data, while the iterative methods are based on either experimental FRF data or experimental modal data. Many of these updating methods are aimed at updating only an undamped FE model, represented by mass and stiffness matrix, while others also consider updating of damping matrix. Since the focus of the current paper is on updating a damped FE model of a structure, further review here is restricted to contributions made in this direction.

The approaches for mass, stiffness and damping matrix identification of a structure can be broadly classified as either the approaches that consider simultaneous updating of mass, stiffness and damping matrix or the approaches that consider updating of these matrices in two stages. Lin and Ewins [5] presented an iterative FRF based method for simultaneous updating of mass, stiffness and damping matrices, in which the difference between the measured and analytical FRFs is linearized with respect to the parameters to be updated. Lin et al. [6] presented a mass, stiffness and damping matrix updating method based on sensitivity of eigendata. Ibrahim et al. [7] presented a technique to directly update mass, stiffness and damping matrices using harmonic input-output. Only the measured input-output responses at a limited number of time instants are required to correct the complete FE model. The popular response function based updating method developed by Lin and Ewins [5 and 8] can update [M] and [K] only. The same method is further extended to deal with complex FRF data and the updating of a proportional damping matrix by Imregun et al. [9]. Friswell et al. [10] extended the direct updating approach to updating of stiffness and damping matrices. Kuo et al. [11] developed computationally efficient techniques for updating mass, damping, and stiffness matrices simultaneously by minimizing an objective function that defines changes in these matrices. Esfandiari et al. [12] proposed an FRF based updating approach with the objective of damage detection by correlating the change in FRFs of a structure to the change of stiffness, mass and damping through sensitivity equations. A case study focusing on changes only in mass and stiffness matrix is investigated. Lin and Zhu [13] further investigated the response function method proposed in [8] for updating damping matrix alongwith mass and stiffness matrix. Hu and Li [14] formulated a procedure that updates the mass, damping, and stiffness matrices of linear dynamic systems simultaneously from modal data. Khanmirza et al. [15] proposed simultaneous identification of mass, stiffness and damping matrices directly from the measured responses using neural networks. Recently, Hernandez et al. [16] proposed an iterative time domain formulation for finite element model updating that updates stiffness and damping parameters. It is noted that simultaneous updating of mass, stiffness and damping matrices may present difficulty in the practical implementation since quite often the magnitude of the stiffness and mass matrix elements are much more than that of the damping matrix elements (Chen et al. [17], Friswell et al. [10]). In such a situation, updating itera-

tions are more influenced by the stiffness and mass matrix than the damping matrix. This may lead to an inaccurate identification of the damping matrix.

The approaches based on two stages of updating typically involve updating of the mass and stiffness in first stage followed by updating of damping in second stage. For lightly damped structures, Brown et al. [18] developed a two-stage approach based on complex eigendata sensitivity. Reix et al. [19] considered updating of damping matrix assuming that the mass and stiffness matrices are perfectly known through a prior updating of them using experimental modal data. The coefficients of a hysteretic damping matrix are then updated using FRF data through least squares estimation. Halevi and Kenigsbuch [20] perform updating of the damping matrix using complex eigenvectors by assuming that an accurate knowledge of stiffness and mass matrices is available. Measured complex eigenvectors are corrected first so as to satisfy orthogonality relations. This is followed by updating of the damping matrix so as to satisfy eigenvalue equation. Lu and Tu [21] proposed a two level neural network scheme for updating including damping matrix for the case of lightly damped structure. In the first stage effect of damping is neglected and structural parameters are updated using natural frequencies and mode shapes, while in the second stage, updating of damping matrix is carried out using FRF data. Datta et al. [22] proposed a two-stage direct updating procedure for mass and damping matrix updating using quadratic orthogonality orthogonality criterion.

It is seen that many of these approaches are based on the assumption of light damping and hence are not applicable to a general class of structures. Some other methods are based on accurate knowledge of mass and stiffness matrices, an assumption which may not always be satisfied in practice. An another strategy which has also been employed is to utilize the real part of the FRFs in the first stage to update mass and stiffness matrices and utilize imaginary part of FRFs or the complex FRFs themselves for updating damping in the second stage. This approach is also not strictly correct since real part of FRF is also affected by damping.

Recently authors have proposed two independent methods for updating for mass and stiffness matrix and damping matrix [23, 24]. These methods do not have shortcomings mentioned above. These two approaches provide a theoretically consistent formulation for updating mass and stiffness matrix and damping matrix respectively. These two approaches have been independently validated through numerical studies. However, for updating all the three matrices, these two approaches need to be used in a sequential manner in a two-stage framework. Updating in a sequential manner couples the performance of the damping matrix updating in the second stage to mass/stiffness matrix updating in the first stage. Inaccuracies in the updated matrices in first stage may have an adverse impact on the performance of the second stage and this coupling of performance needs to be investigated. The incompleteness of the reference or measured data and any noise in it also plays a role in making the second stage performance dependent on the first stage. The performance of the two-stage updating framework in the presence of actual experimental data also needs to be assessed. These are the issues, related to two-stage updating of mass/stiffness and damping matrices, which form the subject matter of this paper. It undertakes numerical and experimental studies with the objective of analyzing above issues. A numerical study of a fixed-fixed beam structure is presented followed by an experimental study of an F shape structure. A new method called 'hybrid' method to deal with data incompleteness in the context of two-stage updating is suggested. Finally, a case study to test effectiveness of the two-stage approach when updating parameters are not chosen correctly is considered.

2 DESCRIPTION OF TWO-STAGE FE MODEL UPDATING PROCEDURE

This section describes the two stage updating procedure which is the subject of numerical and experimental studies presented in this paper. In the two-stage FE model updating procedure, the updating of mass and stiffness matrices is performed in the first stage using the Normal Response Function Method (NRFM) [23]. Updating of damping matrix is performed in the second stage using the complex Response Function Method [24]. The formulations for these two stages of updating are briefly described below.

2.1 Stage I: Mass and Stiffness matrix updating

The updating of mass and stiffness matrices carried out in stage-I is done through an approach that is based on normal FRFs of a structure.

The governing equations of motion of a multi degree of freedom (DOF) structure with structural damping can be written in matrix form as,

$$M\,\ddot{\bar{x}}(t)^c + iD\bar{x}(t)^c + K\bar{x}(t)^c = \bar{f}(t) \tag{1}$$

Where M, K, and D are n × n mass, stiffness and structural damping matrix respectively. All these are real matrices. $x(t)^c$ and $f(t)$ are n × 1 vectors of time-varying displacements and forces and 'n' is the total number of degrees of freedom in the finite element model. The superscript 'c' indicates the quantity corresponding to the damped system. For harmonic excitation,

$$\bar{f}(t) = f(t)e^{j\omega t} \quad \text{and} \quad \bar{x}(t)^c = x(t)^c e^{j\omega t} \tag{2}$$

Let α_A^N represent the normal FRF matrix corresponding to the FE model of the structure. This can be easily found using following equation

$$\alpha(\omega)_A^N = (-\omega^2 M_A + K_A)^{-1} \tag{3}$$

Let the normal FRF matrix for the actual structure be represented by α_X^N. α_X^N represents the 'measured' normal FRF matrix of the structure in the hypothetical situation when the structure is undamped. Since it is not possible to remove damping from the actual structure, hence it is not possible to measure its normal FRF matrix. The FRFs measured on the actual structure are complex, represented by complex FRF matrix α_X^C. Chen et al [17] has shown that there exist a direct relationship between the measured complex FRF matrix α_X^C and the normal FRF matrix α_X^N. The α_X^N can directly be computed from α_X^C using following relationship.

$$\alpha(\omega)_X^N = \alpha(\omega)_R^C + \alpha(\omega)_I^C (\alpha(\omega)_R^C)^{-1} \alpha(\omega)_I^C \tag{4}$$

Where $\alpha(\omega)_R^C$ and $\alpha(\omega)_I^C$ are the real and imaginary parts of $\alpha(\omega)_X^C$.The analytical normal FRF matrix of the structure $\alpha(\omega)_A^N$, measured normal FRF matrix α_X^N, and change in the normal dynamic stiffness matrix of the analytical model ΔZ_A^N are related by, [24],

$$\alpha(\omega)_A^N \Delta Z_A^N \alpha(\omega)_X^N = \alpha(\omega)_A^N - \alpha(\omega)_X^N \tag{5}$$

Where ΔZ_A^N is given by,

$$\Delta Z_A^N = \Delta K_A - \omega^2 \Delta M_A \tag{6}$$

Thus, it is seen that the updating Eq. (5) involves only those properties that are dependent on only stiffness and mass properties of the structure and don't depend on its damping property. In view of this, updating of mass and stiffness matrices based on Eq. (5) is a theoretically consistent formulation which isolates the process of K and M updating.

Eq. (5) written for the jth column of $\alpha(\omega)_X^N$ and $\alpha(\omega)_A^N$ yields following equation. The symbol '(ω)' showing the dependence on frequency has been dropped for the sake of brevity.

$$\alpha_A^N \Delta Z_A^N \alpha_{X,j}^N = \alpha_{A,j}^N - \alpha_{X,j}^N \tag{7}$$

Let $p = \{p_1, p_2, ..., p_{nu}\}$ be the vector of 'nu' number of stiffness and mass related physical parameters of the structure which are to be updated during updating. Linearizing ΔZ_A^N with respect to 'p' gives,

$$\Delta Z_A^N = \sum_{i=1}^{nu} \left(\frac{\partial Z_A^N}{\partial p_i} . \Delta p_i \right) \tag{8}$$

Z_A^N can be replaced by $K_A - \omega^2 M_A$. Dividing and multiplying each term of above equation by 'pi' and then writing 'ui' in place of $\Delta p_i / p_i$, the above equation becomes,

$$\Delta Z_A^N = \sum_{i=1}^{nu} \left(\frac{\partial (K_A - \omega^2 M_A)}{\partial p_i} . p_i \right) . u_i \tag{9}$$

$u = \{u_1, u_2, ..., u_{nu}\}$ is the vector of unknown updating parameters. The individual parameters u_i^s represent fractional correction in the chosen updating parameters p_i^s.

Eq. (7) after making substitution for ΔZ_A^N from Eq. (9) can be written at 'nf' number of frequency points chosen from the frequency range of interest. The resulting equations can be framed in the following matrix form,

$$S^N{}_{(n \times nf) \times (nu)} \quad u_{nu \times 1} = \Delta \alpha^N{}_{(n \times nf) \times 1} \quad Ax = b \tag{10}$$

Where S^N is the normal sensitivity matrix and $\Delta \alpha^N$ is vector of differences in the FRFs on the right hand side of Eq. (7).

The vector 'u' found by solution of Eq. (10) is used to update vector of physical variables 'p' and then an updated version of the FE model is built using the new set of physical variables. This process is repeated in an iterative way until convergence is obtained.

It should be noted that the uj found in jth iteration represents the vector of fractional correction factors for the current '*p*', i.e. p_j, and does not represent a cumulative correction with respect to the '*p*' existing before updating, the p_0. In view of this, at the end of jth iteration the ith cumulative fractional correction factor, is given by,

$$\bar{u}_i = \left(1+u_i^1\right)\cdot\left(1+u_i^2\right).....\left(1+u_i^j\right)-1 \tag{11}$$

In this way, after convergence, the final set of updating parameters, stored in vector $\bar{u}_i$, can be used to obtain the updated mass and stiffness matrix.

2.2 Stage II: Damping matrix updating

Once mass and stiffness matrices have been updated the updating of damping matrix is carried out in stage-II using complex FRFs. The basic updating equations involved in this stage are described below.

The dynamic stiffness matrix (DSM) corresponding to FE model can be written as,

$$Z_A^C = Z_A^N + j\bar{Z}_A \tag{12}$$

where Z_A^N is the normal DSM, corresponding to the undamped FE model and $\bar{Z}_A$ is the DSM due to damping in the FE model. For a structure with structural damping the $\bar{Z}_A$ can be written as,

$$\bar{Z}_A = D_A \tag{13}$$

Where 'D' is the structural damping matrix. Let ΔD_A represent some change in D_A. Hence,

$$\Delta\bar{Z}_A = \Delta D_A \tag{14}$$

The measured complex FRF matrix of the structure α_X^C, measured normal FRF matrix α_X^N, damping matrix D_A and change in damping matrix ΔD_A are related by, [24],

$$\alpha_X^C - \alpha_X^N = -j\alpha_X^N(\bar{Z}_A + \Delta\bar{Z}_A)\alpha_X^C \tag{15}$$

The left hand side of Eq. (15) is nothing but difference between the 'measured' complex FRFs and corresponding normal FRFs. Since the effect of mass and stiffness properties of the structure on the frequency response is completely quantified or captured by α_X^N, the difference appearing on the left hand side of Eq. (15) quantifies the influence of the damping on the frequency response. This means that if α_X^C and α_X^N is completely known then the left hand side is completely independent of mass and stiffness characteristics of the structure. On the right hand side of the Eq. (15) we again have α_X^C and α_X^N that relates to 'measured' FRFs. Thus, it's only the damping matrix of FE model which appears in Eq. (15) and therefore the updating equation for damping is unaffected by mass and stiffness characteristics of the FE

model. Thus, the updating Eq. (15) allows to completely isolate updating of damping matrix in stage-II from that of updating of mass and stiffness matrix in stage-I. This is a very useful characteristic of the two stage updating procedure.

Eq. (15) written using the rth column of LHS is,

$$\alpha_{X,r}^{C} - \alpha_{X,r}^{N} = -j\alpha_{X}^{N}(\overline{Z}_{A} + \Delta\overline{Z}_{A})\alpha_{X,r}^{C} \tag{16}$$

$$j(\alpha_{X,r}^{C} - \alpha_{X,r}^{N}) - \alpha_{X}^{N}\overline{Z}_{A}\alpha_{X,r}^{C} = \alpha_{X}^{N}\Delta\overline{Z}_{A}\alpha_{X,r}^{C} \tag{17}$$

Representing LHS of Eq. (17) by vector 'br' we get,

$$\alpha_{X}^{N}\Delta\overline{Z}_{A}\ \alpha_{X,r}^{C} = b_{r} \tag{18}$$

The updating parameters 'p' are chosen as the correction factors, β_q, to the element damping matrices of the FE model. Therefore, the change in the damping matrix can be expressed in terms of the updating parameters as,

$$\Delta D_{A} = \sum_{q=1}^{Ne} \beta_{q} D_{A}^{q} \tag{19}$$

where D_A^q is the qth element damping matrix, β_q is the corresponding updating parameter and $\sum_{q=1}^{Ne}$ indicates assembly over 'Ne' number of finite element or their groups whose coefficients are selected for correction.

Substitution of Eqs. (14) and (19) in Eq. (18) gives,

$$\alpha_{X}^{N}\left(\sum_{q=1}^{Ne}\beta_{q}D_{A}^{q}\right)\alpha_{X,r}^{C} = b_{r} \tag{20}$$

After expanding element damping matrix D_A^q to the size of the FE model, Eq. (20) can be written as,

$$\sum_{q=1}^{Ne}\alpha_{X}^{N}D_{A}^{q}\alpha_{X,r}^{C}\beta_{q} = b_{r} \tag{21}$$

Eq. (21) written down at 'nf ' number of frequency points chosen from the frequency range of interest can be combined and expressed in the following matrix form,

$$S(\omega)_{(n\times nf)\times(ne)}\beta_{ne\times 1} = b_{r}(\omega)_{(n\times nf)\times 1} \tag{22}$$

Where 'n' is the DOF of the FE model and 'β' is the vector of 'ne' correction factors.

Eq. (22) is implemented iteratively till the convergence is obtained. Let β_i^j is the ith correction factor found in jth iteration. Its cumulative value, $\overline{\beta}_i$, at the end of 'j' number of iterations can be calculated as,

$$\overline{\beta}_i = (1+\beta_i^1).(1+\beta_i^2).....(1+\beta_i^j)-1 \tag{23}$$

The final values of the damping correction factors are used to find the updated damping matrix using equations (13), (14) and (19).

2.3 Algorithm of two-stage updating method

Based on the mathematical formulations described in sections 2.1 and 2.2, the algorithm of the two-stage updating approach can be summarized below and the flowchart of the method is depicted by Figure 1.

Stage-I updating:

1) Construct an (initial) FE model of the structure using the knowledge of geometry, material properties and the boundary conditions.
2) Decide measurement points and measure FRFs at these points. These are complex FRFs.
3) Estimate normal FRFs from the measured complex FRFs using Eq. (4).
4) Choose mass and stiffness related updating parameters.
5) Compute analytical FRFs corresponding to the undamped FE model
6) Set updating Eq. (7), and then convert it into (10), using estimate of normal FRFs and the undamped analytical FRFs.
7) Find 'u' by least square solution of Eq. (10). Using 'u' calculate modified value of vector of updating parameters 'p'. The element mass and stiffness matrices are computed using these parameters and assembled to obtain global updated mass and stiffness matrices.
8) Check for convergence. If convergence criterion is not satisfied then iterate by going to step 5) else stop with the current updated mass and stiffness matrix representing the updated undamped FE model.

Stage-II updating:

1) Construct an initial estimate of FE damping matrix of the structure.
2) Use the normal FRFs, corresponding to 'measured' complex FRFs, estimated in step 3 of stage-I.
3) Choose updating parameters as the correction factors β_q, to the elemental FE damping matrices or the groups formed by them.
4) Set updating Eq. (18), and then convert it into (22), using estimate of normal FRFs, the 'measured' complex FRFs and the current knowledge of the damping matrix
5) Find 'β' by least square solution of Eq. (22).Construct the updated damping matrix using equations (13), (14) and (19).
6) Check for convergence. If convergence criterion is not satisfied then iterate by going to step (4) else stop with the damping matrix constructed in step 5) taken as the final updated damping matrix.

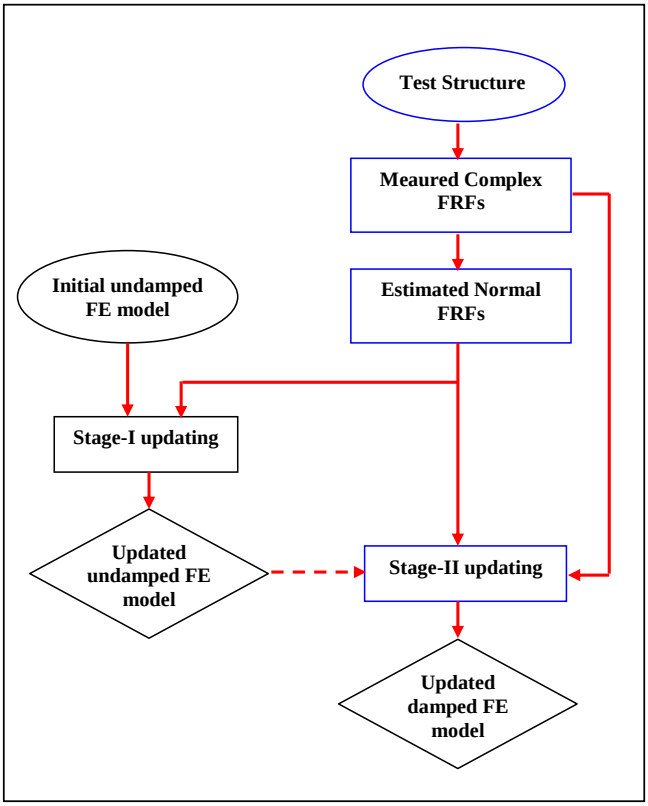


Figure 1: Flow chart of two-stage updating method

3 ISSUES TO BE ADDRESSED IN TWO-STAGE UPDATING

This section identifies the issues related to measurement and estimation that need to be addressed in stage I and II updating and identifies the link between the two stages of updating.

3.1 Issues in Stage I updating

A. Estimation of reference data used in updating:
The first stage of updating uses Normal FRFs as reference data in model updating. The expression for estimating this is given in section 2.1. This expression requires full measured FRF matrix to be known for estimation. This is a major issue to be addressed in stage-I updating because the measured data is generally incomplete. It has been shown in reference [23] that one strategy to obtained reasonably accurate estimate of Normal FRFs using incomplete data is to have measurement of sufficiently large number of translational FRFs. This strategy will be followed in the numerical and Experimental investigations carried out in this paper. However, truncation of the measured data does introduce some errors in the estimation.

B. Incompleteness of measured FRFs:
Incompleteness of measured FRFs also affects setting up of updating equations. This is dealt by replacing the Normal FRFs corresponding to unmeasured DOFs by their FE model counterparts. Once updating equations have been set the equations corresponding to unmeasured DOFs are dropped.

C. Noise in measured FRFs:

The measured FRFs generally have some random noise. This adversely affects the estimation of Normal FRFs.

It is noted that all the above three issues may affect accuracy of mass and stiffness matrix updating in stage-I. This may also affect the performance of stage-II updating as explained below.

3.2 Issues in Stage II updating

A. Estimation of reference data used in updating:

LHS of Eq. (16) is the difference between the measured FRFs and the corresponding estimated Normal FRFs and can be looked upon as reference data for damping matrix updating. This clearly indicates that reference data for second stage updating is also dependent on Normal FRFs and hence is affected by accuracy of their estimation.

B. Incompleteness of measured FRFs:

In Eq. (16), α_X^N needs to be completely known for setting up of updating equations. The strategy followed is to replace the Normal FRFs corresponding to unmeasured DOFs by their FE model counterparts.

C. Influence of stage-I updating:

It is mentioned in part B above that incompleteness is dealt by replacing the Normal FRFs corresponding to unmeasured DOFs by their FE model counterparts. This helps to overcome the problem of incompleteness but requires FE mass and stiffness matrix to compute normal FRFs. It is at this place that the updated mass and stiffness matrix from stage-I chip in and starts influencing stage-II updating. This is how stage-II updating gets coupled to stage-I updating. In this way all the possible sources of errors in stage I updating, mentioned in section 3.1, indirectly start affecting performance in Stage II updating since output of stage I needs to be used in stage II updating.

D. Noise:

Noise in measured FRFs affects estimation of Normal FRFs and thereby directly affects the reference data used for stage-II updating.

4 NUMERICAL STUDY

This section investigates the performance of two stag updating procedure through a numerical example of a simple but representative fixed-fixed beam structure, shown in Figure 2. The objective of the study is to test the effectiveness of the two-stage approach for updating of mass, stiffness and damping matrix and to evaluate the influence of incompleteness of the experimental data on it. Another important point of investigation is to study the influence of performance of updating in the first stage on the second stage. The effect of simulated 'noise' on updating is also studied.

4.1 Details of case study

The size of beam structure is 900 mm × 50 mm × 5 mm. The modulus of elasticity and density of the structure is taken as 2.0e+11 N/m^2 and 7800 kg/m^3 respectively. The initial FE model of the beam is built using thirty 2D beam elements with node at ends fixed giving a total of 29 nodes with two degrees of freedom (translational and rotational) at each node. The damping in the structure is modeled through a proportional structural damping matrix in the initial FE model.

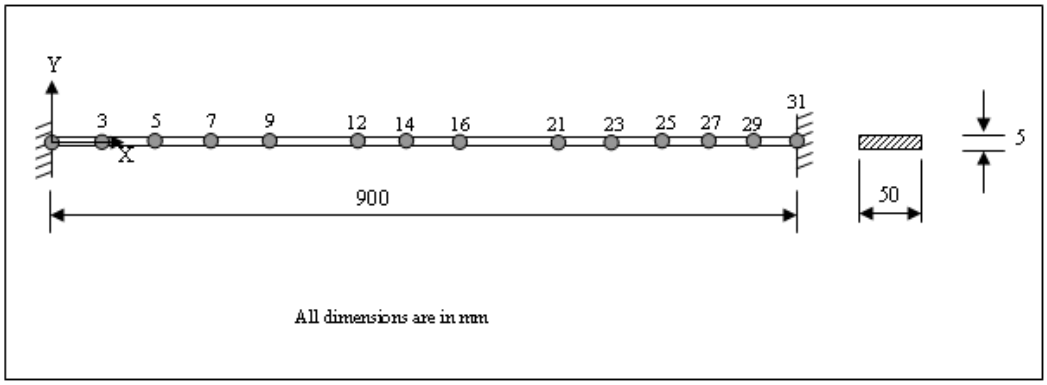


Figure 2: Details of beam structure.

The simulated experimental data is obtained by introducing certain known discrepancies in the initial FE model as follows:

a) Young's moduli of thirty finite elements are perturbed as detailed in Table 1.

b) The damping matrix D_X of the simulated structure is represented as

$$D_X = \sum_{i=1}^{Ne} \left(1 + \frac{\beta_i}{100}\right) D_{A,e}^{i} \tag{24}$$

The summation sign represents assembly of the elemental matrices in the above equation. $D_{A,e}^{i}$ represents the ith elemental damping matrix of the initial FE model. The scalar β_i in the Eq. (24) represents the percentage deviation in the ith elemental damping matrix. The β_i^S used to obtain D_X are also given in Table 1. This gives a non proportional structural damping matrix.

Group No.	Element Numbers	% Deviation in Young's modulus	% Deviation in β_S
1	1-3	+70%	+8000%
2	4-6	+10%	+6000%
3	7-9	+50%	+9000%
4	10-12	+30%	+5000%
5	13-15	+20%	+8000%
6	16-18	+60%	+4000%
7	19-21	+40%	+10000%
8	22-24	+10%	+7000%
9	25-27	+40%	+5000%
10	28-30	+70%	+9000%

Table 1: Discrepancies between the finite element and the simulated 'experimental' model for beam with structural damping.

The model obtained in the above manner thus represents the simulated experimental structure. This simulated experimental structure is solved for obtaining its frequency response. This frequency response is treated as 'measured' frequency response in the study.

For the stage-I updating in which mass and stiffness matrices are updated, the modulus of elasticity of the finite elements are updated. Thirty elements are grouped into ten groups of three finite elements each. The fractional correction to modulus of elasticity of finite elements of each group is treated as an updating parameter thus giving a total of 10 updating parameters. Similarly for stage-II a common fractional correction to damping matrix of three finite elements in each group is taken as an updating parameter. This also gives 10 number of updating parameters for damping matrix updating. The values shown in Table 1 are, therefore, nothing but the correct value of above two sets of updating parameters.

4.2 Updating using incomplete 'experimental' data

In practice, it is not realistic that the FRFs corresponding to all the coordinates specified in an FE model have been measured, either due to physical inaccessibility or due to difficulties faced in the measurement like that for measurement of rotational degrees of freedom. It is therefore assumed that the measurements are not available at all the degrees of freedom of the finite element model. Moreover, it is also generally not desirable to measure the complete FRF matrix due to the reasons of time and economy. Two levels of incompleteness are considered by assuming that translational FRFs are available at all the nodes and then at only half of the nodes of the FE model. These have been referred as cases of 50% and 25% incomplete data respectively, the percentages representing the proportion of the total degrees of freedom of an FE model that are taken as 'measured'. Measurement of limited number of FRFs poses a couple of challenges in the implementation of two-stage updating. The first challenge relates to estimation of normal FRFs and second challenge relates to implementation of updating equations.

Estimation of normal FRFs: The updating in the two stages requires a prior estimation of normal FRFs (α_X^N) for the 'experimental structure' from the knowledge of its complex FRFs (α_X^C). This estimation is based on equation (4) which requires a square α_X^C matrix. This estimation is faced with two types of FRF data incompleteness. The first problem related to incompleteness is that FRFs at all the DOFs of FE model can not be measured e.g. for beam and plate like structures generally only translational FRFs are measured while FRFs corresponding to rotational DOFs (RDOFs) are unmeasured. It is shown that if FRFs at a sufficient number of translational DOFs (TDOFs) are measured then the estimation of normal FRFs using only the translational FRFs gives a quite close estimate of the translational normal FRFs [23]. This strategy is adopted to make up for non-measurement of RDOF-FRFs. However, it should be noted that rotational normal FRFs still remain unknown.

The second problem related to incompleteness is that even the whole FRF matrix corresponding to all the TDOFs, as required above, is not measured and the general practice has been to measure FRFs corresponding to either one row or one column of TDOF-FRF matrix. In view of this, the completeness of the α_X^C is doubly hampered as far as estimation of normal FRFs is concerned. This second incompleteness related to the unmeasured FRF matrix can be resolved by regenerating the 'unmeasured' TDOF-FRFs in other rows and columns using the modal model identified based on the 'measured' row/column of translational FRFs. A normal FRF estimated using above considerations, for the case of 25% incomplete data, is shown overlaid on the exact normal FRF in Figure 3. It is seen that the error between the es-

timated normal FRF and the exact normal FRF is negligible and hence the above strategy to deal with FRF data incompleteness is effective for the estimation of normal FRFs.

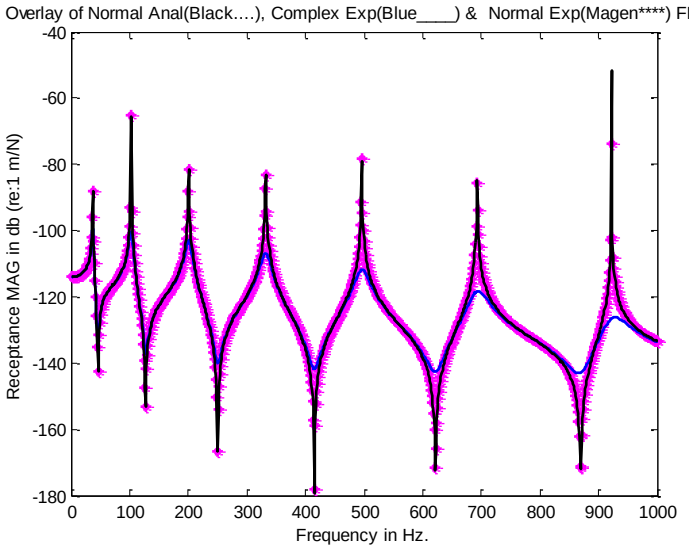


Figure 3: Overlay of Simulated experimental, Exact normal and Estimated normal FRF based on 14 TDOFs: Case of 25% coordinate incompleteness.

Stage-I updating: The incompleteness referred in above section also influences the setting-up of updating equation (7) (and hence (10)). This equation requires knowledge of complete normal FRF matrix, which include both translational and rotational FRFs (in case of a beam or plate like structure). The translational normal FRFs are already estimated and the next difficulty now is associated with the estimation of rotational normal FRFs. In this section, the rotational normal FRFs are approximated by their analytical counterparts. With this replacement the updating equation (10) can be framed and updating carried out. Figure 4(a) shows a plot of stiffness updating parameters estimated during stage-I updating for the case of 25% incomplete data. A comparison with the correct updating parameters value given in Table 1 indicates that the estimated parameters are exact.

Stage-II updating: For updating of damping matrix again the updating equations require full FRF matrix. However, since data is incomplete, the FRFs are available only at limited number of DOFs. Similar to the previous section, incompleteness of FRF data related to unmeasured RDOF-FRFs is dealt by replacing the 'unmeasured' FRFs by their analytical counterparts. Figure 4(b) shows a plot of damping updating parameters estimated during stage-II updating for the case of 25% incomplete data. A comparison with the correct updating parameters value given in Table 1 indicates that the estimated parameters are nearly exact. It is noted that the computation of the analytical FRFs for dealing with incompleteness related to unmeasured RDOF-FRFs require the FE model stiffness and the mass matrix obtained at the end of stage-I updating. Since the mass and stiffness matrices could be accurately updated in stage-I, there was no unfavorable influence of them on damping matrix updating in stage-II.

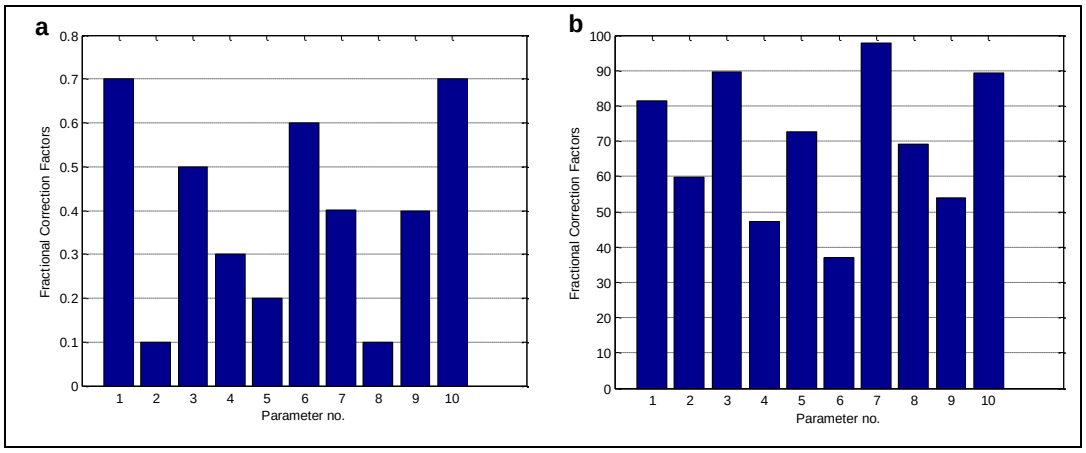


Figure 4: Final values of the updating parameters: Case of 25% incomplete data. (a) updated stiffness parameters after stage-I and (b) updated damping parameters after stage-II.

FRF Comparison after two stages of updating: An overlay of an 'experimental' and the corresponding FE model FRF before updating is shown in Figure 5. The overlay of these two FRFs after stage-I updating is shown in Figure 6(a). It is seen from the overlay that stage-I updating has been able to remove stiffness/mass matrix modeling errors and hence a good FRF match is seen away from the resonances and antiresonances. The overlay of above two FRFs after stage-II updating is shown in Figure 6(b). The overlay shows a perfect match between the 'experimental' and FE model FRF after stage-II updating.

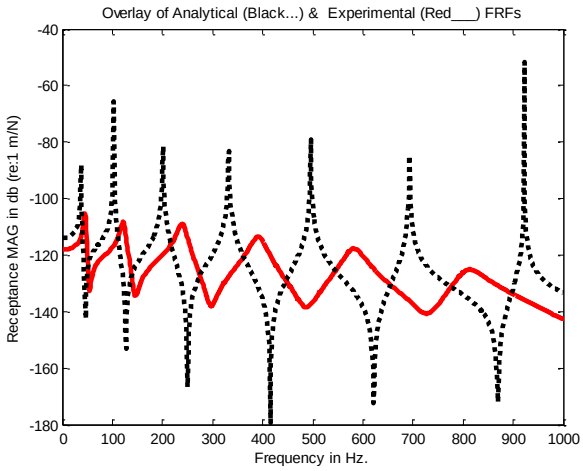


Figure 5: FRF overlay before stage-I updating: Case of 25% incomplete data FRF overlay before stage-I updating: Case of 25% incomplete data ('experimental' complex ('——' (red)) and FE model ('-----'(black)) FRFs)

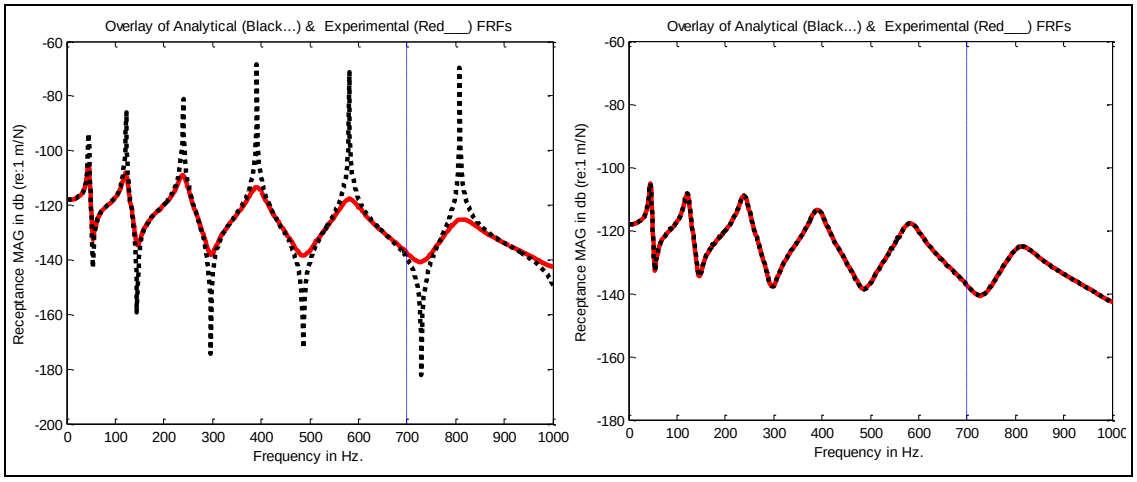


Figure 6: FRF overlay after updating: Case of 25% incomplete data (a) after stage-I (b) after stage-II.

4.3 Updating using noisy incomplete 'experimental' data

In practical measurements, the measured FRFs are generally contaminated by measurement noise. To check the robustness of the method under such conditions, the complex FRFs, are polluted with 2% random noise to obtain noisy complex FRFs. The incompleteness of 'measured' data is again dealt by replacing the 'unmeasured' FRFs by their analytical counter parts computed using latest available estimate of FE mass (M_A) and stiffness (K_A) matrices at any stage. For the case of 50% incompleteness and 1% noise, Figure 7(a) and (b) show plots of updated stiffness parameters and corresponding individual percentage error respectively.

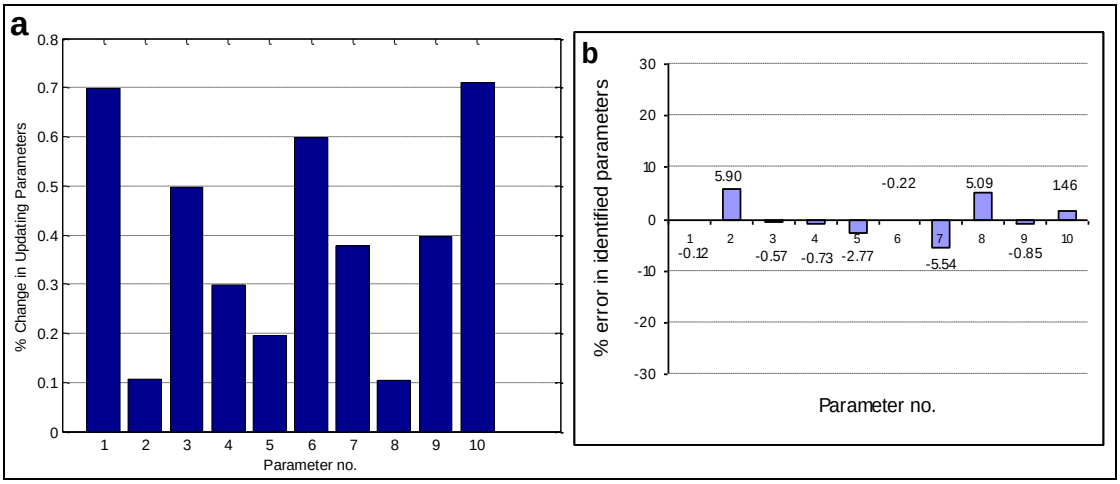


Figure 7: Final values of the updating parameters after stage-I updating: Case of 50% incomplete data with 1% noise (Analytical data approach) (a) updated stiffness parameters (b) % error in updated stiffness parameters.

Similarly, Figure 8(a) and (b) show updated damping parameters and corresponding percentage error respectively. It is seen that the maximum percentage error in stiffness updating

parameters is 5.9 %, while the maximum percentage error in damping updating parameters is 24.79%. Figure 9 (a) and (b) show overlays of an FE model FRF and the corresponding 'measured' complex FRF after stage-I and II updating respectively. It is seen from the above results that stage-I and II updating have been quite successful in terms of FRF matching, even though there is some error in the updated parameters in the two stages. Updating for the case of 50% incompleteness and 2% noise is also done and it is seen that not only the maximum percentage error in both the stages of updating have increased but the FRF- match after stage-II is also not so good in the higher frequency range. The situation is further deteriorated with 25% incompleteness and 1% noise. It is seen from FRF comparison that the mismatch of FRF is localized around resonant and anti-resonant frequency indicating that it is the updating in stage-II that is being more affected as compared to updating in stage-I.

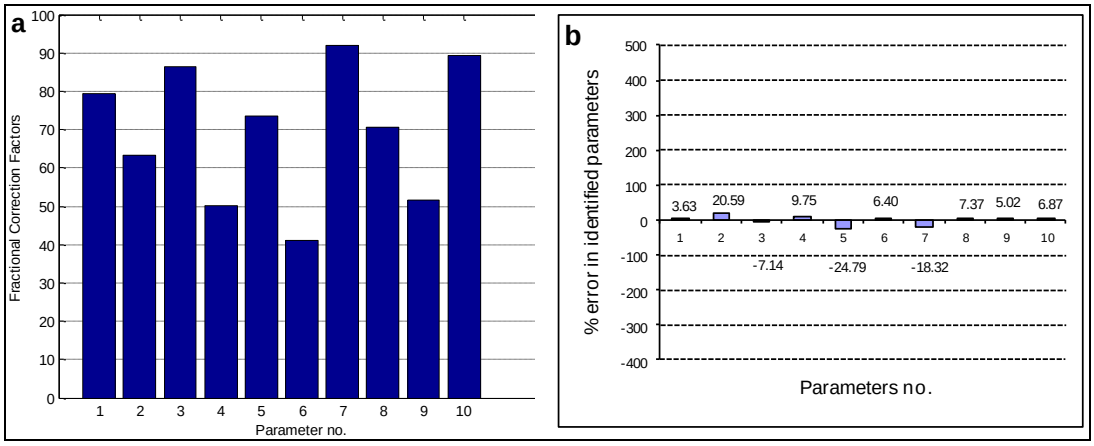


Figure 8: Final values of the updating parameters after stage-II updating: Case of 50% incomplete data with 1% noise (Analytical data approach). (a) updated damping parameters (b) % error in updated damping parameters.

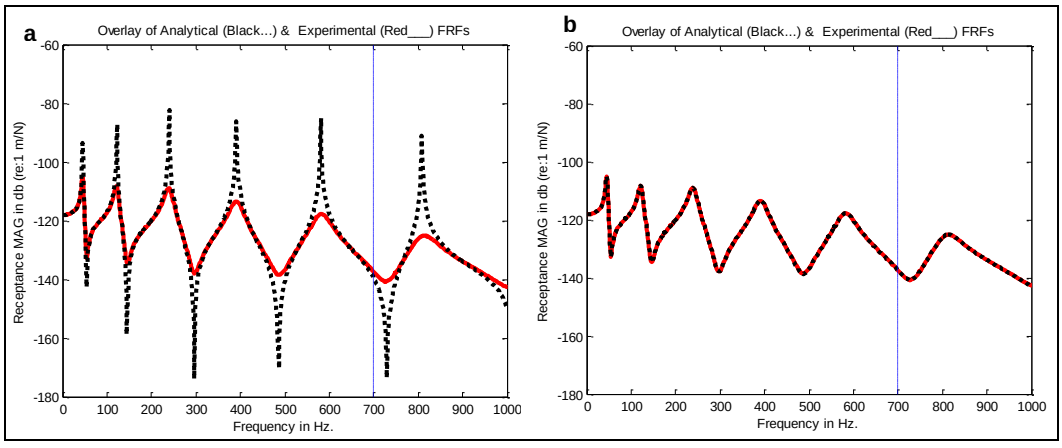


Figure 9: FRF overlay: Case of 50% incomplete data with 1% noise. (Analytical data approach) (a) after stage-I updating (b) after stage-II updating

4.4 Treatment of 'experimental' data incompleteness using Hybrid data

It is observed from results given in previous section that

a) in both the stages of updating, higher is the level of incompleteness, higher is the error in the identified updating parameters. This is due to the fact that the incompleteness of 'experimental' data related to the unmeasured rotational FRFs is dealt by substituting the corresponding data from the analytical model. Since the analytical model is not accurate it leads to inaccuracies in the estimation of updating parameters.

b) the percentage error in stage-II updating is on higher side as compared to stage-I updating. Due to noise in the 'measured' FRFs, stiffness and mass matrix is not updated accurately in stage-I and therefore have some error left in them. The updated mass and stiffness matrix are subsequently used in stage-II for computation of FRFs corresponding to unmeasured DOFs to tackle data incompleteness. This develops the link between the stage-I updating and the stage-II. Thus, the lack of complete data causes the linking of stage-II with stage-I. Due to this, stage-II updating is affected as a result of any inaccuracies that might be left in stage-I updating. Lesser the degree of incompleteness, lesser would be the influence of stage-I updating errors on stage-II updating.

An improvement in the method to deal with incompleteness is suggested here in the framework of proposed two-stage updating approach to reduce its unfavorable influence on updating. This improvement is based on using a combination of FE model and 'experimental' data. In the modified method, the 'unmeasured' complex FRFs are not directly computed using the updated mass and stiffness matrix and the current knowledge of damping matrix as is done in previous sections, but, are regenerated using the modal data. For this purpose the complex 'measured' FRFs are analyzed to obtain an estimate of 'experimental' natural frequencies and the corresponding damping factors. The mode shapes are obtained by solving eigenvalue problem using the updated M_A and K_A matrices. In this way, 'experimental' natural frequencies and the damping factors along with FE model mode shapes are used to regenerate 'unmeasured' complex FRFs.

In stage-I updating, for the case of 50% incompleteness and 1 % noisy data, the identified parameters are nearly the same using both the analytical and hybrid data based strategies. This is clear from the comparison of percentage errors in updating parameters shown in Figure 10. It is noted that both the strategies involving replacing the 'unmeasured' FRF data with some approximation of them are self-corrective in nature, because as the FE model improves over the iterations, the approximation also improves and hence in the limit the error of approximation may get eliminated if FE model indeed converges to the 'correct' model. This is the reason why the parameters identified by both the approaches are not much different. However, in practice, this self-corrective property will be less effective with analytical data based approach if one is not able to choose a 'correct' set of updating parameters. With hybrid data approach self-corrective property may still be at least partially effective. It is however noted that there is a marginal improvement in the convergence characteristics of the updating parameters in stage-I updating based on hybrid data strategy. Hybrid strategy is found to require fewer numbers of iterations for the convergence. This is because of the fact that the hybrid data based approach uses a correct estimate of some of the natural frequencies and corresponding damping factors right from the first iteration resulting into a faster convergence. With hybrid data approach to deal with incompleteness, the parameters and errors in stage-II updating as shown in Figure 11(a) and (b) are more accurate than those with analytical data based approach as shown in Figure 8(a) and (b).

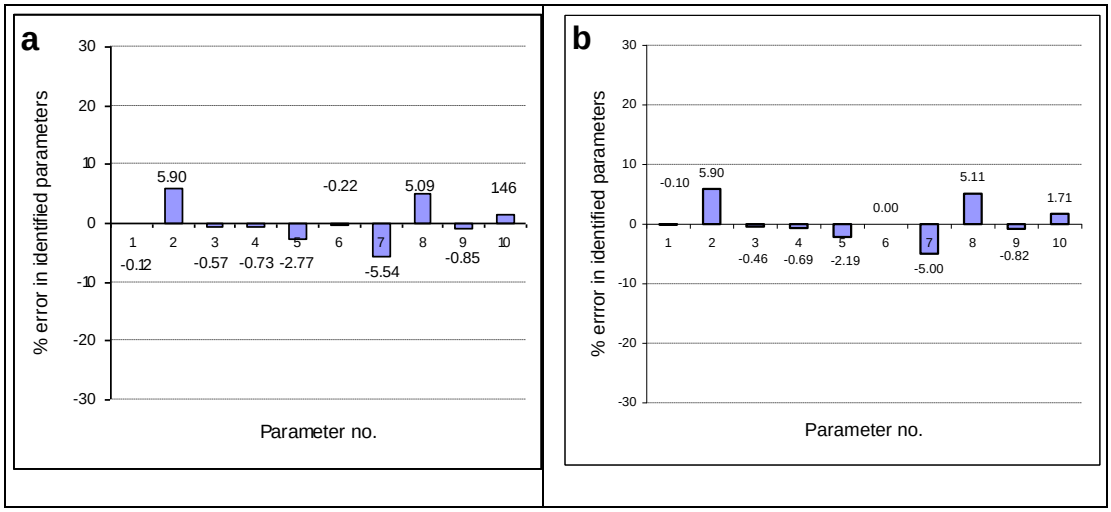


Figure 10: Percentage error in updated stiffness parameters after stage-I updating: Case of 50% incomplete data with 1% noise. (a) Analytical data approach (b) Hybrid data approach

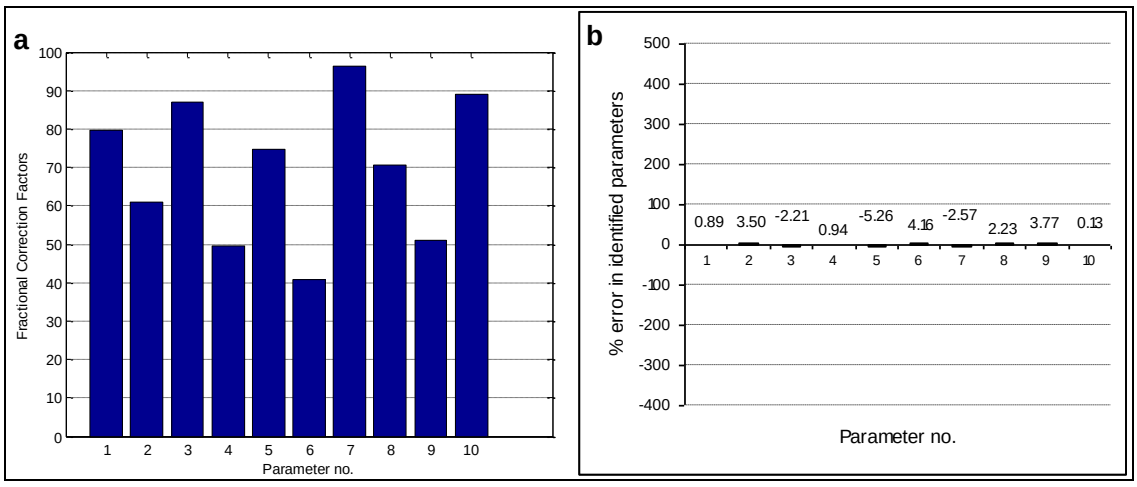


Figure 11: Final values of the updating parameters after stage-II updating: Case of 50% incomplete data with 1% noise (Hybrid data approach) (a) updated damping parameters (b) % error in updated damping parameters.

Similarly, for the case of 50% incompleteness and 2% noisy data, the errors in stage-II updating are reduced from a maximum error of 263.27% obtained using analytical data approach to 7.32% (Figure 12(a) and (b)) obtained using hybrid data approach. This indicates that the hybrid method is a more effective procedure of dealing with data incompleteness in stage-II because a partial use of 'experimental' data to regenerate 'unmeasured' FRFs helps to reduce the influence of any errors in mass and stiffness matrix in stage-I updating flowing down to damping matrix updating in stage-II. Overlays of FE model and 'measured' complex FRF after stage-II updating using hybrid data approach for the case of 50% incompleteness with 1% and 2% noisy data are shown in Figure 13(a) and (b) respectively. These overlays further reflect that the matching of FRFs is much improved when incompleteness is resolved using

hybrid data approach. Hybrid data approach also behaves well when the incompleteness is further increased to 25% as seen from the Figures 14 and 15 which clearly indicate that the percentage errors in updating parameters are lower and the FRF overlay is better as compared to corresponding updating with analytical model based approach.

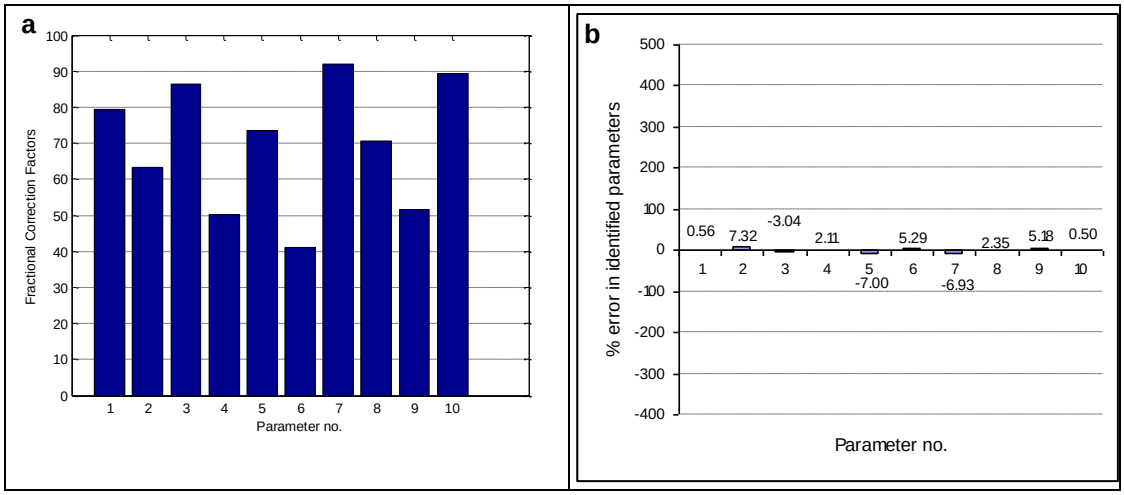


Figure 12: Final values of the updating parameters after stage-II updating: Case of 50% incomplete data with 2% noise (Hybrid data approach) (a) updated damping parameters (b) % error in updated damping parameters.

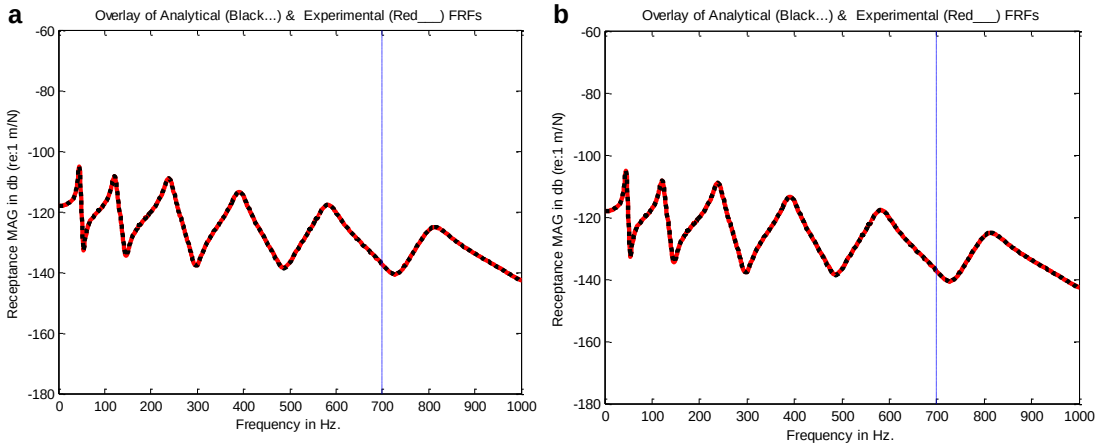


Figure 13: Comparison of FRF overlay after stage-II updating: Case of 50% incomplete data (Hybrid data approach) (a) with 1% noise and (b) with 2% noise ('experimental' complex ('——' (red)) and updated FE model ('-----'(black)) FRFs).

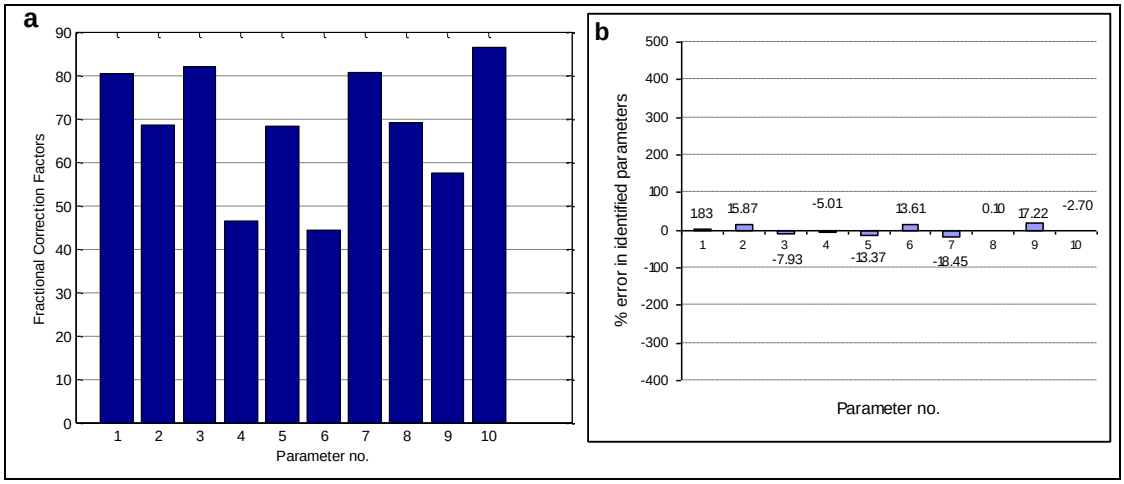


Figure 14: Final values of the updating parameters after stage-II updating: Case of 25% incomplete data with 1% noise (Hybrid data approach) (a) updated damping parameters (b) % error in updated damping parameters.

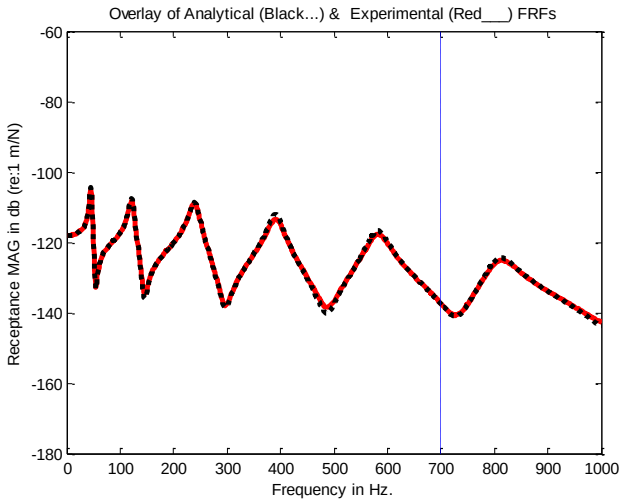


Figure 15: FRF overlay after stage-II updating (Hybrid data approach): Case of 25% incomplete data with 1% noise.

5 UPDATING USING EQUIVALENT UPDATING PARAMETERS

In the previous sections the parameters that need to be updated are assumed to be correctly known. For example, the errors simulated in the FE model were related to modulus of elasticity and the parameters updated were also the modulus of elasticity of individual finite elements.

However, in practice, it's not always possible to correctly identify the parameters that should be updated and most often it is the engineering judgment, coupled sometimes with sensitivity analysis, which is generally resorted to in choosing updating parameters. If parameters chosen in this manner don't match with the 'correct' parameters then such updated parameters can be viewed as a set of equivalent parameters yielding correction in the structural matrices that try to reduce the error between the 'experimental' and the analytical data. This

section is devoted to simulate above situation to test effectiveness of the proposed two-stage updating procedure for its robustness in giving an improved FRF correlation when updating parameters chosen don't contain those parameters that are in error. 'Measured' data is generated through an 'experimental' beam structure in which stiffness and damping discrepancies are introduced in the form of torsional spring stiffnesses (kt1 and kt2) and torsional damping coefficients (dt1, dt2) at the two ends. Table 2 gives the value of these parameters. 'Experimental' complex FRFs are generated through this model from which normal FRFs are computed as explained before.

kt1 (in N-m/radian)	kt2 (in N-m/radian)	dt1 (in N-m-sec/radian)	dt2 (in N-m-sec/radian)
1.0e+04	1.0e+04	0.7e+04	0.7e+04

Table 2: Torsional spring stiffnesses (kt1 and kt2) and torsional damping coefficients (dt1, dt2) at the two ends of the 'experimental' beam structure.

The FE model of the beam structure is same as used in the previous sections. The updating parameters for the two stages are also the same i.e. the fractional correction to the modulus of elasticity of the thirty updating parameters for stage-I and coefficients of the elemental damping matrices for stage-II. It is noted that the parameters to be updated don't exactly contain the parameters that are actually in error. Updating using two-stage procedure is performed using complete 'measured' FRF data. Figure 16 (a) and (b) show bar chart of the identified updating parameters in stage-I and II respectively. It is seen that stage-I shows a significant drop in the Young's modulus of the finite elements at the ends while the Young's modulus of other finite elements show only a relatively smaller change. The values of the updating parameters therefore indicate that the stiffness modeling error is situated at the two ends. Similarly, stage-II updating shows a large change in the damping matrix coefficients of the finite elements at the ends indicating that the damping modeling errors are localized near the two ends. In this way, the two stages of the updating are able to correctly localize the zones of the modeling errors, which in this case are the two ends of the beam, and perform an equivalent adjustment of the chosen updating parameters.

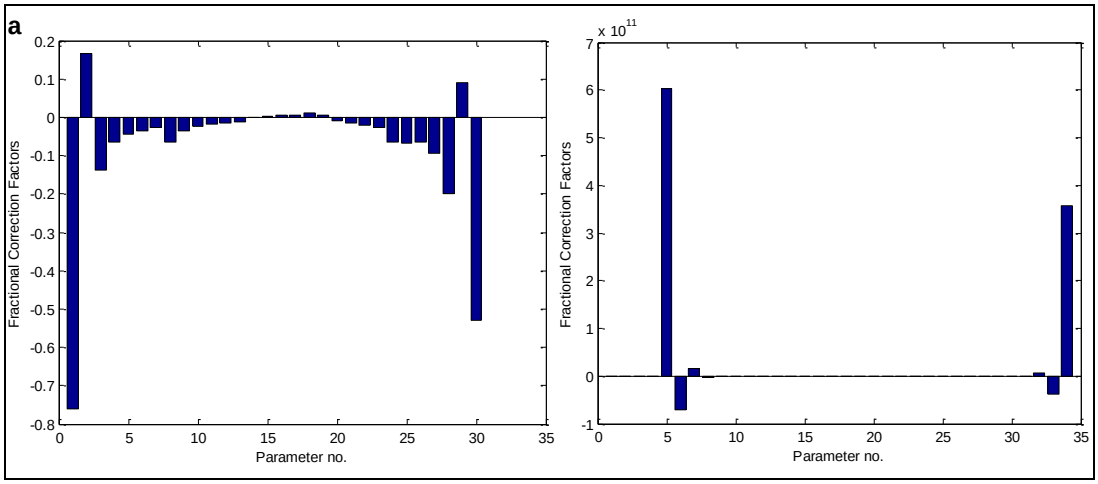


Figure 16: Final values of the updating parameters: Case of equivalent updating parameters. (a) updated stiffness parameters after stage-I and (b) updated damping parameters after stage-II.

An overlay of an 'experimental' and the corresponding FE model FRF before updating is shown in Figure 17. The overlay of these two FRFs after stage-I updating is shown in Figure 18(a). It is seen from the overlay that stage-I updating has been able to make equivalent corrections in the stiffness/mass matrix and hence a good FRF match is seen away from the resonances and antiresonances. The overlay of above two FRFs after stage-II updating is shown in Figure 18(b). The overlay shows a good match between the 'experimental' and FE model FRF after stage-II updating. In this way, it is seen that the two-stage updating procedure has successfully made an equivalent correction sequentially in the mass/stiffness matrix and damping matrix.

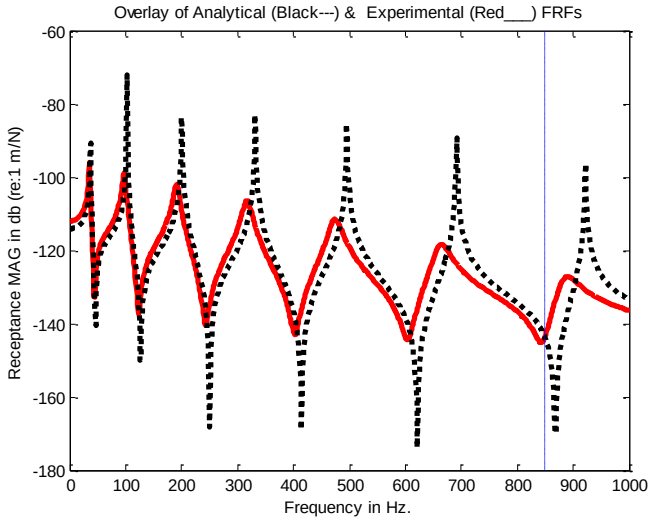


Figure 17: Analytical and 'experimental' FRF overlay before stage-I updating: Case of equivalent updating parameters.

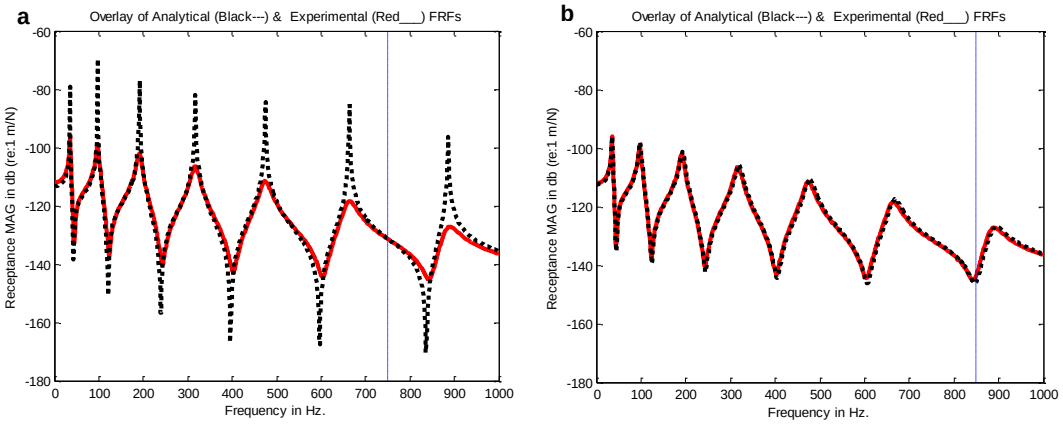


Figure 18: Analytical and 'experimental' FRF overlay: Case of equivalent updating parameters (a) after stage-I updating (b) after stage-II updating

The case study in this section demonstrates that even when the updating parameters cannot be chosen correctly, but the chosen parameters have the ability to capture the influence of the

modeling error in an equivalent way, then the proposed two-stage updating procedure is effective in yielding an updated model that has a good correlation with the measured FRF data.

6 EXPERIMENTAL STUDY ON AN F-SHAPED STRUCTURE

This section presents experimental investigation into two-stage updating of an FE model of an F-shape structure that resembles the skeleton of a drilling or milling machine tool.

6.1 Details of case study

The F-shape structure has been built by bolting horizontally the two beam members to a vertical beam member, which in turn has been welded at the bottom to a base plate. All the beam members have a square cross-section of side 37.7 mm. Figure 19 shows the basic dimensions of the F-structure used in the study.

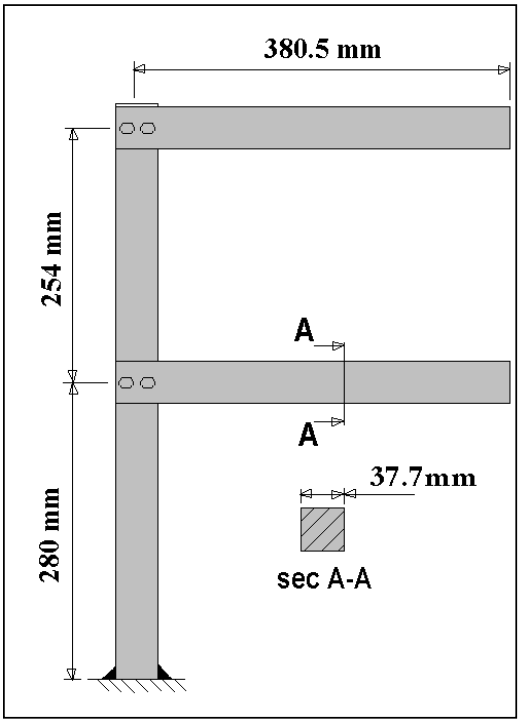


Figure 19: F-Shape-Structure.

A finite element model of the structure is built using forty eight 2-D-frame elements and a total of 52 nodes with three degrees of freedom (two displacements and one rotation) at each of the nodes. The FE mesh is shown in Figure 20. The values for the modulus of elasticity and the density are taken as 2.0e11 N/m^2 and 7800 kg/m^3 respectively. In the present case due to the presence of three joints the modeling of stiffness at these places is expected to be a dominant source of modeling inaccuracy in the FE model. In view of this, the three joints present are modeled by taking coincident nodes at each of them. Thus, there are two geometrically coincident nodes at a joint instead of just one node. The three corresponding degrees of freedom at the two nodes are coupled through three springs respectively. The stiffness of these springs could be the potential updating parameters for accounting the flexibilities that might

be there at the joints. Onosokki make dual channel FFT analyzer, CF-7200A, is used to measure the frequency response function using an accelerometer (B&K model 4368) and an impact hammer (B&K model 8202).

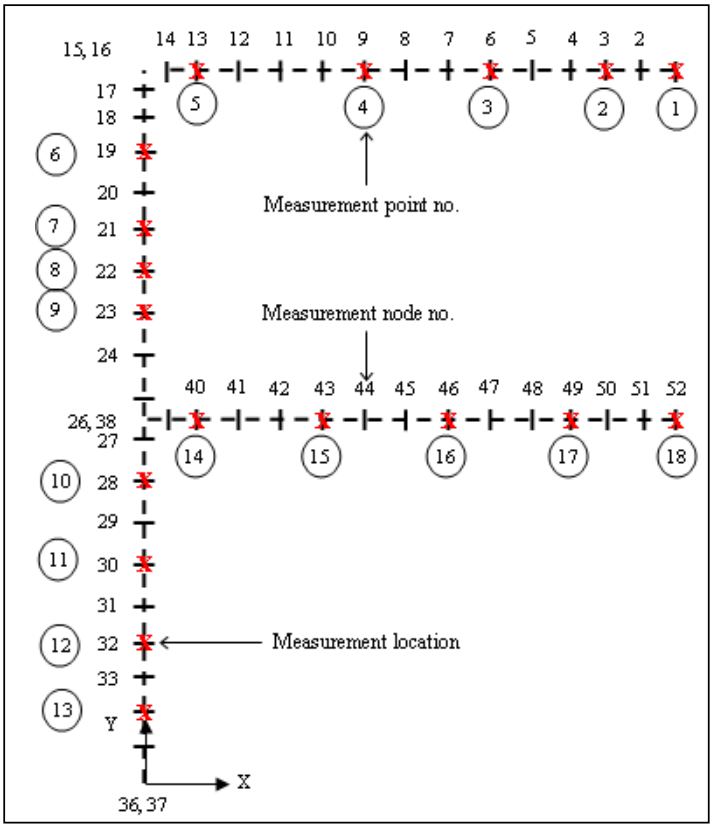


Figure 20: Details of measurement points on F shape structure used in updating.

The FRF is measured over a frequency range of 1 KHz by exciting the structure at above locations with an impact hammer and measuring the response with an accelerometer kept fixed at one of the locations. This gives one row of translational FRF matrix corresponding to 18 nodes. For the estimation of normal FRFs from the measured complex FRFs, a full square complex FRF matrix is required. In this work, this is done by measurement of all the rows of the translational FRF matrix. This is accomplished by changing the accelerometer position to other nodes and again measuring all the FRFs as explained above. In this way the lower triangular part of the FRF is completely measured which effectively gives the full FRF matrix, of order 18 x 18, under the assumption of symmetricity of the FRF matrix as a result of reciprocity theorem.

6.2 Stage-I updating

This section presents results of mass and stiffness matrix updating performed in stage-I.

Estimation of normal FRFs: Identification of mass, stiffness and damping matrix through the FE model updating method explained in section on theory related to stage-I updating requires normal FRFs of the structure which can be computed from equation (4). The measured FRF data is generally incomplete. The strategy followed here is similar to that mentioned in section on 'Updating using incomplete 'experimental' data' of the numerical study, which is based on estimating normal FRFs using a sufficiently large number of measured translational FRFs. In view of this the measured translational FRF matrix of order 18 x 18 is used to compute normal FRFs.

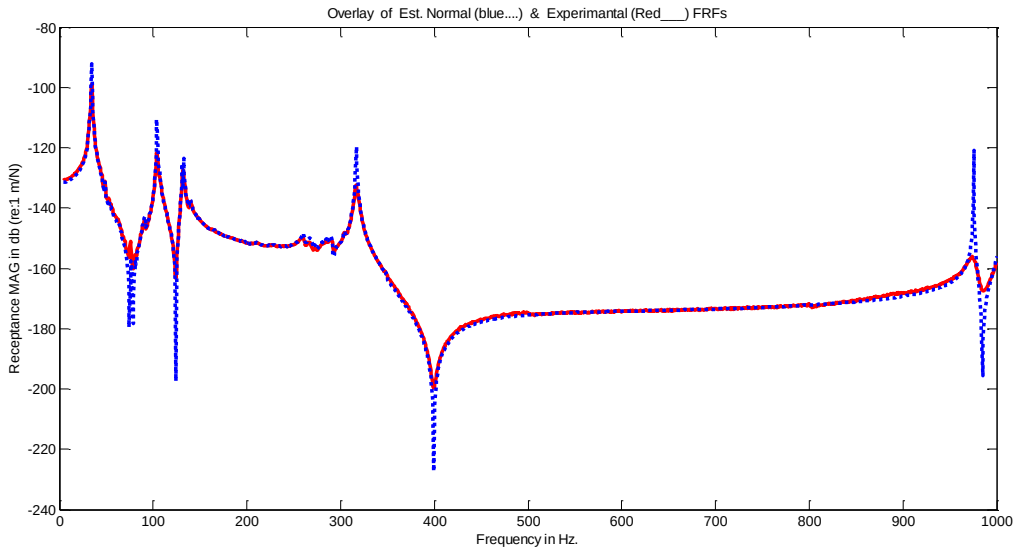


Figure 21: Overlay of experimental ('——' (red)) and estimated normal FRFs ('…….'(blue)) $\alpha_{55\times94}$ with 18 TDOFs only.

Figure 21 shows a plot of an estimated normal FRF corresponding to the FRF $\alpha_{55\times94}$, which indicates response at node 55 due to excitation at node 94, using above strategy. For comparison the corresponding measured complex FRF is also shown. The estimated Normal FRF shows quite sharp peaks and valleys at resonance and antiresonance respectively as compared to damped peaks and valleys in the experimental FRF. It is seen that the computed Normal FRFs display an expected character of a normal FRF and hence seem to represent well the FRFs of a hypothetical 'undamped' F shape structure.

With a view to see the effect of number of translational FRFs used in the estimation of normal FRFs, estimation is done using complex square Translational FRF matrix corresponding to only 12 nodes. Figure 22 shows a normal FRF computed in this manner with the corresponding measured FRFs ($\alpha_{55\times94}$) overlaid on them. It is observed that the estimated normal FRF is still accurate though error in estimation can be seen at some frequency points.

Above results validate the strategy of estimation of normal FRFs even in the case of experimental data as the results indicate that the estimation is reasonably accurate when number of translational FRFs is 'sufficient'.

Choice of updating parameters for Stage-I: One of the most important issues in FE model updating using iterative methods is the selection of the updating parameters. In case of iterative methods, the selection of updating parameters would decide how good a match is ob-

tained between an FE model data and the experimental data. Choice of updating parameters on the basis of engineering judgment about the possible locations of modeling error in a structure is one of the strategies to ensure that only the physically meaningful corrections are made.

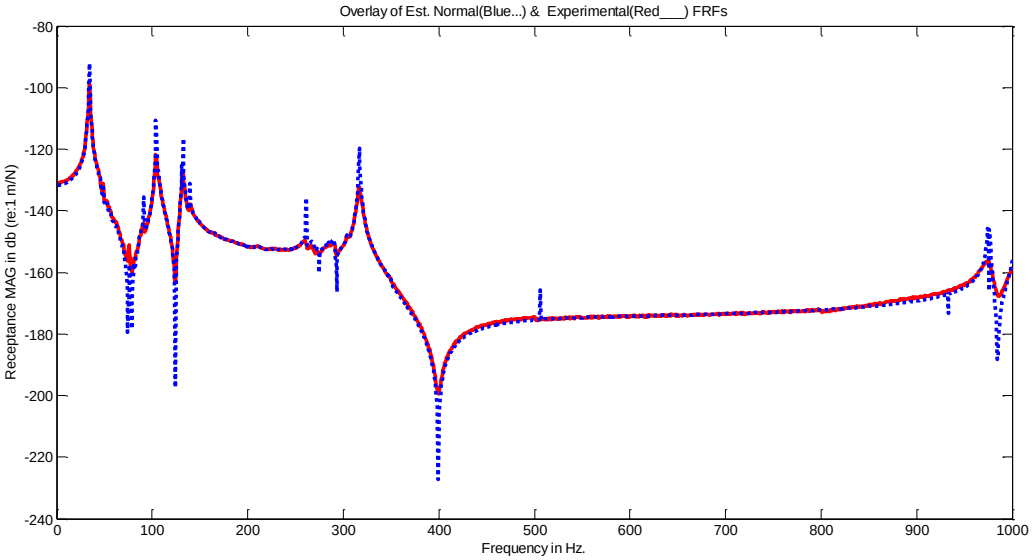


Figure 22: Overlay of experimental ('——' (red)) and extracted normal FRFs ('…….'(blue)) $\alpha_{55\times94}$ with 12 TDOFs only.

In the present structure due to the presence of three joints the modeling of stiffness at these places is expected to be a dominant source of localized modeling inaccuracy in the FE model. The stiffness of these springs, Kx, Ky and Kt respectively, could be the potential updating parameters allowing to account for the deviation in the stiffness of the regions covered by the joints. A sensitivity analysis is performed to further reduce the number of unknowns and it is noticed that the eigenvalues are much more sensitive to the torsional stiffness at the three joints than to other spring-stiffness parameters. In the light of this observation, the three torsional stiffness parameters are chosen as updating variables for updating mass and stiffness matrix. The other stiffness values are taken very large to represent rigid coupling of the corresponding degrees of freedom.

Results of stage-I updating: The undamped FE model of the F structure is now updated with three torsional spring stiffness parameters. Table 3 shows values of the updating parameters before and after updating. Updating is seen to predict lower torsional stiffnesses at the three joints. Figure 23 shows a comparison of undamped FE model point FRF $\alpha_{64\times64}$ and the corresponding normal FRF computed from the measured FRFs. The comparison shows a significant discrepancy between the two FRFs. A similar comparison but carried out after updating is shown in Figure 24 from which it is seen that the updated undamped model FRF matches very well with the normal FRF of the structure.

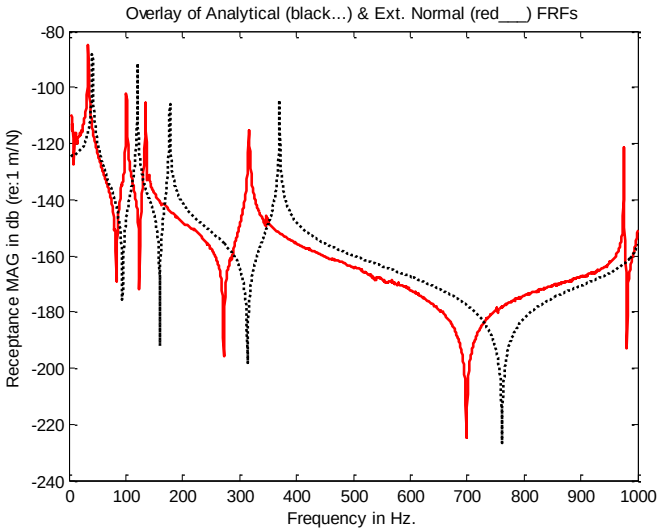


Figure 23: Overlay of FRF $\alpha_{64\times64}$ before stage-I updating: experimental normal ('——' (red)) and undamped FE model ('…….'(black)) FRFs.

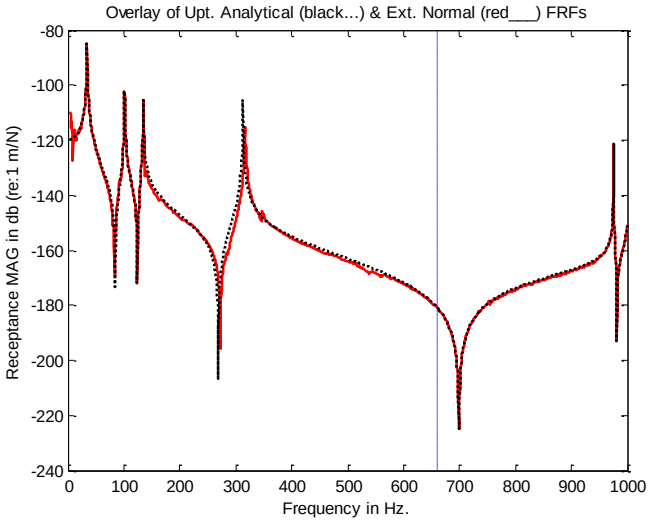


Figure 24: Overlay of FRF $\alpha_{64\times64}$ after stage-I updating: experimental normal ('——' (red)) and updated undamped FE model ('…….'(black)) FRFs.

Updating Parameters	Initial Value (in N-m/radian)	Updated Value (in N-m/radian)
Kt1	3.3E+06	2.9129e+005
Kt2	3.3E+06	2.9956e+005
Kt3	3.3E+06	3.1126e+005

Table 3: Values of the updating parameters for Stage-I updating of F-structure.

The frequency points chosen during updating were restricted to the left side of the vertical line shown in Figure 24 indicating an updating frequency range of 0-680 Hz. These figures also show comparison of FRFs outside the updating frequency range (i.e. over a range of 680-1000 Hz). The updated undamped FE model is found to predict FRF accurately even in this range from where no frequency points were used in updating indicating that the corrections suggested are not only able to give an improved FRF prediction but also are physically meaningful.

Mode Number	Measured Natural Frequency (Hz)	Initial FE model Natural Frequency (Hz)	Initial Percentage Error (%)	Updated FE model Natural Frequency (Hz)	Percentage Error after updating (%)
1	34.35	41.5	17.2	34.10	-0.73
2	103.78	120.7	14.0	101.52	-2.22
3	133.56	177.2	24.6	134.72	0.86
4	316.88	370.2	14.4	312.92	-1.26
5	979.48	1013.4	3.34	977.67	-0.18

Table 4: Correlation of measured and FE model natural frequencies for F-structure.

A comparison of the measured and the updated model natural frequencies is given in Table 4. With stage-I updating, the error in natural frequencies has been reduced substantially in all the modes.

6.3 Stage-II updating

At the end of stage-I, now we have updated undamped FE model, in the form of updated mass and stiffness matrix, and complex FRFs corresponding to the experimental structure. At this stage, a comparison of updated undamped FE model FRF $\alpha_{64\times64}$ and the corresponding measured FRF is shown in Figure 25. The comparison indicates that the FRFs match very well in terms of frequency of the resonance peaks and antiresonances, indicating that the updated mass and stiffness matrix represent the 'undamped' behavior of the experimental F structure accurately. It is however noted that, there is a significant difference in the FRF magnitude between the FE model and the experimental FRF at and around resonances and antiresonances. This difference in the two FRFs is due to the damping model that is missing from the undamped FE model and this difference would form the basis for identifying a structural damping matrix via updating in stage-II.

Choice of updating parameters: The damping in the structural members and the joints is the source of energy dissipation in the F shape structure. To capture the influence of these sources, the complete structure with 48 finite elements is divided into 7 groups. These groups are shown diagrammatically in Figure 26 and the details of the finite elements in each group

are given in Table 5. Damping in groups 1, 3, 7 and 5 represent structural damping in beam members, while damping in groups 2, 4 and 6 represent equivalent structural damping in the zones containing joints. In this way there are seven updating parameters, which are nothing but the correction factors to the coefficients of the damping matrix of each group (represented by variables β_q in equation (19)).

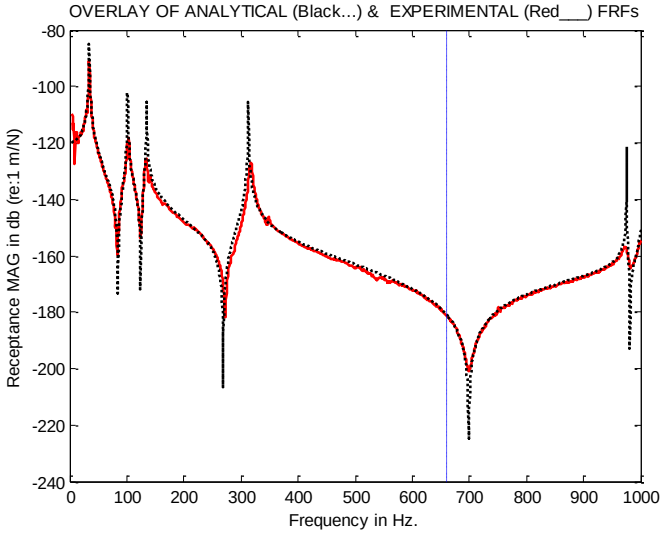


Figure 25: Overlay of FRF $\alpha_{64\times64}$ after stage-I updating: experimental complex ('——' (red)) and updated undamped FE model ('…….'(black)) FRFs.

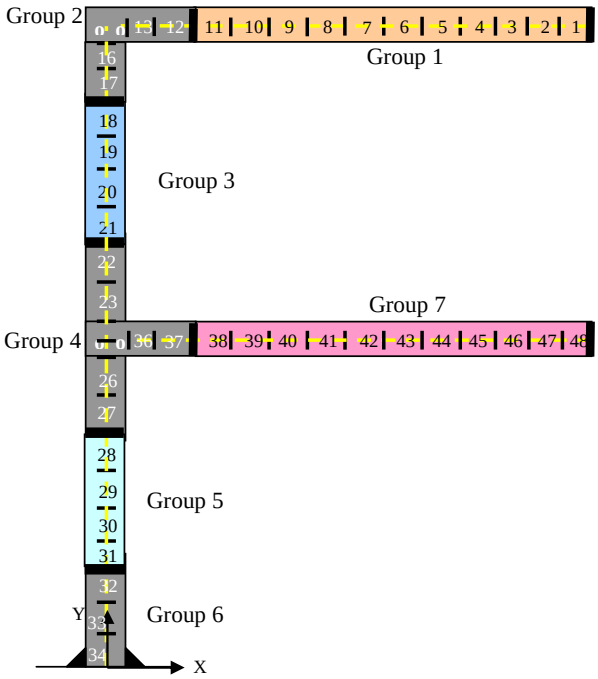


Figure 26: Groups of finite elements for choosing updating parameters for stage-II.

Results of stage-II updating: Damping matrix identification is performed using the algorithm explained in 'stage-II updating theory' in 'Two-stage updating method section'. It is noted that normal FRFs need to be estimated only once as has been done in above section. However, the unmeasured complex FRFs need to be computed at each iteration using the updated mass and stiffness matrix and the knowledge of damping matrix in the current iteration.

Group no.	Finite Elements in the group
1	1, 2, 3, 4, 5, 6, 7, 8, 9, 10, 11
2	12, 13, 14, 15, 16, 17
3	18, 19, 20, 21
4	22, 23, 24, 25, 26, 27, 35, 36, 37
5	28, 29, 30, 31
6	32, 33, 34
7	38, 39, 40, 41, 42, 43, 44, 45, 46, 47, 48

Table 5: Groups of finite elements for Stage-II updating for F-structure.

Updating Parameters	Initial Value	Group number	Updated Value
β_q	0.0001	Group1	0.0102
		Group 2	0.0169
		Group 3	0.0121
		Group 4	0.0174
		Group 5	0.0123
		Group 6	0.0135
		Group 7	0.009

Table 6: Values of the updating parameters for Stage-II updating for F-structure.

The initial damping matrix before updating is taken as proportional to the stiffness matrix with constant of proportionality being 0.0001. A total of 10 frequency points chosen in the updating frequency range (0-680 Hz) were used in updating. Table 6 shows the values of coefficients of the damping matrix of the seven groups, while Figure 27 shows a bar chart of the percentage change in the coefficients. The identified correction factors for groups 1,3,7 and 5, representing structural beam members, are not very much different, while the identified correction factors for groups 2, 4 and 6, representing zones of joints, are higher, suggesting a higher level of damping in the joints. Overlay of the $\alpha_{64\times64}$ updated FE model and the corresponding measured complex FRFs, after stage-II updating is shown in Figure 28. The updated FE model FRF is seen to have a very good match with the corresponding experimental FRF both inside as well as the outside the updating frequency range.

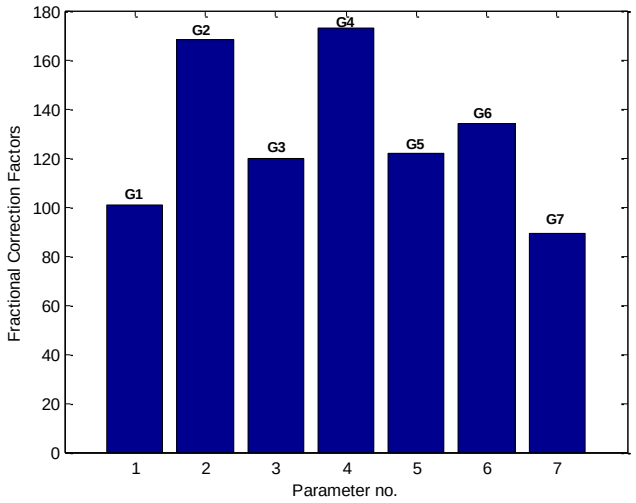


Figure 27. Correction factors to the elemental matrices: Change in updating parameters- stage II

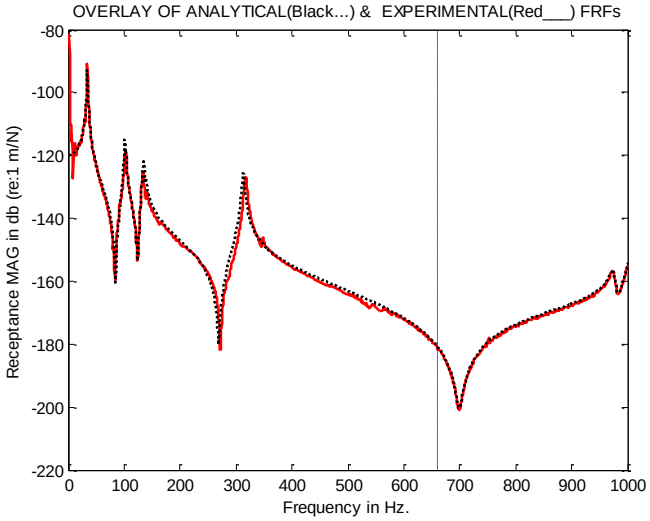


Figure 28. Overlay of FRF $\alpha_{64\times64}$ after stage-II updating: experimental complex ('——' (red)) and updated FE model ('…….'(black)) FRFs

7 CONCLUSIONS

This paper presents numerical and experimental investigations into FE model updating through a two-stage approach. The two-stage procedure investigated has the unique characteristic that the first stage updating is carried out using an estimate of experimental 'undamped' FRFs, referred as normal FRFs, instead of the complex measured FRFs used by other existing methods. This theoretically eliminates any possibility of effect of contribution of damping in the measured complex FRFs on mass and stiffness matrix updating and hence results into their more accurate updating. In the second stage, updating of damping matrix is driven by difference of measured complex FRFs and an estimate of experimental 'undamped' FRFs.

Since this difference solely represents contribution of damping to the measured FRFs, the updating carried out in stage-II is theoretically insulated from stiffness and mass matrix updating in stage-I.

The two-stage procedure is first investigated on a simulated beam structure. Through this study it is found that if complete 'measured' data is available then stage-II updating involving damping matrix updating is completely insulated from the stage-I updating. However, this is found not to be completely true if the 'measured' data is incomplete. Two methods are suggested to deal with incompleteness in the context of two-stage updating procedure. The first is based on using the current analytical model to compute substitutions for 'unmeasured' FRFs. The second method suggested makes use of 'hybrid' data that is a combination of using experimentally identified natural frequencies and damping factors and analytically obtained mode shapes to regenerate unmeasured FRFs. It is found that the hybrid data based method to deal with incompleteness results into a more accurate updated model and helps partially restore the insulation of stage-II from stage-I updating.

Simulated study incorporating 'measurement' noise and data incompleteness shows that the two-stage procedure is able to yield a close match between the FE and 'measured' FRFs, though the updated parameters are found to have small deviations from their exact value. The data incompleteness necessiates the use of updated mass and stiffness matrix in stage-II updating for computation of unmeasured FRFs. This causes linking of stage-II to stage-I updating that otherwise was insulated from stage-I in the case of complete data. It is however concluded that if mass and stiffness matrix are updated accurately in stage-I then stage-II updating also leads to a more accurate identification of damping matrix.

The two-stage procedure is then investigated on an experimental F shape structure. This structure being assembled from beam members through joints makes it challengeable for stiffness and damping matrix modeling. For the experimental structure the normal FRFs could be estimated well using only the translational FRFs. Stage-I updating is found to yield an accurate stiffness and mass matrix that predicted accurately the FRFs of hypothetical 'undamped' experimental structure. Stage-II updating also yielded an accurate equivalent model of structural damping matrix appropriately capturing the distribution of damping in the structural beam members and the joints.

The numerical and experimental investigations into a two-stage updating approach thus indicate that the updating of mass and stiffness matrix followed by updating of damping matrix is a theoretically consistent, numerically superior and robust approach to mass. stiffness and damping matrix updating. The results of the investigations carried out in this paper would be helpful in proper implementation and application of two-stage updating method in practice.

Nomenclature

M_A	Analytical mass matrix	$x(\omega)$	Displacement vector
M_X	Experimental mass matrix	$f(\omega)$	Force vector
K_A	Analytical Stiffness matrix	α^N	Normal frequency response functions
K_X	Experimental Stiffness matrix	α^C	Complex frequency response functions
		α_R^C	Real part of complex FRFs
D	Structural damping matrix	α_I^C	Imaginary part of complex FRFs
DSM	Dynamic stiffness matrix	Z^C	Complex DSM
Z_A	Analytical DSM	Z^N	Normal DSM
Z_X	Experimental DSM	ΔZ^C	Change in Complex DSM

S	Sensitivity matrix	RFM:	Response function method
U	Fractional correction factors to the updating parameters	NRFM	Normal Response Function Method
p	Vector of physical parameters to be updated	nu:	Number of updating parameters
DOFs	Degrees of freedom	ΔZ^N	Change in Normal DSM
TDOF	Translational Degree of freedom	$\overline{Z}$	DSM portion corresponding to damping
RDOF	Rotational Degree of freedom	$\Delta\overline{Z}$	Change in damping DSM portion
FRFs	Frequency Response functions	u, β	Vectors of physical parameters to be updated for stage-I and II respectively

REFERENCES

[1] M. Imregun, W. J. Visser, A review of model updating techniques. *The Shock and Vibration Digest*, **23**, 141–162, 1991.

[2] J. E. Mottershead, M. I. Friswell, Model updating in structural dynamics: a survey. *Journal of Sound and Vibration*, **167**, 347–375, 1993.

[3] M. I. Friswell, J. E. Mottershead, *Finite Element Model Updating in Structural Dynamics*. Kluwer Academic Publishers, Dordrecht, 1995.

[4] J.E. Mottershead and B.N. Datta Special issue on 'Inverse Problems in MSSP'. *Mechanical Systems and Signal Processing*, **23(6)**, 1731-1733, 2009.

[5] R.M. Lin, D.J. Ewins, Model updating using FRF data. *Proceedings of 15th International modal analysis seminar*, K.U.Leuven, Belgium, 141-163, 1990.

[6] R.M. Lin, M.K. Lim, H. Du, A New Complex inverse eigensensitivity method for structural damping model identification. *Computers and Structures*, **52 (5)**, 905-915, 1994.

[7] S.R. Ibrahim, W. D'ambrogio, P. Salvini, A. Sestieri, Direct Updating of Nonconservative Finite Element Models using Measured Input-Output. *Proceedings of the X*, IMAC, 202-210, 1992.

[8] R.M. Lin, D.J. Ewins, Analytical model improvement using frequency response functions. *Mechanical Systems and Signal Processing*, **8(4)**, 437–458, 1994.

[9] M. Imregun, W.J. Visser, D.J. Ewins, Finite element model updating using Frequency response function data–I: theory and initial investigation. *Mechanical Systems and Signal Processing*, **9(2)**, 187–202, 1995.

[10] M.I. Friswell, D.J. Inman, D.F. Pilkey, Direct updating of damping and stiffness matrices. *AIAA Journal*, **36 (3)**, 491-493, 1998.

[11] Y. Kuo, W. Lin, S. Xu, New Methods for Finite Element Model Updating Problems. *AIAA Journal*, **44(6)**, 1310-1316, 2006.

[12] A. Esfandiari, F. Bakhtiari-Nejad, M. Sanayei, A. Rahai, Structural finite element model updating using transfer function data. *Computers and Structures*, **88(1-2)**, 54-64, 2010.

[13] R.M. Lin, J. Zhu, Model updating of damped structures using FRF data. *Mechanical Systems and Signal Processing*, **20**, 2200-2218, 2006.

[14] S. J. Hu, , H. Li, , S. Wang, Cross-Model Cross-Mode Method for Model Updating, *Mechanical Systems and Signal Processing*, **21(4)**, 1690-1703, 2007.

[15] E. Khanmirza, N. Khaji, V. Johari Majd, Model updating of multistory shear buildings for simultaneous identification of mass, stiffness and damping matrices using two different soft-computing methods. *Expert Systems with Applications*, **38(5)**, 5320-5329, 2011.

[16] E. M. Hernandez, D. Bernal, Iterative finite element model updating in the time domain. *Mechanical Systems and Signal Processing*, **34(1–2)**, 39-46, 2013.

[17] S.Y. Chen, M.S. Ju, Y.G. Tsuei, Estimation of mass stiffness and damping matrices from frequency response function. *ASME Journal of Vibration and Acoustics*, **118**, 78-82, 1996.

[18] G.W. Brown, C. Farahat, F.M. Hemez, Extending sensitivity to lightly damped structures. *AIAA Journal*, **35 (8)**, 1369-1377, 1997.

[19] C. Reix, Tombini, A. Gerard, J. Strobbe, E. Dascotte, Updating the Damping Matrix using Frequency Response Data. *Proceedings of the XIV*, IMAC, Dearborn, Michigan, 585-590, 1996.

[20] Y. Halevi, R. Kenigsbuch, Model updating of the complex modeshapes and the damping matrix. *Inverse Problems in Engineering*, **8**, 143-162, 2000.

[21] Y. Lu, Zhenguo Tu , A two-level neural network approach for dynamic FE model updating including damping. *Journal of Sound and Vibration*, **275**, 931-952, 2004.

[22] B.N. Datta, S.V. Deng, O. Sokolov, D.R. Sarkissian, An optimization technique for damped model updating with measured data satisfying quadratic orthogonality constraint. *Mechanical Systems and Signal Processing*, **23 (4)**, 1759-1772, 2009.

[23] S. Pradhan, S.V.Modak, Normal response function method for mass and stiffness matrix updating using complex FRFs. *Mechanical Systems and Signal Processing*, **32**, 232–250, 2012.

[24] S. Pradhan, S.V.Modak, A method for damping matrix identification using frequency response data. *Mechanical Systems and Signal Processing*, **33**, 69–82, 2012.

International Conference on Engineering Vibration
Ljubljana, Slovenia, 7-10 September 2015

NON-LINEAR DYNAMIC ANALYSIS OF PLANE FRAME STRUCTURES UNDER SEISMIC LOAD IN FREQUENCY DOMAIN

Luis F. Paullo Muñoz*[1], Paulo B. Gonçalves[1], Ricardo A.M. Silveira[2], Andréa Silva[2]

[1]Civil Engineering Department of Pontifical Catholic University of Rio de Janeiro
lfernand@tecgraf.puc-rio.br, paulo@puc-rio.br

[2]Civil Engineering Department of Federal University of Ouro Preto
ramsilveira@yahoo.com.br, andreadiassilva@yahoo.com.br

Keywords: Nonlinear Dynamic Analysis, Analysis in Frequency Domain, Dynamic instability.

Abstract. *The dynamic response of large structures in the main resonance regions is a topic of great importance in the analysis of structures under time varying loads. In complex problems, the determination of the response in the frequency domain, characterized by the resonance curves is, in some cases, indirectly obtained through a series of analyses in time domain, which leads to huge computational effort when analyzing structures with a large number of degrees of freedom. In nonlinear cases, the response in the frequency domain becomes even more cumbersome because of the possibility of multiple solutions for certain forcing frequencies. Those solutions can be stable and unstable, and bifurcations can appear, in particular saddle-node bifurcation at the turning points along the resonance curves. In this work, an incremental technique for direct calculation of the nonlinear dynamic response in frequency domain of nonlinear plane frames discretized by the finite element method and subjected to base excitation is proposed. The transformation of discretized equations of motion, in the finite element method context, to the frequency domain is made here through the classical harmonic balance method in conjunction with the Galerkin method. The resulting system of nonlinear equations in terms of the modal amplitudes and forcing frequency is solved by the Newton-Raphson method together with an arc-length procedure to obtain the nonlinear resonance curves. Suitable examples are presented, and the influence of the frame geometric parameters and base motion on the nonlinear resonance curves is investigated.*

1 INTRODUCTION

The dynamic response of large structures in the main resonance regions is an important topic in the analysis of structures under time varying loads. In complex problems, the determination of the response in the frequency domain, characterized by the resonance curves is, in some cases, indirectly obtained through a series of analyses in time domain, as in Galvão [1] and Silva [2], which leads to huge computational effort when analysing structures with a large number of degrees of freedom. In nonlinear cases, the response in the frequency domain becomes even more cumbersome because of the possibility of multiple solutions for certain forcing frequencies. Those solutions can be stable and unstable, and bifurcations can appear, in particular saddle-node bifurcation at the turning points along the resonance curves.

In structures subjected to seismic loads (earthquakes), there is a great interest to know the response of structure in frequency domain, since the vulnerability of structure during an earthquake is related of the relations between the natural vibration frequencies of the structure and the frequency content in the seismic load.

In this work, an incremental technique for the direct calculation of the nonlinear dynamic response in frequency domain of nonlinear plane frames discretized by the finite element method and subjected to a base excitation is proposed. The transformation of discretized equations of motion, in the finite element method context, to the frequency domain is accomplished here through the classical harmonic balance method (HBM), following the formulation presented in Pasquetti [3] for the linear case. For the non-linear analysis, a particular adaptation of the HBM-Galerkin methodology presented by Cheung and Chen [4] and generalized for the use in FEM context by Chen et al [5] is here proposed. The resulting system of nonlinear equations in terms of the modal amplitudes and forcing frequency is solved by the Newton-Raphson method together with an arc-length procedure to obtain the nonlinear resonance curves. Suitable examples are presented, and the influence of the frame geometric parameters and base motion on the nonlinear resonance curves is investigated.

2 FORMULATION

2.1 Equilibrium equations and resonance curves by time domain analysis

One classic way to determinate the resonance curves or bifurcation diagram of a structure is through a time domain analysis, such as the brute force method (Parker et al. [6]). For this, it is supposed that the structure is under the action of a harmonic load with a prescribed forcing frequency ω. The dynamic equilibrium is defined by:

$$\boldsymbol{M}.\ddot{\boldsymbol{u}}(t) + \boldsymbol{C}.\dot{\boldsymbol{u}}(t) + \boldsymbol{Fi}(\boldsymbol{u}(t)) = F.\cos(\omega t).\boldsymbol{f} \tag{1}$$

where $\boldsymbol{M}$, $\boldsymbol{C}$ and $\boldsymbol{Fi}$ are the mass matrix, damping matrix and the internal forces vector, respectively, being $\boldsymbol{Fi}$ dependent on the nodal displacement vector $\boldsymbol{u}(t)$, and on the geometric non-linear formulation (Silveira [7] and Tokami et al. [8]) , $\boldsymbol{f}$ is the nodal external reference load vector, and F and ω are the amplitude and frequency of the harmonic excitation, respectively.

To obtain the resonance curves, it is necessary to make multiples time domain analyses by direct integration of the equations of motion and increasing step by step the excitation frequency (Parker et al. [6]). The analysis must be long enough to achieve the steady state response, as shown in Fig. 1. The resonance curve is obtained by mapping the maximum displacements in the steady state stage for each frequency value.

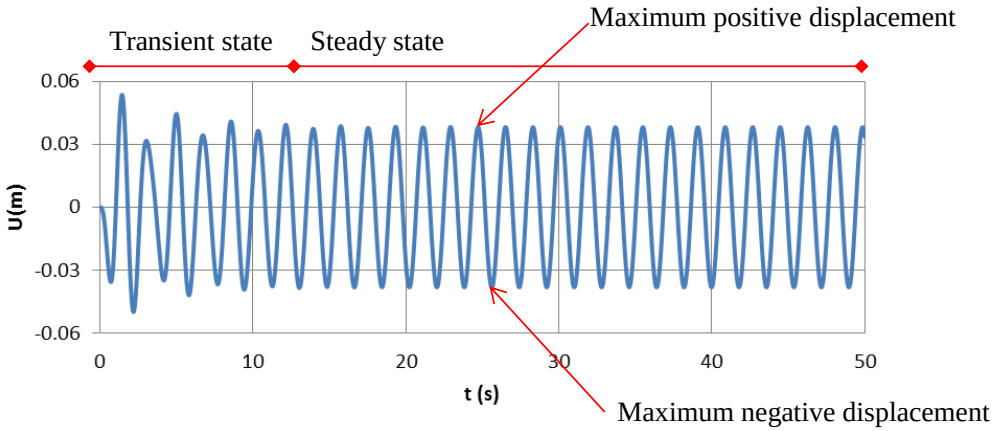


Figure 1. Transient and steady state response in time domain of a system under harmonic excitation.

A disadvantage of this method, even in the linear case is that, after each frequency increase, it is necessary to integrate the equations of motion long enough to reach the steady state response, which depends directly on the damping of the system, the frequency step and on the non-linearity, leading to a huge computational effort for systems with a large number of degrees of freedom. Another disadvantage is the difficulty of mapping all fixed points in regions where coexisting stable and unstable solutions may occur (Parker et al. [6]).

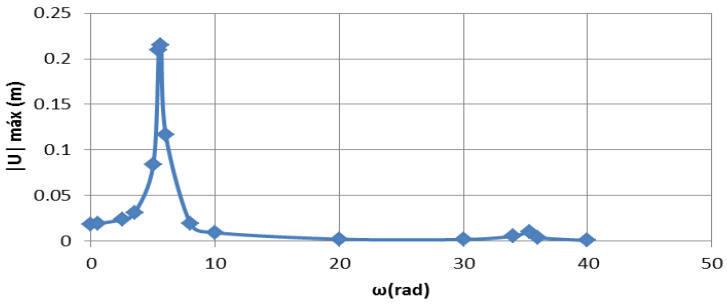


Figure 2. Resonance curve of a 2-DOFs obtained through time domain analysis (25 simulations).

2.2 Classic Balance Harmonic Method (HBM) for Linear Analysis

The HBM is one the most popular methods for the nonlinear analysis of dynamical systems. In this method, the displacement field is approximated by a finite Fourier series, that is:

$$\boldsymbol{u}(t) = \sum_{n=0}^{N}[\boldsymbol{A}_n cos(n\omega t) + \boldsymbol{B}_n sin(n\omega t)] \quad (2)$$

where $\boldsymbol{A}_n$ and $\boldsymbol{B}_n$ are the modal amplitude vectors corresponding to the n^{th} harmonic, and N is the number of terms considered in the approximation. For the linear damped case, it is only

necessary to retain the second term in (2). Thus, the nodal displacement vector can be approximated by:

$$\boldsymbol{u}(t) = \boldsymbol{A}_1 cos(\omega t) + \boldsymbol{B}_1 sin(\omega t) \tag{3}$$

Introducing Eq. (3) in Eq. (1) results in:

$$(\omega \boldsymbol{C}.\boldsymbol{A}_1 - \omega^2 \boldsymbol{M}.\boldsymbol{B}_1)cos(\omega t) - (\omega^2 \boldsymbol{M}.\boldsymbol{A}_1 + \omega \boldsymbol{C}.\boldsymbol{B}_1)sin(\omega t) = F.\boldsymbol{f}\cos(\omega t) \tag{4}$$

Taking $F.\boldsymbol{f} = \boldsymbol{F_0}$ and $\boldsymbol{F_i} = \boldsymbol{K}.\boldsymbol{u}(t)$, where $\boldsymbol{K}$ is the linear stiffness matrix, and applying the harmonic balance to equation Eq. (4) the following system is obtained:

$$\begin{bmatrix} \omega \boldsymbol{C} & -\omega^2 \boldsymbol{M} + \boldsymbol{K} \\ -\omega^2 \boldsymbol{M} + \boldsymbol{K} & -\omega \boldsymbol{C} \end{bmatrix} \begin{Bmatrix} \boldsymbol{A}_1 \\ \boldsymbol{B}_1 \end{Bmatrix} = \begin{Bmatrix} \boldsymbol{F_0} \\ \boldsymbol{0} \end{Bmatrix} \tag{5}$$

Eq. (5) can be expressed in a more compact form as:

$$\overline{\mathbf{K}}(\omega).\overline{\boldsymbol{A}} - \overline{\boldsymbol{F}} = \boldsymbol{0} \tag{6}$$

where

$$\overline{\mathbf{K}}(\omega) = \begin{bmatrix} \omega \boldsymbol{C} & -\omega^2 \boldsymbol{M} + \boldsymbol{K} \\ -\omega^2 \boldsymbol{M} + \boldsymbol{K} & -\omega \boldsymbol{C} \end{bmatrix}, \quad \overline{\boldsymbol{A}} = \begin{Bmatrix} \boldsymbol{A}_1 \\ \boldsymbol{B}_1 \end{Bmatrix}, \quad \overline{\boldsymbol{F}} = \begin{Bmatrix} \boldsymbol{F_0} \\ \boldsymbol{0} \end{Bmatrix} \tag{7}$$

The forcing frequency ω and the modal amplitude vector $\overline{\boldsymbol{A}}$ are the unknowns in Eq. (7). Even in the linear case, the transformation of Eq. (1) to the frequency domain leads to a non-linear system of algebraic equations, being necessary to use of the Newton-Raphson method to solve Eq. (7).

2.3 HBM-Galerkin for Non-Linear Analysis

For the non-linear analysis, the approach proposed by Cheung and Chen [4] and generalized for the use in a finite element formulation by Chen et al [5] is used. In this case, and considering that in steady state phase the response is periodic, it is convenient to use a periodic non-dimensional time variable defined as:

$$\tau = \omega t \tag{8}$$

Substituting Eq. (8) into Eq.(1), the equation of motion can be rewritten as:

$$\omega^2 \boldsymbol{M}.\ddot{\boldsymbol{u}}(\tau) + \omega \boldsymbol{C}.\dot{\boldsymbol{u}}(\tau) + \boldsymbol{Fi}(\boldsymbol{u}(\tau)) = \boldsymbol{F_0}\cos(\tau) \tag{9}$$

and each component of the displacement vector can be approximated by:

$$u_i(\tau) = \sum_{n=0}^{N}\left[a_{i,n}cos(\tau) + b_{i,n}sin(\tau)\right] \tag{10}$$

For systems with quadratic and cubic non-linearity, at least the first two terms of the Fourier series must be considered (Nayfeh and Mook [9]):

$$u_i(\tau) = a_{i,0} + b_{i,1}cos(\tau) + c_{i,1}sin(\tau) \tag{11}$$

For system with cubic nonlinearity it is necessary to consider at least the terms (Nayfeh and Mook [9]):

$$u_i(\tau) = a_{i,1}cos(\tau) + b_{i,1}sin(\tau) \tag{12}$$

Defining:

$$u_i = \boldsymbol{C}\overline{\boldsymbol{a}}_i \tag{13}$$

With

$$\boldsymbol{C}(\tau) = \langle 1, sen(\tau), \cos(\tau) \rangle, \ \overline{\boldsymbol{a}}_i = \langle a_{i,0}, b_{i,1}, c_{i,1} \rangle^{\boldsymbol{T}} \tag{14}$$

considering the following relation:

$$\boldsymbol{u}(\tau) = \boldsymbol{S}(\tau).\overline{\boldsymbol{A}} \tag{15}$$

where,

$$\boldsymbol{S}(\tau) = \begin{bmatrix} \boldsymbol{C}(\tau) & \boldsymbol{0} & \boldsymbol{0} & \boldsymbol{0} & \dots & \boldsymbol{0} \\ \boldsymbol{0} & \boldsymbol{C}(\tau) & \boldsymbol{0} & \boldsymbol{0} & \dots & \boldsymbol{0} \\ \boldsymbol{0} & \boldsymbol{0} & \boldsymbol{C}(\tau) & \boldsymbol{0} & \dots & \boldsymbol{0} \\ \boldsymbol{0} & \boldsymbol{0} & \boldsymbol{0} & \boldsymbol{C}(\tau) & \dots & \vdots \\ \vdots & \vdots & \vdots & \vdots & \ddots & \boldsymbol{0} \\ \boldsymbol{0} & \boldsymbol{0} & \boldsymbol{0} & \dots & \boldsymbol{0} & \boldsymbol{C}(\tau) \end{bmatrix}_{Nx3N}, \overline{\boldsymbol{A}} = \langle \overline{\boldsymbol{a}}_1, \overline{\boldsymbol{a}}_2, \dots, \overline{\boldsymbol{a}}_N \rangle_{1x3N}{}^{\boldsymbol{T}} \tag{16}$$

N = Total number of the degrees of freedom.

and introducing Eq. (15) into Eq. (9), the following matrix equation is obtained:

$$\omega^2 \boldsymbol{M}.\ddot{\boldsymbol{S}}(\tau)\overline{\boldsymbol{A}} + \omega \boldsymbol{C}.\dot{\boldsymbol{S}}(\tau)\boldsymbol{A} + \boldsymbol{Fi}(\boldsymbol{S}(\tau).\overline{\boldsymbol{A}}) = \boldsymbol{F_0}\cos(\tau) \tag{17}$$

Considering that the solution is periodic, multiplying both of sides of the equations Eq. (17) by $\boldsymbol{S}(\tau)^{\boldsymbol{T}}$ and integrating the resulting expression over a period, one obtains (Bouc [10]):

$$\int_0^{2\pi} \boldsymbol{S}(\tau)^{\boldsymbol{T}} \left[\omega^2 \boldsymbol{M}.\ddot{\boldsymbol{S}}(\tau)\overline{\boldsymbol{A}} + \omega \boldsymbol{C}.\dot{\boldsymbol{S}}(\tau)\boldsymbol{A} + \boldsymbol{Fi}(\boldsymbol{S}(\tau).\overline{\boldsymbol{A}})\right] d\tau = \int_0^{\boldsymbol{2\pi}} \boldsymbol{S}(\tau)^{\boldsymbol{T}} \boldsymbol{F_0}\cos(\tau) d\tau \tag{18}$$

In a compact form, Eq. (18) can be expressed as:

$$\omega^2 \overline{\boldsymbol{M}}.\overline{\boldsymbol{A}} + \omega \overline{\boldsymbol{C}}.\overline{\boldsymbol{A}} + \overline{\boldsymbol{Fi}}(\overline{\boldsymbol{A}}) = \overline{\boldsymbol{F}} \tag{19}$$

where:

$$\overline{\boldsymbol{M}} = \int_0^{2\pi} \boldsymbol{S}(\tau)^{\boldsymbol{T}}.\boldsymbol{M}.\ddot{\boldsymbol{S}}(\tau).d\tau, \qquad \overline{\boldsymbol{C}} = \int_0^{2\pi} \boldsymbol{S}(\tau)^{\boldsymbol{T}}.\boldsymbol{C}.\dot{\boldsymbol{S}}(\tau).d\tau$$

$$\overline{\boldsymbol{F}} = \int_0^{\boldsymbol{2\pi}} \boldsymbol{S}(\tau)^{\boldsymbol{T}} \boldsymbol{F_0}\cos(\tau) d\tau, \quad \overline{\boldsymbol{Fi}}(\overline{\boldsymbol{A}}) = \int_0^{2\pi} \boldsymbol{S}(\tau)^{\boldsymbol{T}} \boldsymbol{Fi}(\boldsymbol{S}(\tau).\overline{\boldsymbol{A}}) d\tau \tag{20}$$

Equation Eq. (19) is a non-linear system of algebraic equations in which the unknowns are the frequency ω and the modal amplitude vector $\overline{\boldsymbol{A}}$. The internal force vector in frequency domain $\overline{\boldsymbol{Fi}}(\overline{\boldsymbol{A}})$ is obtained from the transformation of $\boldsymbol{Fi}(\boldsymbol{u}(\tau))$. In this context, it is necessary an explicit expression for $\boldsymbol{Fi}(\boldsymbol{u}(\tau))$. The next step is the solution of the non-linear system of equation.

2.4 Solution of Non-linear System of Equations

The transformation of the equations of motion from time to frequency domain results in a non-linear system of algebraic equation both for the linear and non-linear cases, as shown by Eq. (6) and Eq. (19), being the unknown variables the forcing frequency and the modal amplitudes. In this section, the technique to solve the non-linear system of equation is described, considering the possibility of frequency and amplitude limit points. In this context, the equation Eq. (6) can be defined in general form as:

$$\boldsymbol{R}(\omega, \overline{\boldsymbol{A}}) = \boldsymbol{0} \tag{21}$$

Through an incremental analysis the dynamic equilibrium in the i^{th} step is given by:

$$\boldsymbol{R}(\omega_i, \overline{\boldsymbol{A}}_i) = \boldsymbol{0} \tag{22}$$

The unknown variables in the i^{th} step are obtained by the incremental analysis as:

$$\omega_i = \omega_{i-1} + \Delta\omega_i, \; \overline{\boldsymbol{A}}_i = \overline{\boldsymbol{A}}_{i-1} + \Delta\overline{\boldsymbol{A}}_i \tag{23}$$

Introducing Eq. (22) into Eq. (21) results in:

$$\boldsymbol{R}(\omega_{i-1} + \Delta\omega_i, \overline{\boldsymbol{A}}_{i-1} + \Delta\overline{\boldsymbol{A}}_i) = \boldsymbol{0} \tag{24}$$

The frequency and amplitude increments $\Delta\omega_i$ and $\Delta\overline{\boldsymbol{A}}_i$ can be calculated iteratively as:

$$\Delta{\omega_i}^k = \Delta{\omega_i}^{k-1} + \delta{\omega_i}^k, \; \Delta{\overline{\boldsymbol{A}}_i}^k = \Delta{\overline{\boldsymbol{A}}_i}^{k-1} + \delta{\overline{\boldsymbol{A}}_i}^k \tag{25}$$

where $\delta{\omega_i}^k$ and $\delta{\overline{\boldsymbol{A}}_i}^k$ are the correctors which can be obtained through the first variation of Eq. (24) as:

$$\delta\boldsymbol{R}^k = \frac{\partial \boldsymbol{R}^{k-1}}{\partial \overline{\boldsymbol{A}}_i}.\delta{\overline{\boldsymbol{A}}_i}^k + \frac{\partial \boldsymbol{R}^{k-1}}{\partial \omega_i}\delta{\omega_i}^k \tag{26}$$

or, in a more compact form, as:

$$\overline{\boldsymbol{Km}}^{k-1}.\delta{\overline{\boldsymbol{A}}_i}^k + \delta{\omega_i}^k\overline{\boldsymbol{f}}^{k-1} = \delta\boldsymbol{R}^k \tag{27}$$

It is necessary the addition of a constrain equation to solve Eq. (17). In this work, a spherical arc-length control method (Crisfield [11]; Ramm [12]) is used to solve the non-linear system defined by Eq. (27). More details about the adaptation of arc-length control methods to solve dynamic problems in frequency domain can be found in Ferreira and Serpa [13] and in Pasquetti [3]. In this work a particular adaptation of the spherical arc-length method is used. In this case the spherical arc-length constrain equation is given by:

$$\Delta{\overline{\boldsymbol{A}}_i}^T.\Delta\overline{\boldsymbol{A}}_i + \left(\Delta{\omega_i}^k\right)^2\overline{\boldsymbol{f}}^{k-1^T}.\overline{\boldsymbol{f}}^{k-1} - \Delta{l_i}^2 = 0 \tag{28}$$

From equations Eq. (24), Eq. (25), Eq. (27) and Eq. (28), it is possible to obtain the iterative frequency corrector as:

$$\delta{\omega_i}^k = \begin{cases} \pm\dfrac{\Delta{l_i}^2}{\sqrt{\boldsymbol{v}^T.\boldsymbol{v} + \overline{\boldsymbol{f}}^{k-1^T}.\overline{\boldsymbol{f}}^{k-1}}} & for\ k = 1 \\ -\dfrac{\boldsymbol{r}^{k^T}.\boldsymbol{v}^k}{\boldsymbol{v}^{k^T}.\boldsymbol{v}^k} & for\ k > 1 \end{cases} \tag{29}$$

where

$$\boldsymbol{v}^k = (\overline{\boldsymbol{Km}}^{k-1})^{-1}.\overline{\boldsymbol{f}}^{k-1}, \; \boldsymbol{r}^k = (\overline{\boldsymbol{Km}}^{k-1})^{-1}.\boldsymbol{R}^{k-1} \tag{30}$$

The signal of the first frequency corrector, also called frequency predictor, can be obtained using the positive work criterion as:

$$sign\left(\delta{\omega_i}^1\right) = sign\left((\boldsymbol{v}^k)^T.\overline{\boldsymbol{f}}^{k-1}\right) \tag{31}$$

For linear systems, it can be defined by the following expressions:

$$\overline{\boldsymbol{Km}} = \begin{bmatrix} \omega\boldsymbol{C} & -\omega^2\boldsymbol{M} + \boldsymbol{K} \\ -\omega^2\boldsymbol{M} + \boldsymbol{K} & -\omega\boldsymbol{C} \end{bmatrix}, \; \overline{\boldsymbol{f}} = \begin{bmatrix} \boldsymbol{C} & -2\omega\boldsymbol{M} \\ -2\omega\boldsymbol{M} & -\boldsymbol{C} \end{bmatrix}.\overline{\boldsymbol{A}} \tag{32}$$

Analogously, for the non-linear case, it can be obtained from the following relations:

$$\overline{\boldsymbol{Km}} = \omega^2\overline{\boldsymbol{M}}.+\omega\overline{\boldsymbol{C}} + \frac{\partial\overline{\boldsymbol{Fi}}(\overline{\boldsymbol{A}})}{\partial\overline{\boldsymbol{A}}}, \;\; \overline{\boldsymbol{f}} = (2\omega\overline{\boldsymbol{M}} + \overline{\boldsymbol{C}}).\overline{\boldsymbol{A}} \tag{33}$$

3 NUMERICAL EXAMPLES

As first example, a simple tower model with a concentrated mass at the top and an elastic rotational support at the base is studied to validate de linear formulation. The finite element model is composed by 10 beam-column Euler-Bernoulli elements. The geometrical and material properties are shown in Figure 3. The tower is under the action of horizontal harmonic base-displacement (Paullo et al. [14]).

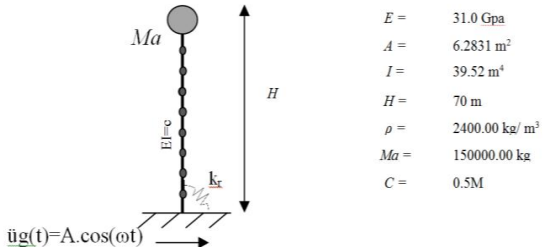


Figure 3: Tower model with concentrate mass at top and elasto-plastic support.

Figure 7 shows the resonance curves of the displacement at top of the tower, considering two values of the elastic support stiffness. The results obtained with the present formulation agree with the results obtained from a time domain analysis. This shows the coherence of the result obtained with the proposed method. It can be also observed that the present method is able to obtain the resonance curve with more accuracy in the vicinity of first resonant frequency.

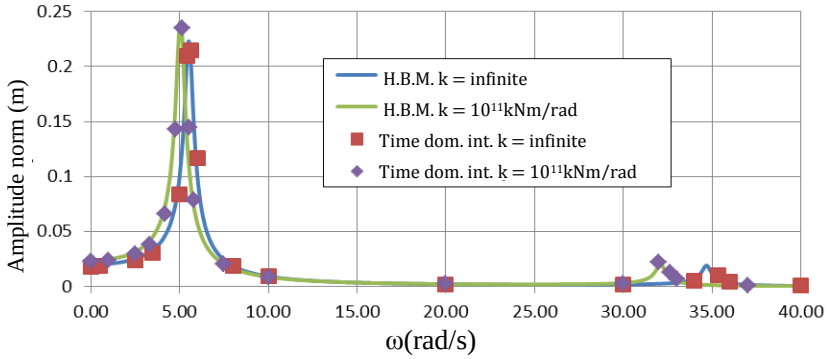


Figure 4: Maximum amplitude norm at top vs. frequency. A=0.8g.

As second example, a simple mass with a non-linear elastic spring under harmonic load is studied to validate the non-linear formulation. The schematic representation of the system and relevant properties are show in Figure 5. For this example, damping is not considered.

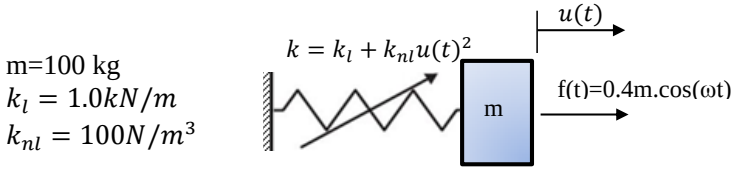


Figure 5: 1-DOFs model with cubic non-linear stiffness under harmonic excitation.

Figure 6 shows frequency-amplitude relation obtained through HBM-Galerkin and time domain simulations. The results obtained with the present HBM-Galerkin scheme and with time domain simulations are very close, validating the non-linear formulation. The effect of positive cubic non-linearity on the response is clear; the resonance curve exhibits a strong hardening behavior with three coexisting solutions in a large frequency range. It can be also observed that the algorithm is able to bypass the limit point associated with a saddle-node bifurcation.

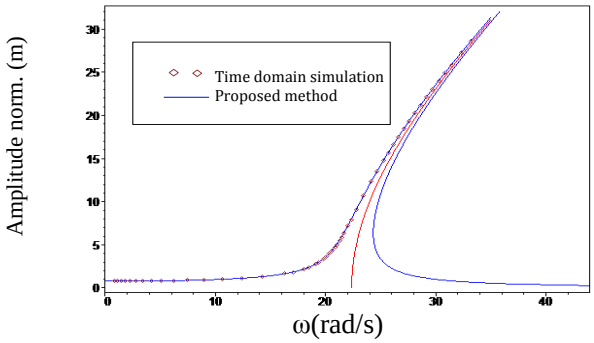


Figure 6: Maximum amplitude vs. frequency

As a last example, a frame with a pitched-roof fixed at the base and with a constant cross section is studied to assess the behavior of this structure under horizontal and vertical base excitation. The vertical vibration is directly proportional to the horizontal vibration, following the criteria of some seismic code, such as Peruvian seismic-code RNE-E030 [15]. In this work it is considered that the intensity of the vertical base motion is 0.67 times the intensity of the horizontal base motion. The geometry and material properties of frame are shown in Figure 7, as well as the configuration of the first four natural vibration modes, being the first and third antisymmetric and the second and fourth symmetric . It is also studied the influence of the roof height on the response. The structure is modeled with twenty bean-column elements; 8 elements of the same size elements for the columns and 12 elements for the roof.

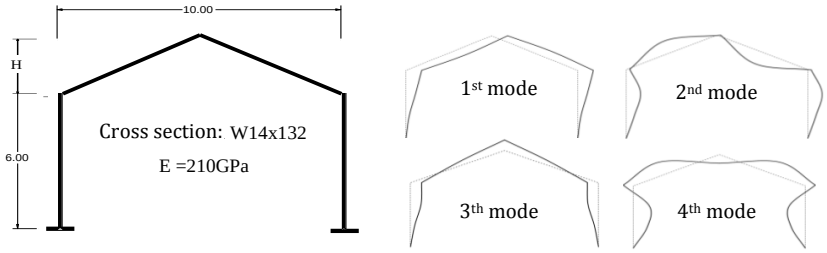


Figure 7 – Pitched-roof frame model and four first natural mode of vibration.

H (m)	Natural frequency of vibration (rad/s)			
	1st Mode	2nd Mode	3th Mode	4th Mode
0.0	25.57	57.23	152.20	186.91
3.0	22.60	54.81	126.16	184.20
6.0	18.00	42.31	94.18	105.35

Table 1: Four first natural frequency of pitched-roof frame

Table 1 shows the first four natural frequencies for the three values of H considered in the analysis. Figure 8 shows the variation of the horizontal (A_x) and vertical displacements (A_y) at the top of frame, considering both a linear (blue) and non-linear (red) formulation. All vibration modes are excited. The influence of geometric non-linearity is evident in the two first resonance regions, where a hardening behavior leading to possible dynamic jumps is observed. As the roof height increases, the magnitude of A_x corresponding to the first resonant peak increases, while the magnitude of second peak decreases. On the other hand, the magnitude of vertical displacement A_y is reduced in the two first resonance regions with the increase of the roof height. It is important to point out that the non-linear resonance curves exhibit amplitude and frequency limit points, which can only be mapped by the use of continuation techniques.

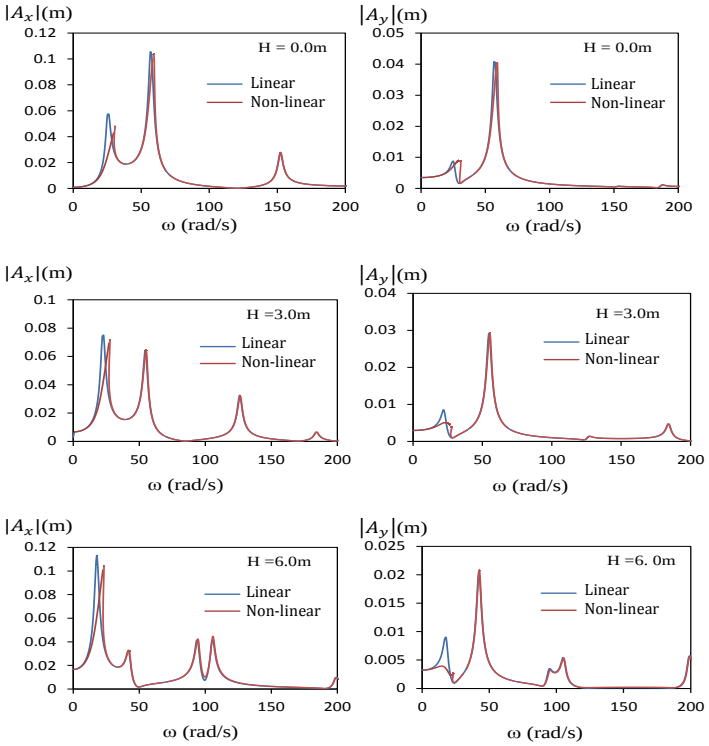


Figure 8: Horizontal and vertical amplitude norm vs. frequency. Agx = 0.8g, Agy = 0.667Agx.

4 CONCLUSIONS

In this work, an incremental technique for the direct calculation of the nonlinear resonance curves of plane frames discretized by the finite element method and subjected to a base excitation is proposed. The transformation of discretized equations of motion, in the finite element method context, to the frequency domain is accomplished here through the classical harmonic balance method together with the Galerkin method. The resulting system of nonlinear equations in terms of the modal amplitudes and forcing frequency is solved by the Newton-Raphson method together with an arc-length procedure to obtain the nonlinear resonance curves. The formulation of the proposed method is validated comparing the present results with time domain simulations showing coherence and precision. The algorithm is able to map regions with coexisting stable and unstable solutions. A pitched-roof frame under horizontal

and vertical base excitation is studied. The results show a nonlinear hardening behavior with more influence in the two first resonance regions. The roof height has a strong influence on the resonant peaks. The proposed method is shown to be a useful method for the analysis of slender frame structures in frequency domain, since it is able to obtain the resonance curves with precision and small computational effort.

REFERENCES

[1] A. S. Galvão, *Instabilidade Estática e Dinâmica de Pórticos Planos com Ligações Semi-rígidas.* DSc. thesis, Civil Engineering Department-PUC-Rio/Rio de Janeiro, Brazil, 2004.

[2] A.R.D. Silva, *Sistema Computacional para Análise Avançada Estática e Dinâmica de Estruturas Metálicas*. DSc thesis, Departamento de Engenharia Civil Escola de Minas UFOP/Ouro Preto, Brazil, 2009.

[3] E. Pasquetti, *Métodos aproximados de Solução de Sistemas Dinâmicos Não-Lineares*. DSc thesis, Civil Engineering Department-PUC-Rio/Rio de Janeiro. Brazil, 2008.

[4] Y.K. Cheun and S.H. Chen, Application of the incremental harmonic balance method to cubic non-linearity systems. *Journal of Sound and Vibration*, **140** (2), 273–286, 1990.

[5] S.H. Chen, Y.K. Cheun and H.X. Xing, Nonlinear vibration of plane structures by finite element and incremental harmonic balance method. *Nonlinear Dynamics*, **26**, 87-104 , 2001.

[6] T. S. Parker and L.O. Chua, *Practical numerical algorithms for chaotic systems*. New York: Springer, 1989.

[7] R.A.M. Silveira, *Análise de Elementos Estruturais Esbeltos com Restrições Unilaterais de Contato*. Dsc thesis, Civil Engineering Department-PUC-Rio/Rio de Janeiro. Brazil, 1995.

[8] M.A.M. Torkamani, M. Sonmez and J.E. Cao, Second-order elastic plane-frame analysis using finite-element method. *Journal of Structural Engineering*, **12 (**9), 1225-1235, 1997.

[9] A. H. Nayfeh and D.T. Mook, *Nonlinear oscillations*. John Wiley & Sons, 2008.

[10] R. Bouc, Sur la méthode de Galerkin-Urabe pour les systèmes différentiels périodiques. *International Journal of Non-Linear Mechanics*, **7** (2), 175-188, 1972.

[11] M.A. Crisfield, A fast incremental/iterative solution procedure that handles snapthrough. *Computers & Structures*, **13**, 52-62, 1981.

[12] E. Ramm, Strategies for Tracing the Non-Linear Response Near Limit-Points. W. Wunderlich, Springer-Verlag eds. *Nonlinear Finite Element Analysis in Structural Mechanics*, Berlin, Germany, 63-89, 1981.

[13] J.V. Ferreira and A.L. Serpa, Aplication of the arc-length method in nonlinear frequency response. *Jornal of Sound and Vibration*, **284**, 133-149, 2005.

[14] L.F. Paullo, P.B. Gonçalves, R.A.M. Silveira and A.R.D. Silva, Nonlinear Dynamic Analysis of Frame Structures under Seismic Excitation Considering Soil-Structure Interaction and Elasto-Plastic Soil Behavior. Z. Dimitrovová et al. eds. *11th International Conference on Vibration* Problems, Lisbon, Portugal, 2013.

[15] V.C. Ministério, RNE E030: Norma de diseño sirmorresistente. *Reglamento Nacional De construcciones*. Lima, Perú, 2007.

11th International Conference on Engineering Vibration
Ljubljana, Slovenia, 7–10 September 2015

DIRECT DAMPING IDENTIFICATION METHODS IN FREQUENCY DOMAIN

M. Brumat[1], **J. Slavič**[1], **M. Boltežar***[1]

[1]University of Ljubljana, Faculty of Mechanical Engineering, Laboratory for Dynamics of Machines and Structures, Aškerčeva 6, 1000 Ljubljana
miha.boltezar@fs.uni-lj.si

Keywords: Experimental Dynamics, Viscous Damping Identification, Frequency Response, Structural Dynamics, Beam, Plate.

Abstract. *Damping combined with mass and stiffness represents dynamic properties of a structure. Standard procedure is to assign proportional damping in physical coordinates which does not reflect true damping distribution. Direct damping methods were developed to improve identification of damping distribution with direct identification of damping from measured signals without transformation to modal coordinates. The Lee-Kim and local equation of motion methods were experimentally tested against: modal and spatial incompleteness and the effect of the damping treatments. It was found that the relation between physical location of damping treatment and location of large numerical values in identified damping matrix is not always straightforward.*

1 Introduction

Numerical and analytical prediction of the structural responses depends on the identified spatial damping throughout the structure. Good damping prediction is important for validation of analytical/numerical models in civil, mechanical and aerospace engineering. Damping in linear mechanical systems is usually identified using one of the methods such as logarithmic decay [1] in time domain, continuous wavelet transform [2] in time-frequency domain or half-power point [1] and first order perturbation [3] in frequency domain. Damping identification methods form the basis of several model updating methods [4, 5], where accurate damping identification can further improve numerical models [6, 7]. Two other examples where exact damping spatial location is needed are: identification of damping sources on existing structures and precise application of damping treatment. However, typically used damping identification methods [1, 6] do not provide spatial information (damping distribution throughout the structure).

An alternative approach is to use direct damping identification methods that were developed for identification of damping distribution directly from the frequency response functions (FRF) without the transformation to the modal coordinates. One of the typically used direct methods is the Lee and Kim's dynamic stiffness method [8]. The core of the method is a inverse identification of linear damping model from the complex part of the measured data which have been found to be very sensitive to real world problems in most follow-on studies, e.g. phase error [9], noise when the modal overlap is low [3] and leakage [10]. Ozgen and Kim [10] proposed a new experimental procedure with simultaneous excitation of all nodes to overcome described measurement errors, but th procedure is not practical with lots of measurement degrees of freedom because demands as many shakers as there are measurement degrees of freedom.

To further improve damping identification on real structures Arora *et al.* [4] proposed a two-step procedure. In the first step, mass and stiffness matrices are updated using FRF data and in the second step, damping matrix is identified using updated mass and stiffness matrices from the previous step. The two step approach relates displacements with material properties which can also be made using the local equation of motion method [11], presented recently by Ablitzer *et al*. Some direct methods, not considered in this research, are reviewed in [12, 3, 9].

Besides theoretical and experimental comparison of the methods, this research focuses on the modal and spatial incompleteness. Modal incompleteness deals with limited frequency span over number of modes whereas spatial incompleteness covers effects of non-measured points on the structure [13]. Modal and spatial incompleteness for spatial damping have been studied numerically [3, 14] and experimentally [9] on low DOF models.

This research is organized as follows. Section 2 gives theoretical background to different frequency-domain direct damping identification methods and extension of local method of motion with viscous damping and beam structure. In Section 3, the experimental research is presented. Analysis and discussion follow in the Section 4 and finally conclusions are drawn in Section 5.

2 Theoretical background

In this section the background of direct damping identification methods is briefly presented. Lee and Kim method is a matrix method and requires full measured frequency response function (FRF) matrix $\mathbf{H}$ whereas local method of motion requires excitation in one point only and full response vector. Both methods will be presented for viscous and hysteretic damping.

2.1 Lee and Kim's method

Starting point for the matrix based direct damping identification methods is the FRF matrix $\mathbf{H}(\omega)$. We begin with the general, second-order, matrix differential equation [1]:

$$\mathbf{M}\,\ddot{\boldsymbol{x}}(t) + \mathbf{C}\,\dot{\boldsymbol{x}}(t) + \mathbf{K}\,\boldsymbol{x}(t) = \boldsymbol{f}(t), \tag{1}$$

where $\mathbf{M}$ is the mass matrix, $\mathbf{C}$ is the viscous damping matrix and $\mathbf{K}$ is the stiffness matrix, respectively. Remaining parts of (1) are the response vector $\boldsymbol{x}(t)$ and the force vector $\boldsymbol{f}(t)$. Assuming a linear system and harmonic excitation/response, the equation (1) can be rewritten in frequency domain as:

$$\left[\mathbf{K} - \omega^2\,\mathbf{M} + \mathrm{i}\,\omega\,\mathbf{C}\right]\ \boldsymbol{X}(\omega) = \boldsymbol{F}(\omega) \tag{2}$$

From (2), the FRF matrix is defined as ratio [1]:

$$\frac{\boldsymbol{X}(\omega)}{\boldsymbol{F}(\omega)} = \mathbf{H}(\omega) = \frac{1}{\left[\mathbf{K} - \omega^2\,\mathbf{M} + \mathrm{i}\,\omega\,\mathbf{C}\right]} \tag{3}$$

and dynamic stiffness matrix $\mathbf{Z}(\omega)$ is defined as matrix inverse of $\mathbf{H}(\omega)$ at each frequency point ω:

$$\mathbf{Z}(\omega) = \mathbf{H}(\omega)^{-1} = \frac{\boldsymbol{F}(\omega)}{\boldsymbol{X}(\omega)} = \left[\mathbf{K} - \omega^2\,\mathbf{M} + \mathrm{i}\,\omega\,\mathbf{C}\right] \tag{4}$$

Using (4) viscous damping matrix might be obtained directly from imaginary part of the dynamic stiffness matrix $\mathbf{Z}(\omega)$:

$$\mathrm{imag}(\mathbf{Z}(\omega)) = \mathrm{imag}([\mathbf{H}(\omega)]^{-1}) = \omega\,\mathbf{C}, \tag{5}$$

Rearranging (5) to isolate viscous damping matrix $\mathbf{C}$ gives:

$$\mathbf{C} = \frac{1}{\omega}\,\mathrm{imag}([\mathbf{H}(\omega)]^{-1}) \tag{6}$$

Method (6) is not limited to viscous damping [10], for example hysteretic damping matrix version is:

$$\mathbf{D} = \mathrm{imag}([\mathbf{H}(\omega)]^{-1}) \tag{7}$$

2.2 Local equation of motion method

The method recently presented by Ablitzer *et al.* [11] is in this paper extended for beam structures and for viscous damping. Equation of motion for the displacement response w of isotropic Euler-Bernoulli beam with hysteretic damping in the steady state is [15]:

$$\rho\,A\,\frac{\partial^2 w}{\partial t^2} + E(1 + \mathrm{i}\,\eta)\,I\,\frac{\partial^4 w}{\partial x^4} = f(x,t) \tag{8}$$

where ρ is the density, A is the cross section, E is the elastic modulus, η is the hysteretic damping ratio, I is the second moment of area and $f(x,t)$ is the point harmonic excitation force at frequency ω, respectively. Viscous damping [16] equation differs only slightly:

$$\rho\,A\,\frac{\partial^2 w}{\partial t^2} + E\,I\,\frac{\partial^4 w}{\partial x^4} + \gamma\,\frac{\partial w}{\partial t} = f(x,t) \tag{9}$$

where γ is the viscous damping constant per unit length. Harmonic response $w(x,t)$ can be written using the method of separation of variables as:

$$w(x,t) = W(x)\,\sin(\omega\,t) \tag{10}$$

where W is response of beam and is only dependable on position on the beam x. Designation of dependency on x will be from here on omitted due to clarity. Partial time derivatives in (8) and (9) can be then expressed as:

$$\frac{\partial^2 w}{\partial t^2} = -\omega^2\,W\,\sin(\omega\,t) \tag{11}$$

and:

$$\frac{\partial w}{\partial t} = \mathrm{i}\,\omega\,W\,\sin(\omega\,t) \tag{12}$$

The fourth derivative is approximated at measurement point j by the finite difference scheme δ_j^4:

$$\frac{\partial^4 w}{\partial x^4} = \delta_j^4\,\sin(\omega\,t) \tag{13}$$

$$\delta_j^4 = \frac{1}{\Delta_x^4}\,(W_{j+2} - 4\,W_{j+1} + 6\,W_j - 4\,W_{j-1} + W_{j-2}) \tag{14}$$

where Δ_x is the measurement mesh spacing. Combining (8) with (11) and (13) for measurement point j we get:

$$-\rho\,A\,\omega^2\,W_j\,\sin(\omega\,t) + E_j(1+\mathrm{i}\,\eta_j)\,I\,\delta_j^4\sin(\omega\,t) = f(x_j,\,t) \tag{15}$$

When excitation is applied outside observation area, right-hand side of (15) is $f(x_j,\,t) = 0$ and equation (15) can be separated in real and imaginary part:

$$E_j = \frac{\rho\,A\,\omega^2}{I}\,\mathrm{real}\left[\frac{W_j}{\delta_j^4}\right] \tag{16}$$

$$\eta_j = \frac{\rho\,A\,\omega^2}{E\,I}\,\mathrm{imag}\left[\frac{W_j}{\delta_j^4}\right] \tag{17}$$

For a viscous system real part is same as in (16) and damping per unit length γ_j in measurement point j is:

$$\gamma_j = -\,\frac{E_j\,I}{\omega}\,\mathrm{imag}\left[\frac{\delta_j^4}{W_j}\right] \tag{18}$$

Discrete viscous damping c_j is obtained from damping per unit length γ_j as:

$$c_j = \gamma_j\,\Delta_x \tag{19}$$

The presented approach is straightforward to use, but better results due to measurement noise amplification in the fourth-order derivation can be obtained with two-step regularization [11]. First, both fields δ_j^4 and W_j are multiplied by a spatial Tukey window for boundary effects attenuation and in the second step each field is convolved with the discrete spatial response of a low-pass filter. Width of the filter kernel is defined with the spatial cut-off wavelength λ_c, e.g. $\lambda_c = 50$ mm, details are given in [11].

3 Experiments

An experiment was conducted on the three equal sized free-free beam specimens to compare direct damping identification methods. The specimens are: a) plain beam - beam A, b) with asymmetrically added local viscous damper - beam B and c) with constrained layer damping (CLD) - beam C, see Fig. 1. Beam specimens B and C have asymmetrically applied damping treatment over restricted area of the beam in order to know damping spatial location. Three samples were considered to emphasize effect of different damping treatments on the identified spatial location in later discussion. The beam A was a plain steel beam with constant cross-section $h \times b = 1\,\text{mm} \times 30\,\text{mm}$, length $l = 400\,\text{mm}$, mass $m = 92.6\,\text{g}$ and Young modulus $E = 210000\,\text{MPa}$. Beam dimensions were selected to have low modal overlap and to have large number of modes in the frequency span up to 3000 Hz. Beam is shown in Fig. 1(a). Two soft springs (stiffness ≈ 50 N/m) were used at each beam boundary in y-direction to limit rigid body translation after impact. The beam B was a similar steel beam as beam A, but additional viscous damper was added between points 5-8, see Fig. 1(b). Discrete damper is based on the design by Rijnen *et. al.* [17], each damper is made from two rubber blocks of a size 5x5x1 mm glued with the cyanoacrylate to the beam and connected with the aluminium struts of the size 80x5x5 mm. The beam C was the steel beam used as beam A, but had attached a constrained layer damper as shown in Fig. 1(c). The visco-elastic layer for application was 3M 112P02 damping material [18]. Steel constraining layer was of the same material and thickness as the beam to maximize damping [18]. Holes were drilled in constraining layer to measure responses of the beam, only.

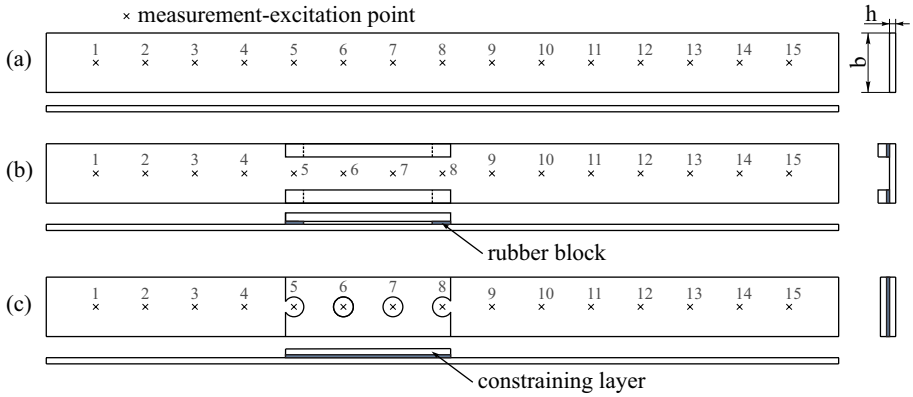


Figure 1: (a) plain beam specimen - beam A, (b) beam with added discrete viscous damper - beam B, (c) beam with added constrained layer damper - beam C

3.1 Measurement setup

Measurement setup is shown in the Fig. 2. Custom made solenoid impactor with PCB 086E80 force sensor was used for repeatable impulse excitation. Response (velocity) measurements employed Polytec PDV100 laser vibrometer. Impactor/laser based measurement allows for non-contact measurement without structural modification due to added stiffness or mass from sensors or shakers. Data acquisition and signal processing were undertaken in custom python software environment using pyDAQmx library [19] to interface NI 9215 acquisition hardware. Sampling rate was 100 kHz and signal was captured for 10 seconds.

To obtain full FRF matrix $\mathbf{H}$ the structure was sequentially excited at 15 points and responses are measured at the same 15 points (15x15 excitation-response pairs, $n = 15$), as shown in Fig 2. For local equation of motion method (see section 2.2) a denser measurement mesh is needed. Structure was excited in point 15 and within the line between points 3 and 11 additional 100 equally spaced responses were measured to obtain 2.5 mm measurement mesh. Each excitation-response point was measured three times to obtain the averaged H_1 estimator (mobility FRF) and later divided by $\mathrm{i}\,\omega$ in the frequency-domain to obtain receptance FRFs [1].

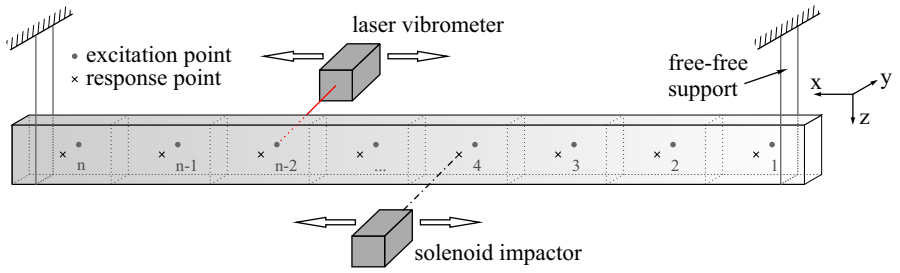


Figure 2: Measurement setup.

4 Analysis and discussion

For each beam 675 (225 points with 3 averages) measured responses were assembled into a full FRF matrix of size 15×15 used by the direct damping identification methods. Fig. 3 shows example of the measured receptance magnitude FRF at the pair 15-10 for all three beams; where 15-10 denotes 15th excitation and 10th response point (the designation will be used throughout this paper). From the FRF's it can be seen that the damping treatment of beams B and C affects high-frequency region more than the low-frequency. Further, the added stiffness and mass due to damping treatment barely shifts eigenfrequencies, see Fig. 3.

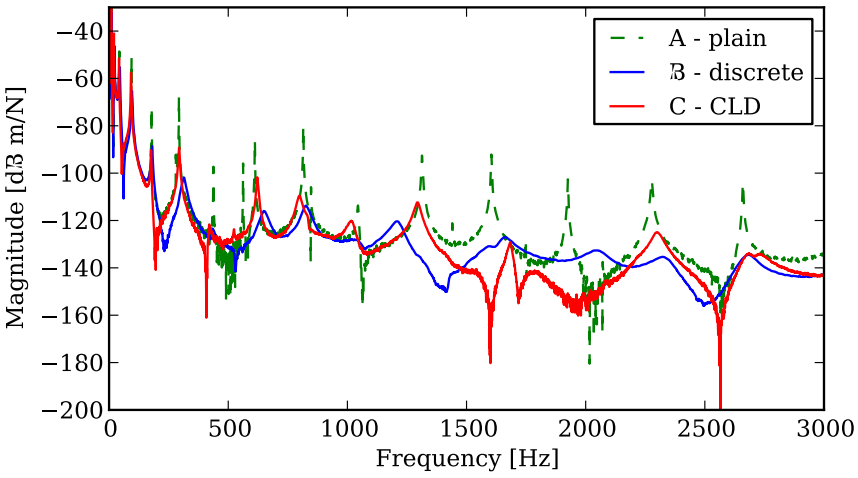


Figure 3: Receptance magnitude FRF plot for point 15-10.

In contrast to damping amplitudes at eigenfrequencies, the damping spatial location is in focus of this research.

4.1 Modal incompleteness

The modal incompleteness is in detail presented with the Lee-Kim method (6). Fig. 4 shows values of identified viscous damping matrix $\mathbf{C}$ for beam B using frequency range of five (0-200 Hz), ten (0-1100 Hz) and fifteen modes (0-3000 Hz). Larger numerical values (e.g. 150 Ns/m in Fig. 4) represent areas of higher damping.

Comparing high modal incompleteness with low incompleteness model it can be seen that the spatial location of damping becomes localised when the modal incompleteness is sufficiently low. Frequency range of ten modes was considered sufficient for accurate viscous damping location - similar conclusions were found in theoretical study [14].

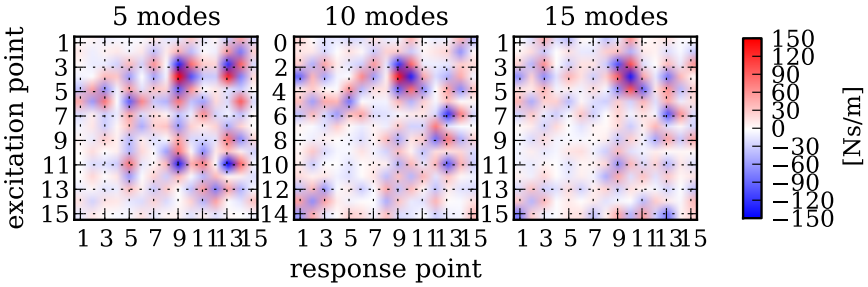


Figure 4: Identified viscous damping matrix for beam B, 5, 10 and 15 modes.

Focusing to identified values in the Fig. 4 show higher damping values at the points of applied damping for beam B (left point 4 and right point 9 of the discrete damper). We see high damping at the pair 4-9; however, in reverse the pair 9-4 has low damping. It is obvious that the identified damping matrix is non-symmetric, what is often the case in experimental measurements [20, 9]. The non-symmetry can be due to the fact that exciting the beam-B at the points 9 to 11 does not induce large strains in the rubber block and consequently damping [17].

Direct comparison of the results from Fig. 4 with the local equation of motion is not possible; result of the local equation of motion method is not damping matrix $\mathbf{C}$ but the local damping value at each measuring point. Damping is also identified at selected frequency, only.

Fig. 5 shows the identified damping with the local equation of motion method at the frequencies 1150, 1840 and 3100 Hz with the spatial cut-off of $\lambda_c = 20$ mm at the location between 30-240 mm of the discretely damped beam - B. Higher damping values can be found at 120 mm and at 200 mm (location of the discrete damper), see Fig. 1. Lower frequencies are more contaminated with noise (locations 50-100 mm).

4.2 Spatial incompleteness

Spatial incompleteness test was done using the full FRF matrix (15 modes) with deleted rows and columns. Deleted rows and columns can be understood as degrees of freedom (DOF) that were not measured (columns represent response DOFs and rows represent excitation DOFs). Fig. 6 shows the identified matrix using Lee-Kim method for four DOFs (i.e. 1, 5, 10, 15) and eight DOFs (i.e. 1, 3, 5, 7, 9, 11, 13, 15). Comparing the results for 15 modes shown in Fig. 4

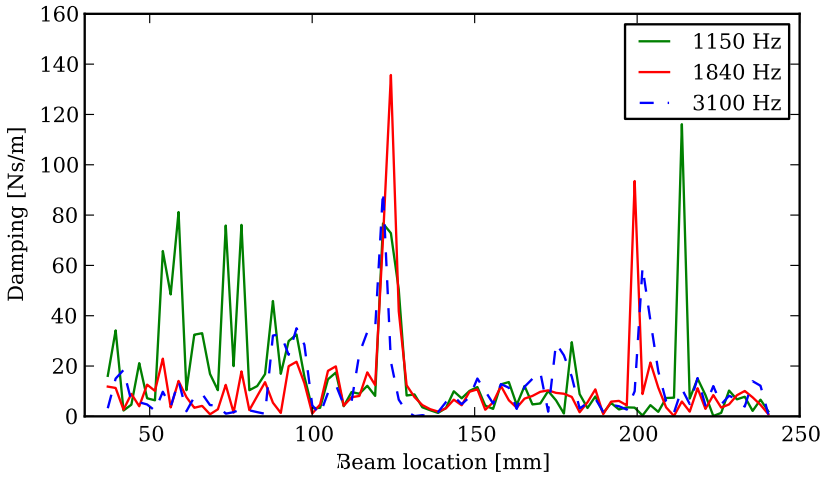


Figure 5: Identified viscous damping for local equation of motion for beam B at 1150, 1840 and 3100 Hz.

with Fig. 6 the redistribution of damping over neighbouring spatial location is observed. High damping area around pair 4-9 in Fig. 4 (15 modes) is in the spatial incomplete cases redistributed due to the missing information. In case of 8 DOF the redistribution is to the pair 5-7 and in case of 4 DOF over the complete damping matrix. The 4 DOF model is also symmetric - the non-symmetry observed in full model is now unexposed due to low DOF model. Low DOF models also tend to have larger damping values because the amount of damping present in the structure is redistributed to less DOFs.

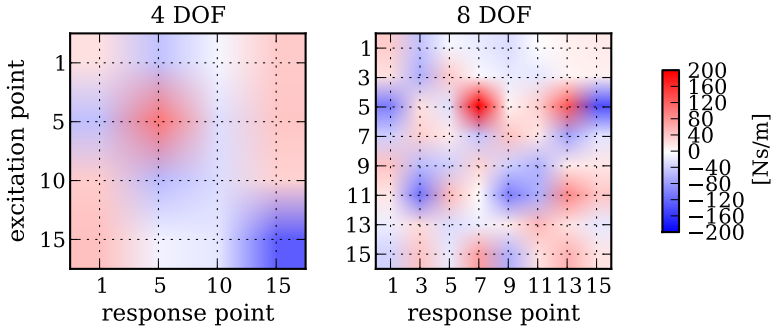


Figure 6: Identified viscous damping matrix for the beam B of the reduced FRF matrix.

4.3 Damping treatment effect on spatial location

In this section Lee-Kim method at frequency span of 15 modes is used to evaluate the remaining beams A and C. Identified viscous matrices for the two beams are shown in Fig. 7. On the plain beam A there are higher damping values identified at the points corresponding to the beam boundaries where the beam was suspended and additional soft spring was attached i.e. at 1-1 and 15-15. Beam C has more pronounced damping values around points 5-8, which corresponds to location of constraining layer damping treatment. Identified damping matrices

of beams A and C are close to symmetric.

The relation between physical location of damping treatment and location of damping values in identified damping matrix is not always straightforward (example of the identified damping of the beams B and C, see Fig. 4 and Fig. 7).

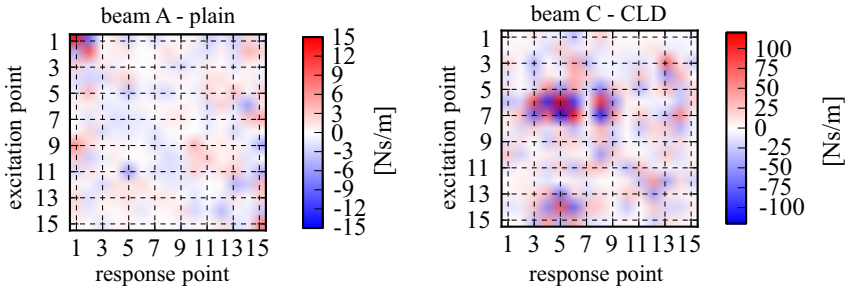


Figure 7: Identified viscous damping matrices for beams A and C. Reader should be aware of different scales.

5 Conclusion

The effectiveness of experimental viscous damping spatial location identification have been analysed. Special measuring setup was made to measure full FRF matrix of size 15×15 for three different beam configurations (plain and with discrete and constrained layer damping treatments). If the structure has known equation of motion (plate, beam) then local equation of motion method gives more precise location of damping. The Lee-Kim method can also identify spatial damping but the numerical and measuring effort raises by square of measuring points. Following conclusions can be drawn:

- In experiment frequency range of 10 modes is sufficient for spatial location identification on the beam, similar to the theoretical findings of Prandina *et. al.* [14].
- Spatial incompleteness can affect identified damping distribution.
- Damping spatial location of CLD treatment (beam C) significantly differs from the discretely damped beam B (even if it was applied at the same locations).

6 Acknowledgements

The financial support of the Young Researchers Programme provided by the Slovenian Research Agency is gratefully acknowledged.

REFERENCES

[1] D.J. Ewins. *Modal testing: theory, practice and application, 2nd ed.* Research Studies Press, 2000.

[2] J. Slavič, I. Simonovski, and M. Boltežar. Damping identification using a continuous wavelet transform: application to real data. *Journal of Sound and Vibration*, 262(2):291–307, 2003.

[3] A. Srikantha Phani and J. Woodhouse. Viscous damping identification in linear vibration. *Journal of Sound and Vibration*, 303(35):475 – 500, 2007.

[4] V. Arora, S.P. Singh, and T.K. Kundra. Finite element model updating with damping identification. *Journal of Sound and Vibration*, 324(35):1111 – 1123, 2009.

[5] S. Pradhan and S.V. Modak. A method for damping matrix identification using frequency response data. *Mechanical Systems and Signal Processing*, 33:69–82, 2012.

[6] M.I. Friswell and J.E. Mottershead. *Finite Element Model Updating in Structural Dynamics*. Kluwer, 1995.

[7] J.E. Mottershead, M. Link, and M.I. Friswell. The sensitivity method in finite element model updating: A tutorial. *Mechanical Systems and Signal Processing*, 25(7):2275–2296, 2011.

[8] J.-H. Lee and J. Kim. Development and Validation of a New Experimental Method to Identify Damping Matrices of a Dynamic System. *Journal of Sound Vibration*, 246:505–524, 2001.

[9] A. Srikantha Phani and J. Woodhouse. Experimental identification of viscous damping in linear vibration. *Journal of Sound and Vibration*, 319(35):832 – 849, 2009.

[10] G.O. Ozgen and J.H. Kim. Error analysis and feasibility study of dynamic stiffness matrix-based damping matrix identification. *Journal of Sound Vibration*, 320:60–83, 2009.

[11] F. Ablitzer, C. Pézerat, J.-M. Génevaux, and J. Bégué. Identification of stiffness and damping properties of plates by using the local equation of motion. *Journal of Sound and Vibration*, 333(9):2454–2468, 2014.

[12] D.F. Pilkey and D.J. Inman. A survey of damping matrix identification. In *16th International Modal Analysis Conference*. SEM, 1998.

[13] A. Berman and W.G. Flannelly. Theory of Incomplete Models of Dynamic Structures. *AIAA Journal*, 9(8):1481–1487, 1971.

[14] M. Prandina, J.E. Mottershead, and E. Bonisoli. An assessment of damping identification methods. *Journal of Sound and Vibration*, 323(35):662 – 676, 2009.

[15] J.-L. Guyader. *Vibration in continuous media*. ISTE, Newport Beach, CA, 2006.

[16] H.T. Banks and D.J. Inman. On damping mechanisms in beams. *Transaction of ASME, Journal of Applied Mechanics*, 58:716–723, 1991.

[17] M.W.L.M. Rijnen, F. Pasteuning, R.H.B. Fey, G. van Schothorst, and H. Nijmeijer. A numerical and experimental study on viscoelastic damping of a 3d structure. *Journal of Sound and Vibration*, In Press, Corrected Proof.

[18] 3M^{TM} viscoelastic damping polymeres 112-130 technical data, 2012.

[19] P. Cladé. *pyDAQmx: a Python interface to the National Instruments DAQmx driver*, 2015.

[20] F.E. Udwadia. A Note on Nonproportional Damping. *Journal of Engineering Mechanics*, 2009.

International Conference on Engineering Vibration
Ljubljana, Slovenia, 7-10 September 2015

Damage identification in beam structure using mode shape data: from spatial continuous wavelet transform to mode shape curvature methods

Rims Janeliukstis*[1], Sandris Rucevskis[1], Miroslaw Wesolowski[2], Andris Chate[1], Andrejs Kovalovs[1]

[1]Institute of Materials and Structures, Riga Technical University, Riga, Latvia
*Rims.Janeliukstis@rtu.lv, sandris.rucevskis@rtu.lv,andrejs.kovalovs@rtu.lv, and_cate@latnet.lv

[2]Department of Structural Mechanics, Faculty of Civil Engineering, Environment and Geodesy, Koszalin University of Technology, Koszalin, Poland
miroslaw.wesolowski@tu.koszalin.pl

Keywords: Wavelets, Mode Shape Curvature, Damage Identification, Damage Estimate Reliability, Scanning Laser Vibrometer.

Abstract. *In this paper, the applicability of spatial continuous wavelet transform (CWT) technique for damage identification in beam structures is analysed by the application of different wavelet functions and scales. The scale, which is most suitable for damage identification, is found by calculating standardized damage index (SDI) and the index, - called damage estimate reliability (DER) for the scales under investigation. Another method, based on mode shape curvature squares (MSCS), is also applied to identify the damage. It is shown that CWT and MSCS methods use exclusively mode shape data from the damaged structure. Damage identification results in terms of DER are compared for both methods. To examine the limitations of the proposed methods, different numbers of measurement points along the beam's axis are used. Effectiveness and robustness of the proposed algorithms are demonstrated experimentally on two aluminium beams containing single mill-cut damage and subjected to different boundary conditions. The modal frequencies and the corresponding operational deflection shapes are obtained by using scanning laser vibrometer with PZT actuator as vibration excitation source.*

1 INTRODUCTION

Different modern engineering structures, including but not limited to buildings, bridges, dams, stadiums, tunnels, automotive and aerospace facilities have to maintain their integrity and functionality under prolonged exploitation and severe environmental conditions. Failure of these structures may lead to tragic consequences and therefore costly and time-consuming inspections must be carried out on a regular basis. As a result, non-destructive structural health monitoring (SHM) methods have become an important research area in civil, mechanical and aerospace communities.

Numerous methods in the area of vibration-based damage detection are proposed. These methods are based on the fact that dynamic characteristics, namely, resonant frequencies, mode shapes and damping are directly related to the stiffness of the structure. Therefore, changes in these characteristics will also indicate the changes in the stiffness. Literature review on the methods for detecting, localizing, and characterizing damage by examining the changes in the dynamic response of a structure can be found in [1,2]. In many studies [3-8], mode shape transformations have been proved to be highly sensitive to damage and could be used for damage detection and quantification. However, the major drawback of those methods is a need for the data of a healthy structure, which sometimes can be difficult or even impossible to obtain. Possible solutions to this issue are employment of Gapped Smoothing Techniques to generate a smoothed surface of mode shape curvature, thus simulating a healthy state of the structure or using wavelet transform (WT) technique. WT was introduced in the 1980`s by Grossman and Morlet and was mainly used for signal singularity detection [9], signal denoising and image compression [10]. Later, in the 1990's, wavelet transform technique was used on vibrational data for damage detection for the first time by Newland. He studied the effects of damage due to building vibrations, caused by underground trains and road traffic [9, 11, 12]. Studies in [11] showed that local perturbations in beam deflection profile are induced by crack and revealed through wavelet transform.

In this paper, the method based on wavelet transform technique for damage detection in beam structure is described and compared to the well-known MSCS method. The drawback of this method – a need for the data of the healthy structure – is solved using an interpolation technique with a Fourier series approximation, simulating smooth mode shape curvature surface of the healthy structure. The absolute difference between square of the measured curvature and the smoothed approximation, representing the healthy structure, is defined as damage index and maximum value indicates the location and size of the damage. Applicability and effectiveness of the proposed algorithms are demonstrated experimentally on aluminium beams containing single mill-cut damage and subjected to different boundary conditions.

2 DAMAGE DETECTION ALGORITHMS

2.1 Continuous wavelet transform

Wavelets are special functions, which are generally used to analyse different signals in time domain. Wavelet transform is simply a mathematical method to transform the original signal into a different domain where additional data analysis becomes possible, therefore damage-affected signal portion is revealed. In spatial analysis, time is simply replaced with a spatial coordinate, say, x, giving rise to spatial signal $f(x)$ [11]. If $\psi(x)$ is a wavelet function, also called *mother wavelet*, then the set of wavelet family functions $\psi_{s,t}(x)$ is created by *translating* (parameter t) and *dilating* (parameter s) the $\psi(x)$ as [13, 14]:

$$\psi_{s,t}(x) = \frac{1}{\sqrt{|s|}} \cdot \psi\left(\frac{x-t}{s}\right) (1).$$

Parameter s is essential in noise reduction [15], and it is a real number. If $0 < s < 1$, the function is expanded, if $s > 1$, it is compressed [16]. In time domain, s is associated with signal`s frequency and t – location of wavelet in time. CWT is given by [14, 15]

$$W_{s,t} = \int_{-\infty}^{\infty} f(x) \cdot \frac{1}{\sqrt{|s|}} \cdot \psi^*\left(\frac{x-t}{s}\right) dx = \int_{-\infty}^{\infty} f(x) \cdot \psi_{s,t}{}^*(x) dx \quad (2),$$

where asterisk denotes complex conjugation. Using Eq. (2), CWT coefficients are calculated. These coefficients are extremely sensitive to any discontinuities and singularities of signal $f(x)$, therefore damage due to a sudden loss of stiffness can be detected in mode shapes that have large amplitude wavelet coefficients. It is a damaged location. This perturbation of wavelet coefficients due to this damage is clearer in the finest scales of the CWT [8].

CWT for mode shapes is depicted as follows (recall Eq. 2)

$$DI^n{}_{i\ CWT} = W^n{}_{i\ s,t} = \int_L w_i^n \cdot \psi_{s,t}{}^*(x) dx \, (3),$$

where L is a length of the beam, w^n is transverse displacement of the structure, n is a mode number, i is number of grid points in x direction. The $\psi_{s,t}{}^*(x)$ was chosen to be complex Gauss wavelets – cGs1, cGs2, cGs3, cGs4, cGs5, complex Morlet wavelets – cMor1, cMor2, cMor3, cMor4 and Shannon wavelets – Shan1, Shan2, Shan3, Shan4, Shan5. $DI_i^n{}_{CWT}$ is a damage index for each mode.

In practice, however, experimentally measured mode shapes are inevitably corrupted by measurement noise causing local perturbations into the mode shape, which can lead to false peaks in damage index profiles. These peaks could be mistakenly interpreted as damage or they could mask the peaks induced by real damage and lead to false or missed detection of the damage. To overcome this problem, it is proposed to summarize the results for all modes. The summarized damage index is then defined as the average summation of damage indices for all modes N, normalized with respect to the largest value of each mode

$$DI_i = \frac{1}{N} \cdot \sum_{n=1}^{N} \frac{DI_i^n}{DI_{i,\max}^n} \quad (4).$$

According to [17], the damage indices, determined for each element, are then standardized and a concept of statistical hypothesis testing is applied to classify damaged and healthy elements and to localize damage depending on the pre-defined damage threshold value. In hypothesis testing, the null hypothesis and alternate hypothesis are defined as H_0 (element i of the structure is healthy); H_1 (element i of the structure is damaged), respectively. In order to test the hypothesis, the summarized damage index, given in Eq. 4, is standardized

$$Z_i = \frac{DI_i - \mu_{DI}}{\sigma_{DI}} \quad (5),$$

where μ_{DI} and σ_{DI} are mean value and standard deviation of damage indices in Eq. 4, respectively. The decision for the localization of damage is established based on the level of significance used in the hypothesis test, which can be determined from a pre-assigned classification criterion: choose H_0 if $Z_i < C_r$ or choose H_1 if $Z_i \geq C_r$, where C_r is a threshold

value. Typical values of C_r, widely used in literature are 1.28, 2 and 3 for 90 %, 95 % and 99 % confidence levels for the presence of damage.

To quantify the reliability of wavelets to identify damage location, a new parameter, called „*damage estimate reliability*" (DER) is introduced and calculated as follows:

- The whole interval along the axis of the beam (x axis) is split into 3 parts:

the first part is the one in which 0 mm < x < 750 mm (part a), the second part is 750 mm < x < 800 mm (part b) and the third part is 800 mm < x < 1250 mm (part c).

- In each of these parts standardized damage indices (SDIs) from Eq. 5 of a respective wavelet are summed and divided by the number of data points in this particular interval, giving average amplitude of SDI ($\overline{Z_i}$) in a respective part.
- DER is equal to average SDI in the middle part (the damaged area or part b in our case) divided by average SDI in all parts combined. It is expressed in percentage as:

$$DER_i = \frac{\overline{Z_i}(b)}{\overline{Z_i}(a) + \overline{Z_i}(b) + \overline{Z_i}(c)} \cdot 100\% \quad (6).$$

2.2 Mode shape curvature squares

Most of the mode shape curvature damage detection methods require the baseline data of the healthy structure for inspection of the change in the modal parameters due to damage. In many cases, such as for structures that are already in service for some time, the baseline modal parameters are rarely available.

In this paper, an interpolation technique with a Fourier series approximation is applied on a mode shape curvature data of the damaged structure, generating smooth mode shape curvature surfaces that are estimates of the healthy structure.

The Fourier series is a sum of sine and cosine functions that describes a periodic signal. The trigonometric Fourier series form is

$$\kappa(x) = a_0 + \sum_{i=1}^{n} a_i \cdot \cos(n \cdot \omega \cdot x) + b_i \cdot \sin(n \cdot \omega \cdot x) \quad (7)$$

where a_0 models a constant (intercept) term in the data and is associated with the $i = 0$ cosine term, ω is the fundamental frequency of the signal, n is the number of terms (harmonics) in the series, and $1 \leq n \leq 8$ [18].

In this study, mode shape curvature data was approximated with Fourier series functions of orders 2-8. The obtained coefficient values a_0, a_i, b_i and ω were used to reconstruct the approximation of mode shape curvature data using Eq. 8. The damage index is defined as the absolute difference between the measured curvature of the damaged structure and reconstruction of the mode shape curvature approximation with Fourier series representing the healthy structure. The maximum value indicates the location of damage. The damage index for the mode at grid point i is expressed as follows

$$DI_i^{n}{}_{MSCS} = \left| \left(\frac{\partial^2 w^n}{\partial x^2} \right)_i^2 - \left(\kappa_x^n \right)_i^2 \right| \quad (8)$$

where w^n is measured transverse displacement of the structure, $\kappa_x{}^n$ is reconstruction of Fourier series approximation of mode shape curvature data in x direction, n is a mode number, i is number of grid points in x direction. It must be noted that the value of the calculated mode shape curvature as well as approximation reconstruction at grid point are normalized with

respect to the largest value of each component. The mode shape curvatures are calculated from the mode shapes by the central difference approximation at grid point *i* as:

$$\left(\frac{\partial^2 w^n}{\partial x^2}\right)_i = \frac{\left(w_{i+1}^n - 2w_i^n + w_{i-1}^n\right)}{h^2} \quad (9)$$

where *h* is the distance between two successive nodes or measured points. For more than one mode used, the damage index is calculated using Eq. 4. Afterwards, this damage index is also standardized (refer to Eq. 5), leading to SDI. DER values are also obtained.

3 EXPERIMENT

Specimens under test were 2 aluminium beams with the following dimensions – $length_1$ = 1250 mm, $length_2$ = 1500 mm (along the *x* axis for both beams), $width_{1,2}$ = 50 mm, $height_{1,2}$ = 5 mm. A single mill-cut damage ($width_1$ – 50 mm, $width_2$ = 100 mm, $depth_{1,2}$ – 2 mm) was introduced in a location at 750 mm from one edge of a *Beam 1* and at 950 mm from one edge of *Beam 2* (Figure 1 (a)).

The resonant frequencies and corresponding operational deflection shapes of the beams are measured by a POLYTEC PSV-400-B scanning laser vibrometer. General experiment set-up consists of a PSV-I-400 LR optical scanning head equipped with a sensitive vibrometer sensor (OFV-505), OFV-5000 controller, PSV-E-400 junction box, a Bruel & Kjaer type 2732 amplifier, and a computer system with a data acquisition board and PSV software (Figure 1 (b)). PSV system requires defining the outer edges and geometry of the object and setting up a scanning grid, which consists of number of points where vibrations are measured. 126 and 151 equally spaced scanning grid points are used with the step of 1 cm to cover the area of *Beam 1* and *Beam 2*, respectively. Free-free (all edges free) boundary conditions (FBC) are simulated by suspending the beam with two thin threads under a frame. In order to simulate clamped-clamped (two ends fixed) boundary conditions (CBC) experimentally, two vices are used to fix the ends of the beam (10 mm from both sides) with the clamped torque of 20 Nm. The beams are excited by a periodic input chirp signal generated by the internal generator with a 1600 Hz bandwidth through piezoelectric actuator discs. After the frequency response function and resonant frequencies have been obtained, the beam is excited by a periodic sine wave signal with a frequency corresponding to each resonant frequency in order to obtain the corresponding mode shape. When the measurement is performed in one point, the vibrometer automatically moves the laser beam to another point of the scan grid, measures the response using the Doppler principle and validates the measurement with the signal-to-noise ratio. The procedure is repeated until all scan points have been measured. More details about the proper arrangement of the experiment set-up can be found in [19].

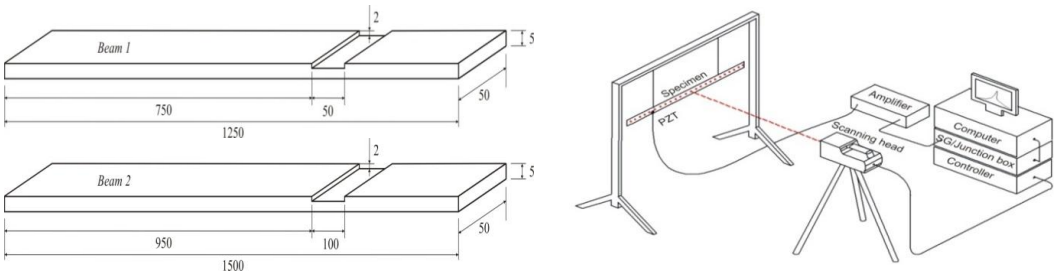


Figure 1. Left: geometry (in mm) of tested beams, right: experimental set – up.

4 RESULTS AND DISCUSSION

SDI values were calculated for complex wavelets, mentioned in section 2.3 for scales s = from 1 to 128. For each of these 128 SDI values one DER value from Eq. 6 was calculated. This result is shown in Figures 3 and 4 only for wavelet with highest maximum DER value at all scales. The number of measured operational deflection shape data points was divided by minimum value of 1 and maximum value of 6, depicted by p = 1 (149 measurement points) and p = 6 (25 measurement points), respectively. DER results, calculated at each p value for both beams at FBC and CBC are summarized in Table 1. DER values were also calculated, using MSCS method. Fourier series approximations are depicted with F2-F8. Respective results are shown in Table 2.

p	Wavelet				DER (%)				Scale			
	Beam1		Beam2		Beam1		Beam2		Beam1		Beam2	
	CBC	FBC	CBC	FBC	CBC	FBC	CBC	FBC	CBC	FBC	CBC	FBC
1	cMor2	cMor3	cMor2	cGs5	89.0	62.7	86.7	89.8	7	84	8	4
2	cMor2	cGs5	cMor2	cMor2	88.0	67.0	80.5	78.9	4	3	4	4
3	cMor1	cMor3	cMor1	Shan5	81.9	68.2	74.9	65.6	4	21	5	14
4	cMor1	Shan2	cMor1	cMor2	73.8	65.7	76.0	68.2	4	74	4	73
5	Shan5	Shan4	cMor1	Shan4	76.6	73.6	71.2	69.9	6	8	4	22
6	cMor4	cMor4	cMor4	cMor4	73.6	76.5	73.8	72.7	81	45	82	119

Table 1: DER values for wavelets with highest maximum DER at different numbers of measurement points.

p	Number of measurement points	Approximation function				DER (%)			
		Beam1		Beam2		Beam1		Beam2	
		CBC	FBC	CBC	FBC	CBC	FBC	CBC	FBC
1	149	F6	F8	F5	F8	93.3	84.1	89.6	86.8
2	75	F2	F3	F2	F2	93.5	91.3	92.5	90.1
3	50	F6	F7	F2	F2	93.3	92.0	92.1	89.5
4	38	F6	F6	F6	F2	94.4	92.7	92.2	90.6
5	30	F6	F6	F3	F3	93.6	93.4	91.0	90.7
6	25	F2	F2	F3	F3	90.1	90.8	92.2	91.8

Table 2: DER values for approximation functions with highest maximum DER at different numbers of measurement points.

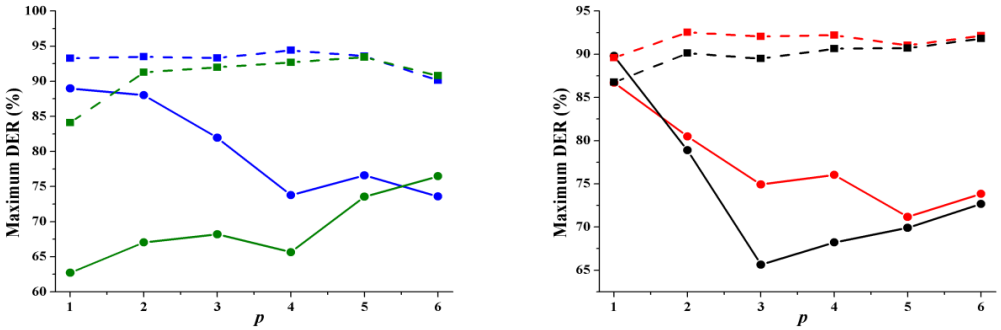


Figure 2: Maximum DER(p). Solid lines – wavelets, dashed lines – MSCS. Blue and red – clamped, green and black – free. Left – Beam1, right – Beam 2.

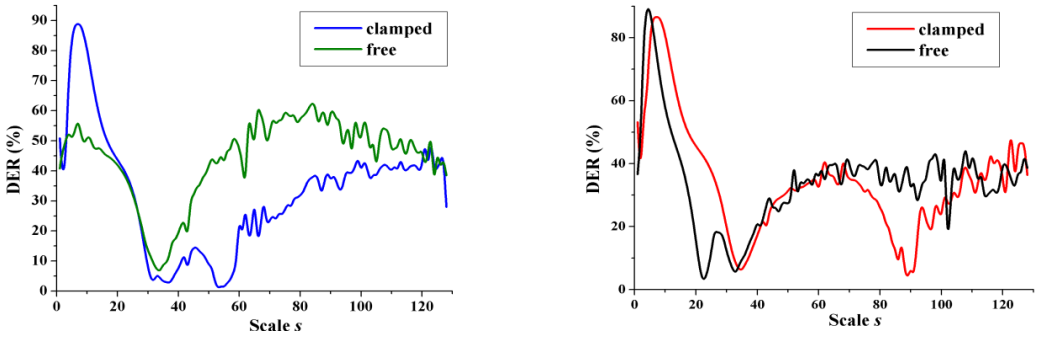


Figure 3: DER(*s*) for wavelets with highest DER at p = 1. Left – Beam1, right – Beam 2.

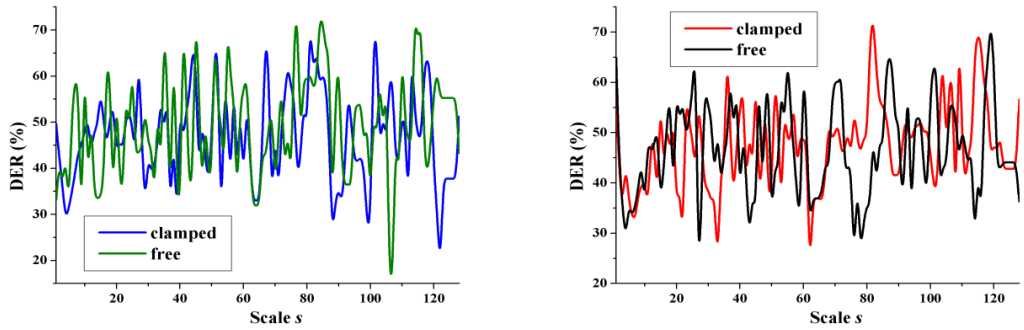


Figure 4: DER(*s*) for wavelets with highest DER at p = 6. Left – Beam1, right – Beam 2.

As one can see in Figure 2, results obtained with MSCS method are better for both beams and at both boundary conditions. Also, DER values are a bit higher for CBC as opposed to FBC, although, as number of measured mode shape data points decreases (p increases), this difference diminishes. There is a minimum at p = 4 for wavelet case, meaning that such a number of data points is not recommended at all. Figures 3-4 indicate that, as p increases, DER dependence on scale becomes more chaotic, resembling noise. On the other hand, at original set of data, there are clear DER peaks at smaller scales, namely at $s < 10$. Therefore scales larger than 10 can easily be dismissed.

SDI distribution over beam longitudinal coordinate x was calculated at scales were highest DER peaks appeared (Figures 5-6). Again, results are shown only for cases p = 1 and p = 6. At p = 1 wavelets manage to identify the damaged location fairly good, especially for CBC with DER values of about 89 % and 90 % for Beam 1 and Beam 2, respectively. Results for FBC are worse for Beam 1– about 63 % but 90 % for Beam 2. As expected, damage identification results were worse for case p = 6 (refer to Table 1). The same procedure involving SDI distribution over beam coordinate was done with MSCS method (Figures 7-8). Results are very stable – even at p = 6, the method manages to identify damage very good. Respective DER values are p = 1: 93 % for CBC and 84 % for FBC (Beam 1) and 90 % for CBC and 87 % for FBC (Beam 2), p = 6: 91 % for CBC and 92 % for FBC (Beam 1) and 92 % for CBC and 93 % for FBC (Beam 2).

Although the peak SDI values occur at the pre–determined location, large values alsoemerged at the boundaries of beams. The boundary distortion problem is caused by discontinuity of mode shapes at their ends due to boundary conditions. Commonly, two methods are used to reduce the boundary effect [5]. One method is to extend the mode shape data beyond the original boundary by cubic spline extrapolation based on points near the

boundaries. The other method is simply to ignore those values near the boundaries by cutting them off or setting them to zeros. In this study, the latter method is adapted – values of data points, corresponding to edges were set to zero for both beams. It should be noted that neither of both methods are capable of detecting damage close to boundaries, since both of them smooth out the information near the boundaries.

Figure 9 shows SDI(x) for Beam 2 using SDI threshold value of 1.28 to filter out smaller peaks that do not contribute to damage. With this approach, damage identification results significantly improved.

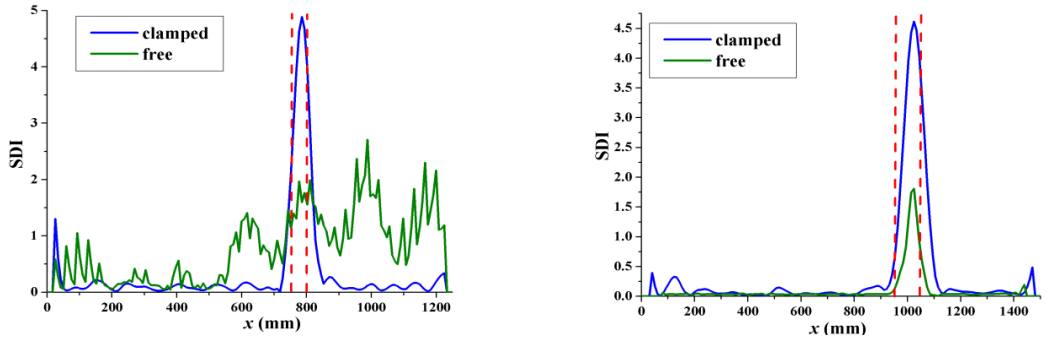


Figure 5: SDI(x) for wavelets with highest DER at p = 1. Left – Beam1, right – Beam 2.

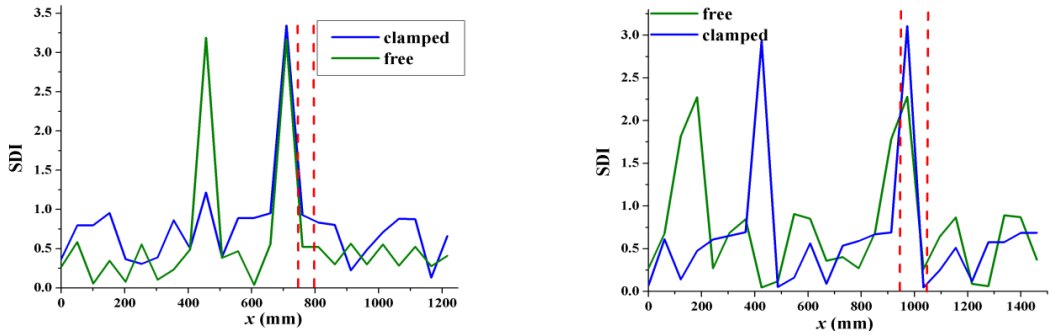


Figure 6: SDI(x) for wavelets with highest DER at p = 6. Left – Beam1, right – Beam 2.

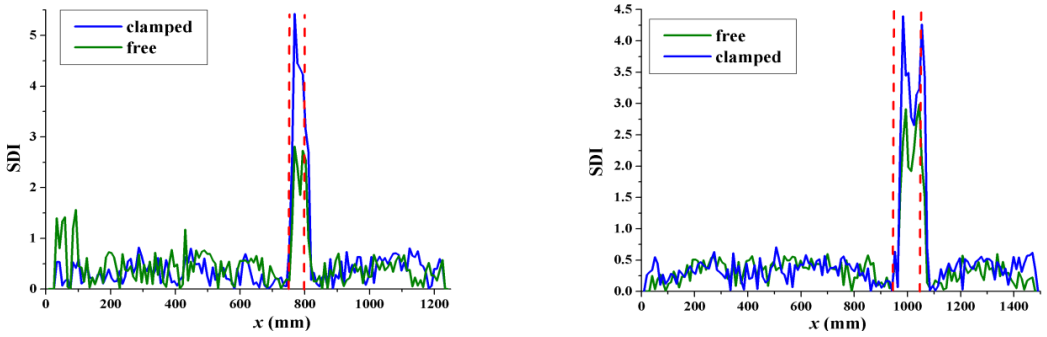


Figure 7: SDI(x) for MSCS with highest DER at p = 1. Left – Beam1, right – Beam 2.

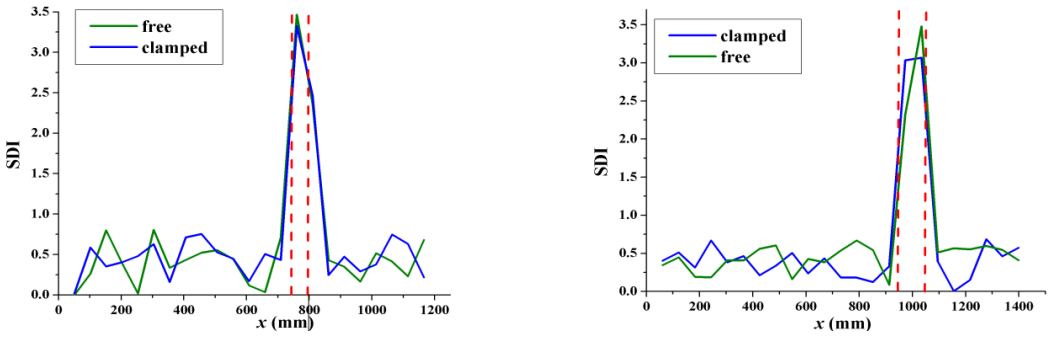


Figure 8: SDI(x) for MSCS with highest DER at p = 6. Left – Beam1, right – Beam 2.

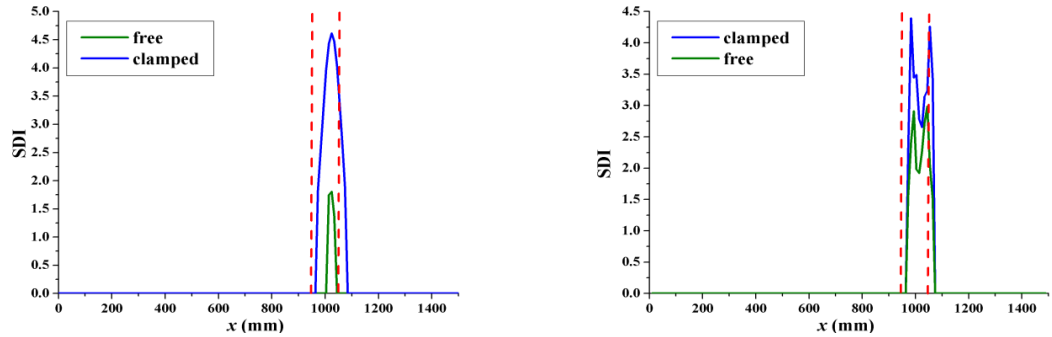


Figure 9: SDI(x) at p = 1 for Beam 2. Left – CWT, right – MSCS.

5 CONCLUSIONS

In this paper, an experimental study on the applicability of mode shape based spatial CWT technique and MSCS method for detection and localization of damage in beam structure are presented and results are compared. Success of damage detection was demonstrated using statistical hypothesis approach, exploiting CWT and MSCS. The obtained results show that both methods provide reliable information about the location of damage in two aluminium beams containing different length single mill-cut damage. Overall, 14 different wavelets were tested at scale parameters from 1 to 128.

While both methods – CWT and MSCS – offer an advantage that there is no need for mode shape information of a healthy structure, results, obtained with MSCS method are slightly better – DER values were higher for all studied cases. Also, there is no need to analyse results at different parameter values (scales for wavelets), meaning much less different combinations (different wavelets at different scales) of calculations. Note that only best results were shown, meaning that there is a considerable variation in DER values for wavelets.

However, in practical situations when location of damage in not known, one must still perform standardized damage index calculations for different approximation functions and wavelet functions for MSCS and CWT methods, respectively, and compare damage detection results obtained with different functions, relying on the results that are similar among the majority of functions, while dismissing those functions that have located damage in a completely different position.

ACKNOWLEDGEMENT

The research leading to these results has received the funding from Latvia state research programme under grant agreement "Innovative Materials and Smart Technologies for Environmental Safety, IMATEH"

REFERENCES

[1] M.I. Friswell, Damage identification using inverse methods. *Philosophical Transactions of the Royal Society A*, **365**, 393–410, 2007.
[2] W. Fan, P. Qiao, Vibration-based damage identification methods: a review and comparative study. *Structural Health Monitoring*, **10**, 83–111, 2011.
[3] Wu, D. and Law S.S., Damage Localization in Plate Structures from Uniform Load Surface Curvature. *Journal of Sound and Vibration*, **276**, 227–244, 2004.
[4] Fan, W., Qiao, P, A 2-D continuous wavelet transform of mode shape data for damage detection of plate structures. *International Journal of Solids and Structures*, **46**, 4379–4395, 2009.
[5] N.T. Khiem, H.T. Tran, A procedure for multiple crack identification in beam-like structures from natural vibration mode. *Journal of Vibration Control*, **20**, 1417–1427, 2014.
[6] S. Rucevskis, M. Wesolowski, A. Chate, Damage detection in laminated composite beam by using vibration data. *Journal of Vibroengineering*, **11**, 363–373, 2009.
[7] S. Ručevskis, M. Wesolowski, A. Chate, Vibration-based damage detection in a beam structure with multiple damage locations. *Aviation*, **13**, 61-71, 2009.
[8] S. Rucevskis, M.A. Sumbatyan, P. Akishin, A. Chate, Tikhonov's regularization approach in mode shape curvature analysis applied to damage detection, *Mechanics Research Communications*, **65**, 9-16, 2015.
[9] R. S. Estrada, Damage detection in bridges through vibration monitoring: evaluation and application. Universidade do Minho, 2008, http://hdl.handle.net/1822/9023
[10] A. J. Jerri, *Introduction to Wavelets, 1st edition*. Sampling Publishing, Potsdam, New York, 2011.
[11] N. Wu, Q. Wang, Experimental studies on damage detection of beam structures with wavelet transform. *International Journal of Engineering Science*, **49**, 253-261, 2011.
[12] H. Kim, H. Melhem, Damage detection of structures by wavelet analysis. *Engineering Structures*, **26**, 347–362, 2004.
[13] M. Solís, M. Algaba, P. Galvín, Continuous wavelet analysis of mode shapes differences for damage detection. *Mechanical Systems and Signal Processing*, **40**, 645 – 666, 2013.
[14] H. Adeli, H. Kim, *Wavelet-Based Vibration Control of Smart Buildings and Bridges*. CRC Press, Taylor and Francis Group, Boca Raton, London, New York, 2009.
[15] A. Gentile, A. Messina, On the continuous wavelet transforms applied to discrete vibration data for detecting open cracks in damaged beams. *International Journal of Solids and Structures*, **40**, 295–315, 2003.
[16] M. Weeks, *Digital Signal Processing Using Matlab and Wavelets, 2nd Edition*. Jones and Bartlett Publishers, Sudbury, Massachusetts, 2011.
[17] W.L. Bayissaa, N. Haritosa, S. Thelandersson, Vibration-based structural damage identification using wavelet transform. *Mechanical Systems and Signal Processing*, **22**, 1194–1215, 2008.
[18] Matlab R2014a: http://se.mathworks.com/help/curvefit/fourier.html.
[19] E. Barkanov, M. Wesolowski, W. Hufenbach, M. Dannemann, An effectiveness improvement of the inverse technique based on vibration tests. *Computers & Structures*, **146**, 152-162, 2015.

11th International Conference on Engineering Vibration
Ljubljana, Slovenia, 7–10 September 2015

BIODYNAMIC BASED EXPERIMENTAL VALIDATION OF A HUMAN FINGER MODEL

Luka Knez*[1], Janko Slavič[1], Miha Boltežar[1]

[1]University of Ljubljana, Faculty of Mechanical Engineering, Slovenia
luka.knez, janko.slavic, miha.boltezar@fs.uni-lj.si

Keywords: Biodynamic Response, Human Finger Model, Explicit Calculation of Finger Response, Biodynamic Mechanical Model.

Abstract. *Mechanical models have been used to predict the biodynamic responses of the human body and hand exposed to vibration but there has been little research on finger modeling. A detailed model is necessary to get an accurate response at the fingers but such a model often leads to coupled equations which prove difficult to solve. To overcome this problem a new approach is proposed in this study, which uses explicit instead of the usual implicit calculation of the dynamic response of the finger model. The multi-degree-of-freedom model parameters were identified from the biodynamic responses and forces measured on the index finger exposed to single-axial broadband excitation (5 to 500 Hz, 10 ms2). To measure the responses a special measuring handle equipped with a force transducer and an accelerometer was used. Reasonable agreement was achieved between the measurements and the model predicted results and the study also confirmed that the proposed finger model is acceptable for further biodynamic studies of the finger. More importantly the proposed procedure enables a systematic approach to modeling, which helps the researchers solve more detail and complex mechanical models.*

1 INTRODUCTION

Prolonged exposure of the human hand-arm system (HAS) to vibration leads to different vibration-induced injuries, which are collectively known as the hand-arm vibration syndrome (HAVS) [1]. One of the most common injuries is the white fingers syndrome where the symptoms are localized in parts of the fingers. To reduce the risk of white fingers syndrome and help interpret the observed phenomena in epidemiological and physiological studies the complex dynamic responses of the fingers are measured and modeled [2].

The biodynamic response method [2, 3] is the most commonly used method for dynamic response measurements of the hand. It was also recently improved to measure the fingers besides the usual palm responses [4, 5, 6]. The method is based on the biodynamic parameters [1, 3]: the apparent mass, mechanical impedance and apparent stiffness, which are derived from measurements done on a vibrating handle. Hand-tool excitations are simulated and simultaneous measurements of the dynamic motion and forces on the hand at the hand-handle interface are required to calculate the biodynamic parameters. To ensure comparable results the push force and the operator's posture are also monitored during the testing as advised by researchers [7].

The measured biodynamic parameters of the palm and the fingers are used to develop mechanical models of the hand [2]. Until recently, only the biodynamic response of the entire hand has been measured, therefore models have focused on the hand as a whole. Newer mechanical models [2, 8, 9, 10] however have started modeling the palm and fingers separately, but the fingers are crudely represented *i.e.* only one or two lumped mass elements are used for all five fingers.

Another approach used by researchers for detailed finger modeling is the use of FE models. Srinivasan *et al.* [11] proposed a two-dimensional FE fingertip model composing of soft tissue, bone and nail. The model simulates stress/strain distributions in the fingertip that is indented by rectangular gratings. Similarly, researchers [12] have used two-point tactile discrimination tests to derive models for stress/strain distributions in the finger soft tissue. Wu *et al.* [13] developed a hybrid FE hand gripping model, which combined the features of conventional FE models with multi-body mechanical models. The model simulated the hand-gripping on a cylindrical handle with covering materials of different softness levels and showed that maximal compressive stress and strain in the soft tissue can be reduced by reducing the stiffness of the covering material. The setback of the current FE finger models is that while good at predicting local tissue responses they are difficult to use for biodynamic response modeling of the entire finger, due to quasi-static loadings and local finger tissue experimental data.

This study focuses on a systematic approach to finger modeling that is based on the biodynamic response (in our case the apparent mass) of the index finger. The biodynamic data is derived using a purpose built measuring device, which was developed for single finger measurements taking into consideration experience from previous research [4, 5, 6, 14]. A mechanical model of the index finger is proposed and, since detailed mechanical models often lead to coupled equations, a new approach of equation solving is proposed in this study. The systems equations of motion are solved explicitly using forward time integration instead of the usual implicit calculation. The Fourier transform is then used to transform the data from the time domain into the frequency domain. Finally, the parameters of the model are obtained by data fitting. This is done sequentially at each part of the finger using the Levenberg-Marquardt method.

2 BIODYNAMIC RESPONSE MEASUREMENT OF THE FINGER

2.1 Biodynamic theory

This subsection presents a brief overview of the theory, which is used to derive the biodynamic response of the index finger, researched in this study. A more detailed explanation - typically used for the entire HAS - can be found in [1, 3].

The response of a biodynamic system is characterised by three parameters: the apparent mass (AM), the mechanical impedance (MI) and the apparent stiffness (AS). The AM was chosen for this study, since it emphasizes the low-frequency components [6] of the biodynamic response. The AM is defined as:

$$AM = \frac{\tilde{F}}{\tilde{A}}\,, \tag{1}$$

where $\tilde{F}$ is the dynamic force, and $\tilde{A}$ is the dynamic acceleration at the finger-measuring device interface. Both parameters must be measured simultaneously and in the direction of excitation. Once the AM is know, the MI and the AS can also be computed using the obtained AM data.

The apparent mass in the frequency domain is calculated by:

$$AM(\omega) = \frac{G_{fa}(\omega)}{G_{aa}(\omega)}\,, \tag{2}$$

where G_{fa} is the cross-spectrum of the force and the acceleration, and G_{aa} is the auto-spectrum of the acceleration. The obtained results are mathematically complex, comprising of both the real and imaginary component.

The measured dynamic force of the finger $\tilde{F}$ is in fact a combination of the finger biodynamic force and the inertial force of the measuring device. To calculate the exact AM of the finger AM_{Finger} it is therefore necessary to deduct the effect of the measuring device AM_{Device} from the total AM (finger and device) $AM_{\text{TotalFinger}}$:

$$AM_{\text{Finger}}(\omega) = AM_{\text{TotalFinger}}(\omega) - AM_{\text{Device}}(\omega)\,. \tag{3}$$

The AM_{Device} in Eq. 3 can be calculated from the data measured on an empty measuring device, where the dynamic force is purely the result of the measuring device mass.

2.2 The measuring device

A special device capable of accurately measuring the small AM of a single finger has been developed. The general measuring principle from previous research [4, 5, 6, 14] was modified to reduced the number of sensors needed, thereby reducing the mass of the measuring device. The device shown in Figure 1 consists of a finger support rectangle on the bottom side of which an accelerometer was attached using adhesive. The rectangle is screwed onto a force sensor and the force sensor onto an aluminum base. The bottom of the aluminum base is circular shaped with a pattern of holes that are used for fixation to a electrodynamic shaker.

A Kistler force sensor type 9317B is used to measure the dynamic forces in the excitation direction. The piezoelectric force transducer together with the Kistler 5073 charge amplifier[1] can measure dynamic as well as quasi-static forces, that are applied on the finger support rectangle. Every force signal measured therefore contains dynamic as well as static components. The

[1]The selected charge amplifier has a low zero-drift, which was appropriately corrected.

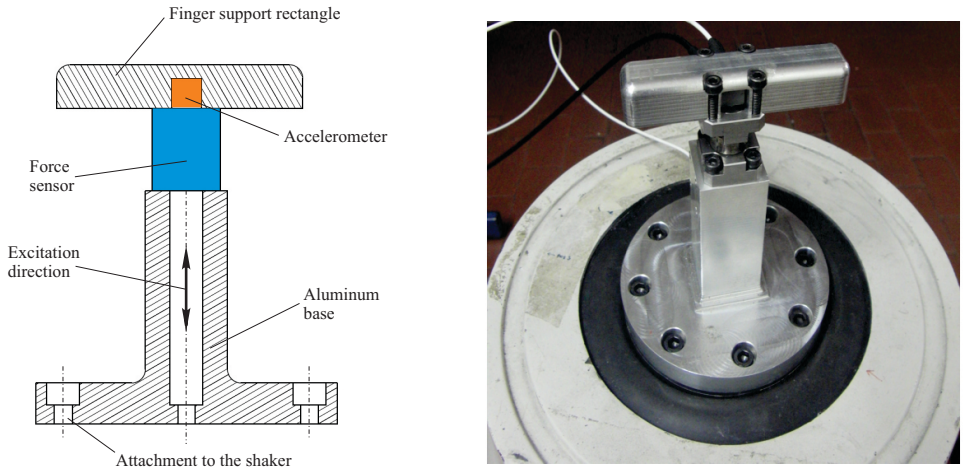


Figure 1: The measuring device: Left - a sketch of the device; Right - a photography of the device.

dynamic component is used for AM calculations and the static component is displayed to the operator for push force adjustments. To measure the accelerations of the finger an accelerometer type PCB T333B30 was used, which was attached to the middle of the finger support rectangle.

2.3 Experimental setup

The experimental setup used in this study is illustrated in Figure 2. The measuring device was fixed on a LDS V555 electrodynamic shaker which was tilted for vertical excitation. Broadband random excitation from 5 to 500 Hz with a power spectral density (PSD) of 10 $(\mathrm{m/s^2})^2/\mathrm{Hz}$ was used.

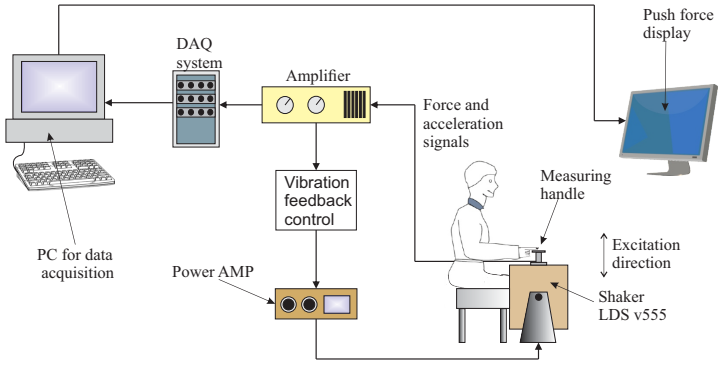


Figure 2: Experimental setup for the finger apparent mass measurements.

Since previous researchers [7] found the posture important, the operator was seated adjacent to the shaker and the angle of the elbow was adjusted to 90°. The operator was asked to push down on the measuring rectangle with his right index finger and to hold his forearm pronated. The amplitude of the push force was held constant at 2 N by the operator with the help of a visual feedback display. The operator conducted three sets of measurements: one with the

entire finger (named three-phalanx measurement), one with the middle and distal phalanx (two-phalanx measurement) and one with only the distal phalanx (one-phalanx measurement) on the instrument handle.

The measurement data were acquired at a sampling rate of 10 kHz using a National Instruments 9234 acquisition module and the National Instruments 9178 DAQ system. The signals were appropriately filtered with low-pass filters to avoid aliasing. National Instruments LabVIEW 2010 was used for data acquisition and Matlab 2012 software for data analysis.

2.4 Identifying the apparent mass

The measured force $F(t)$ and acceleration $A(t)$ at the finger-handle interface are transformed into the frequency domain using the Fourier transform (Hamming window; sampling frequency 10 kHz; 20000 samples per segment; 50% overlap). The frequency-domain forces and accelerations of the finger and measuring device are denoted as: $\tilde{F}_{\text{TotalFingers}}$ and $\tilde{A}_{\text{TotalFingers}}$ and the AM per segment i is obtained as:

$$AM_{\text{TotalFingers,i}}(\omega) = \frac{\tilde{F}_{\text{TotalFingers}}(\omega)}{\tilde{A}_{\text{TotalFingers}}(\omega)}, \tag{4}$$

where the division needs to be performed at the element level.

The AM of the fingers and measuring device is obtained by segment averaging (35 averages have been used):

$$AM_{\text{TotalFingers}}(\omega) = \frac{1}{35}\sum_{i=1}^{35} AM_{\text{TotalFingers,i}}(\omega). \tag{5}$$

Finally, the finger AM can be identified from Eq. 3, as discussed above.

In addition to the dynamic forces, the static push forces need to be measured and shown on a display to provide feedback for the operator. To obtain the static push force component F_{p}, the measured samples are averaged in the time-domain (the averaging period was 0.5 s, which corresponds to 5000 measured samples):

$$F_{\text{p}} = \text{Mean}(\tilde{F}(t))\,. \tag{6}$$

3 FINGER MODELING AND PARAMETER IDENTIFICATION

3.1 Model configurations

Figure 3 shows all the model configurations used in this study. The models were denoted: 2 DOF, 3 DOF and 4 DOF; where DOF means degrees of freedom.

The first body (m_1) and joint (cr_1, kr_1) in all the models represent the part of the finger and hand that is not directly on the measuring handle but also contributes to the measured AM. The rest of the bodies in the model are directly in contact with the vibrating handle and this is simulated by applying an external force F. Since the handle measures only one force the distribution of the force is uniform on all the finger phalanxes. In the 4 DOF model the parameters m_2, cr_2, kr_2 represent the proximal phalanx and connection to the rest of the hand; m_3, cr_3, kr_3 represent the middle phalanx and proximal interphalangeal joint; and m_4, cr_4, kr_4 the distal phalanx and the distal interphalangeal joint.

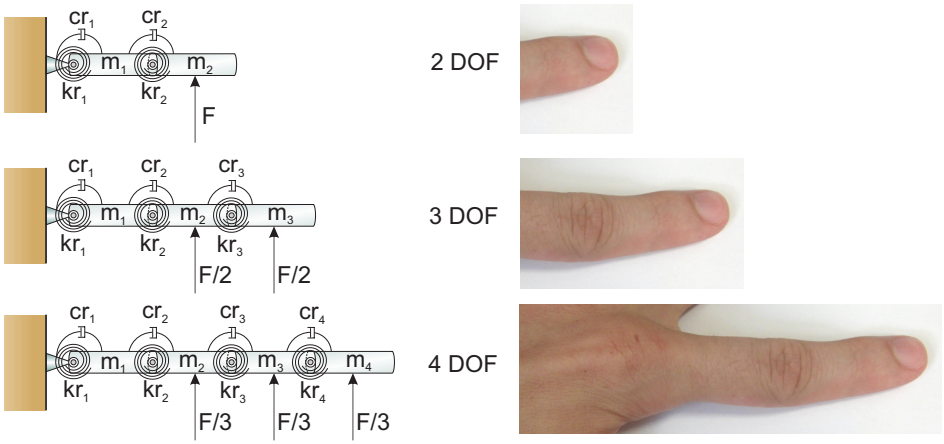


Figure 3: 2 DOF, 3 DOF and 4 DOF model configurations.

3.2 Derivation of equations of motion and model apparent mass calculation

This subsection presents the basics of computational dynamics used to derive the equations of motion, which are then forward integrated in time. The advantage of such an approach is that the models are easy to upgrade and the equations are ready for direct computer implementation. The full theory of the computational dynamics and the time integration can be found in [15].

The motion of *n* interconnected rigid bodies is governed by:

$$\mathbf{M}\,\ddot{\mathbf{q}} = \mathbf{Q}_e + \mathbf{Q}_c\,, \tag{7}$$

where $\mathbf{M}$ is the system mass matrix, $\ddot{\mathbf{q}}$ the total vector of system-generalized accelerations, $\mathbf{Q}_e$ is the vector of system external forces and $\mathbf{Q}_c$ the vector of system constraint forces.

Since the initial conditions can be estimated and the external forces are measured via the measuring handle Eq. 7 can be solved for independent as well as dependent coordinates. Once the accelerations of the multi-body system in the time domain are known the Fourier transform is used for frequency domain transformation; the measured finger forces are also transformed into the frequency domain. The AM of the model can then be calculated using:

$$AM(\omega) = \sum_{i=1}^{n} \frac{\frac{1}{i}\,F(\omega)}{\ddot{q}_i(\omega)}\,, \tag{8}$$

where *n* is the number of bodies in the model that are directly excited via an external force and is dependent on the model configuration; $F(\omega)$ is the force measured on the instrument handle and $\ddot{q}_i(\omega)$ are the calculated accelerations for each of the bodies.

3.3 Model constraints

The validity of the obtained results and the speed and stability of the computational algorithm depend largely on suitable constraints of the model parameters. It is difficult to determine reasonable ranges for damping cr_i and stiffness kr_i parameters but it is possible to define a relatively small range for the mass parameters m_i since each mass in the model represents a physical part of the index finger.

Based on the models configurations the constraints can be divided into two parts:

$$
\begin{gathered}
0.009 < m_1 < 0.250 \text{ kg} \\
0.007 < m_2, m_3, m_4 < 0.020 \text{ kg} \\
\text{5e-4} < cr_1 < \text{5e-2 Ns m/rad} \\
\text{5e-4} < cr_2, cr_3, cr_4 < \text{5e-3 Ns m/rad} \\
0.100 < kr_1 < 1000 \text{ Nm/rad} \\
0.010 < kr_2, kr_3, kr_4 < 10 \text{ Nm/rad},
\end{gathered}
$$

where m_1, cr_1, kr_1 are the constraints used for the first body and joint in the models. Since they represent a portion of the hand that is also indirectly measured, they have higher values compared to the rest of the bodies and joints. It has proven difficult to determine exactly how much mass is added by the hand during measurements.

3.4 Parameter identification

The parameters for each model were determined with data fitting based on the measured AM. The Levenberg-Marquardt algorithm was used:

$$
\left[\mathbf{J}^{\mathrm{T}}\,\mathbf{W}\,\mathbf{J} + \lambda\,\mathrm{diag}(\mathbf{J}^{\mathrm{T}}\,\mathbf{W}\,\mathbf{J})\right]\Delta = \mathbf{J}^{\mathrm{T}}\,\mathbf{W}\left(y_{\mathrm{Mea}} - y_{\mathrm{Mod}}\right), \tag{9}
$$

where $\mathbf{J}$ is the Jacobian matrix and was determined numerically, $\mathbf{W}$ is a weighting matrix, λ is an algorithmic parameter, Δ is the perturbation that moves the parameters in the direction of the solution, y_{Mea} is the measured data and y_{Mod} is the model data.

In the case of this study the y_{Mea} is represented by the measured finger AM and the y_{Mod} is the calculated AM of the model and the fitting was done in the frequency domain from 5 to 500 Hz at 0.5 Hz steps. The 2 DOF model parameters were determined first and then used in the 3 DOF model parameter search. The same procedure was also used for the 4 DOF model.

4 RESULTS AND DISCUSSION

Figures 4-6 show the comparison of the models magnitude and phase responses (designated "Model") with the measured biodynamic data (designated "Measured"). The parameters identified for each of the models are listed in Table 1.

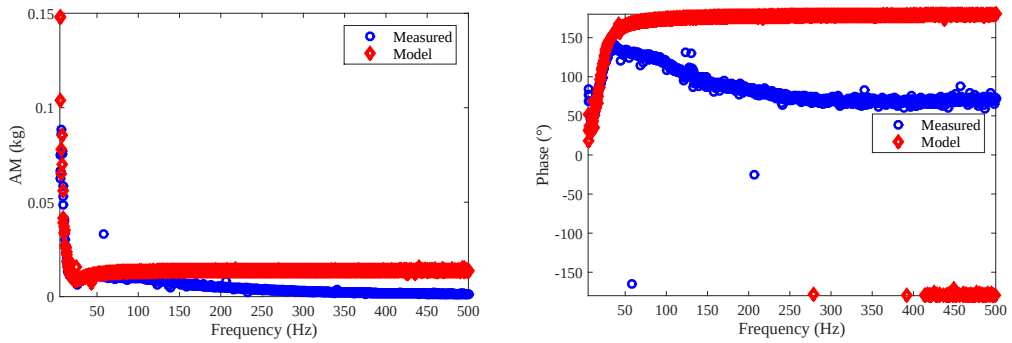


Figure 4: Comparison of measured and 2 DOF model apparent mass results: Left - magnitude; Right - phase.

The AM values of the one-phalanx, two-phalanx and three-phalanx measurements significantly decrease with higher frequencies, therefore model fitting was mostly focused from 5 to

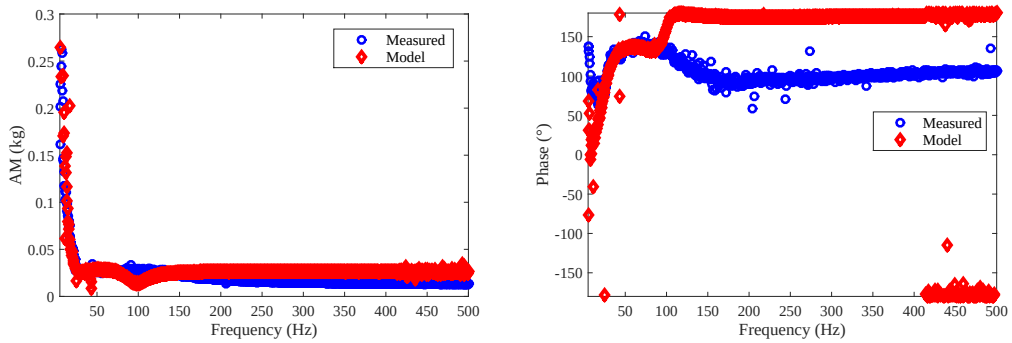


Figure 5: Comparison of measured and 3 DOF model apparent mass results: Left - magnitude; Right - phase.

150 Hz. Also, the relatively high values of AM up to 10 Hz are caused by the rest of the hand that is indirectly measured by the instrumental handle.

The 2 DOF model AM prediction is in good agreement with the measurements up to 100 Hz where the measured AM starts to drop but the model values remain constant. A more detailed model with translational joint components is probably needed to achieve better agreement at higher frequencies. The 3 DOF and 4 DOF models AM fit well with the measured data and the only deviations are observed around 100 Hz (for 3 DOF model) and 40 Hz (for 4 DOF model).

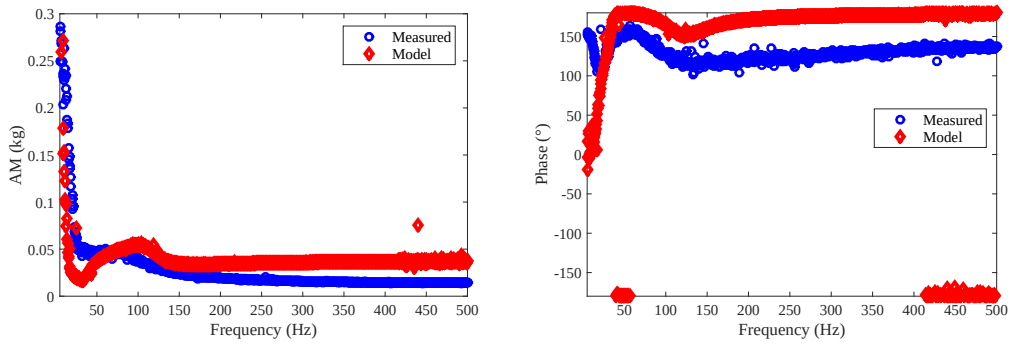


Figure 6: Comparison of measured and 4 DOF model apparent mass results: Left - magnitude; Right - phase.

The phase results for all three models show noticeable deviations from 100 Hz upward but the trend of predicted responses improves with higher DOF models. These deviations can be attributed to three possible reasons: the lack of translational components in joint modeling; the lumped representation of visco-elastic properties of the tissues and joints; and equal distribution of the measured force an all of the model elements. The actual distribution of the excitation force may vary from phalanx to phalanx but the current instrument device measures only the sum force exerted by the finger.

The masses of the phalanxes (see Table 1) obtained in all three models have reasonable values compared to the static masses of the finger phalanxes. The obtained dampness and stiffness

Parameter	Unit	2 DOF	3 DOF	4 DOF
m_1	kg	0.0900	0.0510	0.0607
m_2	kg	0.0100	0.0090	0.0110
m_3	kg	/	0.0100	0.0090
m_4	kg	/	/	0.0100
cr_1	Ns m/rad	0.0033	0.0034	0.0059
cr_2	Ns m/rad	0.0013	0.0020	0.0033
cr_3	Ns m/rad	/	0.0013	0.0020
cr_4	Ns m/rad	/	/	0.0013
kr_1	Nm/rad	1.0667	140.0	150.0
kr_2	Nm/rad	0.0651	0.8501	13.00
kr_3	Nm/rad	/	0.0651	0.8501
kr_4	Nm/rad	/	/	0.0651

Table 1: Parameters of the biodynamic response-based models determined with data fitting.

values are however significantly smaller compared to other research (e.g. [2, 9, 10]). The reason for the variations is mainly due to the differences in finger measurements and modeling. Other researchers measured all five fingers together at higher push forces while in this study only the index finger was measured at a low push force. The finger was therefore relaxed and the tissue during measurements was relatively soft. Also, as was expected from the measurements, the parameters m_1, cr_1, kr_1 vary with each model since a different part of the finger/hand is indirectly measured. The stiffness kr_1 rises as more phalanxes are added, which is again the result of a greater part of the stiffer hand influencing the measurements.

5 CONCLUSIONS

A novel approach to biodynamic modeling was proposed in this study. The usual implicit calculation of the equations of motion was replaced with explicit calculation *i.e.* forward time integration and the Fourier transform was then used to derive the biodynamic responses in the frequency domain. Mechanical models of the index finger were developed and the parameters were derived by minimizing the errors between the models and the measured AM. The required AM was measured with a newly developed instrument handle capable of single finger measurements. The modeling approach was sequential: only one phalanx of the finger was measured and modeled first. The obtained 2 DOF parameters were then used in the two-phalanx finger model and the obtained 3 DOF parameters were then used for the 4 DOF model. This procedure helps establish a systematic approach to biodynamic modeling, which can be used for more detailed and complex mechanical models beyond the finger. Reasonable agreement was achieved between the measured and predicted results and the study also confirmed that the proposed index finger model is an acceptable basis for further biodynamic studies.

REFERENCES

[1] M. J. Griffin, *Handbook of Human Vibration*. Academic Press, London, UK, 1990.

[2] R. Dong, J. Wu, D. Welcome, Recent advances in biodynamics of human hand-arm system. *Industrial Health*, **43 (3)**, 449–471, 2005.

[3] R. Dong, D. Welcome, T. McDowell, J. Wu, Measurement of biodynamic response of human hand-arm system. *Journal of Sound and Vibration*, **294 (4-5)**, 807–827, 2006.

[4] L. Knez, J. Slavič, M. Boltežar, Vibration transmissibilities of the human hand arm system exposed to Zh- and Yh- axes vibration. *Proceedings of the Kuhljevi dnevi conference*, 97–104, 2011.

[5] L. Knez, J. Slavič, M. Boltežar, A multi-axis biodynamic measuring handle for a human hand-arm system. *Journal of Mechanical Engineering*, **59 (2)**, 71–80, 2013.

[6] R. G. Dong, D. E. Welcome, X. S. Xu, C. Warren, J. Z. Wu, S. Rakheja, Mechanical impedances distributed at the fingers and palm of the human hand in three orthogonal directions. *Journal of Sound and Vibration*, **331 (5)**, 1191–1206, 2012.

[7] S. A. Adewusi, S. Rakheja, P. Marcotte, J. Boutin, Vibration transmissibility characteristics of the human hand-arm system under different postures, hand forces and excitation levels. *Journal of Sound and Vibration*, **329 (14)**, 2953–2971, 2010.

[8] R. G. Dong, S. Rakheja, T. W. McDowell, D. E. Welcome, J. Z. Wu, Estimation of the biodynamic responses distributed at fingers and palm based on the total response of the hand-arm system. *International Journal of Industrial Ergonomics*, **40**, 425–436, 2010.

[9] R. G. Dong, J. H. Dong, J. Z. Wu, S. Rakheja, Modeling of biodynamic responses distributed at the fingers and the palm of the human hand-arm system. *Journal of Biomechanics*, **40**, 2335–2340, 2007.

[10] R. G. Dong, D. E. Welcome, T. W. McDowell, J. Z. Wu, Modeling of the biodynamic responses distributed at the fingers and palm of the hand in three orthogonal directions. *Journal of Sound and Vibration*, **332**, 1125–1140, 2013.

[11] M. Srinivasan, K. Dandekar, An investigation of the mechanics of tactile sense using two-dimensional models of the primate fingertip. *Journal of Biomechanics*, **118**, 48–55, 1996.

[12] J. Z. Wu, R. G. Dong, S. Rakheja, A. W. Schopper, W. P. Smutz, A structural fingertip model for simulating of the biomechanics of tactile sensation. *Medical Engineering & Physics*, **26**, 165–175, 2004.

[13] J. Z. Wu, R. G. Dong, C. M. Warren, D. E. Welcome, T. W. McDowell, Analysis of the effects of surface stiffness on the contact interaction between a finger and a cylindrical handle using a three-dimensional hybrid model. *Medical Engineering & Physics*, **36**, 831–841, 2014.

[14] E. Concettoni, M. Griffin, The apparent mass and mechanical impedance of the hand and the transmission of vibration to the fingers, hand, and arm. *Journal of Sound and Vibration*, **325 (3)**, 664–678, 2009.

[15] A. A. Shabana, *Computational Dynamics, Third Edition*. Wiley, West Sussex, UK, 2010.

11th International Conference on Engineering Vibration
Ljubljana, Slovenia, 7–10 September 2015

DIRECT MATRIX UPDATING METHOD FOR STRUCTURAL MODELS BASED ON MEASURED RESPONSE

S.B.Cooper*[1] D.Di.Maio[2] and A.delliCarri[3]

[1]University of Bristol
sc14784@bristol.ac.uk

[2]University of Bristol
dario.dimaio,A.dellicarri@bristol.ac.uk

Keywords: Matrix updating method, Model updating, Mass matrix, Stiffness matrix, Measured response, and Structural modelling

Abstract. *Model updating is an important aspect of structural engineering as a result of its regular application in structural vibration control and structural health monitoring, finite element method (FEM) has become one of the most common approach of understanding and representing the dynamic characteristics of various engineering structures. However, the present FEM is not able to provide acceptable finite element (FE) models that are in adequate agreement when compared with measured results. To narrow the gap between the output of the finite element model and the output of a measured response, model-updating technique has been introduced and used widely to update or correct the analytical FE models using measured modal data. Identification of modal frequencies and mode shapes using output-only data has been in existence in conjunction with many other consistent modal identification methods. In this paper, a differential method for updating the mass and stiffness matrices of a structural model to replicate the measured frequency of the structure is proposed. As an initial simplified step, only the first eigen mode of the structure is considered, the updating process is carried out by applying the orthogonality conditions for the eigenvector. The technique is then generalised to assess scenarios where the first few eigen modes of the structure are measured. To validate the efficiency of the proposed method, numerical simulation based on a cantilever beam test structure is presented. The result obtained demonstrated that the differential updating method can be used to simultaneously update the analytical mass and stiffness of the model using measured vibration data. The advantage of the presented model is its simplicity and precision in computation, it can also be applied to structures with large degrees of freedom.*

1 INTRODUCTION

The use of consistent mathematical models to represent the dynamic behaviour of engineering structures is a technique which has been adopted by various engineers and researchers. These technique are often applied to cases where the reliability, safety and control of the structure depends greatly on the dynamic characteristics of the structure. According to most vibration engineering text books [1][2], the dynamic analysis of a structure can be divided into two different sections. The first section is called numerical or analytical modelling which often involves the use of finite element models, while the second section is vibration testing where the experimental modal parameters are obtained. Both techniques have their advantages and limitations, for example the numerical modelling often contains too many assumptions which doesn't replicate the actual application of the structure while the vibration test could be limited by available resources or difficulties in the experimental set-up and size of the structure. It is therefore important to develop methods that would narrow the gap between the results obtained from both analysis technique, these methods are often referred to as model correlation and/or model updating [3].The process of altering or amending an existing analytical model in light of the result measured from a vibration test is called *Model Updating*.Once the alteration process has been carried out, the updated model is expected to produce a more accurate dynamic behaviour of the structure.[4]. A range of model updating methods have been introduced over the last few decades as indicated in the survey conducted by Mottershead and Friswell in [5]. The Lagrange method which is based on the assumption of an initial correct mass and stiffness matrices was introduced by Berman [6] and Baruch [7]. The method involves the use of an objective function with constraint enforced using the Lagrange multiplier to generate an updated system of matrices. The Error matrix method proposed by Sidhu and Ewins estimated the error mass and stiffness matrices based on the assumptions that the error differences are small when compared with the analytical matrices. [8]. A method which requires the combination of an experimental modal data with the analytical data to construct the inverse of the mass and stiffness matrices was introduced by Link et al [9] and Caesar [10], this method is often referred to as the matrix mixing method. A more parametric updating method became more dominant in the 1990s, this method is called the iterative method. It also includes the eigensensitivity methods and frequency response function (FRF) method, the advantage associated with the method is its ability to preserve the physical connectivity. The eigensensitivity based method introduced in [11],[12] is founded on updating the parameters of the FE model iteratively, this is done by using the analytical modal data to calculate the pseudo-inverse of the sensitivity matrix. The drawback to this method is that the solution obtained is non-unique due to the under-determined nature of the sensitivity matrix. However the FRF updating methods uses measured FRF data to directly improve the different types of error function as shown in [13] and [14]. An iterative FRF method which involves expressing the difference between the analytical and measured receptances as a linear function of the parameter which is to be updated is presented by Lin and Ewins in [15],[16]. The method uses iteration process to yield an accurate updated system matrices. Other updating methods have also been introduced and applied on real engineering structures ever since the parametric updating became more central, a quicker method of generating accurate updated models is the use of Neural Networks in [17]. This method is achieved once an accurate training process has been obtained, however the accuracy of the updated model depends on how well the network is trained and the architecture of the network. Lu and Tu also presented a two-step neural network based model updating procedure for lightly damped structures in [18], the method involves updating the mass matrix in the first step and the damping

matrix in the second step. In this paper a differential method for updating the mass and stiffness matrices is presented, the updated matrices are derived from the orthogonality conditions for eigenvectors. The proposed is validated by conducting a numerical simulation and experimental test on a *Cantilever beam test structure*, the result obtained are discussed with the advantage of the proposed method.

2 Theoretical Formulation of Mass Matrix Updating Considering only the First Mode

Considering the mass and stiffness matrices of the finite element model of a structure with N degree of freedom (DOF), the properties of the modal model possesses some significant features which are called the *Orthogonality properties*.The following represents the orthogonal and normalised conditions for the *ith* eigenvectors.

$$[\psi_a]_i^T[M_a][\psi_a]_j = 0; i \neq j \tag{1}$$

$$[\psi_a]_i^T[K_a][\psi_a]_j = 0; i \neq j \tag{2}$$

where $[M_a]$,$[K_a]$ and $[\psi_a]_i$ in Eq. 1 and Eq. 2 represent the analytical mass and stiffness matrices, and the eigenvalue for a computed model. In practical application both the mass and stiffness matrices of the analytical model is often not the same as the experimental mass $[M_e]$ and stiffness $[K_e]$ matrices of the real structure. In a vibration test only the first few modes of vibration of a structure is often made available hence this formulation uses the natural frequency and first mode shape for the matrix updating. According to [1] for an element in the mass and stiffness matrices, the relationship between the experimental and analytical mass matrix and mode shape of the element can be expressed as:

$$[M_e] = [\Delta M] + [M_a] \tag{3}$$

$$[\psi_e]_1 = [\Delta\psi]_1 + [\psi_a]_1 \tag{4}$$

In Eq. 3 and Eq. 4 $[M_e]$ and $[\psi_e]_1$ represents the experimental mass matrix and mode shape while $[\Delta M]$ and $[\Delta\psi]_1$ is the error mass matrix and the difference in mode shape.Again referring back to Eq. 1 with the consideration of the first mode of an experimental model, the normalisation condition for the structure can be written in the form:

$$[\psi_e]_1^T[M_e][\psi_e]_1 = 1 \tag{5}$$

By substituting Eq. 3 and Eq. 4 into Eq. 5, the following expression is form

$$([\psi_a]_1 + [\Delta\psi]_1)^T([M_a] + [\Delta M])([\psi_a]_1 + [\Delta\psi]_1) = 1 \tag{6}$$

performing an algebraic expansion, Eq. 6 can be rewritten in the form:

$$\begin{aligned}[\psi_a]_1^T[M_a][\psi_e]_1 + [\psi_a]_1^T[\Delta M][\psi_a]_1 + 2[\Delta\psi]_1{}^T[M_a][\psi_a]_1 + \\ 2[\Delta\psi]_1{}^T[\Delta M][\psi_a]_1 + [\Delta\psi]_1{}^T[M_a][\Delta\psi]_1 + [\Delta\psi]_1{}^T[\Delta M][\Delta\psi]_1 = 1\end{aligned} \tag{7}$$

Neglecting the high oder terms, the above equation is reduced to the form:

$$[\psi_a]_1^T[\Delta M][\psi_a]_1 = -2[\Delta\psi]_1{}^T[M_a][\psi_a]_1 \tag{8}$$

From Eq. 8, it can be observed that the terms in both sides of the equation are scalar with an unknown $[\Delta M]$, Eq. 8 therefore becomes undetermined. However this type of problem can be solved using the *Singular Value Decomposition* (SVD), the disadvantage with using the SVD method is the fact that the bigger the dimension of the updating matrix the more unreliable the result. To overcome the challenge with number of unknown terms in the set of equations derived above, it is worth referring to the modal matrix [Φ]of the structure which cannot be obtained for the real structure. However since the modal matrix has been normalised with the experimental mass matrix then the principle in Eq. 9 is applicable.

$$[\Phi][\Phi]^T = [M_e]^{-1} \tag{9}$$

It is therefore possible to replace the analytical mode shape $[\psi_a]_1$ on the left hand side of Eq. 8 with the modal matrix [Φ] and post multiply the right hand side of the equation by the unit identity matrix [I]. By pre and post multiplying Eq. 8 by [Φ] and $[\Phi]^T$

$$[\Phi][\Phi]^T[\Delta M][\Phi][\Phi]^T = [\Phi](-2[\Delta\psi]_1^T[M_a][\psi_a]_1)[I][\Phi]^T \tag{10}$$

By substituting Eq. 9 into Eq. 10, the following expression is obtained

$$[\Delta M] = (-2[\Delta\psi]_1^T[M_a][\psi_a]_1)[M_e] \tag{11}$$

Eq. 3 shows the relationship between the analytical and the experimental mass matrix, by substituting Eq. 3 into Eq. 11 and rearranging an expression for the error mass matrix can be obtained in the form

$$[\Delta M] = \frac{(-2[\Delta\psi]_1^T[M_a][\psi_a]_1)}{1-(-2[\Delta\psi]_1^T[M_a][\psi_a]_1)}[M_a] \tag{12}$$

The mass matrix of the structure can now be update using the following equation

$$[M_e] = [M_a] + \frac{(-2[\Delta\psi]_1^T[M_a][\psi_a]_1)}{1-(-2[\Delta\psi]_1^T[M_a][\psi_a]_1)}[M_a] = \frac{P_M}{1-P_M}[M_a] \tag{13}$$

Where $[P_M]$ in Eq. 13 is -2$[\Delta\psi]_1^T[M_a][\psi_a]_1$, which can also be referred to as the correction factor for the mass matrix. The final equation for the mass matrix update can be expressed in both $[M_e]$ and $[M_a]$:

$$[M_e] = [M_a] + \frac{P_M}{1-P_M}[M_a] \tag{14}$$

It is worth noticing that even though the real modal matrix of the structure which is unobtainable has been used in the derivation for the mass matrix updating formula , the only values required in the final updating equation are the analytical eigenvector and the mode shape corrector.

3 Formulation of Stiffness Matrix Updating

The same procedure used for updating the mass matrix is also considered for the stiffness matrix update, an equation which relates the analytical and experimental stiffness matrix similar to Eq. 3 is formulated below where $[\Delta K]$ is the difference between the experimental and analytical stiffness matrices.

$$[K_e] = [\Delta K] + [K_a] \tag{15}$$

The normalisation conditions for first eigenvector of the analytical stiffness matrix is stated in Eq. 3 while the condition for first eigenvector of the experimental model is expressed in the form as shown in:

$$[\psi_e]_1^T[K_e][\psi_e]_1 = (\omega_e)_1^2 \tag{16}$$

By substituting Eq. 4 and Eq. 15 into Eq. 16, expanding the new equation and reducing the higher order terms would yield the following expression:

$$[\psi_a]_1^T[\Delta K][\psi_a]_1 = (\omega_e)_1^2 - (\omega_a)_1^2 - 2[\Delta\psi]_1^T[K_a][\psi_a]_1 \tag{17}$$

From the equation above it can be said that both sides of the equation have scalar terms and the stiffness error matrix $[\Delta K]$ is unknown, it is therefore not possible to solve the equation directly. However by substituting the analytical mode shapes in the left hand side of Eq. 17 for the real modal matrix of the structure $[\Phi]$ and post multiplying the right hand side of the equation by a unit matrix [I]. Then further pre and post multiplying the equation by $[\Phi]$ and $[\Phi]^T$, the following expression is obtained:

$$[\Phi][\Phi]^T[\Delta K][\Phi]\Phi]^T = [\Phi]((\omega_e)_1^2 - (\omega_a)_1^2 - 2[\Delta\psi]_1^T[K_a][\psi_a]_1)[I][\Phi]^T \tag{18}$$

Using the same principle for the modal normalisation with the experimental mass matrix as shown in Eq. 9, Eq. 18 can therefore be used to obtain an expression for the error stiffness matrix:

$$[\Delta K] = ((\omega_e)_1^2 - (\omega_a)_1^2 - 2[\Delta\psi]_1^T[K_a][\psi_a]_1)[M_e] = P_K[M_e] \tag{19}$$

The final equation used for updating the stiffness matrix can be expressed in the following format:

$$[K_e] = [K_a] + P_K[M_e] \tag{20}$$

Where $[P_K]$ in the equation Eq. 19 is $((\omega_e)_1^2 - (\omega_a)_1^2 - 2[\Delta\psi]_1^T[K_a][\psi_a]_1)$ it is said to be the correction factor for the stiffness matrix. Even though the process for deriving the stiffness is straightforward, it is important to keep in mind that only the first mode of a vibration test is considered. Also only the first modal vector of the analytical model and the first eigenvalues of real structure and analytical model has been used in the derivation. For the purpose of clarity during the updating process, any zero entries in the analytical mass and stiffness matrices are still kept as zero in the new updated matrices.

4 Overview of the Theory Considering More Modes

The mathematical derivation for the matrices updating so far has only taken into account the first vibration mode of the real structure, this section aims to provide a generalised formulation for a model where the first few experimental modes of vibration are available. For the purpose of this derivation, a model with *nDOF* is considered. Referring back to the scalar terms in the right hand side of Eq. 17 and representing it in the form of a *n*n matrix*. Then the equation is written in the form:

$$[(\omega_e^2)^n] - [(\omega_a^2)^n] - 2[(\Delta\psi)^n]^T[K_a][(\psi_a)^n] \tag{21}$$

The dimensions of the parameters in Eq. 21 depends on the number of the DOF that is being considered and the n ranking depends greatly on the number of measured vibration modes, with this new ranking notation Eq. 18 can now be rewritten accordingly:

$$[\Phi][\Phi]^T[\Delta K][\Phi]\Phi]^T = [\Phi]([(\omega_e^2)^n] - [(\omega_a^2)^n] - 2[(\Delta\psi)^n]^T[K_a][(\psi_a)^n])[\Phi]^T \tag{22}$$

Using the same normalisation relationship in Eq. 9, Eq. 22 can be expressed as

$$[\Delta K] = [\Phi][M_e]([(\omega_e^2)^n] - [(\omega_a^2)^n] - 2[(\Delta\psi)^n]^T[K_a][(\psi_a)^n])[\Phi]^T[M_e] \tag{23}$$

It can be noted that the major difference between Eq. 19 for the first mode and Eq. 23 for n number of modes is the modal matrix present in Eq. 23, the updating process is better improved by replacing the modal matrix [Φ] with the corresponding mode shape matrix [$(\psi_a)^n$] that is being considered in the analysis. Therefore Eq. 23 can be rewritten in the form:

$$\begin{aligned}[\Delta K] = [M_e][(\psi_a)^n]([(\omega_e^2)^n] - [(\omega_a^2)^n] - [(\Delta\psi)^n]^T[K_a][(\psi_a)^n] \\ -[(\psi_a)^n]^T[K_a][(\Delta\psi)^n])[(\psi_a)^n]^T[M_e]\end{aligned} \tag{24}$$

The final expression used fro updating the stiffness matrix can be written as follows:

$$\begin{aligned}[K_e] = [K_a] + [M_e][(\psi_a)^n][P_K][(\psi_a)^n]^T[M_e] \\ P_K = [(\omega_e^2)^n] - [(\omega_a^2)^n] - [(\Delta\psi)^n]^T[K_a][(\psi_a)^n] - [(\psi_a)^n]^T[K_a][(\Delta\psi)^n]\end{aligned} \tag{25}$$

The corresponding mass matrix can be updated using a similar expression as shown in the equation below:

$$\begin{aligned}[M_e] = [M_a] + [M_a][(\psi_a)^n][P_M][(\psi_a)^n]^T[M_a] \\ P_M = [(\Delta\psi)^n]^T[M_a][(\psi_a)^n] - [(\psi_a)^n]^T[M_a][(\Delta\psi)^n]\end{aligned} \tag{26}$$

5 Case Study

To verify the efficiency of the proposed method, a simulation case study is presented below. The model considered is a damped cantilever beam with the following dimensions and properties: length of the beam =0.3m, cross section area= 0.025x0.012=0.0003m^2, density =8050kg/m^3, elastic modulus E=198Gpa and the poisson ratio =0.3. The beam is modelled in a 2D planar space using *ABAQUS*, the beam is divided into 3 elements with 4 nodes. The length between each node is 0.1m, the total DOF of the model is 12, however the beam is fixed at the base which reduces the considered DOF of the model to 9. The analytical mass and stiffness matrices are generated from the results of a basic modal analysis simulation in ABAQUS. Solving the associated eigenvalue problem, the analytical natural frequencies and mode shapes are obtained. These values will be used later to generate the frequency response plot for the analytical model.

5.1 Experimental Test

To simulate the errors between the test model and the analytical model, a cantilever beam with the same dimension as the analytical model is fixed on a clamped base. A basic modal testing was carried out on the beam by exciting the tip of the beam to obtain measured response. The response of the beam is measured with 3 acceleration sensors attached to the structure at specific location related to the analytical node numbers. Figure 1 shows an illustration of the experimental set-up and the corresponding measured response from the modal test, the aim of the test is to show the dynamic response of the structure in certain frequency range. The measurement is also designed for clear identification of the first few modes.

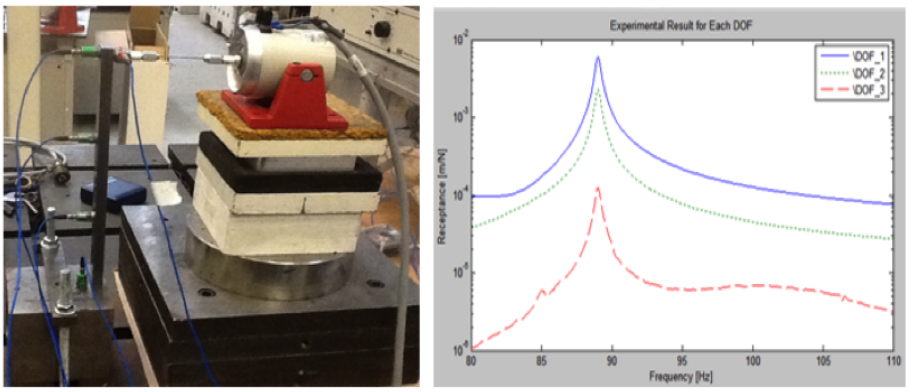


Figure 1: Experiment Setup and Response plot for Each DOF

5.2 Modal Parameter Estimation

To obtain accurate modal data from the experimental result, modal parameter estimation is used. This section covers the type of method used for estimating the modal parameter. The circle fitting method is the chosen method used to estimate the damped natural frequency, damping loss factor, and the normalised modal mass. The circle fitting is a single degree of freedom *SDOF* method based upon the modal model in the frequency domain, the method works by fitting a circle to the real and imaginary part of the frequency response data. It also minimises the error between the radius of the fitted circle and the measured response, the modal coefficient is then obtained from the diameter of the circle and the damping can be projected from the spacing along the nyquist plot. For the case of this example with light damping, the basic underlying function which is required to obtain the modal parameter is:

$$\alpha_{jk}(\omega) = \sum_{r=1}^{N} \frac{{}_rA_{jk}}{\omega_r^2 - \omega^2 + i\eta_r\omega_r^2} \tag{27}$$

where $({}_rA_{jk})$ and (η_r) and are the modal constant and damping loss factor, it is worth mentioning that Eq. 27 is used to extract each corresponding FRF element for the analytical and updated model.

5.3 Model Updating using the first mode

Now that the experimental mode shape and natural frequency have been obtained using the circle fit method, the values for the first mode shape and natural frequency is then substituted into Eq. 12 and Eq. 19 to calculate the correction factor for the mass and stiffness matrix. The correction factors are then substituted into Eq. 14 and Eq. 20 to calculate the updated mass and stiffness matrix. The natural frequencies and mode shapes for the analytical and updated model are obtained by solving the eigenvalue problem. Using the expression in Eq. 27 the general term in the frequency response function matrix, it is appropriate to use the estimated modal parameter with the analytical and updated mass and stiffness matrix to generate an individual FRF plot for each active DOF. However the challenge that was encountered whilst trying to obtain a response plot is the fact that the number of DOF of the analytical model exceeds the measured DOF in the experimental test. To match up both models, a method introduced in

[19] which is often referred to as *Modal Coordinate Method* was used to evaluate the missing DOF of the experimental mode shapes. This method is operated by defining the experimental mode shapes as a linear combination of the analytical mode shapes as described in Eq. 28, the coefficient q is calculated using the active DOF of the analytical model and the measured DOF.

$$[\psi_A]^e = [\psi_A]^a[q] \qquad (28)$$
$$[q] = [\psi_A]^{a+}[\psi_A]^e$$

With the complete DOF, the corresponding frequency response function for each element in the response matrix is obtained for both the analytical and updated model. A comparison of the response for the initial analytical model and the experimental model which corresponds to the the first active DOF is shown in the left hand side of Figure 2. From the response plot in the left

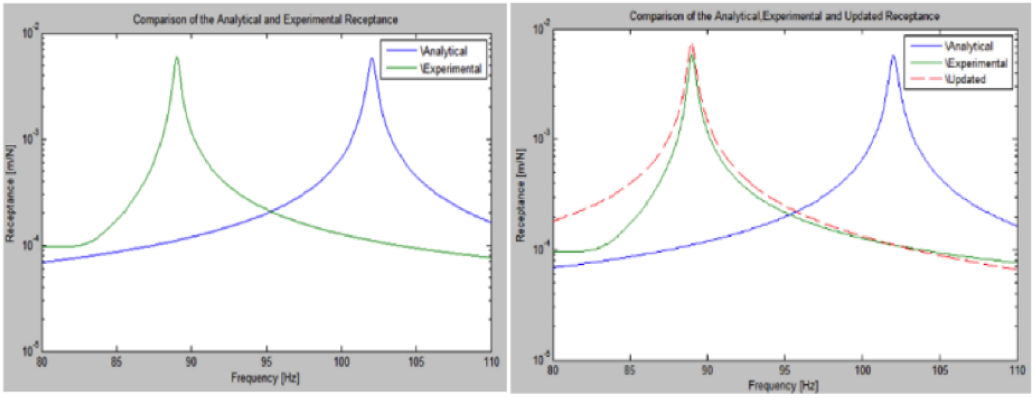


Figure 2: Comparison of Experimental, Analytical with Updated Response

hand side of Figure 2 it can be observed that there is a deviation between the experimental and analytical natural frequency, the overall shape of both plots are largely different which shows that the mass and stiffness matrices needs to be updated. Using the updating method presented, a response plot illustrating the difference between the analytical, experimental and the updated model is presented on the right hand side of Figure 2. It is obvious that excellent results have been achieved for the first mode of the beam using the updating technique, the error between the natural frequencies for the analytical and experimental model was 14.7% with the updating process the error between the updated response and the measured response have been reduced to 0.008% respectively, the difference between the experimental and updated mass line are caused by modelling error.

5.4 Model Updating for a 2DOF Model

Furthermore to test the applicability of the updating method on a multiple degree of freedom system, the response for the first DOF which corresponds to the accelerometer at the tip of the beam and the third DOF which corresponds to the last accelerometer attached to the beam was measured and analysed. The corresponding analytical response for the DOF associated to the measured point was also analysed, the plot on the left hand side of Figure 3 shows a graphical comparison of the experimental and analytical response for both DOF. Repeating the updating process presented, the response for both DOF were updated successfully as shown in the graph

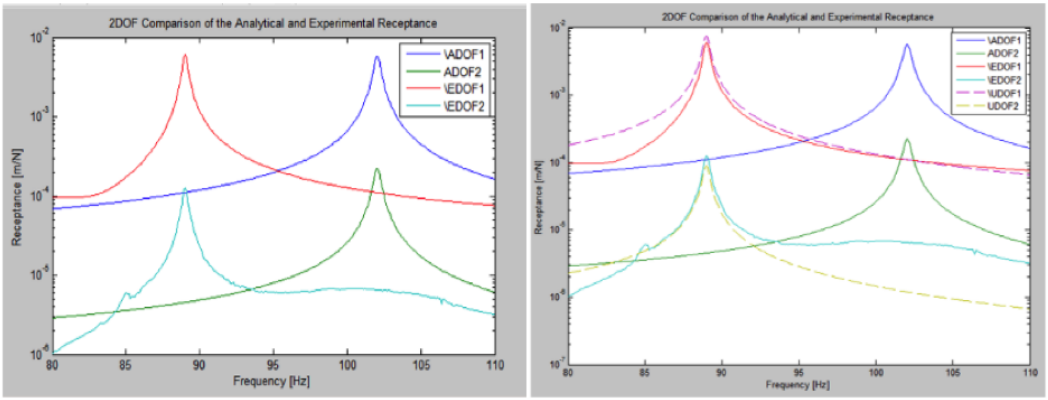


Figure 3: Comparison of Experimental, Analytical with Updated Response for the 1st and 3rd DOF

at the right side of Figure 3. The results obtained from the updating process have demonstrated it is possible to use this technique to simultaneously as many DOF for a model, although the are still some discrepancies between the mass and stiffness line of the updated model when compared with the measured data these errors can be narrowed down to modelling errors and other errors from the modal parameter estimation and experimental errors.

6 CONCLUSIONS

A new direct method for updating the mass and stiffness matrices of a structure to generate a response that would match the experimental measured response using estimated modal parameters is proposed. The matrix updating process was achieved by applying the orthogonality conditions for the eigenvectors and also making use of the mass normalisation principle to solve the problem of unknown terms in the derived equation. By substituting the modal vector with the modal matrix and considering the first mode, a correction factor was obtained. The correction factor was used to update the mass and stiffness matrices.The same process was also used to derive a generalised correction factor for the case where the first few modes of the structure are made available. The efficiency of the proposed method was demonstrated by updating the FRF response of a cantilever beam test structure, the results obtained from the case study illustrates that it is possible to simultaneously update the analytical mass and stiffness matrices of a multiple degree of freedom model using estimated parameters of the first few modes of a structure from a vibration test. The significance of the proposed method is it mathematical simplicity and its computational accuracy, the results obtained from the case study can also be further improved by choosing a material property such as the Young's modulus, density or poision's ratio to update or correct to the properties of the physical structure. The proposed method can also be used to update structures with large degrees of freedom once modal parameters are made available.

REFERENCES

[1] D.J.Ewins, *MODAL TESTING-Theory, Practice and Application*. Baldock, Hertfordshire, England, 2000.

[2] N.M.Maia,J.M.Silva, et,al *Theoretical and Experimental Modal Analysis*. Taunton, Somerset, England, 1997.

[3] M.I.Friswell and J.E.Mottershead *Finite Element Model Updating in Structural Dynamics*. Dordrecht, the Netherlands, 1995.

[4] M.I.Friswell, D.J.Inman and D.F.Pilkey *The Direct Updating of Damping and Stiffness Matrices Journal of AIAA*, **36**, 491–493, 1998.

[5] J.E.Mottershead,M.I.Friswell, *Model Updating in Structural Dynamics: A Survey Journal of Sound and Vibration*, **2**, 347–375, 1993.

[6] A.Berman, E.J.Nagy, *Improved of a Large Analytical Model Using Test Data Journal of American Institute of Aeronautics and Astronautics*, **8**, 1168–1173, 1983.

[7] M.Baruch *Optimal Correlation of Mass and Stiffness Matrices Using Measured Modes Journal of American Institute of Aeronautics and Astronautics*, **11**, 1623–1626, 1982.

[8] J.Sidhu, D.J.Ewins *Correlation of Finite Element and Modal Testing Studies of a Practical Structure Proceedings of the Second IMAC*, **12**, 756–762, 1984.

[9] M.Link, M.Weiland, J.M.Barragan *Direct Physical Matrix Identification as Compared to Phase Resonance Testing Proceedings of the Fifth IMAC*, **12**, 804–811, 1987.

[10] B.Caesar *Updating System Matrices Using Modal Testing Data Proceedings of the Fifth IMAC*, **12**, 453–459, 1987.

[11] H.Jung *Structural Dynamics Model Updating Using Eigensensitivity Analysis P.h.D Thesis, Department of Mechanical Engineering, Imperial College*, London ,UK. 1992.

[12] R.M.Lin, M.K.Lim, H.Du *Improved Inverse Eigensensitivity Method For Structural Analytical Model Updating Journal of Vibration and Acoustics*, **2**, 192–198, 1995.

[13] H.G.Natke, *Updating Computational Models in The Frequency Domain Based on Measured Data: A Survey Journal of Probabilistic Engineering Mechanics*, **1**, 28–35, 1988.

[14] C.P.Friten,S.Zhu *Updating of Finite Element Models by Means of Measured Data Journal of Computer and Structures* , **2**, 475–486, 1991.

[15] R.M.Lin,D.J.Ewins *Model Updating Using FRF Data 15th International Modal Analysis Seminar, K.U.Leuven,Belgium*, 141–163, 1990.

[16] R.M.Lin,D.J.Ewins *Analytical Model Improvement Using Frequency Response Function Journal of Mechanical System and Signal Processing*, *4* 437–458, 1994.

[17] J.Attala Mauro, *On Model Updating Using Neural Network Journal of Mechanical System and Signal Processing*, *1* 135–161, 1998.

[18] Y.Lu,Z.Tu, *A Two-level Neural Network Approach for Dynamic FE Model Updating Including Damping Journal of Sound and Vibration* , **2**, 931–952, 2004.

[19] J.Lipkens,U.Vandeurzen, *The Use of Smoothing Techniques for Structural Modification Application Proceedings of the 12th International Seminar On Modal Analysis, Leuven*, *Paper C1-3*, 1987.

11th International Conference on Engineering Vibration
Ljubljana, Slovenia, 7–10 September 2015

STOCHASTIC MODEL FOR THERMORHEOLOGICALLY SIMPLE MATERIALS USING FRACTIONAL DERIVATIVE OPERATORS

William Pinto Hernandez[1], **Daniel Alves Castello**[1], **Flavia Borges**[1], **Ney Roitman**[1], **Carlos Magluta**[1]

[1]Federal University of Rio de Janeiro, Brazil
pintoso84@gmail.com

Abstract. *The dynamic properties of thermorheological materials are highly frequency -and temperature-dependent. Numerical methods of structural systems require the mathematical model for these dependencies. The present work is a natural continuation of the research work concerning modeling and parameter identification of thermorheologically simple materials. The material behavior is modeled according to a fractional derivative operators model and it also considers a nonlinear relationship for the temperature dependence of the material. Shear complex modulus data for several temperatures of a material are obtained by dynamic tests in an experimental set-up. The goal of the present work is to propose a model calibration strategy for thermorheologically simple materials using the Bayesian Framework, where the parameter identification was performed using Markov Chain Monte Carlo (MCMC) approach. The utilized MCMC method enables us to generate a stochastic model for the thermorheologically simple material with frequency and temperature dependency.*

Fluid-Structure Interactions (TP09)

International Conference on Engineering Vibration
Ljubljana, Slovenia, 7-10 September 2015

PAPER INSTRUCTIONS FOR THE INTERNATIONAL CONFERENCE ON ENGINEERING VIBRATION

First A. Author*[1], Second B. Author[2], Third C. Author[2]

[1]Affiliation of the first author
name@e-mail.address

[2]Affiliation of second (and third) author
{name2,name3}@e-mail.address

Keywords: Instructions, Conference, Vibration, Experimental Dynamics, Wave Problems, Modal Analysis.

Abstract. *This document provides information and instructions for preparing a paper to be included in the Proceedings of the International Conference on Engineering Vibration. The paper can be written in Latex or Word. The first page is reserved for the title of the paper, the authors, affiliations, keywords and the abstract. The introduction must begin at the top of the second page.*

1 INTRODUCTION

The proceedings will be edited in an electronic form and saved on a pen-drive. The paper should be written following the Latex and Word templates for submission. The file has to be converted to Portable Document Format (PDF) before submission. Authors should submit the paper electronically in an archive file (using Zip or any other equivalent program) that must contain the PDF document and the original Word or Latex files and figures used for the manuscript.

The organizers do not commit themselves to include in the Proceedings any paper received later than the official deadline for paper submissions. The presenting author (assigned by *) must register and pay his/her registration fee for inclusion of the paper in the Proceedings.

2 GENERAL SPECIFICATIONS

The paper must be written in English U.K. within a printing box of 16 cm x 24 cm, centred in the A4 page, meaning that margins of 2.85cm should be assigned to the top and bottom and 2.5cm to the right and left. The paper including figures, tables and references must have a minimum length of 6 pages and must not exceed 10 pages, except for Invited lectures that are not subjected to page limits. The style implemented in the Times New Roman or similar, designated further for simplicity just Roman.

3 TITLE, AUTHORS, AFFILIATION, KEYWORDS

The first page must contain the Title, Author(s), Affiliation(s), Keywords and the Abstract. The second page must begin with the Introduction. There is a 58pt space between the Title and the editorial heading, thus the first line of the title is located 3 cm from the top of the printing box.

3.1 Title

The title should be written centred, in 14pt, boldface Roman, all capital letters. It should be single spaced if the title is more than one line long.

3.2 Author

The author's name should include first name, middle initial and surname. It should be written centred, in 12pt boldface Roman, 12pt below the title. The presenting author should be distinguished by *.

3.3 Affiliation

Author's affiliation should be written centred, in 11pt Roman, 12pt below the list of authors. A 12pt space should separate two different affiliations. Different affiliations should be distinguished by superscript with Arabic numbers that should also be included next to the corresponding author's surname.

3.4 Keywords

Please, write no more than six keywords. They should be written left aligned, in 12pt Roman, and the line must begin with the word **Keywords:** boldfaced. A 30pt space should separate the keywords from the affiliations.

3.5 Abstract

Use 12pt Italic Roman for the abstract. The word **Abstract** must be set in boldface, not italicized, at the beginning of the first line. The abstract text should be justified and separated 12pt from the keywords, as shown in the first page of these instructions. The abstract should neither be too short nor exceed the first page.

4 HEADINGS

4.1 Main headings

The main headings should be written left aligned, in 12pt, boldface and all capital Roman letters. There should be a 12pt space before and 6pt after the main headings. Use automatic single Arabic numbering with hanging of 0.7 cm.

4.2 Secondary headings

Secondary headings should be written left aligned, 12 pt, boldface Roman, with an initial capital for first word only. There should be a 12pt space before and 6pt after the secondary headings. Use automatic double Arabic numbering with hanging of 0.6 cm.

5 EDITORIAL HEADING

The first page will include the Editorial Heading, as shown in the first page of these instructions. In addition, successive pages will include the name of the authors. The Editorial Heading must be included in the paper by the authors.

6 TEXT

The normal text should be written single-spaced, justified, using 12pt Roman in one column. The first line of each paragraph must be indented 0.5 cm. Do not use any interparagraph spacing.

7 PAGE NUMBERS

The page numbers should be placed centred at the bottom of each page, with 12pt Roman. Note that the page numbers are not included in the printing box.

8 FIGURES

All figures should be numbered consecutively by Arabic numbers and captioned. The caption title should be written centred, in 10pt Roman, with upper and lower case letters, starting by Figure 1: and ended by a dot. Figures should be referred in the text by Figure 1.

A 12pt space should separate the figure from the text, a 6pt space should separate the figure from the caption, and again a 12pt space should separate the caption from the further text.

Figures should be included within the text.

9 EQUATIONS

A displayed equation should be numbered, using Arabic numbers in parentheses. It should be centred, leaving a 6pt space above and below to separate it from the surrounding text. It should be refereed in the text by Eq. (1) or Eqs. (1-3) or Eqs. (1), (4) or Eqs. (1) and (4).

The following example is a single line equation:

$$Ax = b \tag{1}$$

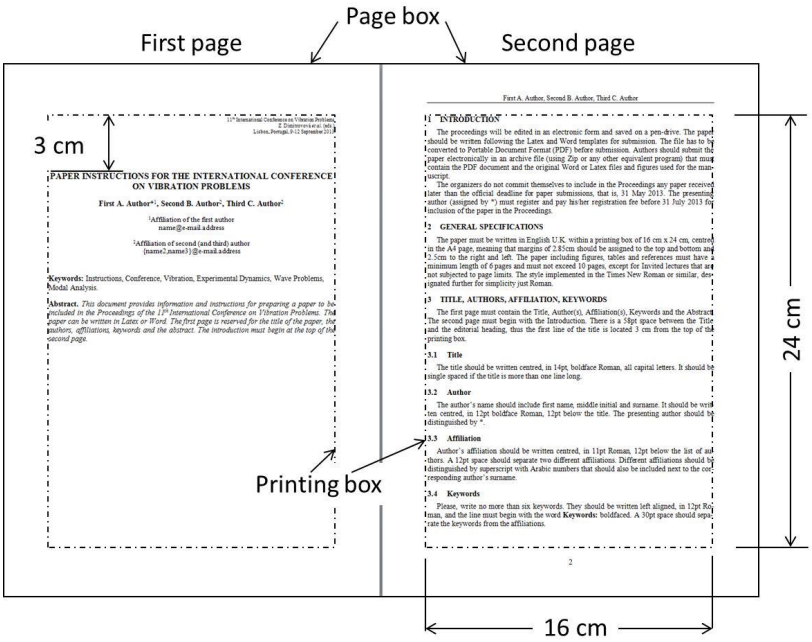


Figure 1: Page layout.

The next example is a multi-line equation:

$$\begin{aligned} Ax &= b \\ Bx &= c \end{aligned} \tag{2}$$

10 TABLES

All tables should be numbered consecutively by Arabic numbers and captioned, the caption should be 10pt Roman, upper and lower case letters, starting by Table 1: and ended by a dot.

Title 1	Title 2	Title 3
C21	C22	C23
C31	C32	C33
C41	C42	C43
C51	C52	C53

Table 1: Example of the construction of one table.

A 12pt space should separate the table from the text, a 6pt space should separate the table from the caption, and again a 12pt space should separate the caption from the further text. Tables should be refereed in the text by Table 1.

11 FORMAT OF REFERENCES

References should be quoted in the text by numbers [1] or [1, 2] or [1-3] or [1-3, 5] and grouped together at the end of the paper in numerical order as shown in these instructions.

They are separate by a 36pt space from the text. They start with **REFERENCES** in bold capital Roman. There is a 6pt space between this title and the first reference. There is always a 6pt space between consecutive references. For automatic numbering use 0.7 cm indentation and hanging of 0.3 cm. Kindly consult the examples of book [1], article in journal [2] and article in proceedings [3] examples at the end of these instructions.

12 CONCLUSIONS

- Papers should be submitted electronically.
- The paper should be written following the Latex and Word templates for submission.
- The paper must be converted to Portable Document Format (PDF) before submission through the conference web site.
- Deadline for the submission: see www.icoev.org.
- The presenting author must register and pay his/her registration fee for inclusion of the paper in the Proceedings.

REFERENCES

[1] P. Nikravesh, *Computer-aided analysis of mechanical systems*. Prentice-Hall, Englewood Cliffs, New Jersey, 1988.

[2] W. Schiehlen, Multibody system dynamics: Roots and perspectives. *Multibody System Dynamics*, **1**, 149–188, 1997.

[3] F. Armero and S. Glaser, Enhanced strain finite element methods for finite deformation problems. M. Doblaré, J.M. Correas, E. Alarcón, L. Gavete and M. Pastor eds. *III Congreso de Métodos Numéricos en Ingeniería*, SEMNI, Barcelona, Spain, 423-437, 1996.

11th International Conference on Engineering Vibration
Ljubljana, Slovenia, 7–10 September 2015

STABILIZATION CONTROL OF SELF-EXCITED VIBRATIONS IN A FLEXIBLE FLUID-CONVEYING PIPE

Xiaoxin Chen*[1], Hiroshi Yabuno[2], Kiyotaka Yamashita[3]

[1]Department of Intelligent Interaction Technologies , University of Tsukuba
s1420847@u.tsukuba.ac.jp

[2]Department of Intelligent Interaction Technologies , University of Tsukuba
yabuno@esys.tsukuba.ac.jp

[3]Fukui University of Technology
yamakiyo@ca2.so-net.ne.jp

Keywords: Nonlinear Dynamics, Stabilization Control, Self-Excited Vibration, Fluid-Conveying Pipe.

Abstract. *This paper presents a theoretical and experimental investigations of stabilization control of self-excited vibrations of a pipe conveying fluid due to non-conservative force. There is a long history of studies on the unstable phenomena of a flexible fluid-conveying pipe. In contrast with the studies on the mechanisms of the unstable phenomena, there are few studies on the stabilization control method for the flexible fluid-conveying pipe. Because most control methods do not take into account the non self-adjointness and employ the eigenmodes of the pipe without fluid flow, the unstable mode is approximated by the linear combination of them. Therefore, many sensors are required and neglected higher modes can cause the spillover. On the other hand, in this study, we try to directly derive the unstable eigenmode by using power series. By using this unstable mode, it is possible to carry out the stabilize control without spillover using one sensor. In this presentation, we derive the method of the unstable eignemode and discuss an experimental result of destabilized a flexible fluid-conveying pipe. A stabilization control method of self-excited vibrations of a fluid-conveying pipe is proposed based on the velocity feedback of the pipe displacement. Then, according to the proposed feedback rule, a bending moment on the top end of the pipe is applied by a piezo actuator. The validity of the proposed stabilization control method is experimentally confirmed.*

11th International Conference on Engineering Vibration
Ljubljana, Slovenia, 7–10 September 2015

INVESTIGATION OF TYPICAL SECTION AERODYNAMIC TRANSFER FUNCTIONS USING A VISCOUS CFD FORMULATION

Rafael N. Ihi[1], **João Luiz F. Azevedo**[2]

[1]Instituto Tecnológico de Aeronáutica, DCTA/ITA, São José dos Campos, SP, Brazil
rafael.ihi@hotmail.com

[2]Instituto de Aeronáutica e Espaço, DCTA/IAE/ALA, São José dos Campos, SP, Brazil
joaoluiz.azevedo@gmail.com

Keywords: Aeroelasticity, Fluid-structure interaction, CFD, Free and forced oscillations.

Abstract. *The fluid-structure interaction problem plays an important role in many industrial applications of engineering systems. In aeronautics, for instance, it is a crucial item to be considered, since this interaction generates vibrations, which in turn can cause structural fatigue and even aeroelastic phenomena, such as buffeting, aileron reversal, or flutter, for example. These problems are often very complex, involving the coupling effects of the fluid flow interacting with a moving structure. Recent advances in computational performance and in computational fluid dynamics (CFD) techniques have made the numerical approach to this problem feasible in an industrial setting. Nevertheless, there is still considerable room for improvement in this research area. In this context, the present work addresses the use of high-fidelity CFD formulations in the construction of the aerodynamic operator for aeroelastic stability analyses. In particular, the work is concerned with studying the effects of the inclusion of the viscous terms in the aerodynamic formulation, as compared to previous inviscid results. Hence, the flows of interest are assumed to be adequately modeled either by the 2-D Euler equations or the 2-D Reynolds-averaged Navier-Stokes (RANS) equations with appropriate turbulence closures. All turbulent results included in the present paper have used the Spalart-Allmaras turbulence model. The dynamic system is represented by the NACA 0012 airfoil typical section with two degrees of freedom, namely, plunge and pitch. The purely aerodynamic test cases considered for the airfoil, in the transonic regime, include steady cases and harmonically prescribed motions. Indicial aerodynamic responses of the airfoil, with the current flow solver formulation, are compared to purely inviscid calculations. These responses are used to construct aerodynamic transfer functions, which then allow for aeroelastic analyses in state space format. The comparison of viscous and inviscid results presents the expected trends.*

1 INTRODUCTION

Aeroelasticity is the science that is concerned with the interaction between aerodynamic, elastic and inertial forces [1]. As one of the most important aeroelastic phenomena in aircraft design, flutter can potentially lead to structural failure. Hence, a structural reinforcement is required to avoid such phenomena. Although the industry and most of the current analysis have relied on linear methods for the flutter prediction, this is not an ideal scenario, especially in the transonic flight regime. In fact, aeroelastic problems are always subjected to nonlinearities, to a greater or lesser extent. The nonlinearity may arise by many mechanisms associated to aerodynamics, structure or control system causes [2].

In transonic flows, for instance, in which the aeroelastic system is investigated in this work, the nonlinearity can be caused by the movement of shock waves. Traditionally, the industry deals with the nonlinearity in flutter analysis by adding safety margins. However, this implies in a heavier aircraft and, in some cases, in restrictions on the flight envelope to avoid potentially dangerous conditions [2]. As noted by Ashley [3], the phase lag in the shock motion over an airfoil, typical in transonic flows, causes a lowering of the flutter speed, which is typically known in the literature as the transonic dip. Hence, the envelope region in which linear methods are less effective is also the most likely for flutter occurrence. In addition, although the study of limit cycle oscillations is not part of this work scope, such studies also require the consideration of nonlinear aerodynamics. Therefore, a higher level of fidelity than the ones used in traditional approaches for the fluid representation is required for an accurate flutter prediction.

The present work is focused on the numerical investigation of the fluid-structure interaction for transonic flows over the NACA 0012 airfoil, and the validation of a CFD tool developed for such aeroelastic application through the comparison of aerodynamic coefficients. The Reynolds number (Re) considered for the simulations is $Re = 12 \times 10^6$. Simulations are based on the Euler and the 2-D Reynolds-averaged Navier-Stokes (RANS) equations, and no deformation of the airfoil is considered. A typical section airfoil system is used, in which the torsion and flexure of a real wing configuration are represented by the pitch and plunge degrees of freedom of the typical section model, respectively. The unsteady flows deal with prescribed step and sinusoidal motions of the airfoil. In the former case, lift and moment coefficients are compared to the inviscid results of Ref. [4] in order to validate the implementation of the viscous terms, recently accomplished. For harmonic motions, the aerodynamic hysteresis is investigated and compared to the literature data.

2 GENERAL FORMULATION

2.1 Aeroelasticity

The aeroelastic structural model is represented by the typical section [1, 5]. This system consists of a rigid airfoil, mounted on torsional and cross-flow springs, as shown in Fig. 1. The airfoil has two degrees of freedom, plunge and pitch, and it is able move under the effect of the aerodynamic, inertial and elastic loadings. A state space representation of the typical section system can be written as

$$\left[\tilde{M}\right]\{\dot{\chi}(t^*)\} + \left[\tilde{K}\right]\{\chi(t^*)\} = \{\tilde{Q}_a(t^*)\}\,, \tag{1}$$

where $\{\chi(t^*)\}$ is the system state vector,

$$\{\chi_1(t^*)\} = \{\eta(t^*)\}\,, \tag{2}$$

$$\{\chi_2(t^*)\} = \{\dot{\eta}(t^*)\} = \{\dot{\chi}_1(t^*)\}\,, \tag{3}$$

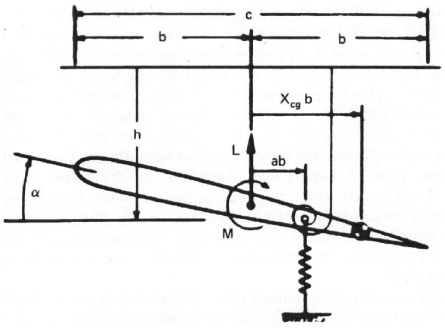


Figure 1: Typical section airfoil.

$$\{\chi(t^*)\} = \left\{ \begin{array}{c} \{\chi_2(t^*)\} \\ \{\chi_1(t^*)\} \end{array} \right\} . \tag{4}$$

The dimensionless mass and stiffness matrices, $[\tilde{M}]$ and $[\tilde{K}]$, are defined, respectively, as

$$[\tilde{M}] = \left[\begin{array}{cc} [M^*] & [0_{2\times2}] \\ [0_{2\times2}] & [I_{2\times2}] \end{array} \right] , \; [\tilde{K}] = \left[\begin{array}{cc} [0_{2\times2}] & [K^*] \\ [-I_{2\times2}] & [0_{2\times2}] \end{array} \right] , \tag{5}$$

where the $[M^*]$ and $[K^*]$ matrices are defined in Ref. [6], and the forcing term is given by

$$\{\tilde{Q}_a(t^*)\} = \left\{ \begin{array}{c} \{{Q_a}^*(t^*)\} \\ \{0_{2\times1}\} \end{array} \right\} , \tag{6}$$

here, $\{{Q_a}^*(t^*)\}$ is the appropriately normalized vector of the generalized modal aerodynamic forces. Applying the Laplace transform to Eq. 1, one obtains

$$s^* \left[\tilde{M}\right] \{X(s^*)\} + \left[\tilde{K}\right] \{X(s^*)\} = \{\tilde{Q}_a(s^*)\} , \tag{7}$$

where

$$s^* = \frac{s}{\omega_r} . \tag{8}$$

The general state space representation of the typical section aeroelastic system is described by the following expression

$$\{\dot{\mathcal{Z}}(t^*)\} = [D] \{\mathcal{Z}(t^*)\} , \tag{9}$$

where the stability matrix, $[D]$, is defined in Ref. [6] and $\{\mathcal{Z}(t^*)\}$ is the new state vector that results from the addition of the aerodynamic state variables. This vector is written as

$$\{\mathcal{Z}(t^*)\} = \left\{ \begin{array}{c} \{\dot{\eta}(t^*)\} \\ \{\eta(t^*)\} \\ \{\eta_a(t^*)\}_1 \\ \vdots \\ \{\eta_a(t^*)\}_{n_a} \end{array} \right\} , \tag{10}$$

and

$$\{\eta_a(t^*)\}_n = \int_0^{t^*} \{\eta(\tau)\} e^{[-V^*\beta_n(t^*-\tau)]} d\tau , \tag{11}$$

where the β_n variables introduce the aerodynamic lags with respect to the structural modes and n_a is the number of added aerodynamic state variables. Furthermore, the generalized aerodynamic force vector is, then, written in terms of the new aerodynamic state variables as

$$\{Q_a(t^*)\} = \frac{(V^*)^2}{\pi\mu_r}\left([A_0]\{\eta(t^*)\} + \frac{1}{V^*}[A_1]\{\dot{\eta}(t^*)\} + \right. \\ \left. + \frac{1}{(V^*)^2}[A_2]\{\ddot{\eta}(t^*)\} + \sum_{n=1}^{n_\beta}\left[A_{(n+2)}\right]\{\eta_a(t^*)\}_n\right) . \quad (12)$$

Here, the $[A_n]$ matrices are the approximating coefficient matrices. Furthermore,

$$[{Q_a}^*(t^*)] = \frac{1}{\omega_r^2}\left[Q_a(t^*)\right] . \quad (13)$$

The aeroelastic stability analysis can be reduced to the classical eigenvalue problem as

$$\left([D] - s^*\left[I_{n\times n}\right]\right)\left\{\mathcal{Z}\left(s^*\right)\right\} = \left\{0_{n\times 1}\right\} . \quad (14)$$

The objective here is to evaluate the behavior of this system as a function of the characteristic speed, V^*, which is defined as

$$V^* = \frac{U_\infty}{b\omega_r} , \quad (15)$$

where b is the airfoil half chord and ω_r is the circular reference frequency.

2.2 Aerodynamics

The CFD tool used in this work is based on the 2-D RANS equations, which represent a two dimensional flow of a compressible viscous fluid through a continuous medium in the transient regime. In a finite volume approach, these equations can be written in Cartesian coordinates as

$$\frac{\partial}{\partial t}\int_{V_i} Q dx dy + \oint_{S_i}(E dy - F dx) = 0 . \quad (16)$$

In Eq. 16, V represents the control volume or the area, and S is the length of the edges of the cells. Q is the vector of conserved properties, and E and F are the flux vectors in the x and y directions, respectively. These variables are written

$$Q = \left[\ \rho \quad \rho u \quad \rho v \quad e\ \right]^T , \qquad E = E_e - E_v, \qquad F = F_e - F_v . \quad (17)$$

Here, E_e and F_e represent the inviscid fluxes, or Euler fluxes, whereas E_v and F_v represent the viscous terms [7]. In addition, the set of Euler equations are obtained from the Navier-Stokes equations by neglecting all viscous stresses and heat conduction terms.

In the present work, turbulence closure is achieved with the Spalart-Allmaras (SA) turbulence model [8]. It is implemented in the solver in accordance to the formulation presented in Ref. [8]. The model is concurrently integrated with the 2-D RANS equations in a loosely coupled approach [9].

2.3 Spatial Discretization

The numerical scheme adopted in this work is a cell centered finite volume method [7]. Here, for each control volume face, flux information of flow field variables are computed from i-th and n_b-th control volumes which share a k-th face. The flux computation is, then, accordingly distributed back to the i-th and n_b-th control volumes. Moreover, all variables or parameters necessary at face are computed by a simple average procedure. Further details can be found in Refs. [4, 7, 10].

2.4 Time Discretization

For calculations without dual time stepping (DTS), an explicit, 2nd-order, 5-stage Runge-Kutta scheme [4] is used to integrate the RANS equations in time, while a 1st-order implicit Euler method [9] is used to time advance the turbulence model equation. For applications in which a dual time stepping method is required, a 2nd-order implicit backward Euler scheme [11] is used to discretize the physical time derivatives for the RANS equations, whereas the same explicit 5-stage Runge-Kutta scheme [4] is used for time stepping in pseudo time. As before, the turbulence modeling equation is time-marched with the 1st-order implicit Euler method [9]. This equation is not subjected to dual time stepping, since the flow and the turbulence model equations are time marched in a loosely coupled fashion. The approach is able to increase the stability range of the method, allowing larger time steps which are, therefore, only bound by the physical frequencies one wishes to resolve in the unsteady simulations.

3 RESULTS

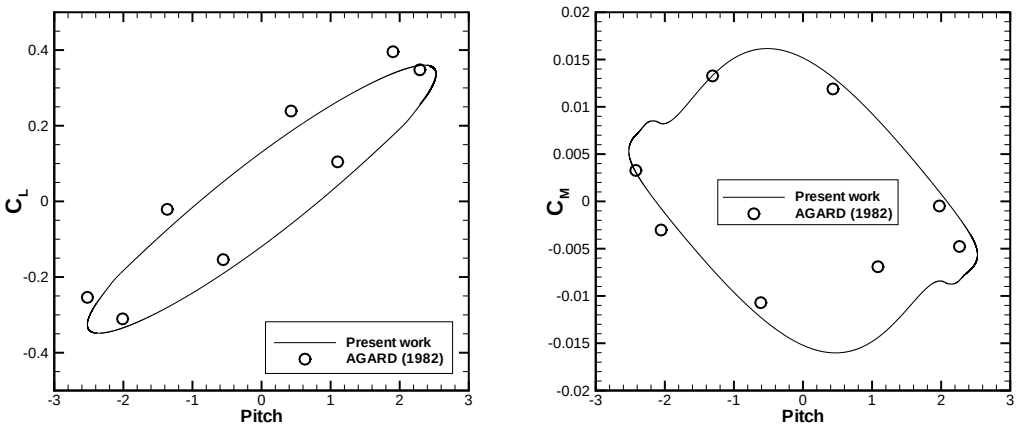
3.1 Validation of the Unsteady Solver

The investigation of aerodynamic hysteresis in unsteady transonic flows is very important as a form of characterizing the behavior of the flow simulation code under controlled unsteady conditions and for very smooth motions. Moreover, such investigation allows a verification of the mesh movement procedures implemented in the solver. This aerodynamic hysteresis phenomenon can be used to validate the unsteady results against data available in the literature, as well as it can be used to estimate the effect of the phase lag between the motion and the aerodynamic response. In the present work, the oscillatory motion of the harmonically pitching airfoil is obtained by specifying the angle of attack variation.

The NACA 0012 airfoil is forced by a harmonic oscillation in the pitch degree of freedom about the quarter chord point. The simulations are performed using an Euler formulation. The unsteady lift and moment coefficients for the pitching NACA 0012 airfoil at $M_\infty = 0.755$, $\alpha_0 = 0.016$ deg., $\Delta\alpha = 2.51$ deg., and $k = 0.0814$ are presented in Fig. 2. Here, α_0 is the initial mean flow angle of attack, $\Delta\alpha$ is the pitch oscillation amplitude and k is the reduced frequency. The simulations are performed until the solution reaches a periodic state, which in this case is obtained after four cycles of motion. The dimensionless time step is 0.001. A comparison of the present Euler results is made with the experimental data from AGARD [12], and good agreement is observed. Moreover, it is quite possible that the differences between the numerical and experimental results would be even smaller for viscous runs. The present simulation has also been used as a form of validating the DTS scheme, which is essential for dealing with the stiffness problem created by the very fine meshes required for viscous turbulent calculations. Further details can be found in Ref. [13], which shows that the implemented algorithm is producing the expected results, once convergence in the inner iterations had been achieved.

3.2 Indicial Response

As demonstrated in Ref. [14], a series of time-shifted and scaled step functions are equivalent to any continuous function. Hence, the convolution integral of an indicial response with the input time derivative is an approximation of the system response to an arbitrary input. The determination of the indicial response of an aerodynamic system is, therefore, sufficient to know the complete unsteady behavior of that system. These calculations are essential in order



(a) Unsteady lift coefficient response.

(b) Unsteady moment coefficient response.

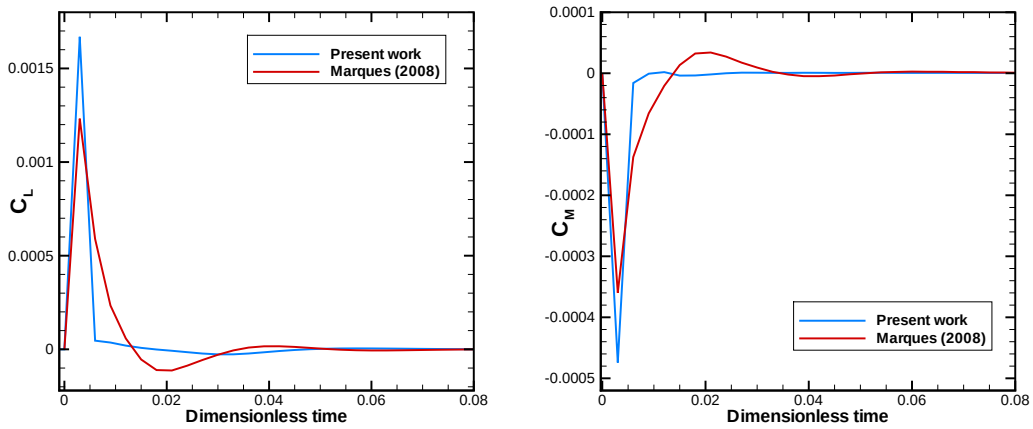
Figure 2: Sinusoidal pitch oscillations of a NACA 0012 airfoil at $M_\infty = 0.755$ and $k = 0.0814$.

to allow the uncoupling of the dynamic equations of motion from the aerodynamic response in aeroelastic problems such as the ones of interest here. In other words, the governing equations for the structural dynamics may be solved separately from the aerodynamic equations.

The investigation on the effects of the inclusion of the viscous terms is performed in comparison with a purely inviscid calculation, obtained in Ref. [4]. Discrete step functions, or DS, are also used to prescribe the airfoil motion, with the intention of measuring the unsteady aerodynamic response. As discussed, the correct calculation of the aerodynamic response for such functions is essential in order to be able to generate aerodynamic transfer functions that would allow performing the stability analysis of the aeroelastic system in the frequency domain.

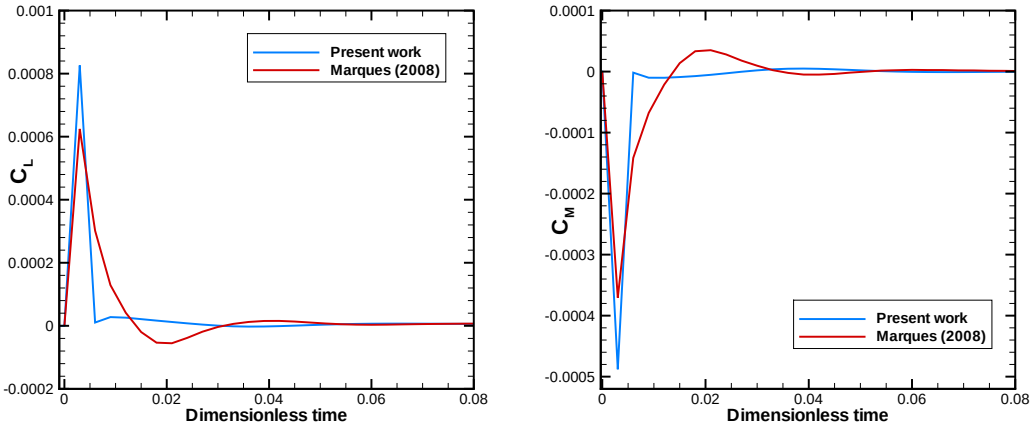
Freestream conditions considered in these simulations are $M_\infty = 0.8$ and initial steady angle of attack $\alpha_0 = 0$ deg. For the viscous calculations, the freestream Reynolds number considered is $Re = 12 \times 10^6$, based on the airfoil chord. Furthermore, the SA turbulence model is used for turbulence closure in the viscous simulations. The amplitude of the DS input is 0.000001 dimensionless chord units in plunge and 0.0001 deg. in pitch. The time step reported in the inviscid calculations in Ref. [4] is 0.003 dimensionless time units. A DTS scheme is used to time march the aerodynamic equations, using the same physical time step as the one employed by the reference. The initial 0.15 dimensionless time units of simulation were performed, here, using 1000 inner iterations for each physical time step. Reference [13] demonstrates that this number of inner iterations is enough to achieve convergence during the initial stage of the DS input excitation. After this initial period of 0.15 time units, the number of inner iterations decreases to 100. This procedure was necessary to allow the feasibility of the computational cost regarding the turbulent flow simulations.

The lift and moment coefficient responses of a NACA 0012 airfoil subjected to a DS input in plunge and pitch are shown in Figs. 3 and 4, respectively. In these figures, the current results are compared to the ones obtained in Ref. [4] for a similar study. Figures 3 and 4 indicate that the variation of the aerodynamic responses becomes much smoother after a short period of time from the onset of the DS perturbation. Hence, it is expected that the number of inner iterations required to achieve convergence of the inner iterations would also follow the same tendency of the aerodynamic coefficients time histories, *i.e.*, it would be smaller. Moreover, despite having



(a) Unsteady lift coefficient response. (b) Unsteady moment coefficient response.

Figure 3: Aerodynamic response to a discrete step in plunge for a NACA 0012 airfoil at $M_\infty = 0.8$ and $\alpha_0 = 0$ deg.



(a) Unsteady lift coefficient response. (b) Unsteady moment coefficient response.

Figure 4: Aerodynamic response to a discrete step in pitch for a NACA 0012 airfoil at $M_\infty = 0.8$ and $\alpha_0 = 0$ deg.

a fairly pronounced initial peak, the viscous response is damped faster than the inviscid one, for all cases, as expected. Additionally, the higher amplitude observed in the initial part of the viscous flow response seems to make sense if one considers the development of a leading edge vortex caused by the unsteady motion. Thus, such vortical structures are responsible for a pressure drop in their vicinity, increasing the lift. Naturally, the lift gain is temporary, once the vortex is quickly convected away from the airfoil, which would explain the damped behavior of the viscous flow response afterwards.

3.3 Aerodynamic Transfer Functions

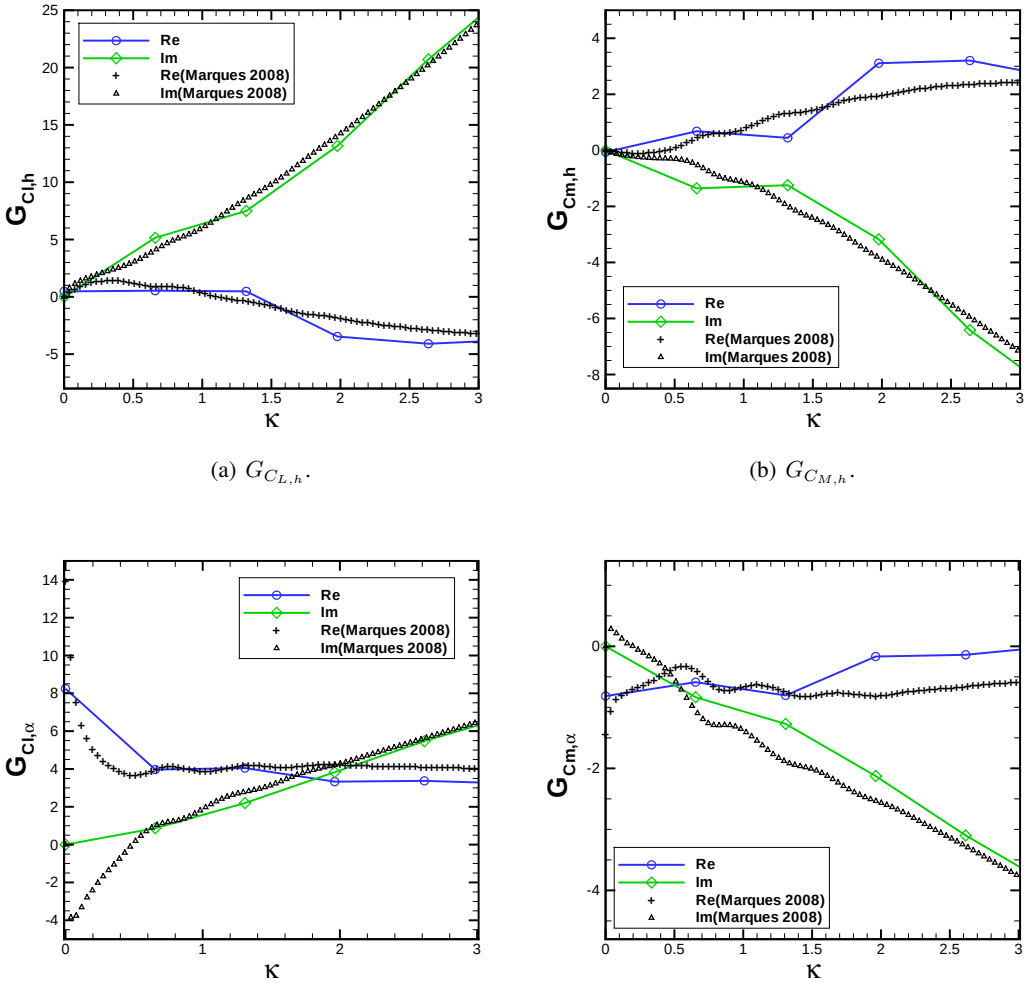
The major interest, considering the perspective of performing aeroelastic stability analyses, consists in obtaining aerodynamic states from the unsteady aerodynamic responses. The calculation of such aerodynamic states concerns the calculation of aerodynamic transfer functions in the frequency domain and the approximation of such transfer functions using rational polynomials as discussed in Refs. [4, 15]. In the case of the present work, the aerodynamic transfer functions are calculated from performing power spectral density calculations of the previous unsteady aerodynamic results, as discussed in detail in Ref. [15].

The aerodynamic transfer functions are presented in Fig. 5. This figure presents the results in terms of real and imaginary parts of the lift and moment coefficients due to plunge and due to pitch. The present results are compared to those reported in Ref. [4], which considered an inviscid flow. Clearly, the frequency content of the current results does not have the same level of resolution as the ones of the literature. The interval of two consecutive points in the frequency domain of the aerodynamic transfer functions is inversely proportional to the total integration time of the aerodynamic solution [15]. Figure 5 clearly indicates that a much longer integration time would be required in order to achieve the same frequency resolution of the results presented in Ref. [4]. However, the figure already indicates that the same general trends, shown in the inviscid solution, seem to be followed by the viscous calculations. Unfortunately, with such results, it is still premature to attempt to conclude on whether there is significant effect, or not, from the inclusion of the viscous terms in the formulation. The simulations are still running and it is hoped that more conclusive data will be available at the conference.

4 CONCLUDING REMARKS

A comparative study of the use of inviscid and viscous aerodynamic formulations is performed in order to obtain the aerodynamic loads for aeroelastic analyses using computational fluid dynamics (CFD) techniques in the development of the aerodynamic operator. The work addresses transonic flows over a NACA 0012 airfoil, and it uses the Spalart-Allmaras turbulence model for turbulence closure when using a viscous formulation, considering the high Reynolds numbers for the flows of interest here. Viscous unsteady aerodynamic calculations here performed are compared to inviscid results previously obtained in the research group. As expected, the oscillations in the aerodynamic responses for the viscous formulation are damped faster than those in the corresponding inviscid results.

The total integration time for the viscous calculations, however, is still quite shorter than it is necessary to achieve a comparable frequency resolution, with respect to the inviscid cases, in the aerodynamic transfer functions. Therefore, at this point, it is not yet possible to conclude on the effects of the inclusion of the viscous terms in the formulation. It should be understood that, for this particular test case, one does not expect to see too much effect of the inclusion of the viscous terms, since the transonic shock occurs fairly upstream over the airfoil and, hence, in a region in which the boundary layer is still quite thin for the present Reynolds number. In other words, there should not be too much shock–boundary layer interaction. The test case was considered here precisely due to this reason. In any event, comparable frequency resolution transfer functions must be achieved in order to have more conclusive indication of the effects of the viscous terms in the aeroelastic analyses.



(a) $G_{C_{L,h}}$.

(b) $G_{C_{M,h}}$.

(c) $G_{C_{L,\alpha}}$.

(d) $G_{C_{M,\alpha}}$.

Figure 5: Aerodynamic transfer functions.

ACKNOWLEDGMENTS

The authors gratefully acknowledge the partial support for this research provided by Conselho Nacional de Desenvolvimento Científico e Tecnológico, CNPq, under the Research Grants No. 309985/2013-7, No. 400844/2014-1 and No. 443839/2014-0. The work was also supported by Fundação de Amparo à Pesquisa do Estado de São Paulo, FAPESP, under the Research Grant No. 2013/07375-0.

REFERENCES

[1] R. L. Bisplinghoff, H. Ashley and R. L. Halfman, *Aeroelasticity*. Addison-Wesley, Cambridge, MA, 1995.

[2] M. J. C. Henshaw, K. J. Badcock, G. A. Vio, C. B. Allen, J. Chamberlain, I. Kaynes, G. Dimitriadis, J. E. Cooper, M. A. Woodgate, A. M. Rampurawala, D. Jones, C. Fenwick, A. L. Gaitonde, N. V. Taylor, D. S. Amor, T. A. Eccles and C. J. Denley, *Non-linear aeroelastic prediction for aircraft applications*. Progress in Aerospace Sciences, 43, 65–137, 2007.

[3] H. Ashley, *Role of Shocks in the Sub-Transonic Flutter Phenomena*. Journal of Aircraft, 17, 187–197, 1980.

[4] A. N. Marques and J. L. F. Azevedo, *Numerical Calculation of Impulsive and Indicial Aerodynamic Responses Using Computational Aerodynamics Techniques*. Journal of Aircraft, 45, 1112–1135, 2008.

[5] T. A. Weisshaar, *Static and Dynamic Aeroelasticity. Encyclopedia of Aerospace Engineering*. John Wiley & Sons, 2010.

[6] A. N. Marques and J. L. F. Azevedo, *A z-Transform Discrete-Time State-Space Formulation for Aeroelastic Stability Analysis*. Journal of Aircraft, 45, 1564–1578, 2008.

[7] J. L. F. Azevedo, L. A. C. A. Schiavo, R. N. Ihi, J. H. A. Azevedo and W. R. Wolf, *Fluid-Structure Interaction Coupling on Free Moving Cylinders in Low Reynolds Number Flows*. Proceedings of the 11th International Conference on Vibration Problems, Lisbon, 2013.

[8] P. R. Spalart and S. R. Allmaras, *A One-Equation Turbulence Model for Aerodynamic Flows*. La Recherche Aerospastiale, 1, 5–21, 1994.

[9] E. D. V. Bigarella and J. L. F. Azevedo, *Advanced Eddy-Viscosity and Reynolds-Stress Turbulence Model Simulations of Aerospace Applications*. AIAA Journal, 45, 2369–2390, 2007.

[10] A. Jameson and D. Mavriplis, *Finite-Volume Solution of the Two-Dimensional Euler Equations on a Regular Triangle Mesh*. AIAA Journal, 24, 611–618, 1986.

[11] H. Lomax, T. H. Pulliam and D. W. Zingg, *Fundamentals of Computational Fluid Dynamics*. Springer, New York, 2001.

[12] AGARD, *Compendium of Unsteady Aerodynamic Measurements*. AGARD-R-702, 1982.

[13] R. N. Ihi and J. L. F. Azevedo, *Comparison of Viscous and Inviscid Unsteady Aerodynamic Loads for Aeroelastic Analyses*. Proceedings of the 53rd 53rd AIAA Aerospace Sciences Meeting, 2015.

[14] W. F. Ballhaus and P. M. Goorjian, *Computation of Unsteady Transonic Flows by the Indicial Method*. AIAA Journal, 16, 117–124, 1978.

[15] J. H. A. Azevedo, J. L. F. Azevedo and R. G. A. Silva, *Efficient Calculation of Aerodynamic States for Aeroelastic Analyses in the Frequency Domain*. Proceedings of the 53rd AIAA/ASME/ASCE/AHS/ASC Structures, Structural Dynamics and Materials Conference, Honolulu, Hawaii, 2012.

International Conference on Engineering Vibration
Ljubljana, Slovenia, 7-10 September 2015

TRANSVERSE SEISMIC RESPONSE ANALYSIS OF SUBMERGED FLOATING TUNNEL CONSIDERING BOUNDARY SOIL PROPERTY

XIANG Yi-qiang *[1], CHAO Chun-feng [2]

[1] Department of Civil Engineering, Zhejiang University, Hangzhou 310058, China;
Cyrus Tang Center for Sensor Materials and Applications, Zhejiang University, Hangzhou, 310058, China
xiangyiq@zju.edu.cn, Anzhong Building B718, Yuhangtang Rd.866 Zijingang Campus, Hangzhou, 310058, Zhejiang University, P.R. China

[2] Zhejiang Scientific Research Institute of Transportation, Hangzhou, 310006, China
ccfzju@163.com

Keywords: Submerged Floating Tunnel, Seismic Response, Revetment Structure, Geotechnical Property, Large Mass Method

Abstract. *Analysis of seismic response of submerged floating tunnel(SFT) is important task for ensuring the safety of this new structure. But existing researches often neglected impact of the real connection form between revetment structures and SFT tube, and only simplified the constraint supports simple or fixed support in calculation. In this paper, the seismic response characteristics of SFT in the lateral earthquake were studied by considering the impact of the geotechnical properties around the revetment structures. The transverse displacement, bending moment and torque of tube and cables tension of SFT were calculated by using large mass method, in the case of the seabed geotechnical condition in the South Sea of China and the Messina Strait SFT design scheme. The parametric study was finished for the revetment structure length L_{sh} and cohesive soil shear modulus G. The results showed that the maximum displacement and bending moment of tube appeared at the mid-span, the maximum torque arised at both ends, and the maximum incremental of cable tension occurred in the shortest cables. The elastic support of SFT considering the impact of the practical geotechnical properties around the revetment structures was conducive to reduce the forces of the tube segment structure, but not to control some of cables tension. The seismic response characteristics of SFT were significantly influenced by the revetment structure length L_{sh} and cohesive soil shear modulus G. But the impact was complicated, which may be related to the dynamic characteristics of SFT structure and the parameters of the seismic waves exerted on SFT.*

1 INTRODUCTION

Submerged Floating Tunnel (SFT) is a new transport structure to across the long or deep water areas. It has strong competitiveness and great development potential compared with the general bridges or tunnels. SFT is designed to be suspended in water, so the impact of SFT on surrounding environment will be completely different from that of general bridges or tunnels. The service behavior of SFT will be affected vulnerably by wave, flow, traffic loads, earthquake and otherwise (Ahrens 1997; Xiang and Chao 2002, 2013) [1]-[7].

One of the future potential SFT construction regions in China is located in China's eastern or southern coast. However, this region is belonged to the circum-Pacific seismic belt, which means that if we want to build the SFT in this region in the future we must consider the earthquake response of SFT. It is necessary to investigate the dynamic characteristics of SFT under earthquake. In recent years, many researchers have carried out a lot of work in various countries. The fluid-solid interaction calculation formula was deduced through an analysis of the dynamic response of the SFT with two different supporting frames under the effects of seismic load (Brancaleoni et al. 1989) [8]. Fogazzi (2000) [9] and Di Pilato (2008) [10]developed a calculation program for simulating water-structure coupling and soil-structure coupling, and constructing large deformation cable element. The seismic response of SFT under the multi-point support earthquake effect was analyzed by the proposed method. Luca et al. (2010, 2011) [11,12]presented a 3-node cable element by considering water action and realized the nonlinear seismic response analysis based on median pseudo-acceleration spectra. Martire et al. (2010) [13] carried out the analysis of SFT structural response by considering a ground multi-support excitation and the propagation of the vertical ground motion into the water and the fluid-structure interaction. Xiao and Huang (2010) [14] investigated the transverse seismic response of SFT with different types of connection between the ends of SFT and the shore bank. Chen et al. (2010) [15] studied the seismic response of SFT under the seismic traveling wave effect by the large mass method. Sun (2008) [16] carried out the experiments on seismic response of SFT, and simulated the interactions between structures and fluid under the seismic excitation by using numerical method.

In above studies, the connections between the ends of SFT and the shore were all simplified into rigid connection, hinged connection or elastic bearing connection, without and the interaction between the soil and revetment structure. So, it is necessary to explore the impact of the revetment structure boundary conditions on the transverse seismic response of SFT. This paper investigated the seismic response of SFT by considering the geotechnical properties of soil around the revetment structure. The numerical model of SFT with three-dimensional soil spring constraints was established by taking the design parameters of Messina Strait SFT and typical geotechnical properties parameters. The seismic response was analyzed by using Large Mass Method.

2 CALCULATION MODEL

2.1 Simplification and simulation of Mechanical model

The SFT structure anchored to foundation under water by cable (such as the straits of Messina SFT scheme [13]) is shown in figure 1. Both ends of the tube body are inside the revetment structures, buried in the sea bed rock and soil. The middle tube body of SFT is the sealed tube body suspended in the water, which is anchored to sea bottom foundation under water by cable. In the Marine environment, long-term circle action of water, wave forces can make the properties of revetment structure boundary soil change. Here the change of soil properties underwater foundation boundary is temporarily not considered. Therefore, the re-

striction of both ends soil on the tube body of SFT adopts three directions of linear spring element to approximately simulate, and the soil spring stiffness is changed to simulate the change of soil properties. The effect of the surrounding water of the structure on structure approximately simulate by the Morison equation. The impact of seismic wave transmission in the water on dynamic water pressure of the structure is also temporary not considered.

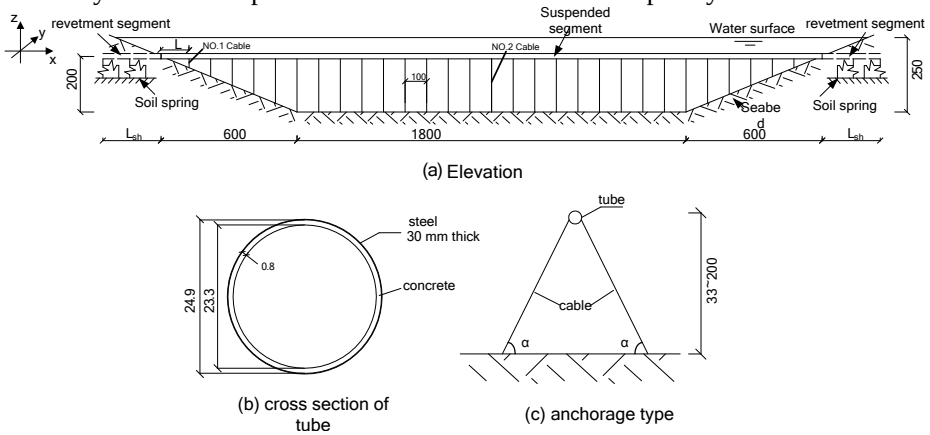


Figure 1: Sketch of submerged floating tunnel model (Dimension unit:m)

2.2 Soil spring dynamic stiffness

According to whether soil has the cohesion or not, the soil can be divided into cohesive soil (clay) and the non-cohesive soil (sand). During SFT service, the properties of soil surrounding revetment structure will change with the various factors such as the environment and stress condition. The basic parameters that affect soil properties include plastic index, shear strength, porosity, cycle times etc., which can be given by the geological survey report.

The dynamic vertical stiffness of soil spring (z direction) [17] is defined as: $K_{\mathrm{V}} = \Delta F_{\mathrm{V}} / \Delta \delta_{\mathrm{V}}$, where ΔF_{V} is dynamic vertical force between revetment section and soil for the unit length. $\Delta \delta_{\mathrm{V}}$ is the vertical displacement of revetment. The dynamic stiffness of soil transverse (y) or longitudinal (x) spring [17] is defined as $K_{\mathrm{L}} = \Delta F_{\mathrm{L}} / \Delta \delta_{\mathrm{L}}$, where ΔF_{L} is the dynamic lateral or longitudinal force between soil and revetment section, $\Delta \delta_{\mathrm{L}}$ is the lateral or longitudinal displacement of revetment.

When the segment length of revetment L_{sh} is more than 10 times the contact width B between the tube body and the soil, the revetment section of the SFT tube body can be equivalent to semi-infinite long beam on elastic foundation. The dynamic vertical, horizontal and longitudinal stiffness of soil spring can be respectively expressed as[15]:

$$K_{\mathrm{V}} = \frac{0.88 \cdot G}{1-\nu} \tag{1}$$

$$K_{\mathrm{L}} = 0.76 \cdot G \cdot (1+\nu) \tag{2}$$

where: ν is Poisson's ratio of the soil, for sand $\nu = 0.35$, for clay $\nu = 0.45$。

Under the condition of small strain, the maximum shear modulus of soil $G_{\max}$ can be calculated by formula (3) [17]:

$$G_{\max} = 625 \cdot \frac{OCR^{k_s}}{0.3 + 0.7 e_s^2} \sqrt{\sigma_a \sigma_s} \tag{3}$$

Where, σ_a is atmospheric pressure, it is 100 *kPa*. σ_s is the average effective stress of soil. OCR is over-consolidation ratio of cohesive soil. For sandy soil, OCR is 1.0. e_s is the void ratio. k_s is the coefficient related to the plastic index.

$$\sigma_{\mathrm{s}} = B\gamma_{\mathrm{soil}} + \frac{q}{3B}\left(1 + \frac{L}{2L_{\mathrm{sh}}}\right) \tag{4}$$

Where, B is the contact width between tube body and soil of revetment structure. γ_{soil} and q respectively are weight of the soil mass per unit volume under water (unit: kN/m^3) and weight per unit length tube body underwater (unit: *kN/m*). L is the length of SFT segment connected to the revetment segment. L_{sh} is the revetment length.

Maximum shear modulus of small strain for clay can be expressed as [17] :

$$G_{\max} = 300\frac{S_{\mathrm{u}}}{I_{\mathrm{p}}} \tag{5}$$

Where, S_{u} is the undrained shear strength for clay, I_{p} is the plastic index.

2.3 Water pressure model

The force of cylinder per unit length by water pressure when it moves in static water can be given by Morison equation [18]:

$$F_{\mathrm{D}} = \frac{1}{2}\rho_w D C_{\mathrm{D}} \dot{U}\left|\dot{U}\right| + \frac{\pi D^2}{4}\rho_w C_{\mathrm{m}} \ddot{U} \tag{6}$$

Where, C_D the drag coefficient of cylinder, such as anchor cable or tube, C_m is added mass coefficient and U is cylinder displacement relative to water. ρ_w is water density, D is the characteristic length for the cylinder. For cylinder, when Reynolds number $\mathrm{Re} > 2.5\times10^5$, $C_D = 0.7$ 、 $C_m = 1.0$.

When the actual earthquake occurred, the movement of SFT is multidimensional. The coupling of water action force in different direction movement is not considered. Hence, the motion of the cylinder is decomposed into three mutually perpendicular components. When cylinder move in a different direction, the water pressure acted on cylinder can be calculated, the mechanical model is shown in figure 2. It is assumed that in local coordinates, when the cylinder moves along the axial direction (x´ axis), it is not influenced by water pressure, when the cylinder moves respectively along lateral (y´axis) and vertical direction (z´ axis), it is subject to action of f_{Dz} and f_{Dy}.

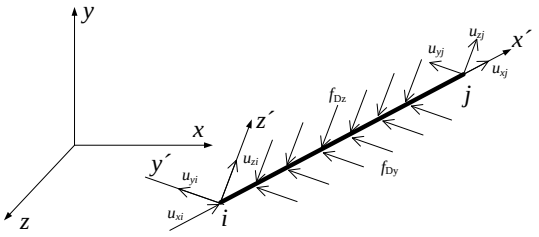


Figure 2: Motion of column in the local coordinate and global coordinate

3 NUMERICAL MODEL AND SOLVING METHOD

3.1 Multipoint input motion equation by considering the water action of SFT

Vibration equation of SFT is:

$$M\ddot{U} + C\dot{U} + KU = f \tag{7}$$

Where, *M, C, K* are respectively the mass matrix, damping matrix and stiffness matrix, $\ddot{U}$, $\dot{U}$, U are respectively acceleration column vector, velocity column vector and displacement column vector, f is a nodal forces column vector of external loads. Eq. (7) is expressed by the block matrix as:

$$\begin{bmatrix} m_{\mathrm{ff}} & m_{\mathrm{fs}} \\ m_{\mathrm{sf}} & m_{\mathrm{ss}} \end{bmatrix}\begin{bmatrix} \ddot{u}_{\mathrm{f}} \\ \ddot{u}_{\mathrm{s}} \end{bmatrix}+\begin{bmatrix} c_{\mathrm{ff}} & c_{\mathrm{fs}} \\ c_{\mathrm{sf}} & c_{\mathrm{ss}} \end{bmatrix}\begin{bmatrix} \dot{u}_{\mathrm{f}} \\ \dot{u}_{\mathrm{s}} \end{bmatrix}+\begin{bmatrix} k_{\mathrm{ff}} & k_{\mathrm{fs}} \\ k_{\mathrm{sf}} & k_{\mathrm{ss}} \end{bmatrix}\begin{bmatrix} u_{\mathrm{f}} \\ u_{\mathrm{s}} \end{bmatrix}=\begin{bmatrix} f_{\mathrm{f}} \\ f_{\mathrm{s}} \end{bmatrix} \tag{8}$$

Where, subscript *f* indicates that the node is freedom node; subscript *s* indicates that the node is a constraint node.

3.2 Solve vibration equation by a large mass method

In this paper, SFT vibration equation with both ends of the elastic support can be solved by Large mass method:

$$\begin{bmatrix} m_{\mathrm{ff}} & m_{\mathrm{fs}} \\ m_{\mathrm{sf}} & m_{\mathrm{ss}}+M_{\mathrm{ss}} \end{bmatrix}\begin{bmatrix} \ddot{u}_{\mathrm{f}} \\ \ddot{u}_{\mathrm{s}} \end{bmatrix}+\begin{bmatrix} c_{\mathrm{ff}} & c_{\mathrm{fs}} \\ c_{\mathrm{sf}} & c_{\mathrm{ss}} \end{bmatrix}\begin{bmatrix} \dot{u}_{\mathrm{f}} \\ \dot{u}_{\mathrm{s}} \end{bmatrix}+\begin{bmatrix} k_{\mathrm{ff}} & k_{\mathrm{fs}} \\ k_{\mathrm{sf}} & k_{\mathrm{ss}} \end{bmatrix}\begin{bmatrix} u_{\mathrm{f}} \\ u_{\mathrm{s}} \end{bmatrix}=\begin{bmatrix} 0 \\ M_{\mathrm{ss}} \end{bmatrix}\cdot\ddot{\delta}-\begin{bmatrix} f_{\mathrm{Df}} \\ f_{\mathrm{Ds}} \end{bmatrix} \tag{9}$$

Where M_{ss} is exert on a large mass at the support point, its value must be much greater than the overall mass of the structure. $\ddot{\delta}$ is the seismic wave acceleration. f_{Df} and f_{Ds} are the node forces of water action load acted on nodes gained by Eq. (6).

4 MODEL PARAMETERS OF TYPICAL CASES

No SFT has been built in the world up to now. Therefore, this paper takes SFT design project of the Messina Strait as case study [13]. The standard cable of the SFT has the length of 231 *m*, the diameter of 0.41 *m*, the density of 7800 kg/m^3, initial tension force of 174810 *kN* and the tilted angle of 60°. The standard segment of the SFT tube is the length of 100 *m*, the outer diameter of 24.9 *m*, elastic modulus of steel pipe of 2.05×10^5 *MPa* , elastic modulus of concrete of 3.45×10^4 *MPa*. Density of concrete is 2500 kg/m^3. Density of steel is 7800 kg/m^3. The ratio of the gravity and buoyancy is 0.35. The density of sea water is approximately 1000 $kg/m.^3$ The contact width between the tube body and soil is 24.9 *m*. Maximum shear modulus G of soil is 300 *kPa*. Seismic wave is typical El Centro wave.

Based on the basis of this SFT design scheme, parametric analysis is finished by the proposed theory. The impact of different the border soil nature of SFT on the seismic response characteristics is discussed in detail.

5 SEISMIC RESPONSE ANALYSIS AND COMPARISON

5.1 Establishment of the numerical model

After SFT built and put into normal service, the tube segment of SFT will be subject to currents, waves and moving vehicles et al. alternating loads, and transmitted supporting soil or foundation through the revetment structure and cable. Under action of this cycle vibration loads, the changes in pore pressure and the strength of the boundary soil at the both ends of

SFT will take place. The soil constraints capacity of revetment structure will vary with it. Finally, it affects the seismic response of the SFT. Here we focus on the impact of the clay nature change on the earthquake response characteristics of SFT.

For the selected typical SFT with design parameters, the appropriate numerical model is establish by using the finite element method, while the boundary condition and the action force of water are processed and input in accordance with the aforementioned methods. Tube and anchor cable elements are 3D spatial beam elements for the finite element web division. The total number of elements is 640 and total number of nodes is 667.

To explore the impact of SFT boundary soil property on the characteristics of the seismic response, this paper calculated the transverse seismic response of SFT for the different revetment length L_{sh}, shear modulus G of cohesive clay and other parameters etc.

5.2 Impact of SFT boundary condition on the transverse seismic response

For research on the dynamic characteristics of SFT, the constraints of the revetment segment structure are generally simplified hinged or clamped, and the actual situation is between these two constraints. Figure 3 shows the maximum transverse displacement envelope (a), the maximum bending moment envelope (b), anchor cable force increment (c) and the maximum torque envelope (d) of SFT in different constraints way of the revetment segments structures under transverse El Centro wave.

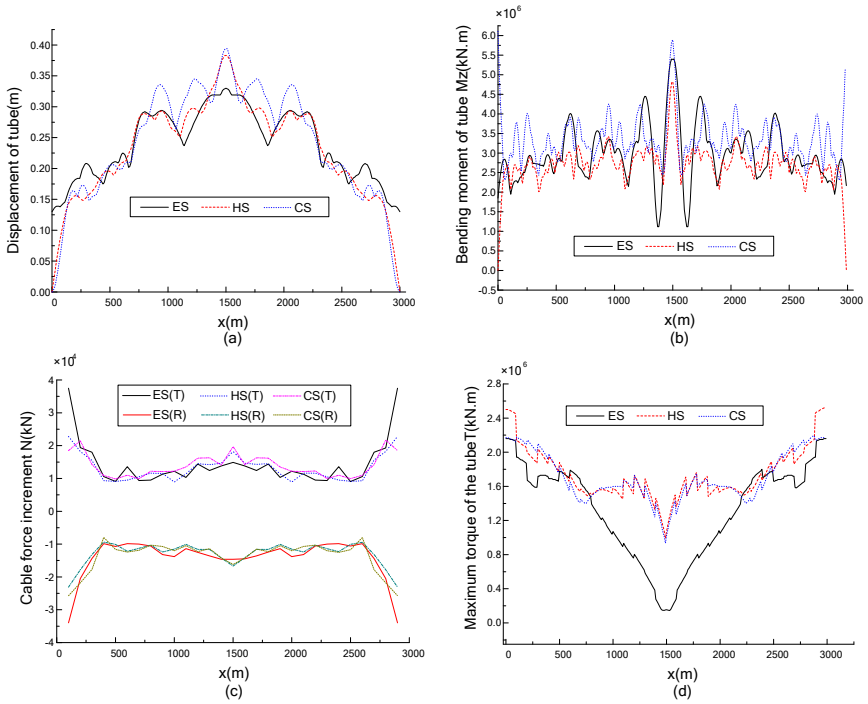


Figure 3: The envelope curve of SFT in different boundary condition under transverse seismic wave
a) transverse maximum displacement of the tube, b) *Mz* bending moment of the tube
（ES: Elastic support; HS: Hinged support; CS: clamped support; T: Tension; R: Relaxation）

It can be seen from Figure 3, the maximum transverse displacement of the SFT under earthquake occurs in the mid-span. The maximum transverse displacement value of SFT in the elastic support (soil spring) is significantly less than the values in the hinged or clamped constraint case. The reducing the amplitude is about 14% and 16% for hinged and clamped

constraint. The maximum bending moment *Mz* of SFT tube occurs also in mid-span under different constraints. The bending moment value of SFT for elastic support is greater than one for hinged support, and less than one for the clamped supported. For anchor cable force increment, the maximum values appear in both ends of SFT (short cable). The values in elastic support are about 1.5 times values in hinge or a clamped support. The anchor cable force increment in mid-span in elastic support is slightly smaller than hinge or clamped support. The maximum torque value of tube body also appears in both ends of SFT (torque constraint points). The end torque values with elastic support are slightly smaller than one with hinge support, and it is almost the same one with clamped support. But the torque values in mid-span with elastic support are significantly less than ones with hinge and clamped support. As a result, it can be seen that simply simplifying the revetment structure constraint as hinged and clamped support is not reasonable, especially for the cable force, which will lead to insecurity of anchor cable design.

5.3 Impact of the revetment length L_{sh} on the transverse seismic response

Changes of revetment structure length will lead to changes in the overall constraint state of SFT. With the increase of revetment structure length L_{sh}, the impact scope of tube segment of revetment on boundaries soil around them will increase. Currently there is no relevant research and recommendations on soil interaction model and calculating length of the L_{sh} of SFT revetment segment. For this, the paper studied calculating length of the L_{sh} of SFT revetment segment. For further calculating, the maximum transverse displacement (a), the maximum bending moment (b), anchor cable force increment (c) and the maximum torque envelope (d) of SFT with different lengths of revetment structure are shown in Figure 4. It can be seen that the changes of calculating length of the segment have a greater impact on the transverse displacement, bending moment of SFT tube segment and anchor cable forces.

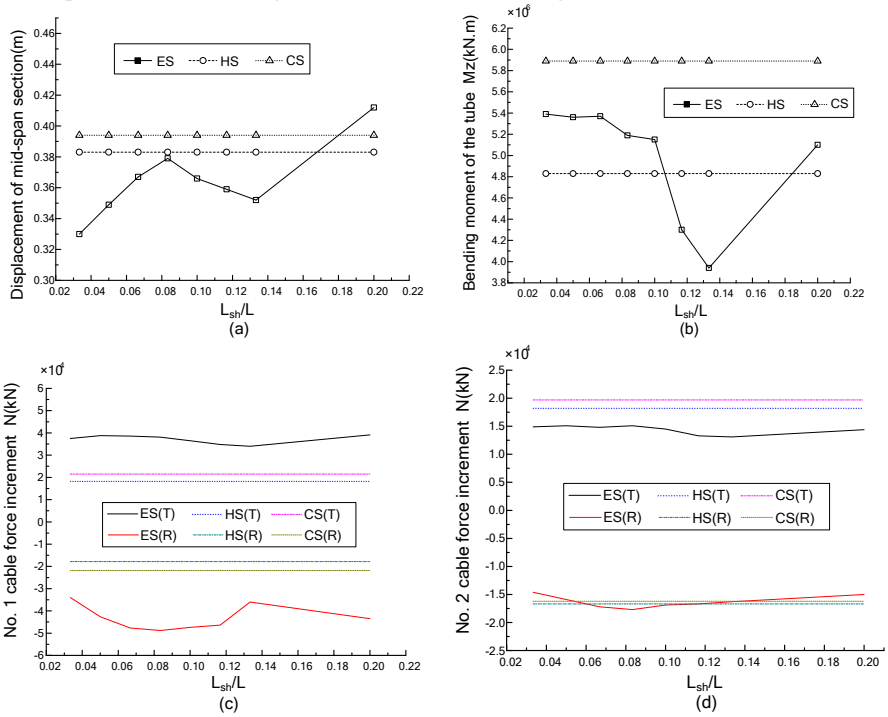


Figure 4: The results of SFT with different lengths of revetment structure(L_{sh}) under transverse seismic wave

When the calculating length of the revetment segment is L_{sh} =100m ~400 m (L_{sh}/L = 0.033 ~ 0.13), the transverse displacement, bending moment in mid-span and anchor cable force have a significant wave with increasing the length of the tube revetment. Which maximum variation amplitude of displacement in span-span is 15%, the biggest change in the magnitude of the bending moment in mid-span is 27%, the maximum variation of No.1 cable force incremental is 12% for tension and 30% for relaxation force. The maximum change amount in the magnitude of No. 2 cable force is 13% for tension and 17% for relaxation force. But with the continued increase in calculating length of the revetment segment to great than 400m, the transverse displacement in mid-span will be substantially increased, the transverse bending moments of tube in mid-span and anchor cable force also increased significantly. Therefore, the design of SFT revetment segments needs to consider a number of factors, which calculating length must be determined by the actual selection. It may result in large errors when assume to be a simple constraint.

5.4 Impact of shear modulus *G* of different boundary soil on the transverse seismic response

In order to analyze effect of soil property around revetment structure of SFT on seismic response, the different state of soil is selected. Change in clay nature can be expressed by shear modulus G or S_u and I_p. The S_u/I_p reflects the type of clay. The clay is classified into very soft, soft, medium and hard, hard state in terms of small to big S_u/I_p. Here, the physical parameters of the clay material from a typical engineering investigation data in South China Sea [19] are adopted to obtain dynamic shear modulus of the soil of the border by using eq. (5). Then it is substituted into Eq. (1) to get the dynamic stiffness of the soil spring. The variation of the maximum transverse displacement in mid-span, the maximum bending moment in mid-span, two typical anchor cable force increments with S_u/I_p are shown in Figure 5.

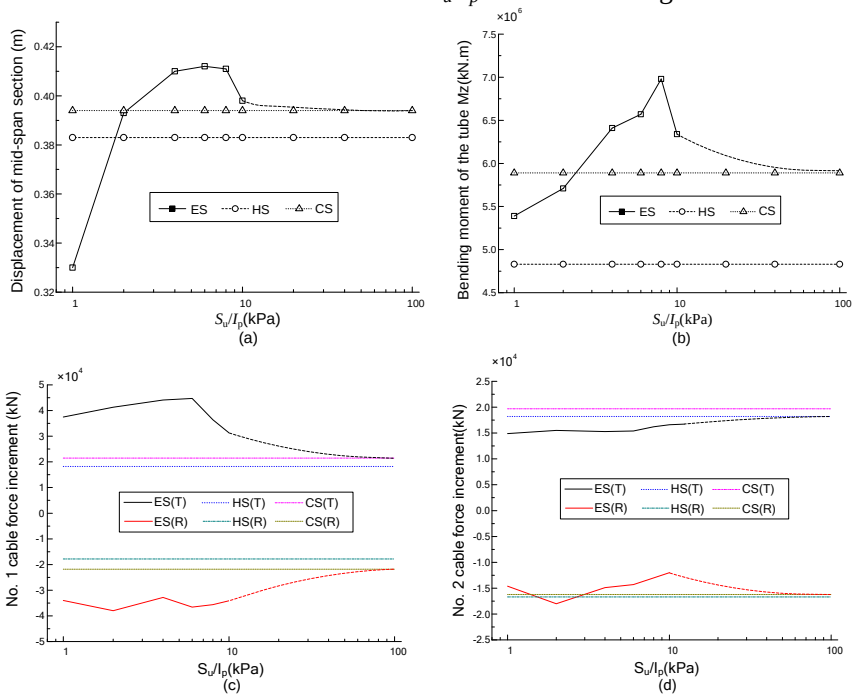


Figure 5: The results of SFT with different shear modulus of clay (G) or S_u/I_p under transverse seismic wave

It can be found from the figure 5, with the increase of S_u/I_p, the overall trend of the displacement and bending moment of tube body in mid-span is significant increase, while No.1 cable force increment is greatly reduced. This is because the larger elastic restraint is more close to the clamped constraints. No. 2 cable force increment also appears obvious fluctuation. At the same time, it is noted the effect of clay S_u/I_p change on the seismic responses of SFT is not linear, sometime it fluctuate. When S_u/I_p is less than or equal to 8, the displacement increment of tube body in mid-span is 25%, when S_u/I_p is more than 8, the biggest change range is within 5%. When S_u/I_p is less than or equal to 8, the bending moment increment of tube body in mid-span is 29%, when S_u/I_p is more than 8, the biggest change range is within 16%. Anchor cable force incremental change is relatively complex. When S_u/I_p is less than or equal to 6, the tension increment of No.1 cable force is 19%. Then it is slashed 35% reduction and tend to be stable. The relaxation force decrease of No.1 cable force is relatively flat and near 35% reduction, and gradually tend to be values in clamped constraint. No. 2 cable force and incremental change is different from the No. 1. Its maximum tension variation was 15%, the biggest change in relaxation force is about 50%. When S_u/I_p is more than 10, the structural stiffness matrix is close to morbid matrix, the results cannot be admissible. But in terms of common sense, when the clay becomes harder, boundary condition is closer to clamped restrain. Therefore, the dotted line in the figure 5 gives its tendency. From the above results, we can see changes in soil properties around revetment structure have a tremendous impact on the results of SFT. But its influence law is not clear. It needs to be further calculated to give proper results according to various practical situations. It brings a certain degree of difficulty to design and built SFT for the future.

6 CONCLUSIONS

- Under the lateral earthquake, the maximum transverse displacement, bending moment and torque of SFT tube occur in the mid-span. Maximum increment of anchor cable tensions occurs in short cable. In the case of elastic support, the maximum transverse displacement and torque of SFT tube in mid-span will be reduced, the maximum transverse bending moment is between hinged and clamped support, and increment of shorter cable forces are significantly increases.
- Changes in calculating length of revetment segment have a greater impact on the transverse displacement, bending moment of SFT tube and anchor cable forces. Changes in soil properties around revetment structure have a tremendous impact on seismic response of SFT.
- In seismic response analysis of SFT, it is not reasonable that the constraints of revetment structure are simply simplified as hinged and clamped support, especially for the cable force, which will lead to insecurity of anchor cable design. The practical constraints situation must be considered.

ACKNOWLEDGEMENT

This work was financially supported by the National Natural Science Foundation of China (51279178) and Cyrus Tang Foundation in China.

REFERENCES

[1] Ahrens D. Submerged floating tunnels—A concept whose time has arrived. *Tunneling and Underground Space Technology*, 12(2): 317-336, 1997.

[2] Xiang Yiqiang, Xue Jinping. Study on submerged floating tunnels in the world. *Journal of China & Foreign highway*, (6):49-52,2002

[3] Xiang Yiqiang, Chao Chunfeng. Vortex- induced dynamic response for the combined action of tube and cable of submerged floating tunnel. *Journal of Zhejiang University(Engineering Science).*, 46(3): 409-415, 2012

[4] Xiang Yiqiang, Zhang keqian. Calculation of Wave Force Acting on Submerged Floating Tunnel. *Journal of Zhejiang University(Engineering Science).* (8):1399-1404,2011

[5] Xiang Yiqiang, Chao Chunfeng. Vortex-Induced Dynamic Response Analysis for the Submerged Floating Tunnel System under the Effect of Currents. *Journal of Waterway, Port, Coastal, and Ocean Engineering*,138:183-189 /(ASCE) , 2013

[6] Xiang Yiqiang, Liu Chengxi, Zhang Keqian, Wu Qiangqiang. Risk analysis and management of submerged floating tunnel and its application. *Proceedings of first international symposium on Archimedes Bridge*, Chun'an, China, **Procedia Engineering**, 4, 117-125, 2010

[7] Zhang Keqiana, Xiang Yiqiang, Du Yinguang. Research on Tubular Segment Design of Submerged Floating Tunnel. *Proceedings of first international symposium on Archimedes Bridge.* Chun'an, China, **Procedia Engineering**, 4:199-205, 2010

[8] Branchaleoni F, Castellani A, D'Asdia P. The response of submerged tunnels to their environment. *Engineering Structures*, 11: 47–56 , 1989

[9] Fogazzi P, Perotti F. The dynamic response of seabed anchored floating tunnels under seismic excitation. *Earthquake Engineering and Structural Dynamics*, 29: 273–95, 2000

[10] Di Pilato M, Perotti F, Fogazzi P. 3D dynamic response of submerged floating tunnels under seismic and hydrodynamic excitation. *Engineering Structures*; 30(1): 268–281, 2008

[11] Luca Martinelli, Gianluca Barbella, Anna Feriani. Modeling of Qiandao Lake submerged floating tunnel subject to multi-support seismic input. *Proceedings of first international symposium on Archimedes Bridge*, Chun'an, China, **Procedia Engineering**, 4: 311–318, 2010

[12] Luca Martinelli, Gianluca Barbella, Anna Feriani. A numerical procedure for simulating the multi-support seismic response of submerged floating tunnels anchored by cables. *Engineering Structures*, 33:2850-2860, 2011

[13] G. Martire, B. Faggianoa, F.M. Mazzolani et al. Seismic analysis of a SFT solution for the Messina Strait crossing. *Proceedings of first international symposium on Archimedes Bridge*, Chun'an, China, **Procedia Engineering**, 4: 303–310, 2010

[14] Xiao Jian, Huang Guojun. Transverse earthquake response and design analysis of submerged floating tunnels with various shore connections. *Proceedings of first international symposium on Archimedes Bridge*, Chun'an, China, **Procedia Engineering**, 4: 233–242, 2010

[15] Chen Wenjun, Huang Guojun. Seismic wave passage effect on dynamic response of submerged floating tunnels. *Proceedings of first international symposium on Archimedes Bridge*, Chun'an, China, **Procedia Engineering**, 4: 217–224, 2010

[16] Sun Shengnan. Dynamic response analysis of submerged floating tunnel. Dalian university of technology. Dalian, 2008

[17] Det Norske Veritas. DNV Recommend Practice, Free Spanning Pipeline. Norway: Det Norske Veritas, 2006

[18] R. Adrezin, H. Benaroya. Non-linear stochastic dynamics of tension leg platforms. *Journal of Sound and Vibration*, 220(1):27-65, 1999

[19] Zhi-chang zheng, Jun-ren Chen, Zhao-yu Zhu. Preliminary study on the south China sea seabed soil physical and mechanical characteristics and its geological environment. *Hydrological and engineering geology*, 31 (4):50-54, 2004

[20] CHAO Chunfeng; XIANG Yiqiang, Hydrodynamic load on SFT tube in ideal fluid layer under the action of earthquake P-wave. *Acta Oceanologica Sinica*，35（5）：156-161, 2013

11th International Conference on Engineering Vibration
Ljubljana, Slovenia, 7–10 September 2015

CFD CALIBRATED WAKE OSCILLATOR MODEL FOR VORTEX-INDUCED VIBRATIONS

Ekaterina Pavlovskaia[1], **Andrey Postnikov**[1], **Marian Wiercigroch**[1]

[1] Centre for Applied Dynamics Research, School of Engineering, University of Aberdeen, Aberdeen AB24 3UE, UK
e.pavlovskaia@abdn.ac.uk

Keywords: Wake Oscillator, Vortex Induced Vibrations, CFD

Abstract. *In this study we investigate vortex-induced vibrations of elastically supported cylinders capable of moving in cross-flow and in-line directions. Two approaches are adopted to analyse the considered system. First the amplitudes of cross-flow and in-line vibrations under variation of the fluid flow velocity are calculated using CFD for various mass ratio. Analysis is performed initially for a cylinder restricted to move in cross-flow direction only and then for the cylinder capable of moving in both directions. It is shown that when a light cylinder is moving in the fluid flow (mass ratio is low), the in-line motion becomes significant resulting in the increase of the cross-flow displacement amplitudes, thus confirming the presence of the "supper-upper" branch earlier obtained in the experimental studies. In the second part of the paper, a new two degrees-of-freedom wake oscillator model is proposed where vortex-induced lift and drag are modelled with two nonlinear self-excited oscillators of van der Pol type. Total hydrodynamic force is obtained here as a sum of lift and drag forces, which are defined as being proportional to the square of the magnitude of the relative flow velocity around the cylinder. The two van der Pol type oscillators are then used to model fluctuating drag and lift coefficients. As the relative velocity around the cylinder depends both on the fluid flow velocity and the velocity of the cylinder, the equations of motions of the cylinder in cross-flow and in-line directions become coupled through the fluid forces. It is shown that such approximation of the fluid forces allows to obtain the well known low dimensional models in the limit case and the model proposed by Facchinetti et al. [1] to describe the cross-flow vibrations is used an example. The CFD results are utilised to calibrate the proposed wake oscillator model and to compare of the cross-flow displacement amplitudes obtain by CDF and using new wake oscillator model for different mass ratios. Some insight into the influence of main coefficients of the wake oscillators and fluid forces coefficients on the cross-flow displacement amplitudes are also presented.*

REFERENCES

[1] Facchinetti M.L., de Langre E., Biolley F., 2004, "Coupling of Structure and Wake Oscillators in Vortex-Induced Vibrations", Journal of Fluids and Structures 19, 123-140.

Identification and Modal Analysis (TP10)

International Conference on Engineering Vibration
Ljubljana, Slovenia, 7-10 September 2015

APPLICATION OF EFFECTIVE MATERIAL PROPERTIES IN FREE VIBRATION ANALYSIS OF A PARTIALLY PERFORATED PLATE WITH TRIANGULAR PENETRATION PATTERN

Kyeong-Hoon Jeong*[1], Myng-Jo. Jhung[2], Jong-Wook. Kim[1]

[1]Korea Atomic Energy Research Institute, SMART Development Division
{khjeong, kjwook}@kaeri.re.kr

[2]Korea Institute of Nuclear Safety, Division of Safety Research
mjj@kins.re.kr

Keywords: Perforated Rectangular Plate, Triangular Hole Pattern; Effective Modulus of Elasticity, Rayleigh–Ritz Method, Ligament Efficiency, Natural Frequency.

Abstract. *A theoretical analysis for free vibration of a perforated rectangular plate with a fixed boundary condition and a triangular penetration pattern, is suggested. The natural frequencies of the perforated plate gradually decrease with a hole size, because the structural stiffness of the perforated plate is reduced severely than mass inertia according to increase of hole size. In the study, the natural frequencies of the perforated square plate are obtained as a function of ligament efficiency using commercial finite element analysis code, ANSYS. Additionally they are used to extract the effective modulus of elasticity under an assumption of constant Poisson's ratio. The effective modulus of elasticity for the fully perforated square plate is applied to modal analysis of a partially perforated rectangular plate using a homogeneous finite element analysis model. The natural frequencies and the corresponding mode shapes of the homogeneous model are compared with the results of the detailed finite element analysis model of the partially perforated rectangular plate in order to check the validity of the effective modulus of elasticity. In addition, theoretical method to calculate the natural frequencies of a partially perforated rectangular plate with fixed edges is suggested according to the Rayleigh-Ritz method. The suggested effective modulus of elasticity can be applicable to the perforated plates of reactor internal structure which will reduce the finite element analysis model size and contribute an effective modal analysis and seismic analysis based on the finite element analysis.*

1 INTRODUCTION

Perforated plates are used in various industrial applications such as sorting and screening any material from others. They are also utilized extensively in heating and ventilating installations, acoustics proofing. Perforated plates also have been used for reactor internal structures in nuclear engineering fields. The perforated structures usually support components and a reactor coolant flows through the perforated plates. The reactor internals shall be designed to withstand not only normal operating loads but also seismic loads. To check the design requirements, the dynamic responses of the reactor internals due to the forcing functions of normal operation and earthquakes are computed by the commercial computer codes. The adequacy of seismic loadings used for the design of the reactor internals are confirmed by the methods of dynamic analysis employing time history and response spectrum techniques. Before the time history or response spectrum analysis, finite element modal analyses of the reactor internals are performed for the appropriate equivalent lumped-mass stick models. It is necessary to idealize a mathematical model consisting of lumped masses connected by elastic massless members to reduce computation time and storage memory. As the perforated structures of the reactor internals require a lot of elements for finite element modal analysis, the finite element model for the perforated structures cannot be constructed as they are. Application of effective properties of the perforated structures for the finite element analysis can be an efficient analysis method. There are many potential applications where perforated materials could be used. In many of these uses, however, the strength and stiffness properties of the perforated plate are very important. Since perforated structures can potentially be used in so many applications in reactor internals involving different geometries, materials and loading conditions, the effective material properties for design data will be given in a general form. The ratio of the effective elastic modulus of the perforated material, E^*, to the elastic modulus of the imperforated solid material, E, will be given, but the Poisson's ratio, μ, assumed to be constant regardless of the ligament efficiency, η (= $(p - d)/p$). The hole diameter is given as d and the pitch between the hole centers is indicated by p.

By evaluating the effect of the perforations, the effective elastic modulus of the perforated material, E^*, was obtained as a function of the elastic modulus of the solid or imperforated material, E. In addition, the effective Poisson's ratio, μ^*, of the perforated material was suggested in ASME PVP code [1]. The Poisson's ratio may be used in cases where correction for the load biaxiality is important. The effective elastic constants presented herein are for plane stress conditions and apply to the in-plane loading of the thin perforated sheets of interest. However, the suggested effective properties are based on the in-plane loading. The plane stress effective elastic constants given in Reference [2] by O'Donnell, may be conservatively used for all loading conditions. Using these effective elastic properties, the designer is able to determine the deflections of the perforated sheet for any geometry of application and any loading conditions using available elastic solutions. However the effective elastic constants given in Reference [2] are not confirmed for the modal analysis of the perforated plates. We cannot convince that the effective elastic constants are constant regardless of vibration modes.

Additionally, the suggested effective Poisson's ratio, μ^*, is greater than 0.5 in the small ligament efficiency, approximately less than $\eta = 0.2$. Generally, it cannot be applicable in the commercial finite element analysis computer codes for the modal analysis. Therefore, this paper will suggest the mode dependent elastic modulus (E^*) for the perforated rectangular plate with a fixed boundary condition as a function of the ligament efficiency (η). Finally an example of a partially perforated rectangular plate will be given to check validity of the newly suggested elastic modulus (E^*).

2 NATURAL FREQUENCY AND ELASTIC CONSTANT

2.1 Perforated plate model

A mathematical model of a partially perforated plate with a triangular penetration pattern is shown in Figure 1, where *A*, *B* and *h* are the width, length and thickness of the plate, respectively. The effective material properties for a perforated region of the plate are followings; the effective modulus of elasticity of E^*, the equivalent mass density of ρ^*. The modulus of elasticity, mass density and Poisson's ratio of the solid plate region are given as E, ρ and μ, respectively. The width of peripheral solid region is given as *G* and the width of the central perforated region is *L*. The length of peripheral solid region is indicated as *S* and the width of the central perforated region is *K*. To apply the Rayleigh-Ritz approach to free vibration analysis of the perforated rectangular plate, each wet mode shape is approximated by a combination of a finite number of admissible functions, $W_{mn}(x,y)$, and an appropriate unknown coefficient, q_{mn}:

$$w(x,y,t) = \sum_{m=1}^{M} \sum_{n=1}^{N} q_{mn} W_{mn}(x,y) \exp(\mathrm{i}\omega t), \tag{1}$$

where $\mathrm{i} = \sqrt{-1}$ and ω is the circular natural frequency of the plate. The indices *m* and *n* indicate the *m*-th order polynomial in the *x*–direction, and *n*-th order polynomial in the *y*–direction, respectively. The transverse modal function can be defined by a multiplication of the *x*– and *y*– directional admissible functions, $X_m(x)$ and $Y_n(y)$:

$$W_{mn}(x,y) = X_m(x)\, Y_n(y). \tag{2}$$

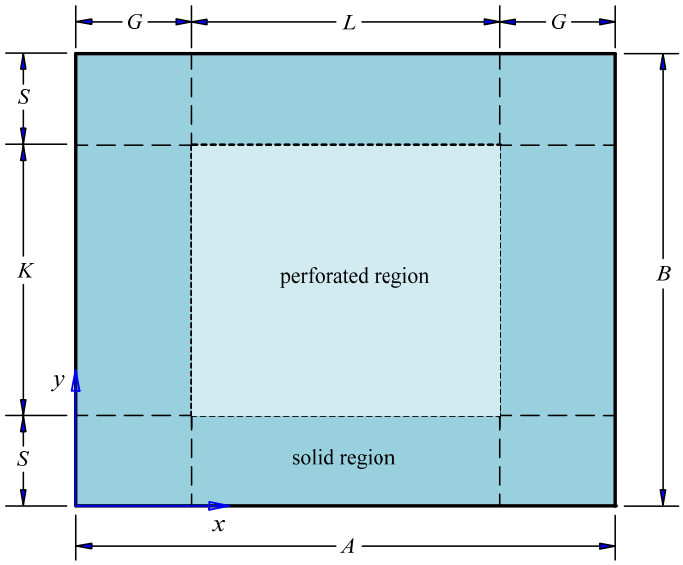


Figure 1: A partially perforated rectangular plate with fixed edges.

The total reference kinetic energy, *T* of the partially perforated rectangular plate can be obtained by summation in the imperforated peripheral and the central perforated regions:

$$T = \frac{h}{2}\boldsymbol{q}^T\left[\rho\,\boldsymbol{Z}_o + \left(\rho^* - \rho\right)\boldsymbol{Z}_c\right]\boldsymbol{q}\,, \tag{3}$$

where

$$\boldsymbol{q} = \left\{q_{11}\ q_{12}\ q_{13}\cdots q_{1N}\ q_{21}\ q_{22}\ q_{23}\cdots q_{MN}\right\}^T. \tag{4}$$

$$\rho^* = \rho\left[1 - \pi\left(d/p\right)^2/2\sqrt{3}\right] \tag{5}$$

The matrices $\boldsymbol{Z}_o$ and $\boldsymbol{Z}_c$ of Eq. (3) can be defined as:

$$Z_o = \int_0^A \int_0^B W_{mn}\,W_{uv}\,dy\,dx = AB\,, \qquad Z_c = \int_G^{A-G} \int_S^{B-S} W_{mn}\,W_{uv}\,dy\,dx\,. \tag{6, 7}$$

The admissible functions of Eq. (2) can be defined as a set of orthogonal poliynomial functions satisfying the geometric boundary conditions of the plate [3-5]. Since the admissible functions are orthogonal to each other, Eq. (6) should be satisfied. The total maximum potential energy, V of the plate can be computed by integrating the derivatives of the admissible modal functions along the imperforated peripheral and central perforated regions. The total maximum potential energy of the partially perforated rectangular plate is given as a matrix form of Eq. (8) by inserting the admissible functions into Eqs. (9) and (10):

$$U = \frac{1}{2}\boldsymbol{q}^T\left[D\,\boldsymbol{V}_o + \left(D^* - D\right)\boldsymbol{V}_c\right]\boldsymbol{q}\,, \tag{8}$$

where

$$V_o = \frac{1}{2}\int_0^B \int_0^A \left[\left\{\frac{\partial^2 W_{mn}}{\partial x^2}\frac{\partial^2 W_{uv}}{\partial x^2}\right\} + \left\{\frac{\partial^2 W_{mn}}{\partial y^2}\frac{\partial^2 W_{uv}}{\partial y^2}\right\} + \mu\left\{\frac{\partial^2 W_{mn}}{\partial x^2}\frac{\partial^2 W_{uv}}{\partial y^2} + \frac{\partial^2 W_{uv}}{\partial x^2}\frac{\partial^2 W_{mn}}{\partial y^2}\right\} + 2(1-\mu)\left\{\frac{\partial^2 W_{mn}}{\partial x\,\partial y}\frac{\partial^2 W_{uv}}{\partial x\,\partial y}\right\}\right] dx\,dy\,, \tag{9}$$

$$V_c = \frac{1}{2}\int_S^{B-S} \int_G^{A-G} \left[\left\{\frac{\partial^2 W_{mn}}{\partial x^2}\frac{\partial^2 W_{uv}}{\partial x^2}\right\} + \left\{\frac{\partial^2 W_{mn}}{\partial y^2}\frac{\partial^2 W_{uv}}{\partial y^2}\right\} + \mu\left\{\frac{\partial^2 W_{mn}}{\partial x^2}\frac{\partial^2 W_{uv}}{\partial y^2} + \frac{\partial^2 W_{uv}}{\partial x^2}\frac{\partial^2 W_{mn}}{\partial y^2}\right\} + 2(1-\mu)\left\{\frac{\partial^2 W_{mn}}{\partial x\,\partial y}\frac{\partial^2 W_{uv}}{\partial x\,\partial y}\right\}\right] dx\,dy\,, \tag{10}$$

The matrices V_o and V_c for indices m , n and u, v can also be derived as

$$V_o = \Delta 1_{mu}\,\Gamma 2_{nv} + \Delta 2_{mu}\,\Gamma 1_{nv} + 2\nu\,\Delta 3_{mu}\,\Gamma 3_{nv} + 2(1-\nu)\,\Delta 4_{mu}\,\Gamma 4_{nv}\,, \tag{11}$$

$$V_c = \Xi 1_{mu}\,\Theta 2_{nv} + \Xi 2_{mu}\,\Theta 1_{nv} + 2\nu\,\Xi 3_{mu}\,\Theta 3_{nv} + 2(1-\nu)\,\Xi 4_{mu}\,\Theta 4_{nv}\,, \tag{12}$$

where

$$\Delta 1_{mu} = \int_0^A X_m''(x)\,X_u''(x)\,dx\,, \qquad \Delta 2_{mu} = \int_0^A X_m(x)\,X_u(x)\,dx\,, \tag{13, 14}$$

$$\Delta 3_{mu} = \int_0^A X_m''(x)\,X_u(x)\,dx\,, \qquad \Delta 4_{mu} = \int_0^A X_m'(x)\,X_u'(x)\,dx\,, \tag{15, 16}$$

$$\Xi 1_{mu} = \int_G^{A-G} X_m(x)\, X_u(x)\, dx, \qquad \Xi 2_{mu} = \int_G^{A-G} X_m''(x)\, X_u''(x)\, dx, \tag{17, 18}$$

$$\Xi 3_{mu} = \int_G^{A-G} X_m(x)\, X_u''(x)\, dx, \qquad \Xi 4_{mu} = \int_G^{A-G} X_m'(x)\, X_u'(x)\, dx. \tag{19, 20}$$

The apostrophe (') in Eqs. (13-20) also indicates a derivative with respect to the corresponding variable. The coefficients, $\Xi 1_{mu}$, $\Xi 2_{mu}$,..., $\Theta 1_{nv}$, $\Theta 2_{nv}$, …, in Eq. (12) can be similarly obtained for the *y*–direction. Minimizing the Rayleigh quotient with respect to the unknown parameters $\boldsymbol{q}$, the Galerkin equation yields

$$\left[D\boldsymbol{V}_o + \left(D^* - D\right)\boldsymbol{V}_c \right]\boldsymbol{q} - \omega^2 h \left[\rho \boldsymbol{Z}_o + \left(\rho^* - \rho\right)\boldsymbol{Z}_c \right]\boldsymbol{q} = \{0\}. \tag{21}$$

2.2 Imperforated square plate

Before we embark upon the analysis of a perforated rectangular plate, the admissible functions shall be briefly examined. To check the adequacy of the Rayleigh-Ritz method and admissible functions, two analysis was performed for a imperforated solid square plate. The 10 admissible functions for each direction are used in the theoretical calculation of the natural frequencies for the solid square plate. Finite element analyses for the same plate were carried out for the fixed boundary condition using commercial software ANSYS (release 14) with Block Lanczos method [6]. The finite element analysis models were constructed with the geometry, boundary condition and material properties used in the theoretical calculation. The geometry and the material properties of the solid square plate are given in Figure 2 with a zero hole diameter. The natural frequencies of the solid square plate are listed in Table 1. Discrepancies between the theoretical natural frequencies and results from the finite element analysis for the solid square plate are negligible as shown in Table 1. Therefore, it is clear that the admissible functions is suitable to describe the dynamic motion and the considered total number of the polynomial functions is enough to obtain the converged results. The mode shapes are symmetric or anti-symmetric with respect to the centerlines or diagonal of the plate.

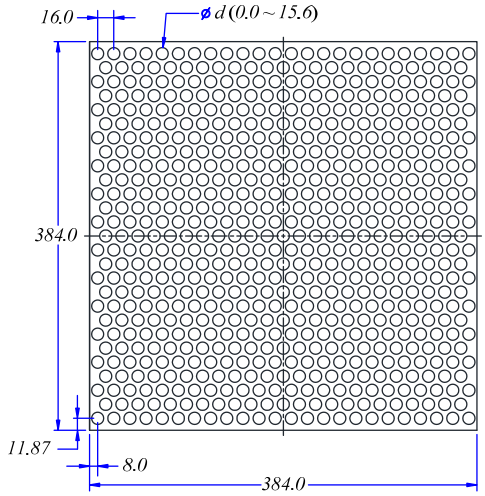
Mode no.	Natural frequency (Hz)		Discrepancy (%)	Mode no.	Natural frequency (Hz)		Discrepancy (%)
	Theory	FEM			Theory	FEM	
1	180.13	180.12	0.005	7	1053.8	1053.6	0.018
2	367.39	367.35	0.011	8	1101.4	1101.0	0.036
3	541.70	541.58	0.022	9	1212.1	1211.7	0.033
4	658.66	658.56	0.015	10	1217.1	1216.7	0.033
5	661.78	661.69	0.014	11	1483.4	1482.6	0.054
6	825.95	825.71	0.029	12	1547.1	1545.9	0.078

Table 1: Natural frequencies of a solid square plate with fixed edges.

2.3 Extraction of effective modulus of elasticity

To extract the effective modulus of elasticity as a function of ligament efficiency, a perforated square plate with a triangular penetration pattern of holes was examined using the finite element analysis. The geometry and physical properties of a fully perforated square plate model are listed in Figure 2. The configuration of the perforated square plate illustrated

in Figure 2 is used to extract the effective modulus of elasticity. The number of circular holes in the plate is enough to extract the effective properties. The finite element analysis was carried out using commercial computer software, ANSYS. The natural frequencies of the perforated plate are normalized with respect to that of imperforated solid plate as a function of the ligament efficiency, η, which is defined as the ligament gap divided by the pitch.



Modulus of elasticity	E	69 GPa
Poisson's ratio	μ	0.33
Density	ρ	2700 kg/m^3
Perforated area	a	384 mm × 384 mm
Hole diameter	d	0 ~ 15.6 mm
Pitch	p	16.0 mm
Thickness	h	3 mm

Unit : mm

Figure 2: A perforated square plate model to extract effective material properties.

Figure 3 shows normalized natural frequencies of the perforated square plate with fixed edges. As the flexural rigidity of the plate is reduced rapidly but the inertia of the plate is proportionally reduced with the hole area, the normalized natural frequencies are decrease with the hole diameter. The normalized natural frequencies, τ of the fixed plate can be categorized into three regions; the first region approximately between $\eta = 0.8$ and $\eta = 1.0$,

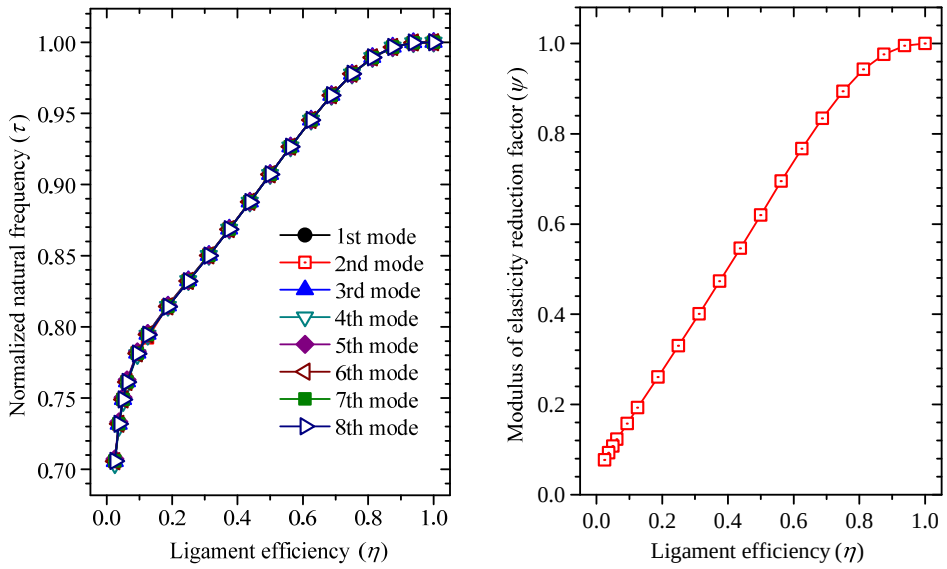


Figure 3: Normalized natural frequency and modulus of elasticity of a perforated square plate with fixed edges

shows a slow reduction in normalized natural frequencies; the second region approximately between η = 0.8 and η = 0.2, represents a linear reduction of normalized natural frequencies, finally; the third region, less than η = 0.2, reveals a drastic reduction in normalized natural frequencies. As a rule, for the fixed case, the normalized natural frequencies of the perforated square plate do not depend on the mode number but the ligament efficiency only as illustrated in Figure 3.

The effective modulus of elasticity of the perforated square plate are obtained using an inverse method as shown in Figure 3. The effective modulus of elasticity for the perforated square plate with the fixed edges approximately does not depend upon the mode number, but they can be given as a function of the ligament efficiency. The normalized effective modulus of elasticity, $\psi = E^* / E$, can be approximated by a polynomial function given by Eq. (22) using a curve fitting.

$$\psi = 0.03945 + 1.26910\,\eta - 0.51685\,\eta^2 + 1.26780\,\eta^3 - 1.06239\,\eta^4 \tag{22}$$

2.4 Application to Partially Perforated Rectangular Plate

The elastic constant extracted through section 2.3 is checked whether it can be applicable to the partially perforated rectangular plate. An example with a triangular penetration pattern is selected as shown in Figure 4. The geometry and material properties are listed in Table 2. The partially perforated plates are regarded as a rectangular plate which is divided into two regions as shown in Figure 1. The one is the inner perforated region and the other is the peripheral solid region. As the inner perforated region can be regarded as a homogeneous plate which has an effective modulus of elasticity and an equivalent mass density, but the outer peripheral solid region has an original modulus of elasticity and mass density. The effective modulus of elasticity of the inner perforated region is determined by Eq. (22) and the equivalent mass density can be calculated by Eq. (5). Finally, the theoretical natural frequencies can be calculated using Eq. (21). Finite element analyses for the partially perforated rectangular plate defined by Figure 4 and Table 2 were performed to confirm the theoretical method characterized by Eq. (21) using ANSYS (release 14). The natural frequencies of the partially perforated rectangular plate are extracted by the suggested theory and two finite element analyses. The results from finite element analysis using effective modulus of elasticity (E^*) are compared with those from finite element analyses of the perforated plate model. It will show validity of the effective modulus of elasticity for the perforated rectangular plate modal analysis. The effective modulus of elasticity (E^*) calculated by Eq. (22) and the equivalent density (ρ^*) given by Eq. (5) are used in the finite element analysis with the homogeneous finite element analysis model.

Physical properties in solid plate	Modulus of elasticity	E	195 GPa
	Poisson's ratio	μ	0.30
	Density	ρ	7770 kg/m^3
Rectangular plate geometry	Total plate area	$A \times B$	1600 mm × 1200 mm
	Perforated area	$L \times K$	1305 mm × 980 mm
	Hole diameter	d	30 mm
	Pitch	p	45 mm
	Thickness	h	8 mm

Table 2: Geometry and physical properties of a partially perforated rectangular plate model.

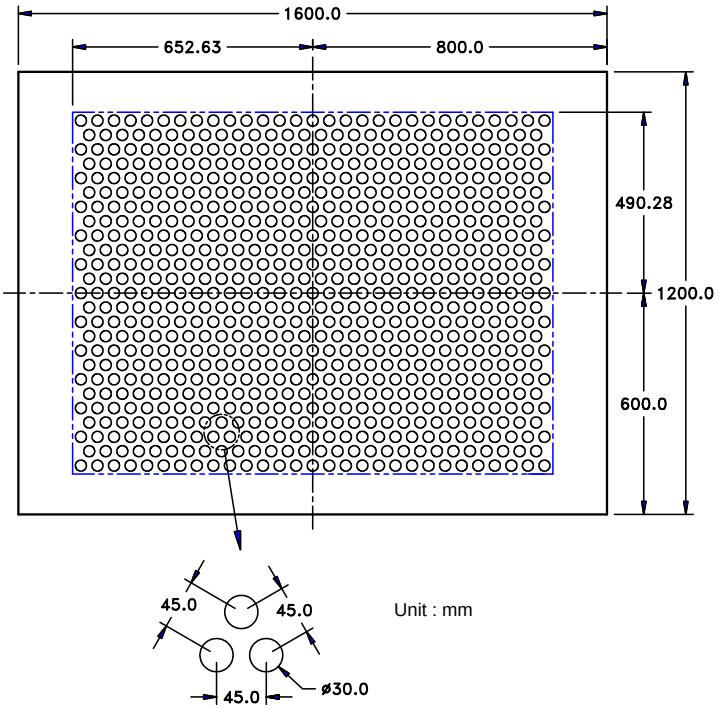


Figure 4: Model of a partially perforated rectangular plate with a triangular penetration pattern.

Serial mode number	Natural frequency (Hz)			Discrepancy between FEM results (%)	Discrepancy between theory and FEM result (%)
	Theory	FEM (ANSYS)			
		Perforated model	Homogeneous model		
1	38.56	38.35	38.81	0.55	1.20
2	63.11	62.78	63.73	0.53	1.51
3	88.64	87.70	89.04	1.07	1.53
4	102.8	101.4	103.31	1.38	1.88
5	110.5	109.9	111.95	0.55	1.87
6	147.6	146.3	149.51	0.89	2.19
7	155.5	152.0	155.43	2.30	2.26
8	160.7	159.6	162.34	0.69	1.72
9	181.8	181.1	184.66	0.39	1.97
10	199.3	195.5	200.30	1.94	2.46
11	217.4	214.5	219.31	1.35	2.24
12	220.4	216.4	221.36	1.85	2.29

Table 3: Natural frequencies of a partially perforated rectangular plate with fixed edges.

3 RESULTS AND DISCUSSION

Tables 3 shows the 12 natural frequencies of the partially perforated rectangular plate with fixed edges. The discrepancies between FEM results and theoretical natural frequencies are

less than 3%. It is clear that the Rayleigh-Ritz method applying the effective modulus of elasticity and the equivalent density is valid in the analysis of the partially perforated rectangular plate with fixed edges. The mode shapes of the simplified homogeneous model are shown in Figure 5, and those of the detailed perforated plate model are illustrated in Figure 6. It can be observed that the each mode shape of the two finite element analyses is identical.

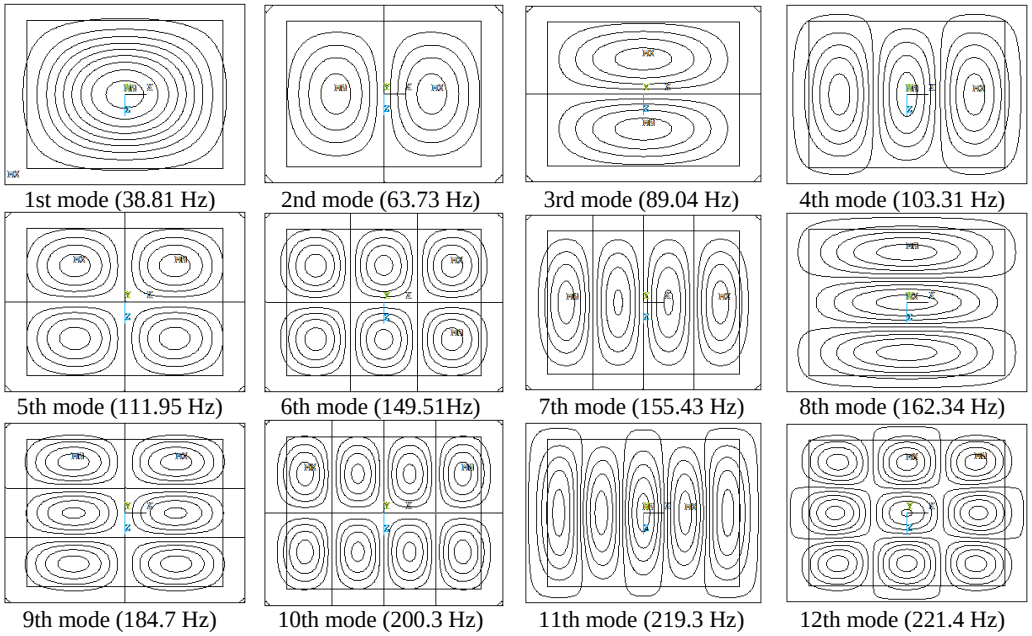


Figure 5: Mode shapes for a partially perforated rectangular plate with fixed edges using effective material properties.

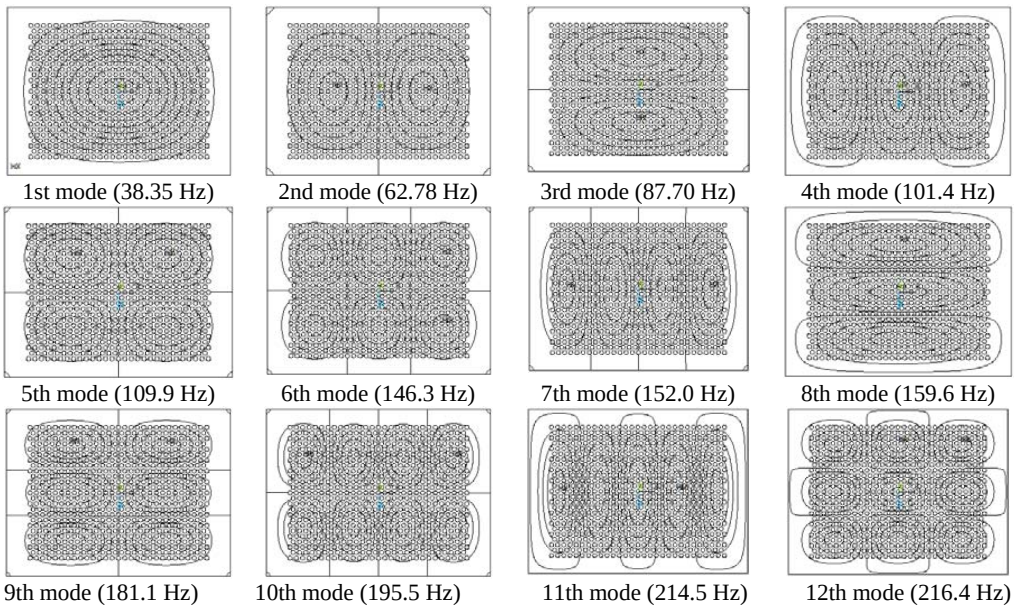


Figure 6: Mode shapes for a partially perforated rectangular plate with fixed edges.

4 CONCLUSIONS

A theoretical analysis for free vibration of a partially perforated rectangular plate with triangular penetration pattern is suggested. It is found that the natural frequencies of the perforated plate gradually decrease with a hole size. In the study, the natural frequencies of the perforated rectangular plate are obtained as a function of ligament efficiency using commercial finite element analysis code, ANSYS. Additionally, they are used to extract the effective modulus of elasticity under an assumption of constant Poisson's ratio. The effective modulus of elasticity of the fully perforated square plate is applied to the modal analysis of a partially perforated rectangular plate using a homogeneous finite element analysis model. The natural frequencies and the corresponding mode shapes of the simplified homogeneous model are compared with those of the detailed finite element analysis model of the partially perforated rectangular plate in order to check the validity of the effective modulus of elasticity. The theoretical method based on the Rayleigh-Ritz method to calculate the natural frequencies of a partially perforated rectangular plate is suggested. It is clear that the suggested effective modulus of elasticity and the Rayleigh-Ritz method can be applicable to the perforated plates with the fixed boundary condition.

ACKNOWLEDGEMENT

This work was supported by the National Research Foundation of Korea grant funded by the Korea government MSIP (No. 2012M2A8A4026290).

REFERENCES

[1] ASME PVP Code, Section III, Division 1, Appendices, Non-mandatory Appendix A, Article A–8000, *Stresses in perforated flat plates*, 2007.

[2] W. J. O'Donnell, Effective elastic constants for the bending of thin perforated plates with triangular and square penetration patterns, *Journal of Engineering for Industry*, **95**, 121–128, 1973.

[3] T. Slot, and W. J. O'Donnell, Effective elastic constants for thick perforated plates with triangular and square penetration patterns, *Journal of Engineering for Industry*, **93** (4), 935–942, 1971.

[4] P. Cupial, Calculation of the natural frequencies of composite plates by the Rayleigh–Ritz method with orthogonal polynomials, *Journal of Sound and Vibration*, **201**(3), 385–387, 1997.

[5] S. M. Dickinson and A. Di Blasio, On the use of orthogonal polynomials in the Rayleigh–Ritz method for the study of the flexural vibration and buckling of isotropic and orthotropic rectangular plates, *Journal of Sound and Vibration*, **108**(1), 51–62, 1986.

[6] R. G. Grimes, J. G. Lewis, and H. D. Simon, A shifted block Lanczos algorithm for solving sparse symmetric generalized eigen problems, *SIAM Journal on Matrix Analysis and Applications*, **15**(1), 228–272, 1994.

International Conference on Engineering Vibration
Ljubljana, Slovenia, 7-10 September 2015

HIGH-FREQUENCY CONTROL OF THE THE SLOW MOTIONS

Eugen Kremer*[1]

[1] Department of Finite Elements
LuK GmbH & Co. KG
Industriestr. 3
77815 Bühl / Germany
Eugen.Kremer@Schaeffler.com

Keywords: non-linear systems, vibrational mechanics, multi-scale, high-frequency control

Abstract. *A non-linear system with essentially different time scales is considered. It is well known, that slow motions in non-linear systems are generally dependant on the high-frequency excitation, which can modify the characteristics of the system with respect to slow motions. This effect is a central issue in the concept of the vibrational mechanics by Prof. I.I.Blekhman. This concept is developed here further on the base of multi-scale asymptotic technique. It was succeeded to obtain the equations describing only the slow motions in a rather general case of analytical systems. It enables us to analyze how the structure of the original equations effects the structure of the equations for the slow motions. These results give a possibility for constructing a high-frequency control to provide requested properties of the the system relating to slow motions. For example, a high-frequency excitation transforms a non-linear friction in a controlled linear friction with essential bigger damping ratio. The theoretical results are verified numerically.*

11th International Conference on Engineering Vibration
Ljubljana, Slovenia, 7–10 September 2015

STRATEGY FOR IDENTIFICATION OF DAMPING RATIO USING MORLET WAVE DAMPING IDENTIFICATION METHOD

I. Tomac*, Ž. Lozina, D. Sedlar

University of Split – Faculty of Electrical Engineering, Mechanical Engineering and Naval Architecture in Split
itomac@fesb.hr

{lozina,dsedlar}@fesb.hr

Keywords: Modal Analysis, Damping ratio, Identification, Continious wavelet transform, Gabor wavelet.

Abstract. *A strategy for the identification of damping ratios in structures with a Morlet Wave Damping Identification method is proposed. Generally, this method is based on extracting damping ratios for a given natural frequency from only two wavelet coefficients. The considerable sensitivity of the identified values is noticed even for a small change of the parameters of the wavelet functions. To raise a certainty in the identified values we propose identification of damping ratio for the whole range of feasible wavelet functions parameters. Decision criteria are based on lowest fluctuation of the identified damping ratio. This strategy resulted in the raising the level of automation and reducing the operator interaction. Method is tested on the simulated responses and the experimentally measured responses. In both cases, the results of the damping ratios identification are compared with numerous independent traditional methods. Traditional identification methods applied in comparative analysis were available as in house code or commercial software.*

1 INTRODUCTION

Parameter identification is a fundamental problem in vibration engineering practice. It is concerned with the estimation of system parameters like natural frequencies, damping ratios and mode shapes. With these parameters, one can obtain the mathematical model for representing a system's input - output relationship that are typically identified form system's Frequency Response Function (FRF), Impulse Response Function (IRF), or a scalogram which depends on method used for the identification. In practice the damping parameter in multi-degree-of-freedom (MDOF) systems are the most critical to estimate. It is well known that they are the most sensitive to noise, measurement errors, inadequate excitation, etc. There are plenty of different techniques developed for the identification of modal parameters, such as: Ibrahim time domain (ITD) method [1, 2, 3], the least square complex exponential (LSCE) method [4] and the minimum eigensystem realisation algorithm (ERA) method which for identification uses signal in time domain. The methods which rely on the analysis in frequency domain are: e.g the rational fraction polynomial (RFP) method [5, 6], the orthogonal polynomial (OP) method [7, 8] and the complex exponential frequencydomain (CEFD) method. The modern frequency approach includes a two-step technique: least square complex frequency-domain (LSCF) and least square frequencydomain (LSFD) [9, 10]. The complex approach is reported as the method of choice in commercial softwares, e.g. MEScope – OP [11] and ModalVIEW – LSCF and LSCE [12]. Methods that for identification use scalogram are based on the continuous wavelet transform (CWT), the extensive research of these method can be found in [13]-[16]. Lately another method based on CWT has been presented by [17] for identification of damping ratio called Morlet wave damping identification method. In this paper we present a simple upgrade of MWDI method. It is noticed that identification results are sensitive on the change of parameters that control method. We suggest identification of damping ratio for the range of feasible parameters and by defining a criteria for choosing damping ratio. Method upgrade is tested experimentally on two numerical test cases and one experimental test case. Results are compared to the existing methodology for identification of damping using CWT and also with traditional methodology which is implemented in commercial software which authors posses (ME'Scope and ModalVIEW). Since MWDI method is based on CWT, the basic concepts of modal parameters identification are explained in section 2. In section 3 the MWDI method is briefly explained and proposed strategy presented. Sections 4 and 5 contain test results of proposed strategy for identification of damping ratio.

2 MODAL PARAMETERS IDENTIFICATION USING CWT - THEORETICAL BACKGROUND

2.1 Continuous Wavelet Transform

Integral transform such as CWT transforms one dimensional time signal into two dimensional translation-scale domain. It is achieved by an inner product of the time signal with a basic wavelet function, show in Eq. 1.

$$W_x^{\psi}(u,s) = \int_{-\infty}^{\infty} x(t)\psi_{u,s}^*(t)dt \tag{1}$$

where, $x(t)$ is a signal and $\psi_{u,s}^*(t)$ complex conjugated basic wavelet function which is shifted along the time axis with a translation parameter u and scaled with the parameter s along the scale axis. The scaled and translated WF is shown in Eq. 2.

$$\psi_{u,s}(t) = \frac{1}{\sqrt{s}}\,\psi\left(\frac{t-u}{s}\right) \tag{2}$$

where the reciprocal square root of the scale parameter suppresses an influence of the scale parameter on energy of the CWT coefficients. The basic wavelet function is generally a window function in both, time and frequency domains. A complex wavelet functions such as: Gabor WF, Morlet WF, Cauchy WF, General harmonic WF are used in modal analysis, [13, 14, 15]. The normalised Gabor WF is shown in Eq. 3.

$$\psi(t) = \frac{1}{\sqrt[4]{\pi\sigma^2}}\exp\left(-\frac{t^2}{2\sigma^2} + i\eta t\right) \tag{3}$$

where η is a basic frequency of the WF and σ defines the window width which allows the manipulation of a time spread – σ_ψ and a frequency spread – $\sigma_{\hat{\psi}}$ of the WF. Time spread and frequency spread are defined as standard deviation of WF in time and frequency domain from its centre values. Furthermore, using the Gabor WF, frequency and scale are related with the expression $\omega = \eta/s$.

2.2 Wavelet transform of the SDOF

The free response of the SDOF mechanical system expressed exponentially with modal parameters, is show in Eq. 4.

$$x(t) = \frac{1}{2}A\exp(-\zeta\omega_{\mathrm{n}}t)\left[\exp(i(\omega_{\mathrm{d}}t-\chi)) + \exp(-i(\omega_{\mathrm{d}}t-\chi))\right] \tag{4}$$

where A and χ depend on the initial conditions, ζ – damping ratio, ω_{n} – undamped natural frequency, ω_{n} – damped natural frequency. The free response from eq. 4 can be integrated with Gabor WF (Eq. 3) using the Eq. 1, which gives an analytical expression of the CWT of the SDOF system (Eq. 5), [16].

$$W_x^{\psi}(u,s) = \frac{A\sqrt[4]{\pi\sigma^2 s^2}}{\sqrt{2}}\exp\left[-u\zeta\omega_{\mathrm{n}} + \alpha(s,\sigma,\eta) - i(-\omega_{\mathrm{d}}u + \beta(s,\sigma,\eta))\right] \tag{5}$$

where $\alpha(s,\sigma,\eta) = 1/2(-\eta^2\sigma^2 - s^2\sigma^2\omega_{\mathrm{d}}^2 + s^2\zeta^2\sigma^2\omega_{\mathrm{n}}^2) + s\eta\sigma^2\omega_{\mathrm{d}}$ and $\beta(s,\sigma,\eta) = \chi + s^2\zeta\sigma^2\omega_{\mathrm{d}}\omega_{\mathrm{n}} - s\zeta\eta\sigma^2\omega_{\mathrm{n}}$. In Eq. 5 can be seen how the modal parameters are integrated in the CWT. So, different approaches can be established for detection.

2.3 Identification of Modal parameters

The extreme values of Eq. 5 are located on the scale equal to the system's natural frequency – s_{d}, which is equal to: $s_{\mathrm{d}} = \eta/\omega_{\mathrm{d}}$. If the scale s_{d} is inserted into Eq. 5 the extreme values along the translation axis u are obtained (Eq. 6).

$$W_x^{\psi}(u,s_{\mathrm{d}}) = \frac{A\sqrt[4]{\pi\sigma^2 s_{\mathrm{d}}^2}}{\sqrt{2}}\exp\left(-u\zeta\omega_{\mathrm{n}} + s_{\mathrm{d}}^2\zeta^2\sigma^2\omega_{\mathrm{n}}^2/2\right)\exp\left(i\omega_{\mathrm{d}}u - \chi\right) \tag{6}$$

Damped natural frequency is detected from the slope of the wavelet instantaneous phase which is equal to: $\Phi(u, s_\mathrm{d}) = \omega_\mathrm{d} u - \chi$. The damping ratio is contained in two members of the instantaneous amplitude of the Eq. 6. This way two different methods for detection of the damping ratio can be established:

- Logarithmic Decrement method, [13]: $-u\zeta\omega_\mathrm{n}$
- Morlet Wave Damping Identification method, [17]: $\alpha(s_\mathrm{d}, \sigma, \eta) = s_\mathrm{d}^2\zeta^2\sigma^2\omega_\mathrm{n}^2/2$

The second method assumes $\sigma = 1$. This value makes Gabor WF identical to Morlet WF. Difference between these two WFs is that window width can be changed independently of scale on Gabor WF, while on Morlet WF window width is changed by scale.

3 BASICS OF THE MWDI METHOD

Methodology for the extraction of the damping ratio can be found in [17]. Only the main parts of this methodology are shown here. Basically, a ratio of the two wavelet coefficients with the same translation and a scale, but with different time spreads are calculated. In order to have a better control of WF's frequency spread, desired frequency, and its position three new parameters were introduced instead of scale, shift and basic frequency. New parameters are: n – controls the time spread of the WF, k – defines the length of the basic WF (T_ψ) expressed in the number of cycles on the designated frequency ω, which is a third parameter. The length of the WF is equal to $T_\psi = 2k\pi/\omega$. The ratio of the amplitude of two wavelet coefficients is calculated by keeping the same length and the position of the WF, changing only the time spread of the basic WF, as shown in Eq. 7.

$$M(n_1, n_2, k, \omega) = \frac{|I_1(n_1, k, \omega)|}{|I_2(n_2, k, \omega)|} \tag{7}$$

The use of the parameter k causes generated WF to be shorter than the measured signal which has the length T_x, so $T_\psi \leq T_x$. This also means that by increasing the parameter k, not only the length of the basic WF changes, but it also shifts the generated WF toward $T = T_x/2$. For that purpose the shift parameter of the basic WF is equal to $u = k\pi\omega$. The scale parameter is related to the time spread $\sigma_\psi(s) = s/\sqrt{2}$, introducing a new parameter n as the following product: $T_\psi = n\sigma_\psi$. Now dilation is expressed as: $s = 2k\pi\sqrt{2}/(n\omega)$. The basic frequency of the WF is expressed in a similar manner: $\eta = 2k\pi\sqrt{2}/\omega$. The basic WF expressed with new parameters is shown in the Eq. 8.

$$\psi(n, k, \omega) = (2\pi)^{-\frac{3}{4}}\sqrt{\frac{n\omega}{k}}\exp\left[-\left(\frac{n(k\pi - \omega t)}{4k\pi}\right)^2 + i(k\pi - \omega t)\right] \tag{8}$$

Each wavelet coefficient is calculated using the expression shown in Eq. 1. Typically the inner product between WF and the signal is calculated using the boundaries of $t \in [0, T_x]$, but here because of the parameter k, which leads to the condition $T_\psi \leq T_x$, integral boundaries are changed, too. So, the inner product is calculated on the boundaries of $t \in [0, T_\psi]$ and the amplitude ratio (Eq. 7), using WF from Eq. 8 can be calculated. The calculated ratio can be expressed with analytical expression in the same manner as in the Eq. 5. The analytical expression of the ratio $M(n_1, n_2, k, \omega)$ is shown in Eq. 9.

$$M(n_1, n_2, k, \omega) = \exp\left[4\pi k\zeta \frac{n_2^2 - n_1^2}{n_1 n_2}\right] \sqrt{\frac{n_2}{n_1}}\,\varepsilon \tag{9}$$

where ε contains error functions – $\mathrm{erf}(k, n_1, n_2, \zeta)$ which is a result of integrating Gaussian window function on the finite interval.

The ratio $M(n_1, n_2, k, \omega)$ from the Eq. 9 is obtained from the measured signal which leads to solving a non-linear equation using the simple numerical method like Newton-Raphson to find the damping ratio.

3.1 Parameters selection

The authors of [17] gave directions for the selection of parameters $n_{1,2}, k$, but the problem of certainty in the identified result remains open. This is especially a problem when a physical system is being identified where the result is not known in the advance. In order to raise a level of certainty in identified damping rations, in this paper we propose identification for the whole range of feasible parameters. For the sake of completeness these conditions are listed here too. The first condition defines the theoretical range of the WF number of cycles: $(-\ln 0.3)/(2\pi\zeta)) \leq k \leq n_1^2/(8\zeta\pi)$, the second condition defines the frequency resolution of the WF in the case of close modes in MDOF systems: $\max(\omega_j, \omega_{j+1})\, n_2/(4\pi k) < |\omega_j - \omega_{j+1}|$, the third condition limits the maximum length of the WF related to the length of the signal: $T_\psi = 2k\pi/\omega \leq T_x$. Parameter which controls width of the first WF is set constant $n_1 = 5$. The second WF width parameter n_2 is varied in interval $n_1 < n_2 \leq 2n_1$. The parameter k is set in the range taking into account above mentioned conditions. It is noticed that identified result vary with a change of parameters n_2 and k. This can be seen in the figure 1a, where on the 3D plot is show identification of the ideal case from the numerical example 1 which is defined later in the text.

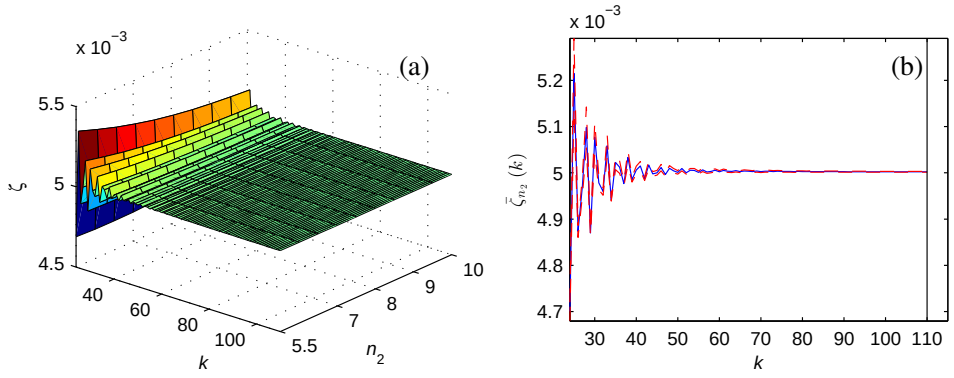


Figure 1: Relative damping coefficient identified using the MWDI method for the range of WF parameters. Figure (a) shows the 3D plot of all identified relative damping coefficients. Figure (b) depicts mean values of the relative damping coefficient along the n_2 axis (blue solid line) and standard deviations from the mean value (red dashed line), vertical black solid line marks the relative damping coefficient with the minimal deviation from the mean value.

On the figure 1 can be seen that with the increase of the parameter k fluctuations of the identified results are reducing. These fluctuations are relatively small, because it is an ideal

case without influence of the errors in signal. In case when signal is disrupted with errors fluctuations of damping ratio are higher. This makes the identification process difficult because the uncertainty in selected parameters of the WF is higher. So we propose a following decision criteria for choosing the identified damping ratio.

3.2 Decision criteria

Procedure for the identification of damping ration:

- Identify damping ratio for the whole range of feasible parameters n_2 and k,
- Calculate a mean value of the identified damping ratios, along the n_2 axis, which is calculated using the following expression:

$$\bar{\zeta}(k_i) = \frac{1}{N}\sum_{j=0}^{N}\zeta_{i,j} \tag{10}$$

  where index i represents the k axis, index j represents the n_2 axis, N is the number of identified damping ratios on the n_2 axis. Equation 10 is depicted on the Figure 1b with the sold blue line.

- Calculate the standard deviation from the calculated mean values – $\mathrm{stdev}(\bar{\zeta}_i)$, which is depicted with red dashed lines on the Figure 1b.
- Chose that value which has minimal standard deviation from the mean value $\zeta = \min\left\{\mathrm{stdev}(\bar{\zeta}_i)\right\}$

The proposed procedure also makes the identification process more autonomous. The validity of this procedure is tested on the following examples with numerically simulated responses with added errors and experimentally measured responses.

4 NUMERICAL TEST CASES

Proposed strategy for identification of the damping ratio is tested on the numerically simulated responses of the mechanical 2DOF system (Figure 2). Two examples are presented, one with distant natural frequencies and second one with close natural frequencies. Both systems have proportional damping. Simulated responses are disrupted with errors in signal in the form

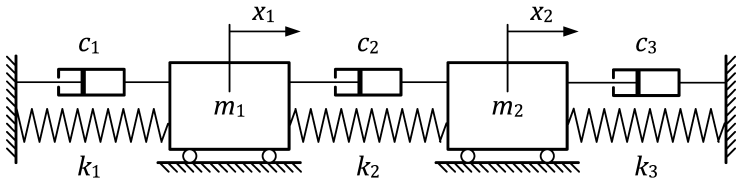


Figure 2: 2DOF system

of a white noise. The white noise is added on three levels of signal-to-noise (SNR) ratios: 24dB, 12dB and 6dB (Eq. 11).

$$\mathrm{SNR} = 10\log\left(\frac{\sigma_x}{\sigma_w}\right)^2 \tag{11}$$

where σ_x is standard deviation of the signal from the mean value and σ_w is standard deviation of the noise from the mean value. All impulse response functions are simulated with same signal parameters set, that are: sampling frequency of 128 Ss^{-1} and 16 s signal duration. Results are shown on diagrams (Figures 4 and 6) where a horizontal axis of the diagram shows the method used for identification and a vertical axis shows an relative error of detected values from the calculated value of the damping ration. Meaning of abbreviations on the horizontal axis are: LD-CWT – CWT, Logarithmic Decrement method; MWDI – Morlet Wave Damping Identification method; ME'S – results obtained using MEScope commercial software; MV-LSCE – results obtained with ModalView commercial software using the Last Square Complex Exponential method; MV-LSCF – results obtained with ModalView commercial software using the Last Square Complex Frequency method.

4.1 Example 1 Weakly coupled 2DOF system

System impulse response functions are generated for the following parameter set: $m_1 = m_2 = 1$ kg, $k_1 = k_3 = 2500$ Nm^{-1}, $k_2 = 2000$ Nm^{-1}, $c_1 = c_3 = 0.5$ Nsm^{-1}, $c_2 = 0.5\,k_2/k_1$ Nsm^{-1}. Referent modal parameters are calculated form these values and they are shown in Table 1.

DOF	$f_{i,\mathrm{n}}$ (Hz)	$\zeta_{i,\mathrm{ideal}}$ ( )
1	7.9577	0.005
2	12.831	0.0081

Table 1: Referent values of the modal parameters for the weakly coupled system.

Detection of the damping ratio using the MWDI method is done in two ranges of k parameter, one range for each natural frequency. On the first natural frequency: $k \in [40, 126]$, and on the second natural frequency: $k \in [33, 121]$. The first parameter is constant: $n_1 = 5$ and the second parameter is set in range: $n_2 \in [5.5, 10]$. Results of the identification using the proposed strategy are shown on the Figure 3.

The results of MWDI method are compared to the other methods and they are displayed in the comparative diagrams (Figure 4).

4.2 Example 2 Strongly coupled 2DOF system

System parameters of this example are the same as for the previous example, only the coupling stiffness is different which is equal to: $k_2 = 200$ Nm^{-1}. Referent modal parameters are calculated form these values and they are shown in Table 2.

DOF	$f_{i,\mathrm{n}}$ (Hz)	$\zeta_{i,\mathrm{ideal}}$ ( )
1	7.9577	0.005
2	8.5708	0.0054

Table 2: Referent values of the modal parameters for the strongly coupled system.

Two ranges of k parameter, one range for each natural frequency are introduced here too. On the first natural frequency: $k \in [41, 127]$, and on the second natural frequency: $k \in [41, 137]$.

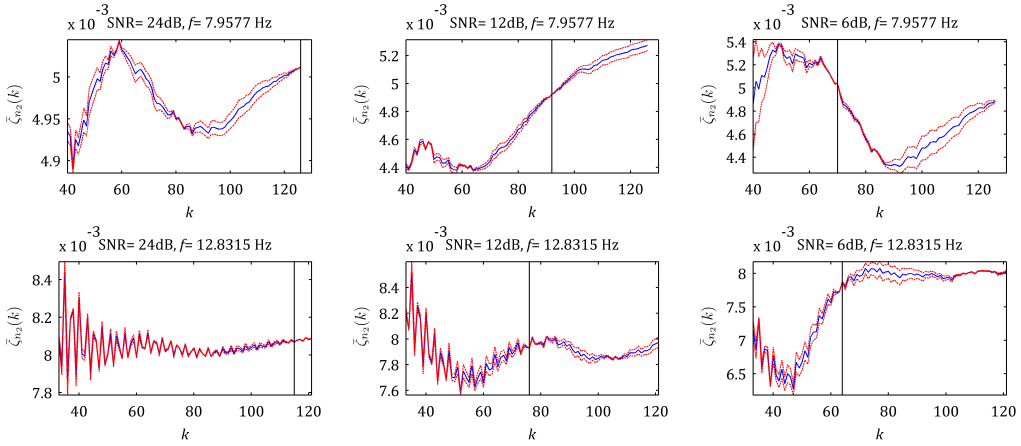


Figure 3: Results of damping ratio detection on the example 1, using proposed strategy with MWDI method. Mean values of the relative damping coefficient along the n_2 axis are plotted with blue solid line and a standard deviations from the mean values are plotted with red dotted line, vertical black solid line marks the relative damping coefficient with the minimal deviation from the mean value.

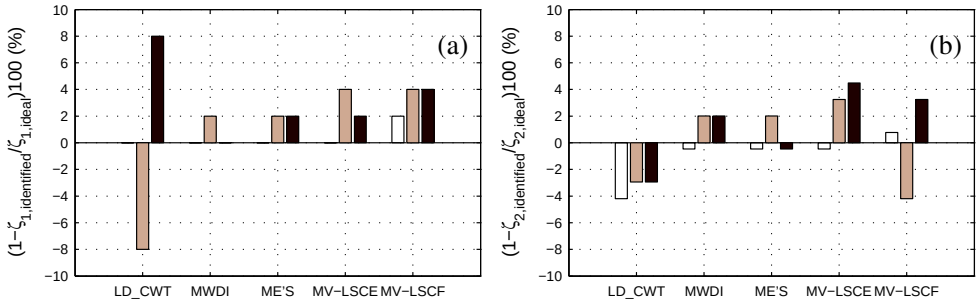


Figure 4: Comparative display of damping ratios for the weakly coupled system. Figure (a) corresponds to the damping ratio of the first natural frequency and Figure (b) to the damping ratio of the second natural frequency. Colour of bars corresponds to the level of SNR in the following order: white 24dB, pink 12dB, dark 6dB.

The first parameter is constant: $n_1 = 5$ and the second parameter is set in range: $n_2 \in [5.5, 10]$. Results of the identification using the proposed strategy are shown on the Figure 5.

The results of MWDI method are compared to the other methods and they are displayed in the comparative diagrams (Figure 6).

In the following chapter proposed strategy is tested on the laboratory test model.

5 EXPERIMENTAL TEST CASE

Damping ratios and natural frequencies are identified on the 2DOF laboratory model which is consisted of two beams that are on the one side attached to the structure with bearing and the free side is attached to the surrounding structure with springs (Figure 7).

System is excited using the impact hammer taking care of small displacements. Both responses and the impact are measured simultaneously, and processed to obtain impulse response function using the following equipment:

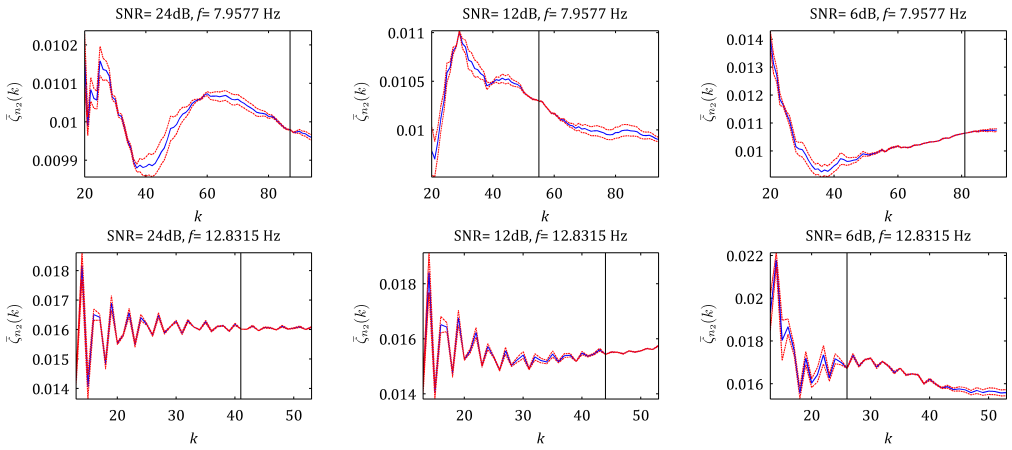


Figure 5: Results of damping ratio detection on the example 2, using proposed strategy with MWDI method. Mean values of the relative damping coefficient along the n_2 axis are plotted with blue solid line and a standard deviations from the mean values are plotted with red dotted line, vertical black solid line marks the relative damping coefficient with the minimal deviation from the mean value.

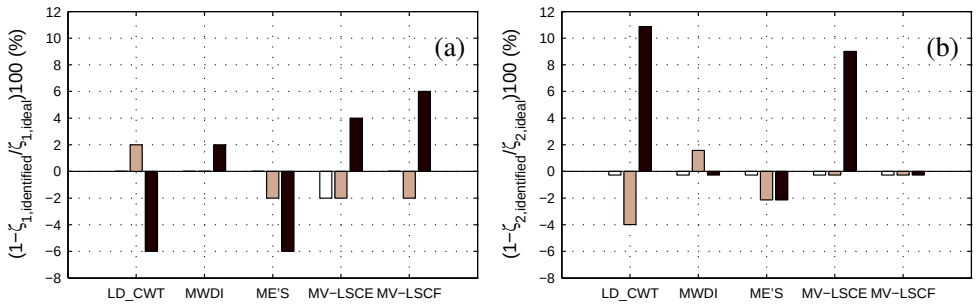


Figure 6: Comparative display of damping ratios for the strongly coupled system. Figure (a) corresponds to the damping ratio of the first natural frequency and Figure (b) to the damping ratio of the second natural frequency. Colour of bars corresponds to the level of SNR in the following order: white 24dB, pink 12dB, dark 6dB.

1. Sensors:
   - Force: B&K impact hammer type 8206-001
   - Accelerometers: MMF type KS95B100
2. Data acquisition hardware:
   - 24bit – NI PXI 4472B
3. Software:
   - Measurement: ME'Scope
   - Signal Processing: Matlab

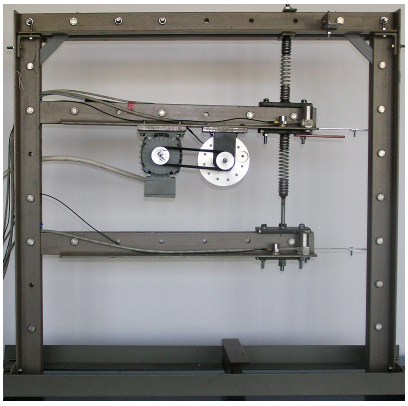


Figure 7: Weakly coupled laboratory model

Signal is measured with a sampling frequency $f_s = 1000$ Ss^{-1} with a signal length of 4096 S using the averaging technique (5 averages). Measured signal is downsampled so that the sampling frequency is similar to the sampling frequency used in numerical examples. Impulse response functions and the frequency response functions obtained from measured signal are shown on the Fig. 8.

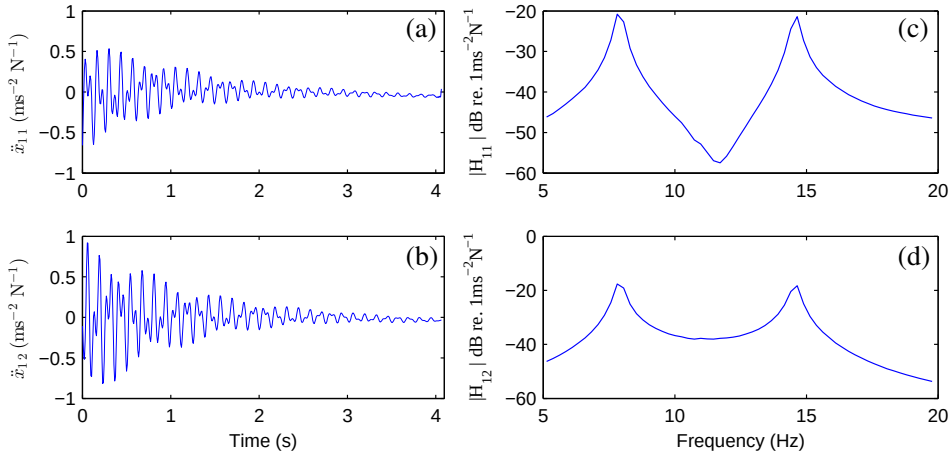


Figure 8: Experimentally measured data from the laboratory test model. Impulse response functions are shown on figures (a) and (b) and frequency response functions are shown on Figures (c) and (d).

Impulse response function from the first mass ($\ddot{x}_{11}$) is used for identification of damping ratio using the MWDI method. Since the natural frequency is not known it should be identified first. Natural frequencies can be identified approximately by detecting peeks on the FRF plot (Figure 8b,d) or more precisely by using other more precise methods. Here, natural frequencies are detected from the wavelet instantaneous phase. Two ranges of k parameter, one range for each natural frequency are used. On the first natural frequency: $k \in [12, 30]$ and on the second natural frequency: $k \in [23, 57]$. The first parameter is constant: $n_1 = 5$ and the second parameter is set in range of: $n_2 \in [5.5, 10]$. Results of the identification using the proposed strategy are shown

on the Figure 9.

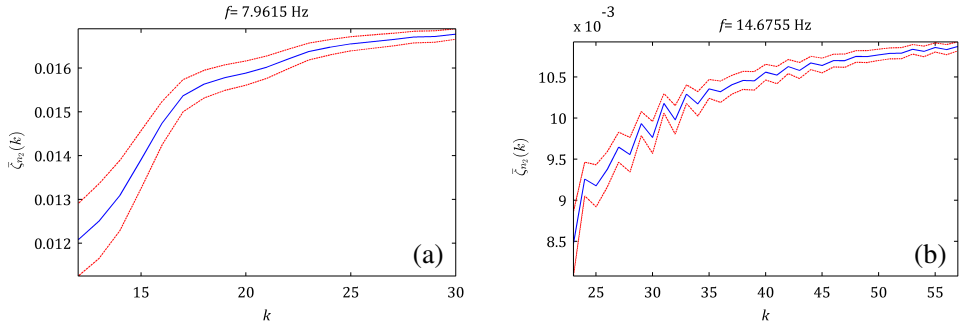


Figure 9: Damping ratios identified on the experimental test case, using the proposed strategy. Mean values of the damping ratio along the n_2 axis are plotted with blue solid line and a standard deviations from the mean values are plotted with red dotted line, vertical black solid line marks the damping ratio with the minimal deviation from the mean value which overlaps with right border of diagrams (a) and (b).

Detected damping ratios and the corresponding value of the parameter k are listed in the table 3.

	ζ_1 ( )	k	ζ_2 ( )	k
MWDI	0.0168	30	0.0109	57

Table 3: Identified damping ratio and the corresponding value of the parameter k.

Now the identification results of MWDI method (table 3) are compared to the results of other methods which are shown on the diagrams in figure 10.

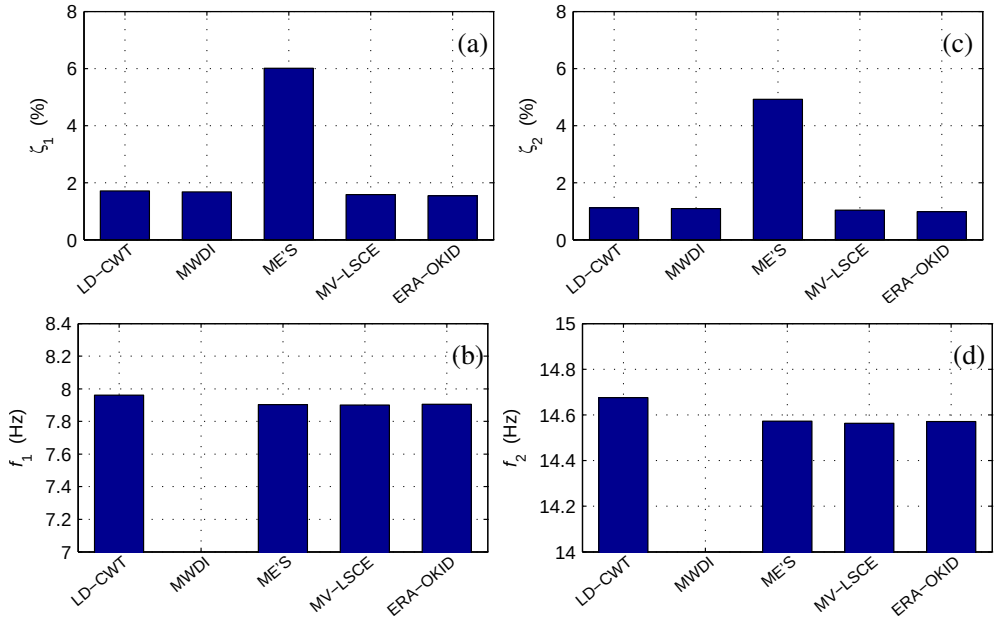


Figure 10: Comparative display of identified damping ratios and the natural frequencies for the experimental test case. Figure (a) shows damping ratio of the first natural frequency (Figure (b)). Figure (c) shows damping ratio of the second natural frequency (Figure (d)).

6 CONCLUSIONS

- Theoretical background of the MWDI method is presented and the strategy for identification of damping ratio which upgrades the MWDI method is given too.
- The intent of a proposed strategy is explained on the theoretical example.
- The proposed strategy is tested on two test cases with numerically simulated responses and one test case where the excitation and responses were experimentally measured.
- Results obtained with proposed strategy were compared to the results of traditional modal identification methods that are implemented in commercial software and a newer method that uses continuous wavelet transform.
- Comparison of results for numerical test cases and the experimental test case to the traditional modal identification methods implemented in commercial software are supplied.
- Results are compared to the relatively new method for identification of modal parameters which ih logarithmic decrement applied on ridges which are extracted from the observed system scalogram, too.
- Results of proposed strategy for damping identification proved to be in correlation with results obtained with comparing methods.
- This strategy makes easier use of MWDI method, because an operator does not need to tune parameters of the method.

REFERENCES

[1] S.R. Ibrahim, E.C. Mikulicik, The Shock and vibration bulletin: A time Domain Modal Vibration Test Technique. *The Shock and vibration bulletin*, **4**, 21–37, 1973.

[2] S.R. Ibrahim, E.C. Mikulicik, The Shock and vibration bulletin: A Methof for Direct Identification of Vibration Parameters form the Force Response. *The Shock and vibration bulletin*, **4**, 183–198, 1977.

[3] R.S. Pappa, S.R. Ibrahim, The Shock and vibration bulletin: A parameter study of the Ibrahim Time Domain Identification Algorithm. *The Shock and vibration bulletin*, **3**, 43–73, 1981.

[4] D.L. Brown, R.J. Allemang, R. Zimmerman, M. Mergeay, SEA Technical paper series: Parameter Estimation Technique for Modal Analysis. *SEA Technical paper series*, **790221**, 15–24, 1979.

[5] M.H. Richardson, D.L. Formenti, Parameter Estimation from Frequency response measurements using rational fraction polynomials. *Proceedings of the 1st International Modal Analysis Conference & Exhibit*, Orlando, Florida, 176–181, 1982.

[6] M.H. Richardson, D.L. Formenti, Global Curve Fitting of Frequency Response Measurements Using The Rational Polynomial Method. *Proceedings of the 3rd International Modal Analysis Conference & Exhibit*, Orlando, Florida, 390–397, 1985.

[7] H. Vold, Orthogonal Polynomials in the polyreference method. *Proceedings of Eleventh International Seminar on Modal Analysis*, Katholieke University of Leuven, Belgium, 1986.

[8] H. Van der Auweraer, J. Leuridan, Mechanical Systems and Signal Processing: Multiple Input Orthogonal Polynomial Parameter Estimation. *Mechanical Systems and Signal Processing*, **3**, 259–272, 1987.

[9] B. Peeters, H. Van Der Auweraer, P. Guillaume and J. Leuridan, Shock and Vibration: Multiple Input Orthogonal Polynomial Parameter Estimation. *Shock and Vibration*, **3-4**, 395–409, 2004

[10] T. De Troyer, P. Guillaume, R. Pintelon and S. Vanlanduit, Mechanical Systems and Signal Processing: Fast calculation of confidence intervals on parameter estimates of least-squares frequency-domain estimators. *Mechanical Systems and Signal Processing*, **2**, 261–273, 2009.

[11] MEscopeVES 5.0 Reference Manual Volume IIB - Options, Vibrant Technology, 2008, http://vibetech.com/go.cfm/en-us/content/mescope

[12] ModalVIEW Operating Tutorial, ABSignal, 2011, http://absignal.com/index.php

[13] W. J. Staszewski, Journal of Sound and Vibration: Identification of damping in MDOF systems using time-scale decomposition. *Journal of Sound and Vibration*, **2**, 283–305, 1997.

[14] J. Slavič, I. Simonovski, M. Boltežar, Journal of Sound and Vibration: Damping identification using a continuous wavelet transform. *Journal of Sound and Vibration*, **2**, 291–307, 2003.

[15] T. P. Le, P. Argoul, Journal of Sound and Vibration: Continuous wavelet transform for modal identification using free decay response,. *Journal of Sound and Vibration*, **1-2**, 73–100, 2004.

[16] S.-L. Chen, J.-J. Liu, H.-C. Lai, Journal of Sound and Vibration: Wavelet analysis for identification of damping ratios and natural frequencies. *Journal of Sound and Vibration*, **1-2**, 103–247, 2009.

[17] J. Slavič, M. Boltežar, Mechanical Systems and Signal Processing: Damping identification using a continuous wavelet transform. *Mechanical Systems and Signal Processing*, **5**, 1632–1645, 2011.

International Conference on Engineering Vibration
Ljubljana, Slovenia, 7-10 September 2015

BIOMECHANICAL MODEL OF A SMART MIDDLE EAR PROSTHESIS

Rafal Rusinek*[1], Jerzy Warminski[1], Krzysztof Kozik[1], Marcin Szymanski[2]

[1]Lublin University of Technology, Department of Applied Mechanics
{r.rusinek,j.warminski,k.kozik}@pollub.pl

[2]Medical University of Lublin
marcinszym@poczta.onet.pl

Keywords: Middle Ear Vibrations, Smart Prosthesis, Shape Memory Alloy.

Abstract. *In the paper an experimental results of stapes motion in an intact middle ear are presented and compared with numerical outcomes, which are obtained from the three degrees of freedom nonlinear model of an intact middle ear. Next, a new concept of smart prosthesis is proposed to reconstruct a damaged ossicular chain. The smart prosthesis, made of shape memory alloy, is described by a polynomial model. Finally, the dynamics of the middle ear with smart prosthesis is analysed as a response on external excitation.*

1 INTRODUCTION

The human middle ear is a biomechanical system which consists of three ossicles: a malleus, an incus and a stapes. The ossicles create a system, which conducts sound from the external ear to the inner ear. The ossicles are connected with each other by the incudo-stapedial joint and incudo-mallear joint. Moreover, the ossicular chain is supported by two muscles to a temporal bone. The malleus is also connected to the tympanic membrane while stapes is attached to the bony walls of the oval window by annular ligament. Such a complex bio-system is modelled in the literature from the last half century [1]. The first study in this field was published by Moller [2] in 1961. Similar model was tested by Zwislocki [3]. Authors of both publications are testing an electrical circuit to analyse middle ear system. They based on Bárány theory which says that the ossicles rotate about an axis through the head of the malleus and the short process of the incus. In this theory there is a rigid connection between the incus and the maleus. Usually, ossicular chain is modelled as several rigid bodies connected by springs and dash-pots. This approach gives the natural frequencies of vibration. A complicated procedure for obtaining the damping and stiffness coefficient of the real middle ear system is the cause of a small number of dynamic models. Therefore, development of the finite element methods (FEM) has improved this situation. In the 1978 for modelling phenomena occurring in the middle ear FEM was used [4–8]. FEA method is popular because allows to obtain the most accurate results, but their quality depends on properly selected parameters to analysis and material properties.

The middle ear is exposed to a number of conditions such as inflammation or abscesses. They lead to the destruction of ossicles that can be rebuild by surgery operations that implements an artificial prosthesis replacing a damaged ossicular chain. During the treatment, an important issue is the selection of the type of prosthesis, a material with will be made, size and fit the individual characteristics of the patient. The biggest problem now is to adjust the size of the prosthesis to the individual patient properties aimed at reducing to a minimum the duration of treatment. A classical prostheses TORP (Total Ossicular Replacement Prosthesis) and PORP (Partial Ossicular Replacement Prosthesis) are made of titanium. Their length can be adjusted but only once during operations and if the prosthesis is too short, reuse of it is impossible. Our idea consists in developing the smart prosthesis made of modern shape memory alloy (SMA), which would be able to adjust its size and shaped according to requirements. Generally, SMAs are a family of metals with the ability of changing their shape depending on their temperature [9]. SMAs undergo thermoelastic phase transformations, which can be induced either by temperature or stress. Thermomechanical properties of SMA can be modelled either by microscopic or macroscopic point of view. The microscopic approach treats phenomena in molecular level while from our point of view macroscopic approach is more interesting because takes into account phenomenological features.

A smart prosthesis can be made of NiTi alloy e.g. Nitinol is one of the most popular materials for medical applications: orthodontic, dental, intravascular stents, bones fracture etc. [10,11]. The most important properties of NiTi are an unique thermomechanical behavior based on martensitic phase transformations, shape memory effect, enhanced biocompatibility, superelasticity and high damping properties [12]. Low elastic module of NiTi which is closer to the module of bone than that of any other surgical material, makes nitinol especially attractive as a material which can substitute bone [13,14]. While there are some reports on release of Ni from NiTi implants might lead to allergic reactions in some cases, thus, limiting the applications in medicine and others re action. However, the amount of nickel released is much lower than that which might cause the negative reactions [12] and all alloy covering by the titanium oxide.

NiTinol can have one or two-way shape memory effect (SME). The basic difference between one-way and two-way SME is that no reverse change of SMA's shape occurs in case of one-way SME after subsequent cooling while two-way SME is characterized by a change of SMA's shape during cooling. For our smart prosthesis we use Nitinol element with one-way SME because the prosthesis should change shape only after heating and must not recover back when cooling.

This paper presents an idea of shape memory prosthesis (SMP) made of nitinol as a simple bar which can change its shape and length. First, dynamics of an intact middle ear is presented on the basis of a three degrees of freedom model, Next, the smart prosthesis is introduced into the middle ear system instead of the maleus and the incus. Then, a sensibility of the system dynamics on an external excitation is investigated.

2 INTACT MIDDLE EAR VIBRATIONS

Usually, vibrations of a human middle ear are depicted in the form of frequency transfer function where a system response (output) is referred to an excitation (input). From medical point of view information about stapes amplitude in the range of audibility is very important. Therefore, at the first stage of investigations, measurements of ossicular chain vibrations are performed in order to evaluate spring and damping constants. Next, a three degrees of freedom system is built to simulate behaviour of intact ossicular chain. The research focuses on stapes vibrations because its motion is directly connected with sound transmission to inner ear.

2.1 Experiment

Temporal bones are prepared in a classical way described in details in [15]. Here, the same procedure of sample preparation is shortly mentioned. The soft tissue is removed and a standard antromastoidectomy with posterior tympanotomy is performed. The mastoid facial nerve is removed to visualize the stapes arch end footplate. The ear canal is drilled leaving about 2-3 mm of bone around tympanic annulus. An artificial external ear canal of 25 mm length and 9 mm diameter is then attached to the bone with epoxy resin. The artificial canal has two ports. One for a microphone (ER-7C Etymotic Reserch) and a second for a sound source (ER2 Etymotic Reserch) placed about 2 mm from the tympanic membrane. The artificial canal is closed with a glass plate to create a sound seal chamber. A pieces of a retroleflective tape (0,5 mm^2) weighing less than 0,05 mg, are placed on the footplate of the stapes. The temporal bone specimen is then embedded in dental cement and put in a temporal bone holder.

The measurements of stapes vibrations are performed on an anti-vibration table inside a sound booth. Sound stimuli are frequency sweeps from 0,2 to 8 kHz at 80-110 dB sound pressure level (SPL). The experimental setup presented in Figure 1, is composed of the sound source (ER2 Etymotic Reserch) with the power amplifier (AP-12), the hear microphone (ER-7C Etymotic Reserch) and the Laser Doppler Vibrometer (LDV, Polytec) system equipped with the controller (OFV-5000), the velocity decoder (PVD-06) and the sensor head (OFV-534). The helium-neon laser beam is directed with the micromanipulator on retroreflective targets on the object of investigations through the artificial ear canal. The stapes footplate velocity is measured and additionally, sound pressure level (SPL) in order to build the transfer function between velocity of the stapes footplate (output) and the excited sound pressure (input). The measurements have been recorded using processing board NI6210 (National Instrument) and DasyLab software.

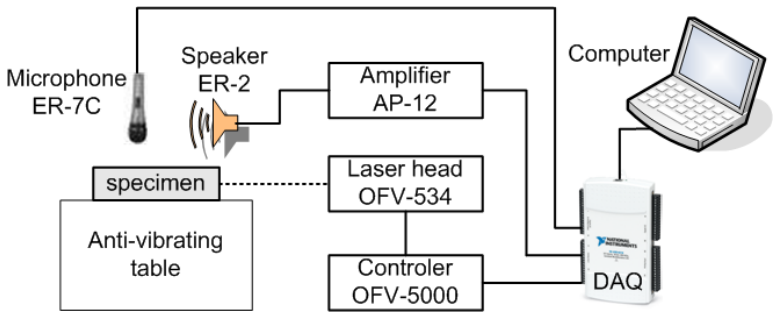


Figure 1: Scheme of experimental setup.

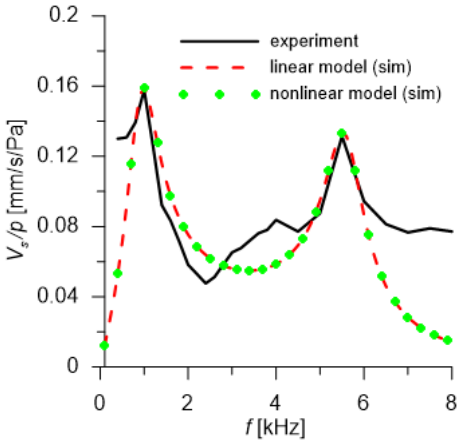


Figure 2: Transfer function of stapes vibrations.

The results of measurements are presented graphically in Figure 2 (black line) in the form of transfer function. v_s means stapes velocity, p is sound pressure. Middle ear system exhibits two resonances. The first natural frequency is about 1kHz and the second about 5.5kHz. Next, a three degrees of freedom model (3dof) of intact middle ear is built to obtain the proper system parameters, that is stiffness and damping ratio. Finally, the intact middle ear model is reduced to two degrees of freedom (2dof) one but with shape memory prosthesis (SMP).

2.2 Modelling and numerical results

The human middle ear mechanism is presented as 3dof model consisting of three lumped masses suspended with seven springs and dashpots (Figure 3). The three ossicular bones: malleus, incus, and stapes are represented by masses m_M, m_I, m_S, respectively**.** The malleus (m_M) is jointed with a tympanic membrane (TM) with spring and dashpot k_{TM} and c_{TM}. An anterior malleal ligament (AML) suspending the malleus is simulated as spring k_{AML} and dashpot c_{AML}. The malleus is connected with the incus by incudomalleal joint (IMJ) represented by spring k_{IMJ} and dashpot c_{IMJ}. Next, the incus and stapes are supported by posterior incudal ligament (PIL) and annular ligament (AL) that are modelled as springs with stiffness k_{PIL} and k_{AL}, and dashpots c_{PIL} and c_{AL}. The incudostapedial joint (ISJ) is shown as spring k_{ISJ} and dashpot c_{ISJ}. Finally, the stapes motion is transferred to cochlea (C) which stiffness and damping is simulated by spring k_C and dashpot c_C.

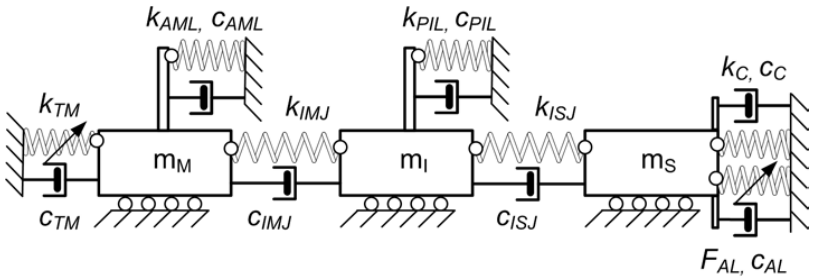


Figure 3: Three degrees of freedom model of intact middle ear.

This model is governed by three differential equations of motion in the form:

$$\begin{aligned} &m_M\ddot{x}_M + k_{TM}x_M + k_{AML}x_M + k_{IMJ}\left(x_M - x_I\right) + c_{TM}\dot{x}_M + c_{AML}\dot{x}_M + c_{IMJ}\left(\dot{x}_M - \dot{x}_I\right) = Q\sin\omega\tau \\ &m_I\ddot{x}_I + k_{IMJ}\left(x_I - x_M\right) + k_{PIL}x_I + k_{ISJ}\left(x_I - x_S\right) + c_{IMJ}\left(\dot{x}_I - \dot{x}_M\right) + c_{PIL}\dot{x}_I + c_{ISJ}\left(\dot{x}_I - \dot{x}_S\right) = 0 \\ &m_S\ddot{x}_S + k_{ISJ}\left(x_S - x_I\right) + k_C x_S + k_{AL}x_S + k_{2AL}x_S^{\,2} + k_{3AL}x_S^{\,3} + c_{ISJ}\left(\dot{x}_S - \dot{x}_I\right) + c_C\dot{x}_S + c_{AL}\dot{x}_S = 0 \end{aligned} \quad (1)$$

The spring force of annular ligament F_{AL} has a linear part $k_{1AL}x_S$ and nonlinear $k_{2AL}x_S^{\,2} + k_{3AL}x_S^{\,3}$, then:

$$F_{AL} = k_{1AL}x_S + k_{2AL}x_S^{\,2} + k_{3AL}x_S^{\,3} \quad (2)$$

Damping and stiffness coefficients of the model are identified from the experiment. The proper value, presented in Table 1, are obtained in such a way to get similar transfer function from the experiment and numerical simulation. The external excitation amplitude Q=0.12mM

Mass [mg]	Stiffness [N/m]	Damping ratio [Ns/m]
m_M=25	k_{TM}=300	c_{TM}=0.06
m_I=28	k_{AML}=800	c_{AML}=0.125
m_S=1.78	k_{IMJ}=1000000	c_{IMJ}=0.359
	k_{PIL}=400	c_{PIL}=0.055
	k_{ISJ}=1350	c_{ISJ}=0.0079
	k_C=200	c_C=0.0017
	k_{AL}=623	c_{AL}=0.00004
	k_{2AL}=3*10^8	
	k_{3AL}=2.25*10^{15}	

Table 1: Parameters of 3dof middle ear model.

The transfer function of 3dof model of the intact middle ear is presented in Figure 2. The red dashed line depicts solutions of linear model (k_{2AL}= k_{2AL} = 0) while the green points represents outcomes of the nonlinear model. Both linear and weak nonlinear approach is consistent with the experiment because the resonances and maxima are conserved.

3 SMART PROSTHESIS OF MIDDLE EAR

When middle ear are damaged, a prosthesis of ossicular chain must be implemented. Here, a new type of smart prosthesis placed instead of a malleus and incus, made of the nitinol is proposed. Then, the 3dof model of intact ear is reduced to 2dof system presented in Figure 4. The simplest design of smart prosthesis as a rod of diameter d, final length L, mass m and cross section A is presented in Figure 5. Initial shape and length of the smart prosthesis (Figure 5a) can be changed when a portion of heat is supplied. Then, the prosthesis takes the final

shape and length shown in Figure 5b. In the model (Figure 4) the prosthesis is represented as a spring (SMA) with restoring spring force *FSMA* given as

$$F_{SMA} = a_1(T - T_M)(x_p - x_s) - a_2(x_p - x_s)^3 + a_3(x_p - x_s)^5 \tag{3}$$

This polynomial model of shape memory alloy (SMA) is proposed by Falk [16] and applied for various applications, for instance by Paiva et.al. [17]. Coefficients a_1, a_2, a_3 depend on the nitinol properties and prosthesis dimension i.e. the final length (L) and the diameter of the rod (d). T means temperature, T_M – temperature when martensite is stable.

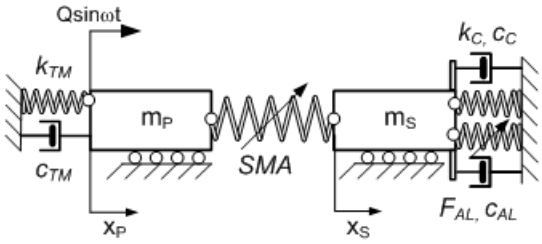


Figure 4: Two degrees of freedom model of middle ear with smart prosthesis.

a) **b)**

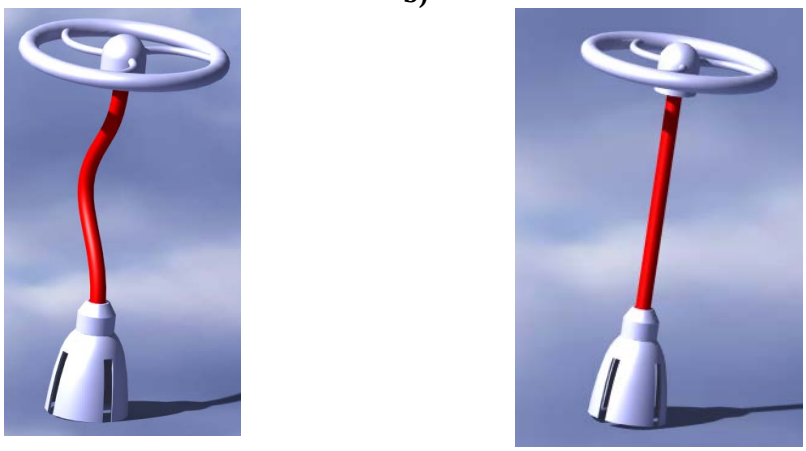


Figure 5: Smart middle ear prosthesis made of the nitinol, initial shape (a), final shape (b).

The differential equations of motion, governing the model presented in Figure 4, is presented in the form

$$\begin{aligned} &m_P\ddot{x}_P + k_{TM}x_P + c_{TM}\dot{x}_P + F_{SMA} = Q\sin\omega\tau \\ &m_S\ddot{x}_S + k_C x_S + k_{AL}x_S + k_{2AL}x_S^2 + k_{3AL}x_S^3 + c_C\dot{x}_S + c_{AL}\dot{x}_S - F_{SMA} = 0 \end{aligned} \tag{4}$$

where, x_p and m_p means a prosthesis displacement and mass, respectively.

In this research, it is assumed that the prosthesis work at temperature T= 36.6 ^{o}C and has the length L=5mm the diameter d=1mm and the mass m_p=25.525mg. Then a_1 =1.5708e5 N/(mK), a_2 =2.5133e14 N/(m^{3}K), a_3 =3.8666e21 N/(m^{3}K^2). The prosthesis (rod) diameter is 1mm because this value provides the first natural frequency of the system equals about 1 kHz. This can be observed in bifurcation diagram shown in Figure 6 where stapes vibrations (x_s) are represented by stroboscopic points. The second natural frequency is far from the range of audibility therefore it does not have any influence on the system dynamics.

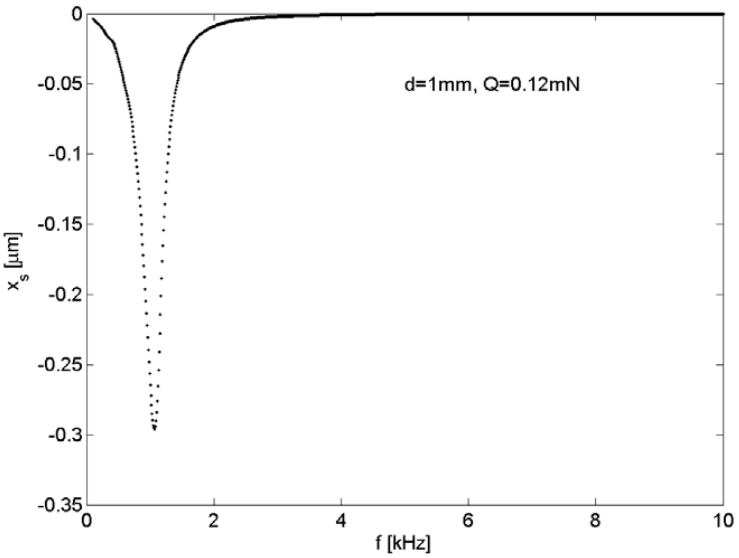


Figure 6: Bifurcation diagram, stapes vibrations versus excitation frequency.

Now, the sensitivity of system response on the amplitude of external excitation at the first natural frequency (f=1020Hz) is analysed (Figure 7). The periodic solutions represented by single lines in bifurcation diagrams (Figure 7a) are repeated periodically while excitation frequency increases.

Interestingly, the period of the periodic solutions does not equal the excitation frequency as the typical stroboscopic Poincaré section suggests (Figure 7a). The same bifurcation diagram made when the stapes velocity is zero (v_s=0) exhibits periodic but not harmonic motion (Figure 7b) as shown in the phase space diagram (Figure 8a). Moreover, the stapes motion can have more harmonic components for instance where Q=6.5N (Figure8b). Then the system response is higher frequency comparing to the external force frequency. Probably, a large excitation can lead to chaotic vibrations but this aspect will be analysed by mean of the Lyapunov exponent in an extended work.

From practical point of view, the excitation amplitude depends on loudness level. A real typical excitation in human ear does not exceed 1mN. Then, the stapes vibrations are significantly smaller and first of all, they are regular and correspond the excitation frequency. Since, the smart prosthesis works at constant temperature of 36.6^{o}C, its influence of middle ear dynamics is omitted here. However, the dynamics can be important during implementation when the prosthesis is heated to obtain a desired shape.

a)

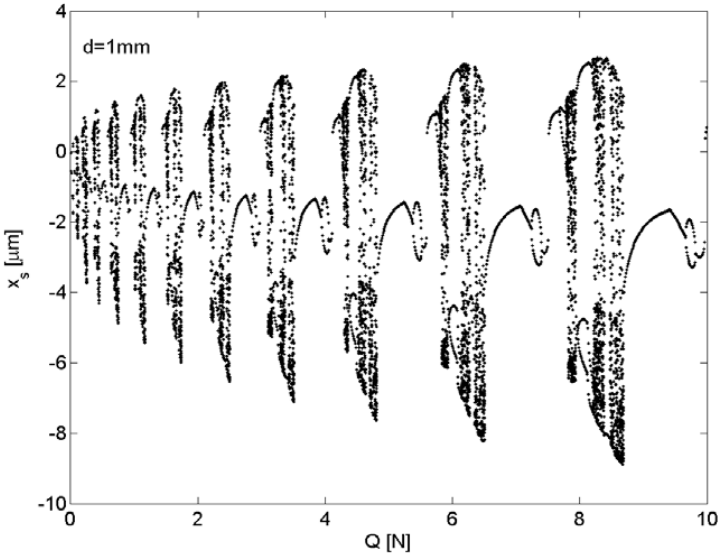


Figure 7: Bifurcation diagram of stapes vibrations versus excitation amplitude as stroboscopic map (a).

b)

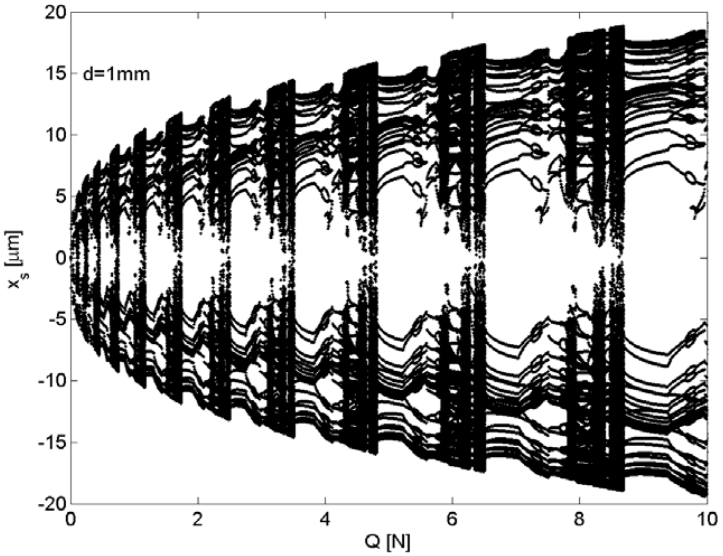


Figure 7: Bifurcation diagram of stapes displacement collected at zero velocity (v_s=0) versus excitation amplitude (b).

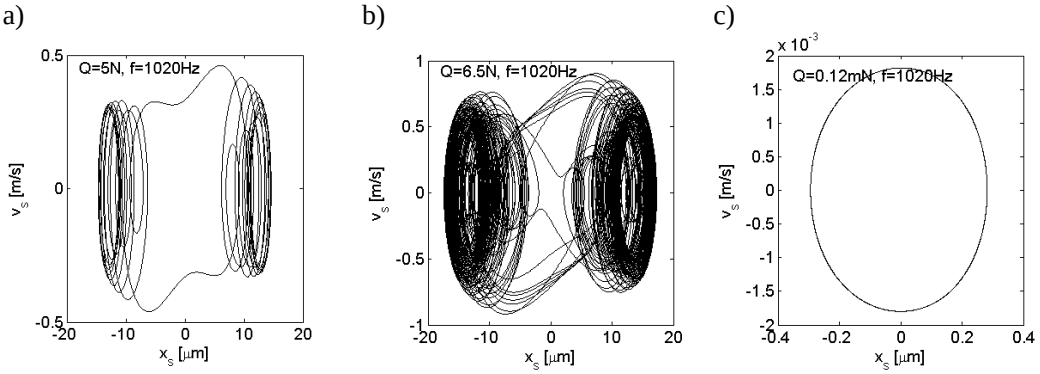


Figure 8: Phase diagrams of stapes motion for Q=5N (a) and Q=6.5N (b), Q=0.12mN (c).

4 CONCLUSIONS

- Smart prosthesis of human middle ear, made of shape memory alloy is an interesting alternative for classical prosthesis for the sake of possibility of easy adjustment its length and shape to individual medical case.
- The regular stapes vibrations of intact human middle ear are also achieved for a reconstructed ossicluar chain in case of for relatively small external excitation which are similar to a real force acting on eardrum.
- Strong external excitation of middle ear system with the smart prosthesis generates periodic vibrations with higher frequencies. This can lead to deterministic chaos.

ACKNOWLEDGEMENT

The work is financially supported under the project of National Science Centre (Poland) no. 2014/13/B/ST8/04047.

REFERENCES

[1] Q.L. Sun, K.H. Chang, K.J. Dormer, R.K. Dyer, R.Z. Gan, An advanced computer-aided geometric modeling and fabrication method for human middle ear. *Medical Engineering & Physics*, 24, 595–606, 2002.

[2] A.R. Moller, Network Model of the Middle Ear. *Journal of the Acoustical Society of America* 33, 168–176, 1961.

[3] J. Zwislocki, Analysis of the Middle-Ear Function. Part I: Input Impedance. *Journal of the Acoustical Society of America*, 34, 1514–1523, 1962.

[4] C. Dai, T. Cheng, M.W. Wood, R.Z. Gan, Fixation and detachment of superior and anterior malleolar ligaments in human middle ear: Experiment and modeling. *Hearing Research*, 230, 24–33, 2007.

[5] A. Eiber, Mechanical Modeling and Dynamical Bhavior of the Human Middle Ear. *Audiology & Neuro-Otology*, 4, 170–177, 1999.

[6] R.Z. Gan, Q. Sun, Finite element modeling of human ear with external ear canal and middle ear cavity. *Second Joint Embs-Bmes Conference*, Conference Proceedings vols 1-3, 264–265, 2002.
[7] R.Z. Gan, Q.L. Sun, R.K. Dyer, K.H. Chang, K.J. Dormer, Three-dimensional modeling of middle ear biomechanics and its applications. *Otology & Neurotology*, 23, 271–280 2002.
[8] Q. Sun, R.Z. Gan, K.H. Chang, K.J. Dormer, Computer-integrated finite element modeling of human middle ear. *Biomechanics and Modeling in Mechanobiology*, 1, 109–122, 2002.
[9] S. Sun, Rajapakse,R. K. N. D., Simulation of pseudoelastic behaviour of SMA under cyclic loading. *Computational Materials Science*, 28, 663–674, 2003.
[10] H. Funakubo, *Shape Memory Alloys*. Gordon and Breach Sci. Publ., New York, USA, 1975.
[11] K. Otsuka, C.M. Wayman, *Shape Memory Materials*. Cambridge Univ. Press,, Cambrigde, 1998.
[12] M. Geetha, A.K. Singh, R. Asokamani, A.K. Gogia, Ti based biomaterials, the ultimate choice for orthopaedic implants – A review. *Progress in Materials Science*, 54, 397–425, 2009.
[13] J. Ryhänen, E. Niemi, W. Serlo, E. Niemelä, P. Sandvik, H. Pernu, T. Salo, Biocompatibility of nickel-titanium shape memory metal and its corrosion behavior in human cell cultures. *Journal of Biomedical Materials Research*, 35, 451-457, 1997.
[14] D.J. Wever, A.G. Veldhuizen, M.M. Sanders, J.M. Schakenraad, J.R. van Horn, Cytotoxic, allergic and genotoxic activity of a nickel-titanium alloy. *Biomaterials*, 18, 1115–1120, 1997.
[15] A.M. Abrao, D. Aspinwall, Cutting Forces Assessment when Turning Hardened Bearing Steel. *Journal of the Braz.Soc.Mechanical Sciences*, XVII, 353–359, 1995.
[16] F. Falk, Model free energy, mechanics, and thermodynamics of shape memory alloys. *Acta Metallurgica*, 28, 1773–1780, 1980.
[17] A. Paiva, M.A. Savi, An overview of constitutive models for shape memory alloys. *Mathematical Problems in Engineering*. 2006, 1–31, 2006.

International Conference on Engineering Vibration
Ljubljana, Slovenia, 7-10 September 2015

NUMERICAL TRANSFER PATH ANALYSIS FOR THE ASSESSMENT OF AIR-BORNE NOISE IN INTERNAL COMBUSTION ENGINES

A. Acri[1,3 *], **G. Offner**[1], **E. Nijman**[2], **R. Corradi**[3]

[1]AVL List GmbH
Antonio.Acri@avl.com, Guenter.Offner@avl.com

[2] ViF, Kompetenzzentrum – Das Virtuelle Fahrzeug Forschungsgesellschaft mbH
Eugene.Nijman@v2c2.at

[3] Dipartimento di Ingegneria Meccanica, Politecnico di Milano
antonio.acri@polimi.it, roberto.corradi@polimi.it

Keywords: Numerical TPA, noise source identification, vibro-acoustics.

Abstract. *Noise legislation and the increasing customer demands determine the NVH (Noise Vibration and Harshness) development of modern commercial vehicles. In order to meet the stringent legislative requirements for the vehicle noise emission, more accurate understanding of all vehicle noise sources and their acoustic behavior is required.*
Transfer Path Analysis (TPA) is a fairly well established technique for estimating and ranking individual low-frequency noise or vibration contributions via the different transmission paths. Transmission paths from different sources to target points of interest and their contributions can be analyzed by applying TPA. This technique is applied on test measurements, which can only be available on prototypes, at the end of the designing process.
In order to overcome the limits of TPA, a Numerical Transfer Path Analysis (NTPA) method, based on numerical simulation, is proposed in this paper. The main target of NTPA methodology is to get information of noise source contribution and noise transmission paths, starting from the first steps of the designing process. The structure-borne noise is computed with a multi-body dynamic model and the results are used to compute the acoustic radiation in the far field with the Wave Based Technique (WBT).
In this paper, a short introduction on NTPA will be provided. Then, the investigated model, a 4-cylinder internal combustion engine, will be described. Finally, the relationships between forces and responses are computed with NTPA methodology and the main noise contributions are identified and analyzed.
The aim of this work is to identify and rank main noise sources of an engine, showing the advantages and benefits of the proposed methodology.

1 INTRODUCTION

TPA is a test-based method, which allows to distinguish between the contributions of different sources or transfer paths to the receiver signal [1]. Typically it is adopted to identify noise contributions in the low frequency range, even though, different formulations, based on the response statistics of multimodal vibro-acoustic systems with strong modal overlap, can be applied for higher frequency range [2].

TPA is based on a load-response relationship. Hence, it has the disadvantage of having individual measurements of each single path from a source to a receiver. A variation of the classical TPA method is the Operational TPA (OTPA), [3,4], which has been developed to get around this disadvantage: OTPA is a response-response relationship model.

The TPA technique is adopted in automotive industry since 1970's and so far it is still a useful tool for the NVH assessment of vehicles and mechanical structures. It is commonly applied for the analysis of interior and radiated noise and the identification of different noise paths in vehicles.

Although TPA is useful for the identification of vehicle noise sources, it is difficult to perform substantial modifications to the system by using experiments for the reduction of the vibration and noise. In order to solve this problem some Hybrid TPA methods (HTPA) were developed. HTPA uses simulated excitation force as input force for TPA analysis, where the vibro-acoustic transfer functions are measured [5].

In this paper, a Numerical Transfer Path Analysis methodology (NTPA) is discussed. The aim of this methodology is to give information about the noise paths and noise contributions with the advantage of being based on numerical simulations. In NTPA it is not necessary to evaluate the vibro-acoustic transfer functions between excitations and responses. Compared with TPA, NTPA can be applied already during the first steps of the designing process. Moreover, with a numerical methodology it is possible to overcome some of the obvious limitations related to an experimental methodology, such as the identification of the operating forces and the reduction of the measurement based error, described in [6] and [7]. The only limitation of NTPA relies on the accuracy of the numerical solution.

The identification of noise sources in internal combustion engines is a challenging task required for the purpose of effective noise reduction. Experimental analysis of noise sources and their transfer paths can be found in literature. In [8] and [9], the contributions of different structure-borne noise sources are investigated with the coherence method, focusing mainly on combustion and piston slap noise: in both cases the predominant low frequency noise source of the investigated engines is the combustion noise, even though it is highlighted that, due to physical limitations, it is not easy to clearly distinguish the different noise sources in an experimental analysis. As concern the acoustic radiation of different engine surfaces, in [9] and [10], some analyses were performed with the aim of ranking the different radiating surfaces of the engine in terms of sound intensity and sound power.

In order to introduce NTPA, a theoretical introduction will be presented in the following section. Then, NTPA methodology is used to identify the air-borne noise sources of a numerical model of an engine. In this paper, the acoustic radiation of an engine is investigated with the advantage of clearly distinguish combustion noise sources from mechanical noise sources.

2 NTPA METHODOLOGY

Numerical Transfer Path Analysis is a numerical methodology, which is able to identify vibro-acoustic sources and noise paths of a vibro-acoustic system. The main difference between TPA and NTPA, is that the latter does not require the evaluation of the transfer functions

because the partial contributions are evaluated applying the excitation forces directly on the system. A comparison between the two methodologies can be found in [11].

NTPA is based on the reduction of the global dynamic system into a vibrating subsystem which considers only the investigated geometry, which is excited with N different sets of operating forces. The investigated subsystem on which the analysis is done must necessarily be linear, whereas all non-linearities of the global dynamic system are included in the sets of operating forces. Each set of forces represent a different load case which is separately applied to the subsystem. The global solution is finally obtained summing all solutions of all cases.

In a first step, the whole dynamic system is computed with numerical methods, such as a flexible multi-body dynamic simulation that considers gross and local vibration motions of linear elastic bodies considering highly nonlinear contacts [12]. The numerical modelling of the dynamic system is based on Newton's equation of momentum and Euler's equation of angular momentum assuming linear elastic structural properties. With reference to local vibration motions, the vibration equation for the investigated geometry can be formulated with respect to a body fixed coordinate system (floating reference frame) with:

$$M \cdot \ddot{q} + D \cdot \dot{q} + K \cdot q = f \tag{1}$$

M, D and K denote the bodies mass, damping and stiffness matrix; q, $\dot{q}$ and $\ddot{q}$ denote the displacement, velocity and acceleration vectors; f is the vector of applied forces.

In a second step, the original system is decomposed and only the investigated geometry is considered in the subsystem: all other bodies and joints are replaced with appropriate forces. Forces acting on the investigated geometry are collected and grouped in N different sets. Each set of forces, f_k, represents a specific excitation acting on the subsystem. The subsystem is excited with only one set of forces per time:

$$M \cdot \ddot{q}_k + D \cdot \dot{q}_k + K \cdot q_k = f_k \tag{2}$$

With this methodology the solution q, $\dot{q}$ and $\ddot{q}$, obtained when a single load case is applied on the subsystem, is directly the contribution of the related set of forces.

Finally, if the considered subsystem is linear, the sum of each contribution is equal to the global response:

$$q = \sum_{k=1}^{N} q_k ; \qquad \dot{q} = \sum_{k=1}^{N} \dot{q}_k ; \qquad \ddot{q} = \sum_{k=1}^{N} \ddot{q}_k \tag{3}$$

3 INVESTIGATION OF ACOUSTIC NOISE SOURCES OF AN INTERNAL COMBUSTION ENGINE

3.1 The model investigated

In this section the NTPA algorithm is performed on a dynamic system for the evaluation of the air-borne noise contributions up to 3 kHz. An application of NTPA methodology for the investigation of the structure-borne noise can be found in [13].

Prior to investigate the air-borne noise contributions, it is necessary to perform a simulation of the dynamic system. Then it is possible to apply a NTPA analysis for the evaluation of the structure-borne noise contribution to the whole exterior surface of the engine. Finally, the structural normal velocities on the engine surface are adopted as boundary conditions for the evaluation of the acoustic radiation.

The system investigated is a four-cylinder internal combustion engine running at a full load conditions with constant engine cycle averaged speed of 3000 rpm, even though NTPA methodology can be applied for any engine running condition.

The simulation of the dynamic system is carried out in time domain using the software AVL EXCITE [14]. The simulation procedure of the structural dynamics consists of three main steps: pre-processing, simulation and post-processing.

In the first step the geometry is prepared and entered in the model. Since the total amount of time, which is needed for the computation, is significantly influenced by the number of Degrees of Freedom (DOF), a condensed model with a reduced number of DOF, equivalent to the full model [15,16], is considered for the simulation (see Figure 1: highlighted in red, the nodes of the condensed mesh). Joints, cylinders and connecting rods are numbered from front to rear engine. The x, y and z directions of the Cartesian coordinate reference system are associated with rotation axis, thrust and vertical directions respectively. In the second step, the dynamic system of equations is solved in time domain. In the last step, result data are extracted in time and transformed into frequency domain.

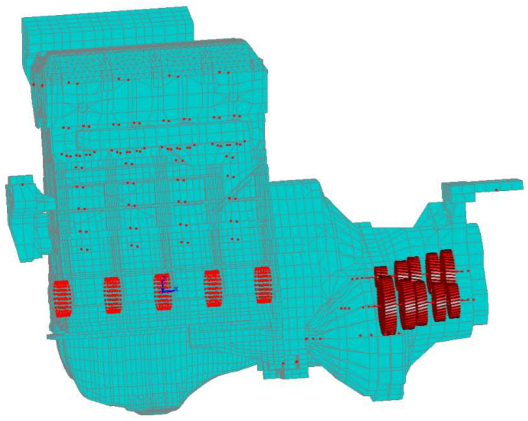


Figure 1: Mesh of the investigated engine. In red the nodes of the condensed mesh and the gears.

In order to perform structure-borne NTPA analysis, all forces acting on the structure of the power unit are collected and grouped in sets. The collected forces are the ones, which are transmitted from joints, from the auxiliary components on engine top head (valves and cams) and the combustion acting in the combustion chamber. Each set of forces contains the forces applied on the structure from the same joint, i.e. from the same excitation. All forces transmitted from cams and valves are considered in two different sets respectively. The subsystem contains only the power unit structure (engine block and the gear box), set of linear mountings (that connect the structure to the chassis) and the rigid static chassis. The subsystem is excited with only one set of forces at the time.

Twenty-two different load cases, i.e. twenty-two different paths, are analyzed. The following cases are identified:

- 4 combustion chambers (corresponding to the noise transmitted directly from the walls of the combustion chambers; from “Comb1 to 4” in Figures from 3 to 7)
- 5 radial bearings (corresponding to the main bearings of the crankshaft; from “Bearing1 to 5” in Figures from 3 to 7)
- 4 guidance for connecting rod small ends (which represent the piston-liner interaction; from “Guide1 to 4” in Figures from 3 to 7)
- 5 roller bearings (corresponding to the roller bearings of primary and secondary gear shafts, respectively “PSRB1 and 2” and “SSRB1 to 3” in Figures from 3 to 7)
- Supports of differential (“Diff” in Figures from 3 to 7)
- Axial bearings

- Valve contacts
- Cam contacts

The cases containing differential supports, axial bearings, valve and cam contacts depict sums of individual contact types.

Once the structural normal velocities on the engine surface are computed for each load case, it is possible to compute the air-borne noise contributions. The acoustic radiation is computed with the Wave Based Technique, implemented in AVL EXCITE [14], adopting the surface normal velocities as boundary conditions for the evaluation of the acoustic radiation, [17]. The acoustic pressure is evaluated in a field point node located 1m distant from the rear of the engine as shown in Figure 2. The position of the investigated node is chosen in order to emphasize some of the well-known acoustic phenomena occurring in engine noise radiation problems.

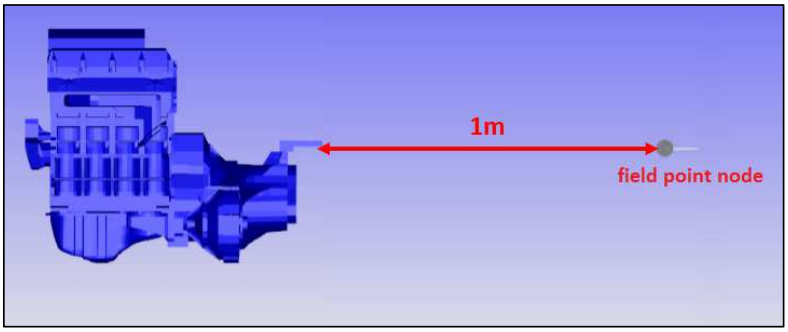


Figure 2: Position of the field point node where the sound pressure is computed.

3.2 Analysis of the different noise sources

The noise generated from combustion and mechanical forces is transmitted into the structure and radiated from its surface into the air. The different contributions to the global Sound Pressure Level (SPL) computed in the field point node (see Figure 2) are displayed in Figure 3.

It can be stated that in this model the noise reaching the field point node is mainly generated at low frequencies and transmitted through the walls of the combustion chambers and radial bearing contacts, even though, some relevant middle and high frequency phenomena transmitted from roller bearings can be detected.

In particular it is possible to clearly distinguish the gear whine noise occurring at 36^{th} order. This is a well-known phenomenon which generation mechanisms are described in [18,19]. With this analysis it is possible to understand how impact forces acting on gears produce noise which propagate mainly through gear shafts and differential. This noise reaches the external surface of the engine, and then the acoustic media, taking six different main paths: two roller bearings, which support the primary shaft (“PSRB1” and “PSRB2”), three roller bearings, which support the secondary shaft (“SSRB1”, “SSRB2” and “SSRB3”) and the supports of the differential (considered as a single path named “Diff”).

Depending on the directivity of the sound emitted by the engine, some phenomena can be heard in some positions but not in others. In order to have an idea of the overall sound power radiated from the whole engine, the active acoustic input power is computed for each different path and shown in Figure 4, even though it is not possible to talk about contributions considering power quantities.

In general, it is possible to state that the main noise contribution of this engine is combustion noise transmitted at low frequency from combustion chamber walls and radial bearings, even though some tonal phenomena at mid-high frequency occur.

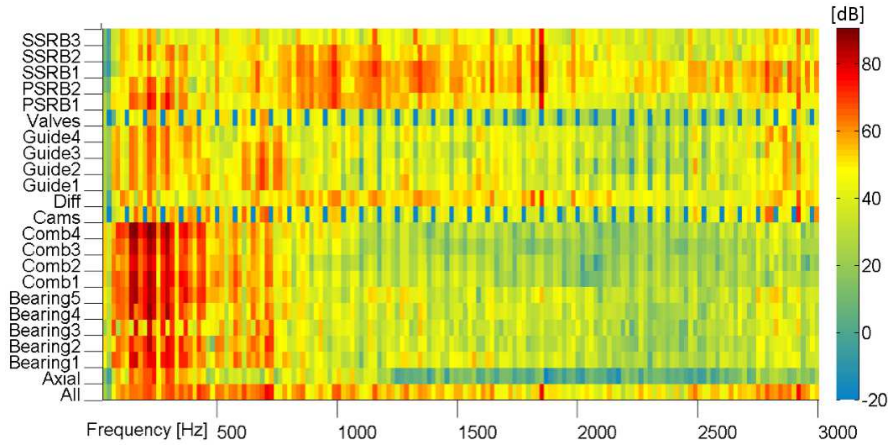


Figure 3: SPL contributions in field point node.

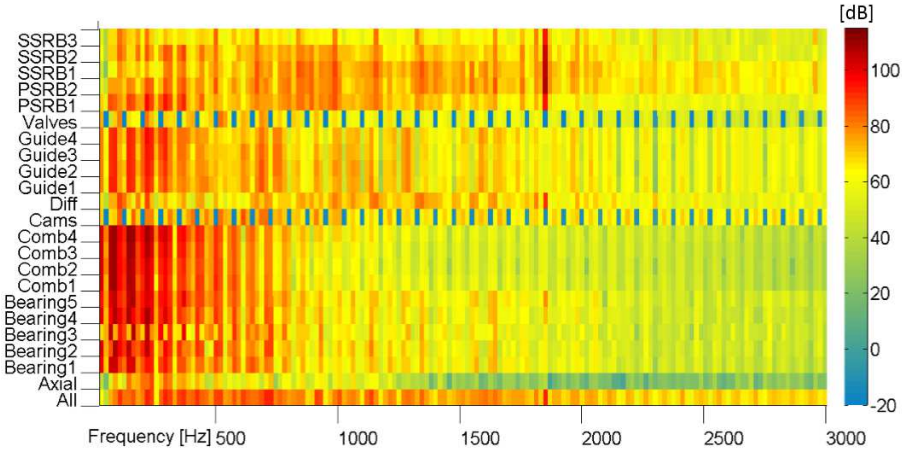


Figure 4: Acoustic input power on model mesh.

Similar results were obtained in [8] and [9], where the experimental analysis was conducted on two different 4-stroke Diesel engines running at constant speed of 2500 rpm. These analyses show that, at low-mid frequency, the most relevant noise contribution is combustion noise (transmitted through radial bearings and combustion chamber walls) under full load conditions. In [9] a TPA analysis, which considers also other sources, was also performed. It shows how noise, which is transmitted from other sources, like valve contacts or oil pump (the latter is not considered in this analysis), is less effective.

3.3 Combined contribution analysis

In Figure 3 the noise contributions of each investigated path are displayed in terms of SPL. In this section also phase information is considered in order to get a clear understanding of the combination of all contributions. The polar graphs in Figure 5 show the noise contributions in terms of sound pressure and phase. Only the biggest five noise contributions in terms of magnitude are considered. For the sake of simplicity, only results at 14^{th} and 36^{th} order are

displayed in Figure 5, because of the high noise level computed at these orders (see Figure 3). However, similar considerations can be done at every frequency.

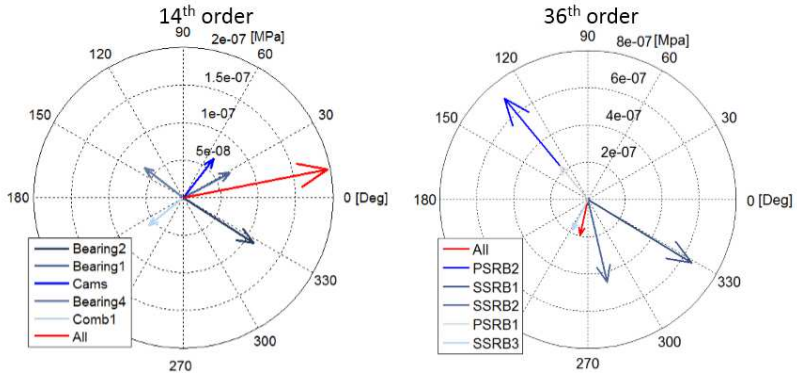


Figure 5: Sound Pressure components in field point node: Investigation of five biggest pressure contributions at 14th and 36th order.

At 36th order, "PSRB2" and "SSRB1" are bigger in magnitude than the overall combination (red arrow in Figure 5). Hence, it is clear that these effects cancel each other. In fact, they are almost opposite in phase. To understand how these differences in phase influence the combined response, all contributions are projected with respect of the phase of the combined response. The projection of a single contribution at a specific frequency can be expressed as:

$$p_p = p_m \cos(\varphi_m - \varphi_u) \tag{4}$$

p_p is the projected pressure component, p_m is the pressure magnitude of the considered noise contribution, φ_m is the phase of the considered noise contribution and φ_u is the phase of the combined response.

The projected components give information about the effective contribution of each noise path to the overall response. In Figure 6, the projected noise contributions are displayed.

The discussions, which arise from the results displayed in Figure 6, depict two different situations. At 36th order, noise is mainly generated and transmitted through a limited number of noise paths, because the main occurring noise phenomenon is gear noise (see discussions in section 3.2). Conversely, at 14th order, different noise phenomena (combustion and mechanical noise from combustion chambers and bearings, cam noise and piston-liner interactions) transmitted from different paths concur to increase the overall noise level.

In conclusion, the different noise contributions are ranked with reference to the projected components. In Figure 7 the projected pressure contributions in field point node are displayed up to 3 kHz. The results are normalized with overall noise magnitude, i.e. positive contributions enhance the total noise level, while negatives contrast the dominant phenomena. In order to simplify the discussion, only positive values are displayed in Figure 7.

From Figure 7 it is clear that the dominant phenomena below 500 Hz in the investigated field point node occur in combustion chambers and radial bearings, while at mid-high frequencies the noise is mainly transmitted through gear shafts roller bearings. Piston-Liner interactions are mainly relevant around 700 Hz and 1700-1900 Hz.

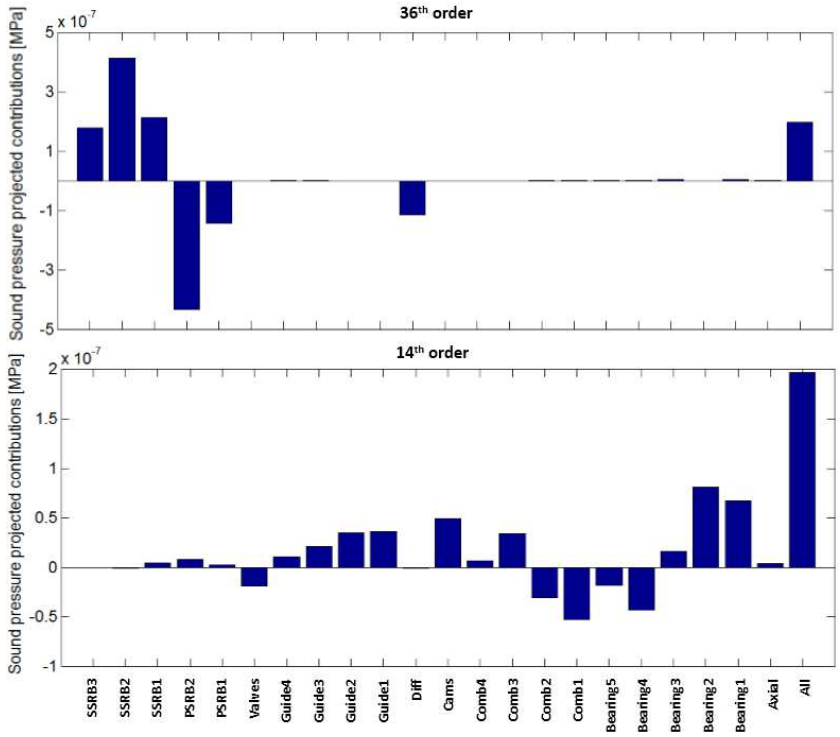


Figure 6: Investigation of projected pressure contributions at 14th and 36th order in field point node.

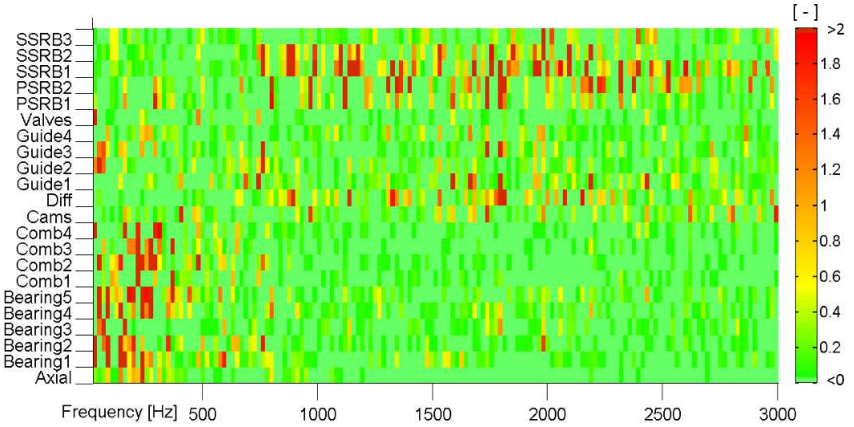


Figure 7: Relative projected contributions in field point node, sound pressure components.

3.4 Signal reconstruction

In order to verify the accuracy of the NTPA methodology, all contributions are summed and compared with the signal evaluated when all excitations are applied together to the structure. The comparison and the relative error are displayed in Figure 8.

The relative error, displayed in Figure 8, is defined as

$$error = 100 * \left| \frac{full_simulation_results - NTPA_results}{full_simulation_results} \right| \quad (5)$$

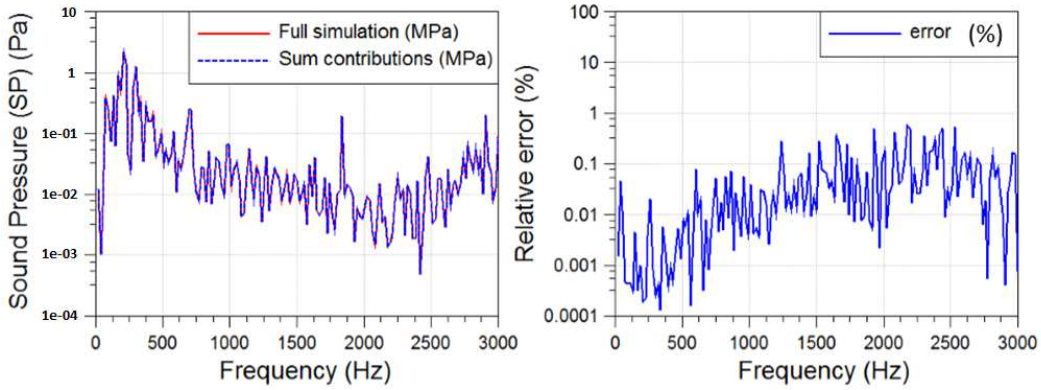


Figure 8: Comparison between the reconstruction of NTPA contributions (NTPA – dotted blue line) and signal obtained when all excitation are applied concurrently on the engine body (Full Simulation – red line). Relative error between the two curves.

4 CONCLUSIONS

In this paper a NTPA methodology is applied to investigate a four cylinder internal combustion engine. With NTPA analysis different noise mechanisms transmitted through different paths are analyzed. Compared with an experimental analysis, a numerical analysis is able to clearly distinguish different noise sources. Furthermore, analyzing the results obtained from NTPA analysis, with reference to the projected components, the different noise contributions are ranked in order to understand which of them contribute to increase or decrease the overall noise in the investigated response node.

5 ACKNOWLEDGEMENTS

The authors gratefully acknowledge the European Commission for their support with the ITN Marie Curie project No. 605867 “BATWOMAN” (Basic Acoustics Training - & Workprogram on Methodologies for Acoustics – Network).

Antonio Acri is a PhD student at the Department of Mechanical Engineering - Politecnico di Milano, via La Masa 1, 20156 Milano (Italy).

REFERENCES

[1] “Transfer Path Analysis: the qualification and quantification of vibro-acoustic transfer paths”, LMS International, Application Notes, 1995.

[2] J. Plunt, “Strategy for transfer path analysis (TPA) applied to vibro-acoustic systems at medium and high frequencies”, Proceedings of ISMA 23, Leuven, Belgium, 16-18 September 1998.

[3] K. Noumura, J. Yoshida, “Method for transfer path analysis for interior vehicle sound by actual measurement”, Japan Society of Automotive Engineers, Proceedings of the Annual Congress 55(06):7-12, 2006.

[4] D. de Klerk, A. Ossipov, “Operational transfer path analysis: Theory, guidelines and tire noise application”, Mechanical System and Signal Processing, volume 24, Special Issue: ISMA 2010, October 2010, pp. 1950-1962.

[5] S.J. Kim, S.K. Lee, "Prediction of interior noise by excitation force of the powertrain based on hybrid transfer path analysis" International Journal of Automotive Technology, Vol. 9, No. 5, 2008, pp. 577-583.

[6] S. Brandl, F. Brandl, W. Biermayer, R. Hoeldrich, A. Sontacchi, "Optimised TPA approach for improving interior sound engineering", Proceedings of 5th ISNVH Congress, Graz, Austria, June 4-6 2008.

[7] P. Gajdatsy, K. Janssens, L. Gielen, P. Mas, H. van der Auweraer, "Critical assessment of operational path analysis: effect of neglected paths", Proceedings of 15th International Congress on Sound and Vibration, Daejon, Korea, 6-10 July 2008.

[8] Y. Yawata, M.J. Crocker, "Identification of internal noise sources in diesel engines". No. 831330. SAE Technical Paper, 1983.

[9] H. Kanda, M. Okubo, T. Yonezawa, "Analysis of noise sources and their transfer paths in diesel engines", No. 900014. SAE Technical Paper, 1990.

[10] C.V. Bedil, A. Rust, M. Rasser, "Key Steps and Methods in the Development of Low Noise Engines", SV Sound and vibration 35.4, pp. 48-54, 2001.

[11] A. Acri, G. Offner, E. Nijman, "Numerical Transfer path analysis for structure-borne and air-borne problems in internal combustion engines", Proceedings of International Conference on Structural Engineering Dynamics ICEDyn2015, Lagos, Algarve, Portugal, 22-24 June 2015.

[12] G. Offner, H.H. Priebsch, "Flexible multi-body dynamics simulation – a powerful method for prediction of structure borne noise of internal combustion engines", Proceedings of ISMA2006, Leuven Belgium, 18-20 September 2006.

[13] A. Acri, G. Offner, E. Nijman, J. Rejlek, "Application of numerical transfer path analysis method for noise source identification in internal combustion engines", Proceedings of International Conference on Structural Engineering Dynamics ICEDyn2015, Lagos, Algarve, Portugal, 22-24 June 2015.

[14] AVL LIST GmbH: AVL-Excite Reference Manual, Version 2014.

[15] J. Gerstmayr, J.A.C. Ambrosio, "Component mode synthesis with constant mass and stiffness matrices applied to flexible multi-body systems", Int. J. Numer. Methods Eng., 73, 1518-1546, 2008.

[16] G. Offner, "Modelling of condensed flexible bodies considering non-linear inertia effects resulting from gross motion", Proceedings of the Institution of Mechanical Engineers Part K, Journal of Multi-body Dynamics, 225(3):204-219, 2011.

[17] T. Moscai, H.H. Priebsch, F. Diwoky, A. Hepberger, "Engine radiation simulation up to 3 kHz using the Wave Based Technique", Proceedings of the 2009 International Congress of Sound and Vibration ICSV, Vol. 16, 5-9 July 2009.

[18] M. Ognjanović, S.C. Kostić, "Gear Unit Housing Effect on the Noise Generation Caused by Gear Teeth Impacts" Strojniški vestnik-Journal of Mechanical Engineering 58.5, pp. 327-337, 2012.

[19] J.D. Smith, "Gear noise and vibration", CRC Press, 2003.

International Conference on Engineering Vibration
Ljubljana, Slovenia, 7-10 September 2015

FAST ONLINE MONITORING AND SYSTEM IDENTIFICATION FOR THE APPLICATION IN THE FIELD OF AEROELASTICITY

Goran Jeličić*[1], Jan Schwochow[2], Yves Govers[2], Anne Hebler [2], Marc Böswald[2]

[1]German Aerospace Centre – Institute of Aeroelasticity
goran.jelicic@dlr.de

[2]German Aerospace Centre – Institute of Aeroelasticity
{jan.schwochow, yves.govers, anne.hebler, marc.boeswald}@dlr.de

Keywords: Flutter, Operational Modal Analysis

Abstract. *During the development of new aircraft wind tunnel testing of 2D and 3D aerofoils or even complete aircraft is essential. The structural integrity of the wind tunnel model needs to be assured for the test campaign because a failure can cause severe damage on the wind tunnel facility and means the loss of the costly model itself. To enhance the level of safety, a detection of the flutter stability while testing is desirable. This new development utilizes experimental and operational modal analysis methods for fast and reliable online identification of a system's eigenvalues and eigenvectors. The developed code presented here uses efficient and novel implementations of signal processing and system identification algorithms coupled with new ones for mode selection and tracking, to achieve a computation time in the order of seconds, thus allowing a responsive temporal tracking of varying parameters. The code developed at the Institute of Aeroelasticity at the German Aerospace Centre (DLR) is written in MATLAB, is hardware-agnostic and its performance has been assessed with different models. The main focus of the discussion is the time efficiency of various algorithms which enable the online monitoring of system parameters, with an overlook of the influence on speed of various parameters along with presentation of results of a flutter test conducted in the Transonic Wind tunnel in Göttingen.*

1 INTRODUCTION

The flutter phenomenon involves an aeroelastic structural instability that may be violent in nature (explosive flutter) and may therefore exhibit a rapid deterioration of modal damping with speed increase. Flutter characteristics of models of complete aircraft or their components are experimentally determined in wind tunnels with the risk of model damage due to the destructive oscillations that occur at flutter. This risk is reduced if the flutter onset can be predicted below the flutter boundary by identifying the critical vibration modes, including their damping and frequencies. These modes must be tracked while test conditions are varied until a damping trend can reliably extrapolate the flutter condition.

In this study, the modal characteristics of an aeroelastic aerofoil model are observed during operation in the *Transonic Wind tunnel Göttingen* (TWG) as operating conditions are being varied to study its interaction with airflow. The damping and eigenfrequency trends of the flutter experiments are monitored to safely approach the unstable boundary, which requires quasi "real time assessment" of the flutter stability during operation.

2 AEROELASTIC SYSTEM IDENTIFICATION

Real-time automated modal analysis describes a procedure by which time data is continually collected, processed and automatically analysed to identify the modal parameters of a system. The onset of an unstable state can be predicted by analysing these parameters. In the framework of *experimental modal analysis* (EMA) the excitations and responses of a system are both measured and their relationship is described by estimating the system's frequency response matrix. If ambient excitation cannot be measured or eliminated, only vibration responses are acquired. Without knowledge of the excitations, quantitative information about the cause of the vibration is missing, thus resulting in lower data quality susceptible to stochastic errors, although eigenvalues and eigenmodes can still be identified without their modal scaling factors using the methods of *operational modal analysis* (OMA). Different system identification methods are available for OMA operating in time domain (e.g. the stochastic subspace identification – SSI family [1][4]) or in frequency domain (e.g. least-square complex frequency estimator – LSCF family [2][3]).

The sampling rate constrains the maximal observable eigenfrequency of a system ($f_N = f_s/2$) and acquisition time determines the minimal achievable frequency resolution ($\Delta f = 1/T_s$); both fix the maximal number of data points in the frequency axis at $N_s = f_s/\Delta f/2$. Several identification algorithms are not efficient and consistent [7][10], therefore acquisition parameters must be conveniently chosen to offset bias, stochastic and leakage effects as they negatively affect the estimated values of the modal parameters. These requirements impose a time delay between data acquisition and the first system identification.

2.1 Theory

Several algorithms handle large and noisy data sets in frequency domain from modal analysis tests containing multiple sensors and multiple exciters. The LSCF estimator in particular is described in this text due to its speed, with some insights on computational complexity and comparisons with the related popular poly-reference pLSCF (PolyMAX) estimator. LSCF identifies a dynamic system's modal parameters in the frequency domain by estimating polynomial coefficients of the LTI system minimizing a certain error function. The LSCF family consists of different implementations, each with different asymptotic properties in the least-squares (LS), total least-squares (TLS), generalized total least-squares (GTLS) and maximum likelihood (ML) senses [8]. There are further distinctions about how poles and modal participation factors are obtained (e.g. left and right matrix fraction models…).

An LTI system with N_y outputs (sensors) and N_u inputs (excitations) can be conveniently described in the frequency domain. If inputs are unknown, only cross-power spectral densities are available. Assuming the excitation is constant in the frequency range of interest, the power spectra $S_{yy} \in \mathbb{C}^{N_y \times N_y}$ of the outputs relay information about the system's dynamics:

$$S_{yy}(\omega) = H(\omega) S_{uu}(\omega) H^H(\omega) \xrightarrow{S_{uu}=const} S_{yy}(\omega) = S_{uu} \cdot H(\omega) H^H(\omega) \tag{1}$$

with $S_{uu}(\omega) \in \mathbb{C}^{N_u \times N_u}$ the cross-power spectral densities of the unknown input forces and $H(\omega) \in \mathbb{C}^{N_y \times N_u}$ the frequency response matrix. The poles and mode shapes of the system can be identified, though the missing information about excitation precludes the determination of the modal scale factors. The double-sided cross-power spectral density of responses *y* with references *x* for each frequency *k* are estimated using Welch's modified periodogram:

$$S_{yx}(\omega_k) = \frac{1}{N_w |W|^2} \sum_{n=1}^{N_w} \mathrm{Y}_n(\omega_k) \mathrm{X}_n(\omega_k)^H \in \mathbb{C}^{N_y \times N_x} \tag{2}$$

with $\mathrm{Y}_n(\omega) \in \mathbb{C}^{N_y \times N}$ and $\mathrm{X}_n(\omega) \in \mathbb{C}^{N_x \times N}$ the windowed Fourier transforms of the *n*-th time data block; the number of averages determines the bias and variance of the estimated spectra.
In the periodogram approach for spectral estimation a window function of size $N<N_s$ reduces data noise by averaging over many data blocks, but increases frequency resolution by a factor N_s/N, thus increasing acquisition time in order to satisfy the same Δf requirement; the local polynomial method [7] keeps full frequency resolution in exchange for higher computation time. The cross-power spectral density can be described in terms of coefficients of its Laplace transform for the i-th entry of the S_{yx} matrix:

$$S_i(\omega) = \frac{\sum_{n=0}^{N_p-1} B_{n,i} (i\omega)^n}{\sum_{n=0}^{N_p-1} a_n (i\omega)^n} \in \mathbb{C}^{N \times 1} \tag{3}$$

with N_p defined as the highest polynomial order plus one (for later convenience).
The unknowns a_n and B_n are found by calculating the system Jacobian and solving:

$$J^H J \theta = 0 \tag{4}$$

where $J^H J$ is the system's Jacobian matrix and the vector θ contains the stacked polynomial coefficients:

$$\theta = \begin{Bmatrix} \beta_1 & \beta_2 & \cdots & \beta_{N_y N_x} & \alpha \end{Bmatrix}^T \quad \text{with} \quad \begin{matrix} \beta_i = \begin{Bmatrix} b_{i,0} & \cdots & b_{i,N_p-1} \end{Bmatrix}^T \\ \alpha = \{ a_0 \quad \cdots \quad a_{N_p-1} \}^T \end{matrix} \tag{5}$$

$J^H J \theta = 0$ can be rewritten as:

$$\begin{bmatrix} M_1 & \cdots & 0 & Q_1 \\ \vdots & \ddots & \vdots & \vdots \\ 0 & \cdots & M_{N_y N_x} & Q_{N_y N_x} \\ Q_1^H & \dots & Q_{N_y N_x}^H & \sum_i^{N_y N_x} T_i \end{bmatrix} \begin{Bmatrix} \beta_1 \\ \vdots \\ \beta_{N_y N_x} \\ \alpha \end{Bmatrix} = 0 \qquad M, Q, T \in \mathbb{C}^{N_p \times N_p} \tag{6}$$

The entries *(p,q)* of the $N_y N_x$ reduced matrices M, Q, T can be expressed as:

$$\begin{aligned} M_{i(p,q)} &\stackrel{\text{def}}{=} \sum_{k=1}^{N} W_{i,k} \cdot z_k^{p-q} \\ Q_{i(p,q)} &\stackrel{\text{def}}{=} \sum_{k=1}^{N} W_{i,k} \cdot S_{i,k} z_k^{p-q} \\ T_{i(p,q)} &\stackrel{\text{def}}{=} \sum_{k=1}^{N} W_{i,k} \cdot S_{i,k} \overline{S_{i,k}} z_k^{p-q} \end{aligned} \tag{7}$$

with W a weighting function in the frequency-domain. A poly-reference algorithm like pLSCF calculates N_y reduced matrices of size $\mathbb{C}^{N_x N_p \times N_x N_p}$.
Carrying out the matrix multiplication of the above, one obtains:

$$\begin{cases} \beta_i = -M_i^{-1} Q_i \alpha \\ D\alpha = 0 \end{cases} \quad \text{with} \quad D \stackrel{\text{def}}{=} \sum_{i=1}^{N_y N_x} (T_i - Q_i^H M_i^{-1} Q_i) \in \mathbb{C}^{N_p \times N_p} \tag{8}$$

where D is called *reduced Jacobian matrix*. The pLSCF version will similarly calculate $D \in \mathbb{C}^{N_x N_p \times N_x N_p}$ by summing N_y reduced matrices M, Q, T [10].

In order to remove the parameter redundancy and calculate "unstable" poles [10], $a_0 = 1$ is imposed, therefore the least-squares solution of the reduced normal equations for each n-th of the N_o requested model orders is:

$$\alpha_n = \{1 \quad -D^{-1}_{(1:n+1,2:n+1)} D_{(1:n+1,1)}\}^T \in \mathbb{C}^{(n+1)\times 1} \tag{9}$$

The pLSCF version computes similarly $\alpha \in \mathbb{C}^{N_x(n+1)\times N_x}$ [10].

For each model order n, the complex poles of the system are the roots ζ_n of the denominator polynomial in the z-domain, i.e. the eigenvalues of the companion matrix of vector α_n.

$$\sum_{k=0}^{n} a_k z^k \quad \overset{roots}{\Longrightarrow} \quad a_n \prod_{k=1}^{n}(z-\zeta_k) \quad \overset{\zeta = e^{\lambda \Delta t} e^{i\varphi}}{\Longrightarrow} \quad \lambda_{k,n} \qquad \forall \text{ model order } n \tag{10}$$

pLSCF similarly constructs a companion matrix from α_n and calculates its eigenvalues [10].

The stabilization diagram is built by repeating (9) (10) for the N_o requested model orders. The vast majority of the calculated roots are purely mathematical, the physical poles of the system are found by imposing $0 < -\Re(\lambda) < |\lambda|$ (poles must be underdamped) and $\Im(\lambda) > 0$ (eigenfrequencies must be positive). At the end of this step, for each model order n, $N_m(n) \leq n/2$ physical poles are known for plotting the stabilization diagram. Instead of calculating β_i from (8), the mode shapes are determined applying the Least Squares Frequency Domain (LSFD) method with the selected eigenvalues λ of the system:

$$S(\omega) = \sum_{m=1}^{N_m} \left(\frac{R_{m,1}}{i\omega - \lambda_m} + \frac{\bar{R}_{m,1}}{i\omega - \bar{\lambda}_m} + \frac{R_{m,2}}{-i\omega - \lambda_m} + \frac{\bar{R}_{m,2}}{-i\omega - \bar{\lambda}_m} \right) - \frac{L_R}{s^4} + U_R \in \mathbb{C}^{N \times N_y N_x} \tag{11}$$

with

$$R_{m,1} = \psi_m L_m^T, \quad \bar{R}_{m,1} = \bar{\psi}_m L_m^T, \quad R_{m,2} = L_m \psi_m^T, \quad \bar{R}_{m,2} = \bar{L}_m \psi_m^T \tag{12}$$

where each of the N_m residue matrices $R_m \in \mathbb{C}^{N_y \times N_x}$ is the product of mode shapes ψ_m and operational deflection vectors L_m^T. The upper and lower residuals U_R and L_R account for the effects of the modes outside the current frequency band. Since the poles are already known, a linear least-squares problem in the parameters R, U_R and L_R must be solved:

$$[S] = [A][R] \quad \overset{solve}{\Longrightarrow} \quad [R] = [A]^+ [S] \tag{13}$$

where $A \in \mathbb{C}^{N \times (N_m + 2)}$ contains the various known $[1/(i\omega - \lambda_m) \quad \cdots \quad -1/s^4 \quad 1]$ terms, S the measured cross-power spectral density matrix and $[R] \in \mathbb{C}^{N_y(N_m+2)\times N_x}$ the unknown stacked residue matrices and upper and lower residuals. The singular value decomposition of the m-th residue delivers the mode shape ψ_m corresponding to the m-th eigenfrequency:

$$R_m = U \Sigma V^T \longrightarrow \psi_m = k U_{(:,1)} \tag{14}$$

The first column of the left-singular vectors U represents the mode shape ψ_m times some scale factor k. At this point, a set of eigenvectors is available for different model orders and time instants but it is unknown which mode shapes are related and some poles appear and disappear due to stochastic effects, therefore *tracking* is desirable to clean the stabilization diagram and to monitor modal parameters as a function of other system variables. The tracking algorithm evaluates the degree of linearity between successive mode shape sets using the modal assurance criterion and assesses concurrently the quality of the identified modes with the mode indicator function, mean phase deviation and modal phase collinearity [11]. Eigenvalues and eigenvectors identified over different model orders or instants belonging to the same physical mode are iteratively flagged as related and recognized, after which stochastic, lone and badly identified modes are spotted and removed. Tracking does not per se identify more precisely physical modes of the system, but instead recognizes modes and sorts them together, allowing the calculation of sample covariance.

2.2 Overview of time complexity

The entire CPSD matrix (2) is calculated at once by taking advantage of symmetry, vectorisation, indexing and benefits from the speed of the FFT algorithm. In most applications the number of sensors and measurement time during OMA are small and this step is only performed once, whereas subsequent steps once per *each* frequency band.

The order of magnitude of computation time is presented for typical practical cases using the authors' notebook as reference (i7 Intel, 8GB RAM, SSD, year 2013). The most important calculation steps are summarized in Table 1:

Calculation	*LSCF*	*pLSCF*	Operation
Build reduced matrices (7)	$N_y N_x \cdot \mathcal{O}(N \log N)$	$N_y N_x^2 \cdot \mathcal{O}(N \log N)$	Fast Fourier Transform
Build reduced Jacobian (8)	$N_y N_x \cdot \mathcal{O}(N_p^3)$	$N_y \cdot \mathcal{O}(N_x^3 N_p^3)$	Matrix multiplication and inversion
Solve normal equations (9)	$N_o \cdot \mathcal{O}(N_p^3)$	$N_o \cdot \mathcal{O}(N_x^3 N_p^3)$	Matrix pseudoinverse
Calculate system poles (10)	$N_o \cdot \mathcal{O}(N_p^3)$	$N_o \cdot \mathcal{O}(N_x^3 N_p^3)$	Eigendecomposition of companion mat.
Calculate residues (13)	$N_o \cdot \mathcal{O}(N_m^3 + N N_m^2)$		Matrix pseudoinverse using SVD
Calculate mode shapes (14)	$N_o \cdot N_m \cdot \mathcal{O}(N_m^3)$		Singular values decomposition

Table 1: Time complexity *per frequency band*, worst-case scenario.

Overall performance of the identification process is most sensitive to the model order required to construct a stabilization diagram. The reduced matrices (7) are reformulated to be Hermitian with real positive diagonal in order to calculate their inverse faster using Cholesky decomposition. Since M_i, Q_i, T_i have Toeplitz structure, only the first N_p terms of their DFT are needed to reconstruct the whole matrix and calculated in parallel [2]. An overview of the computational aspects of the reduced Jacobian matrices is given in [9]. Assuming a model order of one hundred, and hundreds of responses and reference channels, the three reduced matrices are calculated in less than one second. Calculating all poles up to model order one hundred lasts tenths of a second per frequency band. Time complexity for non-sparse matrix multiplication and matrix inversion is conservatively assumed to be $\mathcal{O}(n^3)$ (asymptotically faster algorithms exist). The complexity of the two-step singular value decomposition algorithm when left-singular and right-singular vectors are not required is $\mathcal{O}(N_m^3)$ [12]. After poles have been identified, residuals and mode shapes are calculated according to eq. (13)(14). The tracking algorithm tracks a variable number of modes with an upper bound defined by half the model order; the effective time complexity of the tracking algorithm is that of the matrix operations required to calculate the modes' quality parameters. In practical cases, selecting, sorting and tracking thousands of modes requires less than a tenth of a second.

The computational complexity of iterative and poly-reference methods restrains their applicability in real-time automated modal analysis. An iterative Maximum-Likelihood method has the same complexity as the two mentioned cases times the number of iterations required for convergence: in the current implementation parameters are updated automatically in the available CPU time before the next data block arrives using a maximum-likelihood approach.

2.3 Overview of MATLAB implementation

The MATLAB implementation of the analysis program is almost entirely vectorised and features minimal use of loops and conditional statements. The program favours low CPU load over memory efficiency and the *parallel processing toolbox* is not employed for compatibility and cost. The GUI's CPU time is negligible compared to mathematical operations and does not need to be discussed; its overall performance is competitive with similar software developed at DLR in C# or .NET. MATLAB uses multithreading for `mldivide`, `fft`, `eig`, `svd`, `sort`, thus offering a considerable speedup for the most computationally intensive and common operations, however bottlenecks such as `for` loops are difficult to eliminate completely. Some specific `.set` and `.get` commands are overloaded, there are faster implementations of default functions (`repmat`, `unique`,…), built-in and undocumented functions (`ismembc`,…), and new MEX files. Some parameters are known in advance from experience and user input can be used to "teach" the program how to better analyse data.

The automated analysis program running on a notebook in MATLAB accesses the sensor's signals via an *ActiveX* interface with a *National Instruments* or *Dewesoft* client application. For this test, a *Dewetron* measurement system [13] recorded pressure, force, and acceleration signals. The measurement system allows direct remote access to networked clients running the *Dewesoft* software.

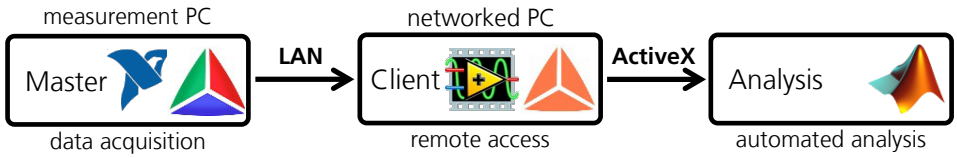


Figure 1: Diagram of the automated system identification's data flow

The user is given real-time control over *measurement setup, signal processing, system identification, mode tracking, plotting*. Various estimation algorithms are available (LSCF and SSI families) and the modular architecture allows any new algorithms to be integrated easily. A fully functional graphical user interface provides options to explore data and results. The program can perform indifferently *both experimental and operational modal analysis*.

3 TEST SETUP

The present wind tunnel investigation was carried out in the *Transonic Wind Tunnel Göttingen DNW-TWG*. It is a continuously-operating facility with a *1×1 m* adaptive test section. The stagnation temperature in this wind tunnel is kept constant by a closed-loop control of a cooler, while Mach number and stagnation pressure may be varied independently. The experimental setup allows free heave and pitch motions of the aerofoil model (see Figure 2**)**.

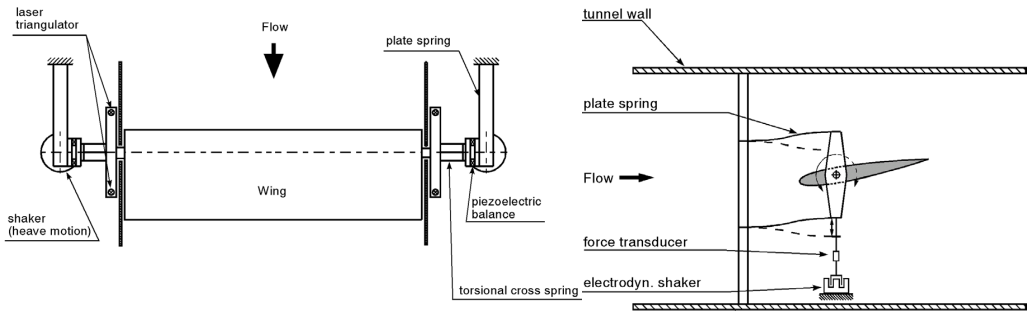


Figure 2: Model of the structural dynamics and test setup in the wind tunnel

A two-dimensional Dornier CAST 10-2 aerofoil is used. The top and bottom walls were adapted to the stationary flow at the mean angle of attack of the aerofoil, where the static aeroelastic equation must be satisfied. The inflow Mach number is kept constant by a closed-loop control using the measured ratio of the static pressure to the stagnation pressure in the test section. The six internal *PCB 352C22* accelerometers measuring perpendicularly to the wing plane are installed at *y/b = 0.15, 0.50, 0.85* span-wise and at *x/c = 0.083, 0.873* in the direction of the flow. The eigenfrequencies of the flutter test setup and the flutter frequencies are well below the first deformation eigenfrequency of the aerofoil model headings. The mean angle of attack of the aeroelastic system under air loads depends on the structural dynamics parameters, the off-wind angle of attack and the flow parameters. The entire test model can be rotated around the elastic axis of the aeroelastic system in order to tune the angle of attack to a given value while the wind tunnel is functioning, thus a target mean angle of attack can be achieved while fulfilling the static aeroelastic equilibrium. The aerofoil is mounted on each side on a piezoelectric balance with high stiffness in order to measure the steady and unsteady lift, drag and pitching moment; two laser triangulators on each side of the wind tunnel measure the instantaneous heave and pitch of the model.

4 MONITORING OF FLUTTER EXPERIMENT

Measurements were conducted in the range $0.5 \leq Ma \leq 0.85$ with control accuracy $\Delta Ma = 0.001$ and at static pressures of $40\ kPa \leq p_0 \leq 90\ kPa$ resulting in Reynolds numbers of $1.0 \cdot 10^6 \leq Re \leq 3.5 \cdot 10^6$. Since the evacuation of the chamber takes time, the static pressure is hold held constant during one measurement series, while the flow rate is increased in steps from minimum Mach number to maximum. Static pressure, Mach number and mean angle of attack can be used to control the flow conditions.

For the current investigation it is assumed that classical aeroelastic instability with two degrees of freedom might occur by coupling of the heave and pitch modes. On the other hand, flutter of the pitch mode might arise because of the indifferent equilibrium of the aerodynamic loading with respect to the rotation axis. To eliminate boundary layer effects, the transition of the flow around the aerofoil was enforced by installation of a turbulator strip at the leading edge. It is assumed that the flow's vorticity and turbulence possess broadband spectra that excite all relevant modes of the aeroelastic system. The model is mass mass-balanced to the rotational axis by two masses installed on the lever arms.

4.1 Analysis

The update rate of the online real-time analysis is a compromise between responsiveness and required calculation time – usually two seconds. Data is sampled at *4* kHz and collected into data blocks; these data blocks are then stacked into a data buffer *~30÷60s* in length and results are updated with every new block. Data is fed directly to time-domain identification algorithms (SSI) or used to estimate the spectra for frequency-domain methods (Figure 3). An instantaneous stabilization in diagram is built to display the currently identified poles and animated mode shapes (Figure 4 and Figure 5). Sets of identified mode shapes are organized depending on the current operating conditions, in this case static pressure and Mach number (Figure 6). All identified mode shapes are grouped into families as new data arrives and compared to the reference mode set obtained with the hammer test of the aerofoil model.

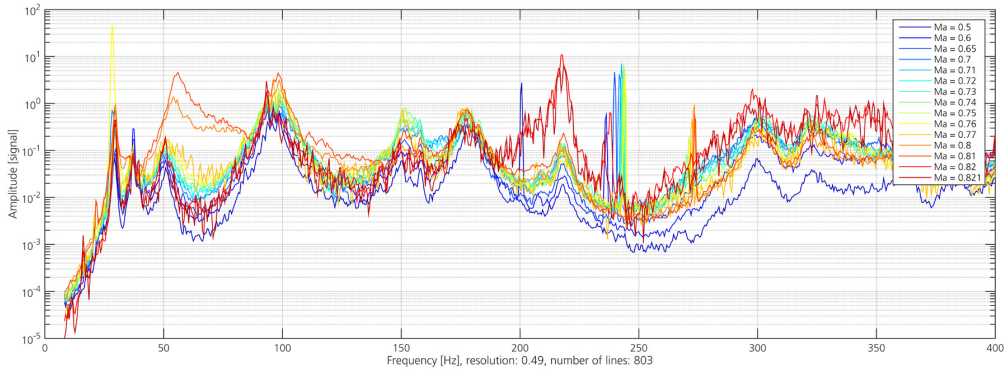


Figure 3: Accelerometers' cross-power spectra from $Ma_\infty = 0.5$ to $Ma_\infty = 0.82$ (flutter)

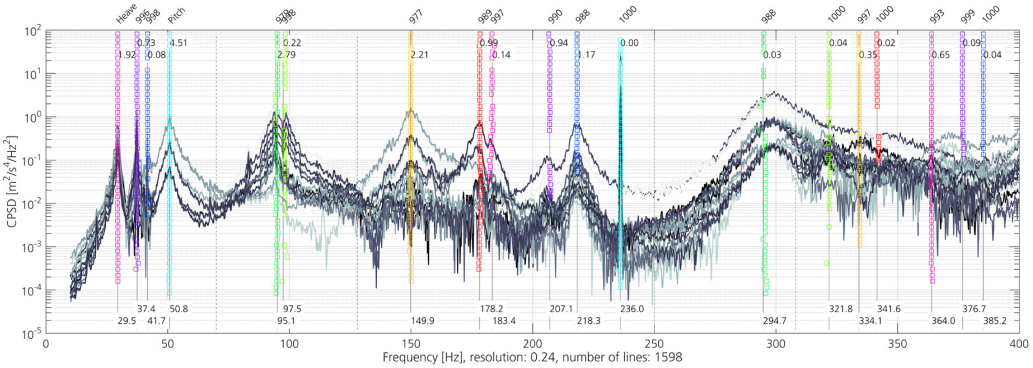


Figure 4: Automated stabilization diagram at $Ma_\infty = 0.65$, OMA-ML-LSCF

Figure 5: First five mode shapes: heave, pitch, in-plane bending, sym. bending, antisym. bending, torsion

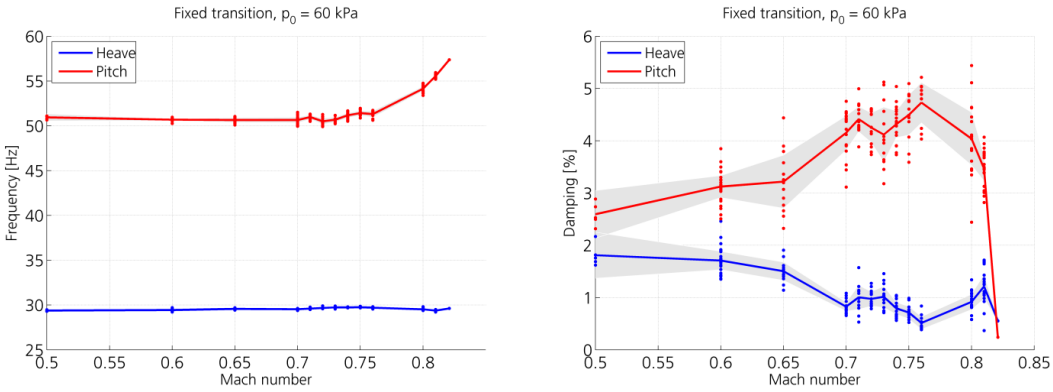


Figure 6: Heave and pitch eigenfrequencies and damping for different Mach numbers

Figure 6 displays the identified eigenfrequencies and damping for the heave and pitch modes over the Mach number. Each point in the plots represents a system identification elaborated from *65536* measured time data samples (all accelerometers as references, *5–400Hz*). The lines connect the average values at each Mach number and the 95% confidence interval in grey is calculated assuming a *t*-distribution of samples.

The eigenfrequency of the heave mode does not change much, while the eigenfrequency of the pitch mode starts rising markedly from $Ma_\infty = 0.77$. This behaviour can be explained with the rear loading effect of the aerofoil at higher Mach numbers where the additional lift generated at oscillating angle of attack acts as a moment in opposite rotation to the angle. It appears as additional aerodynamic stiffness which results in the eigenfrequency increase of the aeroelastic system. On the right side of Figure 6 the damping curves show significant scatter. The damping trend of the heave mode decreases up to $Ma_\infty = 0.77$ and then becomes more stable again. The pitch mode shows the opposite behaviour. The damping trend increases up to $Ma_\infty = 0.77$ and then slopes down to zero level, where self-excited flutter of the model occurs until the brake in the wind tunnel is triggered by the excessive deflection amplitudes.

5 CONCLUSIONS

The presented program for *online automated output-only modal analysis* is based on a fast implementation of the well-known frequency-domain LSCF and pLSCF identification algorithms. Some insights about the different time complexities of both algorithms are given, highlighting parameters to which computation time is sensible. It is shown that a MATLAB implementation of the data processing and analysis program will fully-functioning GUI can be successfully employed in the real-time monitoring of an aeroelastic experiment in a wind-tunnel facility in combination with a commercial data acquisition hardware and software. The experimental frequency and damping trends over Mach number of an instrumented aerofoil model in the subsonic to transonic regimes are presented, including the onset of aeroelastic instabilities. The current program implementation is used flexibly for both OMA and EMA, with both time-domain and frequency-domain identification algorithms. The code has been tested on simple beams, wind gallery models, an aircraft model, a sailplane, a helicopter rotor testbed and on a full-scale aircraft ground vibration test data.

6 OUTLOOK

For the assessment of the flutter stability the damping trends must be extrapolated for higher speeds based on the identified damping and eigenfrequencies at lower speeds. The Zimmerman-Weissenburger method [14] predicts the critical speed of flutter onset by interpolating with quadratic polynomials the identified poles at three different flow speeds. It is assumed, that the unstable coupling is caused by the contribution of only two mode shapes, one with heave character and the other with pitch character. In [15] this method is expanded to multimode unstable couplings, although the underlying assumption for the extrapolation is based on constant aerodynamic lift and moment slope; the Zimmerman-Weissenburger method is therefore not applicable with adequate reliability.

The intended future work in monitoring aeroelastic experiments will include more sophisticated unsteady aerodynamic models for flutter prediction. In this framework, some possible developments are fast maximum-likelihood estimators, algorithms with better tolerance to noisy data, delegation of intensive calculations to external code, different mode tracking algorithms. Finally a future application will not only be monitoring of aeroelastic wind tunnel experiments but also flight flutter testing.

REFERENCES

[1] P. van Overschee, B. De Moor: *Subspace Identification for Linear Systems*. Kluwer Academic Publishers, 1996.

[2] J. Schoukens, Y. Rolain, F. Gustaffson, R. Pintelon: *Fast calculation of least-squares estimates for system identification*. Proceedings of the 32nd Decision and Control Conference, p. 3408-3410, Tampa, FL, USA, 1998.

[3] B. Peeters, G. Lowet, H. van der Auweraer: *A new procedure for modal parameter estimation*, Sound and Vibration, January 2004.

[4] B. Peeters, G. De Roeck: *Reference-based stochastic subspace identification for output-only modal analysis*. Mechanical Systems and Signal Processing, 13 (6) (1999), pp. 855–878.

[5] E. Reynders, R. Pintelon, G. de Roeck: *Uncertainty bounds on modal parameters obtained from stochastic subspace identification.* Mechanical Systems and Signal Processing, Volume 22, Issue 4, May 2008, pp 948-969.

[6] M. Goursat, M. Doehler, L. Mevel, P. Andersen: *Crystal Clear SSI for Operational Modal Analysis of Aerospace Vehicles*, 28th International Modal Analysis Conference IMAC-XXVIII, 2010.

[7] R. Pintelon, J. Schoukens, *System identification – a frequency domain approach*, IEEE Press, 1st edition, 2001.

[8] R. Pintelon, P. Guillaume, Y. Rolain, J. Schoukens, H. van Hamme: *Parametric identification of transfer functions in the frequency domain: a survey.* IEEE Transactrions on Automatic Control, 39(11):2245-2260, 1994.

[9] P. Verboven: *Frequency-domain system identification for modal analysis.* PhD thesis, Dept. of Mechanical Engineering, Vrije Universiteit Brussel, Belgium, 2002.

[10] B. Cauberghe: *Applied frequency-domain system identification in the field of experimental and operational modal analysis*. PhD thesis, Dept. of Mechanical Engineering, Vrije Universiteit Brussel, Belgium, 2004.

[11] J. Schwochow, G. Jelicic: *Automated operational modal analysis for aeroelastic apploications*, IOMAC'15 conference proceedings

[12] G. H. Golub, C. F. van Loan: *Matrix computations*, third edition, Johns Hopkins University Press, 1996.

[13] N.N.: *DEWETRON*, http://www.dewetron.com/applications/aerospace-defense/wind-tunnel-test/

[14] N. H. Zimmerman, J. T. Weissenburger: *Prediction of Flutter Onset Speed Based on Flight Testing at Subcritical Speeds*, Journal of Aircraft, Vol.1 No.4 (1964), pp. 190–202.

[15] R. Lind: *Flutter Margins for Multimode Unstable Couplings with Associated Flutter Confidence,* Journal of Aircraft, Vol.46 No.45 (2009), pp. 1563–1569.

International Conference on Engineering Vibration
Ljubljana, Slovenia, 7-10 September 2015

INDUSTRIAL USE OF METHODS FOR MODAL ANALYSIS OF SMALL AND LIGHT STRUCTURES

Domen Rovščeк*[1], Janko Slavič[2], Miha Boltežar[2], Vitoslav Bratuš[1], Tomaž Mlakar[1]

[1]Hidria AET d.o.o.
domen.rovscek@hidria.com

[2]Faculty of Mechanical Engineering, University of Ljubljana
miha.boltezar@fs.uni-lj.si

Keywords: Experimental modal analysis, small structures, light structures, numerical model, model validation.

Abstract. *When dealing with small and light structures, difficulties occur when measuring the modal parameters. The resonant frequencies are usually relatively high and therefore a wide frequency range is needed for the measurement. Furthermore, the mass that is added to the structure by the sensors causes structural modifications. Three innovative procedures for the experimental modal analysis of small and light structures were developed in this study and the most appropriate of them was used for the modal analysis of an industrial product. The procedure that was used involves a measurement of the excitation force, which was performed by a piezo strain-gauge. The main advantage of this sensor in comparison to other devices used for force measurements is that it adds a very small mass to the measured structure ($\approx$ 0.4 gram) but at the same time enables an accurate measurement of the modal parameters in a wide frequency range (up to 20 kHz). This makes it suitable for the measurement of the frequency-response functions of light structures that have high resonant frequencies. Consequently, an experimental modal analysis of the aforementioned structures with free-free support can be performed. The results of the modal analysis were used to validate the numerical model of the product. The development and functioning of the numerical model is also presented in this study.*

1 INTRODUCTION

Small and light structures (mass < 50 gram) have some distinctive features that intensify the difficulties of measuring their modal parameters. Their resonant frequencies are usually relatively high; therefore, a wide frequency range of measurement is needed. The mass that is added to the structure by the sensors cannot be neglected and there are also difficulties with ensuring the proper excitation, so that all the measured modes are well excited and that at the same time the excitation level is not too large, which would cause a larger response of the structure than the measuring range of the sensors can cover. Three innovative procedures for the experimental and operational modal analysis of small and light structures were developed in this study and the most appropriate of them was used for the modal analysis of an industrial product.

The first procedure is a classical Experimental Modal Analysis (EMA) that involves a measurement of the excitation force. The force measurement was performed by a custom made sensor based on a piezo strain gauge that enables an analysis of the aforementioned structures with free-free support. The main advantage of this sensor in comparison to other devices used for force measurements is that it adds a very small mass to the measured structure (0.4 gram) but at the same time enables an accurate measurement of the modal parameters in a wide frequency range (up to 20 kHz). This makes it suitable for a measurement of the frequency-response functions of light structures that have high resonant frequencies.

The second procedure is an Operational Modal Analysis (OMA) that takes into account the influence of the accelerometer added mass on the mode shapes. The normalisation of the operational mode shapes is based on a sensitivity analysis and a variation of the modal parameters due to the structural modification (as shown by Parloo et al. [1]). The main advantage of this method compared to the sensitivity based operational mode-shape normalisation proposed by Parloo et al. [1] is that it also takes into account the mode shape variation, which occurs due to the added mass of the accelerometer.

The third procedure is non-contact; therefore, there is no added mass of the sensors to the structure. The structure is acoustically excited with a pure sine signal that is tuned to each resonant frequency. A single response measurement with the laser Doppler vibrometer in individual points is needed to determine the modal parameters. A mass-change strategy is used for the mass-normalisation of the measured mode shapes.

To measure the modal parameters of the industrial product named Pressure Sensor Glow-plug (PSG) a proper procedure was needed. The first of the three developed procedures for modal analysis of small and light structures was chosen as the most appropriate. The measured modal parameters were used for the validation of the numerical model that was later used to validate the design of the PSG. The numerical model is being constantly updated and upgraded to enable additional mechanical and thermal simulations of this product.

2 THEORETICAL BACKGROUND

The operational mode shapes are not mass normalised, since the excitation force is not measured when performing the OMA. Therefore, a new approach was proposed by Parloo et al. [1] and later more thoroughly analysed by Lopez-Aenlle et al. [2] to normalise the operational mode shapes. The main idea of this approach is to mass normalise the mode shapes by multiplying them with scaling factors. The scaling factors are calculated on the basis of the modal sensitivity of the structure. By adding a known mass to the selected points of the structure the resonant frequencies shift. From these shifts the scaling factors for each mode shape can be calculated using the sensitivity analysis. This method is usually denoted as the Sensitivity-based operational mode-shape normalisation (sometimes also the Mass-change strategy).

2.1 Sensitivity-based operational mode-shape normalisation

A known mass $[\Delta M]$ needs to be added to the structure to perform the mass-change strategy. The change of the mass matrix causes a variation of the modal parameters. If the modal parameters of the unmodified and modified structure are measured, then the scaling factors α_i can be calculated, as shown in Equation (1)

$$\alpha_i = \sqrt{\frac{\left(\omega_i^2 - \omega_{i,M}^2\right)}{\omega_{i,M}^2 \{\psi_i\}^T [\Delta M] \{\psi_i\}}} \tag{1}$$

where ω_i denotes the i-th resonant frequency of the unmodified structure and $\omega_{i,M}$ is the i-th resonant frequency of the modified structure (when the mass $[\Delta M]$ is added). $\{\psi_i\}$ is the unnormalised mode shape of the structure. A detailed derivation of Equation (1) can be found in [1], where a presumption is made that the mode shapes do not change significantly when adding the mass to the structure ($\{\psi\} \approx \{\psi_i\} \approx \{\psi_{i,\mathrm{M}}\}$). The mass-normalised mode shapes $\{\phi_i\}$ can then be obtained by multiplying the unnormalised mode shapes $\{\psi_i\}$ by the scaling factors α_i, as shown in Equation (2):

$$\{\phi_i\} = \alpha_i \{\psi_i\} \tag{2}$$

3 SAMPLE

To compare different methods for modal analysis, a sample of simple geometry with the proper geometrical and modal characteristics was needed. A steel sample of circular cross-section with 6-mm diameter, 108-mm length and 21-gram mass was used, as shown in Figure 1. Its geometry was chosen in such a way as to ensure one axial-mode, one torsional-mode, and many bending-mode shapes in the frequency range of the measurement (0-20 kHz). The sample that was used for this study is a homogenous structure without any joints. It has well-known material characteristics and geometry; therefore, a relatively accurate FEM model was formed based on this.

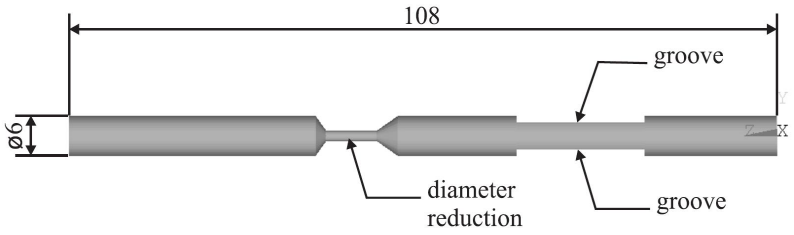


Figure 1: Sample that was used for the evaluation of the developed procedures for modal analysis of small and light structures.

4 MODAL ANALYSIS OF SMALL AND LIGHT STRUCTURES

Three procedures for modal analysis of small and light structures were developed in this study. They are presented in the sections 4.1, 4.2 and 4.3. The comparison of these procedures will not be presented in detail, only the basic set-up. For additional information see articles [3-5] by Rovšček et al.

4.1 EMA

Measurements of the FRFs were performed by monitoring the excitation force and the response (velocity) of the structure simultaneously. The sample and the LDS V-101 electromagnetic shaker (excitation device) were suspended by strings to simulate the free-free support, as shown in Figure 2. The measurement of the response was performed using a LDV Polytec PDV-100 at fifteen points.

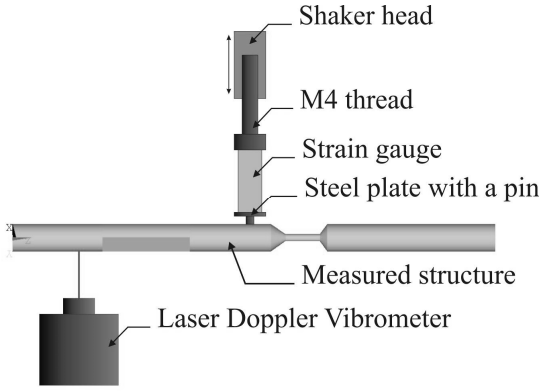


Figure 2: EMA measurement procedure for small and light structures.

A custom made sensor was developed to measure the excitation force and transfer it from the shaker to the sample. This sensor is based on a piezo strain gauge (PCB 740B02). Its structure and functioning are described in an article by Rovšček et al. [3], where a detailed description of the EMA procedure can also be found. The effect of the added mass of the force sensor on the structure was small (0.4 gram) and neglected in the calculation of the modal parameters.

4.2 OMA

The sample was suspended by two strings when performing the OMA. The ambient excitation was carried out using a small steel ball (4 mm diameter) that was glued to a string and swung into the structure to achieve impact excitation. The reference response was measured by a B&K 4517-002 accelerometer. The response in different points on the structure was measured using a LDV Polytec PDV-100. The resonant frequencies ω_i and unnormalised mode shapes $\{\psi_i\}$ were extracted from the response measurements. For the normalisation of the mode shapes with the mass-change strategy, eight magnets, each with a mass of 0.21 gram, were added on the structure and the resonant frequencies $\omega_{i,M}$ of the changed structure were measured, as shown in Figure 3. Then the scaling factors α_i were calculated, as shown in Equations (1) and (2), to normalise the operational mode shapes of the structure with the accelerometer. The mode shapes of the structure itself (without the accelerometer) were obtained by using the method described by Chen [6]. A detailed description of the OMA procedure can be found in an article by Rovšček et al. [4].

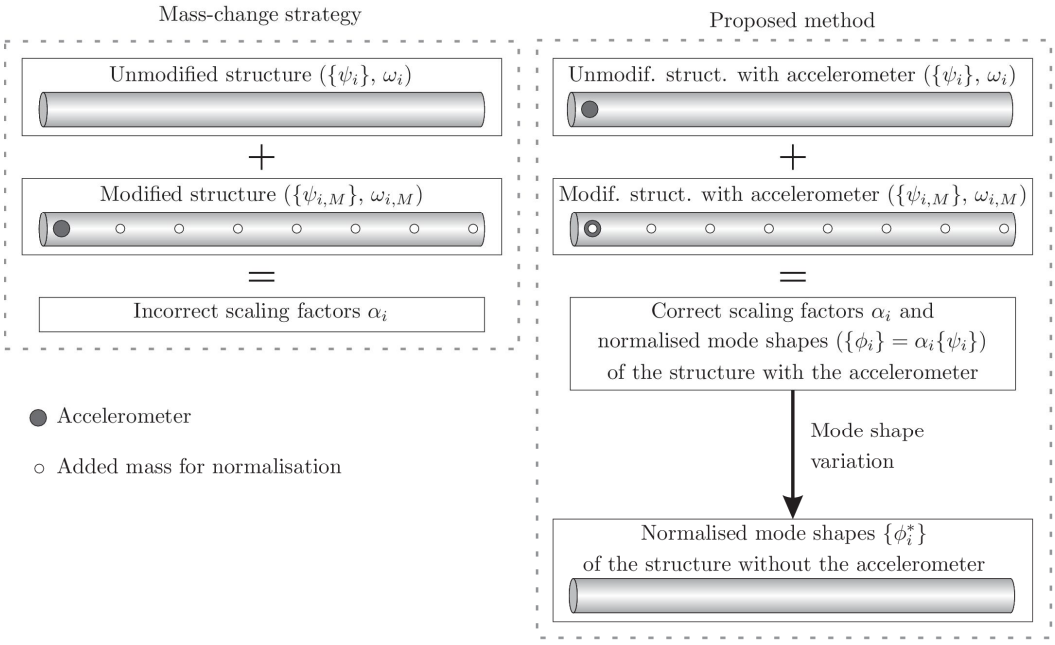


Figure 3: OMA measurement protocol for small and light structures.

4.3 Tuned-Sinusoidal Method

The basic idea of the tuned-sinusoidal method is presented in Figure 4. First, the response of the structure, excited by an unknown force, is measured. Different excitation techniques, such as sound excitation, impact excitation, etc., can be used, as long as the spectral density of the excitation is constant across the whole frequency range of the measurement (white noise excitation). The resonant frequencies ω_r are on the peaks of the measured frequency spectrum. Next, the mode shapes $\{\psi_r\}$ are measured. The structure is subjected to the acoustic excitation (with a loudspeaker) and only the response of the individual point on the structure is measured. If the structure is acoustically excited with a sine that is tuned to the resonant frequency ω_r, then the structure will respond with an Operating Deflection Shape (ODS) that can be used as an un-normalised mode shape $\{\psi_r\}$. This assumption is valid because the mode shape that corresponds to the frequency ω_r prevails over all the other mode shapes in the response of the structure. Therefore, the response of the structure is almost a pure sine with a frequency ω_r.

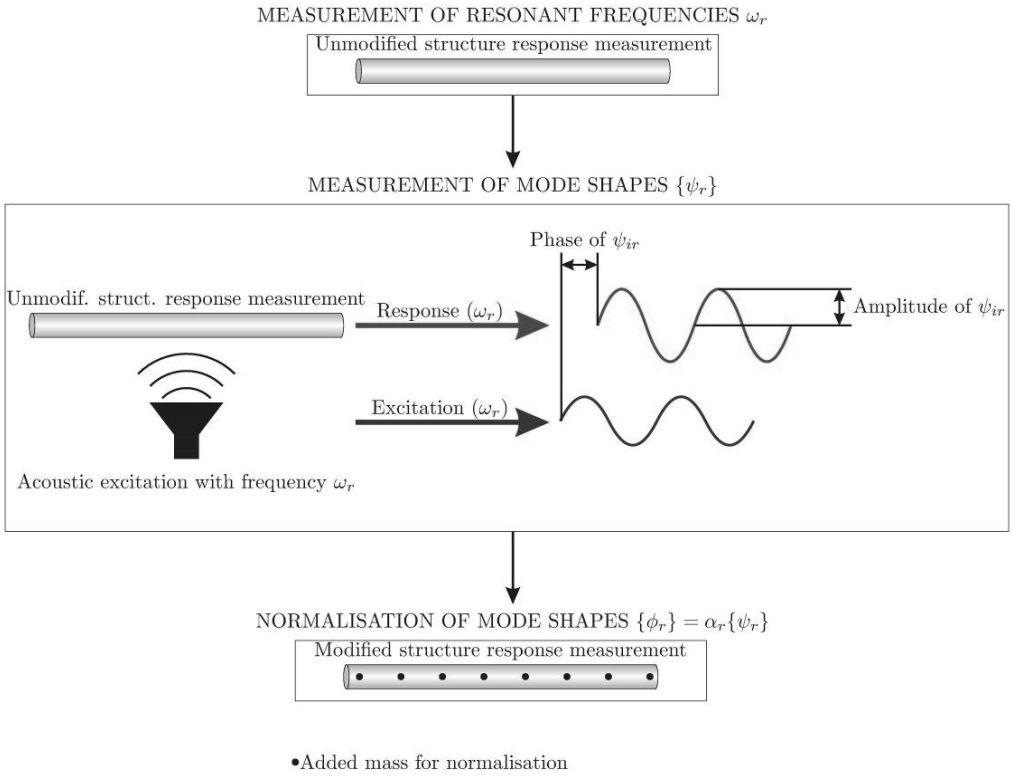


Figure 4: Tuned-Sinusoidal Method for small and light structures.

The structure needs to be excited with all the individual resonant frequencies ω_r and the responses at all the points of the structure need to be measured for each resonant frequency. The phase between the sine of the excitation and response signal is used as a phase of individual component ψ_{ir} of the mode shape $\{\psi_r\}$. The amplitude of the response sine signal defines the amplitude of the individual component ψ_{ir} of the mode shape $\{\psi_r\}$. Therefore, the structure has to be excited and the response needs to be measured for every (i-th) measurement point at all the resonant frequencies ω_r to obtain the amplitude and phase of each component ψ_{ir}. At

last, the scaling factors α_r are calculated, as shown in Equation (2), to normalise the mode shapes $\{\psi_r\}$ of the structure. The name tuned sinusoidal method is used for the described method since the acoustic sine excitation is tuned to the measured resonant frequencies. A detailed description of the Tuned-sinusoidal Method can be found in an article by Rovšček et al. [5].

5 APPLICATION OF THE EMA PROCEDURE ON AN INDUSTRIAL PRODUCT

All three presented procedures can be used for modal analysis of small and light structures. However, for the application that will be presented in this study the EMA was chosen as the most appropriate, because it does not need additional measurements for mode shape normalisation. It also gives accurate results in the frequency range of interest (between 0.5 kHz and 20 kHz) and adds only a small negligible mass to the structure (0.4 gram).

The presented procedure for EMA of small and light structures was applied on a product named Pressure Sensor Glow-plug (PSG) that is shown in Figure 5. Innovative cylinder pressure sensing technology integrated in the glow plug enables extremely high accuracy real time measurement of pressure during combustion process. The pressure information, amplified, calibrated and filtered by exclusive integrated ASIC is transmitted to the engine control unit to enable engine closed loop control, bringing improved fuel burn and reduced engine out emissions.



Figure 5: EMA of the PSG.

The results of the EMA were used to validate the PSG numerical model that helps to improve the design of the product. The developed numerical model (shown in Figure 6) in combination with field measurements is a strong tool for verification of different designs of PSG and is being constantly updated and upgraded. The current version of the model enables the following analyses:

- Modal and harmonic analysis.
- Calculation of stress and strain at different loading conditions (related to fatigue).
- Thermal analysis (glowing of the heater, engine operating conditions…).
- Thermal expansion.

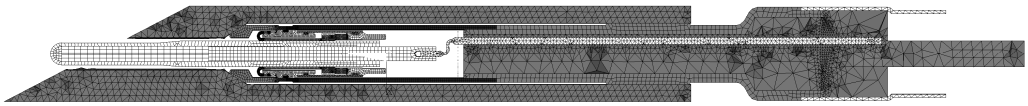


Figure 6: Numerical FEM model of the PSG.

6 CONCLUSIONS

- Three innovative procedures for EMA and OMA of small and light structures were developed.
- All three procedures were tested on a sample of small dimensions and mass.
- The EMA procedure was chosen as the most appropriate for the application on an industrial product, because it enables accurate measurements in the frequency range of interest and it is also more straightforward to use than the other two developed procedures.
- The EMA was used to identify the modal parameters of a product named Pressure Sensor Glow plug (PSG).
- The measured modal parameters were used to build and validate the numerical FEM model of the PSG.
- The model was later used for structural and thermal simulation of the PSG and is being constantly updated and upgraded based on the measurements.

REFERENCES

[1] E. Parloo, P. Verboven, P. Guillaume, M. Van Overmeire, Sensitivity-based operational mode shape normalisation. *Mechanical Systems and Signal Processing*, **16(5)**, 757–767, 2002.

[2] M. Lopez-Aenlle, P. Fernandez, R. Brincker, A. Fernandez-Canteli, Scaling-factor estimation using an optimized mass-change strategy (Correction of: **24(5)**, 1260-1273, 2010). *Mechanical Systems and Signal Processing* **24(8)**, 3061–3074, 2010.

[3] D. Rovšček, J. Slavič, M. Boltežar, The use of strain sensors in an experimental modal analysis of small and light structures with free-free boundary conditions. *Journal of Vibration and Control*, **19(7)**, 1072-1079, 2012.

[4] D. Rovšček, J. Slavič, M. Boltežar, Operational mode-shape normalisation with a structural modification for small and light structures. *Mechanical Systems and Signal Processing*, **42(1-2)**, 1-13, 2013.

[5] D. Rovšček, J. Slavič, M. Boltežar, Tuned-Sinusoidal Method for the Operational Modal Analysis of Small and Light Structures. *Strojniški vestnik - Journal of Mechanical Engineering*, **60(3)**, 187-194, 2014.

[6] H.P. Chen, Efficient methods for determining modal parameters of dynamic structures with large modifications. *Journal of Sound and Vibration*, **298(1-2)**, 462–470, 2006.

11th International Conference on Engineering Vibration
Ljubljana, Slovenia, 7–10 September 2015

FDD MODAL IDENTIFICATION FROM EARTHQUAKE RESPONSE DATA WITH EVALUATION OF SOIL-STRUCTURE INTERACTION EFFECTS

Fabio PIOLDI[1], **Jonathan SALVI**[1], **Egidio RIZZI**[*1]

[1] Università di Bergamo, Dipartimento di Ingegneria e Scienze Applicate,
viale G. Marconi 5, I-24044 Dalmine (BG), Italy
[*] Corresponding Author: egidio.rizzi@unibg.it

Keywords: Modal dynamic identification, Operational Modal Analysis with eXogenous input (OMAX), refined Frequency Domain Decomposition (rFDD), seismic input, Soil Structure Interaction (SSI).

Abstract. *"Non-parametric" system identification via a refined FDD (rFDD) algorithm is developed to evaluate current modal properties of civil engineering buildings subjected to earthquake excitation. Innovatively, the algorithm operates in an OMAX (Operational Modal Analysis with eXogenous input) environment on base-excited buildings, to detect also potential Soil-Structure Interaction (SSI) effects. At first, the identification technique is explored analytically, dealing with a variable stiffness and damping foundation system. The OMAX condition comes from the use of base excitation records, which are employed as exogenous input. The standard fixed-base condition may simulate well the response to ambient loading or weak seismic excitations; rather, the flexible-base model shall deal with more realistic seismic responses of buildings, which may embed interactions between soil and structure. The developed analyses are performed on synthetic response signals, which are computed from a benchmark structure. Simulated signals are generated prior to dynamic identification, by adopting a given seismic input with variable foundation properties. The method demonstrates its full effectiveness, also for the detection of close modes and for the identification of high modal damping ratios. Issues pertaining to earthquake record processing are specifically addressed. The present work proves a necessary condition for the effectiveness of the present rFDD algorithm as a robust method to inspect current flexible-base strong ground motion modal parameters. This shall help in identifying possible variations of structural features and SSI effects along experienced seismic histories, and providing an effective tool towards Earthquake Engineering and Structural Health Monitoring purposes.*

1 INTRODUCTION

The determination of unknown dynamical properties of a given structural system constitutes a main target of modal identification. Towards that purpose, both input-output and output-only techniques may be adopted. Natural frequencies, mode shapes and damping ratios can be estimated, as connected to the dynamic characterization of real engineering structures. In the context of seismic engineering, modal parameters may be detected by dedicated identification procedures, towards the quantification of the structural response to earthquake ground motion.

In this context, seismic Soil-Structure Interaction (SSI) [1, 2] may play a considerable role. The dynamic response of a structure laying on a soft soil may substantially differ, in amplitude and frequency content, from the response of an identical structure based on firm ground [1]. A building subjected to SSI displays a coupling between the foundation and the superstructure motions. The recorded dominant frequency is always smaller than that of the fixed-base building, and of the foundation itself, when no building is present [3].

If the local SSI effect is small, the recorded responses at the foundation level are not influenced by the motions of the upper stories, and the building may be assumed as laying on a "fixed-base" [4]. The motions at the foundation level may be taken as base-excitation for the adopted model. Otherwise, if SSI becomes significant, this assumption is no longer valid, since the foundation input motion and the output response of the structure turn out to be coupled [2]. Then, the response of the building is characterized by a "flexible-base" condition.

Knowing the recordings from the building, the identification of SSI effects may be possible if acquisitions are available also from the foundations, or from free-field or downhole nearby locations. During the last decades, several studies on SSI identification and quantification have been thoroughly attempted, see e.g. [3, 5–9]. By using Operational Modal Analysis (OMA), some attempts have been performed, specifically in the present context, by accounting for SSI effects on buildings, as e.g. in [10, 11].

Within such an OMA field, the present paper investigates the application of a refined Frequency Domain Decomposition (rFDD) algorithm [12–16] to recorded earthquake responses of buildings, in order to identify flexible-base structural modal parameters. Innovatively, the algorithm operates in an OMAX (OMA with eXogenous input) environment [17]. This concept takes benefit from the advantages of both Operational and Experimental Modal Analyses: operational (unknown) forces (causing the earthquake response of the superstructure) as well as artificial (known) forces (free-field and foundation recordings) are processed simultaneously by the present rFDD algorithm, towards a correct detection of potential SSI effects and an effective estimate of flexible- and fixed-base modal parameters. Foundation and free-field recordings are adopted as (exogenous) input for the algorithm, which develops in a self-contained framework some tools for SSI detection and quantification, taken and re-elaborated from [3, 5].

The analyses are performed on synthetic response signals, which are computed from a literature-based real structure. Starting from this model, four different types of soil have been considered, in order to investigate SSI effects on the structural response. These signals are generated before dynamic identification, by adopting the given seismic input at variable foundation properties. Then, they are taken as input (accelerations) to feed the rFDD-OMAX algorithm, towards achieving consistent estimates of flexible- and fixed-base modal parameters.

First, the developed SSI model, the soil properties and the algorithm adopted for flexible-base modal identification are outlined in Section 2. Then, the performed analyses and results obtained from the application of the rFDD-OMAX algorithm are presented in Sections 3 and 4. Main conclusions are finally gathered in Section 5.

2 SSI MODELING AND ALGORITHM OF SYSTEM IDENTIFICATION

The input response channels to be fed to the rFDD-OMAX algorithm, i.e. storey accelerations, are obtained from calculated synthetic response signals. These are generated by taking as benchmark seismic ground motion the El Centro earthquake (see Table 1), as excitation acting on the bedrock of a five-storey Sway-Rocking model adapted from [10]. The simulated responses are calculated by direct time integration of the equations of motion, via Newmark's method (average acceleration). The use of simulated signals shall fulfill a necessary condition for the algorithm's efficiency, since flexible- and fixed-base modal parameters are determined via modal analysis before identification, and then adopted as targets for validation purposes. Further seismic input could be considered at a later stage, after basic features on modal identification under seismic SSI effects are revealed at this stage.

Earthquake	*Date*	*Station*	*Duration* [s]	f_s[Hz]	*M*	*Comp.*	*PGA* [g]
El Centro (EC)	18/05/1940	0117	40	100	7.1	NS	0.312

Table 1: Main characteristics of the adopted benchmark earthquake.

2.1 Idealization of a shear-type frame with SSI effects

An n-storey shear-type superstructure with an underlying Sway-Rocking (SR) SSI model [4, 18] is adopted as a benchmark structure for the present study. This section shows an overview on the developed model; a detailed description is going to be reported elsewhere [16]. In Fig. 1, the initial geometry, the lumped-mass scheme and the displacements of the SR model are represented.

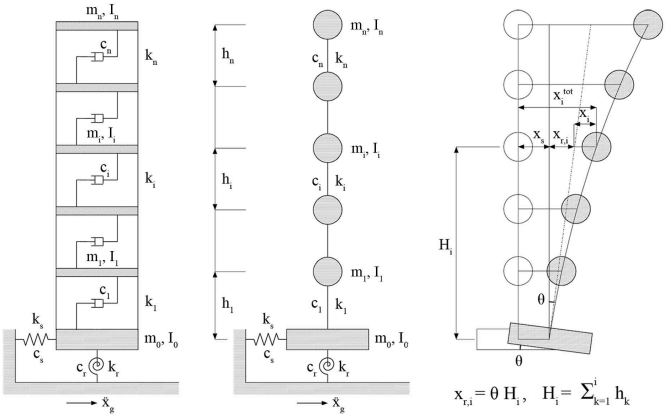


Figure 1: Adopted Sway-Rocking model of a shear-type frame.

Specifically, m_i, c_i, k_i, I_i and x_i are the mass, damping, stiffness, mass moment of inertia and displacement of the i^{th} shear-type frame floor, respectively. The foundation displays mass m_0 and mass moment of inertia $I_0 = m_0 r^2/4$, and is modeled as a rigid circular disc footing (with radius r) of negligible thickness, attached to the surface of a linear elastic halfspace, representing the soil [4]. With respect to the fixed-base model, the sway-rocking model shall be described by two additional degrees of freedom, i.e. the horizontal sway x_s (with k_s and c_s associated stiffness and damping coefficients) and the system rocking θ (with k_r and c_r associated

stiffness and damping coefficients). Then, $\ddot{x}_g$ represents the horizontal acceleration related to the free-field motion x_g, to which the building-foundation system is subjected to. The total displacement x_i^{tot} along the i^{th} translational DOF may be then computed as $x_i^{tot} = x_g + x_s + x_{r,i} + x_i$. Finally, h_i and H_i are the i^{th} relative and absolute floor heights, respectively.

The $n + 2$ equations of motion of the so-assembled SR model may be written as (see also complementary information in [19]):

$$\begin{cases} \mathbf{M}\left(\ddot{\mathbf{x}} + \mathbf{r}\ddot{x}_g + \mathbf{r}\ddot{x}_0 + \mathbf{z}\ddot{\theta}\right) + \mathbf{C}\dot{\mathbf{x}} + \mathbf{K}\mathbf{x} = \mathbf{0} & (1) \\ \mathbf{r}^{\mathrm{T}}\mathbf{M}\left(\ddot{\mathbf{x}} + \mathbf{r}\ddot{x}_g + \mathbf{r}\ddot{x}_0 + \mathbf{z}\ddot{\theta}\right) + m_0\left(\ddot{x}_g + \ddot{x}_0\right) + k_s x_0 = 0 & (2) \\ \mathbf{z}^{\mathrm{T}}\mathbf{M}\left(\ddot{\mathbf{x}} + \mathbf{r}\ddot{x}_g + \mathbf{r}\ddot{x}_0 + \mathbf{z}\ddot{\theta}\right) + I_t\ddot{\theta} + k_r\theta = 0 & (3) \end{cases}$$

where $\mathbf{M}$, $\mathbf{C}$ and $\mathbf{K}$ are the $n \times n$ mass, damping and stiffness matrices of the superstructure (shear-type frame), $\mathbf{r}$ is a rigid body motion vector of unitary components ($n \times 1$), $\mathbf{z}$ is the vector of the absolute floor heights H_i ($n \times 1$), $I_t = I_0 + \sum_{i=1}^{n} I_i$ is the sum of the mass moment of inertia of the foundation-superstructure system; superscript 'T' marks transpose.

Then, starting from the previous equations of motion, the responses of the Sway-Rocking model may be calculated numerically, solving for each of the $n + 2$ DOFs of the system.

2.2 Numerical models

The analytical model proposed in Section 2.1 is assumed for a numerical analysis as a 5-storey shear-type building with a Sway-Rocking foundation. This model is taken in common with companion work [19], where the role of an optimized Tuned Mass Damper is investigated for potential vibration mitigation and control. The structure is assumed to be laying on four types of soil, i.e. *very soft, soft, medium and dense*, as represented by different characteristic parameters. Also, the standard fixed-base frame is considered as basic reference, too.

The inter-storey height is assumed to be equal to $4\,\mathrm{m}$. The floor mass and mass moment of inertia of each floor are taken as $m_i = 3 \times 10^5\,\mathrm{kg}$ and $I_i = 7.5 \times 10^6\,\mathrm{kg\,m^2}$. Inter-storey stiffnesses, from the first to the fifth, are assumed as $7k$, $5k$, $3k$, $2k$ and k, respectively, where $k = 5 \times 10^7\,\mathrm{N/m}$. Two separate cases of superstructure damping have been investigated:

- (ζ_{M}) mass proportional damping, with $\zeta_{\mathrm{M}} = 10\%$ for the first mode;
- (ζ_{R}) Rayleigh damping (linear combination of mass and stiffness matrices), with $\zeta_{\mathrm{R}} = 2\%$ and 2.25% for the first and second modes, respectively.

The circular foundation adopted to explore SSI effects displays the following characteristics: $r = 10\,\mathrm{m}$, $m_0 = 5 \times 10^5\,\mathrm{kg}$ and $I_0 = 7.5 \times 10^6\,\mathrm{kg\,m^2}$. Further, Table 2 summarizes the assumed parameters of the analyzed soils and the stiffness and damping characteristics of the Sway-Rocking model, as taken and re-elaborated from [18].

The spring and dashpot coefficients are obtained from the frequency-dependent impedance function of the soil [1, 20], for the static case (frequency-dependence is removed):

$$k_s = \frac{8\,\mathrm{G}\,r}{2-\nu}, \quad c_s = \frac{4.6}{2-\nu}\,\rho\,V_s\,r^2, \quad k_r = \frac{8\,\mathrm{G}\,r^3}{3\,(1-\nu)}, \quad c_r = \frac{0.4}{1-\nu}\,\rho\,V_s\,r^4 \tag{4}$$

where G, ν, ρ and $V_s = \sqrt{\mathrm{G}/\rho}$ are the shear modulus, Poisson's ratio, mass density and shear-wave velocity of the adopted soil.

Soil type	ν [1]	G [MPa]	ρ [kg/m^3]	V_s [m/s]	k_s [N/m]	k_r [N m]	c_s [N s/m]	c_r [N s m]
Very soft	0.49	4	1600	50	2.12×10^8	2.09×10^{10}	2.44×10^7	6.27×10^8
Soft	0.49	18	1800	100	9.54×10^8	9.41×10^{10}	5.48×10^7	1.41×10^9
Medium	0.48	171	1900	300	9.00×10^9	8.77×10^{11}	1.73×10^8	4.38×10^9
Dense	0.33	600	2400	500	2.87×10^{10}	2.39×10^{12}	3.31×10^8	7.16×10^9

Table 2: Characteristic parameters of the soil/foundation system.

2.3 Modal parameter estimates via the rFDD algorithm

Classical FDD methods [21] are based on the Fourier transform of time-correlated signals, aiming at the evaluation of the Power Spectral Density (PSD) functions of the system responses. Further, a SVD is performed at each line of the frequency spectrum, achieving a modal decomposition of the output PSD matrix. Then, the obtained set of singular values (SV) and singular vectors makes it possible for the estimation of natural frequencies and mode shapes.

The adopted rFDD method, whose original theoretical background is reported in [12, 15], conceptually derives from classical EFDD [21], but considers dedicated refinements and improvements, allowing for better modal estimates, especially at seismic input and concomitant heavy damping. Salient features of the present rFDD algorithm are the following:

- Post-processing of the auto- and cross-correlation matrix, helping in removing possible troubles related to weakly- or non-stationary data;
- Integrated PSD computation, implementing simultaneously both Wiener-Khinchin and Welch's modified periodogram methods;
- Iterative loop and optimization algorithm for effective modal damping ratio estimates;
- Estimation of modal parameters by operating on different SVs and on their composition, without the need of Blind Source Separation methods;
- Specific data filtering applied to the input signals before the identification procedure;
- Inner procedure for the enhancement of the frequency resolution, without the need of higher frequency sampling;
- Combined use of different Modal Assurance Criterion (MAC) indexes for modal validation purposes.

Finally, the rFDD algorithm has been extended to obtain an OMAX technique, towards the identification of fixed-base modal parameters and SSI effects, as shown in the following sections. There, the results arising from the application of the rFDD-OMAX algorithm to the numerical models are presented, focusing specifically on the evaluation of SSI effects and on their implications on the targeted modal identification.

3 RESULTS FROM rFDD MODAL IDENTIFICATION

Taking El Centro earthquake as base excitation, the dynamic analyses have been performed with the present rFDD algorithm, using time series lengths of $400\,\mathrm{s}$ and frequency resolution of $0.0025\,\mathrm{Hz}$. In this first step, flexible-base modal parameters have been estimated by using only storey accelerations (5 channels). In the following section, also the sway and rocking accelerations are considered, by applying the OMAX conditions for SSI identification (7 channels).

Considering flexible-base conditions, every soil-case takes different target parameters. For the sake of compactness, only the reference modal frequencies of the structural system are reported here in Table 3.

Mode, f_n [Hz]	1	2	3	4	5	*6*	*7*
Very-soft soil	0.8002	2.2035	3.3550	4.1185	5.1056	*6.7280*	*9.2036*
Soft soil	1.0169	2.4687	3.8872	5.4386	7.4337	*7.8733*	*11.159*
Medium soil	1.1004	2.5499	4.0301	5.6424	8.0882	*22.393*	*28.124*
Dense soil	1.1076	2.5578	4.0416	5.6579	8.1204	*36.773*	*49.567*
Fixed-base model	1.1115	2.5601	4.0570	5.6650	8.1345	–	–

Table 3: Targeted natural frequencies of the five-storey SR frames at variable soil properties.

Results on the achieved modal estimates are reported in Figs. 2-4, for mass-proportional (ζ_{M}) and Rayleigh damping (ζ_{R}), in terms of deviations of the estimated natural frequencies and damping ratios from the target parameters, and of MAC indexes for the estimated mode shapes. Detailed analyses and results, considering further structures and earthquakes, are going to be reported elsewhere [16].

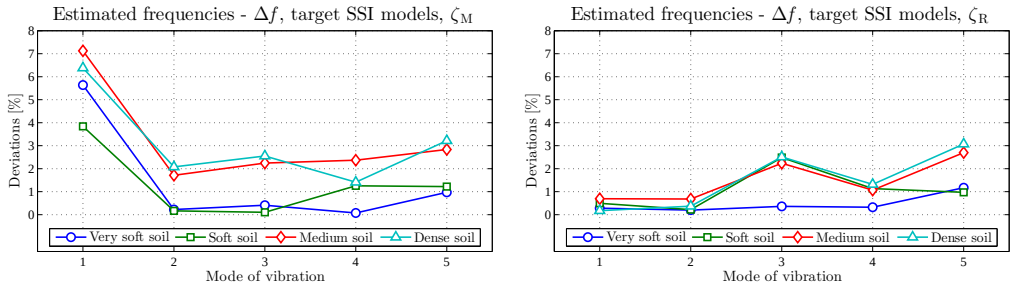


Figure 2: Deviations of estimated frequencies for the flexible-base models.

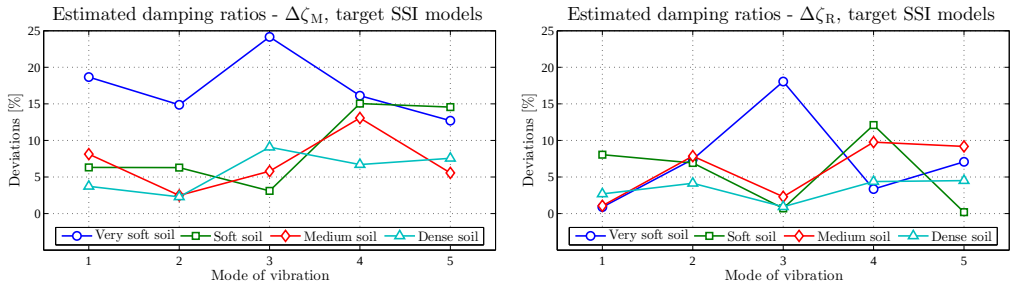


Figure 3: Deviations of estimated modal damping ratios for the flexible-base models.

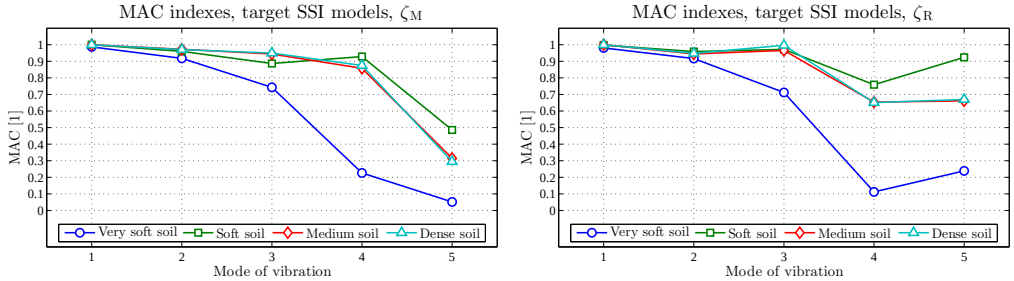


Figure 4: MAC calculated between estimated and target flexible-base mode shapes.

The estimated frequencies show deviations that are always below 4%, except for the first modes of the ζ_{M} cases, where deviations increase up to 7%, due to the related heavy damping (10%). MAC values are always higher than 0.9 for the first three modes, except for the very-soft case, where the tough soil conditions make it harder for the correct mode shape detection. In fact, only the last modes show rather inaccurate values for this case. Finally, the estimated modal damping ratios display suitable deviations, at around 10%, for all the cases. Again, slightly larger deviations are recorded only for the very-soft case, though looking still acceptable in engineering terms. In conclusion, all the obtained results confirm the effectiveness of the developed rFDD algorithm for the detection of flexible-base modal parameters.

4 OMAX EVALUATION OF SSI EFFECTS

The evaluation of SSI effects operates in an OMAX environment [17], as described and analyzed in [16]. The free-field and foundation (Sway and Rocking) recordings (2 signals) are processed jointly with the output-only structural responses of the floors (5 signals), by the present rFDD algorithm. The tools adopted for SSI detection are taken from works [3, 5] and rely on two different approaches, as detailed in the two subsections below.

4.1 Identification of SSI conditions

Specifically, from the recordings of the foundation and of the upper storey accelerations, a first immediate procedure refers to the extraction of the fixed-base building and of the foundation natural frequencies. This is possible since the ratio of the Fourier amplitude spectra between storey and foundation accelerations allows for the identification of the fixed-base building natural frequencies [3]. Starting from:

$$|\mathrm{R}| = \frac{|\mathcal{H}_{b,i}|}{|\mathcal{H}_{f,k}|} = \frac{|\mathscr{F}\{\ddot{x}_{b,i}\}|}{|\mathscr{F}\{\ddot{x}_{f,k}\}|} \tag{5}$$

where $|\mathrm{R}|$ is the absolute value (or amplitude) of the ratio of the system Transfer Functions (TF), $|\mathcal{H}_{b,i}|$ and $|\mathcal{H}_{f,k}|$ are the building and foundation TF amplitudes (referred to the selected $x_{b,i}$ and $x_{f,k}$ building and foundation DOFs), $\mathscr{F}$ represents Fourier transform and $\ddot{x}_{b,i}$, $\ddot{x}_{f,k}$ are the accelerations of the selected DOFs. In the present work, the selected DOFs from which acceleration signals are considered are the top-storey displacement and the foundation sway. In Fig. 5 a clear representation of Fourier transform and TF modulus can be appreciated, by taking mass proportional damping (ζ_{M}), for the very-soft soil and for the fixed-base cases.

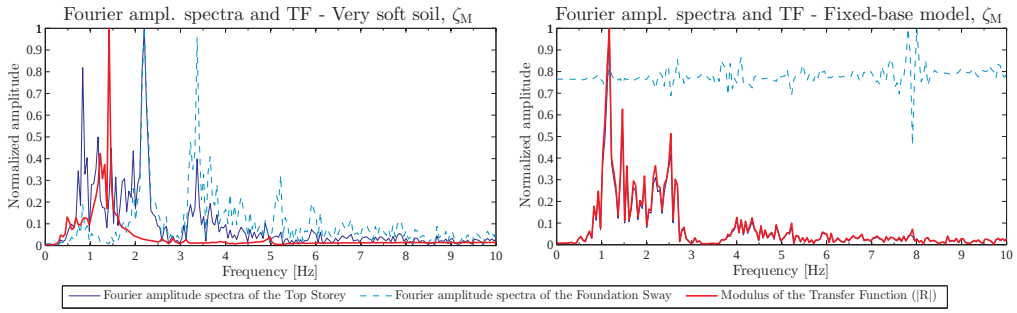


Figure 5: Fourier amplitude spectra of the Top-storey and Foundation-Sway and their Ratio ($|\mathrm{R}|$) for the very-soft soil and for the fixed-base cases, with ζ_{M} damping.

It is demonstrated [3] that $|\mathrm{R}|$ is not influenced by the dynamic characteristics of the foundation, and it always displays a peak at or near the fundamental frequency of the fixed-base building. The coupling between building and foundation is present in the TF, which is a complex-valued quantity. Then, this coupling alters the phase of the TF, but not its amplitude. In fact, this is feasible by observing the curves represented in Fig. 5. For the fixed-base model, the two Fourier amplitudes and the modulus of the TF clearly mark the same frequency, that is the fundamental frequency of this case. For the very-soft soil model, instead, the fundamental frequencies of the three curves are clearly decoupled, suggesting the presence of SSI effects. This feature is also confirmed by the results for all the remaining flexible-base models, not reported here, proving the effectiveness of the present methodology.

4.2 Empirical method for the estimation of SSI effects

A second approach belongs to a simplified empirical method for assessing seismic SSI effects on ordinary shear-type buildings. The analyzed structures, by using the estimated parameters from the previous identification on flexible-base models (Section 3), are then modeled as an equivalent single degree of freedom (SDOF) system [5]. This is developed for each mode of vibration, in order to apply a simple analytical and non-dimensional relationship for the estimation of seismic SSI effects, in terms of modified period (and attached natural frequency) [5].

From this method, the statistical model describing the relationship between the fixed-base (unknown) and the flexible-base (known, estimated) periods, T_i and $\tilde{T}_i$, respectively, for the i^{th} mode of vibration, may be deduced as [5]:

$$y_i = \frac{\tilde{T}_i}{T_i} = 1 + 0.7698 \left(\frac{h_{eq,i}}{T_i\, V_s}\right)^{1.663} \left(\frac{r}{H_{dep}}\right)^{-0.1359} \left(\frac{h_{eq,i}}{r}\right)^{0.8443} \tag{6}$$

where $h_{eq,i} = (\mathbf{H}^{\mathrm{T}}\mathbf{M}\hat{\boldsymbol{\phi}})/(\mathbf{r}^{\mathrm{T}}\mathbf{M}\hat{\boldsymbol{\phi}})$ is the equivalent height of the SDOF system for each considered mode, $\hat{\boldsymbol{\phi}}$ the related mode shape estimate, V_s the shear-wave velocity, r the radius of the foundation and H_{dep} the depth assumed for the bedrock, here taken equal to $50\,\mathrm{m}$. The statistical model y_i in Eq. (6) provides a frequency correction, which applied in an inverse way to each estimated flexible-base frequency $\tilde{f}_i$, allows for the estimation of the original fixed-base ones. The latter may be directly related to ambient vibration conditions, which jointly to the flexible-base characteristics (seismic SSI effects) of the analyzed structures, aims at a complete determination of their dynamic behavior.

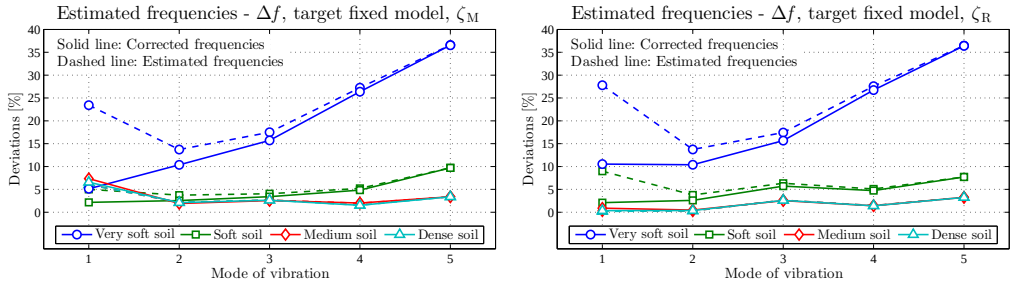


Figure 6: Deviations of the estimated (flexible-base) and of the corrected (fixed-base) frequencies with respect to the targets calculated from the fixed-base model.

Fig. 6 represents the deviations of the estimated (flexible-base) and of the corrected (fixed-base) frequencies, with respect to the target frequencies of the fixed-base model. It is clearly

visible that the deviations, especially for the first modes, take significant benefit from the application of this correction, aiming at a closer representation of the fixed-base conditions and also of the SSI effects read on the structure.

5 CONCLUSIONS

The present work has outlined some preliminary results towards the use of a rFDD-OMAX algorithm for the determination of flexible- and fixed-base modal properties of buildings subjected to SSI effects. Also, seismic input and heavy-damping cases have been considered, getting closer to real earthquake engineering applications. A five-storey SR model has been analyzed, by taking El Centro earthquake as benchmark excitation at the base of the bedrock and two types of damping models for the superstructure.

The effectiveness of the achieved results marks the validity of the present methodology, standing from the goodness of the estimated natural frequencies, modal damping ratios and mode shapes, for both fixed- and flexible-base conditions. This proves that the present rFDD technique can be used for an up-to-date detection of building modal properties in the earthquake engineering range, considering SSI effects.

Summarizing main outcomes and results, the following salient issues may be briefly outlined:

- The integrated approach for PSD matrix computation leads to fundamental support, since the correct modal peak individuation may become very difficult under the presence of SSI effects;
- The estimation of modal damping ratios takes significant advantage from the devised iterative loop and optimization algorithm for the modal damping ratio estimates;
- The enhancement of the frequency resolution appears to be a fundamental step towards achieving reliable modal parameter estimates;
- The OMAX condition belongs to the joint use of output-only response signals and free-field, foundation and/or downhole acquisitions;
- The detection and quantification of SSI effects with the present rFDD-OMAX technique appears quite challenging in the dedicated literature;
- Additional analyses, numerical results and theoretical explanations and investigations are under target, in terms of both applicability of the present rFDD identification technique in the outlined structural context and readability of SSI effects through it. Further output is currently scheduled in [16].

Acknowledgements
The Authors would like to acknowledge public research support from *"Fondi di Ricerca d'Ateneo ex 60%"* and a ministerial doctoral grant and funds at the ISA Doctoral School, University of Bergamo, Department of Engineering and Applied Sciences (Dalmine).

REFERENCES

[1] J.P. Wolf, *Dynamic Soil–Structure Interaction*. Prentice-Hall, Englewood Cliffs, New Jersey, 1985.

[2] S.L. Kramer, *Geotechnical Earthquake Engineering*. Prentice-Hall, Upper Saddle River, New Jersey, 1996.

[3] E. Safak, Detection and identification of soil–structure interaction in buildings from vibration recordings. *Journal of Structural Engineering*, **121**(5), 899–906, 1995.

[4] A.K. Chopra and J.A. Gutierrez, Earthquake response analysis of multistory buildings including foundation interaction. *Earthquake Engineering and Structural Dynamics*, **3** (1), 65–77, 1974.

[5] S. Renzi, C. Madiai and G. Vannucchi, A simplified empirical method for assessing seismic soil-structure interaction effects on ordinary shear-type buildings. *Soil Dynamics and Earthquake Engineering*, **55**, 100–107, 2013.

[6] J.P. Stewart and G. Fenves, System identification for evaluating soil–structure interaction effects in buildings from strong motion recordings. *Earthquake Engineering and Structural Dynamics*, **27**(8), 869–885, 1998.

[7] M.D. Trifunac, S.S. Ivanovic and M.I. Todorovska, Apparent periods of a building. I: Fourier analysis. *Journal of Structural Engineering*, **127**(5), 517–526, 2001.

[8] J.S. Choi, J.S. Lee and C.B. Yun, Identification of the soil-structure interaction system using earthquake response data. *Journal of Engineering Mechanics*, **130**(7), 753–761, 2004.

[9] J.E. Luco, M.D. Trifunac and H.L. Long, Isolation of soil-structure interaction effects by full-scale forced vibration tests. *Earthquake Engineering and Structural Dynamics*, **116**(1), 1–21, 1988.

[10] S. Ghahari, F. Abazarsa, M. Ghannad and E. Taciroglu, Response-only modal identification of structures using strong motion data. *Earthquake Engineering and Structural Dynamics*, **42**(11), 1221–1242, 2013.

[11] S. Ghahari, M. Ghannad and E. Taciroglu, Blind identification of soil–structure systems. *Soil Dynamics and Earthquake Engineering*, **45**, 56–69, 2013.

[12] F. Pioldi, R. Ferrari and E. Rizzi, Output-only modal dynamic identification of frames by a refined FDD algorithm at seismic input and high damping, *Submitted for publication*, 2014.

[13] F. Pioldi, R. Ferrari and E. Rizzi, A refined FDD algorithm for Operational Modal Analysis of buildings under earthquake loading. P. Sas, D. Moens and H. Denayer Eds. *Proceedings of the 26th International Conference on Noise and Vibration Engineering (ISMA2014)*, Leuven, Belgium, 15-17 September 2014, 3353–3368, 2014.

[14] F. Pioldi, R. Ferrari and E. Rizzi, Earthquake FDD modal identification of current building properties from real strong motion structural response signals. *Submitted for publication*, 2014.

[15] F. Pioldi, R. Ferrari and E. Rizzi, Earthquake structural modal estimates of multi-storey frames by a refined FDD algorithm. *Submitted for publication*, 2015.

[16] F. Pioldi and E. Rizzi, Refined FDD Modal identification from earthquake response data with evaluation of Soil-Structure Interaction effects. *In preparation*, 2015.

[17] P. Guillaume, T. De Troyer, C. Devriendt, and G. De Sitter, OMAX: Operational modal analysis in presence of eXogenous inputs. T. Proulx Ed. *Proceedings of the 25th International Modal Analysis Conference (IMAC-XXV)*, Orlando, Florida, 19-22 February 2007.

[18] M.Y. Liu, W.L. Chiang, J.H. Hwang and C.R. Chu, Wind-induced vibration of high-rise building with tuned mass damper including soil–structure interaction. *Journal of Wind Engineering and Industrial Aerodynamics*, **96**(6), 1092–1102, 2008.

[19] J. Salvi, F. Pioldi and E. Rizzi, Effectiveness of seismic-tuned passive tuned mass dampers accounting for soil-structure interaction. *Proceedings of the International Conference on Engineering Vibration (ICoEV)*, Ljubljana, Slovenia, 7-10 September 2015.

[20] A. Pais and E. Kausel, Approximate formulas for dynamic stiffnesses of rigid foundations. *Soil Dynamics and Earthquake Engineering*, **7**(4), 213–227, 1988.

[21] R. Brincker, L. Zhang and P. Andersen, Modal identification of output-only systems using Frequency Domain Decomposition. *Smart Materials and Structures*, **10**(3), 441–445, 2001.

International Conference on Engineering Vibration
Ljubljana, Slovenia, 7-10 September 2015

ASSESSMENT OF DAMPING PROPERTIES OF LARGE 2-STROKE MARINE DIESEL ENGINES

Thomas Secall Wimmel*[1], Dominic Müller [2], Jürg Meier[3]

[1]Winterthur Gas & Diesel Ltd. (former Wärtsilä Switzerland Ltd.)
thomas.secallwimmel@wingd.com

[2]Zürcher Hochschule für Angewandte Wissenschaften
dominic.mueller@zhaw.ch

[3]Zürcher Hochschule für Angewandte Wissenschaften
juerg.meier@zhaw.ch

Keywords: Modal Damping Ratio, Eigenfrequency, Mode Shape, Reciprocating Engine, Vibration Measurement, Vibration Simulation.

Abstract. *When simulating the vibration behaviour of large 2-stroke marine diesel engines the damping properties are an important parameter to be considered. Simulations only allow determining realistic vibration amplitudes if the engine's damping characteristic is known. Modal damping ratios of reciprocating engines vary depending on which parts of the engine interact during oscillation and on how energy is dissipated while vibrating. Therefore different damping ratios can be expected for different engine mode shapes.*

For determining typical modal damping ratios of a diesel engine a methodology for an automated analysis of vibration measurement data was developed: After identifying N resonance peaks in a measured vibration spectrum a spectral curve corresponding to a simple mass-spring-damper system with N degrees of freedom is automatically fitted onto the measured curve by parameter optimization. At the end of this iterative process the damping properties of the substituting mass-spring-damper-system, whose curve adjusts most precisely to the measured spectrum, are attributed to the measured resonances. In addition to determining modal damping ratios and eigenfrequencies the procedure allows separating overlapping resonance peaks.

The analysis process was applied on vibration measurement results of a series of different marine diesel engines and characteristic modal damping ratios could be determined for the engine's principal mode shapes. Considering the determined modal damping properties when performing forced response simulations of the engine by modal superposition in the frequency domain allowed to achieve a higher accuracy in the calculated vibration amplitudes.

1 NUMERICAL VIBRATION ASSESSMENT ON LARGE 2-STROKE MARINE ENGINES

Prototyping of large 2-stroke marine engines is almost impossible due to their large dimensions (Figure 1). Due to the engine's extreme manufacturing costs and time only minor changes are allowed on the machine after the first unit is built. Therefore simulation plays an important role in the engine's design process.

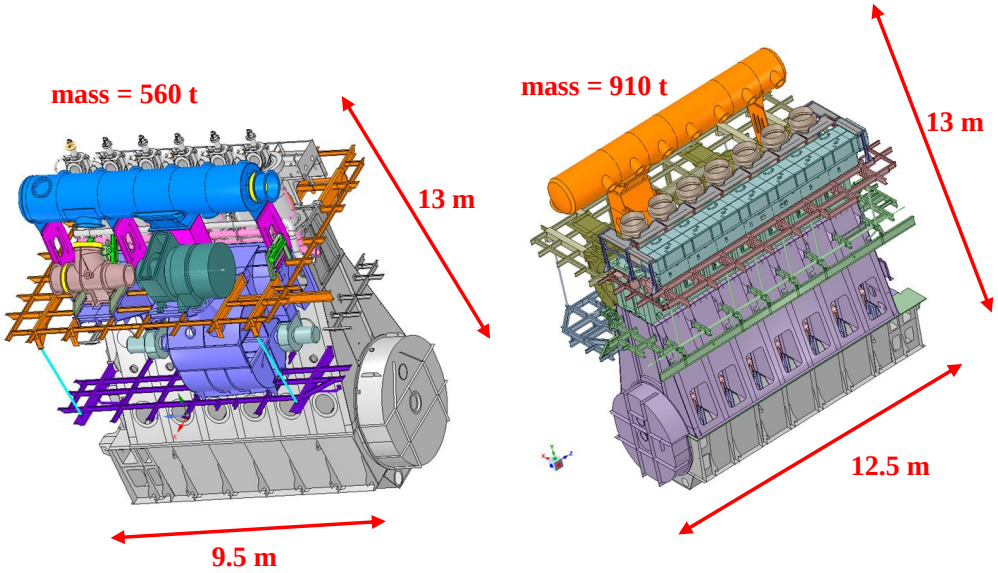


Figure 1: Approximate dimensions of a Wärtsilä 6- (left) and 7-cylinder 2-stroke engine (right) for the propulsion of large cargo vessels.

For assuring the engine's vibration safety a numerical modal analysis and a harmonic response simulation are carried out by means of finite element analysis (FE) [1].

For the modal analysis the equation of motion for an undamped system without excitation is considered:

$$\underline{M} \cdot \ddot{\vec{x}} + \underline{K} \cdot \vec{x} = \vec{0} \tag{1}$$

In this expression $\underline{M}$ is the mass matrix, $\underline{K}$ the stiffness matrix and $\vec{x}$ the position vector. By pre-multiplication with the inverse of the mass matrix $\underline{M}^{-1}$ the equation can be reformulated:

$$\underline{I} \cdot \ddot{\vec{x}} + \underline{A} \cdot \vec{x} = \vec{0} \tag{2}$$

Where $\underline{I}$ is the identity matrix and

$$\underline{A} = \underline{M}^{-1} \cdot \underline{K} \tag{3}$$

This differential equation can be solved by assuming the following solution:

$$\vec{x} = \vec{X} \cdot e^{i\omega t} \tag{4}$$

With Eq. (4) and Eq. (2) the following eigenvalue problem can be formulated:

$$\left[\underline{A} - \lambda_j \cdot \underline{I}\right] \cdot \vec{X}_j = \vec{0} \tag{5}$$

The relation between the eigenvalues λ_j, the angular eigenfrequency ω_j and the eigenfrequency f_j is:

$$\lambda_j = \omega_j{}^2 = 4 \cdot \pi^2 \cdot f_j{}^2 \tag{6}$$

The eigenvalue problem is solved iteratively during the modal analysis by application of the Lanczos solver. With the calculated eigenvectors $\vec{X}_j$ the procedure reveals the mode shapes that the engine structure can adopt while it vibrates and allows to understand the vibration mechanism (Figure 2). Eigenvectors permit to identify the points on the engine on which to apply a design modification for avoiding that a determined mode shape occurs. Additionally the modal analysis supplies the eigenfrequencies ω_j which help to pre-estimate if a mode shape can be excited on a determined engine speed range. [2]

But a numerical modal analysis does not supply any information about the excitability of mode shapes during engine service. Therefore a harmonic response analysis by modal superposition based on the eigenvectors that were determined in a previously performed modal analysis is carried out. [4]-[7]

The base for this analysis is the modal matrix in which the calculated eigenvectors are arranged columnwise:

$$\underline{P} = \left[\vec{X}_1, \vec{X}_2, ..., \vec{X}_N\right] \tag{7}$$

In [3] the orthogonality of the eigenvectors $\underline{X}_j$ with respect to the mass matrix $\underline{M}$ and the stiffness matrix $\underline{K}$ is demonstrated. These properties imply:

$$\underline{P}^T \cdot \underline{M} \cdot \underline{P} = \begin{bmatrix} M_1 & 0 & ... & 0 \\ 0 & M_2 & ... & 0 \\ ... & ... & ... & ... \\ 0 & 0 & ... & M_N \end{bmatrix} \quad \text{where the generalized mass is} \quad M_j = \vec{X}_j{}^T \cdot \underline{M} \cdot \vec{X}_j$$

$$\underline{P}^T \cdot \underline{K} \cdot \underline{P} = \begin{bmatrix} K_1 & 0 & ... & 0 \\ 0 & K_2 & ... & 0 \\ ... & ... & ... & ... \\ 0 & 0 & ... & K_N \end{bmatrix} \quad \text{where the generalized stiffness is} \quad K_j = \vec{X}_j{}^T \cdot \underline{K} \cdot \vec{X}_j \tag{8}$$

If additionally the modal matrix is mass normalized by dividing each eigenvector $\vec{X}_j$ in $\underline{P}$ by the square root of the generalized mass M_j the resulting weighed modal matrix $\underline{\tilde{P}}$ has the following properties [3]:

$$\underline{\tilde{P}}^T \cdot \underline{M} \cdot \underline{\tilde{P}} = \underline{I}$$
$$\underline{\tilde{P}}^T \cdot \underline{K} \cdot \underline{\tilde{P}} = \begin{bmatrix} \lambda_1 & 0 & ... & 0 \\ 0 & \lambda_2 & ... & 0 \\ ... & ... & ... & ... \\ 0 & 0 & ... & \lambda_N \end{bmatrix} = \underline{\Lambda} \tag{9}$$

By means of harmonic response simulations the engine structure's answer to stimulating gas and mass forces $\vec{f}(t)$ is determined. Also the damping properties (described by matrix $\underline{C}$) determine the structure's response amplitude. Therefore the equation of motion (1) has to be reformulated:

$$\underline{M} \cdot \ddot{\vec{x}} + \underline{C} \cdot \dot{\vec{x}} + \underline{K} \cdot \vec{x} = \vec{f}(t) \tag{10}$$

The orthogonality is usually not given with respect to the damping matrix $\underline{C}$. Therefore Raileigh damping is assumed, so that the damping matrix is expressed by a mass and by a stiffness proportional term with the constants α and β:

$$\underline{C} = \alpha \cdot \underline{M} + \beta \cdot \underline{K} \tag{11}$$

Additionally a coordinate transformation into a modal coordinate system with position vector $\vec{y}$ is performed by expressing $\vec{x}$ as a linear combination of the eigenvectors $\vec{X}_i$:

$$\vec{x} = \underline{\tilde{P}} \cdot \vec{y} \tag{12}$$

With Eqs. (11) and (12) the equation of motion (10) can be rewritten as:

$$\underline{M} \cdot \underline{\tilde{P}} \cdot \ddot{\vec{y}} + \left(\alpha \cdot \underline{M} \cdot \underline{\tilde{P}} + \beta \cdot \underline{K} \cdot \underline{\tilde{P}}\right) \cdot \dot{\vec{y}} + \underline{K} \cdot \underline{\tilde{P}} \cdot \vec{y} = \vec{f}(t) \tag{13}$$

After pre-multiplying Eq. (13) with the transposed mass normalized modal matrix $\underline{\tilde{P}}^T$ and by considering the properties that are expressed by Eq. (9) the following expression is obtained:

$$\ddot{\vec{y}} + \left(\alpha \cdot \underline{I} + \beta \cdot \underline{\Lambda}\right) \cdot \dot{\vec{y}} + \underline{\Lambda} \cdot \vec{y} = \underline{\tilde{P}}^T \cdot \vec{f}(t) \tag{14}$$

Eq. 14 is equivalent with the following set of *N* (number of degrees of freedom of the simulated system) uncoupled differential equations:

$$\ddot{y}_j + \left(\alpha + \beta \cdot \omega_j{}^2\right) \cdot \dot{y}_j + \omega_j{}^2 \cdot y_j = \sum_{k=1}^{N} \tilde{P}_{kj} \cdot f_k(t) = \tilde{\vec{X}}_j{}^T \cdot \vec{f}(t) \quad \text{with} \quad j \in [1, N] \tag{15}$$

Where $\tilde{\vec{X}}$ is the mass normalized eigenvector. The modal damping ξ_j is defined by the following equation:

$$2 \cdot \xi_j \cdot \omega_j = \alpha + \beta \cdot \omega_j{}^2 \tag{16}$$

With Eq. (16) the set of differential equations (15) can be rewritten as:

$$\ddot{y}_j + 2 \cdot \xi_j \cdot \omega_j \cdot \dot{y}_j + \omega_j{}^2 \cdot y_j = \sum_{k=1}^{N} \tilde{P}_{kj} \cdot f_k(t) = \tilde{\vec{X}}_j{}^T \cdot \vec{f}(t) \quad \text{with} \quad j \in [1, N] \tag{17}$$

Equation set (17) is the base for the harmonic response analysis. The excitation forces $\vec{f}(t)$ correspond to the gas and mass forces acting on the engine structure [8]. The eigenvectors $\vec{X}_j$ or the modal matrix $\underline{\tilde{P}}$ respectively and the eigenfrequencies ω_j are determined by means of the previously run modal analysis. The values of the modal damping ratios ξ_j were experience values up to now.

For a large number of degrees of freedom *N* solving the equation system (17) can be a cost intensive computation. But, if the number of considered eigenvectors in the modal matrix $\underline{P}$ in equation (12) is limited to only a small subset of modal vectors this method becomes a very powerful procedure for determining the dynamic properties of a vibrating system. When putting into practice this technique only those mode shapes that can be excited by the stimulating forces $\vec{f}(t)$ are considered. Mode shapes with a considerably larger eigenfrequency ω_i than the largest excitation frequency are omitted in the modal superposition. In case of the simulated combustion engines the experience showed that considering 200 mode shapes is sufficient for obtaining acceptable results.

For the analysed reciprocating combustion engines the equation system (17) is computed by using a commercial FE-solver. At the end of the calculation the solver performs the transformation from modal coordinates *y* back to real world coordinates *x* by application of expression (12).

Using an appropriate modal damping ratio ξ_j in the simulation model is important for reproducing vibration amplitudes correctly. Damping properties vary among mode shapes because for each mode different engine parts interact with each other. Figure 2 shows the example of an H-mode (transversal bending), where most deformation occurs in the region of the engine bed. In case of the X-mode (torsion around the vertical axis) the main deformation occurs on the engine column and on the cylinder jacket. Therefore the energy that is dissipated by friction among the interacting engine regions is also unequal for different mode shapes, which explains that the modal damping ratio varies for different vibration shapes.

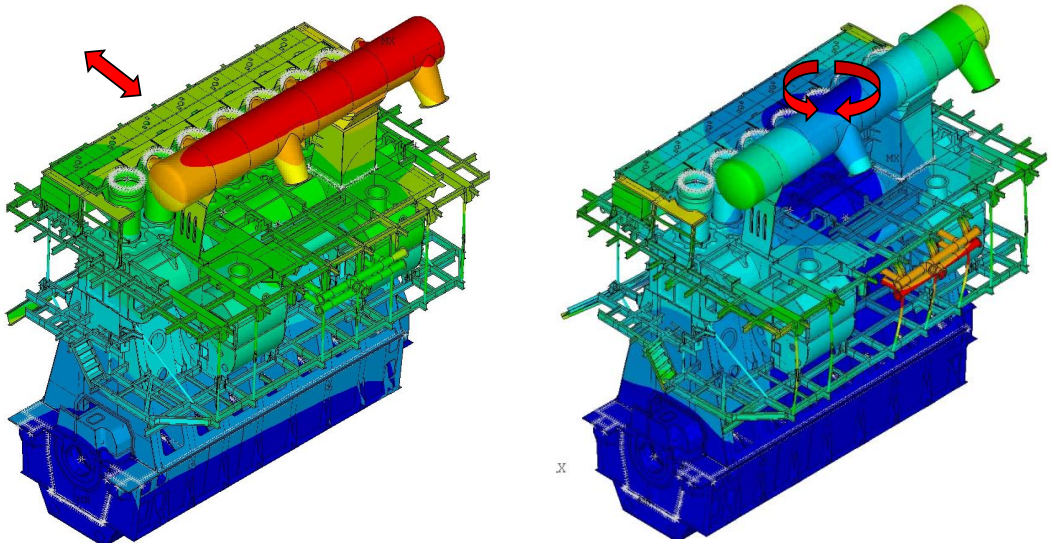


Figure 2: H-mode (transversal bending) and X-mode (torsion around the vertical axis) of a large marine engine

2 DEVELOPMENT OF A METHODOLOGY FOR DETERMINING DAMPING PROPERTIES FROM VIBRATION MEASUREMENT RESULTS

Up to now the value of the modal damping ratio ξ_j was always uncertain and had to be estimated. Therefore vibration amplitudes that were obtained by simulation often differed from the magnitudes that were obtained by measurement. For gaining experience regarding damping properties of large 2-stroke marine engines a methodology was developed for determining modal damping ratios from measured vibration spectra [9] and [10]. In the present case a modal based system identification method is most appropriate. For a measured response spectrum with N resonance peaks a substitutory spring-mass-damper-system with N degrees of freedom, whose vibration properties are equivalent with those of the measured structure, is determined by application of a heuristic algorithm [11].

The following approach functions are introduced into equation system (17) which corresponds to the equations of motion for a spring-mass-damper system with N degrees of freedom in modal coordinates:

$$y_j = Y_j \cdot e^{i\cdot(\Omega\cdot t-\phi)} = \left(Y_j \cdot e^{-i\cdot\phi}\right)\cdot e^{i\cdot\Omega\cdot t}$$
$$\vec{f}(t) = \vec{F}\cdot e^{i\cdot\Omega\cdot t} \tag{18}$$

In Eq. (18) ϕ is the phase angle between excitation and response and Ω the stimulation frequency. After application of the approach the equation system (17) transforms into:

$$Y_j = \frac{e^{i\cdot\phi}}{{\omega_j}^2 - \Omega^2 + 2\cdot i\cdot\xi_j\cdot\omega_j\cdot\Omega}\cdot \tilde{\vec{X}}_j^{\,T}\cdot\vec{F} \tag{19}$$

Being Eq. 19 equivalent to:

$$Y_j = \frac{\tilde{\tilde{X}}_j^{\,T} \cdot \vec{F}}{\sqrt{\left(\omega_j{}^2 - \Omega^2\right)^2 + \left(2 \cdot \xi_j \cdot \omega_j \cdot \Omega\right)^2}} \cdot e^{i \cdot \left(\phi - arctg \frac{2 \cdot \xi_j \cdot \omega_j \cdot \Omega}{\omega_j{}^2 - \Omega^2}\right)} \tag{20}$$

After transforming Eq. (20) from the modal coordinate system back to real coordinates by application of expression (12) the following expression is obtained:

$$\chi_j = \sum_{k=1}^{N} \frac{\tilde{\tilde{X}}_k^{\,T} \cdot \vec{F} \cdot \tilde{P}_{jk}}{\sqrt{\left(\omega_k{}^2 - \Omega^2\right)^2 + \left(2 \cdot \xi_k \cdot \omega_k \cdot \Omega\right)^2}} \cdot e^{i \cdot \left(\phi - arctg \frac{2 \cdot \xi_k \cdot \omega_k \cdot \Omega}{\omega_k{}^2 - \Omega^2}\right)} \tag{21}$$

It is assumed that a spectrum with N resonance peaks that was obtained with a measurement sensor attains to Eq. (21), which can be simplified as:

$$A = \sum_{k=1}^{N} \frac{Q_k}{\sqrt{\left(\omega_k{}^2 - \Omega^2\right)^2 + \left(2 \cdot \xi_k \cdot \omega_k \cdot \Omega\right)^2}} \cdot e^{i \cdot \left(\phi - arctg \frac{2 \cdot \xi_k \cdot \omega_k \cdot \Omega}{\omega_k{}^2 - \Omega^2}\right)} = \sum_{k=1}^{N} a_k \cdot e^{i \cdot \varphi_k} \tag{22}$$

The amplitudes in the sensor's spectrum should be equivalent with the magnitude of A:

$$|A| = \sqrt{\left(\sum_{k=1}^{N} a_k \cdot \cos(\varphi_k)\right)^2 + \left(\sum_{k=1}^{N} a_k \cdot \sin(\varphi_k)\right)^2} \tag{23}$$

For fitting the curve of the substitutory system into the measured frequency response function the $3 \cdot N$ parameters ω_1, ω_2,..., ω_N, ξ_1, ξ_2,…, ξ_N, Q_1, Q_2,…, Q_N are optimized by the method of the least squares, so that the function $|A|$ adapts best to the sensor's spectrum. The algorithm's target is minimizing the residual function R:

$$R^2 = \sum_{j=1}^{M} w_j \cdot \left(m_j - |A(\omega_1, \omega_2, ..., \omega_N, \xi_1, \xi_2, ..., \xi_N, Q_1, Q_2, ..., Q_N)|\right)^2 \tag{24}$$

Where w_j is a weighing factor that is large in regions of small measurement point density and small in regions where measurement points are very close. m_j are the measured spectrum points.

Figure 3 shows the importance of considering the correct phase relations among the summands $a_k \cdot e^{i \cdot \varphi_k}$ in Eq. (22). If erroneously the frequency response function is built by adding the magnitudes of the summands (dashed curve) amplitudes might be overestimated between 2 overlapping resonance peaks. Due to a phase shift of 180° when trespassing resonances the summands are not in phase anymore. This explains why the phase correct superposition spectrum (green curve) always shows less amplitude between overlapping resonance peaks. With increasing modal damping ratios this effect is more significant because the 180° frequency shift occurs over a larger frequency range.

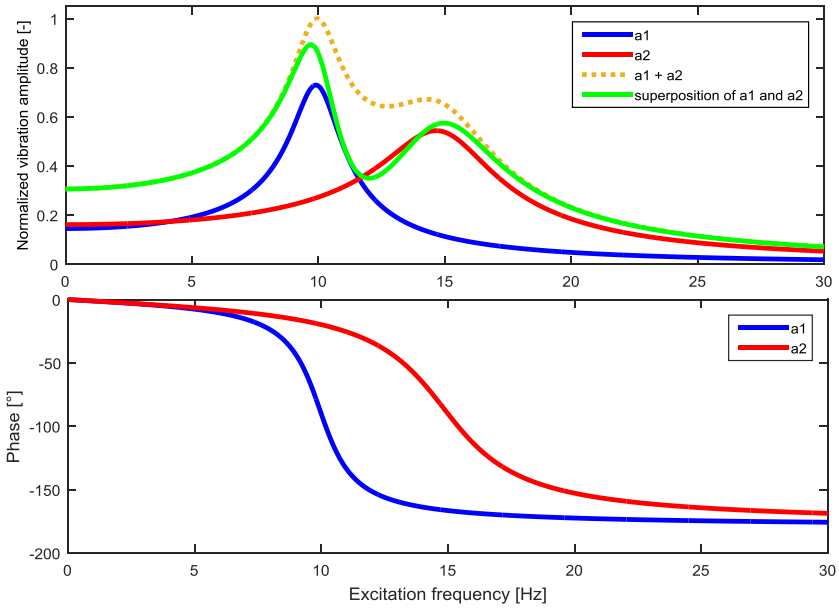


Figure 3: Spectrum for a 2 degree of freedom spring-mass-damper system with eigenfrequencies ω_1=10Hz and ω_2=15Hz and modal damping ratios ξ_1=0.1 and ξ_2=0.15 with amplitude (top) and phase (bottom).

The proposed method for determining modal damping values from measurement data was coded and automatized for efficiently being applied on large 2-stroke engines.

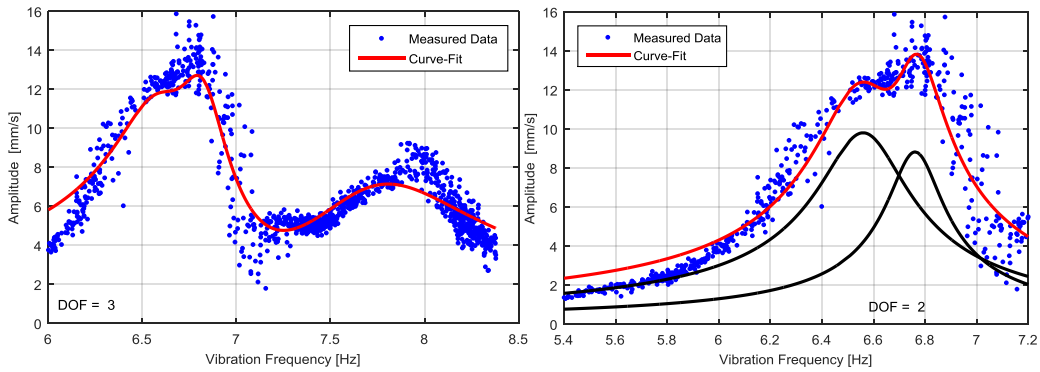


Figure 4: The developed method allows to reproduce the measured spectrum by means of a substitutory spring-mass-damper system and allows to separate overlapping resonance peaks.

Figure 4 demonstrates that the developed tool successfully reproduces the measured spectrum curves. In the shown example (left) a curve with 3 resonance peaks is identified by means of a 3 degree of freedom substitutory spring-mass-damper-system. As output the eigenfrequencies and the damping ratios for this best fitting system are obtained. It can also be seen that overlapping resonance peaks can easily be separated and identified with the procedure. In case of the depicted frequency response function with 2 overlapping resonance peaks (right) the substitutory 2 degree of freedom system allows to visualize the single peaks that compose the spectrum.

3 APPLICATION OF THE METHOD ON MARINE ENGINES

The developed code was applied for determining damping properties of large 2-stroke marine diesel engines from a series of measurement spectra that were registered on different engines. For the analysed reciprocating marine diesel engines a damping ratio ξ between 0.020 and 0.046 could be identified. As expected, the modal damping ratios differ among the 3 main engine mode shapes H-mode (transversal bending), L-mode (longitudinal mode) and the X-mode (torsion around the vertical axis), being the largest ones those for the X-mode.

The obtained values for the engine's damping ratio were used in a harmonic response simulation by modal superposition with a commercial FE-solver (Figure 5). The measured amplitude spectrum for the H-mode of a 6-cylinder engine (blue measurement points) is compared with two calculated frequency response curves. The first one (green curve) was obtained by performing a harmonic response simulation with the lower limit for the modal damping ratio (ξ=0.020) and the other (red curve) with the top border value (ξ=0.046). The satisfactory results show that the measured amplitude is inside the interval that is delimited by the two extreme numerical curves. The eigenfrequency that was obtained by simulation is only approximately 2% lower than the measured one.

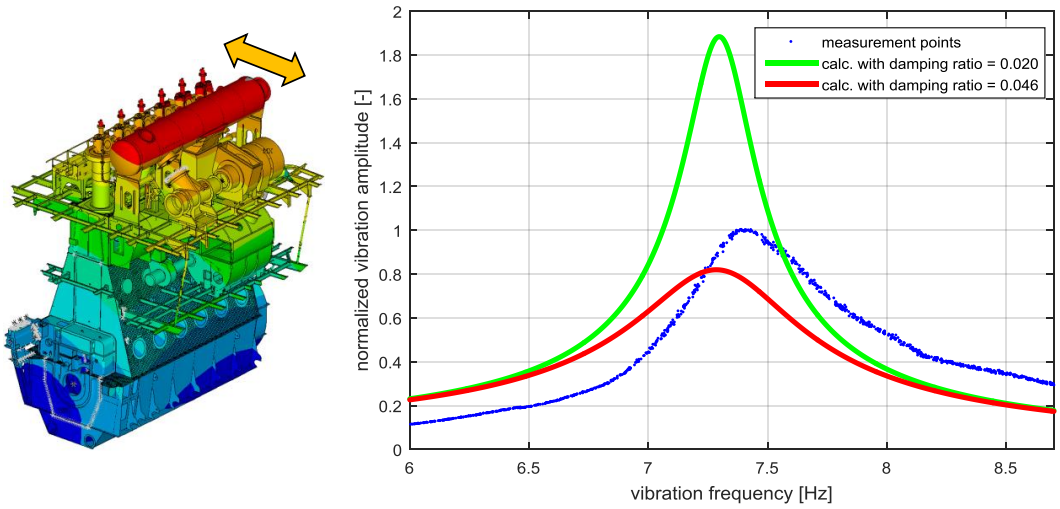


Figure 5: Measured spectrum for the H-mode of a 6-cylinder marine 2-stroke engine and frequency response curves that were obtained numerically by using the determined limit damping ratio values in a harmonic response simulation.

4 CONCLUSIONS

- For vibration assessment of large marine engines a modal analysis and a harmonic response simulation by modal superposition are performed.
- Modal damping has to be known for obtaining correct vibration amplitudes from a harmonic response simulation. Therefore a method to estimate damping properties from measurement data was developed.
- The algorithm allows to identify eigenfrequencies and the modal damping ratio from measurement data of a vibrating system and allows to separate overlapping mode shapes.
- Modal damping ratios for the main engine mode shapes could be determined and tabularized for being used in harmonic response simulations.

REFERENCES

[1] T. Secall Wimmel, *Numerical Vibration Assessment on Large 2-stroke Marine Diesel Engines*. 11th International Conference on Vibration Problems, Lisbon, Portugal, 9-12 September 2013.

[2] C. Pestelli, F. Palloni, L. Bergant and F. Castellani, *Dynamic Properties Assessment and Updating of Large Diesel Ship Engines*, The Thirteenth International Conference on Sound and Vibration, Vienna, Austria, 2-6 July 2006.

[3] W. T. Thomson, *Theory of Vibration With Applications*, Prentice Hall

[4] J. Zhang and J. Han, *CAE process to simulate and optimise engine noise and vibration*, Mechanical Systems and Signal Processing, 20, 1400-1409, 2006

[5] I. Kuninori, S. Nobuaki and K. Kenichi, *Vibration Reduction of Reciprocating Engines*, 7th International Symposium on Marine Engineering, Tokyo, Japan, October 24-28, 2005

[6] H. Tienhaara and H. Mikonaho, *Engine Dynamics and Vibration Control*, Conseil International des Machines a Combustion, Vienna, Austria, 203, 2007

[7] R. Nordrik and H. Solbakken, *Vibration characteristics of a V20 medium speed gas engine. Simulation and measurement*, Conseil International des Machines a Combustion, Bergen, Norway, 51, 2010

[8] W. Schiffer, *Advanced methods for static and dynamic shafting calculations*, ISME International Symposium on Marine Engineering, Tokyo, Japan, 2005

[9] T. Arakawa and K. Yamamoto, *Frequencies and Damping Ratios of a High Rise Building Based on Microtremor Measurement*, 13th World Conference on Earthquake Engineering, Vancouver, B.C., Canada, August 1-6, 2004

[10] J. Butterworth, J. H. Lee and B. Davidson, *Experimental Determination of Modal Damping from Full Scale Testing*, 13th World Conference on Earthquake Engineering, Vancouver, B.C., Canada, August 1-6, 2004

[11] D. Müller, *Vibration Analysis of 2-Stroke Marine Engines*, Master Thesis (Mechanical Engineering), Zürcher Hochschule für Angewadte Wissenschaften, Winterthur, Switzerland, 30.01.2015

International Conference on Engineering Vibration
Ljubljana, Slovenia, 7-10 September 2015

DYNAMIC TESTS FOR THE DESIGN OF A VIBRATION-BASED SHM SYSTEM FOR PROMPT ASSESSMENT OF HEALTH FACILITIES

D. Gargaro[1], **C. Rainieri**[2], **G. Fabbrocino**[3]

[1] Ph.D. Candidate, Di.B.T. Dept., University of Molise, Campobasso, Italy
danilo.gargaro@unimol.it

[2] Post-doctoral researcher, Di.B.T. Dept., University of Molise, Campobasso, Italy
carlo.rainieri@unimol.it

[3] Full Professor, Di.B.T. Dept., University of Molise, Campobasso, Italy
giovanni.fabbrocino@unimol.it

Keywords: Structural Health Monitoring, Health facilities, Operational modal analysis

Abstract. *Health facilities play a primary role in post-earthquake emergency management. They are required to be fully operational after frequent earthquakes and they must ensure life safety and support rescue operations in the case of strong motion.*

A number of structural monitoring programs have been recently issued worldwide in order to quickly assess the health state of health facilities after earthquakes. In particular, the most recent research programs are focusing the attention also on condition assessment of non-structural components, equipment and installations.

This paper describes the dynamic identification tests carried out on one of the buildings of the Main Hospital in Foggia (Southern Italy) in view of design and installation of a permanent vibration-based monitoring system. The building consists of three adjacent structures and it is representative of typical layouts of existing health facilities. The first objective of the tests was the quantitative assessment of the effectiveness of joints separating the different blocks. The obtained results have been also used to define the sensor layout of a continuous vibration-based Structural Health Monitoring system for rapid condition assessment after earthquakes.

1 INTRODUCTION

Life safety and assistance to injured people are the priority after a seismic event. Thus, hospitals play a key role in the post earthquake emergency management. Health facilities are usually very complex systems. They host a large number of functions from health care to administration, and due to their strategic relevance, they must remain fully operational after earthquakes.

Existing hospitals are rarely out of service after an earthquake because of structural damage. Functional breakdown is usually the reason for service interruption [1], as demonstrated also by recent earthquakes in Italy [2]. Thus, an effective protection strategy has to ensure not only that hospitals remain standing in the case of an earthquake, but above all that they remain in service without interruption, in order to accomplish the following tasks [3]:

- Protect the life of patients, visitors and hospital staff;
- Protect the investment in equipment and furnishing;
- Protect the performance of the health facility.

The primary influence of non-structural components, equipment and installations (such as electro-mechanical and medical equipment, tanks and distribution systems, heat ventilation and air conditioning systems) on the performance of health facilities fosters the development of specific analysis and monitoring strategies aimed at promptly assessing their respective conditions. Such an integrated approach to Structural Health Monitoring (SHM) leads to the development of the so-called "smart health facility" (SHF). This can represent an innovative tool to reduce the administrative and organizational vulnerability by increasing the preparedness of the medical staff in the case of an earthquake and supporting the management and maintenance of structural and non-structural components over the structure lifetime. In fact, combining monitoring and early warning strategies can provide additional seismic protection at relatively low cost. Moreover, continuously monitoring the health state and performance of hospitals can support the formulation of disaster mitigation plans and the definition of investment priorities to ensure safety of lives and goods.

Ensuring the resilience of health facilities to seismic events is critical to protect the public investment [4] in specialized personnel and sophisticated and costly equipment, but this is not a trivial task, since functions and resilience of the system as a whole depend also on the ability of inspectors and managers to integrate theoretical evaluations with field measurements and their effective physical interpretation [5, 6]. In the present paper criteria and methods to design a prototype SHF in a seismically prone area are discussed. The results of dynamic identification tests carried out on one of the buildings of the Main Hospital in Foggia (Southern Italy) are presented and critically analyzed in view of design of the permanent vibration-based monitoring system. The main issues in the development of a continuous vibration-based SHM system are illustrated and a sensor layout for continuous vibration-based SHM and rapid condition assessment after earthquakes is proposed. Attention is focused, in particular, on the sustainable implementation of an SHF able to cover the needs of knowledge, storage and monitoring of crucial information and physical data by taking advantage of the most recent developments in sensing, data acquisition and signal processing.

2 STRUCTURAL MONITORING OF HEALTH FACILITIES

A number of hospitals are currently permanently monitored throughout the world. The U.S. Geological Survey, in the framework of the National Strong Motion Project (NSMP; *http://nsmp.wr.usgs.gov/*) and in cooperation with the U.S. Department of Veterans Affairs (VA), has installed seismic monitoring systems on 28 VA hospitals located in seismically ac-

tive regions of the United States, Alaska, and Puerto Rico, collecting data about their response to earthquake shaking [7].

In the last decade the Italian Department of Civil Protection has issued the National Network for seismic monitoring of strategic and relevant structures OSS (Osservatorio Sismico delle Strutture). The seismic response of 149 public structures (45% schools, 21% town hall, 17% hospitals, 17% other buildings), 7 bridges and 1 dam is currently monitored. All these structures are located in areas exposed to high seismic risk [8].

The monitoring systems installed in the USA are based on high performance accelerometers and real-time computer calculations to assess the structural health of each hospital right after an event. The typical architecture of the monitoring systems is illustrated in Figure 1.

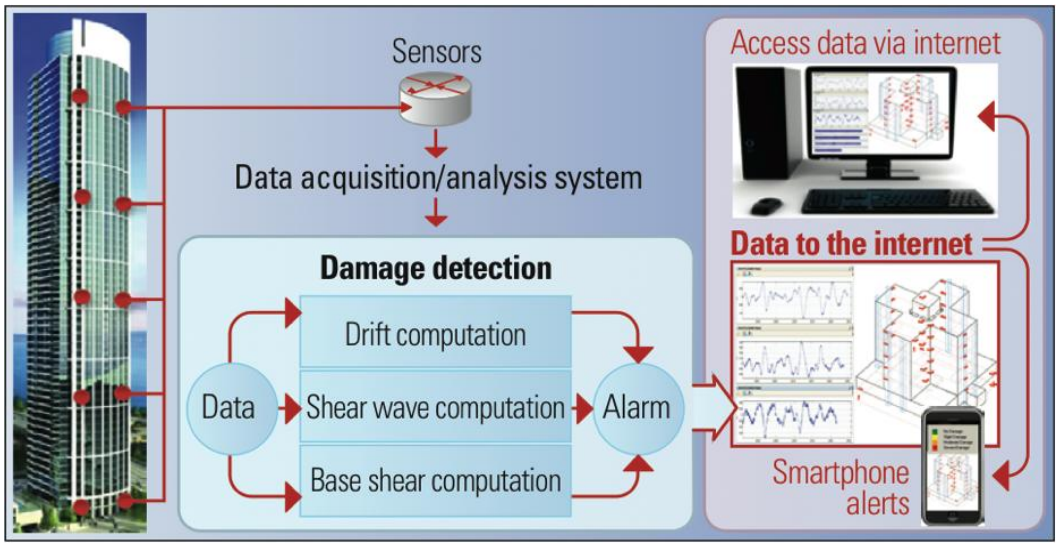


Figure 1: Schematic architecture of a monitoring system for health facilities in the U.S.A.(http://earthquake.usgs.gov/monitoring/).

The number of installed sensors depends on the floor area, the number of stories and the number of blocks. For instance, the main building of the VA medical center in San Diego, California, is monitored by 60 sensors. Sensor locations are defined by estimating where the maximum response of the structure is expected. Every story in each instrumented building is equipped with at least three seismic sensors, horizontally oriented along two orthogonal directions. Each building is also equipped with a triaxial sensor located on the ground floor to records the input motions. The installed instrumentation is sensitive enough to record the earthquake response of the building to small local earthquakes as well as to ambient vibrations. Additional seismic sensors are installed away from the monitored building to record free-field ground shaking [7]. The monitoring systems are designed to provide information about the health status of the structure, swaying and twisting of the building, inter-story drift at each floor level, amount of time seismic waves take to travel from the foundation to the roof.

The monitoring systems installed on the Italian hospitals are also designed to assess the structural health right after a seismic event. They mainly consist of high sensitivity accelerometers and LVDT displacement sensors. The monitoring systems collect and store the acceleration response of the structure when it exceeds 1‰ of the gravity acceleration. The

collected data are transmitted in real-time to the central server in Rome, which analyzes the data and determines the modal parameters of the structure during the seismic event. The estimated modal parameters are finally compared with those estimated from the undamaged structure to detect eventual structural damage.

Each structure belonging to the Italian OSS is monitored by a number of force balance accelerometers ranging from a minimum of 15 to a maximum of 32. The actual number depends on the dimensions and complexity of the structure. Sensor locations are defined by estimating where the maximum response of the structure is expected. A free-field station is always present to measure the seismic input. In many cases the monitored hospitals consists of adjacent structures. Thus, LVDT displacement transducers are also installed to monitor the relative displacements on the top floor [8].

The analysis of the previously described monitoring systems for health facilities highlights that they focus the attention on structural health only. The response of non-structural components, equipment and installations, such as electro-mechanical and medical equipment, tanks and distribution systems, heat ventilation and air conditioning (HVAC) systems, is not monitored. However, the recent earthquakes occurred in Italy and in the rest of the world have remarked the critical role of non-structural components, equipment and installation in ensuring that the hospital remains fully operational after an earthquake. Thus, an effective monitoring system for health facilities cannot neglect the assessment of the performance of those primary components for the functionality of the hospitals.

3 TOWARDS THE DESIGN OF AN SHF: PRELIMINARY DYNAMIC TESTS

This section describes the dynamic identification tests carried out on the building of the Main Hospital in Foggia (Southern Italy) that houses the maternity department (Figure 2). The objective of the test is the definition of an appropriate sensor layout for continuous vibration-based monitoring of the structure.

The building dimensions are 64 m x 13.8 m in plan and 16.20 m in elevation. The building consists of three adjacent reinforced concrete moment frame structures and it is representative of typical layouts of existing facilities. Two blocks host the maternity department, while the third is orthogonal to the others and hosts stairs and elevators. About the first two blocks, the largest one (Figure 2a) covers a rectangular area of 36 m x 13.8 m, while the other (Figure 2b) covers a rectangular area of 28 m x 13.8 m.



(a) (b)

Figure 2: Left (a) and right (b) block of the maternity department at the Main Hospital in Foggia.

Three tests characterized by different sensor layouts have been carried out in order to quantitatively assess the effectiveness of the joints separating the different blocks. The first two tests analyzed the structural response of the left and right block separately. The third test, instead, was aimed at assessing eventual interactions between the two above-mentioned blocks [9], and between those blocks and the orthogonal structure.

In each test 15 piezoelectric accelerometers (Figure 3) have been installed at different levels of the structure and along two orthogonal directions (Figure 4). In particular, in the first two tests, the sensors have been placed at opposite corners of the plan in order to ensure observability of translational as well as torsional modes. The characteristics of the sensors are reported in Table 1. They have been selected in order to ensure high quality measurements in operational conditions.



Figure 3: Piezoelectric sensors.

Sensors	Measurement directions	Sensitivity [V/g]	Full scale range [g]	Resolution [g rms]	Bandwidth [Hz]	Transverse sensitivity
PCB IEPE 393B31	1	10.0	0.5	0.000001	0.1-200	≤5%
PCB IEPE 393B12	1	10.0	0.5	0.000008	0.05-4000	≤7%

Table 1: Sensor characteristics.

Vibration data have been acquired through a customized 24 bit data acquisition recorder based on programmable hardware. Coaxial cables connected the sensors with the measurement system. Cables have been clamped to the structure in order to avoid introduction of

measurement noise by triboelectric effects. Tests have been carried out by simultaneously acquiring data, at a sampling frequency equal to 100 Hz, from the 15 accelerometers. Each record was 3600 s long. The tests did not interfere with the normal use of the structure.

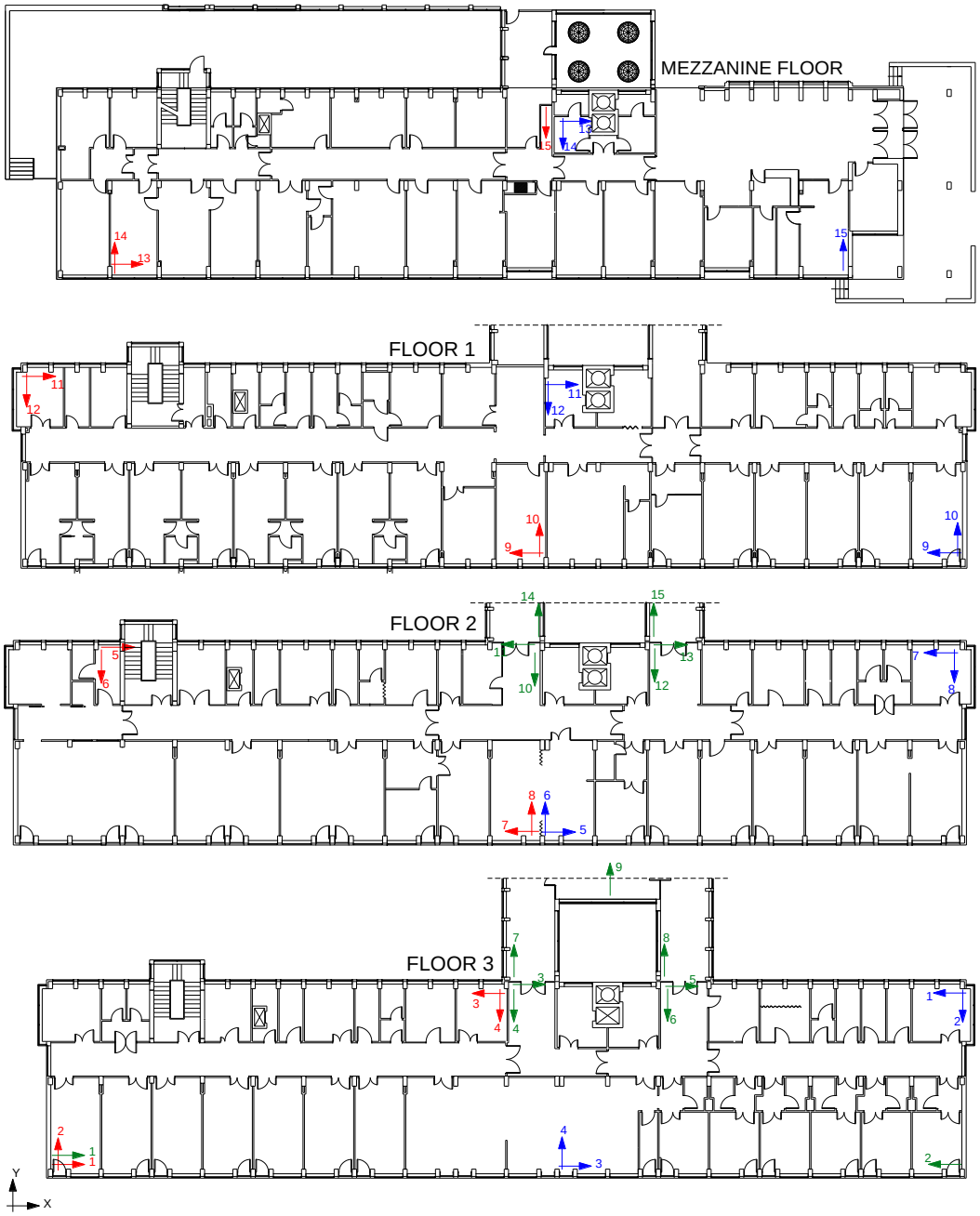


Figure 4: Sensor layouts – test #1 (red arrows), test #2 (blue arrows), test #3 (green arrows).

3.1 Modal identification procedures

Output-only modal parameter estimation has been carried out according to the Covariance Driven Stochastic Subspace Identification (Cov-SSI) [10, 11] and the Frequency Domain Decomposition (FDD) [10, 12, 13] method. The present section briefly reports the basics of the above mentioned procedures.

The FDD is based on the Singular Value Decomposition (SVD) of the output Power Spectral Density (PSD) matrix. As described in the original paper [12], structural resonances are identified from the singular value plots by peak picking; the corresponding singular vectors are good estimates of the corresponding mode shapes.

The SSI method works in time domain and it is based on a state space description of the dynamic problem [11, 15]. In fact, the second order problem, stated by the differential equation of motion, is converted into two first order problems, defined by the so-called ‘‘state equation’’ and ‘‘observation equation’’. Such equations, in the output-only case, can be written as follows for the generic discrete time instant $t = k\Delta t$ with $k \in N$, where Δt is the sampling interval:

$$\{x_{k+1}\}=[A]\{x_k\}+\{w_k\} \quad (1)$$

$$\{y_k\}=[C]\{x_k\}+\{v_k\} \quad (2)$$

where $\{x_k\} = \{x(k\Delta t)\}$ is the discrete-time state vector yielding the sampled displacements and velocities, $\{y_k\}$ is the sampled output, $[A]$ is the discrete state matrix, $[C]$ is the discrete output matrix, $\{w_k\}$ is the ‘‘process noise’’ due to disturbances and model inaccuracies, $\{v_k\}$ is the ‘‘measurement noise’’ due to sensor inaccuracy.

These vector signals are both immeasurable. They are assumed to be zero mean Gaussian white noise processes described by their covariance matrices.

In the stochastic framework that characterizes OMA, due to the lack of information about the input, it is implicitly modeled by the noise terms $\{w_k\}$ and $\{v_k\}$. The white noise assumption about $\{w_k\}$ and $\{v_k\}$ cannot be omitted for the proof of this class of identification methods [15]. Covariance Driven (Cov-SSI) and Data Driven (DD-SSI) SSI are two algorithms for the estimation of system matrices and, therefore, of eigenproperties. The main difference is related to the fact that Cov-SSI works on the output correlations while DD-SSI works directly on the raw data.

Before modal parameter estimation, the acquired data have been accurately inspected in order to assess their quality. Offsets and spurious trends have been removed. Data have been also low-pass filtered and decimated in order to get a final sampling rate of 20 Hz. 66% overlap and Hanning window have been adopted for spectrum estimation. The number of block-rows in SSI was set by means of a sensitivity analysis to optimize the quality of the stabilization diagram quality. This was built for a maximum model order of 80.

3.2 Test results

Analyzing the acquired time series and comparing the results provided by the previously described output-only modal identification methods, the first five modes of the structures have been identified. Results in terms of natural frequencies and damping ratios are reported in Table 2.

The comparison of the results obtained from the different tests pointed out that the joint between the two blocks of the maternity department is not effective at low levels of vibration. Thus, the two blocks act as a single structure. The analysis of the Complexity Plots (Figure 5 and Figure 6) pointed out that all the identified modes are normal. The identified mode shapes are schematically illustrated in Figure 7.

	Test #1		Test #2		Test #3	
Mode	f [Hz]	ξ [%]	f [Hz]	ξ [%]	f [Hz]	ξ [%]
I (translation - x)	3.01	1.7	3.02	1.8	2.99	1.6
II (coupled)	3.38	1.7	3.39	1.8	3.35	1.2
III (translation - y)	3.66	1.9	3.68	2.0	3.63	2.1
IV (torsion)	4.01	1.6	4.01	1.6	4.01	1.5
V (bending of the ends)	4.64	2.2	4.67	2.1	4.62	2.1

Table 2: Identified natural frequencies and damping ratios.

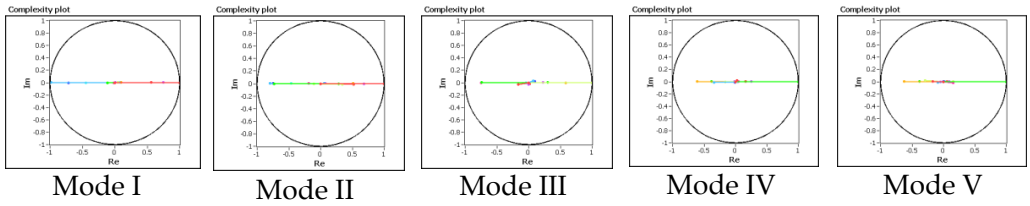


Figure 5: Complexity plots of the identified mode shapes: left block.

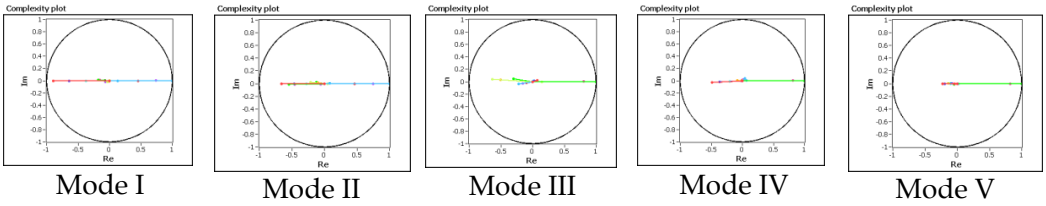


Figure 6: Complexity plots of the identified mode shapes: right block.

4 SENSORS AND ARCHITECTURE FOR VIBRATION-BASED SHM

An effective SHM system for health facilities requires the installation of an appropriate number of sensors, of different types and performance, and, above all, an efficient data processing system. The latter acquires sensor output, processes data and eventually provides an alarm.

About the choice of sensors, they must be able to resolve the system response in operational conditions as well as in the case of an earthquake. The type of sensors also depends on the monitoring requirements. A global assessment based on a number of accelerometers deployed on the structure and vibration based damage detection algorithms can provide relevant information about the health state of the structure. However, additional sensors, different in nature, and appropriate data processing strategies are required to assess health state and performance of non-structural elements, equipment and installations. For instance, connections and anchorages of tanks, large medical devices (CAT scanners, Xray machines) can be more effectively monitored by strain gauges, settlements of distribution systems by FBG sensors, losses in tanks and distribution systems by pressure measurements, while medical equipment sensitive to vibrations also require acceleration measurements [16].

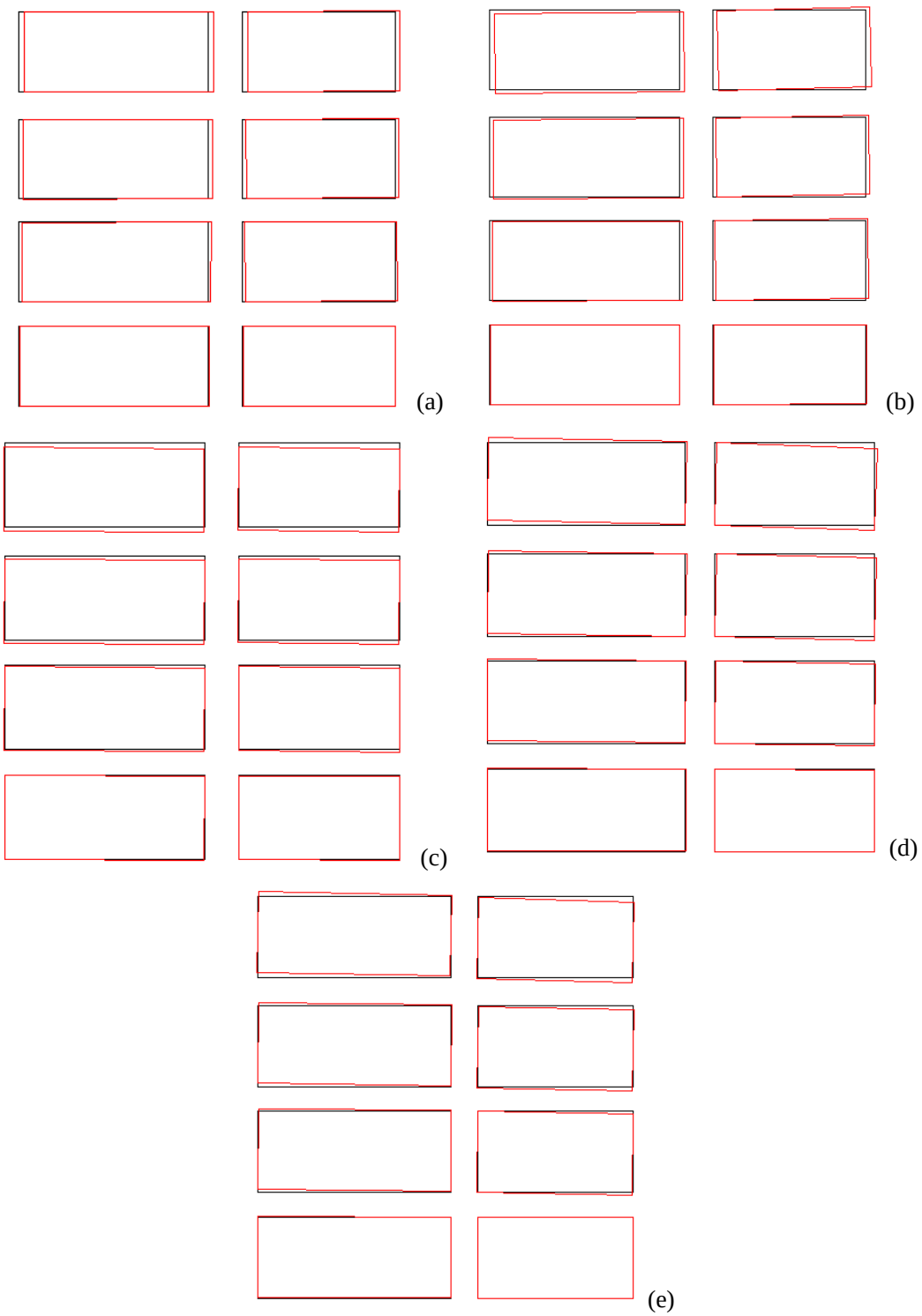


Figure 7: Schematic illustration of the identified mode shapes: mode I (a), II (b), III (c), IV (d), V (e).

The proposed architecture for continuous monitoring of health facilities is sketched in Figure 8. In order to minimize the impact of the monitoring system on the functions of the hospital, wireless sensing units can be adopted. The role of the centralized data server is to aggregate, store and process the data. Data coming from the sensors are continuously stored in local database. The centralized server continuously interrogates the local server to get the raw data and analyze them in order to extract information about the health state of the structure.

Taking into account the results of the dynamic tests carried out on the building hosting the maternity department at the Foggia's Main Hospital, monitoring of the structural response can neglect the presence of the joint between the two blocks. The sensors have to be installed in opposite corners at each level and along two orthogonal directions in order to properly observe the fundamental modes of the structure.

In addition to the vibration measurements, temperature sensors have to be installed to quantify and remove the environmental influence on modal parameter estimates. In the case of the maternity department of the Foggia's Main Hospital, at least one temperature sensor per façade of the building is necessary.

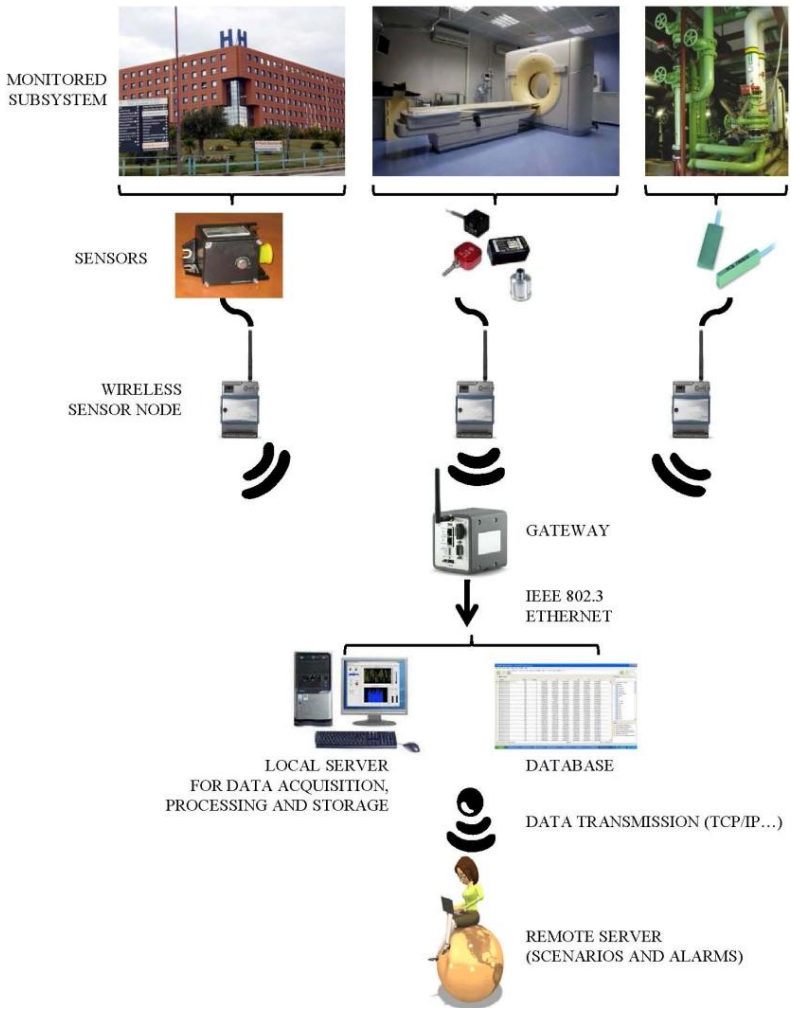


Figure 8: Schematic architecture of an integrated monitoring system for a Health Facility.

5 CONCLUSIONS

In the present paper the main monitoring programs focused on post-earthquake damage assessment of health facilities are reviewed, pointing out their limitations in assessing the performance of non-structural components, equipment and installations. In view of the development of an innovative SHM program for health facilities able to take into account the response of non-structural elements, too, some output-only modal identification tests have been carried out to characterize the dynamic response of the maternity department at the Foggia's Main Hospital. In particular, the test results have provided relevant information for a proper design of the sensor layout and the measurement chain. The architecture of the prototype monitoring system has been finally described, defining the basic requirements of the system and possible solutions to minimize the interference with the normal use of the structure. Different types of sensors are necessary to monitor the response of structural as well as non-structural elements, taking into account that the latter are often more sensitive to displacements than to vibrations. Effective data mining and data fusion procedures are also needed to manage large amount of heterogeneous data.

6 ACKNOWLEDGMENTS

The present work has been partially supported by the ReLuis-DPC Executive Project 2014-2016, Special Project RS9 "Health facilities", whose contribution is gratefully acknowledged.

REFERENCES

[1] C.C. Jacques, J. McIntosh, S. Giovinazzi, T.D. Kirsch, T. Wilson, and J. Mitrani-Reiser, Resilience of the Canterbury Hospital System to the 2011 Christchurch Earthquake. *Earthquake Spectra*, **30**, 533-554, 2014.

[2] A. Masi, G. Santarsiero, M.R. Gallipoli, M. Mucciarelli, V. Manfredi, A. Dusi, and T.A. Stabile, Performance of the health facilities during the 2012 Emilia (Italy) earthquake and analysis of the Mirandola hospital case study. *Bulletin of Earthquake Engineering*, **12**, 2419-2443, 2014.

[3] Pan American Health Organization, *Hospital Safety Index – Guide for Evaluators*, Washington, USA, 2008.

[4] Ministero della Salute, *Raccomandazioni per il miglioramento della sicurezza sismica e della funzionalità degli ospedali*, Rome, Italy, 2003 (in Italian).

[5] ATC 51-1, *Recommended U.S. – Italy collaborative procedures for earthquake emergency response planning for hospitals in Italy*. Applied Technology Council, Redwood City, USA, 2002.

[6] ATC 51-2, *Recommended U.S. – Italy collaborative guidelines for bracing and anchoring non-structural components in Italian hospitals*. Applied Technology Council, Redwood City, USA, 2003.

[7] E. Kalkan, K. Banga, H.S. Ulusoy, J.P.B. Fletcher, W.S. Leith, S. Reza, and T. Cheng, *Advanced earthquake monitoring system for U.S. Department of Veterans Affairs medical buildings—instrumentation*. U.S. Geological Survey Open-File Report 2012–1241, 2012.

[8] M. Dolce, M. Nicoletti, A. De Sortis, S. Marchesini, D. Spina, and F. Talanas, Osservatorio sismico delle strutture: the Italian structural seismic monitoring network. *Bulletin of Earthquake Engineering*, **1**, 2015.

[9] C. Rainieri, G. Fabbrocino, G. Manfredi, and M. Dolce, Robust output-only modal identification and monitoring of buildings in the presence of dynamic interactions for rapid post-earthquake emergency management. *Engineering Structures,* **34**, 436–446, 2012.

[10] C. Rainieri, and G. Fabbrocino, *Operational Modal Analysis of civil engineering structures: An Introduction and Guide for Applications*, Springer, New York, 2014.

[11] B. Peeters, *System identification and damage detection in civil engineering*. PhD thesis, Katholieke Universiteit Leuven, Leuven, Belgium, 2000.

[12] R. Brincker, L. Zhang, and P. Andersen, Modal identification from ambient responses using frequency domain decomposition. *The 18th SEM International Modal Analysis Conference*, San Antonio, TX, USA, 625–630, 2000.

[13] S. Gade, N.B. Møller, H. Herlufsen, and H. Konstantin-Hansen, Frequency domain techniques for operational modal analysis. *The 1st International Operational Modal Analysis Conference*, Copenhagen, Denmark, 261–271, 2005.

[14] R.J. Allemang, and D.L. Brown, A correlation coefficient for modal vector analysis. *The 1st SEM International Modal Analysis Conference*, Orlando, FL, USA, 110–116, 1982.

[15] P. Van Overschee, and B. De Moor, *Subspace identification for linear systems: theory–implementation–applications*. Kluwer Academic Publishers, Dordrecht, The Netherlands, 1996.

[16] C. Rainieri, and G. Fabbrocino, Technologies for seismic safety management of existing health facilities. *Conference Proceedings of the Society for Experimental Mechanics Series*, 199-206, 2013.

Dynamics of Rotating Systems (TP12)

International Conference on Engineering Vibration
Ljubljana, Slovenia, 7-10 September 2015

EVALUATION OF THE DYNAMIC CHARACTERISTICS OF THE THREE-LOBE JOURNAL BEARING WITH FINITE LENGTH USING ANALYTICAL METHODS

Athanasios C. Chasalevris

ALSTOM Power Ltd, TTT Industrial Steam Turbines, Newbold Road CV12NH, Rugby, UK
chasalevris@sdy.tu-darmstadt.de

Keywords: Three-Lobe Bearing, Analytical Solution, Finite Length, Bearing Characteristics.

Abstract. *A recent analytical solution for the lubrication problem of the plain cylindrical journal bearing is applied in this paper in the three-lobe journal bearing geometry that is commonly applied in the large scale rotational machinery. The aim of this paper is to present the procedure of the analytical solution of the Reynolds equation for each one of the lobes of the bearing that is considered to be of finite length and to present results for static and dynamic characteristics of the journal bearing. Charts for eccentricity ratio and equilibrium locus are presented comparing analytical numerical and experimental results. Additionally, stiffness and damping coefficients are evaluated under the analytical solution and compared with the literature.*

1 INTRODUCTION

Due to stability (and not only) issues, the plain cylindrical journal bearing is now partially replaced in large-scale rotor-bearing systems in turbines and generators by two types of journal bearings in most cases, the tilting-pad journal bearing and the lobed journal bearing. Additionally, in high speed systems and especially turbochargers there is a trend for substituting plain cylindrical full floating bearings with floating ring bearings that introduce a lobed geometry in their inner clearances. In both medium and high speed applications , the aim is the same: to prevent the system from developing oil whirl instability or to reduce its amplitude of response when oil whirl instability takes place. Lobed bearings offer a wide range of possibilities for supplying the required stiffness and damping characteristics to the designed system and for providing the required load capacity and stability. The geometric design parameters introduced with lobed journal bearings are the number of pads, pad orientations, clearances, preload factors, and offset factors, and the identical combination of their values can create a very efficient journal bearing with advanced bearing characteristics.

Pinkus [1] was the first to present theoretical analysis of two- and three-lobe bearings using numerical methods while Lund [2] and Lund and Thomsen [3] developed technical reports with design data of noncircular bearings. The calculation methods for several multi-lobe bearings used in the literature are time-consuming; examples are presented by many authors [4-6], adopting perturbation techniques requiring the eight times solution of the Reynolds equation for the evaluation of stiffness and damping coefficients. On the contrary, Shang and Dien [7] evaluated stiffness and damping characteristics for two-lobe bearings by solving the Reynolds Equation only once and using the matrix method.

Elrod [9] included the JFO boundary conditions for bearing analysis within an algorithm based on mass conservation that can predicts cavitation and the form of the fluid in the cavitating area of the bearing. His algorithm was then applied in noncircular lubricating surfaces by Vijadyanathan and Keith [10] where they used the switch of the differencing of the shear flow from central to upwind.

Experimental research on the dynamic characteristics of fixed-geometry journal bearings was performed from Swanson and Kirk [11]. Kostrzewsky et al. [12] compared experimental and theoretical results on the dynamic coefficients of grooved and lobed bearings.

The Elrod's fundamental equation [9] with JFO boundary conditions was expressed by Rao and Sawicky [13] in linear regimes of journal motion using Taylor series and in this way they managed to predict multi-lobed bearing dynamic coefficients.

Stifness and damping coefficients of grooved multi-lobed bearings were theoretically evaluated by Dargaiah et al [14] where he applied theoretical outcome by Shang and Dien [7] for dynamic analysis of multi-lobe bearings. Four different bearing configurations were implemented and static and dynamic characteristics were evaluated.

Malik et al [15] reported the design data of three-lobe bearings for both laminar and turbulent regimes. The theoretical analysis of bearings was based on the usual form solution of the Reynolds equation for laminar regime and the modified Reynolds equation of Ng and Pan [16] for turbulent regime.

Recently, the experimental works of Khatri and Childs [18] present the dynamic performance of the three-lobe bearing for various orientations of the radial static load. One bearing is tested in various speeds of operation and the dynamic results include damping and stiffness coefficients of the oil film with temperature measurements to be taken as well. Pettinato and Flack [19] and Flack and Allaire [20] presented also test results on the static and dynamic characteristics of three-lobe bearings. They used a highly preloaded three-lobe bearing and studied the effect of load orientation to the bearing operational characteristics. Furthermore,

experimental works on journal bearings have been performed recently by Wilkes [21] but they incorporate tilting-pad bearing configuration.

This paper presents an illustration of how to theoretically provide the design data for three-lobe bearings in an analytical solution of the Reynolds equation. The paper aims to provide closed-form analytical expressions that can be easily implemented into rotordynamic algorithms and increase the evaluation speed of rotor-bearing system simulation.

2 THE ANALYTICAL SOLUTION FOR THE LUBRICATION OF THE THREE-LOBE BEARING OF FINITE LENGTH

The geometric definition of a typical symmetric three-lobe bearing is shown in Fig. 1. The radius of curvature for each lobe is R_p. The largest shaft that can fit into the bearing has a radius of $R_b = R + c_b$. A positively preloaded lobe bearing creates a converging-diverging wedge in each pad and thus the load is generated; this happens when $R_p > R_b$. The preload factor m is defined as $m = 1 - c_b / \left(R_p - R\right)$ where c_b is the lobe clearance shown in Fig. 1. $a = \beta / \chi$ is the offset factor, β is the angle between the end of converging portion of pad and the leading edge, see Fig. 1, and χ is the pad arc length. The lobe clearance is defined as c_p, see also Fig. 1.

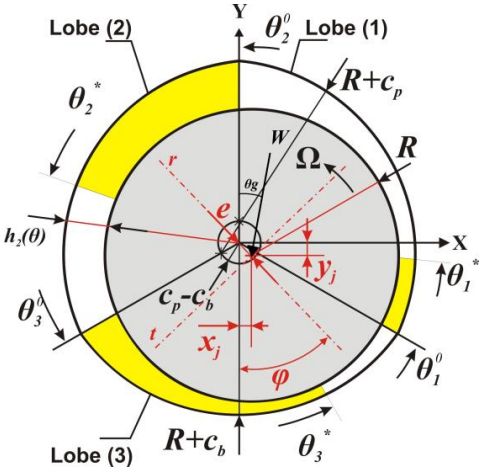


Figure 1: Definition of the geometric properties of a three-lobe journal bearing

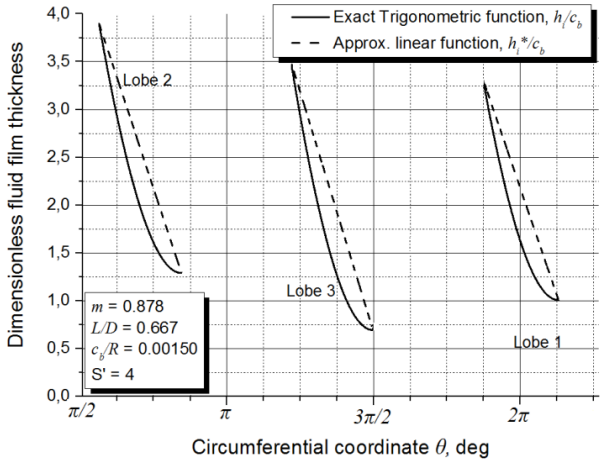


Figure 2: Fluid film thickness function h_i / c_b as a function of circumferential coordinate θ

The journal of radius R and length L_b is assumed to be rotating with a constant rotational speed Ω and to be located in a point of eccentricity e with respect to the geometric centre of the bearing with length L_b after application of a load W as shown in Fig. 1. The journal and the bearing are assumed to be in parallel (aligned bearing) and the fluid film thickness function for the i_{th} lobe is defined as $h_i = c_p - \left(x_j - x_L^i\right)\cos\left(\theta\right) - \left(y_j - y_L^i\right)\sin\left(\theta\right)$ or $h_i = c_p - a_i\cos\left(\theta\right) - \beta_i\sin\left(\theta\right)$ for simplicity where x_j and y_j are the coordinates of the journal centre, x_L^i and y_L^i are the coordinates of centre of the i_{th} lobe, and c_p is the minimum film thickness for centred journal (clearance); also $a_i = x_j - x_L^i$, $\beta_i = y_j - y_L^i$. The time derivative of the fluid film function is defined as $\dot{h}_i = -\dot{x}_j\cos\left(\theta\right) - \dot{y}_j\sin\left(\theta\right)$ where $\dot{x}_j$ and $\dot{y}_j$ are the translational velocities of the journal centre in the horizontal and vertical direction respective-

ly, see Fig. 1; subsequently, the definitions $\dot{x}_j = \dot{a}$ and $\dot{y}_j = \dot{\beta}$ will also be used. The derivative of the fluid film thickness function with respect to θ is defined as $h_i' = \alpha_i \sin(\theta) - \beta_i \cos(\theta)$.

The dynamic viscosity of the lubricant is assumed to be constant and equal to μ through the entire control volume. The attitude angle of the journal is defined as ϕ with respect to the vertical coordinate axis (see Fig. 1). The journal eccentricity is defined as $e = \sqrt{x_j^2 + y_j^2}$ and the relative eccentricity (or eccentricity ratio) as $\varepsilon = e / \mathrm{c}_b$. Under dynamic conditions, the eccentricity rate of change is defined as $\dot{e} = \left(x_j \dot{x}_j + y_j \dot{y}_j\right)/e$ while $\dot{\varepsilon} = \dot{e} / \mathrm{c}_b$. The rate of change of the attitude angle is defined as $\dot{\phi} = \left(-y_j \dot{x}_j + x_j \dot{y}_j\right)/e^2$ and the effective rotational speed as $\Omega_{eff} = \Omega - 2\dot{\phi}$.In this work, all the results are evaluated considering cavitation at the fluid film pressure distribution with the pressure becoming zero exactly at the location of the minimum fluid film thickness at each lobe (Gümbel). The definition of the pressure distribution function is briefly presented in this section, and in correspondence to [25]. The detailed path for obtaining the solution is given in [22, 23]. The starting point is the Reynolds equation, which is expressed in Eq. (1) for the i_{th} lobe, for laminar, isothermal flow. The assumption for the Reynolds equation solution is defined in Eq. (2) [22].

$$\frac{\partial}{\partial z}\left(\frac{h_i^3}{6\mu}\frac{\partial P_i(z,\theta)}{\partial z}\right) + \frac{1}{R^2}\frac{\partial}{\partial \theta}\left(\frac{h_i^3}{6\mu}\frac{\partial P_i(z,\theta)}{\partial \theta}\right) = \Omega_{eff}\frac{\partial h_i}{\partial \theta} + 2\dot{h}_i, \quad i = 1,2,3. \tag{1}$$

$$P_i(z,\theta) = \underbrace{u_i(z,\theta)}_{\text{particular}} + \underbrace{g_i(z,\theta)}_{\text{homogeneous}}, \; i = 1,2,3. \tag{2}$$

The particular and the homogeneous solution of the Reynolds equation are of the form of Eqs. (3-4) and this assumption leads to four Sturm-Liouville problems for the corresponding functions $\varphi_i(\theta), \psi_i(z), f_i(\theta)$ and $m_i(z)$ [22-24], as in follow.

$$u_i(z,\theta) = \varphi_i(\theta) + \psi_i(z), \qquad i = 1,2,3. \tag{3}$$

$$g_i(z,\theta) = f_i(\theta) m_i(z), \qquad i = 1,2,3. \tag{4}$$

When the particular solution of the Reynolds equation $u_i(z,\theta)$ defined in Eq. (3) is substituted for $P_i(z,\theta)$ in Eq. (1), after some calculations Eq. (5) is obtained. When the homogenous solution of the Reynolds equation $g_i(z,\theta)$ defined in Eq. (4) is substituted for $P_i(z,\theta)$ in Eq. (1), after some calculations Eq. (6) is obtained.

$$-\frac{d^2\psi_i(z)}{dz^2} = \frac{1}{R^2}\frac{d^2\varphi_i(\theta)}{d\theta^2} + \frac{3h_i'}{R^2 h_i}\frac{d\varphi_i(\theta)}{d\theta} - \frac{6\mu\Omega_{eff}h_i' + 12\mu\dot{h}_i}{h_i^3}, \qquad i = 1,2,3. \tag{5}$$

$$-\frac{m_i''(z)}{m_i(z)} = \frac{1}{R^2}\frac{f_i''(\theta)}{f_i(\theta)} + \frac{1}{R^2}\frac{3h_i'}{h_i}\frac{f_i'(\theta)}{f_i(\theta)}, \; i = 1,2,3. \tag{6}$$

Eqs. (5-6) are equations with separated variables and each side of them can be assumed equal to a real constant; thus, four ODEs are formed, each one for $\varphi_i(\theta), \psi_i(z), f_i(\theta)$

and $m_i(z)$ individually. The direct analytical solution for $\varphi_i(\theta)$ is presented in Eq. (7). The direct analytical solution for $\psi_i(z)$ is selected to be the trivial [24]; thus, $\psi_i(z) \equiv 0$. The direct analytical solution for $m_i(z)$ is defined in Eq. (8). The ODE for $f_i(\theta)$ does not have direct analytical solution when h_i is trigonometrical and this is the case here. If h_i is a polynomial function $h_i = A_i\theta + B_i$ [25-27], see Figure 2, then the direct analytical solution for $f_i(\theta)$ exists and is given using Bessel's functions. After an approximation of the Bessel's function using trigonometric terms, $f_i(\theta)$ is defined as in Eq. (9) [24]. Further definitions for the variables found in Eqs. (7-9) are presented in Eqs. (10-11).

$$\varphi_i(\theta) = c_{1,i} + \operatorname{atanh}\left(\frac{c_p + a_i - \beta_i}{\sqrt{\upsilon_i}}\tan\left(\frac{\theta}{2}\right)\right)\upsilon_i^{-5/2}\sigma_i + \frac{\beta_i\sigma_i - 3\xi_i\sin(\theta)}{2a_i h_i \upsilon_i^{\,2}} + \frac{\tau_i\sin(\theta) - \vartheta_i}{2a_i h_i^2 \upsilon_i} \tag{7}$$

$$m_{i,j}(z) = \frac{e^{L_b k_j/2}}{1+e^{L_b k_j}}\left(e^{k_j z} + e^{-k_j z}\right), \qquad i = 1,2,3(\text{Lobe}),\ j = 1,2,...(\text{Eigenfunction}), \tag{8}$$

$$f_i(\theta) = \sqrt{\frac{2A_i}{kR\pi\left(A_i\theta + B_i\right)^3}}\left(c_{1,i}\cos\left(\frac{kR\left(A_i\theta + B_i\right)}{A_i} - \frac{3\pi}{4}\right) + c_{2,i}\sin\left(\frac{kR\left(A_i\theta + B_i\right)}{A_i} - \frac{3\pi}{4}\right)\right) \tag{9}$$

$$a_i = x_j - x_L^i, \quad \beta_i = y_j - y_L^i, \quad \dot{a} = \dot{x}_j,\ \dot{\beta} = \dot{y}_j \tag{10}$$

$$\begin{gathered}
\zeta_i = 2\dot{a}\beta_i - 2a_i\dot{\beta} + \left(a_i^2 + \beta_i^2\right)\Omega_{eff} \\
\vartheta_i = -12\mu R^2 a_i\left(a_i\dot{a} + \beta_i\dot{\beta}\right) + 6\mu R^2 c_p^2\left(2\dot{a} + \beta_i\Omega_{eff}\right) + c_{2,i}c_p\beta_i \\
\xi_i = \left(2\mu R^2 c_p^2 + 4\mu R^2\left(a_i^2 + \beta_i^2\right)\right)\zeta_i + c_{2,i}c_p\left(a_i^2 + \beta_i^2\right) \\
\sigma_i = 18\mu R^2 c_p\zeta_i + c_{2,i}\left(a_i^{\,2} + \beta_i^2 + 2c_p^2\right), \tau_i = 6\mu R^2 c_p\zeta_i + c_{2,i}\left(a_i^2 + \beta_i^2\right), \upsilon_i = -c_p^2 + a_i^2 + \beta_i^2
\end{gathered} \tag{11}$$

$$P_i(\mathrm{z},\theta) = \varphi_i(\theta) + \sum_{j=1}^{\infty} c_{i,j}\cdot\left(\frac{e^{L_b k_j/2}}{1+e^{L_b k_j}}\left(e^{k_j z} + e^{-k_j z}\right)\bar{f}_{i,j}(\theta)\right) \tag{12}$$

$$\begin{gathered}
F_X = -\sum_{i=1}^{3}\left(\int_{\theta_i^0}^{\theta_i^*}\int_{-L_b/2}^{L_b/2} P_i(\mathrm{z},\theta)\cos(\theta)R\,dz\,d\theta\right) = \\
-\sum_{i=1}^{3}\left(\int_{\theta_i^0}^{\theta_i^*}\varphi_i(\theta)\cos(\theta)d\theta + 4R\sum_{j=1}^{\infty}\left(\int_{\theta_i^0}^{\theta_i^*}\frac{c_{i,j}}{k_j}\frac{e^{L_b k_j/2}}{1+e^{L_b k_j}}\sinh\left(k_j L_b/2\right)\cos(\theta)\,\bar{f}_{i,j}(\theta)\right)\right)
\end{gathered} \tag{13}$$

With the application of Gumbel's boundary condition and after the normalization of the j_{th} eigenfunction for $f_i(\theta)$ [24], the resulting pressure distribution in each lobe is given in Eq. (12) in closed form expression. Double integration of the pressure distribution through the axial and circumferential direction (multiplied by the appropriate trigonometrical term) will yield the resulting horizontal and vertical impedance forces as in Eqs. (13-14).

$$F_Y = -\sum_{i=1}^{3}\left(\int_{\theta_i^0}^{\theta_i^*}\int_{-L_b/2}^{L_b/2} P_i(\mathrm{z},\theta)\sin(\theta)R\,dz\,d\theta\right) = \\ -\sum_{i=1}^{3}\left(\int_{\theta_i^0}^{\theta_i^*} RL_b\varphi_i(\theta)\sin(\theta)d\theta + 4R\sum_{j=1}^{\infty}\left(\int_{\theta_i^0}^{\theta_i^*}\frac{c_{i,j}}{k_j}\frac{e^{L_b k_j/2}}{1+e^{L_b k_j}}\sinh\left(k_j L_b/2\right)\sin(\theta)\,\bar{f}_{i,j}(\theta)\right)\right) \tag{14}$$

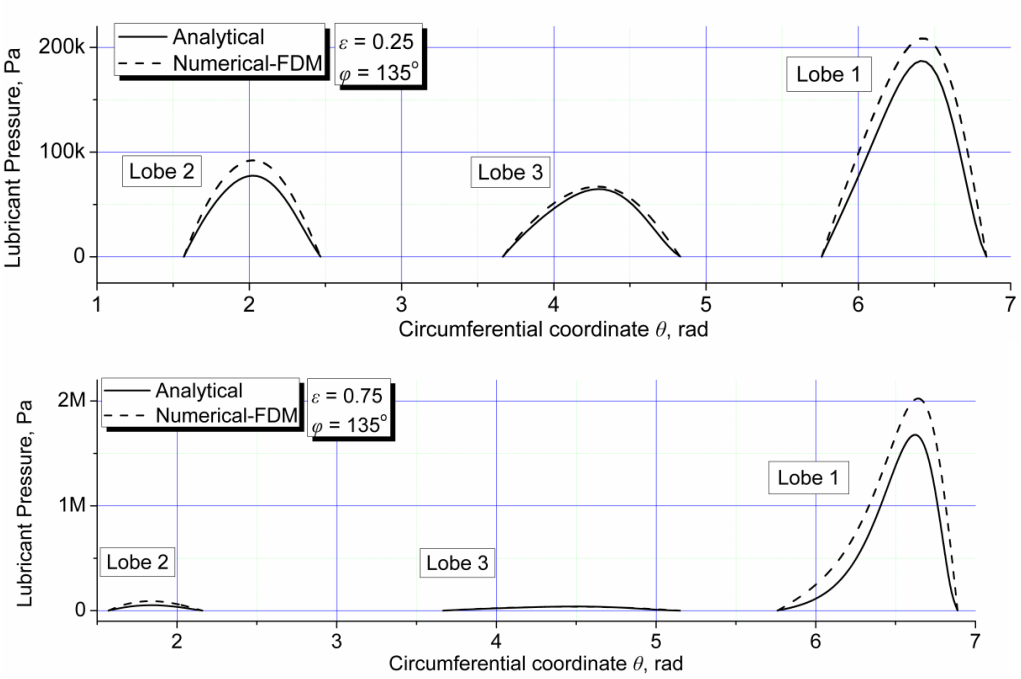


Figure 3: Evaluated pressure distribution of the bearing for static condition using analytical and numerical solution. Above) $\varepsilon = 0.25$ and $\varphi = 135^o$, below) $\varepsilon = 0.75$ and $\varphi = 135^o$.

The resulting pressure and impedance forces for a three-lobe bearing configuration of $c_p = 2.522e-4\mathrm{m}$, $c_b = 9.4713e-5\mathrm{m}$, $R = 0.06\mathrm{m}$, $L_b = 0.04\mathrm{m}$, $\mu = 0.0166\mathrm{Pas}$ and at $\Omega = 140.43\mathrm{rad/s}$ are evaluated both with the presented analytical solution and with a numerical solution using the Finite Differences Method (FDM) [23]. The results consider a light loaded ($\varepsilon = 0.25$) and a heavy loaded ($\varepsilon = 0.75$) bearing, see Figure 3.

In Figure 3 it is seen that the approximate analytical solution can diverge from the numerical solution in some regions through the bearing's circumference. However, this diversion does not yield significant difference in the resulting impedance forces and the equilibrium position of the journal a sit will be shown in next section.

The comparison of evaluation time between the present analytical solution and the numerical solution using FDM (Finite Difference Method) is a first indication that the current approach yields the pressure distribution quite faster, see Table 1. The analytical solution in some cases can even need half the time the numerical solution needs to produce the result. The factors influencing the evaluation time of the analytical solution are the number of eigenfunctions needed and the number of points through circumferential direction in which the pressure is evaluated and then post-processed to yield the impedance forces. The second pa-

rameter does not influence the accuracy of the solution for pressure distribution but influences the evaluation accuracy of the impedance forces; the more the points, the more precise the numerical integration of the pressure field is.

Analytical Solution				
Accuracy	Number of Eigfs.	Intervals	Time for Pressure (s)	Time for Force(s)
1/1000	**4**	30	**0.0019**	**~0.0019**
		60	**0.0041**	**~0.0041**
		90	**0.0051**	**~0.0051**
1/10	**7**	30	**0.0025**	**~0.0025**
		60	**0.0044**	**~0.0044**
		90	**0.0058**	**~0.0058**
10	**10**	30	**0.0028**	**~0.0028**
		60	**0.0056**	**~0.0056**
		90	**0.0078**	**~0.0078**
Numerical Solution Using FDM				
Accuracy	Iterations	Grid size	Time for Pressure (s)	Time for Force (s)
1000Pa	**52**	10x30	**0.0049**	**0.0051**
	153	20x60	**0.0252**	**0.0254**
	277	30x90	**0.0761**	**0.0778**
100Pa	**75**	10x30	**0.0057**	**0.0059**
	242	20x60	**0.0324**	**0.0335**
	469	30x90	**0.1106**	**0.1145**
10Pa	**98**	10x30	**0.0063**	**0.0068**
	337	20x60	**0.0412**	**0.0418**
	678	30x90	**0.1411**	**0.1469**

Table 1: Evaluation time for pressure distribution and impedance bearing forces for the analytical and numerical solution under variable solution parameters

3 EVALUATION OF THE BEARING STATIC CHARACTERISTICS

In this section, two different geometries of the three-lobed bearing are tested and the static operating characteristics are evaluated analytically. The results are compared with numerical and experimental results from the literature [20]. The theoretical analysis used for comparison [20] was performed with Finite Element Method (FEM) for the solution of the Reynolds equation. Turbulence correction factor formulas where included in the Reynolds equation and ambient and supply pressures were assumed to be zero. Furthermore, the half-Sommerfeld (Gümbel) boundary conditions were used in the definition of the bearing model and in some cases the Reynolds boundary condition was also implemented without significant differences compared to those using the half-Sommerfeld boundary condition. Parameters of operation and geometric configuration of the two bearings analysed are presented in Table 2.

Bearing	Ω, RPM	μ, Pas	m	L/D	Rp, m	c_b, m	c_p, m	R, m
1	1350	0.0166	0.898	0.333	0.06073838	8.09e-5	0.0007933	0.06
2	1466	0.0166	0.706	0.667	0.06022841	8.33e-5	0.0002834	0.06

Table 2: Geometric and physical properties and operating conditions of the analysed three-lobe bearings for the static characteristics

In Bearing #1, the eccentricity ratio and the equilibrium locus are evaluated analytically as presented in section 1 and the results are plotted in Figure 4 as a function of the Sommerfeld number and compared to the corresponding values from the literature [20], obtained through numerical simulation and experimental testing. Lower values for the S' express the more heavy loaded bearing operations. The analytically evaluated eccentricity ratio for case

$\theta g = 0^o$, see Figure 4 (left), diverges much from the numerically evaluated but is much closer to the experimental values. For case $\theta g = 30^o$ the analytically and the numerically estimated values are found to diverge almost 0.1 from each other at the variation of S' in lower values. For $\theta g = -30^o$ the eccentricity is predicted in very good agreement between the analytical and the numerical method at the entire range of S'. The equilibrium locus, see Figure 4 (right), is found in very good agreement between the analytical and numerical method both for $\theta g = \pm 30^o$ and converge well with experimental values for $\theta g = -30^o$. The analytically estimated equilibrium locus for $\theta g = 0^o$ diverges from the numerical and experimental values that are found in good agreement with each other.

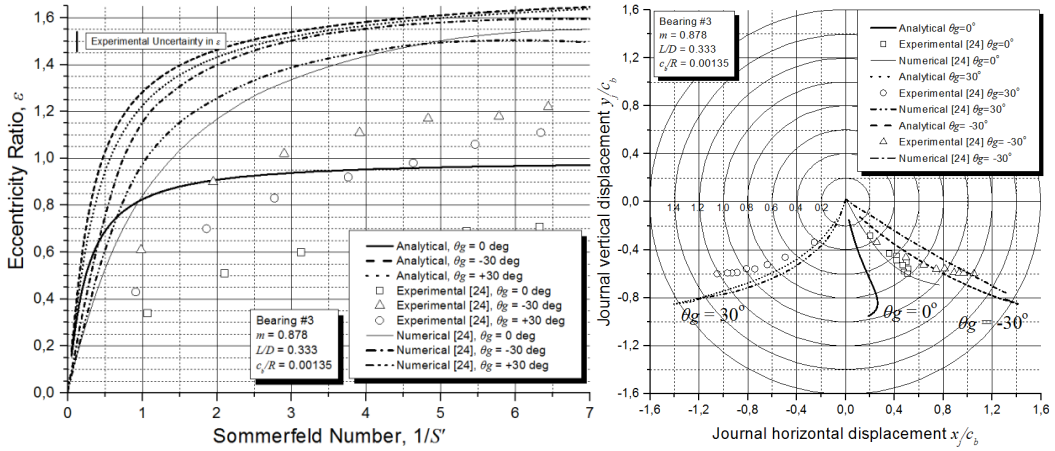


Figure 4: left) eccentricity ratio ε as a function of Sommerfeld number S' and right) equilibrium locus for $m = 0.898$ and $L/D = 0.333$.

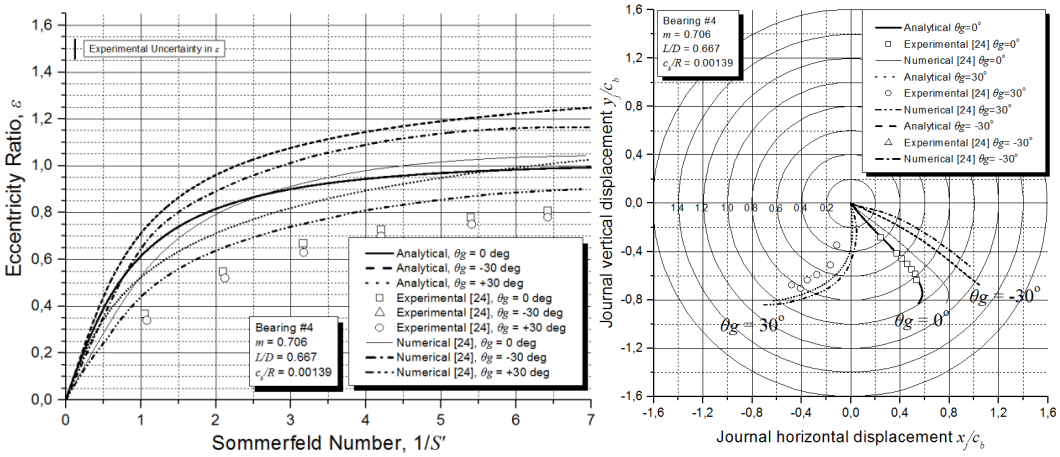


Figure 5: left) eccentricity ratio ε as a function of Sommerfeld number S' and right) equilibrium locus for $m = 0.706$ and $L/D = 0.667$.

In Bearing #2 and for $\theta g = 0^o$ the eccentricity ratio is found in very good agreement between the analytical and the numerical solution in the entire range of S' variation, see Figure 5 (left). Furthermore, for $\theta g = -30^o$ the agreement between analytical and numerical values is quite good while for $\theta g = 30^o$ they still converge well with each other in the entire range of

S' variation. The equilibrium locus estimated analytically for $\theta g = 0^o$ is found exactly equal to the experimental while the numerical estimation diverges slightly, see Figure 5 (right). For $\theta g = 30^o$ the analytical equilibrium locus is found in good agreement with the numerical and both diverge slightly from the experimental values. A similar behaviour is notified also for $\theta g = -30^o$ but in this case no experimental data are provided in [20].

4 ANALYTICAL EVALUATION OF THE STIFFNESS AND DAMPING COEFFICIENTS

This section evaluates the analytical expressions for the stiffness and damping coefficients of three-lobe bearings with finite length for four cases of geometric configuration, the first with $L/D = 0.25$, the second with $L/D = 0.5$ and the 3rd and 4th with $L/D = 0.75$ and $L/D = 1.00$ respectively, see Table 3. The partial derivatives of the journal bearing impedance forces given as a result of the approximate analytical solution are evaluated with respect to displacements, to give the direct and cross-coupled stiffness coefficients and with respect to the journal centre velocities, to give the direct and cross-coupled damping coefficients.

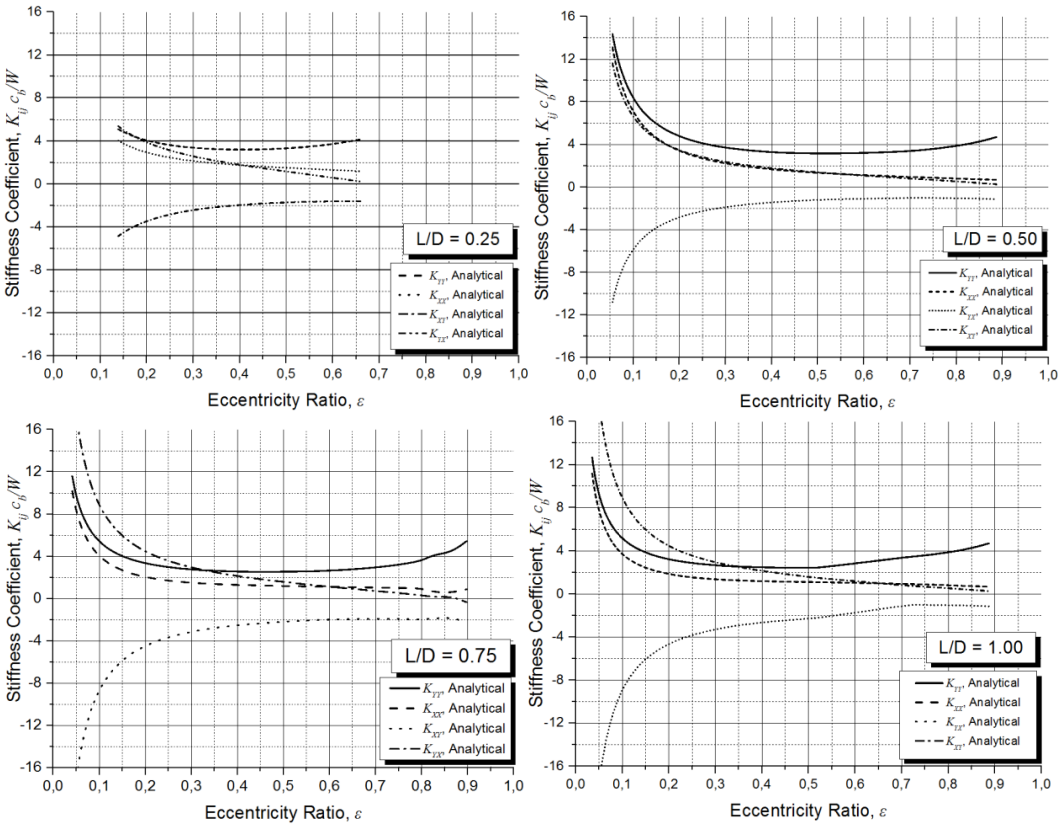


Figure 6: Stiffness coefficients K_{ij} as a function of eccentricity ratio ε for above left) $L/D = 0.25$, above right) $L/D = 0.5$, below left) $L/D = 0.75$ and below right) $L/D = 1.0$.

The evaluation of the stiffness and damping coefficients is done in some chosen values of displacement x_j and y_j corresponding to the equilibrium root locus in the domain of $0.1 < S' < 20$ depending on geometric configuration.

In this section, the simulated bearings have equal geometric and physical properties, as presented in Table 3.

Bear-ing	Ω,RPM	μ, Pas	m	L/D	Rp, m	c_b, m	c_p, m	R, m
1	2000	0.0147	0.5	0.25	0.0601894	9.47 e-5	1.894e-4	0.06
2	2000	0.0147	0.5	0.50	0.0601894	9.47 e-5	1.894e-4	0.06
3	2000	0.0147	0.5	0.75	0.0601894	9.47 e-5	1.894e-4	0.06
4	2000	0.0147	0.5	1.00	0.0601894	9.47 e-5	1.894e-4	0.06

Table 3: Geometric and physical properties and operating conditions of the analysed three-lobe bearings for the static characteristics

$$K_{YY}=\frac{\partial F_Y}{\partial y}=-RL_b\frac{\partial}{\partial y}\left(\sum_{i=1}^{3}\int_{\theta_i^0}^{\theta_i^*}\varphi_i(\theta)\sin(\theta)d\theta+\frac{4}{L_b}\sum_{i=1}^{3}\sum_{j=1}^{\infty}\int_{\theta_i^0}^{\theta_i^*}\frac{c_{i,j}}{k_j}\frac{e^{L_bk_j/2}}{1+e^{L_bk_j}}\sinh\left(\frac{k_jL_b}{2}\right)\sin(\theta)\,\bar{f}_{i,j}(\theta)\right) \quad (15)$$

$$K_{XX}=\frac{\partial F_X}{\partial x}=-RL_b\frac{\partial}{\partial x}\left(\sum_{i=1}^{3}\int_{\theta_i^0}^{\theta_i^*}\varphi_i(\theta)\cos(\theta)d\theta+\frac{4}{L_b}\sum_{i=1}^{3}\sum_{j=1}^{\infty}\int_{\theta_i^0}^{\theta_i^*}\frac{c_{i,j}}{k_j}\frac{e^{L_bk_j/2}}{1+e^{L_bk_j}}\sinh\left(\frac{k_jL_b}{2}\right)\cos(\theta)\,\bar{f}_{i,j}(\theta)\right) \quad (16)$$

$$K_{YX}=\frac{\partial F_Y}{\partial x}=-RL_b\frac{\partial}{\partial x}\left(\sum_{i=1}^{3}\int_{\theta_i^0}^{\theta_i^*}\varphi_i(\theta)\sin(\theta)d\theta+\frac{4}{L_b}\sum_{i=1}^{3}\sum_{j=1}^{\infty}\int_{\theta_i^0}^{\theta_i^*}\frac{c_{i,j}}{k_j}\frac{e^{L_bk_j/2}}{1+e^{L_bk_j}}\sinh\left(\frac{k_jL_b}{2}\right)\sin(\theta)\,\bar{f}_{i,j}(\theta)\right) \quad (17)$$

$$K_{XY}=\frac{\partial F_X}{\partial y}=-RL_b\frac{\partial}{\partial y}\left(\sum_{i=1}^{3}\int_{\theta_i^0}^{\theta_i^*}\varphi_i(\theta)\cos(\theta)d\theta+\frac{4}{L_b}\sum_{i=1}^{3}\sum_{j=1}^{\infty}\int_{\theta_i^0}^{\theta_i^*}\frac{c_{i,j}}{k_j}\frac{e^{L_bk_j/2}}{1+e^{L_bk_j}}\sinh\left(\frac{k_jL_b}{2}\right)\cos(\theta)\,\bar{f}_{i,j}(\theta)\right) \quad (18)$$

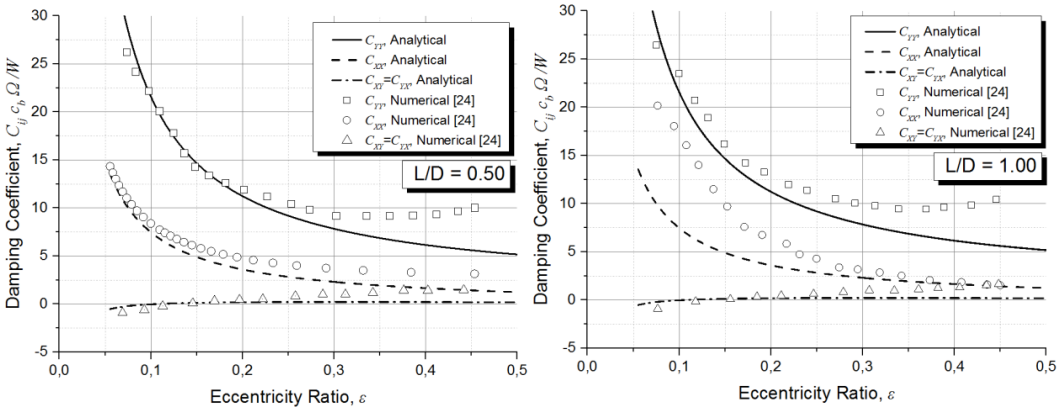


Figure 7: Damping coefficients C_{ij} as a function of eccentricity ratio ε for a) $L/D=0.25$, b) $L/D=0.5$, c) $L/D=0.75$ and d) $L/D=1.0$.

The analytical expression of the fluid film pressure distribution of Eq. (28) with the use of the analytical expressions for the impedance forces of Eqs. (29) and (30) yields the closed-form expressions for the stiffness and the damping coefficients as shown after some math in Eqs. (31) and (32) correspondingly. The derivatives of the impedance forces of Eqs. (29) and (30) with respect to $\dot{x}_j$ and $\dot{y}_j$ at every equilibrium position for $0.1<S'<20$ yield the damping coefficients as in Eq. (32) and plotted in Fig. 7.

5 CONCLUSIONS

The convergence of the presented results provided from the approximate analytical solutions to those provided from numerical solutions or experiments is dependable from the bearing geometrical properties and the operational conditions of the bearing. There are cases of bearing preload factor, L/D ratio and other design parameters that the analytically evaluated static characteristics are very close to the experimental or to those numerically evaluated. Regarding the dynamic characteristics, the analytical formula of resulting pressure in combination or not with numerical post-processing yield the values for stiffness and damping coefficients that can be integrated to the simulation of the rotor-bearing system at every time moment of response evaluation. The incorporation of the analytical formulas instead of the numerical evaluation of the bearing forces provides to the rotor-bearing simulation algorithm reduced evaluation time. The reduced evaluation time is an important parameter of consideration especially at the simulation of systems of high rotating speed..

ACKNOWLEDGMENT

The work was performed in BorgWarner Turbosystems GmbH during the author's R&D activity in Turbosystems. The author would like to thank Dr. Dimitrios Sfyris (Foundation for Research and Technology - Hellas) for his valuable contribution in the analytical solution of the Reynolds Equation for the finite floating-ring bearing.

REFERENCES

[1] Pinkus, O., 1956, "Analysis of Elliptical Bearings," Trans. ASME, 78, p. 965-973.

[2] Lund, J. W., 1965, "Rotor-Bearing Dynamics Design Technology, Part III: Design Handbook for FIuid-Film Type Bearings." Tech. Rept. AFAPL- TR-65-45. Mechanical Technology Inc.

[3] Lund, J. W., and Thomsen. K. K., 1978, "A Calculation method and Data for the Dynamic Coefficients of Oil-Lubricated Journal Bearings", Topics in Fluid Film Bearing and Rotor Bearing System Design and Optimization, The ASME Design Engineering Conference. pp 1-29.

[4] Knight, J.D., and Barrett, L. E., 1983, "An Approximate Solution Technique for Multi-Lobe Journal Bearings including Thermal Effects, with Comparison to Experiment," ASME Trans., 26, 4, pp 501-508.

[5] Glienicke. J., Han, D. C., and Leonhard. M., 1980, "Practical Determination and Use of Bearing Dynamic Coefficients", Trib. Int., 13. pp. 297-309.

[6] Eierman, R. G., 1976, "Stability Analvsis and Transient Motion of Axial Groove Multi-Lobe and Tilting-Pad Bearings," M. S. Thesis, University of Virginia.

[7] Shang, L., and Dien, L. K., 1989, "A Matrix Method for Computing the Stiffness and Damping Coefficients of Multi-Arc Journal Bearings", Trib. Trans., 32, 3, pp 396-404.

[8] Someya, T., 1989, "Journal Bearing Design Data Book", Springer-Verlag, Berlin.

[9] Elrod, H. G., 1981, "A Cavitation Algorithm", ASME Journ. of Lubr. Tech., 103, pp 350-354.

[10] Vaidyanathan, K., and Keith, T. G., 1989, "Numerical Prediction of Cavitation in Noncircular Journal Bearings", Trib. Trans., 32, pp 215-221

[11] Swanson E. E. and Kirk. R. G., "Survey of Experimental Data for Fixed Geometry Hydrodynamic Journal Bearings." ASME Jour. of Trib., 119, pp 704-710 (1997).

[12] Kostrzewsky, G. J., Flack, R. D., and Barett, L. E., 1998, "Comparison Between Measured and Predicted Performance of a Two-Axial Groove Journal Bearing", Trib. Trans., 39, pp 571-578.

[13] Rao, T. V. V. L. N., and Sawicki, J. T., 2002, "Linear Stability Analysis for a Hydrodynamic Journal Bearing Considering Cavitation Effects", Trib. Trans., 45, pp 450-456.

[14] Dargaiah, K., Parthasarathy, K., and Prabhu, B. S., 1993, "Finite Element Method for Computing Dynamic Coefficients of Multilobe Bearings", Trib. Trans., 36, pp 73-83.

[15] Malik, M., Sinhasan, R., and Chandra M., 1981, "Design Data for Three-Lobe Bearings", Trib. Trans., 24, pp 345-353.

[16] Ng, C. W., and Pan, C. H. T., 1965, "A Linearized Turbulent Lubrication Theory." Trans. ASME. J. of Basic Eng., 87, pp 675-688.

[17] Sinhasan, R., Malik, M., and Chandra, M., 1980, "Analysis of Two-Lobe Porous Hydrodynamic Journal Bearings", Wear, 64, pp 343-357.

[18] Khatri, R., and Childs, D., 2014, "An Experimental Investigation of the Dynamic Performance of a Vertical-Application Three-Lobe Bearing", Proc. Of the ASME Turbo Expo 2014, paper No. GT2014-25483.

[19] Pettinato, B., and Flack, R.D., 2015, "Test Results for a Highly Preloaded Three-Lobe Journal Bearing-Effect of Load Orientation on Static and Dynamic Characteristis", J. Society of Tribologists and Lubrication Engineers, 57 (9), pp. 23-30.

[20] Flack, R. D., and Allaire, P. E., 1982 "An Experimental and Theoretical Examination of the Static Characteristics of Three-Lobe Bearings", Trib. Trans., 25, pp 88-94.

[21] Wilkes, J., 2011, "Measured and Predicted Transfer Functions Between Rotor Motion and Pad Motion for a Rocker-Back Tilting-Pad Bearing in LOP Configuration", Proceedings of the ASME Turbo Expo, ASME, Vancouver, Canada.

[22] Sfyris, D. and Chasalevris, A., 2012, "An exact analytical solution of the Reynolds equation for the finite journal bearing". Trib. Int. 55, pp 46-58.

[23] Chasalevris, A. and Sfyris, D., 2013, "Evaluation of the Finite Journal Bearing Characteristics Using the Exact Analytical Solution of the Reynolds Equation", Trib. Int. 57, pp 216-234.

[24] Chasalevris, A., 2015, "Analytical Evaluation of the Static and Dynamic Characteristics of Three-Lobe Journal Bearings With Finite Length", ASME Journal of Tribology. 137, Paper No. 041701-1.

[25] Vogelpohl, G., 1943, ''Zur Integration der Reynoldsschen Gleichung für das Zapfenlager endlicher Breite. Ingenieur Archiv'' (In German).

[26] Michell, A., 1929, ''Progress in Fluid film lubrication'', Trans. ASME MSP-51-21, vol. 51, p. 153-163.

[27] Duffing, G., 1931, ''Die Schmiermittelreibung bei Gleitflächen von endlicher Breite'', Handbucher phys. U. techn.; Mechanik von Auerbach-Hort, Bd. 5. Leipzig; Barth, p. 839-850 (In German).

International Conference on Engineering Vibration
Ljubljana, Slovenia, 7-10 September 2015

EVALUATION OF THE FLOATING-RING BEARING CHARACTERISTICS USING ANALYTICAL METHODS

Athanasios C. Chasalevris

ALSTOM Power, TTT Industrial Steam Turbines, Newbold Road CV12NH, Rugby, UK
chasalevris@sdy.tu-darmstadt.de

Keywords: Floating Ring Bearing, Analytical Solution, Finite Length, Bearing Characteristics.

Abstract. *The floating ring bearings widely used in turbosystems are usually incorporated in rotordynamic algorithms under short bearing approximation or by using numerical solutions. As an effort to improve both evaluation time and accuracy of the pressure distribution in a floating ring, a recent achievement of an analytical solution for the plain cylindrical journal bearing is applied to the floating ring bearing model. After the procedure of exact and approximate analytical solution of the Reynolds equation for the floating ring bearing, the static characteristics are evaluated and compared with the corresponding results under short bearing approximation and numerical methods. Design characteristics and operational parameters such as ring seed ratio, inner and outer eccentricity, and friction coefficient are presented and compared.*

1 INTRODUCTION

The Floating ring bearings are a type of hydrodynamically lubricated journal bearings with special applications, usually in high-speed rotating systems. In this type of bearings, a ring is interfered between the bearing casing and the rotating journal and it is floating in the lubricant after it has obtained a certain percentage of the rotating speed of the journal. In normal operating conditions the ring is fully separated from the journal and the casing by the lubricating films that are both capable of receiving load [1].

There are advantages and disadvantages considering the operational characteristics of a floating ring bearing. The contribution of the outer fluid film in additional damping to the system is considered to be very beneficial especially in applications of high-speed systems, e.g. turbosystems, where the instability response that occurs can be sufficiently damped giving the ability to the system to operate without its integrity to be compromised. The generated heat is less than in a plain cylindrical journal bearing and the thermal distortion does not result in severe shape deformation of the cylindrical surfaces. Additionally, floating ring bearings present lower frictional losses compared to fixed sleeve bearings. However, the existence of two clearances in the radial direction can yield poor shaft centring [2]. Furthermore, the demand of suppling lubricant in two fluid films and the potential demand for an unloaded start up may discard floating ring bearings from some applications.

The fundamental theory for the operation of floating ring bearings has been widely investigated in past [1, 3-5] and recent literature as well [6-7]. The computational power nowadays permits the application of very accurate numerical solutions for the floating ring bearings into rotordynamic algorithms. Approximate analytical solutions considering usually short bearing geometry may be sufficient for certain applications of floating ring bearings. However, in rotordynamic case studies for the design of a high-speed system, the proposal of a fast and accurate analytical solutions for the floating ring bearings can be still of interest. An accurate analytical model for the floating ring lubrication offers the ability to formulate the nonlinear dynamics of such systems in a complete analytical concept and thus further investigations can be performed regarding the dependence of e.g. thresholds of instability and other parameters of design to the bearing geometry. The bearing geometrical configuration does not always correspond to a short bearing. Under these considerations, a recent analytical solution for the plain cylindrical bearing of finite length [8-9] is applied in this paper to the concept of the floating ring bearing.

The solution of the Reynolds equation for the lubrication of the finite length floating ring bearing is presented in this paper in detail in analytical closed form expressions. The fluid film pressure distribution, the impedance forces and some important operational characteristics are evaluated analytically for various cases of bearing operation and parameters of the solution. The bearing eccentricity, the friction coefficient, and the ring speed ratio are evaluated for various values of the load criterion (Sommerfeld number) and compared among the proposed exact analytical solution for the finite length bearing, a numerical solution for the finite length bearing and an analytical solution under the short bearing approximation. The ring speed ratio that is a parameter that significantly influences the thresholds of instability in high-speed systems is presented with differences among the aforementioned solutions. The loading capacity and the frictional losses may also differ among the solutions for various operational conditions of the bearing. The evaluation time needed for the exact analytical solution together with its accuracy and simplicity encourages its application to rotordynamic algorithms for high-speed systems.

2 ANALYTICAL MODELS FOR THE FLOATING-RING BEARING OF FINITE LENGTH

In a fluid film consisted of two cylindrical surfaces of finite length (journal and bearing), see Figure 1 (outer or inner fluid film), let c be the radial clearance, e the eccentricity, μ the dynamic viscosity of the lubricant, Ω_{eff} the effective rotational speed in the fluid film, L_b the length of the fluid film, and R the smallest of the radius of the surfaces that consist each of the fluid film; then, the fluid film thickness with respect to the angular coordinate θ of the film of consideration is defined as $h = c + e\cos(\theta)$ and the developed pressure distribution $P(x,\theta)$ of the lubricant through the coordinates θ and x, see Figure 1, will be given from the analytical solution of the Reynolds equation written as in equation (1).

$$\frac{h^3}{\mu R^2}\frac{\partial P^2(x,\theta)}{\partial \theta^2} - \frac{3eh^2\sin(\theta)}{\mu R^2}\frac{\partial P(x,\theta)}{\partial \theta} + \frac{h^3}{\mu}\frac{\partial P^2(x,\theta)}{\partial x^2} == 12\dot{e}\cos(\theta) - 6e\Omega_{eff}\sin(\theta) \quad (1)$$

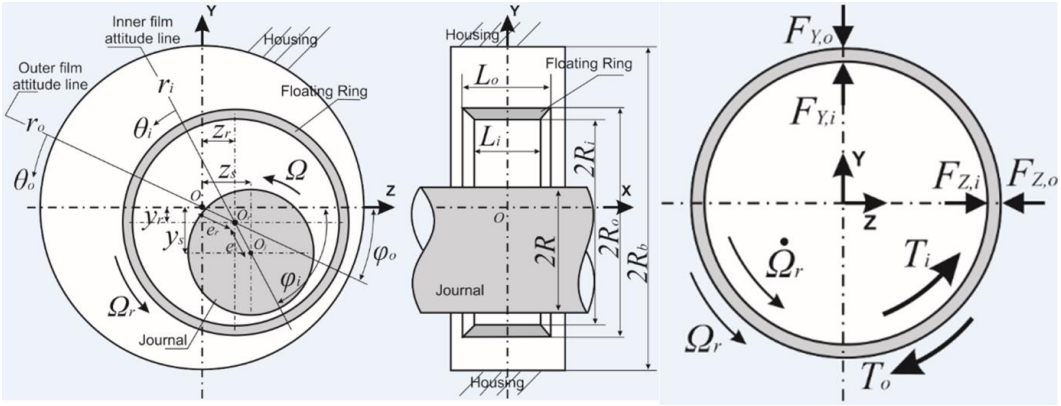


Figure 1: Definition of the geometry and parameters of operation of a plain cylindrical floating ring bearing and representation of the forces and moments acting at the floating ring.

The problem is considered to be dynamic and the journal and the ring are supposed to execute any planar trajectories inside the clearance area of each film; The rotating speed of the rings is defined as $\Omega_{r,1} = \dot{\vartheta}_1$ and $\Omega_{r,2} = \dot{\vartheta}_2$, and then the effective rotating speed on each of the four fluid films can be defined as in equation (2) for the inner and the outer films.

$$\begin{aligned} \Omega_{eff,i,1} &= \Omega + \Omega_{r,1} - 2\dot{\varphi}_{i,1}, & \Omega_{eff,i,2} &= \Omega + \Omega_{r,2} - 2\dot{\varphi}_{i,2} \\ \Omega_{eff,o,1} &= \Omega_{r,1} - 2\dot{\varphi}_{o,1}, & \Omega_{eff,o,2} &= \Omega_{r,2} - 2\dot{\varphi}_{o,2} \end{aligned} \quad (2)$$

Referring to the recent achievement of the analytical solution of the Reynolds equation for the plain cylindrical journal bearing [8-9], only the milestones of the analytical procedure will presented at this section. The procedure concerns one fluid film and the definitions of the paragraph above will be used.

The solution of the Reynolds equation $P(x,\theta)$ is expressed as the sum of a particular solution of the Reynolds, $u(x,\theta)$, and of the solution of the homogenous Reynolds, $g(x,\theta)$, as $P(x,\theta)=u(x,\theta)+g(x,\theta)$ [8-9].

The particular solution will be given using the additive separation of variables and the homogenous solution will be given using the multiplicative separation of variables. Thus, the particular solution $u(x,\theta)$ is expressed as the sum of the single variable functions $\Psi(x)$ and $\Phi(\theta)$, $u(x,\theta)=\Psi(x)+\Phi(\theta)$ while the homogenous solution $g(x,\theta)$ is expressed as the product of the single variable functions $m(x)$ and $f(\theta)$, as $g(x,\theta)=m(x)f(\theta)$. In this way the Reynolds equation is separated in four Sturm-Liuville problems as in Eqs. (3-6).

$$\frac{1}{R^2}\frac{d^2\Phi(\theta)}{d\theta^2}+\frac{3}{R^2}\frac{1}{h}\frac{dh}{d\theta}\frac{d\Phi(\theta)}{d\theta}-\left(\frac{6\mu\Omega_{eff}}{h^3}\frac{dh}{d\theta}+\frac{12\mu}{h^3}\frac{dh}{dt}\right)=0,\ \Phi(0)=\Phi(2\pi)=0 \tag{3}$$

$$\frac{d^2\Psi(x)}{dx^2}=0,\ \ \Psi(-L_b/2)=\Psi(L_b/2)=0 \tag{4}$$

$$\frac{d^2m(x)}{dx^2}=k^2m(x), m(-L_b/2)=m(L_b/2)=1, k\in\mathbf{R}^* \tag{5}$$

$$\frac{d^2f(\theta)}{d\theta^2}+\frac{3}{h}\frac{dh}{d\theta}\frac{df(\theta)}{d\theta}+k^2R^2f(\theta)=0,\ f(0)=f(2\pi)=0, k\in\mathbf{R}^* \tag{6}$$

The first ODE in equation (3) has direct analytical solution, the second ODE in equation (4) is chosen to have the trivial solution $\Psi(x)\equiv 0$ [9], and the third ODE in equation (5) has direct analytical solution. The fourth ODE in equation (6) does not have direct analytical solution and its solution is achieved either using Power Series [8] or using numerical method (e.g. finite difference method). For certain values for the parameters of the solution (e.g. number of eigenfunctions used, number of Power Series, number of finite differences) both solutions are in absolute agreement to each other. Using a linear approximation for the fluid film thickness function the ODE in equation (6) has a direct analytical solution using Bessel's functions [8-9] (approximate analytical solution). The detailed definitions of the problems, the sequence of evaluations and various results regarding the pressure distribution profile, static and dynamic characteristics and operational parameters of the bearing can be found in recent literature [8-9].

The SLP (Sturm-Liouville Problem) of equation (6) is solved numerically using 1-D FDM (Finite Difference Method) . Dimension θ is discretized in NFD (Number of Finite Differences) points as $\theta_i=(i-1)\delta\theta$ for $i=2,3,\ldots,\text{NFD}$, with $\delta\theta=2\pi/\text{NFD}$. Then, the SLP problem of equation (6) is written as in equation (7).

$$\begin{cases} \dfrac{f_{i+1}-2f_i+f_{i-1}}{\delta\theta^2}-\dfrac{3e\sin(\theta_i)}{c+e\cos(\theta_i)}\dfrac{f_{i+1}-f_{i-1}}{2\delta\theta}+k^2R^2f_i=0,\ for\ i=2,3,\ldots NFD \\ f_1=f_{\mathrm{NFD}+1}=0 \end{cases} \tag{7}$$

Then, a linear algebraic system is defined as in equation (8)

$$[\mathbf{A}]_{(\mathrm{NFD}-1)\times(\mathrm{NFD}-1)}[\boldsymbol{\sigma}]_{(\mathrm{NFD}-1)\times 1}=[0]_{(\mathrm{NFD}-1)\times 1}, \tag{8}$$

where $[\boldsymbol{\sigma}]_{(\mathrm{NFD}-1)\times 1}=[\,f_2\ f_3\ldots f_{\mathrm{NFD}}\,]^{\mathrm{T}}$. The elements of matrix $[\mathbf{A}]_{(\mathrm{NFD}-1)\times(\mathrm{NFD}-1)}$ can be simply defined as in equation (9).

$$\begin{cases} \alpha_{i,i}=-\dfrac{2}{\delta\theta^2}+k^2R^2, i=1,2,\ldots,\mathrm{NFD}-1 \\ \alpha_{i,i-1}=\dfrac{1}{\delta\theta^2}+\dfrac{3e\,\sin(\theta_{i+1})}{2\delta\theta\left(c+e\,\cos(\theta_{i+1})\right)}, i=2,3,\ldots,\mathrm{NFD}-2 \\ \alpha_{i,i+1}=\dfrac{1}{\delta\theta^2}-\dfrac{3e\,\sin(\theta_{i+1})}{2\delta\theta\left(c+e\,\cos(\theta_{i+1})\right)}, i=2,3,\ldots,\mathrm{NFD}-2 \end{cases} \tag{9}$$

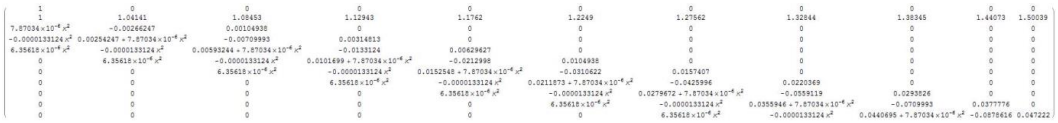


Figure 2. Example of matrix $[\mathbf{A}]_{11\times 11}$ for $K=10$: a sparse matrix consisted of 5 diagonals. The first two lines correspond always to the two boundary conditions.

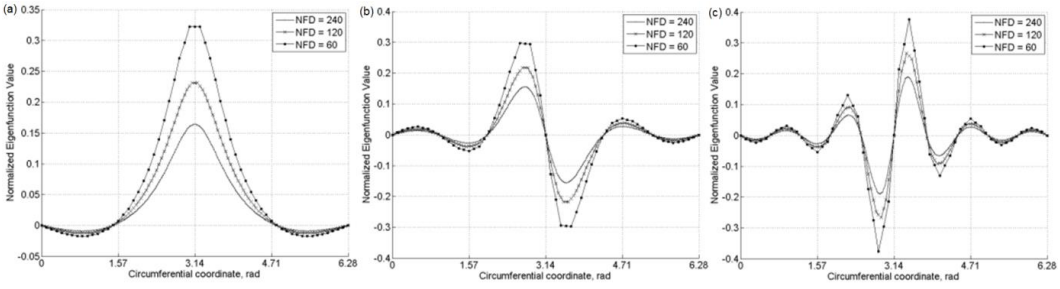


Figure 3. The a) 3rd, b) 6th and c) 9th eigenfunction f_i evaluated in each diagram for a different Number of Finite Differences (NFD).

The definition of $\alpha_{i,i}$ in equation (9) shows that matrix $[\mathbf{A}]_{(\mathrm{NFD}-1)\times(\mathrm{NFD}-1)}$ can be defined as $[\mathbf{A}]=[\mathbf{A}']+\lambda[\mathbf{I}]$ with $\alpha'_{i,i}=-2/\delta\theta^2$ and $\lambda=k^2R^2$. Matrix $[\mathbf{A}]_{(\mathrm{NFD}-1)\times(\mathrm{NFD}-1)}$ is a five-diagonal matrix, see Figure 2, and its j_{th} eigenvalue $\lambda_j=k_j^2R^2$ can be easily evaluated; then, k_j can be evaluated as $k_j=\sqrt{\lambda_j}/R$. The f_i values (i=2,3,…, NFD) through dimension θ can be evaluated for the j_{th} eigenvalue of the system, consisting the j_{th} eigenfunction. For a set of

bearing geometry, the 3rd, 6th and 9th eigenfunction are evaluated and plotted in Figure 3 for three cases of NFD: $\mathrm{NFD}=60$, $\mathrm{NFD}=120$, and $\mathrm{NFD}=240$.

Although the curves in each chart of Figure 3 are different regarding the NFD, at the end they do not have a significant influence on the general solution of Reynolds. This happens because the j_{th} eigenfunction for e.g. $\mathrm{NFD}=60$ is analogue to the j_{th} eigenfunction for e.g. $\mathrm{NFD}=120$; the normalization of the eigenfunctions before they are added together to form the homogeneous solution, see equations (53-55), excludes the difference regarding NFD and yields very similar homogenous solutions even for small NFD, e.g. $10 \sim 20$.

$$\left[\mathbf{A}\right]_{(\mathrm{NFD}-1)\times(\mathrm{NFD}-1)}\left[\boldsymbol{\sigma}\right]_{(\mathrm{NFD}-1)\times 1}=\left[0\right]_{(\mathrm{NFD}-1)\times 1} \tag{10}$$

$$\left[\mathbf{A}\right]_{(\mathrm{NFD}-1)\times(\mathrm{NFD}-1)}\left[\boldsymbol{\sigma}\right]_{(\mathrm{NFD}-1)\times 1}=\left[0\right]_{(\mathrm{NFD}-1)\times 1} \tag{11}$$

$$\left[\mathbf{A}\right]_{(\mathrm{NFD}-1)\times(\mathrm{NFD}-1)}\left[\boldsymbol{\sigma}\right]_{(\mathrm{NFD}-1)\times 1}=\left[0\right]_{(\mathrm{NFD}-1)\times 1} \tag{12}$$

4. EVALUATION OF THE PRESSURE DISTRIBUTION

This section presents a comparison of the evaluated fluid film pressure distribution for the different theories of solution concerning the cases: a) exact analytical solution, b) numerical solution using FDM, and c) approximate analytical solution using short bearing approximation.

In high-speed rotor bearing systems like those in automotive turbochargers, the fluid films of the floating rings present a length to diameter ratio close to $L_b/(2R) = 0.25, 0.5, 0.75$. The pressure distribution under short bearing approximation, see equation (13), is commonly used for the modelling of floating ring bearings into rotordynamic algorithms of such systems.

$$P(x,\theta)=\frac{3\mu\left(2\dot{e}\cos(\theta)-e\Omega_{eff}\sin(\theta)\right)}{\left(c+e\cos(\theta)\right)^3}\left(x^2-\frac{L_b^2}{4}\right) \tag{13}$$

The three cases of $L_b/(2R) = 0.25$ are considered for two cases of eccentricity ratio $e = 0.25c$ and $e = 0.75c$ while the $\dot{e}$ obtains values of $\dot{e} = 0$, $\dot{e} = 0.001\Omega R$ and $\dot{e} = 0.1\Omega R$, see Figure 4. In Figure 4, we note an almost absolute agreement between the exact analytical solution and the numerical solution using FDM and this agreement goes for all the analyzed cases, static and dynamic, with low or high $\dot{e}$ and for low or high e. Furthermore, a very good agreement is noted between the short bearing approximation and the other two solutions, the exact analytical and the numerical using FDM, especially in the case of low $\dot{e}$. In the case of high $\dot{e}$ a slight divergence is noted in comparing the short bearing approximation with the exact analytical or the numerical solution. The approximate analytical solution seems to be in acceptable agreement with the other three cases only in the static case, $\dot{e} = 0$, and for a low eccentricity ratio. In the dynamic cases and for small eccentricity ratios, a divergence is noted and becomes even higher when the eccentricity ratio becomes higher. As shown in a following section, the approximate analytical solution yields quite different results for stability margins and developed harmonics than those of the other three solutions. Regarding the applicability of the approximate analytical solution, it should be preferably used in rotor-bearing systems that experience linear dynamic behaviour in their journal trajectories. Further discussion is added in the conclusions.

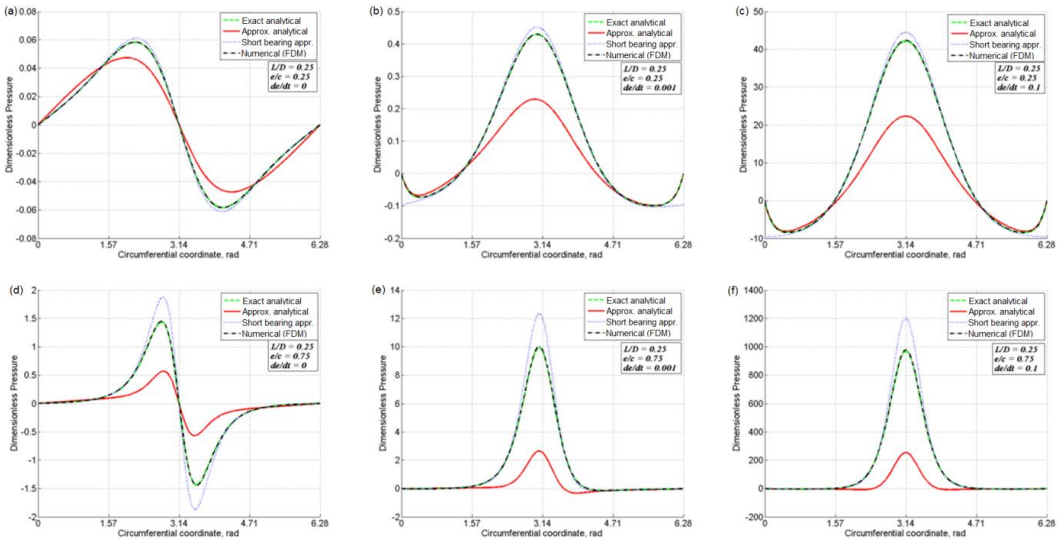


Figure 4. Pressure distribution evaluated through circumferential direction for $L_b/(2R) = 0.25$ for various cases of eccentricity and its rate of change. a) $e/c = 0.25, \dot{e} = 0$, b) $e/c = 0.25, \dot{e} = 0.001\Omega R$, c) $e/c = 0.25, \dot{e} = 0.1\Omega R$, d) $e/c = 0.75, \dot{e} = 0$, e) $e/c = 0.75, \dot{e} = 0.001\Omega R$, f) $e/c = 0.75, \dot{e} = 0.1\Omega R$.

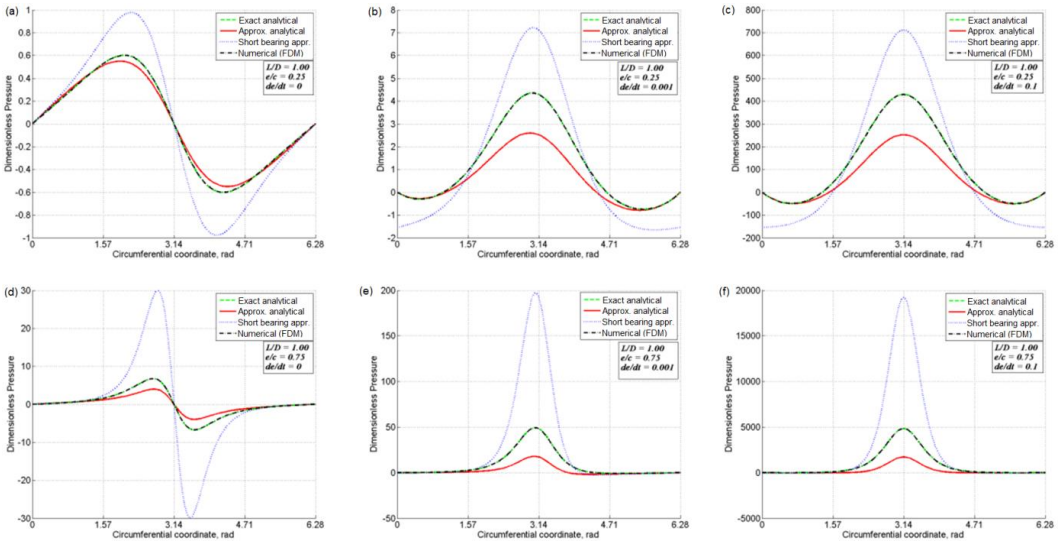


Figure 5. Pressure distribution evaluated through circumferential direction for $L_b/(2R) = 1.00$ for various cases of eccentricity and its rate of change. a) $e/c = 0.25, \dot{e} = 0$, b) $e/c = 0.25, \dot{e} = 0.001\Omega R$, c) $e/c = 0.25, \dot{e} = 0.1\Omega R$, d) $e/c = 0.75, \dot{e} = 0$, e) $e/c = 0.75, \dot{e} = 0.001\Omega R$, f) $e/c = 0.75, \dot{e} = 0.1\Omega R$.

An $L_b/(2R) = 1.00$ is the second analysed geometric configuration for the same cases of eccentricity ratio $e = 0.25c$ and $e = 0.75c$ as before, and with $\dot{e}$ to obtain again values of $\dot{e} = 0$, $\dot{e} = 0.001\Omega R$ and $\dot{e} = 0.1\Omega R$, see Figure 5. In Figure 5, again an almost absolute agreement is noted between the exact analytical solution and the numerical solution using FDM and this agreement goes for all the analyzed cases, static and dynamic, with low or high

$\dot{e}$ and for low or high e. The length to diameter ratio does not correspond to a short bearing, so the agreement between the short bearing approximation and the other two solutions, the exact analytical and the numerical using FDM, is not satisfied, in either dynamic or static cases. The approximate analytical solution is in acceptable agreement with the other two cases, exact analytical and numerical using FDM again only in the static case, $\dot{e} = 0$, and for low eccentricity ratios, but, compared to the short bearing approximation, presents a better convergence to the exact analytical and numerical solution.

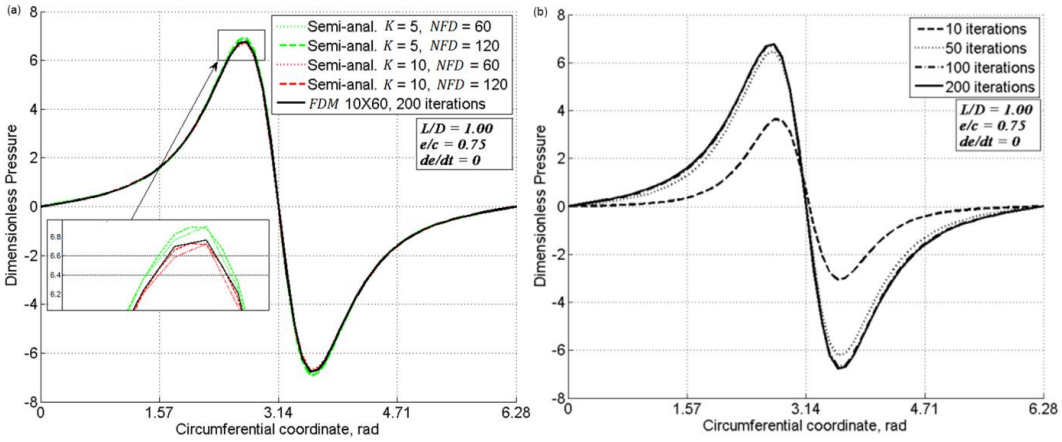


Figure 6. Comparison of the evaluated pressure distribution through the circumferential direction of the film; a) two cases of NFD for the same number of eigenfunctions used, $K = 5$ and $K = 10$; the numerical solution is also presented for comparison. b) The result of the numerical solution for different number of iterations of the iterative solver ADI.

Exact Analytical Solution				
Accuracy	Number of Eigfs.	Intervals	Time for Pressure (s)	Time for Force (s)
(not influenced at the maximum pressure)	5	60	**~0.0017**	**~0.0018**
		120	**~0.0039**	**~0.0040**
		240	**~0.0047**	**~0.0050**
	9	60	**~0.0022**	**~0.0023**
		120	**~0.0040**	**~0.0043**
		240	**~0.0051**	**~0.0056**
	12	60	**~0.0022**	**~0.0025**
		120	**~0.0051**	**~0.0053**
		240	**~0.0072**	**~0.0074**
Numerical Solution Using FDM				
Accuracy	Iterations	Grid size	Time for Pressure (s)	Time for Force (s)
1000Pa	52	10x30	**~0.0049**	**0.0051**
	153	20x60	**~0.0252**	**0.0254**
	277	30x90	**~0.0761**	**0.0778**
100Pa	75	10x30	**~0.0057**	**0.0059**
	242	20x60	**~0.0324**	**0.0335**
	469	30x90	**~0.1106**	**0.1145**
10Pa	98	10x30	**~0.0063**	**0.0068**
	337	20x60	**~0.0412**	**0.0418**
	678	30x90	**~0.1411**	**0.1469**

Table 1: Comparison of evaluation time for fluid film pressure distribution and impedance forces among the cases of Reynold solution.

The pressure distribution in the circumferential direction under the numerical solution using FDM is evaluated and plotted as a reference, see Figure 6, considering an $L_b/(2R) =$

1.00. Then, the exact analytical solution is evaluated using numerically solved eigenfunctions and for two cases of $K = 5$ and $K = 10$ are evaluated for two cases of $NFD = 60$ and $NFD = 120$ each, see Figure 6a. The agreement in the pressure distribution among the four different values of the parameters tested is found absolute almost through the entire circumference of the bearing, with only the peak pressure to diverge slightly among the cases tested, see Figure 6a. Additionally, a test on the convergence of the iterative solver of the numerical solution using FDM is presented in Figure 6b, showing that after 100 iterations the solver converges to the final pressure distribution, always discussing a specific case of parameters for bearing operation. The fact that only $K = 5$ or even fewer eigenfunctions are enough to accurately evaluate the pressure distribution enhances the applicability of the exact analytical solution to rotor dynamic algorithms regarding accuracy and evaluation time.
The evaluation time on the bearing subroutines each time they are called during the evaluation of the pressure distribution and impedance forces is presented in Table 1 where it is seen that the exact analytical solution is even faster from a simple numerical solution using FDM. Additionally, the exact analytical solution can exclude the one from two integrations for the evaluation of the impedance force; the integration through the axial direction of the bearing can be performed analytically and this provides an even faster bearing algorithm.

5. EVALUATION OF BEARING OPERATING PARAMETERS

Various cases of geometric configuration of a floating ring have been simulated under the exact analytical solution and the parameters of eccentricity ratio, friction coefficient and ring speed ratio are presented in this section. The following charts were produced with the variation of the vertical load on the journal with all the rest parameters of bearing operation to remain constant. In Figures 7 and 8, the inner eccentricity ratio is plotted as a function of the outer eccentricity ratio in the floating ring bearing for six different assumptions for inner to outer clearance ratio and three different assumptions for the outer to inner radius ratio of the floating ring and thus 18 geometrical bearing configurations were simulated. The same configurations were used for the friction coefficient, see Figure 9, and for the evaluation of the ring to shaft speed ratio, see Figures 10 and 11.

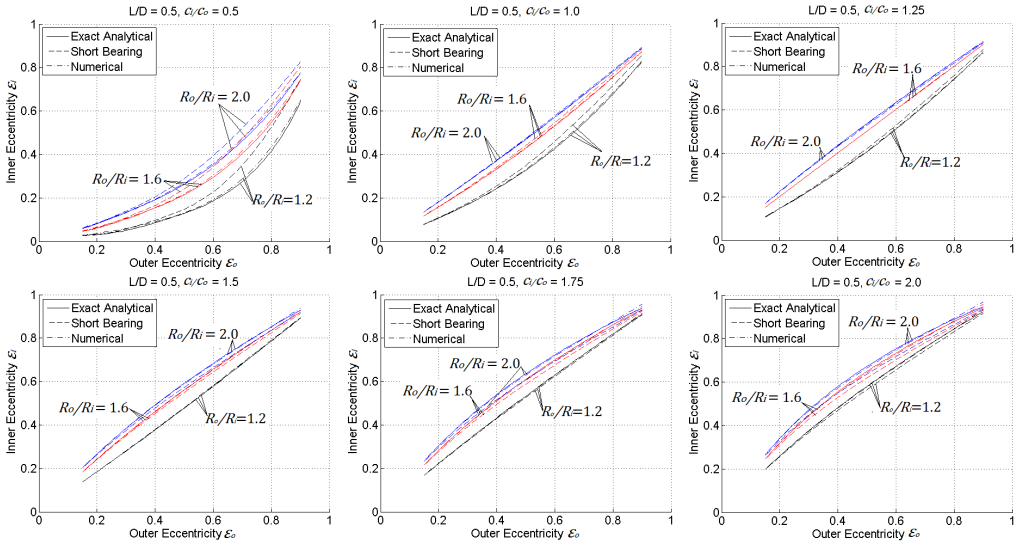


Figure 7. Inner eccentricity ratio as a function of outer eccentricity ratio for various cases of bearing geometry regarding radius and radial clearance and for L/D = 0.5.

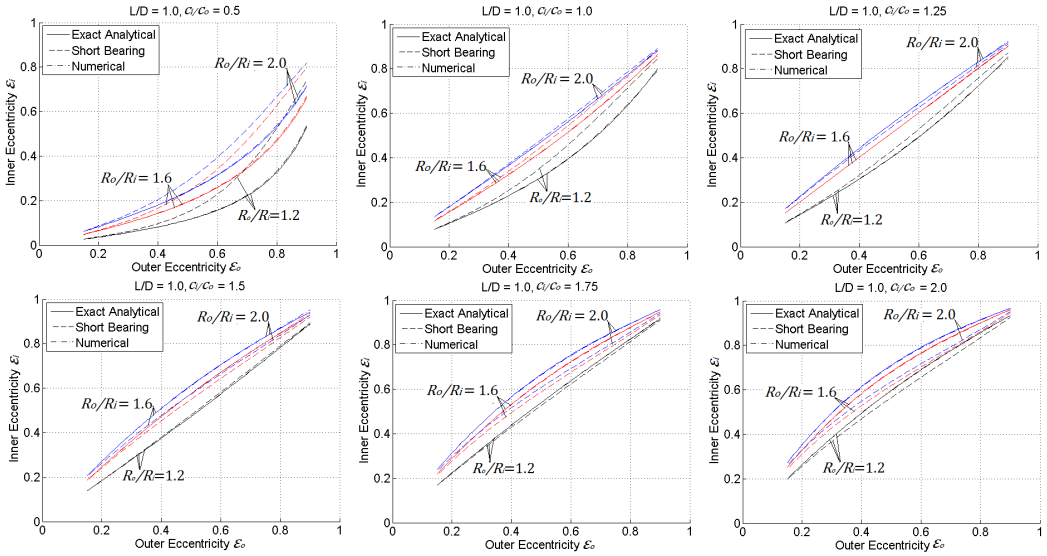


Figure 8. Inner eccentricity ratio as a function of outer eccentricity ratio for various cases of bearing geometry regarding radius and radial clearance and for L/D = 1.0.

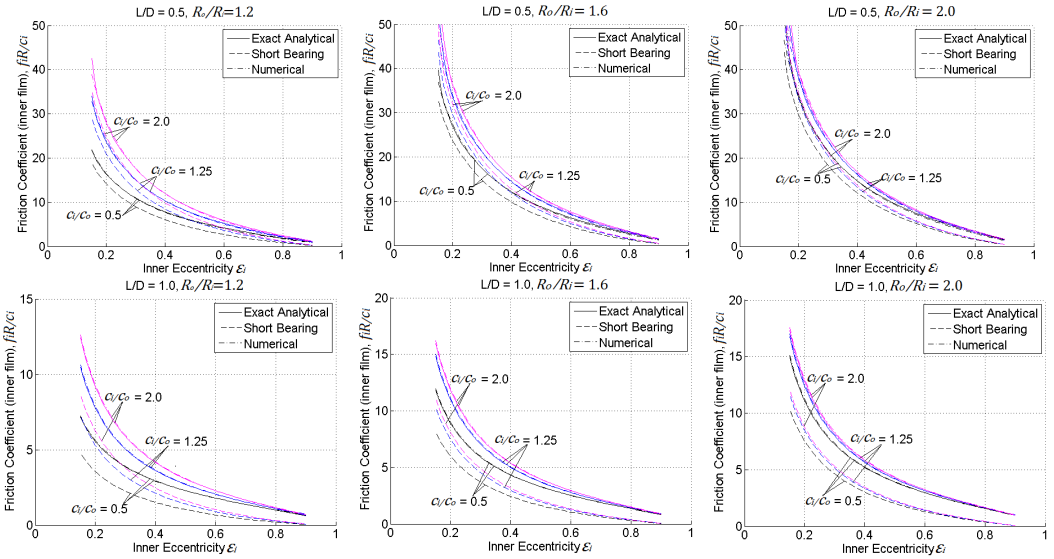


Figure 9. Friction coefficient at the inner film as a function of the inner eccentricity for various cases of bearing geometry regarding radius and radial clearance for L/D = 0.5 (above) and L/D = 1.0 (below).

The exact analytical solution is in a very good agreement with the numerical solution for the finite bearing for almost all cases of bearing configuration and for all three parameters of eccentricity, rotor to ring speed ration and friction coefficient. Both exact analytical and numerical solution present a divergence from the short bearing approximating solution. The divergence gets higher for the case of the L/D = 1 (finite length bearing) while for L/D = 0.5 (short bearing) the divergence gets lower.

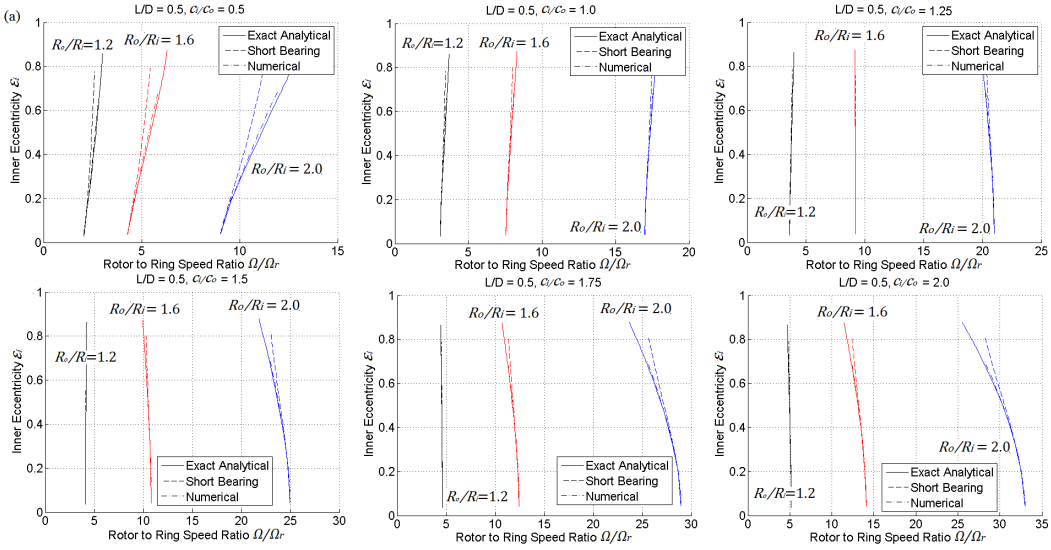


Figure 10. Inner eccentricity ratio as a function of rotor to ring speed ratio for various cases of bearing geometry regarding radius and radial clearance and for L/D = 0.5.

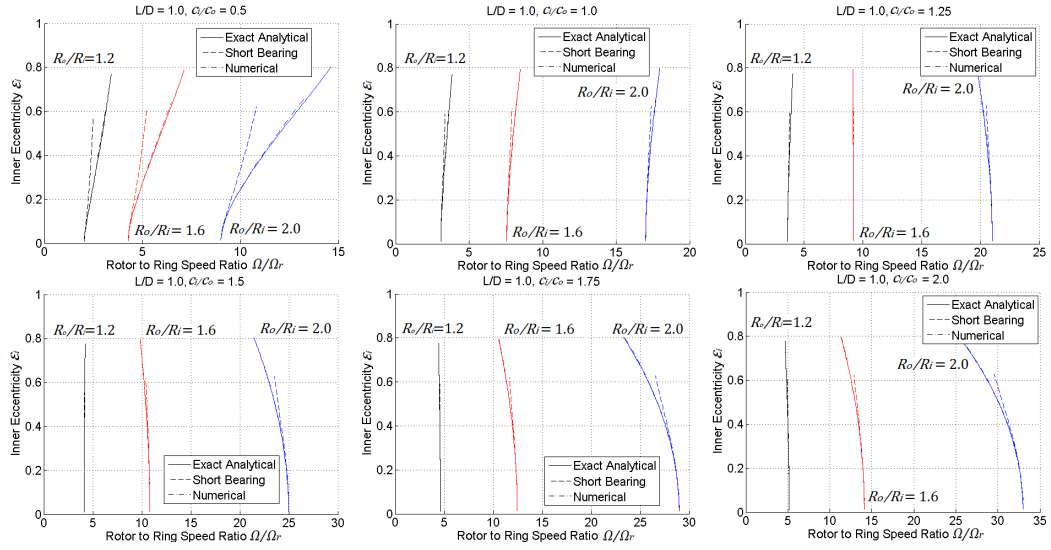


Figure 11. Inner eccentricity ratio as a function of rotor to ring speed ratio for various cases of bearing geometry regarding radius and radial clearance and for L/D = 1.0.

CONCLUSIONS

An exact analytical solution for the lubrication of the plain cylindrical finite length floating ring bearing was presented in this paper. The solution was compared with a numerical solution and a short bearing approximation in operating parameters of major importance such as eccentricity ratio, ring speed ratio and friction coefficient. The solutions were found to differ for some cases of bearing operation while for others they were found in good agreement to each other. The exact analytical solution is in a very good agreement to the numerical solution using Finite Difference Method. Considering the accuracy, the reduced evaluation time and

the further possibilities for the analytical treatment of the nonlinear dynamics of floating ring bearings, the exact analytical solution is proposed to be applied in rotordynamic algorithms.

ACKNOWLEDGMENT

This work was performed during the activity of the author in the research and development of turbosystems in the company BorgWarner Turbosystems GmbH. The author would like to thank Dr. Dimitrios Sfyris (Foundation for Research and Technology - Hellas) for his valuable contribution in the analytical solution of the Reynolds Equation for the finite length floating ring bearing and Dr. Panagiotis Koutsovasilis (BorgWarner Turbosystems GmbH - Germany) for the valuable discussions in turbosystem rotordynamics.

REFERENCES

[1] O. Pinkus and B. Sternlicht, Theory of hydrodynamic lubrication. McGraw Hill, New York, 1961.

[2] P. Orlov, Fundamentals of Machine Design. Part IV. Mir Publishers, Moscow, 1977.

[3] E. Nakagawa and H. Aoki, Unbalance vibrations of a rotor-bearing system supported by floating ring journal bearings. Bull ASME 16 (93), 503-512, 1973.

[4] F. Orcutt and C. Ng, Steady state and dynamic properties of floating ring journal bearings. ASME Journal of Lubrication Technology, Series F, 90 (1), 243-254, 1968.

[5] M. Mokhtar, Floating ring journal bearings: theory, design and optimization. Tribology International, 0301-679X/81/020113, 113-119, 1981.

[6] B. Schweizer, Oilwhirl, oilwhip and whirl/whip synchronization occurring in rotor systems with full-floating ring bearings. Journal of Nonlinear Dynamics doi:10. 1007/s11071-009-9466-3, 2009.

[7] L. San Andrés, J.C. Rivadeneira, K. Gjika, C. Groves, and G. LaRue, Rotordynamics of Small Turbochargers Supported on Floating Ring Bearings – Highlights in Bearing Analysis and Experimental Validation, ASME Journal of Tribology, 129, 391-397, 2007.

[8] D. Sfyris and A. Chasalevris, An exact analytical solution of the Reynolds equation for the finite journal bearing. Tribology International 55, 46-58, 2012.

[9] A. Chasalevris and D. Sfyris, Evaluation of the Finite Journal Bearing Characteristics Using the Exact Analytical Solution of the Reynolds Equation. Tribology International 57, 216-234, 2013.

11th International Conference on Engineering Vibration
Ljubljana, Slovenia, 7–10 September 2015

INFLUENCE OF THE OIL TEMPERATURE OF THRUST BEARINGS ON THE VIBRATORY BEHAVIOR OF SMALL TURBOCHARGERS

Ioannis Chatzisavvas*[1], Aydin Boyaci[1], Panagiotis Koutsovasilis[2], Bernhard Schweizer[1]

[1]Institute of Applied Dynamics, TU Darmstadt
{chatzisavvas, boyaci, schweizer}@sds.tu-darmstadt.de

[2]Rotordynamics & Preventive Acoustics, Global Engineering Core Science, BorgWarner Turbo Systems Engineering, DE-67292 Kirchheimbolanden
pkoutsovasilis@borgwarner.com

Keywords: Thrust Bearing, Reynolds Equation, Energy Equation, Thermohydrodynamic Lubrication, Turbocharger, Nonlinear Oscillations.

Abstract. *In this contribution, the effect of thrust bearings on the nonlinear oscillations of small turbocharger rotors is investigated. The oil-film forces from each pad of a thrust bearing are calculated using the Reynolds equation. The oil-temperature, which is determined with an appropriate energy equation, affects the pressure distribution and thereby the hydrodynamic forces from the thrust bearing. The Reynolds and the energy equation are coupled. In general, the two equations should be solved simultaneously at each time integration step of a transient simulation. The immense computational effort for the solution of these equations can be relaxed using a well-established simplified form of the energy equation. This simplification allows the decoupling of the energy equation from the Reynolds equation. Run-up simulations are performed with isothermal and thermohydrodynamic thrust bearing models, where the pressure fields from the thrust bearing are calculated. Moreover, the influence of the thrust bearing on the rotordynamic system is investigated in transient simulations.*

1 INTRODUCTION

Hydrodynamics thrust bearings are used in turbochargers for axial load support and rotor positioning. The axial loads, which are speed and gas-pressure dependent, are mainly created by the differing strength of the gas forces acting on compressor and turbine wheels. The Reynolds equation is used for the determination of the non-linear hydrodynamic bearing forces. In [1–4] it was shown that the isothermal Reynolds equation does not accurately describe the pressure distribution of the oil-film. The energy equation, which governs the temperature distribution of the lubricant, should be solved simultaneously with the Reynolds equation to account for the thermohydrodynamic lubrication problem. Theoretical and experimental investigations of thermohydrodynamic lubrication problems can be found in [5–7]. However, the computational effort for the solution of the pertinent equations is inappropriate for transient rotordynamic simulations. In [8] several reductions approaches were presented to diminish the size of the problem. A method to avoid this computational effort for thrust and journal bearings was presented in [9] and [10], respectively. This approach decouples the two equations by ignoring the pressure gradients in the energy equation (decoupled-adiabatic model). Therefore, the simultaneous solution of the coupled system is replaced by a sequential solution of the Reynolds and the energy equation. The heat losses to the bearing pads and the runner are neglected. Additionally the temperature is assumed constant across the oil-film [10].

The current work is organized as follows: initially, the pertinent equations (the Reynolds and the energy equation) and the assumptions for the decoupled-adiabatic thrust bearing model are discussed. Transient simulations of a turbocharger rotor/bearing system are carried out with isothermal models using different values of constant oil-viscosity. Finally, the decoupled-adiabatic bearing model is compared with the corresponding isothermal model and the influence of the variable oil-viscosity on the non oscillations, i.e. onset and amplitude, is investigated.

2 THRUST BEARING THERMOHYDRODYNAMIC MODELING

Turbochargers are usually equipped with taper flat thrust bearings. The geometric characteristics of a n-pad taper flat thrust bearing are shown in Figure 1. The angular extent of a pad is θ_0, the inner radius is r_1 and the outer radius is r_2. L is the circumferential length at the middle radius of a pad and L_{wed} is the length of the inclined part. The minimum distance between a pad and the aligned runner is $h_0(t)$; C_{wed} is the taper height.

2.1 Reynolds and energy equation

The oil-film pressure distribution $p(r,\theta)$ of a thrust bearing is governed by the Reynolds equation

$$\frac{\partial}{\partial r}\left(\frac{rh^3}{\mu}\frac{\partial p}{\partial r}\right)+\frac{1}{r}\frac{\partial}{\partial \theta}\left(\frac{h^3}{\mu}\frac{\partial p}{\partial \theta}\right)=6\omega r\frac{\partial h}{\partial \theta}+12r\frac{\partial h}{\partial t}, \tag{2.1}$$

where ω is the rotational speed of the rotor and t the time. The circumferential and radial coordinates are represented by the spatial variables θ and r, respectively. The oil-viscosity μvaries along r and θ, i.e. $\mu(r,\theta)$. The oil-film thickness $h(r,\theta,h_0(t),\alpha(t),\beta(t))$ is given by

$$h=\begin{cases} h_0(t)+C_{\text{wed}}-C_{\text{wed}}\dfrac{\theta-\Theta_i}{\theta_0\dfrac{L_{\text{wed}}}{L}}+r(\alpha(t)\cos\theta+\beta(t)\sin\theta) & \text{(Inclined Part)} \\ h_0(t)+r(\alpha(t)\cos\theta+\beta(t)\sin\theta) & \text{(Flat Part)} \end{cases}, \tag{2.2}$$

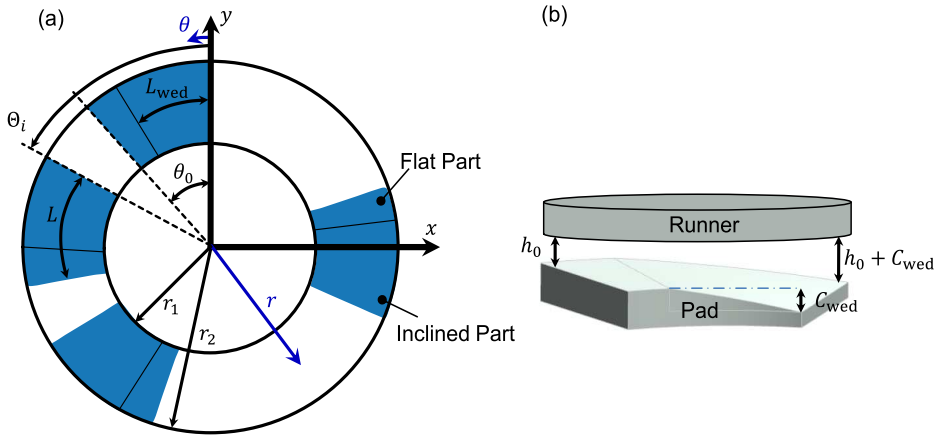


Figure 1: Thrust bearing: (a) bearing geometry, (b) pad geometry.

where $\alpha(t)$ and $\beta(t)$ are the first and the second Bryant angles [11]. Θ_i is the angle of the leading edge of the pad i as shown in Figure 1 . Under the assumption that the oil is incompressible, the oil-temperature distribution $T(r,\theta)$ is calculated using the energy equation

$$\rho c_p \left(\frac{\partial T}{\partial t} + u_r \frac{\partial T}{\partial r} + \frac{u_\theta}{r} \frac{\partial T}{\partial \theta} + u_z \frac{\partial T}{\partial z} \right) = k \left(\frac{1}{r^2} \frac{\partial^2 T}{\partial \theta^2} + \frac{1}{r} \frac{\partial T}{\partial r} \left(r \frac{\partial T}{\partial r} \right) + \frac{\partial^2 T}{\partial z^2} \right) + \Phi, \quad (2.3)$$

where k is the thermal conductivity, ρ is the density and c_p is the specific heat of the oil. The velocities in radial, circumferential and axial direction are u_r, u_θ and u_z, respectively. The term on the left hand side of Eq. 2.3 describes the convection in the oil-film including the temperature time-dependent term. On the right hand side, the first term represents the conduction in the oil-film and the second the viscous dissipation. The assumption in the Reynolds equation (Eq. 2.1) that the temperature is constant across the film thickness is also adopted into the energy equation, i.e. the convection term $\frac{\partial T}{\partial z}$ and the conduction term $\frac{\partial^2 T}{\partial z^2}$ are ignored. It is additionally assumed here that no heat is conducted away by the oil-film and therefore, all the conduction terms will be neglected. Furthermore, the temperature time-dependent term $\frac{\partial T}{\partial t}$ is neglected as in [12]. The viscous dissipation Φ after an order of magnitude analysis [1] is reduced to the form:

$$\Phi = \mu \left(\left(\frac{\partial u_r}{\partial z} \right)^2 + \left(\frac{\partial u_\theta}{\partial z} \right)^2 \right). \quad (2.4)$$

With the above assumptions, the quasistatic energy equation reads:

$$\rho c_p \left(u_r \frac{\partial T}{\partial r} + \frac{u_\theta}{r} \frac{\partial T}{\partial \theta} \right) = \mu \left(\left(\frac{\partial u_r}{\partial z} \right)^2 + \left(\frac{\partial u_\theta}{\partial z} \right)^2 \right). \quad (2.5)$$

Equation 2.5 presents the balance between the heat convected away by the fluid and that generated at any point in the area between the bearing pads and the runner. For the determination of the temperature distribution it is assumed that the inlet temperature T_{in} of every pad is constant i.e. $T(r,\Theta_i) = T_{\text{in}}$. The mixing between the fresh oil and the oil coming from a previous pad is neglected.

2.2 Decoupled-adiabatic thrust bearing model

The computational effort of solving the Reynolds and the energy equation simultaneously can be avoided by ignoring the pressure gradients from the radial and circumferential velocities in the energy equation [9]. Thus, the two equations are decoupled and they can be solved independently through a sequential procedure. Namely, the energy equation is solved for the oil-viscosity, which is then substituted in the Reynolds equation for the determination of the pressure distribution. The decoupled-adiabatic energy equation, outlined above, reads:

$$\rho c_p \left(\frac{\omega}{2} \frac{\partial T}{\partial \theta} \right) = \mu \left(\frac{r\omega}{h} \right)^2 . \tag{2.6}$$

A simple relationship between temperature and viscosity is used:

$$\mu = \mu_{\text{in}} e^{-\lambda (T - T_{\text{in}})}, \tag{2.7}$$

where λ is the temperature-viscosity coefficient, μ_{in} is the inlet oil-viscosity and T_{in} is the inlet oil-temperature at Θ_i for every pad i.

3 NUMERICAL SIMULATIONS

Transient simulations of a turbocharger rotor/bearing system are performed considering the isothermal and the decoupled-adiabatic thrust bearing model. The influence of the former on the nonlinear oscillations of the rotor, is investigated using various values of constant oil-viscosity. Additionally, the decoupled-adiabatic model is compared with the corresponding isothermal during a rotor run-up.

3.1 Mechanical model of a turbocharger rotor/bearing system

A typical turbocharger rotor/bearing system is illustrated in Figure 2 [13, 14]. It consists of a shaft and two wheels, the compressor and the turbine. The shaft is supported by full-floating ring bearings. Unbalance masses are attached at the same phase angle on the com-

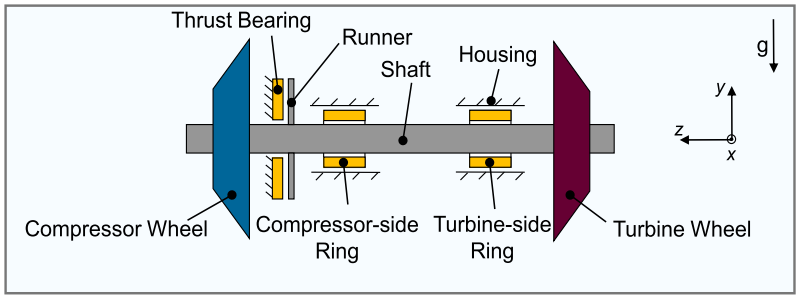


Figure 2: Schematic sketch of a turbocharger rotor/bearing system.

pressor ($u_{\text{C}} = 0.15\,\text{gmm}$) and on the turbine ($u_{\text{T}} = 0.2\,\text{gmm}$) wheel. The pressure distribution from the full-floating ring bearings is modeled using the short bearing theory. For pronouncing the effect of the thrust bearing, the oil-viscosity of the radial bearings is assumed constant in all the current simulations. The shaft (mass $m_{\text{S}} \approx 0.02\,\text{kg}$) is a model order reduced flexible body [15–17]. The turbine (mass $m_{\text{T}} \approx 0.06\,\text{kg}$) and the compressor (mass $m_{\text{C}} \approx 0.02\,\text{kg}$)

wheels are considered as rigid bodies fixed on the shaft. The floating rings are also modeled as rigid bodies. The relevant values of the parameters considered in the simulations are given in Table 1. This work mainly focuses on the subsynchronous oscillations of the turbocharger

Parameter	Description	Value
r_1	inner radius	3.55 mm
r_2	outer radius	6.3 mm
θ_0	angular extent of pad	0.775 rad
L_{wed}/L	ratio of lengths (inclined/full part)	0.7
C_{wed}	taper height	10 μm
ρ	density of the oil	874.5 kg/m^3
c_p	specific heat of the oil	2010 J/(kg K)
λ	temperature-viscosity coefficient	0.0225 1/K

Table 1: Simulation parameters of a taper flat thrust bearing.

rotor. The notation followed here is the one used in [18]. The gyroscopic forward conical mode excited by the inner oil film generates the first subsynchronous oscillations (*sub 1*), the gyroscopic forward cylindrical mode excited by the inner oil film generates the second subsynchronous oscillations (*sub 2*) and the gyroscopic forward conical mode excited by the outer oil film generates the third subsynchronous oscillations (*sub 3*).

The axial force from the gases varies in real applications. Here, it is assumed that this force is $F_{\mathrm{axial}} = 100\,\mathrm{N}$. In the following transient numerical simulations, the rotational speed of the rotor ω and the externally applied axial force $F_{\mathrm{axial}}(t)$ acting in the positive z-direction are prescribed as shown in Figure 3.

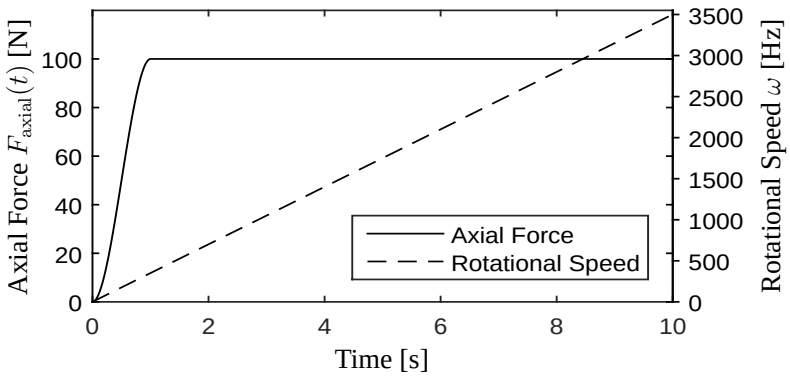


Figure 3: External axial force and rotational speed of the turbocharger rotor.

3.2 Simulations with isothermal thrust bearing model

Transient simulations are performed for oil-temperatures of $T = 40\,^{\circ}\mathrm{C}$, $T = 80\,^{\circ}\mathrm{C}$ and $T = 120\,^{\circ}\mathrm{C}$. In Figure 4, the axial displacements of the rotor are presented for different values

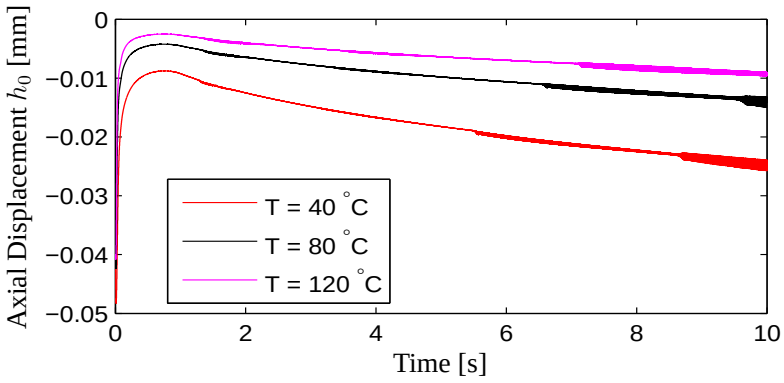


Figure 4: Axial displacements of the rotor for different values of constant oil-temperature.

of constant oil-temperature of a 6-pad thrust bearing. The negative axial displacement implies that the bearing is on the left side of the runner (see Figure 2). As the oil-temperature decreases, each pad can support a higher load for a given axial distance [2]. Since the external axial bearing force is constant ($F_{\text{axial}} = 100\,\text{N}$ for $t > 1\,\text{s}$), the axial distance between the runner and the bearing pads is larger in the model with the higher oil-viscosity.

The vertical displacement of the turbine wheel for each prescribed temperature are shown in Figure 5. At $t \approx 1.2\,\text{s}$ the *sub 1* oscillations appear. The onset point of these oscillations is almost unaffected by the oil-temperature. The *sub 2* oscillations occur at $t \approx 3.1\,\text{s}$ for $T = 40\,^{\circ}\text{C}$, at $t \approx 3.3\,\text{s}$ for $T = 80\,^{\circ}\text{C}$ and at $t \approx 3.5\,\text{s}$ for $T = 120\,^{\circ}\text{C}$. The amplitudes of the *sub 2* oscillations are quite lower than those of *sub 1*. The *sub 3* oscillations are significantly affected

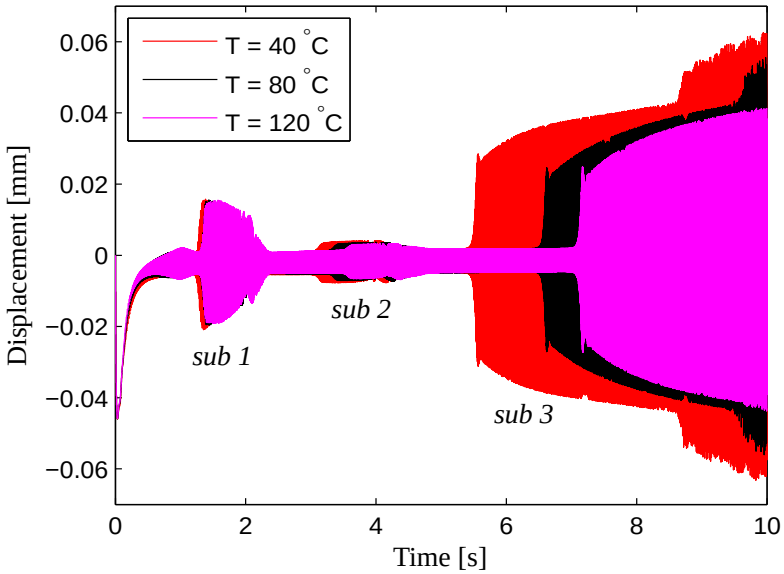


Figure 5: Vertical displacements of the turbine wheel for different values of constant oil-temperature.

from the oil-temperature. With higher oil-viscosity ($T = 40\,^{\circ}\mathrm{C}$) the *sub 3* oscillations become apparent at $t \approx 5.5\,\mathrm{s}$. As the oil-viscosity decreases ($T = 120\,^{\circ}\mathrm{C}$) they are seen at $t \approx 7.1\,\mathrm{s}$.

The difference in the onset points of the *sub 3* oscillations between the isothermal models can be explained as follows: For smaller axial distances h_0 between the runner and the bearing pads, the angular stiffness (and damping) provided from the thrust bearing becomes larger. Therefore, the subsynchronous oscillations appear at higher rotational speeds when the axial distance is lower. Furthermore, the axial distance decreases as the value of the oil-temperature becomes higher (see Figure 4). It can be concluded that for larger oil-temperatures, the *sub 3* oscillations are encountered in higher rotational speeds. The increase of the angular stiffness of the thrust bearing mainly affects the subsynchronous oscillations related with the conical mode of the system. The effect of the angular stiffness on the *sub 1* oscillations is very small, since in lower rotational speeds, the influence of the thrust bearing is less evident.

Figure 6 shows the Short Time Fourier Transform of the turbine displacements for a constant oil-temperature of $T = 120\,^{\circ}\mathrm{C}$. Low amplitude synchronous oscillations are observed due to the unbalance masses on the turbine and compressor wheels.

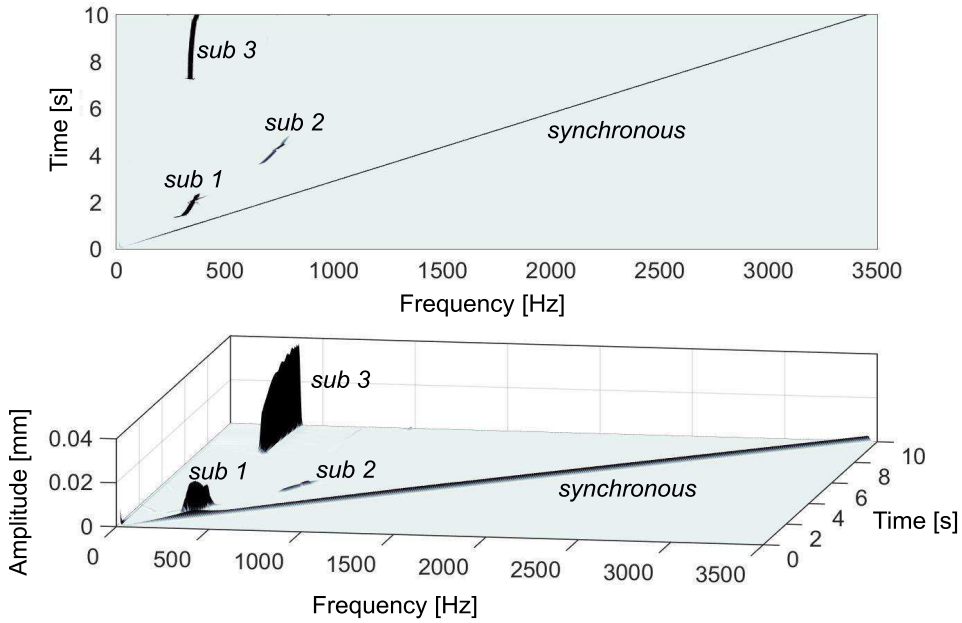


Figure 6: Short Time Fourier Transform (2D and 3D) of the turbine displacements in vertical direction for $T = 120\,^{\circ}\mathrm{C}$.

3.3 Simulations with decoupled-adiabatic thrust bearing model

The decoupled-adiabatic thrust bearing model is compared with the isothermal in a transient simulation. Figure 7 shows the axial displacements of the rotor for the two considered models. The inlet temperature in both cases is assumed $T_{\mathrm{in}} = 100\,^{\circ}\mathrm{C}$. The oil-temperature at all points of the bearing pads is higher for the decoupled-adiabatic model due to viscous dissipation. As explained in section 3.2, the axial distance between the runner and the pads is higher in the isothermal case.

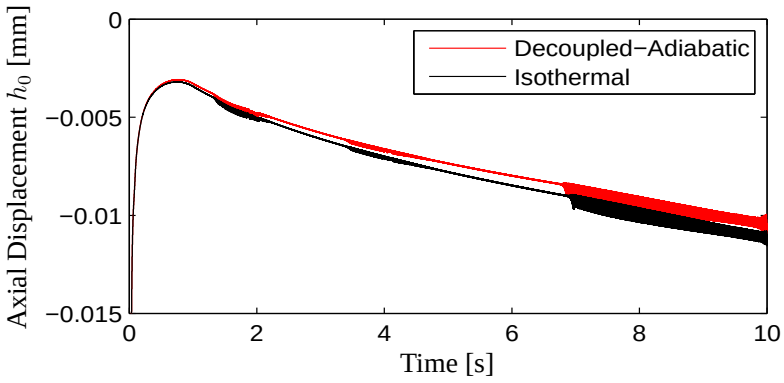


Figure 7: Axial displacements of the rotor for the isothermal and the decoupled-adiabatic thrust bearing model.

The vertical displacements of the turbine wheel for the isothermal and the decoupled-adiabatic case are shown in Figure 8. The *sub 1* and *sub 2* oscillations are almost unaffected using the thermohydrodynamic model as compared with the isothermal. Additionally, the influence on the *sub 3* oscillations is rather small. Figure 9 shows the mean temperature of a bearing pad during the run-up. The presented mean temperature of the decoupled-adiabatic model is calculated from the averaged temperature over a rotation using Eq. 2.7. Since the mean temperature exhibits only a slightly increase, the thermal effects predicted from the decoupled-adiabatic model exert minor influence on the dynamics of the system in the current simulations.

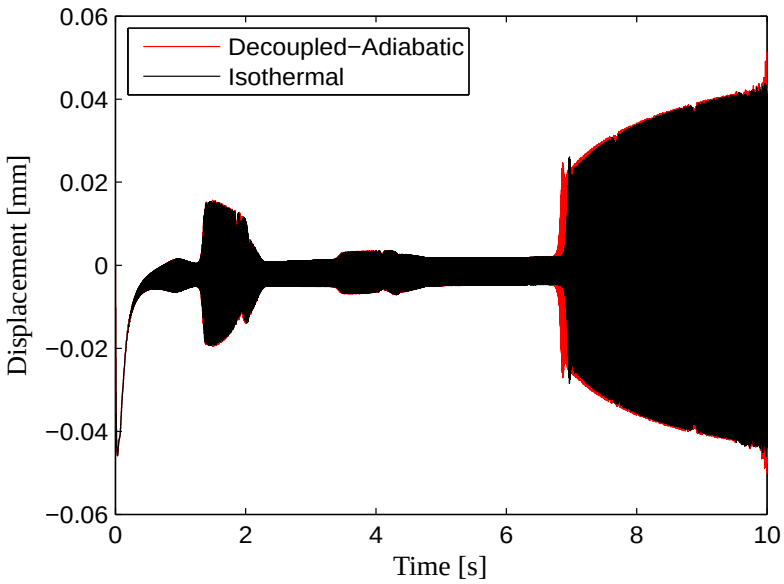


Figure 8: Vertical displacements of the turbine wheel for the isothermal and the decoupled-adiabatic thrust bearing model.

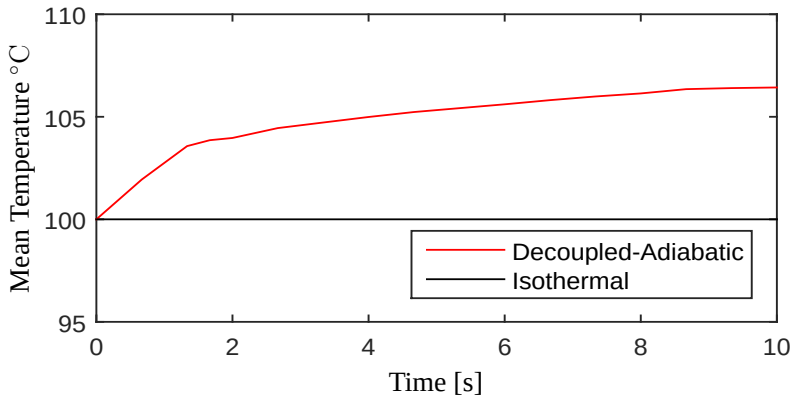


Figure 9: Mean temperature of one pad for the isothermal and the decoupled-adiabatic thrust bearing model.

4 CONCLUSIONS

The influence of the oil-temperature of thrust bearings on the nonlinear oscillations of a turbocharger rotor was investigated. The Reynolds and the energy equations, that govern the thermohydrodynamic lubrication of thrust bearings, may be decoupled allowing for time-efficient transient simulations. Considering the isothermal model, the oil-viscosity affects the axial distance between the runner and the bearing pads as well as the onset point of the subsynchronous oscillations, mainly the sub 3. The decrease of oil-viscosity dictates a smaller distance between the runner and the bearing pads. Additionally, the subsynchronous oscillations are shifted to higher rotational speeds with the increase of temperature. The decoupled-adiabatic model predicted a slightly higher mean oil-temperature during the run-up simulation. Therefore, the influence of the thermohydrodynamic model had a minor effect on the nonlinear oscillations in these simulations compared with the corresponding isothermal.

REFERENCES

[1] D. Dowson, A generalized Reynolds equation for fluid-film lubrication. *Journal of Mechanical Sciences*, **4** (2), 159–170, 1962.

[2] K. H. Huebner, A three-dimensional thermohydrodynamic analysis of sector thrust bearings. *ASLE Transactions*, **109** (17), 62–73, 1974.

[3] A. Fogg, Fluid film lubrication of parallel thrust surfaces. *Proceedings of the Institution of Mechanical Engineers*, **155** (1), 49–67, 1946.

[4] A. A. Raimondi, An adiabatic solution for the finite slider bearing (L/B = 1). *ASLE Transactions*, **101** (9), 283–298, 1966.

[5] A. Dadouche and M. Fillon and J.C. Bligoud, Experiments on thermal effects in a hydrodynamic thrust bearing. *Tribology International*, **33**, 167–174, 2000.

[6] A. Dadouche and M. Fillon and W. Dmochowski, Performance of a hydrodynamic fixed geometry thrust bearing: Comparison between experimental data and numerical results. *Tribology Transactions*, **49**, 419–426, 2006.

[7] Y. Henry and J. Bouyer and M. Fillon, An experimental hydrodynamic thrust bearing device and its application to the study of a tapered-land thrust bearing. *Journal of Tribology*, **136** (2), 021703-1–021703-11, 2014.

[8] M. Mahner and A. Lehn and B. Schweizer, Thermogas- and thermohydrodynamic simulation of thrust and slider bearings: Convergence and efficiency of different reduction approaches. *Tribology International*, **0** , 0–0, 2015.

[9] H. Heshmat and O. Pinkus, Misalignment in thrust bearings including thermal and cavitation effects. *Journal of Tribology*, **109** (1), 108–114, 1987.

[10] O. Pinkus and S. S. Bupara, Adiabatic solutions for finite journal bearings. *Journal of Tribology*, **101** (4), 492–496, 1979.

[11] I. Chatzisavvas, A. Boyaci and B. Schweizer, Efficient thrust bearing model for high speed rotordynamic applications. P. Pennacchi ed. *Proceedings of the 9th IFToMM International Conference on Rotor Dynamics Mechanisms and Machine Science*, **21**, 969–980, 2015.

[12] M. Fillon and H. Desbordes and J. Frene and C. Chan Hew Wai, A global approach of thermal effects including pad deformations in tilting-pad Journal bearings submitted to unbalance load. *Journal of Tribology*, **118** (1), 169–174, 1996.

[13] B. Schweizer, Dynamics and stability of turbocharger rotors. *Archive of Applied Mechanics*, **80** (9), 1017–1043, 2010.

[14] R. G. Kirk and A. A. Alsaeed, Induced unbalance as a method for improving the dynamic stability of high-speed turbochargers. *International Journal of Rotating Machinery*, **2011** (Article ID 952869), 9 pages, 2011.

[15] P. Koutsovasilis, Model order reduction in structural mechanics: coupling the rigid and elastic multi-body dynamics. *PhD thesis, Technische Universitt Dresden*, 2009.

[16] P. Koutsovasilis, Improved component mode synthesis and variants. *Multibody System Dynamics*, **29**, 343–359, 2013.

[17] M. C. C. Bampton and R. R. Craig jr., Coupling of substructures in dynamic analysis. *AIAA Journal*, **6** (7), 1313–1319 1968.

[18] B. Schweizer, Total instability of turbocharger rotors – Physical explanation of the dynamic failure of rotors with full-floating ring bearings. *Journal of Sound and Vibration*, **328** (1), 156–190, 2009.

International Conference on Engineering Vibration
Ljubljana, Slovenia, 7-10 September 2015

ROTOR UNBALANCE ESTIMATION USING A SINGLE MACHINE RUNDOWN WITH REDUCED NUMBER OF SENSORS

Sami M. Ibn Shamsah*[1, 2], Jyoti K. Sinha[1]

[1] School of Mechanical, Aerospace and Civil Engineering (MACE), The University of Manchester, Manchester, UK
{sami.ibnshamsah, jyoti.sinha}@manchester.ac.uk

[2] Ministry of Education: Saudi Arabia

Keywords: Rotor unbalance, Foundation model, Vibration monitoring, Fault diagnosis, Rotating machinery.

Abstract. *Earlier proposed methods in the literature on the rotor unbalance and foundation model estimation using a single machine rundown data have used vibration measurements at all bearing pedestals in both lateral and vertical orthogonal directions. It is generally believed that the measurement in both directions provides the bigger picture of machine dynamical behaviour. However, in the present study the concept of the earlier method is used again but with reduced number of sensors. Instead of using 2 vibration sensors at a bearing pedestal in both lateral and vertical directions, just a single sensor is used at each pedestal, hence reducing the number of sensors by 50%. The sensor is mounted in the radial direction (45 degree to both lateral and vertical directions) so that the measured vibration data will have significant content of vibration behaviour from both directions. The concept is applied to a simple simulated rig of a rotor having a balance disc and supported on either side through ball bearing on flexible foundation. The paper presents the modelling details and comparison of several unbalance estimations in the simulated rig example.*

1 INTRODUCTION

The reliability of rotor machines is essential to industries and plants around the world as most of their activities rely on this class of machines. Over the years, with the development of engineering and material science, industries have tended to use high-speed flexible rotor machines which are supported by lightweight fabricated steel structures and run for long periods of time. As these flexible foundations usually have natural frequencies below the operating speed of the machine, their effect should be taken in consideration in the routine condition monitoring and associated maintenance strategy. Neto *et al*. [1] have highlighted the effects of the flexible foundation on the rotor machine by presenting some real case studies.

Many researchers proposed methods for the identification of rotor machines foundation model [2]. Overview of the different experimental modal analysis approaches was provided by Irretier [3]. Stephenson *et al*. [4] applied modal analysis methods to determine the foundation dynamic characteristics from test in terms of FRFs. Lees *et al*. [5] gave an overview of the researches on the model based identification of foundation model as well as presenting a brief theory of this approach. It has been found that using measured vibration response at the bearing locations together with an acceptable numerical model for the rotor and a reasonably accurate model for the bearings seems to be the most promising approach to identify the foundation model and rotor faults simultaneously [5-7]. Some researchers recently proposed vibration based condition monitoring (VCM) techniques that use few number of sensors, without necessarily compromising the valuable information required for the diagnosis [8, 9].

The existing rotor unbalance and foundation model identification approaches [7, 10] used two vibration sensors per bearing location. These methods are not very practical for large and complex rotating machines as they could be computationally involved and time-consuming as well as significantly relying on experience and engineering judgment during data analysis. Therefore, the current study aims to improve the existing approaches by presenting a simplified and computational efficient method for identifying and quantifying state of rotor unbalance and foundation model in rotor machines using response from a single vibration sensor per bearing location and vibration measurements from a single machine run.

2 EARLIER METHOD [10]

Earlier rotor fault identification method [10] used vibration response measurements from vertical and lateral directions, i.e.v_k and u_k in Figure 1(b) respectively, to estimate the state of rotor unbalance (both amplitude and phase) and foundation model from a single machine coast-down (Figure 1). In their model, each node consists of 4 degrees of freedom (2 translational and 2 rotational), i.e. $[u, v, \theta, \Psi]^T$, as shown in Figure 2.

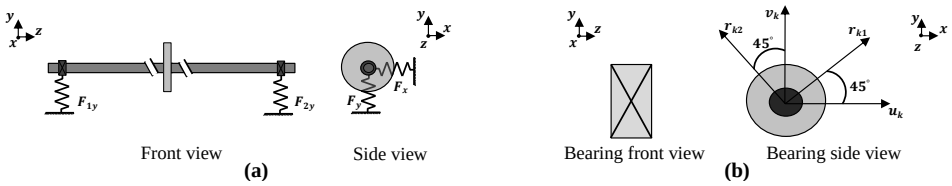


Figure 1: (a) Schematic representation of the rig (b) Directions where measurements are taken from.

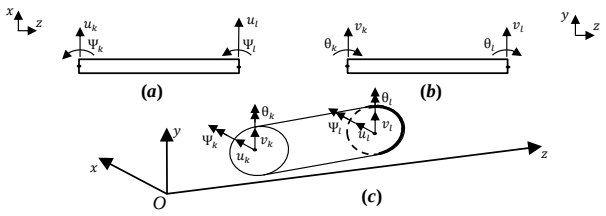


Figure 2: A rotor element with degrees of freedom (a) Horizontal plane, (b) Vertical plane, (c) Combination of horizontal and vertical.

3 PROPOSED METHOD

The current approach aims to investigate the feasibility of estimating the foundation model and state of rotor unbalance using reduced number of vibration measurements from a single machine run. Same formulation as the earlier method [10] is used, but instead of using two vibration sensors per bearing location, i.e. one measures vertical response and the other measures lateral response, only one sensor is used. In order to have significant content of vibration behaviour from vertical and horizontal directions, the response is taken from the radial direction, i.e. r_{k1} and r_{k2} in Figure 1(b). Schematic representation of the rig used in the numerical simulation is shown in Figure 3.

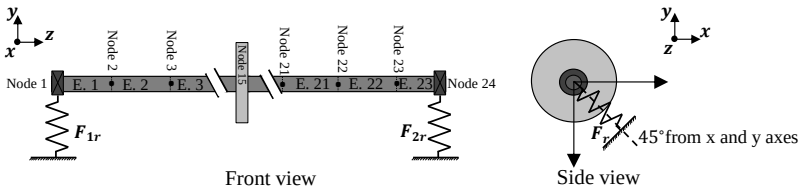


Figure 3: Schematic representation of the rotor.

3.1 Theory

In the construction of typical rotor machinery, the rotor, bearings and machine supporting structure (foundation) are often considered as the major components, where the rotor is connected to the flexible machine supporting structure through the bearings. The equation of motion of such structure can be written [11] as

$$\begin{bmatrix} \mathbf{Z}_{R,ii} & \mathbf{Z}_{R,if} & 0 \\ \mathbf{Z}_{R,fi} & \left(\mathbf{Z}_{R,ff}+\mathbf{Z}_{F,ff}\right) & -\mathbf{Z}_{F,fi} \\ 0 & -\mathbf{Z}_{F,if} & \mathbf{Z}_{F,ii} \end{bmatrix} \begin{Bmatrix} \mathbf{d}_{R,i} \\ \mathbf{d}_{R,f} \\ \mathbf{d}_{F,i} \end{Bmatrix} = \begin{Bmatrix} \mathbf{f}_u \\ 0 \\ 0 \end{Bmatrix} \tag{1}$$

where $\mathbf{Z}$, $\mathbf{d}$ and $\mathbf{f}_u$ are the dynamic stiffness matrix, displacement and unbalance forces respectively, and the subscripts F, R, i and f denote the foundation, rotor, internal degrees of freedom and connection degrees of freedom respectively. In this method, the dynamic stiffness matrix of each element is reduced from 8 by 8 to 4 by 4 related to degrees of freedom $[u_k, v_k, \theta_k, \Psi_k, u_l, v_l, \theta_l, \Psi_l]^T$ to $[r_k, \Psi_{rk}, r_l, \Psi_{rl}]^T$ respectively. Therefore, the total size of the dynamic stiffness matrix of the system is reduced by half. As a result, the time and computational effort in the signal processing will reduce significantly. The unbalance forces are assumed to be applied only at the rotor internal degrees of freedom. It is also assumed that the bearings are rigid connections between the rotor and foundation. The foundation at

bearings locations can be modelled by using the degrees of freedom of the rotor only; hence the foundation internal degrees of freedom are eliminated. Therefore, Eq. (1) is reduced to

$$\begin{bmatrix} \mathbf{Z}_{R,ii} & \mathbf{Z}_{R,if} \\ \mathbf{Z}_{R,fi} & \left(\mathbf{Z}_{R,ff}+\mathbf{Z}_{F,ff}\right) \end{bmatrix} \begin{Bmatrix} \mathbf{d}_{R,i} \\ \mathbf{d}_{R,f} \end{Bmatrix} = \begin{Bmatrix} \mathbf{f}_u \\ 0 \end{Bmatrix} \tag{2}$$

Eq. (2) may be expressed as

$$[\mathbf{Z}_{R,ii}]\{\mathbf{d}_{R,i}\} + [\mathbf{Z}_{R,if}]\{\mathbf{d}_{R,f}\} = \{\mathbf{f}_u\} \tag{3}$$

and

$$[\mathbf{Z}_{R,fi}]\{\mathbf{d}_{R,i}\} + [(\mathbf{Z}_{R,ff} + \mathbf{Z}_{F,ff})]\{\mathbf{d}_{R,f}\} = \{0\} \tag{4}$$

Eq. (3) can be rearranged as

$$\{\mathbf{d}_{R,i}\} = [\mathbf{Z}_{R,ii}]^{-1}[\{\mathbf{f}_u\} - [\mathbf{Z}_{R,if}]\{\mathbf{d}_{R,f}\}] \tag{5}$$

The unknown response can be eliminated by substituting Eq. (5) into Eq. (4) as follows

$$[\mathbf{Z}_{R,fi}][\mathbf{Z}_{R,ii}]^{-1}[\{\mathbf{f}_u\} - [\mathbf{Z}_{R,if}]\{\mathbf{d}_{R,f}\}] + [(\mathbf{Z}_{R,ff} + \mathbf{Z}_{F,ff})]\{\mathbf{d}_{R,f}\} = \{0\} \tag{6}$$

It is assumed that a reasonably accurate model for the rotor is available and the response is measured. Thus, the foundation model and unbalance forces are the only unknowns in Eq. (6).

By inspecting Figure 4, it can be figured out that (x, y) coordinates of a point P can be written in terms of (x', y') as follows

$$x = x'cos(\beta) - y'sin(\beta)$$
$$y = x'sin(\beta) + y'cos(\beta)$$

In matrix form,

$$\begin{bmatrix} x \\ y \end{bmatrix} = \begin{bmatrix} \cos(\beta) & -\sin(\beta) \\ \sin(\beta) & \cos(\beta) \end{bmatrix} \begin{bmatrix} x' \\ y' \end{bmatrix}$$

Hence,

$$\begin{bmatrix} x' \\ y' \end{bmatrix} = \begin{bmatrix} \cos(\beta) & \sin(\beta) \\ -\sin(\beta) & \cos(\beta) \end{bmatrix} \begin{bmatrix} x \\ y \end{bmatrix}$$

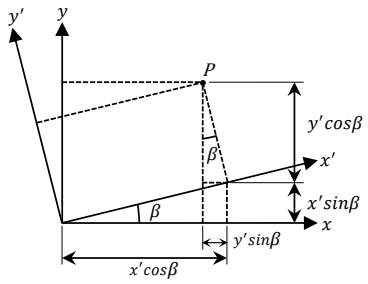


Figure 4: Coordinates of a point in two systems.

Therefore, in order to get the radial response, the vertical and horizontal responses of each bearing are multiplied by the following transformation matrix

$$\mathbf{T}_r = \begin{bmatrix} \cos(45) & \sin(45) \\ -\sin(45) & \cos(45) \end{bmatrix} \tag{7}$$

3.2 Parameter estimation

The unbalance planes are assumed to be positioned at nodes n_1, n_2,…, n_p where p is the number of planes. The amplitude of unbalance may be defined as

$$u_{n_i} = m_{u_i} e_i \tag{8}$$

where m_{u_i} is the unbalance mass at plane i, and e is the eccentric radius of the unbalance mass. In terms of matrices, the amplitude of unbalance and the phase angles associated to the unbalance planes can be written as $\left[u_{n_1}, u_{n_2}, u_{n_3}, \ldots, u_{n_p}\right]^{\mathrm{T}}$ and $\left[\alpha_{n_1}, \alpha_{n_2}, \alpha_{n_3}, \ldots, \alpha_{n_p}\right]^{\mathrm{T}}$ respectively. Therefore, the complex quantity of the rotor unbalance may be expressed as

$$u_{n_i} \exp(\mathrm{j}\alpha_{n_i}) = a_{n_i} + \mathrm{j}b_{n_i} \tag{9}$$

where a_{n_i} and b_{n_i} can be defined as

$$a_{n_i} = m_i\, e_i \cos(\alpha) \quad \text{and} \quad b_{n_i} = m_i\, e_i \cos\left(\alpha + \frac{\pi}{2}\right) = m_i\, e_i \sin(\alpha) \tag{10}$$

Hence, the unbalance forces can be written as

$$\mathbf{f}_u = \omega^2 \begin{Bmatrix} 0 \\ 0 \\ m_1\, e_1(cos(\alpha_1) + j\, sin(\alpha_1)) \\ 0 \\ \vdots \\ 0 \\ m_p\, e_p(cos(\alpha_p) + j\, sin(\alpha_p)) \\ 0 \\ \vdots \\ 0 \end{Bmatrix} = \omega^2 \begin{Bmatrix} 0 \\ 0 \\ a_{n_1} + jb_{n_1} \\ 0 \\ \vdots \\ 0 \\ a_{n_p} + jb_{n_p} \\ 0 \\ \vdots \\ 0 \end{Bmatrix} \tag{11}$$

where the locations in the unbalance force vector depend on the nodal locations of the unbalance planes. Eq. (11) may be further simplified as

$$\mathbf{f}_u = \omega^2 \mathbf{T}\mathbf{g} \tag{12}$$

where $\mathbf{g} = \left[a_{n_1}\ b_{n_1}\ a_{n_2}\ b_{n_2}\ \cdots\ a_{n_p}\ b_{n_p}\right]^T$ and $\mathbf{T}$ is the transformation matrix that is defined such that Eqs. (11) and (12) are equivalent. Substituting Eq. (12) into Eq. (6) gives,

$$[\mathbf{Z}_{R,fi}\mathbf{Z}_{R,ii}{}^{-1}\mathbf{Z}_{R,if} - \mathbf{Z}_{R,ff}]\{\mathbf{d}_{R,f}\} - [\mathbf{Z}_{F,ff}]\{\mathbf{d}_{R,f}\} = \omega^2[\mathbf{Z}_{R,fi}\mathbf{Z}_{R,ii}{}^{-1}\mathbf{T}]\mathbf{g} \tag{13}$$

In order to identify the rotor unbalance in a least-square sense, the foundation parameters are grouped into vectors $\mathbf{v_o}$, $\mathbf{v_1}$ and $\mathbf{v_2}$. Assume that the foundation dynamic stiffness matrix $(\mathbf{Z}_{F,ff})$ is written in terms of mass, damping and stiffness matrices. If there are n measured degrees of freedom at the foundation-bearing interface, then $\mathbf{v_o}$, $\mathbf{v_1}$ and $\mathbf{v_2}$ may be written as

$$\mathbf{v_o} = [k_{F,11}\, k_{F,12}\ \ldots\ k_{F,nn}],\ \mathbf{v_1} = [c_{F,11}\, c_{F,12}\ \ldots\ c_{F,nn}],\ \mathbf{v_2} = [m_{F,11}\, m_{F,12}\ \ldots\ m_{F,nn}] \tag{14}$$

$\mathbf{v_o}$, $\mathbf{v_1}$ and $\mathbf{v_2}$ can be collected in one matrix as follows

$$\mathbf{v} = [\mathbf{v_o}\ \mathbf{v_1}\ \mathbf{v_2}]^{\mathrm{T}} \tag{15}$$

With this definition of $\mathbf{v}$, there is a linear transformation such that

$$[\mathbf{Z}_{F,ff}]\{\mathbf{d}_{R,f}\} = [\mathrm{W}]\{\mathbf{v}\} \tag{16}$$

where W contains the measured response terms at each frequency. For the N_{th} measured frequency

$$\mathrm{W}(\omega_N) = [\mathrm{W}_o(\omega_N)\ \mathrm{W}_1(\omega_N)\ \mathrm{W}_2(\omega_N)]^T \tag{17}$$

If all elements of the foundation mass, damping and stiffness matrices are identified, then

$$W_k(\omega_N)[v_k]^T = (j\omega_N)^k \begin{bmatrix} d_{Rf1}(\omega_N) & \cdots & d_{Rf,n}(\omega_N) & 0 & & & \cdots & 0 \\ 0 & \cdots & 0 & d_{Rf1}(\omega_N) & \cdots & d_{Rf,n}(\omega_N) & \cdots & 0 \\ \vdots & & \vdots & \vdots & & \vdots & & \vdots \\ 0 & 0 & 0 & 0 & 0 & 0 & d_{Rf1}(\omega_N) & d_{Rf,n}(\omega_N) \end{bmatrix} [v_k]^T \quad (18)$$

where $k = 0,1,2$. Eq. (13), then, becomes

$$[\mathbf{Z}_{R,fi}\mathbf{Z}_{R,ii}{}^{-1}\mathbf{Z}_{R,if} - \mathbf{Z}_{R,ff}]\{\mathbf{d}_{R,f}\} - [W]\{v\} = \omega^2[\mathbf{Z}_{R,fi}\mathbf{Z}_{R,ii}{}^{-1}\mathbf{T}]\mathbf{g} \quad (19)$$

Let

$$R(\omega_N) = \omega_N^2[\mathbf{Z}_{R,fi}\mathbf{Z}_{R,ii}{}^{-1}\mathbf{T}] \quad (20)$$

and

$$H(\omega_N) = [\mathbf{Z}_{R,fi}\mathbf{Z}_{R,ii}{}^{-1}\mathbf{Z}_{R,if} - \mathbf{Z}_{R,ff}]\{\mathbf{d}_{R,f}\} \quad (21)$$

Hence, Eq. (19) becomes

$$H(\omega_N) - [W(\omega_N)]\{v\} = [R(\omega_N)]\{\mathbf{g}\} \xrightarrow{yields} [W(\omega_N)]\{v\} + [R(\omega_N)]\{\mathbf{g}\} = H(\omega_N) \quad (22)$$

Eq. (22) may be rewritten as

$$[W(\omega_N)\ R(\omega_N)]\begin{Bmatrix} v \\ \mathbf{g} \end{Bmatrix} = [H(\omega_N)] \quad (23)$$

Suppose that the response is measured for frequencies starting from 1 Hz to q Hz. All measurements are used at ones, and one estimation of the rotor unbalance is produced. Thus, Eq. (23) is repeated q times to give

$$\begin{bmatrix} W_0(\omega_1) & W_1(\omega_1) & W_2(\omega_1) & R(\omega_1) \\ W_0(\omega_2) & W_1(\omega_2) & W_2(\omega_2) & R(\omega_2) \\ \vdots & \vdots & \vdots & \vdots \\ W_0(\omega_q) & W_1(\omega_q) & W_2(\omega_q) & R(\omega_q) \end{bmatrix} \begin{Bmatrix} v \\ \mathbf{g} \end{Bmatrix} = \begin{bmatrix} H(\omega_1) \\ H(\omega_2) \\ \vdots \\ H(\omega_q) \end{bmatrix} \quad (24)$$

Eq. (23) is a least square problem where the number of equations is more than the number of unknowns. Therefore, in order to obtain the rotor unbalance, Eq. (23) may be rewritten as

$$\begin{Bmatrix} v \\ \mathbf{g} \end{Bmatrix} = [W(\omega_q)\ R(\omega_q)]^+ H(\omega_q) \quad (25)$$

where $[W(\omega_q)\ R(\omega_q)]^+$ is the Moore-Penrose pseudo-inverse of $[W(\omega_q)\ R(\omega_q)]$, and can be written as

$$[W(\omega_q)\ R(\omega_q)]^+ = \left[[W(\omega_q)\ R(\omega_q)]^T[W(\omega_q)\ R(\omega_q)]\right]^{-1}[W(\omega_q)\ R(\omega_q)]^T \quad (26)$$

Although Eq. (23) may be solved in a least-squares sense directly as shown in Eq. (25), it is not computationally efficient to invert the normal equations matrix. Therefore, the solution via the singular-value decomposition (SVD) or QR-decomposition approaches is more numerically stable.

The condition number of the inverse problem (Eq. (23)) is relatively large, which implies that any small perturbation in the input may result in large errors in the output data. Therefore, in order to solve this ill conditioned problem, column scaling regularization is applied.

4 SIMULATED EXAMPLE

The proposed method was applied to a numerical simulated machine, where a flexible rotor was mounted on two bearings fitted on a flexible foundation. The bearings were assumed to be rigid joints between the rotor and foundation. The rotor in this example consists of one steel shaft of 600 mm long, with nominal diameter of 20 mm. Balancing disk with diameter of 125 mm and thickness of 10 mm was located at 100 mm away from the centre. The Young's

modulus and density of the rotor and disk material are 200 GPa and 7850 kg/m^3 respectively. The rotor was created with 24 two-noded Timoshenko beam elements, as shown in Figure 3, where each node has 2 degrees of freedom. The torsional and axial vibrations were assumed to be negligible.

5 RESULTS AND DISCUSSION

The estimation process was done through two steps. First, Eq. (2) was used to calculate response at the normal directions of the two bearings using assumed foundation model and a given rotor unbalance. The response vector was ordered as

$$\mathbf{d}_{R,f} = [u_{b1} \quad v_{b1} \quad u_{b2} \quad v_{b2}]^{\mathrm{T}} \tag{27}$$

where the subscript b denotes the bearings. Then, the responses in r_{k1} and r_{k2} directions were calculated by multiplying the responses in the normal directions by Eq. (7). The foundation mass and damping matrices were considered as

$$\mathrm{M}_F = \mathrm{diag}\,[5 \;\; 5 \;\; 5 \;\; 5]\,\mathrm{kg}\,, \quad \mathrm{C}_F = \mathrm{diag}\,[150 \;\; 150 \;\; 150 \;\; 150]\,\mathrm{N}\;{}^{s}/_{m} \tag{28}$$

At each unbalance configuration, three different stiffness combinations were used. First, the horizontal and vertical stiffnesses were assumed to be identical. Then, the horizontal stiffness was reduced to 80% and 50% of the vertical stiffness. The different unbalance and foundation stiffness configurations are listed in Table 1. The numerically modelled machine was run up from 1 to 400 Hz with measurements taken at spacing of 0.5 Hz. The parameter estimation process was done four times where every time the response of one of the four directions was assumed as the only measured response. The results of the different directions are presented in the next three subsections.

Configuration no.	Run no.	Foundation Stiffness V (MN/m)	Foundation Stiffness H (MN/m)	Unbalance (g.m)	Phase (deg.) w.r.t horizontal direction
	1		10.00		
1	2	10.00	8.00	3.20E-04	30.00
	3		5.00		
	4		10.00		
2	5	10.00	8.00	7.20E-04	105.00
	6		5.00		
	7		10.00		
3	8	10.00	8.00	9.00E-04	220.00
	9		5.00		
	10		10.00		
4	11	10.00	8.00	1.80E-03	320.00
	12		5.00		

Table 1: The unbalance and foundation stiffness configurations for the simulated examples.

5.1 Vertical response only

Only the vertical vibration response of the two bearings was assumed as the measured response and used to estimate the foundation model and the amplitude and phase of the rotor unbalance. The estimated rotor unbalances for the different runs are listed in Table 2. It can be seen that the maximum error in the identified unbalances is less than 1%, which indicates that the estimated unbalances are reasonably accurate. As can be seen in Table 2, when the measurements from the vertical direction were used in the unbalance estimation, the estimated phase angles were found to be 90 degrees more than the actual ones. This is due to the fact that the actual phase angles have been measured with respect to the horizontal axis (Figure 5).

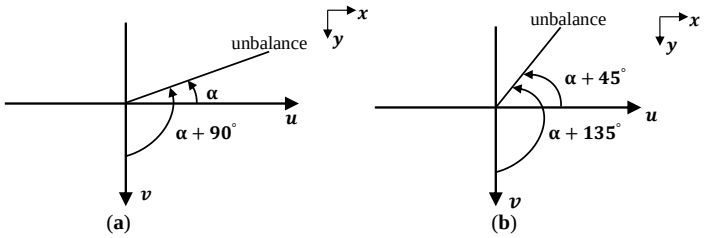


Figure 5: Phase angles with respect to vertical and horizontal axes in cases of (a) Response taken at normal directions and (b) Response taken at radial directions.

5.2 Horizontal response only

The horizontal response was assumed as the measured response and the estimation process was done again. When the horizontal and vertical stiffnesses are identical, the unbalance that was estimated using response from the horizontal direction is same as the vertical direction. However, when the horizontal and vertical stiffnesses are different, the estimated rotor unbalance is not same. The identified rotor unbalances for the 12 runs are presented in Table 2.

Run no.	Vertical direction only					Horizontal direction only			
	Unbalance (kg.m)	Unbalance error (%)	Phase (deg.)	Angle w.r.t horizontal (phase-90)	Phase error (%)	Unbalance (kg.m)	Unbalance error (%)	Phase (deg.)	Phase error (%)
1	3.1781e-04	0.6833	120	30.00	0	3.1781e-04	0.6833	30	0
2	3.1781e-04	0.6833	120	30.00	0	3.1941e-04	0.1834	30	0
3	3.1781e-04	0.6833	120	30.00	0	3.1952e-04	0.1499	30	0
4	7.1509e-04	0.6824	195	105.00	0	7.1509e-04	0.6824	105	0
5	7.1509e-04	0.6824	195	105.00	0	7.1866e-04	0.1859	105	0
6	7.1509e-04	0.6824	195	105.00	0	7.1889e-04	0.1544	105	0
7	8.9387e-04	0.6807	310	220.00	0	8.9387e-04	0.6807	220	0
8	8.9387e-04	0.6807	310	220.00	0	8.9831e-04	0.1881	220	0
9	8.9387e-04	0.6807	310	220.00	0	8.9861e-04	0.1546	220	0
10	0.0017382	0.6767	50	320.00	0	0.0017	0.6767	320	0
11	0.0017382	0.6767	50	320.00	0	0.001747	0.1958	320	0
12	0.0017382	0.6767	50	320.00	0	0.0017471	0.1632	320	0

Table 2: The estimated unbalance for the simulated examples using vertical and horizontal directions separately.

5.3 Radial responses only

The rotor unbalance and foundation model were, first, estimated using the measured vibration response from the first radial direction r_{k1} only. Then, the estimation process was repeated using responses from the second radial direction r_{k2} only. The results of the different runs for both cases are shown in Table 3. The rotor response may be estimated using the identified parameters from either r_{k1} or r_{k2} directions. This is because the estimated parameters which were calculated using responses from either r_{k1} or r_{k2} directions include a significant content of vibration behaviour from the vertical and horizontal directions. A comparison between the actual and estimated responses is shown in Figures 6 and 7. By looking at these two figures, it can be said that the estimated foundation model is of a good quality.

Run no.	r_{k1} direction only					r_{k2} direction only				
	Unbalance (g.m)	Unbalance error (%)	Phase (deg.)	Angle w.r.t horizontal (phase-135)	Phase error (%)	Unbalance (g.m)	Unbalance error (%)	Phase (deg.)	Angle w.r.t horizontal (phase-45)	Phase error (%)
1	3.1785e-04	0.6724	75	30	0	3.1785e-04	0.6724	165	30	0
2	3.1888e-04	0.3492	75	30	0	3.1769e-04	0.7220	165	30	0
3	3.1869e-04	0.4081	75	30	0	3.1733e-04	0.8331	165	30	0
4	7.1515e-04	0.6733	150	105	0	7.1515e-04	0.6733	240	105	0
5	7.1755e-04	0.3406	150	105	0	7.1475e-04	0.7294	240	105	0
6	7.1712e-04	0.4007	150	105	0	7.1393e-04	0.8426	240	105	0
7	8.9392e-04	0.6751	265	220	0	8.9392e-04	0.6751	355	220	0
8	8.9683e-04	0.3518	265	220	0	8.9355e-04	0.7167	355	220	0
9	8.9632e-04	0.4094	265	220	0	8.9255e-04	0.8274	355	220	0
10	0.001738	0.6790	5	320	0	0.001738	0.6790	95	320	0
11	0.0017438	0.3503	5	320	0	0.0017375	0.7141	95	320	0
12	0.001743	0.4069	5	320	0	0.001736	0.8253	95	320	0

Table 3: The estimated unbalance for the simulated examples using r_{k1} and r_{k2} directions separately.

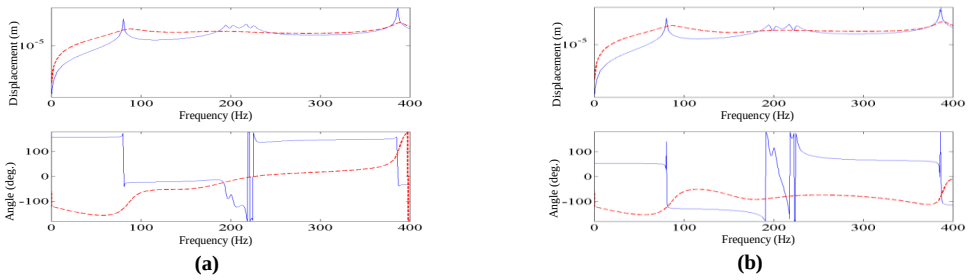


Figure 6: Comparison between the actual and estimated responses at (a) bearing 1 r_{k1} and (b) bearing 2 r_{k1}, for run number 5: —, actual ; - - -, estimated.

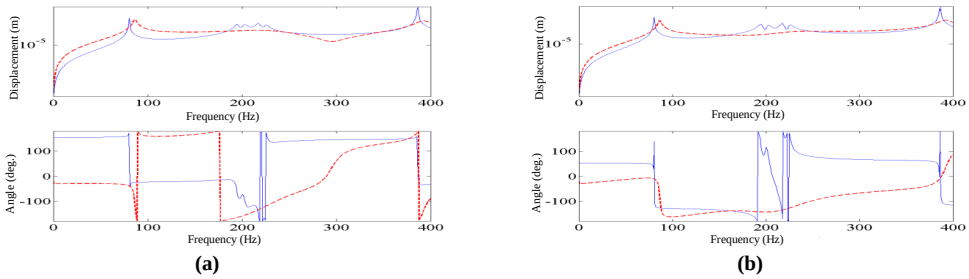


Figure 7: Comparison between the actual and estimated responses at (a) bearing 1 r_{k2} and (b) bearing 2 r_{k2}, for run number 5: —, actual; - - -, estimated.

6 CONCLUSION

This paper has presented a simplified and computational efficient method for identifying and quantifying state of rotor unbalance and foundation model in rotating machines using response from a single vibration sensor per bearing location and vibration measurements from a single machine run. The vibration sensors have been located in the radial direction (45 degree to both lateral and vertical directions) in order to include the effect of the vertical and horizontal directions. Numerical simulation has been done on a rotor-bearing-foundation system with different unbalance and stiffness configurations. Vibration measurements have been collected during a single coast-up and used in the parameter estimation process. The

estimated rotor unbalance and foundation model of the different configurations were close to the actual ones, which indicates the potentials of the technique for practical applications.

REFERENCES

[1] Neto, R. R., Bogh, D. L., and Flammia, M., *Some experiences on rigid and flexible rotors in induction motors driving critical equipment in petroleum and chemical plants*. in *Petroleum and Chemical Industry Conference, 2006. PCIC'06. Record of Conference Papers-IEEE Industry Applications Society 53rd Annual*. 2006. IEEE.

[2] Cavalca, K. L., Cavalcante, F., and Okabe, E. P., *An investigation on the influence of the supporting structure on the dynamics of the rotor system.* Mechanical Systems and Signal Processing, 2005. **19**(1): p. 157-174.

[3] Irretier, H. D., *History and development of frequency domain methods in experimental modal analysis.* J. Phys. IV France, 2002. **12**(11): p. 91-100.

[4] Stephenson, R. W., and Rouch, K. E., *Generating matrices of the foundation structure of a rotor system from test data.* Journal of Sound and Vibration, 1992. **154**(3): p. 467-484.

[5] Lees, A. W., Sinha, J. K., and Friswell, M. I., *Model-based identification of rotating machines.* Mechanical Systems and Signal Processing, 2009. **23**(6): p. 1884-1893.

[6] Edwards, S., Lees, A. W., and Friswell, M. I., *Experimental identification of excitation and support parameters of a flexible rotor-bearings-foundation system from a single run-down.* Journal of Sound and Vibration, 2000. **232**(5): p. 963-992.

[7] Lees, A. W., Sinha, J. K., and Friswell, M. I., *The identification of the unbalance of a flexible rotating machine from a single rundown*. Journal of Engineering for Gas Turbines and Power-Transactions of the Asme, 2004. **126**(2): p. 416-421.

[8] Nembhard, A. D., Sinha, J. K., Pinkerton, A. J., and Elbhbah, K.,*Condition monitoring of rotating machines using vibration and bearing temperature measurements*, in *Advances in Condition Monitoring of Machinery in Non-Stationary Operations*. 2014, Springer. p. 159-169.

[9] Sudhakar, G.N.D.S., and Sekhar, A. S., *Identification of unbalance in a rotor bearing system.* Journal of Sound and Vibration, 2011. **330**(10): p. 2299-2313.

[10] Sinha, J. K., Friswell, M. I., and Lees, A. W., *The identification of the unbalance and the foundation model of a flexible rotating machine from a single run-down.* Mechanical Systems and Signal Processing, 2002. **16**(2-3): p. 255-271.

[11] Smart, M. G., Friswell, M. I., and Lees, A. W., *Estimating turbogenerator foundation parameters: model selection and regularization.* Proceedings of the Royal Society a-Mathematical Physical and Engineering Sciences, 2000. **456**(1999): p. 1583-1607.

11th International Conference on Engineering Vibration
Ljubljana, Slovenia, 7–10 September 2015

DYNAMICS OF A ROTATING HUB-BLADE STRUCTURE WITH NONIDEAL ENERGY SOURCE

Jerzy Warminski*[1], Jaroslaw Latalski[1], Zofia Szmit[1]

[1]Department of Applied Mechanics, Lublin University of Technology, 20-618, Lublin, Poland
j.warminski@pollub.pl; j.latalski@pollub.pl; z.szmit@pollub.pl

Keywords: rotating composite beam, thin-walled structure, coupled vibration modes, non-ideal system, Sommerfeld effect

Abstract. *The paper presents dynamics of a rotating structure composed of two nominally identical flexible thin-walled beams attached to a rigid hub. The structure is excited by a DC motor which may be considered as an ideal or a non-ideal energy source. Both beams are made of unidirectional composite material with reinforcing fibers skewed with respect to their longitudinal axis. The applied lamination pattern in cross-sections flanges and webs results in circumferentially asymmetric stiffness (CAS) property, thus vibrating beams exhibit combined flapwise bending-shear-twisting mode.*

The equations of motion of the structure are derived according to Hamilton's least action principle. These are supplemented by an additional equation incorporating characteristics of the driving DC motor. The Galerkin method is used to convert continuous differential equations to a discrete problem. Finally, the dimensionless form of the governing equations is given.

Vibrations of individual beams and hub are analysed. An influence of the energy source output considered as an ideal and non-ideal one on rotor dynamics is demonstrated. The results of numerical simulation show that the oscillations of the beams and the hub are fully synchronized. This phenomenon is observed either for the ideal and the non-ideal system cases. Although, in the case of non-ideal system both beams are been synchronized after passing a certain transient domain. Moreover, ani-resonance phenomena is observed.

1 INTRODUCTION

Rotating beams are important structural elements commonly used in mechanical, power energy and aerospace engineering. The typical examples are turbine blades, various cooling fans, windmill blades, helicopter rotor blades, airplane propellers etc.

A vast majority of papers dealing with rotating slender elements consider them as separate members, ignoring the dynamics of the driving unit and hub assembly. Therefore, within this research, the structure is considered to be driven by an ideal power supply system – i.e. the one where the engine remains uninfluenced by the driven system dynamics.

However, this assumption is a significant simplification of the actual problem. The real driving power units like brushed DC electric motors or induction motors are typical examples of power sources that are influenced by the response of the structure to which they supply power. These vibrating systems where the power resource is limited and/or influenced by the driven sub-system are referred to as the non-ideal ones. The dynamic behaviour of these non-ideal systems may significantly differ from the corresponding idealized case [10]. It has been shown, that to properly incorporate the discussed phenomena the mathematical model of the non-ideal system has to include an additional equation while compared to that of the corresponding ideal system [1]. This equation describes the interaction between the energy source and the driven structure.

Although the non-ideal power supply assumption is a more realistic approach, the available literature on this topic is rather confined. A comprehensive review paper on the research dealing with the main properties of non-ideal vibrating systems was published by Balthazar in [2] and later on by Cvetićanin [4].

The non-ideal power supply systems were studied also by Warminski and Balthazar in [13]. Authors modelled a rotating Euler-Bernoulli beam made of isotropic material driven by a non-ideal energy source. In the performed analysis geometrical nonlinearities and nonconstant rotating speed were taken into account; moreover the hub inertia was also considered. The authors showed transitions through the resonances for a reduced order discrete system.

More research on blades and hub interactions on complete rotor assembly dynamic characteristics was done later on by Warminski et al. in [14]. In that paper a model of a nonlinear system composed of a hub with attached two pendula rotating in a horizontal plane was studied. Each single pendulum was treated as a massless, non-deformable rod with a lumped mass at the tip and connected to the hub by a flapping hinge. The system was excited by an external torque generated by a DC motor. It was considered as an ideal system with torque given by a harmonic function. An influence of the structural parameters like mass of the hub and pendula length on natural end excited vibrations was studied. The complete synchronization, phase synchronization, bifurcations and transition through resonances were analyzed considering the influence of the mass of the hub. The existence of chaotic oscillations of the system and paths leading to chaos were demonstrated as well.

In the current paper the research is extended to the analysis of a system composed of two flexible beams mounted to the rigid hub. The system is driven by a DC motor that is considered to be a non-ideal power source unit. Both beams are made of composite material exhibiting coupled lead-lag bending and torsional vibrations. In the analysis several nonclassical effects like shear deformation, cross-sectional rotatory inertia and driving hub inertia are taken into account.

2 PROBLEM FORMULATION

Let us consider a system consisting of two nominally identical elastic composite thin-walled beams clamped at the rigid hub of radius R_0 as shown in Figure 1. The hub may rotate or oscillate about vertical axis CZ_O and its current position is described by an angle ψ with respect to inertial reference frame (X_O, Y_O, Z_O). The structure is driven by a DC motor, which we consider in two variants: (a) as an ideal energy source where the output torque is precisely defined by a time dependent function or (b) as limited power supply source, where the actual motor characteristic is influenced by the response of the driven system.

The length of each beam is denoted by l_i, its wall thickness by h_i and width and height of the cross-section by d_i and c_i respectively, where $i = 1, 2$. The composite material of the beams is linearly elastic. The fibres in plies are skewed with respect to the longitudinal beam axis x by angle α and follow the circumferentially asymmetric stiffness (CAS) configuration. This arrangement implies the ply-angle distribution $\alpha(y) = -\alpha(-y)$ in the top and bottom walls of the box beam (flanges) and $\alpha(z) = -\alpha(-z)$ in the lateral walls (webs) – see Figure 1(b). This fabric configuration decouples the full set of six equations of motion (6 d.o.f.) into two subsystems: one exhibiting flapwise bending–shear–twisting coupling and the second one where axial stretching and chordwise bending–shear modes are coupled [6],[12]. Therefore, setting the beam at 90° angle in the hub results in specimen lead-lag deformation to be coupled with twisting.

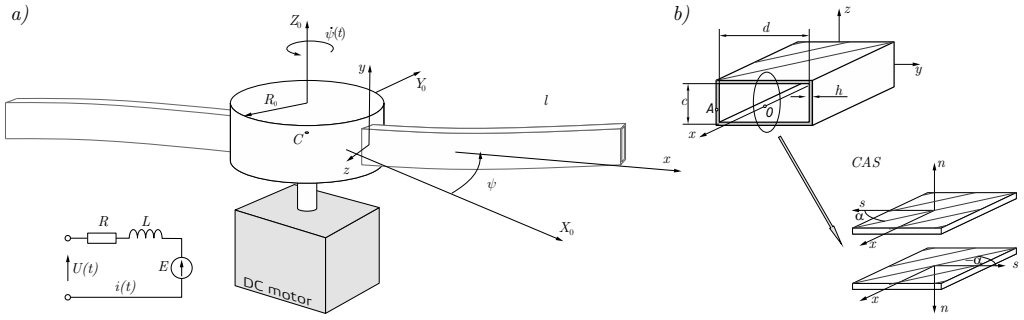


Figure 1: Rotating thin-walled beam under consideration (a) and CAS lamination scheme (b)

3 MATHEMATICAL MODEL

Consider an arbitrary point A located on the beam profile mid-line that is specified by its position vector $\mathbf{r} = \{x, y, z\}^\mathsf{T}$ in the local beam coordinate system — see Figure 1. As the system rotates by $\psi(t)$ about CZ_0 axis and simultaneously the beam experiences an elastic deformation the discussed point A occupies a new position in space that is defined in fixed inertial frame as follows:

$$\mathbf{R} = \begin{Bmatrix} (D_x + x + R_0)\cos\psi(t) + \left(D_z + z - n\frac{dy}{ds}\right)\sin\psi(t) \\ (D_x + x + R_0)\sin\psi(t) - \left(D_z + z - n\frac{dy}{ds}\right)\cos\psi(t) \\ (D_y + y + n\frac{dz}{ds}) \end{Bmatrix}, \tag{1}$$

where D_x, D_y and D_z are individual terms of deformation vector $\mathbf{D}$ given in local coordinates

$$
\begin{aligned}
D_x &= u_0(x,t) + \vartheta_y(x,t)\big(z - n\tfrac{dy}{ds}\big) + \vartheta_z(x,t)\big(y + n\tfrac{dz}{ds}\big) - G(n,s)\varphi'(x,t),\\
D_y &= v_0\,(x,t) - (y + n\tfrac{dz}{ds} - y_0)\big(1 - \cos\varphi(x,t)\big) - (z - n\tfrac{dy}{ds} - z_0)\sin\varphi(x,t)\\
&\approx v_0\,(x,t) - \tfrac{1}{2}(y + n\tfrac{dz}{ds} - y_0)\varphi^2(x,t) - (z - n\tfrac{dy}{ds} - z_0)\varphi(x,t),\\
D_z &= w_0\,(x,t) + (y + n\tfrac{dz}{ds} - y_0)\sin\varphi(x,t) - (z - n\tfrac{dy}{ds} - z_0)\big(1 - \cos\varphi(x,t)\big)\\
&\approx w_0\,(x,t) + (y + n\tfrac{dz}{ds} - y_0)\varphi(x,t) - \tfrac{1}{2}(z - n\tfrac{dy}{ds} - z_0)\varphi^2(x,t).
\end{aligned}
\tag{2}
$$

In the above u_0, v_0, w_0 are displacements of the pole point 0 that corresponds to the arbitrary chosen A (i.e. the point 0 lays on longitudinal x axis and belongs to the same cross-section as the discussed point A), $\varphi(x,t)$ denotes rotation of the cross-section (twist angle). Angles $\vartheta_y(x,t) = \gamma_{xz} - w_0'$ and $\vartheta_z(x,t) = \gamma_{xy} - v_0'$ represent rigid cross-sections rotations about respective axes y and z. These six variables constitute a set of basic unknowns of the 1-D problem equivalent to the original 3-D one as formulated for the single beam of the structure. The first equation in set (2) includes warping effect due to the warping function term $G(s,n)$. Moreover, in the second and third equation the moderately large rotations are allowed by the approximation $\cos\varphi \approx 1 - \varphi^2/2$. The later linearisation of the respective resulting equations is performed after taking into account this approximation. Details concerning the derivation of the given above formula for a general case of arbitrary beam presetting angle are given in [5].

3.1 Velocity vector

The velocity vector of an arbitrary point A of the elastic body in the inertial frame can be obtained by differentiating the position vector (1) with respect to time. After appropriate manipulations one arrives at

$$
\begin{aligned}
\dot{R}_x &= \big[-(D_x + x + R_0)\sin\psi(t) + (D_z + Z)\cos\psi(t)\big]\dot{\psi}(t) + \dot{D}_x\cos\psi(t) + \dot{D}_z\sin\psi(t)\\
\dot{R}_y &= \big[(D_x + x + R_0)\cos\psi(t) + (D_z + Z)\sin\psi(t)\big]\dot{\psi}(t) + \dot{D}_x\sin\psi(t) - \dot{D}_z\cos\psi(t)\\
\dot{R}_z &= \dot{D}_y
\end{aligned}
\tag{3}
$$

where overdot means time derivative, so $\dot{D}_x$, $\dot{D}_y$ and $\dot{D}_z$ terms correspond to the velocities of deformation.

3.2 Strains

We restrict our mathematical model to linear elastic range, therefore only linear strains are considered. The axial and circumferential-axial ones are split into mid-line terms (superscript $(\centerdot)^{(0)}$) and off-mid-line ones (superscript $(\centerdot)^{(1)}$) as proposed by Librescu and Song [6]

$$
\varepsilon_{xx} = \varepsilon_{xx}^{(0)} + n\varepsilon_{xx}^{(1)} \qquad \gamma_{xs} = \gamma_{xs}^{(0)} + n\gamma_{xs}^{(1)} \qquad \gamma_{xn} = \gamma_{xn}^{(0)} \tag{4}
$$

It should be noted that considering linearised displacement field of equations (2) the three remaining strains ($\varepsilon_{yy} = \varepsilon_{zz} = \gamma_{yz}$) are identically zero – so each cross-section of the beam stays rigid in its plane, but is allowed to warp out of its plane. The appropriate components of strains

(4) are defined by the following mid-line expressions

$$\begin{aligned}
\varepsilon_{xx}^{(0)} &= u_0' + z\vartheta_y' + y\vartheta_z' - G^{(0)}(s)\varphi'' + \tfrac{1}{2}\left(v_0' - z\varphi'\right)^2 + \tfrac{1}{2}\left(w_0' + y\varphi'\right)^2 \\
\varepsilon_{xx}^{(1)} &= -\frac{dy}{ds}\vartheta_y' + \frac{dz}{ds}\vartheta_z' - G^{(1)}(s)\varphi'' \\
\gamma_{xs}^{(0)} &= (\vartheta_y + w_0')\frac{dz}{ds} + (\vartheta_z + v_0')\frac{dy}{ds} + g^{(0)}(s)\varphi' \qquad \gamma_{xs}^{(1)} = g^{(1)}(s)\varphi' \\
\gamma_{xn}^{(0)} &= -(\vartheta_y + w_0')\frac{dy}{ds} + (\vartheta_z + v_0')\frac{dz}{ds},
\end{aligned} \tag{5a–d}$$

where $G^{(0)}(s)$, $G^{(1)}(s)$ and $g^{(0)}$, $g^{(1)}$ stay for primary and secondary warping functions given explicitly in [5].

At this point, a word of comment about the axial strain expression is in order. Although the mathematical model of the beam is limited to the linear case the higher order terms associated with flapwise and chordwise displacements are taken into account in (5-a). Incorporating these components is obligatory to ensure proper modelling of the blade stiffening effect arising from the system rotation. For detailed analysis of geometric stiffening effects and their different formulations please consult papers [8], [9], [11].

4 EQUATIONS OF MOTION

Taking into account the given above formula for strains and position vector, setting expressions for potential and kinetic energy in Hamilton's principle and after performing necessary mathematical manipulations one arrives at the system of equations for each of the beams plus an additional equation for the hub dynamics. Beam equations are:

- $w_{o(i)}$ in plane (lead-lag) displacement

$$\begin{aligned}
b_{1(i)}\ddot{w}_{o(i)} - 2b_{1(i)}\dot{u}_{o(i)}\,\dot{\psi}(t) - b_{1(i)}w_{o(i)}\dot{\psi}^2(t) - b_{1(i)}(R_0 + x_i)\ddot{\psi}(t) \\
-a_{55(i)}\vartheta_{y(i)}' - a_{55(i)}w_{o(i)}'' - \left(T_{x(i)}w_{o(i)}'\right)' = 0
\end{aligned}$$

with boundary conditions

$$w_{o(i)}\big|_{x_i=0} = 0, \qquad \left(\vartheta_{y(i)} + w_{o(i)}'\right)\big|_{x_i=l} = 0 \tag{6}$$

- $\vartheta_{y(i)}$ in plane transverse shear angle

$$B_{4(i)}\ddot{\vartheta}_{y(i)} - B_{4(i)}\dot{\psi}^2(t)\vartheta_{y(i)} + B_{4(i)}\ddot{\psi}(t) + a_{55(i)}(\vartheta_{y(i)} + w_{o(i)}') - a_{33(i)}\vartheta_{y(i)}'' - a_{37(i)}\varphi_{(i)}'' = 0$$

with boundary conditions

$$\vartheta_{y(i)}\big|_{x_i=0} = 0, \qquad \left(a_{55(i)}\vartheta_{y(i)}' + a_{37(i)}\varphi_{(i)}'\right)\big|_{x_i=l} = 0, \tag{7}$$

- $\varphi_{(i)}$ twist angle

$$(B_{4(i)} + B_{5(i)})\ddot{\varphi}_{(i)} + (B_{4(i)} - B_{5(i)})\dot{\psi}^2(t)\varphi_{(i)} - a_{37(i)}\vartheta_{y(i)}'' - a_{77(i)}\varphi_{(i)}'' - (T_{r(i)}\varphi_{(i)}')' = 0,$$

with boundary conditions,

$$\varphi_{(i)}\big|_{x_i=0} = 0, \qquad \left(a_{37(i)}\vartheta_{y(i)}' + a_{77(i)}\varphi_{(i)}'\right)\big|_{x_i=l} = 0, \tag{8}$$

In foregoing relations $B_{k(i)}$ and $b_{k(i)}$ factors depict the inertia terms and $a_{kj(i)}$ ones correspond to beam stiffnesses; the last subscript letter ($i = 1, 2$) given in parentheses corresponds successively to each of the two beams considered. The detailed definitions of inertia and stiffness coefficients are given in [5]. Terms $T_{x(i)}(x_i)$ and $T_{r(i)}(x_i)$ correspond to structural stiffening effect due to rotation and they are defined as follows:

$$T_{x(i)}(x_i) = b_{1(i)}(L_i - x_i)\big[R_0 + 0.5(L_i + x_i)\big]\dot{\psi}^2(t) \qquad T_{r(i)}(x_i) = \frac{B_{4(i)} + B_{5(i)}}{m_{0(i)}\beta_{(i)}} T_{x(i)}(x_i) \quad (9)$$

where $m_{0(i)}$ is mass of the i-th beam per its unit length and $\beta_{(i)}$ is a perimeter of its mid-line cross-section.

The hub equation is as follows:

- rotation angle ψ

$$\begin{aligned} &J_{hub}\ddot{\psi}(t) + \sum_{i=1}^{i=2}(b_{22(i)} + B_{4(i)}l_i)\ddot{\psi}(t) \\ &+ \sum_{i=1}^{i=2}\int_0^{l_i}\Big\{b_{1(i)}(R_0 + x_i)\left[2u_{o(i)}\ddot{\psi}(t) + 2\dot{u}_{o(i)}\dot{\psi}(t) - \ddot{w}_{o(i)}\right] + B_{4(i)}\ddot{\vartheta}_{y(i)}\Big\}dx_i = M(t) \end{aligned} \quad (10)$$

where the J_{hub} represents the total mass moment of inertia of the hub and motor shaft assembly and the right hand side term $M(t)$ represents the driving torque delivered by DC motor.

To analyse the flexible system given by eqs. (6)–(8) the Galerkin method is used and partial differential equations are reduced to their state-space form. The representations of the individual unknown generalized displacements functions are

$$w(x,t) = \sum_{n=1}^{N} W_n(x)q_{wn}(t) \quad \vartheta_y(x,t) = \sum_{n=1}^{N} Y_n(x)q_{yn}(t) \quad \varphi(x,t) = \sum_{n=1}^{N} \Phi_n(x)q_{\varphi n}(t) \quad (11)$$

where $W_n(x), Y_n(x), \Phi_n(x)$ are consistent admissible functions – i.e. suitable trial functions that satisfy the geometric boundary conditions and do not prevent the natural boundary conditions from being satisfied; terms $q_{wn}, q_{yn}, q_{\varphi n}$ are relevant generalized coordinates.

Substituting (11) into linear form of (6)–(8), multiplying by successive appropriate shape functions and performing integrations results in an eigenvalue problem. Its solution are N natural frequencies and corresponding mode shapes of the linear system. These modes are $3N$ size vectors with components coming from N displacement, shear and twisting combined deformations.

In the next step the first mode shape is used to discretize the full system of equations (6)–(8). The required axial deformation u_0 (present in e.g. Coriolis term) is determined from the postulate that fixed-free elements may be approximated as inextensional members in the absence of large axial forces [7]. Thus the inextensionality constraint is

$$(1 + u_0')^2 + w_0'^2 = 1 \quad (12)$$

where chordwise displacement is ignored due to aforementioned mode decoupling.

Finally, the discretized, full system of equations (6)–(8) is transformed into dimensionless form by setting $\eta = x/l_1$ and $\tau = t \cdot \omega_0$ where $\omega_0 = \sqrt{a_{33(1)}/b_{1(1)}l_1^4}$ (term l_1 denotes the length

of the first beam, $a_{33(1)}$ and $b_{1(1)}$ are its stiffness and inertia coefficients). After conversion the set of governing equations is:

$$\begin{aligned} \ddot{q}_1+\zeta_1\dot{q}_1+\alpha_{12}\ddot{\psi}+(\alpha_{11}+\alpha_{13}\dot{\psi}^2)q_1+\alpha_{14}\dot{\psi}\dot{q}_1 &= 0 \\ \ddot{q}_2+\zeta_2\dot{q}_2+\alpha_{22}\ddot{\psi}+(\alpha_{21}+\alpha_{23}\dot{\psi}^2)q_2+\alpha_{24}\dot{\psi}\dot{q}_2 &= 0 \\ (1+\widetilde{J}_h+\widetilde{J}_b+\alpha_{h12}q_1+\alpha_{h22}q_2)\ddot{\psi}+\zeta_h\dot{\psi} & \\ +\alpha_{h11}\ddot{q}_1+\alpha_{h21}\ddot{q}_2+\alpha_{h13}\dot{\psi}\dot{q}_1+\alpha_{h23}\dot{\psi}\dot{q}_2 &= \mu \end{aligned} \tag{13}$$

where q_1 and q_2 are the generalized coordinates corresponding to the studied coupled flexural-torsional modes of corresponding beams. Coefficients α_{ij} ($i=1,2,h$; $j=1,\ldots,4$) result from Galerkin projection, ζ_1, ζ_2, ζ_h are beams and the hub damping coefficients respectively; $\widetilde{J}_h$ and $\widetilde{J}_b$ are dimensionless mass moment of inertia of the hub and dimensionless mass moment of inertia of the second beam respectively expressed as a magnitude of the first beam inertia.

Right hand-side quantity μ corresponds to dimensionless driving torque that may be expressed by any arbitrary function – e.g. as a sum of constant and periodic components $\mu = \mu_0 + \rho\sin\omega t$ independent of the current rotor speed (ideal system) or just as a function of the DC motor parameters $\mu = \alpha_{hm}\widetilde{i}$ where

$$\frac{d\widetilde{i}}{d\tau} = -\alpha_{m1}\widetilde{i} - \alpha_{m2}\dot{\psi} + \alpha_{m3}\widetilde{U} \tag{14}$$

and

$$\alpha_{hm} = \frac{c_\varphi i_{max}}{(b_{22(1)}+B_{4(1)}l)\omega_0^2} \quad \alpha_{m1} = \frac{R}{L\omega_0} \quad \alpha_{m2} = \frac{c_\varphi}{Li_{max}} \quad \alpha_{m3} = \frac{U_{max}}{Li_{max}\omega_0}.$$

The given above R, L, c_φ parameters are resistance, inductance and electric constant dependent on stator magnetic flux respectively; these are specific for the given DC motor [3].

5 NUMERICAL SIMULATIONS

Numerical simulations have been performed for a two blade rotor system, considering two variants of the power supply: (a) the ideal system when the torque is given by the function $\mu = \mu_0+\rho\sin\omega t$ and (b) the non-ideal system when the full electromechanical system is studied so the supplied dimensionless voltage is given by harmonic formula $U^* = U_0 + U_A\sin\omega t$.

For the numerical studies the following dimensionless coefficients are used, based on the real physical system:

$$\begin{aligned} &\alpha_{11}=\alpha_{21}=3.58191, && \alpha_{12}=\alpha_{22}=-2.78170, && \alpha_{13}=\alpha_{23}=0.397499, \\ &\alpha_{14}=\alpha_{24}=0.49708, && \alpha_{h11}=\alpha_{h21}=-0.33119, && \alpha_{h12}=\alpha_{h22}=-0.16341, \\ &\alpha_{h13}=\alpha_{h23}=-0.16341, && \alpha_{hm}=0.14656, && \alpha_{m1}=0.53865, \\ &\alpha_{m2}=21.7111, && \alpha_{m3}=5.08462, && J_h=1, \\ &\zeta_h=0.1, && \zeta_1=\zeta_2=0.01\times\omega_{beam} && \omega_{beam}=1.8926. \end{aligned} \tag{15}$$

We note that the structure is fully symmetric therefore all coefficients of both beams are equal.

Excitation amplitude and frequency or related voltage supplied to DC motor are varied in a wide range of magnitude to demonstrate rezonanse zones. In Figure 2 we can observe response of the ideal system excited by harmonic function $\mu = \mu_0 + \rho\sin\omega t$, where simulations have been performed for $\mu_0 = 0$ and three selected excitation levels $\rho = 0.005$ – blue, $\rho = 0.01$ –

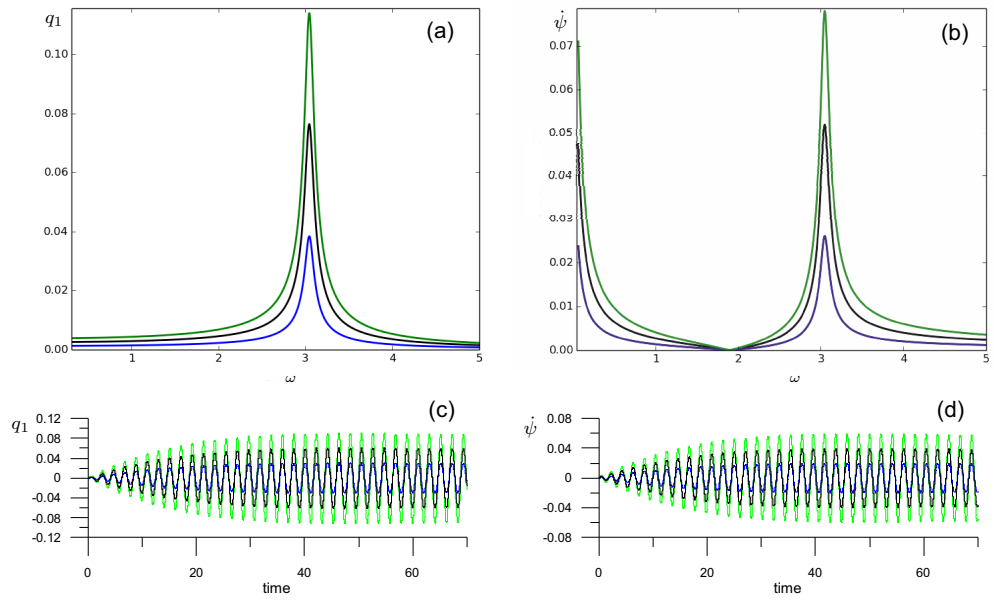


Figure 2: Amplitudes q_1 of the beam (a) and amplitude $\dot{\psi}$ of hub angular velocity (b) versus excitation frequency for $\mu_0 = 0$, $\rho = 0.005$ – blue, $\rho = 0.01$ – black, $\rho = 0.015$ – green, and corresponding time histories of the blade (c) and the hub (d)

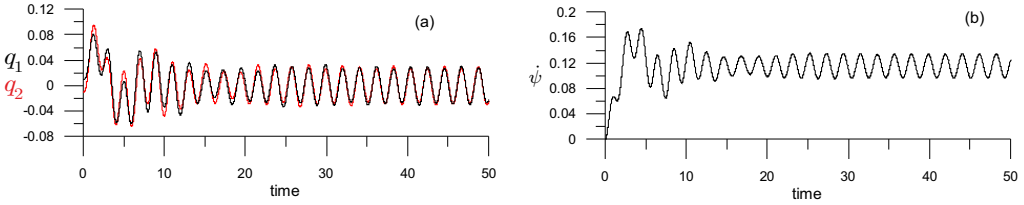


Figure 3: Time histories of beams coordinates q_1 – black, q_2 – red (a) and hub angular velocity $\dot{\psi}$ (b) for the full electromechanical system $U_0 = 0.5$, $U_A = 0.15$, $\omega = 3$

black, $\rho = 0.015$ – green. Amplitude of the first beam represented by coordinate q_1 is presented in Figure 2(a) with resonance close to $\omega \approx 3$. Response of the second beam q_2, due to the symmetry is exactly the same.

Then, the amplitude of angular velocity of the hub is shown in Figure 2(b). We see the shape of the rezonanse curve corresponding to a linear system with increasing response for higher excitation amplitudes. However, the course of the angular velocity is different. Apart from the same resonance next to $\omega \approx 3$ we observe oscillations with a very small amplitude, near $\omega \approx 1.89$. This frequency correspond to the first natural frequency of the beam. Corresponding time histories of the beam and the hub are presented in Figure 2 (c) and (d).

At the next stage numerical studies have been repeated for the full electromechanical system. The supplied voltage has a constant component $U_0 = 0.5$, and a variable one given by amplitude $U_A = 0.15$ and frequency $\omega = 3$. The obtained results for the first beam one the second one are presented in Figure 3(a) in black and red colour respectively. The angular velocity of the hub in

given in Figure 3(b). One can observe, the amplitude of both beams differs at the beginning of the motion, but after transient time domain they become fully synchronised.

6 CONCLUSIONS

The dynamics of a double blade rotor are studied in the paper. The system in considered in two possible configurations, as ideal and non-ideal one. The composite beam model have been derived taking into account CAS reinforcing fibres configuration which results in strong coupling of flexural and torsional modes. The PDEs have been transformed to a set of ODEs by one-mode projection using the extracted torsional-flexural mode. The derived model takes into account nonconstant angular velocity, related centrifugal forces and furthermore nonlinear terms resulting from Coriolis forces. In the present study a fully symmetric structure has been studied. The obtained by numerical simulation resonance curves demonstrate almost linear dynamic properties with hardly present impact of nonlinear terms. For the symmetric structure the oscillations of the beams and the hub are fully synchronized. This phenomenon has been observed either for the ideal and the non-ideal system cases. Although, in the case of non-ideal system both beams have been synchronized after passing a certain transient domain. In the discussed rotor configuration the hub has an important impact on the system dynamics that is observed by a kind of anti-resonance phenomena if excitation frequency is close to the natural frequency of the beam.

In further work the dynamics of slightly detuned beams will be studied. For the nonsymmetric structure authors expect to get more complex response with not complectly synchronized motion.

Acknowledgement

The work is financially supported by grant DEC-2012/07/B/ST8/03931 from the Polish National Science Centre.

REFERENCES

[1] A.A. Alifov, K.V. Frolov, *Interaction of Non-linear Oscillatory Systems with Energy Sources*. Taylor & Francis, London, 1990.

[2] J.M. Balthazar, D.T. Mook, H.I. Weber, R.M.L.R.F. Brasil, A. Fenili, D. Belato, J.L.P. Felix, An overview on non-ideal vibrations. *Meccanica* **38**, 613–621, 2003.

[3] R.M.L.R.F. Brasil, L.C. Feitosa, J.M. Balthazar, A structure excited by a DC motor of limited power supply and controlled by a pendulum like device. In Volume 5: *ASME 2007 International Design Engineering Technical Conferences and Computers and Information in Engineering Conference* Las Vegas, Nevada, USA, September 4-7, 2007. Technical publication DETC2007-35102, 1721–1725, 2008.

[4] L. Cvetićanin, Dynamics of the non-ideal mechanical systems: A review. *Journal of the Serbian Society for Computational Mechanics*, **4**(2), 75–86, 2010.

[5] F. Georgiades, J. Latalski and J. Warminski, Equations of motion of rotating composite beam with a nonconstant rotation speed and an arbitrary preset angle. *Meccanica*, **49**, 1833–1858, 2014.

[6] L. Librescu, O. Song, *Thin-walled composite beams. Theory and application*. Springer, Dordrecht, the Netherlands, 2006.

[7] P. Malatkar, *Nonlinear Vibrations of Cantilever Beams and Plates*, PhD Thesis. Virginia Polytechnic Institute and State University, Blacksburg, Virginia, 2003.

[8] J. Mayo, D. García-Vallejo and J. Domínguez, Study of the geometric stiffening effect: comparison of different formulations. *Multibody System Dynamics*, **11**(4), 321–341, 2004.

[9] J.C. Piedbœuf, and B. Moore, On the foreshortening effects of a rotating flexible beam using different modeling methods. *Mechanics of Structures and Machines*, **30**(1), 83–102, 2002.

[10] A.K. Samantaray, S.S. Dasgupta, R. Bhattacharyya, Sommerfeld effect in rotationally symmetric planar dynamical systems. *International Journal of Engineering Science*. **48**, 21–36, 2010.

[11] I. Sharf, Geometric stiffening in multibody dynamics formulations. *Journal of Guidance, Control, and Dynamics*, **18**(4), 882–890, 1995.

[12] Warminski J., Latalski J., Szmit Z., Coupled flexural-torsional vibrations of a composite beam attached to a rotating hub. A. Cunha, E. Caetano, P. Ribeiro, G. Müller eds. *IX International Conference on Structural Dynamics, EURODYN2014*, Porto, Portugal, 423–437, 2014.

[13] J. Warminski, J.M. Balthazar, Nonlinear vibrations of a beam with a tip mass attached to a rotating hub. In Volume 1: *20th Biennial Conference on Mechanical Vibration and Noise*. Long Beach, California, USA, September 24-28, 2005. Technical publication DETC2005-84518, 1619–1624, 2005.

[14] J. Warminski, Z. Szmit, J. Latalski, Nonlinear dynamics and synchronization of pendula attached to a rotating hub. *The European Physical Journal Special Topics*, **223**, 827–847, 2014.

A International Conference on Engineering Vibration
Ljubljana, Slovenia, 7-10 September 2015

ANALIZING THE STIFFNESS OF A ROTOR WITH TRIANGULAR CROSS FRACTURE

Homero J. R.[1], **Benjamín V. G.**[2], **Gilberto A. M.***[3]

[1]Metropolitan Autonomous University. Azcapotzalco. Division of Basic and Engineering Sciences. Department of Energy. 180 San Pablo Avenue, Colonia Reynosa Tamaulipas. Delegation Azcapotzalco. México Federal District. MÉXICO. hjr@correo.azc.uam.mx

[2]Metropolitan Autonomous University. Azcapotzalco. Division of Basic and Engineering Sciences. Department of Energy. 180 San Pablo Avenue, Colonia Reynosa Tamaulipas. Delegation Azcapotzalco. México Federal District. MÉXICO. bvg@correo.azc.uam.mx

[3]Metropolitan Autonomous University. Azcapotzalco. Division of Basic and Engineering Sciences. Department of Energy. 180 San Pablo Avenue, Colonia Reynosa Tamaulipas. Delegation Azcapotzalco. Mexico Federal District. MÉXICO. gdam@correo.azc.uam.mx

Keywords: Stiffness, Fracture, Resonance, Numerical Integration, Numerical Simulation.

Abstract. *In this work, the stiffness of a rotor with triangular cross fracture in the middle part, within its elastic range, in static condition, simply supported at its ends and middle concentrated load is determined. The functional relationship for the variation of second area moment of their different cross sections is deduced. It was calculated the slope and deflection by numerical integration double obtaining its elastic curve and the frequency range in which the fractured rotor resonates. Additionally the numerical solution to the critical orientation of the fracture was obtained. The calculated values for the rotor fractured are compared with corresponding values to the rotor without fracture, including the comparison the result of the numerical solution. The above parameters were calculated based on the angle of orientation of the fracture with respect to the normal line. From the values obtained it is concluded that, given the geometry of the rotor and of the fracture, the load applied, the support conditions and physical properties of the material and considering the birth and growth of the fracture; there are some frequencies of resonance for the rotor with fracture, in relation with the rotor without fracture, where the last one just have one resonance frequency. The variation between the first resonance frequency of the rotor with fracture and the value of the frequency of the rotor without fracture is of the order of a quarter for the same conditions.*

Homero J. R.[1], **Benjamín V. G.**[2], **Gilberto A. M.***[3]

1 INTRODUCTION

The birth and growth of a fracture in a rotor can cause rupture with catastrophic effects [1]. In recent years there have been investigations to timely detection of a rotor fracture, monitoring the mechanical, thermal and acoustic fields. On the other hand, it also has been studied the influence of the opening and closing mechanism in the performance of the rotor. Additional to this, the variation of second area moment of their different cross sections, as a function of the orientation of the fracture in the life of the rotor were also investigated.

Numerous fracture modelling techniques were reported by G. Sabnavis, R. G. Kirk, M. Kasarda and D. Quinn [2] and by V. Kumar and C. Rastogi [3]

2 NOTATION

a = Fracture width = 1 mm.
b = Fracture depth (mm).
$\frac{dY}{dX}$ = Slope, dimensionless.
E = Young's modulus [2] = $1.94 * 10^6 \frac{Kg}{cm^2} = 190314 \frac{N}{mm^2}$, stainless steel 18-8.
F = Vertical force applied in the middle of the rotor = 100 N.
I_{sf} = Second area moment, no fracture, with respect to X (mm^4).
I_{cf} = Second area moment, fractured, with respect to X (mm^4).
I_c = Second area moment, a circle, with respect to X (mm^4).
I_{sc} = Second area moment, the circular sector, with respect to X (mm^4).
I_{st} = Second area moment, the triangular sector, with respect to X (mm^4).
k = Stiffness N/mm.
L = Rotor length = 160 mm.
M = Bending moment (N.mm).
p = Maximum depth of fracture = 1.25 mm.
r = Rotor radius = 5 mm.
(X, Y, Z) = Inertial coordinate system.
X = Longitudinal coordinates of the rotor.
Y = Vertical transverse coordinates the rotor.
Z = Horizontal transverse coordinates the rotor.
(x, y, z) = Coordinates system fixed to the rotor.
x = Longitudinal coordinates of the rotor.
y = Transverse coordinates of the rotor, in first position, vertical.
z = Transverse coordinates of the rotor, in first position, horizontal.
α = Orientation angle of the fracture = angle between the z axis and Z axis, in first position $\alpha = 0^0$.
β = Fracture angle in the xz plane, invariant without opening and closing = $21.\ 80140949^0$.
δ = Fracture angle parallel to yz plane, variable depending on x.
Δ = Maximum deflection of the rotor (mm).
γ = Maximum angle of fracture on plane parallel to yz = 41.40962211^0.
$\varphi_i = \alpha - \delta$ = Angle, with respect to Z axis, in which initiates the fracture on plane parallel to yz plane.
$\varphi_f = \alpha + \delta$ = Angle, with respect to Z axis, in which ends the fracture on plane parallel to yz plane.
ρ = Density of the rotor [3] = 0.000007817 Kg/(mm^3), stainless steel 18-8.
ω = Resonance frequency in radian per second.

3 COORDINATES SYSTEMS

The origin of inertial coordinate system (X, Y, Z), is located on the middle of the left side of the rotor cross section as shown in Figure 1. The X axis coincides with the longitudinal axis of the rotor. The Y axis is transverse to the rotor and vertical. The Z axis is transverse to the rotor and horizontal.

The origin of the coordinates system fixed to the rotor, (x, y, z), coincides with the origin of the inertial coordinates system (X, Y, Z). The x axis coincides at all times with the X axis. The z and y axes are moved together with the rotor. In Figure 1 is shown the condition of the rotor for $\alpha = 0°$, that is, consider that the fracture is represented by its external surface, then it is possible to assign a normal unit vector to this surface, then $\alpha = 0°$ if the normal unit vector of the surface is parallel and with the same sense to the Z axis. In Figure 2 it is shown the condition for $\alpha = 90°$. From Figures 1 and 2 it follows that the rotation is positive in the counterclockwise observed from the left side of the rotor.

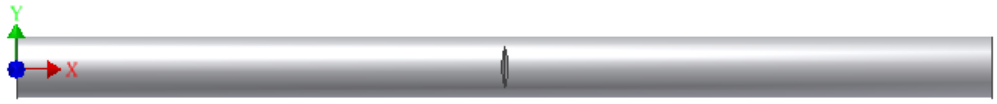


Figure 1: Inertial coordinates system, with the rotor in starting position, $\alpha = 0°$.

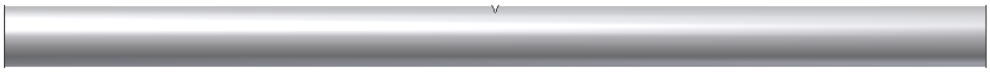


Figure 2: Fracture in the rotor oriented in the direction and sense of Y axis, $\alpha = 90°$.

4 SECOND AREA MOMENT

For the second area moment, in Figure 3 the dimensions of the rotor are shown along with its longitudinal axis, in Figure 4, a detail of the longitudinal section in the x-z plane is shown; from these figures, the Eqs. (1-3) are obtained:

$$\beta = arc\,tg\left(\frac{a}{2p}\right) \tag{1}$$

$$\frac{a}{2p} = \frac{x-0.5(L-a)}{b} \tag{2}$$

$$b = \frac{2px-p(L-a)}{a} \tag{3}$$

Where $a = 2\overline{AE}$, $p = \overline{AB}$ and $b = \overline{CD}$.

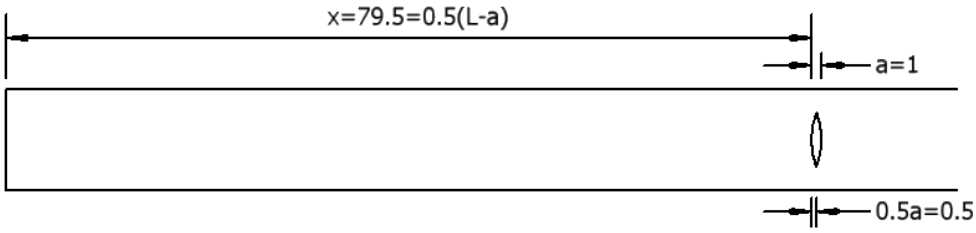


Figure 3: Rotor dimensions along the X axis.

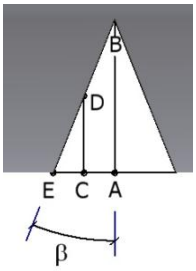


Figure 4: Fracture detail, α = -90°.

A representation of the cross section rotor along with its fracture is represented by a combination of several sections, complete circular section of radius *r*, a circular sector and a triangular sector [4] as shown in Figure 5; from which Eq. (4) is obtained. In the limit, when the parameter *b* tends to parameter *p*, Eq. (4) becomes in Eq. (5).

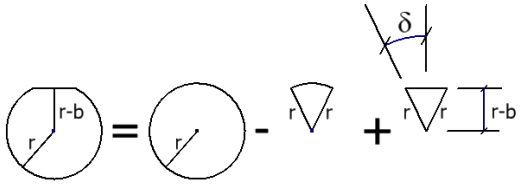


Figure 5: Cross Section CD, in plane parallel to the yz plane.

$$\delta = arc\,cos\left(\frac{r-b}{r}\right) \tag{4}$$

$$\gamma = arc\,cos\left(\frac{r-p}{r}\right) \tag{5}$$

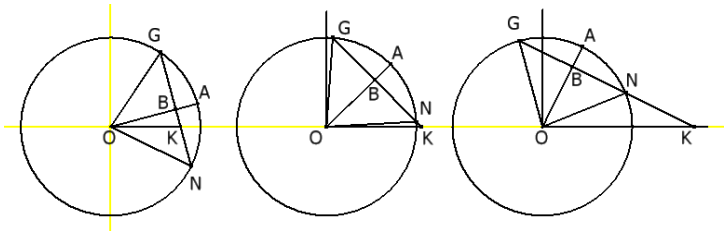
In Fig. 5, the second area moment can be obtained with Eq. (6) in which the moment Ic and the moment Isc, parameters are given by Eqs. (7-8).

$$I_{cf} = I_c - I_{sc} + I_{st} \tag{6}$$

$$I_c = \pi \frac{r^4}{4} \tag{7}$$

$$I_{sc} = \frac{(\varphi_f - sen\,\varphi_f cos\varphi_f) - (\varphi_i - sen\,\varphi_i cos\varphi_i)}{2} \frac{r^4}{4} \tag{8}$$

A cross section of the rotor in the area of the fracture when growing α is shown in Figures 6.a, 6.b and 6.c. The fissure is represented by the AGNA area. For subparagraph a of Figure 6 the triangular OGNO area, is equal to the OGKO area plus OKNO area; for b and c of Figure 6 is equal to the OGKO area minus OKNO area.



a) b) c)

Figure 6: Cross section of the rotor in the area of the fracture, $\alpha = BOK$.

The Eq. (9) is obtained from Figures 6 a), b) and c), along with Figure 5. This equation is transformed in Eq. (10), using trigonometric identities and simplifying.

$$I_{St} = \frac{1}{12}\left(\frac{r-b}{cos\propto}\right)[r\ sen\ (\propto + \delta)]^3 - \frac{1}{12}\left(\frac{r-b}{cos\propto}\right)[r\ sen\ (\propto - \delta)]^3 \tag{9}$$

$$I_{st} = \frac{r^4[3sen\delta(sen\alpha)^2(cos\delta)^3 + cos\delta(cos\alpha)^2(sen\delta)^3]}{6} \tag{10}$$

Substituting the equations (7), (8) and (10) into (6) we obtain the expression of the second area moment I_{cf}, in the zone of the fracture, this expression is parameterized in terms of α and X. In Figure 7 is shown the variations of the I_{cf} for four values of α and X.

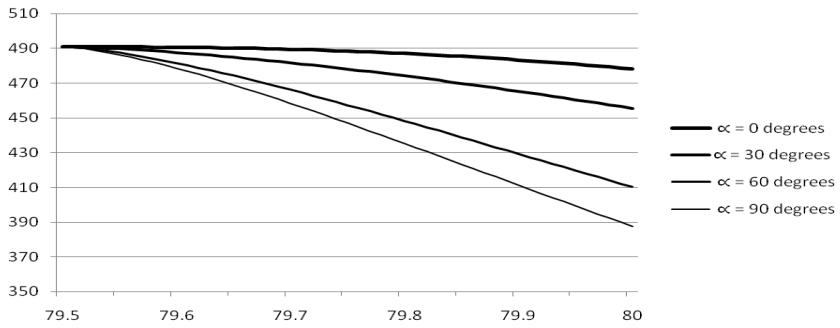


Figure 7: Second area moment in the fracture for α = 0°, 30°, 60° and 90°.

Note that in the fracture region (79.5 - 80 mm.) I_{cf} decreases while X increases, on the other hand, the influence of α on I_{cf} affects significantly, when α increases, I_{cf} not only decreases, the ratio of decreasing is greater.

5 SLOPES AND DEFLECTIONS

The slopes and the deflections denote mechanical characteristics on the dynamics rotors, the structural behaviour of rotors is affected by the presences of fractures, and then in this section we analyze the presence of a fracture, evaluating the slopes and deflection of the rotor near to its fracture.

Applying the Timoshenko beam theory and by numerical integration procedure to Eq. (11), the slopes and deflections of the rotor are obtained. In Figures 8 and 10, the slops and deflections of the rotor are shown respectively, and corresponds to half of the rotor (X=0, X=80).

In Figures 9 and 11, the slopes and deflections are shown for the case near of half of the fracture (X=79.5-ε, X=80), where $|\varepsilon| = 0.1$. In each case, the slopes and deflections are shown for α = 0^0, 30^0, 60^0 and 90°, Figures 8 and 10 are displayed as a single curve due to the scale. In Figures 9 and 11 are clearly differentiated the four curves.

$$\frac{d^2Y}{dX^2} = \frac{0.5F}{E}\frac{X}{I_{cf}} \tag{11}$$

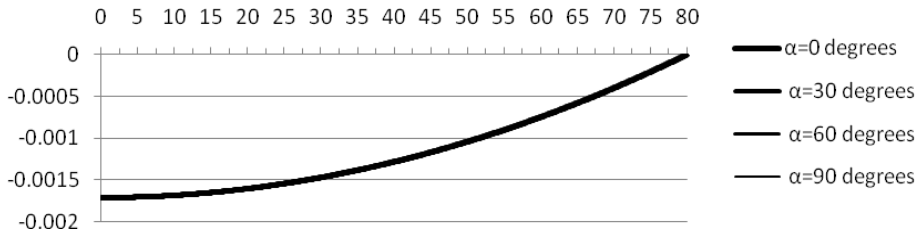


Figure 8: Slopes for α = 0°, 30°, 60° and 90 °, for (X=0, X=80).

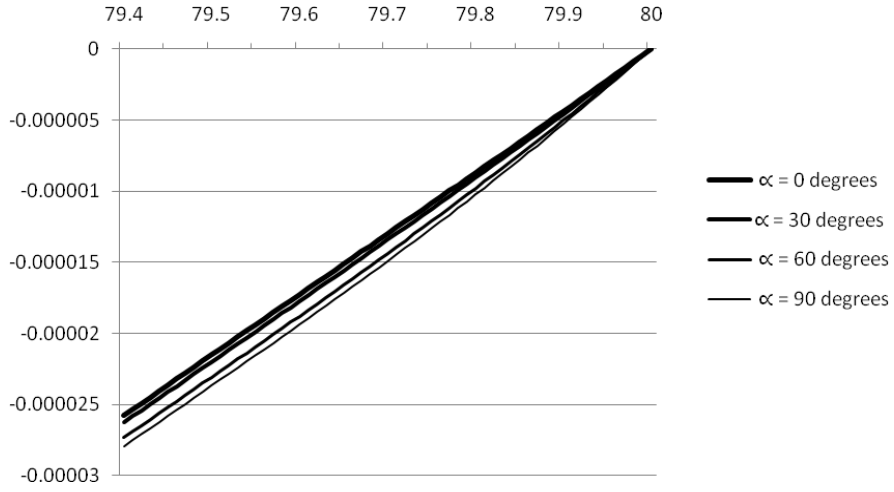


Figure 9: Slopes in the zone of the fracture for α = 0°, 30°, 60° and 90°, for range near to the fracture (X=79.4, X=80)

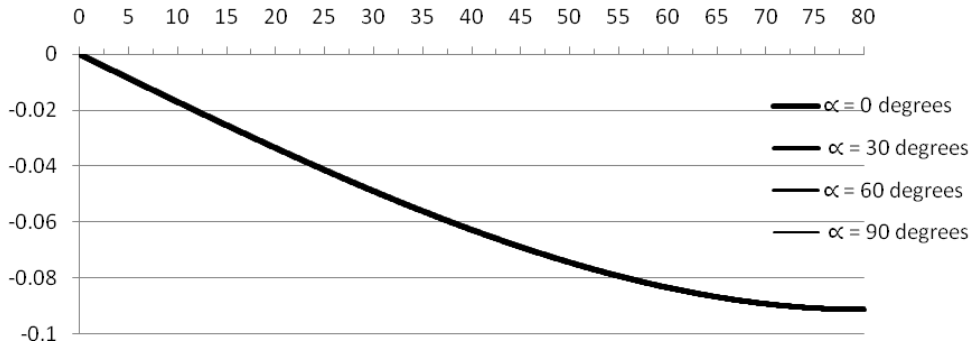


Figure 10: Deflections for α = 0°, 30°, 60° and 90°, for (X=0, X=80).

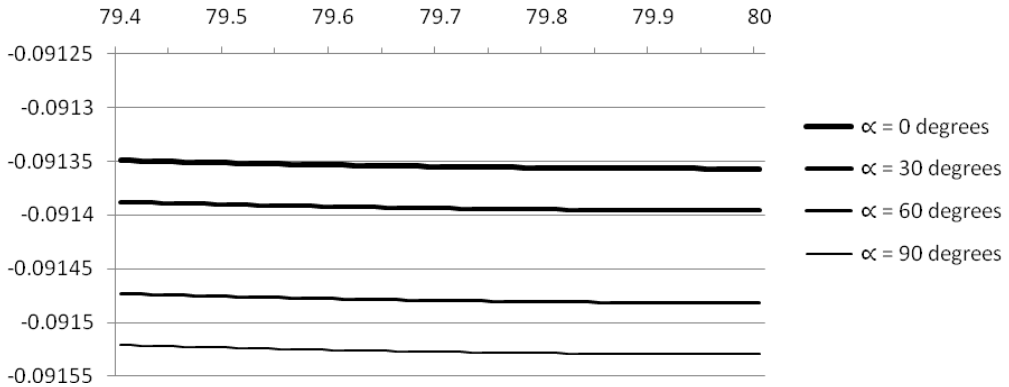


Figure 11: Deflections in the zone of the fracture to α = 0°, 30°, 60° and 90°, for range near to the fracture (X=79.4, X=80)

6 STIFFNESS AND RESONANCE FREQUENCY

From the numeric results of the deflections of the rotor with a fracture, we have determined a correlation between the stiffness of the rotor and its natural frequency. In Figure 11 is shown a graphic of the deflections for α = 0°, 30°, 60° and 90°, then considering the expression for the natural frequency of a rotor on static conditions, which depends on the deflections, then we can determine a spectrum of natural frequencies, that for each α, there exists one deformation and one natural frequency. We must mention that in this case the fracture was modelled without damping, for this reason the resonance frequency, approaches to the natural frequency.

In Figures 12 shown the range of stiffness calculated from the deflections. For this range the spectrum of resonance frequencies is shown in Figure 13.

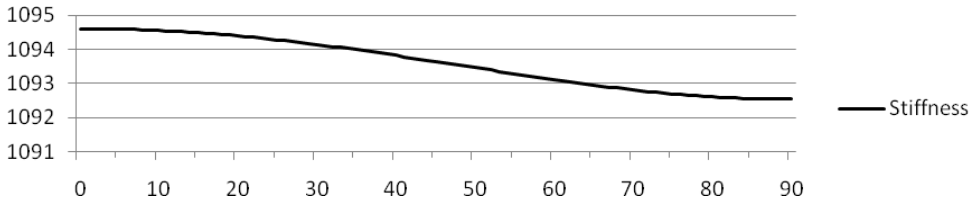


Figure 12: Stiffness depending on α.

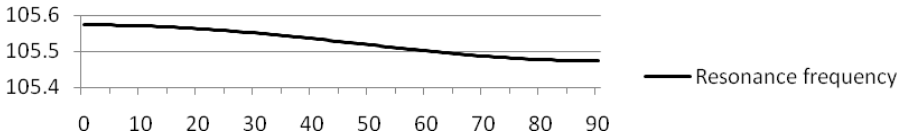


Figure 13: Resonance frequency based on α.

7 NUMERICAL SIMULATION

Numerical simulations was performed using the finite element method, in Figure 14 is shown the rotor with the fracture in the most critical orientation, that is, the simulation includes a fracture for α = -90°, in this situation the deflection determined was of 0.1646 mm.

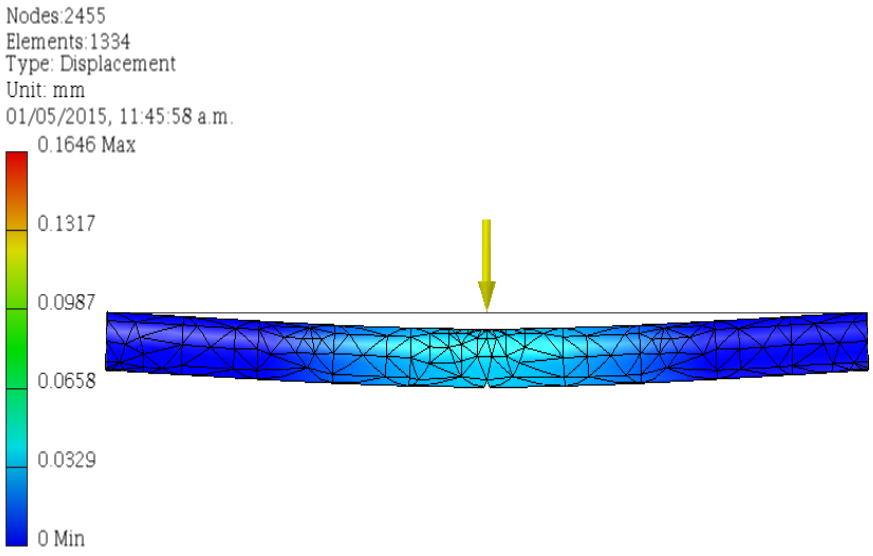


Figure 14: Deflection for α = -90°.

8 COMPARATIVE ANALYSIS

Since the analytical solution, the rotor material is considered homogeneous, isotropic and continuous; discontinuity in the fracture was not considered; the numerical simulation was performed to obtain by this method, the parameters obtained analytically. Figure 14 shows the results.

In Table 1 is shown the deflection, stiffness and resonance frequency obtained analytically for the rotor without fracture.

$\Delta\,(mm)$	k $\frac{N}{mm}$	$\omega\ \frac{rad}{s}$
0.09134359	1094.76757	105.568895

Table 1: Parameters obtained analytically for the rotor without fracture.

In Table 2 is shown the deflection, stiffness and resonance frequency obtained analytically for the rotor with fracture for the four values considered of α.

α°	$\Delta\,(mm)$	k $\frac{N}{mm}$	$\omega\ \frac{rad}{s}$
0	0.09135695	1094.60749	105.573078
30	0.0913958	1094.14219	105.550637
60	0.09148179	1093.11367	105.501015
90	0.09152965	1092.54218	105.473433

Table 2: Parameters obtained analytically for the rotor with fracture.

Finally, in Table 3 is shown the deflection, stiffness and resonance frequency obtained numerically for the rotor with fracture for α=–90°.

α°	$\Delta\,(mm)$	k $\frac{N}{mm}$	$\omega\ \frac{rad}{s}$
-90	0.1646	607.533414	78.6518713

Table 3: Parameters obtained numerically for the rotor with fracture.

The effects of the fractures in the dynamical behaviour of rotors, leads us to evaluate the natural frequencies and then the resonance frequencies, in this work we have obtained resonance frequencies for three different methods, analytical without fracture, analytical with fracture and numerical with fracture. From the results we can compare in the following sense.

Comparing the results of the frequencies from Table 1 and Table 2 (α=90°), then the resonance in the rotor fracture present in a range of 0.1% below the resonance in the rotor without fracture, comparing the results of the frequencies from Table 2 (α=90°) and Table 3, it follows that resonance, obtained analytically, is approximately 34% higher than the corresponding obtained numerically.

Finally, comparing results of the frequencies from Table 1 and Table 3, it follows that the rotor fractured enter into resonance at a frequency range of approximately 25.5% below the resonant frequency of the rotor without fracture.

We considered that the case α=90° corresponds to the case α=–90° for the analytical procedure, in both of the cases the deflections are equivalent, if is not considered stress concentrations and other dynamics conditions.

9 CONCLUSIONS.

In this paper we have analyzed the case of a rotor with a fracture since the point of view of the second area moment. The analysis was performed using basically the finite element method and an analytical procedure, in both of the cases we determined, stiffness and deflections of a fractured rotor. In the analytical procedure, we considered a fracture in different orientations and their effect in the deflections. Then for each orientations of the fracture there is a particular deflection and in consequence a corresponding natural frequency and the associated resonance frequency. In the case of the comparing between the rotor without fracture and with fracture, from the results, we can conclude while the rotor without fracture just it has associated one deflections, in the case of the rotor with fracture, the fracture induces a range of deflections because the second area moment varies continuously. Any way we have analyzed just for cases, or four orientations.

REFERENCES

[1] T. Morais, Control of the breathing mechanism of a cracked rotor by using electromagnetic actuator numerical study. *Latin American Journal of Solids and Structures*, **3**, 2013.

[2] G.Sabnavis, R. G. Kirk, M. Kasarda, D. Quinn, Cracked shaft detection and diagnostics: a literature review. *Shock-Vibration Digest*, 2004.

[3] V. Kumar, C. Rastogi, A brief review on dynamics of a cracked rotor. International Journal of Rotating Machinery, 2009.

[4] Ferdinand P. Beer, E. Russell Johnston, Vector Mechanics for Engineers: Statics and Dynamics, McGraw-Hill, 2010.

International Conference on Engineering Vibration
Ljubljana, Slovenia, 7-10 September 2015

DYNAMICS OF THE ROTOR WITH FOIL BEARINGS AT AN ELEVATED TEMPERATURE

Slawomir Banaszek*[1], **Grzegorz Zywica**[1], **Pawel Baginski**[1]

[1]Institute of Fluid-Flow Machinery, Polish Academy of Sciences, Gdansk, Poland
slawomir.banaszek@imp.gda.pl

gzywica@imp.gda.pl

pbaginski@imp.gda.pl

Keywords: Foil Bearings, Rotor Dynamics, Micro-turbines, High-speed Rotors.

Abstract. *The paper presents the results of investigations of the dynamic state of the rotor founded on foil bearings at higher temperature. Bearings are intended for application in micro power turbine. Measurements of the temperature and vibrations of the rotor were made at room and elevated temperature as it is expected in the real machine. The results of measurements of foil temperature distribution and the rotor vibration are presented.*

.

1 INTRODUCTION

Advantages of foil bearings make them ideal for application in technologically advanced machinery and they are frequently used today as a substitute for other bearing systems applied so far. Properly designed foil bearings provide reduction of friction and very good dynamic properties of rotor, ensuring long-term service, even under difficult operating conditions, such as high rotational speed or elevated temperature [1-7].

Foil bearings have also some limitations and should not be perceived as a one-size-fits-all solution in rotor machines. Gas is most often used as a lubricant, so such bearings have limited capacity, particularly at lower speeds. High start-up torque is also troublesome, especially if the foil set is clenched around the journal. [1-5, 8, 9].

The paper presents the results of investigations of dynamic state of a rotor founded on foil bearings at room and elevated temperature. Gas (air) foil bearings with aerodynamic lubrication were applied (no external delivery of air into the bearings). The bearings are intended to be implemented in a micro-turbine for micro-power plant (about 2 kW of electrical power), which was designed in the Institute of Fluid Flow Machinery (IMP PAN) for dispersed power generation [5, 7, 8]. The expected temperature inside such micro-turbine can reach 160ºC and more. That's why the bearing and the shaft were heated to obtain higher temperature and simulate conditions of real work of rotor-bearing system. The test rig of rotor dynamics and results of measurements are presented in the following.

2 THE TEST RIG

2.1 General description

The experiments were carried out on a rotor dynamics test rig, equipped with a rotor founded on two gas foil bearings. A massive steel plate with threaded mounting holes is a base of the stand, together with a 'table-like' supporting structure. Bearings' pedestals and holders of sensors are mounted on the plate. The rotor is driven with high-speed electrospindle. Each bearing pedestal is split to provide relatively quick and easy replacement of bearing bushes. Basic technical specification of the test rig is presented in the Table 1.

length of the shaft	435 mm
maximum rotational speed	24 000 rpm
rated rotational speed	18 000 rpm
rated diameter of the shaft	34 mm
internal diameter of the bearing bush	35.07 mm

Table 1: Basic technical specifications of the test rig.

Heating devices, namely a heat gun and infrared radiators are placed close to the bearing No.2. The heat gun consists of a tube with heating elements inside and a channel fan, which forces the air flow through the tube on the bearing No.2 and on the free end of the shaft. The infrared radiators warm up the shaft between the bearings' pedestals (close to the bearing No.2) as auxiliary warming elements. The bearing No.2 and the heated part of the rotor can be covered with the glass box to prevent the hot air from rapid escape from the heating zone. It shortens the warming up time and makes the temperature distribution around the rotor more uniform. Figures 1 and 2 present the views of the test rig.

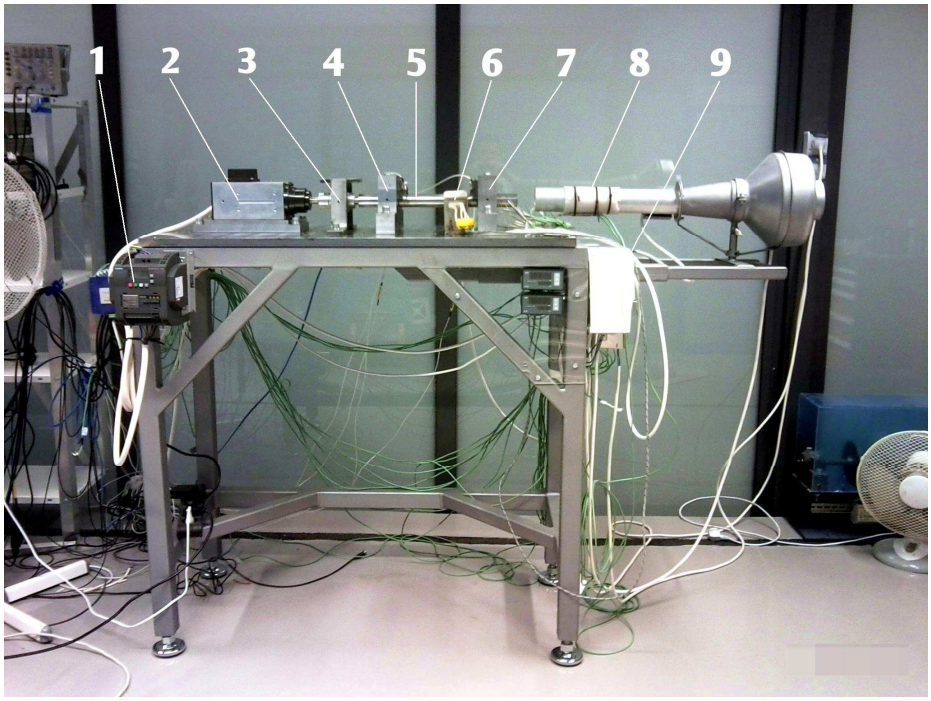


Figure 1: The rotor dynamics test rig (general view): 1 drive control unit, 2 driving motor (electrospindle), 3 clutch, 4 bearing No.1 pedestal, 5 shaft, 6 infra-red radiators, 7 bearing No.2 pedestal, 8 "heat gun", 9 warming elements' control unit.

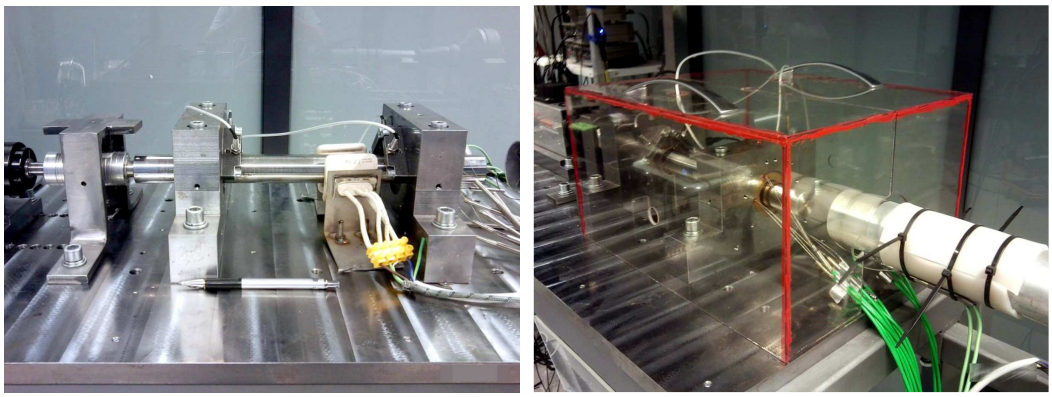


Figure 2: The laboratory rotor: general view (left) and the view of the glass cover keeping the hot air around the shaft.

2.2 The foil bearings

The foil bearings is presented on the Figure 3. Aerodynamic foil bearings were applied. The foil set was made of Inconel 618 and the top foil was coated with an AS20 fluorine polymeric anti-friction coating.



Figure 3: The bearing bush with the assembled foil set.

In order not to interfere with the bearing functioning, the thermocouples are delivered to the top foil through 12 holes made in the bearing sleeve. These holes were drilled inside additional grooves enabling thermocouples insertion and mounting the complete bush with the thermocouples into the housing. The holes were arranged in such a way that thermocouple tips are accurately positioned and have direct contact with top foil between notches in bump foil (3 thermocouples in each of 4 grooves, see Figure 4). The thermocouple tips were additionally joined with the top foil using thermally conductive paste. Due to the presence of a notch intended to secure the foil, one of the grooves was relocated by 20 degrees. The rest of the grooves was equally distributed, 90 degrees from each other.

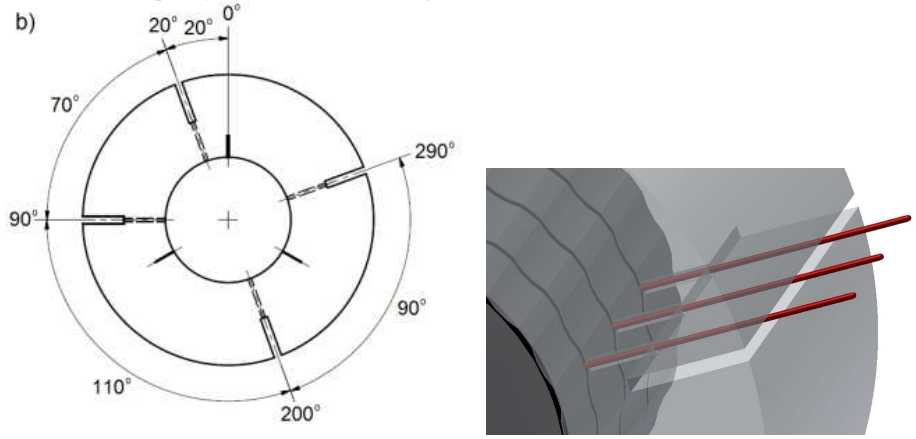


Figure 4: The geometry of the bearing bush (left) and the way of thermocouples delivering to the top foil (right).

2.3 A measurement equipment

A multi-channel LMS SCADAS Mobile analyzer was used with the following sensors applied:

- thermocouples – for measurement of the foil temperature inside the bearing (12 points of measurement),
- tachometer – for rotational speed measurement,
- eddy-current sensors – for measurement of the shaft relative vibration (4 points).

With the use of the mentioned equipment the following tests were carried out: measurements at room temperature (with no heating the shaft) and at elevated temperature, when the heating devices were switched on. Temperature values of the foil inside the bearing were measured as well as the relative vibration of the rotor. A thermovision camera was used for measurement of the surface temperature of the elements consisting the test rig. Thermovision images were frequently taken from the bearing journals' surfaces (as close as possible to the bearing).

3 THE MEASUREMENT AT ROOM TEMPERATURE

The first session of measurement was carried out at room temperature (about 20ºC), with no external heating of the shaft. The rotor was running up for the first 60 s and then it was driven with the maximum rotational speed (24,000 rpm). The measurement time was 1906 s. The Figures 5-7 present the time histories of the temperature measured in 12 point at the bearing, the journals' position inside the bearings (the relative values, taken from the eddy-current probes) and the amplitudes of vibration. Figure 8 shows the chosen thermovision images of the bearing No.1.

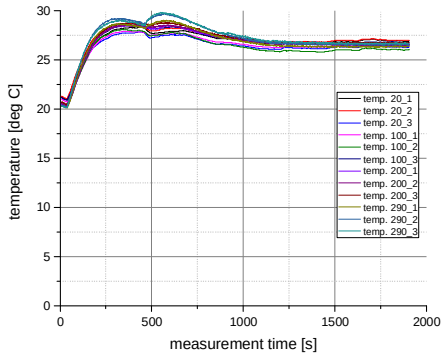


Figure 5: The foil temperature distribution at the test at room temperature.

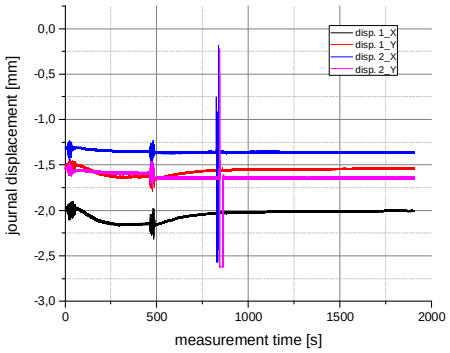


Figure 6: The time history of the bearing journals' locations inside the bearings at the test at room temperature.

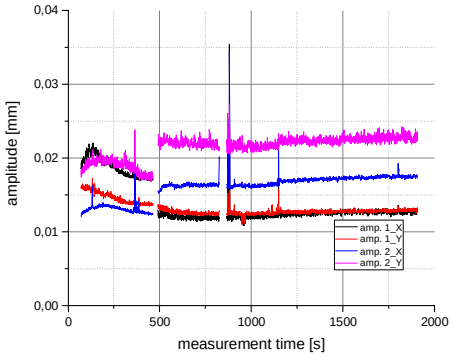


Figure 7: The time history of relative vibration amplitudes at the test at room temperature.

The temperature in the bearing No.2 did not exceed 30°C in the first period of measurement and then it decreased to about 27°C. The spread of the temperature values was close to 1ºC, so the temperature of the bearing was almost constant and it was less then 10ºC higher then the starting temperature.

The rotor at the run-up underwent significant vibration because the journals were supported on the foils only. Since the air layer appeared between the journals and the top-foil (at about 9000 rpm), the vibration and audible noise significantly reduced. The amplitudes of X and Y components were about 13-20 µm and after 240 s they were slightly decreasing.

At the same period of time we can see growing negative values referred to the shaft position inside the bearing No.1. It means, the shaft was relatively receding from the probes. After 450 s sudden large vibration and noise appeared and the amplitudes rose over 0.2 mm. After the next 60 s they decreased again. The thermovision images taken before and after that show significant reduction of the temperature: from 115ºC to about 50ºC (see Figure 8). The possible explanation of that phenomenon is, that the foils bearing clenched around the journal and all of the bearing elements were heated because of friction. The internal diameter of the bearing grew and the stiffness of the foils decreased due to high temperature, so it led the foil set to adjust and adopt to the present conditions. After that both bearings were working stable.

After 800 s the test rig was unintentially pushed. The vibration rose for some time but it was quickly damped down. It revealed good damping properties of the gas foil bearings.

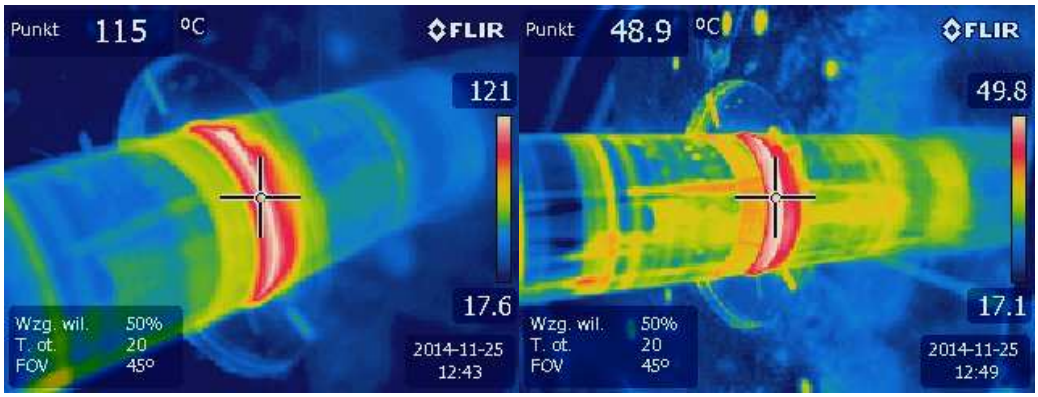


Figure 8: The temperatures of sliding layer of the bearing No.1 journal before and after the foil adjustment.

4 THE MEASUREMENT AT THE ELEVATED TEMPERATURE

The rotor was turning at 24 000 rpm for 300 s, then the heating devices were switched on. The measurement stopped after 3566 s. The Figures 9-11 present the temperatures of the bearing No.2, the displacements of the shaft inside the bearing No.1 and No.2, and the vibration amplitudes. They show clearly the changes of the dynamic behaviour of bearings since the heating devices are switched on. The temperature values on the thermocouples reached 100-112ºC. The highest values appear at the side of the bearing which the hot air from the heat-gun is blown on. The inner thermocouple on the angle of 290º exhibits some malfunction.

Figure 10 presents the transition of the bearing journals inside the bearing clearance. The rotor is receding from the probes and the amplitudes are rising. It is the result of the heating of the bearing. The bearing clearance is growing due to the thermal expansion of the bush and housing. The stiffness of the foil set decreases at higher temperature. The amplitudes reach 30 µm, which is rather high value.

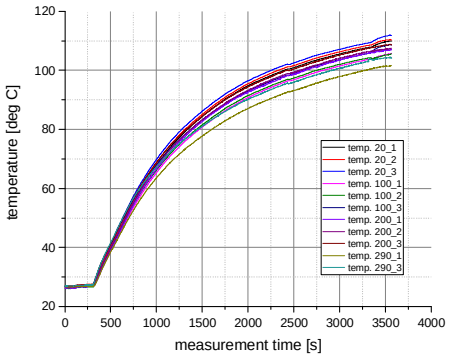


Figure 9: The foil temperature distribution at the test at the elevated temperature.

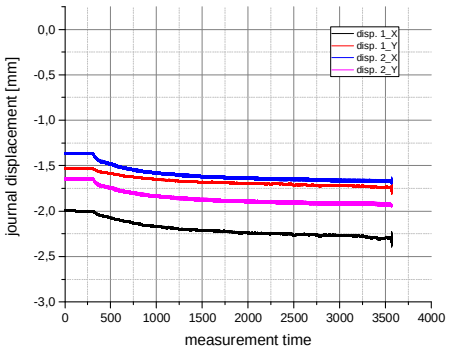


Figure 10: The time history of the bearing journals' locations inside the bearings at the test at the elevated temperature.

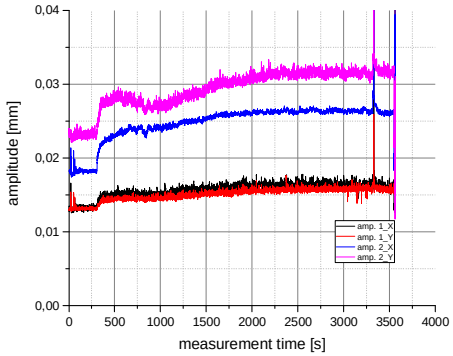


Figure 11: The time history of relative vibration amplitudes at the test at the elevated temperature.

5 TRANSIENT TESTS

The Figure 12 presents the amplitudes obtained at the transient tests at room and elevated temperature. It shows clearly that in the higher temperature the amplitude values rise and the critical speed reduces from 8400 to 7800 rpm. The Figure 13 shows the vibration orbits of the journals at room and elevated temperature at 8000 rpm, which is undercritical at room temperature and overcritical when the rotor is heated. The Figure 13 shows the comparison of the orbits of the journals at 8000 rpm.

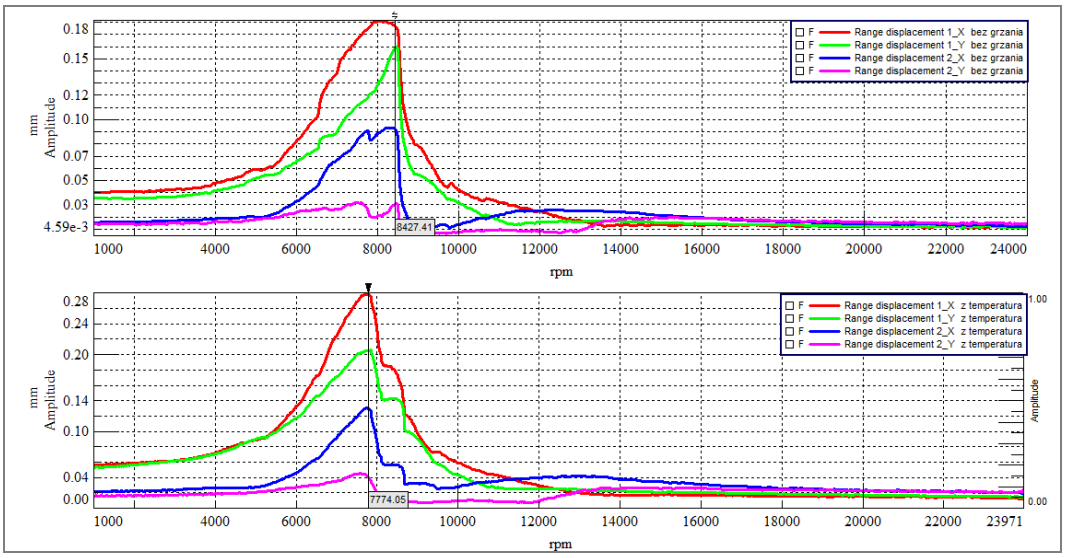


Figure 12: The comparison of relative vibration amplitudes at transient tests at room (up) and elevated temperature (down).

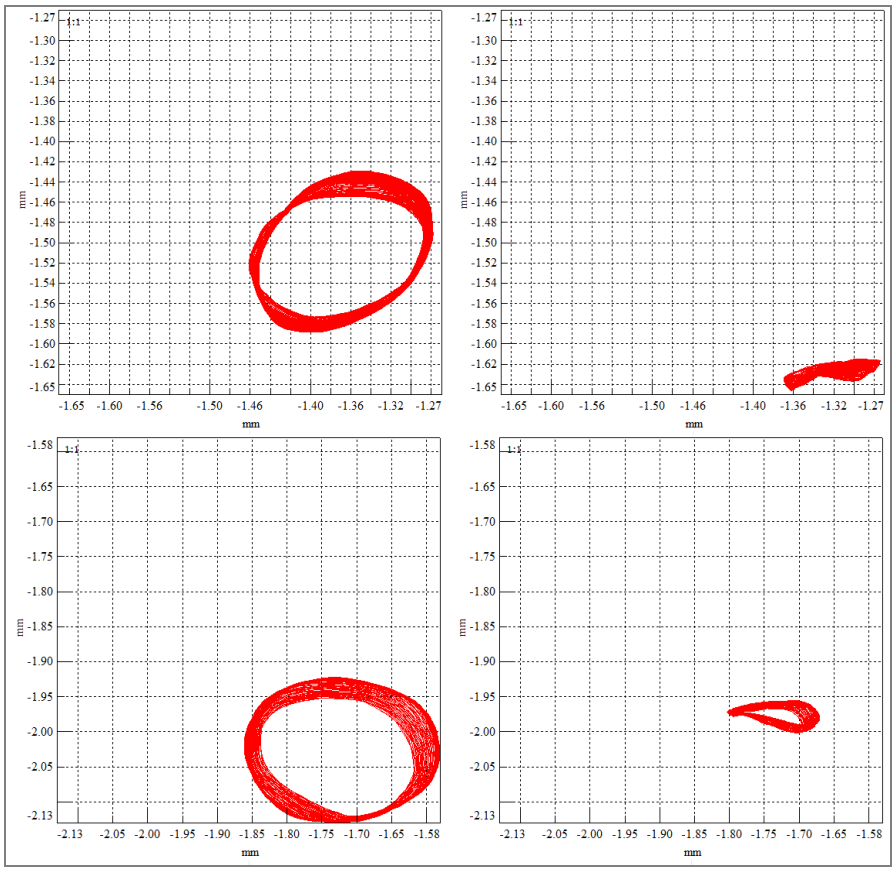


Figure 13: The comparison of the vibration orbits in the bearing No.1 (left) and No.2 (right) at 8000 rpm at room (up) and elevated temperature (down).

6 CLOSING REMARKS

The investigations showed that the temperature of the gas (air) foil bearings considerably influences on the dynamics of the rotor. On one hand, the foil bearings exhibited good damping properties and they revealed their adjustability to the operational conditions. After the generation of the air lubricating layer the rotor turns stable. On the other hand, the excentricity of the journal inside the bearing gap rises in higher temperature, so do amplitudes. These are the results of the thermal expansion of the elements of bearing – the inner diameter of the bearing expands, the bearing clearance rises and the stiffness of the foil set reduces.

The dynamic state of the rotor can change in the higher temperatures. It requires very careful design of the gas foil bearings, especially in microturbines, because of very small clearances over the blades.

REFERENCES

[1] Ch. DellaCorte, *Oil-Free shaft support system rotordynamics: Past, present and future challenges and opportunities*, Mechanical Systems and Signal Processing 29, pp. 67–76, 2012.

[2] R. J. Bruckner, *An assessment of gas foil bearing scalability and the potential benefits to civilian turbofan engines*, Proceedings of ASME Turbo Expo 2010, Glasgow, UK, 2010.

[3] T. H. Kim, L. San Andres, *Analysis of advanced gas foil bearings with piecewise linear elastic supports*, Tribology International 40, pp. 1239-1245, 2007.

[4] Y.-B. Lee, D.-J. Park, Ch.-H. Kim, S.-J. Kim, *Operating characteristics of the bump foil journal bearings with top foil bending phenomenon and correlation among bump foils*, Tribology International 41, pp. 221–233, 2008.

[5] J. Kiciński, G. Żywica, *Steam Microturbines in Distributed Cogeneration*, Springer 2014.

[6] K. Nalepa, P. Pietkiewicz, G. Żywica, *Development of the Foil Bearing Technology*, Technical Sciences, No 12, pp. 229-240, 2009.

[7] J. Kicinski, G. Zywica, *The numerical analysis of the steam microturbine rotor supported on foil bearings*, Advances in Vibration Engineering, Vol. 11(2), pp. 113-120, 2012

[8] J. Kicinski, G. Zywica, P. Baginski, *Thermal studies on foil bearings with a sliding coating made of plastic material*, 9th IFToMM International Conference on Rotor Dynamics, Milan, Italy, 2014.

[9] D. Kozanecka, Z. Kozanecki, E. Tkacz, J. Łagodziński, *Experimental research of oil-free support systems to predict the high-speed rotor bearing dynamics*, Int. J. Dynam. Control, March 2014

International Conference on Engineering Vibration
Ljubljana, Slovenia, 7-10 September 2015

VIBRATION OF TWO DEGREES OF FREEDOM AIR BEARING-ROTOR SYSTEM WITH ASYMMETRIC SUPPLY PRESSURE

Abdurrahim Dal*[1], Tuncay Karaçay[2]

[1]Gazi University
abdurrahimdal@gazi.edu.tr

[2]Gazi University
karacay@gazi.edu.tr

Keywords: Externally Pressurized Air Bearing, Asymmetric Supply Pressure, Rotor Dynamics

Abstract. *In externally pressurized air lubricated bearing, air is generally supplied with constant pressure by orifices. Radial loads (rotor mass or external forces on rotor) make a relative eccentricity between bearing and rotor. And the relationship between the load and the eccentricity is nonlinear due to compressibility of air. Increase in the eccentricity may reach to a critical value, if the rotor is close to the bearing wall. Because the air film thickness may not be sufficient to carry applied load. In order to avoid high value of eccentricity, the load carrying capacity of the bearing must be increased. In this study, in order to increasing the stiffness (load carrying capacity) of the bearing directionally, the supply pressure of the orifices, which are opposite to the loading direction, are increased. However, in this approach although air consumption is lower than the increasing pressure in all orifices, the asymmetric stiffness of the bearing along the orthogonal direction will affect the dynamics of the rotor. In order to investigate the dynamics behaviour of the rotor, the air bearing is analyzed numerically. The bearing-rotor system is modelled in two degree of freedom and it is simulated for different asymmetric supply pressure.*

1 INTRODUCTION

Aerostatic bearings are generally preferred for supported ultra high speed spindles, high precision machine tools and laboratory equipments due to their absolute advantages of low friction loss and high accuracy. In aerostatic bearings, externally pressurized air flows radial clearance between rotor and bearing surfaces by passing through orifices. Most of the aerostatic bearing applications, air is supplied with constant pressure by orifices. Radial loads (rotor mass or external forces on rotor) make a relative eccentricity between bearing and rotor. And the relationship between the load and the eccentricity is nonlinear due to compressibility of air. Increase in the eccentricity may reach to a critical value, if the rotor is close to the bearing wall. Because the air film thickness may not be sufficient to carry applied load. In order to avoid high value of eccentricity, the load carrying capacity of the bearing must be increased. The load carrying capacity could be increased with operating high value supply pressure. Air consumption is also increased with increasing supply pressure. Instead of increasing supply pressure of all orifices, in order to increasing the stiffness (load carrying capacity) of the bearing directionally, the supply pressure of the orifices, which are opposite to the loading direction, could be increased. So, in this approach although air consumption is lower than the increasing pressure in all orifices.

In the aerostatic bearings, the load carrying capacity is strongly related mass flow rate and mass flow rate is also affect supply pressure, orifices geometry and number of orifices. In literature, many researcher analyzed effect of mass flow rate on load carrying capacity and they researched how to increasing load carrying capacity, in other words mass flow rate, using different type orifices or high supply pressure. Fleming et al., performed a small eccentricity analysis on a aerostatic bearing having two feeding planes and they obtained load and attitude angle with speed at different supply pressure and feeding parameter for steady state conditions [1]. Fourka and Bonis analyzed the effect of feeding system type on the performance characteristics of externally pressurized gas bearings. They compared the optimum bearing characteristics such as load capacity, stiffness and flow rate using different kinds of externally pressurized air bearing which have multiple inlets specifically designed with orifices or porous compensation. They concluded that optimum performance may be achieved for each of these different feeding systems, which depend on an optimum number of orifices, position of orifices, or permeability coefficient of the porous material [2]. Czolczynski theoretically analyzed the self excited vibrations of rigid symmetrical rotor supported in two externally pressurized air bearings and additional air rings. He concluded that the set of parameters of such a additional air ring is optimal when the bearing has a chamber feeding systems [3]. Renn and Hsrao in an experimental and CFD study, investigated on the mass flow-rate characteristic through an orifice-type restrictor in aerostatic bearings which radial clearances are 12 and 18 μm. They concluded that the mass flow-rate characteristic through an orifice is different from that through a nozzle and the conventional model to determine the mass flow-rate through an orifice-type restrictor in aerostatic bearings may have to be updated to the proposed new model for more precise design and modelling of the gas-lubricated aerostatic bearings. [4]. Park and Kim theoretically and experimentally investigated on a new type of slot-restricted gas journal bearing with non-uniform slot clearance in the circumferential direction. They analyzed effect of slot restricted on the stability of rotor-bearing system and they concluded that, the proposed new type of the slot-restricted air journal bearings is much more stable than conventional slot-restricted bearing [5]. Su and Lie investigated dynamics of rotor supported hybrid air journal bearings with multi array of 1, 2, 3, 4, or 5 row orifice feedings with multi-array of 1, 2, 3, 4, or 5-row orifice and porous feeding systems. They concluded that the porous bearing is more stable than the orifice feeding bearing at lower rotation speeds or at

higher rotation speeds with lower feeding parameter and the 5-row orifice feeding bearing is more stable than the porous bearing at moderate speeds with lower feeding parameters [6]. Lo et al. discretized Reynold's equation by use Newton method and investigated load carrying capacity and stiffness for different supply pressure, L/D ratio and clearance [7]. Colombo et al. considered, in a theoretical study, the effect of orifice feeding and supply pressure on the load capacity and stiffness externally pressurized gas bearings which have one and two sets of orifices and 38 μm radial clearance. They concluded that the load capacity and stiffness could be improved with high supply pressure and increased orifice diameter [8]. Colombo et al. compared radial stiffness and pressure distribution for three externally pressurized gas bearing at different air consumption rates [9]. Yang et al., studied the influences of both the number and locations of entry holes on the stability of a rigid rotational rotor supported by two double-row, orifice compensated aerostatic bearings. They analyzed of effect of orifices on the whirl stability and load carrying capacity [10]. Chen et al., theoretically and experimentally investigated stiffness of various geometric designs of aerostatic journal bearings for high-speed spindles under different operating conditions. They measured the stiffness of the front and rear journal bearings using the relationship of force and displacement at different supply pressures (6-9 bar). They developed a numerical model to simulate journal-bearing stiffness under the same pressure range to validate the results and calculated the stiffness of the designs with various geometric parameters, including bearing length/diameter (L/D) ratios of 0.5, 1.0, and 1.5; different types of restrictor designs (e.g., pocketed orifice versus inherent orifice); supply orifice diameter; radius gap; supply pressures of 6, 7, 8, and 9 bar [11]. Otsu et al., numerically and experimentally investigated the instability of a rigid rotor supported by aerostatic journal bearings with compound restrictors. They concluded that this type of aerostatic bearings showed a much higher threshold speed for instability compared with bearings with inherently compensated restrictors [12]. Chen et al., investigated static and dynamic characteristics of a rigid spindle supported by aerostatic bearings which are compensated by orifices and inherences. They compared restriction effect both orifice and inherence for various eccentricities, rotor speeds and restriction parameters are taken into considerations for the comparisons of restriction effect between both orifice and inherence [13].

In order to increasing load carrying capacity, high supply pressure or effective feeding systems are generally preferred in the aerostatic air bearing applications. In literature, many studies are also investigated effect of supply pressure [6-8,10], orifices geometry [3,4,10] and feeding system type [5-13] on the load carrying capacity and stability of rotor-bearing systems. In these investigations, in order to obtain high load carrying capacity, the supply pressure and orifice diameter were increased at all orifices, in other words, externally pressurized air was supplied with constant mass flow rate. However, radial loads (rotor mass or external forces on rotor) make a relative eccentricity between bearing and rotor. So, increasing supply pressure of the orifices, which are only opposite to the loading direction could be sufficient. In this study, in order to increasing the stiffness (load carrying capacity) of the bearing directionally, the supply pressure of the orifices, which are opposite to the loading direction, are increased. However, in this approach although air consumption is lower than the increasing pressure in all orifices, the asymmetric stiffness of the bearing along the orthogonal direction will affect the dynamics of the rotor. In order to investigate the dynamics behaviour of the rotor, the air bearing is analyzed numerically. The bearing-rotor system is modelled in two degree of freedom and it is simulated for different asymmetric supply pressure.

2 MATHEMATICAL MODELS

In the aerostatic bearings, externally supplied air is separated bearing and rotor surfaces and is generated a lubrication film. This lubrication air film is supported rotor and is affected

dynamics of aerostatic bearing-rotor system. Mathematical model of air flow and aerostatic bearing-rotor system are given in this chapter.

2.1 Mathematical Model of Air Flow

The aerostatic bearing-rotor system, orifices position and coordinate system using for mathematical models are illustrated Fig. 1.

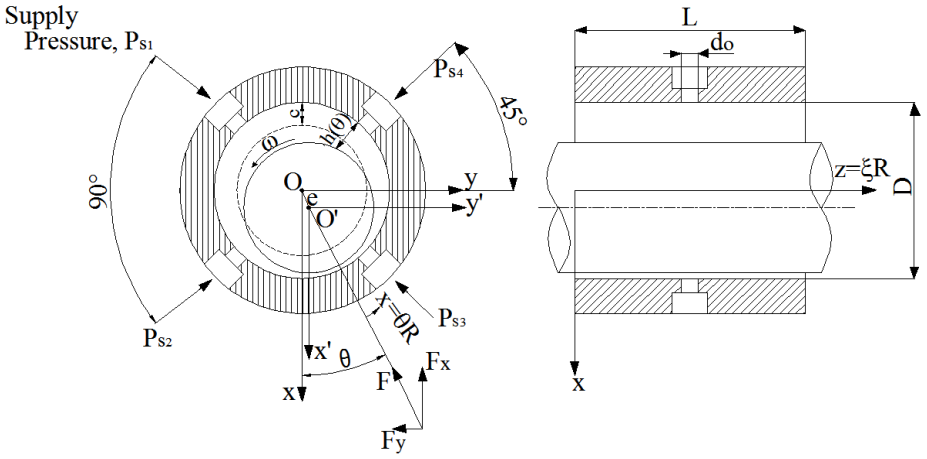


Figure 1: Configuration of aerostatic bearing-rotor system and axes of coordinate

Air flow is modeled using Reynold's equation and it is given in Eq. (1) for compressible fluid and isothermal flow, negligible inertia effect and constant viscosity assumptions.

$$\frac{\partial}{\partial x}\left[\frac{h^3 p}{\mu}\frac{\partial p}{\partial x}\right]+\frac{\partial}{\partial z}\left[\frac{h^3 p}{\mu}\frac{\partial p}{\partial z}\right]+12R^0T^0\dot{m}=12\frac{\partial}{\partial t}(ph)+6U\frac{\partial}{\partial x}(ph) \tag{1}$$

where radial clearance function h is defined as in Eq. (2) and $\dot{m}$ is mass flow rate which is a function of orifice diameter, clearance and supply pressure.

$$h(\theta)=c+e\cos(\theta) \tag{2}$$

Reynold's equation could be given Eq. (3) with using dimensionless parameters which is given below;

$$P=pP_a,\ H=h/c,\ \theta=x/R,\ \xi=z/R,\ U=r\omega$$

$$-\frac{\partial}{\partial\theta}\left[H^3P\frac{\partial P}{\partial\theta}\right]-\frac{\partial}{\partial\xi}\left[H^3P\frac{\partial P}{\partial\xi}\right]+\Lambda\frac{\partial}{\partial\theta}(PH)+\sigma\frac{\partial}{\partial t}(PH)=\dot{M} \tag{3}$$

where squeeze number (σ) and dimensionless bearing number (Λ) are given in Eq. (4) and Eq. (5) respectively.

$$\sigma=\frac{12\mu}{P_a}\left(\frac{R}{c}\right)^2 \tag{4}$$

$$\Lambda=\frac{6\mu\omega}{P_a}\left(\frac{R}{c}\right)^2 \tag{5}$$

In the dimensionless Reynold's equation which is given in Eq. (3), dimensionless mass flow rate which passes through an orifice could be given as in Eq. (6).

$$\dot{M} = \Gamma_o P_s H \Phi(P) \tag{6}$$

where dimensionless feeding parameter and orifice function are defined in Eq. (7) and Eq. (8) respectively.

$$\Gamma_o = \frac{12\pi d_o^2 \mu \sqrt{R^0 T^0}}{p_a c^2 \Delta\theta \Delta\xi} \tag{7}$$

$$\Phi(P) = \begin{cases} \sqrt{\dfrac{2k}{k-1}\left[\left(\dfrac{p_d}{p_u}\right)^{\frac{2}{k}} - \left(\dfrac{p_d}{p_u}\right)^{\frac{k+1}{k}}\right]} & \text{for} \quad 1 > \dfrac{p_d}{p_u} \geq r_p \\ \dfrac{2k}{k+1}^{\frac{1}{2}} \left(\dfrac{2}{k+1}\right)^{\frac{1}{k-1}} & \text{for} \quad \dfrac{p_d}{p_u} < r_p \end{cases} \tag{8}$$

where r_p is the critical pressure ratio, k is specific heat ratio and equal to 1.4, p_d and p_u are downstream and upper stream pressure at the orifice respectively.

2.2 Mathematical Model of Bearing-Rotor System

Rotor-bearing systems which is supported externally pressurized air bearing could be modelled using equation of motions. Radial motion of the rotor-bearing system are modelled in two degree of freedom using Cartesian coordinate system (see Fig. 1) and give in Eq. (9).

$$\begin{aligned} m\ddot{x} + F_x &= 0 \\ m\ddot{y} + F_y &= 0 \end{aligned} \tag{9}$$

where F_x and F_y are air film forces and in order to calculated these forces, pressure distribution of air film between rotor and bearing surfaces must be obtained to solving Reynold's equation. So the forces components could be expressed as Eq. (10).

$$\begin{aligned} F_x &= p_a R^2 \int_0^{2\pi} \int_0^{L/R} P(\xi,\theta) \cos\theta \, d\xi \, d\theta \\ F_y &= p_a R^2 \int_0^{2\pi} \int_0^{L/R} P(\xi,\theta) \sin\theta \, d\xi \, d\theta \end{aligned} \tag{10}$$

In the equation of motions of the rotor-bearing system, there is no external force applied the rotor-bearing system and the rotor was assumed balanced.

3 NUMERICAL SOLUTION OF MATHEMATICAL MODELS

3.1 Numerical Analysis of Reynold's Equation

Reynold's equation which is given in Eq. 1, is in the form of parabolic differential equation and this equation could be solved numerically. In this study the Reynold's equation is solved by alternating direction implicit (ADI) using the scheme which is given in detail in [14]. In this study, in order to guaranteed the develop of fluid (air) flow within the radial clearance, a convergence criteria is defined in the routine of ADI as Eq. 11.

$$\frac{\left|P_{i,j}^{\,n+1} - P_{i,j}^{\,n}\right|}{P_{i,j}^{\,n+1}} \le 10^{-6} \tag{11}$$

If the pressure distribution function is defined as $P(\xi,\theta)$, the initial and boundary conditions could be given as follows;

- Pressure values are equal to atmospheric pressure at the initial time step
- Pressure values are equal to atmospheric pressure on the both ends of the bearing, $P(0,\theta)= P(L,\theta)=P_a$
- Pressure distribution is a periodic function;

$$P(\xi,\theta)=P(\xi,\theta+2\pi),\ \left.\frac{\partial P}{\partial \theta}\right|_{\theta} = \left.\frac{\partial P}{\partial \theta}\right|_{\theta+2\pi} \tag{12}$$

- Pressure distribution is symmetric to the centre of bearing length.

3.2 Solution of Equations of Motion

Equation of motions of the rotor-bearing system supported by air bearing is already given in Eq. (9). Dynamic motions of the rotor depend on to the flow of the air between the rotor and the bearing surfaces. So, an iterative procedure must be used to obtain radial motion of the rotor. Because at every iteration step fluid flow and so the supporting pressure on the rotor must be calculated. In this study, dynamics motions of the rotor-bearing system are obtained to using an iterative procedure which is given in detail in [14].

4 RESULTS AND DISCUSSIONS

In this study, effects of asymmetric supply pressure, in other words increasing the supply pressure of the orifices, which are opposite to the loading direction, on dynamic behaviours of the rotor-bearing system are investigated. Air bearing geometrical properties used in simulation are given in Table 1.

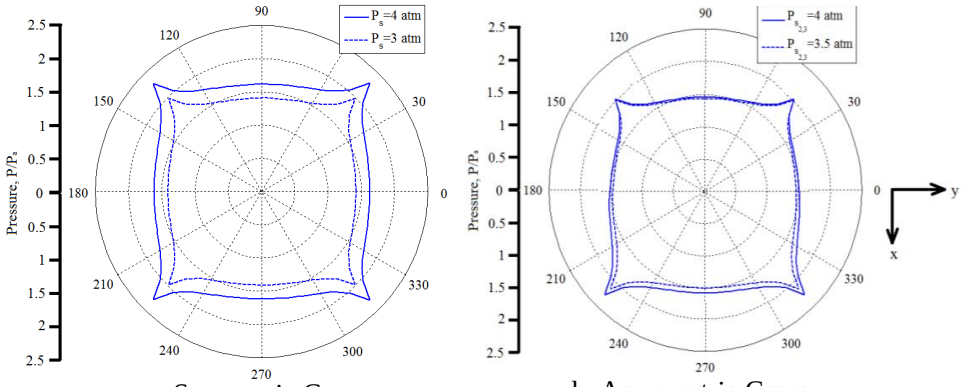
Quantity	Symbol	Value
Radial Clearance	c	125 μm
Bearing Radius	R	12.5 mm
Orifice Diameter	d_o	3 mm
Absolute Viscosity	μ	$18.4\text{x}10^{-6}$ Pa.s
Gas Constant	R^0	287.6 J/Kg K°
Absolute Temperature	T^0	298.15 K°
Rotor Mass	m	0.5 kg
Number of Orifices		4
L/D ratio		2

Table 1. Air bearing detail

4.1 Pressure Distribution

Pressures values along the circumferential direction are given in Fig. 2 for symmetric and asymmetric supply pressure on polar graphic. In these simulation, firstly pressure distribution is obtained for equivalent supply pressure ($P_{s1}= P_{s2}= P_{s3} = P_{s4}$=3 atm and 4 atm). Secondly, the pressure distribution is obtained for asymmetric supply pressure, in other words higher supply pressure at orifices where opposite to the radial load direction ($P_{s2} = P_{s3}$=3.5 atm and 4 atm, $P_{s1}= P_{s4}$=3 atm for two asymmetric cases). The pressure value increase as supply pressure increased at each point for both cases. And, this is reasonable because the gap volume

increase for the same mass flow rate. On the other hand the pressure values at opposite to the radial load direction for asymmetric supply pressure are higher than the bearing with symmetric supply pressure as expected.



a. Symmetric Cases b. Asymmetric Cases

Figure 2. Pressure value of air bearing at circumferential axis

4.2 Mass Flow Rate

In the air bearing, load carrying capacity could be increased with high values of mass flow rate. The mass flow rate is function of supply pressure and orifice diameter as well as clearance between rotor and bearing surfaces. So mass flow rate are affected by changing supply pressure, radial clearance and orifice diameter. Total mass flow rates passing through all orifices are given in Fig. 3 for different symmetric and asymmetric supply pressure cases. It is clear that mass flow rate increases when radial clearance is increased almost linearly. Besides, mass flow rate increases as supply pressure is increased (Fig. 3). In addition to total mass flow rate is lower value for increasing the supply pressure of the orifices where are only opposite to the loading direction (x-direction), in other words, asymmetric supply pressure cases.

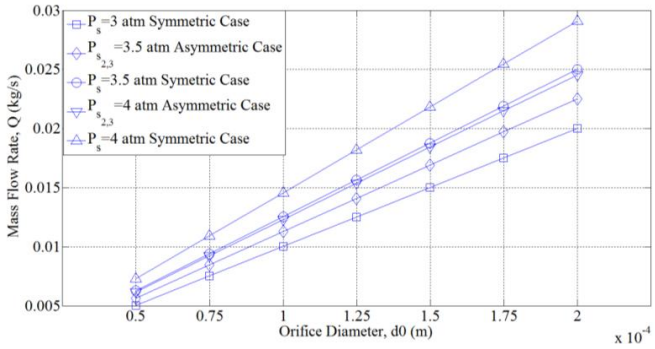


Figure 3. Mass flow rate vs. radial clearance for different symmetric and asymmetric supply pressure cases (In all asymmetric case $P_{s1,4}$ =3 atm)

4.3 Load Carrying Capacity

Load carrying capacity is the sum of forces applied to the shaft produced by pressure distribution between shaft and bearing. It is affected by all of the parameters that effect the pressure distribution. And the load carrying capacity is directly related to the dynamic of rotor

supported as defined in equation of motion which is given in (10). In order to investigate effect of asymmetric supply pressure on the load carrying capacity, a serial cases are simulated and changing load carrying capacity with eccentricity ratio is shown in Fig. 4. It is clear that the load carrying capacity increases with increasing eccentricity value as well as supply pressure. However, in asymmetric supply pressure case as the load carrying capacity increase, the air consumption (mass flow rate) is still lower than symmetric case (see Fig. 3) for same load carrying capacity.

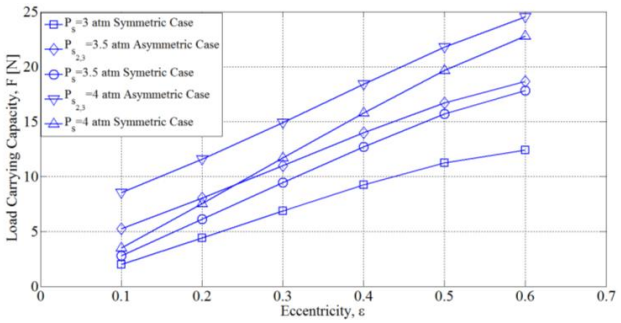


Figure 4. Load carrying capacity vs. eccentricity for different symmetric and asymmetric supply pressure cases (Radial clearance, c=75 μm)

4.4 Vibration of Rotor-Bearing System

The asymmetric load carrying capacity (stiffness) of the bearing along the orthogonal direction will affect the dynamics of the rotor. In order to investigate the dynamics behaviour of the rotor, the bearing-rotor system is modelled in two degree of freedom and it is simulated for different asymmetric supply pressure. Fig. 5a shows vibration of the rotor along the vertical direction (x) for symmetric supply pressure case (P_{s1}=P_{s2}=P_{s3}=P_{s4}=3 atm) and Fig. 5b shows vibration of the rotor along the vertical direction (x) for asymmetric supply pressure case (P_{s2}=P_{s3}=3.5 atm and P_{s1}=P_{s4}=3 atm). In the symmetric case, rotor oscillates more close to the centre of the bearing due to increased the load carrying capacity (stiffness) along x-direction as seen in Fig. 5b. In addition, the rotor also vibrates in low amplitude.

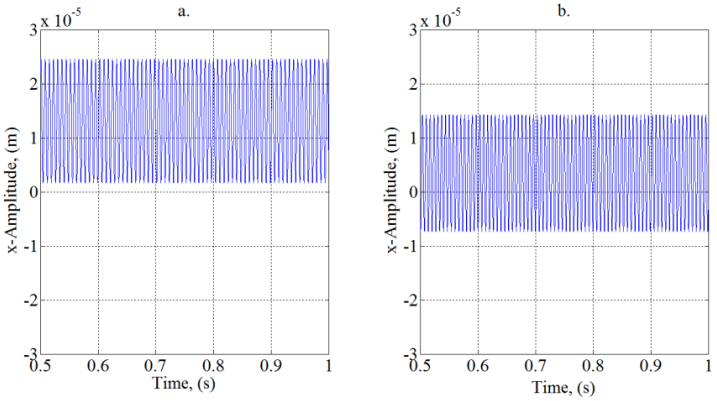


Figure 5. Vibration of rotor at x-direction for ω=1000 rad/s a. Symmetric case (P_{s1}=P_{s2}=P_{s3}=P_{s4}=3 atm) b. Asymmetric case (P_{s2}=P_{s3}=3.5 atm and P_{s1}=P_{s4}=3 atm)

Fig. 6a shows vibration of the rotor along the vertical direction (x) for symmetric supply pressure case (P_{s1}=P_{s2}=P_{s3}=P_{s4}=3 atm) and Fig. 6b shows vibration of the rotor along the ver-

tical direction (x) for asymmetric supply pressure case (P_{s2}=P_{s3}=3.5 atm and P_{s1}=P_{s4}=3 atm). Fig. 6b show that the orbit cycle of rotor is smaller for asymmetric supply pressure.

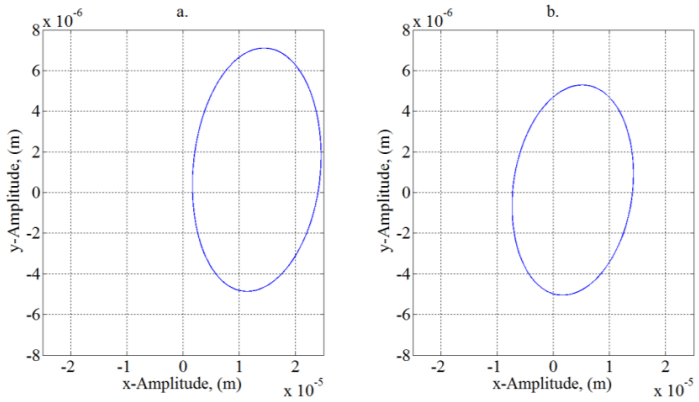


Figure 6. Orbit of the rotor center a. Symmetric case (P_{s1}=P_{s2}=P_{s3}=P_{s4}=3 atm) b. Asymmetric case (P_{s2}=P_{s3}=3.5 atm and P_{s1}=P_{s4}=3 atm)

5 CONCLUSION

In this study, dynamics of the rotor supported by air bearing are investigated for different asymmetric case. In order to increase the stiffness (load carrying capacity) of the bearing directionally, the supply pressure of the orifices, which are opposite to the loading direction, are increased. In this approach air consumption could be kept lower than the increasing pressure in all orifices. On the other hand the asymmetric stiffness of the bearing along the orthogonal direction will also affect the dynamics of the rotor. So, in order to investigate the dynamics behaviour of the rotor, the air bearing is analyzed numerically. The bearing-rotor system is modelled in two degree of freedom and it is simulated for different asymmetric supply pressure. Results show that;

- The load carrying capacity is increased directionally for asymmetric supply pressure
- Amplitudes of vibration of the rotor-bearing system decreased for asymmetric supply pressure
- The rotor oscillates more close to the bearing center.

REFERENCES

[1] D. Fleming, P. Cunningham and W. J. Cunningham, Stability Analysis For Unloaded Externally Pressurized Gas-Lubricated Bearings With Journal Rotation, Technical Report, TN D-4934, NASA Lewis Research Center, United States, 1968.

[2] M. Fourka and M. Bonis, Comparison between externally pressurized gas thrust bearings with different orifice and porous feeding systems, *Wear*, Vol. 210 (1997), pp. 311-317, 1997.

[3] K. CzoŁczyñski, Stability of the rotor supported in gas journal bearings with a chamber feeding system, *Wear*, Vol. 210, Issues 1–2, 220-236, 1997.

[4] J-C. Renn, C-H. Hsiao, Experimental and CFD study on the mass flow-rate characteristic of gas through orifice-type restrictor in aerostatic bearings, *Tribology International*, Vol. 37, pp. 309-315, 2004.

[5] J. Park and K. Kim, Stability analysis and experiments of spindle using new type of slot restricted gas journal bearings, *Tribology International*, vol. 37, pp. 451-462, 2004.

[6] J. C. T. Su, K.N. Lie, Rotor dynamic instability analysis on hybrid air journal bearings, Tribology International, Vol. 39, Issue 3, 238-248, 2006.

[7] C. Lo, C. Wang, and Y. Lee, Performance Analysis Of High-Speed Spindle Aerostatic Bearings, *Tribology International*, Vol. 38, pp. 5–14, 2005.

[8] F. Colombo, T. Raparelli, and V. Viktorov, Externally Pressurized Gas Bearings: A Comparison Between Two Supply Holes Configurations," *Tribology International, Vol. 42*, pp. 303–310, 2009.

[9] F. Colombo, T. Raparelli, and V. Viktorov, Comparison Between Different Supply Port Configurations İn Gas Journal Bearings, *New Tribological Ways*, *Vol. 23*, pp. 477-498, 2009.

[10] D. Yang, C. Chen, Y. Kang, R. Hwang, and S. Shyr, Influence Of Orifices On Stability Of Rotor-Aerostatic Bearing System, *Tribology International*, *Vol. 42*, pp. 1206–1219, 2009.

[11] Y.S. Chen, C.C. Chiu, Y.D. Cheng, Influences of operational conditions and geometric parameters on the stiffness of aerostatic journal bearings, *Precision Engineering*, Vol. 34, Issue 4, 722-734, 2010.

[12] Y. Otsu, K. Somaya, S. Yoshimoto, High-speed stability of a rigid rotor supported by aerostatic journal bearings with compound restrictors, *Tribology International*, Vol. 44, Issue 1, 9-17, 2011.

[13] C-H. Chen, T-H. Tsai, D-W. Yang, Y. Kang, J-H. Chen, The comparison in stability of rotor-aerostatic bearing system compensated by orifices and inherences, *Tribology International*, Vol. 43, Issue 8, 1360-1373, 2010.

[14] A. Dal and T. Karaçay, Dynamics of Externally Pressurized Air Bearing with High Values of Clearance, *ASME 2014 12th Biennial Conference on Engineering Systems Design and Analysis*. Copenhagen, 2014.

11th International Conference on Engineering Vibration
Ljubljana, Slovenia, 7–10 September 2015

EFFECTS OF A JOURNAL BEARING CLEARANCE ON ROTORDYNAMICS OF TURBOCHARGERS

Luboš Smolík*[1], Michal Hajžman[1], Miroslav Byrtus[1]

[1]Department of Mechanics, Faculty of Applied Sciences, University of West Bohemia
{carlist,mbyrtus,mhajzman}@kme.zcu.cz

Keywords: Rotordynamics, Turbocharger, Journal Bearings, Floating Bearings, Steady-state Response.

Abstract. *In the recent years, turbocharged engines have become more common because of better power-to-weight ratio (and thus lower consumption and emission of air pollutants). However, the better performance comes at a price because turbochargers operate at high speeds — usually hundreds of thousands revolutions per minute — and tend to be fatigue and stability prone. For this reason, a turbocharger rotor has to be designed carefully with respect to its dynamic properties. The influence of a bearing clearance on stiffness and damping of a single-film journal bearing is well known and documented. Turbochargers, however, are often supported by floating journal bearings, which have two oil films linked by oil feed-holes. Such a bearing have two bearing clearances — between journal and floating ring and between floating ring and housing — which are determined by different temperatures of oil films and also dimensional tolerances. The following paper deals with differences between nominal (cold) and operational (hot) bearing clearances. The influence of the dimensional tolerances on the values of bearing clearances and turbocharger dynamics is also discussed.*

1 INTRODUCTION

In the recent years, turbocharged engines have become more common because of better power-to-weight ratio (and thus lower consumption and emission of air pollutants). However, the better performance comes at a price because turbochargers operate at high speeds usually hundreds of thousands revolutions per minute and tend to be fatigue and stability prone. For this reason, a turbocharger rotor has to be designed carefully with respect to its dynamic properties, which could be a very interesting task due to the high non-linearity of turbocharger's behaviour, especially for floating ring bearings with a free ring between inner and outer fluid films [1].

The modelling of turbochargers consists of two main tasks. The equations of motion of a standalone rotor (shaft with compressor and turbine wheel) should be created on one hand and the problem of forces transmitted byt floating ring bearings on the other hand. Lumped parameter models [1, 2] and nowadays more finite element models [3, 4] are employed for the rotor modelling. Modelling and analysis of floating ring bearings is rather complex and can be performed using various methods, which should capture the non-linear behaviour of bearing forces. Impedance method for evaluation of floating ring bearing forces was used in [5]. Analytical expressions based on the solution of the Reynolds equation were employed in [4]. Other numerical approaches for the Reynolds equation solution are based on the finite element method [6, 3] and the finite difference method [7]. There exist also applications based on computational fluid dynamics approaches [8].

The important parameters of the floating ring bearing, which could strongly influence its dynamic behaviour, are clearances of the inner and outer films. Their uncertainty in reality is affected by manufacturing tolerances and different temperatures of the turbocharger. Authors of [3] studied the effect of manufacturing tolerances for limit values of both film clearances and observed that the non-linear response can change qualitatively with changing clearances. The effect of outer clearance with fixed inner clearance values was investigated in [4]. Stability of a turbocharger with respect to the values of bearing clearances were studied in [9]. Special type of gas-foil bearings applied in turbochargers and effects of their clearance were mentioned in [10]. Issues of the temperature and heat transfer in turbochargers are commented in [11, 12].

This paper deals with differences between nominal (cold) and operational (hot) bearing clearances. The influence of the dimensional tolerances on the values of bearing clearances and turbocharger dynamics is also discussed.

2 DETAILED PROBLEM DESCRIPTION

Real turbocharger, whose geometry and mass parameters are introduced in Figure 1 and Table 1, is examined employing AVL EXCITE software. As can be seen in Figure 1, the turbocharger rotor is supported by two radial journal bearings. Each of these bearings connects three bodies – a journal, a floating ring (also called bushing) and a housing. Thus there are two oil films in each radial bearing – between journal and floating ring and between floating ring and housing. Both films are connected through the ring by four feed-holes positioned according to Figure 2. Each of four films is operating under different temperature and (hot) clearance, for more information see Table 2. Values of nominal clearances are shown in the Table 2. The real values can slightly differ in dependence on machining accuracy. Acceptable tolerance limits for bodies situated in radial bearing can be found in Table 3.

The rotor is axially supported by hydrodynamic thrust bearing which is located on the compressor side. Since there are no external forces acting in the axial direction in the model, the axial bearing was modelled as a simple linear spring/damper (10^6 N·m, 100 N·m·s^{-1}).

The turbocharger is examined in the speed interval 20,000–200,000 rpm with ca. 130,000 rpm being nominal speed. The motion of all body coordinate systems and response of rotor in radial bearings, between bearings and in centres of mass of blade wheels is computed and stored both in time and frequency domain. Basic tribological characteristics of radial bearings such as power loss, peak pressure, minimum film height and journal orbits are also stored. No external forces are acting, excitation is caused solely by unbalance and hydrodynamic forces. Such a case corresponds with a rotor run-down.

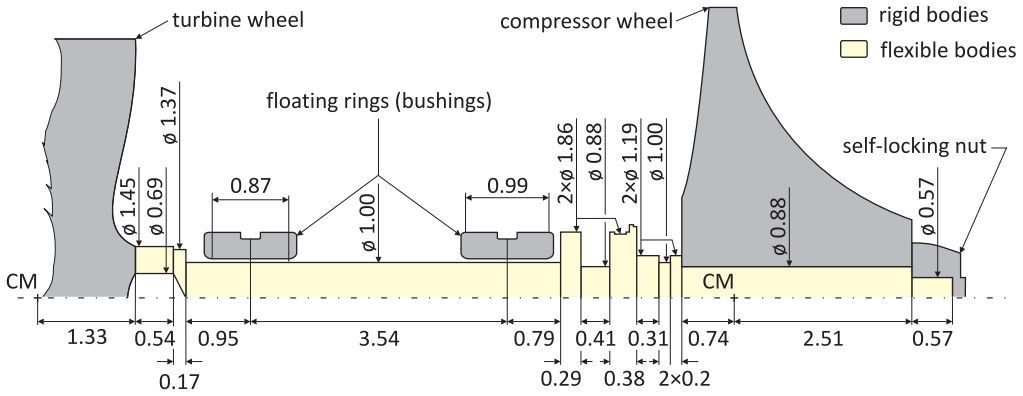


Figure 1: Depicted dimensions of the analysed turbocharger model are relative to diameter of a journal. CM denotes positions of centres of mass of blade wheels.

Body	*Body type*	*Mass* [-]	I_x [-]	I [-]	*Unbalance* [10^{-3}]
compressor wheel	rigid	0.63	1.930	1.238	0.722
housing	reference frame	0.00	0.000	0.000	0.000
floating ring	rigid	0.11	0.046	0.035	0.000
self-locking nut	rigid	0.04	0.007	0.006	0.000
shaft	flexible	1.00	0.195	9.506	0.000
turbine wheel	rigid	2.15	3.757	3.342	2.466

Table 1: Dimensionless values of mass, moment of inertia about axis of rotation I_x, moment of inertia about transverse axes I and unbalance. Dimensionless moments of inertia and unbalances are derived from dimensionless mass and length. Overall weight of the rotor is approximately 200 g.

Oil Film	*Side*	*Diameter* [-]	*Width* [-]	*Clearance Cold / Hot* [‰]	*Temperature* [°C]	*Oil*
inner film	turbine	1.00	0.87	3.43 / 4.10	180	15W-40
inner film	compressor	1.00	0.87	3.43 / 4.24	130	15W-40
outer film	turbine	1.54	0.99	4.83 / 3.56	140	15W-40
outer film	compressor	1.54	0.99	4.83 / 3.70	120	15W-40

Table 2: Operating parameters of all four oil films.

Body	*Material*	*Coeff. of thermal expansion* $[10^{-6}\ ^{\circ}\mathrm{C}^{-1}]$	*Diameter*	*Tolerance limits* [‰]
journal	steel	9,0	outer	$-0.80\ +0.00$
floating ring	leaded bronze	20,4	inner	$-0.00\ +0.80$
			outer	$-0.67\ +0.00$
housing	cast iron	11,0	inner	$-0.00\ +0.75$

Table 3: Bodies acting in radial bearings and their respective materials, coefficients of thermal expansion and relative tolerance limits.

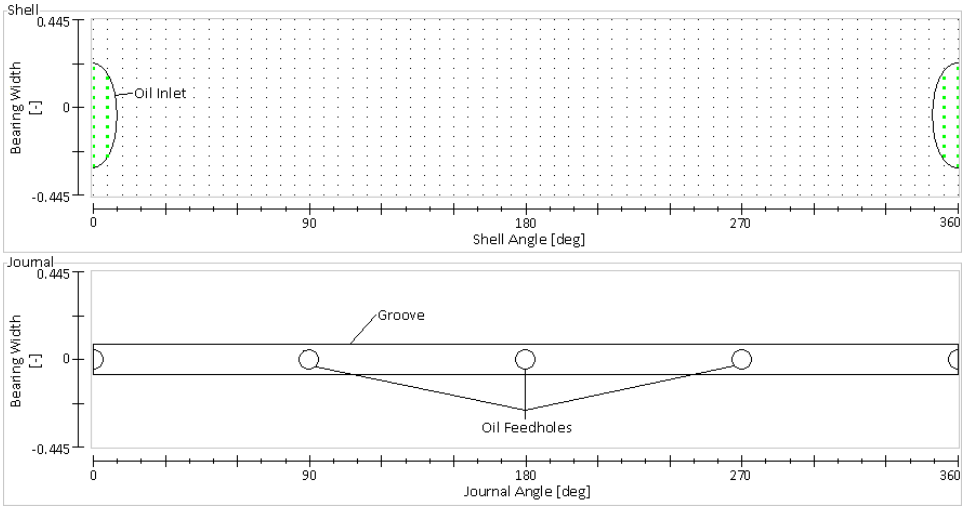


Figure 2: Boundary conditions for outer film on the turbine side of the rotor were taken directly from CAD geometry. The upper diagram shows shell (housing) side of the film, the lower shows journal (bushing) side. Conditions for the inner film are more simple – there are just four feedholes in shell (bushing) side.

3 MATHEMATICAL MODEL

3.1 Elastohydrodynamic (EHD) Lubrication

In the previous section only model of the axial bearing was described. Since the linearisation of the journal bearing with the fully floating ring can cause differences between a model and an actual situation [13], solving the distribution of hydrodynamic pressure in all films and in each time step is necessary in order to obtain accurate results.

Distribution of the hydrodynamic pressure $p = p(x, z, t)$ in flexible possibly cavitated bearing is under laminar flow condition described by modified Reynolds equation in the form [14]

$$\frac{1}{12}\frac{\partial}{\partial x}\left(\frac{\phi_x\,\theta\,h^3}{\eta}\frac{\partial p}{\partial x}\right)+\frac{1}{12}\frac{\partial}{\partial z}\left(\frac{\phi_z\,\theta\,h^3}{\eta}\frac{\partial p}{\partial z}\right)=\frac{1}{2}\frac{\partial\left(\theta\,\gamma\,\zeta\right)}{\partial x}+\frac{\partial\left(\theta\,h_d\right)}{\partial t}, \tag{1}$$

with coefficient γ given by Eq. 2:

$$\gamma=\left(u_j+u_s\right)h_d+\left(u_j-u_s\right)\sigma_c\,\phi_c. \tag{2}$$

x and z in Eq. 1 are circumferential and axial coordinates in a coordinate frame fixed to a shell, $\theta = \theta(x, z, t)$ is the fill ratio, $h = h(x, z, t)$ and $h_d = h_d(x, z, t)$ are nominal and actual

local gaps between surfaces of journal and shell. Actual local gap is the gap between deformed bodies, while nominal gap is related to undeformed geometry. This concept is explained by Figure 3. ϕ_x, ϕ_z and ϕ_c are flow factors dependent on deformed geometry [15], η is the dynamic viscosity of the oil, u_j and u_s are the surface velocities of the journal and the shell, $\sigma_c = \sqrt{\sigma_j^2 + \sigma_s^2}$ is the composite roughness of the bearing with σ_j and σ_s being roughnesses of the journal and the shell and ζ is the oil starvation which is the function of the term $\frac{\partial h}{\partial x}$ and lies within the interval $\langle 0, 1\rangle$ [14].

Note there are two unknowns in Eq. 1: p and θ. For $t = 0$, fill ratio is defined using initial condition (usually $\theta \equiv 1$) and Eq. 1 is solved for p. If p in any region drops below critical value of cavitation pressure p_c then $p = p_c$ in that region and Eq. 1 is solved for θ.

Once the pressure distribution is obtained, the acting EHD forces can be expressed by integrating p over the bearing surface. An exact process is described in [12].

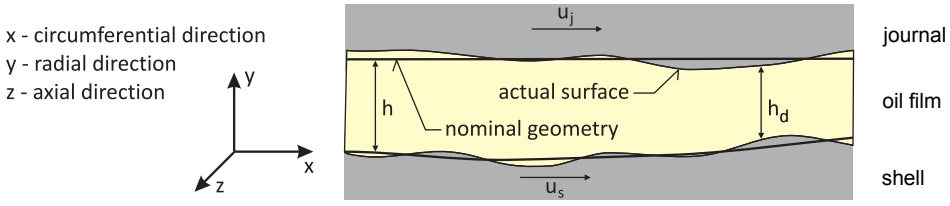


Figure 3: llustration of gaps, surface velocities and coordinate system employed in Eq. 3.

3.2 Turbocharger as Multi-body System (MBS)

In AVL EXCITE multi-body system is treated as a system of partial masses, which can be linked together by complex non-linear joints. Equation of motion of such MBS can be generally expressed as [14, 16]

$$\boldsymbol{M}\,\ddot{\boldsymbol{q}}(t) + \boldsymbol{D}\,\dot{\boldsymbol{q}}(t) + \boldsymbol{K}\,\boldsymbol{q}(t) = \boldsymbol{f}^e(t) + \boldsymbol{f}^j(\dot{\boldsymbol{q}}, \boldsymbol{q}, t) + \boldsymbol{p}^i(\ddot{\boldsymbol{q}}, \dot{\boldsymbol{q}}, \boldsymbol{q}, t), \tag{3}$$

where $\boldsymbol{M}$, $\boldsymbol{D} = \alpha\,\boldsymbol{M} + \beta\,\boldsymbol{K}$, $\boldsymbol{K}$ are diagonal mass matrix and symmetric damping and stiffness matrices of bodies respectively, $\boldsymbol{q}$ is the general displacement vector consisting of global coordinates related to each body in the system and relative coordinates linked deformation of flexible bodies. $\boldsymbol{f}^e$ is the vector describing external loads, $\boldsymbol{f}^j$ is the vector of internal excitation caused by joints and contacts, and $\boldsymbol{p}^i$ describes non-linear inertia terms and gyroscopic effects. $\boldsymbol{p}^i$ stems in the coordinate transformation from global coordinate systems to the bodies relative systems and is derived in [14, 16].

3.3 Solution of the Equation of Motion

Eq. 3 describes the motion of highly non-linear system and generally cannot be solved in the frequency domain. Analytical solution in the time domain can be found only in some special cases and thus Eq. 3 can be solved numerically employing e.g. backward differentiation formulas (BDFs). By omitting $\dot{\boldsymbol{q}}$ and $\boldsymbol{q}$ in arguments and defining

$$\boldsymbol{v}(t) = \dot{\boldsymbol{q}}(t), \tag{4}$$

$$\boldsymbol{p}^i(t) = \boldsymbol{f}^{gyros}(t) - \boldsymbol{f}^{rbAcc}(t), \tag{5}$$

where $\boldsymbol{f}^{gyros}$ is the vector of gyroscopic effects and $\boldsymbol{f}^{rbAcc}$ is the vector of rigid body acceleration [14], the second order Eq. 3 can be rewritten as the first order system

$$\begin{aligned} \boldsymbol{M}\,\dot{\boldsymbol{v}}(t) + \boldsymbol{D}\,\boldsymbol{v}(t) + \boldsymbol{K}\,\boldsymbol{q}(t) - \boldsymbol{f}^{e}(t) - \boldsymbol{f}^{j}(t) - \boldsymbol{f}^{gyros}(t) + \boldsymbol{f}^{rbAcc}(t) = 0, \\ \boldsymbol{v}(t) - \dot{\boldsymbol{q}}(t) = 0. \end{aligned} \tag{6}$$

Substituting BDF for general implicit equation system of the first order

$$F(\dot{\boldsymbol{z}}(t_{i+1}), \boldsymbol{z}(t_{i+1}), t_{i+1}) = F\left(\dot{\tau}_{k,i+1}\,\boldsymbol{z}_{i+1} + \sum_{j=1}^{k} \tau_{k,i+1-j}(t)\,\boldsymbol{z}_{i+1-j}, \boldsymbol{z}_{i+1}, t_{i+1}\right) = 0 \tag{7}$$

into Eq. 6 and evaluating at $t = t_{i+1}$ yields a system of non-linear equations

$$\begin{aligned} \boldsymbol{M}\,\boldsymbol{v}_{i+1} + \boldsymbol{f}^{rbAcc}_{i+1} &= \frac{\boldsymbol{f}^{e}_{i+1} + \boldsymbol{f}^{j}_{i+1} + \boldsymbol{f}^{gyros}_{i+1} - \boldsymbol{D}\,\boldsymbol{v}_{i+1} - \boldsymbol{K}\,\boldsymbol{q}_{i+1} - \boldsymbol{M}\,\hat{\boldsymbol{v}}_{k,i+1} - \hat{\boldsymbol{f}}^{rbAcc}_{k,i+1}}{\dot{\tau}_{k,i+1}}, \\ \mathbf{q}_{i+1} &= \frac{\mathbf{v}_{i+1} - \mathbf{q}_{k,i+1}}{\dot{\tau}_{k,i+1}}, \end{aligned} \tag{8}$$

where

$$\hat{\boldsymbol{z}}_{k,i+1} = \sum_{j=1}^{k} \dot{\tau}_{k,i+1-j}\,\boldsymbol{z}_{i+1-j}, \qquad \boldsymbol{z}_i = \{\boldsymbol{v}_i, \boldsymbol{f}^{rbAcc}_i\}, \tag{9}$$

$$\tau_{k,i+1-j}(t) = \prod_{\substack{l=0 \\ l\neq j}}^{k} \frac{t - t_{i+1-l}}{t_{i+1-j} - t_{i+1-l}}, \tag{10}$$

$$\dot{\tau}_{k,i+1-j}(t) = \sum_{\substack{m=0 \\ m\neq j}}^{k} \frac{1}{t_{i+1-j} - t_{i+1-m}} \prod_{\substack{l=0 \\ l\neq j,m}}^{k} \frac{t - t_{i+1-l}}{t_{i+1-j} - t_{i+1-l}} \tag{11}$$

are terms related to Lagrangian interpolation of the solution in the k previous time steps t_{i+1-j}, which can be also viewed as approximation of the differentiation operator by a finite differences. k denotes the BDF order — in AVL EXCITE $k = 2$.

From Eq. 8 only the local coordinates in $\boldsymbol{q}(t)$ and their respective derivatives can be computed. In order to calculate the global coordinates from $\boldsymbol{q}(t)$, Eq. 8 has to be further extended by the following equations [14]:

$$\boldsymbol{x}_{B,i+1} = \frac{\boldsymbol{v}_{B,i+1} - \boldsymbol{x}_{B,k,i+1}}{\dot{\tau}_{k,i+1}}, \tag{12}$$

$$\boldsymbol{S}(\boldsymbol{\theta}_{B,i+1})\,\boldsymbol{\theta}_{B,i+1} = \frac{\boldsymbol{\Omega}_{i+1} + \boldsymbol{S}(\boldsymbol{\theta}_{B,i+1})\,\hat{\boldsymbol{\theta}}_{B,k,i+1}}{\dot{\tau}_{k,i+1}}, \tag{13}$$

$$\boldsymbol{\theta}^{\top}_{B,i+1}\,\boldsymbol{\theta}_{B,i+1} = 1, \tag{14}$$

$$\boldsymbol{r}(\boldsymbol{q}_{i+1}) = \mathbf{0}. \tag{15}$$

4 RESULTS

Since the turbocharger is examined in the speed interval 20,000–200,000 rpm, Campbell diagrams are used to visualise results. The diagrams are drawn using steady-state response analysis results. The analysis is performed in the time domain for discrete spin speed with the step of 10,000 rpm. The response in the frequency domain is computed internally in AVL EXCITE employing standard FFT algorithm, diagrams are drawn employing MATLAB. The first five cycles (turbocharger revolutions) are omitted from the analysis because model is initiating and response does not behave as steady-state. Relatively poor resolution in presented diagrams is due to the total length of the analysis is significantly shorter than 1 s — if a signal is 1 s long and the sampling frequency is sufficient, FFT analysis resolution is 1 Hz — and AVL EXCITE does not support FFT zoom algorithm.

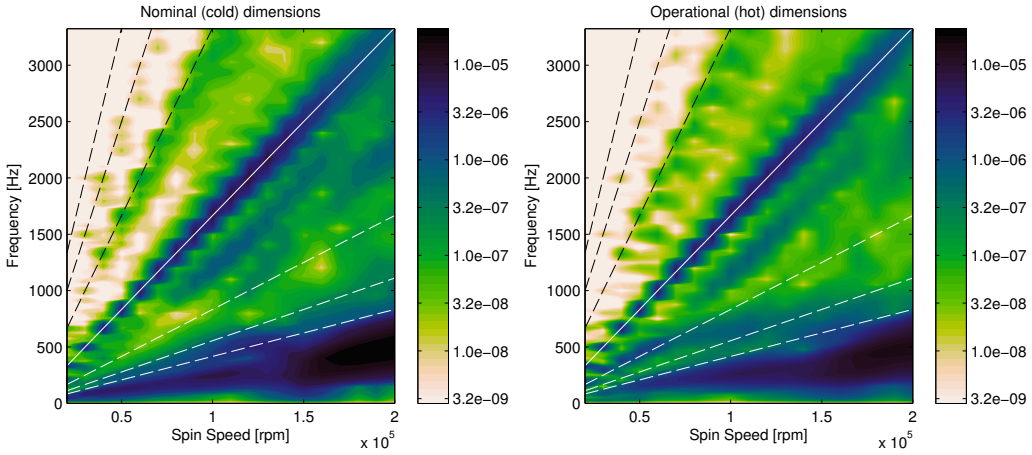


Figure 4: Campbell diagrams for journal in the bearing on compressor side and unbalance phase angle 0°.

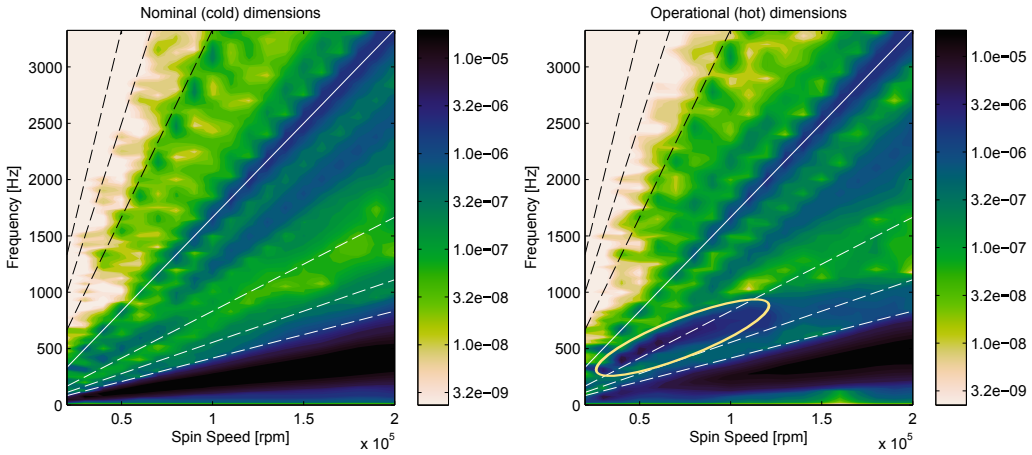


Figure 5: Campbell diagrams for journal in the bearing on compressor side and unbalance phase angle 180°. Marked is the sub-synchronous component, which is present only under the hot conditions.

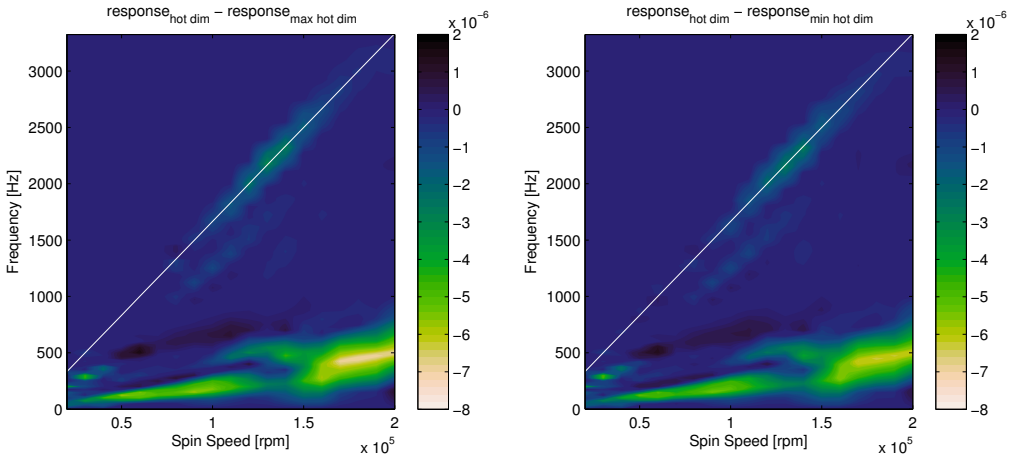


Figure 6: Differences (hot dimensions minus hot dimensions affected by tolerances) in response when upper tolerances are considered for journal in the bearing on the compressor side and unbalance phase angle $0°$.

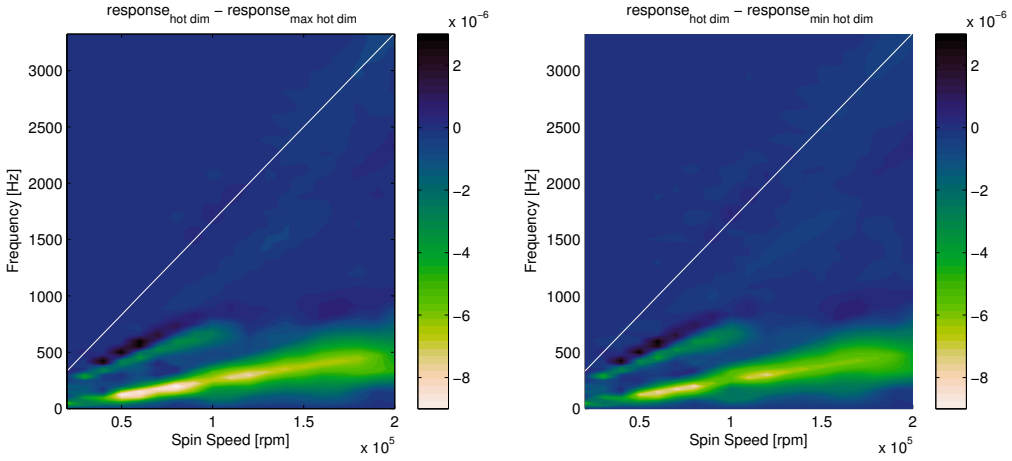


Figure 7: Differences (hot dimensions minus hot dimensions affected by tolerances) in response when upper tolerances are considered for journal in the bearing on the compressor side and unbalance phase angle $180°$.

As can be seen in Figures 4 and 5, the performance of turbocharger differs under cold and hot conditions. The new sub-synchronous component of the response comes into existence under the hot conditions. This component is more apparent as phase angle between unbalance vectors gets higher. Also the sub-synchronous component with the highest amplitudes is slightly lower under these conditions and some new components originating from modulation due to system non-linearity have different amplitudes.

The influence of the dimensional tolerances is not as significant as the operation under the hot conditions. Since Campbell diagrams for hot dimensions and hot dimensions modified by minimum and maximum tolerance limits are fairly similar, differences between these diagrams are visualised in Figure 6 for $0°$ phase angle between unbalance vectors and in Figure 7 for $180°$ angle. The major sub-synchronous component is the most affected by amplitude changes and

is amplified when tolerances are considered. The amplification is more apparent as phase angle rises. The component marked in Figure 5 is subject to frequency shift, especially for angle $180°$. Consideration of the tolerances does not cause a disappearance of any response component.

5 CONCLUSIONS

The presented work suggests that the changes of radial clearances caused by the operational temperature should be respected when analysis of turbocharger dynamical response is performed because of high non-linearity of the system. There were observed not only changes in frequencies and amplitudes of existing response components, but also emergence of new ones.

The influence of the dimensional tolerances is distinguishable but affects just amplitude and frequency of some components, not their existence. This phenomenon could explain observations made by a manufacturer when both vibrations and noise of various turbocharger rotors of the same type were slightly different. It can be also suggested that when the analysis of the particular turbocharger have to be performed and the dimensions measured by micrometer are available, they should be used.

The presented work will be verified experimentally.

ACKNOWLEDGEMENT

The work presented in this article was supported by SGS-2013-036 project of University of West Bohemia.

The usage of the AVL EXCITE software in the framework of the University Partnership Program of AVL List GmbH is greatly acknowledged.

REFERENCES

[1] C.H. Li, Dynamics of rotor bearing systems supported by floating ring bearings. *Journal of Lubrication Technology*, **104**, 469-476, 1982.

[2] B. Schweizer, Oil whirl, oil whip and whirl/whip synchronization occurring in rotor systems with full-floating ring bearings. *Nonlinear Dynamics*, **57**, 509-532, 2009.

[3] L. Wang, G. Bin, X. Li, X. Zhang, Effects of floating ring bearing manufacturing tolerance clearances on the dynamic characteristics for turbocharger. *Chinese Journal of Mechanical Engineering*, **28**, 530-540, 2015.

[4] L. Tian, W.J. Wang, Z.J. Peng, Effects of bearing outer clearance on the dynamic behaviours of the full floating ring bearing supported turbocharger rotor. *Mechanical Systems and Signal Processing*, **31**, 155-175, 2012.

[5] C.H. Li, S.M. Rohde, On the steady state and dynamics performance characteristics of floating ring bearings. *Journal of Lubrication Technology*, **103**, 389-397, 1981.

[6] L. San Andrés, J. Kerth, Thermal effects on the performance of floating ring bearings for turbochargers. *Proceedings of Institution of Mechanichal Engineers, Part J: Journal of Engineering Tribology*, **218**, 437–450, 2004.

[7] H. Zhang, Z. Shi, F. Gu, A. Ball, Modelling of outer and inner film oil pressure for floating ring bearing clearance in turbochargers. *Journal of Physics: Conference Series*, **305**, 012021, 2011.

[8] M. Deligant, P. Podevin, G. Descombes, CFD model for turbocharger journal bearing performances. *Applied Thermal Engineering*, **31**, 811–819, 2011.

[9] H. Zhang, Z. Shi, D. Zhen, F. Gu, A. Ball, Stability analysis of a turbocharger rotor system supported on floating ring bearings. *Journal of Physics: Conference Series*, **364**, 012032, 2012.

[10] K. Sim, Y.B. Lee, T.H. Kim, Effects of mechanical preload and bearing clearance on rotordynamic performance of lobed gas foil bearings for oil-free turbochargers. *Tribology Transactions*, **56**, 224–235, 2013.

[11] A. Romagnoli, R. Martinez-Botas, Heat transfer analysis in a turbocharger turbine: An experimental and computational evaluation. *Applied Thermal Engineering*, **38**, 58–77, 2012.

[12] Y. Hori, *Hydrodynamic Lubrication*. Springer, Tokyo, 2006.

[13] L. Tian, W.J. Wang and Z.J. Peng, Dynamic behaviours of a full floating ring bearing supported turbocharger rotor with engine excitation. *Journal of Sound and Vibration*, **330**, 4851–4874, 2011.

[14] G. Offner et al., *AVL EXCITE Power Unit version 2014: Theory*. AVL Group, Graz, 2014.

[15] M. Prat, F. Plourab and N. Letalleur, Averaged Reynolds Equation for Flows between Rough Surfaces in Sliding Motion. *Transport in Porous Media*, **48**(3), 291–313, 2002.

[16] G. Genta, *Dynamics of Rotating Systems*. Springer Verlag, 2005.

11th International Conference on Engineering Vibration
Ljubljana, Slovenia, 7–10 September 2015

A NUMERICAL INVESTIGATION INTO THE EFFECT OF THE SUPPORTS ON THE VIBRATION OF ROTATING SHAFTS

A. A. Zakaria*[1], E. Rustighi[2], N. S. Ferguson[3]

Institute of Sound and Vibration Research, University of Southampton

[1]aaz1v13@soton.ac.uk

[2]er@isvr.soton.ac.uk

[3]nsf@isvr.soton.ac.uk

Keywords: Rotordynamics, Lateral Vibration, Bearings, Viscoelastic.

Abstract. *Vibration is typically encountered by rotating equipment during its start-up, running operation and shutdown. The severity of the oscillation, which depends on the critical speed and natural frequencies of the system, could cause serious malfunction of the device and affect its operating performance. A simplified lumped parameter model of a rotor system is typically used for the study of the shaft dynamics of a single rotor on bearing supports. Bearing supports are the means of connecting a device between the rotor and supporting structure, which are of different forms and designs. They can be a simple bushing, rolling-element or journal types for light, medium and large load applications respectively. Particularly in this work, flexible supports made of rubber are considered by implementing viscoelastic material into the rotor bearing system. Viscoelastic material is well known to be a good choice for use within isolation systems, due to it being easily available and possessing high damping characteristics over a wide temperature and frequency range. However, the change of mechanical properties with frequency and temperature makes it difficult to design a viscoelastically device that works over a large range of operating conditions. Thus numerical analysis, which focuses on the simple rotor model supported on a range of different flexible supports, will be presented and compared.*

1 INTRODUCTION

Rotating machinery is known to encounter lateral vibration during its range of operating service. Imbalance of uneven mass distribution of the rotor, instability of the supporting device or structure of the shaft and other potential external forces acting on the system can result in serious malfunction of the rotor-bearing system. As the operational speed varies, the critical speed and natural frequency of the system will alter accordingly and affect the performance of the system.

A simplified lumped parameter model of a rotor-bearing system is a popular model used to analyze the dynamics of single rotor supported on bearings. Bearings can be many forms, which depend upon specific assumptions, such as simple bushing, rolling-element and a wide range of journal types. These bearings are normally assumed to be attached on a fixed support, so that performance of the bearings can be evaluated specifically for the whole system dynamics.

In this work, the dynamics of a simple rotor-bearing system on flexible supports will be examined. As the system is supported on two bearings at the two ends of a shaft, it is assumed that the bearings will be mounted on flexible material. The main focus of this work is to implement viscoelastic material into the system. In parallel with the advancement of modelling viscoelastic material [1-7], which help to describe the complexity of the material properties, the application of viscoelastic components in rotordynamics has generally increased as well. Effects on the threshold speed, natural frequency and temperature sensitive behaviour on dynamics characteristics have been discussed in [8, 9] and [10] respectively as viscoleastic support properties vary. Furthermore viscoelastic supports in rotor-bearings systems are reported to be beneficial to attenuate noise and vibration [11, 12].

2 MATHEMATICAL MODEL

In this section, the mathematical modelling of a rigid rotor supported on flexible supports is demonstrated. Generally, the equations of motion of a rigid rotor mounted on flexible supports are derived where the latter are comprised of elastic or viscoelastic supports. The elastic support model is assumed to have a linear spring and viscous damping in parallel, while the viscoelastic support model is based on the standard linear model. For both type of supports, the rotor-bearing system is assumed to consist of a rigid rotor, a massless and rigid shaft supported on two identical short bearings, and the bearings are flexibly supported in both the horizontal and vertical directions.

A right-handed coordinate system is utilized to to define the motion of the rotor-bearing system as shown by Figure 1. The rigid rotor of mass m, spins around the Z-axis with angular velocity Ω and moves horizontally and vertically in the X and Y axes respectively. Gyroscopic couples act on the system by definition of angular momentum conservation that are perpendicular to the axis of spin. The direction of the moments about the X and Y axes are specified by angular direction of ψ and θ shown in Figure 1 respectively.

2.1 Viscously damped supports

From first principles, the equations of motion for the rigid rotor supported by viscously damped flexible supports including unbalance and external moments are

$$\begin{aligned} m\ddot{x} + c_{xT}\dot{x} + c_{xC}\dot{\psi} + k_{xT}x + k_{xC}\psi &= m\varepsilon\Omega^2\cos(\Omega t + \delta) \\ m\ddot{y} + c_{yT}\dot{y} - c_{yC}\dot{\theta} + k_{yT}y - k_{yC}\theta &= m\varepsilon\Omega^2\sin(\Omega t + \delta) \\ I_d\ddot{\psi} - I_p\Omega\dot{\theta} + c_{xC}\dot{x} + c_{xR}\dot{\psi} + k_{xC}x + k_{xR}\psi &= (I_d - I_p)\beta\Omega^2\cos(\Omega t + \gamma) \\ I_d\ddot{\theta} + I_p\Omega\dot{\psi} - c_{yC}\dot{y} + c_{yR}\dot{\theta} - k_{yC}y + k_{yR}\theta &= (I_p - I_d)\beta\Omega^2\sin(\Omega t + \gamma) \end{aligned} \tag{1}$$

where I_d and I_p are the diametral and polar moment of inertia of the rotor respectively. ϵ and β are the rotor eccentricity and skewed centerline angle respectively. δ and γ are the initial condition values of each horizontal, vertical and two angular displacements of the rotor.

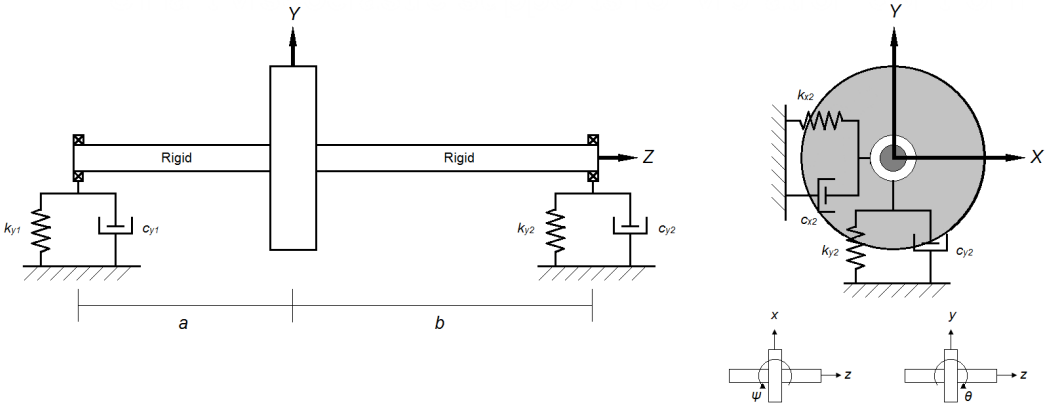


Figure 1: A rigid axisymmetric rotor on viscously damped supports and with definition of the coordinate system *X*, *Y*, and *Z*, origin at the static centre of mass of the rotor.

Stiffness and damping coefficients in Eq. (1) are expressed in term of a combination of each element from the two bearings by

$$\begin{aligned} S_{iT} &= S_{i1} + S_{i2} \\ S_{iC} &= -aS_{i1} + bS_{i2} \\ S_{iR} &= a^2S_{i1} + b^2S_{i2} \end{aligned} \tag{2}$$

where *S* are *k* or *c* for stiffness or damping coefficients respectively, and *i* is either *x* or *y*. The subscript *T*, *C* and *R* are used to describe the translational coefficient (*T*), coupling coefficient between translational and rotation (*C*) and rotational coefficient (*R*).

For free vibration analysis, all right hand terms in Eq. (1) are set to be 0. For convenience it can be converted to a state-space equation in the form of

$$\mathbf{A}\dot{\mathbf{x}} + \mathbf{B}\mathbf{x} = \mathbf{0} \tag{3}$$

where the arrangement of Eq. (1), as in Eq. (3) can be written as

$$\begin{bmatrix}\mathbf{C} & \mathbf{M}\\ \mathbf{M} & \mathbf{0}\end{bmatrix}\frac{\mathrm{d}}{\mathrm{d}t}\begin{Bmatrix}\mathbf{q}\\ \dot{\mathbf{q}}\end{Bmatrix}+\begin{bmatrix}\mathbf{K} & \mathbf{0}\\ \mathbf{0} & -\mathbf{M}\end{bmatrix}\begin{Bmatrix}\mathbf{q}\\ \dot{\mathbf{q}}\end{Bmatrix}=\begin{Bmatrix}\mathbf{0}\\ \mathbf{0}\end{Bmatrix} \tag{4}$$

where

$$\mathbf{A}=\begin{bmatrix}\mathbf{C} & \mathbf{M}\\ \mathbf{M} & \mathbf{0}\end{bmatrix},\mathbf{B}=\begin{bmatrix}\mathbf{K} & \mathbf{0}\\ \mathbf{0} & -\mathbf{M}\end{bmatrix},\dot{\mathbf{x}}=\frac{\mathrm{d}}{\mathrm{d}t}\begin{Bmatrix}\mathbf{q}\\ \dot{\mathbf{q}}\end{Bmatrix},\mathbf{x}=\begin{Bmatrix}\mathbf{q}\\ \dot{\mathbf{q}}\end{Bmatrix} \tag{5}$$

The corresponding mass $\mathbf{M}$, damping and gyroscopic $\mathbf{C}$, and stiffness $\mathbf{K}$ matrices are

$$\mathbf{M}=\begin{bmatrix}m & 0 & 0 & 0\\ 0 & m & 0 & 0\\ 0 & 0 & I_d & 0\\ 0 & 0 & 0 & I_d\end{bmatrix},\mathbf{C}=\begin{bmatrix}c_{xT} & 0 & c_{xC} & 0\\ 0 & c_{yT} & 0 & -c_{yC}\\ c_{xC} & 0 & c_{xR} & -I_p\Omega\\ 0 & -c_{yC} & I_p\Omega & c_{yR}\end{bmatrix},\mathbf{K}=\begin{bmatrix}k_{xT} & 0 & k_{xC} & 0\\ 0 & k_{yT} & 0 & -k_{yC}\\ k_{xC} & 0 & k_{xR} & 0\\ 0 & -k_{yC} & 0 & k_{yR}\end{bmatrix} \tag{6}$$

and the degrees of freedom are represented as

$$\mathbf{q}=\begin{Bmatrix}x & y & \psi & \theta\end{Bmatrix}^T \tag{7}$$

The state-space matrix of Eq. (4) can be solved numerically for a single value rotor speed Ω and the respective complex eigenvalues S_n will represent the damping ratio ζ and damped natural frequency ω_d, which are in the form

$$\begin{aligned}s_n &= -\zeta_n + i\omega_{dn}\\ s_{n+4} &= -\zeta_n - i\omega_{dn}\end{aligned} \tag{8}$$

where n is 1,2, 3, or 4. The relationship between the damped natural frequency ω_{dn} and natural frequency of the particular system ω_n is assumed to be given, as for the single degree of freedom viscously damped system [13], by

$$\omega_{dn}=\omega_n\sqrt{1-\zeta_n^2} \tag{9}$$

Since the motion of the rotor is defined in four degrees of freedom, so the roots of s_n and s_{n+4} form a complex conjugate pair for each n.

2.2 Viscoelastic supports

For viscoelastic materials, the viscously damped flexible supports in Figure 1 are replaced by the standard linear model viscoelastic supports that comprise an internal variable approach to incorporate the frequency dependence of the support modulus, as depicted in Figure 2

Referring to Figure 2, k_∞ is the stiffness constant, α and τ are viscoelastic material properties that can be obtained from material testing procedure [14]. Curve fitting of the data provides the τ and α coefficients which are used to determine the complex moduli behaviour of the viscoelastic component. From Figure 2, forces exerted on the bearings by viscoelastic supports are derived from first principle, which consider a single internal variable or degree of freedom *p*, at each support for both the *x* and *y* directions.

$$\begin{aligned}f_{x1} &= k_\infty(1+\alpha)(x-a\psi)-k_\infty\alpha p_{x1}\\ f_{y1} &= k_\infty(1+\alpha)(y+a\theta)-k_\infty\alpha p_{y1}\\ f_{x2} &= k_\infty(1+\alpha)(x+b\psi)-k_\infty\alpha p_{x2}\\ f_{y2} &= k_\infty(1+\alpha)(y-b\theta)-k_\infty\alpha p_{y2}\end{aligned} \tag{10}$$

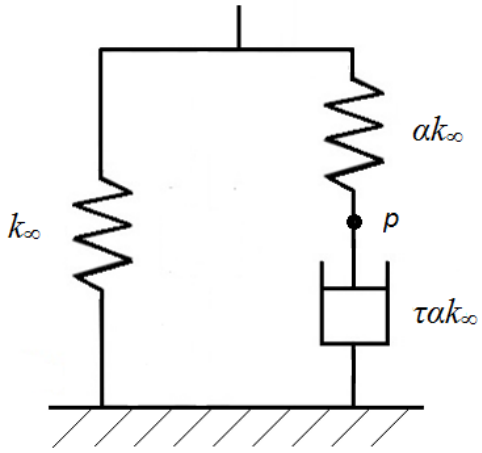


Figure 2: Standard linear model viscoelastic supports

By substituting Eq. (10) into Eq. (1), the equations of motion for rigid rotor mounted on identical viscoelastic supports are expressed as

$$\begin{aligned}
\ddot{x} &= -\frac{2\hat{k}}{m}x + \frac{\hat{k}(a-b)}{m}\psi + \frac{\hat{a}}{m}(p_{x1}+p_{x2}) + \varepsilon\Omega^2\cos(\Omega t+\delta)\\
\ddot{y} &= -\frac{2\hat{k}}{m}y - \frac{\hat{k}(a-b)}{m}\theta + \frac{\hat{a}}{m}(p_{y1}+p_{y2}) + \varepsilon\Omega^2\sin(\Omega t+\delta)\\
\ddot{\psi} &= \frac{I_p\Omega}{I_d}\dot{\theta} + \frac{\hat{k}(a-b)}{I_d}x - \frac{\hat{k}(a^2+b^2)}{I_d}\psi - \frac{\hat{a}a}{I_d}p_{x1} + \frac{\hat{a}b}{I_d}p_{x2} + \left(1-\frac{I_p}{I_d}\right)\beta\Omega^2\cos(\Omega t+\gamma)\\
\ddot{\theta} &= -\frac{I_p\Omega}{I_d}\dot{\psi} - \frac{\hat{k}(a-b)}{I_d}y - \frac{\hat{k}(a^2+b^2)}{I_d}\theta + \frac{\hat{a}a}{I_d}p_{y1} - \frac{\hat{a}b}{I_d}p_{y2} - \left(1-\frac{I_p}{I_d}\right)\beta\Omega^2\sin(\Omega t+\gamma)
\end{aligned} \tag{11}$$

where $\hat{k} = k_\infty(1+\alpha)$ and $\hat{a} = k_\infty\alpha$. By introducing the additional degrees of freedom, the equations of motion that describe the velocity displacement relationship of the internal variables can be written as

$$\begin{aligned}
\dot{p}_{x1} &= \frac{1}{\tau}(x - a\psi - p_{x1})\\
\dot{p}_{y1} &= \frac{1}{\tau}(y + a\theta - p_{y1})\\
\dot{p}_{x2} &= \frac{1}{\tau}(x + b\psi - p_{x2})\\
\dot{p}_{y2} &= \frac{1}{\tau}(y - b\theta - p_{y2})
\end{aligned} \tag{12}$$

The resulting equations of motion in Eqs. (11) and (12) can be written in state space equation [13] as

$$\dot{\mathbf{r}} = \mathbf{D}\mathbf{r} + \mathbf{w}(t) \tag{13}$$

where

$$\mathbf{r} = \begin{Bmatrix} \dot{\mathbf{q}} \\ \mathbf{q} \\ \mathbf{u} \end{Bmatrix} \tag{14}$$

as

$$\mathbf{u} = \begin{Bmatrix} p_{x1} & p_{y1} & p_{x2} & p_{y2} \end{Bmatrix}^T \tag{15}$$

and

$$\mathbf{D} = \begin{bmatrix} \bar{\mathbf{G}} & \bar{\mathbf{K}} & \bar{\mathbf{V}} \\ \boldsymbol{I} & \mathbf{0} & \mathbf{0} \\ \mathbf{0} & \bar{\mathbf{T}} & \bar{\mathbf{H}} \end{bmatrix} \tag{16}$$

Each element of $\mathbf{D}$ is 4×4 matrix where

$$\bar{\mathbf{G}} = \begin{bmatrix} 0 & 0 & 0 & 0 \\ 0 & 0 & 0 & 0 \\ 0 & 0 & 0 & \frac{I_p\Omega}{I_d} \\ 0 & 0 & -\frac{I_p\Omega}{I_d} & 0 \end{bmatrix}, \bar{\mathbf{K}} = \begin{bmatrix} -\frac{2\hat{k}}{m} & 0 & \frac{\hat{k}(a-b)}{m} & 0 \\ 0 & -\frac{2\hat{k}}{m} & 0 & -\frac{\hat{k}(a-b)}{m} \\ \frac{\hat{k}(a-b)}{I_d} & 0 & -\frac{\hat{k}(a^2+b^2)}{I_d} & 0 \\ 0 & -\frac{\hat{k}(a-b)}{I_d} & 0 & -\frac{\hat{k}(a^2+b^2)}{I_d} \end{bmatrix},$$

$$\bar{\mathbf{V}} = \begin{bmatrix} \frac{\hat{a}}{m} & 0 & \frac{\hat{a}}{m} & 0 \\ 0 & \frac{\hat{a}}{m} & 0 & \frac{\hat{a}}{m} \\ -\frac{\hat{a}a}{I_d} & 0 & \frac{\hat{a}b}{I_d} & 0 \\ 0 & \frac{\hat{a}a}{I_d} & 0 & -\frac{\hat{a}b}{I_d} \end{bmatrix}, \bar{\mathbf{T}} = \begin{bmatrix} \frac{1}{\tau} & 0 & -\frac{a}{\tau} & 0 \\ 0 & \frac{1}{\tau} & 0 & \frac{a}{\tau} \\ \frac{1}{\tau} & 0 & \frac{b}{\tau} & 0 \\ 0 & \frac{1}{\tau} & 0 & -\frac{b}{\tau} \end{bmatrix},$$

$$\bar{\mathbf{H}} = \begin{bmatrix} -\frac{1}{\tau} & 0 & 0 & 0 \\ 0 & -\frac{1}{\tau} & 0 & 0 \\ 0 & 0 & -\frac{1}{\tau} & 0 \\ 0 & 0 & 0 & -\frac{1}{\tau} \end{bmatrix}$$

For the forced vibration case, due to mass unbalance,

$$\mathbf{w}(t) = \begin{bmatrix} \varepsilon\Omega^2 \cos(\Omega t + \delta) \\ \varepsilon\Omega^2 \sin(\Omega t + \delta) \\ +\left(1 - \frac{I_p}{I_d}\right)\beta\Omega^2 \cos(\Omega t + \gamma) \\ -\left(1 - \frac{I_p}{I_d}\right)\beta\Omega^2 \sin(\Omega t + \gamma) \end{bmatrix}$$

$\mathbf{w}(t)$ can be set to zero for the free vibration case and then a standard eigenvalue problem has to be solved. Because of the additional degrees of freedom introduced from the internal variables as in Eq. (14), the complex conjugate eigenvalues of S_n of Eq. (8) are now expanded to six pairs instead of four.

3 NUMERICAL SIMULATIONS

In this section, several examples will be shown for the free vibration of a rigid rotor mounted on elastic, viscously damped and viscoelastic supports. Subsequently the forced vibration analysis will be presented for specifically a rotor-bearing system supported on identical viscoelastic supports at both ends. In general, the state space matrix solutions of $\dot{\mathbf{x}}$ and $\dot{\mathbf{r}}$ depend on the rotor rotational speed for Eqs. (3) and (14) respectively. It is convenient to determine the way in which the roots change with the rotational speed graphically by plotting a Campbell diagram where the rotational speed on a horizontal axis and the natural frequencies on vertical axis. Consider a uniform rigid rotor of mass $m = 122.68$ kg, diametral moment of inertia $I_d = 2.8625$ kgm^2 and polar moment of inertia $I_p = 0.6134$ kgm^2 mounted on flexible supports. The rotor is located at the geometric centre of the system, 0.25 m from each support.

3.1 Free vibrations

The parameter values for each support configuration are given in Table 1 specifically for free vibration analysis.

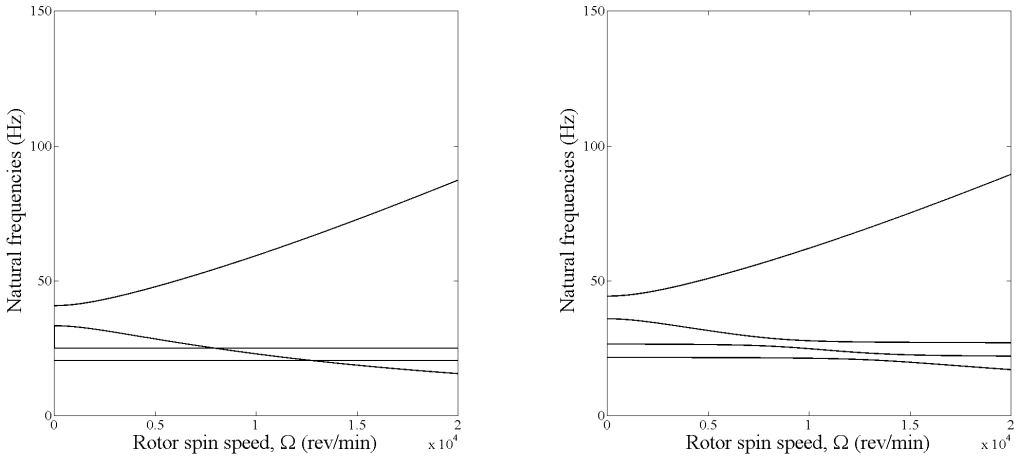
Type of Flexible Support	Uncoupled system	Coupled system
Undamped	$k_{x1} = 1.0$ MN/m	$k_{x1} = 1.0$ MN/m
	$k_{y1} = 1.5$ MN/m	$k_{y1} = 1.5$ MN/m
	$k_{x2} = 1.0$ MN/m	$k_{x2} = 1.3$ MN/m
	$k_{y2} = 1.5$ MN/m	$k_{y2} = 2.0$ MN/m
Viscously damped	$k_{x1} = k_{y1} = 1.0$ MN/m	$k_{x1} = k_{y1} = 1.0$ MN/m
	$k_{x2} = k_{y2} = 1.0$ MN/m	$k_{x2} = k_{y2} = 1.3$ MN/m
	$c_{x1} = c_{x2} = 1.0$ kNs/m	$c_{x1} = c_{x2} = 0.1$ kNs/m
	$c_{y1} = c_{y2} = 1.2$ kNs/m	$c_{y1} = c_{y2} = 0.3$ kNs/m
Viscoelastic	$k_\infty = 1.5$ MN/m	$k_\infty = 1.5$ MN/m
	$\alpha = 10$	$\alpha = 1$
	$\tau = 8.6667\text{x}10^{-4}$	$\tau = 8.6667\text{x}10^{-3}$

Table 1: Type of rigid rotor supports and its corresponding parameters for free vibration analysis. The uncoupled system corresponds to symmetric geometry of the rotor and shaft with equal supports at both ends

An example of a rigid rotor mounted on uncoupled anisotropic bearings produces the natural frequency map shown in Figure 3a. By substituting the corresponding parameters into Eq. (2), the coupling stiffnesses k_{xC} and k_{yC} are found to be zero. Thus, the first and second equations of Eq. (1), for which all the right hand terms are neglected, are uncoupled from the main system and are independent of rotor angular speed, Ω. Since the stiffnesses in both the horizontal and vertical directions are different, then the two natural frequencies that are determined from these equations in x and y are different. When the rotor is not rotating, the remaining two solutions of Eq. (1) are also uncoupled with two distinct natural frequencies. However as the rotor speed increases the two equations are coupled by gyroscopic terms and one of the natural frequency is decreasing whilst the other is increasing. It can be seen that the natural frequencies are converging on account of the gyroscopic effect. The decreasing line is one whereby the whirl is opposed to the rotor rotation direction, Ω and the increasing line is one where the whirl and the rotation directions, Ω are the same. The decreasing natural frequency also intersects with two constant natural frequencies lines at about 8000 and 13000 rev/min. This is a result of the equations of motion being uncoupled and independent of one another (i.e. x and ψ are

uncoupled as the terms in the equations satisfy $k_{xC}x = k_{xC}\psi = 0$).

The natural frequency map for a rigid rotor supported on coupled anisotropic bearings is depicted in Figure 3b. It can be seen from this figure that all of the natural frequency lines do not intersect, which imply all of the equations in Eq. (1) are coupled.



(a) Uncoupled system ($k_{iC} = 0$)

(b) Coupled system ($k_{iC} \neq 0$)

Figure 3: Natural frequency map for a rigid rotor mounted on flexible undamped supports. Cases (a) and (b) refer to a system with symmetric supports or different supports at the two ends respectively.

Figure 4 illustrates the mode shapes for a rigid rotor when the two support bearings are coupled anisotropic bearings, having the same parameters as in the example used for Figure 3b, at four different rotor speeds. The rotor displacement at both bearing locations are depicted. Solid lines connecting the two bearings are established by extending a straight line between each bearing at the same instant. For the first two modes, conical whirl can be observed for all of the rotor speeds except for the first mode at 10000 rev/min. The direction of the rotation is deduced by referring to Figure 4, where counterclockwise motion or forward whirl is positive rotation about the Z axis. However, cylindrical whirls occurred at all speeds, which are backward and forward whirl, for the third and fourth mode respectively except for third mode at 10000 rev/min.

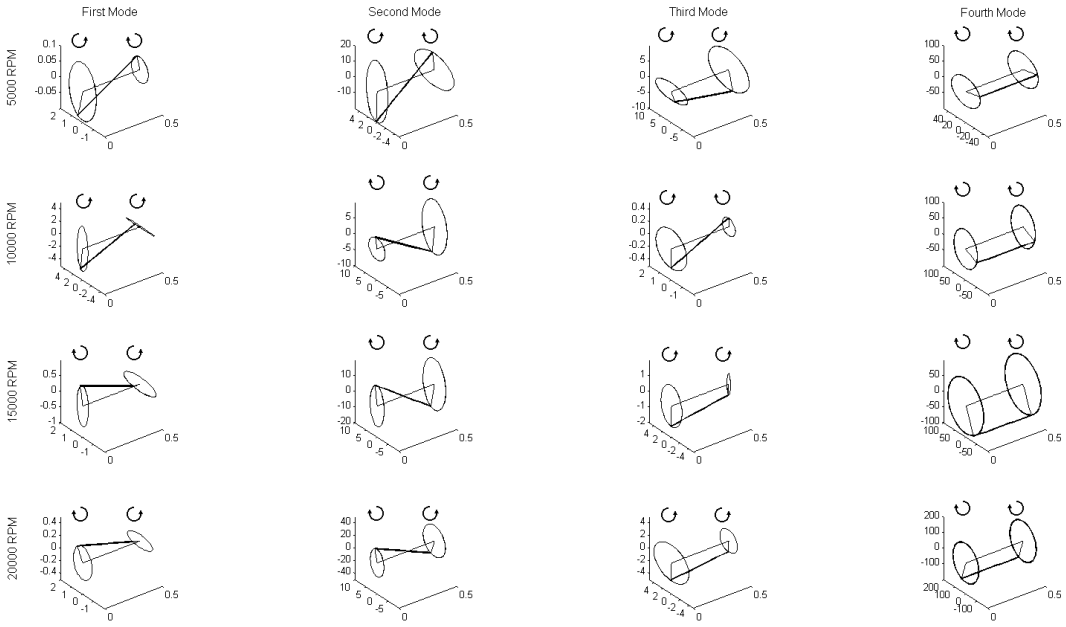
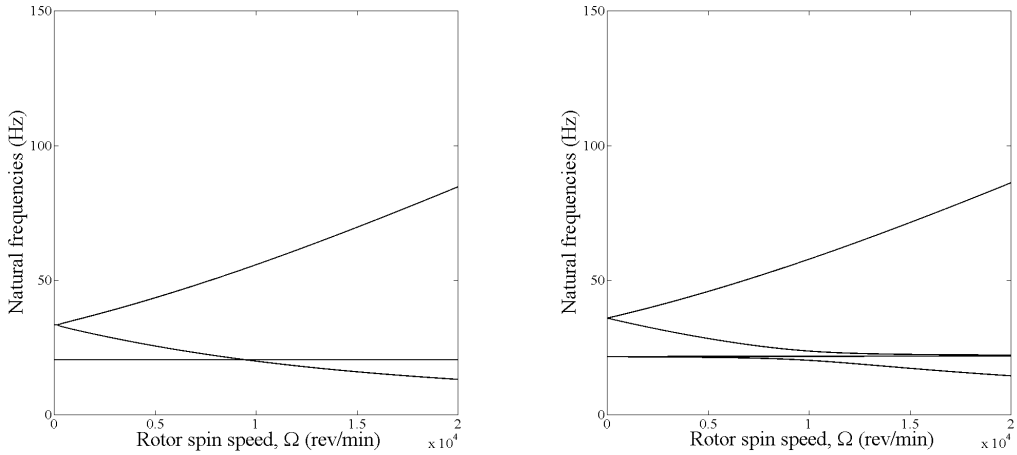


Figure 4: Mode shapes for a rigid rotor mounted on different undamped supports at the ends.

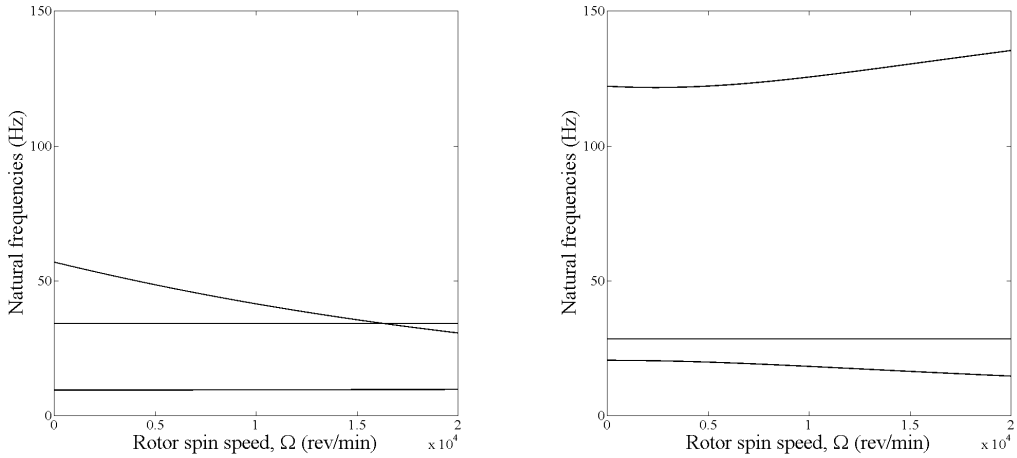
For cases of viscously damped supports, Figure 5 shows comparison of two types of systems namely uncoupled and coupled systems. It can be seen that from case (a) of Figure 5a, two identical natural frequency lines result from solutions of the first and second equations of Eq. (1) because of identical support stiffnesses in the x and y directions. A coupled system is observed in Figure 5b when all the coupling stiffness terms are not the same. Thus the natural frequency lines do not intersect but mode veering [15] is observed for the second and third natural frequency lines.

For the next example, identical viscoelastic supports are consider at both ends of the shaft where the properties of the material are assumed to be identical the x and y directions. Thus is similar to case (a) for viscously damped supports, which have identical stiffnesses in both horizontal and vertical directions at both support ends. Figures 6a and 6b show three different natural frequency lines. From Eq. (10), the first two equations are uncoupled due to the position of the rotor being at the middle of the shaft. Thus the natural frequencies derived from these two equations are identical and independent of Ω. Specifically for case (a) as shown in Figure 6a, the lines of constant natural frequency intersect with a decreasing natural frequency line at about 16000 rev/min. Therefore the first and second equations of Eq. (10) are uncoupled from the third and fourth. For case (b) as in Figure 6b, two distinct natural frequency lines converge as the rotor speed increases due to the gyroscopic terms in the third and fourth equations of Eq. (10).



(a) Uncoupled system ($S_{iC} = 0$) (b) Coupled system ($S_{iC} \neq 0$)

Figure 5: Natural frequency map for a rigid rotor mounted on isotropic viscously damped supports.



(a) Uncoupled system (b) Coupled system

Figure 6: Natural frequency map for a rigid rotor mounted on identical isotropic viscoelastic supports.

3.2 Forced vibration

In this section, forced vibration analysis is demonstrated specifically for a rotor-bearing system mounted on identical viscoelastic supports, modelled by the standard linear type viscoelastic support with one internal variable. The equations of motion given in Eqs. (11) and (12) are directly integrated using the Runge-Kutta method (available in MATLAB). The steady-state rotor response is obtained at specific rotor speed Ω after considering several thousands cycles of t and plotted throughout certain range of Ω. The response is defined by the x and y displacements of the rotor center and its magnitude is observed from the numerical analysis. Figures 7 and 8 show the displacement magnitude responses of the rotor center and the corresponding loss factor for three different samples of viscoelastic supports respectively. The associated dashed lines with similar colour legend indicates the frequency at which the loss factors are maximum. For both samples A and B, the maximum magnitude of rotor center response are at much lower frequency than corresponding dashed line where frequencies loss factor are 77912 rev/min and 7791 rev/min for sample A and B respectively. Reduction of maximum magnitude response is observed as τ is increased, but the most significant reduction can be seen for sample C where its maximum magnitude response located above its corresponding frequency of maximum loss factor, 779 rev/min. Thus it is suggested that high damping behaviour and higher response attenuation are observed at transition region of the viscoelastic material.

Figure 9 depicts surface plots of the maximum magnitude of the rotor centre and its corresponding resonance frequency. Each of the value is plotted against the pair of $\tau\alpha k_\infty$ and αk_∞ values which corresponds to the damping and stiffness coefficients in Figure 2 respectively. Stiffness value of k_∞ is fix as in Table 1 and variation of α is from 1 to 10 and τ is from $8.6667\text{x}10^{-4}$ to $8.6667\text{x}10^{-3}$. It can be seen that from Figure 9a, in general, the maximum rotor center magnitude responses are decreasing when $\tau\alpha k_\infty$ increases for a specific value of αk_∞. However different observations are found as the stiffness component of αk_∞ is increased for each value of $\tau\alpha k_\infty$. This suggests the prominent effect of the damping element in the viscoelastic material for reducing vibration level of rotor motion. The corresponding resonance frequency at which maximum rotor response occurred is shown by Figure 9b. In general, again, increased values of $\tau\alpha k_\infty$ have a greater effect of shifting the resonance frequency to higher values compared to αk_∞, where the effect can only be seen at medium to high range of $\tau\alpha k_\infty$. This is due to the fact that the stiffness and damper are in parallel in the viscoelastic model introduced.

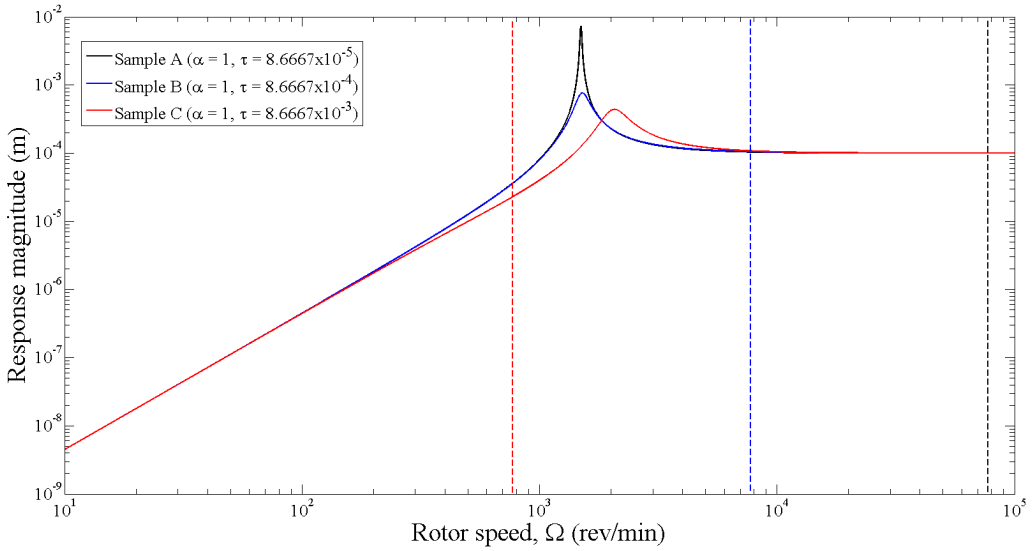


Figure 7: Magnitude of the rotor center displacement response of a rigid rotor mounted on three different samples of identical viscoelastic supports at both shaft's ends (stiff = Sample A, stiffer = Sample B, stiffest = Sample C).

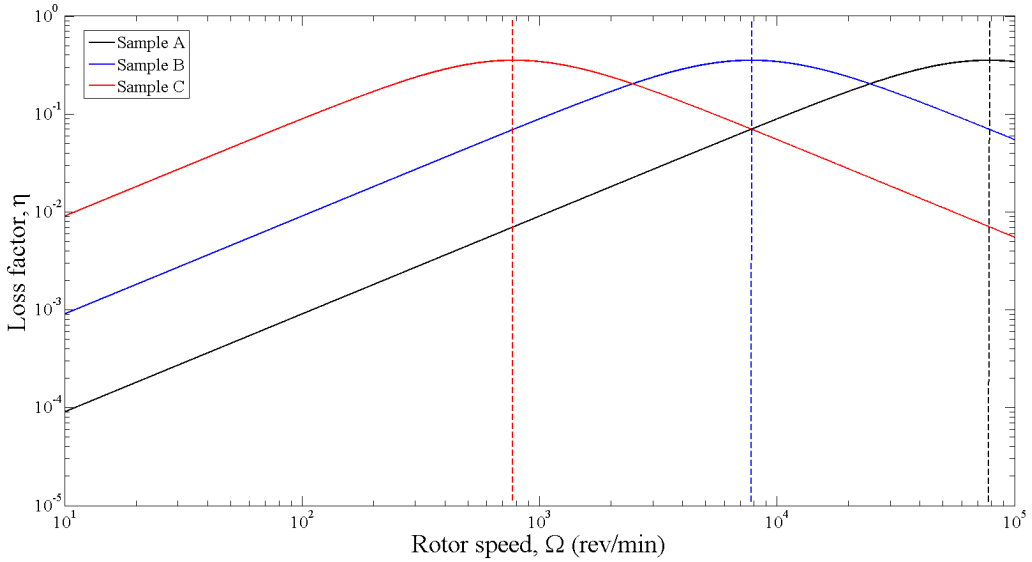
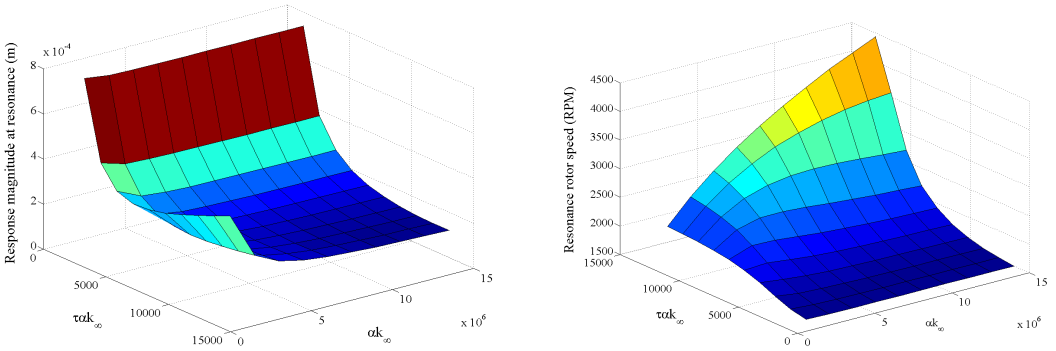


Figure 8: Loss factor of a rigid rotor mounted on three different samples of identical viscoelastic supports (stiff = Sample A, stiffer = Sample B, stiffest = Sample C).



(a) Resonant response magnitude.

(b) Rotor speed for the resonant response.

Figure 9: Resonance speed and maximum displacement response magnitude for a rigid rotor mounted viscoelastic supports.

4 Conclusions

In conclusion, the effect of the stiffness coefficients are dominant in determining the dynamics of the rotor for both elastic and viscoelastic supports. Specifically in terms of mode coupling, the stiffness is significant especially when the supports are not identical at both ends. Furthermore the influence of damping is prominent for attenuating the vibration response explicitly at transition region of viscoelastic material.

REFERENCES

[1] M. Stiassnie, On the application of fractional calculus for the formulation of viscoelastic models. *Applied Mathematical Modelling*, 3(**4**), 300–302, 1979.

[2] A. D. Nashif and J. P. Henderson, *Vibration damping*. John Wiley & Sons, 1985.

[3] R. Fosdick and Y. Ketema, A thermoviscoelastic dynamic vibration absorber. *Journal of Applied Mechanics*, 65(**1**), 17–24, 1998.

[4] M. M. Sjöberg and L. Kari, Non-linear behavior of a rubber isolator system using fractional derivatives. *Vehicle System Dynamics*, 37(**3**), 217–236, 2002.

[5] K. Adolfsson, M. Enelund and P. Olsson, On the fractional order model of viscoelasticity. *Mechanics of Time-Dependent Materials*, 9(**1**), 15–34, 2005.

[6] L. A. Silva, E. M. Austin and D. J. Inman, Time-varying controller for temperature dependent viscoelasticity. *Journal of Vibration and Acoustics*, 127(**3**), 215–222, 2005.

[7] N. Gil-Negrete, J. Vinolas and L. Kari, A nonlinear rubber material model combining fractional order viscoelasticity and amplitude dependent effects. *Journal of Applied Mechanics*, 76(**1**), 011009, 2009.

[8] J. Dutt and B. Nakra, Stability characteristics of rotating systems with journal bearings on viscoelastic support. *Mechanism and Machine Theory*, 31(**6**), 771–779, 1996.

[9] N. Shabaneh and J. W. Zu, Dynamic analysis of rotor–shaft systems with viscoelastically supported bearings. *Mechanism and Machine Theory*, 35(**9**), 1313–1330, 2000.

[10] M. I. Friswell, J. T. Sawicki, D. Inman and A. Lees, The response of rotating machines on viscoelastic supports. *International Review of Mechanical Engineering*, 1(**1**), 32–40, 2007.

[11] H. G. Tillema, Noise reduction of rotating machinery by viscoelastic bearing supports (PhD thesis). *University of Twente*, 2003.

[12] C. A. Bavastri, E. M. d. S. Ferreira, J. J. d. Espíndola and E. M. d. O. Lopes, Modeling of dynamic rotors with flexible bearings due to the use of viscoelastic materials. *Journal of the Brazilian Society of Mechanical Sciences and Engineering*, 30(**1**), 22–29, 2008.

[13] M. I. Friswell, *Dynamics of rotating machines*. Cambridge University Press, 2010.

[14] L. A. Silva, Internal Variable and Temperature Modeling Behavior of Viscoelastic Structures–A Control Analysis (PhD thesis). *Virginia Polytechnic Institute and State University*, 2003.

[15] B. R. Mace and E. Manconi, Wave motion and dispersion phenomena: Veering, locking and strong coupling effects. *The Journal of the Acoustical Society of America*, 131(**2**), 1015–1028, 2012.

11th International Conference on Engineering Vibration
Ljubljana, Slovenia, 7–10 September 2015

STRUCTURAL DYNAMICS OF A WIND TURBINE DRIVE TRAIN HIGH SPEED SUBSYSTEM: MATHEMATICAL MODELLING AND VALIDATION

Saeed Asadi*, Viktor Berbyuk, Håkan Johansson

Department of Applied Mechanics
Chalmers University of Technology
SE-41296, Gothenburg, Sweden

{saeed.asadi,viktor.berbyuk,hakan.johansson}@chalmers.se

Keywords: Wind turbine drive train, High speed shaft subsystem, Torsional vibrations, Model validation, Motor model

Abstract. *The paper studies the dynamics of a wind turbine drive train high speed subsystem, both by modelling and experiments with focus on system torsional vibration and transient events which can reduce fatigue life of functional components (gearbox, bearings, shafts, couplings, others). A scaled down drive train high speed shaft test rig has been developed. Main components of the test rig are six-pole motor with variable frequency drive controller (up to 1000 rpm), shafts' disk coupling and flexible mounting structure representing gearbox housing with output high speed bearing. The test rig is equipped with measurement system comprising a set of accelerometers and displacement sensors, strain gauges and telemeter system, data acquisition hardware and software (SKF WindCon3.0). Mathematical and computational models of the test rig have been developed and went through validation tests. The system dynamic response is studied for different operational scenarios and structural parameters (run-shut down case with and without eccentric mass). The ultimate goal of the test rig is to get insight into interaction between internal dynamics of drive train mechanical and electrical functional components and to develop novel methods to detect, predict and prevent faults and failures in wind turbine drive trains arising due to misalignments and transient external loads.*

1 INTRODUCTION

Wind energy conversion systems are one of the fastest growing global source of new electric generation and it is estimated to remain so for some time. Since mechanical vibrations of wind turbine drive train system become coupled with the electrical vibrations of currents in the motor winding, therefore it is important to include electromechanical interaction between different components in wind turbine system modelling. This leads to improve reliability by better prediction of the risk for different kinds of faults arising due to electromechanical failures demanding for better understanding of motor behaviors. A comprehensive yet ever growing list of the researches dealing with diagnostic problem of electric machines are presented in [1, 2].

In order to model and predict these electromechanical faults in drive train, the motor must be modeled in a sufficiently enough detail yet simple to avoid the complexity [3]. In many cases, this simplifications yield sufficiently useful results, but since many qualitative dynamic properties of the mechanical systems (their mass distribution, torsional flexibility and damping effects) are being neglected, they can lead to inaccuracies.

In wind turbine industry, Special attention was directed to induction motor (and squirrel cage which is used for grid connection) because of known reason such as size, cost, efficiency [4]. Therefore it is expected to model this specific motor. The model must describe the torsional oscillation phenomenon occurring in a multiple winding induction machine. The simplified faults in the induction motors can be categorized as induction motor mechanical faults (bearing, gearbox, oscilation and eccentricity) and electrical faults such as rotor (broken rotor bar and end rings) and stator faults (windings and external faults) [5].
A Gomez-Espinosa and V.M. Hernandez-Guzman have presented a new self-tuning algorithm which is developed for determining the Fourier Series controller coefficients with the aim of reducing the torque ripple in a PMSM, thus allowing for a smoother operation [6].
To support ongoing research with the aim to better predict what kinds of loads and electromechanical interactions that arise in a wind turbine drive train, a scaled down test rig relevant to the high speed subsystem of an indirect drive wind turbine has been developed [7, 8].

In this contribution, the mechanical characteristics of the test rig focusing on the motor response and torsional vibration, are presented, and used to validate its mechanical model. A simplistic model for the induction 3 phase motor is proposed by considering slip and torque ripple causing the failures. After model validation, the influence of eccentric mass and run-shut down case both in different motor speeds and corresponding modal analysis is studied, and the paper ends with conclusion and outlook.

2 DRIVE TRAIN HIGH SPEED SUBSYSTEM TEST RIG

2.1 Mechanical setup and instrumentation

To investigate wind turbine drive train system dynamics, a scaled down test rig has been built and instrumented. It entails a motor, rotor disk with shaft, where the rotor shaft is passing through the bearing housing and connected to the motor by a coupling. A small eccentric mass can be added on the rotor disk to give a uneven inertia distribution and in this way introduce to

the rotor system varying dynamic load. The setup of the drive train high speed subsystem test rig is depicted in Fig. 1.

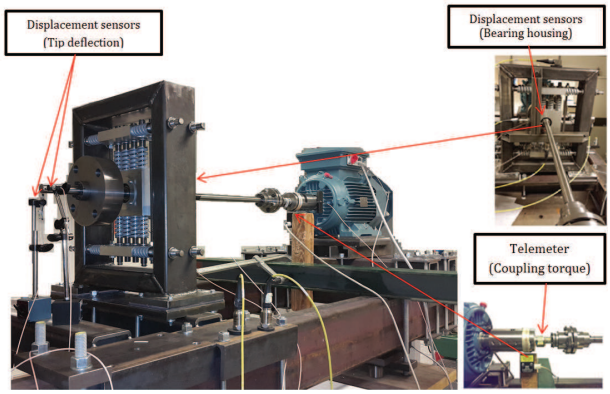


Figure 1: The test rig and its main components with sensors location

The main components of the test rig are ABB motor model M3BP160 MLA 6 (6 pole, 75 kW), with a frequency converter that controls motor speed up to 1000 rpm, motor shaft adapter, shaft's coupling, bearing housing with flexible support, a disk on which an eccentric mass can be added, bedplate on which all the components are mounted. The data acquisition has been done by SKF @ptitude Observer, that SKF offers under its WindCon3.0 condition monitoring system. The set of sensors comprise accelerometers (CMSS 7799 LF, CMSS 2200), and 4 Eddy probes displacement sensors (CMSS 665), which are used to assess vibrations in the test rig and deflection at both shafts tip and bearing housing. Additionally, in order to measure the torque in coupling, full bridge strain gauges are put on the motor shaft, and the signal is acquired using a telemeter system (TEL 1-PCM). Detailed specification of the sensors and their location are presented in Tab. 1.

Table 1 Sensors specifications and locations

Sensor name	Sensitivity	Range	Location
CMSS 7799 LF	500 mV/g	10 g peaks	Bearing housing
CMSS 2200	100 mV/g	80 g peaks	Bearing housing
CMSS 665	7.87 mV/μ m	[0.2, 2.3] mm	Bearing housing and tip
Strain gauge (full bridge) with TEL 1-PCM	0.065 mV/Nm	50 V	Coupling
ABB motor model M3BP160 MLA 6			

2.2 Test rig characterization

2.2.1 Torque ripple in the motor

When running the motor frequency converter with 0 Hz frequency, there are some vibrations which can be seen in the motor, 50 Hz frequency appears in the frequency domain which reveals the existence of torque ripple in the motor torque (see Fig. 2).

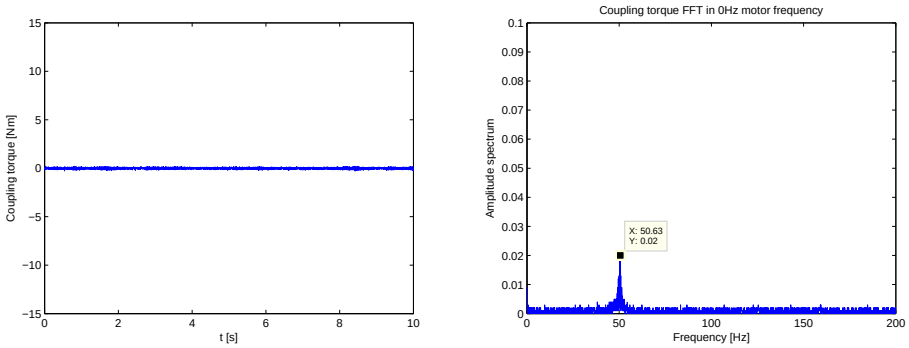


Figure 2: Coupling torsional torque, converter on with 0 Hz frequency (no running) (left) and corresponding FFT (right)

2.2.2 Knock test

In order to investigate the torsional eigenfrequency of the structure, knock test has been performed as shown in Fig. 3.

- A single pronounced peak around 49.5 Hz was seen in frequency diagram which refers to the fundamental torsional eigenmode (6 repetitions gave $f = [49.438, 49.406, 49.406, 49.531, 49.281, 49.344]$ Hz). Since the motor adds substantial damping to the system, it is expected that a measured vibration will be at a somewhat lower frequency (in subsequent analyses a peak at 48.5 Hz was often seen during running).
- In the amplitude spectrum, a small peak at 50 Hz was also seen which seems to be due to a leaking current or some other electrical interference from grid.

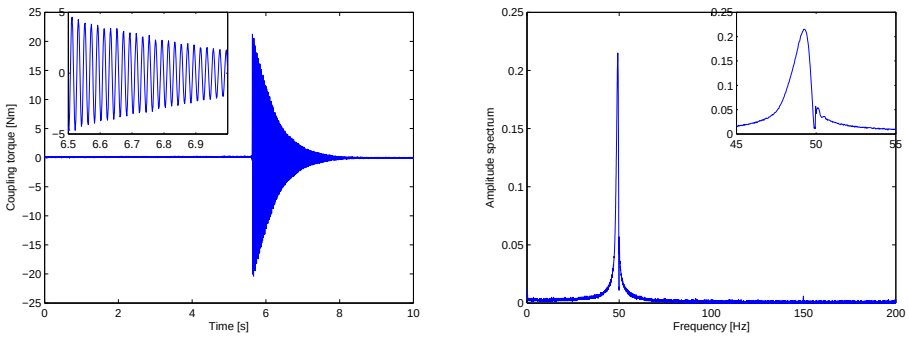


Figure 3: Coupling torsional torque in the knock test (left) and corresponding FFT (right)

2.2.3 Direct connection to the grid

In order to understand the effects of the motor converter to the response of the system, a test is run when motor is fed by direct connection to the grid (50 Hz) circumventing the converter.

Here is the results which are different compared to previous case.

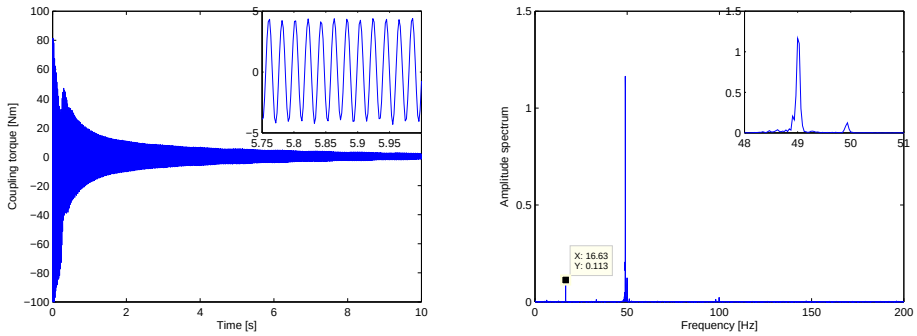


Figure 4: Coupling torsional torque in direct connection to grid, 50 Hz (left) and corresponding FFT (right)

The peaks in the frequency domain, correspond to motor mechanical (16.63 Hz) and electrical (50 Hz) frequencies since the motor is 3 phase. Also since the motor is directly supplied from the grid, we do not see any torque ripple in the steady state regime.

3 TORSIONAL VIBRATION MODEL OF DRIVE TRAIN TEST RIG

An engineering model and the sketch of the test rig are shown in Fig. 1 and Fig. 6 respectively. The mechanical model has been developed based on both rigid and flexible shaft assumption in bending modes, considering that the torsional flexibility is concentrated at coupling. The shaft twist is represented by $\Delta \stackrel{def}{=} \phi_g - \phi_r$, where $\phi_r(t)$ and $\phi_g(t)$ correspond to the rotor and motor shafts' angles, respectively. The motor is rigidly attached to the bedplate, the bearing housing flexibility is assumed linear.
In order to have a better insight into different operation points, Campbell diagram is shown in Fig. 5. Here, the torsional frequency and bending frequency related to the first bending eigenmode [9], the operating motor speed and 3X motor speed have been illustrated. Results below are considered motor speeds 600, 800, 1000 rpm, indicated as vertical lines.

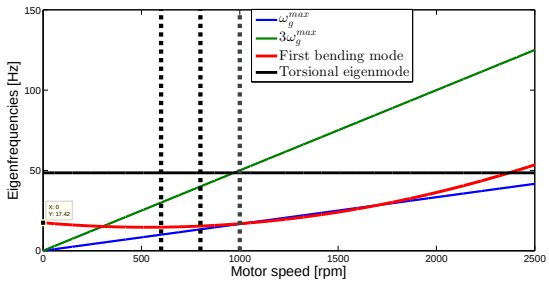


Figure 5: Campbell diagram

It could be perceived that since the second bending eigenmode is higher than the relevant

excitation frequency, it is sufficient to define the deflection field based on the first bending eigenmode (17.42 Hz). Furthermore, a motor speed of 1000 rpm is close to a critical speed.

A model for shaft bending and twist was developed in [10] where it was found that a torsional and deflection fields do not affect significantly and for studying of the torsional response of the test rig, assuming the pure torsional model is sufficient [10].

Here, we shall focus on a lumped torsion vibration model for the drive train test rig. An engineering abstract of the model is depicted in Fig. 6 and entails two inertias, disk J_r and generator rotor J_g, respectively. Each of these inertias are supported by bearings, whose internal friction is represented by torsion dashpots. The shaft and coupling flexibility is lumped together and represented by a torsion spring. Due to gravity and eccentric mass, there will be an external torque $M_r(= m_e r_e g \cos\phi_r)$ acting on the disk, and the induced electrical torque from the motor M_g acts on the generator rotor.

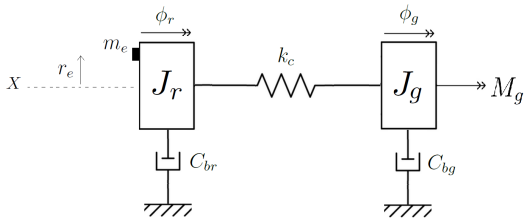


Figure 6: Engineering abstract of the test rig in torsional vibration

Hence, we have the following set of equations to describe the test rig torsional vibration response:

$$J_r\ddot{\phi}_r + C_{br}\dot{\phi}_r + k_c(\phi_r - \phi_g) = -m_e r_e g\cos\phi_r \tag{1}$$

$$J_g\ddot{\phi}_g + C_{bg}\dot{\phi}_g + k_c(\phi_g - \phi_r) = M_g(t) \tag{2}$$

The motor is a 6 pole induction machine with rated power 7.5 kW at speed 975 rpm. The speed is set from a frequency converter, such that the torque is given by the difference from set speed ω_g^{set} and actual speed $\dot{\phi}_g$. A cycle of ramp startup - steady state - shut down can thus be described by:

$$M_{\text{mech}} = \frac{M_{\text{mark}}}{\Delta\omega_{\text{mark}}}\left(\omega_g^{set} - \dot{\phi}_g\right) \quad \text{where} \begin{cases} \omega_g^{set} = \frac{t}{t_0}\omega_g^{max} & t < t_0 \\ \omega_g^{set} = \omega_g^{max} & t_0 \le t < t_1 \\ M_{\text{mark}} = 0 & t_1 \le t \end{cases} \tag{3}$$

where $\Delta\omega_{\text{mark}} = 25/60 \times 2\pi$ rad/s, $M_{\text{mark}} = 73.4561$ Nm, t_0 is the startup-time, and t_1 is the instance when motor is turned off (without braking). From electrical measurement of the voltage from the frequency converter, it was found that in addition to M_{mech}, there is a small periodic torque (ripple) acting on the generator rotor with at frequencies ω_g^{set}, $3\omega_g^{set}$ and $6\omega_g^{set}$. Hence, the following electrical torque is considered

$$M_g(t) = \frac{M_{\text{mark}}}{\Delta\omega_{\text{mark}}}\left(\omega_g^{set} - \dot{\phi}_g\right) + M_{rip1}\sin(\phi_g) + M_{rip2}\sin(3\phi_g) + M_{rip3}\sin(6\phi_g) \tag{4}$$

where $M_{rip1,2,3}$ ($= 10$ Nm) are coefficients that contribute to torque ripple with corresponding frequencies and have been obtained based on comparison of the torque ripple range in steady state in simulation and experiments.

The parameters and their numerical values used in the model are given in Tab. 2.

Table 2 Test rig numerical parameters

Parameter	Symbol	Value
Rotor inertia with respect to ϕ_r	J_r	J_r = 0.095 kgm^2
Rotor inertia	J_g	J_g = 0.087 kgm^2
Coupling torsional stiffness	k_c	$k_c = 2600$ N/rad
Rotor torsional damping coefficient	C_{br}	$C_{br} = 0.006$ N/m
Motor torsional damping coefficient	C_{bg}	$C_{bg} = 0.006$ N/m
Eccentric mass mounted in the rotor disk	m_e	$m_e = 74.4$ gr
Distance of eccentric mass from center	r_e	$r_e = 8$ cm

4 EXPERIMENTAL AND SIMULATION RESULTS

The torsional vibrations of the system in both experiment and simulation have been analyzed and qualitatively validate the mechanical model for torsional response in time and frequency domains.
The coupling torque in the mechanical model is computed as: $M_\Delta(\Delta(t)) = k_c \times \Delta$. The following plots show the coupling torsional torque representing the torsional dynamic response of the system.

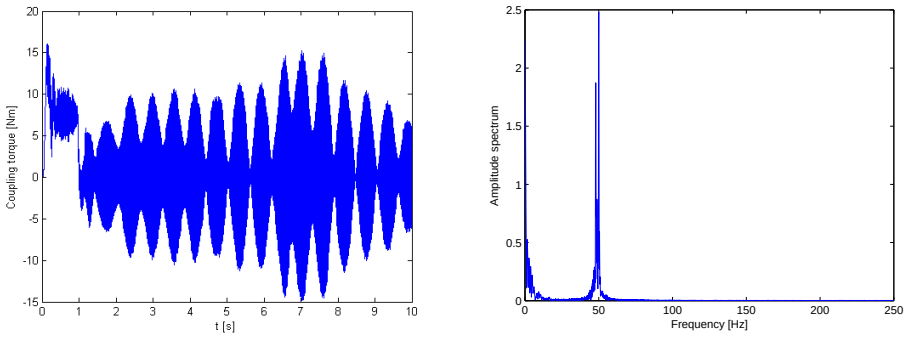


Figure 7: Coupling torsional torque (with frequncy converter) in experiment in 50 Hz (left) and corresponding FFT (right)

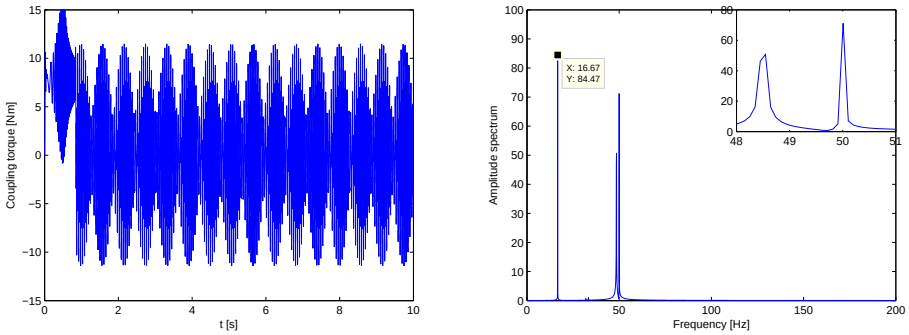


Figure 8: Coupling torsional torque in simulation in 50 Hz (left) and corresponding FFT (right)

As demonstrated by Fig. 7 and Fig. 8, the responses of the system in both simulation and experimental test data in terms of coupling torque are quite similar with respect to amplitude and frequency in steady state phase, but not so much similar in transient phase. The experimental results on coupling torque show a strong modulated oscillation, which seems to be due to motor excitation close to torsional eigenmode, as in the mechanical model it has been modeled as motor torque ripple.
As part of the model validation, the steady state responses of the system from experiment and simulation, with respect to different motor speeds are in Fig. 9.

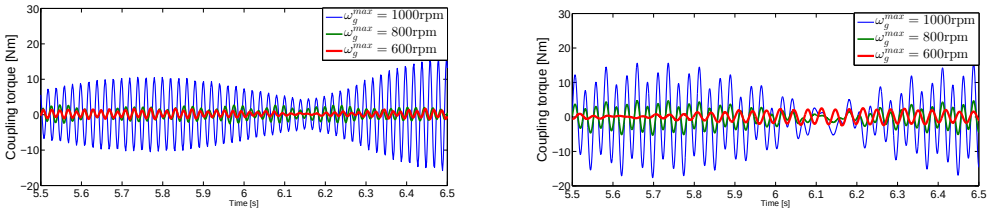


Figure 9: Coupling torsional torque in steady state regime experiment (left) and simulation (right) wrt different motor frequencies

As interpreted from Fig. 9, in the simulation results, the coupling torque range is smoothly decreasing by smaller motor frequency, whereby this decrease in the experiment is significant. This might be due to the nonlinear dependency of the ripple coefficients in the Eqn. 4 ($M_{rip1,2,3}$).

The following graphs show the load cycle defined in Eq. 3 in both simulation and experiment with and without eccentric mass, in different motor speeds. It must be noted that in the experiment, the minor fluctuations in the starting time of data acquisitions and shut down time are due to that they are manually imposed. Also in the simulation, the steady state time span runs for 10 seconds (in $[1, 11]$ sec).

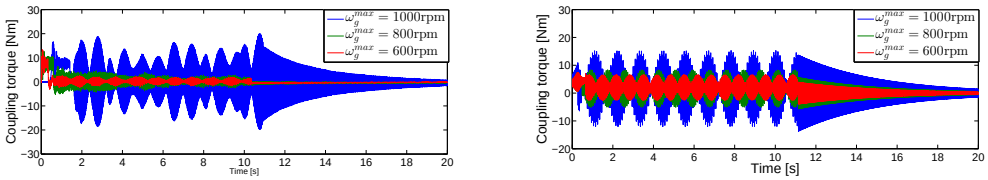


Figure 10: Coupling torsional torque in run-shut down in experiment (left) and simulation (right)

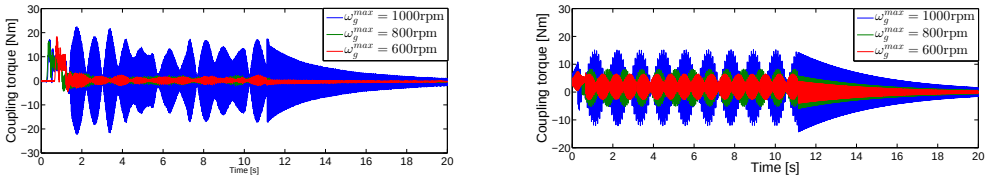


Figure 11: Coupling torsional torque in run-shut down in experiment (left) and simulation (right) with no eccentric mass ($m_e = 0$)

As demonstrated from Fig. 10 and Fig. 11, the simulation response in run-shut down case is quite similar to the experiment, specially in steady state and shut down regime. Also, an experiment without any eccentric mass was conducted. Now, consider the eccentric mass effect as a external torque. Comparing eccentric case and no eccentric case, the range of coupling torque when the eccentric mass is applied, is increased since there is more external torque applied to the system.

5 CONCLUSION AND OUTLOOK

The test rig has been developed to study the dynamics of high speed shaft subsystem of wind turbine drive train. The mathematical and computational models of the test rig have been developed by taking into account torsional flexibility of shafts and coupling and qualitatively validated. The simulation results have been represented based on different operational scenarios (different motor speed, run-shut down case). The results allow one to analyze a dynamic response of a misaligned shaft and coupling as well as reactions that affect bearing.
The proposition for the future works could be outlined as follows:

1. Define more realistic ripple coefficients contributing the specific frequencies in torque ripple.
2. Employ the Park model [2] to better describe the induction motor, where the development of its current, torque and power relationships are based on the assumptions that the rotating magneto motive force produced by stator winding excitation is sinusoidally distributed in space and that the rotor mmf due to the slip frequency induced currents is similarly distributed. The stator currents should in this case be given correspondiong to the pertinent frequency controller output.

Acknowledgment This project is financed through the Swedish Wind Power Technology Centre (SWPTC). SWPTC is a research centre for design of wind turbines. The purpose of the centre is to support Swedish industry with knowledge of design techniques as well as maintenance in the field of wind power. The Centre is funded by the Swedish Energy Agency, Chalmers University of Technology as well as academic and industrial partners. In particular,

donations of motors and frequency converters by ABB CR, WindCon3.0 condition monitoring system and set of sensors by SKF are gratefully acknowledged. Besides, the authors would like to thank Jan M´oller for his contribution in the laboratory.

REFERENCES

[1] M. Benbouzid, Bibliography on induction motors faults detection and diagnosis, IEEE Trans. on Energy Conversion, vol. 14, no. 4, pp. 10651074, 1999. [Online]. Available: http://dx.doi.org/ 10.1109/60.815029

[2] T. Lindh, On the Condition Monitoring of Induction Machines. Lappeenranta: Lappeenranta University of Technology, 2003.

[3] T. Szolc, R. Konowrocki, M. Michajlow, A. Pregowska, An investigation of dynamic electromechanical coupling effect in machine drive systems driven by asynchronous motors, Mechanical systems and signal processing, 4(2), pp.118-134, 2014

[4] R. You, B. Barahona, J. Chai, N. A Cutululis, A Novel Wind Turbine Concept Based on an Electromagnetic Coupler and the Study of Its Fault Ride-through Capability, 11/2013; 6(11):6120-6136. DOI: 10.3390/en6116120

[5] K.S. Gaeid, H. Wooi Ping, M. Khalid, A. Lauy Salih, Fault Diagnosis of Induction Motor Using MCSA and FFT, Electrical and electronic engineering. 1(2), pp.85-92 2011. DOI: 10.5923/jeee.20110102.14.

[6] A. Gomez-Espinosa, V. M. Hernandez-Guzman, M. Bandala-Sanchez, A New Adaptive Self-Tuning Fourier Coefficients Algorithm for Periodic Torque Ripple Minimization in Permanent Magnet Synchronous Motors (PMSM), International Journal of advanced manufacturing technology, 2013, 13(3), 3831-3847; doi:10.3390/s130303831.

[7] McCainn, S.G., 2013:30, Design of Experiments and Analysis for Drive Train Test Rig, Masters Thesis, Department of Applied Mechanics, Chalmers University of Technology, Goteborg, Sweden

[8] Squires, J.C., 2014:36, Measurement System Design and Experimental Study of Drive Train Test Rig, Masters Thesis, Department of Applied Mechanics, Chalmers University of Technology, Goteborg, Sweden

[9] Silva, T., Maia, N., 2011, Elastically restrained Euler-Bernoulli beams applied to rotary machinery modelling, Acta Mech Sin, 27(1), pp. 5662.

[10] Asadi. S, Berbyuk. V, Johansson. H, 2015:30, Vibration Dynamics of a Wind Turbine Drive Train High Speed Subsystem: Modelling and Validation, ASME 2015 International Design Engineering Technical Conferences Computers and Information in Engineering Conference. 2015: August 2-5, 2015, Boston, Massachusetts, USA, paper DETC2015-46016.

International Conference on Engineering Vibration
Ljubljana, Slovenia, 7-10 September 2015

MODELLING OF MAGNETORHEOLOGICAL OILS IN ROTORDYNAMIC DAMPING DEVICES BY BILINEAR MATERIAL

Jaroslav Zapomel*[1,2], Petr Ferfecki[2], Jan Kozanek[1]

[1]Institute of Thermomechanics, The Czech Academy of Sciences, Prague, Czech Republic
zapomel@it.cas.cz
kozanek@it.cas.cz

[2]Department of Applied Mechanics, VSB-Technical University of Ostrava, Ostrava, Czech Republic
jaroslav.zapomel@vsb.cz
petr.ferfecki@vsb.cz

Keywords: Magnetorheological Squeeze Film Damper, Magnetorheological Oil, Bilinear Material, Rigid Rotor, Frequency Response.

Abstract. *To reduce lateral vibrations of rotors excited by unbalance of the rotating parts the damping devices are added to the rotor supports. To achieve their optimum performance their damping effect must be controllable. This is offered by magnetorheological squeeze film dampers whose damping force is produced by squeezing a thin layer of magnetorheological fluid between two concentric rings. The damping element is equipped with an electric coil that generates magnetic flux passing through the lubricating oil. As its resistance against the flow depends on magnetic induction, the change of the current can be used to control the damping force. The development of a new mathematical model of a magnetorheological squeeze film damper is based on assumptions of the classical theory of lubrication except that for the lubricant. Because the magnetorheological oils affected by a magnetic field belong to the class of liquids with a yielding shear stress, the lubricant is represented by a bilinear theoretical material. The pressure distribution in the full oil film is then described by a modified Reynolds equation. In addition, the influence of cavitation and of the magnetic forces, by which the damping device acts on the rotor journal, were taken into account. The advantage of the developed mathematical model is that unlike the Bingham or Herschel-Bulkley materials the flow curve of the bilinear liquid is continuous. It reduces nonlinear character of the damping forces and thus rises numerical stability of the computational procedures. The simulations show that changing the magnetic induction in the lubricating film makes it possible to achieve the optimum performance of the damping device in a wide range of the rotor operation speeds. The carried out calculations confirmed that application of the new model increased numerical stability of the simulation procedures.*

1 INTRODUCTION

To reduce amplitude of the lateral vibrations of rotors excited by unbalance of the rotating parts the damping devices added to the rotor supports are frequently used. To achieve their optimum performance in a wide range of rotational speeds their damping effect must be controllable, as widely discussed in [1]. Some mechanical, hydraulic and electromagnetic principles applicable to control the damping force are reported in [2-4]. A new concept is represented by the squeeze film dampers lubricated by magnetorheological oils. The derivation of the relations governing the pressure distribution in the full oil film and some experimental results concerning application of the magnetorheological dampers in the field of rotordynamics can be found in [5-7].

The magnetorheological oils when effected by a magnetic field behave as fluids with a yielding shear stress. It means their flow occurs only if the shear stress between two adjacent layers exceeds a limit value - a yielding shear stress. In areas, called a core, where the yielding shear stress is not reached, the magnetorheological liquids exhibit properties close to solid materials.

The main parts of a magnetorheological squeeze film damper are two concentric rings between which there is a layer of magnetorheological oil (Fig. 1). The inner ring is coupled with the rotor journal by a rolling element bearing and with the damper housing by a squirrel spring. The lateral vibration of the rotor squeezes the oil layer which produces the damping effect. The damping device is equipped with an electric coil generating magnetic flux passing through the lubricating oil. As resistance against its flow depends on magnetic induction, the change of the applied current can be used to control the damping force.

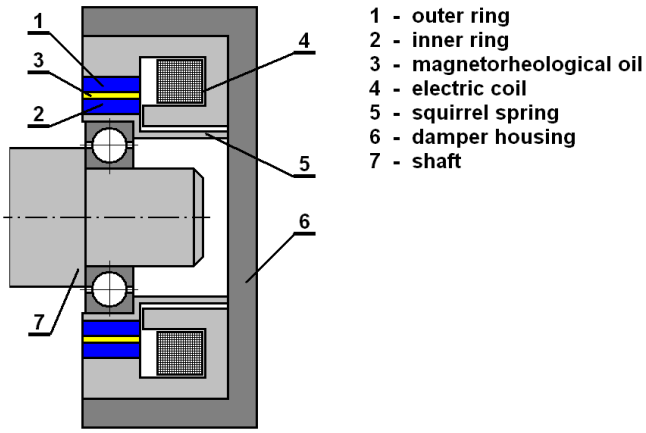


Figure 1: A magnetorheological squeeze film damper.

In mathematical models the magnetorheological liquids are usually represented by Bingham or Herschel-Bulkley theoretical materials. In this paper the development of a new and enhanced mathematical model of a short magnetorheological squeeze film damper based on representing the magnetorheological oil by bilinear material is reported. Unlike the Bingham fluid, its flow curve is continuous which contributes to reducing the nonlinear character of the damping forces. In addition, the influence of magnetic forces by which the damping device acts on the rotor journal and thus influences the damping effect is taken into account. The performed computational simulations show that the new mathematical model increases the com-

putational stability of procedures for determination of the steady state vibrations of rotors comparing to those based on modelling the magnetorheological oil by Bingham material.

The development of a new and enhanced mathematical model of a short squeeze film damper, consideration of influence of magnetic forces on the damping process and learning more on the effect of magnetorheological damping devices on the vibration attenuation of rotating machines are the main contributions of the presented article.

2 HYDRAULIC PRESSURE IN THE MAGNETORHEOLOGICAL OIL FILM

The new mathematical model of a magnetorheological squeeze film damper is developed on assumptions of the classical theory of lubrication [8-9] except that for the lubricant. The magnetorheological oil is represented by bilinear material whose yielding shear stress depends on magnetic induction. In addition, it is assumed that both the geometric and design parameters of the damper enable to consider it as short [8-9].

The derivation of the relations for the pressure distribution in the full oil film starts from the equation of continuity (1), the equation of equilibrium of an infinitesimal element specified in the oil film (2) and from the constitutive relationship of bilinear material (3) - (5).

$$\frac{\partial w}{\partial Z}+\frac{\partial v}{\partial Y}=0 \tag{1}$$

$$\frac{\partial p}{\partial Z}=\frac{\partial \tau}{\partial Y} \tag{2}$$

$$\tau=+\tau_y+\eta\frac{\mathrm{d}w}{\mathrm{d}Y} \qquad \text{for} \qquad \tau_C<\tau \tag{3}$$

$$\tau=\eta_C\frac{\mathrm{d}w}{\mathrm{d}Y} \qquad \text{for} \qquad -\tau_C\le\tau\le\tau_C \tag{4}$$

$$\tau=-\tau_y+\eta\frac{\mathrm{d}w}{\mathrm{d}Y} \qquad \text{for} \qquad \tau<-\tau_C \tag{5}$$

p is the pressure, τ is the shear stress, Y, Z are the radial and axial coordinates defining positions in the oil film (Fig. 2), v, w are the radial and axial velocity components of the oil flow, τ_y is the yielding shear stress, τ_C is the shear stress at the core border and η_C, η are dynamic viscosities of the oil in and outside the core area respectively.

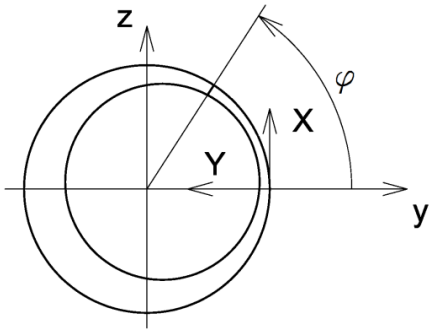


Figure 2: The coordinate systems.

Two areas are constituted in the oil film. In the one closer to the damper middle plane the core extends across the whole width of the damper gap and touches the damper surfaces. In the second area, there is, except the core, also a region where the oil flows. The relations for the axial coordinate Z_C, which defines the border between these two regions, and the corresponding pressure gradient in the axial direction p'_C at that location read

$$Z_C = -\frac{\tau_C h^2}{6\eta_C \dot{h}}, \tag{6}$$

$$p'_C = -\frac{2\tau_C}{h}. \tag{7}$$

h is the oil film thickness (more details for its determination can be found in [8-9]) and $(\dot{\cdot})$ denotes the first derivative with respect to time.

The pressure profile in the oil film is governed by the relations

$$p = \frac{6\eta_C \dot{h}}{h^3}\left(Z^2 - Z_C^2\right) + p_C \qquad \text{for} \qquad 0 \le Z < Z_C, \tag{8}$$

$$h^3\eta_C p'^3 + \left[3h^2\tau_y\eta_C - \left(12\dot{h}Z + C_1\right)\eta\eta_C\right]p'^2 + 8\tau_C^3\eta_C - 12\tau_y\tau_C^2\eta_C - 8\tau_C^3\eta = 0 \quad \text{for} \quad Z > Z_C. \tag{9}$$

C_1 is the integration constant and p_C is the pressure at location specified by the coordinate Z_C. The boundary conditions needed for solving equation (9) are

$$p = p_A \qquad \text{for} \qquad Z = \frac{L}{2}, \tag{10}$$

$$p' = p'_C \qquad \text{for} \qquad Z = Z_C. \tag{11}$$

p_A is the atmospheric pressure and L is the damper length. More details on solving equation (9) can be found in [4].

If the core fulfills the whole cross section of the oil film ($Z_C > L/2$), then the pressure profile in the axial direction is described by relation (12)

$$p = -\frac{6\eta_C \dot{h}}{h^3}\left(\frac{L^2}{4} - Z^2\right) + p_A. \tag{12}$$

In areas where the pressure drops to a critical level a cavitation takes place. In the developed mathematical model it is assumed that pressure of the medium in cavitated areas remains constant and equal to the pressure in the ambient space. This implies the cavitation extends over one half of the damper circumference and occurs at that part of the damper gap where its width rises with time.

Based on measurements the dependence of the yielding shear stress on magnetic induction can be approximated by a power function

$$\tau_y = k_y B^{n_y}. \tag{13}$$

B is magnetic induction and k_y and n_y are the proportional and exponential material constants of the magnetorheological oil. In the simplest design variant the inner and outer rings of damper can be considered as a divided core on an electromagnet with the gap filled with the magnetorheological oil. Then magnetic induction in the lubricating film can be expressed

$$B = k_B \mu_0 \mu_r \frac{I}{h}. \tag{14}$$

μ_0 is the vacuum permeability, μ_r is the relative permeability of the magnetorheological oil, I is the applied current and k_B is the design parameter that depends on the number of the coil turns and on the shape and arrangement of the damping element.

The consideration that the rings form a divided core on an electromagnet makes it possible to express the specific magnetic force p_m (magnetic force per a square unit) attracting the damper rings

$$p_m = \frac{B^2}{2\mu_0 \mu_r}. \tag{15}$$

3 HYDRAULIC AND MAGNETIC FORCES ACTING ON THE SHAFT JOURNAL

Two main forces act between the damper rings: hydraulic and magnetic. The hydraulic force is produced by squeezing the magnetorheological oil film and pushes the rings one from another. On the contrary, the magnetic force is attracting and is induced by the magnetic flux generated in the electric coils. The components of both forces are obtained by integration of the hydraulic and magnetic pressure distributions around the circumference and along the length of the damper gap

$$F_{mry} = -2R \int_0^{\frac{L}{2}} \int_0^{2\pi} p_d \cos\varphi \, \mathrm{d}\varphi \, \mathrm{d}Z \tag{16}$$

$$F_{mrz} = -2R \int_0^{\frac{L}{2}} \int_0^{2\pi} p_d \sin\varphi \, \mathrm{d}\varphi \, \mathrm{d}Z \tag{17}$$

$$F_{magy} = +2R \int_0^{\frac{L}{2}} \int_0^{2\pi} p_m \cos\varphi \, \mathrm{d}\varphi \, \mathrm{d}Z \tag{18}$$

$$F_{magz} = +2R \int_0^{\frac{L}{2}} \int_0^{2\pi} p_m \sin\varphi \, \mathrm{d}\varphi \, \mathrm{d}Z \tag{19}$$

F_{mry}, F_{mrz}, F_{magy}, F_{magz} are the y and z components of the magnetorheological damping and magnetic forces respectively, R is the middle radius of the damper gap, p_d is the hydraulic pressure distribution taking into account different pressure profiles in noncavitated and cavitated regions and φ is the circumferential coordinate (Fig. 2).

4 THE ANALYZED ROTOR SYSTEM

The investigated rotor is rigid (Fig. 3). It is composed of a shaft and one disc attached on it. At both its ends it is supported by magnetorheological squeeze film dampers. The rotor rotates at constant angular speed and is loaded by its weight and by the disc unbalance. The squirrel springs of both dampers are prestressed to be eliminated their deflection caused the rotor weight. The whole system can be considered as symmetric relative to the disc middle plane. The task was to analyze amplitude of the rotor vibrations.

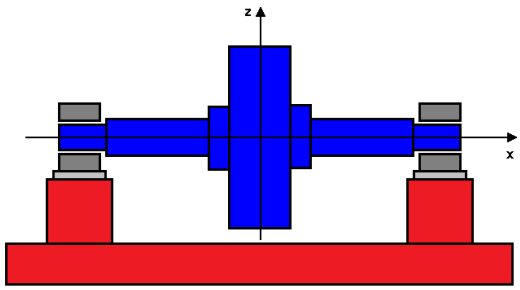


Figure 3: The investigated rotor.

In the computational model the rotor is considered to be absolutely rigid. The magnetorheological squeeze film dampers are implemented by spring elements and nonlinear force couplings.

Because of the symmetry lateral vibration of the rotor is described by two nonlinear equations of motion

$$m\ddot{y} + b_P\dot{y} + 2k_D y = me_T\omega^2\cos\omega t + 2F_{mry} + 2F_{magy}, \tag{20}$$

$$m\ddot{z} + b_P\dot{z} + 2k_D z = me_T\omega^2\sin\omega t - mg + 2F_{mrz} + 2F_{magz} + 2F_{PS} \tag{21}$$

where m is the rotor mass, k_D is the stiffness of one squirrel spring, b_P is the coefficient of the rotor damping produced by the environment, ω is the angular speed of the rotor rotation, t is the time, g is the gravity acceleration, e_T is the rotor center of gravity, y, z are the horizontal and vertical displacements of the rotor center, F_{PS} is the force prestressing one squirrel spring and (¨) notates the second derivative with respect to time.

To obtain the steady state solution of the equations of motion a trigonometric collocation method was applied.

5 THE COMPUTATIONAL SIMULATIONS

The design parameters and operation data of the analyzed system are: the rotor mass 450 kg, the squirrel spring stiffness 2.0 MN/m, the coefficient of the rotor external damping 50 Ns/m, the rotor imbalance, the damper length/diameter 50/150 mm, the width of the damper gap 0.9 mm, the oil dynamic viscosity not effected by a magnetic field 0.3 Pas, the oil dynamic viscosity in the core 300, the magnetorheological oil proportional and exponential constants 2000, 1.1 and its relative permeability 5 and the damper design parameter 60.

Fig. 4 shows the frequency response of the rotor excited by the disc unbalance for several magnitudes of the applied current (0.0 A, 0.1 A, 0.3 A, 0.6 A). It is evident that for lower velocities (approximately lower than the critical speed) rising current reduces amplitude of the vibrations. In the range of higher angular speeds increasing current has little influence on the rotor vibration and even it can arrive at the slight increase of its amplitude. This is confirmed also by Fig. 5 where the steady state orbits for two applied currents (0.0 A, 0.3 A) are depicted. The force transmitted between the rotor and the stationary part is constituted of three components: elastic, hydraulic and magnetic. The results in Fig. 6 show that the time history of the hydraulic force is shifted relative to those of the elastic and magnetic forces. This confirms that it depends mostly on velocity of the rotor journal while the elastic and magnetic components only of the squirrel springs deformation.

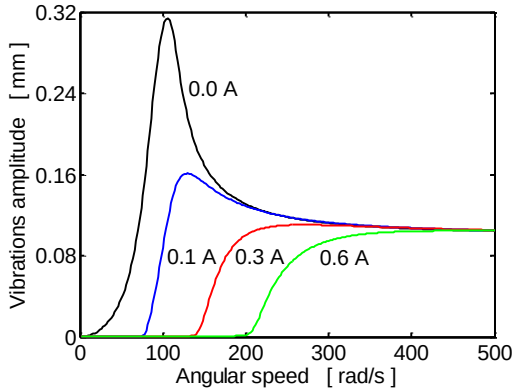


Figure 4: Frequency response of the rotor.

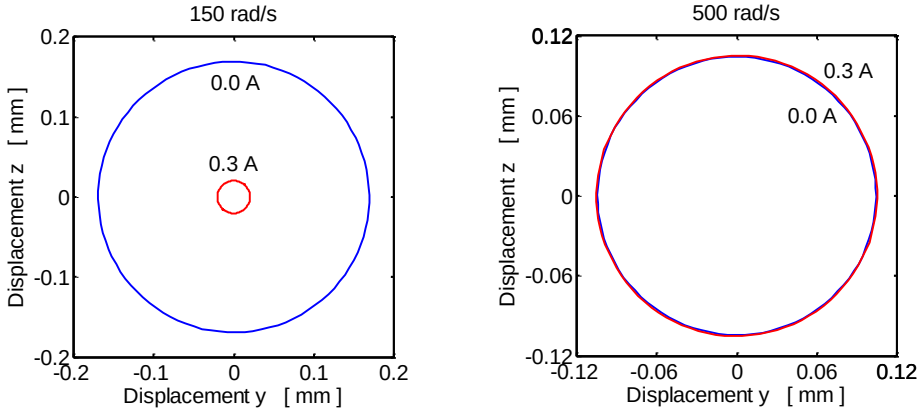


Figure 5: Orbits of the rotor center for speeds of rotation 150 rad/s, 500 rad/s and currents 0.0 A, 0.3 A.

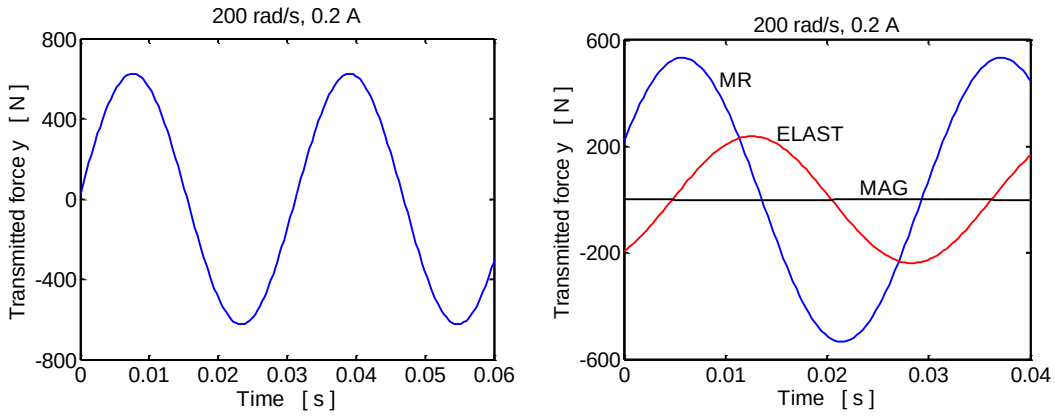


Figure 6: Force transmitted to the rotor frame and its components.

6 CONCLUSIONS

The main contributions of the work presented in this article are the development of a new and enhanced mathematical model of a short squeeze film damper for the rotordynamic applications, consideration of influence of the magnetic forces on the damping process and learning more on the effect of magnetorheological damping devices on the vibration attenuation of rotating machines. The new model is based on the assumptions of the magnetorheological oil by bilinear material whose yielding shear stress depends on magnetic induction. Its behavior is described by a continuous flow curve which reduces nonlinear character of the equations governing the rotor vibrations and thus increases computational stability of the procedures applied for their solving. The computational simulations showed that adapting the damping force to the operating speed by means of changing the applied current enabled to optimize the damper performance in a wide range of velocities. The simulations also confirmed that the developed model increased stability of the computational procedures comparing with those based on modelling the magnetorheological oil by Bingham material.

Acknowledgement: This work has been supported by the Czech Science Foundation 15-06621S and the European Regional Development Fund CZ.1.05/1.1.00/02.0070.

REFERENCES

[1] J. Zapoměl, P. Ferfecki P. and J. Kozánek, Determination of the transient vibrations of a rigid rotor attenuated by a semiactive magnetorheological damping device by means of computational modelling. *Applied and Computational Mechanics*, **7**(2), 223-234, 2013.

[2] C. Mu, J. Darling and C. R. Burrows, An appraisal of a proposed active squeeze film damper. *ASME Journal of Tribology*, **113**(4), 750-754, 1991.

[3] A. El-Shafei and M. El-Hakim, Experimental investigation of adaptive control applied to HSFD supported rotors. *ASME Journal of Engineering for Gas Turbines and Power*, **122**(4), 685-692, 2000.

[4] M. E. F. Kasarda, P. E. Allaire, R. R. Humphirs and L. E. Barret, A magnetic damper for the first-mode vibration reduction in multimass flexible rotors. *Journal of Engineering for Gas Turbines and Power*, **112**(4), 463-469, 1990.

[5] J. Zapoměl, P. Ferfecki and P. Forte, A computational investigation of the transient response of an unbalanced rigid rotor flexibly supported and damped by short magnetorheological squeeze film dampers. *Smart Materials and Structures* **21**(10), 1–12, 2012.

[6] J. Zapoměl and P. Ferfecki, Mathematical modelling of a long squeeze film magnetorheological damper for rotor systems. *Modelling and Optimization of Physical Systems*, 97-102, 2010.

[7] C. Carmignani, P. Forte and E. Rustighi, Design of a novel magneto-rheological squeeze-film damper. *Smart Materials and Structures*, **15** (1), 164-170, 2006.

[8] J. Zapoměl, *Computer modelling of lateral vibration of rotors supported by hydrodynamical bearings and squeeze film dampers*. VSB-Technical University of Ostrava, Ostrava, 2007 (in Czech).

[9] A. Z. Szeri, *Tribology: Friction, Lubrication, and Wear*. Hemisphere, Publishing Corporation, Washington, New York, London, 1980.

International Conference on Engineering Vibration
Ljubljana, Slovenia, 7-10 September 2015

INVESTIGATION OF HIGH VIBRATION ON LARGE FAN MOTOR

Keri A. Elbhbah*[1], Ian. Andrew[2], Jyoti K. Sinha[1], Erfan. Asnaashari[1], Wolfgang. Hahn[2]

[1]School of Mechanical; Aerospace & Civil Engineering (MACE);
University of Manchester
keri.elbhbah@postgrad.manchester.ac.uk; Jyoti.sinha@manchester.ac.uk
Erfan.Asnaashari@postgrad.manchester.ac.uk

[2]West Burton Power Station; EDF Energy
Ian.andrew@edfenergy.com; Wolfgang.Hahn@edfenergy.com

Keywords: Power Generation; Steam Turbine; Primary Air Fan; Condition Monitoring; Vibration.

Abstract. *The West Burton power plant (a subsidiary of EDF Company) commissioned between 1967 and 1969 is a 2000MW capacity power station consists of four similarly Boiler and Turbo Generator (TG) sets (generating unit). Each of the generating units is made up of several turbine stages (i.e. high pressure (HP) turbine; an intermediate pressure (IP) turbine and three low pressure (LP) turbines), in addition to a generator and an exciter. Along with the main generating units' assets, there are number of auxiliary equipments such as; condenser; air ejector; feed water pumps and primary air (PA) fans. Each boiler has two primary air (PA) fans, used for supplying primary air to the mills and conveying pulverised fuel into the boiler unit. As part of operational performance enhancement strategies, two of the boilers' (unit 1 & 4) PA-fans have been retrofitted with new electric motors, while the other two boilers (units 2 & 3) still possess their original electric motors. High levels of vibration readings were recorded on unit 3 PA-fan-B' electric motor' bearings on both; drive and non-drive ends. Hence a number of vibration measurements were conducted on this machine to find out the root cause of the increase on the machine vibration.*

1 INTRODUCTION

West Burton Power Plant, UK owned by EDF Energy has 4 boilers and steam turbo-generator (TG) sets (generating unit) for the power generation [1]. Each generating unit consists of number of the main equipments such as; turbines; generator and an exciter and also number of auxiliary equipments. The primary air PA fans are generally considered as one of the most critical auxiliary equipment, owing to the fact that operational faults on any of these fans will eventually result to a shutdown of the entire unit which consequently lead to a loss of electricity production. Hence, the continuous monitoring of such critical machines so as to detect emerging operational defects at their early stages is of immense importance. Each PA fan is a 10-bladed fan, supported by two journal bearings and connected by a Bibby coupling to a 4 pole squirrel cage, 3kV, 3-phase, 50 Hz, 1.2MW induction electric motor, as a picture and schematic diagram show in Figure 1.

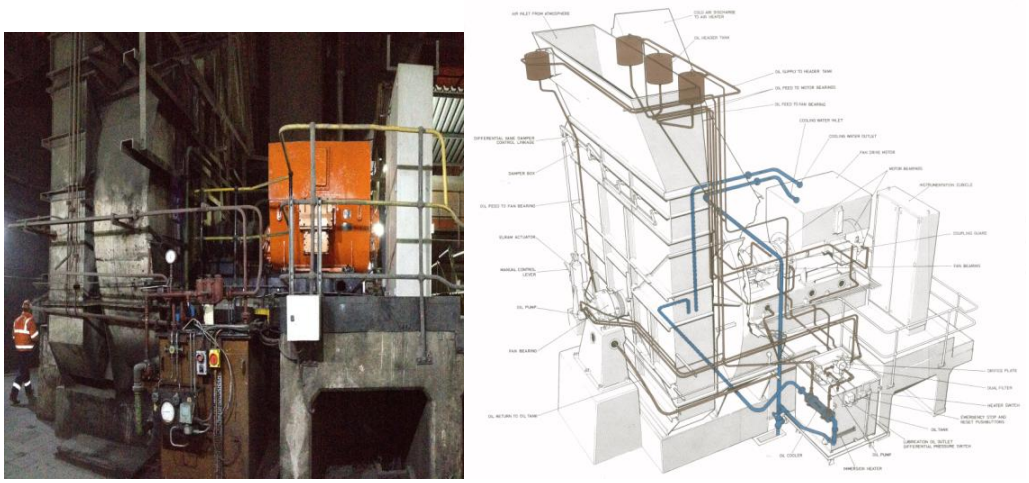


Figure 1: Picture and schematic diagram of PA-Fan.

On July 2012 unit 3 was taken to a major outage and came back to service on November 2012. High levels of vibration readings were recorded in the vertical and horizontal directions of both drive and non-drive ends' bearings of the electric motor of the PA-fan-B. Hence, this motor vibration was closely monitored for a period of approximately sixteen months (November 2012 to March 2014). The trend of overall RMS velocity of the vibration at the motor drive end bearing (B3) in horizontal direction is typically shown in Figure 3 where it is obvious that the change in the vibration is significant after the outage (November 2012).

The vibration level was just close to satisfactory limit before the outage in July 2012. However it became close to unsatisfactory limit of 7.1mm/s (RMS velocity) to unacceptable limit (above 7.1mm/s RMS velocity) as per ISO 10816-3 codes where the allowable and satisfactory vibration limits should be 2.3mm/s (RMS velocity) and 4.5 mm/s (RMS velocity) respectively for this machine assuming the rigid foundation. Also, figure 2 clearly shows the increasing trend in the vibration and this resulted in the stoppage of the TG unit 3 in February 2014 and hence the loss of power production.

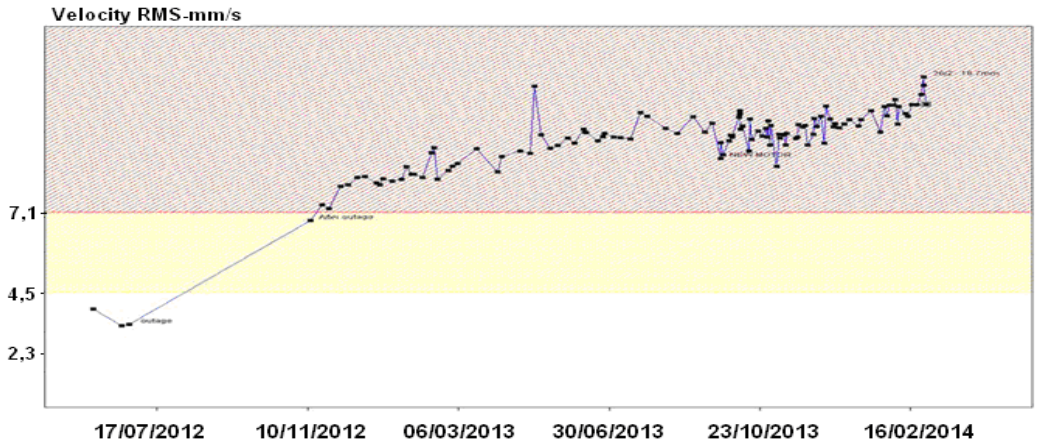


Figure 2: PA Fan B vibration trend at the motor drive end bearing (B3) in horizontal direction.

2 VIBRATION MEASUREMENT & ANALYSIS

Numbers of vibration measurements were carried on unit 3' PA-fan-B during its steady state operation at 1500RPM (25Hz) and also experimental modal analysis was conducted under static conditions (i.e. zero speed) to identify the motors' critical speeds. Mainly vibration measurements were carried at the housing for both the fan and the motor bearings in the vertical and horizontal directions. Accelerometers of sensitivity of 100mV/g with linear frequency measurement range up to 10 kHz were used. The vibration data were then collected through 4 channels CompactDAQ 24-bit data acquisition analogue to digital device for further signals processing using Matlab program.

2.1 Spectrum Analysis

Initially, the averaged spectra have been computed for all the measured vibration data during machines' normal operations speed at the machines' four bearings (B1; B2; B3 and B4) at both vertical and horizontal directions. Frequency resolution of 0.75Hz (number of data points, N=32768 for the sampling frequency, f_s=24576Hz) with Hanning window were used in the data analysis.

The amplitude spectra for the vibration data measured at the fan side' two bearings (B1&B2) at both vertical and horizontal directions show relatively small peaks at the first harmonic (25 Hz) with some peaks at its higher harmonics with higher amplitude on the driven side close to the coupling (B2) as shown in Figure 3. The typical computed amplitude spectra for the vibration measured data on the motor side (B3 & B4) show significant higher peaks on the fundamental speed of 25 Hz (1x) amplitude with also some peaks at the speeds' higher harmonics as shown in Figure 4.

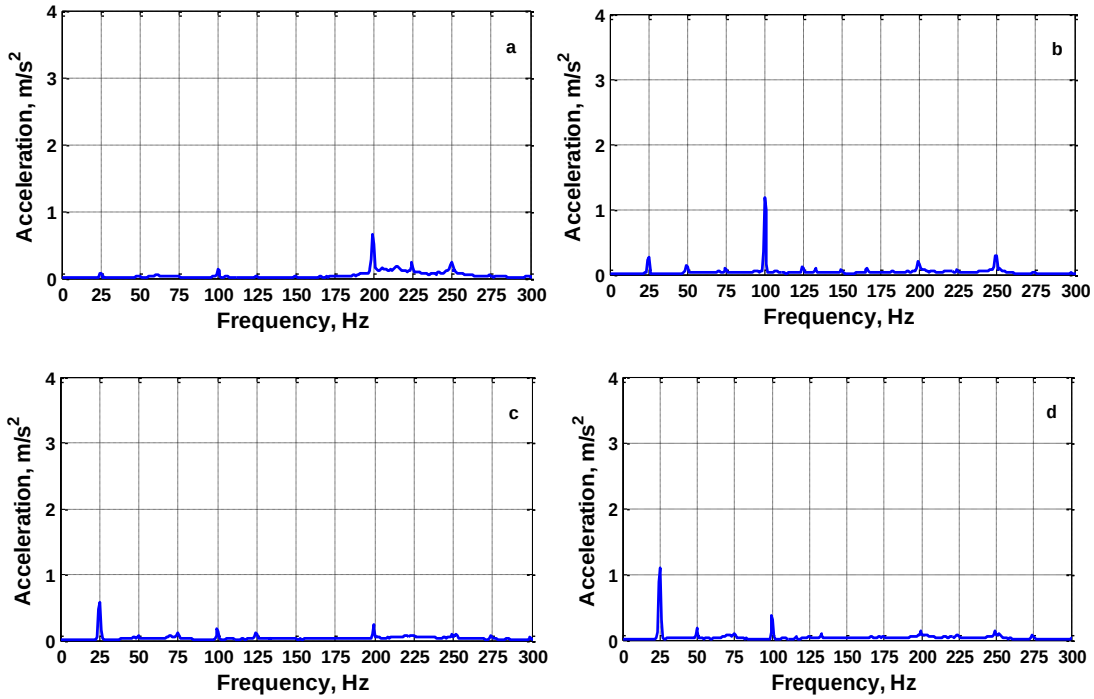


Figure 3: Typical amplitude spectra for fan; a. Drive-End vertical; b. Drive-End horizontal; c. Non- Drive-End vertical; d. Non- Drive-End horizontal.

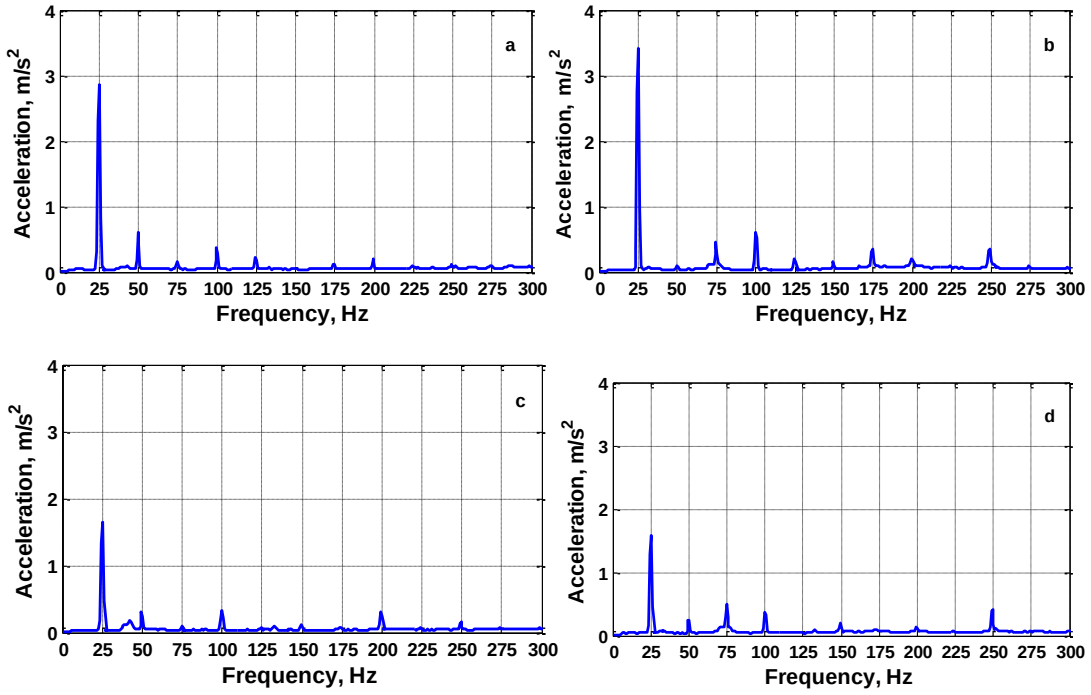


Figure 4: Typical amplitude spectra for motor; a. Drive-End vertical; b. Drive-End horizontal; c. Non- Drive-End vertical; d. Non- Drive-End horizontal.

2.2 Dynamic Characterisation

In order to foster a better understanding of the dynamic characteristics of the monitored machine, experimental modal analysis was also conducted using the impulse-response method where the motor was excited by a PCB instrumented hammer and the vibration responses were measured by PCB accelerometers under static conditions (i.e. zero speed) [2]. The FRF amplitude and phase plots shown in Figure 5 clearly show that non of the machine natural frequencies coincide with its rotation speed (25Hz) or any of its higher harmonics which confirms that there was no possible source of resonance.

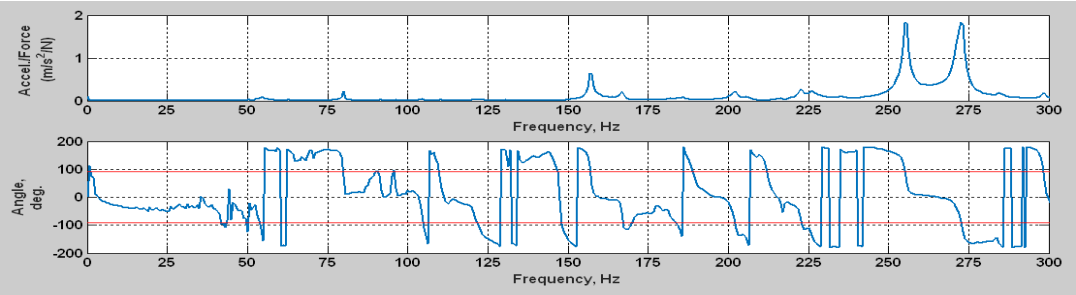


Figure 5: Typical amplitude FRF for Unit 3 PA-Fan-B motor.

The high vibration has impacted the fan assembly over the period of fan operation which led to the motor drive ends' bearing failure. This resulted in the stoppage of the complete unit and hence the loss of power production. A typical failed bearing of the motor is shown in Figure 6.

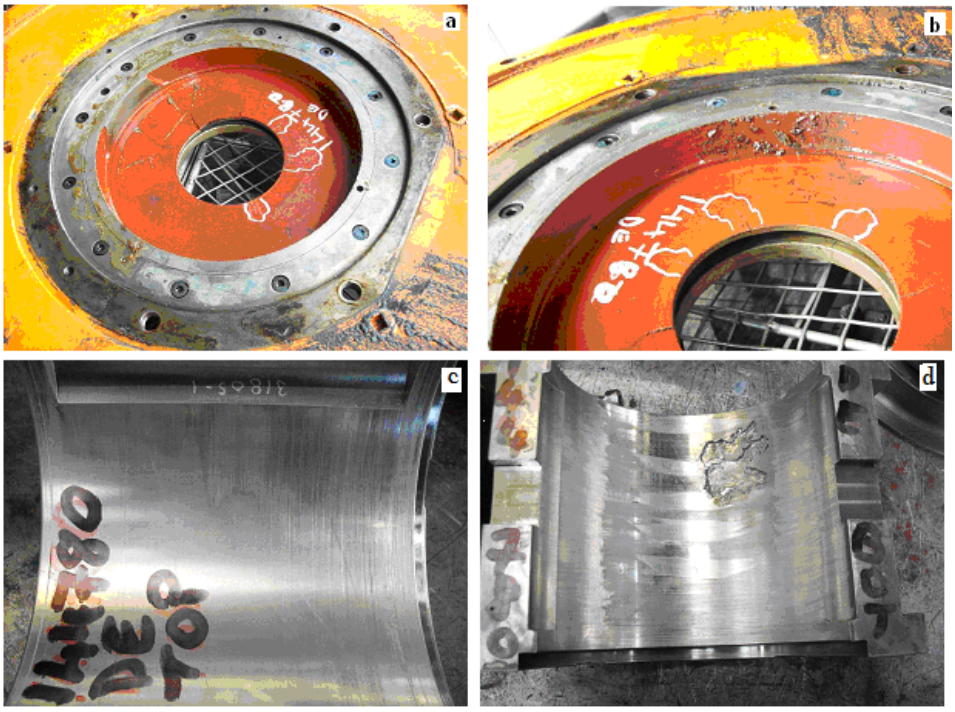


Figure 6: Failed drive end motor bearing.

The motor then was put back into the operation after balancing the motor and repairing its faulty bearing. The vibration measurements were carried out after this correction at all the 4 bearings during its normal operational speed of 1500RPM (25Hz) in both vertical and horizontal directions. Once again the overall RMS vibration velocity at the motors' drive end bearing was found to be in the unacceptable level (zone D - sufficient severity to cause damage to the machine) with 11mm/s-RMS.

3. REMEDIAL ACTIONS

The fan unit had been thoroughly investigated and no obvious reason for the high vibration was observed. The *in-situ* modal testing also confirms that there was no possible source of resonance at 25Hz that resulting into high vibration. Also, There was no significant peak at the blade passing frequency at 250Hz (10x – fan speed of 25Hz times 10 number of fan blades). The rotational speed dominant peak in the computed spectra might indicate unbalance case and after balancing the fan and the motor, the suspicion was that the coupling element between the motor and fan shafts may not be perfectly balanced and due its position it may introduces large rotor unbalance. Hence the coupling was step-by-step rotated by 90 degrees to observe the impact on the vibration readings. Big improvement on the overall vibration reading was recorded with 3 mm/s (RMS velocity) when the coupling was rotated by 270 degrees from its original position which is within the satisfactory limit as per the ISO 10816-3 codes. The motors' measured acceleration vibration spectra in Figure 7 also show significantly reduced vibration at 1x.

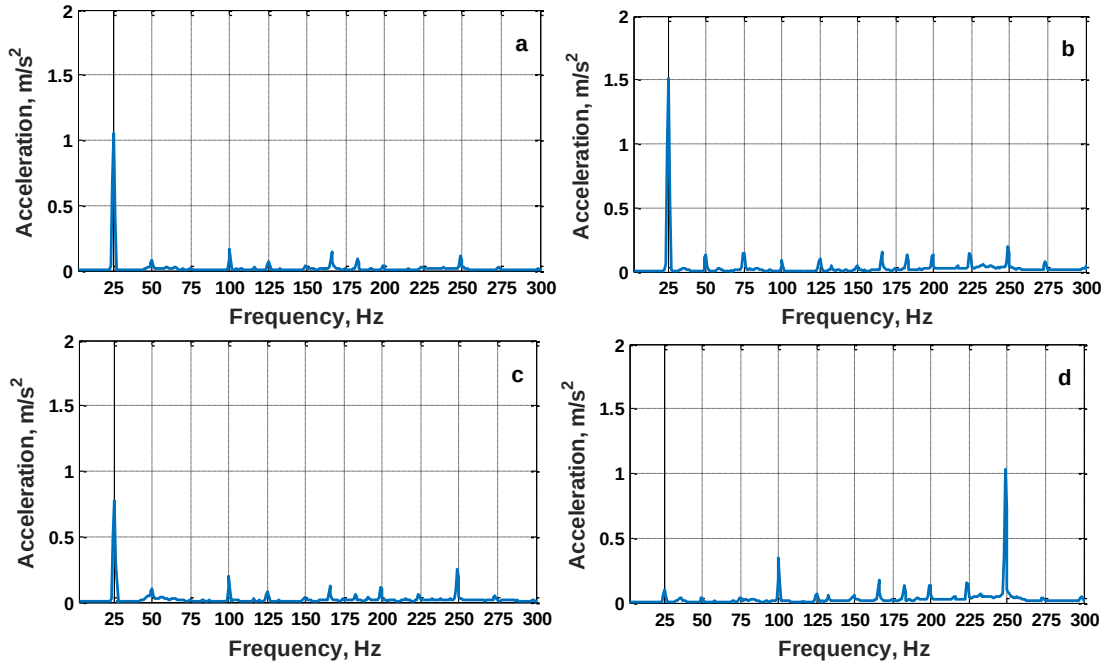


Figure 7: Typical amplitude spectra for motor; a. Drive-End vertical; b. Drive-End horizontal;

4 CONCLUSION

West Burton power plant was the first 2000MW power station. It consists of four turbo generation sets (500 MW each). Each TG set consists of multi stage turbines with a generator and an exciter. Along with the main generating units' main assets, there are number of the auxiliary equipments. PA Fans is considered as one of the most critical auxiliary equipment due to the fact that its failure leads to shut down the complete unit which cost huge amount of money especially when the power demand is high. High vibration was recorded on one of the unit 3' PA-Fans which eventually led to the stoppage of the entire unit. Numbers of vibration measurements were conducted to find out the rout cause of the vibration. After balancing the motor and repairing its faulty bearing it is discovered that the coupling was the main source of the vibration increase and rotating it from its original position made big improvement on the vibration readings up to the acceptable level.

REFERENCES

[1] J.K. Sinha, W. Hahn, K. Elbhbah, G. Tasker and I. Ullah, Vibration investigation for low pressure turbine last stage blade failure in steam turbines of a power plant, ASME Turbo Expo 2012, Turbine Technical Conference & Exposition. Copenhagen, Denmark, June 11-15, 2012.

[2] D.J. Ewins, Modal Testing, Theory, Practice and application (Mechanical Engineering Research Study: Engineering Dynamics Series), 2nd Edition, 2000.

International Conference on Engineering Vibration
Ljubljana, Slovenia, 7-10 September 2015

EVALUATION OF THE DYNAMIC RESPONSE OF HIGH-SPEED SYSTEMS USING AN ANALYTICAL MODEL FOR THE FLOATING RING BEARINGS OF FINITE LENGTH

Athanasios C. Chasalevris*

ALSTOM Power, TTT Industrial Steam Turbines, Newbold Road CV12NH, Rugby, UK
chasalevris@sdy.tu-darmstadt.de

Keywords: Floating-Ring Bearing, Analytical Solution, High-Speed System.

Abstract. *The paper presents a model of a high-speed rotor-bearing system consisting of a rigid rotor mounted on nonlinear floating ring journal bearings of finite length that are incorporated using a recently developed analytical solution for the Reynold's equation. The analytical solution for the floating ring bearing of finite length offers the ability of introducing the bearing forces to the rotordynamic algorithm using closed form expressions. The paper aims to the investigation of the dynamics and stability of high-speed systems under an analytical nonlinear-dynamic model that focuses on the influence of the nonlinear fluid film forces. The evaluated response and the developed eccentricities in the fluid films during a transient start-up of the system cover the majority of the results. Time-frequency decompositions of the system's transient response support this investigation of the fundamental dynamic effects that appear in high-speed systems with floating ring bearings. The results are compared to those obtained using numerical methods for the simulation of floating ring bearings and to those obtained using infinitely short bearing approximation.*

1 INTRODUCTION

In the design of high-speed systems numerous simulations can be demanded considering different geometric and physical parameters of the floating ring bearing elements. Unfortunately, the luck of the possibility of expressing the dynamic response of the rotating system in direct relevance to the bearing design parameters leads to numerous case studies considering transient response analysis under various combinations of the bearing geometry that is interpreted to variation of bearing radial clearance and of bearing width through a specified range of values. The nonlinear response of such systems contains the most times additional sub-/super-harmonics that are responsible for leading the system out of the demands for maximum response amplitude, bearing eccentricities, power losses, acoustic emission etc. More specifically, the developed eccentricities of the bearings are of crucial importance since they are supposed to be the first indication for the systems durability considering its millions of run-ups and run-downs in applications of automotive turbochargers.

In a run-up of an automotive turbocharger, three domains of rotational speed usually provoke the three corresponding instabilities at the inner and outer fluid films of the floating ring bearings [1, 2]. There is additionally the total instability at even higher speeds that leads soon to systems failure [3]. The three sub-synchronous components of the response, referred as sub-1, sub-2, and sub-3 that are developed due to the oil whirl/whip instability are influenced in their amplitude and duration from the bearing physical and geometric parameters. The canal through which the bearing geometric and physical configuration influences the bearing instability is the resulting forces/moments of impedance and friction; these phenomena have been widely explained in [1-4]. Therefore, the model for evaluating the oil film pressure distribution and then the impedance forces and moments from the fluid film to reaction parts (shaft, ring and housing) defines in crucial sense the rotational speed in which the instability will occur (or not) and the amplitude with which the sub-synchronous/sub-harmonic response will be developed.

The possibilities of incorporating floating ring bearing simulation into rotordynamic dynamic algorithms are many and there can be found extensively discussed in the literature. The numerical solution of the Reynolds equation for both inner and outer oil films has been performed with numerical methods such as FDM, FEM and CFD [5-9]. Such methods are quite accurate but even after the development of very efficient solvers they can be judged slower in comparison to direct formulas for the bearing impedance forces yielded from short/long bearing approximation. However the incorporation of axial grooves and holes in the floating ring geometry does not leave possibilities for non-numerical treatment of the Reynolds full equation.

The short/long bearing approximation has been widely used in the literature and there is a considerable amount of rotordynamic investigations of turbosystems under this assumption [10-13]. However the length to diameter ratio that is presented in the inner and outer film of the floating ring bearings is not always below or near L/D = 0.5; in the automotive turbochargers it is very common for the outer fluid film to be defined with a ratio near or even higher of L/D = 0.75. The short bearing approximation will give a different pressure distribution especially for high eccentricities and high eccentricity rate of change in comparison to the pressure distribution evaluated numerically. However the difference in the final outcome, that is impedance force, is not really significant, so still the approximation can be acceptable for the demands of rotor-bearing design. Considering further the operating parameters of the bearing such as power loss in the lubricant, developed shearing stresses in it, resulting torque from the oil to the ring and increment of ring speed, the method of the evaluation of pressure distribution can lead to different results regarding the occurrence of instabilities and their

characteristics. The present paper aims to highlight the evaluated ring speed under two different solutions for the pressure distribution based a recent achievement of analytical solution of the Reynolds equation in journal bearings of finite length [14-16] and leading to an exact and an approximate analytical solution.

Both theoretical bearing models (exact and approximate) express the impedance forces and moments of the bearing in closed form expressions and they are presented in a couple of lines in the form of subroutines that are proved to be very fast.

The results incorporate evaluated time histories for a geometric configuration of the rotor-bearing system; The bearing eccentricities, the compressor wheel response and the trajectories of the rotor and the floating rings during run-up are of major interest and they are compared among the different bearing simulation.

2 MODEL OF THE HIGH-SPEED ROTOR-BEARING SYSTEM

In the present analysis, a rigid rotor and two rigid wheels, with their masses concentrated at a point, are fixed to each other and rotate with a rotational speed Ω around the rotor center line as shown in Figure 1. The three components (CW, TW, and Rotor) are supposed to have a total mass M, a total moment of inertia (polar) J_P with respect to the rotor center line, and a total diametric moment of inertia J_T with respect to the vertical and horizontal axes that pass through the center of mass of the system, see Figure 1. A global rectangular coordinate system XYZ has its center at the system reference line at the plane of the center of mass of the system, see Figure 1. Since the system is not supposed to obtain any axial displacement (hypothesis of plane orbits), the coordinate system XYZ is fixed and with respect to this system all the lateral displacements will be defined.

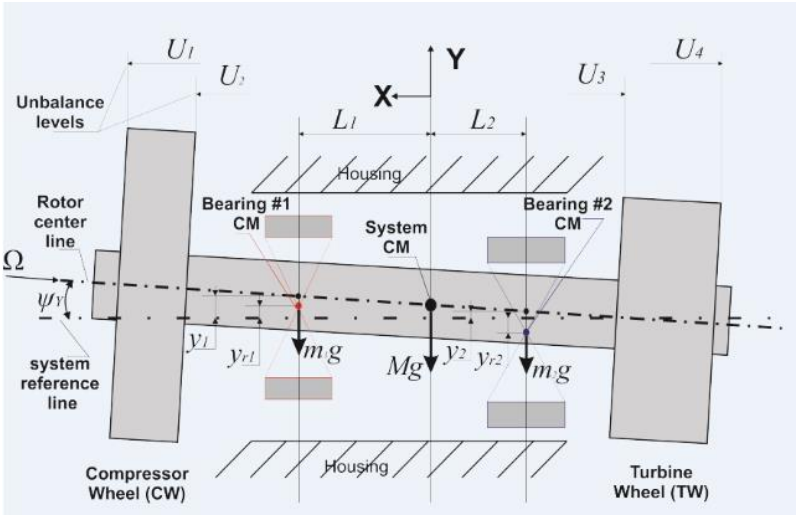


Figure 1: Representation and definition of the physical and geometrical parameters of the rotor-bearing system consisted of a rigid rotor carrying two wheels at its ends and be mounted on two floating ring bearings and of the floating ring bearing.

The changes of the momentum and the angular momentum of the rotor (and wheels) per unit time are represented by the left-hand sides of equations (1-4) [17]. Due to the impedance forces of the bearings, due to the gravity forces, and due to the unbalance forces that act on

the system, resultant forces and moments act to the system; these are expressed by the right hand side of equations (1-4) refereed to its CM.

$$M\ddot{y}_{CM} = F_{g,1} + F_{Y,1} + F_{g,2} + F_{Y,2} + \sum_{j=1}^{4} F_{u,y,j} \tag{1}$$

$$M\ddot{z}_{CM} = F_{Z,1} + F_{Z,2} - \sum_{j=1}^{4} F_{u,z,j} \tag{2}$$

$$J_T\ddot{\psi}_Y + J_P\Omega\dot{\psi}_Z = F_{Y,1}L_1 - F_{Y,2}L_2 + F_{u,y,1}U_1 + F_{u,y,2}U_2 - F_{u,y,3}U_3 - F_{u,y,4}U_4 \tag{3}$$

$$J_T\ddot{\psi}_Z - J_P\Omega\dot{\psi}_Y = F_{Z,1}L_1 - F_{Z,2}L_2 - F_{u,z,1}U_1 - F_{u,z,2}U_2 + F_{u,z,3}U_3 + F_{u,z,4}U_4 \tag{4}$$

The four unbalance forces are applied on the planes defined at a distance U_j from the plane of CM (see Figure 1); their definition is given in equation (5).

$$F_{u,y,j} = u_j\Omega^2\cos\left(\frac{1}{2}\Omega t\right),\ F_{u,z,j} = u_j\Omega^2\sin\left(\frac{1}{2}\Omega t\right),\ j = 1,2,3,4 \tag{5}$$

$$F_{g,1} = -MgL_2/(L_1+L_2),\ F_{g,2} = -MgL_1/(L_1+L_2) \tag{6}$$

$$y_1 = y_{CM} + L_1\psi_Y, y_2 = y_{CM} - L_2\psi_Y, z_1 = z_{CM} + L_1\psi_Z, z_2 = z_{CM} - L_2\psi_Z \tag{7}$$

$$\psi_Y = (y_1 - y_2)/(L_1+L_2), \psi_Z = (z_1 - z_2)/(L_1+L_2) \tag{8}$$

The total gravity forces of the rotor and of the wheels that are transferred to the bearings are defined in equation (6) for each bearing; in all definitions subscript '1' implies bearing #1 while the subscript '2' implies bearing #2.

The formulas of equations (7) and (8) are used to express the motion of the CM and the tilting angles of the system with the four variables y_1, y_2, z_1, z_2. After some math the equations of motion expressed at the equations (1-4), are expressed as in equations (9-12).

$$\ddot{y}_1 = \frac{L_1+L_2}{ML_2}\left(F_{g,1} + F_{Y,1} + F_{g,2} + F_{Y,2} + \sum_{j=1}^{4} F_{u,y,j}\right) - \frac{L_1}{L_2}\ddot{y}_2 \tag{9}$$

$$\ddot{z}_1 = \frac{L_1+L_2}{ML_2}\left(F_{Z,1} + F_{Z,2} - \sum_{j=1}^{4} F_{u,z,j}\right) - \frac{L_1}{L_2}\ddot{z}_2 \tag{10}$$

$$\ddot{y}_2 = -\frac{L_1+L_2}{J_T}\left(F_{Y,1}L_1 - F_{Y,2}L_2 + F_{u,y,1}U_1 + F_{u,y,2}U_2 - F_{u,y,3}U_3 - F_{u,y,4}U_4\right) + \frac{J_P\Omega}{J_T}\left(\dot{y}_1 - \dot{y}_2\right) + \ddot{z}_1 \tag{11}$$

$$\ddot{z}_2 = -\frac{L_1+L_2}{J_T}\left(F_{Z,1}L_1 - F_{Z,2}L_2 - F_{u,z,1}U_1 - F_{u,z,2}U_2 + F_{u,z,3}U_3 + F_{u,z,4}U_4\right) - \frac{J_P\Omega}{J_T}\left(\dot{z}_1 - \dot{z}_2\right) + \ddot{y}_1 \tag{12}$$

The gravity forces at the floating rings are also incorporated and they are supposed to act on the vertical direction at the CM of each ring with magnitudes $m_1 g$ and $m_2 g$. Under the action of the forces and moments from the fluid films to the rings, each ring (at bearing #1 and bearing #2) obtains angular rotation ϑ_1 and ϑ_2, rotating speed $\Omega_{r,1} = \dot{\vartheta}_1$ and $\Omega_{r,2} = \dot{\vartheta}_2$ and rotational acceleration $\dot{\Omega}_{r,1} = \ddot{\vartheta}_1$ and $\dot{\Omega}_{r,2} = \ddot{\vartheta}_2$ respectively. The motion of each ring is defined at the global coordinate system, see Figure 1, by the planar displacements of their CM, $y_{r,1}$

and $y_{r,2}$ at the vertical direction, and $z_{r,1}$ and $z_{r,2}$ at the horizontal direction for the bearing #1 and bearing #2 correspondingly. Three independent coordinates are demanded for the definition of the motion of each ring at every discrete time moment: the two planar displacements and the angle of rotation. Therefore, 6 more DoFs are added for the simulation of the rotor-bearing system. Letting $I_{P,1}$ and $I_{P,2}$ be the mass moment of inertia of each ring with respect to its axis of rotation and m_1 and m_2 to be the mass of each of them, the equations of motion are defined as in equations (13-15) for the first and the second ring correspondingly.

$$m_1\ddot{y}_{r,1} = -m_1 g + F_{Y,o,1} - F_{Y,i,1}, \quad m_2\ddot{y}_{r,2} = -m_2 g + F_{Y,o,2} - F_{Y,i,2} \tag{13}$$

$$m_1\ddot{z}_{r,1} = F_{Z,o,1} - F_{Z,i,1}, \quad m_2\ddot{z}_{r,2} = F_{Z,o,2} - F_{Z,i,2} \tag{14}$$

$$I_{P,1}\ddot{\vartheta}_1 = T_{i,1} - T_{o,1}, \qquad I_{P,2}\ddot{\vartheta}_2 = T_{i,2} - T_{o,2} \tag{15}$$

Since the nonlinear fluid film bearing forces are evaluated through the dynamic motion of the floating rings, the equations (9-15) consist a nonlinear system of 2nd order. After an order reduction the 2nd order 10×10 system of equations of motion (equations (9-12)) can be reduced to a 20×20 system of 1st order.

The 20×20 system can be solved with various methods of numerical integration of ODEs. According to the parameters of geometry and operation of the rotor-bearing system, the 20×20 system can be less or more stiff. The Matlab® solver "ode15s" integrates the 20×20 system of differential equations in a discrete time domain after setting the initial conditions and the absolute and relevant error tolerance. During a run-up the system experiences operational conditions that rise or decrease the nonlinearity of the fluid film forces and the suggested solver adopts its step on the progress of the solution.

3 ANALYTICAL SOLUTION FOR THE FLOATING-RING BEARING OF FINITE LENGTH

With reference to Figure 2, the inner eccentricities are defined as $e_1 = \sqrt{\left(y_1 - y_{r,1}\right)^2 + \left(z_1 - z_{r,1}\right)^2}$, $e_2 = \sqrt{\left(y_2 - y_{r,2}\right)^2 + \left(z_2 - z_{r,2}\right)^2}$ for both bearings; subscript "1" refer always to the left bearing (bearing #1) and subscript "2" refer always to the right bearing (bearing #2), see also Figure 1.

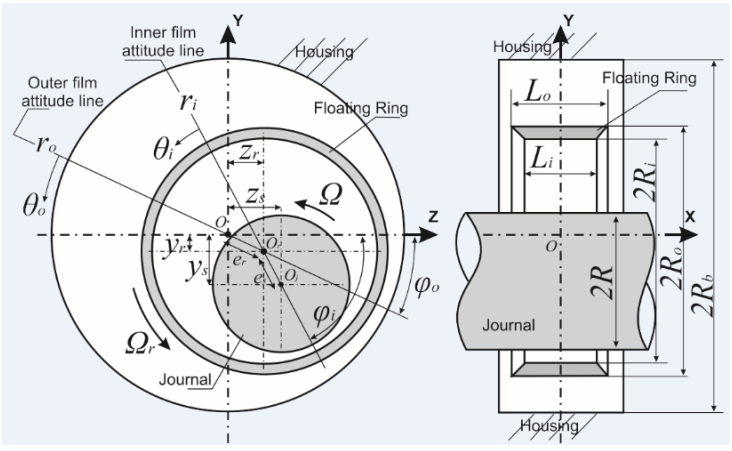


Figure 2: Definition of the geometry and parameters of operation of a plain cylindrical floating ring bearing

The outer eccentricities are defined as $e_{r,1}=\sqrt{{y_{r,1}}^2+{z_{r,1}}^2}$ and $e_{r,2}=\sqrt{{y_{r,2}}^2+{z_{r,2}}^2}$. By defining the radial clearances as $c_i=R_i-R$ and $c_o=R_b-R_o$ the eccentricity ratios are defined for the inner films as $\varepsilon_{i,1}=e_1/c_{i,1}$, $\varepsilon_{i,2}=e_2/c_{i,2}$, and for the outer films as $\varepsilon_{o,1}=e_{r,1}/c_{o,1}$, $\varepsilon_{o,2}=e_{r,2}/c_{o,2}$. The problem is considered to be dynamic and the journal and the ring are supposed to execute any planar trajectories inside the clearance area of each film; the inner and outer eccentricity rate of change at the bearing #1is defined as in equation (16) and at the bearing #2 as in equation (17).

$$\dot{e}_1=\left(\left(y_{s,1}-y_{r,1}\right)\left(\dot{y}_{s,1}-\dot{y}_{r,1}\right)+\left(z_{s,1}-z_{r,1}\right)\left(\dot{z}_{s,1}-\dot{z}_{r,1}\right)\right)/e_1,\qquad \dot{e}_{r,1}=\left(y_{r,1}\dot{y}_{r,1}+z_{r,1}\dot{z}_{r,1}\right)/e_{r,1} \quad (16)$$

$$\dot{e}_2=\left(\left(y_{s,2}-y_{r,2}\right)\left(\dot{y}_{s,2}-\dot{y}_{r,2}\right)+\left(z_{s,2}-z_{r,2}\right)\left(\dot{z}_{s,2}-\dot{z}_{r,2}\right)\right)/e_2,\quad \dot{e}_{r,2}=\left(y_{r,2}\dot{y}_{r,2}+z_{r,2}\dot{z}_{r,2}\right)/e_{r,2} \quad (17)$$

The rate of change of the attitude angle, see Figure 2, of the inner and outer films are defined in equation (18) for the bearing #1 and in equation (19) for the bearing #2.

$$\dot{e}_1=\left(\left(y_{s,1}-y_{r,1}\right)\left(\dot{y}_{s,1}-\dot{y}_{r,1}\right)+\left(z_{s,1}-z_{r,1}\right)\left(\dot{z}_{s,1}-\dot{z}_{r,1}\right)\right)/e_1,\qquad \dot{e}_{r,1}=\left(y_{r,1}\dot{y}_{r,1}+z_{r,1}\dot{z}_{r,1}\right)/e_{r,1} \quad (18)$$

$$\dot{e}_2=\left(\left(y_{s,2}-y_{r,2}\right)\left(\dot{y}_{s,2}-\dot{y}_{r,2}\right)+\left(z_{s,2}-z_{r,2}\right)\left(\dot{z}_{s,2}-\dot{z}_{r,2}\right)\right)/e_2,\quad \dot{e}_{r,2}=\left(y_{r,2}\dot{y}_{r,2}+z_{r,2}\dot{z}_{r,2}\right)/e_{r,2} \quad (19)$$

The rotating speed of the rings is defined as $\Omega_{r,1}=\dot{\vartheta}_1$ and $\Omega_{r,2}=\dot{\vartheta}_2$,

and then the effective rotating speed on each of the four fluid films can be defined as in equation (20) for the inner and the outer films.

$$\begin{aligned}&\Omega_{eff,i,1}=\Omega+\Omega_{r,1}-2\dot{\varphi}_{i,1}, && \Omega_{eff,i,2}=\Omega+\Omega_{r,2}-2\dot{\varphi}_{i,2}\\ &\Omega_{eff,o,1}=\Omega_{r,1}-2\dot{\varphi}_{o,1}, && \Omega_{eff,o,2}=\Omega_{r,2}-2\dot{\varphi}_{o,2}\end{aligned} \quad (20)$$

In a fluid film consisted of two cylindrical surfaces of finite length (journal and bearing), see Figure 2, let c be the radial clearance, e the eccentricity, μ the dynamic viscosity of the lubricant, Ω_{eff} the effective rotational speed in the fluid film, L_b the length of the fluid film, and R the smallest of the radius of the surfaces that consist each of the fluid film; then, the fluid film thickness with respect to the angular coordinate θ of the film of consideration is defined as $h=c+e\cos(\theta)$ and the developed pressure distribution $P(x,\theta)$ of the lubricant through the coordinates θ and x, see Figure 2, will be given from the analytical solution of the Reynolds equation written as in equation (21).

$$\frac{h^3}{\mu R^2}\frac{\partial P^2(x,\theta)}{\partial\theta^2}-\frac{3eh^2\sin(\theta)}{\mu R^2}\frac{\partial P(x,\theta)}{\partial\theta}+\frac{h^3}{\mu}\frac{\partial P^2(x,\theta)}{\partial x^2}==12\dot{e}\cos(\theta)-6e\Omega_{eff}\sin(\theta) \quad (21)$$

Referring to the recent achievement of the analytical solution of the Reynolds equation for the plain cylindrical journal bearing [14, 15], only the milestones of the analytical procedure will presented at this section. The procedure affords one fluid film and the definitions of the paragraph above will be used.

The solution of the Reynolds equation $P(x,\theta)$ is expressed as the sum of a particular solution of the Reynolds, $u(x,\theta)$, and of the solution of the homogenous Reynolds, $g(x,\theta)$, as $P(x,\theta)=u(x,\theta)+g(x,\theta)$ [14, 15].

The particular solution will be given using the additive separation of variables and the homogenous solution will be given using the multiplicative separation of variables. Thus, the particular solution $u(x,\theta)$ is expressed as the sum of the single variable functions $\Psi(x)$ and $\Phi(\theta)$, $u(x,\theta)=\Psi(x)+\Phi(\theta)$ while the homogenous solution $g(x,\theta)$ is expressed as the product of the single variable functions $m(x)$ and $f(\theta)$, as $g(x,\theta)=m(x)f(\theta)$. In this way the Reynolds equation is separated in four Sturm-Liuville problems as in Eqs. (22-25) [14, 15].

$$\frac{1}{R^2}\frac{d^2\Phi(\theta)}{d\theta^2}+\frac{3}{R^2}\frac{1}{h}\frac{dh}{d\theta}\frac{d\Phi(\theta)}{d\theta}-\left(\frac{6\mu\Omega_{eff}}{h^3}\frac{dh}{d\theta}+\frac{12\mu}{h^3}\frac{dh}{dt}\right)=0,\ \Phi(0)=\Phi(2\pi)=0 \tag{22}$$

$$\frac{d^2\Psi(x)}{dx^2}=0,\ \ \Psi(-L_b/2)=\Psi(L_b/2)=0 \tag{23}$$

$$\frac{d^2m(x)}{dx^2}=k^2m(x),m(-L_b/2)=m(L_b/2)=1,k\in\mathbf{R}^* \tag{24}$$

$$\frac{d^2f(\theta)}{d\theta^2}+\frac{3}{h}\frac{dh}{d\theta}\frac{df(\theta)}{d\theta}+k^2R^2f(\theta)=0,\ f(0)=f(2\pi)=0,k\in\mathbf{R}^* \tag{25}$$

The first ODE in equation (22) has direct analytical solution [18], the second ODE in equation (23) is chosen to have the trivial solution $\Psi(x)\equiv 0$ [14-16], the third ODE in equation (24) has direct analytical solution [18]. The fourth ODE in equation (25) does not have direct analytical solution and regarding its solution, approximate analytical [19-21] or semi-analytical [22], the solution of the Reynolds is defined similarly [14-16]. Using a linear approximation for the fluid film thickness function the ODE in equation (22) has a direct analytical solution using Bessel's functions [14-16] (approximate analytical solution) while using the exact fluid film thickness function and a numerical solution (e.g. finite difference method) the solution is defined as exact semi-analytical. The detailed definitions of the problems, the sequence of evaluations and various results regarding the pressure distribution profile, static and dynamic characteristics and operational parameters of the bearing can be found in recent literature [14-16].

4 RESULTS AND POST-PROCESSING

A rotor-bearing system of high speed, taken from applications of automotive turbochargers, is analysed in this section. The geometric configuration is described in main dimensions in Figure 3. In such systems only a slight change in their dimensions and especially in the dimensions of the bearings can yield far different results regarding the instability response. The system is supposed to have an ending speed of 171900RPM (2865Hz) in real

conditions of operation. The detailed geometrical and physical configuration of the system is presented in Table 1.

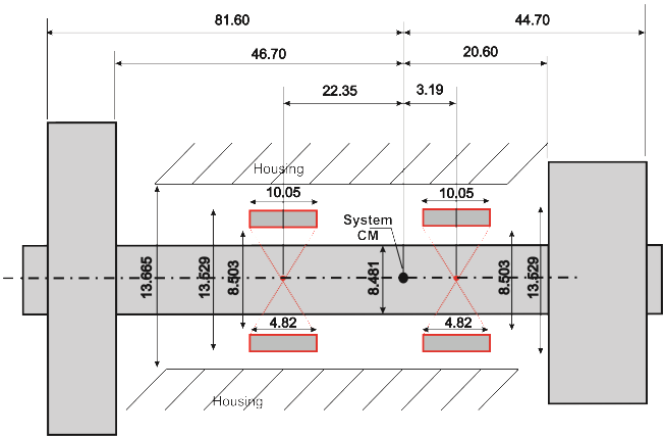


Figure 3: Basic dimensions of the high-speed rotor-bearing system, in mm.

Rotor	Bearing #1	Bearing #2
$M = 0.246$kg	$c_{i,1} = 34$e-6m	$c_{i,2} = 34$e-6m
$J_P = 36.47$e-6kgm^2	$c_{o,1} = 68$e-6m	$c_{o,2} = 68$e-6m
$J_T = 524.26$e-6kgm^2	$m_1 = 0.00605$kg	$m_2 = 0.00605$kg
$L_1 = 0.02235$m	$R_1 = 0.0042405$m	$R_2 = 0.0042405$m
$L_2 = 0.00319$m	$R_{i,1} = 0.0042515$m	$R_{i,2} = 0.0042515$m
$\dot{\Omega} = 1800.13$rad/s^2	$R_{o,1} = 0.0067645$m	$R_{o,2} = 0.0067645$m
$\Omega_{max} = 18001.33$rad/s (171900RPM)	$L_{i,1} = 0.00482$m	$L_{i,2} = 0.00482$m
$t_{max} = 10$s	$L_{o,1} = 0.01005$m	$L_{o,2} = 0.01005$m
$U_1 = 0.08160$m	$I_{P,1} = 0.197$e-6kgm^2	$I_{P,2} = 0.197$e-6kgm^2
$U_2 = 0.04670$m	$T_{i,1} = 150$°C	$T_{i,2} = 150$°C
$U_3 = 0.02060$m	$T_{o,1} = 140$°C	$T_{o,2} = 140$°C
$U_4 = 0.04470$m	$\mu_{i,1} = 0.0028$Pas	$\mu_{i,2} = 0.0028$Pas
$u_i = 1$e-7kgm, $i = 1,2,3,4$	$\mu_{o,1} = 0.0033$Pas	$\mu_{o,2} = 0.0033$Pas

Table 1: Definition of the geometric and physical properties of the simulated system

The system is characterized from symmetry in its bearing properties and it is simulated under the following cases for rotor and bearing simulation, described shortly as $\dot{\Omega}$ in Table 2. The system performs a transient run-up under constant rotational acceleration that results to linear speed variation and thus linear driving frequency variation from zero to the ending speed $\Omega_{\max}$ defined in Table 1.

Case	Rotor Model	Bearing model	Bearing Solution
#1	Rigid	Finite length Bearing	Approximate analytical solution - Bessel eigfs.
#2	Rigid	Short bearing approximation	Approximate analytical solution
#3	Rigid	Finite length Bearing	Exact analytical solution - Numer. Eigfs.

Table 2: Definition/description of the cases of simulation for the high-speed rotor-bearing systems

The response time-series are evaluated and post-processed as follows. The vertical response of the rotor at the locations of the bearings is plotted in Figure 4 for the various cases of bearing solution. In Figure 4 there is the first indication of how sensitive is the systems re-

sponse regarding to the bearing simulation and the impedance forces. The approximate analytical and the short bearing approximation (Case #1 and Case#2) produce similar response regarding its progress and its amplitude. The corresponding notification is made also regarding the progress of the eccentricities during the run-up of the system, see Figure 5.

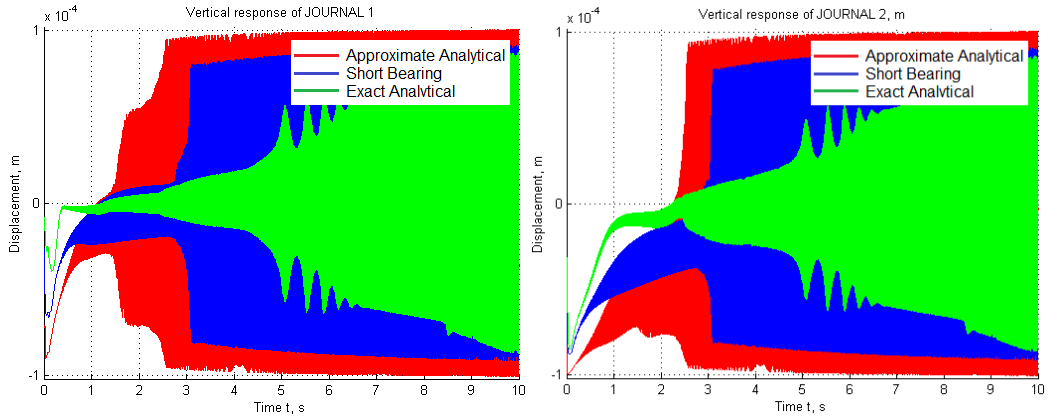


Figure 4: vertical displacement of the journal vs time for the different cases of simulation; left) Bearing #1, and right) Bearing #2

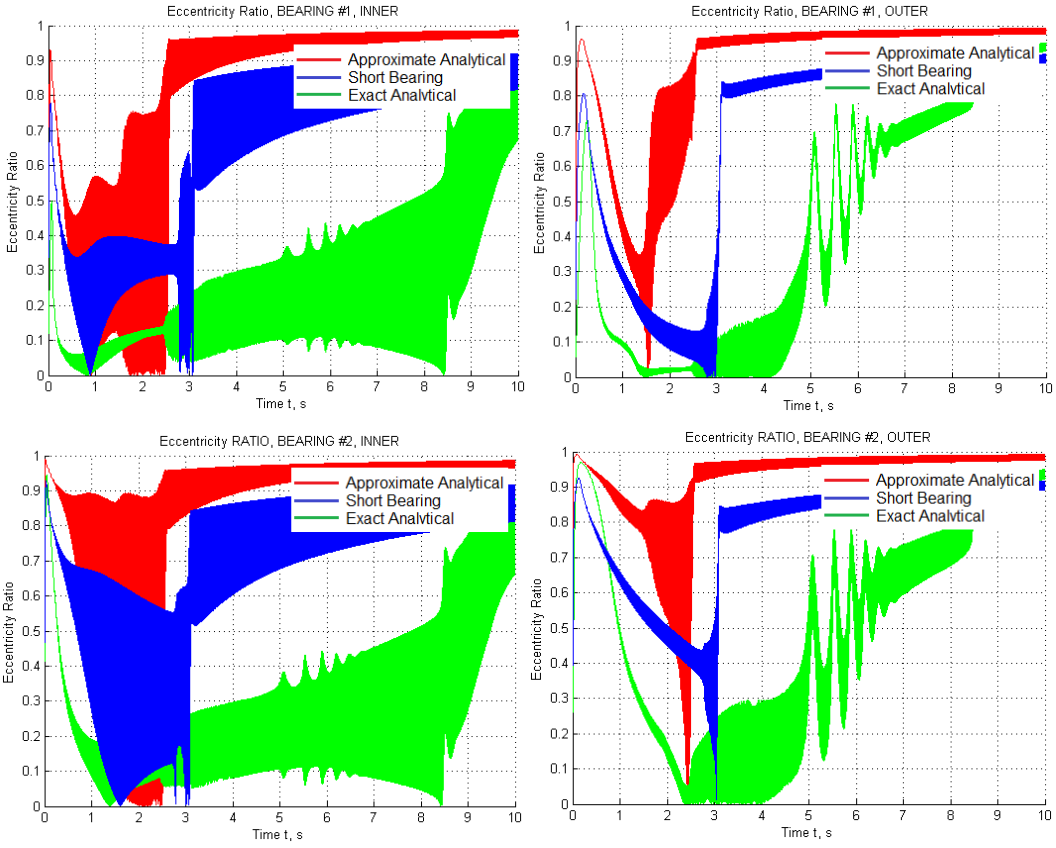


Figure 5: eccentricity ratio vs time for the different cases of simulation; upper left) Bearing #1-inner film, upper right) Bearing #1-outer film, below left) Bearing #2-inner film and below right) Bearing #2-outer film.

Time-Frequency decomposition of the time series of Figure 4 is performed using Short Time Fourier Transform (STFT) and the corresponding spectrograms are plotted in Figure 7. In Figure 4 it is seen that all three simulations present instability and the response amplitude increase with speed/time. The approximate analytical presents the less damping from the outer film and thus the response is presented with higher amplitude than this of short bearing approximation and exact analytical solution. The exact analytical solution yields a response of higher damping and the increment of the amplitude occurs gradually as the speed increases. The threshold of instability occurs later in exact analytical simulation than in the other two simulations that present it similarly in time between 2nd and 3rd second during the run-up.

The significant for the design parameter of bearing eccentricity is evaluated and plotted in Figure 5. The progress of eccentricity declares clearly the thresholds of instability in the approximate analytical and short bearing solution. The ring speed, which is plotted in Figure 6, gradually increases up to a certain value and after the instability occurs, it 'locks' in relative constant value in the cases of approximate analytical and short bearing simulation while the exact analytical yields relatively similar progress up to when the instability occurs.

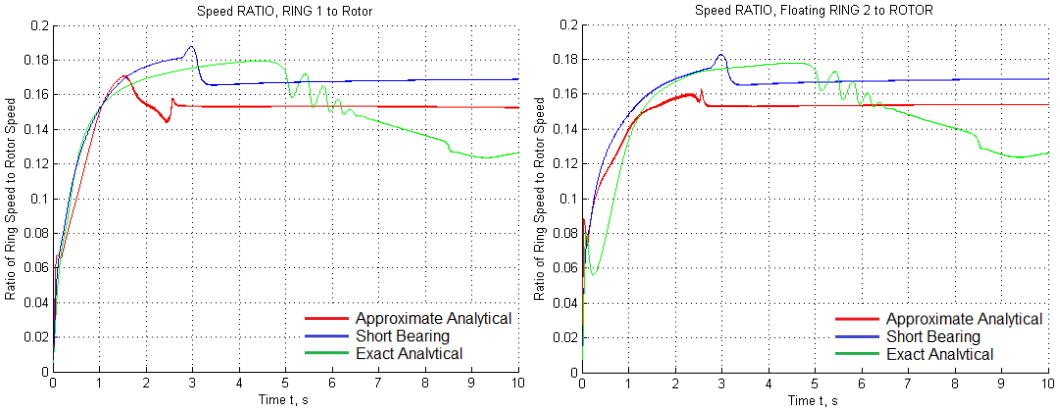


Figure 6: ratio of the speed of the floating ring to the rotor's speed vs time for the different cases of simulation; left) Bearing #1 and right) Bearing #2

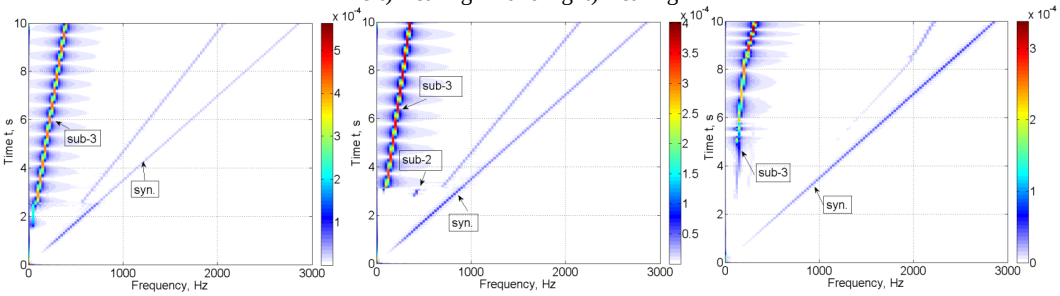


Figure 7: Time-Frequency decomposition using STFT of the transient response of the journal of Bearing #1 for the simulation of upper left) Case #1, upper right) Case #2, below left) Case #3 and below right) Case #4.

In Figure 7, the time-frequency analysis presents the developed sub-3 component near the 2nd second in the approximate analytical, near the 3rd second in the short bearing approximation, and near the 4th second in the exact analytical simulation. With the time-frequency analysis the occurrence of instability is declared clearly regarding time and frequency; the amplitude of the sub-3 component is of similar value among the cases of simulation. The synchronous components are also clearly presented.

5. CONCLUSIONS

The investigation of the high-speed rotordynamics on a turbosystem under three different solutions for the floating-ring bearings declared that the bearing forces and their model are of significant importance and have decisive role in the design of a turbosystem regarding its amplitude of response and the instability threshold. There are also investigated cases of the turbosystem geometry that yielded totally different dynamic behavior among the different cases of bearing simulation, e.g. different sub-components may occur for each case of bearing simulation. As an outcome, the turbosystem rotordynamics may differ significant among the different bearing models. The recent achievement of the exact analytical solution of the Reynolds equation results in relatively different response compared to approximate analytical bearing models that were found in relative agreement.

ACKNOWLEDGMENT

This work was performed during the activity of the author in the research and development of turbosystems in the company BorgWarner Turbosystems GmbH. The author would like to thank Dr. Dimitrios Sfyris (Foundation for Research and Technology - Hellas) for his valuable contribution in the analytical solution of the Reynolds Equation for the finite floating-ring bearing and Dr. Panagiotis Koutsovasilis (BorgWarner Turbosystems GmbH - Germany) for the valuable discussions in turbosystem rotordynamics.

REFERENCES

[1] Schweizer, B.; Sievert, M.: Nonlinear oscillations of automotive turbocharger turbines, Journal of Sound and Vibration, Vol. 321, pp. 955-975, 2009.

[2] Schweizer, B.: Oilwhirl, oilwhip and whirl/whip synchronization occurring in rotor systems with full-floating ring bearings. Journal of Nonlinear Dynamics doi:10. 1007/s11071-009-9466-3 (2009)

[3] Schweizer, B.: Total Instability of Turbocharger rotors-Physical Explanation of the Dynamic Failure of Rotors with Full-Floating Ring Bearings, Journal of Sound and Vibration, Vol. 328, No. 1-2, pp. 156-190, 2009.

[4] Schweizer, B.: Dynamics and Stability of Turbocharger Rotors. Archive of Applied Mechanics, Vol. 80, No. 9, pp. 1017-1043, 2010.

[5] Tatara, A.: Vibration suppressing effect of floating bush bearings. Report of the Research Group of High-Speed Rotating Machinery. J. JSME **72**, 1565–1569 (1969)

[6] Tanaka, M., Hori, Y.: Stability characteristics of floating bush bearings. ASME J. Lubr. Technol. **94** 248–259 (1972)

[7] Hatakenaka, K., Tanaka, M., Suzuki, K.: A theoretical analysis of floating bush journal bearing with axial oil film rupture being considered. ASME J. Tribol. **124**, 494-505 (2002)

[8] Seemann,W., Proppe, C., Knoll, G.: Multibody run-up simulation of turbocharger rotors with nonlinear modeled floating ring bearings. Report No. R 542 Research Association Engine/Turbomachinery, Semi-Annual Congress Spring 2008, Frankfurt am Main (Germany) (2008)

[9] Koutsovasilis, P., Driot, N., Lu, D., Schweizer, B.: Quantification of sub-synchronous vibrations for turbocharger rotors with full-floating ring bearings. Archive of Applied Mechanics. DOI 10.1007/s11071-008-9403-x (2014)

[10] Chen, W.J., Gunter, E.: Introduction to dynamics of rotor-bearing systems. RODYN vibration analysis Inc. Charlottesville, Virginia (US)(2005)

[11] Adiletta, G., Guido, A.R., Rossi, C.: Chaotic motions of a rigid rotor in short journal bearings Nonlinear Dynamics 10, 251-269 (1996)

[12] Adiletta, G., Guido, A.R., Rossi, C.: Nonlinear Dynamics of a Rigid Unbalanced Rotor in Journal Bearings. Part I: Theoretical Analysis. Nonlinear Dynamics 14, 57-87 (1997)

[13] Trippett, R., Li, D.: High-speed floating-ring bearing test and analysis. ASLE Trans. **27** (1), 73–81 (1984)

[14] Sfyris, D., Chasalevris, A.: An exact analytical solution of the Reynolds equation for the finite journal bearing. Tribology International 55, 46-58 (2012)

[15] Chasalevris, A., Sfyris, D.: Evaluation of the Finite Journal Bearing Characteristics Using the Exact Analytical Solution of the Reynolds Equation. Tribology International 57, 216-234 (2013)

[16] Chasalevris, A.: Analytical Evaluation of the Static and Dynamic Characteristics of the Three-Lobe Journal Bearing with Finite Length. ASME Journal of Tribology, doi: 10.1115/1.4030023 (2015)

[17] Yamamoto, T., Ishida, Y.: Linear and nonlinear rotordynamics. John Wiley and Sons Inc., New York (US) (2001)

[18] Polyanin, A., Zaitsev, V.: Handbook of exact solutions for ordinary differential equations. Chapman & Hall/CRC (2003)

[19] Vogelpohl, G.: Zur Integration der Reynoldschen Gleichung für das Zapfenlager endlicher Breite. Ingenieur Archiv (1943). (In German)

[20] Vogelpohl, G.: Beiträge zur Kenntnis der Gleitlagerreibung. VDI-Forsch.-Heft 386, 3-5 (1937) (In German)

[21] Michell, A.: Progress in Fluid film lubrication. Trans. ASME MSP-51-21, 51, 153-163 (1929)

[22] Chasalevris, A.: Evaluation of the Floating Ring Bearing Characteristics Using Analytical Methods. Proceedings of the International Conference on Engineering Vibration, ICOEV, Ljubljana, Slovenia, 2015.

Vibration Control and Isolation (TP14)

International Conference on Engineering Vibration
Ljubljana, Slovenia, 7-10 September 2015

ON THE REMOVAL OF BREAK SQUEAL BY TUNED MASS DAMPERS

Simon Gekeler, Oskar Glück, Ashish Srivastava, Rolf Steinbuch

Reutlingen University, Reutlingen Germany

Simon.Gekeler@Reutlingen-University.DE
Oskar.Glück@Student.Reutlingen-University.DE
Ashish.Srivastava@Reutlingen-University.DE
Steinbuch@Reutlingen-University.DE

Keywords: brake squeal reduction, Tuned Mass Dampers, cooling channel, adaption, optimization.

Abstract. *Break squeal is one of the most disruptive noises produced especially by upper class vehicles. The non-symmetric contact between pads and disc excites resonant frequencies of the disc, producing a shrill sound which is unacceptable to most drivers. Methods for reducing break squeal without major alterations to the axis geometry must reduce the stiffness and the forces acting on the vibration system. However, these reductions severely decrease brake performance.*

Tuned Mass Dampers are a broadly accepted tool to reduce unwanted vibrations. The additional masses of the Tuned Mass Dampers are coupled via a defined stiffness to the vibrating system, such that excited parts will transmit their energy to the damper. To reduce the break squeal problem the masses must be applied to the rotating disk without contacting the pads. As many modern break discs are supplied with cooling channels the dampers could be placed into some of them. A set of such dampers could be designed to cover the range of critical frequencies over the lifetime of the disc. A problem of this design lies in the limited mass of dampers able to be placed into the cooling channels. Furthermore, the reduction of the flow of air through the channels may cause local deformations.

The basic principle is outlined, design proposals are demonstrated and applications shown. The idea may help to reduce break squeal, or even remove it entirely.

International Conference on Engineering Vibration
Ljubljana, Slovenia, 7-10 September 2015

TECHNIQUE TO OVERCOME PIEZO STACK ACTUATOR SATURATION USING PARALLEL STIFFNESS COMBINATION FOR AN ACTIVE SUSPENDED HANDLE

Ahmad Zhafran Ahmad Mazlan*[1] and Zaidi Mohd Ripin[2]

[1,2] The Vibration Lab, School of Mechanical Engineering, Universiti Sains Malaysia, 14300 Nibong Tebal, Pulau Pinang, MALAYSIA
[1]zulryan_85@yahoo.com, [2]mezaidi@usm.my

Keywords: Active Suspended Handle, Parallel Stiffness Combination, PID Controller, Piezo Stack Actuator, Die Grinder.

Abstract. *This paper presents a technique to overcome piezo stack actuator saturation using parallel stiffness combination (PSC) based on the deflection shape of an active suspended handle. Three types of stiffness are designed at the center, center-end and at the end of the lower handle structure to strengthen the active area of piezo stack actuator. The combination of these stiffness show a significant improvement of the structure by shifting the modes of the structure outside of the operating frequency range of an active suspended handle. The PSC is realized in the form of material modification for the actual active suspended handle with an equal total stiffness value. Experimental modal analysis is carried out to validate the model of the modified active suspended handle. A real-time proportional-integral-derivative (PID) controller is developed to provide a counter voltage for the active vibration control (AVC) system. Using this technique, the effective frequency range of isolation is improved and reduced the vibration transmissibility of the handle. The modified active suspended handle is then attached to a die grinder to prove its effectiveness.*

1 INTRODUCTION

Structural dynamic modification (SDM) is generally applied for an improvement of a structure. It is a technique where the dynamic properties of the structure are modified, as a prediction to the physical structure alteration. The modified parameters including mass [1], damping [2], stiffness [2] and the addition of dynamic vibration absorber (DVA) [3]. The main reason of using SDM is because of unsatisfied dynamic characteristic of the structure such as natural frequencies, undesired vibration response and dynamic instability of the structure. SDM has been widely applied in automotive and power tools applications. For example, two types of stiffeners are added to the brake shoe of the vehicle to eliminate the brake squeal noise [2] and DVA is applied to the grass trimmer shaft to reduce the transmitted vibration to the operator [3]. Not limited to the passive vibration control application, some SDM method such as DVA has also been applied to improve the performance of an active vibration control (AVC) system [4-5].

In AVC system, actuator selection is a main criterion that needs to be decided. There are many type of actuators can be used such as hydraulic, electromagnetic and piezoelectric actuators [6-8]. Hydraulic actuator is working on the basis of fluid that translated into a mechanical movement, while electromagnetic actuator provides a mechanical movement due to the internal electromagnetic field such as solenoid. Both can produced high force and displacement, but only effective at low frequency range [7]. Piezoelectric actuator is known for their compact size, high frequency response and high stiffness, but limited by displacement [8]. The limitation of piezoelectric actuator displacement can contribute to the non-linear saturation if it is mounted in parallel or series with the structure [9-10]. SDM is one of the technique that can improved the performance of the AVC system, but rarely been studied to overcome the piezoelectric actuator saturation. A minor modification of the structure will allow a reduction in term of operating voltage for the piezoelectric actuator. Basically, when the amplitude of the vibrating structure is reduced, the necessary voltage needed to counteract the vibration will wane, and at the same time can produce a better vibration reduction for the structure.

This study investigates the effectiveness of using SDM technique in overcoming piezo stack actuator saturation for an active suspended handle. This approach is novel since this is the first time the SDM using parallel stiffness combination (PSC) is applied together with the AVC in attenuating the vibration of the suspended handle. The PSC is realized in the form of material modification of the lower handle structure for an actual active suspended handle. Experimental modal analysis is carrying out to validate the predicted frequency response function (FRF). A real time PID controller is designed to generate a counter voltage for the piezo stack actuator in attenuating the vibration transmitted to the handle. A new effective frequency range for the modified active suspended handle is determined and compared. A die grinder is chosen as an apparatus to demonstrate the performance of the modified active suspended handle.

2 DESIGN OF AN EXISTING ACTIVE SUSPENDED HANDLE

Figure 1(a) shows the design of an existing active suspended handle with parallel coupled piezo stack actuator [11]. From Figure 1(a), the active suspended handle consists of two main parts; handle and moving base. Two springs are mounted in the handle to preload the piezo stack actuator (P-010.00) and the load cell is placed on top of the actuator to measure the force $F_a(t)$.Since the piezo stack actuator is mounted in parallel with the springs and handle, the displacement saturation effects of the actuator must be considered. The equation of motion

of the active suspended handle in Figure 1(a), with a non-linear saturation effect of the piezo stack actuator can be written as:

$$m\ddot{x}_1(t) + c(\dot{x}_1 - \dot{x}_0)(t) + k(x_1 - x_0)(t) = F_a(t) \quad (1)$$

$$\text{Where, } x_1(t) - x_0(t) \geq x_{asat}(t); F_{asat}(t) = \alpha_{(V,f)} V_{asat}(t)$$

From Eq. (1), m, c and k are the mass, damping and stiffness of the handle. When the displacement difference of the handle $x_1(t)$ and the base $x_0(t)$ is equal or exceeded the maximum actuator displacement $x_{sat}(t)$, the system is saturated including the force $F_{a\,sat}(t)$ and the voltage $V_{a\,sat}(t)$.

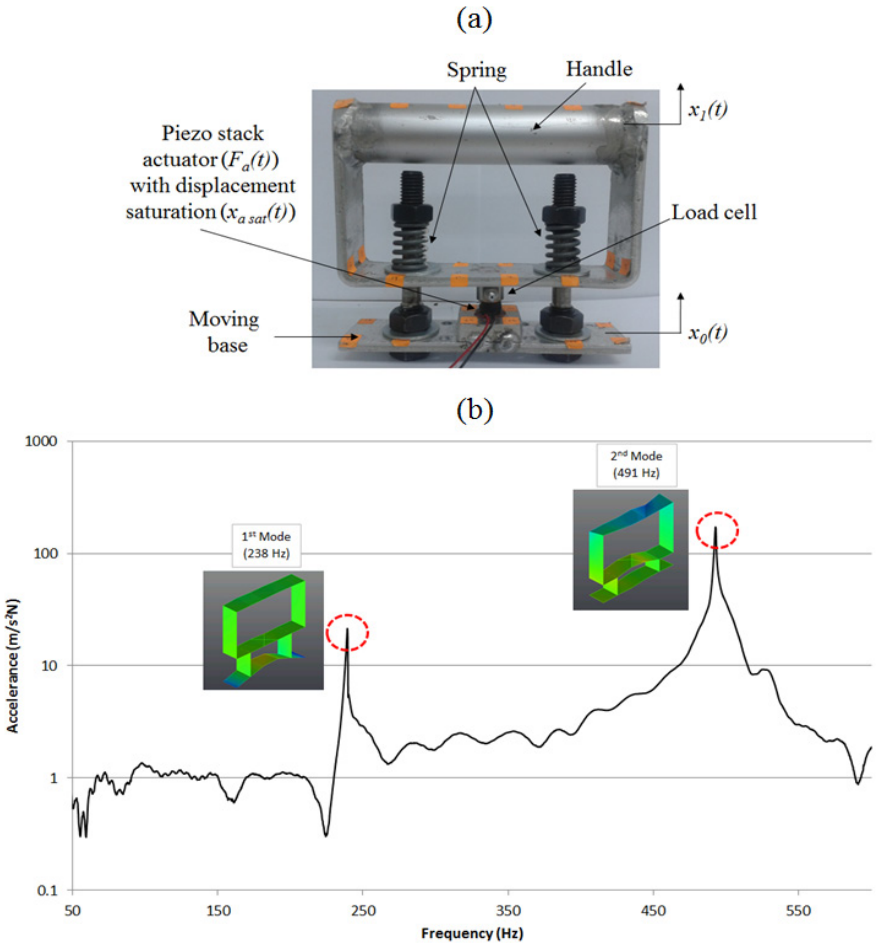


Figure 1: (a) Design of existing active suspended handle [11] and (b) Experimental FRF of the active suspended handle.

Figure 1(b) shows the measured accelerance FRF including the mode shapes of the active suspended handle. From the figure, there are two modes at 238 Hz and 491 Hz for the frequency range between 50 ~ 500 Hz. At the first mode (238 Hz), there is a bending of the base while at the second mode (491 Hz), the whole suspended handle is deformed. In this case, the second mode is more dominant with a higher accelerance FRF output. Since the active suspended handle will be operated within this frequency range, there is a possibility that the

piezo stack actuator will be saturated at these two natural frequencies because of the large displacement difference between the handle and the base [11]. SDM is one of the solutions that can be applied to overcome this phenomenon.

3 SDM TO OVERCOME PIEZO STACK ACTUATOR SATURATION

3.1 Theory to overcome piezo stack actuator saturation

Figure 2 shows the theory to overcome the piezo stack actuator non-linear saturation using the SDM method.

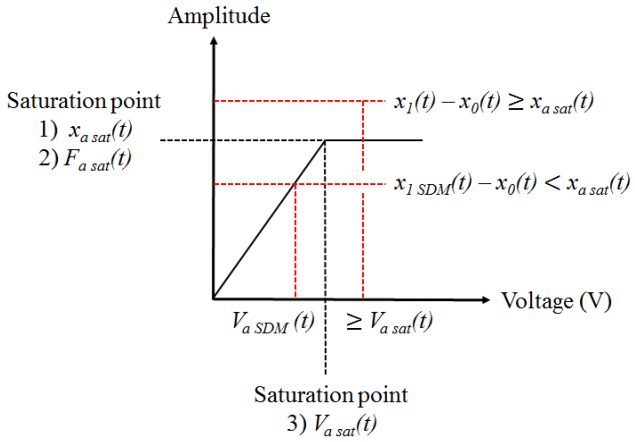


Figure 2: Theory to overcome piezo stack actuator non-linear saturation.

From the figure, the implementation of the SDM method can reduce the displacement produced by the handle x_{1SDM} well below the maximum displacement of the piezo stack actuator. As shown Figure 2, the effect of SDM to the condition in Eq. (1) can be rewritten as:

$$x_{1SDM}(t) - x_0(t) < x_{asat}(t); F_{aSDM}(t) = \alpha_{(V,f)} V_{aSDM}(t) \tag{2}$$

Where, $x_{1SDM}(t)$ and $F_{a\,SDM}(t)$ are the displacement and force produced by the modified (SDM) handle with the respect of supplied voltage $V_{a\,SDM}(t)$.

3.2 Parallel stiffness combination (PSC)

The SDM prediction is carried out using LMS software based on the mode shapes of the active suspended handle in Figure 1(b). The SDM is focused at the lower handle structure to strengthen the active area of the piezo stack actuator. Figure 3(a) shows the SDM prediction at the lower handle using stiffness modification method [2] and Figure 3(b) shows the modified active suspended handle model in LMS software. From Figure 3(a), there are three main core stiffness combination of $\mathbf{\Delta K_1}$, $\mathbf{\Delta K_2}$ and $\mathbf{\Delta K_3}$ at the centre, centre-end and at the end of the lower handle. These core stiffness are then combined in parallel to produce another stiffness of $\mathbf{\Delta K_4}$, $\mathbf{\Delta K_5}$, $\mathbf{\Delta K_6}$ and $\mathbf{\Delta K_7}$. The detail components of each stiffness can be written as:

$$\mathbf{\Delta K_1} = \begin{bmatrix} k_1 & k_2 \\ k_3 & k_4 \end{bmatrix}, \mathbf{\Delta K_2} = \begin{bmatrix} k_5 & k_6 \\ k_7 & k_8 \end{bmatrix}, \mathbf{\Delta K_3} = \begin{bmatrix} k_9 & k_{10} \\ k_{11} & k_{12} \end{bmatrix}, \mathbf{\Delta K_4} = \mathbf{\Delta K_1} + \mathbf{\Delta K_2}, \mathbf{\Delta K_5} = \mathbf{\Delta K_1} + \mathbf{\Delta K_3}$$

$$\mathbf{\Delta K_6} = \mathbf{\Delta K_2} + \mathbf{\Delta K_3}, \mathbf{\Delta K_7} = \mathbf{\Delta K_1} + \mathbf{\Delta K_2} + \mathbf{\Delta K_3} \tag{3}$$

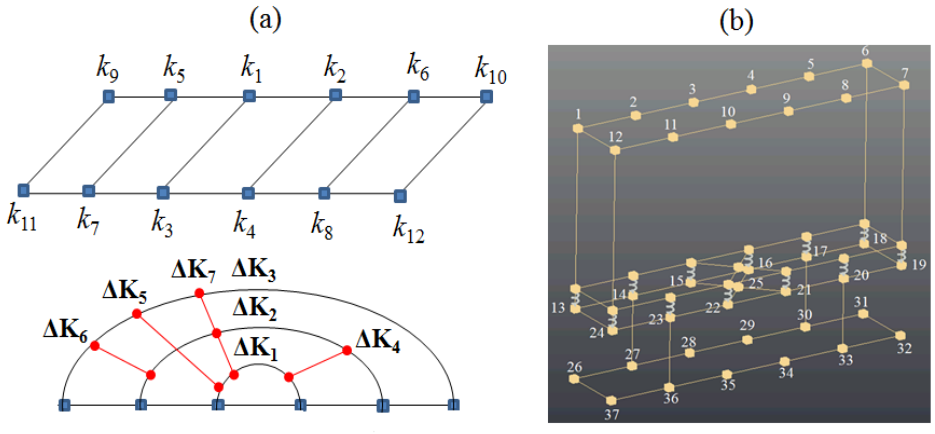


Figure 3: (a) Stiffness modification at lower handle and (b) modified active suspended handle in LMS software.

Table 1 shows the shifted natural frequencies and the damping ratio for stiffness $\mathbf{\Delta K_1}$ ~ $\mathbf{\Delta K_7}$. Generally, the addition of stiffness has significantly shifted the natural frequency of the active suspended handle above 500 Hz.

Stiffness	Type	Natural frequency, f_n (Hz)	Damping ratio, ζ (%)
$\mathbf{\Delta K_1}$	Core	495	0.39
$\mathbf{\Delta K_2}$		501	0.14
$\mathbf{\Delta K_3}$		515	1.91
$\mathbf{\Delta K_4}$	Parallel	504	0.29
$\mathbf{\Delta K_5}$		518	2.04
$\mathbf{\Delta K_6}$		523	1.78
$\mathbf{\Delta K_7}$		529	1.90

Table 1: Shifted natural frequencies and damping ratio from the SDM prediction.

From Table 1, the core stiffness $\mathbf{\Delta K_3}$ produced the largest shifted frequency of 515 Hz with increased damping ratio of 1.91 %. Meanwhile, for $\mathbf{\Delta K_1}$ and $\mathbf{\Delta K_2}$, there were small effects on the natural frequencies which $\mathbf{\Delta K_2}$ reduced the damping ratio to 0.14 %. For the parallel combined stiffness, $\mathbf{\Delta K_5}$ increased the damping ratio up to 2.04 %, but there was only 3 Hz of frequency difference compared to core stiffness $\mathbf{\Delta K_3}$. The combination of all core stiffness can shift the natural frequency wider to 529 Hz with damping ratio of 1.90 %, as shown by $\mathbf{\Delta K_7}$. From this result, all core stiffness play an important role in completing the modification of the suspended handle with $\mathbf{\Delta K_3}$ gives the most significant effect since it will strengthen the connection of the lower-upper handle.

3.3 SDM Implementation

Figure 4(a) shows the design of the modified active suspended. From Eq. (3), the PSC of $\mathbf{\Delta K_7}$ is designed at the lower handle structure, as shown in Figure 3(b). This is then translated to the material modification of the lower handle structure with an equal total stiffness value of 3 x 10^6 N/m, as shown in Figure 4(a). The aluminium lower handle in previous suspended handle is replaced with a mild steel material, which mounted at both sides of the handle. This translation gives a significant contribution for the suspended handle in terms of maintaining

overall handle shape and increased structural strength with a reduction of material thickness by 2 mm.

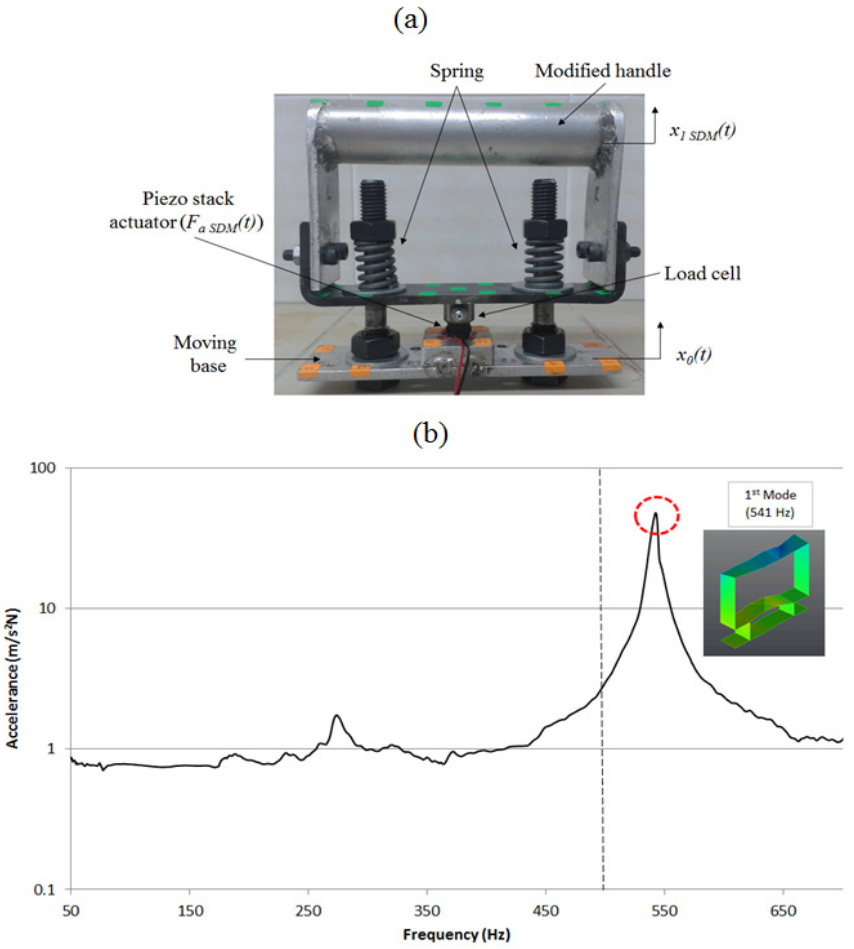


Figure 4: (a) Design of modified active suspended handle and (b) Experimental FRF of the modified active suspended handle.

Figure 4(b) shows the measured accelerance FRF including the mode shape of the modified active suspended handle. From the figure, the implementation of the new lower handle to the active suspended handle has shifted the natural frequency to 541 Hz with a damping ratio of 0.52 %. It can also be observed that the experimental and predicted $\mathbf{\Delta K_7}$ natural frequencies are closed to each other with percentage difference of 2.2 %. From this result, the purpose of shifting the natural frequencies of the active suspended handle outside the operating frequency range of 50 ~ 500 Hz is realized.

4 AVC EXPERIMENT AND RESULTS

4.1 Acceleration transmissibility measurement of modified active suspended handle

Figure 5 shows the schematic diagram of an experiment to measure the acceleration transmissibility of the modified active suspended handle.

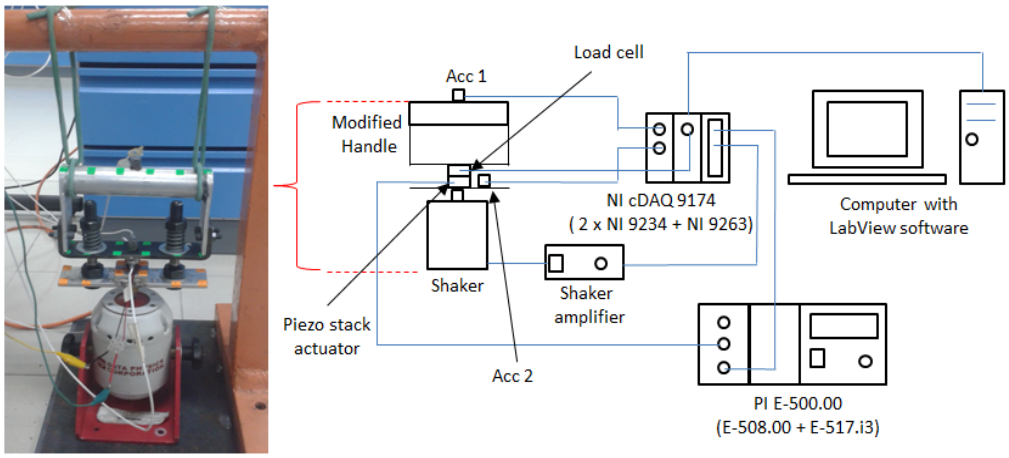


Figure 5: Experimental setup for modified active suspended handle

From Figure 5, a frequency dependent sine wave signal of 50 ~ 500 Hz is generated from the LabView software to the shaker through the NI 9263 module and the shaker amplifier. Two accelerometers (1 and 2) are mounted on the handle and the base to measure the vibration transmissibility of the active suspended handle and the data is sent to the computer through NI 9234 module for analyses. A real time PID controller is developed in the LabView software to produce a counter voltage signal to the piezo stack actuator. This signal is amplified by E-508.00 piezo amplifier and display E-517 is used to monitor the voltage.

4.2 Experimental results and discussion

Figure 6(a) shows the acceleration transmissibility of an existing and the modified active suspended handles.

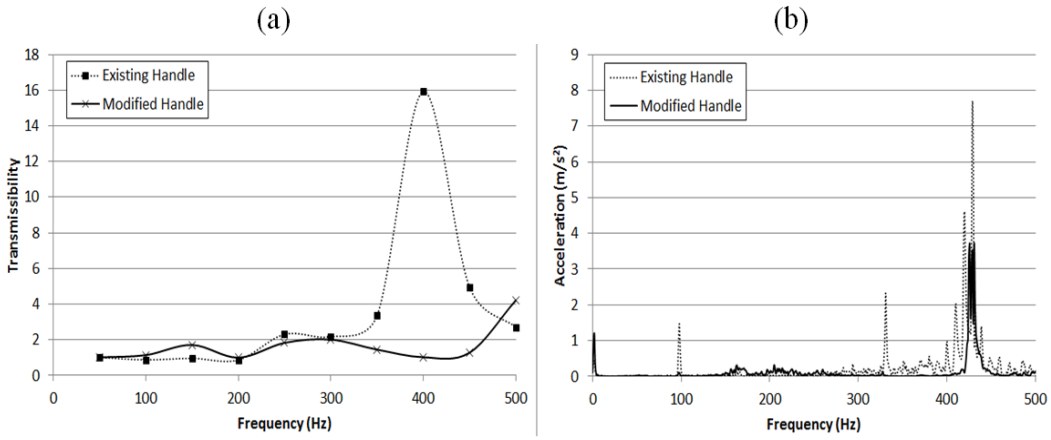


Figure 6: (a) Acceleration transmissibility and (b) Performance of an existing and modified active suspended handle mounted on a die grinder

From Figure 6(a), the acceleration transmissibility of an existing active suspended handle is slightly low at frequency below 200 Hz. The first peak of transmissibility is shown at frequency 250 Hz, which near to the first natural frequency (238 Hz) of the handle, as shown

previously in Figure 1(b). The acceleration transmissibility continues to increase and the maximum transmissibility occurred at frequency 400 Hz (15.9) [11]. At this frequency, the displacement difference between the base and handle is high, which contribute to the saturation of piezo stack actuator. For the case of modified active suspended handle, there is no significant effect at the frequency below 300 Hz compared to the existing active suspended handle. However, there is a large transmissibility reduction between 300 Hz to 480 Hz with the lowest transmissibility occurred at 400 Hz (1.03). At this frequency, the acceleration transmissibility of the active suspended handle reduced by 93 %.

Both existing and modified active suspended handles are mounted to the die grinder with rotating speed of 25000 rpm (416 Hz) to prove the effectiveness of the handle. This power tool is chosen based on the effective frequency range of the modified active suspended handle. Figure 6(b) shows the comparison of acceleration frequency response for both handles. At the operating frequency of 416 Hz, the transmitted acceleration is reduced from 7.7 m/s^2 to 3.6 m/s^2 by using the modified active suspended handle. This shows about 53 % of vibration reduction compared to the existing active suspended handle and the effectiveness of the SDM method to the active suspended handle is proven.

5 CONCLUSIONS

- The existing design of an active suspended handle produced two modes (238 Hz and 491 Hz) within the frequency range (50 ~ 500 Hz) which affected the performance of the piezo stack actuator.
- SDM by using PSC method is introduced in this study and successfully shifted out both natural frequencies of the handle outside the operating frequency range with lower accelerance output.
- The PSC is realized in the form of material modification of the lower handle and the experimental validation shows a small error (2.2 %) between them.
- The saturation effect of the piezo stack actuator in the existing active suspended handle is successfully overcome between the frequency range 300 ~ 480 Hz with the lowest transmissibility output (1.03) occurred at 400 Hz.
- The effectiveness of the modified active suspended handle is proven by 53 % of transmitted vibration reduction from the die grinder.

REFERENCES

[1] T. K. Kundra, Structural dynamic modification via models. *Sadhana*, **25**, 261-276, 2000.

[2] M. N. A. Hamid, C. Y. Teoh, Z. M. Ripin, The operational deflection shapes and transient analysis of the brake shoes in drum brake squeal. *Proceedings of the Institution of Mechanical Engineers, Part D: Journal of Automobile Engineering*, **277**, 866-884, 2013.

[3] K. Y. Hao, L. X. Mei, Z. M. Ripin, Tuned vibration absorber for suppression of hand-arm vibration in electric grass trimmer. *International Journal of Industrial Ergonomics*, **41**, 494-508, 2011.

[4] R. Rohling, An active dynamic vibration absorber for a hand-held vibro-elastography probe. *Journal of Vibration and Acoustics*, **129**, 101-112, 2007.

[5] Y. Du, R. A. Burdisso, E, Nikolaidis, Control of internal resonances in vibration isolators using passive and hybrid dynamic vibration absorbers. *Journal of Sound and Vibration*, **286**, 697-727, 2005.

[6] G. Priyandoko, M. Mailah, H. Jamaluddin, Vehicle active suspension system using skyhook adaptive neuro active force control. *Mechanical Systems and Signal Processing*, **23**, 855-868, 2009.

[7] J. W. Sohn, Y. S. Paeng, S. B. Choi, An active mount using an electromagnetic actuator for vibration control: Experimental investigation. *Proceedings of the Institution of Mechanical Engineers, Part C: Journal of Mechanical Engineering Science*, **224**, 1617-1625, 2010.

[8] S. B. Choi, M. S. Seong, S. H. Ha, J. Jeon, J. W. Sohn, Design of a piezostack-based inertial actuator and application to vibration control: Experimental investigation. *Proceedings of the Institution of Mechanical Engineers, Part I: Journal of Systems and Control Engineering*, **225**, 1115-1124, 2011.

[9] L. Zhenming, O. Guangyao, Z. Jiadong, Development of an electromechanical model for piezo actuated common rail injectors. *International Conference on Intelligent Computation Technology and Automation*, ICICTA, Changsha, China, 98-101, 2010.

[10] A. A. Hanieh, A. Preumont, Multi-axis vibration isolation using different active techniques of frequency reduction. *Journal of Vibration and Control*, **17**, 759-768, 2011.

[11] A. Z. A. Mazlan, Z. M. Ripin, Frequency dependent vibration attenuation of a suspended handle using piezo stack actuator. *Applied Mechanics and Materials*, **761**, 211-215, 2015.

11th International Conference on Engineering Vibration
Ljubljana, Slovenia, 7–10 September 2015

A CONTRIBUTION TO THE REDUCTION OF SELF-EXCITED VIBRATIONS OF DYNAMICAL SYSTEMS BY IMPULSIVE PARAMETRIC EXCITATION

T. Pumhoessel*[1]

[1]Institute of Mechatronic Design and Production, Johannes Kepler University Linz, Austria
thomas.pumhoessel@jku.at

Keywords: Impulsive Parametric Excitation, Modal Energy Transfer, Self-Excited Vibrations.

Abstract. *In this paper, the possibilities of reducing self-excited vibrations of dynamical systems by using stiffness excitation of impulsive type are investigated. The self-excitation mechanism is modeled by a linearized Rayleigh approach, describing self-excited vibrations which originate from fluid flows with constant velocity, for example. A stiffness element, which is capable of changing its stiffness value is introduced to affect the dynamical behavior of the mechanical system in a targeted manner. The proposed approach for the reduction of vibrations is based on the theory of impulsive parametric excitation. Therewith, the effect of parametric impulses of Dirac delta type to the modal energy content of mechanical systems can be investigated analytically.*

Self-excited vibrations result in an increasing energy content of a mechanical system. It is shown in this contribution that a proper impulsive parametric excitation, applied in a state-dependent manner, allows to shift kinetic energy from lower, to higher modes of vibration. As higher modes possess enhanced damping properties compared to lower ones, the damping properties of the mechanical system are utilized more effectively. In the theoretical case of applying parametric impulses of Dirac delta type, it is shown that certain states of the mechanical system exist, which allow a modal energy transfer to higher modes where no external energy is required, i.e. the total energy content of the mechanical system remains unchanged. This may results in a stabilization of the otherwise unstable system, which is demonstrated with a numerical example with three degrees of freedom, where the stiffness impulses of Dirac delta type are replaced by rectangular shaped ones.

1 INTRODUCTION

The phenomenon of self-excited vibrations occurs in many fields of engineering. In rotor dynamics, for example, a source of self-excitation is the internal damping of rotor shafts. A well-known reason of self-excitation in civil engineering can be a constant wind flow acting on a structure. As self-excited vibrations lead to increasing vibration amplitudes which may result in a damage or breakdown of structures, they have to be avoided in any case. An interesting possibility to suppress self-excited vibrations was discovered by A. Tondl, see [1]. He investigated mechanical systems with continuous, time-periodic stiffness coefficients and found out that, if the frequency of the stiffness variation is equal or close to certain combinations of the natural frequencies, which he denoted as anti-resonance frequencies, self-excited vibrations can be suppressed. First numerical results about suppressing self-excited rotor vibrations using the anti-resonance effect can be found in [2]. Comprehensive analytical as well as numerical investigations were done by H. Ecker and F. Dohnal, see [3], [4] and [5], for example. From a physical point of view, excitation at anti-resonance frequencies results in a bi-directional energy transfer between participating modes of vibration, see [5, 6, 7], as well as a concentration of the vibrational energy in only a few modes, see [8].
A different strategy for suppressing self-excited vibrations is proposed in this contribution, based on the theory of impulsive parametric excitation, developed by C.S. Hsu, see [9] and [10]. It was shown in [11], and [12] by T. Pumhoessel et al., that stiffness impulses are capable to shift vibration energy from a set of lower modes to a set of higher modes, where in the theoretical case of parametric impulses of Dirac delta type, no external energy is necessary therefore. It will be shown in the following, that applying parametric impulses in a state-dependent manner allows to transfer energy, which was fed to the mechanical system by a self-excitation mechanism, to higher modes of vibration. As higher modes possess enhanced damping properties compared to lower ones, the damping properties of the mechanical system are utilized more effectively, which may results in suppressing self-excited vibrations.

2 THEORETICAL INVESTIGATIONS

The equations of motion of a mechanical system may have the form

$$\mathbf{M}\mathbf{x}'' + (\mathbf{C} + \mathbf{C}_{se})\mathbf{x}' + \mathbf{K}\mathbf{x} + p(\tau)\mathbf{K}_P\mathbf{x} = \mathbf{0}, \tag{1}$$

where $\mathbf{M}$, $\mathbf{C}$ and $\mathbf{K}$ represent the constant and symmetric $(n \times n)$-mass, -damping and -stiffness matrices. A self-excitation mechanism is introduced via the matrix $\mathbf{C}_{se}$. It is assumed that the stiffness of the mechanical system can be affected in a targeted manner. Therefore, the term $p(\tau)\mathbf{K}_P$, where $\mathbf{K}_P$ is a constant matrix, and $p(\tau)$ represents a sum of scalar rectangular shaped impulsive functions according to

$$p(\tau) = \sum_{k=1}^{K} p_k(\tau), \tag{2}$$

is introduced. In (2),

$$p_k(\tau) = \begin{cases} \bar{p}_k & \text{if } (\tau_k - \tau_p/2) \leq \tau \leq (\tau_k + \tau_p/2), \text{ and} \\ 0 & \text{otherwise,} \end{cases} \tag{3}$$

i.e., a sequence of K rectangular shaped parametric impulses with the center at τ_k, a pulse-width τ_p, and a pulse-height $\bar{p}_k$ are applied to the mechanical system. It has to be pointed out, that the

instants of time τ_k are neither a-priori defined, nor necessarily equidistant.
Replacing the rectangular-shaped parametric impulses by Dirac delta ones located at τ_k, and applying a modal transformation $\mathbf{x} = \mathbf{\Phi y}$, where $\mathbf{\Phi}$ comprises the natural modeshapes of the undamped mechanical system without parametric- and self-excitation, leads to the equations of motion in the form

$$\mathbf{M}^*\mathbf{y}'' + (\mathbf{C}^* + \mathbf{C}^*_{se})\mathbf{y}' + \mathbf{K}^*\mathbf{y} + \left\{\sum_{k=1}^{K} \varepsilon_k \delta(\tau - \tau_k)\right\} \mathbf{K}^*_P \mathbf{y} = \mathbf{0}. \tag{4}$$

Therein, $\mathbf{M}^* = \text{diag}(\mu_1, \mu_2, \dots \mu_n)$, $\mathbf{K}^* = \text{diag}(\nu_1, \nu_2, \dots \nu_n)$ and $\varepsilon_k = \tau_p \bar{p}_k$ holds. For the sake of simplicity, a stiffness proportional damping $\mathbf{C}^* = \alpha \mathbf{K}^*$ is assumed. The matrices $\mathbf{C}^*_{se}$ and $\mathbf{K}^*_P$ are, in general, not of diagonal form, i.e. $\mathbf{K}^*_P = [k_{p,ij}]$ and $\mathbf{C}^*_{se} = [c_{se,ij}]$, $i, j = 1, \dots n$. Moreover, $\mathbf{y} = [y_1, y_2, \dots y_n]^T$ holds. The effect of parametric impulses of Dirac delta type to the displacements and velocities of mechanical systems was investigated by C.S. Hsu, see [9]. He introduced a jump-transfer matrix $\mathbf{J}_k$, relating the state vector just before the application of a parametric impulse at the instant of time τ_k, to the state-vector just after the impulse, according to

$$\begin{bmatrix} \mathbf{y}_{k+} \\ \mathbf{y}'_{k+} \end{bmatrix} = \underbrace{\begin{bmatrix} \mathbf{I} & \mathbf{0} \\ -\varepsilon_k \mathbf{M}^{*^{-1}} \mathbf{K}^*_P & \mathbf{I} \end{bmatrix}}_{\mathbf{J}_k} \begin{bmatrix} \mathbf{y}_{k-} \\ \mathbf{y}'_{k-} \end{bmatrix}, \tag{5}$$

where $\mathbf{I}$ denotes the identity-matrix. It can be concluded from Eq. (5), that the potential energy of the mechanical system remains unchanged across a parametric impulse of Dirac delta type, whereas the kinetic energy is subject of variation, as $\mathbf{y}'_{k+} \neq \mathbf{y}'_{k-}$, in general. To investigate the effect of a parametric Dirac impulse to the mechanical system in more detail, the total energy content of a mode i, consisting of kinetic energy T_i and potential energy U_i, according to

$$E_i(\tau) = T_i + U_i = \frac{1}{2}(\mu_i y_i'^2(\tau) + \nu_i y_i^2(\tau)), \tag{6}$$

is introduced. Equations (5) and (6) allow to express the variation of the modal energy content in the form

$$\Delta E_{i,k} = -\varepsilon_k \beta_{i,k-} \left[y'_{i,k-} - \frac{1}{2\mu_i} \varepsilon_k \beta_{i,k-} \right], \tag{7}$$

where $\beta_{i,k-} = \sum_{j=1}^{n} k_{p,ij} y_{j,k-}$. The variation of the overall energy content ΔE_k reads

$$\Delta E_k = \sum_{i=1}^{n} \Delta E_{i,k} = -\varepsilon_k \sum_{i=1}^{n} \beta_{i,k-} y'_{i,k-} + \frac{1}{2}\varepsilon_k^2 \sum_{i=1}^{n} \frac{\beta^2_{i,k-}}{\mu_i}, \tag{8}$$

which is a quadratic function of the impulsive strength factor ε_k. It can easily be seen, that ΔE_k is zero for $\varepsilon_k = 0$, and for

$$\varepsilon_k = \varepsilon_{S,k} = \frac{\sum_{i=1}^{n} (y'_{i,k-} \sum_{j=1}^{n} k_{p,ij} y_{j,k-})}{\frac{1}{2} \sum_{i=1}^{n} \frac{1}{\mu_i} (\sum_{j=1}^{n} k_{p,ij} y_{j,k-})^2}. \tag{9}$$

Within the interval $]0, \varepsilon_{S,k}[$, $\Delta E_k < 0$, and $\Delta E_k > 0$ outside this interval. If a parametric impulse of Dirac delta type, with an impulsive strength factor $\varepsilon_k = \varepsilon_{S,k}$ according to Eq. (9)

is applied, the overall energy content of the mechanical system does not change, i.e. the work of the impulsive force is equal to zero. However, it does not prevent the energy content of each single mode of vibration from being subject of variation. This can be utilized to affect the dynamic behavior of the mechanical system in a targeted manner, as described in the following. The impulsive strength $\varepsilon_{S,k}$ was the outcome of the condition

$$\Delta E_{1,k} + \Delta E_{2,k} + \ldots + \Delta E_{n,k} = 0, \tag{10}$$

which can be written in the form

$$\Delta E_{1,k} + \ldots + \Delta E_{m,k} = -(\Delta E_{m+1,k} + \ldots + \Delta E_{n,k}). \tag{11}$$

This means, that a Dirac impulse with a strength equal to $\varepsilon_{S,k}$ is capable of shifting vibration energy from a set of modes, consisting of modes 1 to m, to another set, comprising modes $m+1$ to n. The required work of the impulsive forces vanishes, i.e. no external work is necessary to transfer energy. It has to be pointed out, that this holds only for the theoretic case of Dirac delta impulses. An approximation with rectangular shaped impulses may results in extracting energy from, or feeding external energy to the mechanical system, concurrently to the modal transfer of energy. Introducing the mode-sets

$$A = \{1, \ldots m\} \text{ and } B = \{m+1, \ldots n\}, \tag{12}$$

Eq. (11) can be written in the form

$$\Delta E_{A,k} = -\Delta E_{B,k}. \tag{13}$$

The direction of energy transfer, i.e. if energy is shifted from set A to set B or vice versa, depends on the values of the state variables at the instant of time the impulse is applied. If energy should be transferred exclusively in one direction, for example $A \rightarrow B$, parametric impulses with $\varepsilon_k = \varepsilon_{S,k}$ have to be applied only if $\Delta E_{A,k} < 0$ holds, i.e. in the sense of a control-loop, requiring the actual state-vector of the mechanical system.
If the set A is specified as a set of lower modes of vibration, and set B comprises the remaining higher modes, a transfer of energy $A \rightarrow B$ can be beneficial for the vibration behavior of the mechanical system, as it will be shown in the following with a numerical example.

3 NUMERICAL RESULTS

Figure (1) displays a sketch of the investigated mechanical system with three degrees of freedom. It is assumed, that the mass m_3 is subjected to a lateral flow with constant velocity U. Using a linearized Rayleigh model for the self-excitation mechanism, the resulting force acting on the mass m_3 in the direction of x_3 can be written in the form

$$F_{se} = (a - bU^2)\dot{x}_3. \tag{14}$$

With the abbreviation $c_{se} = a - bU^2$, self-excitation takes place if $c_{se} < 0$ holds, i.e. external energy is fed to the mechanical system. Parametric excitation is introduced via the time-dependent stiffness $k(t) = k_{01}(1 + p(t))$. Introducing a time transformation $\tau = \Omega_R t$, where $\Omega_R = \sqrt{k_R/m_R}$ represents a reference angular velocity, using the non-dimensional system parameters

$$M_i = \frac{m_i}{m_R},\ C_{i-1,i} = \frac{c_{i-1,i}\Omega_R}{k_R},\ C_{se} = \frac{c_{se}\Omega_R}{k_R},\ K_{i-1,i} = \frac{k_{i-1,i}}{k_R}, \tag{15}$$

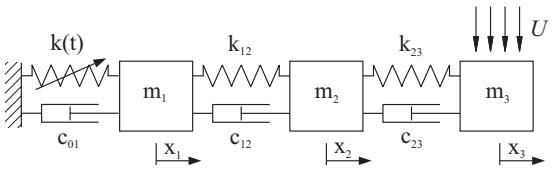


Figure 1: Sketch of the investigated mechanical system with self- and parametric excitation.

$i = 1, \ldots 3$, and applying a modal transformation, the equations of motion are of the form of Eq. (4). The application of the parametric impulses is done in the following way. At any instant of time τ, it is checked if a Dirac impulse at a future point in time $\tau + \Delta\tau$ results in the desired transfer of energy from set A to set B of modes. If so, the Dirac impulse is approximated by a rectangular shaped impulse with the center at $\tau_k = \tau + \Delta\tau$, a width of τ_p, and a height according to $\bar{p}_k = \varepsilon_{S,k}/\tau_p$. Moreover, the impulsive strength factor is restricted to $0 \leq \varepsilon_{S,k} \leq \varepsilon_{max}$. Applying this procedure repeatedly may results in a sequence of parametric impulses. The non-dimensional system parameters

$$\begin{aligned} M_1 = M_2 = M_3 = 1, K_{01} = 1.5, K_{12} = K_{23} = 1, \\ \alpha = 0.01, C_{se} = -0.02, \varepsilon_{max} = 0.4, \Delta\tau = 0.15, \tau_p = 0.1 \end{aligned} \tag{16}$$

are used for the following numerical investigations. As initial conditions, a shock load at mass m_3 according to $\mathbf{x}'(\tau = 0) = [0, 0, 1]^T$ and $\mathbf{x}(\tau = 0) = [0, 0, 0]^T$ is used.

3.1 Transfer of energy in the Hamiltonian case without self-excitation

To demonstrate the capability of parametric impulses to transfer energy across sets of modes, structural damping as well as self-excitation are neglected first, i.e. $\alpha = 0$ and $c_{se} = 0$. Figure (2) (left) shows the results for transferring energy from set $A = \{1\}$ to set $B = \{2, 3\}$. Within the first 50 time-units, parametric excitation is switched off, and hence, the mechanical system exhibits vibrations with constant amplitudes. Accordingly, the total energy content E_{tot} remains constant, see Fig. (2) (left, bottom). Switching on parametric excitation at $\tau = 50$ results in the occurrence of a sequence of parametric impulses, see the timeseries of p. Each impulse causes a reduction of the energy content E_1 of the first mode of vibration and, at the same instant of time, an increase of the energy content $E_2 + E_3$ of second and third mode of vibration. The total energy content E_{tot} of the mechanical system remains almost constant throughout all the time. (In the case parametric impulses of Dirac delta type are used, E_{tot} remains exactly constant.)

Transferring energy to a set of modes consisting of $(n - m) > 1$ modes addresses the target modes as a whole, which means that energy is shifted to a group of modes. This may results in inter-set energy transfers within the target mode-set, i.e. in the preceding case, shifting energy from mode one to modes two and three is possibly accompanied by shifting energy from mode two to mode three or vice versa. However, the summed energy content of both modes $E_2 + E_3$ is increased.

In the autonomous case, i.e. within the first 50 time-units, the mechanical system exhibits mixed-mode vibrations comprising all three modes due to the selected initial conditions. With each impulse, energy is shifted to the higher mode-set, i.e. E_1 decreases and $E_2 + E_3$ increases. Finally, almost all energy is contained within modes two and three, i.e. first mode vibrations

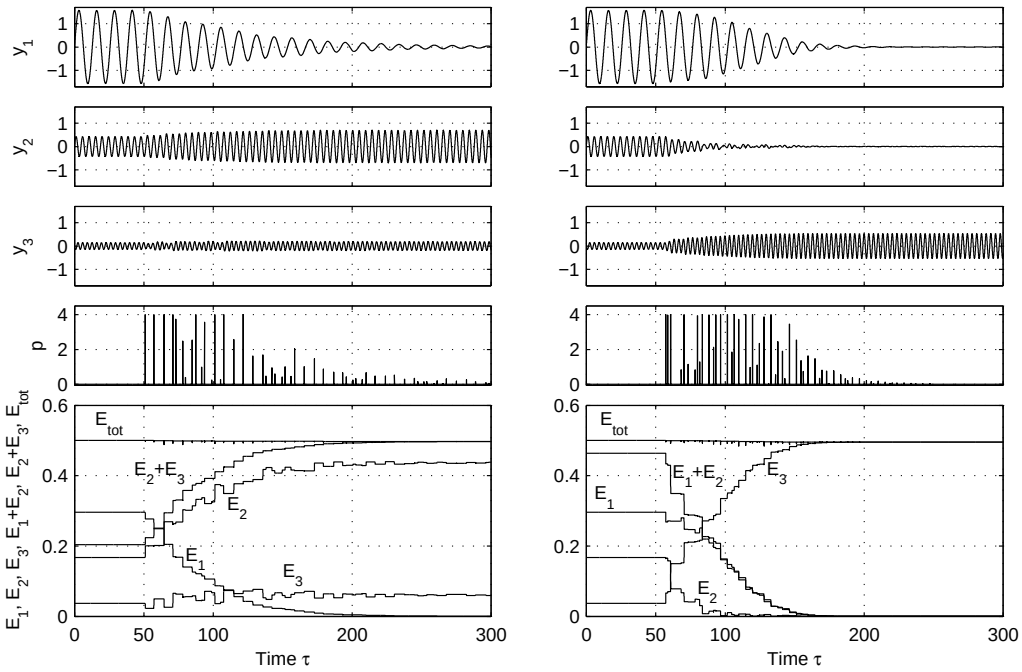


Figure 2: Transfer of energy from set $A = \{1\}$ to set $B = \{2, 3\}$ (left), and from set $A = \{1, 2\}$ to set $B = \{3\}$ (right) in the absence of structural damping and self-excitation. Timeseries of modal coordinates y_1, y_2 and y_3, stiffness scaling factor p and modal energies E_1, E_2 and E_3.

have almost vanished, and the mechanical system exhibits only second and third mode vibrations. Interestingly, the second mode contains the majority of energy, this means that the applied parametric impulses have addressed primarily the second mode of vibration.
If we want to transfer energy to a single mode of vibration, the target mode-set should be selected appropriately. Figure (2) (right) displays the numerical results for selecting the mode-sets $A = \{1, 2\}$ and $B = \{3\}$. In this case, energy is extracted from first and second mode of vibration, and shifted to the third mode, where the total energy content E_{tot} remains almost constant. Finally, all energy is primarily contained within mode three, and the mechanical system exhibits exclusively third mode vibrations.
Hence, parametric excitation of impulsive type is capable of transferring energy across sets of modes of vibration where the total energy content of the mechanical system remains unchanged, i.e. we can affect the active modes of vibration of a mechanical system in a targeted manner. This is may beneficial if the vibration frequency spectrum of a mechanical system should comprise only selected modes.

3.2 Transfer of energy in the damped case where self-excitation is present

Introducing structural damping reveals another advantage of shifting vibration energy across mode-sets. As higher modes usually possess enhanced damping properties compared to lower ones, shifting vibration energy to higher modes may results in a faster decrease of vibrations compared to the case where no impulsive parametric excitation is present, see [12].
In the following, it is demonstrated that applying parametric impulses in a targeted manner

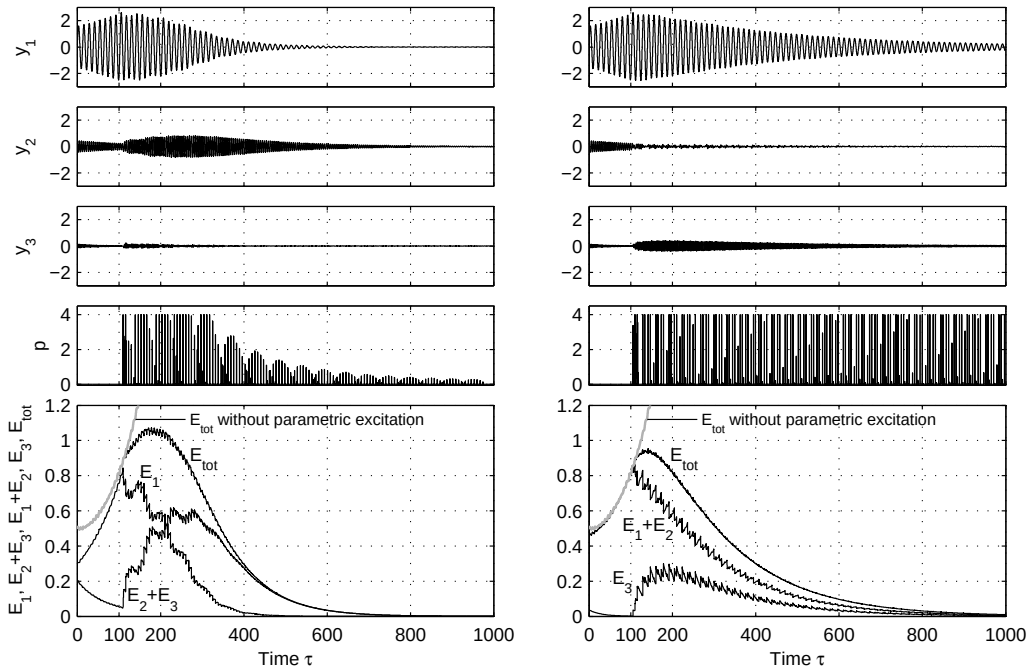


Figure 3: Transfer of energy from set $A = \{1\}$ to set $B = \{2, 3\}$ (left), and from set $A = \{1, 2\}$ to set $B = \{3\}$ (right) in the presence of structural damping and self-excitation. Timeseries of modal coordinates y_1, y_2 and y_3, stiffness scaling factor p and modal energies E_1, E_2 and E_3.

allows to suppress self-excited vibrations. Figure (3) (left) shows first results. Within the timespan $[0, 100]$, impulsive parametric excitation is switched off. The lateral flow on mass m_3 results in a self-excitation mechanism, and hence, the total energy content E_{tot} of the mechanical system increases, see Fig. (3) (left, bottom). At $\tau = 100$, impulsive parametric excitation is switched on, where the mode sets are selected as $A = \{1\}$ and $B = \{2, 3\}$. As a consequence, the initially increasing first mode vibrations y_1, caused by the self-excitation mechanism, decrease. Concurrently, second mode vibrations y_2 increase, and to a much smaller extent third mode vibrations y_3 as well. Most of the energy of the first mode is shifted to mode two, as in the previous case, see Fig. (2) (left). The corresponding energy contents are shown in Fig. (3) (left, bottom). Switching on parametric excitation at $\tau = 100$ results in a decrease of the energy content E_1 of the first mode, accompanied by an increase of the energy content $E_2 + E_3$ of second and third mode. The growth of the total energy content E_{tot} slows down, compared to E_{tot} without parametric excitation (see grey-colored line in Fig. (3) (left, bottom)). At $\tau \approx 175$ time-units, E_{tot} starts decreasing, and finally, comes to zero. All vibration signals y_1, y_2 and y_3 have almost vanished. Hence, self-excited vibrations have been successfully suppressed by the use of impulsive parametric excitation. As described previously, this effect is based on utilizing the enhanced damping properties of higher modes, inherent to the mechanical system, more effectively. In the present case, energy was transferred to modes two and three. Possibly, better results, i.e. a faster decrease of the total energy E_{tot} can be expected if all energy is transferred to mode three, which possesses the best damping properties. The corresponding results are presented in Fig. (3) (right), where energy is shifted from mode-set $A = \{1, 2\}$ to set $B = \{3\}$. As

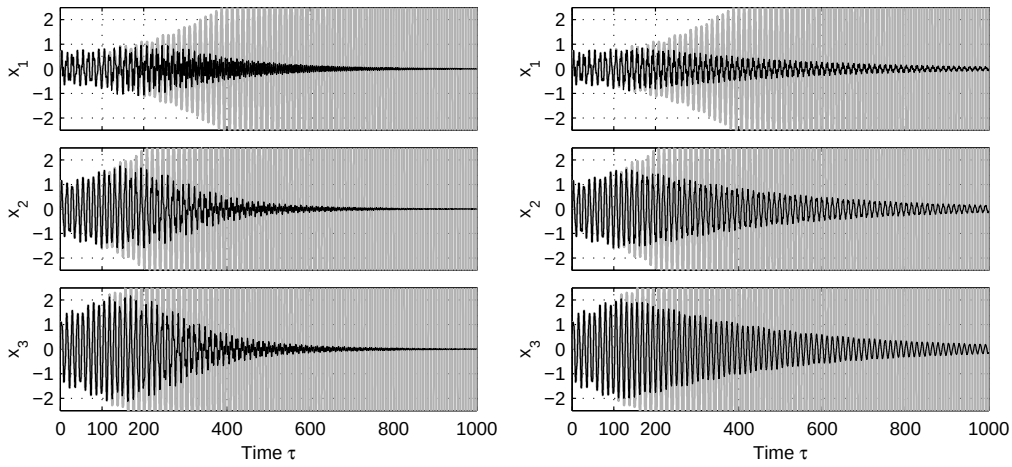


Figure 4: Timeseries of physical coordinates x_1, x_2 and x_3 for transfer of energy from set $A = \{1\}$ to set $B = \{2, 3\}$ (left), and from set $A = \{1, 2\}$ to set $B = \{3\}$ (right) in the presence of structural damping and self-excitation.

previously, parametric excitation is switched on at $\tau = 100$ time-units, resulting in a decrease of the energy content $E_1 + E_2$ of first and second mode, and an initial increase of E_3 of the third mode, until E_3 starts decreasing. Also in this case, the self-excited vibrations are suppressed. Comparing E_{tot} with the case where the target mode-set was selected as $B = \{2, 3\}$, see Fig. (3) (left), shifting energy to the third mode exclusively, results in an increase of E_{tot} to a lower maximum value until the drop of E_{tot} starts. Until about $\tau \approx 400$ time-units, E_{tot} is smaller than in the case shown in Fig. (3) (left). Thereafter, shifting energy to modes two and three results in a faster decrease of E_{tot}.

Figure (4) depicts the effect on the corresponding physical coordinates x_1, x_2 and x_3 for transferring energy from set $A = \{1\}$ to set $B = \{2, 3\}$ (left), and from set $A = \{1, 2\}$ to set $B = \{3\}$ (right). Therein, the grey-colored lines represent the results without impulsive parametric excitation, i.e. show the unstable behavior of the mechanical system. Both diagrams clearly indicate that impulsive parametric excitation is capable of suppressing self-excited vibrations.

A comparison of the total energy content E_{tot} for different values of ε_{max}, and transferring energy from set $A = \{1\}$ to set $B = \{2, 3\}$ is depicted in Fig. (5). Impulsive parametric excitation is switched on at $\tau = 100$. As expected, allowing a larger ε_{max} leads to a faster decrease of the total energy E_{tot}, where the gain is larger for smaller values of ε_{max}.

4 CONCLUSIONS

In this contribution, it was shown that impulsive stiffness excitation allows to suppress self-excited vibrations of mechanical systems effectively. Applying parametric impulses in a state-dependent manner, where the impulsive strength is derived from energy-considerations, allows a transfer of vibration energy between sets of modes without changing the overall energy content of the mechanical system. Moreover, it was demonstrated that transferring energy from a set of lower modes of vibration to a set of higher modes is capable of suppressing self-excited vibrations. This is based on the fact that higher modes usually possess enhanced damping

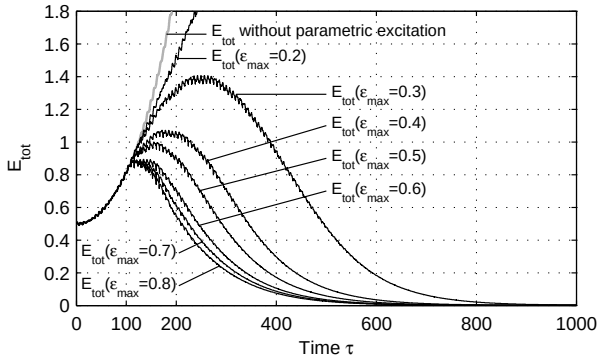


Figure 5: Timeseries of total energy content E_{tot} for different values of ε_{max} and transfer of energy from set $A = \{1\}$ to set $B = \{2, 3\}$ in the presence of structural damping and self-excitation.

properties compared to lower ones. This means, that with parametric stiffness impulses applied according to the proposed approach, the damping properties of the mechanical system can be utilized more effectively than without impulsive parametric excitation.

5 ACKNOWLEDGEMENT

This work has been supported by the Austrian COMET-K2 programme of the Linz Center of Mechatronics (LCM), and has been funded by the Austrian federal government and the federal state of Upper Austria.

REFERENCES

[1] A. Tondl, To the problem of quenching self-excited vibrations. *Acta Technica CSAV*, **43**, 109–116, 1998.

[2] H. Ecker, T. Pumhoessel, A. Tondl, A Study on Parametric Excitation for Suppressing Self-excited Rotor Vibrations, In: *Proc. of the 6th Int. Conference on Rotor Dynamics (IFToMM)*, Sydney, Australia, 2002.

[3] H. Ecker, *Suppression of Self-Excited Vibrations in Mechanical Systems by Parametric Stiffness Excitation.* ASIM Fortschrittsberichte Simulation, Vol. 11, 2005.

[4] F. Dohnal, *Damping of mechanical vibrations by parametric excitation.* PhD Thesis, Vienna University of Technology, Vienna, Austria, 2005.

[5] F. Dohnal, *A contribution to the mitigation of transient vibrations, Parametric anti-resonance: theory, experiment and interpretation.* Habilitation Thesis, Technische Universität Darmstadt, Germany, 2012.

[6] H. Ecker, T. Pumhössel, Vibration suppression and energy transfer by parametric excitation in drive systems. *Proc. IMechE Part C: J. Mechanical Engineering Science*, **226**(8), 2000–2014, 2012.

[7] F. Dohnal, Damping by Parametric Stiffness Excitation: Resonance and Anti-Resonance. *Journal of Vibration and Control*, **4**, 669–688, 2008.

[8] T. Pumhössel, P. Hehenberger, K. Zeman, Reduced-order modelling of self-excited, time-periodic systems using the method of Proper Orthogonal Decomposition and the Floquet theory. *Mathematical and Computer Modelling of Dynamical Systems: Methods, Tools and Applications in Engineering and Related Sciences*, **20**(6), 528–545, 2014.

[9] C.S. Hsu, Impulsive Parametric Excitation: Theory. *Journal of Applied Mechanics*, **39**(2), 551–558, 1972.

[10] C.S. Hsu, W.-H. Cheng, Applications of the Theory of Impulsive Parametric Excitation and New Treatments of General Parametric Excitation Problems. *Journal of Applied Mechanics*, **40**(1), 78–86, 1973.

[11] T. Pumhoessel, P. Hehenberger, K. Zeman, On the effect of impulsive parametric excitation to the modal energy content of Hamiltonian systems, In: *Proc. of the 11th International Conference on Vibration Problems (ICOVP)*, Lisbon, Portugal, 2013.

[12] T. Pumhoessel, P. Hehenberger, Impulsive parametric excitation as a means to transfer energy between modes of vibration. In: *Proc. of 8th European Nonlinear Dynamics Conference (ENOC)*, Vienna, Austria, 2014.

International Conference on Engineering Vibration
Ljubljana, Slovenia, 7-10 September 2015

ACTIVE SUSPENSION LQ CONTROL FOR IMPROVING RIDING COMFORT

Francesco Cosco[1, 2], Ion Borozan*[2], Stefano Candreva[3], Domenico Mundo[3]

[1] Department of Mechanical Engineering, KU Leuven, Celestijnenlaan 300B, 3001 Leuven, Belgium
francesco.cosco@kuleuven.be

[2] G&G Design and Engineering SRL, Via G. Barrio, SN 87100 Cosenza, Italy
{francesco.cosco, ionutz_borozan}@gegde.com

[3]University of Calabria, Cosenza, Italy
{stefano.candreva, domenico.mundo}@unical.it

Keywords: quarter-car, driver model, active suspension, optimal control, comfort

Abstract. *The purpose of this research is to improve the perceived comfort in passenger's cars, by means of a properly tuned optimally controlled active suspension, exploiting conceptual human body models as a tool for virtually sense human body vibrations. Canonical approaches achieve comfort performance by reducing vehicle body accelerations. Complimentary, our approach aims to reduce also human body vibrations, taking into account their estimation by means of a simplified human body model.*

In order to assess whether and to what extent the proposed approach improves comfort, we defined a case study where just vertical vibrations are considered. In this scenario, several conceptual human body models are available in literature, specifically designed for capturing the vertical vibrational behaviour of the driver while in the seated position. By coupling such a two degrees-of-freedom (DOFs) human body model with a standard two DOFs quarter car model we get a four DOFs driver-car system on which the linear quadratic optimal control design was performed to obtain the optimally controlled behaviour. For validating the approach, we derived also the optimal control of the active suspension in a canonical sense (i.e. by aiming at reducing vehicle body vibrations) which we adopted as the reference model. By use of numerical simulations, we finally compared the proposed active suspension optimal control highlighting the main differences with respect to the reference model in terms of head vibrations (vertical accelerations), vehicle body vibrations, suspension travel, and tire deflection. In particular, we considered two different scenarios: one where the vehicle travels just over the planar straight road roughness at a constant speed of 72 km/h, and the other one where the vehicle passes over a sinusoidal bump. Numerical results demonstrate that the proposed controller is able to reduce the driver head's vibrations in both situations more than the standard approach, leading this way to an improvement of passenger's comfort.

1 INTRODUCTION

A vehicle's suspension system typically consists of springs and shock absorbers that help to isolate the vehicle chassis and occupants from sudden vertical displacements of the wheel assemblies when driving. A well-tuned suspension system is important for the comfort and safety of the vehicle occupants as well as the long-term durability of the vehicle's electronic and mechanical components. The vehicle suspension provides a means of isolating the vehicle's body, and thus the passengers, from the road inputs.

Occupant comfort requires the minimization of sprung mass accelerations [1], as well as the optimization of the seating design [2-4]. Because of its response to varying road conditions, active suspensions offer superior handling, road feel, responsiveness and safety compared to passive suspension systems. For instance, in a passive suspension system each improvement comes at the expense of performance in another area. In general, passive suspensions are the best solution when considering a single operating point, situation not common in real life. While adding complexity, active suspensions have shown an ability to minimize vehicle accelerations, rattle space utilization, or to improve road holding to various degrees over certain frequency ranges.

One common control technique that is based on full state feedback relates with the Linear Quadratic Regulator (LQR). Many works are available in the literature regarding LQR optimal control design of active suspension based on quarter car, half car and also full car models. In our work, we take into account a quarter car model coupled with a two DOFs lumped parameters human body model, with the aim of designing the active suspension also from the driver point of view, i.e. taking into account body and head accelerations.

In the following sections the driver-car system model is first presented (Section 2), then exploited for the optimal design of the LQR (Section 3). Numerical simulation results of the obtained controlled suspension are presented for two different scenarios: random road roughness, and a speed bumper, both engaged at constant speed. For each scenario, a comparison between the passive solution, the reference controller (i.e. a controller obtained optimizing the performance in a canonical sense), and the proposed controller are presented and discussed in Section 4. Numerical results demonstrate that the proposed controller is able to reduce the driver head's vibrations in both situations more than the standard approach, leading this way to an improvement of comfort.

2 DRIVER-CAR SYSTEM MODEL

Several authors already addressed the problem of capturing the vertical dynamics of a car by means of lumped parameters models [5]. The use of quarter-car, half-car and even full car models is a well-established technique with widespread application in the field of vehicle dynamics and control. In the particular case of improving ride quality, Wakeham and Rideout highlighted that using two quarter-car-based LQ controllers better performance are achieved compared to half-car-based LQ controller[1], unless pitch control is of great importance.

As a consequence, the model used along this paper, extends the 'quarter-car' model, in order to add a physical and compact description of the vertical vibrational behaviour of the driver. To this end, several lumped-parameters models were proposed in literature [6-12], all considering the human body as several concentrated masses, interconnected by springs and dampers. As reported in a recent survey [10], complexity of these models ranges from simple one DOF, to increasing levels of detail alternatives, like the dedicated eleven DOFs model proposed by Quassem et al. to capture the effect of pregnant women [11].

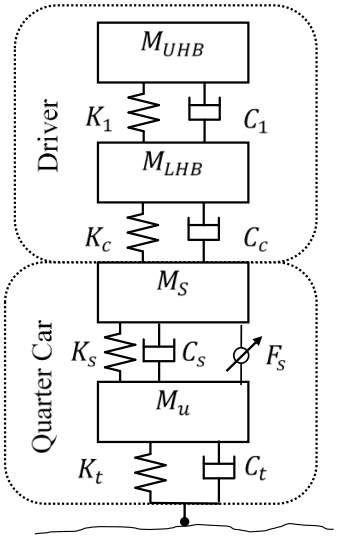


Figure 1. System lumped-parameters model

After considering all alternatives, and taking into account the goal of this research, i.e. the synthesis of a LQR, we choose the two DOF model representation developed by Allen in [12]. As depicted in Figure 1, the driver body is composed of two masses, M_H and M_B, corresponding to the head and the rest of the body respectively, which are inter-connected by a spring-damper element (K_N and C_N) representing the neck articulation. The driver model is attached to the car model by means of a soft connection (K_C and C_C).

This connection was modelled assuming that the seat mass foreseen by the Allen model is part of the *sprung* mass, M_S, of the quarter car system. The remaining mass, M_u, completes the system model, by concentrating the inertia of the *unsprung* elements of the suspension; with the passive stiffness and damping of the suspension being concentrated in K_S and C_S. Whereas, the stiffness and damping of the tyre is modelled by K_t and C_t. Values of the lumped parameters used in this work are listed in table 1.

Driver model(M = 56.8 kg) [10, 12]		Quarter car model parameters [5]	
M_H [Kg]	5.5	M_S [Kg]	240
M_B [Kg]	51.3	M_U [Kg]	36
K_N [N/m]	41000	Ks [N/m]	16000
C_N [N s/m]	318	Cs [N s/m]	980
K_C [N/m]	74300	K_T [N/m]	160000
C_C [N s/m]	2807	C_T [N s/m]	0

Table 1: List of the lumped parameters used for the Driver-Car system model.

3 LQ CONTROLLER DESIGN

For the design of the regulator gains, we extended the approach suggested by Wakeham and Rideout [1], by adopting the extended four DOFs quarter car model (as described in the previous section). The corresponding general linear system expressed in the state-space form is described as follows:

$$\dot{\boldsymbol{x}} = A\boldsymbol{x} + B\boldsymbol{u} + C\boldsymbol{d} \tag{1}$$

where the system states vector,

$$\boldsymbol{x} = [v_h \quad v_b \quad v_s \quad v_t \quad z_{hb} \quad z_{bs} \quad z_{st} \quad z_{tr}]^T \tag{2}$$

is defined considering the head, body, sprung and unsprung velocities, followed by neck, cushion, suspensions and tire deflections. Moreover, vectors **u** and **d** represent the control action (force actuation) and the external disturbance (time derivative of the road profile variations) respectively.
Given the state variables, the state transition matrix A, as well as the control matrix, B, and the disturbance matrix C, are derived as follows:

$$A = \begin{bmatrix} -\frac{c_h}{m_h} & \frac{c_h}{m_h} & 0 & 0 & -\frac{k_h}{m_h} & 0 & 0 & 0 \\ \frac{c_h}{m_b} & -\frac{c_h+c_c}{m_b} & \frac{c_c}{m_b} & 0 & \frac{k_h}{m_b} & -\frac{k_c}{m_b} & 0 & 0 \\ 0 & \frac{c_c}{m_s} & -\frac{c_c+c_s}{m_s} & \frac{c_s}{m_s} & 0 & \frac{k_s}{m_s} & -\frac{k_s}{m_s} & 0 \\ 0 & 0 & \frac{c_s}{m_u} & -\frac{c_s+c_t}{m_u} & 0 & 0 & \frac{k_s}{m_u} & -\frac{k_t}{m_u} \\ 1 & -1 & 0 & 0 & 0 & 0 & 0 & 0 \\ 0 & 1 & -1 & 0 & 0 & 0 & 0 & 0 \\ 0 & 0 & 1 & -1 & 0 & 0 & 0 & 0 \\ 0 & 0 & 0 & 1 & 0 & 0 & 0 & 0 \end{bmatrix} \tag{3}$$

$$B = \begin{bmatrix} 0 & 0 & \frac{1}{m_s} & -\frac{1}{m_u} & 0 & 0 & 0 & 0 \end{bmatrix}^T \tag{4}$$

$$C = [0 \quad 0 \quad 0 \quad 0 \quad 0 \quad 0 \quad 0 \quad -1]^T \tag{5}$$

According to the LQR method, a parametric performance index needs to be defined, in order to retrieve the corresponding optimal gains. The proposed performance index is derived as an extension of [1]:

$$\mathrm{J} = \int_0^\infty \ddot{z}_s^2 + \rho_1 z_{st}^2 + \rho_2 \dot{z}_s + \rho_3 z_{tr}^2 + \rho_4 \dot{z}_u + \rho_5 \ddot{z}_h^2 + \rho_6 \ddot{z}_b^2 \, dt \tag{6}$$

where two extra terms (last two terms in eq. 6) were added to allow the regulator minimizing the performance also from the perspective of the human body vibrations.

4 SIMULATIONS RESULTS

We performed a set of time-domain simulations, which highlight the performances of the proposed approach with respect to the reference regulator obtained in [1], in two different scenarios: a sinusoidal bump and a random road profile, according to the ISO 8606 specification.Weights tuned for the design of the optimal LQ regulators are summarized in table 2.

	2DOF-LQR (Reference)	4DOF-LQR
ρ_1	0.4	0.4
ρ_2	0.16	0.16
ρ_3	0.4	0.4
ρ_4	0.16	0.16
ρ_5	-	100
ρ_6	-	100

Table 2: LQR weights for the design of the reference 2 DOFs regulator, and the proposed 4DOFs regulator.

For both situations, the following discretized form of equation (1) is first derived, by considering an exponential integrator scheme, with a fixed time-step $h = 4ms$:

$$x_{k+1} = A_d x_k + B_d u_k + C_d d_k \tag{7}$$

with:

$$A_d = e^{h \cdot A} \tag{8}$$

$$B_d = A^{-1}\,(A_d - I)\,B \tag{9}$$

$$C_d = A^{-1}\,(A_d - I)\,C \tag{10}$$

The optimal gains, K, obtained from the LQR design are used *online* to get the full-state control feedback:

$$u_{k-1} = K\,x_{k-1} \tag{11}$$

4.1 Sinusoidal bump

For the discrete bump scenario, the input disturbance (i.e. road profile height, as showed in Figure 1) was defined according to the following continuous function:

$$Z_r(t) = \begin{cases} \frac{a}{2}\left(1 - \cos\left(2\pi \frac{V}{L} t\right)\right), & t_0 \le t \le t_0 + \frac{L}{V} \\ 0 & otherwise \end{cases} \tag{12}$$

The input disturbance series, d_k, for simulating the scenario was then computed by differentiating the given formula for a speed, *V*, of 50 km/h; a bump height, *a*, of 0.1 m; and a bump length, *L* of 2 m.

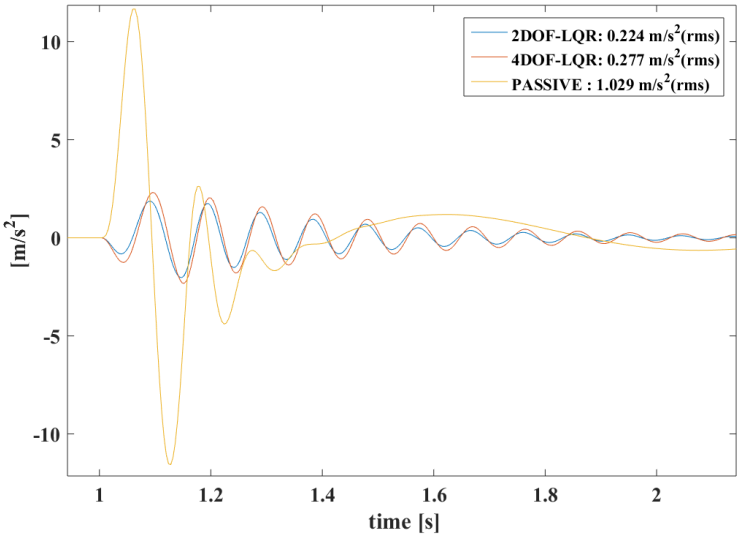


Figure 2. Sinusoidal bump: sprung mass acceleration (Conventional-Ride quality)

As depicted in Figure 2, both the optimal regulators outperforms the passive solutions in term of ride quality. In particular the 4DOFs solution tends to allow slightly larger vibrations of the sprung mass,of ride quality. In particular the 4DOFs solution tends to allow slightly larger vibrations of the sprung mass, but obtains a substantial reduction (about two order of magnitudes) of the vibration transmitted to the driver head (Figure 3). This results are achieved without compromising neither the force demanded by the actuators (Figure 4), nor the road-holding performance estimated by considering the tire deflections (Figure 5).

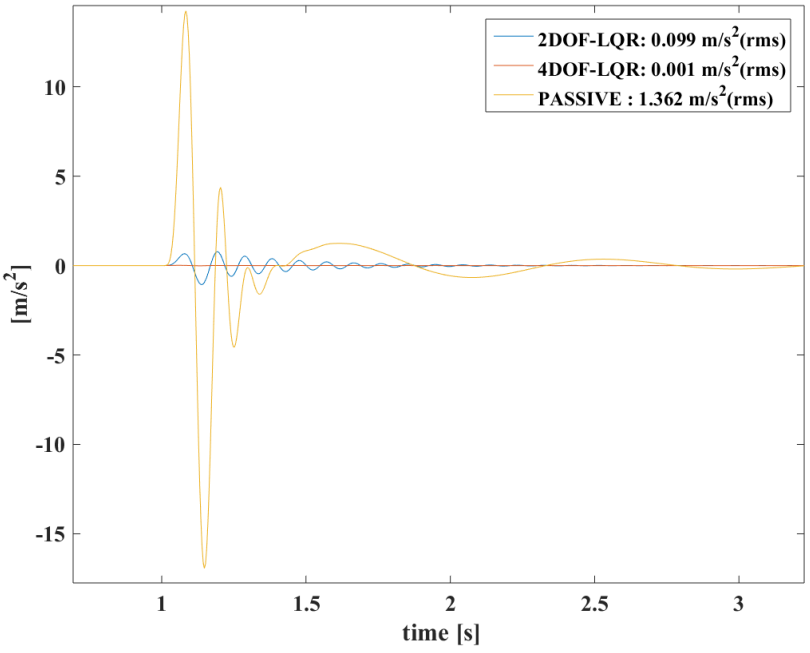


Figure 3. Sinusoidal bump: driver head acceleration (Objective ride quality)

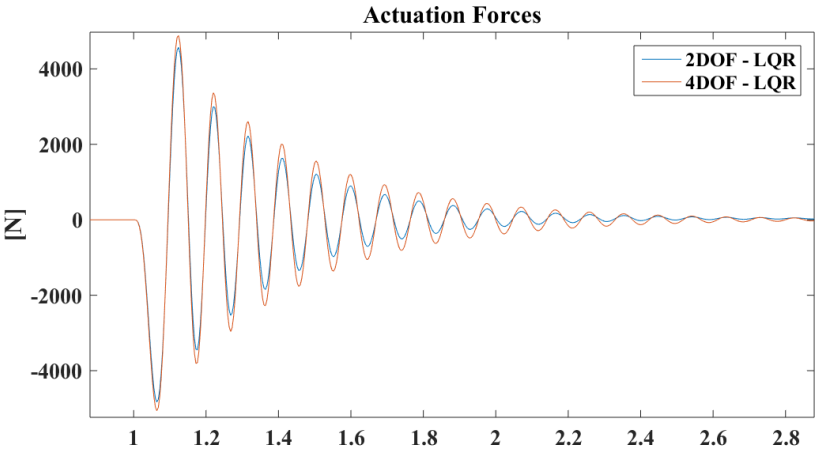


Figure 4. Sinusoidal bump: force demanded by the controllers

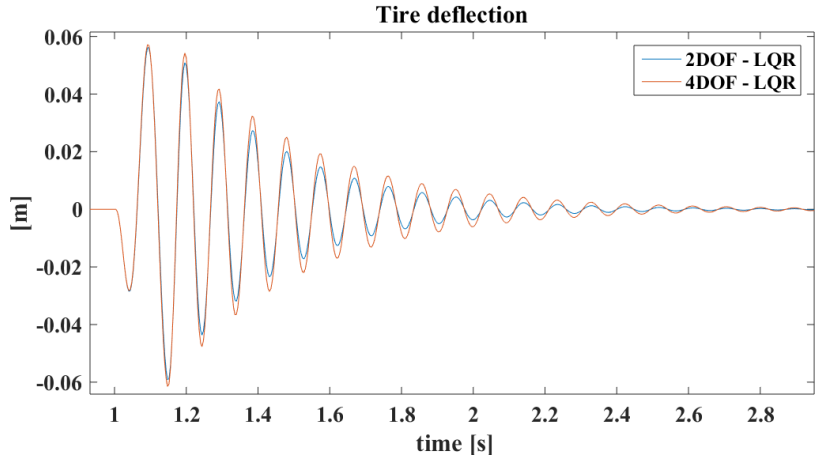


Figure 5. Sinusoidal bump: tire deflections (Road holding performance)

4.2 Random road profile

Following the approach described in [13], a class 'E' rough road profile (ISO 8606), corresponding to a road with a rating of very poor quality, was generated. For this test, the velocity of the car is assumed to remain constant at 72 km/h (20 m/s). The corresponding disturbance signal in time domain is showed in Figure 6.

Simulation results of the random input are qualitatively identical to those related to the sinusoidal bump scenario. As depicted in Figures 7 to 10, both the controllers outperform the passive suspension, with the 4DOFs presenting again a small performance reduction in terms of sprung mass acceleration (Figure 7), force actuation (Figure 9) and road holding (Figure 10), but with great improvements (Figure 8: the rms of the head vibrations scales from 0.2 to 0.002 m/s^2) in term of head and body vibrations.

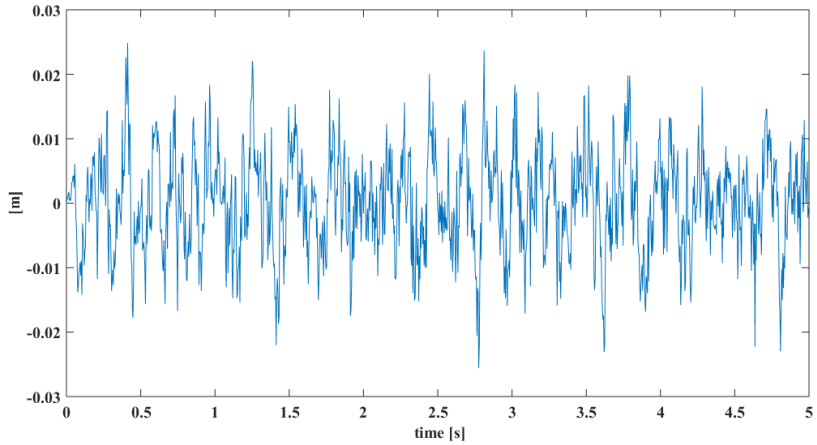


Figure 6. Random road profile, ISO 8606 class E engaged at 72 km/h

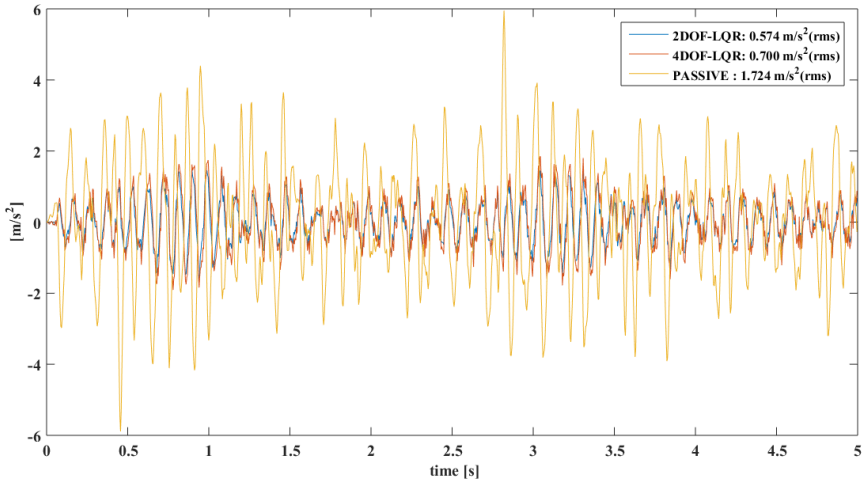


Figure 7. Random road profile: sprung mass acceleration (Conventional-Ride quality)

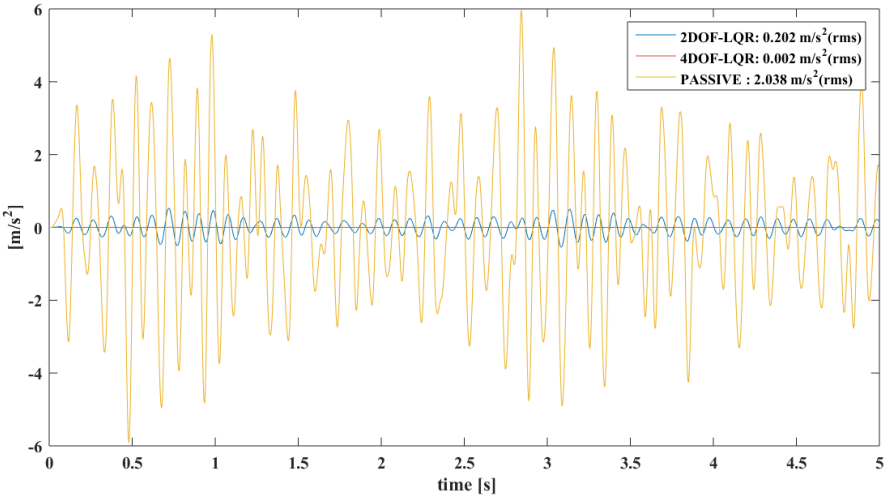


Figure 8. Random road profile: driver head acceleration (Objective ride quality)

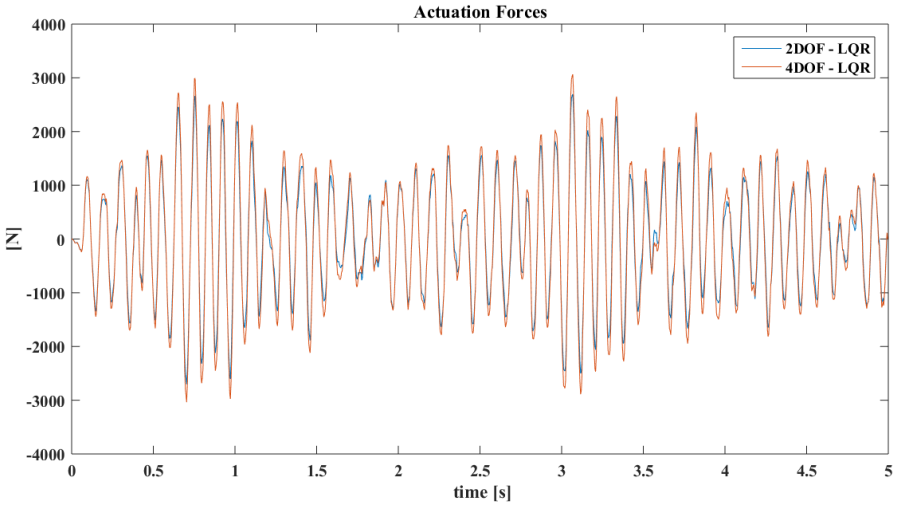


Figure 9. Random road profile: force demanded by the controllers

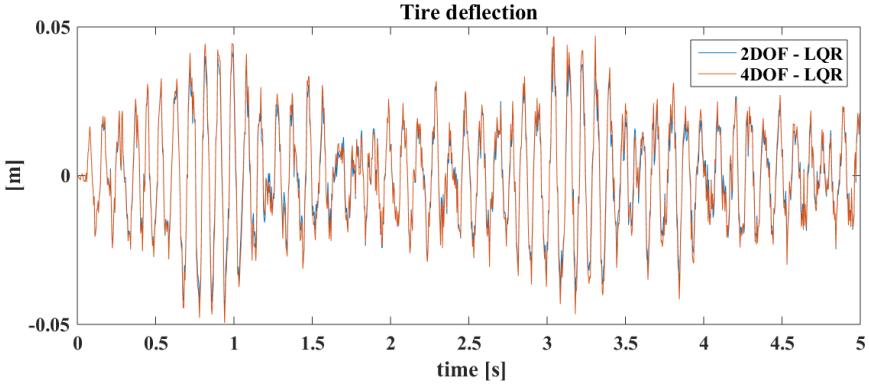


Figure 10. Random road profile: tire deflections (Road holding performance)

5 CONCLUSIONS

A novel approach for designing LQR optimal control of an active suspension system was presented, whose peculiarity lies in expanding the well-known quarter car model by adding the inertia, stiffness and damping elements required to capture human vibrational behaviour. After dealing with the mathematical background of the used models, and the derivation of a suitable performance index, the LQR was applied to derive the controlled suspension.

Numerical results demonstrate that the proposed controller is able to reduce the driver head's vibrations in the two driving scenarios analysed in the present work more than the standard approach, leading this way to a deep improvement of comfort, which in both of our test cases was in the range of two orders of magnitude.

AKNOWLEDGEMNENTS

The research leading to these results has received funding from the People Programme (Marie Curie Actions) of the European Union's Seventh Framework Programme FP7/2007-2013/

under REA grant agreement n° [285808] – INTERACTIVE: Innovative Concept Modelling Techniques for Multi-Attribute Optimization of Active Vehicles (www.fp7interactive.eu).

REFERENCES

[1] K. J., Wakeham, and D. Geoff Rideout. *Model complexity requirements in design of half car active suspension controllers* ASME 2011 Dynamic Systems and Control Conference. American Society of Mechanical Engineers, 2011.

[2] W. Abbas, O. B. Abouelatta, M. El-Azab, M. Elsaidy, A. A. Megahed, *Optimization of biodynamic seated human models using genetic algorithms*, Engineering (2010), 2, 710-719.

[3] Ö. Gündoğdu, *Optimal seat and suspension design for a quarter car with driver model using genetic algorithms*, International Journal of Industrial Ergonomics 37 (2007), 327-332

[4] M. Patil, M. Palachinamy, D. Ghista, *Man-tractor system dynamics: Towards a better suspension system for human ride comfort*, Journal of Biomechanics, Vol. 11(1978) 397-406.

[5] T. Gillespie, *Fundamentals of Vehicle Dynamics*, Society of Automotive Engineers, Warrendale, 1992

[6] P. Boileau, S. Rakheja, *Whole-body vertical biodynamic response characteristics of the seated vehicle driver measurement and model development*, International Journal of Industrial Ergonomics 22 (1998) 449- 472.

[7] P. Boileau, *A body mass dependent mechanical impedance model for applications in vibrations seat testing*, Journal of Sound and Vibration (2002) 253(1), 243-264.

[8] Z. Gan, A. Hillis, J. Darling, *Biodynamic modelling of seated human subjects exposed to whole-body vibration in both vertical and fore-and-aft directions*, 2015

[9] L. Wei, M.J. Griffin, *Mathematical models for the apparent mass of the seated human body exposed to vertical vibration*, Journal of Sound and Vibration 212 (1998) 855–874.

[10] C. Liang, C Chiang, *A study on biodynamic models of seated human subjects exposed to vertical vibration*, International Journal of Industrial Ergonomics 36 (2006) 869–890.

[11] W. Qassem, M.O. Othman, *Vibration effects on sitting pregnant women—subjects of various masses*, Journal of Biomechanics 29 (4), 493–501, 1996

[12] G. Allen. *A critical look at biomechanical modeling in relation to specifications for human tolerance of vibration and shock*. AGARD Conference Proceedings No. 253, Paper A25-5, Paris, France, pp. 6–10, 1978

[13] J.Y. Wong. *Theory of Ground Vehicles*, Wiley; 4 edition, 2008

International Conference on Engineering Vibration
Ljubljana, Slovenia, 7-10 September 2015

FRACTIONAL PID CONTROLLER TO AN ACTIVE IMAGE STABILIZATION SYSTEM

***S. A. David [1], R. V. de Sousa [1], C. A. Valentim Jr. [1], L. R. Trevisan[1], L. P. Magalhães[1], J.M. Balthazar[2]**

[1] *University of São Paulo at Pirassununga -USP*
sergiodavid@usp.br,rafael.sousa@usp.br,carlos.valentim@usp.br,lucas.renato.trevisan@usp.br, leonardo.magalhaes@usp.br

[2] *Aeronautics Technological Institute - ITA*
jmbaltha@ita.br.

Keywords: Fractional Calculus; Control Action; Modeling and Simulation; Displacement Compensation

Abstract. *Recent demands in sophisticated agricultural machinery require passive or active image sensors to be mounted on the vehicle frame. The impact caused by vertical displacement due to the tire-soil interaction and the mechanical engine vibration cause oscillations that interfering with the precision of any activity performed by the camera, spectroradiometer, scanner laser and hence reducing data quality. The paper presents the modeling and simulation of an active system for stabilization of oscillations using a fractional order PID (Proportional-Integrative-Derivative) controller. It is described the modeling of the stabilization controller system as well as it is applied a method for tuning the fractional order PID parameters. Experiments are performed to compare the response from both fractional and integer order PID controllers, using typical excitations found in studies of agricultural machinery vibrations. The results show the better performance of the fractional order PID controller demonstrated through parameters of the responses related to step reference inputs. Also, it is demonstrated the robustness of the fractional order PID controller in attenuating the disturbance inputs compared to the integer order PID controller.*

.

1 INTRODUCTION

The dynamics and control of vibration systems require modelling and accurate control project in order to mitigate or suppress unwanted vibrations. The mechanical vibrations are frequently inconvenient because provokes oscillations that can have very significant effects on the final outcome desired. Sophisticated vehicles, including mobile robot and agricultural machinery, require passive or active image stabilization system (AIS) to be mounted on the vehicle frame for attenuating excitations due to the tire-soil interaction and to the mechanical engine that produces vibrations [1].

Applications of machine vision in agriculture have been researched in recent decades mainly for non-destructive measurement, visual navigation and behavioural surveillance [2]. In particular, the development of autonomous agricultural vehicles or mobile robots for different kinds of applications depends on the development of such technologies [3]. However, there are still significant challenges to overcome to enable commercial agricultural technologies for both the processing and the image acquisition system [4]. One of these challenges corresponds to the vibrations of the machines themselves that harm the acquisition of images. Vibrations of parts of machinery can lead to blurry images that have a negative impact on the accuracy of measurement applications for the machine vision system. Furthermore, continuous vibration can damage the electronics components of this system [1]. In this context, AIS has interests in areas such as robotics to eliminate or reduce unwanted fluctuations in the acquired images [5]. The AIS involves applying movement in opposition to unwanted movement of the mechanism where the image acquisition system is mounted. The unintentional movements are identified by inertial sensors and a controller determines commands to an active stabilizing mechanism [6]. Advanced control methods have been researched to improve accuracy AIS [7]

Studies proposed recently employ Fractional Calculus (FC) in control systems. Fractional controllers have attracted a considerable attention, however a small part of them are investigated to agricultural machinery applications. Recent history, basic concepts and several applications involving FC were presented in [8-13]. Investigations using fractional controllers' applications such as a controller of variable order for an electromagnetic servo used in industrial knitting were conducted in [14]. A controller of the type PI^{λ} was used in the control of an engine that triggers a flexible robotic joint, showing a better performance when compared to the integer order controller [15]. The side controller of an autonomous vehicle was proposed in order to adjust the gains of the feedforward controller in [16]. An analysis of the project of digital fractional order control systems as well as fractional control of force/position of robotic manipulators was approached in [17] and [18]. Also, a Fractional Order PID Controller (FOPID) was examined on a benchmark position servomechanism control system considering actuator saturation and the shaft torsional flexibility in [19].

The fact that the fractional controllers have been successfully applied in control engineering motivated the choice for an appropriate FOPID applied to AIS for agricultural machinery. In this study, it is investigate the impacts resulting from the project and introduction of a FOPID for an active stabilization system on agricultural vehicle subject to external excitations. The modelling of the stabilization controller system as well as a method for tuning the fractional order PID parameters is proposed. Numerical experiments are performed to compare the response from both FOPID and PID controllers, using typical excitations found in studies of agricultural machinery vibrations [20,21].

This paper is organized in four sections. In Section 2, it presents the modeling and control. In section 3, it is shown some numerical simulation results and performed comparisons be-

tween integer PID and FOPID controllers' performances. Finally, in Section 4, we highlight the main concluding comments.

2 MODELLING AND CONTROL

In this work, it is considered an oscillatory platform that can be used such as in image acquisition on the field through a camera, a spectroradiometer or a scanner laser mounted on the frame of a vehicle (or mobile agricultural robot), which moves in a rough ground (Figure 1). Recently, the image acquisition is a very investigated theme in agriculture, mostly for post processing of these images for several purposes, such as automatic fruit recognition and counting [22], determination of crop coefficient [23], weed recognition [24], identification of diseases on the surface of plants [25] and others.

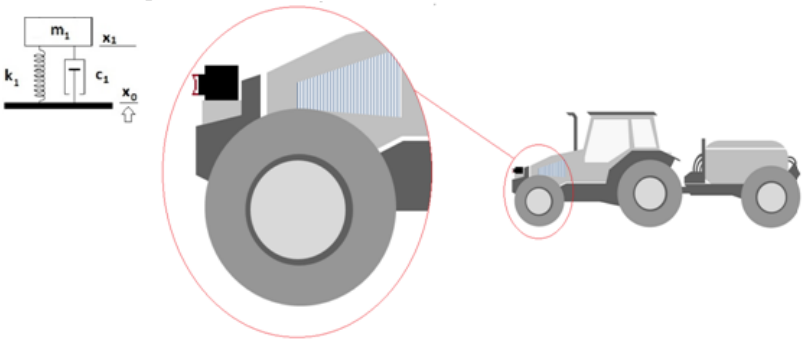


Figure 1: Model

However, the impact caused by irregularities on the ground during displacement of the platform causes oscillations, interfering with the accuracy of any activity performed by a sensor, hence reducing the data quality. Therefore, may be convenient or even necessary a better attenuation or suppression of these vibrations.

The oscillatory mechanical platform is modelled by a spring-mass-damper system and an external force is added to the model in order to characterize an AIS. For the closed-loop control systems, there are four possible situations, namely: 1) Traditional Modelling (Integer Order plant) with Traditional Control (Integer Order Controller; 2) Traditional Modelling (Integer Order plant) with Fractional Control (Fractional Order Controller); 3) Fractional Modelling (Fractional Order plant) with Tradicional Control (Integer Order Controller) and 4) Fractional Modelling (Fractional Order plant) with Fractional Control (Fractional Order Controller).

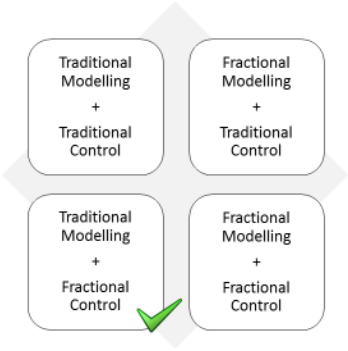


Figure 2: Modelling and Control

Considering the scenario described and adopting the situation highlighted in the Figure 2 (situation 2), the modelling based on FOPID controller is proposed and evaluated.

2.1 Modelling – plant

In Figure 1, m_1 represents the mass of the image acquisition system. The parameters k_1 and c_1 are the stiffness and damping coefficients of the system, respectively. The position, x_1, is considered to be the displacement of the system out from equilibrium. Also, x_0 and $\dot{x_0}$ denote, respectively, the system displacement and its velocity relative to the vehicle. Finally, f represents the force exerted by an active stabilization actuator on the mass m_1.

According to Newton's second law and free body diagram approach (Figure 1), the equation of motion for the system is written in (1).

$$\ddot{x_1} = -\frac{k_1 x_1}{m_1} - \frac{c_1 \dot{x_1}}{m_1} + \frac{k_1 x_0}{m_1} + \frac{c_1 \dot{x_0}}{m_1} + \frac{f}{m_1} \tag{1}$$

Assuming the state variables as $\mathbf{x_s} = [x_1\ x_2\ ]^T$, where $x_2 = \dot{x_1}$, and defining the input variables as $\mathbf{u} = [x_0\ \dot{x_0}\ f]^T$, the equation (1) can be rewritten in the state space form as

$$\dot{\mathbf{x}}_\mathbf{s} = \begin{bmatrix} 0 & 1 \\ \frac{-k_1}{m_1} & \frac{-c_1}{m_1} \end{bmatrix} \mathbf{x_s} + \begin{bmatrix} 0 & 0 & 0 \\ \frac{k_1}{m_1} & \frac{c_1}{m_1} & \frac{1}{m_1} \end{bmatrix} \boldsymbol{u} \tag{2}$$

The desired output of the system is the position x_1, which represents the position out from equilibrium point (Figure 1). In the state-space form, the output is represented as

$$\boldsymbol{y} = [1\ 0]\ \mathbf{x_s} \tag{3}$$

2.2 FOPID Controller

The PID controller is the most popular algorithms of feedback control. PID controllers are today found in all areas where control is used. Simple controllers like the PI and PID controller are naturally not suitable for all processes. PID control is not suitable for processes that are highly oscillatory or when the requirements are extreme. In this context, the FOPID controller is proposed in order to verify its performance and establish comparisons with traditional PID.

The most common way of representing a FOPID controller is designing it as a $PI^{\lambda}D^{\mu}$ controller in which λ and μ represent arbitrary orders that may be integer (classical case) or not (fractional case) [26]. The transfer function of such a controller has the form [19]

$$G(s) = K_p + \frac{K_I}{s^{\lambda}} + K_D s^{\mu} \quad , \qquad (\lambda, \mu > 0) \tag{4}$$

The control signal can be expressed in time domain as

$$u(t) = K_p e(t) + K_I D^{-\lambda} e(t) + K_D D^{\mu} e(t) \tag{5}$$

where $e(t)$ is the error signal. If $\lambda = \mu = 1$, we have a integer PID controller .

A modified approximate Oustaloup's method for fractional derivative [27] is used in this work. The Matlab/Simulink® software, the solver "ode45" in Simulink and the algorithm "active-set" in the Matlab optimisation are also used. The values of the parameters are listed in Table 1.

Table 1: Parameters (SI*).

Parameter	Value
Block mass	m1=15
Elasticity constant	k1 = 5000
Damping constant	c1 = 1500

* International system of unities

The ITAE method [27] is adopted and the Figure 3 illustrates the optimisation scheme.

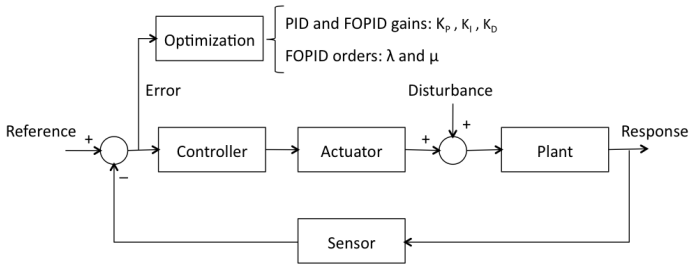


Figure 3. Optimisation scheme

For investigating the effect of a vibration disturbance, it was assumed the input reference is null and applied a sinusoidal disturbance using typical excitations found in studies of agricultural machinery vibrations with frequency of 4 Hz [20, 21].

3 RESULTS AND DISCUSSION

In this section, it presents the results related to the tuning process, the transient response for a step input excitation (desired position) and the disturbance responses for pulse and sinusoidal inputs (vibration profiles simulation). It is analysed, by means of numerical simulations, the behavior of the closed-loop system in both three cases: without a controller, with integer PID controller and with the proposed FOPID controller.

Simulations of the closed-loop AIS system model without a controller for controlling the position x_1 were carried out based on the parameters placed in Table 1. Figure 4 shows the response curve for this model applying a step input of 0.1 m and assuming that the null disturbance. It is possible to identify in Figure 4 a significant steady-state error (offset).

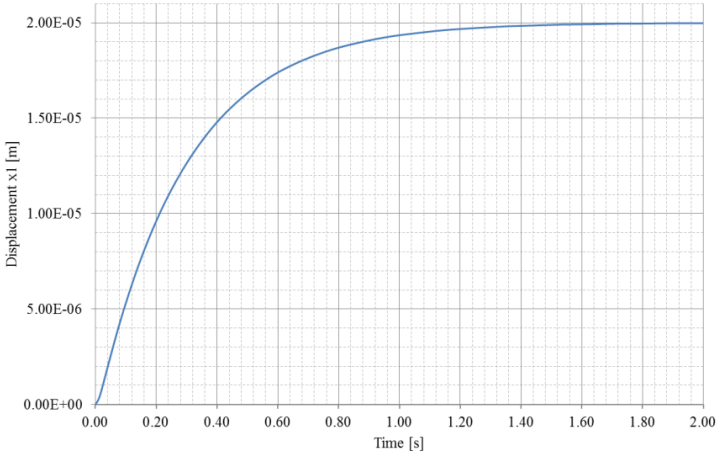


Figure 4. Step response for a closed-loop without controller

For investigating the effect of a vibration disturbance, it was assumed the input reference is null and applied a sinusoidal disturbance input with amplitude of 0.1 m and frequency of 4 Hz. Figure 5 shows the response curve related to these input settings.

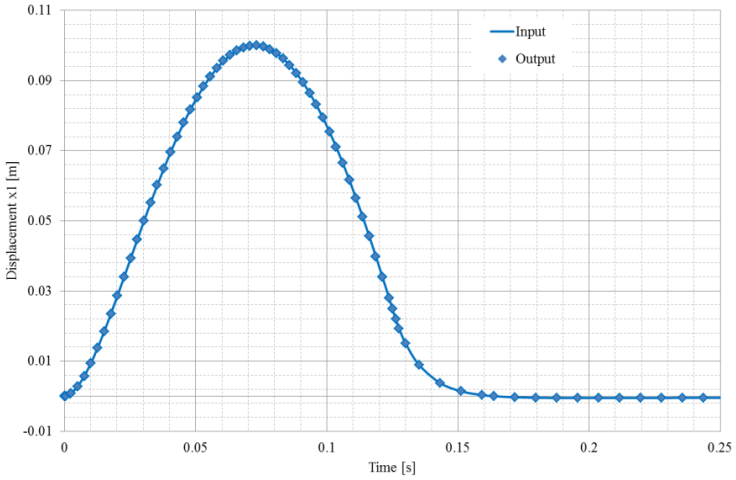


Figure 5. Response for sinusoidal disturbance for closed-loop without controller

Analysing the responses in Figure 4 and Figure 5, it is possible see that the closed-loop system without a controller is stable, however there is a large offset related to the reference input and there is no rejection to the disturbance input. Thereby, the use of a controller is required to improve the response to the input reference while reducing the influence of the disturbance.

3.1Tuning controllers and step response

For tuning the controller, the reference inputs of the closed-loop systems were treated independently. The controller gains of the integer PID and FOPID controllers were obtained using the tuning algorithm based on ITAE method for the step reference input of 0.1 m and the null disturbance. The gains are listed in Table 2 wherein the integral order of $\lambda = 0.7$ and derivative order of $\mu = 0.7$ related to the FOPID gains were obtained in the same tuning process.

Table 2. Gains of the controllers

	K_P	K_I	K_D
PID Controller	0.2291×10^4	1.4064×10^4	0.003×10^4
FOPID Controller	1.7785×10^4	7.0557×10^4	0.1956×10^4

From the values listed on the Table 2 and the related integral orders, it was generated the continuous transfer function of PID controller that is given by (6) and the continuous transfer function of FOPID controller that is given by (7),

$$G(s) = 0.2291 \times 10^4 + \frac{1.4064 \times 10^4}{s} + 0.003 \times 10^4 \times s \quad (6)$$

$$G(s) = 1.7785 \times 10^4 + \frac{7.0557 \times 10^4}{s^{0.7}} + 0.1956 \times 10^4 \times s^{0.7} \quad (7)$$

The controllers defined by (6) and (7) were used for simulations with input step of 0.1 m from which were obtained the response curves showed in Figure 6.

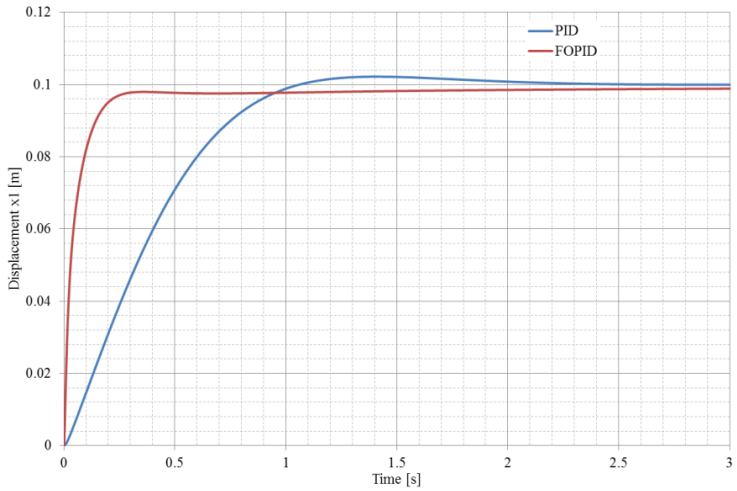


Figure 6. Step responses for the systems with integer PID and FOPID controller

Figure 6 shows the system with FOPID controller response with faster convergence and less overshoot in comparison to the system with integer PID controller. Such comparison is confirmed by the step response parameters taken from simulations and presented in Table 3.

Table 3. Step response parameters

	Peak	**Peak Time**	**Overshoot**	**Settl. Time**
PID Controller	0.12500 m	1.2657 s	0.12500 m	2.1250 s
FOPID Controller	0.09949 m	0.3687 s	0	1.1750 s

For the active stabilization system is necessary to compromise between the magnitude of the peak time, overshoot and settling time to a step input. In the response parameters system listed in Table 3, a reasonable compromise could be reached by using FOPID. It is possible to note that the performance of the FOPID gave a quick response identified by the smaller value for both peak time and settling time, while presents a lower magnitude for the overshoot. These entire responses characteristics guarantee to the FOPID based system a fast stabilization without large displacements if it is compared to the integer PID performance.

3.2 Response to disturbance by vibration

The efficient stabilization by controller demands that the system is still stable even the disturbance signal is intruded on the plant. Therefore, to establish the effectiveness of the controller is also analysed the robustness for disturbance rejection. After the tuning values of the FOPID controller have been obtained, two types of disturbances (pulse and sinusoidal) are applied in turn to assessment the robustness of the FOPID controller. The disturbance input of the closed-loop system was treated independently assuming null the reference input.

The pulse input disturbance has been applied to simulate a fast component of vibration profile. This signal was applied to closed-loop model system with amplitude of 0.1 m and period of 0.01 s for both systems based on integer PID and system based on FOPID. The pulse responses related x_1 displacement were obtained by simulations and compared in Figure 7.

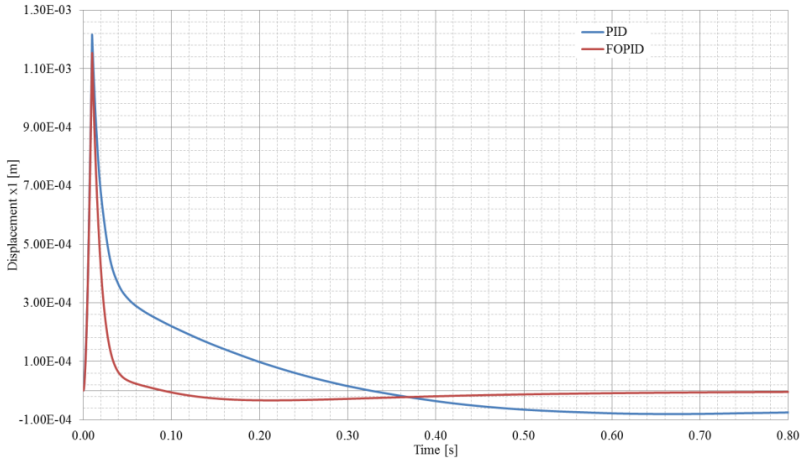


Figure 7. Pulse responses for the systems with integer PID and FOPID controllers

It is possible to see in Figure 7 that the system with FOPID controller effectively rejects the pulse disturbance compared to the system with the integer PID controller. The peak values for both responses are markedly smaller than the amplitude of the input signal, with the peak value for the response of the system based on FOPID is slightly smaller than the peak amplitude of the response for the system based on PID. More importantly, considering the settling time in 2 % of the largest response amplitude it is possible to assess that the value of this parameter is 0.34 s for the system response with the FOPID controller that is significantly smaller than the value of the 1.33 s for system response with the PID controller.

The sinusoidal input disturbance has been applied to closed-loop models based on integer PID and FOPID as typical component of vibration profile. This vibration component was modelled by a half period of a sine signal with frequency of 4 Hz and amplitude of 0.1 m. The sinusoidal responses related x_1 were obtained by simulations and compared in Figure 8.

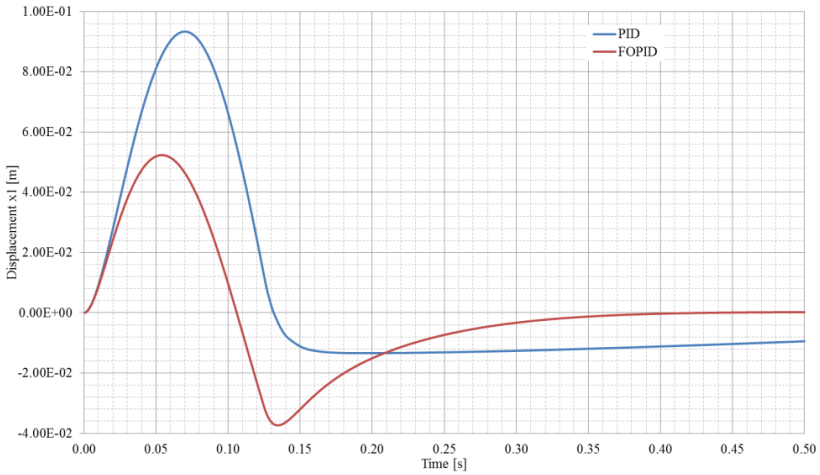


Figure 8. Response for sinusoidal disturbance for the systems with integer PID and FOPID

The curves presented in Fig. 8 shows the system with FOPID controller attenuated the sinusoidal disturbance compared to the system with integer PID. The peak value 0.05235 m for the system response based on FOPID controller is smaller than the peak value 0.09336 m for the system based on integer PID controller. Also, considering the settling time in 2 % of the

largest response amplitude it is possible to assess that the value of this parameter is 0.33 s for the system response with the FOPID controller that is significantly smaller than the value of the 1.06 s for system response with the PID controller

4 CONCLUSIONS

A methodology was proposed to design a FOPID controller for an AIS system applied to compensate the unwanted movement or vibration of the mechanism where the vision system is mounted on agricultural machinery frame. The evaluation of the model was performed by simulation using the FOPID response and compared to the performance of the closed-loop system for both without controller and with classical PID controller. Using reference signal excitation, step and pulse, it was possible to observe that the applying of the active element allows reaching a better performance for FOPID than that of using a pure closed-loop system without a controller or with a classical PID controller. Also, the ITAE criterion was an optimum method in finding the robust FOPID and PID parameters. The robustness for disturbance rejection of typical vibrations components of agricultural machinery demonstrated the benefits of the AIS and it shows the better performance FOPID in attenuating the disturbance inputs compared to the integer order PID controller. The modelling and simulation accelerated the study of stabilization controllers for AIS as well as the modelling of FOPID controller opens up new possibilities for designing of optimal controllers for these systems.

Acknowledgements

The authors wish to acknowledge the FAPESP (São Paulo Research Foundation, grant 2014/02041-9).

REFERENCES

[1] Y. W. Choi, T. H. Kang and S. G. Lee. Development of Image Stabilization System Using Extended Kalman Filter for a Mobile Robot. Advances in Swarm Intelligence. Lecture Notes in Computer Science Vol. 6145, 2010, pp 675-682.

[2] J. Xue, L. Zhang, T. E. Grift. Variable field-of-view machine vision based row guidance of an agricultural robot. Comput. and Electron. in Agriculture, Vol. 84, June 2012, pp. 85-91.

[3] B.Åstrand, A.J. Baerveldt,. A vision based row-following system for agricultural field machinery. Mechatronics, 2005, 15 (2), 251–269.

[4] S.A. Hiremath, G. W.A.M. van der Heijden, F. K. van Evert, A. Stein, C. J.F. ter Braak. Laser range finder model for autonomous navigation of a robot in a maize field using a particle filter Computers and Electronics in Agriculture, Vol. 100, January 2014, pp. 41-50.

[5] K. Janschek, V. Tchernykh and S. Dyblenko, Performance Analysis of Opto-mechatronic Image Stabilization for a Compact Space Camera, Control Eng. Practice, 2007, 15: 333-347.

[6] A.Gasteratos, "Active Camera Stabilization with a Fuzzy-grey Controller", European Journal of Mech. and Environmental Eng., 2009,Vol 2009-2, pp 18-20.

[7] N. Marichal, M. Tomas-Rodriguez, A. Hernandez, S. Castillo and P. Campoy. Vibration reduction for vision systems on board UAV using a neuro-fuzzy controller. Journal of Vibration and Control, Jun 2013, pp. 1-12.

[8] J.A.T. Machado, V. Kiryakova, F. Mainardi, Recent history of fractional calculus, Communications in Nonlinear Science and Numerical Simulation; 2011; 16 (3), 1140-1153.

[9] D. Valerio, J.J. Trujillo, M. Rivero, J.A.T. Machado, D. Baleanu, Fractional calculus: A survey of useful formulas, Eur. Phys. J. Special Topics, 222, 2013, 1827–1846, doi: 10.1140/epjst/e2013-01967-y.

[10] S. A. David, J.L. Linares, E.M.J.A. Pallone, Fractional order calculus: historical apologia, basic concepts and some applications, Rev. Bras. de Ensino de Física, 2011, 33 (4), http://dx.doi.org/10.1590/S1806-11172011000400002.

[11] E. C. de Oliveira and J. A. T.Machado, A Review of Definitions for Fractional Derivatives and Integral, Mathematical Problems in Engineering, 2014, http://dx.doi.org/10.1155/2014/238459

[12] K. B. Oldham, J. Spanier, The Fractional Calculus: Theory and Applications of Differentiation and Integration to Arbitrary Order 2006 (Dover Publication, Mineola).

[13] I. Podlubny, Fractional differential equations. New York. Academic Press, 1999.

[14] Ostalczyk P, Rybicki T. Variable-fractional-order Dead-beat Control of an Electromagnetic Servo. J Vib Control 2008;14:1457–71.

[15] Bohannan GW. Analog Fractional Order Controller in Temperature and Motor Control Applications. J Vib Control 2008;14:1487–98.

[16] J.I. Suarez, B. M. Vinagre A Fractional Adaptation Scheme for Lateral Control of an AGV. J Vib Control 2008;14:1499–511.

[17] J.A.T. Machado. Analysis and design of fractional-order digital control systems n.d.

[18] J.A.T. Machado, A. Azenha Position/force fractional control of mechanical manipulators. Adv Motion Control, AMC ’98-Coimbra, 1998 5th Int Work 1998:216–21.

[19] D. Xue,C. Zhao, Y. Chen. Fractional order PID control of a DC-motor with elastic shaft: a case study. Proc. Am. Control Conf., Minneapolis, MN: IEEE; 2006, p. 3182–7.

[20] A.J. Scarlett, J.S. Price, R.M. Stayner. Whole-body vibration: evaluation of emission and exposure levels arising from agricultural tractors. J Terramech, 44 (2007), pp. 65–73

[21] F. Shams. Tractors cabin's passive suspension parameters optimization via experimental and numeral methods. Journal of Terramechanics, 2011, v. 48, n. 6, p. 439-450.

[22] Y. Song, C.A. Glasbey, G.W. Horgan, G. Polder, J.A. Dieleman, G.W.A.M. van der Heijden.Automatic fruit recog. counting from multiple images.Biosyst Eng.2014;118:203–15.

[23] D.G. Fernández-Pacheco, D. Escarabajal-Henarejos, A. Ruiz-Canales, J. Conesa, J.M. Molina-Martínez. A digital image-processing-based method for determining the crop coefficient of lettuce crops in the southeast of Spain. Biosyst Eng 2014;117:23–34.

[24] Z. Peng, C. Jun. Weed recognition using image blur information. Biosyst Eng 2011;110:198–205.

[25] A. Camargo, J.S. Smith. An image-processing based algorithm to automatically identify plant disease visual symptoms. Biosyst Eng 2009;102:9–21.

[26] I. Podlubny. Fractional-order systems and PI/sup /spl lambda//D/sup /spl mu//-controllers. IEEE Trans Automat Contr 1999;44:208–14.

[27] D. Xue, C. Zhao, Y. Chen . A modified approximation method of fractional order system. Proc. Int. Conf. on Mechatronics and Automation, IEEE;2006, p. 1043-8.

International Conference on Engineering Vibration
Ljubljana, Slovenia, 7-10 September 2015

VIBRATION PROTECTION OF OBJECTS WITH HELP OF THIN-LAYERED RUBBER-METAL ELEMENTS

Svetlana N. Polukoshko*[1], **Vladimirs F. Gonca**[2]

[2] Ventspils University College, Engineering Research Institute "VSRC", Ventspils, Latvia
pol.svet@inbox.lv

[1]Riga Technical University, Institute of Mechanics, Riga, Latvia
vladimirs.gonca@rtu.lv

Keywords: Elastomers, Bonded Elastomeric Layers, Vibration Damping, Rabotnov's Kernel,Viscoelastic Behaviour.

Abstract. *Rubber and rubber-metal (RM) elements are successfully used as bearing, joints, compensating devices, vibration and shock absorbers in civil engineering and machine building because of rubber and rubberlike materials (elastomers) have a capability of absorbing input energy much better than other construction materials. The elastic properties of rubber in such supports allows reverse backward to its original position under dynamic load action. Along with the immediate elastic deformation these materials exhibit a retarded elastic deformation, viscous flow (creep) and relaxation. The mechanical properties of rubber which are necessary for the optimal design of antivibration devices are next: bulk modulus of compression, dynamic and static shear modulus, energy dissipation factor. To describe the relationship between the compressive (or shear) stress $\sigma(t)$ and strain $\varepsilon(t)$ the creep and relaxation kernels, taking into account the viscoelastic properties of the rubber, are used. In this paper the flat-type RM absorber with kinematic harmonic excitation is considered. For the accounting of dissipative properties of the rubber Rabotnov's kernel is used, the energy loss during one oscillation period is calculated. Damping properties are expressed by the ratio of amplitude of the driving vibration to the amplitude of the forced oscillations of object.*

1 INTRODUCTION

Nowadays under conditions of intensification of production processes, increasing of the equipment capacity and high-speed vehicles creation the question of preventing the harmful effects of vibration requires special attention. In the most cases it is necessary to provide of shock and vibration protection devices at the design stage [1–5]. Elastomers (rubber and rubber-like materials) are the most suitable material for anti-vibration devices due to its adhesive characteristics, the ability to acquire a predetermined shape at press processing after curing, high elasticity and high internal damping. The elastic properties of rubber characterized by a large difference between bulk and shear moduli (K/ G ratio reaches 500 ÷ 5000) [3, 6–10]. The high elasticity of rubbers allows them to withstand the large elongation without breaking. Consequently, the rubber has a greater capacity to store energy per unit volume compared with other materials.

Rubber and rubber-metal parts (rubber and metal connected by vulcanization or gluing) are used as elastic supports of veicle and machinery and are designed to reduce the dynamic loads of the working machines on their foundations or floors of buildings or for the protection of equipment and devices from bumps, shock and vibration loading operating on their base. The packages of thin-layered rubber-metal elements (rubber layer widh/height ratio > 10) are also successfully used. Thin-layered rubber-metal elements (TRME) - essentially anisotropic elastic element made of rubber (or other elastomeric) and metal (or hard plastic) assembled in a package of two or more layers having a high load capacity (more than 200 MPa in the normal to layer direction) and higher compliance (50 ... 200% from relative deformation) in the transverse direction [9–13]. In practice TRME packages of different geometric shapes are used: flat, cylindrical, conical and others, number of layers may be different, at least three (Fig. 1).

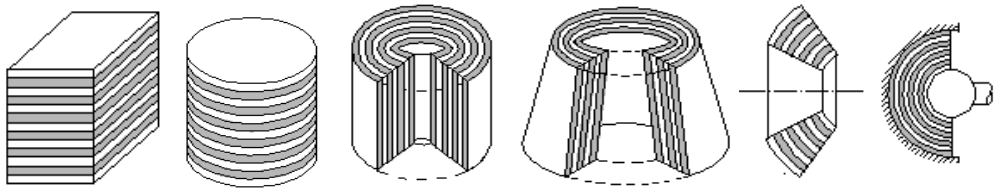


Figure 1: Multilayered elastomeric structures examples; a) flat rectangular, b) flat circular, c) cylindrical, d) conical, e) and f) spherical

Elastomers offer many engineering advantages because of their small volume compressibility and ability to maintain large elastic deformation. Reinforced elastomeric structures consist of alternating thin layers of rubber and adhesive – bonded reinforcing layers of much more rigid material (usually metal); geometric shapes and number of layers may be different. Packages of thin-layered rubber-metal elements (TRME) are successfully used in civil engineering and machine building. The elastic compensation device mounted between the vibrating base and protecting object is the main element of any the passive vibration protection system. Natural frequency of vibrating mass may be estimated if stiffness characteristics of vibroisolator are known, i.e. the analytical dependence of the relationship between imposed external compressive or share forces and corresponding displacements. As an example the flat multilayered TRME package of rectangular form under axial compression is presented. It is shown that for a given layers geometry neglecting the weak compressibility and deformation of the elastomeric and intermediate non-elastomeric layers leads to significant errors.

Rubber is a material that has a clearly defined relaxation properties, so its mechanical properties strongly depend on the time of application of external loads, that is, the mode of de-

formation [10, 14–18]. If the duration of the force causing a deformation equal to the time of relaxation processes in the rubber, the elastic deformation is fully manifested, and this mode of deformation will correspond to well-defined modulus of rubber. When rate of deforming load application increases modulus of elasticity will be changing, and its magnitude will be more than elastic modulus for the mode with full implementation of the elastic process.

Since many rubber-metal products serve as elastic links experience an impulsive load, alternating-sign load, periodical and non-periodical high-frequency load, it is necessary to to take into account the characteristics of the mechanical properties of rubber under dynamic loads [9–13].

In this paper the vibration absorber operating under uniaxial deformation (compression or shear) is considered. In Fig. 2 the scheme of mounting of this device are shown: RM absorber with flat layers (cylindrical or prismatic form) is placed between protected object and base. Rubber layers 1 are reinforced by perfectly rigid undeformable plates 2, which is cured on to the elastomers by vulcanizing.

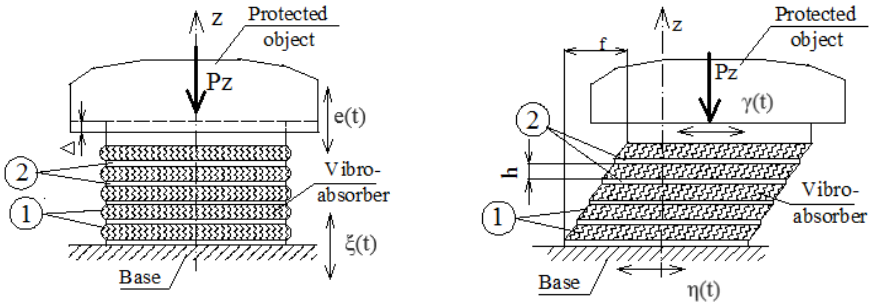


Figure 2: Scheme of the installed absorbers: (a) anti-vertical vibrations, (b) anti-horizontal vibrations; 1-rubber layers of height *h*, 2 –metal layer.

The aim of this work is to determine the dependence of this absorber dissipative and damping properties on the viscoelastic behaviour of elastomer, on the forced vibration frequency and natural frequency of the system for the model with one degree of freedom (ODF) under the action of harmonic excitation. Mass of isolator is not taken into account because of its smallness. The damping properties are determined by the ratio of the amplitude of the upper plate forced oscillations to the amplitude of the forcing oscillation of lower plate. Dissipative properties of vibroabsorber are estimated by the energy loss during one period of oscillation. Such approach allows to appoint the dimentions of antivibration devices at design stage.

2 MATHEMATICAL MODELS OF RUBER-METAL ELEMENT

2.1 Visco-elastic properties in rubber model

In the mechanical properties of rubber a set of features manifest itself: alongside with the instantaneous elastic deformation these materials exhibit retarding elastic deformation, viscous flow (creep) and relaxation. For the description of the elastic and dissipative processes for the most materials a combination of two types of mechanical elements, elastic and viscous, may be used. Elastic element is controlled by Hooke's law, viscous - by Newton's law of flow. Connections of them in series or in parallel joint (Maxwell model or Kelvin-Voigt model) approximately describes the visco-elastic behaviour of the material [17–19].

The most common relationship between stress and strain may be expressed by means of integral equations of relaxation and creep. In this case accounting of the time factor influence is

reduced to solving systems of integro-differential equations. Methods of solving such systems are very diverse, the most widely used methods based on the use of integral transforms, especially Laplace and Fourier transforms, and also integral operators Volterra's type [13].

In the case of axial deformation for weakly filled rubbers and small deformation ($\varepsilon \le 20\%$), when the linear dependence between stress and strain exists, the dependence is valid:

$$\sigma(t) = E_t \varepsilon(t),$$

where E_t – time operator, which does not depend on σ and ε and reflects the viscoelastic behaviour of system.

This dependence may be written in the form of an integral equation of Volterra:

$$\sigma(t) = E_0 \left[\varepsilon(t) - \int_0^t R(t-\tau)\varepsilon(\tau)d\tau \right], \tag{1}$$

where: E_0 – instantaneous compressive modulus (or G_0 – instantaneous shear modulus), which specifies the instantaneous stiffness in the classical sense; $R(t - \tau)$ – relaxation kernel describing the viscoelastic properties of the rubber.

The presence of relaxation kernel determines the dissipative properties of rubber.

Using Fourier – images transform of $\sigma(\omega)$, $\varepsilon(\omega)$ and R(ω), equation (1) may be written as:

$$\sigma(\omega) = E_0(1 - R(\omega))\varepsilon(\omega) = E(\omega)\varepsilon(\omega), \tag{2}$$

where $E(\omega)$ – dynamic compression modulus of elasticity (it may be also $G(\omega)$ – shear modulus).

$$\sigma(\omega) = \int_{-\infty}^{\infty} \sigma(t) e^{-i\omega t} dt,$$

analogically for $\varepsilon(\omega)$, $R(\omega)$.

The elastic compressive modulus $E(\omega)$ expressed as complex modulus is:

$$E(\omega) = E'(\omega) + iE''(\omega).$$

Splitting $E_0(1-R(\omega))$ in Eq. (2) into real and imaginary parts we obtain:

$$E'(\omega) = E_0 \operatorname{Re}(1 - R(\omega)), \qquad E''(\omega) = -E_0 \operatorname{Im} R(\omega). \tag{3}$$

Let's denote

$$\operatorname{Re}(1 - R(\omega)) = B_1(\omega), \qquad -\operatorname{Im} R(\omega) = B_2(\omega),$$

and rewrite the elastic complex modulus $E(\omega)$ as:

$$E(\omega) = E_0 B_1(\omega) + iE_0 B_2(\omega).$$

Proposed by A. Rzhanitsin, Y. Rabotnov and M. Koltunov kernels are in most common use. These kernels allow satisfactory describing the mechanical properties of rubber in the medium frequency range $10^{-3} < \omega < 10^3$ s^{-1}. In this work the Rabotnov's kernel is considered, which represents fractional exponential function $R(t - \tau) = Э_\alpha(-\beta, t - \tau)$:

$$R(t-\tau) = (1-\tau)^{\alpha} \sum_{n=0}^{\infty} \frac{(-\beta)^n (t-\tau)^{n(1-\alpha)}}{\Gamma[(n+1)(1+\alpha)]}, \tag{4}$$

where Γ – gamma-function, $-1 < \alpha < 0$, $\beta > 0$.

In this equation α – parameter of fractionality, expressed in terms of the maximum value of the spectrum of relaxation times and modulus defect, β – rheological characteristics of rubber equal to:

$$\beta = t_0^{-1-\alpha},$$

where t_0 – generalized relaxation time.
Rheological parameters are tabulated for many types rubbers.

Fourier image for Rabotnov's kernel is:

$$R(\omega) = \frac{1}{(i\omega)^{(i+\alpha)} + \beta}. \tag{5}$$

Taking into account Eq. (3) real and imaginary parts we obtain from Eq. (5):

$$B_1(\omega) = \frac{\omega^{1+\alpha}\cos\delta + \beta}{\omega^{2(1+\alpha)} + 2\omega^{1+\alpha}\beta\cos\delta + \beta^2}, \qquad B_2(\omega) = \frac{\omega^{1+\alpha}\sin\delta}{\omega^{2(1+\alpha)} + 2\omega^{1+\alpha}\beta\cos\delta + \beta^2}, \quad \delta = \frac{\pi}{2}(1+\alpha). \tag{6}$$

The coefficients B_1 and B_2 are the Fourier cosine transform and sinus transform of the fractional exponential function (4):

$$B_1 = \int_0^\infty R(z)\cos(\omega z)dz, \qquad B_2 = \int_0^\infty R(z)\sin(\omega z)dz.$$

If the deformation of the elastomer is harmonic, equation (1) may be written as:

$$\sigma(t) = E_t\varepsilon_0\sin(\omega t) = E_0\varepsilon_0\left[\sin(\omega t) - \int_{-\infty}^{t} R(t-\tau)\sin(\omega\tau)d\tau\right] = E_0\varepsilon_0\left[(1-B_1)\sin(\omega t) + B_2\cos(\omega t)\right]. \tag{7}$$

The coefficients B_1 and B_2 are the same for compression and shear deformation. In the case of share:

$$G'(\omega) = G_0B_1(\omega) \text{ and } G''(\omega) = G_0B_2(\omega).$$

In this case stress is calculated by the same way.

2.2 Model of damping system with one degree of freedom

Most clearly it is possible to estimate the dynamic properties of the RME in the frame of the simplified one-degree-of-freedom model, which allows to obtain explicit analytical dependences for dissipation and damping characteristics of RME. Such model, presented in Fig.1, is considered below. Protected object is represented as a point mass, vibration isolator is placed between the protected object and the vibrating base with kinematic excitation in accordance with time dependence of $\xi(t)$. The time dependence of the movement of the protected object is $e(t)$.

Since ξ and e are defined in the inertial system, the relative motion of the object and base will be equal to $\xi(t) - e(t)$, and the deformation of compression of the elastomer layers with total thickness h_Σ is equal to:

$$\varepsilon(t) = \frac{\xi(t) - e(t)}{h_\Sigma}. \tag{8}$$

Let function $\xi(t)$ is periodic with amplitude ξ_0:

$$\xi(t) = \xi_0 \sin(\omega t). \tag{9}$$

Since the system is linear, for the harmonic input function (e. g. deformation) all caused by its output processes (e. g. stress) will also be harmonic functions with the same frequency. Then it is natural to assume that function *e (t)* will be as follows:

$$e(t) = e_0 \sin(\omega t + \varphi), \tag{10}$$

where e_0 – amplitude vibrations of steady-state vibrations of mass, φ – angle of lag.
The force imposed on the object with mass *m* from the TRM support is equal to:

$$F = A\sigma(t),$$

where A – area of the upper face of the vibration.
The equation of motion of mass *m* in the *z* direction is:

$$m\ddot{e}(t) = -A\sigma(t).$$

Let us find the mass displacementdepending on the viscoelastic properties of the rubber. Taking into account Eq. (1) we have:

$$m\ddot{e}(t) = -AE_0\left[\varepsilon(t) - \int_{-\infty}^{t} R(t-\tau)\varepsilon(\tau)d\tau\right] \tag{11}$$

Let denote the natural frequency of vibrating mass as ω_0, taking into account Eq. (8):

$$\omega_0 = \sqrt{\frac{AE_0}{h_\Sigma m}} \tag{12}$$

Substituting Eqs. (8–10) into Eq. (11) and taking into account Eq. (12) we received the equation of the object motion in the form:

$$\ddot{e}(t) - {\omega_0}^2\left[(\xi(t) - e(t)) - \int_{-\infty}^{t} R(t-\tau)(\xi(\tau) - e(t))d\tau\right] = 0 \qquad \text{or:}$$

$$\ddot{e}(t) + {\omega_0}^2 e_0 \sin(\omega t + \varphi) - {\omega_0}^2 \xi_0 \sin(\omega t) - \omega_0^2\left[\int_{-\infty}^{t} R(t-\tau)(\xi \sin(\omega\tau) - e\sin(\omega\tau + \varphi))d\tau\right] = 0 \tag{13}$$

For harmonic deformation taking into account linear independency of the functions $\sin(\omega t)$ and $\cos(\omega t)$, using the property $R(t-\tau) = 0$ if $t < \tau$, the system of the equations is obtained from Eq. (13):

$$\begin{vmatrix}\cos(\varphi) & -\sin(\varphi)\\ \sin(\varphi) & \cos(\varphi)\end{vmatrix} \cdot \begin{vmatrix}(1 - B_1(\omega)) - b^2\\ B_2(\omega)\end{vmatrix} = \frac{\xi_0}{e_0}\begin{vmatrix}(1 - B_1(\omega))\\ B_2(\omega)\end{vmatrix}, \quad b = \frac{\omega}{\omega_0}. \tag{14}$$

From system (14) we can define the amplitude of the forced vibration e_0 of mass and the angle of lag φ:

$$\frac{e_0}{\xi_0}(\omega) = \frac{{B_1}^2 - 2B_1 + {B_2}^2 + 1}{\sqrt{\left(B_2 b^2\right)^2 + \left({B_1}^2 + B_1 b^2 - 2B_1 + {B_2}^2 - b^2 + 1\right)^2}}, \quad . \tag{15}$$

$$\varphi(\omega) = arctan\frac{-B_2(\omega)b^2}{B_1(\omega)^2 + B_1(\omega)b^2 - 2B_1(\omega) + B_2(\omega)^2 - b^2 + 1}, \quad b = \frac{\omega}{\omega_0}. \tag{16}$$

$B_1=B_1(\omega)$ and $B_2=B_2(\omega)$ – functions of excitation frequency, calculated in accordance with Eq. (6).

2.3 Dissipative properties of rubber elements

The expression (1) is the generalized Hooke's law, here E_0 defines the instantaneous stiffness of rubber in classic sense, but relaxation kernel defines the dissipative properties of rubber. Further we can calculate the work of compressive (or shear) stress per unit volume during the all-time of the existence of deformations $\varepsilon(t)$.

$$A = \int_{-\infty}^{\infty} \sigma(t) d\varepsilon(t) = \int_{-\infty}^{\infty} \sigma(t) \dot{\varepsilon}(t) dt \tag{17}$$

Expressing $\sigma(t)$ and $\varepsilon(t)$ in terms of Fourier components we receive:

$$\int_{-\infty}^{\infty} \sigma(t) \dot{\varepsilon}(t) dt = \frac{1}{4\pi^2} \int_{-\infty}^{\infty} dt \int_{-\infty}^{\infty} E(\omega') e^{i\omega t} d\omega' \int_{-\infty}^{\infty} i\omega \varepsilon(\omega) e^{i\omega t} d\omega,$$

after transformation:

$$A = \int_{-\infty}^{\infty} \sigma(t) d\varepsilon(t) = \int_{-\infty}^{\infty} \omega E''(t) |\varepsilon(\omega)|^2 d\omega.$$

It is seen that $\omega E''(\omega)$ defines the density of the energy dissipation due to viscoelastic rheology of rubber. This expression may be used for the estimation of the volume density of energy release. Generally speaking, at an orbitrally point of time it is impossible to divide dissipative loss and elastic energy, saved in the RM support. For the harmonic loading the loss of energy during the period of vibration may be calculated as:

$$U_T(\omega) = \pi m \omega_0^2 B_2(\omega) b^4 \frac{{\xi_0}^2}{B_2(\omega)^2 + \left[1 - B_1(\omega) - b^2\right]^2}, \quad b = \frac{\omega}{\omega_0}. \tag{18}$$

Energy loss depends on natural frequency ω_0, excitation frequency ω, vibration amplitude ξ_0 of the base, as well as B_1 and B_2 coefficients. It is necessary to take into account, that ω_0 in turn depends on vibrating mass.

This expression is necessary for attenuation factor definition, if vibration motion of the object is describe approximately, for example, by viscoelastic Maxwell model.

3 NUMERICAL SOLUTION AND EXPERIMENTAL RESULTS

The results of the calculation of damping properties of RM elements in accordance with above algorithm and equations are given below. Numerical examples was solved with help of Mathcad program.

In Fig. 3 (a), (b) plots of dependence the amplitudes ratio on excitation frequency for natural frequencies ω_0 = 1, 5, 10, 15 and 20 s^{-1} for low-filled rubber 2959 (α = -0.6 and factor β =1.062) are presented.

From Fig. 3 (b) we can see that under the excitation frequency ω =3, 15, 30, 45 and 60 s^{-1} the amplitude of the forced vibration of the objects becames in 10 times smaller for natural frequencies ω_0 = 1, 5, 10, 15 and 20 s^{-1} respectively. This confirm the well-known fact from vibration protection theory. From this graphs it is seen that RM absorber diminishes the vibration action on the object if it's natural frequency much less than forcing frequency.

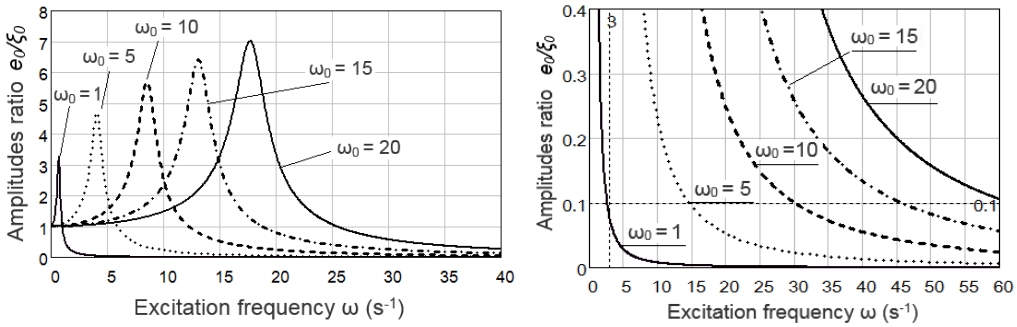


Figure 3: Plots of dependence the amplitude ratio on excitation frequency for different natural frequencies ω_0 and factor β =1.062. (a) – full- scale plots, (b) – lower part of plots.

Plots of dependence the lag angle φ on excitation frequency for different natural frequencies ω_0 are presented in Fig. 4; factor β = 1.062, α = - 0.6.

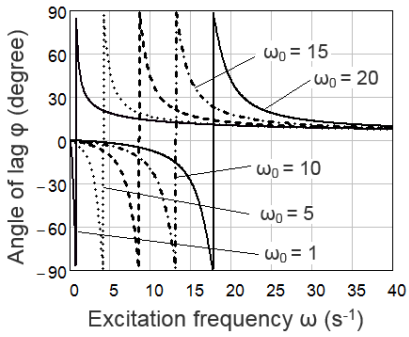


Figure 4: Plots of dependence the lag angle φ on excitation frequency for different natural frequencies ω_0; factor β = 1.062, α = -0.6.

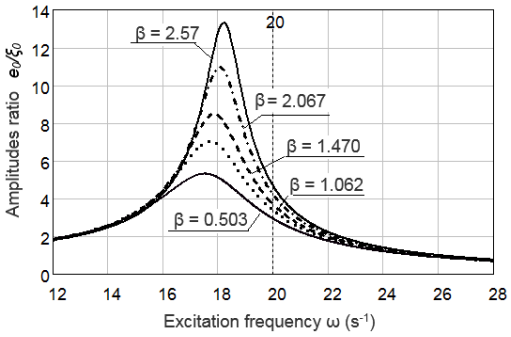


Figure 5: Plots of dependence the amplitude ratio on excitation frequency for rubbers with α = -0.6 and different β factor, natural frequency ω_0 = 20 s^{-1}.

In Fig. 5 plots of dependence the amplitudes ratio on factor β for different rubbers for natural frequencies ω_0 = 20 s^{-1} are shown, for all rubber α = - 0.6.

Energy loss according to Eq. (18) is studied for RM absorbers with excitation amplitude ξ_0 = 0.5 mm, factors β = 1.062 and α = - 0.6. Plots in Fig. 6 shows the dependence of energy loss per period U_T on excitation frequency for mass 200 kg and 400 kg (ω_0 = 14.09 s^{-1} and 9.96 s^{-1} respectively). Reinforced RM absorber of the cylindrical form with rubber part radius r = 18 mm and total rubber height h_Σ = 40 mm is studied, G_0 =1.76·10^6 N/m^2.

It is seen from the plots that the energy loss per period is identical for different mass if excitation frequency is equal to the natural frequency.

In Fig. 7 plots of the dependence of energy loss per period U_T on excitation frequency for mass 200 kg are presented for RM absorbers with h_Σ = 40 mm, radii 15, 18 and 25 mm (natural frequency ω_0=11.74 s^{-1}, 14.09 s^{-1} and 19.57 s^{-1} respectively).

Loss of energy more distinguishes in the post-resonance zone; absorbers with radius 20 mm deposes the energy twice as large than absorber with r=18 mm.

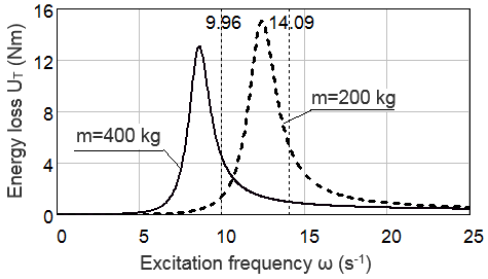


Figure 6: Plots of dependence energy loss per period U_T on excitation frequency for mass 400 kg with $\omega_0 = 9.96\ s^{-1}$ and for mass 200 kg, $\omega_0 = 14.09\ s^{-1}$.

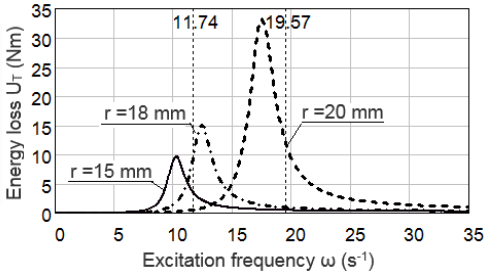


Figure 7: Plots of dependence energy loss per period U_T on excitation frequency for mass 200 kg and natural frequencies $\omega_0 = 11.74\ s^{-1}$, 14.09 s^{-1},19.57 s^{-1}.

4 CONCLUSIONS

- This paper presents the procedure of the estimation of damping and dissipative properties of rubber-metal absorber devices for ODF system under harmonic exitation. Definition of damping properties is fulfilled for one degree-of-freedom system with kinematic excitation.
- Damping properties are expressed by the ratio of the amplitude of the driving lower base to the amplitude of the forced oscillations of the upper base and the object**.** Estimation of the dissipative properties are expressed by the energy loss per period of oscillation.
- The flat rubber – metal absorber of cylindrical form is calculated as the examples. Numerical examples was solved with help of Mathcad -15 program.
- The fulfilled calculations confirm the known fact of the theory of vibration protection: if the natural frequency of the object is three times lower than the frequency of the forcing oscillationsos, the forced oscillation amplitude is attenuated approximately in ten times.
- It can be concluded that the proposed approach is suitable for dimensioning of RM absorber on the design stage depending on the prevented object mass, its operating mode and taking into account physical - mechanical properties of the elastomeric layers.
- Experimental study of the dissipative and damping properties of rubber-metal vibration absorber will be the next step of the current research work.

REFERENCES

[1] J. M. Kelly and D. A. Konstantinidas, *Mechanics of Rubber Bearings for Seismic and Vibration Isolation.* UK: John Wiley & Sons, 2011.

[2] A. N. Gent, *Engineering with Rubber: How to Design Rubber Components.* Munich, Carl Hanser Verlag, 2011.

[3] J. T. Bauman, J. T., *Fatigue, Stress and Strain of Rubber Components: Guide for Design Engineers.* Munich, Carl Hanser Verlag, 2008.

[4] D. Konstantinidis, J.M. Kelly, Advances in Low-Cost Seismic Isolation with Rubber. *Proceedings of the 10th National Conference in Earthquake Engineering*, July 21-25, 2014, Earthquake Engineering Research Institute, Anchorage, AK, 2014.

[5] Lihua Zou, Kai Huang, Yu Rao, Ran Guo, Zhixu Xu, Research on isolation property of prestressed thick rubber bearings. *JVE Journal of Vibroengineering*, March 2013, Volume 15, Issue 1. pp. 383-394.

[6] V. A. Lepetov, *Rubber technical products.* Moscow, Chemistry, 1972.

[7] V. T. Lyapunov, E. E. Lavendel and S.A. Shlyapochnikov, *Rubber vibration isolators. Habdbook.* Russia, Leningrad, Sudostrojenie, 1988.

[8] S. I. Dimnikov, *Design of Rubber Elements of Structures.* Latvia, Riga: Zinatne, 1991.

[9] E. E. Lavendel, *Design of Rubber Products.* Moscow: Mashinostroenie, 1976.

[10] V. M. Malkov, *Mechanics of Multi-layered Elastomeric Structures.* St.-Petersburg, Russia, St.-Petersburg University Press, 1998.

[11] N. S. Gusyatinskaya, *Application of Thin Layer Rubber-Metal Elements in Machine-Tools and Other Engines*. Moscow, Mashinostroenie, 1978.

[12] N. N. Frolov, S. J. Moldovanov and S. B. Lozovoy, *Mechanics of Thin Rubber Elements*, Kuban State Technological University, Krasnodar, Publishing House "Jug", 2011.

[13] N. A. Leykand, E. E. Lavendel and V. A. Hrichikova, Calculation of Compression Rigidity of Thin-layer Rubber-Metal Elements. In book*: Problems of Dynamics and Strength*, Issue 38, pp. 57-63, Riga, 1981.

[14] T. O. Ormonbekov and U. T. Begaliev, *Use of Thin Rubber-Metal Elements in Earthquake Protection of Buildings, Engineering Constructions and Equipments.* Kyrgyzstan, Bishkek, Ilim, 1996.

[15] A.R.Bhuiyan, A.F.M.S. Amin, T. Hossain, Y. Okui, Nonlinear viscosity law for rate-dependent response of high damping rubber: FE implementation and verification. *Constitutive Models for Rubber V* – Boukamel, Laiarinandrasana, Meo & Verron (eds), Taylor & Francis Group, London, 2008, pp. 279-284.

[16] A.S. Kravchuk, A.I. Kravchuk, Simulation on creep by hereditary theory in a simple model of constant thickness deformed coating. *Electronic scientific journal, Apriori. Series: natural and technical sciences.* № 2, 2014, Available: http://apriori-journal.ru/seria2/2-2014/Kravchuk-Kravchuk.pdf

[17] V. N. Poturaev and V. I. Dyrda, *Rubber Machine Elements.* Voscow, Mashinostrojenie, 1977.

[18] A. R. Bhuiyan, Y. Okui, H. Mitamurab, T. Imaic, A Rheology Model of High Damping Rubber Bearings for Seismic Analysis: Identification of nonlinear viscosity. *International Journal of Solids and Structures*, 46, pp. 1778–1792, 2009, Available: http://www.sciencedirect.com/science/article/pii/S0020768309000298

[19] A. F. M. S. Amin, M. S. Alam and Y. Okui, Measurement of Lateral Deformation in Natural and High Damping Rubbers in Large Deformation Uniaxial Tests. *Journal of Testing and Evaluation*, Vol. 31, No 6, pp. 524-532, Nov. 2003, Available: http://www.saifulamin.info/publication/journals/j4.pdf

11th International Conference on Engineering Vibration
Ljubljana, Slovenia, 7–10 September 2015

EFFECTIVENESS OF SEISMIC-TUNED PASSIVE TUNED MASS DAMPERS ACCOUNTING FOR SOIL-STRUCTURE INTERACTION

Jonathan SALVI[1], **Fabio PIOLDI**[1], **Egidio RIZZI**[*1]

[1]Università di Bergamo, Dipartimento di Ingegneria e Scienze Applicate,
viale G. Marconi 5, I-24044 Dalmine (BG), Italy
[*]Corresponding Author: egidio.rizzi@unibg.it

Keywords: Tuned Mass Damper (TMD), Earthquake Tuning, Soil-Structure Interaction (SSI), Frame Structures.

Abstract. *Tuned Mass Damper (TMD) devices are generally considered as valuable means for reduction and control of undesired vibrations and excessive dynamic responses of structural systems. The expectable level of performance of TMDs in the framework of earthquake engineering, a research topic widely studied and still debated, doubtlessly plays an important role, since TMDs may represent a convenient intervention solution for both aseismic structural design and seismic retrofitting of existing structures. The present paper is placed within such a research context, aiming at investigating the potential effectiveness of an optimum passive TMD in reducing the structural response to strong-motion earthquakes of a given set of MDOF shear-type frame structures. One of the most relevant features of this study is the proposal of a seismic-tuned TMD, optimised through an innovative numerical method, apt to provide the optimum configuration of the control device for a given combination of host structure and seismic event. A further important aspect is the consideration, within the structural and dynamic model, of Soil-Structure Interaction (SSI) effects, which looks crucial for a comprehensive analysis of the whole context. Moreover, being SSI embedded within the tuning process, an influence on both optimum TMD parameters and achievable TMD performance is recorded and quantified. The obtained results, focussing on the relations between all considered features (including soil parameters) and arising TMD effectiveness in terms of reduced seismic response, also for post-tuning trials, provide crucial information towards the final evaluation of TMDs as possible useful control devices in earthquake engineering applications.*

1 INTRODUCTION

The subject discussed here concerns the performance of seismic-tuned passive Tuned Mass Damper (TMD) devices for the reduction of the earthquake response of frame buildings, with consideration of Soil-Structure Interaction (SSI) effects. In particular, the optimum TMD setting is achieved through an original seismic tuning method [5], apt to provide the best selection for a given structure-earthquake case, developed within a wider research stream [1–9].

The need for seismic protection of buildings motivated, during the last decades, the investigation on different suitable devices. In this sense, TMDs appear as one of the most validated solutions for the mitigation of structural vibrations, with many existing examples of application to high-rise buildings. Specifically, the adoption of TMDs in earthquake engineering is considered a strategic and currently-discussed topic.

The determination of the optimum TMD setting may be easily achieved through available tuning formulas, for related benchmark ideal excitations. Work [8] provided a unified approach in that sense, by proposing simple relationships for different loading cases, obtained from a common polynomial form. On the other hand, the contextualisation of TMDs into seismic engineering scenarios shall require a dedicated approach. Besides first fundamental studies, the last decade counts various works on this topic, with tuning methods based either on the characteristics of the host structure [10] or on the features of the seismic events [11].

The common point of all these studies concerns the hypothesis of a fixed-base system. However, the seismic behaviour of structures may be considerably affected by the interaction of the surface or the embedded foundation with the adjoint soil layer [12–14], with potential viewable changes of the modal parameters. This issue turns out important in light of the TMD tuning process, since the effectiveness of this narrow-band device may be easily compromised by a misplaced evaluation of the structural parameters.

Hence, in recent works SSI started to be implemented within the tuning problem. Study [15] analysed the seismic behaviour of a single-degree-of-freedom (SDOF) primary structure with attached TMD, placed on a flexible base, in the frequency domain, recovering a remarkable difference of dynamic response, as compared to the fixed-base case, with consequent loss of reliability of the TMD tuning. In [16], the wind-induced oscillation of a forty-storey frame building with a TMD added on top has been investigated, with the assumption of three different soil cases, as compared to the fixed-base case. As a main outcome, it appeared that the presence of SSI would turn out more important for the case of soft soil, while for stiff soil its effect appeared smaller, also in terms of tuning and efficiency of the TMD. A similar study [17] in the seismic context proposed an optimum TMD developed through an Ant Colony Optimisation (ACO) method, confirming a significant influence of SSI on the TMD parameters and on the arising seismic response.

The present paper, placed within this research stream and in connection to a complementary study devoted to a Frequency Domain Decomposition model dynamic identification in the same seismic and SSI context [18], is organised as follows. In Section 2, the main characteristics of the structural and dynamical framework are reported, with focus on the implementation of SSI effects into the whole model. Two multi-degree-of-freedom (MDOF) buildings are considered (a five- and a forty-storey shear-type frame structure), placed on three different soil types (the fixed-base case is also considered for comparison purposes) and subjected to five different seismic events, for a total of forty cases of analysis. Section 3 outlines the key-point features of the proposed seismic tuning method, and presents a significant extract of the numerical results. Finally, Section 4 summarises the salient concluding considerations of the whole study.

2 STRUCTURAL AND DYNAMIC CONTEXT

2.1 Structural system and SSI model

The five- and forty-storey shear-type frame buildings, presented in [19] and in [16], respectively, have been assumed as primary structures for this study, with main modal parameters resumed in Table 1. They are characterised by a diagonal mass matrix $\mathbf{M}_S$, a tridiagonal stiffness matrix $\mathbf{K}_S$ and a viscous damping matrix $\mathbf{C}_S$, the latter being modelled through a classical Rayleigh damping assumption, as simply proportional to the stiffness matrix [10]:

$$\mathbf{C}_S = \beta \mathbf{K}_S \,, \qquad \beta = \frac{2\,\zeta_{S,I}}{\omega_{S,I}} \tag{1}$$

where $\zeta_{S,I}$ and $\omega_{S,I}$ are the given structural damping ratio and the angular frequency of the primary structure referred to its first mode of vibration, respectively. In particular, the first mode damping ratio has been taken here as $\zeta_{S,I} = 2\%$.

Building	Mode	$f_{S,i}$ [Hz]	$T_{S,i}$ [s]	$M_{meff,S,i}$ [%]
Five-storey [19]	I	1.112	0.900	71.1
	II	2.560	0.391	15.5
	III	4.047	0.247	7.2
	IV	5.665	0.177	3.6
	V	8.135	0.123	2.5
Forty-storey [16]	I	0.261	3.830	78.7
	II	0.731	1.368	10.6
	III	1.210	0.827	3.9
	IV	1.688	0.593	2.0
	V	2.164	0.462	1.2

Table 1: Main modal parameters of the assumed primary shear-type frame structures.

The TMD mechanical parameters are the mass m_T, the constant stiffness k_T and the viscous damping coefficient c_T. The TMD angular frequency and damping ratio are classically defined as follows:

$$\omega_T = \sqrt{\frac{k_T}{m_T}}, \qquad \zeta_T = \frac{c_T}{2\sqrt{k_T m_T}} \tag{2}$$

Besides for the TMD damping ratio ζ_T, the other free parameters useful for the optimum tuning process of the control device are the mass ratio μ and the frequency ratio f, defined as follows:

$$\mu = \frac{m_T}{\Phi_{S,I}^T \mathbf{M}_S \Phi_{S,I}} \,, \qquad f = \frac{\omega_T}{\omega_{S,I}} \tag{3}$$

where $\Phi_{S,I}$ is the first mode shape of the primary structure (with fixed base), normalised so as to exhibit a unit value at the top storey.

The structural system, composed of a n-degree-of-freedom primary structure and a TMD added on top, is represented by the equations of motion of the structural system. By taking into account Sway-Rocking SSI effects, these take the following form:

$$\mathbf{M}\ddot{\mathbf{x}}(t) + \mathbf{C}\dot{\mathbf{x}}(t) + \mathbf{K}\mathbf{x}(t) = -\mathbf{m}^* \ddot{x}_g(t) \tag{4}$$

where the $\big((n{+}3){\times}(n{+}3)\big)$ global structural matrices $\mathbf{M}$, $\mathbf{C}$ and $\mathbf{K}$, and the $\big((n{+}3){\times}1\big)$ mass vector of the right term $\mathbf{m}^*$ related to earthquake excitation, are stated as follows [12] (see also complementary information in [18]):

$$\mathbf{M} = \begin{bmatrix} \mathbf{M}_{SS} & \mathbf{M}_{SS}\mathbf{r} & \mathbf{M}_{SS}\mathbf{z} \\ \mathbf{r}^T\mathbf{M}_{SS} & m_{_F} + \sum_{i=1}^{n} m_{S,i} + m_{_T} & \sum_{i=1}^{n} m_{S,i} z_i + m_{_T} z_n \\ \mathbf{z}^T\mathbf{M}_{SS} & \sum_{i=1}^{n} m_{S,i} z_i + m_{_T} z_n & I_{_F} + \sum_{i=1}^{n} (I_{S,i} + m_{S,i} z_i^2) + m_{_T} z_n^2 \end{bmatrix} \tag{5}$$

$$\mathbf{K} = \begin{bmatrix} \mathbf{K}_{SS} & \mathbf{0}_{(n+1)\times 1} & \mathbf{0}_{(n+1)\times 1} \\ \mathbf{0}_{1\times(n+1)} & k_{_h} & 0 \\ \mathbf{0}_{1\times(n+1)} & 0 & k_{_\theta} \end{bmatrix} \tag{6}$$

$$\mathbf{C} = \begin{bmatrix} \mathbf{C}_{SS} & \mathbf{0}_{(n+1)\times 1} & \mathbf{0}_{(n+1)\times 1} \\ \mathbf{0}_{1\times(n+1)} & c_{_h} & 0 \\ \mathbf{0}_{1\times(n+1)} & 0 & c_{_\theta} \end{bmatrix} \tag{7}$$

$$\mathbf{m}^* = \begin{bmatrix} \mathbf{M}_{SS}\mathbf{r} \\ m_{_F} + \sum_{i=1}^{n} m_{S,i} + m_{_T} \\ \sum_{i=1}^{n} m_{S,i} z_i + m_{_T} z_n \end{bmatrix} \tag{8}$$

where $\mathbf{x}(t) = [x_{_1}(t), \ldots, x_{_{n+1}}(t); x_{_f}(t), \theta(t)]^T$ is the $\big((n{+}3){\times}1\big)$ vector of degrees of freedom; $\mathbf{M}_{SS}$, $\mathbf{C}_{SS}$ and $\mathbf{K}_{SS}$ are the $\big((n{+}1){\times}(n{+}1)\big)$ mass, damping and stiffness matrixes of the structural system (host structure + TMD), respectively; $I_{_i}$ is the mass moment of inertia of the i-th floor; $m_{_F}$, $I_{_F}$ are the mass and the moment of inertia of the foundation, respectively; $\ddot{x}_{_g}(t)$ is the seismic ground acceleration; $\mathbf{r}$ is a $\big((n{+}1){\times}1\big)$ unit vector; $\mathbf{z}$ is the $\big((n{+}1){\times}1\big)$ vector of absolute (referred to the ground) heights of the floors.

Tables 2 and 3 display the characteristics of the three considered soil cases ($\nu_{_s}$ Poisson's ratio, $G_{_s}$ shear modulus, $\rho_{_s}$ mass density, $V_{_s} = \sqrt{G_{_s}/\rho_{_s}}$ shear wave velocity), as stated in [16, 17], and the parameters of the circular foundation of the two host structures ($R_{_F}$ radius, $m_{_F}$ mass, $I_{_F}$ mass moment of inertia), respectively.

The values of soil stiffness and damping $k_{_h}$, $k_{_\theta}$, $c_{_h}$, $c_{_\theta}$ (h subscript = swaying effect, θ subscript = rocking effect), reported in Table 4, are determined as indicated in [13, 18]. The fixed-base case has been also considered for comparison purposes.

Soil type	$\nu_{_s}$	$G_{_s}$ [N/m^2]	$\rho_{_s}$ [kg/m^3]	$V_{_s}$ [m/s]
Soft soil	0.49	$1.80{\times}10^7$	1800	100
Medium soil	0.48	$1.71{\times}10^8$	1900	300
Dense soil	0.33	$6.00{\times}10^8$	2400	500

Table 2: Parameters of the considered soil cases [16].

Building	R_F [m]	m_F [kg]	I_F [kg m^2]
Five-storey [19]	10	3×10^5	7.5×10^6
Forty-storey [16]	20	1.96×10^6	1.96×10^8

Table 3: Foundation parameters of the assumed host structures [16, 19].

Building	Soil type	$k_{s,h}$ [N/m]	$k_{s,\theta}$ [N m]	$c_{s,h}$ [N s/m]	$c_{s,\theta}$ [N s m]
Five-storey [19]	Soft soil	9.54×10^8	9.41×10^{10}	5.48×10^7	1.41×10^9
	Medium soil	9.00×10^9	8.77×10^{11}	1.73×10^8	4.39×10^9
	Dense soil	2.87×10^{10}	2.39×10^{12}	3.31×10^8	7.16×10^9
Forty-storey [16]	Soft soil	1.91×10^9	7.53×10^{11}	2.19×10^8	2.26×10^{10}
	Medium soil	1.80×10^{10}	7.02×10^{12}	6.90×10^8	7.02×10^{10}
	Dense soil	5.75×10^{10}	1.91×10^{13}	1.32×10^9	1.15×10^{11}

Table 4: Stiffness and damping coefficients for the considered flexible-base cases [16, 19].

2.2 Seismic input

The five considered seismic input signals (with main features listed in Table 5) are the following: Imperial Valley 1940 (I1940, El Centro station, S00E component [10]), Loma Prieta 1989 (L1989, Corralitos station, 0 component [4]), L'Aquila 2009 (A2009, Valle Aterno station, WE component [5]), Tohoku 2011 (T2011, Sendai station, NS component [5]), Katmandu 2015 (K2015, Kanti Path station, NS component). The selected events exhibit different characteristics, magnitude and duration, in order to exploit possible consequences within the tuning process. Also, the latter two records have been corrected through a two-stage process, composed of a baseline removal (mean value) and a Butterworth filtering.

Earthquake	M	Duration [s]	PGA [g]	PSa^{max} [g]	T(PSa^{max}) [s]
Imperial Valley 1940 (I1940)	6.9	40	0.359	1.265	0.460
Loma Prieta 1989 (L1989)	7.0	25	0.801	3.795	0.329
L'Aquila 2009 (A2009)	5.8	50	0.676	2.534	0.111
Tohoku 2011 (T2011)	9.0	180	2.667	3.814	0.655
Katmandu 2015 (K2015)	7.8	100	0.164	0.940	0.530

Table 5: Seismic input signals main data.

3 OPTIMUM TMD AND RESPONSE REDUCTION

3.1 Seismic tuning of TMDs

The seismic tuning process adopted in this study concerns the optimisation of the TMD for a specific seismic input, by involving the earthquake signal within the optimisation routine. The main task of such an operating way is the achievement of the optimum TMD for each selected seismic event [1, 5]. This method has been developed in the time domain, i.e. the optimisation process is looped with a time solver based on classical Newmark's average acceleration method.

The tuning of TMDs can be easily stated and managed by a classical optimisation problem, where the free parameters of the control device play the role of optimisation variables:

$$\min_{\mathbf{p}} \mathbf{J}(\mathbf{p}), \qquad \mathbf{l}_b \leq \mathbf{p} \leq \mathbf{u}_b \tag{9}$$

where $\mathbf{p}$, $\mathbf{J}(\mathbf{p})$, $\mathbf{l}_b$ and $\mathbf{u}_b$ represent the optimisation variables, the objective function, the lower and upper bounds on the optimisation variables, respectively.

The usual approach adopted in the literature has been considered here, where the frequency ratio f and the TMD damping ratio ζ_T are taken as optimisation variables, namely $\mathbf{p} = [f, \zeta_T]$, while the mass ratio μ is assumed to be set constant (equal to $\mu = 0.02$), which is potentially representative of real application cases. Since the main goal is the reduction of the whole structural seismic response, the Root Mean Square (RMS) estimate of the displacement of the primary structure has been taken as objective function. Motivations of such a choice have been widely discussed in [1, 5].

The numerical optimisation takes advantage of a classical nonlinear gradient-based optimisation algorithm available within MATLAB, based on Sequential Quadratic Programming (SQP), which ensures fast convergence and high level of accuracy. A flowchart of the algorithm is available in [9].

The initial evaluation of the tuning variables necessary for launching the optimisation process has been set through well-known Den Hartog's tuning formulas [20], depending only on the assumed mass ratio μ. Alterative start-point assumptions from different possible tuning formulas, also with consideration of inherent damping (e.g. those proposed in [2]), would not affect the final estimation of the optimum TMD parameters obtained by the optimisation algorithm.

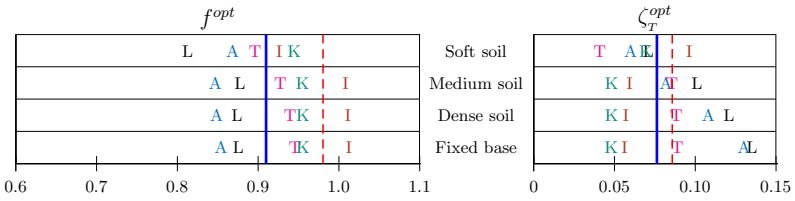
3.2 Optimum TMD parameters

The optimum TMD parameters, achieved through the proposed method, are displayed in Fig. 1, together with those obtained by Den Hartog's tuning formulas [20], reported here for reference purposes.

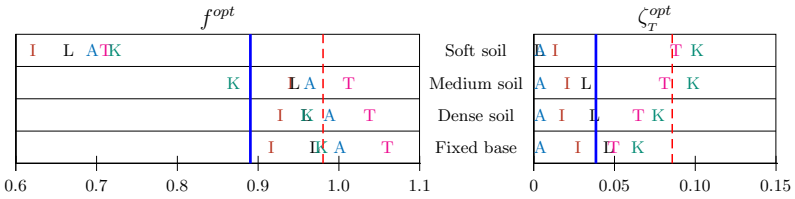
The five-storey building (Fig. 1a) exhibits a spread but rather homogeneous distribution of optimum TMD parameters, with suitable values (i.e. close to those usually obtainable for benchmark excitations); it looks that no particular trends related to soil type and seismic event could be traced. Perhaps, clearer scenarios could be recovered by considering a wider number of cases and partially compensating the randomness of the seismic excitation.

A wider spread of optimum TMD parameters is achieved for the forty-storey building, especially concerning the case of soft soil (Fig. 1b). Indeed, in this case optimum TMDs are characterised by very small frequency ratio f^{opt} and low TMD damping ratio ζ_T^{opt}. Such a trend could likely be motivated by a sort of higher connection between the soil and the structural system, with respect to cases with harder soil. Thus, the behaviour of the TMD takes into account an actually different modal and dynamic context, witnessed by apparently anomalous values of f^{opt}. Moreover, this fact occurs for all the considered seismic events, which are instead quite different from each other. Hence, the modal parameters of the host structure appear to play an important role into the tuning process.

In Fig. 1 also notice globally that mean trends are always on the left from Den Hartog's reference, with wider spread for the higher building.



(a) Five-storey building.



(b) Forty-storey building.

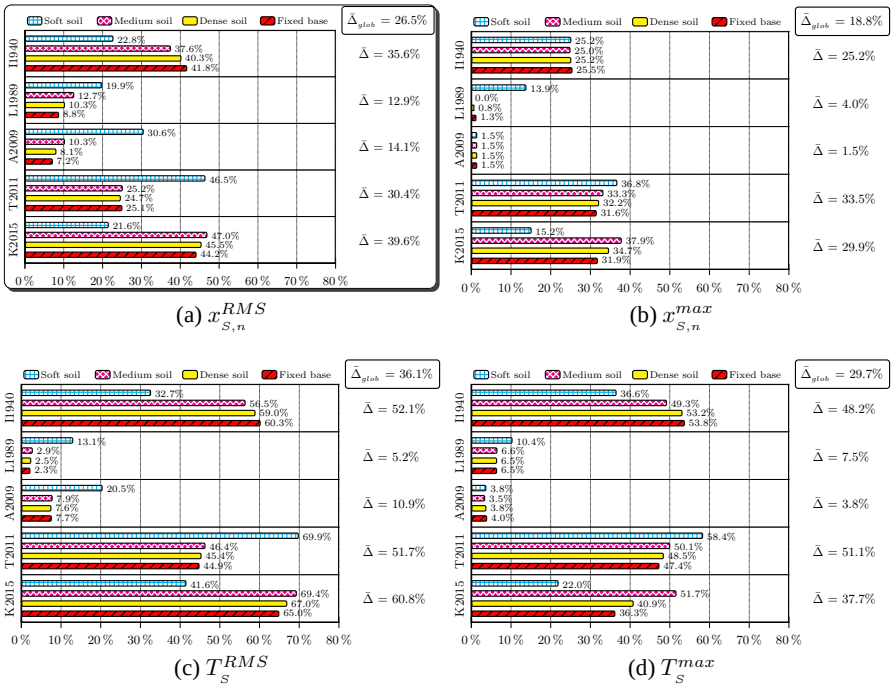
Figure 1: *Optimum TMD parameters, mean values (thick blue line) and Den Hartog's values (dashed red line) (seismic events: I = I1940, L = L1989, A = A2009, T = T2011, K = K2015; assumed inherent damping ratio $\zeta_{S,I}$ = 0.02).*

3.3 Seismic TMD performance

A significant extract of the numerical results in terms of seismic response reduction has been reported in Figs. 2–3, related to the five- and the forty-storey structure, respectively. In particular, Figs. 2a and 3a represent the main outcomes, i.e. on the RMS estimate of the top-storey displacement $x_{S,n}$, adopted here as objective function. The other plots complete the reading of the seismic response scenario, by considering the peak top-storey displacement (Figs. 2b and 3b) and the RMS and peak kinetic energy of the primary structure (Figs. 2c and 3c, 2d and 3d), as a result of the TMD optimisation process targeted merely on $x_{S,n}^{RMS}$.

Fig. 2 for the five-storey frame points out a fact common to all the analysed response indexes, that is a general low performance for the seismic events L1989 and A2009, with values smaller than 10%, while for the remaining earthquakes significant response reductions have been obtained, with better results for the RMS estimate and for the kinetic energy, with respect to the peak estimate and the top-storey displacement, respectively. A further interesting consideration comes from the different performance arising between the soft soil and the other soil cases, with either higher or lower results, but dissimilar. Such a fact occurs independently of the earthquakes, and therefore it may be related to the specific interaction between soil and structural system, specifically on the modification of the frequency contents.

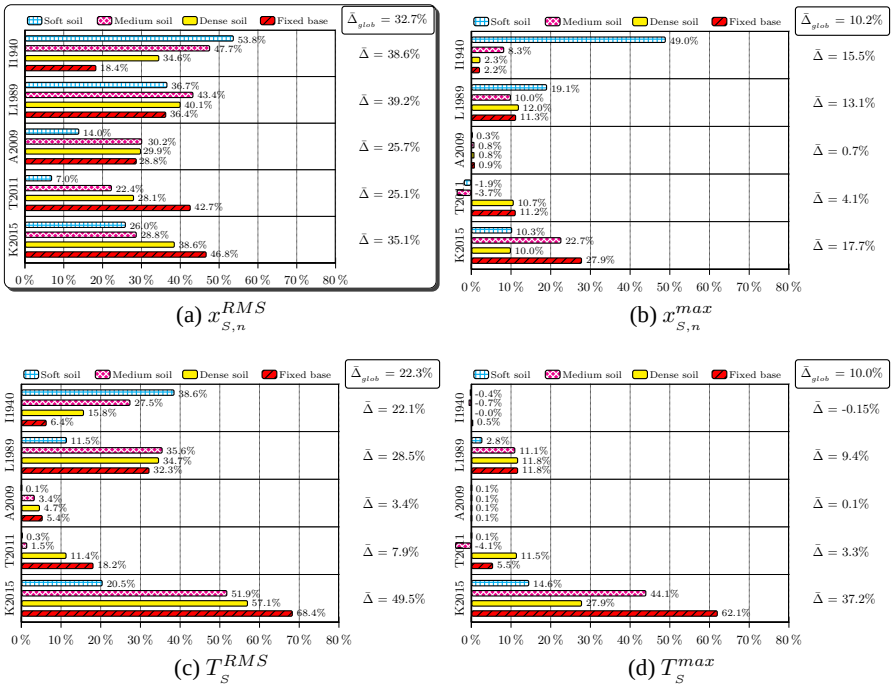
The situation of the forty-storey building, presented in Fig. 3, displays an overall lower TMD effect on response abatement, especially concerning the peak indexes; in this sense, A2009 still looks as the earthquake with smallest response reduction, while K2015 exhibits the highest performance. The only homogeneous index, in the sense of seismic events, is the RMS displacement (Fig. 3a), while all the others are characterised by quite different TMD performance for each earthquake. Again, the case of soft soil represents an exception among all those considered in this study, with always the smallest response decrease. This fact could mean that a soft soil shall somehow be able to provide an intrinsic response reduction, being less "connected" to the structural system. Hence, the TMD seems to work just as a sort of complementary measure, in this situation.



(a) $x_{S,n}^{RMS}$ (b) $x_{S,n}^{max}$

(c) T_S^{RMS} (d) T_S^{max}

Figure 2: *Response reduction in terms of (a),(b) top-storey displacement and (c),(d) kinetic energy for the five-storey building. Frame on (a) highlights the assumed objective function.*



(a) $x_{S,n}^{RMS}$ (b) $x_{S,n}^{max}$

(c) T_S^{RMS} (d) T_S^{max}

Figure 3: *Response reduction in terms of (a),(b) top-storey displacement and (c),(d) kinetic energy for the forty-storey building. Frame on (a) highlights the assumed objective function.*

4 CONCLUSIONS

The influence of SSI effects on the seismic performance of TMDs has been investigated here, by exploiting an innovative and specific seismic tuning method, and by considering different primary structures, soil cases and earthquake events.

The achieved optimum TMD parameters, as a result of the optimisation process targeted on the top-storey RMS displacement, pointed out what follows:

- A larger spread is recovered for the forty-storey building, because of the soft soil case (very low frequency and TMD damping ratio);
- The mean values are always lower than those obtained by Den Hartog's formulas.

The salient remarks in terms of achieved seismic response reduction of the structural system with TMD and accounting for SSI effects could be listed as:

- The RMS response is more reduced than the peak response;
- The kinetic energy response is more reduced than for the top-storey displacement;
- The TMD performance is quite different in the case of soft soil with respect to the other soil cases, and usually much lower;
- The higher TMD effect in response abatement is recorded for the five-storey building than that for the forty-storey building;
- Better results are achieved for the T2011 and K2015 earthquakes; small TMD effect is recorded for the A2009 seismic event.

In general, the TMD appears to sort more benefit on the seismic response reduction in case of medium and hard soil, as clearly pointed out by the obtained outcomes. This fact strongly motivated the introduction of SSI effects within both the tuning process and the post-tuning seismic analysis, and may lead to unexpected modifications of the best set up of TMDs, which shall be characterised by lower frequencies in the case of soft soil, thus far from the resonance conditions. Indeed, for the latter case the host structure looks somehow more "connected" to the soil, which acts like an implicit damper, therefore making the TMD just a sort of complementary control device.

Another important issue, already detected in previous works [9], is represented by the connection between the modal characteristics and the features of the earthquake events, as proved by the large difference of modal parameters, followed by a respective difference of TMD effect between the two considered primary structures. The main example in this sense concerns the forty-storey building, with very high natural periods, less sensitive (on non-objective function indexes) to the TMD insertion, especially when earthquakes with low-period PGA occur (e.g. like A2009), able to cause just small seismic vibration.

It could be globally affirmed that the TMD appears able to provide a remarkable seismic response reduction *when it appears really necessary towards that*, concerning the seismic effect on the host structure and the contribution of the soil characteristics in reducing the whole seismic response.

ACKNOWLEDGEMENTS

The Authors would like to acknowledge public research funding from *"Fondi di Ricerca d'Ateneo ex 60%"* and a former ministerial doctoral grant at the University of Bergamo, School of Engineering (Dalmine).

REFERENCES

[1] J. Salvi, E. Rizzi, Minimax optimization of Tuned Mass Dampers under seismic excitation, Proc. of the 8th Int. Conf. on Struct. Dyn. (EURODYN 2011), Leuven, Belgium, 4–7 July 2011, 8 pages, 2011.

[2] J. Salvi, E. Rizzi, A numerical approach towards best tuning of Tuned Mass Dampers, Proc. of the 25th Int. Conf. on Noise and Vibr. Engng. (ISMA 2012), Leuven, Belgium, 17–19 September 2012, 16 pages, 2012.

[3] J. Salvi, E. Rizzi, E. Rustighi, N.S. Ferguson, Analysis and optimisation of Tuned Mass Dampers for impulsive excitation, Proc. of the 11th Int. Conf. on Recent Adv. in Struct. Dyn. (RASD 2013), Pisa, Italy, 1–3 July 2013, 15 pages, 2013.

[4] J. Salvi, E. Rizzi, M. Gavazzeni, Analysis on the optimum performance of Tuned Mass Damper devices in the context of earthquake engineering, Proc. of the 9th Int. Conf. on Struct. Dyn. (EURODYN 2014), Porto, Portugal, 30 June–2 July 2014, 8 pages, 2014.

[5] J. Salvi, E. Rizzi, "Optimum tuning of Tuned Mass Dampers for frame structures under earthquake excitation", *Struct. Contr. and Health Monit.*, doi: 10.1002/stc.1710, **22**(4):707-715, 2015.

[6] J. Salvi, E. Rizzi, E. Rustighi, N.S. Ferguson, On the optimisation of a hybrid Tuned Mass Damper for impulse loading, *Smart Mater. Struct.*, In press, 2015.

[7] J. Salvi, E. Rizzi, E. Rustighi, N.S. Ferguson, Optimum tuning of passive Tuned Mass Dampers for the mitigation of pulse-like responses, Sub. for publ., 2014.

[8] J. Salvi, E. Rizzi, Closed-form optimum tuning formulas for passive Tuned Mass Dampers under benchmark excitations, Sub. for publ., 2014.

[9] J. Salvi, E. Rizzi, Performance of optimum seismic-tuned TMDs for frame buildings, Sub. for publ., 2015.

[10] R. Villaverde, L.A. Koyama, Damped resonant appendages to increase inherent damping in buildings, *Earthq. Engng. and Struct. Dyn.*, **22**(6):491–507, 1993.

[11] G. Bekdaş, S.M. Nigdeli, Estimating optimum parameters of tuned mass dampers using harmony search, *Engng. Struct.*, **33**(9):2716–2723, 2011.

[12] A.K. Chopra, J.A. Gutierrez, Earthquake response analysis of multistorey buildings including foundation interaction, *Earthq. Engng. and Struct. Dyn.*, **3**(1):65–77, 1974.

[13] T.K. Datta, *Seismic Analysis of Structures*, Wiley, 1st Ed., 2010.

[14] J.P. Wolf, *Dynamic Soil-Structure Interaction*, Prentice-Hall, 1st Ed., 1985.

[15] A. Ghosh, B. Basu, Effect of soil interaction on the performance of tuned mass dampers for seismic applications, *J. of Sound and Vibr.*, **274**(3–5):1079–1090, 2004.

[16] M.-Y. Liu, W.-L. Chiang, J.-H. Hwang, C.-R. Chu, Wind-induced vibration of high-rise building with tuned mass damper including soil-structure interaction, *J. of Wind Engng. and Ind. Aerodyn.*, **96**(6–7):1092–1102, 2008.

[17] A. Farshidianfar, S. Soheili, Ant colony optimization of tuned mass dampers for earthquake oscillations of high-rise structures including soil-structure interaction, *Soil Dyn. and Earthq. Engng.*, **51**(1):14–22, 2013.

[18] F. Pioldi, J. Salvi, E. Rizzi, FDD modal identification from earthquake response data with evaluation of soil-structure interaction effects, 11th Int. Conf. on Engineering Vibration (ICoEV 2015), Liubljana, Slovenia, 7–10 September 2015.

[19] S.F. Ghahari, F. Abazarsa, M.A. Ghannad, E. Taciroglu, Response-only modal identification of structures using strong motion data, *Earthq. Engng. and Struct. Dyn.*, **42**(8):1221–1242, 2013.

[20] J.P. Den Hartog, *Mechanical Vibrations*, McGraw-Hill, 4th ed., 1956.

International Conference on Engineering Vibration
Ljubljana, Slovenia, 7-10 September 2015

A METHODOLOGY TO DECOUPLE THE TONAL NOISE SOURCES OF A COMPRESSOR SYSTEM

Roberto Faventi*[1], Adrien Gomar[1], Hugh Hopper[1] & Ludovic Desvard[1]

[1]Dyson Ltd
*roberto.faventi@dyson.com

Keywords: Vibro-Acoustics, Compressor Noise, Source Breakdown, Sound Quality

Abstract. *Fans and compressors generate noise which can be split into two main components: aerodynamic and structure borne noise. In the case of a small compressor for domestic appliances, the aerodynamic noise dictates the broadband signature and hence the overall sound power level, but also generates tonal content. Structure borne noise also contributes to the sound power level, but it originates from the vibration generated due to rotating unbalance and therefore has a predominately tonal characteristic that is detrimental to the sound quality. To control the structure borne noise the mount scheme must adequately isolate the vibration generated.*

In this paper a methodology is proposed to experimentally decouple the aerodynamic and the structure borne tonal noise. Experimentation was performed on a compressor that is mounted with different schemes, ranging from a rigidly coupled to a soft mounted system. For each of these schemes the contribution of the structure borne and aerodynamic tonal content is evaluated and compared with the ideal noise floor represented by the broadband level. The broadband signature is evaluated using a median filter, which replaces each data point with the median of its neighbouring values, thus removing the tonal content from the power spectrum.

It was initially established that the mount scheme design was crucial in order to control the structure borne noise contribution to the sound power level. Furthermore, the tonal sources were decoupled using the technique outlined in order to categorise and weight the different transmission paths contribution. This information, which dictates the appropriate noise control solution, is valuable to improve the sound quality of such compressor systems.

1 INTRODUCTION

Domestic products often incorporate fans or compressors. The noise generated by the compressor is usually the main acoustic source and therefore can drive the sound power level (SWL) of the full product. In addition to this, sound quality, such as the tonality, must also be considered, as for manufacturers of consumer goods the subjective impression of the user is of highest importance. Therefore, it is crucial to accurately characterise the noise sources of the compressor system in order to subsequently guide the acoustic development.

Characteristically, compressors generate both aerodynamic and structure borne noise [1]. The aerodynamic noise has both broadband and tonal content [2]. On the other hand the structure borne noise has a predominantly tonal characteristic as it originates from vibration generated due to rotating unbalance. In order to control this contribution, a suitable mount scheme should be designed to isolate this vibration. However, to establish if the scheme is adequate, the contribution of the structure borne noise to the overall acoustic response must be understood.

This study focuses on an experimental method used to decouple the acoustic sources. Initially a simplified set-up is considered to understand the sources in isolation. Subsequently two different mount schemes are considered. In both cases, the influence of the mount scheme on the acoustic response is investigated as it is sought to establish a link between the mount scheme properties and the vibro-acoustic response of the system. Lastly, the relationship between the tonal noise and the sound quality is established, leading to appropriate noise control solutions being proposed.

2 INFLUENCE OF TONAL NOISE TO THE SWL

A standalone rig has been designed to measure the sound power level of a prototype compressor in isolation. To ensure that the results are representative of the noise that will be generated when the system is integrated into a product, it is paramount that the acoustic response is not affected by the interaction of the compressor with the rig. Therefore the structure borne contribution must be adequately controlled using a suitable mount as would be expected in product. In order to demonstrate the necessity of controlling the structure borne noise, the acoustic response of a rigidly mounted compressor is compared with a soft mounted system.

2.1 Test set-up

The SWL was measured in a hemi-anechoic sound chamber using a 10 microphone 2 m hemisphere arrangement as outlined in ISO 3744 [3]. The schematic of the test set-up is shown in Figure 1. The compressor system was run at a constant power across a range of flow rates by varying the restriction using ball valve that was ducted outside the sound chamber.

As mentioned previously, the structure borne noise is expected to be predominantly tonal, associated with the rotating unbalance. In order to establish the contribution of this tonal noise on the SWL, a median filter was applied [4] to artificially remove the acoustic energy at the rotational frequency of the compressor, f_r (Hz), as shown in Figure 2. This reduces the sound pressure level (SPL) to the broadband noise floor associated with the aerodynamic package of the compressor. By subsequently integrating over frequency, to compute the SWL, the influence of the energy associated at f_r could be deduced.

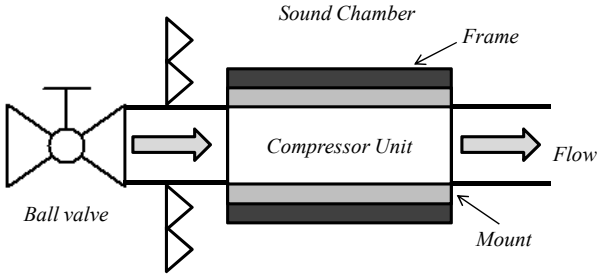


Figure 1: Schematic of the test set-up of the compressor in isolation.

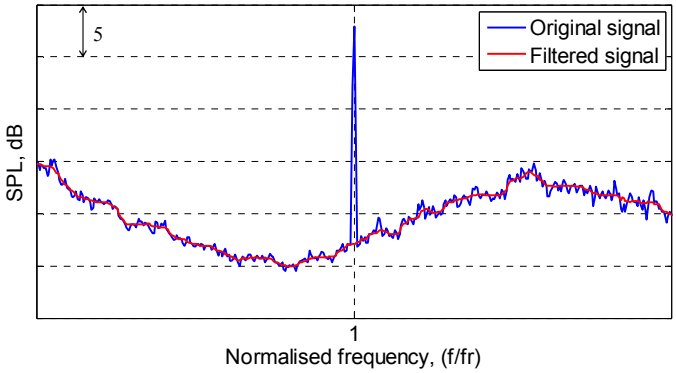


Figure 2: An example of the original acoustic spectra along with the median filtered response showing the removal of energy at the rotational frequency of the compressor.

2.2 Results & discussion

Across the range of flow rates measured, the SWL of the soft mounted compressor unit is quieter than the rigidly mounted setup by around 2 dB as seen in Figure 3. When the median filter is applied, the SWL reaches its floor dictated by the broadband signature associated with the aerodynamic package.

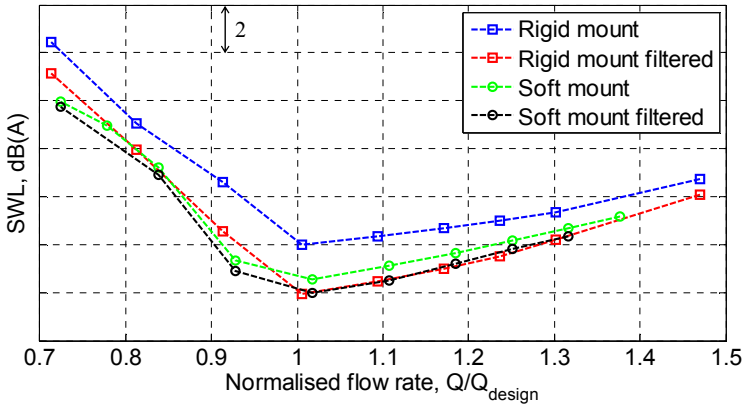


Figure 3: Sound power level against the normalised flow rate of the compressor mounted with the rigid and soft mount compared to the median filtered data.

In the case of the soft mount scheme the SWL approaches this floor implying that the structure borne noise is adequately controlled. This also outlines that the increase in SWL seen for the rigidly mounted scheme can be attributed to the tonal noise at f_r and clearly demonstrates the requirement for a suitable mount scheme, even when testing the compressor in isolation.

Additionally this implies that if the aerodynamic noise dominates the broadband signature of the compressor unit, then the expected SWL of the system in isolation can be established relatively quickly by implementing a rigid mount and subsequently applying a median filter. However, this technique is clearly not ideal and best used for a rough estimate.

3 MOUNT SCHEME CHARACTERISATION

Having outlined the influence of the mount scheme on the acoustic response, two different schemes have been designed. The properties of these mounts have been characterised to better understand the vibro-acoustic response. The different schemes were integrated into the test rig shown in Figure 4. This was then rigidly coupled to a shaker table that was used to excite the system across a suitable frequency range. The transfer function between the compressor unit and the frame was then calculated from the measured vibration data in each location.

The frequency responses of the two systems excited radially are shown in Figure 5. The radial plane is of prime interest as this corresponds to the direction of the rotating unbalance force. As the mass of the compressor unit is known, the mount scheme's radial stiffness (k) can be determined from the frequency associated with this mode. Also, the vibration isolation performance can be estimated directly from the response and is dictated by the shift in amplitude of the two curves in the frequency region of interest.

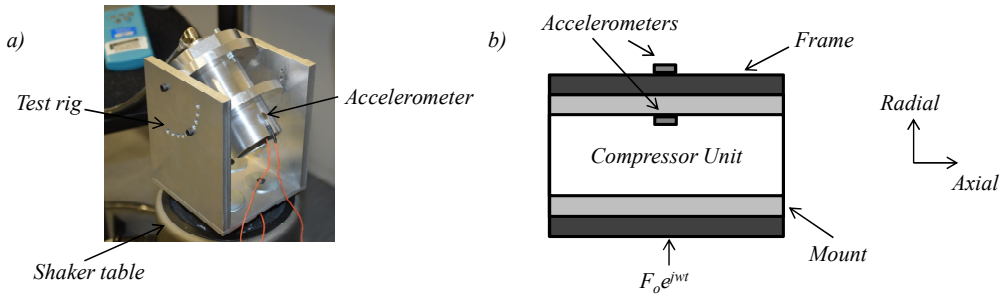


Figure 4: a) Test rig connected to the shaker table, b) Schematic of the set-up.

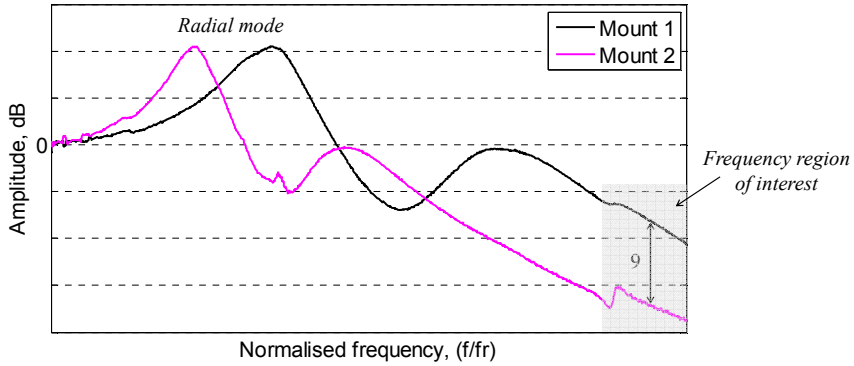


Figure 5: Transfer function estimate between the compressor unit and the frame for the two mount schemes.

From this testing it was established that mount 2 has a lower radial stiffness; $k_2 = 0.44k_1$. This difference in stiffness corresponds to a 9 dB reduction in transmitted vibration in the frequency region of interest. In a product application mount 2 should therefore be expected to exhibit a reduced level of structure borne noise.

4 TONAL SOURCE BREAKDOWN

The results in section 2 showed that without a suitable mount scheme the tonal noise contributed undesirably to the SWL. For an adequate mount scheme, the contribution to SWL will ideally be negligible. Additionally the remaining tonal noise must also be considered as it directly relates to the user's perception of the product, as demonstrated in previous studies [5].

The level of tonal noise is affected by both direct airborne radiation of the aerodynamic noise and vibration transmitted through the structure from the compressor unit. An experimental methodology has been implemented to decouple these sources and thus better understand the contribution of each transmission path. Furthermore, a correlation between the acoustics and the measured vibration response is outlined.

4.1 Acoustic source breakdown set-up

Acoustic testing was performed as outlined in section 2.1. The compressor unit was housed using the two mounts characterised in the previous section. For this testing, measurements were taken at 3 operating flow rates, being the design point of the compressor and subsequently one point above and below it. This was useful to assess the system response over a realistic operating range. To understand the contribution of the aerodynamic and structure borne noise to the overall acoustic response, each transmission pathway was physically isolated as shown in Figure 6.

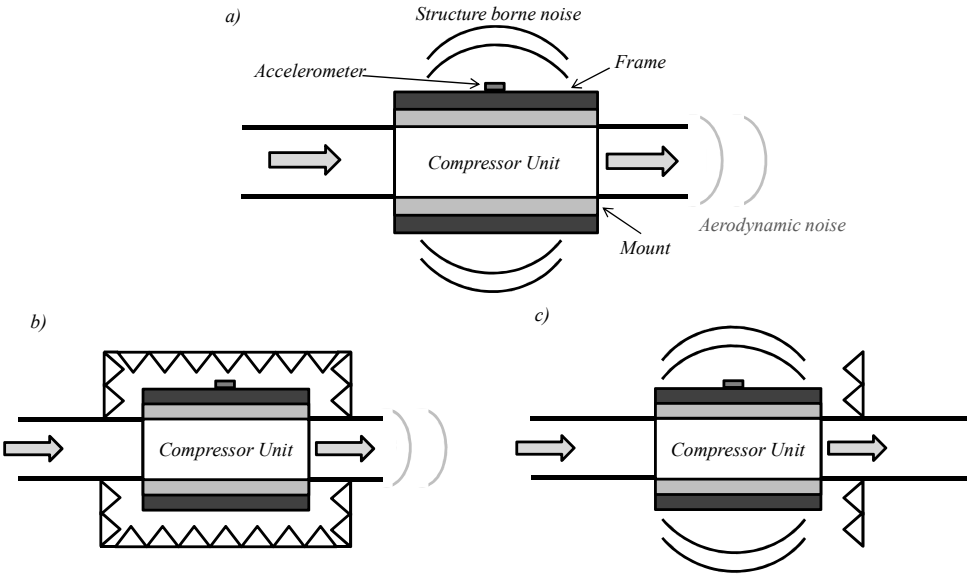


Figure 6: Schematic of the experimental set-up used to breakdown the acoustic sources of the compressor unit, a) combined sources, b) aerodynamic noise only and c) structure borne noise only.

The structural noise was isolated by piping the compressor exhaust outside of the sound chamber. The airborne noise was isolated by placing the compressor assembly inside a *heavy* box lined with acoustic media, which should impede any noise radiated from the structure. A

combined measurement where both pathways were radiating into the sound chamber was also conducted. Additionally, the vibration transmitted to the frame was recorded to understand the relationship with the radiated structure borne noise.

4.2 Estimate of SWL

As in section 2 it is initially sought to assess the influence of the mount on the SWL. Once again the median filter is applied to remove the tonal content associated with f_r. In this case the combined test and structural borne only test cases are evaluated with the compressor running at its design point.

In Table 1, for the combined test case, the change in SWL is less than 0.1 dB for both mounts. As the tonal noise does not contribute significantly to the SWL, it implies that the broadband noise generated by the aerodynamic package is the dominant source. Furthermore it outlines that the tonal noise associated with vibration is adequately controlled by both mounts with respect to the SWL.

Considering the structure borne only test, the change in SWL is no longer negligible which shows that now tonal noise is contributing to it. This is not a surprise as the aerodynamic source is no longer driving the broadband level in this test set-up. For mount 1 the change in SWL is greater than that for mount 2 which implies that tonal noise is more significant for this scheme. This result is in line with the expectation from section 3, being that mount 2 should provide better vibration isolation than mount 1 and hence generate less structure borne noise. However, to breakdown the tonal noise sources, spectral analysis is performed in section 4.3 for each test case outlined in Figure 6.

	Mount 1		Mount 2	
Test case	Combined	Structure borne	Combined	Structure borne
Change in SWL, dB	0.04	2.4	0.03	1.1

Table 1: The change in SWL when removing the tonal content associated with the rotational frequency of the system using a median filter for the two mount schemes whilst the compressor is operating at its design point.

4.3 Spectral analysis and tonal breakdown

As previously mentioned, it is desired to decouple the acoustic sources of the compressor unit to better understand the noise generation mechanisms. Therefore, the acoustic spectra for each test case are analysed. In Figure 7, the acoustic signatures of the combined and airborne only tests are very similar. This shows that the broadband level is purely driven by the aerodynamic (airborne) contribution which in turn drives the SWL as outlined in section 4.2. The main discrepancy seen between the airborne only and combined test scenario (grey box) around 1.6 f_r is likely due to slight differences in ducting between these measurements. This changes the acoustic impedance and hence the measured broadband response in this region.

Considering the structure borne only test the broadband level is noticeably lower than the airborne only test though the tonal content at f_r is of the same order of magnitude. This outlines that both of these transmission paths can contribute to this tone and therefore need to be decoupled in order to distinguish how to control this noise.

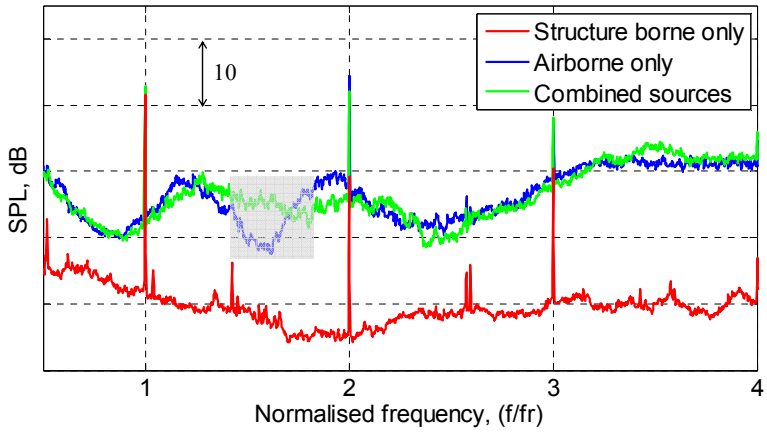


Figure 7: Acoustic spectra for each test case with the compressor running at its design point for mount 1.

By extracting the level of the tone at f_r according to DIN 45681 [6], shown in Figure 8, the contribution of each source to overall SPL can be established. Firstly it is seen that for the structure borne only tests the spread in the SPL is fairly consistent for both mounts. On the other hand, the airborne only test has a bigger spread in the data. This suggests that when the compressor is run off of its design point the acoustic response is affected to a greater extent. Despite this, trends can still be established.

With mount 1 implemented the structure borne tonal noise is the dominant source as the SPL is approximately 4-5 dB greater than that for the airborne only test. With mount 2, the more compliant system, the structure borne SPL at f_r is reduced by 5 dB which shows the benefit of implementing this scheme.

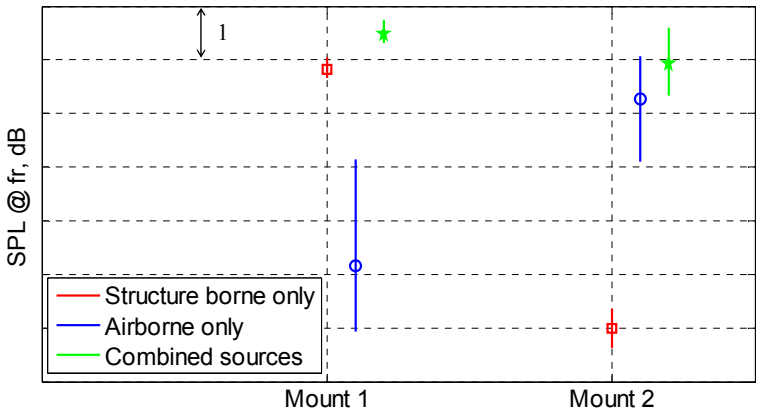


Figure 8: The sound pressure level at the rotational frequency of the compressor unit for each test case implementing mount 1 and mount 2. The symbols represent the mean value for the 3 flow rates whilst the extremities of the associated lines represent the minima and maxima.

It is also interesting to note that with mount 2, the airborne only test shows an increase in the level of the tone at f_r. This may be due to greater displacement of the compressor unit itself causing direct radiation of the tone into the air pathway. The greater displacement is expected due to the reduced stiffness of this mount. Ideally an accelerometer would have been attached to the compressor unit during the acoustic testing to assess this; however for this test set-up it was unfeasible.

Overall, by performing this breakdown an understanding of the two transmission paths has been established and should help to guide the acoustic development of the compressor unit. To guide the compressor unit's mount design a relationship between the transmitted vibration and structure borne noise is required for the two schemes tested.

4.4 Vibro-acoustic analysis

To control the structure borne tonal noise it is sought to establish a relationship with the transmitted vibration and subsequently link this back to the underlying mount properties outlined in section 3. Considering Figure 9, it is shown that the majority of the vibration energy transmitted to the compressor frame is at the fundamental excitation frequency, f_r, associated with rotating unbalance. At higher harmonic frequencies (2 f_r, 3 f_r), the vibration level is noticeably reduced. Referring back to Figure 7, these same trends are seen for the structure borne noise test case, outlining the connection between the vibration and acoustics.

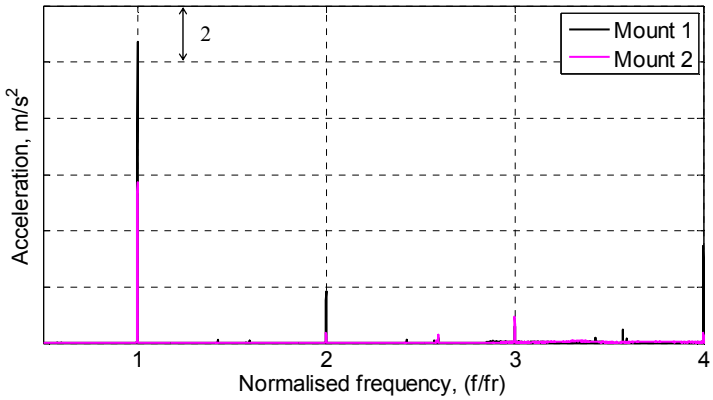


Figure 9: The vibration spectra measured on the frame for both mount schemes with the compressor running at its design point.

To assess this further, the transmitted vibration and the structure borne SPL at f_r for the two mount schemes is presented in Figure 10. A clear correlation can be seen. On average there is a 5-6 dB reduction in the transmitted vibration between the two mounts. From the preliminary mount characterisation the predicted reduction in transmitted vibration was 9 dB. The discrepancy could be related to the fact that the shaker table response outlines the difference in the two schemes assuming constant source strength (i.e. initial vibration level); in reality it is likely to be greater for the more compliant mount. Additionally the shaker table only provides loading in one continuous direction, whereas during operation the rotating unbalance force is constantly changing its relative radial direction.

Despite this, the results outlined still provide good guidance and can dictate any future mount development work. For example if the structure borne tonal noise contribution is required to be reduced by a specified value then a target vibration level on the frame can be outlined. By estimating the mount properties and source strength a suitable arrangement can be designed and considered for product integration. Only the combined sources test case would be required to be measured in the sound chamber. The contribution of structure borne SPL at f_r could be estimated by simultaneously measuring the transmitted vibration and thus the source breakdown could be approximated. By doing so, this would reduce the amount of testing required and therefore speed up the acoustic development of the compressor units.

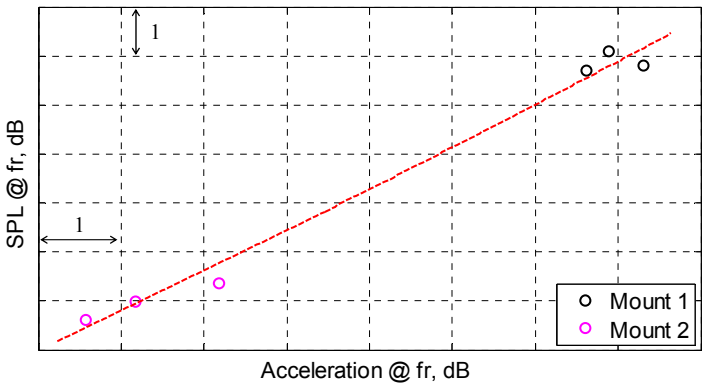


Figure 10: Relationship between the level of vibration transmitted to the compressor unit frame and corresponding structure borne sound pressure level at the running speed of the system.

5 CONSIDERING THE SOUND QUALITY

In section 4.2 it was established that the compressor unit's SWL was unaffected by the tonal noise at f_r when suitable mount schemes were implemented. However, it is expected that the sound quality would be affected. To investigate this further the tonality, which is a measure of the perceived pitch strength, was deemed to be a suitable sound quality metric to characterise the acoustic response. A high tonality is often associated with an annoying, whining sound that is detrimental to the user's perception.

The tonal noise at f_r was incrementally reduced using a notch filter and the relationship to the tonality, calculated according to Terhardt [7], was deduced as shown in Figure 11a). A notch filter is preferred over the median filter as it allows more control over the amount of attenuation applied to the tone. The median filter is only beneficial to quickly see the effect of completely removing the tonal content i.e. decoupling the tonal noise from the broadband signature.

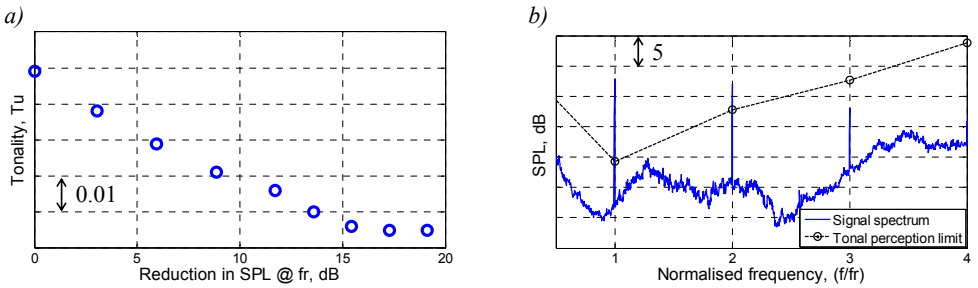


Figure 11: a) The relationship between the sound pressure level at the rotational frequency of the compressor and tonality and b) the acoustic spectra of the combined sources test case, for the compressor unit operating at its design point with mount 1, along with the tonal perception limit.

It can be seen that the level of the tone at f_r directly influences the tonality, for example, a reduction of 6 dB would lead to a 0.02 Tu decrease. Also there is a large scope to improve the sound quality by a means of reducing this tone as there is linear reduction in the tonality for a change in SPL of up to 16 dB. However, considering Figure 11b), the higher frequency tones are close or below the threshold of perception and hence have less influence on the tonality.

For this reason the tonal noise at f_r is the prime focus for this system and should be tackled by targeting each transmission path according to their relative contribution.

For example if the structure borne path is dominant then the transmitted vibration must be primarily targeted. This can be done by reducing the transmitted vibration as shown in section 4.4. If the aerodynamic source is dominant then airborne silencing solutions could be implemented, such as Helmholtz resonators as in [8].

This ultimately shows the benefit of breaking down the compressor unit's tonal sources in order to establish which noise control solutions should be implemented. Additionally by understanding the influence of the tonal noise to the sound quality, the control solutions can be designed accordingly to provide the desired attenuation level.

6 CONCLUSION

The paper presented a methodology to decouple the noise sources of compressor unit integrated into a domestic appliance. Initially, the importance of having a suitable mount scheme was outlined. When the mount scheme was not adequately isolating the vibration then the SWL was detrimentally affected by the associated structure borne tonal noise generated. It was also shown that by applying a median filter to the spectra, the broadband signature relating to the aerodynamic package could be isolated, and subsequently allowed the associated SWL floor to be predicted.

However, it was also outlined that the tonal noise of the system influences the sound quality as well. Therefore a methodology was implemented to decouple the aerodynamic and structure borne noise to understand the relative contribution of each source to the overall acoustic response. By doing so, suitable noise control solutions have been proposed to target each transmission path to achieve a desired sound quality. Additionally by establishing a correlation between the transmitted vibration and structure borne noise, in future, mount scheme properties can be tailored to control this source as required.

7 REFERENCES

[1] S. Parrang et al, Aeroacoustic noise prediction for SRM. *7th IET International Conference on Power Electronics, Machines and Drives,* Manchester, United Kingdom. pp.0293, 2014.

[2] S.E Wright, The acoustic spectrum of axial flow machines. *Journal of Sound and Vibration*, **45(2)**, 165-223, 1976.

[3] ISO 3744, *Acoustics – Determination of sound power levels and sound energy levels of noise sources using sound pressure – Engineering methods for an essentially free field over a reflecting plane.* 2010

[4] W.K Pratt, *Digital Image Processing 4th ed*. John Wiley & Sons, Hoboken, NJ, 2007.

[5] L. Desvard et al, An investigation of the effect of uneven blade spacing on the tonal noise generated by a mixed flow fan, *Fan 2012,* Senlis, France, 2012.

[6] DIN 45681, *Acoustics – Determination of tonal components of noise and determination of a tone adjustment for the assessment of noise emissions*. 2005-03.

[7] E. Terhardt et al, Algorithm for extraction of pitch and pitch salience from complex tonal signals. *Journal of the Acoustical Society of America*, **Vol. 71**, pp. 679-688, 1981.

[8] N. Etaix et al, Sound quality improvement of a high speed hand dryer, *CFA 2014, Congrès Français d'Acoustique*, Poitiers, France, 2014.

Non-linear Dynamics and Dynamic Stability (MS01)

11th International Conference on Engineering Vibration
Ljubljana, Slovenia, 7–10 September 2015

QUASI-PERIODIC RESPONSE TYPES OF A SINGLE NON-LINEAR DYNAMIC SYSTEM IN RESONANCE AND OUT OF RESONANCE DOMAINS

Jiří Náprstek*[1], Cyril Fischer[1]

[1]Institute of Theoretical and Applied Mechanics ASCR, v.v.i.
{naprstek,fischerc}@itam.cas.cz

Keywords: Non-linear dynamics, Quasi-periodic response, Post-critical processes, Dynamic stability.

Abstract. *The exact coincidence of external excitation and basic eigen-frequency of a single degree of freedom (SDOF) non-linear system produces stationary response with constant amplitude and phase shift. When the excitation frequency differs from the system eigen-frequency, various types of quasi-periodic response occur having a character of a beating process. The period of beating changes from infinity in the resonance point until a couple of excitation periods outside the resonance area. The above phenomena have been identified qualitatively in many papers including authors contributions. Nevertheless investigation of internal structure of a quasi-period and its dependence on the difference of excitation and eigen-frequency is still missing. Combinations of harmonic balance and small parameter methods are used for qualitative analysis of the system in mono- and multi-harmonic versions. They lead to non-linear differential and algebraic equations serving as a basis for qualitative analytic estimation or numerical description of characteristics of quasi-periodic system response. Zero, first and second level perturbation techniques are used. Appearance, stability and neighborhood of limit cycles is evaluated. Numerical phases are based on simulation processes and numerical continuation tools. Parametric evaluation and illustrating examples are presented.*

1 INTRODUCTION

Nonlinear dynamic systems are distinguished mostly by a complex response structure in resonance zone and in its surrounding area. It applies to Single Degree of Freedom (SDOF) as well as Multi-degree of Freedom (MDOF) systems. This process has very often a character of a post-critical response, which is called quasi-periodic response. There are two main components of this process: auto-oscillations related with relevant eigen frequency and stationary forced vibration. They can emerge either isolated or in combination. The latter one results in a beating effect. Each of both components can be stable or instable which manifests in the final shape of the system response. Consequently, the pattern of the resulting process is strongly dependent on parameters of the system and mainly on the excitation amplitude and difference of the excitation and eigen frequency - detuning. When the system eigen frequency and frequency of excitation coincide, no quasi-periodic response emerges and the system response is stationary. The quasi-period length vanishes in a certain distance from the resonance. Then auto-oscillation component disappears and only forced vibration part remains and represents the response.

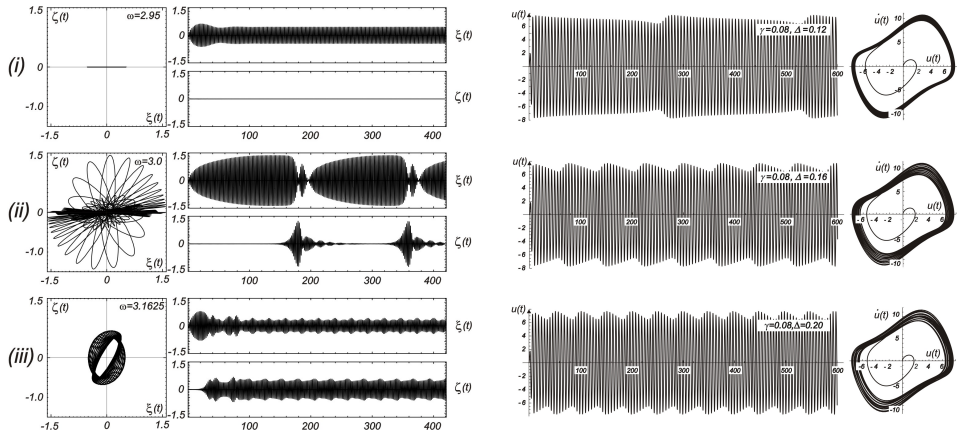
Despite of a wide variety of knowledge the systematic investigation of internal structure of a quasi-period and its dependence on detuning is still missing. The reason motivating theoretical investigations of the resonance zone and relevant quasi-periodic response consists in the need to protect systems against this phenomenon and, on the other hand, in wide possibilities of sophisticated applications in practice. A few papers deal with the close topic of quasi-periodicity discussing theoretical aspects, e.g. [1], [2], [3], as well as some experimentalist's view [4]. An interesting study comes also from the astrophysics [5], and many other areas. The process of quasi-periodicity is rather deterministic although it moves nearby zero of the Lyapunov exponent. Hence a temporary or permanent passage to chaotic regime is also possible.

2 QUASI-PERIODIC RESPONSE

Certain classes of non-linear systems are characterized by a quasi-periodic response when the excitation frequency is close to basic eigen-frequency (small detuning – the system is working in the resonance zone). The beating effect can be observed in systems with softening stiffness, small or zero linear damping, where the non-linear part stabilizes the response process, etc.

Two examples are demonstrated at Figure 1, pictures (a) and (b), see e.g. [6] or [7]. The Figure 1a represents the time history of horizontal response components of a spherical pendulum under horizontal kinematic excitation along ξ coordinate in the suspension point nearby the basic eigen-frequency (simulation). The left column of the picture (a) demonstrates the vertical view of the response process demonstrating character of the attractor. The right column shows time history of length coordinate $\xi(t)$ and cross coordinate $\zeta(t)$. The first group (i) marks the resonance (zero detuning, see Eq. (4) for definition), the second (ii) shows beating effect for a small detuning (large quasi-period) and the third (iii) means the state at the boundary of the resonance zone (short quasi-period and high proportion of the stationary component representing forced vibration). It is obvious that the part of energy absorbed by quasi-periodic part with increasing detuning is dropping for the sake of the stationary part until the quasi-periodic part disappears completely. This state corresponds to vanishing of auto-oscillation part and domination of forced vibration.

The second example is the generalized Van der Pol or Rayleigh equation; both are widely used for modelling of various physical processes exhibiting limit cycles or homoclinic orbits. See Figure 1b. Although the shape of the response envelope looks simpler, its character is similar concerning the dependence on the detuning. The left column shows the time history



(a) (b)

Figure 1: Quasi-periodic response of systems nearby the resonance point; (a) the spherical pendulum with kinematic horizontal excitation in the suspension point in length coordinate $\xi(t)$ (cross coordinate $\zeta(t)$); (b) the Van der Pol equation response nearby the basic eigen-frequency.

of the system response for three values of detuning $\Delta = 0.12, 0.16, 0.20$ with respect to eigen frequency $\omega_0^2 = 1$; the right column demonstrates the time history plotted in the Poincaré plane. Finally the orbit passes into a stable closed trajectory, unless we are not in the proximity of an unstable limit cycle.

Studies dealing with the resonance zone concerning MDOF and continuous systems including homoclinic and more complicated orbits have been studied as well. They represent valuable contribution to the general problem analysis, although their aim is slightly different than the focus of this paper. These papers discuss influence of various types of internal resonance onto processes within the resonance zone, see e.g. [8], [9]. The parametric identification in resonance zone is treated in papers, e.g., [10], [11], [12] as well as multi-harmonic processes [13], etc. There can be found many inspiration steps regarding problems of quasi-periodic processes nearby eigen frequencies and dealing with sub and super-harmonic synchronization. Interesting results referring multi frequency quasi-periodicity provides paper [2], which deals with the state of the chaos onset. In such a case the limit cycle is replaced by an attractor with parameters adequate to the detuning and system properties, see e.g., [14], [15].

We can see that the beating nearby the resonance of the nonlinear system is very important phenomenon in engineering and physical applications having negative but also positive influence. It is worthy to be thoroughly investigated using semi-analytic and numerical (simulation) approaches in order to compare results obtained using various procedures and with respect to experimental verification. Hence we start with semi-analytic investigation and try to explore at least qualitatively the character of quasi-periodic processes concentrating at the SDOF system. The investigation will be based on analysis of the response time history envelope being complemented by the relevant response phase shift.

With respect to results of experimental investigation and comprehensive numerical simulation let us consider an SDOF system described by the generalized Van der Pol equation:

$$\ddot{u} - (\eta - \nu u^2 + \vartheta u^4)\dot{u} + \omega_0^2 u \;=\; P\omega^2 \cos \omega t \tag{1}$$

where: $\omega^2 = K/m$ - eigen frequency of the associated linear system with stiffness K and concentrated mass m; μ, ν, ϑ - coefficients of linear viscous and nonlinear damping; ω - exci-

tation frequency; $P\omega^2 = F\omega^2/m$ - amplitude of the excitation force (per unit mass), P can be interpreted as an eccentricity of a mass m rotating with a frequency ω. The equation (1) characterizes nonlinear vibration of an SDOF system modelling the reduced flutter as one of post-critical response types of an aeroelastic system. In general, this equation describes state when the total linear damping component drops below zero due to aeroelastic effects and only nonlinear effects should try to stabilize the system on the level of a limit cycle (if stable), see, e.g., [16] and others.

Similar applications can be found also in mechanical engineering and theoretical physics. See for instance problems of blade lattice in turbines, vehicle dynamics, dynamics of turbulent streaming, hot plasma movement, dynamics of musical instruments, electronics, etc. A couple of problems motivated by these branches have been referred in [17] [18] [19] together with a numerical study [20]. An approach dealing with type-II intermittency in the driven double scroll circuit has been presented [21]. In this paper has been brought the experimental evidences, confirmed by numerical results, that a homoclinic saddle connection is the nonlinear mechanism responsible for the re-injection of the trajectory around a repulsing focus.

3 RESPONSE TYPES AND STABILITY

Let us use for $u(t)$ a harmonic approximation together with the 1st and 2nd derivatives:

$$\begin{aligned} u &= U\cos(\omega t+\varphi) \\ \dot{u} &= -U\omega\sin(\omega t+\varphi) \\ \ddot{u} &= -U\omega(\omega+2\dot{\varphi})\cos(\omega t+\varphi) - 2\dot{U}\omega\sin(\omega t+\varphi) \end{aligned} \tag{2}$$

where the following auxiliary constraint has been adopted due to increase of unknowns number from one to two:

$$\dot{U}\cos(\omega t+\varphi) - U\dot{\varphi}\sin(\omega t+\varphi) \;=\; 0 \tag{3}$$

Substituting Eqs (2) into Eq. (1) and employing harmonic balance procedure, we eliminate the "fast" time and obtain following equations in "slow" time for amplitude A and phase shift φ:

$$\begin{aligned} \dot{A} &= \frac{\eta}{2}A(1-A^2+2\gamma A^4) - \frac{\eta}{2}Q\omega\sin\varphi, \qquad \text{(a)} \\ \dot{\varphi} &= \Delta - \frac{\eta}{2A}Q\omega\cos\varphi, \qquad \text{(b)} \end{aligned} \tag{4}$$

$$\Delta \;=\; \frac{\omega_0^2-\omega^2}{2\omega} \approx \omega_0-\omega, \;\; A^2 = \frac{1}{4}\frac{\nu}{\eta}U^2, \;\; \gamma = \frac{\vartheta\eta}{\nu^2}, \;\; \delta^2 = \frac{\Delta^2}{\eta^2}, \;\; Q^2 = \frac{\nu P^2}{4\eta^3}.$$

where for detuning Δ the exact or the approximate expression will be used following the level of the difference of excitation and eigen-frequency. Take a note that the monochromatic approach Eq. (2) is a coarse approximation. However, it can be adopted when the damping parameter η and particularly the generalized damping γ are small. Otherwise, another approximation type should be used being based on a small value of the inertia or restoring force. In such a case the final orbit or possible limit cycle has no more the ellipse-like form. See also [22] and other resources concerning limit cycles and their stability.

As the first step we investigate the stationary solution of Eqs (4). We put $\dot{A} = \dot{\varphi} = 0$ and subsequently an equation for amplitude A can be carried out:

$$((1-A^2+2\gamma A^4)^2 + 4\delta^2)A^2 \;=\; Q^2\omega^2 \tag{5}$$

Character of the amplitude A^2 depends on detuning $\delta^2 = \Delta^2/\eta^2$ and excitation amplitude $Q^2\omega^2$, while damping ratio γ influences the basic character of the resonance picture. Eq. (5)

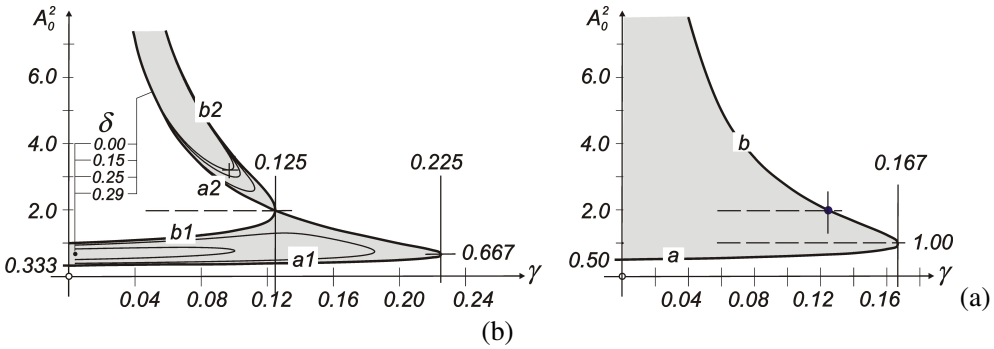


Figure 2: Positive and negative (shadow area) value of the inequalities (8); picture (a), ineq. (8a) - limits: bold $\delta = 0$, thin $\delta = 0.15, 0.25, 0.29$; picture (b), ineq. (8b)

can accommodate one, three or five real roots A^2 depending on parameters γ, δ^2, Q^2. The roots can provide stable and unstable solution of the system Eqs (4).

In order to assess parameter areas leading to the stable/unstable response we suppose that linearization in the stationary point is regular. Hence we can write out the linear system associated with original system Eqs (4) for small deviations ξ, ψ from stationary solution A_0, φ_0. The weakly perturbed stationary solution can be written in a form:

$$A \;=\; A_0 + \xi, \qquad \varphi \;=\; \varphi_0 + \psi \tag{6}$$

Substitution of Eq. (6) into the system Eqs (4) provides a linear system for perturbations ξ, ψ:

$$\begin{aligned} \dot{\xi} \;&=\; \tfrac{1}{2}\eta(1 - 3A_0^2 + 10\gamma A_0^4)\cdot\xi \qquad - A_0\Delta\cdot\psi \qquad \text{(a)} \\ \dot{\psi} \;&=\; + \tfrac{\Delta}{A_0}\cdot\xi \;+\; \tfrac{1}{2}\eta(1 - A_0^2 + 2\gamma A_0^4)\cdot\psi \qquad \text{(b)} \end{aligned} \tag{7}$$

The linear system Eqs (7) is stable with respect to Routh-Hurwitz conditions if it holds:

$$\begin{aligned} (1 - 3A_0^2 + 10\gamma A_0^4)(1 - A_0^2 + 2\gamma A_0^4) + 4\delta^2 \;&\geq\; 0 \qquad \text{(a)} \\ 6\gamma A_0^4 - 2A_0^2 + 1 \;&\geq\; 0 \qquad \text{(b)} \end{aligned} \tag{8}$$

The condition Eq. (8a) could be brought to the depressed quartic inequality. However, still it is not suitable for further analytical investigation. Nevertheless, a qualitative answer can be obtained putting $\delta^2 = 0$, when Eq. (8a) splits into two quadratic conditions which yield:

$$\begin{aligned} A_0^2 \;&\leq\; \frac{1}{4\gamma}\left(1 - \sqrt{1 - 8\gamma}\right), \quad \text{(a1)}, \qquad A_0^2 \;\geq\; \frac{1}{4\gamma}\left(1 + \sqrt{1 - 8\gamma}\right), \quad \text{(a2)}, \\ A_0^2 \;&\leq\; \frac{1}{20\gamma}\left(3 - \sqrt{9 - 40\gamma}\right), \quad \text{(b1)}, \qquad A_0^2 \;\geq\; \frac{1}{20\gamma}\left(3 + \sqrt{9 - 40\gamma}\right), \quad \text{(b2)}. \end{aligned} \tag{9}$$

Character of inequalities Eq. (9) is outlined in Fig. 2a. The shadow areas within bold curves represent domains where the expression Eq. (8a) gives negative values for $\delta = 0$ and the condition is not fulfilled. Here the solution becomes instable. The thin curves which mean limits for several $\delta > 0$ have been evaluated numerically. It is obvious that for increasing detuning δ the lower shadow area diminishes rapidly and for $\delta \approx 0.29$ disappears completely. Then only the upper part should be considered starting $A_0^2 \geq 3.16$. So that with increasing amplitude A_0^2 the system is becoming less and less sensitive to the emergence of instability.

For $\gamma > 0.225$ negative value of the expression on the left side of Eq. (8) cannot occur and only stable solutions are to be expected. Such a result is obvious when we realize that increasing damping ratio has always a stabilizing influence.

The condition Eq. (8b) is independent from δ. It is fulfilled for any amplitude A_0^2 if the damping ratio $\gamma < 1/6$. Otherwise one of two following conditions should be valid:

$$A_0^2 \le \frac{1}{6\gamma}(1 - \sqrt{1-6\gamma}),\ \text{(a)}, \qquad A_0^2 \ge \frac{1}{6\gamma}(1 + \sqrt{1-6\gamma}),\ \text{(b)}. \tag{10}$$

The inequalities Eq. (10) are demonstrated in the Fig. 2b. Positive values of Eq. (8b) arise outside the shadow area. The picture is δ^2 independent, so that the upper limit of Eq. (8b) is fixed. Take a note that the curve following from Eqs (10) passes through the same point where intersect both limits specified by Eqs (9).

It implies from Fig. 2a that four intervals γ should be distinguished. They are separated by points $\gamma = 0, 0.125, 0.167, 0.225, +\infty$. The first interval $\gamma \in (0, 0.125)$ produces two instable intervals on the A_0^2 axis, while in the interval $\gamma \in (0, 0.125)$ only one instable zone emerges. In the interval $\gamma \ge 0.225$ no instable cases occur.

Let us evaluate now information about system stability discussing the Fig. 3. Six plots for damping ratio $\gamma = 0.075, 0.100, 0.125, 0.150, 0.175, 0.225$ demonstrate the response amplitude

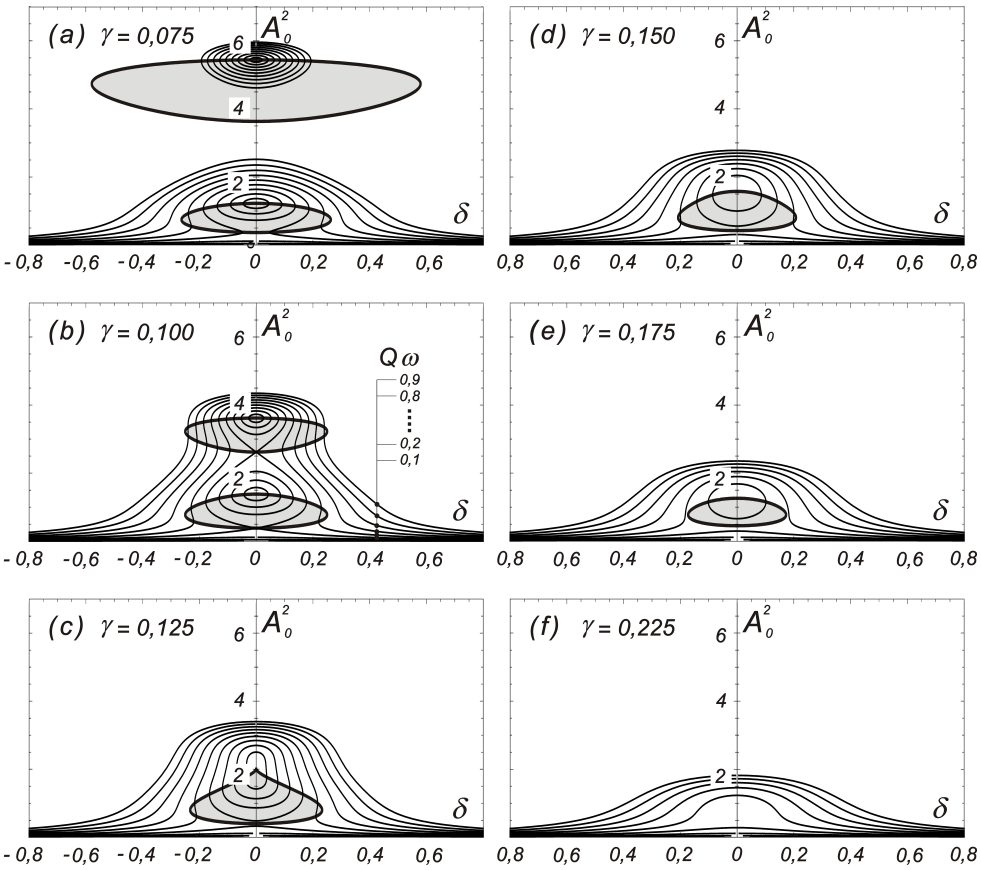


Figure 3: Resonance curves in the plane (δ, A_0^2) for various excitation amplitudes $Q\omega$; (a) $\gamma = 0.075$, (b) $\gamma = 0.100$, (c) $\gamma = 0.125$, (d) $\gamma = 0.150$, (e) $\gamma = 0.175$, (f) $\gamma = 0.225$.

A_0^2 in the plane (δ, A_0^2) as it follows from Eq. (5). Values γ have been selected with respect to important points separating the axis γ into four intervals mentioned above. In every interval γ more or less qualitatively different shape of the resonance picture in the plane (δ, A_0^2) and different stability properties of the system arises. Differences consist in number and type of individual resonance curves. Fig. 3a,b demonstrate the system attributes in the interval $\gamma \in (0, 0.125)$. For small excitation amplitudes the resonant curve splits into three curves, where two of them are closed making detached resonance zones. It is markedly visible in the picture 3a. Increasing the excitation amplitude the lower detached zone disappears as it corresponds with tendency of disappearing of the lower instability domain in Fig. 2a for increasing $\delta > 0.0833$. A transition case represents Fig. 3c separating two intervals in $\gamma = 0.125$. Final disappearance of the upper instability zone is obvious. Furthermore only three real roots A_0^2 exist. Nevertheless, a gradual decrease in the number of real roots is also associated with an increasing detuning.

In intervals $\gamma \in (0.125, 0.167) \bigcup (0.167, 0.225)$ the shapes are similar in general, see Fig. 3d,e. The resonance curve includes one closed detached zone for small excitation amplitude. For large $\gamma > 0.225$ only one open curve exists remembering conventional linear cases Fig. 3f. Only one real root A_0^2 exists whatever is detuning δ or, in other words, one set of open resonance curves characterizes the system.

Take a note that the derivative in points separating stable and instable parts of curves in Fig. 3 is infinite (the tangent is vertical). They are the points characterized by relations Eqs (8) being considered as equations. Graphically expressed, they are represented in the Fig. 3 by bold closed curves with shadow filling. They appear nearby the limit cycles of the system (if any), see [16]. This referenced paper also classifies intervals of the damping ratio where one stable or one stable+one unstable or no limit cycle exist. Just remember that these zones lead to Hopf bifurcation as a rule, see, e.g., [22], [23] and other resources.

It comes to light that in parameter configurations leading to more real roots (e.g. five) the highest and lowest curve represents the stable roots as a rule. If there exists only one real root it is stable in a certain interval of detuning δ^2, or everywhere if $\gamma \geq 0.167$. The auto-oscillations in eigen frequency emerge for $\gamma \leq 0.167$, in a certain interval of detuning δ^2 and excitation amplitude. This state leads to failure of the synchronous regime and beatings arise. If $\gamma > 0.167$, auto-oscillations don't occur and whatever detuning leads to forced vibrations only.

Another aspect more should be remarked. The Fig. 4 demonstrates dependence of the re-

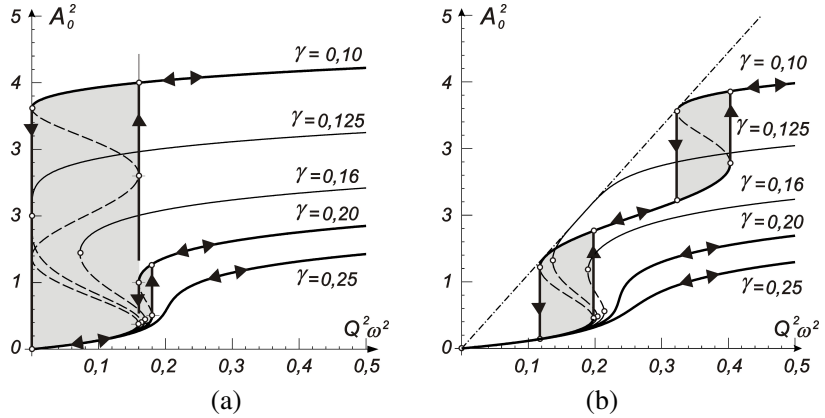


Figure 4: Dependence of the response amplitude A_0^2 on excitation amplitude (factor $Q^2\omega^2$) for damping ratio $\gamma = 0.10, 0.125, 0.16, 0.20, 0.25$; (a) detuning $\delta = 0.0$, (b) $\delta = 0.15$.

sponse amplitude A_0^2 on the excitation amplitude $Q^2\omega^2$ moving up and going down. Pictures (a) and (b) depict A_0^2 for detuning $\delta = 0.00, 0.15$, each of them five curves for damping ratio $\gamma = 0.10, 0.125, 0.16, 0.20, 0.25$. Instable zones are obvious. In general, the relevant hysteresis zones reduce their size with increasing damping ratio and ascending detuning as far as disappear completely.

Let us follow this process for zero detuning - picture (a). For $\gamma < 0.125$ (curve 1) and small excitation amplitude two stable stationary response types exist: (i) forced vibrations with a small amplitude A_0^2, (ii) synchronous auto-oscillations with large amplitude A_0^2. Increasing the excitation amplitude starting the level $Q^2\omega^2 \approx 0.16$ only synchronous vibrations can exist. When the factor $Q^2\omega^2$ is then descending from the level above 0.16, it follows the upper stable curve as far as the zero. The hysteresis loop created by this curve is the largest one.

In the interval $\gamma \in (0.125, 0.225)$ the small excitation amplitudes produce forced vibrations only. Increasing the excitation amplitude also auto-oscillations are possible and beatings emerge. A hysteresis loop is smaller. For $\gamma > 0.225$ only forced vibrations can be seen and no hysteresis appears. Amplitude of forced vibration is decreasing with rising damping ratio γ.

Concerning cases with non-zero detuning, the picture (a) remains partly in force. Only a straight line $4\delta^2 A^2$ is added to the picture (a) which is skewed adequately. The hysteresis loops generally diminish and disappear sooner in the picture (b) then those in the picture (a). Take a note that the hysteresis loop can split into two separate zones which are followed adequately when the excitation amplitude is changing. It is also to see markedly that the response amplitude is dropping rapidly with rising damping.

4 CONCLUSIONS

The qualitative analysis of a nonlinear dynamic system response has been performed. A complex picture of stability regarding system parameters and those of external excitation has been investigated and physically interpreted. The character of beatings and conditions of their stable existence have been set. The variability of the quasi-period of a beating effect including description of its components have been assessed in dependence on the detuning. Synchronous and asynchronous regimes and their stability have been described. It has been shown that the shape of the response amplitude envelope within one quasi-period changes from a constant (stationary process) dramatically when the detuning is rising. The ratio of energy content of quasi-periodic and stationary component is decreasing in the same time. Starting a certain frequency the quasi-periodic part fully vanishes and the stationary component absorbs whole amount of the response energy. It should be noted, that appearance and vanishing of the quasi-periodic response component can proceed smoothly or suddenly when sweeping the excitation frequency up and down. Different branches of the response amplitude can be followed depending on the excitation amplitude, damping parameters and initial conditions. Appearance, stability and neighborhood of limit cycles has been evaluated as an isolated response type as well as being a component of a more complex beating effect.

Analytic qualitative methods have been used together with numerical evaluation in order to verify results of the analytical approach. Detailed discussion has been performed to interpret physical meaning of theoretical results comparing both analytical and numerical results. The full numerical simulation as an absolute comparative tool has been started. Relevant results will be published in due time. The preliminary results are promising. Therefore we can conclude that the semi-analytic approach approved very well its efficiency and seems to be applicable for investigation of systems with more degrees of freedom.

ACKNOWLEDGEMENT

The kind support of the Czech Science Foundation project No. 15-01035S and the institutional support No. RVO 68378297 are gratefully acknowledged.

REFERENCES

[1] S. Ostlund, D. Randt, J. Sethna, E. Siggia, Universal properties of the transition from quasi-periodicity to chaos in dissipative systems, *Physica D*, 8, 303-342, 1983.

[2] P.S. Linsay, A.W. Cumming, Three-frequency quasiperiodicity, phase locking, and the onset of chaos, *Physica D*, 40, 196-217, 1989.

[3] N.V. Stankevich, J. Kurths, A.P. Kuznetsov, Forced synchronization of quasiperiodic oscillations, *Commun Nonlinear Sci Numer Simulat*, 20, 316-323, 2015.

[4] J.A. Glazier, A. Libchaber, Quasi-periodicity and dynamical systems: An experimentalist's view, *IEEE Transactions on circuits and systems*, 35(7), 790-809, 1988.

[5] L. Titarchuk, Effects of resonance in quasiperiodic oscillators of neutron star binaries, *Astrophysical Journal Letters*, August, 1-11, 2002.

[6] J. Náprstek, C.Fischer, Auto-parametric semi-trivial and post-critical response of a spherical pendulum damper, *Computers and Structures*, 87, 1204-1215, 2009.

[7] J. Náprstek, C.Fischer, Types and stability of quasi-periodic response of a spherical pendulum, *Computers and Structures*, 124, 74-87, 2013.

[8] D.T. Mook, N. HaQuang, R.H. Plaut, The influence of an internal resonance on nonlinear structural vibrations under combination resonance conditions, *Jour. Sound and Vibration*, 104(2), 229-241, 1986.

[9] G. Kerschen, A.F. Vakakis, Y.S. Lee, D.M. McFarland, J.J. Kowtko, L.A. Bergman, Energy transfers in a system of two coupled oscillators with essential nonlinearity: 1:1 resonance manifold and transient bridging orbits, *Nonlinear Dynamics*, 42, 283-303, 2005.

[10] A.H. Nayfeh, Parametric excitation of two internally resonant oscillators, *Jour. Sound and Vibration*, 119(1), 95-109, 1987.

[11] L.D. Zavodney, A.H. Nayfeh, The response of a single-degree-of-freedom system with quadratic and cubic non-linearities to a fundamental parametric resonance, *Jour. Sound and Vibration*, 120(1), 63-93, 1988.

[12] P.F. Pai, Time-frequency analysis for parametric and non-parametric identification of nonlinear dynamical systems, *Mechanical Systems and Signal Processing*, 36, 332-353, 2013.

[13] A.H. Nayfeh, A.E.S. Jebril, The response of two-degree-of-freedom systems with quadratic and cubic non-linearities to multifrequency parametric excitations, *Jour. Sound and Vibration*, 115(1), 83-101, 1987.

[14] A.J. Lichtenberg, M.A. Lieberman, *Regular and Chaotic Dynamics*, Springer, New York, 1992.

[15] C. Grebogi, E. Ott, J.A. Yorke, Attractors on an N-torus: quasiperiodicity versus chaos, *Physica D*, 15, 354-373, 1985.

[16] J. Náprstek, C.Fischer, Stability of limit cycles in autonomous nonlinear systems, *Meccanica*, 8, 1929-1943, 2014.

[17] K.Y. Plaksiy, Y.V. Mikhlin, Dynamics of nonlinear dissipative systems in the vicinity of resonance, *"Jour. Sound and Vibration*, 334, 319-337, 2015.

[18] A. Kozmin, Yu. Mikhlin, C. Pierre, Transient in a two-DOF nonlinear system, *Nonlinear Dynamics*, 51, 141-154, 2008.

[19] Xing Jian Jing, Zi Qiang Lang, Frequency domain analysis of a dimensionless cubic nonlinear damping system subject to harmonic input, *Nonlinear Dynamics*, 58, 469-485, 2009.

[20] R.P. Eason, A.J. Dick, S. Nagarajaiah, Numerical investigation of coexisting high and low amplitude responses and safe basin erosion for a coupled linear oscillator and nonlinear absorber system, *Jour. Sound and Vibration*, 333, 1390-3504, 2014.

[21] M.S. Baptista, I.L. Caldas, Type-II intermittency in the driven Double Scroll Circuit, *Physica D*, 132, 325-338, 1999.

[22] Yu.A. Kuznetsov, *Elements of Applied Bifurcation Theory*, 3rd edition, Springer, Berlin, Heidelberg, New York, 2004.

[23] J.C. Ji, Non-resonant Hopf bifurcations of a controlled van der Pol-Duffing oscillator, *Journal of Sound and Vibration*, 297, 183-199, 2006.

International Conference on Engineering Vibration
Ljubljana, Slovenia, 7-10 September 2015

INTERACTION OF FRICTIONAL AND REGENERATIVE MECHANISM OF CHATTER VIBRATION

R. Rusinek*[1], M. Wiercigroch[2]

[1]Lublin University of Technology, Department of Applied Mechanics
r.rusinek@pollub.pl

[2]University of Aberdeen, Centre for Applied Dynamics Research
m.wiercigroch@abdn.ac.uk

Keywords: Cutting process, frictional chatter, dry friction, regenerative chatter.

Abstract. *This paper presents new model of frictional chatter extended with regenerative effect due to modulation of cutting depth. These both chatter mechanisms interact each other giving interesting effect of nonlinear dynamics. Nonlinear behaviour is examined with the help of bifurcation diagrams where cutting velocity is chosen as the bifurcation parameters.*

1 INTRODUCTION

During machining operations, vibrations called chatter may occur between the workpiece and the tool. This phenomenon generates dimensional and geometrical inaccuracies, a poor surface finish, faster tool wear and reduction of spindle life. Therefore, it is necessary to understand and control chatter vibrations. There are four types of chatter mechanism: regenerative, frictional, mode coupling and thermos-mechanical ones [1,2]. Frictional and regenerative chatter are the most important from practical point of view. The base of regenerative vibrations go back to the 1950s when Tobias [3] and Tlusty [4] explained the regenerative chatter mechanism in orthogonal cutting and developed the stability lobes theory. This theory makes it possible to predict the cutting depth for a given spindle speed in order to void harmful chatter vibrations. In the middle of 1990s Altintas [5] presented an analytical form of stability lobes theory dedicated for milling. This theory is still widely applied, although many researchers modify the cutting force definition [6–15].

Model of cutting process with frictional chatter was developed later in 1986 by Grabec [6]. Grabec considered both velocity dependent cutting forces as well as dry friction between the chip and the workpiece. This study exhibits possibility of chaos generating during metal cutting. Modelling of cutting process is still ongoing and new models are still being developed wherein various nonlinearities of the cutting forces are introduced. Most researchers focus on cutting forces that depend on the axial width of cut, the chip thickness or the cutting speed but ignore the possibility of the tool losing contact with the workpiece which introduces significant nonlinear responses like chaos. Grabec [6] and Wiercigroch el.al [1,2,16] were the first to account for discontinuous behaviour in their studies of frictional chatter. The models presented by Wiercigroch and co-workers improves the physical modelling of the cutting force characteristics as it accounts for the possibility of a negative relative velocity between the tool and the workpiece related to model proposed by Grabec [6]. However, the models do not take into account the forces acting on flank face. Recently, Rusinek et.al [17] have improved model of orthogonal cutting. They propose the model which considers the forces acting both on the tool face as well as the tool flank.

Usually in the literature the problem of regenerative and frictional chatter mechanisms are investigated separately, although friction phenomena exist always in case of contact problem. Therefore, this approach describes the model of orthogonal cutting both with regenerative and frictional effect. The model of frictional chatter, presented in [17], is completed with regenerative effect. An interaction between the two phenomena gives interesting nonlinear behaviour when cutting speed is used as a bifurcation parameters.

2 MODEL OF ORTHOGONAL CUTTING

Here, we consider an orthogonal cutting process modelled as a two-degrees-of-freedom spring-mass-damper system with effective modal stiffness and damping in two orthogonal directions: the cutting direction and perpendicular to the workpiece along the tool axis (Figure 1a). Figure 1b presents the force distribution on the tool edge separately for the rake face and flank face. This is a quite new approach because classical analysis takes into account only the rake face forces or resultant force acting on the tool [2]. Here, the resultant cutting force is distributed on the normal force on the rake (N_1) and face (N_2) force. The normal forces together with friction between the tool and the workpiece cause the friction force F_1 and F_2 on the rake and the flank face, respectively. This approach of cutting force distribution is presented more detailed in the paper [17]. The normal and the friction force are defined as follows:

$$N_1 = Q_o a_p \left(c_1 (v_r - 1)^2 + 1\right) H(a_p) H(v_r),$$
$$N_2 = K_{con} a_p H(a_p), \tag{1}$$

$$F_1 = N_1 \mu_x \left(\mathrm{sgn}(v_f) - \alpha_x v_f + \beta_x {v_f}^3\right),$$
$$F_2 = N_2 \mu_y \left(\mathrm{sgn}(v_r) - \alpha_y v_r + \beta_y {v_r}^3\right), \tag{2}$$

where Q_o represents the specific cutting force modulus, a_p is the instantaneous penetration of the tool into the workpiece (depth of cut), c_1 is a constant controlling the dependence of the cutting force on the relative velocity between the tool and the workpiece (v_r), K_{con} is the contact stiffness and $H()$ represents the Heaviside function. Note that the $H(v_r)$ takes care of the loss of contact between the tool and the chip while $H(a_p)$ accounts for the tool coming out of the workpiece. In the friction forces (Eqs.(2)) μ_x , μ_y denote the static coefficient of friction between the tool and the workpiece, and the tool and the chip, respectively, α_x, β_x, α_y, β_y are constants which regulate the nonlinear characteristics of the friction forces between the respective surfaces in contact. v_r and v_f are the relative velocities between the tool and the workpiece, and the tool and the chip, respectively and sgn() represents the sign function.

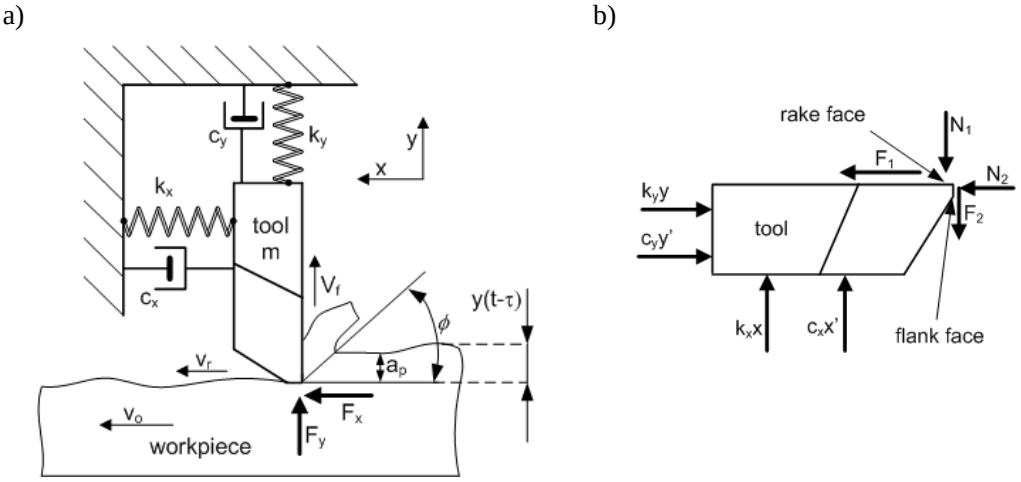


Figure 1: Two degrees of freedom model of orthogonal cutting (a), force distribution on tool edge (b).

Now, the normal and the friction forces are replaced by equivalent forces (F_x and F_y) acting in two orthogonal directions, which are obtained by summing the forces in the vertical and the horizontal directions

$$F_x = Q_o a_p \left(c_1 (v_r - 1)^2 + 1\right) H(a_p) H(v_r) + K_{con} a_p \mu_y \left(\mathrm{sgn}(v_r) - \alpha_y v_r + \beta_y {v_r}^3\right) H(a_p),$$
$$F_y = K_{con} a_p H(a_p) + Q_o a_p \left(c_1 (v_r - 1)^2 + 1\right) \mu_x \left(\mathrm{sgn}(v_f) - \alpha_x v_f + \beta_x {v_f}^3\right) H(a_p) H(v_r). \tag{3}$$

The presented above model from [17] is additionally extended with regenerative phenomenon, that is a novelty of the paper. Regenerative mechanism comes from wavy workpiece geometry from the previous pass of a vibrating tool, which produces a fluctuating cutting force caus-

ing self-excited vibrations. Thus, the instantaneous penetration of the tool into the workpiece or the cutting depth a_p can be written in terms of the specified depth of cut a_{po}, the tool motion y and the tool motion one rotation before $y(t-\tau)$ as

$$a_p = a_{po} - y + y(t-\tau). \tag{4}$$

Time delay τ is connected with a spindle or a workpiece speed Ω by equation

$$\tau = 2\pi / \Omega \tag{5}$$

The relative velocities between the tool and the workpiece (v_r), and the tool and the chip (v_f) are related to the nominal cutting speed v_o, the shear angle of the workpiece material ϕ and the tool velocities by

$$v_r = v_o - \dot{x}, \quad v_f = v_r \tan\phi - \dot{y}. \tag{6}$$

Finally, the nondimensional equations of motion I defined in the form

$$\begin{aligned} &\ddot{x} + 2z_x\dot{x} + x = f_x, \\ &\ddot{y} + 2z_y\sqrt{\alpha}\dot{y} + \alpha y = f_y, \end{aligned} \tag{7}$$

where

$$\alpha = \frac{k_y}{k_x}, \quad \omega_x{}^2 = \frac{k_x}{m}, \quad \omega_y{}^2 = \frac{k_y}{m} = \alpha\,\omega_x{}^2, \quad z_x = \frac{c_x}{2m\omega_x}, \quad z_y = \frac{c_y}{2m\omega_y} \tag{8}$$

and the forces are given by

$$\begin{aligned} f_x &= q_o a_p \left(c_1(v_r-1)^2+1\right) H(a_p)H(v_r) + k_{con} a_p H(a_p)\mu_y \left(\mathrm{sgn}(v_r) - \alpha_y v_r + \beta_y v_r{}^3\right), \\ f_y &= k_{con} a_p H(a_p) + q_o a_p \left(c_1(v_r-1)^2+1\right) H(a_p)H(v_r)\mu_x \left(\mathrm{sgn}(v_f) - \alpha_x v_f + \beta_x v_f{}^3\right), \end{aligned} \tag{9}$$

where all the constants are nondimensional.
In order to avoid some problems with numerical integration, the discontinuous Heaviside and sign function is replaced by

$$\mathrm{sgn}(x) = \tanh(\sigma x), \quad H(x) = \frac{1}{1+e^{-\sigma x}}, \tag{10}$$

where σ is a large number; in our computation we assume $\sigma = 500$.

3 INFLUENCE OF REGENERATIVE EFECT

The main aim of the analysis is to reveal the nonlinear phenomena caused by the regenerative mechanism as a connection with friction one. The presented in previous section model is analysed by mean of MATLAB using the inbuilt command *ode45* with a specified tolerance of *1e-6* for numerical integration. Numerical research are presented as bifurcation diagrams where cutting velocity is used as a parameter. Moreover, the influence on the stiffness ratio α is analysed. Since, the system do not have any external periodic excitation the displacements when the velocities are zero ($\dot{x}=0$, $\dot{y}=0$) is plotted in the bifurcation diagrams. Numerical simulations are performed using the parameters adopted from [17] and given by z_x=z_y= 0.01, a_{po}= 0.5, v_o=0.5, q_o=0.9, α=1, α_x=α_y=0.3, β_x=β_y=0.1, μ_x=μ_y=0.5, $\tan\phi$=0.45, k_{con}=0.5, c_1=0.3,

$\Omega = v_o$. Figure 2 – 4 show bifurcation diagrams for various stiffness ratio α. The diagrams (a) and (b) represent the system only with frictional effect while (c) and (d) the system with frictional and regenerative chatter mechanisms.

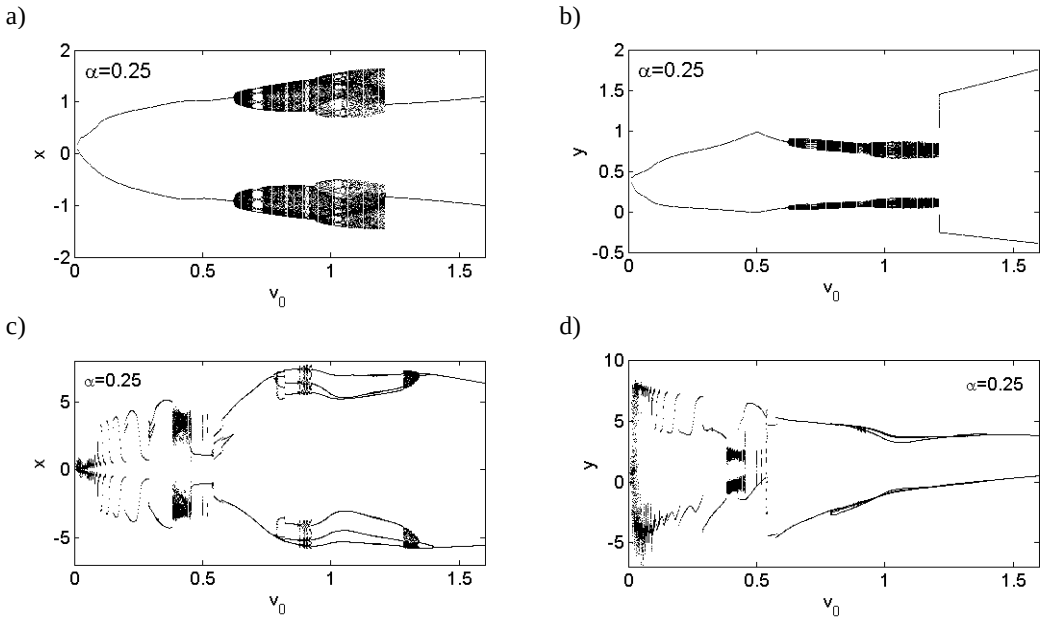


Figure 2: Bifurcation diagram for α=0.25, system without time delay (a, b) and with time delay (c, d).

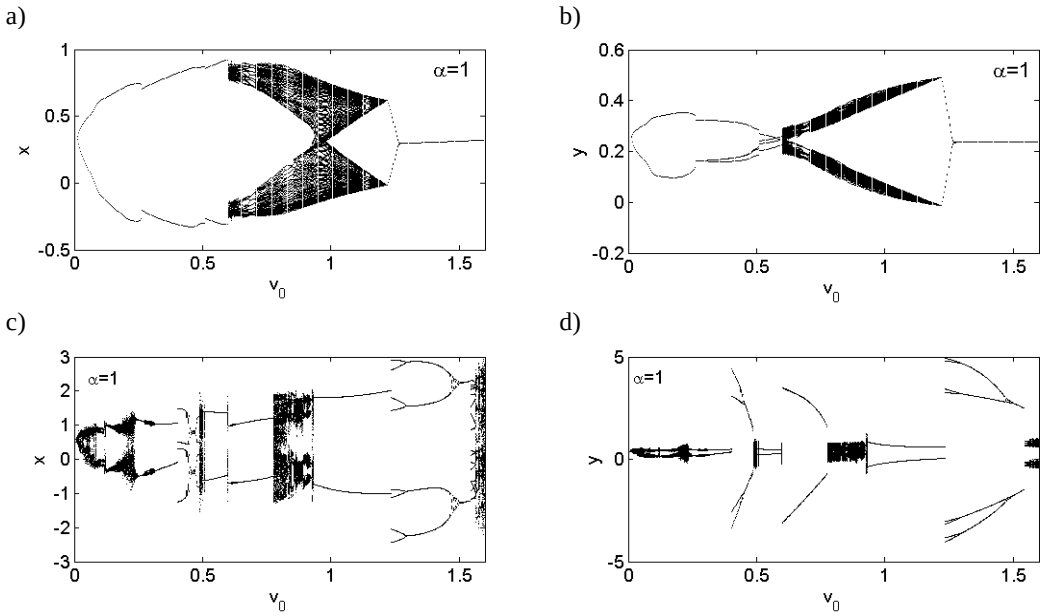


Figure 3: Bifurcation diagram for α=1, system without time delay (a, b) and with time delay (c, d).

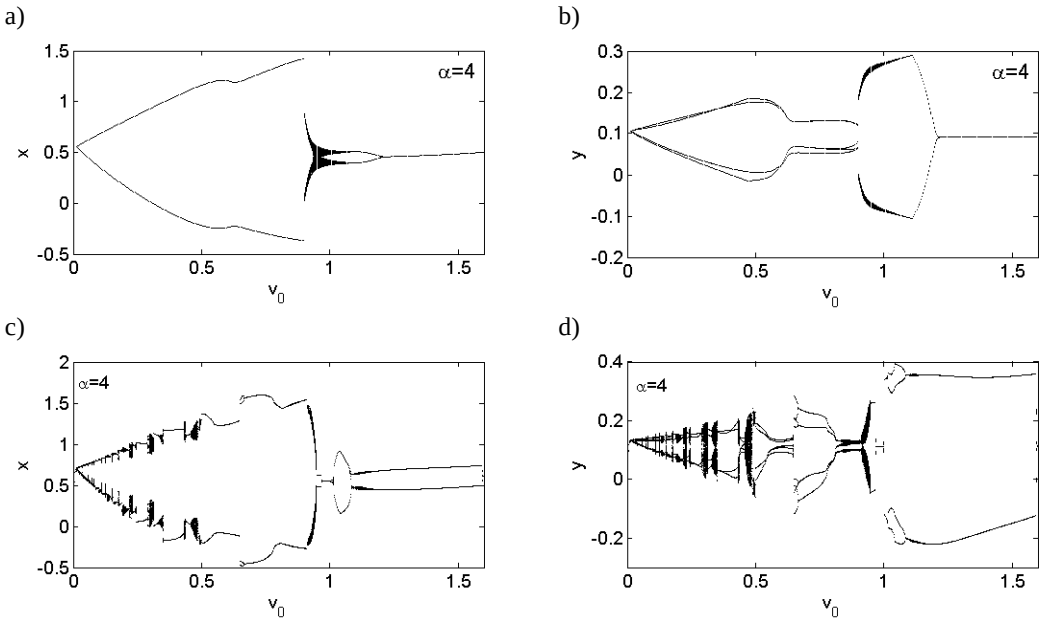


Figure 4: Bifurcation diagram for α=4, system without time delay (a, b) and with time delay (c, d).

Generally, the system with two chatter mechanisms has much bigger vibrations compared to the system with only frictional effect. Moreover, modulations of vibrations amplitude are visible. In case of α=0.25 (Figure 2c, d) strong influence of velocity change is observable specially in the range of v_o between 0 and 0.5. Next, the periodic solutions and period doubling bifurcation area exists for $0.8<v_o<1.3$. The dark regions on the diagrams are suspected on chaotic or quasi-periodic motion. Self-excited systems without external excitation do not have pure periodic response therefore, their frequency never equal the natural frequency of the system but they are close to the natural frequency. From that reason, the Lyapunov exponents analysis is the best method of chaos recognition. Since, calculations of the Lyapunov exponents in systems with time delay need special procedure, this problem will be discusses in next paper.

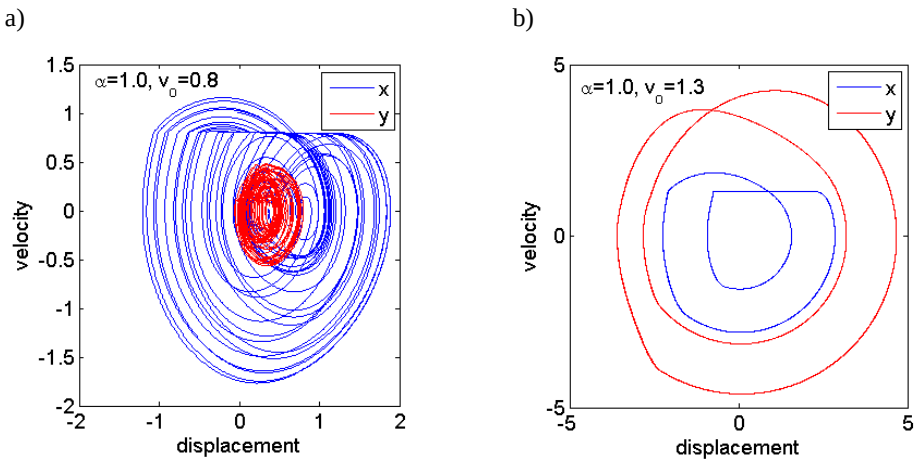


Figure 5: Phase space for α=1, v_0=0.8(a), v_0=1.3 (b).

From practical point of view, the case when the stiffness in both directions are the same (α=1) is the most common. Then the system dynamics is still richer in relation to the pure frictional model. Period doubling bifurcation leading to motion of period 2 and 4 occur (Figure 3c, d). Moreover the symptom of chaos is noticeable as well. The evidence of chaos is presented on the phase space for the chosen cutting velocity presented in Figure 5a. Vibrations of period 2 are also shown in Figure 5b.

The last case presented here, when α=4 demonstrates relatively small increase of vibrations (Figure 4c, d) compared to the fictional model (Figure 4a, b). Interestingly, that for higher cutting speed v_o >1.2 the pure frictional model presents the response without chatter vibrations while the model with fictional and regenerative mechanisms give periodic response (period 1). Moreover, there are more dark regions testifying for irregular responses.

4 CONCLUSIONS

- Pure frictional model of orthogonal cutting process generates smaller chatter vibrations compared to the model with frictional and regenerative mechanisms.
- Dynamics of the presented model is more complex than the frictional one. Quasi- periodic, sub-harmonic and chaotic motion occur more often.
- Modulation of chatter amplitude caused by variable time delay are observed.
- Machining with high speed (like HSM) which is developed only on the basis of regenerative model in order to improve productivity and avoid chatter, does not have to be beneficial because of interaction between regenerative and frictional chatter mechanisms.

ACKNOWLEDGEMENTS

Financial support of Structural Funds in the Operational Programme - Innovative Economy (IE OP) financed from the European Regional Development Fund - Project "Modern material technologies in aerospace industry", POIG.01.01.02-00-015/08-00 is gratefully acknowledged.

REFERENCES

[1] M. Wiercigroch, E. Budak, Sources of nonlinearities, chatter generation and suppression in metal cutting, Philosophical Transactions of the Royal Society A: Mathematical, Physical and Engineering Sciences 359 (2001) 663–693.
[2] M. Wiercigroch, A.M. Krivtsov, Frictional Chatter in Orthogonal Metal Cutting, Phil.Trans.The Royal Society Society of London A Mathematical Physical And Engineering Science 359 (2001) 713–738.
[3] S.A. Tobias, Machine Tool Vibration, John Wiley, New York, USA, 1965.
[4] J. Tlusty, M. Polacek (Eds.), Stability of Machine Tools Against Self-Excited Vibration in Machining, Proc. ASME Prod. Eng. Res. Conf, 1963.
[5] Y. Altintas, E. Budak, Analytical Prediction of Stability Lobes in Milling, CIRP Annals - Manufacturing Technology 44 (1995) 357–362.
[6] I. Grabec, Chaos Generated by the Cutting Process, Physics Letters A A117 (1986) 384–386.

[7] N.S. Namachchivaya, R. Beddini, Spindle Speed Variation for the Suppression of Regenerative Chatter, J.Nonlinear Sci. 13 (2003) 265–288.
[8] G. Stepan, Modelling Nonlinear Regenerative Effect in Metal Cutting, Philosophical Transactions of the Royal Society A: Mathematical, Physical and Engineering Sciences 1781 (2001) 739–757.
[9] N. Deshpande, M.S. Fofana, Nonlinear regenerative chatter in turning, Robotics and Computer Integrated Manufacturing 17 (2001) 107–112.
[10] M.S. Fofana, Delay dynamical system and applications to nonlinear machine tool chatter, Chaos Solitons and Fractals 17 (2003) 731–747.
[11] G. Litak, Chaotic Vibrations in a Regenerative Cutting Process, Chaos Solitons and Fractals 13 (2002) 1531–1535.
[12] G. Stepan, R. Szalai, T. Insperger, Nonlinear Dynamics of High-speed Milling Subjected to Regenerative Effect, in: G. Radons, R. Neugebauer (Eds.), Nonlinear Dynamics of Production Systems, Wiley-VCH, Weinheim, 2004, pp. 111–127.
[13] G. Stepan, Kalmar-Nagy T. (Eds.), Nonlinear Regenerative Machine Tool Vibrations, 1997.
[14] Wahi P., Chatterjee A., Self-interrupted regenerative metal cutting in turning, Journal of Non-Linear Mechanics 43 (2008) 111–123.
[15] P. Wahi, A. Chatterjee, Regenerative tool chatter near a codimension 2 Hopf point using multiple scales, Nonlinear Dyn 40 (2005) 323–338.
[16] M. Wiercigroch, A.H.-D. Cheng, Chaotic and Stochastic Dynamics of Orthogonal Metal Cutting, Chaos Solitons and Fractals 8 (1997) 715–726.
[17] R. Rusinek, M. Wiercigroch, P. Wahi, Modelling of Frictional Chatter in Metal Cutting, International Journal of Mechanical Science 89 (2014) 167–176.

International Conference on Engineering Vibration
Ljubljana, Slovenia, 7-10 September 2015

INFLUENCE OF SHEAR DEFORMABILITY AND AXIAL/ROTATIONAL INERTIA IN THE NONLINEAR FREE VIBRATIONS OF BEAMS WITH DIFFERENT BOUNDARY CONDITIONS

Stefano Lenci*[1], Giuseppe Rega[2]

[1]Polytechnic University of Marche, via Brecce Bianche, I-60131 Ancona, Italy
lenci@univpm.it

[2]Sapienza University of Rome, via A. Gramsci, I-00197 Rome, Italy
Giuseppe.rega@uniroma1.it

Keywords: Nonlinear oscillations, hardening vs softening behaviour, hinged vs supported boundary conditions, asymptotic methods.

Abstract. *Nonlinear free oscillations of elastic beams have been investigated in the past aimed at highlighting the effects of kinematical and dynamical assumptions under different boundary conditions. Yet, open issues still occur as regards the influence of the various assumptions (concerned with axial inertia, rotational inertia, shear deformability, and nonlinear curvature) in variable geometrical situations. This paper aims at highlighting their importance via a unified treatment of the nonlinear free vibrations of hinged beams with either an axially restrained (hinged-hinged) or free (hinged-supported) end.*

Three geometrically exact equations of free motion in the axial and transverse displacement and in the shear angle are obtained. They are strongly nonlinear and cannot be solved in closed form, so an asymptotic method is applied to obtain an analytical solution approximate to the third order. Longitudinal and transverse dynamics are decoupled at first order, which allows to assume vanishing (first order) axial displacement and obtain the equation of motion in the sole transverse displacement. It provides the first order normal mode and the linear natural (circular) frequencies of the system, both of which do not depend on the type of the boundary condition in the axial direction. The second order problem provides the axial displacement, which instead depends on the type of boundary conditions. The second order (nonlinear) frequency is provided by the solvability conditions of the third order problem; it gives the bending of the so-called "backbone" curve.

The main goal consists of studying the dependence of the second order frequency on the axial and rotational inertia, on the shear stiffness and, mainly, on the kind of axial (immovable or movable) boundary. The accomplished comprehensive treatment allows to resume and properly framework literature results, while also shedding new light on the comparative importance of the beam geometrical and mechanical properties.

11th International Conference on Engineering Vibration
Ljubljana, Slovenia, 7–10 September 2015

MULTI-MODE SOLUTIONS IN A PERIODIC ARRAY OF COUPLED NONLINEAR PENDULUMS UNDER PRIMARY RESONANCE

D. Bitar*[1], N. Kacem[1], N. Bouhaddi[1]

[1] FEMTO-ST Institute, UMR 6174, Applied Mechanics Department, University of Franche-Comté, UBFC, 24 Chemin de l'Épitaphe, F 25000, Besançon, France
{diala.bitar,najib.kacem,noureddine.bouhaddi}@femto-st.fr

Keywords: Collective Dynamics, Periodic Structures, Nonlinear Pendulums, Modal Interactions, Asymptotic Numerical Method

Abstract. *The collective nonlinear dynamics of a periodic structure of coupled pendulums is investigated under primary resonance. The coupled equations governing the nonlinear vibrations of the considered system are normalized and transformed into a set of coupled complex algebraic equations using the multiple scales method coupled with standing wave decomposition. The resulting nonlinear system is numerically solved using the asymptotic numerical continuation technique. It is shown that the number of additional multi-mode solutions is large even for an array of few pendulums and the stability of the corresponding branches can be tuned with respect to the design parameters. In practice, the nonlinear stiffness can be functionalized in order to enhance the performances of the system in term of energy transfer.*

1 INTRODUCTION

Nonlinear periodic systems are frequently encountered in serval scientific domains such as biology, optics, acoustics and mechanics. For instance, in the field of acoustics, Narisetti *et al.* [1] analyzed the influence of nonlinearity and wave amplitude on the dispersion properties of plane waves in nonlinear periodic materials, particularly in uniform granular media. In optics, Heinrich *et al.* [2] introduced optomechanical arrays as a new system to study collective oscillator dynamics. Moreover, in micro and nanotechnology, dynamic behavior investigations of an array of N nonlinearly coupled microbeams have been performed by Lifshitz *et al.* [3] using a discrete model.

In mechanics, the array of coupled pendulums represents a famous example of periodic nonlinear structures which can be described by the sine-Gordon model. The latter is suitable for a large variety of physical systems, which explains the vast research area developed around this field. Several theorems on the existence of oscillatory, rotary, and mixed periodic motions of n coupled simple pendulums were proved by Marlin [4] *et al.*, and Cai *et al.* [5] identified two distinct regimes for a damped sine Gordon chain driven by the spatio-temporal periodic potential. For a single monochromatic driving, Khomeriki *et al.* [6] demonstrated numerically and experimentally the existence of three tristable stationary states. Recently, Liang *et al.* [7] reported an undergraduate experiment using a coupled-pendulum chain to demonstrate various aspects of wave motion, while Jallouli *et al.* [8] investigated the nonlinear dynamics of a 2D array of coupled pendulums under parametric excitation.

In addition, Intrinsic Localized Modes (ILMs), existing as exact solutions in nonlinear lattices have been widely studied, particularly for an array of coupled pendulums [9] which is an ideal playground for showcasing many interesting features of discrete breathers [10] which can be stabilized in the presence of driving and damping [11] or propagate energy in a forbidden band-gap [12]. However, the nonlinear coupling and decoupling between ILM and third allowed plane-wave mode, as well as both modes interaction with the driver, give rise to pulsating breather instability [13]. Although the dynamics of coupled nonlinear pendulums was thoroughly investigated in the frequency and time-space domains, there is a real need to perform profound analysis of the collective dynamics of such systems in order to identify practical relations with the nonlinear energy localization phenomena in terms of modal interactions and bifurcation topologies [14].

In this paper, we investigate the collective dynamics of a periodic array of coupled pendulums under primary resonance. The coupled nonlinear equations of motion were transformed to a set of complex algebraic equations, which are numerically solved. The stability, the modal interactions and the bifurcation topologies of small size pendulum arrays (two and three pendulums) are analyzed in the frequency domain for a given set of design parameters. The main goal is to understand how nonlinearities may be tuned to control the stability of multimode solutions in coupled pendulums.

2 MODEL

Figure 1 shows the theoretical model of an array composed by a horizontal axle, containing N identical pendulums separated by an equal distance. Each pendulum is designed as pendulum n attached perpendicularly to the axle, with a mass m and length l. θ_n is the inclination angle of the n^{th} pendulum measured from its equilibrium position. The pendulums n and $n+1$ are connected together by a linear torsional spring, with spring constant k. We denote by c the viscous damping coefficient of the dissipative force acting on the supporting point of the n^{th}

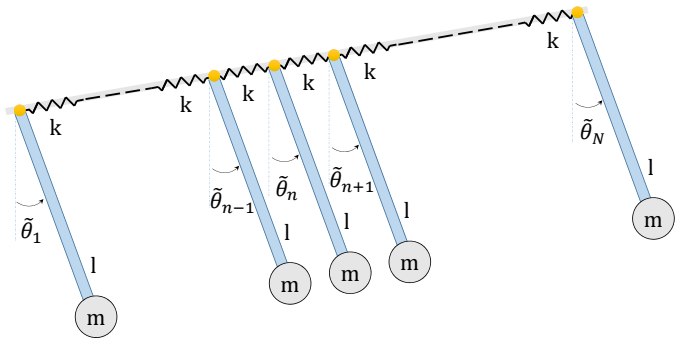


Figure 1: A chain of externally excited pendulums sharing a common axle and coupled by linear torsional springs.

pendulum. Each pendulum is subjected to an external excitation $Fcos(\Omega t)$.

2.1 Equations of motion

The kinetic energy T of the system can be expressed as

$$T = \frac{1}{2}\sum_{n=1}^{N} m(\dot{\widetilde{x}}_n^2 + \dot{\widetilde{y}}_n^2). \tag{1}$$

Where $(\widetilde{x}_n, \widetilde{y}_n)$ represents the Cartesian coordinates system of the n^{th} pendulum and the dot denotes the derivative with respect to time, $\widetilde{x}_n$ and $\widetilde{y}_n$ are given as

$$\widetilde{x}_n = l\sin\widetilde{\theta}_n, \quad \widetilde{y}_n = -l\cos\widetilde{\theta}_n. \tag{2}$$

by substituting Eq. (2) into Eq. (1) the kinetic energy becomes

$$T = \frac{1}{2}\sum_{n=1}^{N} ml^2\dot{\widetilde{\theta}}_n^2. \tag{3}$$

The potential energy V of the system can be written as

$$V = \sum_{n=1}^{N} mgl(1-\cos\widetilde{\theta}_n) + \frac{1}{2}\sum_{n=1}^{N-1} k(\widetilde{\theta}_{n+1} - \widetilde{\theta}_n)^2. \tag{4}$$

Where g represents the acceleration due to gravity. The dissipation energy D of the system is given by

$$D = \frac{1}{2}\sum_{n=1}^{N} \alpha l\dot{\widetilde{\theta}}_n^2. \tag{5}$$

The Lagrange equation can be written in the following form

$$\frac{d}{d\widetilde{t}}\left(\frac{\partial L}{\partial \dot{\widetilde{\theta}}_n}\right) - \frac{\partial L}{\partial \widetilde{\theta}_n} + \frac{\partial D}{\partial \dot{\widetilde{\theta}}_n} = Q_n. \tag{6}$$

With L the Lagrangian operator defined by $L = T - V$. Substituting Eqs. (3) - (5) into Eq. (6) and expanding $\sin(\theta)$ as the sum of its Taylor series centered at 0 up to the third order, lead to the following equation of motion of the nth pendulum

$$ml^2\ddot{\widetilde{\theta}}_n + \alpha l\dot{\widetilde{\theta}}_n + k(2\widetilde{\theta}_n - \widetilde{\theta}_{n-1} - \widetilde{\theta}_{n+1}) + mgl(\widetilde{\theta}_n - \frac{1}{3}\widetilde{\theta}_n^3) = F\cos(\Omega t) \qquad (n = 1, \ldots, N) \quad (7)$$

2.2 Normalized equations

For convenience and equation simplicity, the following nondimensional variables are introduced:

$$\theta_n = \frac{\widetilde{\theta}_n}{\widetilde{\theta}_D}, \qquad t = \omega_0\widetilde{t}. \tag{8}$$

Where $\widetilde{\theta}_D = \frac{F\omega_0}{\alpha g}$ is the dynamic displacement of the associated linear system. After dropping Eqs. (8) into Eq. (7), we obtain the following nondimensional system of equations

$$\ddot{\theta}_n + \frac{1}{Q}\dot{\theta}_n + \theta_n + \frac{k}{mgl}(2\theta_n - \theta_{n-1} - \theta_{n+1}) - \frac{1}{6}\frac{F^2}{\alpha^2 gl}\theta_n^3 = \frac{\alpha}{\omega_0 ml}\cos(\frac{\Omega}{\omega_0}t) \tag{9}$$

In the following section, we shall solve these equations using multiple-scale perturbation theory [15], by introducing the following parameters and setting the external frequency an amount $\varepsilon\omega_0\Omega_D$ away from the resonant frequency, whereby they contribute to the equations of amplitude

$$\frac{1}{Q} = \varepsilon c, \quad \frac{k}{mgl} = \frac{1}{2}\varepsilon\gamma, \quad \frac{F^2}{\alpha^2 gl} = \xi, \quad \frac{\alpha}{\omega_0 ml} = \varepsilon^{\frac{3}{2}} f. \tag{10}$$

2.3 Derivation of amplitude equations

We expand $\theta_n(t)$ as a sum of standing-wave modes with slowly varying amplitudes

$$\begin{aligned} \theta_n(t) &= \varepsilon^{\frac{1}{2}} \sum_{m=1}^{N} (A_m(T)\sin(nq_m)e^{it} + c.c.) \\ &\quad + \varepsilon^{\frac{3}{2}}\theta_n^{(1)}(t) + \cdots, \qquad n = 1, \cdots, N \end{aligned} \tag{11}$$

where $T = \varepsilon t$ is a slow time variable. Since the boundary conditions are such that there are two additional fixed pendulums labeled 0 and $N + 1$ (θ_0= θ_{N+1}= 0), the possible wave components q_m can be given as

$$q_m = \frac{\pi}{N+1} \tag{12}$$

After replacing Eq. (11), into the EOM, we can get at the order of $\varepsilon^{\frac{3}{2}}$, N equations of the form:

$$\ddot{\theta}_n^{(1)} + \theta_n^{(1)} = \sum_m (m^{th}\text{secular term})e^{it} + \text{other terms}$$

On the right hand side, we have N secular terms that act to drive the coupled oscillators $u_n^{(1)}$ at their resonance frequencies. We require them to be vanished so that $\theta_n^{(1)}$ remain finite, and thus we obtain the equations for the slowly varying amplitudes $A_m(T)$. To extract the equation for the m^{th} amplitude $A_m(T)$, we make use of the orthogonality of the modes, by multiplying

the m^{th} secular term by $\sin(nq_m)$ and summing over n. We find that the equation of the m^{th} amplitude $A_m(T)$ is given by:

$$2i\frac{dA_m}{dT} + icA_m + 2\gamma\sin^2(\frac{q_m}{2})A_m - \frac{3}{4}\sum_{j,k,l} A_j A_k A *_l \Delta^{(1)}_{jkl,m} = \frac{g}{N+1}e^{i\Omega_D T}\sum_{n=1}^{N}\sin(nq_m) \quad (13)$$

Neglecting initial transients, we try a steady-state solution of the form

$$A_m = a_m e^{i\Omega_D T} \quad (14)$$

Substituting Eq. (14) into Eq. (13), we obtain the required equation for the fixed complex amplitudes a_m.

$$(ic - 2\Omega_D)a_m + 2\gamma\sin^2(\frac{q_m}{2})a_m - \frac{3}{4}\sum_{j,k,l} a_j a_k a *_l \Delta^{(1)}_{jkl,m} = \frac{g}{N+1}\sum_{n=1}^{N}\sin(nq_m) \quad (15)$$

3 RESULTS AND DISCUSSION

In order to study the collective nonlinear dynamics, we started by solving the algebraic system for a small number of coupled pendulums. As a first step, the system (15) was solved for N=2. The coupled algebraic equations were solved numerically for $N = 2$, for several values of the detuning parameter Ω_D in the frequency domain where the whole response is represented. The stability analysis of each point was performed based on the eigenvalues of the Jacobian matrix of the differential system (13). For the case of $N = 3$, a continuation technique based on the prediction-correction method such as the Asymptotic Numerical Method (ANM) was considered after transforming Eq. (13) into its cartesian form [16].

Table 1: Design parameters for the corresponding periodic structure depicted in Figure 1

M (kg)	g $(M.s^{-2})$	l (m)	k $(N.m^{-1})$	α $(Kg.s^{-1})$	F (N)
0.02	9.81	0.25	0.0003	0.01	0.065

Figure 2 represents the response intensities of two coupled pendulums as a function of the detuning parameter Ω_D, for the set of design parameters given in Table 1. Although, we have two coupled pendulums, there are regions in where three stable solutions can exist for a given frequency. The Single Mode (SM) corresponds to the frequency response of a single forced Duffing oscillator for the first intensity and a null trivial solution for the second one. The Double Mode (DM) results from the coupling between the two pendulums. By zooming over a precise frequency range, we can clearly see that we have modal interaction and bifurcation topology transfer between these two intensity responses.

Figure 3 displays the response intensities of three coupled pendulums under external excitation, as a function of the detuning parameter Ω_D for the set of design parameters given in Table 1. Remarkably, the only SM corresponds to the null trivial solution of $|a_2|^2$ for N=3 and m=2, while all solutions of $|a_1|^2$ and $|a_3|^2$ are multimodal. The DM solution branches generated by the coupling between the first and the third pendulums are denoted by Di_j with $i \in \{1, 2\}$ and $j \in \{1, 2, 3, 4\}$.

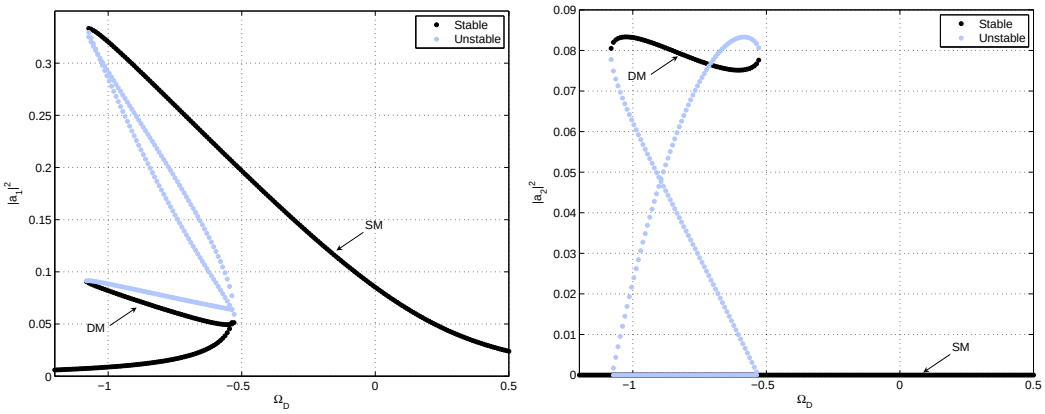


Figure 2: Response intensity of two pendulums as a function of the detuning parameter Ω_D under primary resonance for the set of design parameters given in Table 1, where Black curves indicate stable solutions. The Single and Double-Mode solution branches are labeled SM and DM respectively.

In addition, the interactions between the three pendulums gives rise to the Triple Mode (TM) branches denoted by Tk_l with $k \in \{1, 2, 3\}$ and $l \in \{1, 2\}$. Thus, the response intensities of the first and the third pendulums are completely driven by the collective dynamics due to the modal interaction between the pendulums. Moreover, it is noticeable that each bifurcation point due to a multi-modal solution has a correspondence on the two other intensity responses, which proves that the bifurcation topology transfer is general for any number of oscillators.

These curves were plotted to underline the large number of stable solution branches, even for a small number of coupled oscillators. Indeed, the intensity responses of $|a_1|^2$ and $|a_3|^2$ are highly multistable with up to six stable non-trivial solutions for a given frequency (four double mode and two triple mode solutions).

4 CONCLUSION

The collective nonlinear dynamics of a periodic array of coupled pendulums was modeled under primary resonance. The equations of motion have been derived and solved using the secular perturbation theory, combined with standing wave decomposition and the asymptotic numerical method. The cases of two and three coupled pendulums were investigated, where we demonstrate the complexity of the resulting nonlinear frequency curves in terms of modal interactions and bifurcation topology transfer. The complex response curves were shown to emphasize the large number of nontrivial solution branches, even for a small number of coupled pendulums. As a work in progress, the basins of attraction will be analyzed in the multistability domain in order to investigate the robustness of the multimode solutions which can be tuned with respect to design parameters.

ACKNOWLEDGMENTS

This project has been performed in cooperation with the Labex ACTION program (contract ANR-11-LABX-01-01).

REFERENCES

[1] R. K. Narisetti, M. Ruzzene, and M. J. Leamy. Study of wave propagation in strongly nonlinear periodic lattices using a harmonic balance approach. *Wave Motion*, **49**(2):394 – 410, 2012.

[2] G. Heinrich, M. Ludwig, J. Qian, B. Kubala, and F. Marquardt. Collective dynamics in optomechanical arrays. *Phys. Rev. Lett.*, **107**:043603, 2011.

[3] R. Lifshitz and M. C. Cross. *Nonlinear Dynamics of Nanomechanical and Micromechanical Resonators*. Wiley, 2008.

[4] J. A. Marlin. Periodic motions of coupled simple pendulums with periodic disturbances. *International Journal of Non-Linear Mechanics*, **3**(4):439 – 447, 1968.

[5] D. Cai, A. R. Bishop, and A. Sánchez. Length-scale competition in the damped sine-gordon chain with spatiotemporal periodic driving. *Phys. Rev. E*, **48**:1447–1452, 1993.

[6] R. Khomeriki and J. Leon. Tristability in the pendula chain. *Phys. Rev. E*, **78**:057202, 2008.

[7] C. Liang, W. Ke, M. Fu, C. Wang, and X. Chen. An undergraduate experiment of wave motion using a coupled-pendulum chain. *American Journal of Physics*, **83**(5):389–394, 2015.

[8] A. Jallouli, N. Kacem, and N. Bouhaddi. Nonlinear dynamics of a 2D array of coupled pendulums under parametric excitation. In *5th ECCOMAS Thematic Conference on Computational Methods in Structural Dynamics and Earthquake Engineering (COMPDYN 2015)*, page 8 p, 2015.

[9] T. Ikeda, Y. Harata, and K. Nishimura. Intrinsic localized modes of harmonic oscillations in pendulum arrays subjected to horizontal excitation. *Journal of Computational and Nonlinear Dynamics*, **10**, 2013.

[10] J. Cuevas, L. Q. English, P. G. Kevrekidis, and M. Anderson. Discrete breathers in a forced-damped array of coupled pendula: Modeling, computation, and experiment. *Phys. Rev. Lett.*, **102**:224101, 2009.

[11] L. Q. English. Experimental results for the sine-gordon equation in arrays of coupled torsion pendula. In Jess Cuevas-Maraver, Panayotis G. Kevrekidis, and Floyd Williams, editors, *The sine-Gordon Model and its Applications*, volume **10** of *Nonlinear Systems and Complexity*, pages 111–129. Springer International Publishing, 2014.

[12] F. Geniet and J. Leon. Energy transmission in the forbidden band gap of a nonlinear chain. *Phys. Rev. Lett.*, **89**:134102, 2002.

[13] R. B. Thakur, L. Q. English, and A. J. Sievers. Driven intrinsic localized modes in a coupled pendulum array. *Journal of Physics D: Applied Physics*, **41**(1):015503, 2008.

[14] D. Bitar, N. Kacem, N. Bouhaddi, and M. Collet. Collective dynamics of periodic nonlinear oscillators under simultaneous parametric and external excitations. *Nonlinear Dynamics*, pages 1–18, 2015.

[15] A. H. Nayfeh and D. T. Mook. *Nonlinear Oscillations*. Wiley Classics Library. Wiley, 2008.

[16] B. Cochelin, N. Damil, and M. Potier-Ferry. *Méthode asymptotique numérique*. Methodes numériques. Hermes Lavoissier, 2007.

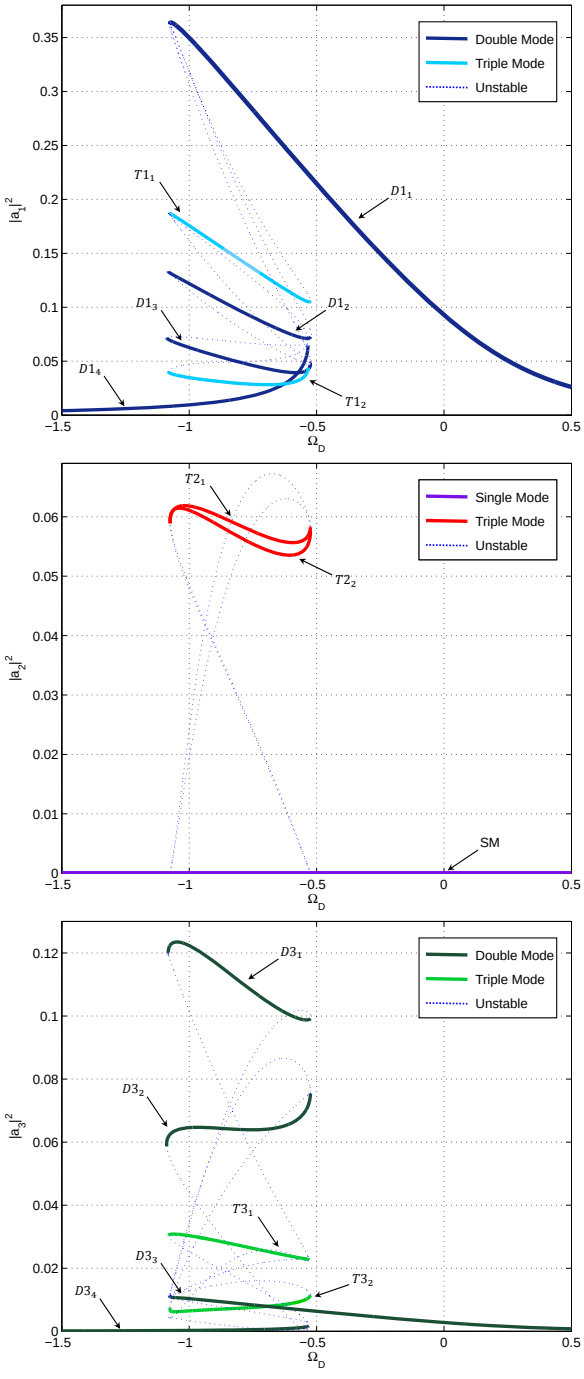


Figure 3: Response intensity of three coupled pendulums as a function of the detuning parameter Ω_D, under primary resonance, for the set of design parameters given in Table 1. The Double and Triple Mode solution branches are respectively denoted by: Di_j and Tk_l for $i \in \{1,3\}, j \in \{1,2,3,4\}, k \in \{1,2,3\}$ and $l \in \{1,2\}$. The only Single Mode denoted by SM corresponds to the trivial null solution of Equation (15), for $N = 3$ and $m = 2$.

11th International Conference on Engineering Vibration
Ljubljana, Slovenia, 7–10 September 2015

A PARAMETRIC STUDY OF THE NON-LINEAR RESPONSE OF PLANE FRAME STRUCTURES UNDER SEISMIC LOADS IN FREQUENCY DOMAIN

Luis Fernando Paullo Munoz[1], **Paulo Gonçalves**[1], **Ricardo Silveira**[2], **Andréa Silva**[2]

[1]Pontifical Catholic University of Rio de Janeiro
f_pm21@hotmail.com

[2]Federal University of Ouro Preto

Abstract. *The structural dynamic analysis in the frequency domain is a topic with great importance in the analysis of structures. In complex problems, the determination of the response in frequency domain, characterized by the resonance curves, is, in some cases, indirectly obtained through analysis in time domain, which leads to big computational efforts when analyzing structures with several number of degrees of freedom. In non-linear cases, the response in frequency domain becomes more complex than in linear cases because of the possibility of multiple solutions for certain frequencies. Those solutions can be stable, unstable or bifurcations, which create the conditions for the appearance of different limit points on resonance curves. In this work, an incremental technique for direct calculation of the non-linear dynamic response in frequency domain of plane frame systems subjected to seismic actions is presented. The transformation of discretized motion equations system, in the context of the Finite Element Method, to the frequency domain is made through the classical Harmonic Balance Method for the linear case. For non-linear analysis, a variant of the Harmonic Balance Method in conjunction with the Galerkin Method to obtain the non-linear algebraic equations in the frequency domain is used. For the non-linear analysis, geometric non-linear formulation is considered. To obtain the resonance curves, the arc-lentgh control method is adopted for the solution of the algebraic non-linear system of equations. The influence of geometric parameters of the structure system over resonance curves is studied as well.*

11th International Conference on Engineering Vibration
Ljubljana, Slovenia, 7–10 September 2015

NUMERICAL AND EXPERIMENTAL INVESTIGATION OF AN UNDERPLATFORM DAMPER TEST RIG

L.Pesaresi*[1], C.W.Schwingshackl[1], L.Salles[1], R.Elliott[2], A.Jones[2], J.S.Green[2]

[1]Imperial College London
*luca.pesaresi12@imperial.ac.uk

[2]Rolls-Royce plc

Keywords: Nonlinear dynamics, Vibrations, Underplatform dampers, Experimental test rig

Abstract. *During operation mechanical structures can experience large vibration amplitudes. One of the challenges encountered in gas-turbine blade design is avoiding high-cycle fatigue failure usually caused by large resonance stresses driven by aeroelastic excitation. A common approach to control the amplitude levels relies on increasing friction damping by incorporating underplatform dampers (UPD). An accurate prediction of the dynamics of a blade-damper system is quite challenging, due to the highly nonlinear nature of the friction interfaces and detailed validation is required to ensure that a good modelling approach is selected. To support the validation process, a newly developed experimental damper rig will be presented, based on a set of newly introduced non-dimensional parameters that ensure a similar dynamic behaviour of the test rig to a real turbine blade-damper system. An initial experimental investigation highlighted the sensitivity of the measured response with regards to settling and running in of the damper, and further measurements identified a strong dependence of the nonlinear behaviour to localised damper motion. Numerical simulations of the damper rig with a simple macroslip damper model were performed during the preliminary design, and a comparison to the measured data highlighted the ability of the basic implicit model to capture the resonance frequencies of the system accurately.*

1 INTRODUCTION

One of the main problems encountered in turbine blade design is avoiding high-cycle fatigue caused by large resonance stresses [1]. Different approaches for lowering the amplitude levels and the stresses in a turbine are available, one of the most common relying on energy dissipation at dry friction contacts of the blade. This energy dissipation can reduce the vibration amplitude significantly, but it also leads to shifts in the resonance frequencies of the bladed disk. Dry friction can occur in various locations in a blade (root, shrouds etc.), however the most effective practical solution is an underplatform damper [2]. The underplatform damper consists of a metal device which sits in a groove on the underside of the platform between adjacent blades, and it is kept in place and loaded by the centrifugal force (see Fig. 1). When the blades vibrate, the relative motion between the blades and the damper leads to friction in the contact interface, which in turn provides energy dissipation and damping to the system.

The dynamics of a bladed disk assembly, with underplatform dampers, is governed by nonlinear differential equations [3–5]. Many studies on damper modelling have been conducted in the past [6–11], but despite all the research efforts, there is still not a standardised approach for the analysis. For this study initially, the blade was modelled as a single degree of freedom system [7, 12], followed by multi-degrees of freedom models with some kinematic hypothesis on the damper motion (eg. parallel platform and damper surfaces during motion) [8, 10, 13]. More recently detailed full 3D models were introduced to more accurately capture the damper motion [11]. The modelling approaches developed must be validated against experimental data to ensure the correct prediction of the nonlinear behaviour. The most common experimental set-up is a double beam with platforms and a damper fitted in between with centrifugal load provided via wires [10, 14, 15]. A complete rotating blisk with cottage-roof dampers has also been tested [16] allowing full engine order excitation. A full not rotating blisk has recently been developed by Berruti et al. [17, 18] overcoming the lack of symmetry in the double beam set up. Test rigs based on blisks can better mimic the effect of dampers on a real turbine stage, but the inevitable mistuning introduced due to the manufacturing and the asymmetries in the loading of the dampers makes the analysis more complicated. Most of these rigs focused on capturing the nonlinear effect correctly, but did not consider a realistic blade-platform motion in great detail.

To overcome these difficulties a new experimental underplatform damper rig is presented in this paper, which follows the scheme of previously developed rigs [10, 14] with two pseudo-blades and one damper. However the geometry has been tuned to allow a more realistic damper motion and a similar friction damping on the blade dynamics. For this purpose, a set of non-dimensional parameters partly new and partly selected from literature, has been used. Nonlinear simulations with an implicit damper model [19] have been performed to support the design and a study on their abilities to capture the experimental FRFs of the introduced test rig will be presented.

2 UPD RIG DEVELOPMENT

2.1 Rig concept

The underplatform damper (UPD) test rig is an experimental set up that allows the effect of UPDs on blade like structures to be evaluated. A static rig design was chosen, to isolate the effect of the damper on the dynamics from the mistuning effect and to create a simplified experimental set up. The basic concept of the rig can be seen in Fig. 1. Two pseudo beam like blades are fixed on a common base, which simulates a rigid disk. The damper is a wedge type, [10], which has a triangular cross section with a characteristic angle. Unlike a real high pressure

turbine blade (HPT), the aerofoil is substituted by a straight rectangular cross-section beam, given the similar vibration modes of the beam like blade to a real blade. These simplifications may lead to a different nonlinear dynamic behaviour, and for this reason, it is important to tune the geometry to minimise this difference.

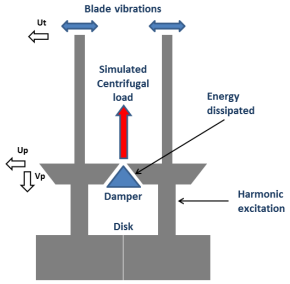


Figure 1: Basic concept of the UPD rig

2.2 Non-dimensional parameters

In order to make the design of the test rig as realistic as possible, it is necessary to tune the geometry to reflect the dynamics of real blades. For this purpose a set of non-dimensional design parameters (Table 1) characterising the main aspects of the dynamic behaviour of a turbine blade has been introduced. These parameters, in part selected from the literature [10, 12, 20] and in part newly defined, are:

A) The *force ratio* [12] of the centrifugal load over the excitation force controls the regime in which the damper is operating. At a low ratio, the excitation force is predominant and the damper is in slip condition, whereas at very high levels the damper is in full stuck condition. During the measurement this parameter can be varied by modifying the damper pull load or the shaker force.

B) The *acceleration ratio*, in a real engine, represents the ratio between the centrifugal acceleration of the damper, due to the rotational speed, and the acceleration of the blade platform projected along the same direction. This parameter controls whether the damper separates from the platform when the damper acceleration is exceeded by the platform acceleration. In the simplified test rig the damper maximum acceleration is governed by the flexibility of the wire-pulley system.

C) The *displacement ratio* [20] is the ratio between the horizontal displacement of the platform and the horizontal displacement of the blade tip in the first flexural mode of the blade. Higher values cause more relative motion at the damper interface leading to more energy dissipated. It allows similar mode shapes between the real blade and the test rig.

D) The *platform displacement ratio* is the ratio between the horizontal and vertical displacement of the platform. This parameter influences the kinematics of the damper during a vibration cycle and ensures realistic damper motions.

	Description	Expression
A)	Force ratio	$\frac{CF}{F_{exc}}$
B)	Acceleration ratio	$\frac{r\Omega^2}{a\omega^2}$
C)	Displacement ratio	$\frac{u_p}{u_t}$
D)	Platform displacement ratio	$\frac{u_p}{v_p}$
E)	Frequency shift	$\frac{\omega_d}{\omega_u}$
F)	Energy ratio	$\frac{E_{fri}}{E_{tot}}$
G)	Contact strain	$\frac{\sigma}{E}$

Table 1: Non-dimensional parameters.

E) The *frequency shift* [10] indicates the change in frequency caused by the damper compared to the baseline configuration (no damper) . The damper causes a stiffening of the system due to the coupling of the blades which depends on the load, on the mode considered, and on the platform and damper geometry. It will ensure that the chosen design leads to realistic frequency shifts.

F) The *energy ratio* considers the energy dissipated by the friction damping and the energy dissipated due to the material hysteresis. It quantifies the contribution of the damper to the total energy dissipation in the dynamic system.

G) The *contact strain* is the ratio between the contact pressure and the Young′s modulus of the material used at the interface. Keeping it similar to a real blade allows the rig to reproduce a similar pressure distribution and similar wear behaviour.

2.3 Design features and measurement set-up

The design process of the UPD test rig was driven by the above mentioned parameters and by minimising external factors that would affect the quality of the nonlinear measurements. The geometry of the blade was defined and optimised using linear FE and nonlinear dynamic analysis, leading to the final design shown in Fig. 2. In particular, the beam length relative to the platform height was adjusted in order to match the displacement ratio and frequency shift of a real blade. In addition, the platform displacement ratio was directly influenced by changing the platform width. The correct contact strain at the blade-platform interface was reached by adjusting the damper dimensions. The centrifugal force, which the damper experiences in a real engine, is simulated with a pulley system and a set of variable weights. In order to have a correct acceleration ratio (defined above) to control damper separation and clapping, the stiffness K of the stainless steel pulling wire is chosen to satisfy the following relation:

$$K_w = \frac{E_w A}{l} > m\omega^2 \tag{1}$$

where K_w is the stiffness of the wire, E_w is the equivalent Young's modulus of the wire, A is the nominal cross section area of the wire, l is the free length between the damper and the first pulley, m is the mass of the damper and ω is the vibration frequency of the blades. It must be noted that the equivalent Young's modulus E is not constant and it increases with the load, since the strands of the wire tend to get closer. The energy parameter, newly introduced here, is affected by all the other parameters, and reasonable values can be achieved only after some design iterations. Compared to a real HPT blade, the fir-tree attachment used to connect the blade to the disk is removed in order to minimise the number of friction joints and focus the non linear rig dynamics on the damper effects alone. The correct alignment between two consecutive platforms, which guarantees a symmetrical loading of the damper, is ensured by a shim between the two blocks (see Fig. 2). The test rig was manufactured to the defined design and the blades were then clamped tightly to a 2 tons inertia block via a newly developed hydraulic vice capable of 200 kN clamping force. The measurement set up can be seen in Fig. 2. The excitation is provided by an electrodynamic shaker, attached below the platform, and the response is measured with two non-contact laser doppler vibrometers (LDV) focused near the tip of each blade.

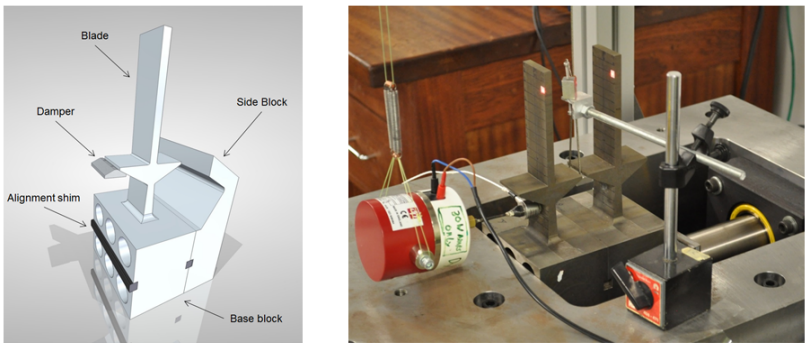


Figure 2: Rig design and lab set-up

3 MEASUREMENTS

3.1 Rig set-up assessment

When evaluating the non linear dynamic response caused by friction damping, it is very important that the underlying dynamic system without a damper is linear and the nonlinearities introduced by the clamping are minimal. For this reason, frequency sweeps of the rig without the damper at increasing clamping forces have been performed, and the modal parameters were extracted (Fig. 3a) to obtain an understanding of the damping performance.

Both loss factor and resonance frequency show some small variations at low clamping forces but seem to converge above 30 kN. The small influence of the clamp on the dynamics is confirmed by the values of the loss factor which are below 0.1 %, which is very close to the free-free

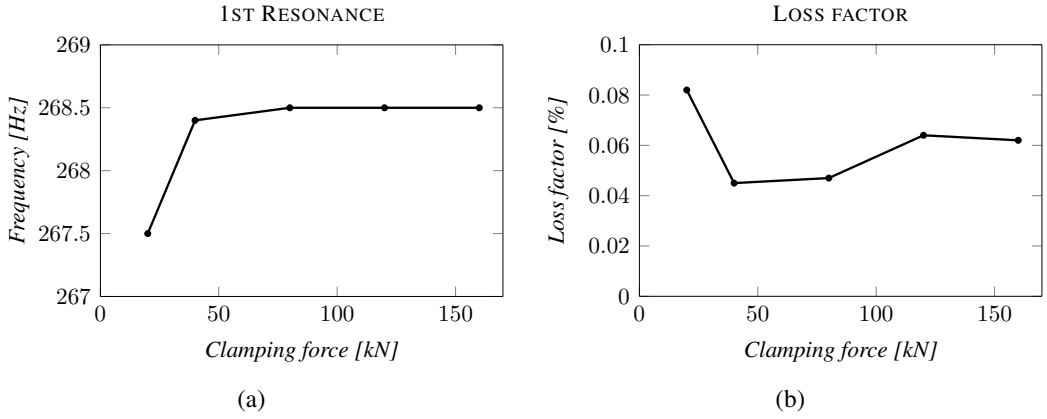


Figure 3: Clamping effect on the 1F modal parameters a) Resonance frequency b) Loss factor

configuration of the blade. In order to evaluate the nonlinear behaviour of the rig at a given force ratio, which should guarantee a constant response as suggested in the literature [7, 12, 15], various FRFs have been measured over a wide range of damper loads, each time adjusting the harmonic excitation to maintain the same force ratio. In this condition, the FRFs should be similar, since similar levels of nonlinearities are triggered, however, our findings (Fig. 4) show a clear change in the resonance frequency at low damper load. A possible explanation could be an inaccurate settling of the damper, leading to a non uniform contact at the interface. When the damper load exceeds 700 N the resonance frequency of the first mode stabilises, providing a minimum loading condition for the subsequent tests.

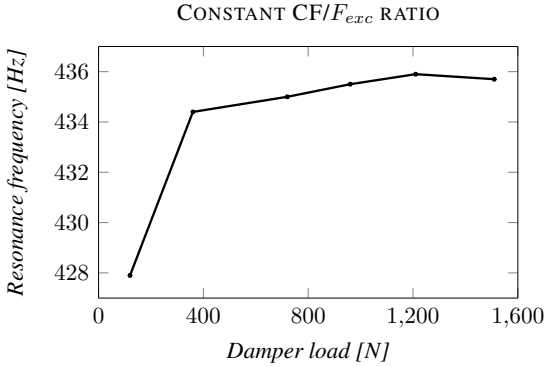


Figure 4: FRFs at constant force ratio and variable damper load

3.2 Non-linear measurements

The initial nonlinear measurements focussed on the first flexural mode (1F), as it normally leads to the highest alternating stresses near the blade root. The double blade configuration of the rig leads to an in phase (IP) and out of phase (OoP) 1F mode, whereas in a real engine, the inter blade phase angle (phase between two consecutive blades) will be between these two

extreme values depending on the nodal diameter excited. The pulling load for the damper was kept at a high level (960 N) to ensure a good conformity at the contact interface. A stepped sine test with a Data Physics SignalCalc ACE card was performed around each resonance at various levels of excitation, from 0.01 N to 17 N. A feedback control kept the excitation force constant throughout the sweep, which guarantees that the nonlinear behaviour is activated every time in a similar way.

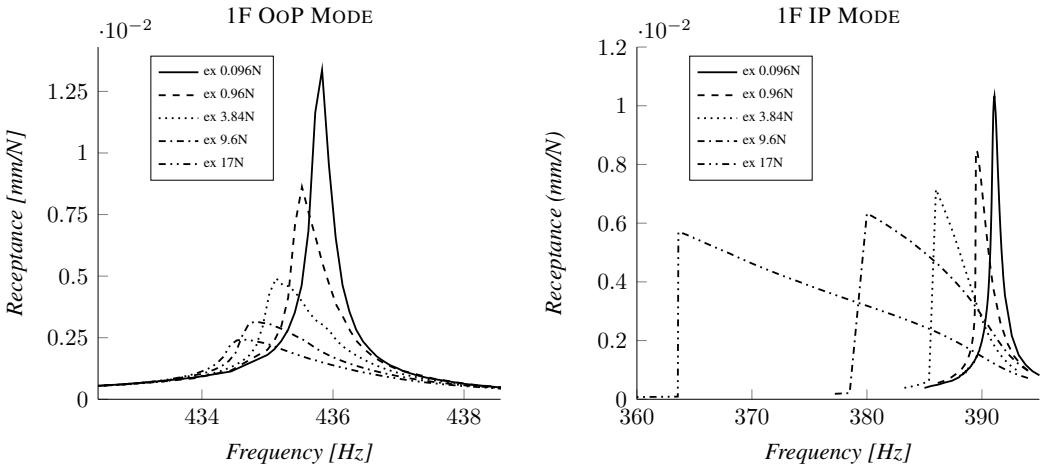


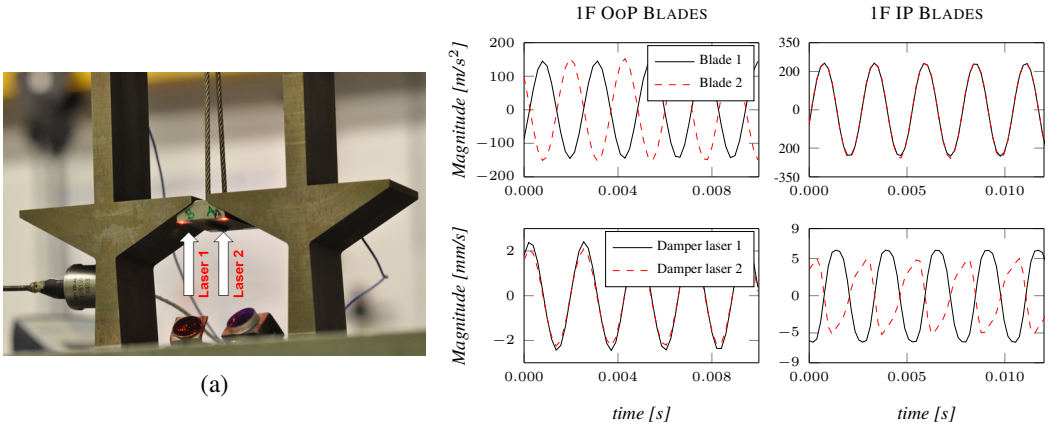
Figure 5: Experimental FRFs at various excitation forces and constant damper load (960 N)

The out of phase mode (OOP) in Fig. 5a shows a significant amplitude reduction from the nearly linear case ($CF/F_{exc} = 10000$) increasing the excitation force. This could be explained by the strong contribution of the local microslip on the energy dissipation mechanism as, even at low excitation levels, when the macroslip is not triggered, the damper is still effective. A very slight frequency shift can also be observed (less than 1%) from the linear to the more damped measurements.

The in phase mode (Fig. 5b), shows a slightly lower amplitude reduction, and in addition large jumps appear at low force ratios due to the strong nonlinear softening in the system. Different maxima are reached when the sweep direction is changed, as the position of the jump, on the two stable FRF branches, shifts. The strong softening effect observed in the in phase FRFs (see Fig. 5b) has a significant impact on the blade dynamics, as it causes large shifts in the resonance frequency compared to the linear case. A possible explanation could be based on the tendency of the damper to roll in the IP mode [10, 15], which can reduce the damper-platform contact area at higher amplitudes, leading to a softer system. In particular, the contact on the platform which is lifting tends to shift down close to the lower edge and the contact on the platform which is lowering tends to move up close to the upper edge.

To confirm the previous assumption on the damper motion, a local measurement of the damper kinematics has been performed for the IP and OOP modes. Two LDV single-point lasers were directed by two mirrors to the bottom corners of the damper as shown in Fig. 6a similarly to the set up shown in [15]. It can be seen that for the IP mode the corners of the damper are moving out of phase, causing a rolling motion, whereas the OOP mode shows a

pure translation of the damper (Fig. 6b). This confirms the strong difference in damper motion between the IP and OOP mode, and highlights the significance on the overall blade behaviour.



(a)

(b)

Figure 6: a) Damper kinematics measurement position, b) Damper motion for the IP and OoP blades modes

4 NUMERICAL SIMULATIONS

4.1 Model

A model of the rig was generated in order to help with the understanding of the damper behaviour and identify possible uncertainties with the rig design. The analysis, conducted in FORSE (Forced Response SuitE), is based on a multi-harmonic balance solver with a powerful model reduction technique [21–23]. To allow a fast computation, an implicit model of the wedge damper [19] was used in this investigation, which consists of a lumped mass at the centre of gravity of the damper, coupled to the blade platforms by the macroslip friction elements as shown in Fig. 7.

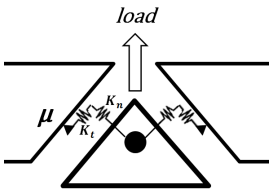


Figure 7: Cottage-roof damper model

Normal load variation, including separation of the contact interface is considered in the model, as well as the tangential friction forces, responsible for the stick-slip transitions. The interface parameters required for the contact model are the friction coefficient μ, and the normal and tangential contact stiffness kn and kt. No limiting hypothesis is made on the damper

motion, which is calculated instead iteratively as a result of the coupled blade-damper dynamic problem. The element allows for 3D translational motion, but no rotating DOFs are considered.

For the analysis, a detailed FE model of the UPD rig was created, and updated to accurately represent the dynamics of the linear rig without a damper. Great care was taken to identify the correct interface parameters for the nonlinear element, as they can significantly influence the results [24]. Measured values for the tangential and normal contact stiffness and the friction coefficient ($\mu = 0.6$) were used to ensure a realistic model [25, 26]. The UPD element is connected to a central node at the contact interface of the linear FE model and the contact area of each damper side must be specified. The initial static normal load N_1 and N_2 for each side of the damper is calculated by taking friction into account [19]:

$$N_1 = N_2 = \frac{1}{2}\frac{F}{(cos(\alpha) + \mu sin(\alpha))} \tag{2}$$

where F is the radial force due to the CF loading and α is the damper angle.

For the multiharmonic analysis, the first three harmonics were included in the Fourier series, as it has been shown that this allowed the most significant nonlinear phenomena to be accurately captured [24] in most cases. Modal damping extracted from a single blade test was used as baseline material damping ($\zeta = 0.05\%$). The position of the sinusoidal excitation and the location of the output response was chosen to coincide with the experiment (see Fig. 2).

4.2 Results

The plot in Fig. 8a shows a numerical FRF for the IP (left peak) and OOP (right peak) first flexural mode at the lowest excitation level (force ratio = 10000). At this level, both friction contact elements at the two sides of the damper are stuck, and therefore, no energy dissipation occurs. The magnitude of the OOP mode is close to the measurements in the linear case, however the IP mode results in much higher amplitudes, indicating a possible dissipation in the test rig even at very low amplitudes, which is not captured correctly with the implicit damper model. A possible explanation for this could be the detected rolling motion of the damper in the IP mode, which can not be described by the basic UPD model. The shifted resonance frequencies are close to the measured ones, with the IP mode about 3% higher, and the OOP about 5% lower, which highlights the capability of the element to introduce the correct stiffness between the two blades.

The nonlinear analysis was focused on the OOP mode due to the difficulty of this modelling approach to capture the IP mode correctly. The amplitude reduction caused by the friction dampers was one of the main design concerns during the initial investigation, and it can be used to evaluate the accuracy of the modelling approach. Fig. 8b shows the peak magnitude of the receptance for the OOP mode at different excitation levels, both experimental and numerical. In the experimental curves, a drop in peak amplitude can be observed, even at very low force levels, indicating unexpected energy dissipation. The model, based on the measured contact interface parameters, is unable to correctly capture this initial drop, but it tends to get closer to the experimental amplitudes at higher excitation levels. This difference may indicate that microslip phenomena are taking place at the contact interface, which can not be captured with the basic macroslip model, leading to incorrect amplitude predictions at very low excitation levels. To better capture the contribution of the microslip with a macroslip model, the friction contact parameters were adjusted to achieve a better match at lower amplitudes as suggested in [27]. With a friction coefficient of $\mu = 0.2$, much better results were obtained at high

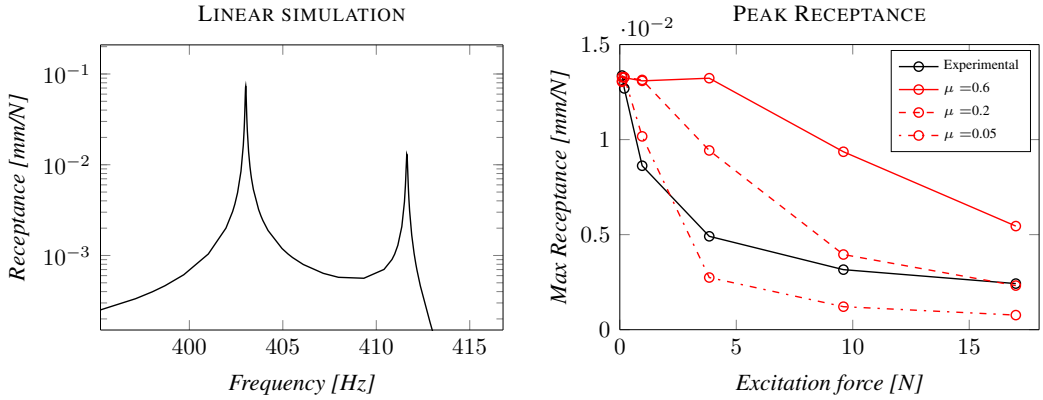


Figure 8: a) IP (left) and OoP (right) linear simulation, b) OoP Numerical NL simulation and experiments

excitation levels (see Fig. 8b), but still some discrepancies were observed for lower excitation levels. A further decrease in the friction coefficient to a very low value of $\mu = 0.05$ helped to get a good match in the low excitation zone, however it overestimates the damping effect at higher forcing levels. For these reasons, a simple macroslip UPD element is a very helpful tool during preliminary design stages to capture the shifts in frequencies in the model, but care needs to be taken in the prediction of the resulting amplitudes, due to its intrinsic inability to correctly capture microslip phenomena. Tuning the friction coefficient could improve the results, however it is hard to find an optimal value for a wide range of excitation forces. In addition, the IP mode dynamics, which seems to be strongly influenced by the rotation of the damper, can not be captured correctly by this simple implicit damper model.

5 CONCLUSIONS

A new static underplatform damper test rig, made of two pseudo blades has been designed and commissioned. A set of non-dimensional parameters has been suggested to ensure a dynamic behaviour of the test rig with realistic loading, displacement and stiffness characteristics. During commissioning of the rig, the settling of the damper was identified as the main issue affecting the quality of the measurements. Nonlinear measurements were performed for the first bending IP and OOP mode at a range of forcing levels, to explore the dynamic behaviour of the rig. The OOP mode showed significant nonlinear damping, whereas the IP mode showed a marked softening effect, which reflects the influence of the rotation of the damper.

A simple UPD model with two macroslip friction elements was used for the analysis of the real damper. This approach allowed a fast computation during the preliminary design phase and a comparison with the final rig behaviour demonstrated a good representation of the frequency shifts caused by the damper. However, the macroslip nature of the UPD element did not allow small excitation amplitudes to be captured accurately, due to an expected presence of microslip in the rig. Using the friction coefficient as a tuning parameter led to a slightly better damping prediction, but relatively low values were required, which may not have a physical meaning for a dry friction interface. Due to the inability of the model to capture the rotation of the damper and its effect on the dynamics, particular care needs to be taken when evaluating lower nodal diameters of the bladed disks where the dynamic behaviour of adjacent blades approaches an

IP mode. When more accurate predictions are required over a wide range of force levels, some more advanced modelling approaches that can capture the microslip phenomena and rotational effects are required.

ACKNOWLEDGEMENTS

The authors are grateful to Rolls-Royce Plc. and Innovate UK for providing the financial support for this project and for giving permission to publish this work.

REFERENCES

[1] B.A.Cowles, "High cycle fatigue in aircraft gas turbine - an industry prospective," *International Journal of Fracture*, vol. 80, pp. 147–163, 1996.

[2] J. H. Griffin, "A review of friction damping of turbine blade vibration," *International Journal of Turbo and Jet Engines*, vol. 7, pp. 297–307, 1990.

[3] B. Feeny, N. Hinrichs, and K. Popp, "A historical review on dry friction and stick-slip phenomena," *Applied Mechanics Reviews*, vol. 51, no. 5, pp. 321–341, 1998.

[4] L. Gaul and R. Nitsche, "The role of friction In mechanical joints," *Applied Mechanics Reviews*, 2001.

[5] J. P. Den Hartog, "Forced vibrations with combined coulomb and viscous friction," *ASME trans.*, pp. 107–115, 1931.

[6] G. C. K. Yeh, "Forced vibrations of a two degree of freedom system with combined coulomb and viscous damping," *The Journal of the Acoustical Society of America*, vol. 39, no. 1, 1966.

[7] J. H. Griffin, "Friction Damping of Resonant Stresses in Gas Turbine Engine Airfoils," *Journal of Engineering for Power*, vol. 102, pp. 329–333, 1980.

[8] B. D. Yang and C. H. Menq, "Characterization of Contact Kinematics and Application to the Design of Wedge Dampers in Turbomachinery Blading : Part 1 Stick-Slip Contact Kinematics," *Journal of Engineering for Gas Turbines and Power*, vol. 120, no. April 1998, pp. 410–417, 1998.

[9] J. H. Wang and W. K. Chen, "Investigation of the Vibration of a Blade With Friction Damper by HBM," *Journal of Engineering for Gas Turbines and Power*, vol. 115, no. April 1993, pp. 294–299, 1993.

[10] K. Y. Sanliturk, D. J. Ewins, and A. B. Stanbridge, "Underplatform Dampers for Turbine Blades: Theoretical Modeling, Analysis, and Comparison With Experimental Data," *Journal of Engineering for Gas Turbines and Power*, vol. 123, no. 4, p. 919, 2001.

[11] E. P. Petrov, "Explicit Finite Element Models of Friction Dampers in Forced Response Analysis of Bladed Disks," *Journal of Engineering for Gas Turbines and Power*, vol. 130, no. 2, p. 022502, 2008.

[12] J. H. Griffin, "An Integrated Approach for Friction Damper Design," *Journal of Vibration and Acoustics*, vol. 1, no. April 1990, pp. 175–181, 1990.

[13] M. H. Jareland, "A parametric study of a cottage-roof damper and comparison with experimental results," in *Proceedings of ASME TURBOEXPO*, pp. 1–9, 2001.

[14] L. Panning, W. Sextro, and K. Popp, "Optimization of interblade friction damper design," in *Proceedings of ASME TURBOEXPO*, pp. 1–8, 2000.

[15] C. M. Firrone, "Measurement of the kinematics of two underplatform dampers with different geometry and comparison with numerical simulation," *Journal of Sound and Vibration*, vol. 323, pp. 313–333, June 2009.

[16] I. a. Sever, E. P. Petrov, and D. J. Ewins, "Experimental and Numerical Investigation of Rotating Bladed Disk Forced Response Using Underplatform Friction Dampers," *Journal of Engineering for Gas Turbines and Power*, vol. 130, no. 4, p. 042503, 2008.

[17] T. Berruti, "A test rig for the investigation of the dynamic response of a bladed disk with underplatform dampers," *Mechanics Research Communications*, vol. 37, pp. 581–583, Sept. 2010.

[18] T. Berruti, C. M. Firrone, and M. M. Gola, "A Test Rig for Noncontact Traveling Wave Excitation of a Bladed Disk With Underplatform Dampers," *Journal of Engineering for Gas Turbines and Power*, vol. 133, no. 3, p. 032502, 2011.

[19] E. P. Petrov and D. J. Ewins, "Advanced Modeling of Underplatform Friction Dampers for Analysis of Bladed Disk Vibration," *Journal of Turbomachinery*, vol. 129, no. 1, p. 143, 2007.

[20] R. K. Giridhar, P. V. Ramaiah, G. Krishnaiah, and S. G. Barad, "Gas Turbine Blade Damper Optimization Methodology," *Advances in Acoustics and Vibration*, vol. 2012, pp. 1–13, 2012.

[21] E. P. Petrov and D. J. Ewins, "State-of-the-art dynamic analysis for non-linear gas turbine structures," *Proceedings of the Institution of Mechanical Engineers, Part G: Journal of Aerospace Engineering*, vol. 218, pp. 199–211, Jan. 2004.

[22] E. P. Petrov and D. J. Ewins, "Analytical Formulation of Friction Interface Elements for Analysis of Nonlinear Multi-Harmonic Vibrations of Bladed Disks," *Journal of Turbomachinery*, vol. 125, no. 2, p. 364, 2003.

[23] E. P. Petrov, "A High-Accuracy Model Reduction for Analysis of Nonlinear Vibrations in Structures With Contact Interfaces," *Journal of Engineering for Gas Turbines and Power*, vol. 133, no. 10, p. 102503, 2011.

[24] C. W. Schwingshackl, E. P. Petrov, and D. J. Ewins, "Effects of Contact Interface Parameters on Vibration of Turbine Bladed Disks With Underplatform Dampers," *Journal of Engineering for Gas Turbines and Power*, vol. 134, no. 3, p. 032507, 2012.

[25] C. W. Schwingshackl, E. P. Petrov, and D. J. Ewins, "Measured and estimated friction interface parameters in a nonlinear dynamic analysis," *Mechanical Systems and Signal Processing*, vol. 28, pp. 574–584, Apr. 2012.

[26] C. W. Schwingshackl, "Measurement of Friction Contact Parameters for Nonlinear Dynamic Analysis," in *Proceedings of the SEM IMAC Conference*, 2012.

[27] J. S. Green, *Controlling Forced Response of a High Pressure Turbine Blade*. PhD thesis, KTH Royal Institute of Technology, 2006.

11th International Conference on Engineering Vibration
Ljubljana, Slovenia, 7–10 September 2015

A ROTATING PENDULUM WITH IRRATIONAL NONLINEARITY

Ning Han*[1], Qingjie Cao[1]

[1] Centre for Nonlinear Dynamics Research, Harbin Institute of Technology,
School of Astronautics, Harbin 150001 China
Email: hanning.bing@163.com qingjiecao@hotmail.com

Keywords: Rotating Pendulum, Irrational nonlinearity, SD oscillator, Equilibrium bifurcation, Chaos.

Abstract. *In this paper, we consider a novel model which comprises a rotating pendulum linked by a pair of linear springs with fixed ends. This model provides a typically cylindrical dynamical system with irrational nonlinearity due to the geometry configuration. This system exhibits smooth or discontinuous characteristics depending on a mechanical parameter, which is similar to the conventional pendulum coupled with SD oscillator. We discuss the irrational restoring force, potential energy, equilibrium bifurcations and transitions of phase portraits for the unperturbed dynamics. The primary responses of the small angle oscillation can be studied by means of the averaging method under the perturbation of viscous damping and external harmonic forcing. Finally, numerical simulations is carried out to investigate the complicated dynamics behavior of periodic and chaotic motions in both smooth and discontinuous case.*

1 INTRODUCTION

The study of the nonlinear dynamics of pendulum is one of the oldest scientific topics, and dates back at least to Galileo and Huygens. By the middle of the 20th century, the interest in the study of pendulum has grown nearly in an exponential manner due to the invention of digital computers. Nowadays, its interest extends from science to civil, education [1], military [2] and industry [3] owing to the wide range of application.

Many kinds of pendulum system or systems containing pendulum have been studied by using experimental method, numerical method and analytical method, which greatly enrich the research content of pendulum. For example, a new concept of using mechanical pendulum systems for wave energy extraction has been given in [4, 5]. Synchronization of pendulum hanging on a common movable beam has been the subject of the research by a number of authors [6, 7, 8]. Chaotic dynamics in pendulum-like system has received a great deal of treatment [9, 10]. The oscillatory and rotary motion of pendulum is among the most widely investigated motions in physics and many nonlinear phenomena in the real world [11, 12].

Recently, a rotating pendulum linked by an oblique spring with fixed end have been proposed and investigated in [13]. This system is a cylindrical dynamical system with irrational characters whose phase portraits of free motion is similar to the conventional pendulum coupled with SD oscillator [14, 15, 16] of the homoclinic orbits of the first and second type. We introduce a cylindrical approximate system which is topologically equivalent to the original system to detect the chaotic boundary in smooth case [17]. Then the chaotic boundary of discontinuous case with a pair of heteroclinic-like orbits [18] are obtained by using semi-analytical method.

In this paper, we present a rotating pendulum linked by a pair of springs pinned to rigid supports. This particular system provides a novel cylindrical system with both smooth and discontinuous dynamic characteristics. The phase portraits of the unperturbed regime bears significant similarities to the conventional pendulum coupled with GSD oscillator [19] of a single, double and triple well surrounded by the homoclinic orbits of the second type, respectively.

2 MATHEMATICAL MODEL

Consider this novel model which comprises a rotating pendulum linked by a pair of linear springs with fixed ends, as shown in Figure 1a and 1b. Now suppose this pendulum is perturbed

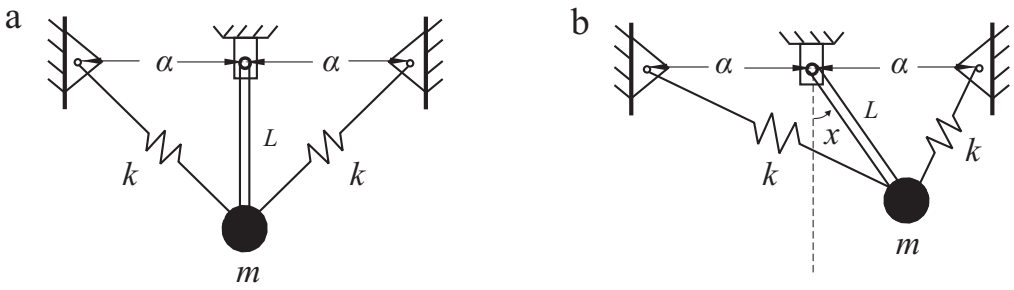


Figure 1: The proposed model of the rotating pendulum linked by a pair of linear springs with fixed ends.

by a viscous damping $CL\dot{x}$ and an external harmonic excitation of amplitude F_0 and frequency

ω, this leads to the following system,

$$\begin{aligned} &mL\ddot{x} + CL\dot{x} + mg\sin x + \\ &kL\alpha\cos x\left(\frac{l}{\sqrt{L^2+\alpha^2-2L\alpha\sin x}} - \frac{l}{\sqrt{L^2+\alpha^2+2L\alpha\sin x}}\right) = F_0\cos\omega t, \end{aligned} \tag{1}$$

where the dot denotes derivative with respect to t, m is the pendulum mass, L is pendulum length, k and l are the stiffness and relax length of the spring, g is the acceleration due to gravity, α is the half distance between the rigid supports, always assumed $h \geq L$ respectively.

The dimensionless form of equation (1) can be written in the following form

$$\ddot{x} + 2\xi\dot{x} + g\sin x + \omega_0^2\alpha\cos x\left(\frac{1}{\sqrt{1+\alpha^2-2\alpha\sin x}} - \frac{1}{\sqrt{1+\alpha^2+2\alpha\sin x}}\right) = f_0\cos\omega t, \tag{2}$$

where

$$\xi = \frac{C}{2m},\ \omega_0^2 = \frac{k}{m}l,\ f_0 = \frac{F_0}{mL},\ L = 1.$$

It is worth pointing out that this system can be smooth or discontinuous depending on the value of the smoothness parameter α. The smooth dynamics appears when $\alpha > L$, while the discontinuous dynamic behavior occurs when $\alpha = L$.

3 UNPERTURBED DYNAMICS

In this section, the unperturbed dynamics of Eq. (2) including the irrational restoring force, stability of equilibria, potential energy, hamiltonian function and phase portraits are discussed by using nonlinear dynamical technique in both smooth and discontinuous case, respectively.

When $\xi = 0$ and $f_0 = 0$, the unperturbed dynamics of Eq. (2) can be written as

$$\dot{x} = y,\ \ \dot{y} = -g\sin x - \omega_0^2\alpha\cos x\left(\frac{1}{\sqrt{1+\alpha^2-2\alpha\sin x}} - \frac{1}{\sqrt{1+\alpha^2+2\alpha\sin x}}\right), \tag{3}$$

of which the nonlinear restoring force

$$F(x,\alpha,\omega_0) = -g\sin x - \omega_0^2\alpha\cos x\left(\frac{1}{\sqrt{1+\alpha^2-2\alpha\sin x}} - \frac{1}{\sqrt{1+\alpha^2+2\alpha\sin x}}\right), \tag{4}$$

is plotted for $\alpha = 1.1$ in Figure 2a for different values of parameter ω_0, the blue, black, red lines mark the smooth case, for $\omega_0 = 3.0, 3.6$ and 4.0, respectively. The corresponding potential energy $V(x) = \int_0^x F(x,\alpha,\omega_0)\,dx$ is shown in Figure 2c. When $\alpha = 1$, the nonlinear restoring force of discontinuous system can be written as

$$\begin{aligned} &F_d(x,\omega_0) = -g\sin x - \\ &\frac{\omega_0^2}{\sqrt{2}}\left(\left(\cos\frac{x}{2}+\sin\frac{x}{2}\right)\ \text{Sign}\left(\cos\frac{x}{2}-\sin\frac{x}{2}\right) - \left(\cos\frac{x}{2}-\sin\frac{x}{2}\right)\ \text{Sign}\left(\cos\frac{x}{2}+\sin\frac{x}{2}\right)\right). \end{aligned} \tag{5}$$

Figure 2b show the nonlinear restoring force of discontinuous system for different values of parameter ω_0, colored the blue, black, red lines for $\omega_0 = \sqrt{15}, \sqrt{20}$ and $\sqrt{30}$, respectively. The corresponding potential energy is plotted in Figure 2d. It is worth pointing out that the yellow line is represented the restoring force of conventional pendulum for $\omega_0 = 0$. Even

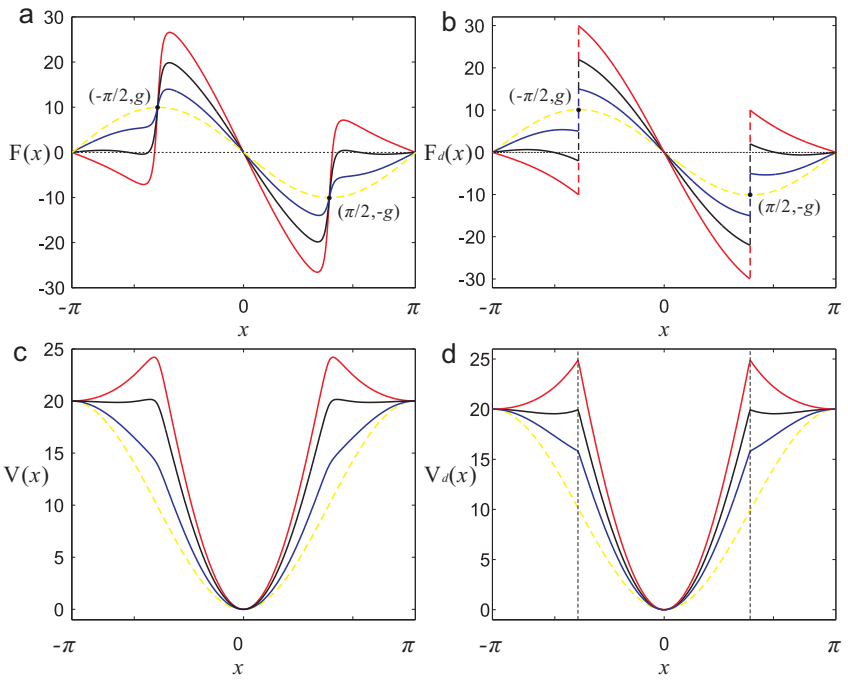


Figure 2: (a) The nonlinear restoring force of smooth case for $\alpha = 1.1$ and corresponding potential energy (c); (b) nonlinear restoring force of discontinuous case for $\alpha = 1$ and corresponding potential energy (d).

the stiffness of the spring is linear and the resistance force supplied to the system is strongly irrational nonlinearity due to geometry configuration.

It can be seen that the equilibrium set $F(x, \alpha, \omega_0) = 0$, of system (3) is a three-dimensional surface in (x, α, ω_0) space, as shown in Figure 3a. Even though we can not obtain the analytical form for $x = x(\alpha, \omega_0)$ explicitly in terms of α and ω_0, we can know the structure of the surface by fixing α, in order to cut the equilibrium surface and intersections are obtained as shown in Figure 3b the discontinuous bifurcation, Figure 3c hysteresis bifurcation and Figure 3d pitchfork bifurcation. We calculate the transient sets on the surface of $F(x, \alpha, \omega_0) = 0$ in the parameter space (ω_0, α) plane

$$\Sigma = \mathscr{B}_1 \cup \mathscr{B}_2 \cup \mathscr{B}_3 \cup \mathscr{H}, \tag{6}$$

where $\mathscr{B}_1$, $\mathscr{B}_2$, $\mathscr{B}_3$ and $\mathscr{H}$ correspond to the subcritical pitchfork bifurcation set, the supercritical pitchfork bifurcation set, the saddle-node bifurcation set and the homo-heteroclinic orbits transition set, respectively, denoted as

$$\begin{aligned}
\mathscr{B}_1 &= \left\{(\omega_0, \alpha) \mid\ g - 2\omega_0^2\alpha^2(1+\alpha^2)^{-1.5} = 0,\ F_x(\pi) = 0,\ \ \alpha > \sqrt{\left(3+\sqrt{5}\right)/2}\right\},\\
\mathscr{B}_2 &= \left\{(\omega_0, \alpha) \mid\ g - 2\omega_0^2\alpha^2(1+\alpha^2)^{-1.5} = 0,\ F_x(\pi) = 0,\ \ \alpha < \sqrt{\left(3+\sqrt{5}\right)/2}\right\},\\
\mathscr{B}_3 &= \left\{(\omega_0, \alpha) \mid\ \ F_x(x_2(\omega_0, \alpha)) = 0\right\},\\
\mathscr{H} &= \left\{(\omega_0, \alpha) \mid\ \ \int_{x_1(\omega_0,\alpha)}^{\pi} F(x) = 0\right\},
\end{aligned} \tag{7}$$

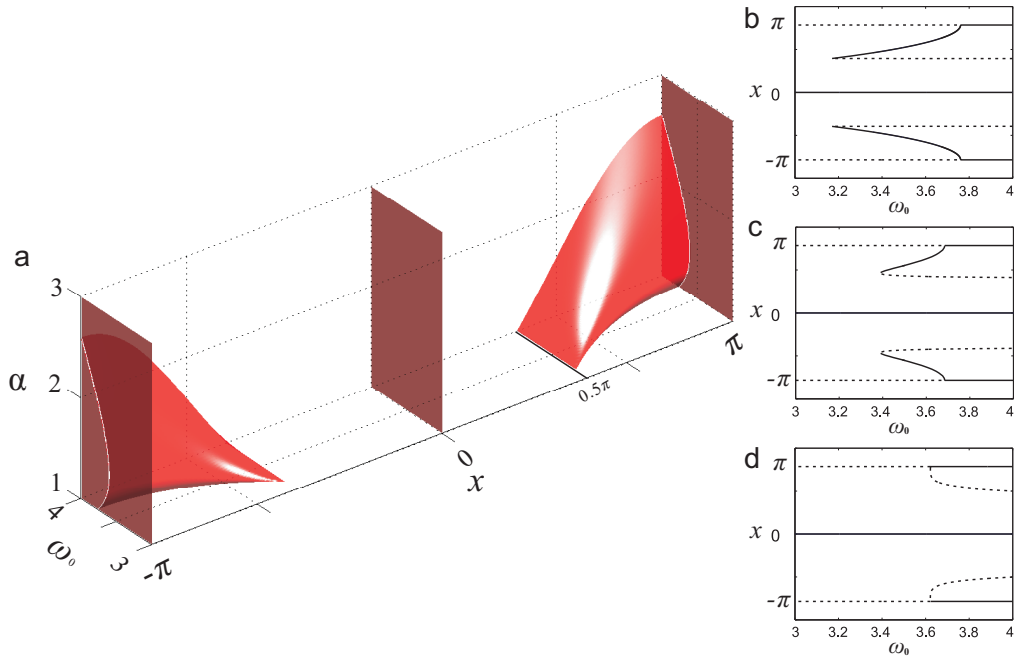


Figure 3: Equilibrium surface in (x, ω_0, α) space and its intersections (the solid and dashed curves represent stable and unstable branches); (a) equilibrium surface, (b) the discontinuous bifurcation, (c) hysteresis bifurcation, (d) pitchfork bifurcation.

and the catastrophe points are obtained as follow

$$\begin{aligned} A\ (\omega_0, \alpha) &= \left(\sqrt{g}, 1\right), \\ B\ (\omega_0, \alpha) &= \left(\sqrt{\sqrt{50 - 10\sqrt{5}}g/4}, \sqrt{\left(3 + \sqrt{5}\right)/2}\right), \\ C\ (\omega_0, \alpha) &= \left(\sqrt{\left(\sqrt{2} + 1\right)g/2}, 1\right), \\ D\ (\omega_0, \alpha) &= \left(\sqrt{\sqrt{2}\, g}, 1\right), \end{aligned} \tag{8}$$

The Hamiltonian function of system (3) is as follow

$$\begin{aligned} &H(x, y) = \frac{y^2}{2} + \\ &g(1 - \cos x) - \omega_0^2 \left(\sqrt{1 + \alpha^2 - 2\alpha \sin x} + \sqrt{1 + \alpha^2 + 2\alpha \sin x} - 2\sqrt{1 + \alpha^2}\right). \end{aligned} \tag{9}$$

With the help of the Hamiltonian function, the trajectories can be classified and analyzed for different values of $H(x, y) = h$, the detail seen in Figure 4a-n. Smooth dynamics for $\alpha > 1$ is displayed in Figure 4a-4h, demonstrating a subcritical pitchfork bifurcation at $x = \pm\pi$, a supercritical pitchfork bifurcation at $x = \pm\pi$, seen in Figure 4a, 4b, 4c and Figure 4c, 4d, 4e and a saddle-node bifurcation Figure 4a, 4h, 4g, respectively. The transitions of the singular orbits undergo from a pair of homoclinic orbits with red line denoted *hom*1 and a pair of heteroclinic orbits denoted *het*, Figure 4e, to three heteroclinic orbits with red line marked *het*, Figure 4f,

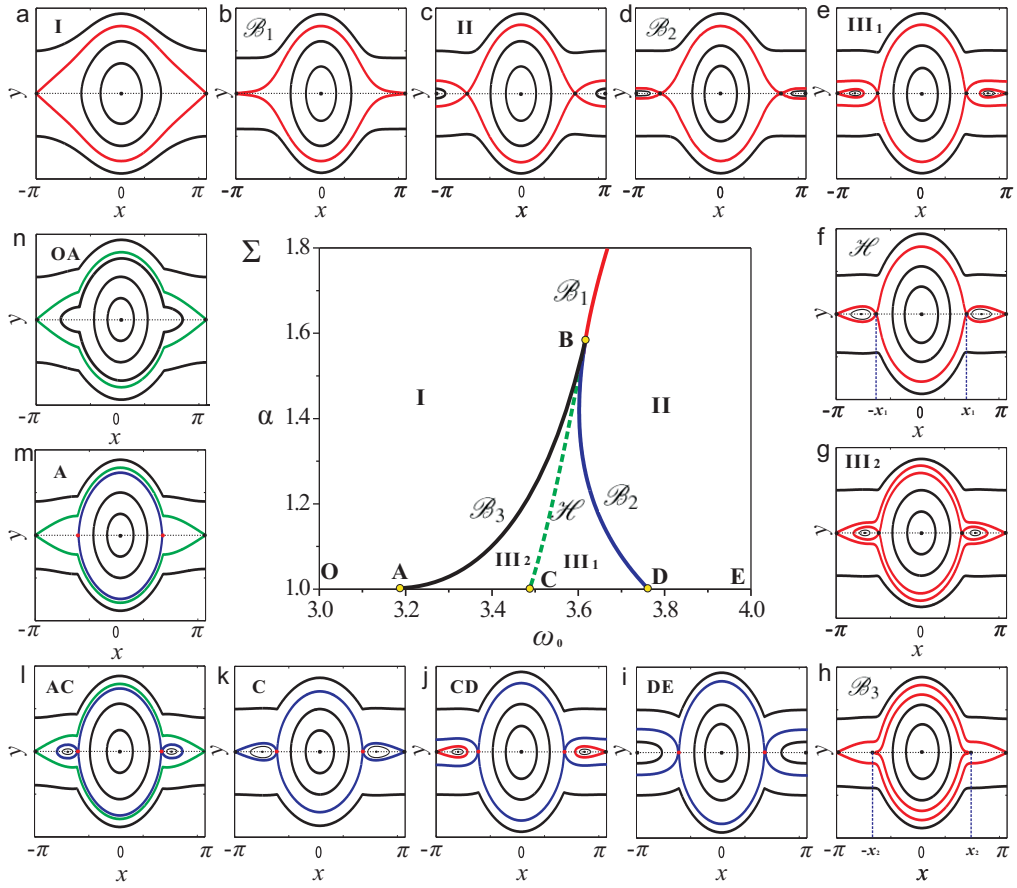


Figure 4: Graph of transition set Σ and the corresponding phase portraits, (a)-(n).

bifurcating to a pair of homoclinic orbits and a pair of heteroclinic orbits colored red line, seen in Figure 4g. It is worth reiterating here that the smooth dynamics Figure 4a becomes discontinuous dynamics Figure 4n by decreasing the smoothness parameter α to 1. Similarly, the discontinuous dynamics for $\alpha = 1$ is plotted in Figure 4i-n, demonstrating a discontinuous bifurcation and a pitchfork bifurcation at $x = \pm\pi$, seen in Figure 4n, 4m, 4l and Figure 4i, 4j. The transitions of the singular orbits of the discontinuous case is displayed in Figure 4j-l, colored blue line. The singular orbits colored green is a special heteroclinic orbits connecting the points $(-\pi, 0)$ and $(\pi, 0)$, which exhibits non-smooth dynamics at $(x, y) = (\pm\pi/2, g)$. It is worth pointing out that the phase portraits is similar to the conventional pendulum coupled with GSD oscillator [19] of a single, double and triple well surrounded by the homoclinic orbits of the second type, respectively.

4 ANALYTICAL STUDIES OF SMALL OSILLATING MOTION

In this section, the primary resonance of the small angle oscillations is studied by using analytical method [20].

Letting $\sin x \approx x$ and $\cos x \approx 1$, the small angle oscillations of Eq. (2) is given by

$$\ddot{x} + 2\xi\dot{x} + gx + \omega_0^2\alpha\left(\frac{1}{\sqrt{1+\alpha^2-2\alpha x}} - \frac{1}{\sqrt{1+\alpha^2+2\alpha x}}\right) = f_0\cos\omega t. \tag{10}$$

Define $\omega^2 = g(1+\sigma)$, system (10) becomes

$$\ddot{x} + \omega^2 x = f_0\cos\omega t + g\sigma x - 2\xi\dot{x} - \omega_0^2\alpha\left(\frac{1}{\sqrt{1+\alpha^2-2\alpha x}} - \frac{1}{\sqrt{1+\alpha^2+2\alpha x}}\right), \tag{11}$$

Introduce periodic solution in the form of slowly varying amplitude and phase

$$x = A\cos\varphi, \;\; \dot{x} = -A\omega\sin\varphi, \;\; \varphi = \omega t + \theta. \tag{12}$$

By means of averaging method, the averaged equation is obtained as follow

$$\begin{cases} \dot{A} = -\dfrac{1}{2\omega}(2\xi\omega A + f_0\sin\theta), \\ \dot{\theta} = -\dfrac{1}{2\omega A}(G(A) + g\sigma A + f_0\cos\theta). \end{cases} \tag{13}$$

where

$$\begin{aligned} G(A) &= \frac{4\omega_0^2}{A\pi}\left(\sqrt{1+\alpha^2+2A\alpha}\,\text{EllipticE}\left[\overline{k}\right] - \frac{1+\alpha^2}{\sqrt{1+\alpha^2+2A\alpha}}\,\text{EllipticK}\left[\overline{k}\right]\right), \\ \overline{k} &= \sqrt{\frac{4A\alpha}{1+\alpha^2+2A\alpha}}. \end{aligned} \tag{14}$$

The amplitude-frequency curve equation is given by

$$(G(A) + A(\omega^2 - g))^2 + (2\xi\omega A)^2 = f_0^2. \tag{15}$$

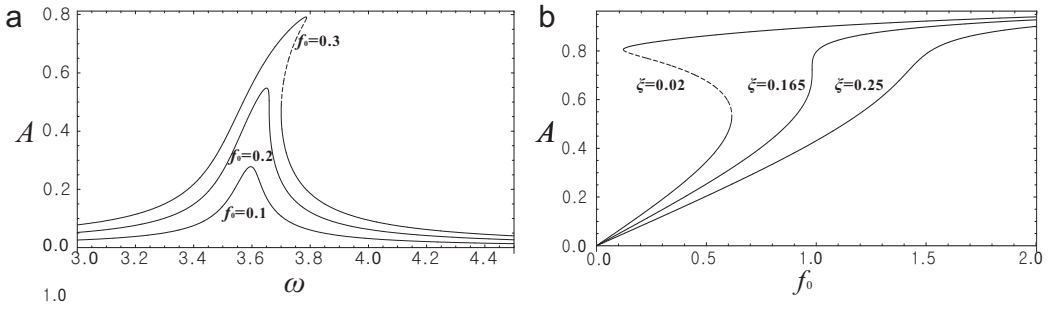


Figure 5: Response curves of system (10): (a) response curves $\{\omega, A, f_0\}$ for $\alpha = 1, \xi = 0.05, \omega_0 = 2$; (b) response curves $\{f_0, A, \xi\}$ for $\alpha = 1, \omega = 3.8, \omega_0 = 2$.

Based upon Eq. (15), the response curves near $(x, y) = (0, 0)$ are displayed in Figure 5, whose stable and unstable branches are marked with solid and dashed lines respectively. The response curves $\{\omega, A\}$ for different values of parameter $f_0 = 0.1, 0.2, 0.3$ are plotted for $\alpha = 1, \xi = 0.05, \omega_0 = 2$, as shown in Figure 5a. When increases f_0 smoothly, changes occur in the response curves, for example, when $f_0 = 0.2$ the hysteresis phenomenon appears. Similarly, Figure 5b show the response curves $\{f_0, A\}$ for different values of parameter $\xi = 0.02, 0.165, 0.25$ with $\alpha = 1, \omega = 3.8, \omega_0 = 2$. It is clear that the hysteresis phenomenon appears at $\xi = 0.165$.

5 NUMERICAL ANALYSIS

In this section, the numerical analysis is carried out to investigate the global behavior [21] for the system (2).

Figure 6a shows the bifurcation diagram for α versus x for parameter $\xi = 0.15, \omega_0 = 3.4, f_0 = 8, \omega = 4$. A periodic-1 solution is displayed for $\alpha = 1.5$ in Figure 6b. Figure 6c and Figure 6d present the chaotic transition between the smooth and discontinuous regimes for $\alpha = 1.15$ and $\alpha = 1$, the details can be seen in the corresponding captions.

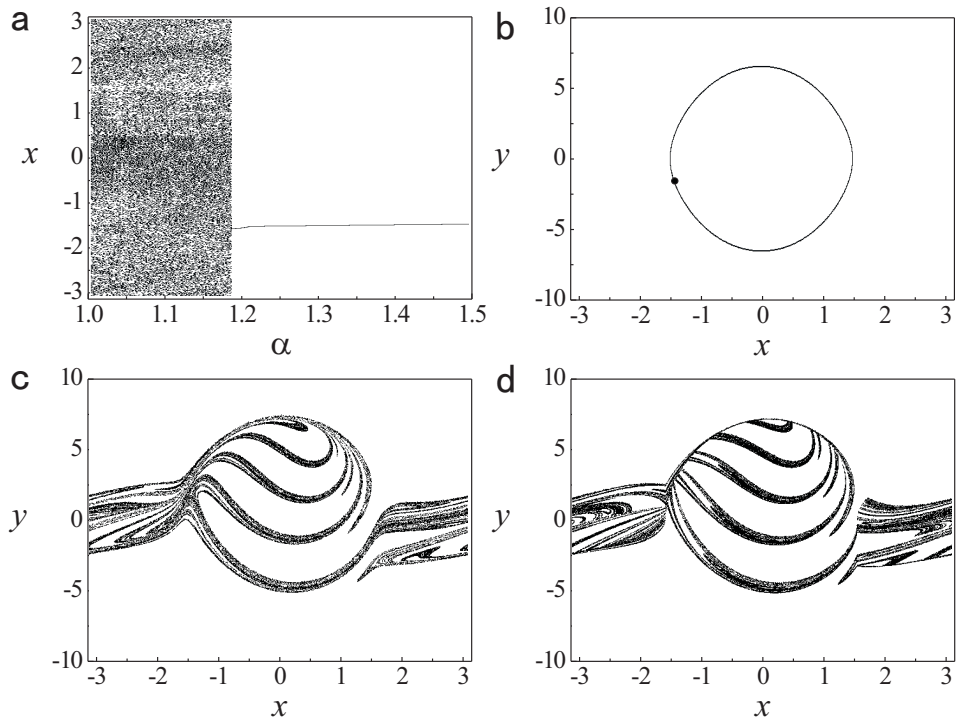


Figure 6: (a) Bifurcation diagram for x versus α with $\xi = 0.15, \omega_0 = 3.4, f_0 = 8, \omega = 4$; (b) the periodic -1 solution; (c) smooth chaotic attractor for $\alpha = 1.15$ with their Lyapunov characteristics $(\lambda_1, \lambda_2) = (0.685119, -0.985123), D_L = 1.69547$; (d) discontinuous chaotic attractor for $\alpha = 1.15$ with their Lyapunov characteristics $(\lambda_1, \lambda_2) = (0.189547, -0.483208), D_L = 1.3921$.

6 CONCLUSIONS

In summary, we have proposed a new-type of pendulum system with complicated nonlinear behavior for both smooth and discontinuous regimes. All the possible trajectory patterns of the unperturbed system have been demonstrated for the chosen parameters ω_0 and α with multiple homoclinic and heteroclinic orbits. Under the perturbation of viscous damping and external harmonic forcing, the primary responses of the small angle oscillation has been investigated analytically by means of the averaging method. Finally, we display a brief description of global behavior including periodic solution and chaotic motion.

7 ACKNOWLEDGEMENT

The authors would like to acknowledge the financial support from the Natural Science Foundation of China (Grant No. 11372082) and the National Basic Research Program of China (Grant No. 2015CB057400).

REFERENCES

[1] R. Whitaker, Types of two-dimensional pendulums and their uses in education. *Sci. Educat.*, **13**, 401-415, 2004.

[2] Y. Kim, S. Kim, Y. Kwak, Dynamic analysis of a non-holonomic two-wheeled inverted pendulum robot. *J. Intell. Robot. Syst.* **44**, 25-46, 2005.

[3] D. Anh, H. Matsuhisa, L. Viet, M. Yasuda, Vibration control of an inverted pendulum type strcture by passive mass-spring-pendulum dynamics vibration absorber. *J. Sound Vib.* **307**, 187-201, 2007.

[4] B. Horton, M. Wiercigroch, X. Xu, Transient tumbling chaos and damping identification for parametric pendulum. *Philos. Trans. R. Soc. A*, **366**, 767-84, 2008.

[5] A. Najdecka, S. Narayanan, M. Wiercigroch, Rotary motion of the parametric and planar pendulum under stochastic wave excitation. *Int. J. Nonlinear Mech.*, **71**, 30-38, 2015.

[6] M. Kapitaniak, K. Czolczynski, P. Perlikowski, T. Kapitaniak, Synchronization of clocks. *Phys. Rep.*, **517**, 1-69, 2012.

[7] A. Fradkov, B. Andrievsky, Synchronization and phase relations in the motion of two pendulum system. *Int. J. Nonlinear Mech.*, **43**, 462-473, 2007.

[8] M. Senator, Synchronization of two coupled escapement-driven pendulum clocks. *J. Sound Vib.*, **291**(3), 566-603, 2006.

[9] K. Kwek, J. Li, Chaotic dynamics and subharmonic bifurcations in a nonlinear system. *Int. J. Nonlinear Mech.* , **31**(3), 277-295, 1996.

[10] Albert C. Luo, Chaotic motions in the resonant separatrix band of a parametrically excited pendulum. Commun. Nonlinear Sci. Numer. Simulat., **5**(4), 135-140, 2000.

[11] X. Xu, M. Wiercigroch, M. Cartmell, Rotating orbits of a parametrically excited pendulum. *Chaos Soliton Fract.***23**(5), 1537-1548, 2005.

[12] X. Xu, M. Wiercigroch, Approximate analytical solutions for oscillatory and rotational motion of a parametric pendulum. *Nonlinear Dyn.*, **47**, 311-420, 2007.

[13] Q. Cao, N. Han, R. Tian, A rotating pendulum linked by an oblique spring. *Chin. Phys. Lett.* **28**(6), 060502:1-4, 2011.

[14] Q. Cao, M. Wiercigroch, EE. Pavlovskaia, C. Grebogi, JMT. Thompson, An archetypal oscillator for smooth and discontinuous dynamics. *Phys. Rev. E* **74**, 046218, 2006.

[15] Q. Cao, M. Wiercigroch, EE. Pavlovskaia, C. Grebogi, JMT. Thompson, Piecewise linear approach to an archetypal oscillator for smooth and discontinuous dynamics. *Philos. Trans. R. Soc. A* **366**, 635-652, 2008.

[16] Q. Cao, M. Wiercigroch, EE. Pavlovskaia, C. Grebogi, JMT. Thompson, The limit case response of the archetypal oscillator for smooth and discontinuous dynamics. *Int. J. Nonlinear Mech.* **43**, 462-473, 2008.

[17] N. Han, Q. Cao, Estimation of the chaotic thresholds for the recently proposed rotating penulum. *Int. j. Bifurcat. Chaos* **23**(4), 1350074:1-22, 2013.

[18] N. Han, Q. Cao, A rotating disk linked by a pair of springs. *Nonlinear Dyn.* **79**, 1275-1291, 2015.

[19] Y. Han, Q. Cao, A novel smooth and discontinuous oscillator with strong irrational nonlinearities. *Science China*. **55**, 1-12, 2012.

[20] Z. Li, Q. Cao, M. Wiercigroch, A. Léger, Analysis of the periodic solutions of a smooth and discontinuous oscillator. *Acta Mech. Sinica* **29**(4), 575-582, 2013.

[21] J. Guckenheimer and P. Holmes, *Nonlinear Oscillations, Dynamical Systems, and Bifurcations of Vector Fields*, Springer, New York, 1983.

11th International Conference on Engineering Vibration
Ljubljana, Slovenia, 7–10 September 2015

DISCONTINUITY INDUCED BIFURCATIONS IN HIGHER DIMENSIONAL FILIPPOV SYSTEMS

B Santhosh, S Narayanan*, C Padmanabhan

Department of Mechanical Engineering, Indian Institute of Technology Madras
Chennai, India 600036
santhoshbpillai@gmail.com, narayans@iitm.ac.in, mouli@iitm.ac.in

Keywords: Discontinuous systems, Filippov models, Discontinuity induced bifurcations

Abstract. *Nonlinear systems with discontinuous nonlinearities involving impact, friction exhibit discontinuity induced bifurcation like sliding and grazing bifurcations. These bifurcations take place when periodic trajectories interact with a discontinuity surface. The sudden onset of chaos and stick-slip phenomena in dry friction systems can be explained in terms of these bifurcations. In this paper, numeric and numeric-analytic methods are used to study the dynamics of harmonically excited nonlinear systems with discontinuous nonlinearities by modeling them as Filippov systems. The switch model based numerical integration in combination with the shooting method is used to obtain the periodic solutions and the bifurcations. The smooth and discontinuous (SD) oscillator and systems with friction are considered as examples. The sudden transition of the periodic solution to chaotic solution in these systems are due to the grazing bifurcation. The Lyapunov exponents corresponding to the chaotic solution can be obtained by the chaos synchronization method. The system thus becomes a two dimensional Filippov system. A method to solve the higher dimensional Filippov system based on the switch model based numerical integration is also outlined.*

1 INTRODUCTION

Nonlinear dynamical systems can have either continuous or discontinuous nonlinearities or both. Rotor-stator rub interaction in gas turbines, dry friction damping in turbomachinery bladed systems, complex frictional contact and backlash in gear teeth, intermittent separation and contact of tool and work piece in metal cutting and switching electrical circuits are examples of systems with discontinuous nonlinearities. The equation of motion suddenly changes depending on the transition of a particular state of the system crossing a barrier. Accurate modeling and efficient analysis framework are necessary to obtain the dynamics of these systems. The order of the time for transition from one state to another in these systems is very small compared to the overall dynamics of the system which allows the use of smooth functions to replace the discontinuous nonlinearities. The main disadvantages of this approximation are the loss of essential dynamics in the system and computational expense as the system of equations becomes stiff.

Nonlinear systems with discontinuous nonlinearities can be modeled as Filippov systems, where the state space is divided into subspaces separated by non-overlapping boundaries [1]. In the subspaces the system is smooth and along the boundaries, the system is discontinuous and the system behavior in the boundaries is represented by a convex combination of the smooth vector fields representing the system behavior along the subspaces. This method allows the use of event driven numerical integration or shooting method based on a switch model representation for the integration of the equation of motion through the discontinuity on the boundary [2]. Such modeling and integration procedures enable the identification of classical bifurcations and a special class of bifurcations in these systems known as the discontinuity induced bifurcations (DIBs).

In this paper, the Filippov model representation and the event based numerical integration or the shooting method based on switch model are applied to two example problems, the harmonically excited smooth and discontinuous (SD) oscillator and a harmonically excited single degree of freedom (sdf) nonlinear system with damping and stiffness nonlinearities on a moving belt with Coulomb friction between the belt and the mass. The bifurcation diagrams are obtained by numerical integration and the DIBs are identified in both the cases. In the case of the SD oscillator the sudden transition to chaos from a period 1 solution is through a grazing bifurcation and in the case of the friction oscillator it is through a grazing sliding bifurcation. In the case of the friction oscillator other DIBs such as adding sliding, switching sliding and crossing sliding bifurcations are also identified. The procedure for the solution of two dimensional Filippov system based on the switch model representation is outlined.

2 FILIPPOV SYSTEMS AND DISCONTINUITY INDUCED BIFURCATIONS

2.1 Filippov systems

In the Filippov representation, the phase space is divided into a number of subspaces separated by switching boundaries. Consider only two regions S_1 and S_2 with smooth vector fields F_1 and F_2 in phase space separated by a single switching boundary Σ. The differential equation becomes a differential inclusion of the form

$$\dot{\mathbf{x}} \in F(\mathbf{x}) = \begin{cases} F_1(\mathbf{x}) & \mathbf{x} \in S_1 \\ \overline{co}(F_1(\mathbf{x}), F_2(\mathbf{x})) & \mathbf{x} \in \Sigma \end{cases} \tag{1}$$

where $\overline{co}$ is the convex combination of F_1 and F_2 given by

$$\overline{co}(F_1(\mathbf{x}), F_2(\mathbf{x})) = \{f_F : x \in \mathbb{R}^n \to \mathbb{R}^n : f_F = (1-\alpha_1)F_1 + \alpha_1 F_2, \alpha_1 \in [0,1]\} \quad (2)$$

The discontinuity surface Σ is represented by a scalar function $H(\mathbf{x})$ with a non-vanishing gradient. The region S_1 corresponds to $H(\mathbf{x}) > 0$, the region S_2 corresponds to $H(\mathbf{x}) < 0$ and the discontinuity surface Σ corresponds to $H(\mathbf{x}) = 0$.

The state of the system can initially be in one of the subspaces. As time unwinds, it may reach the discontinuity boundary and cross to reach the other subspace (transversal intersection) or can slide along the discontinuity surface (sliding) depending on the signs of the projection of the vector fields along the normal to the discontinuity surface [3]. The Filippov systems can be integrated numerically based on an event based numerical integration or a switch model based integration in combination with the shooting method to obtain periodic solutions. [2].

2.2 Discontinuity induced bifurcations

Discontinuous systems exhibit a class of bifurcations known as the discontinuity induced bifurcations (DIBs), which happen when the periodic trajectory interacts with the boundary of the discontinuity surface. The four co-dimension one bifurcations are (i) crossing sliding (ii) grazing sliding (iii) switching sliding and (iv) adding sliding bifurcations which are shown respectively in Fig. 1(a)-(d). G_1 and G_2 are the two smooth regions and the plane corresponds to the discontinuity surface. The shaded region corresponds to the part of the discontinuity surface over which the sliding takes place.

In crossing sliding bifurcation (Fig. 1(a)), with parameter variation, the trajectory hits the boundary of the discontinuity surface (trajectory b) and crosses to the other subspace. Further variation of the parameter causes a part of the trajectory to slide over the discontinuity surface (trajectory c). In grazing sliding bifurcation (Fig. 1(b)), the trajectory initially lying in one of the subspaces (trajectory a) grazes the sliding surface with the variation of the parameter (trajectory b). Occasionally, the grazing bifurcation leads to the sudden onset of chaos from a periodic solution. In switching sliding bifurcation (Fig. 1(c)), the trajectory initially confined to one of the subspaces and the sliding region (trajectory c), intersects the boundary of the sliding surface and passes to the other subspace and then back to the sliding surface (trajectory a). In adding sliding bifurcation (Fig. 1(d)), the segment of trajectory which undergoes bifurcation lies within the sliding region (trajectory a). As the parameter is varied, a sliding portion of the trajectory hits tangentially the boundary of the sliding region (trajectory b). Further variation of the parameter leads to the formation of an additional segment of trajectory above or below the sliding region (trajectory c). These bifurcations satisfy appropriate analytical conditions [3].

3 ILLUSTRATIVE EXAMPLES

The dynamics of the harmonically excited snap through oscillator also called as the smooth and discontinuous(SD) oscillator and the harmonically excited sdf system with Coulomb friction are investigated by modeling them as Filippov systems.

3.1 The Smooth and Discontinuous (SD) oscillator

The non dimensional equation of motion for the harmonically excited SD oscillator (Fig. 2) is given by [4]

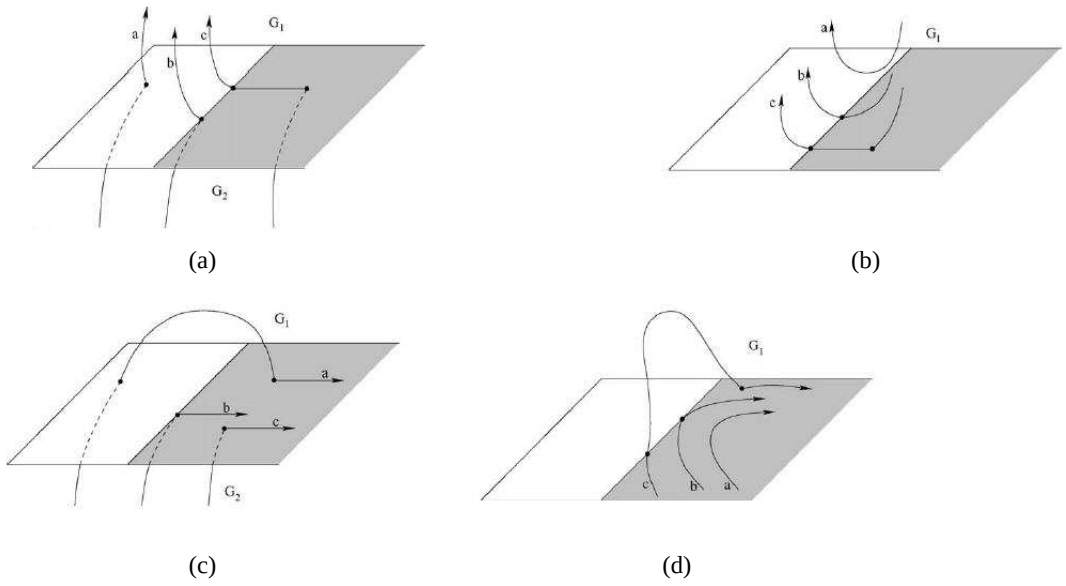


Figure 1: Sliding bifurcations in Filippov systems (a) Crossing sliding bifurcation (b) Grazing sliding bifurcation (c) Switching sliding bifurcation and (d) Adding sliding bifurcation [3].

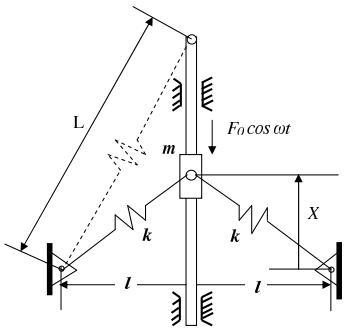


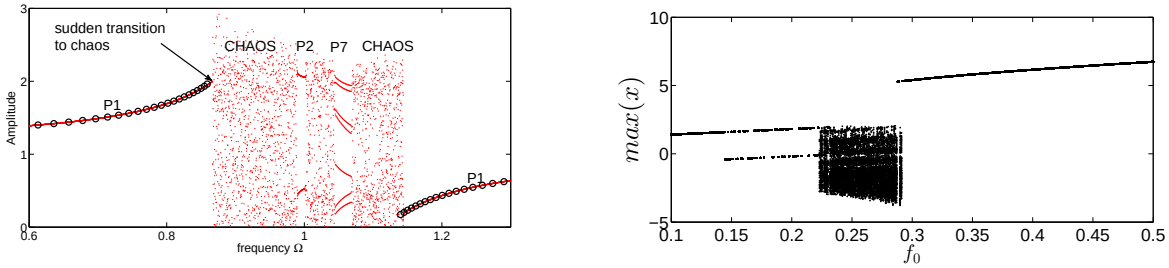
Figure 2: The smooth and discontinuous oscillator.

where $\alpha = \frac{l}{L}$ is the smoothness parameter. For $\alpha = 0$, the system is discontinuous and the equation of motion reduces to

$$x'' + 2\zeta x' + x - sgn(x) = f_0 \cos \Omega\tau \tag{4}$$

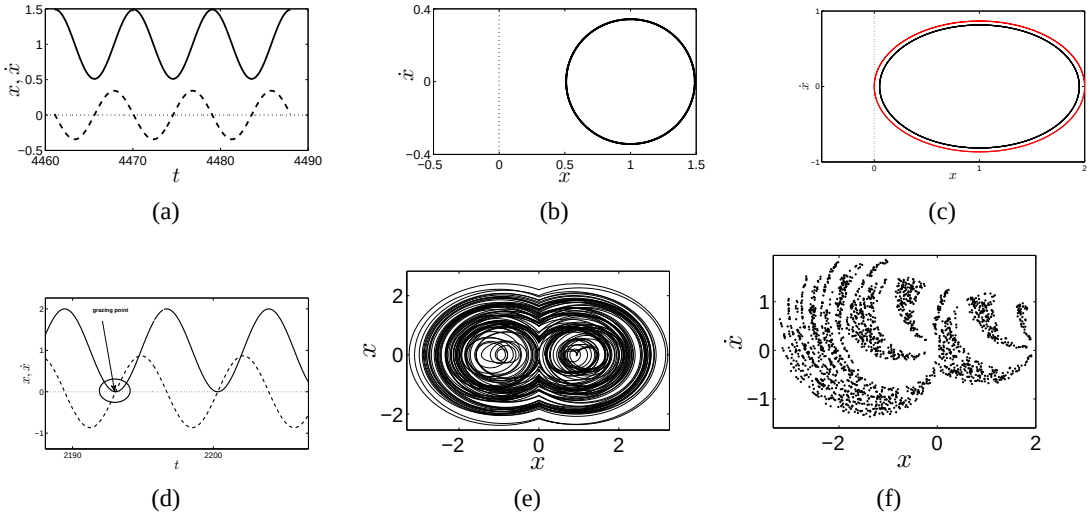
where sgn is the signum function. The discontinuous oscillator given by Eq.(4) is represented as a Filippov system and integrated numerically using an event based numerical integration scheme. The bifurcation diagrams obtained with Ω and f_0 as the parameters are shown in Fig. 3.

When Ω is increased from a lower value, the discontinuous oscillator has a large amplitude period 1 (P1) motion which suddenly bifurcates to a chaotic solution at $\Omega = 0.8667$. At $\Omega = 1.145$, the chaotic solution suddenly changes to a P1 solution. The bifurcation diagram with f_0 as the parameter also shows a sudden transition of period 1 solution to chaotic solution for $f_0 = 0.21$. The sudden transition of the periodic solution to chaotic solution in the bifurcation



(a) (b)

Figure 3: Bifurcation diagrams (a) with Ω as the parameter ($\zeta = 0.0141, f_0 = 0.25$) (b) with f_0 as the parameter($\zeta = 0.01, \Omega = 0.85$)



(a) (b) (c)

(d) (e) (f)

Figure 4: (a)-(b) time histories and phase plane plot before grazing (c)-(d) time histories and phase plane plot at the time of grazing (e)-(f) phase plane plot of the chaotic solution and the corresponding Poincare section.

The periodic solution is confined to the smooth region S_1 where $h(x) = x > 0$. The discontinuity surface is shown by the dotted line in the time histories and phase plane plots. When the parameter Ω is varied, the amplitude of the motion grows and when $\Omega = 0.866715$, the periodic orbit grazes the discontinuity surface tangentially as shown in Fig. 4(c) and (d). The phase plane plot shows the periodic orbit just before grazing (black) and the periodic orbit at the time of grazing (red). From the time histories it is observed that the displacement and velocity both are zero at the time of grazing. The sudden onset of chaos beyond the bifurcation value $\Omega = 0.86667$ is thus due to the grazing bifurcation which is a discontinuity induced bifurcation. The phase plane plot and the strange attractor for $\Omega = 0.87$ are shown in Figs. 4(e) and (f).

3.2 Dynamics of a friction oscillator

The equation of motion for the harmonically excited sdf system shown in Fig. 5 is given by

$$m\ddot{x} - c_1(\dot{x} - v) + c_2(\dot{x} - v)^3 + k_1 x + k_2 x^3 + \mu mg\ sgn(\dot{x} - v) = F_0 \cos \omega t \qquad (5)$$

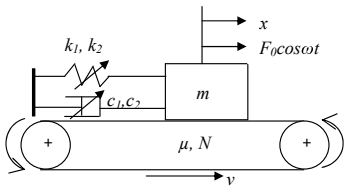


Figure 5: Mass on a moving belt with additional nonlinearities.

restoring force is able to overcome the frictional force, then the mass starts slipping over the belt. The equation of motion can be expressed as

$$\ddot{x} - \alpha g(\dot{x} - v) + \beta g(\dot{x} - v)^3 + \gamma_1 x + \gamma_2 x^3 + \mu g \; sgn(\dot{x} - v) = f_0 \cos \omega t \tag{6}$$

with parameters $\alpha = \frac{c_1}{mg}, \beta = \frac{c_2}{mg}, \gamma_1 = \frac{k_1}{m}, \gamma_2 = \frac{k_2}{m}$ and $f_0 = \frac{F_0}{m}$.

In this study, the dynamics of the system is investigated by modeling it as a Filippov system. The two smooth vector fields S_1 and S_2 correspond to the value of the scalar function $\dot{x} - v$. The equations of motion are integrated numerically employing a switch model for the following parameters, $f_0 = 10m/s^2, \mu = 0.6, \alpha = -0.05s/m, \beta = 0, \gamma_1 = 10/s^2, \gamma_2 = 0, v = 1m/s$. The frequency response of the system is shown in Fig. 6. The dotted line corresponds to $\dot{x} = v = 1m/s$. Once the solution undergoes sliding (sticking of the mass to the belt), the

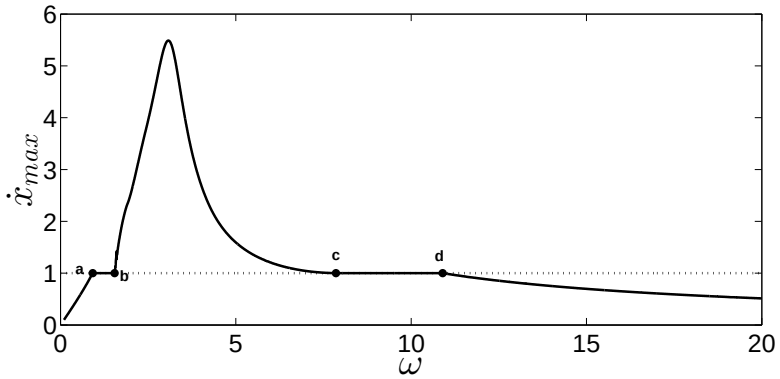


Figure 6: Frequency Response.

response remains in the sliding region for a finite duration of time period. For the two regions **a-b** and **c-d**, a part of the trajectory undergoes sliding and the other part is confined to one of the smooth regions (the mass is slipping). To explain the different dynamic phenomena associated with this system, the phase plane plots of the response for different ω values along the frequency response curve in Fig. 6 are obtained by the shooting method and are shown in Fig. 7.

When $\omega = 0.92$ (point **a**), the solution grazes the discontinuity surface (Fig. 7(b)) which was initially confined to one of the subspace (Fig. 7(a)). Further increase of ω causes a part of the trajectory to slide as shown in Fig. 7(c). When $\omega = 1.55$, marked by the point **b** in Fig. 6, a segment of the trajectory crosses the sliding region and joins back the sliding surface as shown in Fig. 7(d). This is the case of adding sliding bifurcation. The zoomed view of the same is also shown in the figure. With further increase of ω, this slipping segment grows in size and it

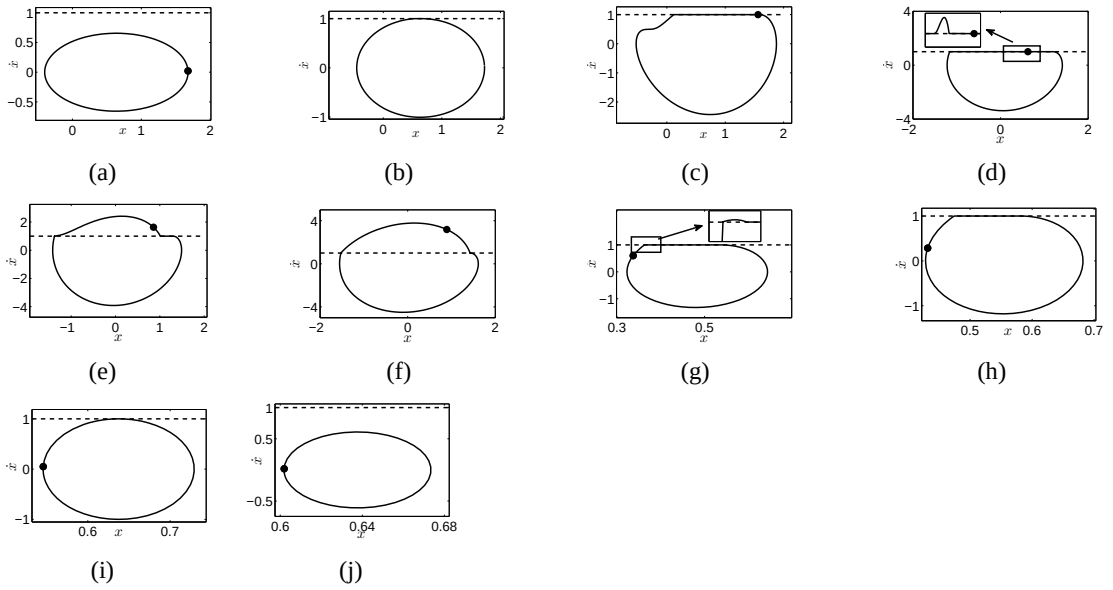


Figure 7: Phase plots (a) $\omega = 0.63$ (b) $\omega = 0.92$ [**a**] (c) $\omega = 1.3$ (d) $\omega = 1.55$ [**b**] (e) $\omega = 1.95$ (f) $\omega = 2.44$ (g) $\omega = 7.85$ [**c**] (h) $\omega = 9.1$, (i) $\omega = 10.9$ [**d**] (i) $\omega = 17$.(Letters in square brackets corresponds to the points marked in Fig.6). ● - Poincare points.

bifurcation. With further increase in ω, the sliding region on the right of the phase plane also disappears and the solution after reaching the sliding surface from one of the subspace does not remain on the sliding surface but moves to the other subspace. When $\omega = 7.85$, marked by the point **c** in Fig. 7 the sliding segment shows the generation of an additional slipping segment at the boundary. This region is marked with a rectangle and the zoomed view of the same is shown in Fig. 7(g). This is the case of switching sliding bifurcation.

The dynamics is further investigated by considering the following parameters $f_0 = 10m/s^2, g = 9.81m/s^2, \mu = 0.6, \alpha = -0.05s/m, \beta = 0, \gamma_1 = 0, \gamma_2 = 10000m/s^2 and v = 1m/s$. The bifurcation diagram obtained for the range $4.7 \leq \omega \leq 4.7$ is shown in Fig. 8(a) which shows a P1 solution suddenly bifurcating into a chaotic solution. This transition takes place at $\omega = 4.565$. The phase plane plots of the P1 solution for $\omega = 4.56$ is shown in Fig. 8(b). With slight increase in the value of ω, the P1 solution grazes the discontinuity surface. With further increase in the value of ω, the solution starts sliding over the discontinuity surface. The grazing phenomenon can lead to a sudden onset of chaos. The phase plane plot of the chaotic solution is shown in Fig. 8(c).

4 TWO DIMENSIONAL FILIPPOV SYSTEMS

One of the ways to characterize chaos in nonlinear systems is by calculating the Lyapunov exponent. The method of chaos synchronization can be used to obtain the Lyapunov exponents [5] which uses the principle that there exists a linear dependence between the synchronization value of the coupling coefficient of the two identical continuous dynamical systems and the largest value of the Lyapunov exponent of such coupled systems. For this purpose the equations of motion along with the augmented set of equation should be represented in the state space form. These systems of equations are thus integrated numerically till a synchronization takes

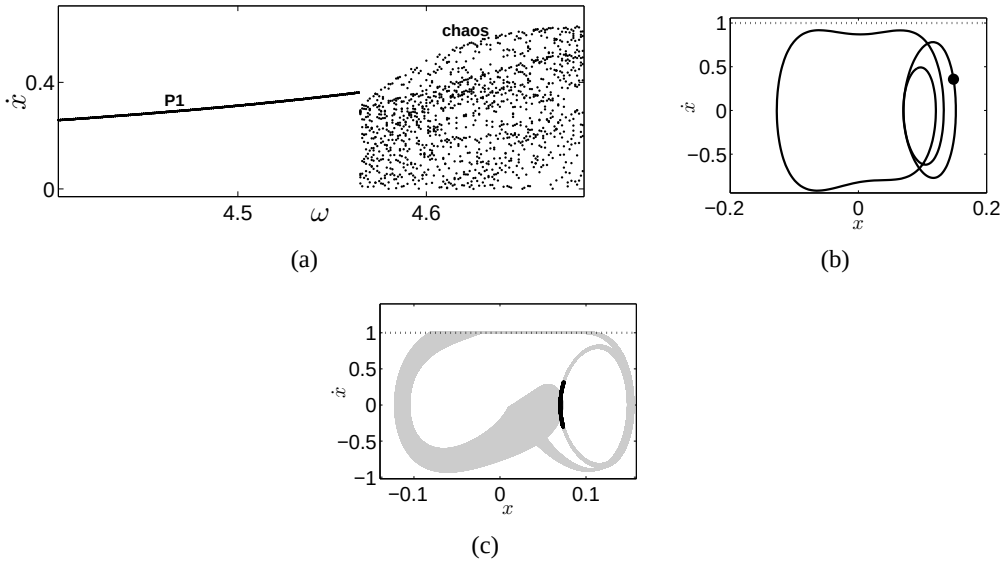


Figure 8: (a)Bifurcation diagram with ω as the parameter (b) phase plane plot of the P1 solution before grazing (c) phase plane plot of the chaotic solution after grazing.

motion for the mass on a moving belt (Eq. (6)) with a synchronizing similar system can be expressed in state space form as

$$\begin{aligned}
\dot{x}_1 &= x_2 \\
\dot{x}_2 &= f_0 \cos\omega t + \alpha g(x_2 - v) - \beta g(x_2 - v)^3 - \gamma_1 x_1 - \gamma_2 x_1^3 - \mu g sgn(x_2 - v) \\
\dot{x}_3 &= x_4 + \lambda(x_1 - x_3) \\
\dot{x}_4 &= f_0 \cos\omega t + \alpha g(x_4 - v) - \beta g(x_4 - v)^3 - \gamma_1 x_3 - \gamma_2 x_3^3 - \mu g sgn(x_4 - v) + \lambda(x_2 - x_4)
\end{aligned} \tag{7}$$

where λ is the coupling parameter.

The above system of equations when represented in the Filippov form corresponds to a two dimensional Filippov system with the two indicator functions $x_2 - v = 0$ and $x_4 - v = 0$. The switch model representation of the two dimensional system is shown in Fig. 9 The state space

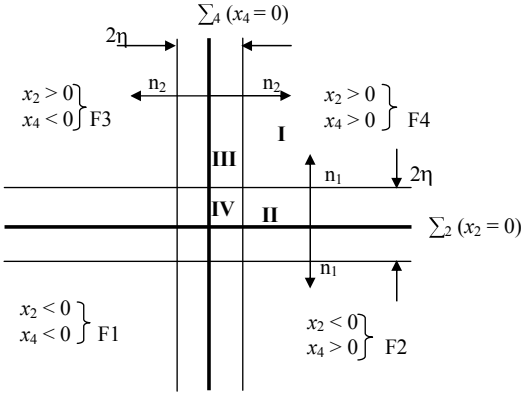


Figure 9: Switch model representation of a two dimensional Filippov system

denoted by F_1, F_2, F_3 and F_4. The discontinuity surfaces are represented as Σ_2 and Σ_4. Along the length of the discontinuity surfaces, a small band of width η is considered. The normals to the discontinuity surfaces are represented by n_1 and n_2.

Let the state of the system be in the first quadrant where the vector field is F_4. During integration of the equation of motion, the state of the system may remain at **I** or move to **II,III** or **IV**. If the state is at **II** or **III** the different possibilities for the state to move are same as that of the one dimensional case ie. (i) transversal intersection from F_4-F_2 / F_4-F_3 (ii) sliding along Σ_2/Σ_4 with vector field as a convex combination of the corresponding two vector fields or (iii) remain as F_2. When the state of the system reaches **IV**, the three vector fields F_4, F_3 and F_2 will be involved. Apart from the transversal intersection, sliding along one of the discontinuity surface, the third possibility is the sliding along the intersection of the two discontinuity surfaces Σ_2 and Σ_4. Analytical conditions in terms of the dot product of the normal along the discontinuity surface and the vector fields can be established for this case and the vector field chosen will be a convex combination of the four vector fields F_1, F_2, F_3 and F_4. For example if $n_1^T F_4 < 0, n_1^T F_2 > 0, n_2^T F_4 < 0$ and $n_2^T F_3 > 0$, then the sliding will take place simultaneously along both the discontinuity surfaces. The sliding modes in this case is generally assumed to be attractive. The two possibilities of attractive sliding modes are (i) nodal attractivity and (ii) spiral attractivity [6]. The vector field for the case of sliding along the intersection can be expressed as

$$\dot{x} = (1-\alpha)(1-\beta)F_1 + (1-\alpha)\beta F_2 + \alpha(1-\beta)F_3 + \alpha\beta F_4 \tag{8}$$

with $\alpha, \beta \in [0, 1]$. The switch model based integration procedure can thus be used to solve the two dimensional Filippov system. The values of alpha and beta are governed by a set of nonlinear algebraic equations [6] which can be solved and the vector field corresponding to the sliding on both the sliding surfaces can be obtained.

5 CONCLUSIONS

In this work, discontinuity induced bifurcations in systems modeled as Filippov systems are investigated. The harmonically excited SD oscillator and the sdf friction oscillator are considered as examples. These systems exhibit grazing bifurcation which leads to the sudden onset of chaos. The dry friction damped systems show adding sliding, crossing sliding and switching sliding bifurcations. The method of chaos synchronization for the calculation of the largest Lyapunov exponent necessitates the consideration of a two dimensional Filippov system. The procedure for the analysis of two dimensional Filippov system based on the switch model representation is briefly presented.

REFERENCES

[1] A. F Filippov, Differential equations with discontinuous right hand side. *Americak Mathematical Society Transl.*, **42**, 199-231, 1964.

[2] R. I Leine and H. Nijmeijer, *Dynamics and bifurcations of non-smooth mechanical systems*. Springer Science and Business, 2013.

[3] Di Bernardo, M. Kowalczyk and M. P. Nordmark, Sliding bifurcations: a novel mechanism

[4] Q. Cao, M. Wiercigroch, E.E. Pavlovskaia, C. Grebogi and J. M. T. Thompson, Archetypal oscillator for smooth and discontinuous dynamics. *Physical Review E*, **74(4)**, 046218, 2006.

[5] A. Stefanski, Using chaos synchronization to estimate the largest Lyapunov exponent of nonsmooth systems. *Discrete Dynamics in Nature and Society*, **4(3)**, 207-215, 2000.

[6] L. Dieci and L. Lopez, Sliding motion on discontinuity surfaces of high co-dimension. A construction for selecting a Filippov vector field. *Numerische Mathematik*, **117(4)**, 779-811, 2011.

Frequency-based spectral methods for vibration random fatigue (MS02)

International Conference on Engineering Vibration
Ljubljana, Slovenia, 7-10 September 2015

DERIVATION OF EQUIVALENT POWER SPECTRAL DENSITY SPECIFICATIONS FOR SWEPT SINE-ON-RANDOM ENVIRONMENTS VIA FATIGUE DAMAGE SPECTRA

Tom Irvine

Dynamic Concepts, Inc.
tirvine@dynamic-concepts.com

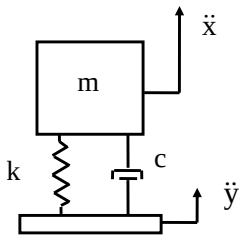
Keywords: Sine, Random, Vibration, Rainflow, Power Spectral Density, Fatigue.

Abstract. *Launch vehicles may encounter a variety of mixed sine and random vibration environments during liftoff and powered flight. The vehicle is subjected to an external oblique incident acoustic field during liftoff, as well as to direct structural-borne vibration. As the vehicle accelerates through the transonic velocity and encounters its maximum dynamic pressure condition, the random vibration is driven by turbulent boundary layers, shock waves, and other aerodynamic flow effects. The sine vibration may be due to a thrust oscillation for the case of a solid motor. Liquid engines may also have sinusoidal sloshing or combustion instabilities. Furthermore, the sinusoidal oscillation frequency and amplitude may each vary with time. Both the sine and random environments may thus be nonstationary. Avionics components must be designed and tested to withstand the composite vibration environment. A single power spectral density specification which envelops the complete environment is usually desired for simplicity. Furthermore, the power spectral density specification is assumed to have a corresponding time history which is both stationary and Gaussian. Traditional specification derivation methods involve assuming piecewise stationary flight data and making a maximum power spectral density envelope from the piecewise segments. A more discerning method is to use the fatigue damage spectrum method to derive a stationary power spectral density which yields the equivalent fatigue damage of the composite nonstationary flight data. This paper demonstrates this fatigue damage enveloping method. The envelope then becomes the basis for the specification derivation with the addition of the appropriate statistical uncertainty margin.*

1 INTRODUCTION

The effect of dissimilar base inputs on a given component can be compared in terms of the response fatigue damage spectra. This is an indirect method of comparing the severity of the inputs. The component is treated as a single-degree-of-freedom as shown in Figure 1 for this purpose. The fatigue damage spectrum (FDS) expresses the relative damage as a function of natural frequency for a given amplification factor and fatigue exponent.

Furthermore, the fatigue damage spectrum may be calculated from either a time domain or power spectral density (PSD) base input. The time domain data may be measured nonstationary vibration, such as swept sine-on-random, or any other mixed vibration. A PSD can then be carefully constructed which meets or exceeds the damage potential of the measured data at each potential component natural frequency, as demonstrated by the examples in this paper.



m = mass
c = damping coefficient
k = stiffness
ẍ = response acceleration
ÿ = base acceleration

Figure 1. Single-degree-of-freedom System Subject to Base Acceleration

2 MEASURED TIME HISTORY FATIGUE DAMAGE SPECTRA

The first step is to calculate the time domain responses of an array of single-degree-of-freedom (SDOF) systems to the base input per Reference 1. The natural frequency fn is an independent variable. The amplification factor Q and the fatigue exponent b are fixed for a given case but are varied between cases. A rainflow cycle count is made for each response time history as a function of fn and Q, using the method in Reference 2. A relative damage index D can be calculated for each case using

$$D = \sum_{i=1}^{m} A_i^b \, n_i \tag{1}$$

where

A_i is the *response* amplitude from the rainflow analysis

n_i is the corresponding number of cycles

b is the fatigue exponent

Note that the response amplitude convention for this paper is: (peak-valley)/2. The amplitude may be in terms of acceleration, pseudo velocity, or relative displacement, depending on the component sensitivity, potential failure modes, etc. Acceleration is used for the examples in this paper. The fatigue damage spectrum expresses the relative damage as a function of

natural frequency for each of the cases. Two Q and two b cases are used for the examples in this paper, with a total of four FDS permutations.

3 OPTIMIZED PSD ENVELOPE DERIVATION

The following description applies to the examples in this paper, as based on Reference 3. The method is flexible and can be tailored to other data sets. The following steps are to be performed after the time domain calculation described in the previous section.

The next step is to generate a candidate base input PSD over the frequency domain from 20 to 2000 Hz. The PSD may have an arbitrary number of breakpoints, but simplicity is better. A PSD with four points will be generated, with each having a ramp-plateau-ramp design. The PSD coordinates may be arbitrary using random numbers, as long as the starting and ending frequencies are 20 and 2000 Hz, respectively.

The response PSD can then be calculated for each candidate input PSD. This is done for each natural frequency fn of interest and for each Q value. Again, the fn values will be varied in octave fraction steps from 20 to 2000 Hz. The Dirlik rainflow cycle counting method is then performed for each response PSD per the method in Reference 4 and 5.

The candidate base input PSD is then scaled so that each of its four fatigue damage spectra envelops those of the measured acceleration time history, while keeping the PSD levels as small as possible. This process can be repeated for a few hundred candidate PSDs in order to find the least one which still satisfies the fatigue damage enveloping requirement for the four cases. The method is flexible in that the PSDs can be ranked in terms of the respective overall displacement, velocity, or acceleration levels, or some combination thereof, in order to determine which is least.

4 EXAMPLE ASSUMPTIONS

The test item is assumed to be a single-degree-of-freedom system in each of the two examples. The natural frequency is an independent variable from 20 to 2000 Hz. The amplification factor is varied as Q=10 and 30. The fatigue exponent is varied as b=4 and 6.4. There are thus four combinations of Q and b. A wide spread of values for each of these parameters is needed because avionics components are often “black boxes” for mechanical engineering purposes.

A PSD envelope is developed using trial-and-error to cover all four cases. The FDS of the PSD must envelope that of the time history for each of the four cases. The PSD is also optimized to give the least possible overall levels for a fixed number of breakpoints while still satisfying the enveloping requirement. The calculation is performed using a function within the Vibrationdata Matlab GUI package. The function within this package is “PSD Envelope via FDS.”

5 EXAMPLE 1

The time history in Figure 2 is actual flight accelerometer data from an unnamed suborbital launch vehicle during stage 2 burn. The vibration is predominantly sine sweep due to a solid rocket motor thrust oscillation, as shown in the Figure 3 Waterfall FFT. The main oscillation sweeps downward from 530 to 450 Hz. There is also some background random vibration.

A PSD envelope is derived for this segment as shown in the following plots. The PSD duration is set as 20 seconds, but this value can be varied. The PSD in Figure 4 envelops the swept sine time history in Figure 2 in terms of fatigue damage spectra. The justification is shown via the fatigue damage spectra in Figure 5.

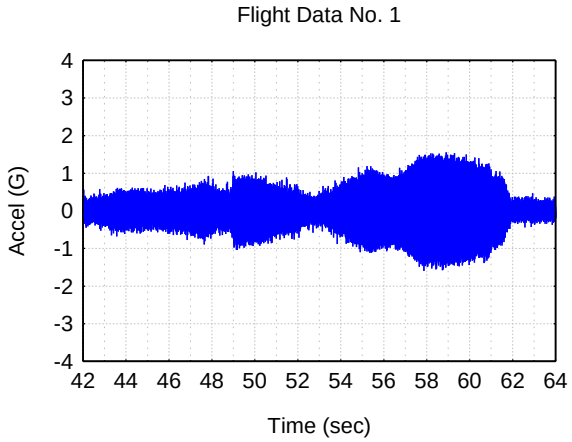


Figure 2. Example 1, Time History

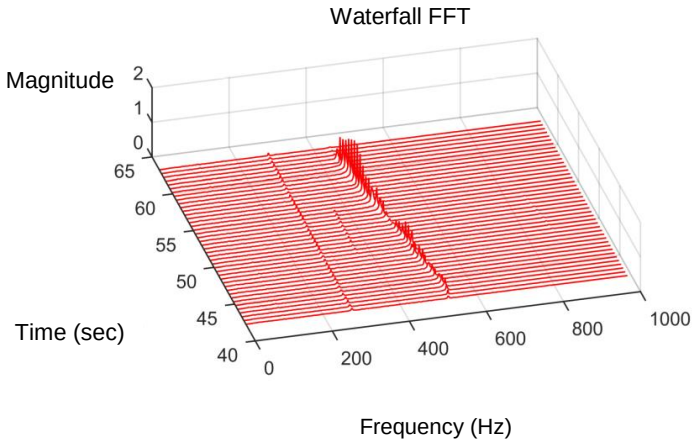


Figure 3. Example 1, Waterfall FFT

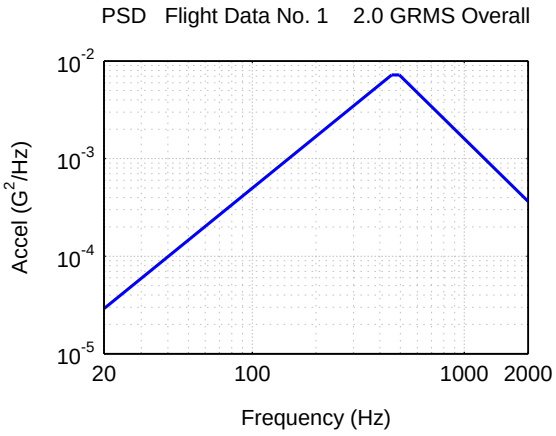


Figure 4. Example 1, PSD Envelope

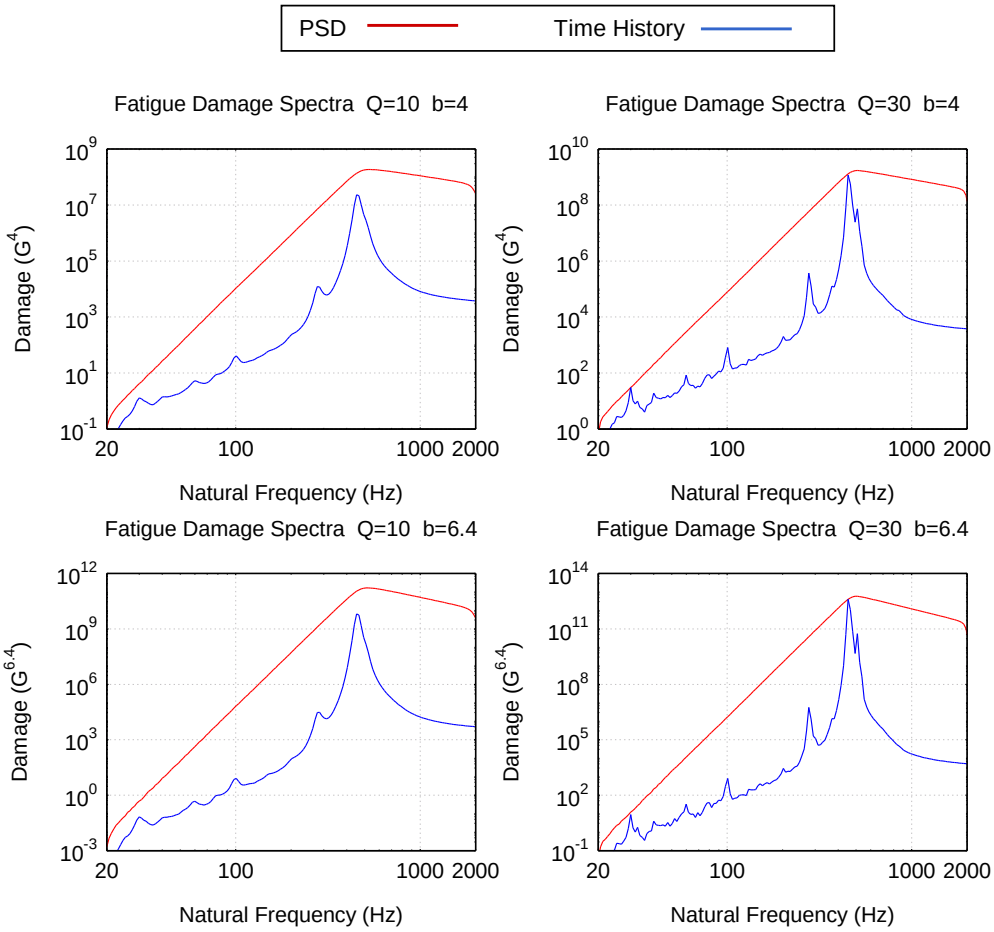


Figure 5. Example 1, FDS Comparison for Four Cases

The FDS of the PSD envelops that of the flight accelerometer time history for each of the four cases and over the entire natural frequency domain. The two Q=30 cases drive the PSD envelope. The PSD envelope is conservative within the stated assumptions.

6 EXAMPLE 2

The time history in Figure 5 is actually a combination of flight from two different vehicles. The idea was to create a rigorous data set where several different effects occurred, including random, sine, and sine sweep. A PSD envelope is derived for this hybrid data as shown in the following plots. The PSD duration is set as 60 seconds, but this value can be varied. The waterfall FFT in Figure 7 shows a mixture of vibration events. Random vibration due to aerodynamic effects dominates the response from 10 to 30 seconds. A sine sweep occurs from 30 to 50 seconds due to a simulated thrust oscillation. Sinusoidal spectra occur near the end of the record.

The PSD in Figure 8 envelops the swept sine time history in Figure 6 in terms of fatigue damage spectra. The justification is shown via the fatigue damage spectra in Figure 9.

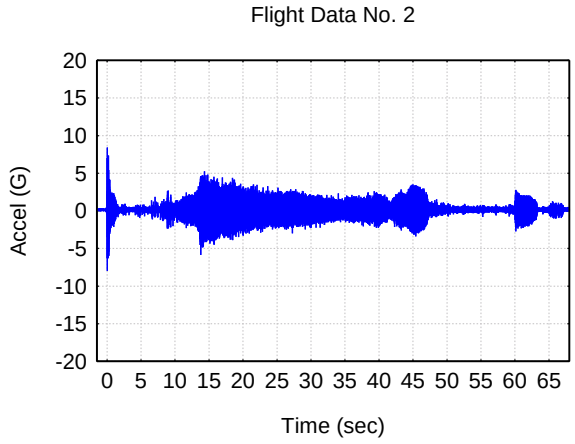


Figure 6. Example 2, Time History

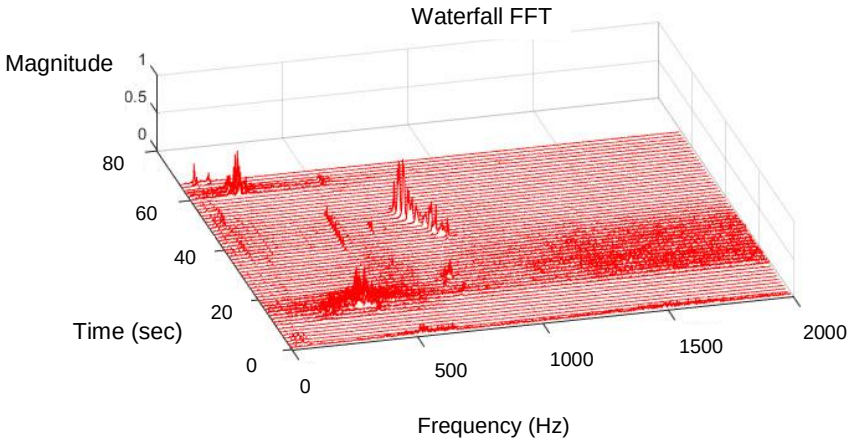


Figure 7. Example 2, Waterfall FFT

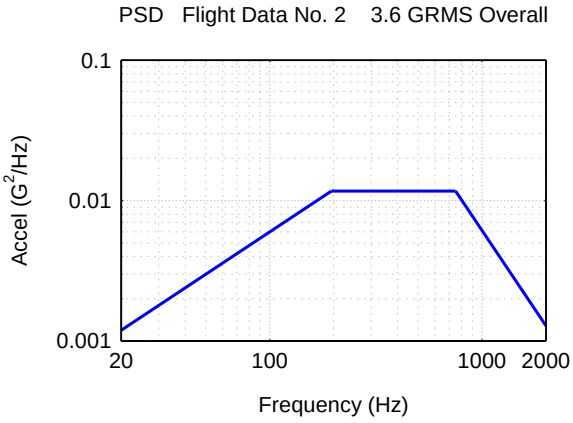


Figure 8. Example 2, PSD Envelope

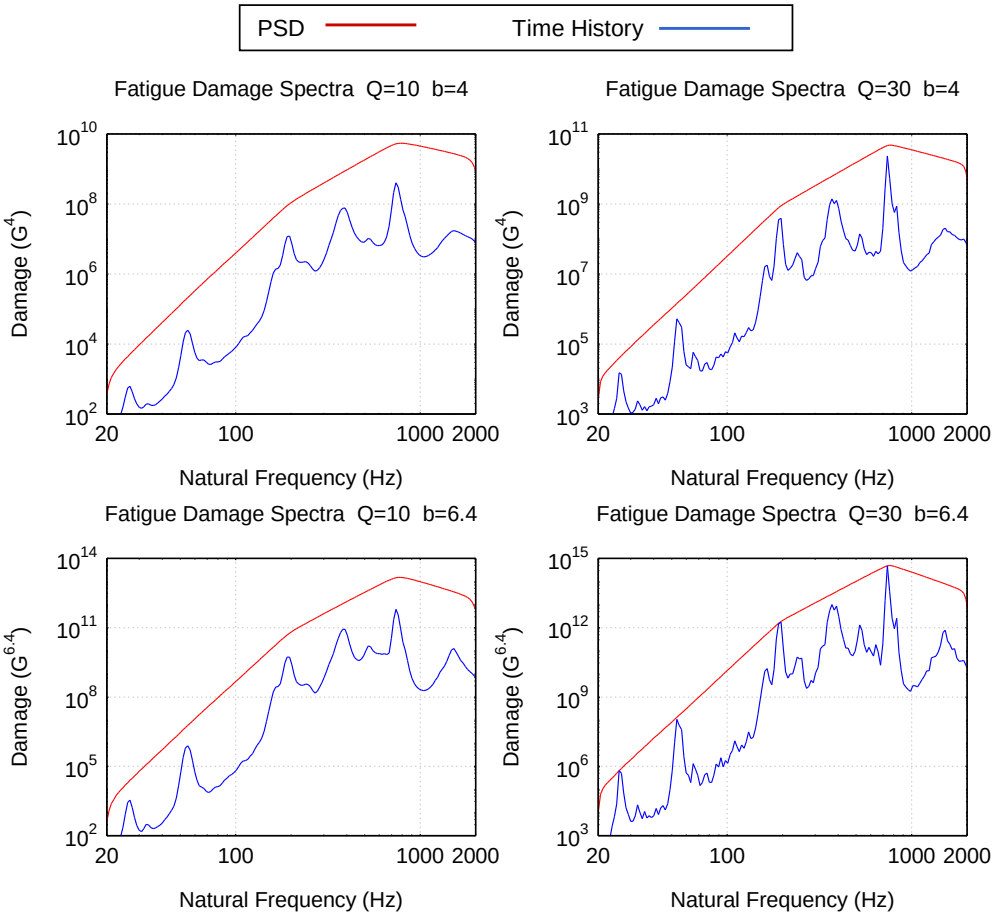


Figure 9. Example 2, FDS Comparison for Four Cases

The FDS of the PSD envelops that of the flight accelerometer time history for each of the four cases and over the entire natural frequency domain. The (Q=30, b=6.4) case is the driver. The PSD envelope is conservative within the stated assumptions.

7 CONCLUSIONS

The fatigue damage spectrum is a useful method for enveloping a nonstationary vibration environment in terms of a stationary power spectral density with an implied Gaussian distribution. The nonstationary environments may include a mixture of sine, swept-sine and random vibration, as shown in the previous examples.

Application of the method requires a framework of assumptions. Engineering judgment is needed to estimate the component natural frequency, amplification factor and fatigue exponent for cases where these values are unknown. The natural frequency can be varied in octave fraction steps over a wide domain. Permutations of upper and lower estimates of the amplification factor and fatigue exponent can then be used to derive a conservative envelope. The enveloping method for the examples was carried out via a set of Matlab scripts. Researchers may contact the author via Email for complimentary access to the scripts.

Derivation of the maximum expected flight level (MEFL) requires adding a statistical uncertainty margin to the envelope level. The margin may account for flight-to-flight variation as well as spatial variation. Margin guidelines are given in References 6 through 8. The MEFL can then be taken as the component acceptance specification along with the possible inclusion of a minimum workmanship level. The component qualification level is typically set as the acceptance level plus 3 to 6 dB. The acceptance test is performed on the actual flight component via a shaker table. The qualification test is more rigorous and is only performed on a non-flight unit to verify design. One-of-kind components may be tested to an intermediate proto-flight level.

REFERENCES

[1] David O. Smallwood, *An Improved Recursive Formula for Calculating Shock Response Spectra*, Shock and Vibration Bulletin, No. 51, May 1981.

[2] ASTM E 1049-85 (2005) *Rainflow Counting Method*, American Society for Testing and Materials, 1987.

[3] T. Irvine, *Optimized PSD Envelope for Nonstationary Vibration*, Revision A, Vibrationdata, 2014.

[4] Halfpenny & Kim, *Rainflow Cycle Counting and Acoustic Fatigue Analysis Techniques for Random Loading*, RASD 2010 Conference, Southampton, UK.

[5] Halfpenny, *A Frequency Domain Approach for Fatigue Life Estimation from Finite Element Analysis*, nCode International Ltd., Sheffield, UK.

[6] NASA-HDBK-7005, *Handbook for Dynamic Environmental Criteria*, 2001.

[7] NASA-STD-7001A, *Payload Vibroacoustic Test Criteria*, 2011.

[8] MIL-HDBK-340A, *Military Handbook: Test Requirements for Launch, Upper-Stage, and Space Vehicles*, U.S. Department of Defense, 1999.

11th International Conference on Engineering Vibration
Ljubljana, Slovenia, 7–10 September 2015

FATIGUE ASSESSMENT OF NON GAUSSIAN RANDOM VIBRATIONS BY USING DECOMPOSITIONS IN GAUSSIAN PORTIONS

Peter Wolfsteiner*[1]

[1]University of Applied Sciences Munich
Lothstr. 34
80335 München, Germany
peter.wolfsteiner@hm.edu

Keywords: Power Spectral Density, Random Vibrations, Fatigue Strength, Numerical Modeling, Railway Engineering, Shaker Testing.

Abstract. *For the analysis of random vibrations a well established set of tools is available based on the assumption of a Gaussian distribution of the analyzed signals. These tools may, for example, be applied very efficiently in the area of structural dynamics to perform a simulation based fatigue strength analysis. The procedure is based on the application of the power spectral density (PSD) of a given excitation signal, the frequency response functions of the analyzed structure, special methods (e.g. Dirlik's Method) for the estimation of load spectra directly from stress response PSDs and a method for the derivation of equivalent fatigue values from these stress load spectra (e.g. Miner's rule). These procedures are based on the assumption that the analyzed time signals have Gaussian distribution; any deviation from this theoretical distribution can cause conservative or non conservative deviations from the real fatigue damage value. Unfortunately lots of real excitation signals show such a deviation. Consequently, the above presented methods can not be used for reliable fatigue strength predictions. Therefore alternative methods are available, usually coming along with certain drawbacks. This paper introduces a new method for the substitution of a non Gaussian signal by a combination of several Gaussian signals (each having its own PSD) by preserving the spectral properties and the fatigue damage potential of the initial non Gaussian signal. By going back to these Gaussian distributions all the well established methods for Gaussian signals may still be applied without any extensions or modifications. The primary focus of this paper is the simulation based fatigue strength analysis; the results may also be applied to experimental procedures.*

1 INTRODUCTION

Usually fatigue strength calculations are carried out in the time domain, because for the simulation of stress loads in dynamical systems (Finite Element Method, Multibody Systems) as well as for the derivation of load spectra (Rainflow Counting), well established methods are available. However, this approach is not capable of covering all possible applications of fatigue strength calculations. Especially in the area of random vibrations, the time domain approach has some major drawbacks. Time domain simulations are not always suitable for covering random vibration problems because of their restriction to limited time intervals used in the simulation. The used time samples often cover just a fraction of time and usually do not have the same statistical properties compared to the real signal. In combination with computing time limitations, this problem even gets worse, because Finite Element simulations are not capable of processing long excitation time samples in combination with huge vibrating structures. For this special purpose, frequency domain methods are available (see e.g. [1]) capable of modeling random vibrations in an adequate way and also offering the possibility of much faster simulations. Therefore [2] gives a detailed introduction with concrete practical examples. [3] gives an overview for the available methods for load spectra estimation directly from PSDs. Especially for this area lots of research work has been done to find reliable techniques (see e.g. [4, 5, 6, 7, 8]). The drawback of this set of PSD based methods is their assumption of Gaussian distributions of the underlying time signals. If applied for Gaussian or nearly Gaussian distributed signals small deviations in the fatigue strength results may occur. For major deviations from the Gaussian distribution these fatigue strength results just serve as a rough approximation because of enormous deviations (e.g. see [9, 10]).

From literature a technique is known that approximates non Gaussian distributions by a composition of Gaussian distributed signals. [11, 12] used this technique of synthesizing non Gaussian vibration signals by composing Gaussian signals with equally shaped PSDs but with different standard deviations. This idea was analyzed in [9] for certain types of railroad track excitations by using an algorithm for cutting a time signal into Gaussian portions according to predefined classes and than reassembling them corresponding to their classes. The resulting nearly Gaussian distributed signals (each having a different PSD with its own shape and standard deviation) replace the original measured non Gaussian signal. The results proved the potential of this idea. But it also turned out, that inaccuracies in the fatigue load may occur, caused by the cutting of the signals in pieces and also by deviations from the Gaussian distribution.

The work presented here proposes a solution for this issue by introducing a new method still based on the idea of a decomposition of the non Gaussian time signal in Gaussian parts, but with a systematic derivation of the PSDs. Therefore the measured, non Gaussian signal $u_M(t)$ will be replaced by R Gaussian signals $u_{G,r}(t)$:

$$u_M(t) \text{ for: } t = 0 \dots T \quad \Longrightarrow \quad \begin{cases} u_{G,1}(t) & \text{for:} & 0 & \leq t < & T_{G,1} \\ u_{G,2}(t) & \text{for:} & T_{G,1} & \leq t < & (T_{G,1} + T_{G,2}) \\ \vdots & & & & \\ u_{G,R}(t) & \text{for:} & (T - T_{G,R}) & \leq t < & T \end{cases} \tag{1}$$

where $T = \sum_{r=1}^{R} T_{G,r}$ corresponds to the length of time of the measured non Gaussian signal $u_M(t)$, $T_{G,r}$ to the length of time of the Gaussian portions $u_{G,r}(t)$ and $p_r = T_{G,r}/T$ to the corresponding time portion (with $\sum_{r=1}^{R} p_r = 1$). The derivation of these Gaussian signals $u_{G,r}(t)$ is based on the finding that the deviation in the signal $u_M(t)$ from a Gaussian distribution is not

just one single characteristic of the signal. A filtering of non Gaussian time signals $u_M(t)$ for limited frequency bands Δf usually shows a non constant deviation from a Gaussian distribution over the frequency spectrum of these time signals [13]. The new approach proposed in the presented work respects this frequency dependent probability distribution. This approach improves the accuracy especially for applications with dynamic structures because these structures act like frequency filters based on their specific frequency response function. Due to the amplification or reduction of certain frequency bands, a non respected frequency dependent probability distribution may cause inaccurate distributions in the calculated vibration responses.

2 ANALYSIS OF A NON GAUSSIAN SIGNAL

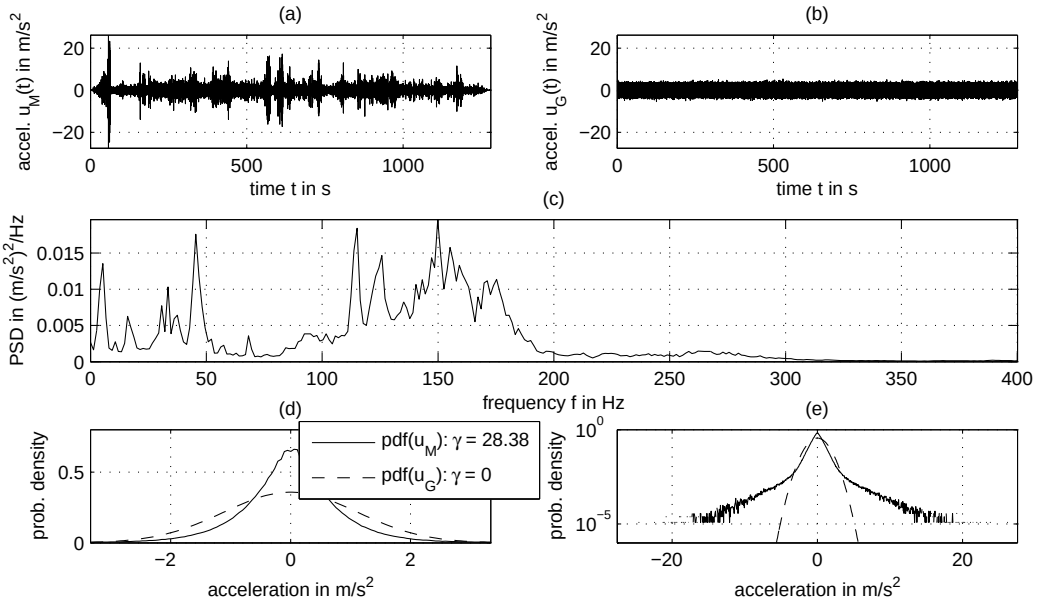


Figure 1: Measured axle box acceleration of a railway vehicle. (a): total time signal $u_M(t)$ (standard deviation $\sigma = 1.1132\frac{m}{s^2}$); (b): from PSD of $u_M(t)$ reconstructed Gaussian signal $u_G(t)$; (c): PSD of $u_M(t)$; (d): probability distribution of signals $u_M(t)$ and $u_G(t)$; (e): plot (d) with a logarithmic scaled ordinate.

Figure 1(a) shows the measurement $u_M(t)$ of an axle box acceleration of a railway vehicle (given in digitally sampled form $u(t_k) = u_k(t_k)$). The corresponding probability density function $pdf(u_M)$ of $u_M(t)$ is depicted in Figure 1(d). As a comparison, also the Gaussian distribution $pdf(u_G)$ is shown according to Eq. 2 based on the standard deviation σ of signal $u_M(t)$. The standard deviation σ is related to the second moment m_2; m_i is a general statistical moment.

$$pdf(u_G) = \frac{1}{\sigma\sqrt{2\pi}} e^{-\frac{1}{2}\left(\frac{u_G-\bar{u}}{\sigma}\right)^2}; \quad \text{with:} \quad \sigma^2 = m_2;\ \bar{u} = \frac{1}{K}\sum_{k=1}^{K} u_k;\ m_i = \frac{1}{K}\sum_{k=1}^{K}\left(u_k - \bar{u}\right)^i; \tag{2}$$

In addition Figure 1(e) shows plot (d) with a logarithmic scaled ordinate. Also a realization of a synthetically generated stationary Gaussian distributed signal $u_G(t)$ (Figure 1(b)) was derived from the PSD of $u_M(t)$ under the assumption of a uniform distribution of phase angles in the Fourier series, see e.g. [9]. The differences between $u_G(t)$ and $u_M(t)$ as well as between $pdf(u_G)$ and $pdf(u_M)$ are obvious. In particular, the frequency of occurrence of very small

values and also of very large values is higher compared to the theoretical Gaussian distribution. The kurtosis γ may be used to quantify this deviation [1]. It is derived from the second (m_2) and the fourth moment (m_4) of the distribution of the signal $u_M(t)$ according to:

$$\gamma = \frac{m_4}{m_2^2} - 3; \tag{3}$$

where $\gamma = 0$ corresponds to a Gaussian distribution, $\gamma > 0$ corresponds to a leptokurtic, $\gamma < 0$ to a platykurtic distribution. To obtain information on the probability distribution depending on the frequency f of the signal $u_M(t)$ a filtering for frequency intervals Δf may be used. Figure 2(a) shows the $N = 50$ second moments $m_{2,n}$ of the filtered signals $u_{f,n}(t)$ for frequency intervals of $\Delta f = 8Hz$ in the relevant frequency band from 0 to $400Hz$ (corresponding to $n = 1 \ldots N$). Based on an alternative definition of the second moment:

$$m_2 = \sigma^2 = \int S(f)\, \mathrm{d}f \tag{4}$$

m_2 may also be expressed by the PSD $S(f)$. Consequently the moment $m_{2,n}$ of frequency interval n may also be understood as the corresponding PSD S_n of the signal $u_{f,n}(t)$; the corresponding fourth moment $m_{M4,n}$ may be used to derive the kurtosis γ_n (Figure 2 summarizes the results; Figure 2(b) also shows the average kurtosis $\gamma = 28.38$ of the total signal $u_M(t)$):

$$S_n = \frac{m_{M2,n}}{\Delta f} = \frac{\sigma_n^2}{\Delta f}; \qquad \gamma_n = \frac{m_{M4,n}}{(m_{M2,n})^2} - 3; \tag{5}$$

As the kurtosis may be understood as a measure for the deviation from a Gaussian distribution, this result clearly highlights the fact that this deviation is not constant for the entire frequency spectrum of the signal. It has a distribution depending on the signal frequency. Consequently an accurate analysis of random vibrations requests to respect this frequency dependent, non constant deviation from the Gaussian distribution.

3 DECOMPOSITION BASED ON STATISTICAL MOMENTS

As a basic introduction to the concept presented here Figure 3 shows respectively the probability distributions $pdf(u_M)$ and $pdf(u_G)$ of an assumed measured non Gaussian signal $u_M(t)$ and the corresponding Gaussian signal $u_G(t)$ as well as their corresponding PSD $S(f)$. These

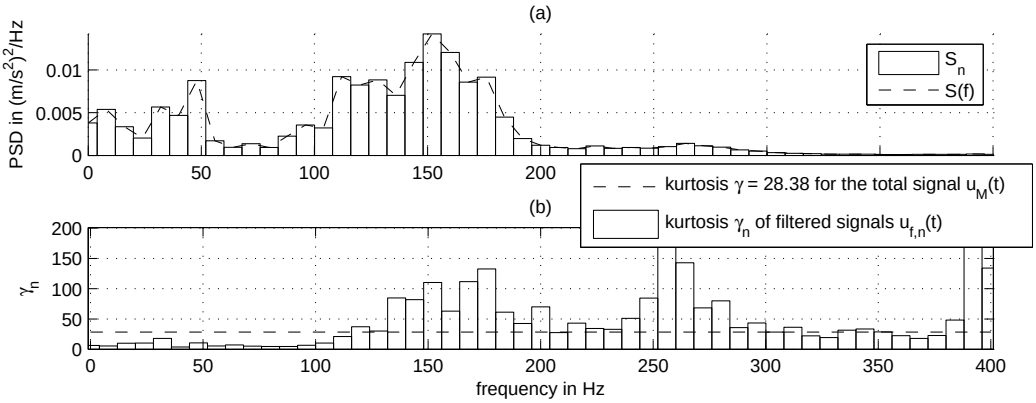


Figure 2: Moments of filtered signals $u_{f,n}(t)$ (frequency interval $\Delta f = 8$Hz). (a): PSD; (b): kurtosis.

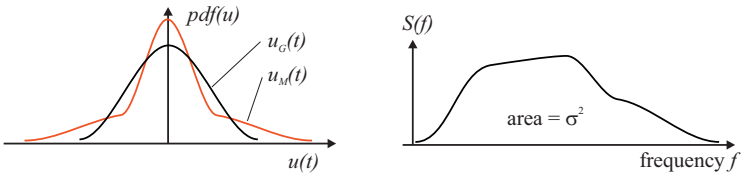


Figure 3: Probability distributions $pdf(u_M)$ and $pdf(u_G)$ of non Gaussian signal $u_M(t)$ and Gaussian signal $u_G(t)$ with their corresponding PSD $S(f)$.

two different signals have the same PSD $S(f)$ even though their probability distributions differ. Based on the approach expressed in Eq. 1 (saying that a non Gaussian signal $u_M(t)$ may be replaced by a composition of several Gaussian signals $u_{G,r}(t)$) the non Gaussian distribution $pdf(u_M)$ in Figure 3 may be approximated by the sum of several Gaussian distributions $pdf(u_{G,r})$ ($r = 1 \ldots R$). The corresponding Gaussian signals $u_{G,r}(t)$ defined by the given PSDs $S_r(f)$, their standard deviations σ_r (Eq. 4) and their time portions p_r (Eq. 1). These PSDs $S_r(f)$ are assumed to have the same shape. Figure 4 demonstrates this concept based on $R = 3$. Eq. 6

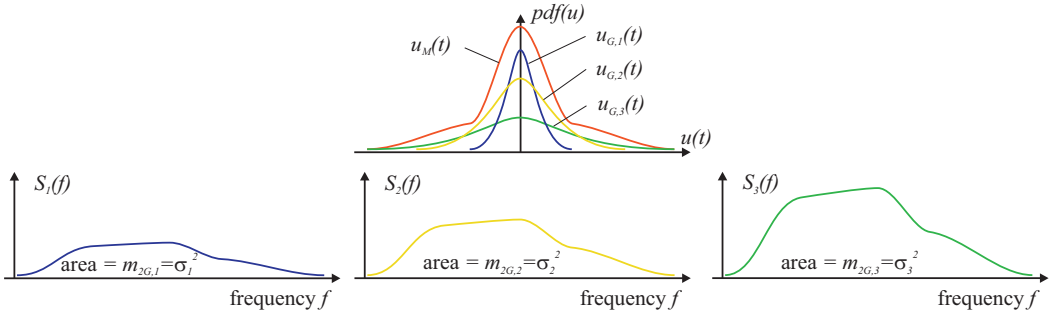


Figure 4: Approximation of a non Gaussian distribution $pdf(u_M)$ by a superposition of three Gaussian distributions $pdf(u_{G,1})$, $pdf(u_{G,2})$ and $pdf(u_{G,3})$ (with the corresponding PSDs $S_1(f)$, $S_2(f)$ and $S_3(f)$).

expresses this superposition based on the Gaussian distributions $pdf(u_{G,r})$ and the corresponding time portions p_r for $R = 3$.

$$pdf(u_M) = p_1\ pdf(u_{G,1}) \ + \ p_2\ pdf(u_{G,2}) \ + \ p_3\ pdf(u_{G,3}) \tag{6}$$

To enable a mathematical description of this approximation the underlying statistical moments m_i are used (see Eq. 2). As a Gaussian distribution is uniquely described by its standard deviation $\sigma = \sqrt{m_2}$ (Eq. 2) all the higher moments may be derived from it. For a centered Gaussian distribution ($\bar{u}_G = 0$) the higher moments are related to the second moment m_2 as follows [1]:

$$m_0 = 1;\ m_2 = \sigma^2;\ m_4 = 3\,\sigma^4;\ m_6 = 15\,\sigma^6;\ m_8 = 105\,\sigma^8;\ m_{10} = 945\,\sigma^{10};\ m_{12} = \ldots \tag{7}$$

To keep the presentation of the concept simple, the odd moments $m_3, m_5, m_7, \ldots$ are considered to be zero based on the assumption of a centered and symmetric distribution. For a non Gaussian signal $u_M(t)$ the moments m_4 and higher deviate from the corresponding Gaussian values and have to be calculated corresponding to Eq. 2 (the relations $m_0 = 1$, $m_1 = \bar{u}$ and $m_2 = \sigma^2$ are still valid!). Based on these facts the sum of the probability density functions (Eq. 6) may be replaced by the sums of the corresponding statistical moments m_i of the distributions (here for

$R = 3$):

$$\begin{array}{rcllllll} 1 & = & p_1 & + & p_2 & + & p_3 & \\ m_{2M} & = & p_1\, m_{2G,1} & + & p_2\, m_{2G,2} & + & p_3\, m_{2G,3} & = \quad (p_1\,\sigma_1^2 + p_2\,\sigma_2^2 + p_3\,\sigma_3^2) \\ m_{4M} & = & p_1\, m_{4G,1} & + & p_2\, m_{4G,2} & + & p_3\, m_{4G,3} & = 3 \quad (p_1\,\sigma_1^4 + p_2\,\sigma_2^4 + p_3\,\sigma_3^4) \\ m_{6M} & = & p_1\, m_{6G,1} & + & p_2\, m_{6G,2} & + & p_3\, m_{6G,3} & = 15 \quad (p_1\,\sigma_1^6 + p_2\,\sigma_2^6 + p_3\,\sigma_3^6) \\ m_{8M} & = & p_1\, m_{8G,1} & + & p_2\, m_{8G,2} & + & p_3\, m_{8G,3} & = 105 \quad (p_1\,\sigma_1^8 + p_2\,\sigma_2^8 + p_3\,\sigma_3^8) \\ \vdots & & & & & & & \end{array} \tag{8}$$

As the moments m_{2M}, m_{4M}, m_{6M} and m_{8M} (and may be even more higher moments) are defined by the measured non Gaussian signal $u_M(t)$, the Eqn. (8) can be solved for p_1, p_2, p_3, σ_1, σ_2 and σ_3 with an appropriate numerical method. The number of higher moments (here m_{4M}, m_{6M}, m_{8M}) as well as the number of decompositions (here $R = 3$) can be adjusted according to the individual requirements of the underlying problem.

However, this method does not produce results with sufficient accuracy. As shown in [9] the assumption of similar PSDs $S_1(f)$, $S_2(f)$ and $S_3(f)$ of the decomposed Gaussian signals $u_{G,1}(t)$, $u_{G,2}(t)$ and $u_{G,3}(t)$ does not match with reality. This causes deviations from the correct modeling of the fatigue potential of the measured signal $u_M(t)$ on the way of its decomposition to $u_{G,1}(t)$, $u_{G,2}(t)$ and $u_{G,3}(t)$. The central point of the presented paper is the solution of this issue by skipping the limitation to similar PSDs by applying the above presented concept on the level of frequency intervals Δf. Therefore it is necessary to perform a filtering of the measured non Gaussian signal $u_M(t)$ in intervals Δf in a first step. The resulting N filtered signals $u_{f,n}(t)$ may than be analyzed for the corresponding moments $m_{2M,n}$, $m_{4M,n}$, $m_{6M,n}$, ... In a second step the above sketched approach may than be applied for all N single frequency intervals Δf. Figure 5 demonstrates this concept. Consequently the above developed Eq. 8 has to be

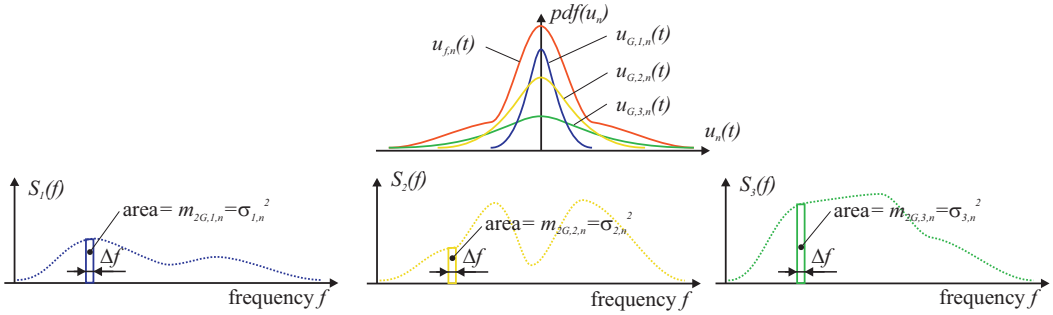


Figure 5: Approximation of non Gaussian distribution $pdf(u_{f,n})$ of frequency interval n by superposition of Gaussian distributions $pdf(u_{G,1,n})$, $pdf(u_{G,2,n})$ and $pdf(u_{G,3,n})$ (with standard deviations $\sigma_{1,n}$, $\sigma_{2,n}$ and $\sigma_{3,n}$).

applied analogously to all N frequency intervals Δf. The unknowns of this set of equations are again the time portions p_1, p_2 and p_3 as well as the PSDs $S_1(f)$, $S_2(f)$ and $S_3(f)$ whereat each of these consists of N data points ($S_1(f)$: $\sigma_{1,1} \ldots \sigma_{1,n} \ldots \sigma_{1,N}$ / $S_2(f)$: $\sigma_{2,1} \ldots \sigma_{2,n} \ldots \sigma_{2,N}$ / $S_3(f)$: $\sigma_{3,1} \ldots \sigma_{3,n} \ldots \sigma_{3,N}$). The relation between $\sigma_{r,n}$ and $S_{r,n}$ per frequency interval Δf is given by Eq. 5.

4 APPLICATION TO MEASURED DATA

To demonstrate the performance of the proposed method an analysis of the measured data $u_M(t)$ from Figure 1 is presented here. It starts with the comparison of the higher statistical moments $m_{M4,n}$, $m_{M6,n}$ derived from the filtered signals $u_{f,n}(t)$ to the theoretical moments

$m_{G4,n}$, $m_{G6,n}$ of the corresponding Gaussian distribution based on the above introduced $N = 50$ frequency intervals (Figure 6(a) and 6(b)). As already shown before for the kurtosis the higher

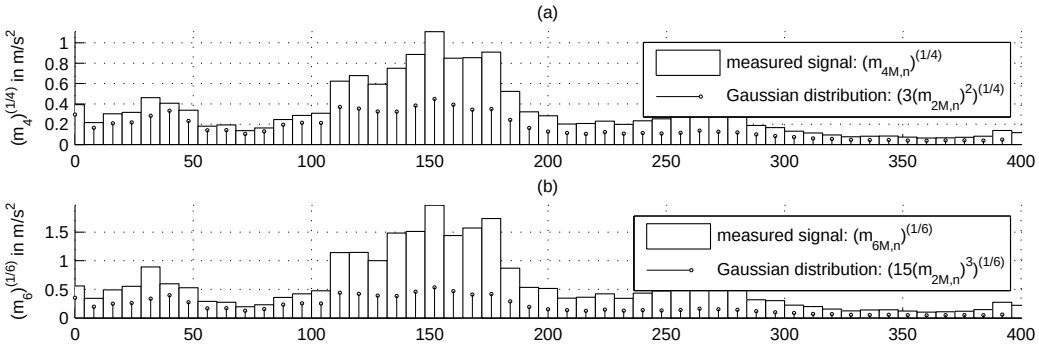


Figure 6: Higher order statistical moments of N filtered signals $u_{f,n}(t)$. (a): N moments $m_{4M,n}$ of measured signal and Gaussian moments $m_{4G,n} = 3(m_{2M,n})^2$; (b): N moments $m_{6M,n}$ of measured signal and Gaussian moments $m_{6G,n} = 15(m_{2M,n})^3$; each for $n = 1 \ldots 50$ and a frequency interval $\Delta f = 8$Hz.

moments have a clear deviation from the theoretical Gaussian distribution. These data have been used to set up an optimization problem with $R = 4$ PSDs $S_1(f)$, $S_2(f)$, $S_3(f)$ and $S_4(f)$. Figure 7 summarizes the results. The objective of this optimization was to fulfill Eqn. (8) by adjusting $p_1 \ldots p_4$, $\sigma_{1,1} \ldots \sigma_{1,n}$, $\sigma_{2,1} \ldots \sigma_{2,n}$, $\sigma_{3,1} \ldots \sigma_{3,n}$ and $\sigma_{4,1} \ldots \sigma_{4,n}$.

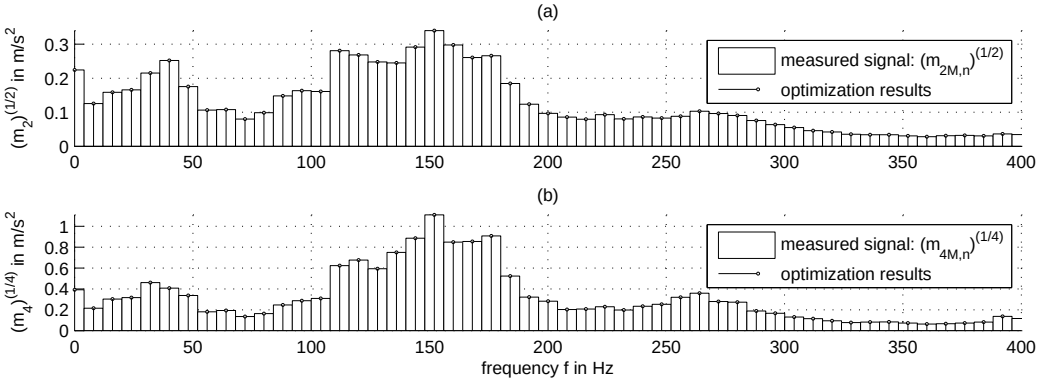


Figure 7: Results for statistical moments from optimization in comparison to moments of measurement. (a): N moments $m_{2M,n}$ of filtered measured signal $u_{f,n}(t)$ and summarized moments $\sum_{r=1}^{R} p_r \ \sigma_{r,n}^2$; (b): N moments $m_{4M,n}$ and $\sum_{r=1}^{R} 3 \ p_r \ \sigma_{r,n}^2$; each for $n = 1 \ldots 50$ and frequency intervals $\Delta f = 8$Hz (compare to Figure 6).

It is obvious that the approximation of the moments m_{2M} and m_{4M} is achieved by the numerical optimization. The PSDs $S_1(f)$, $S_2(f)$, $S_3(f)$ and $S_4(f)$ derived from these results are plotted in Figure 8. They are shown as continuous functions $S_r(f)$ and each one is compared to the PSD $S(f)$ of the measured signal $u_M(t)$ (see Figure 2). These results show increasing values for $S_r(f)$ combined with decreasing time portions p_r.

To assess the presented results, a comparison of the probability distribution is presented here. Figure 9 shows the distribution $pdf(u_M)$ of the measured signal $u_M(t)$ compared to the summarized distribution $pdf(u_{G,1}, u_{G,2}, u_{G,3}, u_{G,4})$ (right side of Eq. 6) of the four PSD based signals $S_1(f)$, $S_2(f)$, $S_3(f)$, $S_4(f)$. Also plotted is the distribution of the signal $pdf(u_G)$ under the assumption of a Gaussian distribution (see Figure 1(b)). These results confirm a good

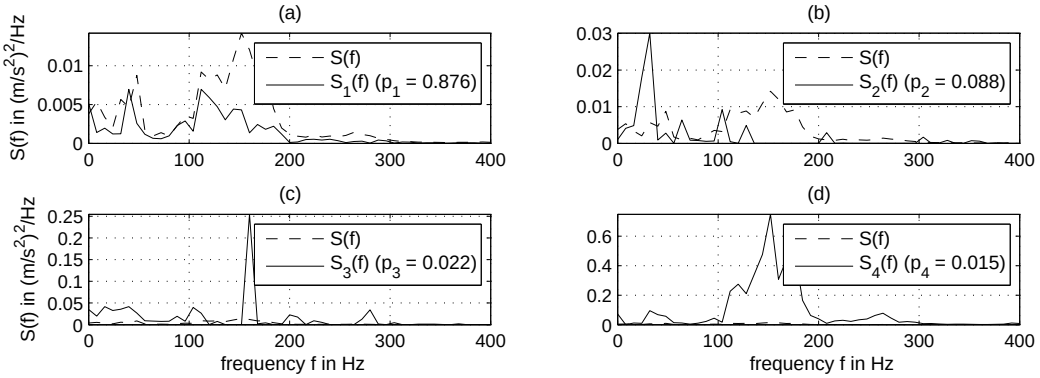


Figure 8: PSDs (with $n = 1 \ldots 50$ data points) resulting from optimization compared to PSD $S(f)$ of measurement $u_M(t)$. (a): $r = 1$; $S_1(f)$ with portion p_1 ($T_{G,1} = 1121.1s$); (b): $r = 2$; $S_2(f)$ with portion p_2 ($T_{G,2} = 112.1s$); (c): $r = 3$; $S_3(f)$ with portion p_3 ($T_{G,3} = 28.2s$); (d): $r = 4$; $S_4(f)$ with portion p_4 ($T_{G,4} = 18.8s$).

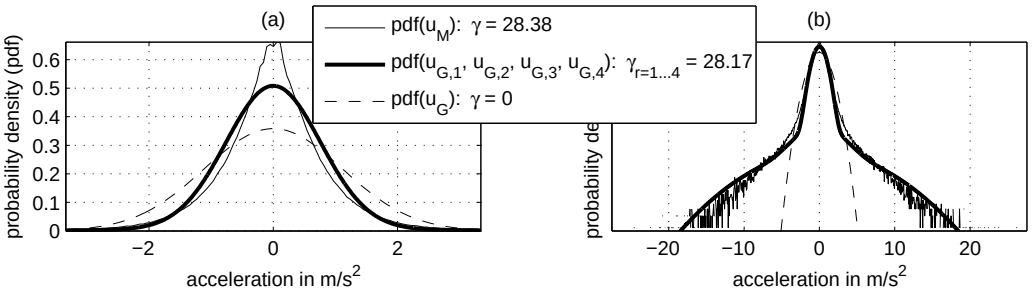


Figure 9: Probability distributions. (a): $pdf(u_M)$ of measured signal $u_M(t)$, $pdf(u_G)$ of signal $u_G(t)$ under assumption of a Gaussian distribution, $pdf(u_{G,1}, u_{G,2}, u_{G,3}, u_{G,4})$ of summarized PSDs $S_1(f)$, $S_2(f)$, $S_3(f)$ and $S_4(f)$; (b): plot (a) with logarithmic scaled ordinate.

approximation of the non Gaussian distribution by the summation of the four Gaussian signals $u_{G,1}(t)$, $u_{G,2}(t)$, $u_{G,3}(t)$ and $u_{G,4}(t)$; a comparison of the corresponding kurtosis values fits as well (measurement: $\gamma = 28.38$, summation of Gaussian signals: $\gamma_{r=1\ldots4} = 28.17$). The ranges of low probability are particularly modeled much better compared to the assumption of a Gaussian distribution $pdf(u_G)$.

5 VERIFICATION BASED ON FATIGUE LOADS

The main intention of the presented method is the replacement of a non Gaussian signal $u_M(t)$ by several Gaussian signals having in total the same spectral properties and the same fatigue damage potential under consideration of its spectral distribution. The following analyses intend to prove the correct modeling by testing for the equivalent fatigue load u_{equ} of the generated signals. For the derivation of load spectra from time signals $u_M(t)$ the Rainflow Counting method is used (without respecting the mean stresses corresponding to Dirlik's Method); for the PSDs $S_r(f)$ Dirlik's Method [3] is used. To reduce the resulting load spectra to single equivalent fatigue damage values u_{equ} a usual fatigue accumulation hypothesis like Miner's rule is applied. It summarizes the cycles of the load spectrum to a single equivalent fatigue value u_{equ} under consideration of a specific slope k of the S-N-diagram. To assess the proper modeling of the equivalent fatigue damage load of the signal $u_M(t)$ it has to be compared to the corresponding sum of the four signals $S_r(f)$. This comparison was done for each of all $n = 1 \ldots 50$ filtered

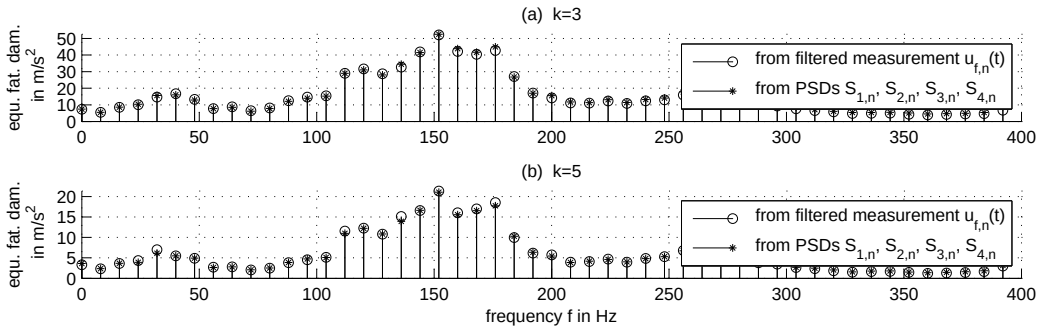


Figure 10: Comparison of equivalent fatigue loads of n filtered measurements $u_{f,n}(t)$ to sum of fatigue loads of corresponding Gaussian signals $u_{G1,n}(t)$, $u_{G2,n}(t)$, $u_{G3,n}(t)$, $u_{G4,n}(t)$. (a): for an exponent of $k = 3$ of the S-N-diagram; (b): for $k = 5$.

time signals $u_{f,n}(t)$ in reference to the sum of each of the fatigue damage values of $S_{1,n}(f)$, $S_{2,n}(f)$, $S_{3,n}(f)$ and $S_{4,n}(f)$ for all corresponding frequency intervals. Figure 10 shows the results for different typical exponents of the S-N-diagram ($k = 3$ and 5) and an assumed number of reference load cycles $N_{\text{equ}} = 1$. The comparison shows clearly that the example analyzed here shows a good accordance achieved for these usual values of k.

In addition another test for proving the proper modeling of the fatigue damage of the signal itself is presented; it looks at the equivalent fatigue load in the total signal. It compares the equivalent fatigue damage load u_{equ} of the complete measured signal $u_M(t)$ without any filtering (Table 1, line 2) to the corresponding value resulting from the sum of equivalent fatigue damage loads of the Gaussian signals $u_{G,1}(t)$, $u_{G,2}(t)$, $u_{G,3}(t)$ and $u_{G,4}(t)$ which were derived from the PSDs $S_1(f)$, $S_2(f)$, $S_3(f)$ and $S_4(f)$ (Table 1, line 4). This result proves that also the sum of fatigue damages of the four generated Gaussian signals corresponds to the fatigue damage of the non Gaussian signal $u_M(t)$. The remaining small deviations may be further minimized by comprising more higher moments and more Gaussian signals $u_{G,r}(t)$ (with their corresponding PSDs $S_r(f)$). As a comparison also the equivalent fatigue damage value of the Gaussian signal $u_G(t)$ is listed in Table 1 (line 3); it clearly expresses the need of the method presented.

equivalent load u_{equ} from:	$k = 3$	$k = 5$
measured vibration $u_M(t)$ (Figure 1(a))	100%	100%
Gaussian vibration $u_G(t)$ (Figure 1(c))	69.67%	43.11%
Gaussian vibrations $u_{G,1}(t)$, $u_{G,2}(t)$, $u_{G,3}(t)$, $u_{G,4}(t)$	97.29%	98.12%

Table 1: Comparison of equivalent fatigue damage loads in percent

6 CONCLUSIONS

This paper introduced a new method for the substitution of a non Gaussian time signal by a combination of several different Gaussian time signals with the objective of making a correct frequency domain based fatigue load calculation possible. They are derived under the condition of keeping the spectral properties and the fatigue damage load of the initial non Gaussian signal. The method is based on an analysis of the distribution of statistical moments over the relevant frequency band of the given time signal. Based on a systematic mathematical approach, these higher order moments of the probability distributions are approximated by a combination of the corresponding moments of Gaussian distributions. The resulting signals respect the frequency

distribution of these moments and also the fatigue load distribution. The concept has been tested in terms of correct modeling of fatigue damage loads and their distribution in the frequency spectrum by analyzing real non Gaussian measurements from the area of railway vehicles. This method is useful in the framework of fatigue damage calculations in the frequency domain because available tools are often limited to Gaussian distributions. Based on the extension from the presented work, all these well established methods can still be used without any limitations. Another field of application is the fatigue oriented experimental shaker testing of structures subjected to non Gaussian loads. With the presented methods, all the well developed procedures from the area of Gaussian signal processing can be used for non Gaussian signals as well.

ACKNOWLEDGMENT

The analyzed measurements were provided by Siemens AG Graz.

REFERENCES

[1] J. S. Bendat, A. G. Piersol, *Random Data: Analysis and Measurement Procedures*, John Wiley & Sons, 2010.

[2] N.W.M. Bishop, Spectral methods for estimating the integrity of structural components subjected to random loading, *Handbook of Fatigue Crack Propagation in Metallic Structures*, Elsevier Science B.V., 1994.

[3] F. Sherrat, N.W.M. Bishop, T. Dirlik, Predicting fatigue life from frequency-domain data, current methods, part A, *Engineering Integrity*, Volume 18, September 2005, pp. 12-16.

[4] J.W. Miles, On structural fatigue under random loading, *Journal of Aeronautical Sciences*, Jahrgang 21, 1994, S. 753-762.

[5] W. Zhao, M.J. Baker, On the probability density function of rainflow stress ranges for stationary Gaussian processes, *Int. Journal of Fatigue*, Vol. 14, 1992, S.121-135.

[6] X. Wang, J.Q. Sun, Effect of skewness on fatigue life with mean stress correction, *Journal of Sound and Vibration* 282 (2005), pp. 1231-1237.

[7] D. Benasciutti, B. Tovo, Fatigue life assessment in non-Gaussian random loadings, *International Journal of Fatigue*, 28, pp. 733-746, 2005.

[8] M. Mršnik, J. Slavič, M. Boltežar, Frequency-domain methods for a vibration-fatigue-life estimation - Application to real data, *International Journal of Fatigue*, Volume 47, February 2013, Pages 8-17.

[9] P. Wolfsteiner, W. Breuer, Fatigue assessment of vibrating rail vehicle bogie components under non-Gaussian random excitations using power spectral densities, *Journal of Sound and Vibration* 322 (2013) 5867-5882.

[10] C. Braccesi, F. Cianetti, G. Lori, D. Pioli, The frequency domain approach in virtual fatigue estimation of non-linear systems: the problem of non-gaussian states of stress, *International Journal of Fatigue*, Volume 31, 2009, Pages 766-775.

[11] D. Charles, Derivation of Environment Descriptions and Test Severities from Measured Road Transportation Data, *Journal of the IES*, Vol. 36, Number 1, 1993, pp. 37-42.

[12] V. Rouillard, On the Non Gaussian Nature of Random Vehicle Vibrations, *Proceedings of the World Congress on Engineering 2007* Vol. II, July 2-4, 2007, London, U.K.

[13] P. Wolfsteiner, S. Sedlmair, Deriving Gaussian Fatigue Test Spectra from Measured non Gaussian Service Spectra, *Proceedings of the 3rd International Conference on Material and Component Performance under Variable Amplitude Loading (Procedia Engineering)* Vol. 101, 2015, p. 543-551.

International Conference on Engineering Vibration
Ljubljana, Slovenia, 7-10 September 2015

AN ANALYTICAL APPROACH TO MEASURE THE ACCURACY OF VARIOUS DEFINITIONS OF THE "EQUIVALENT VON MISES STRESS" IN VIBRATION MULTIAXIAL FATIGUE

Denis Benasciutti

Università di Udine, Dipartimento di Ingegneria Elettrica Gestionale Meccanica (DIEGM), via delle Scienze 208, 33100 Udine, Italy
denis.benasciutti@uniud.it

Keywords: vibration fatigue, multiaxial stresses, von Mises stress, Power Spectral Density.

Abstract. *This paper aims to review and compare various definitions of the "equivalent von Mises stress" (EMVS), which is used as a criterion to analyse multiaxial stationary Gaussian random stresses in the frequency-domain. Since the original definition of EVMS proposed in 1994 by Preumont and Piéfort, several modified formulations have been suggested by other authors. In particular, this paper focuses on the definitions proposed by Braccesi et al. (2008) and Niesłony (2008). Such modified formulations aimed to correct some incoherencies in the Preumont's definition of EVMS, which can lead to inaccurate estimations for particular combinations of material fatigue properties. In this work, analytical expressions are derived to check the accuracy of the original and modified EVMS criterion for different random loading types (e.g. pure bending, pure torsion, combined bending plus torsion). Such analytical expressions will allow engineers to understand when the original EVMS criterion and its modifications can safely be applied in fatigue design.*

1 INTRODUCTION

The "equivalent von Mises stress" (EVMS), first proposed in 1994 by Preumont and Piéfort, is a uniaxial normal stress used to analyse multiaxial stationary Gaussian random stresses in the frequency-domain [1-2]. The Preumont's EVMS is based on two hypotheses: i) S-N lines for normal and shear stress have equal slopes, ii) the fatigue strengths for normal and shear stress are scaled by $\sqrt{3}$. If these hypotheses are not satisfied, the EVMS criterion may lead to inaccurate damage estimations. These potential drawbacks were firstly pointed out in Refs. [3, 4] and further remarked in Refs. [5, 6-7], which also proposed modifications of Preumont's EVMS original definition.

This paper will derive analytical expressions to evaluate and to compare the accuracy of damage estimations given by several formulations of EVMS criterion, applied to different random loading types (e.g. pure bending, pure torsion, combined bending plus torsion). The obtain results can be used to understand which combinations of material fatigue properties allow each EVMS formulation to provide sufficiently accurate estimations.

2 SPECTRAL DESCRIPTION OF MULTIAXIAL RANDOM PROCESS

A zero-mean stationary random stress $x(t)$ is characterised in the frequency-domain by a two-sided power spectral density (PSD) function $S(f)$. The spectral moments of $S(f)$ are:

$$\lambda_n = \int_{-\infty}^{\infty} |f|^n \, S(f)\,\mathrm{d}f \qquad n = 1,2,\ldots \tag{1}$$

The variance is $Var(x(t))=\lambda_0$ and the frequency (Hz) of upward crossings of mean value is $\nu_0 = \sqrt{\lambda_2/\lambda_0}$. Spectral moments are also combined to define bandwidth parameters (as for example α_1, α_2 [8]), which are dimensionless numbers (between 0 and 1) that measure the frequency bandwidth of $S(f)$ (e.g. α_1, α_2 are close to unity for a narrow-band process).

A multi-axial random stress is usually represented by a six-dimensional vector process $\mathbf{x}(t) = \left[\sigma_{xx}(t), \sigma_{yy}(t), \sigma_{zz}(t), \tau_{xy}(t), \tau_{yz}(t), \tau_{zx}(t)\right]$, where σ and τ are normal and shear stress, respectively. The vector process $\mathbf{x}(t)$ is characterised in frequency-domain by a two-sided PSD Hermitian 6x6 matrix:

$$\mathbf{S}(f) = \begin{bmatrix} S_{xx,xx}(f) & \cdots & S_{xx,zx}(f) \\ \vdots & \ddots & \vdots \\ S_{zx,xx}(f) & \cdots & S_{zx,zx}(f) \end{bmatrix} \tag{2}$$

where diagonal elements $S_{hh}(f)$ are auto-PSDs, while out-of-diagonal elements $S_{hk}(f)$ are cross-PSDs of stress components (which in general are complex functions of f). The covariance matrix of the multi-axial random stress $\mathbf{x}(t)$ is:

$$\mathbf{C} = \int_{-\infty}^{\infty} \mathbf{S}(f)\,\mathrm{d}f = \begin{bmatrix} C_{xx,xx} & \cdots & C_{xx,zx} \\ \vdots & \ddots & \vdots \\ C_{zx,xx} & \cdots & C_{zx,zx} \end{bmatrix} \tag{3}$$

In matrix $\mathbf{C}$, the diagonal element $\lambda_{0,hh}=Var(x_h(t))$ is the variance of stress $x_h(t)$, while the out-of-diagonal element $\lambda_{0,hk}=Cov(x_h(t),x_k(t))$ (with $h\neq k$) is the covariance between stress components $x_h(t)$ and $x_k(t)$. The phase lag (i.e. degree of proportionality) between stresses $x_h(t)$,

$x_k(t)$ is measured by the correlation coefficient $\rho_{hk} = C_{hk} \Big/ \sqrt{\lambda_{0,hh}\, \lambda_{0,kk}}$. It is ρ_{hk}=1 for proportional (totally correlated) stresses, ρ_{hk}=0 for non-proportional (uncorrelated) stresses.

3 SPECTRAL METHODS FOR UNIAXIAL RANDOM PROCESSES

The fatigue damage of rainflow cycles, under the Palmgren-Miner rule, can be estimated in frequency-domain by analytical expressions given by spectral methods. A well-known example is the damage per time unit of a uniaxial random process with narrow-band PSD [8]:

$$d_{NB} = \frac{\nu_0}{C} \left(\sqrt{2\,\lambda_0}\right)^k \Gamma\left(1+\frac{k}{2}\right) \tag{4}$$

where $\Gamma(-)$ is the Gamma function and C, k are the fatigue strength coefficient and the inverse slope (exponent) of the S-N curve $s_a^k N = C$. Symbol N denotes the number of cycles to failure at constant amplitude s_a. The fatigue strength coefficient is usually defined as $C = s_A^k N_A$, where s_A is the fatigue strength amplitude at N_A cycles (typically N_A=2×10^6).

Expression (4) is correct only for a narrow-band random stress, while it gives too conservative estimates with a wide-band stress. A simple way to improve the damage estimated by Eq. (4) is to introduce a correction factor η, which accounts for the bandwidth of the PSD ($0 \le \eta \le 1$, with η=1 for a narrow-band stress, η<1 for a wide-band stress):

$$d_{WB} = \eta \frac{\nu_0}{C} \left(\sqrt{2\,\lambda_0}\right)^k \Gamma\left(1+\frac{k}{2}\right) \tag{5}$$

The parameter η only depends on the shape of the PSD $S(f)$ of the uniaxial stress $x(t)$ and it is usually a combination of spectral parameters [8]. An example is the TB method, where the correction factor is $\eta_{TB} = \left[\, b + (1-b)\, \alpha_2^{k-1} \,\right]$, where b parameter depends on α_1, α_2 [9].

The damage equation (5) is very general and applies to any type of stress (e.g. normal stress in axial or bending loading, shear stress in torsion loading), provided that the parameters C, k are those of the S-N curve for the considered loading type (axial, bending or torsion). For example, the stress amplitude s_a in the S-N curve $s_a^k N = C$ is a normal stress σ_a (in axial or bending loadings), or a shear stress τ_a in torsion loading.

Material	σ_A (MPa)	τ_A (MPa)	k_σ	k_τ	$c_{-1} = \frac{\sigma_A}{\tau_A}$	k_τ/k_σ	$r_{d,Pre}$	$r_{d,BC}$, $r_{d,N}$
CuZn40Pb2	216	187	5.9	17.2	1.16	2.93	$2\cdot10^9$	$1.86\cdot10^8$
34CrMo4	375	261.1	15.3	11.4	1.44	0.74	0.008	0.0005
18G2A (S255 J0)	189.6	141.9	7.9	12.3	1.34	1.56	$5\cdot10^3$	594
Ck 45 (SAE1045)	357	226	7.7	13.4	1.58	1.74	10^5	$5\cdot10^4$

Table 1: Experimental S-N parameters for several materials (more data are given in Ref. [10]). The last two columns show the calculated values of damage ratio r_d of EVMS criterion applied to pure torsion loading.

Experimental fatigue data confirm that S-N lines depend on the type of loading (bending, torsion); two separate equations must be defined: $\sigma_a^{k_\sigma} N = C_\sigma$ for normal stress and $\tau_a^{k_\tau} N = C_\tau$ for shear stress, where k_σ, k_τ are the exponents and $C_\sigma = \sigma_A^{k_\sigma} N_A$, $C_\tau = \tau_A^{k_\tau} N_A$ the fatigue strength coefficients for normal and shear S-N curves. The previous two equations can be the

design S-N lines, which are estimated by statistical analysis of experimental data, with reference to an assumed survival probability (e.g. P_s=90% or 97.7%).

4 MULTIAXIAL SPECTRAL METHODS BASED ON THE "EQUIVALENT VON MISES STRESS"

This section presents a short survey on the original definition of the "equivalent von Mises stress" by Preumont (as it is often misunderstood in the literature), as well as on some modifications. Without loss of generality, but for the sake of simplicity, the EVMS criteria reviewed in the next Sections will be presented for a biaxial state of stress ($\sigma_{xx}(t)$, $\sigma_{yy}(t)$, $\tau_{xy}(t)$).

4.1 Preumont's definition (1994) [1,2]

For a biaxial state of stress, the von Mises stress is:

$$\sigma_{vm}^2(t) = \sigma_{xx}^2(t) + \sigma_{yy}^2(t) - \sigma_{xx}(t)\sigma_{yy}(t) + 3\tau_{xy}^2(t) \tag{6}$$

Owing to the quadratic form of Eq. (6), the von Mises stress is a random process that is always positive, non-Gaussian and with positive mean value, even if all stress components are zero-mean Gaussian random processes. Furthermore, the frequency content of $\sigma_{vm}(t)$ is not consistent with that of stress components. In fact, in Eq. (6) the squared terms give frequency peaks at twice the frequencies (doubling) of the original PSDs, while the cross-product $\sigma_{xx}(t)\cdot\sigma_{yy}(t)$ gives additional contributions by a frequency shift of the original PSDs of $\sigma_{xx}(t)$ and $\sigma_{yy}(t)$. Therefore, the PSD of von Mises stress cannot be obtained by a simple linear combination of the PSDs of stress components.

To overcome the foregoing problems, Preumont and co-workers transformed expression (6) into the frequency-domain and demonstrated the following relationship [1,2]:

$$E\left[\sigma_{vm}^2(t)\right] = \text{Trace}\{\mathbf{Q}_{Pre}\,\mathbf{C}\} = \lambda_{0,xx} + \lambda_{0,yy} - \lambda_{0,xxyy} + 3\lambda_{0,xy} \tag{7}$$

which links the mean-square value of the von Mises stress to the covariance matrix $\mathbf{C}$ of the multi-axial random stress, by introducing the constant matrix:

$$\mathbf{Q}_{Pre} = \begin{bmatrix} 1 & -0.5 & 0 \\ -0.5 & 1 & 0 \\ 0 & 0 & 3 \end{bmatrix} \tag{8}$$

Expression (8) shows that the mean-square value of von Mises stress is simply the sum of variances of normal and shear stress, and covariances of normal stresses, in the multi-axial loading. As shown in Eq. (3), the covariance matrix $\mathbf{C}$ is equal to the integral (i.e. area) of PSD matrix $\mathbf{S}(f)$. Similarly, the mean-square value $E\left[\sigma_{vm}^2(t)\right]$ can be related to the area of a suitable PSD function $S_{eq}(f)$ and then equation (7) can be rewritten as:

$$E\left[\sigma_{vm}^2(t)\right] = \int_{-\infty}^{\infty} S_{eq}(f)\,df = \int_{-\infty}^{\infty} \text{Trace}\{\mathbf{Q}_{Pre}\,\mathbf{S}(f)\}\,df \tag{9}$$

Expression (9) is true without any particular hypothesis. The exact shape of $S_{eq}(f)$ is, however, not known, because *infinite* functions $S_{eq}(f)$ can be solutions of the integral equality in Eq. (9). Among all possible functions $S_{eq}(f)$, Preumont and Piéfort take the following PSD:

$$S_{eq}(f) = \text{Trace}\{\mathbf{Q}_{Pre}\,\mathbf{S}(f)\} = S_{xx}(f) + S_{yy}(f) - \text{Re}\{S_{xx,yy}(f)\} + 3S_{xy}(f) \tag{10}$$

which is obtained by combining, for each frequency f, the PSDs of stress components exactly by the quadratic combination rule that defines the von Mises stress (this is equivalent to eliminate the symbol of integration in Eq. (9)).

Once a suitable PSD function $S_{eq}(f)$ has been computed from the PSD matrix $\mathbf{S}(f)$, Preumont and co-workers *postulate* that $S_{eq}(f)$ represents the PSD of a uniaxial stationary, Gaussian zero-mean random process $\sigma_{eq}(t)$, which they call "equivalent von Mises stress" (EVMS). It has to be remarked that the stress $\sigma_{eq}(t)$ is a conventional definition and, of course, it has not to be confused with von Mises stress $\sigma_{vm}(t)$ of Eq. (6). On the other hand, the stress $\sigma_{eq}(t)$ solves all the problems mentioned above for the von Mises stress $\sigma_{vm}(t)$, as it has exactly all the properties we were looking for: (i) it is Gaussian with zero mean (by construction), (ii) it reduces to a uniaxial random stress if the loading is uniaxial, (iii) its frequency content is consistent with that the stress components of the multi-axial process. Note, however, that the definition in Eq. (10) ignores the cross-correlations between normal stresses $\sigma_{xx}(t)$, $\sigma_{yy}(t)$ and the shear $\tau_{xy}(t)$ stress.

The multi-axial fatigue criterion based on the EVMS assumes that the uniaxial equivalent random stress $\sigma_{eq}(t)$ gives the same amount of fatigue damage as that caused by the multi-axial random stress (as, for example, the biaxial stress $\sigma_{xx}(t)$, $\sigma_{yy}(t)$, $\tau_{xy}(t)$ considered above). The fatigue damage d_{eq} of stress $\sigma_{eq}(t)$ can be estimated by spectral methods for uniaxial random processes. Since $\sigma_{eq}(t)$ is a normal stress, the damage d_{eq} is evaluated on the S-N curve $\sigma_a^{k_\sigma} N = C_\sigma$ for normal stress, with coefficients $C=C_\sigma$ and $k=k_\sigma$ in the damage equation (5).

4.2 Braccesi and Cianetti definition (2008) [5]

The Preumont's definition of the EVMS adopts a coefficient 3 to multiply the PSD of shear stresses, which implies that the fatigue strength amplitudes σ_A, τ_A for normal and shear stress are scaled exactly by a factor $\sqrt{3}$. In a modification of Preumont's EVMS suggested by Braccesi et al. [5], the coefficient $\sqrt{3}$ is replaced by $c_{-1} = \sigma_A / \tau_A$ (in Ref. [5], the fatigue limits f_{-1} and t_{-1} for fully-reversed bending and torsion are considered in place of σ_A, τ_A. However, this distinction does not modify the following arguments).

The constant matrix $\mathbf{Q}_{Pre}$ in Eq. (7) then modifies as:

$$\mathbf{Q}_{BC} = \begin{bmatrix} 1 & -0.5 & 0 \\ -0.5 & 1 & 0 \\ 0 & 0 & c_{-1}^2 \end{bmatrix} \tag{11}$$

In Ref. [5] the authors write: "*The only difference consists in the last term of the main diagonal which Preumont puts close to* 3 *according to the classical formulation of von Mises stress; in the proposed definition we have preferred the value* c_{-1}^2 *in better agreement with the experimental results*".

For example, for a biaxial state of stress, the PSD function of the EVMS-BC becomes:

$$S_{eq,BC}(f) = \text{Trace}\{\mathbf{Q}_{BC}\,\mathbf{S}(f)\} = S_{xx}(f) + S_{yy}(f) - \text{Re}\{S_{xx,yy}(f)\} + c_{-1}^2 S_{xy}(f) \tag{12}$$

The Braccesi-Cianetti (BC) formulation of EVMS coincides with Preumont's definition for materials characterised by $c_{-1} = \sigma_A / \tau_A = \sqrt{3}$.

4.3 Niesłony definition (2008) [6,7]

In Ref. [6,7], Niesłony recognised that the Preumont's EVMS criterion can safely be applied only to materials having S-N lines for normal and shear stress with equal slopes (k_σ=k_τ) and fatigue strengths scaled as $\sigma_A = \sqrt{3}\tau_A$. However, he assumed that the condition $\sigma_A = \sqrt{3}\tau_A$ is more important than k_σ=k_τ, "*because a wide range of materials does not satisfy it. However, it is possible to formulate a criterion in the frequency domain without this restriction, which allows one to obtain correct values under simple loading states, i.e. tension compression and torsion*". The EVMS modified by Niesłony, which is based on the definition of the octahedral plane, has a PSD defined as:

$$S_{\mathrm{eq,N}}(f) = a_\mathrm{N}^2\, S_{\tau\mathrm{os}}(f) + b_\mathrm{N}^2\, S_{\sigma\mathrm{os}}(f) + 2\, a_\mathrm{N}^2\, b_\mathrm{N}^2\, \mathrm{Re}\left\{S_{\tau\mathrm{os},\sigma\mathrm{on}}(f)\right\} \tag{13}$$

where $S_{\tau\mathrm{os}}(f)$, $S_{\sigma,\mathrm{on}}(f)$, $S_{\tau\mathrm{os},\sigma\mathrm{on}}(f)$ are, respectively, the auto- and cross-PSD of shear $\tau_{\mathrm{os}}(t)$ and normal $\sigma_{\mathrm{os}}(t)$ stresses on the octahedral plane. The auto-PSDs are calculated as:

$$S_{\tau\mathrm{os}}(f) = \mathrm{Trace}\left\{\mathbf{Q}_{\mathrm{os}}\,\mathbf{S}(f)\right\} \quad , \quad S_{\sigma\mathrm{on}}(f) = \mathrm{Trace}\left\{\mathbf{Q}_{\mathrm{on}}\,\mathbf{S}(f)\right\} \tag{14}$$

by using the constant matrices:

$$\mathbf{Q}_{\mathrm{os}} = \frac{1}{9}\begin{bmatrix} 2 & -1 & 0 \\ -1 & 2 & 0 \\ 0 & 0 & 6 \end{bmatrix} \quad , \quad \mathbf{Q}_{\mathrm{on}} = \frac{1}{9}\begin{bmatrix} 1 & 1 & 0 \\ 1 & 1 & 0 \\ 0 & 0 & 0 \end{bmatrix} \tag{15}$$

The coefficients in expression (13) are defined as [6,7]:

$$a_\mathrm{N} = \sqrt{6}\, c_{-1}/2 \quad , \quad b_\mathrm{N} = -\sqrt{3}\, c_{-1}\, r_{\tau\mathrm{os},\sigma\mathrm{on}} + \sqrt{9 - 3c_{-1}^2\left(1 - r_{\tau\mathrm{os},\sigma\mathrm{on}}^2\right)} \tag{16}$$

where $r_{\sigma\mathrm{os},\tau\mathrm{os}}$ is the correlation coefficient between $\sigma_{\mathrm{os}}(t)$ and $\tau_{\mathrm{os}}(t)$. Note that Eq. (16) adopts a slightly different notation from [6,7] to point out the dependence on coefficient c_{-1} also used in the definition of Braccesi et al. The EVMS formulation proposed by Niesłony, similarly to that of Braccesi et al., only accounts for the ratio σ_A/τ_A, but not for the inverse slopes k_σ and k_τ.

5 ACCURACY OF EVMS CRITERIA WITH UNIAXIAL RANDOM STRESS

A requirement for any multi-axial fatigue criterion is that its estimate must be consistent with uniaxial fatigue data. In this Section, the EVMS multi-axial criterion is tested in the limiting case of a uniaxial normal $\sigma(t)$ or shear $\tau(t)$ random stress (as given by pure axial/bending loading or pure torsion). The estimations by EVMS criterion (with different formulations) are compared with damage estimated directly on the S-N line pertinent to the uniaxial stress:

$$d_\sigma = \eta_\sigma \frac{\nu_{0,\sigma}}{C_\sigma}\left(\sqrt{2V_\sigma}\right)^{k_\sigma}\Gamma\left(1+\frac{k_\sigma}{2}\right) \quad , \quad d_\tau = \eta_\tau \frac{\nu_{0,\tau}}{c_\tau}\left(\sqrt{2V_\tau}\right)^{k_\tau}\Gamma\left(1+\frac{k_\tau}{2}\right) \tag{17}$$

where V_σ=$Var(\sigma(t))$, V_τ=$Var(\tau(t))$ are the variances, $\nu_{0,\sigma}$ and $\nu_{0,\tau}$ the frequencies of upcrossing of the mean value, η_σ and η_τ the bandwidth correction factors that quantify the spectrum width of $S_\sigma(f)$, $S_\tau(f)$, i.e. the PSDs of uniaxial stresses $\sigma(t)$ and $\tau(t)$. Of course, the values d_σ , d_τ have to be interpreted as the "true" fatigue damage, as they are calculated directly from the PSD $S_\sigma(f)$, $S_\tau(f)$ of normal and shear stress by using the appropriate S-N curve.

5.1 Accuracy of EVMS criterion by Preumont

For a uniaxial normal stress $\sigma(t)$ with PSD $S_\sigma(f)$, the PSD of the EVMS is $S_{eq}(f)=S_\sigma(f)$, see Eq. (10). Coincident spectra clearly have identical spectral parameters: $V_{eq}=Var(\sigma_{eq}(t))=V_\sigma$, $\nu_{0,eq}=\nu_{0,\sigma}$ and $\eta_{eq}=\eta_\sigma$. The damage d_{eq} of $\sigma_{eq}(t)$ calculated by Eq. (5) is thus equal to the damage of $\sigma(t)$, in symbols $d_{eq}=d_\sigma$. For a uniaxial normal stress $\sigma(t)$, the damage estimated by EVMS criterion thus exactly agrees with the damage of the uniaxial stress: $r_d=d_{eq}/d_\sigma=1$.

For a random shear stress $\tau(t)$ with PSD $S_\tau(f)$, the PSD of the EVMS is $S_{eq}(f)=3S_\tau(f)$, see Eq. (10). Since the spectrum $S_{eq}(f)$ has the same shape of $S_\tau(f)$ – it is just increased three times – its spectral moments are $\lambda_{n,eq}=3\lambda_{n,\tau}$, where $\lambda_{n,\tau}$ are the spectral moments of $S_\tau(f)$. The equivalent stress $\sigma_{eq}(t)$ has variance $Var(\sigma_{eq}(t))=3V_\tau$, same frequency of mean-upcrossings $\nu_{0,eq}=\nu_{0,\tau}$ and correction factor $\eta_{eq}=\eta_\tau$.

The EVMS criterion assumes that $\sigma_{eq}(t)$ causes the same damage of $\tau(t)$. The damage of $\sigma_{eq}(t)$ must be computed by Eq. (5) by using the parameters of the S-N line for normal stress:

$$d_{eq} = \eta_{eq} \frac{\nu_{0,eq}}{C_\sigma} \left(\sqrt{2V_{eq}}\right)^{k_\sigma} \Gamma\left(1+\frac{k_\sigma}{2}\right) \tag{18}$$

As already said, d_τ is the "true" fatigue damage; instead, d_{eq} is the estimate given by EVMS criterion. Therefore, the accuracy of EVMS criterion with a uniaxial random shear stress is measured by the ratio $r_d=d_{eq}/d_\tau$, which after some simplifications becomes [10]:

$$r_{d,Pre} = \frac{d_{eq}}{d_\tau} = \frac{\tau_A^{k_\tau}}{\left(\sigma_A/\sqrt{3}\right)^{k_\sigma}} \frac{\Gamma\left(1+k_\sigma/2\right)}{\Gamma\left(1+k_\tau/2\right)} \left(\sqrt{2V_\tau}\right)^{k_\sigma-k_\tau} \tag{19}$$

A perfect agreement is when $r_d=1$, while other values indicate over-conservative ($r_d>1$) or unsafe ($r_d<1$) damage estimations by Preumont's EVMS criterion.

5.2 Accuracy of EVMS criterion by Braccesi et al.

An approach similar to that used in the previous Section can be applied also to test the accuracy of BC-EVMS criterion modified by Braccesi et al. For a pure normal stress $\sigma(t)$ with PSD $S_\sigma(f)$, the PSD of the BC-EVMS is $S_{eq,BC}(f)=S_\sigma(f)$, as given by Eq. (12). As for Preumont's definition, it follows that $d_{eq,BC}=d_\sigma$ and the damage ratio $r_{d,BC}=d_{eq,BC}/d_\sigma=1$ measures a perfect agreement.

For a pure shear stress $\tau(t)$ with PSD $S_\tau(f)$, the PSD of the BC-EVMS calculated by Eq. (12) is $S_{eq,BC}(f)=c_{-1}^2\,S_\tau(f)$. Since the spectrum $S_{eq,BC}(f)$ has the same shape of $S_\tau(f)$ – it is just increased by a factor c_{-1}^2 – its spectral moments are $\lambda_{n,eq,BC}=c_{-1}^2\lambda_{n,\tau}$, where $\lambda_{n,\tau}$ are the spectral moments of $S_\tau(f)$. The equivalent stress $\sigma_{eq,BC}(t)$ has variance $Var(\sigma_{eq,BC}(t))=c_{-1}^2V_\tau$, same frequency of mean-upcrossings $\nu_{0,eq,BC}=\nu_{0,\tau}$ and correction factor $\eta_{eq,BC}=\eta_\tau$. The same arguments used for Preumont's EVMS criterion lead to the following damage ratio for the BC-EVMS:

$$r_{d,BC} = \frac{d_{eq}}{d_\tau} = \frac{\tau_A^{k_\tau}}{\left(\sigma_A/c_{-1}\right)^{k_\sigma}} \frac{\Gamma\left(1+k_\sigma/2\right)}{\Gamma\left(1+k_\tau/2\right)} \left(\sqrt{2V_\tau}\right)^{k_\sigma-k_\tau} \tag{20}$$

where c_{-1} simply replaces $\sqrt{3}$ in Eq. (19); when $c_{-1}=\sigma_A/\tau_A=\sqrt{3}$, it is $r_{d,BC}=r_{d,Pre}$.

5.3 Accuracy of EVMS by Niesłony

For a pure normal stress $\sigma(t)$ with PSD $S_\sigma(f)$, the PSDs of shear and normal stress on the octahedral plane, calculated by Eq. (14) are $S_{\tau os}(f)=(2/9)\cdot S_\sigma(f)$ and $S_{\sigma on}(f)=S_\sigma(f)/9$. The PSD of the equivalent stress, computed by Eq. (13) with $r_{\sigma os,\tau os}=0$, is $S_{eq,N}(f)=S_\sigma(f)$. Therefore, similarly to other criteria, the N-EVMS method gives a damage ratio $r_{d,N}=d_{eq,BC}/d_\sigma=1$ for a pure normal stress.

For a pure shear stress $\tau(t)$ with PSD $S_\tau(f)$, the PSDs of shear and normal stress on the octahedral plane are $S_{\tau os}(f)=(2/3)S_\tau(f)$ and $S_{\sigma on}(f)=0$, then $r_{\sigma os,\tau os}=0$. The PSD of the N-EVMS by Niesłony, as obtained by Eq. (13), is $S_{eq,BC}(f)=c_{-1}^2\,S_\tau(f)$, i.e. it is exactly equal to that computed by BC-EVMS of Braccesi et al. Therefore, for the N-EVMS the damage ratio $d_{eq,N}$ for a pure shear stress can be computed by Eq. (20); of course, it is $d_{eq,N}=d_{eq,BC}$.

6 SENSITIVITY ANALYSIS

6.1 Trends of r_d for pure torsion random loading

Similarly to the study in [10], some trends of the damage ratio r_d in expressions (19) and (20) are calculated by varying the material parameters $c_{-1}=\sigma_A/\tau_A$, $r_k=k_\tau/k_\sigma$ and the variance V_τ. The following ranges of values are considered: $V_\tau=100$ MPa^2, $r_{\sigma\tau}=1\div2.5$ (with $\sigma_A=100$, 300 MPa), $r_k=0.67$, 1, 1.33, 1.67, 2 (with $k_\sigma=3$, 6) [10].

An example of result is shown in Figure 1, which compares $r_{d,Pre}$ with $r_{d,BC}$ and $r_{d,N}$. The horizontal line marks a perfect prediction by EVMS criterion applied to torsion loading. Remarkably, the overall accuracy of Preumont's EVMS criterion is anything but satisfactory, as r_d varies in a wide interval of several orders of magnitude even for relatively small variations in S-N parameters. In particular, both $r_d>1$ (conservative) and $r_d<1$ (unsafe) estimations are obtained, with a largely inaccurate estimations ($r_d>>1$ and $r_d<<1$) observed for specific combinations of fatigue properties.

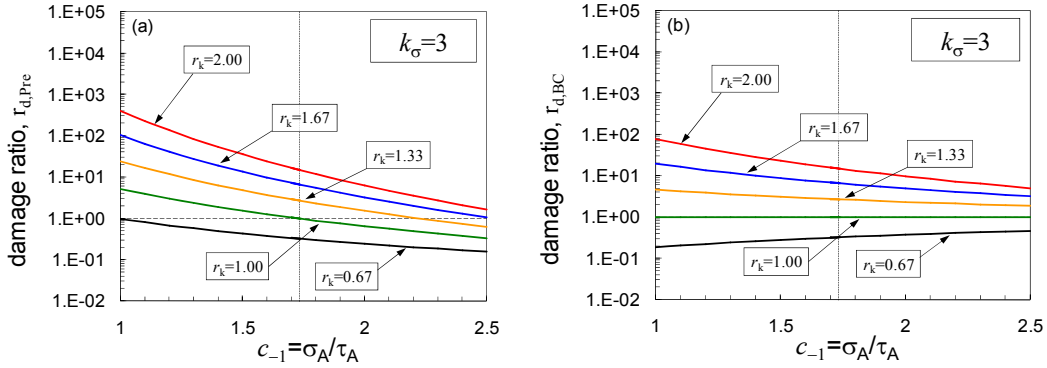


Figure 1: Damage ratio for torsion loading: (a) $r_{d,Pre}$ (Preumont); (b) $r_{d,BC}$ (Braccesi et al.) and $r_{d,N}$ (Niesłony).

The BC/N-EVMS criteria, instead, provide slightly better estimations, which also are less sensitive to the parameter $c_{-1}=\sigma_A/\tau_A$ (i.e. the damage ratio r_d is more constant over c_{-1}). In particular, equal slopes $k_\tau=k_\sigma$ give a perfect estimation $r_d=1$ for any value of c_{-1}.

6.2 Trends of r_d for bending-torsion random loading

Unfortunately, no analytical approach can be devised to check the accuracy of EVMS criterion with multiaxial loading, even for a simple biaxial state of stress (σ_{xx}, σ_{yy}, τ_{xy}). An ana-

lytical result could be obtained, however, at least for a combined normal and shear random stresses, by interpolating the estimation error calculated for the limiting case of pure normal stress (r_d=1) and pure shear stress (r_d>1 or r_d <1), see Eqs. (19)-(20). In a biaxial state with normal σ(t) and shear τ(t) stresses, V_τ=0 indicates only a normal stress, whereas V_σ=0 indicates only shear stress, where V_σ, V_τ are the variances of stress. The damage estimation index, say i_d, then changes from 1 to r_d as the variance ratio v_r=V_τ/V_σ moves from 0 (only normal stress, V_τ=0) to ∞ (only shear stress, V_σ=0); intermediate values of i_d characterise the values 0<v_r<∞.

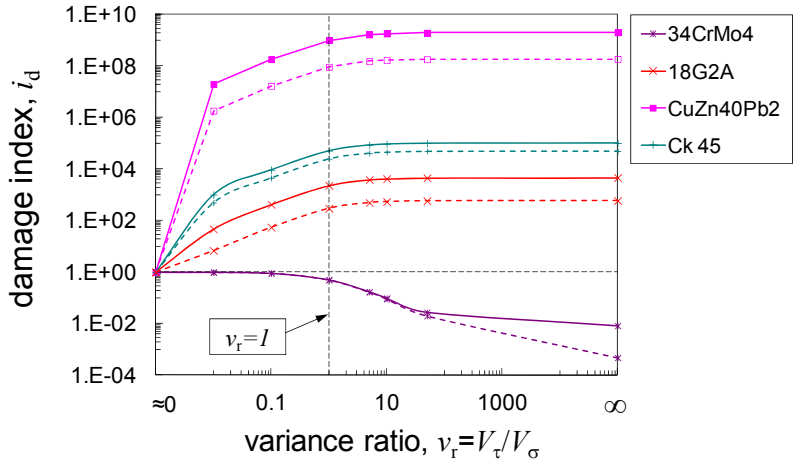


Figure 2: Comparison of damage ratio $r_{d,Pre}$ with $r_{d,BC}$ and $r_{d,N}$.

Without any information from experimental data, this expression has been proposed in [10]:

$$i_d = r_{d,*} - \frac{r_{d,*} - 1}{v_r + 1} \tag{21}$$

where symbol $r_{d,*}$ is the damage ratio for pure torsion as obtained by EVMS criterion formulated by Preumont's ($r_{d,*}$= $r_{d,Pre}$ in Eq. (19)) or by either Niesłony or Braccesi et al. ($r_{d,*}$=$r_{d,BC}$=$r_{d,N}$ in Eq. (20)). The values of the damage index $r_{d,Pre}$, $r_{d,BC}$, $r_{d,N}$ $r_{d,*}$ for pure shear stress are reported in the last two columns of Table 1. As an example, Figure 2 shows the trends of the damage index for four metallic alloys, which are characterised by the largest damage ratios r_d among those calculated. In general, BC/N-EVMS criteria tend to give better estimations than P-EVMS, with only the exception of 34CrMo4 steel, which has a ratio r_k<1.

7 CONCLUSIONS

The obtained results allow drawing the following conclusions:

- with a uniaxial random normal stress σ(*t*), all definitions of the EVMS give a perfect damage estimate (r_d=1), regardless of S-N parameters. Instead, with a uniaxial random shear stress τ(*t*), the damage estimate varies in a large interval, depending on the particular combinations of S-N parameters;
- the EVMS by Braccesi et al. and the EVMS by Niesłony are characterised by the same damage ratio for a pure torsion random loading, i.e. $r_{d,BC}$=$r_{d,N}$;

- When $c_{-1} = \sigma_A / \tau_A = \sqrt{3}$, the EVMS by Braccesi et al. and by Niesłony gives the same damage ratio as the EVMS by Preumont, that is $r_{d,Pre}=r_{d,BC}=r_{d,N}$, irrespective of the values of $r_k=k_\tau/k_\sigma$;
- When $k_\tau=k_\sigma$, the EVMS by Braccesi and Niesłony give an exact damage estimate for pure torsion loading, for any combination of $c_{-1}=\sigma_A/\tau_A$ values; instead, the estimate of EVMS by Preumont is exact only when $c_{-1} = \sigma_A / \tau_A = \sqrt{3}$;
- with a biaxial normal+shear random stress, the accuracy of EVMS criterion strongly depends on the particular combination of S-N parameters and also on the relative intensity (variance) of normal and shear stresses. Quite good estimations are obtained for materials characterised by $k_\tau \approx k_\sigma$, whereas larger errors are obtained for other.

The above conclusions then suggest a great caution when using the EVMS criterion, especially when the requirement $k_\tau=k_\sigma$ is not satisfied; the S-N fatigue parameters should be checked very carefully to find out possible large estimation errors. To mitigate possible errors, it is recommended to use EVMS formulations by Braccesi et al. and by Niesłony (this latter, in particular, can also account for correlations between normal and shear stress).

REFERENCES

[1] A. Preumont and V. Piéfort, Predicting random high-cycle fatigue life with finite elements. *J. Vibration and Acoustics*, **116**(2), 245-248, 1994.

[2] X. Pitoiset and A. Preumont, Spectral methods for multiaxial random fatigue analysis of metallic structures. *International Journal of Fatigue*, **22**, 541-550, 2000.

[3] R. Tovo, D. Benasciutti, A. Cristofori, L. Susmel, Studio degli approcci in frequenza nella fatica multiassiale ad ampiezza variabile, AIAS Congress, Ancona, September 2006 (in Italian).

[4] A. Cristofori, *A new perspective in multiaxial fatigue damage estimation*. PhD Thesis, University of Ferrara, March 2007.

[5] C. Braccesi, F. Cianetti, G. Lori and D. Pioli, An equivalent uniaxial stress process for fatigue life estimation of mechanical components under multiaxial stress conditions. *International Journal of Fatigue*, **30**(8), 1479–1497, 2008.

[6] A. Niesłony, Comparison of some selected multiaxial fatigue failure criteria dedicated for spectral method, *J. Theoretical and Applied Mechanics*, **48**(1), 233-254, 2010.

[7] A. Niesłony and C.M. Sonsino, Comparison of some selected multiaxial fatigue assessment criteria, *LBF Fraunhofer Institute, Darmstadt*, Report No. FB-234 (2008).

[8] L.D. Lutes and S. Sarkani, *Random vibrations: analysis of structural and mechanical systems*, Elsevier, US, MA, 2004.

[9] D. Benasciutti, R. Tovo, Spectral methods for lifetime prediction under wide-band stationary random processes, *International Journal of Fatigue*, **27**(8), 867-877, 2005.

[10] D. Benasciutti, Some analytical expressions to measure the accuracy of the "equivalent von Mises stress" in vibration multiaxial fatigue. *Journal Sound and Vibration*, **333**(18), 4326-4340, 2014.

International Conference on Engineering Vibration
Ljubljana, Slovenia, 7-10 September 2015

SIMULATION OF THE WHOLE WIND-INDUCED FATIGUE LIFE OF A SLENDER STEEL STRUCTURE

Maria P. Repetto*[1]

[1]Department of Civil, Chemical and Environmental Engineering, University of Genova, Italy
repetto@dicca.unige.it

Keywords: Instructions, Conference, Vibration, Experimental Dynamics, Wave Problems, Modal Analysis.

Abstract. *An extensive simulation of wind-induced fatigue loading of a slender steel structure has been developed, containing both macro- and micro-meteorological fluctuations, coherent with the parent distribution and the velocity spectrum of the same 'probable' wind during the whole structural life. The corresponding cycles histogram and fatigue damage are obtained post-processing the stress time-history by numerical Rainflow counting algorithm, to obtain a benchmark solution of the fatigue analysis. The results are compared with a simplified fatigue estimation methods proposed in literature*

1 INTRODUCTION

Wind-induced fatigue is a key issue in design of many slender structures, such as wind turbines, cranes, poles and towers. Wind-induced loads on structures constitute a non-stationary, non-Gaussian random process. The methods for fatigue analysis generally define a series of independent loading conditions, each corresponding to a fixed value of mean wind velocity and direction. The fluctuating wind-induced effect is usually schematized as a stationary Gaussian process superimposed to a mean static effect associated to the mean wind velocity. The long-term time variation of the mean static effect is taken into account probabilistically.

The wind effects associated to the loading conditions are usually evaluated in applications adopting two different approaches. The first, referred to as time-domain procedure, requires the acquisition of stress time series corresponding to all the considered loading conditions, by means of measurements or numerical simulation techniques. The samples have to be post-processed by numerical algorithms, such as the Rainflow counting method, in order to build the cycles histogram, from which the mean damage can be estimated. The time domain methods are numerically burdensome and time-consuming, however they are still largely adopted in many practical problems [1] and standards codes.

The second approach makes recourse to analytical methods in frequency domain. The wind effects associated to the loading conditions are treated as stationary, Gaussian processes; the fatigue damage induced by the considered loading conditions is obtained adopting analytical formulations based on the spectral properties of loads, on the basis of narrow-band hypothesis [2], wide band hypothesis [3] or bi-modal hypothesis for the loading spectral shape [4-5]. The frequency domain methods can be adopted to derive engineering procedures for simple structures [6] but are still unsuitable for extensive application in complex structures design.

The two approaches have mutual strengths and weaknesses and none of them meet with the general approvals of the technical community. Long-term simulations of the wind-induced loads have be adopted as reference results to discuss the criticisms of different methods. Kelley et al [7] created a series of 144, 10-minute inflow records that are likely to occur individually within a 24-hour period at two distinct locations, discussing the effects of the diurnal loading variation on a wind turbine. Moriarty [8] simulated a total of 5 years of operational wind turbine loading conditions, to test loads extrapolation techniques used in wind turbine design, highlighting that discrete load cases currently represented in the standard can be reproduced by stochastic simulations as long as they are run for a sufficient length of time. More recently Barone et al [9] performed 96 years of operational wind turbine load simulations. This huge amount of data have been used to assess extreme load design standards [10] but they still have not been used to analyse fatigue procedures.

The author of the present paper contributed to the discussion, presenting the results of a long-term simulation of fatigue damage of a steel lighting pole, corresponding to 50 years of structural life containing both macro- and micro-meteorological fluctuations of the same 'probable' wind [11-12]. The present paper resumes the results previously obtained, discussing and extending the analysis in two directions. Firstly, the benchmark result is firstly used to discuss the reliability of time-domain methods, with reference to the uncertainties related to the transition cycles of fragmented time-histories and to the time length of independent loading conditions; then, it is compared with the most relevant frequency domain methods and with the statistical extrapolation method, to assess their suitability for modelling the wind-induced fatigue phenomenon in slender structures.

2 CLASSICAL FRAMEWORK OF FATIGUE ANALYSIS: STATE APPROACH

The wind speed in the atmospheric boundary layer can be expressed as the superposition of two independent components, referred to as macro- and micro-meteorological components. Let us subdivide the time t into successive ΔT intervals falling into the spectral gap (10-60 min); the macro-meteorological component varies so slowly on ΔT, which can be described with constant intensity $\overline{V}$ and direction φ; the micro-meteorological component V', associated to the atmospheric turbulence, can be treated as a stationary Gaussian nil mean process.

Considering a time interval T much greater than ΔT, the time variation of the macro-meteorological component of the wind velocity shall be taken into account. A 'state approach' is generally adopted for the evaluation of the wind-induced fatigue, considering the wind loading effects induced on a structure during T as a series of independent loading conditions, each corresponding to a ΔT step, and macro-meteorological variation of the wind velocity is treated probabilistically. Disregarding the directional effect, a series of equally spaced speed classes $\Delta\overline{V}_i$ (i=1,2…) can be defined, each of them associated to a loading condition. P_i is the probability that $\overline{V} \in \Delta\overline{V}_i$, then the state approach assumes that the structure undergoes the i-th loading condition for an effective duration time $T_i=TP_i$.

For structures with linear behaviour, the wind loading effect associated to the i-th loading condition is given by:

$$e_i(t) = \overline{e}_i + e'_i(t) \tag{1}$$

where $\overline{e}_i$ and $e'_i(t)$ and are the mean and nil mean fluctuating components, respectively.

Disregarding the effects of the original load cycles sequence, the total damage accumulated during the whole structure's life is evaluated collecting the cycles deriving from all wind loading conditions into a discrete cycles histogram. Considering a series of stress cycle amplitude Δk (k=1,2…), is the mean number of stress cycles $\overline{n}_{ik}$ with amplitude Δκ and mean value $\overline{e}_i$ is proportional to T_i and can be obtained applying a suitable cycle counting method to the fluctuating process.

Adopting the Palmgren-Miner linear rule, the fraction of damage induced by stress cycles $\overline{n}_{ik}$ is given by:

$$\overline{d}_{ik}(T) = \overline{n}_{ik}(T) / N_{ik} \tag{2}$$

where N_{ik} is the number of the stress cycles with amplitude Δ_k and mean stress $\overline{s}_i$ given by the S-N fatigue resistance curve of the structural detail.

The total accumulated damage $\overline{D}(T)$ is given by the sum of the contribution of $\overline{d}_{ik}(T)$. Assuming that the collapse occurs when $\overline{D}(T)$ reaches the unit, and being $\overline{D}(1)$ is the yearly accumulated damage, the mean fatigue life in years can be estimated by:

$$\hat{T}_F = 1 / \overline{D}(1) \tag{3}$$

3 NUMERICAL SIMULATION OF WIND-INDUCED FATIGUE

3.1 Case study

The analyses take into account the alongwind-induced fatigue of the urban light pole shown in Figure 1, where R is the radius, μ is the mass per unit length, and ψ_1 is the first modal shape. The pole is h = 14 m high with an octagonal section of constant thickness t = 4 mm. The light device has a mass of 145 kg, with the centre of gravity at 14.9 m height, and an exposed surface of 3.33 m2. The fundamental frequency is $_{n1}$ = 0.54 Hz; the damping ratio is ξ = 0.005. The drag coefficient of the shaft and of the light device are 1.2 and 0.3, respectively. In the present application, the structure is placed in Province of Rome, Italy.

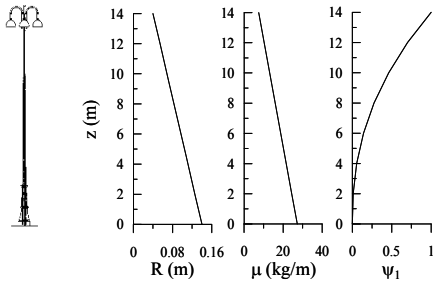


Figure 1: Light pole: scheme, radius, mass per unit length and first modal shape.

According to the Italian Standard Codes [13], the mean wind velocity with return period R=50 years is $\bar{u}_{ref}$ = 27m/s. The Weibull parameters have been estimated by means of a climatologycal analysis in the zone. In particular, k=1.155.

In accordance with the Eurocode 3 [14], the base section is classified as Category 36. The equivalent static stress associated to $\bar{V}_{ref}$ is $\bar{s}_{ref}$ = 57 MPa, the static stress due to permanent loads is $\bar{s}_p$ = 1.1 MPa., the material ultimate stress is s_u = 510 MPa.

3.2 Numerical simulation of wind-induced stress

Long-term time series of wind-induced stress are generated by means of a 3-step procedure. First, 50 years of 10-min mean wind observations spaced 10 min apart are generated by means of the Monte Carlo (MC) procedure reported in [11]. Then, 50 years of synthetic measurements of the bending moment at the base of a lighting pole $M(t)$ are generated applying additional MC conditional simulations. Finally, the time series of the stress $s(t)$ are trivially derived from the time series of $M(t)$ through linear relationships.

The wind speed statistics are based on the anemometric analysis reported in Torrielli et al., adopting wind measurements recorded by 6 anemometers spread out over an area of approximately 200 km in diameter in the central part of Italy. The features of the local terrain where the anemometers are sited are taken into account by transforming the wind data - affected by the local roughness and topography - into speed values corresponding to a unique reference condition, i.e. a height of 10 m on a flat terrain with a roughness length z_0 = 0.05 m .

The 6 wind records are processed to describe the probability distribution and the power spectrum of the of mean wind velocity process. This can be ascribed to a ‘probable’ wind climate, so called because it cannot be retraced to a single site of measurement, but it is physically ‘probable’ since it derives from real wind observations in a limited area.

The Hybrid Weibull (HW) model is used to describe the parent distribution, with F_0=0.118, c=3.91 m/s and k=1.155.

The simulation algorithm described in [11] is used for the generation of 50 years of 10-min mean wind observation spaced 10 min apart. This algorithm pursues the generation of data sample with the desired probability distribution and power spectrum through iterative corrections of the probabilistic and spectral contents. The power spectrum of the resulting time series matches perfectly the target, while the CDF slightly deviates from the target distribution in the upper tail region. Such discrepancies may affect an extreme value analysis but should be less significant for a fatigue analysis, where the contribution to the damage provided by the rare high speeds conditions is expected to be minor.

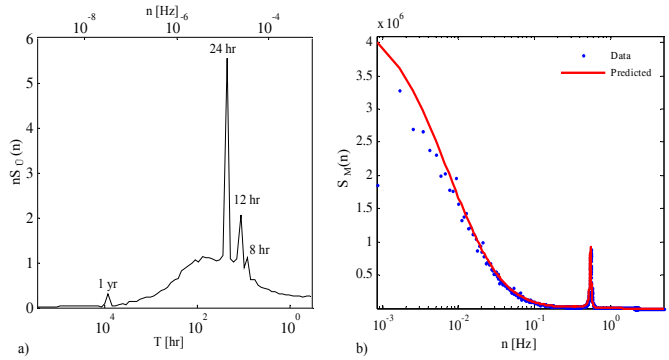


Figure 2: Spectra of the mean wind velocity (a) and fluctuating component of the bending moment (b).

This study fixes a priori the length T of the response signal, which is analyzed for assessing independent estimates of the fatigue damage, namely T=3 days. This choice takes into regard the macro-meteorological fluctuations without exceeding the correlation time of the response process linked to fatigue damage phenomenon. Taking into account this, the 1-year time series of M(t) is obtained by joining multiple independent 3-day simulation, each based on the consecutive 3-days segments of the aforementioned time histories of the mean wind speed. In this way the following estimate of the yearly fatigue damage will take into account the different loading conditions occurring during the whole year. Since the response simulation is independent from segment to segment, below the focus is on a single segment. The statistics of the bending moment are derived by adopting the formulation proposed in [15]. Analogously to the wind velocity, M(t) can be regarded as the superposition of two components, the mean $\bar{M}$ and the nil mean fluctuation M'(t) (Eq. (1)). Once the time series of the mean wind velocity $\bar{V}$ is known, $\bar{M}$ can be deterministically evaluated thanks to the analytical expressions of the response statistics. Much more complex is the definition of M'(t), as no analytic expression for this is known in literature. However, an interesting novel expression for the spectrum in frequency (n) of M'(t) has been proposed in [12], taking into account the resonant structural response associated with the first vibration mode only.

Figure 2b (—) shows the spectrum of the quasi-static part, magnification factor and the global spectrum of M'(t) associated with a mean wind velocity $\bar{V}$=15 m/s.

The 3-day time series of M(t) are simulated considering $\bar{V}$(t) as a sequence of speed values $\bar{V}_i$ on consecutive ΔT time steps and by superimposing the corresponding fluctuating nil mean Gaussian-distributed component M_i'(t). This simple simulation procedure does not provide the continuity of M(t), because a jump occurs at the end of each ΔT step, on which $\bar{V}_i$ remains unchanged. The last step of the procedure correct simulated signal at i-th time inter-

val by considering the bending moment simulated at the end of the previous (i-1)-th, restoring the continuity of the process. Figure 3 shows the result of the above procedure, showing a large and zoomed time window of the simulated bending moment (Fig. 3 a,b) due to given mean wind velocity (Fig. 3 c,d). Considering in particular Fig. 3 b, which zooms the time series displayed in Fig. 3 a at the vertical solid line, the blue dotted line represents the 2-step procedure, highlighting a jump in the time-history in the time step boundary; the red line shows the final 3-step procedure result, with continuity restores.

The spectrum of the resulting $M_i'(t)$ is displayed (•) in Fig. 2 b, revealing a very good agreement with the spectrum analytically predicted (—).

The procedure described above is sequentially applied for simulating 3-day time series of $M(t)$, which rest on consecutive 3-day segments; then the derived response functions are serially concatenated so as to yield a 1-year time history of the bending moment.

For each 1-year time series of the bending moment $M(t)$ at the base of the lighting pole, the relative stress series is easily derived as $s(t) = [M(t)/J]R$, where R=0.14 m is the radius at the base of the pole, J=3.303x10-5 m^4 is the second moment of area of the cross section.

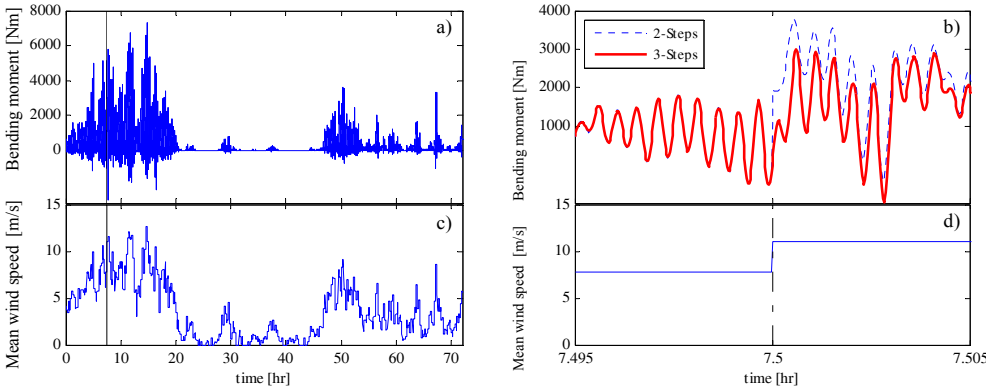


Figure 3: 3-day time histories of the bending moment (a,b) and mean wind velocity (c,d).

3.3 Benchmark solution of wind-induced fatigue damage

The annual cycle histograms is obtained by applying the Rainflow counting method to the synthetic time series of the stresses. Consistently with the previous assumption of a structural correlation time of 3 days, the 1-year time series of $s(t)$ is viewed as a sequence of 3-day segments, which are independently processed by the Rainflow method. In order to consider properly how the mean part of the stress affects the fatigue analysis, the cycles amplitude is transformed into "equivalent amplitude" according with Goodman law [16]. After setting a series of equally spaced intervals of equivalent amplitude, the annual cycle histogram is derived by summing the number of cycles, related to a given class, over all the 3-day segments forming 1 year time series of $s(t)$, i.e. 121 items. The analysis of 3-day continuous segment of $s(t)$ ensures that also the low-frequency cycles are included in the fatigue analysis, and the problem of the transition cycles between consecutive ΔT time steps is avoid. Second, the analysis of multiple segments of $s(t)$, based on 1 year of synthetic wind observations, ensures that the daily, seasonal and annual climatologic features of the local wind climate are taken into account in the fatigue analysis. In light of these remarks, the annual cycle histogram based on the analysis of 3-day segments is viewed as a benchmark, for the current case study, since it involves all the cycles relevant for the fatigue analysis.

For each of the 50, 1-year time-series of s(t) the relative annual cycles histogram is evaluated. The annual damage $D(1)$ relative to the 50, 1-year time-series of $s(t)$ is computed applying the Palmgren-Miner linear accumulation rule to each one of the annual cycles histograms.

Table 1 proves numerically the variability of D(1) reporting the minimum, maximum and mean values, besides the standard deviation (Std) and the coefficient of variation (CoV) of the annual damage.

	Minimum	Maximum	Mean	Std	CoV [%]
D(1)	0.00147	0.10931	0.01353	0.01688	125

Table 1: The annual damage from a sample of 50 years of synthetic stresses.

Note that the difference between the minimum and maximum values of D(1) exceeds 2 order of magnitude, and the CoV is greater than 100%. The high variability of the random variable annual damage makes the mean value a poor estimator. The fatigue lifetime corresponding to the mean value of D(1) is equal T_F=74 years.

4 COMPARISON WITH CLASSICAL TIME-DOMAIN METHOD

The application of the State Approach in time-domain is generally fulfilled by simulating a certain number of 10-min time-histories for each loading conditions. The theoretical number of time-histories for each loading conditions can be obtained by dividing the effective duration time of the i -th loading condition, T_i, by the duration of simulated time history segment, ΔT, usually 10 minutes, and can be expressed by:

$$\Pi_i(1) = \frac{T_i}{\Delta T} = \frac{365 \cdot 24 \cdot 60 \cdot 60}{\Delta T} P_i \tag{4}$$

The extrapolation of the damage associated to a loading condition from a number of simulations lower that the theoretical number expressed in Eq. (4) can induce relevant errors in the results. As an example, Figure 5 shows the normalized damage trajectory based on the sequential analysis of the 10-min simulations associated to some loading conditions for a particular simulated year, adopting a graphical representation already used in [1]. In each plot, the damage obtained from all the 10-min simulations is normalized to one. The sequential count is referred to the average nominal damage, plotted as a function of the number of 10-min records included in the average (black dots in Figure 5), in the order in which they appear in the complete yearly simulation time-history. The upper and lower bounds (red continuous and blue dashed lines in Figure 5) are obtained adding the 10-min records contribution in the order of the damage they contain, sorted in descending order for the upper bound and in ascending order for the lower bound, respectively. For each loading conditions, these trajectories quantify the overestimation and the underestimation of the 10-min simulation containing the largest and the smallest damage, respectively, when used to extrapolate the average yearly damage of the loading condition. Loading conditions at moderate wind velocities are characterized by relatively high probability of occurrence; in this case the theoretical number of 10-min simulation (Eq. 4) is high, thus the single 10 min simulation is poorly representative and the errors in the extrapolation of the mean yearly damage can reach two orders of magnitude. On the contrary, the loading conditions at high wind velocities are characterized by relatively low probability of occurrence; in this case the theoretical number of 10-min simulation (Eq. 5) is low, thus the single 10 min simulation is quite representative and the errors in the extrapolation of the mean yearly decreases to more suitable values.

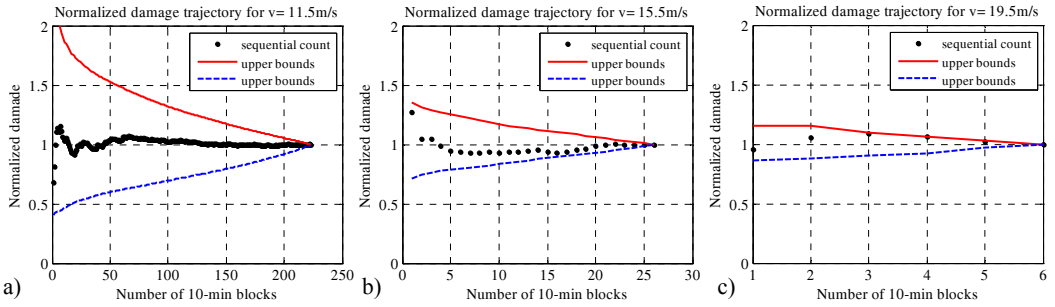


Figure 5: Normalized damage sequence trajectories for loading conditions at $\bar{V}_i$ =11.5 m/s (a), $\bar{V}_i$ =15.5 m/s (b), $\bar{V}_i$ =19.5 m/s (c).

5 COMPARISON WITH FREQUENCY-DOMAIN METHOD

A large number of frequency domain methods has been proposed in literature for fatigue analysis under random excitation. In particular, the author have developed a wide research program on wind-induced fatigue of slender structures, providing a broad band of closed form solutions (CFS) [17]. In general, the mean total damage in the unit time (Eq. (10) can be expressed by:

$$\bar{D}(1) = \bar{D}_0(1) C_{BM} C_{MS} C_{SN} \tag{5}$$

where $\bar{D}_0(1)$ is referred to as the 0 level solution, CBM is the bi-modal factor, CMS is the mean stress factor, and CSN is the fatigue curve factor.

The 0 level solution adopts three classic simplifications traditionally used in the technical literature: 1) the stress process is narrow band; 2) the stress process is zero mean; and, 3) the fatigue curve is a straight line on a log (stress range) – log (number of cycles that cause the collapse) diagram. CBM, CMS and CSN are obtained by removing, independently, the three previous hypotheses and are furnished in different CFS at different level of approximation [17]. A good compromise between simplicity and approximation can be obtained expressing the basic stress parameters as a power law of the mean wind velocity $\bar{V}$ and regressing the exponent of the law by imposing the passage of the function on two points, corresponding to the classical design wind velocity, $\bar{V}_{ref}$, and a 'fatigue' wind velocity , $\bar{V}_{fat}$, representative of the velocity range where fatigue damage is maximum. Such value usually falls into the range 0.35-0.65 $\bar{V}_{ref}$. For the Italian territory $\bar{V}_{fat}$ = 0.5 $\bar{V}_{ref}$ represents a reasonable and simple estimate. The complete results are reported in [17]. In the present example, the following formulation has been applied:

$$\bar{D}_0(1) = \frac{24\pi}{a_1} \nu_{ref} \sigma_{ref}^3 (0,2k - 0,12)^{3\alpha_\sigma} \left(\frac{3\alpha_\sigma}{k} + 1 \right)^{\left(\frac{3\alpha_\sigma}{k} + \frac{1}{2} \right)} \left(\frac{1}{e} \right)^{\left(\frac{3\alpha_\sigma}{k} + 1 \right)} \tag{6}$$

$$C_{BM} = \frac{\nu_{Q,ref}}{\nu_{ref}} + \frac{n_1}{\nu_{ref}} \lambda_{D,ref}^{3/2} (0,2k - 0,12)^{\frac{3\alpha_\lambda}{2}} \left(\frac{3\alpha_\sigma}{k} + 1 \right)^{\frac{3\alpha_\lambda}{2k}} \tag{7}$$

$$C_{MS} = \left[\frac{s_u}{(s_u - \bar{s}_P)} \right]^3 \left[1 + \frac{3\bar{s}_{ref}}{(s_u - \bar{s}_P)} (0,2k - 0,12)^2 \left(\frac{3\alpha_\sigma}{k} + 1 \right)^{\frac{2}{k}} \right] \tag{8}$$

$$C_{SN}=1-exp\left\{-342,25\left(\frac{\sigma_{ref}}{\Delta_C}\right)^{\frac{2k}{\alpha_\sigma}}\left(0,2k-0,12\right)^{2k}\right\} \quad (9$$

$$\kappa\left(\bar{V}\right)=\kappa_{ref}\left(\frac{\bar{V}}{\bar{V}_{ref}}\right)^{\alpha_\kappa};\alpha_\kappa=\frac{1}{ln\left(\bar{V}_{fat}/\bar{V}_{ref}\right)}\cdot ln\left(\frac{\kappa_{fat}}{\kappa_{ref}}\right); \quad (\kappa=\sigma,\lambda D) \quad (10)$$

where Δ_C and a_1 are the S-N fatigue curve parameters of the joint, in particular Δ_C is the detail category, corresponding generally to $N_C = 2x10^6$; and the parameter $a_1=N_C\Delta_C^3$; s_u is the material ultimate stress; $\kappa_{ref}=\kappa(\bar{V}_{ref})$ are the basic stress parameters evaluated at the design wind velocity $\bar{V}_{ref}$, associated with the design return R = 50 years, $\kappa=\sigma, \nu, \nu_Q, \lambda_D$ being, respectively, the standard deviation of the fluctuating stress *s'*, the expected frequency of *s'*, the expected frequency of the quasi static part of the stress, s_Q', the normalized variance of the resonant part the stress s_D'. Eurocode 1 [18] reports complete procedures to evaluate such parameters. Applying the above procedure to the lighting pole, the yearly total damage results $\bar{D}(1)$ =0.013 and the corresponding fatigue lifetime is T_F=77 years. Table 2 summarizes the input parameters involved. Tt is worth noting the very good agreement between the mean yearly damage obtained with the simplified procedure and the numerical benchmark solution obtained in Section 3.

$\bar{V}_{ref}$ (m/s)	σ_{ref}(MPa)	ν_{ref}	$\nu_{Q,ref}$	$\lambda_{D,ref}$	α_σ	α_λ	$\bar{D}_0(1)$	C_{BM}	C_{MS}	C_{SN}
27	27	0.414	0.078	0.55	2.037	0.234	0.024	0.623	1.107	0.785

Table 2: The parameters for analytical yearly damage estimation from Eqs (6)- (10).

6 CONCLUSIONS

The wind-induced fatigue analysis of slender and lightweight structures is a very complex phenomenon, whose complete understanding and awareness in the designers entourage is still inadequate. This paper contribute to the discussion, presenting the results of a research program, still in course, started with the numerical simulation of the whole design structural life time series of the wind-induced stress at the base of a lighting pole. These contain both macro- and micro-meteorological fluctuations, coherent with the parent distribution and the power spectrum of mean wind speed. The stress time series are processed by numerical Rainflow counting algorithm, obtaining the corresponding cycle histograms and yearly fatigue damage. On the basis of the he benchmark mean damage solution, the classical time-domain approach has been discussed, showing that the numerical simulation of short stress time histories for each loading condition can lead to very large uncertainties and the time length of simulations should be related to the probability of occurrence of the loading condition. On the contrary, the benchmark mean damage solution is surprisingly very close to the simplified solution proposed in [17]. Even this results is preliminary, it put in evidence that probabilistic approach can have the potentiality of catching the main features of the wind-induced fatigue phenomenon, giving rise to good results with simplified procedures engineering design oriented.

REFERENCES

[1] H.J. Sutherland, *On the Fatigue analysis of Wind turbines*. SAND99-0089, Sandia National Laboratories, Albuquerque, NM, 1999.

[2] M.P. Repetto, G. Solari, Directional wind-induced fatigue of slender vertical structures. *J. Struct. Eng., ASCE*, **130**(7), 1032-1040, 2004.

[3] P.H. Wirsching, M.C. Light, Fatigue under wide band random stresses. *J. Struct. Div. ASCE*, **106**, 1593–1607, 1980.

[4] G. Jiao, T. Moan, Probabilistic Analysis of Fatigue due to Gaussian Load Processes. *Prob Eng Mech*, **5:2**, 76-83, 1992.

[5] M.P. Repetto, G. Solari, Bimodal alongwind fatigue of structures. *J Struct Eng ASCE*, **132**, 899–908, 2006.

[6] M.P. Repetto, G. Solari, Closed-Form Prediction of the Alongwind-Induced Fatigue of Structures, *J. Struct. Eng. ASCE*, **138**, 1149-1160, 2012.

[7] N.D.Kelley, A.D.Wright, M.L. Buhl, J.L.Tangler, Long-Term Simulation of Turbulence-Induced Loads Using the SNLWIND-3D, FAST2, YAWDYN, and ADAMS Numerical Codes. *16th ASME/AIAA Wind Energy Symposium*, Reno, Nevada, 1997

[8] P.Moriarty, Database for validation of design load extrapolation techniques. *Wind Energy*, **11**, 559-576, 2008.

[9] M.F. Barone, J. Paquette, B. Resort, L. Manuel, Decades of wind turbine load simulation. *50th AIAA Aerospace Sciences Meeting*, Nashville, Tennessee, 2012.

[10] L. Manuel, H.H. Nguyen, M.F. Barone, On the use of a large database of simulated wind turbine loads to aid in assessing design standard provision. *50st AIAA Aerospace Sciences Meeting*, Grapevine, Texas, 2013.

[11] A. Torrielli, M.P. Repetto, G. Solari, Long-term simulations of the mean wind velocity. *J Wind Eng Ind Aerodyn*, **99**, 1139-1150, 2011.

[12] M.P. Repetto, A. Torrielli, Comparison between analytical and simulation-based wind-induced fatigue analyses, *13th International Conference on Wind Engineering (ICWE13)*, Amstrerdam, The Netherlands, 2011.

[13] CNR (Italian National Research Council), *Istruzioni per la valutazione delle azioni e degli effetti del vento sulle costruzioni*. CNR-DT 207/2008, 2008.

[14] Eurocode 3: *Design of steel structures, Part 1-9:Fatigue*. EN 1993-1-9, 2005.

[15] G.Piccardo, G.Solari, 3-D gust effect factor for slender vertical structures. *Prob. Eng. Mech.*, 17, 143-155, 2002.

[16] J. Goodman, *Mechanics applied to engineering*. Longmans Green, London, U.K., 1930.

[17] M.P. Repetto, G. Solari, Closed-Form Prediction of the Alongwind-Induced Fatigue of Structures, J. *Struct. Eng. ASCE*, **138**, 1149-1160, 2012.

[18] Eurocode 1: *Basis of Design and Actions on Structures, Part 2-4:Wind Actions*. ENV 1991-2-4, 1994.

International Conference on Engineering Vibration
Ljubljana, Slovenia, 7-10 September 2015

SHAKER TESTING SIMULATION OF NON-GAUSSIAN RANDOM EXCITATIONS WITH THE FATIGUE DAMAGE SPECTRUM AS A CRITERION OF MISSION SIGNAL SYNTHESIS

Bram Cornelis*[1], **Alexander Steinwolf**[1,2], **Marco Troncossi**[3], **Alessandro Rivola**[3]

[1]Siemens Industry Software NV, Interleuvenlaan 68, B-3001 Leuven, Belgium.
bram.cornelis@siemens.com

[2]AST Consulting Ltd, 14A Croydon Road, New Lynn, 0600 Auckland, New Zealand
astc.info@vodafone.co.nz

[3]University of Bologna, DIN – Department of Engineering for Industry,
via Fontanelle 40, I-47121, Forlì, Italy.
{marco.troncossi, alessandro.rivola}@unibo.it

Keywords: random vibration shaker testing, kurtosis control, accelerated lifetime testing

Abstract. *Experimental simulations of random excitations are nowadays performed digitally by applying the Inverse Fast Fourier Transform (IFFT) to the desired Power Spectral Density (PSD) profile, in combination with randomized IFFT phases. However, the excitations generated in this way will always have a Gaussian probability distribution, whereas real-life random excitations are typically non-Gaussian. For example, in the case of land transportation some distinctive peaks will occur which exceed the average level of vehicle vibration. The statistical parameter known as kurtosis can characterize this feature and could be controlled in experimental simulations in addition to the PSD. The so-called "kurtosis control" can be achieved by special phase manipulation instead of selecting the phases randomly. By increasing the kurtosis, it is furthermore also possible to obtain an accelerated qualification test, whereby the time-to-failure (TTF) is decreased in a controlled manner. It is known that the response of a lightly-damped linear system is closer to Gaussian than the applied excitation. Therefore, in order to increase the response kurtosis in an accelerated test, the kurtosis control method must be able to effectively generate extra kurtosis. In this work a method was used which indeed achieves a high excitation kurtosis, which moreover passes into the response of the structure. According to the Fatigue Damage Spectrum (FDS) model, a single-degree-of-freedom system was hereby considered in order to calculate the structural response. Furthermore, the rainflow counting procedure and the Miner damage accumulation rule were employed to predict relative TTFs for operational excitation and accelerated test mission. Finally, the considered method of non-Gaussian shaker testing simulation was also advanced from kurtosis control to direct application of the FDS as a criterion for mission signal synthesis. An extensive experimental campaign was carried out, where an example of a real-life vibration excitation measured on the cabin floor of a car was considered. Shaker testing was performed for a cantilevered test specimen subjected to various simulated Gaussian, non-Gaussian, accelerated non-Gaussian, and real road excitations.*

1 INTRODUCTION

In applications such as automotive and aerospace engineering, components are exposed to dynamic vibration loads that may induce failures due to (resonant) fatigue phenomena. To validate whether the components will remain operational during the service life, they are subjected to extensive vibration tests on electrodynamic shakers, i.e. so-called qualification tests [1]-[4]. It has become standard practice to develop a qualification test specification based on the actual environmental conditions where the components are deployed, a procedure referred to as "test tailoring" or "mission synthesis" [1]-[3]. The objective is to have damage equivalence between the in-field operational data and the qualification test profile, meaning that the damage accumulated over the operational lifetime of the component has to be recreated in the qualification test. The method therefore tries to match the so-called Fatigue Damage Spectrum (FDS) [3], which quantifies the damage potential of the operational excitations.

When performing qualification tests in the laboratory, it is of particular interest to shorten the required testing time, i.e. to obtain an "accelerated" lifetime test where the total test duration is reduced in a controlled manner [4]. Essentially, the time-to-failure (TTF) of the test has to be decreased while preserving the total accumulated lifetime damage (so that there is still damage equivalence between the in-field operational data and the qualification test). When designing an accelerated lifetime test, a damage model such as a Wöhler curve (S-N curve) is typically assumed [4]. Applied to random vibration excitations specified by a Power Spectral Density (PSD), this results in a simple power scaling law: in order to decrease the duration of the test, the overall PSD level has to be increased [4]. There are however several caveats when using this approach [3]-[6]. If the PSD level is increased, (*i*) the failure mode of the component may no longer be due to fatigue, (*ii*) and/or the structure may start behaving non-linearly whereas a linear system response was assumed. For materials with an endurance limit, (*iii*) previously small non-damaging cycles may suddenly be scaled over the limit, so that the accumulated damage becomes higher than expected. Finally, (*iv*) there is a high sensitivity to the assumed parameters in the fatigue damage model, in particular the slope of the Wöhler curve. For all these reasons, the standards suggest that the "test exaggeration factor" (i.e. the ratio of test PSD level over operational PSD level) should be kept to a minimum [2].

Modern shaker control systems can generate random excitations with any prescribed PSD profile, so that they can be used for the previously described accelerated lifetime testing (with the mentioned caveats). A recent development is so-called "kurtosis control" [7], where the kurtosis (i.e., the fourth order statistical moment) can be controlled in addition to the PSD. Compared to the methods where only the PSD is controlled (implying Gaussian random excitation), the additional control of kurtosis allows for shaker signal simulations which better represent non-Gaussian excitations, with the presence of high peaks, occurring in real-life (e.g. land transportation [8]). Furthermore, there is an increasing interest to combine higher kurtosis generation with accelerated lifetime testing [9]. In such an approach, the test acceleration could be achieved by increasing the kurtosis, while the PSD level can be preserved (hence, avoiding the previously discussed problems associated with increasing the PSD level). However, this is a non-trivial task: it is known that due to the Central Limit Theorem (CLT), the response of a lightly-damped linear system is closer to Gaussian than the original excitation. It has been verified numerically [10] and experimentally [11] that, even though an excitation possesses a higher kurtosis, it may not be sufficient to decrease the TTF compared to a Gaussian signal, namely in case the kurtosis does not transfer through the structural resonances.

This paper considers a kurtosis control method which is effective at generating high kurtosis signals which moreover transfer into a structural resonance. The method is also advanced from kurtosis control to direct application of the FDS as a criterion for mission signal synthe-

sis, so that accelerated lifetime testing (without increasing the PSD level) is enabled. Finally, the method is evaluated through an extensive experimental campaign, where an example of a real-life vibration excitation measured on the cabin floor of a car is considered, and where shaker testing is carried out for a cantilevered test specimen.

The paper is organized as follows. Section 2 reviews qualification testing and in particular the FDS function for assessing the damage potential of signals. Section 3 describes the analytical kurtosis control method which is applied in this work. Section 4 discusses the results of the experimental validation. Finally, Section 5 presents the conclusions of the paper.

2 QUALIFICATION TESTING USING THE FATIGUE DAMAGE SPECTRUM

The main objective of a qualification test is to replicate the "effect" of the operational environments on the tested component, e.g. the accumulated damage due to vibration fatigue phenomena [1]. Instead of calculating or measuring the stress response at the critical locations of the component, typically a working assumption is made whereby a fictitious single-degree-of-freedom (SDOF) reference system with a variable resonance frequency is assumed. The SDOF reference system allows for an assessment and comparison of the different environmental input excitations, independently from the actual component-under-test (similarly to the Shock Response Spectrum, SRS). The damage potential of different input excitations can then be quantified by the so-called Fatigue Damage Spectrum (FDS) function [1][3].

In order to calculate the FDS, first a simulation is made where a given (measured) input acceleration is applied to the base of an SDOF system with an assumed resonance frequency f_n and damping factor ζ, resulting in a relative displacement response [1][3]. The simulated response is subsequently processed by a cycle counting algorithm (e.g. the rainflow counting method [12]). Finally, the fatigue damage can be calculated based on three main assumptions [6]: it is assumed that (*i*) the stress response is proportional to the relative displacement response, (*ii*) the fatigue damage model can be described by a Wöhler curve without endurance limit, and (*iii*) the fatigue damage accumulation follows the Miner [13] linear damage accumulation rule. It should be noted that there are certain assumed normalization constants in the calculation, so that the obtained absolute damage value does not have a true physical meaning (sometimes, the term "pseudo-damage" is used). However, this is not a problem as the objective is only to make relative comparisons of the potential damage induced by different excitations.

The described methodology is typically applied for different assumed resonance frequencies f_n, so that a damage result in function of f_n is obtained ("a spectrum"), i.e. the aforementioned FDS. However, if the reliability of a particular component with known resonance frequency has to be experimentally investigated (e.g. to study possible design improvements), it can alternatively be of importance to only focus on one point of the FDS (i.e. the known resonance frequency), as will be demonstrated in Section 4.

Finally, for the purpose of qualification testing, a random shaker excitation signal can be "synthesized" which matches the FDS calculated for the operational data (so that the qualification test has the same damage potential as the operational data). In the current practice, only Gaussian random excitations (described by the PSD) can be obtained, as an analytical expression which directly relates the FDS to the shaker PSD profile is utilized [1]. An accelerated test is then obtained by reducing the specified time duration (an explicit parameter in the analytical expression), which leads to an increase of the prescribed PSD level (with the associated problems discussed previously). In Section 4, it will be demonstrated how the FDS can be combined with non-Gaussian kurtosis control methods, so that accelerated lifetime testing without increasing the PSD level is enabled.

3 KURTOSIS CONTROL BY ANALYTICAL PHASE SELECTION METHOD

Modern computer systems have made it possible to generate random excitations for shaker testing in random vibration control mode. A common technique is to reconstruct time histories from the prescribed PSD by the Inverse Fast Fourier Transform (IFFT). It means that the shaker is driven by a multi-frequency signal with a large number of harmonics *N*,

$$x(t) = \sum_{n=1}^{N} A_n \sin(2\pi n \Delta f t + \varphi_n) \tag{1}$$

The phase angles φ_n are usually defined as random variables uniformly distributed in the range from $-\pi$ to $+\pi$ radians. The amplitudes of the harmonics A_n are determined according to the PSD shape $S(f)$ discretized with the frequency increment Δf, i.e.

$$A_n = \sqrt{2\Delta f S(n\Delta f)} \tag{2}$$

A shaker excitation obtained in the above way is a pseudo-random signal with a probability distribution close to a Gaussian model, which can describe time history peaks with a height up to 3 root-mean-square (RMS) values of the signal. However, this Gaussian model based on the PSD as a single characteristic becomes insufficient for many real-life environments, e.g. vehicle vibration data [8], where higher peaks can occur (especially for rougher roads and higher vehicle speeds). It means that, along with the PSD, some other characteristics must be involved to describe the non-Gaussian extreme peaks in vehicle vibration data. For this purpose, so-called kurtosis control methods have been developed [7], which in addition to the PSD also control the kurtosis. To simulate higher and more severe non-Gaussian peaks typical of vehicle vibration, the kurtosis parameter of the shaker-generated excitation should be increased with respect to the Gaussian kurtosis value of 3.

For the pseudo-random multi-frequency signal which is given analytically by Eq. (1), there is an opportunity to express the kurtosis via amplitudes A_n and phases φ_n of the multi-frequency signal, and moreover to use this expression for manipulating the amplitudes and phases in order to control kurtosis in addition to the ordinary PSD control. An analytical equation expressing the kurtosis (*K*) via parameters A_n and φ_n was obtained in the following form [14]:

$$\begin{aligned} K = 3 - \frac{3}{2}\Big(\sum_{n=1}^{N} A_n^2\Big)^{-2} \sum_{n=1}^{N} A_n^4 + 2\Big(\sum_{n=1}^{N} A_n^2\Big)^{-2} \Bigg\{ & 6 \sum_{\substack{j+k=m+n \\ j<k,m<n,m<j}} A_j A_k A_m A_n \cos(\varphi_j + \varphi_k - \varphi_m - \varphi_n) \\ & + 6 \sum_{\substack{j+k+m=n \\ j<k<m}} A_j A_k A_m A_n \cos(\varphi_j + \varphi_k + \varphi_m - \varphi_n) + \sum_{j=3k} A_j A_k^3 \cos(\varphi_j - 3\varphi_k) \\ & + 3 \sum_{\substack{j=k+2m \\ k \neq m}} A_j A_k A_m^2 \cos(\varphi_j - \varphi_k - 2\varphi_m) + 3 \sum_{\substack{j+k=2m \\ j<k}} A_j A_k A_m^2 \cos(\varphi_j + \varphi_k - 2\varphi_m) \Bigg\}, \end{aligned} \tag{3}$$

where special conditions must be observed for the sums in the curly brackets. The summation is performed only for those combinations of subscripts *j, k, m, n* that satisfy equalities and inequalities written under the summation symbols.

It is clear from the above equation that the kurtosis can be changed by manipulating the phases, while keeping the amplitudes fixed to preserve the specified PSD. If the argument of a cosine function in Eq. (3) is set to zero by virtue of one of the phases being expressed via the

others, then the corresponding member of the summation is forced into its largest possible value. If a similar phase selection is made not for one subscript group *j, k, m, n* but for many of them and also for other summation terms of Eq. (3), this results in a tendency for kurtosis increase. This is the essence for the kurtosis control method used in this work.

4 EXPERIMENTAL VALIDATION

4.1 Experimental setup

With the aim of experimentally verifying the actual effects of the generated input signals on real mechanical components, a number of tests were performed at the DIN laboratory (Bologna, Italy). A simple specimen was designed for this purpose (cf. Fig. 1): it is a flat specimen with rectangular shape and rectangular section, 165 mm long, 25 mm wide, and 3 mm thick. The material is the Aluminium alloy 6082. The specimen is rigidly mounted with four screws on a stiff fixture in a cantilever configuration and carries an additional mass of about 1.8 kg close to its free end. The specimen presents its first natural frequency (corresponding to a flexural mode shape) at about 12 Hz.

The specimen is excited by imposing a vertical vibratory motion to its base. The input motion is provided by a single-axis electrodynamic shaker (Dongling ES-2-150), controlled at a sampling frequency of 200 Hz and with a resolution of 1024 spectral lines. The software tools used to control the shaker and to acquire the vibratory signals are a number of modules provided by LMS Test.Lab, depending on the kind of input signal that had to be implemented. Four piezoelectric accelerometers (models PCB 353B03 and PCB 333B32) are used to measure (i) the base vertical acceleration, (ii) the mass vertical acceleration, (iii) the mass transversal acceleration, in order to verify the possible excitation of torsional modes, and (iv) the vertical acceleration of a section close to the specimen fixed constrain. In this paper, only the signals measured by the base and mass vertical accelerometers are presented and discussed.

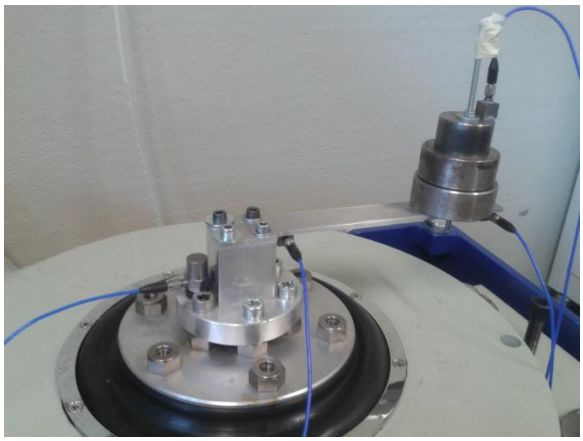


Figure 1: Experimental setup: cantilevered specimen mounted on shaker.

4.2 Methodology

The analytical phase selection method can be incorporated into an automatic closed-loop shaker controller, but in this research it was set up as a manual open-loop iterative procedure to assess all intermediate results. On each iteration, a drive signal for the shaker amplifier input was prepared as a result of analysis of the shaker acceleration feedback signal from the previous iteration. The PSD of the shaker vibration was controlled in the following way.

The height of a certain spectrum line $S_i^{vib}(n\Delta f)$ located at the frequency $f = n\Delta f$ in the feedback signal PSD on i-th iteration may become more (or less) than what it should be according to the test specification $S_{spec}(n\Delta f)$ at this frequency. To compensate for the difference between $S_i^{vib}(n\Delta f)$ and $S_{spec}(n\Delta f)$, the height of the same spectrum line $S_{i+1}^{dr}(n\Delta f)$ in the drive signal PSD on the next (i+1)-th iteration should be decreased (or increased) compared to what it was on the previous iteration $S_i^{dr}(n\Delta f)$. Mathematically this is expressed as

$$S_{i+1}^{dr}(n\Delta f) = S_i^{dr}(n\Delta f)\frac{S_{spec}(n\Delta f)}{S_i^{vib}(n\Delta f)}, \qquad n = 1, 2, 3, \ldots, N. \tag{4}$$

Eq. (4) repeated for each of N spectrum lines gives the full PSD of the drive signal for the next iteration. Then all discrete spectrum values $S_{i+1}^{dr}(n\Delta f)$ obtained are substituted into Eq. (2) for harmonics amplitudes and a new drive signal time history is generated according to Eq. (1). Such iterations are continued until the feedback signal spectrum $S_i^{vib}(n\Delta f)$ is close enough to the specified target profile $S_{spec}(n\Delta f)$ and, thus, the PSD simulation requirement is fulfilled.

This classic technique for simulating random excitations on shakers was developed further [7] to involve kurtosis and to control it in the same iterative manner as the PSD. If the kurtosis value K_i^{dr} of drive signal is increased, the kurtosis of the acceleration feedback K_i^{vib} will follow or vice versa if the kurtosis decrease is needed. Hence the kurtosis can be adjusted similarly to how it was discussed above for the height of a PSD line

$$K_{i+1}^{dr} = K_i^{dr}\frac{K_{spec}}{K_i^{vib}}, \tag{5}$$

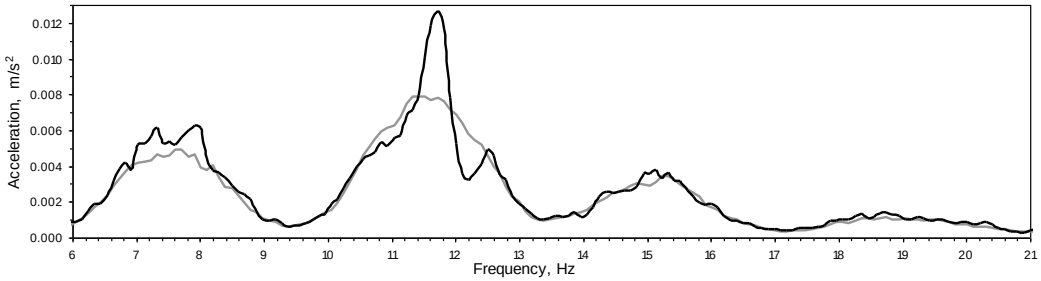
with only one such correction for the entire random signal, not N corrections for every spectrum line.

For comparison purpose, a standard Gaussian random control method, where only the PSD is controlled as in Eq. (4), will also be evaluated in the following section.

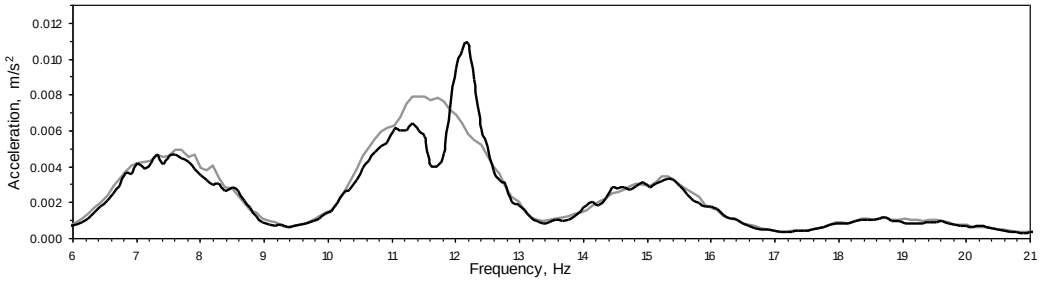
4.3 Results

Experimental results of the described iteration process of simultaneously controlling the PSD and kurtosis of the shaker excitation are shown in Fig. 2, where the gray curve is the target PSD profile of a car vibration recorded on a country road which had the kurtosis value of 5.7. On the first iteration (Fig 2,a), the PSD of the acceleration feedback signal (black curve) was essentially different from the target profile in the vicinity of the second peak (11.5 Hz) of the car vibration PSD, mildly different in the vicinity of the first PSD peak (7.7 Hz), and slightly different at the third PSD peak (15.3 Hz). The shaker vibration kurtosis value $K_1^{vib} = 9.6$ obtained on the first iteration was larger than the target kurtosis $K_{spec} = 5.7$ of the car vibration. It means that the drive signal kurtosis K_2^{dr} for the next (second) iteration should be lower than it was on the first iteration. This K_2^{dr} value was calculated by Eq (5).

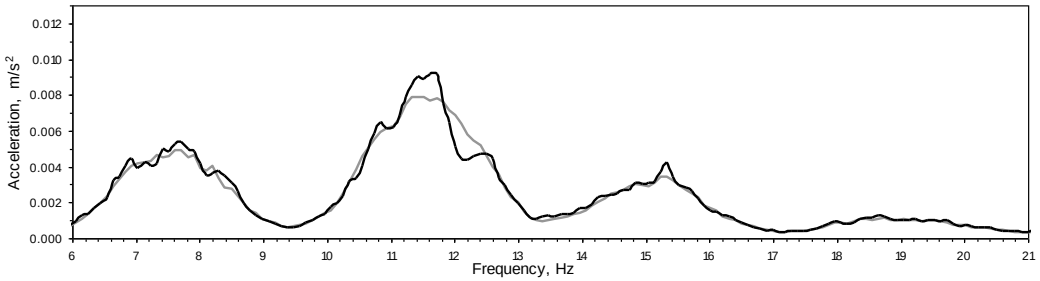
On the second (Fig 2,b) and third (Fig 2,c) iterations, the PSD and kurtosis simulation continued to improve. On the fourth iteration (Fig 2,d), a K_4^{vib}=6.1 value was obtained with the shaker vibration PSD simultaneously achieving a good match with the car vibration PSD. Thus, no further PSD corrections were needed and one more, fifth iteration (not shown), with the same drive signal PSD was carried out in order to refine the kurtosis value only. This resulted in the final kurtosis of K_5^{vib}=5.8.



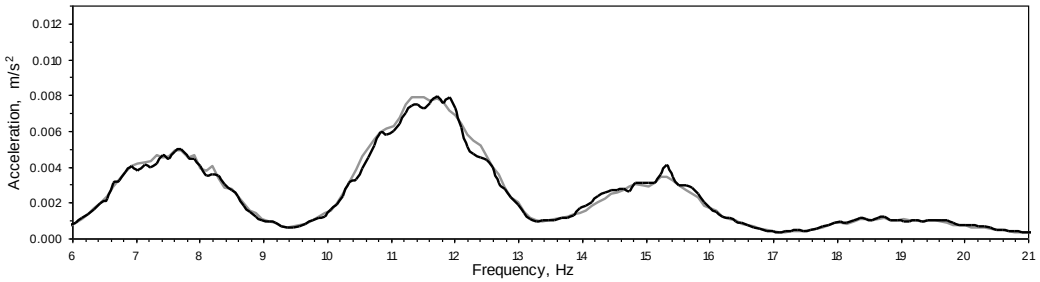
a) First iteration: shaker vibration kurtosis $K_i^{vib} = 9.6$ was much higher than the target kurtosis $K_{spec} = 5.7$



b) Second iteration: shaker vibration kurtosis $K_i^{vib} = 5.2$ was lower than the target kurtosis $K_{spec} = 5.7$



c) Third iteration: shaker vibration kurtosis $K_i^{vib} = 6.3$ was higher than the target kurtosis $K_{spec} = 5.7$



d) Fourth iteration: shaker vibration kurtosis $K_i^{vib} = 6.1$ was slightly higher than the target kurtosis $K_{spec} = 5.7$

Figure 2: PSDs of shaker vibration in random control mode (black curves) with high kurtosis by analytical phase selection method and the target PSD of car vibration recorded on a country road (gray curve).

When the shaker control setup is finished and the shaker vibration acceleration signal is recorded, the FDS can be calculated and its results compared for different methods of simulating environmental excitations. The FDS was calculated assuming a damping factor ζ=2.8% and a Wöhler curve slope b=5.8. These parameters were previously determined for the considered specimens of the experimental setup. In the research reported in this paper, the focus is only on a single point of the FDS curve, i.e. the point being at 12 Hz which is the resonance frequency of the cantilevered specimen mounted on the shaker. The damage values obtained for the two aforementioned methods (Gaussian random and non-Gaussian with kurtosis by the analytical phase selection method) were converted into TTF predictions with these quantities being relative to the TTF predicted for the real-life measured car body vibration example under consideration. The relative TTF results expressed in percentage form are presented in Table 1 alongside with experimental kurtosis values for the shaker vibration and mass responses. These kurtosis values are certainly related to the resulting TTF values for the compared methods: if the kurtosis value of the mass response is higher, it can be expected that more cycles with larger amplitudes will be encountered in the stress time history and, consequently, more severe damage can be inflicted upon the component under test.

It can be seen from Table 1 that, if only standard Gaussian random testing were implemented, the TTF would be more than 6 times longer than the TTF predicted for the real road excitation, thus resulting in a significant undertesting. For the analytical phase selection method, the result presented in the second row of Table 1 is opposite: the relative TTF estimated in this case is 62% of the TTF for the excitation from car vibration. Obviously, this implies an overtesting, whereby the generated shaker vibration imposes the same kurtosis (i.e. 5.7), but inflicts more damage than the road excitation (for which the mass response kurtosis is 6.4). Therefore further action was taken to make the shaker excitation less damaging and to bring the corresponding TTF closer to the TTF estimated for the road excitation.

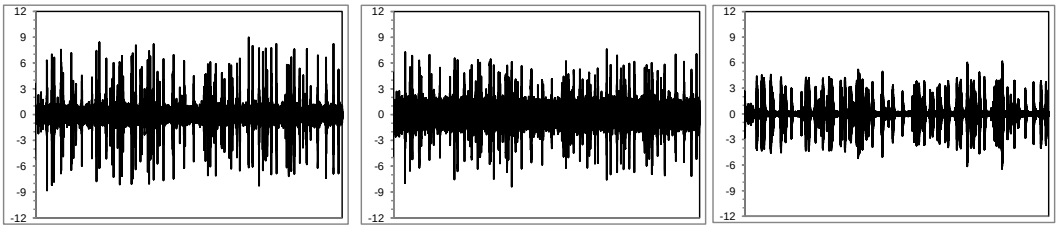
Two more shaker control iterations were performed with the drive signal PSD unchanged and the kurtosis value decreasing. The result is presented in the third row of Table 1. When the shaker vibration kurtosis was reduced to 4, the mass response kurtosis dropped from 7.8 to 6.9, and the TTF value has become equal to the road TTF. This is the requirement for obtaining a fully equivalent qualification test, i.e. where the lab test causes equivalent damage as the road excitation. To achieve accelerated testing, where the TTF is less than the TTF for the road excitation, one needs to return to control iterations again and now select IFFT phases in such a way that the kurtosis of drive signals is again increasing. The analytical phase selection method has the potential of doing so.

The last row of Table 1 contains results of accelerated testing achieved by the analytical phase selection method. More phases were involved in the phase manipulation process and a much higher kurtosis value was needed for the drive signal to increase the shaker vibration kurtosis from K=5.7 (kurtosis of the road excitation), to K=10.1 in order to make the shaker excitation more severe than the road excitation so that an accelerated lifetime test is realized. The mass response kurtosis also increased from K=6.9 to K=9.2. The time histories of all three signals involved are illustrated in Figure 3.

The above results and their discussion demonstrate that the analytical phase selection method is capable of controlling the FDS value and, by doing so, to achieve various TTF values, ranging from a TTF which is equivalent to realistic vehicle vibration with severe non-Gaussian peaks, to a TTF enabling an accelerated lifetime test, whereby the test duration is reduced by a factor 3 (compared to the equivalent testing situation where no test acceleration is applied). However, it should be noted that this research work focused on a single point of the FDS curve, i.e. taking explicitly into account that the specimen has its resonance at 12 Hz.

Random Control Methods	Shaker vibration kurtosis	Mass response kurtosis	TTF relative to road TTF	IFFT phase selection
Standard Gaussian random testing	3.0	3.0	630%	no phase manipulation, all phases are random
Analytical phase selection to get shaker excitation kurtosis equal to that of car vibration on the road	5.7	7.8	62%	phases from 8.3 to 14 Hz are manipulated but other phases remain random
Equivalent shaker testing by analytical phase selection to generate high-kurtosis shaker excitation leading to TTF equal to TTF for the road excitation	4.0	6.9	100%	phases from 9.6 to 12.5 Hz are manipulated but other phases remain random
Accelerated shaker testing by analytical phase selection to generate high-kurtosis shaker excitation leading to TTF less than the road excitation TTF	10.1	9.2	36%	phases from 5.8 to 13.4 Hz are manipulated but other phases remain random

Table 1: Results of shaker testing for car vibration with PSD specified in frequency interval from 5 to 45 Hz.



a) Drive signal (K=19) b) Shaker vibration (K=10.1) c) Mass response (K=9.2)

Figure 3: Excitation and response signals in accelerated testing by the analytical phase selection method with the TTF for shaker excitation estimated to be 36% of the TTF for road excitation.

Normally the FDS assessment is a curve drawn over a certain frequency interval, cf. Figure 4. This curve was calculated for the shaker excitation time history shown in Fig 3,b for the frequency interval from 5.8 to 13.4 Hz, where the IFFT phases of the input drive signal were manipulated by the analytical phase selection method in order to achieve the relative TTF of 36% at the frequency of 12 Hz (cf. Table 1). As can be seen from Figure 4, accelerated testing was also ensured for most of the other frequencies in the considered interval. However, in the vicinity of 8 Hz, the estimated TTF for the shaker excitation appears to be longer than for the road excitation. Further work of the authors is underway now in order to investigate whether it is possible to control the complete shape of the FDS curve, in similar way as the complete PSD shape is controlled in modern shaker controllers.

5 CONCLUSION

This paper presented a kurtosis control method which enables qualification testing using damage equivalent non-Gaussian random vibration excitations. It is moreover possible to achieve an accelerated lifetime test, where the time-to-failure at a particular resonance frequency is decreased in a controlled manner, by increasing the kurtosis while the PSD level is preserved. In order to assess the damage potential of the various excitations, the Fatigue Damage Spectrum (FDS) was employed. The phase selection method has been assessed by an extensive experimental campaign. The work paves the way to advance kurtosis control methods towards direct application of the FDS as a criterion for mission signal synthesis.

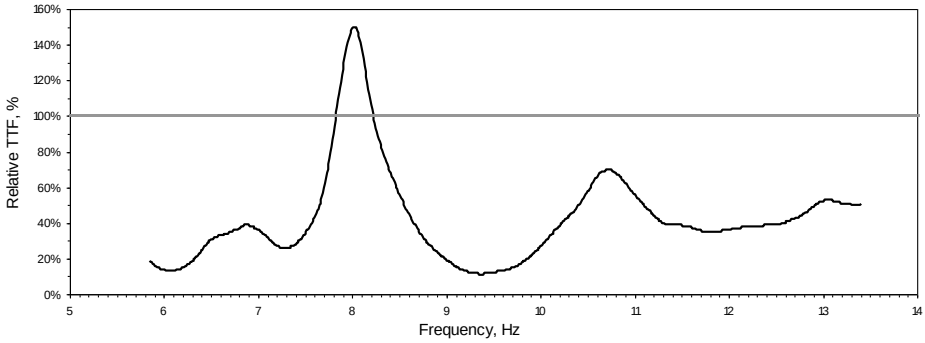


Figure 4: TTF for accelerated testing by analytical phase selection, relative to TTF for the road excitation.

ACKNOWLEDGEMENT

This research was supported by a Marie Curie International Incoming Fellowship (Project N° 328961 "RANGE") within the 7th European Community Framework Programme.

REFERENCES

[1] Y.-L. Lee, H.-T. Kang, "Vibration Fatigue Testing and Analysis", Ch. 9 in Y.-L. Lee, M.E. Barkey, H.-T. Kang, Eds., *Metal Fatigue Analysis Handbook: Practical Problem-Solving Techniques for Computer-Aided Engineering*, Waltham, MA, USA, Butterworth-Heinemann/Elsevier, (2011).

[2] US Department of Defense, *MIL-STD-810G*, Department of Defense Test Method Standard for Environmental Engineering Considerations and Laboratory Tests, (2008).

[3] C. Lalanne, *Mechanical Vibration and Shock Analysis – Volume 5: Specification Development*, 3rd edition, John Wiley & Sons, Inc - ISTE, London, (2014).

[4] A.G. Piersol, "Accelerated Vibration Testing-Proceed With Caution", *Tustin Training News* (1993).

[5] G. M. Hieber, "Use and Abuse of Test Time Exaggeration Factors", *TEST Engineering and Management*, pp. 14-16, Apr/May, (1999).

[6] M. Troncossi, R. Cipollini, A. Rivola, "Experimental Evaluation of the FDS-based Equivalence Approach for the Mission Synthesis in Accelerated Life Tests", *Proc. International Conference on Sound & Vibration (ICSV)*, Bangkok (Thailand), Jul. 7-11, (2013), ISBN: 978-618-551-682-2, ISSN: 2329-3675.

[7] A. Steinwolf, "Vibration testing of vehicle components by random excitations with increased kurtosis", *Int. Journal of Vehicle Noise and Vibration*, 11 (1), 39-66, (2015).

[8] D. Charles, "Derivation of environment descriptions and test severities from measured road transportation data", *Environmental Engineering*, 5 (4), 28-30, (1992).

[9] J. Minderhoud, P. Van Baren, "Using Kurtosion® to Accelerate Structural Life Testing", *Sound and Vibration* 44.10: 8, (2010).

[10] S.A. Rizzi, A. Przekop, T.L. Turner, "On the response of a nonlinear structure to high kurtosis non-Gaussian random loadings", *Proc. 8th International Conference on Structural Dynamics (EURODYN)*, Leuven (Belgium), Paper 41, July 4-6, (2011).

[11] M. Troncossi, A. Rivola, "Response analysis of specimens excited with non-Gaussian acceleration profiles", *Proc. 26th Int. Conf. Noise and Vibration Engineering - ISMA2014*, Leuven (Belgium), pp. 799-808, September 15-17, (2014).

[12] M. Matsuishi, T. Endo, "Fatigue of metals subjected to varying stress", *Japan Society of Mechanical Engineers*, Fukuoka, Japan, (1968).

[13] M.A. Miner, "Cumulative Damage in Fatigue", *J. Applied Mechanics*, Vol. 67, A159-A164, (1945).

[14] A. Steinwolf, "Approximation and simulation of probability distributions with a variable kurtosis value", *Computational Statistics and Data Analysis*, 21 (2), 163-180, (1996).

11th International Conference on Engineering Vibration
Ljubljana, Slovenia, 7–10 September 2015

FULL FIELD EXPERIMENTAL MODELLING IN SPECTRAL APPROACHES TO FATIGUE PREDICTIONS

Alessandro Zanarini[1,2]

[1]University of Bologna, DIN - Industrial Engineering Dept., Italy
a.zanarini@unibo.it

[2]Vienna University of Technology, Institute of Mechanics & Mechatronics, Austria
alessandro.zanarini@tuwien.ac.at

Keywords: Full field vibration measurements, Frequency Response Functions, Optical metrology, experimental dynamic strain & stress maps, spectral methods in fatigue life assessment.

Abstract. *Experimental techniques based on optical dynamic measurements with high spatial definition proved to be able to model dynamic strain maps on the surface of components by means of corresponding strain frequency response functions. By means of a constitutive model, dynamic stress FRFs can be modelled directly from receptance estimations, avoiding the costly & time-consuming steps of building and tuning a numerical dynamic model of a flexible component or a structure in real life conditions. Once dynamic stress FRFs are obtained, spectral fatigue approaches can predict the life of a component in different excitation conditions.*

In this paper high quality receptance maps from three different full field technologies (SLDV, Hi-Speed DIC and dynamic ESPI), estimated on a thin plate as light-weight structure with broad band dynamics and high modal density in a unique comparative set-up, are used to obtain the dynamic stress FRFs. Different spectral shaping of the excitation can be used to enhance the comparison in the framework of the spectral approaches for fatigue life calculations.

The fatigue life predictions from the three optical measuring techniques are compared and discussed in detail, highlighting benefits and drawbacks of a direct experimental approach to failure & risk assessment in structural dynamics.

1 INTRODUCTION

One possible path in advancing failure analysis is to raise the quality of the numerical models by means of better assumptions in the formulation of the elements, a close geometrical relationship with the actual component (as really manufactured, not only on drawings), by means of extensive material tests and overall model updating, to tune the numerical model on the structural dynamics responses, such as displacement, velocity or acceleration measurements in many points of the structure, plus the awaited rotations[1, 2], as the answer to a dynamic event. But, faulty, too many times the model updating stage is easily forgotten or strongly simplified for the costs, leaving an unpredictable and unreliable numerical model to forecast the behaviour of an unreal structure, even when the model is complex and with millions of degrees of freedom, albeit very expensive as computational cost. Even if the model updating stage is performed (leaving anyway a discrepancy with reality), again the lumped sensor placement is not completely answered, because is inherent with the whole dynamics under investigation and the choice of sensor type. Problems like effective sensor placement, spatial averaging, mass burden and lumped measurements could affect conventional techniques like strain gauge arrays. Multi-modal and multi-axis dynamics might be not adequately described by a limited number of sensors placed using brittle lacquer coatings or without an accurate dynamic analysis. Did we use the right sensor in the best position? Can that location be optimal for any kind of sensor and in the whole frequency range of interest?

Even using virtual models, fatigue analysis might be a non-trivial effort: model updating requires precise tests when the inherent structural dynamics and boundary constraints display high modal density with complex displacement patterns and strain fields. This paper explores the suitability of full field experimental impedance models for fatigue life prediction considering the whole structural dynamics of the specimen under real test, extending previous research work [3, 4] taking into account the dynamic contribution at every frequency line of the domain. With the derivation approach applied in [1, 2] and with material appropriate constitutive laws, strain & stress fields can be numerically obtained at each frequency line from any full field optical technique, without the aid of numerical structural models, and taking into account real experiment-related boundary conditions and constraints. Dirlik spectral method [5] is applied for high cycle fatigue cumulative damage calculation, together with appropriate $S - N$ curves for material and power spectral density of Von Mises equivalent stresses at every measurement point. Time-to-failure of the test specimen is thus mapped in each measuring location by means of different combination of coloured noise, leading to an experiment-based fatigue life assessment procedure. The whole approach is reported in detail by means of the measurements acquired on an aluminium rectangular plate, as fully described in [1, 6].

2 NOMENCLATURE

$\boldsymbol{\varepsilon}(x, y)$ strain tensor map
$\boldsymbol{\sigma}(x, y)$ stress tensor map
E, ν elastic modulus, Poisson ratio
G, Λ shear modulus, Lamé constant
K_r, b fatigue strength coefficient and exponent
$S_r(\omega, x, y)$ map of stress cycle ranges at frequency ω
$S_{eq}(x, y)$ map of equivalent range of broad band stress cycles

3 DYNAMIC STRAIN-STRESS FIELDS FROM OPTICAL MEASUREMENTS

The great amount of experimental degrees-of-freedom (dofs) typical of full-field techniques for vibration patterns reduces the uncertainty in choosing the best sensor locations, in the presence of complex-shaped multi-modal displacement patterns and experimental boundaries, simply by dramatically increasing the spatial sampling in respect to more traditional equipment. Further, conventional instruments like strain gauges, due to their physical dimension and set-up complexity, give an intrinsic local-area averaging effect, which is reduced by optical high resolution gear. But of major concerns is the possibility to have a precise description of the sample dynamics, without any simplification, since complex-shaped patterns are complex-valued measurable at extremely high frequencies, with high spatial description, as obtained in [6, 2], from which the experimental results are processed.

3.1 Stress fields

$\boldsymbol{\sigma}$-tensor can be evaluated in every point from the experimental $\boldsymbol{\varepsilon}$-tensor using proper constitutive model. A linear elastic and low-strain/high-cycle fatigue behaviour of the material is expected in the following applications. The material is assumed isotropic, but would not be a problem for the measuring systems if anisotropic (but different constitutive models have to be taken into consideration). The experimental full-field *impedance* model can extend the simulations, in the assumption of linear behaviour, also to higher response ranges and many different exciting spectra.

3.1.1 Constitutive model

A linear isotropic constitutive model is outlined as the complex-valued tensor expression of Hooke's law. The complex-valued principal strains and stresses can be then easily evaluated, together with their principal directions. The material parameters in Eq.1 are: *E*, elastic modulus; ν, Poisson ratio; *G*, shear modulus; Λ, Lamé constant.

$$\begin{aligned} \sigma_\omega(x,y)_{ii} &= 2G\varepsilon_\omega(x,y)_{ii} + \Lambda\left(\varepsilon_\omega(x,y)_{xx} + \varepsilon_\omega(x,y)_{yy}\right),\ \sigma_\omega(x,y)_{ij} = 2G\varepsilon_\omega(x,y)_{ij}, \\ G &= E/2\left(1+\nu\right),\ \Lambda = E\nu/\left(\left(1+\nu\right)\left(1-2\nu\right)\right) \end{aligned} \tag{1}$$

3.1.2 Failure criteria for multi-axis equivalence

An equivalence criteria has to be formulated to compare the multi-axis loading conditions of real samples with results from mono-axial loading fatigue tests on materials [7]. A general comprehensive theory is awaited[8] to relate fatigue limits among different stress states.

In each (x, y) location of the maps complex-valued Von Mises equivalent stresses are evaluated. A completely reversed-stress is expected from single frequency forced-vibration tests and no mean stress effect is taken into account here. Full field measurements become an alternative to the assumption of stress concentration factors: thus they might be seen as a means to reduce uncertainty in life assessment, through better estimates of the values and locations of complex-valued strain&stress in multi-axis loading sequences.

4 CUMULATIVE DAMAGE IN FATIGUE LIFE ASSESSMENT

In long-life up to giga-cycle (10^6-10^9 cycles) fatigue, low stress-strain is expected and elastic behaviour of material is assumed: stress-based Stress-Number-of-cycles ($S-N$) curves are widely used. Long-life fatigue tests are time-demanding experiments and ask for accelerated

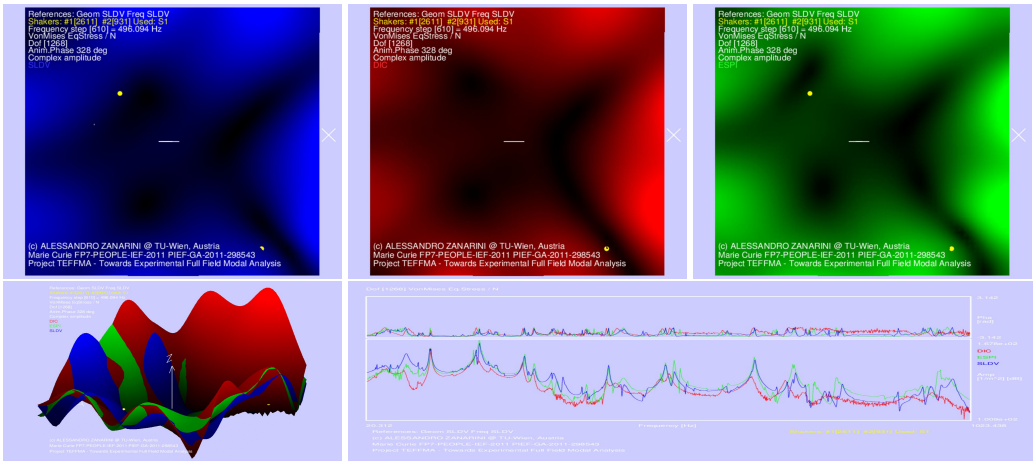


Figure 1: Comparison of VonMises equivalent stress FRF maps at 496Hz, of single functions at dof 1268 in the whole frequency domain from SLDV, DIC and ESPI, excitation from shaker 1

tests: an example of the researches carried on this latter aspect is given in [7], where a very fast vibration-based fatigue testing procedure is proposed, exploiting the designed sample&test-rig in a forced vibration-based fatiguing procedure, to achieve a basic understanding of the effects of frequency shifts due to crack growth and stop, bi-axial stress state and stress gradient in bending.

Though many damage models have been developed, none of them enjoys universal acceptance [9] because many specific aspects need consideration, as can be found in the specialised literature. Consequently, the basic Palmgren-Miner linear damage rule is still dominantly used in design, in spite of its major shortcomings (absence of loading interaction, sequencing and memory effects, failure with a wide range of the total damage).

This paper does not pretend to illustrate new fatigue models; it shows instead a promising evolution of accepted procedures towards the use of full-field measurements, pointing to obtain the prediction without selecting *a priori* the location of the sensors on the surface under

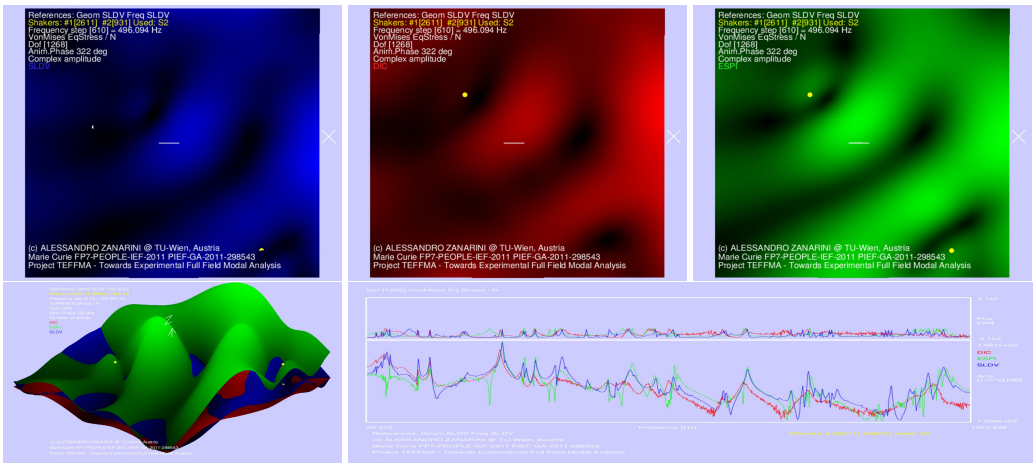


Figure 2: Comparison of VonMises equivalent stress FRF maps at 496Hz, of single functions at dof 1268 in the whole frequency domain from SLDV, DIC and ESPI, excitation from shaker 2

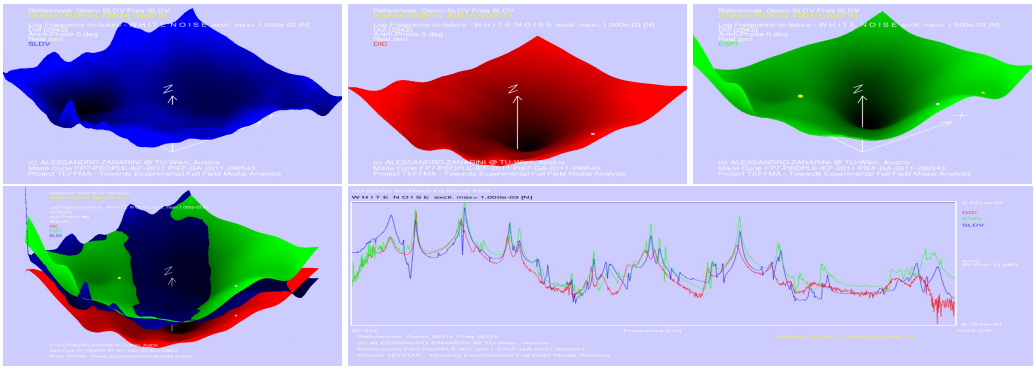


Figure 3: Comparison of failure frequencies maps, of single VonMises equivalent stress PSD at dof 2542 in the whole frequency domain from SLDV, DIC and ESPI, white noise excitation from shaker 1

analysis and without simplifying the dynamic behaviour of the sample, even in high-frequency ranges where complex-shaped patterns are expected due to high modal superposition. The procedure here outlined aims at considering a precise experimental characterization of the spatial and frequency domains in the structural dynamics of the components under test. This paper then follows the approach proposed by ESDU [10, 11, 5] in low-stress / high-cycles random loading for isotropic metal alloys, extending the evaluations over a high number of experimental measurement points. Furthermore, full field measurement-based predictions can be extracted exploiting also other fatigue assessment approaches.

4.1 *S - N* curves in high-cycles fatigue

The experimental $S-N$ curves (from reversed bending or acoustic excitation testing on standard isotropic metal samples) can be modelled as Basquin's exponential law, once the material specific parameters (fatigue strength coefficient K_r and exponent b) are least-squared identified in a log-log plot of number-of-cycles-to-failure N and stress cycle range S_r [5]. Here no environmental effect is considered in $S-N$ curves, and it must be underlined that full field measurement-based fatigue estimations might be suited for most finishing pattern. Further, neither stress concentration nor size factors have to be considered when exploiting high resolution optical-based maps, because just measuring the whole field. Part of the design of the experi-

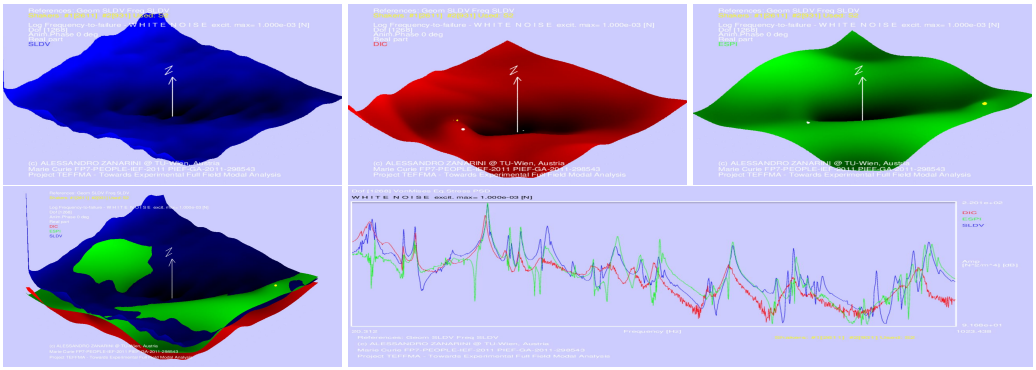


Figure 4: Comparison of failure frequencies maps, of single VonMises equivalent stress PSD at dof 1268 in the whole frequency domain from SLDV, DIC and ESPI, white noise excitation from shaker 2

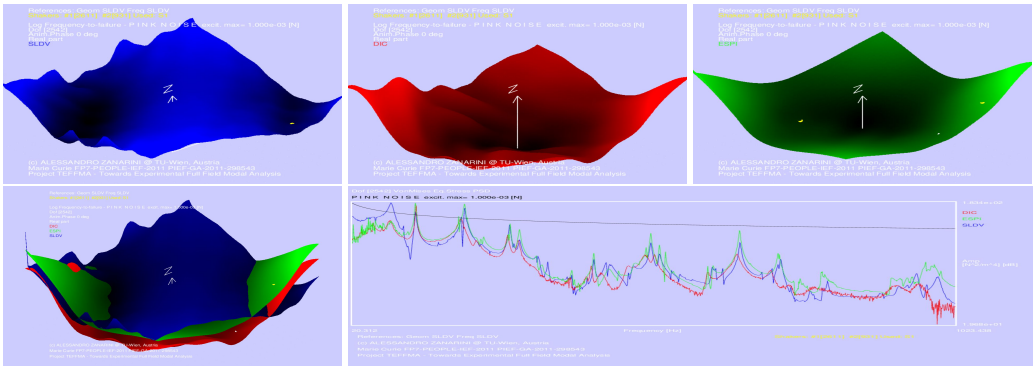


Figure 5: Comparison of failure frequencies maps, of single VonMises equivalent stress PSD at dof 2542 in the whole frequency domain from SLDV, DIC and ESPI, pink noise excitation from shaker 1

ment that normally becomes an important part of fatigue testing could be already addressed by full field optical testing, with its intrinsic high spatial resolution and no need of *a priori* sensor placement evaluations. Nevertheless, testing more similar samples can increase the statistical awareness of the experiment based methodology here proposed.

Having obtained from full field calculations a spatial distribution of Von Mises equivalent stress cycle ranges $S_r(\omega, x, y)$ as in Figures 1-2, also the number of cycles to failure becomes function of the location as $N(\omega, x, y)$:

$$N(\omega, x, y) S_r^b(\omega, x, y) = K_r \tag{2}$$

4.2 Spectral cumulative damage methods

A strong simplification of the dynamic behaviour is often imposed in cumulative damage calculations by means of either neglecting the damage associated with the higher frequency modes of stress response, or by means of assuming that the damage of the lowest resonance frequency f_n has an *rms*-value based on the whole broad band process [5]. Instead, the full field experiment-based approach aims here at avoiding any simplification of the structural behaviour, taking into account the multi-axial dynamics especially at higher frequencies by means of the broad collection of experiment-based results.

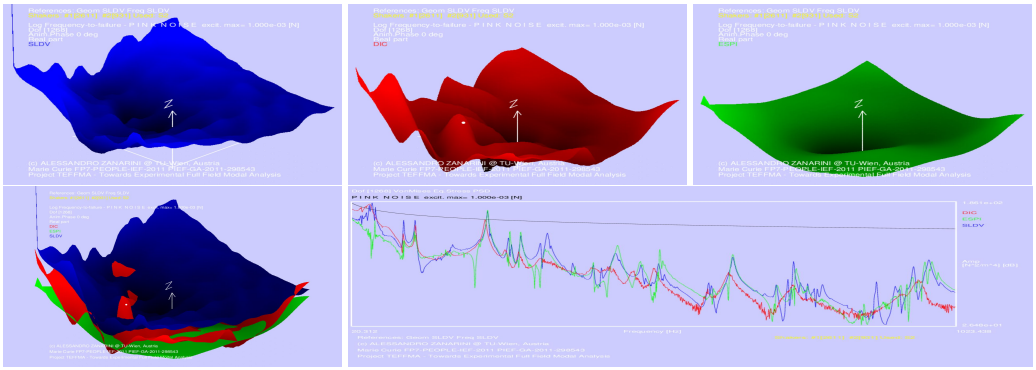


Figure 6: Comparison of failure frequencies maps, of single VonMises equivalent stress PSD at dof 1268 in the whole frequency domain from SLDV, DIC and ESPI, pink noise excitation from shaker 2

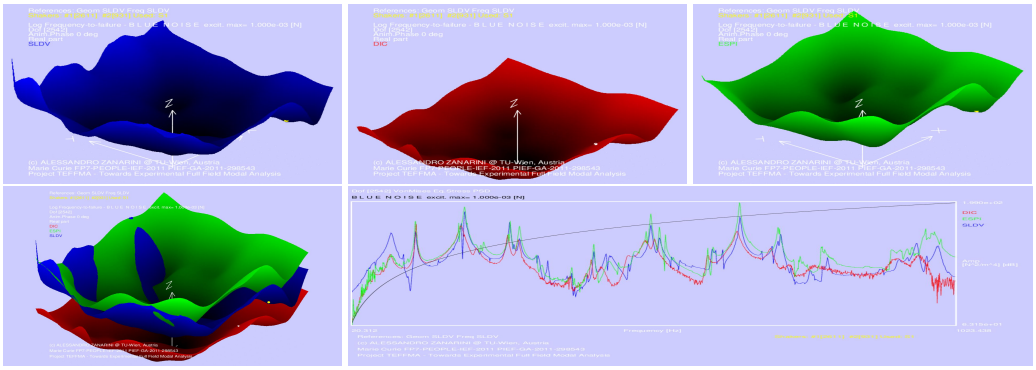


Figure 7: Comparison of failure frequencies maps, of single VonMises equivalent stress PSD at dof 2542 in the whole frequency domain from SLDV, DIC and ESPI, blue noise excitation from shaker 1

In this paper procedure, no time-domain approach is adopted. Instead spectral cumulative damage methods [10, 11, 5] are applied to evaluate an equivalent range of stress cycles $S_{eq}(x,y)$ representative of the damage inferred by the whole spectrum of the retained dynamics. Spectral methods were developed as early as the 1980s for high-cycles domain to accelerate the testing, exploiting the growing FFT analysers, signal processing techniques and the analogy with rain-flow cycle counting and statistical parameters in time domain. They assume the stress ranges as ergodic random, stationary and Gaussian processes. Being $p(S_r(\omega,x,y))$ the probability density function (pdf) of $S_r(\omega,x,y)$, adopting the proper $S-N$ curve, the total damage $D(x,y)$ accumulated in $N_{eq}(x,y)$ equivalent cycles of broad band spectrum loading becomes:

$$D(x,y) = \frac{N_{eq}(x,y)}{K_r} S^b_{eq}(x,y) = \frac{N_{eq}(x,y)}{K_r} \int_0^\infty S^b_r(\omega,x,y) p\left(S_r(\omega,x,y)\right) dS_r(\omega,x,y) \quad (3)$$

4.2.1 Spectral method parameters

From [5] follows the description of the parameters of the spectral methods to obtain the equivalent range of stress cycles $S_{eq}(x,y)$ in Eq.3. In a full field experiment-based procedure the parameters need to be considered as maps, but here the suffix (x,y) is omitted for space limitations. The spectral methods are based on k-th order moments $m_k = \int_0^\infty f^k PSD_{VM}(\omega) d\omega$ of

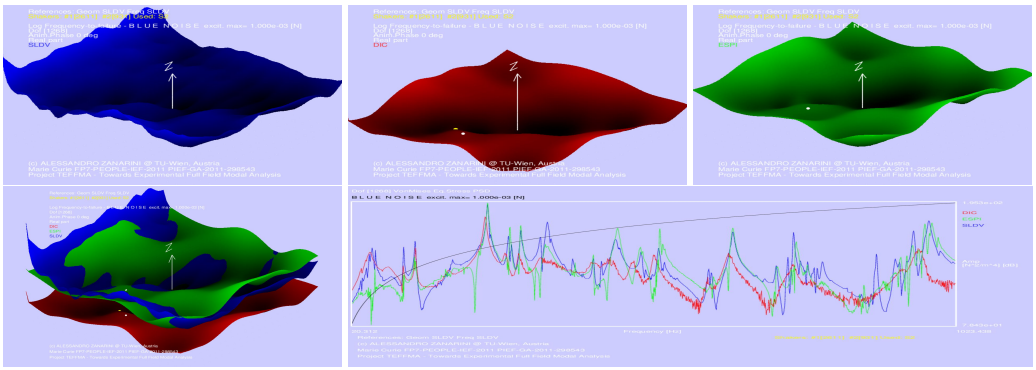


Figure 8: Comparison of failure frequencies maps, of single VonMises equivalent stress PSD at dof 1268 in the whole frequency domain from SLDV, DIC and ESPI, blue noise excitation from shaker 2

the frequency by the power spectral density (PSD) of the Von Mises equivalent stress $PSD_{VM}(\omega)$; on characteristic frequencies $F_k = (m_k/m_0)^{1/k}$; and on a whole class of bandwidth parameters $\gamma_k = m_k/\left(m_0 m_{2k}\right)^{1/2}$ to describe the distribution of the stationary and Gaussian processes. For what follows, some more specific expressions are evaluated:

effective frequency: $F_{zerocrossing} = F_{zc} = \sqrt{m_2/m_0}$

expected number of peaks per unit time: $F_{peaks} = F_p = \sqrt{m_4/m_2}$

irregularity factor: $\gamma = \gamma_2 = F_{zc}/F_p = m_2/\sqrt{m_0 m_4}$

Underlining that full field techniques can be exploited by any cumulative damage model, in this paper is adopted the Dirlik method, as suggested in [5], where Dirlik semi-empirical spectral method is regarded as giving the best prediction of the fatigue life, especially for wide band spectra of stress responses. Below is reported the formulation:

$$\begin{array}{l} \chi_m = (m_1/m_0)\,(m_2/m_4)^{1/2}\,, D_1 = 2\,(\chi_m - \gamma^2)\,/\,(1+\gamma^2) \\ R = (\gamma - \chi_m - D_1^2)\,/\,(1-\gamma-D_1+D_1^2)\,, D_2 = (1-\gamma-D_1+D_1^2)\,/\,(1-R) \\ D_3 = 1 - D_1 - D_2, Q = 1.25\,(\gamma - D_3 - D_2 R)\,/D_1 \\ S_{eq}^b = D_1(2\sqrt{m_0}Q)^b\Gamma(b+1) + (2^{3/2}\sqrt{m_0})^b\Gamma(1+b/2)[D_2 R^b + D_3] \end{array} \tag{4}$$

Finally the time-to-failure distribution is given by:

$$T_{failure}(x,y) = K_r/\big(F_p(x,y)S_{eq}^b(x,y)\big) \tag{5}$$

5 CUMULATIVE FATIGUE CALCULATION ON A PLATE WITH COLOURED NOISE EXCITATION

The constitutive model and $S-N$ curve parameters were taken from the Aluminium 7075T6 properties [5]: E= 7.0e+10 Pa, ν=0.33, b=4.81, K_r=4.4200e+43 Pa^b.

The definition of $PSD_{VM}(\omega)$ takes into account the complex-valued nature of VonMises equivalent stress and the spectra of the input shaping selected as coloured noise, as can be seen in the single functions of Figures 3-8. Dirlik semi-empirical spectral method can be thus followed as in Eq.4, and the map of time-to-failure is obtained as in Eq.5 for each excitation considered. Table 1 gives some parameters regarding evaluated life distributions; the calculations were run on the *receptance* FRF and impedance strain model maps calculated in [6, 2], to assess the fatigue life of the component as subjected to an input force with coloured noise spectrum of 0.001 N maximum amplitude. The location of the calculated failing points (corresponding to the minimum time-to-failure or maximal frequency-to-failure) was always on the corners of the plate, followed by the borders, as might have been expected. Nevertheless the distributions of critical locations inside the area, and Table 1 results, demonstrate to be deeply linked with the dynamic behaviour retained in the elaborated data, in terms of emphasised spectral part and excitation point, as shown in Figures 3-8 by sketching the frequency-to-failure distribution as the inverse of Eq.5, in a logarithmic scale (the brighter is the colour or higher is the point, the shorter is the time-to-failure or higher is the damage reached in the corresponding point).

There is tough a marked dependency on the full field technology adopted to extract the *receptances*, not only in terms of extrema, but also in terms of simulated distribution of damage: the scattering of SLDV maps and some artefacts of DIC, highlighted in [1, 6, 2] increase the uncertainty of the predictions; ESPI, with its superior continuity in spatial domain, released much smoother cumulated damage surfaces. Besides, any input spectra, e.g. standardized flight loads, can be simulated by means of the *receptance* FRF and VonMises equivalent stress impedance model, within the linearity assumption.

Shaker	Noise color	Technology	Min	[dof]	Max	[dof]	Mean
S1	WHITE	SLDV	9.632730e+04	1	8.437879e+08	699	1.469646e+08
S2	WHITE	SLDV	3.937123e+03	1	1.574594e+09	1452	1.637552e+08
S1	PINK	SLDV	2.949305e+09	1	5.461020e+12	756	8.577066e+11
S2	PINK	SLDV	3.765489e+06	1	1.154861e+13	1277	5.104718e+11
S1	BLUE	SLDV	2.759115e+08	1	1.672918e+12	1687	1.676004e+11
S2	BLUE	SLDV	1.158575e+08	1	5.424645e+11	2325	7.487253e+10
S1	WHITE	DIC	2.260433e+07	2907	2.004491e+11	1569	5.798740e+09
S2	WHITE	DIC	3.722684e+07	58	6.895290e+10	1456	3.583005e+09
S1	PINK	DIC	1.623319e+10	2907	4.470353e+14	1626	2.680125e+13
S2	PINK	DIC	3.477011e+09	1	1.044501e+15	1276	1.520427e+13
S1	BLUE	DIC	6.670324e+10	2851	5.701700e+13	1513	4.604659e+12
S2	BLUE	DIC	1.207647e+11	1	1.127806e+13	1803	1.812633e+12
S1	WHITE	ESPI	5.715910e+05	58	4.797944e+09	1399	2.560428e+08
S2	WHITE	ESPI	1.717253e+07	28	4.614659e+09	1222	3.526391e+08
S1	PINK	ESPI	4.030778e+09	2907	1.380882e+13	1286	2.509488e+12
S2	PINK	ESPI	4.565073e+10	58	6.900680e+14	1222	1.687894e+13
S1	BLUE	ESPI	4.253744e+08	2851	8.853231e+11	1455	5.787530e+10
S2	BLUE	ESPI	3.791790e+09	2878	3.166121e+11	1574	5.312801e+10

Table 1: Evaluated time-to-failure distribution [hours] as function of excitation & measurement technology.

6 CONCLUSIONS

This paper has extended what proposed already in [3, 4] showing a promising experiment-based procedure to assess the fatigue life on a component, by means of full field optical measurements obtained from different gears. By applying numerical differentiation, material constitutive laws and a cumulative damage model, the time/frequency-to-failure distribution of the component under test was evaluated without the need of any analytical/numerical structural model. Further, the experiments were performed by non-contact full-field optical techniques on a lightweight structure, freeing the researcher from any *a priori* identification of the best location of the sensors. This latter aspect might become of uttermost importance in dealing with detailed multi-modal behaviour with complex-shaped patterns in the whole frequency domain of interest. The evaluation of detailed experimental *receptance* FRF maps becomes a promising approach to simulate fatigue life as function of the varying input spectra, excitation point and measurement technology, without the aid of structural or virtual models, when measurement uncertainty is under control. Certainly, verification of life estimates should be considered an important activity to confirm the calculations of this experiment-based approach.

Acknowledgements

This activity is part of the Project TEFFMA - Towards Experimental Full Field Modal Analysis, funded by the European Commission at the Technische Universitaet Wien, through the Marie Curie FP7-PEOPLE-IEF-2011 PIEF-GA-2011-298543 grant, for which the Research Executive Agency is greatly acknowledged. This work is intended to be part of the spreading of the results thereof. Vienna University of Technology, in the person of Prof. Wassermann and his staff, are kindly acknowledged for hosting the TEFFMA project of the author at the *Schwingungs- und Strukturanalyse* / Optical Vibration Measurement Laboratory. Dantecdynamics GmbH (Ulm, Germany) is also acknowledged for the precious technical support given for DIC and ESPI equipment used in the project.

REFERENCES

[1] Zanarini, A., 2014. *On the estimation of frequency response functions, dynamic rotational degrees of freedom and strain maps from different full field optical techniques*. In Proceedings of the ISMA2014 International Conference on Noise and Vibration Engineering, Leuven, Belgium, September 15-17, KU Leuven, pp. 1–15. paper ID676.

[2] Zanarini, A., 2015. *Accurate FRFs estimation of derivative quantities from different full field measuring technologies*. In Proceedings of the ICoEV2015 International Conference on Engineering Vibration, Ljubljana, Slovenia, September 7-10, IFToMM, pp. 1–10. ID192.

[3] Zanarini, A., 2008. *Full field ESPI vibration measurements to predict fatigue behaviour*. In Proceedings of the IMECE2008 ASME International Mechanical Engineering Congress and Exposition, October 31- November 6, Boston (MA) USA, ASME, pp. 1–10. Paper imece2008-68727.

[4] Zanarini, A., 2008. *ESPI measurements in structural dynamics: fatigue life assessment*. In Proceedings of the Dantec Dynamics 15th International Conference and User Meeting, Dantecdynamics GmbH, pp. 1–20.

[5] ESDU, 2006. "Spectral methods for the estimation of fatigue life 06011". In *Estimation of fatigue life of structures subjected to random loading*, Vol. 9 of *Vibration and Acoustic Fatigue Series*. ESDU International Plc, London, November.

[6] Zanarini, A., 2015. *Comparative studies on full field FRFs estimation from competing optical instruments*. In Proceedings of the ICoEV2015 International Conference on Engineering Vibration, Ljubljana, Slovenia, September 7-10, IFToMM, pp. 1–10. ID191.

[7] George, T. J., Seidt, J., Shen, M. H. H., Nicholas, T., and Cross, C. J., 2004. "Development of a novel vibration-based fatigue testing methodology". *Int. J. Fatigue,* **26**, pp. 474–486. Elsevier Science Ltd.

[8] McDowell, D. L., 1996. "Multiaxial fatigue strength". In *Fatigue and Fracture*, Vol. 19 of *ASM Handbook*. ASM International Handbook Committee.

[9] Fatemi, A., and Yang, L., 1998. "Cumulative fatigue damage and life prediction theories: a survey of the state of the art for homogeneous materials". *Int. J. Fatigue,* **20**, pp. 9–34. Elsevier Science Ltd.

[10] ESDU, 2006. "Fatigue damage and life under random loading 06009". In *Estimation of fatigue life of structures subjected to random loading*, Vol. 9 of *Vibration and Acoustic Fatigue Series*. ESDU International Plc, London, May.

[11] ESDU, 2006. "Cycle counting methods for the estimation of fatigue life 06010". In *Estimation of fatigue life of structures subjected to random loading*, Vol. 9 of *Vibration and Acoustic Fatigue Series*. ESDU International Plc, London, August.

11th International Conference on Engineering Vibration
Ljubljana, Slovenia, 7–10 September 2015

EXPERIMENTAL COMPARISON OF MULTIAXIAL-CRITERIA IN FREQUENCY-DOMAIN

Matjaž Mršnik*[1], Janko Slavič[1], Miha Boltežar[1]

[1]University of Ljubljana, Faculty of Mechanical Engineering
matjaz.mrsnik@fs.uni-lj.si

Keywords: Vibration Fatiuge, Multiaxial criteria, Structural dynamics

Abstract. *Vibration endurance must be ensured for structures that will be exposed to different vibratory loads, originating from environment and rotating and other machinery. Tests are usually done in the lab to that end, using shakers and other equipment. With the help of some state-of-art vibration fatigue methods vibration endurance can be analyzed and estimated already beforehand. The analysis procedure consists of structural dynamics analysis and is followed by fatigue analysis made on the resulting stress states. For broad-band excitation these are of random nature and very suitable for frequency-domain approach, e.g. fatigue cycle analysis of (equivalent) uni-axial stress which is well researched. This study researches the multi-axial criteria that are used to reduce the complex multi-axial stress state to an equivalent uniaxial stress. Several multi-axial criteria formulated for the frequency-domain can be found in literature. However, experimental studies exploiting natural response to induce multi-axial stress state are less frequent. This research first presents and then theoretically and experimentally compares selected multi-axial criteria for analysis in frequency-domain. The criteria of maximum normal stress, maximum shear stress and the C-S criterion are considered. Next, an experiment is performed to provide experimental data which serves as a basis for experimental comparison of selected multi-axial criteria. A special specimen is used with significant resonances present in the frequency range of applied vibration. Two broadband excitation sources are used to excite the specimen simultaneously. Time-to-failure results are compared across multi-axial criteria and with experimental data. Accuracy of multi-axial criteria is assessed with the aim of choosing the criterion that is most suitable for analysis of random stress response. Experimental data also show that selected methods give reliable time-to-failure estimates and can be used for fatigue analysis of mechanical structures exposed to broadband random vibration.*

1 INTRODUCTION

Prolonged exposure to a broad-band random stress load is known to cause material fatigue [1, 2]. Most of established fatigue analysis procedures (e.g. Palmgren-Miner, S/N curve [3, 4, 5]) are derived for analysis of uniaxial stress. In real structure, a complex multiaxial stress state develops. Furthermore, in the presence of more than one vibration source, the principal stresses are not proportional and the orientation of principal axes changes in time [2]. Such stress state cannot be directly analyzed for fatigue but is rather reduced to a uniaxial stress state through the use of a multiaxial criterion [1, 2, 6].

Characterization of vibration fatigue calls for special methods that can be applied in the frequency-domain, on random response states. The process of analysis consists of multiple steps. Stress responses are deduced first [7, 8]. An equivalent uniaxial stress is calculated next [1, 2]. Finally, the cycle counting and damage summation is performed [9, 10].

This study focuses on experimental comparison of multiaxial criteria in the frequency-domain, quite a few of which can be found in literature [1, 6, 11, 12, 13] as well as some comparison studies [6, 13, 12]. This study experimentally compares side-by-side the following multiaxial criteria in the frequency-domain: maximum normal stress, maximum shear stress and the CS criterion. Experimental results are obtained using a Y-shaped specimen, which is excited until failure using predefined loads.

The emphasis is on the analysis of a multiaxial stress state, resulting from multiple broad-band random loads.The Y-sample is excited with two electro-dynamic shakers in perpendicular directions, each producing random vibration in the frequency range of one particular modal shape. The stresses are calculated using the FEM method and actual measured loads from experiment. Multiaxial criteria are used to get the equivalent uniaxial stress and Tovo-Benasciutti [9] method is used to calculate time-to-failure. Numerical results are then compared across different multiaxial criteria and with experiment.

2 THEORETICAL BACKGROUND

To facilitate a better understanding of vibration fatigue and multiaxial criteria, theoretical fundamentals are presented in this section. Initially, some details on the random processes [14] are given. Next, some structural dynamics [7] details are presented for their crucial role in deducing the stresses that arise in material due to vibratory loads. Finally, the procedure of calculating equivalent stresses (i.e. the multiaxial criteria) is presented [1].

2.1 Random processes

Most research in the field of vibration fatigue is based on normal-distributed random processes, ordinarily described by a one-sided power-spectral density $G(\omega)$ (PSD) as a function of angular frequency ω. The random process is further characterized by moments of the PSD m_i, which give information about properties of the process in time-domain, such as variance $\sigma^2 = m_0$ or peak rate ν:

$$m_i = \int_0^\infty \omega^i \, G(\omega) \mathrm{d}\omega \tag{1}$$

$$\nu = \sqrt{\frac{m_4}{m_2}} \tag{2}$$

Based on these moments, cycle amplitude distribution of the random process can be es-

timated, using cycle-counting methods in frequency domain, such as Dirlik [10] or Tovo-Benasciutti [9]. Using material data in the form of an S/N curve and Palmgren-Miner hypothesis [4, 5], fatigue damage or time-to-failure can be deduced, which is part of the standard high-cycle fatigue analysis routine. This is for a simple uniaxial stress state, while complex multiaxial stress states calls for special approach with multiaxial criteria.

2.2 Structural dynamics analysis

Structure can be modeled with FEM method as a linear multi-degree-of-freedom system. Frequency analysis solution provides a modal model (i.e. eigenfrequencies, eigenvectors) which can be used to deduce the transfer functions from one point on the structure to the next. For the case of kinematic excitation, the structural modification approach [8] is used to obtain the appropriate transfer functions. Knowing the correct transfer function matrices $\boldsymbol{H_{as}}(\omega)$ (accelerations-to-stress) and $\boldsymbol{H_{fs}}(\omega)$ (force-to-stress) the random stress responses can then be calculated in the following way:

$$\boldsymbol{G}_s = \boldsymbol{H_{as}}(\omega)\, \boldsymbol{a}(\omega) \tag{3}$$

where the stress tensor components are described in the frequency domain by a 6-by-6 cross-correlation matrix $\boldsymbol{G}_s$:

$$\boldsymbol{S}_s = \begin{bmatrix} S_{xx,xx}(\omega) & \dots & S_{xx,yz}(\omega) \\ \vdots & \ddots & \vdots \\ S_{yz,xx}(\omega) & \dots & S_{yz,yz}(\omega) \end{bmatrix} \tag{4}$$

2.3 Multiaxial criteria

The conventional methods for fatigue analysis are based on uniaxial stress state. Multiaxial criteria are used to calculate an equivalent uniaxial stress state from a stress tensor and enable the use of cycle counting methods. These criteria are often based on failure and yield criteria used in static analyses, such as maximum normal stress criterion or von Mises. For vibration fatigue analysis, they are formulated in the frequency domain. The stress tensor in frequency domain $\boldsymbol{G}_s(\omega)$, obtained using modal analysis is a 6-by-6 matrix from eq. (4), which has to be converted to a scalar function of angular frequency $G_{s_{eq}}$. The process of reduction constitutes a multiaxial criterion in frequency domain. The equivalent stress $G_{s_{eq}}$ on the critical plane is determined from the components of the original stress tensor, by means of directional cosines l_j, m_j and n_j with $j = 1, 2, 3$ for the respective axis. The following multiaxial criteria are presented and compared side-by-side in this study: maximum normal stress, maximum shear stress and CS criterion.

2.4 Criteria of maximum normal stress and maximum shear stress

The maximum normal stress and maximum shear stress can be calculated in time-domain from the time-dependent stress tensor components. A method based on six-input physical system (described in [1]) derives the equivalent stress PSD directly from frequency-domain PSD matrices from eq. (4):

$$G_{seq} = \boldsymbol{a}\, \boldsymbol{G}_s(\omega) \boldsymbol{a}^T \tag{5}$$

where $\boldsymbol{a}$ is a vector of coefficients, defined for the two criteria in Table 1.

Table 1: Coefficients defining the multi-axial criteria.

$\mathbf{a}$	Max. normal	Max. shear
a_1	l_1^2	$(l_1^2 - l_3^2)$
a_2	m_1^2	$(m_1^2 - m_3^2)$
a_3	n_1^2	$(n_1^2 - n_3^2)$
a_4	$2\,l_1\,m_1$	$2\,(l_1\,m_1 - l_3\,m_3)$
a_5	$2\,l_1\,n_1$	$2\,(l_1\,n_1 - l_3\,n_3)$
a_6	$2\,m_1\,n_1$	$2\,(m_1\,n_1 - m_3\,n_3)$

All of these criteria are applied on the critical plane, which has to be determined beforehand. The straightforward way of doing this would be to calculate the value of the criterion on equally spaced planes and choose the plane that produces the most damaging spectrum. However, the calculation is much faster if only the variance of the criterion is compared for equally spaced planes. In the case of using the latter approach, there is only one value to deal with at each plane as opposed to a frequency-spectrum for total damage calculation. For that purpose, the covariance matrix $\boldsymbol{C}$ is calculated first:

$$\mathbf{C} = \begin{bmatrix} \sigma^2_{xx,xx} & \cdots & \sigma^2_{xx,yz} \\ \vdots & \ddots & \vdots \\ \sigma^2_{yz,xx} & \cdots & \sigma^2_{yz,yz}(\omega) \end{bmatrix} \tag{6}$$

and the plane is then searched, that gives the maximum variance of the multiaxial criterion. This is done in accordance with eq. (5):

$$\sigma^2_{s_{eq}} = \boldsymbol{a}\,\boldsymbol{C}\boldsymbol{a}^T \tag{7}$$

2.5 C-S criterion

Carpinteri et al. proposed a way to calculate the mean principal stress directions based on cross-correlation matrix $\boldsymbol{G}_s(\omega)$ [6]. The rotation matrix $\boldsymbol{C}_{CS}$ is obtained by applying 5 successive rotations with 3 of them being based on the orientation of the mean principal angles (see [6] for more details). When the position of the critical plane is determined, the equivalent uniaxial stress $G_{s_{eq}}$ is calculated as a combination, dependent on fully reversed bending and torsion limit $\sigma_{af,-1}$ and $\tau_{af,-1}$:

$$\boldsymbol{G}_{CS}(\omega) = \boldsymbol{C}_{CS}\,\boldsymbol{G}_s(\omega)\,\boldsymbol{C}_{CS}^T \tag{8}$$

$$S_{eq} = S_{zz} + \left(\frac{\sigma_{fr}}{\tau_{fr}}\right) S_{yz} \tag{9}$$

3 EXPERIMENT

Two excitation sources – electro-dynamic shakers are used, to provide a sufficiently complex and general stress state inside the material, as shown in Figure 1. In the vertical direction, the sample is excited using kinematical excitation with a controlled acceleration profile. In the horizontal direction, the specimen is excited using open-loop force excitation. Measured are the acceleration responses, mounted on the top of the sample with the purpose of extracting the respective modal shapes. Force load is measured at the tip of the stinger. Masses of 104.5g

are mounted on the Y-sample on each branch, pushing the mode frequencies in the desired frequency range.

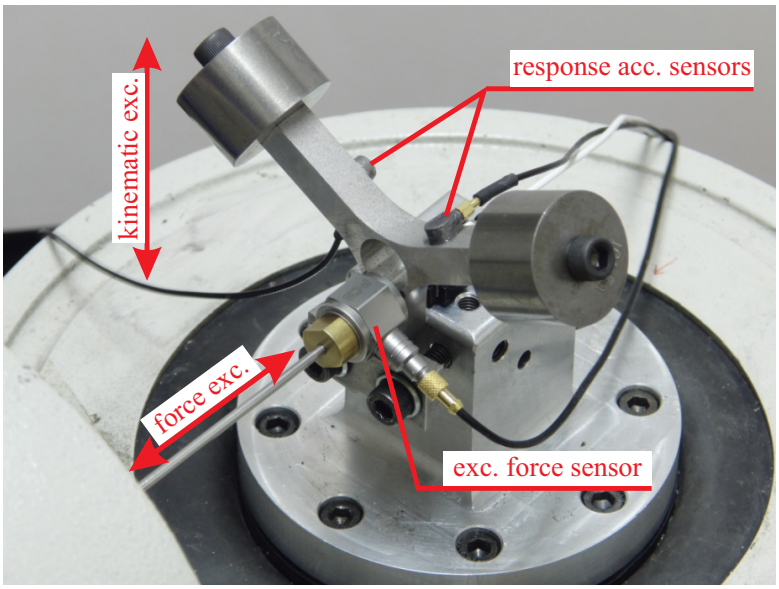


Figure 1: Experimental setup.

At the beginning of the experiment both excitation sources are powered on with predefined loads, consisting of uniform spectra in the specified range. For kinematic excitation, a uniform profile of amplitude x is controlled in the frequency range of 380 - 480 Hz. For force excitation, the current is applied to the amplifier with a uniform profile of y in the frequency range of 290 - 390 Hz. Due to fatigue, the structural response changes; when at least one of the modes which are monitored continuously goes out of the excited frequency range, the experiment is aborted. The load amplitudes for kinematic excitation are in the range of 0.7 - 1.7 GRMS and actively controlled. The load amplitudes for force excitation are in the range of 4 - 20 NRMS and are not actively controlled.

4 NUMERICAL MODEL

The Y-shaped specimen was analyzed using FEM method to extract the eigenmodes (see Figure 2). Acceleration and stress-response functions were deduced based on eigenmodes, according to modal superposition method. Structural modification approach [8] was used for calculating response functions for kinematic base excitation. Viscous damping was applied in this process, identified on experimental data using the circle-fit method [7].

Multiaxial criteria from section 2.3 were applied in combination with the Tovo-Benasciutti [9] cycle counting method. Maximum variance method is applied to find the critical plane. Fully reversed bending and torsion limits, needed for the C-S criterion, were not known for the aluminum alloy tested (AlSi7Cu3). The following values were instead taken from literature [15] for alloy AlCuMg1: $\sigma_{af,-1} = 161$ and $\tau_{af,-1} = 97$. The time-to-failure for each specimen was obtained from experiment and was taken when any mode frequency drops for more than 5%. Material parameters were searched that minimized the deviation of calculated time-to-failures

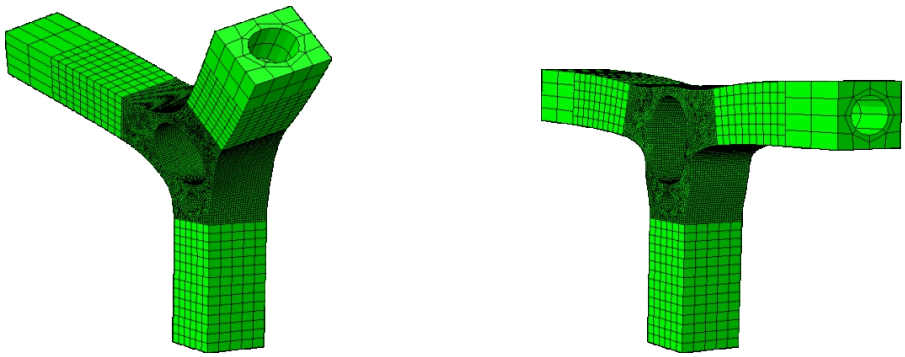


Figure 2: Mode shapes for force response (left) and kinematic response (right).

from experimental results, for each multiaxial criterion.

5 RESULTS AND COMPARISON

The comparison of numerical and experimental results is shown in Figures 3 to 5. Results are well within the 300% band. It can be concluded that all specimens were loaded in the high-cycle fatigue regime, ranging from the estimated 1.5×10^6 of loading cycles for the shortest time-to-failure to the 7.9×10^6 loading cycles for the longest run.

Estimates are better for the maximum shear stress criterion and for the C-S criterion. Furthermore, both maximum shear and C-S criteria give results that are very close. It should be mentioned, that the C-S criterion performance depends on some additional material parameters, namely fully reversed bending and torsion fatigue limit. These results were not obtained for the material used but from literature for another aluminum alloy.

In general, all of the compared criteria give quite good estimate of time-to-failure for high-cycle fatigue of aluminum alloy component.

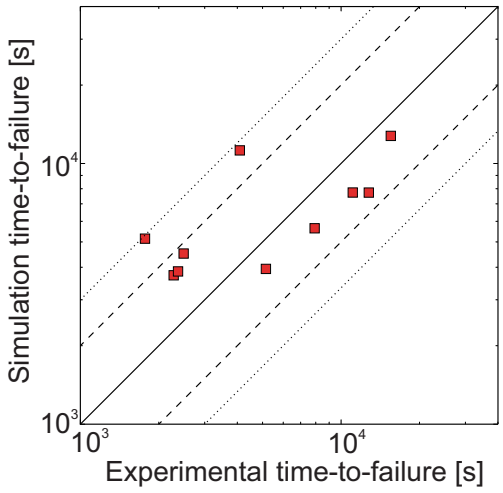


Figure 3: Comparison of numerical and theoretical results for the maximum normal stress criterion.

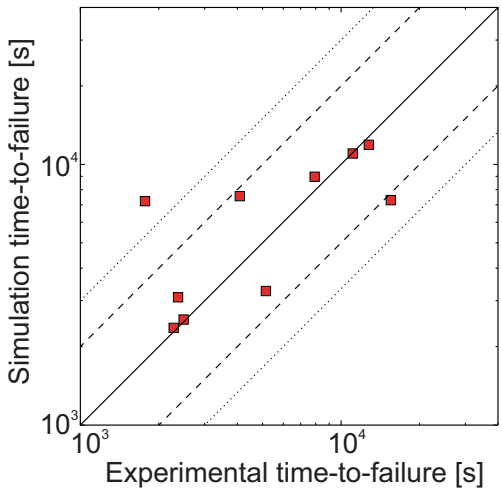


Figure 4: Comparison of numerical and theoretical results for the maximum shear stress criterion.

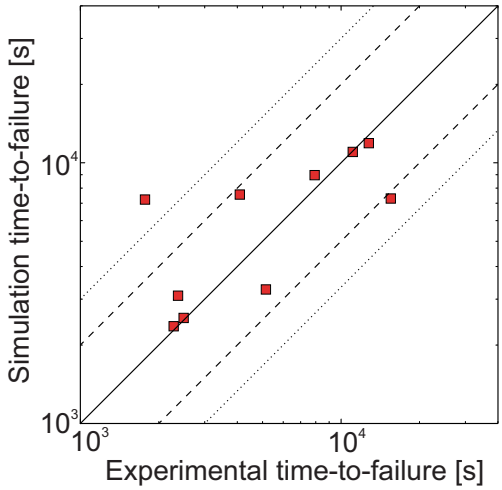


Figure 5: Comparison of numerical and theoretical results for the C-S criterion.

6 CONCLUSIONS

A group of multiaxial criteria, namely the maximum normal stress, maximum shear stress and the C-S criterion, were compared experimentally. 10 samples were used in comparison. They were exposed to broad-band excitation originating from two uncorrelated sources of vibration until a crack was well-developed. Two different mode shapes, producing a complex multiaxial stress state in material, participated in fatigue failure. Time-to-failure was defined with a relative fall of frequency (5%).

Vibration fatigue analysis was performed on a FEM model resulting in a time-to-failure estimate on a critical point on the model. Analysis proved to be quite reliable for a respective

multiaxial criteria. It should be noted though, that implicitly estimated material parameters vary significantly between different criteria and should be thus chosen carefully in a real application.

Large scatter is common in material fatigue analyses. However in this case, more than one source of error might be responsible, as the vibration fatigue analysis consists of multiple steps. An error in stress-response deduction is propagated and amplified due to the highly-nonlinear nature of material fatigue properties. With this in mind it should be stated here that while the second mode (kinematic excitation) was modeled well, the 1st mode (force excitation) deviated quite a bit from experimentally measured data and could not be fitted perfectly. This might be due to the way that force is applied in experiment.

To sum up, all of the criteria, experimentally compared in the course of this study, can provide acceptable, although reasonably scattered time-to-failure estimates for high-cycle fatigue of an aluminum component.

REFERENCES

[1] Adam Niesłony and Ewald Macha. *Spectral Method in Multiaxial Fatigue*. Springer-Verlag Berlin Heidelberg, 2007.

[2] Darrell F. Socie and Gary B. Marquis. *Multiaxial Fatigue*. Society of Automotive Engineers Inc, 1999.

[3] M. Matsuishi and T. Endo. Fatigue of metals subject to varying stress. *Paper presented to Japan Society of Mechanical Engineers, Fukuoka, Japan*, 1968.

[4] A. Palmgren. Die lebensdauer von kugellagern. *VDI-Zeitschrift*, 68:339–341, 1924.

[5] MA Miner. Cumulative damage in fatigue. *J. Appl. Mech.*, 12:A159–A164, 1945.

[6] Andrea Carpinteri, Andrea Spagnoli, and Sabrina Vantadori. Reformulation in the frequency domain of a critical plane-based multiaxial fatigue criterion. *International Journal of Fatigue*, 67:55–61, 2014.

[7] N. M. M. Maia and J. M. M. Silva. *Theoretical and Experimental Modal Analysis*. Research Studies Press, 1997.

[8] Martin Česnik, Janko Slavič, Primož Čermelj, and Miha Boltežar. Frequency-based structural modification for the case of base excitation. *Journal of Sound and Vibration*, 332(20):5029–5039, 2013.

[9] D. Benasciutti and R. Tovo. Spectral methods for lifetime prediction under wide-band stationary random processes. *Int. J. Fatigue*, 27(8):867–877, August 2005.

[10] T. Dirlik. *Application of Computers in Fatigue Analysis*. PhD thesis, The University of Warwick, 1985.

[11] A. Preumont and V. Pifort. Predicting random high cycle fatigue life with finite elements. *Journal of Vibration and Acoustics*, 116:245–248, 1994.

[12] A. Cristofori, D. Benasciutti, and Tovo R. A stress invariant based spectral method to estimate fatigue life under multiaxial random loading. *International Journal of Fatigue*, 33:887–899, 2011.

[13] Adam Niesłony. Comparison of some selected multiaxial fatigue failure criteria dedicated for spectral method. *Journal of Theoretical and Applied Mechanics*, 48:233–254, 2010.

[14] Julius S. Bendat and Allan G. Piersol. *Random Data: Analysis and Measurement Procedures*. Wiley, 2010.

[15] M. Kurek and Łagoda T. Comparison of the fatigue characteristics for some selected structural materials under bending and torsion. *Journal of Materials Science*, 47:59–67, 2011.

11th International Conference on Engineering Vibration
Ljubljana, Slovenia, 7–10 September 2015

A REVIEW AND COMPARISON OF CYCLE IDENTIFICATION METHODS FOR FATIGUE AND FRACTURE ANALYSIS

Curtis Larsen[1], **Tom Irvine** [2]

[1]NASA Engineering and Safety Center, NASA Langley Research Center, USA
curtis.e.larsen@nasa.gov

[2]Dynamic Concepts, Inc., Huntsville, AL, USA

Abstract. *A comprehensive review of fatigue cycle identification (counting) methods is presented for the purpose of encouraging a common standard of practice within the NASA and aerospace contractor community of practice. The primary source of commonly accepted standard cycle identification methods used in this review is ASTM E1049 - 85(2011)e1, ?Standard Practices for Cycle Counting in Fatigue Analysis?. An independent comparison of these methods, as well as other methods available in the literature, is presented by application of the methods to a number of time histories synthesized from numerous example power spectral densities (PSDs). The PSDs are selected to span a large range of bandwidth and spectral shapes to elicit cases for which particular counting methods may be best or poorly suited. Other factors influencing the selection of a cycle identification method, such as the specifics of the resulting fatigue spectrum?s application in a fracture mechanics analysis (as by NASGRO for example), are discussed. Time domain cycle counting methods are also compared with some common spectral methods such as the Rayleigh, Wirsching-Light, Ortiz-Chen, Dirlik, Benasciutti-Tovo, Zhao-Baker, and Single-Moment.*

Vibration Problems in the Solids Systems With Dry Friction (MS03)

11th International Conference on Engineering Vibration
Ljubljana, Slovenia, 7–10 September 2015

ON VIBRATIONAL SMOOTHING OF DRY FRICTION AND ITS APPLICATION TO REVOLUTE JOINTS

Simon Kapelke*, Wolfgang Seemann

Karlsruhe Institute of Technology (KIT), Institute of Engineering Mechanics
Kaiserstr. 10, 76131 Karlsruhe
simon.kapelke@kit.edu

Keywords: Dry Friction, Vibrational Smoothing, Friction Reduction, Averaging.

Abstract. *The effect of vibrational smoothing of dry friction has been subject of many publications in the past. High-frequency vibrations have been shown to smooth the average characteristics of dry friction at low sliding velocities and, consequently, avoid undesired friction induced phenomena such as stick-slip motion. Intending an improvement in process quality, this effect is used in industrial manufacturing, especially in the field of metal forming.*
Concerning other manufacturing processes or in particular positioning applications, accuracy may be limited by joint friction. In order to overcome this problem, it is the objective to develop a revolute joint with little clearance but without undesired phenomena caused by dry friction. Avoiding lubrication, the effect of vibrational smoothing is to be used in order to ensure the intended properties of the joint.
Yielding improved understanding of the underlying mechanisms, the effect of transverse high-frequency vibrations on a 1-DoF-friction oscillator is investigated here. Using a point contact model, the importance of contact compliance is carved out. Based on the friction model suggested by Dahl, a reduction of the smoothing effect is observed compared to classical Coulomb friction results. Finally, the application to revolute joints is discussed.

1 INTRODUCTION

In modern industrial manufacturing, it is essential to achieve as small tolerances as possible. However, process accuracy may be limited dramatically by undesired motion in joint structures. As a consequence, joint clearance has to be reduced in order to ensure the desired kinematics. On the other hand, reducing the clearance or even setting it to zero or below makes the surface pressure increase and gives rise to friction induced phenomena. However, providing a sufficient lubrication may be impossible in some applications.
Especially friction induced oscillations have been subject of numerous publications in the past. Motivated by mostly automotive applications, several mechanisms have been investigated leading to friction induced instabilities and high-amplitude oscillations [3, 12]. One of the most prominent among them is the instability of steady-state sliding caused by a negative gradient of the friction-velocity characteristics.
If a lubrication is not possible, high-frequency vibrations may be utilised in order to avoid friction induced instabilities. It has been shown that the effective friction characteristics can be smoothed when providing an appropriate excitation. As a consequence, the negative gradient can be overcome and friction induced oscillations are quenched [10].
This effect of vibrational smoothing has been investigated by many researchers [4, 8, 9] and is used in a number of applications. In the field of manufacturing, the most prominent applications of friction reduction are metal forming and cutting processes [5, 7].
While related publications focus on classical Coulomb friction, the effect of contact compliance on vibrational smoothing is considered here. As joint structures may contain compliant materials, the use of a rigid contact model appears to be a very strong assumption, which is rejected within this contribution. Due to practical aspects concerning revolute joints, the subsequent analysis is restricted to excitation transverse to the macroscopic sliding direction.
In section 2, the mechanical model under investigation is introduced. Recapitulating the classical results using Coulomb friction, the required mathematical tools are presented. In section 3, the model is refined using Dahl's friction model and accounting for contact compliance. Some further mathematical aspects are discussed and numerical results are carried out. Section 4 contains practical aspects concerning the application of vibrational smoothing to revolute joints. Finally, the present investigation is concluded and a brief outlook is formulated.

2 VIBRATIONAL SMOOTHING: RIGID CONTACT

It is well known that a negative gradient in the friction-velocity characteristics corresponds to negative damping. Thus, steady-state sliding may become unstable and friction induced oscillations arise. However, it has been shown that high-frequency vibrations may be utilised in order to suppress the negative gradient and, consequently, quench friction induced oscillations [10].
The basic underlying mechanisms can be investigated using a simple 1-DoF-friction oscillator. The corresponding equation of motion can be stated as

$$m\frac{\mathrm{d}^2\xi}{\mathrm{d}\tilde{t}^2} + c\xi = F_R. \tag{1}$$

Using $\omega_0^2 = \frac{c}{m}$ and introducing the time scale $t = \omega_0\tilde{t}$, the dimensionless equation of motion reads

$$\ddot{x} + x = f_R, \tag{2}$$

where $f_R = \frac{F_R}{cL}$ is the dimensionless friction force and $x = \frac{\xi}{L}$.

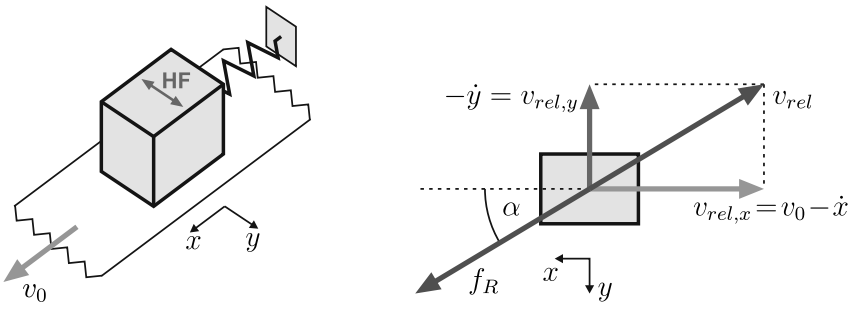


Figure 1: 1-DoF-friction oscillator under high-frequency excitation and corresponding velocity sketch.

For the present analysis, the model has to be extended in order to account for the excitation transverse to the direction of macroscopic sliding (cf. fig. 1). Assuming high-frequency vibrations in transverse direction to provide an excitation of inertia type, the equations of motion are given by

$$\ddot{x} + x = f_R \cos\alpha, \tag{3}$$

$$\ddot{y} = f_R \sin\alpha + a\omega^2 \sin\omega t. \tag{4}$$

Herein, $a \ll 1$ and $\omega \gg 1$ are dimensionless excitation amplitude and angular frequency, respectively, such that for the excitation velocity $a\omega = \mathcal{O}(1)$ holds. Concerning high-frequency and especially ultrasonic applications, the smallness of the excitation amplitude is a reasonable and common assumption [8, 9].
Furthermore, α is introduced as the angle between friction force and velocity of the underground (cf. fig. 1). Kinematic considerations yield

$$\cos\alpha = \frac{v_0 - \dot{x}}{\sqrt{(v_0 - \dot{x})^2 + \dot{y}^2}}, \quad \sin\alpha = \frac{-\dot{y}}{\sqrt{(v_0 - \dot{x})^2 + \dot{y}^2}}. \tag{5}$$

In order to analyse the effect of high-frequency excitation, it is helpful to rewrite the equations of motion as a system of first order equations. Introducing the fast time scale $\tau = \omega t$, $(\cdot)' = \frac{\partial}{\partial\tau}$, the equations of motion read

$$\mathbf{x}' = \varepsilon\mathbf{v}, \tag{6}$$

$$\mathbf{v}' = \varepsilon(-\mathbf{x}_r + \mathbf{f}_R) + \mathbf{h}(\tau), \tag{7}$$

where $\mathbf{x} = [x; y]$, $\mathbf{v} = [\dot{x}; \dot{y}]$, $\mathbf{x}_r = [x; 0]$, $\mathbf{f}_R = [f_R \cos\alpha; f_R \sin\alpha]$ and $\mathbf{h}(\tau) = [0; a\omega \sin\tau]$. $\varepsilon = \frac{1}{\omega} \ll 1$ is a small parameter.
As a first step, it is reasonable to start with the analysis of the corresponding unperturbed problem ($\varepsilon = 0$). Its solution is easy to calculate and can be used as a transformation of variables. The resulting equations of motion read

$$\mathbf{X}' = \varepsilon\mathbf{v}^*, \tag{8}$$

$$\mathbf{V}' = \varepsilon(-\mathbf{X}_r + \mathbf{f}_R), \tag{9}$$

where $\mathbf{X}$, $\mathbf{V}$ capture the slow motions of the system and $\mathbf{v}^* = [V_x; V_y - a\omega\cos\tau]$.
As all terms on the right hand sides are multiplied by the small parameter ε, the system is now

suitable for averaging. Returning to equations of second order, the slow motions of the system can be described by

$$\ddot{X} + X = \langle f_R \cos\alpha \rangle, \tag{10}$$

$$\ddot{Y} = \langle f_R \sin\alpha \rangle, \tag{11}$$

where $\langle\cdot\rangle$ denotes averaging with respect to the fast time scale τ.
The resulting equations resemble the classical equations for the friction oscillator without excitation, but with the right hand sides averaged over one period of the fast excitation.
Using $\dot{x} = V_x$ and $\dot{y} = V_y - a\omega\cos\omega t$, (5) can be used in order to calculate the averaged friction characteristics. Assuming for simplicity $f_R = \mu f_N = \text{const.}$, the corresponding expressions can be calculated as

$$\langle \cos\alpha \rangle = \frac{2}{\pi} \frac{V_{rel}}{\sqrt{V_{rel}^2 + (a\omega)^2}} K_1 \left(\frac{a\omega}{\sqrt{V_{rel}^2 + (a\omega)^2}} \right), \tag{12}$$

$$\langle \sin\alpha \rangle = 0. \tag{13}$$

Herein, $V_{rel} = v_0 - V_x$ has been introduced as the macroscopic relative velocity between underground and sliding mass and K_1 is the complete elliptic integral of first kind.

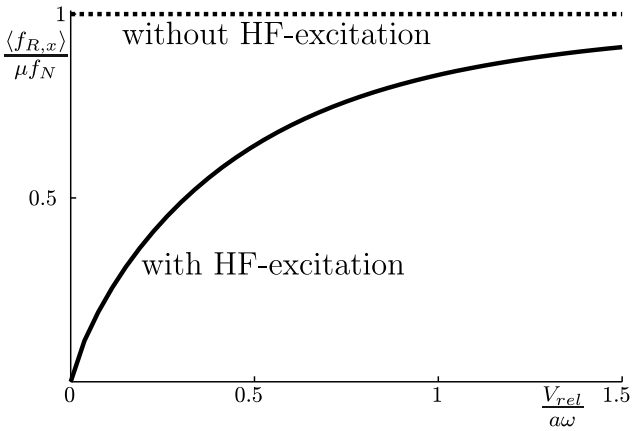


Figure 2: Rigid contact: friction-velocity characteristics.

The resulting effective friction characteristics are visualised in fig. 2. What can be observed is a reduction of the effective friction force especially for low sliding velocities. This yields a smoothing effect and overcomes the discontinuity at $v = 0$.
The same qualitative results are obtained for $\mu = \mu(v_{rel})$, which can be verified by numerical calculations. Providing appropriate high-frequency excitation, the friction characteristics are smoothed and a negative gradient can be suppressed.

3 VIBRATIONAL SMOOTHING: COMPLIANT CONTACT

One of the simplest models accounting for contact compliance has been worked out by Dahl. Motivated by friction in ball bearings, the following friction-displacement relationship was for-

mulated [1]:

$$\frac{\mathrm{d}F_R}{\mathrm{d}\xi} = c_0 \left| 1 - \frac{F_R}{\mu F_N} \mathrm{sign} \frac{\mathrm{d}\xi}{\mathrm{d}\tilde{t}} \right|^i \mathrm{sign} \left(1 - \frac{F}{\mu F_N} \mathrm{sign} \frac{\mathrm{d}\xi}{\mathrm{d}\tilde{t}} \right). \tag{14}$$

In order to investigate the effect of transverse high-frequency vibrations, the friction model has to be extended to planar motions. Using the same dimensionless parameters as before, the vector quantities $\mathbf{f}_R = [f_{R,x}; f_{R,y}]$ and $\mathbf{v}_{rel} = [v_0 - \dot{x}; -\dot{y}]$ are introduced. Setting $i = 1$, the dimensionless friction model can be stated as

$$\dot{\mathbf{f}}_R = \sigma_0 \left(\mathbf{v}_{rel} - |\mathbf{v}_{rel}| \frac{\mathbf{f}_R}{\mu f_N} \right), \tag{15}$$

where $\sigma_0 = \frac{c_0}{c}$ is the dimensionless contact stiffness [6].
Using the derived friction model and transforming to a system of first order equations, the equations of motion for the friction oscillator under transverse high-frequency excitation read

$$\mathbf{x}' = \varepsilon \mathbf{v}, \tag{16}$$

$$\mathbf{v}' = \varepsilon(-\mathbf{x}_r + \mathbf{f}_R) + \mathbf{h}(\tau), \tag{17}$$

$$\mathbf{f}_R' = \beta \left(\mathbf{v}_{rel} - |\mathbf{v}_{rel}| \frac{\mathbf{f}_R}{\mu f_N} \right), \tag{18}$$

where $\varepsilon = \frac{1}{\omega} \ll 1$ is still a small parameter and $\beta = \frac{\sigma_0}{\omega} = \mathcal{O}(1)$.
Considering again the corresponding unperturbed problem, a harmonic velocity distribution $\mathbf{v}^* = [V_x; V_y - a\omega \cos\tau]$ and a corresponding periodic friction force $\mathbf{f}_R = \mathbf{f}_0(\tau)$ can be obtained. Using this solution as a transformation of variables, the equations of motion read

$$\mathbf{X}' = \varepsilon \mathbf{v}^*, \tag{19}$$

$$\mathbf{V}' = \varepsilon(-\mathbf{X}_r + \mathbf{f}_0(\tau) + \mathbf{\Phi}), \tag{20}$$

$$\mathbf{\Phi}' = -\beta |\mathbf{v}^*_{rel}| \frac{\mathbf{\Phi}}{\mu f_N}. \tag{21}$$

While the first two equations show the small parameter ε or their right hand sides and seem to be suitable for averaging, the third equation does not show the required properties. As the coefficient on the right hand side is strictly negative and $\beta = \mathcal{O}(1)$, (21) can be identified as a strongly damped subsystem: $\mathbf{\Phi}$ will decay very fast compared to the evolution of $\mathbf{X}$ and $\mathbf{V}$.
For strongly damped systems, the averaging procedure can be modified as follows: As a first step, a particular solution is calculated for the fast subsystem. The solution is substituted into the slow subsystem and the slow evolution of the system can be determined by averaging the slow subsystem [2].
For the present analysis the slow motions of the system are captured by the averaged equations

$$\ddot{X} + X = \langle f_{0,x}(\tau) \rangle, \tag{22}$$

$$\ddot{Y} = \langle f_{0,y}(\tau) \rangle. \tag{23}$$

The results are carried out numerically. As expected, $\langle f_{0,y}(\tau) \rangle = 0$. The averaged friction force in x-direction is visualised in fig. 3.
Qualitatively, the extended model shows the same properties as the simple model using Coulomb friction and agrees with the results obtained in [11]. A smoothing effect can be observed for low sliding velocities, while the friction force approaches the original characteristics without

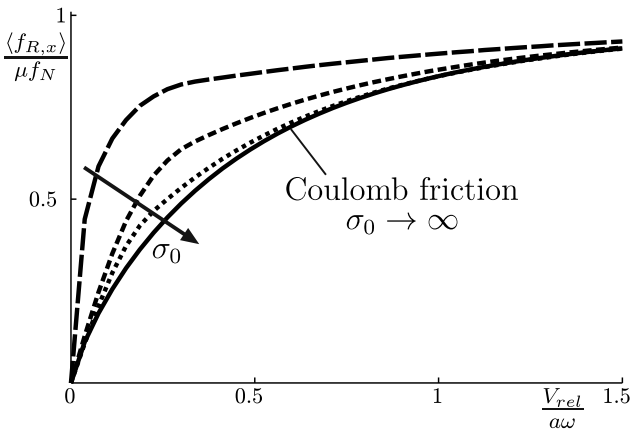


Figure 3: Compliant contact: friction-velocity characteristics.

high-frequency excitation at higher velocities.
In contrast to the classical results, the averaged friction force is increased when accounting for contact compliance. Depending on the stiffness ratio σ_0, the Coulomb friction model seems to highly overestimate the smoothing effect.
Similar results can easily be obtained for velocity dependent friction models such as the LuGre friction model.

4 APPLICATION TO REVOLUTE JOINTS

In the previous chapters it has been shown that high-frequency vibrations can reduce the effective friction characteristics of a system and overcome undesired friction induced phenomena. This effect is used in several manufacturing processes in order to improve process quality. Concerning positioning applications, it is the goal to develop a revolute joint with little or even without clearance, where the effect of vibrational smoothing is used in order to ensure the desired joint properties, while lubrication is avoided.
A simple model of such a revolute joint is depicted in fig. 4. The joint consists of a cylindrical bolt, which is connected to the housing by frictional bearings. A rod is located between the two housing bearings, which can rotate about the bolt axis.
The circumferential motion of the rod is subjected to friction between bolt and bearing structures and may show undesired phenomena. Consequently, the rod motion is to be influenced by high-frequency vibrations. In order to provide an appropriate transverse high-frequency motion, the bolt is excited in its axial direction by a piezoelectric transducer that is pre-stressed by a spring. By using piezoelectric transducers, high excitation frequencies can be achieved, while the amplitude of excitation, and thus the superposed motion, remains small.
In order to verify the calculated results experimentally, a test set-up was developed from the simple model in fig. 4. The housing was made of aluminium, while a steel bolt (6mm diameter) was chosen in order to ensure the desired contact properties. Polymer journal bearings (IGUS iglidur J) were designed as sockets with transition fit. In order to provide the high-frequency excitation, a PICA stack actuator P-007 (PI) was used.
Starting from a static displacement of the rod, it could be observed that the break away force of the joint is reduced in presence of high-frequency excitation. Depending on the surface

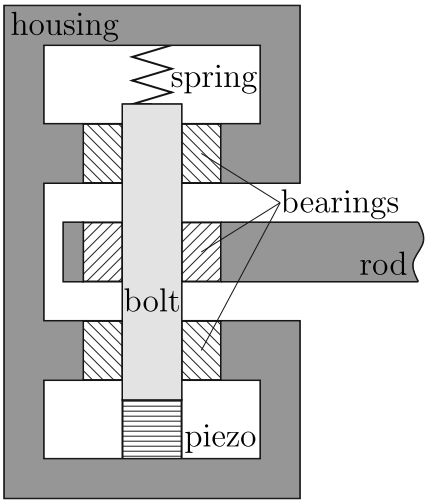


Figure 4: Model of a revolute joint with piezoelectric excitation.

pressure, one of the main problems is to provide a sufficient high-frequency motion within the bearing structures. Very detailed knowledge concerning the pressure distribution is necessary in order to ensure the intended transverse motion.
On the other hand, it is useful to increase amplitude and frequency of the high-frequency motion. An improvement of the results can be obtained by adding a second transducer with the same polarity on the opposite side of the bolt. An increased power input ensures the desired high-frequency motion at least in the two housing bearings, yielding vibrational smoothing between bearing structures and bolt. A corresponding modification of the set-up will be established in a next step.
Further experimental results, especially quantitative results, still have to be carried out. Apart from reducing the static break away forces, the reduction of sliding friction in presence of high-frequency vibrations still has to be verified in this application.

5 CONCLUSIONS

Within this contribution, the effect of transverse high-frequency vibrations on a 1-DoF-friction oscillator has been discussed. Using a Coulomb friction law, the classical results have been recapitulated showing a smoothing effect of the friction-velocity characteristics.
Yielding an improved modelling, the friction model has been refined and results have been carried out using Dahl's friction model. When accounting for contact compliance, vibrational smoothing is still observed, while the calculated friction forces are higher than the corresponding results using a rigid contact. As a consequence, it has to be stated that the Coulomb friction model overestimates the effect of friction reduction.
Concerning the application to revolute joints, a test set-up has been designed in order to validate the calculated results. While the break away force has been shown to reduce in presence of high-frequency excitation, further investigations still have to be performed.

REFERENCES

[1] P. R. Dahl, Solid friction damping of mechanical vibrations. *AIAA Journal*, **14**, 1675–1682, 1976.

[2] A. Fidlin and J. J. Thomsen, Non-trivial effects of high-frequency excitation for strongly damped mechanical systems. *International journal of non-linear mechanics*, **43**, 569–578, 2008.

[3] R. A. Ibrahim, Friction-induced vibration, chatter, squeal, and chaospart II: dynamics and modeling. *Applied Mechanics Reviews*, **47**, 227–253, 1994.

[4] V. C. Kumar and I. M. Hutchings, Reduction of the sliding friction of metals by the application of longitudinal or transverse ultrasonic vibration. *Tribology International*, **37**, 833–840, 2004.

[5] R. Pohlman and E. Lehfeldt, Influence of ultrasonic vibration on metallic friction. *Ultrasonics*, **4**, 178–185, 1966.

[6] H. Olsson and K. J. Åström and C. Canudas de Wit and M. Gäfvert and P. Lischinsky, Friction models and friction compensation. *European journal of control*, **4**, 176–195, 1998.

[7] K. Siegert and J. Ulmer, Superimposing ultrasonic waves on the dies in tube and wire drawing. *Journal of Engineering Materials and technology*, **123**, 517–523, 2001.

[8] H. Storck and W. Littmann and J. Wallaschek and M. Mracek, The effect of friction reduction in presence of ultrasonic vibrations and its relevance to travelling wave ultrasonic motors. *Ultrasonics*, **40**, 379–383, 2002.

[9] E. Teidelt and J. Starcevic and V. L. Popov, Influence of ultrasonic oscillation on static and sliding friction. *Tribology Letters*, **48**, 51–62, 2012.

[10] J. J. Thomsen, Using fast vibrations to quench friction-induced oscillations. *Journal of Sound and Vibration*, **228**, 1079–1102, 1999.

[11] C. C. Tsai and C. H. Tseng, The effect of friction reduction in the presence of in-plane vibrations. *Archive of Applied Mechanics*, **75**, 164–176, 2006.

[12] U. von Wagner and D. Hochlenert and P. Hagedorn, Minimal models for disk brake squeal. *Journal of Sound and Vibration*, **302**, 527–539, 2007.

11th International Conference on Engineering Vibration
Ljubljana, Slovenia, 7–10 September 2015

IDENTIFICATION STRATEGIES FOR FRICTION LAWS: A NUMERICAL STUDY

Andrew McKay*[1], Jim Woodhouse[1], Thibaut Putelat[2]

[1]Dept. of Engineering, University of Cambridge
am2198@cam.ac.uk

[2]Dept. of Engineering Mathematics, University of Bristol

Keywords: Friction, Friction-induced vibration, Stick-slip, Rate-and-state friction.

Abstract. *Many friction laws have been proposed but a law capable of accurately predicting all aspects of dynamic frictional behaviour from frictional damping to the thresholds and transients of stick-slip remains to be found. This paper describes an approach to identifying which features of a stick-slip waveform may be useful for experimental identification of a friction law; this will then aid the design of experimental procedures.*

A numerical study of a single degree of freedom oscillator driven by the Spinodal rate and state friction law has been performed. A number of metrics that describe features of the waveforms have been extracted from the simulated data to produce surfaces across a parameter plane where experimental conditions are varied in one direction and a feature of the friction law is varied in the other. The surface then shows whether the metrics are sensitive to the friction law and/or to experimental conditions and so whether they are useful for experimentally discriminating between laws.

For rate and state laws the loop-area in the friction force − sliding velocity plane and the skew of the velocity waveform were seen to vary with both the normal load and with the timescale of the state evolution law which means these metrics may be useful experimentally. On the other hand, metrics such as the proportion of the period spent sticking only vary with the normal load, which makes them less useful experimentally.

1 INTRODUCTION

For cases of steady sliding, measurement procedures for friction force are well established, but for the prediction of the onset of stick-slip and the characteristics of the resulting waveform the task of creating a suitable friction law is more difficult, see Woodhouse et al. [1]. Stick-slip is a common phenomenon seen in brake squeal, the bowing of a violin [2] and even in earthquakes [3] and so a law capable of making accurate predictions would be useful across a wide range of fields.

Experiments performed by Dieterich et al. [4] revealed that in response to an instantaneous increase in sliding speed there is a gradual relaxation to a new friction level. It was suggested that an underlying steady-state curve determines the new level which the friction relaxes to but an internal state variable controls the transition to the new level. Multiple internal state variables can be introduced with various physical interpretations such as the average age of the contact or the temperature of the interface, physical justification for these laws is made by Putelat et al. [5]. This type of law is known as a rate and state friction law and the general form of these laws is

$$\mu = F(v, \psi) \tag{1}$$

$$\dot{\psi} = -G(v, \psi) \tag{2}$$

where μ is the coefficient of friction, v the interfacial slip rate, and ψ the state variable as proposed by Rice et al. [6]. For the following numerical study the 'Spinodal' friction law proposed by Putelat et al. [7] is used

$$\mu = a \sinh^{-1}\left\{\frac{v}{2V_*}\exp\left[\frac{\mu_*}{a} + \frac{b}{a}\ln(c+\psi)\right]\right\} \tag{3}$$

$$\dot{\psi} = \frac{1-\psi}{t_{**}} - \frac{|v|\psi}{L} \tag{4}$$

where $a, b, c, \mu_*, V_*, t_{**}, L$ are constants that depend on the materials in contact. The law consists of a friction law which is a regularised form of the Dieterich-Ruina law [8] (the regularisation removes a $\ln(v)$ term which is problematic when $v = 0$) and a state evolution law where the internal state saturates at a chosen value giving the interface finite strength after a rest period. Earlier state evolution laws allowed unbounded strengthening during a rest period which does not agree with experiments (e.g. Rabinowicz [9], Dieterich [4] and also early experiments by Coulomb). The steady-state friction curve is obtained by substituting the equation for $\phi_{ss}(v)$ into F, this describes the friction force for a given velocity after the transients due to ψ have died out, for the Spinodal law this curve has an N shape.

2 NUMERICAL STUDY

In this study we are simulating stick-slip of a single degree of freedom mass-spring system driven by the Spinodal friction law. The rapid fluctuations in friction force seen in stick-slip mean that the internal state variable may be extremely active and so it may be a useful phenomenon to measure in order to see ψ's effect. The shape of the resulting limit cycle and the stability boundary where the onset of stick-slip occurs will both be revealing of required features of a friction model.

From the waveform it is possible to extract a variety of metrics. It is relatively straightforward to take measurements that give information about the steady-state characteristics of friction

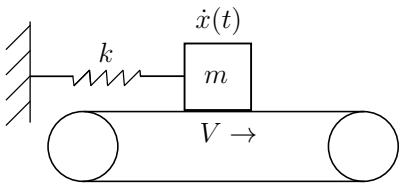


Figure 1: Schematic of the simulated single degree of freedom oscillator driven by a belt.

so we are looking for a metric which reveals the most information about the behaviour of an internal state variable. To enable this a scaling term λ is introduced to the state evolution law

$$\dot{\psi} = -G(v, \psi)/\lambda \tag{5}$$

This has the effect of changing how quickly the internal state evolves: for large values of λ the value of $\dot{\psi}$ is scaled down so that the evolution is slow, for small values of λ the evolution is sped up. Changing λ varies how much the motion of the system is affected by the internal state since ψ reaches its largest values when $v = 0$ but with small values of λ the state decays so rapidly that it will have little effect on the system's dynamics. In fact as $\lambda \to 0$ the friction law approaches the underlying steady-state friction law.

By calculating the metrics in a plane where the scaling λ is varied in one direction and an experimental parameter is varied in the other we can see which metrics are a feature of the dynamic response of the internal state. If such a metric is revealed then it may be useful to measure experimentally in order to discriminate between candidate models. The simulated system is a single degree of freedom oscillator driven by the Spinodal friction law. The oscillator is driven at a constant velocity V and it is the difference between this and the block's velocity $\dot{x}$ that give the interfacial slip rate v on which friction depends.

The equations of motion of the simulated system are

$$m\ddot{x} = N\mu(v, \psi) - kx \tag{6}$$

$$\dot{\psi} = -G(v, \psi)/\lambda \tag{7}$$

where μ and G are defined by equations (3) and (4). The varied experimental parameter will be the normal load N, along with driving velocity V: this is one of the simplest parameters to vary in an experimental set-up. The mass m and stiffness k of the oscillator to be described in Section 3 would be more difficult to vary as it will be machined from one piece of steel.

2.1 Results and extracting metrics

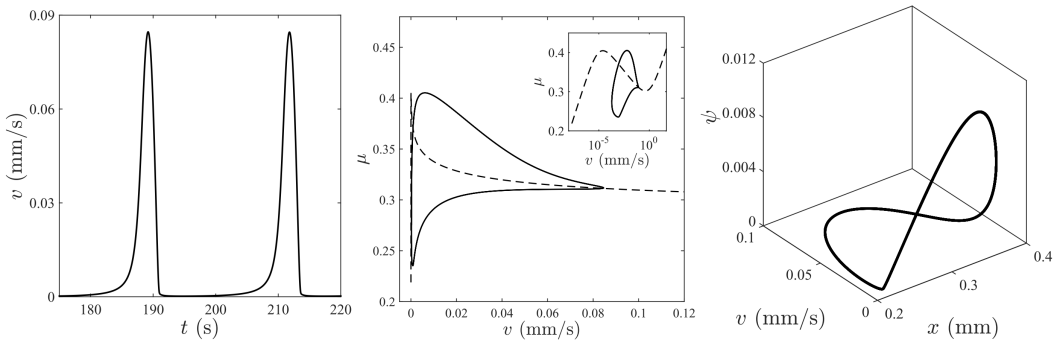
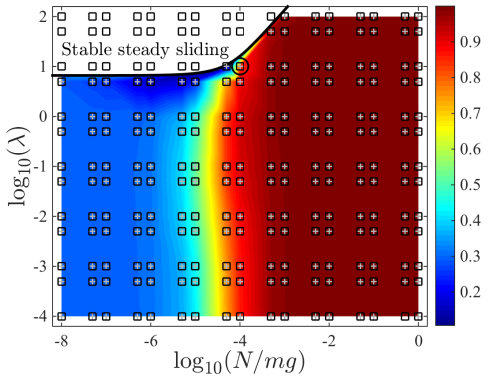


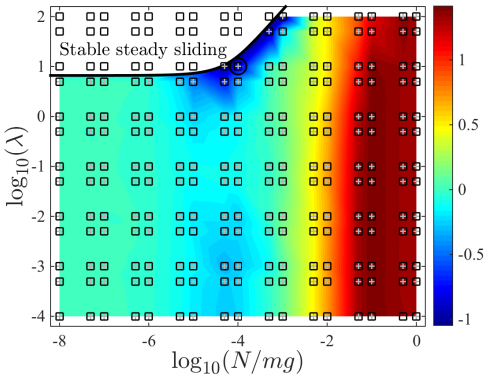
Figure 2: Simulation of a mass-spring driven by a Spinodal friction law for $m = 1$ kg, k =1.09 N/m, $V = 10^{-2}$ mm/s, $\lambda = 10$ and $N/mg = 10^{-4}$: a) Velocity waveform; b) Trajectory in the $\mu - v$ plane for the Spinodal law (solid line) and the steady state sliding relation $\mu_{ss}(v)$ (dashed line); c) 3D phase portrait. The inset in b shows the same data on a logarithmic scale for consistency with earlier work [7].

Figure 2 shows the same simulation plotted in various forms to highlight potential metrics. Figure 2a highlights the proportion of the stick-slip cycle spent sticking and also the skew of the waveform i.e. the length and direction of the tail, figure 2b shows the hysteresis of the trajectory in the $\mu - v$ plane - the value of μ is highest as gross sliding starts and the block returns to sticking at a lower value. A measure of this hysteresis is represented in the area of the loop formed. Finally figure 2c shows the sharpness of the corner at breakaway compared to that as the block returns to sticking - a sharper curve means ψ has decayed rapidly at the onset of slip and has little influence on the block dynamics.

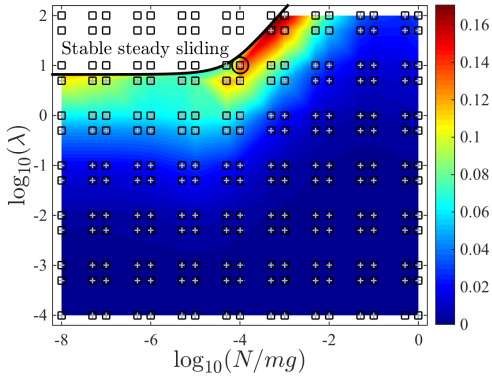
The loop area, skew and sharpness metrics in particular indicate the effect of the state on friction — with a rate only law there can be no hysteresis in the $\mu - v$ plane and the phase portrait becomes 2D and symmetric. The aim of the simulation study is to identify metrics which will be useful for experimentally discriminating between friction laws and so the sharpness metric can be ruled out since ψ is not directly measurable.



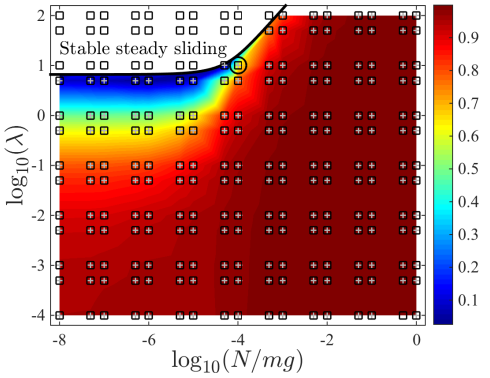
(a) Proportion of period spent sticking



(b) Skew of the velocity waveform



(c) Normalised loop area in the $\mu - v$ plane



(d) Sharpness in the $\psi - v$ curve at breakaway

Figure 3: Variation of metrics across the $\lambda - N/mg$ parameter plane. The solid line shows the linearised stability threshold, □ marks a simulated run, + marks runs detected as stick slip and the circled run is the simulation shown in figure 2.

Figure 3a shows that the proportion of the stick-slip cycle spent sticking is largely dependent on the normal load and has very little sensitivity to the value of λ. This suggests that the metric will be less useful for experimentally determining the influence of ψ.

The skew of the velocity waveform in figure 3b shows that for the majority of the parameter plane the dependence is only on the normal load but in the region of the bend in the stability boundary there is a small region where the skew is as low as negative one which means a longer tail on the left of the waveform and elsewhere in the plane the skew is around zero and above. The same metric can be found experimentally and the dependence on λ and N/mg seen in figure 3b suggests it may be useful for discriminating between laws.

Figure 3c shows us that the loop area is a useful metric for discriminating between results as the normal load is varied but also as λ is scaled. For larger values of λ we see that the loop area increases, especially in the region close to the stability boundary, and so the loop area is a good indicator of how strong the state dependence is. These results suggest that a useful experiment should focus on the measurement of the loop area in order to gauge the state dependence. Hysteresis of the trajectory in the $\mu - v$ plane was experimentally observed by

Woodhouse [10] for the case of the bowing of a violin string where the interfacial temperature plays a significant role.

Finally figure 3d shows the sharpness of the corner in the $\psi - v$ curve at breakaway. As expected there is a strong dependence on λ but only for $N/mg < 10^{-4}$. Again, this metric is not observable since ψ is an internal variable.

Most of the interesting activity of the metrics occurs in the region close to the bend in the stability threshold. Where a dependence on λ and N/mg is seen a potential experiment may compare friction laws by first seeking out the stability boundary, then varying the normal load and comparing the metrics with the results along a horizontal line in these surfaces.

3 DESIGN OF AN EXPERIMENT

The measurement of stick-slip is part of a range of tests being performed to probe friction from a number of angles. The tests are all performed on a pin-on-disc rig where the pin is a small hemisphere of a chosen polymer and the disc has a glass surface, the same rig has previously been used to calculate a frictional frequency response function as described in [11]. The contact geometry and materials are the same for the various tests which allows the results to be compared between tests with confidence.

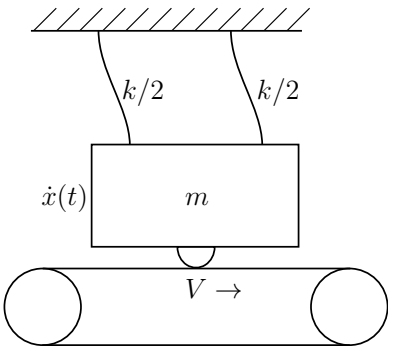


Figure 4: Schematic of the oscillating head.

For stick-slip measurements a hemispherical contact is again used but it will be attached to a new sensored head which approximates a single degree of freedom oscillator and minimises any rolling that would change the area of contact. The head will be instrumented with piezo and strain gauges to measure force in normal and frictional directions. A laser vibrometer will also measure the motion in the frictional direction.

4 CONCLUSIONS

Past experiments have shown that steady-state friction measurements are not sufficient to reveal everything we need to know about friction. Instead we must find measurements which also reveal information about internal state variables. Speed jumps as performed by Dieterich [4] exposed the presence of an internal state, but the relaxation that is seen is over a relatively slow time scale. It remains to be seen whether the same rate and state laws can be used in situations where the timescales are much shorter, such as in friction-induced vibration relevant to engineering applications.

This study focused on the simulation of stick-slip and the calculation of metrics extracted from the waveform. Of the metrics explored the loop area in the $\mu - v$ plane and the skew of the velocity waveform were the most promising for revealing the influence of the internal state variable on observable dynamics. With this in mind the next stage is to develop an experiment which can accurately measure stick-slip waveforms and allow a variety of experimental parameters to be varied. From the experimental results the metrics can be calculated and compared with surfaces from a range of laws in order to discriminate between laws.

An approximation of a single degree of freedom oscillator driven by a rotating disc is currently being developed as part of a range of other tests all using the same disc and contact conditions in order to explore friction from many angles.

REFERENCES

[1] J. Woodhouse, T. Putelat and A. McKay, Are there reliable constitutive laws for dynamic friction? *Philosophical Transactions of the Royal Society of London A: Mathematical, Physical and Engineering Sciences, In Press.*

[2] J.W.S. Rayleigh, *The Theory of Sound: Vol 1*. Dover Publications Inc., 1998.

[3] W. Brace and J. Byerlee, Stick-slip as a mechanism for earthquakes. *Science*, **153**, 990–992, 1966.

[4] J. Dieterich, Modeling of rock friction: 1. Experimental results and constitutive equations. *Journal of Geophysical Research*, **9**, 2161–2168, 1979.

[5] T. Putelat, J. Dawes and J. Willis, On the microphysical foundations of rate-and-state friction. *Journal of the Mechanics and Physics of Solids*, **59**, 1062–1075, 2011.

[6] J. Rice, N. Lapusta and K. Ranjith, Rate and state dependent friction and the stability of sliding between elastically deformable solids. *Journal of the Mechanics and Physics of Solids*, **49**, 1865–1898, 2001.

[7] T. Putelat, J. Dawes and J. Willis, Sliding modes of two interacting frictional interfaces. *Journal of the Mechanics and Physics of Solids*, **55**, 2073–2105, 2007.

[8] A. Ruina, Slip instability and state variable friction laws. *Journal of Geophysical Research*, **88**, 10359, 1983.

[9] E. Rabinowicz, *Friction and wear of materials*. Wiley-Interscience, 1965.

[10] J. Woodhouse, The physics of the violin. *Contemporary Physics*, **27**, 61–62, 1986.

[11] S. Wang, J. Woodhouse, The frequency response of dynamic friction: A new view of sliding interfaces. *Journal of the Mechanics and Physics of Solids*, **59**, 1020–1036, 2011.

International Conference on Engineering Vibration
Ljubljana, Slovenia, 7-10 September 2015

INFLUENCE OF CONTACT CHARACTERISTICS ON THE DYNAMIC BEHAVIOR OF RUBBING STRUCTURES

M-A. Douville*[1], B. Faverjon, G. Jacquet-Richardet

[1] Université de Lyon, CNRS, INSA-Lyon, LaMCoS, UMR5259, France F-69621LaMCoS
marc-andre.douville@insa-lyon.fr

Keywords: Vibration, Friction, Nonlinear behavior, Experimental Dynamics, Numerical modelling

Abstract. *The present study deals with the effects of contact characteristics on the vibratory response of a beam that can be associated with several rubbing devices. Experimentally several contact configurations are tested by varying the contact area size and roughness of the samples. For each tests, the frequency response functions (FRF) are measured and then superimposed with the other configurations. Numerically, temporal calculations are presented and compared to the measured data using Masing's contact model with updated parameter values and averaged estimated values.*

1 INTRODUCTION

The modelling of the vibratory response of jointed structures can become a very delicate task due to the nonlinear behavior induced by dry friction occurring at the interfaces. Sticking, macro or micro slipping between interfaces have non negligible effects on both the natural frequencies and damping properties.

Dealing with complex structures containing many joints, reduced-order friction models are required. However due to the diversity of contact configurations, a large number of these models are non-generalizable making them useful only case by case. Indeed in practice, such as in [1], experimental hysteresis curves are almost always needed to identify:

- which type of friction is occurring at the interfaces (based on the shape of the hysteresis curve)
- The contact parameters such as the friction coefficient and/or the joint stiffness

This is a major issue because engineers and researchers (assuming that they are using the right contact models) are strongly dependent on these experimental data that are not always available. Thus it is legitimate to ask the fallowing question: Is it possible to have access to accurate parameter values (or at least good estimations) without any prior frictional experiments?

To answer this question, the first and most common way is to use parameter values available on databases. In [2] for example, the authors propose estimated friction coefficients and contact stiffness values based on a very large experimental campaign they have carried.

The second possibility is given by more physics-based models. Many researchers such as Eriten et al [3-5] have worked on developing models that only take into account the material and geometrical properties of the contacting surfaces, surfaces roughness data, and contact loading. The main advantage is that no prior friction hysteresis curves is required.

The principle behind these models is based on the pioneer work of Greenwood and Williamson on rough contacts [6]. Knowing the behavior of an individual spherical asperity pressed against a flat surface it is possible, thanks to statistical summation, to simulate the global behavior of two rough flat-on-flat surfaces rubbing against each other.

In the current study, a simple, yet easily customizable test rig has been developed to measure the dynamic response of a steel beam associated with several friction devices. The set-up allows for punctual or surface to surface contact configurations. In the case of the surface to surface contact, devices with various area size, shape and roughness are tested in order to assess their influence on the FRF. Two friction models are considered here and are compared to the experimental data. Model 1 uses identified friction parameter values, it will serve as a reference. Model 2 uses the same model as in model 1, yet the parameter values will be estimated as suggested the literature such as in [2]. This study is a preliminary step toward the contribution of a FE model using minimal to no contact parameter identification.

2 THE TEST RIG

2.1 Description of the test rig

The studied structure is a cantilever steel beam with a rectangular cross section of 0.008 m by 0.04 m and a length of 0.50 m. At its the free end, the beam can be associated with a rubbing device (Figure 1).

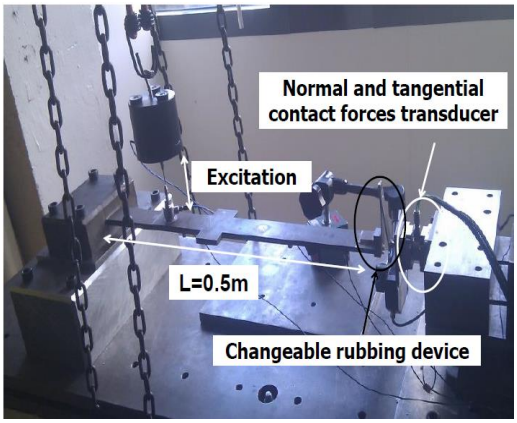
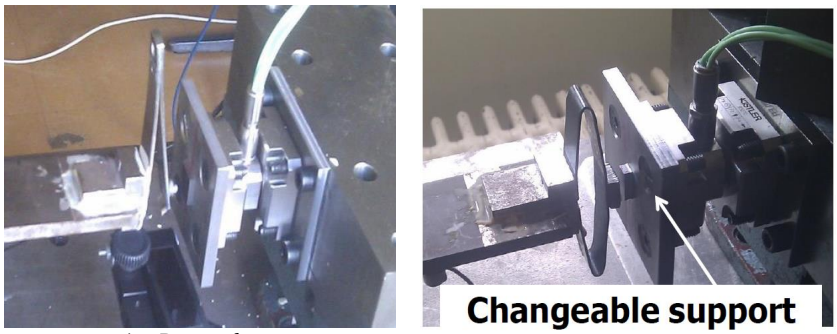


Figure 1: Experimental set up – cantilever steel beam.

The experimental set-up allows the measurement of the displacement at 0.35 m of the clamped end of the beam by mean of an accelerometer (the measured signal is then integrated twice). The excitation force which is provided by a shaker is measured by a force sensor located at the end of the shaker's push rod. Similarly to the excitation force, the normal and tangential contact forces are also measured using a force sensor.

Two types of devices were chosen in order to allow punctual contact or surface to surface contact (Figure 2). For both contact configurations sine sweeps (harmonic excitation) are performed at constant excitation force amplitude in a [15-130] Hz frequency range for various normal contact forces. The measured FRF are then superimposed in order to identify the different global behaviour.



a) Punctual contact b) Surface to surface contact

Figure 2: Rubbing devices.

2.2 Physical phenomenon

In Figure 3, an example of a typical measured FRF for the punctual contact case is shown. Here the influence of the normal contact load on the vibratory response of the beam is exhibited.

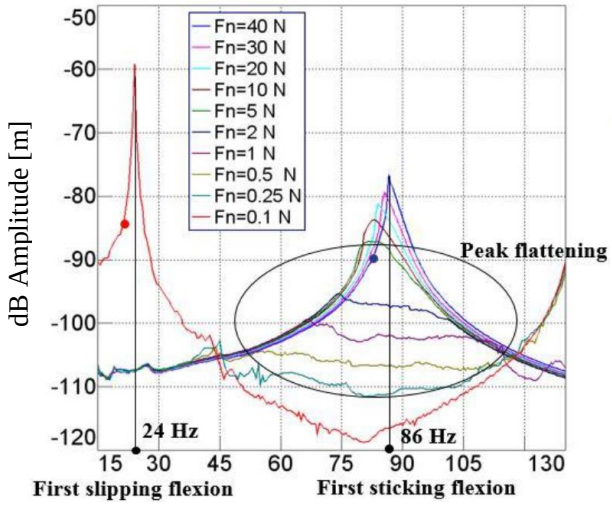
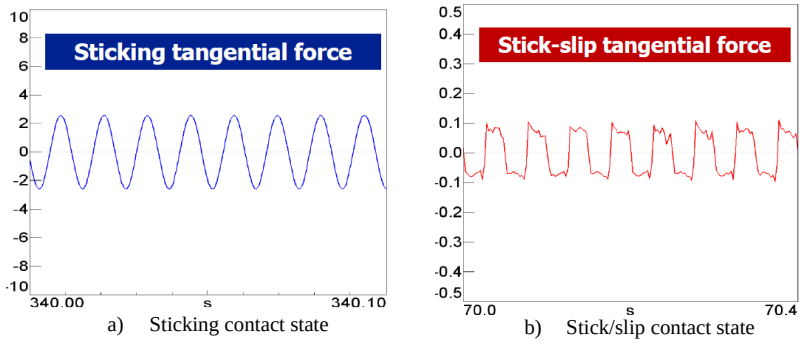


Figure 3: FRF vs normal load.

For high normal load (Fn=40 N), in comparison to an excitation force of 2 N, the contact is stuck. The FRF exhibits a linear behaviour with a peak resonance at 86 Hz. As the normal load is lowered (from 30 N to 0.25 N), relative displacement is allowed in the contact region (presence of stick/slip) and the vibration amplitudes located around the 86 Hz resonance peak drops to the point of becoming nearly flat. Finally, for Fn=0.1 N, the contact is in a slip state, a high peak resonance is observed at 24Hz.

In Figure 4, an example of measured tangential force in sticking and stick/slip states is shown. When the contact is in a stuck state the tangential force is proportional to the displacement at the same point (sinusoidal signal). On the other hand, when the contact is in a stick/slip state the tangential force is proportional to the displacement at the same point in stuck phase while it cannot be above a limit value of ±μFn (μ: friction coefficient) in the slip phase.



a) Sticking contact state b) Stick/slip contact state

Figure 4 : Measured tangential force.

3 DYNAMIC RESPONSE OF THE STRUCTURE

In this section, only the results regarding surface to surface contact configurations are presented. Surfaces with various areas were chosen (13x13 mm^2, 9x9 mm^2, 13x5 mm^2, 5x5 mm^2 in Figure 5) and each sample came in two surface finish, one rough and one smooth. The surface finish is described here by the average roughness (Ra) that is defined by [7]:

$$R_a = \frac{1}{L}\int_0^L |z(x)|dx \tag{1}$$

Where $z(x)$ is the height of the surface above the datum and L is the sampling length.

In Figure 6, the profile of the 13x13 mm^2 samples are presented. The smooth one has a Ra of 0.714 µm while the rough one has a Ra of 3.76 µm. Let us precise that only the faces that are to be in contact are treated to be smooth or rough. Regarding the external forces, normal loads varied within the range [0.1 – 80] N and the excitation force amplitude remained at 2N.

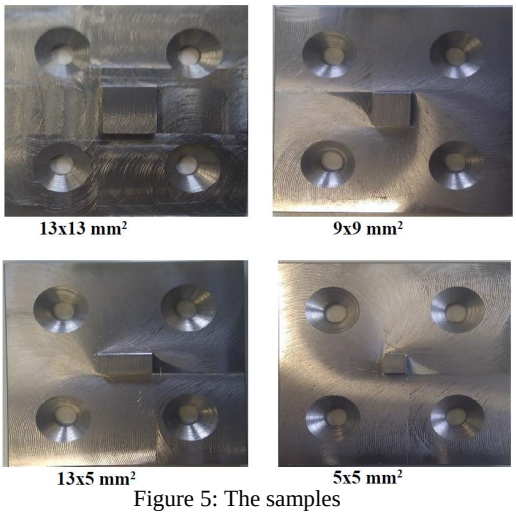
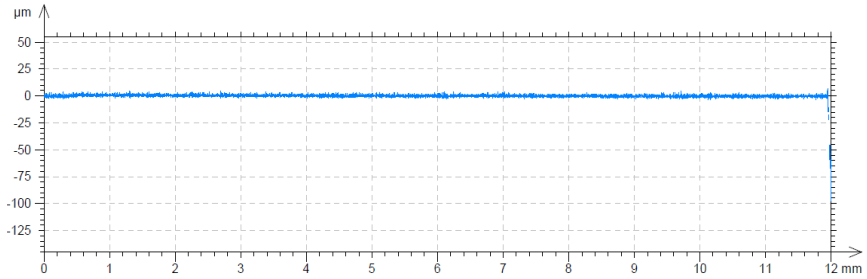
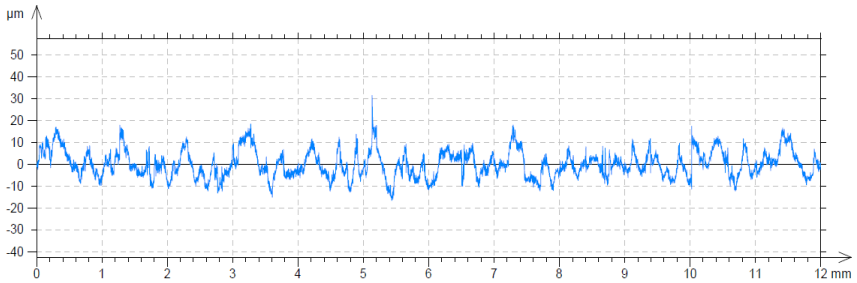


Figure 5: The samples



a) Profile of the smooth 13x13 mm^2 sample : Ra=0.714 µm



b) Profile of rough 13x13 mm^2 sample : Ra=3.76 µm

Figure 6: Profile of the 13x13 mm^2 specimens.

3.1 Area size and roughness effects on FRF

As a first result, for normal contact loads Fn of [0.1-2-10-80] N and an excitation force amplitude of 2N, contact area size does not affect significantly the dynamics of the assembly. As shown in Figure 7, the superposition of FRFs of the four smooth samples for a normal load of 2N does not display much differences. The same observations were made when assessing the influence of surface roughness.

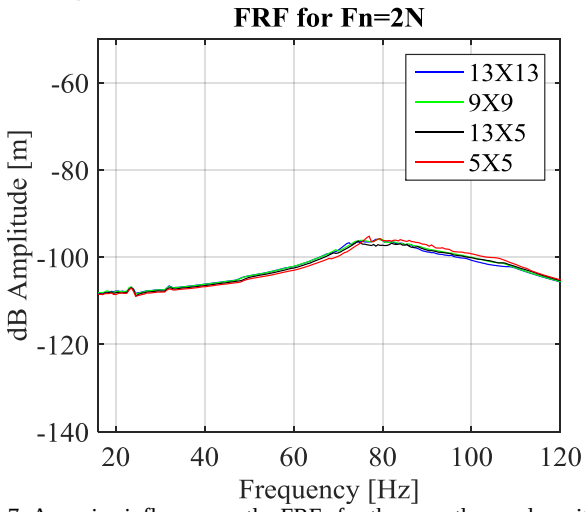


Figure 7: Area size influence on the FRFs for the smooth samples with Fn=2 N.

In the fallowing, we present results concerning surface 13x13 mm^2 and 5x5 mm^2 only. We will evaluate the discrepancies via three quantities: the maximum displacement amplitudes, the frequency at which the maximum displacement amplitudes is obtained and the damping ratios. The assessment of area size effect is summarized in Table 1 and Table 2 while the effect of roughness is summarized in Table 3 and Table 4.

	Fn=0.1 N	Fn=2 N	Fn=10 N	Fn=80 N
Amplitude differences.	-5.2 %	0.7 %	1.5 %	0.8 %
Frequency of the maximum amplitudes.	0 %	3 %	-1.1 %	0 %
Damping ratio differences.		-0.44 %	0.91 %	0.27 %

Table 1: Effect of area size: 13x13 mm^2 smooth versus 5x5 mm^2 smooth.

	Fn=0.1 N	Fn=2 N	Fn=10 N	Fn=80 N
Amplitude differences.	4 %	1.7 %	1.3 %	3.3 %
Frequency of the maximum amplitudes.	0 %	0 %	0 %	1.6%
Damping ratio differences.		6.9 %	0.59 %	0.81 %

Table 2: Effect of area size: 13x13 mm^2 rough versus 5x5 mm^2 rough.

As shown in Table 1 and Table 2, discrepancies between surface 13x13 and 5x5 are limited. Differences between maximum displacement amplitudes does not exceed 5.2 %. Also, the frequencies of the maximum amplitudes and damping are not affected significantly, with one exception (6.9 % discrepancy on damping for Fn=2 N).

	Fn=0.1 N	Fn=2 N	Fn=10 N	Fn=80 N
Amplitude differences.	-0.31 %	2.4 %	0.85 %	-0.2 %
Frequency of the maximum amplitudes.	0 %	5.8 %	2.8 %	1.6 %
Damping ratio differences.		-11.3 %	-1 %	0 %

Table 3: Influence of roughness: 13x13 mm^2 smooth versus 13x13 mm^2 rough.

	Fn=0.1 N	Fn=2 N	Fn=10 N	Fn=80 N
Amplitude differences.	8.4 %	-1.5 %	-1 %	2.32 %
Frequency of the maximum amplitudes.	0 %	5.8 %	4 %	1.6 %
Damping ratio differences.		-4.1 %	-1.36 %	0.81 %

Table 4: Influence of roughness: 5x5 mm^2 smooth versus 5x5 mm^2 rough.

The former conclusions remain when considering the effects of roughness on the dynamics of the assembly as shown in Table 3 and Table 4.

3.2 Numerical modelling

A finite element model of the structure has been constructed using beam, shell and 8 nodes brick elements. As for the contact interface, zero thickness elements are used with Masing's tangential contact model. It is a combination of a Coulomb's contact model with a spring as illustrated in Figure 8 with 1 dof mass-spring system.

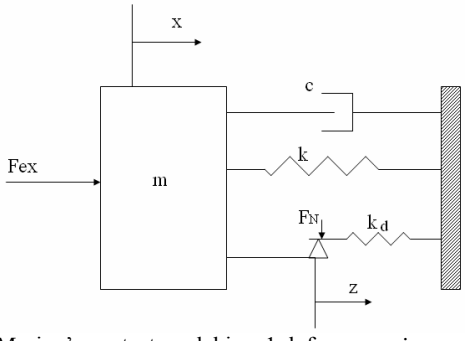


Figure 8: Masing's contact model in a 1 dof mass-spring system

The tangential contact force Ft is given by the fallowing equations:

$$F_t = sgn(\dot{x})\mu Fn \quad \text{for slipping contact}$$
$$F_t = -sgn(\dot{x})\mu Fn + k_d(x - z) \quad \text{for sticking contact} \tag{2}$$

Where μ is the friction coefficient, F_n the normal contact load, k_d the contact stiffness, x the displacement of the mass, $\dot{x}$ its the velocity and z is the internal slipping variable.

Due to the nonlinear nature of the problem, the solution is obtained using a Newmark time integration scheme with Newton-Raphson iterations. Depending on the circumstances, two different models we will used. The first is based on parameters (μ and k_d) that are obtained from model updating, in the case when experimental data are available. The second model uses estimated averaged parameters given in [2], as the authors suggest useful when experimental data are unavailable: friction coefficient of 0.66 and contact stiffness of 3e7 N/m. Table 5 gives the parameters used for the smooth surface with an area of 13x13 mm^2 for model 1 and 2. It is noticeable that parameters suggested in [2] are higher than the identified values.

	Friction coefficient	**Contact stiffness**
Model 1	0.45	3.9e5 N/m
Model 1	0.66	3e7 N/m

Table 5: Parameter values for the smooth surface 13x13 mm^2

In Figure 9, comparisons between the numerical and experimental results are presented. In the case of model 2, the comparisons were done only with two normal loads due to calculation time. The graphics clearly show that on one hand model 1 reproduces with good accuracy the experimental FRFs as on the other there is a shift of 10 Hz between model 2 and experiments. We can also notice that minimal discrepancy is observed on the maximum displacement amplitudes for both models.

While a 10 Hz frequency shift is not dramatic considering that no experimental data is available, it shows the need of more accurate parameter estimation. A third model, which will not be presented in this paper will focus on this aspect.

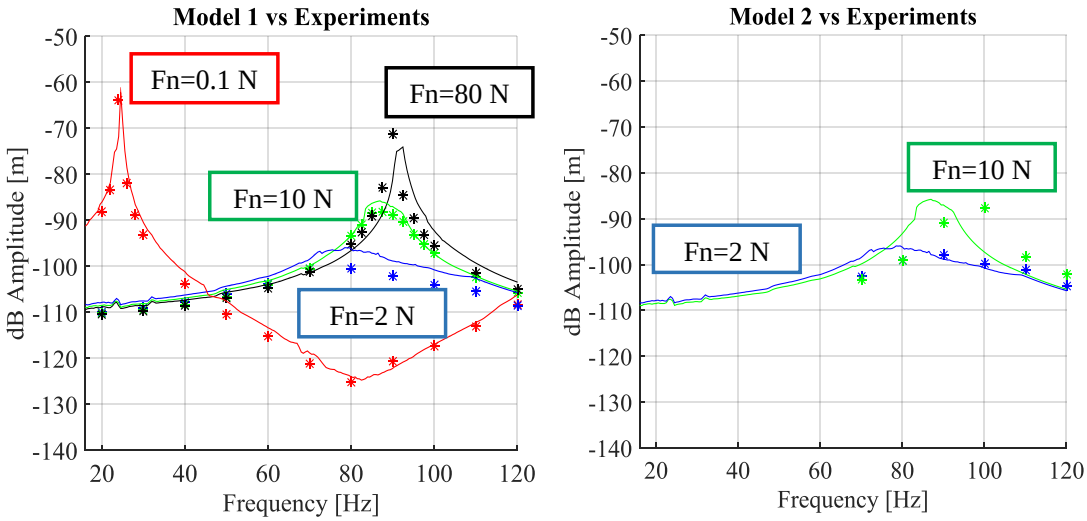


Figure 9: Model 1 and 2 versus experiments

Similarly to what has been done experimentally, numerical studies with various contact area size and roughness were done. The numerical modeling shows little to no influence of area size and surface roughness on the dynamic response of the assembly. Thus confirming the experimental results. An example of comparison between surface 13x13 and 5x5 is shown in Table 6.

	Fn=0.1 N	Fn=2 N	Fn=10 N	Fn=80 N
Amplitude differences.	0 %	1.4 %	2.2 %	-3.1 %
Frequency of the maximum amplitudes.	0 %	0 %	0 %	0 %
Damping ratio differences.		1.7 %	1.6 %	0.23 %

Table 6: Contact area size effect on the FRF – smooth 13x13mm^2 versus smooth 5x5 mm^2

Numerical calculations for higher normal loads (120 – 160 – 200 N) and excitation amplitude loads (2 – 20 – 40 - 100 N) were done in order to see in what range of Fn and Fex contact area size and roughness may have more influence. In Figure 10, smooth surface 13x13 and the rough surface 13x13 are compared for Fn=120 N and Fex=40 N. The maximum amplitude discrepancy is of 6.1 % and the smooth surface dissipates more energy than the rough one. The other calculations show an increase of the influence of contact characteristics for higher external loads (Fn and Fex). However, the observed discrepancies remain limited as they do not exceed 10% for maximum amplitude for instance.

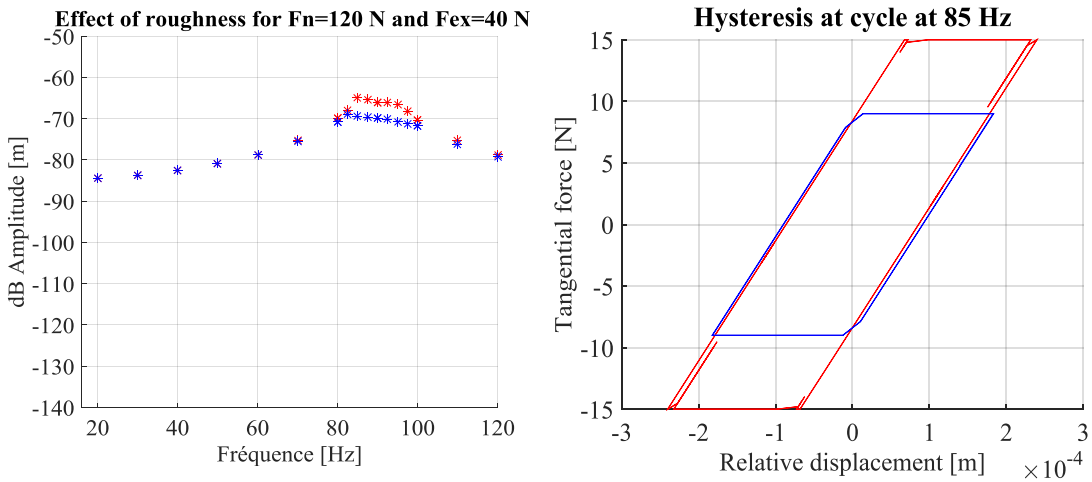


Figure 10: Smooth surfaces (red color) versus rough surface (blue color) for 13x13 sample, Fn=120 N and Fex=40 N.

4 CONCLUSIONS

This study was focused on the dynamics of a beam associated with rubbing devices. Both experimental and numerical results are presented. Different configurations were tested in order to assess the effect of contact area size and roughness of the assembly. It was shown that the influence of such characteristics is limited when considering the discrepancies on maximum amplitude of displacements, frequencies of peak displacements and damping ratios.

Numerically, calculations with Masing's model were done. In the case when experimental data is available, the comparison between the model and experiments agrees well hence validating the fact that contact area size and roughness have limited effects on the FRF. On the other hand, when measured data is not readily available, the correlation between the model (using averaged estimated values) and experiments is more delicate as a shift between the peak frequencies is observed. This is due to the fact that the contact stiffness estimation is too high. However a good agreement was noticed on maximum amplitudes. This last results leads us to believe that a work on the estimation of contact parameters is needed. A model which does not require prior experimental friction tests such as in [5] is under development.

REFERENCES

[1] L. Gaul, J. Lenz, Nonlinear dynamics of structures assembled by bolted joints. *Acta Mechanica*, **125**, 169–181, 1997.

[2] C.W. Schwingshackl, E.P. Petrov, D.J. Ewins, Measured and estimated friction interface parameters in a nonlinear dynamic analysis. *Mechanical Systems and Signal Processing*, **28**, 574–584, 2012.

[3] M. Eriten, A.A. Polycarpou, L.A. Bergman, Physics-based modeling for partial slip behavior of spherical contacts. *International Journal of Solids and Structures*, **47**, 2554–2567, 2010.

[4] M. Eriten, A.A. Polycarpou, L.A. Bergman, Physics-based modeling for fretting behavior of nominally flat rough surfaces. *International Journal of Solids and Structures*, **48**, 1436–1450, 2011.

[5] M. Eriten, A.A. Polycarpou, L.A. Bergman, A Physics-Based Friction Model and Integration to a Simple Dynamical System. *Journal of Vibration and Acoustics*, **134**, 051012, 2012.

[6] J. A. Greenwood, J. B. P. Williamson, *Contact of Nominally Flat Surfaces*. Proc. R. Soc. A, **295** (1442), 300–319, 1966.

[7] K. Johnson, *Contact Mechanics*, Cambridge University Press, Cambridge, 1985.

International Conference on Engineering Vibration
Ljubljana, Slovenia, 7-10 September 2015

ON THE DYNAMICS OF THE SYMMETRICAL SOLIDS ON A VIBRATION RUBBED HORIZONTAL PLANE

Alexey A. Kireenkov*[1]

[1]Institute for Problems in Mechanics of the Russian Academy of Sciences
kireenk@ipmnet.ru, kireenk@mail.ru

Keywords: Multi-Components Dry Friction, Dynamics of the Symmetrical Solids on Vibrated Rubbed Horizontal Plane.

Abstract. *It is considered the influence of the combined dry friction on a free motion of the symmetrical solids on rubbed plane which is performing periodical oscillation in the vertical direction. Arising dry friction effects are described with aid of theory of multicomponent dry friction based on analytical approximants of the exact integral dry friction models. As example, a free motion of the heavy disk on rubbed plane which is performing periodical oscillation in the vertical direction is considered. Disk has form of the short circle cylinder, one of base of which is found on the plane, and, consequently, the normal contact stresses distribution is obeyed by Galin's law. It is supposed that disk is performing a free combined motion: simultaneously sliding and spinning.*

1 INTRODUCTION

A problem about the symmetrical solids dynamics on the horizontal rubbed plane is one of the classical problems of theoretical mechanics. It was investigated in many publications. Most arise effects are caused by the influence of the combined dry friction.

One of the first works, in which there was carried out a detailed study of the dynamics of a heavy circular cylinder on a rough plane under the assumption of uniform distribution of normal contact stress inside of the contact area, was made by a group of Russian scientists under under the leadership of A.Yu. Ishlinsky [1].

With that, a specialists in the field of theory of elasticity are well known that distribution of normal contact stress in the case of the indentation of cylindrical punch into an elastic half-space distribution of is obeys by Galin law [2]. However, the use of the real law of the normal contact stresses distribution in the dynamics problems was complicated by cumbersome methods of investigations. Progress was made only after the establishment of the theory of multicomponent friction.

Fact is that researchers in the field of dry friction has long been known that in case of combined of the kinematics, when the rubbed solids are participated, simultaneously, in the sliding, spinning and rolling motion, the use of the classical Coulomb's law is not correct, and the friction law is undergoing significant changes.

One of the first attempts to describe the relationship of friction and spinning in the case of non-point contact of moving solids was undertaken by Contensou The principle new development of the theory was given by Zhuravlev in [4]. Zhuravlev’s theory was used in [5] to investigate the dynamics of heavy disk on a rough plane in the case of combined kinematics in assumption that distribution of normal contact stresses is described by Galin law.

Just after the publication of [4-5], the theory of multicomponent dry friction had begun the development. The main distinguishing feature of this theory is that, at first, under the assumption of validity both the classical Coulomb's law in differential form for small element of the area inside the contact area and its generalized forms, there are constructed the exact coupled integral dry friction model, obtained by integrating the differentials of the principal vector and torque on the contact spot. In addition, in process of the exact integral models construction there are is used well known results from the theory of elasticity that tangent stresses lead to shift in the symmetric diagram of the normal contact stresses in the direction of the instantaneous sliding or rolling velocities [6]. To apply the theory of elasticity results in the dynamics problems, it is used the simple asymptotic representations for the contact stresses distributions based on their general properties known from the theoretical results of the theory of elasticity [7-8].

To this exact form, to facilitate its use in the dynamics problems, Pade expansions [9] or Zhuravlev’s approximations [7], based on the analytic properties of integral models, are applied. The approximate models preserve all properties of the models based on the exact integral expressions and correctly describe the behaviour of the net vector and torque of the friction forces and their first derivatives at zero and infinity. They are considered as phenomenological, as their coefficients are numbers that can be determined from the experiment that completely avoids the necessity to calculate the double integrals over the contact spot.

It is worth explain the used the "exact integral model" term because any model can not be exact, because it is only an approximation to a real phenomenon. This notion is used in the sense that, after the initial assumptions about the validity of Coulomb's law in classical and generalized differential form and general properties of the normal contact distributions inside of contact spot, all other computations, from a mathematical point of view, are being made exactly, without the use of approximate methods. Thus, after writing expressions for the dif-

ferentials of the dry friction principal vector and torque, all subsequent transformations are exact results, reflecting the nature of the phenomenon.

Another important fact that affects on the construction of a friction model is a dynamic coupling of components that determine the force state of rubbed solids, appearing in case of combined kinematics due to skew in symmetric distribution chart of the normal contact stresses [10].

The investigation of the a heavy disk dynamics on the vibration rubbed plane, presented below, are took into account both the dynamic coupling between components that determine the force state of the rubbed solids, as well as a generalized differential form of Coulomb's law.

2 FRICTION MODELS OF THE HEAVY DISK FREE MOTION ON THE RUBBED HORIZONTAL PLANE

Friction models of the heavy disk free motion on the rubbed horizontal plane are constructed under the assumption that the Coulomb law in differential form holds for the small surface element dS in the interior of the contact spot, according to which the differentials of the resultant vector $d\mathbf{F}$ and the moment of friction dM_C with respect to the disk center are determined by the formulas:

$$d\mathbf{F} = -f\sigma\frac{\mathbf{V}}{|\mathbf{V}|}\left(1+\mu_1|\mathbf{V}|^3-\mu_2|\mathbf{V}|\right)dS,\ \ dM_C = -f\sigma\frac{\mathbf{r}\times\mathbf{V}}{|\mathbf{V}|}\left(1+\mu_1|\mathbf{V}|^3-\mu_2|\mathbf{V}|\right)dS, \qquad (1)$$
$$\mathbf{V} = (v-\omega y, \omega x),\ \mathbf{r} = (x, y)$$

where f is the coefficient of friction, $\mathbf{r} = (x, y)$ is the position vector of an elemental area in the interior of the contact spot with respect to its center (Fig. 1), R - radius of contact spot, x - axe of the rectangular coordination systems with origin in the center of contact circle which is directed parallelly to velocity of instantaneous sliding v, ω is the angular velocity of rotation of the contact spot center, but μ_1 and μ_2 are the coefficients which can be defined in practice from experiments.

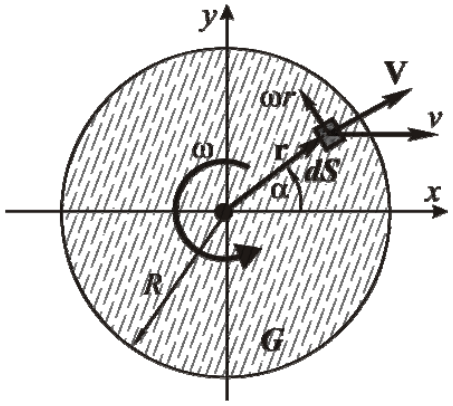


Figure 1: Kinematics inside the contact spot.

To use the theory of elasticity results in the dynamics problems, a simple linear approximation of the normal contact stresses distribution is proposed:

$$\sigma(x,y)=\sigma_0\left(1+kx/R\right) \tag{2}$$

where $\sigma_0=\sigma_0(r), r=|\mathbf{r}|$ - Galin distribution of normal contact stresses at absence of motion having the properties of central symmetry:

$$\sigma_0=N\Big/\left(2\pi R^2\sqrt{1-r^2/R^2}\right) \tag{3}$$

where N - normal reaction force.

To calculate coefficient k it is used the condition of equality of the external force F torque to the normal reaction force N torque which is appears from the shifting of the center of gravity of the contact spot in the direction of sliding on the value s:

$$Fh=Ns \tag{4}$$

where h - distance from the disk center mass to the plane of sliding.

On the other hand the shifting s of the gravity center relatively of the contact spot center can be defined by the following formula:

$$s=\iint\limits_G x\sigma(x,y)dxdy\Big/\iint\limits_G \sigma(x,y)dxdy,\ G=\{(x,y):x^2+y^2\le R^2\} \tag{5}$$

Substitution of the normal contact stresses distribution (3) to formula (4) yields:

$$s=\frac{\pi k}{R}\int\limits_0^R\sigma_0(r)r^3dr=\frac{R}{3} \tag{6}$$

Equalization values s calculated by the formulas (3) and (5) allows to define coefficient k which is characterized the dynamical coupling of the components defining the force state inside of contact spot.

2.1 Integral model

To obtain the resultant vector and the moment of friction, it is necessary to integrate the expressions (1) over the contact spot. The obtained dependencies, where $F_{\parallel}$ and $F_{\perp}$ denote the respective components of the resultant vector directed along the tangent and the normal to the trajectory of motion, present an exact integral friction model of the disk motion on rubbed horizontal plane.

At the supposition that external forces are absence, the coefficient k in formula (1) is defined by the friction force component $F_{\parallel}$ and the model has the following form:

$$\begin{aligned}
F_{\parallel}&=fN\int\limits_0^{2\pi}\int\limits_0^1\frac{(v-ur\sin\alpha)r\sigma_0(r)}{\sqrt{u^2r^2+v^2-2uvr\sin\alpha}}drd\alpha+2\pi f\left((\mu_1v^3-\mu_2v)I_1+2\mu_1vu^2I_3\right)\\
F_{\perp}&=kfN\int\limits_0^{2\pi}\int\limits_0^1\frac{ur^3\sigma_0(r)\cos^2\alpha}{\sqrt{u^2r^2+v^2-2uvr\sin\alpha}}drd\alpha,\ k=\frac{fhR}{\pi I_3}\int\limits_0^{2\pi}\int\limits_0^1\frac{(v-ur\sin\alpha)r\sigma_0(r)}{\sqrt{u^2r^2+v^2-2uvr\sin\alpha}}drd\alpha\\
M_C&=fRN\int\limits_0^{2\pi}\int\limits_0^1\frac{(ur^2-vr\sin\alpha)r\sigma_0(r)}{\sqrt{u^2r^2+v^2-2uvr\sin\alpha}}drd\varphi+2\pi f\left((2\mu_1v^2-\mu_2)uI_3+\mu_1u^3I_5\right)
\end{aligned} \tag{7}$$

where coefficients of polynomials terms in formulas (7) are the first moments of the normal contact stresses distribution: $I_1 = \int_0^1 r\sigma_0(r)dr = \frac{1}{2\pi}$ - moment of the first order, $I_3 = \int_0^1 r^3\sigma_0(r)dr = \frac{1}{3\pi}$ - moment of the third order and $I_5 = \int_0^1 r^5\sigma_0(r)dr = \frac{4}{15\pi}$ - moment of the fifth order.

2.2 Models based on Pade expansions

Double integrals in formulas (7) can be calculated in elementary function [10-11], but much more convenient to use they direct approximations based on Pade expansions. The simplest of them for the torque M_C and for the tangent force component $F_{\parallel}$ are the linear-fractional approximations. But, for the normal friction force component, corresponded Pade approximation, naturally, became of the second order:

$$
\begin{aligned}
&M_C = M_0\left(\frac{u}{u+mv} + 2\pi\left((2\mu_1 v^2 - \mu_2)uI_3 + \mu_1 u^3 I_5\right)\right),\ \frac{1}{m} = \frac{3\pi}{4}\\
&F_{\parallel} = F_0\left(\frac{v}{v+au} + 2\pi\left((\mu_1 v^3 - \mu_2 v)I_1 + 2\mu_1 v u^2 I_3\right)\right),\ \frac{1}{a} = \frac{4}{\pi}\\
&F_{\perp} = \frac{\mu F_0 uv}{(u+bv)(v+au)},\ \frac{1}{b} = \frac{4\pi^2}{3}
\end{aligned}
\qquad (8)
$$

The model of the first order (8) preserves the values of the functions $F_{\parallel}(u,v)$, $F_{\perp}(u,v)$ and $M_C(u,v)$ defined by the formulas (7) at zero, as well as their behavior and the behavior of their first derivatives at infinity. But model of this type cannot completely preserve the values of all first partial derivatives of these functions at zero. To obtain a correct description of the behavior of the first derivatives at zero, it is required to use the second-order Pade´ approximations:

$$
\begin{aligned}
&M_C = M_0\left(\frac{u^2+muv}{v^2+muv+u^2} + 2\pi\left((2\mu_1 v^2 - \mu_2)uI_3 + \mu_1 u^3 I_5\right)\right),\ m = \frac{4}{3\pi}\\
&F_{\parallel} = F_0\left(\frac{v^2+auv}{v^2+auv+u^2} + 2\pi\left((\mu_1 v^3 - \mu_2 v)I_1 + 2\mu_1 v u^2 I_3\right)\right),\ a = \frac{\pi}{4}\\
&F_{\perp} = \frac{\mu F_0 uv}{(u+bu)(v+au)},\ \frac{1}{b} = \frac{4\pi^2}{3}
\end{aligned}
\qquad (9)
$$

The second-order model (9) completely satisfies to the all integral model analytical properties.

The approximations (8) and (9) hold for positive values of u and v. They can be easily generalized to the case of arbitrary (in sign) velocities u and v by a formal change by absolute values in the denominators of the corresponding expressions.

2.3 Models based on new type of approxomations

Another kind of the approximations which will be valid for all ranges of the velocities variation is approximations, firstly mentioned but not calculated in [7]:

$$
\begin{aligned}
M_C &= M_0\left(\frac{u}{\sqrt{u^2+mv^2}}+2\pi\left((2\mu_1 v^2-\mu_2)uI_3+\mu_1 u^3 I_5\right)\right),\ \frac{1}{m}=\frac{16}{9\pi^2}\\
F_{\parallel} &= F_0\left(\frac{v}{\sqrt{v^2+au^2}}+2\pi\left((\mu_1 v^3-\mu_2 v)I_1+2\mu_1 vu^2 I_3\right)\right),\ \frac{1}{a}=\frac{16}{\pi^2}\\
F_{\perp} &= \frac{\mu F_0 uv}{\sqrt{(u^2+bv^2)(v^2+au^2)}},\ \frac{1}{b}=\frac{16\pi^4}{9}
\end{aligned}
\tag{10}
$$

This model permits to escape using not smooth functions in the cases when velocities are changed their signs. Moreover, model (10) are defines by the same coefficients amounts as models based on Pade expansions.

3 DISK DYNAMICS

The equations of motion of a disk of radius R and mass m_d considered at the projections on the axes of fixed coordinate system $\{XY\}$ (Fig.2) hardly connected with vibration plane are:

$$
\begin{aligned}
&J\dot{\omega} = -M_C,\ m_d\ddot{\mathbf{r}} = \mathbf{F},\ \mathbf{r}=(x,y),\mathbf{F}=(F_x,F_y)\\
&N = m_d g - A_z m_d \nu_z^2 \sin\nu_z t
\end{aligned}
\tag{11}
$$

where A_z and ν_z are the amplitude and frequency of the plane oscillations, but $J = m_d R^2/2$ is the disk moment of inertia.

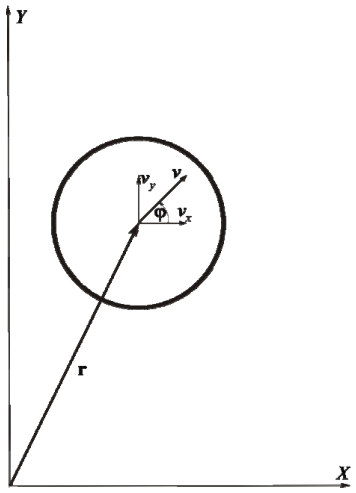


Figure 2: Disk kinematics.

Velocities of disk center mass are defined by formulas: $v_x = \dot{x}, v_y = \dot{y}$. In the moving polar coordinates system $\{v,\varphi\}$ with origin in projection of the mass center to the sliding plane (center of contact spot) they has form: $v_x = v\cos\varphi, v_y = v\sin\varphi, \dot{\varphi} = \omega$.

Connections of the net vector **F** components in fixed coordinate system with their components in moving coordinate systems with origin at the center of contact circle are given by the formulas:

$$\begin{aligned} F_x &= -F_{\|}\cos\varphi + F_{\perp}\sin(\varphi) \\ F_y &= -F_{\|}\sin\varphi - F_{\perp}\cos(\varphi) \end{aligned} \tag{12}$$

Here $F_{\|}$ and $F_{\perp}$ can be defined as by formulas (8)-(9) as formulas (10). Because the sliding velocity v can change the sign, it is convenient to use the model (10), in which:

$$\begin{aligned} F_0 &= fN = f(m_d g - A_z m_d \nu_z^2 \sin\nu_z t) \\ M_0 &= fNR = fR(m_d g - A_z m_d \nu_z^2 \sin\nu_z t) \end{aligned} \tag{13}$$

In result, the full equation system of the disk dynamics on the vibration rubbed plane has form:

$$J\dot{\omega} = -M_C,\ m_d\dot{v}_x = F_x,\ m_d\dot{v}_y = F_y \tag{14}$$

Transition from variables $(\omega, \dot{v}_x, \dot{v}_y)$ to variables (u, v, φ) gives:

$$J\dot{u} = -RM_C,\ m_d\dot{v} = -F_{\|},\ m_d v\dot{\varphi} = -F_{\perp} \tag{15}$$

From the last equation of this system (16) immediately follows conclusion about the shift of the disk trajectory from the straight line because $\dot{\varphi} \neq 0$ at $F_{\perp} \neq 0$. The first two equations are separated and, consequently, can be solve independently, because $M_C = M_C(u, v)$, $F_{\|} = F_{\|}(u, v)$. Moreover, presence the periodic functions caused the periodic disk motion.

4 CONCLUSIONS

- The combined dry friction effects have a basic influence on the solids dynamics.
- The periodic oscillations in vertical directions of the plane on which the disk is rest caused its periodic motion.

REFERENCES

[1] A.Yu.Ishlinsky, B.N. Sokolov and F.L. Chernous'ko, On the motion of plane bodies subject to dry friction. *Izv.ANSSSR.MTT[Mechanics of Solids]*, **4**, 17–28, 1981.

[2] A. Galin, *Contact Problems of Elasticity and Viscoelasticity*. Nauka, Moscow, 1980.

[3] P. Contensou, Couplage entre frottement de glissement et Ftottement depivotement dans la theorie de la touplie. in Kreisel probleme Gyrodynamics*: IUTAM Symp. Celerina*, 1962, Springer, Berlin, 201-216, 1963.

[4] V.Ph. Zhuravlev, On the model of dry friction in the problem of rolling of rigid bodies. *J. Appl. Math. Mech.*, **62(5)**, 762–767, 1998.

[5] A.A. Kireenkov, On the motion of a homogeneous rotating disk along a plane in the case of combined friction. *Mechanics of Solids*, **37(1)**, 47–53, 2002.

[6] I.G. Goryacheva, *Mechanics of friction interaction*. Moscow: Nauka, 2001.

[7] V.V. Andronov, V.Ph. Zhuravlev, *Dry Friction in Problems of Mechanics*. Moscow-Izhevsk: NITs Reg. Khaot. Dinam., 2010.

[8] A.A. Kireenkov, Coupled Model of Sliding and Spinning Friction. *Doklady Akademii Nauk*, **441(6)**, 750–755, 2011.

[9] J.A. Baker, P. Graves-Morris, *Pade approximants*. Addison-Wesley Publishing Co, London, Amsterdam, Don-Mills, Ontario, Sydney, Tokyo, 1981.

[10] A.P. Ivanov, A dynamically consistent model of the contact stresses in the plane motion of a rigid body, *Prikl. Mat. Mekh.*, **73(2)**, 134-144, 2009.

[11] A.A. Kireenkov, Generalized two dimensional model of the sliding and spinning friction. *Doklady Akademii Nauk*, **431(4)**, 482–486, 2010.

5

Falling Motion of a Circular Cylinder Interacting Dynamically with a Point Vortex

Sergei V. Sokolov

Аннотация

The dynamical behavior of a heavy circular cylinder and N point vortices in an unbounded volume of ideal liquid is considered. The liquid is assumed to be irrotational and at rest at infinity. The circulation about the cylinder is different from zero. The governing equations are presented in Hamiltonian form. Integrals of motion are found. Allowable types of trajectories are discussed in the case $N = 1$. The stability of finding equilibrium solutions is investigated and some remarkable types of partial solutions of the system are presented. Poincaré sections of the system demonstrate chaotic behavior of dynamics, which indicates a non-integrability of the system.

point vortices, Hamiltonian systems, reduction, stability of equilibrium solutions

1. INTRODUCTION

The problem of falling motion of a body in fluid has a long history and was considered in a series of the classical [14, 22, 23] and modern papers [2, 12]. Some of the effects described in the papers, such as periodic rotation (tumbling), can be encountered only in viscous fluids and thus demand for their proper treatment the use of the Navier–Stokes equations with boundary conditions specified on the body's surface. As a rule, such problems are hardly amenable to analytical analysis and can be addressed only numerically. Another approach is to use (instead of the exact Navier–Stokes equations) some phenomenological ODE models which capture the viscous effects only qualitatively. For example, in [21] approximate expressions for the drag and lift on the body are used and the translational and rotational motions of the body are assumed to be independent. Evidently, the validity and accuracy of such models and approaches remain open for discussion.

The fluid's viscosity imposes resistive forces on the body. These forces manifest themselves not only through the skin friction but they also serve a source of vortex generation. To evaluate a model which is a more or less realistic and at the same time amenable to analytical treatment it is customary to assume the liquid to be ideal and add the vorticity *ad hoc* meaning that we postulate the existence of, say, circulation, point vortices or vortex sheets etc. The simplest manifestation of vorticity is the presence of circulatory motion about the body.

The falling motion of a body with circulation was considered in [7, 13, 16]. It is shown in [16] that the lift on the body due to circulation prevents the body from actually falling and forces it to travel within a horizontal strip of finite width. To move further in understanding the role of vorticity it seems reasonable to investigate the interaction of a rigid body with point vortices. Kirchhoff [11] was the first who obtained the Hamiltonian form of the equations of motion for point vortices. In [3, 6, 17, 18] this Hamiltonian formalism was extended to the case when point vortices are dynamically interacting with a 2D rigid body (in the absence of gravity). In [17] and then in [18] *exact* governing ODEs were obtained. The integrability of the system of circular cylinder interacting with a single point vortex was proved in [3]. Some partial cases, reduction and the general analysis of motion in this problem were performed in [6].

The next step was the Brown and Michael model (which dates from 1960s) where the shedding of new vortices from body's sharp edges is postulated since it is well known that vorticity cannot be generated in ideal fluid. The intensity of each newborn vortex varies with time so as to fulfill the Kutta–Zhukovsky condition at the edge and maybe some other restrictions (depending on the modification of the model adopted) that stem from the conservation laws. Within the framework of this model the falling motion of a body was recently investigated in [15].

The falling card problem in the presence of distributed vorticity was considered in [9]. The flow was assumed two-dimensional and to consist of a bound vortex sheet coincident with the plate and two free vortex sheets that emanate from each of the plate's two sharp edges. Though the governing equations (ODEs) in [9, 15] are exact, they are investigated only numerically due to their complexity.

In [10] the motion of a point vortex in the flow generated by a translationally moving circular cylinder is considered. Thus the problem is purely kinematical and does not account for the forces the vortex exerts on the cylinder. The paper [10] is focused on the analysis of chaotic behavior of the vortex when the cylinder's motion is perturbed.

In previous works [19, 20] the problem of motion of the heavy cylinder under the action of gravity and a single point vortex was investigated with non-zero circulation.

In this paper we study the influence of the vorticity on the falling body in a trivial setting: a body (circular cylinder) subject to gravity is interacting dynamically with N point vortices. The circulation around the cylinder is not necessarily zero. So the model we consider here is exact and, at the same time, not so despairingly complex as most of the existing models are.

2. SETTING UP OF THE PROBLEM

Consider a circular cylinder subject to gravity moving in an unbounded volume of ideal liquid at rest at infinity. The cylinder's element is orthogonal to the flow; thus the problem is essentially two-dimensional. There are N vortex filaments (point vortices) of strength Γ_i parallel to the cylinder's element, here $i = \overline{1, N}$.

The circulation Γ of the flow around the cylinder is, generally, different from zero (Fig. 1). Our goal is to detect and investigate the main features of the system.

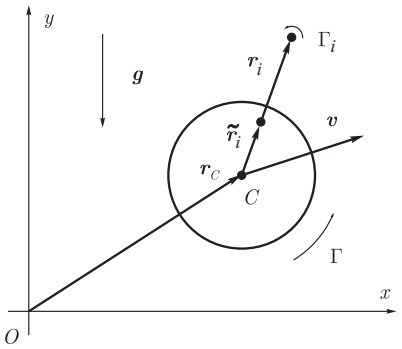


Рис. 1. Circular cylinder and point vortices in the gravity field.

3. GOVERNING EQUATIONS

According to [17], the equations of motion for a cylinder and point vortices in the presence of gravity can be written as

$$\begin{aligned}
&\dot{\boldsymbol{r}}_i = -\boldsymbol{v} + \operatorname{grad}\widetilde{\varphi}_i(\boldsymbol{r})|_{\boldsymbol{r}=\boldsymbol{r}_i}\,,\\
&\dot{\boldsymbol{r}}_c = \boldsymbol{v},\\
&a\dot{v}_1 = \lambda v_2 - \sum_{i=1}^{N}\lambda_i(\dot{\widetilde{y}}_i - \dot{y}_i),\\
&a\dot{v}_2 = -\lambda v_1 + \sum_{i=1}^{N}\lambda_i(\dot{\widetilde{x}}_i - \dot{x}_i) - ag,
\end{aligned} \tag{1}$$

Here $\boldsymbol{r}_c = (x_c,\, y_c)$ is the radius-vector from the origin of a laboratory frame of reference Oxy to the cylinder's center, $\boldsymbol{v} = (v_1,\, v_2)$ is the velocity of the cylinder, the radius-vector $\boldsymbol{r}_i = (x_i,\, y_i)$ is from the center of the cylinder to the i-th vortex, and $\widetilde{\boldsymbol{r}}_i = (\widetilde{x}_i,\, \widetilde{y}_i) = \dfrac{R^2\boldsymbol{r}_i}{r_i^2}$ is the radius-vector from the center of the cylinder to the image of the i-th vortex (Fig. 1), R — the radius of the cylinder, the constant a is the mass plus the added mass of the cylinder, the constant ag is a gravity force applied to the cylinder, the constants λ and λ_i are related to the circulation and vortex's strength $\lambda = \dfrac{\Gamma}{2\pi}$, $\lambda_i = \dfrac{\Gamma_i}{2\pi}$. The density of the fluid is assumed to be 2π. The function $\widetilde{\varphi}_i(\boldsymbol{r})$ represents that portion of the velocity

potential $\varphi(\boldsymbol{r})$ which does not have a singularity at the point $\boldsymbol{r} = \boldsymbol{r}_i$:

$$\varphi(\boldsymbol{r}) = -\frac{R^2}{r^2}(\boldsymbol{r},\, \boldsymbol{v}) - \lambda \operatorname{arctg}\frac{y}{x} + \sum_{i=1}^{N} \lambda_i \left(\operatorname{arctg}\left(\frac{y-\widetilde{y}_i}{x-\widetilde{x}_i}\right) - \operatorname{arctg}\left(\frac{y-y_i}{x-x_i}\right)\right). \tag{2}$$

The equations (1) are identical to those from [17] except for the term that accounts for the gravity force.

As in [3], one can note that the finite-dimensional system (1), which governs the motion of a cylinder and vortices in the gravity field, preserves the standard measure and can be represented in the Hamiltonian form.

Proposition. *The equations of motion* (1) *can be represented as follows:*

$$\dot{\zeta}_i = \{\zeta_i,\, H\} = \sum_k \{\zeta_i,\, \zeta_k\} \frac{\partial H}{\partial \zeta_k}, \tag{3}$$

where ζ_i *is the phase vector of the system* (1)*, that is,*

$$\zeta = \{x_1,\, y_1,\, \ldots,\, x_N,\, y_N,\, v_1,\, v_2,\, x_c,\, y_c\},$$

H *is the Hamiltonian function, and the components of the skew-symmetric tensor of the Poisson structure* $J_{ij}(\zeta) = \{\zeta_i,\, \zeta_j\}$ *satisfy the Jacobi identity*:

$$\sum_l \left(J_{il}\frac{\partial J_{jk}}{\partial \zeta_l} + J_{kl}\frac{\partial J_{ij}}{\partial \zeta_l} + J_{jl}\frac{\partial J_{ki}}{\partial \zeta_l}\right) = 0, \quad \forall i,\, j,\, k.$$

Доказательство.

It is straightforward to check that the system (1) has a constant of motion which can be interpreted as the energy integral

$$H = \frac{1}{2}av^2 + \frac{1}{2}\sum_{i=1}^{N}\left(\lambda_i^2 \ln(r_i^2 - R^2) - \lambda_i \lambda \ln r_i^2\right) + \frac{1}{2}\sum_{i<j}\lambda_i\lambda_j \ln\frac{R^4 - 2R^2(\boldsymbol{r}_i,\, \boldsymbol{r}_j) + r_i^2 r_j^2}{|\boldsymbol{r}_i - \boldsymbol{r}_j|^2} + agy_c. \tag{4}$$

Assuming H be the Hamiltonian of our system, we now choose the components J_{ij} for the equations of motion (3) to be identical with the equations (1). The non-zero tensor components (as in [3]) read

$$\begin{gathered}
\{v_1,\, x_i\} = \frac{1}{a}\frac{r_i^4 - R^2(x_i^2 - y_i^2)}{r_i^4}, \quad \{v_1,\, y_i\} = -\frac{1}{a}\frac{2R^2 x_i y_i}{r_i^4}, \\
\{v_2,\, x_i\} = -\frac{1}{a}\frac{2R^2 x_i y_i}{r_i^4}, \quad \{v_2,\, y_i\} = \frac{1}{a}\frac{r_i^4 + R^2(x_i^2 - y_i^2)}{r_i^4}, \\
\{v_1,\, v_2\} = \frac{\lambda}{a^2} - \sum_{i=1}^{N}\frac{\lambda_i}{a^2}\frac{r_i^4 - R^4}{r_i^4}, \quad \{x_i,\, y_i\} = -\frac{1}{\lambda_i}, \\
\{x_c,\, v_1\} = \{y_c,\, v_2\} = \frac{1}{a}.
\end{gathered} \tag{5}$$

The check of the validity of the Jacoby identity for the components of (5) is a matter of straightforward computation. □

Thus, the fact that the equations (1) are Hamiltonian allows application of standard tools (e.g. for the stability analysis) from the extensively developed theory of Hamiltonian systems.

4. FIRST INTEGRALS AND REDUCTION

The presence of gravity breaks the rotational symmetry of the system, which implies the absence of an additional integral of motion which existed in the case $g = 0$ (see [3]). However, the system has two integrals of motion due to the translational symmetry: an autonomous integral P — projection of the system's linear momentum on the horizontal axis and a non-autonomous Q — projection of the system's linear momentum on the vertical axis:

$$\begin{aligned} Q &= a(v_2 + gt) + \lambda x_c - \sum_{i=1}^{N} \lambda_i(\widetilde{x}_i - x_i), \\ P &= av_1 - \lambda y_c + \sum_{i=1}^{N} \lambda_i(\widetilde{y}_i - y_i). \end{aligned} \tag{6}$$

Now we reduce the order of our system in the case $N = 1$. The system does not seem to have any additional constants of motion which is confirmed by chaotic behavior of solutions on the Poincaré section surface (Fig. 6, 7). A rigorous proof of non-itegrability of the system consisting of a body (with unequal added masses) with non-zero circulation around it falling in an ideal fluid is given in [5].

Using the autonomous integral P, one can reduce the original three-degree of freedom system to a system with two degrees of freedom.

To do this, put $P = 0$. It is clear that for $\lambda \neq 0$ (the case of $\lambda = 0$ will be addressed elsewhere) this can be always achieved by shifting the origin of the laboratory reference frame. Solving for y_c from the equation $P = 0$, substituting the result into the Hamiltonian (4) and excluding from (1) the equation in $\boldsymbol{r}_c$, we obtain the reduced system:

$$\begin{gathered} \dot{x}_1 = -v_1 + \left.\frac{\partial\widetilde{\varphi}}{\partial x}\right|_{\boldsymbol{r}=\overline{r}_1}, \quad \dot{y}_1 = -v_2 + \left.\frac{\partial\widetilde{\varphi}}{\partial y}\right|_{\boldsymbol{r}=\overline{r}_1}, \\ a\dot{v}_1 = \lambda v_2 - \lambda_1(\dot{\widetilde{y}}_1 - \dot{y}_1), \quad a\dot{v}_2 = -\lambda v_1 + \lambda_1(\dot{\widetilde{x}}_1 - \dot{x}_1) - ag \end{gathered} \tag{7}$$

which remains Hamiltonian with the Hamiltonian function

$$H_c = \frac{1}{2}av^2 + \frac{1}{2}\lambda_1^2 \ln(r_1^2 - R^2) - \frac{1}{2}\lambda_1\lambda \ln r_1^2 + \frac{ag}{\lambda}(av_1 + \lambda_1(\widetilde{y}_1 - y_1))$$

and the bracket structure obtained from (5) by eliminating the rows and columns corresponding to x_c and y_c.

5. CLASSIFICATION OF MOTIONS

Though our system is (comparatively) trivial, very few results concerned with the classification of the possible types of the cylinder and vortex trajectories can be obtained analytically. Numerical evidence show that there exist three types of motion (Fig. 2):

1) the cylinder and vortex are moving close to each other in a horizontal strip of finite width (Fig. 2a);
2) the cylinder "abandons" the vortex and then moves as in the previous case (Fig. 2b);
3) the cylinder "abandons" the vortex and travels down without bound ($y_c \to -\infty$) (Fig. 2c).

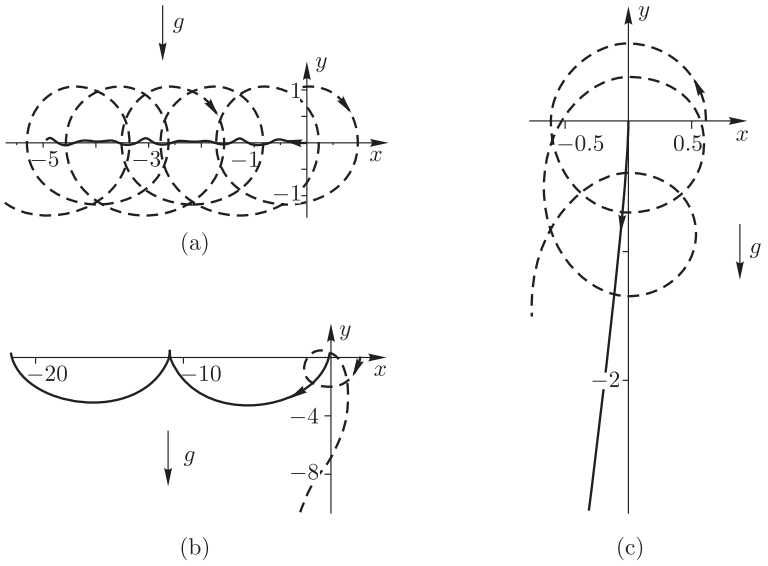


Рис. 2. Motion of the cylinder (solid line) and the vortex (dashed line) in the field of gravity: (a) the cylinder and the vortex are moving in a bounded horizontal strip, the vortex is captured by the cylinder; (b) the cylinder moves in a bounded horizontal strip, the vortex is left behind; (c) the cylinder abandons the vortex and falls down without bound ($\lambda = \lambda_1$).

Thus, we have the capture of the vortex by the cylinder as in [10] and motion in a horizontal strip as described in [13, 16].

So we hypothesize (but cannot prove it) that in the course of motion the cylinder is *always confined to a horizontal strip*, except, maybe, for the case $\lambda = \lambda_1$. If the cylinder falls down without bound (the function $y_c(t)$) tends to $-\infty$) the vortex cannot be captured with the cylinder.

6. RELATIVE EQUILIBRIA AND THEIR STABILITY

The stationary solutions of the reduced system (7) are the relative equilibria for the original system (1).

To find the equilibria we equate the right-hand sides of (7) to zero and thereby immediately obtain $v_2 = 0$, $v_1 = -\dfrac{ag}{\lambda}$. From hydrodynamical considerations it is clear that x_1 is necessarily zero meaning that the vortex and the cylinder's center lie on the same vertical line. (There are two other equilibria lying on the cylinder's surface for which $x_1 \neq 0$; but this case is of little interest as the vortex merely annihilates with its image, so we will not consider it). Substituting the found x_1, v_1, and v_2 into the right-hand side of the first equation (7) yields

$$\overline{y}_1^4 + (\widetilde{\lambda}^2 - \widetilde{\lambda}\widetilde{\lambda}_1)\overline{y}_1^3 - \widetilde{\lambda}^2\overline{y}_1 - 1 = 0. \tag{8}$$

Here the following notation is used $\overline{y}_1 = \dfrac{y_1}{R}$, $\widetilde{\lambda} = \dfrac{\lambda}{\sqrt{agR}}$, $\widetilde{\lambda}_1 = \dfrac{\lambda_1}{\sqrt{agR}}$. It is interesting to note that a similar polynomial equation was obtained in [10] where advection of a point vortex in the field generated by an oscillating cylinder was studied.

Thus, the stationary solution of (7) is given by $(x_1,\, y_1,\, v_1,\, v_2) = \Big(0,\, y_1,\, -\dfrac{ag}{\lambda},\, 0\Big)$, where $y_1 = \overline{y}_1 R$ and $\overline{y}_1$ is a root of (8). For these solutions the cylinder and vortex are moving horizontally along parallel lines at a constant rate. For a hydrodynamically asymmetric body (the added masses are different) the stability of such rectilinear horizontal motions was investigated in [13].

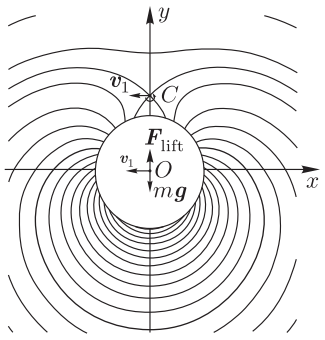


Рис. 3. Cylinder and vortex in the state of relative equilibrium.

Physically, it is clear that for a cylinder to move with a constant speed the external forces applied to it must sum up to zero: the gravity must be compensated with the lift, which is due to the circulation. The vortex placed at the stagnation point C (Fig. 3) (at this point the velocity of the fluid particle relative to the cylinder is zero) does not move relative to the cylinder and therefore neither does its image. In this case the vortex exerts no force on the

cylinder [17] and therefore cannot prevent the cylinder from moving rectilinearly. The stream lines for this equilibrium case are depicted in Fig. 3.

It follows from (8) that the ordinate of the vortex relative equilibrium depends on the two parameters $\widetilde{\lambda}$ and $\widetilde{\lambda}_1$ (normalized circulation and vortex strength). For some value of $(\widetilde{\lambda},\, \widetilde{\lambda}_1)$ there are up to 4 equilibria (Fig. 4). Here an important restriction $|y_1| > R$ must be obeyed for the vortex to be outside the cylinder. Without loss of generality we assume $\widetilde{\lambda} > 0$. A schematic of the many-leaved surface (8) is given in Fig. 4. Consider the main features of the surface.

1. In the second quadrant of the plane $(\widetilde{\lambda}_1,\, \widetilde{\lambda})$, where $\widetilde{\lambda}_1 < 0$, $\widetilde{\lambda} > 0$, there is only one equilibrium below the cylinder (the lower leaf of the surface (8)).

2. In the first quadrant $(\widetilde{\lambda}_1 > 0,\ \widetilde{\lambda} > 0)$ there is an equilibrium above the cylinder (the upper leaf of the surface (8)). The lower leaf has a "fold singularity", therefore, as indicted in Fig. 5, there may occur three equilibria: two below and one above the cylinder.

3. The upper leaf of (8) is truncated along the axis $\widetilde{\lambda}_1 = 0$ by the condition $y_1 > R$, meaning that the equilibria positions tend to the cylinder's surface from above.

4. As in the previous case, the lower leaf and the fold stitched to it are truncated with the condition $y_1 < -R$ meaning that below the cylinder the equilibria exist in any small neighborhood of its surface.

5. Since (8) is unaltered under the transformation $\widetilde{\lambda}_1 \to -\widetilde{\lambda}_1$, $\widetilde{\lambda} \to -\widetilde{\lambda}$, it is clear that in the third and fourth quadrants the surface (8) can be constructed via rotation by 180° about the $\overline{y}_1$-axis of the surface from Fig. 4.

6. In Fig. 4 the stable equilibria defined by (8) dwell only on the intermediate leaf and are shown with dark-grey shading. The unstable equilibria form the entire upper and lower leaves (light-grey shading); the unstable equilibria on the intermediate leaf form the hatched region.

For the stability analysis of the equilibria found we will use the methods and approaches developed in [1]. It is well known that to investigate the stability of an equilibrium solution of a Hamiltonian system the two invariant characteristics of such a solution must be obtained:

1. the index of the quadratic form d^2H_c $\left(\text{i.e. the index of the symmetric } (4\times 4)\text{-matrix } \left\|\frac{\partial^2 H_c}{\partial\zeta_k\,\partial\zeta_j}\right\|\right)$, which can vary from 0 to 4;

2. the type of the equilibrium solution depending on the eigenvalues of the linearized vector field $\left(\text{i. e. the eigenvalues of the symplectic } (4\times 4)\text{-matrix } \left\|\sum_k J_{ik}\frac{\partial^2 H_c}{\partial\zeta_k\,\partial\zeta_j}\right\|\right)$. This type can be one of the following: center–center, saddle–center, saddle–saddle, focus–focus.

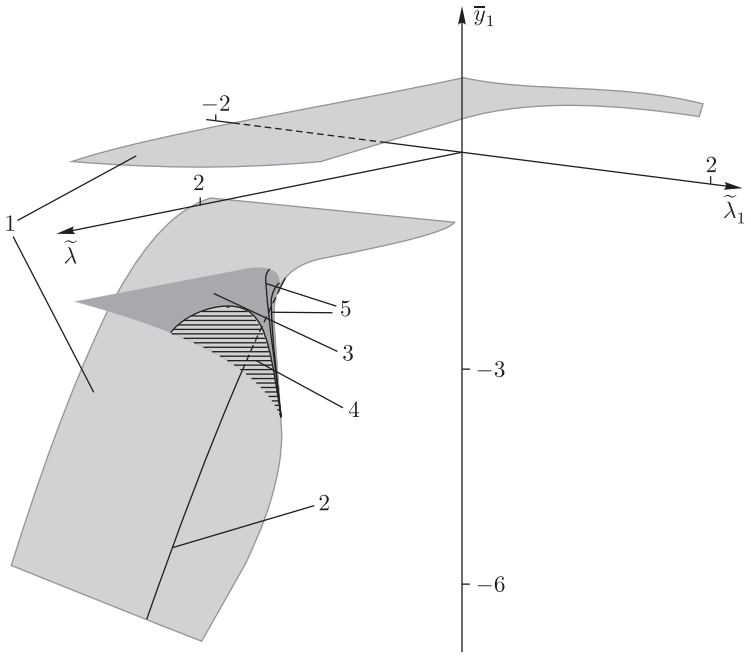


Рис. 4. Equilibrium position $\overline{y}_1$ of the vortex depending on the parameters $\widetilde{\lambda}$, $\widetilde{\lambda}_1$: 1 — unstable equilibria (ind = 1), 2 — unstable equilibria (the form d^2H_c is degenerate, the instability can be deduced from the linearized equations), 3 — stable equilibria of the center-center type (ind = 2), 4 — unstable equilibria of the focus-focus type (ind = 2), 5 — resonance curves.

Like in [1], we mark off the eigenvalues of the linearized vector field, which are the roots of the characteristic polynomial

$$\chi(\mu) = \det\left(\sum_k J_{ik}\frac{\partial^2 H_c}{\partial\zeta_k\,\partial\zeta_j} - \mu E\right) = \mu^4 + a\mu^2 + b, \tag{9}$$

on the plane (a, b) of the polynomial coefficients. In Fig. 5a from [1], one can see stable and unstable regions, the index of the form d^2H_c, and the types of the equilibrium solutions.

In Fig. 4, the upper and lower leaves are comprised of unstable solutions of the saddle–center type because here the index of d^2H_c is 1. These solutions correspond to the region $b < 0$ in Fig. 5a. The points on the intermediate leaf (except for the resonance curves) are either unstable of the focus–focus type or stable of the center–center type; on this leaf the index of d^2H_c is 2.

Consider in greater detail the region in the first quadrant of the plane $(\widetilde{\lambda}_1, \widetilde{\lambda})$ where there are three equilibria. A close up of this part of the surface (8) is given

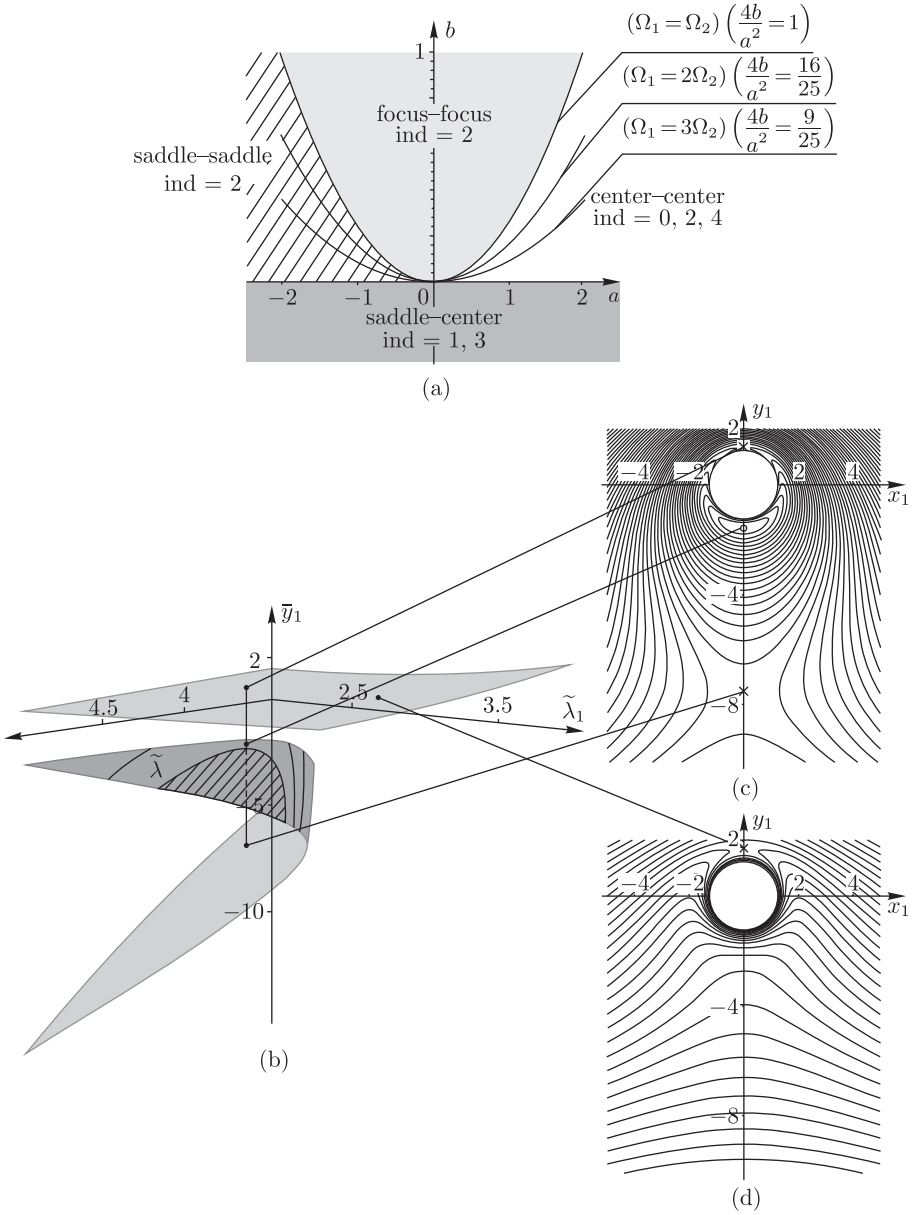


Рис. 5. Equilibrium solutions and their stability. (a) Stable and unstable regions in the (a, b) plane of the characteristic polynomial coefficients. The third- and fourth-order resonance curves are shown. (b) The relative equilibrium position of the vortex versus the parameters $\widetilde{\lambda}$, $\widetilde{\lambda}_1$. Depending on the value of $\widetilde{\lambda}$, $\widetilde{\lambda}_1$ there can be a single equilibrium or even three equilibria. (c) The Hill domain for the three-equilibrium case. (d) The Hill domain for the single equilibrium case. In (c) and (d) the unstable equilibria are marked with crosses and the stable equilibria – with circles.

in Fig. 5b. As in Fig. 4, the lower and upper leaves of the surface (8) represent unstable solutions with of the saddle–center type with ind $= 1$; the leaves correspond to the region $b < 0$ in Fig. 5a. The intermediate leaf contains two types of points: stable (center-center) and unstable (focus–focus); everywhere on this leaf ind $= 2$. The stable solutions correspond to the region $\left(a > 0,\, 0 < b < \frac{a^2}{4}\right)$ in Fig. 5a. The unstable points form the region $b > \frac{a^2}{4}$. In Fig. 5a and Fig. 5b the third- and fourth-order resonances, defined by the equations $b = \frac{4a^2}{25}$ and $b = \frac{9a^2}{100}$, are shown. The resonances lie within the stable area. The analysis of the stability of the solutions on the boundaries $b = 0$, $b = \frac{a^2}{4}$ and the resonance curves is not performed here as it entails a great amount of computation.

Finally, consider the equilibria corresponding to $\widetilde{\lambda}_1 = 2.1$ and $\widetilde{\lambda} = 4$. The Hill domains in the vicinity of these equilibria are depicted in Fig. 5c. The upper and lower equilibria are seen to be unstable and the intermediate one is stable.

Suppose that the circulation around the cylinder increases and the strength of the vortex is fixed. This can be imagined as if a vertical line moves along the $\widetilde{\lambda}$-axis in Fig. 5b. When this line crosses the boundary that corresponds to the parabola $b = \frac{a^2}{4}$ the type of the solution switches from center-center to focus-focus. The Hill domains in the vicinity of these solutions are analogous to those depicted in Fig. 5c. The intermediate solution becomes unstable.

Now let the circulation be fixed and the vortex strength grow. The imaginary vertical line moves along the $\widetilde{\lambda}_1$-axis. The stable center–center solution approaches the unstable focus–focus solution and they finally merge on the curve that corresponds to $b = 0$. As the vortex strength increases further there remains only one equilibrium (which is unstable) of the saddle–center type and located on the upper leaf (above the cylinder). The schematic of the Hill domain is given in Fig. 5d.

It should be noted that the boundaries that separate the stable solutions with ind $= 2$ from the unstable solutions with ind $= 2$ are very sensitive to the choice of the mass and radius of the cylinder a and R. At the same time, the surface (8) is independent of a and R. The type of the equilibria in Figs. 4 and 5 was determined for $a = 1,\ R = 1$.

7. POINCARÉ SECTION AND CHAOTIC BEHAVIOR OF THE DYNAMICAL SYSTEM

It is known that a system with insufficient number of conserved quantities (first integrals) is usually characterized with chaotic behavior of its trajectories. A strict proof of the property of non-integrability usually involves highly non-trivial mathematical argumentation. On the other hand, the chaotic dynamics of the system's solutions (that can be easily revealed via simulations) indicates

the lack of first integrals.

Let us apply this line of reasoning to the system of equations (7), which is a Hamiltonian system with two degrees of freedom. To better understand its dynamics we plot a few Poincaré sections.

The phase vector of the system reads

$$\zeta = \{x_1,\, y_1,\, v_1,\, v_2,\}.$$

We fix $y_1 = 0.9$ thus picking a section plane in a neighborhood of the vortex's relative equilibrium. For $H_c = -17$ the Poincaré section is shown in Fig. 6. The other parameter's values $a = 1$, $R = 0.5$, $g = 10$, $\Gamma = 10$, $\Gamma_1 = 8.4375$.

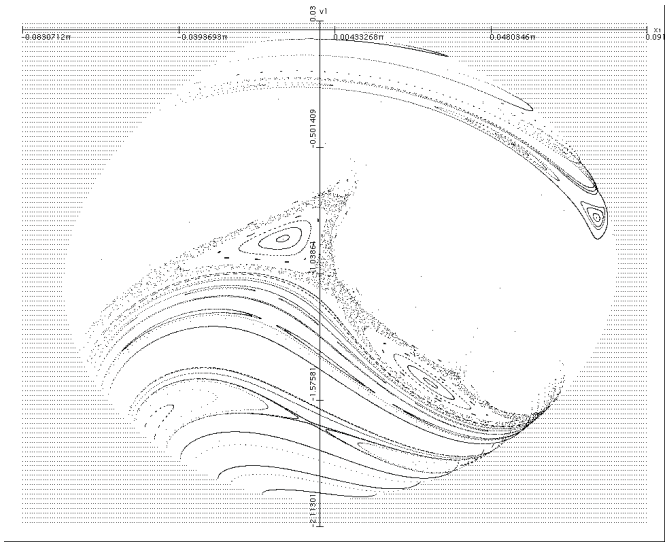


Рис. 6. Poincaré section of the reduced cylinder-vortex system for $Hc = -17$; the system exhibits chaotic behavior.

In Fig. 6 points of the phase plane x_1v_1 which lie outside the region of allowable motion are shown with grey shading. We can see areas of regular dynamics which appear as intersection of the energy level surface and invariant tori. A stochastic layer is presented in the area surrounding second order tori. The appearance of this layer is a striking illustration of chaotic behavior of our system.

We can also build a Poincaré section on the energy level, which permits a spacial separation of points whose projections onto the plane x_1v_1 coincide. Section is depicted in Fig. 7.

In Fig. 7 we can also see regular and chaotic dynamics of the system for the given parameter values. The chaos is evidence of the absence of an additional

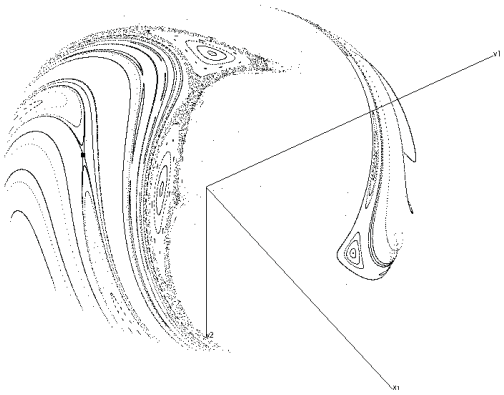


Рис. 7. Poincaré section on the energy level $Hc = -17$ of the reduced cylinder-vortex system (the other parameter values are as those in Fig. 6). The small square marker indicates the position of the hyperbolic fixed point.

integral of motion and confirm the hypothesis about non-integrability of our system. It seems to be curious to further explore the dynamics' evolution and possible scenarios of transition to chaos.

8. DISCUSSION AND FUTURE WORK

In this paper we have considered a system consisting of a heavy circular cylinder interacting dynamically with N point vortices in an unbounded volume of ideal fluid. The Hamiltonian form of the governing equations is obtained and the basic types of motion are outlined. The equilibrium solutions are found and their stability is investigated. The upper and lower equilibria are always unstable. The stability of the intermediate equilibrium depends on the value of the physical parameters of the problem.

Poincaré sections of the reduced cylinder-vortex system are presented. The system exhibits chaotic behavior, which confirms the hypothesis [19, 20] about non-integrability of the system.

Falling motion of a circular cylinder interacting dynamically with two point vortices symmetric about the vertical axis could be an interesting partial solution of the problem of the cylinder with N vortices. That configuration is a generalization of the well-known Föppl problem [4, 8]. An exploration of this case will be the subject of a forthcoming paper.

In the future it seems interesting to consider the case of cylinders of arbitrary shapes. In the current problem the following issues deserve a closer look: 1) the analysis of periodic solutions in the vicinity of the equilibria and existence of choreographies 2) a more accurate (numerical) classification of possible types of motion (Fig. 2) depending on the value of the parameters of the problem and 3) the analysis of the bifurcations underlying the change of number and types of relative equilibria.

My thanks go to A. V. Borisov and I. S. Mamaev for valuable comments and discussion.

Список литературы

[1] Bolsinov, A. V., Borisov, A. V., and Mamaev, I. S., The Bifurcation Analysis and the Conley Index in Mechanics, *Regul. Chaotic Dyn.*, 2012, vol. 17, no. 5, pp. 457–478.

[2] Borisov, A. V., Kozlov, V. V., and Mamaev, I. S., Asymptotic Stability and Associated Problems of Failing Rigid Body, *Regul. Chaotic Dyn.,* 2007, vol. 12, no. 5, pp. 531–565.

[3] Borisov, A. V. and Mamaev, I. S., An Integrability of the Problem on Motion of Cylinder and Vortex in the Ideal Fluid, *Regul. Chaotic Dyn.,* 2003, vol. 8, no. 2, pp. 163–166.

[4] Borisov, A. V. and Mamaev, I. S., *Mathematical methods in the dynamics of vortex structures.* Moscow - Izhevsk: Institute of Computer Science, 2005, 368 p.

[5] Borisov, A. V. and Mamaev, I. S., On the Motion of a Heavy Rigid Body in an Ideal Fluid with Circulation, *Chaos,* 2006, vol. 16, no. 1, 013118, 7 pp.

[6] Borisov, A. V., Mamaev, I. S., and Ramodanov, S. M., Dynamics of a Circular Cylinder Interacting with Point Vortices, *Discrete Contin. Dyn. Syst. Ser. B,* 2005, vol. 5, no. 1, pp. 35–50.

[7] Chaplygin, S. A., On the Motion of Heavy Bodies in an Incompressible Fluid, in *Complete Works: Vol. 1,* Leningrad: Izd. Akad. Nauk SSSR, 1933, pp. 133–150 (This is a Chaplygin's student paper which he wrote in 1890 and published only in 1933).

[8] Föppl L. Wirbelbewegung hinter einem Kreiszylinder. Sitzungsber. K. Baäyr Akad. Wiss. I, (1913); Vortex motion behind a circular cylinder. NASA TM 77015.

[9] Jones, M. A. and Shelly, M. J., Falling Cards, *J. Fluid Mech.,* 2005, vol. 540, pp. 393–425.

[10] Kadtke, J. B. and Novikov, E. A., Chaotic Capture of Vortices by a Moving Body: 1. The Single Point Vortex Case, *Chaos,* 1993, vol. 3, no. 4, pp. 543–553.

[11] Kirchhoff, G. R., *Vorlesungen über mathematische Physik: Bd. 1: Mechanik,* Leipzig: Teubner, 1874.

[12] Kozlov, V. V., On the Problem of Fall of a Rigid Body in a Resisting Medium, *Vestn. Mosk. Univ. Ser. 1 Mat. Mekh.,* 1990, no. 1, pp. 79–86 [*Mosc. Univ. Mech. Bull.,* 1990, vol. 45, no. 1, pp. 30–36].

[13] Kozlov, V. V., On a Heavy Cylindrical Body Falling in a Fluid, *Izv. Ross. Akad. Nauk Mekh. Tverd. Tela,* 1993, no. 4, pp. 113–117 (Russian).

[14] Maxwell, J. K., On a Particular Case of Descent of a Heavy Body in a Resisting Medium, *Cambridge and Dublin Math. Journ.,* 1854, vol. 9, pp. 145–148.

[15] Michelin, S. and Llewellyn Smith, S. G., Falling Cards and Flapping Flags: Understanding Fluid-Solid Interactions Using an Unsteady Point Vortex Model, *Theor. Comp. Fluid Dyn.,* 2010, vol. 24, pp. 195–200.

[16] Ramodanov, S. M., On the Influence of Circulation on the Behavior of a Rigid Body Falling in a Fluid, *Izv. Ross. Akad. Nauk Mekh. Tverd. Tela,* 1996, no. 5, pp. 19–24 (Russian).

[17] Ramodanov, S. M., Motion of a Circular Cylinder and a Vortex in an Ideal Fluid, *Regul. Chaotic Dyn.,* 2001, vol. 6, no. 1, pp. 33–38.

[18] Shashikanth, B. N., Marsden, J. E., Burdick, J. W., and Kelly, S. D., The Hamiltonian Structure of a 2D Rigid Circular Cylinder Interacting Dynamically with N Point Vortices, *Phys. Fluids,* 2002, vol. 14, pp. 1214–1227.

[19] Sokolov S. V., Ramodanov S. M. Falling Motion of a Circular Cylinder Interacting Dynamically with a Point Vortex, *Reg. & Chaot. Dyn.,* 2013, vol. 18, no 1-2, p. 184–193.

[20] Sokolov S. V., Ramodanov S. M. Falling Motion of a Circular Cylinder Interacting Dynamically with a Point Vortex, *Rus. J. Nonlin. Dyn.,* 2012, vol. 8. no 3, pp. 617-628.

[21] Tanabe, Y. and Kaneko, K., Behavior of a Falling Paper, *Phys. Rev. Lett.,* 1994, vol. 73, no. 10, pp. 1372–1375.

[22] Zhukovskii, N. E., On the Falling in the Air of Light Oblong Bodies Rotating About Their Longitudinal Axis, Paper I, *Collected Papers: Vol. 5,* Moscow–Leningrad: Gostekhizdat, 1937, pp. 72–80.

[23] Zhukovskii, N. E., On the Falling in the Air of Light Oblong Bodies Rotating About Their Longitudinal Axis, Paper II, *Collected Papers: Vol. 5,* Moscow–Leningrad: Gostekhizdat, 1937, pp. 100–115.

11th International Conference on Engineering Vibration
Ljubljana, Slovenia, 7–10 September 2015

EXPERIMENTAL INVESTIGATION ON SQUEAL-NOISE OF DISK-BRAKES FOR RAILWAY APPLICATIONS

M. C. De Simone*[1], **D. Guida**[1]

[1]Department of Industrial Engineering
University of Salerno
mdesimone@unisa.it

Keywords: Friction Vibration, Geometrical Instability, Brake Squeal, Modal Analysis, Finite Element Method.

Abstract. *In this paper we propose a theoretical and experimental investigation on noise emitted by a disc brake for railway applications. Even though this analysis has been performed on one class of disc brake systems the results can be useful for better understanding the path which brings to the generation of the brake noise. The system analysed in composed by a steel disk assembly on which acts a pad made of an array of cylinders of friction materials. This pad system makes easy simulations because has no needs to be "discretised", indeed, we can assume that it acts on the disk surface just in some points. The experimental investigation were made on a test-rig in real scale on which we have measured, by means a sound intensity probe, the noise emitted by disc brake and performed on it the FFT for identifying the frequencies with more high amplitude. The numerical results agree with the experimental ones.*

1 INTRODUCTION

Brakes are one of the most important components in terms of safety and performance in vehicles. The problem of noise generation during braking assumes an economic and technical increasingly important in the transport industry. The generation of noise and its suppression have become important considerations to be assessed during the design phase and execution of the brake systems. In fact, as noted by Abendroth and Wernitz [1], many manufacturers of materials for pads spend up to 50% of their budget in engineering activities on noise and vibration problems. In the last decades, a considerable amount of scientific literature has been produced on the possibility to eliminate "Brake noise". Much progress has been made and have been suggested many solutions, for example by reducing the causes, adding constrained layer (shims) or by moving damping modal coupling elements that constitute the brake assembly. Brake noise can be categorized according to the frequencies range in which the phenomenon occurs. We talk about low frequency noise for frequencies between 100 and 1000 Hz [4]; for frequencies above 1000 Hz but below the first in plane mode of the disc we talk about low frequency squeal while high frequency squeal is the noise produced by self-induced vibration [5]. There are two theories that try to describe squeal phenomenon. One theory, ascribes the increase of vibration amplitudes to the stick-slip mechanism. The other, assigns it to geometrical instability of the brake assembly. In spite both approaches agree that squeal phenomenon depends above all on a variation of the friction force. In this paper, we chose to keep constant the friction coefficient μ, since it is possible to obtain variables friction forces due to the presence of variables closing forces [6, 7, 8, 9]. This is the assumption underlying the studies carried out by Spurr, Earles and Soar. In this paper we show that if two modes are geometrically coupled, for increasing values of friction coefficient, frequencies tend to coincide. Once the two modes couple, they can become unstable.

2 MATHEMATICAL MODEL

The system analysed in this paper consists of a *SEE* (mod. 10-9007302) steel disk mechanically coupled to a system of four pads used in railway applications. Each pad, has six pairs of cylinders, made of friction material, connected by a cantilever. The mechanical behaviour of such cantilevers is shown in Figure 1

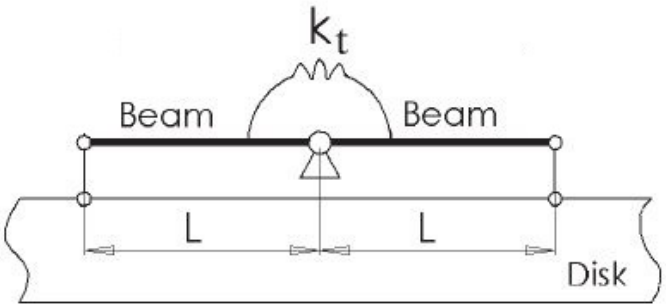


Figure 1: Mechanical scheme for cantilevers

In this way, the disk is always in contact with the 48 cylinders. In Figure 2(a) and 2(b) are indicated respectively the disk and one of the four sub-systems composing the pads. The

disk has a diameter of 640 mm, a thickness of 45 mm and geometrical characteristic indicated in the same figure. The twelve cylinders, which form the pad, have a diameter of 35 mm and a hight of 20 mm. In Figure 3 is reported the assembly model developed in Dassault



(a) Disk (b) Pad

Figure 2: Physical System

Systèmes SolidWorks 3D software. Given the geometry and the materials used for the pad, for the numerical analysis, we considered the four sub-systems rigid except cantilevers and disk modelled as flexible bodies. In Figure 4, we have reported the meshed assembly realized for the subsequent FEM analysis carried out. In the figure, you can distinguish the parts considered flexible (meshed parts) from the ones considered rigid (no-meshed parts).
We developed the differential equations of motion of the system as follows:

$$\mathbf{M}\ddot{\mathbf{q}} + \mathbf{K}\mathbf{q} = \mathbf{Q}_{pad} + \mathbf{Q}_v \tag{1}$$

with $\mathbf{M}$ and $\mathbf{K}$ mass and stiffness matrix of the disk-pad system, respectively; $\mathbf{Q}_{pad}$ is the force field between disk and pads and $\mathbf{Q}_v$ is the quadratic velocity vector resulting from the differentiation of the kinetic energy with respect to time and with respect to the body coordinates. This quadratic velocity vector contains the gyroscopic and Coriolis force components.

$$\mathbf{Q}_v(\mathbf{q}, \dot{\mathbf{q}}) = \mathbf{G}(\Omega)\dot{\mathbf{q}} \tag{2}$$

$\mathbf{Q}_{pad}$ can be seen as a force field proportional to the friction coefficient present between disc and pad.

$$\mathbf{M}\ddot{\mathbf{q}} + \mathbf{G}(\Omega)\dot{\mathbf{q}} + \mathbf{K}\mathbf{q} = \mathbf{Q}_{pad}(\mathbf{q}; \mu) \simeq -\mu\mathbf{K}_p\mathbf{q} \tag{3}$$

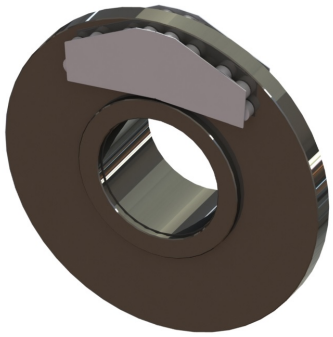
Thus, eq 1 can be rewritten as:

$$\mathbf{M}\ddot{\mathbf{q}} + \mathbf{G}(\mathbf{\Omega})\dot{\mathbf{q}} + (\mathbf{K} + \mu\mathbf{K_p})\,\mathbf{q} = \mathbf{0} \tag{4}$$

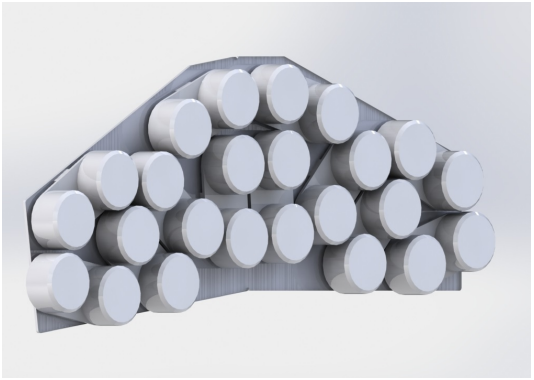
The eigenvalues problem of eq 4 allow us to predict instability forms of the system. The modal parameters of the disk-pad system have been calculated by using ANSYS FEM software.

3 NUMERICAL SIMULATION

Several simulations were conducted under Ansys Workbench, for fixed values of closing force and angular velocity of the disk. The friction coefficient μ is considered constant for



(a) CAD Assemply Model



(b) CAD Pad Model

Figure 3: CAD Assembly

each simulation, and caused to vary from the value 0 to 1 in order to study the influence of dry friction on the occurrence of forms of instability. For simplicity, a Coulomb law characteristic is applied. The upper limit of the frequency range to be studied is fixed at 8000 Hz. To define the contact behaviour between the cylinders and disc, frictional contact has been selected leaving liberty to separate in their normal direction while in tangential direction, sliding occurs only when the shear stress exceeds the value multiplying the normal stress by the constant friction coefficient μ. For ensuring contact compatibility at the interface preventing penetration of the contacting point, Augmented Lagrange formulation has been used providing the normal force $F_n = k_n x_n + \lambda$, with λ contact pressure, whenever a contacting point penetrates normally target face.

In Figure 5 are indicated the real and imaginary part of the eigenvalues which are relative to

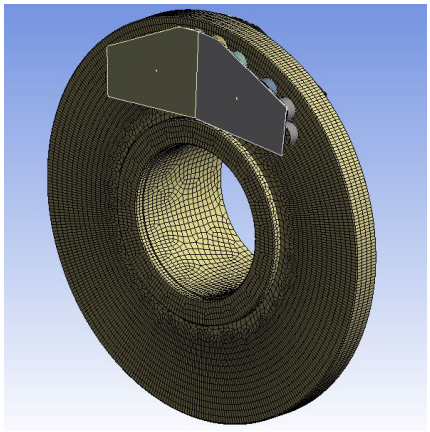


Figure 4: Mesh of brake assembly

unstable modes. Besides a first form of instability that is recorded for values greater than zero of the coefficient of friction, the first unstable mode is recorded around 7500 Hz for values of $\mu > 0.18$ as shown in the top left diagram of Figure 5. Five modes tend to become unstable. In Figure 6 are indicated the natural frequencies versus nodal diameters for the disk-brake analysed. By

the figure can be observed that the pad force field generates modes which become unstable to increase of μ only for $ND = 0$.

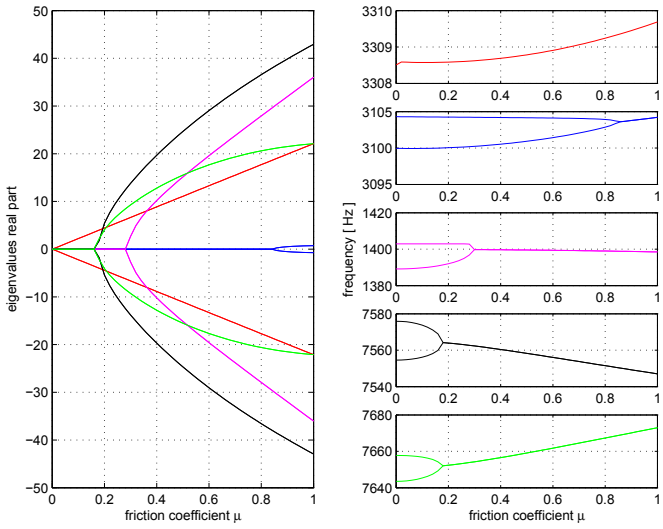


Figure 5: Eigenvalues versus μ

4 EXPERIMENTAL INVESTIGATION

To verify the results obtained numerically by finite element analysis, an experimental investigation was conducted providing sound pressure levels during a braking bench simulation from 70 km/h to zero. In 4 seconds the caliper closing force reaches its maximum value (1000 daN) and then keeps constant. Two microphones were placed one meter close to the disk: one in front of the pads and the other in the opposite side along the disk diameter, as illustrated in Figure 7. Sound pressure frequency spectrum time varying past braking incoming is illustrated in Figure 8. Some peak frequencies increase as caliper closing force grow up, as it can be seen. This can be due to stress-stiffening phenomenon. Furthermore it can be noted that: 1) less than 4000 Hz frequency peaks appear as soon as braking starts; 2) 6000 Hz frequency peak damps in 6 seconds; 3) 7500 and 9300 Hz frequency peaks appear after first 6 sec. Numerical simulations fairly match experimental data. In particular the adopted model can predict geometric instability incoming at frequencies close to 1300, 2100, 3100, 5500 and 6800 Hz, especially in first braking moments. As adopted model does not take in account for stress-stiffening nor friction coefficient dependence by pressure gap is quite small. Model does not predict one important peak only close to 9300 Hz. Considering that the first transversal pad-subsystem beam resonance frequency is close to that value, one can deduce that peak to due to dynamic instability such as stick-slip nor to geometric instability. So it be said that adopted model just cannot predict it. This work confirmed squeal to be a very complicated phenomenon in which dynamic and geometric instability take place simultaneously.

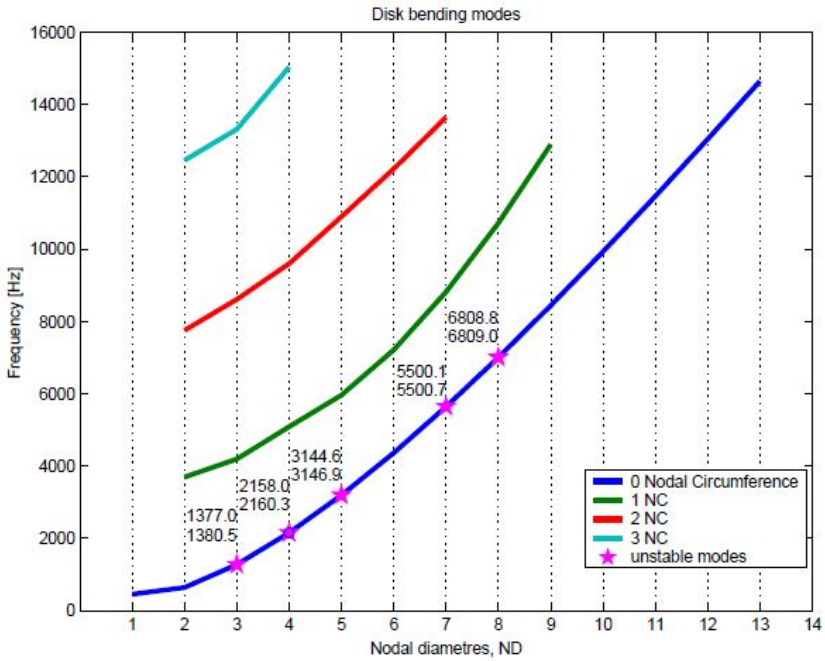


Figure 6: Eigenvalue versus ND

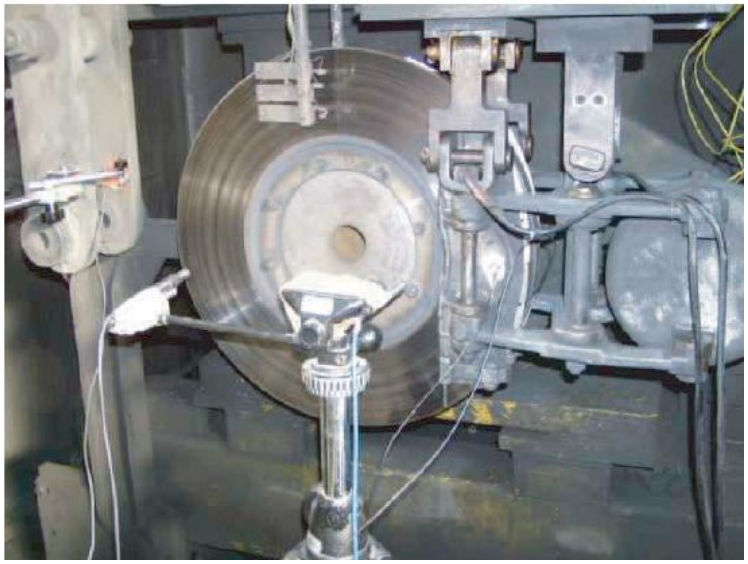
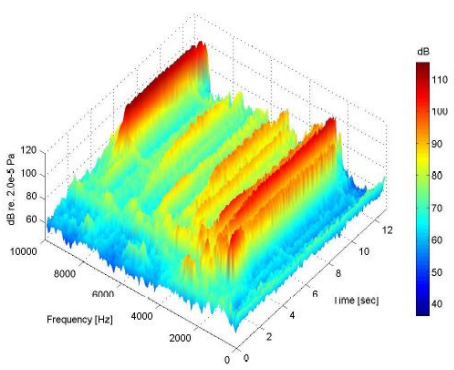
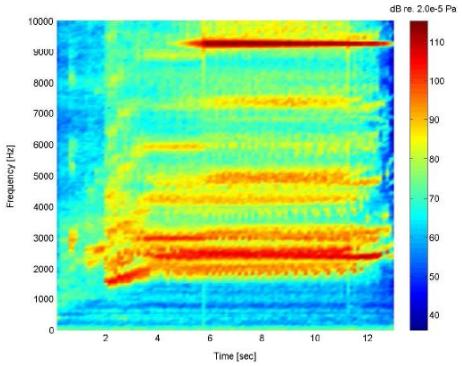


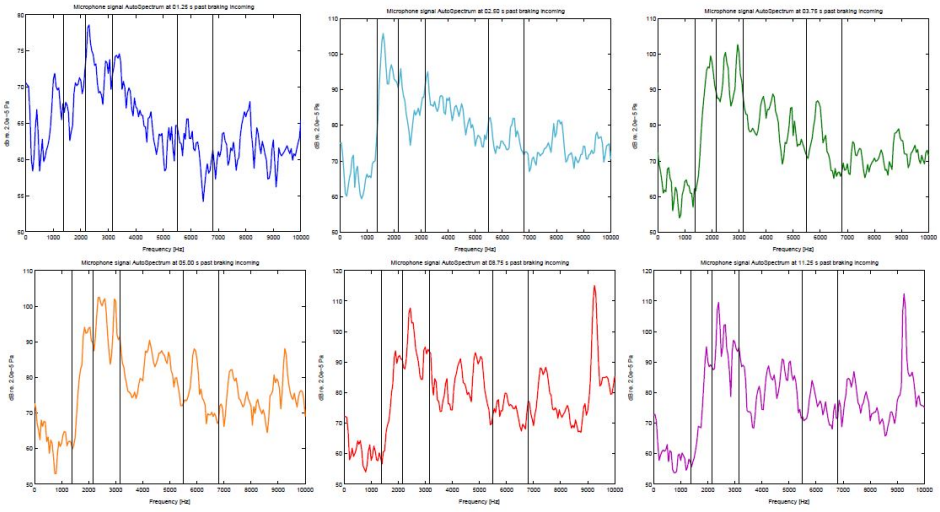
Figure 7: Disk Brake Bench



(a) Sound pressure waterfall



(b) Sound pressure color map



(c) Sound pressure spectrum for t = 1.25s, 2.5s, 3.75s, 5s, 8.75s, 11.25s

Figure 8: Measurements of the experimental apparatus

5 CONCLUSIONS

A theoretical study followed by an experimental activity is presented in this paper . Furthermore we presented a mathematical model to describe the dynamic behaviour of a disk brake system for railways applications. In this system the pad is composed by arrays of pad subsystem elements composed by cylinders mounted at the end of elastic beams. The pad model proposed was realized in order to facilitate variable force fields between disc and pad systems in order to analyse the influence of a variable friction force on the dynamic behaviour of the whole system. The numerical analysis and the subsequent experimental investigation allows to make the following consideration: 1) five modes became instable to increase of the friction coefficient μ; 2)the unstable modes are (0,3), (0,4), (0,5), (0,7) and (0,8); 3) the instability relative to the (0,5) mode occurs for value of the parameter $\mu > 0.5$ and hence it isn't significative for this problem; 4) The experimental data are in a good agreement with the theoretical results; 5) Every instability form predicted by the model occurs in the experimental analysis; 6)Nevertheless in the experimental results appears a frequency component of about 9300 Hz which is not predicted by the theoretical model. This component could be generated by stick slip phenomenon. In fact the pad sub-system beam has a transversal natural frequency close to the foregoing frequency.
This work is the first step of a wide research project on the self-excited vibrations induced by dry friction.

REFERENCES

[1] H. Abendroth, B. Wernitz. *The integrated test concept: Dyno-vehicle, performance-noise* (No. 2000-01-2774). SAE Technical Paper.

[2] W. V. Nack. *Brake squeal analysis by finite elements* (No. 1999-01-1736). SAE technical Paper.

[3] C. H. Chung, W. Steed, K. Kobayashi, H. Nakata. *A new analysis method for brake squeal part I: theory for modal domain formulation and stability analysis* (No. 2001-01-1600). SAE Technical Paper.

[4] S. W. Kung, K. B. Dunlap, R. S. Ballinger. *Complex eigenvalue analysis for reducing low frequency brake squeal* (No. 2000-01-0444). SAE Technical Paper.

[5] G. Capone, V. D'Agostino, D. Guida. *Stick-slip instability analysis.* Meccanica 27.2 (1992): 111-118.

[6] G. Capone, V. D'Agostino, S. Della Valle, D. Guida *Influence of the variation between static and kinetic friction on stick-slip instability.* Wear (1993), 161(1), 121-126.

[7] M. C. De Simone, D. Guida *Dry Friction Influence on Structure Dynamics*, International Conference on Computational Methods in Structural Dynamics and Earthquake Engineering 2015, Crete Island, 2015.

[8] M. C. De Simone, A. Ruggiero, Z. B. R. Chavez, D. Guida *Dry Friction Influence on the Response of a Mechanical System with two DOFs* 6th International Conference on Theoretical and Applied Mechanics (TAM 2015), Salerno, Italy, 27-27 June 2015.

[9] M. C. De Simone, A. Ruggiero, Z. B. R. Chavez, D. Guida *Instability in Disk Brake Systems* 6th International Conference on Theoretical and Applied Mechanics (TAM 2015), Salerno, Italy, 27-27 June 2015.

Optimization on Vibration Control of Seismic Structures (MS04)

International Conference on Engineering Vibration
Ljubljana, Slovenia, 7-10 September 2015

OPTIMIZATION OF TMDS FOR SEISMIC STRUCTURES CONSIDERING NEAR FIELD GROUND MOTION SETS

Gebrail Bekdaş[1], Sinan Melih Nigdeli*[2]

[1]Istanbul University, Civil Engineering Department, 34320 Avcılar, Istanbul, Turkey
bekdas@istanbul.edu.tr

[2] Istanbul University, Civil Engineering Department, 34320 Avcılar, Istanbul, Turkey
melihnig@istanbul.edu.tr

Keywords: Optimization, Tuned mass damper, Near field ground motion sets, Earthquake, seismic structures.

Abstract. *Near field ground motions records may contain pulse-like motions. Forward directivity effect is the main cause of these velocity pulses. The main aim of the study is to find optimum tuned mass damper (TMD) parameters for seismic structures subjected to near-field ground motions. In order to find a global optimum solution, two sets of ground motions including 28 records from 14 stations were used. These sets are presented in FEMA-P695 report for quantification of building seismic performance factors. All records of these sets were taken from the stations which are located less than 10 km from fault rupture. One of the sets contain records strong pulses, while the other one has no records with strong pulses.*

In optimization of TMD, a metaheuristic algorithm called harmony search was used. In the methodology, the objective function of the optimization is to reduce the first story displacement of the structure for the most critical excitation. The design variables include mass, period and damping ratio of the TMD. During optimization time-domain analyses are done for all random design variables assigned by using algorithm rules.

As a numerical example, a ten storey structure is investigated. Two different optimum TMD parameters were searched by using set of records with and without pulses. Thus, the optimum parameters for different types of excitations are compared. The proposed method is effective to find optimum TMD for the structure for both types of excitations. As conclusions, it is possible to reduce structural displacements more effectively for excitations without pulses, but the optimum damping is higher than the optimum results obtained for records with strong pulses.

1 INTRODUCTION

Near field ground motions cause more structural vibrations than the excitations resulting from far fault rupture. This situation is the result of impulsive motions which are seen in near field ground motion records. There are two types of impulsive motions and these motions are directivity effect perpendicular to fault and flint step parallel to fault. Flint steps are known as permanent ground displacements. The major effect of near-field ground motions are strong velocity pulses known as directivity effect. These pulses have high peak velocity and long period. Generally, these pulses occur when forward directivity is seen. If fault rapture propagates towards a site at a velocity close to shear wave velocity, most of the seismic energy arrive at site within a short time. This situation is called as forward directivity.

The types seismic sources are defined in ATC40 [1]. These types are defined with maximum moment magnitude and slip rate as seen in Table 1. Type A sources are capable to cause large magnitude events with a high rate of seismic activity. On the contrary, type C sources cannot cause excitations with specific near-field effects.

Seismic Source Type	Maximum Moment Magnitude, M	Slip Rate, SR (mm/year)
A	$M \geq 7.0$	$SR \geq 5$
B	$6.5 \leq M < 7$	$2 \leq SR < 5$
C	$M < 6.5$	$SR < 2$

Table 1: Seismic sources given in ATC40.

Near-field ground motions are defined in UBC (1997) [2] according to the distance to fault rupture. Type A sources can produce near-field excitations up to 15 km, while type B sources produce near-field ground motions up to 10 km.

In investigation of effects of near-field ground motions on structures, several approaches have been proposed for modelling of impulsive motions [3-7]. The mostly used models were produced by Makris [3] and another type for continuous pulses was proposed by Makris and Chang [4]. These pulse models have been used in several studies separately or superimposed with ground motions as done in the seismic performance simulation of the Bolu (Turkey) viaduct [8] and control of torsionally irregular structures [9]. Also, set of earthquake of earthquake records are given in FEMA P695 [10] for far and near-field ground motions. Near-field sets are the records which are taken from less than 10 km to fault rapture. Two sets are given for near-field excitation. One of the sets contain records including strong pulses, while the other one contains records without pulses.

In this study, optimum tuned mass damper (TMD) parameters were searched by using set of earthquakes. Near-field sets given in FEMA P695 [10] were separately used for excitations with and without pulses. The performance and optimum TMD parameters were compared. The optimization methodology employs a metaheuristic method inspired by musical performances. It is harmony search algorithm developed by Geem et al. [11].

2 METHODOLOGY

Metaheuristic algorithms have been born by making several observations of processes. Harmony search is a music inspired algorithm and it imitates musical performance of a musician. In this performance, the main goal of musician is to gain attention and admiration of listener. Other metaheuristic methods [12-17] and harmony search [18-22] have been employed in several optimization approaches of TMDs in order to reduce structural vibrations. These algorithms generally use a randomization operation of design variables in order to reach optimization objective. Randomization may be global by using a solution range or local by using

the previous random results. Thus, the best solution (exact optimum) can be found around the existing random solution and trapping to a local optimum is prevented by using the whole solution range.

The tuning problem of TMDs cannot be solved by mathematical equations since the main structure has inherent damping. Also, random characteristic of excitations (such as earthquake motions) may affect the optimum parameters. Thus, iterative numerical algorithms such as metaheuristic method is very suitable for the problem.

The optimization methodology is consist of four stages such as data entering, analyses of structure without TMD, generation of initial harmony memory and iterative analyses done for modification of harmony memory in order to reach the global optimum solution. The special properties and advantages of algorithm is used during the process of the last stage.

In the first stage, properties of shear building (mass, stiffness and damping coefficients of all stories), time history data of earthquake excitations, solution range of design variables and several parameters about the algorithm are defined.

The objective function of the optimization is to reduce the ratio of maximum first story displacement of the structures with and without TMD under a user selected value. Thus, dynamic analyses of the structure without TMD must be done before searching optimum TMD parameters.

In the third stage, a harmony memory matrix is constructed. This matrix contains harmony vectors and the number of these vectors are defined with a parameters called harmony memory size (HMS). Randomly assigned design variables are stored in these vectors. These design variables are mass, period and damping ratio of TMD. The analyses of structure with TMD is done for all set of variables and the optimization objectives are calculated for all harmony vectors.

The last stage is iteratively done in order to reach the global optimum value. A new harmony vector is generated. The generation is done in two ways using local and global search. In local search, random variables are searched around an existing vector in harmony memory. The probability of using local search is defined by a parameter called harmony memory considering rate. In global search, the whole solution range is used as done in the generation of initial harmony memory. The new harmony vector is replaced with the worst one in mean of objective function. The iterative process continues until the stopping criterion is provided. According to this criterion, the objective function must be smaller than a user defined value. If it is not physically possible, user defined value can be increased after several iterations. Thus, user defined value can be also entered as zero in order to find minimum possible objective function.

3 NUMERICAL EXAMPLE

A ten story structure is investigated for an application of TMD on the top of the structure. The properties of the structure is given in Table 2. The damping coefficients are taken as 0.0129 times of stiffness coefficients.

The information about earthquake records are shown in Table 3 and 4 for pulse and no-pulse records. The earthquake records used in the study were downloaded by Pacific Earthquake Engineering Research Center NGA database [24]. The optimum TMD parameters are separately searched for both sets of earthquakes. The solution ranges are taken as shown in Table 5. T_{st} and m_{st} are the critical period and total mass of the structure without TMD.

Storey	Mass (t)	Stiffness (kN/m)
10	98	34310
9	107	37430
8	116	40550
7	125	43670
6	134	46790
5	143	49910
4	152	53020
3	161	56140
2	170	52260
1	179	62470

Table 2: Properties of the structure [23].

Earthquake No.	Earthquake Name	Recording Station	Year	Magnitude
1	Imperial Valley-06	El Centro Array #6	1979	6.5
2	Imperial Valley-06	El Centro Array #7	1979	6.5
3	Irpinia, Italy-01	Sturno	1980	6.9
4	Superstition Hills-02	Parachute Test Site	1987	6.5
5	Loma Prieta	Saratoga - Aloha	1989	6.9
6	Erzican, Turkey	Erzican	1992	6.7
7	Cape Mendocino	Petrolia	1992	7.0
8	Landers	Lucerne	1992	7.3
9	Northridge-01	01 Rinaldi Receiving Sta	1994	6.7
10	Northridge-01	01 Sylmar - Olive View	1994	6.7
11	Kocaeli, Turkey	Izmit	1999	7.5
12	Chi-Chi, Taiwan	TCU065	1999	7.6
13	Chi-Chi, Taiwan	TCU102	1999	7.6
14	Duzce, Turkey	Duzce	1999	7.1

Table 3: Earthquake set for near-field excitations with pulses [10].

Earthquake No.	Earthquake Name	Recording Station	Year	Magnitude
1	Gazli, USSR	Karakyr	1976	6.8
2	Imperial Valley-06	El Centro Array #7	1979	6.5
3	Imperial Valley-06	Sturno	1979	6.5
4	Nahanni, Canada	Site 1	1985	6.8
5	Nahanni, Canada	Site 2	1985	6.8
6	Loma Prieta	Bran	1989	6.9
7	Loma Prieta	Corralitos	1989	6.9
8	Cape Mendocino	Cape Mendocino	1992	7.0
9	Northridge-01	LA - Sepulveda VA	1994	6.7
10	Northridge-01	Northridge - Saticoy	1994	6.7
11	Kocaeli, Turkey	Yarimca	1999	7.5
12	Chi-Chi, Taiwan	TCU067	1999	7.6
13	Chi-Chi, Taiwan	TCU084	1999	7.6
14	Denali, Alaska	TAPS Pump Sta. #10	2002	7.9

Table 4: Earthquake set for near-field excitations without pulses [10].

Variable	Symbol	Lower bound	Upper bound
Mass	m_d	$0.01m_{st}$	$0.10m_{st}$
Period	T_d	$0.8T_{st}$	$1.2T_{st}$
Damping ratio	ξ_d	0.05	0.3

Table 5: Solution ranges of optimization.

The optimum parameters are presented in Table 6. Generally, a significant difference is not seen for optimum TMD mass, but other variables are very different. The maximum first storey displacement of the structure are shown in Table 7. It must be noted that the critical excitation for the structure without TMD is not the critical for the structure with TMD. Thus, the usage of multiple records is needed for a global optimum results.

Symbol	Record with pulses	Record without pulses
m_d (t)	138,23	134,99
T_d (s)	2,08	1,82
ξ_d	0,07	0,17

Table 6: Optimum design variables.

Earthquake	Component	Record with pulses		Record without pulses	
		without TMD	with TMD	without TMD	with TMD
1	1	0.0732	0.0591	0.0452	0.0442
1	2	0.0782	0.0813	0.0602	0.0464
2	1	0.0524	0.0433	0.0735	0.0352
2	2	0.0787	0.0733	0.0416	0.0318
3	1	0.0493	0.0376	0.0284	0.0184
3	2	0.0543	0.0572	0.0272	0.0175
4	1	0.1543	0.0948	0.0244	0.0203
4	2	0.0513	0.0468	0.0356	0.0282
5	1	0.0597	0.0359	0.0205	0.0128
5	2	0.0264	0.0312	0.0284	0.0195
6	1	0.0781	0.0557	0.0411	0.0395
6	2	0.1419	0.0862	0.0241	0.0212
7	1	0.0484	0.0393	0.0447	0.0360
7	2	0.0938	0.0615	0.0435	0.0394
8	1	0.0583	0.0696	0.0655	0.0602
8	2	0.0235	0.0259	0.0561	0.0407
9	1	0.1100	0.0909	0.0744	0.0456
9	2	0.1047	0.0649	0.0525	0.0776
10	1	0.1052	0.0656	0.0501	0.0319
10	2	0.1245	0.0964	0.1168	0.0582
11	1	0.0369	0.0254	0.0556	0.0551
11	2	0.0280	0.0200	0.0533	0.0504
12	1	0.1898	0.0787	0.1130	0.0846
12	2	0.1402	0.0915	0.0637	0.0411
13	1	0.0994	0.0688	0.2475	0.0994
13	2	0.1086	0.0876	0.0577	0.0424
14	1	0.0408	0.0459	0.1258	0.0991
14	2	0.1057	0.0451	0.0692	0.0490

Table 7: Maximum displacements for the first story of the structure.

A time history plot (Figs. 1 and 2) for each cases are given in the paper. These plots are for the critical excitation of the structure without TMD. As seen from the time history plots, optimum TMD is very effective on obtaining a steady state response in addition to reduction of maximum displacement.

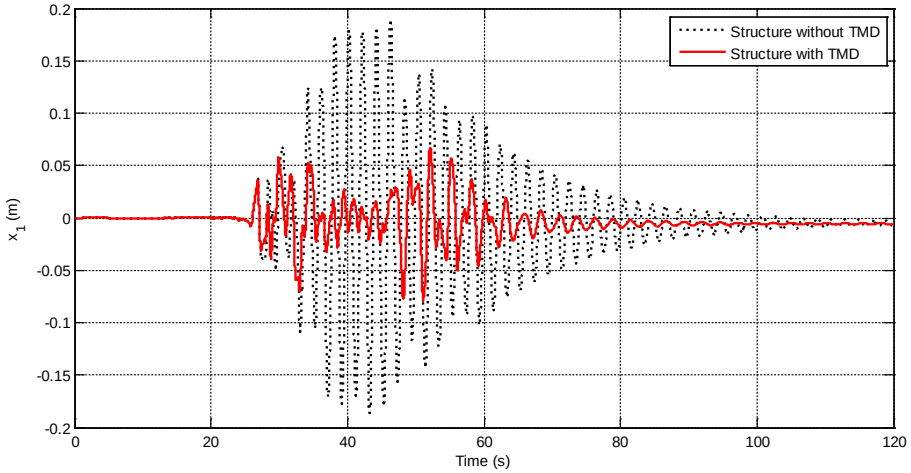


Figure 1: First story time history (records with pulses-Earthquake 12-East component).

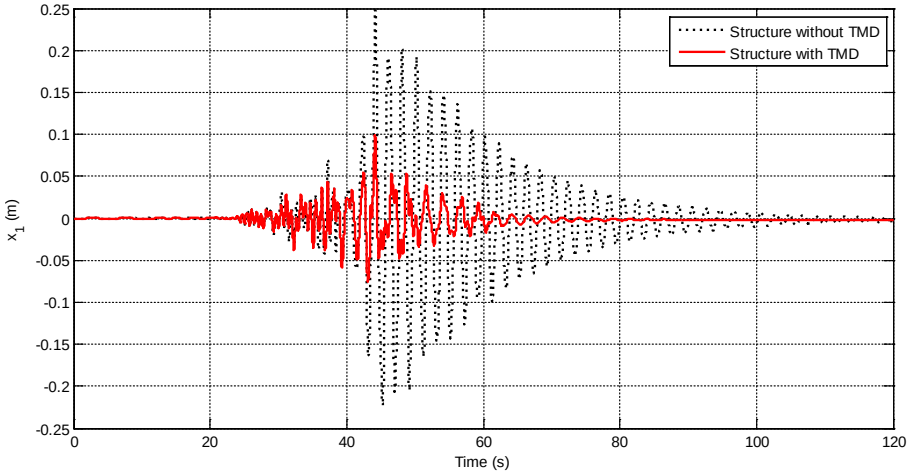


Figure 2: First story time history (records without pulses-Earthquake 13-East component).

4 CONCLUSIONS

In this paper, the optimum TMD parameters are investigated for different types of near-field excitations and the optimum results show significant differences for two cases considering records with and without pulses. According to the optimum TMD results applied for a ten story shear building, 49% reduction is obtained for the first story displacements under records with pulses while a better reduction (60%) is obtained for records without pulses. These re-

duction percentages were calculated according to the maximum responses of all excitations in a set. For the critical excitation, the optimum TMD is more effective to reduce first story displacements according to these percentages but the critic one in a set of records may change for the structure with TMD as also seen in the presented numerical example. Thus, global optimum results can be only found by using a wide variety of excitations.

The optimum TMD results are very different in stiffness and damping while a significant difference is not seen for the mass of TMD. For the case considering records with pulses, the optimum period of TMD is slightly higher than the critical period of main structure while the TMD period for records without pulses is very low according to the critical period of main structure. Additionally, the increase of the damping ratio is effective to obtain excellent reduction for excitations without pulses.

According to the results, the optimum TMD is very effective to reduce displacements at the first story which is the most critical relative displacement of a story. In addition to that, the essential benefit of the TMD application are shown in the time history plots. The optimum TMD supports the structure by damping of structural displacements. Thus, a steady state response is immediately obtained.

The proposed methodology is very effective to obtain global optimum TMD parameters. The importance of the optimization of this tuning problem is clearly seen from the results. The optimum design variables are not found near to the bounds of the solution ranges. Thus, the proposed methodology is very effective and feasible for TMD design.

REFERENCES

[1] ATC (Applied Technology Council), *Seismic evaluation and retrofit of concrete buildings*. ATC 40, Volume 1, Chapter 4, Report No. SSC 96-01, November 1996.

[2] International Code Council, *Earthquake regulations for seismic-isolated structures (Chapter 16)*. Uniform Building Code (UBC), 1997.

[3] N. Makris, Rigidity-plasticity-viscosity: can electrorheological dampers protect base-isolated structures from near-source ground motions?. *Earthquake Engineering and Structural Dynamics*, **26(5)**, 571-591, 1997.

[4] N. Makris and S. Chang, Effect of viscoplastic and friction damping on the responce of seismic isolated structures. *Earthquake Engineering and Structural Dynamics*, **29(1)**, 85-107, 2000.

[5] J.F. Hall, T.H. Heaton, M.W. Halling and D.J.Wald, Near-source ground motion and its effects on flexible buildings. *Earthquake Spectra*, **11(4)**, 569-605, 1995.

[6] B. Alavi and H. Krawinkler, *Effects of near-fault ground motions on frame structures*, The John A. Blume Earthquake Engineering Center, Report 138, 2001.

[7] M. Sasani, New measure for severity of near-source seismic ground motion. *Journal of Structural Engineering*, **132(12)**, 1997-2005, 2006.

[8] S.W. Park, H. Ghasemi, J. Shen, P.G. Somerville, W.P. Yen and M. Yashinsky, Simulation of the seismic performance of the Bolu Viaduct subjected to near-fault ground motions. *Earthquake Engineering and Structural Dynamics*, **33(13)**, 1249-1270, 2004.

[9] S.M. Nigdeli and M.H. Boduroğlu, Active Tendon Control of Torsionally Irregular Structures under Near-Fault Ground Motion Excitation. *Computer-Aided Civil and Infrastructure Engineering*, **28(9)**,718-736, 2013.

[10] FEMA P-695, *Quantification of Building Seismic Performance Factors*, Federal Emergency Management Agency, Washington DC, 2009.

[11] Z.W. Geem, J.H. Kim and G.V. Loganathan, A new heuristic optimization algorithm: harmony search, *Simul.*, **76**, 60–68, 2001.

[12] M.N.S. Hadi and Y. Arfiadi, Optimum design of absorber for MDOF structures. *Journal of Structural Engineering-ASCE*, **124**, 1272-1280, 1998.

[13] M.P. Singh, S. Singh and L.M. Moreschi, Tuned mass dampers for response control of torsional buildings. *Earthquake Engineering and Structural Dynamics*, **31**, 749-769, 2002.

[14] N.B. Desu, S.K. Deb and A. Dutta, Coupled tuned mass dampers for control of coupled vibrations in asymmetric buildings. *Structural Control and Health Monitoring*, **13**, 897-916, 2006.

[15] G.C. Marano, R. Greco and B. Chiaia, A comparison between different optimization criteria for tuned mass dampers design. *Journal of Sound and Vibration*, **329**, 4880-4890, 2010.

[16] A.Y.T. Leung, H. Zhang, C.C. Cheng and Y.Y. Lee, Particle swarm optimization of TMD by non-stationary base excitation during earthquake. *Earthquake Engineering and Structural Dynamics*, **37**, 1223-1246, 2008.

[17] R. Steinbuch, Bionic optimization of the earthquake resistance of high buildings by tuned mass dampers. *Journal of Bionic Engineering*, **8**, 335-344, 2011.

[18] G. Bekdaş and S.M Nigdeli, Estimating Optimum Parameters of Tuned Mass Dampers Using Harmony Search. *Engineering Structures*, **33**, 2716-2723, 2011.

[19] G. Bekdaş and S.M Nigdeli, Optimization of Tuned Mass Damper with Harmony Search. In '*Metaheuristic Applications in Structures and Infrastructures*'. Edited by Amir Hossein Gandomi, Xin-She Yang, Amir Hossein Alavi, Siamak Talatahari, Elsevier, Chapter 14, February 2013.

[20] S.M. Nigdeli and G. Bekdaş, Optimum Tuned Mass Damper Design for Preventing Brittle Fracture of RC Buildings. *Smart Structures and Systems*, **11**, 137-155, 2013.

[21] G. Bekdaş and S.M. Nigdeli, Mass Ratio Factor for Optimum Tuned Mass Damper Strategies. *International Journal of Mechanical Sciences*, **71**, 68-84, 2013.

[22] S.M. Nigdeli and G. Bekdaş, Optimum Tuned Mass Damper Approaches For Adjacent Structures. Earthquakes and Structures, **7(6)**, 1071-1091, 2014.

[23] F. Sadek, B. Mohraz, A. W. Taylor, R. M. Chung, A method of estimating the parameters of tuned mass dampers for seismic applications, *Earthquake Engineering and Structural Dynamics*, **26**, 617–635, 1997.

[24] Pacific Earthquake Engineering Research Center (PEER NGA DATABASE) http://peer.berkeley.edu/nga.

International Conference on Engineering Vibration
Ljubljana, Slovenia, 7-10 September 2015

A ROBUST OPTIMUM DESIGN APPROACH OF TMDS CONSIDERING STRUCTURAL UNCERTANITY

Sinan Melih Nigdeli[1], Gebrail Bekdaş*[2]

[1]Istanbul University, Civil Engineering Department, 34320 Avcılar, Istanbul, Turkey
melihnig@istanbul.edu.tr

[2] Istanbul University, Civil Engineering Department, 34320 Avcılar, Istanbul, Turkey
bekdas@istanbul.edu.tr

Keywords: Optimization, Tuned mass damper, Structural uncertainties, Earthquake, seismic structures.

Abstract. *In the analyses of civil structures, several assumptions are done in determining of structural properties. These assumptions may be the results of unknown live loading conditions or non-linear behaviour of structures during random excitations like earthquakes. The tuned mass dampers (TMD) used for the reduction of structural responses are tuned according to the properties of the structure.*

In this paper, a robust optimization procedure considering five different stiffness of the structure is proposed. A metaheuristic algorithm called harmony search is used in the optimization methodology. All design variables such as mass, period and damping ratio of TMD are iteratively searched according to the employed algorithm. The methodology was applied for ten-story structures. All story stiffness values were changed between ±30%. The methodology considering five different properties of structures is effective to reduce first story displacement under six different excitations by 26% while the reduction is 23% for the optimum values obtained without considering stiffness change. Thus, the proposed methodology is feasible for the tuning problem.

1 INTRODUCTION

Tuned mas dampers (TMD) are vibration absorber devices used with mechanical systems. The performance are depended to the excellent tuning by considering main system properties. The main system properties may not be exactly determined or these properties may change in time according to external excitation.

TMD are also used on the structures in order to damp structural displacements under strong excitations such as winds or earthquakes. Since the civil structures are huge mechanical systems, the uncertainty characteristics are more than any other mechanical systems. The total mass of the civil structures may not be constantly known since the live loads on the structure are already changeable. Additionally, the nonlinear behaviour of structure may change according to the external excitations.

The documented method shows that the performance of the TMD can be defined with a frequency ratio value. The value of the frequency ratio is defined with the mass ratio of TMD and main structure. The change of the frequency of the main structure may lead us to get away from the optimum value if the simple expressions proposed in the documented method are used [1-4].

The change of mass and stiffness has effective on the change of critical frequencies of the structures. By the reduction and increase of the mass because of the live load may be considered as done in the study Bekdas and Nigdeli [5]. The increase of the mass may be a reason of the increase of the external load or the reduction of the mass will decrease the external load and structural responses. The stiffness values may be changed and the nonlinear behaviour of the structure may be also considered. The change of the stiffness value will not show a great different on the earthquake force. In this paper, five different stiffness properties are used in the optimization. These values are calculated with ±30% difference of the constant stiffness values of the structural model. The robust optimization method for TMDs employes harmony search algorithm which is a music inspired metaheuristic method developed by Geem et al. [6].

Several TMD optimization methods using metaheuristic algorithms such as genetic algorithm [7-11], particle swarm optimization [4, 12], bionic algorithm [13] and harmony search algorithm [5, 14-18] have been developed. These numerical searching algorithms are effective on finding optimum TMD properties since the exact optimum values cannot be derived because of inherent damping of main structure, random characteristic of external excitation and degrees of the freedom of multi-story structures.

2 METHODOLOGY

The methodology of optimization process is presented in the flow chart given as Fig. 1. After the design constants, solution ranges and external excitation are defined, the structural responses are calculated by dynamic analyses of the structure without TMD because the aim of the optimization is to reduce structural responses of the structure. The analyses are done for all structural models with different stiffness values.

The optimization starts by generating an initial harmony memory (HM) matrix containing harmony vectors (HV) including randomly assigned design variables such as mass, period and damping coefficient of TMD. The number of these vectors are defined with harmony memory size (HMS). The essential optimization continue by generating new harmony vectors and updating HM with these vectors if the solution is better in mean of optimization objective. The optimization objective is to reduce ratio of maximum first story displacements of the structure with and without TMD. The average of five different structural models are considered for the objective.

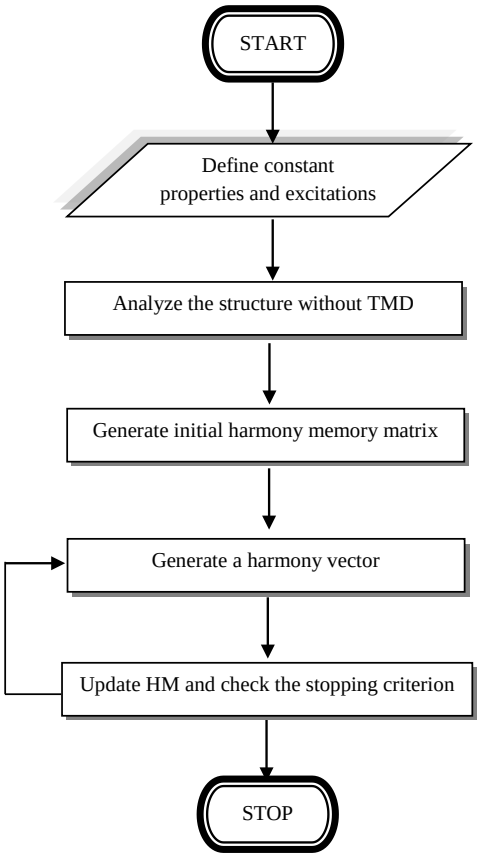


Figure 1: Flow chart of the methodology.

In generation of harmony vectors, two different procedure are applied. With a possibility defined as harmony memory considering rate (HMCR), a new vector is generated around the existing vector in HM by using a compact range according to the pitch adjusting rate (PAR). Otherwise, a new vector is generated from the whole solution range.

The iterative analyses continue until the stopping criterion is supported. The stopping criterion is to reduce the optimization objective under a user defined value. This value is increase after several iterations if a physical solution is not found.

3 NUMERICAL EXAMPLE

A ten story shear building is investigated as a numerical example. The optimum TMD is positioned on the top of the structure. Optimization is done for the structure under six different excitations. The record of excitations were downloaded Pacific Earthquake Engineering Research Centre [19] database and information about the records are shown in Table 1. A story of the structure has 360 t mass, 650 MN/m stiffness coefficient and 6.2 MNs/m damping coefficient [20]. The properties of all stories are the same. The stiffness values of all stories were changed between ±30% and five different models with 15% stiffness difference are generated. The optimum TMD results were also obtained by using a single stiffness value without any modification to the constant stiffness values.

Earthquake	Date	Station	Component	PGA (g)
Imperial Valley	1940	117 El Centro	I-ELC180	0.313
Kobe	1995	0 KJMA	KJM000	0.821
Erzincan	1992	95 Erzincan	ERZ-NS	0.515
Northridge	1994	77 Rinaldi	RRS228	0.838
Northridge	1994	24514 Sylmar	SYL360	0.843
Loma Prieta	1989	16 LGPC	LGP000	0.563

Table 1: Earthquake records used in the optimization.

The optimum results were shown in Table 2 for two approaches. The robust method has higher optimum damping ratio than the other one. Also, the optimum period of the robust optimization approach is nearly equal to the critical period of the structure which has a stiffness coefficient without any difference. Because of these reasons, the optimum TMD properties are effective to reduce structural responses of the structural systems with difference stiffness values (different critical period). The optimum period of the optimization approach done for a single stiffness value is far from the optimum one for a system with different critical period, although the reduction of structural displacement of the first story under the critical excitation is slightly better than the robust approach for the structure without stiffness change. This situation can be seen from the maximum first story displacement results given in Tables 3-5 for structure without TMD, structure with optimum robust TMD and structure with optimum TMD, respectively. The advantages of the robust optimization approach can be clearly seen from the results of the structures with stiffness change.

Variable	Symbol	Robust optimum design	Optimum design	Range
Mass of TMD	m_d (t)	355.40	358.92	36t-360t
Period of TMD	T_d (s)	1.0162	0.9111	0.8-1.2s
Damping ratio of TMD	ξ_d	0.0718	0.0525	0.05-0.3

Table 2: Optimum design variables.

Earthquake	Stiffness change				
	-30%	-15%	0	+15%	+30%
Imperial Valley	0.0235	0.0248	0.0288	0.0250	0.0264
Kobe	0.0690	0.0694	0.0719	0.0775	0.0704
Erzincan	0.0572	0.0511	0.0449	0.0378	0.0316
Northridge (Rinaldi)	0.1101	0.1055	0.0972	0.0881	0.0808
Northridge (Sylmar)	0.0742	0.0636	0.0551	0.0478	0.0407
Loma Prieta	0.0667	0.0600	0.0523	0.0490	0.0539

Table 3: Maximum first story displacement for structure without TMD.

Earthquake	Stiffness change				
	-30%	-15%	0	+15%	+30%
Imperial Valley	0.0147	0.0167	0.0171	0.0163	0.0146
Kobe	0.0693	0.0613	0.0452	0.0432	0.0421
Erzincan	0.0467	0.0361	0.0330	0.0301	0.0275
Northridge (Rinaldi)	0.0807	0.0771	0.0715	0.0663	0.0622
Northridge (Sylmar)	0.0606	0.0522	0.0443	0.0372	0.0306
Loma Prieta	0.0681	0.0584	0.0487	0.0449	0.0438

Table 4: Maximum first story displacement for structure with optimum robust TMD

Earthquake	Stiffness change				
	-30%	-15%	0	+15%	+30%
Imperial Valley	0.0149	0.0174	0.0174	0.0173	0.0155
Kobe	0.0674	0.0569	0.0507	0.0487	0.0448
Erzincan	0.0513	0.0384	0.0330	0.0305	0.0281
Northridge (Rinaldi	0.0920	0.0827	0.0710	0.0660	0.0621
Northridge (Sylmar)	0.0651	0.0534	0.0432	0.0361	0.0296
Loma Prieta	0.0788	0.0631	0.0426	0.0442	0.0506

Table 5: Maximum first story displacement for structure with optimum TMD.

Five different time history plots are presented in Figs. 2-6. In these time histories, first story displacements are shown for structure with and without optimum robust TMD and these time histories are plotted by changing different stiffness values. In all plots, the optimum robust TMD is effective to reduce maximum responses.

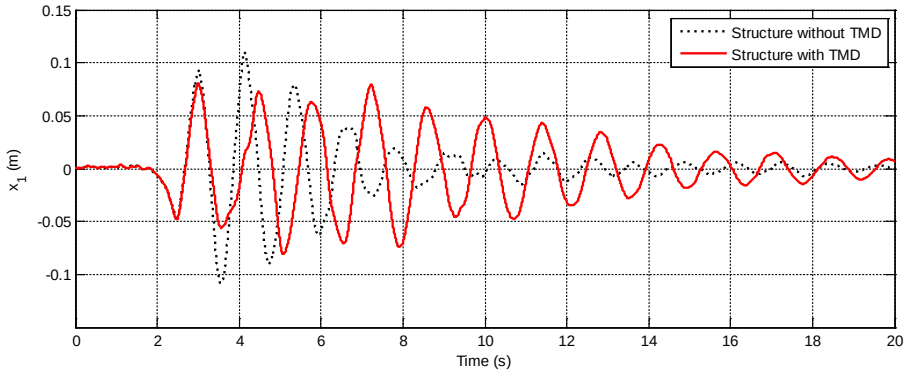


Figure 2: First story plot for structure with -30% stiffness change.

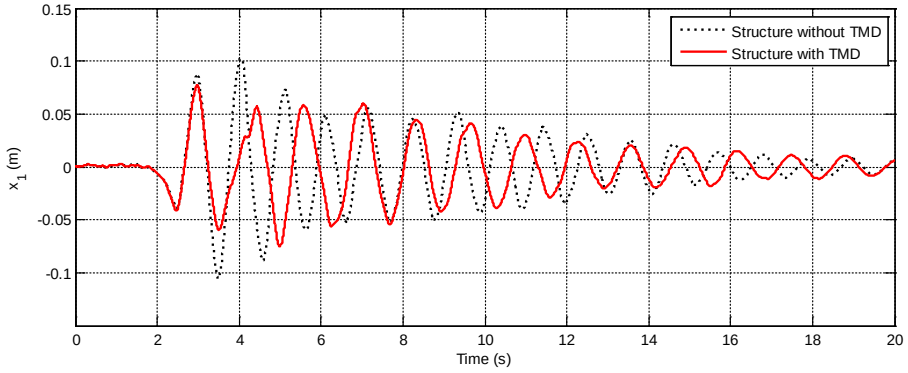


Figure 3: First story plot for structure with -15% stiffness change.

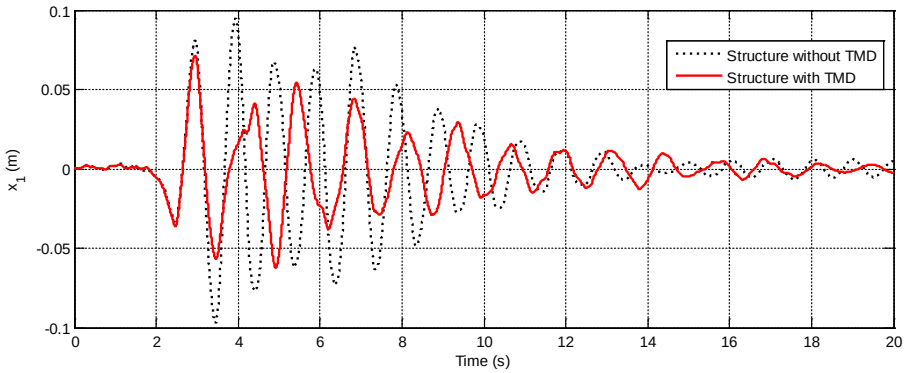


Figure 4: First story plot for structure with 0% stiffness change.

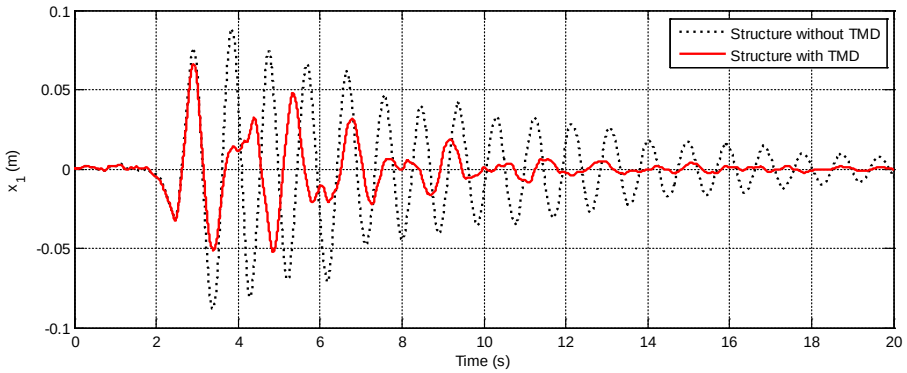


Figure 5: First story plot for structure with +15% stiffness change.

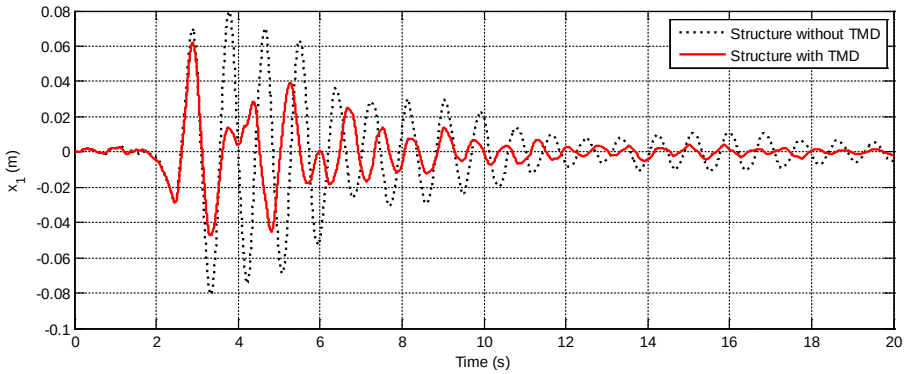


Figure 6: First story plot for structure with +30% stiffness change.

4 CONCLUSIONS

The proposed robust optimization approach is very suitable in order to consider the possible period change of the structure. As known, the damping ratio of the TMD is effective on the robustness of TMD. The optimum results of the method proves that knowledge because the optimum damping ratio for the robust approach is higher than the other approach. Also,

the robust optimum period value is assigned with on average value of the critical period of the structural system. Thus, this value is suitable for all structural systems.

As a conclusion, the proposed robust approach is effective to reduce first story displacement of the five different structural models by 26% while the approach without additional robustness measures is effective to reduce the objective by 23%. The proposed method is feasible to find a robust optimum TMD design.

REFERENCES

[1] J.P. Den Hartog, *Mechanical Vibrations*. McGraw-Hill, New York, 1947.

[2] G.B. Warburton, Optimum absorber parameters for various combinations of response and excitation parameters. *Earthquake Engineering and Structural Dynamics*, **10**, 381-401, 1982.

[3] F. Sadek, B. Mohraz, A.W. Taylor and R.M. Chung, A method of estimating the parameters of tuned mass dampers for seismic applications. *Earthquake Engineering and Structural Dynamics*, **26**, 617-635, 1997.

[4] A.Y.T. Leung and H. Zhang, Particle swarm optimization of tuned mass dampers. *Engineering Structures*, **31**, 715-728, 2009.

[5] G. Bekdaş and S.M Nigdeli, An optimization approach of tuned mass dampers by considering uncertain mass of structures. 11th International Conference on Vibration Problems-ICOVP, Lisbon, Portugal, 9-12 September 2013.

[6] Z.W. Geem, J.H. Kim and G.V. Loganathan, A new heuristic optimization algorithm: harmony search, *Simul.*, **76**, 60–68, 2001.

[7] M.N.S. Hadi and Y. Arfiadi, Optimum design of absorber for MDOF structures. *Journal of Structural Engineering-ASCE*, **124**, 1272-1280, 1998.

[8] M.P. Singh, S. Singh and L.M. Moreschi, Tuned mass dampers for response control of torsional buildings. *Earthquake Engineering and Structural Dynamics*, **31**, 749-769, 2002.

[9] N.B. Desu, S.K. Deb and A. Dutta, Coupled tuned mass dampers for control of coupled vibrations in asymmetric buildings. *Structural Control and Health Monitoring*, **13**, 897-916, 2006.

[10] S. Pourzeynali, H.H. Lavasani, and A.H. Modarayi, Active control of high rise building structures using fuzzy logic and genetic algorithms. *Engineering Structures*, **29**, 346-357, 2007.

[11] G.C. Marano, R. Greco and B. Chiaia, A comparison between different optimization criteria for tuned mass dampers design. *Journal of Sound and Vibration*, **329**, 4880-4890, 2010.

[12] A.Y.T. Leung, H. Zhang, C.C. Cheng and Y.Y. Lee, Particle swarm optimization of TMD by non-stationary base excitation during earthquake. *Earthquake Engineering and Structural Dynamics*, **37**, 1223-1246, 2008.

[13] R. Steinbuch, Bionic optimization of the earthquake resistance of high buildings by tuned mass dampers. *Journal of Bionic Engineering*, **8**, 335-344, 2011.

[14] G. Bekdaş and S.M Nigdeli, Estimating Optimum Parameters of Tuned Mass Dampers Using Harmony Search. *Engineering Structures*, **33**, 2716-2723, 2011.

[15] G. Bekdaş and S.M Nigdeli, *Optimization of Tuned Mass Damper with Harmony Search*. In 'Metaheuristic Applications in Structures and Infrastructures'. Edited by Amir Hossein Gandomi, Xin-She Yang, Amir Hossein Alavi, Siamak Talatahari, Elsevier, Chapter 14, February 2013.

[16] S.M. Nigdeli and G. Bekdaş, Optimum Tuned Mass Damper Design for Preventing Brittle Fracture of RC Buildings. *Smart Structures and Systems*, **12**, 137-155, 2013.

[17] G. Bekdaş, and S.M. Nigdeli, Mass Ratio Factor for Optimum Tuned Mass Damper Strategies. *International Journal of Mechanical Sciences*, **71**, 68-84, 2013.

[18] S.M. Nigdeli and G. Bekdaş, Optimum Tuned Mass Damper Approaches for Adjacent Structures. *Earthquakes and Structures*, **7**, 1071-1091, 2014.

[19] Pacific Earthquake Engineering Research Center (PEER NGA DATABASE) http://peer.berkeley.edu/nga.

[20] M.P. Singh, E.E. Matheu and L.E. Suarez, Active and semi-active control of structures under seismic excitation. *Earthquake Engineering and Structural Dynamics*, **26**, 193-213, 1997.

International Conference on Engineering Vibration
Ljubljana, Slovenia, 7-10 September 2015

EFFECT OF ECCENTRICITY ON ACTIVE CONTROL OF SEISMIC STRUCTURES

Sinan Melih Nigdeli*[1], M. Hasan Boduroğlu[2]

[1]Istanbul University, Department of Civil Engineering, 34320 Avcılar, Istanbul, Turkey
melihnig@istanbul.edu.tr

[2] Deceased Professor of Istanbul Technical University and MEF University, Dep. of Civil Engineering

In memory of Professor M. H. Boduroğlu, Ph.D (1944-2015)

Keywords: Eccentricity, Structural control, Active control, Earthquake, Seismic structures, Torsionally irregular structures.

Abstract. *Generally, all structures are torsionally irregular because of several reasons like the irregularity of plan and accidental torsion. Although a symmetric structure has the same point for centres of mass and rigidity, an amount of torsional effects called as accidental torsion can occur because of different distribution of live loads, torsional effects of earthquake excitations or the difference between computed and actual structural properties. These torsional effects can be reduced by using active control for seismic structures. In this paper, the change of eccentricity is investigated for an active structural control system designed for torsionally irregular structures. A single story torsionally irregular structure using active tendons controlled by Proportional–Integral–Derivative (PID) type controllers was taken as a numerical example. A numerical algorithm which scans the combination of controller parameters such as proportional gain, integral time and derivation time was used in tuning of controller and time delay of the control signal was considered as 20 ms. Error signal is taken as the velocity at the critical direction and sides of the torsionally irregular shear building under bi-directional near-fault earthquake excitation. The system tuned for a constant eccentricity was investigated for different eccentricities. Three different orientations of active tendons were investigated. In the first orientation, the structure is controlled from a single side in critical direction. In the second orientation case, the structure is controlled from the both directions, but only from two sides where the displacements are mostly affected by the torsion. The third orientation is the symmetrically control of structure from all sides. As conclusions, the first two orientations are not physically applicable because the centre of mass or rigidity may change because of uncertainty. Thus, the critical sides or directions may change. The third orientation is robust for different eccentricities in mean of reduction of structural responses and obtaining a steady stead response.*

1 INTRODUCTION

Control is a process in which response of a system excited by an external disturbance is measured and the required interference is done by using mechanical systems in passive control or motor driven systems in active control. Since civil structures are investigated according to principle of mechanics and structures are under excitation of different loads, active and passive control approaches are needed in order to maintain a comfortable and secure condition especially under dynamic forces such as wind, traffic and earthquakes.

Passive and active control systems must be tuned according to the properties of the structures in order to reduce vibrations. In this optimization process, structures are modelled according to major freedoms and corresponding frequencies. Generally, planer systems with translational motion are considered in studies. Because of different center of mass (C.M.) and center of rigidity (C.R.), torsional irregularity occurs (Figure 1). Thus, rotational effects may be investigated and control systems may be tuned by including the rotation of the storey. Additionally, torsional effects may also occur in structures with regular plan because of accidental torsion. The distribution of live loads may change by the time. Thus, in structural design, a certain eccentricity is always considered for regular structures in the plan.

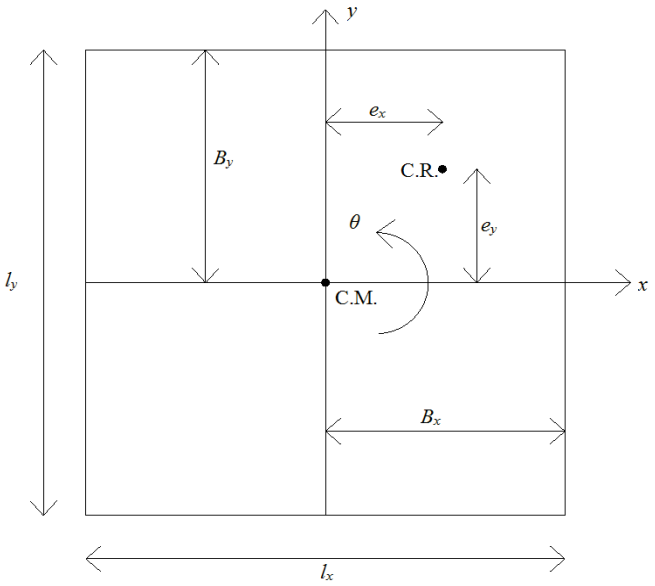


Figure 1: Plan of torsionally irregular structures

Active tendon control systems consisting of actuator driver tendons at the sides of the structures are very suitable and basic way to control rotational responses. By varying the control signal of actuators at the sides of the structure, the rotational control is maintained. Active tendon control systems are investigated for torsionally irregular structures. Lin et al. [1] presented a H_∞ based control algorithm for active tendon control of torsionally irregular structure with soil-structure interaction effects. An active control algorithm optimized with genetic algorithm was developed for 3 dimensional buildings by Cha et al. [2]. Nigdeli and Boduroğlu controlled torsionally irregular structures under near fault excitations with active tendons by using Proportional Integral Derivative (PID) type controllers [3, 4]. Recently, several active structural control methods have been developed [5-10].

In this paper, the effect of eccentricity is investigated. The optimally tuned single storey system with active tendons was checked for different eccentricities different from constant system eccentricity. The evaluation of robustness is done for a near fault Northridge excitation superimposed with additional impulsive pulses given in Nigdeli and Boduroğlu [3, 4].

2 SINGLE STORY TORSIONALLY COUPLED STRUCTURE

As seen in Figure 1., the distance between the centers of mass and rigidity are shown with e_x and e_y. B_x and B_y defines the location of center of rigidity and l_x and l_y are the length of the structure in x and y directions, respectively. The equations of motion of a single story shear building are given in matrix form as

$$\mathbf{M}\ddot{x}(t)+\mathbf{C}\dot{x}(t)+\mathbf{K}x(t)=\mathbf{E}\ddot{z}(t) \tag{1}$$

and

$$\mathbf{M}=\begin{bmatrix} m & 0 & 0 \\ 0 & m & 0 \\ 0 & 0 & J_0 \end{bmatrix}, \tag{2}$$

$$J_0=mr^2, \tag{3}$$

$$\mathbf{C}=\alpha\mathbf{M}+\beta\mathbf{K}, \tag{4}$$

$$\mathbf{K}=\begin{bmatrix} k_x & 0 & -k_x e_y \\ 0 & k_y & k_y e_x \\ -k_x e_y & k_y e_x & k_\theta+k_x e_y^2+k_y e_x^2 \end{bmatrix}, \tag{5}$$

$$x(t)=\begin{bmatrix} x \\ y \\ \theta \end{bmatrix}, \tag{6}$$

$$\mathbf{E}=\begin{bmatrix} -m & 0 \\ 0 & -m \\ 0 & 0 \end{bmatrix}, \tag{7}$$

$$\ddot{z}(t)=\begin{bmatrix} \ddot{x}_g \\ \ddot{y}_g \end{bmatrix}. \tag{8}$$

In the equations, m is story mass; k_x, k_y and k_θ are story stiffnesses in x, y and θ directions, respectively; $\ddot{x}_g$ and $\ddot{y}_g$ are ground accelerations at x and y directions, respectively; J_0 is mass

polar moment of inertia of story; r is radius of gyration of the floor. Damping Matrix (**C**) is taken according to Rayleigh damping and it is proportional to mass and stiffness matrix by using α and β coefficients.

As seen in Figure 2, the active tendon controlled single story torsionally coupled structure is shown. Two parallel crosswise tendons driven by an actuator are placed in spans of the structure. In Figure 2, the actuators are numbered from 1 to 4. The equation for the controlled structure is shown in Equation (9). The symbols in this equation are tendon displacement vector; U(t) (Equation (10)) and tendon location matrix; B (Equation (11)). In tendon location matrix and tendon displacement vector, k_c is stiffness of a tendon; θ_{tx} and θ_{ty} are angles between ground and tendons in x and y directions, respectively. $u_1(t)$, $u_2(t)$, $u_3(t)$ and $u_4(t)$ are control signals (the displacements of actuator arms).

$$\mathbf{M}\ddot{x}(t)+\mathbf{C}\dot{x}(t)+\mathbf{K}x(t)=\mathbf{B}U(t)+\mathbf{E}\ddot{z}(t). \tag{9}$$

$$U(t)=[u_1(t) \quad u_2(t) \quad u_3(t) \quad u_4(t)]^{\mathbf{T}}. \tag{10}$$

$$B=\begin{bmatrix} 4k_c\cos\theta_{tx} & 4k_c\cos\theta_{tx} & 0 & 0 \\ 0 & 0 & 4k_c\cos\theta_{ty} & 4k_c\cos\theta_{ty} \\ -4k_cB_y\cos\theta_{tx} & 4k_c(l_y-B_y)\cos\theta_{tx} & 4k_cB_x\cos\theta_{ty} & -4k_c(l_x-B_x)\cos\theta_{ty} \end{bmatrix}. \tag{11}$$

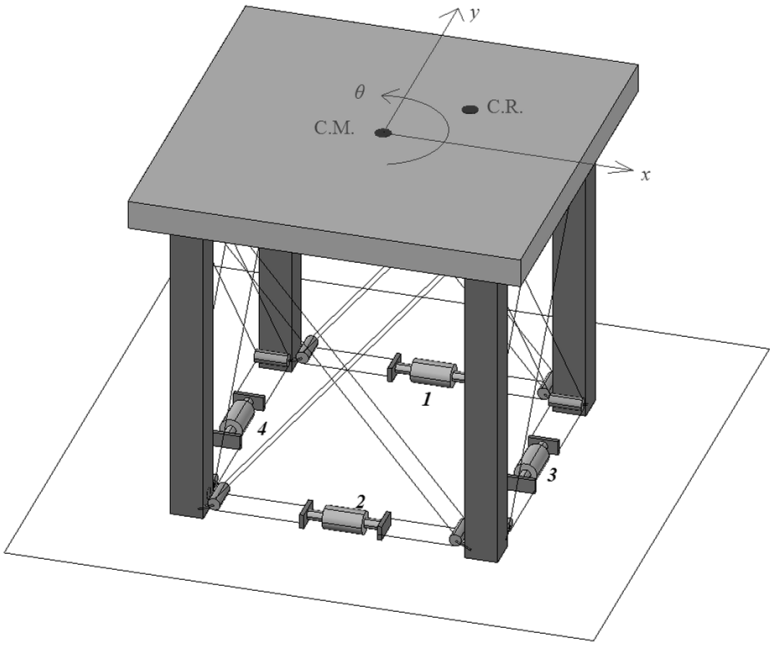


Figure 2: Active tendon controlled irregular structure.

The control signals are generated by Proportional Integral Derivation (PID) type controllers. The equation of PID controllers which transforms error signal (e(t)) into control signal (u(t)), is shown in Equation (12).

$$u(t) = K\left(e(t) + \frac{1}{T_i}\int e(t)dt + T_d \frac{de(t)}{dt} \right) \quad (12)$$

In the equation of controller, K (Proportional gain), T_i (Integral time) and Td (Derivation time) are the parameters of the controller. These parameters were found by a numerical algorithm using an objective to find the best set of parameters from the ranges found by trials for a critical excitation [3,4].

3 NUMERICAL EXAMPLE

A single story torsionally coupled shear building taken from [1] is investigated for different eccentricities. Superimposed Northridge-Sylmar excitation [3, 4] is used in the investigation (Figure 3). The properties of structure are shown in Table 1.

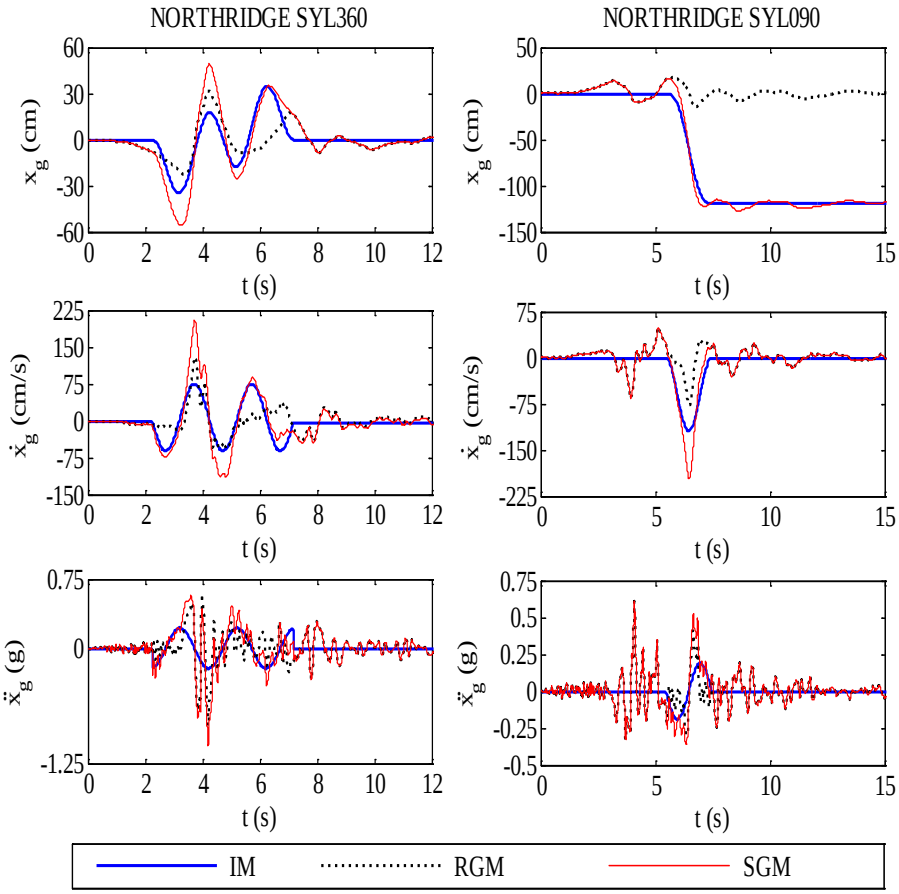


Figure 3: Superimposed excitations (IM: Impulsive motion, RGM: Recorded ground motion, SGM: Superimposed ground motion) [3, 4].

In Nigdeli and Boduroğlu [3,4], three different tendon orientations of active tendons were considered. Active tendons are positioned at the second side in the first case. Active tendons are positioned at the second and fourth side in the second case and the structure is controlled

for two directions. The structure is controlled by all sides in the last case. PID controller parameters are the same for all cases. In the properties given in Table 1, these parameters were found as -0.007 s, 0.005 s and 6 s for K, T_d and T_i, respectively [3, 4].

Story mass	m (kg)	2923.5
Story stiffness in x, y and θ directions	ω_x (Hz)	3.47
	ω_y (Hz)	3.81
	ω_θ (Hz)	4.16
Damping ratios in x and y directions	$\zeta_x = \zeta_y = \zeta_\theta$ (%)	1.24
Stiffness of a tendon	k_c (N/m)	372100
Angles between ground and tendons in x and y directions	$\theta_{tx} = \theta_{ty}$ (◦)	36
Location of the center of rigidity	$e_x/r = e_y/r$	0.3
Location of the center of mass	$B_x/r = B_y/r$	$\sqrt{3/2}$

Table 1: Properties of the structure [1].

4 CONCLUSIONS

The structure is investigated for five eccentricity cases. The maximum results are presented in Tables 2-6 for eccentricity cases which are named as EC1, EC2, EC3, EC4 and EC5 for e_x/r=e_y/r=0, 0.1, 0.3, 0.5 and 0.7, respectively. EC3 is the case used in tuning of PID controller.

	Uncontrolled	***Case 1***	***Case 2***	***Case 3***
$\boldsymbol{x}$ (m)	0.0647	0.0493	0.0489	0.0390
$\dot{\boldsymbol{x}}$ (m/s)	1.0468	0.7723	0.7672	0.5859
$\ddot{\boldsymbol{x}}$ (m/s^2)	21.5477	15.4713	15.3138	11.0634
$\ddot{\boldsymbol{x}} + \ddot{\boldsymbol{x}}_{\boldsymbol{g}}$ (m/s^2)	30.7509	24.4491	24.3067	19.8611
$\boldsymbol{y}$ (m)	0.0162	0.0162	0.0151	0.0129
$\dot{\boldsymbol{y}}$ (m/s)	0.3348	0.3348	0.2802	0.2139
$\ddot{\boldsymbol{y}}$ (m/s^2)	7.8462	7.8462	5.6666	4.5175
$\ddot{\boldsymbol{y}} + \ddot{\boldsymbol{y}}_{\boldsymbol{g}}$ (m/s^2)	9.3056	9.3056	8.4956	7.7302
$\boldsymbol{r\theta}$ (m)	-	0.0086	0.0068	-
$r\dot{\boldsymbol{\theta}}$ (m/s)	-	0.1840	0.1447	-
$r\ddot{\boldsymbol{\theta}}$ (m/s^2)	-	4.0205	3.3282	-
$\mathbf{4k_cCos(\theta_{tx})u_1}$ (N)	-	-	-	4976.11
$\mathbf{4k_cCos(\theta_{tx})u_2}$ (N)	-	5483.70	5760.49	4976.11
$\mathbf{4k_cCos(\theta_{ty})u_3}$ (N)	-	-	-	1810.67
$\mathbf{4k_cCos(\theta_{ty})u_4}$ (N)	-	-	1903.38	1810.67

Table 2: Maximum responses for EC1.

In EC1, regular structure is investigated. Thus, rotational effects are not seen in uncontrolled structure and Case 3. Since active tendons are not symmetric in Case 1 and Case 2, minor torsional effects are seen.

	Uncontrolled	***Case 1***	***Case 2***	***Case 3***
$\boldsymbol{x}$ (m)	0.0674	0.0469	0.0465	0.0393
$\dot{\boldsymbol{x}}$ (m/s)	1.1016	0.7260	0.7260	0.5872
$\ddot{\boldsymbol{x}}$ (m/s^2)	22.6969	14.3911	14.1546	11.1073
$\ddot{\boldsymbol{x}} + \ddot{\boldsymbol{x}}_{\boldsymbol{g}}$ (m/s^2)	31.6159	23.3043	23.1579	19.8710
$\boldsymbol{y}$ (m)	0.0164	0.0174	0.0154	0.0126
$\dot{\boldsymbol{y}}$ (m/s)	0.3243	0.3355	0.2861	0.2043
$\ddot{\boldsymbol{y}}$ (m/s^2)	7.6042	7.7452	6.4324	4.3839
$\ddot{\boldsymbol{y}} + \ddot{\boldsymbol{y}}_{\boldsymbol{g}}$ (m/s^2)	9.5283	10.1208	9.0238	7.5623
$r\boldsymbol{\theta}$ (m)	0.0125	0.0057	0.0064	0.0031
$r\dot{\boldsymbol{\theta}}$ (m/s)	0.2766	0.1350	0.1203	0.0432
$r\ddot{\boldsymbol{\theta}}$ (m/s^2)	6.5037	3.4112	2.8921	0.8658
$\mathbf{4k_c Cos(\theta_{tx})u_1}$ (N)	-	-	-	4605.41
$\mathbf{4k_c Cos(\theta_{tx})u_2}$ (N)	-	6036.54	6334.80	5379.75
$\mathbf{4k_c Cos(\theta_{ty})u_3}$ (N)	-	-	-	2093.24
$\mathbf{4k_c Cos(\theta_{ty})u_4}$ (N)	-	-	1490.26	1456.46

Table 3: Maximum responses for EC2.

For smaller eccentricity than the used in tuning of controller, Case 1 and Case 2 is more effective in percentage. An increase of responses in y direction is observed for the second orientation case because the structure is controlled for only the critical direction.

	Uncontrolled	***Case 1***	***Case 2***	***Case 3***
$\boldsymbol{x}$ (m)	0.0709	0.0458	0.0460	0.0410
$\dot{\boldsymbol{x}}$ (m/s)	1.1073	0.6593	0.6764	0.5906
$\ddot{\boldsymbol{x}}$ (m/s^2)	22.6720	13.2885	13.3427	11.2235
$\ddot{\boldsymbol{x}} + \ddot{\boldsymbol{x}}_{\boldsymbol{g}}$ (m/s^2)	30.4549	21.7653	21.9579	19.7628
$\boldsymbol{y}$ (m)	0.0308	0.0160	0.0130	0.0108
$\dot{\boldsymbol{y}}$ (m/s)	0.5789	0.3199	0.1895	0.1415
$\ddot{\boldsymbol{y}}$ (m/s^2)	13.1997	7.0426	4.3116	3.4818
$\ddot{\boldsymbol{y}} + \ddot{\boldsymbol{y}}_{\boldsymbol{g}}$ (m/s^2)	12.7501	8.4232	8.0869	6.5488
$r\boldsymbol{\theta}$ (m)	0.0345	0.0100	0.0095	0.0086
$r\dot{\boldsymbol{\theta}}$ (m/s)	0.6865	0.1719	0.1322	0.1190
$r\ddot{\boldsymbol{\theta}}$ (m/s^2)	14.2354	4.5542	3.3133	2.2542
$\mathbf{4k_c Cos(\theta_{tx})u_1}$ (N)	-	-	-	4068.57
$\mathbf{4k_c Cos(\theta_{tx})u_2}$ (N)	-	6731.99	6738.45	6080.33
$\mathbf{4k_c Cos(\theta_{ty})u_3}$ (N)	-	-	-	2363.39
$\mathbf{4k_c Cos(\theta_{ty})u_4}$ (N)	-	-	1886.91	1666.17

Table 4: Maximum responses for EC3.

For EC4 and EC5, decrease of responses in x and rotational directions is seen and the effects in y direction are increased. In that situation, active tendon control is effective for all responses.

	Uncontrolled	***Case 1***	***Case 2***	***Case 3***
$\boldsymbol{x}$ (m)	0.0686	0.0446	0.0470	0.0426
$\dot{\boldsymbol{x}}$ (m/s)	0.9681	0.6293	0.6703	0.5725
$\ddot{\boldsymbol{x}}$ (m/s^2)	17.5618	11.8048	12.7761	10.8499
$\ddot{\boldsymbol{x}} + \ddot{\boldsymbol{x}}_{\boldsymbol{g}}$ (m/s^2)	25.2241	20.0619	21.2183	19.0573
$\boldsymbol{y}$ (m)	0.0410	0.0188	0.0141	0.0139
$\dot{\boldsymbol{y}}$ (m/s)	0.7930	0.2881	0.1753	0.1374
$\ddot{\boldsymbol{y}}$ (m/s^2)	15.1999	6.3398	4.2003	3.0341
$\ddot{\boldsymbol{y}} + \ddot{\boldsymbol{y}}_{\boldsymbol{g}}$ (m/s^2)	14.9746	8.0923	7.3536	6.3534
$r\boldsymbol{\theta}$ (m)	0.0377	0.0171	0.0144	0.0124
$r\dot{\boldsymbol{\theta}}$ (m/s)	0.6806	0.2652	0.1981	0.1632
$r\ddot{\boldsymbol{\theta}}$ (m/s^2)	16.3248	5.7743	4.3412	3.3136
$\mathbf{4k_c Cos(\theta_{tx})u_1}$ (N)	-	-	-	3654.85
$\mathbf{4k_c Cos(\theta_{tx})u_2}$ (N)	-	7003.85	6869.22	6385.53
$\mathbf{4k_c Cos(\theta_{ty})u_3}$ (N)	-	-	-	2394.51
$\mathbf{4k_c Cos(\theta_{ty})u_4}$ (N)	-	-	2489.38	2276.25

Table 5: Maximum responses for EC4.

	Uncontrolled	***Case 1***	***Case 2***	***Case 3***
$\boldsymbol{x}$ (m)	0.0544	0.0410	0.0468	0.0432
$\dot{\boldsymbol{x}}$ (m/s)	0.8400	0.5052	0.6070	0.5325
$\ddot{\boldsymbol{x}}$ (m/s^2)	15.2529	10.3692	11.6513	10.0783
$\ddot{\boldsymbol{x}} + \ddot{\boldsymbol{x}}_{\boldsymbol{g}}$ (m/s^2)	18.8396	16.9746	19.3042	18.0233
$\boldsymbol{y}$ (m)	0.0466	0.0229	0.0175	0.0171
$\dot{\boldsymbol{y}}$ (m/s)	0.7224	0.3438	0.2286	0.1456
$\ddot{\boldsymbol{y}}$ (m/s^2)	12.5629	6.8082	5.0210	3.8954
$\ddot{\boldsymbol{y}} + \ddot{\boldsymbol{y}}_{\boldsymbol{g}}$ (m/s^2)	14.8237	8.5510	7.3900	6.8681
$r\boldsymbol{\theta}$ (m)	0.0324	0.0168	0.0144	0.0145
$r\dot{\boldsymbol{\theta}}$ (m/s)	0.5253	0.2352	0.2067	0.1545
$r\ddot{\boldsymbol{\theta}}$ (m/s^2)	9.9248	6.5426	5.0244	3.7247
$\mathbf{4k_c Cos(\theta_{tx})u_1}$ (N)	-	-	-	3492.68
$\mathbf{4k_c Cos(\theta_{tx})u_2}$ (N)	-	6416.62	6985.75	6049.56
$\mathbf{4k_c Cos(\theta_{ty})u_3}$ (N)	-	-	-	2312.89
$\mathbf{4k_c Cos(\theta_{ty})u_4}$ (N)	-	-	3121.01	2708.52

Table 6: Maximum responses for EC5.

Earthquake excitations are unknown, so characteristics of responses of structures may be different according to excitations. Additionally, eccentricities may be in the opposite direction. When the case; e_x/r=e_y/r=-0.5 is investigated, the first and second tendon orientation cases are not effective as seen in Figure 4. Generally, the active control system is robust against the change of eccentricity.

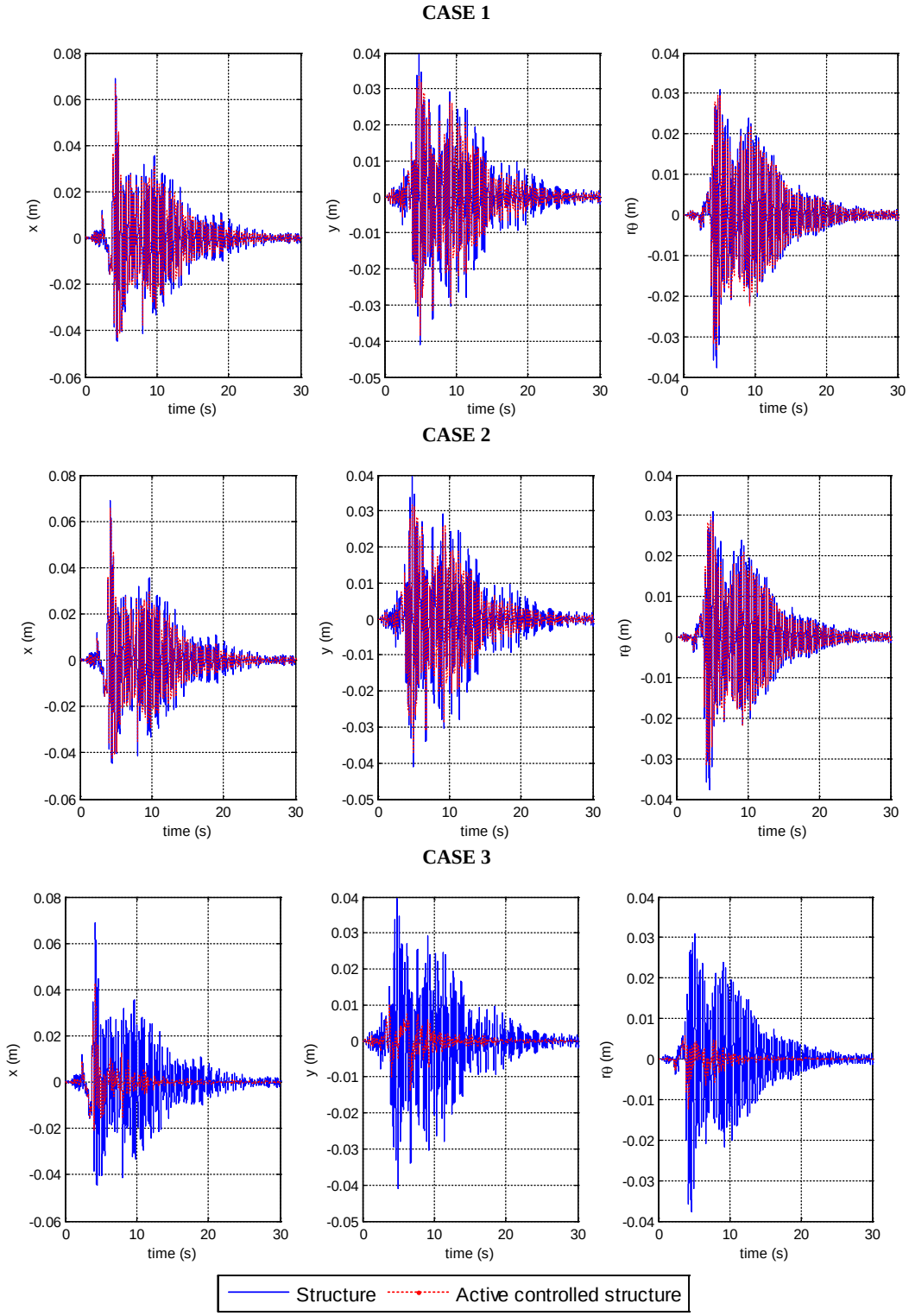


Figure 4: Displacement plots $e_x/r=e_y/r$=-0.5 .

ACKNOWLEDGEMENT

On April 8th, 2015, Professor M. H. Boduroğlu passed away because of a suddenly emerged illness. He was a distinguished academician. As a student of him, the presenter author is grateful to his experience and knowledge in structural and earthquake engineering.

REFERENCES

[1] C. Lin, C. Chang and J. Wang, Active Control of Irregular Buildings Considering Soil-Structure Interaction Effects. *Soil Dynamics and Earthquake Engineering*, **30**, 98-109, 2010.

[2] Cha Y-J., Y. Kim, A. M. Raich and A. K. Agrawal A.K., Multi-objective optimization for actuator and sensor layouts of actively controlled 3D buildings. *Journal of Vibration and Control*, **19**, 942-960, 2013.

[3] S.M. Nigdeli, Lateral Displacement and Torsion Control of Structures with Active Tendons under Near Fault Effects. *PhD. Thesis*, Istanbul Technical University, Graduate School of Science, Engineering and Technology, 2012.

[4] S.M. Nigdeli and M.H. Boduroğlu, Active tendon control of torsionally irregular structures under near-fault ground motion excitation. *Computer-aided civil and infrastructure engineering*, **28**, 718-736, 2013.

[5] O. El-Khoury and H. Adeli, Recent Advances on Vibration Control of Structures under Dynamic Loading. *Archives of Computational Methods in Engineering*, **20**, 353-360, 2013.

[6] A. Yanik, U. Aldemir and M. Bakioglu, A new active control performance index for vibration control of three-dimensional structures. *Engineering Structures*, **62**, 53-64, 2014.

[7] S. M. Nigdeli, Effect of feedback on PID controlled active structures under earthquake excitations. *Earthquakes and Structures* , **6**, 217-235, 2014.

[8] F. Amini and M.Z. Samini, A wavelet-based adaptive pole assignment method for structural control. *Computer-aided civil and infrastructure engineering*, **29**, 464-477, 2014.

[9] H. Ghaffarzadeh and A. Younespour, Active tendons control of structures using block pulse functions. *Structural Control and Health Monitoring*, **21**, 1453-1464, 2014.

[10] N. Wang and H. Adeli, Self-constructing wavelet neural network algorithm for nonlinear control of large structures. *Engineering Applications of Artificial Intelligence*, **41**, 249-258, 2015.

International Conference on Engineering Vibration
Ljubljana, Slovenia, 7-10 September 2015

MULTI OBJCETIVE OPTIMIZATION OF DOUBLE TUNED MASS DAMPERS CONSIDERING MAXIMUM STROKE CAPACITY

Sinan Melih Nigdeli[1], **Gebrail Bekdaş***[2]

[1]Istanbul University, Civil Engineering Department, 34320 Avcılar, Istanbul, Turkey
melihnig@istanbul.edu.tr

[2] Istanbul University, Civil Engineering Department, 34320 Avcılar, Istanbul, Turkey
bekdas@istanbul.edu.tr

Keywords: Multi objective optimization, Double tuned mass damper, Earthquake, Seismic structures, Stroke capacity, Harmony Search.

Abstract. *A multi objective optimization approach is presented for double tıned mass dampers (DTMD) positioned on the top of the seismic structures. In the optimization methodology, set of grouped earthquakes is used in order to find a global optimum solution under two objectives such as minimization of maximum top story displacement and limitation of maximum relative displacement of masses of DTMD (stroke). The optimization problem of DTMD has six design variables such as masses, periods and damping ratios of two masses. Harmony search (HS) algorithm is employed in the optimization process. HS is a music inspired metaheuristic algorithm using iterative stages of local and global search. The optimum design variables were found for a structure with 10 stories and three different limits of the stroke are investigated. According to the results and comparison to single tuned mass dampers, DTMDs are more effective than TMDs in reduction of structural responses.*

1 INTRODUCTION

Tuned mass dampers (TMD) are vibration absorber devices and the properties of these absorbers are tuned according to the frequency behavior of the mechanical systems in order to surpass the vibrations. In the tuning process of the TMDs, optimization is needed in order to consider design constraints for the best efficiency. Also, TMDs have been used on civil structures subjected to the random vibrations of winds, earthquakes and other dynamic excitations. An example structure is shown in Fig. 1.



Figure 1: Berlin TV Tower.

First optimum design of TMDs was proposed by Den Hartog for undamped single degree of freedom (SDOF) main systems [1]. The expressions proposed by Den Hartog for harmonic excitation are still used in practice including multiple degree of freedom structures because Warburton and Ayorinde showed that the structure may be taken as an equivalent SDOF system, if the natural frequencies are well separated [2]. For harmonic and random excitations, Warburton derived simple expressions for frequency and damping ratio of TMDs [3].

The simple expressions cannot be derived when the damping is included in the main system. Thus, Sadek et al. conducted numerical trials and obtained several expressions by using curve fitting. Also, a modification for the expressions was proposed for multiple degree of freedom (MDOF) structures [4]. Rana and Soong employed numerical optimization for tuned mass dampers in control of a single structural mode and proposed multi-tuned mass dampers for possible control of multiple modes [5]. Chang obtained close form expressions for TMDs under wind and earthquake excitations [6]. By investigating the displacement and acceleration response spectra of structures, an extended random decrement method was proposed in reduction of vibration responses [7]. Alternatively, semi-active magnetorheological (MR) damper were employed in the design of TMDs by Aldemir [8]. In order to reduce a performance index value, Lee et al. developed a numerical optimization approach for TMDs [9]. Li and Zhu proposed optimum double tuned mass dampers (DTMD) for seismic structures [10].

Metaheuristic methods have been also used in optimization of TMDs positioned on structures. The metaheuristic methods used in these optimization problems are genetic algorithm [11-15], particle swarm optimization [16-17], bionic optimization [18], harmony search algorithm [19-23], ant colony optimization [24], artificial bee optimization [25] and shuffled complex evolution [26].

In this paper, a multi objective optimization of DTMD parameters is proposed. Harmony search (HS) algorithm developed by Geem et al. [27] is employed for two objectives which are related with the performance and practicability. The first objective is the reduction of

maximum top story displacement. The other objective is about the stroke capacity. A scaled displacement value of DTMD is used in order to consider the stroke capacity of DTMD.

2 EQUATIONS OF TMD PROBLEM FOR EARTHQUAKE EXCITED STRUCTURE

A shear building with a DTMD is physically modelled in Fig. 2. The number of the stories of the structure is *N*. The equations of motion of the structure can be written as

$$\mathrm{M}\ddot{x}(t)+\mathrm{C}\dot{x}(t)+\mathrm{K}x(t)=-\mathrm{M}\{1\}\ddot{x}_g(t) \tag{1}$$

in matrix form for ground acceleration excitation. The *M, C and K m*atrices are diagonal lumped mass, damping and stiffness matrices, respectively and these matrices are given in Eqs. (2)-(4). The x(t), $\ddot{x}_g(t)$ and {1} are the vector containing structural displacements of all stories and DTMD (Eq. (5)), ground acceleration in horizontal direction and a vector of ones with a dimension of (N+2,1), respectively.

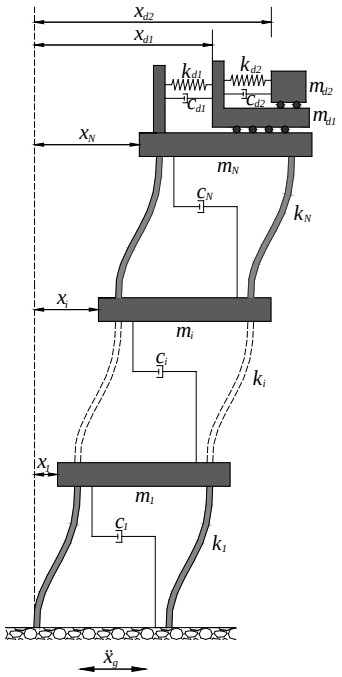


Figure 1: Physical model of N-story shear building including a DTMD.

$$M=\mathrm{diag}[m_1\ m_2\ \ldots\ m_N\ m_{d1} m_{d2}] \tag{2}$$

$$\mathrm{C}=\begin{bmatrix} (c_1+c_2) & -c_2 & & & & & \\ -c_2 & (c_2+c_3) & -c_3 & & & & \\ & . & . & & & & \\ & . & . & . & & & \\ & & . & -c_N & (c_N+c_{d1}) & -c_{d1} & \\ & & & & -c_{d1} & (c_{d1}+c_{d2}) & -c_{d2} \\ & & & & & -c_{d2} & c_{d2} \end{bmatrix} \tag{3}$$

$$K = \begin{bmatrix} (k_1 + k_2) & -k_2 & & & & & & \\ -k_2 & (k_2 + k_3) & -k_3 & & & & & \\ & . & . & & & & & \\ & . & . & . & & & & \\ & & . & -k_N & (k_N + k_{d1}) & -k_{d1} & & \\ & & & & -k_{d1} & (k_{d1} + k_{d2}) & -k_{d2} & \\ & & & & & -k_{d2} & k_{d2} \end{bmatrix} \quad (4)$$

$$\boldsymbol{x}(t) = [x_1\, x_2\, \ldots\, x_N\, x_{d1}\, x_{d1}]^T \quad (5)$$

In the equations, m_i, c_i, k_i *and* x_i *are mass, damping coefficient, stiffness coefficient and displacement of* i_{th} *storey* of structure. The parameters of the DTMD are shown with mass (m_{d1}, m_{d2}), damping coefficient (c_{d1}, c_{d2}) and stiffness coefficient (k_{d1}, k_{d2}). The displacements of the DTMD are x_{d1} and x_{d2}.

3 MULTI OBJECTIVE OPTIMIZATION USING HARMONY SEARCH

Musicians search the best harmony by playing random notes in order to gain the admiration of the audience. Similarly, the best objective function of an engineering problem can be found. For that reason, harmony search (HS) algorithm is developed for optimization. The multi objective optimization methodology can be divided into two sections for initial calculations and iterative optimization.

First structural properties, external excitations and ranges of design variables are defined as optimization constraints. Then, the structure without DTMD is analyzed because one of the objective function depends on it. After that, the initial Harmony Memory (HM) matrix containing Harmony Vectors (HVs) is generated. Each HV contains a possible solution for the masses, periods and damping ratios which are the design variables and these variables are defined with random numbers generated within the range. Also, the optimization objectives are calculated for these set of variables.

The objective functions are given in Eqs. (6) and (7). The first one is the reduction of maximum top story displacement of the structure to a user defined value (x_{max}). If the user defined value is not applicable by using the design variable ranges, this value is iteratively increased. The other objective is related to the stroke capacity of the TMD.

$$|x_N| \le x_{max} \quad (6)$$

$$\max\left[\frac{\max\left[\left|x_{N+2} - x_{N+1}\right|\right]_{with\ DTMD}}{\max\left[\left|x_N\right|\right]_{without\ DTMD}}, \frac{\max\left[\left|x_{N+1} - x_N\right|\right]_{with\ DTMD}}{\max\left[\left|x_N\right|\right]_{without\ DTMD}}\right] \le st_\max \quad (7)$$

After the initial calculations, the iterative optimization process starts. A new HV is generated and calculations of objective functions are done. If the solution of a new vector is better than the existing ones in HM, it is replaced with the worst one. The objective given as Eq. (7) is considered in elimination. If this objective function is lower than *st_max*, the objective function given in Eq. (10) is considered in elimination. This iterative search is done until the criteria given by two objectives are provided.

A new harmony vector is generated in two ways according to a possibility called Harmony Memory Considering Rate (HMCR). The new vector can be generated by a smaller range around an existing vector in HM or by the whole range. The ratio of the small and the whole range is defined with Pitch Adjusting Rate (PAR).

4 NUMERICAL EXAMPLES

A ten story structure with equal properties was optimized [13]. The mass, stiffness coefficient and damping coefficient of a story is 360 t, 6.2 MNs/m and 650 MN/m, respectively. In optimization of DTMD, FEMA P-695 [28] far-fault ground motion set given in Table 1 was used. These records were downloaded from Pacific Earthquake Research Centre (PEER) database [29]. The ranges for the design variables and optimum DTMD parameters are given in Table 2. The *st_max* limitation was taken as 0.8 and 1 for Case 1 and 2, respectively. x_{max} was taken as zero in order to find a solution with maximum efficiency on reduction of displacement.

Earthquake Number	Date	Name	Component 1	Component 2
1	1994	Northridge	NORTHR/MUL009	NORTHR/MUL279
2	1994	Northridge	NORTHR/LOS000	NORTHR/LOS270
3	1999	Duzce, Turkey	DUZCE/BOL000	DUZCE/BOL090
4	1999	Hector Mine	HECTOR/HEC000	HECTOR/HEC090
5	1979	Imperial Valley	IMPVALL/H-DLT262	IMPVALL/H-DLT352
6	1979	Imperial Valley	IMPVALL/H-E11140	IMPVALL/H-E11230
7	1995	Kobe, Japan	KOBE/NIS000	KOBE/NIS090
8	1995	Kobe, Japan	KOBE/SHI000	KOBE/SHI090
9	1999	Kocaeli, Turkey	KOCAELI/DZC180	KOCAELI/DZC270
10	1999	Kocaeli, Turkey	KOCAELI/ARC000	KOCAELI/ARC090
11	1992	Landers	LANDERS/YER270	LANDERS/YER360
12	1992	Landers	LANDERS/CLW-LN	LANDERS/CLW-TR
13	1989	Loma Prieta	LOMAP/CAP000	LOMAP/CAP090
14	1989	Loma Prieta	LOMAP/G03000	LOMAP/G03090
15	1990	Manjil, Iran	MANJIL/ABBAR--L	MANJIL/ABBAR—T
16	1987	Superstition Hills	SUPERST/B-ICC000	SUPERST/B-ICC090
17	1987	Superstition Hills	SUPERST/B-POE270	SUPERST/B-POE360
18	1992	Cape Mendocino	CAPEMEND/RIO270	CAPEMEND/RIO360
19	1999	Chi-Chi, Taiwan	CHICHI/CHY101-E	CHICHI/CHY101-N
20	1999	Chi-Chi, Taiwan	CHICHI/TCU045-E	CHICHI/TCU045-N
21	1971	San Fernando	SFERN/PEL090	SFERN/PEL180
22	1976	Friuli, Italy	FRIULI/A-TMZ000	FRIULI/A-TMZ270

Table 1: FEMA P-695 far-field ground motion records [28].

In order to compare the results, optimum TMD is also investigated by using the same problem, but the maximum mass of TMD is taken as 10% of total mass. Thus, the sum of masses of DTMD is not scanned for higher values than single TMD. The optimum results for single TMD are shown in Table 3.

Design variable	Range definition	Optimum values	
		Case 1	Case 2
Mass (t)	between 0.1% and 5% of total mass of structure	160.18-169.56	178.64-173.16
Period (s)	between 0.5 and 1.5 times of the critical period of structure	0.5666-0.6775	0.6399-0.7077
Damping ratio (%)	between 1% and 30%	28.28-18.68	28.88-9.35

Table 2: The ranges of design variables and optimum values (DTMD).

Design variable	Range definition	Optimum values	
		Case 1	Case 2
Mass (t)	between 0.1% and 10% of total mass of structure	359.06	357.65
Period (s)	between 0.5 and 1.5 times of the critical period of structure	0.9250	1.0470
Damping ratio (%)	between 1% and 30%	28.84	26.26

Table 3: The ranges of design variables and optimum values (TMD).

5 CONCLUSIONS

The optimum results are investigated for 44 far-field excitations and the most critical record is the BOL090 component of Düzce earthquake. The maximum displacement of the structure is 0.4101 m for that excitation. The optimum DTMD is effective to reduce maximum displacement to 0.2771 m and 0.2626 m for Case 1 and 2, respectively. In Figure 2, the first and top storey displacement plots are shown for the first case of DTMD.

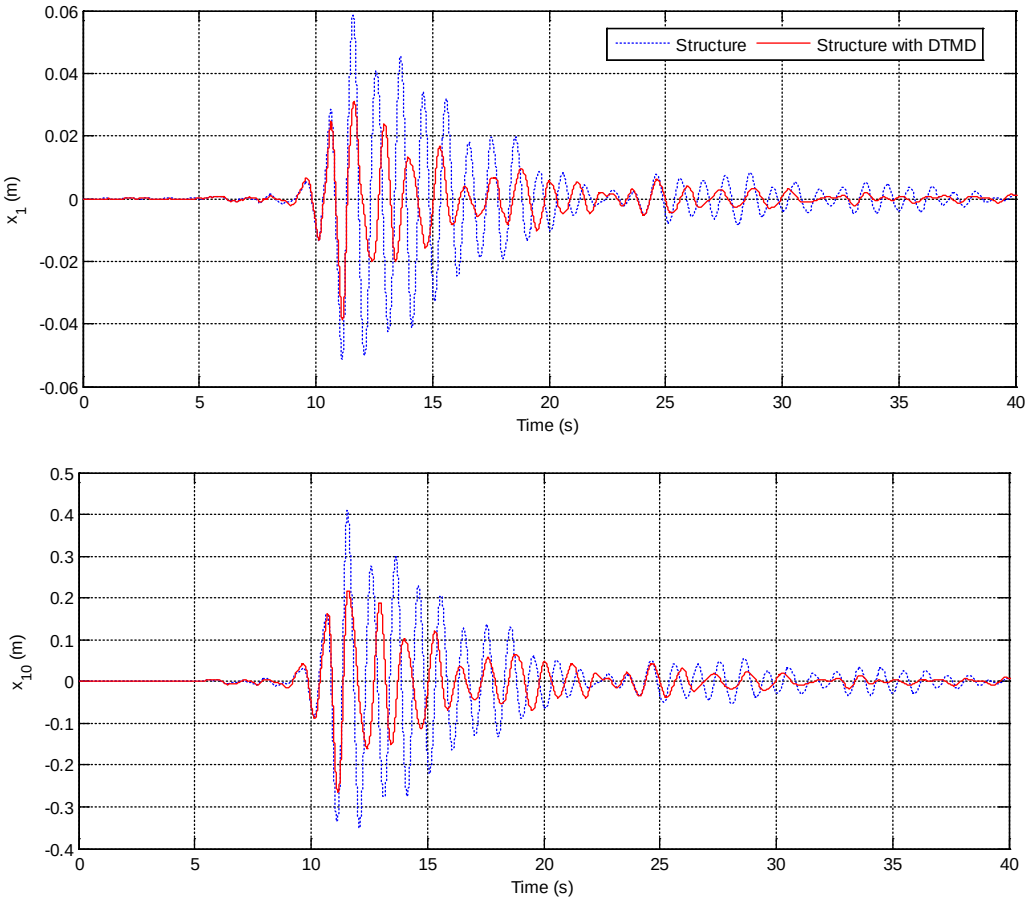


Figure 2: The time history plots for the critical excitation (DTMD- CASE 1)

The effect of reduction of vibrations and immediate damping of vibrations is clearly seen from the plot. The same structural responses of TMD controlled structure are 0.2936 m and 0.2762 m for Case 1 and Case 2, respectively. This result shows that the optimum DTMD is more effective than a single TMD in reduction of structural responses by using the same amount of masses for vibration absorbers.

The optimization approach employing HS algorithm is effective to consider a second objective related to a physical constraint of TMD (stroke capacity) in addition to an index of reduction of structural vibrations. A global optimum solution is found for the numerical example considering 44 records of earthquakes. The proposed approach is effective in finding the best suitable parameters for DTMDs.

REFERENCES

[1] J. P. Den Hartog, Mechanical Vibrations, third ed., Mc Graw-Hill, New York, 1947.

[2] G.B. Warburton, E.O. Ayorinde, Optimum absorber parameters for simple systems, *Earthq. Eng. Struct. D.*, **8**, 197–217, 1980.

[3] G.B. Warburton, Optimum absorber parameters for various combinations of response and excitation parameters, *Earthq. Eng. Struct. D.*, **10**, 381–401, 1982.

[4] F. Sadek, B. Mohraz, A.W. Taylor, R.M. Chung, A method of estimating the parameters of tuned mass dampers for seismic applications, *Earthq. Eng. Struct. D.*, **26**, 617–635, 1997.

[5] R. Rana, T.T. Soong, Parametric study and simplified design of tuned mass dampers, *Eng. Struct.*, **20**, 193–204, 1998.

[6] C.C. Chang, Mass dampers and their optimal designs for building vibration control, *Eng. Struct.*, **21**, 454-463, 1999.

[7] C.C. Lin, J.F. Wang, J.M. Ueng, Vibration Control identification of seismically excited m.d.o.f structure-PTMD systems, *J. Sound Vib.*, **240,** 87–115, 2001.

[8] U. Aldemir, Optimal control of structures with semiactive-tuned mass dampers, *J. Sound Vib.*, **266**, 847–874, 2003.

[9] C.L. Lee, Y.T. Chen, L.L. Chung, Y.P. Wang, Optimal design theories and applications of tuned mass dampers, *Eng. Struct.*, **28**, 43-53, 2006.

[10] C. Li, B. Zhu, Estimating double tuned mass dampers for structures under ground acceleration using a novel optimum criterion, *Journal of Sound and Vibration*, **298**, 280–297, 2006.

[11] M.N.S. Hadi, Y. Arfiadi, Optimum design of absorber for MDOF structures, *J. Struct. Eng.- ASCE*, **124**, 1272–1280, 1998.

[12] G. C. Marano, R. Greco, B. Chiaia, A comparison between different optimization criteria for tuned mass dampers design, *J. Sound Vib.*, **329**, 4880-4890, 2010.

[13] M.P. Singh, S. Singh, L.M. Moreschi, Tuned mass dampers for response control of torsional buildings, *Earthq. Eng. Struct. D.*, **31**, 749–769, 2002.

[14] N.B. Desu, S.K. Deb, A. Dutta, Coupled tuned mass dampers for control of coupled vibrations in asymmetric buildings, *Struct. Control Hlth.*, **13**, 897–916, 2006.

[15] S. Pourzeynali, H.H. Lavasani, A.H. Modarayi, Active control of high rise building structures using fuzzy logic and genetic algorithms, *Eng. Struct.*, **29**, 346-357, 2007.

[16] A.Y.T. Leung, H. Zhang, Particle swarm optimization of tuned mass dampers, *Eng. Struct.*, **31**, 715-728, 2009.

[17] A.Y.T. Leung, H. Zhang, C.C. Cheng, Y.Y. Lee, Particle swarm optimization of TMD by non-stationary base excitation during earthquake, *Earthq. Eng. Struct. D.*, **37**, 1223-1246, 2008.

[18] R. Steinbuch, Bionic optimisation of the earthquake resistance of high buildings by tuned mass dampers, *J. Bionic Eng.*, **8**, 335-344, 2011.

[19] G. Bekdaş, S.M. Nigdeli, Estimating Optimum Parameters of Tuned Mass Dampers Using Harmony Search, *Eng. Struct.*, **33**, 2716-2723, 2011.

[20] G. Bekdaş, S.M. Nigdeli, Optimization of Tuned Mass Damper with Harmony *Search*. In 'Metaheuristic Applications in Structures and Infrastructures'. Edited by Amir Hossein Gandomi, Xin-She Yang, Amir Hossein Alavi, Siamak Talatahari, Elsevier, Chapter 14, February 2013.

[21] G. Bekdaş, S.M. Nigdeli, Mass Ratio Factor for Optimum Tuned Mass Damper Strategies, *Int. J. Mech. Sci.*, **71**, 68-84, 2013.

[22] S.M. Nigdeli, G. Bekdaş, Optimum Tuned Mass Damper Design for Preventing Brittle Fracture of RC Buildings, *Smart Struc. Syst.*, **12(2)**, 137-155, 2013.

[23] Bekdaş G., Nigdeli SM. Optimization of Double Tuned Mass Dampers by using Harmony Search. The Twelfth International Conference on Computational Structures Technology, 2-5 September 2014, Naples, Italy.

[24] A. Farshidianfar, S. Soheili, Ant colony optimization of tuned mass dampers for earthquake oscillations of high-rise structures including soil–structure interaction, *Soil Dyn. Earthquake Eng.*, **51**, 14-22, 2013.

[25] A. Farshidianfar, S. Soheili, ABC optimization of TMD parameters for tall buildings with soil structure interaction, *Interact. Multiscale Mech.*, **6**, 339-356, 2013.

[26] A. Farshidianfar, S. Soheili, Optimization of TMD parameters for Earthquake Vibrations of Tall Buildings Including Soil Structure Interaction, *Int. J. Optim. Civ. Eng.*, **3**, 409-429, 2013.

[27] Z.W. Geem, J.H. Kim and G.V. Loganathan, A new heuristic optimization algorithm: harmony search, *Simul.*, **76**, 60–68, 2001.

[28] FEMA P-695, Quantification of Building Seismic Performance Factors, FederalEmergency Management Agency, Washington DC, 2009.

[29] Pacific Earthquake Engineering Research Center (PEER NGA DATABASE) http://peer.berkeley.edu/nga.

International Conference on Engineering Vibration
Ljubljana, Slovenia, 7-10 September 2015

CONTROLLING OF THE FULL VEHICLE MODEL USING SLIDING MODEL CONTROL OPTIMIZED BY GENETIC ALGORITHM

Alaattin SAYIN*[1], Hasan O. OZER[2]

[1] Istanbul University, Programme of Biomedical Equipment Tech., Vocational School of Technical Science, 34320, Istanbul, Turkey
e-mail: sayina@istanbul.edu.tr

[2] Istanbul University, Programme of Air Conditioning and Refrigeration Technology, Vocational School of Technical Science, 34320, Istanbul, Turkey
e-mail: omurozer@istanbul.edu.tr

Keywords: Full Vehicle Model, Sliding Mode Controller, Genetic Algorithm, Multi-Objective Genetic Algorithm, Simulation of Vehicle Vibrations.

Abstract. *In this study, the dynamic behaviour of a non-linear seven degrees of freedom full vehicle model using linear motor controlled by Sliding Mode Controller optimized Genetic Algorithm controller is examined. Main feature of the study is to isolate car body motion from the road disturbance and improve the ride comfort. The aim of this study is to design Sliding Mode Controller tuned by Multi Objective Genetic Algorithm (MOGA) for providing smooth pitch, yaw and roll motions of car body. Sliding mode control (SMC) has been preferred in many mechanical and structural systems due to its robust character and high control performance. Choosing tuning optimum controller parameters for the vehicle model is an important problem. Therefore, Genetic Algorithm with several fitness functions is used to tuning optimum SMC coefficients. The full vehicle model is excited by road disturbance. Then, simulation results of uncontrolled and MOGA integrated sliding mode controllers models are compared. The results show that the full vehicle model with SMC optimized by MOGA is effective to decrease the effects of road disturbance induced vibrations.*

1 INTRODUCTION

Ride comfort and road holding properties are important research areas for the vehicle dynamics. In this area, many control techniques and vehicle suspension systems have been developed in the recent years. Therefore, passive, semi-active and active suspension systems are currently studied. However, Active suspension systems have more potential to meet high performances requirements [1, 2].

In order to control vibrations more effectively, numerous active control algorithms have been suggested [3, 4, 5]. Huisman et al. [3] presented active control strategy for quarter car model. Teja and Srinivasa [4] investigated a stochastically PID controller for a linear quarter car model.

Sliding Mode Control (SMC) is a variable structure control method and insensitive to parameter variation and external disturbances [5]. Due to these advantages, SMC is commonly used in robotics [6], vibration control at structures [7, 8, 9, 10], flight control [11], and path control of underwater vehicles [12]. Essential requirements for sliding mode control are the hitting time reduction and chattering attenuation [10]. Yagiz [13] applied the non-chattering sliding mode control to a full vehicle model. To select suitable gain switching and sliding surface parameter is significant for system performance. Thus, sliding mode control was combined with fuzzy logic, neural network and genetic algorithm. Huang and Lin [14] proposed an adaptive fuzzy sliding mode controller for a quarter car test rig. Eski and Yildirim [16] used neural network based robust control system for vehicle vibration system. Cheng et al. [5] presented GA-based adaptive fuzzy sliding model controller for a nonlinear system. Javadi-Moghaddama and Bagheri [12] suggested an adaptive neuro-fuzzy sliding-mode-based genetic algorithm control system for a remotely operated vehicle with four degrees of freedom for tracking control. Ozer et al. [10] used sliding mode control based genetic algorithm to decrease vibration at the half vehicle model.

The aim of this study is to improve the ride comfort of the vehicle. Thus, Sliding Mode Controller tuned by Multi Objective Genetic Algorithm (MOGA) has been designed for providing smooth vertical motion of a car body. Firstly, a seven degree of freedom nonlinear full car model is described in detail. Then, the proposed SMC parameters have been tuned by MOGA with several fitness functions to get better dynamic performance. The vehicle model is excited by road data and is simulated with the proposed control system. Finally, the results of proposed controlled and uncontrolled systems are given and discussed.

2 VEHICLE MODEL

In this study, seven degree of freedom vehicle model is used as shown in Figure 1. In this model, y is body bounce, θ is the pitch motion, α is roll motion of the vehicle body; y_1 and y_2 are the displacement of the front wheels and y_3 and y_4 are the displacement of the front wheels.

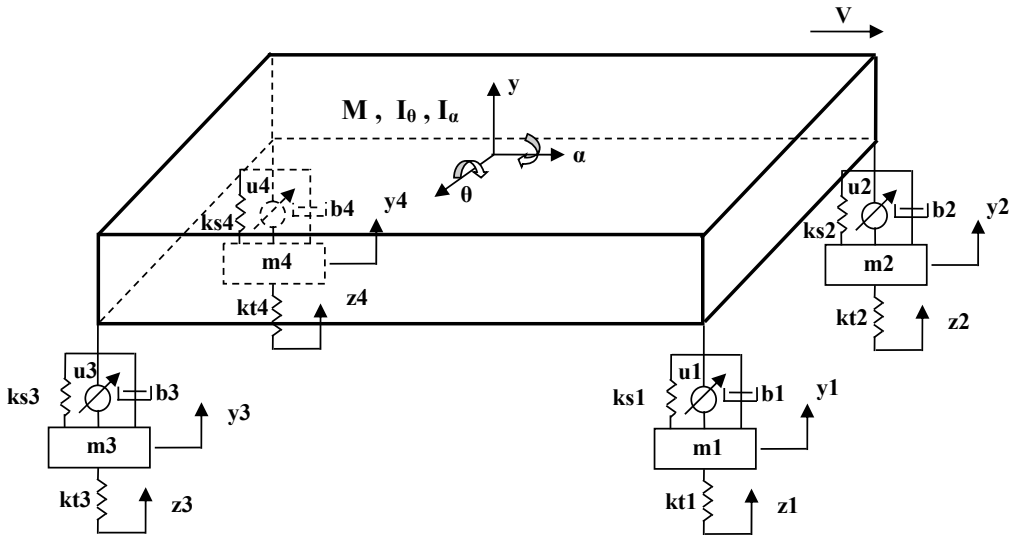


Figure 1: The psychical model of full-vehicle model

Total kinetic, potential and dissipative energy of the model are;

$$K = \frac{1}{2}M\dot{y}^2 + \frac{1}{2}I_z\dot{\theta}^2 + \frac{1}{2}I_x\dot{\alpha}^2 + \frac{1}{2}m_1\dot{y}_1^2 + \frac{1}{2}m_2\dot{y}_2^2 + \frac{1}{2}m_3\dot{y}_3^2 + \frac{1}{2}m_4\dot{y}_4^2 \tag{1}$$

$$\begin{aligned} P = {} & \frac{1}{2}k_{s1}(x_1 - y_1)^2 + \frac{1}{2}k_{s2}(x_2 - y_2)^2 + \frac{1}{2}k_{s3}(x_3 - y_3)^2 + \frac{1}{2}k_{s4}(x_4 - y_4)^2 \\ & + \frac{1}{2}k_{t1}(y_1 - z_1)^2 + \frac{1}{2}k_{t2}(y_2 - z_2)^2 + \frac{1}{2}k_{t3}(y_3 - z_3)^2 + \frac{1}{2}k_{t4}(y_4 - z_4)^2 \end{aligned} \tag{2}$$

$$D = \frac{1}{2}b_1(\dot{x}_1 - \dot{y}_1)^2 + \frac{1}{2}b_2(\dot{x}_2 - \dot{y}_2)^2 + \frac{1}{2}b_3(\dot{x}_3 - \dot{y}_3)^2 + \frac{1}{2}b_4(\dot{x}_4 - \dot{y}_4)^2 \tag{3}$$

The equation of motion is obtained by using Lagrange's equations and can therefore be expressed as,

$$\begin{aligned} & M\ddot{y} + (b_1 + b_2 + b_3 + b_4)\dot{y} + (k_{s1} + k_{s2} + k_{s3} + k_{s4})y + \\ & (a(b_1 + b_2) - b(b_3 + b_4))Cos\theta\dot{\theta} + (a(k_{s1} + k_{s2}) - b(k_{s3} + k_{s4}))Sin\theta + \\ & (d(b_2 + b_4) - c(b_1 + b_3))Cos\alpha\dot{\alpha} + (d(k_{s2} + k_{s4}) - c(k_{s1} + k_{s3}))Sin\alpha \\ & -b_1\dot{y}_1 - k_{s1}y_1 - b_2\dot{y}_2 - k_{s2}y_2 - b_3\dot{y}_3 - k_{s3}y_3 - b_4\dot{y}_4 - k_{s4}y_4 = U_y = u_1 + u_2 + u_3 + u_4 \end{aligned} \tag{4}$$

$$\begin{aligned} & I_z\ddot{\theta} + (a^2(b_1 + b_2) + b^2(b_3 + b_4))Cos^2\theta\dot{\theta} \\ & + (a^2(k_{s1} + k_{s2}) + b^2(k_{s3} + k_{s4}))Cos\theta Sin\theta \\ & + (a(b_1 + b_2) - b(b_3 + b_4))Cos\theta\dot{y} + (a(k_{s1} + k_{s2}) - b(k_{s3} + k_{s4}))Cos\theta\, y \\ & + (d(ab_2 - bb_4) - c(ab_1 - bb_3))Cos\theta Cos\alpha\dot{\alpha} \\ & + (d(ak_{s2} - bk_{s4}) - c(ak_{s1} - bk_{s3}))Cos\theta Sin\alpha \\ & -ab_1 Cos\theta\dot{y}_1 - ak_{s1}Cos\theta\, y_1 - ab_2 Cos\theta\dot{y}_2 - ak_{s2}Cos\theta\, y_2 \\ & +bb_3 Cos\theta\dot{y}_3 + bk_{s3}Cos\theta\, y_3 + bb_4 Cos\theta\dot{y}_4 + bk_{s4}Cos\theta\, y_4 = U_\theta = u_1a - u_3b + u_2a - u_4b \end{aligned} \tag{5}$$

$$
\begin{aligned}
&I_x\,\ddot{\alpha}+\left(c^2\left(b_1+b_3\right)+d^2\left(b_2+b_4\right)\right)Cos^2\alpha\,\dot{\alpha}+\\
&\left(c^2\left(k_{s1}+k_{s3}\right)+d^2\left(k_{s2}+k_{s4}\right)\right)Cos\alpha Sin\alpha+\\
&\left(d\left(b_2+b_4\right)-c\left(b_1+b_3\right)\right)Cos\alpha\,\dot{y}+\left(d\left(k_{s2}+k_{s4}\right)-c\left(k_{s1}+k_{s3}\right)\right)Cos\alpha\,y+\\
&\left(d\left(ab_2-bb_4\right)-c\left(ab_1-bb_3\right)\right)Cos\theta\,Cos\alpha\,\dot{\theta}+\\
&\left(d\left(ak_{s2}-bk_{s4}\right)-c\left(ak_{s1}-bk_{s3}\right)\right)Cos\alpha\,Sin\theta+\\
&cb_1\,Cos\alpha\,\dot{y}_1+ck_{s1}\,Cos\alpha\,y_1-db_2\,Cos\alpha\,\dot{y}_2-dk_{s2}\,Cos\alpha\,y_2+\\
&cb_3\,Cos\alpha\,\dot{y}_3+ck_{s3}\,Cos\alpha\,y_3-db_4\,Cos\alpha\,\dot{y}_4-dk_{s4}\,Cos\alpha\,y_4=U_\alpha=u_2d-u_1c+u_4d-u_3c
\end{aligned}
\tag{6}
$$

$$
\begin{aligned}
&m_1\,\ddot{y}_1+b_1\,\dot{y}_1+\left(k_{s1}+k_{t1}\right)y_1-b_1\,\dot{y}-k_{s1}\,y-a\,b_1\,Cos\theta\,\dot{\theta}-a\,k_{s1}\,Sin\theta+c\,b_1\,Cos\alpha\,\dot{\alpha}\\
&+c\,k_{s1}\,Sin\alpha-k_{t1}\,z_1=-u_1
\end{aligned}
\tag{7}
$$

$$
\begin{aligned}
&m_2\,\ddot{y}_2+b_2\,\dot{y}_2+\left(k_{s2}+k_{t2}\right)y_2-b_2\,\dot{y}-k_{s2}\,y-a\,b_2\,Cos\theta\,\dot{\theta}-a\,k_{s2}\,Sin\theta-d\,b_2\,Cos\alpha\,\dot{\alpha}\\
&-d\,k_{s2}\,Sin\alpha-k_{t2}\,z_2=-u_2
\end{aligned}
\tag{8}
$$

$$
\begin{aligned}
&m_3\,\ddot{y}_3+b_3\,\dot{y}_3+\left(k_{s3}+k_{t3}\right)y_3-b_3\,\dot{y}-k_{s3}\,y+b\,b_3\,Cos\theta\,\dot{\theta}+b\,k_{s3}\,Sin\theta+c\,b_3\,Cos\alpha\,\dot{\alpha}\\
&+c\,k_{s3}\,Sin\alpha-k_{t3}\,z_3=-u_3
\end{aligned}
\tag{9}
$$

$$
\begin{aligned}
&m_4\,\ddot{y}_4+b_4\,\dot{y}_4+\left(k_{s4}+k_{t4}\right)y_4-b_4\,\dot{y}-k_{s4}\,y+b\,b_4\,Cos\theta\,\dot{\theta}+b\,k_{s4}\,Sin\theta-d\,b_4\,Cos\alpha\,\dot{\alpha}\\
&-d\,k_{s4}\,Sin\alpha-k_{t4}\,z_4=-u_4
\end{aligned}
\tag{10}
$$

3 CONTROL STRATEGY

3.1 Sliding Mode Control

Sliding Mode Control is a variable structure control method and design provides a systematic approach to the problem of maintaining stability and consistent performance in the face of modeling imprecision. Sliding mode control theory has been many applications for nonlinear systems. The basics of the control are to bring and keep the error on a sliding surface such that the system is insensitive to the disturbances and parameter changes [22-23-24]. Sliding surface can be chosen as Eq. (12). Δx is error matrix. $[G]$ contains gradient of sliding surface.

$$\sigma=[G][\Delta X]=\underbrace{[G][X_r]}_{A}-[G][X] \tag{11}$$

A chosen Lyapunov function must have a value greater than zero and its derivative should be smaller than zero.

$$V(\sigma)=\left(\sigma^T\sigma\right)/2>0\quad \dot{V}(\sigma)=\sigma^T\dot{\sigma}\le 0 \tag{12}$$

Due to limit situation, the control input in sliding surface can be calculated as below;

$$\dot{\sigma} = \frac{d[A]}{dt} - [G]\{f(x) + [B]u\} = 0 \Rightarrow u_{eq} \tag{13}$$

$$\dot{\sigma} = -[\Gamma](\sigma) \Rightarrow u \tag{14}$$

$$\underbrace{[GB]^{-1}\left\{\frac{d[A]}{dt} - [G]f(x)\right\}}_{u_{eq}} + [GB]^{-1}[\Gamma](\sigma) = u \tag{15}$$

It is suggested that the equivalent control is the average of the total control [6] and the averaging filter is used to calculate the control value. The equivalent control is shown in Eq. (17).

$$\hat{u}_{eq} = \frac{1}{\tau s + 1}u \tag{16}$$

$$u = \hat{u}_{eq} + [GB]^{-1}[\Gamma](\sigma) \tag{17}$$

The system must be defined in state space form as $\dot{x} = f(x) + [B]\underline{u}$

$$\begin{bmatrix} X_1 & X_2 & X_3 & X_4 & X_5 & X_6 & X_7 & X_8 & X_9 & X_{10} & X_{11} & X_{12} & X_{13} & X_{14} \end{bmatrix}^T = \begin{bmatrix} y & \theta & \alpha & y_1 & y_2 & y_3 & y_4 & \dot{y} & \dot{\theta} & \dot{\alpha} & \dot{y}_1 & \dot{y}_2 & \dot{y}_3 & \dot{y}_4 \end{bmatrix}^T \tag{18}$$

$$\begin{bmatrix} \dot{X}_1 \\ \dot{X}_2 \\ \dot{X}_3 \\ \dot{X}_4 \\ \dot{X}_5 \\ \dot{X}_6 \\ \dot{X}_7 \\ \dot{X}_8 \\ \dot{X}_9 \\ \dot{X}_{10} \\ \dot{X}_{11} \\ \dot{X}_{12} \\ \dot{X}_{13} \\ \dot{X}_{14} \end{bmatrix} = \begin{bmatrix} X_8 \\ X_9 \\ X_{10} \\ X_{11} \\ X_{12} \\ X_{13} \\ X_{14} \\ f_{81}(x) \\ f_{91}(x) \\ f_{101}(x) \\ f_{111}(x) \\ f_{121}(x) \\ f_{131}(x) \\ f_{141}(x) \end{bmatrix} + \begin{bmatrix} 1/M & 0 & 0 & 0 & 0 & 0 & 0 \\ 0 & 1/Iz & 0 & 0 & 0 & 0 & 0 \\ 0 & 0 & 1/Ix & 0 & 0 & 0 & 0 \\ 0 & 0 & 0 & 1/m1 & 0 & 0 & 0 \\ 0 & 0 & 0 & 0 & 1/m2 & 0 & 0 \\ 0 & 0 & 0 & 0 & 0 & 1/m3 & 0 \\ 0 & 0 & 0 & 0 & 0 & 0 & 1/m4 \end{bmatrix} \begin{bmatrix} U_y \\ U_\theta \\ U_\alpha \\ u_1 \\ u_2 \\ u_3 \\ u_4 \end{bmatrix} \tag{19}$$

$$f_{81}(x) = \frac{1}{M}\begin{bmatrix} -X_8(b1+b2+b3+b4) - X_1(k_{s1}+k_{s2}+k_{s3}+k_{s4}) - \cos(X_2)X_9[a(b1+b2)-b(b3+b4)] \\ -\sin(X_2)[a(k_{s1}+k_{s2})-b(k_{s3}+k_{s4})] - \cos(X_3)X_{10}[d(b2+b4)-c(b1+b3)] - \sin(X_3)[d(k_{s2}+k_{s4})-c(k_{s1}+k_{s3})] \\ +b_1X_{11}+b_2X_{12}+b_3X_{13}+b_4X_{14}+k_{s1}X_4+k_{s2}X_5+k_{s3}X_6+k_{s4}X_7 \end{bmatrix} \tag{20}$$

$$f_{91}(x) = \frac{1}{I_z}\begin{bmatrix} -\cos^2(X_2)X_9[a^2(b1+b2)+b^2(b3+b4)] - \cos(X_2)\sin(X_2)[a^2(k_{s1}+k_{s2})+b^2(k_{s3}+k_{s4})] \\ -\cos(X_3)X_8[a(b1+b2)-b(b3+b4)] \\ -\cos(X_2)X_1[a(k_{s1}+k_{s2})-b(k_{s3}+k_{s4})] \\ -\cos(X_2)\cos(X_3)X_{10}[d(ab2-bb4)-c(ab1-bb3)] \\ -\cos(X_2)\sin(X_3)[d(ak_{s2}-bk_{s4})-c(ak_{s1}-bk_{s3})] \\ +\cos(X_2)X_{11}ab_1+\cos(X_2)X_4ak_{s1}+\cos(X_2)X_{12}ab_2+\cos(X_2)X_5ak_{s2} \\ -bb_3\cos(X_2)X_{13}-bk_{s3}\cos(X_2)X_6-bb_4\cos(X_2)X_{14}-bk_{s4}\cos(X_2)X_7 \end{bmatrix} \tag{21}$$

$$f_{101}(x)=\frac{1}{I_x}\begin{bmatrix}-\cos^2(X_3)X_{10}[c^2(b1+b3)+d^2(b2+b4)]-\cos(X_3)\sin(X_3)[c^2(k_{s1}+k_{s3})+d^2(k_{s2}+k_{s4})]\\-\cos(X_3)X_8[d(b2+b4)-c(b1+b3)]\\-\cos(X_3)X_1[d(k_{s2}+k_{s4})-c(k_{s1}+k_{s3})]\\-\cos(X_2)\cos(X_3)X_9[d(ab2-bb4)-c(ab1-bb3)]\\-\cos(X_3)\sin(X_2)[d(ak_{s2}-bk_{s4})-c(ak_{s1}-bk_{s3})]\\-\cos(X_3)X_{11}cb_1-\cos(X_3)X_4ck_{s1}+\cos(X_3)X_{12}db_2+\cos(X_3)X_5dk_{s2}\\-cb_3\cos(X_3)X_{13}-ck_{s3}\cos(X_3)X_6+db_4\cos(X_3)X_{14}+dk_{s4}\cos(X_3)X_7\end{bmatrix} \tag{22}$$

$$f_{111}(x)=\frac{1}{m_1}\left[-b_1X_{11}-(k_{s1}+k_{t1})X_4+b_1X_8+k_{s1}X_1+ab_1\cos(X_2)X_9+ak_{s1}\sin(X_2)-cb_1\cos(X_3)X_{10}-ck_{s1}\sin(X_3)+k_{t1}z_1\right] \tag{23}$$

$$f_{121}(x)=\frac{1}{m_2}\left[-b_2X_{12}-(k_{s2}+k_{t2})X_5+b_2X_8+k_{s2}X_1+ab_2\cos(X_2)X_9+ak_{s2}\sin(X_2)+db_2\cos(X_3)X_{10}+dk_{s2}\sin(X_3)+k_{t2}z_2\right] \tag{24}$$

$$f_{131}(x)=\frac{1}{m_3}\left[-b_3X_{13}-(k_{s3}+k_{t3})X_6+b_3X_8+k_{s3}X_1-bb_3\cos(X_2)X_9-bk_{s3}\sin(X_2)-cb_3\cos(X_3)X_{10}-ck_{s3}\sin(X_3)+k_{t3}z_3\right] \tag{25}$$

$$f_{141}(x)=\frac{1}{m_4}\left[-b_4X_{14}-(k_{s4}+k_{t4})X_7+b_4X_8+k_{s4}X_1-bb_4\cos(X_2)X_9-bk_{s4}\sin(X_2)+db_4\cos(X_3)X_{10}+dk_{s4}\sin(X_3)+k_{t4}z_4\right] \tag{26}$$

Anti-roll motion $u_3c=u_4d$

$$u_1=\frac{bdU_y+dU_\theta-(a+b)U_\alpha}{(a+b)(c+d)},\ u_2=\frac{bcU_y+cU_\theta+(a+b)U_\alpha}{(a+b)(c+d)},\ u_3=\frac{d\left(aU_y-U_\theta\right)}{(a+b)(c+d)},\ u_4=\frac{c\left(aU_y-U_\theta\right)}{(a+b)(c+d)} \tag{27}$$

$$[G]=\begin{bmatrix}\alpha_1&0&0&0&0&0&0&1&0&0&0&0&0&0\\0&\alpha_2&0&0&0&0&0&0&1&0&0&0&0&0\\0&0&\alpha_3&0&0&0&0&0&0&1&0&0&0&0\\0&0&0&\alpha_4&0&0&0&0&0&0&1&0&0&0\\0&0&0&0&\alpha_5&0&0&0&0&0&0&1&0&0\\0&0&0&0&0&\alpha_6&0&0&0&0&0&0&1&0\\0&0&0&0&0&0&\alpha_7&0&0&0&0&0&0&1\end{bmatrix}\quad[\Gamma]=\begin{bmatrix}\Gamma_1&0&0&0&0&0&0\\0&\Gamma_2&0&0&0&0&0\\0&0&\Gamma_3&0&0&0&0\\0&0&0&\Gamma_4&0&0&0\\0&0&0&0&\Gamma_5&0&0\\0&0&0&0&0&\Gamma_6&0\\0&0&0&0&0&0&\Gamma_7\end{bmatrix} \tag{28}$$

$$u=\hat{u}_{eq}+\left\{\begin{bmatrix}M\Gamma_1&0&0&0&0&0&0\\0&I_z\Gamma_2&0&0&0&0&0\\0&0&I_x\Gamma_3&0&0&0&0\\0&0&0&m_1\Gamma_4&0&0&0\\0&0&0&0&m_2\Gamma_5&0&0\\0&0&0&0&0&m_3\Gamma_6&0\\0&0&0&0&0&0&m_4\Gamma_7\end{bmatrix}\begin{bmatrix}\alpha_1&0&0&0&0&0&0&1&0&0&0&0&0&0\\0&\alpha_2&0&0&0&0&0&0&1&0&0&0&0&0\\0&0&\alpha_3&0&0&0&0&0&0&1&0&0&0&0\\0&0&0&\alpha_4&0&0&0&0&0&0&1&0&0&0\\0&0&0&0&\alpha_5&0&0&0&0&0&0&1&0&0\\0&0&0&0&0&\alpha_6&0&0&0&0&0&0&1&0\\0&0&0&0&0&0&\alpha_7&0&0&0&0&0&0&1\end{bmatrix}\right\}\begin{bmatrix}X_{1r}-X_1\\X_{2r}-X_2\\X_{3r}-X_3\\X_{4r}-X_4\\X_{5r}-X_5\\X_{6r}-X_6\\X_{7r}-X_7\\X_{8r}-X_8\\X_{9r}-X_9\\X_{10r}-X_{10}\\X_{11r}-X_{11}\\X_{12r}-X_{12}\\X_{13r}-X_{13}\\X_{14r}-X_{14}\end{bmatrix} \tag{29}$$

The control laws can be shown in Eq. (30).

$$\begin{aligned}U_y&=\hat{U}_{y(eq)}+M\Gamma_1\left[\alpha_1\left(X_{1r}-X_1\right)+\left(X_{8r}-X_8\right)\right]\\U_\theta&=\hat{U}_{\theta(eq)}+I_z\Gamma_2\left[\alpha_2\left(X_{2r}-X_2\right)+\left(X_{9r}-X_9\right)\right]\\U_\alpha&=\hat{U}_{\alpha(eq)}+I_x\Gamma_3\left[\alpha_3\left(X_{3r}-X_3\right)+\left(X_{10r}-X_{10}\right)\right]\end{aligned} \tag{30}$$

3.2 Sliding Mode Control Parameters Tuned by Multi Objective Genetic Algorithm

Genetic Algorithms (GAs) has been depended on Darwinian principle in biological mutation and reproduction, survival-of the-fittest. This principle is used to evolve solutions to problems. A genetic algorithm consists of three main operators; reproduction, crossover and mutation operators. A fitness function must be suggested for each problem [19]. Minimum or maximum solution of cost function is the solution of the problem.

The idea of Multi-Objective Optimization with Genetic Algorithm minimizes multiple fitness function simultaneously. The multi objective genetic algorithm is used to solve multi objective optimization problems by identifying the Pareto front - the set of evenly distributed non dominated optimal solutions [20-21].

The proposed method can efficiently choose the appropriate gain parameters α,Γ for sliding mode controller based on two proposed fitness functions. The aim of the fitness function is devised to obtain time responses (displacement and acceleration) reduction for the body, pitch and yaw motion.

MOGA is implemented for tuning of the parameters of sliding mode controller. The optimum value of gain parameters α,Γ obtained by MOGA is used to simulate the vehicle model. The flowchart of the control algorithm is shown as Figure 2.

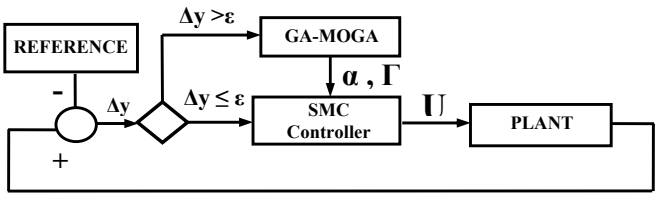


Figure 2: The flowchart of control algorithm

4 SIMULATION RESULTS

4.1 Multi Objective GA's Fitness Functions

Six different cost functions are chosen to get minimum value of the total time responses. The optimum values minimized both displacement and acceleration responses of y, θ and α were researched by Multi Objective genetic algorithm to obtain the controller coefficients, $[\alpha_1\ \Gamma_1],[\alpha_2\ \Gamma_2]$ and $[\alpha_3\ \Gamma_3]$. The objective function is shown below;

$$\phi_y(\alpha_1,\Gamma_1)=\min\sum_{ti}^{tf}x(t),\quad \phi_y(\alpha_1,\Gamma_1)=\min\sum_{ti}^{tf}a(t) \tag{31}$$

$$\phi_\theta(\alpha_2,\Gamma_2)=\min\sum_{ti}^{tf}x(t),\quad \phi_\theta(\alpha_2,\Gamma_2)=\min\sum_{ti}^{tf}a(t) \tag{32}$$

$$\phi_\alpha(\alpha_3,\Gamma_3)=\min\sum_{ti}^{tf}x(t),\quad \phi_\alpha(\alpha_3,\Gamma_3)=\min\sum_{ti}^{tf}a(t) \tag{33}$$

It is clear from this Figure-5 that first and second resonance peak due to a vehicle body are eliminated by SMC MOGA. The human body is more sensitive to vertical vibration between 4 Hz and 8 Hz [2]. Therefore, the elimination of first resonance has improved ride comfort remarkably. The magnitude of the first resonance for pitch and yaw motion is also reduced. Different values of the optimum control coefficients $[\alpha,\Gamma]$ were obtained by multi objective genetic algorithm shown Table 1. Number of iterations is 102.

	α_1	Γ_1	α_2	Γ_2	α_3	Γ_3	$\Sigma x_y(t)$	$\Sigma x_\theta(t)$	$\Sigma x_\alpha(t)$	$\Sigma a_y(t)$	$\Sigma a_\theta(t)$	$\Sigma a_\alpha(t)$
1	21	2	52	8	491	491	4,29	4,62	0,03	4693	4499	1876
2	21	2	52	1	491	491	5,54	5,72	0,03	4767	3785	1866
3	1	475	5	8	2	2	0,25	1,74	2,22	2099	4937	9746
4	1	2	52	1	97	1	4,36	6,93	13,07	4745	3797	6690
5	470	387	5	1	40	393	0,07	2,06	0,43	1092	5911	3927
6	470	475	5	1	2	393	0,05	2,06	0,42	1287	5846	3714
7	21	29	67	33	383	491	1,06	1,26	0,04	4822	5214	1429
8	21	2	5	1	383	491	4,72	1,99	0,04	4705	3617	1445
9	1	236	5	8	2	2	0,43	1,71	2,14	3193	4260	8551
10	21	2	52	1	491	491	5,60	5,83	0,03	4771	3791	1865

Table 1: Several parameters for SMC tuned by MOGA.

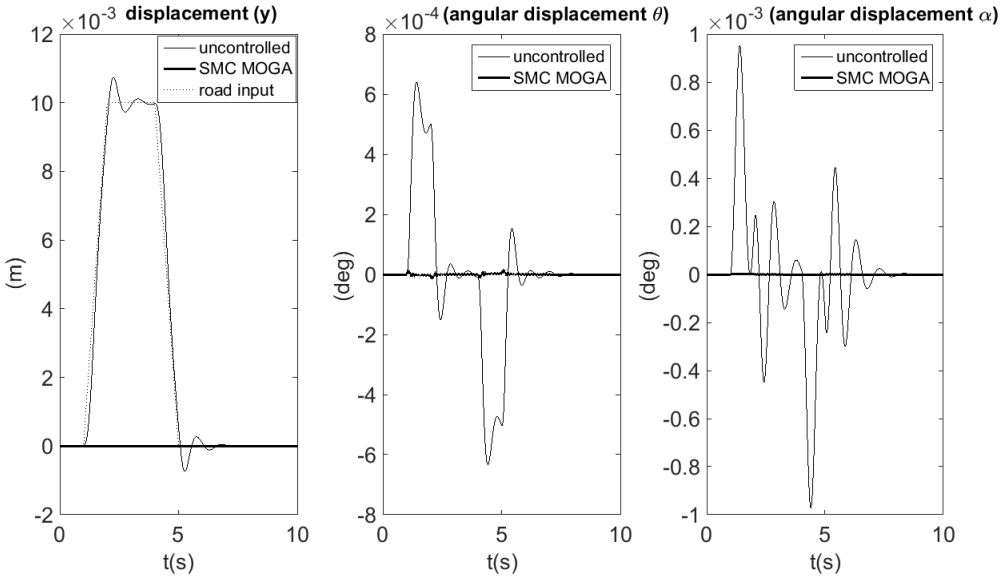


Figure 3: The uncontrolled and SMC MOGA controlled displacement responses: (a) body bounce(y) ($[\alpha\ \Gamma]=[470\ \ 475]$), (b) pitch motion(θ) ($[\alpha\ \Gamma]=[67\ \ 33]$), (c) yaw motion(α) ($[\alpha\ \Gamma]=[40\ \ 393]$)

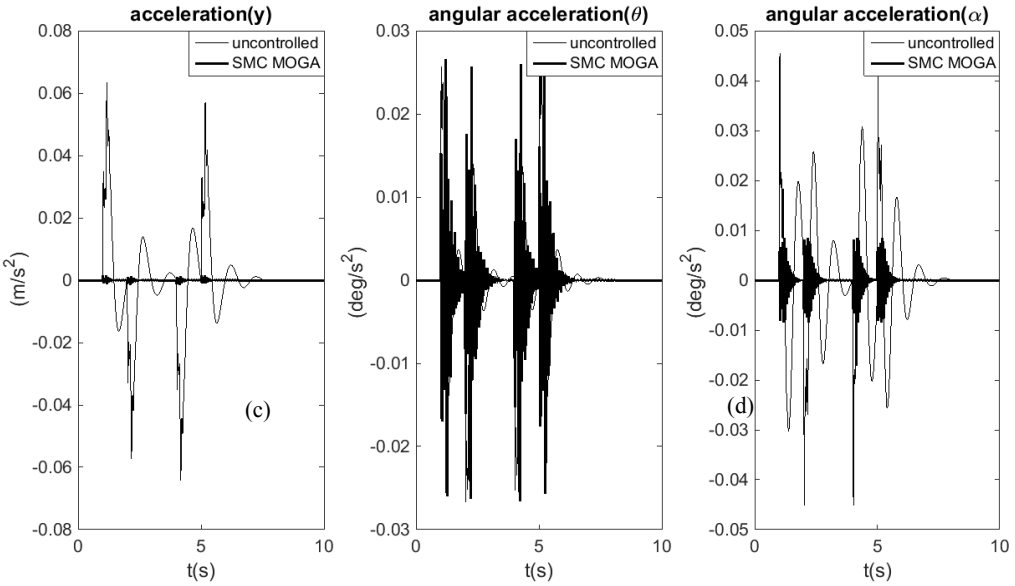


Figure 4: The uncontrolled and SMC MOGA controlled acceleration responses: (a) body bounce(y) ($[\alpha\ \Gamma]=[470\ \ 475]$), (b) pitch motion(θ) ($[\alpha\ \Gamma]=[67\ \ 33]$), (c) yaw motion(α) ($[\alpha\ \Gamma]=[40\ \ 393]$)

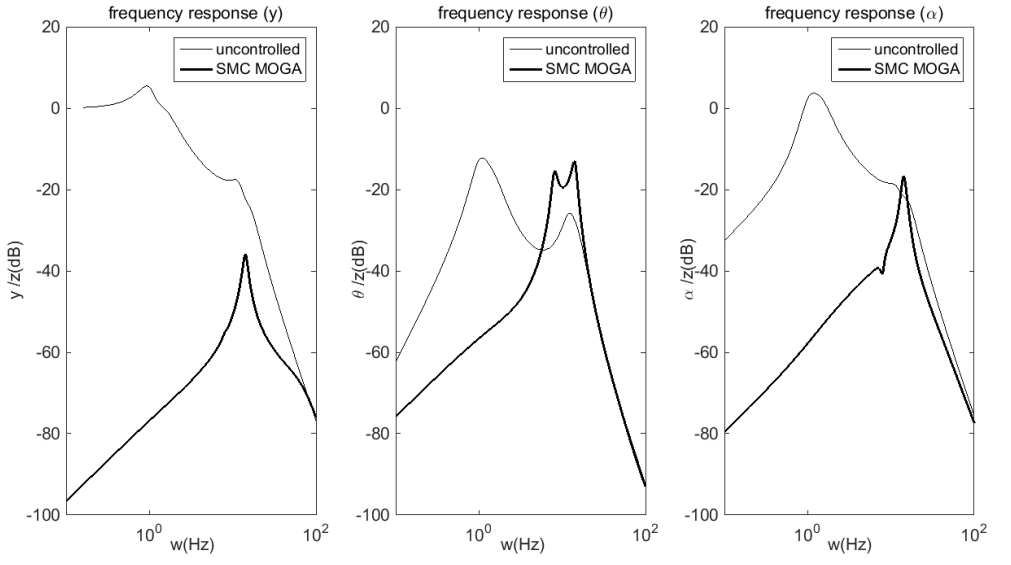


Figure 5: The uncontrolled and SMC MOGA controlled frequency responses: (a) body bounce(y) ($[\alpha\ \Gamma]=[470\ \ 475]$), (b) pitch motion(θ) ($[\alpha\ \Gamma]=[67\ \ 33]$), (c) yaw motion(α) ($[\alpha\ \Gamma]=[40\ \ 393]$)

Although the magnitudes of body bounce, pitch and yaw motion is decreased significantly with respect to uncontrolled model, pitch angular acceleration is worse that the uncontrolled one as shown Figure 3 and 4. Therefore, the responses of acceleration and displacement must be checked before chosen suitable parameters for the system. Optimum values are researched

with multi objective genetic algorithm by using SCM GA values as upper boundary for $[\alpha\ \Gamma]$ values.

At the end of Multi Objective Genetic Algorithm process, optimum controller parameters $[\alpha\ \Gamma]$ were attained. Though these values increase total error of pitch acceleration response, we have significant progress in other responses.

5 CONCLUSIONS

In this study, the optimum values of sliding mode controller parameters $[\alpha\ \Gamma]$ are obtained for the full vehicle model by Multi Objective Genetic Algorithm. The cost function is designed to reduce time responses. The proposed sliding mode controller improves ride comfort with controlling body bounce pitch and yaw motion.

Although genetic algorithm obtains best values for displacement responses, the pitch acceleration responses increase significantly. The controller coefficients (body bounce, pitch and yaw) have been processed simultaneously with the multi-objective genetic algorithm. There is trade-off between displacement response and acceleration. Selected different parameters $[\alpha\ \Gamma]$ at table are used to simulate time responses. The results show that the accelerations of the vehicle increase significantly and displacement responses are quite improved.

Consequently, parameter optimization is useful to obtain optimum results. The parameters of SMC are constant during the simulation. We suggest that using time-invariant coefficients for SMC may be advantage. Therefore, we plan to propose SMC with time-invariant coefficients.

REFERENCES

[1] R.S Sharp and S. A Hassan., An Evaluation of passive automotive suspension systems with variable stiffness and damping parameters. *Vehicle System Dynamics*, **15**, 335-350, 1986.

[2] H Gao,.J Lam, C Wang., Multi-objective control of vehicle active suspension systems via load-dependent controllers. *Journal of Sound and Vibration*, **290.3**, 654-675, 2006.

[3] R. G. M Huisman, F. E Veldpaus, H. J. M Voets and J.J. Kok, An optimal continuous time control strategy for active suspensions with preview. *Vehicle System Dynamics* **22.1**, 43–55 ,1993.

[4] S. R. Teja and Y. G. Srinivasa, Investigations on the stochastically optimized PID controller for a linear quarter-car road vehicle. *Vehicle System Dynamics* **26.2**, 103-116, 1996.

[5] P.C. Chen, C.W. Chen, W.L. Chiang, GA-based modified adaptive fuzzy sliding mode controller for nonlinear systems. *Expert Systems with Applications,* **36.3**, 5872-5879, 2009.

[6] M. Ertugrul, O. Kaynak and A. Sabanovic, A comparison of various VSS techniques on the control of automated guided vehicles. *Industrial Electronics ISIE'95 Proceedings of the IEEE International Symposium* 2, 837-842, 1995.

[7] R. Guclu, H. Yazici, Vibration control of a structure with ATMD against earthquake using fuzzy logic controllers. *Journal of Sound and Vibration,* **318**, 36-49, 2008.

[8] N. Yagiz, Sliding Mode Control of a Multi-Degree-of-Freedom Structural System with Active Tuned Mass Damper. *Tr.J. of Engineering and Environmental Science*, **25,** 651-657, 2001.

[9] A.P. Wang, C.D. Lee, Fuzzy sliding mode control for a building structure based on genetic algorithms. *Earthquake Engineering and Structural Dynamics,* **31**, 881–895,2002.

[10] H. O. Ozer, A. Sayin, N. Korkmaz, N. Yagiz, Genetic Algorithm Integrated Sliding Mode Control Of A Vehicle. *11th World Congress on Computational Mechanics, Barcelona, Spain*, 3857-3868, 2014.

[11] E. M. Jafarov, and R. Tasaltin, Robust sliding mode control for the uncertain MIMO aircraft model F-18. *Aerospace and Electronic Systems IEEE Transactions on*, **36.4**, 1127-1141, 2000.

[12] J. J. Moghaddam and A. Bagheri, An adaptive neuro-fuzzy sliding mode based genetic algorithm control system for under water remotely operated vehicle. *Expert Systems with Applications*, **37.1**, 647-660, 2010.

[13] N. Yagiz, Comparison and evaluation of different control strategies on a full vehicle model with passenger seat using sliding modes. *International Journal Of Vehicle Design*, **34.2**, 168-182, 2004.

[14] S. J. Huang and W. C. Lin, Adaptive fuzzy controller with sliding surface for vehicle suspension control. *Fuzzy Systems, IEEE Transactions on,* **11.4**, 550-559, 2003.

[15] S. B. Choi, C. C. Cheong and D.W. Park, Moving switching surfaces for robust control of second-order variable structure systems. *International Journal of Control*, **58.1**, 229-245, 1993.

[16] I. Eski, S. Yildirim, Vibration control of vehicle active suspension system using a new robust neural network control system. *Simulation Modelling Practice and Theory*, **17.5,** 778-793, 2009.

[17] C.C. Wong, S.Y. Chang, Parameter Selection in the Sliding Mode Control Design Using Genetic Algorithms. *Tamkang Journal of Science and Engineering*, **1,** 115-122,1998.

[18] G. Bartolini, Chattering phenomena in discontinuous control systems. *International Journal of Systems Science,* **20**, 2471-2481, 1989.

[19] H.R. Ji, Y.J. Moon, C.H. Kim, I.W. Lee, Structural Vibration Control Using Semiactive Tuned Mass Damper. *The Eighteenth KKCNN Symposium on Civil Engineering-KAIST6,* 18-20, 2005.

[20] N.N. Bengiamin, B. Kauffmann, Variable structure position control. *Control Systems Magazine IEEE,* **4.3,** 3-8, 1984.

[21] G.C. Hwang, S.C. Lin, A stability approach to fuzzy control design for nonlinear systems. *Fuzzy sets and Systems*, **48.3**, 279-287, 1992.

[22] K. Ogata, *Modern Control Engineering*, Prentice Hall, 1990.

[23] J.J. Slotine, W. Li, *Applied Nonlinear Control*, Prentice Hall, 1991.

[24] V.I. Utkin, *Sliding modes in control optimization*, Springer, 1992.

International Conference on Engineering Vibration
Ljubljana, Slovenia, 7-10 September 2015

SUPPRESSION OF STRUCTURAL VIBRATIONS USING DYNAMIC ABSORBER

Hasan O. OZER[1] , **Nurkan YAGIZ**[2] **, Yuksel HACIOGLU**[2]

[1] Istanbul University, Programme of Air Conditioning and Refrigeration Technology, Vocational School of Technical Science, 34320, Istanbul, Turkey
e-mail: omurozer@istanbul.edu.tr

[2] Istanbul University, Department of Mechanical Engineering , Faculty of Engineering, 34320, Istanbul, Turkey, e-mail: nurkany@istanbul.edu.tr , yukselh@istanbul.edu.tr

Keywords: Dynamic absorber, Building model, Vibration suppression, Experimental results.

Abstract. *Analysis and design of a dynamic absorber for vibration reduction of buildings is studied in this paper. A small two-storey building model consisting of steel plates and columns has been constructed in laboratory. Free vibration tests have been performed on this model in order to obtain parameter values of the physical building model for simulations. Then a dynamic absorber has been designed to suppress the vibrations of the building. The simulation and experimental results have been presented for comparison. Furthermore an optimal mass value for the dynamic absorber has been investigated and obtained. Finally the experimental results for the building vibrations along with the dynamic absorber with optimal mass have been presented. The results have shown that designed dynamic absorber reduced building vibrations effectively.*

1 INTRODUCTION

Earthquakes, winds and moving vehicles have the potential to cause vibrations on buildings. Earthquakes especially may lead to serious structural damage or failure. Therefore, it is very important to protect both the buildings and their occupants from the dangerous effects of those vibrations. Furthermore the need for studies on decreasing the effects of vibrations on buildings has increased during last decades and it is an important research area.

The control of structural vibrations can be realized by using various methods such as modifying rigidities, masses, damping or by providing passive or active counter forces [1, 2, 3]. Structural control methods can be classified as passive, semi-active and active control systems. A passive control system does not require an external power source [4, 5].

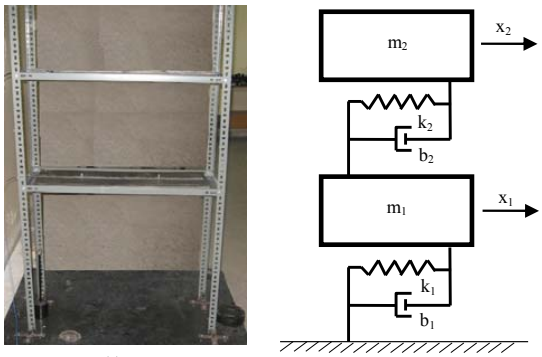
As a passive structural control method, the use of tuned mass dampers (TMDs) have been investigated during last decades. The TMD consists of a mass connected to the structure via a spring and damper. It is aimed that during vibration the TMD will share the energy of the main structure and will result in reduced vibrations. The detailed theory and working principles of damped and undamped TMDs that is used for structural vibration control of a single degree-of-freedom system subjected to a harmonic force has been described by Den Hartog [6]. TMDs have been used in multi-storey buildings since 1971 [7]. They have been successfully used to improve the behavior of the buildings against wind-induced vibrations. Examples are CN Tower in Canada, John Hancock Building in Boston, Center-Point Tower in Sydney, and the Taipei Tower in Taiwan, the tallest building in the world [3]. Dyke and Jensen [8] tried to control vibrations if a single degree-of-freedom model using TMD where a shake table is used to generate external excitation. The cases with different mass ratios were taken into account. Wong and Chee used a six-storey building model with a TMD [9]. They investigated the variation of kinetic, potential and damping energies with different mass ratios. Experiments have shown that the energy of the system was reduced by using TMD. Ji and Zhang proposed that significant reduction of primary resonance vibrations can be achieved by using an absorber mass corresponding to 6% of the mass of the nonlinear oscillator and an absorber spring stiffness corresponding to 4.5% of the linear stiffness of the nonlinear oscillator [10]. Yang and Cheng designed a dynamic vibration absorber to suppress the vibration of a plate in a frequency band [11]. The control mechanism was investigated with respect to different bandwidth, and the coupling was also examined in terms of the resonator location and frequency bandwidth.

Spencer et al. [12] developed an acceleration feedback control strategy whose experimental implementation was made by B.F.Spencer and S.J.Dyke at SUNY-Buffalo National Earthquake Engineering Research Center in 1995. 68 % reduction in acceleration and displacement values and 55% reduction in amplitude-frequency response were achieved by using H2/LQG control methods on three storey model. Nishimura et al. [13] investigated active control of the vibrations of a scale building model using a linear motor placed on base floor and using μ synthesis method. Fukushima et al. [14] developed the active–passive tuned mass damper (APTMD) system by using active and passive tuned mass damper. This system was installed on a 29-story building and the building displacement decreased 14 times if compared to the system without controller. Yagiz [15, 16] designed a sliding mode control method to suppress earthquake or wind induced vibration on multi-degree of freedom buildings. Since the model might have uncertainties and/or parameter changes, sliding mode control is preferred because of its robust character and superior performance. Ozer and Yagiz [17, 18] designed a experimental building model for determine the system parameters. The building model was used to verify the parameters for simulation model.

The study presented in this paper intended to decrease the vibration effects on buildings. Therefore, a two-storey building model is constructed for experiments and it is presented in Section 1. Section 2.1 presents the experimental setup and the Section 2.2 presents the computer search for the optimal mass value of the dynamic absorber. Finally, Section 3 concludes the paper.

2 BUILDING MODEL AND DYNAMIC ABSORBER DESIGN

In this study, a building model with two floors was designed. Each storey of the building was constructed using sheet metal plates and its columns were constructed by using perforated steel sheet profiles. The constructed two-storey building model is presented in Figure 1a.



(a)

Figure 1: Two DOF building (a) experimental model (b) physical model.

In order to be able to study the characteristics of the building model a lumped parameter physical model was also developed and presented in Figure. 1b. The degree- of-freedom (DOF) of the model is two. Column base connections were regarded as fixed and only the horizontal movements of the building model were considered.

In this study a dynamic absorber (DA), which is a tuned mass damper is designed and constructed for the vibration suppression of the building. This tuned mass damper is added to the second floor of the building model as seen in Figure 2a. It is a metal car with plastic wheels as seen Figure 2b. It is expected that this absorber will share the energy of the building during horizontal motions due to external disturbances and thus will decrease the vibrations of the building. The lumped parameter physical model of the constructed building model with dynamic absorber whose total DOF is three is given in Figure 2c.

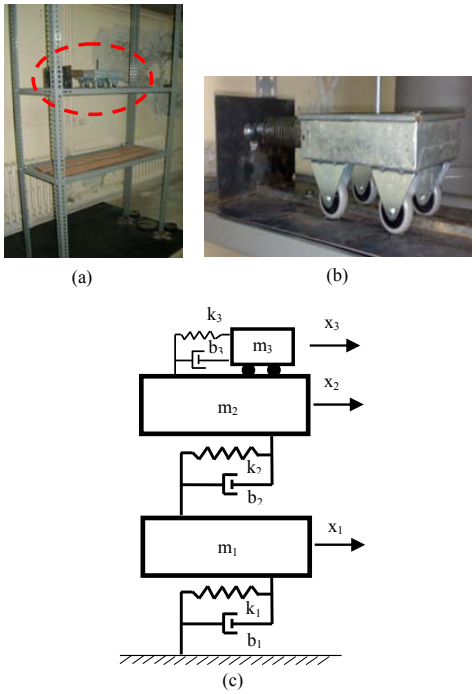


Figure 2: a) Three DOF building model with dynamic absorber (da)
(b) close-up view of the absorber (c) physical model.

The mathematical model of the two-storey building with dynamic absorber was obtained using Lagrange's equations and presented below:

$$m_1\ddot{x}_1 + (b_1 + b_2)\dot{x}_1 + (k_1 + k_2)x_1 - b_2\dot{x}_2 - k_2x_2 = 0 \quad (1)$$

$$m_2\ddot{x}_2 + (b_2 + b_3)\dot{x}_2 + (k_2 + k_3)x_2 - b_2\dot{x}_1 - b_3\dot{x}_3 - k_2x_1 - k_3x_3 = -F_d \quad (2)$$

$$m_3\ddot{x}_3 + b_3(\dot{x}_3 - \dot{x}_2) + k_3(x_3 - x_2) = 0 \quad (3)$$

Here, mi, ki and bi (i = 1, 2) denote the mass, stiffness and damping values related to each storey of the building model and m3, k3 and b3 stand for the mass, stiffness and damping values of the dynamic absorber. F_d is an external disturbance that acts initially only for two sampling time period.

3 SIMULATION AND EXPERIMENTAL RESULTS

In subsection 3.1 parameters of the lumped parameter building model and dynamic absorber are obtained via free vibration tests. Then in subsection 3.2 an optimal mass value for the dynamic absorber is obtained and results are presented

3.1 Experimental Setup and Parameter Identification Of The Building

The parameters of the lumped parameter physical building model were obtained via free vibration tests conducted on the experimental model. The experimental setup is shown in Figure 3.

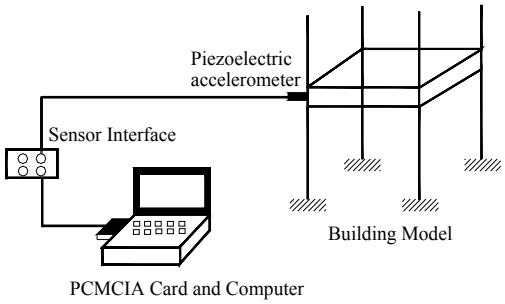


Figure 3: The schema of the experimental setup.

An initial disturbing force was applied to the second floor of the building during free vibration tests. Piezoelectric accelerometers were used in order to measure the horizontal accelerations of the each building storey. A sensor interface and PCMCIA data acquisition card were used for data collection.

Collected acceleration signals were processed using a signal processing software in order to obtain their Auto Power Spectrum (APS). Therefore the Fast Fourier Transform (FFT) of the signals were computed and then Root Mean Square (RMS) power values were calculated from the normalized FFT signals. Figure 4 presents the time data and power RMS data for the accelerations of the building model without dynamic absorber.

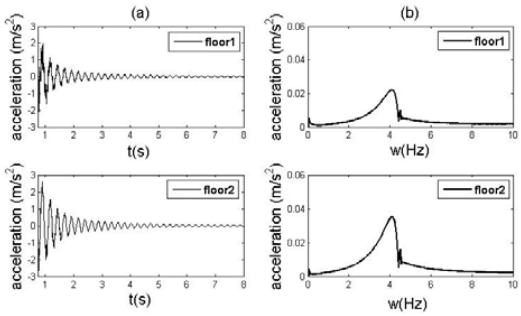


Figure 4: a) Time and b) frequency responses of free vibration experiment on two storey building model.

The parameters of the building model were obtained by simulating the physical model and tuning the building parameters until the acceleration data of simulated and experimental building model coincide with each other. This case can be seen from Figure 5. The obtain parameters of the building model are presented in Table 1.

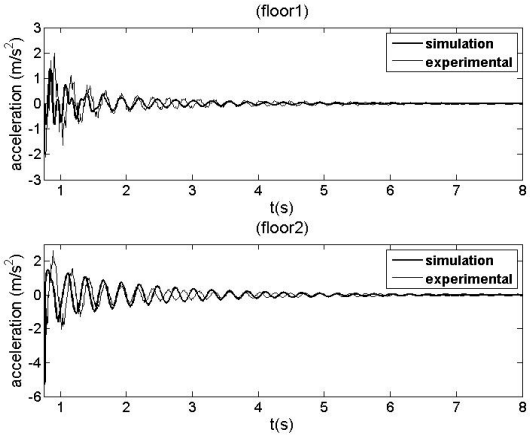


Figure 5: The comparison of the experimental and simulation results.

Parameters	Values
Magnitude of the initial force Fd	93.2 N
The mass of floor1 (m1)	18.3 kg
The mass of floor2 (m2)	17.7 kg
The stiffness coefficient of floor1 (k1)	38000 N/m
The stiffness coefficient of floor2 (k2)	14000 N/m
The damping coefficient of floor1 (b1)	70 Ns/m
The damping coefficient of floor2 (b2)	40 Ns/m
Magnitude of the initial force Fd	93.2 N

Table 1: The parameters of the building model.

The dynamic absorber used in this study was tuned according to the first resonance frequency of the second floor of the building which is 4.094 Hz as seen in Figure 6. Parameters of the dynamic absorber are given in Table 2.

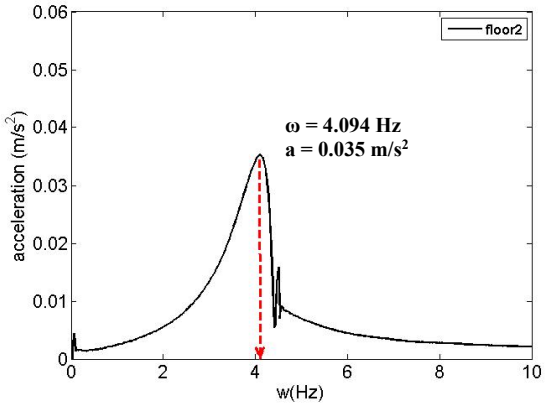


Figure 6: Frequency response used for the tuning of dynamic absorber.

Parameters	Values
ω_e experimental natural frequency	4.094 Hz
The mass of dynamic absorber (m3)	1.40 kg
The spring coefficient of dynamic absorber (k3)	920 N/m
The damping coefficient of dynamic absorber (b3)	4.3867 Ns/m

Table 2: The parameters of dynamic absorber.

Simulation results for the second floor of the building model with and without dynamic absorber are presented in Figure 7. It is seen from the time responses presented in Figure 7a that the dynamic absorber will reduce the horizontal vibrations of the second floor since magnitudes of the accelerations are reduced. This result was also confirmed with the power RMS results of the second storey presented in Figure 7b that magnitudes especially in the vicinity of the first resonance frequency are reduced considerably.

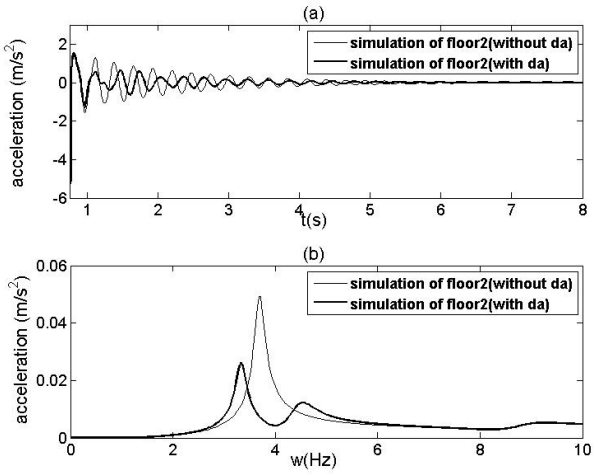


Figure 7: Simulation results for the acceleration of top floor with and without dynamic absorber a) time response, b) power spectrum.

Figure 8 presents the experimental results of the building model with the designed dynamic absorber in comparison with the case without dynamic absorber. The experimental results confirmed the results obtained via simulations. That is, as seen from Figure 8b the dynamic absorber reduced the vibration amplitudes significantly in the vicinity of the first resonance frequency of the second floor. The amplitude of the power RMS reduced to 0.021 m/s^2 from 0.035 m/s^2 by using designed dynamic absorber, which indicates 40 % reduction if compared with the case without dynamic absorber.

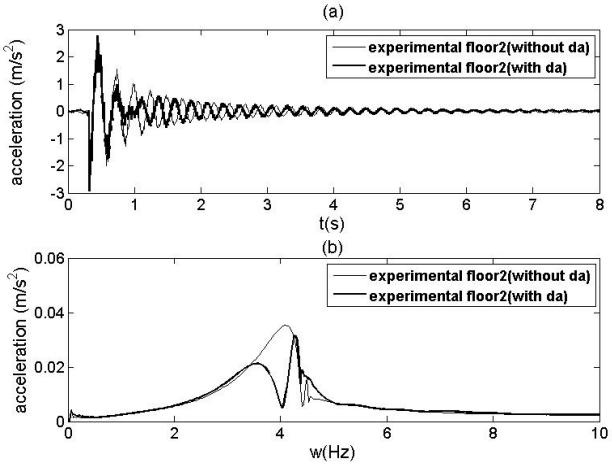


Figure 8: Experimental results for the acceleration of top floor with and without dynamic absorber a) time response, b) power spectrum.

3.2 Computer Search for the Best Mass Value of the Dynamic Absorber

In this section it is aimed to find an optimal value for the absorber mass that minimizes the auto power spectrum (APS) of the acceleration of the second floor. All of the building model parameters are kept constant and by changing the mass of the absorber an optimal value was searched. The flow diagram of the computer search is given in Figure 9.

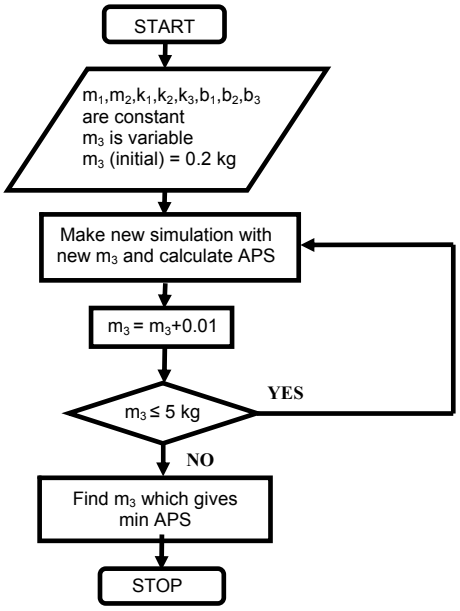


Figure 9: The flow diagram of the computer search.

The result of the computer search can be seen in Figure 10 which presents the second floor acceleration power spectrum versus different mass values for the absorber. It is deduced from

the results that acceleration of the second floor takes minimum value for the absorber mass value m =1.69 kg. This value will now be used for experiments.

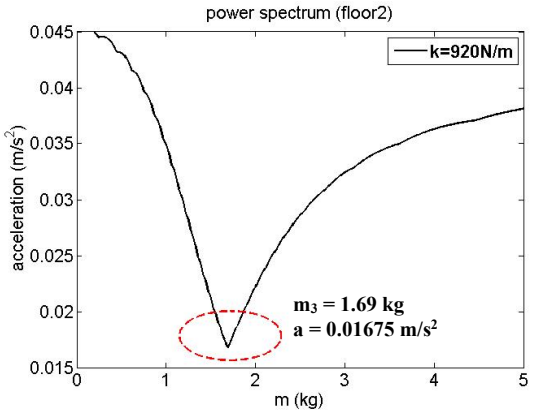


Figure 10: Acceleration power spectrum peak values for different absorber mass values.

The experimental results for the cases with and without dynamic absorber were presented in Figure 11 for comparison. From the time response it is seen that dynamic absorber with optimal mass value reduced the acceleration amplitudes of the second floor of the building. The success of the designed dynamic absorber can be seen especially from the results in frequency domain. It is deduced that by using designed dynamic absorber the acceleration power spectrum magnitudes for the first resonance peak reduced from 0.035 m/s^2 to 0.016 m/s^2. This means that 54 % reduction in acceleration magnitude is achieved. The reduction by the previous dynamic absorber was 40 %. Therefore the results verify the success of the optimal dynamic absorber.

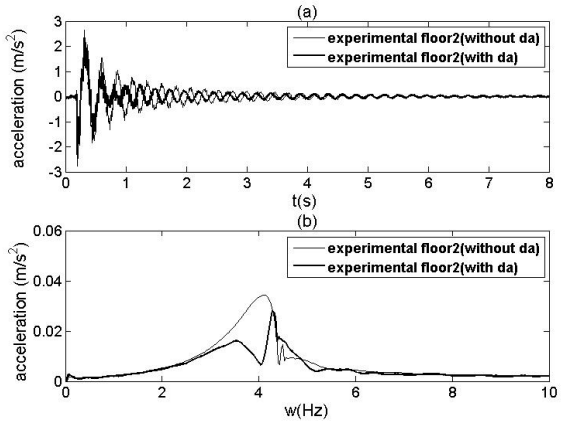


Figure 11: Experimental results for the acceleration of top floor with and without optimal dynamic absorber a) time response, b) power spectrum.

4 CONCLUSIONS

In this study, a building model was constructed, and free vibration experiments were performed to obtain building parameters. Using piezoelectric accelerometers and data acquisition cards, the time responses of these vibrations has been recorded and analyzed both in time and frequency domains. The results of computer simulations and experiments were compared and it was deduced that those results agreed with each other. Then, a dynamic absorber was designed to reduce the building vibrations. The designed dynamic absorber was constructed and used in the experiments. The acceleration responses in the experiments have shown that the dynamic absorber acted for a time and the vibration amplitudes of the building with the dynamic absorber were suppressed significantly in the vicinity of first resonance frequency. By using the dynamic absorber, the amplitude of the acceleration was reduced by 40% if compared to the system without the dynamic absorber. Then optimum mass value for the dynamic absorber was obtained by a computer search, and that value was used in the experiments. It was shown that the amplitude of acceleration was reduced by 54% by using optimal dynamic absorber. Therefore it can be concluded that designed dynamic absorber with optimal mass will effectively reduce the building vibrations caused by possible earthquakes or winds.

REFERENCES

[1] G.W. Housner and S.F. Masri, Eds., Proceedings of the U.S. National Workshop on Structural Control Research. *USC Publications M9013, University of Southern California*, Los Angeles, USA, 1990.

[2] G.W. Housner and S.F. Masri, Proc.of the Int Workshop on Structural Control Research. *USC Publ. No. CE-9311, University of South California*, Los Angeles, USA, 1993.

[3] G.W. Housner, L.A. Bergman ,T.K. Caughey, A.G. Chassiakos, R.O. Claus, S.F. Masri, R.E. Skelton, T.T. Soong, B.F. Spencer and J.T.P. Yao, Structural Control: Past, Present, and Future. *Journal of Engineering Mechanics*, **123(9),** 897-971, 1997.

[4] T. Soong, *Active Structural Control Theory and Practice*. Longman Scientific and Technical, Essex, 1990.

[5] T. Soong and G.F. Dargush, *Passive Energy Dissipation Systems in Structural Engineering*. John Wiley and Sons, New York, 1997.

[6] J.P. Hartog, *Mechanical Vibrations*. McGraw-Hill, New-York, 1956.

[7] C.C. Lins and J.F. Wang, Vibration Control Identification of Seismically Excited m.d.o.f. Structure-PTMD Systems. *Journal of Sound Vibration*, **240 (1)**, 87-115, 2001.

[8] S.J. Dyke and L.M. Jansen, Implications of Control-Structure Interaction in Scaled Structural Control System Testing. *Proceedings of the 1999 International Conference*, **(1)**, Kohala Coast, USA, 339-344, 1999.

[9] K.K.F. Wong and Y.L. Chee, Energy Dissipation of Tuned Mass Dampers during Earthquake Excitations. *The Structural Design of Tall Buildings*, **13**, 105-121, 2004.

[10] J.C. Ji and N. Zhang, Suppression of the Primary Resonance Vibrations of a Forced Nonlinear System Using a Dynamic Vibration Absorber. *Journal of Sound and Vibration*, **329**, 2044–2056, 2010.

[11] C. Yang, D. Li, L. Cheng, Dynamic Vibration Absorbers for Vibration Control within a Frequency Band. *Journal of Sound and Vibration*, **330**, 1582–1598, 2011.

[12] B.F. Spencer, S.J. Dyke, P Quast, Experimental Verification of Acceleration Feedback Control Strategies for an Active Tendon System. *National Center for Earthquake Engineering Research Technical Report NCEER-94-0024*, New-York, USA, 1994.

[13] H. Nishimura, Y. Okhubo, K. Nonami, Active Isolation Control for Multi-degree of Freedom Structural System. *Third International Conference on Motion and Vibration Control*, Chiba, Japan, 82-87, 1996.

[14] I. Fukushima, T. Kobori, M. Sakamoto, N. Koshika, I. Nishimura, K. Sasaki, Vibration Control of a Tall Building Using Active-Passive Composite Tuned Mass Damper. *Third International Conference on Motion and Vibration Control*, Chiba, Japan, 1-6, 1996.

[15] N. Yagiz, Sliding Mode Control of a Multi-Degree-of-Freedom Structural System with Active Tuned Mass Damper. *Tr.J. of Engineering and Environmental Science*, **25,** 651-657, 2001.

[16] N. Yagiz, Vibration control of a building with ATMD under earthquake Excitation. *International Journal of Applied Mechanics and Engineering*, **8-1**, 117-124, 2003.

[17] H.O. Ozer, N. Yagiz, Reducing Vibration Effects on the Two Storey Building Model Using Dynamic Absorber. *Second International Conference on Advances in Mechanical Engineering (AME2011)*, New Delhi, India, 2011.

[18] H.O. Ozer, N. Yagiz, Dynamic Absorber Design for Experimental Two Storey Building Model. *10th International Conference of Numerical Analysis and Applied Mathematics (ICNAAM 2012)*, Kos, Greece, 2012.

International Conference on Engineering Vibration
Ljubljana, Slovenia, 7-10 September 2015

SEISMIC ANALYSIS ON MULTI-LEVEL SUPPORTED PRESSURE RETAINING COMPONENTS IN NPPS BY USING RESPONSE SPECTRUM MOETHD

Gangsig Shin*[1], Jinseong Kim[1]

[1]Korea Institute of Nuclear Safety
k534sks@kins.re.kr

Keywords: Single supported or multi-level supported, seismic analysis, response spectrum analysis, modal analysis, flexible or rigid.

Abstract. *As integrity and/or functionality of pressure retaining components in Nuclear Power Plants (NPPs) is highly important to guaranty more reliable use of nuclear energy and much more acceptance from public.*

To deal with the effect by seismic and vibration, two cases shall be considered. One is single supported case and the other is multi-level supported case. Multiply supported case, again can be categorized into two cases. The first one is flexible component such as pipe system, while the second one is (relatively) rigid component such as pressure retaining components. Multiply supported flexible cases have been studied quite a lot, however, multiply supported (relatively) rigid case have not been studied that much.

So, in this paper, multiply supported NPP pressure retaining components case will be handled. Modal analysis will be performed followed by case by case study. The modal deformation in the frequency range of interest will be considered to study the relation with the deformation by relative movement of multi-level supports, or whole system will be considered as a single supported case.

1 INTRODUCTION

As integrity and/or functionality of pressure retaining components in Nuclear Power Plants (NPPs) is highly important to guaranty more reliable use of nuclear energy and much more acceptance from public. And this has been much more emphasized after Fukushima accident, especially, maintaining integrity and/or functionality of pressure retaining components from the effect of earthquake.

Seismic design and analysis can be done to show that a certain structure or component is safe from the effect of earthquake. To conduct seismic design and analysis, in many cases, the seismic input is applied to just one support of the components or equipment.

However, in some cases, there are some components or equipment which have multiple supports with different seismic accelerations, like piping system with supports in different levels or even different building structures. To deal with this situation, C.W. Lin [1] suggested a method using elastic beam theory and response spectra for various boundary conditions. And since Clough and Penzien [2] published their book containing outline of multiple support excitation analysis, R.W. Wu, et al [3] and K.R Leimbach [4] further studied this topic. Later, Y.K. Wang [5], M. Subudhi and P. Bezler [6] studied independent support motion more and suggested some changes for regulatory guidance. These studies are all focused on piping system with multiple supports in different levels or even different building structures. However, there are some components or equipment with multiple supports in different level as well. Some examples of major pressure retaining components in nuclear power plants are reactor, steam generator and pressurizer. But, little has been studied on the effects of different seismic input from these multiple supports to those components.

In most cases, components are much stiffer than piping systems and can be affected more by relative displacement between supports than piping systems. So, in this paper, the effect by multiple supports with different seismic input is dealt with and case study is conducted by using and comparing the methods suggested by former researches [1-6] and current regulatory guidance [7-9]. To make it simple and to focus on multiple support effect on components only, just a single spatial component (horizontal x-direction) is handled here and combination of spatial responses is left for further research.

2 MULTIPLE EXCITATION SOLUTION METHODS

2.1 Time history method and response spectrum method

There are two methods for multiple excitation solution methods, one is the time history method and the other is response spectrum method. Time history method is straight forward and contains phase information while response spectrum method is easy to use and needs far less computation effort.

Time history methods suggested by former research [1-6] are similar. They considers unconstrained (unsupported) and constrained (supported) displacements (or velocity or acceleration), and external forces and support reactional forces. And make use of modal orthogonality concept for easy calculation.

However, calculating time history response for each support needs much time and computation effort. Moreover, in many cases, time history for each elevation of support are not given. So, we need extra hour and computation effort to get artificial time histories enveloping the given response. Thus, in many cases, response spectrum methods are used instead. Unlike time history method, for response spectrum method make use of readily calculated response spectra curve, it needs less computation effort and extra calculation of input is not needed. As stated by M. Subudhi and P. Bezler [6], response of multiple supported case is considered to be

composed of dynamic component due to dynamics of inertia, and static component due to relative movement of each support. The governing equation for response spectrum method as of Y.K. Wang [5] can be express as:

For the dynamic response case (inertia effect)

$$M\ddot{x}_d + C\dot{x}_d + Kx_d = MK^{-1}K_{AB}\ddot{z} \tag{1}$$

and for the static response case (pseudo-static)

$$x_s = K^{-1}K_{AB}z \tag{2}$$

where, M, C and $K$are mass, damping and stiffness matrix respectively. x_d and x_s are the dynamic and static component of multiply supported response. K_{AB} is the coupling term between the system and support points, z is the ground displacement at the support point.

In case of dynamic component, the response can be calculated by using artificial time history. However, in response spectrum method, spectral acceleration for the support response spectrum, S_a is used. Once maximum modal response has been acquired, maximum dynamic response along the whole system can be calculated by applying mode shape of nth mode.

In case of static component, z can be calculated by below relation [6]:

$$S_d = S_a/\omega^2 \tag{3}$$

Where, S_a is the structural acceleration at the high frequency end of the spectrum curve, S_d is maximum displacement of the support, ω is fundamental frequency of support structure. Thus, from maximum displacement S_d, maximum static response can be calculated.

2.2 Regulatory guidance

Regulatory guidance in Standard Review Plan (SRP) 3.7.2 and 3.7.3 [7, 8] states that both time history method and response spectrum method can be used. Especially, in case of response spectrum method, when it comes to multiply supported cases, it says that uniform support motion (USM) method can be used. In USM method, a uniform response spectrum which envelops all the response spectra applied at each support is applied to all the supports, which producing somewhat conservative result. So, more realistic response spectrum method has been suggested. In SRP 3.7.3 and NUREG-1061 volume 4 [8, 9], independent support motion (ISM) method is suggested. Unlike USM method, distinct response spectrum at each support is used in ISM method, while the other supports are being stationary. And then all the responses by each support input is combined. At both USM and ISM cases, response due to relative support motion shall be calculated separately, and considered in calculating the total maximum response of the system.

3 APPLYICATION OF RESONSE SPECTRUM TO MAJOR NPP COMPONENTS

The above studies [1-6, 9] are all focused in piping system with multiple supports in different levels or even different building structures. However, there are some components or equipment with multiple supports in different level as well. Some examples of these components are reactor, steam generator and pressurizer in nuclear power plants. These components are very important to the safe operation of NPPs. But, little has been studied on the effects of different seismic input from these multiple supports to those components. Thus, in this section, application of response spectrum method to those components is studied and case by case application of each response spectrum method is compared to get find the best method for these multiple supported major NPP components.

3.1 Example model

To make it simple, application to pressurizer is conducted. Pressurizer is a simple pressure vessel controlling pressure of the reactor coolant system, and contains relatively less internal structures. Thus, in this research, a pressurizer is assumed as a simple vertical tank with its skirt support and four keys. The pressurizer is supported at the bottom of skirt to the floor by fixed condition. And it is surrounded by pressurizer room walls and supported by four sliding keys as shown in Figure 1.

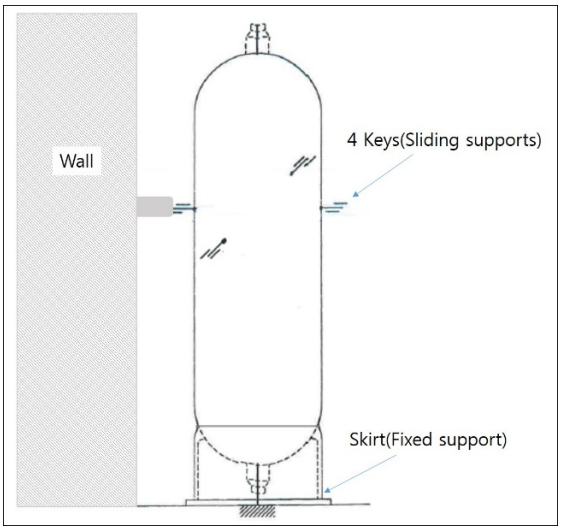


Figure 1: Pressurizer and its support.

The response spectra at both support levels (skirt and keys) are shown in Figure 2. In this case, response spectrum at keys level envelops the other, so this response spectrum is used in USM method.

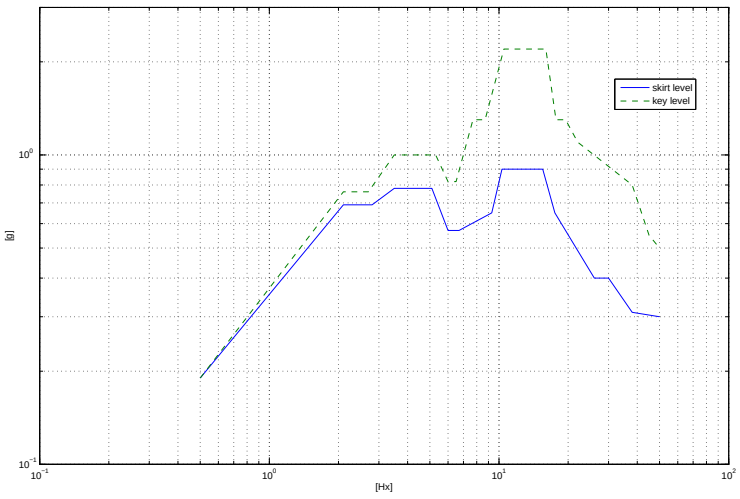


Figure 2: Response Spectra at bottom and key level.

3.2 USM and ISM method

As the first step, modal analysis on the model has been conducted. To conduct the analysis, throughout this paper, ANSYS workbench is used and the FE model is simplified including the pressurizer room walls.

As shown in Table 1, the first two natural frequencies are shell mode frequencies. So, these modes have little meaning in this case. The next two natural frequencies are the first beam mode frequencies, but they are beyond the range of FRS curve shown in Figure 2. As 50Hz (conservatively) is considered as cut-off frequency of rigidity, we can consider that the same response spectrum value is extended beyond 50Hz.

No.	fn	description
1	66.419	1st shell mode
2	68.695	1st shell mode
3	70.598	1st beam mode (x-direction)
4	70.654	1st beam mode (z-direction)
5	119.76	2nd shell mode

Table 1: Natural frequencies of pressurizer in Hz.

By applying key level response spectrum value at both supports, dynamic result by USM method can be calculated. Below table shows the maximum equivalent stress in MPa. Table 2 is the results at key support and table 3 is the results at skirt support.

Method	Dynamic result	Pseudo-static result
USM	5.42	24.92
ISM	4.15	18.31

Table 2: Result by USM and ISM method in MPa at key support.

Method	Dynamic result	Pseudo-static result
USM	2.43	11.38
ISM	1.77	8.358

Table 3: Result by USM and ISM method in MPa at skirt support.

According to the regulatory guidance documents [7-9], in calculating static component when using USM method, relative movement between each support shall be the most unfavourable combination of each support movement. In ISM method, on the other hand, those documents allow engineering judgement on the phase between supports. So, in this paper, pseudo-static result by USM was calculated from the sum of maximum pseudo displacement of both supports. And, ISM case was calculated from the square root of the square sum of each support's movement. That's because the phase of movement between base support and key support is unknown.

As a result, the maximum stresses are shown to be at key support, while the resultant stress values at skirt support are about 45% of those at key supports for both dynamic and pseudo-static cases.

3.3 Pressurizer-wall composite system case

In previous section, the same USM and ISM method that has been applied to piping system by former researcher [1-6] was applied to a pressurizer. As USM and ISM consider not only dynamic response but also pseudo-static response which is comes from relative displacement between supports, and as the pressurizer is stiffer than piping system, the pseudo-static response component can make bigger effect on resultant forces or moments at each supports. As Y.K. Wang [5] has shown in his research, even in case of piping systems, resultant forces or moments by pseudo-static response component are at least 5 times bigger than those by dynamic response component. So, applying USM and ISM to this example can be said to be a reasonable approach. However, as both component and wall share common base excitation and the excitation of key level can be highly related to the base excitation. So, response spectrum analysis on pressurizer-wall composite system was conducted by applying a single response spectrum at the common base as a common excitation.

Firstly, the natural frequencies of pressurizer alone, wall alone and pressurizer-wall composite model, each supported only at the bottom, are calculated.

As shown in table 4, each model including the pressurizer-wall composite system is flexible.

fn[Hz]	A	B	C	
1	11.827	14.221	14.482	1st beam mode (x-direction)
2	11.846	19.472	18.743	1st beam mode (y-direction)
3	53.24	31.825	34.146	Twist mode
4	-	34.398	43.974	-
5	58.097	42.45	44.983	-
6	58.314	44.461	45.602	-
7	61.847	49.571	50.179	-
8	61.903	63.418	55.228	-

Table 4: Natural frequencies of pressurizer (A), wall (B), composite model (C) in Hz

The pressurizer-wall composite case response is calculated by applying a single response spectrum at the bottom support both pressurizer and the wall at the same time. In this paper, let me call it as Composite Single Support (CSS) method. Table 5 shows the maximum equivalent stress results by CSS, ISM and USM method. Here, again, the maximum stress point by CSS method is pressurizer key point.

Method	Result at key support	Result at skirt support
CSS	12.554	10.501
Combined ISM (SRSS)	18.774	8.543
Combined ISM (ABS)	25.26	11.517
Combined USM	25.503	11.637

Table 5: Result by Composite Single Support method and combined results by ISM/USM in MPa.

For CSS method deals with only a single support and the component and the wall are included in the composite model, we don't need to consider pseudo-static component.

As can be seen from above results, USM and ISM method on pressurizer resulted in relatively higher pseudo-static stresses than dynamic ones. This result is somewhat understandable because, pressurizer (as a representative of NPP components) is stiffer if supported at both supports.

To compare the results by USM/ISM with that by CSS method, combined stress of USM and ISM is calculated. In this paper, square root of square sum (SRSS) rule is applied to combine those two components (dynamic and pseudo-static components) as stated in NUREG-1061 [9]. The combined stress results are shown in Table 5. To know the effect to the pseudo-static component by calculation method, Table 5 also shows two separate ISM results by considering pseudo-static component from absolute (ABS) and SRSS displacement difference between supports. The stresses by SRSS pseudo-static components are from table 2 and 3. In case of the stresses by ABS are from those of USM.

In this case, the combined stresses are much higher than those by CSS method, except for the SRSS ISM case at skirt support. As can be seen from table 5, the absolute ISM case has similar results with USM case. So, it can be said that the stress by pseudo-static component is dominant. But, as stated in reference [3], stress developed by pseudo-static component is derived from relative displacement between supporting points, thus, can be categorized as self-limiting secondary stress. So, combining stress by dynamic and pseudo-static component can be somewhat conservative.

4 CONCLUSIONS

- In this paper, various methods for the seismic analysis of multiply supported nuclear power plant components by using simplified example of pressurizer have been conducted and compared.
- As can be seen from the modal analysis result of Table 4, dynamic characteristics of pressurizer-wall composite system is more strongly related to the wall than pressurizer. So, it can be inferred that, the wall plays main role in dynamic behaviour of the composite system. So, this gives some credit on applying SUM and ISM to the pressurizer model.
- The result by USM and ISM has been compared with the result by composite single support (CSS) response spectrum method applied to a pressurized-wall composite system, and it shows that combined stress by USM and ISM is higher than the stress by CSS method at key support. But, the result by CSS at skirt support is higher than the result by SRSS ISM method.
- The big difference between USM and ISM method is mainly due to the pseudo-static components. And the way of calculating the pseudo-static components has big effect on the overall result; calculating the pseudo-static components by absolute displacement or SRSS displacement difference between supports makes big difference.
- As CSS method is somewhat straight forward and it doesn't need to consider the static component of the result, it can be said that CSS method is more realistic and convenient than USM/ISM method which needs separate analysis to get dynamic and static result each.
- Time history analysis, to compare with each method, needs to be conducted as a further study topic along with the analysis on spatial combination of the result by each method.

REFERENCES

[1] C.W. Lin, Response spectral solution for structures with multiple support input. *IAFE, 5WCEE Proceedings*, 1973.

[2] R.W. Clough and J. Penzeien, *Dynamics of Structures*. McGraw-Jill, New York, 1975.

[3] R.W. Wu, F.A. Hussain and L.K. Liu, Seismic response analysis of structural system subjected to multiple support excitation. *Nuclear Engineering and Design*, **47**, 273-282, 1978.

[4] K.R. Leimbach, Comparison of multiple support excitation solution techniques for piping systems. *Nuclear Engineering and Design*, **57**, 295-307, 1980.

[5] Y.K. Wang, BNL-NUREG-32628, Comparison study of time history and response spectrum responses for multiply supproted piping systmes, *7th International conference on structural mechanics in reactor technology*, Chicago, US, 1983

[6] M. Subudhi and P. Bezler, Alternate procedures for the seismic analysis of multiply supproted piping systmes, *8th International conference on structural mechanics in reactor technology*, Brussels, Belgium, 1985

[7] NUREG-0800, Standard Review Plan, *3.7.2 Seismic System Analysis*, USNRC, 2007.

[8] NUREG-0800, Standard Review Plan, *3.7.3 Seismic Subsystem Analysis*, USNRC, 2007.

[9] NUREG-1061 Vol.4, Report of the U.S.Nuclear Regulatory Commission Piping Review Committee *Evaluation of Other Dynamic Loads and Load Combinations*, USNRC, 1984.

International Conference on Engineering Vibration
Ljubljana, Slovenia, 7-10 September 2015

ADAPTIVE INERTIAL SHOCK-ABSORBER FOR VIBRATION DAMPING

Rami Faraj*[1], Jan Holnicki-Szulc[1]

[1]Institute of Fundamental Technological Research, Polish Academy of Sciences, Warsaw, Poland
{rfaraj, holnicki}@ippt.pan.pl

Keywords: Adaptive Impact Absorption, shock-absorber, vibration damping.

Abstract. *The goal of this paper is to briefly describe the concept of a new shock-absorber and to discuss its unique characteristics in reference to the problems of vibration damping. The specific construction of the so-called SPIN-MAN device is introduced and the semi-active control performed on this device is presented. In order to prove the potential of presented shock-absorber, one of possible control strategies is described and results of its numerical simulation are shown. A specific control technique is demonstrated as the main source of significant improvement of the overall impact damping process. Possibility of the shock-absorber application for mitigation of earthquakes effects is investigated and features of the system enabling adaptation to identified impact conditions are indicated. Various applications of the SPIN-MAN are considered and requirements resulting from them are specified. Challenges which have to be overcome are presented and some solutions are proposed.*

1 INTRODUCTION

During the last years, mechanical structures with embedded active and adaptive absorbers or dissipators were investigated in the area of vibration and impact control of structures. Active and adaptive methods of control for absorbers and dissipators can be used for example to emphasize and exploit their non-linear characteristics. Thanks to these features, mechanical structures can automatically adjust their response to compensate for external excitations or loads. Despite the growing amount of research, it is still challenging to design effective absorbers and dissipators and to control structures with such devices. This article presents the general concept of a new shock-absorbing device invented and developed in Institute of Fundamental Technological Research Polish Academy of Sciences, and discusses its special characteristics and possibilities of future applications. Impact absorber so-called SPIN-MAN is based on such a switchable device equipped with rotating rings, which direction of rotation is controllable [4]. The control of spinning (value and direction) – Spinning Management (SPIN-MAN) will be demonstrated to be the main source of significant improvement in the overall efficiency of impact damping process. The proposed damping strategy for impact-born vibrations is based on the on/off type of control. Similarly, on/off type of control have been used for effective damping of impact-born vibrations in the so-called PAR (Prestress Accumulation–Release) technique [5], where a proper timing of instant release/attachment of structural joints leads to an extremely effective management of impact energy absorption.

Currently, adaptive absorbers and dissipators are mainly built based on the so-called smart materials such as magneto-rheological fluids, electro-rheological fluids, piezoelectric materials, shape memory alloys or granular materials [6-11]. A separate type of devices with embedded inertia elements used to accumulate and absorb energy of impact or vibration were proposed by Chen M. Z. Q. et al [3], Smith [12], Gomuła et al. [13] and Lazar et al. [1-2]. They discussed numerous ideas of application of so-called inerter devices in the area of protection of structures against impact and vibration. These devices have similar features to the SPIN-MAN but they are not adaptive so it is impossible to design them optimally for the wide range of load conditions.

Some solutions can be expanded and adjusted to requirements for mitigation of wind and seismic response of buildings and bridges. Seismic protections can be divided into three groups: base isolation e.g. elastomeric bearings, lead rubber bearings, sliding friction pendulum; passive energy dissipation e.g. metallic dampers, friction dampers, viscoelastic dampers, viscous fluid dampers, tuned mass and tuned fluid dampers. The third group, the newest and most effective solution is an active control implemented by active bracing systems, active mass dampers, systems with variable stiffness or damping or smart materials [15]. There also exist so-called semi-active control systems which cannot inject mechanical energy into the controlled system. Performance of appropriately designed semi-active systems is significantly better than performance of passive devices and can be comparable to performance of the fully active systems [14].

2 SPIN-MAN – CONCEPT OF THE CONSTRUCTION

Operation of the SPIN-MAN shock-absorber, shown in Figure 1, is initiated by a linear motion of a rod that is connected with the cushioned structure which is subjected to vibrations or impacts. Linear motion of the rod is converted into the rotary motion of threaded rings, what means that energy of vibrations or impact is converted to the energy of rotational motion of rings. Energy of rotating parts is accumulated and then dissipated using Spinning Management technique.

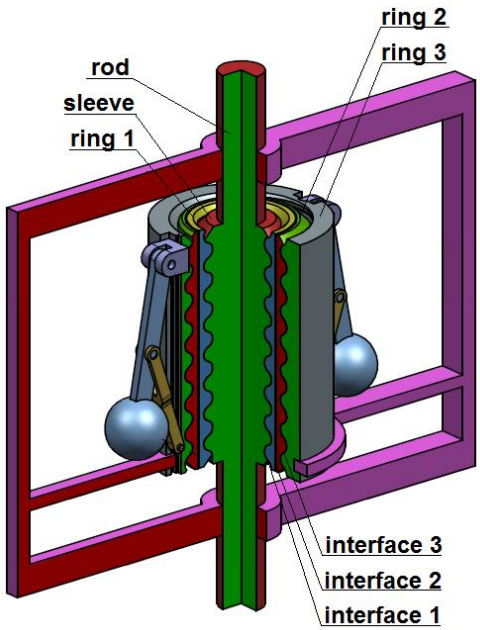


Figure 1: Construction of the SPIN-MAN shock-absorber.

The shock absorber is composed of a threaded sleeve on the rod that is positioned in a frame, three threaded rings and two weights on arms. Inner ring is screwed to the sleeve and has, on its inner surface, a thread compatible with the thread on the sleeve; its outer surface is cylindrical. Middle ring has, on its outer surface, a thread compatible with a thread on the inner surface of the outer ring. Thread of the sleeve and thread of the middle ring provide a rotary motion in the opposite directions. Inner surface of the middle ring and outer surface of the outer ring are cylindrical. A connecting element, so-called energy dissipation surface (EDS), is placed between cylindrical surfaces of the inner ring and the middle ring. This part is a dissipative connection and it can be realized based on an elastomeric ring, a frictional connection or a connection filled with a magneto-rheological fluid, which viscosity (and thus the damping characteristics) can be changed and adjusted to the load conditions, using a magnetic field control. Weights connected with the outer ring are placed on the arms. Such a solution provides the possibility to control the position of the weights and change the moment of inertia of the spinning mass.

Connections of the main components as well as mass parameters have a significant influence on the SPIN-MAN's performance. Each connection is called an interface. A threaded connection of the sleeve with inner ring 1 is the interface 1 and it allows linear and angular relative displacements. Interface 2, between inner ring 1 and middle ring 2 as a dissipative connection – EDS, allows only angular relative displacements. Interface 3 connecting middle ring 2 with outer ring 3 is a threaded connection – thread opposite oriented to the thread of the interface 1. Third connection enables rotation and move in the direction of the rod axis of the middle ring. Outer ring can rotate and cannot move along the rod axis because of the positioning connection with the frame. Each interface is equipped with a blocker of the relative rotary motion that can be separately turned on and turned off leading to a desired sequence of relative rotary motions.

A system of sensors, required for effective system adaptation to the random excitation, should identify precisely main characteristics of the shock. For known parameters of the im-

pact – instant velocity growth and energy of impact, control system determines the required moment of inertia of rotating parts and selects an appropriate control strategy ensuring demanded response of the system. Moreover, for better performance, the moment of inertia of outer ring can be changed during the entire process of shock absorption using the continuous control of weights' position. In addition, it is possible to control the damping characteristics of the interface 2, especially in case of the solution with the magneto-rheological fluid. The large number of controllable parameters of the system allows to change and adjust absorbing characteristics of the SPIN-MAN and obtain required objectives. Simultaneously, the number of variables makes design and optimization processes difficult.

3 OPERATION OF THE SPIN-MAN

A brief discussion on sample operation of introduced shock-absorber is presented and some applications of this device are considered in this section.

3.1 Sample control strategy – numerical simulation

Let us consider a spring-mass system connected with the SPIN-MAN, as shown in Figure 2. Sample simulation of such a system was conducted in ADAMS software environment and some results are presented below. In considered case, the mass of 10 kg is excited with initial velocity of 10 m/s. Spring stiffness and SPIN-MAN's parameters were selected so as to obtain an efficient operation of the shock-absorber. Energy dissipation process was modelled by viscous damping on the EDS. Time of turning on/off actions performed on blockers of interfaces was assumed as 0.4 millisecond. Control of the moment of inertia was not implemented.

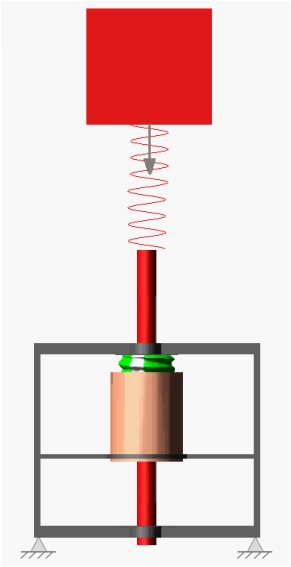


Figure 2: Scheme of analyzed system.

According to the possibility of separate control of each blocker of relative rotation, the Spinning Management technique can be implemented through a large number of different control strategies. One of possible solutions was selected as efficient enough to demonstrate a potential of the SPIN-MAN device. Initially, interface 1 and interface 2 are blocked so the rod

with sleeve, the inner and the middle ring move together. Blocker on interface 3 is released so forward move of mentioned elements lead to the rotary motion of the outer ring, as shown in Figure 3. When value of angular velocity of the outer ring reaches a maximum, interface 1 and interface 2 are released and immediately after that, interface 3 is blocked. These actions lead to the rotation of combined middle and outer rings which pull the inner ring with them, after some decrease of combined rings' angular velocity, inner ring starts rotating in opposite direction to their rotation. Obtained velocity difference between the parts allows to dissipate quickly the energy of rotary motion on the EDS caused by the viscous damping. Phase of energy dissipation is ended with turn on action performed on the blocker of interface 1.

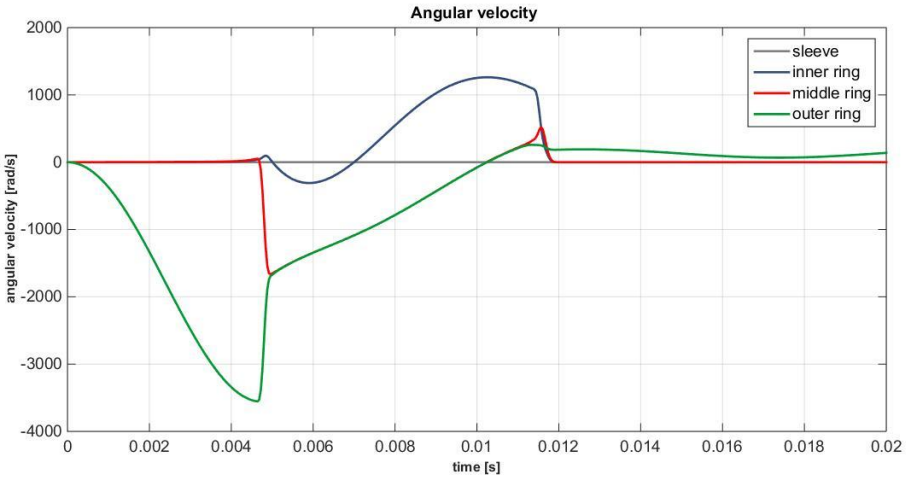


Figure 3: Angular velocity of SPIN-MAN's components.

In accordance with a graph in Figure 4, implementation of described control technique results in 50% reduction of the maximum reaction force in a spring in reference to the spring-mass system and after about 12 milliseconds all movements in the system almost disappear.

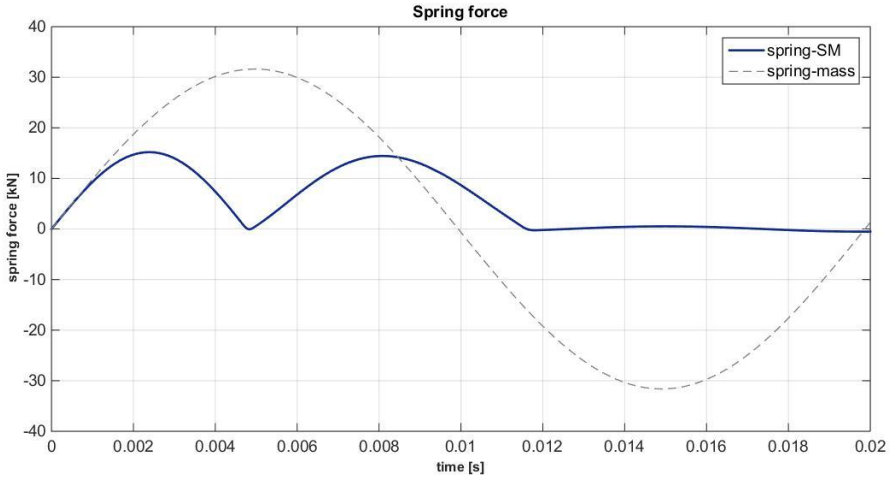


Figure 4: Reduction of the impact force in a spring.

Looking at the graph of energy balance presented in Figure 5, it is easier to understand the operation of the SPIN-MAN. In first phase of operation, kinetic energy of the mass is transferred by the spring to the moving forward elements which convey energy to the outer ring. After the moment when outer ring reaches maximum angular velocity, interface 1 and 2 are released allowing relative rotations between sleeve and inner ring, inner and middle ring so the energy dissipation process on interface 2 is started. Simultaneously, action of the interface 3 blocking causes a fast energy dissipation, energy has to be absorbed by the blocker to combine two rings so blocker with good endurance is needed. When almost all remaining in a system energy is dissipated, blocker on the interface 1 is activated absorbing some amount of energy.

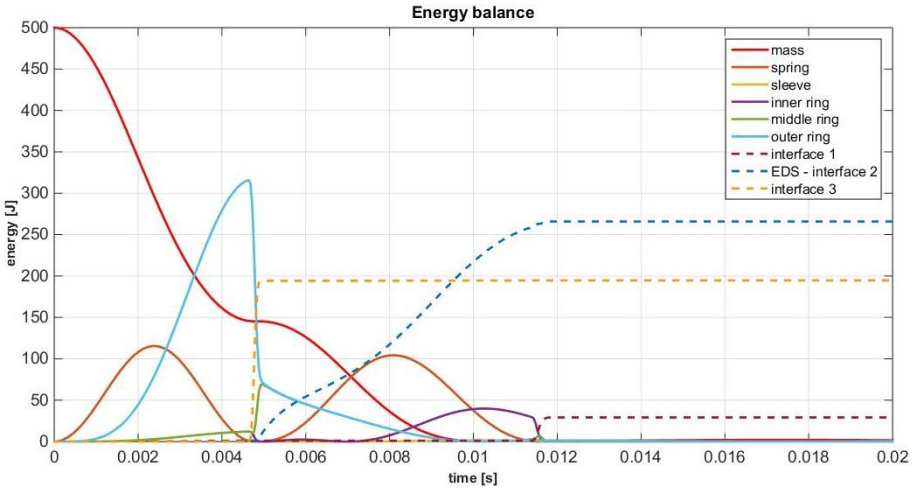


Figure 5: Energy balance - energy transfer and dissipation.

3.2 Short discussion on applications of the SPIN-MAN

The SPIN-MAN shock-absorber seems to be widely applicable because of a large number of implementable control strategies which can be selected and optimized for particular applications. Moreover, construction of this shock-absorber allows it to operate in any spatial orientation. Besides control of blockers and changeable moment of inertia of the outer ring, adaptation of the SPIN-MAN to the random load conditions can be realized using control of damping characteristics of the EDS that can be obtained by for instance version of the shock-absorber with magneto-rheological fluid in interface 2. According to the number of conducted simulations, it is worth mentioning that geometric and mass parameters have significant influence on the performance of this device and for some sets of these parameters providing good performance of the shock-absorber, a small changes can lead to not worse performance but to completely useless operation of this device. For instance threads on interface 1 and 3 should provide easy initiation of accelerating rings – large thread pitches but for effective accumulation of the energy, thread pitches should be small. Geometry of thread pitches can be changeable but this solution makes the SPIN-MAN device significantly more complicated.

The SPIN-MAN shock-absorber can be used in airdrop systems, road barriers, bumpers of trains, etc. For a large number of excitations occurring within a short time, in order to achieve optimal, repetitive effect of energy absorption, system has to quickly return to the initial configuration of all parts. This demand can be achieved by a specially designed spring-back sys-

tem designed for a fast restoration of the initial configuration of the shock-absorber. This solution allows effective reception of frequent, repetitive impacts. The SPIN-MAN prepared for reception of repetitive excitations and smooth energy dissipation can be applied in suspensions of road vehicles, airplanes etc. Other solution but difficult to be obtained is a precise implementation of the Spinning Management technique which should be updated based on the actual load conditions. This solution allows to predict a sequence and timing of blockers' turn on/off actions needed to return to initial configuration of the shock absorber as soon as possible with required efficiency of energy absorption. Moreover, this solution can be amended in order to meet requirements for systems mitigating the wind and seismic response of bridges. In such cases a role of the identification system of load conditions is significant. Nevertheless, construction and control system of the shock-absorber have to be optimized in terms of quick response and fast return to the initial configuration.

4 CONCLUSIONS

This paper introduces a new shock-absorber called SPIN-MAN, a device invented in the Institute of Fundamental Technological Research Polish Academy of Sciences (IPPT PAN). One of possible operation of this device, based on the impact energy management technique was simulated in ADAMS software environment. Implementation of the Spinning Management – a control concept based on switching on/off blockers gives desired results which demonstrate that it is possible to significantly reduce the maximum loads caused by the impact. Moreover, it can be achieved in a very short time, what shows a big potential of this solution. Currently, a demonstrator of the SPIN-MAN device is prepared.

ACKNOWLEDGEMENT

Financial support of Structural Funds in the Operational Programme - Innovative Economy (IE OP) financed from the European Regional Development Fund - Project "Modern material technologies in aerospace industry", Nr POIG.01.01.02-00-015/08-00 is gratefully acknowledged.

REFERENCES

[1] I.F. Lazar, S.A. Neild, D.J. Wagg, Using an inerter-based device for structural vibration suppression. *Earthquake Engineering & Structural Dynamics* **43**(8):1129-1147, 2014.

[2] I.F. Lazar, S.A. Neild, D.J. Wagg, Design and Performance Analysis of Inerter-Based Vibration Control Systems. Proceedings of the 32nd IMAC, A Conference and Exposition on Structural Dynamics, pp. 493-500, 2014.

[3] M.Z.Q. Chen, C. Papageorgiou, F. Scheibe, F.-C. Wang, M.C. Smith, The missing mechanical circuit element. *Circuits and Systems Magazine* **9**(1): 10-26, 2009.

[4] J. Holnicki-Szulc, R. Faraj, A. Mróz, A mean of damping of vibrations excited by a mechanical impact and an inertial damper (in Polish: Sposób tłumienia drgań wywołanych udarem mechanicznym oraz tłumik bezwładnościowy). *Patent pending P.411237.*

[5] A. Mróz, A. Orłowska, J. Holnicki-Szulc,Semi-active damping of vibrations. Prestress Accumulation-Release strategy development. *Shock and Vibration* **17**(2):123-136, 2010.

[6] G. Mikułowski, J. Holnicki-Szulc, Adaptive landing gear concept – feedback control validation. *Smart Materials and Structures* **16**(6):2146, 2007.

[7] G. Mikułowski, R. Wiszowaty, J. Holnicki-Szulc,Characterization of a piezoelectric valve for an adaptive pneumatic shock absorber. *Smart Materials and Structures* **22**(12):125011, 2013.

[8] Makowski M., Knap L., Reduction of wheel force variations with magnetorheological devices, *Journal of Vibration and Control*, Vol. **20**(10) pp. 1552–1564, 2014.

[9] Carlson, J.D. and Spencer Jr. B.F., Magneto-Rheological Fluid Dampers for Semi-Active Seismic Control. Proc. of the 3rd Int. Conf. on Motion and Vibration Control, Chiba, Japan, Vol. 3, pp. 35–40, 1996.

[10] Bajkowski J., Jasiński M., Mączak J., Radkowski S., Zalewski R., 2012, The active magnetorheological support as an element of damping of vibrations transferred from the ground to large-scale structure supports, *Key Engineering Materials*, 518, 350-357.

[11] G. Mikułowski, Ł. Jankowski, Adaptive Landing Gear: optimum control strategy and potential for improvement, *Shock and Vibration* **16**(2), 2009, pp. 175-194.

[12] Smith M. C., Synthesis of Mechanical Networks: The Inerter, EEE TRANSACTIONS ON AUTOMATIC CONTROL, Vol. **47**, No. 10, pp. 1648-1662, 2002.

[13] Gomuła, S., Łągiewka, L., A method of impact and inertia force reduction during collisions between physical objects. Results of experimental investigations. Journal of Technical Physics. Vol. 48, no 1, pp. 13-27, 2007.

[14] Housner, G., Bergman, L., Caughey, T., Chassiakos, A., Claus, R., Masri, S., Skelton, R., Soong, T., Spencer, B., and Yao, J., Structural Control: Past, Present, and Future, Journal of Engineering Mechanics, **123**(9), 897–971, 1997.

[15] T.T. Soong, B.F. Spencer Jr, Supplemental energy dissipation: state-of-the-art and state-of-thepractice, *Engineering Structures* **24**, 243–259, 2002.

Vibration Analysis of Steel and Steel-Concrete Composite Structures (MS05)

International Conference on Engineering Vibration
Ljubljana, Slovenia, 7-10 September 2015

VIBRATION ANALYSIS OF STEEL-CONCRETE COMPOSITE MULTI-STOREY BUILDINGS

Vinícius C. Morais[1], **Rafael R. Barboza**[1], **José Guilherme S da Silva***[2]

[1]Civil Engineering Post-graduate Programme, PGECIV
State University of Rio de Janeiro, UERJ
viniciusmorais.eng@hotmail.com; rafael_engciv@yahoo.com.br

[2]Structural Engineering Department, ESTR
Civil Engineering Post-graduate Programme, PGECIV
State University of Rio de Janeiro, UERJ
jgss@uerj.br

Keywords: Steel-Concrete Composite Buildings, Stochastic Wind Loading, Dynamic Analysis, Human Comfort, Numerical Modelling.

Abstract. *Based on a favourable economic scenario combined with technological advances of the material sciences and construction processes, in the last forty years, the Brazilian cities have presented a substantial growth related to construction of residential and commercial multi-storey steel and steel-concrete buildings. Nowadays, these buildings present greater slenderness and have been constructed with more challenging structures that encompass the experience and knowledge of structural designers by using newly developed materials and technologies boosted by the ever-growing investigations on this field. This way, this work aims to investigate the structural behaviour of a 20 story steel-concrete composite building when subjected to nondeterministic wind dynamic actions. The numerical model was developed using three-dimensional beam finite elements to simulate the steel beams and columns and the reinforced concrete slabs were represented by shell finite elements, based on the use of the ANSYS program. The building bracing system was represented by spatial truss finite elements and three types of bracings are presented and analysed. The present investigation considered the results of a geometric nonlinear analysis for serviceability limit states. The investigated structural models nondeterministic dynamic responses (displacements and peak accelerations) were obtained and compared to the limiting values proposed by several authors and design standards.*

1 INTRODUCTION

Considering the favourable economic scenario and technological advances of material sciences and construction processes, in the last forty years, the Brazilian cities have presented a substantial growth, with respect to construction of residential and commercial multi-storey buildings [1-2].

Nowadays, these buildings present greater slenderness and have been constructed with more challenging structures that encompass the experience and knowledge of structural designers by using newly developed materials and technologies boosted by the ever-growing investigations on this field [1-2].

As the structural designer main objective is related to produce increasingly lighter structures, its conception requires a substantial amount of theoretical knowledge associated to structural design and construction processes, in order to make compatible the requirements of architecture with the necessary conditions for stability [2]. It must be emphasized that this type of construction has become a worldwide phenomenon, which began in developed countries and now it's also present in developing countries such as China, Korea and Malaysia [3].

As a result, these tall buildings have become more sensitive to dynamic excitations by wind loads and thus more vulnerable to problems related to excessive vibrations [4]. The excessive vibrations not only interfere in human comfort, but it also may cause fatigue of the structural elements or even a general collapse of the building in a worst case scenario [5-6].

This way, this research work aims to investigate the static and dynamic structural behaviour of a 20 story steel-concrete composite building, when submitted to the non-deterministic wind dynamic actions [5-6]. The developed computational model adopted the usual mesh refinement techniques present in finite element method simulations implemented in the ANSYS program [7]. The numerical model was developed using three-dimensional beam finite elements to simulate the steel beams and columns and the reinforced concrete slabs were represented by shell finite elements. The building bracing system was represented by spatial truss finite elements and three different types of bracings are presented and analysed [5].

The present study has considered the results of a geometric nonlinear analysis for serviceability limit states [5-6]. The investigated structural model non-deterministic dynamic response, in terms of displacements and peak accelerations, was obtained and compared to the limiting values proposed by several authors and design standards [8-9].

2 NON-DETERMINISTIC WIND MODEL

One of the dynamic loads of great importance to be considered in the structural analysis of tall buildings is related to the wind forces. The buildings wind-induced structural response consists of along-wind response, across-wind response and torsion response. Initially, in this investigation the along-wind response analysis is considered.

In design practice, wind around tall building flows in a very complex and random way, so the wind is a nondeterministic process and presents unstable properties and random characteristics, which indicate that the deterministic consideration should be avoided [5-6]. In order to consider the non-deterministic action of the wind, statistical concepts and numerical simulations are needed [10-14].

This way, aiming to simulate the non-deterministic wind actions, this investigation presents a numerical formulation based on the Monte Carlo's method and the Wind Synthetic Method [10-14]. The Monte Carlo numerical procedure is then used to compute the power spectral density associated to the wind actions and to derive the statistics of the dynamic response, considering the uncertainty of the wind loadings [10-14].

Initially, the fluctuating parcel of the wind is decomposed into a finite number of harmonic functions proportional to the structure resonant frequency with phase angles randomly determined [5-6]. Obata recommends a minimum of 11 harmonic components from intervals of 0.5 seconds to 600 seconds [10]. The present study assumed a frequency range of 0.01 Hz to 3.01 Hz, which corresponded to the first ten vibration modes of the investigated building and a 48 harmonics with an increment frequency equal to 0.0625 Hz.

In the present investigation, the tenth harmonic coincides with the resonant harmonic, while the remaining harmonics are multiples and submultiples of the harmonic resonant, as described in the Wind Synthetic Method [10]. The amplitude of each harmonic is obtained based on a wind power spectrum density function. Considering the existing power spectra density functions determined by formulas of the present representative literature, see Figure 1, in this work the Kaimal spectrum [5-6] was adopted due to consideration of the height z. The power spectrum is given by Eqs. (1) and (2) and the friction velocity is determined by Eq. (3).

$$\frac{f\,S^{V}(f,z)}{u_{*}^{2}} = \frac{200x}{(1+50x)^{5/3}} \tag{1}$$

$$x(f,z) = \frac{f\,z}{V_{z}} \tag{2}$$

$$u_{*} = \frac{k\,\overline{V}_{Z}}{\ln(z/z_{0})} \tag{3}$$

In Eqs. (1) to (3), f represents the frequency, $S^{V}(f)$ is related to the wind power spectral density in the frequency f, x is the dimensionless frequency, Vz is the velocity at height z and k is the Karman constant.

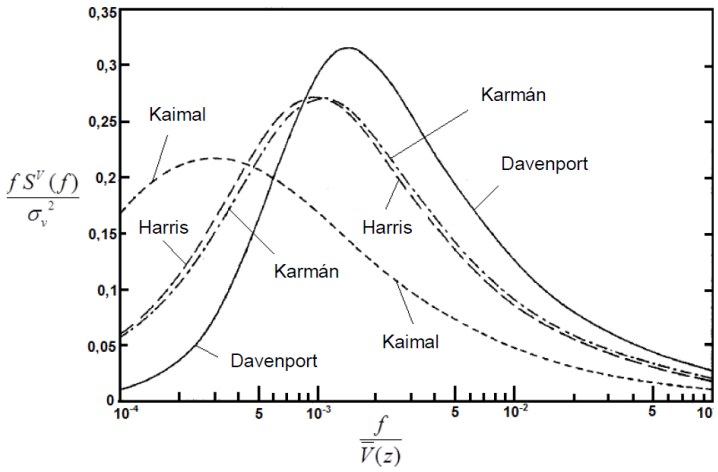


Figure 1: Wind power spectra [5].

Firstly, based on a single harmonic function, the fluctuating parcel of the wind can be represented by Eq. (4), with v_0 representing the basic wind speed [5-6]. In sequence, assuming that the fluctuating parcel of the wind is associated to a second order ergodic stationary random process with mean equal to zero and also considering a superposition of the harmonic waves [5-6], the fluctuations can be expressed as in Eq. (5), where N is the total number of

frequency increments in the power spectrum density, f_i is the frequency related to the harmonic i, Δf is the frequency increment and θ_i is the random phase angle normally distributed in the interval [0-2π]. The amplitude of the functions in time domain is given by Eq. (6) [5-6].

$$v(t) = v_0 \cos(2\pi f t) \tag{4}$$

$$v(t) = \sum_{i=1}^{N} \sqrt{2S^V(f_i)\Delta f} \cos(2\pi f_i t + \theta_i) \tag{5}$$

$$a_i = \sqrt{2S^V(f_i)\Delta f} \tag{6}$$

Finally, based on the Brazilian design code [8] combined with the developed mathematical formulation, see Eqs. (1) to (6), the wind-induced response in along-wind direction can be calculated through the sum of a static parcel (along-wind translation) and a dynamic part (along-wind random vibration) [5-6]. It must be emphasized that the along-wind translation is mainly caused by the wind steady flow. The along-wind vibration is caused by the turbulent flow. The along-wind random vibration includes a quasi-steady background turbulence response to low frequency component and a narrow-band resonant response [13].

3 INVESTIGATED STEEL-CONCRETE COMPOSITE BUILDING

The investigated steel-concrete composite building presents 20 stories, total height of 66 m, storey height equal to 3.3 m and rectangular dimensions of 20 m by 30 m, see Figure 2. The structural system is formed by steel columns and beams and also reinforced concrete slabs with thickness equal to 15 cm [5-6]. In addition, the inner core also contains steel diagonals forming vertical trusses and three types of bracings are presented and analysed, see Figure 3. In sequence, Table 1 and Figure 3 present the European laminated standard profiles adopted in the structural system.

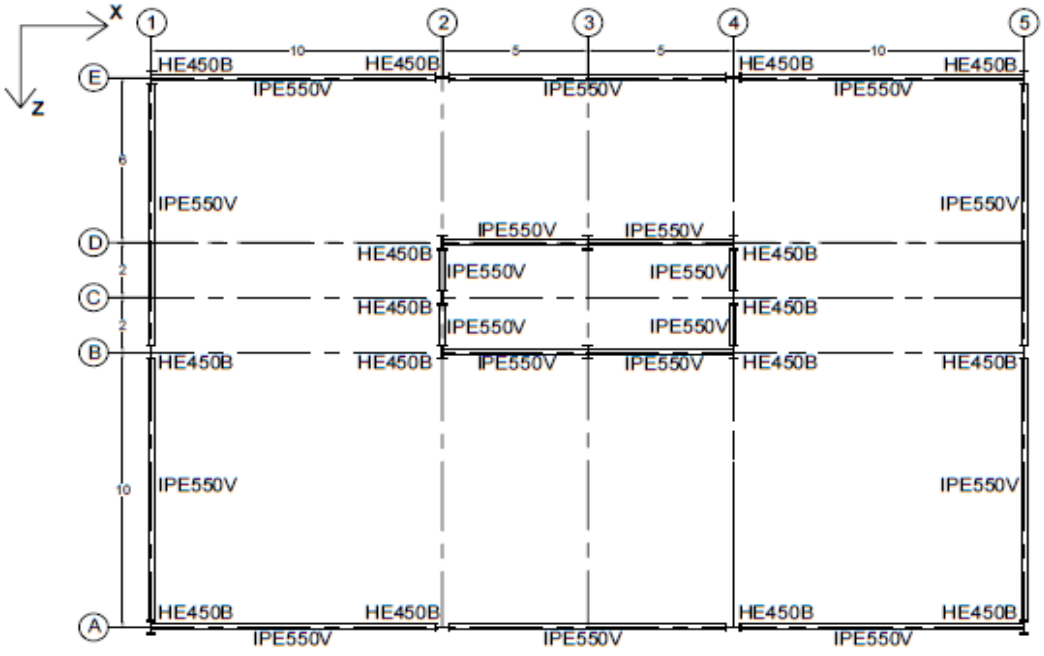


Figure 2: Investigated steel-concrete composite building.

Structural members	Type
Columns (1st to 10th story)	HE450B
Columns (11th to 20th story)	HE450A
Beams	IPE550V
Diagonals	HE260M

Table 1: Steel profiles used in the structural system.

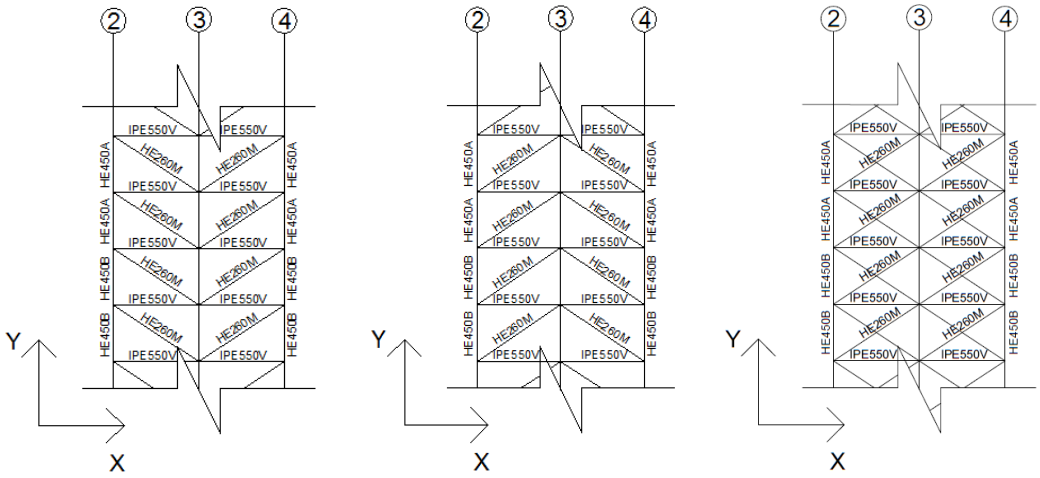


Figure 3: Investigated building bracing systems: V (Model I), Λ (Model II) and XX (Model III).

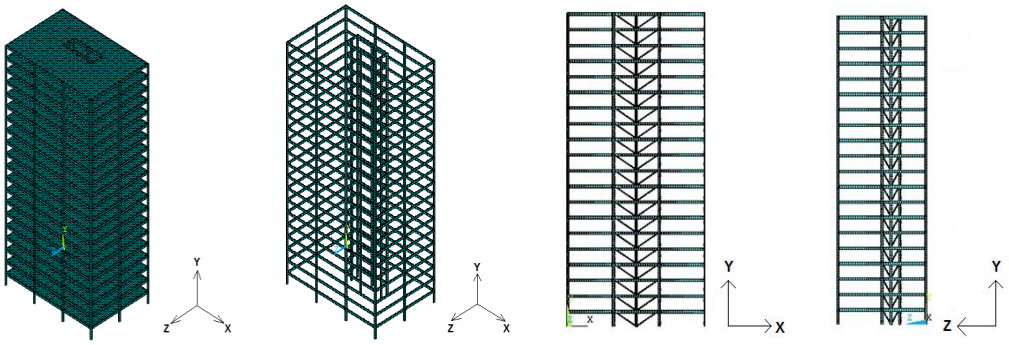
4 FINITE ELEMENT MODELING

The proposed computational model, developed for the building dynamic analysis, adopted the usual mesh refinement techniques present in finite element method simulations implemented in the ANSYS program [7]. In this computational model, floor steel girders were represented by three-dimensional beam elements, where flexural and torsion effects are considered. The composite slab was represented by shell elements. The bracing systems were simulated by three-dimensional truss elements, see Figures 3 and 4.

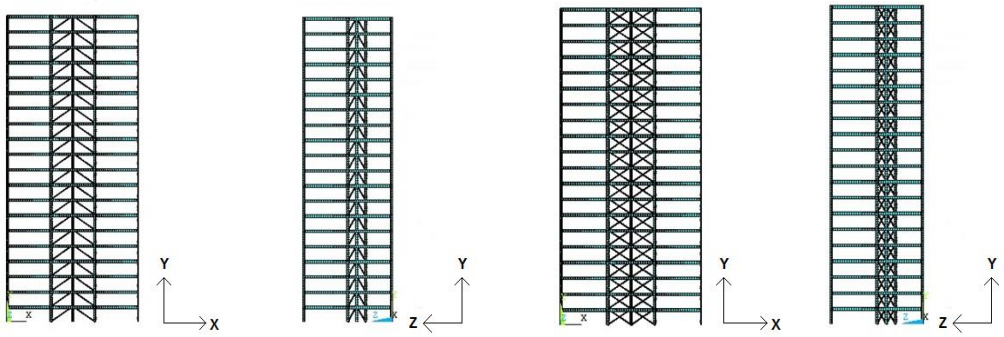
The present investigation considered that both materials (steel and concrete) have an elastic behaviour. The numerical analysis considered full interaction between steel and concrete. The final finite element models presented 49538 nodes and 52560 elements regarding Structural Models I and II (bracing system: V and Λ) and 52680 elements regarding Structural Model III (bracing system: XX), respectively, as presented in Figures 3 and 4.

5 DYNAMIC ANALYSIS

First of all, the steel-concrete composite buildings natural frequencies were determined with the aid of the numerical simulations (Models I, II and III, see Figures 3 and 4), as presented in Table 2, while the corresponding vibration modes are shown in Figure 6. After that, a geometric nonlinear dynamic analysis was performed on the investigated structural models (Models I, II and III, see Figures 3 and 4). The wind actions were simulated considering nondeterministic loadings acting on the negative direction of the global Z axis, see Figure 5. Twenty series of nondeterministic dynamic wind loads were generated [see Eqs. (1) to (6)], based on the appropriate probabilistic treatment and applied to each model, see Figure 4. The maximum displacement and peak accelerations were obtained and analysed at the nodes 1A, 2A, 4A and 5A (66 m) and nodes 6A, 7A, 9A and 10A (62.7 m), as illustrated in Figure 5.



a) Building finite element model with and without slabs b) Structural Model I: frontal and lateral views



b) Structural Model II: frontal and lateral views. c) Structural Model III: frontal and lateral views.

Figure 4: Finite element models of the investigated composite building.

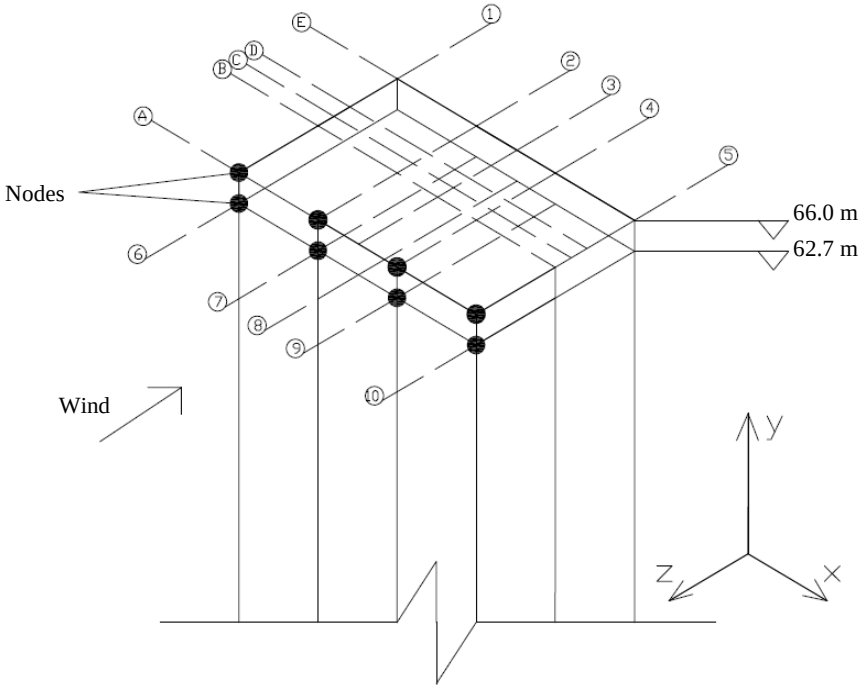
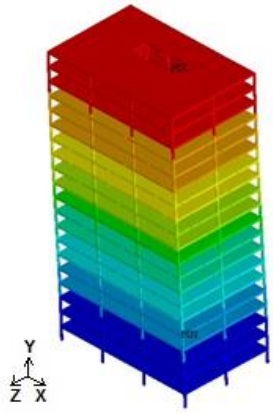


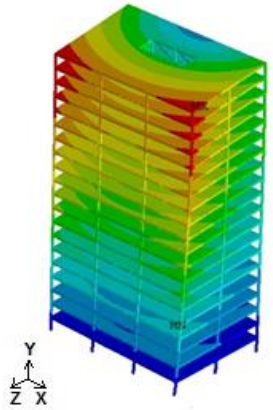
Figure 5: Wind loads direction and investigated nodes for dynamic response evaluation.

Vibration Modes	Model I: V bracing	Model II: Λ bracing	Model III: XX bracing
f_{01}	0.28 Hz	0.29 Hz	0.30 Hz
f_{02}	0.32 Hz	0.32 Hz	0.33 Hz
f_{03}	0.41 Hz	0.42 Hz	0.44 Hz
f_{04}	0.94 Hz	0.97 Hz	1.03 Hz

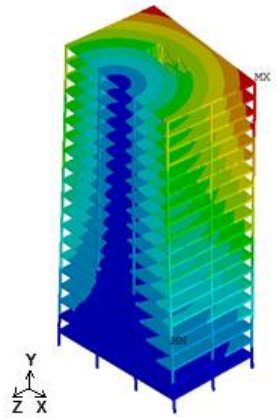
Table 2: Natural frequencies of the investigated structural models.



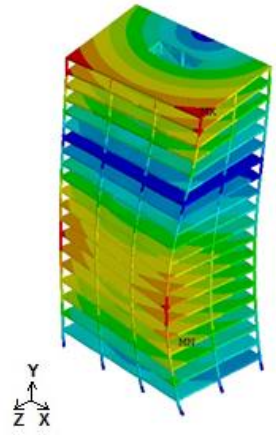
a) 1st Vibration mode (Bending): f_{01} = 0.30 Hz.



b) 2nd Vibration mode (Torsion): f_{02} = 0.33 Hz.



c) 3rd Vibration mode (Torsion): f_{03} = 0.44 Hz.

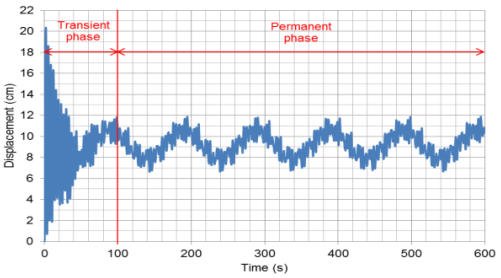


d) 4th Vibration mode (Torsion): f_{04} = 1.03 Hz.

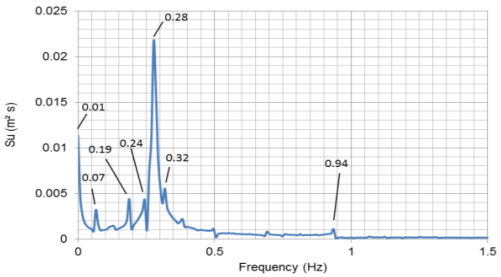
Figure 6: Model III (XX bracing system): vibration modes.

The building dynamic response in terms of the horizontal translational displacements and accelerations of the investigated systems (Models I, II and III, see Figures 3 and 4) were obtained in time and frequency domains. Figures 7 to 9 illustrate the dynamic response of the investigated structural models, when twenty series of nondeterministic wind loads were considered in the analysis. The non-deterministic wind actions require a statistical treatment of the obtained results (displacements and accelerations). Thus, considering a normal distribution, it is possible to obtain the building dynamic response, $R_{z95\%}$, based on the mean maximum values, m, and the standard deviation, σ, with a reliability of 95%, see Eq. (7) [5-6].

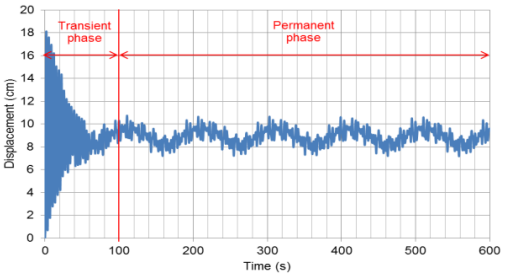
$$R_{z_{95\%}} = 1{,}65\ \sigma + m \tag{7}$$



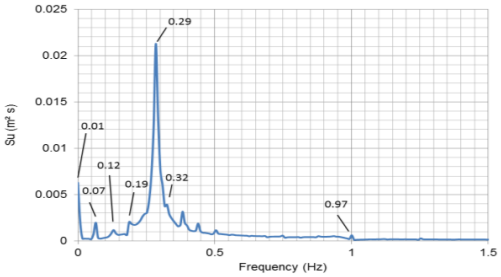
e) Displacements (4th serie of loading). Model I: V bracing system.



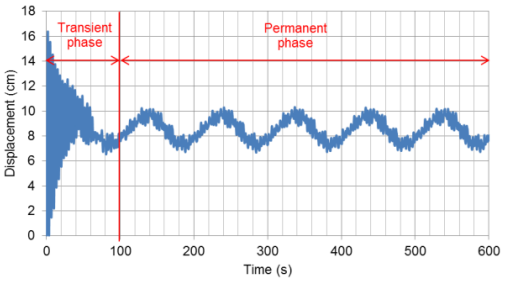
f) Spectral density (4th serie of loading). Model I: V bracing system.



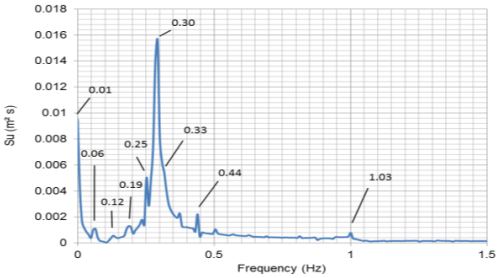
c) Displacements (2nd serie of loading). Model II: Λ bracing system.



d) Spectral density (2nd serie of loading). Model II: Λ bracing system.



a) Displacements (1st serie of loading). Model III: XX bracing system.



b) Spectral density (1st serie of loading). Model III: XX bracing system.

Figure 7: Displacements in time and frequency domains.

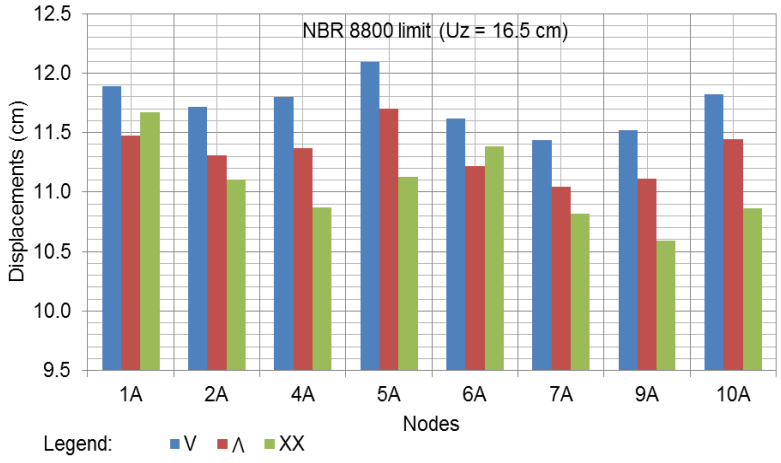


Figure 8: Mean maximum horizontal translational displacements of the investigated structural models.

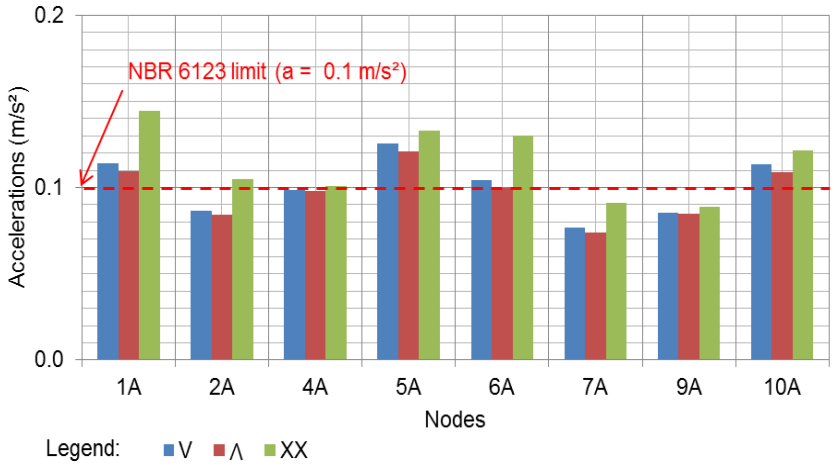


Figure 9: Mean maximum peak accelerations of the investigated structural models.

Based on the results presented in Figures 7 to 9, it can be observed that the maximum horizontal displacement and accelerations values were equal to 12.10 cm (H = 66.0 m)/0.114 m/s² (H = 62.7 m) [Model I: V bracing system]; 11.70 cm (H = 66.0 m)/0.109 m/s² (H = 62.7m) [Model II: Λ bracing system] and 11.67 cm (H = 66.0 m)/0.130 m/s² (H = 62.7 m) [Model III: XX bracing system], respectively. It must be emphasized that the maximum displacements for the three types of bracing systems are according with the limits recommended by NBR 8800 (U_{zlim} = 16.5 cm) [15]. On the other hand, it can be verified that the maximum accelerations surpassed the recommended limit suggested by NBR 8800 (a_{zlim} = 0.10 m/s²) [15].

According to Bachmann [9], the tolerance levels associated to the effects of vibration in buildings when subjected to wind loads are presented in Table 3. This way, considering the maximum accelerations values and the Bachmann's criteria, it can be concluded that the investigated building presents a "perceptible condition" when the human comfort is considered.

Perception	Limit accelerations
Imperceptible	a < 0,005 g
Perceptible	0,005 g < a < 0,015 g
Uncomfortable	0,015 g < a < 0,05 g
Very uncomfortable	0,05 g < a < 0,15 g
Intolerable	a > 0,15 g

Table 3: Tolerance levels related to the effects of vibration in buildings when subjected to wind loads.

6 CONCLUSIONS

- The investigated building presented very low natural frequencies, with the fundamental frequency value around 0.30 Hz. This fact becomes very relevant due to the slenderness of the structure, which may be subjected to excessive vibrations.
- The maximum horizontal translational displacements values are according with the limits recommended by NBR 8800 (U_{zlim} = 16.5 cm) [15]. However, the maximum accelerations violate the human comfort criteria (a_{zlim} = 0.10 m/s²) [15].
- Based on Bachmann's criteria [9], it can be concluded that the building presents a perception level classified as "perceptible", when the human comfort is analysed.

REFERENCES

[1] J. Blessmann, Accidents caused by wind (In Portuguese). UFRGS Ed., Porto Alegre/RS, Brazil, 2001.

[2] R. R. Barboza. Modelling the dynamic behaviour of steel-concrete composite buildings subjected to the wind action. MSc Dissertation (In Portuguese). Civil Engineering Post-graduate Programme, PGECIV. State University of Rio de Janeiro, UERJ, Rio de Janeiro/RJ, Brazil, 2012.

[3] K. S. Moon. Tall building motion control using double skin façades. *Journal of architectural engineering*, **15**, 84-90, 2009.

[4] Q. S. Li, L. H. Zhi, A. Y. Tuan, C. S. Kao, S. C. Su and C. F. Wu. Dynamic behaviour of Taipei 101 Tower: field measurement and numerical analysis. *Journal of Structural Engineering*, **137**, 143-155, 2011.

[5] V. C. Morais. Dynamic analysis of (steel-concrete) composite buildings submitted to the non-deterministic wind action. MSc Dissertation (In Portuguese). Civil Engineering Post-graduate Programme, PGECIV. State University of Rio de Janeiro, UERJ, Rio de Janeiro/RJ, Brazil, 2014.

[6] G. S. Filho. Study of the dynamic behaviour of mixed buildings (steel-concrete) subjected to the non-deterministic wind action. MSc Dissertation (In Portuguese). Civil Engineering Post-graduate Programme, PGECIV. State University of Rio de Janeiro, UERJ, Rio de Janeiro/RJ, Brazil, 2012.

[7] ANSYS Swanson Analysis Systems Inc. Theory Reference (version 12.1), 2009.

[8] NBR 6123: Wind forces in buildings (In Portuguese). Associação Brasileira de Normas Técnicas (ABNT), Rio de Janeiro/RJ, Brazil, 1988.

[9] H. Bachmann. Vibration problems in structures: practical guidelines. Birkhäuser. Berlim, 1995.

[10] S. H. Obata. Synthetic wind and Monte Carlo simulation: a way of considering the random feature and unstable wind loading on structures (In Portuguese). *Exacta*, **7**, 77–85, 2009.

[11] M. A. Smith and L. Caracoglia. A Monte Carlo based method for the dynamic ‘‘fragility analysis’’ of tall buildings under turbulent wind loading. *Engineering Structures*, Boston, **33**, 410-420, 2011.

[12] M. Franco. Direct along-wind dynamics analysis of tall structures. Technical Bulletin of the Polytechnic School (In Portuguese), University of São Paulo, USP, São Paulo/SP, Brazil, 1993.

[13] S. X. Chen. A more precise computation of along wind dynamic response analysis for tall buildings built in urban areas. *Engineering*, **2**, 290-298, 2010.

[14] M. Shinozuka and C. M. Jam. Digital simulation of random process and its applications. *Journal of Sound and Vibration*, **25**, 111-118, 1972.

[15] NBR 8800: Design and construction of steel structures and steel-concrete composite buildings (In Portuguese). Associação Brasileira de Normas Técnicas (ABNT), Rio de Janeiro/RJ, Brazil, 2008.

International Conference on Engineering Vibration
Ljubljana, Slovenia, 7-10 September 2015

HUMAN COMFORT ANALYSIS OF CONCRETE PEDESTRIAN FOOTBRIDGES USING BIODYNAMIC MODELS

Gilvan L. Debona[1], **José Guilherme S. da Silva**[2]

[1]Civil Engineering Post-graduate Programme, PGECIV
State University of Rio de Janeiro, UERJ
gilvanld@yahoo.com.br

[2]Structural Engineering Department, ESTR
Civil Engineering Post-graduate Programme, PGECIV
State University of Rio de Janeiro, UERJ
jgss@uerj.br

Keywords: Footbridges, Structural Dynamics, Dynamic Analysis, Biodynamic Models, Human Comfort, Excessive Vibrations.

Abstract. *Recent publications related to the dynamic behaviour of pedestrian footbridges have been based on a modelling of the pedestrian-structure interaction using biodynamic models. Therefore, this investigation aims to contribute to this scenario by developing a more realistic modelling of the pedestrian-footbridge system taking into account the dynamic characteristics of the pedestrians (mass, stiffness and damping), when crossing the footbridge. This way, the investigated structural model is based on an existing internal concrete footbridge spanning 24.4 m, constituted by concrete beams and slabs, and being currently used for pedestrian crossing. Initially, experimental tests were carried out, in order to determine the dynamic properties of the structural system: natural frequencies, vibration modes and modal damping ratio. The computational model adopted the usual mesh refinement techniques present in finite element method simulations, based on the use of ANSYS program. The finite element model was developed and calibrated with the obtained experimental results. Finally, the pedestrian footbridge human comfort and its associated vibration serviceability limit states were investigated and the peak accelerations values were obtained, based on an extensive parametric study, with the use of biodynamic dynamic loading models.*

1 INTRODUCTION

This research work aims the development of an analysis methodology to investigate the dynamic behaviour of footbridges when subjected to walking of pedestrians. In this investigation, in order to simulate the pedestrian's walking on the structural system biodynamic models were used and simulated by "mass-spring-damper" systems. This way, the effect of the dynamics of the pedestrians while crossing footbridges in crowd situations is analysed and the pedestrian-footbridge dynamic interaction was investigated.

It is noteworthy that recent research papers [1]-[5] using experimental measurements and numerical analysis, related to the human dynamic force associated with the pedestrians walking, confirm the ability of the people to act like a shock absorber for the structural system dynamic response [2]. On the other hand, an increase of the structural system damping rate when a pedestrian crowd is crossing the footbridge in continuous flow was also reported [3].

Another investigated relevant aspect is related to the differences in the pedestrian footbridges natural frequencies values when occupied by a crowd of people [4]. Other research work [5] have demonstrated that the effects of the decisions assigned to each pedestrian, to change its direction (trajectory), frequency, speed and step distance, to overcome other pedestrians or even to change their attitude when walking on the structure should be included in the dynamic analysis in addition to the pedestrian-structure dynamic interaction.

Based on this scenario, this paper aims to investigate the dynamic behaviour of an existing pedestrian footbridge located in the campus of the State University of Rio de Janeiro (UERJ), Rio de Janeiro/RJ, Brazil. The structural system is based on an internal reinforced concrete footbridge spanning 24.4 m, constituted by concrete beams and slabs and being currently used for pedestrian crossing.

A computational model, based on the finite element method (FEM), was developed using the ANSYS program [6]. The numerical model was calibrated with experimental results. This model enabled a complete dynamic evaluation of the investigated footbridge especially in terms of human comfort and its associated vibration serviceability limit states.

Based on the developed analysis methodology, the dynamic response of the footbridge (natural frequencies and peak accelerations) was evaluated and compared with the limit values proposed by international standards and design recommendations [7]-[9], aiming a more rational and realistic assessment of the structure performance related to human comfort.

2 HUMAN WALKING MODELLING

Human loads comprise a large portion of the acting live loads in structures, especially in footbridges. In general, the human live loads are classified into two broad categories: in situ and moving. Periodic jumping due to music, sudden standing of a crowd, and random in-place movements are examples of in situ activities. Walking, marching, and running are examples of moving activities that might specifically act in footbridges. As the main purpose of these structures is the pedestrian's crossing, they must be safe and do not cause discomfort to users [7]-[9]. In addition, human activities produce dynamic forces and their associated vibration levels should not disturb or alarm their users.

In order to model realistically the pedestrian-structure dynamic interaction, representative biodynamic models of people will be considered in this investigation. These models simulate conveniently the dynamic characteristics of the pedestrians (mass, stiffness and damping) and have been used as an efficient alternative to better evaluate the human comfort instead the traditional "hard force" model widely used for dynamic analysis of footbridges.

The biodynamic models can be described by a one degree of freedom (SDOF) or even multi degrees of freedom (MDOF). In the technical literature there are several proposals to

represent the pedestrians in the vertical direction, like representing a person sitting or standing [10], for people jumping [11] or people running [12]. For people walking there are some recent proposals [13]-[14], with different aspects related to the number of degrees of freedom and the mass, damping and stiffness parameters used to simulate the pedestrians.

In this research work, the developed analysis methodology has considered that the pedestrians are modelled as "mass-spring-damper" systems, with a single degree of freedom (SDOF) [1]. These systems corresponding to the biodynamic models are coupled to the finite element model of the structural system (footbridge), in order to reproduce the pedestrian-structure dynamic interaction.

On the other hand, a dynamic force, $F_p(t)$, simulates the pedestrian crossing on the footbridge with a constant velocity v(t), as presented in Figure 1. The walking loading model implemented in this investigation can be represented based on the use of the biodynamic models in addition with a dynamic force produced by a combination of four harmonic forces with frequencies that are multiples or harmonics of the step frequency, fs, for human walking.

The loading model has considered a space and temporal variation of the dynamic action on the structure and the time-dependent repeated force can be represented by the Equation (1). The harmonic forces appear due to interaction between the increasing load represented by a foot and the simultaneous unloading of the other foot. The mathematical representation of the vertical dynamic action induced by human walking is given by Equation (1).

$$F(t) = P\,[\,\sum \alpha_i \cos\left(2\pi i\, f_s\, t + \phi_i\right)\,] \tag{1}$$

Where:

- F(t) : dynamic loading function;
- P : person's weight;
- α_i : dynamic coefficient for the harmonic force (dynamic load factor);
- i : multiple harmonic (1, 2, 3, etc.);
- f_s : step frequency;
- ϕ_i : phase angle for the harmonic i;
- t : time.

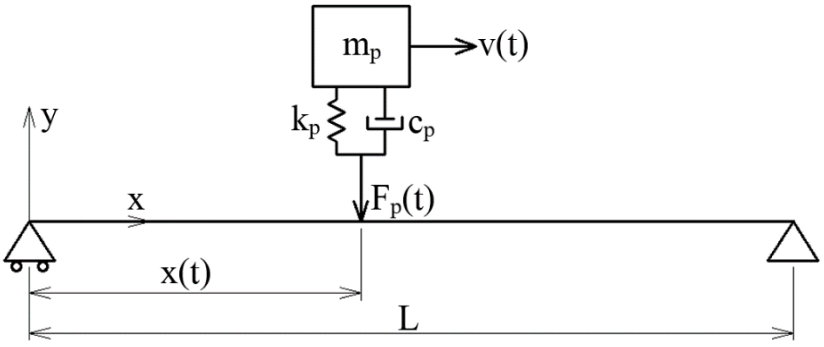


Figure 1: Representation of the human walking on the footbridge.

However, it is also necessary to incorporate several other parameters in the walking representation, like step frequency, step distance and velocity. These variables are related to the excitation frequency values, dynamic coefficients and phase angles. Table 1 presents a description of these parameters adopted in the mathematical representation of the dynamic loading model used in the present investigation.

Harmonic i	Dynamic Coefficient (α_i)	Phase Angle (ϕ_i)
1	0.50	0
2	0.20	$\pi/2$
3	0.10	$\pi/2$
4	0.05	$\pi/2$

Table 1: Dynamic coefficients and phase angles [9].

The parameters of the biodynamic models were considered based on the experimental results as described by Silva [14]. In this investigation, the values equal to 841.56 Ns/m and 15085.56 N/m were considered for the damping (c_p) and stiffness (k_p), respectively. The values associated to the mass (m_p) and the step frequency (f_p) are presented in Table 2.

Parameters	Average Value	Standard Deviation
Mass [m_p (kg)]	68.58	12.42
Step Frequency [f_s (Hz)]	1.88	0.13

Table 2: Parameters of the biodynamic models [14].

3 INVESTIGATED PEDESTRIAN FOOTBRIDGE

The investigated structural model is related to an existing pedestrian footbridge located in the campus of the State University of Rio de Janeiro (UERJ), Rio de Janeiro/RJ, Brazil. The structural system is based on a simply supported internal reinforced concrete footbridge spanning 24.4 m (L = 24.4 m), constituted by concrete beams and slabs, and being currently used for people crossing, as illustrated in Figures 2 to 3. The concrete presents a 14 MPa specified compression strength and a 1.78 x 10^{10} N/m^2 Young's Modulus.



Figure 2: Investigated concrete footbridge: lateral view.



a) Support details.



b) Internal view.

Figure 3: Details of the investigated concrete pedestrian footbridge.

4 EXPERIMENTAL INVESTIGATION

The experimental modal analysis of the investigated footbridge was conducted by dynamic monitoring through accelerometers installed on the structure. The free vibration tests were carried out, in order to obtain the structural model natural frequencies, vibration modes and also the structural damping ratio, as presented in Figures 4 to 6.

The experimental results were obtained using accelerometers (Transducers Capacitive Acceleration Uniaxial), as presented in Figure 4. A data acquisition system ADS-2002 manufactured by LYNX Electronic Technology was used in this investigation, see Figure 5. The experimental responses were measured and recorded in the ADS-2002 system. This system is based on signal conditioners that turn the sign of the variation in electrical engineering value (specific deformation, acceleration and force), controlled by a computer, see Figure 5.



Figure 4: Accelerometers.



Figure 5: ADS-2002 system and computer.

The experimental results of the footbridge free vibration analysis are presented in Figure 6. Three accelerometers were located on the concrete slab of the investigated pedestrian footbridge at 0.25L (AC1), 0.50L (AC2) and 0.75L (AC3) of the span length (L = 24.4m). The free vibration tests consisted to excite the footbridge with a hammer at the middle span. The pedestrians were not allowed to cross the footbridge during these tests.

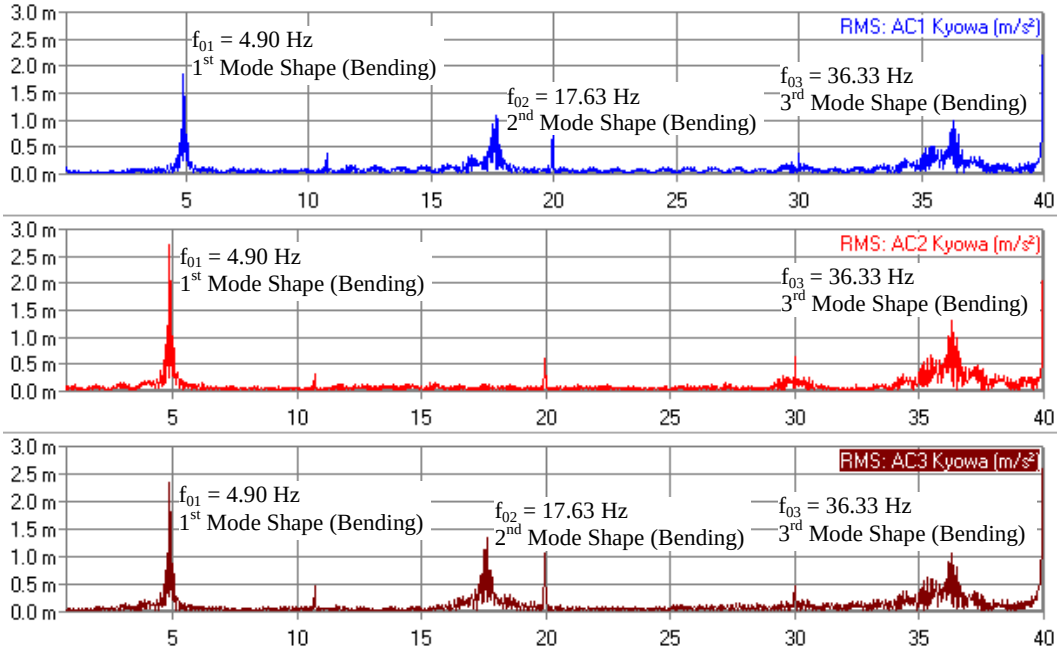


Figure 6: Spectrum of the footbridge natural frequencies.

The results in frequency domain were obtained by a Fast Fourier Transform (FFT) of the time domain signal. The visualization of the mode shapes can be done observing those obtained by the numerical model (see Figure 10). The damping ratios were obtained using the logarithmic decrement method of the signals after filtering them at a short range near the experimental frequencies. The modal damping ratios are equal to 1.8% (1st mode shape), 1.15% (2nd mode shape) and 1.02% (3rd mode shape).

5 NUMERICAL MODELLING OF THE PEDESTRIAN-FOOTBRIDGE SYSTEM

The developed finite element model adopted the usual mesh refinement techniques present in finite element method simulations, based on the ANSYS program [6], as illustrated in Figure 7. In this computational model, all the reinforced concrete sections were represented by shell finite elements (SHELL63). This finite element has both bending and membrane capabilities. The element has six degrees of freedom at each node: translations in the nodal x, y, and z directions and also rotations about the nodal x, y, and z axes.

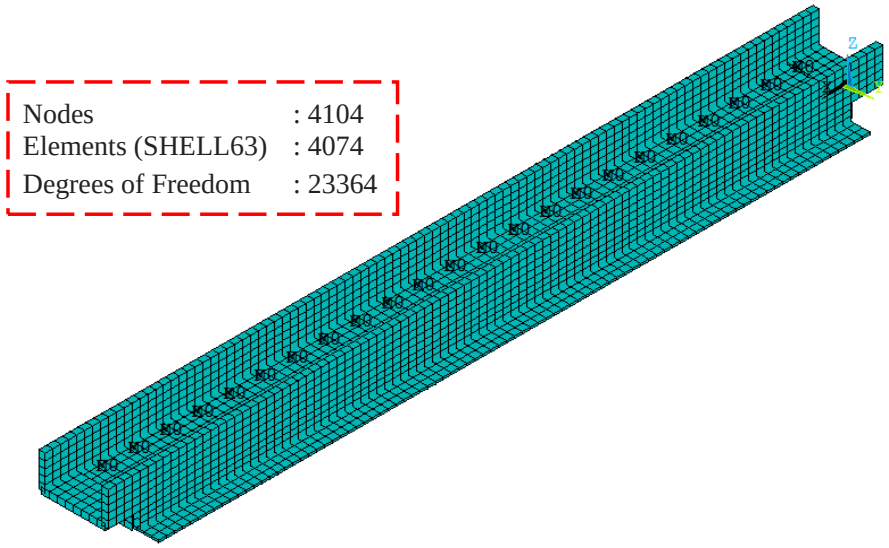


Figure 7: Three dimensional view.

For the simulation of the pedestrians walking on the footbridge, in crowd loads situations, based on the use of the biodynamic models, there are two possibilities to be followed in the modelling process: in the first case, the biodynamic models are moved along the structure together with the dynamic load and in the second modelling strategy the biodynamic models remain in fixed positions at the nodes of the finite element model and only a dynamic force moves throughout the structure.

The second modelling strategy simplifies the processing of the numerical data, which in situations of crowds on the footbridge have presented good results [14]. Thus, the biodynamic models representative of the pedestrians were coupled to the nodes of the investigated footbridge finite element model, see Figure 7, and remain fixed along the dynamic analysis, when the simulation of pedestrians walking is considered, according to Figures 8 and 9. The biodynamic models were uniformly distributed (16 to 50 people) on the structure span, based on the use of single degree of freedom systems (SDOF), as shown in Figures 8 and 9.

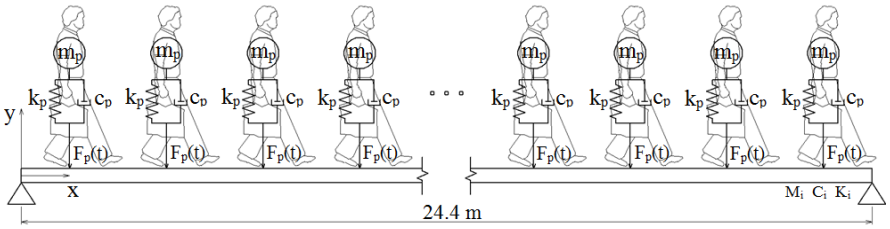


Figure 8: Modelling of pedestrian-footbridge dynamic interaction.

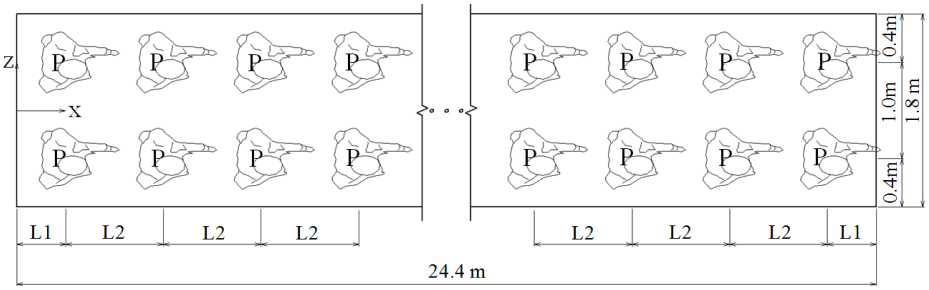


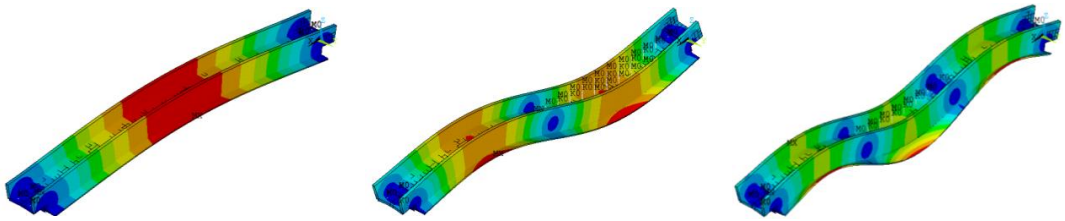
Figure 9: Top view of pedestrian-structure system.

6 PEDESTRIAN-FOOTBRIDGE SYSTEM VIBRATION ANALYSIS

The footbridge natural frequencies, vibration modes and peak accelerations values were determined with the aid of the numerical simulations, based on the finite element method using the ANSYS program [6] and also compared with the experimental results. The maximum accelerations were obtained based on the use of the biodynamic models (pedestrian-footbridge system) and the traditional "hard force" model.

Modal Analysis	Footbridge Natural Frequencies (Hz)		
	f_{01}	f_{02}	f_{03}
Experimental Modal Analysis	4.900	17.630	36.330
Numerical Analysis	4.898	15.923	32.154
Differences (%)	0.04%	10.72%	12.99%

Table 3: Investigated footbridge natural frequencies.



1st Vibration mode (Bending) 2st Vibration mode (Bending) 3st Vibration mode (Bending)

Figure 10: Footbridge natural frequency.

Comparing the footbridge natural frequencies values it is clear from Table 3 results that there is very good agreement between the finite element natural frequencies values and the frequencies obtained based on the experimental modal analysis. Such fact validates the developed numeric modelling, as well as the results and conclusions obtained throughout this work.

The vibration analysis follows with the evaluation of the footbridge performance in terms of vibration serviceability due to dynamic forces induced by people walking. The first step of this investigation concerned the determination of the footbridge peak accelerations, based on a linear time-domain dynamic analysis. The maximum accelerations were obtained adopting an integration time step equal to 10^{-3}s ($\Delta t = 10^{-3}$s). The structural damping ratio considered in the numerical analysis was equal to 0.01 (ξ = 1.18%). The peak accelerations values were obtained based on a step frequency described in item 2, see Table 2. The accelerations were compared to the limits recommended by design standards and recommendations [7]-[9].

Two modelling strategies were investigated in this study: dynamic analysis based on the use of biodynamic models and the traditional analysis related to the simulation of the human walk using "hard force" models. Based on the width of the structural system, the pedestrians walk on two paths and the central section of the footbridge was analysed (Node A), see Figure 11. Figure 12 presents the investigated footbridge dynamic response considering 50 pedestrians walking on the structure. It must be emphasized that the blue and red lines illustrated in Figure 12 are related to the biodynamic and "hard force" models dynamic response, respectively.

In this analysis (forced vibration), the uncertainty related to the pedestrian mass [m_p (kg)] and step frequency [f_s (Hz)] was considered, see Table 2. These uncertainties in pedestrian mass and inter-subject step frequency variability were modelled as random variables and included in the Monte Carlo simulation. In sequence, Table 4 shows the investigated footbridge steady-state dynamic response (peak accelerations) related to the central node of the structural model, see Figure 11.

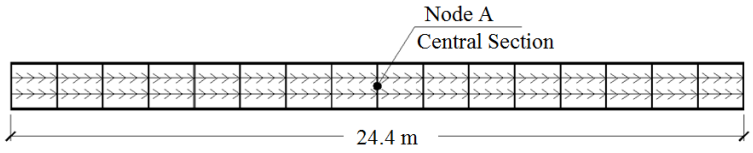


Figure 11: Pedestrians walking on the footbridge.

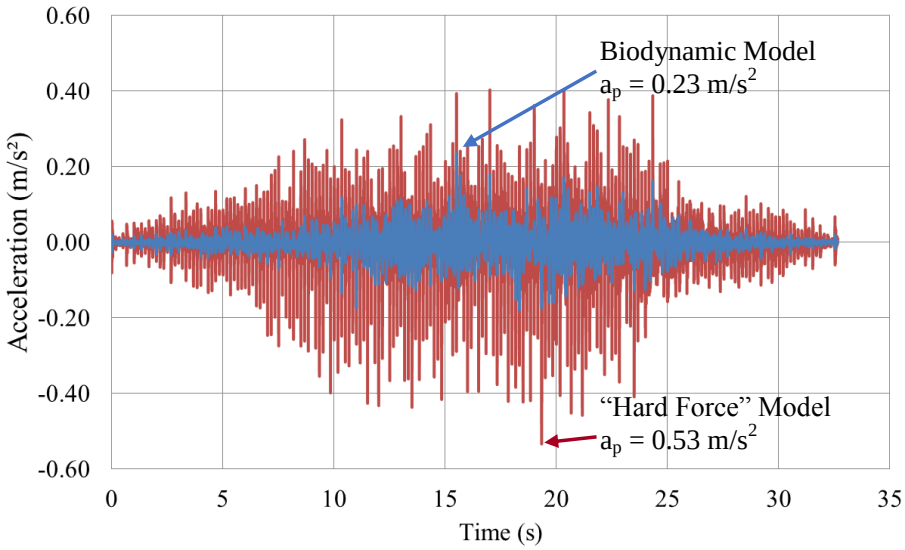


Figure 12: Model with 50 pedestrians walking on the structure by varying the m_p and f_s variables.

Number of Pedestrians	Peak Acceleration a_p (m/s^2)		Human Comfort Level [8]	
	"Hard Force"	Biodynamic	"Hard Force"	Biodynamic
16	0.379	0.139	Maximum	Maximum
20	0.453	0.144	Maximum	Maximum
24	0.634	0.147	Mean	Maximum
32	0.487	0.181	Maximum	Maximum
38	0.597	0.153	Mean	Maximum
50	0.531	0.234	Mean	Maximum

Table 4: Investigated footbridge peak accelerations (Node A).

Based on the results presented in Figure 12 and Table 4, it can be clearly observed a very significant reduction of the maximum values of the accelerations, when the pedestrian-structure interaction is introduced in the footbridge dynamic analysis, compared to the traditional methodology ("hard force model").

The reduction on the peak accelerations values reach up to 76%, see Table 4, when the biodynamic models (pedestrian-structure interaction) are considered in the dynamic analysis. The footbridge human comfort criterion [8] was also modified in situations where the "hard force model" was considered in the dynamic analysis.

It can be concluded that the "mass-spring-damping" systems, used to simulate the pedestrians, coupled on the footbridge finite element model, see Figure 8, works like a vibration absorber system reducing the structural system dynamic response.

Based on the results achieved through this research work, it is clear to the authors that the analysis methodology based on use of the biodynamic models (pedestrian-footbridge interaction), provides peak acceleration values closer to the experimental measurements in real structural systems, when compared to traditional models using "hard force".

The results here presented indicate the relevance of considering the pedestrians dynamic actions on footbridges and also illustrates the impact of more detailed studies about the modelling of the pedestrian walking using more realistic dynamic loading models.

7 CONCLUSION

- This work covers the effect of the pedestrian-structure dynamic interaction on the vibration serviceability of footbridges and tries to give an overview about the assessment of its dynamic behaviour, aiming to help structural engineers to deal with this kind of problem.
- The present investigation was based on the development of a more realistic analysis methodology, in order to consider the pedestrian-footbridge dynamic interaction using biodynamic models that take into consideration the dynamic characteristics of the people (mass, stiffness and damping).
- Based on the results it was verified a very significant reduction of the peak accelerations values of the accelerations, when the pedestrian-structure interaction was introduced in the footbridge dynamic analysis, compared to the traditional methodology ("hard force model"). This reduction on the accelerations values reach up to 76%. This way, it was also concluded that the "mass-spring-damping" systems used to model the pedestrians works like a vibration absorber system reducing the structural system dynamic response.
- Finally, the results of this research suggest the urgency and relevance with respect to the development of more detailed studies associated to the modelling of the pedestrian dynamics to better evaluate the structural performance and human comfort of footbridges.

REFERENCES

[1] G.L. Debona, *"Biodynamic Walking Model for Vibration Serviceability of Steel-Concrete Composite Footbridges Subjected to Pedestrian-Induced Loads"*. PhD Thesis (In Portuguese). Civil Engineering Post-graduate Programme, PGECIV. State University of Rio de Janeiro, UERJ. Rio de Janeiro/RJ, Brazil, 2014 (In development).

[2] J.M.W. Brownjohn and T.N. Fu, "Vibration excitation and control of a pedestrian walkway by individuals and crowds". *Shock and Vibration*, 12, 333-347, 2005.

[3] H. Fernandes, *"Comportamento dinâmico de passarelas modeladas como vigas sujeitas a vibrações na direção vertical induzidas por pedestres"*. PhD Thesis. PPGEM - Graduate Program in Mechanical Engineering, 2007.

[4] C. Butz, M. Feldmann, C. Heinemeyer, G. Sedlacek, B. Chabrolin, A. Lemaire, M. Lukic, P.O. Martin, E. Caetano, A. Cunha, A. Goldack, A. Keil, M. Schlaich, *"Advanced load models for synchronous pedestrian excitation and optimised design guidelines for steel footbridges"*. European Comission, pp. 167, 2008.

[5] F. Venuti, V. Racic, A. Corbetta, "Pedestrian-structure interaction in the vertical direction: coupled oscillator-force model for vibration serviceability assessment". *Proceedings of the 9th International Conference on Structural Dynamics, EURODYN 2014*, 915-920, 2014.

[6] ANSYS, *"Swanson Analysis Systems"*, Inc., P.O. Box 65, Johnson Road, Houston, PA, 15342-0065, Version 10.0, Basic analysis procedures, Second edition, 2009.

[7] H. Bachmann, W.J. Ammann, F. Deischl, J. Eisenmann, J. Floegl, G.H. Hirsch et al., *"Vibration Problems in Structures - Practical Guidelines*"**,** Basel (Switzerland): Institut für Baustatik und Konstruktion, Birkhäuser; 1995.

[8] Sétra, *"Guide méthodologique passerelles piétonnes (Technical guide footbridges: Assement of vibrational behaviour of footbridges under pedestrian loading)"*, 2006.

[9] T.M. Murray, D.E. Allen, E.E. Ungar, *"Floor Vibrations due to Human Activity"*, Steel Design Guide Series, American Institute of Steel Construction, AISC, Chicago, USA, 2003.

[10] ISO 5982, International Organization for Standardization. *"Bases for Design of Structures - Vibration and Shock-Mechanical driving point impedance of the human body"*, 1981.

[11] S. Nhleko, A. Zingoni, P. Moyo, "A variable mass model for describing load impulses due to periodic jumping". *Engineering Structures*, 30, 1760-1769, 2008.

[12] B.M. Nigg, W. Liu, "The effect of muscle stiffness and damping on simulated impact force peaks during running". *Journal of Biomechanics*, 32, pp. 849-856, 1999.

[13] C.C. Caprani, J. Keogh, P. Archbold, P. Fanning, "Characteristic vertical response of a footbridge due to crowd loading", *Proceedings of the 8th International Conference on Structural Dynamics, EURODYN 2011*, Leuven, Belgium, 2011.

[14] F.T. Silva, *"Vibração de passarelas de pedestres na direção vertical considerando modelos biodinâmicos de pessoas caminhando"* (In Portuguese), PhD Thesis, Federal University of Paraiba, Post-Graduate Program in Mechanical Engineering, PPGEM/UFPB, João Pessoa, Paraíba, Brasil, 2011.

International Conference on Engineering Vibration
Ljubljana, Slovenia, 7-10 September 2015

VIBRATION CONTROL AND HUMAN COMFORT EVALUATION OF STEEL-CONCRETE COMPOSITE FLOORS UNDER AEROBICS

Cassio M. R. Gaspar*[1], José Guilherme S. da Silva[2]

[1]Civil Engineering Post-graduate Programme, PGECIV
State University of Rio de Janeiro, UERJ
cgaspac@yahoo.com.br

[2]Structural Engineering Department, ESTR
Civil Engineering Post-graduate Programme, PGECIV
State University of Rio de Janeiro, UERJ
jgss@uerj.br

Keywords: Steel-Concrete Composite Floors, Structural Dynamics, Human Comfort, Excessive Vibrations, Vibration Control.

Abstract. *Vibration problems issues concerning the human comfort of individuals practising aerobic activities has been reported by several researches in the last years. Indeed, there are many causes in which the excessive vibration levels are associated. These causes can be attributed to the new trend concerning the structural design of composite floors as well as the way in which the human activity is carried out on the structural systems. On the other hand, it has been observed in design practice low floor structural damping ratios, which is related to the type of construction, materials, presence of non-structural elements, age and quality of construction. Besides, it is noticeable the design of slender low weight structural floors systems due to the technological advance in the materials field. Consequently, the floors natural frequencies tend to decrease. Therefore, such trend is completely unfavourable in relation to the vibration issues because the harmonics of the human rhythmic may cause resonance with composite floors and then leading the occupants to a very discomforting condition. Thus, considering these aspects, this work investigates a steel-concrete composite floor spanning 40m by 40m, with a total area of 1600m². This system represents a typical interior floor bay of a commercial building used for gym. In this research, an extensive parametric study was developed aiming to obtain the peak accelerations, RMS and VDV values, based on five different mathematical formulations used for modelling human rhythmic actions (aerobics). The dynamic response of the investigated structural model have indicated that the steel-concrete composite floor presented high vibration levels that compromise the human comfort, according to the limiting values proposed by several authors and design standards. On the other hand, a vibration control system based on the use of TMDs (tuned mass dampers) was proposed and installed under the floor in order to mitigate excessive accelerations. It has been found that such vibration control system has reduced significantly the human discomfort.*

1 INTRODUCTION

Structural engineers are constantly faced with an economical design versus the structural safety and serviceability in a general design process. In fact, considering the design of steel-concrete composite floors under human rhythmic activities, one may use some force functions in order to represent the human activity acting on the floor. Namely, some design standards, practical design guides and authors as ISO10137 [1], CEB [2, 3], SCI [4], AISC [5] and FAISCA [6] might be considered.

On the other hand, taking into account that the mathematical representation of human rhythmic activities consists on a very complex problem, most of these force functions does not agree to each other. Consequently, the choice of one or other force function may lead the floor design to a more or less conservative assessment regarding the human comfort serviceability. Besides, it is important to highlight that beyond the design stage evaluation of composite floors, the choice of one of these force functions is likewise significant and plays an important role in relation to already built floors assessment.

In parallel, it must be emphasized that several authors have been related that the current composite floors design might be susceptible to the resonance phenomenon, causing undesirable vibrations in the frequency range that is the most noticeable to humans, i.e. 4 to 8Hz [3-5]. Such condition is in part due to the technological advance in the materials field which has allowed the use of more resistant and low weight materials that result in slender and more flexible structural floor systems. In addition, it has been observed in design practice low floor structural damping ratios, which is related to the type of construction, materials, presence of non-structural elements, age and quality of construction [1]. Therefore, all these combinations make the steel-concrete composite floors very susceptible to annoying vibrations induced by humans. In this sense, this work aims to evaluate the human comfort of a typical composite floor gym subjected to aerobics and afterwards to control the excessive floor vibrations by the use of multiple tuned mass dampers.

2 RHYTHMIC ACTIVITIES REPRESENTATION

The representative mathematical function of the rhythmic dynamic loading can be described by five different experimental approaches such as proposed by ISO10137 [1], CEB [2, 3], SCI [4], AISC [5] and FAISCA [6]. The Figures 1 and 2 show an example of the dynamic force in the time and frequency domain considering a frequency step of 2.57Hz. It is also assumed that a single person's weight is 800N.

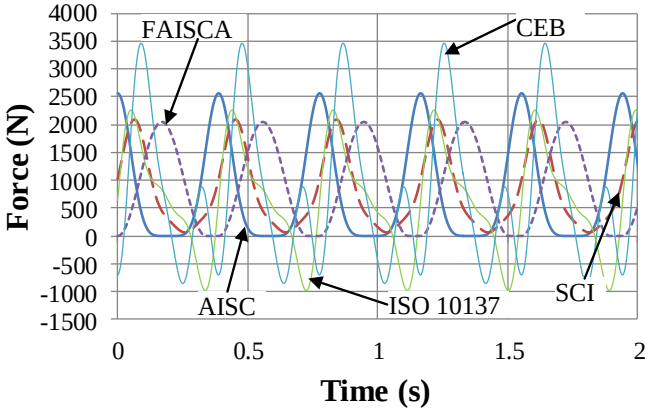
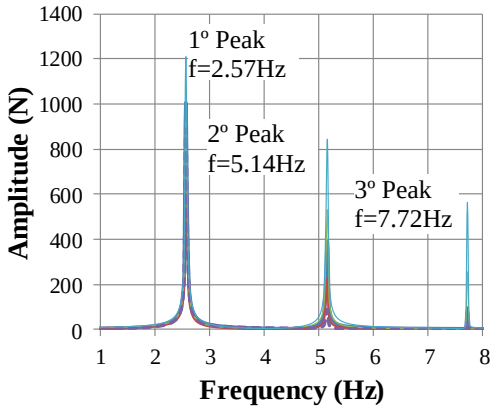
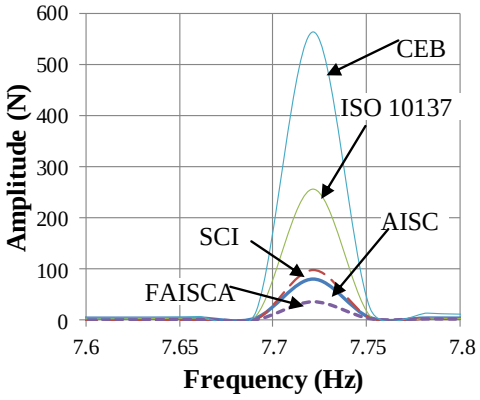


Figure 1: Dynamic loading functions in time domain.



a) The first three harmonics of the force functions.



b) Third harmonic of the force functions.

Figure 2: Dynamic loading functions in frequency domain.

Dynamic loading model	Force frequency range corresponding to the third harmonic of aerobics activities (Hz)
FAISCA [6]	5.66 - 8.57
SCI [4]	4.5 - 8.4
AISC [5]	6.0 - 8.25
CEB [2, 3]	5.4 - 10.2
ISO 10137 [1]	4.5 - 10.5

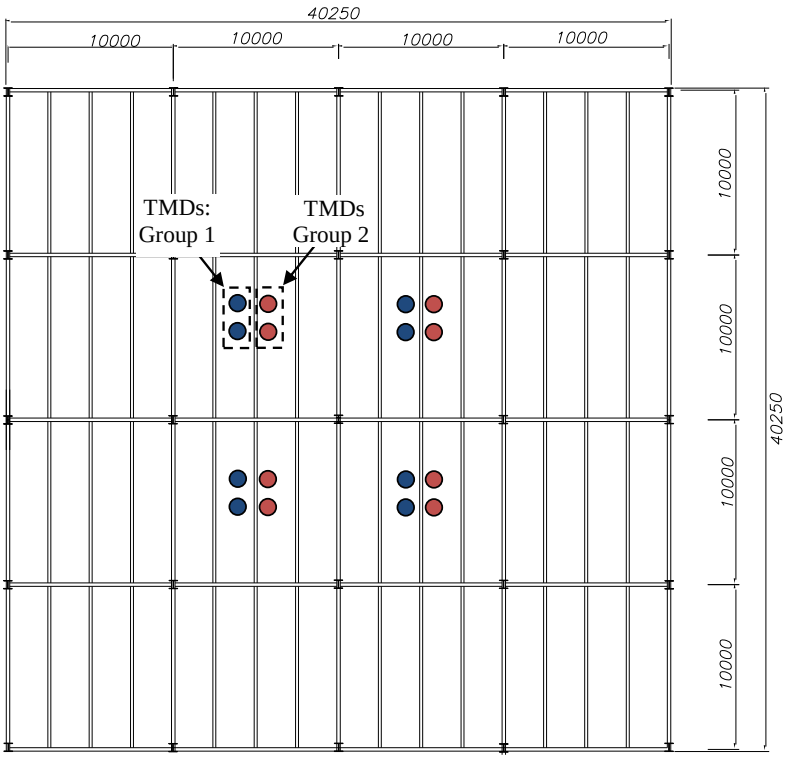
Table 1: Force frequency range corresponding to the third harmonic of aerobic activities.

From Figure 2 one can see that the third Fourier coefficients related to the CEB and ISO 10137 functions are more energetics than the SCI, AISC and FAISCA functions ones. Therefore, this fact will be investigated in this work. Table 1 presents the frequency range related to the third harmonic of aerobics activities. It can be noted that the CEB and ISO 10137 are more conservative in relation to the upper limit frequency range (see Table 1).

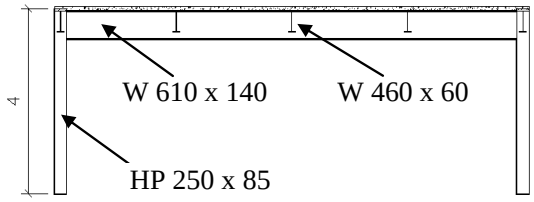
3 FINITE ELEMENT MODELING

The finite element model was based on a real steel-concrete composite floor spanning 40m by 40m with a total area of 1600m² composed by 16 bays of 10x10m. The structural system is made from composite beams and a 100mm thick concrete slab, according to Figure 3. The columns height is equal to 4m. The steel sections used were welded wide flanges (WWF) made from a 345MPa yield stress steel grade. A $205x10^3$MPa Young's modulus was adopted for the steel beams. The concrete slab has a 30MPa specified compression strength and a $26x10^3$ MPa Young's Modulus.

The proposed computational model adopted the usual mesh refinement techniques present in finite element method simulations implemented in the ANSYS program [7], see Figure 4. The floor steel beams were represented by three-dimensional beam elements, where flexural and torsion effects are considered. The composite slab was represented by shell finite elements. Both materials (steel and concrete) have an elastic behaviour.

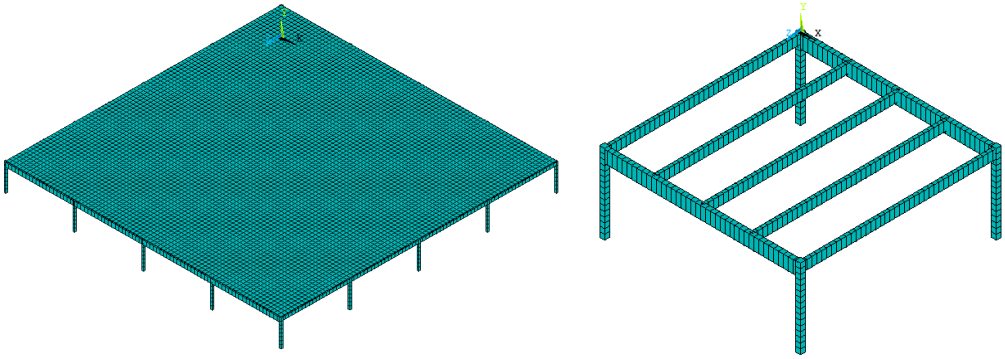


a) Steel-concrete composite floor plan view (dimensions in mm).



b) Typical floor bay cross section (dimensions in m).

Figure 3: Investigated structural model: plan view and typical floor bay cross section.



a) Isometric model view (40x40m). b) Typical isometric floor bay view.

Figure 4: Composite floor (steel-concrete) finite element model.

The complete interaction between the concrete slab and steel beams was considered in the analysis and simulated by spring elements so that the numerical model coupled all the nodes between the beams and slab to prevent the occurrence of any slip. Regarding the behaviour of the structural connections present in the investigated composite floor, the beam-to-beam connections were modelled as flexible joints using spring elements. The beam-to-column connections were considered as rigid joints. The final numerical-computational model was made out of 29874 nodes, 3920 three-dimensional beam elements and 25600 shell elements, resulting in a numerical model with 167069 degrees of freedom.

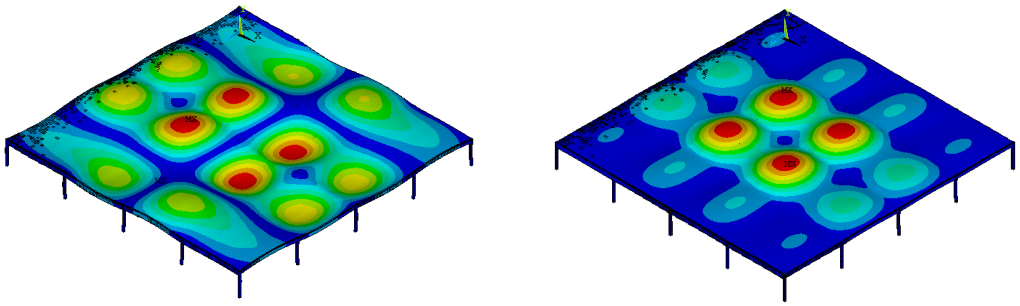
4 STEEL-CONCRETE COMPOSITE FLOOR DYNAMIC ANALYSIS

4.1 Natural Frequencies and Vibration Modes

The modal analysis was carried out and it was verified that the first sixteen natural frequencies of the analysed floor (see Table 2), varying from 6.06Hz to 7.79Hz, are close to the excitation frequency range (aerobics) [4-6]. In this situation, the frequency of the third harmonic of the dynamic loading may match these natural frequencies and therefore lead the composite floor to resonance. Consequently, such situation might result in undesirable vibrations and thus human annoyance. The total structural mass corresponds to 485.3t.

Vibration Modes	Composite Floor Frequencies (Hz)	Modal Mass/Total Structural Mass Ratio (%)	Vibration Modes	Composite Floor Frequencies (Hz)	Modal Mass/Total Structural Mass Ratio (%)
f_{01}	6.06	24.49	f_{11}	7.35	16.17
f_{02}	6.36	18.74	f_{12}	7.44	11.31
f_{03}	6.44	15.01	f_{13}	7.55	11.55
f_{04}	6.65	10.81	f_{14}	7.62	10.04
f_{05}	6.92	13.49	f_{15}	7.72	8.63
f_{06}	7.05	12.37	f_{16}	7.79	11.44
f_{07}	7.11	9.73	f_{17}	8.90	18.79
f_{08}	7.12	10.68	f_{18}	9.30	10.34
f_{09}	7.13	14.58	f_{19}	9.38	19.15
f_{10}	7.27	9.06	f_{20}	9.63	11.16

Table 2: Steel-concrete composite floor natural frequencies and modal masses.



a) 11th Vibration mode (f_{11}=7.35Hz). b) 15th Vibration mode (f_{15}=7.72Hz).

Figure 5: Investigated structural model vibration modes.

Figure 5 presented some vibration modes which might be excited by the dynamic load positioning (see Figure 6). It is must be emphasized that all steel-concrete composite floor vibration modes present a predominant flexural behaviour.

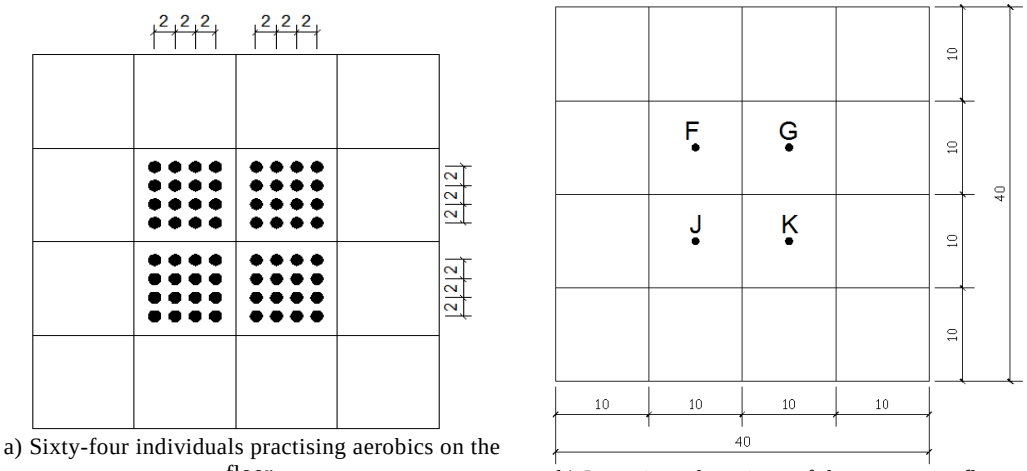
With the objective of avoiding unwanted vibrations the fundamental composite floor frequency should be at least equal to 9.2 Hz (AISC [5]) for aerobics considering the structural system as a light floor or 8.4Hz for rhythmic activities according to SCI [4].

4.2 Human Comfort Assessment

The dynamic transient analysis was performed considering sixty-four individuals practising aerobics (0.25 person/m² [3]) so that the third harmonic of each force function matches the fifteenth vibration mode (f_{15} = 7.72 Hz) aiming to cause a resonant motion state (see Figure 6). It is also assumed that a single person's weight is 800N (0.8kN).

The modal damping ratio of 1% was chosen according to ISO 10137 [1] and lies in the extreme range of 0.5% to 8.0% for fully composite steel beams with shear connectors to concrete slab. The dynamic response of the composite floor was obtained from the central node of each floor bay where the rhythmic activity is taken place, which is represented by the letters F, G, J and K as shown in Figure 6.

Then, the steel-concrete composite floor accelerations herein were evaluated based on peak unweighted accelerations (steady-state response), a_p, RMS weighted accelerations, $a_{w,rms}$, and vibration dose values, VDV. Table 3 shows the unweighted acceleration, RMS weighted accelerations and the VDV acceptance criteria respectively.



a) Sixty-four individuals practising aerobics on the floor.

b) Investigated sections of the composite floor.

Figure 6: Persons' positioning on the floor. Dimensions in (m).

AISC[5]	SCI [4]	Ellis and Littler [8]	Setareh [9]	Person's Reaction
a_p (m/s²)	$a_{w,rms}$ (m/s²)	VDV (m/s$^{1.75}$)	VDV (m/s$^{1.75}$)	
0.5	< 0.35	< 0.66	< 0.50	Reasonable limit: passive persons
	0.35 - 1.27	0.66 - 2.38	0.50 - 3.50	Disturbing
	1.27 - 2.47	2.38 - 4.64	3.50 - 6.90	Unacceptable
	> 2.47	> 4.64	> 6.90	Probably causing panic

Table 3: Human comfort acceptance criteria.

Dynamic loading model	Resonance with the 15th Vibration mode (f_{15}=7.72Hz).			
	Person's Reaction	Acceleration (m/s²)		VDV (m/s$^{1.75}$)
		a_p	$a_{w,rms}$	
FAISCA [6]	Disturbing	1.72	1.04	2.15
SCI [4]	Unacceptable/ Panic	4.83	3.08	6.28
AISC [5]	Unacceptable/ Panic	4.23	2.58	5.25
ISO 10137 [1]	Panic	11.77	6.71	12.09
CEB [2]	Panic	25.36	14.31	25.48

Table 4: Composite floor dynamic response. Nodes F, G, J and K.

From a comparison between Tables 3 and 4, it can be observed that all acceleration values are greater than the human comfort criteria reasonable limits (Table 3) for all cases. Indeed, such condition might be expected once the natural frequencies and vibration modes of the composite floor lie in the third harmonic of the force functions ranges. Therefore, the sixty-four individuals who were practising aerobics might be subjected to extremely annoying vibrations. Figures 7 and 8 present the steel-concrete composite floor dynamic response in time domain and frequency domain.

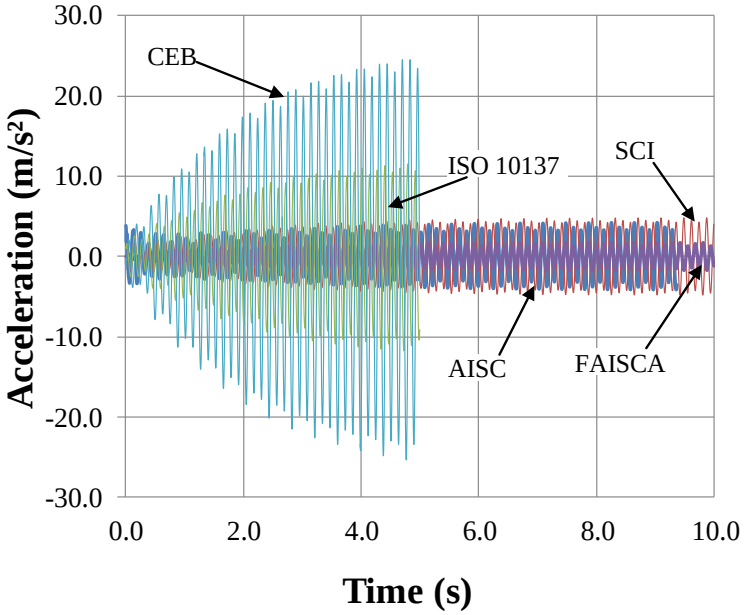


Figure 7: Investigated steel-concrete composite floor time domain response.

With respect to Figure 7, one can note the steady-state acceleration in the time domain from 5s. In relation to Figure 8, it can be seen that the ISO 10137 [1] and CEB [2] force functions presented the third harmonic more energetic than those compared to SCI, AISC and FAISCA [6]. Note that this result could be expected from Figure 2.

In general, the accelerations obtained by the ISO 10137 [1] and CEB [2] functions were very conservative in terms of the Fourier coefficients corresponding to the third harmonic. In fact, CEB [2] was the most conservative one. The SCI [4] and AISC [5] functions presented accelerations at the same level whereas the lowest accelerations values were obtained according to the FAISCA [6] function. However, the acceleration results from FAISCA [6] were still found in disturbing vibration levels.

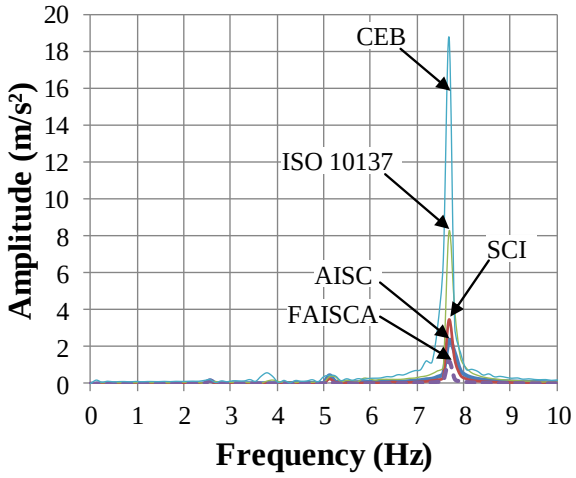


Figure 8: Investigated steel-concrete composite floor frequency response.

5 VIBRATION CONTROL

In order to improve the human comfort of the occupants the dynamic loading model I (Faisca [6]) was chosen in order to design the MTMDs based on absorber system proposed by Varela [10]. This choice was made based on recent studies once the Faisca function [6] have presented a more reasonable and economical dynamic loading model used to evaluate the human comfort of composite floors [11].

Therefore, from an extensive dynamic parametric analysis two TMD groups were tuned to the eleventh (group 1: f_{11} = 7.35 Hz) and fifteenth (group 2: f_{15} = 7.72 Hz) vibration modes, in order to minimize unwanted floor vibrations in case of resonance state. Thus, the two TMD groups were divided proportionally in eight TMDs with the same tuning, totalling sixteen TMDs, aiming to make them lighter and easier to be attached on the floor bottom (see Figure 3). The effective mass of each TMD is equal to 130 kg, which corresponds to five steel plates of 26 kg. Note that each TMD does not have a physical dashpot, but an inherent damping due to its mechanism and the friction between the steel plates (Figure 9). The damping value obtained experimentally varies in the range of 1 to 1.5 % and in the present investigation was considered equal to 1.5 %. Figure 9 shows the properties of each individual TMD corresponding to each group. The TMDs were designed according to the Den Hartog's formulation [12].

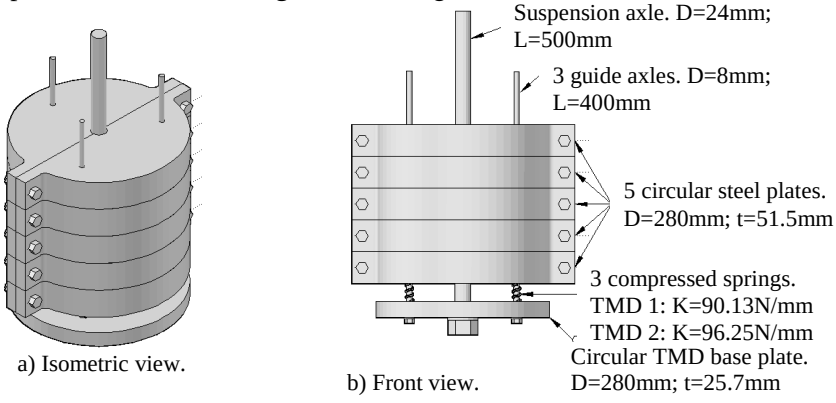


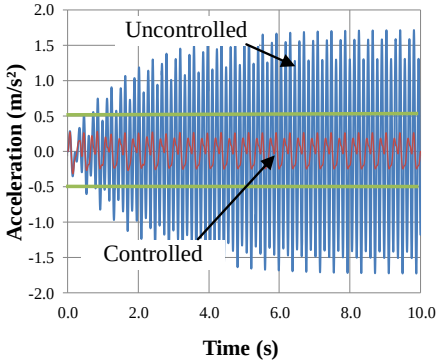
Figure 9: TMDs physical characteristics.

Vibration mode (Hz)	Floor Dynamic Response. Resonant motion state. Nodes F, G, J and K			
	Vibration Control	Acceleration (m/s²)		VDV (m/s$^{1.75}$)
		a_p	$a_{w,rms}$	
f_{15} = 7.72	uncontrolled	1.725	1.045	2.155
	controlled	0.285	0.143	0.298
	reduction (%)	-84	-86	-86
f_{11} = 7.35	uncontrolled	0.677	0.291	0.616
	controlled	0.288	0.146	0.329
	reduction (%)	-57	-50	-47

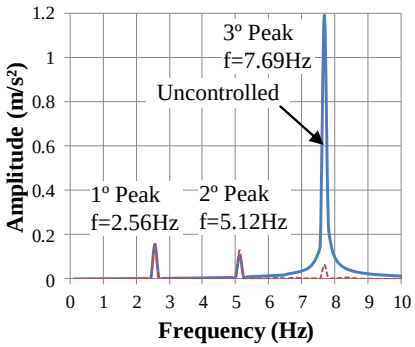
Table 5: TMDs effectiveness comparison. Resonant motion state. Nodes F, G, J and K.

Based on Table 5 results, a very good percentage reduction of 84%, 86% and 86% (Resonant motion state with the fifteenth mode: peak unweighted acceleration, RMS acceleration and VDV values, respectively) and of 57%, 50% and 47% (Resonant motion state with the eleventh mode: peak unweighted acceleration, RMS acceleration and VDV values respectively) was obtained for sixty-four persons practising aerobics on the investigated building steel-concrete composite floor. Moreover, regarding the human comfort acceptance criteria (compare Tables 3 and 5), these reduction values were enough to satisfy all evaluation methods.

The steel-concrete composite floor dynamic responses in time and frequency domain for the worst case are shown in Figure 10, respectively. Note that the red dashed line in this Figure is related to the steel-concrete composite floor controlled response.



a) Nodes F, G, J and K. Time Domain.



b) Nodes F, G, J and K. Frequency Domain.

Figure 10: Composite floor controlled dynamic response. Resonant motion state (f_{15} = 7.72Hz).

6 CONCLUSIONS

- This investigation analysed the dynamic behaviour of a steel-concrete composite floor spanning 40m by 40m used for human rhythmic activities. The modal analysis performed indicated that the frequency of the third harmonic of the dynamic loadings may match the natural frequencies of the floor and therefore lead the composite floor to resonance.
- The dynamic analysis showed that the accelerations values obtained when sixty-four persons practising aerobics were higher than the human comfort criteria according to five different human rhythmic force functions [ISO10137, CEB, SCI, AISC and FAISCA]. This situation led to human discomfort for the individuals practising aerobics on the floor. It was verified that most of these force functions does not agree to each other. Conse-

quently, the choice of one or other dynamic loading function may lead the floor design to a more or less conservative assessment regarding the human comfort serviceability.

- A passive control system based on the use of multiple tuned mass damper systems (MTMDs) was used aiming to control the excessive floor vibrations. This way, the controlled composite floor dynamic response attended the human comfort criteria for the occupants.
- The use of tuned mass damper systems developed herein might be an alternative solution, in order to respect human comfort criteria for composite floors when subjected to human rhythm activities whenever it is not possible to make significant changes in structural elements due to either structural and architectural factors or even economic ones.

REFERENCES

[1] International Standard Organization. Bases for design of structures - Serviceability of buildings and walkways against vibrations, ISO 10137, 2007.

[2] Comité Euro-International du Béton. CEB. Vibration problems in structures: Practical guidelines. Bulletin d'Information 209, London: Thomas Telford Services, 1993.

[3] H. Bachmann et al., "Vibration problems in structures - practical guidelines", Basel (Switzerland):Institut für Baustatik und Konstruktion, Birkhäuser; 1995.

[4] A.L. Smith, S.J Hicks, P.J. Devine,. "Design of floors for vibrations: A new approach", SCI Publication P354, Ascot, 2009.

[5] T.M. Murray, D.E. Allen, E.E. Ungar, "Floor Vibrations due to Human Activity", Steel Design Guide Series, American Institute of Steel Construction, AISC, Chicago, USA, 2003.

[6] R.G. Faisca, "Characterization of Dynamic Loads due to Human Activities", PhD Thesis (In Portuguese), COPPE/UFRJ, Rio de Janeiro/RJ, Brazil, 2003.

[7] ANSYS Swanson Analysis Systems, Inc., Release 11.0, SP1 UP20070830, Products ANSYS Academic Research, 2007.

[8] B.R. Ellis and J.D. Littler, "Response of cantilever grandstands to crowd loads. Part I: Serviceability evaluation", in Proceedings of the Institution of Civil Engineers – Structures and Buildings 157(SB4): 235-241, 2004.

[9] M. Setareh, "Evaluation and assessment of vibrations owing to human activity", in Proceedings of the Institution of Civil Engineers – Structures and Buildings 165(SB5): 219–231, 2012.

[10] W.D. Varela and R.C. Battista, Control of vibrations induced by people walking on large span composite floor decks. *Engineering Structures*, **33**(9), 2485-2494, 2011.

[11] C.M.R. Gaspar and J.G.S. da Silva, Influence of the human rhythmic activities modelling on the composite floors dynamic response. *Journal of Civil Engineering and Architecture Research*, **2**, 429-438, 2015.

[12] J.P.D. Hartog, *Mechanical Vibrations*, Mcgraw-Hill, 1956.

Vibration of Solids and Structures Under Moving Loads: Modelling and Analysis (MS06)

International Conference on Engineering Vibration
Ljubljana, Slovenia, 7-10 September 2015

MULTIPOINT CONTACT MODEL FOR DYNAMIC INTERACTION ANALYSIS OF HIGH-SPEED TRAIN AND RAILWAY STRUCTURE AFTER DERAILMENT DURING AN EARTHQUAKE

M. Tanabe*[1], M. Sogabe[2], H. Wakui[2] and Y. Tanabe[3]

[1] Kanagawa Institute of Technology
tanabe@sd.kanagawa-it. ac.jp

[2] Railway Technical Research Institute
sogabe@rtri.or.jp, wakui@rtri.or.jp

[3] Laboratory for Computational Mechanics Inc.

Keywords: Dynamic interaction, train, railway structure, contact, post-derailment, multibody dynamics, FEM.

Abstract. *An efficent computational method to solve the dynamic interaction of a high-speed train and railway structure during and after derailment under an earthquake is given. The motion of the train with nonlinear springs and dampers is modeled in multibody dynamics. Mechanical models to express contact-impact behaviors between wheel and rail before derailment and between wheel and the track structure after derailment are given to solve the interaction during an earthquake. A simple contact model based on multipoint contact springs on the contact surface between wheel and the track structure after derailment are presented. The contact area between wheel and track structure is divided as many sections needed in the rail direction where a contact spring is given in each section to express the contact-impact behavior.*

The railway structure is modeled with various finite elements. The combined dynamic response of the train and railway structure during an earthquake is obtained by solving nonlinear equations of motions of the train and the railway structure subjected to the interactions between wheel and rail before derailment and between wheel and the track structure after derailment. Numerical examples are demonstrated.

1 INTRODUCTION

There is a radical dynamic interaction between the train and railway structure during a strong earthquake. The huge impact force between the wheel and rail may cause lifting of the wheel, derailment and post-derailment behaviors.

Regarding the wheel-rail contact Pombo et al. [1] presented a generic contact detection formulation that allows the lead and lag flange contact in the rail direction. Ju [2] studied the method to express the vertical stiffness between the wheel and rail as a power function of changing contact force and developed a nonlinear moving wheel element to solve the contact problem of a moving train. Montenegro et al. [3] presented an algorithm to express the nonlinear vehicle-structure interaction by constraint equations and solve them by Lagrange multipliers based on the Newton method due to the nonlinearity.

Regarding the derailment behavior in the dynamic interaction between the train and railway structure during an earthquake, Xiao et al. [4] studied the derailment criteria based on the derailment coefficient that is defined as the ratio of the lateral force to vertical force of the wheel to predict the derailment and evaluate the vehicle running safety for the various operation speeds of the train and earthquake motions. Ju [5] developed a moving wheel finite element to investigate the derailment behavior of a high-speed train moving on simply supported bridges, where derailment coefficients were used to study the derailment under seismic loads. Sumami et al. [6] studied the way to solve the impact behavior between the derailed wheel and sleeper based on a wheel-sleeper impact model and investigated the derailed vehicle motion. However, very little work related to the computational method to solve derailment and post-derailment behaviors in the dynamic interaction between the train and railway structure during an earthquake has been reported so far.

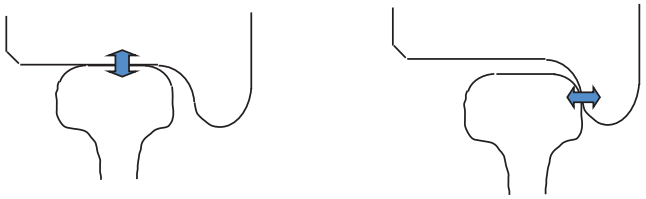
In this paper an efficient computational method to solve the dynamic interaction of a high-speed train and railway structure including derailment and post-derailment behaviors during an earthquake is given. Mechanical models to express contact-impact behaviors between the wheel and rail before derailment and between the wheel and the track structure after derailment are given to solve the interaction during an earthquake effectively. A contact model based on multipoint contact springs on the contact surface between wheel and the track structure with irregularities after derailment is presented. The contact area between wheel and track structure is divided as many sections needed in the rail direction where a contact spring is given in each section to express the contact-impact behavior.

For nonlinear equations of the combined motion of the train and railway structure, a modal reduction is applied to solve large-scale nonlinear equations effectively. Equations of motions of the train and the structure are solved in modal coordinates. However, since the equations are strongly nonlinear, iterative calculations are made during each time increment until the unbalanced force between the train and railway structure becomes small enough within a tolerance specified. Based on the present method a simulation program has been developed to solve the interaction including derailment and post-derailment behaviors during an earthquake. Numerical examples are demonstrated.

2 INTERACTION BETWEEN WHEEL AND TRACK STRUCTURE

2.1 Contact between wheel and rail before derailment

Assuming that the yawing and rolling of wheel-set are relatively small for the contact behavior between wheel and rail, two dimensional geometries of the cross sections of wheel and rail are considered, and the contact-impact behavior in the normal direction on the contact surface between wheel and rail is modeled simply in two modes of the contact in the vertical and transverse directions as shown in Fig. 2 [7].



(a) Vertical direction (b) Transverse direction

Fig. 1 Contact modes between wheel and rail

Regarding the vertical mode of the contact the contact displacement between wheel and rail in the vertical direction, δ_Z, is expressed as a function of displacements of the rail z_R and the wheel z_W in the vertical direction, the relative displacement on the contact surface between wheel and rail in the transverse direction d_y, and also the rail irregularity in the vertical direction ε_z as follows

$$\delta_Z = \delta_Z(z_R, z_W, d_y, \varepsilon_z). \tag{1}$$

The contact displacement δ in the normal direction on the contact surface between wheel and rail is obtained from the contact angle at the contact position. When wheel contacts on rail, there is a contact force created on the contact surface. The contact force on the contact surface between wheel and rail in the normal direction, H, is expressed as a function of δ and d_y as follows

$$H = H(\delta, d_y). \tag{2}$$

Regarding the transverse mode of the contact between wheel and rail, the contact displacement in the transverse direction δ_y is also expressed as a function of d_y, δ_Z and the rail irregularity in the transverse direction ε_y as

$$\delta_y = \delta_y(d_y, \delta_Z, \varepsilon_y). \tag{3}$$

When a wheel contacts on the rail in the transverse direction, the contact force is obtained in the same manner as the contact mode in the vertical direction described above.

Regarding the tangential and longitudinal directions on the contact surface between wheel and rail, constitutive equations to describe the relationship between creep forces and slipping rates of wheel are given [8]. The creep force in the tangential direction Q_c and yaw moment T_c due to the creep force in the longitudinal direction on the contact surface between wheel and rail are described mathematically here as functions of slipping rates of wheel in the longitudinal and tangential directions, S_x and S_t, and also of the spin rate around the normal vector on the contact surface, S_n, as [9]

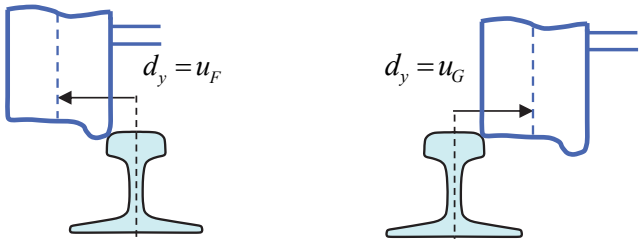
$$Q_c = Q_c(S_x, S_t, S_n) \tag{4}$$

$$T_c = T_c(S_x). \tag{5}$$

When a wheel lifts on the rail, there is no impact and creep forces created between the wheel and the rail.

2.2 Derailment Criterion

When the relative displacement between the wheel and rail in the transverse direction, d_y, exceeds derailment criteria u_F in the field side and u_G in the gauge side as shown in Fig. 2, derailments in the field side and gauge side are initiated, respectively. After the derailment of the wheel from rail during an earthquake the wheel touches down on the track structure and the post-derailment behavior of the wheel on the track structure comes to start.



(a) Field-side derailment (b) Gauge-side derailment

Fig. 2 Derailment criterion of left wheel

2.3 Contact between wheel and track surface after derailment

1) Vertical direction

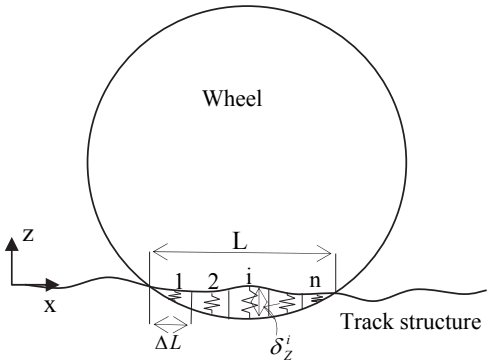


Fig.3 Multipoint contact spring model

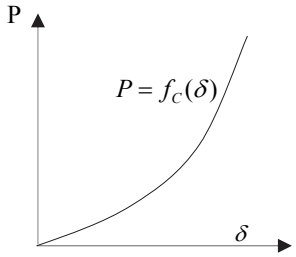


Fig.4 contact force-displacement relationship

Of the contact between wheel and track structure in the vertical direction after derailment, the contact area with the length of L is divided into n sections with the same length in the rail direction as shown in Fig.3, where n is an odd positive integer so that the center section corresponds to the bottom of wheel. The length of each section ΔL is obtained as L/n. The contact displacement in the vertical direction between wheel and track structure in the section i , δ_Z^i, is expressed as a function of displacements of the wheel z_W^i and the track structure z_S^i in the section in the vertical direction and also the irregularity of the track structure in the section in the vertical direction ε_z^i as follows

$$\delta_Z^i = \delta_Z^i(z_W^i, z_S^i, \varepsilon_z^i) \tag{6}$$

The contact force P_Z^i in the section i is expressed as a function of the contact displacement δ_Z^i

$$P_Z^i = f_C(\delta_Z^i) \tag{7}$$

where f_C expresses the relationship between the contact force and contact displacement in the each section with the length of ΔL (Fig.4). The total contact force P_Z between wheel and contact surface is written as

$$P_Z = \sum_{i=1,n} f_C(\delta_Z^i) \tag{8}$$

When the contact behavior in the each section is elastic with a spring constant of k_C, Eq.(7) and (8) are simply written respectively as

$$P_Z^i = k_C \delta_Z^i \tag{9}$$

$$P_Z = k_C \sum_{i=1,n} \delta_Z^i \tag{10}$$

Then

$$k_C = P_Z / (\sum_{i=1,n} \delta_Z^i) \tag{11}$$

The contact spring k_C is obtained from Herz solution for the contact problem between wheel and the track structure depending on the geometries of the surfaces, or static loading tests using an actual wheel on the track structure, or the finite element static contact anaysis of the wheel on the track structure.

2) Contact-impact behavior in the lateral direction after derailment

When a wheel slips in the transverse direction on the track surface after derailment, there is a friction force Q_{Ty} created on the contact surface in the transverse direction (Fig. 5). The friction force is modeled here with Coulomb friction law.

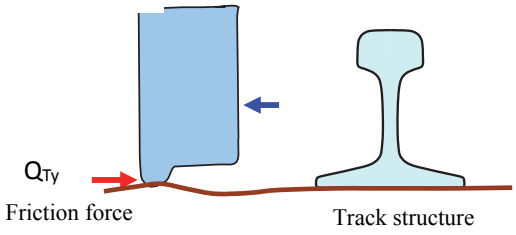


Fig.5 Contact between wheel and track surface in the transverse direction after derailment

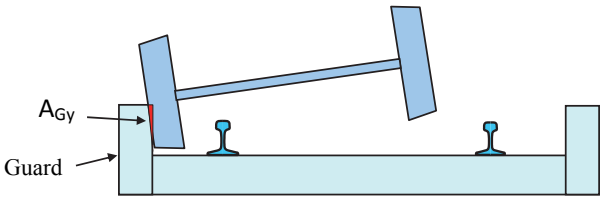


Fig. 6 Contact between wheel and guard on the track structure in the transverse direction

Guards are attached on the track structure to prevent the wheel deviating from the track even after the derailment during an earthquake to build an earthquake-safe railway system [10] as shown in Fig. 6. After the derailment of wheel, it contacts on the guard of the track structure in the transverse direction. The contact force Q_{Gy} is expressed here as a function of the embedded area A_{Gy} between the wheel and the guard in Fig. 6 as

$$Q_{Gy} = Q_{Gy}(A_{Gy}). \tag{12}$$

The relationship in Eq. (12) is obtained from static loading tests using an actual wheel on the guard of the track structure, or the finite element static contact analysis of the wheel on the guard. If the guard has the enough height and strength for the impact force between the wheel and guard, the wheel is guided well between left and right guards in the rail direction preventing wheel deviating from the track even after derailment during an earthquake.

2.4 Track element

Based on the contact model after derailment described above, a track element has been developed to express the contact-impact behavior between wheel and the long track structure after derailment, where the motion in plane of the cross-section of the track structure is expressed in multibody dynamics and the motion in out-of-plane of the cross-section is expressed by FEM. Fig. 7 shows the track element with a guard attached to prevent wheel deviating from the track after derailment. Irregularities along longitudinal direction are given in the track element as geometric attributes defined on the surface in the vertical and transverse directions.

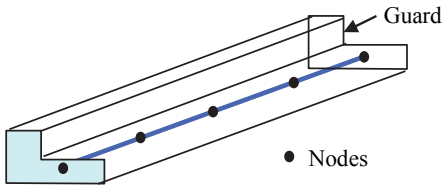


Fig.7 Track element

3 EQUATION OF MOTION OF THE TRAIN AND RAILWAY STRUCTURE

The motion of the train is modeled in multibody dynamics with nonlinear springs and dampers to connect all components. Assuming that the train runs at a constant speed, the nonlinear equation of motion of the train is derived and written as follows [11]

$$M^V \ddot{X}^V + D^V(\dot{X}^V) + K^V(X^V) = F^V \tag{13}$$

where X^v and F^v are displacement and load vectors of the train, M^v is the mass matrix, and $D^V(\dot{X}^V)$ and $K^V(X^V)$ are the damping and internal force vectors which are nonlinear depending on the velocity and displacement vectors, respectively.

A railway structure made of rail, rail pad, sleeper, ballast, bridge are modelled with various finite elements such as truss, beam, shell, solid, mass and damper elements, and nonlinear spring element that is to model simply a concrete structure with an elastic-plastic behaviour appeared under cyclic loads during an earthquake [11], and also with track elements for long railway components, and the whole equation of motion of a railway structure is written in a matrix form as

$$M^b \ddot{X}^b + D^b(\dot{X}^b) + K^b(X^b) = F^b \tag{14}$$

where X^b and F^b are displacement and load vectors of the railway structure, M^b is the mass matrix, and $D^b(\dot{X}^b)$ and $K^b(X^b)$ are the damping and internal force vectors which are non-linear depending on the velocity and displacement vectors, respectively.

The combined dynamic response of the train and railway structure during an earthquake is obtained by solving nonlinear equations of motions of the train and the railway structure in Eqs. (13) and (14) subjected to the interactions between wheel and rail before derailment and between wheel and the track structure after derailment. However, modal reduction to displacement vectors of the train and railway structure is made to solve the combined response of a large-scale railway system during an earthquake effectively. Equations of motions of the train and the structure are solved in modal coordinates for each time increment. Since the equations are strongly nonlinear iterative calculations are made during each time increment until they converge within a small tolerance specified.

Based on the present method a computer program DIASTARS has been developed for the simulation of a Shinkansen train (high speed train in Japan) running at high speed on the railway structure including derailment and post-derailment behaviors during an earthquake.

4 NUMERICAL EXAMPLES

4.1 Contact spring of wheel on the rail

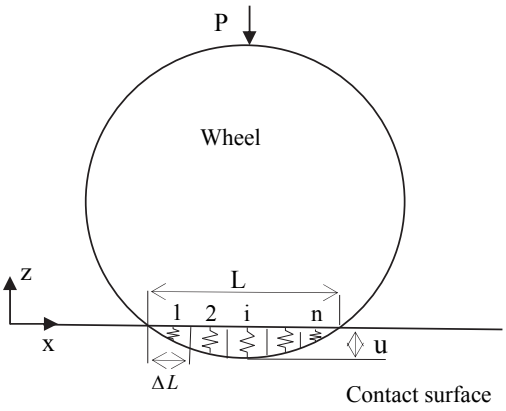


Fig.8 Contact between wheel and rail

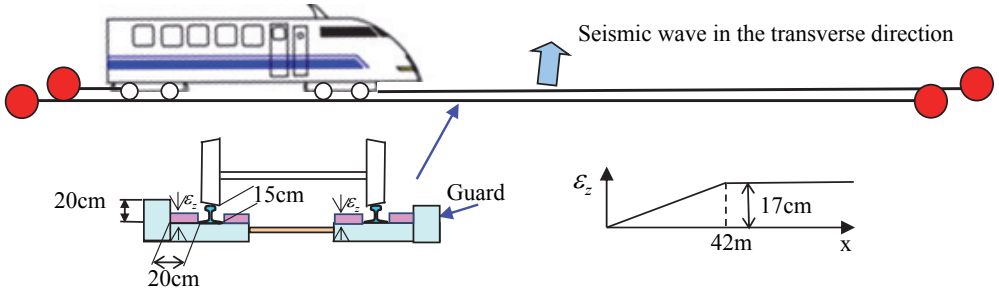
Fig.8 shows a contact problem of a wheel on the rail [12] for various wheel load P given on the wheel. Tab.1 shows contact displacement u and the contact length L obtained from Hertz solution for various load P. The contact length L is divided in n sections. Assuming elastic deformation of wheel on the rail the contact spring k_C obtained from Eq.(11) is given there. The contact spring between wheel and rail k_C for the unit length obtained from Hertz solution is shown to be almost same for various load P.

The contact spring k_C between wheel and the track structure is obtained from Herz solution for the contact problem depending on geometries of the contact surfaces, or static loading tests using an actual wheel on the track structure, or the finite element static contact anaysis.

Table 1 Contact spring k_C for various wheel loads

P (kN)	u (mm)	L (mm)	n	k_C (kN/mm)
82	0.087	18.799	21	70.6
200	0.16	25.493	27	69.1
400	0.25	31.865	35	70.7

4.2 Simulation of a Shinkansen car running on the ladder track with guards attached during an earthquake



(a) Cross-section of ladder track with guards (b) Track irregularity in the vertical direction ε_z

Fig.9 A Shinkansen car running on the ladder track with guards attached during an earthquake

The simulation of a Shinkansen car running at a speed of 300km/h on the ladder track given along the rigid track during a sinusoidal seismic wave with the frequency of 1 Hz, the maximum amplitude of 4.8m/s^2 and wave number of 5 given from the base in the transverse direction has been conducted (Fig.9). The ladder track is made of ladder-shaped composite concrete beams to support rails with guards attached, where the track irregularity in the vertical direction ε_z is given in the rail direction x as shown in Fig.9(a),(b). The ladder track is modeled with the track element with the irregularity. The number of divisions n used for the contact area between wheel and the track in the rail direction in Eq.(10) is 31. The seismic wave of 1 Hz is very severe frequency for the car as it is close to the resonance frequency of the rolling motion of the body, truck and wheel-set that leads to the derailment easily. Fig. 10 and 11 show the vertical displacement responses of the left and right wheels at the 1st wheel-set. It is shown that wheel runs onto the rail due to the impact between the wheel and rail in the transverse and vertical directions, lifts off, derails, touches down on the track, and goes up due to the vertical irregularity ε_z on the track surface and lifts off the surface during the earthquake. Fig. 12 shows the relative displacement response between the left wheel and rail in the transverse direction, d_y, at the 1st wheel-set. When d_y exceeds u_F (7cm in this case) shown in Fig.2, the derailment to the field side is initiated, the wheel touches down on the surface of the ladder track in the vertical direction, impacts on the guard of the track in the

transverse direction and rebounds. Fig. 13 shows the impact force of left wheel on the guard. Maximum impact force is shown to be 15.6 tonf.

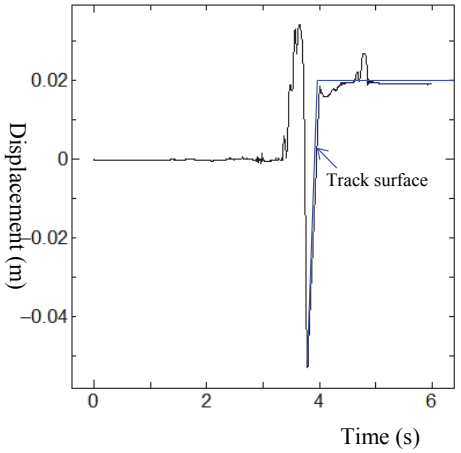


Fig.10 Vertical displacement of the left wheel

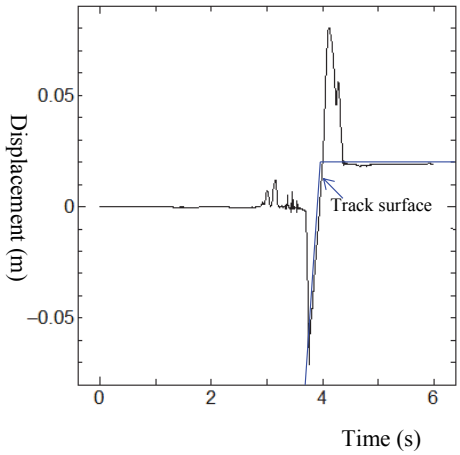


Fig.11 Vertical displacement of the right wheel

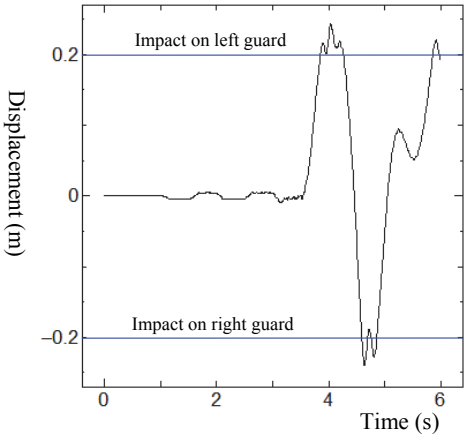


Fig.12 Relative displacement between left wheel and rail in the transverse direction

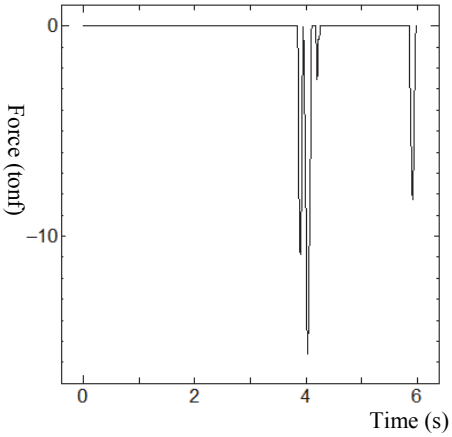


Fig.13 Impact force of the left wheel on the guard

5 CONCLUSIONS

The computational method to solve for the dynamic interaction of a high-speed train and railway structure including derailment and post-derailment during an earthquake was given. Mechanical models to express contact-impact behaviors between the wheel and rail before derailment and between the wheel and the track structure after derailment were given to solve the interaction during an earthquake effectively. A contact model based on multipoint contact springs on the contact surface between wheel and the track structure with irregularities after derailment was presented. The contact area between wheel and track structure was divided as many sections needed in the rail direction where a contact spring is given in each section to express the contact-impact behavior. Based on the contact model after derailment, a track element has been developed to solve the contact problem between wheel and the long track

structure effectively. A simulation of a Shinkansen car running at high speed on the ladder track with guards attached where the irregularity in the transverse direction was given was conducted to study the interaction between wheel and track structure including derailment and post-derailment behaviors.

The computational method developed here would be effective to design an earthquake-safe railway system.

REFERENCES

[1] J. Pombo, J. Ambrosio, and M. Silva, A new wheel-rail contact model for railway dynamics, *Vehicle System Dynamics*, 45, No. 2, 165-189, 2007.

[2] S. H. Ju, A simple finite element for nonlinear wheel/rail contact and separation simulations, *J. Vibration and Control* ,20, No.3, 330-338, 2014.

[3] P. A. Montenegro, S. G. M. Neves, R. Calcada, M. Tanabe, M. Sogabe, Wheel-rail contact formulation for analyzing the lateral train-structure dynamic interaction, *Computers & Structures*, 152, 200-214. DOI:10.1016/j.compstruc.2015.01.004, 2015.

[4] X. Xiao, L. Ling, X. Jin, A study of the derailment mechanism of a high speed train due to an earthquake, *Vehicle System Dynamics*, 50, No.3, 449-470, 2012.

[5] S. H. Ju, Nonlinear analysis of high-speed trains moving on bridges during earthquakes, *Nonlinear Dynamics*, 69, No.1-2, 173-183, 2012.

[6] H. Sunami, Y. Termichi, M. Adachi, An analytical study of derailed vehicle motion from wheel-sleeper impacts, *J. Railway Technology*, 2, Issue 2,35-63, 2013.

[7] M. Tanabe, N. Matsumoto, H. Wakui, M. Sogabe, H. Okuda and Y. Tanabe, A simple and efficient numerical method for dynamic interaction analysis of a high-speed train and railway structure during an earthquake, *J. Computational and Nonlinear Dynamics*, 3/ 041002, ASME, 2008.

[8] J. J. Kalker, *Three-dimensional elastic bodies in rolling contact,* Kluwer, 1990.

[9] *Dynamics of railway vehicle,* JSME, 1994.

[10] K. Asanuma, M. Sogabe, T. Watanabe, J. Okayama and H. Wakui, Development of a Ballasted ladder track equipped with a vehicle guide device, *RTRI Report,* 23, No.2, 27-32, 2009.

[11] M. Tanabe, N. Matsumoto, H. Wakui, M. Sogabe, Simulation of a Shinkansen train on the railway structure during an earthquake, *Japan J. Indust. Appl. Math.,* 28, 223-236, 2011.

[12] R. G. Dong, S. Sankar, R.V. Dukkipati, A finite element model of railway track and its application to the wheel flat problem, CONCAVE Research Centre, Concordia University, Canada, ImechE Part F: *Journal of Rail and Rapid Transit*, 208, 61-72,1994.

International Conference on Engineering Vibration
Ljubljana, Slovenia, 7-10 September 2015

AN ABAQUS NUMERICAL METHOD TO PREDICT GROUND VIBRATIONS INDUCED BY HIGH-SPEED RAILWAY LINES

Yanmei CAO*[1], Fu-xing Wang[1], Ying Wang[2]

[1]School of Civil Engineering, Beijing Jiaotong University, Beijing, 100044, China
ymcao@bjtu.edu.cn

[2]Beijing Grand Mentality Information Technology Co. LTD., Beijing, 100080, China
heroym@163.com

Keywords: Ground vibration, High-speed railway, Numerical method, Attenuation laws.

Abstract. *A numerical method is proposed to predict the ground vibrations induced by the high-speed surface lines and the attenuation laws of wave propagating through the subsoil are studied. The train-track-subsoil finite element model is established, in which the dynamic interactions between adjacent parts are taken into account and the high-speed train is simulated by the rigid body and the moving axle load, respectively. In addition, a dynamic coupling model of finite elements and infinite elements for simulating infinite subsoil is put forward to prevent the reflection of vibration waves on the boundaries of a subsoil model. Moreover, the numerical modeling of track irregularity sample in time domain is generated using the inverse Fourier transformation, on the basis of the Germany interference spectrum with low power. The results from the proposed numerical model agree well with those from existing references with an acceptable accuracy, so the numerical method can be used to make a preliminary prediction of ground vibrations induced by high speed railway lines.*

1 INTRODUCTION

The problem of environmental vibration related to the increase of the train speed has been frequently reported since the opening of the Swedish line between Göteborg and Malmö in 1997. In that case the excessive vibration levels were detected both in the railway embankment and surrounding soil when the X-2000 train travelled at speeds around 200 km/h[1]. The high vibration levels were explained by the increase of the train speed, which approached the R-wave velocity of the soil, causing the resonance of the track-soil system and resulting in the potential instability of the train. Therefore, in planning high-speed railways, it is important to predict whether there will be sections of the line where the vibrations induced by the passage of the train might be problematic, which is the motivation of the present paper.

The earlier works assumed that the problem of vibrations induced by moving vehicles can be described by two-dimensional models. For example, Gutowski and Dym[2] mentioned that the vibrations generated along a road or a railway track could be modeled as a line source as long as the roadway was relatively uniform and the receiver was in the far field. In fact, however, the phenomenon is a three-dimensional problem, namely, the vehicle moves in one direction while the waves propagate in the soil in all three directions, so the use of three-dimensional models comes forward, such as finite element method (FEM), boundary element method (BEM), combined FEM-BEM method. Ju[3] used the 3D FEM with first-order absorbing boundaries to simulate soil vibrations due to a high-speed train crossing a bridge and to study the efficiency of soil improvement as a countermeasure. Masafumi et al[4] adopted a 3D viscoelastic staggered-grid finite difference method with fourth-order accuracy in space to study the mechanism of ground vibrations induced by a high-speed train. Bode et al[5] used the BEM to model the half-space soil and the FEM to simulate the sleepers and the rails, and the vibrations in the free field and the influence of the soil-sleeper coupling are analyzed in time domain. A similar strategy was followed by O'Brien and Rizos[6], but instead of half-space Green's function, they used full-space Green's function. Auersch[7] presented a combined FEM/BEM model for soil and track and a multi-DOF model for the vehicle.

In recent years, some authors considered that the geometry is invariant in the longitudinal direction, and after performing a Fourier transform of the field of variables in that direction, they reduced the three-dimensional problem to a set of 2-dimensional problems in the hybrid space-wavenumber-frequency domain, which is the so-called 2.5-dimensional (2.5D) approach. Takemiya[8] proposed a 2.5D finite model considering the irregular topographies of the track. Yang and Hung[9] established a 2.5D finite/infinite element approach to study the transmissibility of soils for vibrations induced by moving trains. François et al[10] used a 2.5D coupled FE-BE methodology to solve the dynamic interaction between longitudinally invariant structures and a layered half-space. Costa[11] presented a numerical study to understand the dynamic behavior of ballasted tracks with mats by means of 2.5D FEM-BEM formulation including train-track-ground interaction.

In this paper, a numerical method is proposed to predict the ground vibrations induced by the high-speed surface lines and the attenuation laws of wave propagating through the subsoil are studied. The ground vibrations induced by high-speed trains are obtained by establishing the semi-analytical train-track-subsoil interaction model, which ensures the efficiency of calculation.

2 FEM-IFEM SOIL MODEL

The soil is simulated by the finite/infinite (FEM-IFEM) method established by the software of ABAQUS. Figure 1 illustrates a three-dimensional (3D) FEM-IFEM layered subsoil model, in which l_x, l_y and l_z are the size of subsoil model along the x-, y-, and z-direction, respectively.

In the soil model, the elastic-plastic solid element is adopted, and the stress-strain relationship accords with Mohr-Coulomb yield criterion. At the bottom of the soil model, all the freedoms of each joint are fixed. For the other sides except the surface, the 3D infinite elements are employed to satisfy the condition of outward wave propagation on the boundary, and they are coupled with the finite elements in near field by connecting common joints on the interfaces. The soil parameters adopted in this paper are listed in Table 1.

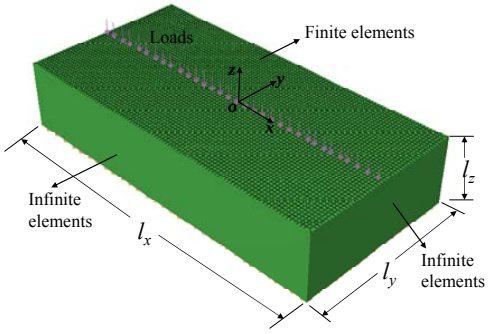


Figure 1: A three-dimensional finite/infinite subsoil model.

The soil model can simulate ground vibration by all types of loading. For example, a non-moving unit harmonic loading $F_z(t) = 1 \cdot e^{i\varpi t}$ is vertically applied to the origin O (0, 0, 0) on ground surface, in which $\varpi = 2\pi f_0$ is the angle frequency of source. In this paper, only the vertical displacement is taken into account. Figure 2 demonstrates the soil displacements at a moment subjected to a centric harmonic load with the frequency of f_0 = 25 Hz and f_0 = 35 Hz, respectively. The calculated results show that the harmonic load generates the steady vibration of subsoil with frequency almost equal to f_0, and it can be seen that the frequency of source has obvious effect on the propagation modes of wave. It also indicates the wave fronts of a spherical wave emerge when a non-moving harmonic point load is applied, and the higher the frequency is, the more obvious the spherical wave fronts are.

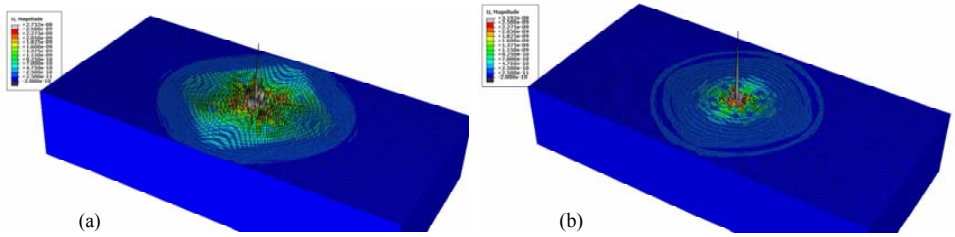


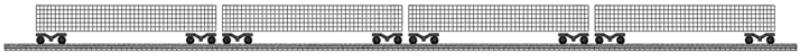
Figure 2: Soil displacements subjected to a point harmonic load: (a) f_0=25 Hz (b) f_0=35 Hz.

3 NUMERICAL MODEL OF TRAIN-TRACK-SUBGRADE-SOIL

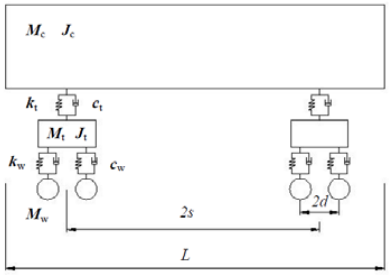
3.1 Train model

The train is composed of several locomotives and passenger cars, and each vehicle is a multiple-DOF vibration system consisting of a car-body, bogies, and wheel-sets, as shown in

Figure 3. The individual parts of the train are regarded as rigid body, and are connected with spring-damper suspension cell.



(a) Marshalling of train model



(b) Vehicle components and parameters

Figure 3: Train model.

The four passages of German ICE3 is adopted herein to simulate the whole process of coming to and leaving off the ground, and the velocity is V=250km/h.

3.2 Track and subgrade model

The parameters of the ballastless track of CRTS I and the subgrade are listed in Table 1. In the model, the track slab, CA mortar cushion, concrete base, and the subgrade are simulated by the 8-node linear reduced integrated solid element.

Structural layer	Width (m)	Depth (m)	Density (kg/m^3)	Elastic modulus (MPa)	Poisson ratio
Rail	0.1	0.2	7800	2.06×10^5	0.25
Track slab	2.4	0.2	2600	3.5×10^4	0.167
CA mortar cushion	2.4	0.05	1800	9.2	0.4
Concrete base	3	0.3	2500	2.4×10^4	0.2
Top subgrade	-	0.4	2184	120	0.3
Bottom subgrade	-	2.3	1939	70	0.3
Embankment	-	3.6	1837	50	0.35

Table 1: Parameters of ballastless track and subgrade.

Also, the fasteners are nonlinear spring-damper cell which cannot sustain compression. In addition, the wheel-track contact is regarded as hard contact allowing separation in the normal direction and as zero-friction contact in the tangential direction. The track irregularity is generated by low interference power spectral density function of German high-speed railway and inverse Fourier transformation. The subgrade layers accords to Drucker-Prager plastic constitutive model.

3.3 Train-track-subgrade-soil model

The train-track-subgrade-soil interaction model is established, as shown in Figure 4. The soil model can be seen in Figure 1, in which l_x=300m, l_y =150m, and l_z =60m.

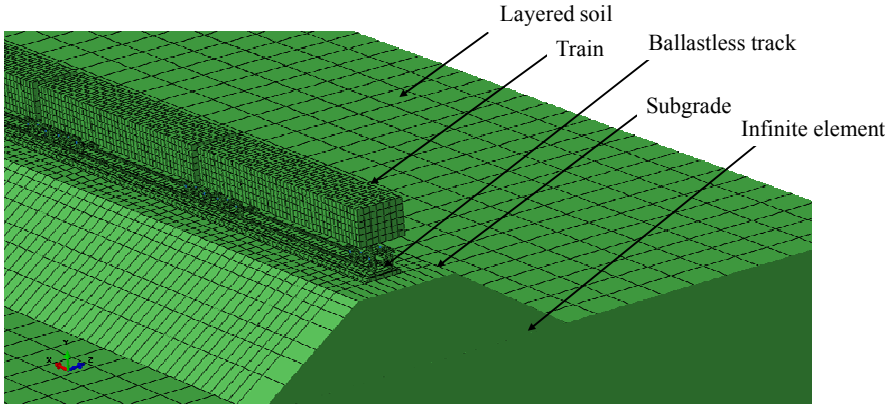


Figure 4: Train-track-subgrade-soil interaction numerical model.

The parameters of the FEM-IFEM soil model are listed in Table 2. The mesh size of soil model is closely related to the velocity V_s of S-wave and circular frequency ω in soil, and is no more than $2\pi\times V_s/(14\times\omega)$ [12]. Herein, the mesh size is 3m.

Soil layer	Depth (m)	Density (kg/m^3)	Elastic modulus(MPa)	Poisson ratio	Velocity of S-wave (m/s)	Damping ratio
Silty clay	6	1898	124	0.302	158.40	0.02
Silt clay	9	1704	111.2	0.31	157.82	0.02
Sandy silt	24	1847	159.2	0.318	180.83	0.02
Half-space	21	1900	141	0.33	167.03	0.02

Table 2: Parameters of layered soil [13].

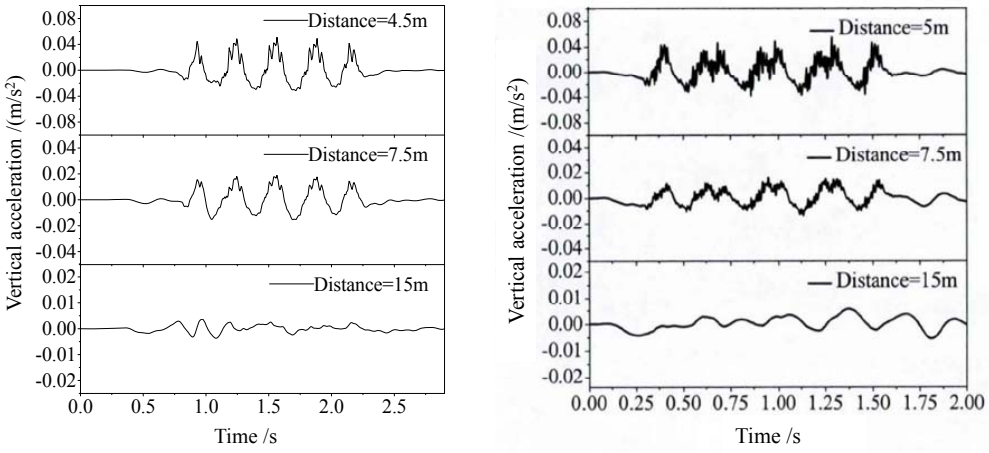
3.4 Validation of the train-track-subgrade-soil numerical model

The finite element method and infinite element method are combined to solve the dynamic equations of the whole train-track-subgrade-subsoil system, in which the Newmark-β integral method is adopted.

The calculated ground accelerations of D=4.5m, D=7.5m, and D=15m are showed in Figure 5(a). Simultaneously, the results in Reference [12] are illustrated in Figure (b) to validate the numerical model established herein. By comparison, it can be found that the two results are very similar, which proves the effectiveness of the numerical method established in this paper.

4 GROUND STRESS AND DISPLACEMENT INDUCED BY HIGH-SPEED TRAIN

Figure 6 and Figure 7 shows the mise stress and vertical displacement distribution of ground vibrations when a train with the speed of V=250km/h. It can be seen that the distribution of ground dynamic stress has obvious correspondence with the position of train wheelsets, and the higher are the stress and the displacement, the nearer they are to the position of train axle loads. In addition, the clear Mach cone appears on the ground displacement distribution, that is because the speed of moving train (V=69.45m/s) is more than the velocity of Rayleigh wave (C_R=52.06m/s) of the top soil layer and close to that of the second soil layer (C_R=72.36m/s).



(a) Results in this paper (b) Results in Reference [13]

Figure 5: Comparison of vertical acceleration of the ground point calculated here and in [13].

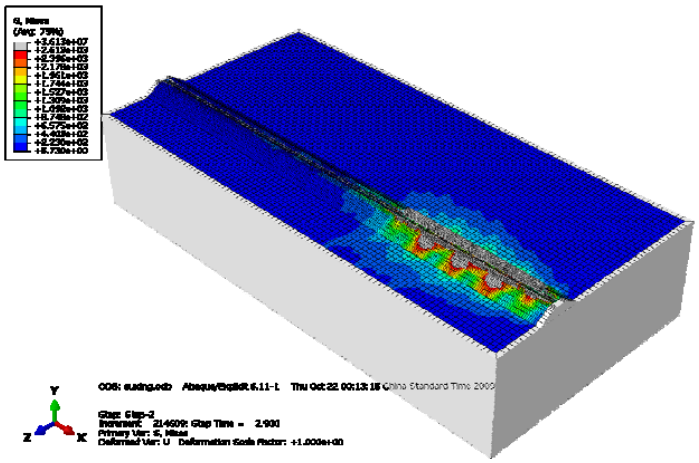


Figure 6: Mise stress distribution graph of the train-track-subsoil model.

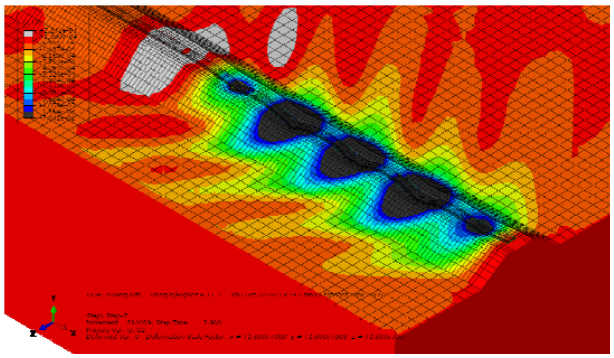


Figure 7: Vertical displacement distribution graph of the train-track-subsoil model.

5 CONCLUSIONS

- A numerical method is proposed to predict the ground vibrations induced by the high-speed surface lines and is validated.
- A dynamic coupling model of finite elements and infinite elements for simulating infinite subsoil is put forward to prevent the reflection of vibration waves on the boundaries of a subsoil model.
- The results from the proposed numerical model agree well with those from an existing reference with an acceptable accuracy, so the numerical method can be used to make a preliminary prediction of ground vibrations induced by high speed railway lines.

6 ACKNOWLEDGEMENTS

The research is sponsored by the Major State Basic Research Development Program of China (‘‘973’’ Program: 2013CB036203), Beijing Higher Education Young Elite Teacher Project (Grant No. YETP0557), and the Fundamental Research Funds for the Central Universities (Grant No.2014JBM091).

REFERENCES

[1] Madshus C, Kaynia A M, High-speed railway lines on soft ground: dynamic behavior at critical train speed. *Journal of Sound and Vibration*, 231(3): 689−701, 2000.

[2] Gutowski T, Dym C, Propagation of ground vibration: a review. *Journal of Sound and Vibration*, 49 (2): 179-193, 1976.

[3] Ju S H, Three-dimensional analyses of wave barriers for reduction of train-induced vibrations. *Journal of geotechnical and geoenvironmental engineering*, 130 (7): 740-748, 2004.

[4] Masafumi K, Toshifumi M, Osamu Y, et al, Numerical simulation study of ground vibrations using forces from wheels of a running high-speed train. *Journal of Sound and Vibration*, 318: 830-849, 2008.

[5] Bode C R, Hirschauer R, Savidis S A, Soil-structure interaction in the time domain using halfspace Green’s function. *Soil Dynamics and Earthquake Engineering*, 22(4): 283-295, 2002.

[6] O’Brien J, Rizos D, A 3D BEM-FEM methodology for simulation of high speed train induced vibrations. *Soil Dynamics and Earthquake Engineering*, 25(4): 289-301, 2005.

[7] Auersch L, The excitation of ground vibration by rail traffic: theory of vehicle–track–soil interaction and measurements of high-speed lines. *Journal of Sound and Vibration*, 284, 103-132, 2005.

[8] Takemiya H, Simulation of track-ground vibrations due to a high-speed train: the case of X-2000 at Ledsgard. *Journal of Sound and Vibration*, 261, 503-526, 2003.

[9] Yang Y B, Hung H H, *Wave Propagation for train-induced vibrations*. Singapore: World Scientific Publishing Co. Pte. Ltd. 2009.

[10] François S, Schevenels M, Galvín P, et al, A 2.5 D coupled FE-BE methodology for the dynamic interaction between longitudinally invariant structures and a layered halfspace.

Computer methods in applied mechanics and Engineering, 199(23-24): 1536-1548, 2010.

[11] Costa P, Calcada R, Cardoso A S, Ballast mats for the reduction of railway traffic vibrations. Numerical study. *Soil Dynamics and Earthquake Engineering*, 42: 137-150, 2012.

[12] Pengbo WEI, *Prediction and Evaluation of Environmental Vibrations induced by Urban Rail Traffic*. Beijing, Beijing Jiaotong University, 68-69, 2009.

[13] Haiyan Han, *Numerical Simulation of Ground Vibrations of Soft Soil induced by High-speed Railway*. Xinan Jiaotong University, 51-67, 2012.

International Conference on Engineering Vibration
Ljubljana, Slovenia, 7-10 September 2015

ENERGY HARVESTING FROM MOVING LOADS ON A BEAM WITH ELASTIC FOUNDATION

M. Ghandchi Tehrani*[1], M. Hussein[2]

[1]University of Southampton
m.ghandchi-tehrani@soton.ac.uk

[2] Qatar University
mhussein@qu.edu.qa

Keywords: Energy harvesting, Moving loads, Beams on elastic foundations

Abstract. *In this paper, the problem of energy harvesting from the vibrations of a moving load is presented. Potential application is in the rail industry, in which the passage of the train can induce vibration. The vibrational energy can be harvested to power up for example the sensors that are mounted on the rail track for structural health monitoring. An infinite beam on an elastic foundation under quasi-static moving load is considered. The response of the beam is obtained analytically. A single-degree-of-freedom energy harvester subject to beam vibration is designed to harvest energy from the motion of the moving load. The frequency of the harvester is tuned to match the excitation frequency in order to maximise the amount of the harvested energy. The maximum relative displacement between the harvester and the beam and the amount of the harvested energy at several excitation frequencies are obtained. The effect of the velocity of the moving load on the harvested energy is also discussed.*

1 INTRODUCTION

An infinite beam with elastic foundation has been considered as a model for railway tracks, which was first presented by Winkler in 1867 [1]. This model consists of a single infinite beam supported on a foundation with constant stiffness. Mathews [2] calculated the steady-state response of an Euler–Bernoulli beam on an elastic foundation under an oscillating moving load. The Fourier transformation was used to calculate a closed form solution for the response using contour integrals and the residue theorem. A more complicated problem in which the complete solution (transient and steady state) of a beam on elastic foundation under an oscillating moving mass, was calculated by Duffy [3]. Fourier transformation was used to transform the differential equation with respect to space, while Laplace transformation is used with respect to time. Hussein et al. [4] considered a model of floating-slab track as a model of the track and investigated its dynamics under oscillating moving loads.

When a load moves on an elastic beam, the beam deflects vertically due to the load. The vertical displacement of the elastic beam under the weight of a moving load can engage regenerative devices such as a vibration energy harvester. The generated power can be stored and used to power electronic devices.

Piezoelectric and electromagnetic energy harvesters have been widely used in energy harvesting technologies. A British company Perpetuum Ltd [5] developed an energy harvester, which can harvest mWatts of power. The French national railway system, SNCF [6] also investigated the problem of energy harvesting from train vibrations. Recently, Ghandchi Tehrani et al [7] carried out simulations on the measured data from an Intercity125 train to investigate the amount of the harvested energy. Nelson et al [8] designed an electromagnetic harvester, which was able to harvest an average power of 0.22 Watts for a loaded train passing at 11.5 mph at in-field test. Wang et al. [9] built a prototype of an electromagnetic energy harvester to harness the vibrational power from the railroad deflections due to passing trains. The irregular pulse-type track vibrations was converted into unidirectional rotation of the generator, enabling the electrical generator to operate at more efficient speeds. However, the efficiency of their device is still less than ideal, largely due to mechanical friction. Z.F. Mian [10] generated power by placing an electromagnetic coil near the rail, so that when the train wheel passes by, the coil will generate electricity due to changing magnetic flux. An Israeli company Innowattech Ltd [11] developed an energy harvesting pad composed of piezoelectric stacks. These pads can replace the conventional railway track damping pad. Nelson et al [12] also studied piezoelectric techniques for harvesting power from railcar traffic.

In this paper, first the dynamic response of an infinite elastic beam subject to a moving load is obtained analytically. Then, a single-degree-of-freedom mechanical oscillator is designed as an energy harvester. The amount of energy harvested from such a system is obtained analytically using the relative velocity between the elastic beam and the harvester. Finally, simulations are carried out on a numerical example to analyse the response of a moving train on an elastic beam and to calculate the harvested energy.

2 VIBRATIONS OF A BEAM ON ELASTIC FOUNDATION SUBJECT TO HARMONIC MOVING LOAD

An infinite beam on an elastic foundation, shown in Figure 1 is considered to be as a model of a rail track. A harmonic moving load is travelling on the beam with a constant velocity v, having the rotational frequency of ω_0.

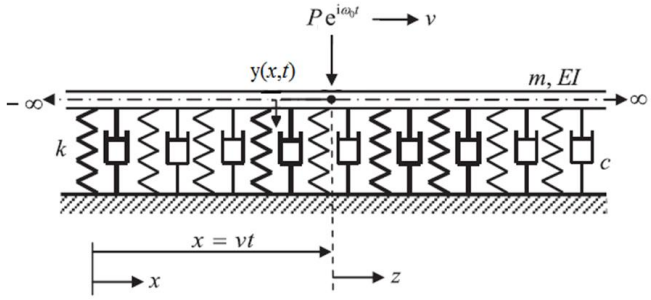


Figure 1: Infinite beam on elastic foundation under harmonic moving Load

The governing differential equation for the beam can be written as,

$$EI\frac{\partial^4 y(x,t)}{\partial x^4}+m\frac{\partial^2 y(x,t)}{\partial^2 t}+c\frac{\partial y(x,t)}{\partial t}+ky(x,t)=F(x,t) \tag{1}$$

where, $y(x,t)$ is the transverse deflection of the beam, x is the space coordinate along the length of the beam, t is time and the harmonic moving load per unit length of the beam is $F(x,t)$.

The constant parameters are EI , which is the bending rigidity of the beam and m , c and k , which are the mass, damping and stiffness per unit length of the beam, respectively.

The harmonic moving load acts on the beam at a certain time t at the point x_0+vt along the beam, where x_0 is the initial position of the load, i.e. at t=0. The force can be expressed as,

$$F(x,t)=Pe^{i\omega_0 t}\delta(x-x_0-vt) \tag{2}$$

where, δ is the Delta function and is defined as,

$$\delta(t)=\frac{1}{2\pi}\int_{-\infty}^{\infty}e^{-it\tau}d\tau \tag{3}$$

A characteristic of the Delta function is,

$$\int_{-\infty}^{\infty}\delta(x-x_0)f(x)dx=f(x_0) \tag{4}$$

Since Eq. (1) is a space-time differential equation, double Fourier integral transform is used to solve the equation and to change it to wavenumber-frequency equation [Hussein and Hunt 2006]. After finding the response in this domain, inverse double Fourier transform is then used to obtain the response in space-time domain.

By implementing double Fourier transform, Eq. (1) can be written in an algebraic form,

$$EI\xi^4\tilde{y}(\xi,\omega)-m\omega^2\tilde{y}(\xi,\omega)+ic\omega\tilde{y}(\xi,\omega)+k\tilde{y}(\xi,\omega)=\tilde{F}(\xi,\omega) \tag{5}$$

where, $\tilde{y}(\xi,\omega)$ and $\tilde{F}(\xi,\omega)$ are the double Fourier transform of the response $y(x,t)$ and applied load $F(x,t)$, respectively. Applying double Fourier transform to the moving load, yields,

$$\tilde{F}(\xi,\omega)=\int_{-\infty}^{\infty}\int_{-\infty}^{\infty}Pe^{i\omega_0 t}\delta(x-x_0-vt)e^{-i(\xi x+\omega t)}dxdt \tag{6}$$

using the definition of the Delta function , Eq. (3), and the convolution integral, Eq. (4), leads to,

$$\tilde{F}(\xi,\omega)=2\pi Pe^{-i\xi x_0}\delta(\omega+v\xi-\omega_0). \tag{7}$$

Substituting Eq. (7) into Eq. (5) and rearranging leads to the response of the beam in wave-number-frequency domain as,

$$\tilde{y}(\xi,\omega)=\frac{2\pi Pe^{-i\xi x_0}\delta(\omega+v\xi-\omega_0)}{EI\xi^4-m\omega^2+ic\omega+k} \tag{8}$$

To obtain the response in space-time domain, the inverse Fourier transform is applied, which results in,

$$y(x,t)=\frac{1}{(2\pi)^2}\int_{-\infty}^{\infty}\int_{-\infty}^{\infty}\frac{2\pi Pe^{-i\xi x_0}\delta(\omega+v\xi-\omega_0)}{EI\xi^4-m\omega^2+ic\omega+k}e^{i(\xi x+\omega t)}d\xi d\omega \tag{9}$$

Using the property of the Delta function, Eq. (6), yields,

$$y(x,t)=\frac{Pe^{i\omega_0 t}}{(2\pi)}\int_{-\infty}^{\infty}\frac{e^{i\xi(x-x_0-vt)}}{EI\xi^4-mv^2\xi^2+(2mv\omega_0-icv)\xi-m\omega_0^2+ic\omega_0+k}d\xi \tag{10}$$

To integrate Eq. (10), the complex analysis theory as discussed in [4] is used. This theory requires calculating the residues of the function and the roots of the denominator of the function, the poles, ξ_j. If the poles of the characteristic equation in Eq. (10) are complex, it is shown that the response in space-time can be obtained from,

$$y(x,t)=\begin{cases}-iPe^{i\omega_0 t}\sum\limits_{\mathrm{Im}(\xi_j)<0}\dfrac{e^{i\xi_j(x-x_0-vt)}}{(\xi_j-\xi_1)\ldots(\xi_j-\xi_{j-1})(\xi_j-\xi_{j+1})(\xi_j-\xi_4)} & x-x_0-vt<0\\ iPe^{i\omega_0 t}\sum\limits_{\mathrm{Im}(\xi_j)>0}\dfrac{e^{i\xi_j(x-x_0-vt)}}{(\xi_j-\xi_1)\ldots(\xi_j-\xi_{j-1})(\xi_j-\xi_{j+1})(\xi_j-\xi_4)} & x-x_0-vt\geq 0\end{cases} \tag{11}$$

3 ENERGY HARVESTING

A single degree-of-freedom energy harvester system (spring-mass-damper), is attached to the infinite elastic beam as shown in Figure 2, where m_h is the mass, k_h is the suspension stiffness, c_h is the damping of the harvester that is used for energy harvesting, x_h is the displacement of the harvester, and $y(x_h,t)$ is the base displacement at the location of the harvester, x_h. The energy harvester is excited by the vibration transmitted from the moving load y to the harvester.

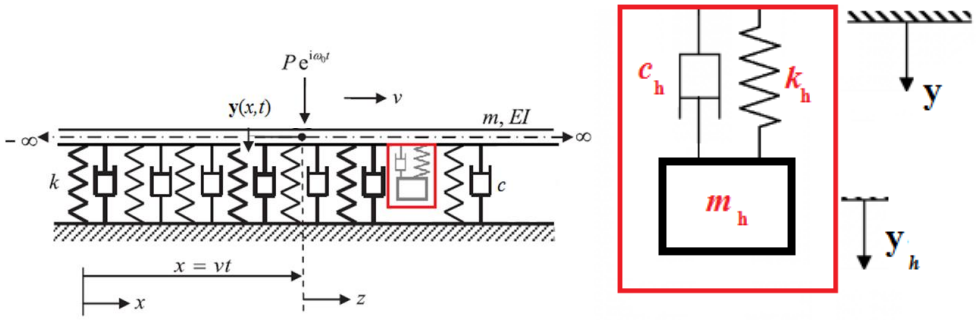


Figure 2: A harvester attached to the beam subject to harmonic moving load

The governing dynamic equation can be written as:

$$m_h\ddot{y}_h + c_h(\dot{y}_h - \dot{y}) + k_h(y_h - y) = 0 \tag{12}$$

Denoting, $z(t) = y_h(t) - y(t)$ as the relative displacement between the base and the mass, yields to

$$m_h\ddot{z}(t) + c_h\dot{z}(t) + k_h z(t) = -m_h\ddot{y}(t) \tag{13}$$

The location of the harvester is known, therefore Eq. (13) is entirely in time domain. Taking Fourier transform, we can convert Eq. (13) into frequency domain,

$$\tilde{z}(\omega) = \frac{m_h\omega^2\tilde{y}(\omega)}{-m_h\omega^2 + ic_h\omega + k_h} \tag{14}$$

Applying Fourier transform to Eq. (11) leads to $\tilde{y}(\omega)$. For example, for the case where $x_h - x_0 - vt \geq 0$,

$$\tilde{y}(\omega) = iP\sum_{\mathrm{Im}(\xi_j)<0} \frac{e^{i\xi_j(x_h-x_0)}\int_{-\infty}^{\infty} e^{i(\omega_0-\omega-\xi_j v)t}dt}{(\xi_j-\xi_1)\ldots(\xi_j-\xi_{j-1})(\xi_j-\xi_{j+1})(\xi_j-\xi_4)} \tag{15}$$

Applying the definition of Delta function,

$$\tilde{y}(\omega) = i2\pi P\sum_{\mathrm{Im}(\xi_j)>0} \frac{e^{i\xi_j(x_h-x_0)}\delta(\omega+\xi_j v-\omega_0)}{(\xi_j-\xi_1)\ldots(\xi_j-\xi_{j-1})(\xi_j-\xi_{j+1})(\xi_j-\xi_4)} \tag{16}$$

, and substituting Eq. (16) into Eq. (14), yields the frequency response of the energy harvester,

$$\tilde{z}(\omega) = \begin{cases} \dfrac{-i(2\pi)Pm_h\omega^2}{-m_h\omega^2 + ic_h\omega + k_h}\displaystyle\sum_{\mathrm{Im}(\xi_j)<0} \frac{e^{i\xi_j(x_h-x_0)}\delta(\omega+\xi_j v-\omega_0)}{(\xi_j-\xi_1)\ldots(\xi_j-\xi_{j-1})(\xi_j-\xi_{j+1})(\xi_j-\xi_4)} & x_h - x_0 - vt < 0 \\ \dfrac{i(2\pi)Pm_h\omega^2}{-m_h\omega^2 + ic_h\omega + k_h}\displaystyle\sum_{\mathrm{Im}(\xi_j)>0} \frac{e^{i\xi_j(x_h-x_0)}\delta(\omega+\xi_j v-\omega_0)}{(\xi_j-\xi_1)\ldots(\xi_j-\xi_{j-1})(\xi_j-\xi_{j+1})(\xi_j-\xi_4)} & x_h - x_0 - vt \geq 0 \end{cases} \tag{17}$$

Applying inverse Fourier transform to Eq. (17), we can find the response of the harvester subject to harmonic moving load. For example, for the case of $x_h - x_0 - vt \geq 0$,

$$z(t)=\frac{1}{2\pi}\int_{-\infty}^{\infty}\frac{i(2\pi)Pm_h\omega^2}{-m_h\omega^2+ic_h\omega+k_h}\sum_{\mathrm{Im}(\xi_j)<0}\frac{e^{i\xi_j(x_h-x_0)}\delta(\omega+\xi_j v-\omega_0)}{(\xi_j-\xi_1)\ldots(\xi_j-\xi_{j-1})(\xi_j-\xi_{j+1})(\xi_j-\xi_4)}e^{i\omega t} \tag{18}$$

Applying the property of the Delta function, the relative displacement is,

$$z(t)=\begin{cases}-iPm_h e^{i\omega_0 t}\sum_{\mathrm{Im}(\xi_j)<0}\frac{e^{i\xi_j(x_h-x_0-vt)}(-\xi_j v+\omega_0)^2}{(\xi_j-\xi_1)\ldots(\xi_j-\xi_{j-1})(\xi_j-\xi_{j+1})(\xi_j-\xi_4)\left(-m_h(-\xi_j v+\omega_0)^2+ic_h(-\xi_j v+\omega_0)+k_h\right)} & x_h-x_0-vt<0\\ iPm_h e^{i\omega_0 t}\sum_{\mathrm{Im}(\xi_j)>0}\frac{e^{i\xi_j(x_h-x_0-vt)}(-\xi_j v+\omega_0)^2}{(\xi_j-\xi_1)\ldots(\xi_j-\xi_{j-1})(\xi_j-\xi_{j+1})(\xi_j-\xi_4)\left(-m_h(-\xi_j v+\omega_0)^2+ic_h(-\xi_j v+\omega_0)+k_h\right)} & x_h-x_0-vt\geq 0\end{cases} \tag{19}$$

The instantaneous power can be obtained from the damping force multiplied by the relative velocity,

$$P_{ins}=c_h\dot{z}^2(t) \tag{20}$$

Therefore, the derivative of the displacement response of Eq. (20) is required. The harvested energy from the measured time t_0 to t_f, can be calculated from,

$$E=c_h\int_{t_0}^{t_f}\dot{z}^2(t)dt \tag{21}$$

4 NUMERICAL SIMULATIONS

4.1 Response under a quasi-static moving train

In this section, the response of the elastic beam under a moving train is obtained. The parameters for the elastic beam are chosen to be,

$$EI=2.5MNm^2,\ m=50kg/m,\ v=50m/s,\ k=70MN/m^2,\ c=8kNs/m^2.$$

The train is simplified as a 2D object. It has seven carriages. Each carriage is 23m long and has two bogies and each bogie has two wheels. The distance between the two wheels of a bogie is $l_1=2.5m$. The distance between the wheels of the two adjacent bogie is $l_2=13.5m$ and the distance between the wheels between the two adjacent carriages is $l_3=6.5m$, as shown in Figure 3.

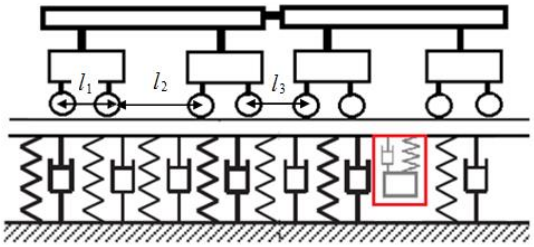


Figure 3: Infinite beam on an elastic foundation under a quasi-static moving train

The static mass of one carriage of the train is 45 tones. Therefore the static force per unit length for each carriage is $19KN$. In this example, the angular velocity of the wheels are zero, $\omega_0=0$ and we have a static force.

Response under a single carriage.

To obtain the response of the beam at $x = 500m$, Eq. (11) is used. The coordinates x_0 for the four wheels from the right to the left of the first carriage are $0, -l_1, -(l_1 + l_2), -(2l_1 + l_2)$. The response of the beam subject to each individual moving wheel is obtained as shown in Figure 4.

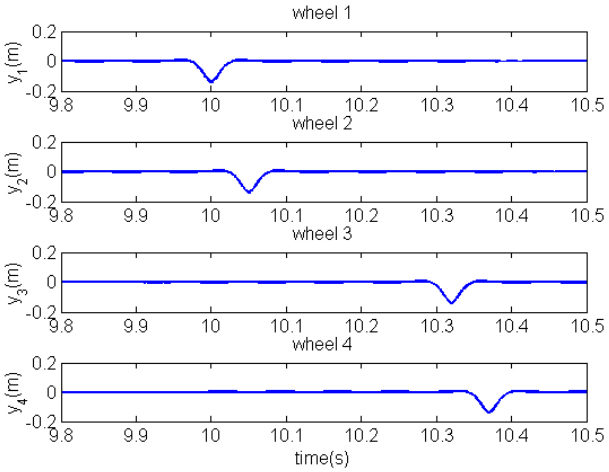


Figure 4: Response of the beam at $x = 500m$ under the individual wheels of a single carriage

Since, the beam is linear, its total response from the single carriage at the measured point can be found from adding all the individual responses due to each moving wheel, as shown in Figure 5.

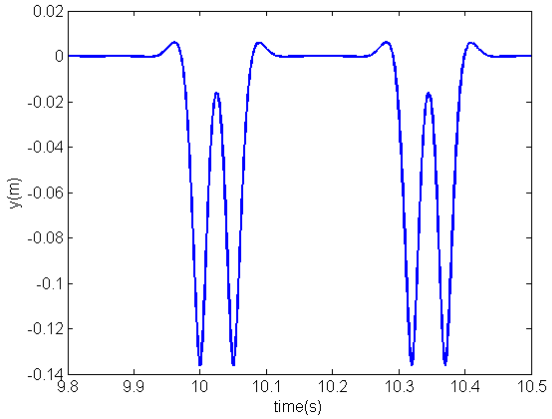


Figure 5: Response of the beam at $x = 500m$ under a single carriage

Response under a train with seven carriages.

Similarly, the response of the beam at the location of $x = 500m$ under seven carriages can be obtained by linear superposition of all the responses due to each carriage. Figure 6 shows the total displacement response measured from 9.8s to 13.4 seconds.

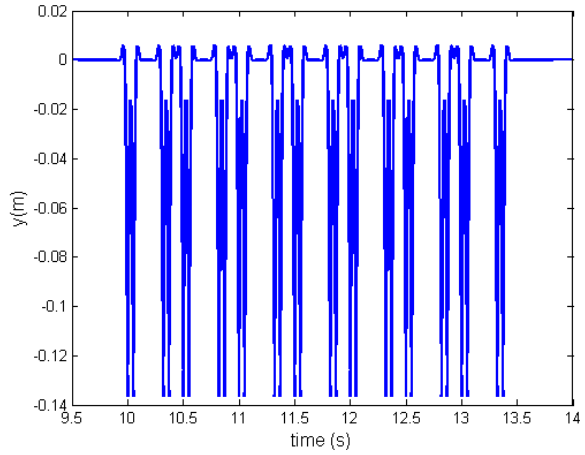
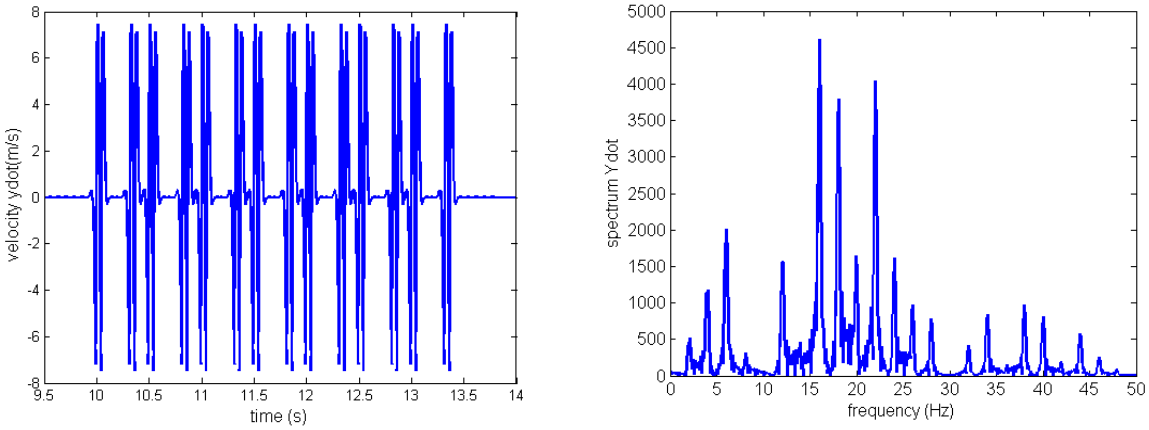


Figure 6: Response of the beam at $x = 500m$ due to the passage of the train

4.2 Energy harvesting using the response of seven carriages

In this section, an investigation is made on how much energy can be harvested from a beam subject to the moving train with speed of 50m/s.

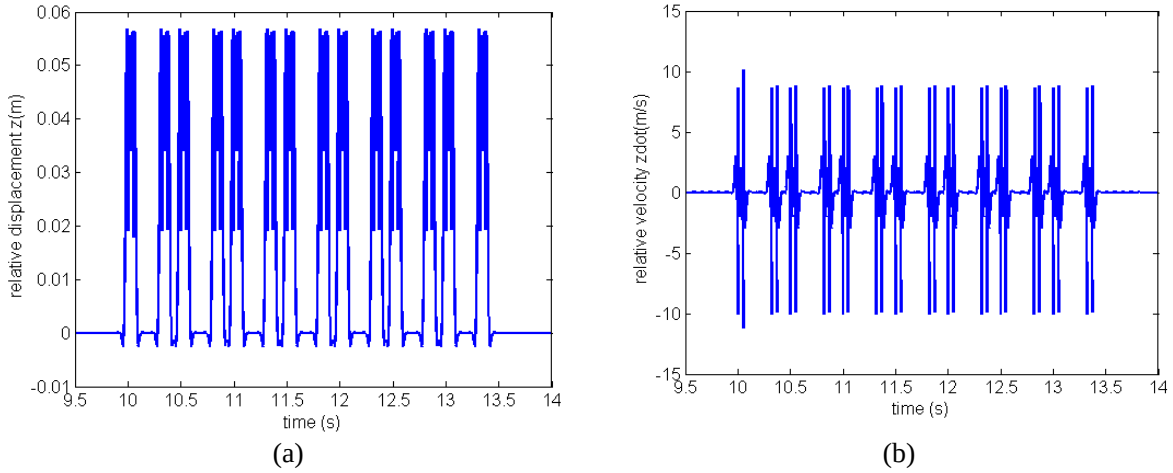
The energy harvester is chosen to have a fixed mass of $m_h = 1kg$ and a damping value of $c_h = 0.5Ns/m$. The performance of the harvester is maximum when the natural frequency of the harvester is tuned at the excitation frequency. Therefore, the velocity $\dot{y}(t)$ and its spectrum $Y(\omega)$ are plotted in Figure 7 in order to define the dominant excitation frequencies due to the passage of the train.



(a) (b)

Figure 7: Velocity response of the beam at $x = 500m$ (a) time history, $\dot{y}(t)$ (b) velocity spectrum $\dot{Y}(\omega)$

The three dominant peaks in Figure 7(b) are about 16Hz, 18Hz and 21Hz. The stiffness of the harvester can be chosen such that the harvester has the natural frequency equal to one of these dominant peaks. In this case, the stiffness of the harvester is chosen to be $k_h = 10.095 kN/m$ which is tuned to the highest peak at 16Hz.
Using these parameters for the harvester, the relative displacement and relative velocity of the harvester can be obtained from Eq. (19) and its derivative as shown in Figure 8.



(a) (b)

Figure 8: (a) Relative displacement and (b) relative velocity between the beam and the harvester

The amount of the energy harvested is calculated from Eq(20) and is about 9.12kJ.
Simulation was also carried out to calculate the energy harvested for stiffness of the harvester varying between 0 to $98.6 kN/m$. Figure 9 shows the energy harvested as a function of the natural frequency of the harvester. It can be seen that significant amount of energy can be harvested at frequencies below 50 Hz.

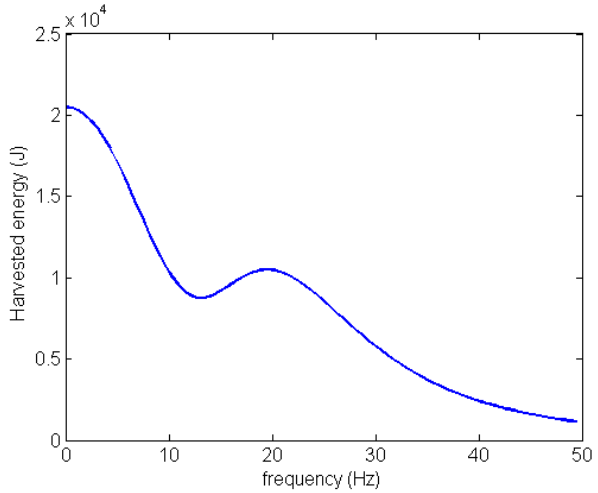
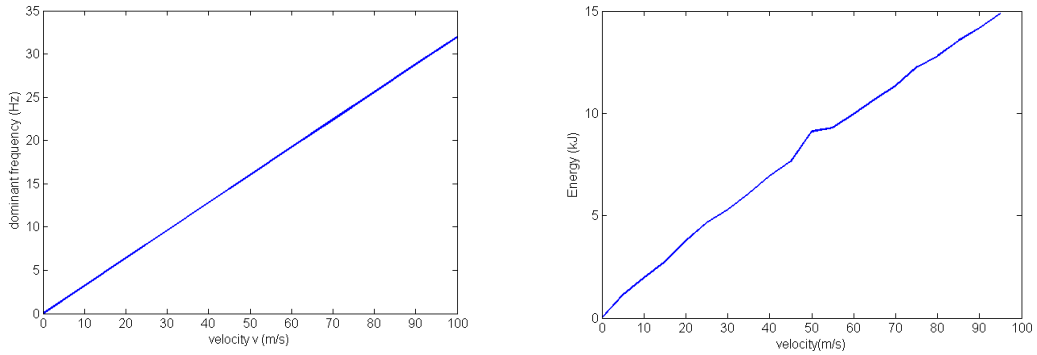


Figure 9: Harvested energy as a function of the natural frequency of the harvester

The effect of the velocity of the train on the dominant frequency is also investigated. Ju et al [13] showed that the dominant frequency has a linear relationship with the velocity of the train and the simulation result in Fig 10(a) also confirms this. Figure 10(b) shows the amount of harvested energy as a function of velocity. The harvested energy increases also linearly between the speed of 0 to 100m/s.



(a) (b)

Figure 10: Harvested energy as a function of the natural frequency of the harvester

5 CONCLUSIONS

In this paper, the problem of energy harvesting from a moving load on an elastic foundation was considered. An energy harvester was considered as a single dof oscillator and was designed to harvest maximum energy from the vibrations of the beam due to the passage of the train. The train was modelled as a 2D object with seven carriages. Each carriage has two bogies and each bogie has four wheels. The train has the speed of 50m/s. The deflection of the beam due to the passage of the train was derived analytically at the location of the harvester. Then the relative displacement between the harvester and the beam was obtained. The harvester was designed such that the amount of the energy harvested is maximum. The velocity spectrum has dominant frequencies with the maximum peak at 16 Hz. The harvester was designed so that its natural frequency is equal to the excitation frequency. It was shown that about 10k J was harvested at this frequency. Then the stiffness of the harvester was varied so that its natural frequency changes between 0 to 50 Hz. The harvested energy was calculated as a function of the stiffness of the harvester or the natural frequency of the device to demonstrate its variation.

REFERENCES

[1] L. Fryba, History of Winkler foundation, Vehicle System Dynamics Supplement, 24, 7–12, 1995.

[2] P.M. Mathews, Vibrations of a beam on elastic foundation, *Zeitschrift fu¨r Angewandte Mathematik und Mechanik* 38 ,105–115, 1958.

[3] D.G. Duffy, The response of an infinite railroad track to a moving, vibrating mass, Journal of Applied Mechanics, *Transaction of the American Society of Mechanical Engineers ASME*, 57, 66–73, 1990.

[4] M.F. Hussein, and H.E. M. Hunt, Modelling of floating-slab tracks with continuous slabs under oscillating moving loads, *Journal of Sound and Vibration*, 297(1), 37-54, 2006.

[5] Perpetuum Ltd, Southampton, UK, http://www.perpetuum.com/

[6] O. Gatin and B. Lhenoret, 2009, WSN and Energy harvesting for railway applications, Presentation at Energy Harvesting & Storage USA 2009, Denver, CO.

[7] M. Ghandchi Tehrani, G. Gatti, G., M.J. Brennan, and D.J. Thompson, Energy harvesting from train vibrations, *Proceedings of 11th International Conference on Vibration Problems (ICOVP 2013)*, Lisbon, Portugal, 19-21, 2013.

[8] C.A. Nelson, S.R. Platt, D. Albrecht, V. Kamarajugadda, and M. Fateh, Power harvesting for rail road track health monitoring using piezoelectric and inductive devices. *Proc. of the SPIE: Active and Passive Smart Structures and Integrated Systems*, 6928(1), 2008.

[9] J.J. Wang, G.P. Penamalli and L. Zuo, Electromagnetic energy harvesting from train induced railway track vibrations, *IEEE*, 29-34, 2012.

[10] Z. F. Mian, 2009, Wireless railroad monitoring US patent 12/493,789.

[11] Innowattech Ltd., Technion City, Haifa, Israel

[12] C A. Nelson, S R Plattb, S E. Hansen, M Fateh, Power harvesting for railroad track safety enhancement using vertical track displacement, *Proc. of SPIE: Active and Passive Smart Structures and Integrated Systems*, Vol. 7288, 2009.

[13] S. Ju, H. Ling, J. Huang, Dominant frequencies of train-induced vibrations, *Journal of Sound and Vibration*, 319, 247-259. 2009.

International Conference on Engineering Vibration
Ljubljana, Slovenia, 7-10 September 2015

ANALYTICAL MODELLING OF RAILWAY TRACK DYNAMICS

P. Koziol

Cracow University of Technology, Faculty of Civil Engineering, Institute of Road and Railway Engineering
pkoziol@pk.edu.pl

Keywords: Railway dynamics, One-layer model, Two-layer model, Vertical vibrations, Analytical solution, Experimental validation.

Abstract. *Analytical procedures leading to effective parametrical analysis of structures subjected to dynamic excitations are of importance in recent railroads investigations. Improvements of existing structures and new techniques of modelling and design are sought by researchers and railways industry. Experimental measurements show that railway track imperfections can produce noticeably significant changes in the structure response associated with quasi-static force. The paper shows analytical solution representing railway track vibrations due to moving train. Two theoretical models are analysed. The first one is described by the dynamic equation of beam resting on viscoelastic foundation and the second one consists of two layers. The first layer is modelled by the Euler-Bernoulli beam on viscoelastic foundation (representing rail with fasteners) and the second one is the sleepers' layer (rigid bodies without bending) on viscoelastic foundation (ballast and subgrade). The rail modelled by infinitely long beam is subjected to a set of moving forces related to a wheelset of single wagon. Each of wheels produces load harmonically varying in time with frequency calculated on the basis of distances between wheels and considered type of rail imperfections. The steady-state response of the beam is obtained by applying the moving coordinate system and coiflet based approximation of the Fourier transform, leading to analytical estimation of vertical vibrations amplitude. It is shown that the analysed models taking into account viscous damping of foundation can be considered as good enough representation of realistic railway track behaviour. Numerical examples using parameters taken from measurements carried out for Polish railway network during passage of fast train Pendolino EMU250 are presented. The obtained results are in accordance with measured data in wide range of physical parameters. A comparative study of two considered models of railway track is carried out for different types of load distributions.*

1 INTRODUCTION

Intensive development of railways during last decades leads to a necessity of deeper investigations with regard to modelling of railway structures and especially railway tracks. One can observe a lack of effective procedures allowing parametrical analysis of models describing transportation systems. Whereas laborious and very often doubtful numerical computations are used in the investigation of such structures, new mathematical tools might bring an improvement of analytical solutions being more reliable benchmark for further studies [1,2].

Various problems related to moving loads and masses analysis are widely discussed in the literature [3]. Theoretical modelling of beams vibrations generated by moving loads is of great significance in railway engineering. Nevertheless, the analytical and closed form solutions are possible for significantly simplified models only. When it comes to more realistic systems, available methods are not enough for their solution. Therefore many models of rail tracks on rigid foundation are considered by scientists and engineers in order to avoid computational difficulties and, at the same time, to reflect all important features of existing structures fairly enough. This process leads to simplification of studies. A good balance between modelling complexity and solving ability must be found in order to achieve proper representation of realistic structures behaviour.

The wavelet based approximation of the Fourier transform is one of relatively new methods which might help in solving more complex dynamic models, especially when computationally difficult assumptions are introduced, e.g. nonlinear or stochastic properties [2,4,5]. Although this method already gave a number of important new results in the subject of moving loads analysis, it still needs experimental validation in order to show its advantages and limitations when applied to systems describing real scenarios [6-10].

The railway track is modelled very often either as the one-layer system described by the dynamic equation of beam or the two-layer system consisting of a beam on viscoelastic foundation (representing rail with fasteners) and separated sleepers' layer (rigid bodies without bending) on viscoelastic foundation representing ballast and subgrade.

In this paper, these two models are solved by using the coiflet based approximation instead of direct computation of the Fourier integrals [2,11]. The solutions are obtained for realistic physical parameters and validated by using measurements taken for Polish Railway network and the fast train Pendolino EMU-250 [12]. The reference results show accordance with wavelet based simulations in wide range of physical parameters, which can be treated as a fundamental and preliminary experimental validation of the proposed method adapted to transportation investigations [2,13].

The force produced by train is modelled by more realistic load representation, compared to previous publications, cf. [7,8,10,13], consisting of a quasi-static part coming from weight of wagon and a dynamic part produced by rail irregularities. A set of four wheels with axles configuration related to Pendolino train is considered. Regular track imperfections are described theoretically as the factor generating additional dynamic load. Physical parameters related to existing operational systems are taken into account for numerical comparisons.

2 MODEL FORMULATION

Two models of railway track are considered. The first one is described by the dynamic equation of the Euler-Bernoulli beam resting on viscoelastic foundation:

$$EI\frac{\partial^4 \widetilde{w}(\widetilde{x},t)}{\partial \widetilde{x}^4}+\rho_B\frac{\partial^2 \widetilde{w}(\widetilde{x},t)}{\partial t^2}+c\frac{\partial \widetilde{w}(\widetilde{x},t)}{\partial t}+k\widetilde{w}(\widetilde{x},t)=P(\widetilde{x},t) \tag{1}$$

where $\widetilde{w}(\widetilde{x},t)$ is the beam vibration, EI is the bending stiffness, ρ_B is the linear density of the rail, c is the viscous damping of foundation and k is the coefficient of foundation stiffness. $P(\widetilde{x},t)$ represents the vertical moving force. This force is composed of four distributed loads related to wheels of one wagon, each of them consisting of a quasi-static part P_{St} and a harmonically varying part P_D representing variations produced by track irregularities:

$$P(\widetilde{x},t) = P_{St}(\widetilde{x},t) + P_D(\widetilde{x},t) = \\ = \sum_{l=0}^{3}\left(\frac{\Delta P}{a}e^{i(\Omega t+\varphi_l)} + \frac{P_0}{a}\right)\cos^2\left(\frac{\pi(\widetilde{x}-Vt-s_l)}{2a}\right)H(a^2-(\widetilde{x}-Vt-s_l)^2) \tag{2}$$

$$P_{St}(\widetilde{x},t) = \sum_{l=0}^{3}\frac{\Delta P}{a}e^{i(\Omega t+\varphi_l)}\cos^2\left(\frac{\pi(\widetilde{x}-Vt-s_l)}{2a}\right)H(a^2-(\widetilde{x}-Vt-s_l)^2) \tag{3}$$

$$P_D(\widetilde{x},t) = \sum_{l=0}^{3}\frac{P_0}{a}\cos^2\left(\frac{\pi(\widetilde{x}-Vt-s_l)}{2a}\right)H(a^2-(\widetilde{x}-Vt-s_l)^2)\,. \tag{4}$$

$H(.)$, $2a$ and V are the Heaviside function, the span of load and the speed of train, respectively. $\Omega = 2\pi V/L$ is the angular frequency of vibrations produced by the considered irregularities of rail and φ_l denotes the angular phase associated with different positions of wheels on these rail irregularities. $\Delta P = 0.1\cdot P_0$ is an amplitude of additional harmonically varying force that can be related to imperfections appearing on rail. It is assumed that these irregularities, with length of $L = 0.5\text{m}$, are placed directly side by side, that is with no space between them and their shape is similar to the cosine function with constant amplitude. Other rail imperfections are neglected.

The second model is represented by so called the double-beam system resting on viscoelastic foundation. It allows to consider all important elements of railway tracks such as rails, sleepers, rail pads, floating slabs or slab bearings. The mathematical model consists of an upper Euler-Bernoulli beam to account for rails (with mass m_r and bending stiffness EI_r) and a lower layer without bending to account for sleepers (with mass m_s). There are also two layers, the first one viscoelastic (with stiffness k_r and a viscous damping factor c_r), under the beam, and the second one underneath the slab (with stiffness k_s and viscous damping factor c_s). The transverse vibration of this system can be described by the two coupled partial differential equations of motion:

$$E_r I_r\frac{\partial^4 u}{\partial\widetilde{x}^4} + m_r\frac{\partial^2 u}{\partial t^2} + c_r\left(\frac{\partial u}{\partial t}-\frac{\partial w}{\partial t}\right) + k_r(u-w) = P(\widetilde{x},t) \tag{5}$$

$$m_s\frac{\partial^2 w}{\partial t^2} + c_s\frac{\partial w}{\partial t} + k_s w - c_r\left(\frac{\partial u}{\partial t}-\frac{\partial w}{\partial t}\right) - k_r(u-w) = 0 \tag{6}$$

where u and w are the transverse displacements of the rail and sleepers, respectively, at position $\widetilde{x}$ and time t. For both models, the boundary conditions must reflect the fact that in the area being far from the applied force, the central line deflection, its slope and curvature tend to zero.

Both systems can be solved by introducing the Galilean coordinate transformation $x = \widetilde{x} - Vt$ and by applying the Fourier transform to such obtained ordinary differential equations. Although two described models are relatively easy to solve using classical methods, ei-

ther analytical or numerical ones, the wavelet based approximation using the coiflet type filters is used for calculation of the inverse Fourier transforms [2,5,11]. This is done for two reasons. The first one is an efficiency improvement of hybrid semi-analytical approach, compared with numerical integration, and the second one is an attempt to circumvent laborious calculations related to integration over contour or application of the residues theorem. In addition, such relatively simple implementation of this technique allows to validate the proposed approximation without involvement in more complex considerations related to mechanical aspects of the train-track dynamics. However, it still forms an interesting application important for engineering problems and shows possible advantages of the method when applied to more complicated models. One should underline that the usefulness of the wavelet based approach using the developed estimation was already justified leading to important results in the field of moving load analysis, including stochastic and nonlinear models [2,4-9,13-15]. It was also partially validated in the case of simplified dynamic one-layer model possessing nonlinear properties of foundation stiffness, with its classical cubic form assumed for rail deflection, and compared with the Finite Element Method results in the theoretical case of beam subjected to a concentrated load [9,13]. Yet, the experimental validation for various models is needed in order to recognize probable traps in engineering implementations. This paper shows this kind of validation in the case of two considered linear models of railway track, using the system of parameters determined on the basis of measurements done on the Polish Railways network, the line No. 4 between stations Psary and Góra Włodowska, during passage of EMU-250 (Pendolino) test train [12].

Two different representations of distributed force generated by a single wheel are used: the first one based on description by a constant function spread on the interval of length equal to $2a$ and the second one represented by the square of cosine function (see Eqs. (2-4)). Numerical simulations show that the difference between these two representations of the force applied is negligible for the considered system of physical parameters and train axles configuration, from the engineering point of view. This means that the adopted approximation method works correctly even if some important mathematical features of the used functions are not secured. A more detailed discussion on this problem is presented in past publications (see e.g. [2]). However the second approach, i.e. the square of cosine function, allows to avoid all doubts related to mathematical aspects of the load modelling. The function used in Eqs. (2-4) is differentiable and has compact support. Therefore all calculations needed to solve the problem can be easily done, without additional approximations which are necessary e.g. in the case of the Fourier series applied to rectangular load representation. Nevertheless, one can show examples of sets of parameters for which the two considered loads produce significantly different response. For these cases, the two described approaches cannot be used interchangeably.

3 COIFLET-BASED ESTIMATION

The wavelet theory, a relatively new subject of mathematics, provides interesting tools allowing to improve approximating techniques for various computations, not only numerical ones which are very popular in engineering, but also for analytical formulas describing closed form solutions given by integrals. It is shown that the Fourier transform and the inverse Fourier transform of each function belonging to L^2 space:

$$F[f] = \hat{f}(\omega) = \int_{-\infty}^{\infty} f(x) e^{-i\omega x} dx\,,\ F^{-1}[\hat{f}] = f(x) = \frac{1}{2\pi} \int_{-\infty}^{\infty} \hat{f}(\omega) e^{i\omega x} d\omega \tag{7}$$

can be derived by using the following formulas [2,5,16]:

$$\hat{f}(\omega)=\lim_{n\to\infty}\hat{f}_n(\omega)=\lim_{n\to\infty}2^{-n}\prod_{k=1}^{\infty}\Big(\sum_{j=0}^{3N-1}p_j e^{-ij\omega/2^{n+k}}\Big)\sum_{k=-\infty}^{+\infty}f((k+M)2^{-n})e^{-i\omega k2^{-n}} \tag{8}$$

$$f(x)=\lim_{n\to\infty}f_n(x)=\lim_{n\to\infty}\frac{1}{2^{n+1}\pi}\prod_{k=1}^{\infty}\Big(\sum_{j=0}^{3N-1}p_j e^{ijx/2^{n+k}}\Big)\sum_{k=-\infty}^{+\infty}\hat{f}((k+M)2^{-n})e^{ixk2^{-n}} \tag{9}$$

where $M=\sum_{k=0}^{3N-1}kp_k$ and N is the degree of accuracy of the coiflet filter (p_k), in this paper equal to 6 [11]. The wavelet coefficients associated with coiflets can be estimated analytically due to their property of vanishing moments for both the scaling and the wavelet functions. The only criterion which can be used for determination of the approximation order is the solutions' stabilization [14,15]. For the problem considered in this paper, it is enough to take relatively low order of approximation $n=3$. Therefore one can assume $f(x)\approx f_3(x)$ for further analysis. Hence formulas for the solution in physical domain take the following practical forms:

$$\tilde{w}(x)=\frac{1}{2^4\pi}\prod_{k=1}^{k_p}\sum_{j=0}^{17}p_j\exp(jix/2^{3+k})\sum_{k=k_{\min}}^{k_{\max}}\hat{\tilde{w}}((k+M)/2^3)\exp(ikx/2^3) \tag{10}$$

in the case of Eq. (1) and

$$u(x)=\frac{1}{2^4\pi}\prod_{k=1}^{k_p}\sum_{j=0}^{17}p_j\exp(ij\,x/2^{3+k})\sum_{k=k_{\min}}^{k_{\max}}\hat{u}((k+M)/2^3)\exp(ikx/2^3), \tag{11}$$

$$w(x)=\frac{1}{2^4\pi}\prod_{k=1}^{k_p}\sum_{j=0}^{17}p_j\exp(ij\,x/2^{3+k})\sum_{k=k_{\min}}^{k_{\max}}\hat{w}((k+M)/2^3)\exp(ikx/2^3) \tag{12}$$

in the case of Eqs. (5-6).

k_p is a parameter associated with the used coiflet filter and the order of wavelet approximation n. The value of this parameter is determined by applying the stabilization criterion. The range of summation $k_{\min}(\omega_{\min})=16(\omega_{\min}-1)$ and $k_{\max}(\omega_{\max})=16\omega_{\max}-1$ should be chosen in a way that keeps all values of variable ω having strong influence on behaviour of the solution inside the interval $[\omega_{\min},\omega_{\max}]$.

4 NUMERICAL EXAMPLES AND RESULTS DISCUSSION

The following system of parameters is used for numerical simulations (60E1 rail) [10,12]:

1. For the one-layer model: $k=3.1\cdot10^7\ \mathrm{N/m^2}$ (fasteners' vertical stiffness); $P_0=78329\mathrm{N}$ (average static load of EMU-250); $\Delta P=0.1\cdot P_0$ (the amplitude of harmonically varying load generated by irregularities); $I=3055\cdot10^{-8}\ \mathrm{m^4}$ (moment of inertia of the rail); $EI=2.1\cdot10^{11}\ \mathrm{N/m^2}$ (Young's modulus of the rail); $a=0.0075\,\mathrm{m}$; $c=3768\,\mathrm{Ns/m}$ (damping coefficient of fasteners); $\rho_B=427$ kg/ m (the structure linear mass density);

2. For the two-layer model: $I=3055\cdot10^{-8}\ \mathrm{m^4}$ (moment of inertia of rail), $E=2.1\cdot10^{14}\ \mathrm{N/m^2}$ (Young's modulus of rail), $A=7.69\cdot10^{-3}\ \mathrm{m^2}$ (average cross section area of the rail), $m_r=60\,\mathrm{kg/m}$ (unit mass of rail), $c_r=3950\,\mathrm{Ns/m^2}$ (unit fasteners' damping coefficient), $k_r=9.12\cdot10^7\ \mathrm{N/m^2}$ (unit fasteners' linear stiffness), $m_s=367\,\mathrm{kg/m}$ (unit mass of

sleepers with ballast mass), $k_s = 56.67 \cdot 10^6\,\mathrm{N/m^2}$ (unit sleeper foundation stiffness), $c_s = 81667\,\mathrm{Ns/m^2}$ (sleeper foundation damping coefficient), $\Delta P = 0.1 \cdot P_0$, $a = 0.0075\,\mathrm{m}$. The observation point $\tilde{x} = 0$ and the train speed $V = 240\,\mathrm{km/h}$ are chosen for comparative analysis.

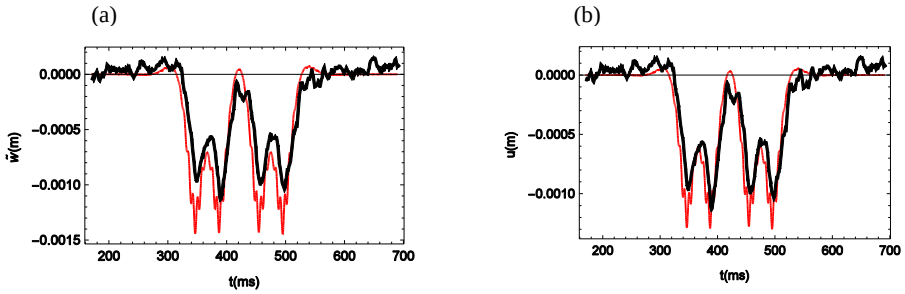


Figure 1: The vertical displacement of rail - experimental (black), coiflet-based solution (red): (a) one-layer model (Eq. (1)); (b) two-layer model (Eqs. (5) and (6)).

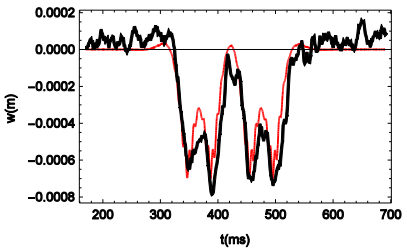


Figure 2: The vertical displacement of sleepers (Eqs. (5) and (6)): experimental (black); coiflet-based solution (red).

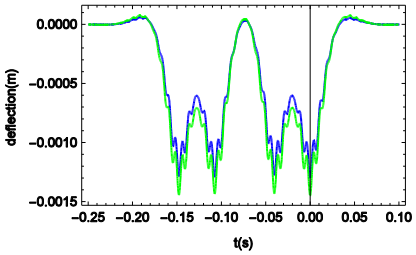


Figure 3: Comparison of vertical displacements of rail obtained for the one-layer model (Eq. (1) - green) and the two-layer model (Eqs. (5) and (6) - blue).

Numerical simulations lead to the conclusion that the two-layer model better reflects physical properties of the railway track. One should underline that the vertical stiffness of ballast and subgrade must be estimated in order to carry out parametrical study. This parameter is determined on the basis of numerical experiments done for two-layer model. This means that the value of this parameter, assumed in this paper as equal to $100\,\mathrm{MN/m^3}$, is chosen in a way which guaranties matching of the calculated rail displacements with experimental data for a

wide range of train speeds with assumed accuracy related to the vibration amplitude. After this, the equivalent stiffness is calculated for the one-layer model. It can be also observed that sleepers' layer vibrations obtained by using the two-layer model are relatively weekly dependent on the vertical stiffness of ballast and subgrade determined experimentally for rails (cf. [10]).

Figure 1 shows rail vibrations obtained via two considered models. One can see that the two-layer model gives results closer to experimental data for the chosen train speed. The two-layer model can be considered as more useful due to the fact that it allows to analyse also sleepers' layer (Figure 2). In this case, the similarity between experimental measurements and analytical results is more stable and independent of speed value.

Figure 3 shows how big differences can be ascertained for the rail vibrations in the case of high speed when both models are used. This leads to necessity of answering the question: When the two-layer model (Eqs. (5) and (6)) can be successfully replaced by much simpler one-layer system (Eq. (1)) in the case of rail vibration analysis only? One can observe in Figure 4 that the relative error between these two solutions grows with increasing speed of train. Therefore one can suggest a great care while using the one-layer system in high speed range.

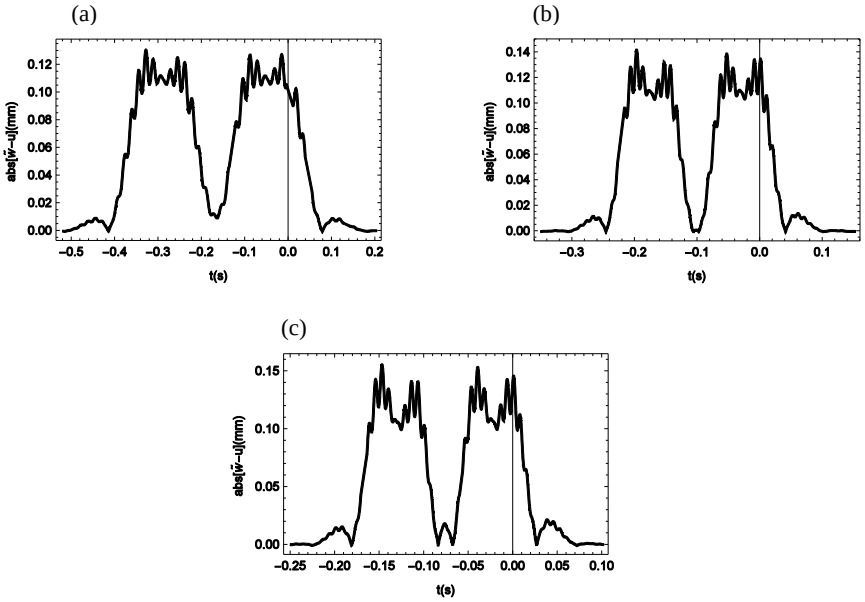


Figure 4: Comparison of rail vertical displacement obtained for the one-layer model and the two-layer model ($|\tilde{w}-u|$): (a) $V=108\,\mathrm{km/h}$; (b) $V=180\,\mathrm{km/h}$; (c) $V=240\,\mathrm{km/h}$.

5 CONCLUSIONS

- Two models of railway tracks are compared and some hints regarding a proper choice of modelling approach are presented. The one-layer model might appear less appropriate for using in the area of high speeds for some systems of physical parameters.
- Semi-analytical results obtained by using the coiflet based approximation of the Fourier transform are compared with experimental measurements showing relatively good matching especially in the case of two-layer model. Comparative studies done for several

sets of parameters can be treated as another validation of the wavelet based approach to vibration analysis applied to railway tracks investigations.

- More reliable representation of the force produced by train is used in this paper. It takes into account a quasi-static force combined with dynamic part of load produced by rail imperfections. Realistic parameters of fast train Pendolino EMU250 are used for modelling of moving load and for numerical simulations of track vibrations.

REFERENCES

[1] V-H. Nguyen, D. Duhamel, Finite element procedures for nonlinear structures in moving coordinates. Part II: Infinite beam under moving harmonic loads. *Computers & Structures*, Elsevier, 86 (21-22), 2056-2063, 2008.

[2] P. Koziol, *Wavelet approach for the vibratory analysis of beam-soil structures: Vibrations of dynamically loaded systems.* VDM Verlag Dr. Müller, Saarbrucken, 2010.

[3] L. Fryba, *Vibrations of Solids and Structures under Moving Loads.* Thomas Telford Ltd., London, 1999.

[4] P. Koziol, C. Mares, Wavelet approach for vibration analysis of fast moving load on a viscoelastic medium. *Shock and Vibration*, 17 (4-5), 461-472, 2010.

[5] P. Koziol, C. Mares, I. Esat, Wavelet approach to vibratory analysis of surface due to a load moving in the layer. *International Journal of Solids and Structures*, 45, 2140-2159, 2008.

[6] P. Koziol, Z. Hryniewicz, Vibrations of beams on a random foundation due to a moving load: wavelet approach. *CC2009, Proceedings of the Twelfth International Conference on Civil, Structural and Environmental Engineering Computing, Funchal, Madeira, 1-4 September 2009*. Edited by B.H.V. Topping, L.F. Costa Neves and R.C. Barros, ISBN 978-1-905088-31-7, Civil-Comp Press, Stirlingshire, United Kingdom, paper 42, doi:10.4203/ccp.91.42.

[7] P.Koziol, Wavelet approximation of Adomian's decomposition applied to the nonlinear problem of a double-beam response subject to a series of moving loads. *Journal of Theoretical and Applied Mechanics*, 52, 3, 687-697, 2014.

[8] P. Koziol, Z. Hryniewicz, Dynamic response of a beam resting on a nonlinear foundation to a moving load: coiflet-based solution. *Shock and Vibration*, 19, 995-1007, 2012.

[9] M. Musuva, P. Koziol, C. Mares, M.M. Neves, The Analysis of Beams subject to Moving Loads using: Coiflets, the Wavelet Finite Element Method and the Finite Element Method. in J. Pombo, (Editor), Proceedings of *the Second International Conference on Railway Technology: Research, Development and Maintenance*, Civil-Comp Press, Stirlingshire, UK, Paper 222, 2014. doi:10.4203/ccp.104.222.

[10] W. Czyczula, D. Kudla, P. Koziol, S. Lisowski, Analytical evaluation of track response in vertical direction due to moving load. *Journal of Vibration and Control*, 2015, in review.

[11] L. Monzon, G. Beylkin, W. Hereman, Compactly supported wavelets based on almost interpolating and nearly linear phase filters (coiflets), *Applied and Computational Harmonic Analysis*, 7, 1999, 184-210.

[12] W. Czyczula, T. Tatara et al. Field investigation of track response under EMU-250 (Pendolino) high speed train (in Polish). *Cracow University of Technology reports*. Krakow 2014.

[13] P. Koziol, Nonlinear response of railway track subjected to a moving train. *Proceedings of the ICEDYN 2015 International Conference on Structural Engineering Dynamics, Lagos, Algarve, Portugal, 22-24 June 2015.* Edited by N.M.M. Maia, M.M. Neves and R.P.C. Sampaio, ISBN 978-989-96276-9-7, paper K03.

[14] P. Koziol, Vibrations of the Euler-Bernoulli beam resting on a nonlinear foundation, *Proceedings of the ICEDYN 2013 International Conference on Structural Engineering Dynamics, Sesimbra, Portugal, 17-19 June 2013.* Edited by Maia N.M.M., Neves M.M., Sampaio R.P.C., ISBN 978-989-96276-4-2, paper K03.

[15] P. Koziol, Vibrations generated by moving train: Coiflet approximation of nonlinear response, *Pojazdy Szynowe 02/2014*, ISSN 0138-0370.

[16] J. Wang, Y. Zhou, H. Gao, Computation of the Laplace inverse transform by application of the wavelet theory. *Communications in Numerical Methods in Engineering*, 19, 959-975, 2003.

International Conference on Engineering Vibration
Ljubljana, Slovenia, 7-10 September 2015

UNIFORMLY MOVING LOAD ON A BEAM SUPPORTED BY A FOUNDATION WITH FINITE DEPTH

Zuzana Dimitrovová*[1]

[1]Departamento de Engenharia Civil, Faculdade de Ciências e Tecnologia, Universidade Nova de Lisboa and IDMEC, Instituto Superior Técnico, Universidade de Lisboa, Lisboa, Portugal
zdim@fct.unl.pt

Keywords: Transverse Vibration, Critical Velocity, Active Soil Depth, Visco-elastic Foundation, Moving Load, Analytical Solution.

Abstract. *In this paper some new analytical solutions for moving load problems are presented. In the first part, a new analytical formula for the critical velocity of a uniformly moving force on a beam supported by a foundation of finite depth is given. This formula just indicates a more realistic estimate of the critical velocity because it considers only the part of the foundation that is dynamically activated. The formula accounts for the effect of the normal force acting on the beam and the shear influence of the foundation. The critical velocity is expressed as a function of the mass ratio that relates the foundation mass with the beam mass. The new formula approaches the classical formula for the low mass ratio and the velocity of propagation of shear waves for the high mass ratio. In the second part, a new analytical formula is presented for the deflection shape of an infinite beam that is traversed by a moving mass and supported by a visco-elastic foundation. In such a case the deflection shape resembles the one associated with the moving force with an additional oscillation around it. The frequency of this oscillation is induced by the foundation characteristics and the amplitude can by derived analytically. It is also shown that if the force associated with the mass has a harmonic component, then its frequency is superposed with the one induced by the foundation.*

1 INTRODUCTION

The investigations on moving load problems were initiated since the early 20th century, when increased importance was attributed to the railway lines performance. Since then, numerous studies have been published on this subject. At first, simple models have been undertaken by analytical and semi-analytical approaches, because of the lack of advanced methods capable to deal with more complex formulations. But these solutions did not lose their utility, because they possess several advantages: they cover only the relevant data, making them easier to analyse; the parameter dependence of the results is preserved, permitting direct sensitivity analysis and providing physical insight into the problem; the numerical evaluation of the results can be carried out for the places of interest only (both in space and time), and more importantly, solving realistic and complicated three-dimensional finite element models still presents some difficulties in form of the high computational cost; necessity to solve the problem over the whole time domain; large number of results to analyse; need for special boundary conditions; several uncertainties in the input data and in the level of discretization, etc.

Regardless the excessive number of published works, there are still some unsolved issues. The aim of this paper is therefore to review some analytical approaches and provide some missing solutions. In Section 2 a simplified model of a beam supported by a foundation with finite depth and subjected to a moving force is introduced. A new analytical formula for the critical velocity of the uniformly moving force is presented. The formula accounts for the effect of the normal force acting on the beam and the shear influence of the foundation. In Section 3 the moving mass problem on a finite beam is reviewed. Then a new analytical formula is presented for the deflection shape of an infinite beam that is traversed by a moving mass and supported by a visco-elastic foundation. In such a case the deflection shape resembles the one associated with the moving force and an additional oscillation around it is induced by the mass. The frequency of this oscillation depends on the foundation characteristics and the amplitude can be derived analytically. It is also proven that if the force associated with the mass has a harmonic component, then its frequency is superposed on the one induced by the foundation. The paper is concluded in Section 4.

2 MOVING FORCE

The problem of a uniformly moving force on a beam supported by a visco-elastic foundation of the Winkler or Pasternak type has an analytical solution for finite as well as infinite beams. Fully analytical closed form solution is only available for simply supported finite beam, thus other cases must be accompanied by a numerical solution of an additional equation, but otherwise the deflection shape of the beam can be presented in a closed explicit form. The most severe simplifications that contradict the railway lines applications are: (i) missing inertial effects of the foundation; and (ii) linearity of the springs representing the foundation, in the sense that the foundation is not tensionless, as it should be.

In this paper one of the possible extensions of the simple beam model is presented, namely, a foundation of a finite depth with inertia and shear effects is introduced. Such a finite depth corresponds to an effective depth of the foundation that is dynamically activated. A uniform motion of a constant vertical force P along a horizontal infinite beam posted on an elastic foundation of finite depth H is assumed (Figure 1). Simplifications for the analysis of beam vertical vibrations are outlined as follows:

(i) the beam obeys linear elastic Euler-Bernoulli theory;
(ii) the beam vertical displacement is measured from the equilibrium deflection position caused by the beam weight;
(iii) the force velocity is maintained constant and no restriction is imposed on its magnitude;

(iv) the foundation is represented by a finite strip of width *b* under plane strain condition.

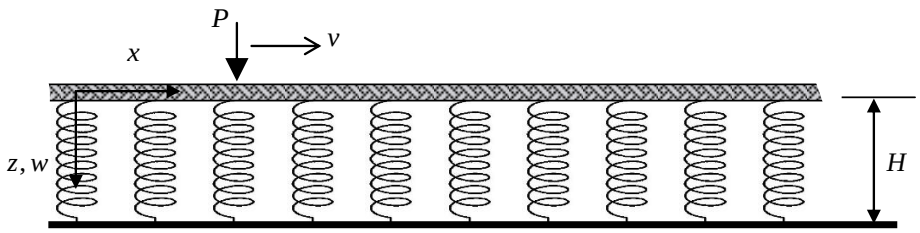


Figure 1: Infinite beam on an elastic foundation of finite depth represented by frequency dependent Winkler's springs, subjected to a moving force.

The governing equation for transverse vibrations $w(x,t)$ can be written as:

$$EIw_{,xxxx} + Nw_{,xx} + mw_{,tt} + c_b w_{,t} + p_s = P\delta(x - vt) \tag{1}$$

where *EI*, *m*, c_b and *N* stand for the bending stiffness, mass per unit length and coefficient of viscous damping of the beam and for the axial force acting on the beam, considered positive when inducing compression. δ is the delta Dirac function, *v* is the force velocity and p_s is the foundation pressure that will be substituted later. Spatial variables are *x* and *z* and *t* is the time. Derivatives are designated by the respective variable in subscript position, preceded by a comma. Initial conditions are assumed as homogeneous.

Some preliminary results are presented in [1]. Further extensions of the analytical solutions presented in [1] are still under review [2], therefore only main features will be given here. The vertical soil displacement is introduced as $u(x,z,t)$, and the necessary boundary conditions are:

$$u(x,0,t) = w(x,t) \text{ and } u(x,H,t) = 0 \tag{2}$$

Then the soil dynamic equilibrium in the vertical direction with the shear influence in a simplified form can be written as:

$$\bar{\rho} u_{,tt} + c_f u_{r,t} = \bar{k}_{st} H u_{,zz} + \bar{G} u_{,xx} \tag{3}$$

where $\bar{\rho}$ and $\bar{G}$ are the density and shear modulus of the foundation soil, where the upper bar means that these values are related to the foundation strip, i.e. multiplied by *b*. c_f is the viscous damping coefficient of the foundation, which can only be introduced correctly if the relative vertical displacement u_r is used. $\bar{k}_{st}$ is the static value of the foundation modulus, $k_{st} = E^{oed} / H$, where E^{oed} is the oedometer modulus of the soil and the upper bar has the same meaning as before. Eqs. (1, 3) can be simplified by introduction of the moving coordinate $s = x - vt$ and further restricted to the steady state conditions:

$$EIw_{,ssss} + \left(N + mv^2\right) w_{,ss} - vc_b w_{,s} + p_s = P\delta(s) \tag{4}$$

$$\bar{\rho} v^2 u_{,ss} - c_f v u_{r,s} = \bar{k}_{st} H u_{,zz} + \bar{G} u_{,ss} \tag{5}$$

Further alterations will involve dimensionless parameters. Displacement components can be divided by the static displacement w_{st} to get dimensionless $\hat{u}_r$ and $\hat{w}$. In addition:

$$\chi = \sqrt[4]{\frac{\bar{k}_{st}}{4EI}},\ w_{st} = \frac{P\chi}{2\bar{k}_{st}},\ \eta_b = \frac{\mathrm{c}_b}{2\sqrt{m\bar{k}_{st}}},\ \eta_f = \frac{c_f H}{\sqrt{\bar{k}_{st} m}},\ \vartheta_s = \frac{v_s}{v_{cr}},\ \alpha = \frac{v}{v_{cr}} \tag{6}$$

and also

$$v_{cr} = \sqrt[4]{\frac{4\bar{k}_{st}EI}{m^2}} = \frac{1}{\chi}\sqrt{\frac{\bar{k}_{st}}{m}},\ \xi = \chi s,\ z = \zeta H,\ \hat{u}_r = \sum_{j=1}^{\infty} U_j \sin\left(j\pi\zeta\right),\ \eta_N = \frac{N}{N_{cr}} = \frac{\mathrm{N}}{2\sqrt{k_{st}EI}} \tag{7}$$

will be used. The soil equilibrium:

$$\begin{aligned}&\left(1-\left(\frac{\vartheta_s}{\alpha}\right)^2\right)\sum_{j=1}^{\infty} U_{j,\xi\xi}\sin\left(j\pi\zeta\right) - \frac{\eta_f}{\alpha\mu^2}\sum_{j=1}^{\infty} U_{j,\xi}\sin\left(j\pi\zeta\right) + \left(\frac{j\pi}{\alpha\mu}\right)^2\sum_{j=1}^{\infty} U_j\sin\left(j\pi\zeta\right)\\ &= -\left(1-\left(\frac{\vartheta_s}{\alpha}\right)^2\right)(1-\zeta)\,\hat{w}_{,\xi\xi\xi}\end{aligned} \tag{8}$$

can be solved by the Fourier transform:

$$U_j^* = \frac{\omega^2\dfrac{2}{j\pi}\left(1-\left(\dfrac{\vartheta_s}{\alpha}\right)^2\right)}{-\omega^2\left(1-\left(\dfrac{\vartheta_s}{\alpha}\right)^2\right) - i\omega\dfrac{\eta_f}{\alpha\mu^2} + \left(\dfrac{j\pi}{\alpha\mu}\right)^2} W^* \tag{9}$$

and then the foundation pressure p_s can be obtained from the contact condition:

$$p_s = -\left(1+i\eta_h\right)\bar{k}_{st}\left(\sum_{j=1}^{\infty} j\pi u_j - w\right) \tag{10}$$

where η_h stands for the hysteretic damping of the foundation. Finally:

$$\hat{w}_{,\xi\xi\xi\xi} + 4\left(\alpha^2+\eta_N\right)\hat{w}_{,\xi\xi} - 8\eta_b\alpha\hat{w}_{,\xi} + 4\left(1+i\eta_h\right)\left(\hat{w} - \sum_{j=1}^{\infty} j\pi U_j\right) = 8\delta\left(\xi\right) \tag{11}$$

which can also be solved by the Fourier transform. At the end, the inverse transform to the time domain has to be done numerically, because of the trigonometric functions that will appear in the Fourier image. By examinations of the deflection shapes, the improved formula for the critical velocity $v_{sh,N}$ is obtained as:

$$v_{sh,N} = v_{cr}\left[\left(\sqrt{1-\eta_N} - \vartheta_s\right)\sqrt{\frac{2}{2+\mu^{2+\sqrt{\vartheta_s}}}} + \vartheta_s\right] \tag{12}$$

where the mass ratio is defined as $\mu = \sqrt{\bar{\rho}H/m}$.

The new formula was checked numerically and some results are presented in Figure 2. In this figure $\eta_N = 0.5$ and the mass ratio is varied between 0 and 10. Three different shear ratios

were tested. It is seen that for the low mass ratio the critical velocity approaches the classical formula and for the high mass ratio it reaches the velocity of propagation of the shear waves in the foundation soil.

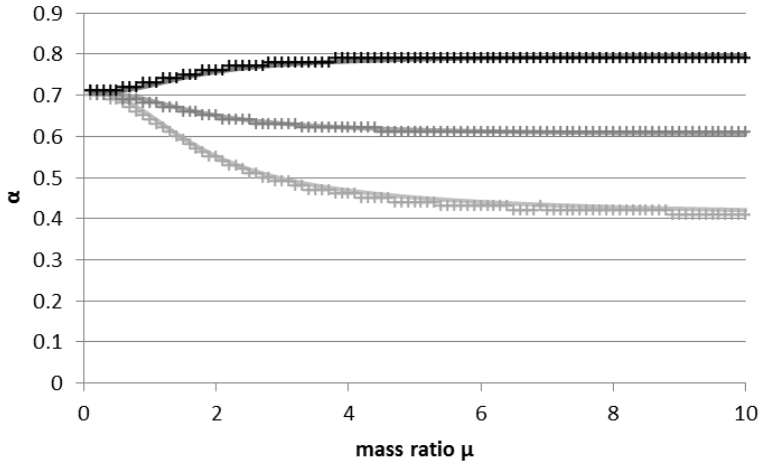


Figure 2: Critical velocity as a function of the mass ratio: full lines represent the prediction according to formula (12) for $\vartheta_s = 0.4$ (light grey), $\vartheta_s = 0.6$ (medium grey) and $\vartheta_s = 0.8$ (dark grey), respectively, crosses represent the numerical values.

3 MOVING MASS

Regarding the finite beam, the solution of the problem of the moving mass can be expressed by the eigenvalue expansion method. The first solution of this kind was presented in [3]. Solution presented in [4] is a semi-analytical one and can be easily extended to Timoshenko beams or account for the effect of the normal force, etc. The disadvantage is that the equations in the modal space are coupled, thus even if no discretization is involved and mode shapes are introduced in their analytical form, the generalized coordinate must be solved numerically.

The equation of motion for the unknown vertical deflection field $w(x,t)$ can be written as:

$$EIw_{,xxxx} + mw_{,tt} + c_b w_{,t} + kw = p(x,t) \tag{13}$$

where k is the Winkler's constant of the foundation. For a constant mass M and an associated constant force P with harmonic component, the loading term $p(x,t)$ can be written as:

$$p(x,t) = \left(P + P_0 \sin\left(\omega_f t + \varphi_f\right) - Mw_{0,tt}(t)\right)\delta(x - vt) \tag{14}$$

Function sine is used to keep this term in the real domain, because then, the whole solution can be solved in the real domain. The mass displacement $w_0(t) = w(vt,t)$, i.e. the mass is always in contact with the beam and its horizontal position is determined by the velocity. Initial conditions are considered as homogeneous. x has its origin at the left extremity of the beam and zero time corresponds to load position at x=0. For the solution it is necessary to remove the additional unknown $w_0(t)$ and express it in terms of the unknown field $w(x,t)$ as:

$$\left(P + P_0 \sin\left(\omega_f t + \varphi_f\right) - M\left(w_{,tt}(x,t) + 2vw_{,xt}(x,t) + v^2 w_{,xx}(x,t)\right)\right)\delta(x - vt) \tag{15}$$

Thus

$$\begin{aligned} &EIw_{,xxxx} + mw_{,tt} + c_b w_{,t} + kw + M\delta\left(x - vt\right)\left(w_{,tt}\left(x,t\right) + 2vw_{,xt}\left(x,t\right) + v^2 w_{,xx}\left(x,t\right)\right) \\ &= \left(P + P_0 \sin\left(\omega_f t + \varphi_f\right)\right)\delta\left(x - vt\right) \end{aligned} \tag{16}$$

Several boundary conditions can be considered.

$$w\left(0,t\right) = 0\,,\ w_{,xx}\left(x,t\right)\big|_{x=0} = 0\,,\ w\left(L,t\right) = 0\,,\ w_{,xx}\left(x,t\right)\big|_{x=L} = 0\,, \tag{17}$$

$$w\left(0,t\right) = 0\,,\ w_{,x}\left(x,t\right)\big|_{x=0} = 0\,,\ w_{,xx}\left(x,t\right)\big|_{x=L} = 0\,,\ w_{,xxx}\left(x,t\right)\big|_{x=L} = 0\,, \tag{18}$$

Above these conditions are written for simply supported beam and left cantilever, respectively, and the beam length is designated as L. Solution of the problem can be obtained by implementing the Fourier method of variable separation and assuming the existence of free harmonic vibrations:

$$w\left(x,t\right) = w\left(x\right)e^{i\omega t}\,,\ i = \sqrt{-1} \tag{19}$$

The frequency ω of these vibrations is named as the natural frequency and it is determined from the eigenvalue problem obtained from the homogeneous governing equation. Then the transient response in the time domain is expressed as infinite series of these modes, where each vibration mode (function of the spatial coordinate x) is multiplied by a generalized displacement (modal coordinate, amplitude function) that is a function of time.

$$w\left(x,t\right) = \sum_{j=1}^{\infty} q_j\left(t\right) w_j\left(x\right) \tag{20}$$

The same designation "w" can be used for the deflection field as well as for the vibration modes, because the vibration modes are distinguished by the corresponding subscript. As usual, the modes are normalized by mass, therefore:

$$\delta_{jk} = \int_0^L m w_j\left(x\right) w_k\left(x\right) dx \tag{21}$$

where δ_{jk} is the Kronecker delta. Modal expansion is commonly governed by undamped vibration modes, because this allows their determination within the real domain and completeness of the eigenspace is guaranteed. Unfortunately, equations in modal space are coupled as shown below:

$$\mathbf{M}\left(t\right)\cdot\ddot{\mathbf{q}}\left(t\right) + \mathbf{C}\left(t\right)\cdot\dot{\mathbf{q}}\left(t\right) + \mathbf{K}\left(t\right)\cdot\mathbf{q}\left(t\right) = \tilde{\mathbf{q}}\left(t\right) \tag{22}$$

In the equation above matrices **M**, **C**, **K** are defined by introduction of vibration modes in their exact analytical form (without any discretization) as:

$$M_{ij} = \delta_{ij} + M w_i\left(vt\right) w_j\left(vt\right) \tag{23}$$

$$C_{ij} = 2Mv w_i\left(vt\right) w_{j,x}\left(vt\right) + \delta_{ij}\frac{c_b}{m} \tag{24}$$

$$K_{ij} = Mv^2 w_i\left(vt\right) w_{j,xx}\left(vt\right) + \delta_{ij}\omega_j^2 \tag{25}$$

$$\tilde{q}_j = \left(P + P_0 \sin\left(\omega_f t + \varphi_f\right)\right) w_j\left(vt\right) \tag{26}$$

Standard techniques can be used for wave numbers λ_j / L determination, it is only recalled that

$$\omega_j = \sqrt{\left(\frac{\lambda_j}{L}\right)^4 \frac{EI}{m} + \frac{k}{m}} \tag{27}$$

The system (22) cannot be solved analytically, but numerically. For numerical solution in Matlab code, the system should be written in the state space form as:

$$\begin{bmatrix} \mathbf{I} & \mathbf{0} \\ \mathbf{0} & \mathbf{M} \end{bmatrix} \begin{Bmatrix} \dot{\mathbf{q}} \\ \ddot{\mathbf{q}} \end{Bmatrix} = \begin{bmatrix} \mathbf{0} & \mathbf{I} \\ -\mathbf{K} & -\mathbf{C} \end{bmatrix} \begin{Bmatrix} \mathbf{q} \\ \dot{\mathbf{q}} \end{Bmatrix} + \begin{Bmatrix} \mathbf{0} \\ \tilde{\mathbf{q}} \end{Bmatrix} \tag{28}$$

$$\begin{Bmatrix} \dot{\mathbf{q}} \\ \ddot{\mathbf{q}} \end{Bmatrix} = \begin{bmatrix} \mathbf{0} & \mathbf{I} \\ -\mathbf{M}^{-1}\mathbf{K} & -\mathbf{M}^{-1}\mathbf{C} \end{bmatrix} \begin{Bmatrix} \mathbf{q} \\ \dot{\mathbf{q}} \end{Bmatrix} + \begin{Bmatrix} \mathbf{0} \\ \mathbf{M}^{-1}\tilde{\mathbf{q}} \end{Bmatrix} \tag{29}$$

Computational time increases exponentially with the number of modes involved. Precision of a solution obtained for a certain number of modes cannot be simply increased by including one more mode, but the whole system must be recalculated again. If there is no elastic foundation, usually low number of modes is sufficient (around 5-10). With the foundation included, the number of modes must be much higher, depending on several factors and it ranges around 100-200, or more. As an example, the solution of the moving mass and its corresponding weight on a cantilever is shown in Figure 3. This is one of the examples that are presented in [3]. Numerical data from [3] are slightly adapted to: L=7.62m, P=25.79kN, M=2629kg, EI=9480.6kNm^2, m=46kg/m, v=50.8m/s. It is seen that in this case the effect of the Coriolis and centrifugal forces is significant. This is, however, not a very good example, since the deflection is quite large and the validity of the Euler-Bernoulli beam theory is compromised.

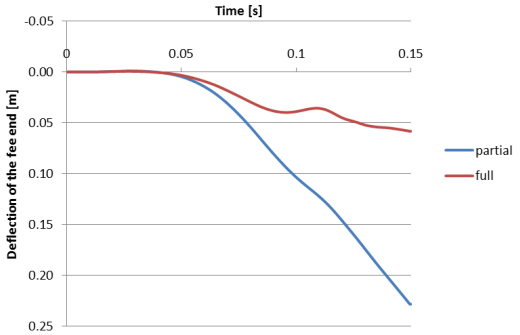


Figure 3: Deflection of the cantilever free end, "partial" means that some terms were omitted as in [3], "full" means that all terms are included.

Another application is a simply supported beam on an elastic foundation (Figure 4). The input data are: L=100m, P=100kN, M=10ton, EI=6.4MNm^2, m=60kg/m, k=4MN/m^2, v=100m/s. The beam and foundation data are related to railway applications. The beam stands for one single rail. In this case 150 modes were necessary for a good accuracy of the solution, but for over 50 modes (even if in this case with purely sinusoidal shape) accumulated numerical errors caused unphysical excessive oscillations when the load approached the right support. The solution of this case is already similar to the one on an infinite beam, thus the new analytical solution that will be presented next, can be checked on it.

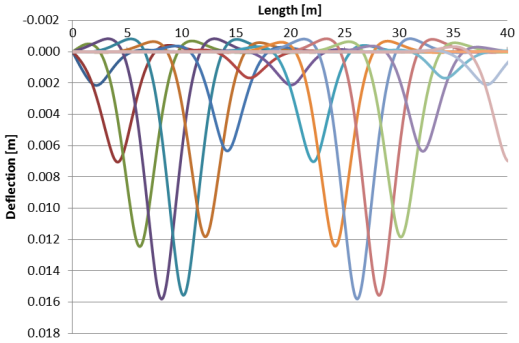


Figure 4: Deflection of the simply supported beam on an elastic foundation, initial 40m of the full length, deflections related to mass position at each 2m.

The governing equation of the vibrations of an infinite beam can be written as:

$$EIw_{,xxxx}+\left(N-k_p\right)w_{,xx}+mw_{,tt}+c_bw_{,t}+kw=-\left(P+P_0e^{i\omega_f t}+Mw_{0,tt}\right)\delta\left(x-vt\right) \tag{30}$$

As compared to Eq. (13), other effects like Pasternak coefficient k_p and the normal force N can be easily introduced. In this formulation there is no problem to express the harmonic component of the force with complex numbers as $P_0e^{i\omega_f t}$. The unknown deflection w is assumed positive when acting upward. Similarly as before the additional unknown $w_0(t)$ must be expressed in terms of the unknown field $w(x,t)$. The moving coordinate $s=x-vt$ and dimensionless parameters can be introduced in accordance with Section 2 to obtain:

$$\begin{aligned}&\hat{w}_{,\xi\xi\xi\xi}+4\left(\eta_N-\eta_S+\alpha^2\right)\hat{w}_{,\xi\xi}+4\hat{w}_{,\tau\tau}-8\alpha\hat{w}_{,\xi\tau}+8\left(\eta_b\hat{w}_{,\tau}-\eta_b\alpha\hat{w}_{,\xi}\right)+4\hat{w}\\&=-4\left(2+2\eta_Pe^{i\hat{\omega}_f\tau}+\eta_M\hat{w}_{,\tau\tau}\right)\delta\left(\xi\right)\end{aligned} \tag{31}$$

where $\bar{k}_{st}$ was substituted by k, and moreover

$$\hat{\omega}_f=\frac{\omega_f}{\chi v_{cr}},\ \eta_S=\frac{k_p}{2\sqrt{kEI}},\ \eta_M=\frac{M\chi}{m},\ \eta_P=\frac{P_0}{P} \tag{32}$$

were used.

It can be shown that by application of the Fourier transform in the form of:

$$F\left(p,q\right)=\int_{-\infty}^{\infty}\int_{-\infty}^{\infty}f\left(\xi,\tau\right)e^{-i\left(p\xi+q\tau\right)}d\xi d\tau \tag{33}$$

The governing equation gets the form:

$$W\left(p,q\right)D\left(p,q\right)=-16\pi\delta\left(q\right)-16\pi\eta_P\delta\left(q-\hat{\omega}_f\right)+4\eta_Mq^2\tilde{W}\left(0,q\right) \tag{34}$$

where

$$D\left(p,q\right)=p^4-4p^2\left(\eta_N-\eta_S+\alpha^2\right)-4q^2+8\alpha pq-8iq\eta_c+8ip\alpha\eta_c+4 \tag{35}$$

and the final solution for the deflection under the load is:

$$w(0,\tau)=-\int_{-\infty}^{\infty}\frac{8i\left[\delta(q)+\eta_P\delta\left(q-\widehat{\omega}_f\right)\right]\left(D_{,p}(p_1,q)+D_{,p}(p_2,q)\right)e^{iq\tau}dq}{\left(D_{,p}(p_1,q)D_{,p}(p_2,q)-4\eta_M q^2 i\left(D_{,p}(p_1,q)+D_{,p}(p_2,q)\right)\right)} \tag{36}$$

where p_1 and p_2 are roots of Eq. (35) according to the integration around upper and lower semi-circle.

From Eq. (36) it is clear that if $\eta_P=0$, then the value of η_M has no influence on the final result and the deflection under the load is constant, i.e. steady, which is not correct. This proves that first Laplace transform must be implemented

$$\tilde{F}(\xi,\bar{q})=\int_0^{\infty}f(\xi,\tau)e^{-\bar{q}\tau}d\tau \tag{37}$$

with the connection to the previous variables $\bar{q}=iq$, and only after that the Fourier one. Then the main difference is already seen in Eq. (34) which has now the form as:

$$W(p,\bar{q})\bar{D}(p,\bar{q})=-\frac{8}{\bar{q}}-\frac{8\eta_P}{\bar{q}-i\widehat{\omega}_f}-4\eta_M\bar{q}^2\tilde{W}(0,\bar{q}) \tag{38}$$

i.e.

$$W(p,q)D(p,q)=+\frac{8i}{q}+\frac{8i\eta_P}{q-\widehat{\omega}_f}+4\eta_M q^2\tilde{W}(0,q) \tag{39}$$

This procedure is described in [5], however, no results of the deflection shape are presented there. It is necessary to solve numerically for the frequency that is induced by the foundation. This can be done by simple iterative algorithm which convergence is secured. Once this is known, the deflection under the load can be expressed analytically by the inverse transform. Its form is quite complicated and thus its presentation is omitted here due to the limited number of pages. Then it is straightforward to join to this result the rest of the full deflection shape. If the applied force is constant, then the mass oscillates around the stationary position, as demonstrated in Figure 4. If the force has a harmonic component, than both harmonic movements are superposed around the stationary position.

4 CONCLUSIONS

In this paper some new analytical solutions for moving load problems were presented. In the first part, a new analytical formula for the critical velocity of a uniformly moving force on a beam supported by a foundation of finite depth was given. The formula accounts for the effect of the normal force acting on the beam and the shear influence of the foundation. The critical velocity is expressed as a function of the mass ratio that relates the foundation mass with the beam mass. The new formula approaches the classical formula for the low mass ratio and the velocity of propagation of shear waves for the high mass ratio.

In the second part, firstly, the analytical solution of the moving mass problem on a finite beam is presented. The importance of the Coriolis and centrifugal forces is highlighted. The solution with elastic foundation indicates the form of the deflection shape on infinite beams. Secondly, a new analytical solution is presented for the deflection shape of an infinite beam that is traversed by a moving mass and supported by a visco-elastic foundation. In such a case the deflection shape resembles the one associated with the moving force with an additional oscillation around it. The frequency of this oscillation is induced by the foundation characteristics and the amplitude can by derived analytically. When the force associated with the mass

has a harmonic component, then its frequency is superposed with the one induced by the foundation.

ACKNOWLEDGEMENTS

This work was supported by the Fundação para a Ciência e a Tecnologia (FCT), Portugal, both directly in the form of a project PTDC/EME-PME/67658/2006 and through IDMEC, under LAETA, project UID/EMS/50022/2013.

REFERENCES

[1] Z. Dimitrovová, Enhanced formula for a critical velocity of a uniformly moving load, *European Congress on Computational Methods in Applied Sciences and Engineering* (ECCOMAS 2012), 11-14 September, 2012, Vienna, Austria, Vienna Technical University, ISBN 978-3-9502481-8-0, proceedings ISBN 978-3-9502481-9-7.

[2] Z. Dimitrovová, Critical velocity of a uniformly moving load on a beam supported by a finite depth foundation, *Journal of Sound and Vibration*, under review, 2015.

[3] J.E. Akin, M. Mofid, Numerical solution for response of beams with moving mass, *ASCE Journal of Structural Engineering*, **115**, 120–31, 1989.

[4] Z. Dimitrovová, On the moving mass versus moving load problem, *IX International Conference on Structural Dynamics* (EURODYN2014), 30 June - 2 July, 2014, Porto, Portugal.

[5] A.V. Metrikine, H.A. Dieterman, Instability of vibrations of a mass moving uniformly along an axially compressed beam on a visco-elastic foundation, *Journal of Sound and Vibration*, **201**, 567–576, 1997.

Nonlinear Dynamic Interactions and Phenomena: Emergent Methods... (MS07)

International Conference on Engineering Vibration
Ljubljana, Slovenia, 7-10 September 2015

FORCED NONLINEAR VIBRATION ANALYSIS OF CYLINDRICAL PANELS

Henrique A. R. Sattler[1], Frederico M. A. Silva[*2], Zenón J. G. N. Del Prado[3], Paulo B. Gonçalves[4]

[1,2,3] School of Civil Engineering, Federal University of Goiás, Brazil
eng.henriquesattler@hotmail.com, {silvafma,zenon}@ufg.br

[4]Department of Civil Engineering, Pontifical Catholic University of Rio de Janeiro, Brazil
paulo@puc-rio.br

Keywords: Panels, Modal Coupling, Nonlinear, Dynamics.

Abstract. *This work analyzes the nonlinear forced vibrations of a cylindrical panel simply supported and excited by a transversely time dependent load. The cylindrical panel is modeled by the nonlinear Donnell shallow shell theory. The lateral displacement field is determined by a perturbation procedure and the axial and circumferential displacement fields are described in terms of lateral displacement, thus generating a precise low-dimensional model. A general expression for the nonlinear vibration modes is provided in this paper, satisfying all boundary conditions. The discretized equations of motion are obtained by applying the Galerkin method. Various numerical techniques are employed to obtain the cylindrical panel resonance curves and bifurcation scenario. The results show the influence of geometry and nonlinear modal coupling on the nonlinear response of the cylindrical panel.*

1 INTRODUCTION

Thin-walled shell panels are structural components found in, among others, civil engineering constructions, aircrafts, tanks, submarines, rockets and other aerospace structures. These structures have efficient load-carrying capabilities, but exhibit the risk of buckling failures under static and dynamic loads. Due to the advances in structural mechanics analyses and structural materials, these structures have become increasingly slender and lighter. Thus, the knowledge of their nonlinear dynamics behavior is of crucial importance in engineering design. These factors motivated several researchers to investigate their behavior under static and dynamic loads. Most publications on the linear and nonlinear vibration analysis of cylindrical panels submitted to static or dynamic loads is focused on their structural stability [1-4]. The effect of material, damping, load type and boundary conditions on their nonlinear response has also been analyzed [5-8].

In 2005 Amabili [2] examined the nonlinear forced vibrations of a simply supported cylindrical panel using Donnell nonlinear shallow shell theory, concluding that the system's behavior is initially of the softening the type, but when the vibration amplitude exceeds the thickness the cylindrical panel a turning point appears, passing to a hardening type behavior. Ribeiro [9] studied the nonlinear vibration of a thin cylindrical panel by finite element method. The results show that the nonlinear vibrations behavior depends markedly on the geometric characteristics of the cylindrical panel.

Amabili and Paidoussis [10] and Alijani and Amabili [11] published an extensive review of works on the nonlinear free or forced vibrations of cylindrical shells, including cylindrical panels. A large number of these works mentions the importance of the correct choice of the modal expansion for the lateral displacement field, as different choices can lead to distinctly different results.

Recently, the authors proposed a new solution method for cylindrical shells well adapted to the derivation of efficient reduced order models [12, 13], based on a perturbation technique proposed initially by Gonçalves and Batista [14]. In the present work this methodology is extended to thin-walled cylindrical panels. A consistent modal expansion for the panel displacement field is thus obtained, satisfying all boundary conditions for a simply supported panel. Based on this modal expansion, a reduced order model is derived to study the nonlinear vibrations of a panel subjected to a lateral harmonic pressure. The obtained results highlight the influence of modal coupling and geometry on the frequency-amplitude relation and resonance curves of the cylindrical panel.

2 MATHEMATICAL FORMULATION

2.1 Panels' equations

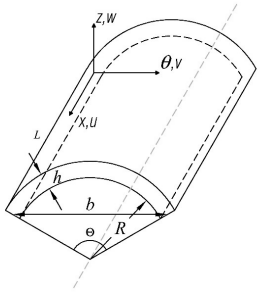


Figure 1 – Cylindrical panel geometry and coordinate system

Consider a cylindrical panel of radius R, sector angle Θ, chord b, thickness h and length L, made of a linear elastic material with Young's modulus E, Poisson coefficient υ and mass density ρ. The three displacement components u, v and w are related to the cylindrical coordinate system x, θ and z, as shown in Figure 1.

The cylindrical panel´s deformations ($\bar{\varepsilon}_x, \bar{\varepsilon}_\theta$ and $\bar{\gamma}_{x\theta}$) at an arbitrary point are given in terms of the middle surface strain ($\varepsilon_x, \varepsilon_\theta$ and $\gamma_{x\theta}$) and change of curvature components (χ_x, χ_θ and $\chi_{x\theta}$) by:

$$\bar{\varepsilon}_x = \varepsilon_x + \chi_x \qquad \bar{\varepsilon}_\theta = \varepsilon_\theta + \chi_\theta \qquad \bar{\gamma}_{x\theta} = \gamma_{x\theta} + 2\,\chi_{x\theta} \tag{1}$$

The middle surface quantities are given, in terms of the displacement components, according to Donnell nonlinear shallow shell theory, by:

$$\begin{aligned} &\varepsilon_x = u_{,x} + \frac{1}{2} w_{,x}^2 \quad \varepsilon_\theta = \frac{1}{R}\left(v_{,\theta} + w\right) + \frac{1}{2R^2} w_{,\theta}^2 \qquad \gamma_{x\theta} = v_{,x} + \frac{1}{R}\left(u_{,\theta} + w_{,x}\, w_{,\theta}\right) \\ &\chi_x = -w_{,xx} \qquad \chi_\theta = -\frac{1}{R^2} w_{,\theta\theta} \qquad\qquad \chi_{x\theta} = -\frac{1}{R} w_{,x\theta} \end{aligned} \tag{2}$$

The cylindrical panel is subjected to a harmonic lateral pressure of the form:

$$p(t) = P \sin\left(\frac{n\pi\theta}{\Theta}\right) \sin\left(\frac{m\pi x}{L}\right) \cos(\Omega t) \tag{3}$$

where P is the pressure magnitude in N/m²; n and m are the number of half-waves in the circumferential and axial direction, respectively, Ω is the excitation frequency and t is time.

The nonlinear equations of motion, considering only the transversal inertia and damping forces, are given in terms of the force and moment resultants by:

$$\begin{aligned} &N_{x,x} + \frac{N_{x\theta,\theta}}{R} = 0 \qquad\qquad N_{x\theta,x} + \frac{N_{\theta,\theta}}{R} = 0 \\ &\rho h \ddot{w} + 2\eta_1 \rho h \Omega_0\, \dot{w} - p(t) - \frac{1}{R^2}\left[R\, M_{x,xx} + 2M_{x\theta,x\theta} + \frac{M_{\theta,\theta\theta}}{R} + R N_x\, w_{,xx} \right. \\ &\left. + N_\theta\left(\frac{w_{,\theta\theta}}{R} - 1\right) + 2 N_{x\theta}\, w_{,x\theta} \right] = 0 \end{aligned} \tag{4}$$

where η_1 is the linear viscous damping coefficient, $D = E\,h^3/12(1-\upsilon^2)$ is the flexural stiffness of the shell, Ω_0 is the lowest vibration frequency and $p(t)$ is the lateral pressure.

The force and moment resultants in Eq. (5) are obtained by integrating the stress components along the cylindrical panel thickness as follows:

$$\begin{aligned} &N_x = \int_{-h/2}^{h/2} \bar{\sigma}_x\, dz \qquad N_\theta = \int_{-h/2}^{h/2} \bar{\sigma}_\theta\, dz \qquad N_{x\theta} = \int_{-h/2}^{h/2} \bar{\tau}_{x\theta}\, dz \\ &M_x = \int_{-h/2}^{h/2} z\,\bar{\sigma}_x\, dz \qquad M_\theta = \int_{-h/2}^{h/2} z\,\bar{\sigma}_\theta\, dz \qquad M_{x\theta} = \int_{-h/2}^{h/2} z\,\bar{\tau}_{x\theta}\, dz \end{aligned} \tag{5}$$

For a simply-supported cylindrical panel along the four edges, the following boundary conditions must be satisfied:

$$w(0,\theta) = w(L,\theta) = 0 \tag{6}$$

$$w(x,0)=w(x,\Theta)=0 \tag{7}$$

$$M_x(0,\theta)=M_x(L,\theta)=0 \tag{8}$$

$$M_\theta(x,0)=M_\theta(x,\Theta)=0 \tag{9}$$

The displacement field, in this work, is also required to satisfy the following condition:

$$u(L/2,\theta)=0 \tag{10}$$

In the foregoing, the following non-dimensional parameters have been introduced:

$$W=\frac{w}{h} \qquad \xi=\frac{x}{L} \qquad \tau=\Omega_0 t \qquad \overline{\Omega}=\frac{\Omega}{\Omega_0} \tag{11}$$

2.2 General solution of the shell displacement field by a perturbation procedure and determination of the in-plane displacements *u* and *v*

The numerical model is developed by expanding the transversal displacement component *w* in series in the circumferential and axial variables. This modal solution must express the nonlinear coupling between the modes and describe consistently the unstable post-buckling response of the shell as well as the correct frequency-amplitude relation [12-17].

By employing a perturbation technique and by imposing the appropriate boundary conditions, a consistent modal solution for the transversal displacements can be obtained as shown in [12-17].

In order to start the perturbation procedure, the fundamental vibration mode is adopted as the seed mode:

$$W=W_{1,1}(t)\sin(m\pi\xi)\sin\left(\frac{n\pi\theta}{\Theta}\right) \tag{12}$$

By applying the perturbation procedures described in previous works [12-13] and by considering the boundary conditions for a simply supported cylindrical panel, Eqs. (7)-(10), the following modal solution is obtained:

$$\begin{aligned} W=&\sum_{i=1,3,5}^{\infty}\sum_{j=1,3,5}^{\infty}W_{i,j}(\tau)\,\sin(im\pi\varepsilon)\sin\left(\frac{jn\pi\theta}{\Theta}\right)\\ &+\sum_{\alpha=0}^{\infty}\sum_{\beta=0}^{\infty}W_{(2+6\beta),(2+6\alpha)}(\tau)\left\{-\frac{(3+6\beta)}{(4+12\beta)}cos(6\beta m\pi\varepsilon)+\cos((2+6\beta)m\pi\varepsilon)\right.\\ &\left.-\frac{(1+6\beta)}{(4+12\beta)}\cos((4+6\beta)m\pi\varepsilon)\right\}\left\{-\frac{(3+6\alpha)}{(4+12\alpha)}cos\left(6\alpha\frac{n\pi\theta}{\Theta}\right)+\cos\left((2+6\alpha)\frac{n\pi\theta}{\Theta}\right)\right.\\ &\left.-\frac{(1+6\alpha)}{(4+12\alpha)}\cos\left((4+6\alpha)\frac{n\pi\theta}{\Theta}\right)\right\} \end{aligned} \tag{13}$$

The in-plane displacements *u* and *v* are obtained by substituting a selected numbers of modes from Eq. (14) into the in-plane equilibrium equations in Eq. (5), and solving the system of linear partial differential equations in *u* and *v* and imposing the relevant boundary and symmetry conditions. Based on this procedure, one selects the necessary number of in-plane modes and write their modal amplitudes in terms of the modal amplitudes W_{ij} in Eq. (14) [12-13]. Finally, by substituting the adopted expansion for the transversal displacement *w* together

with the obtained expressions for u and v into the equation of motion in the transversal direction, third equation in Eq. (5), and by applying the standard Galerkin method, a consistent discretized system of ordinary differential equations of motion is derived.

3 NUMERICAL RESULTS

Consider a perfect cylindrical panel with the following material's properties: E = 2.06 x 10^{11} N/m², υ = 0.3 and ρ = 7850 kg/m³. A cylindrical panel with radius R = 1 m, length L = 0.1 m, thickness h = 0.001 m and different sector angles Θ is adopted in the parametric analysis. Table 1 shows the lowest natural frequency, associated wave numbers and vibration mode profile in the circumferential direction for six selected values of Θ. As the sector angle Θ increase the circumferential half-wave number increases and the natural frequency decreases.

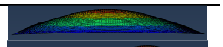
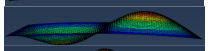
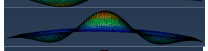
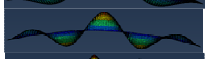
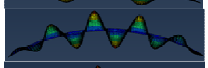
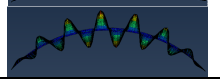
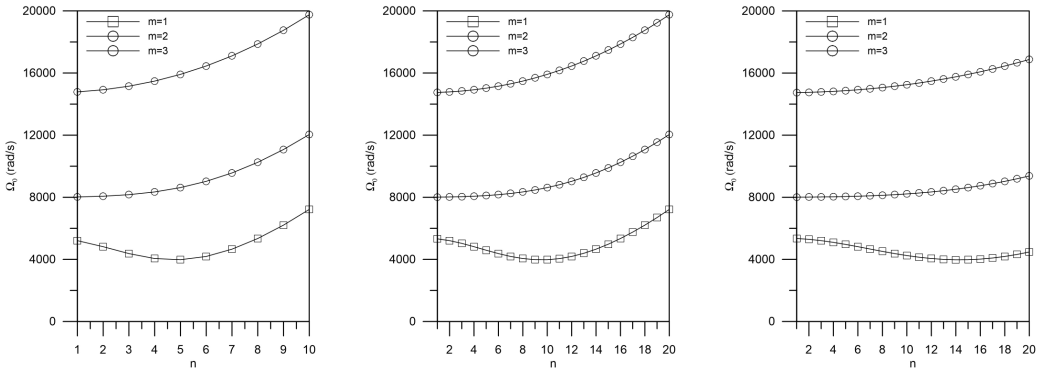
Sector angle – Θ (rad)	Ω_0 (rad/s)	m	n	
0.1	4003.25	1	1	
π/18	4188.21	1	2	
π/9	3982.25	1	3	
π/6	3979.52	1	5	
π/3	3979.52	1	10	
π/2	3973.39	1	14	

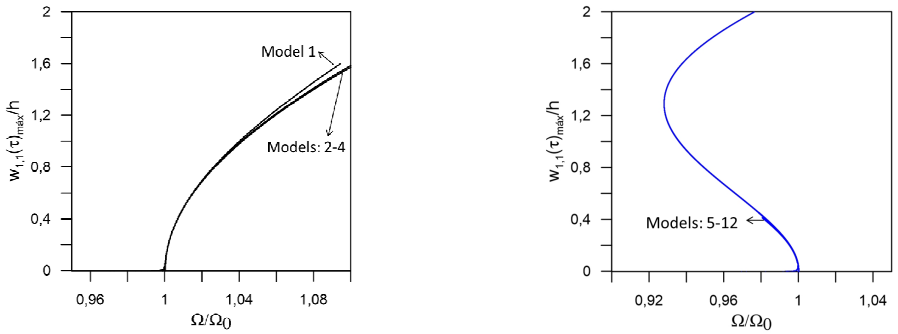
Table 1: Natural frequencies and vibration mode for different cylindrical panels' sector angle Θ.

The frequency spectrum for selected values of Θ are shown in Figure 2, where the dense frequency spectrum characteristic of thin-walled shell structures can be observed.



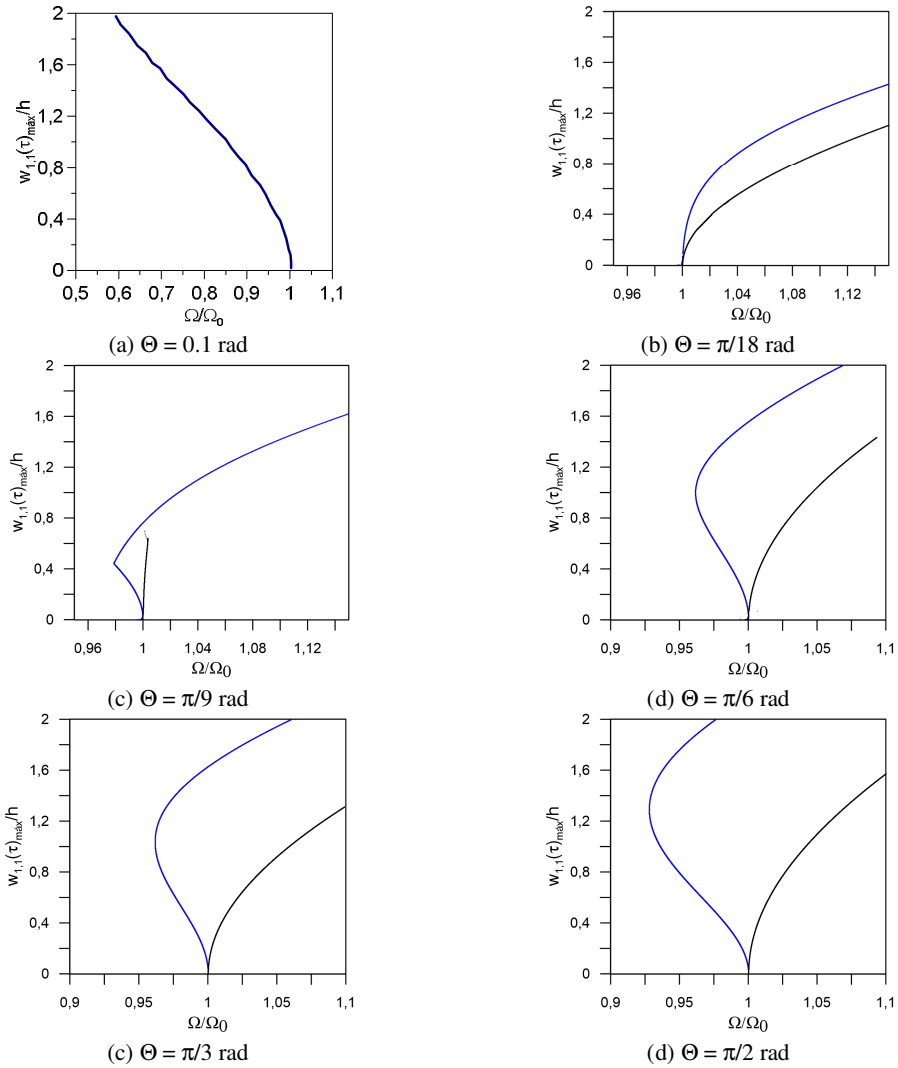
(a) Θ=π/6 (b) Θ=π/3 (c) Θ=π/2

Figure 2 – Frequency spectrum for selected values of Θ.



(a) Models: 1-4 (b) Models: 5-12

Figure 3 - Convergence of the frequency-amplitude relation for Θ=π/2.



(a) Θ = 0.1 rad (b) Θ = π/18 rad

(c) Θ = π/9 rad (d) Θ = π/6 rad

(c) Θ = π/3 rad (d) Θ = π/2 rad

Figure 4 – Frequency-amplitude relation for the cylindrical panel with different sector angles. ($\eta_1 = 0$).

— Model: 1. — Model: 5.

In Figure 3 the frequency-amplitude relations are obtained considering different modal expansions based on Eq. (14). They are: Model 1: $w_{1,1}(\tau)$; Model 2: $w_{1,1}(\tau) + w_{1,3}(\tau)$; Model 3: $w_{1,1}(\tau) + w_{1,3}(\tau) + w_{1,5}(\tau) + w_{1,7}(\tau)$; Model 4: $w_{1,1}(\tau) + w_{1,3}(\tau) + w_{1,5}(\tau) + w_{1,7}(\tau) + w_{3,1}(\tau) + w_{3,3}(\tau) + w_{3,5}(\tau) + w_{3,7}(\tau)$; Model 5: $w_{1,1}(\tau) + \mathbf{w_{2,2}}(\tau)$; Model 6: $w_{1,1}(\tau) + w_{1,3}(\tau) + \mathbf{w_{2,2}}(\tau)$; Model 7: $w_{1,1}(\tau) + w_{1,3}(\tau) + w_{1,5}(\tau) + w_{1,7}(\tau) + \mathbf{w_{2,2}}(\tau)$; Model 8: $w_{1,1}(\tau) + \mathbf{w_{2,2}}(\tau) + \mathbf{w_{2,8}}(\tau)$; Model 9: $w_{1,1}(\tau) + \mathbf{w_{2,2}}(\tau) + \mathbf{w_{8,2}}(\tau)$; Model 10: $w_{1,1}(\tau) + \mathbf{w_{2,2}}(\tau) + \mathbf{w_{8,8}}(\tau)$; Model 11: $w_{1,1}(\tau) + \mathbf{w_{2,2}}(\tau) + \mathbf{w_{2,8}}(\tau) + \mathbf{w_{8,2}}(\tau)$; Model 12: $w_{1,1}(\tau) + \mathbf{w_{2,2}}(\tau) + \mathbf{w_{2,8}}(\tau) + \mathbf{w_{2,14}}(\tau)$. In bold are the coupling terms due to quadratic nonlinearities in Eq. (5).

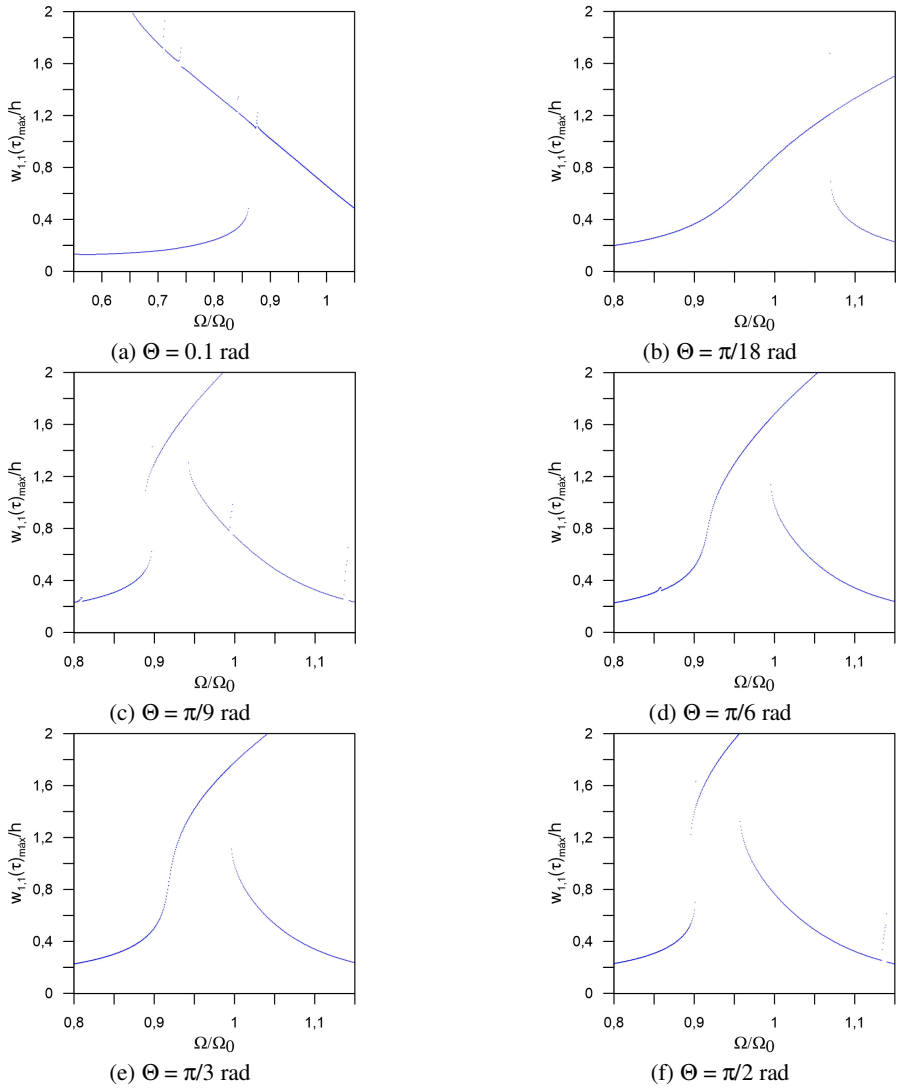
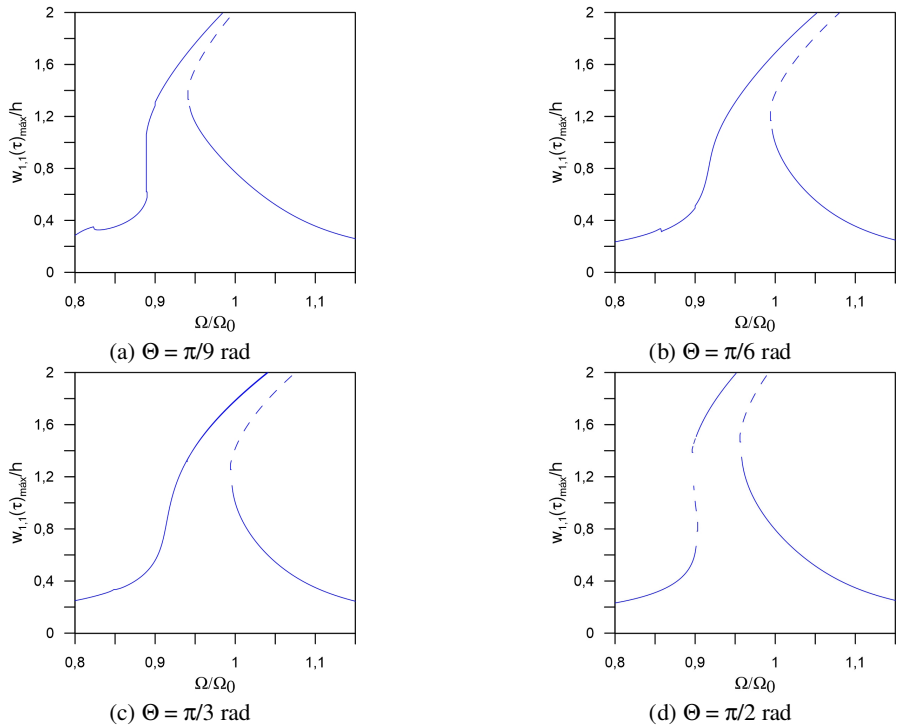


Figure 5 – Resonance curves, maximum lateral deflection versus excitation frequency. Brute force od. Model: 5. η_1 = 1 x 10^{-3} and P = 10 kN/m².

The time-dependent modal amplitudes $w_{i,j}(\tau)$ are, in each case, exactly obtained by the use of the shooting method [18]. Figure 3 shows the convergence of the frequency-amplitude relation up to vibration amplitudes of the order of two times the shell thickness for $\Theta=\pi/2$. It is

observed that a small number of modes is enough to obtain convergence up to very large vibration amplitudes. However, two different types of behavior are distinguished. Models 1-4 lead to a hardening behavior, while Models 5-12 display an initial softening behavior, which is the expected behavior for this panel geometry. This shows the important influence of the coupling terms in bold in Models 5-12 and, consequently, of the quadratic nonlinearity on the nonlinear shell response.



(a) $\Theta = \pi/9$ rad (b) $\Theta = \pi/6$ rad

(c) $\Theta = \pi/3$ rad (d) $\Theta = \pi/2$ rad

Figure 6 – Resonance curves, maximum lateral deflection versus excitation frequency. Continuation techniques. Solid line: stable solution. Dashed line: unstable solution. Model 5. $\eta_1 = 1 \times 10^{-3}$ and P = 10 kN/m².

Figure 4 shows of the frequency-amplitude relation for six selected values of Θ, considering model one and five. For $\Theta = 0.1$ rad (very shallow panel) all models lead to the same softening response, similar to that of a shallow arch. However the response changes to hardening for $\Theta = \pi/18$ rad, but Model 1 displays a stronger hardening behavior. For all other selected values of Θ, Models 1-4 lead to a hardening behavior, while Models 5-12 display an initial softening behavior. Thus, it is shown that the initial softening or hardening behavior is strongly affected by the nonlinear modal coupling present in the transversal displacement field and by the sector angle Θ. If the model contains only the modes with sine functions the nonlinear frequency-amplitude relation displays a hardening behavior for $\Theta > \pi/18$ rad . The addition of any mode with cosine function (bold modes in Models 5 to 12) the frequency-amplitude relation changes to softening and this character is intensified by the increasing of the sector angle Θ. The initially softening behavior turns to hardening for vibration amplitude around the panel thickness, as already observed by Amabili [2].

Figure 5 shows the resonance curve of the cylindrical panel submitted to a harmonic lateral pressure given by Eq. (4), considering Model 5. They are obtained by the brute force method

increasing and decreasing the excitation frequency in the main resonance region. Strong nonlinearity is observed leading to saddle-node bifurcations and dynamic jumps.

Figure 6 shows the resonance curves obtained by continuation techniques where the solid lines represent the stable solution and the dashed lines indicate the unstable solution, confirming the results obtained by the brute force method.

4 CONCLUSIONS

In the present paper, Donnell shallow shell theory has been applied to model the dynamics of a cylindrical panel under lateral harmonic pressure. Based on a modal solution obtained by a perturbation technique, a general solution for the displacement field is obtained satisfying all boundary and symmetry conditions of a simply-supported cylindrical panel. Using different reduced order models for the transversal displacement field, based on the derived general solution, the discretized panel equations are obtained by the standard Galerkin method. The nonlinear frequency-amplitude relation is obtained by the shooting method considering different sector angles, which has a strong influence on the shell nonlinear behavior. The results corroborate the importance of modal coupling between linear and nonlinear modes and quadratic nonlinearities on the frequency-amplitude relation. Based on this analysis, the nonlinear forced vibrations of the panel under harmonic radial pressure are investigated. This is a work in progress; further work will focus on the bifurcation scenario and dynamic integrity.

Acknowledgement

This work was made possible by the support of the Brazilian Ministry of Education – CAPES, CNPq, FAPERJ-CNE and FAPEG.

REFERENCES

[1] M. Amabili and M. Pellegrini, Nonlinear vibrations of circular cylindrical panels. *Computational Fluid and Solid Mechanics,* **2003**, 50-53, 2003.

[2] M. Amabili, Nonlinear vibrations of circular cylindrical panels. *Journal of Sound and Vibration*, **281**, 509-535, 2005.

[3] F. Alijani and M. Amabili, Nonlinear vibrations of thick laminated circular cylindrical panels. *Composite Structures*, **96**, 643-660, 2013.

[4] Y. Zhou, I. Stanciulescu, T. Eason and M. Spottswood, Nonlinear elastic buckling and postbuckling analysis of cylindrical panels. *Finite Elements in Analysis and Design*, **96**, 41-50, 2015.

[5] K.M. Liew, J. Yang and Y.F. Wu, Nonlinear vibration of a coating-FGM-substrate cylindrical panel subjected to a temperature gradient. *Computer Methods in Applied Mechanics and Engineering*, **195**, 1007-1026, 2006.

[6] D. P-Shahraki, A. R. Shahidi, H. R. Mirdamadi and O. Vaseghi, Nonlinear analysis of uni-lateral buckling for cylindrical panels on tensionless foundation. *Thin-Walled Structures*, **62**, 109-117, 2013.

[7] T. Q. Quan, P. Tran, N. D. Tuan and N. D. Duc, Nonlinear dynamic analysis and vibration of shear deformable eccentrically stiffened S-FGM cylindrical panels with metal–ceramic–metal layers resting on elastic foundations. *Composite Structures*, **126**, 16-33, 2015.

[8] H-S Shen and H. Wang, Nonlinear bending of FGM cylindrical panels resting on elastic foundations in thermal environments. *European Journal of Mechanics - A/Solids*, **49**, 49-59, 2015.

[9] P. Ribeiro, Non-linear free periodic vibrations of open cylindrical shallow shells. *Journal of Sound and Vibration*, **313**, 224-245, 2008.

[10] M. Amabili and M. P. Paidoussis, Review of studies on geometrically nonlinear vibrations and dynamics of circular cylindrical shell and panels, with and without fluid-structure interaction. *Applied Mechanics Reviews*, **56**, 349-381, 2003.

[11] F. Alijani and M. Amabili, Non-linear vibrations of shells: a literature review from 2003 to 2013. *International Journal of Non-Linear Mechanics*, **58**; 233-257, 2014.

[12] P. B. Gonçalves, F. M. A. Silva and Z. J. G. N. Prado, Low-dimensional models for the nonlinear vibration analysis of cylindrical shells based on a perturbation procedure and proper orthogonal decomposition. *Journal of Sound and Vibration*, **315**, 641-663, 2008.

[13] F. M. A. Silva, P. B. Gonçalves and Z. J. G. N. Prado, An alternative procedure for the non-linear vibration analysis of fluid-filled cylindrical shells. *Nonlinear Dynamics*, **66**, 303-333, 2011.

[14] P. B. Gonçalves and R. C. Batista, Nonlinear vibration analysis of fluid-filled cylindrical shells. *Journal of Sound and Vibration*, **127**, 133-143, 1988.

[15] G. W. Hunt, K. A. J. Williams and R. G. Cowell, Hidden symmetry concepts in the elastic buckling of axially loaded cylinders. *International Journal of Solid and Structures*, **22**, 1501-1515, 1986.

[16] P. B. Gonçalves and Z. J. G. N. Prado, Nonlinear oscillations and stability of parametrically excited cylindrical shells. *Meccanica*, **37**, 569-597, 2002.

[17] J. Awrejcewicz and A. V. Krys'ko, Analysis of complex parametric vibrations of plates and shells using Bubnov-Galerkin approach. *Archive of Applied Mechanics*, **73**, 495-504, 2003.

[18] R. Seydel, *From Equilibrium to Chaos: Practical Bifurcation and Stability Analysis*. Elsevier Science Publishing, New York, 1988.

International Conference on Engineering Vibration
Ljubljana, Slovenia, 7-10 September 2015

INCREASING PRACTICAL SAFETY OF VON MISES TRUSS VIA CONTROL OF DYNAMIC ESCAPE

Diego Orlando[1], **Paulo B. Gonçalves**[1], **Stefano Lenci**[2], **Giuseppe Rega**[3]

[1] Department of Civil Engineering, Catholic University, PUC-Rio, Rio de Janeiro, Brazil
dgorlando@gmail.com; paulo@puc-rio.br

[2] Dep. Architecture, Buildings and Structures, Polytechnic University of Marche, Ancona, Italy
lenci@univpm.it

[3] Department of Structural and Geotechnical Engineering, Sapienza University of Rome, Roma, Italy
giuseppe.rega@uniroma1.it

Keywords: Von Mises Truss, Nonlinear Vibrations, Escape Control, Dynamic Instability

Abstract. *In this paper a method for controlling the global nonlinear dynamics of mechanical systems is applied to the elastic von Mises truss model, which is a prototype for buckling analysis of several planar and spatial truss systems and shallow lattice shell structures, including the geodesic dome, and which has a theoretical and practical interest. The method consists of the (optimal) elimination of homoclinic intersection by properly adding superharmonic terms to a given harmonic excitation. By means of the solution of an appropriate optimization problem, it is possible to select the amplitudes and the phases of the added superharmonics in such a way that the manifolds distance is as large as possible. This methodology is here applied to increase the integrity of the basins of attraction of the system and its practical safety.*

1 INTRODUCTION

Shallow structures such as shells, arches and reticulated space domes generally have a highly nonlinear behavior with increasing loss of effective stiffness in the presence of compressive stresses, which leads to limit point instability or unstable symmetric bifurcation along the nonlinear equilibrium path before reaching the first limit point [1, 2]. This nonlinearity leads to a complex dynamic behavior and loss of stability under dynamic loads well below the static critical load, making, therefore, of vital importance, the investigation of the nonlinear dynamic behavior of these structures in structural engineering and applied mechanics [3, 4].

Among these shallow structures are shallow space trusses of pyramidal shape, whose planar example is the well-known planar von Mises truss [4-6], which is traditionally used in numerical analysis to test the convergence and accuracy of numerical softwares and algorithms for the analysis of nonlinear structures [7]. Shallow pyramidal trusses are found in various engineering areas [8], as they constitute the basic substructure of several structures, including from large structures like geodesic domes [9] and folding structures [10] to carbon nanostructures [11, 12].

The static stability of this class of structures was studied by [1, 2, 8, 13-19], among others. However, little is known about the nonlinear dynamic behavior of these structures.

In this paper a method for controlling nonlinear dynamics and chaos, which has been recently developed [20] and tested on various mechanical systems [21, 22], is applied to the von Mises truss [8]. The method consists of the (optimal) elimination of homoclinic (or heteroclinic) intersection by properly adding superharmonic terms to a given harmonic excitation. It can be implemented as either a global or a one-side control, the former aiming at eliminating the intersections of the manifolds of a given saddle over the whole phase space, the latter over just one part of it. By means of the solution of an appropriate optimization problem, it is possible to select the amplitudes and the phases of the added superharmonics in such a way that the manifolds distance is as large as possible. The best result is obtained with an infinite number of superharmonics. However, even using few (one or two) controlling superharmonics one is able to have results which are satisfactory from a practical point of view. The elimination of the homoclinic intersections permits to eliminate from the system dynamics various nonlinear phenomena such as chaotic transients, sensitivity to initial conditions and fractal basin boundaries. The latter, in particular, is a very desirable effect since it permits to reduce the basin erosion and thus to increase the dynamical integrity.

2 FORMULATION

The non-linear behavior and stability under static and dynamic loads of the von Mises shallow truss is analyzed in this paper [8]. The model (Figure 1) is composed of two identical elastic bars of length L ($L^2 = H^2 + B^2$), axial stiffness EA and mass per unit length m. The shallow truss has a height H and span $2B$, with $(H/2B) << 1$.

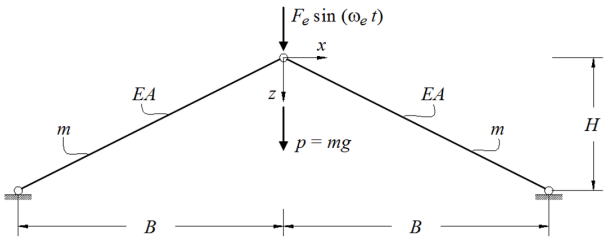


Figure 1: Elastic von Mises truss model.

The potential energy of the truss under a static vertical load p is given by

$$V = EA/4L^3\left(\left(H-z\right)^2 - H^2\right)^2 - pz, \tag{1}$$

Adopting the nondimensional parameters $w = z/H$, $\alpha = B/H$ and $\lambda = p/EA$, the nonlinear equilibrium path is described by:

$$\lambda = \frac{w\left(2-w\right)\left(1-w\right)}{\left(\sqrt{1+\alpha^2}\right)^3}, \tag{2}$$

Having as a reference a static equilibrium configuration w_i, the nondimensional potential energy $\bar{V}$ can be written as

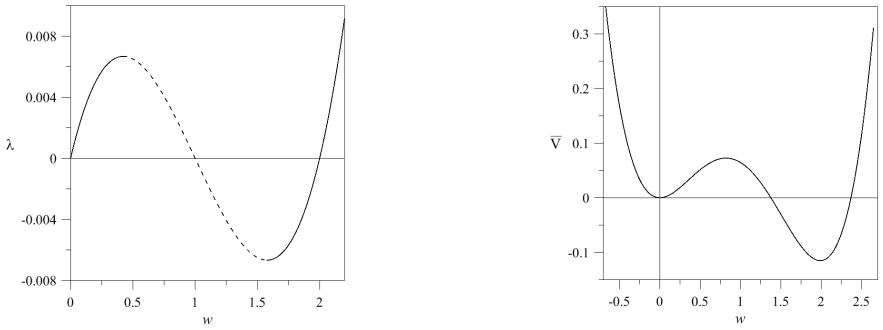
$$\bar{V} = \frac{w^2}{2}\left(1-3w_i+\frac{3}{2}w_i^2\right) - \frac{1}{2}w^3\left(1-w_i\right) + \frac{1}{8}w^4, \tag{3}$$

For a prescribed static load level p between the two limit points, there are three equilibrium positions w_i (i=1, 2, 3) (two stable and one unstable), as illustrated in Figure 2(a) for $B/H = 1/\tan\left(15°\right)$. The observed nonlinear behavior is typical of shallow structures. Figure 2(b) shows the potential energy of the system under a load level equal to 30% of the snap-through load ($w_i = 0.0636$). For the loaded structure the first safe well is smaller than the second well associated with the buckled configuration. So, preventing the escape from the pre-buckling well becomes an important issue in design. To this aim, we intend to control the global bifurcation associated with the homoclinic orbit (one-side control) defining the safe potential well, as suggested in [20-22].

The nondimensional nonlinear equation of motion, having as a reference a static equilibrium configuration w_i, is given by

$$w_{,\tau\tau} + 2\xi w_{,\tau} + w\left(1-3w_i+3/2\,w_i^2\right) - 3/2\,w^2\left(1-w_i\right) + 1/2\,w^3 = F\sin\left(\Omega\tau\right), \tag{4}$$

Here, $\tau = \omega_0 t$, $c/m = 2\xi\omega_0$ and $\Omega = \omega_e/\omega_0$, where $\omega_0 = \sqrt{2EAH^2/mL^3}$ is the natural frequency of the unloaded structure, ω_e is the excitation frequency, c is the damping, F ($F = F_e/mH\omega_0^2$) is the amplitude of the dynamic excitation.

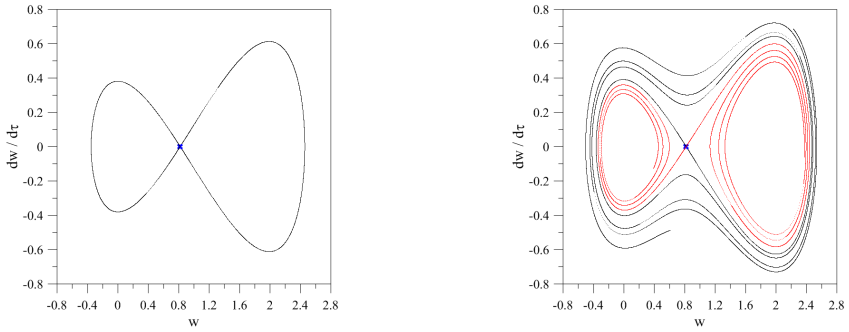


(a) (b)

Figure 2: (a) Nonlinear equilibrium path; (b) Potential energy.

3 DINAMIC ANALYSIS

The phase portrait of the unforced ($F = 0$) system with a static load level equal to 30% of the snap-through load (stable pre-buckling position $w_i = 0.0636$), which can be easily obtained by the conservation of energy equation $\overline{T} + \overline{V} = const.$, is reported in Figure 3(a) in the undamped case ($\xi = 0$), and in Figure 3(b) in the damped case ($\xi = 0.01$). From these figures it is possible to see that the safe potential well of the von Mises shallow truss is bounded by a homoclinic orbit. The safe pre-buckling basin decreases with the static load level and becomes zero at the limit point.



(a) (b)

Figure 3: Homoclinic orbit (a) $\xi = 0.0$; (b) $\xi = 0.01$.

Before proceeding with the analysis of the beneficial effects of control, it is worth to shortly discuss the overall dynamical scenario for the uncontrolled case, i.e. the system subjected to harmonic excitation (static load level equal to 30% of the snap-through load). The behavior charts for the von Mises shallow truss around the main resonance are reported in Figure 4, where the thresholds of the relevant bifurcations are reported along with the regions of inevitable escape from the pre-buckling well. The overall threshold of the escape region is obtained as the envelop of the different loci of local bifurcations – obtained by extensive numerical simulations of (4) – which govern the onset of escape in various frequency ranges. Note that the main resonance occurs for an $\Omega = \omega_e / \omega_o$ value (e.g., $\Omega = 0.902889$) which corresponds to the fundamental resonance of the model.

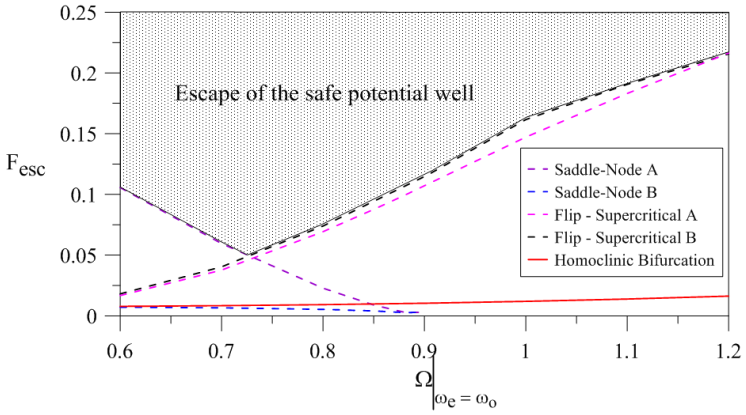


Figure 4: Behavior charts in the main resonance region.

4 CONTROL METHOD

Among several existing control techniques, one which consists of modifying the excitation of the system by adding a superharmonic force to a basic harmonic excitation is a technique of low computational cost and very viable [20, 23-25]. The method consists of looking for the excitation which avoids, in an optimal manner, the intersection of the stable and unstable perturbed manifolds, which delimits the safe region, and comprises the following steps:

1. determination of the homoclinic bifurcation (critical excitation amplitude), e.g. by the method of Melnikov;

2. analysis of the dependence of homoclinic bifurcation on the shape of the excitation, i.e. on the controlling superharmonic terms;

3. formulation and solution of the mathematical optimization problem, which consists of determining the theoretical optimal excitation that maximizes the distance between the stable and unstable manifolds for fixed excitation amplitude or, equivalently, the critical amplitude where the global bifurcation occurs;

4. numerical implementation of optimal excitation needed to confirm the theoretical predictions and to verify the feasibility and performance of the control technique.

Following this procedure, the excitation is taken in the form:

$$\overline{F}(\tau) = -F\left(\sin(\Omega\tau) + \sum_{j=2}^{n} \frac{F_j}{F} \sin(j\Omega\tau + \nu_j) \right), \tag{5}$$

where F_j and ν_j, j=2,3,…, are the amplitudes and phases of the controlling superharmonics added to the reference harmonic one, whereas F is the overall excitation amplitude.

Computing by the Melnikov method the global bifurcation thresholds without and with control, and comparing these two values to ascertain the effect of control, one obtains:

$$G = \frac{F_{cr}^{cont}}{F_{cr}^{h}} = \frac{1}{\max_{m\in[0,2\pi]}\{\gamma(m)\}} = \frac{1}{\overline{m}}, \tag{6}$$

where (more information about $\alpha_2(j)$ see [22])

$$\gamma(m) = \sin(\eta + m) + \sum_{j=2}^{n} h_j \sin(\overline{\eta}_j + jm + \nu_j), \qquad h_j = \frac{F_j}{F}\frac{\alpha_2(j)}{\alpha_2(1)}. \tag{7}$$

The aim of the procedure, as shown in [25], is to obtain the lowest value of $\overline{m} < 1$ that leads to the largest (optimal) value of F_{cr}^{cont}. Thus, the optimization problem can be written as:

$$\max\{G\} \text{ by varying the Fourier coefficients } h_j \text{ and } \nu_j,\ j=2,3,\ldots n., \tag{8}$$

The solution of the previous problem, which is independent of the specific mechanical system, is obtained in [23, 24] and is reported in Table 1.

n	G_n	h_2, ν_2	h_3, ν_3	h_4, ν_4	h_5, ν_5
2	1.4142	0.353553, π			
3	1.6180	0.552756, π	0.170789, 0		
4	1.7321	0.673525, π	0.333274, 0	0.096175, π	
5	1.8019	0.751654, π	0.462136, 0	0.215156, π	0.059632, 0
...	....	...	...	...	...
∞	2	1, π	1, 0	1, π	1, 0

Table 1: Results of the optimization problems with increasing number of superharmonics.

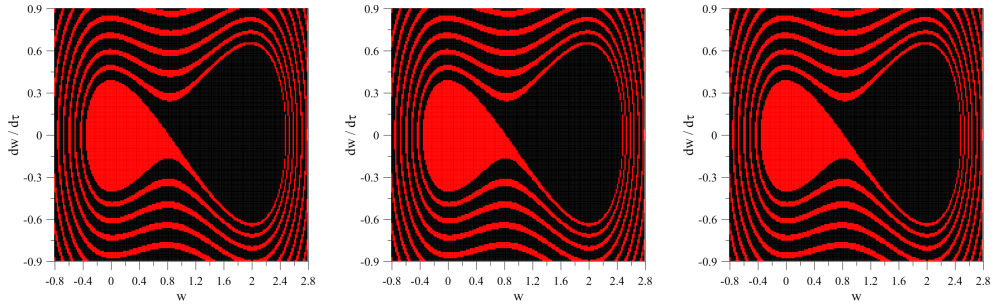
By using the values of Table 1, the magnitude of each controlling superharmonic is simply given by:

$$F_j = F h_j \frac{\alpha_2(1)}{\alpha_2(j)}. \tag{9}$$

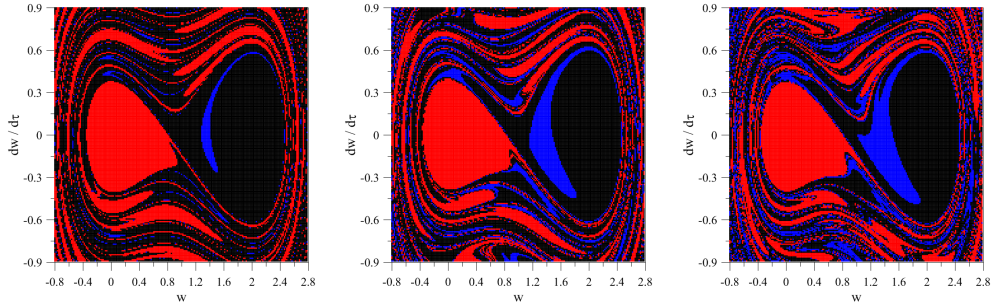
The column of gains G_n in Table 1 allows us to observe that, in general, the gain increases with increasing number of superharmonics, as expected. The last line presents, for comparison purposes, the values of the optimal gain G_∞ and of the optimal coefficients h_j considering an infinite number of superharmonics (i.e. a completely free periodic shape of the excitation). These values represent the upper bound of optimal solutions. Comparing G_n with G_∞ it is possible to conclude that even using a limited number of controlling superharmonics, it is possible to obtain quite satisfactory results, at least from a practical point of view. Actually, checking the practical effectiveness of the theoretical results of Table 1 constitutes the object of the next section.

4.1 Numerical Verification of the Control Effectiveness

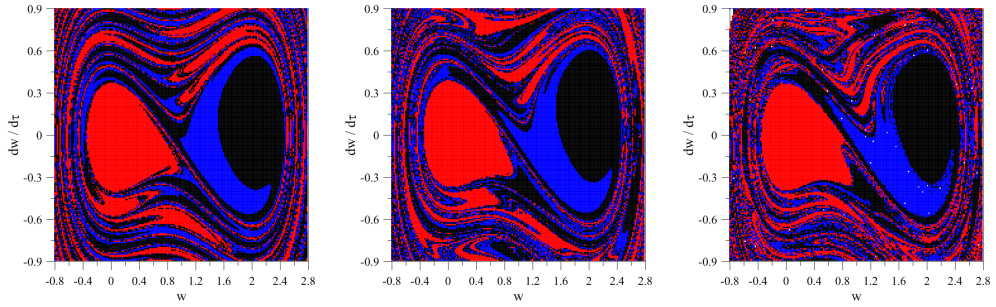
In order to verify the control effectiveness two cases are considered here: (a) one controlling superharmonic, n=2 in (7), and (b) two controlling superharmonics, n=3 in (7). These are sufficient to check the efficiency of the method, since better results are of course expected using more superharmonics. The performances of control in reducing the fractal basin erosion are first shown in Figure 5. The left column shows how the erosion develops in the case of harmonic excitation. For the same values of F, the results in the medium and right columns show that the erosion of the red safe basin by the competing black basin is postponed in the controlled cases. The beneficial effects of control are visible in Figures 5(b) and 5(c) as regards the occurrence of both a widened core basin and of a relevant smoother boundary.



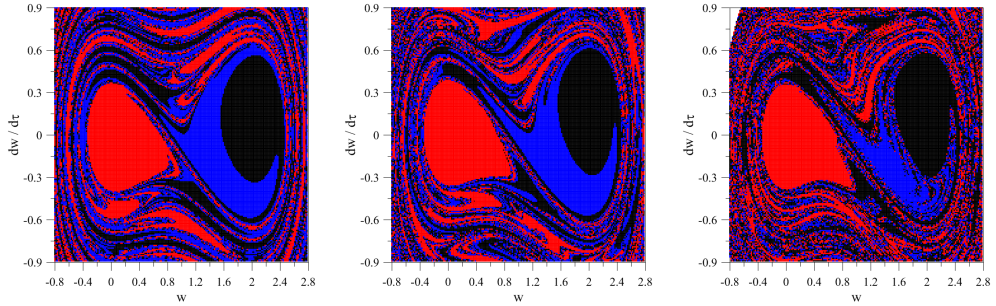
(a) F = 0.0



(b) F = 0.01



(c) F = 0.0165



(d) F = 0.02

Figure 5: Basins of attraction for uncontrolled (left column), controlled 1 (medium column, one superharmonic, $F_2 = 1.1605F$ and $\nu_2 = \pi$) and controlled 2 (right column, two superharmonics, $F_2 = 2.5756F$, $\nu_2 = \pi$, $F_3 = 4.9331F$, $\nu_3 = 0$). Static load level equal to 30% of the snap-through load, $\Omega = 0.902889$ and $\xi = 0.01$.

By building a sufficient number of basins of attractions such as those in Figure 6 it is possible to construct the so called erosion profiles [26], which report a measure of the basin dynamical integrity (i.e. of the safety of the structure) versus the increasing excitation amplitude. Two different integrity measures are here considered [26]: the GIM, which measures the entire safe area, and the IF, which measure the radius of the largest circle inscribed in the same area safe. In both cases, the integrity measure is normalized with respect to its magnitude for $F = 0$. The IF has been introduced to rule out from the integrity measure the fractal parts of the basins, which clearly do not contribute to the safety of the structure, even if they may have a large area (and thus a large GIM). The IF integrity profiles are reported in Figure 6(a) for both the controlled and the uncontrolled case, while the GIM integrity profiles are reported in Figure 6(b). These curves clearly show that a gain of about 40% (one controlling superharmonic) and 60% (two controlling superharmonics) is confirmed by numerical simulations, even in the case of a single controlling superharmonic: the erosion of safe basin in the controlled model starts later (see Figure 5), increasing the magnitude of the disturbances that the structure can undergo without practically losing its stability and consequently its safety margin in a dynamic environment.

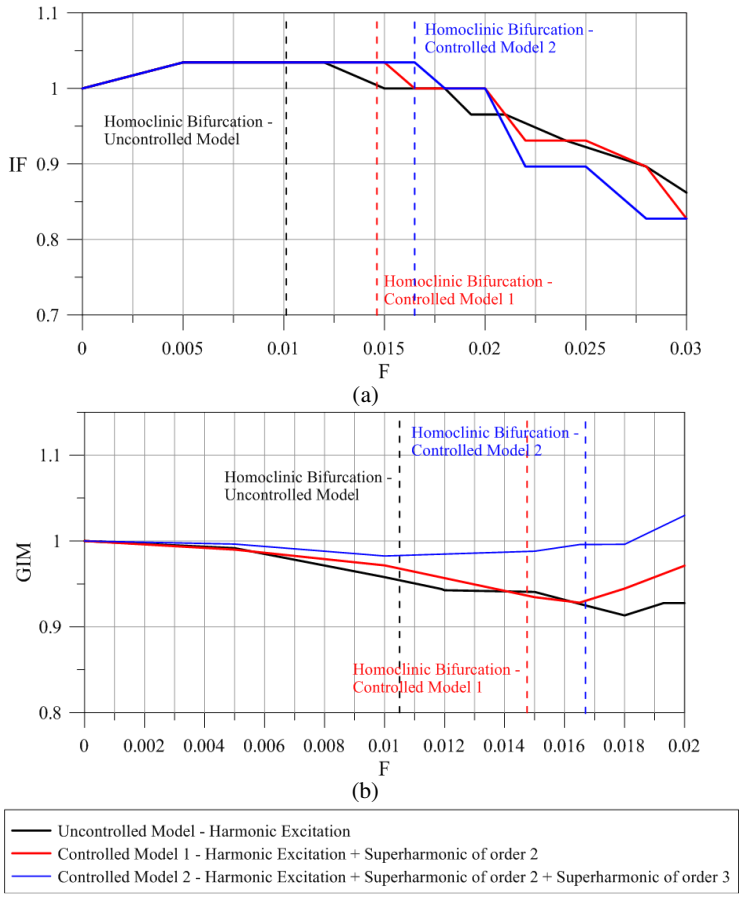


Figure 7: Integrity profiles for increasing load. (a) IF; (b) GIM. Controlled 1 (one superharmonic, $F_2 = 1.1605F$ and $\nu_2 = \pi$) and controlled 2 (two superharmonics, $F_2 = 2.5756F$, $\nu_2 = \pi$, $F_3 = 4.9331F$, $\nu_3 = 0$). Static load level equal to 30% of the snap-through load, $\Omega = 0.902889$ and $\xi = 0.01$.

Looking at Figures 6(a) and 6(b) we conclude that in the present case IF and GIM are able to reliably catch the system safety, contrary to what happens in other situations, where GIM overestimates it [26]. Likely this occurs because we have a strongly softening system. In fact, in weakly softening or hardening systems, the GIM measure (which considers the fractal part as safe) often overestimates the real safety of the structure. These points also hold when the control is applied, since it does not modify the global behaviour of the system.

5 CONCLUSIONS

In this paper a method for controlling nonlinear dynamics and chaos is applied to a structural system liable to unstable buckling behavior, the von Mises truss, with the aim of increasing its load carrying capacity, or, equivalently, the "practical" stability threshold. After having summarized the main features of the control method, which has been developed elsewhere, it has been applied to the considered structural system. The results of extensive numerical simulations show that the methodology leads to an increment of the integrity of the basins of attraction in the excitation ranges where the erosion takes place, thus increasing (i) its performance in a dynamic environment, and (ii) its "practical" safety and thus its load carrying capacity.

REFERENCES

[1] J. M. T. Thompson and G. W. Hunt, *Elastic instability phenomena*. London, Great Britain: John Wiley and Sons, 1984.

[2] Z. Bazant and L. Cedolin, *Stability of structures: elastic, inelastic, fracture and damage theories*. Oxford: UK: Oxford University Press, 1991.

[3] M. S. Soliman and P. B. Gonçalves, Chaotic behavior resulting in transient and steady state instabilities of pressure-loaded shallow spherical shells. *Journal of Sound and Vibration*, **259**(3), 497-512, 2003.

[4] M. A. Savi, and J. B. Nogueira, Nonlinear dynamics and chaos in a pseudoelastic two-bar truss. *Smart Materials and Structures*, **19**(11), 1-11, 2010.

[5] M. Greco, and W. S. Venturin, Stability analysis of three-dimensional trusses. *Latin American Journal of Solids and Structures*, **3**(3), 325-344, 2006.

[6] L. Kwasniewski, Complete equilibrium paths for Mises trusses. *International Journal of Non-Linear Mechanics*, **44**(1), 19-26, 2009.

[7] M. A. Crisfield, *Non-linear finite element analysis of solids and structures: Advanced topics*. John Wiley & Sons, Inc,1997.

[8] S. S. Ligarò and P. S. Valvo, Large displacement analysis of elastic pyramidal trusses. *International Journal of Solids and Structures*, **43**(16), 4867-4887, 2006.

[9] M. P. Saka, Optimum geometry design of geodesic domes using harmony search algorithm. *Advances in Structural Engineering*, **10**(6), 595-606, 2007.

[10] I. Ario, and A. Watson, Dynamic folding analysis for multi-folding structures under impact loading. *Journal of Sound and Vibration*, **308**(3), 591-598, 2007.

[11] H. Kroto, C60, fullerenes, giant fullerenes and soot. *Pure and Applied Chemistry*, **62**(3), 407-415, 1990.

[12] R. B. Ansems and L. T. Scott, Circumtrindene: A geodesic dome of molecular dimensions. Rational synthesis of 60 of C601. *Journal of the American Chemical Society*, **122**(12), 2719-2724, 2000.

[13] D. A. Pecknold, J. Ghaboussi and T. J. Healey, Snap-through and bifurcation in a simple structure. *Journal of Engineering Mechanics*, **111**(7), 909-922, 1985.

[14] A. López, I. Puente and M. A. Serna, Numerical model and experimental tests on single-layer latticed domes with semi-rigid joints. *Computers & Structures*, **85**, 360-374, 2007.

[15] T. Schioler and S. Pellegrino, Space frames with multiple stable configurations. *AIAA Journal*, **45**, 1740-1747, 2007.

[16] G.A. Hrinda, Snap-through instability patterns in truss structures. *NASA Langley Research Center*, Hampton, Virginia, 23831, 2010.

[17] F. Fan, Z. Cao and S. Shen, Elasto-plastic stability of single-layer reticulated shells. *Thin-Walled Structures*, **48**, 827-836, 2010.

[18] H. Saffari, N. M. Mirzai, I. Mansouri and M. H. Bagheripour, Efficient numerical method in second-order inelastic analysis of space trusses. *Journal of Computing in Civil Engineering*, **27**, 129-138, 2012.

[19] S. D. Shon, S. J. Lee and K. G. Lee, Characteristics of bifurcation and buckling load of space truss in consideration of initial imperfection and load mode. *Journal of Zhejiang*, **14**, 206-218, 2013.

[20] S. Lenci and G. Rega, A procedure for reducing the chaotic response region in an impact mechanical system. *Nonlinear Dynamics*, **15**(4), 391-409, 1998.

[21] G. Rega and S. Lenci, Recent advances in control of complex dynamics in mechanical and structural systems. In M.A.F. Sanjuan, C. Grebogi (Eds.), *Recent Progress in Controlling Chaos*, Series on Stability Vibration and Control of Systems, **16**, 189-237, 2009.

[22] S. Lenci, D. Orlando, G. Rega, P. B. Gonçalves, Controlling practical stability and safety of mechanical systems by exploiting chaos properties. *Chaos*, **22**, 047502-1-15 , 2012.

[23] S. Lenci and G. Rega, Optimal control of nonregular dynamics in a Duffing oscillator. *Nonlinear Dynamics*, **33,** 71-86, 2003.

[24] S. Lenci and G. Rega, Optimal control of homoclinic bifurcation: Theoretical treatment and practical reduction of safe basin erosion in the Helmholtz oscillator. *Journal of Vibration and Control*, **9**, 281-315, 2003.

[25] S. Lenci and G. Rega, Global optimal control and system-dependent solutions in the hardening Helmholtz-Duffing oscillator. *Chaos, Solitons & Fractals*, **21**, 1031-1046, 2004.

[26] G. Rega and S. Lenci, Dynamical integrity and control of nonlinear mechanical oscillators. *Journal of Vibration and Control*, **14**, 159-179, 2008.

11th International Conference on Engineering Vibration
Ljubljana, Slovenia, 7–10 September 2015

CUBIC SOFTENING NONLINEAR ELASTICITY MEASUREMENT OF MAGNETIC ATTRACTION MODEL USING SELF-EXCITED OSCILLATION

Yudai Tanaka*[1], Hiroshi Yabuno*[2]

[1]University of Tsukuba
s1520801@u.tsukuba.ac.jp

[2]University of Tsukuba
yabuno@esys.tsukuba.ac.jp

Keywords: nonlinear dynamics, softening nonlinear stiffness, negative linear stiffness self-excited oscillation, van der Pol oscillator

Abstract. *In this paper, a stiffness sensor for measuring cubic softening nonlinear elasticity is developed. The measurement system consists of an oscillator and a feedback circuit, and achieves the dynamics of van der Pol oscillator in the oscillator by the positive linear velocity feedback and the nonlinear feedback proportional to the squared position and the velocity. Then, the tuning of the nonlinear feedback gain can realize any setting of the magnitude of the response amplitude. It is well known that the natural frequency depends on the response amplitude in the case with nonlinearity in the system. Therefore, we can experimentally describe the backbone curve from the relationship between the response amplitudes, which are set by various nonlinear feedback gains, and the corresponding response frequencies and identify the nonlinear elasticity. In experiments, we employ a magnetic attraction model as a measurement object with negative linear elasticity and cubic softening nonlinear elasticity. Similar to the measurement for the model with hardening nonlinear elasticity, softening nonlinear elasticity is also measured by setting a sign of the coefficient of the nonlinear feedback appropriately to produce the stable limit cycle.*

International Conference on Engineering Vibration
Ljubljana, Slovenia, 7-10 September 2015

PARAMETRIC STUDY OF A MACRO-SCALE TUNING FORK GYROSCOPE

M. Ghandchi Tehrani*[1], J. M. Balthazar[2,3], M. Silveira[3]

[1]University of Southampton, Institute of Sound and Vibration Research, Southampton, UK
m.ghandchi-tehrani@soton.ac.uk

[2]ITA (Aeronautics Technological Institute), Mechanical-Aeronautics Division, São josé dos campos, SP, Brazil
jmbaltha@gmail.com

[3] São Paulo State University UNESP-Bauru, Mechanical Engineering department, SP, Brazil
m.silveira@feb.unesp.br

Keywords: Tuning fork Gyroscope, Parametric excitation, Nonlinear dynamics

Abstract.
In this paper, the dynamic behaviour of a macro-scale tuning gyroscope is presented. The gyroscope consists of two inverted pendulums on a suspension mass. The suspension mass is subjected to force excitation generated by an electromagnetic shaker. The dynamics of the shaker are included in the analysis. It is shown that the system is a parametrically excited system. Parametric excitation can lead to vibration in the horizontal motion of the suspension mass, when the two pendulums are in phase. The problem is particularly interesting for energy harvesting. Due to the interaction between the system's degrees-of-freedom, the energy is transferred from vertical (base excitation) to horizontal direction. Initial parametric studies are carried out to analyse the dynamic behaviour of the system by varying the initial conditions, base excitation frequency and amplitude. It is demonstrated that under certain parameters the system can exhibit complex dynamic behaviour such as chaotic motion.

1 INTRODUCTION

Vibratory gyroscopes are used to measure the angular velocity. They are non-rotating devices and work based on Coriolis acceleration effect. The tuning-fork gyroscopes is a typical example of vibratory gryroscopes. They consist of two tines, which vibrate in opposite direction to measure the angular velocity.

The performance of the micro tuning fork gyroscopes is limited due to its small size and imperfection in fabrication. A small imperfection in fabrication can cause significant error in operation of such devices. The increase of input or drive velocity can enhance its performance, however this depends on the power provided by the external source. Parametric excitation can be used to increase the amplitude of vibrations of the two tines.

Ghandchi Tehrani et al [1] experimentally investigated the instability caused by parametric excitation on a beam attached to a shaker subject to base excitation. When the base excitation frequency is twice the natural frequency of the beam, large amplitudes of vibration can occur in the direction perpendicular to the vibrating motion. Lee [2] has demonstrated the response of a tuning fork beam subject to parametric excitation in an experiment. He has shown that parametric excitation can be taken advantage of, in order to increase the sensitivity of the tuning fork gyroscopes [3]. Vibrations of a parametrically excited system with ideal and non-ideal energy sources have been investigated [4, 5]. The dynamic interaction between a parametric pendulum and an electro-dynamic shaker has been considered [6]. Xu et al. [7] employed both numerical and analytical techniques to explore the dynamics of the harmonically excited parametric pendulum when it exhibits rotational orbits.

In this paper, a macro model of a tuning fork gyroscope is considered. It consists of two pendulums and a suspension mass, which can vibrate in both horizontal and vertical motion. The system is subject to base excitation through an electrodynamic shaker. The dynamics of the shaker interacts with the structure. The problem is complex, since there is coupling between the degrees of freedom through parametric excitation, inertia and geometric nonlinearities. First, the governing dynamic equations are provided using Lagrange method. Then, the dynamic equations are solved numerically using Matlab Runge-Kutta method to obtain the responses. Parametric study is carried out to investigate the effect of initial conditions, the amplitude and frequency of excitation.

2 DYNAMIC EQUATIONS OF A TUNING-FORK GYROSCOPE

Figure 1 shows the tuning fork gyroscope. It consists of two pendulums attached to a suspension mass. Each pendulum has a lumped mass, m_1 and m_2 which is connected to a massless rod, whose length is l_1 and the other one is connected to l_2. The stiffness of the pendulums are k_1 and k_2, which includes linear and nonlinear springs. The mass M is suspended via horizontal and vertical springs, k_3 and k_4, respectively to an electrodynamic shaker. There are five degrees of freedom, two rotations of the pendulums θ_1, θ_2, horizontal x and vertical motion y of the suspended mass M and the electrical charge q of the shaker. The shaker generates a base displacement, along the vertical direction and has an electrical circuit with resistance, R, inductance, L and capacitance C.

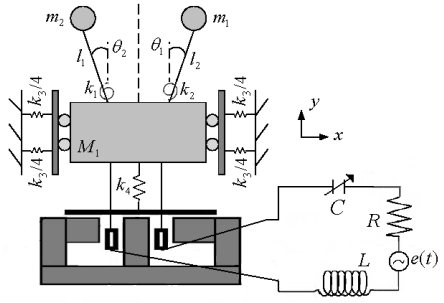


Figure 1: A tuning fork gyroscope

Using Lagrange method, the dynamic equations can be obtained. The governing equations of motion s in the non-dimensional form can be written as,

$$\begin{aligned}
&\theta_1'' + \delta_1\theta_1 + \lambda_1\theta_1^3 + \mu_1\theta_1' - \eta_1\left(\mathrm{X}''\cos\theta_1 + \left(\mathrm{Y}'' + g_1\right)\sin\theta_1\right) = 0\\
&\theta_2'' + \delta_2\theta_2 + \lambda_2\theta_2^3 + \mu_2\theta_2' - \eta_2\left(\mathrm{X}''\cos\theta_2 + \left(\mathrm{Y}'' + g_1\right)\sin\theta_2\right) = 0\\
&\mathrm{X}'' + \mu_4\mathrm{X}' + \omega_x^2\mathrm{X} - \sum_{i=1}^{2} F_i\left(\theta_i''\cos\theta_i - \theta_i'^2\sin\theta_i\right) = 0\\
&\mathrm{Y}'' + \mu_5\mathrm{Y}' + \omega_y^2\mathrm{Y} - \sum_{i=1}^{2} F_i\left(\theta_i''\sin\theta_i - \theta_i'^2\cos\theta_i\right) - \gamma_1\mathrm{Q}' = 0\\
&\mathrm{Q}'' + \mu_3\mathrm{Q}' + \mathrm{Q} + \lambda_3\mathrm{Q}^3 + \gamma_2\mathrm{Y}' = E_0\cos\left(\omega\tau\right)
\end{aligned} \tag{1-5}$$

where, the non-dimensional parameters are provided as,

$$\mathrm{X} = \frac{x}{l_c}, \mathrm{Y} = \frac{y}{l_c}, \mathrm{Q} = \frac{q}{q_0}, \omega_e = \frac{1}{\sqrt{LC_0}}, \omega = \frac{\Omega}{\omega_e}, \tau = \omega_e t, g_1 = \frac{g}{\omega_e^2 l_c}, \delta_1 = \frac{k_1}{m_1 l_1^2 \omega_e^2},\ \delta_2 = \frac{k_2}{m_2 l_2^2 \omega_e^2},$$

$$\omega_x = \sqrt{\frac{k_x}{M_t\omega_e^2}}, \omega_y = \sqrt{\frac{k_y}{M_t\omega_e^2}}, \eta_1 = \frac{l_1}{l_c}, \eta_2 = \frac{l_2}{l_c}, F_1 = \frac{m_1 l_1}{M_t l_c}, F_2 = \frac{m_2 l_2}{M_t l_c}, \lambda_1 = \frac{h_1}{m_1 l_1^2 \omega_e^2}, \lambda_2 = \frac{h_2}{m_2 l_2^2 \omega_e^2},$$

$$\lambda_3 = \frac{\alpha_3 q_0^2}{L\omega_e^2}, \mu_1 = \frac{c_1}{m_1\omega_e}, \mu_2 = \frac{c_2}{m_2\omega_e}, \mu_4 = \frac{c_4}{M_t\omega_e}, \mu_5 = \frac{c_5}{M_t\omega_e}, \mu_3 = \frac{R}{L\omega_e}, \gamma_1 = \frac{Kq_0}{M_t\omega_e l_c}, \gamma_2 = \frac{Kl_c}{M_t\omega_e q_0},$$

$$E_0 = \frac{e_0}{L\omega_e^2 q_0}.$$

We can write the equations of motion (1-5) in a matrix form.

$$\tilde{\mathbf{M}}\ddot{\mathbf{z}} + \tilde{\mathbf{C}}\dot{\mathbf{z}} + \tilde{\mathbf{K}}\mathbf{z} + \tilde{\mathbf{G}}\sin(\mathbf{z}) = \mathbf{f} \tag{6}$$

where, $\mathbf{z} = \left[\theta_1 \quad \theta_2 \quad \mathrm{X} \quad \mathrm{Y} \quad \mathrm{Z}\right]^T$, $\mathbf{f} = \left[0 \quad 0 \quad 0 \quad 0 \quad E_0\cos\omega\tau\right]^T$.

The nonlinear mass matrix is,

$$\tilde{\mathbf{M}} = \begin{bmatrix} 1 & 0 & -\eta_1\cos\theta_1 & -\eta_1\sin\theta_1 & 0\\ 0 & 1 & -\eta_2\cos\theta_2 & -\eta_2\sin\theta_2 & 0\\ -F_1\cos\theta_1 & -F_2\cos\theta_2 & 1 & 0 & 0\\ -F_1\sin\theta_1 & -F_2\sin\theta_2 & 0 & 1 & 0\\ 0 & 0 & 0 & 0 & 1 \end{bmatrix}, \tag{7}$$

the nonlinear damping and the stiffness matrices are,

$$\tilde{\mathbf{C}} = \begin{bmatrix} \mu_1 & 0 & 0 & 0 & 0 \\ 0 & \mu_2 & 0 & 0 & 0 \\ F_1 \sin\theta_1\theta_1' & F_2 \sin\theta_2\theta_2' & \mu_4 & 0 & 0 \\ -F_1 \cos\theta_1\theta' & -F_2 \cos\theta_2\theta_2' & 0 & \mu_5 & -\gamma_1 \\ 0 & 0 & 0 & \gamma_2 & \mu_3 \end{bmatrix}, \mathbf{K} = \begin{bmatrix} \delta_1 + \lambda_1\theta_1^2 & 0 & 0 & 0 & 0 \\ & \delta_2 + \lambda_2\theta_2^2 & 0 & 0 & 0 \\ & & \omega_x^2 & 0 & 0 \\ & & & \omega_y^2 & 0 \\ & & & & 1+\lambda_3 q^2 \end{bmatrix}, \tag{8,9}$$

,and the nonlinear matrix corresponds to $\sin(\mathbf{z})$ is,

$$\tilde{\mathbf{G}} = \begin{bmatrix} -\eta_1 g_1 & 0 & 0 & 0 & 0 \\ & -\eta_2 g_1 & 0 & 0 & 0 \\ & & 0 & 0 & 0 \\ & & & 0 & 0 \\ & & & & 0 \end{bmatrix}. \tag{10}$$

3 NUMERICAL SIMULATION

The equations of motion are solved numerically using Matlab ode45 to find the response of the system. Numerical parametric study has been carried out to understand the dynamic behaviour of such systems. The dynamics is complex, since there is nonlinearity as well as parametric excitation.

For simulation, the following system parameters are used:

$$\delta_1 = \delta_2 = 1, \omega_x = \omega_y = 1, \omega_e = 1, F_1 = F_2 = 0.1, \eta_1 = \eta_2 = 1.01, g_1 = 1, \lambda_1 = \lambda_2 = 0.75, \mu_1 = \mu_2 = 0.01,$$
$$\mu_4 = \mu_5 = 0, \lambda_3 = 0.95, \mu_3 = 0.05, \gamma_1 = 0.4, \gamma_2 = 0.2$$

3.1 Effect of initial conditions $\theta_1(0), \theta_2(0)$

The response of nonlinear systems is sensitive to initial conditions. When the two initial conditions for the angular displacements of the pendulums are the same, the motion of the two pendulums is in-phase. For this simulation, $\omega = 1.8$ and $E_0 = 0.1$. Figure 2(a) shows the time histories of the inverted pendulums on an in-phase motion, with same initial conditions $\theta_1(0) = \theta_2(0) = 0.01$. The two pendulums oscillate about the angular position of 0.1. The two pendulums have the out-of-phase motion when the initial conditions have the opposite sign, $\theta_1(0) = -\theta_2(0) = 0.01$, as shown in Figure 2(b). The right pendulum oscillates about the angle of 0.1 and the left one oscillates about -0.1.

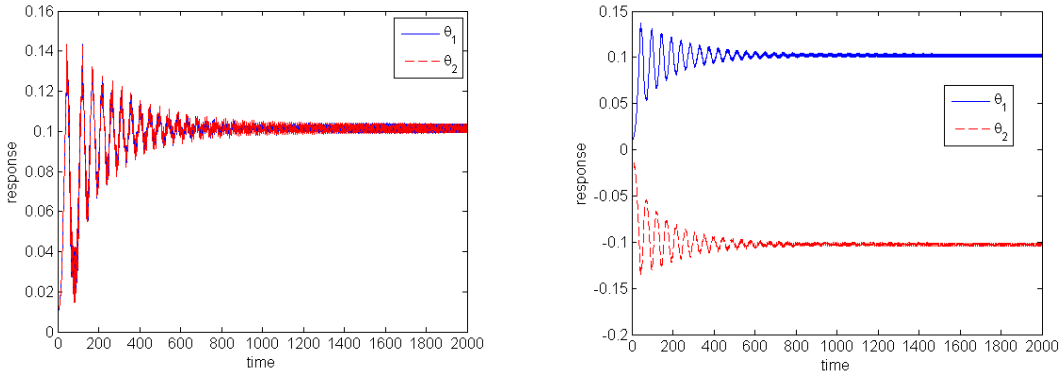


Figure 2: Angular positions of the two pendulums θ_1 (blue solid line), and θ_2 (red dashed line)with $\omega = 1.8$ and $E_0 = 0.1$ (a) in-phase motion with initial conditions $\theta_1(0) = \theta_2(0) = 0.01$, (b) out-of-phase motion with initial conditions $\theta_1(0) = -\theta_2(0) = 0.01$.

The in-phase motion of the two pendulums leads to the transfer of energy from Y-direction to X-direction, as illustrated in Figure 3(a). The blue solid line is the displacement of the suspension mass in Y direction and the red dashed line is for the X-direction. When the two pendulums are out-of-phase, no vibration can be observed in X-direction, as illustrated in Figure 3(b).

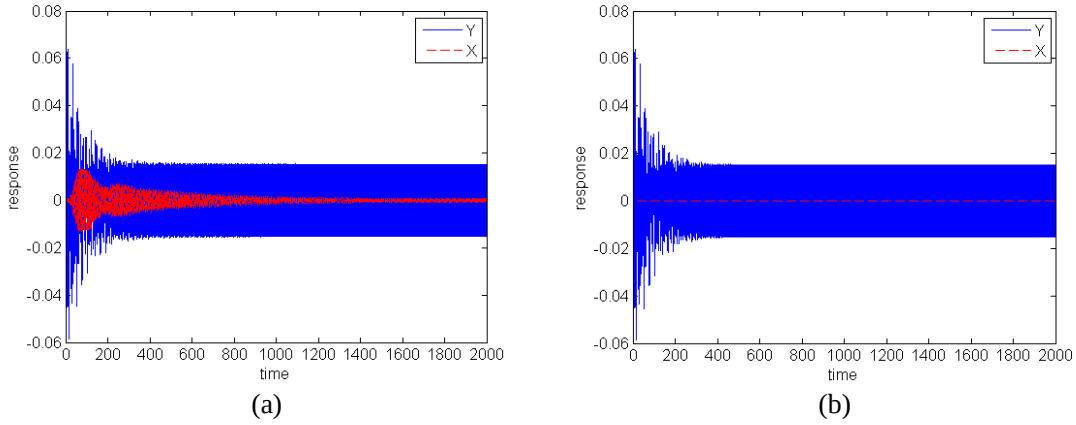


Figure 3: Displacements of the mass in vertical Y (blue line) and horizontal motion X (red dashed line), with $\omega = 1.8$ and $E_0 = 0.1$ (a) in-phase, (b) out-of-phase

The in-phase motion can transfer energy from Y-direction to X-direction and therefore, we investigate the dynamics when the initial conditions have the same sign.

3. 2 Effect of base excitation amplitude E_0, and frequency ω

Numerical simulations are carried out for different base excitation amplitudes and the results for the responses, power spectrum and the phase portraits are provided for two excitation

amplitudes of $E_0 = 0.1$ and $E_0 = 1$ in Figures 4-6, when the two pendulums are in-phase with initial conditions of $\theta_1(0) = \theta_2(0) = 0.01$ and the excitation frequency of $\omega = 1.8$. The increase of the base excitation amplitude increases the amplitude of vibrations in both X and Y directions. When excitation is large, the systems exhibits chaotic behaviour as can be seen in the time responses in Figure 4(d-f).

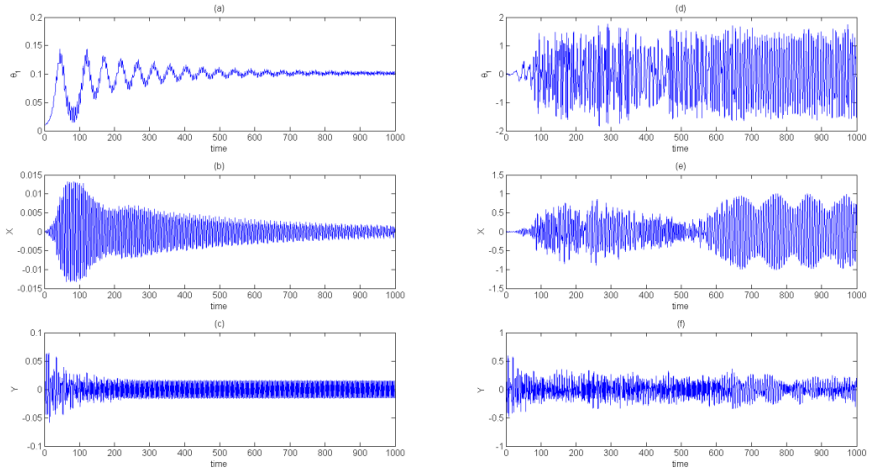


Figure 4: time responses, (a-c) $E_0 = 0.1$ and (d-f) $E_0 = 1$

The power spectrum is obtained by taking FFT using the sampling frequency of 10Hz , Hanning window and 50% overlap. For low level of excitation, there is still coupling between X and Y motions. By increasing the excitation level to $E_0 = 1$, the coupling can be seen between all the degrees of freedom. The frequency of about 0.9 exists in power spectrum of Fig.5(d-f).

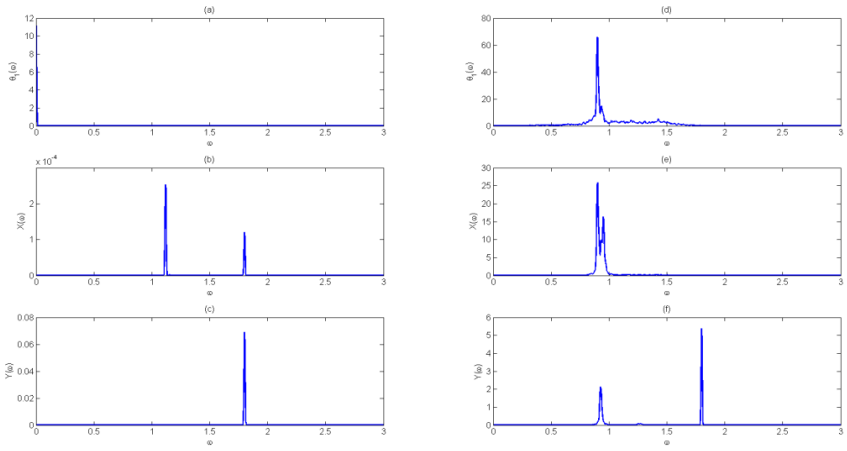


Figure 5: Power spectrum, (a-c) $E_0 = 0.1$ and (d-f) $E_0 = 1$

The phase portraits conform the existence of chaotic behaviour as shown in Fig. 6(d-f).

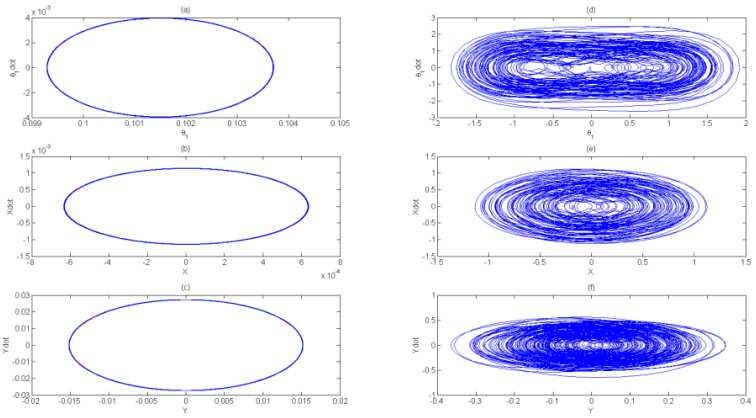


Figure 6: Phase portraits, (a-c) $E_0 = 0.1$ and (d-f) $E_0 = 1$

3. 3 Effect of base excitation frequency ω

Time-domain simulations are also carried out for two different excitation frequencies ω. The response at $\omega = 1.1$ is chaotic.

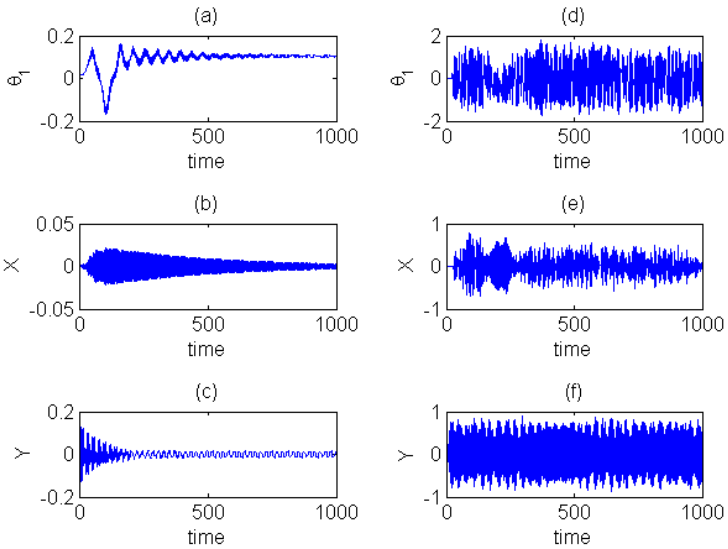


Figure 7: Responses at two different excitation frequencies, (a-c) $\omega = 0.3$, (d-f) $\omega = 1.1$.

Power spectrum of the time signals are also provided, which confirms the chaotic behaviour of the system when $\omega = 1.1$. The power spectrum of the response covers a frequency band-width of 0.7 to 1.6 for excitation frequency of $\omega = 1.1$.

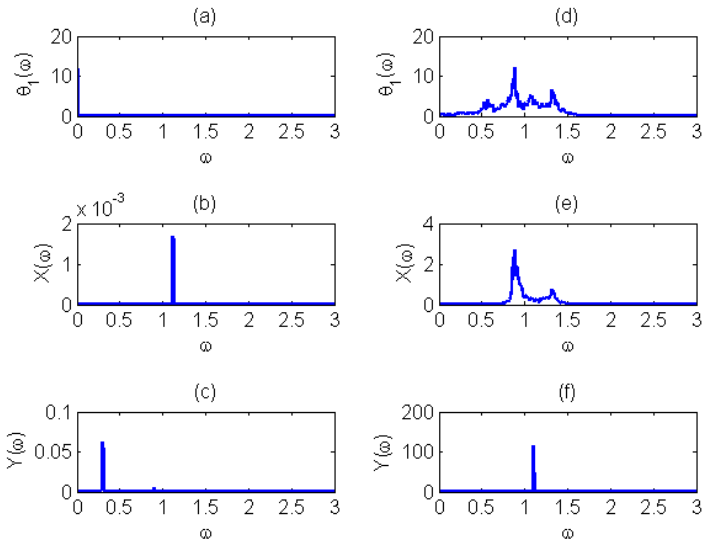


Figure 8: Power spectrum of the displacements at two different excitation frequencies, (a-c) $\omega = 0.3$, (d-f) $\omega = 1.1$.

The phase portraits are also provided, as shown in Figure 9. The periodic motion can be seen when $\omega = 0.3$, however quasi- periodic and chaotic motion is observed for $\omega = 1.1$.

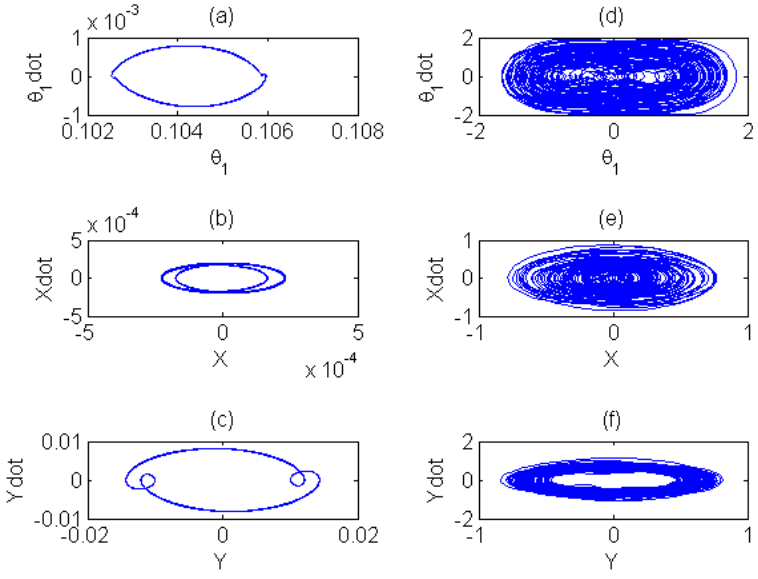


Figure 9: Phase portraits of the responses at two different excitation frequencies, (a-c) $\omega = 0.3$, (d-f) $\omega = 1.1$.

A statistical '0–1' test method has been applied to reveal the nature of the response of the system [8]. The chaotic and regular solutions can be determined by the value of '0-1' test. The

zero value of K indicates the regular motion, while the value of K close to one represents the chaotic behaviour. The excitation frequency varies from 0 to 2 and the statistical measure is calculated from [].

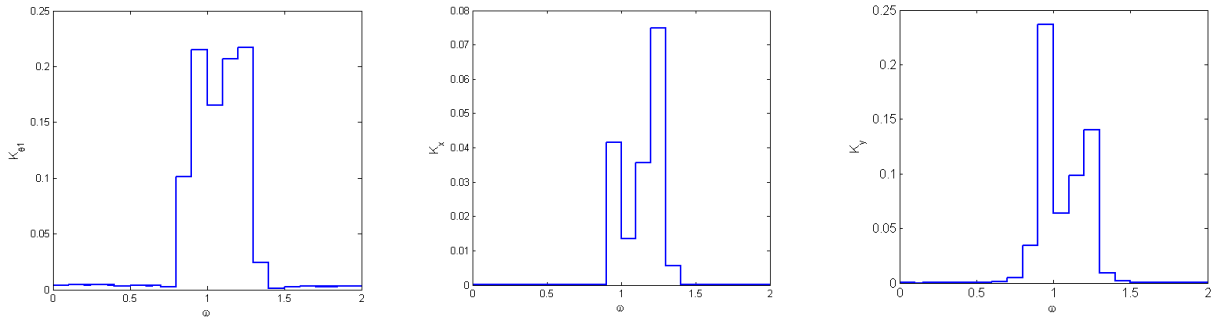


Figure 10: "0-1 test", (a) K_{θ_1}, (b) K_x and (c) K_y

The maximum displacement of the overall response including transient response is plotted in Figure 1 in which the displacement has got its maximum values between the frequency range of 0.7 to 1.4.

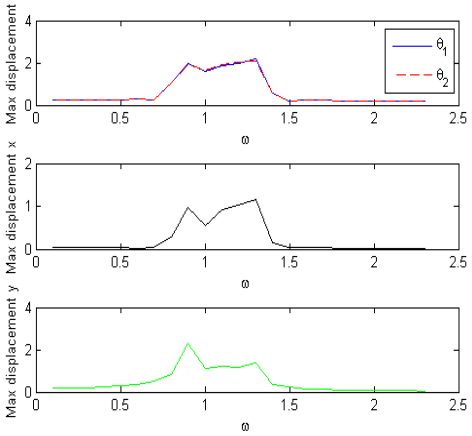


Figure 11: Maximum displacement

4 CONCLUSIONS

In this paper, a numerical study is carried out on a macro-scale tuning gyroscope. The gyroscope consists of two inverted pendulums on a suspension mass. The suspension mass is subjected to base excitation generated by an electromagnetic shaker. It is demonstrated that the system can have periodic, quasi-periodic and chaotic behaviour depending on the parameters using different representations such as time responses, power spectrum, phase portraits, maximum displacements and "0-1" test. Due to the interaction between the system degrees-of-freedom, the energy is transferred from vertical to horizontal direction. The problem is interesting from the energy harvesting point of view.

ACKNOWLEDGEMENTS

Dr Ghandchi Tehrani would like to acknowledge the support provided by the State University of Sao Paolo UNESP for the visiting academic position (PROPG-PVExt). She also would like to acknowledge EPSRC for the first grant scheme (ref: EP/K005456/1). The second author acknowledges CAPES and CNPQ , both Brazilian financial agencies.

REFERENCES

[1] M. Ghandchi Tehrani and M. Kalkowski, Active control of parametrically excited systems, Journal of Intelligent Material Systems and Structures, accepted for pubmication, 2015.

[2] Y. Lee, A study of parametric excitation applied to a MEMS tuning fork gyroscope, Phd dissertation , Faculty of the Graduate School – University of Missouri – Columbia, 2007.

[3] Y. Lee, P. Frank , Z. C. Feng , Nonlinear complex response of a parametrically excited tuning fork, *Mechanical Systems and Signal Processing*, 22(5), 2008, 1146-1156.

[4] J. Warminski, J.M. Balthazar, Vibration of a parametrically and self-excited system with ideal and non-ideal energy source, RBCM-Journal of the Brazilian Society, mechanical Sciences, 25(4),2003,413-420.

[5] J.M. Balthazar J.M., J.L.P Felix., Revisited nonlinear non-ideal vibration. In: Vibration Problems ICOVP (Supplement), Technical University of Liberec, Prague, Czech Public, pp.84-89, 2011.

[6] X. Xu, E. Pavlovskaia, M. Wiercigroch., F. Romeo, S. Lenci, Dynamic interactions between parametric pendulum and electro-dynamical shaker – ZAMM, Journal of Applied Mathematics and Mechanics, 87, 2, 172-186, 2007.

[7] X. Xu, M. Wiercigroch, M. P. Cartmell, Rotating orbits of a parametrically-excited pendulum – Science Direct – Chaos, Solitons and Fractals, 1538-1548pp., June, 2004.

[8] G. A. Gottwald and I. Melbourne. A new test for chaos in deterministic systems. Proc. Roy. Soc. A 460 (2004) 603–61

International Conference on Engineering Vibration
Ljubljana, Slovenia, 7-10 September 2015

ON ENERGY TRANSFER BETWEEN VIBRATION MODES AND THE FREQUENCY-VARYING EXCITATIONS FOR ENERGY HARVESTING

Jorge L.P. Felix[1], Rafael Bianchinr[1], Alan Almeida[1], José M. Balthazar[2], Rodrigo T. Rocha [3], Reyolando M.L.R.F. Brasil [4]

[1]Federal University of Pampa – Technological Center of Alegrete, RS, Brazil
jorge.felix@unipampa.edu.br, rafaelpbianchin@gmail.com, alan.almeida@hotmail.com.br

[2,3]Aeronautics Technological Institute, Mechanical-Aeronautics Division,são José dos Campos.,SP, Brazil,jmbaltha.gmail.com

[3] UNESP – São Paulo State University, Bauru, SP, Brazil ,digao.rocha@gmail.com

[4] Federal University of ABC, CECS, Santo André,SP, Brazil
reyolando.brasil@gmail.com

Keywords: Energy Harvesting, Time-Varying Frequency, Flexible Portal Frame, Saturation Phenomenon.

Abstract. *In summary, this paper presents an analytical and numerical analysis of vibration energy harvesting from the dynamic interaction and energy transfer between the two vibration modes of a 2-D-O-F model of a flexible portal frame. The frequencies of these modes are set in a two-to-one internal resonance condition. Excitation is provided by eccentric rotating mass-motor captured in external resonance. Next, we consider the same flexible portal frame excited from various directions with time-variable frequency. A piezoelectric device gives energy harvesting. Depending on how the piezoelectric energy harvester is installed (or coupled) different gains are obtained. Good performance of the harvester generator is detected. We also observed periodic, quasi-periodic or chaotic oscillations, depending on the saturation phenomenon.*

1 INTRODUCTION

Recent years have seen a study increase in large-scale vibration energy harvesting, for example, some device converts the vibrations of buildings or bridges, vehicle systems, even rotating machinery into useful electric energy that can be used for monitoring.

All the review articles and the majorities of the research on vibration energy harvesting using piezoelectric materials have been studied in the last decade. The importance of the configurations nonlinearities and tested under sinusoidal and random vibrations in the process of harvesting are studied by [1-8].

The linear and nonlinear dynamics of portal frame systems with model different of external excitation has received considerable attention in the literature. Brasil examined the nonlinear oscillations a portal frame driven by several unbalanced rotating machines by means of perturbation technique such as the method of multiple timescales [9]. De Paula and co-workers employed the numerical technique to examine the nonlinear dynamics of a nonlinear flexible portal frame under support excitation by an electrodynamics shaker [10]. Balthazar and co-investigators introduced various mathematical models of non-ideal systems [11]. Balthazar and co-workers introduced the mathematical model of two eccentric motors with limited power supply supported by a nonlinear flexible portal frame and was studied the self-synchronization of this motors [12]. Palacios-Felix and co-workers examined analytical and numerically the dynamics of the saturation phenomenon induced by quadratic nonlinearities, 1:2 internal resonance between the vertical and lateral modes of a flexible portal frame structure under non-ideal excitation [13-15]. Substantial theoretical and experimental work has also been achieved to bring a better understanding of vibrating system excited by an unbalanced dc motor with limited power supply [16-17].

Iliuk and co-workers examined the piezoelectric energy harvesting from portal frame using non-ideal excitation sources as alternative of ambient vibration [18-20].

In the present study, the proposed of a flexible frame-type vibration harvester under a external mechanical force with time-varying frequency for energy harvesting, is analytical and numerically investigated, considering that the portal frame possesses a two-to-one internal resonance between the first two vibration modes known as saturation phenomenon and an unbalanced mass rotate as excitation source from two directions (The rotating mass controlled by an electric device will be discussed a future work, here no dwell on). The method of Jacobi-Anger expansion is employed to solve the differential equations with harmonic force of varying frequency. Direct time integration of the governing equations is performed to study the global dynamics of the system via resonance curves.

2 ECCENTRIC ROTATING MASS AS AMBIENT VIBRATION

In this section, we summarize the electromechanical modeling of the nonlinear portal frame that supporting the piezoelectric materials and as ambient vibration was considered an eccentric rotating mass provided by a small DC motor, was mounted rigidly on the top shown in Figure 1. The schematic representation of a flexible portal frame structure having two columns clamped at their bases, with height h and constant cross section of area A_c and moment of inertia I_c, with concentrated weights at their tops of the columns of mass m. The horizontal beam is pinned to the columns at both ends with length L and constant cross section, of area A_b and moment of inertia I_b. A linear elastic material is considered whose Young modulus is E.

The two piezoelectric devices are installed to the vertical and horizontal beams and an electric circuit is connected to the piezoelectric material in order to produce the voltage output v .

Figure 2, shows the motion of the portal frame is represented for the generalized coordinates, q_1 is related to the horizontal displacement of the central section of the beam in the sway mode (with natural frequency ω_1) and q_2 to the mid-span vertical displacement of the same section of the beam in the first symmetrical mode (with natural frequency ω_2).

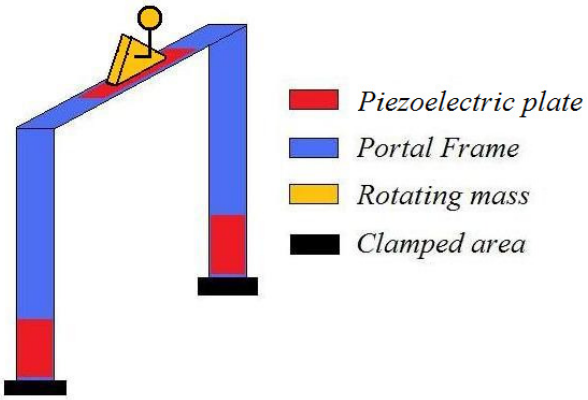


Figure 1: Proposed frame-type vibration Harvester with eccentric rotating mass

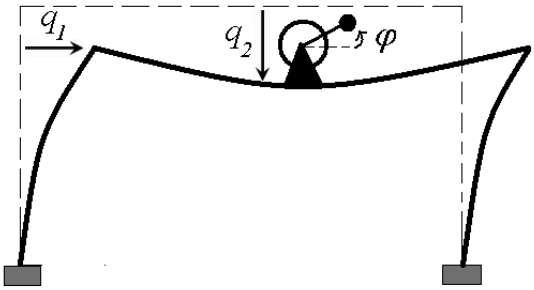


Figure 2: Schematic of vibration modes and eccentric mass motion

The schematic representation for the excitation was considered an eccentric mass m_0 at a distance r from the axis drive by small DC motor and is placed at the mid-span of the beam. The angular displacement of this mass is adopted as generalized coordinate $q_3 = \varphi$. The physical and geometric properties of the frame are chosen to tune the natural frequencies of these two modes into a 1:2 internal resonance ($\omega_2 \approx 2\omega_1$). The control of passing through resonances or resonance capture of the angular velocity ($\frac{d\varphi}{dt} \approx \omega_2$ and $\frac{d\varphi}{dt} \approx \omega_1$) is drive by a rotational actuator $u(t)$ with various constants torques levels. c_φ is the coefficient of rotation torque resisting. The dimensionless motion equations characterizing the portal frame electromechanical system [14, 15] and the energy harvester device [3] are following:

$$\ddot{q}_1 + \omega_1^2 q_1 = -\alpha_5 q_1 q_2 + \alpha_1(\ddot{q}_3 \sin q_3 + \dot{q}_3^2 \cos q_3) - \mu_1 \dot{q}_1 + \chi_1 v$$

$$\ddot{q}_2 + \omega_2^2 q_2 = -\alpha_6 q_1^2 + \alpha_2(-\ddot{q}_3 \cos q_3 + \dot{q}_3^2 \sin q_3) - \mu_2 \dot{q}_2 + \chi_2 v \tag{1}$$
$$\ddot{q}_3 = \alpha_3 \ddot{q}_1 \sin q_3 - \alpha_4 \ddot{q}_2 \cos q_3 - \alpha_7 \cos q_3 + u(t) - c_\varphi \dot{q}_3$$
$$\dot{v} + \lambda v + \kappa_1 \dot{q}_1 + \kappa_2 \dot{q}_2 = 0$$

v is the dimensionless voltage across the load resistor, χ is the dimensionless piezoelectric coupling term in the mechanical equation, κ is the dimensionless piezoelectric coupling term in the electrical equation, $\lambda = 1/RC_P$ is the reciprocal of the dimensionless time constant of the electrical circuit, R is the load resistance, and C_P is the capacitance of the piezoelectric material.

3 CASE OF STUDY TIME-VARYING FREQUENCY EXCITATION

In this section, we consider the harmonic force in two directions (horizontal and vertical) with time-varying frequency from an eccentric mass that rotate due by a torque actuator.

According to Prof.Kononenko, the variable angular velocity can be approximated by [16]:

$$\frac{d\varphi}{dt} = \Omega_0 + a_0 \cos(b_0 \Omega_0 t + c_0) \tag{2}$$

Where Ω_0 is a constant obtained from the averaging of the angular frequency at resonance. The parameters a_0, b_0 and c_0 are defined by the active interaction between the oscillating system and the excitation source. Furthermore, are considered as control parameters. If $a_0 = 0$, then $q_3 = \varphi = \Omega_0 t$ corresponding to harmonic excitation.

The governing equations of motion were obtained from Eq. (1), without consider the dynamic equation of the eccentric mass, in a modified form

$$\ddot{x} + 2\zeta_1 \dot{x} + \omega_1^2 x + \alpha_1 xy - \chi v = f_0 \cos[\Omega_0 t + a_0 \sin(b_0 \Omega_0 t + c_0)] \tag{3}$$
$$\ddot{y} + 2\zeta_2 \dot{y} + \omega_2^2 y + \alpha_2 x^2 - \chi v = g_0 \sin[\Omega_0 t + a_0 \sin(b_0 \Omega_0 t + c_0)] \tag{4}$$
$$\dot{v} + \lambda v + \kappa \dot{x} + \kappa \dot{y} = 0 \tag{5}$$

where the constants f_0, g_0 are the amplitudes of excitation in horizontal and vertical direction respectively with excitation frequency Ω_0. Furthermore $x = q_1$ and $y = q_2$.

Using the Jacobi-Anger expansion, the sine and cosine terms can be written as:

$$\cos(z \sin\theta) = \sum_{k=-\infty}^{\infty} J_k(z) \cos(k\theta) \tag{6}$$

$$\sin(z \sin\theta) = \sum_{k=-\infty}^{\infty} J_k(z) \sin(k\theta) \tag{7}$$

where $J_k(z)$ is the k-th Bessel function.

Using Eqs. (6) and (9), we will obtain the trigonometric functions of Eqs. (3) and (4) of the form:

$$\cos[\Omega_0 t + a_0 \sin(b_0 \Omega_0 t + c_0)] = \sum_{k=-\infty}^{\infty} J_k(a_0) \cos(\Omega_k t + k c_0), \tag{8}$$

$$\sin[\Omega_0 t + a_0 \sin(b_0 \Omega_0 t + c_0)] = \sum_{k=-\infty}^{\infty} J_k(a_0) \sin(\Omega_k t + k c_0), \tag{9}$$

where $\Omega_k = \Omega_0 + k b_0 \Omega_0$.

Substituting Eqs. (8) and (9) into Eqs. (3) and (4) yields

$$\ddot{x} + 2\varsigma_1\dot{x} + \omega_1^2 x + \alpha_1 xy - \chi v = f_0 \sum_{k=-\infty}^{\infty} J_k(a_0)\cos(\Omega_k t + kc_0) \tag{10}$$

$$\ddot{y} + 2\varsigma_2\dot{y} + \omega_2^2 y + \alpha_2 x^2 - \chi v = g_0 \sum_{k=-\infty}^{\infty} J_k(a_0)\sin(\Omega_k t + kc_0) \tag{11}$$

$$\dot{v} + \lambda v + \kappa\dot{x} + \kappa\dot{y} = 0 \tag{12}$$

We change the Eqs. (10-12) into:

$$\ddot{x} + 2\varsigma_1\dot{x} + \omega_1^2 x + \alpha_1 xy - \chi v = f_0 J_k(a_0)\cos(\Omega_k t + kc_0) \tag{13}$$

$$\ddot{y} + 2\varsigma_2\dot{y} + \omega_2^2 y + \alpha_2 x^2 - \chi v = g_0 J_k(a_0)\sin(\Omega_k t + kc_0) \tag{14}$$

$$\dot{v} + \lambda v + \kappa\dot{x} + \kappa\dot{y} = 0 \qquad k = -\infty\cdots,-1,0,1,\cdots\infty \tag{15}$$

It is important to note that the Eq. (13) and (14) are similar to a system with harmonic excitation for each k. If (x_k, y_k, v_k) is solution for each k of the system (13-15), then, using the general principle of superposition, the solution of the system (10-12) will be of the form:

$$x = \sum_{k=-\infty}^{\infty} x_k \ , \ y = \sum_{k=-\infty}^{\infty} y_k \ , \ v = \sum_{k=-\infty}^{\infty} v_k \ . \tag{16}$$

The electric power generated by the system is defined by:

$$P = \frac{v^2}{R} \tag{17}$$

The numerical solutions were carried out using MATLAB®. The dimensionless parameters values used are shown in Table 1.

Parameters	Values
ς_1 ς_2 ω_1 ω_2	0.01 0.01 1.0 2.0
f_0 g_0 a_0 b_0	0.2 0.2 2.0 0.001
χ λ κ	0.05 0.001 0.5
α_1 α_2 R c_0	0.3 0.4 1.0 0.0

Table 1. Dimensionless parameters of the electro mechanical system.

Figures 3 and 4 exhibit the numerical simulations using a harmonic excitation. In this particular case, we take into account that $a_0 = 0$, $b_0 = 0$ in Eqs. (3-5) and others numerical parameters of Table 1 are fixed. Figure 3 shows the maximum amplitudes (in steady state regime) of the plane portal frame structure.

We denote in blue line the column x motion, in red the horizontal beam y motion and in green it is shown the amplitudes of the voltage v. Taking into account the internal resonance $\omega_2 = 2\omega_1$, we may observe that in the region of second resonance $\Omega_0 \approx \omega_2$, the saturation phenomenon occurs, that is, from a critical point of $\Omega_0 = \Omega_c$, the amplitudes of oscillations y stops growing (or saturates) (red line) while x increased drastically (blue line).

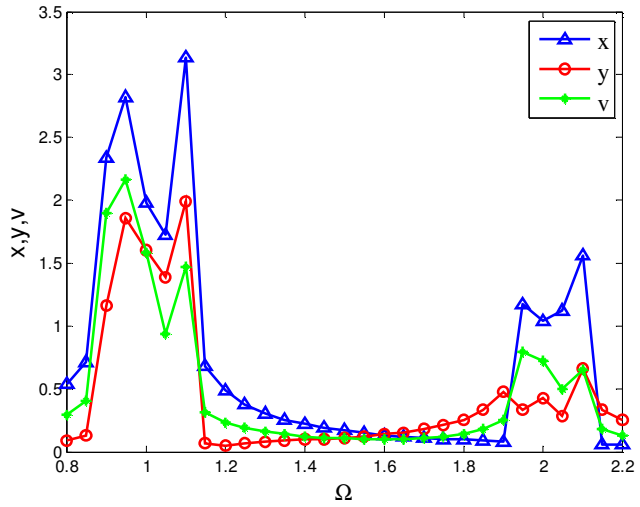


Figure 3: Harmonic excitation case. Curves (x, y, v) versus Ω_0 in the passage through resonance ($\Omega_0 \approx \omega_1$ and $\Omega_0 \approx \omega_2$) and internal resonance ($\omega_2 = 2\omega_1$).

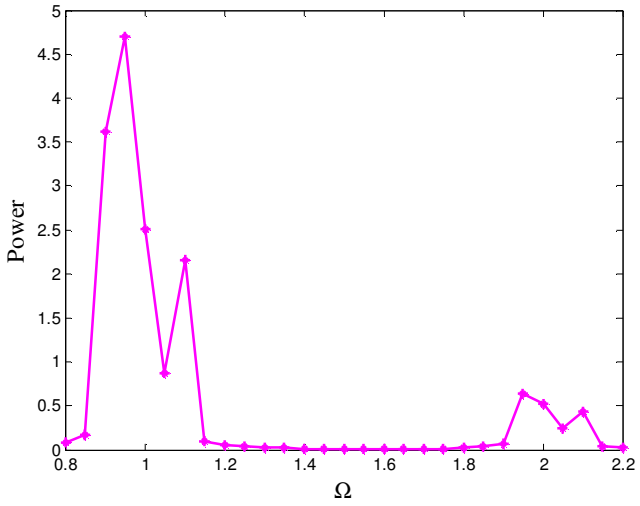


Figure 4: Electric Power output for harmonic excitation.

The response of the voltage (green line) is highly influenced by the response of the column. In the first region of resonance $\Omega_0 \approx \omega_1$, with internal resonance $\omega_2 = 2\omega_1$, it is easy to note that the voltage predominates over the second resonance region**.** Figure 4 shows the electric power generated when the excitation frequency passes through the resonance regions.

Next, we present numerical simulations using Eqs. (3-5) for the time-varying frequency excitation case using Table 1.

The influence of the time-varying frequency excitation on the electromechanical system is presented in Figures 5 and 6. By comparisons with the results obtained in Figures 3 and 4, one can see the excellent result of the electric power generated by the proposed model in the passage through resonance.

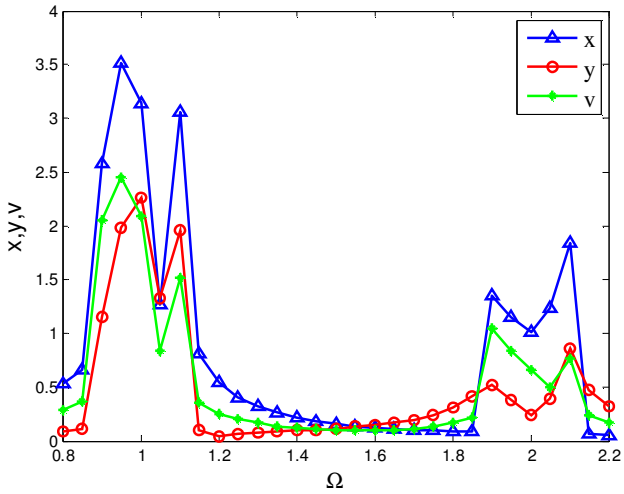


Figure 5. Time-varying frequency excitation Case – Curves (x , y , v) versus Ω_0 in the passage through resonance ($\Omega_0 \approx \omega_1$ e $\Omega_0 \approx \omega_2$) and internal resonance ($\omega_2 = 2\omega_1$).

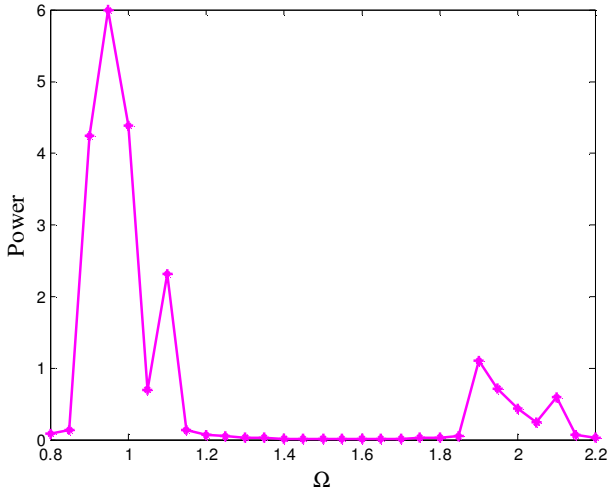


Figure 6: Electric power output for time-varying frequency excitation**.**

Although the excitation frequency parameters are determined by the host structure and therefore are not controllable, we wish to study their effect on the output power in order to design harvesters that can harness energy efficiently from time-varying frequency excitations. In the range $0 < a_0 < 4$, exponentially increase the portal frame amplitudes then we have the performance of the output power. Furthermore, in the resonance region $\Omega_0 \approx 1$ and $\Omega_0 \approx 2$ we observer the chaotic behaviour while in other region is quasi-periodic. The results are displayed in Figs. 7-9

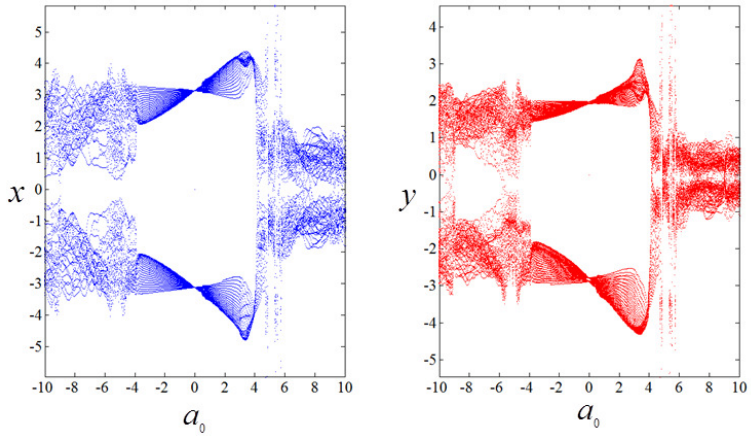


Figure 7. Bifurcation diagram for the variable a_0 from Eqs. (3)-(5).

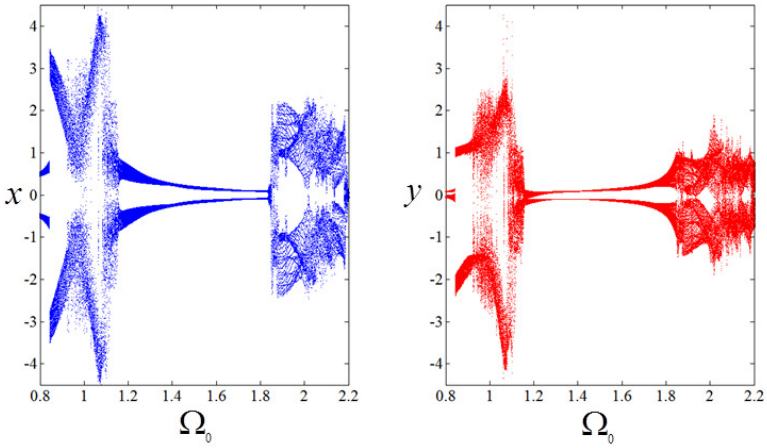


Figure 8. Bifurcation diagram for the variable Ω_0 from Eqs. (3)-(5).

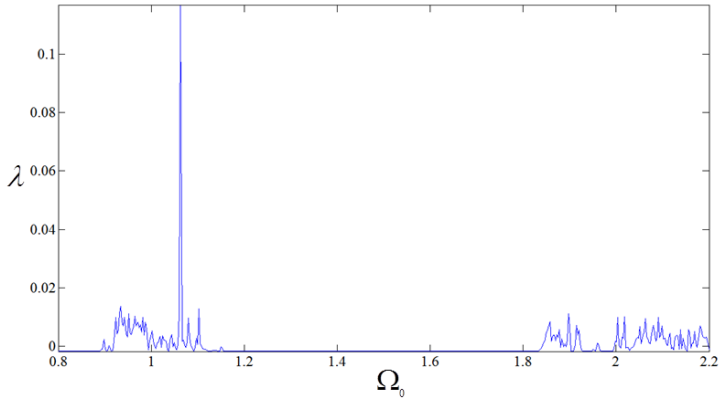


Figure 9. Bifurcation diagram of Lyapunov exponent maximum for the variable Ω_0 .

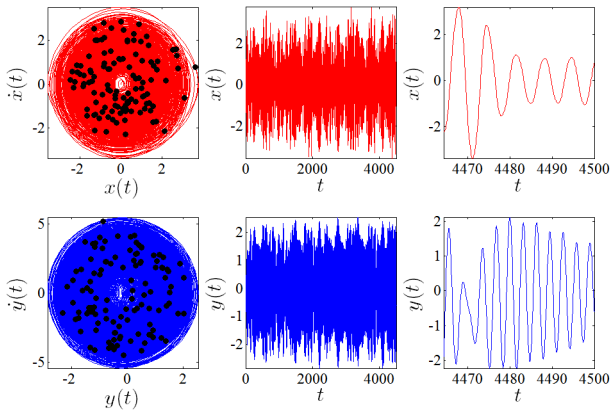


Figure 10. Time history and Poincare section for Ω_0 =1.

4 CONCLUSIONS

This paper proposes a frame portal-type vibration harvester of energy harvester taking into account the mutual interaction between two vibration modes with saturation phenomenon under a excitation source from various directions with time-variable frequency. Furthermore, depending as was installed the piezoelectric in each beam of portal frame.

ACKNOWLEDGEMENTS

The authors acknowledge support by (PDA) UNIPAMPA, CNPq, FAPERGS, FAPESP and CAPES, all Brazilian research funding agencies.

REFERENCES

[1] S.R Anton and H.A Sodano, A review of power harvesting using piezoelectric materials, *Smart Materials and Structures*, Vol. 16, No 3, R1–R21, 2007.

[2] M. F. Daqaq, R. Masana, A. Erturk and D. Quinn, On the Role of Nonlinearities in the Transduction of Energy Harvesters: A Critical Review and Discussion, *Appl. Mech. Rev*. 66(4), 040801(23 pgs), 2014.

[3] A. Ertuk, J. Hoffman and D.J. Inman, A piezomagnetoelastic structure for broadband vibration energy harvesting, *Appl. Phys. Lett*. 94, 254102, 2009.

[4] A. Erturk and D.J. Inman, *Piezoelectric energy harvesting*, John Wiley & Sons, Ltd, 2011.

[5] G. Litak, M.I. Friswell, C. A. K. Kwuimy, S. Adhikari and M. Borowiec, Energy harvesting by two magnetopiezoelastic oscillators with mistuning, *Theoretical & Applied Mechanics Letters*, 2(4), 043009:1-5, 2012.

[6] N.G. Stephen, On energy harvesting from ambient vibration, *Journal of Sound and Vibration* 293, 409-425, 2006.

[7] A.M. Triplett and D.D. Quinn, The effect of non-linear piezoelectric coupling vibration-based energy harvesting, *J. of Intelligent Material Systems and Structures*, Vol. 20, 1959-1967, 2009.

[8] Brasil R.M.L.R.F., Multiple scales analysis of nonlinear oscillations of a portal frame foundation for several machines, *Journal of the Brazilian Society of Mechanical Sciences* 21(4), 641–654, (1999).

[9] A. S De Paula, J.M. Balthazar and J.L. Palacios-Felix, Some comments on the nonlinear dynamics of a portal frame under base excitation, *Shock and Vibration* 20, 1093–1101, 2013.

[10] J.M. Balthazar, D.T. Mook, H.I. Weber, R.M.L.R.F. Brasil, A. Fenili, D. Belato and J.L.P. Felix, An overview on non-ideal vibrations, *Meccanica* 38, 613–621, 2003.

[11] JM Balthazar, JLP Felix, and RMLRF. Brasil, Short comments on self-synchronization of Two non- ideal sources supported by a flexible portal frame, *Journal of Vibration and Control*, 10, 2, 1739-1748, 2004.

[12] J.L.P. Felix, J.M. Balthazar and R.M.L.R.F. Brasil, On saturation control of a non-ideal vibrating portal frame foundation type shear-building, *Journal of Vibration and Control*, 11, 121-136, 2005.

[13] J. L. P. Felix, *Theory of Non-ideal and Nonlinear Portal Frame Vibrating System*, doctoral thesis, in portuguese, UNICAMP, Brazil, 181p, 2002a.

[14] J.L.P. Felix, J.M. Balthazar and R.M.L.R.F. Brasil, On non-ideal and nonlinear portal frame dynamic analysis: using Bogoliubov perturbation method, *J. of the Brazilian Society of Mechanical Systems*, Vol. XXIV, No 4, 257-265, 2002b.

[15] J.L.P. Felix, J.M. Balthazar and R.M.L.R.F. Brasil, Comments on nonlinear dynamics of a non-ideal Duffing-Rayleigh oscillator: Numerical and analytical approaches, *Journal of Sound and Vibration* 319, 1136-1149, 2009.

[16] P.J.P. Gonçalves, M. Silveira, B.R. Pontes Jr, J.M. Balthazar, The dynamic behavior of a cantilever beam coupled to a non-ideal unbalanced motor through numerical and experimental analysis, *Journal of Sound and Vibration, Volume 333,* Issue 20, 29, 5115-5129, 2014.

[17] V. O. Kononenko, Vibrating Systems with a Limited Power Supply. Illife Books, London, 1969.

[18] I. Iliuk, J.M. Balthazar, A.M. Tusset, J.L. Palacios-Felix, and B.R. Pontes JR, On non-ideal and chaotic energy harvester behavior, *Differ. Equations and Dynamical. Syst*., 21, (1-2), 93–104, 2013a.

[19] I. Iliuk, J.M. Balthazar, A.M. Tusset, J.R.C. Piqueira, B.R. Pontes Jr, J.L.P. Felix and A.M. Bueno, A non-ideal portal frame energy harvester Controlled using a pendulum, *The European Physical Journal Special Topics*, **222**(7), 1575-1586, 2013b.

[20] I. Iliuk, J.M. Balthazar, A.M. Tusset, J.R.C. Piqueira, B.R. Pontes Jr, J.L.P. Felix and A.M. Bueno, Application of passive control to energy Harvester efficiency using a non-ideal portal frame structural support system, *Journal of Intelligent Material Systems and Structures*, V. 25, n. 4, 417-429, 2014a.

International Conference on Engineering Vibration
Ljubljana, Slovenia, 7-10 September 2015

DYNAMICAL VIBRATION ABSORBER BY USING SHAPE MEMORY MATERIALS

Vinícius Piccirillo*[1], José Manoel Balthazar[2], Angelo Marcelo Tusset[1], Davide Bernardini[3], Giuseppe Rega[3]

[1]UTFPR - Federal Technological University of Parana, Brazil
piccirillo@utfpr.edu.br, a.m.tusset@gmail.com

[2]UNESP – São Paulo State University, CP 473, 17033-360, Bauru, SP, Brazil
jmbaltha@gmail.com

[3]Dipartimento di Ingegneria Strutturale e Geotecnica, Sapienza Università di Roma.
davide.bernardini@uniroma1.it, giuseppe.rega@uniroma1.it

Keywords: Shape memory materials, Dynamical Vibration Absorber, Nonlinear Dynamics

Abstract. *The dynamic response of structures subjected to high-amplitude vibration is often dangerous and undesirable. Dynamic vibration absorbers have received special attention in recent years due to vibration attenuation offered by them. Thus, the present study analyzes the nonlinear dynamics of a system with a dynamic vibration absorber using a shape memory material (SMM) whose characteristics are highly dependent upon temperature. Numerical simulations show the effectiveness of using the SMM in reducing oscillations of a harmonic oscillator.*

1 INTRODUCTION

Dynamic vibration absorbers (DVAs) are devices used to control the undesirable vibration amplitudes of a system at certain frequencies, especially close to resonance. The first study concerning the role of this device to suppress the vibration amplitudes of a primary system was made by [1]. A secondary mass attached by a spring to a main system was considered with the aim to syntonize the two oscillators in such a manner to have a resonance frequency coincident with a given frequency of interest. When this coupled system vibrates near this frequency, the vibration amplitudes of the primary system are significantly reduced, if compared with those observed without the absorber. This system was called tuned mass damper (TMD).

In order to obtain an optimum solution of a damped DVA, in [2] a method was proposed to adjust the best values of the absorber stiffness and damping. Den Hartog utilized the feature of ‘‘fixed-point’’ frequencies, i.e., frequencies at which the response amplitude of the primary mass is independent of the absorber damping. Based on the ‘‘fixed-points’’ theory, Den Hartog found the optimum tuning parameter and the optimum absorber damping.

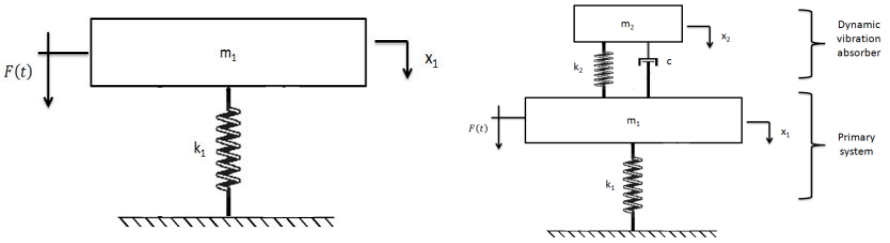
On the other hand, the initial study about the influence of non-linearity over the frequency-range of absorption was reported in [3]. As a result of the increasing interest on nonlinear absorbers, several works [4, 5] were developed to provide a better understanding of their behavior. On the other hand, many efforts were invested to design adaptive TMDs (ATMD), able to change their own features in order to follow possible changes of the behavior of the primary system. Different materials and physical principles have been considered [6-7] to make a TMD adaptive.

This work presents a preliminary study on the design and optimization on a nonlinear vibration absorber based on SMA. In this article, the optimum damping ratio of the proposed absorber is determined via numerical simulations, based on performance indexes such as the H_∞ norm for minimizing the maximum am-

plitude response of the main mass or the H_2 norm for minimizing its mean square motion.

2 MATHEMATICAL MODEL

Figure 1 shows a primary vibratory system (m_1, k_1) without (Fig. 1(a)) or with (Fig. 1(b)) a DVA (m_2, k_2, c) with viscous damper. In both cases a harmonic force $F(t)$ is applied to the main mass m_1.



(a) (b)

Figure 1: Schematic representation of a single degree of freedom oscillator without (a) and with (b) a damped DVA.

2.1 Equation of motion

The equations of motion are obtained by the Lagrange equations where the generalized coordinates are the displacements of the primary system (x_1) and of the absorber (x_2), and the applied force on the primary mass is given as $F(t) = A\cos(\omega t)$. Therefore, the nondimensional form of the equations of motion are obtained for the single-DOF

$$\ddot{u}_1 + u_1 = A\cos(\Omega\tau) \tag{1}$$

and the two-DOF system

$$\begin{cases} \ddot{u}_1 - 2\zeta_1\left(\dot{u}_2 - \dot{u}_1\right) + \varepsilon u_1 - \sigma\varepsilon\left(u_2 - u_1\right) = A\cos\left(\Omega\tau\right) \\ \\ \ddot{u}_2 + 2\zeta_2\left(\dot{u}_2 - \dot{u}_1\right) + \left(u_2 - u_1\right) = 0 \end{cases} \tag{2}$$

where: $\omega_1 = \sqrt{\frac{k_1}{m_1}}$, $\omega_2 = \sqrt{\frac{k_2}{m_2}}$, $\zeta_1 = \frac{c}{2m_1\omega_2}$, $\zeta_2 = \frac{c}{2m_2\omega_2}$ $\sigma = \frac{k_1}{k_2}$, $A = \frac{F_0}{m_1\omega_2^2 x_{est}}$, $\Omega = \frac{\omega}{\omega_1}$, $\varepsilon = \frac{m_2}{m_1}$

3 SMA MATHEMATICAL MODEL

In this section, a dynamic vibration absorber is characterized by a Shape Memory Device (SMD) that provides a restoring force against the relative displacements between the primary structure and the absorber. In this work the attention is focused on SMDs with pseudoelastic behavior. Here, the thermomechanical model for devices with pseudoelastic behavior used for the SMA restoring force follows the formulation proposed by [8]. The model takes into account several aspects of SMM behavior by means of seven model parameters. The system studied is modeled as a two-degree-of-freedom oscillator. A mechanical model of this system can be observed in Fig. 2. The dimensionless equations of motion from the energy balance read:

$$\begin{cases} \ddot{u}_1 - \zeta_1\left(\dot{u}_2 - \dot{u}_1\right) + \varepsilon\bar{K}u_1 - \\ \varepsilon\left[\left(u_2 - u_1\right) - sgn\left(u_2 - u_1\right)\lambda\xi\right] = A\cos\left(\Omega t\right) \\ \ddot{u}_2 + \zeta_2\left(\dot{u}_2 - \dot{u}_1\right) + \left[\left(u_2 - u_1\right) - sgn\left(u_2 - u_1\right)\lambda\xi\right] = 0 \end{cases} \tag{3}$$

The system response depends on 7 model parameters, J, λ, q_1, q_2, q_3, L, h whose physical meaning is discussed later (see also [8]). Here the non-dimensional quantities are: $\tau = \alpha t$,

$$u_1 = \frac{x_1}{x_{MS}},\ u_2 = \frac{x_2}{x_{MS}},\ \alpha = \sqrt{\frac{K}{m_2}},\ \ \zeta_1 = \frac{c}{2m_1\alpha}, \zeta_2 = \frac{c}{2m_2\alpha}\ ,\ \bar{K} = \frac{k_1}{K},$$

$$A = \frac{F_0}{m_1\alpha^2 x_{MS}},\ \Omega = \frac{\omega}{\alpha},\ \varepsilon = \frac{m_2}{m_1}$$

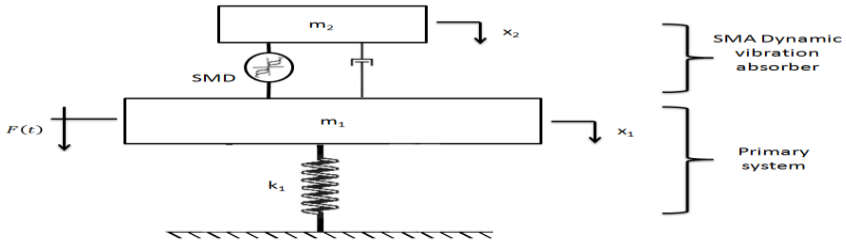


Figure 2: Oscillator with SMA Dynamical Vibration Absorber

4 NUMERICAL RESULTS

4.1 Linear Absorber Design

Den Hartog proposed to optimize the parameters of the absorber in such a way to have the two fixed points of equal amplitude in the frequency-response curve. This methodology to design the stiffness and damping of the absorber was called equal-peak method and, under such circumstances, Den Hartog [2] derived approximate analytic formulas for the absorber stiffness and damping, respectively. The optimal frequency ratio f (i.e., the ratio between the frequency of the TMD by itself and that of the main structure) and optimal damping ratio ζ for a damped TMD can be expressed as

$$f_{optimal} = \frac{\omega_2}{\omega_1} = \frac{\sqrt{k_2 m_1}}{\sqrt{k_1 m_2}} = \frac{1}{1+\mu}, \zeta_{optimal} = \frac{c}{2m_1\omega_1} = \sqrt{\frac{3\mu}{8(1+\mu)^3}} \quad (4)$$

where μ is the mass ratio (i.e., the relation between the absorber mass and the main mass). The values of the material parameters used in the current numerical investigations were taken from [6] and are as follows: $m_1 = 1\,kg$, $k_1 = 1\,N/m$, and we assume that the absorber mass is 5% of the main mass, and thus

$\mu = 0.05$. Using the equal-peak theory, the optimized $f_{optimal}$ and $\zeta_{optimal}$ parameters are 0.9524 and 0.1473, respectively.

The optimization theory of linear absorbers is well established. Now, we formulate an optimization problem that provides a set of physical parameters for the absorbers introduced in the main system (linear or SMA absorbers).

Due to difficulties in determining an exact closed-form solution for the SMA absorbers, in our work we compare the Den Hartog optimization theory with the H_2-norm and H_∞-norm, of the response curve in the maximum amplitude-frequency plane first in the case of the standard linear absorber, in order to demonstrate the viability of these two norms. Then the procedure is extended to the analysis to a SMA nonlinear absorber.

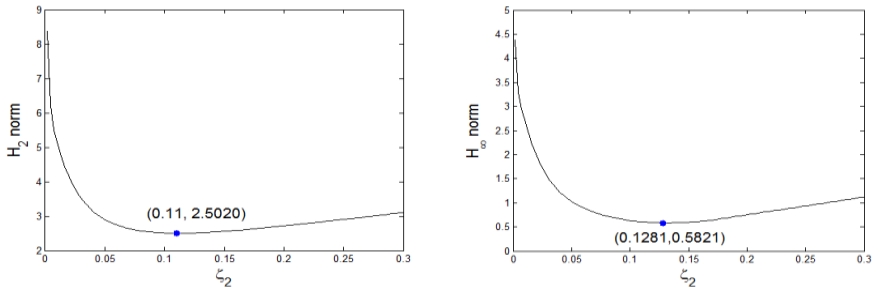
More specifically, the frequency response curves (FRC) are used to evaluate the effectiveness of the SMA absorber. For selected range of ζ_2 the FRCs are computed for the frequency interval $\Omega \in [0.1, 2]$. Then, based on the FRCs, the corresponding H_2-norm and H_∞-norm are computed taking into account the presence of the absorber:

$$H_2 = \left(\int_{0.1}^{2} \left| \max\left(u_1\right) \right|^2 d\Omega \right)^{1/2}, H_\infty = \max_{i=1}^{N} \left(\left| u_1\left(\Omega_i\right) \right| \right) \qquad (5)$$

where $\Omega_1 = 0.1$ and $\Omega_N = 2$.

Therefore, the optimization problem described above implies the minimization of the two equations quantities; The above dynamic optimization problem determines the absorber parameters that minimize the H_2-norm and H_∞-norm. Fig. 4 shows the H_2-norm and H_∞-norm of the FRCs of the damped linear absorber for different values of ζ_2. The dot indicates the minimum value reached for the corresponding norm. Figure 4(a) shows that in the H_2-norm curve the minimum value of ζ_2 occurs for 0.11, and in Fig. 4(b) the minimum value of the H_∞-norm occurs for $\zeta_2 = 0.1281$. If we compare the equal-peak methodology with

the H_2-norm and H_∞-norm the difference among them is 0.0373 and 0.0192, respectively. In terms of percentage, $\zeta_2 = 0.11$(H_2-norm) corresponds to 75% and $\zeta_2 = 0.1281$(H_∞-norm) to 87% of $\zeta_2 = 0.1473$ obtained by the equal-peak theory (Den Hartog). In order to quantify the structure associated with the maximal amplitude, we construct the FRC diagram for frequency excitation Ω versus damping factor ζ_2, as shown in Fig. 5. The optimal points corresponding to each optimization criterion are plotted in Fig. 5 in the tri-dimensional space.



(a) (b)

Figure 4: Linear absorber. (a) H_2-norm vs ζ_2 of the RFCs and (b) H_∞-norm vs ζ_2 of the RFCs

4.2 SMA Absorber

The numerical simulation of the vibrating system was carried out for values of the mechanical parameters which correspond to those in [10]. Due to nonlinearities, the SMA absorber responses are more complex than the linear oscillator absorber response. Through the Den Hartog methodology, in this study, the parameter σ (see Eq. 2) that represents the relation between the stiffnesses of the main system and of the absorber $\left(\sigma = \frac{k_1}{k_2}\right)$ is given the value $\sigma = 22.02$. In order to try to obtain consistent results with regard to the linear absorber we conjecture that the relation between the stiffnesses of the main system and of the

SMA absorber $\left(\bar{K} = \frac{k_1}{K}\right)$ is equal to that of the linear system, namely, $\bar{K} = 22.02$. Therefore, in the SMA absorber context, we establish that $\bar{K} = 22.02$ (in Eq. 3), and in order to obtain the optimal damper coefficient we use the H_2-norm and H_∞-norm. Fig. 6 shows the H_2-norm and H_∞-norm curves plotted as function of the ζ_2. Both curves present a global minimum corresponding to an optimal solution. It should be observed that the absolute minimum of the H_∞-norm is lower than the minimum of the H_2-norm. Again, the optimal points of the SMA absorber corresponding to each optimization criterion are plotted in Fig.7 in the tri-dimensional space. Figure 8 shows a comparison between the undamped single-degree of freedom (1 DOF) oscillator and the SMA nonlinear absorber with $\zeta_2 = 0.1889$ (H_∞-norm). The 1 DOF oscillator presents amplitudes that increase indefinitely when $\Omega \approx 1$, while the SMA absorber tends to limit the amplitude increase. It can be observed that for $\Omega \approx 1$, which is the critical resonant situation for the 1DOF oscillator, the absorber reduces the amplitude of the primary system response. Nevertheless, the new degree of freedom related to the secondary system introduces a new resonant frequency, identified as $\Omega \approx 1.06$. Figure 8 shows that the SMA absorber is able to attenuate the vibration of the primary system when $\zeta_2 = 0.1889$.

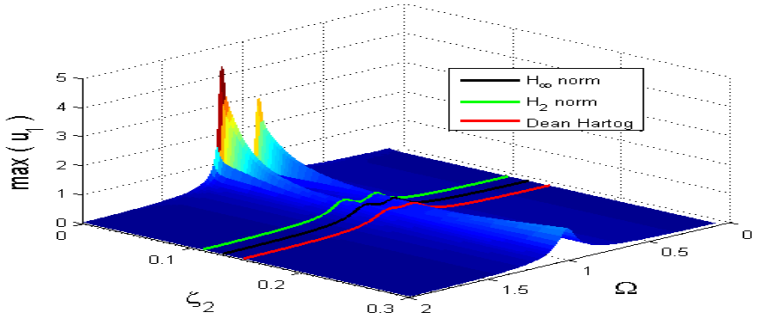
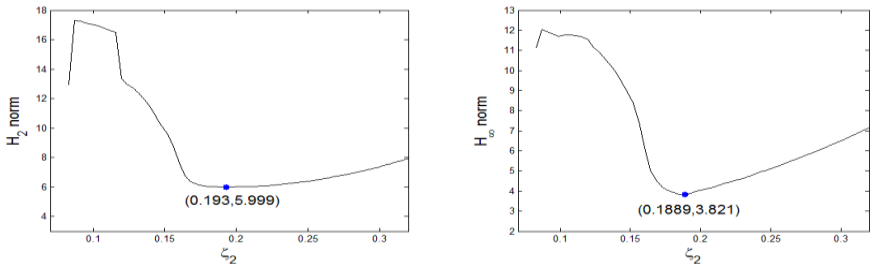


Figure 5: Frequency Response Curves corresponding to a linear absorber



(a) (b)

Figure 6: SMA absorber. (a) H_2-norm vs ζ_2 of the RFCs and (b) H_∞-norm vs ζ_2 of the RFCs for $\bar{K} = 22.02$

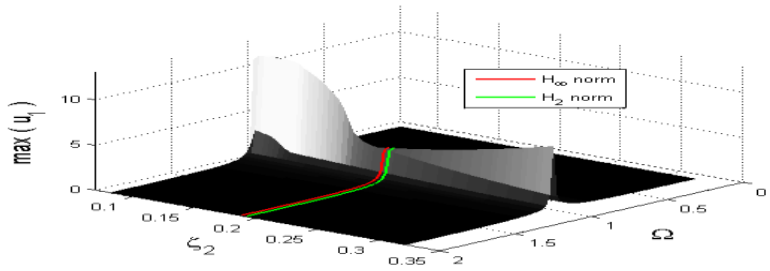
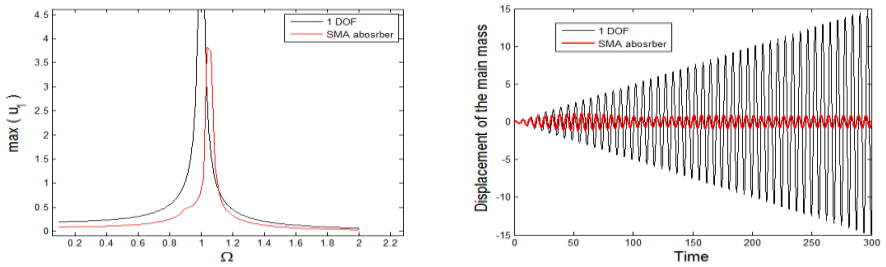


Figure 7: Frequency Response Curves corresponding to a SMA nonlinear absorber for $\bar{K} = 22.02$



(a) (b)

Figure 8: Linear vs SMA absorber. (a) Frequency Response Curves and (b) time history for $\zeta_2 = 0.1889$ and $\bar{K} = 22.02$

5 CONCLUSIONS

In this work, the effectiveness of a SMA absorber device with hysteretic behaviour in reducing the oscillations of a mechanical model has been investigated. In order to develop an optimization procedure, two performance indices have been compared. The

H_2-norm and the H_∞-norm of the FRC of the main mass, which have been evaluated and compared with the traditional equal-peak methodology. The selection criterion aims to minimize the maximum amplitude values of the FRC diagram, the damping ratio being considered as design parameter. The obtained results point out that the SMA absorber can be an efficient tool towards the reduction of the vibration amplitude of the main system and then the possible damage of the structure.

REFERENCES

[1] H. Frahm, Device for damping vibrations of bodies, US Patent No. 989,958, 1911.

[2] J.P. Den Hartog, Mechanical Vibrations, McGraw-Hill, New York, 1934.

[3] Roberson, R.E., Synthesis of a nonlinear dynamic vibration absorber. *Journal of the Franklin Institute*, **254**, 205 – 220, 1952.

[4] Shaw, J., Shaw, S.W. and Haddow, A.G., On the response of the non-linear vibration absorber. *International Journal of Non-Linear Mechanics*, 24, 281 – 293, 1989.

[5] Viguié, R. and Kerschen, G., On the functional form of a nonlinear vibration absorber, *Journal of Sound and Vibration*, **329**, 5225 – 5232, 2010.

[6] P. Bonello, M.J. Brennan, S.J. Elliott, Vibration control using an adaptive tuned vibration absorber with a variable curvature stiffness element, *Smart Materials and Structures*, **14**, 1055-1065, 2005.

[7] K. Williams, G. Chiu, R. Bernhard, Adaptive-passive absorbers using shape-memory alloys, *Journal of Sound and Vibration*, **249**. 835–848, 2002.

[8] D. Bernardini, G. Rega, Thermomechanical modelling, nonlinear dynamics and chaos in shape memory oscillators, *Mathematical and Computer Modelling of Dynamical Systems*, **11**,291–314, 2005.

International Conference on Engineering Vibration
Ljubljana, Slovenia, 7-10 September 2015

NONLINEAR DISCONTINOUS PHENOMENA IN ATOMIC FORCE MICROSCOPY

Laura Ruzziconi*[1,2], Mohammad I. Younis[3,4], Stefano Lenci[2]

[1] eCampus University, via Isimbardi 10, 22060 Novedrate, Italy
laura.ruzziconi@uniecampus.it

[2] Polytechnic University of Marche, via Brecce Bianche, 60131 Ancona, Italy
lenci@univpm.it

[3] King Abdullah University of Science and Technology (KAUST), Thuwal 23955-6900, Saudi Arabia
mohammad.younis@kaust.edu.sa

[4] State University of New York at Binghamton, Binghamton, 13902 NY, USA
myounis@binghamton.edu

Keywords: AFM, Multistability, Nonlinear Dynamics.

Abstract. *This study is motivated by the increasing attention toward nonlinear discontinous phenomena in atomic force microscopy. After introducing a reduced-order model which is able to take into account the most relevant aspects of the system dynamics, the overall scenario of the structure response is investigated. Extensive numerical simulations are performed. The AFM behavior is examined, with special attention devoted to the analysis of discontinuity-induced bifurcations. The nonlinear response is highlighted. Competing attractors with different characteristics are observed. Physical meaning and practical relevance of the nonlinear features are discussed. Multistability is examined in detail via the combined use of behavior charts and basin-of-attraction analysis.*

11th International Conference on Engineering Vibration
Ljubljana, Slovenia, 7–10 September 2015

DYNAMICS OF BEAMS AND PLATES UNDER COUPLED THERMO-MECHANICAL LOADING

Anna Warminska*[1], Emil Manoach[2], Jerzy Warminski[3]

[1]Department of Thermodynamics, Fluid Mechanics and Aviation Propulsion Systems, Lublin University of Technology, 20-618, Lublin, Poland
a.warminska@pollub.pl

[2]Institute of Mechanics, Bulgarian Academy of Sciences, Acad. G. Bonchev 4, 1113, Sofia, Bulgaria
e.manoach@imbm.bas.bg

[3]Department of Applied Mechanics, Lublin University of Technology, 20-618, Lublin, Poland
j.warminski@pollub.pl

Keywords: Beams and Plates Dynamics, Nonlinear Oscillations, Thermo-Elasticity, Bifurcations, Modal Reduction.

Abstract. *An effect of thermal load on vibrations of beams and plates is investigated in the paper. Two types of elements are investigated: (a) a beam considered as an extended Timoshenko model with nonlinear terms resulted from large deflections and (b) a circular plate represented by the geometrically nonlinear Mindlin model. Dynamics of both structures is analysed under thermal and mechanical loadings. The importance of the elevated temperature around the selected resonance conditions are presented. The nonlinear characteristics with bifurcation points have been demonstrated.*

1 INTRODUCTION

Thermal loadings play an important role in dynamics of structural elements, in particular if they operate close to critical - bifurcation points. In many branches as aviation and aerospace engineering, nuclear and chemical technologies, micro- or nano-electro-mechanical systems (MEMS or NEMS), structural elements may be subjected to large mechanical and thermal loadings leading to large amplitude vibrations. Furthermore, due to varied temperature some dynamic phenomena can be changed or masked [1]. The beam and plates are fundamental structural elements and they are widely applied in mentioned above technologies [2]–[7]. Many thermoelastic problems have been treated by lot of authors using different approaches during the past decades. Due to the fact that these problems are quite complicated from a computational point of view, several authors have applied techniques which allow reducing the number of equations by transforming the discretized governing equations into the modal coordinates [2, 8, 9, 10, 11]. The cost of solving coupled nonlinear thermo-mechanical problems should be reduced because the regular finite element or finite difference analysis yields a large set of nonlinear equations.

Most of the papers treating thermoelastic vibrations of plates concern the case when structures subjected to mechanical loading are in a high temperature environment and the structural elements beams or plates get the elevated temperature instantaneously.

The temperature usually is considered as uniformly distributed along the structures length and thickness. The elevated temperature can cause buckling in the structures and several authors studied buckling and postbuckling behavior of structures subjected to mechanical loads at elevated temperatures [12, 13]. In many cases this approach is well accepted, as the heat process is much slower than the mechanical oscillations. In the steady state cases the propagation of the temperature along the structure can be neglected. Of course for the intensive heat flux and studying transient dynamics we have to solve the fully coupled thermoelastic problem [14, 15].

In this study we present a reduced model of a nonlinear Timoshenko beam and a thermoelastic model of circular Midlin plate. Dynamics of the Timoshenko beam is based on derivation published in papers [10, 11] and then the study is extended for a circular plate. The numerical investigations are developed in order to clarify the influence of the thermal loadings on the response of the beams and plates.

2 A nonlinear thermo-elastic beam model

A beam model is based on nonlinear strain relationships, shear deformation, and a linear curvature associated with the mid-axes . The assumed model which is valid for large displacements can be expressed as:

$$\varepsilon_x^0 = \frac{\partial u}{\partial x} + \frac{1}{2}\left(\frac{\partial w}{\partial x}\right)^2, \varepsilon_{xz}^0 = \frac{\partial w}{\partial x} - \psi, \kappa^0 = -\frac{\partial \psi}{\partial x} \tag{1}$$

with the strain vector expressed as:

$$\varepsilon_x = \varepsilon_x^0 + z\kappa_x^0,\ \varepsilon_{xz} = f(z)\varepsilon_{xz}^0 \tag{2}$$

where $f(z)$ is a function describing the distribution of the shear strain along the beam thickness, $u(x,t)$ is the longitudinal displacement, $w(x,t)$ is the transverse displacement in the z direction and $\psi(x,t)$ is the rotation angle of the cross section to the longitudinal axis. Assuming that the beam material is linear elastic and isotropic the constitutive equations take the form

$$\sigma_x = E\left[\varepsilon_x - \alpha_T(T - T_0)\right], \sigma_{xz} = G\varepsilon_{xz} \tag{3}$$

where E is the Young modulus, G is the shear modulus and α_T is the coefficient of thermal expansion. The bending moment M, the shear force Q and the in-plane stress σ_{xz} resultant per unit length are expressed by the stresses as follows

$$M = b \int_{-h/2}^{h/2} \sigma_x z \, dz, \quad Q = b \int_{-h/2}^{h/2} \sigma_{xz} \, dz \quad , \quad N = b \int_{-h/2}^{h/2} \sigma_x \, dz \tag{4}$$

where b is the beam width. The equations describing the coupled problem of the temperature distribution and the beam vibrations as a result of the action of a heat flow with intensity $q(x,t)$ and of a mechanical load with intensity $p(x,t)$ are:

$$\begin{aligned} \frac{c_p}{\lambda_T}\frac{\partial T}{\partial t} &= \frac{\partial^2 T}{\partial x^2} - \frac{\partial^2 T}{\partial z^2} - \frac{\alpha_T E T_0}{\lambda_T}\frac{\partial \varepsilon}{\partial t} \\ \frac{\partial N}{\partial x} - c_1\frac{\partial u}{\partial t} - \rho F\frac{\partial^2 u}{\partial t^2} &= 0 \\ -\frac{\partial M}{\partial x} + Q - c_2\frac{\partial \psi}{\partial t} - \rho I\frac{\partial^2 \psi}{\partial t^2} &= 0 \\ \frac{\partial Q}{\partial x} + N\left(\frac{\partial^2 w}{\partial x^2}\right) + \frac{\partial N}{\partial x}\frac{\partial w}{\partial x} - c_1\frac{\partial w}{\partial t} - \rho F\frac{\partial^2 w}{\partial t^2} &= -p(x,t) \end{aligned} \tag{5}$$

where F is the area of the beam cross-section, l is the beam length, I geometrical inertia moment of the cross-section with respect to neutral bending axis, T is current temperature, T_0 is the initial constant temperature, λ_T is the thermal conductivity and c_p is the heat capacity per unit volume, c_1, c_2 damping coefficients, and

$$\varepsilon = -z\frac{\partial \psi}{\partial x} + \alpha_T (T - T_0) + \frac{\partial u}{\partial x} + \frac{1}{2}\left(\frac{\partial w}{\partial x}\right)^2 \tag{6}$$

According to the paper [10] longitudinal displacement can be found assuming that longitudinal acceleration is equal to zero and the model can be simplified to two partial differential equations in the dimensionless form [10]:

$$\begin{aligned} \frac{\partial^2 \psi}{\partial x^2} + \beta\alpha\left(\frac{\partial w}{\partial x} - \psi\right) - d_2\frac{\partial \psi}{\partial t} - \frac{\partial^2 \psi}{\partial t^2} &= 0 \\ \beta\left(\frac{\partial^2 w}{\partial x^2} - \frac{\partial \psi}{\partial x}\right) - d_1\frac{\partial w}{\partial t} - \frac{\partial^2 w}{\partial t^2} &= -p + G_2^T + G_2^L \end{aligned} \tag{7}$$

The components G_2^T, G_2^L are defined as:

$$G_2^T = \alpha_T \gamma_\theta \frac{\partial^2 w}{\partial x^2}, \quad G_2^L = K\frac{\partial^2 w}{\partial x^2}, \quad K = -\int_0^1 \xi \frac{\partial w}{\partial \xi}\frac{\partial^2 w}{\partial \xi^2} d\xi \tag{8}$$

α_T is a linear coefficient of a thermal expansion, and

$$\chi_\theta = \int_{-1/2}^{1/2} \theta(x,z,t) z dz, \quad \gamma_\theta = \int_{-1/2}^{1/2} \theta(x,z,t) dz \, . \tag{9}$$

where $\theta(x,z,t)$ is a space and time dependent dimensionless function of a temperature distribution. Assuming that the distribution of temperature along x and z axis is constant: $\theta(x,z) = const.$, we get: $\chi_\theta = 0$, $\gamma_\theta = \Delta T$, where ΔT is a difference between the reference temperature and the current temperature. We note that the dimensionless displacement of the beam is expressed versus beam's length $w = w^*/l$, where w^* is the displacement in physical units.

The model of a beam has been reduced from Partial Differential Equations (PDE) to Ordinary Differential Equations (ODE) by means of modal projection and then by using Galerkin's orthogonalisation method. For this purpose the generalized displacements vector is expanded as a sum of the product of the quasi-normal modes $w_n(x)$, $\psi_n(x)$ and the time dependent functions $q_n(t)$:

$$w(x,t) = \sum_{n=1}^{N_f} w_n(x) q_n(t), \quad \psi(x,t) = \sum_{n=1}^{N_f} \psi_n(x) q_n(t) \tag{10}$$

Assuming proportional damping the equations are transformed into the form:

$$\ddot{q}_n(t) + 2\xi_n \omega_n \dot{q}_n(t) + \omega_n^2 q_n(t) = \int_0^1 \left[p(x,t) w_n(x) - G_2^L(x,t) w_n(x) - G_2^T(x,t) w_n \right] dx \tag{11}$$

where, ω_n is the ***n-th*** natural frequency of the linear undamped Timoshenko beam and ξ_n is a dimensionless modal damping coefficient and

$$G_2^L = K \sum_{n=1}^{N_f} q_n(t) \frac{d^2 w_n}{dx^2}, \quad G_2^T = \alpha_T \Delta T \sum_{n=1}^{N_f} q_n(t) \frac{d^2 w_n}{dx^2} \tag{12}$$

$$p = p(x,t), \; K = -\int_0^1 \sum_{n=1}^{N_f} \sum_{j=1}^{N_f} \xi q_n \frac{dw_n(\xi)}{d\xi} q_j \frac{d^2 w_j(\xi)}{d\xi^2} d\xi .$$

Considering one mode reduction ($n = 1$), substituting (10) and (12) into (11) we get a reduced nonlinear ordinary differential equations of the problem

$$\ddot{q}_1 + 2\xi_1 \omega_1 \dot{q}_1 + \omega_1^2 q_1 + C_{1,111} q_1^3 + C_1^T \Delta T q_1 = p_1 \sin \Omega t \tag{13}$$

2.1 A thermo-elastic model of a circular plate

The thermo-elastic model of a circular plate is based on Midlin model which takes into account large deflections and linear curvatures and shear deformation

$$\varepsilon_r^0 = \frac{\partial u}{\partial r} + \frac{1}{2}\left(\frac{\partial w}{\partial r}\right)^2, \; \varepsilon_t^0 = \frac{u}{r}, \; \varepsilon_{rz}^0 = \psi + \frac{\partial w}{\partial r}, \; \kappa_r^0 = \frac{\partial \psi}{\partial r}, \; \kappa_t^0 = \frac{\psi}{r} \tag{14}$$

and

$$\varepsilon_r = \varepsilon r^0 + z k_r^0, \; \varepsilon_t = \varepsilon_t^0 + z k_r^0, \; \varepsilon_{rz} = f(z) \varepsilon_{rz}^0 \tag{15}$$

where $f(z)$ is a function describing the distribution of the shear strain along the plate thickness, $u(r,t)$ is the in-plane displacement, $w(r,t)$ is the transverse displacement, $\psi(r,t)$ is the rotation angle, r and ψ are polar coordinates. Considering linear material properties the plate constitutive equations have the form

$$\sigma_r = \frac{E}{1-\nu^2}\left(\varepsilon_r + \nu\varepsilon_t\right) - \frac{E}{1-\nu^2}\alpha_T(T-T_0), \tag{16}$$
$$\sigma_t = \frac{E}{1-\nu^2}\left(\varepsilon_t + \nu\varepsilon_r\right) - \frac{E}{1-\nu^2}\alpha_T(T-T_0), \quad \sigma_{rz} = kG\varepsilon_{rz}$$

The equations describing the coupled problem of the temperature distribution and the plate vibrations as a result of the action of a heat flow with intensity $q(r,t)$ and of a mechanical load with intensity $p(r,t)$ are:

$$\frac{\rho c_p}{\lambda_T}\frac{\partial T}{\partial t} = \frac{\partial^2 T}{\partial r^2} + \frac{1}{r}\frac{\partial T}{\partial r} - \frac{\partial^2 T}{\partial z^2} - \frac{\alpha_T E T_0}{(1-2\nu)\lambda_T}\frac{\partial \varepsilon}{\partial t} \tag{17}$$
$$\frac{\partial N_r}{\partial r} + \frac{N_r - N_t}{r} - \rho h\frac{\partial^2 u}{\partial t^2} = 0$$
$$\frac{\partial M_r}{\partial r} + \frac{M_r - M_t}{r} - Q_r - c_2\frac{\partial \psi}{\partial t} - \frac{\rho h^3}{12}\frac{\partial^2 \psi}{\partial t^2} = 0$$
$$\frac{\partial Q_r}{\partial r} + \frac{Q_r}{r} + N_r\left(\frac{\partial^2 w}{\partial r^2} + \frac{1}{r}\frac{\partial w}{\partial r}\right) + \frac{\partial N_r}{\partial r}\frac{\partial w}{\partial r} - c_1\frac{\partial w}{\partial t} - \rho h\frac{\partial^2 w}{\partial t^2} = -p(r,t)$$

$T(x,z,t)$ is current temperature, T_0 is the initial temperature, λ_T is the thermal conductivity, c_p is the heat capacity per unit volume, c_1 and c_2 denote the damping coefficients, and

$$\varepsilon = z\frac{\partial \psi}{\partial r} + \frac{z}{r}\psi + \frac{1}{r}u + 2\alpha_T\left(T - T_0\right) + \frac{\partial u}{\partial r} + \frac{1}{2}\left(\frac{\partial w}{\partial r}\right)^2 \tag{18}$$

Substituting (14)-(16) and (18)) into (17) we get a set of partial differential equations of the analysed problem

$$Ah\left[\frac{\partial^2 u}{\partial r^2} + \frac{\partial w}{\partial r}\frac{\partial^2 w}{\partial r^2} + \frac{1}{r}\frac{\partial u}{\partial r} - \frac{u}{r^2} + \frac{1}{2r}(1-\nu)\left(\frac{\partial w}{\partial r}\right)^2\right] = A(1+\nu)\alpha_T\frac{\partial \gamma_T}{\partial r} \tag{19}$$
$$D\left[\frac{\partial^2 \psi}{\partial r^2} + \frac{1}{r}\frac{\partial \psi}{\partial r} - \frac{\psi}{r^2}\right] - k^2 Gh\left(\frac{\partial w}{\partial r} + \psi\right) - c_2\frac{\partial \psi}{\partial t} - \frac{\rho h^3}{12}\frac{\partial^2 \psi}{\partial t^2} = A(1+\nu)\alpha_T\frac{\partial \kappa^T}{\partial r},$$
$$k^2 Gh\left(\frac{\partial^2 w}{\partial r^2} + \frac{1}{r}\frac{\partial w}{\partial r} + \frac{\partial \psi}{\partial r} + \frac{\psi}{r}\right) + Ah\left[\frac{\partial u}{\partial r} + \frac{1}{2}\left(\frac{\partial w}{\partial r}\right)^2 + \frac{\nu}{r}u - \frac{1+\nu}{h}\alpha_T\gamma_T\right]\left(\frac{\partial^2 w}{\partial r^2} + \frac{1}{r}\frac{\partial w}{\partial r}\right)$$
$$+Ah\left(\frac{\partial^2 u}{\partial r^2} + \frac{\nu}{r}\frac{\partial u}{\partial r} - \frac{\nu}{r^2}u + \frac{\partial w}{\partial r}\frac{\partial^2 w}{\partial r^2} - \frac{1+\nu}{h}\alpha_T\frac{\partial \gamma_T}{\partial r}\right)\frac{\partial w}{\partial r} + c_1\frac{\partial w}{\partial t} - \rho h\frac{\partial^2 w}{\partial t^2} = -p(r,t)$$

The associated boundary conditions have to take into account mechanical and also heat propagation aspects. The boundary conditions for studied particular cases are commented in numerical simulation sections.

3 Numerical analysis of beam and plate dynamics

The numerical examples aim to illustrate and to clarify the influence of the parameters which define the impact of the thermal and mechanical loadings on the structures response. The vibrations of heated beams and plates, are considered in order to show the difference in the structures

response depending on the thermal loading. The results shown here are obtained for the simply supported beam and clamped circular plate. As regards the thermal flow we demonstrate the simplest case taking into account the influence of uniformly distributed elevated temperature.

The beam and plates are assumed to have the same material parameters

$$\rho = 0.2778 \times 10^4 kg/m^3,\ E = 0.7 \times 10^{11}\ N/m^2,\ G = 2.612 \times 10^{10} N/m^2,$$
$$\nu = 0.34,\ \alpha_T = 2.39 \times 10^{-5} K^{-1}\,.$$

Geometrical parameters have values:
for the beam

$$l = 0.5\ m,\ h = 0.05\ m,\ b = 0.05\ m,\ k = 0.833$$

for the plate

$$R = 0.1m,\ h = 0.01m\,.$$

3.1 Dynamics of a beam at elevated temperature

The dynamics of the beam is based on equation (13) which is solved numerically and then a continuation method is used. At first we determined the resonance curve wihtout temperature influence, for $\Delta T = 0$, fixed mechanical loading $p_1 = 1 \times 10^{-5}$ and varied excitation frequency around the first beam natural frequency. The nonlinear terms included in the model are visible

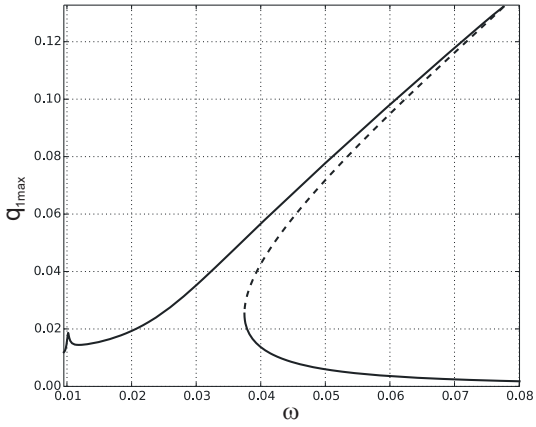


Figure 1: Resonance curves for temperature $\Delta T = 0$, $p_1 = 1 \times 10^{-5}$

by stiffening effect on the resonance curve in Fig.1 which is of classical Duffing type with stable and unstable branches (dashed line).

Next, the influence of the elevated temperature is analysed for fixed mechanical loading. We selected the point located on lower resonance branch for $\omega = 0.05$, $p_1 = 1 \times 10^{-5}$. Temperature is varied in a very wide range from $\Delta T = -100$ to $\Delta T = +400$. In Fig.2(a) we see very rich dynamics of the beam caused by varied temperature. Starting from $\Delta T = 0$ and following the lower branch for the temperature about $\Delta T = 38$, a new branch occurs (branch point). This region is enlarged in Fig.2(b). For about $\Delta T = 49$ the curve is unstable with arising, after a period doubling bifurcation, a new solution around $\Delta T = 58$. This is the next period doubling point. The time histories of the beam response are presented in Fig.3, respectively, before the

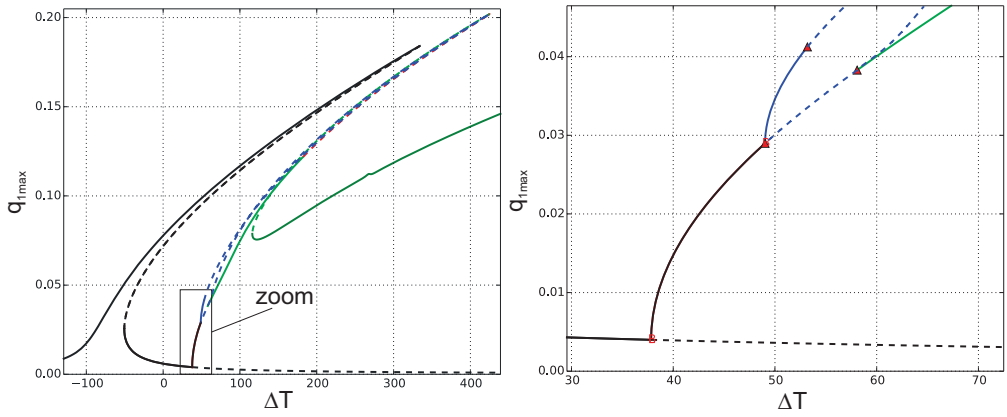


Figure 2: Amplitude against temperature ΔT (a) and a zoom nearby the bifurcation point (b); $\omega = 0.05$, $p_1 = 1 \times 10^{-5}$

branch point for $\Delta T = 35$, after the branch point for $\Delta T = 45$, and after the period doubling bifurcation for $\Delta T = 50$. For temperature $\Delta T = 50$, Fig.3(c) three different solutions are possible: the symmetric response with a doubled period (black line) and two different solutions with small oscillations, shifted in a positive (green line) or negative (blue line) direction.

3.2 Dynamics of a circular plate at elevated temperature

The solutions for the thermo-elastic vibrations of the plate are obtained by algorithms developed in [14, 15]. They are based on the successive solution of the equations for the mechanical vibrations of the structure and for the heat transfer. The nonlinear equations for mechanical vibrations are solved by using pseudo-load mode superposition method where the nonlinear terms (including the ones from the temperature heating) are considered as pseudo-loads. The heat transfer equation is solved by discretizing them by finite differences method and the obtained system of ODE is solved by the Gear method.

In Fig.4(a) the displacements of the plate center at different temperatures are displayed. The applied mechanical loading is distributed uniformly along the plates upper surface and varied periodically in time $p = p_0 \sin \omega_e t$ with frequency ω_e equal to the half of the first natural plate frequency $\omega_e = \omega_1/2$, where $\omega_e = 15300\, rad/s$, and $p_0 = 1500\, N$. The elevated temperature (varied from $\Delta T = 0$ to $\Delta T = 400$) not only increased the amplitudes but also changed qualitatively the response. The corresponding Poincaré maps are presented in Fig.4(b).

The behavior of the plate in a case when it is excited with the same loading but with excitation frequency equal to the first natural frequency $\omega_e = \omega_1$ is quite different. Time histories for this case and for different elevated temperatures are presented in Fig.5(a).

Due to the fact that the excitation frequency is close to the first natural frequency of the nonlinear system, a beating phenomenon is observed in the unheated plate. The amplitude of vibrations increases if the temperature rises, till $\Delta T = 100$. For $\Delta T > 100$ however the amplitude of vibrations decreases. This is in a contrast to the case of excitation $\omega_e = \omega_1/2$, in which the amplitude increases in the entire temperature domain. The variation of the amplitude against temperature is presented in Fig.5(b) for $\omega_e = \omega_1$ (red line) and $\omega_e = \omega_1/2$ (black line). The explanation of this phenomenon is that the elevated temperature leads to a rise of in plane stresses which changes the real resonance frequencies and thus deflections decrease.

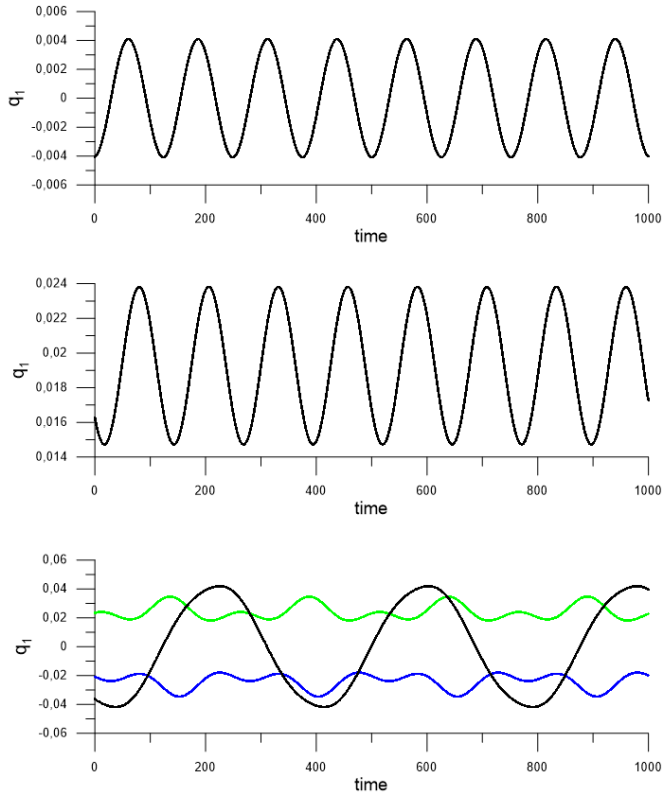


Figure 3: Time histories for different temperature levels (a) $\Delta T = 35$, (b) $\Delta T = 45$, (c) $\Delta T = 50$, $\omega = 0.05$, $p_1 = 1 \times 10^{-5}$

4 CONCLUSIONS

The nonlinear models of the beam and plate presented in the paper allows investigations of large oscillations induced by mechanical and thermal loadings. The thermal field has been taken into account by analysing uniformly distributed heat caused by elevated temperature. However, the derived partial differential equations enable to study a fully coupled problem with mon-uniformly distributed heat flow.

The beam model has been reduced to one nonlinear ordinary differential equation. This allowed extensive parametric studies by the continuation method. We have demonstrated the nonlinear resonance curve with hardening characteristic of Duffing type. The elevated temperature influenced the resonance zone and an occurrence of the bifurcation points and new solutions with different amplitudes and periods has been observed. The period doubling bifurcation has been detected.

The circular plate dynamics has been investigated directly from partial differential equations which, similar to the beam model, included the nonlinear displacement field. The influence of the thermal field has been limited to the uniformly distributed elevated temperature and for mechanical loading exciting the plate with half of the first natural frequency and close to the first natural frequency. In the former case the impact of elevated temperature has been observed by increased vibrations while for the latter case above a certain threshold the vibrations decreased. This phenomenon can be explained by more complex dynamics nearby the resonance region.

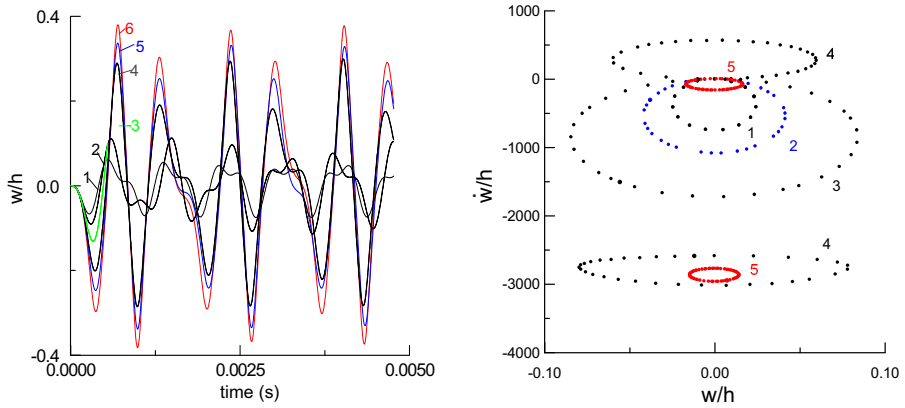


Figure 4: Time histories of the plate center (a) and corresponding Poinceré maps (b) at different temperatures. Harmonic loading with $\omega_e = \omega_1/2$; 1- $\Delta T = 0$, 2- $\Delta T = 100$, 3- $\Delta T = 200$, 4- $\Delta T = 300$, 5 - $\Delta T = 350$, 6- $\Delta T = 400$; $\zeta_n = 0$, $p_0 = 1500N$.

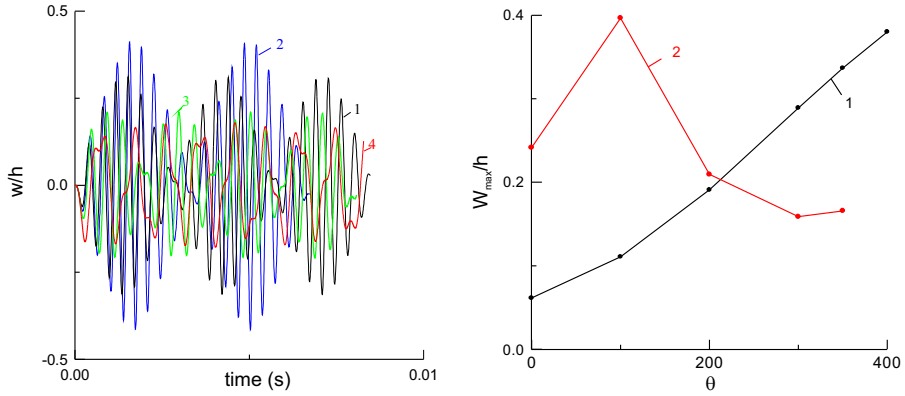


Figure 5: Time histories of the plate center (a) at different temperatures and harmonic loading with $\omega_e = \omega_1$; 1- $\Delta T = 0$, 2- $\Delta T = 100$, 3- $\Delta T = 200$, 4- $\Delta T = 350$; $\zeta_n = 0$, $p_0 = 1500N$; and (b) variation of maximal amplitude versus elevated temperature for: 1- $\omega_e = \omega_1/2$, 2- $\omega_e = \omega_1$.

More detailed parametric studies will be performed in future analysis of the reduced low order plate model, similar to the performed beam analysis.

ACKNOWLEDGMENTS

Financial support of Structural Funds in the Operational Programme - Innovative Economy (IE OP) financed from the European Regional Development Fund - Project No POIG.0101.02-00-015/08 is gratefully acknowledged. The second author would like to acknowledge the partial support received through Bulgarian NSF Grant DUNK-01/3 .

REFERENCES

[1] E. Manoach, S. Samborski, A. Mitura, J. Warminski, Vibration based damage detection in composite beams under temperature variations using Poincare maps, *Int. Journal of*

Mechanical Sciences, **62**, 1, 120–132, 2012.

[2] J.M. Dhainaut, B. Duan, C. Mei, C.S.M Spottswood, H. Wolfe, Non-linear response of composite panels to random excitations at elevated temperatures, *Proc. of 7th Int. Conf. Recent Advances in Str. Dynamics*, Southampton, **Vol. 2**, 769–784, 2000.

[3] X.M. Su, J.H. Zhang, J. Wang, Y.Q. BI, D.F. Qie, Z.H. XIANG, M.D. Xue, Experimental investigation of the thermally induced vibration of a space boom section, *Sci China-Phys Mech Astron*, **58**:044601, 2015, doi: 10.1007/s11433-014-5622-y

[4] E.A. Thorton, *Thermal structures for aerospace applications*. AIAA Education Series, 1996.

[5] W. Nowacki, *Dynamic problems of thermoelasticity*, The Netherlands, Noordhoff, Leyden, 1975.

[6] M. Amabili, S. Carra, Thermal effects on geometrically nonlinear vibrations of rectangular plates with fixed edges, *Journal of Sound and Vibration* **321**, 2, 936-954, 2009.

[7] S. Kazemirad, M. H. Ghayesh, M. Amabili, Thermo-mechanical nonlinear dynamics of a buckled axially moving beam, *Archive of Applied Mechanics*, **Vol.83**, Issue 1, 25–42, 2013.

[8] R.C. Zhou, D.Y. Xue, C. Mei, Finite element time time domain modal formulation for nonlinear flutter of composite panels, *AIAA Journal*, **32** (10), 2044–2052, 1994.

[9] Y. Shi, R.Y.Y. Lee, C. Mei, Thermal postbuckling of composite plates using the finite element modal coordinate method. *AIAA Journal*, **37**, 1035-1032, 1999

[10] A. Warminska, E. Manoach, J. Warminski, Nonlinear dynamics of a reduced multimodal Timoshenko beam subjected to thermal and mechanical loadings, *Meccanica*, **49**,8, 1775–1793, 2014.

[11] A. Warminska, E. Manoach, J. Warminski, S. Samborski, Regular and chaotic oscillations of a Timoshenko beam subjected to mechanical and thermal loadings, *Continuum Mechanics and Thermodynamics*, 2014, DOI 10.1007/s00161-014-0381-6.

[12] C. Mei, K. Abdel-Motagaly, R. Chen, Review of nonlinear panel flutter at supersonic and hypersonic speeds. *Appl. Mech. Rev.*, **52** (10), 321–332, 1999.

[13] H. Chen, L. N. Virgin, Dynamic analysis of modal shifting and mode jumping in thermally buckled plates, *J. Sound and Vibration*, **278**, 233-256, 2004.

[14] E. Manoach, P. Ribeiro, Coupled, thermoelastic, large amplitude vibrations of Timoshenko beams, *Int. J. Mech. Sci.*, **46**, 1589–1606, 2004.

[15] P. Ribeiro, E. Manoach, The effect of temperature on the large amplitude vibrations of curved beams, *J. Sound and Vibrations*, **285**, 1093–1107, 2005.

Influencing Vibrations by Dissipative Effects (MS08)

11th International Conference on Engineering Vibration
Ljubljana, Slovenia, 7–10 September 2015

CONFERENCE PAPER ABSTRACT - TEMPORARY VERSION

First A. Author*[1], Second B. Author[2], Third C. Author[2]

[1]Affiliation of first author
name@e-mail.address

[2]Affiliation of second (and third) author
{name2,name3}@e-mail.address

Keywords: Instructions, Conference, Vibration, Experimental Dynamics, Wave Problems, Modal Analysis.

Abstract. *This document provides information and instructions for preparing a paper to be included in the Proceedings of the International Conference on Engineering Vibration. The paper can be written in Latex or Word. The first page is reserved for the title of the paper, the authors, affiliations, keywords and the abstract. The introduction must begin at the top of the second page.*

11th International Conference on Engineering Vibration
Ljubljana, Slovenia, 7–10 September 2015

PRELIMINARY STUDY INVESTIGATING THE CAPABILITY OF EULERIAN- AND LAGRANGIAN-ACOUSTIC ELEMENTS TO DESCRIBE THE COCHLEAR FLUID-STRUCTURE INTERACTIONS

Philipp Wahl*, Sebastian Ihrle, Pascal Ziegler, and Peter Eberhard

Institute of Engineering and Computational Mechanics, University of Stuttgart,
Pfaffenwaldring 9, 70569 Stuttgart, Germany
{philipp.wahl, sebastian.ihrle, pascal.ziegler, peter.eberhard}@itm.uni-stuttgart.de

Keywords: Fluid-Structure Interaction, Enclosed Fluid, Acoustic Elements, Biomechanics, Human Hearing, Cochlea.

Abstract. *The human inner ear or cochlea can be considered as a closed hydraulic system, where pressure changes in the slightly compressible fluid, induced by vibrations of the middle-ear ossicles, lead to the vibration of the compliant basilar membrane, which in turn results in hearing nerve stimulation. In order to understand the intracochlear dynamics in detail, the development of a mechanical simulation model is required. Not only will this provide a deeper insight into the cochlear processes, but also this numerical model will allow to address clinical aspects like the effect of prosthesis on the hearing impression or to predict the impact of pathological changes.*

For this purpose, the fluid-structure interaction between the enclosed fluid and the soft membranes has to be described. Therefore, a simplified finite element model with a fluid domain, enclosed by two compliant membranes and a rigid wall is used in this study to investigate the capability of two different element formulations, i.e. pressure- and displacement-formulated acoustic elements, to describe the fluid-structure interaction. The two different element formulations, their specific coupling at the fluid-structure interfaces as well as the modeling of the boundary conditions are described. To verify the fluid-structure interaction, the coupled system is excited with a pressure impulse and the transient system response is evaluated. The results obtained for the model with pressure-formulated acoustic elements were compared with those obtained with displacement-formulated acoustic elements. Further, a harmonically varying load is applied to the system to obtain the frequency responses with Eulerian-based and Lagrangian-based acoustic elements, respectively. These results show, that the transfer behavior for higher frequencies differs depending on the acoustic element formulation being used. Further, the fluid viscosity has different impacts on the frequency responses obtained for pressure- and displacement-formulated acoustic elements.

1 INTRODUCTION

The inner ear or cochlea is the sensory organ where mechanical vibrations are transferred to nerve stimuli. It is a bone structure of spiral shape and is composed of conical chambers which are filled with fluid and separated by a soft membrane, the basilar membrane. The chambers are closed by the stapes footplate and the round window membrane, respectively. The cochlea can, therefore, be considered as a closed hydraulic system with fluid properties similar to water.

For a normal ear, sound is received by the eardrum, transmitted through the middle ear ossicles chain and finally excites the hydraulic system through the vibration of the stapes footplate. The stapedial vibrations lead to the propagation of pressure waves in the cochlear fluid which in turn results in the characteristic vibration behavior of the basilar membrane. Depending on the excitation frequency, the oscillation of the basilar membrane reaches the maximum amplitude at a characteristic location along the cochlear partition. Hair cells on the basilar membrane are stimulated particularly at this location and cause hearing nerve stimulation.

Since the dynamic behavior of the cochlea, especially of the basilar membrane, is almost impossible to measure, the development of a simulation model of the inner ear is necessary. Due to the complex structure of the inner ear, the Finite Element (FE) analysis is one common method to describe the fluid-structure interactions between the inner ear fluid and the compliant structures. Since the slightly compressible fluid is an enclosed volume with no mean flow, acoustic elements may be capable to describe the cochlear fluid behavior, as described in [1] and [2].

In this paper, we present simulation results for a first simplified model with fluid-structure interaction consisting of a fluid with a cylindrical shape enclosed by two soft membranes and a rigid wall. The results using Lagrangian-formulated acoustic elements for the fluid domain are compared with those obtained for Eulerian-formulated elements. In addition, the two different element formulations and the modeling at the fluid-structure interfaces are described.

2 FE-MODEL AND ACOUSTIC ELEMENT FORMULATIONS

In the following section, first the geometry, material properties and boundary conditions for the simplified FE-model are presented. In the second part, the two different formulations of acoustic-elements being investigated in this study are provided.

2.1 Geometry, material properties and boundary conditions

The FE-model comprises the enclosed fluid domain of cylindrical shape, two soft membranes and a rigid wall, represented as a fluid boundary condition. The geometry is shown in Figure 1, the material properties and dimensions are listed in Table 1. Latter ones are scaled up compared to the cochlea, since laboratory experiments are intended in further investigations to validate the simulation results.

For the fluid, the dynamic viscosity η_f, the bulk modulus ζ_f, the density ρ_f and the sound velocity c_f for water were used. Assuming small structural deflections, a linear elastic material behavior for the membranes with similar properties to a silicon film is used, as a model for the behavior of human tissues. The rims of both membranes have fixed translations and the left membrane is loaded with a time-varying pressure $P(t)$.

The FE-model has been created using ANSYS Mechanical APDL 15.0. The membranes were meshed with standard shell elements of type SHELL181. For the fluid domain the pressure-formulated or Eulerian-based acoustic elements are used, refered to as FLUID30, and the displacement-formulated or Lagrangian-based acoustic elements, refered to as FLUID80, re-

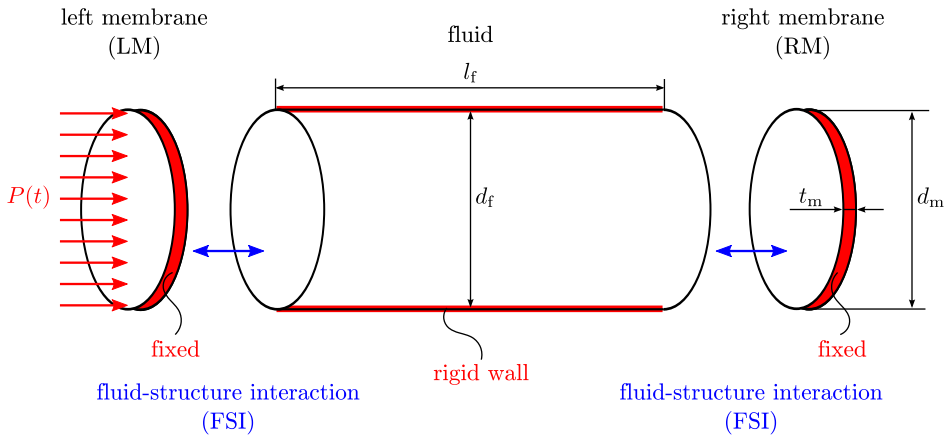


Figure 1: Geometry of the FE-model and applied boundary conditions.

fluid					
d_f [mm]	l_f [mm]	ρ_f [kg/m^3]	ζ_f [Pa]	η_f [Pa·s]	c_f [m/s]
10	50	988	$2.08{\cdot}10^9$	$8.9{\cdot}10^{-4}$	1492
membranes					
d_m [mm]	t_m [mm]	ρ_m [kg/m^3]	E_m [N/m^2]	μ_m [-]	
10	0.25	1200	$3{\cdot}10^6$	0.49	

Table 1: Dimensions and material properties of the FE-model.

spectively. The formulation of the fluid-structure interactions depends on the acoustic element formulation being used, as described in the following sections.

2.2 Pressure-formulated acoustic elements

For the pressure-formulated acoustic elements, the Navier-Stokes equations are simplified to form the acoustic wave equation

$$\nabla^2 p - \frac{1}{c_\mathrm{f}^2}\frac{\partial^2 p}{\partial t^2} + \frac{4\eta_\mathrm{f}}{3\rho_\mathrm{f} c_\mathrm{f}^2}\nabla^2\frac{\partial p}{\partial t} = 0. \tag{1}$$

The equation describes the spatial propagation of pressure waves in a fluid with no net flow rate and no source, neglecting effects of thermal conductivity. Further, a compressible fluid where density changes are due to pressure variations is assumed and the equation is limited to relatively small pressures, such that the changes in density are small compared to the mean density. By discretizing Eq. 1, the finite element equation for the pressure-formulated, linear acoustic element is

$$\mathbf{M}_\mathrm{f}\,\ddot{\mathbf{p}} + \mathbf{C}_\mathrm{f}\,\dot{\mathbf{p}} + \mathbf{K}_\mathrm{f}\,\mathbf{p} = \mathbf{F}_\mathrm{f}, \tag{2}$$

where $\mathbf{M}_\mathrm{f}$, $\mathbf{C}_\mathrm{f}$ and $\mathbf{K}_\mathrm{f}$ are the equivalent fluid mass, damping and stiffness matrices. Further, $\mathbf{F}_\mathrm{f}$ represents the vector of applied fluid loads and $\mathbf{p}$ the vector of the unknown nodal acoustic

pressures. At the interfaces between fluid and membranes, the acoustic pressure is related to the resulting normal displacement of the structure, using a coupling matrix $\mathbf{R}$ that accounts for the effective surface area associated with each node on the interface. This leads to the equations of the two-way coupled fluid-structure interaction problem

$$\begin{aligned} \mathbf{M}_\mathrm{f}\,\ddot{\mathbf{p}} + \mathbf{C}_\mathrm{f}\,\dot{\mathbf{p}} + \mathbf{K}_\mathrm{f}\,\mathbf{p} &= \mathbf{F}_\mathrm{f} - \rho_\mathrm{f}\mathbf{R}^T\ddot{\mathbf{u}}, \\ \mathbf{M}_\mathrm{s}\,\ddot{\mathbf{u}} + \mathbf{C}_\mathrm{s}\,\dot{\mathbf{u}} + \mathbf{K}_\mathrm{s}\,\mathbf{u} &= \mathbf{F}_\mathrm{s} + \mathbf{R}\mathbf{p}. \end{aligned} \tag{3}$$

There, $\mathbf{M}_\mathrm{s}$, $\mathbf{C}_\mathrm{s}$ and $\mathbf{K}_\mathrm{s}$ are the structural fluid mass, damping and stiffness matrices, $\mathbf{F}_\mathrm{s}$ is the vector of applied structural loads and $\mathbf{u}$ is the vector of unknown nodal displacements. These equations can be formed into a matrix equation, where the assembled mass and stiffness matrices are unsymmetric. Using the linear pressure-formulated acoustic elements to model the fluid domain, the FLUID30-element in ANSYS has one pressure DOF and three additional displacement DOFs at the fluid-structure interface. However, elements inside the fluid domain have only pressure DOFs.

To accurately represent the coupling between the translational DOFs of FLUID30- and SHELL181-elements, coincident nodes for the fluid and structure have to be defined at the interfaces. The use of a shell with pressure-load on the exterior surface and fluid-structure interaction on the interior surface, as present in the FE-model for the left membrane, will not work, since each node in the shell-element can either take the pressure value of the load or the pressure value available at the fluid-structure interface. Therefore, two layers with separated node sets were created for the shell, coupling their displacement DOFs. The nodes of the shell-layer located closer to the fluid are merged with the fluid-nodes at the interface. To represent the behavior of a single shell, the Young's modulus E_m and the density ρ_m of the membranes were halved. The Poisson ratio μ_m and thickness t_m remain unaltered, according to the procedure described in [3]. Additionally, the absorption coefficient is set to zero for the FLUID30-elements located on the cylindrical surface, representing the rigid wall boundary condition.

2.3 Displacement-formulated acoustic elements

The Lagrangian-acoustic elements are based on the nodal displacements of modified standard, linear solid elements, altering the underlying material behavior to reflect the behavior of a fluid. The adiabatic process of an ideal gas can be described by

$$p = p_0 V_0^\kappa V^{-\kappa} \tag{4}$$

with the heat capacity ratio κ and the volumes V_0 and V. The derivative of the pressure with respect to the volume can therefore be expressed as

$$\frac{dp}{dV} = -p\frac{\kappa}{V}. \tag{5}$$

By using Eq. 5, the Taylor series, neglecting terms of second and higher order, can be formed

$$p\left(V_0 + \Delta V\right) = p_0 + \Delta p = p_0 + \left.\frac{dp}{dV}\right|_{V_0} \Delta V = p_0 + \left(-p\left.\frac{\kappa}{V}\right|_{V_0}\right)\Delta V \tag{6}$$

which leads to the linear relationship for small pressure changes

$$\Delta p = -p\kappa\varepsilon_b \tag{7}$$

with the bulk strain $\varepsilon_b = \frac{\Delta V}{V_0}$. The fundamental equation used for the displacement-formulated acoustic elements is formed by combining Eqs. 7 and 5 by use of the bulk modulus $\zeta_\mathrm{f} = -V\frac{dp}{dV}$

$$p = -\zeta_\mathrm{f}\varepsilon_b = -\zeta_\mathrm{f}\nabla\cdot\mathbf{u}. \tag{8}$$

The displacement-formulated acoustic elements, FLUID80, available in ANSYS, are based on modified SOLID45-elements. The stiffness matrix $\mathbf{K_f}$ with $S_\mathrm{f} = \zeta_\mathrm{f}10^{-9}$ is represented by

$$\mathbf{K}_\mathrm{f} = \begin{bmatrix} \frac{1}{\zeta_\mathrm{f}} & 0 & 0 & 0 & 0 & 0 & 0 \\ 0 & \frac{1}{S_\mathrm{f}} & 0 & 0 & 0 & 0 & 0 \\ 0 & 0 & \frac{1}{S_\mathrm{f}} & 0 & 0 & 0 & 0 \\ 0 & 0 & 0 & \frac{1}{S_\mathrm{f}} & 0 & 0 & 0 \\ 0 & 0 & 0 & 0 & \frac{1}{S_\mathrm{f}} & 0 & 0 \\ 0 & 0 & 0 & 0 & 0 & \frac{1}{S_\mathrm{f}} & 0 \\ 0 & 0 & 0 & 0 & 0 & 0 & \frac{1}{S_\mathrm{f}} \end{bmatrix} \tag{9}$$

where the Young's modulus is set equal to the bulk modulus ζ_f of the fluid and the stiffness terms associated with the shear stresses are set to near zero. Therefore, the FLUID80-element has a significantly low ability to resist shear stress. Each FLUID80-element in ANSYS has three nodal displacement DOFs and should be of rectangular shape whenever possible, as results are known to be of lower accuracy for non-brick-shape elements. The resulting assembled system matrices of the coupled problem using displacement-formulated acoustic elements are symmetric, since the interaction between fluid and structural elements is performed by coupling directly the nodal displacement DOFs. However, only the nodal displacements of the acoustic elements pointing normal to the interface are coupled with the structural displacement DOFs, since only out-of-plane motions of the structure generate acoustic pressure.

In the present FE-model, separate but coincident node sets for the membrane and fluid were created at the fluid-structure interface and the longitudinal nodal displacements of FLUID80- and SHELL181-elements were coupled. Representing the fluid boundary condition of a rigid wall, the nodal coordinate systems of the exterior fluid-elements were rotated normal to the cylindrical surface. Then, the normal translational DOFs were constrained, while the tangential DOFs were left unconstrained.

2.4 FE-model

The entire FE-model with its global coordinate system is shown in Figure 2, consisting of 15600 acoustic elements for the fluid domain. For the FE-model with FLUID30, 1248 shell elements were used for each membrane comprising two layers. With FLUID80-elements only half of the shell elements per membrane were required.

3 RESULTS

The FE-model is used to investigate the transient and frequency response of the coupled system comparing the results obtained for pressure-formulated and displacement-formulated acoustic elements.

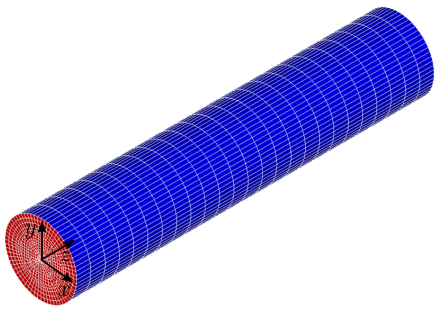


Figure 2: Discretization of the FE-model and its global coordinate system.

3.1 Pressure impulse and transient system response

The left membrane of the coupled system is now excited by the pressure impulse, as illustrated in Figure 3 with an amplitude of 250 Pa. The transient acoustic-pressure and structural responses were conducted over 25 ms with a time step of 1 μs. The excitation of the coupled system leads to the propagation of pressure waves in the fluid domain travelling towards the right membrane. In Figure 3 the transient pressure responses in the middle of the cylinder axis are given, obtained from the FE-model with FLUID30- and FLUID80-elements, respectively.

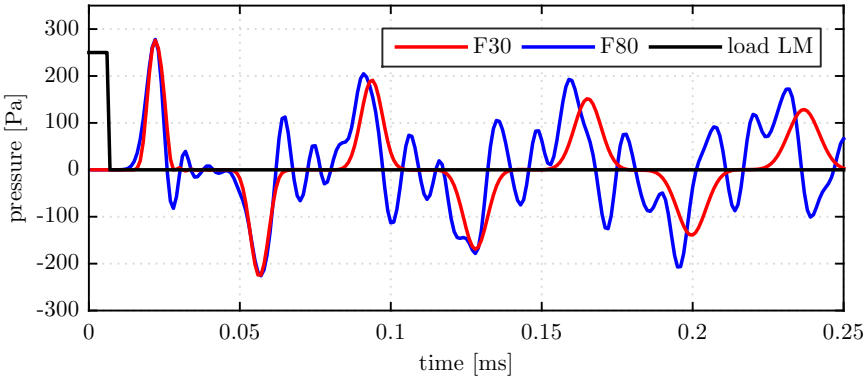


Figure 3: Applied pressure impulse on left membrane (LM) and resulting pressure responses for FLUID30 and FLUID80 at $x = 0\,\mathrm{mm}$, $y = 0\,\mathrm{mm}$, $z = 25\,\mathrm{mm}$.

At $t = 22\,\mu$s, the wave front crosses the middle of the fluid domain, indicated by a sharp pressure peak. Reaching the right membrane, reflection of the wave front occurs, travelling back towards the left membrane with a negative pressure amplitude. Thereby, the reflected wave front crosses the middle of the fluid domain at $t = 57\,\mu$s and gets superimposed with subsequent waves travelling towards the right membrane. Due to the increasing superposition of the acoustic waves over time, the previously clearly visible wave fronts get blurred and the pressure amplitude decreases. The time shift between the first up- and downstream travelling pressure wave front of $\Delta t_\mathrm{s} = 35\,\mu$s seems physical compared to $\Delta t_\mathrm{a} = 34\,\mu$s obtained for the sound velocity $c_\mathrm{f} = 1492\,\mathrm{m/s}$ and travelled distance of $\Delta z = 50\,\mathrm{mm}$, whereas latter one does not take the deformation at the fluid-structure interface into account.

While FLUID30-elements inside the domain stay undeformed and the pressure is calculated by the acoustic wave equation provided at each node, the pressure provided in the center of FLUID80-elements is obtained by evaluating the bulk strain of the element. Considering two adjacent elements, a compression of one element, resulting in a positive acoustic pressure, leads to the expansion of the adjacent element, resulting in a negative pressure and vice versa. This leads to a negative pressure wave front of small amplitude, travelling just behind the positive wave front, as shown in Figure 3 at $t = 28\,\mu$s. Consequently, this results in a smoother curve shape for results obtained with FLUID30-elements. Besides, the transient acoustic pressure responses obtained for FLUID30- and FLUID80-elements show for $t \leq 70\,\mu$s quite similar results. For $t > 70\,\mu$s differences in the results for FLUID30- and FLUID80-elements regarding the amplitudes and travel times of the pressure wave fronts occur.

Further, the displaced volumes at the left and right membrane were evaluated based on the calculated membrane deflections. The transient behavior of the displaced volumes for the FE-model with FLUID30- and FLUID80-elements are shown in Figure 4.

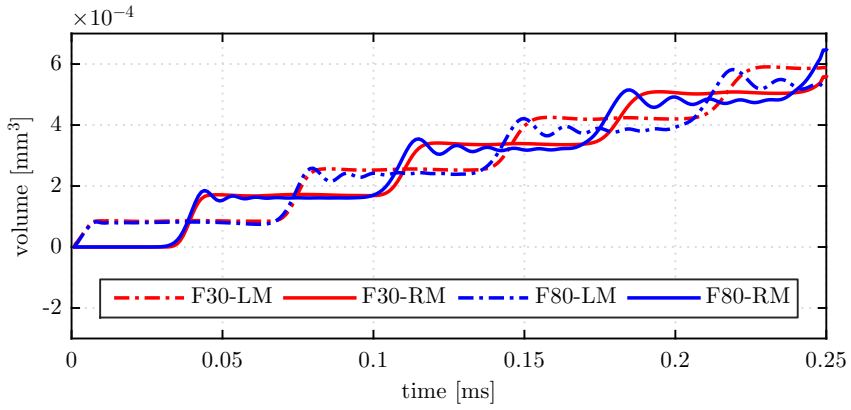


Figure 4: Transient behavior of the displaced volume at the left (LM) and right (RM) membrane obtained for the FE-model with FLUID30- and FLUID80-elements, respectively.

The displaced volume increases stepwise with time, whereas the first increase in volume at the left membrane starting at $t = 0\,\mu$s represents the applied pressure impulse. Each time a pressure wave front reaches the left or right membrane, it leads to an abrupt increase in volume. The time delay between two steps in volume for the same membrane correlates closely to $\Delta t_\mathrm{a} = 70\,\mu$s, obtained for the distance of $\Delta z = 100\,\mathrm{mm}$ and the sound velocity of $c_\mathrm{f} = 1492\,\mathrm{m/s}$. For $t > 100\,\mu$s, the abrupt increase of volume at the left and right membrane, calculated using FLUID30-elements, occur slightly time-delayed compared to the results for FLUID80 and the amplitude is readily increased. With time, the acoustic pressure waves travelling through the fluid-domain get superimposed and single wave fronts are no longer visible. The coupled system then converges to the steady state and oscillates harmonically, as illustrated in Figure 5.

With the equality of displaced volumes at the left and right membrane, the results verify the compliance with the continuity equation. The resulting oscillation frequency for the FE-model with FLUID80-elements is slightly reduced compared to the results with FLUID30, but with around 41 Hz the results for both models are in a similar range. According to [3], for acoustic elements based on the lossy wave equation, Eq. 1, the dimensionless coefficient

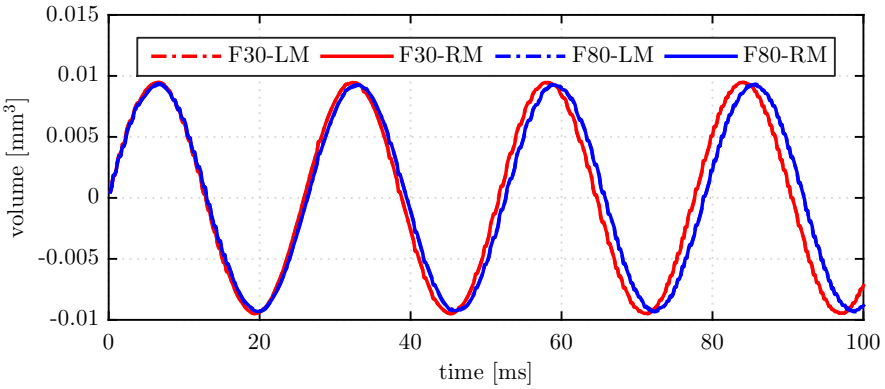


Figure 5: Displaced volume at the left (LM) and right (RM) membrane converging to the steady state of the coupled system.

$$\alpha = \frac{2\pi f \eta_\mathrm{f}}{\rho_\mathrm{f} {c_\mathrm{f}}^2} \tag{10}$$

represents how fast the acoustic field with the frequency f is attenuated by the effects of the fluid viscosity η_f. Since for $\alpha \ll 1$ the wave number is almost real, the viscous affects are negligible. However, for higher frequencies, when the dimensionless coefficient approaches unity, viscous losses due to fluid viscosity can be significant. In this case, the coupled system leads to a steady oscillation with about $f = 41\,\mathrm{Hz}$. For the fluid properties, given in Table 1, the dimensionless coefficient is about $\alpha = 10^{-10}$. Therefore, it can be assumed, that the results obtained with FLUID30-elements do not include any viscous losses. Thus, the slightly different results obtained with Fluid30- and Fluid80-elements may be caused by the different formulations of the damping matrices, accounting for viscous fluid losses.

3.2 Harmonic pressure excitation, frequency response and corresponding mode shapes

The left membrane is excited with a harmonic varying pressure and the displaced volume at the right membrane is calculated for the FE-model with FLUID30- and FLUID80-elements, respectively. The frequency response analyses were conducted for the frequency ranges 0.1 Hz to 100 Hz and 100 Hz to 1100 Hz. For the first range an increment of $\Delta f = 0.1\,\mathrm{Hz}$ and a pressure amplitude of 100 Pa, for the second range an increment of $\Delta f = 1\,\mathrm{Hz}$ and a pressure amplitude of 1000 Pa were used. The frequency response curves for the displaced volume of the right membrane are shown in Figure 6 and 7. For the lower frequency range, one single resonance peak appears at about $f_{\mathrm{F80},1} \approx f_{\mathrm{F30},1} \approx 38\,\mathrm{Hz}$ for both FE-models. These resonance frequencies are in a similar range as the oscillating frequency obtained in Figure 5 and correspond to the first mode shape of the coupled system, shown in Figure 8(a).

For excitation frequencies above 100 Hz, the frequency response curves for the FE-model with FLUID80-elements show two further resonance peaks at $f_{\mathrm{F80},4} = 330\,\mathrm{Hz}$ and $f_{\mathrm{F80},7} = 680\,\mathrm{Hz}$. These resonance frequencies are related to the fourth and seventh mode shape, illustrated in Figure 8(b) and (c). In contrast, these resonance frequencies are shifted to $f_{\mathrm{F30},4} = 458\,\mathrm{Hz}$ and $f_{\mathrm{F30},7} = 1066\,\mathrm{Hz}$ for the FE-model using FLUID30-elements. Table 2 summarizes further resonance frequencies within the analyzed frequency range. Since for the

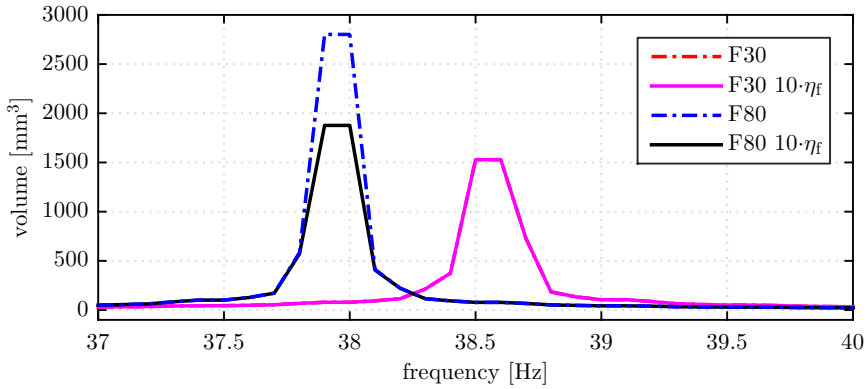


Figure 6: Frequency response for the displaced volume at the right membrane (RM) resulting from the harmonic pressure load with an amplitude of 100 Pa applied at the left membrane (LM).

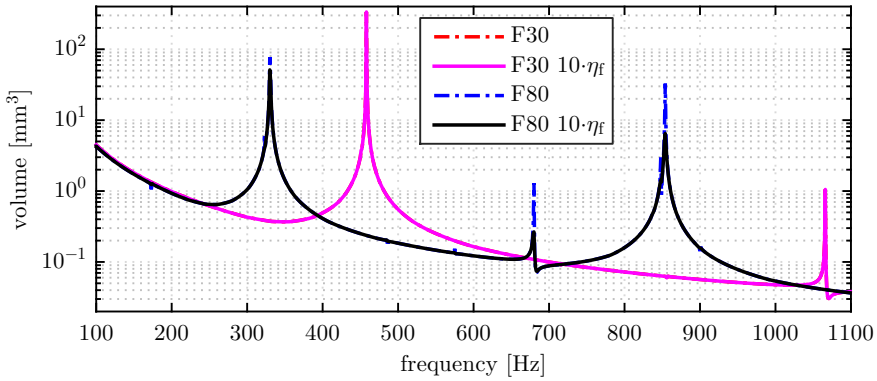
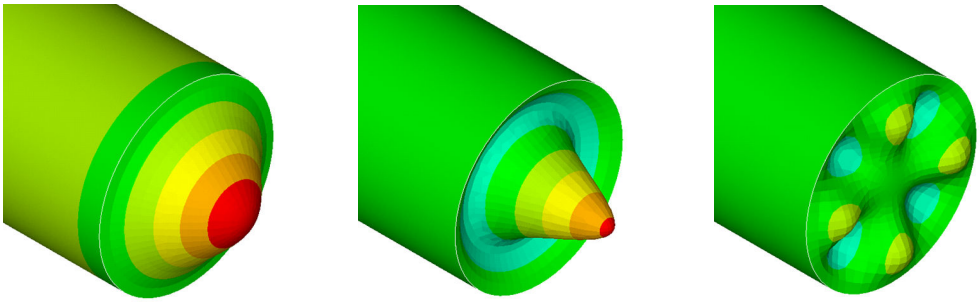


Figure 7: Frequency response for the displaced volume at the right membrane (RM) resulting from the harmonic pressure load with an amplitude of 1000 Pa applied at the left membrane (LM).

corresponding mode shapes the displaced volume at the right membrane balances itself, these resonance frequencies do not appear in the frequency responses illustrated in Figure 7.

Obviously, the transfer behavior obtained with displacement-formulated acoustic elements differs for higher frequencies from the transfer characteristic obtained with pressure-formulated acoustic elements. Furthermore, the frequency responses with an increased fluid viscosity were calculated for both FE-models and compared to the transfer behavior using the default viscosity value for water. Increasing the fluid viscosity by 10-fold, the transfer behavior of the coupled system using FLUID30-elements does not alter significantly, see Figure 6 and 7. For the highest analyzed frequency of 1100 Hz and the increased fluid viscosity $\eta_f = 8.9 \cdot 10^{-3}$ Pa·s, the dimensionless coefficient is $\alpha = 2.7 \cdot 10^{-8}$, thus damping effects due to fluid viscosity are not expected for results obtained with pressure-based acoustic elements. In contrast, the frequency response obtained with FLUID80-elements changes considerably resulting in strongly damped resonance peaks due to increased viscous damping.



(a) $f_{\mathrm{F80,1}}$=$f_{\mathrm{F30,1}}$=38 Hz (b) $f_{\mathrm{F80,4}}$=330 Hz, $f_{\mathrm{F30,4}}$=458 Hz (c) $f_{\mathrm{F80,7}}$=680 Hz, $f_{\mathrm{F30,7}}$=1066 Hz

Figure 8: Resonance frequencies and corresponding mode shapes of the right membrane for the FE-model with FLUID30- and FLUID80-elements.

	i=1	i=2	i=3	i=4	i=5	i=6	i=7
$f_{\mathrm{F80,i}}$ [Hz]	38	173	316	330	486	575	680
$f_{\mathrm{F30,i}}$ [Hz]	38	217	433	458	716	856	1066

Table 2: Resonance frequencies of right membrane resulting from the harmonic pressure load applied at the left membrane.

4 CONCLUSIONS

For the development of a numerical model of the human cochlea, the fluid-structure interaction between a slightly compressible, enclosed fluid and compliant membranes has to be described. Therefore, we investigated the capability of Eulerian and Lagrangian acoustic elements to describe the cochlear fluid-structure interaction using a simplified FE-model with scaled up dimensions comparable to the inner ear. We describe the different formulations of the acoustic elements being investigated as well as the element-specific modeling at the interfaces and the definition of the boundary conditions. The transient response of the coupled-system due to a pressure impulse was evaluated and compared for both acoustic elements formulations. The resulting structural vibrations verify the successful modeling of the fluid-structure interaction and the resulting oscillating frequencies are in a similar range. Furthermore, the frequency response and corresponding mode shapes are obtained, exciting the coupled system with a harmonically varying pressure. Whereas the transfer behavior for low frequencies is in a similar range for both acoustic element formulations, the frequency responses for higher excitation frequencies differ significantly. In addition, the fluid viscosity has a different impact on the frequency response depending on the acoustic element formulation being used.

REFERENCES

[1] M.Kwacz, P. Marek, P. Borkowski and W. Gambin: Effect of different stapes prostheses on the passive vibration of the basilar membrane, *Hearing Research*, 310, 13-26, 2014.

[2] R.Z. Gan, B.P. Reeves and X. Wang: Modelling of sound transmission from ear canal to cochlea, *Biomedical Engineering*, 35, 2180-2195, 2007.

[3] C.Q. Howard and B.S. Cazzolato: Acoustic analyses using MATLAB and ANSYS, 2015.

11th International Conference on Engineering Vibration
Ljubljana, Slovenia, 7–10 September 2015

NUMERICAL AND EXPERIMENTAL INVESTIGATION OF THE EFFECT OF A FLUID PIPE ON SYSTEMS SUBJECTED TO FORCED VIBRATIONS

Georg Jehle*[1], Alexander Fidlin[1]

[1]Karlsruhe Institute of Technology
{georg.jehle, alexander.fidlin}@kit.edu

Keywords: Oscillating fluid, fluid-structure interaction, experiment.

Abstract. *There are several reasons why unwanted vibrations can arise in a shift gearbox. For example, it can be caused by a friction-induced instability during shifting[1]. In such a situation, some structural components can be seen as vibration inducer (clutch disc, shafts, gears), whereas other parts are forced to resonate (housing, control elements). Besides their actual purpose, hydraulic control elements such as fluid pipes of the actuation system can contribute to the passive amplification and/or suppression of vibrations.*

In order to get a first idea of the effect of a hydraulic aggregate on vibrations of a shift gearbox, two models of oscillating fluid pipes are analyzed. The first model is a rigid pipe with only one translational DoF in its own axial direction. It is hinged on a translational spring and force-excited. The two exits of the pipe are both closed; inside, hydraulic oil is situated, which can flow weakly because of its own compressibility and additional capacitances. The second model has the same structure as the previous one, but an additional cylinder is situated inside the fluid. The fluid pipe and the diving cylinder are connected to each other by a translational spring.

The analysis consists of a numerical and an experimental part. For the numerical analysis, equations to describe the fluid dynamics are derived from the Navier-Stokes equations and the equation of continuity. Galerkin's method and a finite differences discretization are applied in order to obtain an ODE approach. The experimental setup consists of a closed pipe on a rail which is connected to a frame by a leaf spring and force-excited by a shaker. The hydraulic oil and the diving mass are optional components.

When the pipe is forced to vibrate, it is observed that the stress acting between fluid and structure reduces the vibration amplitude. This effect works best when the first fluid eigenfrequency hits the eigenfrequency of the corresponding 1-DoF-oscillator (system without fluid). The diving cylinder increases the dissipative effect. A good correlation is found between the analytical results and the experiment.

1 INTRODUCTION

Most of today's mechanical applications are unthinkable to operate without the help of hydraulic fluid. There are many examples where hydraulics acts as element of control or power transmission: lifting platforms, transmissions, positioning of the clutch disc in a shift gearbox etc. One reason for the widespread use is the favorable relation between transmittable power and low loss.
Several model descriptions are available a pipe flow. The most prominent one is the Hagen-Poiseuille model [2], which is a suitable description of a 1D unidirectional flow through a rigid pipe. For most situations in engineering (e.g. the flow through a straight pipe in the positioning aggregate of a clutch disc), this approach is sufficient for the design of mechanics and control.
The situation changes when the considered system is subjected to high frequency vibrations [3]. Then, the inertia of the fluid becomes important, even in a pipe with a small cross-section, and the primitive model is not applicable any more. Forced vibrations in fluids may occur because of an oscillating flow source, vibrating actuation cylinders or pipe vibrations. A lot of literature considers vibrating fluids and fluid-structure interaction. For the special case of fluid in a cylindrical pipe with negligible elasticity, oscillations of laminar flow are discussed in [4, 5]. Here, a space-fixed pipe was assumed. The extension a non inertial-fixed environment is given in [6].
The aim of the present study is the application of the theory to a more complex geometry, and the comparison between simulation and experiments. Therefore, in section 2 the equations of motion are derived, in section 3 the experimental setup is explained, and in section 4 results are shown and discussed.

2 MATHEMATICAL MODEL OF FLUID IN A PIPE

The system of consideration is a rotationally symmetric, rigid fluid pipe, which contains fluid, and which is able to translate in axial direction. The pipe is limited by two ends. Here, cavities separated by elastic membranes are enclosed. Temperature changes and heat transfer effects are neglected.
The physical quantities to describe the fluid dynamics are the pressure p and the velocity $\boldsymbol{u} = \boldsymbol{u}_r + \boldsymbol{u}_\varphi + \boldsymbol{u}_z$. In order to determine the evolution of these variables with respect to time, a simplification of the Navier-stokes equations is solved. The assumptions are as follows:

- 1-dimensional flow with rotational symmetry. Then, $\boldsymbol{u} \equiv \boldsymbol{u}_z = u\boldsymbol{e}_z$ and $\frac{\partial(\cdot)}{\partial\varphi} = 0$
- Newtonian fluid and laminar flow. Then, the shear stress $\boldsymbol{\tau} = \rho\nu\text{grad}(\boldsymbol{u})$.
- The fluid velocity is small (smaller than c). Then, convection terms can be neglected.
- Volume forces are neglected.

This leads to field equations [5]

$$\begin{aligned} \rho\dot{u} &= -\frac{\partial p}{\partial z} + \rho\nu\left(\frac{\partial^2 u}{\partial r^2} + \frac{1}{r}\frac{\partial u}{\partial r}\right) , \\ \dot{p} &= -E\frac{\partial u}{\partial z} , \end{aligned} \tag{1}$$

with ρ the mass density of the fluid, ν the kinematic viscosity and E the bulk modulus, r the radial and z the axial coordinate of the pipe. At the radial boundary of the pipe ($\partial\Omega_1$), the

no-slip condition

$$u|_{\partial\Omega_1} = \dot{w}_1 \tag{2}$$

holds, with $\dot{w}_1$ the translational velocity of the pipe. At the ends of the pipe ($\partial\Omega_2$ and $\partial\Omega_3$), the total volume is conserved:

$$\begin{aligned} C_h\dot{p}(z=0) &= \dot{V}_{in}(z=0) - \dot{V}_{out}(z=0), \\ C_h\dot{p}(z=\ell) &= \dot{V}_{in}(z=\ell) - \dot{V}_{out}(z=\ell), \end{aligned} \tag{3}$$

with $\dot{V}$ the volume flow, ℓ the length of the pipe, and C_h the capacitance of the cavity-membrane-assemblage. Before further processing the equations, two kinds of shape of the fluid domain are introduced. The first *shape (I)* has a cylindrical cross-section (outer radius r_o, cf. Figure 1). A more complex case is *shape (II)* (Figure 2), where the fluid flows between an inner and an outer cylinder (radii r_i and r_o). Both cylinders have a translational DoF (w_1 and w_2).

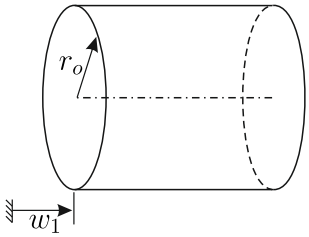


Figure 1: Pipe shape (I): plain cylinder.

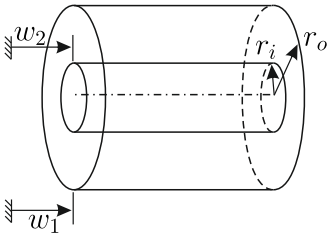


Figure 2: Pipe shape (II): hollow cylinder.

Now, an approach is elaborated in order to approximate the set of PDEs by ODEs on the respective shape. First, the transformation $u(r,z,t) = \dot{w}_1(t) + u_{fl}(r,z,t)$ is introduced, with $u_{fl}(r,z,t)$ the axial fluid velocity relative to the pipe. Then, the separation of variables is applied as $u_{fl}(r,z,t) = \sum_{k=0}^{n_m} A_k(r)B_k(z,t)$, where $n_m \in \mathbb{N}$. The last step is a discretization of the z-dependency, such that $z_j = j\Delta\ell$, where $j \in \{1,...,n_{el}\}$ and $n_{el} = \ell/\Delta\ell \in \mathbb{N}$. Thus,

$$\begin{aligned} u^{(I)}(r,z_j,t) &\approx \dot{w}_1 + \sum_{k=1}^{n_m} A_k^{(I)}(r)B_{k,j}^{(I)}(t)\,, \\ u^{(II)}(r,z_j,t) &\approx \dot{w}_1 + (\dot{w}_2 - \dot{w}_1)\frac{\ln(\frac{r}{r_o})}{\ln(\frac{r_i}{r_o})} + \sum_{k=1}^{n_m} A_k^{(II)}(r)B_{k,j}^{(II)}(t)\,, \\ p(z_j,t) &= p_j(t)\,, \end{aligned} \tag{4}$$

where the index (I) or (II) denotes the shape on which the approach is valid. The trial functions $A_k(r)$ have to be $\mathcal{C}^2[0,r_o]$ or $\mathcal{C}^2[r_i,r_o]$ and linearly independent, and to fulfill the radial boundary conditions (Eq. (2)). Thus, they are chosen as

$$\begin{aligned} A_k^{(I)}(r) &= J_0\left(\frac{r}{r_o}\kappa_k\right), \\ A_k^{(II)}(r) &= J_0\left(\frac{r}{r_i}\xi_k\right) - \frac{J_0(\xi_k)}{Y_0(\xi_k)}Y_0\left(\frac{r}{r_i}\xi_k\right), \end{aligned} \tag{5}$$

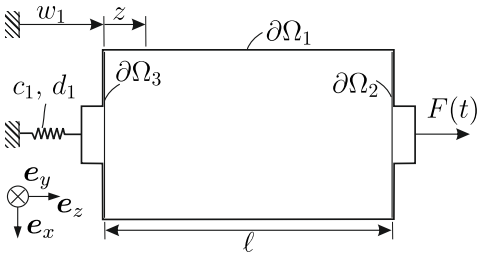


Figure 3: First pipe model.

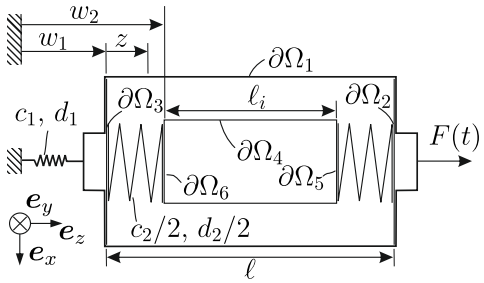


Figure 4: Second pipe model.

with κ_k the roots of $J_0(\kappa)$ and ξ_k the roots of $G(\xi, \frac{r_o}{r_i}) = J_0\left(\frac{r_o}{r_i}\xi\right) - \frac{J_0(\xi)}{Y_0(\xi)} Y_0\left(\frac{r_o}{r_i}\xi_k\right)$. Substituting this approach in Eq. (1) and introducing finite differences yields an error $e_{k,j}$, whose projection onto the space of trial functions must be minimal according to Galerkin's method. This requirement results in a set of discretized field equations on shape (I)

$$\begin{aligned} \dot{B}^{(I)}_{k,j} &= -\nu \left(\frac{\kappa_k}{r_o}\right)^2 B^{(I)}_{k,j} - \frac{2}{\kappa_k J_1(\kappa_k)} \left(\ddot{w}_1 + \frac{p^{(I)}_{j+1} - p^{(I)}_j}{\rho \Delta \ell}\right) , \\ \dot{p}^{(I)}_j &= -\frac{2E}{\Delta \ell} \sum_{k=1}^{n_m} \frac{J_1(\kappa_k)}{\kappa_k} \left(B^{(I)}_{k,j} - B^{(I)}_{k,j-1}\right) , \end{aligned} \tag{6}$$

and on shape (II)

$$\begin{aligned} \dot{B}^{(II)}_{k,j} &= -\nu \left(\frac{\xi_k}{r_i}\right)^2 B^{(II)}_{k,j} - \frac{g_{1,k}}{g_{3,k}}(\ddot{w}_2 - \ddot{w}_1) - \frac{g_{2,k}}{g_{3,k}} \left(\ddot{w}_1 + \frac{p^{(II)}_{j+1} - p^{(II)}_j}{\rho \Delta \ell}\right), \\ \dot{p}^{(II)}_j &= -\frac{2E}{\Delta \ell} \frac{r_i^2}{r_o^2 - r_i^2} \sum_{k=1}^{n_m} g_{2,k} \left(B^{(II)}_{k,j} - B^{(II)}_{k,j-1}\right), \end{aligned} \tag{7}$$

where the integrals

$$g_{1,k} = \int_1^{\frac{r_o}{r_i}} \frac{\ln\left(\frac{r_o}{r_i}\right) - \ln(\bar{r})}{\ln(\frac{r_o}{r_i})} G_k(\bar{r}) \bar{r} d\bar{r}, \quad g_{2,k} = \int_1^{\frac{r_o}{r_i}} G_k(\bar{r}) \bar{r} d\bar{r}, \quad g_{3,k} = \int_1^{\frac{r_o}{r_i}} G_k^2(\bar{r}) \bar{r} d\bar{r} \tag{8}$$

and $G_k(\bar{r}) = G(\xi_k, \bar{r})$.

The first model to be investigated is presented in Figure 3. The cross-section is purely of shape (I), the pipe with mass m_1 is connected by a spring-damper element (c_1, d_1) to inertial space, and force-excited by $F(t)$. The equations of motion are

$$\begin{aligned} F(t) &= m_1 \ddot{w}_1 + d_1 \dot{w}_1 + c_1 w_1 + \boldsymbol{f}_o \cdot \boldsymbol{e}_z, \\ \boldsymbol{f}_o &= \int_{\partial\Omega_1} \boldsymbol{\sigma} d\boldsymbol{a} + \int_{\partial\Omega_2} \boldsymbol{\sigma} d\boldsymbol{a} + \int_{\partial\Omega_3} \boldsymbol{\sigma} d\boldsymbol{a}, \end{aligned} \tag{9}$$

in addition to Eqs. (3) and (6). The stress on $\partial\Omega_1$ is $\boldsymbol{\sigma} d\boldsymbol{a} = \tau_{rz} \boldsymbol{e}_z da = \rho\nu \frac{\partial u_{fl}}{\partial r} \boldsymbol{e}_z da$, whereas on $\partial\Omega_2$ and $\partial\Omega_3$, $\boldsymbol{\sigma} d\boldsymbol{a} = p \boldsymbol{e}_z da$.

The model of comparison is presented in Figure 4: It is the expansion of the first model by an

inner cylinder with mass m_2, which is connected to the pipe by a spring-damper element (c_2, d_2). The fluid domain is a stringing together of shapes (I) and (II). Thus, the equations of motion are

$$\begin{aligned} F(t) &= m_1\ddot{w}_1 + d_1\dot{w}_1 + c_1 w_1 + d_2(\dot{w}_1 - \dot{w}_2) + c_2(w_1 - w_2) + \boldsymbol{f}_o \cdot \boldsymbol{e}_z, \\ 0 &= m_2\ddot{w}_2 + d_2(\dot{w}_2 - \dot{w}_1) + c_2(w_2 - w_1) + \boldsymbol{f}_i \cdot \boldsymbol{e}_z, \\ \boldsymbol{f}_o &= \int_{\partial\Omega_1} \boldsymbol{\sigma} d\boldsymbol{a} + \int_{\partial\Omega_2} \boldsymbol{\sigma} d\boldsymbol{a} + \int_{\partial\Omega_3} \boldsymbol{\sigma} d\boldsymbol{a}, \\ \boldsymbol{f}_i &= \int_{\partial\Omega_4} \boldsymbol{\sigma} d\boldsymbol{a} + \int_{\partial\Omega_5} \boldsymbol{\sigma} d\boldsymbol{a} + \int_{\partial\Omega_6} \boldsymbol{\sigma} d\boldsymbol{a}, \end{aligned} \tag{10}$$

again together with Eqs. (3) and (6), and the conservation of mass condition between shapes (I) and (II).
The sets of Eqs. (9) and (10) can be solved numerically by an ODE solver. According to the assumptions, both models are linear. However, since the number of equations is large and the evaluation of shear forces costful, the use of a fast algorithm is recommended. In this work, an OPENMP[1] implementation was chosen.

3 EXPERIMENTAL SETUP AND MEASUREMENT DATA PROCESSION

In Figure 5, the test rig is illustrated schematically. It consists of the pipe, which is connected to a leaf spring (c_1, d_1), a force transducer to measure $F(t)$, and a shaker which excites the system. The shaker and the spring are suspended on a common rack. An accelerometer is situated on the pipe.
As Figure 7 reveals, the excitation signal is produced by a signal generator and amplified by a power amplifier. The force signal as well as the acceleration are entered into a frontend, which besides A-D conversion provides the connection to a PC.

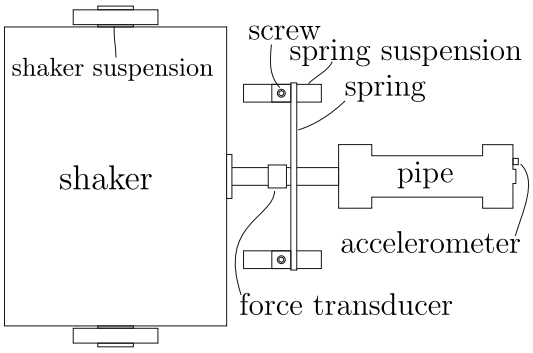


Figure 5: Measurement setup.

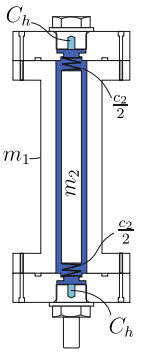


Figure 6: Pipe in detail.

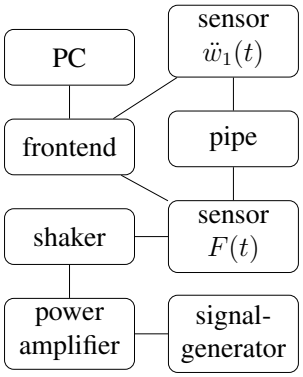


Figure 7: Wiring of the test rig.

The stiffness of the leaf spring is determined in a static Euler-Bernoulli beam model. As in the experiment, a beam of length 2ℓ is suspended at its ends and subjected to a single load applying in the middle. With $v(x)$ the deflection ($x \in [0, 2\ell]$), the reduced spring stiffness is $c_1 = F/v(\ell)$.

[1] www.openmp.org

Because the nature of the suspension is somewhere in between fixed- and pin-ended type, the limits

$$3\frac{EI_y}{\ell^3} \leq c_1 \leq 12\frac{EI_y}{\ell^3} \tag{11}$$

hold, where E is the Young's modulus of the beam and I_y the second moment of area. With two screws determining the prestess between the leaf spring and its suspension (cf. Figure 5), c_1 is adjustable in between this interval.
The capacitance results from the elastic properties of a membrane fixed on a cavity in the locking screw of the pipe (cf. Figure 6). The membrane material is freely selectable, but must have a thickness not larger than 1mm. The diameter of the cavity is $\varnothing = 4$mm, its deepness $h = 6$mm. As in the numerical approach, the system behaviour is linear for small excitation – therefore, one possible aim is the estimation of the transfer function in frequency domain

$$G(i\omega) = \frac{\mathcal{F}\{w_1\}(i\omega)}{\mathcal{F}\{F\}(i\omega)} = -\frac{\mathcal{F}\{\ddot{w}_1\}(i\omega)}{\omega^2\mathcal{F}\{F\}(i\omega)}\,, \tag{12}$$

with $\mathcal{F}\{s\}(i\omega)$ the Fourier transformation of $s(t)$. Denoting $r_{sq}(\tau) = E\{s(t)q(t+\tau)\}$ the cross correlation function of $s(t)$ and $q(t)$ and $R_{sq}(i\omega) = \mathcal{F}\{r_{sq}\}(i\omega)$ the cross-spectral density, the transfer function can be expressed as [7]

$$G_1(i\omega) = -\frac{R_{F\ddot{w}_1}(i\omega)}{\omega^2 R_{FF}(i\omega)}, \quad G_2(i\omega) = -\frac{R_{\ddot{w}_1\ddot{w}_1}(i\omega)}{\omega^2 R_{\ddot{w}_1 F}(i\omega)}, \quad |G_{00}(i\omega)| = \frac{1}{\omega^2}\sqrt{\frac{|R_{\ddot{w}_1\ddot{w}_1}(i\omega)|}{|R_{FF}(i\omega)|}}. \tag{13}$$

Both the measures of $F(t)$ and $\ddot{w}_1(t)$ contain uncertainties, which have different impacts on the relative error of the estimates G_1, G_2 and G_{00}. In literature, it is found that

$$|G_1(i\omega)| \leq |G(i\omega)| \leq |G_2(i\omega)| \qquad \text{and} \qquad |G_{00}(i\omega)| \approx |G_m(i\omega)|\,, \tag{14}$$

where $|G_m(i\omega)| = \frac{1}{2}\left(|G_1(i\omega)| + |G_2(i\omega)|\right)$. As this relation is found to be true and the estimates are very close to one another, in the diagrams of section 4.2 $G_m(i\omega)$ is analyzed.

4 RESULTS AND DISCUSSION

4.1 Numerical results

In order to obtain a first insight into the dynamics of models 1 and 2, a simulation with stationary frequency is performed, and the velocity is analyzed. The chosen parameters are those listed in Tables 1 and 2 and a capacitance of $C_h = 50 \cdot 10^{-14}$m^3/Pa. In Figure 8, the velocity profile is presented at $z = \ell/2$. This diagram confirms that the higher n_m is chosen, the better the convergence (cf. [5]). In particular, the simulation of model 2 (Fig. 8 below) with $n_m < 3$ makes no sense, whereas the apparent relative error is small at $n_m = 5$.
In Figure 9, the mean axial fluid velocity $U(z)$ is presented. Obviously the radius r_o has an impact on the overall compliance, which is why the gradient of $U(z)$ increases towards higher values of r_o. Because of the conservation of mass at the transition between shapes (I) and (II), in model 2 there is a velocity jump. Combining the information of Figures 8 and 9 reveals the fluid motion in the pipe in this frequency region: Apart from the boundary, it translates "en bloc", like a rigid body with very little compression.

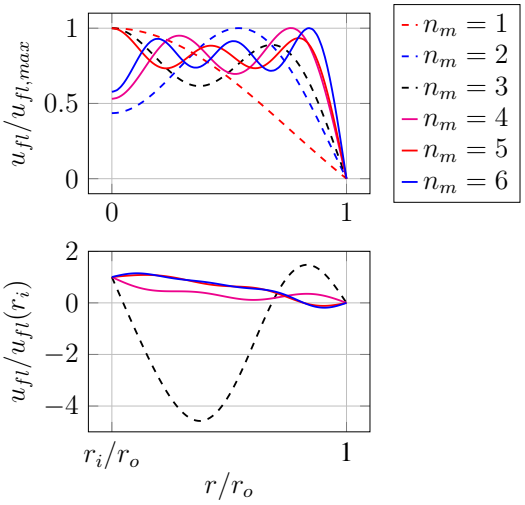


Figure 8: Calculated velocity profile for an excitation frequency $f = 300$Hz and for different radial discretization n_m. Above: pipe model 1, below: pipe model 2.

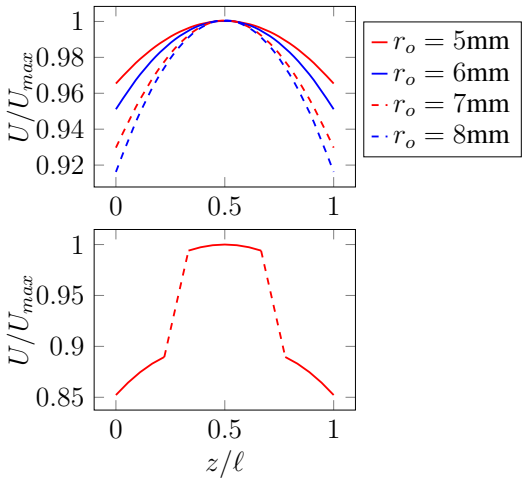


Figure 9: Mean fluid velocity at $f = 300$Hz. The radius r_o influences the dependency on z in model 1 (above). The diving mass in model 2 causes a velocity jump (below).

The absolute value of the transfer function $|G(i\omega)|$ is plotted for both models in Figure 10. Here, the most significant effect is vibration absorption at the frequency corresponding to the first fluid eingenfrequency. In the diagram, the evolution of the resonance amplitudes with respect to a change of c_1 is illustrated.

4.2 Experimental results

The previously discussed effects are to be carried out and continued in experiment, but the main aim of this work is the achievement of accordance to the simulation models. The first task is the estimation of parameters. Masses are determined by scales, stiffnesses can be found by comparing the transfer functions of the empty pipe in simulation and experiment. Hence, the unknowns are E and C_h. There is a manufacturer specification of E for hydraulic oil without

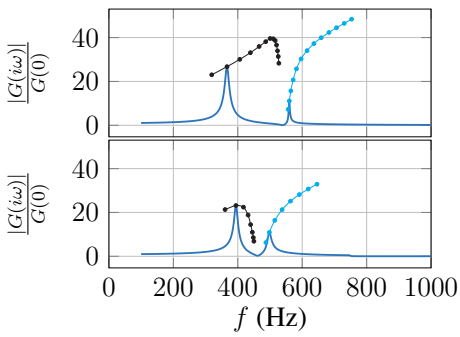


Figure 10: Transfer function of model 1 (above) and model 2 (below). As c_1 changes, the vibration absorption can be visualized.

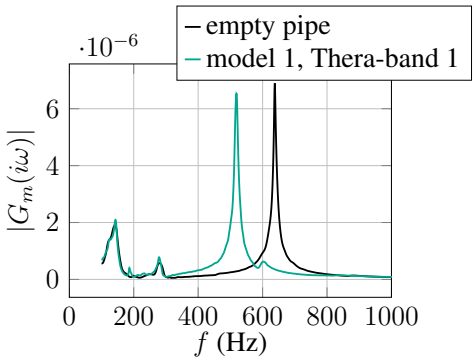


Figure 11: Transfer function from experiment: comparison of the empty pipe with model 1, capacitance modeled with a Thera-Band membrane.

air, but it is not clear whether the experiment leads to a critical amount of dissolved air, and how important is the impact. Therefore, its value is tried to be identified.
In pipe model 1 without membranes, the first fluid eigenfrequency is purely determined by the fluid properties. Neglecting the viscosity ν, the first eigenfrequency is $f_1 \approx \frac{1}{\pi\ell}\sqrt{\frac{E}{\rho}}$; Thus, when f_1 is found and ρ and ℓ known, E can be reconstructed. This is done by comparing $G_m(i\omega)$ of the empty and the filled pipe. Unfortunately, the vibration amplitude of the fluid is too small to clearly identify f_1, which is why the given value of E is assumed.
After this first attempt, membranes of different materials are mounted on the cavity in order to assess their effect on the transfer function. Figure 11 reveals that in model 1, besides the main resonance and some test rig-related parasitic oscillations at low frequencies, an amplitude appears at $f = 600$Hz. This recalls that here, the first fluid eigenfrequency is defined primarily by the boundary conditions. From a check against the simulation model with same parameters ($\ell = 20$cm, $r_o = 10$mm), it is now possible to estimate C_h of the respective material (cf. Table 3). The adjustment criterion is that the frequency of vibration absorption – the minimum of $|G(i\omega)|$ between the two peaks – has to match.

Par.	Value	Unit
m_1	0.7	kg
m_2	0.09	kg
c_1	$5-15$	MN/m
c_2	500	N/m
d_1	60	N/(ms)
d_2	60	N/(ms)

Table 1: Parameters 1.

Par.	Value	Unit
r_o	7.5, 10	mm
r_i	$6-9$	mm
ℓ	11, 20	cm
ℓ_i	10	cm
ν	26	mm^2/s
ρ	840	kg/m^3
E	17	kbar

Table 2: Parameters 2.

Membrane	C_h (10^{-14}m^3/Pa)
Acetate	10
Transparent film	7
Scotch tape	9
Thera-Band 1	22
Thera-Band 2	25
Thera-Band 3	24

Table 3: Capacitances.

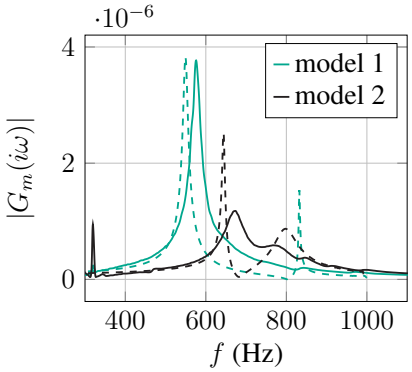


Figure 12: Comparison of the transfer function of models 1 and 2 in simulation (dashed line) and experiment (solid line).

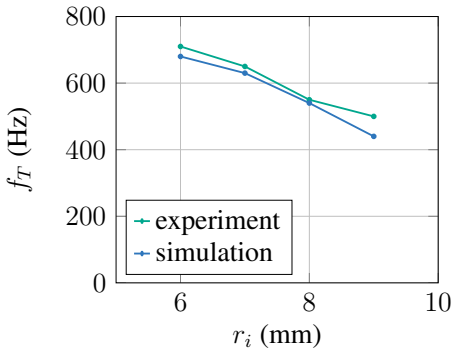


Figure 13: Frequency of vibration absorption in simulation and in experiment for different r_i.

The last stage is the validation between simulation and experiment. Therefore, the assemblage with $C_h = 25 \cdot 10^{-14}$m^3/Pa (softest Thera-Band) is taken, but the geometry changed: First, the length of the model 1-pipe is set to $\ell = 11$cm, then the diving cylinder ($r_i = 6$mm) mounted in order to obtain model 2. Figure 12 points out that the frequency of vibration absorption from

simulation and from experiment match very well in both combinations, but there are noticeable differences concerning the resonance amplitudes. In general, there is more dissipation in experiment than in simulation. Possible effects that cause damping are a radial flow around the diving cylinder, an orifice effect at the inlet geometry, or damping in the membranes.
The fact that the frequency of vibration absorption is found in good concordance persists when the radius of the diving mass r_i is changed (cf. Figure 13). This again emphasizes the qualitative correctness of the model, but the lack of quantitative agreement.

5 CONCLUSIONS

In this contribution, an oscillating fluid flow was analyzed in simulation and in experiment. The principal behaviour was investigated in two models: a cylindric geometry (model 1) and a cylinder with diving mass (model 2). It became visible that the fluid itself is very little compressed and moves like an additional almost-rigid body. As a key result, it was found that this body acts like a vibration absorber at the first fluid eigenfrequency.
A qualitative validation between simulation and experiments was achieved. The frequency of vibration absorption was found in very good accordance, whereas the agreement concerning the amplitudes was of less quality. Possible reasons are a more complex flow in the reality than assumed (maybe radial components), an orifice effect at the inlet, and the purely conservative formulation of the axial boundary conditions.

ACKNOWLEDGEMENTS

The authors like to thank Ruijin Shi who set up the test rig in his master's thesis [8].

REFERENCES

[1] G. Jehle and A. Fidlin. Friction induced vibrations in shift gearboxes. *ZAMM-Journal of Applied Mathematics and Mechanics/Zeitschrift für Angewandte Mathematik und Mechanik*, 2014.

[2] H. Oertel, M. Böhle, and U. Dohrmann. Strömungsmechanik. *Wiesbaden: Vieweg*, 2002.

[3] R.E. Goodson and R.G. Leonard. A survey of modeling techniques for fluid line transients. *Journal of Fluids Engineering*, 94(2):474–482, 1972.

[4] A.F. D'Souza and R. Oldenburger. Dynamic response of fluid lines. *Journal of Fluids Engineering*, 86(3):589–598, 1964.

[5] M. Jelali and A. Kroll. *Hydraulic servo-systems: modelling, identification and control*. Springer, 2003.

[6] G. Jehle, M. Koester, A. Fidlin, and A. Fridrich. On the influence of the fluid pipe on the stability of a mechanical system subjected to friction-induced vibrations. In *Proceedings of ENOC 2014, 8. EUROMECH Nonlinear Dynamics Conference*, 2014.

[7] R. Scheithauer. *Signale und Systeme*, volume 2. Teubner Stuttgart, 1998.

[8] R. Shi. Experimentelle Untersuchung einer axialschwingenden Hydraulikleitung zur Ansteuerung von Schaltgetrieben. Master's thesis, Institut für Technische Mechanik, Karlsruher Institut für Technologie, 2015.

International Conference on Engineering Vibration
Ljubljana, Slovenia, 7-10 September 2015

ON THE INFLUENCE OF DAMPING ON BRAKE VIBRATIONS

Nils Gräbner*[1], Holger Gödecker[1], Utz von Wagner[1]

[1] Department of Applied Mechanics, Chair of Mechatronics and Machine Dynamics, Technische Universität Berlin.

nils.graebner@tu-berlin.de, holger.goedecker@tu-berlin.de, utz.vonwagner@tu-berlin.de

Keywords: Brake Vibrations, Noise Vibration Harshness, Self Excitation, Damping.

Abstract. *Brake vibrations are prominent examples of NVH (Noise, Vibration, Harshness) problems in automotive engineering. Most brake vibrations are self-excited oscillations where energy is transferred from the rotation of the brake disk via the friction forces into a vibration of the brake system. If the self-excitation prevails the damping, increasing vibrations occur finally in most cases ending in stable limit cycles. Therefore, beside the excitation effect by the friction forces, damping plays a decisive role, whether oscillations occur or not in brakes.*

This paper shows some results of theoretical investigations on the influence of non-conservative forces in brakes. In linear models stability analysis can be performed by a calculation of the complex eigenvalues. The influence of nonlinearities is also discussed.

1 INTRODUCTION

Brake squeal is a high-frequent noise phenomenon in the audible frequency range between 1 and 15 kHz. Squealing automotive brakes are usually not accepted by customers. This results in high costs for warranty adjustments and high effort in the development of silent brakes. An earlier review of the corresponding problems and modeling is given in [1], a newer one in [2]. There are other applications than automotive disk brake squeal where friction induced vibrations may not be just a comfort problem but can lead to a system's failure, e.g. as described in [3]. If brake squeal is investigated experimentally, the observed phenomenon is an approximately monofrequent vibration of the brake structure, i.e. disk, calliper and carrier perform vibrations with displacement amplitudes in the µm-range and frequency independent from rotation speed.
Using a rough estimation comparing the in-plane velocity of the pad to the circumferential velocity of the disk, it can be concluded that squeal is not (at least not macroscopically) a stick-slip phenomenon as the disk has always (at least not for vehicle speeds very close to standstill) a much larger velocity than the pads.
Models for brake squeal are in general nonlinear and, for validity, must contain the self-excitation mechanism by the non-conservative friction force and nonlinearities for restricting the vibrations to a limit cycle, representing the experimentally observed stationary monofrequent vibration during squeal. Nonlinear discretised models of automotive disk brakes can generally be written as

$$\boldsymbol{M}\ddot{\boldsymbol{y}} + (\boldsymbol{D} + \boldsymbol{G})\dot{\boldsymbol{y}} + (\boldsymbol{K} + \boldsymbol{N})\boldsymbol{y} + \boldsymbol{f}_{\mathrm{nl}} = \boldsymbol{0}, \tag{1}$$

therefore, a system containing a symmetric and positive definite mass matrix $\boldsymbol{M}$, symmetric and positive semi-definite damping matrix $\boldsymbol{D}$ and stiffness matrix $\boldsymbol{K}$ as well as skew symmetric gyroscopic matrix $\boldsymbol{G}$ and circulatory matrix $\boldsymbol{N}$ and the vector of nonlinearities $\boldsymbol{f}_{\mathrm{nl}}$.These equations can result from industrial FE modeling with 10^6 degrees of freedom or simple minimal models with two degrees of freedom, where the structure is always the same.

It is still state of the art, to use linearised models for the description of squeal, in which the instability of the desired quiet solution is interpreted as squeal. If mathematical models for brake squeal are linearised with respect to a certain operation state, the result is

$$\boldsymbol{M}\ddot{\boldsymbol{y}} + (\boldsymbol{D} + \boldsymbol{G})\dot{\boldsymbol{y}} + (\boldsymbol{K} + \boldsymbol{N})\boldsymbol{y} = \boldsymbol{0}. \tag{2}$$

If a complex eigenvalue analysis of such a system is performed (in automotive industry called CEA) the results are either pairs of conjugate complex eigenvalues or real eigenvalues. At least one single positive real part of an eigenvalue results in instability of the trivial solution of (2) and may be interpreted as potential squeal. Beside the excitation mechanism to be found in $\boldsymbol{N}$ and the gyroscopic terms, the damping matrix $\boldsymbol{D}$ has a decisive influence on the stability behavior of the system, but can stabilise as well as destabilise [4]. Therefore, this paper focuses on the influence of linear and nonlinear damping on brake squeal. A study on the influence of parameter uncertainty is performed in [4].

Fundamental investigations on the construction of stabilising or destabilising damping matrices can be found in [5]. Damping in a brake system can be either distributed (e.g. in material damping) or concentrated, e.g. in joints or bearings. In [6] the authors found that distributed damping lowers the system's tendency to squeal while concentrated damping may have the opposite effect. Additional investigations on the theoretical/numerical influence of damping

on the problem can be found in [7] and [8]. A very popular countermeasure against squeal are so called "shims", a multilayered device fixed on the brake pads' backplates, e.g. described in [9], [10], [11] and [12]. In [13], experimental investigations are performed on a beam on disk system with added damping layers on both, beam and disk. Material damping of the brake disk is well known to have a significant influence on the problem. The influence of damping and the microstructure of brake disk materials is examined in [14]. The influence of damping in joints has been investigated in [15] and [16] while damping due to interaction of structure and brake fluid via piston and seal is researched in [17]. There is also some work on the influence of added damping devices to brake systems, e.g. in [18] and for integrated shunted piezoceramics or of a fuzzy damper in [19].
For a fundamental understanding of self-excited vibrations in brakes, minimal models, as in [20], can be used while for the detailed modeling of a specific brake Finite Element (FE) modeling is necessary. Therefore, large linearised FE models are used for complex eigenvalue analysis (CEA) as state of the art in industry. As damping can be decisive for stability behavior, the question on how these effects can be introduced in FE modeling is of vital interest. This is discussed in the following sections 2 and 3 with the linear effects of friction induced damping and material damping. It was shown in [15] that friction in joints can have a strong influence. These effects are nonlinear and therefore, not a linearised FE model but an extended minimal model based on [20] is investigated in section 4 for this influence, e.g. on limit cycle behavior.

2 FRICTION INDUCED DAMPING

The starting point of the investigation is the consideration of friction induced damping, i.e. velocity proportional forces or torques proportional to the friction coefficient μ. This phenomenon appears in frictional contacts with a relative velocity normal to an oscillation and has been shown to appear for a minimal model of disk brake squeal in [20] and was described more detailed in [21]. In the case of brake squeal, this effect can stabilise the solution and is therefore not negligible in the simulation. To analyse whether the effect of friction induced damping is well represented in the FE Models which are used in an industrial environment, the minimal model shown in Figure 1 exhibiting this effect is introduced and solved by using the CEA and analytical methods. Finally, the results are compared to see if the implementation in the FE-Tool is correct.

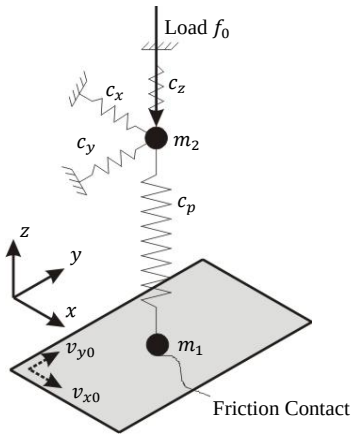


Figure 1: Investigated minimal model

Two point-masses are coupled elastically in z-direction with a spring (stiffness c_p) and coupled rigidly together in the other two directions. The lower point-mass is in contact with a moving layer assuming Coulomb friction in the contact. The layer is moving with the constant velocities v_{x0} in x-direction and v_{y0} in y-direction. The upper point-mass is elastically suspended in all three direction and a load f_0 is applied in negative z-direction. Thereby, the system has three degrees of freedom (the displacement of the upper point-mass) summarised in the vector $\boldsymbol{q} = (u, v, w)^T$. A dynamic equilibrium leads, after linearisation, to the equations of motion

$$\boldsymbol{M}\ddot{\boldsymbol{q}} + \boldsymbol{P}\dot{\boldsymbol{q}} + \boldsymbol{Q}\boldsymbol{q} = \boldsymbol{f} \tag{3}$$

with

$$\boldsymbol{f} = \begin{pmatrix} 0 \\ 0 \\ -f_0 \end{pmatrix}, \boldsymbol{M} = \begin{pmatrix} m_1+m_2 & 0 & 0 \\ 0 & m_1+m_2 & 0 \\ 0 & 0 & m_2 \end{pmatrix}, \boldsymbol{P} = \begin{pmatrix} \frac{v_{y0}^2}{(v_{x0}^2+v_{y0}^2)^{3/2}} & -\frac{v_{x0}v_{y0}}{(v_{x0}^2+v_{y0}^2)^{3/2}} & 0 \\ -\frac{v_{x0}v_{y0}}{(v_{x0}^2+v_{y0}^2)^{3/2}} & \frac{v_{x0}^2}{(v_{x0}^2+v_{y0}^2)^{3/2}} & 0 \\ 0 & 0 & 0 \end{pmatrix} \frac{\mu c_p f_0}{c_p + c_z}, \boldsymbol{Q} = \begin{pmatrix} c_x & 0 & -\frac{\mu c_p v_{x0}}{\sqrt{v_{x0}^2+v_{y0}^2}} \\ 0 & c_y & -\frac{\mu c_p v_{y0}}{\sqrt{v_{x0}^2+v_{y0}^2}} \\ 0 & 0 & c_p + c_z \end{pmatrix}. \tag{4}$$

The introduction of the friction contact results in a symmetric damping matrix $\boldsymbol{P} = \boldsymbol{D}$ while the model includes no dampers. Furthermore, additional entries in $\boldsymbol{K}$ appear due to the frictional contact which leads to an asymmetric matrix $\boldsymbol{K}$. The velocities v_{x0} and v_{y0} are given as

$$v_{x0} = \cos(k\pi)\frac{\mathrm{m}}{\mathrm{s}} \text{ and } v_{y0} = \sin(k\pi)\frac{\mathrm{m}}{\mathrm{s}} \tag{5}$$

with the factor k. Variation of this factor leads to a rotation of the vector of velocity in the xy-plane. The eigenvalues can be calculated with an exemplary set of parameters.
In the next step, an FE-model with the same properties as the minimal model in Figure 1 is developed and solved by using the complex eigenvalue analysis which is the state of the art method to simulate brake squeal. In the Figures 2 and 3, the results for the first two pairs of eigenvalues of the analytical calculation (blue line) and the simulation with the FE-model (red dots) for a variation of k are shown.

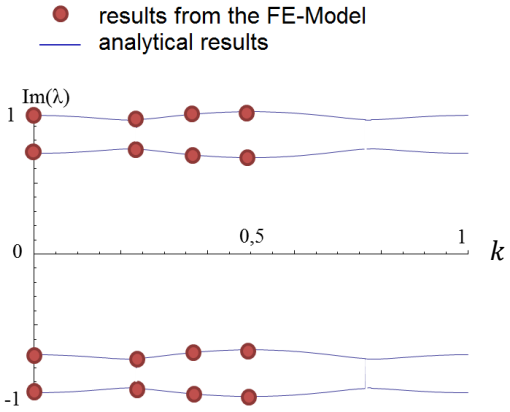


Figure 2: Imaginary part of the first two eigenvalues for a variation of k.

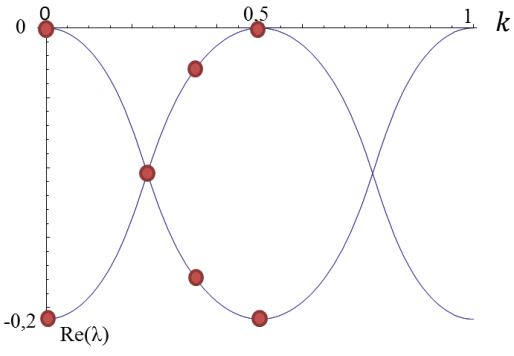


Figure 3: Real part of the first two eigenvalues for a variation of k.

Both results are consistent. This leads to the conclusion, that the effect of friction induced damping is implemented accurately in the complex eigenvalue analysis in the used FE-system PERMAS.

3 MATERIAL DAMPING

Another kind of damping mechanism in real systems is the material damping. As this kind of damping is assumed not to be viscous, a usual way to introduce it to the undamped system described by

$$\boldsymbol{M}\ddot{\boldsymbol{y}} + \boldsymbol{K}\boldsymbol{y} = \boldsymbol{0} \tag{6}$$

is to include a complex stiffness matrix, as shown in [22] and the current PERMAS manual

$$\boldsymbol{M}\ddot{\boldsymbol{y}} + (1 + id)\boldsymbol{K}\boldsymbol{y} = \boldsymbol{0} \tag{7}$$

with the structural damping factor d. For steel for example d ranges between 0.004 and 0.04. With the harmonic ansatz $\boldsymbol{y}(t) = \boldsymbol{r}\cos(\omega t)$ the eigenvalue problem

$$(-\omega^2\boldsymbol{M} + id\boldsymbol{K} + \boldsymbol{K})\boldsymbol{r} = \boldsymbol{0} \tag{8}$$

can be written. In comparison, a system with viscous damping

$$\boldsymbol{M}\ddot{\boldsymbol{y}} + \boldsymbol{D}\dot{\boldsymbol{y}} + \boldsymbol{K}\boldsymbol{y} = \boldsymbol{0} \tag{9}$$

leads to the eigenvalue problem

$$(-\omega^2\boldsymbol{M} + i\omega\boldsymbol{D} + \boldsymbol{K})\boldsymbol{r} = \boldsymbol{0}. \tag{10}$$

It is obvious, that the material damping can be written as an equivalent viscous damping $\boldsymbol{D}_q = d\boldsymbol{K}/\omega$ which is inversely proportional to ω. In order to calculate the eigenvalues ω the characteristic equation

$$\det(-\omega^2\boldsymbol{M} + id\boldsymbol{K} + \boldsymbol{K}) = \boldsymbol{0} \tag{11}$$

needs to be solved. The resulting polynomial is of order $2n$ with complex coefficients. The power of the polynomial is an even number, which leads to complex conjugate pairs of eigenvalues. To calculate the eigenvector $\boldsymbol{r}_i$, the solution ω_i has to be inserted in equation (8). The sum of all solutions $\boldsymbol{y}(t) = \sum_{i=1}^{2n} \boldsymbol{r}_i\cos(\omega_i t)$ is real.

Now the simultaneous appearance of both, viscous and material damping, is considered. The according eigenvalue problem reads as

$$(-\omega^2\boldsymbol{M} + i\omega\boldsymbol{D} + id\boldsymbol{K} + \boldsymbol{K})\boldsymbol{r} = \boldsymbol{0} \tag{12}$$

which leads to the characteristic equation

$$\det(-\omega^2\boldsymbol{M} + i\omega\boldsymbol{D} + id\boldsymbol{K} + \boldsymbol{K}) = \boldsymbol{0}. \tag{13}$$

The resulting polynomial is again of order $2n$ with complex coefficients while the polynominal contains odd and even exponents. Therefore, the sum of all solutions is not real. In FE simulations, the equivalent viscous damping is usually replaced by $\boldsymbol{D_q} = d\boldsymbol{K}/\omega_{ref}$ with a reference angular frequency ω_{ref}. Only if $\omega_{ref} \approx \omega$ the solution of such simulations is correct, what makes the inclusion of material damping in FE difficult.

4 DAMPING EFFECTS IN JOINTS

4.1 General

The different components in a brake are coupled with joints. Each joint has an influence on the overall damping, that can be ten times more than the material damping as shown in [15]. Therefore, it is rather important to implement this kind of damping effect in brake models.

Since the dissipation is a result of friction, the amplitudes of the displacement have a direct influence on the amount of dissipated energy as shown in [15] and [16]. Therefore, this effect is nonlinear and cannot be directly taken into account in linearised FE models. To take it into account, one possibility is to calculate equivalent viscous damping and stiffness parameters for numerical models. This is currently a very complex task and therefore neglected in most numerical studies. Another reason why the effect is not investigated in the industrial CEA models is that the stiffness and damping parameters which represent the joints are of higher order (nonlinear) and thus have no influence on a linearised model. Therefore, a nonlinear simulation is necessary to include the damping effect stemming from the joint. In [23] a method to solve high dimensional nonlinear problems, like in industrial FE models, is presented. To show the basic influence of joint modeling, an extended minimal model based on that in [20] is investigated in the following.

4.2 Influence on the Nonlinearities

To model a joint, a common method is to use a Jenkins element which consists of a linear elastic spring and a friction element (Coulomb friction) in series [24] as shown in Figure 4.

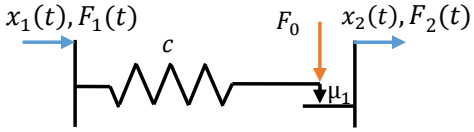


Figure 4: Jenkins-Element with a linear elastic spring and a friction element in series

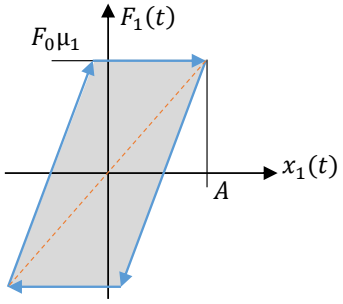


Figure 5: Force-Displacement-Hysteresis of a Jenkins-Element

The parameters for this element include the contact stiffness c, the friction coefficient μ_1 and the preload F_0. Stick-slip transitions are possible. Given $x_2(t) = 0$ and $x_1(t) = A\cos(\omega t)$ the Force displacement hysteresis shown in Figure 5 results. Using the method of energetic balance (see [25]), the Jenkins-Element can be replaced by a parallel-connection of a nonlinear spring with stiffness c^* and a nonlinear damper with d^* with the condition, that the dissipated energy during one oscillation cycle and the maximum of the potential energy is the same. With the ansatz $x_1(t) = A\cos(\omega t)$, this results in

$$\frac{1}{2}c^*A^2 = \frac{1}{2}c\left(\frac{\mu_1 F_0}{c}\right)^2 \tag{14}$$

for the potential energy and

$$d^*\omega\pi A^2 = 4\mu_1 F_0 A\left(1 - \frac{\mu_1 F_0}{cA}\right) \tag{15}$$

for the dissipated energy. Hence, c^* for the nonlinear spring can be written as

$$c^*(A) = \begin{cases} c & \text{für } |A| < \frac{F_0\mu_1}{c} \\ \frac{{\mu_1}^2{F_0}^2}{cA^2} & \text{für } |A| \geq \frac{F_0\mu_1}{c} \end{cases}, \tag{16}$$

while d^* for the nonlinear damper can be written as

$$d^*(A,\omega) = \begin{cases} 0 & \text{für } |A| < \dfrac{F_0\mu_1}{c} \\ \dfrac{4\mu_1 F_0}{\omega\pi|A|}\left(1 - \dfrac{\mu_1 F_0}{c|A|}\right) & \text{für } |A| \geq \dfrac{F_0\mu_1}{c} \end{cases}. \tag{17}$$

In the case of $|A| < \frac{F_0\mu_1}{c}$, the limit of adhesion is not exceeded and only stick occurs, i.e. there is just a stiffness and no dissipative effect.
To investigate the influence of the joints on the onset of squeal in brakes, the extended minimal model from [20] is considered, consisting of a wobbling elastically supported rigid disk in contact with two pads modelled as point masses. In the geometrically linearised model the coordinates q_1 and q_2 describe the wobbling motion of the disk while the nonholonomic constraint of constant disk revolution speed results in an equation of the driving torque. This model is refined with a more detailed modeling of the brake pads, the calliper and the joints as shown in Figure 6 on the left-hand side. Both brake pads are represented by a point mass with two degrees of freedom each (coordinates q_3, q_4, q_5 and q_6). In normal direction, the two point masses are connected by a spring with stiffness k_s which represents the calliper. The elasticity of the carrier is represented by the connection of each point mass with the surrounding in in-plane direction via a spring and a damper (with constants k_{ip} and d_{ip}). The connection of each point mass with the surrounding in normal direction is realised by a Jenkins-Element with c^* and d^* as shown in equations (16) and (17). This represents the connection of the calliper with the carrier in a floating calliper brake as shown in Figure 6 on the right-hand side (the red markings show the sliding bolts of this joint).
Altogether, this is a model with 6 degrees of freedom and the equations of motion can be written as

$$\boldsymbol{M\ddot{q} + P\dot{q} + Qq + f}_{\mathrm{nl}} = \boldsymbol{0}. \tag{18}$$

For more details see equation (20) and (21) in the appendix.

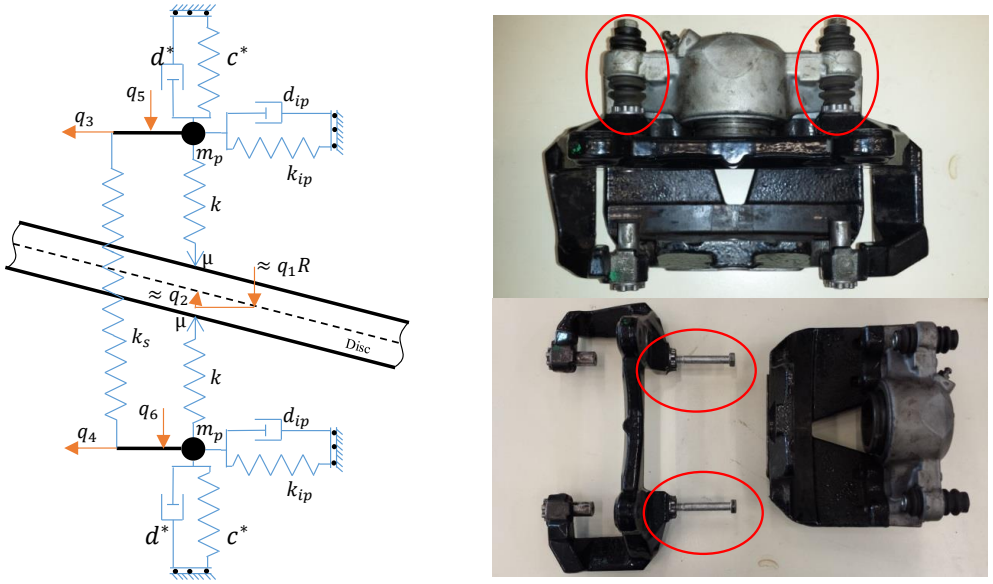


Figure 6: Minimal model from [20] with refined modeling of the brake pads, calliper and joints (left). Floating calliper brake with marked nonlinear modelled joints (right).

Solving the linearised equation

$$\boldsymbol{M\ddot{q} + P\dot{q} + Qq = 0} \tag{19}$$

results in the stability behavior of the trivial solution. The result for given parameters are shown in the appendix Figure 11 and Figure 12.The system becomes unstable with increasing rotational speed with two instable modes. The rotational speed has almost no influence on the frequencies of these modes.

The result for the nonlinear coefficients c^* and d^* varying with the amplitude A for given parameters are shown in Figure 7 and Figure 8 respectively. It is noticeable that for small amplitudes the stiffness is constant and the damping zero. This is the area of stick, where the linear stiffness coefficient is valid. Exceeding the critical amplitude $A > \frac{F_0 \mu_1}{c}$ slip occurs which leads to an increase of damping and to a decrease of the stiffness. For $A \rightarrow \infty$ both, stiffness and damping, are reaching the limit zero.

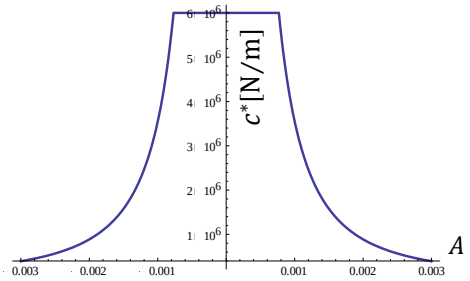


Figure 7: Nonlinear stiffness coefficient c^* over amplitude A

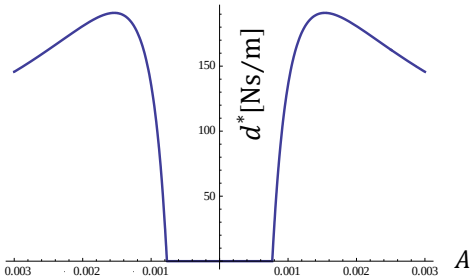


Figure 8: Nonlinear damping d^* coefficient over amplitude A

In the next step, a numerical time integration was performed. The results are shown in Figure 9 and Figure 10 for different friction coefficients. In both cases a limit cycle is reached, which is in reality the squealing of the brake. It can be clearly seen, that the damping in the joint has a strong influence on the resulting limit cycle amplitude.

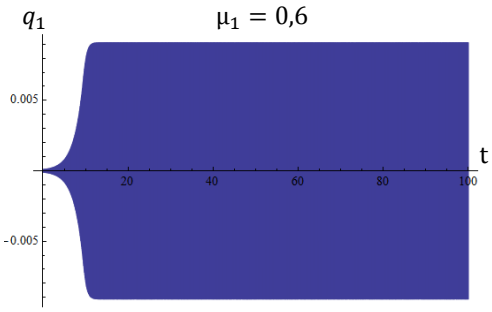


Figure 9: $q_1(t)$ reaching a limit cycle for $\mu_1 = 0{,}6$

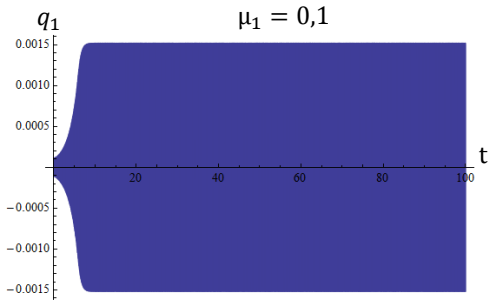


Figure 10: $q_1(t)$ reaching a limit cycle for $\mu_1 = 0{,}1$

5 CONCLUSIONS

Brake vibrations, especially squeal, are self-excited oscillations resulting in NVH problems in automotive engineering. Hereby, energy is transferred from the rotation of the brake disk via friction forces into a vibration of the brake system. If the self-excitation prevails the damping, increasing vibrations occur, finally in most cases ending in stable limit cycles.

Therefore, beside the excitation effect by the friction forces, damping plays a decisive role, whether or not oscillations occur in brakes.

This problem is studied in the present paper by examining different linear and nonlinear damping effects in brakes. Large linear FE models are used as state of the art in industry. Therefore, the possibility of including linear damping effects in FE models is of vital interest. As examples of linear damping the effects of friction induced damping and material damping are considered and the possibility of including these effects in FE models is discussed.

It has recently been shown in [15], that damping in joints may play a dominant role during squeal, which is a limit cycle behavior, i.e. requires a nonlinear modeling if vibration amplitudes shall be calculated. For an extended minimal model from [20], including a Jenkins element for the modeling of the calliper/carrier coupling, the influence of the damping characteristic of the joint on the limit cycle amplitude is demonstrated.

REFERENCES

[1] S. Yang, R.F. Gibson, Brake vibration and noise: reviews, comments, and proposals. *Int. J. of Materials and Product Technology*, **12(4-6)**, 496-513, 1997.

[2] N.M. Kinkaid, O. M. O'Reilly, P. Papadopoulos, Automotive disc brake squeal. *Journal of Sound and Vibration*, **267(1),** 105-166, 2003.

[3] D. Hochlenert, G. Spelsberg-Korspeter, P. Hagedorn, A note on safety-relevant vibrations induced by brake squeal. *Journal of Sound and Vibration*, **329(19)**, 3867-3872, 2010.

[4] A. Nobari, H. Ouyang, P. Bannister, Statistics of complex eigenvalues in friction-induced vibration. *Journal of Sound and Vibration*, **338(3)**, 169-183, 2015.

[5] P. Hagedorn, M. Eckstein, E. Heffel, A. Wagner, Self-Excited Vibrations and Damping in Circulatory Systems. *ASME. J. Appl. Mech.*, **81(10)**, 101009-1-101009-9, 2014.

[6] J.-J. Sinou, L. Jézéquel, The influence of damping on the limit cycles for a self-exciting mechanism. *Journal of Sound and Vibration*, **304(3–5)**, 875-893, 2007.

[7] B. Hervé, J.-J. Sinou, H. Mahé, L. Jézéquel, Analysis of squeal noise and mode coupling instabilities including damping and gyroscopic effects. *European Journal of Mechanics - A/Solids*, **27(2)**, 141-160, 2008.

[8] F. Cantone, F. Massi, A numerical investigation into the squeal instability: Effect of damping. *Mechanical Systems and Signal Processing*, **25(5)**, 1727-1737, 2011.

[9] R. Singh, A. A. Sheikh, M. J. Mitchell, Viscoelastic damping to control disc brake squeal. *Journal of Sound and Vibration*, **32(10)**, 18-22, 1998.

[10] A. M. Balvedi, S. N. Y. Gerges, Squeal Noise in Disc Brakes and the Influence of Damping on the System Dynamic Stability. *Acta Acustica united with Acustica*, **94(2)**, 254-264, 2008.

[11] J. Kang, Finite element modelling for the investigation of in-plane modes and damping shims in disc brake squeal. *Journal of Sound and Vibration*, **331(9)**, 2190-2202, 2012.

[12] H. Festjens, C. Gaël, R. Franck, D. Jean-Luc, L. Remy, Effectiveness of multilayer viscoelastic insulators to prevent occurrences of brake squeal: A numerical study. *Applied Acoustics*, **73(11)**, 1121-1128, 2012.

[13] F. Massi, O. Giannini, Effect of damping on the propensity of squeal instability: an experimental investigation. *J Acoust Soc Am*, **123(4)**, 2017-2023, 2008.

[14] S. Yang, R. F. Gibson, D. Li, R.L. Hecht, Damping and microstructures of brake rotor materials. *International Journal of Materials and Product Technology*, **13(3-6)**, 155-166, 1998.

[15] M. Tiedemann, S. Kruse und N. Hoffmann, Dominant damping effects in friction brake noise, vibration and harshness: the relevance of joints. *Proceedings of the Institution of Mechanical Engineers Part D: Journal of Automobile Engineering*, 2014.

[16] S. Kruse, M. Tiedemann, B. Zeumer, P. Reuss, N. Hoffmann, H. Hetzler, The influence of joints on friction induced vibration in brake squeal. *Journal of Sound and Vibration*, **340**, 239-252, 2015.

[17] J. Liette, J. Dreyer R. Singh, Dynamic characterization of the rectangular piston seal in a disk-caliper braking system using analytical and experimental methods. *Proceedings of the Institution of Mechanical Engineers, Part D: Journal of Automobile Engineering* **226**, 1613-1629, 2012.

[18] M. Neubauer, J. Wallaschek, Vibration damping with shunted piezoceramics: Fundamentals and technical applications. *Mechanical Systems and Signal Processing*, **36(1)**, 36-52, 2013.

[19] O. Giannini, Squeal suppression through a tuned fuzzy damper: A numerical study. *International Journal of Vehicle Design*, **51(1/2)**, 105-123, 2009.

[20] U. von Wagner, D. Hochlenert, P. Hagedorn, Minimal models for disk brake squeal. *Journal of Sound and Vibration*, **302**, 527-539, 2007.

[21] D. Hochlenert: Selbsterregte Schwingungen in Scheibenbremsen: Mathematische Modellbildung und aktive Unterdrückung von Bremsenquietschen, Doctoral Thesis, TU Darmstadt, 2006.

[22] C. W. Bert, Material damping: An introductory review of mathematic measures and experimental technique. *Journal of Sound and Vibration* 29.2 129-153, 1973.

[23] N. Gräbner, M. Tiedemann, U. von Wagner und N. Hoffmann, Nonlinearities in Friction Brake NVH-Experimental and Numerical Studies, *SAE Technical Paper 2014-01-2511*, 2014.

[24] K. Klamt, Zur optimalen Schwingungsdämpfung durch trockene Reibung in lokalen und ausgedehnten Fügestellen. VDI Verlag, 1990.

[25] K. Magnus, Schwingungen, Stuttgart: Teubner-Verlag, 4. Auflage 1986.

APPENDIX

$$\boldsymbol{M} = \begin{pmatrix} \Theta & 0 & 0 & 0 & 0 & 0 \\ 0 & \Theta & 0 & 0 & 0 & 0 \\ 0 & 0 & m_p & 0 & 0 & 0 \\ 0 & 0 & 0 & m_p & 0 & 0 \\ 0 & 0 & 0 & 0 & m_p & 0 \\ 0 & 0 & 0 & 0 & 0 & m_p \end{pmatrix}, \boldsymbol{Q} = \begin{pmatrix} k_t + HN_0 + 2kR^2 & \frac{H^2\mu N_0}{2R} & \frac{H\mu N_0}{2R} & -\frac{H\mu N_0}{2R} & -kR & -kR \\ -Hk\mu R - 2\mu N_0 R & k_t HN_0 + H\mu^2 N_0 & N_0 & -N_0 & \frac{1}{2}Hk\mu & \frac{1}{2}Hk\mu \\ -k\mu R & (1+\mu^2)N_0 & k_{ip} & 0 & k\mu & 0 \\ k\mu R & -(1+\mu^2)N_0 & 0 & k_{ip} & 0 & -k\mu \\ -kR & 0 & 0 & 0 & k + k_s + c & -k_s \\ -kR & 0 & 0 & 0 & -k_s & k + k_s + c \end{pmatrix}, \tag{20}$$

$$\boldsymbol{P} = \begin{pmatrix} \frac{H^2\mu N_0}{2\Omega} & \Omega\Theta_p & 0 & 0 & 0 & 0 \\ -\Omega\Theta_p & 0 & 0 & 0 & 0 & 0 \\ 0 & 0 & d_{pi} & 0 & 0 & 0 \\ 0 & 0 & 0 & d_{pi} & 0 & 0 \\ 0 & 0 & 0 & 0 & 0 & 0 \\ 0 & 0 & 0 & 0 & 0 & 0 \end{pmatrix}, \boldsymbol{f}_{\mathrm{nl}} = \begin{pmatrix} 0 \\ 0 \\ 0 \\ 0 \\ \begin{cases} 0 & \text{für } |q_5| < \frac{F_0\mu_1}{c} \\ \frac{4\mu_1 F_0}{\omega\pi|q_5|}\left(1 - \frac{\mu_1 F_0}{c|q_5|}\right)\dot{q}_5 + \frac{{\mu_1}^2 {F_0}^2}{c{q_5}^2} q_5 & \text{für } |q_5| \geq \frac{F_0\mu_1}{c} \end{cases} \\ \begin{cases} 0 & \text{für } |q_5| < \frac{F_0\mu_1}{c} \\ \frac{4\mu_1 F_0}{\omega\pi|q_5|}\left(1 - \frac{\mu_1 F_0}{c|q_5|}\right)\dot{q}_6 + \frac{{\mu_1}^2 {F_0}^2}{c{q_5}^2} q_6 & \text{für } |q_5| \geq \frac{F_0\mu_1}{c} \end{cases} \end{pmatrix}. \tag{21}$$

Table 1: parameter of the linearized model

Θ	moment of inertia of the disk in the direction q_1 and q_2	0,16	kg m^2
Θ_p	moment of inertia of the disk in the direction z	0,32	kg m^2
m_p	Mass of the brake caliper	0,15	kg
H	Thickness of the disk	0,02	m
R	Radius of the disk	0,13	m
N_0	Preload in the contact interface in normal direction (brake pressure)	3000	N
k	Stiffness of the brake pad	$6 \cdot 10^6$	N/m
k_s	Stiffness of the brake caliper	$1 \cdot 10^6$	N/m
k_t	Torsional stiffness of the mount from the disk in the center	$1{,}88 \cdot 10^7$	Nm
k_{ip}	Stiffness of the carrier	$6 \cdot 10^6$	N/m
d_{ip}	damping of the carrier	0,1	Ns/m
μ	Friction coefficient between the disk and the pad	0,6	1

Table 2: additional parameter of the nonlinear model

F_0	Preload in the Joint	1000	N
c	Tangential stiffness of the Joint	$6 \cdot 10^6$	N/m
ω	Angular frequency of the unstable mode	11 000	1/s
μ_1	Friction coefficient in the Joint	0,6	1

Results from the linear stability analysis.

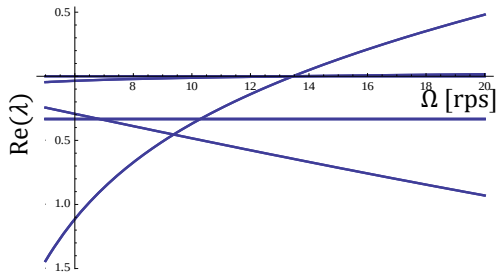


Figure 11: Real parts $\mathrm{Re}(\lambda)$ of the eigenvalues over rotational speed Ω

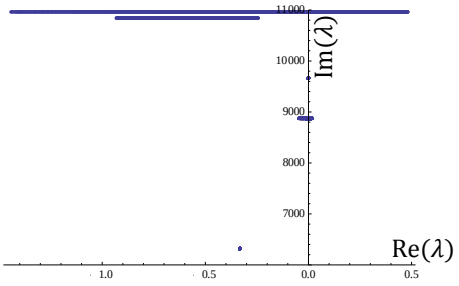


Figure 12: Imaginary parts $\mathrm{Im}(\lambda)$ over real parts $\mathrm{Re}(\lambda)$ of the eigenvalues

International Conference on Engineering Vibration
Ljubljana, Slovenia, 7-10 September 2015

ON THE EFFECT OF THE DISTRIBUTED FRICTION IN THE ARC SPRING ON THE DYNAMIC BEHAVIOR OF THE AUTOMOTIVE TRANSMISSION

Alexander Fidlin*[1], Phillip Mall[2]

[1]Karlsruhe Institute of Technology, Institute of Engineering Mechanics
alexander.fidlin@kit.edu

[2]Porsche AG, Development Drivetrain
philipp.mall@porsche.de

Keywords: Automotive drivetrain, Distributed Friction, Vibrations
Abstract. *Torsional excitation of a combustion engine is usually very strong and requires special solutions for reducing the torsional vibrations in automotive transmissions. Dual mass flywheel (DMF) is one of the most effective devices for this purpose. The main element of the DMF is the "arc spring" which determines the dynamic behavior of the whole system.*
A simplified model of the arc spring is developed. It takes into account both the large deformations of the spring and the distributed friction between the coils of the spring and the wall of the spring channel in the primary flywheel. It is demonstrated that the distributed friction causes extreme nonlinear behavior of the DMF including the distinct memory effect which cannot be described by simplified models of dissipation. The main attention is directed to the modelling of the interaction between the outer and the inner springs which are the usual realization of the bilinear spring characteristic. It is shown that the friction interaction between the springs has to be taken into account in order to obtain realistic results in the overall model of the automotive drivetrain. Especially the "boom" noise of the differential and rattle noise in idle are sensitive for the accurate modelling of the springs.

1 INTRODUCTION

Comfort issues are of significant importance to the automotive industry. Drivetrain including combustion engine and geared transmission is one of the main sources of disturbing noise. Thus, all kinds of efforts are made for minimizing the drivetrain vibrations. Gear rattling is one of the classical acoustical problems in the automotive drivetrains and the most efficient device against it is the Dual Mass Flywheel (DMF) [1, 2]. The core element of the DMF determining the whole dynamics of the drivetrain is the arc spring whose behaviour is strongly nonlinear mainly governed by the distributed friction between the spring coins and the channel in the primary flywheel (cf. Figure 1).

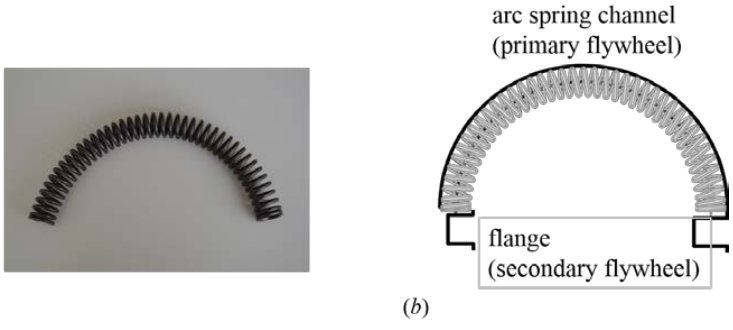


Figure 1: (a) the real arc spring; (b) the model of the arc spring in the channel of the primary flywheel activated by the flange connected to the secondary flywheel.

This paper aims at giving the basic mechanical description of the arc spring and demonstrating the effect of the correct modelling of the friction interactions both between the spring and the channel, and between the inner and the outer spring for “bilinear” arc spring common in some applications.

2 BASIC MODEL OF THE ARC SPRING

The basic properties of the arc spring can be described in a quasi-static continuous model as suggested in [3]. Two types of the modelling are useful for the arc spring. The first one is based on an appropriate discretisation of the spring and its contacts to the channel in the primary flywheel. Such a model is shown in Figure 2 and consists of the usual helix springs and deflecting wedges.

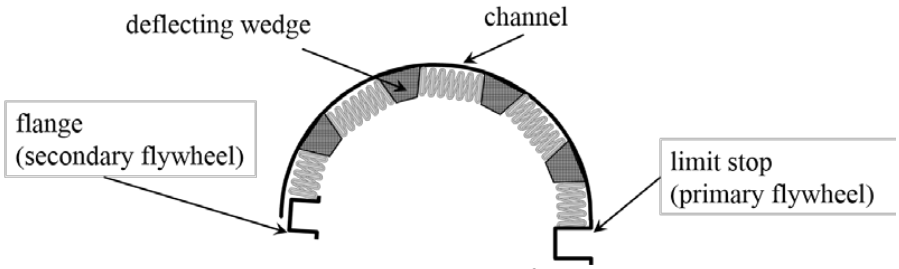


Figure 2: the discretized model of the arc spring.

The number of the elements can be chosen based on the required accuracy of the model. Since each coil of the arc spring is in contact with the channel, the maximal number of the elements is equal to the number of the coils in the arc spring. The mass of the spring can be

considered as concentrated in the wedges, hence the equations of motion for each wedge can be easily formulated as follows (cf. Figure 3):

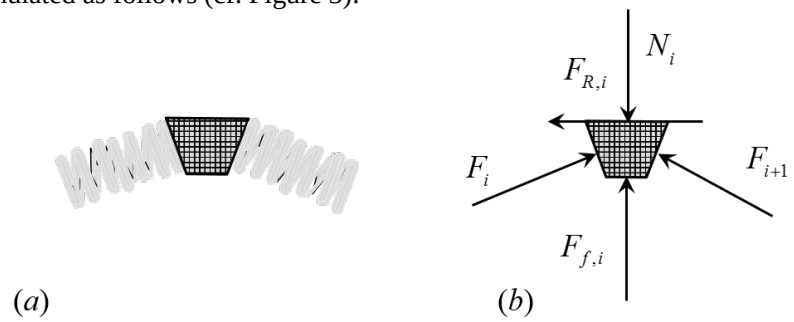


Figure 3: (*a*) the i-th wedge with the adjoining springs; (*b*) the i-th wedge and the applied forces including the reaction forces in the contact with the channel.

$$
\begin{aligned}
&m_{i,eff}\ddot{\varphi}_i + k_{i-1,i}\left(R\left(\varphi_i-\varphi_{i-1}\right)-L_{i-1,i}\right)\cos\left(\frac{1}{2}\left(\varphi_i-\varphi_{i-1}\right)\right)\\
&\qquad -k_{i,i+1}\left(R\left(\varphi_{i+1}-\varphi_i\right)-L_{i,i+1}\right)\cos\left(\frac{1}{2}\left(\varphi_{i+1}-\varphi_i\right)\right)=F_{R,i}\\
&F_{R,i}=-\mu N_i\,\mathrm{sgn}\left(\dot{\varphi}_i-\omega\right) \qquad (1)\\
&N_i = k_{i-1,i}\left(R\left(\varphi_i-\varphi_{i-1}\right)-L_{i-1,i}\right)\sin\left(\frac{1}{2}\left(\varphi_i-\varphi_{i-1}\right)\right)\\
&\qquad +k_{i,i+1}\left(R\left(\varphi_{i+1}-\varphi_i\right)-L_{i,i+1}\right)\sin\left(\frac{1}{2}\left(\varphi_{i+1}-\varphi_i\right)\right)+m_{i,eff}R\dot{\varphi}_i^2
\end{aligned}
$$

The overall characteristic of the spring simulated based on the Eq. (1) is shown in Figure 4.

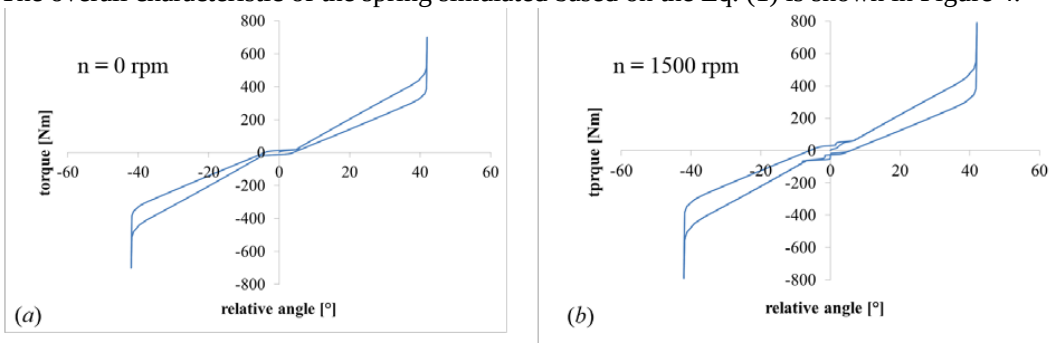


Figure 4: the overall characteristic of the arc spring for different rotation speeds of the flywheel.

However some additional assumptions have been taken into account:

- The springs have been discretised in 6 masses each.
- The basic friction in the bearing between the primary and secondary flywheels has been taken into consideration.
- The finite thickness of the spring wire has been considered; in means that the deformation of each element of the spring is limited by its block length.

The simulations have been performed for both the immobile primary flywheel and slowly oscillating secondary flywheel so that the effects of the centrifugal force are negligible (Figure 4 (a)) and also for the flywheel rotating at 1500 rpm (figure 4 (b)).
The effect which can be noticed in the vicinity of the zero point can be explained as follows. During loading the spring is compressed against its elasticity but also against the friction forces between the spring and the channel. These distributed friction forces are proportional to the normal contact forces which are caused both by the centrifugal forces and by the curvature of the spring middle line or by the angle $\varphi_i - \varphi_{i\pm1}$ in the Eq. (1).
During unloading the friction forces act in the opposite direction and hold the spring slightly compressed in the channel even if there is no more contact between the flange and the spring. If the load direction changes. i.e. the flange comes from the opposite side it meets the preloaded spring and pushes it as a rigid body through the channel until the free end of the spring touches the limit stop (cf. Figure 5).

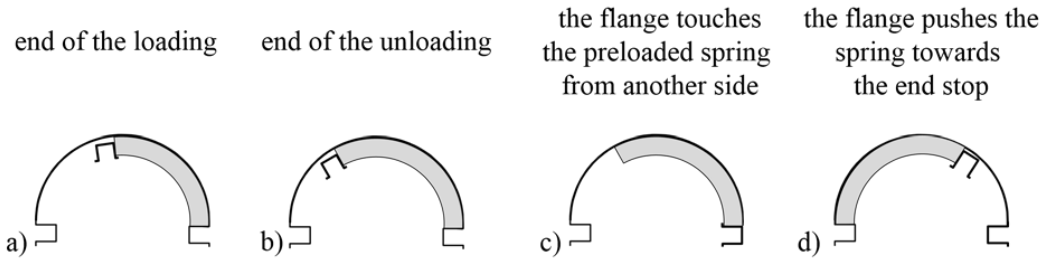


Figure 5: the load history of the spring with the changing load direction.

The numeric results shown in Figure 4 correlate very well with those obtained by the continuous analytical model [3] and with the experimental results published in [1].

3 MODELLING THE INTERACTION BETWEEN OUTER AND INNER SPRINGS IN "BILINEAR ARC SPRINGS"

The described simple arc spring doesn't provide a sufficient isolation in some critical applications. The powerful diesel engines can be mentioned here along with the turbo charged gasoline engines with less than four cylinders. The "bilinear arc spring" is sometimes used in such applications (cf. Figure 6).



Figure 6: (a) the outer and the inner springs; (b) the bilinear spring assembled; (c) the outer spring is longer than the inner spring.

It consists of two arc springs: the outer one with the large coins diameter and the inner one with the smaller coins diameter (Figure 6 (a)). During assembly the inner spring is pushed inside of the outer spring (Figure 6 (b)). The inner spring is shorter than the outer one, hence the last one takes the main part of the load as long as it is sufficiently small. As soon as the load exceeds a certain level, the inner spring also comes into contact with the flange and the effective stiffness of the whole system increases. Thus the characteristics of the spring becomes approximately bilinear.

The described scenario neglects the friction between the outer and the inner spring. However, it is necessary to consider this interaction at least for modelling of the spring's properties at high rotation speeds where the centrifugal forces are dominant.
This task is extremely difficult, because the contact conditions between the deformed coils of the springs are extremely complex and very difficult to calculate.
The simplest possible approach is to replace the spring's assembly by two outer springs which can be simulated independently [4]. The corresponding model is shown schematically in Figure 7. The physically motivated model considering friction between the outer and the inner springs is shown in Figure 8.

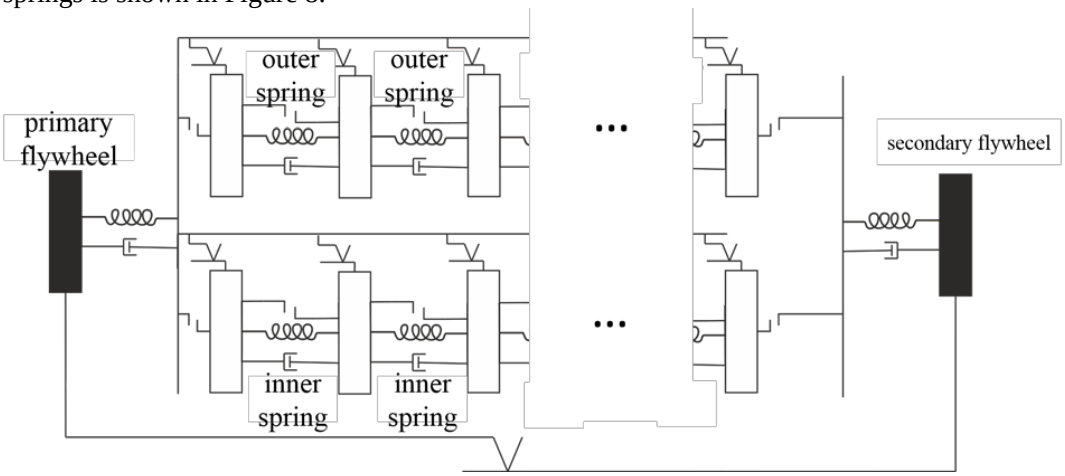


Figure 7: the schematic model of a dual mass flywheel with two "outer springs".

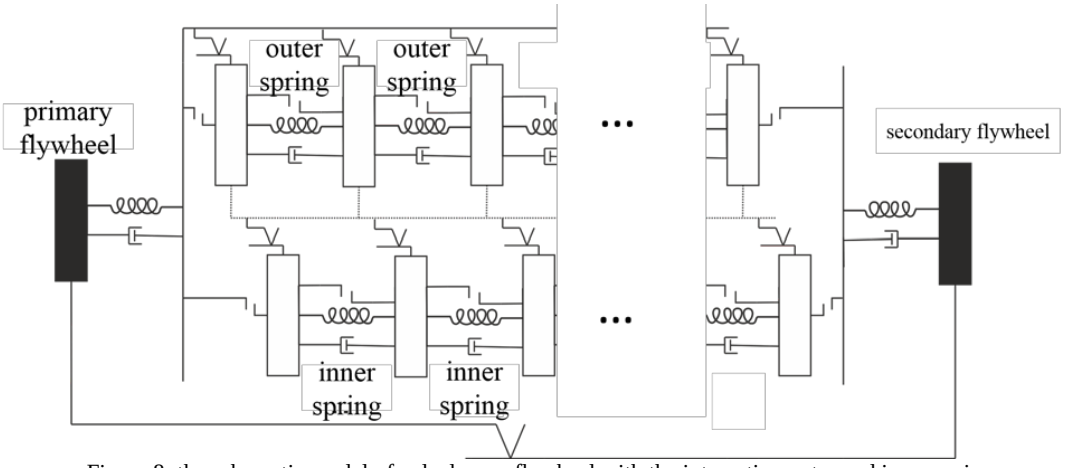


Figure 8: the schematic model of a dual mass flywheel with the interacting outer and inner springs.

In the first model both inner and outer springs interact with the spring channel in the primary flywheel. This is physically incorrect but enables an easy utilization of the existing model and delivers a "visually plausible" bilinear characteristic.
The most important feature of the second model is that there is some kind of a search algorithm enabling to distribute the load from the inner spring to the adjacent elements of the outer spring. Thus, the friction forces are applied on the right position and between the right masses: the additional friction force works against the relative motion between the outer and

the inner springs and not between the inner spring and the spring channel. (The basic friction between the outer spring and the channel is naturally also taken into account).
This model is definitely more realistic than the previous one, but also more elaborate. However it also does not include all effects. The main one is connected to the spatial distribution of the contacts between the inner and outer springs. Both of them are some kind of toroidal helix wrapping and the contact points change rapidly while deforming the springs. This spatial distribution generally increases the friction (due to the simple "wedge effect"). On the other hand it results in a discontinuous jumps of the friction force both in its level and in the spatial position depending on the actual distribution of contact points. This effect is extremely difficult to simulate, thus the main "wedge effect" is often considered by increasing the nominal friction coefficient between the two springs (but not between the outer spring and the channel).

4 THE EFFECT OF THE FRICTION MODEL ON THE STATIC CHARACTERISTIC OF THE SPRING

The next two sections aim at comparing the static characteristics of the described models along with their dynamic behaviour in the complete drivetrain model.
The static characteristics of the spring models are compared in Figure 9.

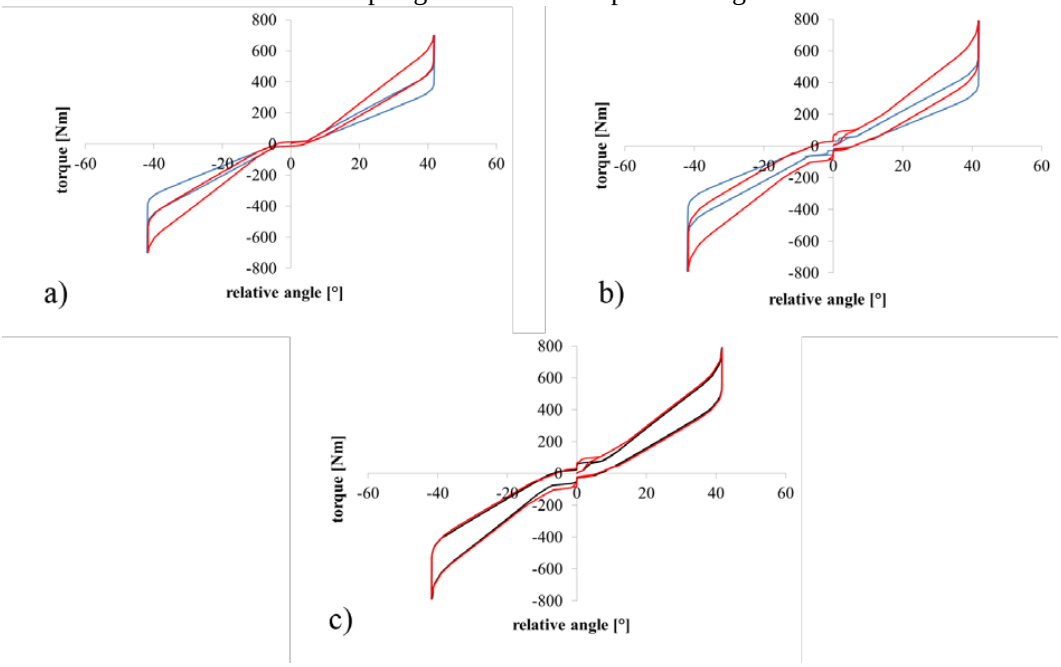


Figure 9: static characteristics of the spring models; (a) n = 0 rpm, only outer spring – the blue line, outer and inner spring – the red line; (b) n = 1500 rpm, only outer spring – the blue line, outer and inner spring – the red line; (c) n = 1500 rpm, outer spring and inner spring modelled as the second outer spring – the black line, outer and inner spring – the red line.

Figure 9 (a) shows the basic effect of the inner spring providing for the bilinear characteristic of the element as a whole. Whereas the red characteristic coincides with the blue one for small relative angles (up to 10°), they diverge for the larger angles. However there is no visible difference between the behaviour of the model with the interacting outer and inner springs

(Figure 8) and that of the model with two outer springs (Figure 7). Thus only one characteristic is shown in the diagram.

The situation changes if the rotation speed of the engine is not equal to zero. Even at the moderate rotation speed of 1500 rpm there is a significant difference between the two models (cf. Figure 9 (b) and (c)). This difference is especially noticeable for small relative angles, where the model with the interacting outer and inner springs demonstrates the larger overall level of hysteresis.

This fact can be emphasized by the comparison between the partial loops of the system obtained for the periodically oscillation load:

$$M = M_0 \sin \omega t;\ M_0 = 100\ \ Nm;\ \ \omega = 1\ \ rad/s \tag{2}$$

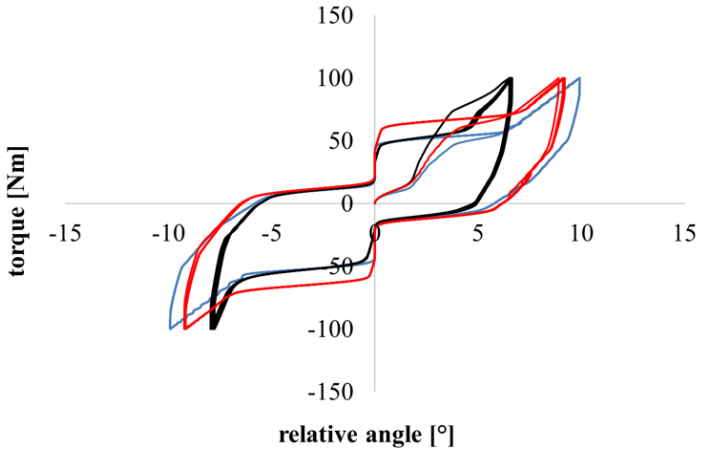


Figure 10: The partial loops in the vicinity of the zero point, the colours are the same as in Figure 9.

The model with two outer springs (the black line) demonstrates the “shortest” loop although the pre-stress and the corresponding torque which is necessary for pushing the whole spring through the channel is slightly lower compared to the model considering the friction interaction between the outer and the inner springs (the red line). The described differences are important for the comfort evaluation of the drivetrain in the idle regime of the combustion engine, which is one of the most sensitive regimes for the drivers [5].

5 THE EFFECT OF THE FRICTION MODEL ON THE ISOLATION OF VIBRATIONS IN THE AUTOMOTIVE DRIVETRAIN

The described models of the arc spring can be implemented into the drivetrain simulation model in order to investigate their influence on the isolation of vibrations during the usual driving. The corresponding model based on that from [3] is shown in Figure 11.

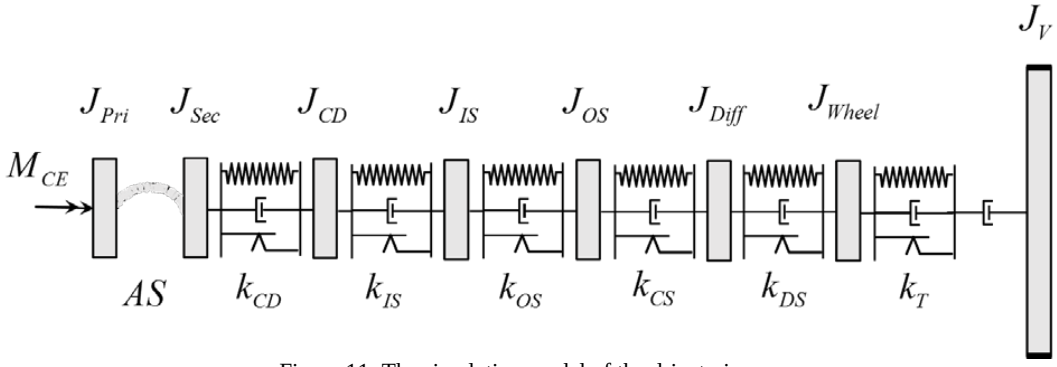


Figure 11: The simulation model of the drivetrain.

The model consists of 8 masses connected to nonlinear elements, including elasticity, linear damping and dry friction. Each of these masses is also connected to damping and friction elements to the inertial space. The last connection isn't shown in Figure 11.

The signs in Figure 11 are as follows:

- J_{Pri} is the inertia of the crankshaft together with the primary flywheel;
- J_{Sec} is the inertia of the secondary flywheel;
- AS is the arc spring between the primary and the secondary flywheel;
- J_{CD} is the inertia of the clutch disc;
- k_{CD} is the force characteristic of the clutch disc;
- J_{IS} is the inertia of the input shaft of the transmission;
- k_{IS} is the force characteristic of the input shaft which is usually linear;
- J_{OS} is the inertia of the output shaft of the transmission;
- k_{OS} is the force characteristic of the output shaft which is usually linear;
- J_{Diff} is the inertia of the differential;
- k_{CS} is the force characteristic of the Cardan shaft;
- J_{Wheel} is the inertia of the wheels;
- k_{DS} is the force characteristic of the drive shafts;
- J_V is the inertia of the vehicle;
- k_T is the force characteristic of the tyres which is usually strongly nonlinear;

The whole system is accelerated by the torque M_{CE} which describes the excitation of the combustion engine. This torque is strongly non-uniform and depends on the position of the crankshaft.

It is common practice to quantitate the amplitude of the oscillating velocity of different drivetrain parts as a measure for evaluating the vibration comfort in the vehicle [2]. The relevant range of the engine speeds for the typical comfort relevant phenomena is between 800 and 3000 rpm. The main disturbing noise in the modern automotive drivetrains with dual mass flywheel is "boom" associated with the resonance of the inertia J_{Diff}. Figure 12 shows the amplitudes obtained by the simulation of the described drivetrain with different models of the arc spring.

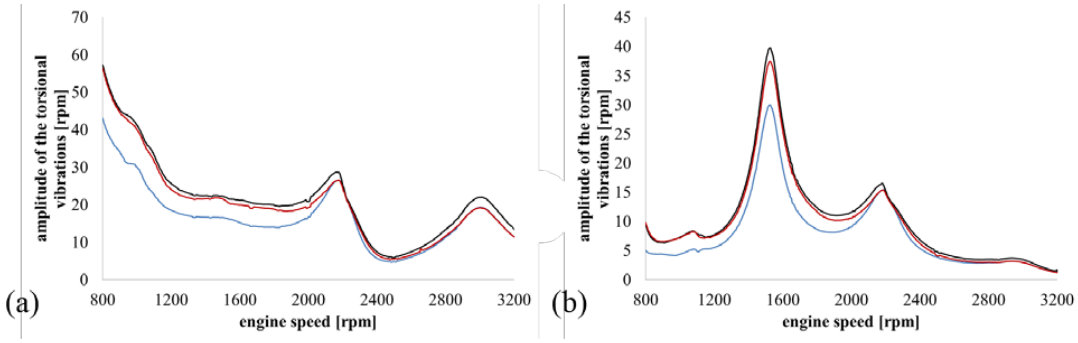


Figure 12: Amplitude of the torsional vibration over the engine's rotation speed during full load acceleration of the vehicle; (a) the amplitude evaluated at the transmission input shaft; (b) the amplitude evaluated at the differential; the colours are the same as in Figure 9.

The most distinctive resonance can be seen in the speed range about 1500 rpm in the velocity of the differential. The difference between the results obtained with different models of the arc spring is quite significant. The lowest resonant amplitude is obtained for the simplest model taking only the outer spring into account. This result is natural, because this model has the lowest effective stiffness. However it is unrealistic, because the simple system with only the outer spring is usually inacceptable due to the problems while starting the combustion engine.

The difference between the two discussed models of the inner spring is also significant. It demonstrates that the simple model with two outer springs overestimate the resonant amplitudes. The model with friction interaction between the outer and the inner springs delivers the intermediate amplitudes although the effective stiffness in this range seems to be the same as in the model with two outer springs. The static force characteristic (Figure 9 (c)) does not explain this difference. Thus the local force loops have to be plotted for better understanding of the results (cf. Figure 13).

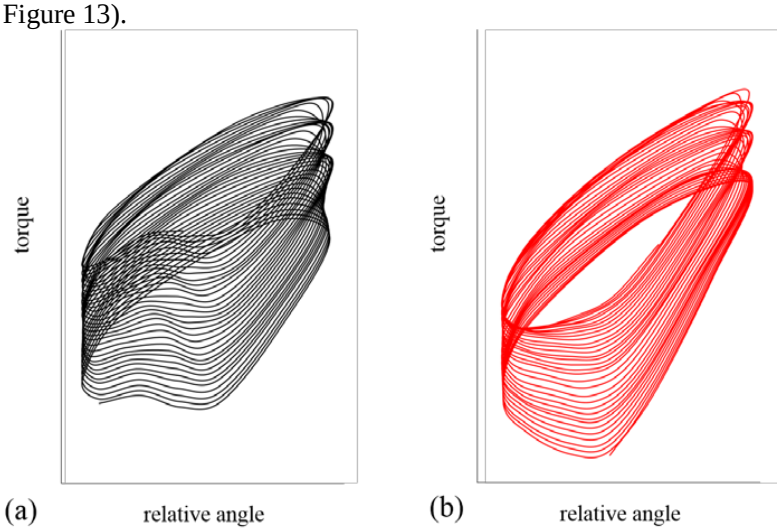


Figure 13: Local force loops in the dynamic simulations in the vicinity of the resonance; (a) the model with "two outer springs"; (b) the model with the friction interaction between the outer and the inner springs.

This figure enables the following interpretation. Although the effective stiffness is in all cases similar, the model with the interacting springs has the lower effective friction than the

model with “two outer springs”. The lower friction in DMF-Systems leads to better isolation in the speed domain beyond the main resonance which is not visible here (it is under the idle speed in the combustion engine). Hence the lower effective friction leads to the lower vibrations amplitude in the critical speed range.

6 CONCLUSIONS

- The basic model of the arc spring has been introduced in order to describe the basic properties of this element.
- Two different simplified models of interaction between the inner and the outer springs in the bilinear arc spring have been discussed and implemented in the simple torsional model of the automotive drivetrain.
- The effect of the modelling of the interaction between the outer and the inner springs have been discussed both for the static force characteristic and for the dynamic behaviour near the resonance corresponding to the “boom” of the differential.
- It is shown that the simple model with two outer springs overestimates the resonant amplitudes.

REFERENCES

[1] A. Albers and A. Krüger, Methodik zur Untersuchung des Übertragungsverhaltens von Antriebselementen am Beispiel eines Zweimassenschwungrads für Kraftfahrzeuge. VDI (Hrsg) Schwingungen in Antrieben 2001 (Würzburg 2001), VDI-Verlag Düsseldorf, 137 – 149, 2001.

[2] D. Balashov, L. Burkovski, F. Ferderer, A. Fidlin, M. Kremer, B. Pennec, R. Seebacher, Simulation bei Drehschwingungsdämpfern“, ATZ 12, 1038 – 1045, 2006.

[3] H. Dresig, A. Fidlin, Schwingungen Mechanischer Antriebssysteme, 3. Auflage, Springer: Berlin – Heidelberg – New York, 2014, 651 S.

[4] A. Fidlin, R. Seebacher, Simulationsgestützte Optimierung von Drehschwingungsdämpfern. In “Systemanalyse in der Kfz-Antriebstechnik III”, Herausgeber: U. Brill, Haus der Technik Fachbuch, Band 44, Expert Verlag, pp. 141 – 159.

[5] R. Fischer, G. Jürgens, F. Küçükay, R. Najork, B. Pollak, Das Getriebebuch, Springer Verlag, Wien – New York, 2012

11th International Conference on Engineering Vibration
Ljubljana, Slovenia, 7–10 September 2015

A MECHANICAL MODEL FOR THE DYNAMICAL CONTACT OF ELASTIC ROUGH BODIES WITH VISCOELASTIC PROPERTIES

Frank Schulte*[1], Jan Neuhaus[2], Walter Sextro[2]

[1]Chair for Mechatronics and Dynamics, University of Paderborn, Germany
Frank.Schulte@uni-paderborn.de

[2]Chair for Mechatronics and Dynamics, University of Paderborn, Germany
{Jan.Neuhaus,Walter.Sextro}@uni-paderborn.de

Keywords: Contact Mechanics, Viscoelastic Material, Adhesive Friction, Hysteresis Friction, Energy Dissipation, Vibration.

Abstract. *The contact between viscoelastic materials e.g. elastomers and a rough surface leads to a special friction characteristic, which differs greatly in its properties comparing to other materials like metals. In practice, this friction combination occurs for example in the tire-road contact, or in the use of rubber gaskets. Due to the frictional forces a system is significantly influenced in its vibrational properties. The friction force is composed of two main components adhesion and hysteresis. The adhesion results from molecular bounds between the contact partners, while the deformation of the viscoelastic material by the roughness of the counter body leads to power loss. This internal friction results in an additional frictional force, which is described by the hysteresis.*

To simulate the frictional behaviour of elastomers on rough surfaces and thus to determine the energy dissipation in contact, it is necessary to develop a mechanical model which considers the roughness of the contact partners, as well as dynamic effects and the dependence on normal pressure and sliding speed. The viscoelastic material behaviour must also be considered. The contact between two rough surfaces is modelled as a rough rigid layer contacting a rough elastic layer. The elastic layer is modelled by point masses connected by Maxwell-elements. This allows the viscoelastic properties of the elastomer to be considered. The behaviour of whole system can be described by equations of motion with integrated constraints. The degrees of freedom of the model depends on the varying contact conditions. A point mass not in contact has two degrees of freedom. A point mass in contact moving along the roughness path can be described by only one degree of freedom. For each Maxwell-Element also an inner coordinate and thus a further degree of freedom is needed. Because of varying contact conditions during the simulation, the simulation interrupts in case the contact conditions change. Then the equations of motions are adapted with respect to the contact constraints.

As a result of the simulation one obtain the energy dissipation and thus the friction characteristic during the friction process. It is possible to use these results in three dimensional point-contact elements in order to model contact surfaces on lager length scales.

1 INTRODUCTION

Friction is the force resisting the relative motion of surfaces sliding against each other. The relative motion in the contact area leads to an energy transformation. The friction converts kinetic energy into thermal energy. Due to this energy dissipation friction plays an important role in dynamical engineering systems. There are different types of dynamic systems. In many systems the friction has to be minimized, so that wear is reduced and the lifetime is increased. On the other hand, there are dynamic systems, where the friction is used to reduce vibration amplitudes or to transmit forces. The reduction of vibration amplitudes leads in an increase of lifetime and safety due to a reduction of alternating stress. Another point is, that the noise development can be reduced, which depends on the vibration frequency and amplitude. For all this reasons, a good knowledge of friction phenomena is necessary to develop an optimized dynamic system.

Viscoelastic materials e.g. elastomers are used in many technical systems. An important field of application is, for example, tire road contact. Driving safety and comfort as well as occurring emissions depend on the contact conditions in the tire contact area. The complex material behavior of these materials results in an special friction characteristic. In the following publication, the elastomer friction is described. Then, the friction characteristics are explained with reference to viscous material properties. A corresponding contact model is presented based on these investigations.

2 ELASTOMER FRICTION

The friction characteristics of viscoelastic materials differ greatly in their properties comparing to other materials like metals. It is not possible to describe these contacts with classic friction laws. Parameter like sliding speed, surface pressure and temperature strongly influence the friction characteristic. Due to the low material stiffness, the elastomer penetrates into the free areas of roughness under normal pressure. This results in a large true contact area compared to other contact pairs, e.g. Steel-Steel. This again leads to high adhesive forces between the contact partners. Due to the material deformation during sliding energy is dissipated in the material which leads to so called hysteresis friction.

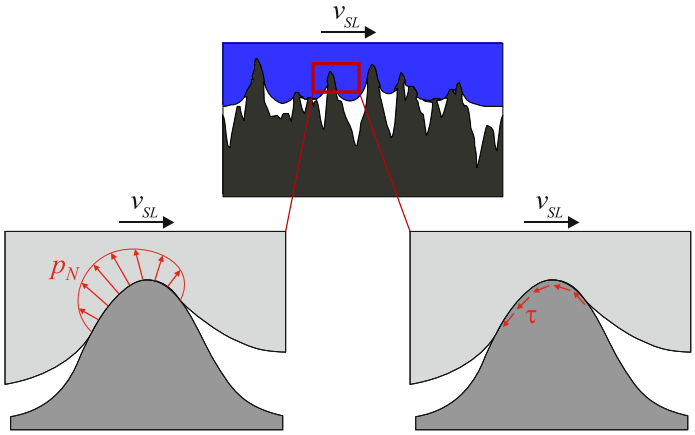


Figure 1: Hysteresis and adhesive friction of viscoelastic materials [1].

Figure 1 shows the two main effects of the friction viscoelastic materials adhesion and hysteresis, which are described in the following.

2.1 Hysteresis friction

The reason for hysteresis friction is the internal damping of viscoelastic materials. During sliding over the rough surface, the material is deformed. Due to the deformations, the material continuously braces and then relaxes again. This process is not adiabatic, so a part of the stored elastic energy is converted into heat. The dissipated energy results macroscopically in an increased frictional force.

The hysteresis friction is deformation-rate dependent. Depending on the roughness, which can be described as self-affine, there is an excitation by various frequencies in contact.These frequencies increase with rising sliding speed. Due to the rate-dependency of viscous properties the dissipated energy and thus the friction coefficient shows a maximum over sliding speed. This maximum is dependent on the wavelength of surface roughness.

2.2 Adhesive friction

Adhesive friction arises due to direct contact of the two friction partners. Between the viscoelastic material and the rough surface intermolecular bonds form, e.g. van der Waals bonds and hydrogen bonds [2]. Molecular compounds can be stretched before they are broken, thereby tension occurs. The constant breaking and formation of bonds is lossy and leads to a sliding resistance. Adhesive friction is directly dependent on the true contact area which again depends on the relative speed. At low speeds, the viscoelastic material can penetrate deeper into the roughness.

3 ELASTOMER PROPERTIES

Hysteresis and adhesive friction can be explained using the mechanical properties of viscoelastic materials. These are strongly dependent on the deformation rate and the temperature. If a sample is excited with a sinusoidal strain ε, results for the stress σ also a sinusoidal profile with a phase shift δ,

$$\begin{aligned} \varepsilon(t) &= \varepsilon_0 sin(\omega t), \\ \sigma(t) &= \sigma_0 sin(\omega t) + \delta. \end{aligned} \tag{1}$$

The relationship between stress and strain can be described by the complex modulus of elasticity E^*. Separation of real and imaginary part leads to

$$E^* = \frac{\sigma^*}{\varepsilon^*} = E^{'} + iE^{''}. \tag{2}$$

The real part $E^{'}$ is called storage module. This module describes the proportion, which oscillates with the excitation in phase. The imagninary part $E^{''}$ is called loss modulus and includes the part which vibrates 90° out of phase with the excitation. The storage and loss module are shown in Figure 2. For small excitation frequencies the storage module is lower compared to high frequencies. Thus the stiffness of the material increase with the frequency. The state above the frequency at which the dynamic stiffening takes place is called glass state. The loss modulus has a maximum in the range of the glass transition.

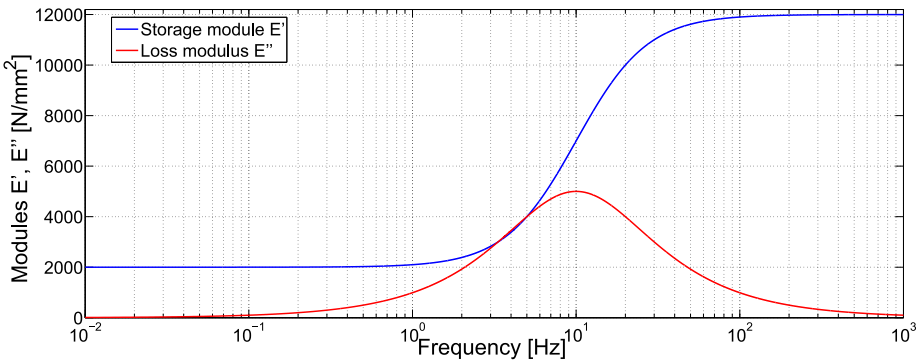


Figure 2: Schematic characteristic of storage and loss modulus.

Considering measured coefficients of friction as a function of relative velocity commonly two maxima are observed [3,4]. One maximum occurs at low speeds another one appears at higher velocities. This curve can be explained by the described effects. The first maximum can be explained by the adhesion. For low speeds the true contact area is large, so that many molecular bonds are formed. At higher velocities the material stiffens and the penetration depth decreases. Thus, the true contact area and the adhesive friction decrease. On the other hand the loss modulus increases, so the hysteresis component of friction increases. Where the loss modulus reaches its maximum, the second maximum of the friction value curve is formed.

To simulate the contact of an elastic body with viscoelastic properties a model is needed that reflects the deformation of the elastomer. For the hysteresis friction the dissipated energy must be calculated in the contact due to these deformations. To calculate the adhesive friction the true contact area needs to be determined. In the following a contact model is presented, which is able to simulate these properties.

4 CONTACT MODEL

The contact model is based on the approaches of [5,6]. The contact between a rough surface and a visoelastic material can be modelled in two dimensions as a rough rigid layer contacting a rough elastic layer. When considering the contact of an elastomer with a hard surface, the stiffness of the hard material can be assumed to be rigid. This is, for example, applicable to the contact tire-road or rubber-steel. As shown in Figure 3, the elastic layer is modelled by discrete elements, while the rigid surface is modelled continuously by cubic splines. The viscoelastic body is reduced to a thin layer modelled by k point-masses.

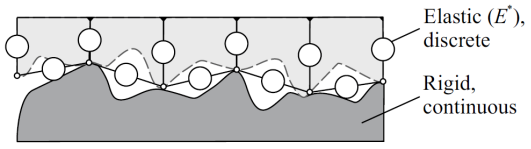


Figure 3: Modelling of two rough surfaces in contact [7].

Figure 4 shows the two dimensional mechanical contact model. The input values for the

roughness of the rigid surface are discrete data points from a computed or measured rough surface. The roughness of the elastic layer is applied as an offset to an initial vertical position of a point mass. The point-masses are connected by spring-, damper- and Maxwell-elements in vertical and horizontal direction. They are also coupled by spring-, damper and Maxwell-elements to the excitation vertically and horizontally. A Maxwell element can simulate the dynamic stiffening of the viscoelastic material as described in the chapter before [8]. The coordinates of the excitation displacement relative to the inertia frame are $u(t)$ and $w(t)$.

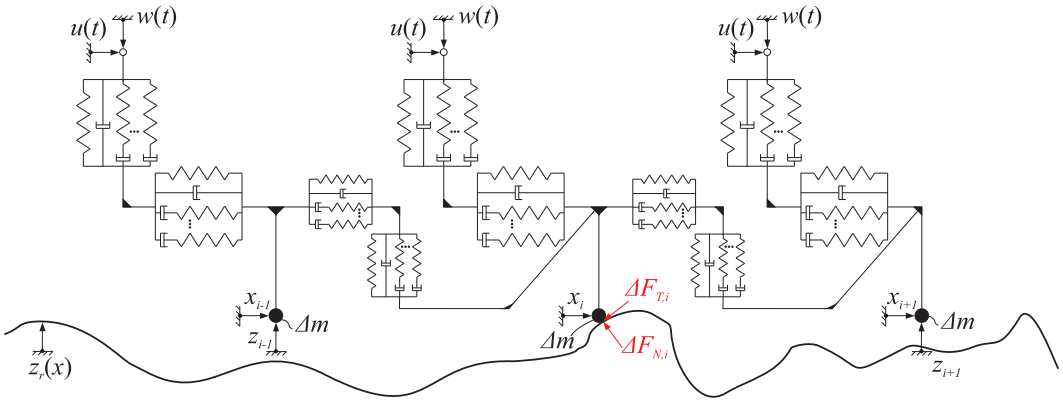


Figure 4: Two-dimensional contact model.

A point-mass without contact has two degrees of freedom, one in the x-direction and one in the z-direction. The equations of motion for an element i are

$$\Delta m_i \ddot{x}_i + F_{c,d,x} + F_{maxwell,x} + F_{c,d,x,l_{i-1\to i}} + F_{maxwell,x,l_{i-1\to i}} - F_{c,d,x,l_{i\to i+1}} - F_{c_{maxwell},x,l_{i\to i+1}} = 0, \tag{3}$$

$$\Delta m_i \ddot{z}_i - F_{c,d,z} - F_{maxwell,z} - F_{c,d,z,l_{i-1\to i}} - F_{maxwell,z,l_{i-1\to i}} + F_{c,d,z,l_{i\to i+1}} + F_{c_{maxwell},z,l_{i\to i+1}} = 0. \tag{4}$$

The equations contain the corresponding spring and damper forces $F_{c,d}$ acting through the external excitation and the adjacent elements on the mass. Furthermore, the force components $F_{maxwell}$ of the n Maxwell-elements are added. The index l describes the coupling between the masses. The number of the Maxwell-elements can be arbitrarily selected, so the model is adaptable to various materials. Every Maxwell element has an internal variable y and is described by a differential equation of 1st order.

Once, an element comes into contact, the equations change. The element can now only move tangentially to the roughness, thus the point-mass has only one degree of freedom.The variable s_i describes the slope at the contact point of the mass Δm_i,

$$s_i = \tan(\varphi_i) = \left.\frac{\partial z_r(x)}{\partial x}\right|_{x=x_i}. \tag{5}$$

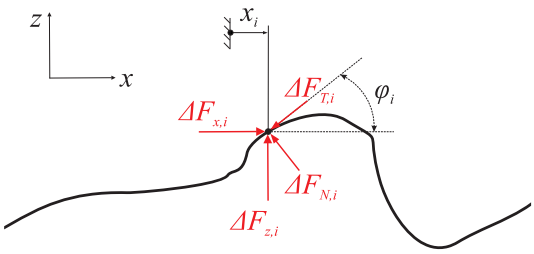


Figure 5: Forces in the contact zone.

The new equation of motion can be derived considering kinematics and the forces acting on the point-mass as depicted in Figure 5. This results in the equations

$$\Delta F_{x_i} = -\frac{\Delta F_{T_i}}{\sqrt{1+s_i^2}} - \frac{\Delta F_{N_i} s_i}{\sqrt{1+s_i^2}}, \tag{6}$$

$$\Delta F_{z_i} = -\frac{\Delta F_{T_i} s_i}{\sqrt{1+s_i^2}} + \frac{\Delta F_{N_i}}{\sqrt{1+s_i^2}}. \tag{7}$$

Rearranging the equation 7 and inserting into equation 6 yields the relation

$$\Delta F_{x_i} + \Delta F_{z_i} s_i = -\Delta F_{T_i} \sqrt{1+s_i^2}. \tag{8}$$

The forces ΔF_{x_i} and ΔF_{z_i} are calculated from the left side of equations 3 and 4. The location of the point-mass in the z-direction and its derivatives are as follows

$$z_i = z_r(x_i), \qquad \dot{z}_i = \frac{\partial z_r}{\partial x}\dot{x}_i, \qquad \ddot{z}_i = \frac{\partial^2 z_r}{\partial x^2}\dot{x}_i^2 + \frac{\partial z_r}{\partial x}\ddot{x}_i. \tag{9}$$

The complete model can described by the system of equations

$$\mathbf{M}\ddot{\mathbf{r}} + \mathbf{D}\dot{\mathbf{r}} + \mathbf{C}\mathbf{r} = \mathbf{B}\mathbf{r}_{\mathbf{exc}} + \mathbf{F}. \tag{10}$$

With the displacement vector

$$\mathbf{r} = [z_1 \ ... \ z_n \ x_1 \ ... \ x_n \ \mathbf{y}]^T \tag{11}$$

and the excitation vector

$$\mathbf{r}_{\mathbf{exc}} = [w(t) \ u(t) \ \dot{w}(t) \ \dot{u}(t)]^T. \tag{12}$$

The vector $\mathbf{y}$ within the displacement vector contains the internal variables of each Maxwell elements. Mass matrix $\mathbf{M}$, damping matrix $\mathbf{D}$, stiffness matrix $\mathbf{C}$ and excitation matrix $\mathbf{B}$ are

divided into separate sub-matrices because these can be generated automatically in Matlab due to their simple structure, with

$$\mathbf{M} = \begin{bmatrix} \mathbf{M_{11}(r)} & \mathbf{0} \\ \mathbf{0} & \mathbf{0} \end{bmatrix}, \quad \mathbf{D} = \begin{bmatrix} \mathbf{D_{11}(r)} & \mathbf{0} \\ \mathbf{D_{21}} & \mathbf{D_{22}} \end{bmatrix}, \tag{13}$$

$$\mathbf{C} = \begin{bmatrix} \mathbf{C_{11}(r)} & \mathbf{C_{12}(r)} \\ \mathbf{C_{21}} & \mathbf{C_{22}} \end{bmatrix}, \quad \mathbf{B} = \begin{bmatrix} \mathbf{B_{11}(r)} & \mathbf{B_{12}(r)} \\ \mathbf{B_{21}} & \mathbf{B_{22}} \end{bmatrix}. \tag{14}$$

The matrices $\mathbf{M_{11}}$, $\mathbf{D_{11}}$, $\mathbf{C_{11}}$, $\mathbf{C_{12}}$, $\mathbf{B_{11}}$ and $\mathbf{B_{12}}$ include the parameters of the equations of motion. The Matrix $\mathbf{C_{12}}$ couples the equations of motion with Maxwell elements. The variables of Maxwell elements are determined by the sub-matrices of the second line. Due to the contact condition of equation 7, the matrices in the first line become position-dependent. Furthermore, due to the contact conditions all matrices are variable in their dimension.

For no point mass in contact, the system has the maximum order $2k + 4kn - 2n$. After applying the contact constraints, the system order and also the system matrices are reduced. The number of internal variables of Maxwell elements remains unchanged, while the degrees of freedom of the masses are variable. The new dimension of the displacement vector is $(2k - k_{contact}) + 4kn - 2n \times 1$.

For simulation the movement differential equations and the differential equations of Maxwell-elements are transformed into a state space. The system equations have the following structure

$$\begin{bmatrix} \dot{\mathbf{r}} \\ \ddot{\mathbf{r}} \\ \dot{\mathbf{y}} \end{bmatrix} = \begin{bmatrix} \mathbf{0} & \mathbf{I} & \mathbf{0} \\ -\mathbf{M_{11}(r)^{-1}C_{11}(r)} & -\mathbf{M_{11}(r)^{-1}D_{11}(r)} & -\mathbf{M_{11}(r)^{-1}C_{12}(r)} \\ -\mathbf{D_{22}^{-1}C_{21}} & -\mathbf{D_{22}^{-1}D_{21}} & -\mathbf{D_{22}^{-1}C_{22}} \end{bmatrix} \begin{bmatrix} \mathbf{r} \\ \dot{\mathbf{r}} \\ \mathbf{y} \end{bmatrix} + \begin{bmatrix} \mathbf{0} \\ -\mathbf{M_{11}(r)^{-1}F} \\ \mathbf{0} \end{bmatrix} + \mathbf{U_{exc}}. \tag{15}$$

The simulation of the contact model is performed using an ODE solver. First of all the corresponding matrices of the state space model are automatically generated in consideration of the initial states. Than the calculation starts with the given initial values and continues until a termination condition is reached. This is the case when a point-contact with the roughness profile comes into contact, or when the normal force of an element becomes equal to zero. The system matrices are adapted to the new contact conditions and initial values. Subsequently, the simulation restarts. Figure 6 shows the simulation process.

5 MODEL RESULTS

In the following, some results of the model are presented. For this purpose, a special case is assumed whereby the model is simplified. The Maxwell-elements are disabled, so only spring and damper act between the masses and the external excitation. In the simulation, a rough rigid surface is vertically pressed against a smooth elastic surface. This process is terminated as soon as a selected nominal pressure is reached. Then a tangential movement of the elastic body on the roughness at low speeds is performed.

Figure 7 shows that the tangential contact stiffness increases when the surface pressure rises. The reason for the increase in stiffness is the higher number of contacting elements. Sliding of all elements is reached when the tangential force no longer increase.

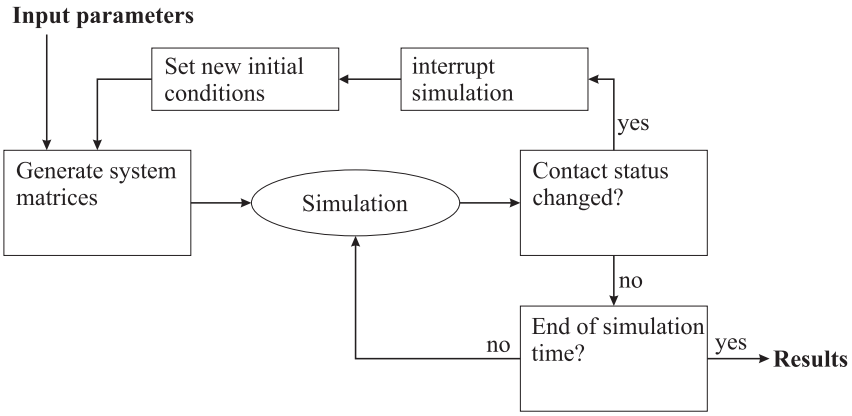


Figure 6: Simulation chart.

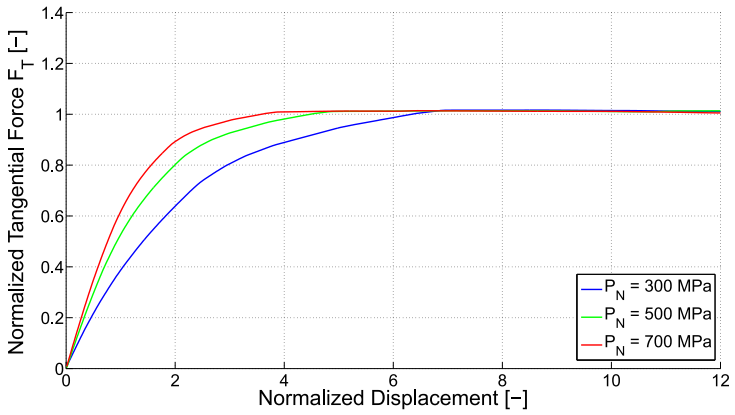


Figure 7: Tangential Force-Displacement Relation.

6 CONCLUSION

Within this work a contact model has been presented to simulate the hysteretic component of rubber friction. The model can discribe the contact behavior on a small length scale. It is possibel to use the results of these simulations for ponit-contact elements, in order to simulate the entire contact surface with unequally distributed normal pressure on a larger scale. For this, the simulation results are stored in lookup tables. The model can correctly represent the viscoelastic material properties, described by the storage and loss modulus. Through the knowledge whether an element is in contact or not, it is possible to draw conclusions about the true contact area. This can be incorporated into an approach for modeling the adhesive friction.

REFERENCES

[1] W.E. Meyer and H.W. Kummer, Die Kraftbertragung zwischen Reifen und Fahrbahn. *ATZ Automobiltechnische Zeitschrift 66, 245–250, 1964.*

[2] P. Moldenhauer, *Modellierung und Simulation der Dynamik und des Kontakts von Reifenprofilbloecken*. Dissertation, Freiberg, 2010.

[3] W. Sextro, *Dynamical Contact Problems with Friction*. Springer Verlag, Berlin, 2007.

[4] B. Lorenz, B.N. Persson, G. Fortunato, M. Giustiniano and F. Baldoni, Rubber friction for tire tread compound on road surfaces. *Journal of Physics: Condensed Matter 25, 2013.*

[5] J. Neuhaus and W. Sextro, A Discrete 2D Model for Dynamical Contact of Rough Surfaces. *3rd International Conference on Computational Contact Mechanics 2013, Lecce, Italy, 51–53, 2013.*

[6] J. Neuhaus and W. Sextro, A Discrete Model for Dynamical Simulation of Normal and Tangential Contact on Rough Surfaces. *Congresss on Numerical Methods in Engineering 2013, Bilbao, Spain, 2013.*

[7] J. Neuhaus and W. Sextro, A Two Dimensional Model for the Dynamical Contact of Elastic Rough Surfaces. *Proceedings in Applied Mathematics and Mechanics Vol.14, 227–228, 2014.*

[8] M. Lindner, W. Sextro, K. Popp, Hysteretic Friction of a Sliding Rubber Element. *Proceedings in Applied Mathematics and Mechanics Vol.4, 101–102, 2004.*

11th International Conference on Engineering Vibration
Ljubljana, Slovenia, 7–10 September 2015

SYNCHRONIZATION VIA DISCONTINUOUS COUPLING

P. Brzeski[1], E. Pavlovskaia[2], T. Kapitaniak[1], P. Perlikowski*[1]

[1]Division of Dynamics, Technical University of Lodz, Stefanowskiego 1/15, 90-924 Lodz, Poland
{piotr.brzeski, tomasz.kapitaniak, przemyslaw.perlikowski}@p.lodz.pl

[2]Centre for Applied Dynamics Research, School of Engineering, University of Aberdeen, AB24 3UE, Aberdeen, Scotland
e.pavlovskaia@abdn.ac.uk

Keywords: Synchronization, Discontinues coupling, Destruction of Solutions.

Abstract. *This paper presents an influence of discontinuous coupling on the dynamics and synchronization of two interacting multistable systems. The model consists of two periodically forced oscillators that can interact via soft impacts. We control parameters two parameters, i.e, the distance between the oscillators and the difference in the phase of the harmonic excitation. When the distance is large two systems do not collide and a numerous of different solutions can be observed in both of them. When decreasing of the distance, after transient impacts the systems settle down on periodic non-impacting attractor. We show that with the properly chosen distance and difference in the phase of the harmonic excitation, we can reduce the number of possible solutions of the coupled systems.*

1 INTRODUCTION

The interaction between impacting systems is nowadays extensively investigated. In many systems like tooling machines, gear boxes, heat exchangers and backlash gear the motion of some elements is limited by a barrier. There are many impact models which give the relations between the interacting system elements. Generally, they can be divided into two groups, i.e., the hard and soft impacts [1, 2].

The numerous works have been devoted to phenomena induced by the the impacts. The bifurcation scenarios and implication of grazing events are quite well understood [3, 4]. There are a few studies which focus on the systems where impacts between coupled oscillators are transient. Blazejczyk-Okolewska *et. al.* [5] show that impacting systems can synchronize (via the exchange of energy during the contact) in anti-phase on chaotic attractor. The impacts can be considered as a noncontinuous transient coupling which disappears once the interacting systems reach the synchronous solutions.

The phenomenon of synchronization is commonly encountered in non-linear systems [6, 7]. We can distinguish many types of synchronous motion. The strongest relation is a complete synchronization where all connected systems perform identical motion [8]. In a phase synchronization the phases of interacting systems are locked while their amplitudes stay uncorrelated [9]. Generally, in coupled mechanical systems one can observe two types of synchronous motion, i.e., the complete and the phase synchronization [10, 11]. As the coupling between mechanical oscillators is always bidirectional; when systems are completely synchronized the value of coupling force is equal to zero, and only if common motion is perturbed the systems once again start to interact. This is the straightforward analogy to the above mentioned noncontinuous transient coupling via impacts, where the perturbation of stable non-impacting solution leads to the appearance of transient impacting motion (coupling).

In this paper we demonstrate the idea and present solution to reduce complexity via transient impacts. We consider systems of two identical oscillators and assume that interaction between them occurs through soft impacts. When the systems are uncoupled we observe multiple stable attractors for each subsystem. Using a piecewise transient coupling to another identical subsystem we can change the number of stable attractors and, in many cases, specify on which attractor both systems settle.

The paper is organized as follows. In Section 2 we consider a simple model which is used to demonstrate the main idea of our approach. Section 3 defines the notations introduced to describe existing periodic states. The numerical resuluts are presented in Section 4 and finally Section 3 presentes the main conclusions.

2 MODEL OF SYSTEM

The system considered in this subsection consists of two identical Duffing oscillators shown in Figure 1. Oscillators in their steady states (at rest) are separated by the distance d , and the impacts which could occur between them are of the soft type due to the presence of a spring with stiffness k_c and a viscous damper with damping coefficient c_c. Two Duffing oscillators have masses M each and are damped by viscous dampers with damping coefficient c. The spring connecting each oscillator to the wall is nonlinear and of hardening type, where both stiffness coefficients are positive: $k_1 > 0$ and $k_2 > 0$. Both Duffing systems are driven by harmonic forces with the amplitude F and the frequency ω but there is a phase shift between these forces. Forcing of the first oscillator has fixed phase (equal to zero) while for the second one there is a phase shift φ which is used as a control parameter ($\varphi \in \langle 0,\ 2\pi)$).

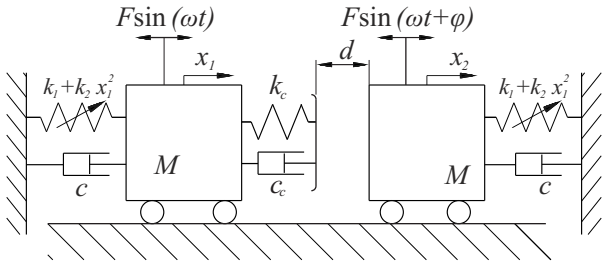


Figure 1: Model of two discontinuously coupled Duffing oscillators.

The whole system is described by the following equations of motion:

$$M\ddot{x}_1 + k_1 x_1 + k_2 x_1^3 + c\dot{x}_1 + F_C = F\sin(\omega t) \tag{1}$$

$$M\ddot{x}_2 + k_1 x_2 + k_2 x_2^3 + c\dot{x}_2 - F_C = F\sin(\omega t + \varphi) \tag{2}$$

where F_C describes the forces generated by the discontinuous coupling and is given by the formula:

$$F_C = \begin{cases} 0 & for \quad x_1 - x_2 > d \\ \\ k_c\left((x_1 - x_2) - d\right) + c_c\left(\dot{x}_1 - \dot{x}_2\right) & for \quad x_1 - x_2 \leqslant d \end{cases} \tag{3}$$

The values of the parameters are as follows: $M = 1.0\,[kg]$, $k_1 = 1.0\,[\frac{N}{m}]$, $k_2 = 0.01\,[\frac{N}{m^3}]$, $c = 0.05\,[\frac{Ns}{m}]$, $F = 1.0\,[N]$, $\omega = 1.3\,[\frac{1}{s}]$, $k_c = 8.0\,[\frac{N}{m}]$, $c_c = 10.0\,[\frac{N}{m}]$, $d = 1.0\,[m]$. Introducing dimensionless time $\tau = t\omega_1$, where $\omega_1 = 1\,[\frac{1}{s}]$, reference length $l_r = 1.0\,[m]$ and mass $m_r = 1\,[kg]$ we transform the equations 1, 2, 3 into dimensionless form in which dimensional parameters are replaced by the following non-dimensional parameters:

$$M' = \frac{M}{m_r},\ k_1' = \frac{k_1 l_0}{m_r\omega_1^2},\ k_2' = \frac{k_2 l_0^2}{m_r\omega_1^2},\ c' = \frac{c}{m_r\omega_1},\ F' = \frac{F}{m_r l_0\omega_1^2},\ \omega' = \frac{\omega}{\omega_1},\ k_c' = \frac{k_c l_0}{m_r\omega_1^2},\ c_c' = \frac{c_c}{m_r\omega_1},$$
$$d' = \frac{d}{l_0}.$$

We perform transformation to the dimensionless form in the way that enables to hold the values of parameters, hence: $M' = 1.0$, $k_1' = 1.0$, $k_2' = 0.01$, $c' = 0.05$, $F' = 1.0$, $\omega' = 1.3$, $k_c' = 8.0$, $c_c' = 10.0$, $d' = 1.0$. For simplicity all of the primes used in definitions of dimensionless parameters will be omitted hereafter in the analysis.

3 NOTATIONS FOR THE PERIODIC SOLUTIONS

We introduce the notations that enable to describe all periodic states of two impacting oscillators, hence we can classify all solutions that can occur in the considered system. To recall, we assume that the left (first) system is a reference system, hence its phase of excitation and position are fixed while for the right (second) system the phase of excitation φ can vary in the range form 0 to 2π and the oscillator's position can be changed to decrease or increase the distance d. The solution of the left oscillator is described in the following way:

$$\mathrm{L}_{pl}^{nl}$$

where: nl is the number of the attractor (in case of multiple attractors of isolated oscillator) and pl is the period of given attractor in respect to the period of excitation (we assume that solutions are periodic). Similarly, the solution of the right oscillator is given by:

$$\mathrm{R}_{pr}^{nr}$$

where: nr is the number of the attractor (in case of multiple attractors of isolated oscillator), pr is the period of given attractor. To define the solution of the interacting oscillators system we will use the following notations:

$$\mathrm{L}_{pl}^{nl}\mathrm{R}_{pr-s}^{nr}.$$

where s is the shift in phase between the systems given by an integer number when the period of solution is longer than the period of excitation i.e, $s = 1$ for 2π shift and so on.

The best example to describe the importance of s is a case when we have two identical systems both with the same period 2 solution (i.e. their response periods are twice longer than the period of excitation). In Poincare map, for both systems, we observe two dots. Let's assume that the position of the first oscillator, at the sampling moment of time, is in one of the dots. Then, the second oscillator can be either in the same position ($s = 0$) or in the second dot when its phase is shifted by one period of excitation ($s = 1$). Number of possible shifts is equal to the greatest common divisor ($\gcd$) of both systems solutions' periods. Let us now consider an example where both oscillators have period 2 and period 5 co-existing solutions. If the first oscillator is on period 2 solution and the second one is on period 5 solution only one configuration is possible because $\gcd(2, 5) = 1$, so we have one possible value of $s = 0$. In the other case where both oscillators have period 4 and period 6 co-existing solutions, the $\gcd(4, 6) = 2$, hence $s = 0$ or $s = 1$.

Figure 2 demonstrates these examples. In Figure 2(a) we show possible configuration for systems with periods 2 and 5. In this case the period of the whole system is equal to 10. The upper row shows the sequence of possible positions of the system with period 2 (1st or 2nd dot on Poincare map), while the lower row presents the possible positions of the system with period 5 (1st to 5th dot on Poincare map). It is easy to see that along one period of the whole system all possible pairs of numbers are created, hence no more states can occur and any shift makes no difference. In Figure 2(b) we show the second example when two possible configurations for systems with periods 4 and 6. The first case for $s = 0$ (upper) where both system start form dot No. 1 (one in the lower and the upper row) and the second case for $s = 1$ when the first oscillator starts motion from dot No. 1 and the second system from dot No. 2. Analysing the graph we see that shifts $s = 0$ and $s = 1$ create all possible pairs of dots on Poincare map.

For example, if each oscillator has only one period 2 solution, the solutions of the interacting system can be described as $\mathrm{L}_2^1\mathrm{R}_{2-0}^1$ and $\mathrm{L}_2^1\mathrm{R}_{2-1}^1$. More examples and the detailed explanations for the possible solutions in the system with co-existing attractors are given in the following sections.

It should be noted that in our investigations we use the relative position of two oscillators on their attractors which depend on the phase shift of excitation φ. Therefore, in the plots each presented solution is marked as

$$\mathrm{L}_{pl}^{nl}\mathrm{R}_{pr-s}^{nr}(\varphi).$$

4 POSSIBLE NON-IMPACTING STATES OF THE CONSIDERED SYSTEM

After defining the notations we can continue the analysis of two Duffing systems introduced at the beginning of this section. For the assumed parameters single Duffing oscillator has two

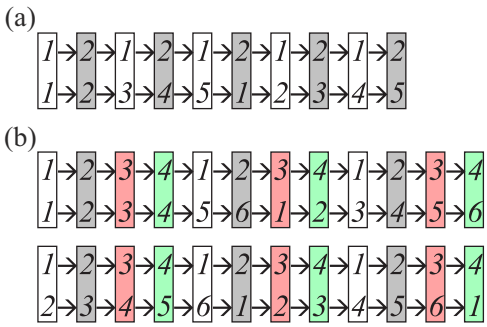


Figure 2: The possible combinations of the system states for (a) period 2 and period 5 solutions and (b) period 4 and period 6.

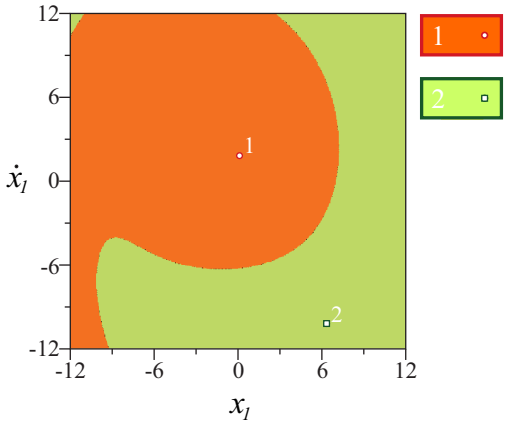


Figure 3: Basins of attraction for one Duffing oscillator. ($M = 1.0$, $k_1 = 1.0$, $k_2 = 0.01$, $c = 0.05$, $F = 1.0$, $\omega = 1.3$).

period 1 solutions with large and small amplitude respectively. Their basins of attraction are shown in Figure 3, where the solution with small amplitude is marked by No. 1 (orange basin) and the solution with large amplitude by No. 2 (green basin). The basins' boundary is a smooth curve so it is clear which attractor is reachable for the given initial condition.

For two identical systems shown in Figure 1, trajectories of two coexisting period 1 solutions on the phase plane are presented in Figure 4 (a) for the following values of the system parameters ($M = 1.0$, $k_1 = 1.0$, $k_2 = 0.01$, $c = 0.05$, $F = 1.0$, $\omega = 1.3$). According to the introduced notation, the solution of the left system can be either the period 1 attractor with small amplitude (small loop) denoted by L_1^1 or the period 1 attractor with large amplitude (large loop) denoted by L_1^2. The dots on small and large loops of the left oscillator's trajectories correspond to the maximum displacements which the oscillator could reach. When the left system is in the point L_1^1 the solution of the right system can be either on the small amplitude period 1 attractor represented by the dot on the small loop or on the large amplitude period 1 attractor (the dot on the large loop) - this corresponds to solutions $L_1^1 R_{1-0}^1(0)$ (red dot) or $L_1^1 R_{1-0}^2(0)$ (green dot). When the left system is in the point L_1^2, the possible locations of the second oscillator are $L_1^2 R_{1-0}^1(0)$ (yellow dot) and $L_1^2 R_{1-0}^2(0)$ (black dot). Note that when the systems are on the different trajectories (the left on the small and the right on the large and vice verse) their positions are shifted in phase without the phase shift in excitation ($\varphi = 0$). The detailed scheme of solutions is shown

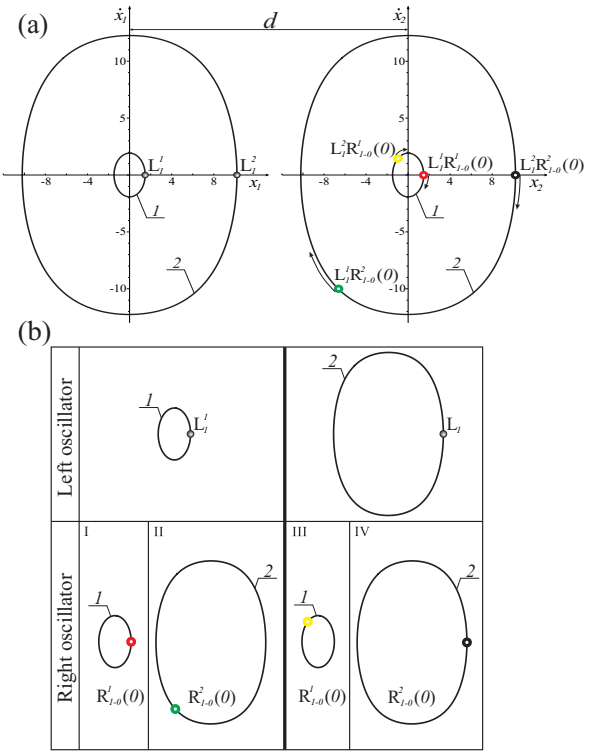


Figure 4: Possible attractors of two Duffing oscillators for in-phase forcing ($\varphi = 0$) (a) and four possible solutions of the system that consists of two Duffing oscillators (b). ($M = 1.0$, $k_1 = 1.0$, $k_2 = 0.01$, $c = 0.05$, $F = 1.0$, $\omega = 1.3$).

in Figure 4 (b).

As we mention before, our controlling parameters are the phase shift of excitation φ and the initial distance between the oscillators. The current distance between the oscillators can be measured as $x_1 - x_2 - d$ and it depends on the relative position of each oscillator along the trajectory governed by the phase shift φ. Impact between the two oscillators occurs when the distance $x_1 - x_2 - d$ is zero or negative. The presence of impacts in the steady state response introduces new types of solutions in the combined system and depending on the values of d and φ destroys the combinations of period 1 solutions described earlier. In Figure 5(a) two parameters plot is presented showing the boundaries for which given combinations of period-1 solutions exist. Considered system has four possible combinations of the solutions and each of them is marked by a different colour. Solution $L_1^1 R_{1-0}^1(\varphi)$ disappears for all values of d and φ which are located below the red line on the graph. For $\varphi = 0$, the critical distance d is equal to zero because the oscillators are moving in phase, so no collision is possible. For $\varphi = \pi$ oscillators move in anti-phase, hence the impact (destruction of given solution) occurs as soon as trajectories start to overlap.

To calculate the boundaries presented in Figure 5(a), the distance between two oscillators needs to be monitored. In Figures 5(b-d) the difference between the displacements of two oscillators $x_1 - x_2$ over one period of steady state motion for $L_1^2 R_{1-0}^2(\varphi)$ solution is shown for three different cases, i.e, $\varphi = \pi/4$, $\varphi = 3\pi/4$, and $\varphi = \pi$. The red triangle marks indicate the maximum difference between the displacements during one period of this solution. As the

impact occurs when $x_1 - x_2 - d < 0$, choosing the critical distances d_{crit} for given phase shifts φ based on these maximum differences, i.e. (b) $d_{crit} = 7.44466$, (c) $d_{crit} = 18.66971$ and (d) $d_{crit} = 20.40519$, would guarantee that for any $d > d_{crit}$, there will be no collisions between two oscillators and therefore this type of solution will exist. For $d < d_{crit}$ the coupled systems interact and the solution is destroyed. As can be seen from these graphs, the critical distance is a function of the phase shift φ.

The graph shown in Figure 5(a) gives us a clear understanding of how the value of the phase shift φ influences the critical distance d_{crit}. As one can expect, the solution that remains stable for the lowest d is the case when two oscillators are both settled on the small attractors ($L_1^1 R_{1-0}^1(\varphi)$). Such solution exists for all values of d and φ above the red line. Two solutions where one system is on small attractor and the second one is on large attractor (yellow and green curves) disappear around $d = 10$ and are mirrored in respect to $\varphi = \pi$. The biggest influence of the shift phase on critical d is observed for solution $L_1^2 R_{1-0}^2(\varphi)$ marked by black line. The Roman numbers printed in each area indicate which types of solutions are present there. All states are possible above all lines and crossing each line causes disappearance of one of them, finally below the red line no non-impacting solution is present.

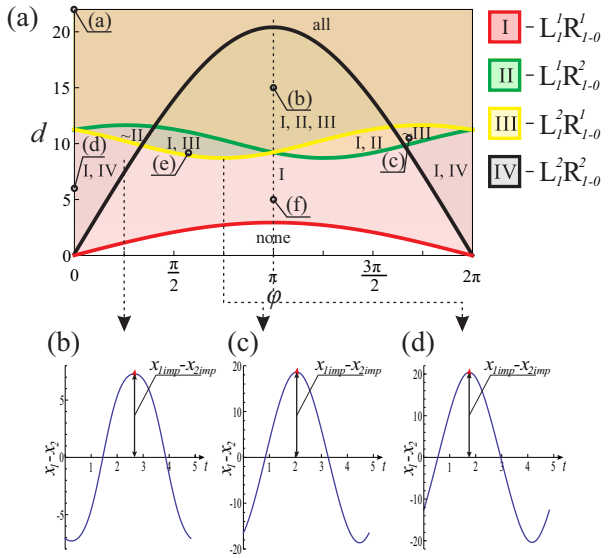


Figure 5: Possible solutions of the system that consists of two Duffing oscillators in the $(d,\ \varphi)$ plane (a). Each type of solution is drawn with line of different color. Subplots (b-d) present trajectory traces of $L_1^2 R_{1-0}^2$ solution in plane (x_1, x_2) for different phase shifts φ, i.e., (a) $\varphi = \pi/4$; (b) $\varphi = 3\pi/4$; (c) $\varphi = \pi$. Red triangles represent the collision points. ($M = 1.0$, $k_1 = 1.0$, $k_2 = 0.01$, $c = 0.05$, $F = 1.0$, $\omega = 1.3$).

In Figure 6 we present six basins of attractions in plane $(x_1,\ x_2)$ calculated for the initial velocities of oscillators fixed to zero, i.e., $\dot{x}_1 = \dot{x}_2 = 0.0$. As the full dimension of phase space is four (i.e. the complete set of initial conditions for the system includes two displacements and two velocities), it is difficult to visualize the basins of attraction for all possible initial states. Therefore, two dimensional cross-sections of the phase space are presented with two most relevant state variables as parameters. Is it clear that in two dimensional projection each oscillator should be represented by one variable. In mechanical systems one can easily control and precisely impose the initial displacements, while such control is impossible or very difficult

for the velocities. Therefore, in the current study the velocities of both systems were fixed as zero and only displacements are varied.

Each basin is computed for different φ and d to show that varying of the phase and the distance between two oscillators changes the number of coexisting solutions. Circles in Figure 5(a) marked by letters (a)-(f) correspond to values of φ and d for which the basins are calculated. Figure 6(a) shows basins for two oscillators calculated for in phase forcing ($\varphi = 0$) and $d = 22$, the boundaries are straight lines and there is no coupling between the systems. When we decrease the distance, oscillators start to interact and one can observe disappearance of one or more solutions. In Figure 6(b) computed for $\varphi = \pi$ and $d = 15.0$, three coexisting solutions are present (Nos. I, II and III). This corresponds to point (b) in Figure 5(a) (below the black line) in plane (φ, d), hence the case where two systems are on big loops is destroyed. In Figure 6(c) one can observe three solutions (Nos. I, III and IV) - disappearance of $L_1^1 R_{1-0}^2(5.28)$. Two next plots correspond to set of parameters for which only two solutions are observed (see Figure 6(d,e)) and the last possibility with just one present solution is shown in Figure 6(f).

It is important to clarify the position of the points marking the different attractors in the Figure 6. As can be seen from this figure, in some cases the attractors shown do not belong to their own basin (i.e. yellow, green and black symbols in Figure 6(a)). This can be explained by the fact that the basins are calculated for the two dimensional projection $(x_1, x_2, 0, 0)$ and the real Poincare section (i.e. values of displacements x_1 and x_2 at moments $t_n = 2\pi n/\omega$) needs to be projected on the chosen plane. The projection of attractor can be then in any place on the two dimensional cross-section, not necessarily within its basin of attraction. Nevertheless, we do not resign form showing attractors because number of dots give information about the periodicity of the solution.

It is interesting to note that in all examples presented in Figure 6, only non impacting solutions were found and the number of them were controlled by the phase shift and the distance between the oscillators. In general, as the distance decreases, the co-existence of the non impacting and impacting solutions becomes likely. For the small distances (below red line given in Figure 5(a)), only impacting solution(s) exist.

5 CONCLUSIONS

In this paper we study the influence of discontinuous coupling on the dynamics of multistable systems. It is shown that with precise selection of the systems' parameters (the gap between the systems or/and phase shift of external excitation) one can easily decrease the number of co-existing solutions via noncontinuous coupling. This idea is verified by performing calculation for Duffing oscillator. When systems are uncoupled ($\forall t \;\; (x_1 - x_2) > d$) there are numerous coexisting non-impacting solutions. When oscillators start to interact we observe impacts. Due to the damper in the stop the energy is dissipated and oscillators settle down on one of the non-impacting solutions and perform the synchronous motion (phase synchronization). The exchange of the energy (impacts) is a transient state lasting up to some minimal distance d for which only impacting solutions are presented. Near the threshold where non-impacting solutions destabilize, one can observe the coexistence of impacting and non-impacting solutions. However, the by the exact selection of stop's parameters we are able to eliminate the impacting solutions. The proposed method is robust and the idea is likely to be applied in gear transmission systems, energy harvesters and in control and danger elimination of impacts between densely located oscillators or structures.

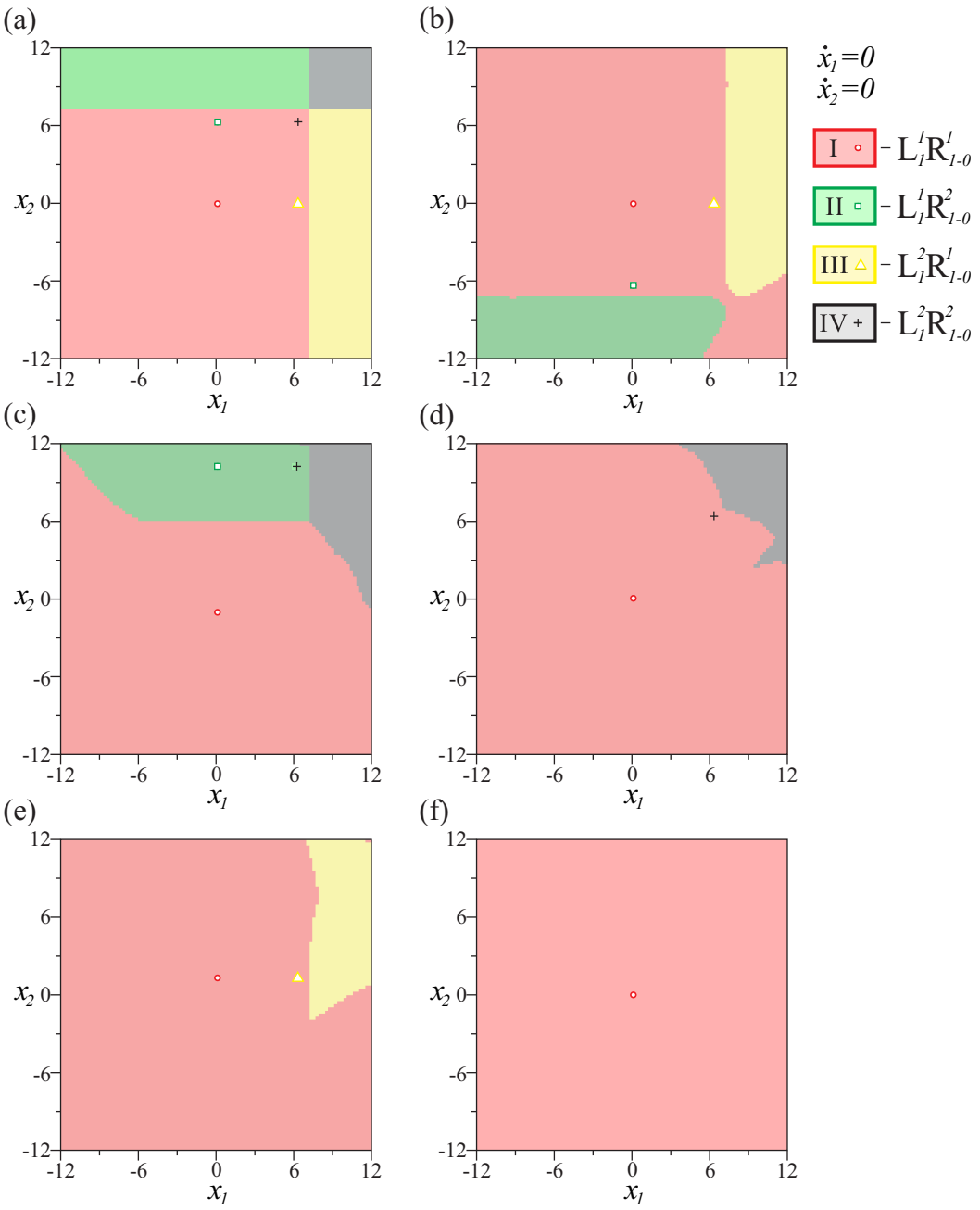


Figure 6: Basins of attraction for two Duffing oscillators for the following values of the system parameters $M = 1.0$, $k_1 = 1.0$, $k_2 = 0.01$, $c = 0.05$, $F = 1.0$, $\omega = 1.3$, $k_c = 8.0$, $c_c = 10.0$ for all subplots except subplot (c) for which $k_c = 10.0$, $c_c = 2.0$. The forcing phase shift and the distance between the oscillators are the following: (a) $\varphi = 0$, $d = 22$ (no impacts); (b) $\varphi = \pi$, $d = 15.0$; (c) $\varphi = 5.28$, $d = 10.5$; (d) $\varphi = 0$, $d = 6.0$; (e) $\varphi = 0.573\pi$, $d = 9$; (f) $\varphi = \pi$, $d = 5.0$. Attractors are marked as dots. Pairs of colours for given attractor and its basin are shown on right side of the figure.

ACKNOWLEDGMENT

This work has been supported by Lodz University of Technology own Scholarship Fund (PB) and by Stipend for Young Outstanding Scientists from Ministry of Science and Higher Education of Poland (PP).

REFERENCES

[1] J. J. Moreau and P. D. Panagiotopoulos *Nonsmooth Mechanics and Its Applications*, Springer Science & Business Media, Udine, 1988.

[2] B. Brogliato. *Nonsmooth mechanics: Models, dynamics and control*, Springer Science & Business Media, London, 1999.

[3] M. Bernardo, C. Budd, A. R. Champneys, and P. Kowalczyk. *Piecewise-smooth dynamical systems: theory and applications*, Springer, 2008.

[4] A. Ganguli and S. Banerjee. Dangerous bifurcation at border collision: When does it occur? *Physical Review E*, **71**, 057202, 2005.

[5] B. Blazejczyk-Okolewska, J. Brindley, K. Czolczynski, and T. Kapitaniak. Antiphase synchronization of chaos by noncontinuous coupling: two impacting oscillators *Chaos, Solitons & Fractals*, **12**, 1823, 2001.

[6] A. Pikovsky, M. Rosenblum, and J. Kurths. *Synchronization. A Universal Concept in Nonlinear Sciences*. Cambridge University Press, 2001.

[7] S. H. Strogatz, D. M. Abrams, A. McRobie, B. Eckhardt, and E. Ott. Theoretical mechanics: Crowd synchrony on the millennium bridge. *Nature*, **438**, 43, 2005.

[8] L. M.. Pecora and T. L. Carroll. Master stability functions for synchronized coupled systems. *Physical Review Letters*, **80**, 2109, 1998.

[9] A. Pikovsky, M. Zaks, M. Rosenblum, G. Osipov, and J. Kurths. Phase synchronization of chaotic oscillations in terms of periodic orbits *Chaos*, **7**, 680, 1997.

[10] I.I. Blekhman, *Synchronization in Science and Technology*, ASME Press, New York, 1988.

[11] H. Fujisaka and T. Yamada, Stability theory of synchronized motion in coupled oscillator systems *Progress Theoretical Physics* **69**, 32, 1983.

[12] P. Brzeski, E. Pavlovskaia, T. Kapitaniak and P. Perlikowski, Controling multistability by discontinuous dissipative coupling. *Submitted*, 2015.

Dynamics Drilling Deep Boreholes - Drillstring and Drillbit Vibrations (MS09)

International Conference on Engineering Vibration
Ljubljana, Slovenia, 7-10 September 2015

AXIAL EXCITATION TOOL STRING MODELLING

Ian Forster*[1]

[1]National Oilwell Varco, Conroe, Texas

United States

ian.forster@nov.com

Keywords: Axial Excitation Tool, String Modelling, Spring Mass Models.

Abstract. *Current types of axial excitation tool have been shown to produce beneficial results – in terms of load transfer to the bit, general reductions in string friction and reductions in drill dysfunctions – such as stick slip.*

The positioning of such tools to achieve optimum benefit is therefore extremely important – in order to maximize the axial excitation to the areas of the string that require a reduction in friction, and also to minimize the axial excitation to the surface and to sensitive string tools (such as MWD)– where damage may occur.

This paper describes a string model that allows the position of axial excitation tools to be assessed – in terms of the string response – both locally and remotely from the tool.

The model breaks the string down in to springs and masses– with 10 nodes in the upper string; and 5 nodes in the BHA. Additional components can also be added to the string – such as shock tools, jars and accelerators – in terms of mass and stiffness. The model is Mathcad based, and as a result, executes very quickly– so allowing comparative studies to be carried out with relative ease. The model has been compared with and ANSYS spring mass model, and good agreement has been reached. Additionally, the model allows more than one axial excitation tool to be added to the string – in order to gauge the benefits of such a configuration.

The results from this model have been used to compare with field test data - derived from a string with instrumentation tool located at various points in the string. The results show that good agreement can be reached between the model and the field test results, however, careful consideration needs to be taken of the damping assumed in the model. The model can, never the less, be used for comparative studies – i.e. tool location, number of tools and optimum frequencies.

Further work is recommended in comparing model results with field test results – in order to get a better understanding of the effect of damping. The damping model could be improved in the model presented here, or alternatively, the lessons learned here could be merged into an existing string model.

Ian Forster

1. Introduction

Axial excitation tools now come in a variety of types, but have become established as a method of reducing drill string friction, improving load transfer to the drilling bit, and also addressing drilling dysfunctions such as stick slip (refs 1 and 2).

The axial excitation generated from the tools has been shown to travel significant distances along the string (ref 3).

The tools can also be used to aid recovery of such items as stuck BHAs and casing components.

However, it is important that the excitation/energy transfer is directed only where it is needed, and does not cause damage to such drill string components as MWDs, other components with electronics and also surface equipment.

Therefore placement of the axial excitation tools is critical.

Up until recently, placement of the tools has been determined by experience/trial and error, and, although this approach is satisfactory for mid and upper string placements – where there are generally no sensitive string tools – for placements closer to BHA components and placements closer to the surface (for shallow fishing operations) requires assessment of the response of the string close to and remote from the axial excitation tool.

The modelling approach in this paper describes a means of determining the string response at different locations.

2. Nomenclature

MWD – measurement while drilling
CAD – computer aided design
BHA – bottom hole assembly
DP – drill pipe
HWDP – heavy weight drill pipe
RMS – root mean squared

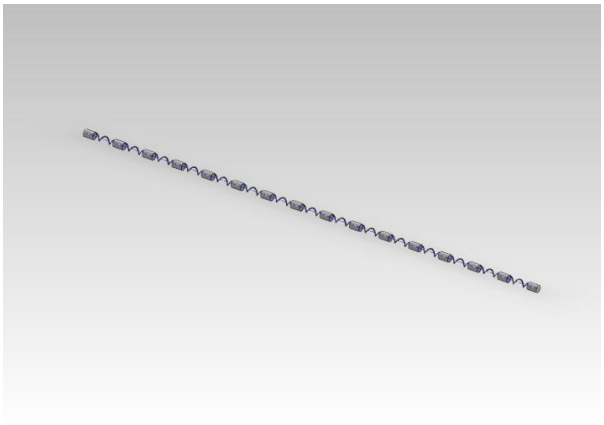
3. Mathcad Model

The modelling approach divides the drill string in to a series of springs and masses – with damping at each mass. This basic approach was described in (ref 4) for fishing/casing pulling specific applications. The difference between the fishing specific approach and this approach, is, that whereas the fishing model only had 3 masses and 3 springs, the model described here has 10 masses and springs for the upper string and 5 masses and springs for the lower string/BHA.

Additionally specific tools can be added to the string – such as shock tools, jars and accelerators. These tools are represented by added concentrated masses and/or added springs. A mass with or without resistance can be added to the bit to represent a casing section.

More than one axial excitation tool can be added to the string if required.

The equation of motion of each mass or node is described as a differential equation, and the equations of motion of all of the nodes are linked by springs connected to each node – fig 1.



$$M \cdot \frac{d^2}{d\tau^2} x(\tau) + c \cdot \frac{d}{d\tau} x(\tau) + k \cdot x(\tau) = 0$$

Fig 1 – spring mass model and equation of motion for each mass M with respect to time τ – x=displacement, c=damping and k=spring stiffness

The 11 differential equations for the complete string are solved simultaneously and numerically in Mathcad (ref 5), and the output, in terms of displacements and velocities and accelerations are represented graphically at each node.

Therefore, the response at different locations in the string can be determined.

An additional modelling approach was used to check the Mathcad model – via ANSYS (ref 6).

In the ANSYS model, the string was also modelled as a series of springs and masses (created as CAD models and in ported into ANSYS) – with the axial excitation tool represented as a harmonic force input.

The response at particular locations can be determined, and an animation of the simulation can be generated.

Good agreement with the Mathcad model was obtained.

4. Case 1

In case 1, the model was tested against already generated field test data in order to determine the effect of damping on the response.

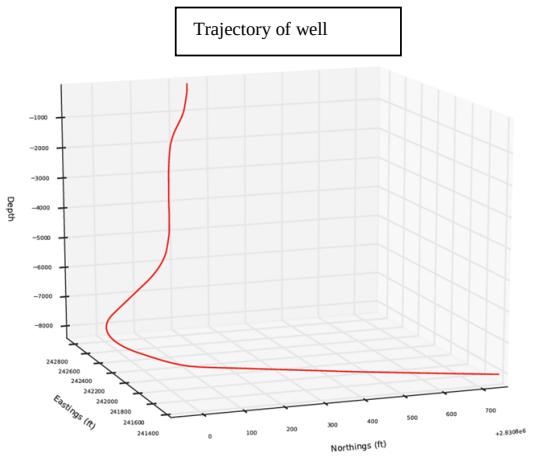
The BHA is shown in fig 2, and comprised two measurement tools in the string (ref 7) – one up hole, immediately above the axial excitation tool, and one downhole from the axial excitation tool approx. 350 feet below. There were also two additional measurement tools in the BHA downhole from the axial excitation tool, but these were in the string to measure whirl.

Case 1 BHA			
Item	Dia in	Length ft	Cum Length ft
PDC	8.5	0.81	0.81
MOTOR	6.75	28.27	29.08
PONY	6.75	14.73	43.81
HELL	6.75	22.22	66.03
NMDC	6.75	30.02	96.05
SLIDE REAMER	8.2	4.94	100.99
WHIRL MEASUREMENT	6.75	4.01	105
XO	7.375	3.63	108.63
HWDP	6.75	276.88	385.51
XO	6.75	3.55	389.06
JAR	6.435	32.18	421.24
XO	7.375	3.63	424.87
HWDP	5.5	92.01	516.88
XO	6.75	3.56	520.44
ACCEL	6.5	31.99	552.43
WHIRL MEASUREMENT	6.75	4.01	556.44
XO	7.375	3.62	560.06
HWDP	5.5	61.11	621.17
DP	5.5	282.66	903.83
MEASUREMENT TOOL	6.75	6.13	909.96
DP	5.5	379.18	1289.14
XO	6.6875	3.1	1292.24
AXIAL EXCITATION TOOL	6.75	12.98	1305.22
SHOCK SUB	6.75	10.47	1315.69
MEASUREMENT TOOL	6.75	7.78	1323.47

Fig 2 – case 1 BHA

Of note is the fact that the lower measurement tool was in DP, and this was found to be in an area of the string that was to affect damping assumptions.

The well trajectory is shown in fig 3 – along with dog leg severity.



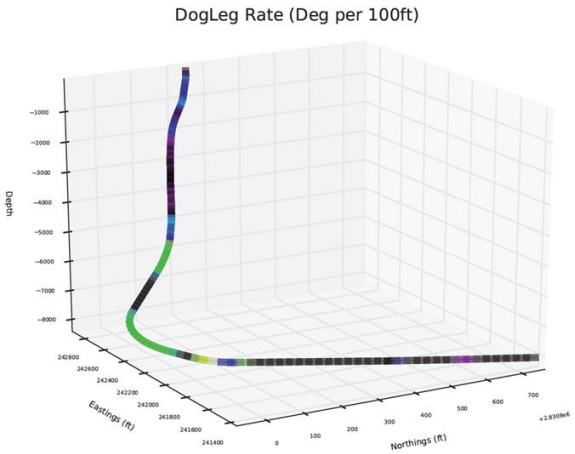
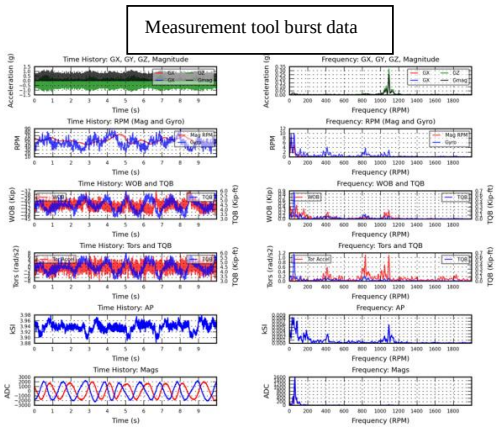


Fig 3 – case 1 well trajectory and dog leg severity

From the results, it was found that, the most significant damping factor for the string was in the vicinity of the lower measurement tool, in the DP - the reason for this being, the fact that the DP would tend to buckle in the build section, and, as a result, the damping would be significantly higher than in other parts of the string. The damping factor was found in this area of the string to be 0.5 – compared to 1.0 for critical damping. Other areas of the string were assigned low damping factors – 0.1 and below.

The field test results at the measurement tool locations are shown in fig 4 – and are plotted at axial g value color contours with frequency over the duration of the test run. The axial excitation tool frequency – 18-18.5 Hz – is dominant, and indicates 0.9 g peak to peak above the axial excitation tool, and 1.0 g peak to peak below the tool. RMS values are shown on the contour plots, but a peak value snap shot during a burst data event is also given.



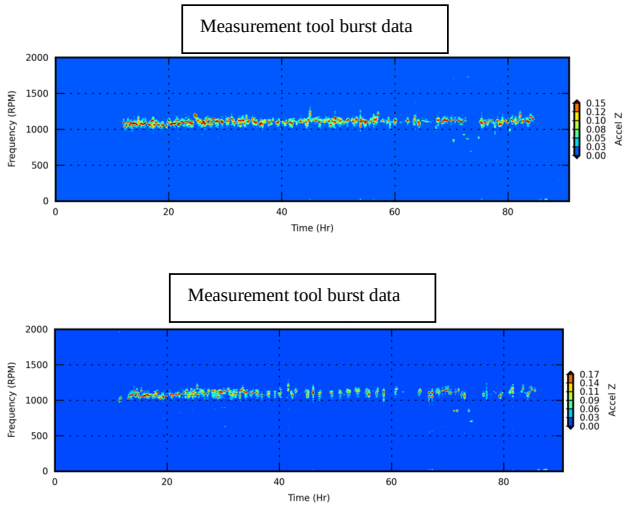
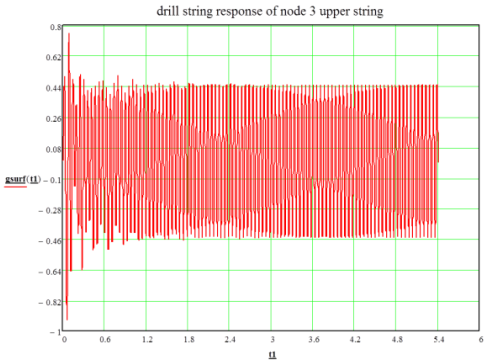


Fig 4 – case 1 field test results

The Mathcad model results are shown in fig 5 – and suggest that agreement can be reached if the damping in the vicinity of the lower measurement tool is increased to reflect the behavior of the DP.



Ems 1



Ems 2

Fig 5 – case 1 Mathcad results

The damping factors in relation to the critical damping were checked by applying a displacement to the model and observing the response – fig 6 – where the response is reasonably close to critical (but tending to be underdamped).

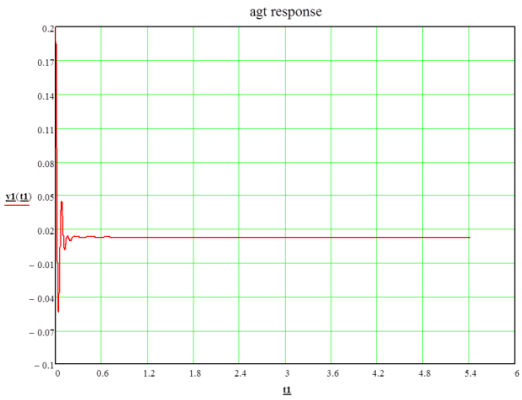


Fig 6 – case 1 critical damping check

Using the information gained with respect to damping factors on this field test, in the following field test, a significantly greater amount of the modelling was done prior to the field test, and the results compared.

5. Case 2

The BHA for case 2 is shown in fig 7, and, as for case 1, has measurement tools - 640 feet above and 620 feet below the axial excitation tool. The lower measurement tool was located just below HWDP.

Case 2 BHA			
Item	Dia in	Length ft	Cum Length ft
PDC	8.5	0.98	0.98
DHM	6.75	30	30.98
NMDC	6.75	15	45.98
IDS	6.75	12.5	58.48
HEL	6.75	18	76.48
NMDC	6.75	30	106.48
Reamer	8.375	8	114.48
XO	7	3	117.48
MEASUREMENT TOOL	6.75	4	121.48
XO	7	3	124.48
HWDP	5.5	279	403.48
XO	7	3	406.48
JAR	6.5	32.58	439.06
XO	7	3	442.06
HWDP	5.5	93	535.06
XO	7	3	538.06
ACCEL	6.5	32	570.06
XO	7	3	573.06
HWDP	5.5	62	635.06
DP	5.5	93	728.06
XO	7	3	731.06
AXIAL EXCITATION TOOL	6.5	11.3	742.36
SHOCK SUB	6.5	11.6	753.96
XO	7	3	756.96
DP	5.5	620	1376.96
XO	7	3	1379.96
MEASUREMENT TOOL	6.75	4	1383.96
XO	7	3	1386.96
DP	5.5	1500	2886.96

Fig 7 – case 2 - BHA

Additionally, in the HWDP was located a jar and accelerator. These were modelled at concentrated springs and masses.

In this case the damping for the BHA was set higher than the rest of the string to allow for the HWDP – set at 0.1 compared with the rest of the string, set at well below 0.1.

The well trajectory is show in fig 8 – along with dog leg severity.

Trajectory of well

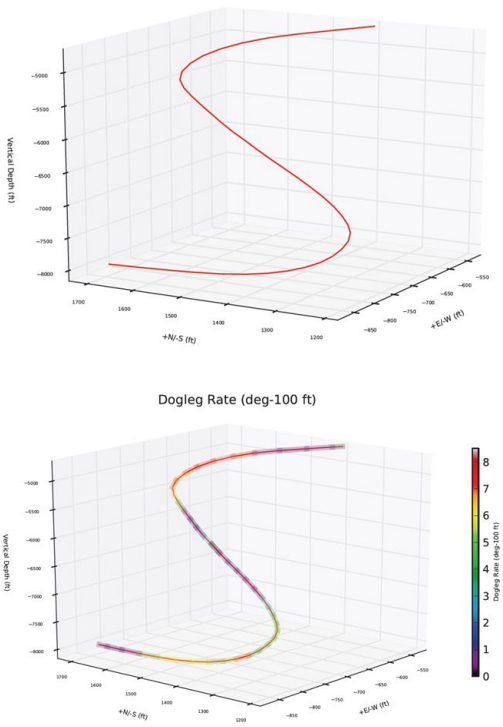
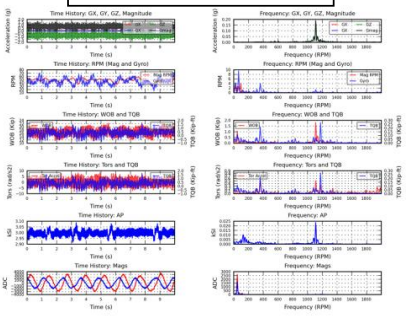


Fig 8 – case 2 well trajectory and dog leg severity

As with case 1, the field test results at the measurement tool locations are shown in fig 9 – and are plotted at axial g value color contours with frequency over the duration of the test run. The axial excitation tool frequency – 18-18.5 Hz – is dominant, and indicates 0.1-0.4 g peak to peak above the axial excitation tool, and 0.06-0.25 g peak to peak below the tool. Again, the contour plots show RMS results, but a peak snap shot is also given.

Measurement tool burst data



Measurement tool burst data

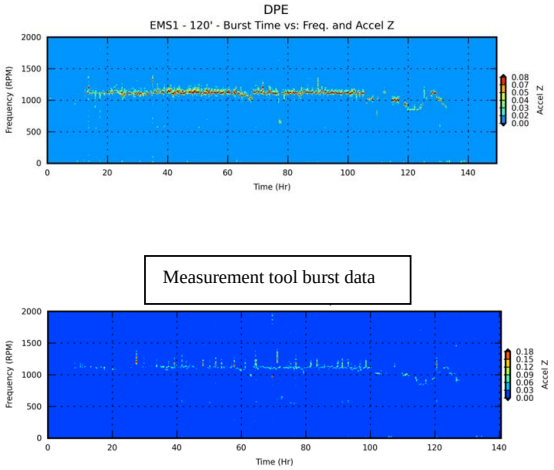


Fig 9 – case 2 field test results

The Mathcad model results in fig 10 show good agreement with the field test results – if account is taken of the increase in damping due to HWDP.

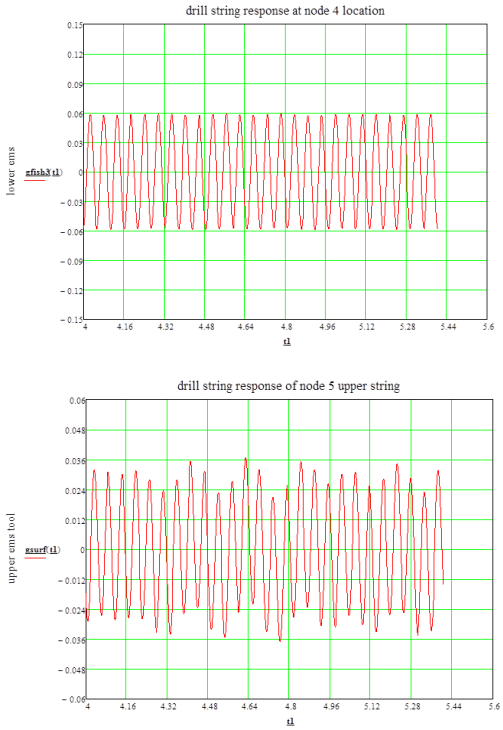


Fig 10 – Mathcad results

Using the knowledge gained in the model comparison, it has also been possible to use the model to predict the potential improvements in response that can be obtained by changes to the string.

These include: moving the axial excitation tool closer the bit; moving the axial excitation tool further from the bit; changing the operating frequency; removing the jar and accelerator; and including a second axial excitation tool – with both tools at the same frequency, and also at different frequencies (with the upper tool more tuned to the upper string natural frequency and the lower tool more tuned to the lower string natural frequency).

These results are shown in table 1 – and indicated the best string response is achieved by two axial excitation tools operating at different frequencies – whilst minimizing the surface response. However, the most desirable response, as far at the customer is concerned, could be determined by the location of sensitive MWD tools close to the bit – i.e. minimizing the response in the vicinity of the MWD and at the surface whilst maximizing response elsewhere. Case 3 is an example of such an application.

Comparison table – g levels with respect to base case – 18.5 hz

Case	Lower measurement tool - MT	Upper measurement tool	Axial excitation tool - AET	Surface	Bit	Node 350 m above upper MT– 2nd AET position	Node 700 m above the upper MT
Base	±0.1-0.2	±0.08	±4.0	±0.005-0.010	±0.1-0.2	±0.016	±0.016
AET 20 m closer to bha	±0.2-0.3	±0.08	±4.0	±0.005-0.010	±0.2-0.3	±0.016	±0.018
Removed jar/accel	±1.1	±0.04	±1.2	±0.005-0.010	±1.1	±0.006	±0.008
Lower freq 13 hz	±0.8-0.9	±0.12-0.18	±3.0-4.0	±0.005-0.010	±0.8-0.9	±0.008-0.026	±0.016
Combined – 20 m closer; removed jar/accel; and 13 hz	±1.0	±0.03-0.04	±1.1	±0.005-0.010	±1.0	±0.009-0.016	±0.006
AET 30 m further from bit	±0.14	±0.1	±3.2	±0.004	±0.14	±0.01-0.02	±0.008
AET 60 m further from bit	±0.18	±0.05-0.1	±3.1	±0.003	±0.18	±0.01	±0.01
AET 90 m further from bit	±0.28	±0.16	±4.8	±0.003	±0.28	±0.01	±0.01
2 AET in phase	±0.13-0.22	±0.08-0.016	±4.0 upper±1.0	±0.005-0.01	±0.13-0.22	±1.0	±0.03-0.06
2 AET out of phase	±0.12-0.21	±0.08-0.012	±4.0 upper±1.2	±0.010-0.028	±0.12-0.21	±1.2	±0.065
2 AET – low freq 13 hz	±0.8-1.0	±0.12-0.18	±3.2 upper±0.75	±0.010	±0.8-1.0	±0.75	±0.05
2 AET different freq – 6hz up; 13 hz down	±0.9-1.2	±0.8-1.2	±3.0-4.0 upper±1.8-2.4	±0.08-0.16	±0.9-1.2	±1.8-2.4	±1.0-1.5

Table 1 – case 2 comparative results

6. Case 3

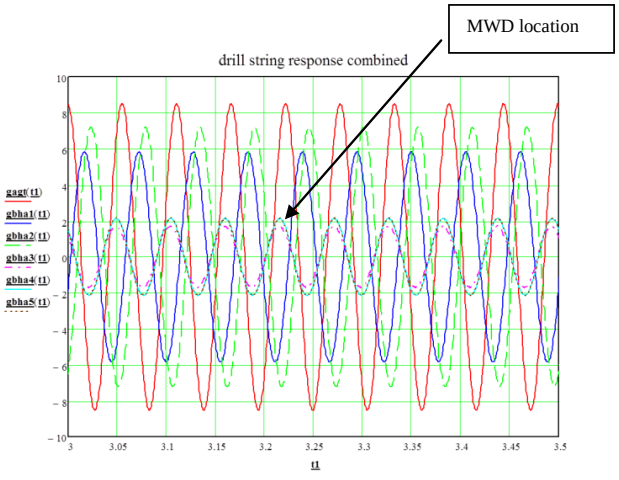
The BHA for case 3 is given in table 2, and shows an axial excitation tool placement proposal - to be located in the 3 ½ DP above an MWD tool.

Case 3 BHA			
Item	Dia in	Length m	Cum Length m
6in PDC Bit	6	0.27	0.27
A475S4535SP	5.875	5.50469	5.77469
Float Sub	4.75	1	6.77469
5 1/2" Stabilizer	5.5	1.524	8.29869
Pony	4.75	4	12.29869
ShortPulse MF	5.25	9.7536	22.05229
4 3/4" NMDC	4.756	9.45	31.50229
Heavy Weight Drill Pipe	4.75	9.27875	40.78104
3-1/2 " 13.30 DPG, Class 2 (50 joints)	5	479.6349	520.41596
Hydra-Jar	4.83	9.4	529.81596
3-1/2 " 13.30 DPG, Class 2 (126 joints)	5	1208.68	1738.49596
X/O	5	0.51	1739.00596
5" 19.50 DPX, Premium	6.1	10	1749.00596

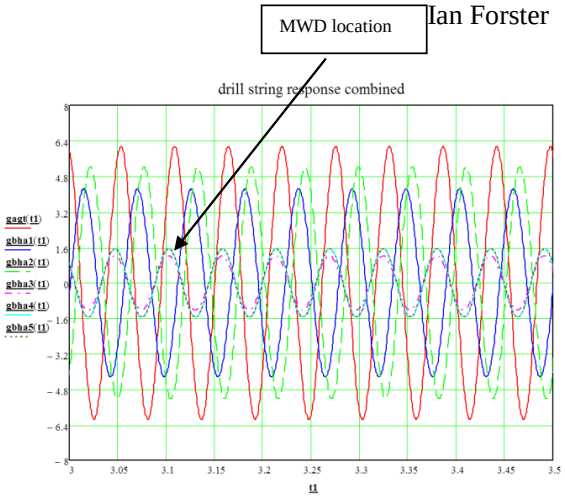
Table 2 – case 3 BHA

For this application, the well trajectory was not as tortuous as the previous two cases, and, as a result, the damping was assumed to be constant throughout the string.

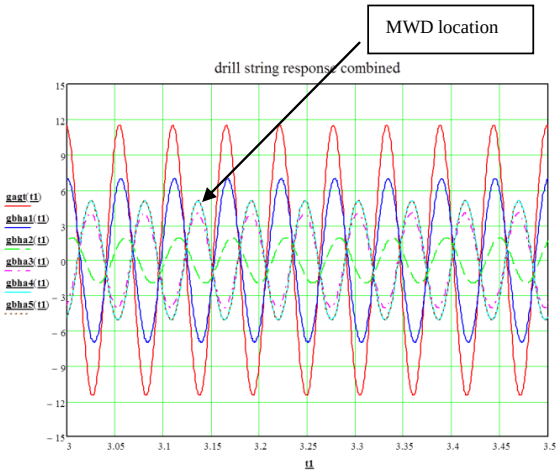
The results in fig 11, show the response at the MWD tool for different axial excitation tool locations – default 300m from the MWD – and for a different shock tool rating.



Low sprung shock tool



Hard sprung shock tool



Low sprung shock tool axial excitation tool 100 m from MWD

Fig 11 – case 3 Mathcad results

The results show that moving that axial excitation tool closer to the MWD results in large g levels at the MWD; whereas increasing the shock tool stiffness above the axial excitation tool will divert energy up hole rather than down hole and result in lower g levels at the MWD.

7. Discussion and Conclusions

From the results presented in the 3 field test cases above, it is shown that the Mathcad string model does produce good agreement with measured results.

However, careful consideration needs to be taken of the damping of the string – particularly at locations where the string is passing though significant build sections with high dog leg severity and with flexible DP or HWDP.

The Mathcad model is also shown to provide results relatively quickly – and so allow comparative studies to be carried out at the pre job planning stage.

Future model developments would include more damping evaluations; and building into the model a damping calculation that accounts for well trajectory and string flexibility automatically. Or alternatively, including/merging the lessons learned in the modelling presented here into existing string models that do account for trajectory and flexibility.

8. Acknowledgements

I acknowledge the help National Oilwell Varco Downhole have given in the preparation of this paper; and I also acknowledge ICoEV2015 for the opportunity to present the work contained within.

9. References

[1] Ian Forster/National Oilwell Varco Downhole Ltd - SPE/IADC 139830 - *Axial Excitation as a Means of stick Slip Mitigation* - Small Scale Rig Testing and Full Scale Field Testing - 2010

[2] J.R. Clausen, A.E. Schen, I. Forster, J. Prill, R. Gee - National Oilwell Varco - SPE 168034-MS - *Drilling with Induced Vibrations Improves ROP and Mitigates Stick/Slip in Vertical and Directional Wells* - 2014

[3] McCarthy, Staines, Clark, Kolker, Leuenberger, Rebellon, Grabski - NOV – IADC/SPE 119958 – *A Step Change in Drilling Efficiency:Quantifying the Effects of Adding an Axial Oscillation Tool Within Challenging Wellbore Environments* – 2009.

[4] Mathcad – hand calculation software v15

[5] ANSYS – FEA software v 14.5

[6] Ian Forster, Robert Grant and NOV Downhole Ltd. - IADC/SPE 151096 *Axial Excitation and Drill String Resonance as a Means of Aiding Tubular Retrieval* - Small Scale Rig Testing and Full Scale Field Testing - 2012

[7] Barton, S., Clarke, A., Garcia, A., Perez, D., NOV/ReedHycalog, Mora, G., Carrion, C., Petroamazonas. 2009. *Improved Drilling Performance: Downhole Dynamic Logging Tools Break Paradigm in Ecuador*. Paper SPE 122208 - 2009

International Conference on Engineering Vibration
Ljubljana, Slovenia, 7-10 September 2015

LOCALIZING THE EXCITATION SOURCE OF HIGH FREQUENCY TORSIONAL OSCILLATIONS

Mathias Tergeist*[1], Hanno Reckmann[2], Michael Neubert[2], Georg-Peter Ostermeyer[1]

[1]Institute of Dynamics and Vibrations, Technische Universität Braunschweig
gp.ostermeyer@tu-braunschweig.de

[2]Baker Hughes CTC
{hanno.reckmann,michael.neubert}@baker-hughes.com

Keywords: Deep Drilling, Self-Excited Vibration, High-Frequency Torsional Oscillation, Instability

Abstract. *Increases in drilling performance and high-bandwidth MWD tools have recently led to the establishment of a new category of drillstring vibration, associated with high loads on the downhole tools, but poor mechanical indication thereof at the surface. High frequency torsional oscillations (HFTO) describe the BHA resonance at a high order natural frequency which corresponds to a mode shape with an anti-node close to the PDC bit. The latter of these points, along with the known weak dependency of HFTO on the WOB and RPM, has led to the hypothesis that the phenomenon is self-excited through bit-rock interaction. Many effects have been discussed in the literature, any of which could potentially be the root mechanism of this excitation. Reliable identification of the root is of high interest towards developing measures to counteract HFTO.*

The three classical categories of self-excitation defined in manufacturing engineering theory are revisited, with regard to their applicability towards drilling: Falling friction characteristics, regenerative chatter vibrations, and mode coupling. The excitation mechanisms that are considered most likely to be the root of HFTO are discussed.

Excitation may be found in the cutting and chip extrusion processes themselves. Rock is commonly understood to experience internal friction, which explains its pressure dependent strength. Friction processes are known to cause self-excitement when large friction forces act on compliant structures, often manifesting itself as squealing. For further analysis, a discrete element method has been developed to model rock at high pressures and high strains. Here, applicability and a high-strain modification are discussed.

1 INTRODUCTION

Throughout decades of drilling dynamics research, a variety of theories about the root cause of stick/slip vibration in deep drilling were proposed and helped develop less susceptible drilling systems and operation awareness. However, the successes of torsional vibration modelling must not detract from the fact that the precise excitation source is not agreed upon.

High-frequency torsional oscillations (HFTO) were noticed through higher bandwidth MWD tools and are part of an active field of research. HFTO differ from stick/slip by affecting a high-order torsional mode instead of the fundamental torsional mode. As justified in [1] HFTO is assumed to be a self-excited phenomenon caused by PDC bits operated in hard low-permeability rocks.

In chapter 2, candidates for excitation sources are compiled that were explicitly published as excitation mechanisms for stick/slip or that are potential excitation mechanisms from a dynamics point of view. In chapter 3, evaluation is presented for a plain bearing theory and the group of rock related theories. In chapter 4, the challenges this problem poses to bonded particle modelling are presented in addition to a lean model extension that enables the application of the method to full rock degradation.

2 SELF-EXCITATION THEORIES: CONCEPTS IN MACHINE TOOL AND DEEP DRILLING RESEARCH

Optimisation of both manufacturing and deep drilling processes aims to stabilise the operation, i.e. the planned steady process is robust against perturbations arising from external and system-inherent sources. In this paper, a planned operation with constant rotary speed (RPM) and weight on bit (WOB) associated with a constant depth of cut (DOC) as the operating point is employed. Technical systems with material and designed damping can develop severe free vibration from instability in absence of external vibration sources (e.g., erratic drive, mass imbalance). Instable processes are characterised by positive feedback to process deviations, which, e.g., is given if rising RPM entails declining resisting torque that causes the RPM to rise even more. This requires power that a certain mechanism transfers from the drive to the vibration. For machine tools, such self-excitation mechanisms were investigated by Daněk [2]; three basic categories are encompassed in elementary literature such as by Milberg [3].

Machine tools	Deep drilling
falling friction characteristic	falling torque characteristic
regenerative chatter vibrations	regenerative coupling
mode coupling	torsional-axial mode coupling

Table 1: Transferring machine tool self-excitation theories to deep drilling.

Although deep drilling's work piece, namely the rock, is inhomogeneous, anisotropic, typically fluid infiltrated and usually uncertainly defined at the time of drilling, close analogies can be drawn (Table 1). The more specific nomenclature from the right column was used for clarity.

$$\begin{bmatrix} m & \\ & \Theta \end{bmatrix} \begin{bmatrix} \ddot{z}_+ \\ \ddot{\varphi}_+ \end{bmatrix} + \boldsymbol{f}\left(\begin{bmatrix} z_+ \\ \varphi_+ \end{bmatrix}, \begin{bmatrix} \dot{z}_+ \\ \dot{\varphi}_+ \end{bmatrix} \right) = 0, \qquad \begin{bmatrix} z_+ \\ \varphi_+ \end{bmatrix} = \begin{bmatrix} z_0 \\ \varphi_0 \end{bmatrix} + \begin{bmatrix} z \\ \varphi \end{bmatrix} \tag{1}$$

Equations of motion in this paper are meant to illustrate the analysis. Therefore, the simplest reasonable case with a single bit mass/node (mass m, rotational inertia Θ) that can

move vertically (coordinate z_+) and rotate around the z_+-axis (coordinate φ_+) is employed in Eq. (1). Therefore, the bit was presumed on center without tilt (lateral influence excluded) and all forces in the system as to be functions $\boldsymbol{f}$ of position and velocity.

The bit motion can be thought of as comprising the operating point where the state variables take values $z_0, \dot{z}_0, \varphi_0, \dot{\varphi}_0$ and deviations in coordinates z, φ. By linearization for the deviations, one obtains Eq. (2) with matrices **D** and **C** holding damping and stiffness parameters.

$$\begin{bmatrix} m & \\ & \Theta \end{bmatrix} \begin{bmatrix} \ddot{z} \\ \ddot{\varphi} \end{bmatrix} + \boldsymbol{D} \begin{bmatrix} \dot{z} \\ \dot{\varphi} \end{bmatrix} + \boldsymbol{C} \begin{bmatrix} z \\ \varphi \end{bmatrix} = 0, \qquad \boldsymbol{C} = \begin{bmatrix} c_{11} & c_{12} \\ c_{21} & c_{22} \end{bmatrix} \tag{2}$$

Contributions to the matrices originate from the drilling system and its interaction with the rock. A simplistic steady-state cutting force model for drag bits adds to the first column of the stiffness matrix which belongs to the DOC: Rock engagement increases the axial stiffness c_{11} and causes torque as described by pseudo-elasticity c_{21}.

For HFTO, the order of magnitude of the vibration amplitude has been estimated based on field accelerometer data [1]. HFTO amplitude has an upper bound defined by bit rest in the minima of $\dot{\varphi}$. Presuming linearity, the amplitudes $\hat{\varphi}, \hat{\dot{\varphi}}$ are dependent on the HFTO frequency; in Eq. (3) separate estimates are given for reasons of clarity.

$$\hat{\varphi} \sim 0.1°, \qquad \hat{\dot{\varphi}} \in [-\dot{\varphi}_0, \dot{\varphi}_0], \qquad \hat{\ddot{\varphi}} \sim 100\ \text{Hz} \cdot 2\pi\hat{\dot{\varphi}} \tag{3}$$

2.1 Falling Torque Characteristics

Torsional self-excitation can be caused by the property of the cutting torque to deliver positive feedback to torsional perturbations. In this case, the instability mechanism can be mathematically described in an uncoupled rotational equation of motion alone.

$$\Theta\ddot{\varphi} + d_{22}\dot{\varphi} + c_{22}\varphi = 0, \qquad d_{22} = \left[\frac{\partial f_2}{\partial \dot{\varphi}_+}\right]_0 = d_{string} + \left[\frac{\partial T}{\partial \dot{\varphi}_+}\right]_0 < 0 \tag{4}$$

In contrast to Eq. (2), axial perturbation is restrained ($z = 0$). An instable process is described if entry d_{22} is negative because of negative slope of bit-rock torque T at the operating point that outweighs the positive damping d_{string} in the drillstring. Self-excitation of this type is determined by the torsional eigen behaviour of the drilling system. Here, self-excited vibration occurs close to the torsional eigen frequency; for more complex models, the most critical torsional eigen frequency can be determined from [4]. Torsional damping is required to suppress vibration.

Most commonly, positive torsional feedback is presented as the outcome of a falling friction characteristic, which is the first of the fundamental instability categories from Table 1. If friction processes at a PDC bit are characterized by a coefficient of friction μ that declines with increasing RPM, falling bit torque is the result in operation at constant WOB. As reported by Brett [5], a falling characteristic is found for the available measure of bit aggressiveness which comprises both frictional and cutting resistance from bit-rock interaction. According to the falling friction theory, high exposure bits run at high weight, i.e. bits with small frictional forces, were expected less prone to stick/slip, which contradicts field tests as performed by Jain [6] and disproves the pure friction approach.

Because cutting torque decreases with decreasing DOC, falling torque characteristics can indirectly result from a mechanism which lowers the DOC at higher RPMs. The resulting bi-directionally coupled equations of motion enable positive torsional feedback through the axial degree of freedom. Systems featuring abundant modal spacing can approximately be viewed

as of the falling torque category because axial eigen behaviour will be negligibly represented in self-excited torsional vibration. HFTO affect high-order torsional eigen modes that typically have close axial counterparts. Coupled torsional-axial vibration therefore must be considered as a source of self-excitation [3], which will be discussed in paragraph 2.3.

2.2 Regenerative Chatter Vibrations

Through DOC variation, axial perturbations cause perturbations of torque. Therefore, a purely axial self-excitation mechanism, if effective, causes persistent forced torsional vibration that is preferably countered by axial damping. In machine tool theory, regenerative chatter can be explained as purely axial.

In turning and milling operations, a singular axial perturbation leaves a bump or wave on the cut surface. When the tool returns to the bump, the DOC is perturbed again, leaving another surface irregularity. Therefore, in a periodic machining process, waviness can amplify and spread on the work piece implicating self-excited axial vibration.

$$\mathrm{m}\ddot{z} + d_{11}\dot{z} + c_{11}z = c_R(z(t) - z(t-\tau)) \tag{5}$$

The mechanism is described in an axial equation of motion with a time delay (Eq. (5)). For clarity, axial stiffness resulting from rock interaction is separated from c_{11} and shown on the right side of the equation as part of the cutting torque term. Accordingly, the DOC depends on axial bit deviation at the time of evaluation and a period τ ago.

Similarly, the cutters on a drag bit leave bumps on the bottomhole and, depending on bit design, a cutter returns to these bumps after a full or partial revolution. Presuming sufficient ductility of the rock, waviness from prior cuts can regenerate. However, for τ to be a constant time delay the RPM is required to be constant, otherwise another case of bi-directionally coupled equations of motion is obtained. In cases of stick/slip, simplifying treatment may be reasonable where large modal spacing is guaranteed. Otherwise, the more general case of coupled torsional-axial vibration must be considered (as analysed by Richard [7]).

2.3 Torsional-Axial Mode Coupling

In machine tool theory, mode coupling can be viewed as an instability mechanism complementing falling friction characteristics and regenerative chatter because it uniquely involves both torsional and axial modes. Under conditions elaborated by Daněk, the stiffness cutting adds to the dynamic system, causes bi-directional coupling and enables synchronization of torsional and axial vibration [2]. The associated modes superpose to a two-dimensional path, on which positive feedback is obtained if the mean DOC is lower on the forward branch ($\dot{\varphi} > 0$) than it is on the reverse ($\dot{\varphi} < 0$) branch.

In drilling systems, the axial degree of freedom, however, is co-linearly aligned with DOC so that with simple cutting force models, torsional perturbation is not reflected in axial motion ($c_{21} = 0$, uni-directional coupling). Thus, for evaluating torsional-axial mode coupling as a source of HFTO, this particular aspect of cutting force modelling is the most crucial. There is little doubt that effects exist, e.g., falling torque and regenerative chatter mechanisms were discussed as potential sources, but their significance for instability remains uncertain.

An intuitive completion of bi-directional torsional-axial coupling is represented by RPM-dependent lift forces at the bit. For constant surface WOB, a reduction of DOC over RPM is the result, which was verified by Brett for a dull PDC bit from full scale laboratory tests under downhole conditions [8]. Laboratory tests typically concern steady drilling (constant or slowly changing RPM) that are representative of HFTO in terms of RPMs. The frequency of HFTO vibration, however, additionally requires very quick DOC adaption to be effective.

Lift forces can originate from mud viscosity, analogously to an axial hydrodynamic plain bearing. In particular on bits featuring rubbing or tracking elements, shallow gaps are formed with the bottomhole that are likely flooded with mud and can enable pressure build-up.

Besides that, literature reports rate dependency of rock in various stages of degradation, from crack initiation to the granular state, usually in the form of strengthening at high cutting rates.

Strengthening can be caused by the pure rock structure. As reviewed by Zhang, rate-dependent rock properties were investigated in dynamic tests, i.a., dynamic triaxial compression tests. The outcome are significant dependence of ductility and strength on strain rate for several rock types that may result of inertial forces impeding crack growth [9].

With advancing deformation, dense rocks experience dilation which causes pore pressure to drop. The effect is used to explain the decline of drilling efficiency over drilling depth. Following Kollé's concept of dynamic confinement, the reduction in pore pressure increases the apparent strength of the rock: the rock appears the stronger, the higher the cutting rate is compared to the re-equilibrating (therefore softening) diffusion rate [10].

When fully crushed, the confined granulate remains strong by virtue of inter-granular frictional forces. Pelfrene suggested viscous pressure build-up in the granular body that is enclosed between cutter face and intact rock by analogy with laboratory shearing experiments in granular networks [11].

An alternate approach explaining DOC reduction was proposed by Richard as part of a stick/slip theory. He considers observed DOC as a mean value of fast axial chatter vibration which increases with vibration amplitude because of non-linearity. For a simplified drillstring and bit model, axial vibration and, therefore, DOC are observed to reduce with increasing RPM [7].

An entirely different class of effects in the cutting process is neither detectable in steady-drilling tests nor is it, to the authors' best knowledge, covered by public drilling models. These effects are governed by inertial forces or require a certain interaction frequency to become effective for drilling dynamics.

Brittle rocks like Carthage limestone form a (quasi-ductile) chip when drilling within downhole conditions. Its considerable confined strength was examined in laboratory tests by Ledgerwood [12]; at the surface, the same chips are easily pulverized between two fingers. The chip's typical lamellar shape documents a discontinuous extrusion process with alternating lock and flow phases. Axial and torsional vibration of the bit, in principle, can interfere and control the transitions if frequent enough and both receive cutting force feedback.

3 EVALUATING SELF-EXCITATION THEORIES

In the previous chapter, two explanations for HFTO excitation were given that do not include specific assumptions about structural cutter-rock interaction. Falling friction characteristics and fluid lift forces are both basic concepts in engineering and they are evaluable for machined interacting surfaces. The significance of the latter is analysed in the first section. The remaining theories include particular assumptions on plastic rock behaviour. In the second section, uncertainties about the rock behaviour are presented.

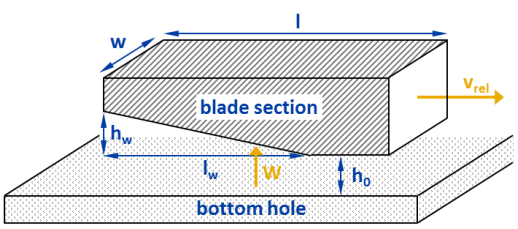
3.1 Plain Bearing Analogy

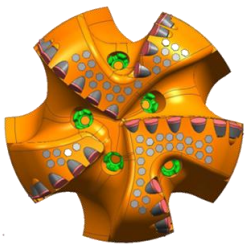
This paragraph evaluates whether DOC reduction can result from hydrodynamic lift forces at the bit nose. Presuming sufficient smoothness of the bit and the bottomhole surfaces and, further, that an effective viscosity is representative of the local non-Newtonian mud, axial plain bearing guidelines (DIN 31653 [13]) can be applied for an estimate. Using Eq. (6) the

maximum gap height h_0 (as shown in Figure 1) is calculated as an indicator of applicability under ideal conditions.

$$h_0 = \sqrt{\eta v_{rel} \cdot Nwl^2 \cdot \frac{\kappa}{W}}, \qquad \kappa = F^{\star}\left(\frac{w}{l}, \frac{l_w}{l}, \frac{h_0}{h_w}\right) \cdot \left(\frac{h_0}{h_w}\right)^2 \tag{6}$$

Herein, η denominates the effective fluid viscosity, v_{rel} the mean relative speed, N, w, l the number, width, and length of bearing sections and W the hydrodynamic lift force. The dimensionless capacity factor κ contains figures from numerical fluid simulations; approximation functions depending on aspect ratios of the bearing sections are provided in the guidelines.





$N = 10$
$l \approx 2$ cm
$w \approx 4$ cm
$\max(\kappa) = 0.138$
$\eta = 50$ mPas
$\Delta v_{rel} = 0.38$ m/s
$\Delta W = 20$ kN

Figure 1: From left to right: Schematic bearing section geometry. Exemplary bit design with large rubbing areas and associated test figures.

Because there are no designated bearing sections, the bit blades inside an 80-mm nose radius are assumed to conform well to the bottomhole by abrasion. Even in worn condition, cutter traces intermit these virtual bearing sections. At best, ten 2x4 cm bearing segments are in use. Pressure buildup requires the gap to narrow over length; the particular wedge geometry is reflected in κ which takes its maximum $\max(\kappa) = 0.138$ (relative wedge length $l_w/l = 0.75$ and relative gap height $h_0/h_w = 0.81$).

As a test case, the idealized bearing setup is expected to deliver a lift force $W > 20$ kN (4.4 klbs) for a significant change in DOC over a delta of 90 RPM ($v_{rel} = 0.38$ m/s) with a high-viscosity drilling mud ($\eta = 50$ mPas). From Eq. (6), $h_0 < 4.6$ µm is obtained, which – given the idealization – for sure must be satisfied. The roughness of a cutter groove was determined after a laboratory single-point cutter test (3,000 psi, oil-based mud, polished cutter) as $R_a \approx 50$ µm in arithmetic average. Consequently, the capacity of fluid pressure build-up is regarded insignificant for a typical drilling process.

3.2 Rock Related Mechanisms

Coupling effects causal for HFTO excitation need to be highly responsive, which moves the focus to the high-frequency dynamics of the rock degradation process. A majority of the compiled self-excitation theories includes specific assumptions on how the rock fails resulting in crucial uncertainties as shown in Table 2.

The inhomogeneous field of strain rates in the rock determines at what rates the rock fails or dilates and is required to estimate the magnitude of viscous forces. The local distribution of those forces around the cutter defines to what extent torque and weight are affected. Regenerative chatter at relevant frequencies requires bottomhole waves mostly shorter than one degree on a bottomhole orbit, which results in bump lengths shorter than two millimetres for all cutters on an 8¾" bit. The formability of the rock and the strength of the waves are uncertain but decisive for the effect. Further it is questionable, whether the chip extrusion

process can be effectively triggered by the drilling system in competition with rock's natural inhomogeneity.

Theory	Rock uncertainty
rate-dependent rock strength viscous pressure equilibration granular viscosity	strain rate field rate significance
regenerative coupling	rock formability
chip extrusion triggering	triggering mechanism

Table 2: Self-excitation theories with corresponding uncertainties about rock behaviour.

4 A PARTICLE APPROACH FOR EVALUATION OF ROCK IN DYNAMIC CUTTING

It was argued that the most promising theories on self-excitement of HFTO through bit-rock interaction include specific assumptions about the rock failure process. These theories were mostly established on experience with drilling and manufacturing and in reference to material properties determined in quasi-static or constant RPM procedures. Recent advances in structural rock cutting simulation shed some light on the rock internal failure process, which to the authors' best knowledge were not checked for consistency with excitation mechanisms. In this last section it shall be discussed what challenges and chances bonded particle methods comprise for the investigation of HFTO excitation. One particular new extension of the tribological particle contact shall be briefly presented.

4.1 Applicability of and Special Requirements to Bonded Particle Methods

A crucial aspect of rock modelling is the dependence of failure mode and strength on the hydrostatic stress; in other words, on confining pressure. With increasing confining pressure, many rocks experience a brittle-to-ductile transition and strengthen. This is commonly understood as an effect of internal friction, which can be imitated in particle methods. Potyondy published a bonded particle method that based on elastic spherical particles and an initial net of bonding beams between neighbour pairs of those reproduces this pressure dependency intrinsically. The particle material obtains shear strength from both the frictional interaction of the particles (grains) and the elastic beam bonds (cement) which fail above a specified shear and tensile load. Isotropy and inhomogeneity of real rock are imitated using normally distributed per-particle (e.g., radius) and per-pair (e.g., bond strengths) properties [14]. Various studies document the potential of the model to match strength and fracturing of rock. Publications cover triaxial compression tests as well as PDC cutting simulations.

In the following, it is presented if similar bonded particle methods are applicable to the investigation of HFTO which are characterised by high frequency and low angular amplitudes. The former property stresses the importance of viscous and inertial forces within the rock and the latter property requires high spatial resolution, both pose typical and special requirements to a bonded particle method.

Fundamentally, distinct element methods are dynamic models, in the sense that particle inertia is considered during simulation. Inertial effects in simulation were reported by Wang who modelled rock strengthening under impact loads in accordance with experiments [15]. In contrast to quasi-static simulations where strong damping can be applied, dynamic evaluation requires realistic damping in the model.

The tangential cutter displacement associated with HFTO vibration lies in the order of the chip thickness. Granular material in front of the cutter can contribute significantly to the

dynamic rock response. Consequently, the material model must capture the full degradation process. The range of length scales from a crushed rock particle to the intermediate cutter chamfer to the full cutter-rock contact requires a large number of particles in the system. A primitive common measure to reduce complexity is the two-dimensional PDC cutter as the simplest meaningful cutting geometry.

4.2 Tribological High-Strain Modification

In this section a lean extension is proposed for two-dimensional bonded particle models to enhance their applicability to states of advanced material degeneration. For clarification of the problem, material degradation without extension is presented in principle using triaxial compression simulations. To disclose the frictional contribution to specimen stress, the results for three numerical rock specimens are contrasted with identical simulations without any beam bonds. In Figure 2 (left) a selection of the obtained stress-strain curves is shown for strains up to 10%. In the case of 2 kpsi confinement pressure (blue), bond failure is concentrated on paths through the specimens that eventually form macroscopic cracks. The rock specimen is split into large chunks, which is brittle failure. Above 2.5% strain, the stress fluctuates approximately two times as high as the stress obtained with the rock powder specimens. In the case of 10 kpsi confinement pressure (red), bond failure spreads over large parts of the specimens, resulting in quasi-ductile barrelling. Above 2.5% strain, the stresses obtained with rock and rock powder specimens remain on a similar level.

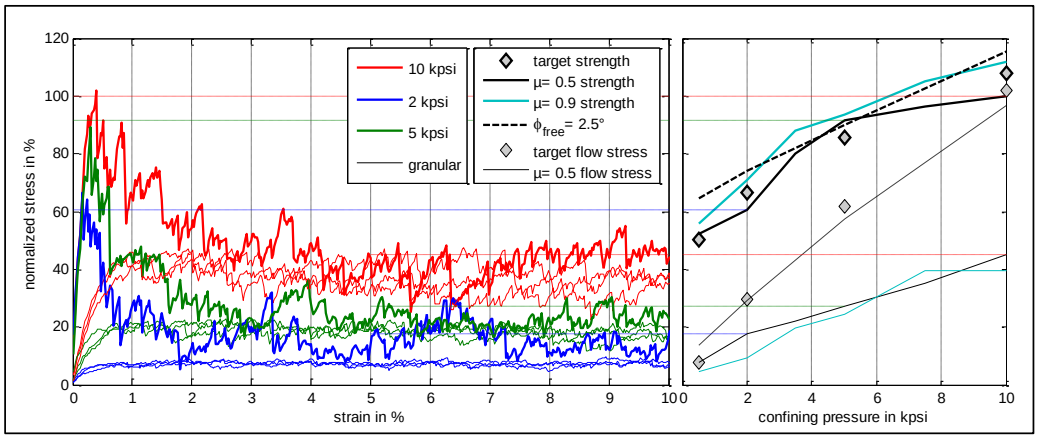


Figure 2: (a) Pressure series of triaxial compression simulations with rock (bold) and granular (light) specimens. (b) Pressure dependence of strength and flow stress for same material (μ=0.5), high-friction material (μ=0.9) and material with high-strain modification compared to target values from tests with real rock (diamonds).

Both, in high- and low-pressure tests, the bonded particle material reaches a stationary state of degradation where bond failure formed shear paths in between chunks or single grains, so that straining proceeds with negligible additional fracturing. Figure 2 (right) shows that for high confinement, the level of the associated stationary flow stress (black) is significantly smaller than for a real reference rock (diamonds). Increasing the coefficient of friction between particles μ from 0.5 to 0.9 does not change the ratio of strength to flow stress significantly (turquoise). This is because sliding resistance is bypassed by free rolling motion when all beam bonds are broken.

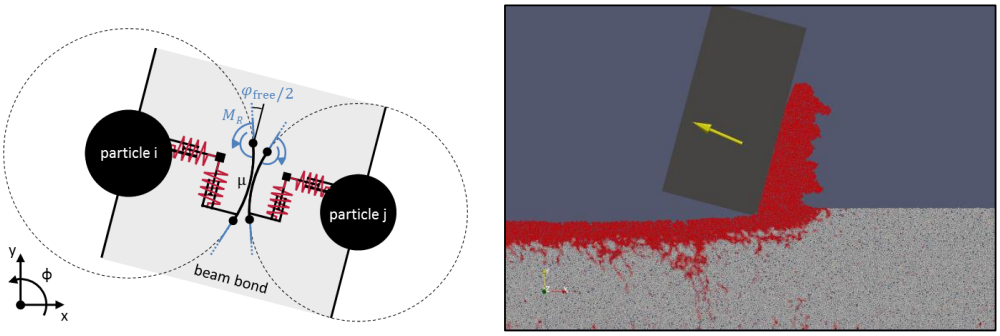


Figure 3: From left to right: Schematics of high-strain modified material. Dynamic single-cutter simulation.

To overcome bypassing, a model extension is proposed following the design principle of bonded particle methods. The behaviour of real pulverized rock depends on the frictional transfer of shear loads through loaded particle contact points and particle interlocking. Rolling resistance in a network of rock grains likely arises from interlocking primarily. It is, therefore, not meaningfully reflected in the basic network of circular particles which aims at efficient neighbour search and evaluation of intersections. Just like for bonding inhomogeneity, a normally distributed property is added to that basic structure. This property φ_{free} measures the angle of relative rotation up to which the surfaces of a grain pair can roll without surface deformation. On either side of the defined free-rolling range, plastic deformation on a sub-particle scale is required and an ideally-plastic constant torque counteracts further rolling (Figure 3, left). Using $\varphi_{\mathrm{free}} = 2.5°$ and a resistance torque $M_R = 22.8\,\mathrm{Nm/m}$ with a particle coefficient of friction $\mu = 0.46$, the flow stress in the fully degraded material remains on a realistic level (Figure 2, right). Plastic shearing of an isolated pair of average diameter particles hereby requires a pair of centroid forces which is four times greater than for sliding under 10 kpsi confinement. The model strengths to reproduce brittle-ductile transition and to simulate strengthening with confinement are not restricted by the modification.

5 CONCLUSIONS AND OUTLOOK

The base-type mechanisms of self-excitation distinguished in machine tool theory are also found in deep drilling and were transferred to the stick/slip phenomenon. Because HFTO affects high-order modes, both, primarily torsional and primarily axial instability merges with the comprehensive category of torsional-axial mode coupling.

The collection of causal mechanisms for HFTO instability is most effectively restricted by the requirement of high responsiveness. Both the friction and hydrodynamic analogue models cannot explain HFTO instability unless used as sub-models towards a larger model of the rock failure process. There is indication that the rock failure process is RPM-dependent and that it interacts with high-frequency vibration.

Bonded particle methods are suggested for numerical investigation of downhole rock dynamics. As one preparation step, a model extension is proposed for matching high-strain flow stresses of rock in steady-state triaxial compression tests. Next steps include simulation of kinematic and dynamic cutting processes under pressure including oscillatory variation of DOC and RPM as shown in Figure 3 (right). An assessment of inertial strengthening and dynamic interaction in representative cutting RPM ranges shall answer whether fluid infiltration of the rock must be included.

REFERENCES

[1] J. R. Jain, H. Oueslati, A. Hohl, H. Reckmann, L. W. Ledgerwood III, M. Tergeist, and G.-P. Ostermeyer, High-Frequency Torsional Dynamics of Drilling Systems: An Analysis of the Bit-System Interaction. *IADC/SPE DC*, Fort Worth, Texas, USA, 2014.

[2] O. Danek, M. Polacek, L. Spacek, and J. Tlusty, *Selbsterregte Schwingungen an Werkzeugmaschinen*. Veb Verlag Technik, Berlin, 1962.

[3] J. Milberg, *Werkzeugmaschinen-Grundlagen: Zerspantechnik, Dynamik, Baugruppen und Steuerungen,* 2nd ed. Springer, Berlin, 1995.

[4] A. Hohl, M. Tergeist, H. Oueslati, J. R. Jain, C. Herbig, G.-P. Ostermeyer, and H. Reckmann, Derivation and experimental validation of an analytical criterion for the identification of self-excited modes in drilling systems. *J. Sound Vib,* **342**, 290–302, 2015.

[5] J. F. Brett, The Genesis of Bit-Induced Torsional Drillstring Vibrations. *SPE Drilling Engineering*, **7**, 168–174, 1992.

[6] J. R. Jain, L. W. Ledgerwood, O. J.-M. Hoffmann, T. Schwefe, and D. M. Fuselier, Mitigation of Torsional Stick-Slip Vibrations in Oil Well Drilling through PDC Bit Design: Putting Theories to the Test. *SPE ATCE*, Denver, Colorado, USA, 2011.

[7] T. Richard, C. Germay, and E. Detournay, A simplified model to explore the root cause of stick–slip vibrations in drilling systems with drag bits. *J. Sound Vib,* **305**, 432–456, 2007.

[8] J. F. Brett, T. M. Warren, and S. M. Behr, Bit Whirl: A New Theory of PDC Bit Failure. *SPE ATCE*, San Antonio, Texas, 1989.

[9] Q. B. Zhang and J. Zhao, A Review of Dynamic Experimental Techniques and Mechanical Behaviour of Rock Materials. *J. Rock Mech. Rock Eng,* **47**, 1411–1478, 2014.

[10] J. J. Kollé, A model of dynamic confinement during drilling in pressurized boreholes. *Int. J. Rock Mech. Min. Sci,* **30**, 1215–1218, 1993.

[11] G. Pelfrene, H. Sellami, and L. Gerbaud, Mitigating Stick-Slip In Deep Drilling Based On Optimization Of PDC Bit Design. *SPE/IADC DC*, Amsterdam, The Netherlands, 2011.

[12] L. W. Ledgerwood, PFC modeling of rock cutting under high pressure conditions. *1st Canada-US Rock Mechanics Symposium*, Vancouver, 2007.

[13] *Plain bearings; hydrodynamic plain thrust bearings under steady-state conditions; permissible operational parameters for calculation of pad thrust bearings*, DIN 31653-3:1991-06.

[14] D. O. Potyondy and P. A. Cundall, A bonded-particle model for rock. *Int. J. Rock Mech. Min. Sci*, **41**, 1329–1364, 2004.

[15] Y. Wang and F. Tonon, Dynamic validation of a discrete element code in modeling rock fragmentation. *Int. J. Rock Mech. Min. Sci,* **48**, 535–545, 2011.

11th International Conference on Engineering Vibration
Ljubljana, Slovenia, 7–10 September 2015

PROPAGATION OF TORSIONAL VIBRATIONS IN DRILLSTRINGS: HOW BOREHOLE GEOMETRY AFFECTS TRANSMISSION AND IMPLICATIONS ON MITIGATION TECHNIQUES

Roman J. Shor*[1], Can Pehlivanturk [1], Behcet Acikmese[1], Eric van Oort[1]

[1]The University of Texas at Austin
roman.shor@utexas.edu

Keywords: Torsional Vibrations, Drillstring Dynamics, Stick-slip, Drilling, Model Analysis, Experimental Dynamics.

Abstract. *Single degree of freedom models have been used extensively to study stick-slip and other torsional vibrations in drill strings over the years and are used in currently deployed vibration mitigation systems. However, these systems cannot account for higher order dynamics, nor can they account for variations in borehole trajectories. This paper proposes a continuous beam model and compares it to an seven-degree of freedom laboratory model to study the effects of drillstring-borehole contact, modeled as distributed damping, on the propagation of torsional waves. By modeling the drillstring as a transmission line, the borehole environment, including borehole fluid, material hysteresis and friction, can be abstracted as distributed damping acting on each model element. The model is first applied to simplified test cases before being used to predict how borehole geometry may complicate the detection of stick-slip at the surface. A demonstration case of an S-shaped well is presented that illustrates how stick slip may be present at the bit without the typical torque and rpm fluctuation signature visible at the surface. An improved controller, based on frequency domain loop shaping techniques, shows that effective in drill-string vibration mitigation can be achieved.*

1 INTRODUCTION

Significant strides have been made to understand the dynamics of of drill strings within boreholes, but the models used for control purposes remain grossly simplified and often cannot capture higher order dynamics. Conditions have been observed in the field where current surface torsional vibration mitigation systems are ineffectual, including in deviated wellbores. This paper proposes to study the effects of well path, wellbore tortuosity, and drillstring composition on the transmission of torsional vibration signals from the bit to the surface by abstracting these distributed effects as damping terms within the lumped mass model. It will conclude with the proposal of advanced mitigation technique from surface based on frequency domain loop shaping.

1.1 Motivation

The underlying goal of control system design is to match an output, y, to a reference signal, $R(s) = \mathcal{L}\{r\}$, while rejecting any disturbances to the system, $D(s) = \mathcal{L}\{d\}$ and reducing the effect of noise, $N(s) = \mathcal{L}\{n\}$, in sensor readings. In the basic control system loop shown in figure 1, the frequency domain output $Y(s) = \mathcal{L}\{y\}$ is given by the expression

$$Y(s) = SL(R - N) + SPD$$

where the sensitivity S is given by

$$S = \frac{1}{1 + C(s)P(s)}$$

and $C(s)$ is the control system and $P(s)$ is the plant

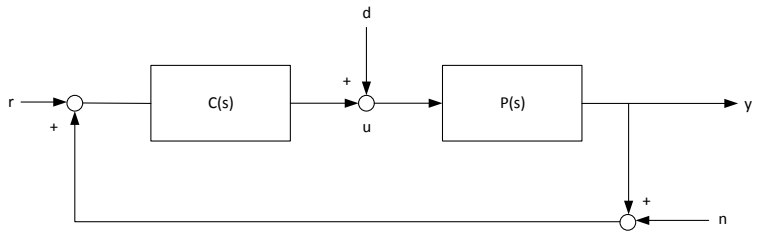


Figure 1: A basic feedback control loop, with r being the reference and y being the output. d and n are the disturbance and sensing noise, respectively.

To design high-order, high performance controllers, we need high order models with better accuracy. However, this requires knowledge of physics of the plant, the drillstring in this case, which is hard to quantify. Existing systems model the drillstring as a lumped mass and torsional spring, as in the case of SoftTorque and SoftSpeed [1, 2, 3], or as a transmission line [6] and treat the wellbore geometry, bit rock interaction, and friction as disturbances to the system. Many of these can be estimated, both during the drilling process or prior during the well planning process, and their incorporation into the plant model would allow for improved controller design.

2 Methodology

The mathematical model of the the drillstring is presented first, both in time and frequency domains, and includes a discretized implementation as both the damped wave equation and a mass-spring-damper system. The model is then be compared to a simple laboratory setup to verify model mechanics. Finally, a control methodology is proposed that successfully mitigates stick-slip in situations where current systems face difficulties.

2.1 Mathematical Model

The drillstring is modeled using the one dimensional damped wave equation and incorporates complexities using boundary conditions and distributed damping. As described by Lee [4], the primary sources of damping are: viscous damping from the borehole fluid, material hysteresis, radiation of energy into the formation, and frictional damping. All of these except for friction can be considered constant along a drillstring. Friction between the drillstring and wellbore is a function of borehole inclination, tortuosity of the wellbore, the existence of ledges or other points of wellbore contact, and the drillstring design, namely the placement of stabilizers.

The angular displacement of the drillstring, ϕ, may be described using:

$$\frac{1}{v^2}\frac{\partial^2\phi}{\partial t^2} = \frac{\partial^2\phi}{\partial x^2} - \frac{D(x,t)}{GJ(x)}\frac{\partial\phi}{\partial t} \tag{1}$$

where $v^2 = \frac{G}{\rho}$ is the wave velocity, D is the damping and J is the moment of inertia. The general model consists of n beam elements, each described by the wave equation, bounded by a surface impedance, representing the top drive, and a bit boundary, representing bit-rock interaction.

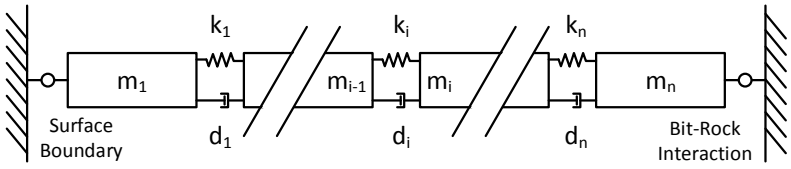


Figure 2: Mathematical model of the drillstring

This model may be simplified further, as shown in Figure 2, by abstracting each mass element as a mass-spring-damper which obeys the following equation.

$$m\frac{d^2\phi}{dt^2} = -k\phi - d\frac{d\phi}{dt} \tag{2}$$

In this case, m is the moment of inertia of each element, $k = \frac{GJ}{L}$ is the torsional spring constant, and d is the damping between elements.

For a n-DOF model, the motion of each mass may be described using:

$$m_i\ddot{\phi}_i = -k_{i-1}\left(\phi_i - \phi_{i-1}\right) - \phi_i\left(\phi_i - \phi_{i+1}\right) - d_i\dot{\phi}_i \tag{3}$$

and the plant transfer function may be obtained, assuming a free bit end condition and an ideal velocity source at the top drive.

For a seven lumped mass model presented here, the states are the angular displacements of the top drive and the seven lumped masses representing the drillpipe and the bit, $\phi = [\phi_1, \phi_2, ..., \phi_8]$ with an ideal velocity source $\dot{\phi}_1 = u$. The system can be expressed as a series of seven second order differential equations in the form $M\ddot{\tilde{\phi}} + D\dot{\tilde{\phi}} + K\tilde{\phi} = k_1 e_1 \phi_1$, where $e_1 \in \mathbf{R}^7$ is the standard basis vector, $\tilde{\phi} = [\phi_2, \phi_3, ..., \phi_8]$ is the new state vector with the angular displacements of seven lumped masses and the M, D and K matrices are the inertia, damping and spring matrices defined as:

$$M = \begin{bmatrix} I_1 & & \\ & \ddots & \\ & & I_7 \end{bmatrix} \quad D = \begin{bmatrix} d_1 & & \\ & \ddots & \\ & & d_7 \end{bmatrix} \quad K = \begin{bmatrix} k_1 + k_2 & -k_2 & & \\ -k_2 & k_2 + k_3 & -k_3 & \\ & & \ddots & \\ & & -k_7 & k_7 \end{bmatrix} \tag{4}$$

Applying the Laplace transform and rearranging gives the transfer function of the plant which will be used in the subsequent control section.

$$\tilde{\Phi}(s) = (Ms^2 + Ds + K)^{-1} k_1 e_1 \frac{1}{s} U(s), \qquad Y(s) = e_7^\top \tilde{\Phi}(s) s \tag{5}$$

$$G(s) = \frac{Y(s)}{U(s)} = k_1 e_7^\top (Ms^2 + Ds + K)^{-1} e_1 \tag{6}$$

This construct may be used in both the frequency domain, for control system design and system response, and in the time domain to analyze transient behavior.

3 EXPERIMENTAL SETUP

Many laboratory models described in literature [5, 6, 7] are single degree of freedom models that model the BHA as a single large inertial mass (typically a disk) and the drillstring as a torsional spring (typically a long slender rod). These models are effective at modeling first order dynamics, but do not take complexities of complex drillstring designs or non-vertical wellbores into account. A seven degree of freedom model is constructed as a proof of concept for a much larger 30 degree of freedom model currently under construction which will emulate a 2km drillstring and will be detailed in a future paper.. These models are based upon a model designed by Shell Research [10] that distributes the inertial masses along the drillstring, but expands on its capabilities by allowing for distributed damping to emulate borehole contact. n inertial masses, the size of which can be varied to match different sections of a BHA, are fixed to a steel rod that acts as a torsional spring between each of the masses. Torsional waves can then be generated, either at the top drive or at the bit and wave propagation can be observed and recorded at each inertial mass.

This paper details a seven-DOF benchtop prototype of the laboratory model that is able to simulate a 320 meter (950 ft) drillstring by using a series of 2.54 cm diameter inertial masses attached to a rubber rod. The masses act to delay a torsional wave that would otherwise travel at 25 m/s down to an effective velocity of 3.3 m/s. Measurement of angular displacement at four points is achieved using rotating stripped disks and photo sensors, giving an estimate of angular velocity. Sensing in the future system will be improved to include numerous measurement points at higher resolutions.

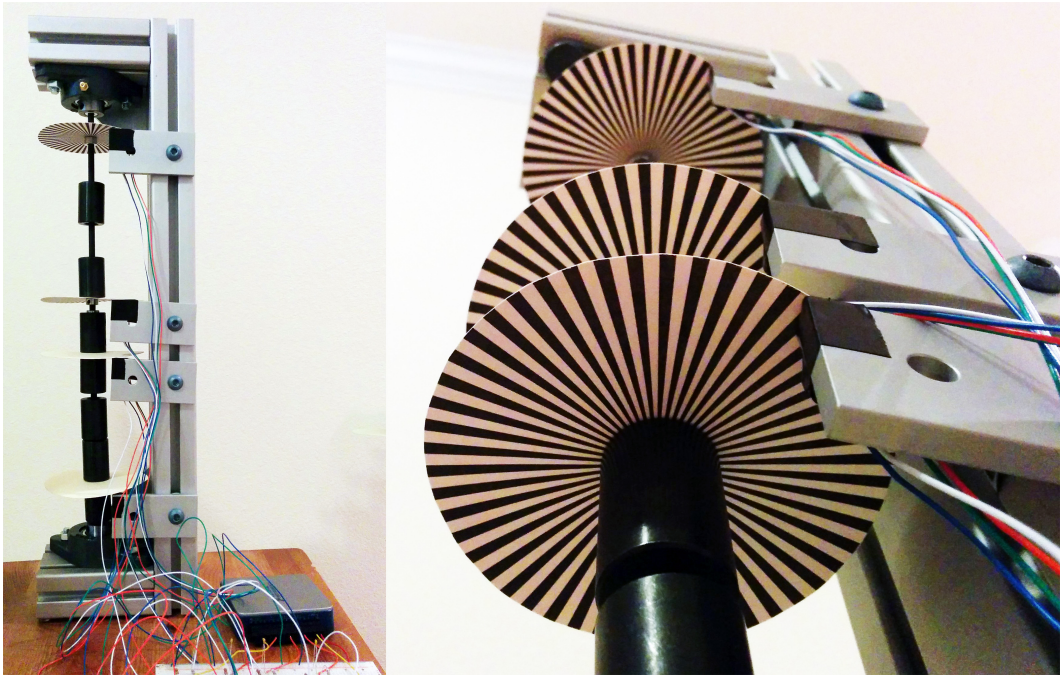


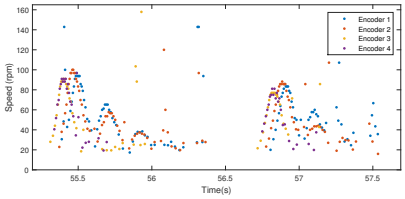
Figure 3: The desktop prototype model showing the full model, sensing and data acquisition (right) and the stripped disks and photo sensors used as rudimentary encoders (left).

The seven degree of freedom mass-spring-damper model described in the previous section is next compared with the velocity distributions generated by the benchtop model to ensure model fidelity.

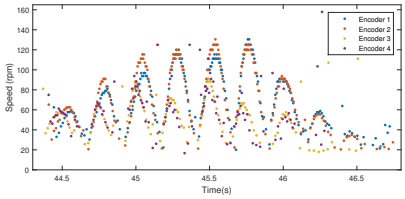
4 MODEL ANALYSIS

A sinusoidal input is placed at bit boundary in the desktop model and velocities are computed from the reflectance values of the photo sensors. The initial wave propagation may be used to compute propagation delay and once the sinusoidal input ceases, the decay of the oscillations may give a damping factor. Of note, the simple encoder discs do not allow for differentiation between forward and reverse motion, so only the absolute value of velocity may be computed from the transit time of a light or dark stripe. Lateral motion is not accounted for in the model physics, but does not affect velocity measurements since sensor radial position does not affect the angular width of a stripe.

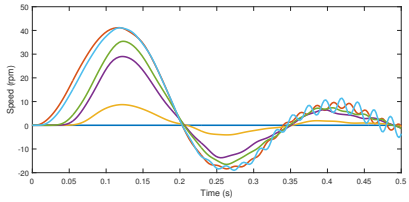
The analytic derivation of the spring constants and mass inertial elements from material constants gives a close approximation of the physical behavior, and as expected, the damping constants, which are constant within the model, require some tuning to match the decay of the observed wave behavior. Consistent behavior of the model, either after a unit cycle or a repeated oscillation cycle indicates that damping may be estimated from the behavior of the top node within a true drillstring.



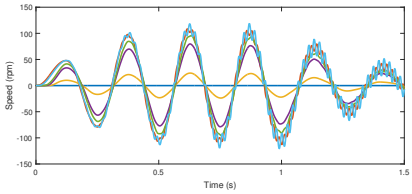
(a) Half period sinusoidal input at the bit



(b) Two period sinusoidal excitation from the bit boundary



(c) Modeled half period sinusoidal excitation from the bit boundary



(d) Modeled four period sinusoidal excitation from the bit boundary

Figure 4: Model output (top) and model results (bottom)

5 FUNDAMENTAL CONTROL

In this section, design of a fundamental PI controller based on frequency domain loop shaping is presented. Figure 5 shows the bode plots of the plant and the loop with the PI controller of the form $K_p + \frac{1}{s}K_i$. The controller is tuned such that the gain cross over frequency is below all natural frequencies and the gain margin is around 6 dB, which occurs at the frequency associated with the first mode.

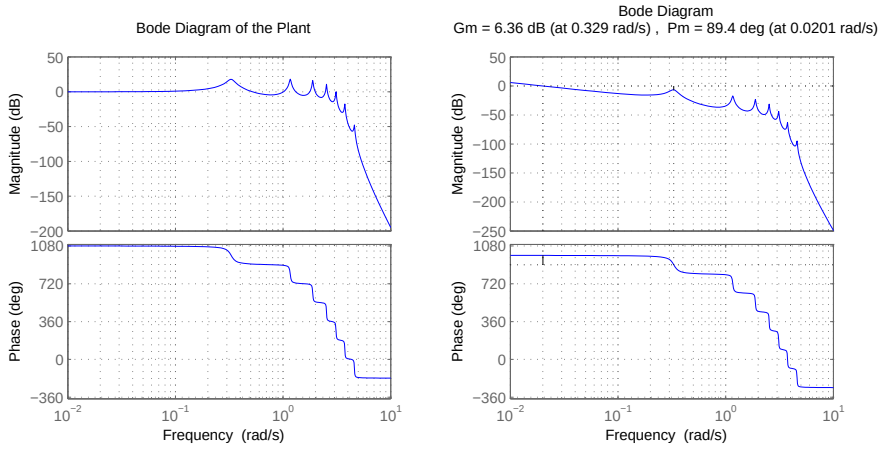


Figure 5: Bode plot of the plant and the loop transfer functions

In the situation where there is a higher damping point midway in the drillstring, such as would be observed in a well with a high angle curve or in the presence of a horizontal section, the same controller remains stable. This is demonstrated in Figure 6. The phase margin is

decreased and can cause instability with very high damping values, such as when stuck pipe situations arise; however, these situations may be detected from surface and drilling ceases.

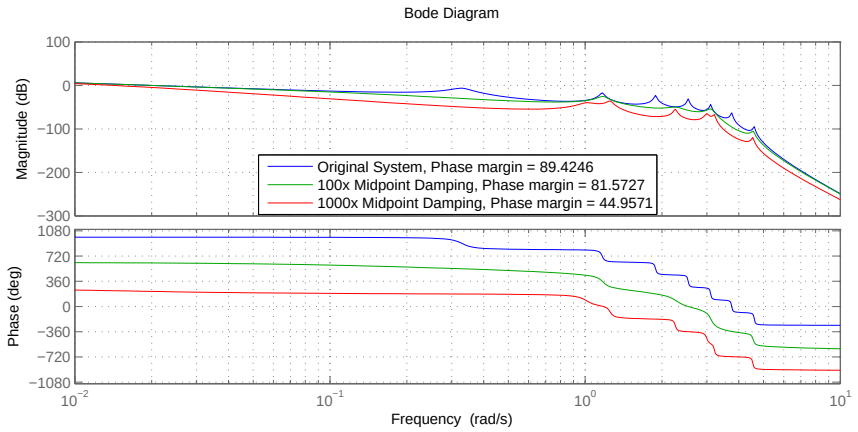


Figure 6: Bode plot of the loop transfer functions with increased damping in midpoint

In Figure 7 the step response of the system with and without the controller is presented. Without the controller, the system has many high amplitude oscillations before being damped by internal friction. The controller successfully reduces these oscillations and eliminates overshoot, which is desired as high or cyclic bit speed may cause damage to the bit. The closed loop system is not sensitive to uncertainties and independent of increased damping points.

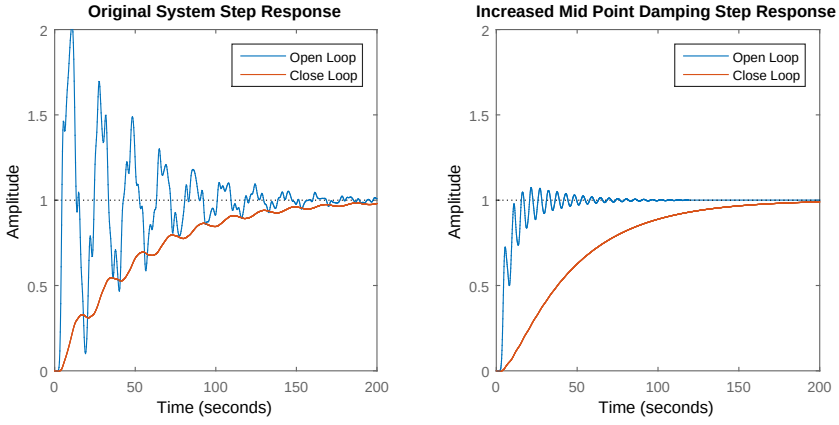


Figure 7: Step response of the system with and without the controller

Once the full scale model is constructed, higher order controllers will be designed to improve the drilling performance while mitigating vibration. This will occur by maximizing the feedback bandwidth through shaping of the feedback loop at higher frequencies while avoiding structural modes. Available feedback will be distributed over the functional bandwidth to

achieve maximum disturbance rejection and improve tracking performance by maximizing the feedback at lower frequencies. Bit-rock interaction and drillstring friction remain difficult to model, and can either be regarded as disturbances or through model predictive control. These two loop shaping tasks mentioned are independent and can be achieved sequentially [9].

6 CONCLUSIONS

A continuous model, based on a damped wave equation, and a lumped mass model, based on a mass-spring-damper system, of a drillstring is presented and compared with a prototype benchtop simulator to verify model mechanics. A controller is then derived that, through frequency domain loop shaping, successfully reduces relaxation time of the system, even in the presence of higher damping in the center of the drillstring. This verifies the basic construct of the model and shows the way forward to a higher fidelity, 30-DOF model, which with improved sensing and actuation, may be used to study and test control schemes for complex drillstrings.

7 ACKNOWLEDGEMENTS

The authors wish to thank Shell International E&P and ConocoPhillips for their support of the research program at the University of Texas at Austin.

REFERENCES

[1] S. Dwars, I. Stulemeijer, I and J.J. Runia, A brief history of the Shell "Soft Torque Rotary System" and some recent case studies, SPE/IADC Drilling Conference, 2013

[2] A. Kyllingstad and P.J. Nessjøen, A new stick-slip prevention system, SPE/IADC Drilling Conference, 2009

[3] A. Kyllingstad and P.J. Nessjøen, Hardware-in-the-Loop Simulations Used as a Cost-Efficient Tool for Developing an Advanced Stick-Slip Prevention System, SPE/IADC Drilling Conference, 2010

[4] H.Y. Lee, Drillstring axial vibration and wave propagation in boreholes, Ph.D. Thesis, MIT, 1991

[5] R.I. Leine, D.H. van Campen and W.J.G. Keultjes, Stick-slip Whirl Interaction in Drillstring Dynamics, *Journal of Vibration and Acoustics*, 124(2), 2002

[6] E. Kreuzer and M. Steidl, A Wave-Based Approach to Adaptively Control Self-Excited Vibrations in Drill-Strings, *Proc. Appl Math Mech*, 10(1), 2010

[7] C. Liao, N. Vlajic, H. Karki and B. Balachandran, Parametric studies on drill-string motions, *International Journal of Mechanical Sciences*, 54(1), 2012

[8] L. Greenhill, L and G. Cornejo, Critical speeds resulting from unbalance excitation of backward whirl modes, Design Engineering Technical Conference, 1995

[9] B. J. Lurie, P. J. Enright. Classical Feedback Control With MATLAB and Simulink Second Edition. Boca Raton: CRC Press, 2012

[10] S. Dwars, Recent Advances in Soft Torque Rotary Systems, SPE/IADC Drilling Conference and Exhibition, 2015

Inverse Problems and Uncertainty Quantification (MS10)

11th International Conference on Engineering Vibration
Ljubljana, Slovenia, 7–10 September 2015

IDENTIFICATION OF UNCERTAIN BOUNDARY CONDITION OF A BEAM MODEL USING THE BAYESIAN APPROACH AND EXPERIMENTAL DATA

T.G. Ritto*[1], Rubens Sampaio[2], R.R. Aguiar[2]

[1]Federal University of Rio de Janeiro, Department of Mechanical Engineering, Brazil
tritto@mecanica.ufrj.br

[2] PUC-Rio, Department of Mechanical Engineering, Brazil, 22453-900
rsampaio@puc-rio.br, aguiar.rr@gmail.com

Keywords: Uncertain boundary condition, clamped beam, Bayesian identification, stochastic dynamics, structural dynamics

Abstract. *In many mechanical applications (wind turbine tower, substructures joints, etc.), the stiffness of the boundary conditions is uncertain and might decrease with time, due to wear and/or looseness. In this paper, a torsional stiffness parameter is used to model the clamped side of a Timoshenko beam. The goal is to perform the identification with experimental data. To represent the decreasing stiffness of the clamped side, an experimental test rig is constructed, where several rubber layers are added to the clamped side, making it softer. The Bayesian approach is applied to update the probabilistic model related to the boundary condition (torsional stiffness parameter).*

1 INTRODUCTION

In many mechanical applications the stiffness of the boundary conditions is uncertain and might decrease with time, due to wear and/or looseness. This article deals with this problem proposing an identification strategy to estimate the stiffness parameter related to the boundary condition.

Although in many situations the boundary conditions of a structure are uncertain, there are few articles related to the modeling of uncertain boundary conditions in structural dynamics. For instance, in [1], boundary conditions of a beam structure are identified using static flexibility measurements. Translational and rotational springs are considered in the clamped side of the beam model. Ritto et al. (2008) [2] propose two probabilistic models to take into account uncertainties on the clamped side of a Timoshenko beam. Mignolet et al. (2013) [3] propose a probabilistic model to model uncertainties on the boundary conditions of linear structures and on the coupling between linear substructures.

In the present paper, the Bayesian approach [4] is employed for the identification of the torsional stiffness parameter, related to the clamped side of a beam model. The Markov Chain Monte Carlo Method (MCMC) is used to sample from the posterior probability density function, such that the prior probability density function is updated with experimental data.

This article is organized as follows. Section 2 presents the dynamical model of the Timoshenko beam, with a torsional stiffness in the clamped side. Section 3 presents the identification strategy, and Section 4 shows the results obtained. Finally, the concluding remarks are made in Section 5.

2 COMPUTATIONAL MODEL

To illustrate the proposed Bayesian update methodology to recursively identify the stiffness of a boundary condition, a Timoshenko beam is considered in the present analysis. The 2D Timoshenko beam element used has three degrees of freedom at each node: axial, vertical and rotational.

The clamped side of the beam is modeled as a torsional spring, with uncertain stiffness. As the value of the stiffness increases, the model approaches to the clamped condition. To developed the element equations, the variational form of the strain energy U and kinetic energy T are given by:

$$\delta U = \int_0^L [\delta u'(EAu') + \delta v''(EIv'') + \delta\theta_z'(GI\theta_z')]dx\,, \tag{1}$$

$$\delta T = \int_0^L \delta u(\rho A\ddot{u}) + \delta v(\rho A\ddot{v})dx\,, \tag{2}$$

where $'$ is the derivative with respect to x ($\partial/\partial x$) and the over dot is the derivative with respect to t ($\partial/\partial t$). The degrees of freedom are: the axial displacement (u); the vertical displacement (v); and the rotation (θ_z). E is the elastic modulus of the material, G is the shearing modulus, I is the area moment of inertia, L is the beam length and A is the cross-sectional area. The system is discretized using the Finite Element Method, and the element matrices are the following ones:

$$[M^{(e)}] = \rho A \frac{h}{420} \begin{bmatrix} 140 & 0 & 0 & 170 & 0 & 0 \\ 0 & 156 & 22h & 0 & 54 & -13h \\ 0 & 22h & 4h^2 & 0 & 13h & -3h^2 \\ 70 & 0 & 0 & 140 & 0 & 0 \\ 0 & 54 & 13h & 0 & 156 & -22h \\ 0 & -13h & -3h^2 & 0 & -22h & 4h^2 \end{bmatrix}$$

$$[K^{(e)}] = \rho \frac{E}{1+m} \begin{bmatrix} A(1+m)/h & 0 & 0 & -A(1+m)/h \\ 0 & 12I/h^3 & 6I/h^2 & 0 \\ 0 & 6I/h^2 & 4I(1+m/4)/h & 0 \\ -A(1+m)/h & 0 & 0 & A(1+m)/h \\ 0 & -12I/h^3 & -6I/h^2 & 0 \\ 0 & 6I/h^2 & 2I(1-m/2)/h & 0 \end{bmatrix}$$

$$\begin{bmatrix} 0 & 0 \\ -12I/h^3 & 6I/h^2 \\ -6I/h^2 & 2I(1-m/2)/h \\ 0 & 0 \\ 12I/h^3 & -6I/h^2 \\ -6I/h^2 & 4I(1+m/4)/h \end{bmatrix},$$

where $m = \left(\frac{12}{h^2}\right)\left(\frac{EI}{GAk_s}\right)$, k_s is the shear correction factor and h is the element size.

On the clamped side, the essential boundary conditions are given by $u(x=0) = 0$ and $v(x=0) = 0$, i.e., axial and vertical displacements are not allowed. And, the torsional stiffness parameter k is added to the component of the stiffness matrix related to the rotation θ_z at $x = 0$. After assembling the matrices, one can write:

$$[M]\ddot{\mathbf{u}}(t) + [C]\dot{\mathbf{u}}(t) + [K]\mathbf{u}(t) = \mathbf{f}(t)\,, \tag{3}$$

where $[M]$, $[C]$ and $[K]$ are the mass, damping and stiffness matrices, which are real and positive-definite. The damping matrix, added a posteriori to the model, is of Rayleigh type, proportional to the mass matrix $c[M]$, where c is the damping constant. The external force is represented by the vector $\mathbf{f}(t) = (f_{1a}, f_{1v}, f_{1r}, f_{2a}, \ldots, f_{nr})$ and the displacements $(u_{1a}, u_{1v}, u_{1r}, u_{2a}, \ldots, u_{nr})$ are the components of the vector $\mathbf{u}(t)$.

In the frequency domain, the system can be written as:

$$(-\omega^2[M] + i\omega[C] + [K])\hat{\mathbf{u}}(\omega) = \hat{\mathbf{f}}(\omega)\,. \tag{4}$$

2.1 NATURAL FREQUENCIES

To calculate the natural frequencies without damping, the following eigenvalue problem must be solved:

$$(-\omega_i^2[M] + [K])\Phi_i = \mathbf{0}\,, \tag{5}$$

where ω_i is the i-th natural frequency and Φ_i is i-th vibration mode. The i-th natural frequency with damping is calculated in the following way:

$$\omega_{di} = \omega_i\sqrt{1-\xi_i^2}\,, \tag{6}$$

where ξ_i is the damping rate of the i-th mode, which can be calculated using the normal modes and the damping matrix:

$$\xi_i = \frac{\Phi_i^T [C] \Phi_i}{2\omega_i} \,. \tag{7}$$

3 IDENTIFICATION STRATEGY

The present work employs the Bayesian strategy to update the prior probability density function (pdf) of the torsional stiffness of the clamped side of a beam. This strategy is used because more information can be extracted from the system, such as the marginal probability density functions of the parameters, updated with the experimental data; and statistical correlations among the response of interest. A similar procedure was considered in [5], where MCMC was applied to identify three parameters of the bit-rock interaction (boundary condition) of a drill-string dynamical model.

Let K be the random variable related to the stiffness parameter k. The prior probability density function is updated with experimental data D. We assume an additive Gaussian noise to model the measurement uncertainties. This is an usual assumption, and it is corroborated by the Maximum Entropy Principle (MaxEnt) [6], if we use the following information for the noise: (1) the support is R^n (where n is the number of points measured), (2) the mean is zero and (3) the variance is finite. With this information, the MaxEnt yields a Gaussian random vector with independent components. Hence, for a given K:

$$\mathbf{Y}^{exp} = \mathbf{f}(K) + \mathbf{N} \,, \tag{8}$$

where $\mathbf{Y}^{exp}$ represents the measured natural frequencies, $\mathbf{f}$ represents the natural frequencies obtained with the computational model, $\mathbf{N}(\lambda) \sim Normal(\mathbf{0}, \sigma_e^2[I])$ is a white noise vector with zero mean and covariance matrix $\sigma_e^2[I]$ (where $[I]$ is the identity matrix). Using the Bayes strategy, we can compute the updated (or posterior) probability density function of K, given data D:

$$p(K|D) \propto p(D|K)p(K) \,, \tag{9}$$

where '$\propto$' means 'proportional to', $p(D|K)$ is the likelihood function, and $p(K)$ is the prior pdf.

To approximate the posterior distribution, which is given up to a normalization constant, the Markov Chain Monte Carlo (MCMC) / Metropolis-Hasting algorithm is applied [7, 8]. The algorithm implemented is the following:

1. Initiate the chain K_n at $n = 0$.
2. Generate a candidate Y from a proposal distribution q.
3. Generate $U \sim \text{Uniform}(0, 1)$.
4. If $U \leq \alpha(K_n, Y)$, accept candidate $K_{n+1} = Y$. Else, reject the candidate and set $K_{n+1} = K_n$.
5. Set $n = n + 1$ and go back to step 2.

where $\alpha(K_n, Y) = posterior(Y)/posterior(K_n)$, and q is the Normal density function with mean K_n and standard deviation σ_q that is chosen such that the acceptance rate is about 50%.

4 RESULTS

The data used for the numerical simulation were: $c = 10$ N/(m.s); $E = 2e11$ Pa; $\rho = 7850$ kg/m^3; $\nu = 0.3$; $G = 0.5E/(1+\nu)$; $k_s = 5/6$; $L = 511$ mm, $b = 30.7$mm; $h = 3.04$mm. It was assumed $\sigma_e = 1$ and $\sigma_q = \{800; 200; 150; 100\}$ for $\{(bc_1); (bc_2); (bc_3, bc_4, bc_5, bc_6, bc_7); bc_8\}$, such that the accepted rate of the chain was about 50%.

To determine the number of elements needed, the error of the sixth natural frequency is calculated. It was necessary 32 elements to have an error lower than 0.1%.

4.1 Experimental results

Rubber layers are included in the clamped side of the beam to emulate the different boundary condition, corresponding to a measurement time. The natural frequencies are obtained from the magnitude signal of both accelerometers and confirmed by the phase chart. The natural frequencies obtained with the experiment (not detailed in this work) are shown in Tab. 1.

Observing the system frequency response function and the data shown in Tab. 1, it can be noticed that there is no variation of the first frequency, but it is worth it to remark that the accuracy of the experiment is 0.25Hz, what makes it difficult to distinguish 9.0Hz from 9.1Hz, for example.

The higher the number of rubber layers more flexible the boundary conditions become and lower the natural frequencies, compared to the condition without rubber layers. A comparison between the opposite sides of the experiment, i.e., the frequency response function of the beam without rubber layers (bc_1) on the clamped side and the system with 10 rubber layers (bc_8) is shown in Fig. 1.

4.2 Identification results

The experimental results shown in Tab. 1 are used to identify the torsional stiffness of the boundary condition for each boundary condition $\{bc_1, bc_2, ..., bc_8\}$, see Tab. 3. For each condition the prior pdf is set to Uniform and the updated pdf is computed simulating a Markov Chain. The prior pdf is set to Uniform, such that the previous boundary condition results do not bias the identification of the next instant.

Table 2 shows the evolution of the mean value and the coefficient of variation (CV) of random variable K. The mean value is very close to the maximum a posterior estimator (MAP). The table also shows the mean square error for each condition analyzed, i.e, for decreasing stiffness on the boundary condition. The uncertainty for bc_1 is higher (9%) than at other instants, where the CV is about 4%. There is a big jump in the mean value of K from bc_1 to bc_2, when a rubber layer is included in the experiments.

Due to experimental uncertainties, see Tab. 1, the 4th and 5th natural frequencies increase from bc_2 to bc_3. This fact explains why the mean value of K increases from bc_2 to bc_3, when we would expect the opposite result. From bc_3 to bc_8 the mean value of K decreases continuously.

Figures 3 and 4 show the prior Uniform pdf of K together with the updated (posterior) pdf for all time instants. To better visualize the probability density functions, they are shown in pairs: pdf(bc_1) with pdf(bc_2), pdf(bc_2) with pdf(bc_3), and so on. Note that the pdf is shifting to the left, because the system is getting less stiff. The biggest shift occurs from bc_1 to bc_2, when the first layer is included in the experiment. As it was noticed before, due to experimental uncertainties, from bc_2 to bc_3 there is a shift to the right, which is not expected.

5 CONCLUSIONS

This paper deals with uncertain boundary conditions. In many applications boundary condition stiffness decreases with time, and this should be taken into account in the computational model. An identification strategy is proposed to update the information related to the stiffness of the boundary condition. For this purpose the Bayesian update is employed with the aide of experimental data. The strategy worked well in the sense that the computational model was able to update the stiffness parameter of the boundary condition and the results were close to the experimental ones.

ACKNOWLEDGEMENTS

The authors would like to thank the financial support of the Brazilian agencies CNPq, CAPES, and Faperj.

REFERENCES

[1] L. Wang, Z. Yang, Identification of boundary conditions of tapered beam-like structures using static flexibility measurements, *Mechanical Systems and Signal Processing*, **25**(7) 2484-2500, 2011.

[2] T.G. Ritto, R. Sampaio, C. Cataldo, Timoshenko beam with uncertainty on the boundary conditions, *Journal of the Brazilian Society of Mechanical Science and Engineering*, **30**(4) 295-303, 2008.

[3] M. P. Mignolet, C. Soize, J, Avalos, Nonparametric stochastic modeling of structures with uncertain boundary conditions/coupling between substructures, *AIAA Journa*l, **51**(6) 1296-1308, 2013.

[4] J. Kaipio, E. Somersalo, *Statistical and Computational Inverse Problem*. Springer, 2005.

[5] T. G. Ritto, Bayesian approach to identify the bit-rock interaction parameters of a drill-string dynamical model, *Journal of the Brazilian Society of Mechanical Science and Engineering*, 2014.

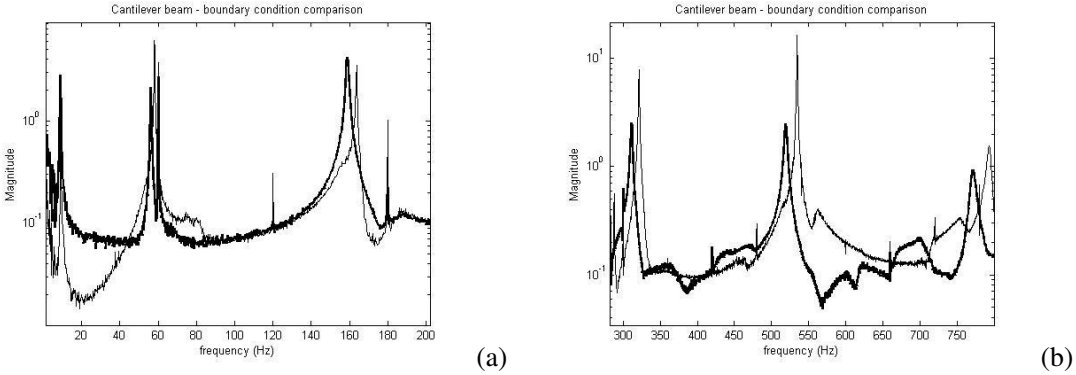
[6] J. N. Kapur, *Maximum Entropy Models in Science and Engineering*, Wiley-Blackwell, 1990.

[7] D. Gamerman, *Markov Chain Monte Carlo: Stochastic Simulation for Bayesian Inference*, Chapman and Hall/CRC, 2nd Edition, 2002.

[8] C. Robert, G. Casella, *Monte Carlo Statistical Methods, Springer*, 2004.

Table 1: Natural frequencies - changing boundary conditions.

natural frequency (Hz) / **Boundary Condition**	**1st**	**2nd**	**3rd**	**4th**	**5th**	**6th**
bc_1	9.25	58.80	163.75	321.50	534.50	793.20
bc_2	9.00	57.00	160.90	315.60	524.75	778.75
bc_3	9.00	57.00	160.75	315.25	525.40	780.00
bc_4	9.00	56.75	160.00	314.00	523.00	777.25
bc_5	9.00	56.75	160.15	314.20	523.00	777.00
bc_6	9.00	56.65	159.90	313.60	522.75	775.75
bc_7	9.00	56.50	159.75	313.20	521.50	773.50
bc_8	9.00	56.25	158.75	311.50	519.25	770.75



(a) (b)

Figure 1: Frequency response, boundary condition comparison. Thin line: 0 rubber layers (bc_1); thick line: 10 rubber layers (bc_8). a) 0-200 Hz, b) 300-800Hz.

Boundary condition	**MAP estimator** ($\times 10^3$ N.m)	**Mean value** ($\times 10^3$ N.m)	**CV**	**Mean Square Error** (Hz^2)
bc_1	3.7	3.8	9.0 %	8.9
bc_2	1.3	1.3	4.5 %	12.3
bc_3	1.4	1.4	4.4 %	10.9
bc_4	1.2	1.2	4.4 %	9.0
bc_5	1.1	1.1	4.4 %	9.9
bc_6	1.1	1.1	4.4 %	13.7
bc_7	1.0	1.0	4.0 %	17.2
bc_8	0.8	0.8	4.0 %	16.3

Table 2: MAP estimator, Mean value, coefficient of variation (CV), and mean square error, at each instant.

Table 3: Methodology - Boundary conditions.

Boundary condition	**Number of rubber layers**
bc_1	0
bc_2	1
bc_3	2
bc_4	3
bc_5	4
bc_6	6
bc_7	8
bc_8	10

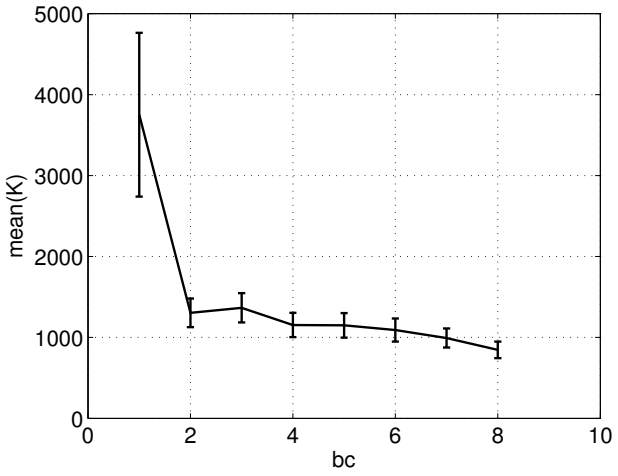


Figure 2: Evolution of the mean value of K together with errorbars; plus or minus two standard deviations.

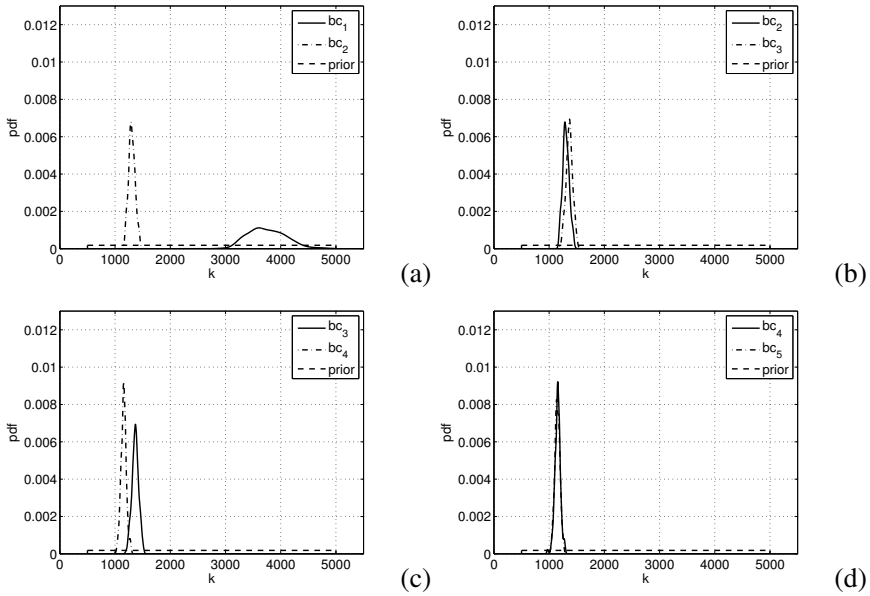


Figure 3: Prior (dashed line) and posteriors pdf of K from bc_1 to bc_4.

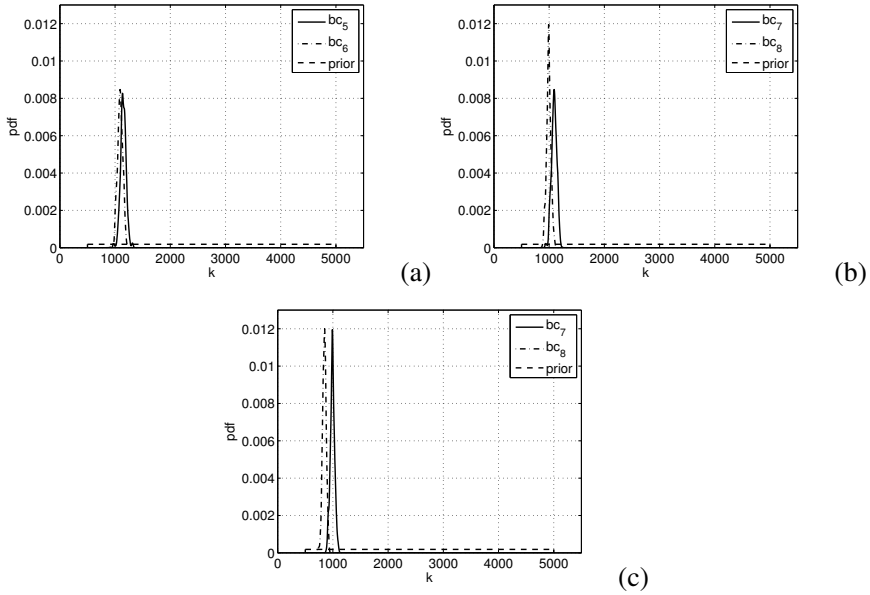


Figure 4: Prior (dashed line) and posteriors pdf of K from bc_4 to bc_8.

11th International Conference on Engineering Vibration
Ljubljana, Slovenia, 7–10 September 2015

ROBUST OPTIMIZATION OF HORIZONTAL DRILLSTRING RATE OF PENETRATION THROUGH A NONLINEAR STOCHASTIC DYNAMIC MODEL

Americo Cunha Jr[1,2,3], Christian Soize[2], and Rubens Sampaio[3]

[1]Universidade do Estado do Rio de Janeiro
americo@ime.uerj.br

[2]Université Paris-Est
christian.soize@univ-paris-est.fr

[3]PUC–Rio
rsampaio@puc-rio.br

Keywords: drillstring dynamics, horizontal drillstring, parametric probabilistic approach, robust optimization

Abstract. *A drillstring is a long column under rotation, composed by a sequence of connected drill-pipes and auxiliary equipment, which is used to drill the soil in oil prospecting. During its operation, this column presents a three-dimensional dynamics, subjected to longitudinal, lateral, and torsional vibrations, besides the effects of friction, shock, and bit-rock interaction. The study of the dynamics of this equipment is very important in many engineering applications, especially to reduce costs in the oil exploration process. In this sense, this work aims to formulate and solve a robust optimization problem that seeks to maximize horizontal drillstrings rate of penetration into of the soil, subjected to the restriction imposed by the structural limits of the column. To analyze the nonlinear dynamics of drillstrings in horizontal configuration, a computational model, which uses a nonlinear beam theory of Timoshenko type is considered. This model also takes into account the effects of friction and shock, induced by the lateral impacts between the drillstring and borehole wall, as well as bit-rock interaction effects. The uncertainties of the bit-rock interaction model are taken into account using a parametric probabilistic approach. Two optimizations problems (one deterministic and one robust), where the objective is to maximize the drillstring rate of penetration (ROP) into the soil, respecting its structural limits, are formulated and solved. In order to optimize the ROP, it is possible to vary the drillstring velocities of translation and rotation. The solutions of these optimization problems provided two different strategies to maximize the ROP.*

1 INTRODUCTION

The process of oil exploration involves very high costs, particularly during the drilling of a well. An effective way to reduce these costs is to optimize the drillstring rate of penetration into the soil, where a drillstring is a long column under rotation, composed by a sequence of connected drill-pipes and auxiliary equipment, which is used to drill the soil until the reservoir level. For this reason, and also because of the complex dynamics of this equipment, several recent studies have devoted attention to its study [12, 13, 1, 10, 4]. Some papers, in particular, focusing their attention on drillstrings in horizontal configuration, such as [14, 5, 11].

In the present work the objective is to formulate and solve a robust optimization problem that seeks to maximize horizontal drillstrings rate of penetration into of the soil, subjected to the restriction imposed by the structural limits of the column. For this purpose, a nonlinear beam theory of Timoshenko type is considered to analyze the nonlinear dynamics of drillstrings in horizontal configuration. Also, the mathematical model also takes into account the effects of friction and shock, induced by the lateral impacts between the drillstring and borehole wall, as well as bit-rock interaction effects. The uncertainties of the bit-rock interaction model are taken into account using a parametric probabilistic approach.

The rest of the paper is organized as follows. Section 2 presents the mathematical modeling of the nonlinear dynamics and the system efficiency analysis. In section 3 it is presented the probabilistic modeling of system parameters uncertainties. The formulation and solution of optimization problems that seek to maximize the drillstring rate of penetration into the soil can be seen in section 4. Finally, in section 5, the conclusions of the work are emphasized.

2 MODELING THE NONLINEAR DYNAMICS

2.1 Mechanical system of interest

The mechanical system of interest is sketched in Figure 1. It consists of a pair of stationary rigid walls, that emulates a horizontal rigid pipe, perpendicular to gravity acceleration g, which contains in its interior a deformable tube under rotation (rotating beam), subjected to three-dimensional displacements. This deformable tube has a length L, cross section area A, and is made of a material with mass density ρ, elastic modulus E, and shear modulus G. It loses energy through a mechanism of viscous dissipation, proportional to the mass operator, with damping coefficient c. Concerning the boundary conditions, the rotating beam is blocked for transversal displacements in both extremes; blocked to transversal rotations on the left extreme; and, on the left extreme, has a constant angular velocity around x equal to Ω, and an imposed longitudinal velocity V_0.

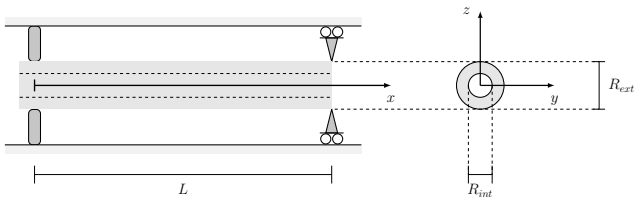


Figure 1: Schematic representation of the rotating beam which models the horizontal drillstring.

The beam theory adopted takes into account the rotatory inertia and shear deformation of beam cross section. Also, it is assumed that the beam is undergoing small rotations in the transverse directions, large rotation in x, and large displacements the three spatial directions, which couples the longitudinal, transverse and torsional vibrations.

In this way, the following kinematic hypothesis is adopted

$$\begin{aligned} u_x(x,y,z,t) &= u - y\theta_z + z\theta_y, \\ u_y(x,y,z,t) &= v + y\left(\cos\theta_x - 1\right) - z\sin\theta_x, \\ u_z(x,y,z,t) &= w + z\left(\cos\theta_x - 1\right) + y\sin\theta_x, \end{aligned} \tag{1}$$

where u_x, u_y, and u_z respectively denote the displacement of a beam point in x, y, and z directions, at the instant t. Also, u, v, and w are the displacements of a beam neutral fiber point in x, y, and z directions, respectively, while θ_x, θ_y, and θ_z represent rotations of the beam around the x, y, and z axes respectively. Note that the physical quantities of interest are the fields u, v, w, θ_x, θ_y, and θ_z, which depend on the position x and the time t.

2.2 Friction and shock effects

This beam is also able to generate shocks and friction effects in random areas of the rigid tube, which are described by the Hunt and Crossley shock model [7], and the standard Coulomb friction model [2].

The normal force of shock is given by

$$F^n_{\text{FS}} = -k_{\text{FS}_1}\,\delta_{\text{FS}} - k_{\text{FS}_2}\,\delta^3_{\text{FS}} - c_{\text{FS}}\,|\delta|^3\dot{\delta}_{\text{FS}}, \tag{2}$$

where k_{FS_1}, k_{FS_2} and c_{FS} are constants of the shock model. The $\dot{}$ is an abbreviation for time derivative, and the parameter $\delta_{FS} = r - \texttt{gap}$, where $r = \sqrt{v^2 + w^2}$, is dubbed *indentation*, and is a measure of penetration in the wall of a beam cross section, such as illustrated in Figure 2.

Once the column is rotating and moving axially, an impact also induces a frictional force in axial direction, F^a_{FS}, and a torsional friction torque, T_{FS}. Both are modeled by Coulomb friction law [2], so that

$$F^a_{\text{FS}} = -\mu_{\text{FS}}\,F^n_{\text{FS}}\,\texttt{sgn}\left(\dot{u}\right), \tag{3}$$

and

$$T_{\text{FS}} = -\mu_{\text{FS}}\,F^n_{\text{FS}}\,R_{bh}\,\texttt{sgn}\left(\dot{\theta}_x\right), \tag{4}$$

being μ_{FS} the friction coefficient, $\texttt{sgn}\left(\cdot\right)$ the sign function, and the radius of the borehole is $R_{bh} = R_{ext} + \texttt{gap}$.

2.3 Bit-rock interaction effects

At the beam right extreme act a force and a torque, which emulate the effects of interaction between the drill-bit and soil. They are respectively given by

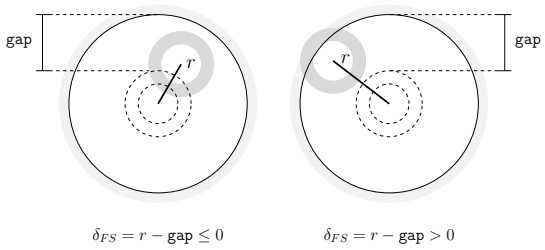


Figure 2: Illustration of indentation parameter in a situation without impact (left) or with impact (right).

$$F_{\mathrm{BR}} = \begin{cases} \Gamma_{\mathrm{BR}} \left(e^{-\alpha_{\mathrm{BR}} \, \dot{u}_{bit}} - 1 \right) & \text{for } \dot{u}_{bit} > 0, \\ 0 & \text{for } \dot{u}_{bit} \leq 0, \end{cases} \tag{5}$$

and

$$T_{\mathrm{BR}} = -\mu_{\mathrm{BR}} \, F_{\mathrm{BR}} \, R_{bh} \, \xi_{\mathrm{BR}} \left(\omega_{bit} \right), \tag{6}$$

where Γ_{BR} is the bit-rock limit force; α_{BR} is the rate of change of bit-rock force; $\dot{u}_{bit} = \dot{u}(L, \cdot)$; μ_{BR} bit-rock friction coefficient; $\omega_{bit} = \dot{\theta}_x(L, \cdot)$; and ξ_{BR} is a regularization function. The expression for the bit-rock interaction models above were, respectively, proposed by [11] and [9].

2.4 Variational formulation of the nonlinear dynamics

Using a modified version of the extended Hamilton's principle, to include the effects of dissipation, one can write the weak equation of motion of the mechanical system as

$$\mathcal{M} \left(\boldsymbol{\psi}, \ddot{\boldsymbol{U}} \right) + \mathcal{C} \left(\boldsymbol{\psi}, \dot{\boldsymbol{U}} \right) + \mathcal{K} \left(\boldsymbol{\psi}, \boldsymbol{U} \right) = \mathcal{F} \left(\boldsymbol{\psi}, \boldsymbol{U}, \dot{\boldsymbol{U}}, \ddot{\boldsymbol{U}} \right), \tag{7}$$

where $\mathcal{M}$ is the mass operator, $\mathcal{C}$ is the damping operator, $\mathcal{K}$ is the stiffness operator, and $\mathcal{F}$ is the force operator. Also, the field variables and their weight functions are lumped in the vectors fields $\boldsymbol{U} = \left(u, v, w, \theta_x, \theta_y, \theta_z \right)$, and $\boldsymbol{\psi} = \left(\psi_u, \psi_v, \psi_w, \psi_{\theta_x}, \psi_{\theta_y}, \psi_{\theta_z} \right)$. To see the definitions of the above operator the reader is referred to [8, 3].

The weak form of the initial conditions reads

$$\mathcal{M} \left(\boldsymbol{\psi}, \boldsymbol{U}(0) \right) = \mathcal{M} \left(\boldsymbol{\psi}, \boldsymbol{U}_0 \right), \tag{8}$$

and

$$\mathcal{M} \left(\boldsymbol{\psi}, \dot{\boldsymbol{U}}(0) \right) = \mathcal{M} \left(\boldsymbol{\psi}, \dot{\boldsymbol{U}}_0 \right), \tag{9}$$

where $\boldsymbol{U}_0$ and $\dot{\boldsymbol{U}}_0$, respectively, denote the initial displacement, and initial velocity fields.

In order to simulate the nonlinear dynamics of the mechanical system, the physical parameters presented in Table 1 are adopted, as well as $L = 100 \ m$, the rotational and axial velocities in x, respectively given by $\Omega = 2\pi \ rad/s$, and $V_0 = 1/180 \ m/s$.

Table 1: Physical parameters of the mechanical system that are used in the simulation.

parameter	value	unit
ρ	7900	kg/m^3
g	9.81	m/s^2
ν	0.3	—
κ_s	6/7	—
c	0.01	—
E	203×10^9	Pa
R_{bh}	95×10^{-3}	m
R_{int}	50×10^{-3}	m
R_{ext}	80×10^{-3}	m

2.5 Discretization of the model equations

After the discretization of Eqs.(7), (8) and (9), by means of finite element method [6], one arrives the following initial value problem

$$[\mathcal{M}]\,\ddot{\boldsymbol{Q}}(t) + [\mathcal{C}]\,\dot{\boldsymbol{Q}}(t) + [\mathcal{K}]\,\boldsymbol{Q}(t) = \boldsymbol{\mathcal{F}}\left(\boldsymbol{Q}, \dot{\boldsymbol{Q}}, \ddot{\boldsymbol{Q}}\right), \tag{10}$$

and

$$[\mathcal{M}]\,\boldsymbol{Q}(0) = \boldsymbol{Q}_0, \qquad \text{and} \qquad [\mathcal{M}]\,\dot{\boldsymbol{Q}}(0) = \dot{\boldsymbol{Q}}_0. \tag{11}$$

where $\boldsymbol{Q}(t)$ is the generalized displacement vector, $\dot{\boldsymbol{Q}}(t)$ is the generalized velocity vector, $\ddot{\boldsymbol{Q}}(t)$ is the generalized acceleration vector, $[\mathcal{M}]$ is the mass matrix, $[\mathcal{C}]$ is the damping matrix, $[\mathcal{K}]$ is the stiffness matrix, and $\boldsymbol{\mathcal{F}}$ is a nonlinear force vector, which contains contributions of an inertial force and a force of geometric stiffness.

The discretization of the structure uses a finite element mesh with 500 elements. As each element has 6 degrees of freedom per node, this results in a semi-discrete model with 3006 degrees of freedom. To reduce the computational cost of the simulations, the initial value problem of Eqs.(10) and (11) is projected in a vector space of dimension 49 to generate a reduced order model, which is integrated for the time interval $[t_0, t_f] = [0, 10]\ s$ using the Newmark method [6], and the nonlinear system of algebraic equations, resulting from the time discretization, is solved by a fixed point iteration. Further details can be seen in [3].

2.6 Analysis of drilling process efficiency

The drilling process efficiency is defined as

$$\mathcal{E} = \frac{\int_{t_0}^{t_f} \mathcal{P}_{out}\, dt}{\int_{t_0}^{t_f} \mathcal{P}_{in}\, dt}, \tag{12}$$

where $\mathcal{P}_{out}$ is the useful (output) power used in the drilling process, and $\mathcal{P}_{in}$ is the total (input) power injected in the system. The output power is due to drill-bit movements of translation and rotation so that

$$\mathcal{P}_{out} = \dot{u}_{bit}^{+}\,(-F_{\text{BR}})^{+} \;+\; \omega_{bit}^{+}\,(-T_{\text{BR}})^{+}, \tag{13}$$

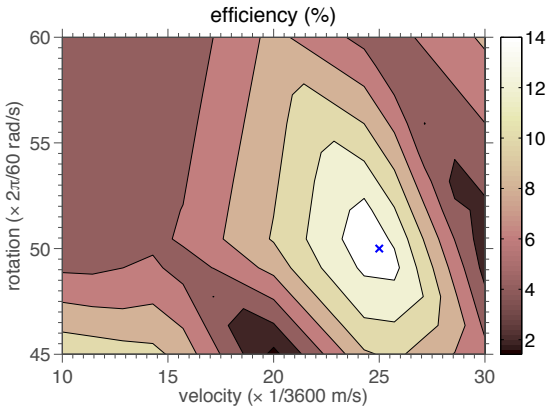


Figure 3: Illustration of efficiency function contour plot, for an "operating window" defined by $1/360\ m/s \leq V_0 \leq 1/120\ m/s$ and $3\pi/2\ rad/s \leq \Omega \leq 2\pi\ rad/s$. The maximum is indicated with a blue cross.

where the upper script $^+$ means the function positive part. The input power is defined as

$$\mathcal{P}_{in} = \dot{u}(0,t)^+ \, (-\lambda_1)^+ \; + \; \dot{\theta}_x(0,t)^+ \, (-\lambda_4)^+, \tag{14}$$

where the first and the fourth Lagrange multipliers, respectively, represent the drilling force and torque on the beam origin.

One can observe the contour map of $\mathcal{E}$, for an "operating window" defined by $1/360\ m/s \leq V_0 \leq 1/120\ m/s$ and $3\pi/2\ rad/s \leq \Omega \leq 2\pi\ rad/s$, in Figure 3.

Accordingly, it can be noted in Figure 3 that the optimum operating condition is obtained at the point $(V_0, \Omega) = (1/144\ m/s, 5\pi/3\ rad/s)$, which is indicated with a blue cross in the graph. This point corresponds to an efficiency of approximately 16%. Suboptimal operation conditions occur in the vicinity of this point, and some points near the "operating window" boundary show lower efficiency.

3 MODELING OF SYSTEM-PARAMETER UNCERTAINTIES

The bit-rock interface law is given by Eqs.(5) and (6), so that this model is characterized by three parameters, namely, α_{BR}, Γ_{BR}, and μ_{BR}. A parametric probabilistic approach [15, 16] is employed to construct the probabilistic model for each one parameter of these parameters, which are respectively modeled by random variables $\mathbb{\alpha}_{\text{BR}}$, $\mathbb{\Gamma}_{\text{BR}}$, and $\mathbb{\mu}_{\text{BR}}$. In this approach, the maximum entropy principle is used to specify the probability distribution of the random parameters, taking into account only the known information about them.

For $\mathbb{\alpha}_{\text{BR}}$, it is assumed that

$$\int_{\alpha=0}^{+\infty} p_{\mathbb{\alpha}_{\text{BR}}}(\alpha)\, d\alpha = 1, \tag{15}$$

$$\mathbb{E}\left[\mathbb{\alpha}_{\text{BR}}\right] = m_{\mathbb{\alpha}_{\text{BR}}} > 0, \tag{16}$$

and

$$\mathbb{E}\left[\ln\left(\mathbb{\alpha}_{\text{BR}}\right)\right] = q_{\mathbb{\alpha}_{\text{BR}}}, \quad |q_{\mathbb{\alpha}_{\text{BR}}}| < +\infty. \tag{17}$$

Thus, the maximum entropy distribution is given by

$$p_{\text{ω}_{\text{BR}}}(\alpha) = \mathbb{1}_{]0,\infty[}(\alpha)\,\frac{1}{m_{\text{ω}_{\text{BR}}}}\left(\frac{1}{\delta^2_{\text{ω}_{\text{BR}}}}\right)^{1/\delta^2_{\text{ω}_{\text{BR}}}} \times \frac{1}{\Gamma(1/\delta^2_{\text{ω}_{\text{BR}}})}\left(\frac{\alpha}{m_{\text{ω}_{\text{BR}}}}\right)^{1/\delta^2_{\text{ω}_{\text{BR}}}-1}\exp\left(\frac{-\alpha}{\delta^2_{\text{ω}_{\text{BR}}}m_{\text{ω}_{\text{BR}}}}\right), \quad (18)$$

which corresponds to the gamma distribution. Similar information are assumed to $\mathbb{\Gamma}_{\text{BR}}$, so that this random variable also presents gamma distribution.

On the other hand, for the variable $\mathbb{\mu}_{\text{BR}}$ one assumes

$$\int_{\mu=0}^{1} p_{\mathbb{\mu}_{\text{BR}}}(\mu)\,d\mu = 1, \quad (19)$$

$$\mathbb{E}\left[\ln\left(\mathbb{\mu}_{\text{BR}}\right)\right] = q^1_{\mathbb{\mu}_{\text{BR}}}, \quad |q^1_{\mathbb{\mu}_{\text{BR}}}| < +\infty, \quad (20)$$

and

$$\mathbb{E}\left[\ln\left(1-\mathbb{\mu}_{\text{BR}}\right)\right] = q^2_{\mathbb{\mu}_{\text{BR}}}, \quad |q^2_{\mathbb{\mu}_{\text{BR}}}| < +\infty, \quad (21)$$

which implies in a maximum entropy distribution of the form

$$p_{\mathbb{\mu}_{\text{BR}}}(\mu) = \mathbb{1}_{[0,1]}(\mu)\,\frac{\Gamma(a+b)}{\Gamma(a)\,\Gamma(b)}\,\mu^{a-1}\,(1-\mu)^{b-1}, \quad (22)$$

that corresponds to the beta distribution.

For the probabilistic analysis of the dynamic system, the random variables of interest are characterized by the mean values $m_{\text{ω}_{\text{BR}}} = 400\ 1/m/s$, $m_{\mathbb{\Gamma}_{\text{BR}}} = 30\times10^3\ N$, and $m_{\mathbb{\mu}_{\text{BR}}} = 0.4$, and the dispersion factors $\delta_{\text{ω}_{\text{BR}}} = 0.5\%$, $\delta_{\mathbb{\Gamma}_{\text{BR}}} = 1\%$, and $\delta_{\mathbb{\mu}_{\text{BR}}} = 0.5\%$.

4 OPTIMIZATION OF THE RATE OF PENETRATION

4.1 Deterministic optimization problem

The instantaneous rate of penetration is given by the function $\dot{u}_{bit}(t)$, defined for all instants of analysis. Meanwhile, only contributes to the column advance, the positive part of this function $\dot{u}^+_{bit}(t)$. In addition, as objective function, it is more convenient to consider a scalar function. Thus, the temporal mean of $\dot{u}^+_{bit}(t)$ is adopted as rate of penetration, and, consequently, objective function of the optimization problem

$$\texttt{rop}(\Omega,\, V_0) = \frac{1}{t_f - t_0}\int_{t=t_0}^{t_f} \dot{u}^+_{bit}(t)\,dt. \quad (23)$$

Furthermore, respect the material structural limits is indispensable to avoid failures in drillstring during the drilling process. For this reason, von Mises criterion of failure is considered, where it is established that, for all pairs $(\Omega,\, V_0)$ in the "operating window", one has

$$\texttt{UTS} - \max_{\substack{0\le x\le L\\ t_0\le t\le t_f}}\left\{\sigma_{VM}(V_0,\,\Omega,\,x,\,t)\right\} \ge 0, \quad (24)$$

where UTS is the material ultimate tensile strength, and σ_{VM} is the von Mises equivalent stress.

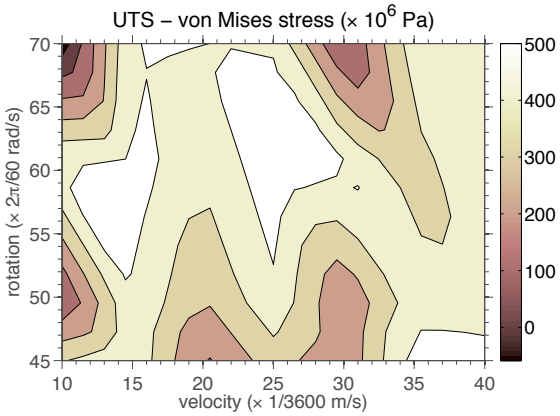


Figure 4: Illustration of maximum von Mises stress contour plot, for an "operating window" defined by $1/360\ m/s \leq V_0 \leq 1/90\ m/s$ and $3\pi/2\ rad/s \leq \Omega \leq 7\pi/3\ rad/s$.

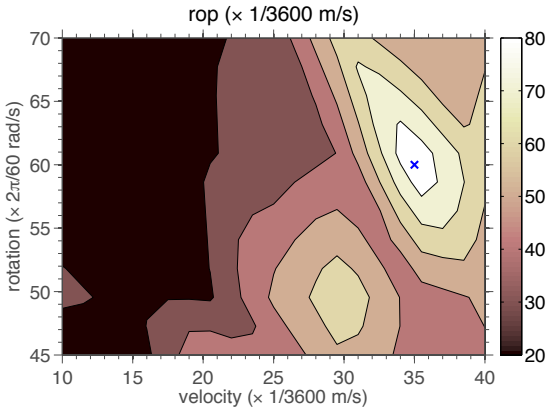


Figure 5: Illustration of rate of penetration function contour plot, for an "operating window" defined by $1/360\ m/s \leq V_0 \leq 1/90\ m/s$ and $3\pi/2\ rad/s \leq \Omega \leq 7\pi/3\ rad/s$. The maximum is indicated with a blue cross.

Regarding the rate of penetration analysis, "operating window" is defined by the inequations $1/360\ m/s \leq V_0 \leq 1/90\ m/s$ and $3\pi/2\ rad/s \leq \Omega \leq 7\pi/3\ rad/s$, and $\texttt{UTS} = 650 \times 10^6\ Pa$.

The contour map of constraint (24), is shown in Figure 4. From the way (24) is written, the Mises criterion is not satisfied when the function is negative, which occurs in a "small neighborhood" of the upper left corner of the rectangle that defines the "operating window". It is noted that all other points respect the material structural limits. In this way, then, the "operating window" *admissible* region consists of all points that satisfy the constraint.

In Figure 5 the reader can see the contour map of `rop` function. Taking into account only points in the admissible region, the maximum of `rop` occurs at $(V_0, \Omega) = (7/720\ m/s, 2\pi\ rad/s)$, which is indicated on the graph with a blue cross. This point corresponds to a mean rate of penetration, during the time interval analyzed, approximately equal to 90 "meters per hour".

4.2 Robust optimization problem

Taking into account the uncertainties, through the parametric approach presented in section 3, drill-bit velocity becomes the stochastic process $\mathbb{U}_{bit}(t,\theta)$, so that the random rate of penetration is defined by

$$\mathbb{ROP}(V_0,\,\Omega,\theta) = \frac{1}{t_f - t_0}\int_{t=t_0}^{t_f} \dot{\mathbb{U}}^{+}_{bit}(t,\theta)\,dt. \tag{25}$$

In the robust optimization problem, who plays the role of objective function is the expected value of the random variable $\mathbb{ROP}(V_0,\,\Omega,\theta)$, i.e., $\mathbb{E}\left[\mathbb{ROP}(V_0,\,\Omega,\theta)\right]$.

Regarding the restriction imposed by the von Mises criteria, now the equivalent stress is the random field $\varpi_{VM}(V_0,\,\Omega,\,x,\,t,\theta)$, so that the inequality is written as

$$\texttt{UTS} - \max_{\substack{0\le x\le L\\ t_0\le t\le t_f}} \left\{\varpi_{VM}(V_0,\,\Omega,\,x,\,t,\theta)\right\} \ge 0. \tag{26}$$

However, the robust optimization problem considers as restriction a probability of the event defined by inequality (26),

$$\mathbb{P}\left\{\texttt{UTS} - \max_{\substack{0\le x\le L\\ t_0\le t\le t_f}} \left\{\varpi_{VM}(V_0,\,\Omega,\,x,\,t,\theta)\right\} \ge 0\right\} \ge 1 - P_{risk}, \tag{27}$$

where $0 < P_{risk} < 1$ is the risk percentage acceptable to the problem.

A robust optimization problem very similar to this one, in the context of a vertical drillstring dynamics, is considered in [13].

To solve this robust optimization problem it is employed a trial strategy which discretizes the "operating window" in a structured grid of points and then evaluates the objective function $\mathbb{E}\left[\mathbb{ROP}(V_0,\,\Omega,\theta)\right]$ and the probabilistic constraint (27) in these points.

Accordingly, it is considered the same "operating window" used in the deterministic optimization problem solved above, i.e., $1/360\ m/s \le V_0 \le 1/90\ m/s$ and $3\pi/2\ rad/s \le \Omega \le 7\pi/3\ rad/s$, in addition to $\texttt{UTS} = 650\times10^6\ Pa$ and $P_{risk} = 10\%$. Each MC simulation in this case used 128 realizations to compute the propagation of uncertainties.

Concerning the simulation results, the probabilistic constraint (27) is respected in all grid points that discretize the "operating window". Thus, the admissible region of robust optimization problem is equal to the "operating window". In what follows, the contour map of function $\mathbb{E}\left[\mathbb{ROP}(V_0,\,\Omega,\theta)\right]$ can be see in Figure 6. Note that the maximum, which is indicated on the graph with a blue cross, occurs at the point $(V_0,\Omega) = (1/90\ m/s, 7\pi/3\ rad/s)$. This point is located in the boundary of the admissible region, in the upper right corner, and corresponds to a expected value of the mean rate of penetration, during the time interval analyzed, approximately equal to 58 "meters per hour".

This result says that, in the "operating window" considered here, increasing drillstring rotational and translational velocities provides the most robust strategy to maximize its ROP into the soil. This is in some ways an intuitive result, but is at odds with the result of the deterministic optimization problem, which provides another strategy to achieve optimum operating condition.

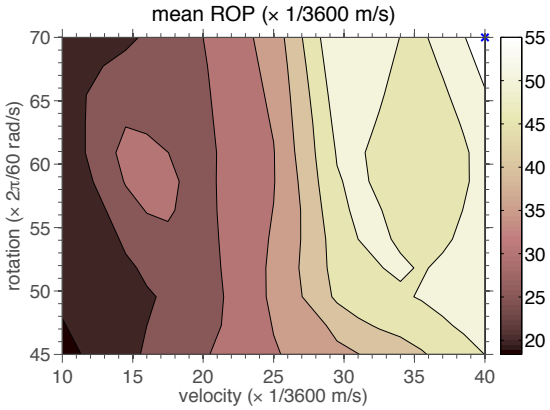


Figure 6: Illustration of the contour plot of the mean rate of penetration function, for an "operating window" defined by $1/360\ m/s \leq V_0 \leq 1/90\ m/s$ and $3\pi/2\ rad/s \leq \Omega \leq 7\pi/3\ rad/s$. The maximum is indicated with a blue cross in the upper right corner.

5 CONCLUDING REMARKS

In this work a model that uses a beam theory, with effects of rotatory inertia and shear deformation, which is capable of reproducing large displacements effects, is employed to describe the nonlinear dynamics of horizontal drillstrings. This model also considers the friction and shock effects due to transversal impacts, as well as, the force and torque induced by bit-rock interaction. The uncertainties of the bit-rock interaction model were taken into account using a parametric probabilistic approach. A study aiming to maximize drilling process efficiency, varying drillstring velocities of translation and rotation was presented. The optimization strategy used a trial approach to seek for a local maximum, which was located within "operating window" and corresponds to an efficiency of approximately 16%. Two optimizations problems, one deterministic and one robust, where the objective was to maximize drillstring rate of penetration into the soil, respecting its structural limits, were formulated and solved. The solutions of these problems provided two different strategies to optimize the ROP.

ACKNOWLEDGEMENTS

The authors are indebted to Brazilian agencies CNPq, CAPES, and FAPERJ, and French agency COFECUB for the financial support given to this research. The first author is grateful for the institutional support received from PUC-Rio and Université Paris-Est to carry out this work.

REFERENCES

[1] I. K. Chatjigeorgiou. Numerical simulation of the chaotic lateral vibrations of long rotating beams. *Applied Mathematics and Computation*, 219:5592–5612, 2013.

[2] S. J. Cull and R. W. Tucker. On the modelling of Coulomb friction. *Journal of Physics A: Mathematical and General*, 32:2103–2113, 1999.

[3] A. Cunha Jr. *Modeling and Uncertainty Quantification in the Nonlinear Stochastic Dynamics of a Horizontal Dsrillstrings*. D.Sc. Thesis, Pontifícia Universidade Católica do Rio de Janeiro / Université Paris-Est, 2015.

[4] A. Depouhon and E. Detournay. Instability regimes and self-excited vibrations in deep drilling systems. *Journal of Sound and Vibration*, 333:2019–2039, 2014.

[5] Y. Hu, Q. Di, W. Zhu, Z. Chen, and W. Wang. Dynamic characteristics analysis of drillstring in the ultra-deep well with spatial curved beam finite element. *Journal of Petroleum Science and Engineering*, 82—83:166–173, 2012.

[6] T. J. R. Hughes. *The Finite Element Method*. Dover Publications, New York, 2000.

[7] K. H. Hunt and F. E. Crossley. Coefficient of restitution interpreted as damping in vibroimpact. *Journal of Applied Mechanics*, 42:440–445, 1975.

[8] A. Cunha Jr, C. Soize, and R. Sampaio. Computational modeling of the nonlinear stochastic dynamics of horizontal drillstrings. *(submitted for publication)*, 2015.

[9] Y. A. Khulief, F. A. Al-Sulaiman, and S. Bashmal. Vibration analysis of drillstrings with self-excited stick–slip oscillations. *Journal of Sound and Vibration*, 299:540–558, 2007.

[10] X. Liu, N. Vlajic, X. Long, G. Meng, and B. Balachandran. Nonlinear motions of a flexible rotor with a drill bit: stick-slip and delay effects. *Nonlinear Dynamics*, 72:61–77, 2013.

[11] T. G. Ritto, M. R. Escalante, R. Sampaio, and M. B. Rosales. Drill-string horizontal dynamics with uncertainty on the frictional force. *Journal of Sound and Vibration*, 332:145–153, 2013.

[12] T. G. Ritto, C. Soize, and R. Sampaio. Non-linear dynamics of a drill-string with uncertain model of the bit–rock interaction. *International Journal of Non-Linear Mechanics*, 44:865–876, 2009.

[13] T. G. Ritto, C. Soize, and R. Sampaio. Robust optimization of the rate of penetration of a drill-string using a stochastic nonlinear dynamical model. *Computational Mechanics*, 45:415–427, 2010.

[14] S. M. Sahebkar, M. R. Ghazavi, S. E. Khadem, and M. H. Ghayesh. Nonlinear vibration analysis of an axially moving drillstring system with time dependent axial load and axial velocity in inclined well. *Mechanism and Machine Theory*, 46:743–760, 2011.

[15] C. Soize. *Stochastic Models of Uncertainties in Computational Mechanics*. Amer Society of Civil Engineers, Reston, 2012.

[16] C. Soize. Stochastic modeling of uncertainties in computational structural dynamics — recent theoretical advances. *Journal of Sound and Vibration*, 332:2379—2395, 2013.

11th International Conference on Engineering Vibration
Ljubljana, Slovenia, 7–10 September 2015

STOCHASTIC STABILITY ANALYSIS OF A WIND TURBINE BLADE VIBRATIONS APPLYING THE FLOQUET THEORY

S. Mohsen Forghani[1] **and T. G. Ritto***[1]

[1] Federal University of Rio de e Janeiro, Department of Mechanical Engineering, Centro de Tecnologia, Ilha do Fundão, 21945-970, Rio de Janeiro, Brazil

mohsen_forghani@hotmail.com
tritto@mecanica.ufrj.br

Keywords: wind turbine blade, blade dynamics, Floquet theory, stochastic stability analysis, linear periodic system.

Abstract. *In many engineering applications, such as wind turbines and helicopter rotor dynamics, the resulting system of differential equations is periodic. In such cases, it is possible to assess the stability of the system applying the Floquet theory. In this work, the stochastic stability of a wind turbine blade is assessed by means of the the Floquet exponents. The uncertain parameter is the wind speed, which is modeled as a random variable. The propagation of the uncertainty is obtained using the Monte Carlo method.*

1 INTRODUCTION

Because of the importance of the wind as a green alternative to fossil energy, the number of researches on the area of modeling and improving the efficiency of wind turbines are increasing day by day.

Usually wind turbines are designed for wind farms with mostly stable wind flow during their operating hours and. When they start to operate, they reach their nominal rotor velocity and become stable. In this case the aerodynamic forces exerted on the blades due to the air flow become constant [6], but wind speed variation with height, and also the gravitational forces, are periodic functions of the angle of rotor, $\theta = \Omega t$, which leads to a periodic function. Therefore, the equations of motion of the blade consist in linear periodic system (LSP).

For a linear periodic system, it is possible to assess its stability by computing the characteristic multipliers using the Floquet theory, thus, integrating the equations only for the time interval of one period of the system [7]. In the Floquet theory, the Floquet exponents define the stability of the solutions of the periodic system.

In this work a numerical model of the transverse vibrations of a wind turbine blade is presented and the stability of its solutions is analyzed applying the Floquet theory. Then, the effect of uncertainties on the Floquet exponents are investigated using a stochastic analysis, where the random parameter is the wind speed.

2 BLADE VIBRATIONS MODEL

If we consider a wind turbine which is located in a place with mean wind speed μ_w (in the upstream) and its operational rotational velocity is Ω, then the differential aerodynamic forces normal and tangent to the plane of the rotation of rotor for any section of the blade are

$$dF_N = \frac{1}{2}\rho_a c \mu_{rel}^2 (C_l \cos\varphi + C_d \sin\varphi) dx \tag{1}$$

$$dF_T = \frac{1}{2}\rho_a c \mu_{rel}^2 (C_l \sin\varphi - C_d \cos\varphi) dx \tag{2}$$

where, x is the is the longitudinal coordinate of the blade, ρ_a is the air density, c is the chord length of the blade section's airfoil, C_l is the lift coefficient of the blade section's airfoil, C_d is the drag coefficient of the blade section's airfoil, φ is the relative wind angle, which is the angle between the wind and the plane of rotation. This angle is the sum of the angle of attack α and the pitch angle θ_p, at any section [4, 6]. The relative wind μ_{rel} is the sum of the wind stream and the rotational wind as shown in Figure 1.

The Beam Element Momentum Theorem (BEM) is considered in the analysis. It assumes that the speed of the wind flow at the plane of the rotation of the blades is $(1-a)\mu_w$ where, a is the axial induction factor. Also, because of the wake rotation ω behind the turbine, the component of the relative wind in the plane of rotation for any section, distant r from the rotor, is $r\Omega + \frac{1}{2}r\omega$. Introducing the angular induction factor $a' = \frac{\omega}{2\Omega}$ leads to $r\Omega(1+a')$ for the relative wind in the plane of rotation for any section distant r from the rotor [6].

Therefore,

$$\tan\varphi = \frac{\mu_w(1-a)}{r\Omega(1+a')} \tag{3}$$

Because the parameters a, a', c, φ, C_l and C_d are functions of the distance x, an iterative approach is needed to solve the equations. In the present paper, an ideal case of flow is considered. In this case, it is assumed that there is now reduction in the wind speed while it passes the

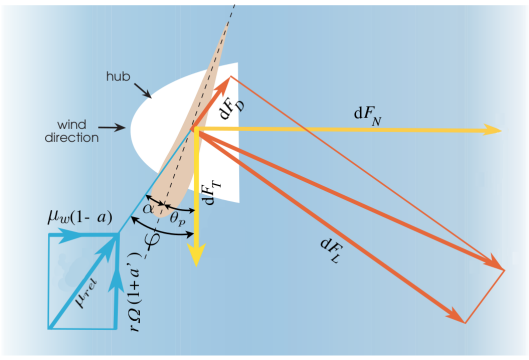


Figure 1: Blade geometry for analysis of a horizontal axis wind turbine [4].

plane of rotation of the blades, which means that $a = 0$. Also, it is assumed that $a' = -1$, or $\omega = -2\Omega$ [4]. With these assumptions and using Eq. 3 for a blade with constant pitch angle θ_p along its longitudinal axis, the angle of attack α will be constant along the longitudinal axis and $\varphi = \pi/2$.

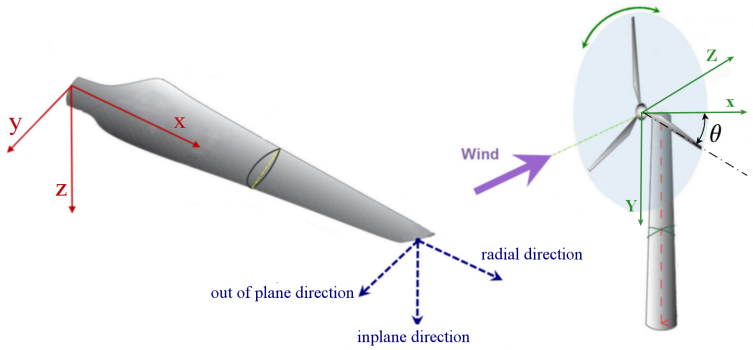


Figure 2: System of coordinates of the wind turbine and direction of vibrations for the blade tip.

Figure 2 shows the coordinate systems for the wind turbine and a blade. As the length L of the blade is much bigger than the chord c, for all airfoil sections of the blade, the Euler-Bernoulli beam model is considered for the transverse vibrations of the blade. If the displacements of the beam in the in-plane direction is w, the equation of motion of the rotating blade under the effect of axial load $P(x,t)$ is

$$\frac{\partial^2}{\partial x^2}\left(EI\frac{\partial^2 w}{\partial x^2}\right) - \frac{\partial}{\partial x}\left(P(x,t)\frac{\partial w}{\partial x}\right) + \rho A\frac{\partial^2 w}{\partial t^2} = \frac{1}{2}\rho_a c\mu_w^2 C_l + \rho A g\cos\theta(t) \tag{4}$$

where, E and ρ are modulus of elasticity and density of the blade material, I is the cross sectional moment of inertia of the blade [8].

Note that because of the simplifying assumptions, the in-plane component of aerodynamic forces of Eq. 2 exerted on the blade is $\frac{1}{2}\rho_a c\mu_w^2 C_l$. While the blade rotates, there exists a periodic

gravitational force $\rho A g \cos\theta(t)$ [4]. Also, the axial force distribution $P(x,t)$ at a blade with length L and cross section airfoil area A is given by

$$P(x,t) = \int_x^L \rho A \left(g \sin(\theta) + r\dot{\theta}^2 \right) dr \tag{5}$$

To solve Eq. 4, the system is discretized by means of the finite element method, where with Hermite polynomials $\phi_i(x)$ is used [4, 9]. Hence, the matrix equation of the assembled system is given by

$$\boldsymbol{M}\ddot{\boldsymbol{q}}(t) + \boldsymbol{C}\dot{\boldsymbol{q}}(t) + \boldsymbol{K}(t)\boldsymbol{q}(t) = \boldsymbol{\psi}(t) \tag{6}$$

where $\boldsymbol{M}$ is the mass matrix, $\boldsymbol{C}$ is the damping matrix, proportional to the mass matrix, and $\boldsymbol{K}(t)$ is the periodic stiffness matrix, in which the element matrices/force are given by

$$M_{ij} = \int_0^L \rho \phi_i(x) \phi_j(x) dx \tag{7}$$

$$K_{ij}(t) = \int_0^L \left(EI \frac{\partial^2 \phi_i(x)}{\partial x^2} \frac{\partial^2 \phi_j(x)}{\partial x^2} + P(x,t) \frac{\partial \phi_i(x)}{\partial x} \frac{\partial \phi_j(x)}{\partial x} \right) dx \tag{8}$$

$$\psi_i(t) = \int_0^L \left(\frac{1}{2} \rho_a c \mu_w^2 C_l + \rho A g \cos\theta(t) \right) \phi_i(x) dx \tag{9}$$

Writing Eq. 6 in state-space form yields

$$\dot{\boldsymbol{y}} = \begin{pmatrix} \dot{\boldsymbol{q}} \\ \ddot{\boldsymbol{q}} \end{pmatrix} = \boldsymbol{A}(t)\boldsymbol{y} + \boldsymbol{B}\boldsymbol{\psi}(t) \tag{10}$$

where,

$$\boldsymbol{A}(t) = \begin{pmatrix} \boldsymbol{0} & \boldsymbol{I} \\ -\boldsymbol{M}^{-1}\boldsymbol{K}(t) & -\boldsymbol{M}^{-1}\boldsymbol{C} \end{pmatrix} \tag{11}$$

and

$$\boldsymbol{B} = \begin{pmatrix} \boldsymbol{0} \\ \boldsymbol{M}^{-1} \end{pmatrix} \tag{12}$$

Eq. 10 is periodic because the components of the stiffness matrix is periodic Eq. 6.

3 FLOQUET STABILITY

Since the analyzed system is linear which periodic coefficients, the the Floquet theory is applied. Therefore, it is possible to define the stability of the system using the Floquet exponents [4, 10].

In this case, it is enough to numerically integrate the equations only over one period of the system to obtain the stability solution.

A convergence analysis, considering the error in the 5th natural frequency, Eq. 6, indicates that for number of elements $N \geq 16$ is needed to have error lower than 0.1%; see Figure 3. It was decided to do the simulations with $N = 20$.

With $N = 20$, the size of matrix A in Eq. 10 is 80 and, therefore, an arbitrary nonsingular 80×80 initial matrix $\boldsymbol{\Phi(0)}$ is chosen. The results of the integration over one period of the system leads to the fundamental matrix $\boldsymbol{\Phi(T)}$ [4].

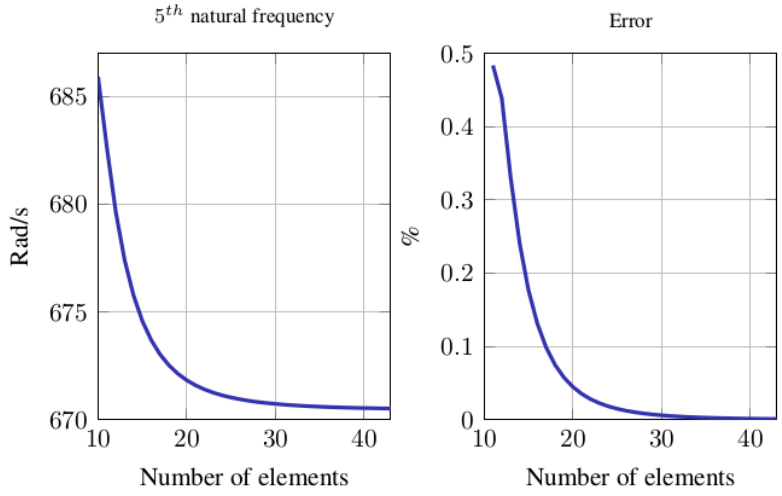


Figure 3: Error in 5^{th} natural frequency calculation versus number of elements.

Configuring the monodromy matrix by

$$\boldsymbol{B} = \boldsymbol{\Phi}^{-1}(0)\boldsymbol{\Phi}(T), \tag{13}$$

and computing its eigenvalues ρ_j, leads to the Floquet exponents μ_j by

$$e^{\mu_j T} = \rho_j, \quad j = 1, 2, \cdots, 4N \tag{14}$$

The stability of the solutions of the periodic systems is defined as [10]:

- if $|\rho| < 1$, then $\mathrm{Re}(\mu) < 0$. Therefore $\lim_{t\to\infty} \boldsymbol{y}(t) = \boldsymbol{0}$ and the solution is *stable*.
- if $|\rho| = 1$ and $\mathrm{Im}(\rho) \neq 0$. Therefore $\mathrm{Re}(\mu) = 0$, $\mathrm{Im}(\mu) \neq 0$ and the solution is *quasi periodic*.
- if $|\rho| = \pm 1$. Therefore $\mathrm{Re}(\mu) = 0$ and the solution is *periodic*.
- if $|\rho| > 1$, then $\mathrm{Re}(\mu) > 0$. Therefore $\lim_{t\to\infty} \boldsymbol{y}(t) = \infty$ and the solution is *unstable*.

Figure 4 shows the real part, imaginary part and the absolute value of the characteristic multipliers of the homogeneous form of Eq. 10 ($\boldsymbol{\psi} = \boldsymbol{0}$) for the wind turbine with parameters of Table 1. Due to the stability conditions of the Floquet theory, the solutions of the periodic system are stable and because the absolute value of most of the multipliers are near 1, the solutions are semi periodic.

4 STOCHASTIC ANALYSIS ON THE FLOQUET EXPONENTS

Table 1 shows the parameters used for numerical modeling of the wind turbine [4].

Previous work of the authors show that the uncertainty in wind speed has solely great effect on the behavior of wind turbine dynamics [3]. To analyze the effect of wind uncertainty on

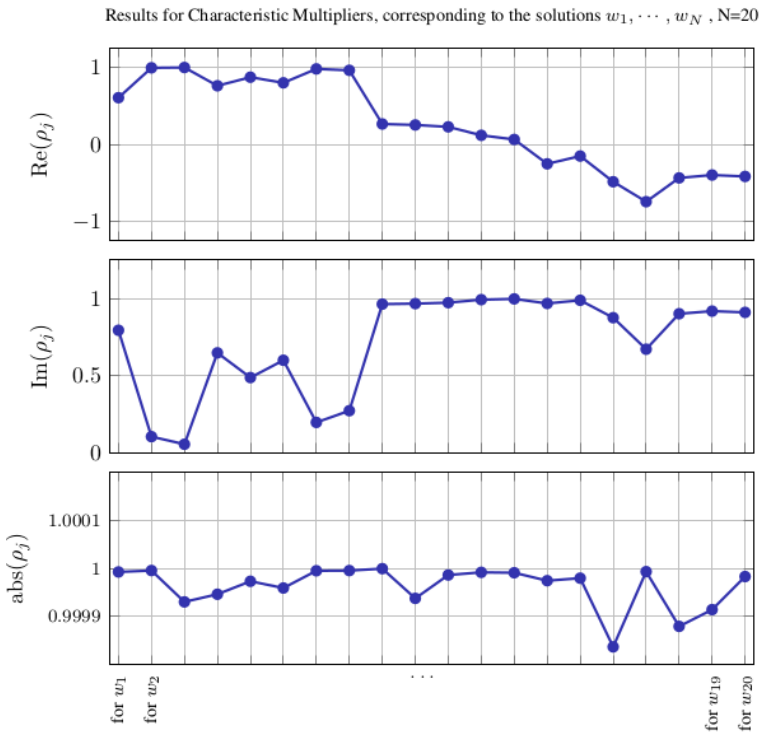


Figure 4: Real part, imaginary part and the absolute value of the characteristic multipliers of free transverse vibrations of the rotating blade with $N = 20$ for the solutions $w_i(t)$, $i = 1, 2, \cdots, N$.

Table 1: Sample wind turbine parameters for numerical modeling, [4]

Parameter	**Abv.**	**Value**	**Unit**
Mean wind speed	μ_w	12	m/s
Air density	ρ_a	1.15	Kg/m^3
Chord of blade	c	1.85	m
Blade length	L	45	m
Lift coefficient	C_l	1.20	–
Drag coefficient	C_d	0.08	–
Density of blade material	ρ	1600	Kg/m^3
Young modulus of blade material	E	$1.45e11$	N/m^3
Moment of cross section of blade	I	1	m^4
Cross section area of blade	A	0.15	m^2

the Floquet exponents of the solutions of a system of Eq. 10, a stochastic analysis is performed using the Monte Carlo method with 1000 random experiments.

Experiments show that the mean wind speed has a normal distribution over short periods of time [6]. Here a normal or Gaussian distribution with coefficient of variation $CV = 10\%$ is used for the wind speed [4].

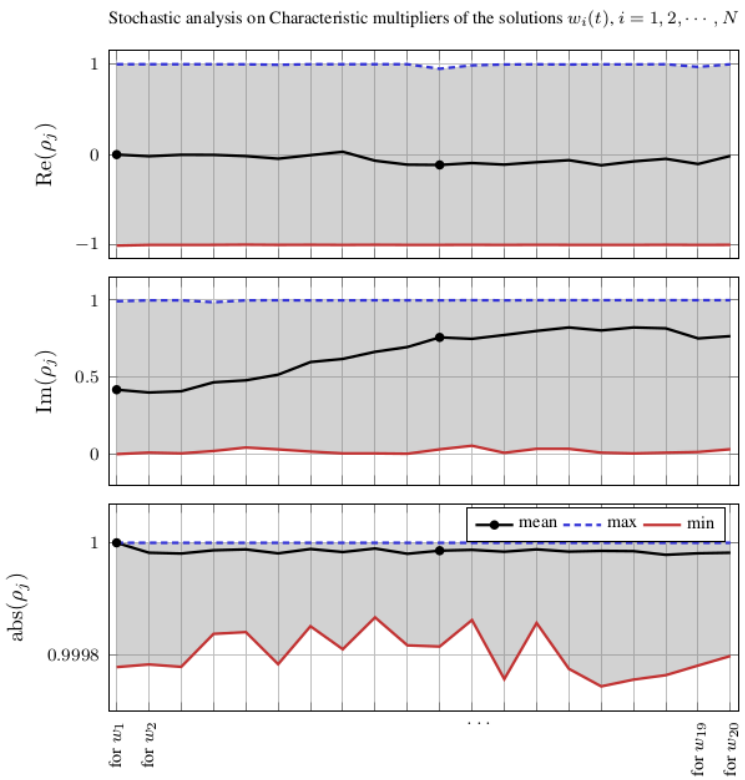


Figure 5: Mean value and confidence limits of results for Characteristic Multipliers of the system corresponding to the solutions $w_i(t)$ in a stochastic analysis of 1000 random experiments.

Figure (5), depicts that in 1000 simulated random experiments with normal distribution for the wind speed, values of $|\rho|$ are lower than or equal to 1 and all values of performed 1000 random analyses are less than 1 but very close to it. This means that the system solutions are mostly periodic or quasi-periodic and the system has a tendency to be stable.

5 CONCLUSIONS

A rotating wind turbine blade is modeled using the Euler-Bernoulli beam equations and discretized by means of the finite element method. The equation of motion is periodic and its stability is investigated using the Floquet theory instead of direct integration over a big time interval or methods such as Lyapunov method.

For the nominal operational deterministic conditions, all of Floquet exponents are inside the stable region for the homogeneous form of Eq. 10. Appearance of absolute value close to 1 for many of characteristic exponents of the system indicates that most of the solutions should be periodic or quasi-periodic.

The wind speed is model as a random variable. To study the effect of uncertainties on the Floquet exponents of the system, a stochastic analysis is performed with 1000 random experiments with the wind speed as the random variable with a Gaussian distribution and $CV = 10\%$ is conducted using the Monte Carlo method. The results show that for the homogeneous system is mostly periodic or quasi-periodic and the system has a tendency to be stable.

As future works we intend to apply the Floquet theory of the general solutions of the system. Also in modeling section, it is assumed a special case of aerodynamic forces with $a = 0$ and $a' = -1$. In general $a = 0$ and $a' = -1$ are not constant and they have to be calculated through an iterative process. As another task it is necessary to combine the nacelle and tower structural dynamics to be able to consider the effects such as gyroscopic effect on the blade dynamics and the stability of the solutions of whole system.

REFERENCES

[1] W. E. Boyce and R. C. DiPrima, *Elementary Differential Equations and Boundary Value Problems*. John Wiley & Sons, Inc., seventh edition, 2000.

[2] S. M. Forghani and T. G. Ritto, Stochastic Modeling of The Dynamics of A Wind Turbine Using MATLAB and MSC.ADAMS. *Mecánica Computacional*, **XXXII**, 615–630, 2013.

[3] S. M. Forghani and T. G. Ritto, Stochastic Modeling of A Simplified Wind Turbine Dynamics. *22nd International Congress in Mechanical Engineering*, COBEM, Ribeirão preto, Brazil, 2013.

[4] S. M. Forghani, *Stochastic Wind Turbine Dynamics and Stability Analysis of The Blade Applying The Floquet Theory*. MSc Thesis, Federal University of Rio de Janeiro, Mechanical Engineering Department, Brazil, 2015.

[5] P. A. Lynn, *Onshore and Offshore Wind Energy, An Introduction*. John Wiley & Sons Inc., 2012.

[6] J. F. Manwell, J. G. Mc Grawman and A. L. Rogers, *Wind Energy Explained, Theory, Design and Application*. John Wiley & Sons Inc, 2002.

[7] A. H. Nayfeh and B. Balachandran, *APPLIED NONLINEAR DYNAMICS: Analytical, Computational and Experimental Methods*. WILEY-VCH Verlag GmbH & Co. KGaA, seventh edition, 2004.

[8] S. S. Rao, *Vibration of Continuous Systems*. John Wiley & Sons, Inc., 2007.

[9] J. N. Reddy, *An Introduction to The Finite Element Method*. McGraw-Hill, Inc., 2nd edition, 1993.

[10] M. J. Ward, Chapter 3: Basic Floquet Theory. `http://www.math.ubc.ca/~ward/teaching/m605/notes2010/every2_floquet1.pdf`.

International Conference on Engineering Vibration
Ljubljana, Slovenia, 7-10 September 2015

PARTIAL EIGENSTRUCTURE ASSIGNMENT IN VIBRATING SYSTEMS THROUGH HOMOTOPY OPTIMIZATION

Roberto Belotti[1], **Ilaria Palomba**[1], **Dario Richiedei***[1], **Alberto Trevisani**[1]

[1]Università degli Studi di Padova
Stradella San Nicola 3,
36100, Vicenza
belotti@gest.unipd.it, ilaria.palomba@unipd.it, dario.richiedei@unipd.it, alberto.trevisani@unipd.it

Keywords: Dynamic Structural modification, Inverse Eigenvalue Problem, Eigenstructure Assignment, Vibratory feeder, Vibrating system design, Homotopy optimization.

Abstract. *Passive eigenstructure assignment on vibrating systems is aimed at computing the modifications of the inertial and elastic parameters ensuring the desired dynamical behaviour, in terms of natural frequency and mode shape. In many cases, it is desirable assigning only the response of some critical parts rather than the response of the whole system. However, the currently available methods do not provide a way to distinguish the degrees of freedom with different levels of interest.*

To solve this relevant open issue, this paper proposes a method intended for the assignment of partial parts of an arbitrary number of eigenvectors. In order to determine the optimal structural modifications satisfying constraints on the feasible values, the assignment problem is cast as an optimization problem solved numerically. The presence of some not-imposed eigenvector entries leads to a non-convex optimization problem. Therefore, to boost the convergence to a global minimum, homotopy optimization is implemented by morphing from a convex relaxation of the problem to the original non-convex one. The convex approximation is performed through some auxiliary variables and the McCormick's relaxation of the bilinear terms.

The proposed approach can handle general assignment tasks, with an arbitrary number of modification parameters and prescribed eigenpairs. Interrelated modifications can be also accounted for.

The method is numerically validated in the dynamic optimization of a vibratory linear feeder. The aim of the system modification is to specify the shape of the displacement of the upper tray where the conveyed parts flow, through the assignment of the eigenvector with the highest participation factor in the forced dynamics. At the same time, the assignment of the related eigenvalue in a neighbourhood of the excitation frequency allows obtaining large amplitude displacements with small driving force. The numerical results show that partial assignment significantly improves the fulfilment of the specifications on the eigenvector entries representing the tray translation, which are those of greater concern.

1 INTRODUCTION

Eigenstructure assignment (EA) techniques on vibrating systems are design methods aimed at modifying the natural frequencies and the mode shapes in order to meet some requirements on the dynamic behaviour. Besides a significant academic and theoretical interest of the subject, the need of effective techniques to perform EA is of primary importance also in industrial applications, since the traditional approaches relying on trial-and-error procedures are usually too time-consuming. A class of methods of EA that is often employed in the scientific literature is that of inverse dynamic structural modification (IDSM), which consists in the computation of the appropriate passive modifications of the inertial and elastic parameters of the system by solving inverse eigenvalue problem. In fact, given an undamped vibrating system whose mass and stiffness matrices are respectively $\mathbf{M}$ and $\mathbf{K}$, it is wanted to find a pair of symmetric matrices $\widetilde{\mathbf{K}} = \mathbf{K} + \mathbf{\Delta K}$ and $\widetilde{\mathbf{M}} = \mathbf{M} + \mathbf{\Delta M}$ that features a certain set of eigenvalues ω_h^2 and eigenvectors $\boldsymbol{u}_h$ (for h =1,...,N_e). Explicitly, the following equations must be satisfied:

$$\left(\omega_h^2 \widetilde{\mathbf{M}} - \widetilde{\mathbf{K}}\right)\boldsymbol{u}_h = 0, \text{ for } h = 1, \dots, N_e. \tag{1}$$

In the present work damping is supposed negligible, otherwise a different mathematical development should be needed.

Over the last years, several numerical methods for IDSM have been proposed in literature to solve such an issue which has some theoretical and computational difficulties, and solutions to a wide variety of EA tasks have been proposed. For instance, Ram and Braun, in their seminal work [1] consider the case of modification of a system which is characterized by incomplete modal data. The ideas introduced in that paper were further developed by Bucher and Braun in [2], where the theory is applied to several special cases and the problem of extracting modal vectors from the FRF matrix is addressed. Sivan and Ram in [3] exploit optimization to deal with the issue of physical feasibility and present two algorithms: one that assures a global solution and another which is more efficient but provides only a local solution. Mottershead in [4] deals with the assignment of natural frequencies and nodes of the modes of vibration using measured receptances, thus without the need of an analytical model of the system. An approach that stands out for its versatility is the one proposed in [5,6,7]. Such a method solves a more general problem, thus assigning an arbitrary number of eigenpairs and including feasibility constraints of the modification parameters, by casting the inverse eigenproblem as a linear least-squares optimization problem. Moreover, the convex formulation guarantees the attainment of a globally optimal solution.

In this work, the method proposed in [5] is extended in order to assign only the response of the most critical parts of the system, rather than the response of the whole system as in the original formulation, so as to fulfil more accurately the design specifications where it is needed most. Such task is referred to as partial eigenstructure assignment (PEA), and it is the topic of the present paper. Indeed, such an issue is only marginally solved in literature, although it is of relevant interest in particular in the presence of large scale models. On the other hand, such a problem has some mathematical difficulties. In this work, the method will be proposed and discussed in detail, with a special attention paid to the computational issues that might arise in the optimization process. Moreover, the design of a mechanical system of practical interest will be addressed for the method validation. Such a system is a linear feeder which is often employed in packaging or manufacturing plants to convey small products along a production line by means of the forced oscillation of a transport surface. The latter is the only part of the system to whom the partial eigenstructure assignment will focus, in order to obtain the desired motion of the conveyed parts.

2 METHOD FORMULATION

2.1 The assignment problem

In order to formulate the assignment problem, the admissible modifications of the inertial and elastic physical parameters of the system are collected in the unknown vector $\boldsymbol{x} \in \mathbb{R}^{N_x}$. The distribution of such parameters, instead, is represented through the additive modification matrices already introduced, $\boldsymbol{\Delta M}(\boldsymbol{x}) \in \mathbb{R}^{N \times N}$ and $\boldsymbol{\Delta K}(\boldsymbol{x}) \in \mathbb{R}^{N \times N}$, where the dependence on $\boldsymbol{x} \in \mathbb{R}^{N_x}$ is supposed to be linear (as it is for most of the type of modifications of interest). Moreover, there is no limitation on the topology of these matrices, except that they must be symmetric in order to ensure the modifications to be physically meaningful.

Let us define $\omega_1, \dots, \omega_{N_e}$ as the natural frequencies (and therefore the eigenvalues) to be assigned, together with the associated mode shapes (eigenvectors) $\boldsymbol{u_1}, \dots, \boldsymbol{u}_{N_e}$. In such eigenvectors, only the components related to the most important parts of the system are to be assigned, and therefore exactly specified, while the other ones are indeterminate and thus are represented as linear functions of some other unknowns $\boldsymbol{y} \in \mathbb{R}^{N_y}$. Hence $\boldsymbol{u}_i = \boldsymbol{u}_i(\boldsymbol{y}), i = 1, \dots, N_e$.

An important issue that must be considered is the technical and economical feasibility of the computed solution; thus the unknowns $\boldsymbol{x}$ and $\boldsymbol{y}$ are constrained into a feasible set Γ. Such a set includes lower and upper bounds on the single variables, but it can also contain constraints simultaneously relating different variables, the latter being represented by N_γ inequalities modelled as a polyhedron, namely a convex set defined as $\mathbf{A}\boldsymbol{x} \leq \boldsymbol{c}$ for some $\mathbf{A} \in \mathbb{R}^{N_\gamma \times N_x}$ and $\mathrm{c} \in \mathbb{R}^{N_\gamma}$. Explicitly,

$$\Gamma = \left\{ \begin{Bmatrix} \boldsymbol{x} \\ \boldsymbol{y} \end{Bmatrix} \in \mathbb{R}^{N_x + N_y} : \boldsymbol{x}^{\mathbf{L}} \leq \boldsymbol{x} \leq \boldsymbol{x}^{\mathbf{U}}, \boldsymbol{y}^{\mathbf{L}} \leq \boldsymbol{y} \leq \boldsymbol{y}^{\mathbf{U}}, \mathbf{A}\boldsymbol{x} \leq \boldsymbol{c} \right\}, \tag{2}$$

where $\boldsymbol{x}^L = \left\{ x_1^L \dots x_{N_x}^L \right\}^T$, $\boldsymbol{x}^U = \left\{ x_1^U \dots x_{N_x}^U \right\}^T$, $\boldsymbol{y}^L = \left\{ y_1^L \dots y_{N_y}^L \right\}^T$ and $\boldsymbol{y}^U = \left\{ y_1^U \dots y_{N_y}^U \right\}^T$ are lower and upper bounds on the problem unknowns.

The solution of the PEA can be computed by finding the values of $\boldsymbol{x}$ and $\boldsymbol{y}$ that satisfy the following system equations:

$$\left[\omega_i^2 \left(\mathbf{M} + \boldsymbol{\Delta M}(\boldsymbol{x}) \right) - \left(\mathbf{K} + \boldsymbol{\Delta K}(\boldsymbol{x}) \right) \right] \boldsymbol{u}_i(\boldsymbol{y}) = 0, \forall i = 1, \dots, N_e, \begin{Bmatrix} \boldsymbol{x} \\ \boldsymbol{y} \end{Bmatrix} \in \Gamma. \tag{3}$$

The solvability of this problem in general is not ensured, given the presence of the constraint set Γ. Therefore it is suggested to minimize in a least-square sense the residuals of Eq. (3) over the feasibility domain Γ:

$$\min \left\{ f(\boldsymbol{x}, \boldsymbol{y}) = \sum_{i=1}^{N_e} \alpha_i \left\| \left[\omega_i^2 \left(\mathbf{M} + \boldsymbol{\Delta M}(\boldsymbol{x}) \right) - \left(\mathbf{K} + \boldsymbol{\Delta K}(\boldsymbol{x}) \right) \right] \boldsymbol{u}_i(\boldsymbol{y}) \right\|^2, \begin{Bmatrix} \boldsymbol{x} \\ \boldsymbol{y} \end{Bmatrix} \in \Gamma \right\}. \tag{4}$$

The scalar positive coefficients α_i allows weighing the relative importance of the assignment of each eigenpair in the case of multiple assignment.

It is important to remark that the cost function f is non-convex, in general. The lack of convexity of the optimization program is the main difference with respect to the formulation adopted in [5], where the cost function has been recast as the squared residuals of a linear system. In the present context, instead, such formulation cannot be achieved, due to the presence of some bilinear terms that appear in the expression of f, i.e. terms like $x_r \cdot y_s$ for some $r = 1, \dots, N_x$ and $s = 1, \dots, N_y$.

In the minimization of non-convex functions, local optimization algorithms are not reliable since such functions have local minima which are not global minima. A possible approach is to adopt one of the numerical methods available for global optimization, which are however

very time consuming and unsuitable for large scale and badly conditioned systems, like PEA problems are. Therefore, this paper proposes a technique based on homotopy optimization to boost the achievement of the global optimum. Although the convergence to the global minimizer is not deterministically ensured, the proposed method allows to improve significantly the chances to effectively attain modifications of the system parameters that lead to an exact fulfilment of the design requirements.

2.2 Homotopy optimization

Homotopy is a well-established technique in global optimization, whose success is due to its very simple and appealing formulation, combined with excellent properties of robustness and stability [8]. The fundamental idea of homotopy optimization is to minimize an auxiliary and simplified function that approximates the cost function of interest, as a first step of optimization. Then the simplified function is gradually morphed back into the original function. Such a transformation is described by the so-called homotopy map, which is usually dependent on a continuous parameter $\lambda \in [0,1]$. Since the homotopy map is continuous, small changes in the parameter λ lead to small changes in the location of the minimal points. Therefore it is possible, in principle, to keep track of the solution of the simplified problem along the transformation, as λ varies from 0 to 1. It has been observed in literature that the final outcome of such a procedure is often a globally optimal solution of the original minimization problem (see for example [9]). For the implementation of homotopy to be effective, it is important to carefully design both the trivially-solvable auxiliary problem that approximates the original one, and the homotopy map. In the rest of this Section, these two important aspects will be discussed in a brief and general way, whereas the details on the implementation of the method will be given in the next Section.

As for the first issue, i.e. the approximation of the cost function f with another function which is easy to minimize, there is a straightforward choice. In fact it is widely known that convex functions have the remarkable property that any local minimum is also a global minimum. Then, provided a convex approximation f_c of the function of interest f, it is easy to obtain a global minimum of f_c by means of a method for convex programming.

The homotopy map must be defined carefully, as well. As a graphical example, let us consider the one-dimensional real function f and its convex approximation f_c, shown in Figure 1.

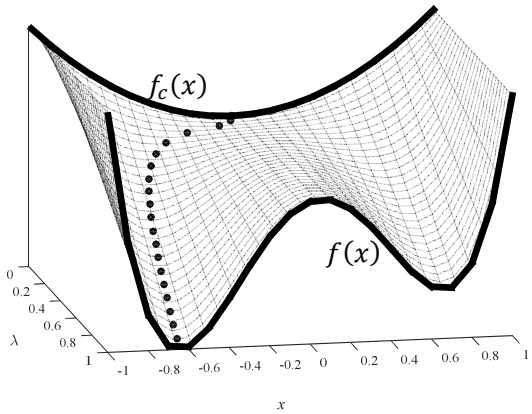


Figure 1: Example of homotopy map; the dots represent the path of optimal points.

A possible way to define the homotopy map is the affine combination of the original cost function and its convexification, that is

$$f_h(x,\lambda) = \lambda f(x) + (1-\lambda) f_c(x). \tag{5}$$

Such a function, represented in the figure by the grid, provides the desired connection between the two functions, in fact it holds that $f_h(x,0) = f_c(x)$ and $f_h(x,1) = f(x)$. This is the basic and usual formulation of the homotopy transformation. The homotopy map employed in the proposed method is, instead, slightly different than the one of Eq. (5), which has been presented only as an explanatory example.

2.3 Formulation of the proposed method

The two issues to be tackled in the design of an homotopy transformation have been carefully investigated to provide an effective solution of the PEA problem.

In order to attain the convex approximation of the cost function f, it is here proposed to replace the bilinear terms $x_r y_s$ that appear in f with an identical number N_t of new auxiliary variables $t_1, \dots, t_{N_t}$:

$$x_r y_s \to t_i. \tag{6}$$

for appropriate values of the indices i, r, s. Since the closed analytic form of the cost function is available, such algorithm is symbolic rather than numeric and hence it is computationally efficient. This definition sets a new function f_c, which can be easily proven to be convex. It is important to note that f_c is defined in a space of higher dimension with respect to the domain of f. In particular $f_c = f_c(\boldsymbol{x}, \boldsymbol{y}, \boldsymbol{t})$, where $\boldsymbol{t} = \{t_1, \dots, t_{N_t}\}^T$ collects all the new auxiliary variables.

Since such variables $t_1, \dots, t_{N_t}$ are still unconstrained, at this point, it is evident that f_c might greatly fail to approximate f. It would be desirable to introduce some constraints aimed at limiting the separation between the original cost function and its convexification. In principle, since the variable t_i replaces the bilinear term $x_r y_s$, for some indices i, r and s, the bilinear constraint $t_i - x_r y_s = 0$ should be added. In practice it is not possible, otherwise convexity of the optimization problem would be lost. In order to introduce this constraint by preserving convexity, an approximation is performed by taking advantage of the results demonstrated in [11], which define the tightest convex envelopes of such constraints. This transformation is known as the so-called McCormick's relaxation. Let $x_r \in [x_r^L, x_r^U]$ and $y_s \in [y_s^L, y_s^U]$ then $t_i = x_r y_s$ implies the following four convex inequalities:

$$\begin{cases} t_i \geq x_r^{\mathrm{L}} y_s + y_s^{\mathrm{L}} x_r - x_r^{\mathrm{L}} y_s^{\mathrm{L}} \\ t_i \geq x_r^{\mathrm{U}} y_s + y_s^{\mathrm{U}} x_r - x_r^{\mathrm{U}} y_s^{\mathrm{U}} \\ t_i \leq x_r^{\mathrm{U}} y_s + y_s^{\mathrm{L}} x_r - x_r^{\mathrm{U}} y_s^{\mathrm{L}} \\ t_i \leq x_r^{\mathrm{L}} y_s + y_s^{\mathrm{U}} x_r - x_r^{\mathrm{L}} y_s^{\mathrm{U}}. \end{cases} \tag{7}$$

In conclusion, the appropriate convex domain for f_c, denoted Γ', is defined by the same inequalities (3) that define Γ, together with the inequalities in (7) for each variable t_i introduced.

Concerning the definition of the homotopy map, rather than directly using the one of Eq. (5), in this work a slightly different strategy is proposed. The idea is inspired by the convexification technique previously discussed. In fact the homotopy map, henceforth denoted by $f_h(\boldsymbol{x}, \boldsymbol{y}, \boldsymbol{t}, \lambda)$, is obtained from f once again by symbolic substitution. In particular each bilinear term $x_r y_s$ is replaced with an affine combination of $x_r y_s$ itself and the associated t_i, based on the homotopy parameter λ:

$$x_r y_s \longrightarrow (1-\lambda)t_i + \lambda x_r y_s. \tag{8}$$

A function f_h defined as $f_h(\boldsymbol{x},\boldsymbol{y},\boldsymbol{t},\lambda)$ is an actual homotopy map that connects f_c and f. In fact it is easy to demonstrate that $f_h(\boldsymbol{x},\boldsymbol{y},\boldsymbol{t},0) \equiv f_c(\boldsymbol{x},\boldsymbol{y},\boldsymbol{t})$ for all $\{\boldsymbol{x}^T,\boldsymbol{y}^T,\boldsymbol{t}^T\}^T \in \Gamma'$ and $f_h(\boldsymbol{x},\boldsymbol{y},\boldsymbol{t},1) \equiv f(\boldsymbol{x},\boldsymbol{y})$, for all $\{\boldsymbol{x}^T,\boldsymbol{y}^T\}^T \in \Gamma$ and $\boldsymbol{t} \in \mathbb{R}^{N_t}$.

2.4 Implementation issues of the proposed method

Finally, it is important to discuss how to implement the solution of the PEA problem in Eq. (4) from a solution of the simplified problem (i.e. the minimization of f_c over Γ') through the homotopy map. In practice, it is necessary to discretize the interval $[0,1]$ where the parameter λ ranges. Then the function $f_h(\boldsymbol{x},\boldsymbol{y},\boldsymbol{t},\lambda)$ is iteratively minimized over Γ' for the selected values of λ. It is usually suggested to space linearly such a range, i.e. $\lambda \in \{0, \Delta\lambda, 2\Delta\lambda, \dots, 1-\Delta\lambda, 1 \subset [0,1]$, where a uniform discretization step $\Delta\lambda$ is assumed, with $\Delta\lambda = 1/(Ni-1)$ and Ni being the number of iterations. The results is not affected by $\Delta\lambda$, unless unreasonable "large values" of $\Delta\lambda$ are assumed. The problem function $f_h(\boldsymbol{x},\boldsymbol{y},\boldsymbol{t},\lambda=0)$, i.e. the one in the first iteration, is a convex optimization program, thus a global minimum, denoted $\left(\boldsymbol{x}_{opt}^{\lambda=0},\boldsymbol{y}_{opt}^{\lambda=0},\boldsymbol{t}_{opt}^{\lambda=0}\right)$, can be found regardless of the initial guess. Afterwards, in any other iteration the cost function is very unlikely convex; hence a solver for non-convex programming must be employed and a great care should be paid in the choice of the initial guess. Therefore, supposed that a minimizer $\left(\boldsymbol{x}_{opt}^{\lambda=\bar{\lambda}},\boldsymbol{y}_{opt}^{\lambda=\bar{\lambda}},\boldsymbol{t}_{opt}^{\lambda=\bar{\lambda}}\right) \in \Gamma'$ of $f_h\left(\boldsymbol{x},\boldsymbol{y},\boldsymbol{t},\bar{\lambda}\right)$ has been found for a certain $\lambda = \bar{\lambda} \in \{0, \Delta\lambda, \dots, 1-\Delta\lambda\}$, then at the subsequent step $f_h\left(\boldsymbol{x},\boldsymbol{y},\boldsymbol{t},\bar{\lambda}+\Delta\lambda\right)$ is minimized using as the initial guess $\left(\boldsymbol{x}_{opt}^{\lambda=\bar{\lambda}},\boldsymbol{y}_{opt}^{\lambda=\bar{\lambda}},\boldsymbol{t}_{opt}^{\lambda=\bar{\lambda}}\right)$. This process is continued until $\lambda = 1$, when the original non-convex problem is morphed back, since $f_h(\boldsymbol{x},\boldsymbol{y},\boldsymbol{t},1) = f(\boldsymbol{x},\boldsymbol{y})$. Finally, the optimal modifications of the mass and stiffness matrices can be computed as $\boldsymbol{\Delta M}_{opt} = \boldsymbol{\Delta M}\left(\boldsymbol{x}_{opt}^{\lambda=1}\right)$ and $\boldsymbol{\Delta K}_{opt} = \boldsymbol{\Delta K}\left(\boldsymbol{x}_{opt}^{\lambda=1}\right)$.

3 NUMERICAL EXAMPLE AND METHOD VALIDATION

3.1 Description of the test-case

The test case assumed for numerical validation is a linear vibratory feeder, of the type usually used to convey small products by means of the oscillatory motion of a surface (the so called tray), excited at resonance by one or more actuators. The system model employed, shown in Figure 2, has 39 degrees-of-freedom. Both the upper beam, which models the feeder tray where the conveyed products move, and the lower one (which behaves as a support beam) are 2 meters long and are modelled through 8 Euler-Bernoulli beam finite elements uniformly spaced. The bending stiffness and linear mass density of such elements in the system original design are, respectively, $EJ_U = 4.5 \cdot 10^3\ Nm^2$ and $\rho A_U = 12.7\ \frac{kg}{m}$ for the upper beam and $EJ_L = 4.5 \cdot 10^4\ Nm^2$ and $\rho A_L = 16\ \frac{kg}{m}$ for the lower one. Two lumped springs, whose stiffness is $k_{f1} = k_{f2} = 50\ \frac{N}{m}$, connect the lower beam to the rigid frame. Six elastic suspensions, modelled as lumped springs, are placed at $0.25\ m$, $0.75\ m$, $1.25\ m$, $1.75\ m$ and at the two ends of the beams to support the tray. Their stiffness will be computed by solving the PEA problem. Three electromagnetic actuators placed at $0.5\ m$, $1\ m$ and $1.5\ m$, and modelled as concentrated masses (whose values are unknown) are also cantilevered to the upper beam by three elastic elements representing the spring leafs (whose stiffness is to be computed). The nominal values of such parameters in the original system design, which can be thought of as either the original system or a first-guess design, are shown in Table 1. It is supposed that all

the lumped parameters can be modified, except the two ground springs, and also that none of the distributed parameters can be altered.

Just one eigenpair is assigned since these devices are forced through single harmonic excitation whose frequency should match the one of a vibrational mode featuring an uniform vertical oscillation of the tray, the so called "working mode". Just the vertical displacements of the tray are therefore assigned at the prescribed values, while all the other system dofs are of less concern and hence belong to the unknown vector $\boldsymbol{y}$. Such entries are therefore constrained to range within the admissible domain (see third column of Table 2). It is only required that the three concentrated masses have the same vertical displacements and that they oscillate in anti-phase with respect to the upper beam, with an arbitrary amplitude. As for the eigenfrequency, it is required to be $40\ Hz$.

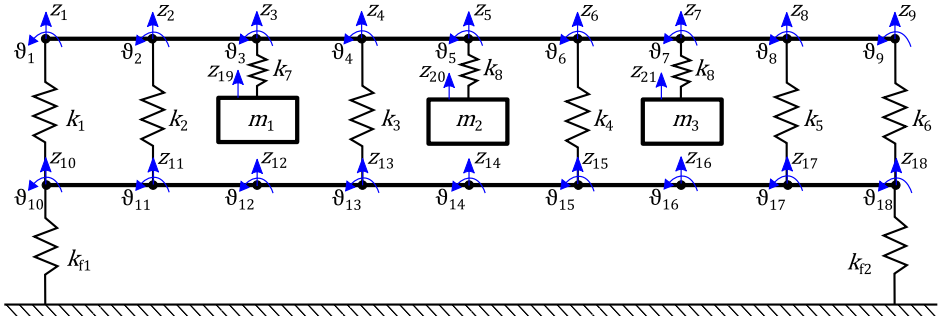


Figure 2: Distributed and lumped parameter system model.

3.2 Numerical results

The implementation of the method has been coded in *Matlab*, using the modelling language of *YALMIP* [12]. The discretization step of the homotopy parameter has been chosen as $\Delta\lambda = 0.02$. The solvers employed are *Mosek* [13] for convex programming and *fmincon* [14], contained in the *Optimization Toolbox* by Mathworks, for non-convex programming.

	Lower bound	Upper bound	Optimal values
$m_1\ (kg)$	0	50	20 + 8.931
$m_2\ (kg)$	0	50	20 + 9.868
$m_3\ (kg)$	0	50	20 + 8.931
$k_1\ (N/m)$	-7*e*3	+2*e*5	8.000*e*3 + 1.062*e*5
$k_2\ (N/m)$	-7*e*3	+2*e*5	8.000*e*3 + 1.875*e*5
$k_3\ (N/m)$	-3*e*4	+2*e*5	4.000*e*4 + 6.764*e*4
$k_4\ (N/m)$	-3*e*4	+2*e*5	4.000*e*4 + 6.764*e*4
$k_5\ (N/m)$	-7*e*3	+2*e*5	8.000*e*3 + 1.875*e*5
$k_6\ (N/m)$	-7*e*3	+2*e*5	8.000*e*3 + 1.062*e*5
$k_7\ (N/m)$	-2*e*5	+2*e*5	2.700*e*5 - 9.524*e*4
$k_8\ (N/m)$	-2*e*5	+2*e*5	2.700*e*5 - 8.958*e*4
$k_9\ (N/m)$	-2*e*5	+2*e*5	2.700*e*5 - 9.524*e*4

Table 1: Optimal modifications.

The computed optimal modifications of the physical parameters are shown in the second column of Table 1. The resulting eigenvector is shown in the first column of Table 2. It fits very accurately the desired one, leading to a MAC (Model Assurance Criteria), computed

with reference to just the assigned entries of the eigenvector, equal to 1.000, and whose eigenfrequency is $\omega = 40.000\,Hz$. As a further and concise evaluation of the accuracy, the final residual is negligible, in fact $\left\|\left[\omega^2\left(\mathbf{M}+\mathbf{\Delta M}_{\text{opt}}\right)-\left(\mathbf{K}+\mathbf{\Delta K}_{\text{opt}}\right)\right]\cdot \boldsymbol{u}_{opt}\right\| = 8.949\cdot 10^{-7}$. The obtained mode shape is depicted in Figure 4, where the displacement of the three concentrated masses with respect to the equilibrium is magnified six times for clarity of representation.

In comparison, Figure 3 shows the mode shape of the original unmodified system with the highest participation factor at 40 Hz, whose eigenfrequency is 40.135 Hz and whose MAC is 0.632. The great improvement obtained, in particular in term of mode shape, is evident. All these results clearly confirm the effectiveness of the proposed method in performing PEA for optimizing the dynamic behaviour of complex vibrating systems.

	Obtained eigenvector	Desired eigenvector
z_1	1.000	1
ϑ_1	0.067	[-20, 20]
z_2	1.000	1
ϑ_2	-0.018	[-20, 20]
z_3	1.000	1
ϑ_3	0.005	[-20, 20]
z_4	1.000	1
ϑ_4	-0.001	[-20, 20]
z_5	1.000	1
ϑ_5	0.000	[-20, 20]
z_6	1.000	1
ϑ_6	0.001	[-20, 20]
z_7	1.000	1
ϑ_7	-0.005	[-20, 20]
z_8	1.000	1
ϑ_8	0.018	[-20, 20]
z_9	1.000	1
ϑ_9	-0.067	[-20, 20]
z_{10}	0.306	[-20, 20]
ϑ_{10}	-1.900	[-20, 20]
…		
z_{11}	-0.164	[-20, 20]
ϑ_{11}	-1.834	[-20, 20]
z_{12}	-0.588	[-20, 20]
ϑ_{12}	-1.489	[-20, 20]
z_{13}	-0.883	[-20, 20]
ϑ_{13}	-0.839	[-20, 20]
z_{14}	-0.991	[-20, 20]
ϑ_{14}	0.000	[-20, 20]
z_{15}	-0.883	[-20, 20]
ϑ_{15}	0.839	[-20, 20]
z_{16}	-0.588	[-20, 20]
ϑ_{16}	1.489	[-20, 20]
z_{17}	-0.164	[-20, 20]
ϑ_{17}	1.834	[-20, 20]
z_{18}	0.306	[-20, 20]
ϑ_{18}	1.900	[-20, 20]
z_{19}	-0.106	[-20, -10^{-8}]
z_{20}	-0.106	[-20, -10^{-8}]
z_{21}	-0.106	[-20, -10^{-8}]

Table 2: Comparison of the obtained and desired eigenvector.

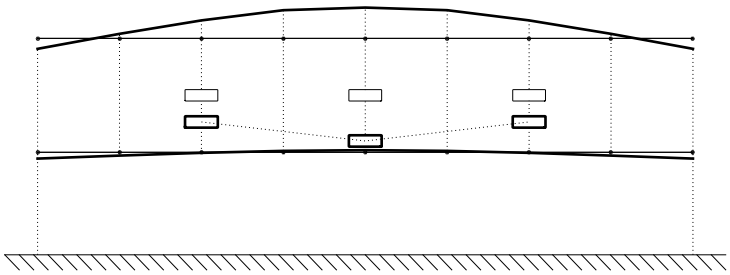


Figure 3: Original mode shape at 40.135 Hz.

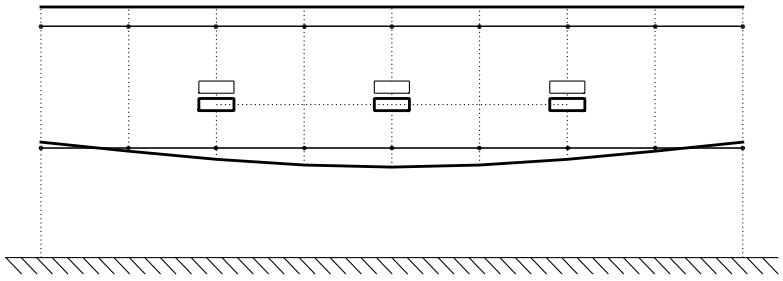


Figure 4: Modified mode shape at 40.000 Hz.

4 CONCLUSIONS

This paper proposes a method for inverse dynamic structural modification (IDSM) to perform partial eigenstructure assignment (PEA), i.e. to make possible the assignment of an arbitrary number of entries of eigenvectors and the related eigenvalues. The method is intended for those cases where it is desirable assigning only the response of some critical parts of the system, rather than the response of the whole system.

In the proposed approach, the components of the eigenvectors related to the most concerning parts of the system are exactly imposed on the basis of the desired dynamic behaviour. Conversely, for the less concerning ones, the related eigenvector entries are considered as optimization variables, and hence it is possible to specify upper and lower bounds. Since the introduction of these new variables makes the problem non-convex, an effective and intuitive homotopy-based approach has been proposed to boost the convergence of the numerical optimization towards a globally optimal solution.

The method has been validated through the partial eigenstructure assignment in a test case of practical interest: a linear vibratory feeder, designed to be excited by a single-harmonic force exerted by three electromagnetic actuators. The assignment involved the natural frequency, which has been asked to approach to the excitation frequency, and the dynamic behaviour of the tray where the products are placed and whose vibration determines the conveyed product motion. In particular the vertical displacement of the tray has been asked to be uniform throughout its length. The rest of the system, instead, has been forced to oscillate within some appropriate bounds.

The results obtained prove that the desired eigenstructure has been achieved with an extremely high accuracy, hence the proposed homotopy optimization technique actually succeeded in finding a global minimum of the cost function, as it is also evident from the computed residual. In conclusion, the performed test suggests that the advantages of Partial Eigenstructure Assignment greatly surpass the drawbacks, which are basically limited to a slightly more laborious computation of the optimal modifications. Therefore, the proposed method, given the good results obtained in the assessment with medium-scale systems, can be considered mature enough to be challenged also with large-scale models.

ACKNOWLEDGEMENT

The first Author acknowledges the financial support of the FSU foundation ("Fondazione Studi Universitari" — Vicenza) through a Ph.D. scholarship.

REFERENCES

[1] Y. Ram and S. Braun, An inverse problem associated with modification of incomplete dynamic systems. *Journal of Applied Mechanics*, **1**, 233–237, 1991.

[2] I. Bucher and S. Braun, The structural modification inverse problem: an exact solution. *Mechanical Systems and Signal Processing*, **3**, 217–238, 1993.

[3] D. Sivan and Y. Ram, Optimal construction of a mass-spring system from prescribed modal and spectral data. *Journal of sound and vibration*, **3**, 323–334, 1997.

[4] J. E. Mottershead, C. Mares and M. I. Friswell, An inverse method for the assignment of vibration nodes. *Mechanical Systems and Signal Processing*, **15**, 87–100, 2001.

[5] D. Richiedei, A. Trevisani and G. Zanardo, A constrained convex approach to modal design optimization of vibrating systems. *Journal of Mechanical Design*, **6**, 061011, 2011.

[6] H. Ouyang, D. Richiedei, A. Trevisani and G. Zanardo, Eigenstructure assignment in undamped vibrating systems: A convex-constrained modification method based on receptances. *Mechanical Systems and Signal Processing*, **27**, 397–409, 2012.

[7] H. Ouyang, D. Richiedei, A. Trevisani and G. Zanardo, Discrete mass and stiffness modifications for the inverse eigenstructure assignment in vibrating systems: Theory and experimental validation. *International Journal of Mechanical Sciences*, **1**, 211–220, 2012.

[8] L. T. Watson, Globally convergent homotopy algorithms for nonlinear systems of equations. *Nonlinear Dynamics*, **1**, 143–191, 1990.

[9] C. P. Vyasarayani, T. Uchida, A. Carvalho and J. McPhee, Parameter identification in dynamic systems using the homotopy optimization approach. *Multibody System Dynamics*, **4**, 411–424, 2011.

[10] E. M. Smith and C. C. Pantelides, A symbolic reformulation/spatial branch-and-bound algorithm for the global optimisation of nonconvex MINLPs. *Computers & Chemical Engineering*, **4**, 457–478, 1999.

[11] F.A. Al-Khayyal and J. E. Falk, Jointly constrained biconvex programming. *Mathematics of Operations Research*, **2**, 273–286, 1983.

[12] J. Löfberg, Yalmip : A toolbox for modeling and optimization in MATLAB. *Proceedings of the CACSD Conference*, Taipei, Taiwan, 2004.

[13] E. D. Andersen and K. D. Andersen, *The MOSEK interior point optimizer for linear programming: an implementation of the homogeneous algorithm*. Springer, 2000.

[14] R. H. Byrd, M. E. Hribar and J. Nocedal, An interior point algorithm for large-scale nonlinear programming. *SIAM Journal on Optimization*, **9**, 877–900, 1999.

International Conference on Engineering Vibration
Ljubljana, Slovenia, 7-10 September 2015

COMPARISON BETWEEN MULTI-OBJECTIVE GENETIC ALGORITHM AND BAYESIAN INFERENCE ON IDENTIFICATION OF ROTATING MACHINERY PARAMETERS.

Andrei B. Rezende, Natalia C. Tyminski, Helio F. de Castro*

University of Campinas, Faculty of Mechanical Engineering - R. Mendeleyev 200, Campinas, SP 13083-860, Brazil
{abavaresco, natalia.tyminski, heliofc}@fem.unicamp.br

Keywords: Multi-objective Genetic Algorithm, Bayesian Inference, unbalance identification, rotordynamics.

Abstract. *Rotating systems are critical components of power generation plants, as they are critical to its operation. Therefore, the study and modeling of Rotating machinery have been developed, where the rotor is modeled by finite element method and the bearings by numerical or analytical approach. These rotating systems have stochastic characteristic, which makes the identification of parameters by model updating (solution of inverse problems) a very complicate procedure, when considered deterministic model responses. This work proposes the use of model updating techniques that take into account the stochastic characteristic of the system. The first method is the application of multi-objective optimization, in order to obtain a feasible region of possible responses (Pareto set). Thus, it is possible to evaluate the effect of model uncertainties on the variability of the Pareto optimal set. The optimization methodology proposed is based on multi-objective genetic algorithms. Another proposed approach is application of Bayesian inference. In this case, it is taken into account a priori distribution, which represents the previous knowledge about the parameters, and a likelihood distribution, represented by a distribution of the difference (or residual) between the experimental results and the response of the dynamic model. In other words, the likelihood distributions typifies the observations. The parameters to be determined correspond to the posterior distribution, which takes into account the prior knowledge and the observations. The solution to this method can be obtained through a numerical search method Monte Carlo Markov Chain (MCMC). For the application of model updating, experimental data from a test-rig will be obtained.*

1 INTRODUCTION

Fault identification is an important issue in rotordynamics field, because rotating machines are widely applied in industries or energy production. Therefore, significant advances in the modeling of rotor-bearing systems have been achieved, see [1-3]. These models are extensively applied on model based identification techniques for fault diagnosis (see, [4-9]).

These model-based techniques are formulated as optimization procedures, whose objective functions are add to a single function through weighting factors. Each objective function represents the residuum between an experimental response and the correspondent degree of freedom of the numerical model. If a bad choice of these weighting factors is made, the fault parameter identification can lead to values that are not the right solution. Therefore, multi-objectives techniques can be used, considering all objective functions (residuum) separately, so that, a Pareto optimal set of solutions can be reached, and then the fault parameters can be identified from this solution set, as proposed by [10].

NSGA-II [11] is a multi-objective optimization technique based on Genetic Algorithm, which means non-dominated sorting genetic algorithm II. The first version of NSGA algorithm was developed in 1995 [12]. For the second version, some improvements were developed as an elitism criterion and no need of a sharing parameter. This method is an interesting option for multi-objective optimization and it were applied on this work for fault identification procedure.

After obtaining the Pareto set, a single solution from this set should be selected. It is proposed the application of maximum likelihood principle to do this choice. In that way, the solution of the Pareto set with higher likelihood function has more probability to be right solution. This is inspired on the application of Bayesian inference for parameter estimation. Tyminski and Castro [13] applied Bayesian inference to unbalance identification. In this case, the likelihood function together with a prior function (information about the parameters before the observations, or residuum calculation) were considered.

The methodology of model updating using Bayesian Inference was also used by [14], where modeling errors were considered. Marwala [15] used Bayesian Inference to updating a finite element model. Ritto [16] applied Bayesi-an inference to parameter identification in drill bits. An important advantage of this proposal is the possibility of identify stochastic information of the parameters.

To achieve the estimated parameters distribution through Bayesian inference, Markov Chain Monte Carlo methods can be considered [17-23]. As Genetic Algorithm, these methods demands many evaluations. So, both techniques take time to converge.

The objective of this work is a comparison between multi-objective genetic algorithm optimization and Bayesian inference for unbalance parameter identification.

2 ROTOR-BEARING MODEL

The representation of mathematical model of a rotating system can be divided in substructures, which are the rotor, the journal bearings, and the support structure (or foundation). The foundation can be considered rigid in a general case. The rotor support is realized by the oil-film bearings, which couple the rotor train and supporting structures. Therefore, hydrodynamics forces are generated in the clearance between the rotating part and the foundation. These forces have a non-linear nature, but it can considered a linear approximation in general, taking into account damping and stiffness coefficients, see [24]. Therefore, the expression of the linearized forces of the oil-film bearing is:

$$\mathbf{F_B} = \mathbf{K_b} \cdot \mathbf{q} + \mathbf{C_b} \cdot \dot{\mathbf{q}} \tag{1}$$

where the bearing stiffness and damping matrices are respectively:

$$\mathbf{K_b} = \begin{bmatrix} \ddots & \vdots & \vdots & \\ \cdots & k_{yy}(\omega) & k_{yz}(\omega) & \cdots \\ \cdots & k_{zy}(\omega) & k_{zz}(\omega) & \cdots \\ & \vdots & \vdots & \ddots \end{bmatrix} \text{ and } \mathbf{C_b} = \begin{bmatrix} \ddots & \vdots & \vdots & \\ \cdots & c_{yy}(\omega) & c_{yz}(\omega) & \cdots \\ \cdots & c_{zy}(\omega) & c_{zz}(\omega) & \cdots \\ & \vdots & \vdots & \ddots \end{bmatrix}. \tag{2}$$

Finite Element method can be applied to model de rotor, which is composed by cylindrical beams elements and rigid discs elements [25]. Therefore, mass and stiffness matrices can be obtained. Equation (3) presents the equation of motion, which depends on the rotor-bearing system matrices **M** (mass), **C** (damping) and **K** (stiffness), the excitation force **f**(*t*), and the bending degree of motion $\mathbf{q}(t)^{\mathrm{T}} = \left\{y_1, z_1, \phi_{y_1}, \phi_{z_1}, \dots, y_n, z_n, \phi_{y_n}, \phi_{z_n}\right\}$, where the horizontal and vertical radial displacements are *y* and *z* and the angular displacement related to *y* and *z* are respectively ϕ_y and ϕ_z.

$$\mathbf{M}\ddot{\mathbf{q}}(t) + (\mathbf{C} + \mathbf{C_b})\dot{\mathbf{q}}(t) + (\mathbf{K} + \mathbf{K_b})\mathbf{q}(t) = \mathbf{f}(t). \tag{3}$$

The shaft damping matrix C contains two parts. The first part is proportional to the stiffness matrix **K** (multiplied by the constant β), and the second part has the gyroscopic effect (**C** = β**K** + ω**G**), also obtained by Finite Element Method. The bearing stiffness and damping coefficients are included in the corresponding degrees of freedom.

Unbalance is the most common failure in rotating system. The synchronous excitation force for a constant rotation speed ω is due to the mass unbalance m, with an eccentricity e and phase angle φ, as it is shown in Eq. (4). The axial position of the unbalance is determined by the finite element discretization node. The unbalance force is included in the degrees of freedom related to that node:

$$\mathbf{f}(t) = m \cdot e \cdot \omega^2 \begin{Bmatrix} \vdots \\ \cos(\omega t - \varphi) \\ \sin(\omega t - \varphi) \\ \vdots \end{Bmatrix} \tag{4}$$

In order to compare the experimental results to the numerical response, the unbalance response in frequency domain is considered, which can be calculated by Eq. (5):

$$Q = \frac{m \cdot e \cdot \omega^2 \cdot \exp(i \cdot \varphi)}{-\omega^2 \mathbf{M} + i \cdot \omega \mathbf{C} + \mathbf{K}} \tag{5}$$

3 EXPERIMENTAL SETUP

Figure 1 illustrates the test-rig used to obtain the real response of unbalance rotor bearing system. The system is composed by two hydrodynamic journal bearings spaced 600 mm, with radial clearance of 90 μm. The bearing length and radius are 20 mm, 31 mm respectively. Located in the middle of a shaft with diameter of 12mm, there are a disc with mass of 2.3 kg, external diameter of 95 mm and length 47 mm. To measure the shaft displacement, two sensors are immersed in the oil film in each bearing.

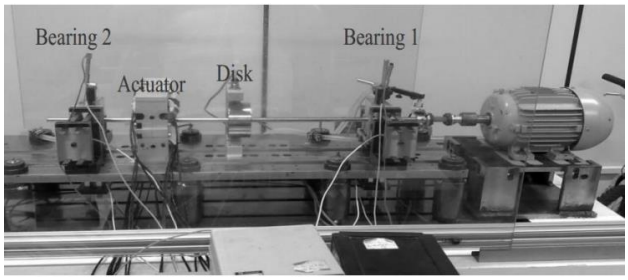


Figure 1: Experimental test-rig, see [8].

4 SEARCH METHODS

4.1 Multi-Objective Genetic Algorithm (NSGA II)

The genetic algorithm is based on the biological evolution theory. Therefore, it considers that an individual of future generations is a descendent of the best-adapted individuals of previous. The main Genetic Algorithm operators is the reproduction, which is a combination of selection, crossover and mutation process that leads to a new generation with the best characteristic of the previous one. It means that the search parameters that corroborate with a better objective function are used to create a new set of parameter for the next iteration. Firstly, it is generated an initial population with the fixed size and its individuals (set of solutions parameters) are coded by a binary string. In each generation, all individuals (or possible solutions) are evaluated concerning their own fitness (or objective functions). In order to generate a new offspring, the operator's selection, crossover and mutation are applied. The selection is an important phase of GA because it selects the most capable individuals to reproduce and participate in the next generation (iteration). The individual's probability to be selected depends on its fitness. The objective of this process is to make copies of good solutions and eliminate bad solutions in a population, while maintaining the size of the population constant. After that, crossover is used by applying crossings to combine different individuals' genes to produce the offspring. It usually selects two individuals and random portions of the genetic material to exchange among them in order to generate new individuals for the next generation. The mutation operator is applied to randomly modify the new individuals' code. The mutation is a critical element of a GA because, instead of guiding the population for the convergence, as the crossover operator, it reintroduces the genetic diversity in the population and allows the search process to escape from local optima.

The NSGA (Non-dominated Sort Genetic Algorithm) is a genetic algorithm multi-objective that results in a selection of the non-dominated solution and maintains the diversity of this solution. To be considered a non-dominated solution, it is necessary that none of the objective functions can be improved in value without degrading some of the other objective values. In each iteration of NSGA, the population is divided in groups that are distributed in

non-dominated front. This process is used to select the individuals that will participate in the process of reproduction.

The NSGA – II is a modified version of NSGA. In NSGA II is included the elitism (the best individuals of a generation are copied to the next one). Besides, a parameter called crowding that is a measure between an individual and its neighbors was refined else the sorting algorithm. In this method after the population are initialized, they are sorted considering the non-dominated into each front. In the first front are this non-dominated individuals and the second front are the dominated individual by the first front. In the first front is attributed a number 1 and the second front the number 2 then a rank is created with this individuals. Therefore, to use the fitness value of each individual, it is considered a crowding distance parameter that shows how the individuals are closed at your neighbors. The binary tournament selection is used to select the individuals that will pass by the reproduction process. The process is repeated considering the rank and the crowding distance on the last front.

For this work, the Pareto set represents the solutions (unbalance moment, phase and position) that minimize the objective functions (residues) of Eq. (6) and Eq. (7). As the choice to the best response is a high order decision, it was proposed a selection method: taking in to account the proximity between the solutions, the possible solutions are separated in groups. After that, it was used the maximum likelihood method, considering a normal distribution with probability density function pdf represented by Φ for each objective function. Therefore, the solution with higher likelihood function L (Eq. (8)) has a higher probability to be a better solution.

$$f_i = \sqrt{(\mathrm{Re}(qe_i) - \mathrm{Re}(qs_i))^2} \tag{6}$$

$$f_{i+ns} = \sqrt{(\mathrm{Im}(qe_{i+ns}) - \mathrm{Im}(qs_{i+ns}))^2} \tag{7}$$

where *ns* is the number of sensors and *i* varies *1* to *ns*, *qe* and *qs* are the experimental and simulated displacements respectively. In this work, it was used two sensors in each bearing, so *ns* is equal to four that totalizes eight objective functions.

$$L = \prod_{i=1}^{2ns} \Phi(f_i) \tag{8}$$

4.2 Bayesian Inference

The Bayesian Inference is a method that considers the Bayes theorem as the principal rule. Through the Bayesian Inference, it is possible estimated a parameter with their uncertainties. The Bayes theorem is given by the Eq. (9):

$$p(\boldsymbol{\theta}|\mathbf{X}) = \frac{p(\mathbf{X}|\boldsymbol{\theta})p(\boldsymbol{\theta})}{p(\mathbf{X})} \tag{9}$$

According to Bayes theorem, the prior information about a parameter of interest is given by a distribution for this parameter, and this is represented by p(θ). The data observation is represented by the likelihood function, represented by the distribution $p(\mathbf{X}|\boldsymbol{\theta})$. This distribution contains the residue between the experiments results and the model. The distribution $p(\mathbf{X})$ does not depends on the parameter θ. In that way, it is considered as a constant of proportionality. The posterior distribution, $p(\boldsymbol{\theta}|\mathbf{X})$, is the distribution for the estimated parameters

and is given by the combination of the prior distribution and the likelihood function. In the case that there is a few information about the parameters, a uniform distribution was considered for prior distribution, the only information necessary is the upper θ_u and lower θ_l bounds of each parameter:

$$p(\boldsymbol{\theta}) = \begin{cases} \dfrac{1}{\boldsymbol{\theta}_u - \boldsymbol{\theta}_l} & \boldsymbol{\theta}_l \leq \boldsymbol{\theta} \leq \boldsymbol{\theta}_u \\ 0 & \boldsymbol{\theta} > \boldsymbol{\theta}_l \quad \text{and} \quad \boldsymbol{\theta} > \boldsymbol{\theta}_u \end{cases} \tag{10}$$

The likelihood distribution $p(\mathbf{X}|\boldsymbol{\theta})$ is assumed to be a Normal distribution, and the difference between experimental and numerical results is the residue ε i. It can be written as [15]:

$$p(\mathbf{X}|\boldsymbol{\theta}) = \exp\left(-\kappa \sum_i^N (\varepsilon_i^2)\right) \tag{11}$$

$$\varepsilon_i^2 = \left[\sum_{i=1}^{ns} w_i (f_i + f_{i+ns})\right]^2 \tag{12}$$

where f_i and f_{i+ns} are the objectives functions of Eqs. (6) and (7) and *w* is a weighting factor to each measured degree of freedom. These factors are used to evidence a higher confidence for a specific measured degree of freedom. In our case, the same importance is considered for all measured signals. The measurement adjustment coefficient is represent by κ. This constant is chosen to increase (or decrease) the relative importance of the likelihood distribution to the prior distribution.

As the analytical calculation of posteriori distribution Eq. (9) is hardly accomplished, the application of sampling techniques, as the Monte Carlo Markov Chain methods, is a reasonable solution.

4.3 Markov Chain Monte Carlo

Markov Chain Monte Carlo (MCMC) method is a class of algorithms to simulate complex multivariate distributions. A Markov chain is a sequence of random elements (X1, X2, X3, … , Xn) where the element Xn+1 only depends on Xn. The method started from the proposal distribution. In each cycle of algorithm, it generates a candidate sample, and this sample may or may not be accepted, according to the criterion of the algorithm. For this work, it was considered the Delayed Rejection Adaptive Metropolis (DRAM) method [13, 18-20]. The final sample will be a distribution, in which through the Monte Carlo integration method, you can get a posteriori distribution of the parameters estimates.

5 METHODOLOGY APPLICATION AND RESULTS

Firstly by the application of an updating model procedure the stiffness and damping coefficients are obtained. This process can be seen in [8]. Then, the parameters of Eq. (2) is obtained and the rotor-bearing model in Eq. (3) completed.

Then, in the center disc of test-rig is set an unbalance mass to obtain the experimental response. Thus, the residual (difference between the experimental and simulated responses) in each bearing degree of freedom were accomplished.. The NSGA II and the Bayesian Inference method are applied to obtain unbalance amplitude ($m \cdot e$), phase angle (φ) and axial position that are the failure parameters.

The parameters of NSGA II can be seen on Table 1. The product of number of generations (iterations) and population size represents the number of evaluation of the objective functions. Others parameters are the probability of crossover and mutation respectively.

NSGA II Parameters			
Number of Iteration	1000	Probability of Mutation	0,2
Population Size	100	Probability of Crossover	0,95

Table 1: NSGA II Parameters.

The solutions obtained after application of NSGA II are illustrated in Figure 2. The Pareto set was separated in groups (represented by different colors) considering the proximity between each element. The target solution (based on the experimental test) is also represented in Figure 2 by a black square, with unbalance moment of 1.425·10-4 kg·m, unbalance phase equal to 0 radians and axial position corresponded by the node 8.

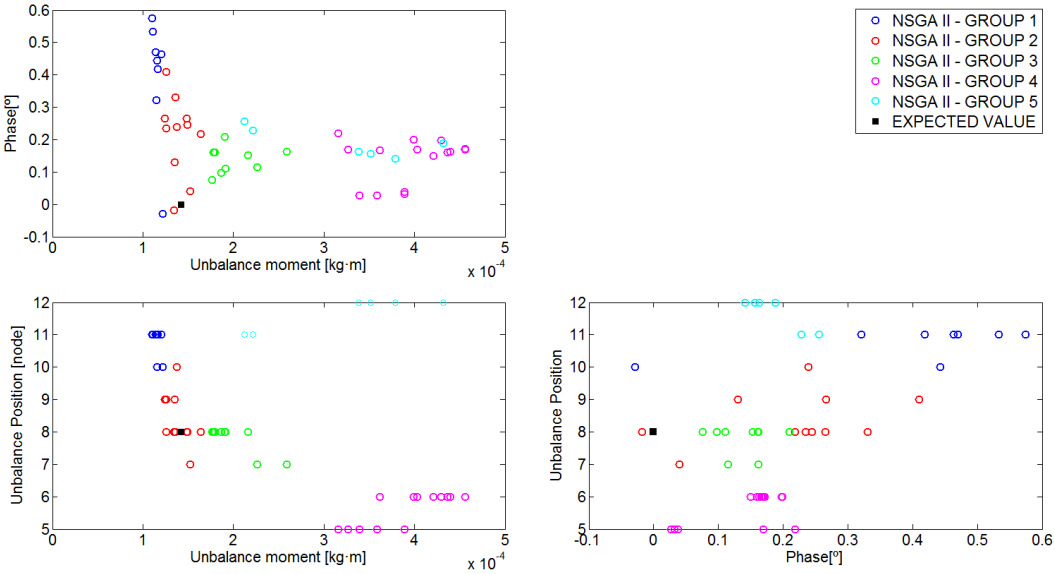


Figure 2: Groups of solutions to NSGAII.

Table 2 presents the best components of group. The classifications is based on the maximum likelihood principle. It is important to highlight that the group 2 presents the results that are the closest to the expected values.

For Bayesian inference evaluation, uniform distribution was used, Eq. (10). Therefore, the lower and upper limit of each parameter should be considered. These limits are presented on Table 3, as well as, the initial value for MCMC procedure, where it was selected 10000 iterations.

The estimated parameter distributions are shown on Figure 3. Besides, the expected values are also highlited (in red) in Figure 3. The expexted values, mean and standard deviation of each parameter are also presentd by Table 4.

Both methods were sucefull to reach close to the expected values. The applications of the Bayesian Inference demanded10000 iterations, while the NSGAII demanded 100000 objective functions (evaluations). On the other hand, the NSGAII was more prescise on the determination of the axial position, because for the group 2 (the best selection by maximum

likelihood method), the node varies from 7 to 11, while values between 6 and 12 were reached on the Bayesian Inference, even considering that most of the estimated values are around 8 and 9. This means that for this parameter, a lower uncertainty could be reached by the aplication of NSGAII.

			Bests Individuals by Group				
			GROUP 1	GROUP 2	GROUP 3	GROUP 4	GROUP 5
NSGA II	X (Solution)	Unbalance Moment [Kg.m]	1,217E-04	1,352E-04	1,783E-04	3,615E-04	3,383E-04
		Unbalance Phase [°]	-0,028	0,130	0,161	0,166	0,163
		Unbalance Position [Node]	10,331	9,205	8,221	6,307	11,547
	Classification through Maximum Likelihood Principle: [Li – min(L)] $.10^{12}$		2,682	3,014	2,738	2,875	2,877

Table 2: Best solutions for each method separated by group according maximum likelihood principle.

Parameter	Lower limit	Upper limit	Initial value
Unbalance moment (kg·m)	$1 \cdot 10^{-5}$	$10 \cdot 10^{-4}$	$\cdot 10^{-4}$
Phase (rad)	$-\pi$	π	0.1745
Axil position (node)	1	17	8

Table3: Inicial parameters for Prior distribution.

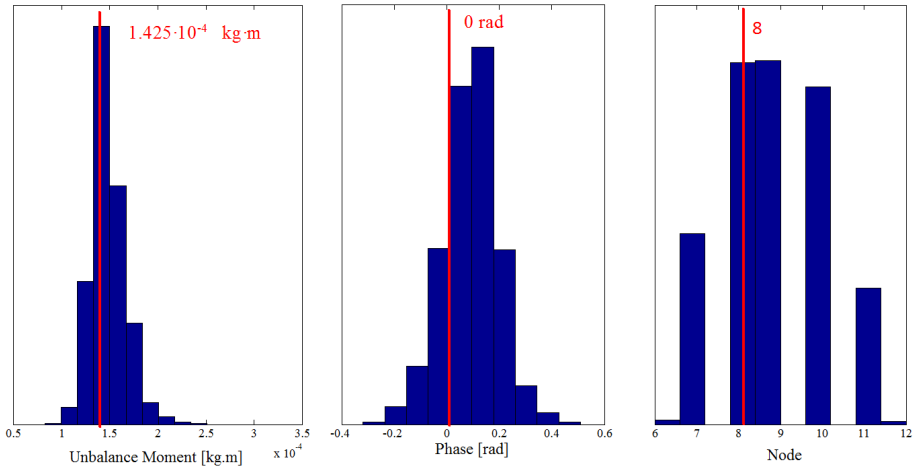


Figure 3: Estimated Parameters distributions and expected values (red)

Parameter	Mean (μ)	Standard deviation (σ)	Expected value
Unbalance moment (kg·m)	$1.4824 \cdot 10^{-4}$	$1.8066 \cdot 10^{-5}$	$1.425 \cdot 10^{-4}$
Phase (rad)	0. 091695	0. 10528	0
Axil position (node)	8. 9066 (9)	1. 2527	8

Table 4: Mean and Standard deviation of the parameters.

6 CONCLUSIONS

This paper proposed the application of multi-objective Genetic Algorithm and Bayesian Inference to estimate the unbalance response of the rotor. These parameters are the unbalance moment, the phase angle and the axial position.

First, the as Non-dominated Sort Genetic Algorithm II (multi-objective Genetic Algorithm) was applied. It was able to reach a non-dominated Pareto set. This solution could be divided in 5 groups of solution, based on distance between the estimated parameters. In order to choose the more adequate solution, the maximum likelihood method was used to indicate the most probable single solution.

On the other hand, it was applied the Monte Carlo Markov Chain methods with the DRAM algorithm to estimate the unbalance parameters. Once estimated the parameters, it was used to simulate the stochastic response of the rotor, using the Monte Carlo simulation.

In both cases, the identified parameters were close to the expected values. However, the NSGAII needed a considerable amount of objective functions evaluation, while the Bayesian Inference accomplished to a axial position distribution with a high dispersion (or uncertainty).

REFERENCES

[1] Nelson, H.D., A Finite Rotating Shaft Element Using Timoshenko Beam Theory. *Journal of Engineering for Industry – Transactions of the ASME*. New York: ASME, 11 p., 1980.

[2] Machado, T.H., Cavalca, K.L. Analysis of the influence of hydrodynamic bearings with geometric discontinuities on the dynamic response of a rotating system. In: *IMechE 2012 - VIRM10 10th International Conference on Vibrations in Rotating Machinery*, London, England, 2012.

[3] Daniel, G.B., Cavalca, K. L. Evaluation of the Thermal Effects in Tilting Pad Bearing. *International Journal of Rotating Machinery*, p. 1-17, 2013.

[4] Lees, A.W., Friswel, M.I.. The evaluation of rotor imbalance in flexibly mounted machines. *Journal of Sound and Vibration*, v.208, pp. 671 -683, 1997.

[5] Pennacchi, P., Vania, A. Analysis of rotor-to-stator rub in a large steam turbogenerator. *International Journal of Rotating Machinery*, 8p, 2007.

[6] Edwards, S., Lees A.W., Friswell M.I. Experimental Identification of Excitation and Support Parameters of a Flexible Rotor-Bearings-Foundation System from a Single Run-Down. *Journal of Soundand Vibration*, vol. 232(5), pp.963-992, 2000.

[7] Camargo, L. W. F., Castro, H. F., Cavalca. K. L. Identification of misaligment and unbalance in rotating machinery using multi-objective genetic algorithms. In: *Proceedings of the 8th IFToMM International Conference on Rotordynamics*, Seoul, Korea, 2010.

[8] Castro, H. F., Cavalca, K. L., Bauer, J., Norrick, N. Convergence on unbalance identification process based on genetic algorithm applied to rotating machinery. In: *Proceedings of the 10th International Conference on Vibrationsin Rotating Machinery*, London, England, 2012.

[9] Castro, H. F. Comparison in the application of genetic algorithm and particle swarm optimization in unbalance identification in rotating machinery. *22rd ABCM International Congress of Mechanical Engineering*, Ribeirão Preto, Brazil, pp. 1-11, 2013.

[10] Christodoulou, K., Ntotsios, E., Papadimitriou, C., Panetsos, P. Structural model updating and prediction variability using Pareto optimal models. *Comput. Methods Appl. Mech. Engrg.* 198. 138–149, 2008.

[11] Deb. K., A. Pratap, S. Agarwal and T. Meyarivan. A fast and elitist multi-objective genetic algorithm: NSGA II. *IEEE Trans. Evol. Comput*., 6: 182-197, 2002.

[12] Srinivas, N. and Deb K. Multi-objective function optimization using non-dominated sorting genetic algorithms. *Evolutionary Computation*, 2(3):221–248, Fall 1995.

[13] Tyminski, N. C., Castro, H. F. Application of Bayesian Inference to unbalance identification in rotors. *9th IFToMM International Conference on Rotor Dynamics* , 2014.

[14] Zhang, E. L., Feissel, P., Antoni, J. A comprehensive Bayesian approach of model updat-ing and quantification of modeling errors. Probabilistic Engineering Mechanics. 26, pp. 550-560, 2011.

[15] Marwala. T. Finite Element Model Updating Using Computational Intelligence Techniques. *Springer Verlag*, London, UK. , 2010.

[16] Ritto, T. G. Bayesian identification of the bit-rock interaction parameters using a simplified drill-string dynamical model. *Proceedings of the XV International Symposium on Dynamic Problems of Mechanics*, pp. 1 -7, 2013.

[17] Boulkaibet, I., Marwala, T., Mthembu, L., Friswell, M.I., Adhikari, S. Sampling Techniques in Bayesian Finite Element Model Updating, *25th International Modal Analysis Conference*, 2012.

[18] Haario H., Saksman E., and Tamminen J. Adaptative proposal distribution for random walk Metropolis algorithm. *Comp. Stat*. 14: 375-395, 1999.

[19] Haario H., Saksman E., and Tamminen J. An adaptive Metropolis algorithm. Bernoulli 7: 223-242, 2001.

[20] Haario H., Laine M., Mira A. and Saksman E. DRAM: Efficient adaptative MCMC. *Comp. Stat*. 16:339-354, 2006.

[21] Tierney L. and Mira A. Some adaptive Monte Carlo methods for Bayesian inference. *Statistics in Medicine* 18:2507-2515, 1999.

[22] Green, P.J. and Mira, A. Delayed rejection in reversible jump Metropolis-Hastings. *Biometrika* 88: 1035-1053, 2001.

[23] Mira A. On Metropolis-Hastings algorithms with delayed rejection. *Metron*, Vol. LIX, (3 -4):231 -241, 2001.

[24] Lund, J. L. Review of the concept of Dynamic Coefficient for Fluid Film Journal Bearings. *Journal of Tribology*, Vol. 109, pp. 37 – 41, 1987.

[25] Tuckmantel, F.W.S., Cavalca, K.L. Integration of rotor-hydrodynamic bearings-support structure systems for numerical resolution. *In: COBEM 2011 - 21st International Congress of Mechanical Engineering*, Natal, Brazil, 2011.

11th International Conference on Engineering Vibration
Ljubljana, Slovenia, 7–10 September 2015

DAMAGE IDENTIFICATION UNDER MODELLING UNCERTAINTIES

Daniel A. Castello*[1], Jari P. Kaipio[2]

[1]Department of Mechanical Engineering. Universidade Federal do Rio de Janeiro
castello@mecanica.ufrj.br

[2]Department oh Mathematics. University of Auckland
j.kaipio@auckland.ac.nz

Keywords: Damage Identification, Model Errors, Marginalization, Vibrations

Abstract. *This work presents a damage identification strategy using reduced computational models. Modelling errors are taken into account as random variables. Model uncertainties are taken into account with the Approximation Error Theory. Uncertainties about the applied load is taken into account. The effectiveness of this approach is assessed using a numerical example.*

1 INTRODUCTION

Structural and mechanical components are subjected to ageing and deterioration that lead to changes into these systems. These changes are generally defined as damage and they affect current and future performance of any component [7]. Therefore, almost every industry wants to detect damage in its preliminary stages [7].

The damage identification literature has increased over the last decades. And, in particular, vibration-based non-destructive testing (NDT) methodologies which are built on computational models have received considerable attention [5], [4], [6]. It seems to be common sense that comprehensive vibration-based damage identification strategies should provide answers to the following questions [7]: (I) Existence: Is there damage in the system ? (II) Location: Where is the damage in the system ? (III) Type: What kind of damage is present ? (IV) Extent: How severe is the damage ? (V) Prognosis: How much useful life remains ? Levels (I), (II) and (IV) are often tackled by means of inverse analysis. Level (V) can be tackled using damage mechanics models [9] combined with Uncertainty Quantification approaches [8].

The present paper presents a novel strategy to be used for damage identification under modelling uncertainties. This strategy is built under the formalism of Statistical Inverse Problems.

2 MATHEMATICAL MODELLING

This section briefly presents the theory proposed for the damage identification approach under modelling uncertainties.

2.1 Governing Equations and Model Parameters

Let's consider a mechanical system whose model predictions $\mathbf{y}^m$ are *accurately* provided by an operator $\bar{\mathbf{A}} : \mathcal{R}^{N_{\bar{\theta}}} \times \mathcal{R}^{N_{\bar{\psi}}} \mapsto \mathcal{R}^d$ as follows

$$\mathbf{y}^m = \bar{\mathbf{A}}(\bar{\boldsymbol{\theta}}, \boldsymbol{\psi}) \tag{1}$$

in which $\bar{\boldsymbol{\theta}}$ and $\bar{\boldsymbol{\psi}}$ are input model parameters. Additionally, let's consider that $\bar{\boldsymbol{\theta}}$ are model parameters of primary interest and $\bar{\boldsymbol{\psi}}$ contains model parameters that are uncertain and are not of primary interest.

2.2 Observation Model and Modelling Errors

Let's assume that the relation between observations $\mathbf{y}$ and accurate model predictions $\mathbf{y}^m$ may be described by an additive error model as follows

$$\mathbf{y} = \mathbf{y}^m + \mathbf{e} = \bar{\mathbf{A}}(\bar{\boldsymbol{\theta}}, \bar{\boldsymbol{\psi}}) + \mathbf{e} \tag{2}$$

in which $\mathbf{e} \sim \mathcal{N}(\mathbf{e}_*, \boldsymbol{\Gamma}_e)$ describes measurement errors. Let's consider one aims at obtaining updated information about the primary model parameters $\bar{\boldsymbol{\theta}}$ given a set of measured data $\mathbf{y}$. Furthermore, let's also suppose that one decides to use a less refined model for the inverse analysis. In essence, we assume that we are going to use an approximative model to get predictions $\mathbf{y}_a^m$ provided by an operator $\mathbf{A} : \mathcal{R}^{N_\theta} \mapsto \mathcal{R}^d$, viz.

$$\mathbf{y}_a^m = \mathbf{A}(\boldsymbol{\theta}, \boldsymbol{\psi}_0) \tag{3}$$

in which the subindex in $\mathbf{y}_a^m$ denotes approximative, $\boldsymbol{\theta} \in \mathcal{R}^{N_\theta}$ corresponds to the projection of $\bar{\boldsymbol{\theta}}$ to a lower dimension via an operator $\mathcal{P} : \mathcal{R}^{N_{\bar{\theta}}} \mapsto \mathcal{R}^{N_\theta}$, i.e., $\boldsymbol{\theta} = \mathcal{P}\bar{\boldsymbol{\theta}}$. Finally, we fix the projection of the random variable $\bar{\boldsymbol{\psi}}$ at a fixed value $\boldsymbol{\psi}_0$.

The observation model can now be rewritten as follows

$$\mathbf{y} = \bar{\mathbf{A}}(\bar{\boldsymbol{\theta}}, \bar{\boldsymbol{\psi}}) + \mathbf{e} = \tag{4}$$

$$= \mathbf{A}(\boldsymbol{\theta}, \boldsymbol{\psi}_0) + [\bar{\mathbf{A}}(\bar{\boldsymbol{\theta}}, \bar{\boldsymbol{\psi}}) - \mathbf{A}(\boldsymbol{\theta}, \boldsymbol{\psi}_0)] + \mathbf{e} = \tag{5}$$

$$= \mathbf{A}(\boldsymbol{\theta}, \boldsymbol{\psi}_0) + \boldsymbol{\xi} + \mathbf{e} \tag{6}$$

in which the modelling errors described by $\boldsymbol{\xi}$ are defined as follows

$$\boldsymbol{\xi} = \bar{\mathbf{A}}(\bar{\boldsymbol{\theta}}, \bar{\boldsymbol{\psi}}) - \mathbf{A}(\boldsymbol{\theta}, \boldsymbol{\psi}_0) \tag{7}$$

The modelling errors in Equation (7) may describe discretization errors, discrepancies between model classes, etc..

2.3 Inverse Problem

Here we briefly introduce the strategy used to obtain information about model parameters. Let's start with a Bayesian framework for inverse problems.

In a Bayesian framework for inverse problems [10]: (i) all the variables are modelled as random variables, (ii) uncertainties about model parameters are described by their probability density functions and (iii) the solution to the model calibration problem corresponds to the posterior density of model parameters.

The inverse problem considering the accurate model casts as follows

$$\pi(\bar{\boldsymbol{\theta}}, \bar{\boldsymbol{\psi}}|\mathbf{y}) = \frac{\pi(\mathbf{y}|\bar{\boldsymbol{\theta}}, \bar{\boldsymbol{\psi}})\pi_{pr}(\bar{\boldsymbol{\theta}}, \bar{\boldsymbol{\psi}})}{\pi(\mathbf{y})} \tag{8}$$

in which $\pi(\bar{\boldsymbol{\theta}}, \bar{\boldsymbol{\psi}}|\mathbf{y})$ corresponds to the posterior density given measurements $\mathbf{y}$, $\pi_{pr}(\bar{\boldsymbol{\theta}}, \bar{\boldsymbol{\psi}})$ is *a priori* (prior) density which describes our currenty state of knowledge about model parameters before acquiring $\mathbf{y}$, $\pi(\mathbf{y}|\bar{\boldsymbol{\theta}}, \bar{\boldsymbol{\psi}})$ is the likelihood function and $\pi(\mathbf{y})$ is a normalising factor.

Equation (8) corresponds to the complete model describing the posterior density of model parameters $(\bar{\boldsymbol{\theta}}, \bar{\boldsymbol{\psi}})$ given a set of measured data $\mathbf{y}$. Nevertheless, one highlights that the main interest here is to use the reduced/approximative model described by $\mathbf{A}(\boldsymbol{\theta}, \boldsymbol{\psi}_0)$ for the inverse analysis instead of using the accurate model described by $\bar{\mathbf{A}}(\bar{\boldsymbol{\theta}}, \bar{\boldsymbol{\psi}})$. Additionally, one may associate the model described by $\mathbf{A}(\boldsymbol{\theta}, \boldsymbol{\psi}_0)$ for situations in which *we think/assume we know* the value of the secondary variable $\bar{\boldsymbol{\psi}}$. This type of situations is quite common in Engineering practice in which one has to describe boundary conditions, initial conditions and environmental excitation or even when dealing with heterogeneous materials, just to cite a few.

As for the use of the approximative model, when assuming $\bar{\boldsymbol{\theta}}$ and $\bar{\boldsymbol{\psi}}$ as random variables in Equation (7), one naturally gets that one gets that $\boldsymbol{\xi}$ is also a random variable. In principle, one may compute the joint density $\pi(\boldsymbol{\xi}, \bar{\boldsymbol{\theta}}, \bar{\boldsymbol{\psi}})$ as well as the associated marginal densities. Nevertheless, in practice one hardly ever gets an analytical expression for such densities. Finally, since our interest is to use the variable $\boldsymbol{\theta}$ for the inverse analysis, henceforth we focus on the joint density $\pi(\boldsymbol{\xi}, \boldsymbol{\theta}, \boldsymbol{\psi})$.

3 APPROXIMATION ERROR APPROACH

The objective of the Approximation Error Approach is to build a computationally efficient approximation $\tilde{\pi}(\boldsymbol{\theta}|\mathbf{y})$ for the target posterior $\pi(\boldsymbol{\theta}|\mathbf{y})$. In other words, the true target is the posterior $\pi(\boldsymbol{\theta}|\mathbf{y})$. Nevertheless, we will work with approximate posterior which beyond allowing efficient computations it also provides a compensation for the modelling error stemming

from the fact the we are using an approximative model to describe the system dynamics, i.e., $\mathbf{A}(\boldsymbol{\theta}, \boldsymbol{\psi}_0)$. This is performed here using the Bayesian Approximation Error Approach (AEA) proposed as presented by Anti Nissinen, Ville Kolehmainen and Jari Kaipio [13]. Next we present in a concisely fashion the basic principles of the AEA.

Let's rewrite the observation model in Equation (6) as follows

$$\mathbf{y} = \mathbf{A}(\boldsymbol{\theta}, \boldsymbol{\psi}_0) + \boldsymbol{\nu}(\boldsymbol{\theta}, \boldsymbol{\psi}, \boldsymbol{\psi}_0) \tag{9}$$

in which $\nu(\boldsymbol{\theta}, \boldsymbol{\psi}, \boldsymbol{\psi}_0) = \boldsymbol{\xi} + \mathrm{e}$. The key-ingredient in the modelling error approach is to obtain information about the density $\pi(\boldsymbol{\nu})$ of the additive error $\boldsymbol{\nu}$ in Equation (9) and to use it for inverse analysis. Unfortunately, for the great majority of problems one deals with nonlinear forward maps and therefore it is not possible to obtain a closed form solution for the density $\boldsymbol{\nu}$. Here we obtain information about the modelling error using stochastic simulations as described Nissinen *et al.* [14].

4 NUMERICAL RESULTS

Next we describe an example presenting a damage identification scenario in which one faces uncertainties associated to mesh discretization along with excitation forces.

4.1 Mechanical System

The mechanical system consists of a prismatic body $\mathcal{B}$ which occupies the region $[0, L] \times [-\frac{h}{2}, \frac{h}{2}] \times [0, w] \subset \Re^3$. The body $\mathcal{B}$ is cantilevered at the left face. The material properties of the beam are: elasticity modulus $E = 209$ MPa, Poisson's ratio $\nu_p = 0.3$ and specific mass $\rho = 7850\, kg/m^3$. Its length is considered to be $L = 1.0m$ and its height $h = \frac{1}{5}m$. The system is assumed to be under plane stress states.

It is considered that one has available ten accelerometers located at the positions $\mathbf{x}_k = (\frac{k}{L}, \frac{h}{2}, 0)$, $k = 1, \ldots, 10$. We also consider that the system is subject to a vertical force $F(t)$ applied at the position of the ninth accelerometer. Additionally, it is considered that $F(t)$ is uncertain. More specifically, it is considered the following parameterization

$$F(t) = \begin{cases} F_0(1 - \cos(2\pi\, f_c\, t)), & t \in [0, \frac{1}{f_c}] \\ 0, & \text{otherwise} \end{cases} \tag{10}$$

in which the environment is such that F_0 and f_c are independent random variables whose distributions are described as follows

$$\pi(F_0) \sim \mathcal{N}(\mu_F, \sigma_F^2) \tag{11}$$

$$\pi(f_c) \sim \mathcal{N}(\mu_c, \sigma_c^2) \tag{12}$$

As for the uncertainties associated to the applied force, they will be used to obtain information about modelling errors.

4.2 Accurate and Approximative Models

The accurate model is built using 8-node quadrilateral finite elements with a mesh containing 60×12 elements. As for the approximative model, it is built using 8-node quadrilateral finite elements with a mesh containing 10×2 elements.

It is considered a scenario in which severe damage is located in the left upper face and in the middle of the body $\mathcal{B}$.

4.3 RESULTS

Figure (1) presents the first results provided by the proposed approach when modelling uncertainties associated to mesh refinement and applied force is present along the inverse analysis.

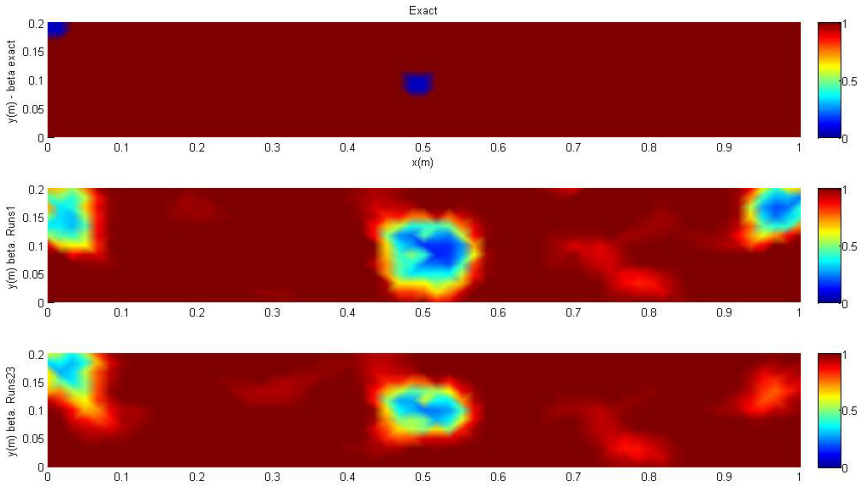


Figure 1: First: True damage field. Second: Recovered damage field. Third: Recovered damage fields averaged with 23 runs.

5 CONCLUSIONS

This work presents the basic principles of a new strategy for damage identification under modelling uncertainties. It is built using the Theory of Approximation Errors. It was presented a first case for analysis which shows the potential of the method.

REFERENCES

[1] E. P. Carden and P. Fanning. 2004. *Vibration based condition monitoring: A review* , Structural Health Monitoring, **3(4)**, pp.355-377, DOI: 10.1177/1475921704047500.

[2] S. W. Doebling, C. R. Farrar, M. B. Prime and D. W. Shevitz. 1996. *Damage Identification and Health Monitoring of Structural and Mechanical Systems from Changes in their Vibration Characteristics: A Literature Review*, Los Alamos National Laboratory report LA-13070-MS.

[3] Fan,W. and Qiao,P. 2011. *Vibration-based damage identification methods: A review and comparative study*, Structural Health Monitoring, 10(1),83-111.

[4] C. R. Farrar and K. Worden. 2007. *An Introduction to Structural Health Monitoring*, Philosophical Transactions of the Royal Society A, 365, 303-315.

[5] C. R. Farrar and Niek A.J. Lieven. 2007. *Damage Prognosis: The Future of Structural Health Monitoring*, Philosophical Transactions of the Royal Society A, 365, 623632.

[6] Lemaitre, J. and Chaboche, J. 1994. *Mechanics of Solids Materials*, Cambridge University Press.

[7] J. P. Kaipio and E. Somersalo. 2005. Statistical and Computational Inverse Problems, Springer, New York.

[8] S. R. Arridge, J. P. Kaipio, V. Kolehmainen, M. Schweiger, E. Somersalo, T. Tarvainen and M. Vauhkonen. 2006. *Approximation Errors and Model Reduction with an Application in Optical Diffusion Tomography*, Inverse Problems 22, 175-195.

[9] V. Kolehmainen, T. Tarvainen, S. R. Arridge and J. P. Kaipio. 2011. *Marginalization of Uninteresting Distributed Parameters in Inverse Problems - Application to diffuse Optical Tomography*, International Journal for Uncertainty Quantification, 1(1), 1-17.

[10] A. Nissinen, V. Kolehmainen, J. P. Kaipio. 2011. *Compensation of Modelling Errors due to Unknown Boundary in Electrical Impedance Tomography*, IEEE Transactions on Medical Imaging, 30(2), 231-242.

[11] A. Nissinen, LM Heikkinen, V Kolehmainen, J. P. Kaipio. 2009. *Compensation of Errors due to Discretization, Domain Truncation and Unknown Contact Impedances in Electrical Impedance Tomography*, Measurement Science and Technology, 29, 1-13.

International Conference on Engineering Vibration
Ljubljana, Slovenia, 7-10 September 2015

DETERIORATION OF TENSILE STRENGTH AND STIFFNESS OF ELASTIC STRUCTURAL ADHESIVE JOINTS DUE TO ENVIRONMENTAL FACTORS

Korneel Van Massenhove*[1], Dirk Vandepitte[2], Stijn Debruyne[1]

[1] KU Leuven Department Mechanical Engineering Technology TC, Technology Campus Ostend
korneel.vanmassenhove@kuleuven.be
stijn.debruyne@kuleuven.be

[2] KU Leuven Department of Mechanical Engineering
dirk.vandepitte@kuleuven.be

Keywords: adhesive, dynamic stiffness, ageing effects, temperature dependence

Abstract. *Adhesive bonding is becoming increasingly popular as an alternative to traditional joining techniques in various industrial applications. However, often its use is limited to statically loaded structures. In case of dynamic loads the structural elasticity and vibration damping properties mostly result from the characteristics of the substrates used, not from the adhesive joint. Many research activities have been conducted on the widely used and more brittle adhesive types like epoxies.*
So far, not much research is performed on the estimation of the durability of bonded joints that use more elastic structural adhesives.
This paper presents a variability study as part of an extensive research project concerning the durability estimation of structural elastic adhesively bonded joints in dynamically loaded structures.
The first part of this paper discusses the main factors that influence the elastic properties and the mechanical durability of the bonded joint. Some environmental ageing factors are discussed.
A second section focusses on the characterisation of the effect of the factors described in the first part on the mechanical behaviour of the joint. This is done by performing uniaxial and dynamic mechanical tests on adhesive samples. These results are then compared to simple but adequate finite element models. These models are used to relate the mechanical properties of the joint with the observed variability in the various experiments.

The final part summarizes and makes important conclusions on the obtained experimental and numerical results. This part also outlines the research prospects concerning durability uncertainty quantification when adhesive ageing is taken into account.

1 INTRODUCTION

The use of elastic adhesives for structural applications has many advantages. Many industrial applications are characterized by sometimes highly dynamic loads. Especially in situations where sound and vibration insulation is of great importance these adhesives can include multiple functions into one adhesive joint. A well designed adhesive joint can fulfil the need for joining, sealing, vibration damping and electrical insulation.

These rather visco-elastic adhesives induce however some challenges to design engineers and machine constructors. In contrast to brittle adhesives, visco-elastic adhesives show a high dependency on environmental conditions such as temperature, frequency of the load, etc. From a designer's point of view this causes problems in predicting [1] the eventual elastic behaviour of an adhesive joint in an actual application. A numerical design approach should always be supported by performing adequate experiments [2].

In the case where the adhesive joints are dynamically loaded an analysis of damping properties is necessary. A number of mathematical models exist to describe the damping properties of (adhesive) materials [3]. However, numerical models tend to become computationally ineffective when highly non-linear material behaviour [4, 5] is included. Moreover, many common finite element software packages only incorporate linear models in case of structural dynamics. Yet, it is still possible to obtain linear numerical models [6] that adequately describe structural dynamics.

The dynamic behaviour of adhesive joints in a certain application is, amongst other factors, strongly influenced by environmental temperature, frequency of the applied load and boundary conditions. This paper discusses the effect of these three parameters.

2 INFLUENCE OF LOAD FREQUENCY

Vibration damping comes down to the dissipation of deformation energy. With visco-elastic materials the damping performance is strongly dependent of excitation frequency. In the context of material elasticity, damping is often related to the loss factor. In dynamic material analysis the energy loss during cyclic loading is coupled to a frequency dependent material stiffness or complex modulus.

Expression (1) relates the loss factor η to the structural damping ratio ξ at resonance.

$$\frac{\omega_2 - \omega_1}{2\omega_n} = \xi = \sqrt{1+\eta} - \sqrt{1-\eta} \approx \frac{\eta}{2} \tag{1}$$

According to Ungar and Kerwin [7], the simplification in expression (3) is good within 1% for general damping cases (not only viscous damping) if the loss factor does not exceed 0.28. A series of dynamic tensile tests is performed on dog bone shaped samples, cut from adhesive sheets with a thickness of 2 mm. The adhesive is of the MS-polymer type. The test specimens are subjected to dynamical material analysis (DMA) within a frequency range of 10 to 120 Hz. In the test set-up, an electro dynamic shaker acts as a vibration actuator and an impedance head measures the applied force and acceleration, as illustrated by figure 1. The applied static strain during the experiments is 5 % and the experiments are conducted at 20 °C.

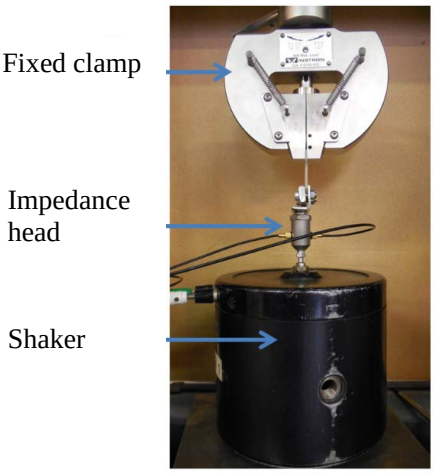


Figure 1: set-up for dynamical material analysis measurements.

Expression (2) calculates the resulting complex modulus E^* from the measured frequency response function.

$$E^*(j\omega) = H(j\omega)\frac{L_0}{S(j\omega)^2} \tag{2}$$

In (2), the frequency response function $H(j\omega)$ is the ratio of the measured force and acceleration signals.
Table 1 gives an overview of the obtained complex Young's moduli at different frequencies from 10 to 120 Hz. The Young's modulus, determined through static tensile tests is also shown as a comparison.

Frequency (Hz)	0	20	40	60	80	100	120
Complex modulus (MPa)	2.8	11.5	12.3	13.2	13.5	13.4	13.9
Loss factor	0	0.11	0.095	0.090	0.087	0.079	0.068

Table 1: Experimentally determined complex Young's moduli of MS – polymer adhesive.

The loss factors in table 1 are calculated from the measured phase shift between the force and acceleration signals of the impedance head. The tangent of this phase angle equals the loss factor. The method that is applied here is referred to in literature as a non-resonant test method.
These tests clearly show that with increasing frequency, the adhesive material tends to act stiffer. In addition, the damping performance decreases.

3 INFLUENCE OF AMBIENT TEMPERATURE

Elastic adhesives are thermoplastic materials. There elastic characteristics are hence strongly dependent on ambient temperature. The same adhesive type as in 2.1 is subjected to dynamic tensile tests under different temperatures, ranging from -15°C to + 40°C. Table 2 summarizes the obtained complex moduli.

Frequency (Hz)	0	20	40	60	80	100	120
Complex modulus (MPa) @ -15°C	3,1	11,8	12,6	13,5	13,8	13,7	14,2
Complex modulus (MPa) @ 0°C	3,0	11,7	12,5	13,4	13,7	13,6	14,1
Complex modulus (MPa) @ 20°C	2.8	11.5	12.3	13.2	13.5	13.4	13.9
Complex modulus (MPa) @ 40°C	2,7	11,4	12,2	13,1	13,4	13,3	13,8

Table 2: Experimentally determined complex Young's moduli of MS-polymer adhesive at different ambient temperatures

Although the temperature effect on the complex modulus is evident from table 2, the analysed adhesive type has a quite constant stiffness over the observed temperature range.

4 INFLUENCE OF BOUNDARY CONDITIONS

The adhesive, used as a test bed in this research work, is commonly used in construction engineering. Therefore it is now applied to joint two concrete plates to form an L-shaped structure. Such a structure is freely suspended and subjected to hammer impact vibration tests. The applied method is clearly a resonant test. Following the process of experimental modal analysis, the complex modulus is estimated through finite element model updating and the loss factors are derived from measured damping ratios at resonance. Table 3 gives an overview of the obtained results from this test, which was conducted at 20°C. The first four eigenmodes were analysed during this test.

Frequency (Hz)	48	77	102	159
Complex modulus (MPa)	18.7	23.4	29.7	39.1
Loss factor	0.11	0.087	0.081	0.077

Table 3: Experimentally determined complex Young's moduli of MS – polymer adhesive by means of an experimental modal analysis.

Table 3 clearly indicates that the adhesive acts stiffer because of the boundary restrictions of the joint. In this test case the joint is a simple face to face joint with the adhesive thickness equal to 6 mm. Currently resonance tests are being conducted to analyse the effect of the adhesive layer thickness.

5 CONCLUSIONS AND ONGOING RESEARCH

This research work is part of an industrial project. Currently ageing tests are being conducted. It concerns 500 and 1000 hours Xenon tests. Initial results from static tensile tests on a pre batch show that elongation at break after 500 hours of Xenon ageing is not significantly different compared to that of an original test sample. After this test the Young's modulus tends to increase in a strain range up to 15 %. A 1000 hours test reduces the elongation at break drastically (by 40 %) and increases the modulus by approximately 6 %.
Other ageing tests like cataplasma are prepared at the moment.

REFERENCES

[1] R.D. Adams, W.C. Wake, *Structural adhesive joints in engineering*,

[2] L. da Silva, A. Öchsner, *Modeling of adhesively bonded joints*,

[3] C. W. Bert, *Material Damping: An Introductory Review of Mathematical Models Measures and Experimental Techniques*, *Journal of Sound and Vibration,* Vol. 29, 1973.

[4] C.T. Sun, Y.P. Lu, *Vibration Damping of Structural Elements*, Prentice-Hall, NJ, 1995.

[5] B.J. Lazan, *Damping of Materials and Members in Structural Mechanics*, Pergamon Press, New York, NY, 1968.

[6] L.D.R. Grant, R.D. Adams, L. da Silva, *Experimental and numerical analysis of single-lap joints for the automotive industry*, International journal of adhesion and adhesives, vol. 29, iss. 4, June 2009, 405-413.

[7] E. Ungar, E. Kerwin, *Loss Factors of Viscoelastic Systems in Terms of Energy Concepts*, Journal of the Acoustical Society of America. 34(7), 1962.

[8] A. Sheppard, D. Kelly, L. Tong, *A damage zone model for failure analysis of adhesively bonded joints*, International Journal of adhesion and adhesives, vol. 18, iss. 16, dec. 1998, 385-400.

[9] K. S. Madhusudhana, R. Narasimhan, *Experimental and numerical investigations of mixed mode crack growth resistance of a ductile adhesive joint*, International journal of engineering fracture mechanics, vol. 69, iss. 7, may 2002, 865-883.

[10] W.C. De Goei, M. J. L. van Tooren, A. Beukers, *Composite adhesive joints under cyclic loading*, International journal of materials and design, vol. 20, iss. 5, October 1999, 213-223.

[11] A. J. Kin Loch, S.J. Shaw, *The fracture resistance of a toughened epoxy adhesive*, international journal of adhesion, vol. 12, iss. 1, 1981, 59-77.

[12] U. Edlung, A. Klarbring, *A coupled elastic-plastic damage model for rubber-modified epoxy adhesives*, International journal of solids and structures, vol. 30, iss. 19, 1993, 2693-2708.

[13] L.D.R. Grant, R.D. Adams, L. da Silva, *Effect of the temperature on the strength of adhesively bonded single lap and T joints for the automotive industry*, International journal of adhesion and adhesives, vol. 29, iss. 5, July 2009, 535-542.

[14] L. da Silva, P. das Neves, R.D. Adams, Wang A., Spelt J.K., *Analytical models of adhesively bonded joints—Part II: Comparative study*, International journal of adhesion and adhesives, vol. 29, iss. 13, 2009, 331-341.

[15] T. Lauwagie, *Vibration-based methods for the identification of the elastic properties of layered materials,* Phd thesis, KU Leuven, D/2005/7515/80, 2005.

[16] G.I. Schuëller, H.J. Pradlwarter, *Uncertain linear systems in dynamics: Retrospective and recent developments by stochastic approaches,* Engineering Structures, Volume 31, Issue 11, November 2009, Pages 2507-2517.

[17] A. Schenk, G.I. Schuëller, *Uncertainty assessment of large finite element systems*, Springer, Innsbruck, 2005.

[18] D. Moens, D. Vandepitte, *A survey of non-probabilistic uncertainty treatment in finite element analysis,* Computer Methods in Applied Mechanics and Engineering, Vol. 194, Nos.12-16, Pages 1527-1555, 2005.

[19] F. Mortensen, O.T. Thomsen, *Analysis of adhesive bonded joints: a unified approach*, International journal of composites science and technology, vol. 62, iss. 7-8, June 2002, 1011-1031.

[20] G. Richardson, A. D. Crocombe, P.A. Smith, *A comparison of two- and three- dimensional finite element analyses of adhesive joints,* International journal of adhesion and adhesives, vol. 13, iss. 3, July 1993, 193-200.

[21] W. Renton, J. Vinson, *Analysis of adhesively bonded joints between panels of composite materials,* International journal of applied mechanics, 44(1), 1977, 101-106.

[22] F. Ascione, *Mechanical behaviour of FRP adhesive joints: A theoretical model,* Composites part B: Engineering, vol. 40, iss. 2, 2009, 116-124.

[23] S. Debruyne, *Estimation of skin and core stiffness properties of honeycomb sandwich panels*, Phd thesis, KU Leuven, D/ 2013/7515/64, 2013.

[24] ISO Standard 6721-3, *Plastics - Determination of Dynamic Mechanical Properties, Part 3: Flexural Vibration-Resonance-Curve Method*, 1994.

Substructuring Techniques in Structural Dynamics (MS11)

11th International Conference on Engineering Vibration
Ljubljana, Slovenia, 7–10 September 2015

SELECTION OF INTERNAL DOFS TO REPLACE HARD TO MEASURE COUPLING DOFS IN SUBSTRUCTURE DECOUPLING

Walter D'Ambrogio*[1], Annalisa Fregolent[2]

[1]Dipartimento di Ingegneria Industriale e dell'Informazione e di Economia,
Università dell'Aquila, Via G. Gronchi, 18 - I-67100, L'Aquila (AQ), Italy
walter.dambrogio@uniroma1.it

[2]Dipartimento di Ingegneria Meccanica e Aerospaziale,
Università di Roma La Sapienza, Via Eudossiana, 18 - I-00184 Roma, Italy
annalisa.fregolent@uniroma1.it

Keywords: Substructure Decoupling, Rotational DoFs, Mixed Interface, Experimental Dynamic Substructuring.

Abstract. *Substructure decoupling consists in the identification of a dynamic model of a structural subsystem, starting from a dynamic model (e.g. FRFs) of both the assembled system and a known portion of it (the so-called residual subsystem). The degrees of freedom (DoFs) of the assembled system can be subdivided into internal DoFs (not belonging to the couplings) and coupling DoFs. To achieve decoupling, a fictitious subsystem that is the negative of the residual subsystem is added to the assembled system, and appropriate compatibility and equilibrium conditions are enforced at interface DoFs. Interface DoFs can include coupling DoFs only (standard interface), additional internal DoFs of the residual subsystem (extended interface), subsets of coupling DoFs and internal DoFs of the residual subsystem (mixed interface), or a subset of internal DoFs of the residual subsystem only (pseudo interface). In previous papers, the use of a mixed interface is applied in order to get rid of hard-to-measure coupling DoFs, such as for instance rotational DoFs at junctions involving bending and/or torsion. In this paper, criteria are sought for an appropriate selection of internal DoFs used to replace coupling DoFs at which it is hard to obtain experimental FRFs.*

1 INTRODUCTION

Substructure decoupling represents a special case of experimental dynamic substructuring. Specifically, it consists in the identification of the dynamic behaviour of a structural subsystem, starting from the dynamic behaviour of both the assembled system and the residual subsystem (the known portion of the assembled system). Decoupling is a need for subsystems that cannot be measured separately, but only when coupled to their neighboring substructure(s), such as fixtures needed for testing. In Frequency Based Substructuring, Frequency Response Functions (FRFs) are used instead of modal parameters to avoid modal truncation problems. A general framework for dynamic substructuring is provided in [1].

A well known issue in experimental dynamic substructuring is related to rotational DoFs: rotational FRFs are quite difficult to be obtained experimentally, both from translational FRFs [2] and by measuring directly the rotational responses [3, 4]. However, whilst rotational FRFs are needed when coupling together different subsystems, they are not essential in substructure decoupling as shown in [5, 6].

To achieve decoupling, a fictitious subsystem that is the negative of the residual subsystem is added to the coupled system, and appropriate compatibility and equilibrium conditions are enforced at interface DoFs. Interface DoFs may include coupling DoFs only (standard interface), additional internal DoFs of the residual subsystem (extended interface), subsets of coupling DoFs and internal DoFs of the residual subsystem (mixed interface), or a subset of internal DoFs of the residual subsystem only (pseudo interface).

In this paper, a mixed interface is used to replace rotational coupling DoFs with translational internal DoFs. Qualitative criteria are sought for an optimal selection of internal DoFs. Such criteria are verified by testing a structure made by a cantilever column with two staggered short arms (residual substructure) coupled to a horizontal beam (unknown substructure).

2 DIRECT DECOUPLING USING DUAL ASSEMBLY

The unknown substructure U (N_U DoFs) is a portion of a larger structure RU (N_{RU} DoFs). The known portion of the assembled structure RU, defined as residual substructure R (N_R DoFs), is joined to the unknown substructure through a number of couplings (see Fig. 1). The degrees of freedom (DoFs) can be partitioned into internal DoFs (not belonging to the couplings) of substructure U (u), internal DoFs of substructure R (r), and coupling DoFs (c).

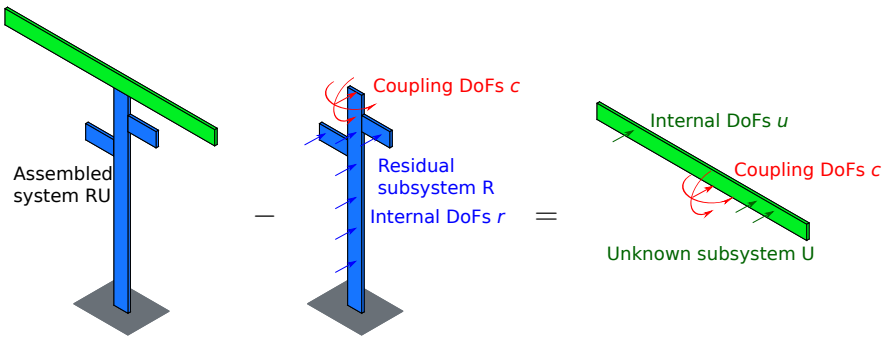


Figure 1: Scheme of the direct decoupling problem.

The goal is to find the FRF of the unknown substructure U starting from the FRFs of the assembled structure RU and of the residual substructure R. The dynamic behaviour of the unknown substructure U can be extracted from that of the assembled structure RU by taking out the dynamic effect of the residual subsystem R. This can be accomplished by considering a negative structure, i.e. by adding to the assembled structure RU a fictitious substructure with a dynamic stiffness opposite to that of the residual substructure R and satisfying compatibility and equilibrium conditions. The dynamic equilibrium of the assembled structure RU and of the negative substructure is expressed in block diagonal format as:

$$\begin{bmatrix} \mathbf{Z^{RU}} & \mathbf{0} \\ \mathbf{0} & -\mathbf{Z^{R}} \end{bmatrix} \begin{Bmatrix} \boldsymbol{u^{RU}} \\ \boldsymbol{u^{R}} \end{Bmatrix} = \begin{Bmatrix} \boldsymbol{f^{RU}} \\ \boldsymbol{f^{R}} \end{Bmatrix} + \begin{Bmatrix} \boldsymbol{g^{RU}} \\ \boldsymbol{g^{R}} \end{Bmatrix} \tag{1}$$

where:

- $\mathbf{Z^{RU}}$, $-\mathbf{Z^{R}}$ are the dynamic stiffness matrices of the assembled structure RU and of the negative structure, respectively;
- $\boldsymbol{u^{RU}}$, $\boldsymbol{u^{R}}$ are the vectors of degrees of freedom of the assembled structure RU and of the negative structure, respectively;
- $\boldsymbol{f^{RU}}$, $\boldsymbol{f^{R}}$ are the external force vectors on the assembled structure RU and on the negative structure, respectively;
- $\boldsymbol{g^{RU}}$, $\boldsymbol{g^{R}}$ are the vectors of disconnection forces between the assembled structure and the negative structure (constraint forces associated with compatibility conditions).

Equilibrium of disconnection forces and compatibility must be considered at the interface between the assembled structure RU and the negative structure: such interface includes not only the coupling DoFs between substructures U and R, but includes as well the internal DoFs of substructure R (the blue part of the structure in Fig. 1). However, it is not required to consider the full set of these interface DoFs, because it is sufficient that the number of interface DoFs be not less than the number of coupling DoFs n_c. Therefore, several options for interface DoFs can be considered:

- standard interface, including only the coupling DoFs (c) between substructures U and R;
- extended interface, including also a subset of internal DoFs ($i \subseteq r$) of substructure R;
- mixed interface, including subsets of coupling DoFs ($d \subset c$) and internal DoFs ($i \subseteq r$);
- pseudo interface, including only internal DoFs ($i \subseteq r$) of substructure R.

The use of a mixed or pseudo interface may allow to ignore rotational coupling DoFs by substituting them with translational internal DoFs.

The compatibility condition at the (standard, extended, mixed, pseudo) interface DoFs implies that any pair of matching DoFs u_l^{RU} and u_m^R, i.e. DoF l on the coupled system RU and DoF m on subsystem R must have the same displacement, that is $u_l^{RU} - u_m^R = 0$. Let the number of interface DoFs on which compatibility is enforced be denoted as N_C.

The compatibility condition can be generally expressed as:

$$\begin{bmatrix} \mathbf{B_C^{RU}} & \mathbf{B_C^{R}} \end{bmatrix} \begin{Bmatrix} \boldsymbol{u^{RU}} \\ \boldsymbol{u^{R}} \end{Bmatrix} = \mathbf{0} \tag{2}$$

where each row of $\mathbf{B_C} = \begin{bmatrix} \mathbf{B_C^{RU}} \, \mathbf{B_C^{R}} \end{bmatrix}$ corresponds to a pair of matching DoFs. Note that $\mathbf{B_C}$ has size $N_C \times (N_{RU} + N_R)$ and is, in most cases, a signed Boolean matrix.

It should be noted that the interface DoFs used to enforce the compatibility condition need not to be the same where equilibrium of disconnection forces is required, provided that compatibility is ensured by disconnection forces applied at such DoFs. If the compatibility and the equilibrium DoFs are not the same, the approach is called non-collocated [7]. The traditional approach, in which compatibility and equilibrium DoFs are the same, is called collocated.

Let N_E denote the number of interface DoFs on which equilibrium is enforced. The equilibrium of disconnection forces implies that their sum must be zero for any pair of matching DoFs belonging to the equilibrium interface, i.e. $g_r^{RU} + g_s^R = 0$. Furthermore, for any DoF k on the coupled system RU (or on the residual subsystem R) not belonging to the equilibrium interface, it must be $g_k^{RU} = 0$ ($g_k^R = 0$). Overall, the previous conditions can be expressed as:

$$\begin{bmatrix} \mathbf{L_E^{RU}} \\ \mathbf{L_E^{R}} \end{bmatrix}^T \begin{Bmatrix} \boldsymbol{g^{RU}} \\ \boldsymbol{g^{R}} \end{Bmatrix} = \mathbf{0} \tag{3}$$

where the matrix $\mathbf{L_E} = \begin{bmatrix} \mathbf{L_E^{RU}} \, \mathbf{L_E^{R}} \end{bmatrix}$ is a Boolean localisation matrix. Note that the number of columns of $\mathbf{L_E}$ is equal to the number N_E of equilibrium interface DoFs plus the number N_{NE} of DoFs not belonging to the equilibrium interface. Note that $N_{NE} = N_{RU} + N_R - 2N_E$: in fact, the number of DoFs belonging to the equilibrium interface must be subtracted once from N_{RU} and once from N_R. Therefore, the size of $\mathbf{L_E}$ is $(N_{RU} + N_R) \times (N_{RU} + N_R - N_E)$.

By gathering Eqs. (1-3), one obtains the so-called 3-field formulation, from which several assembly techniques can be devised, such as: dual assembly [1, 8] where equilibrium is satisfied exactly by defining a unique set of disconnection force intensities; primal assembly [1, 9] where compatibility is satisfied exactly by defining a unique set of interface DoFs; hybrid assembly [10] where both compatibility and equilibrium are satisfied exactly. It can be shown [10] that whenever $N_C = N_E$, i.e. the number of compatibility and equilibrium DoFs is the same, all assembly techniques provide the same result. In the sequel, only the dual assembly is recalled.

2.1 Disconnection force intensities provided by dual assembly

In the dual assembly, the equilibrium condition $g_r^{RU} + g_s^R = 0$ at a pair of equilibrium interface DoFs is ensured by choosing $g_r^{RU} = -\lambda_r$ and $g_s^R = \lambda_r$. If a Boolean matrix $\mathbf{B_E}$ related to interface equilibrium DoFs is defined similarly to $\mathbf{B_C}$, the overall interface equilibrium can be ensured by writing the disconnection forces in the form:

$$\begin{Bmatrix} \boldsymbol{g^{RU}} \\ \boldsymbol{g^{R}} \end{Bmatrix} = - \begin{bmatrix} \mathbf{B_E^{RU}}^T \\ \mathbf{B_E^{R}}^T \end{bmatrix} \boldsymbol{\lambda} \tag{4}$$

where $\boldsymbol{\lambda}$ are Lagrange multipliers corresponding to disconnection force intensities and $\mathbf{B_E}$ is a $N_E \times (N_{RU} + N_R)$ matrix. Since there is a unique disconnection force intensity λ_r for any pair of equilibrium DoFs, the interface equilibrium is satisfied automatically for any $\boldsymbol{\lambda}$, i.e.

$$\begin{bmatrix} \mathbf{L_E^{RU}} \\ \mathbf{L_E^{R}} \end{bmatrix}^T \begin{Bmatrix} \boldsymbol{g^{RU}} \\ \boldsymbol{g^{R}} \end{Bmatrix} = - \begin{bmatrix} \mathbf{L_E^{RU}} \\ \mathbf{L_E^{R}} \end{bmatrix}^T \begin{bmatrix} \mathbf{B_E^{RU}}^T \\ \mathbf{B_E^{R}}^T \end{bmatrix} \boldsymbol{\lambda} = \mathbf{0} \tag{5}$$

In the dual assembly, the total set of DoFs is retained, i.e. each interface DoF appears twice. Since Eq. (5) is always satisfied, the 3-field formulation reduces to:

$$\begin{cases} \begin{bmatrix} \mathbf{Z^{RU}} & \mathbf{0} \\ \mathbf{0} & -\mathbf{Z^{R}} \end{bmatrix} \begin{Bmatrix} \boldsymbol{u}^{RU} \\ \boldsymbol{u}^{R} \end{Bmatrix} + \begin{bmatrix} \mathbf{B_E^{RU}}^T \\ \mathbf{B_E^{R}}^T \end{bmatrix} \boldsymbol{\lambda} = \begin{Bmatrix} \boldsymbol{f}^{RU} \\ \boldsymbol{f}^{R} \end{Bmatrix} & (1^*) \\ \begin{bmatrix} \mathbf{B_C^{RU}} & \mathbf{B_C^{R}} \end{bmatrix} \begin{Bmatrix} \boldsymbol{u}^{RU} \\ \boldsymbol{u}^{R} \end{Bmatrix} = \mathbf{0} & (2) \end{cases}$$

or in more compact form:

$$\begin{cases} \mathbf{Z}\boldsymbol{u} + \mathbf{B_E}^T \boldsymbol{\lambda} = \boldsymbol{f} & (1^*) \\ \mathbf{B_C}\boldsymbol{u} = \mathbf{0} & (2) \end{cases}$$

To obtain $\boldsymbol{\lambda}$, Eq. (1^*) can be written:

$$\boldsymbol{u} = -\mathbf{Z}^{-1}\mathbf{B_E}^T \boldsymbol{\lambda} + \mathbf{Z}^{-1}\boldsymbol{f} \tag{6}$$

i.e., by noting that the inverse of the block diagonal dynamic stiffness matrix $\mathbf{Z}$ is:

$$\begin{bmatrix} \mathbf{Z^{RU}} & \mathbf{0} \\ \mathbf{0} & -\mathbf{Z^{R}} \end{bmatrix}^{-1} = \mathbf{Z}^{-1} = \mathbf{H} = \begin{bmatrix} \mathbf{H^{RU}} & \mathbf{0} \\ \mathbf{0} & -\mathbf{H^{R}} \end{bmatrix} \tag{7}$$

where $\mathbf{H^{RU}}$ and $\mathbf{H^{R}}$ are the FRFs of the assembled structure and of the residual substructure, Eq. (6) becomes:

$$\boldsymbol{u} = -\mathbf{H}\mathbf{B_E}^T \boldsymbol{\lambda} + \mathbf{H}\boldsymbol{f} \tag{8}$$

which substituted in Eq. (2) gives:

$$\mathbf{B_C}\mathbf{H}\mathbf{B_E}^T \boldsymbol{\lambda} = \mathbf{B_C}\mathbf{H}\boldsymbol{f} \tag{9}$$

from which the vector of disconnection force intensities $\boldsymbol{\lambda}$ is found as:

$$\boldsymbol{\lambda} = \left(\mathbf{B_C}\mathbf{H}\mathbf{B_E}^T\right)^+ \mathbf{B_C}\mathbf{H}\boldsymbol{f} \tag{10}$$

To obtain a determined or overdetermined matrix for the generalized inversion operation, the number of rows of $\mathbf{B_C}$ must be greater or equal than the number of rows of $\mathbf{B_E}$, i.e.

$$N_C \geq N_E \geq n_c \tag{11}$$

The set of disconnection forces is not unique since it depends on the choice of equilibrium and compatibility DoFs. However, disconnection forces must be able to cancel constraint forces at the coupling DoFs. If coupling DoFs include rotational DoFs, constraint forces include moments about some given axes. Several sets of disconnection forces can be devised:

- the trivial set, consisting of disconnection forces acting at the coupling DoFs and opposite to the constraint forces;
- non trivial sets of disconnection forces acting at different DoFs but able to cancel the constraint forces at the coupling DoFs.

In the former case, disconnection forces may include disconnection moments opposite to the constraint moments. In the latter case, disconnection moments can be substituted by disconnection forces applied to internal DoFs, but able to provide a moment about the rotation axes. Therefore, a qualitative criterion for the selection of internal DoFs to replace coupling DoFs that are difficult to observe, such as rotational DoFs, is the following:

Internal DoFs must be such that disconnection forces that are applied to them are able to control coupling DoFs, e.g., if one of the coupling DoFs is a rotation about a given axis, the line of action of the substituted force must not intersect such axis.

2.2 Prediction of the FRF of the unknown subsystem

The FRF of the unknown subsystem U can be obtained by back-substituting $\boldsymbol{\lambda}$ in Eq. (1^*), and by isolating $\boldsymbol{u}$ at the left hand side:

$$\boldsymbol{u} = \left(\mathbf{H} - \mathbf{H}\mathbf{B_E}^T \left(\mathbf{B_C}\mathbf{H}\mathbf{B_E}^T\right)^+ \mathbf{B_C}\mathbf{H}\right) \boldsymbol{f} \tag{12}$$

which is in the form $\boldsymbol{u} = \mathbf{H}\boldsymbol{f}$, so that the FRF of the unknown subsystem U is:

$$\mathbf{H^U} = \mathbf{H} - \mathbf{H}\mathbf{B_E}^T \left(\mathbf{B_C}\mathbf{H}\mathbf{B_E}^T\right)^+ \mathbf{B_C}\mathbf{H} \tag{13}$$

With the dual assembly, the rows and the columns of $\mathbf{H^U}$ corresponding to compatibility and equilibrium DoFs appear twice. Furthermore, when using an extended or mixed interface, $\mathbf{H^U}$ contains some meaningless rows and columns: those corresponding to the internal DoFs of the residual substructure R. Obviously, only meaningful and independent entries are retained.

3 TEST BED

The assembled system is an aluminium tree structure (Fig. 2). The residual substructure

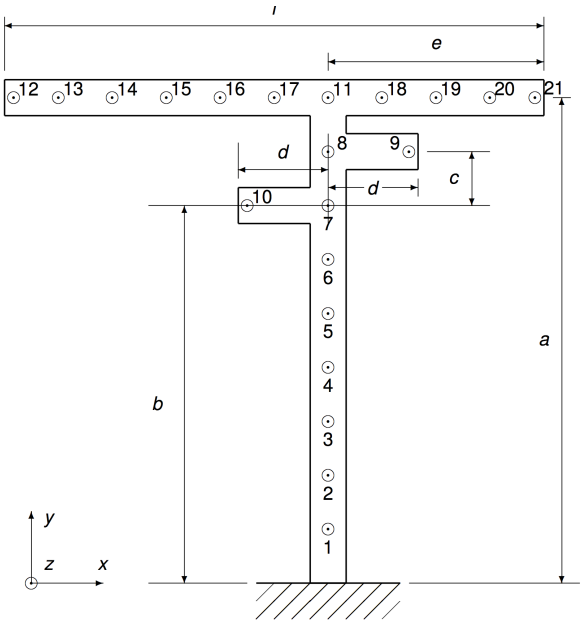


Figure 2: Sketch of the test structure.

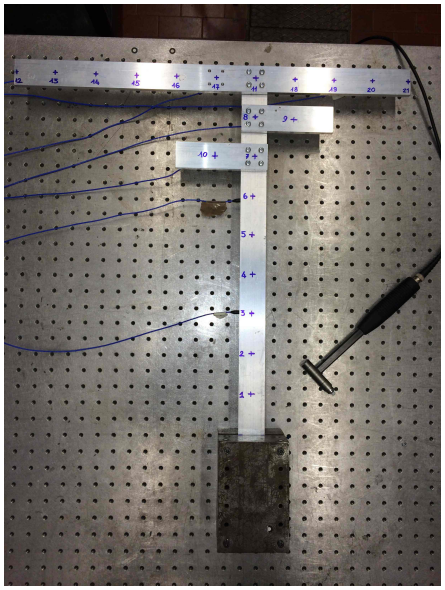


Figure 3: Assembled system.

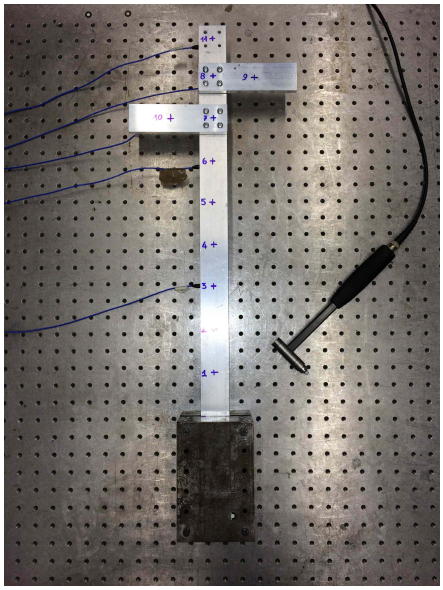


Figure 4: Residual subsystem.

R is a cantilever column with two staggered short arms and the unknown substructure U is a horizontal beam. The horizontal beam is bolted to the top of the column, involving both translational and rotational DoFs. The geometrical dimensions are shown in Table 1. The cross section is 40 mm$\times$8 mm for all beams, with the short side along the z-direction.

The experimental FRFs of the assembled system RU up to 2000 Hz are obtained by applying impact excitation and measuring the resulting accelerations along z-direction at seven locations (3, 6, 9, 10, 11, 13, 20), as shown in Fig. 3. For the residual subsystem R (column) the experimental FRFs are similarly measured at five locations (3, 6, 9, 10, 11), as shown in Fig. 4. Coupling DoFs are: $11z$, $11\vartheta_x$ and $11\vartheta_y$, that is one translational DoF and two rotatonal DoFs.

A detail of the bolted junction between the beam and the column is shown in Fig. 5. Finally, to check decoupling results, FRFs are measured also at three locations (11, 13, 20) of the unknown subsystem U (beam), supported by an inflated rubber tube, shown in Fig. 6, giving rigid body eigenfrequencies well separated from the first flexible mode of the beam.

Measurements are performed by placing the accelerometers at the underside of each (sub)-structure. In order to obtain a complete FRF matrix, as required by the decoupling technique, impact excitation is sequentially provided on all DoFs at the topside of each (sub)-structure.

4 DECOUPLING

The FRFs of subsystem U can be determined by the procedure described previously and summarized in Eq. (13), where compatibility and equilibrium DoFs are defined case by case. A collocated approach is adopted in which compatibility and equilibrium DoFs are the same.

Since rotational DoFs at the junction between the residual subsystem and the unknown sub-

a	b	c	d	e	l
540	420	60	100	240	600

Table 1: Geometrical dimensions [mm]

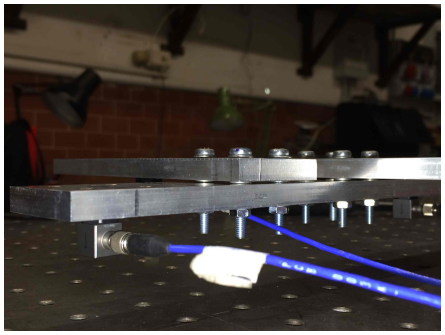


Figure 5: Detail of the bolted junction.

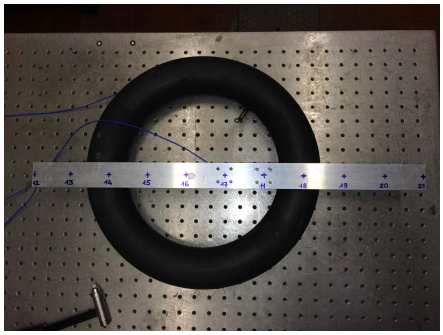


Figure 6: Unknown subsystem.

system can not be measured, neither the standard interface nor the extended interface can be used. Therefore, only mixed interfaces can be considered. FRFs to be used in decoupling can be either the raw FRFs or can be obtained by a curve fitting procedure. Raw FRFs are used.

The number n_c of coupling DoFs is 3 so that it must be $N_E \geq n_c = 3$. Some tests using mixed interfaces with $N_C = N_E = 4$ are performed.

First, a mixed interface including the coupling DoF $11z$ and the internal DoFs $3z$, $6z$ and $9z$ is used. A force applied to DoF $9z$ is able to control the coupling DoF $11\vartheta_y$, whilst forces applied to DoFs $3z$ and $6z$ are able to control the coupling DoF $11\vartheta_x$. Therefore

$$\mathbf{B_C} = \mathbf{B_E} = \begin{array}{c} \begin{matrix} u_{3z}^{RU} & u_{6z}^{RU} & u_{9y}^{RU} & u_{11z}^{RU} & u_{3z}^{R} & u_{6z}^{R} & u_{9z}^{R} & u_{11z}^{R} \end{matrix} \\ \left[\begin{array}{cccc|cccc} 1 & 0 & 0 & 0 & -1 & 0 & 0 & 0 \\ 0 & 1 & 0 & 0 & 0 & -1 & 0 & 0 \\ 0 & 0 & 1 & 0 & 0 & 0 & -1 & 0 \\ 0 & 0 & 0 & 1 & 0 & 0 & 0 & -1 \end{array}\right] \\ \mathbf{B_C^{RU}} \qquad\qquad \mathbf{B_C^{R}} \end{array} \tag{14}$$

The FRF of the unknown substructure U is shown in Fig. 7: the peak around 1000 Hz is not well described and some other peaks are shifted towards higher frequencies.

Another mixed interface including the coupling DoF $11z$ and the internal DoFs $3z$, $9z$ and $10z$ is used. Forces applied to DoFs $9z$ and $10z$ are able to control the coupling DoF $11\vartheta_y$, whilst a force applied to DoF $3z$ is able to control the coupling DoF $11\vartheta_x$. $\mathbf{B_C}$ and $\mathbf{B_E}$ are built similarly to the first case. The FRF of the unknown substructure U is shown in Fig. 8: the peak around 600 Hz is shifted forward and the FRF around it is scattered. However, the peak around 1000 Hz is very well described.

A new set of attempts is performed using mixed interfaces including only 3 DoFs. A mixed interface that includes the coupling DoF $11z$ and the internal DoFs $3z$ and $9z$ is used. A force applied to DoF $9z$ is able to control the coupling DoF $11\vartheta_y$, whilst a force applied to DoF $3z$ is able to control the coupling DoF $11\vartheta_x$. The FRF of the unknown substructure U is shown in Fig. 9: the result is quite clean with no significant drawbacks.

To cross-check this result, a mixed interface that includes the coupling DoF $11z$ and the internal DoFs $3z$ and $6z$ is used. In this case, the coupling DoF $11\vartheta_y$ can not be controlled by any force applied to an internal DoF, so that a bad result is expected. The FRF of the unknown substructure U is shown in Fig. 10. The result is quite bad: the two peaks around 315 Hz and 615 Hz are shifted forward, a spurious peak appears around 500 Hz, and the peak around 1000 Hz is not well described.

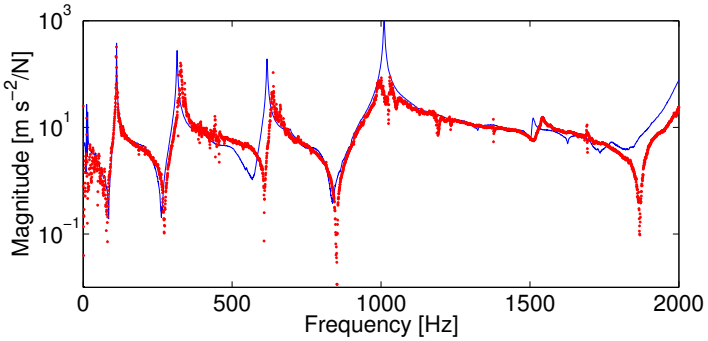


Figure 7: $H^U_{11z,11z}$: measured (—), computed using coupling DoF $11z$ and internal DoFs $3z$, $6z$, $9z$ (***).

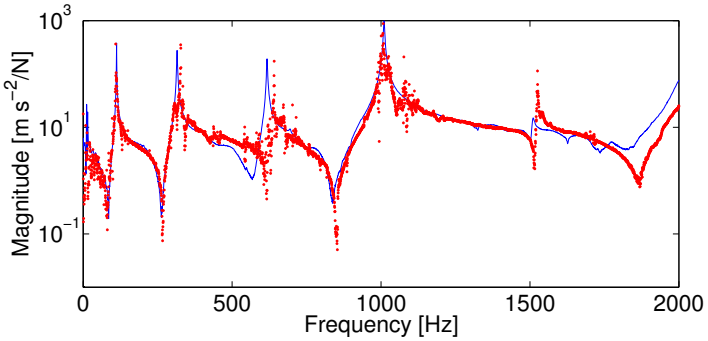


Figure 8: $H^U_{11z,11z}$: measured (—), computed using coupling DoF $11z$ and internal DoFs $3z$, $9z$, $10z$ (***).

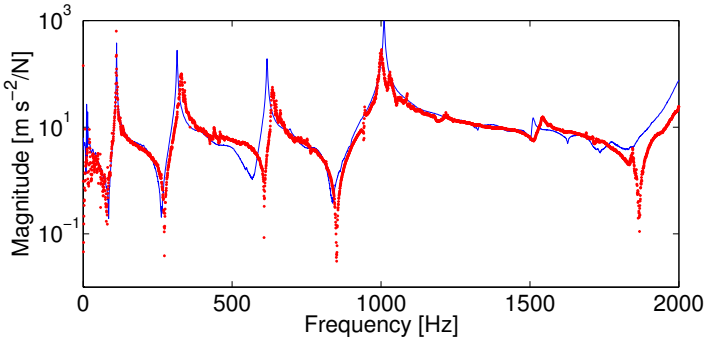


Figure 9: $H^U_{11z,11z}$: measured (—), computed using coupling DoF $11z$ and internal DoFs $3z$, $9z$ (***).

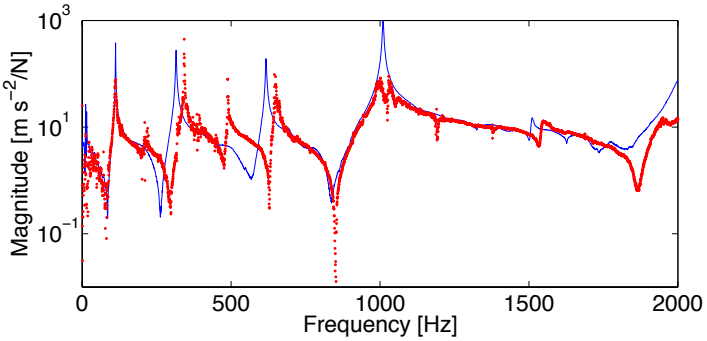


Figure 10: $H^U_{11z,11z}$: measured (—), computed using coupling DoF $11z$ and internal DoFs $3z$, $6z$ (***).

5 CONCLUSIONS

In this paper, qualitative criteria are sought for an optimal selection of translational internal DoFs used to replace rotational coupling DoFs. It is found that internal DoFs must be such that disconnection forces that are applied to them are able to control coupling DoFs.

The criterion is checked on an experimental test bed made by a cantilever column with two staggered short arms coupled to a horizontal beam. This involves both flexural and torsional DoFs, on which rotational FRFs are not measured. It is found that bad results are obtained whenever forces applied to the selected internal DoFs are unable to control coupling DoFs. However, even when internal DoFs are selected correctly, the quality of the results may be affected by systematic errors that are difficult to be detected a priori.

ACKNOWLEDGEMENTS

This research is supported by University of Rome La Sapienza and University of L'Aquila.

REFERENCES

[1] D. de Klerk, D. J. Rixen and S. Voormeeren, General framework for dynamic substructuring: History, review, and classification of techniques. *AIAA J.*, **46**, 1169–1181, 2008.

[2] A. Sestieri, P. Salvini and W. D'Ambrogio, Reducing scatter from derived rotational data to determine the frequency response function of connected structures. *Mech. Syst. Signal Proc.*, **5**, 25–44, 1991.

[3] A. Stanbridge and D. Ewins, Measurement of translational and angular vibration using a scanning laser doppler vibrometer. *Shock and Vibration*, **3**, 141–152, 1996.

[4] M. Bello, A. Sestieri, W. D'Ambrogio and F. La Gala, Development of PZT's as rotational transducers. *Mech. Syst. Signal Proc.*, **17** 1069–1081, 2003.

[5] W. D'Ambrogio and A. Fregolent, Are rotational DoFs essential in substructure decoupling? *Dynamics of Coupled Structures, Vol. 1*. M. Allen, R. Mayes, and D. Rixen, eds. Proceedings of IMAC 32, 27–36, Springer, 2014.

[6] W. D'Ambrogio and A. Fregolent, Ignoring rotational dofs in decoupling structures connected through flexotorsional joints. *Dynamics of Coupled Structures, Vol. 4* M. Allen, R. L. Mayes, and D. J. Rixen, eds. Proceedings of IMAC 33, 57–69, Springer, 2015.

[7] S. N. Voormeeren and D. J. Rixen, A family of substructure decoupling techniques based on a dual assembly approach. *Mech. Syst. Signal Proc.*, **7**, 379–396, 2012.

[8] W. D'Ambrogio and A. Fregolent, The role of interface DoFs in decoupling of substructures based on the dual domain decomposition. *Mech. Syst. Signal Proc.*, **24**, 2035–2048, 2010.

[9] W. D'Ambrogio and A. Fregolent, Direct decoupling of substructures using primal and dual formulation. *Linking Models and Experiments, Vol. 2*. Tom Proulx ed. Proceedings of IMAC 29, 47–76, Springer, 2011.

[10] W. D'Ambrogio and A. Fregolent, Inverse dynamic substructuring using direct hybrid assembly in the frequency domain. *Mech. Syst. Signal Proc.*, **45**, 360–377, 2014.

11th International Conference on Engineering Vibration
Ljubljana, Slovenia, 7–10 September 2015

ADAPTIVE FEEDFORWARD COMPENSATION FOR REALTIME HYBRID TESTING WITH HARMONIC EXCITATION.

Andreas Bartl[1], **Johannes Mayet**[2], **Daniel J. Rixen**[3]

[1]Technische Universität München, andreas.bartl@tum.de

[2]BMW Group, johannes.mayet@bmw.de

[3]Technische Universität München, rixen@tum.de

Keywords: hybrid testing, hardware in the loop, real-time substructuring, interface synchronization, cyber physics

Abstract. *Cyber Physical Testing or Realtime Hybrid Testing is an experimental technique making it possible to test components of structural systems with realistic boundary conditions. The basic idea is to split a given mechanical system into a virtual and an experimental subsystem. Both subsystems are coupled in a real time test. This type of testing can be valuable where neither an experimental test of the overall system nor a full simulation are reasonable or applicable. This study concentrates on the implementation of an adaptive feedforward cancellation algorithm for interface synchronization of the hybrid test. It is applicable in cases with known harmonic excitation. In contrast to existing Realtime Hybrid Testing control schemes we developed an adaptive harmonic excitation generator, which produces harmonic interface forces and the associated interface forces are simultaneously applied on both substructure interfaces. The interface force frequencies are chosen in accordance with the excitation on the numerical substructure. Amplitudes and phases of the harmonic components of the interface force, however, are retrieved from an adaption law which successively minimizes the interface gap.*

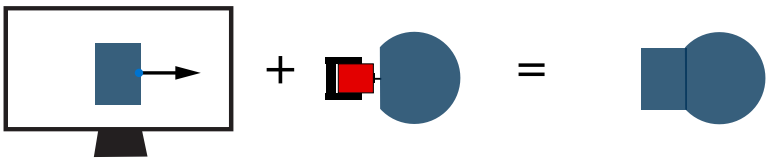


Figure 1: Principle of Real Time Hybrid testing: Virtual and experimental component are coupled with actuators, sensors and a real time control system such that the experimental component deforms as in the assembled product.

1 Introduction

The idea of Real Time Hybrid Testing is to separate a complex product into a virtual and an experimental component. Virtual and experimental components are coupled with actuators, sensors and a real time control system such that the experimental component deforms as if it would be assembled to the overall product (Fig. 1). Potential applications include automotive drivetrains, wind energy drive trains, high precision machinery and structural test of wind turbine blades or satellites (see eg. Bosse et al. [4] and Plummer [13]). First approaches of Real Time Hybrid Testing have been presented by Reinel [14] for satellite testing. Nakashima et al. [12], Horiuchi et al. [8] and Blakeborough et al. [2] applied the technique to the test of components of civil structures under seismic loads. A key problem is the synchronization of the interfaces which corresponds to a compensation of the actuator dynamics. Wagg and Stoten [16] and Stoten and Hyde [15] propose to use Model Reference Adaptive Control (MRAC) for the compensation in Real Time Hybrid Testing. Darby et al. [5] and Horiuchi et al. [8] use feedforward prediction based on polynomials for actuator compensation, which Wallace et al. [17] extended by gain and phase estimation. More recently Li et al. [11] proposed a neuronal network feedforward compensator in Real Time Hybrid Testing and Jungblut et al. [9] synchronize interface deflections using a filtered-x Least-Mean-Square(fxLMS) algorithm.
In this contribution an Adaptive Feedforward Cancelation (AFC) strategy for interface synchronization is proposed. The general AFC strategy, which uses an adaption law with sinusoidal regressors, was proposed by Glover [6] and further investigated by Bodson et al. [3] and Bayard [1]. We introduce an Real Time Hybrid Testing approach, which makes use of AFC. The stability of a simulated test with two lumped mass systems is investigated. Furthermore, we present first experimental results of a Real Time Hybrid Test with a one DoF interface.

2 The Coupling Problem

Starting point for coupling a virtual and an experimental subsystem (Fig. 2) are the interface equilibrium and compatibility conditions given in Eq. (1). The subscripts E and V denote the experimental and the virtual subcomponent. $\mathbf{G}_V$ and $\mathbf{G}_E$ are Boolean matrices assigning global degrees of freedom (DoFs) to interface DoFs.

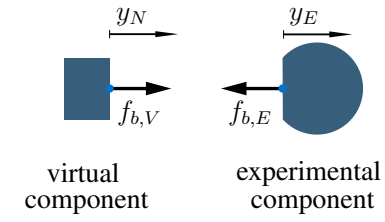


Figure 2: Coupling two subsystems.

$$\mathbf{y}_V - \mathbf{y}_E = \mathbf{0} \quad \text{and} \quad \mathbf{G}_E \mathbf{f}_{b,E} = -\mathbf{G}_V \mathbf{f}_{b,V} = \boldsymbol{\lambda} \tag{1}$$

The equilibrium condition can be satisfied by applying forces with identical magnitude $\boldsymbol{\lambda}$ but opposite sign on both interfaces, which yields the dual formulation (see also Klerk et al. [10]) given in Eq. (2). Forces on the experimental component are applied by actuators. The actuation force is subsequently applied with opposite sign to the virtual component.

$$\begin{bmatrix} \mathbf{M}_V & \mathbf{0} \\ \mathbf{0} & \mathbf{M}_E \end{bmatrix} \begin{bmatrix} \ddot{\mathbf{u}}_V \\ \ddot{\mathbf{u}}_E \end{bmatrix} + \begin{bmatrix} \mathbf{D}_V & \mathbf{0} \\ \mathbf{0} & \mathbf{D}_E \end{bmatrix} \begin{bmatrix} \dot{\mathbf{u}}_V \\ \dot{\mathbf{u}}_E \end{bmatrix} + \begin{bmatrix} \mathbf{K}_V & \mathbf{0} \\ \mathbf{0} & \mathbf{K}_E \end{bmatrix} \begin{bmatrix} \mathbf{u}_V \\ \mathbf{u}_E \end{bmatrix} + \begin{bmatrix} \mathbf{G}_V^T \\ -\mathbf{G}_E^T \end{bmatrix} \boldsymbol{\lambda} = \begin{bmatrix} \mathbf{f}_V \\ \mathbf{f}_E \end{bmatrix} \tag{2}$$

The corresponding state space formulations are given in Eqs. (3) and (4). The external forces $\mathbf{f}_V$ and $\mathbf{f}_E$ are considered as disturbance input, $\boldsymbol{\lambda}$ as input and the interface displacements $\mathbf{y}_E$ and $\mathbf{y}_V$ as outputs.

$$\begin{aligned} \dot{\mathbf{x}}_V &= \underbrace{\begin{bmatrix} \mathbf{0} & \mathbf{I} \\ -\mathbf{M}_V^{-1}\mathbf{K}_V & -\mathbf{M}_V^{-1}\mathbf{D}_V \end{bmatrix}}_{\mathbf{A}_V} \mathbf{x}_V + \underbrace{\begin{bmatrix} \mathbf{0} \\ \mathbf{M}_V^{-1}\mathbf{G}_V^T \end{bmatrix}}_{\mathbf{B}_V} \boldsymbol{\lambda} + \underbrace{\begin{bmatrix} \mathbf{0} \\ \mathbf{M}_V^{-1} \end{bmatrix}}_{\mathbf{E}_V} \mathbf{f}_V \\ \mathbf{y}_V &= \mathbf{G}_V \mathbf{u}_V = \underbrace{\begin{bmatrix} \mathbf{G}_V & \mathbf{0} \end{bmatrix}}_{\mathbf{C}_V} \mathbf{x}_V \end{aligned} \tag{3}$$

$$\begin{aligned} \dot{\mathbf{x}}_E &= \underbrace{\begin{bmatrix} \mathbf{0} & \mathbf{I} \\ -\mathbf{M}_E^{-1}\mathbf{K}_E & -\mathbf{M}_E^{-1}\mathbf{D}_E \end{bmatrix}}_{\mathbf{A}_E} \mathbf{x}_E - \underbrace{\begin{bmatrix} \mathbf{0} \\ \mathbf{M}_E^{-1}\mathbf{G}_E^T \end{bmatrix}}_{\mathbf{B}_E} \boldsymbol{\lambda} + \underbrace{\begin{bmatrix} \mathbf{0} \\ \mathbf{M}_E^{-1} \end{bmatrix}}_{\mathbf{E}_E} \mathbf{f}_E \\ \mathbf{y}_E &= \mathbf{G}_E \mathbf{u}_E = \underbrace{\begin{bmatrix} \mathbf{G}_E & \mathbf{0} \end{bmatrix}}_{\mathbf{C}_E} \mathbf{x}_E \end{aligned} \tag{4}$$

Note that n interface displacements ($\mathbf{y}_V, \mathbf{y}_E \in \mathbb{R}^n$) are measured respectively retrieved from simulation and n interface forces ($\boldsymbol{\lambda} \in \mathbb{R}^n$) are applied on both subsystems. We assume an external excitation given by m harmonics and rewrite the steady-state system output in frequency domain as

$$\begin{aligned} \mathbf{Y}_V(j\omega) &= \mathbf{C}_V(j\omega\mathbf{I} - \mathbf{A}_V)^{-1}\mathbf{B}_V\boldsymbol{\Lambda}(j\omega) + \mathbf{C}_V(j\omega\mathbf{I} - \mathbf{A}_V)^{-1}\mathbf{E}_V\mathbf{F}_{e,V}(j\omega) = \\ &= \mathbf{H}_V(j\omega)\boldsymbol{\Lambda}(j\omega) + \mathbf{H}_{e,V}(j\omega)\mathbf{F}_{e,V}(j\omega) \end{aligned} \tag{5}$$

$$\mathbf{Y}_E(j\omega) = \mathbf{H}_E(j\omega)\boldsymbol{\Lambda}(j\omega) + \mathbf{H}_{e,E}(j\omega)\mathbf{F}_{e,E}(j\omega) \tag{6}$$

where capital symbols are corresponding Fourier transformations. E.g. $\boldsymbol{\Lambda}(j\omega)$ is the Fourier transformation of $\boldsymbol{\lambda}$. We rewrite Eqs. (5) and (6) in time domain in the following form showing that the outputs are a sum of multiple harmonics:

$$\begin{aligned} \mathbf{y}_V &= \sum_{i=1}^{m} \underbrace{\mathbf{W}_i(t)\mathbf{P}_{V,i}\tilde{\boldsymbol{\theta}}_i}_{\substack{\text{influence} \\ \text{interface forces}}} + \underbrace{\mathbf{d}_V}_{\substack{\text{influence external} \\ \text{excitation (disturbance)}}} \\ \mathbf{y}_E &= \sum_{i=1}^{m} \mathbf{W}_i(t)\mathbf{P}_{E,i}\tilde{\boldsymbol{\theta}}_i + \mathbf{d}_E \end{aligned} \tag{7}$$

The interface force signal is generated according to Eq. (8).

$$\boldsymbol{\lambda} = \mathbf{W}\tilde{\boldsymbol{\theta}} \tag{8}$$

The matrix $\mathbf{W}(t)$ contains the sinusoidal functions. The phase angles of the functions is defined as $\alpha_i = \int_0^t \omega_i(t)\mathrm{d}t$ where $\omega_i(t)$ is the excitation frequency.

$$\mathbf{W}_i = \begin{bmatrix} \mathbf{I}_{nn}\cos(\alpha_i) & \mathbf{I}_{nn}\sin(\alpha_i) \end{bmatrix} \qquad \text{with} \quad \mathbf{W}_i \in \mathbb{R}^{n \times 2n}$$

The matrices $\mathbf{P}_{V,i}$ and $\mathbf{P}_{E,i}$ originate from the transfer function $\mathbf{H}_V(j\omega_1)$ and $\mathbf{H}_E(j\omega_1)$ respectively and apply a phase shift and gain to the parameter vector $\tilde{\boldsymbol{\theta}}$.

$$\mathbf{P}_{V,i} = \begin{bmatrix} Re(\mathbf{H}_V(j\omega_i)) & Im(\mathbf{H}_V(j\omega_i)) \\ -Im(\mathbf{H}_V(j\omega_i)) & Re(\mathbf{H}_V(j\omega_i)) \end{bmatrix} = \begin{bmatrix} \mathbf{P}_{R,V,i} & \mathbf{P}_{I,V,i} \\ -\mathbf{P}_{I,V,i} & \mathbf{P}_{R,V,i} \end{bmatrix} \quad \text{with} \quad \mathbf{P}_{V,i} \in \mathbb{R}^{2n\times 2n}$$
$$\mathbf{P}_{E,i} = \begin{bmatrix} Re(\mathbf{H}_E(j\omega_i)) & Im(\mathbf{H}_E(j\omega_i)) \\ -Im(\mathbf{H}_E(j\omega_i)) & Re(\mathbf{H}_E(j\omega_i)) \end{bmatrix} = \begin{bmatrix} \mathbf{P}_{R,E,i} & \mathbf{P}_{I,E,i} \\ -\mathbf{P}_{I,E,i} & \mathbf{P}_{R,E,i} \end{bmatrix} \quad \text{with} \quad \mathbf{P}_{E,i} \in \mathbb{R}^{2n\times 2n}$$

The equivalence can be understood by applying the inverse Fourier transformation to the frequency domain form:

$$\mathcal{F}^{-1}(\mathbf{H}_V(j\omega_1)\mathcal{F}(\mathbf{W})) = \mathcal{F}^{-1}(\begin{bmatrix}\mathbf{H}_V(j\omega_1)\mathcal{F}(\mathbf{I}\cos\alpha_1) & \mathbf{H}_V(j\omega_1)\mathcal{F}(\mathbf{I}\sin\alpha_1) & \dots\end{bmatrix}) = \mathbf{W}\mathbf{P}_V$$

The responses given by Eqs. (7) are finally written in the matrix notation given by Eq. (9).

$$\begin{aligned} \mathbf{y}_V &= \mathbf{W}(t)\mathbf{P}_V\tilde{\boldsymbol{\theta}} + \mathbf{d}_V \quad \text{with} \quad \tilde{\boldsymbol{\theta}} \in \mathbb{R}^{2nm} \\ \mathbf{y}_E &= \mathbf{W}(t)\mathbf{P}_E\tilde{\boldsymbol{\theta}} + \mathbf{d}_E \quad \text{with} \quad \tilde{\boldsymbol{\theta}} \in \mathbb{R}^{2nm} \end{aligned} \tag{9}$$

3 Coupling Harmonically Excited Subsystems with Adaptive Feedforward Cancellation

In order to couple the substructures, our objective is to close the interface gap, which is achieved by applying an appropriate interface force magnitude vector $\boldsymbol{\lambda}$ on the virtual and the experimental subsystem. In contrast to conventional control laws for Real Time Hybrid Testing our objective is not to influence the system dynamics. Small measurement errors may cause instabilities when testing lightly damped structural components or assembled systems. We propose the use of AFC to enforce the interface synchronization where the gap between the two substructures is closed by applying an input signal to the actuator. The control structure is shown in Fig. 3. The input signal is generated from sinusoidal shape functions. As already mentioned the interface force frequencies are the same as the excitation frequencies. The excitation phase angle α_i is either retrieved from the excitation of the virtual subsystem or can be measured directly during operation. As long as the interface gap is not closed we use an adaption algorithm in order to determine the appropriate amplitudes and phases of the interface forces. After a given time a proper stable algorithm will converge to the sought-after solution resulting in a purely harmonic excited system.
The objective of the adaption law is to minimize the cost functional of EQ. (10) with the interface gap $\mathbf{e}$. Note that we take into account the controlled actuator dynamics by expressing the parameter vector as $\tilde{\boldsymbol{\theta}} = \mathbf{P}_A\boldsymbol{\theta}$. The new parameter vector $\boldsymbol{\theta} \in \mathbb{R}^{2nm}$ defines the actuator input signal. The expression $(\mathbf{P}_E - \mathbf{P}_V)\mathbf{P}_A$ is referred to as $\mathbf{P}$ in the following.

$$J = \frac{1}{2}\mathbf{e}^T\mathbf{e} \quad \text{with} \quad \mathbf{e} = \mathbf{y}_E - \mathbf{y}_V = \mathbf{W}\underbrace{(\mathbf{P}_E - \mathbf{P}_V)\mathbf{P}_A}_{\mathbf{P}}\boldsymbol{\theta} + (\mathbf{d}_E - \mathbf{d}_V) \tag{10}$$

The associated adaption law using the cost function gradient $\nabla J = \mathbf{P}^T\mathbf{W}^T\mathbf{e}$ is given in Eq. (11) where $\mathbf{P}$ is additionally replaced by $\mathbf{P}^*$, which is an estimation of the unknown matrix $\mathbf{P}$. However, the entries of $\mathbf{P}^*$ can be retrieved by measurement before the actual test. Note that a relatively rough estimate $\mathbf{P}^*$ is sufficent to achieve stable adaption. In the case of an interface with 1-DoF the correct choice of the correct sign is sufficient. The postive definite adaption gain matrix $\boldsymbol{\Gamma} = \boldsymbol{\Gamma}^T$ controls the performance of the adaption.

$$\dot{\boldsymbol{\theta}} = -\boldsymbol{\Gamma}\nabla J = -\boldsymbol{\Gamma}\mathbf{P}^{*T}\mathbf{W}^T(\mathbf{y}_E - \mathbf{y}_V) \tag{11}$$

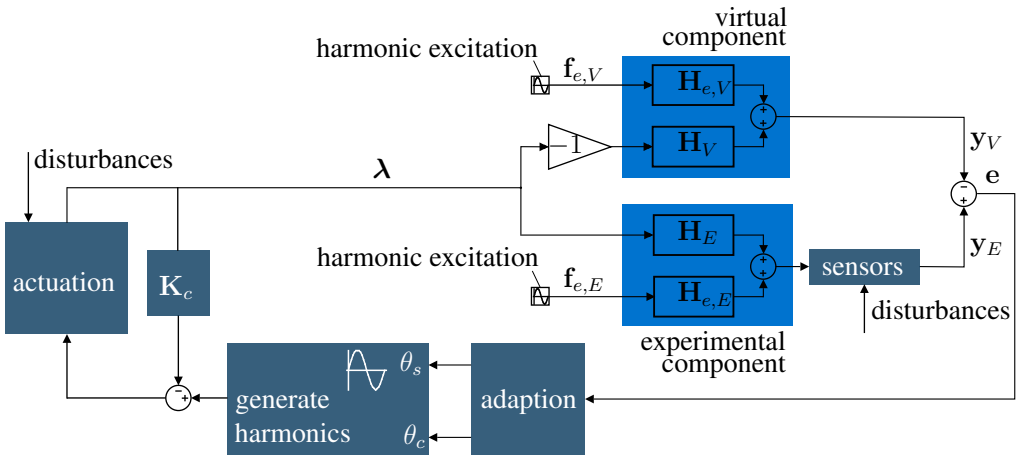


Figure 3: Virtual and experimental component are coupled in the closed-loop system. The interface gap $\mathbf{e}$ is used for the adaption of the harmonic actuator inputs. A simple state feedback $\mathbf{K}_c$ indicates a seperate control loop for the actuator. Both sensors and actuators are subject to disturbances. The forces applied to the experimental component are measured and applied with opposite sign to the virtual component.

4 Equivalent State Space Representation

The stability of the system can be analyzed by transformation of the control law into state space form as described by Guo and Bodson [7]. The adaption law is represented in state space form by using the following coordinate transformations:

$$\mathbf{x}_h = \mathbf{R}\boldsymbol{\theta} \Longleftrightarrow \boldsymbol{\theta} = \mathbf{R}^T\mathbf{x}_h \tag{12}$$

$$\dot{\mathbf{x}}_h = \dot{\mathbf{R}}\boldsymbol{\theta} + \mathbf{R}\dot{\boldsymbol{\theta}} \tag{13}$$

where (14)

$$\mathbf{R} = \begin{bmatrix} \mathbf{R}_1 & \mathbf{0} & \dots & \mathbf{0} \\ 0 & \mathbf{R}_2 & \dots & \mathbf{0} \\ \vdots & \vdots & \ddots & \mathbf{0} \\ \mathbf{0} & \mathbf{0} & \mathbf{0} & \mathbf{R}_m \end{bmatrix} \quad \text{with} \quad \mathbf{R}_i = \begin{bmatrix} \mathbf{I}\cos(\alpha_i) & \mathbf{I}\sin(\alpha_i) \\ -\mathbf{I}\sin(\alpha_i) & \mathbf{I}\cos(\alpha_i) \end{bmatrix}$$

Using Eq. (8), (12) and (13) and replacing $\dot{\boldsymbol{\theta}}$ yields the following linear state space system:

$$\begin{aligned} \dot{\mathbf{x}}_h &= \underbrace{\dot{\mathbf{R}}\mathbf{R}^T}_{\mathbf{A}_h}\mathbf{x}_h \underbrace{-\mathbf{R}\boldsymbol{\Gamma}\mathbf{P}^{*T}\mathbf{W}^T}_{\mathbf{B}_h}(\mathbf{y}_E - \mathbf{y}_V) \\ \boldsymbol{\lambda} &= \underbrace{\mathbf{W}^T\mathbf{R}^T}_{\mathbf{B}_h}\mathbf{x}_h \end{aligned} \tag{15}$$

Note that the state matrix $\mathbf{A}_h = \dot{\mathbf{R}}\mathbf{R}^T$ has the form

$$\mathbf{A}_h = \begin{bmatrix} \mathbf{A}_{h1} & \mathbf{0} & \dots & \mathbf{0} \\ 0 & \mathbf{A}_{h2} & \dots & \mathbf{0} \\ \vdots & \vdots & \ddots & \mathbf{0} \\ \mathbf{0} & \mathbf{0} & \mathbf{0} & \mathbf{A}_{hm} \end{bmatrix} \quad \text{with} \quad \mathbf{A}_{hi} = \begin{bmatrix} \mathbf{0} & \omega_i\mathbf{I} \\ -\omega_i\mathbf{I} & \mathbf{0} \end{bmatrix}$$

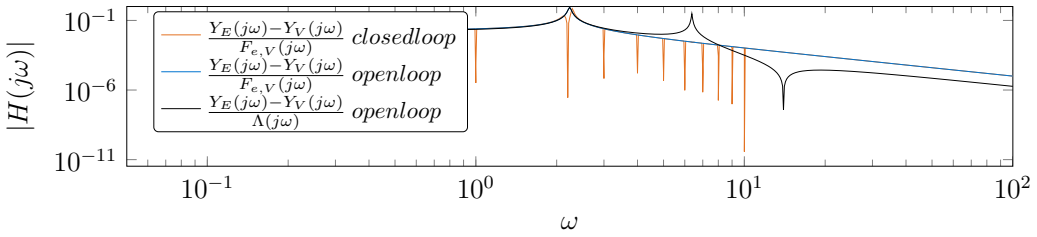


Figure 4: Interface synchronization of the lumped mass example system. Synchronization at the excitation frequencies 1 $\left[\frac{rad}{s}\right]$, 2.2 $\left[\frac{rad}{s}\right]$, 3 $\left[\frac{rad}{s}\right]$, 4 $\left[\frac{rad}{s}\right]$, 5 $\left[\frac{rad}{s}\right]$, 6 $\left[\frac{rad}{s}\right]$, 7 $\left[\frac{rad}{s}\right]$, 8 $\left[\frac{rad}{s}\right]$, 9 $\left[\frac{rad}{s}\right]$, 10 $\left[\frac{rad}{s}\right]$ is indicated by the zeros in the sensitivity function $\frac{Y_E(j\omega)-Y_V(j\omega)}{F_{e,V}(j\omega)}$.

Finally, the state space representation of the overall coupled system is

$$\begin{bmatrix} \dot{\mathbf{x}}_V \\ \dot{\mathbf{x}}_E \\ \dot{\mathbf{x}}_h \end{bmatrix} = \begin{bmatrix} \mathbf{A}_V & \mathbf{0} & \mathbf{B}_V\mathbf{C}_h \\ \mathbf{0} & \mathbf{A}_E & \mathbf{B}_E\mathbf{C}_h \\ -\mathbf{B}_h\mathbf{C}_V & \mathbf{B}_h\mathbf{C}_E & \mathbf{A}_h \end{bmatrix} \begin{bmatrix} \mathbf{x}_V \\ \mathbf{x}_E \\ \mathbf{x}_h \end{bmatrix} + \begin{bmatrix} \mathbf{E}_V & \mathbf{0} \\ \mathbf{0} & \mathbf{E}_E \\ \mathbf{0} & \mathbf{0} \end{bmatrix} \begin{bmatrix} \mathbf{f}_V \\ \mathbf{f}_E \end{bmatrix} \tag{16}$$

5 Example: Synchronizing two lumped mass systems

In order to illustrate the stability properties of a coupled system we consider two mass-spring-damper-systems given by

$$\begin{bmatrix} \dot{u}_V \\ \ddot{u}_V \end{bmatrix} = \underbrace{\begin{bmatrix} 0 & 1 \\ -\frac{k_V}{m_V} & -\frac{d_V}{m_V} \end{bmatrix}}_{\mathbf{A}_V} \underbrace{\begin{bmatrix} u_V \\ \dot{u}_V \end{bmatrix}}_{\mathbf{x}_V} + \underbrace{\begin{bmatrix} 0 \\ -\frac{1}{m_V} \end{bmatrix}}_{\mathbf{B}_V} \lambda + \underbrace{\begin{bmatrix} 0 \\ \frac{1}{m_V} \end{bmatrix}}_{\mathbf{E}_V} F_0 \cos\omega_1 t \tag{17}$$

$$\begin{bmatrix} \dot{u}_E \\ \ddot{u}_E \end{bmatrix} = \underbrace{\begin{bmatrix} 0 & 1 \\ -\frac{k_E}{m_E} & -\frac{d_E}{m_E} \end{bmatrix}}_{\mathbf{A}_E} \underbrace{\begin{bmatrix} u_E \\ \dot{u}_E \end{bmatrix}}_{\mathbf{x}_E} + \underbrace{\begin{bmatrix} 0 \\ \frac{1}{m_E} \end{bmatrix}}_{\mathbf{B}_E} \lambda \tag{18}$$

Since $F_0 \cos\omega_1 t$ is the only external excitation we obtain the following linear time invariant (LTI) state space representation for the AFC:

$$\dot{\mathbf{x}}_h = \underbrace{\begin{bmatrix} 0 & \omega_1 \\ -\omega_1 & 0 \end{bmatrix}}_{\mathbf{A}_h} \mathbf{x}_h \underbrace{-\gamma \begin{bmatrix} P^*_{R,1} \\ P^*_{I,1} \end{bmatrix}}_{\mathbf{B}_h} e$$
$$\lambda = \underbrace{\begin{bmatrix} 1 & 0 \end{bmatrix}}_{\mathbf{C}_h} \mathbf{x}_h$$

The overall system can be written in a state space representation accordingly to Eq. (16). The transfer function of the closed loop system is shown in Fig. 4. In order to understand the properties of AFC controllers and the influence on the choice of filter matrix $\mathbf{P}^*$ we investigate the coupled system with the parameter values $m_1 = 10$, $m_2 = 12$, $d_1 = 0.05$, $d_2 = 0.050$, $k_1 = 50$, $k_2 = 500$ and $\Gamma = 1$. The stability plot of the close-loop system depends on the choice of $\mathbf{P}^*$ as illustrated in Fig. 5. The adaption is robust against the choice of $\mathbf{P}^*$ as the stability border is perpendicular to the line between the origin O and $\mathbf{P}$. In fact, the phase shift estimate

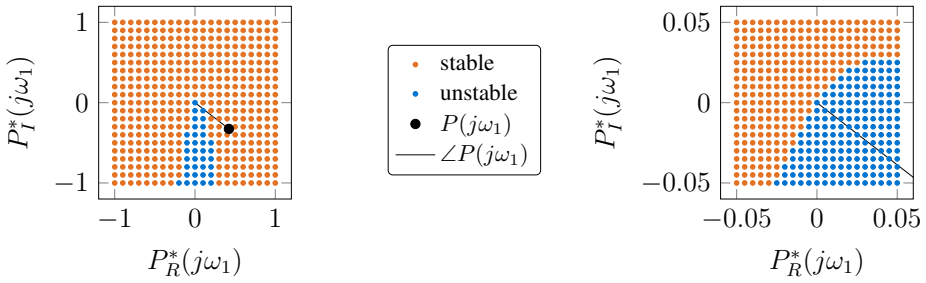


Figure 5: Stability map for the choice of P^* with $\omega_1 = 2.2\left[\frac{rad}{s}\right]$ and $d = 0.05$. Left and right subfigures show different clippings of the same stabilty map.

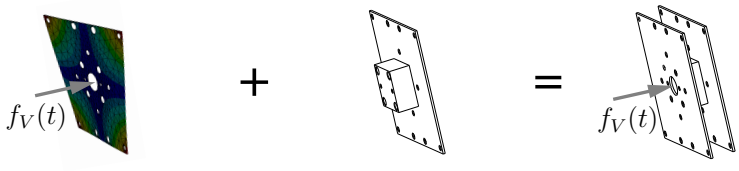


Figure 6: Virtual component, experimental component and coupled reference system used for the validation of the hybrid test with one DoF coupling.

can have a deviation in the range of $-\pi < \angle \mathbf{P}^*(j\omega_i) O \mathbf{P}(j\omega_i) < \pi$ for a stable adaption. An important observation for practice is the following: In cases of small damping and/or excitation frequencies close to resonance the stable parameter regions are smaller. However, stability can always be achieved by the use of a sufficiently small adaption gain Γ (see also section 4).

6 Synchronizing an experiment with a reduced order finite-element model

In order to validate the proposed approach we carried out a hybrid test, where the physical system is a square aluminum plate bolted to an aluminum block and the virtual component is a finite element model of an aluminum plate as illustrated in figure 6. For validation we use an actual physical assembly of the tested system as a reference. The coupling of the Real Time Hybrid Test is performed with a one DoF interface. In order to be able to apply exactly the same force on the reference system and on the virtual component, we excite the reference system with a defined harmonic excitation force. The force is measured and subsequently applied to the virtual component of the Real Time Hybrid Test.

The experimental setup consists of an electro magnetic shaker (RMS SW52), commonly used for vibration and modal tests, an amplifier (RMS TG101), a laser-triangulation displacement sensor (Micro-Epsilon LD1605-10) and a force sensor (PCB M208C02) with an ICP voltage source. Model and synchronization control are run on a Simulink Realtime Target PC, which is controlled and programmed from a host PC. A schematic diagram of the experimental setup is illustrated in Fig. 7. The finite element model of the virtual component is created in ANSYS. The model is subsequently reduced to the coordinate set $\mathbf{q}$ by $\mathbf{u}_V = \Phi\mathbf{q}$ where Φ is a matrix with normal modes. The reduction yields

$$\Phi^T\mathbf{M}_V\Phi\ddot{\mathbf{q}} + \Phi^T\mathbf{C}\Phi\dot{\mathbf{q}} + \Phi^T\mathbf{K}\Phi\mathbf{q} + \Phi^T\mathbf{f}_b = \Phi^T\mathbf{f}_V \tag{19}$$

The interface coordinate y_V is the averaged interface displacement and the interface force is

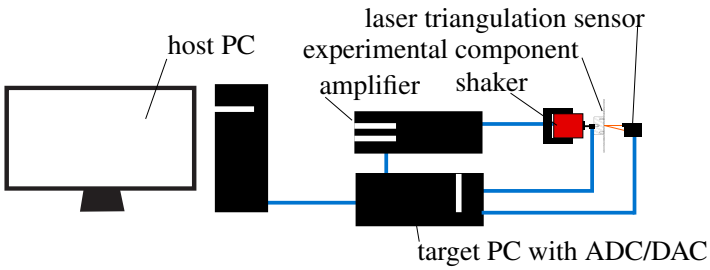


Figure 7: Experimental setup used for validation of the proposed approach: Model and synchronization control run on a real time target PC, which is equipped with a Digital-to-Analog/Analog-to-Digital converter card. The target PC is sending a control signal to an electromagnetic shaker over an amplifier. Displacement and force sensor are connected as inputs to the converter card. The host PC is used for the control and record of the experiment.

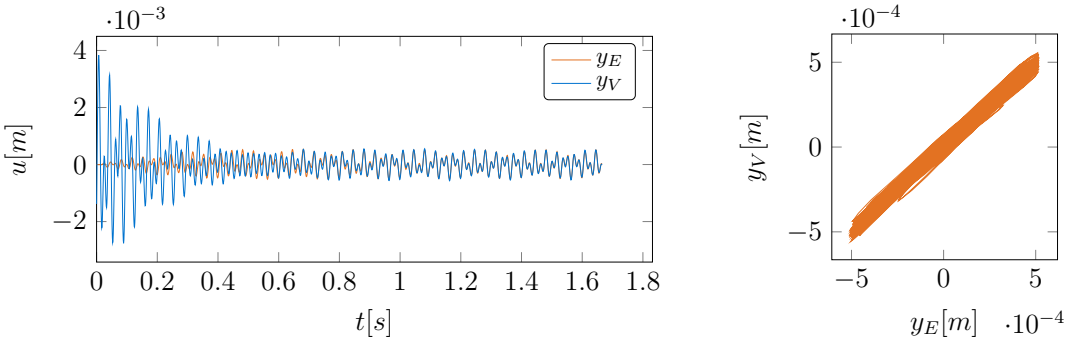


Figure 8: The left subfigure shows the adaption process of the describes experiment. The right subfigure shows the synchronization of virtual and experimental component in adapted state. Optimal synchronization in the synchronization plot would be indicated by a straight line with slope 1.

uniformly distributed on the virtual conponent's interface using the matrix $\tilde{\mathbf{G}}_V$. This procedure implies that the coupling is enforced in a weak sense.

$$y_V = \tilde{\mathbf{G}}_V \Phi \mathbf{q} \tag{20}$$

$$\mathbf{f}_b = \tilde{\mathbf{G}}_V^T \lambda \tag{21}$$

The measurement was performed with an excitation, combining sinusoidal forces with $30[Hz]$ and $55[Hz]$ and amplitudes of $2[N]$ and $8[N]$ on the reference assembly. For the adaption gain matrix $\mathbf{\Gamma} = \mathbf{I} \in \mathbb{R}^{2\times 2}$ the identy matrix is chosen. Virtual and experimental substructure show synchronization on the interface (Fig. 8). Reasons for slight deviation are drift effects caused by low frequency noise content of the measured forces, which are fed back to the virtual component. Note that the adaption converges in less than $2[s]$ in the considered test case. Reference system and Real Time Hybrid Test (Fig. 9) show a high degree of agreement. This indicates a consistent test imitating the reference system.

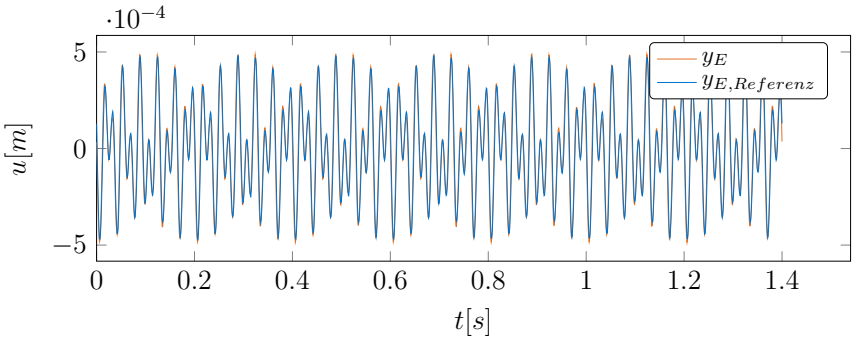


Figure 9: Interface responses of the hybrid realtime test y_E and of a physical reference system $y_{E,Referenz}$.

7 Conclusion

In this contribution we propose the use of Adaptive Feedforward Cancelation for interface synchronization in Real Time Hybrid Testing. The coupling problem is formulated and transferred into a form, which can be handled by AFC. The stability behavior of Real Time Hybrid Test is investigated on a numerical example. The method is then validated on a simple test rig. Adaptive Feedforward Cancelation can be applied to steady state test cases with harmonic excitation. The method shows a satisfactoy convergence time on the test rig, which indicates feasibility for a variety of applications. The dynamics of the system in adapted state is not changed compared to dynamics of the subcomponents. While here the issue of stability can be easily handled, it is noteworhty that in other techniques used in Hybrid Testing, the dynamics of the system have to be very close to instability in order to imitate the overall system's dynamics. Future work will include the online estimation of the plant parameters. This technique could be applied to the coupling of multiple DoF and the coupling of nonlinear substructures. Also strategies, which allow the online adaption of the frequency exist in the control community and can be adapted to Real Time Hybrid Testing.

References

[1] D. S. Bayard. "A general theory of linear time-invariant adaptive feedforward systems with harmonic regressors". In: *IEEE Transactions on Automatic Control* 45.11 (2000), pp. 1983–1996.

[2] A. Blakeborough, A. Darby, and M. Williams. "The development substructure of real-time testing". In: *Pilosophical transactions: Mathematical, Physical and Engineering Sciences* 359.1786 (2001), pp. 1869–1891.

[3] M. Bodson, A. Sacks, and P. Khosla. "Harmonic generation in adaptive feedforward cancellation schemes". In: *IEEE Transactions on Automatic Control* 39.9 (1994), pp. 1939–1944.

[4] D. Bosse, D. Radner, R. Schelenz, and G. Jacobs. "Analysis and Application of Hardware in the Loop Wind Loads for Full Scale Nacelle Ground Testing". In: *DEWI Magazin* 43 (2013), pp. 65–70.

[5] A. P. Darby, M. S. Williams, and A Blakeborough. "Stability and Delay Compensation for Real-Time Substructure Testing". In: *Journal of Engineering Mechanics* 128.Dezember (2002), pp. 1276–1284.

[6] J. Glover. “Adaptive noise canceling applied to sinusoidal interferences”. In: *IEEE Transactions on Acoustics, Speech, and Signal Processing* 25 (1977), pp. 484–491.

[7] X. Guo and M. Bodson. “Equivalence between adaptive feedforward cancellation and disturbance rejection using the internal model principle”. In: *International Journal of Adaptive Control and Singal Processing* 24 (2010), pp. 211–218.

[8] T. Horiuchi, M. Inoue, T. Konno, and Y. Namita. “Real-time hybrid experimental system with actuator delay compensation and its application to a piping system with energy absorber.” In: *Earthquake Engineering and Structural Dynamics* 28.10 (1999), pp. 1121–1141.

[9] T. Jungblut, S. Wolter, M. Matthias, and H. Hanselka. “Using Numerical Models to Complement Experimental Setups by Means of Active Control of Mobility”. In: *Applied Mechanics and Materials* 70 (Aug. 2011), pp. 357–362.

[10] D. D. Klerk, D. J. Rixen, and S. N. Voormeeren. “General Framework for Dynamic Substructuring: History, Review and Classification of Techniques”. In: *AIAA Journal* 46.5 (2008), pp. 1169–1181.

[11] G. Li, J. Na, D. P. Stoten, and X. Ren. “Adaptive neural network feedforward control for dynamically substructured systems”. In: *IEEE Transactions on Control Systems Technology* 22.3 (2014), pp. 944–954.

[12] M. Nakashima, H. Kato, and E. Takaoka. “Development of real-time pseudo dynamic testing”. In: *Earthquake Engineering & Structural Dynamics* (1992), pp. 79–92.

[13] A. Plummer. “Model-in-the-Loop Testing”. In: *Proceedings of the Institution of Mechanical Engineers, Part I: Journal of Systems and Control Engineering* 220 (2006), pp. 183–199.

[14] K Reinel. “Motion Simulation Facility for the Satellite SYMPHONIE.” In: Sonderdruck: Deutsche Forschungs- und Versuchsanst. für Luft- und Raumfahrt. Defense Technical Information Center, 1972.

[15] D. Stoten and R. Hyde. “Adaptive control of dynamically substructured systems: the single-input single-output case”. In: *Proceedings of the Institution of Mechanical Engineers, Part I: Journal of Systems and Control Engineering* 220.2 (Feb. 2006), pp. 63–79.

[16] D. J. Wagg and D. P. Stoten. “Substructuring of dynamical systems via the adaptive minimal control synthesis algorithm”. In: *Earthquake Engineering & Structural Dynamics* 30.6 (2001), pp. 865–877.

[17] M. Wallace, D. Wagg, and S. Neild. “An adaptive polynomial based forward prediction algorithm for multi-actuator real-time dynamic substructuring”. In: *Proceedings of the Royal Society A: Mathematical, Physical and Engineering Sciences* 461.2064 (Dec. 2005), pp. 3807–3826.

11th International Conference on Engineering Vibration
Ljubljana, Slovenia, 7–10 September 2015

COMPARISON BETWEEN PRIMAL AND DUAL CRAIG-BAMPTON SUBSTRUCTURE REDUCTION TECHNIQUES

Fabian M. Gruber*[1], Johannes B. Rutzmoser[2], Daniel J. Rixen[3]

[1,2,3]Institute of Applied Mechanics, Faculty of Mechanical Engineering, Technische Universität München, Boltzmannstr. 15, 85748 Garching, Germany

[1]fabian.gruber@tum.de, [2]johannes.rutzmoser@tum.de, [3]rixen@tum.de

Keywords: Dynamic substructuring, Component mode synthesis, Model order reduction, Dual Assembly, Craig-Bampton method, Free interface method

Abstract. *Dynamic substructuring is an efficient way to reduce the size and to analyse the dynamical behaviour of large models. The most popular approach is a fixed-interface method, the Craig-Bampton method (1968), which is based on fixed-interface vibration modes and interface constraint modes. On the other hand, free-interface methods employing free-interface vibration modes together with attachment modes are also used, e.g. MacNeal's method (1971) and Rubin's method (1975). The methods mentioned so far assemble the substructures using interface displacements (primal assembly). The dual Craig-Bampton method (2004) uses the same ingredients as the methods of MacNeal and Rubin, but assembles the substructures using interface forces (dual assembly). This method enforces only weak interface compatibility between the substructures, thereby avoiding interface locking problems as sometimes experienced in the primal assembly approaches using free-interface modes. Moreover, the dual Craig-Bampton method leads to simpler reduced matrices compared to other free-interface methods and these reduced matrices are similar to the classical Craig-Bampton matrices. In this contribution we want to refine the first formulation of the dual Craig-Bampton method from 2004 and present the derivation in a comprehensible consistent manner. Special attention is directed to the influence of the applied eigensolver for computing the required free-interface vibration modes. Moreover, a detailed comparison between the primal (classical) formulation of the Craig-Bampton method and the dual formulation of the Craig-Bampton method will be given. The presented theory and the comparison between the two substructuring methods will be illustrated on a three-dimensional beam frame and on a two-dimensional solid plane stress problem.*

1 INTRODUCTION

Nowadays the increasing performance of modern computers makes it possible to solve very large linear systems of millions of degrees of freedom (DOF). Nevertheless, since dynamic analysis requires solving a lot of linear systems and since the refinement of finite element models is increasing faster than the computing capabilities, dynamic substructuring still remains an essential tool for analysing dynamical systems in an efficient manner. Building reduced models of subparts of a structure enables sharing models between design groups. Moreover the reduction of the DOF of substructures is also important for building reduced order models for optimisation and control. If a single component of a system is changed, only that component needs to be reanalysed and the system can be analysed at low additional cost. Thus dynamic substructuring offers a flexible and efficient approach to dynamic analysis.

Dynamic substructuring techniques can be classified in two categories depending on the underlying modes which are used. The term mode can refer to all kind of structural shape vectors. The first class consists of methods using fixed-interface vibrations modes and interface constraint modes to represent the substructure dynamics. The method commonly used is the Craig-Bampton method (CBM) [2] which assembles the substructures in a primal way using interface displacements in order to enforce interface compatibility. The second class consists of methods using free-interface vibrations modes and attachment modes. Common representatives of that class are MacNeal's method [4] and Rubin's method [8] using a primal assembly process as well. Herting generalizes in [3] the concept of component mode synthesis to include any kind of interface boundary condition for the modes. In contrast to the aforementioned methods, the dual Craig-Bampton method (DCBM) [5] uses the same ingredients as MacNeal's and Rubin's method, but assembles the substructures in a dual way using interface forces. As a consequence, the DCBM enforces only weak interface compatibility between the substructures, thereby avoiding interface locking problems as sometimes experienced in the primal assembly approaches.

In section 2, the differences between primal and dual assembly are stated. Following this, the formulation of the CBM and the DCBM will be outlined in section 3 explaining general properties. These properties will be illustrated subsequently in detail using a three-dimensional beam frame in section 4 and an two-dimensional solid plane stress problem in section 5. Finally a brief summary and outlook are given in section 6.

2 PRIMAL AND DUAL ASSEMBLY OF SUBSTRUCTURES

Consider a finite element model of a global domain Ω. This domain Ω is divided into N non-overlapping substructures called $\Omega^{(s)}$ such that every node belongs to exactly one substructure except for the nodes on the interface boundaries. The linear/linearized equation of motion of one substructure s is written as

$$\boldsymbol{M}^{(s)}\ddot{\boldsymbol{u}}^{(s)} + \boldsymbol{K}^{(s)}\boldsymbol{u}^{(s)} = \boldsymbol{f}^{(s)} + \boldsymbol{g}^{(s)}, \quad s = 1, \dots, N \tag{1}$$

where the superscript (s) is the label of the particular substructure. $\boldsymbol{M}^{(s)}$, $\boldsymbol{K}^{(s)}$ and $\boldsymbol{u}^{(s)}$ are the mass matrix, the stiffness matrix and the displacement vector of the substructure, respectively. $\boldsymbol{f}^{(s)}$ is the external force vector and $\boldsymbol{g}^{(s)}$ is the vector of reaction forces on the substructure due to its connection to adjacent substructures at its boundary DOF. The local displacements $\boldsymbol{u}^{(s)}$

of each substructure can be divided in local internal DOF $\boldsymbol{u}_i^{(s)}$ and boundary DOF $\boldsymbol{u}_b^{(s)}$:

$$\boldsymbol{u}^{(s)} = \begin{bmatrix} \boldsymbol{u}_b^{(s)} \\ \boldsymbol{u}_i^{(s)} \end{bmatrix} = \begin{bmatrix} \boldsymbol{L}_b^{(s)} & \boldsymbol{0} \\ \boldsymbol{0} & \boldsymbol{I} \end{bmatrix} \begin{bmatrix} \boldsymbol{u}_b \\ \boldsymbol{u}_i^{(s)} \end{bmatrix} \tag{2}$$

The boundary DOF $\boldsymbol{u}_b^{(s)} = \boldsymbol{L}_b^{(s)} \boldsymbol{u}_b$ of the substructure are a subset of the assembled boundary DOF $\boldsymbol{u}_b$ of the global domain Ω. $\boldsymbol{L}_b^{(s)}$ is a Boolean localization matrix relating the assembled boundary DOF $\boldsymbol{u}_b$ of the global domain to the substructure boundary DOF. Consequently, the equation of motion (1) of one substructure s partitioned in the same manner writes

$$\begin{bmatrix} \boldsymbol{M}_{bb}^{(s)} & \boldsymbol{M}_{bi}^{(s)} \\ \boldsymbol{M}_{ib}^{(s)} & \boldsymbol{M}_{ii}^{(s)} \end{bmatrix} \begin{bmatrix} \ddot{\boldsymbol{u}}_b^{(s)} \\ \ddot{\boldsymbol{u}}_i^{(s)} \end{bmatrix} + \begin{bmatrix} \boldsymbol{K}_{bb}^{(s)} & \boldsymbol{K}_{bi}^{(s)} \\ \boldsymbol{K}_{ib}^{(s)} & \boldsymbol{K}_{ii}^{(s)} \end{bmatrix} \begin{bmatrix} \boldsymbol{u}_b^{(s)} \\ \boldsymbol{u}_i^{(s)} \end{bmatrix} = \begin{bmatrix} \boldsymbol{f}_b^{(s)} \\ \boldsymbol{f}_i^{(s)} \end{bmatrix} + \begin{bmatrix} \boldsymbol{g}_b^{(s)} \\ \boldsymbol{0} \end{bmatrix}. \tag{3}$$

2.1 Primal assembly

The Eqs. (1) and (2) of all substructures N can be assembled in a primal way as

$$\boldsymbol{M}_a \ddot{\boldsymbol{u}}_a + \boldsymbol{K}_a \boldsymbol{u}_a = \boldsymbol{f}_a, \tag{4}$$

where

$$\begin{aligned} \boldsymbol{M}_a &= \begin{bmatrix} \sum_{s=1}^{N} \boldsymbol{L}_b^{(s)^T} \boldsymbol{M}_{bb}^{(s)} \boldsymbol{L}_b^{(s)} & \boldsymbol{L}_b^{(1)^T} \boldsymbol{M}_{bi}^{(1)} & \cdots & \boldsymbol{L}_b^{(N)^T} \boldsymbol{M}_{bi}^{(N)} \\ \boldsymbol{M}_{ib}^{(1)} \boldsymbol{L}_b^{(1)} & \boldsymbol{M}_{ii}^{(1)} & & \boldsymbol{0} \\ \vdots & & \ddots & \\ \boldsymbol{M}_{ib}^{(N)} \boldsymbol{L}_b^{(N)} & \boldsymbol{0} & & \boldsymbol{M}_{ii}^{(N)} \end{bmatrix}, \quad \boldsymbol{u}_a = \begin{bmatrix} \boldsymbol{u}_b \\ \boldsymbol{u}_i^{(1)} \\ \vdots \\ \boldsymbol{u}_i^{(N)} \end{bmatrix}, \\ \boldsymbol{K}_a &= \begin{bmatrix} \sum_{s=1}^{N} \boldsymbol{L}_b^{(s)^T} \boldsymbol{K}_{bb}^{(s)} \boldsymbol{L}_b^{(s)} & \boldsymbol{L}_b^{(1)^T} \boldsymbol{K}_{bi}^{(1)} & \cdots & \boldsymbol{L}_b^{(N)^T} \boldsymbol{K}_{bi}^{(N)} \\ \boldsymbol{K}_{ib}^{(1)} \boldsymbol{L}_b^{(1)} & \boldsymbol{K}_{ii}^{(1)} & & \boldsymbol{0} \\ \vdots & & \ddots & \\ \boldsymbol{K}_{ib}^{(N)} \boldsymbol{L}_b^{(N)} & \boldsymbol{0} & & \boldsymbol{K}_{ii}^{(N)} \end{bmatrix}, \quad \boldsymbol{f}_a = \begin{bmatrix} \sum_{s=1}^{N} \boldsymbol{L}_b^{(s)^T} \boldsymbol{f}_b^{(s)} \\ \boldsymbol{f}_i^{(1)} \\ \vdots \\ \boldsymbol{f}_i^{(N)} \end{bmatrix}. \end{aligned} \tag{5}$$

The reaction forces $\boldsymbol{g}^{(s)}$ on the interfaces of the substructures cancel out during assembly. This assembly is called primal assembly since the compatibility between the substructures is enforced using the same boundary displacements for adjacent substructures.

2.2 Dual assembly

Another way to enforce the interface compatibility between the substructures is to consider the interface connecting forces as unknowns. These forces must be determined to satisfy the interface compatibility condition (displacement equality) and the local equation of motion of the substructures:

$$\sum_{s=1}^{N} \boldsymbol{b}^{(s)} \boldsymbol{u}_b^{(s)} = \boldsymbol{0} \tag{6}$$

$$\boldsymbol{M}^{(s)} \ddot{\boldsymbol{u}}^{(s)} + \boldsymbol{K}^{(s)} \boldsymbol{u}^{(s)} + \begin{bmatrix} \boldsymbol{b}^{(s)^T} \boldsymbol{\lambda} \\ \boldsymbol{0} \end{bmatrix} = \boldsymbol{f}^{(s)}, \quad s = 1, \ldots, N \tag{7}$$

$\boldsymbol{b}^{(s)}$ are signed Boolean matrices acting on the substructure interface DOF. $\boldsymbol{b}^{(s)^T}\boldsymbol{\lambda}$ is representing the interconnecting forces between substructures and $\boldsymbol{\lambda}$ is the vector of all Lagrange multipliers acting on the interfaces which are additional unknowns. The displacement vector $\boldsymbol{u}^{(s)}$ is partitioned according to Eq. (2). With the block-diagonal matrices

$$\boldsymbol{M} = \begin{bmatrix} \boldsymbol{M}^{(1)} & & \boldsymbol{0} \\ & \ddots & \\ \boldsymbol{0} & & \boldsymbol{M}^{(N)} \end{bmatrix}, \quad \boldsymbol{K} = \begin{bmatrix} \boldsymbol{K}^{(1)} & & \boldsymbol{0} \\ & \ddots & \\ \boldsymbol{0} & & \boldsymbol{K}^{(N)} \end{bmatrix} \quad \text{and} \tag{8}$$

$$\boldsymbol{u} = \begin{bmatrix} \boldsymbol{u}^{(1)} \\ \vdots \\ \boldsymbol{u}^{(N)} \end{bmatrix}, \quad \boldsymbol{f} = \begin{bmatrix} \boldsymbol{f}^{(1)} \\ \vdots \\ \boldsymbol{f}^{(N)} \end{bmatrix}, \quad \boldsymbol{B} = \begin{bmatrix} \boldsymbol{B}^{(1)} & \cdots & \boldsymbol{B}^{(N)} \end{bmatrix} \quad \text{with} \quad \boldsymbol{B}^{(s)^T} = \begin{bmatrix} \boldsymbol{b}^{(s)^T} \\ \boldsymbol{0} \end{bmatrix} \tag{9}$$

the set of Eqs. (6) and (7) and can be written as

$$\begin{bmatrix} \boldsymbol{M} & \boldsymbol{0} \\ \boldsymbol{0} & \boldsymbol{0} \end{bmatrix} \begin{bmatrix} \ddot{\boldsymbol{u}} \\ \ddot{\boldsymbol{\lambda}} \end{bmatrix} + \begin{bmatrix} \boldsymbol{K} & \boldsymbol{B}^T \\ \boldsymbol{B} & \boldsymbol{0} \end{bmatrix} \begin{bmatrix} \boldsymbol{u} \\ \boldsymbol{\lambda} \end{bmatrix} = \begin{bmatrix} \boldsymbol{f} \\ \boldsymbol{0} \end{bmatrix}. \tag{10}$$

In this hybrid formulation the Lagrange multipliers $\boldsymbol{\lambda}$ enforce the interface compatibility constraints and can be identified as interface forces [7]. The dual assembled system (10) is equivalent to the primal assembled system (4) since both systems express the same local equilibrium for each substructure and enforce the same interface compatibility.

3 CRAIG-BAMPTON AND DUAL CRAIG-BAMPTON METHOD

3.1 Craig-Bampton method (CBM)

Considering the partitioned equation of motion (3), the internal DOF $\boldsymbol{u}_i^{(s)}$ of every substructure s can be seen as being excited by its boundary DOF $\boldsymbol{u}_b^{(s)}$, namely

$$\boldsymbol{M}_{ii}^{(s)}\ddot{\boldsymbol{u}}_i^{(s)} + \boldsymbol{K}_{ii}^{(s)}\boldsymbol{u}_i^{(s)} = \boldsymbol{f}_i^{(s)} - \boldsymbol{K}_{ib}^{(s)}\boldsymbol{u}_b^{(s)} - \boldsymbol{M}_{ib}^{(s)}\ddot{\boldsymbol{u}}_b^{(s)}. \tag{11}$$

This indicates that $\boldsymbol{u}_i^{(s)}$ of each substructure can be approximated by a superposition of a static response and of eigenmodes associated to $\boldsymbol{M}_{ii}^{(s)}$ and $\boldsymbol{K}_{ii}^{(s)}$. The static response is given by

$$\boldsymbol{u}_{i,stat}^{(s)} = -{\boldsymbol{K}_{ii}^{(s)}}^{-1}\boldsymbol{K}_{ib}^{(s)}\boldsymbol{u}_b^{(s)} = \boldsymbol{\Psi}_{ib}^{(s)}\boldsymbol{u}_b^{(s)}, \tag{12}$$

where the columns of matrix $\boldsymbol{\Psi}_{ib}^{(s)}$ are the static response modes. The so-called fixed interface normal modes $\boldsymbol{\phi}_k^{(s)}$ are obtained as eigensolutions of the generalized eigenproblem $\boldsymbol{K}_{ii}^{(s)}\boldsymbol{\phi}_k^{(s)} = {\omega_k^{(s)}}^2\boldsymbol{M}_{ii}^{(s)}\boldsymbol{\phi}_k^{(s)}$. The columns of the $n_i^{(s)} \times n_\phi^{(s)}$ matrix $\boldsymbol{\Phi}_{i\phi}^{(s)}$ contain the first $n_\phi^{(s)}$ fixed interface normal modes $\boldsymbol{\phi}_k^{(s)}$ which can also be considered as the free vibration modes of the substructure s clamped on its boundary DOF $\boldsymbol{u}_b^{(s)}$. The approximation of $\boldsymbol{u}_i^{(s)}$ therefore writes

$$\boldsymbol{u}_i^{(s)} \approx \boldsymbol{u}_{i,stat}^{(s)} + \boldsymbol{\Phi}_{i\phi}^{(s)}\boldsymbol{\eta}^{(s)} = \boldsymbol{\Psi}_{ib}^{(s)}\boldsymbol{u}_b^{(s)} + \boldsymbol{\Phi}_{i\phi}^{(s)}\boldsymbol{\eta}^{(s)} \tag{13}$$

and the displacements of the substructure are approximated by

$$\begin{bmatrix} \boldsymbol{u}_b^{(s)} \\ \boldsymbol{u}_i^{(s)} \end{bmatrix} = \begin{bmatrix} \boldsymbol{I}_{bb}^{(s)} & \boldsymbol{0}_{b\phi}^{(s)} \\ \boldsymbol{\Psi}_{ib}^{(s)} & \boldsymbol{\Phi}_{i\phi}^{(s)} \end{bmatrix} \begin{bmatrix} \boldsymbol{u}_b^{(s)} \\ \boldsymbol{\eta}^{(s)} \end{bmatrix} \tag{14}$$

with the vector of modal parameters $\boldsymbol{\eta}^{(s)}$ of dimension $n_\phi^{(s)}$ corresponding to the amplitudes of the fixed-interface normal modes $\boldsymbol{\Phi}_{i\phi}^{(s)}$. The CBM reduction matrix $\boldsymbol{T}_{CB}$ for reducing the primal assembled system can be defined as

$$\boldsymbol{u}_a = \begin{bmatrix} \boldsymbol{u}_b \\ \boldsymbol{u}_i^{(1)} \\ \vdots \\ \boldsymbol{u}_i^{(N)} \end{bmatrix} \approx \boldsymbol{T}_{CB} \begin{bmatrix} \boldsymbol{u}_b \\ \boldsymbol{\eta}_i^{(1)} \\ \vdots \\ \boldsymbol{\eta}_i^{(N)} \end{bmatrix} = \begin{bmatrix} \boldsymbol{I} & \boldsymbol{0} & \cdots & \boldsymbol{0} \\ \boldsymbol{\Psi}_{ib}^{(1)} \boldsymbol{L}_b^{(1)} & \boldsymbol{\Phi}_{i\phi}^{(1)} & & \boldsymbol{0} \\ \vdots & & \ddots & \\ \boldsymbol{\Psi}_{ib}^{(N)} \boldsymbol{L}_b^{(N)} & 0 & & \boldsymbol{\Phi}_{i\phi}^{(N)} \end{bmatrix} \begin{bmatrix} \boldsymbol{u}_b \\ \boldsymbol{\eta}^{(1)} \\ \vdots \\ \boldsymbol{\eta}^{(N)} \end{bmatrix} \tag{15}$$

and the CBM reduced matrices $\boldsymbol{K}_{CB} = \boldsymbol{T}_{CB}^T \boldsymbol{K}_a \boldsymbol{T}_{CB}$ and $\boldsymbol{M}_{CB} = \boldsymbol{T}_{CB}^T \boldsymbol{M}_a \boldsymbol{T}_{CB}$ are found [2].

3.2 Dual Craig-Bampton method (DCBM)

Considering the equation of motion (7) of substructure s, every substructure can be seen as being excited by the interface connection forces and the external forces. This indicates that the displacements of each substructure $\boldsymbol{u}^{(s)}$ can be expressed in terms of local static solutions $\boldsymbol{u}_{stat}^{(s)}$ and in terms of eigenmodes associated to the substructure matrices $\boldsymbol{K}^{(s)}$ and $\boldsymbol{M}^{(s)}$:

$$\boldsymbol{u}^{(s)} = \underbrace{-\boldsymbol{K}^{(s)^+} \boldsymbol{B}^{(s)^T} \boldsymbol{\lambda} + \sum_{j=1}^{r^{(s)}} \boldsymbol{R}_j^{(s)} \alpha_j^{(s)}}_{\boldsymbol{u}_{stat}^{(s)}} + \sum_{j=1}^{n^{(s)}-r^{(s)}} \boldsymbol{\theta}_j^{(s)} \eta_j^{(s)} \tag{16}$$

$\boldsymbol{K}^{(s)^+}$ is equal to the inverse of $\boldsymbol{K}^{(s)}$ when there are enough boundary condition to prevent the substructure form floating when its interface with neighbouring substructures is free [5]. If a substructure is floating, $\boldsymbol{K}^{(s)^+}$ is a generalized inverse of $\boldsymbol{K}^{(s)}$ and $\boldsymbol{R}^{(s)}$ is the matrix containing the $r^{(s)}$ rigid body modes as columns. The vector $\boldsymbol{\alpha}^{(s)}$ contains the amplitudes $\alpha_j^{(s)}$ of the rigid body modes and the vector $\boldsymbol{\eta}^{(s)}$ contains the amplitudes $\eta_j^{(s)}$ of the local eigenmodes $\boldsymbol{\theta}_j^{(s)}$ being eigensolutions of the generalized eigenproblem $\boldsymbol{K}^{(s)} \boldsymbol{\theta}_j^{(s)} = {\omega_j^{(s)}}^2 \boldsymbol{M}^{(s)} \boldsymbol{\theta}_j^{(s)}$. An approximation is obtained by retaining only the first $n_\theta^{(s)}$ free-interface normal modes $\boldsymbol{\theta}_j^{(s)}$. Calling $\boldsymbol{\Theta}^{(s)}$ the matrix containing only these $n_\theta^{(s)}$ eigenmodes, the approximation of the displacements $\boldsymbol{u}^{(s)}$ of the substructure is given by

$$\boldsymbol{u}^{(s)} \approx -\boldsymbol{K}^{(s)^+} \boldsymbol{B}^{(s)^T} \boldsymbol{\lambda} + \boldsymbol{R}^{(s)} \boldsymbol{\alpha}^{(s)} + \boldsymbol{\Theta}^{(s)} \boldsymbol{\eta}^{(s)}. \tag{17}$$

Since a part of the subspace spanned by $\boldsymbol{\Theta}^{(s)}$ is already included in $\boldsymbol{K}^{(s)^+}$ (which can be seen considering the spectral expansion of $\boldsymbol{K}^{(s)^+}$) the residual flexibility matrix $\boldsymbol{G}_{res}^{(s)}$ can be used instead of $\boldsymbol{K}^{(s)^+}$, which is defined by

$$\boldsymbol{G}_{res}^{(s)} = \sum_{j=n_\theta^{(s)}+1}^{n^{(s)}-r^{(s)}} \frac{\boldsymbol{\theta}_j^{(s)} \boldsymbol{\theta}_j^{(s)^T}}{{\omega_j^{(s)}}^2} = \boldsymbol{K}^{(s)^+} - \sum_{j=1}^{n_\theta^{(s)}} \frac{\boldsymbol{\theta}_j^{(s)} \boldsymbol{\theta}_j^{(s)^T}}{{\omega_j^{(s)}}^2}. \tag{18}$$

Note that, by construction $\boldsymbol{G}_{res}^{(s)} = \boldsymbol{G}_{res}^{(s)^T}$, which is computed using the second equality in Eq. (18). For further properties of $\boldsymbol{G}_{res}^{(s)}$ see [5]. As a result the approximation of one substructure writes

$$\boldsymbol{u}^{(s)} \approx \begin{bmatrix} \boldsymbol{R}^{(s)} & \boldsymbol{\Theta}^{(s)} & -\boldsymbol{G}_{res}^{(s)} \boldsymbol{B}^{(s)^T} \end{bmatrix} \begin{bmatrix} \boldsymbol{\alpha}^{(s)} \\ \boldsymbol{\eta}^{(s)} \\ \boldsymbol{\lambda} \end{bmatrix} \tag{19}$$

and assembling all substructures N, the entire structure can consequently be approximated by

$$\begin{bmatrix} \boldsymbol{u} \\ \boldsymbol{\lambda} \end{bmatrix} \approx \underbrace{\begin{bmatrix} \boldsymbol{R}^{(1)} & \boldsymbol{\Theta}^{(1)} & & & \boldsymbol{0} & -\boldsymbol{G}_{res}^{(1)}\boldsymbol{B}^{(1)^T} \\ & & \ddots & \ddots & & \vdots \\ \boldsymbol{0} & & & \boldsymbol{R}^{(N)} & \boldsymbol{\Theta}^{(N)} & -\boldsymbol{G}_{res}^{(N)}\boldsymbol{B}^{(N)^T} \\ \boldsymbol{0} & & \cdots & \boldsymbol{0} & & \boldsymbol{I} \end{bmatrix}}_{\boldsymbol{T}_{DCB}} \begin{bmatrix} \boldsymbol{\alpha}^{(1)} \\ \boldsymbol{\eta}^{(1)} \\ \vdots \\ \boldsymbol{\alpha}^{(N)} \\ \boldsymbol{\eta}^{(N)} \\ \boldsymbol{\lambda} \end{bmatrix}. \tag{20}$$

Assuming that the rigid body modes $\boldsymbol{R}^{(s)}$ and the elastic modes $\boldsymbol{\Theta}^{(s)}$ are orthonormalized with respect to the mass matrix $\boldsymbol{M}^{(s)}$, the approximation of the dynamic equations of the dual assembled system (10) is

$$\boldsymbol{M}_{DCB} \begin{bmatrix} \ddot{\boldsymbol{\alpha}}^{(1)} \\ \ddot{\boldsymbol{\eta}}^{(1)} \\ \vdots \\ \ddot{\boldsymbol{\alpha}}^{(N)} \\ \ddot{\boldsymbol{\eta}}^{(N)} \\ \ddot{\boldsymbol{\lambda}} \end{bmatrix} + \boldsymbol{K}_{DCB} \begin{bmatrix} \boldsymbol{\alpha}^{(1)} \\ \boldsymbol{\eta}^{(1)} \\ \vdots \\ \boldsymbol{\alpha}^{(N)} \\ \boldsymbol{\eta}^{(N)} \\ \boldsymbol{\lambda} \end{bmatrix} = \boldsymbol{T}_{DCB}^T \boldsymbol{f}. \tag{21}$$

The DCBM reduced mass and stiffness matrices are

$$\boldsymbol{M}_{DCB} = \boldsymbol{T}_{DCB}^T \begin{bmatrix} \boldsymbol{M} & \boldsymbol{0} \\ \boldsymbol{0} & \boldsymbol{0} \end{bmatrix} \boldsymbol{T}_{DCB} = \begin{bmatrix} \boldsymbol{I} & \boldsymbol{0} \\ \boldsymbol{0} & \boldsymbol{M}_{res} \end{bmatrix}, \tag{22}$$

$$\boldsymbol{K}_{DCB} = \begin{bmatrix} \begin{bmatrix} \boldsymbol{0} & \boldsymbol{0} \\ \boldsymbol{0} & \boldsymbol{\Omega}^{(1)^2} \end{bmatrix} & & \boldsymbol{0} & \begin{bmatrix} \boldsymbol{R}^{(1)^T}\boldsymbol{B}^{(1)^T} \\ \boldsymbol{\Theta}^{(1)^T}\boldsymbol{B}^{(1)^T} \end{bmatrix} \\ & \ddots & & \vdots \\ \boldsymbol{0} & & \begin{bmatrix} \boldsymbol{0} & \boldsymbol{0} \\ \boldsymbol{0} & \boldsymbol{\Omega}^{(N)^2} \end{bmatrix} & \begin{bmatrix} \boldsymbol{R}^{(N)^T}\boldsymbol{B}^{(N)^T} \\ \boldsymbol{\Theta}^{(N)^T}\boldsymbol{B}^{(N)^T} \end{bmatrix} \\ \begin{bmatrix} \boldsymbol{B}^{(1)}\boldsymbol{R}^{(1)} & \boldsymbol{B}^{(1)}\boldsymbol{\Theta}^{(1)} \end{bmatrix} & \cdots & \begin{bmatrix} \boldsymbol{B}^{(N)}\boldsymbol{R}^{(N)} & \boldsymbol{B}^{(N)}\boldsymbol{\Theta}^{(N)} \end{bmatrix} & -\boldsymbol{F}_{res} \end{bmatrix}, \tag{23}$$

where

$$\boldsymbol{F}_{res} = \sum_{s=1}^{N} \boldsymbol{B}^{(s)}\boldsymbol{G}_{res}^{(s)}\boldsymbol{B}^{(s)^T}, \qquad \boldsymbol{M}_{res} = \sum_{s=1}^{N} \boldsymbol{B}^{(s)}\boldsymbol{G}_{res}^{(s)}\boldsymbol{M}^{(s)}\boldsymbol{G}_{res}^{(s)}\boldsymbol{B}^{(s)^T} \tag{24}$$

and $\boldsymbol{\Omega}^{(s)}$ being a diagonal matrix containing the remaining $n_\theta^{(s)}$ eigenvalues $\omega_j^{(s)}$. The DCBM enforces only a weak compatibility between the substructures and does not enforce a strong displacement compatibility between the interfaces compared to many other common reduction methods. Considering the system of Eqs. (6) and (7) multiplied by the reduction matrix $\boldsymbol{T}_{DCB}^T$, the last row of Eq. (21) results from

$$\underbrace{\begin{bmatrix} \cdots & -\boldsymbol{B}^{(s)}\boldsymbol{G}_{res}^{(s)} & \cdots & \boldsymbol{I} \end{bmatrix}}_{\text{last row of } \boldsymbol{T}_{DCB}^T} \begin{bmatrix} \vdots \\ \boldsymbol{M}^{(s)}\ddot{\boldsymbol{u}}^{(s)} + \boldsymbol{K}^{(s)}\boldsymbol{u}^{(s)} + \begin{bmatrix} \boldsymbol{b}^{(s)^T}\boldsymbol{\lambda} \\ \boldsymbol{0} \end{bmatrix} = \boldsymbol{f}^{(s)} \\ \vdots \\ \sum_{s=1}^{N} \boldsymbol{B}^{(s)}\boldsymbol{u}^{(s)} = \boldsymbol{0} \end{bmatrix}. \tag{25}$$

Replacing the strong interface compatibility condition of Eq. (6) by the weak form according to Eq. (25) can be interpreted as follows. Denote $\Delta \boldsymbol{f}^{(s)}$ the residual forces of substructure s resulting from the weak satisfaction of the local equilibrium of the substructure approximating the dynamics by a small number of free-interface normal modes. Name $\Delta \boldsymbol{u}^{(s)} = \boldsymbol{G}_{res}^{(s)} \Delta \boldsymbol{f}^{(s)}$ the displacements these residual force $\Delta \boldsymbol{f}^{(s)}$ would create locally. Then the weak interface compatibility condition (25) states that a compatibility error (i.e. an interface displacement jump) equal to the incompatibility of $\Delta \boldsymbol{u}^{(s)}$ is permitted [5]. Compared to MacNeal's and Rubin's method [4, 8], the weak interface compatibility of the DCBM avoids locking problems occuring during the application of the aforementioned methods. Therefore, the approximation accuracy is improved [5]. But the fact that a weak interface compatibility is allowed in the DCBM implies that the infinite eigenvalues related to the Lagrange multipliers $\boldsymbol{\lambda}$ in the non-reduced problem (10) are now becoming finite and negative [6]. In practice those negative eigensolutions will appear only in the higher eigenvalue spectrum if the reduction space is rich enough [6]. Nevertheless, the reduction basis has to be selected with care avoiding potential non-physical effects of the possibly occurring negative eigenvalues.

4 GENERAL PROPERTIES ILLUSTRATED BY A BEAM FRAME

In [5] a frame made of steel beams (density $7500\,\mathrm{kg\,m^{-3}}$, Young's modulus $210\,\mathrm{GPa}$, Poisson's ratio 0.3) schematically shown in Figure 1 is considered. Each cell in the frame has a height of $0.35\,\mathrm{m}$ and a width and depth of $0.5\,\mathrm{m}$. All outer beams have a hollow circular cross-section with the outside and inside diameters $0.02\,\mathrm{m}$ and $0.018\,\mathrm{m}$. The diagonal members inside the cells have a solid circular cross section with diameter $0.008\,\mathrm{m}$. The frame is divided into 5 substructures and the objective is the approximation of the lowest eigenfrequencies ω of the frame. Approximation of the eigenfrequencies of this system with the DCBM with 4 free-interface normal modes per substructure (rigid body modes are not counted as free-interface normal modes) is carried out using a simple Lanczos eigensolver. The results presented in [5] were obtained based erroneously on an incomplete set of free-interface modes in the substructures: modes related to multiple frequencies were not determined by the simple Lanczos algorithm applied in that work. In this work, first we also used a simple Lanczos algorithm and computed the eigenfrequencies ω_{red} by the CBM and the DCBM. Additionally the eigenfrequencies ω_{full} of the full (non-reduced) system are computed. The eigenfrequency relative errors $\varepsilon_{rel} = |\omega_{red} - \omega_{full}|/\omega_{full}$ comparing the eigenfrequencies of the non-reduced model obtained by the two reduction methods are plotted as dashed lines in Figure 2. As already observed in [5], this confirms that the accuracy of the DCBM in the low frequency range is two orders of magnitude better than the CBM.

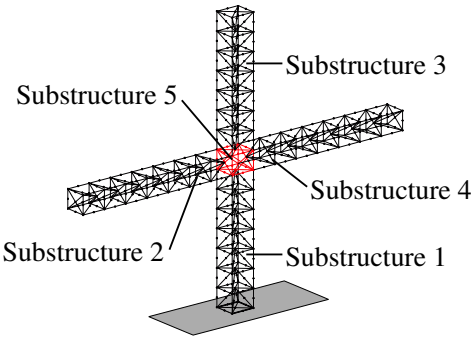


Figure 1: Frame made of steel beams divided into 5 substructures.

Now the attention shall be directed to the applied eigensolver. The simple Lanczos eigensolver (no blocks, no restarts) used in [5] is not capable of determining multiple eigenvalues reliably. Considering the geometry of the beam frame structure of the arms in Figure 1, the symmetry of the substructures is identifiable resulting in multiple eigenfrequencies of the substructures. Hence, when the simple Lanczos algorithm is used to determine the free modes of the substructure, modes that are multiple are missing and the representation of the lower

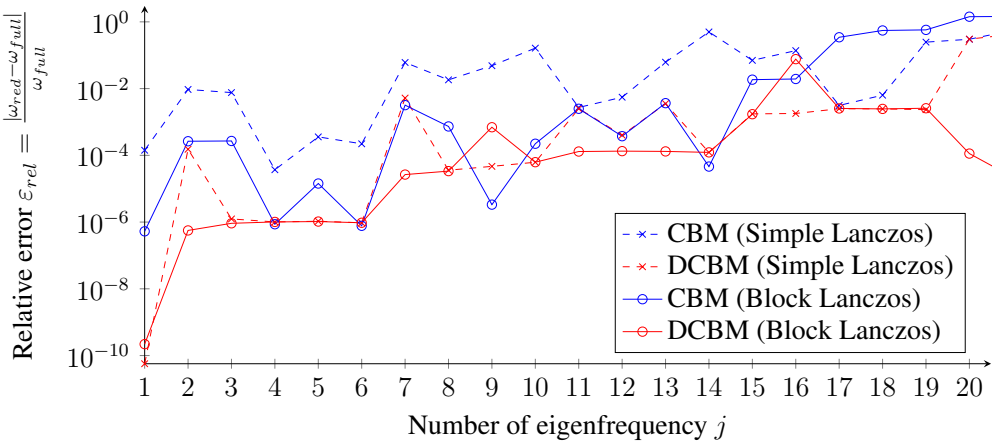


Figure 2: Reduction of the beam frame with the CBM and the DCBM.

spectrum is incomplete. Normal-modes associated to the higher eigenfrequencies computed by the simple Lanczos eigensolver are used leading to poor approximation accuracy. Now using an eigensolver capable of determining multiple eigenvalues (e.g. block Lanczos method) and repeating the analysis described so far, multiple eigenvalues and associated eigenvectors (free-interface normal modes) as reduction basis of the substructures are computed.

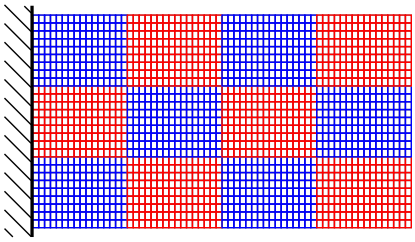
For example, the lowest 4 eigenvalues ω_j^2 of the generalized eigenvalue problem for $\boldsymbol{K}^{(1)}$ and $\boldsymbol{M}^{(1)}$ of substructure 1 are listed in Table 1 once computed with the simple Lanczos algorithm and again computed with the block Lanczos algorithm. One of the eigenvalues $\omega_{3/4}^2 = 1.204\,194 \times 10^5\,\mathrm{s}^{-2}$ of multiplicity 2 and the subspace of the associated eigenvectors is missed by the simple Lanczos eigensolver (compared to the block Lanczos eigensolver). The next higher eigenvalue with associated eigenvector is used instead resulting in a bad approximation of the eigenfrequencies of the full system in the low frequency range. Using the block Lanczos method and taking the lowest eigenfrequencies with associated subspaces of eigenvectors, the accuracy of the eigenfrequencies of the reduced global system obtained by the two reduction methods increases in the low frequency range. The eigenfrequency relative errors ε_{rel} using a block Lanczos algorithm are plotted additionally as solid lines in Figure 2. Especially in the low frequency range the improvement of the accuracy of the approximations is significant.

j	Eigenvalue ω_j^2 $[10^5\,\mathrm{s}^{-2}]$	
	Lanczos	Block Lanczos
1	0.089802	0.089802
2	0.823489	0.823489
3	1.204194	1.204194
4	2.345638	1.204194

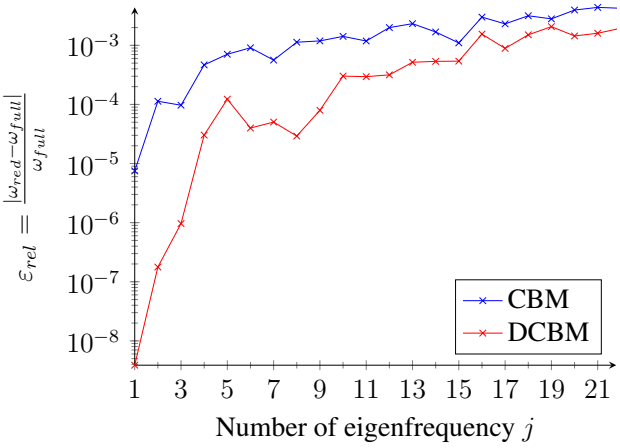
Table 1: First eigenvalues ω_j^2 of the generalized eigenproblem of substructure 1 for $\boldsymbol{K}^{(1)}$ and $\boldsymbol{M}^{(1)}$.

5 EXTENDED EXAMPLE OF A TWO-DIMENSIONAL SOLID

In order to emphasize the weak coupling between the substructure interfaces, as described in section 3.2, the problem of a two dimensional rectangle (density ρ, Young's modulus E, Poisson's ratio $\nu = 0.3$) decomposed in 12 substructures as illustrated in Figure 3a is considered. Each substructure is discretized by 16×9 bilinear four-noded elements (plane stress) and the structure is clamped on the left side in both directions. Again the objective is to ap-



(a) Two dimensional solid problem (dimensionless width $l_x = 16$, height $l_y = 9$) decomposed in 12 substructures. Each substructure is discretized by 16×9 bilinear four-noded elements (plane stress) and the structure is clamped on the left side in both directions.



(b) Relative error ε_{rel} using 8 normal modes per substructure for lowest eigenfrequencies of the entire structure.

Figure 3: Reduction of a two dimensional solid problem.

proximate the lowest eigenfrequencies ω of the full structure with the CBM and the DCBM. Using 8 normal modes per substructure (not including potential rigid body modes) the relative errors $\varepsilon_{rel} = |\omega_{red} - \omega_{full}|/\omega_{full}$ depicted in Figure 3b are resulting. Making use of such a large reduction basis the DCBM gives excellent results in the low frequency range in comparison to the CBM. Approximating the 20 lowest eigenfrequencies of the full structure, neither compatibility problems nor trouble with negative eigenfrequencies occur during the reduction process with the DCBM. Similar graphs depicting the relative errors ε_{rel} as in Figure 3b are obtained using different numbers of normal modes per substructure for the two methods.

When considering a very small reduction basis for the substructures (using only a small number of normal modes), non-physical negative eigenvalues of the reduced problem show up in the low frequency range. Using only 2 normal modes per substructure as reduction basis for this example negative values emerge among the 20 smallest absolute values of eigensolutions ω^2. In this case the first 14 of the lowest absolute values of ω^2 are positive and the associated eigenmodes are approximating the true eigenvalues and eigenmodes of the full system accurately. But, as shown in Table 2, the 15th eigenvalue is negative and the associated eigenmode depicted in Figure 4 shows the non-physical behaviour of this eigensolution. The eigenmodes

j	$\omega_j^2 \frac{\rho}{E}$
1	0.000874
2	0.009729
⋮	⋮
14	0.245011
15	−0.250785
16	0.261676

Table 2: Number j and associated eigenvalue ω_j^2 of the two dimensional solid reduced with the DCBM.

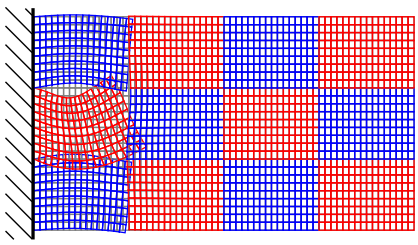


Figure 4: Eigenmode number 15 approximated by the DCBM using 2 free-interface normal modes per substructure ($\omega_{15}^2 = -0.250785 \frac{E}{\rho}$).

corresponding to negative eigensolutions with higher absolute values show similar behaviour. All these negative eigenvalues are related to the weak compatibility on the interfaces and not meaningful from a physical point of view. Consequently detecting and filtering out those negative eigenvalues is an additional step in the DCBM compared to the CBM. This extra step is cheap and therefore does not increase the effort of the reduction process using the DCBM compared to the CBM keeping the DCBM very efficient.

6 CONCLUSIONS AND FUTURE WORK

In this paper the general concepts of the Craig-Bampton method (CBM) and the dual Craig-Bampton method (DCBM) were briefy presented and compared using two examples. The DCBM is outperforming the CBM using the same number of normal modes per substructure as reduction basis with comparable computational effort. Properties of the DCBM were outlined and an additional necessary step, namely filtering out the negative eigensolutions, during the reduction process was illustrated.

Crucial for the application of the DCBM is the usage of a powerful eigensolver being capable to detect multiple eigenvalue for getting the required reduction basis. Non-physical negative eigenvalues of the reduced dual assembled problem are intrinsic in the reduction process using the DCBM caused by the weak compatibility on the interfaces between the substructures. Filtering out these negative eigenvalues is the decisive factor for the excellent approximation quality of the DCBM. The numerical effort adding this additional step is negligible keeping the efficiency of this method. Further research has to be conducted on the negative eigensolutions and their effect on subsequent steps after the reduction.

REFERENCES

[1] R. R. Craig, Coupling of substructures for dynamic analyses: An overview, *Proceedings of AIAA/ASME/ASCE/AHS/ASC structures, structural dynamics, and materials conference and exhibit*, Atlanta, GA, USA, 1573–1584, 2000.

[2] R. R. Craig and M. C. Bampton, Coupling of substructures for dynamic analyses, *AIAA Journal*, **6**, 1313–1319, 1968.

[3] D. N. Herting, A general purpose, multi-stage, component modal synthesis method, *Finite elements in analysis and design*, **1**, 153–164, 1985.

[4] R. H. MacNeal, A hybrid method of component mode synthesis, *Computers & Structures*, **1**, 581–601, 1971.

[5] D. J. Rixen, A dual Craig–Bampton method for dynamic substructuring, *Journal of Computational and Applied Mathematics*, **168**, 383–391, 2004.

[6] D. J. Rixen, Interface Reduction in the Dual Craig-Bampton method based on dual interface modes. *Linking Models and Experiments*, **2**, Conference Proceedings of the Society for Experimental Mechanics Series, 311–328, 2011.

[7] D. J. Rixen, The dual Craig-Bampton method, *Proceedings of the 21st IMAC*, IMAC-XXI, Kissimmee, Florida, USA, 1176–1184, 2003.

[8] S. Rubin, Improved component-mode representation for structural dynamic analysis, *AIAA Journal*, **13**, 995–1006, 1975.

11th International Conference on Engineering Vibration
Ljubljana, Slovenia, 7–10 September 2015

A COMPARISON ON MODEL ORDER REDUCTION TECHNIQUES FOR GEOMETRICALLY NONLINEAR SYSTEMS BASED ON A MODAL DERIVATIVE APPROACH USING SUBSPACE ANGLES

Johannes B. Rutzmoser*[1], Fabian M. Gruber[1], Daniel J. Rixen[1]

[1]Technische Universität München, Institute of Applied Mechanics
{johannes.rutzmoser,fabian.gruber,rixen}@tum.de

Keywords: Structural Dynamics, Model Order Reduction, Geometric Nonlinearity.

Abstract. *As model order reduction is a significant step in the construction of efficient models describing nonlinear structural dynamics, the demand for reduction methods not building on training data sets is very high. While sharp and meaningful error estimates exist for linear systems based on invariants like frequency response functions or the concept of observability and controlability, there is a lack of quantification methods for nonlinear systems.*

In this paper an error quantification method is proposed. This method is built on subspace angles, which are able to describe the differences between subspaces in a mathematical rigorous way. The approach is exemplarily applied to a geometrically nonlinear finite element model, extending reduction techniques based on the linearized system to nonlinearity with modal derivatives. As representative linear methods a modal truncation method, a modal truncation method with augmented static modes and a Krylov subspace method is chosen. The results are compared to perfectly trained POD sets for the given excitations with the proposed method. As the method will show, the extension methods capture essential behaviors of the nonlinear system.

1 INTRODUCTION

Model order reduction is an important step in the computational solution of structural mechanics problems. As the spatial discretization is usually performed with the finite element method, a large number of degrees of freedom is used to describe the kinematics of the elastic structure. Whereas the parametrization of the kinematics by means of the finite element method using local displacements and rotations of nodes is very convenient as they have an intuitive meaning, the size of the problem generated that way is most often too large to handle problems of this type efficiently for time integration schemes.

Thus model order reduction and substructuring techniques were developed in order to shrink the number of degrees of freedom while preserving the accuracy of the dynamical model for the desired task as good as possible.

Especially for linear dynamical systems a huge body of well developed theory and literature exists providing methods and knowhow for the efficient reduction of these models. Most of these reduction techniques make use of the constant system matrices of the linear system. In linear system theory very strong theoretical concepts exist like stability, observability and controlability, modal decoupling, input-output behavior and transfer functions etc., which can all be processed more or less efficiently with linear algebra and the corresponding numerical methods on a computer.

For nonlinear systems, however, most of the concepts do not hold any more or are extremely hard to state theoretically and obtain computationally, as there are in general no constant system matrices which can be efficiently handled with the toolbox of computational linear algebra. Thus in essence two lines established in the projective reduction of nonlinear systems.

The first one is basically data driven. The idea is to perform a training simulation of the full, unreduced model and analyze the data generated by the full training set. The price of these methods is not only the computational cost of the full model, but also a high sensitivity of the reduction quality on the training scenario. When the training scenario and the scenario of the reduced system are very similar, it is to be expected, that the reduction quality is good, i.e. the error between the original model and the reduced model is small. If the training scenario and the reduced scenario are different it is difficult to predict, if the reduction quality is appropriate.

The second line is based on the idea to linearize the nonlinear problem, use a well established reduction technique and enhance the reduction method by trying to capture the effect of the nonlinearity. One approach in this context is the use of so called *modal derivatives*. First introduced by Cardona in 1985 for model order reduction [6, 5], the technique of augmenting the basis of the linearized problem using modal derivatives is used successfully for the reduction of geometrically nonlinear problems [1, 7] and problems with localized nonlinearity [8, 9].

In this paper, the method of augmenting linear reduction techniques with modal derivatives is further investigated. Therefore three very basic linear reduction techniques are briefly explained. Furthermore the properties of the Proper Orthogonal Decomposition (POD) and the associated Singular Value Decomposition (SVD) are in essence highlighted and the concept of modal derivatives for the extension of linear reduction bases is given. Subsequently the concept of subspace angles is introduced. The reduction techniques and the subspace angle concept is applied to a simple geometrically nonlinear test case. At the end a short conclusion is given.

2 REDUCTION TECHNIQUES FOR LINEAR AND NONLINEAR SYSTEMS

Projectional model order reduction techniques base all on the principle of projecting the kinematic variables onto a subspace. Consider the linear and nonlinear mechanical system

obtained through a spatial discretization scheme, for instance finite element method:

$$\boldsymbol{M}\ddot{\boldsymbol{x}} + \boldsymbol{D}\dot{\boldsymbol{x}} + \boldsymbol{K}\boldsymbol{x} = \boldsymbol{F}, \qquad \boldsymbol{M}\ddot{\boldsymbol{x}} + \boldsymbol{f}(\boldsymbol{x}, \dot{\boldsymbol{x}}) = \boldsymbol{F} \tag{1}$$

with the displacement vector $\boldsymbol{x}$, the mass matrix $\boldsymbol{M}$, damping matrix $\boldsymbol{D}$, stiffness matrix $\boldsymbol{K}$ and the external forcing $\boldsymbol{F}$. In the nonlinear case, damping and stiffness are nonlinear functions with respect to the velocities and the displacements and therefore are collected in the nonlinear force vector $\boldsymbol{f}(\boldsymbol{x}, \dot{\boldsymbol{x}})$.

The key idea of projective model order reduction is the expression of the displacements in terms of constant linearly independent basis vectors, $\boldsymbol{v}_1, \ldots, \boldsymbol{v}_n$, which are associated with the time dependent amplitudes $q_1, \ldots, q_n$. If the basis vectors are gathered in the matrix $\boldsymbol{V}$ and the amplitudes are stacked into the vector $\boldsymbol{q}$, the time dependent displacement $\boldsymbol{x}(t)$ can be expressed in terms of the constant basis $\boldsymbol{V}$ and the time dependent amplitude vector $\boldsymbol{q}(t)$:

$$\boldsymbol{x} = \boldsymbol{V}\boldsymbol{q} \tag{2}$$

If the matrix $\boldsymbol{V}$ is square, Eq. (2) is simply a coordinate transformation and the column vectors of $\boldsymbol{V}$ form the new basis. If $\boldsymbol{V}$ contains less columns than rows, Eq. (2) is a kinematic reduction of the displacement variable $\boldsymbol{x}$, which is bound to the subspace spanned by the columns of $\boldsymbol{V}$.

When plugging Eq. (2) with $\boldsymbol{V}$ only containing a small number of columns into Eq. (1), the latter can not be fulfilled exactly, as there are more equations than unknown variables. Thus the residual $\boldsymbol{R}$ expresses the remainder:

$$\boldsymbol{M}\boldsymbol{V}\ddot{\boldsymbol{q}} + \boldsymbol{D}\boldsymbol{V}\dot{\boldsymbol{q}} + \boldsymbol{K}\boldsymbol{V}\boldsymbol{q} = \boldsymbol{F} + \boldsymbol{R}, \qquad \boldsymbol{M}\boldsymbol{V}\ddot{\boldsymbol{q}} + \boldsymbol{f}(\boldsymbol{V}\boldsymbol{q}, \dot{\boldsymbol{V}}\boldsymbol{q}) = \boldsymbol{F} + \boldsymbol{R} \tag{3}$$

Stating that the residual $\boldsymbol{R}$ does not live in the subspace spanned by $\boldsymbol{V}$ yields to the reduced equation as $\boldsymbol{V}^T\boldsymbol{R} = 0$:

$$\begin{aligned} \boldsymbol{V}^T\boldsymbol{M}\boldsymbol{V}\ddot{\boldsymbol{q}} + \boldsymbol{V}^T\boldsymbol{D}\boldsymbol{V}\dot{\boldsymbol{q}} + \boldsymbol{V}^T\boldsymbol{K}\boldsymbol{V}\boldsymbol{q} &= \boldsymbol{V}^T\boldsymbol{F}, & \boldsymbol{V}^T\boldsymbol{M}\boldsymbol{V}\ddot{\boldsymbol{q}} + \boldsymbol{V}^T\boldsymbol{f}(\boldsymbol{V}\boldsymbol{q}, \dot{\boldsymbol{V}}\boldsymbol{q}) &= \boldsymbol{V}^T\boldsymbol{F} \\ \boldsymbol{M}_r\ddot{\boldsymbol{q}} + \boldsymbol{D}_r\dot{\boldsymbol{q}} + \boldsymbol{K}_r\boldsymbol{q} &= \boldsymbol{V}^T\boldsymbol{F}, & \boldsymbol{M}_r\ddot{\boldsymbol{q}} + \boldsymbol{V}^T\boldsymbol{f}(\boldsymbol{V}\boldsymbol{q}, \dot{\boldsymbol{V}}\boldsymbol{q}) &= \boldsymbol{V}^T\boldsymbol{F} \end{aligned} \tag{4}$$

The system matrices are projected onto the the subspace $\boldsymbol{V}$ yielding the reduced system matrices $\boldsymbol{M}_r$, $\boldsymbol{D}_r$ and $\boldsymbol{K}_r$. They can be evaluated in an offline step before time integration or other analyses. The term $\boldsymbol{V}^T\boldsymbol{f}(\boldsymbol{V}\boldsymbol{q}, \dot{\boldsymbol{V}}\boldsymbol{q})$ is usually computationally expensive, as it cannot be precomputed. Thus several attempts were made in order to reduce the nonlinear force term, for which the name *Hyper Reduction* was coined.

The following sections deal with selected methods, which provide a basis $\boldsymbol{V}$ for Eq. (4).

2.1 Linear Model Order Reduction Techniques

The linear model order reduction techniques that will be investigated are briefly introduced. For more details, the reader is referred to [8].

- Modal Truncation:
  In modal reduction, typically the lowest eigenvectors of the generalized eigenvalue problem $\omega_i^2\boldsymbol{M}\boldsymbol{\varphi}_i = \boldsymbol{K}\boldsymbol{\varphi}_i$, also called vibration modes, form the basis $\boldsymbol{V}$. Commonly, only the eigenvectors associated with the lowest eigenfrequencies ω_i are chosen to form the basis. As this choice is not based on the external force $\boldsymbol{F}$, commonly a modal dominance criterion, according to the ranking factor $\alpha_i = \boldsymbol{\varphi}_i^T\boldsymbol{F}$ is used as well.

- Modal Truncation Augmentation:
  As the modal reduction has the disadvantage to be agnostic with respect to the input positions $\boldsymbol{F}$ acts on, one can augment the basis with the static displacement modes. The static displacement modes $\boldsymbol{u}_i$ are the solution of the static displacement equation $\boldsymbol{K}\boldsymbol{u}_i = \boldsymbol{F}_i$ with $\boldsymbol{F}_i$ being a unit force vector on one input position.

- Krylov Subspace Reduction:
  The Krylov Subspace Reduction is based on the approximation of the transfer function, i.e. it makes also use of the input positions. The basic idea is the iterative approximation of the transfer function using rational functions expanded around a point in the complex plane, called the shift. The order of matching is called moment. For structural dynamics, it can be shown, that the basis vectors of the Krylov reduction scheme can be built using the Boolean matrix $\boldsymbol{B}$ defining input locations as $\boldsymbol{V} = [(-\omega^2\boldsymbol{M} + \boldsymbol{K})^{-1}\boldsymbol{B}, (-\omega^2\boldsymbol{M} + \boldsymbol{K})^{-1}\boldsymbol{M}\ (-\omega^2\boldsymbol{M} + \boldsymbol{K})^{-1}\boldsymbol{B}, \ldots, ((-\omega^2\boldsymbol{M} + \boldsymbol{K})^{-1}\boldsymbol{M})^{n-1}\ (-\omega^2\boldsymbol{M} + \boldsymbol{K})^{-1}\boldsymbol{B}]$. The shift ω is a real number and n is the number of moments matched.

2.2 Nonlinear Model Order Reduction Techniques

2.2.1 Proper Orthogonal Decomposition

The idea of the proper orthogonal decomposition is to find the best possible basis $\boldsymbol{V}$ covering the subspace of the displacements of a full model training set.

If $\boldsymbol{x}(t)$ is the continuous solution of Eq. (1) for a given input function $\boldsymbol{F}(t)$, one can sample the solution at M time steps $t_1, \ldots, t_M$ and construct a snapshot matrix $\boldsymbol{S} = [\boldsymbol{x}(t_1), \ldots, \boldsymbol{x}(t_M)]$ representing the displacements of the system at discrete time points.

If the solution $\boldsymbol{x}(t)$ lives only in a subspace, then the snapshot matrix $\boldsymbol{S}$ is rank deficient, as all columns of $\boldsymbol{S}$ are members of the subspace. The goal of the POD is to find the most dominant subspace of the columns of the snapshot matrix $\boldsymbol{S}$, such that $\boldsymbol{S}$ can be reconstructed using only the basis vectors $\boldsymbol{v}_1, \ldots \boldsymbol{v}_n$.

This problem is solved by the Singular Value Decomposition (SVD), which solves, according to the Eckhart-Young Theorem, the optimization problem [4, p.79]

$$\min_{rank(B)=n} ||\boldsymbol{S} - \boldsymbol{B}||_2. \tag{5}$$

If the SVD $\boldsymbol{S} = \boldsymbol{U}\boldsymbol{\Sigma}\boldsymbol{V}^T$ of the snapshot matrix $\boldsymbol{S}$ is computed, the optimization problem (5) is solved via $\boldsymbol{B} = \sum_{i=1}^{n} \boldsymbol{u}_i\sigma_i\boldsymbol{v}_i^T$. This means, that the snapshot matrix is reconstructed by a sum of rank-1 matrices $\boldsymbol{u}_i\sigma_i\boldsymbol{v}_i^T$ giving the best approximation in each case.

Thus, the snapshot matrix $\boldsymbol{S}$ has the optimal approximation in the spectral norm. The basis then consists of the left sided singular vectors $\boldsymbol{u}_i$ corresponding to the largest singular values σ_i. Consequently, it seems straightforward, that the best basis for the particular problem (1) with a given input $\boldsymbol{F}(t)$ are the left hand sided singular vectors of the SVD of the snapshot matrix. Furthermore the singular values σ_i do not only order the importance of the left hand sided singular vectors $\boldsymbol{u}_i$, but they also quantify the contribution to the snapshot matrix. The approximation quality or – looking at the dual statement – the error measure can be precisely given according to the truncated singular values of the SVD.

The downside, as already mentioned, is the sensitivity to the input $\boldsymbol{F}(t)$ and the need to compute the high fidelity model.

The decay rate of the singular values gives insight to the complexity of the problem. When the singular values decay quickly, the snapshot matrix can be approximated better with less

basis vectors. Thus the subspace, in which the main dynamics takes place, is small. In contrast to that, if the singular values decay slowly, the subspace embracing the relevant dynamics is large.

2.2.2 Extension of linear reduction techniques with modal derivatives

Another approach for nonlinear model order reduction used especially in structural dynamics is to augment the basis of the linearized problem with some basis vectors, which capture the behavior of the nonlinearity. As the nonlinearity in the equation of motion Eq. (1) is in the elastic forces, the approach of modal derivatives captures the second order terms of the nonlinear force $\boldsymbol{f}(\boldsymbol{x}, \dot{\boldsymbol{x}} = 0)$ with respect to the displacement. The idea is to augment the basis with the directions of the second order expansion of the nonlinear force.

The first idea of modal derivatives comes from the derivative of the eigenvalue problem $\omega_i^2 \boldsymbol{M}\boldsymbol{\varphi}_i = \boldsymbol{K}\boldsymbol{\varphi}_i$ with respect to a parameter p. As in geometric nonlinear systems the tangential stiffness matrix $\boldsymbol{K} = \boldsymbol{K}(\boldsymbol{x})$ is a function of displacements, one can pick the parameter p as the amplitude of a displacement vector. If the displacement vector is another eigenvector $\boldsymbol{\varphi}_j$ and the amplitude is ν_j, one can compute the modal derivative by differentiating the eigenvalue problem with respect to ν_j.

In the literature [8, 7] the mass influence is often neglected. Thus the statement for the approximated modal derivative is

$$\frac{\partial}{\partial \nu_j} \left(\boldsymbol{K}\boldsymbol{\varphi}_i \right) = 0 \tag{6}$$

leading to

$$\boldsymbol{K} \frac{\partial \boldsymbol{\varphi}_i}{\partial \nu_j} = -\frac{\partial \boldsymbol{K}}{\partial \nu_j} \boldsymbol{\varphi}_i \tag{7}$$

as the equation for the approximated modal derivative $\frac{\partial \boldsymbol{\varphi}_i}{\partial \nu_j}$. The physical interpretation can be given as follows: the partial derivative $\frac{\partial \boldsymbol{\varphi}_i}{\partial \nu_j}$ is the second order term of a variable vector $\boldsymbol{\varphi}_i(\boldsymbol{q})$ compensating the change of the stiffness matrix, if perturbed around the displacement $\boldsymbol{\varphi}_j \nu_j$. This statement is not limited to vibration modes, as the mass influence is neglected and thus no eigenfrequency shows up in Eq. (7), but can be used for any basis vectors.

For model order reduction this technique has proven to give reasonable results, as the second order terms of the static nonlinear displacement are captured and thus the information of the nonlinearity is exploited. The drawback is, that the number of modal derivatives grows quadratically. As the modal derivatives are symmetric, i.e. $\frac{\partial \boldsymbol{\varphi}_i}{\partial \nu_j} = \frac{\partial \boldsymbol{\varphi}_j}{\partial \nu_i}$, for i modes, there exist $\frac{i(i+1)}{2}$ modal derivatives.

In order to keep the number of basis vectors for augmentation small, different heuristics exist for the selection of modal derivatives for the reduction basis, see [1, 7].

3 INSPECTION THROUGH SUBSPACE PRINCIPAL ANGLES

The concept of principal angles between subspaces is known and used in mathematics [3, 4], whereas it is rarely used, if ever, in the model order reduction community. The basic idea is, that two subspaces $\mathcal{S}_1$ and $\mathcal{S}_2$ are orthogonal to each other, if the inner product of any normalized vector $\boldsymbol{g} \in \mathcal{S}_1, ||\boldsymbol{g}|| = 1$ of Subspace 1 is orthogonal to any other normalized vector $\boldsymbol{f} \in \mathcal{S}_2, ||\boldsymbol{f}|| = 1$ of subspace 2, i.e. the angle between the two subspaces is $\theta = 90°$, as $\boldsymbol{f}^T\boldsymbol{g} = \cos\theta$. In contrast to that, the two subspaces are identical, if $\boldsymbol{f}^T\boldsymbol{g} = 1 = \cos\theta$, which gives $\theta = 0°$.

Furthermore, there exist the principal vectors $\boldsymbol{g}_i \in \mathcal{S}_1$ and $\boldsymbol{f}_i \in \mathcal{S}_2$ and the corresponding principal angle θ_i, which can be *recursively* defined as [4, p.329]

$$\cos\theta_i = \max \boldsymbol{f}_i^T \boldsymbol{g}_i, \qquad \boldsymbol{f}_i^T[\boldsymbol{f}_1, \dots, \boldsymbol{f}_{i-1}] = 0, \quad \boldsymbol{g}_i^T[\boldsymbol{g}_1, \dots, \boldsymbol{g}_{i-1}] = 0. \tag{8}$$

This means, that the i-th principal angle of the two subspaces is the minimum angle of a vector pair $\boldsymbol{f}_i$ and $\boldsymbol{g}_i$ being member of $\mathcal{S}_1$ or $\mathcal{S}_2$ respectively, with the principal vectors being orthogonal to all previous principal vectors of the same subspace.

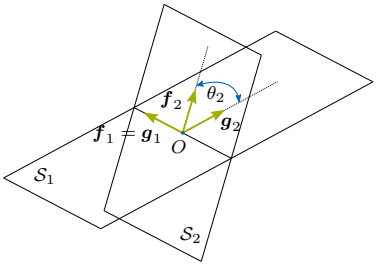


Figure 1: Illustration of two-dimensional Subspaces $\mathcal{S}_1$ and $\mathcal{S}_2$ in the three-dimensional space with the subspace angles $\theta_1 = 0$ and θ_2 and the principal vectors.

If the subspaces are interpreted as planes in three-dimensional space, see Figure 1, than the first principal angle is zero, $\theta_1 = 0$, with the first principal vectors $\boldsymbol{f}_1 = \boldsymbol{g}_1 = \mathcal{S}_1 \cap \mathcal{S}_2$ being the intersection line. The second principal angle, θ_2, is the angle between the two planes, and the second principal vectors, $\boldsymbol{g}_2$ and $\boldsymbol{f}_2$, form the vectors in the two planes which enclose the angle θ_2.

As can be seen from this simple example, the subspace angles are a powerful tool for the analysis of reduction bases, as not the basis itself, but the subspace spanned by the basis is relevant. If two subspaces differ fundamentally, their principal angles are all close to $90°$. If they fall into each other, their principal angles are all zeros.

Furthermore, the concept of subspace angles is not restricted to subspaces of equal size, but also different dimensions of subspaces can be compared. This gives the possibility to quantify, how good one basis is embraced by another basis. Sticking to the example of three-dimensional space above, one can compute the angle between a line and a plane. By definition, the line and the plane go through the origin. The line is a member of the plane, if the angle θ is zero, and is orthogonal, if $\theta = 90°$.

The computation of principal angles and vectors is as follows [4, pp.329]. Given two subspaces defined by the basis $\boldsymbol{V}_1 \in \mathbb{R}^{N\times p}$ and $\boldsymbol{V}_2 \in \mathbb{R}^{N\times q}$ with $p \leq q$, go through the following steps:

1. Orthogonalize the basis matrices $\boldsymbol{V}_1$ and $\boldsymbol{V}_2$ via QR-Decomposition:
   $\boldsymbol{V}_1 = \boldsymbol{Q}_1\boldsymbol{R}_1, \qquad \boldsymbol{V}_2 = \boldsymbol{Q}_2\boldsymbol{R}_2$
2. Compute the correlation matrix $\boldsymbol{C} = \boldsymbol{Q}_1^T\boldsymbol{Q}_2$ of the two orthogonalized subspaces.
3. Compute the SVD of the correlation matrix $\boldsymbol{C} = \boldsymbol{U}\boldsymbol{\Sigma}\boldsymbol{V}^T$. The singular values are the cosines of the principal angles: $\sigma_i = \cos\theta_i$.
4. Compute the principal vectors, if necessary:
   $\boldsymbol{G} = \begin{pmatrix}\boldsymbol{g}_1 & \dots & \boldsymbol{g}_p\end{pmatrix} = \boldsymbol{Q}_1\boldsymbol{U}$, $\boldsymbol{F} = \begin{pmatrix}\boldsymbol{f}_1 & \dots & \boldsymbol{f}_q\end{pmatrix} = \boldsymbol{Q}_2\boldsymbol{V}$

4 NUMERICAL EXAMPLE

4.1 Numerical test case

In order to measure the quality of the approximation of linear reduction techniques designed for the treatment of geometric nonlinearity, a planar geometrically nonlinear finite element test case is set up, see Figure 2. The test case consists of a U-shaped geometry discretized with

452 triangular finite elements and a total of 600 DoFs with applied boundary conditions. The element formulation is Total Lagrangian using linear shape functions and Kirchhoff material law. These elements can display arbitrary large rotations and constant strains and stresses [2]. The U-shaped geometry is fixed at one end and subjected to a non follower harmonic loading at the other end. The material properties are: Young's modulus $E = 210\ GPa$, Poisson's ratio $\nu = 0.3$, density $\rho = 10\,000\ \frac{kg}{m^3}$ and thickness $d = 1\ m$. The lowest eigenfrequencies of the linearized system are $f_1 = 3.054$ Hz, $f_2 = 6.173$ Hz, $f_3 = 19.94$ Hz and $f_4 = 52.41$ Hz.

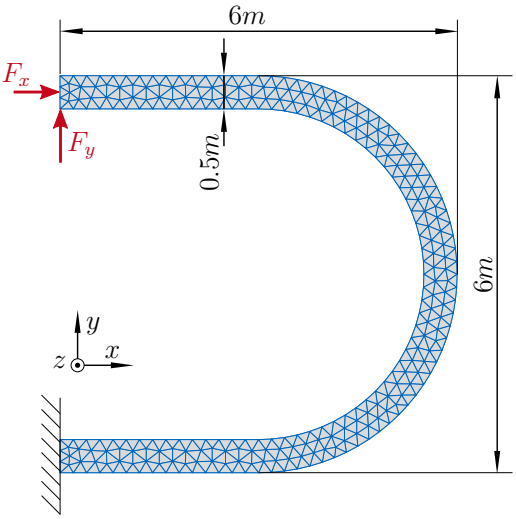


Figure 2: Geometry of the investigated test case.

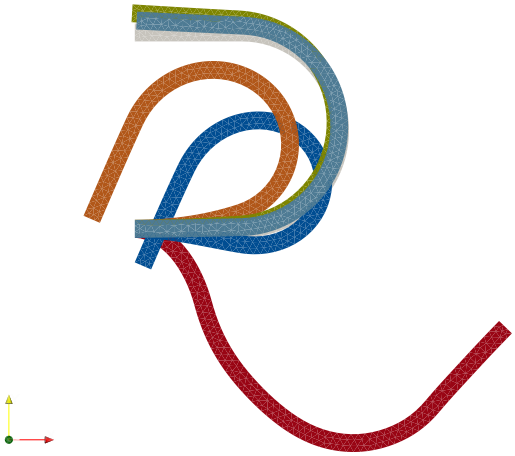


Figure 3: Configurations representing the range of displacements for the given test case at $t = 2.661\ s$. The color coding is given in Table 1

For the analysis of the structure five test cases were chosen, which have all harmonic loadings close to the first two eigenfrequencies in order to obtain reasonably large geometric nonlinear deformations. Furthermore the load steps are varying, including the range of almost linear behavior up to very large almost chaotic dynamics. All investigations were performed using a total simulation time of $3s$ with a generalized-α integration scheme with time step size $2 \cdot 10^{-1}s$ and the numerical damping factor $\alpha = 0$. In table 1 the load cases are listed and in Figure 3 displacements of the test cases are shown in order to give an impression of the displacement magnitude.

Table 1: Load cases of the finite element structures.

	Loading x-direction		Loading y-direction	
Test Case	Amplitude	Frequency	Amplitude	Frequency
A	5 10^4 N	3 Hz	5 10^4 N	6 Hz
B	1 10^5 N	3 Hz	1 10^5 N	6 Hz
C	5 10^5 N	3 Hz	5 10^5 N	6 Hz
D	1 10^6 N	3 Hz	1 10^6 N	6 Hz
E	1.5 10^6 N	3 Hz	2 10^6 N	6 Hz

4.2 Proper Orthogonal Decompostion

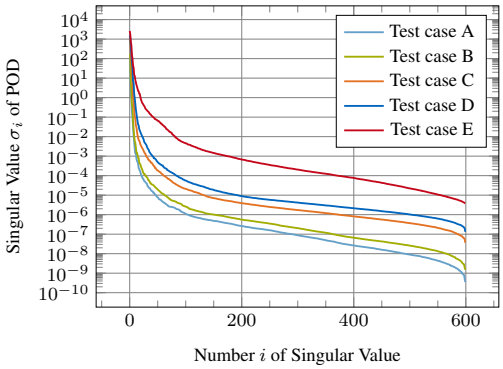


Figure 4: Singular values of the POD of the full simulation. As the decay rate is indicator of the complexity of the motion, it can clearly be seen that the complexity increases with stronger loading from test case A to E.

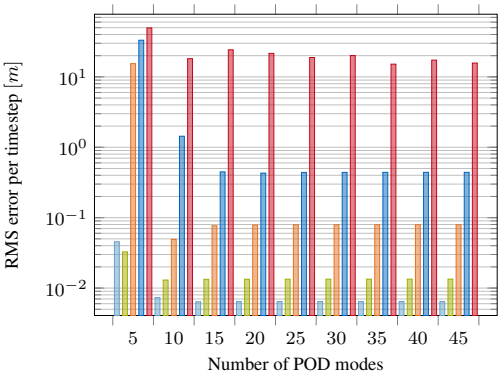


Figure 5: Average root mean square error of displacements of time simulation with POD basis.

In order to quantify the number of modes, which are at minimum necessary to make a good reduction, the solution of the full problem is computed for all five test cases and a POD is carried out. Figure 4 shows the singular values, highlighting the increasing complexity of the solution from A to E. As also can be seen in Figure 3, the displacements of test cases with higher loading are more complex requiring more basis vectors to be reconstructed.

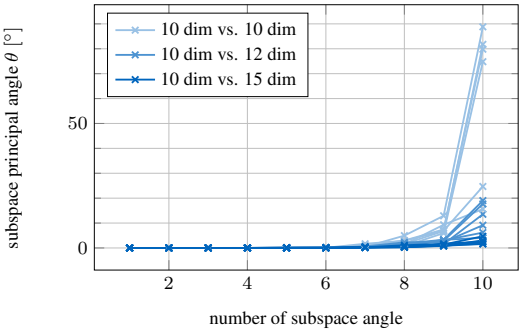


Figure 6: Principal angles between the POD subspaces of the five test cases. Not only two ten-dimensional subspaces are compared, but also larger dimensional ones with smaller ones shedding light on how one POD subspace embraces the other.

The question of the appropriate size of the subspace still remains, as it is not the error in the kinematic projection, which is relevant, but the result of the dynamic equation. Thus, a reduced simulation is performed using the POD basis of each test case with different numbers of basis vectors. The average root mean square error of the displacement is given in Figure 5, which shows clearly, that a basis of five POD vectors produces a huge error for all test cases. But already with ten POD basis vectors, the error of the reduced simulation seems to be more or less converged for four of the five test cases. This impression is not only due to the values of the RMS error, but also the video of the simulation shows clear overlapping for test cases A, B, C and D, whereas for test case E even the basis of 50 POD vectors does not produce an overlapping reduced simulation.

When looking at the subspace angles of the POD basis vectors, it is notable, that the ten-dimensional POD subspaces have a certain degree of overlapping. In Figure 6 the subspace angles between the ten-dimensional POD bases of all five test cases are shown. As can be seen, eight to nine dimensions practically overlap. The hypothesis, that the POD bases are sort of

similar independently of the load case, gets stronger when the subspaces are compared with one subspace getting additional two or five more dimensions. Then, as the subspace angles in Figure 6 suggest, the 15-dimensional POD subspace of one test case practically embraces almost the ten-dimensional POD subspace of another test case.

4.3 Linear reduction techniques augmented with modal derivaitives

Based on the assumption, that basically ten POD vectors represent the kinematics of the problems A to D reasonably sufficiently, these ten POD basis vectors are taken as the reference basis vectors. The investigated reduction techniques should embrace the reference subspace, as it is a good basis for the problem. For the following investigations test case D was chosen for further inspection. This test case is complex enough to go strongly into nonlinearity while having not the complex behavior of test case E, which is even hard to approximate via a POD basis of dimension 50.

First results of linear reduction techniques are shown in Figure 7. The principal angles show, that – independent of the reduction technique – the POD subspace is only fitted for three to four basis vectors. Increasing the number of basis modes does not improve the number of principal vectors that coincide. This means, that the linear basis misses additional subspaces for the reduction of geometrically nonlinear systems.

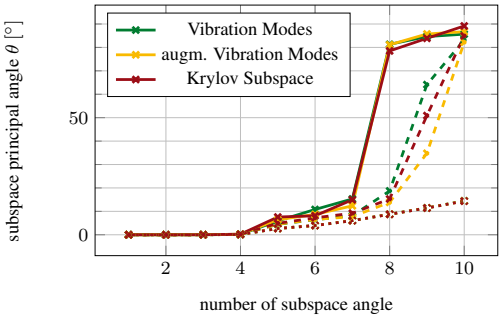


Figure 7: Subspace principal angles between 10 POD vectors and the linear reduction methods. The solid line displays the angles with 10 linear basis vectors, the dashed line with 15 linear basis vectors and the dotted line with 50 linear basis vectors.

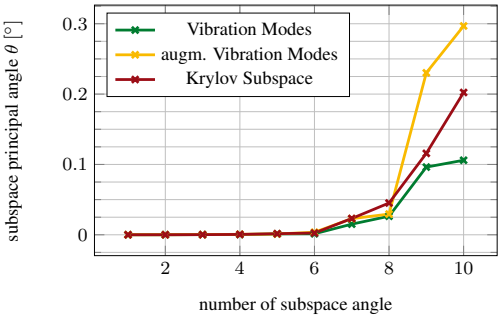


Figure 8: Subspace principal angles between 10 POD vectors and the linear reduction methods augmented with modal derivative basis. 8 basis vectors from the linear reduction technique were used augmented with the corresponding 36 modal derivatives.

Secondly the basis vectors gathered from the linear reduction techniques are enriched by the modal derivative vectors as described in section 2.2.2. For the example shown in Figure 8, eight basis vectors augmented with the modal derivatives are used to build the basis. As depicted, the subspace angles converge much stronger to zero than in the linear case in Figure 7 – note the scaling of the ordinate. There is also no real winner to be found, as all three methods perform comparably well in this scenario. Also the other test cases A, B, C and E show similar behavior – no method shows superiority over the other.

The same result is obtained with video inspection of the displacements over time, where the test cases A - D almost perfectly overlap compared to the full reference simulation. Test case E is once again too hard to approximate exactly, though the subspace spanned by the first POD modes gets similarly approximated as for the other test cases.

5 CONCLUSION

The classification of the reduction quality for nonlinear models is very difficult, as many techniques from linear system theory are not extensible to nonlinear models. In this paper, subspace angles are proposed as a mathematically rigorous comparison tool for nonlinear model order reduction. With this technique the necessity for augmentation a linear basis with modal derivatives can be verified, which was conducted on an example using geometrically nonlinear finite elements.

Furthermore, the augmentation of three linear reduction techniques – modal truncation, modal truncation augmentation and Krylov subspace – with its static modal derivatives was investigated. Both, time integration of the reduced models as well as the investigation with subspace angles does not find a clear winner of these techniques, as they all deliver good results.

As the investigation of subspace angles is not established in the model order reduction community, further research is necessary as open questions remain. It is not clear, which angles can be classified as large and which as practically zero. The observations in this paper showed, that a subspace seems to be grasped when the angle is smaller than one to two degrees. Furthermore the concept of subspace angles was used in Euclidean space. It is an open question, if other concepts of spaces, like the in structural dynamics common $\boldsymbol{M}$ and $\boldsymbol{K}$-spaces deliver more accurate descriptions.

REFERENCES

[1] Jernej Barbič and Doug L James. *Real-Time subspace integration for St. Venant-Kirchhoff deformable models*. In *ACM Transactions on Graphics (TOG)*, volume 24, pages 982–990. ACM, 2005.

[2] Ted Belytschko, Wing Kam Liu, and Brian Moran. *Nonlinear Finite Elements for Continua and Structures*. John Wiley & Sons, 2000.

[3] Åke Björck and Gene H Golub. *Numerical methods for computing angles between linear subspaces*. Mathematics of computation, 27(123):579–594, 1973.

[4] Gene H Golub and Charles F Van Loan. *Matrix computations*, volume 3. JHU Press, 2012.

[5] Sergio R Idelsohn and Alberto Cardona. *A load-dependent basis for reduced nonlinear structural dynamics*. Computers & Structures, 20(1):203–210, 1985.

[6] Sergio R Idelsohn and Alberto Cardona. *A reduction method for nonlinear structural dynamic analysis*. Computer Methods in Applied Mechanics and Engineering, 49(3):253–279, 1985.

[7] PMA Slaats, J De Jongh, and AAHJ Sauren. *Model reduction tools for nonlinear structural dynamics*. Computers & structures, 54(6):1155–1171, 1995.

[8] Wolfgang Witteveen. *On the Modal and Non-Modal Model Reduction of Metallic Structures with Variable Boundary Conditions*. World Journal of Mechanics, 2:311, 2012.

[9] Wolfgang Witteveen and Florian Pichler. *Efficient Model Order Reduction for the Dynamics of Nonlinear Multilayer Sheet Structures with Trial Vector Derivatives*. Shock and Vibration, 2014, 2014.

11th International Conference on Engineering Vibration
Ljubljana, Slovenia, 7–10 September 2015

AN INTERFACE FORCE MEASUREMENTS-BASED SUBSTRUCTURE IDENTIFICATION

Kranjc, T.*[1], Slavič, J.[2], Boltežar, M.[2]

[1] Ydria motors d.o.o.
tadej.kranjc@ydria-motors.si

[2] Faculty of mechanical engineering, Ljubljana
{janko.slavic, miha.boltezar}@fs.uni-lj.si

Keywords: substructure decoupling, interface force identification.

Abstract. *Substructure-decoupling techniques are used to identify a substructure as a stand-alone system while it is coupled to a complex structure (an assembly of substructures). These recently introduced techniques can be used for various applications,* e.g.*, when modal testing methods are not appropriate due to the limits of the measurement equipment, when the substructure cannot be measured separately from the complex structure and for vibration-control techniques. The complex structure consists of the unknown substructure and the remaining structure. A drawback of the available substructure-decoupling techniques is that they require a model of the remaining substructure. However, when the model cannot be calculated or (experimentally) identified, the substructure-decoupling techniques cannot be used. In this paper a new approach is presented that does not require a model of the remaining substructure, but is based on an experimental identification of the interface forces. To research the application possibilities for real situations, complex structures with beam-like coupling elements are investigated. The article includes numerical and experimental test cases.*

1 Introduction

In the field of substructure-decoupling techniques the complex structure is usually divided into the unknown and the remaining substructures. The result of the substructure-decoupling technique is a model of the unknown substructure, which is identified from the complex structure. The substructure-decoupling techniques can be classified as the inverse and the direct decoupling techniques [1]. The inverse techniques are based on coupling equations, that are rearranged in such a way that the model of the unknown substructure is isolated [1]. Examples of the inverse techniques are the impedance [2, 3, 4] and the mobility [3, 4, 5] substructure-decoupling techniques. The direct decoupling techniques are based on the adding of a fictitious subsystem to the model of the complex structure, that is the negative of the residual substructure [1, 6, 7].

It is a common feature of all the available decoupling techniques that they require a dynamical model of the complex and the remaining substructures. The model of the complex structure is identified experimentally and the model of the remaining substructure is calculated or experimentally identified. A drawback of the substructure-decoupling techniques is that the calculation or identification of the remaining substructure's model requires an additional effort. When the remaining substructure is too complicated to be calculated or experimentally identified, the substructure-decoupling techniques cannot be used.

In this research a new approach to linear substructure decoupling is introduced that does not require a model of the remaining substructure [8]. This approach is based on measuring the interface forces [9, 10, 11]. The interface forces of the complex structures usually cannot be measured directly; therefore, an identification is made. The approach was validated by numerical simulations and experimental tests on a beam structure [8].

2 The responses of the coupled substructure

The substructure decoupling will be considered for the complex structure AB (Fig. 1a) that is assembled from the substructures A and B. It is assumed that the considered systems are linear and time invariant. In this article all the quantities are functions of frequency, except for the constants and integers. The subscripts a, b and c correspond to the substructures A, B and the coupling degrees of freedom (DOF), respectively. The structure AB is excited with the external excitation forces $\mathbf{f}_a$ and $\mathbf{f}_b$ (Fig. 1a).

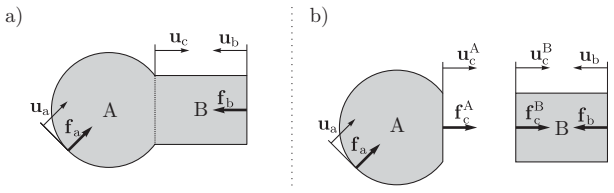


Fig. 1: a) The complex structure AB; b) The coupled substructures A and B

Using the interface forces $\mathbf{f}_c^B$ the response of the coupled substructure B can be written

as [12]:

$$\begin{bmatrix} \mathbf{u}_c^B \\ \mathbf{u}_b \end{bmatrix} = \underbrace{\begin{bmatrix} \mathbf{H}_{cc}^B & \mathbf{H}_{cb}^B \\ \mathbf{H}_{bc}^B & \mathbf{H}_{bb}^B \end{bmatrix}}_{\mathbf{H}^B} \begin{bmatrix} \mathbf{f}_c^B \\ \mathbf{f}_b \end{bmatrix} \tag{1}$$

where $\mathbf{H}^B$ is the FRF matrix of the substructure B. When the substructures A and B are assembled, the compatibility and equilibrium conditions are satisfied for the coupling DOF.

3 The substructure-decoupling procedure

The proposed approach is based on the decoupling technique presented by Sjövall and Abrahamsson [5] and further developed by Voormeeren and Rixen [12]. The existing technique requires a response model A for the interface force identification. With the proposed technique the interface forces $\mathbf{f}_c^B$ are identified experimentally, where the mathematical model of the substructure A is not needed. This section briefly describes the general procedure for the proposed substructure decoupling. More details are given in the following sections. The technique is schematically shown in Fig. 2. At the ith linearly-independent excitation step the structure AB is excited with the external forces ${}_i\mathbf{f}_a$ and ${}_i\mathbf{f}_b$ (Section 3.1). In this research the linear independence of the excitation forces is achieved by changing the number, location and magnitudes of the excitation forces. At each excitation step the responses ${}_i\mathbf{u}_b$, ${}_i\mathbf{u}_c$ are measured (Section 3.1) and the interface forces ${}_i\mathbf{f}_c^B$ are identified (Section 3.2). After m excitation steps (m is defined in Section 3.3) the measured (identified) quantities are used to identify the substructure-B response model with the approach that is introduced in Section 3.3.

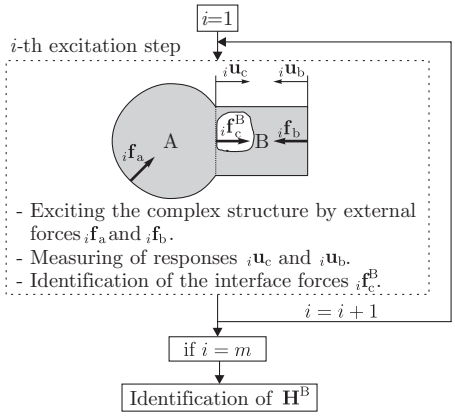


Fig. 2: The substructure-decoupling technique

3.1 The structure excitations and response measurements

Under laboratory conditions the testing process can be controlled by exciting the structure in a similar way as in the experimental modal analysis (EMA) [9, 10, 11] with a modal hammer

or an electrodynamic shaker. The responses can be measured with a motion sensor (*e.g.*, a piezoelectric accelerometer or a laser vibrometer).

3.2 The identification of the interface forces for the beams

In this section the interface force identification is presented that is based on the response measurements only. It does not require the FRF matrix of the substructure A. When the coupling element between the substructures A and B is a beam (Fig. 3) the interface forces are normal ($N_{x,\mathrm{c}}$) and the shear forces ($T_{y,\mathrm{c}}$, $T_{z,\mathrm{c}}$), bending ($M_{y,\mathrm{c}}$, $M_{z,\mathrm{c}}$) and torsion ($M_{x,\mathrm{c}}$) moments. However, it is assumed in this research that the coupling element is a uniform Euler-Bernoulli beam in pure planar bending in the plane xz; therefore, only the bending moments $M_{y,\mathrm{c}}$ and the shear forces $T_{z,\mathrm{c}}$ are analyzed [13]. A vector of the interface forces $\mathbf{f}_{\mathrm{c}}^{\mathrm{B}}$ for the coupling DOF c (Fig. 3) is written as:

$$\mathbf{f}_{\mathrm{c}}^{\mathrm{B}} = [-T_{z,\mathrm{c}} \quad -M_{y,\mathrm{c}}]^{\mathrm{T}} \tag{2}$$

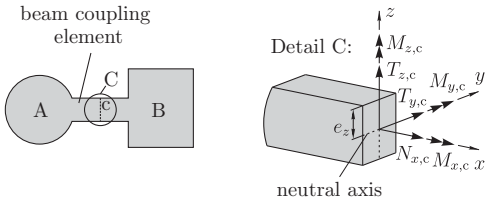


Fig. 3: The complex structure with the beam coupling element

In this section a procedure for the identification of the interface forces $\mathbf{f}_{\mathrm{c}}^{\mathrm{B}}$ is presented. The bending moments M_y result in the normal stress σ_{xx}. σ_{xx} varies linearly with the distance e_z from the neutral axis (see Fig. 3 and 5), where the normal stress and strain equal zero [14]. The normal stress at the surface is written as [14, 15]:

$$\sigma_{xx,\mathrm{s}} = \frac{M_y}{I_y}\, e_z, \tag{3}$$

where I_y is the area moment of inertia around the y-axis and e_z (Fig. 3) is the distance between the neutral axis [14] and the surface. By considering Hooke's law, the relationship between the bending moment and the strain $\varepsilon_{xx,\mathrm{s}}$ at the surface can be written as:

$$M_y = E\, \varepsilon_{xx,\mathrm{s}}\, \frac{I_y}{e_z} \tag{4}$$

where E is the Young's modulus. The shear force T_z is the first partial derivative of the bending moment with respect to x [13]:

$$T_z = \frac{\partial M_y}{\partial x} \tag{5}$$

Eq. (5) can be written in terms of the central difference formula for the first derivative [16]. In this research the identification of the bending moment $M_{y,\mathrm{c}}$ and the shear force $T_{z,\mathrm{c}}$ is based

on measuring the strain responses (with piezoelectric strain gauges [17, 18]) at two structure points, which are located symmetrically around the coupling DOF (see Fig. 3 and 4) with the spacing s. When I_y is constant, $T_{z,\mathrm{c}}$ can be identified with the following equation:

$$T_{z,\mathrm{c}} \approx \frac{M_{y,\mathrm{c_b}} - M_{y,\mathrm{c_a}}}{s} \tag{6}$$

$M_{y,\mathrm{c_a}}$ and $M_{y,\mathrm{c_b}}$ are bending moments, corresponding to the points $\mathrm{c_a}$ and $\mathrm{c_b}$, respectively (Fig. 4). $M_{y,\mathrm{c_a}}$ and $M_{y,\mathrm{c_b}}$ are calculated with Eq. (4). When the strain responses are measured at the points $\mathrm{c_a}$ and $\mathrm{c_b}$, the bending moment at the point c can be obtained by calculating the average value:

$$M_{y,\mathrm{c}} \approx \frac{M_{y,\mathrm{c_a}} + M_{y,\mathrm{c_b}}}{2} \tag{7}$$

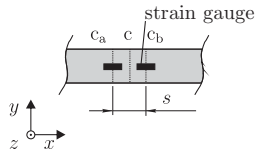


Fig. 4: The strain gauges for the interface force identification

Using the strain FRF matrix [17, 19] of the structure AB the bending moment $M_{y,\mathrm{c}}$ (Eq. (7)) can be calculated with the following equation:

$$M_{y,\mathrm{c}} = \frac{1}{2}\,\frac{I_y}{e_z}\,E\,\begin{bmatrix}\mathbf{H}^{\mathrm{AB},\varepsilon_{xx}}_{\mathrm{c_a a}} + \mathbf{H}^{\mathrm{AB},\varepsilon_{xx}}_{\mathrm{c_b a}} & \mathbf{H}^{\mathrm{AB},\varepsilon_{xx}}_{\mathrm{c_a b}} + \mathbf{H}^{\mathrm{AB},\varepsilon_{xx}}_{\mathrm{c_b b}}\end{bmatrix}\begin{bmatrix}\mathbf{f}_{\mathrm{a}}\\ \mathbf{f}_{\mathrm{b}}\end{bmatrix} \tag{8}$$

where $\mathbf{H}^{\mathrm{AB},\varepsilon_{xx}}$ is the strain FRF matrix of the complex structure. An element of $\mathbf{H}^{\mathrm{AB},\varepsilon_{xx}}$ can be written as [17, 19]:

$$H^{\mathrm{AB},\varepsilon_{xx}}_{jk} = \frac{\varepsilon_{xx,\,k}}{F_j} \tag{9}$$

where $\varepsilon_{xx,\,k}$ is the normal strain in the x-direction and F_j is the excitation force. The shear force (6) can be written in a similar way as Eq. (8):

$$T_{z,\mathrm{c}} = \frac{I_y}{e_z\,s}\,E\,\begin{bmatrix}\mathbf{H}^{\mathrm{AB},\varepsilon_{xx}}_{\mathrm{c_b a}} - \mathbf{H}^{\mathrm{AB},\varepsilon_{xx}}_{\mathrm{c_a a}} & \mathbf{H}^{\mathrm{AB},\varepsilon_{xx}}_{\mathrm{c_b b}} - \mathbf{H}^{\mathrm{AB},\varepsilon_{xx}}_{\mathrm{c_a b}}\end{bmatrix}\begin{bmatrix}\mathbf{f}_{\mathrm{a}}\\ \mathbf{f}_{\mathrm{b}}\end{bmatrix} \tag{10}$$

Eq. (8) and (10) can be used for numerical simulations. The derivations for $M_{z,\mathrm{c}}$ and $T_{y,\mathrm{c}}$ can be performed in a similar way as for $M_{y,\mathrm{c}}$ and $T_{z,\mathrm{c}}$, respectively (Fig. 4).

3.3 The Identification of the substructure's FRF matrix

The coupled substructure B (Fig. 1b) can be considered as a stand-alone system that is manipulated with the excitation force $\mathbf{f}^{\mathrm{B}}$ (see Eq. (1)):

$$\mathbf{f}^{\mathrm{B}} = \begin{bmatrix} \mathbf{f}_{\mathrm{c}}^{\mathrm{B}} \\ \mathbf{f}_{\mathrm{b}} \end{bmatrix}_{n_{\mathbf{F}}} \tag{11}$$

where $n_{\mathbf{F}}$ is the number of excitation forces corresponding to the coupled substructure B. The excitation forces that excite the coupled substructure B, corresponding to the m linearly independent load steps can be collected in the matrix $\mathbf{F}^{\mathrm{B}}$:

$$\mathbf{F}^{\mathrm{B}} = \begin{bmatrix} {}_1\mathbf{f}^{\mathrm{B}} & \cdots & {}_i\mathbf{f}^{\mathrm{B}} & \cdots & {}_m\mathbf{f}^{\mathrm{B}} \end{bmatrix}_{n_{\mathbf{F}} \times m} \tag{12}$$

The responses of the structure B that correspond to the m linearly independent load steps can be written as:

$$\mathbf{U}^{\mathrm{B}} = \begin{bmatrix} {}_1\mathbf{u}_{\mathrm{c}} & \cdots & {}_i\mathbf{u}_{\mathrm{c}} & \cdots & {}_m\mathbf{u}_{\mathrm{c}} \\ {}_1\mathbf{u}_{\mathrm{b}} & \cdots & {}_i\mathbf{u}_{\mathrm{b}} & \cdots & {}_m\mathbf{u}_{\mathrm{b}} \end{bmatrix}_{n_{\mathbf{U}} \times m} \tag{13}$$

where $n_{\mathbf{U}}$ is the number of responses. For the theoretical analysis the response and excitation points correspond to the DOFs of the substructure B; therefore, $n_{\mathbf{U}}$ and $n_{\mathbf{F}}$ are equal to the number of substructure B DOFs n_{B}. The relation between $\mathbf{U}^{\mathrm{B}}$ and $\mathbf{F}^{\mathrm{B}}$ can be written as [5, 12]:

$$\mathbf{U}^{\mathrm{B}} = \mathbf{H}^{\mathrm{B}}\,\mathbf{F}^{\mathrm{B}} \tag{14}$$

where $\mathbf{H}^{\mathrm{B}}$ is the FRF matrix of the subsystem B (as a stand-alone structure). Eq. (14) is determined or over-determined when the number of linearly independent excitation steps m is equal to or higher than n_{B} ($m \geq n_{\mathrm{B}}$) [5, 12, 20]. When Eq. (14) is over-determined $\mathbf{H}^{\mathrm{B}}$ can be solved using the least-squares solution of Eq. (14) [5, 12]:

$$\mathbf{H}^{\mathrm{B}} = \mathbf{U}^{\mathrm{B}}\,\mathbf{F}^{\mathrm{B}\,+} \tag{15}$$

where $^+$ denotes the generalized inverse of the matrix. When m equals n_{B} the matrices $\mathbf{U}^{\mathrm{B}}$ and $\mathbf{F}^{\mathrm{B}}$ become square and the regular matrix inversion can be made. In practice, where the real structures are tested, the number of response points and excitation points (corresponding to the substructure B) is usually not the same. In this case Eq. (14) is determined or over-determined when $m \geq n_{\mathbf{F}}$.

4 Case study

The validation (numerical and experimental) of the proposed approach was conducted on a steel, 1-m-long, free-free supported beam with a rectangular, 0.01×0.03 m^2 cross-section (Fig. 5). Only the bending modes in the plane xz are considered, which result in displacements in the z-direction and normal strains in the x-direction [13]. The beam is considered as a structure AB, which is assembled from the substructures A and B (see Fig. 5). The case study 2 includes the numerical simulations and the experimental tests.

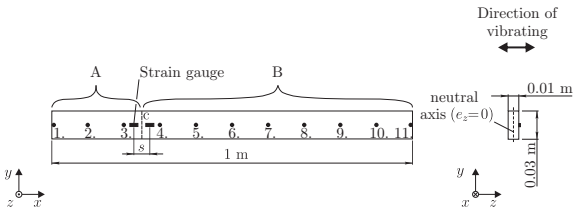


Fig. 5: The tested beam

4.1 Numerical simulations

In this section the substructure decoupling is based on the quantities (with the frequency resolution of 1 Hz) that are calculated using (FEM) harmonic analysis. The proportional hysteretic damping model was assumed with the constant damping loss factor $\eta = 8 \times 10^{-4}$.

The numerical simulations were made with the same quantities (motion and strain responses) as for the experimental test (Section 4.2). The structure AB was excited at the points 1 and 3 with the excitation forces. To obtain the interface forces between the substructures A and B the shear forces (T_z, c) and the bending moments (M_y, c) were calculated at the point c. The responses were calculated at the point 11. These quantities are used for the identification of the substructure B. The sizes of the excitation (a column of $\mathbf{F}^{\mathrm{B}}$) and the response vector (a column of $\mathbf{U}^{\mathrm{B}}$) are two ($n_{\mathbf{F}} = 2$) and one ($n_{\mathbf{U}} = 1$), respectively (see Eq. (12) and (13)). To ensure that Eq. (14) is determined, two excitation steps are required. The structure excitation was made as follows: In the first and second steps the structure was excited with the unit force (a constant value over the whole frequency range) at the points 1 and 2, respectively. The results of the substructure decoupling are the FRFs of the substructure B as a stand-alone dynamical system. The input data enable the identification of the motion (translational) and moment (rotational) FRFs between the response point 11 and the excitation point c. Fig. 6 shows the accelerance of the substructure B between the response point 11 and the excitation point c ($\hat{A}^{\mathrm{B}}_{11\,\mathrm{c}}$) that was identified using the proposed approach, the true accelerance of the substructure B ($A^{\mathrm{B}}_{11\,\mathrm{c}}$) and the accelerance corresponding to the structure AB ($A^{\mathrm{AB}}_{11\,\mathrm{c}}$). The identified accelerance $\hat{A}^{\mathrm{B}}_{11\,\mathrm{c}}$ matches the true accelerance $A^{\mathrm{B}}_{11\,\mathrm{c}}$.

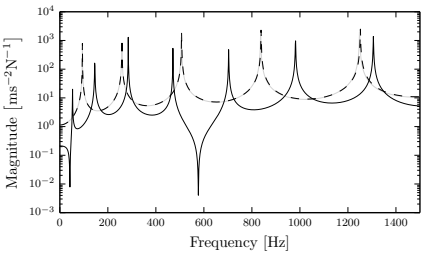
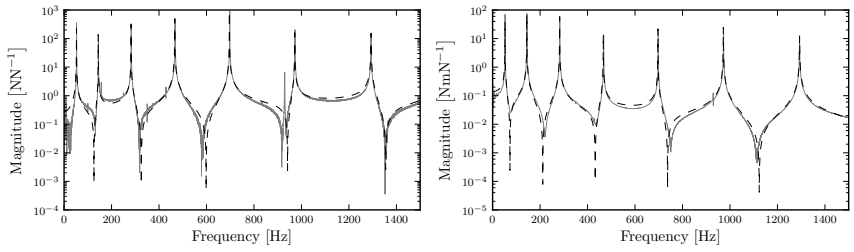


Fig. 6: The accelerances of substructure B ($A^{\mathrm{B}}_{11\,\mathrm{c}}$): Identified (black - - -), True (grey —); The accelerance of the structure AB ($A^{\mathrm{AB}}_{11\,\mathrm{c}}$): (black —)

4.2 Experimental testing

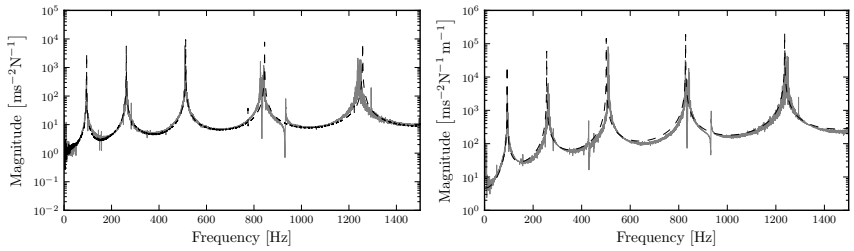
This section introduces the results of the experimental testing on the real beam. The free-free boundary conditions of the beam were achieved by suspending the structure from thin ropes. During the experimental testing the structure was excited with a modal hammer (B&K Type 8206-002). The strain responses were measured with two piezoelectric strain gauges (PCB 740B02 [18]), which were attached symmetrically around the point c. The attaching of the the strain gauges is shown in Fig. 5. The spacing between the strain gauges was 20 mm. The motion responses were measured at point 11 with the piezoelectric accelerometer (B&K Type 4517-002). To compare the identified interface forces with the calculated ones using the validated finite-element (FE) model the results are plotted as the FRFs between the shear force (bending moment) and the external excitation force. Fig. 7(a) shows the FRF between $T_{z,\mathrm{c}}$ and the excitation point 1. FRF between $M_{y,\mathrm{c}}$ and excitation point 1 is shown in Fig. 7(b). The frequency resolution of the quantities that are plotted in this section is 0.1 Hz. Fig. 7(a) and 7(b) show that the identified interface forces match the calculated ones well.

The linearly independent excitation steps were made in the same way as for the numerical simulations. The measured responses, (identified) shear forces and bending moments were used to identify the substructure B FRFs. The identified accelerance $\hat{A}^{\mathrm{B}}_{11\,\mathrm{c}}$ (between the points 11 and c) is plotted together with the measured one (Fig. 8(a)), where the free-free supported beam with the length L=750 mm was tested. The identified moment accelerance $\hat{A}^{M,\mathrm{B}}_{11\,\mathrm{c}}$ is plotted together with the calculated one (from the validated FE model) in Fig. 8(b). Fig. 8(a) and 8(b) show that the experimental results match the calculated ones well.



(a) (b)

Fig. 7: a) The accelerance of the substructure B ($A^{\mathrm{B}}_{11\,\mathrm{c}}$): Identified (grey —) and measured for the 0.75-m-long beam (black - - -), FRF between the bending moment and the excitation force: Identified (grey —) and calculated (black - - -).



(a) (b)

Fig. 8: a) The accelerance of the substructure B ($A^{\mathrm{B}}_{11\,\mathrm{c}}$): Identified (grey —) and measured for the 0.75-m-long beam (black - - -), b) The moment accelerance of the substructure B ($A^{M,\mathrm{B}}_{\mathrm{c}\,11}$): identified (grey —) and calculated (black - - -).

5 Conclusion

A drawback of the current substructure decoupling techniques is that the response model of the remaining substructure is required. In this article a new approach is introduced that does not require the response model of the remaining substructure. The proposed approach is based on an experimental identification of the interface forces.

The proposed approach was validated on a beam structure. The tests included numerical simulations and experimental testing. The results of the numerical simulations showed that the identified FRFs of the substructure match the true ones well. The experimental testing showed that the identified accelerances and moment accelerances correspond to the calculated values.

REFERENCES

[1] W. DAmbrogio, A. Fregolent, Direct decoupling of substructures using primal and dual formulation. *Proceedings of the 27 International Modal Analysis Conference (IMAC XXIX)*, SEM, 2011, pp. 4776.

[2] P. Ind, D. Ewins, Impedance based decoupling and its application to indirect modal testing and component measurement: a numerical investigation. *Proceedings of 21th International Modal Analysis Conference, Kissimmee*, FL, Society for Experimental Mechanics, Bethel, CT, 2003.

[3] D. Cloutier, P. Avitabile, Investigation on the use of various decoupling approaches. *Proceedings of the 28 International Modal Analysis Conference (IMAC XXVIII)*, Jacksonville, Florida, Society for Experimantal Mechanics Inc., 2010, pp. 679687.

[4] W. DAmbrogio, A. Fregolent, Promises and pitfalls of decoupling procedures. *Proceedings of the 26 International Modal Analysis Conference (IMAC XXVI)*, Orlando, Florida, 2008.

[5] P. Sjovall, T. Abrahamsson, Substructure system identification from coupled system test data. *Mechanical Systems and Signal Processing*, 22 (1), 15 33, 2008.

[6] S. Voormeeren, D. Rixen, A family of substructure decoupling techniques based on a dual assembly approach. *Mechanical Systems and Signal Processing*, 27 (0), 379 396, 2012.

[7] S. Voormeeren, D. Rixen, A dual approach to substructure decoupling techniques. *Proceedings of the 28th International Modal Analysis Conference IMAC-XXVIII*, Jacksonville, Florida USA, Society for Experimantal Mechanics Inc., 2010, pp. 601616.

[8] T. Kranjc, J. Slavič, M. Boltežar, An interface force measurements-based substructure identification and an analysis of the uncertainty propagation. *Mechanical Systems and Signal Processing*, 56-57 (0), 2-14, 2015.

[9] N. M. N. Maia, J. M. M. Silva, *Theoretical and Experimental Modal Analysis*. Research studies press Ltd., Baldock, Hertfordshire, England, 1997.

[10] W. Heylen, S. Lammers and P. Sas, *Modal Analysis Theory and Testing*. Katholieke Universiteit Leuven, Haverlee, Belgium, 2007.

[11] D. J. Ewins, *Modal testing: Theory and Practice*. Research studies press Ltd., Baldock, Hertgordshire, England, 1984.

[12] S. Voormeeren, D. Rixen, Substructure decoupling techniques - a review and uncertainty propagation analysis. *Proceedings of the International Modal Analysis Conference IMAC-XXVII*, Orlando, Florida, USA, SEM, 2009.

[13] S. S. Rao, *Mechanical Vibrations*. Prentice Hall, Upper Saddle River, NJ., 2010.

[14] M. Kutz, *Mechanical Engineers' Handbook*. Wiley, 1998.

[15] K. Washizu, *Variational Methods in Elasticity and Plasticity*. Elsevier Science & Technology, 1974.

[16] R. Burden, J. Faires, *Numerical Analysis*. Brooks/Cole, Cengage Learning, 2011.

[17] T. Kranjc, J. Slavič, M. Boltežar, The mass normalization of the displacement and strain mode shapes in a strain experimental modal analysis using the mass-change strategy. *Journal of Sound and Vibration*, 332 (26), 6968 6981, 2013.

[18] J. J. Dosch, Piezoelectric strain sensor. *Proceedings of the International Modal Analysis Conference IMAC* , SEM, Bethel, CT, United States, 1999.

[19] T. Kranjc, J. Slavič, M. Boltežar, A comparison of strain and classic experimental modal analysis, *Journal of Vibration and Control*, Published online April 29, 2014.

[20] D. Čelič, M. Boltežar, The influence of the coordinate reduction on the identification of the joint dynamic properties. *Mechanical Systems and Signal Processing*, 23 (4), 1260 1271, 2009.

11th International Conference on Engineering Vibration
Ljubljana, Slovenia, 7–10 September 2015

EFFECTS OF INTERFACE LOADING IN DYNAMIC SUBSTRUCTURING

Andreas Linderholt[1], **Maren Scheel**[2] **Anders T. Johansson**[2]

[1]Linnaeus University, Växjö Sweden
andreas.linderholt@lnu.se

[2]Chalmers University of Technology, Gothenburg Sweden

Keywords: A600 wind turbine, dynamic substructuring, decoupling, transmission simulator

Abstract. *Over the last few IMAC conferences, the SEM substructuring focus group's benchmark; the Ampair A600 wind turbine, has been thoroughly studied, at substructure as well as system levels but also by implementation of different substructuring techniques for assembling experimental and/or analytical component models.*

Within the focus group, work dedicated to appropriate interfacing between substructures has furthermore been an area of increased interest. This is notable through the use of the transmission simulator method. This paper draws on that paradigm in studying the end effects on assembled structures of using nominally identical substructure models derived from experimental setups with different levels of mass loading at the interface. Specifically, experimental models for an A600 blade and bracket system attached to dummy masses of different sizes are coupled to an analytical model of the hub. The results are compared to analytical results of the full system.

1 INTRODUCTION

Dynamic substructuring is a mature tool of structural analysis which has been subjected to renewed interest from researchers in recent years [1]. The conceptual idea is that a complex structure can be decomposed into a number of simpler components, called substructures, which interact with each other through compatibility of motion and equilibrium of forces at the interfaces.

The use of substructuring has been integrated into many commercial finite element codes, predominantly by using the Craig-Bampton technique [2]. This technique, while being very successful in accurately reproducing the effect of a substructure using a limited set of modes, requires interface modes that are typically not available for experimentally derived models. Thus, when trying to synthesise experimental models, alternative methods have been proposed, either using only FRFs, such as in the early works by Bishop [3] and Jetmundsen [4], or using free-free modes as described for instance in the book by Meirovitch [5]. Comparisons of FRF and modal techniques have been presented by Allen and Mayes [6] and by DeKlerk et al [1]. The latter paper also presents an extensive expos of the history of dynamic substructuring.

Recently, a series of papers have been published which address two shortcomings of experimental dynamic substructuring: Firstly, any interface which is not readily modelled as rigid runs the risk of causing lockdown when coupling is attempted and secondly that models identified from measurements in free-free conditions are poor representations of the motion of the subcomponent when coupled to the rest of the structure [6, 7, 8]. The technique used to solve this is referred to as the transmission simulator method. It works by adding a well-known structure to the system which is to be experimentally modelled; the effects of this is then removed by adding the negative of the same to the system. By using this process, the modes of the well-known structure - the transmission simulator - are used to describe the motion of the interface between the bodies in a relaxed sense. The method can hence be seen as an extension of using a mass loading of the interface, as was advocated by e.g. Chandler and Tinker [9].

In this paper, the transmission simulator technique in modal form is applied to the Ampair 600W dynamic substructuring benchmark structure [10], a structure which has been studied extensively by the SEM dynamic substructuring focus group. Dynamic substructuring of the Ampair test bed using the transmission simulator technique was studied earlier by e g Rohe [11] and Macknelly [12]. There is also a wiki page for the interested reader [13].

This study aims at investigating the effects of changing the mass of the transmission simulator by using rigid transmission simulators of different weights to one of the blades of the Ampair test bed and subsequently couple the blade model, after removal of the transmission simulator, to a Finite Element model of the hub with two other blades. Three different transmission simulators have been tested, all assumed being rigid and weighing 1.5, 2.5 and 4.5kg, approximately.

2 THEORY

The following short description of dynamic substructuring and transmission simulator theory leans heavily on the work in [1] and [7].

It is commonplace to assume that the motion of a deformable body is described by a set of partial differential equations which, when discretised in the spatial domain, gives rise to ordinary differential equations of the form:

$$\mathbf{M}_p^{(s)}\ddot{\mathbf{q}}^{(s)}(t) + \mathbf{V}_p^{(s)}\dot{\mathbf{q}}^{(s)}(t) + \mathbf{K}_p^{(s)}\mathbf{q}^{(s)}(t) = \mathbf{f}_p^{(s)}(t) + \mathbf{g}_p^{(s)}(t) \tag{1}$$

Here $\mathbf{M}$, $\mathbf{V}$ and $\mathbf{K}$, are referred to as mass, damping and stiffness matrices, respectively. The notation $\mathbf{q}$ stands for displacement, while $\mathbf{f}$ and $\mathbf{g}$ represent external and connection forces, respectively. The superscript s indicates that the equation is valid for substructure number s. The subscript p stands for physical. Assuming that there are h substructures, the equations of motion of all of them may be written in compact block diagonal form as

$$\mathbf{M}_p\ddot{\mathbf{q}}(t) + \mathbf{V}_p\dot{\mathbf{q}}(t) + \mathbf{K}_p\mathbf{q}(t) = \mathbf{f}_p(t) + \mathbf{g}_p(t) \tag{2}$$

Where $\mathbf{M}_p = diag\left(\mathbf{M}_p^{(1)}, ..., \mathbf{M}_p^{(h)}\right)$, $\mathbf{V}_p = diag\left(\mathbf{V}_p^{(1)}, ..., \mathbf{V}_p^{(h)}\right)$, $\mathbf{K}_p = diag\left(\mathbf{K}_p^{(1)}, ..., \mathbf{K}_p^{(h)}\right)$, $\mathbf{q}^T = \left[\left(\mathbf{q}^{(1)}\right)^T, ..., \left(\mathbf{q}^{(h)}\right)^T\right]$, $\mathbf{f}_p^T = \left[\left(\mathbf{f}_p^{(1)}\right)^T, ..., \left(\mathbf{f}_p^{(h)}\right)^T\right]$ and $\mathbf{g}_p^T = \left[\left(\mathbf{g}_p^{(1)}\right)^T, ..., \left(\mathbf{g}_p^{(h)}\right)^T\right]$.

The degrees of freedom of the structures are often replaced by a set of generalized coordinates η obtained by reduction using a matrix $\mathbf{R}$. For an uncoupled compound system described as in (2), the reduction matrix $\mathbf{R}$ consists of the individual reduction matrices $\mathbf{R}^{(s)}$ of the h substructures. Pre-multiplying equation 2 by $\mathbf{R}^T$, the uncoupled compound system can be expressed in the generalized coordinates (where residual terms from the reduction have been suppressed by the pre-multiplication) as:

$$\mathbf{M}\ddot{\eta}(t) + \mathbf{V}\dot{\eta}(t) + \mathbf{K}\eta(t) = \mathbf{f}(t) + \mathbf{g}(t) \tag{3}$$

Where $\mathbf{M} = \mathbf{R}^T\mathbf{M}_p\mathbf{R}, \quad \mathbf{V} = \mathbf{R}^T\mathbf{V}_p\mathbf{R}, \quad \mathbf{K} = \mathbf{R}^T\mathbf{K}_p\mathbf{R}, \quad \mathbf{f} = \mathbf{R}^T\mathbf{f}_p, \quad \mathbf{g} = \mathbf{R}^T\mathbf{g}_p.$

Conditions enforcing compatibility and equilibrium, such that displacements at the interface are equal and interface forces cancel each other out, can be compactly expressed in terms of matrix relations as [1]:

$$\mathbf{E}_p\mathbf{q} = \mathbf{E}_p\mathbf{R}\boldsymbol{\eta} = \mathbf{E}\boldsymbol{\eta} = \mathbf{0} \tag{4}$$

$$\mathbf{L}^T\mathbf{R}^T\mathbf{g}_p = \mathbf{L}^T\mathbf{g} = \mathbf{0} \tag{5}$$

and a unique set of coordinates is

$$\boldsymbol{\eta} = \mathbf{L}\boldsymbol{\xi} \tag{6}$$

where $\mathbf{L} = null(\mathbf{E})$. Using the differential equation with coordinates $\boldsymbol{\xi}$ pre-multiplied with $\mathbf{L}^T$ and the information of the coupling conditions, a coupled system in generalized coordinates can be described by

$$\bar{\mathbf{M}}\ddot{\boldsymbol{\xi}} + \bar{\mathbf{V}}\dot{\boldsymbol{\xi}} + \bar{\mathbf{K}}\boldsymbol{\xi} = \bar{\mathbf{f}} \tag{7}$$

Where $\bar{\mathbf{M}} = \mathbf{L}^T\mathbf{M}\mathbf{L}, \quad \bar{\mathbf{V}} = \mathbf{L}^T\mathbf{V}\mathbf{L}, \quad \bar{\mathbf{K}} = \mathbf{L}^T\mathbf{K}\mathbf{L}, \quad \bar{\mathbf{f}} = \mathbf{L}^T\mathbf{f}.$

The effect of subtracting a system can be achieved by simply adding the negative of that system [7]. That is, adding a system with negative mass, damping and stiffness, to the coupled system in the generalized domain as described above:

$$\begin{bmatrix} \mathbf{M}^{(1)} & 0 \\ 0 & -\mathbf{M}^{(2)} \end{bmatrix} \begin{Bmatrix} \ddot{\boldsymbol{\eta}}^{(1)} \\ \ddot{\boldsymbol{\eta}}^{(2)} \end{Bmatrix} + \begin{bmatrix} \mathbf{V}^{(1)} & 0 \\ 0 & -\mathbf{V}^{(2)} \end{bmatrix} \begin{Bmatrix} \dot{\boldsymbol{\eta}}^{(1)} \\ \dot{\boldsymbol{\eta}}^{(2)} \end{Bmatrix} + \begin{bmatrix} \mathbf{K}^{(1)} & 0 \\ 0 & -\mathbf{K}^{(2)} \end{bmatrix} \begin{Bmatrix} \boldsymbol{\eta}^{(1)} \\ \boldsymbol{\eta}^{(2)} \end{Bmatrix} = \begin{Bmatrix} \mathbf{f}^{(1)} \\ \mathbf{f}^{(2)} \end{Bmatrix} + \begin{Bmatrix} \mathbf{g}^{(1)} \\ \mathbf{g}^{(2)} \end{Bmatrix} \tag{8}$$

In the following, structure 1 is called (tot), indicating the measured coupled structure, and structure 2 is denoted (ts), for the transmission simulator to be subtracted. Earlier, $\boldsymbol{\eta}$ denoted generalized coordinates; it will henceforth specifically denote modal coordinates, such that $\mathbf{R} = \boldsymbol{\Phi}$.

It has been noted that problems occur if it is not possible to estimate the motion of the connection points from the motion of the measurement points. A solution to this was described by Allen et al [7]. The Modal Constraints for Fixture and Subsystem (MCFS) method, enforces the compatibility by constraining the displacement of all measurement points on the transmission simulator to the motion of the analytical transmission simulator model:

$$\mathbf{q}_{(meas)}^{(tot)} = \mathbf{q}_{(meas)}^{(ts)} \tag{9}$$

$\mathbf{q}_{(meas)}^{(ts)}$ and $\mathbf{q}_{(meas)}^{(tot)}$ have the same size since $\mathbf{q}_{(meas)}^{(tot)}$ stands for the measurement points on the part of the total structure that belongs to the transmission simulator and $\mathbf{q}_{(meas)}^{(ts)}$ is the displacement of the analytical model at the points corresponding to the measurements.

In a practical application, Allen et al advocate more measurement points on the transmission simulator than transmission simulator modes to be used, leaving some coupling conditions redundant. To ensure that this does not cause lockdown phenomena, the constraints are applied on the modal coordinates of the transmission simulator and their orthogonal projection onto the total systems' motion. Expressed mathematically:

$$\boldsymbol{\eta}^{(ts)} = {\boldsymbol{\Phi}_{(meas)}^{(ts)}}^{+} \mathbf{q}_{(meas)}^{(ts)} = {\boldsymbol{\Phi}_{(meas)}^{(ts)}}^{+} \mathbf{q}_{(meas)}^{(tot)} = {\boldsymbol{\Phi}_{(meas)}^{(ts)}}^{+} \boldsymbol{\Phi}_{(meas)}^{(tot)} \boldsymbol{\eta}^{(tot)} \tag{10}$$

Here, there are as many equations as transmission simulator modes. If a lower number of modes than measurement points are considered, the constraints do not enforce strict equality of the displacements but the compatibility condition will be fulfilled in a relaxed, least-square sense. In matrix notation the full coupling condition becomes:

$$\begin{aligned} {\boldsymbol{\Phi}_{(meas)}^{(ts)}}^{+} \begin{bmatrix} \mathbf{I} & -\mathbf{I} \end{bmatrix} \begin{Bmatrix} \mathbf{q}_{(meas)}^{(tot)} \\ \mathbf{q}_{(meas)}^{(ts)} \end{Bmatrix} &= {\boldsymbol{\Phi}_{(meas)}^{(ts)}}^{+} \begin{bmatrix} \mathbf{I} & -\mathbf{I} \end{bmatrix} \begin{bmatrix} \boldsymbol{\Phi}_{(meas)}^{(tot)} & \mathbf{0} \\ \mathbf{0} & \boldsymbol{\Phi}_{(meas)}^{(ts)} \end{bmatrix} \begin{Bmatrix} \boldsymbol{\eta}^{(tot)} \\ \boldsymbol{\eta}^{(ts)} \end{Bmatrix} \\ &= \begin{bmatrix} {\boldsymbol{\Phi}_{(meas)}^{(ts)}}^{+} \boldsymbol{\Phi}_{(meas)}^{(tot)} & -\mathbf{I} \end{bmatrix} \begin{Bmatrix} \boldsymbol{\eta}^{(tot)} \\ \boldsymbol{\eta}^{(ts)} \end{Bmatrix} = \tilde{\mathbf{E}}_{MCFS} \begin{Bmatrix} \boldsymbol{\eta}^{(tot)} \\ \boldsymbol{\eta}^{(ts)} \end{Bmatrix} = \mathbf{0} \end{aligned} \tag{11}$$

and $\tilde{\mathbf{L}}_{MCFS} = null(\tilde{\mathbf{E}}_{MCFS})$. Here, the first identity matrix $\mathbf{I}$ has as many rows and columns as there are measurement points whereas the second has as many rows and columns as there are modes of the transmission simulator.

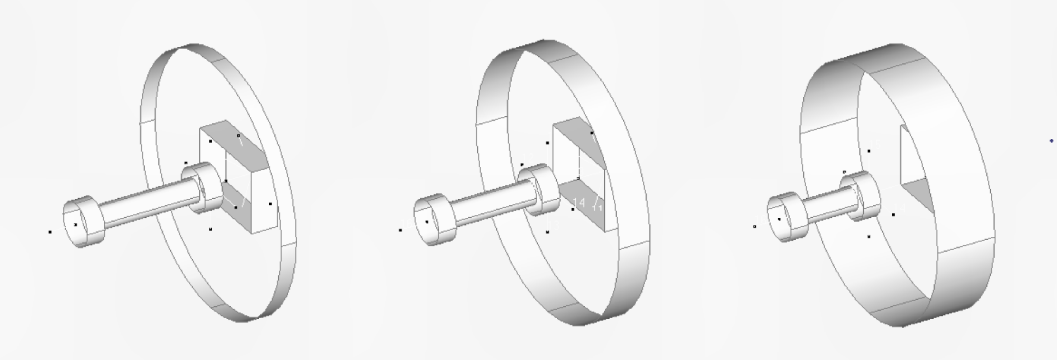


Figure 1: Models of the three transmission simulators used. The mass of the models is respectively 1.36, 2.43 and 4.34kg. The discs are made of steel and have a diameter of 0.14m.

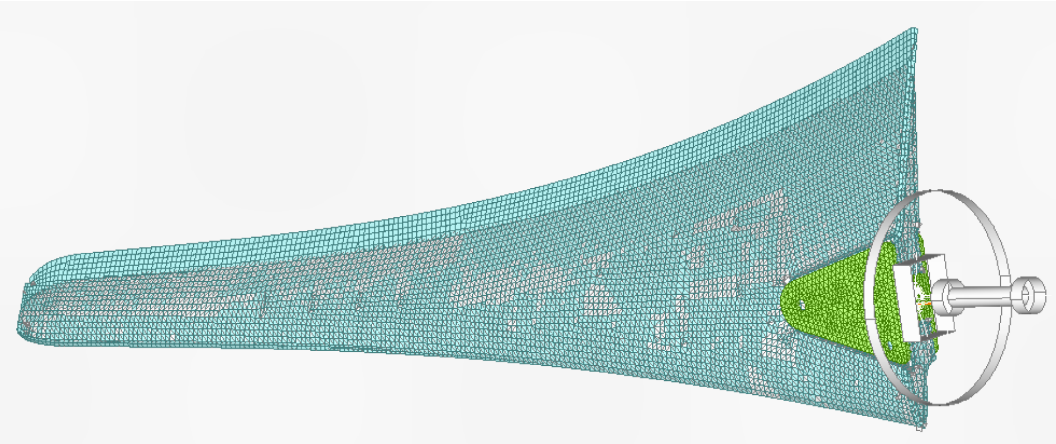


Figure 2: FE model of blade with transmission simulator of 1.36kg attached.

An advantage of the MCFS is that it is robust against measurement errors. Moreover, only translational measurements of the transmission simulator are necessary, circumventing the problem of trying to measure rotational degrees of freedom. Also, no forces or moments on the connection points need to be applied. The methods described in this section are implemented in a toolbox for Matlab available at the Matlab file central [14].

3 FINITE ELEMENT MODELS

A number of Finite Element models have been used in this study: A model of the transmission simulator has been used in the manner described in the theory section above. Further, a model of the blade with a transmission simulator attached was used to decide on an adequate sensor set for the measurements. A two-bladed hub model was used to which the experimentally derived substructures were coupled. Finally, two versions of the fully assembled system were used for comparison.

The transmission simulators were modelled using beam elements with different cross sec-

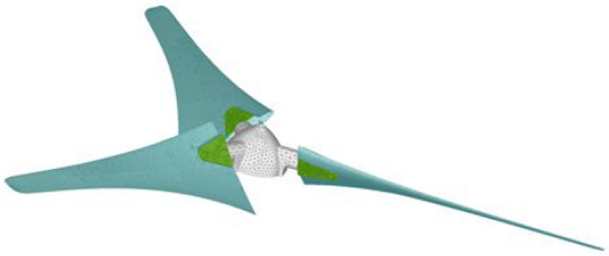


Figure 3: FE model of hub with three blades attached. The same model but with only two blades attached was the target model to which the experimentally derived blades were attached.

tions. The three models used can be seen in figure 1. Rigid elements were used to map the motion of the beam nodes to the surfaces of the transmission simulator. These models were used to remove the effect of the respective transmission simulators. In all substructuring cases, the transmission simulators were assumed rigid, that is, only six rigid body modes were considered.

Finite Element models of the blade with the transmission simulators attached were built for deciding how many sensors were needed to come up with reliable results when decoupling the transmission simulator. A numerical study, detailed in the next section, concluded that five triaxial measurement locations was sufficient to accurately describe the motion of the coupling point at the interface between the transmission simulator and the blade. The model with the 1.36kg transmission simulator is shown in figure 2.

The final Finite Element models of this study are models of the compound system. First, a hub with three attached blades, see figure 3, is used for comparison. The experimentally derived blades are coupled to a two-bladed hub, which has furthermore been augmented by the addition of rigid body elements to create one coupling node. For a fair comparison, similar rigid body elements were added to a version of the three-bladed hub model.

4 NUMERICAL PRESTUDIES

Before conducting the experiments, a numerical study of the sensor placement was performed using a transmission simulator with 1/100 of the mass of the lightest transmission simulator used in the actual tests. The underlying assumption is that this will ensure that the effect of the transmission simulator will be negligible, such that if removed properly the resulting model will behave as the FE model of the blade without a transmission simulator. Six different sensor configurations were compared, and a set using five triaxial sensors was chosen, see figure 4.

The weights of the transmission simulators used in the experiments were based on a second pre-study. The effect on the natural frequencies is shown in figure 5. Transmission simulators weighing 10 and 100kg were also tested, but suffered numerical difficulties, limiting the scope to approximately 5kg.

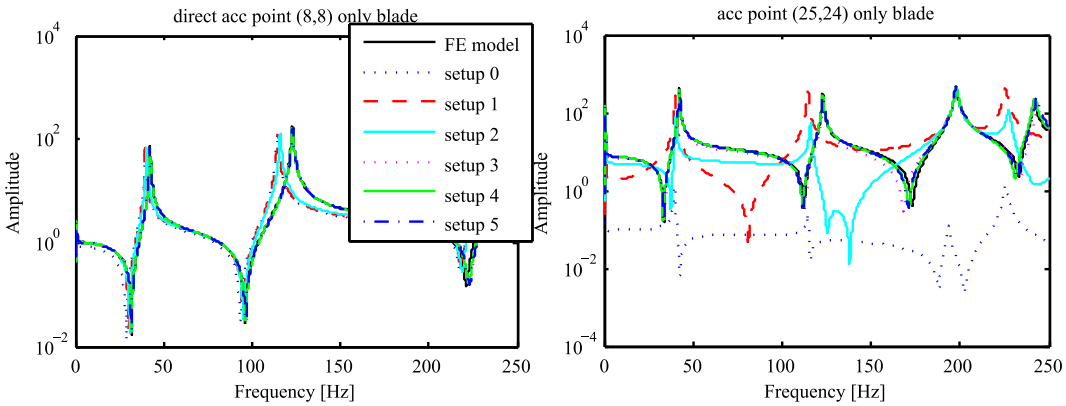


Figure 4: Comparison of different sensor layouts for the transmission simulator. Numerical results using the blade and transmission simulator model with a transmission simulator weighing only 13.6g. The sensor configurations are: FE blade - only the blade without a transmission simulator. 0 - 9 uniaxial sensors positioned in such a way that the the spin rigid body mode of the transmission simulator is not observable. 1 - as 0 but with an extra uniaxial sensor to ensure observability. 2, 3 and 4 - using 4 tri- and 5 uniaxial, 5 tri- and 4 uniaxial and only 4 triaxial sensors, respectively. 5 - the chosen set, using 5 triaxial sensors, one on each surface of the cube and one at the tip of the bolt. To the left: Direct accelerance at drive point of measurement. To the right: Accelerance from input at one rotational dof at coupling point to another.

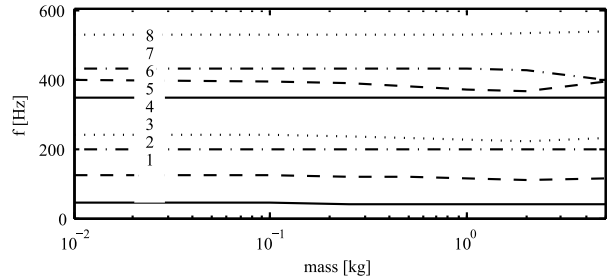


Figure 5: Comparison of the effects of the transmission simulator weight on the eigenfrequency of the decoupled blade. Results from the numerical study.

5 EXPERIMENTS

The measurements were performed in Växjö, Sweden, in the vibration laboratory at the Linnaeus University. One triaxial accelerometer was mounted at the middle of each surface of the rectangular plate belonging to the transmission simulator, having normal directions in the y-z-plane, see figure 6. Furthermore, one triaxial accelerometer was mounted on the top of the bolt head. Hence, 15 degrees-of-freedom were used to describe the response of the system at the transmission simulator. The system was excited using a modal shaker. To firmly attach the impedance head used, the discs used as weights on the transmission simulator were slightly modified by cutting out an angle into which the impedance head was attached. The degree-of-freedom associated with the impedance head was only used to enable mass normalization of the mode shapes and was not a part of the modal vectors used in the substructure decoupling process. The assembled structure was hanged in a steel wire at the bolt head nut. This suspension system may have added stiffness and/or damping to an assumed free-free structure.

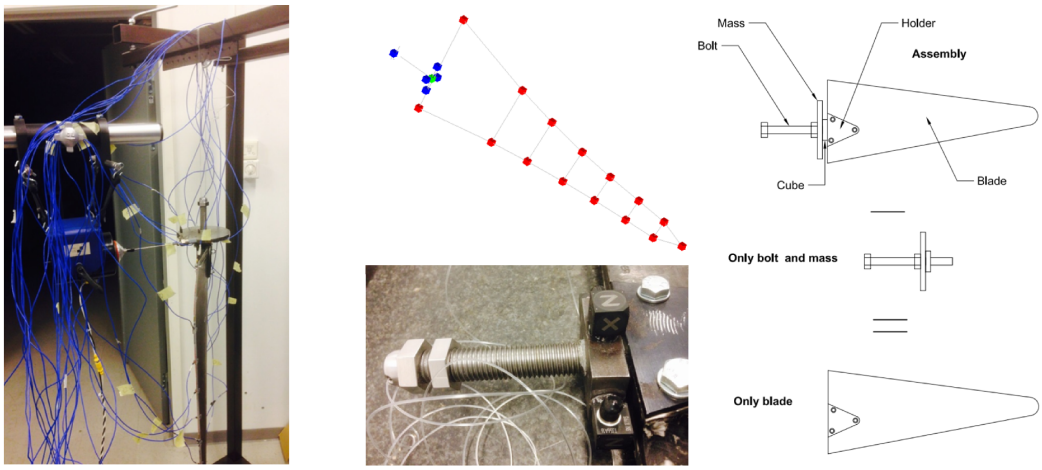


Figure 6: Details of experimental study. Left: Blade with transmission simulator suspended for vibration testing. Center, top: Schematic view of sensor locations, where blue squares indicate triaxial sensors on the transmission simulator, red indicate uniaxial sensors measuring perpendicular to the blade and the green square is the virtual coupling point where the system is attached to the hub using six degrees of freedom. Center, bottom: Detail of the transmission simulator without weight, showing the position of the triaxial sensors. Right: Schematic description of the construction of the transmission simulator used.

	1 kg			2 kg			4kg		
	f_{FE}	f_{meas}	MAC	f_{FE}	f_{meas}	MAC	f_{FE}	f_{meas}	MAC
1st bending	38.2	34.4	0.97	37.3	33.6	0.97	36.1	32.0	0.97
2nd bending	110.7	101.3	0.96	108.4	98.6	0.97	104.7	94.3	0.97
1st torsion	192.9	163.0	0.98	191.6	162.4	0.98	190.6	163.1	0.98
3d bending	218.7	194.2	0.93	215.3	189.4	0.93	209.1	180.7	0.85
2nd torsion	330.6	275.2	0.91	326.5	269.4	0.91	321.0	249.7	0.64

Table 1: Comparison of the first elastic natural frequencies, in [Hz], and the corresponding MAC values of the blade and transmission simulators stemming from FEM and experiments.

6 RESULTS

The study was performed in three steps: First, measurements of natural frequencies and mode shapes were performed of the blade with transmission simulators with different weights attached, see table 1. Second, the transmission simulators were decoupled from the blade using the technique described in the theory section, the results of which can be seen in table 2. It should be noted here that this process caused one higher frequency modes of each system to exhibit negative mass, a problem which has been reported to occur. There are also methods for dealing with these non-physical modes in the literature [15]. Since the negative mass occured outside the frequency range of interest, it was not concerned further in this paper. The final comparison is performed when the blade is coupled to an FE model of a two-bladed hub, the results of which is presented in table 3.

		1 kg			2 kg			4kg		
	f_{FE}	f_{meas}	MAC		f_{meas}	MAC		f_{meas}	MAC	
1st bending	42.4	38.7	0.22	0.98	39.3	0.24	0.98	36.2	0.25	0.98
2nd bending	122.8	111.3	0.11	0.99	115.6	0.14	0.99	104.0	0.15	0.96
1st torsion	197.7	169.1	0.91	0.95	163.1	0.73	0.96	163.2	0.67	0.96
3d bending	241.6	207.3	0.03	0.73	237.0	0.06	0.91	205.8	0.11	0.85
2nd torsion	347.2	307.0	0.78	0.90	285.8	0.66	0.81	260.0	0.46	0.65

Table 2: Comparison of elastic natural frequencies of experimental models when the transmission simulators have been removed through decoupling. Two MAC values are presented: The first MAC column contains the values when the virtual coupling point is included, while the latter considers only the measurement locations on the blade. Frequencies are presented in Hz.

FE		1 kg		2 kg		4kg	
f_1	f_2	f_{meas}	MAC	f_{meas}	MAC	f_{meas}	MAC
22.4	22.5	23.9	0.63	23.9	0.63	23.9	0.63
28.7	28.7	29.6	0.87	29.7	0.86	29.8	0.84
28.7	28.8	65.3	0.30	62.2	0.35	61.9	0.36
77.3	77.6	77.7	0.61	77.8	0.66	77.8	0.67
80.3	80.3	82.3	0.73	81.9	0.82	82.1	0.83

Table 3: Comparison of elastic modes of the fully coupled system. The two FE models in the table differ in that the second column has been modified by rigid elements in one blade to mimic the effect of a one-node connection as in the substructured cases. Frequencies in Hz. MAC values have been calculated with respect to the second FE model.

7 CONCLUSIONS

A study of the effects of interface loading in dynamic substructuring has been performed. It was found that the sensor placement on the transmission simulator, and specifically the observability of the modes of the transmission simulator used, is of great importance. Comparing with FE models, it seems that the virtual coupling point is still suffering from difficulties, which has also been stated in literature previously. It is difficult to draw conclusions on which transmission simulator was better; the results are comparable.

8 ACKNOWLEDGEMENTS

The authors would like to take this opportunity to acknowledge the contribution by Mr. Ahmed Akaysee and Mr. Marek Wronski, who worked with design and preliminary measurements during the work with their MSc thesis at the Linnaeus University during the spring of 2014. The Finite Element models used have been prepared by Mr. Mladen Gibanica during his MSc thesis work at Chalmers during the spring of 2013.

REFERENCES

[1] Dennis de Klerk, Daniel J. Rixen, and Sven N. Voormeeren. General framework for dynamic substructuring: History, review and classification of techniques. *AIAA Journal*, 46(5):1169–1181, 2008.

[2] R R Craig Jr and M C C Bampton. Coupling of substructures for dynamic analyses. *AIAA Journal*, 6:1313–1319, 1968.

[3] R. E. D. Bishop and D. C. Johnson. *The Mechanics of Vibration*. Cambridge University Press, 1960.

[4] Bjorn Jetmundsen, Richard L. Bielawa, and William G. Flannelly. Generalized frequency domain substructure synthesis. *Journal of the American Helicopter Society*, 33(1):55–54, 1988.

[5] Leonard Meirovitch. *Computational Methods in Structural Dynamics*. Sijthoff & Noordhoff, 1980.

[6] Matthew S. Allen and Randall L. Mayes. Comparison of frf and modal methods for combining experimental and analytical substructures. *Conference Proceedings of the Society for Experimental Mechanics Series. 25th IMAC, A Conference on Structural Dynamics*, 2007.

[7] Matthew S. Allen, Randy L. Mayes, and Elizabeth J. Bergman. Experimental modal substructuring to couple and uncouple substructures with flexible fixtures and multi-point connections. *Journal of Sound and Vibration*, 329:4891–4906, 2010.

[8] Randy L. Mayes. Tutorial on experimental dynamic substructuring using the transmission simulator method. *Conference Proceedings of the Society for Experimental Mechanics Series. 30th IMAC, A Conference on Structural Dynamics*, pages 1–9, 2012.

[9] Kathy O. Chandler and Michael L. Tinker. A general mass-additive method for component mode synthesis. *AIAA 38th Structures, Structural Dynamics and Materials Conference*, 1997.

[10] Randy L. Mayes. An introduction to the sem substructures focus group test bed - the ampair 600 wind turbine. *Conference Proceedings of the Society for Experimental Mechanics Series. 30th IMAC, A Conference on Structural Dynamics*, pages 61–71, 2012.

[11] Daniel P. Rohe. Validation of experimental-analytical substructuring using the transmission simulator method. Master's thesis, 2012.

[12] David Macknelly, Mohsin Nurbhai, and Nicholas Monk. Additional modal testing of turbine blades and the application of transmission simulator substructuring methodology for coupling. *Conference Proceedings of the Society for Experimental Mechanics Series. 31th IMAC, A Conference on Structural Dynamics*, 2013.

[13] Sem substructuring wiki, `http://substructure.engr.wisc.edu/substwiki/`, June 2013.

[14] Modal substructuring (cms) and modal substructure modification, http://www.mathworks.com/matlabcentral/fileexchange/28063-modal-substructuring--cms--and-modal-substructure-modification, June 2013.

[15] Randy L. Mayes, Mathew S. Allen, and Daniel C. Kammer. Correcting indefinite mass matrices due to substructure uncoupling. *Journal of Sound and Vibration*, 332:5856–5866, 2013.

Gresimo (MS12)

International Conference on Engineering Vibration
Ljubljana, Slovenia, 7-10 September 2015

DYNAMIC RESPONSE OF LAMINATED STRUCTURES USING A REFINED ZIGZAG THEORY (RZT) SHELL ELEMENT

Alessandra Treviso*[1,2], Domenico Mundo[2], Michel Tournour[1]

[1]Siemens Industry Software nv, Leuven, Belgium
alessandra.treviso@siemens.com
michel.tournour@siemens.com
[2]University of Calabria – Department of Mechanical, Energy and Management Engineering, Rende, Italy
domenico.mundo@unical.it

Keywords: laminates, shell, zigzag theories

Abstract. *Shell-like structures are common in many engineering applications such as aerospace structures, civil constructions and automotive components. In all these fields, composite materials and laminated sandwich are used as a viable lightweight alternative to standard engineering materials.*
Simulations of multilayer structures often require explicit modelling in the through-the-thickness direction to account for properties discontinuities. This is especially true in sandwich structures, where stiff layers are interleaved with soft viscoelastic layers for vibration attenuation. However, the use of solid elements significantly increases the time necessary to build and analyse the models.
Reduction of both modelling and computational costs can be achieved by the use of equivalents single layer models. However, equivalent single layer theories fail to represent the piecewise distribution of displacements in the through-the-thickness direction. This is where Zigzag Theories *find application. Zigzag theories, which were first proposed by Di Sciuva and Averill, combine an equivalent single layer approach with a linear piecewise function of the thickness coordinate.*
Di Sciuva and Averill zigzag functions presented few shortcomings, such as the vanishing of reaction forces at clamps and the layer-dependent function definition. These drawbacks are overcome by the Refined Zigzag Theory *proposed by Tessler.*
Tessler zigzag formulation is hereby used in the framework of a shell element for vibration analysis of standard laminates and laminated sandwich structures.
The main objective of the paper is to show that zigzag refined elements can be effectively used to reduce the computational cost of simulations within a reasonable level of accuracy.

1. Introduction

The use of composite materials and multi-layer laminated structures has increased in the last years due to increasingly stringent requirements on CO_2 emissions and fuel consumption. This trend has motivated much effort to search for new modelling strategies to tackle the complexity of these new materials. The biggest difficulty to deal with is the variation of material properties in the thickness direction which causes the rise of transverse shear stresses at the layers' interface due to properties mismatch. When the thickness of the laminates is low, the Classical Lamination Theory (CLT), based on the same hypotheses of the Classical Plate Theory [1], can be effectively used. In thick laminates, however, the transverse shear stresses are no longer negligible and refinements are required to truly capture the structure behaviour [2].

A first improvement is attained by relaxing the third hypothesis of the Classical Plate Theory, therefore allowing for the independent rotation of the plate transverse section. This theory is known as the *First Order Shear Deformation Theory* (FSDT), and its formulation was obtained by Reissner and Mindlin [3, 4]. The resulting stresses are generally multiplied by a shear correction factor which compensates the linear distribution of the shear stresses in the thickness direction eventually giving an energetically equivalent stress distribution. Further refinements of the CLT have been proposed through the years which use higher order expansions of the axial displacement in the transverse direction in order to increase the accuracy. Among the others, the Reddy's Third Order Theory [5] had a lot of success, but second-order and higher than the third order formulations have been equally proposed [6].

The abovementioned models all belong to the family of the *Equivalent Single Layer Theories* (ESLT), which represent the multi-layer structure as an equivalent homogenised single layer structure. All of them share the underlying assumption that displacements are continuous at layers' interface, according to the expansion order used [7]. Such assumption however is in contrast with the elasticity solution obtained by Pagano, which shows that the axial displacements are actually piecewise in the thickness direction [8]. Such difference has an impact on thick laminates because it prevents from a realistic description of the laminate response with undesirable consequences. For example, free edge transverse stresses are responsible for delamination [9] and in the case of viscoelastic treatment, is the deformation in shear which contributes the most to the energy dissipation [10-12].

An easy though expensive way to overcome these issues is to use 3D models to accurately describe the full behaviour of the structure. However, for complex geometries this may result in long computations that are not affordable in today's industrial environment. In response to the need of cheaper model two modelling strategies have been developed: *layerwise formulations* and *zigzag theories*.

The first one leads to a quasi-3D description of the structure, using 2D elements for the in-plane behaviour, employing one layer per physical ply, which are then linked by 1D elements which provide information on the through-the-thickness response. One of the first layerwise formulations was proposed by Reddy [13]. A lot of freedom is left to the engineer in the choice of the in-plane and through-the-thickness elements, leading to the desired level of accuracy. Nonetheless, the number of total degrees of freedom will be proportional to the number of physical layers, making this approach unfeasible for thicker structures.

The second method starts from an Equivalent Single Layer Theory and adds a piecewise function in the thickness coordinate to the in-plane displacements [14]. The main advantage is that the number of degrees of freedom no longer depends on the number of layers.

In the present paper the Refined Zigzag Theory (RZT) first proposed by Tessler [15] is used to develop a C^0-continuous shell element for the dynamic simulation of flat and curved sandwich structures.

2. The refined Zigzag Theory

The investigation on Zigzag theories were first addressed by Di Sciuva [16] who proposed the refinement of a FSDT with a linear [17] and a cubic [18, 19] piecewise function. The added kinematic is determined by imposing the continuity of transverse shear stresses in the through-the-thickness direction. The resulting model has a number of kinematic unknowns that is fixed in number and does not depend on the number of layers of the structure. Shortly after, Averill proposed a variation of Di Sciuva's model. His model stems from Timoshenko FSDT theory and adds a kinematic variable for the zigzag contribution together with a penalty term in the variational formulation.

Both Di Sciuva and Averill models suffer from a major drawback, that is the inability to model clamped boundary conditions since the integration of transverse shear stresses over the cross section at clamps differ from the resultant obtained by the equilibrium equations.

It is also worth to mention the development of a Zigzag function by Murakami [21] who proposed a geometry-based model. The slope of the piecewise function in each layer is a function of the layer thickness and the sign changes at every interface. Murakami derived his function for multi-layered structures with periodic geometry, i.e. layer thickness, and material properties and warns on the accuracy of his model for other types of structures.

The Refined Zigzag Theory (RZT) proposed by Tessler overcomes the abovementioned shortcomings and is suitable for both periodic and non-periodic structures, thus including sandwiches with thick soft cores [22].

The RZT stems from a FSDT of the form:

$$\boldsymbol{u_1}(\boldsymbol{x},\boldsymbol{y},\boldsymbol{z}) = \boldsymbol{u}(\boldsymbol{x},\boldsymbol{y}) + \boldsymbol{z}\boldsymbol{\theta_1}(\boldsymbol{x},\boldsymbol{y}) \quad \textbf{(Eq. 1)}$$

$$\boldsymbol{u_2}(\boldsymbol{x},\boldsymbol{y},\boldsymbol{z}) = \boldsymbol{v}(\boldsymbol{x},\boldsymbol{y}) + \boldsymbol{z}\boldsymbol{\theta_2}(\boldsymbol{x},\boldsymbol{y}) \quad \textbf{(Eq. 2)}$$

$$\boldsymbol{u_z}(\boldsymbol{x},\boldsymbol{y},\boldsymbol{z}) = \boldsymbol{w}(\boldsymbol{x},\boldsymbol{y}) \quad \textbf{(Eq. 3)}$$

The quantities in Eq. 1-3 are defined as follow:

$\boldsymbol{u},\boldsymbol{v} = uniform\ through-the-thicknes\ displacement\ in\ the\ x\ and\ y\ direction\ respectively$

$\boldsymbol{\theta_x}, \boldsymbol{\theta_y}$ = *average bending rotation of the normal to the mid-plane about the +y and –x axes*

$\boldsymbol{w} = transverse\ deflection$

A zigzag function is then superposed to the in-plane displacement to obtain a refined kinematic formulation.

In particular, the RZT is obtained by imposing the vanishing of the transverse shear stresses at the top and bottom layer, as prescribed by the elasticity theory, unlike Di Sciuva and Averill models where vanishing was imposed within the laminate, thus creating a dependency issue between the chosen layer and the final form assumed by the zigzag function. Unlike Murakami zigzag function, the RZT is based on both geometry considerations and material properties enabling a more physical description of the zigzag effect occurring within multi layered structures.

The RZT reads [23]

$$\boldsymbol{u_1^{(k)}}(\boldsymbol{x},\boldsymbol{y},\boldsymbol{z}) = \boldsymbol{u}(\boldsymbol{x},\boldsymbol{y}) + \boldsymbol{z}\boldsymbol{\theta_1}(\boldsymbol{x},\boldsymbol{y}) + \boldsymbol{\phi_1^{(k)}}(\boldsymbol{z})\,\boldsymbol{\psi_1}(\boldsymbol{x},\boldsymbol{y}) \quad \textbf{(Eq. 4)}$$

$$\boldsymbol{u_2^{(k)}}(\boldsymbol{x},\boldsymbol{y},\boldsymbol{z}) = \boldsymbol{v}(\boldsymbol{x},\boldsymbol{y}) + \boldsymbol{z}\boldsymbol{\theta_2}(\boldsymbol{x},\boldsymbol{y}) + \boldsymbol{\phi_2^{(k)}}(\boldsymbol{z})\,\boldsymbol{\psi_2}(\boldsymbol{x},\boldsymbol{y}) \quad \textbf{(Eq. 5)}$$

$$\boldsymbol{u_z}(\boldsymbol{x},\boldsymbol{y},\boldsymbol{z}) = \boldsymbol{w}(\boldsymbol{x},\boldsymbol{y}) \quad \textbf{(Eq. 6)}$$

The superscript *k* refers to layer quantities. The additional kinematic variables appearing in Eq 4-5, ψ_x and ψ_y, represent the zigzag contribution to the overall rotation of the transverse normals about the y and x axes respectively; the two functions, $\phi_x^{(k)}(z)$ and $\phi_y^{(k)}(z)$, define their variation in the thickness direction in a piecewise manner. They are defined in terms of the interfacial displacements as

$$\phi_1^{(k)}(z) \equiv \frac{1}{2}\left(1 - \xi^{(k)}\right)u^{(k-1)} + \frac{1}{2}\left(1 - \xi^{(k)}\right)u^{(k)} \quad \textbf{(Eq. 7)}$$

$$\phi_2^{(k)}(z) \equiv \frac{1}{2}\left(1 - \xi^{(k)}\right)v^{(k-1)} + \frac{1}{2}\left(1 - \xi^{(k)}\right)v^{(k)} \quad \textbf{(Eq. 8)}$$

being $\xi^{(k)}$ a local non-dimensional coordinate whose origin lies on the *k-th* layer mid-plane and defined as

$$\xi^{(k)} = \frac{z - (z^{(k-1)} + h^{(k)})}{h^{(k)}} \quad \textbf{(Eq. 9)}$$

From the above equations and by imposing that the transverse shear stresses are zero at the top and bottom layers it is possible to define the functions

$$\beta_1^{(k)} \equiv \phi_{1,z}^{(k)} = \frac{u^{(k)} - u^{(k-1)}}{2h^{(k)}} \quad \textbf{(Eq. 10)}$$

$$\beta_2^{(k)} \equiv \phi_{2,z}^{(k)} = \frac{v^{(k)} - v^{(k-1)}}{2h^{(k)}} \quad \textbf{(Eq. 11)}$$

Which represent the slopes of the zigzag function. As the transverse shear stresses on the top and bottom layer vanish, so does the zigzag function. A direct consequence is that integration of Eq.10-11 over the thickness of the laminate returns zero.

By combination of the above equations with the laminate constitutive relation it is possible to write the slope $\beta^{(k)}$ as a function of the thickness and of the transverse shear moduli of the *k-th* layer.

$$\beta_1^{(k)} = \frac{G_1}{Q_{11}^{(k)} - 1} \quad \textbf{(Eq. 12)}$$

$$\beta_2^{(k)} = \frac{G_2}{Q_{22}^{(k)} - 1} \quad \textbf{(Eq. 13)}$$

$G_1$and G_2 are constant and they are obtained by integration of Eq. 12-13 over the thickness and remembering that the integral of $\beta^{(k)}$ on *z* is zero.

$$G_1 = \frac{1}{h}\sum_{k=1}^{N}\frac{h^{(k)}}{Q_{11}^{(k)}} \quad \textbf{(Eq. 14)}$$

$$G_2 = \frac{1}{h}\sum_{k=1}^{N}\frac{h^{(k)}}{Q_{22}^{(k)}} \quad \textbf{(Eq. 15)}$$

As Eq.14-15 show, the slope of the zigzag function depends on both the thickness of the *k-th* layer and the lamina stiffness coefficients.

The abovementioned theory was integrated into a pre-existing Mindlin shell element by addition of the pertaining degrees of freedoms. The implementation has been performed in LMS Samtech Samcef.

To test the validity of the new element, two test cases have been considered: a flat sandwich panel and a curved sandwich laminate. The following paragraphs will detail the geometry and material properties of the selected cases and will provide the results of modal analysis.

3. Undamped Free vibration of flat sandwich panels

The first case considered is a flat sandwich panel (Fig. 1). The face-sheets are made of a 2-layer carbon/epoxy laminate while the core is made of PVC. Two different lamination sequences are chosen. Table 1-2 summarise material properties, geometric and lamination parameters respectively.

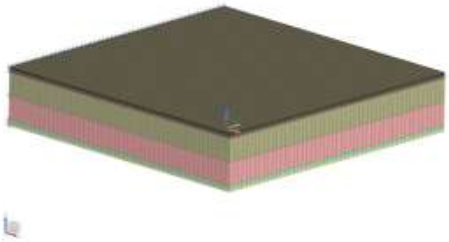


Figure 1

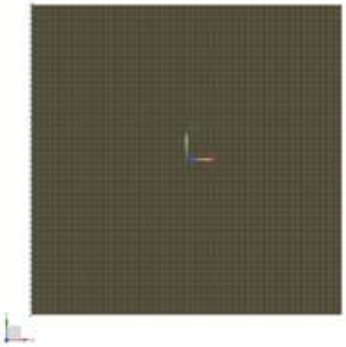


Figure 2

Materials properties	
Face sheets	***Core***
E_1= 157.9 GPa, E_2= 9.584 GPa, E_3= 9.584 GPa	E=104 Mpa
G_{12}= 5.930 GPa, G_{23}= 3.227 GPa, G_{13}= 5.930 GPa	G=40 Mpa
ν_{12}= ν_{13} = 0.32, ν_{23} = 0.49	ν=0.3
ρ = 1600 kg/m^3	ρ = 1350 kg/m^3

Table 1

Geometry and Layup
L=0.1 m
t_f = 0.001 m
t_c = 0.016 m
$Layup_1$ = [0/90/Core/90/0]
$Layup_2$ = [30/-45/Core/45/-30]

Table 2

The panel is clamped on one side only. The choice of fixed boundary conditions relates to the major drawbacks that it caused in previously proposed zigzag theories and asymmetry is to emphasise possible modes coupling and its handling by the zigzag function.

The eigenfrequencies obtained with the Zigzag shell are then compared to those obtained using a 3D model and a standard shell model. Both the standard shell and 3D models were built in NX Nastran using the NX Laminate module. In Samcef and NX alike, basic draping operations are performed to account for eventual distortions of fibres from the nominal orientation which will affect the overall stiffness and strength properties of the manufactured part [24].

Table 3 compares the eigenfrequencies obtained using the different modelling strategies outlined above.

$Layup_1$ =[30/-45/Core/45/30]					
Mode	***NX Laminated shell***	***Error (%)***	***Samcef Zigzag model***	***Error (%)***	***NX 3D model***
1	415.9	6.0	443.9	-0.3	442.5
2	824.3	3.3	858.1	-0.7	852.4
3	1244.0	10.1	1393.0	-0.7	1383.0
4	1522.5	10.8	1718.0	-0.7	1706.0
5	1655.1	5.8	1769.0	-0.7	1757.0
6	2095.1	13.2	2434.0	-0.8	2414.0
7	2144.5	15.2	2567.0	-1.5	2528.0
8	2301.1	13.2	2745.0	-3.6	2650.0
9	2453.6	8.8	2824.0	-5.0	2690.0
10	2721.8	2.5	2873.0	-2.9	2791.0
11	279.2	16.7	3397.0	-1.3	3354.0

12	2849.5	16.9	3473.0	-1.3	3428.0
13	3014.9	22.0	3944.0	-2.1	3864.0
14	3126.4	20.3	3997.0	-1.9	3923.0
15	3291.1	17.9	4173.0	-4.1	4007.0

Table 3

A further check can be performed on the mode shapes. In particular, it is interesting to look at the correlation between each of the shell models and the 3D model. Correlation is measured through the *Modal Assurance Criterion* (MAC) [25]. The MAC is generally used to compare experimental and numerical mode shapes but it can be used to correlate different numerical model as well, as in this case. The MAC is a scalar value obtained by

$$MAC\ (N_1, N_2) = \left| \sum_{j=1}^{N} (\psi_{N_1})_j \, (\psi_{N_2})_j^* \right|^2 \Bigg/ \left\{ \left(\sum_{j=1}^{N} (\psi_{N_1})_j \, (\psi_{N_1})_j^* \right) \cdot \left(\sum_{j=1}^{N} (\psi_{N_2})_j \, (\psi_{N_2})_j^* \right) \right\} \qquad \textbf{(Eq. 16)}$$

Where the subscripts N_1 and N_2 refer to the first and the second numerical model to compare and the index j runs over the number of normal modes.
MAC values vary between 0 and 1 with the following meaning:

- MAC=0: the two modes do not correlate, i.e. they do not correspond to each other
- MAC=1: the two modes are identical.

The result of the correlation operation is generally represented in matrix form, a diagonal matrix meaning in general a good correlation between the models. However, obtaining exactly unit values for all the modes is difficult because of intrinsic differences between the models that are to be correlated and/or because of the uncertainties involved in the experimental measures; therefore, it is general practice to define a threshold value above which the correlation is regarded as good. Most textbooks report this value to be MAC=0.8 [26]. The pictures (Figure 3 and 4) below show the MAC matrices for the *Zigzag Shell – 3D Model* and the *NX Laminated Shell - 3D Model* respectively.

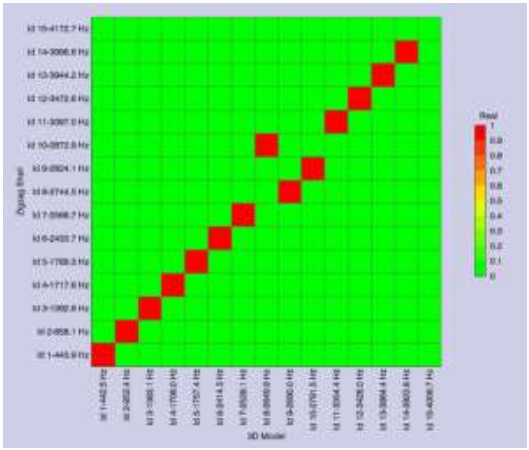


Figure 3

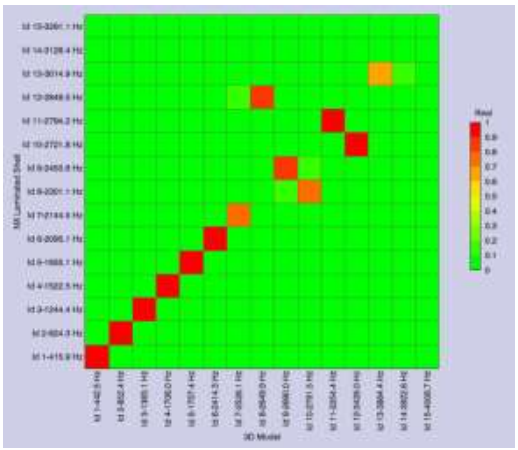


Figure 4

The analysis of the results highlights in general a better performance of the zigzag shell in predicting the mode shapes, even though modes 8, 9 and 10 do not show a one-to-one correspondence. A closer look at the frequencies, however, reveals that those three modes in particular are closely spaced and in such circumstances the MAC may not give reliable results [27]. Not only Figure 4 shows a greater scatter around the diagonal but modes 7, 8 and 13 have a MAC below the aforementioned threshold and modes 14 and 15 have a zero MAC.

4. Undamped Free vibration of curved sandwich panels

Modal analysis has been performed also on a curved sandwich panel, as shown in Figure 3-4.



Figure 5

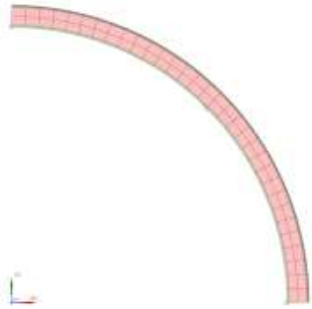


Figure 6

Each layer is made of Carbon/Epoxy and the core of PVC, whose material properties are reported in Table 1. The lamination scheme for the face sheets are the same as for the flat panel. The geometric parameters are described in Table 4. The panel is fixed on all sides.

Draping simulations are automatically run during the laminate definition in both Samcef and NX. Analysis of the manufacturing simulations shows that the curvature of the panel introduces a slight deviation in fibre orientation with respect to the nominal angle. The actual angle is taken into account during the stiffness matrix calculation in both solvers and is fully compatible with the proposed zigzag element.

Table 5 shows the eigenvalues for the generic laminate.

Results show that despite the difference between the standard shell and the zigzag element is not constant, the use of the zigzag shell systematically reduces the error compared to the 3D model, especially at higher frequencies.

Layup$_1$ =[30/-45/Core/45/30]					
Mode	***NX Laminated shell***	***Error (%)***	***Samcef Zigzag model***	***Error (%)***	***NX 3D model***
1	972.90	3.48	1007.04	0.10	1008.00
2	983.00	2.48	1015.62	-0.76	1008.00
3	1193.00	4.41	1284.04	3.00	1248.00
4	1273.00	3.85	1359.94	-2.71	1324.00
5	1389.00	5.32	1471.05	-0.28	1467.00
6	1396.00	5.03	1478.37	-0.57	1470.00
7	1521.00	2.81	1628.12	-4.03	1565.00
8	1535.00	6.63	1670.99	-1.64	1644.00
9	1547.00	5.96	1684.33	-2.39	1645.00
10	1578.00	4.94	1719.34	-3.57	1660.00
11	1702.00	-3.07	1730.09	-2.19	1693.00
12	1745.00	-0.80	1818.65	-3.33	1760.00
13	1774.00	3.16	1884.33	-2.80	1833.00
14	1775.00	6.31	1930.62	-1.56	1901.00
15	1781.00	6.36	1932.28	-1.59	1902.00

Table 4

As for the flat panel, the influence of the zigzag function on response prediction is tested also by means of the MAC, figure 7-8.

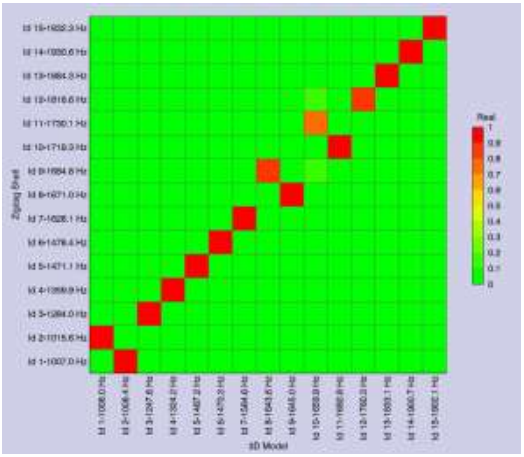


Figure 7

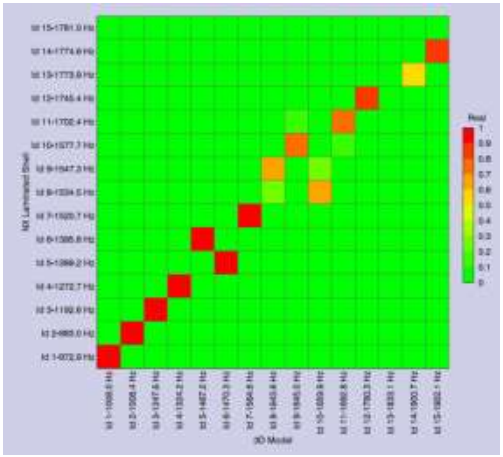


Figure 8

Figure 7 shows the correlation between the zigzag element and the 3D model. Beside mode inversion, the MAC values always stay above the threshold value of 0.8. This is not the case for the NX laminated shell which not only shows mode inversion but also MAC values as low as 0.6 already for mode 8.

5. Conclusions

The paper presented a new shell element based on the Refined Zigzag Theory for the dynamic simulations of sandwich and composite laminates. A flat sandwich panel and a curved composite panel have been considered as examples to prove the capabilities of the proposed formulation.

In both cases the use of the zigzag function allows for a more accurate stiffness estimation as it can be seen by analysing the natural frequencies of the two panels and comparing them to the frequencies estimated by a reference 3D model. Computation of the MAC matrix also shows that the Zigzag Shell is generally performing better than the standard shell

For the curved panel the zigzag formulation is combined with the draping simulation capabilities of LMS Samtech Samcef proving its compatibility.

Acknowledgements

This research is supported by the European Commission under the 7th Framework Programme through the GRESIMO Marie Curie Initial Training Network (GA 290050).

References

[1] S. Timoshenko, S. Woinowsky-Krieger. *Theory of plates and shells.* McGraw-Hill Classic Textbooks Reissue, 2nd Edition, 1959.

[2] R. Gibson. *Principle of Composite Materials Mechanics.* CRC Press, 3rd Edition, 2012.

[3] R. D. Mindlin. *Influence of rotatory inertia and shear on flexural motions of isotropic, elastic plates.* J Appl Mech-T ASME 1951, 18:31–38.

[4] E. Reissner. *The effect of transverse shear deformation on the bending of elastic plates.* J. Appl. Mech. (1945), 12:A69–76.

[5] J. N. Reddy. *A refined shear deformation theory for the analysis of laminated plates.* NASA Contractor Report 3955.
[6] T. Kant, K. Swaminathan. Free Vibration of Isotropic, Orthotropic, and Multilayer Plates Based on Higher Order Refined Theories. J Sound Vib 2001;241:319–27.
[7] O. O. Ochoa, J. N. reddy. *Finite Element Analysis of Composite Laminates.* Kluwer Academic Publishers, 1992.
[8] N. J. Pagano. *Exact Solutions for Composite Laminates in Cylindrical Bending.* J. Compos. Mater. (1969), 3:398.
[9] N.J. Pagano. *Free edge stress fields in composite laminates.* Int. J. Solids Struct. (1978), 14, 3:401-406.
[10] R. Adams, D. Bacon. *Effect of fibre orientation and laminate geometry on the dynamic properties of CFRP.* (1973), 7, 4:402-428.
[11] A. Araújo et al. *Finite element model for hybrid active-passive damping analysis of anisotropic laminated sandwich structures.* J. Sandw. Struct. Mater. (2009), 12, 4:397-419.
[12] E. Fotsing et al. *Lightweight damping of composite sandwich beams: experimental analysis.* J. Compos. Mater. (2012), 47, 12:1501-1511.
[13] J. N. Reddy. *Mechanics of Laminated Composite Plates and Shells – Theory and Analysis.* CRC Press, 2nd Edition, 2003.
[14] E. Carrera. Theories and finite elements for multilayered, anisotropic, composite plates and shells. Arch Comput Methods Eng 2002;9:87–140.
[15] A. Tessler et al. *Refinement of Timoshenko Beam Theory for Composite and Sandwich Beams using Zigzag Kinematics*. NASA Technical Publication (November 2007).
[16] M. Di Sciuva. *A refined transverse shear deformation theory for multi-layered anisotropic plates.* Atti Accademia delle Scienze di Torino (1984), 118:279-295.
[17] M. Di Sciuva. *Bending, vibration and buckling of simply supported thick multilayered orthotropic plates: an evaluation of a new displacement model.* J Sound Vib 1986; 105 (3):425-442.
[18] M. Di Sciuva. M*ultilayered anisotropic plate models with continuous interlaminar stresses*. Comput Struct 1992;22:149–167.
[19] M. Di Sciuva. *A general quadrilateral multilayered plate element with continuous interlaminar stresses*. Comput Struct 1993;41:91–105.
[20] R. C. Averill. *Static and Dynamic Response of Moderately Thick Laminated Beams with Damage*. Compos Eng 1994; 4(4): 381–395.
[21] H. Murakami. *Laminated plate theory with improved in-plane response.* J Appl Mech 1986; 53:661-666.
[22] A. Tessler et al. *Refined Zigzag Theory for homogeneous, laminated composite and sandwich plates: a homogeneous limit methodology for Zigzag function selection.* NASA Technical Publication (March 2010).
[23] A. Tessler at al. *A consistent refinement of first-order shear deformation theory for laminated composite and sandwich plates using improved zigzag kinematics.* J Mech Mater Struct 2010; 5 (2): 341-367.
[24] A. Treviso et al. *NVH Assessment of polymer-based composite structures.* Proceedings of 26th International Conference on Noise and Vibration Engineering (ISMA), Leuven, Sept. 15-17 2014.
[25] D. J. Ewins. *Model validation: Correlation for updating.* Sadhana-Acad P Eng S 2000; 25 (3):221-234.
[26] W. Haylen et al. *Modal Analysis Theory and Testing.* Katholieke Universiteit Leuven - PMA Division, 2007.

[27] H. Walther et al. *Model Correlation with Closely Spaced Modes.* Proceedings of 2004 IMAC XXII: Conference & Exposition on Structural Dynamics, Dearborn, Michigan.

11th International Conference on Engineering Vibration
Ljubljana, Slovenia, 7–10 September 2015

SURFACE IMPEDANCE PREDICTION USING PHASED GEOMETRICAL ACOUSTICS, A SMALL REVERBERANT CHAMBER AND OPTIMIZATION

Matthew Boucher*[1], Bert Pluymers[1], Wim Desmet[1]

[1]KU Leuven, Department of Mechanical Engineering,
Celestijnenlaan 300B, B-3001, Heverlee, Belgium
matt.boucher@kuleuven.be

Keywords: Geometrical Acoustics, Beam Tracing, Inverse Method, Optimization.

Abstract. *An inverse method is proposed to determine the normal surface impedance of acoustic materials using phased geometrical acoustics and a least-squares optimization algorithm inside a small reverberant chamber. A material with unknown impedance is placed on the floor of the reverberant chamber, and the steady-state acoustic pressure is measured. Then the surface impedance of the material is predicted using an optimization algorithm and phased beam tracing as the forward model. In phased beam tracing, the center ray of a triangular beam is traced specularly throughout the acoustic cavity. During this analysis, incident angles, indices of reflection and total distance traveled are saved for each image source detected. The strength of each image source is then the product of all successive plane wave reflection coefficients, which are dependent upon the surface impedance of each reflecting surface encountered. The calculation time of the cost function is greatly reduced, because beams do not need to be recast in order to calculate the simulated pressure for different impedance values and because the image sources are separated based on whether or not they depend on the floor. The reverberant chamber used is a multifunctional vibro-acoustic test rig common in the automotive industry. Beam tracing results with added noise are used as the known values. The optimization is more robust and accurate if more than 40 frequencies and if more than two receivers are used. The outputs of this prediction technique are the real and imaginary parts of the normal surface impedance for different 3^{rd}-octave bands of a material placed on the floor of a small reverberant chamber.*

1 INTRODUCTION

Measuring the surface properties of acoustic materials is usually done in a reverberation chamber or by using an impedance tube. Assumptions are that the sound field is diffuse or that only a plane wave is present, respectively. In the former, a large room is required in order to produce a diffuse field at sufficiently low frequencies while in the latter, results are only valid below the first transverse resonance of the tube. An alternative measurement technique is proposed here that combines phased triangular beam tracing with an optimization algorithm when an acoustic material is placed on the floor of a small reverberant chamber. This technique can be classified as an inverse technique, because it involves the determination of model inputs from model outputs. Since there are two model inputs, *i.e.*, the real and imaginary parts of the impedance of the acoustic material, the system is overdetermined if the vector-valued cost function is longer than two data points. Overdetermination is then enforced by using more than one microphone or by evaluating the cost function at more than one frequency.

Inverse methods in acoustics is not a new class of problems, and in fact, recent attention has been given to the prediction of surface impedances using different numerical methods combined with measurements. Antonello [1] uses a finite difference time domain method and a Gauss-Newton optimization algorithm to retrieve surface impedances inside a room. The problem can also be formulated in the frequency domain, which was done by Nava [2] where the forward model used was the boundary element method. Although not intended for surface property prediction, optimization and ray tracing is available in the latest version of ODEON [3] in order to find optimal surface absorption coefficients so that simulations better fit measurements.

The technique applied in this work is formulated in the frequency domain and is applied to the PMA SoundBox, see Fig. 1, which is a multi-functional vibro-acoustic test rig. An unknown absorbing material is placed on the floor ($z = 0$), the other five boundaries being concrete with known absorption coefficients for each 3^{rd}-octave band. The geometry of the acoustic cavity is convex, and there are no scattering objects, which simplifies the beam tracing method, *i.e.*, the Uniform Theory of Diffraction is not needed. The PMA SoundBox has already been used for absorption coefficient measurements using techniques similar to that for a large reverberation room [4] and normal incidence impedance using a combined experimental-numerical method [5].

This work is organized as follows: first, the forward beam tracing model is briefly presented; secondly, the formulation of a least-squares optimization problem is presented that uses all known information given by a beam tracing analysis and finally, the impedance prediction method is tested using beam tracing results with added noise as the known values.

2 PHASED TRIANGULAR BEAM TRACING

Phased triangular beam tracing makes most of the same assumptions as geometrical acoustics, including (1) wavelengths are assumed to be small compared to the characteristic dimensions of the room, (2) the medium is homogeneous, meaning sound travels in straight lines as rays and (3) rays lose energy as $1/r^2$ where r is the distance traveled; consequently, pressure decreases as $1/r$ [6]. In addition, *phased* geometrical acoustics includes a phase factor that is based on the total distance traveled. The beam tracing method used in this work is similar to and includes aspects of the image source method [7], the ray tracing method [8] and the beam tracing method [9]. The center axis of a triangular beam is traced specularly throughout an acoustic enclosure, and valid image sources are detected if they lie inside the viewing angle of the beam. The applicable frequency range for phased beam tracing is suggested to be between

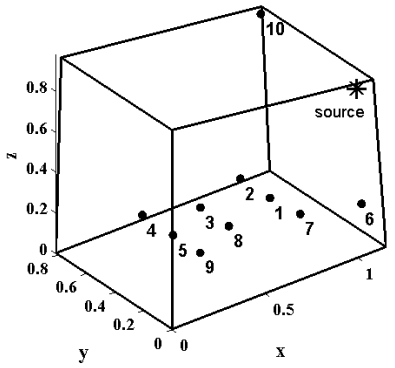


Figure 1: PMA SoundBox with 9 receivers in the $z = 0.18\,\mathrm{m}$ plane, the 10th receiver in the the top, back left corner and a loudspeaker in the top, back right corner (as viewed in the + x direction).

the Schroeder frequency, f_{sch}, and $4f_{sch}$ [10], although this range may be extended in some situations [11].

In order to cover the entire solid angle of 4π without any overlaps or gaps [9], a large number of triangular beams are sent out in all directions from a single point to simulate an acoustic point source with uniform directivity. As shown in Fig. 2, starting with an icosahedron shown in Fig. 2(a), each face is divided into smaller triangular faces, as shown in Fig. 2(b). Then, all points are projected back onto the circumscribed sphere, Fig. 2(c). Finally, a triangular beam is shown in Fig. 2(d) and consists of one of the smaller faces and the center of the sphere.

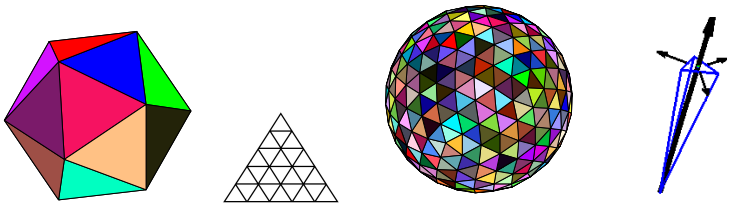
The center ray of each beam is traced throughout a geometrical enclosure. At each reflection, an image beam is found whose vertex is a possibly valid image source. The image source is valid if the receiver point lies in the path of the image beam. Through this process, all valid image sources are found and stored. In addition, the index of reflections of the beam is also recorded so that an effective reflection coefficient may be calculated (described below).

The tracing of one beam is limited by either the number of reflections or by setting a maximum distance from image source to receiver. For a particular source/receiver pair, $\vec{x}_{src}/\vec{x}_{rec}$, this yields a number of valid raypaths, N, each representing one image source. For each valid raypath, n, the beam undergoes M_n reflections.

In order to calculate the complex, steady-state acoustic pressure, each image source is assumed to radiate as a point source in free-space [12] multiplied by an effective reflection coefficient, which takes into account the attenuation at each reflection . Since the initial magnitude of the source is assumed to be $1\,\mathrm{kg/s^2}$, the steady-state pressure contribution of the n-th image source is then given by

$$\widetilde{p}_n\left(f, \vec{x}_{rec}, \vec{x}_{IS,n}\right) = \widetilde{R}_{eff,n}\frac{e^{-\mathrm{j}kr_n}}{r_n} \tag{1}$$

where f is the frequency, $\mathrm{j} = \sqrt{-1}$, k is the wavenumber ($k = 2\pi f/c$), c is the speed of sound and $r_n = \|\vec{x}_{rec} - \vec{x}_{IS,n}\|$ is the distance from receiver to the n-th image source. Complex quantities are denoted by $\widetilde{\ }$. The effective reflection coefficient for the n-th valid raypath is given by $\widetilde{R}_{eff,n} = \prod_{m=1}^{M_n}\widetilde{R}_{n,m}$ where $\widetilde{R}_{n,m}$ is the plane wave reflection coefficient of the n-th



(a) (b) (c) (d)

Figure 2: Geodesic subdivision of an icosahedron to model an omnidirectional beam source [9].

raypath at its m-th reflection, given by

$$\widetilde{R}_{n,m} = \frac{\widetilde{Z}_{n,m}\cos\theta_{n,m} - \rho c}{\widetilde{Z}_{n,m}\cos\theta_{n,m} + \rho c} \tag{2}$$

where $\widetilde{Z}_{n,m}$ and $\theta_{n,m}$ are the normal surface impedance and the angle of incidence, respectively, at the m-th reflection. Finally, the total steady-state sound pressure, $\widetilde{p}\left(f, \vec{x}_{rec}, \vec{x}_{src}\right) = \sum_{n=1}^{N} \widetilde{p}_n\left(f, \vec{x}_{rec}, \vec{x}_{IS,n}\right)$, due to all image sources is

$$\widetilde{p}\left(f, \vec{x}_{rec}, \vec{x}_{src}\right) = \sum_{n=1}^{N} \widetilde{R}_{eff,n} \frac{e^{-\mathrm{j}kr_n}}{r_n} \tag{3}$$

.

The methods described in this section are implemented in MATLAB [13]. The inputs are the room geometry, locations of the source and receivers, the number of beams to be traced and the number of reflections of interest. In this work, $10,000$ beams are traced up to a maximum of 35 reflections, which leads to steady-state results for the boundary conditions used (described below). For 10 receivers, all r_n, $\theta_{n,m}$ and indices of reflection are stored and used in the optimization algorithm. More details may be found in [14].

Under these conditions, the beam tracing analysis takes $218.2\,\mathrm{s}$, and an additional $68.2\,\mathrm{s}$ is used to separate the raypaths based on their dependence on the floor (using an i5 $2.60\,\mathrm{GHz}$ processor with $8\,\mathrm{GB}$ of RAM). The amount of image sources detected ranges from $32,544$ for receiver 10 to $52,490$ for receiver 3.

The boundary conditions and frequency values are not used until post-processing when the effective reflection coefficients are calculated, making this method ideally suited for an optimization problem where the pressure must be evaluated for many different values of the surface impedance.

3 OPTIMIZATION

In order to extract the impedance of the unknown acoustic material placed on the floor, the following optimization problem must be solved,

$$\min_{x\in\mathbb{R}^2} \frac{1}{2}\|\widetilde{\eta} - \widetilde{\mathrm{M}}(x)\|_2^2 \tag{4}$$

where $x = [R_\perp \quad X_\perp]^T$ are the design variables and $\widetilde{Z} = R_\perp + \mathrm{j}X_\perp$. The cost function, $|\widetilde{\eta} - \widetilde{\mathrm{M}}(x)|$, is the complex modulus of the difference between the known values, $\widetilde{\eta}$, and the forward beam tracing model, $\widetilde{\mathrm{M}}(x)$. The l_2-norm is denoted by $\|\cdot\|_2$. The optimization problem is

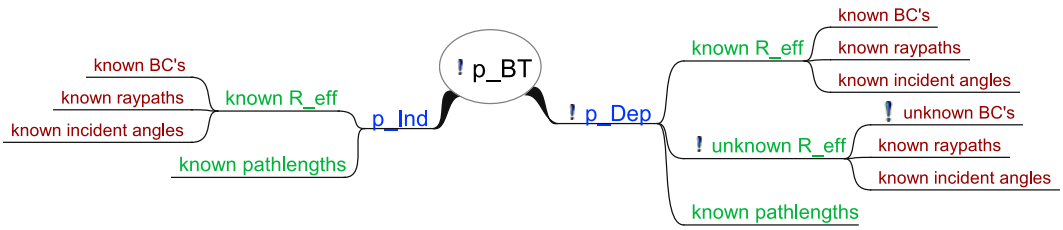


Figure 3: Decomposition of the beam tracing model. Quantities denoted by ! are dependent upon the impedance of the acoustic material placed on the floor.

solved using the non-linear least squares algorithm $lsqnonlin$ in MATLAB and a 'trust-region-reflective' algorithm with a tolerance of $1\text{x}10^{-6}$. Iterating from an initial guess of $10,000(1 + \text{j})\,\text{rayl}$ and constraining the design variables to be on the interval $(-1, 1)\text{x}10^{6}$, the optimal values for the real and imaginary parts of the surface impedance may be found. The impedance of the other 5 walls is assumed to be $1\text{x}10^{6}\,\text{rayl}$, which is representative of the concrete walls of the PMA SoundBox [4]. The known values, $\widetilde{\eta}$, come from a beam tracing model with added noise.

3.1 Redefining the cost function in terms of dependent and independent raypaths

The acoustic pressure calculated from the beam tracing model, $\widetilde{\text{M}}(x)$, is divided into two parts: $\widetilde{p}_I$, the pressure which is a sum of raypaths independent of the floor impedance and $\widetilde{p}_D$, the pressure which is a sum of raypaths dependent on the floor impedance, where $\widetilde{\text{M}}(x) = \widetilde{p}_I + \widetilde{p}_D(x)$. The cost function then becomes

$$|\widetilde{\eta} - \widetilde{p}_I - \widetilde{p}_D(x)| \tag{5}$$

where

$$\widetilde{\text{M}}(x) = \widetilde{p}_I + \sum_{n=1}^{N} \widetilde{R}_{D,n}(x) \frac{e^{-\text{j}kr_{D,n}}}{r_{D,n}} \tag{6}$$

and $\widetilde{R}_{D,n}(x)$ is the effective reflection coefficient for the n-th valid image source that involves a reflection about the floor.

There is yet more information that can be extracted from the beam tracing model, that is, $\widetilde{R}_{D,n}(x)$ also involves reflections from surfaces with known boundary conditions. Dividing the effective reflection coefficient into known and unknown parts, $\widetilde{R}_{D,n}(x) = \widetilde{R}_{K,D,n}\widetilde{R}_{UK,D,n}(x)$, $\widetilde{M}(x)$ can be written as

$$\widetilde{\text{M}}(x) = \widetilde{p}_I + \sum_{n=1}^{N} \widetilde{R}_{K,D,n}\widetilde{R}_{UK,D,n}(x) \frac{e^{-\text{j}kr_{D,n}}}{r_{D,n}} \tag{7}$$

where $\widetilde{R}_{K,D,n}$ and $\widetilde{R}_{UK,D,n}(x)$ are product series of reflection coefficients of known and unknown surfaces, respectively, for raypaths dependent upon the floor.

An outline of the components of $\widetilde{\text{M}}(x)$ is shown in Figure 3 and shows the motivation for splitting up the beam tracing pressure, which is to exploit the vast amount of information that can come out of a beam tracing model and to reduce computation time. The information separated includes lengths of raypaths, index of reflecting walls, incident angles at each reflection

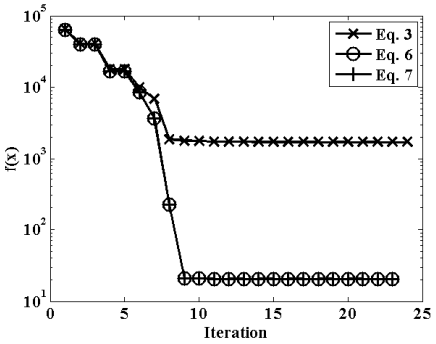


Figure 4: Cost function versus iteration for the 3^{rd}-oct. band with center frequency of $1000\,\mathrm{Hz}$, 232 frequencies and 1 receiver, $\widetilde{Z} = 2000\,\mathrm{rayl}$.

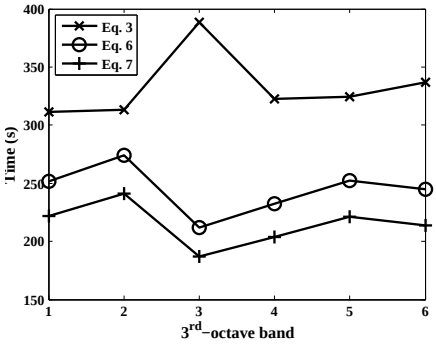


Figure 5: Computation time for different expressions of $\widetilde{\mathrm{M}}(x)$ for 3^{rd}-octave bands at center frequencies of 800, 1000, 1250, 1600, 2000 and 2500 Hz.

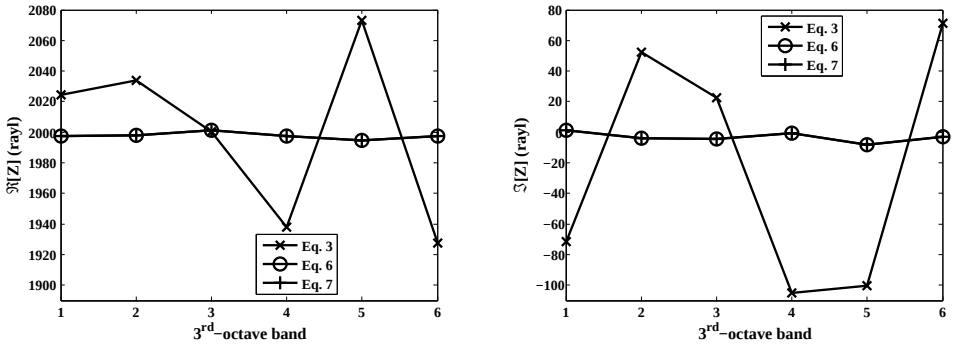
and known boundary conditions. By doing this, quantities that are constant relative to the design variables are isolated and calculated only once. The effect of splitting up the various data depicted in Fig. 3 is analyzed in the next section.

4 RESULTS

In this section, the real and imaginary parts of the impedance are predicted where $\widetilde{\eta}$ is given by a beam tracing model with added noise. $\widetilde{\mathrm{M}}(x)$ is given by Eqs. 3, 6 or 7, successively representing more detailed use of the quantities in Fig. 3. White Gaussian noise with a signal-to-noise ratio (SNR) of $30\,\mathrm{dB}$ is included in $\widetilde{\eta}$. First, the three different equations for $\widetilde{\mathrm{M}}(x)$ are compared based on computation time and accuracy. Then, Eq. 7 is used for $\widetilde{\mathrm{M}}(x)$ to test the optimization's performance relative to how many frequencies and receivers are used.

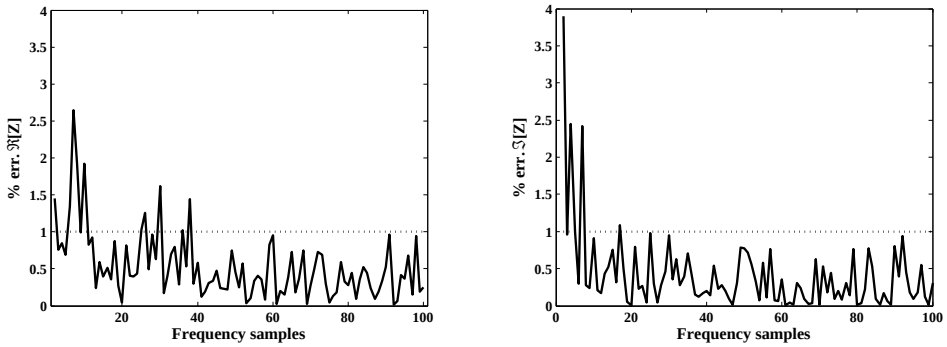
Fig. 4 shows the average value of the cost function, $f(x)$, at each iteration of the optimization algorithm. Using any one of the three expressions for $\widetilde{\mathrm{M}}(x)$, the optimization initially converges at a similar rate. However, after 9 iterations, $f(x)$ is already around two orders of magnitude smaller when Eqs. 6 and 7 are used as compared to using Eq. 3.

The computation time needed to predict an impedance of $Z = 2000\,\mathrm{rayl}$ for different 3^{rd}-octave bands is shown in Fig. 5. For the 3^{rd}-octave band with center frequency of $2000\,\mathrm{Hz}$, reductions of 22% and 31% are seen using Eqs. 6 and 7, respectively. Similar results are found for various 3^{rd}-octave bands. The optimal values for the real and imaginary parts of $\widetilde{Z}$ are



(a) (b)

Figure 6: Predicted $R_\perp$ and $X_\perp$, (a) and (b), respectively, for different expressions of $\widetilde{\mathrm{M}}(x)$ for 3^{rd}-octave bands at center frequencies of 800, 1000, 1250, 1600, 2000 and 2500 Hz. True values are $R_\perp = 2000$ and $X_\perp = 0$.



(a) (b)

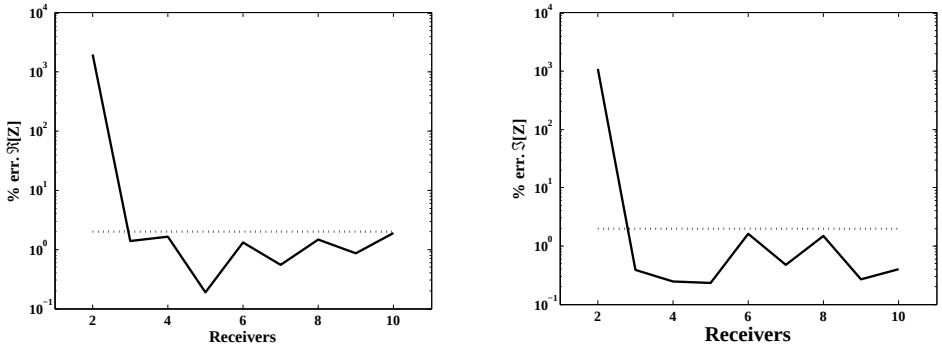
Figure 7: Percent error for predicted $R_\perp$ and $X_\perp$, (a) and (b), respectively, as a function of number of frequency samples (1 receiver). True values are $R_\perp = 1400$ and $X_\perp = 1400$. Samples are distributed evenly across the 3^{rd}-octave band with 1250 Hz center frequency. 1% reference line $(\cdots)$.

shown in Fig. 6, indicating the improved accuracy using Eqs. 6 and 7.

In Figs. 7–8, the accuracy of the prediction method using Eq. 7 is tested, as well as its dependence on the length of the cost function vector. Specifically, Fig. 7 shows the dependence on using more frequency points for only one receiver, while Fig. 8 shows the dependence on using more receivers for only one frequency. The true value of the impedance is $\widetilde{Z} = 1400\,(1 + \mathrm{j})\,\mathrm{rayl}$. The results show that the percent error in the predicted real and imaginary parts of the impedance is less than 1% if at least 40 frequency samples are used. Similarly, if at least 3 receivers are used, the percent error is less than 2%.

5 CONCLUSIONS

A surface impedance prediction technique is proposed based on minimizing the difference between known pressure values and those calculated with a phased beam tracing model with an acoustic material placed on the floor of a small reverberant chamber. With this method, the real and imaginary parts of the normal surface impedance may be calculated using measurements and an optimization algorithm. This is in contrast to traditional, direct measurements such



(a) (b)

Figure 8: Percent error for predicted $R_\perp$ and $X_\perp$, (a) and (b), respectively, as a function of number of receivers ($f = 1250\,\mathrm{Hz}$). True values are $R_\perp = 1400$ and $X_\perp = 1400$. 2% reference line ($\cdots$).

as reverberation room and impedance tube techniques. The diffuse field assumption is not required, a relaxation of the reverberation room technique, which is also limited in that only absorption coefficients, lacking phase information, may be measured. Furthermore, since this method is applicable in the frequency range of $(f_{sch}, 4f_{sch})$, it may cover higher frequencies than some impedance tubes. The proposed technique is applied to the convex geometry of the PMA SoundBox, a small reverberant chamber similar to those found in the automotive industry. Separating the beam tracing model into raypaths that are independent of and dependent on the bottom surface decreases computation time and increases accuracy. When the known values are a beam tracing model with SNR of $30\,\mathrm{dB}$, including more than 40 frequencies over a 3^{rd}-octave band increases the robustness and reliability of the optimization. Including more receivers in the cost function has a less significant effect, although using at least 3 receivers consistently gives more accurate results.

ACKNOWLEDGEMENTS

The authors wish to acknowledge the European Commission and the Marie Curie Initial Training Network No. 290050 GRESIMO for supporting this research. The IWT Flanders and the Research Fund KU Leuven are also gratefully acknowledged for their support. Niccolo Antonello and Kunmo Koo also provided meaningful feedback and discussions.

REFERENCES

[1] N. Antonello, T. van Waterschoot, M. Moonen, P. A. Naylor, *Identification of surface acoustic impedances in a reverberant room using the FDTD method*. Proceedings of 14th International Workshop on Acoustic Signal Enhancement, pp. 114–118, 2014.

[2] G. P. Nava, Y. Yasuda, Y. Sato, S. Sakamoto, *On the in situ estimation of surface acoustic impedance in interiors of arbitrary shape by acoustical inverse methods*. Acoust. Sci. & Tech., **30**, No. 2, pp. 100–109, 2009.

[3] G. Naylor, *ODEON - Another hybrid room acoustical model*. Applied Acoustics, **38**, pp. 131–143, 1993.

[4] M. Vivolo, *Vibro-acoustic characterization of lightweight panels by using a small cabin*. PhD Thesis, KU Leuven, 2013.

[5] M. Vivolo, B. Pluymers, D. Vandepitte, W. Desmet, *Normal-incidence sound absorption measurements by means of a small cabin*. Proceedings of AIA-DAGA, Meran, March 18–22, 2013.

[6] H. Kuttruff, *Room Acoustics*. Spon Press, London & New York, 5th edition, 2009.

[7] J. B. Allen, D. A. Berkley, *Image method for efficiently simulating small-room acoustics*. J. Acoust. Soc. Am., **65**, No. 4, pp. 943–950, 1979.

[8] A. Krokstad, S. Strom, S. Sorsdal, *Calculating the acoustical room response by the use of a ray tracing technique*. J. Sound Vib., **8**, No. 1, pp. 118–125, 1968.

[9] T. Lewers, *A combined beam tracing and radiant exchange computer model of room acoustics*. Applied Acoustics, **38**, pp. 161–178, 1993.

[10] C.-H. Jeong, J.-G. Ih, J.H. Rindel, *An approximate treatment of reflection coefficient in the phased beam tracing method for the simulation of enclosed sound fields at medium frequencies*. Applied Acoustics, **69**, pp. 601–613, 2008.

[11] H.-C. Shin, J.-G. Ih, *Acoustic analysis of interior spaces by using the phased geometric acoustic model*. J. Acoust. Soc. Korea, **17**, pp. 54–61, 1998.

[12] A. Wareing, M. Hodgson, *Beam-tracing model for predicting sound fields in rooms with multilayer bounding surfaces*. J. Acoust. Soc. Am., **118**, No. 4, pp. 2321–2331, 2005.

[13] MATLAB R2012b. Natick, Massachusetts: The MathWorks Inc., 2012.

[14] M. Boucher, B. Pluymers, W. Desmet, *Phased geometrical acoustics in a small cabin*. Proceedings of the Leuven Conference on Noise and Vibration Engineering, Leuven, Belgium, 15–17 September, 2014.

International Conference on Engineering Vibration
Ljubljana, Slovenia, 7-10 September 2015

ON THE EFFECTS OF DAMPING ON WAVE PROPAGATION IN PERIODIC VIBRO-ACOUSTIC META-MATERIALS

A. Nateghi*[1], C. Claeys[1], E. Deckers[1], B. Pluymers[1], W. Desmet[1]

[1]KU Leuven, Department of Mechanical Engineering, Celestijnenlaan 300, 3001 Heverlee, Belgium
Alireza.nateghi@kuleuven.be

Keywords: Meta-materials, Bloch-Floquet, Dispersion behaviour, Damping, Complex *k*-space.

Abstract. *In search for novel materials which combine lightweight characteristics with good acoustical behaviour, triggered by ecological and economic reasons, resonant meta-materials come to attention, be it at least in some targeted and tunable frequency ranges, referred to as stop bands. Meta-materials are defined as the general family of materials engineered to have specific properties, uncommon in nature, for dedicated applications. In this paper, an infinite periodic meta-material panel composed of unit cells with local resonators is discussed. The panel is designed to obtain stop band behaviour for bending waves in vibro-acoustic applications. As the panel is periodic, a single unit cell contains all essential information and the Bloch-Floquet theorem can be applied to reduce the computational effort required to analyze its dispersion behaviour. More specifically, the effects of damping are investigated, since this can have an important influence on wave propagation. In order to capture both propagating and attenuated parts of waves, an alternative formulation of the Bloch-Floquet theorem is employed to scan the k-space (wavenumber) for a given frequency and evaluate the dispersion behaviour. Unlike the classic Bloch-Floquet approach, this approach captures complex wavenumbers as the governing equations are reformulated to form a quadratic eigenvalue problem with respect to wavenumber. This allows the investigation of the dispersion behaviour in the complex k-space providing more information on attenuating waves. The alternative formulation can also facilitate the analysis of structures with complex damping configurations allowing direct inclusion of damping in the constitutive law with a more detailed description. In addition, it reduces the computational effort required to analyze structures with frequency-dependent properties as the eigenvalue problem is solved for eigen-wavenumbers at discrete frequency steps. Finally, the dispersion behaviours of infinite structures with various levels of structural damping are compared to capture the effects of damping on wave propagation of such periodic meta-materials.*

1 INTRODUCTION

In the recent years, restrictive regulations regarding CO level have persuaded the transportation industry to look at Electric or hybrid vehicles as a possible alternative for classical gasoline consuming vehicles. On the other hand, reducing the weight of the vehicle is becoming a common fashion mainly due to the energy limitations of electric batteries resulting in lightweight (LW) vehicle designs with possible unsatisfactory dynamic behaviour. In many cases, these LW designs fail to satisfy the legal regulations regarding the acoustic behaviour of vehicles. The two often contradictory criteria of LW design and efficient vibro-acoustic behaviour ask for new and innovative acoustic solutions. These solutions should be kept as simple, cheap and easy to apply as possible.

As one of these efficient LW acoustic solutions, acoustic and vibro-acoustic metamaterials are becoming more and more of interest to many researchers [1-3]. Metamaterials have shown a promising potential in efficiently insulating noise and vibration in the host structure at least in targeted frequency ranges [4]. These targeted frequency ranges are commonly referred to as stop bands since in these bands no free wave propagation can occur. One of the major benefits of such metamaterials is that unlike phononic crystals their stop band behaviour is independent of the periodicity which gives the designer more freedom [5]. While in phononic crystals Bragg scattering is responsible for the acoustic behaviour, in metamaterials the stop band behaviour is the result of local resonances of resonant cells distributed in a subwavelength scale and can be explained based of Fano-type interference [6].

As stated the periodicity is not a necessary property of local resonant metamaterials, but considering a periodic metamaterial can highly reduce the computational costs in the first stages of design. A periodic structure is defined as a structure which consists of repeating unit cells; while a unit cell is defined as the smallest portion of a periodic structure which includes all of the essential information to describe the behaviour of the structure. Therefore, in a periodic structure, it is possible to analyse the behaviour of the entire structure by studying the unit cell and using the Bloch-Floquet theorem to relate the behaviour of the unit cell to those of the entire structure [7, 8]. In the usual implementation of the Bloch-Floquet theorem in such problems, the dispersion equations are derived and solved at certain wavenumbers as an eigenvalue problem for frequency to evaluate the Brillouin contours [9].

In this paper, the main concentration would be on the effects of damping on dispersion behaviour of metamaterials. Considering that introducing damping or frequency dependant properties to the structure reduces the efficiency of the classical Bloch-Floquet decomposition significantly, an alternative Bloch-Floquet based approach is adopted [10, 11]. Using this technique, the dispersion relation is reformulated as a quadratic eigenvalue form and eigenwavenumbers are calculated at given frequencies by scanning the k-space (complex wavenumbers). Other than tackling the problems arising from frequency dependency and damping, the main benefit of the method is its capability to evaluate both attenuated and propagating parts of waves. This extra information is of more importance when dealing with damped structures since the attenuation plays a more significant role in presence of structural damping. In the following sections the formulation of the alternative approach is briefly reviewed. For a more detailed explanation of the approach, readers are referred to Collet et al. [10, 11]. In addition, numerical results of the wave dispersion in an infinite periodic metamaterial composed of repetitive locally resonant unit cells are discussed. Through the paper, structural damping as a widely used damping model is considered to further investigate the complex wavenumbers. Finally, the effects of mechanical damping on the dispersion behaviour of an infinite periodic plate composed of local resonant unit cells are investigated through comparison of the results obtained considering different values of loss factor in the plate.

2 FORMULATION

2.1 Bloch-Floquet Decomposition

Without going into details, Bloch-Floquet decomposition [7, 8] states that in a three dimensional infinite structure composed of periodically repetitive unit cells, the response of a random point in the structure can be expressed in terms of the response of its corresponding point in a reference unit cell together with the phase shift which is related to the distance of the point to the unit cell as shown in Figure 1.

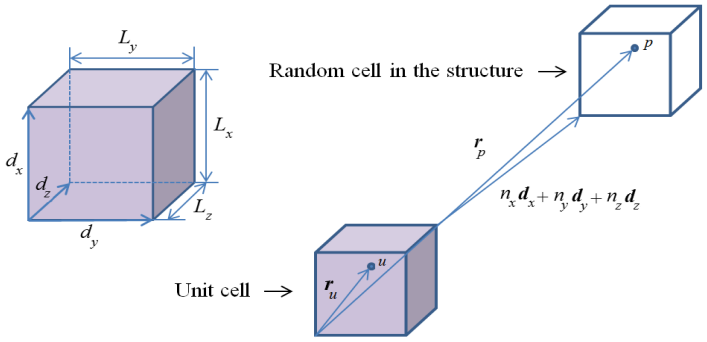


Figure 1: Schematics of the unit cell in the periodic structure.

As one can see in Figure 1, the location of the random point "p" can be described in terms of the location of the corresponding point "u" in the unit cell as follows:

$$\boldsymbol{r}_p = \boldsymbol{r}_u + n_x\boldsymbol{d}_x + n_y\boldsymbol{d}_y + n_z\boldsymbol{d}_z \tag{1}$$

in which $\boldsymbol{d_x}$, $\boldsymbol{d_y}$ and $\boldsymbol{d_z}$ are the basis vectors of the unit cell and n_x, n_y and n_z are number of cells between the random cell and the reference unit cell in d_x, d_y and d_z directions, respectively. Based on Bloch-Floquet theorem, the response of point "p" can also be expressed in terms of the response of point "u" together with the exponential term which defines the amplitude and the phase shift between the two points, respectively:

$$\boldsymbol{u}\left(\boldsymbol{r}_p,\omega\right) = \boldsymbol{u}\left(\boldsymbol{r}_u,\omega\right) e^{\boldsymbol{k}.(n_x\boldsymbol{d}_x + n_y\boldsymbol{d}_y + n_z\boldsymbol{d}_z)} = \boldsymbol{u}\left(\boldsymbol{r}_u,\omega\right) e^{\boldsymbol{\mu}.\mathbf{n}} \tag{2}$$

where "." means an scalar product, ω represents frequency, $\boldsymbol{k}$ is the wavenumber vector and $\boldsymbol{\mu} = \boldsymbol{k}.\boldsymbol{d}$ is the propagation vector which expresses the complex phase shift between the two points.

2.2 Application to elasto-dynamic problems

In general, the dynamic equilibrium of any infinite homogeneous structure can be represented with the following partial differential equation:

$$\nabla.\boldsymbol{\sigma} = \rho\ddot{\boldsymbol{u}} \tag{3}$$

where ρ is the density, $\ddot{\boldsymbol{u}}$ is the second time derivative of the displacement field and $\nabla.\boldsymbol{\sigma}$ represents the divergence of the stress tensor. The stress tensor can be defined in terms of strain tensor ε as follows:

$$\boldsymbol{\sigma} = \boldsymbol{C} : \boldsymbol{\varepsilon} \tag{4}$$

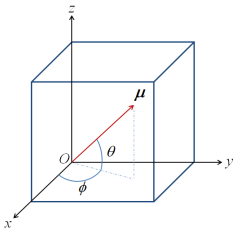
where $\boldsymbol{C}$ is the compliance tensor related to the mechanical properties of the material and ":" is the tensor double dot product. Finally the strain tensor can expressed in terms of the displacement field as follows:

$$\varepsilon_{ij} = \frac{1}{2}\left(\frac{\partial u_i}{\partial x_j} + \frac{\partial u_j}{\partial x_i}\right) \quad , \quad i, j = 1,2,3 \tag{5}$$

Assuming periodicity in the infinite structure and based on the Bloch-Floquet theorem, Bloch eigenmodes [7] and the dispersion functions can be investigated considering the following displacement field:

$$\boldsymbol{u} = \boldsymbol{U} e^{i\boldsymbol{\mu}.\boldsymbol{r}} e^{i\omega t} \tag{6}$$

where $\boldsymbol{U}$ represents the periodic magnitude of the displacement field, the first exponential term defines the propagation phase shift through the infinite structure with $\boldsymbol{\mu}$ being the complex wavenumber vector and the second exponential term represents the time dependency of the displacement field.



$$\boldsymbol{\mu} = \mu_0 \begin{bmatrix} \cos(\theta)\cos(\phi) \\ \cos(\theta)\sin(\phi) \\ \sin(\theta) \end{bmatrix} = \mu_0 \boldsymbol{\Phi}$$

Figure 2: Representation of the wavenumber vector in the unit cell.

In a three dimensional periodic structure, the complex wavenumber can be expressed as shown in Figure 2 where θ and φ are angles of the wavenumber vector with respect to z-axis and x-axis, respectively.

Substituting the proposed displacement field of Eq. (6) into the equations of motion, Eq. (3), leads to the following form of equations of motion:

$$\left(\rho\omega^2 \boldsymbol{U} + \nabla.(\boldsymbol{C} : \boldsymbol{\Xi}) + i\mu_0 \nabla.(\boldsymbol{C} : \boldsymbol{\kappa}) + i\mu_0 (\boldsymbol{C} : \boldsymbol{\Xi}).\boldsymbol{\Phi} - \mu_0^{\,2} (\boldsymbol{C} : \boldsymbol{\kappa}).\boldsymbol{\Phi}\right) e^{i\boldsymbol{\mu}.\boldsymbol{r}} e^{i\omega t} = 0 \tag{7}$$

which then consequently leads to the following quadratic eigenvalue problem in terms of the complex wave number μ:

$$\rho\omega^2 \boldsymbol{U} + \nabla.(\boldsymbol{C} : \boldsymbol{\Xi}) + i\mu_0 \nabla.(\boldsymbol{C} : \boldsymbol{\kappa}) + i\mu_0 (\boldsymbol{C} : \boldsymbol{\Xi}).\boldsymbol{\Phi} - \mu_0^{\,2} (\boldsymbol{C} : \boldsymbol{\kappa}).\boldsymbol{\Phi} = 0 \quad \forall \boldsymbol{r} \in \Omega_R \tag{8}$$

with the following boundary condition:

$$\boldsymbol{U}_{(r_i - L_i.\mathrm{d}_i, \mu)} = \boldsymbol{U}_{(r_i, \mu)} \quad for\, i = x, y, z \quad \forall \boldsymbol{r} \in \Gamma_R \tag{9}$$

where Ω_R and Γ_R are the entire domain and boundaries of the infinite structure, respectively. The boundary condition given by Eq. (9) simply ensures that the symmetrical periodicity condition of the unit cell, represented in Figure 2, is met on parallel boundaries. In addition, in Eqs. (7) and (8), Ξ and $\boldsymbol{\kappa}$ are defined as:

$$\Xi_{ij} = \frac{1}{2}\left(\frac{\partial U_i}{\partial x_j} + \frac{\partial U_j}{\partial x_i}\right) \quad \& \quad \kappa_{ij} = \frac{1}{2}\left(U_i \Phi_j + U_j \Phi_i\right) \quad for \;\; i, j = 1,\; 2 \; and \; 3 \tag{10}$$

2.3 Weak formulation and numerical computation of the dispersion equation

In order to obtain the dispersion curves of an infinite periodic structure, the quadratic eigenvalue problem given by Eqs. (8-9) should be numerically solved. To this end, Finite Element Method is adopted as the numerical tool. In order to use the formulations discussed in the previous section in FEM, one needs to obtain the weak form of the stated equations. If $\boldsymbol{U}$ is a solution of Eq. (8) which satisfies the boundary condition of Eq. (9), the weak form of the problem can be expressed as:

$$\begin{aligned}\delta\Pi = \int_{\Omega_R} \big(&\rho\omega^2\delta(\boldsymbol{U})\boldsymbol{U} - \delta(\boldsymbol{\Xi}):(\boldsymbol{C}:\boldsymbol{\Xi}) - i\mu_0.\delta(\boldsymbol{\Xi}):(\boldsymbol{C}:\boldsymbol{\kappa}) \\ &+ i\mu_0.\delta(\boldsymbol{\kappa}):(\boldsymbol{C}:\boldsymbol{\Xi}) - {\mu_0}^2\delta(\boldsymbol{\kappa}):(\boldsymbol{C}:\boldsymbol{\kappa})\big)dv = 0 \qquad \forall\delta(\boldsymbol{U}) \\ &\delta\left(\boldsymbol{U}_{(r_i - L_i.\mathrm{d}_i,\mu)}\right) = \delta\left(\boldsymbol{U}_{(r_i,\mu)}\right) \quad for\, i = x, y, z \qquad \forall \boldsymbol{r} \in \Gamma_R\end{aligned} \tag{11}$$

The sign δ in Eq. (11) specifies the test functions. Now, this weak form can be used together with any standard FEM discretization to assemble the matrix equations, forming the following quadratic eigenvalue problem in the wavenumber domain:

$${\mu_0}^2 H + i\mu_0 L + \left(K - \omega^2 M\right) = 0 \tag{12}$$

H, *L*, *K* and *M* are matrices defined based on Eq. (11). In absence of damping, the solution of Eq. (12) provides pairs of eigen-wavenumbers in the form of $(\mu, -\mu, i\mu, -i\mu)$, where the real roots represent the propagative waves and the imaginary ones represent evanescent waves while the sign of the roots indicates the direction of propagation (i.e. going and coming waves). In presence of the damping the solution of Eq. (12) is in the form of complex roots of $(\mu, -\mu, \mu^*, -\mu^*)$ where the sign "*" depicts complex conjugate. The complex wave solution provided by this approach is especially of importance when dealing with damped mechanical structures. While the real part of the solution defines the propagating part of the wavenumber, the imaginary part is an indicator of the amount of wave attenuation. In this paper, the following criterion is used to differentiate propagating and non-propagating waves:

$$\frac{\mathrm{Im}(\mu)}{|\mu|} \le 0.05 \tag{13}$$

where "Im" represents the imaginary part of the solution which corresponds to the wave attenuation. The current approach is also of interest for being more flexible in case of dealing with frequency dependant material properties, which could be the case especially when dealing with highly damped structures, composed of viscoelastic or poroelastic materials. Therefore, since the problem is solved for eigen-wavenumbers at given frequencies, instead of searching for eigen-frequencies, adding frequency dependant material properties do not add much more effort and time to the solution process. As stated, any standard FEM packages could be used for discretization of the model. In this paper COMSOL Multiphysics® as a flexible tool is used to solve the eigenvalue problem of Eq. (12).

3 CASE STUDY

3.1 Infinite panel composed of periodic local resonant unit cells

The schematics of the analysed unit cell are given in Figure 3.

As explained before, the main benefit of using metamaterials is in their engineered properties which can ensure a satisfactory behaviour at least for certain applications. Metamaterials are being used in various applications such as in acoustics, optics, electromagnetics, etc.; therefore, the mechanisms based on which they function differ significantly, but in all of cases, the properties of metamaterials are different from those found in nature.

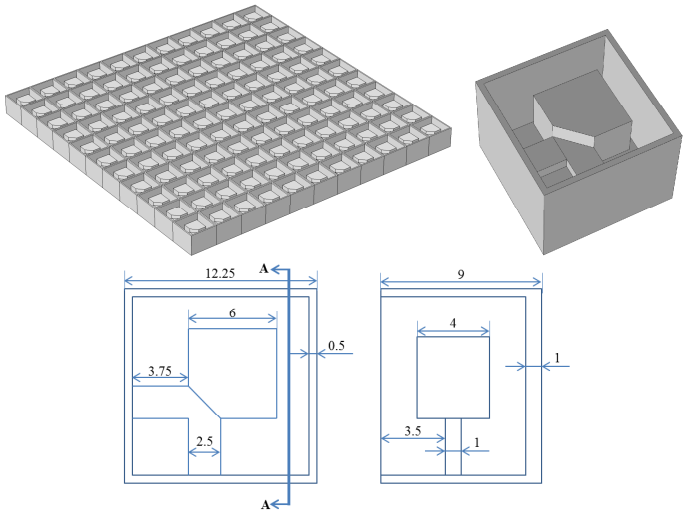


Figure 3: Schematic of the infinite plate and the specifications of the unit cell (all dimensions are in mm).

In this paper, the behaviour of a local resonant metamaterial which can be used in vibro-acoustic applications is investigated. Considering an infinite plate composed of periodically repeating unit cells shown in Figure 3, one can use the method explained in the previous section to analyse the dispersion behaviour of the structure. The unit cell is tuned to introduce a low frequency local resonance in the flexural mode [12]. This local mode can introduce a gap in the dispersion curves of the flexural mode (the so-called stop band) by destructive interference with the flexural mode of the host structure. The schematics and geometrical measurements of the unit cell are represented in Figure 3. The infinite plate is composed of polyamide with the material properties given in Table 1.As explained before, the unit cell is designed to have a local flexural mode at a low frequency. Based on the material properties of Table 1 and the measurements given in Figure 3, this resonance can be found at 1098.4 Hz. This mode is evaluated using COMSOL Multiphysics® and is shown in Figure 4. Fixed boundary conditions are assumed for the surfaces which connect the resonator to the enclosure of the unit cell. The resonator is meshed using the auto-mesher provided by the software. The mesh consists of 16136 tetrahedron solid elements with 71211 degrees of freedom to ensure the convergence of the first mode of vibration with an error less than 0.1%. In Figure 4, the deformed configuration is presented together with the wireframe which represents the undeformed configuration of the resonator.

Property	Value
Young modulus E	1.65 GPa
Poisson ratio ν	0.4
Density ρ	950 kg/m^3

Table 1: Material properties of the polyamide infinite plate.

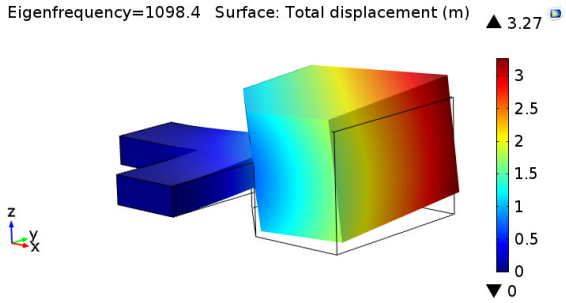


Figure 4: First bending mode in the resonator at frequency of 1098.4 Hz.

3.2 Numerical results

The weak form of Eq. (11) is implemented in COMSOL Multiphysics® to derive the dispersion relation for the unit cell explained in section 3.1. The unit cell is discretised to 9468 tetrahedron solid elements with 51231 degrees of freedom to ensure the convergence of the results up to 1% in the frequency range of 0-1500 Hz.

To analyse dispersion in the infinite plate the quadratic eigenvalue problem of Eq. (12) should be solved. Therefore, a sweep is done in the frequency zone of 0 to 1500 Hz with steps of 10 Hz. In addition, considering the wave vector of section 2.2, in order to include all the possible waves propagating in the infinite flat plate in the solution, θ should be set to zero while φ should vary from 0 to 2π. Considering that the solution of the eigenvalue problem is of the form $\left(\mu,-\mu,\mu^{*},-\mu^{*}\right)$, the solution for φ varying from 0-π are symmetrically equal to those obtained in the range of π-2π which represent the going and coming waves, respectively. In addition, considering the geometrical symmetries of the unit cell, it is sufficient to solve the problem for waves propagating in the directions corresponding to $\varphi=0$- $\pi/4$ and $\pi/2$-$3\pi/4$. Therefore a sweep is done for φ with steps of $\pi/20$ in the stated zones.

In this paper, structural damping model is adopted to represent the mechanical dissipation mechanism in the unit cell. To this end, the Young modulus E is replaced with a complex modulus $E\,(1+i.\eta)$ in which η is called the loss factor and determines the amount of dissipated mechanical energy. In order to study the effect of damping on dispersion behaviour of the plate, three different values of 0, 0.01 and 0.1 are considered for the loss factor to simulate the three conditions of undamped, lowly damped and highly damped structure. Finally, the criterion given by Eq. (13) is used to divide the propagating and highly attenuated waves.

First to validate the model, results obtained for a flat infinite plate composed of the material given in Table 1 are compared with the analytical solution [13]. The plate is assumed to have a thickness of 1 mm. A unit cell of 12.25 mm by 12.25 mm is chosen and meshed in COMSOL Multiphysics® with 2504 tetrahedron solid elements forming 13239 degrees of freedom. As it can be seen in Figure 5, the shear and flexural wavenumbers found using the current model have a good agreement with those obtained from the analytical solution.

The dispersion curves in y-direction ($\varphi= \pi/2$) of an infinite plate composed of empty inclusions without the local resonators are given in Figure 6. Since the wavenumbers are normalized using the length of the unit cell, all the possible solutions in the first Brillouin zone lie between $-\pi$ to π. As expected, the dispersion curves are symmetric with respect to μ=0 representing waves which are propagating in opposite directions. As it can be seen, there are three pairs of possible solutions in the frequency range of 0-1500 Hz. As the plate is considered to be undamped all of the evaluated wavenumbers are either purely imaginary or purely real. The curves which are numbered as **1** in the figure correspond to the dilatational and shear

modes of vibration while the curves shown by number **2** are related to the flexural waves. Dilatational and shear waves are not of interest to this paper, since they do not contribute to the acoustic radiation of the plate. The left figure shows all of the possible solutions including evanescence and propagative waves while the right figure depicts only the propagative parts of the waves.

These figures can be used to compare the results obtained for the infinite plate with the local resonators to give a better understanding on the effects of their addition. As it can be seen in the figures, there is no stop band behaviour in the host structure without the local resonator.

Figure 7 depicts the dispersion curves for all the waves which can propagate through y-direction ($\varphi = \pi/2$) of the infinite plate of Figure 3 with different values of loss factor. The results show that addition of the local resonant has introduced a gap in the dispersion curve corresponding to the flexural mode around the frequency of this resonant. Moreover, it can be seen that the addition of damping increases the frequency range of the gap in the dispersion curve significantly while for the highly damped case of 10%, the gaps are also observed for longitudinal waves. These additional gaps and the width of band gap in flexural waves are highly related to the criterion used to separate propagating waves from the evanescence ones.

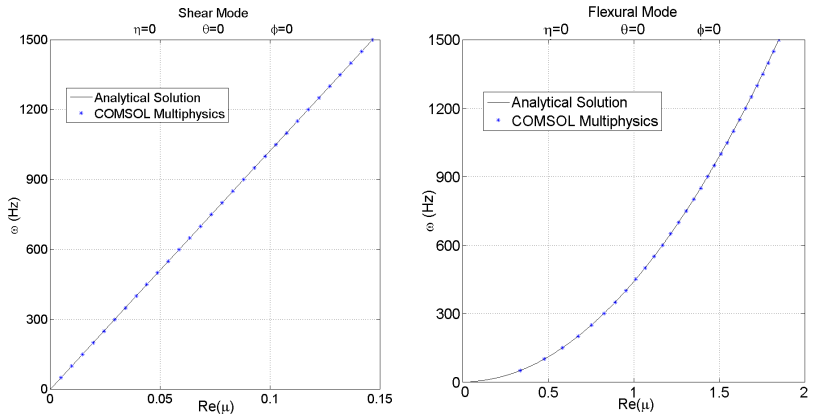


Figure 5: Shear and Flexural wave in a flat infinite plate.

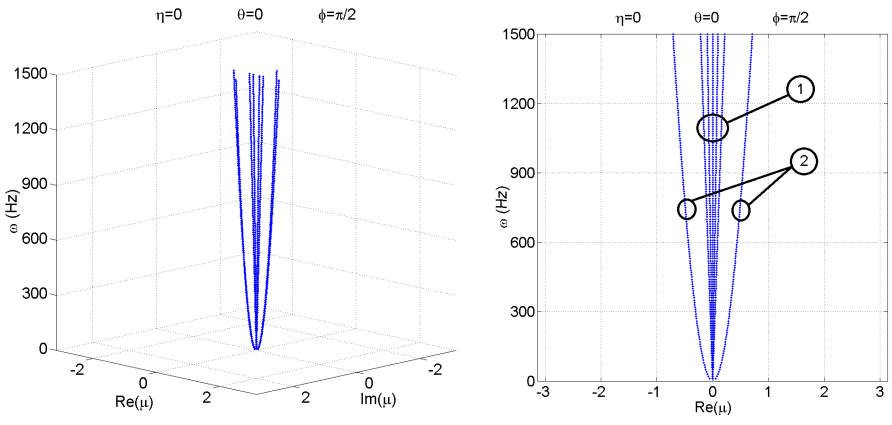


Figure 6: Dispersion curves in y-direction ($\varphi = \pi/2$) of an inclusion without the resonator.

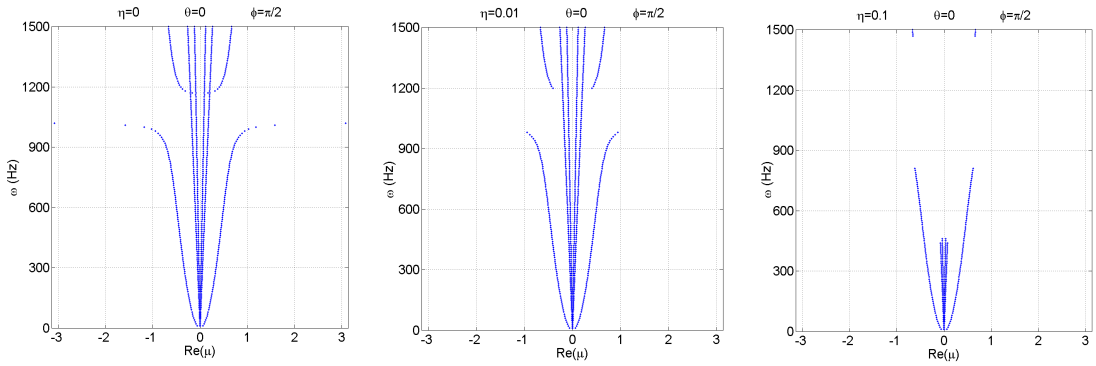


Figure 7: Dispersion curves of waves propagating in y-direction ($\varphi = \pi/2$) in the unit cells depicted in Figure 3 considering various damping cases.

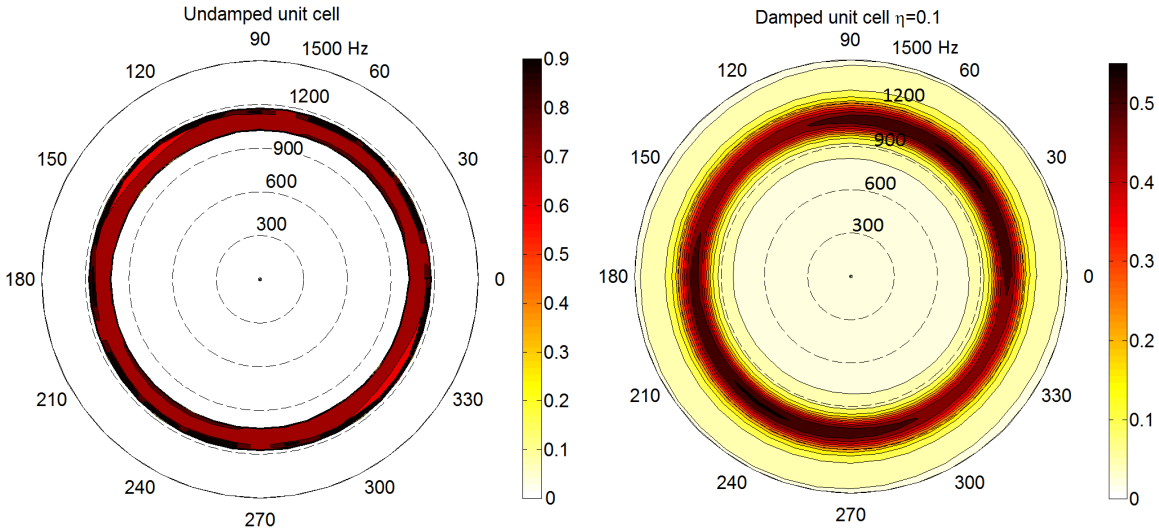


Figure 8: Evanescence indicator for Flexural mode in the undamped (left) and 10% damped (right) infinite plate composed of the unit cells depicted in Figure 3.

It should be noted that the gaps observed in Figure 7 do not necessarily represent a stop band, since a stop band is a frequency range in which there is no free wave propagation in any direction; therefore, to determine the stop band, the previously explained sweep should be done on φ. The contours presented in Figure 8 are plotted by sweeping on φ as explained before. In this figure, an evanescence indicator is plotted for different wave propagation direction and at different frequencies. The evanescence indicator is defined as follows:

$$Indicator = \min_n \left(\frac{\mathrm{Im}(\mu_n)}{|\mu_n|} \right) \tag{14}$$

in which "n" is the number of calculated wavenumbers. It is obvious that higher values of this indicator represent highly attenuated waves. As it can be seen in Figure 8, around the frequency range of the local resonance, a region of high attenuation exist and since this region can be observed in all possible propagation directions, this region can now be called a stop band. It is

also noted that addition of damping increases the size of this band which is in agreement with results presented in Figure 7. It is also worth noting that introducing damping to the plate has decreased the maximum amount of attenuation. This observation will be further investigated in the following pages.

In order to understand the effect of damping on the dispersion of waves, it is important to look at the entire complex solution found for the dispersion relation. Figures 9-11 represent the complex wavenumber solutions found for Eq. (11) in the first Brillouin zone including all three types of evanescence, attenuating and propagating waves. In these figures, the 3D view is companied with top views of the curves for more clarity. As it can be seen in Figure 9, in the case of an undamped infinite plate, the dispersion curves of the flexural waves come in two pairs of purely real and purely imaginary wavenumbers at frequencies below and above the stop band while in the frequency range of the stop band these curves are replaced with four complex curves. This phenomena means through the stop band, evanescence and propagative waves are replaced by highly attenuated waves.

Figure 10 shows the complex dispersion curves for an infinite plate with 1% damping. It can be seen that unlike the undamped case the curves below and above the stop band are not purely real or imaginary anymore. In presence of damping the change from a propagative/evanescence wave to attenuated waves occur gradually while in the undamped case this change was abrupt at the lower limit of the stop band. It can also be noted that unlike undamped case the dispersion curves are not "discontinuous" in the stop band zone anymore, instead they from lopes in which the propagative/evanescence waves become attenuated waves and turn back into propagative/evanescence waves. Therefore, in the presence of damping the stop band phenomenon does not really apply anymore. In such a case, instead of having a stop band, the dispersion curves include a highly attenuated region; nonetheless, the frequency range of this highly attenuated region can be tuned by manipulation of the first flexural mode of the local resonator.

Comparison between the dispersion curves of Figures 10 and 11 shows that increasing the amount of damping increases the frequency range in which waves are highly attenuated. But further investigation of these results also show a reduction in the highest amount of attenuation for the case of highly damped platen which is in agreement with results shown in Figure 8. Therefore, when dealing with damping, one should be careful about its two contradictory effects on wave dispersion behaviour.

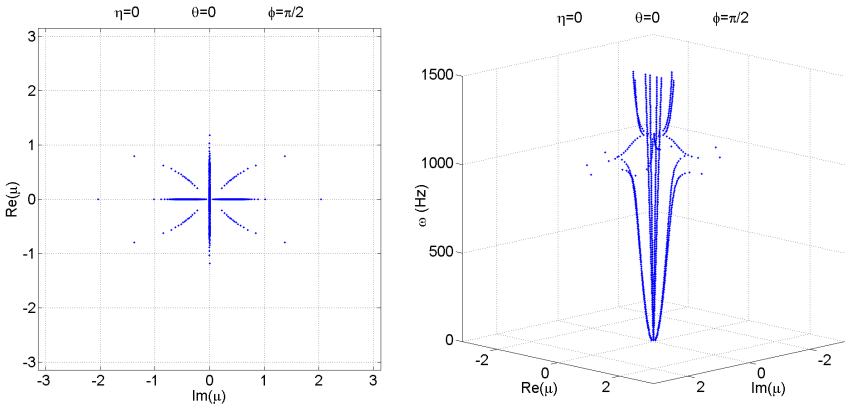


Figure 9: Complex dispersion curves of the infinite plate composed of the unit cells depicted in Figure 3.

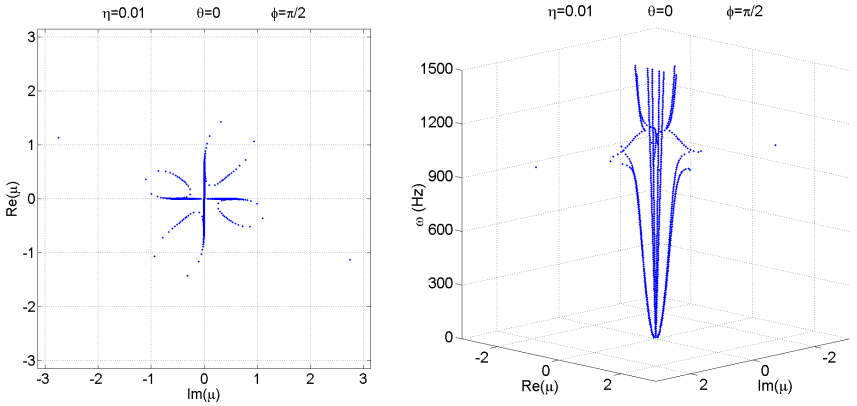


Figure 10: Complex dispersion curves of the infinite plate composed of the unit cells depicted in Figure 3 with 1% damping.

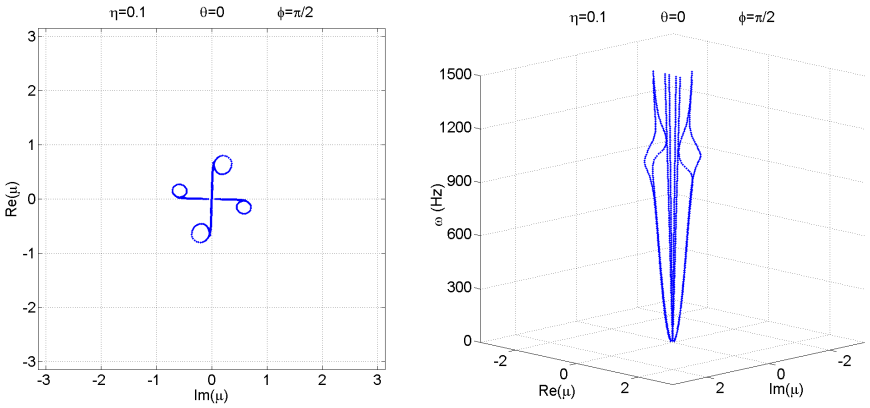


Figure 11: Complex dispersion curves of the infinite plate composed of the unit cells depicted in Figure 3 with 10% damping.

4 CONCLUSION

In this paper, the dispersion behaviour in an infinite plate composed of periodically distributed local resonant based metamaterial unit cells was investigated. Given the periodicity, an alternative Bloch-Floquet decomposition was adopted to reduce the computational effort required to analyse the structure. Using Bloch-Floquet decomposition, the infinite periodic plate can be represented by a single unit cell which includes all the necessary information. The alternative approach is especially of interest when dealing with damped structures or structures with frequency dependant material properties. The results presented in the paper, proves that adding local resonances to an infinite plate can introduce a gap in the dispersion curves around the frequency range of this resonance. This gap, commonly known as stop band, is a frequency range in which there is no free wave propagation through the structure. In addition, the effects of damping on dispersion behaviour of such structures were investigated by considering different amount of structural damping in the infinite plate. It was shown that the stop band phenomenon no longer exists in damped structures; instead the dispersion curves show a zone of highly attenuated waves. It is also shown that increasing the amount of damping wid-

ens the frequency range of this high attenuation zone while in return it decreases the maximum amount of attenuation. These two contradictory effects of structural damping on wave dispersion should be taken into account when dealing with damped structures.

ACKNOWLEDGEMENT

The European Commission is gratefully acknowledged for their support of the GRESIMO research project (GA 290050). The Fund for Scientific Research Flanders (F.W.O.) is gratefully acknowledged for its support. The research of Elke Deckers is funded by a grant from the Fund for Scientific Research-Flanders (F.W.O.). The Research Fund KU Leuven is gratefully acknowledged for its support.

REFERENCES

[1] C. Claeys, K. Vergote, P. Sas, W. Desmet, On the potential of tuned resonators to obtain low-frequency vibrational stop bands in periodic panels. *Journal of Sound and Vibration*, **332**(6), 1418–1436, 2013.

[2] Y. Xiao, J. Wen, D. Yu, X. Wen, Flexural wave propagation in beams with periodically attached vibration absorbers: band-gap behaviour and band formation mechanisms. *Journal of Sound and Vibration*, **332**, 867–893, 2012.

[3] M. Shen, W. Cao, Acoustic band-gap engineering using finite-size layered structures of multiple periodicity. *Applied Physics Letters*, **75**, 3713–3715, 1999.

[4] C. Claeys, P. Sas, W. Desmet, On the acoustic radiation efficiency of local resonance based stop band materials. *Journal of Sound and Vibration*, **333**(14), 3203-3213, 2014.

[5] J.B. Pendry, A.J. Holden, D.J. Robbins, W.J. Stewart, Magnetism from conductors and enhanced nonlinear phenomena. *Microwave Theory and Techniques*, IEEE Transactions on **47**(11), 2075–2084, 1999.

[6] F. Lemoult, N. Kaina, M. Fink, G. Lerosey, Wave propagation control at the deep subwavelength scale in metamaterials. *Nature Physics*, **9**, 55–60, 2012.

[7] F. Bloch, Über die Quantenmechanik der Electron in Kristallgittern. *Zeitschrift für Physik*, **52**, 550–600, 1928.

[8] G. Floquet, Sur les équations diff Trentielles linéaires a coefficients périodiques. *Annales de l'Ecole Normale Supérieure*, **12**, 47–88, 1883.

[9] L. Brillouin. *Wave propagation in periodic structures*. Dover Publication, 1953.

[10] M. Collet, M. Ouisse, M. Ruzzene, M.N. Ichchou, Floquet–Bloch decomposition for the computation of dispersion of two-dimensional periodic, damped mechanical systems. *International Journal of Solids and Structures*, **48**, 2837–2848, 2011.

[11] M. Collet, M. Ouisse, M. Ruzzene, M. Ichchou, A Floquet-Bloch decomposition of the elastodynamical equations for the computation of wave's dispersion in damped mechanical systems. *ISMA2010*, Leuven, Belgium, 2010.

[12] C. Claeys. Design and analysis of resonant metamaterials for acoustic insulation. Ph.D. dissertation, KU Leuven, April 2014.

[13] F. Fahy. *Sound and structural vibration*. Academic Press, London, 1987.

11th International Conference on Engineering Vibration
Ljubljana, Slovenia, 7–10 September 2015

ANALYSIS OF THE PERFORMANCES OF AUTOMOTIVE CAR BODIES WITH DIFFERENT STRUCTURAL CONTRASTS

M. Nobou Dassi*[1,2], A. Gaudin[1], Z. Abbadi[1], L. Gagliardini[1], C. Pézerat[2], F. Gautier[2]

[1]PSA Peugeot Citroën, Direction de la Recherche et de l'Ingénierie Avancée
Route de Gisy 78140 Vélizy, France
martial.noboudassi@mpsa.com

[2]Laboratoire d'Acoustique de l'Université du Maine,
Rue Aristote, 72085 Le Mans cedex 9, France

Keywords: Vibration, NVH performances, Structural contrast, Mobility, Automotive.

Abstract. *To reduce the greenhouse gas emissions produced by cars, one solution considered is to reduce their masses by using composite materials. However, the introduction of such orthotropic materials can significantly modify the automotive design due to the new distribution of local stiffnesses. These modifications may result in very different vibroacoustic behaviours and therefore different NVH performances. Indeed, the panels can participate more greatly to the overall stiffness of the car, reducing the ratio of frame in the architecture and therefore changing the structural contrast between frame and panels. The objective of this work is to investigate the NVH performances of several car body models built with different structural contrasts.*

Several strategies can be used to highlight the structural contrast of a mechanical system made of frame and panels. In this work, this concept is developed by calculating the input point mobilities. This approach allows building maps which are representative of the vibrational behaviour of the car body. On such maps, the areas corresponding to the presence of stiffeners (frame) can be identified, and a histogram containing the input points mobilities values allows the definition of a dynamic structural contrast indicator. This indicator can be used to evaluate the level of contrast of any kind of models.

1 INTRODUCTION

Since several years, the mass reduction of structures linked to CO_2 emissions in the automotive industry has become one of the main topics of industrial research. The main impact of introducing lightweight materials such as composite materials in a car is the very poor performance in terms of vibroacoustic behaviour. This performance is directly linked to some structural parts of the car body. As it happens, the resistance to external efforts is conventionally ensured by the frame, whereas the tightness is ensured by the panels. It seems obvious that this conventional configuration may change, due to the specific properties of the new used materials. In this context, panels made with composites materials may for example participate more greatly to the overall stiffness of a car.
Design an efficient architecture of car body suitable to the lightweight materials, highlight the main parameters that control the behaviour and evaluate the resulting NVH performance are the main topics that we are interested in. To achieve this, we will use a simplified model of car, which will be declined in several models with different configurations. The study of these models will allow bringing out the concept of structural contrast.

2 THE GENERAL AUTOMOTIVE NVH

The Noise and Vibration Harshness (NVH) of a car body is generally defined as the study and the modification of the noise and vibration characteristics of a vehicle to achieve a given performance target. In the automotive industry, the targeted performance is related to needs expressed by the customers, which are representative of the overall comfort feeling of the car. The expressed needs are accurately studied by techniques like System Engineering, which allow identification of subsystems that control the overall behaviour. This approach therefore leads to the definition of a functional and a component architectures, which ensure the coherence between the subsystems behaviours and the NVH performance.

2.1 The automotive NVH behaviour

During his life cycle, a car body is subjected to several kinds of excitations that generate operating organs vibrations and noise inside the air cavity. To reduce the noise and vibrations, Cremer [1] explains that one should control the phenomena bellow:

- the generation defined as the origin of an oscillation;
- the transmission of oscillatory energy to a passive structure;
- the propagation of the transmitted energy throughout the structural systems;
- the radiation of power from involved subsystems to the connected fluid.

These phenomena can be presented as shown in figure 1.
The figure 1 highlights the fact that some subsystems have to be accurately designed in order to satisfy the needs expressed by the stakeholders. To ensure the NVH performance, each subsystem shall fill specific functions. The set of functions to be filled by the subsystems defines *the functional architecture* of the car.

2.2 The automotive NVH performances

The NVH performance is defined for each considered frequency range. Indeed, each frequency range matches a particular behaviour, and therefore a specific definition of performance.

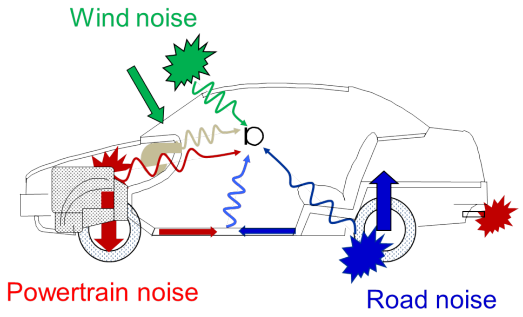


Figure 1: Noise sources and transfer paths on a car body.

The automotive frequencies ranges can be defined as following:

- *the Very Low Frequencies* (VLF) range, which corresponds to the zone where appear the first global deformation modes of the car body (torsional mode, bending modes...), vehicle suspension modes and the mounted powertrain modes. This range also correspond to the zone where appear the human being modes, which need to be carefully avoided;
- *the Low Frequencies* (LF) range, which corresponds to the zone where the car body has a modal behaviour, with distinct and isolated resonance peaks;
- *the Mid-Frequencies* (MF) range, reveals a mixed behaviour. While some areas of the car continue to have a modal behaviour, others have a more homogeneous behaviour with a high level of overlap between adjacent peaks. This dual behaviour makes this range difficult to analyse because it involves the use of both deterministic and statistical techniques;
- *the High Frequency* (HF) range corresponds to the zone where the response is almost uniform throughout the car. This behaviour allows the use of assumptions like diffuse field and energetic techniques on the overall car body.

Regarding the introduction of composites materials in the car and therefore the structural contrast, we are particularly interested in the NVH performance on the LF and the MF ranges.

2.2.1 The performance on the Low Frequency range

The LF range is related to a particular field of the mechanics which introduces all the deterministic methods and allows an accurate study of complex systems. These methods use appropriate mathematical developments in order to predict the response of a system in terms of displacement or pressure field for a given and well described excitation.
To meet the expressed needs, one should control the vibrational behaviour of the car and the pressure field in the air cavity, which represents the noise level felt by passengers. The vibro-acoustic performance will therefore be defined as the ability to guarantee a low level of vibration on the structure and a low level of pressure in the air cavity for a deterministic load applied to the system.

2.2.2 The performance on the Mid Frequency range

The MF range is characterised by a dual behaviour, representative to both LF and HF ranges. This dual behaviour requires the introduction of energetic approaches, which allow taking into account both stochastic and deterministic behaviours. Energy averages are then made to characterize the behaviour of the structure and the cavity.
To properly design on this frequency band, one should control the energetic vibrational levels on the structure and the energetic noise levels in the cavity. The NVH performance is therefore defined as the ability to guarantee a low energetic vibrational level on structural subsystems and a low energetic pressure level in the air cavity.

3 DESIGNING A SIMPLIFIED MODEL OF CAR FOR THE ANALYSIS

The models of cars presented in this section were already used by the authors in [4] and [3] in the general context of understanding the consequences of introducing composites materials in the automotive design. These models are simplified finite element models of a Citroën C3. The original model is a finite element body in white as shown in Figure 2. This original model has a mass of $284kg$ and $1,150,000$ degrees of freedom.

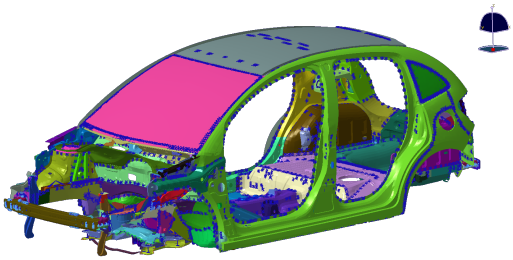


Figure 2: Original Finite Element Model

The simplified model car is obtained from this original model by introducing two main simplifications. The simplifications aim to provide an easy-to-use model, with sufficiently representative results compare to the original car body. The first simplification consists in representing the hollow sections by rectangular section beams, as presented in figure 3. This simplification reduces the number of degrees of freedom of the system (and therefore saves computation time). It also facilitates changing the thickness and inertia (without remeshing or morphing). Applying this on all the car body's hollow sections leads to the definition of the simplified model's frame.

The second simplification introduced consists in modelling some car body panels by introducing an orthotropic behaviour. This allows as presented in figure 4 to take into account both ribbed floors and composites materials panels behaviours. The application of this procedure leads to the definition of the simplified model's panels.
Assembling frame and panels allows the definition of the simplified model of car as presented in figure 5. This simplified model has only $200,000$ degrees of freedom.

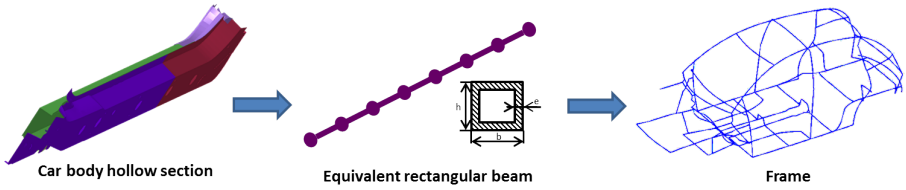


Figure 3: Designing the frame

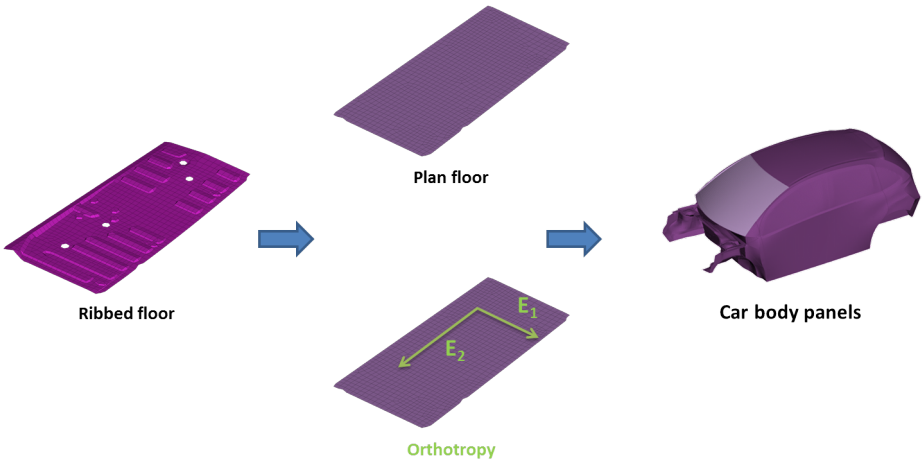


Figure 4: Modelling panels on the simplified models

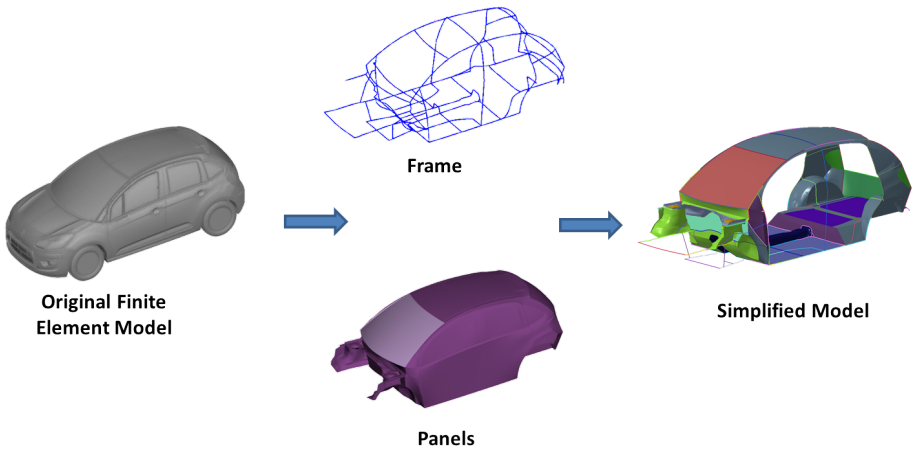


Figure 5: Simplified model of car body

4 THE CAR BODY MOBILITIES MAPS

A car body system generally has a high complexity, due to the presence of different component parts. The separation of the car body in a frame and a set of panels constitutes a first step of sub-structuring in order to overcome this complexity. The frame in this context represents the part that ensures resistance to the overall system, while the panels ensures tightness. To efficiently introduce the composites materials in the cars, we propose a point mobilities approach related to the energy balance of the car to characterize the contrast between the frame and the panels and identify the configuration which leads to the best performance compromise.

4.1 The car body point mobilities

The equation of the structure discretized by the finite element method is conventionally written in the harmonic domain as follows:

$$\left(K + jK_\eta + j\omega C - \omega^2 M\right) \mathrm{u}\left(\omega\right) = F\left(\omega\right), \tag{1}$$

where M, C and K are respectively the mass, the damping and the stiffness matrices. K_η is the structural damping matrix, associate to the loss factor η. ω is the pulsation, u is the displacement field and F is the applied force vector.
The projection on the eigen modes basis allows writing equation 1 as presented in equation 2, by introducing the eigen vectors matrix ϕ defined by $\mathrm{u} = \phi\mathrm{q}$:

$$\left(\phi^t K\phi + j\phi^t K_\eta\phi + j\omega\phi^t C\phi - \omega^2\phi^t M\phi\right) \mathrm{q}\left(\omega\right) = \phi^t F\left(\omega\right), \tag{2}$$

where q is the modal coordinates vector. If the damping is small enough, all projected matrices are diagonal. The terms of the diagonal can be written as follows:

$$\phi^t K\phi = [k_p] \tag{3}$$
$$\phi^t K_\eta\phi = [\eta_p k_p] \tag{4}$$
$$\phi^t C\phi = [c_p] \tag{5}$$
$$\phi^t M\phi = [m_p] \tag{6}$$

Equation 2 can therefore be written as:

$$\left(k_p(1 + j\eta_p) + j\omega c_p - \omega^2 m_p\right) \mathrm{q}_p\left(\omega\right) = \phi_p^t F\left(\omega\right), \tag{7}$$

The response of the system is then written as a sum of independent modal contributions as presented in equation 8:

$$\mathrm{u}\left(\omega\right) = \sum_{p=1}^{n} \frac{\phi_p\phi_p^t}{k_p(1 + j\eta_p) + j\omega c_p - \omega^2 m_p} F\left(\omega\right), \tag{8}$$

The input point mobility of a structure is the ratio between the velocity at the degree of freedom M_i and the applied force at the same degree of freedom as presented in equation 9:

$$Y_{M_i,M_i} = \frac{j\omega \mathbf{u}_{M_i}}{F_{M_i}}. \tag{9}$$

The transfer mobility of a structure is the ratio between the velocity at the degree of freedom M_i and the applied force at another degree of freedom Q_i as presented in equation 14:

$$Y_{M_i,Q_i} = \frac{j\omega \mathbf{u}_{M_i}}{F_{Q_i}}. \tag{10}$$

The damping is generally introduced either in viscous form or as a structural damping. The correspondence is ensured by writing at the resonance $\eta_p = 2\xi_p$. It is also possible to introduce the concepts of effective modal masses, effective modal forces and generalized modal pulsation respectively defined as:

$$m_p^{eff} = \frac{\phi_p^t M \phi_p}{\phi_p^t \phi_p} \tag{11}$$

$$F_p^{eff} = \frac{\phi_p^t F}{\phi_p^t \phi_p} \tag{12}$$

$$\widehat{\omega}_p^2 = \omega^2(1 - j\eta_p) \tag{13}$$

The mobility can therefore been written as:

$$Y_{M_i,Q_i}(\omega) = \sum_{p=1}^{n} \frac{j\omega}{\widehat{\omega}_p^2 + 2j\xi_p\omega_p\omega - \omega^2} \frac{\phi_p^M \phi_p^Q}{m_p}. \tag{14}$$

4.2 The energy balance and mobilities maps

The energy balance of a structure is done by introducing the terms of injected and dissipated power. The injected power due to an excitation force F is conventionally written as presented in equation 15:

$$\Pi_F = \mathbb{R}e\left(\mathrm{V}^* F\right), \tag{15}$$

where V^* is the conjugate transpose of the velocity. For an isolated system, the dissipated power equals the injected power. If the damping is introduced by a constant loss factor, the vibrational energy is proportional to the average power dissipated through the structural loss factor.
To study the power injected into the structure, we assume a force having constant spectral power density and which is therefore frequency independent. Using the definition of the input point mobility in a modal approach, the mean injected power $\langle \Pi_F \rangle$ is written as follows:

$$\langle \Pi_F \rangle_{\Delta\omega} = \int_{\Delta\omega} \mathbb{R}e\left\{F^* Y^* F\right\} d\omega \tag{16}$$

$$= \int_{\Delta\omega} \mathbb{R}e\left(\sum_{p=1}^{n} \frac{j\omega}{\widehat{\omega}_p^2 + 2j\xi_p\omega_p\omega - \omega^2} \frac{F^t \phi_p \phi_p^t \overline{F}}{m_p}\right) d\omega \tag{17}$$

$$\langle \Pi_F \rangle_{\Delta\omega} = \sum_{p=1}^{n} \frac{\left|\phi_p^t F\right|^2}{m_p} \int_{\Delta\omega} \mathbb{R}e\left(\frac{j\omega}{\widehat{\omega}_p^2 + 2j\xi_p\omega_p\omega - \omega^2}\right) d\omega. \tag{18}$$

The term in the integral tends to $\frac{\pi}{2}$ when the resonance frequency is included the band $\Delta\omega$ and is equal to zero otherwise. The mean injected power therefore becomes:

$$\langle \Pi_F \rangle_{\Delta\omega} \approx \frac{\pi}{2} \sum_{\omega_k \in \Delta\omega} \frac{\left|\phi_k^t F\right|^2}{m_k}. \tag{19}$$

For mass normalized modes, the mean mobility at the degree of freedom M_i is therefore written as:

$$\langle Y_{M_i,M_i} \rangle_{\Delta\omega} \approx \frac{\pi}{2} \sum_{\omega_k \in \Delta\omega} \frac{\phi_k^2(M_i)}{\Delta\omega}, \tag{20}$$

In the case of a 3D structure, the point mobility correspond to a matrix. To characterize the excitability of a structure, it is logical to consider the mobility in the direction of maximum excitability. This quantity calculated at each node of the model allows building of a mobilities map, which shows the stiffness behaviour of each zone of the car. An example of mobilities map for the frequency band $[500 - 1000]$Hz is presented in figure 6.

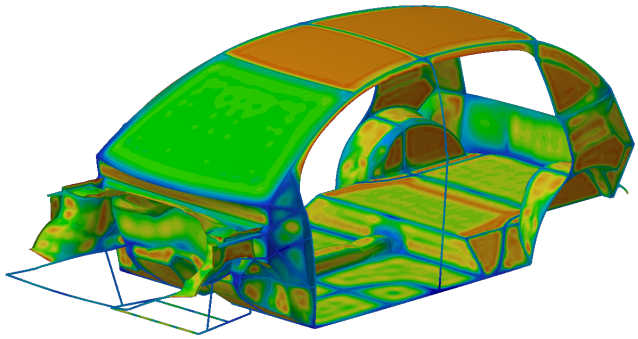


Figure 6: Mobilities map of the simplified model of car

On such a map, the areas corresponding to the presence of stiffeners (frame) can be identified easily. We are interested in understanding the evolutions of mobilities values obtained on this map.
Let us consider some elements of the model and compare the obtained mobilities with corresponding analytical values. Studying evolution of point mobilities between the different areas of the structure will allow highlighting a structural contrast. Cremer [1] gives the as presented in equation 21 an analytical expression of point mobility for an infinite plate, computed in its center:

$$Y_{Ana} = \frac{1}{4}\sqrt{\frac{3(1-\nu^2)}{\rho E h^4}}, \tag{21}$$

where ν is the Poisson ratio of the material, ρ is the mass density, E is the Young modulus and h is the thickness of the plate. Let us consider the roof, the windscreen and the rear floor pan having different mobilities values as highlighted in figure 7.
These panels have the properties presented in table 1

	$E[MPa]$	$\rho[\frac{t}{mm^3}]$	ν	$h[mm]$
Roof	$2.10\ e^{+5}$	$7.85\ e^{-9}$	0.3	0.67
Windscreen	$7\ e^{+4}$	$2.5\ e^{-9}$	0.22	4.4
Rear floor pan	$13.65\ e^{+6}$	$7.85\ e^{-9}$	0.3	0.67

Table 1: Selected panel's properties

As explained during the presentation of the simplified model, some panels have an orthotropic behaviour. The rear floor pan is one of those panels. Since the values displayed on each node correspond to the mobilities in the direction of maximum excitability, the Young modulus used

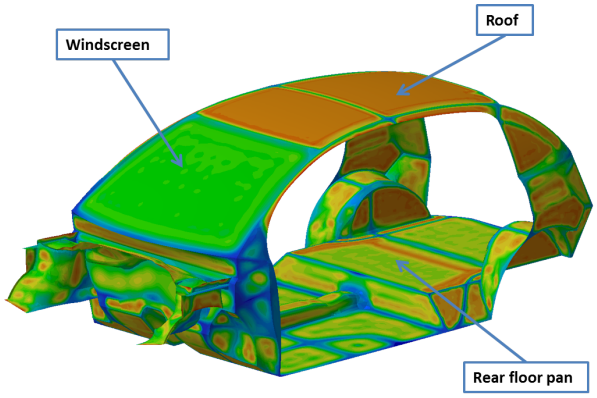


Figure 7: Selected panels mobilities

to calculate the analytic values is taken in the same direction. Applying these properties in equation 21 leads to the analytical mobilities Y_{Ana} presented in table 2. The table also presents the numerical mobilities values Y_{Num}, obtained on the built map.

	Roof	Windscreen	Rear floor pan
$Y_{Ana}[(\frac{mm}{t.N})^{\frac{1}{2}}]$	22.66	1.65	2.8
$Y_{Num}[(\frac{mm}{t.N})^{\frac{1}{2}}]$	19.2	1.1	3

Table 2: Comparison of analytical and numerical mobility

The mobilities levels obtained analytically and numerically are close enough to validate the developed approach. The small differences between the values can be attributed to the fact that the selected panels are not infinite (as considered in the analytical approach), and the selected panels interact with other subsystems having different mobilities levels.
Cremer also give an analytical expression of point mobility for an infinite beam. This mobility computed in the center of the beam is written as presented in equation 22:

$$Y_{Ana} = \frac{1}{4\sqrt{\omega}} \frac{1-j}{(EI)^{\frac{1}{4}}(\rho A)^{\frac{3}{4}}}, \tag{22}$$

where j is the imaginary unit, I is the moment of inertia of the beam and A is the section area of the beam. Let us consider (as done for the panels) the roof reinforcing crosspiece, the engine support and the centre pillar as highlighted in figure 8.
These beams have the properties presented in table 3

	$E[MPa]$	$\rho[\frac{t}{mm^3}]$	ν	$I[mm^4]$	$A[mm^2]$
Roof reinforcing crosspiece	$2.10\ e^{+5}$	$7.80\ e^{-9}$	0.3	$2.78\ e^{+3}$	173.32
Engine support	$2.10\ e^{+5}$	$7.80\ e^{-9}$	0.3	$2.32\ e^{+2}$	30.84
Centre pillar	$2.10\ e^{+5}$	$7.80\ e^{-9}$	0.3	$3.05\ e^{+5}$	720.44

Table 3: Selected beam's properties

As explained in the case of the panels, the mobilities are computed in the direction of maximum

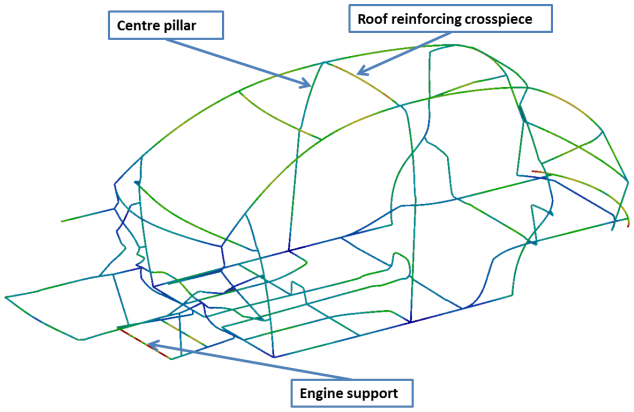


Figure 8: Selected beams mobilities

excitability. The moments of inertia here presented are thus taken in the same direction. Applying these properties in equation 22 leads to the analytical mobilities values Y_{Ana} presented in table 4. The table also presents the numerical mobilities values Y_{Num}, obtained on the built map.

	Roof reinforcing crosspiece	Engine support	Centre pillar
$Y_{Ana}[(\frac{mm}{t.N})^{\frac{1}{2}}]$	0.72	4.91	0.076
$Y_{Num}[(\frac{mm}{t.N})^{\frac{1}{2}}]$	0.68	4.69	0.07

Table 4: Comparison of analytical and numerical mobility

Table 4 allows validating the beam's mobilities values obtained on the maps. The observed differences can be attributed to the nature of the beams (not infinite as supposed in the analytical expression), to the presence of adjacent elements, and also to the curvature.
This approach brings out the fact that an automotive structure has areas with different mobility levels, due to local stiffness differences. These differences can be characterized by introducing the concept of structural contrast. We are interested in defining a related indicator which helps understanding the impact of changing materials on the vibroacoustic performances of a car.

5 LIGHTWEIGHT MODELS AND DEFINITION OF THE CONTRAST INDICATOR

5.1 Definition of lightweight models

The use of composites materials in the automotive design has significant advantages that Giocasa presents in his work [2] as following:

- a low mass density of the final structure;
- the possibility to obtain structures with complex geometry by moulding and over-moulding;
- the use of the optimum amount of material required for the desired function;
- removing machining.

Such materials may however introduce difficulties, due to the new distribution of local stiffnesses. To analyse their impacts on the design, one solution is to build a comparative analysis with models having different design scenarios and therefore different structural contrast levels. In order to achieve this, we propose to change the Young modulus used for the frame, from a very low value corresponding to a polymer (E $\approx 8 * 10^8$ Pa) to a high value corresponding to a carbon fiber (E $\approx 4 * 10^{11}$ Pa). Switching from one model to another, the Young modulus is doubled while the Poisson ratio and mass density are kept constant in order to observe only the effect of the structural contrast. Thus, the 10 built models have the frame material properties presented in table 5.

Model	1	2	3	4	5	6	7	8	9	10
$E[Pa]$	$8.20\ e^5$	$1.64\ e^6$	$3.28\ e^6$	$6.56\ e^6$	$1.31\ e^7$	$2.63\ e^7$	$5.25\ e^7$	$1.05\ e^8$	$2.10\ e^8$	$4.20\ e^8$
ν	0.3	0.3	0.3	0.3	0.3	0.3	0.3	0.3	0.3	0.3
$\rho[\frac{kg}{m^3}]$	$7.8\ e^3$	$7.8\ e^3$	$7.8\ e^3$	$7.8\ e^3$	$7.8\ e^3$	$7.8\ e^3$	$7.8\ e^3$	$7.8\ e^3$	$7.8\ e^3$	$7.8\ e^3$

Table 5: Frame material's properties

5.2 Mobilities histogram and contrast indicator

For each of the defined models, a study of the structural contrast is done on the frequency band $[0 - 1000]$ Hz, in order to highlight the evolution of the structural contrast while the frequency increases. A mobilities map of each model is built. Figure 9 presents mobilities maps of the models 1, 6 and 10. These models are chosen because they allow to observe major changes in structural contrasts.

To understand the results provided by the maps, let us introduce some parameters used in the image theory. An image histogram is conventionally defined as the function that associates to each intensity value the number of pixels having that value. There are several definitions of contrast of an image. Peli [5] presents in his work a common way to define the contrast of an image, so that the contrasts of several images can be compared. He used the root-mean-square contrast definition presented in equation 23.

$$rms = \sqrt{\frac{1}{N-1}\sum_{n=1}^{N}(x_n - \overline{x})^2}, \tag{23}$$

where x_n is a normalized grey-level value and $\overline{x}$ is the mean normalized gray level. To characterize the structural contrast of a car, we are interested in building similar parameters based on a mobilities map. Let us consider at each node the trace of the real part of the mobilities matrix, corresponding to the sum of translational mobilities as defined in equation 24.

$$Y_i = Y_{x_i} + Y_{y_i} + Y_{z_i}. \tag{24}$$

This definition allows building histograms related to mobilities maps as presented in figure 9 for models 1, 6 and 10. On such histograms, the main differences between the models appear on the nodes having low mobilities level, and corresponding to the frame. Indeed, since the panels have not been changed, their average mobilities remain unchanged as visible from ≈ 3 to 200 [mm/s/N]. It is also possible to notice that the more the frame is stiffened, the more low mobilities nodes we have. Finally, we note that the windscreen properties remain unchanged,

and his mean mobility correspond to the peak near 1 [mm/s/N]. Since the firsts (more flexible) models have more nodes with that mobilities level, it seems that the more stiff the model is, the less nodes with that mobility level we have. To summarize:

- we observe four sets of nodes with the same mean mobility level. These sets can be attributed to zones of the maps as highlighted in figure 9;
- the number of sets in the histogram (four in this case) can be used to characterized the global behaviour of the car;
- when the contrast increases (in this design case), the number of nodes in the lowest mobility set increases, the one in an intermediate set decrease and the one in the highest mobility set remains constant.

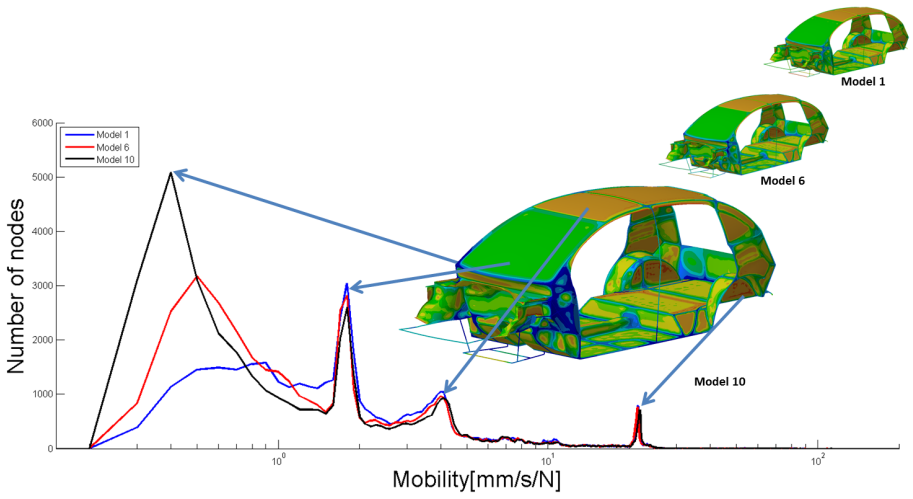


Figure 9: Mobilities histogram of models 1, 6 and 10

To quantitatively characterize the structural contrast of the models, let us introduce the *structural contrast indicator* (SCI) defined as presented in the equation 25. Such an indicator is dimensionless and consistent with the defined concept of an image contrast.

$$SCI = \frac{\{rms\}^2}{\overline{x}}. \tag{25}$$

Since we are interested in the dynamic behaviour of the system when the contrast increases, we present in figure 10 the evolution of the SCI function of the frequency, in third octave average for the models 1, 6 and 10.
The figure 10 give a dynamic structural contrast indicator on the band $[200 - 800]$ Hz. The band $[0 - 200]$ Hz is indeed dominated by a modal behaviour, with resonant nodes (so very high mobilities) somewhere and non-resonant nodes elsewhere. The structural contrast therefore has no physical meaning on such a band.

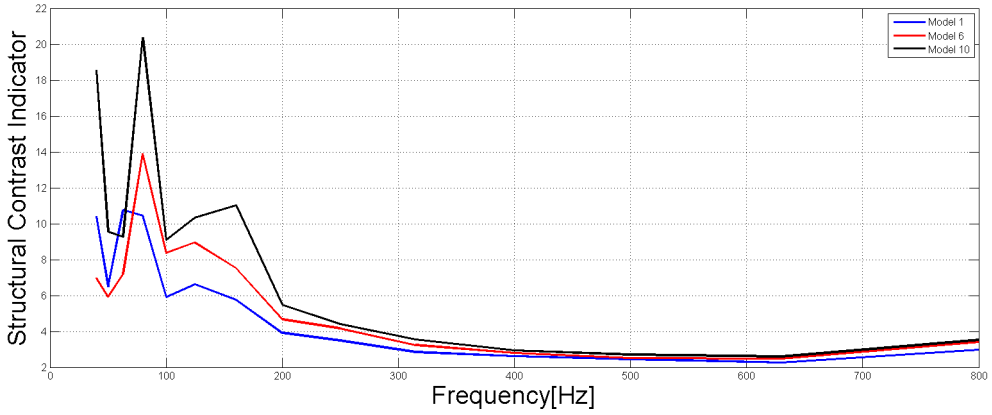


Figure 10: Structural Contrast Indicator of the models function of frequency

6 CONCLUSIONS

This study focussed on the main consequences of changing materials in a car, in the global context of automotive lightweight design. The new distribution of local stiffnesses due to the introduction of orthotropic materials leads to models with different structural contrasts. This concept has been highlighted, by using an input point mobility approach. Built mobilities maps allowed studying the distribution of stiffness on the models, and defining a kind of characteristics mobility sets. A dynamic structural contrast indicator is proposed, consistently to the image theory. This work is continuing in order to understand the relation between the structural contrast and the vibroacoustic performance of a car, defined in terms displacement levels on the structure and pressure levels in the air cavity.

ACKNOWLEDGMENTS

The authors would like to thank the Marie Curie Foundation which finances this research through the GRESIMO Initial Training Network project.

REFERENCES

[1] Lothar Cremer, M. Heckl, and B. A. T. Petersson. *Structure-borne sound structural vibrations and sound radiation at audio frequencies*. Springer, Berlin; New York, 2005.

[2] Alain Giocosa. *Les composites dans l'industrie automobile*. Techniques Ingnieur, 1999.

[3] Martial Nobou Dassi and Al. Vibro-acoustic specifications and design indicators for lightweight vehicles. *International Conference on Noise and Vibration Engineering*, Leuven 2014.

[4] Martial Nobou Dassi and Al. Conception vibro-acoustique de caisses autmobiles allégés : Analyse par games de fréquences et indicateurs associés. *Congrès Francais d'Acoustique*, Poitiers 2014.

[5] Eli Peli. Contrast in complex images. *Journal of the Optical Society of America*, 7(10), October 1990.

International Conference on Engineering Vibration
Ljubljana, Slovenia, 7-10 September 2015

ON VARIABLE SCREENING AND OPTIMIZATION OF CAR BODY STRUCTURES SUBJECT TO MULTIDISCIPLINARY CONSTRAINTS

R. Sala*[1], N. Baldanzini[1], M. Pierini[1]

[1]Università di Firenze, Dipartimento di Ingegneria Industriale
*ramses.sala@unifi.it

Keywords: Eigenfrequency Optimization, Variable Screening, Multidisciplinary Design Optimization, Crashworthiness, Lightweight Design.

Abstract. *Besides eigenfrequency and other NVH related targets vehicle structures are required to satisfy multidisciplinary design criteria. Efficient multidisciplinary design while taking in to account conflicting structural requirements for car body structures comes with many challenges: the large number of parameters or design variables spans a vast high dimensional search space; the high computation cost for crashworthiness simulations strongly limits the number of available design evaluations; and the highly non-linear and non-convex simulation model responses complicate the search procedure for global optimization algorithms. There are various state of the art techniques that could be used to deal with these challenges separately, there are however only few significant guidelines available in the literature that help to select effective methods for the application to vehicle design problems which involve NVH, crashworthiness and light weight criteria, and the resulting previously mentioned challenges.*
Variable screening and sensitivity analysis methods can be applied in order to reduce the dimensionality of the search space by selecting the most relevant design variables, this comes however at additional function evaluation and computation cost. For the optimization of highly nonlinear and non-convex multidisciplinary structural problems many nature inspired optimization algorithms have been proposed, the selection of efficient optimization algorithms remains however difficult.
This communication presents an interdisciplinary review of state of the art on variable screening, sensitivity analysis, and optimization methods and comparisons on their performance to deal with some typical challenges that occur in the design of automotive structures. Since the design of car body structures deals with expensive simulations the performance of the methods are compared in terms of the computational effort and efficiency. Also the combined effects of variable screening based dimension reductions on the optimization efficiency will be assessed, to identify effective design strategies.

11th International Conference on Engineering Vibration
Ljubljana, Slovenia, 7–10 September 2015

THE IMPACT OF THE STRUCTURAL NON-LINEARITY ON THE VIBRATION FATIGUE DAMAGE ACCUMULATION

Uroš Proso*[1], Janko Slavič[2], Miha Boltežar[2]

[1]Faculty of Mechanical Engineering, University of Ljubljana, Slovenia
uros.proso@fs.uni-lj.si

[2]Faculty of Mechanical Engineering, University of Ljubljana, Slovenia
{janko.slavic, miha.boltezar}@fs.uni-lj.si

Keywords: Vibration Fatigue, Damage Accumulation, Structural Non-linearity, Structural Dynamics.

Abstract. *High cycle vibration fatigue is the main cause for the damage in structural components which accumulates while structure is excited by random dynamic loads. Significant influence of the structural non-linearity on the damage accumulation is supposed. A validated numeric investigation of a linear dynamic structure is used for vibration fatigue damage-accumulation estimation. The accelerated vibration tests are performed for vibration fatigue lifetime determination and non-linearity quantification. The structure is excited at increasing excitation levels where an increasing level of non-linearity is observed by a FRF based approach. The FRF based structural non-linearity rate is used for the linear damage accumulation correction. The research is expected to give results with applicability to similar cases and opens up new potential in the field of structural - vibration fatigue optimization.*

1 INTRODUCTION

Fatigue failures in metallic structures are a well-known technical problem [1]. Fatigue damage increases with applied load cycles in a cumulative manner. Probably the first systematic fatigue testing was undertaken by Wöhler [2] who concluded that cyclic stress range is more important than peak stress and introduces the concept of endurance limit. Palmgren [3] introduced the first damage accumulation theory which is now known as linear rule and Miner [4] expressed the linear rule in a mathematical form as a summation of the damages with different loadings which were calculated as a ratio between the number of applied cycles and the number of total cycles until failure for ith constant amplitude loading level. Marco and Starkey [5] proposed a non-linear load dependent damage rule based on an exponentiated Miner's damage accumulation of the coefficients depending on ith load level. Recently Aid et al.[6] proposed a new damage model for fatigue life prediction under variable loading based on the stress history which includes a load depended non-linear damage accumulation. Huffman and Beckman [7] used strain load history in their approach to predict fatigue life time due to damage accumulation process at different loading levels.
High cycle, vibration fatigue, related to structural dynamics is the focus of this research. Fatigue life-time and damage accumulation issues in relation with the change of the structural dynamics i.e. structure's frequency response functions, were extensively studied [8, 9, 10, 11]. Shang et al. [8, 9] experimentally and numerically investigated effects of fatigue damage accumulation on the natural frequency response. They identified a non-linear change of the natural frequencies as the damage propagates. Shang [9] proposed a new damage accumulation variable according to the non-linear change of the natural frequencies. Dattoma et al. [10] deal with the application of a technique based on the natural frequencies and damping to predict fatigue failure of closed cell aluminium foams. Česnik et al. [11] presented an improved accelerated fatigue - testing methodology based on the dynamic response of the test specimen to the harmonic excitation in the near-resonant area with simultaneous monitoring of the modal parameters.
This research deals with the effects of the structure's non-linearity on the damage accumulation. Non-linearity arises as a results of changes in geometries of the structure during the test. Rate of structure's non-linearity is estimated via the change of the amplitude in the experimentally measured frequency response functions (Section 2). Numerical investigation, shown in Section 3, is performed to obtain the linear damage accumulation of the structure which is combined with non-linearity rates to obtain real damage accumulation used for the life-time assessment. Accelerated vibration tests shown in Section 4 are performed to validate numerical model by the operational modal analysis, identify real fatigue lifetimes and non-linearity of the structures at different excitation levels. Results and discussions are presented in Sections 4 and 5.

2 THEORETICAL BACKGROUND

One of the most common causes of the structural damage is the material fatigue. Under the concept of the material fatigue is considered defect of the material under dynamic load which is always less than static[12]. The damage due to fatigue process does not occur instantly. It starts with an initial crack in places of stress concentration and propagates to the total damage [13].
Initially, the linear damage accumulation theory is presented which will support the later introduced non-linearity to the damage accumulation.

2.1 Linear Damage Accumulation

Here, for the damage accumulation analysis, the high-cycle fatigue stress-based method is used [2, 13, 14]. Wöhler [2] investigated fatigue and used the stress-cycles (S-N) curve to characterise the fatigue behaviour of materials. Wöhler's curve can be represented in the Basquin's equation [15]:

$$\sigma = C\, N^{-\frac{1}{b}}, \tag{1}$$

where b is the fatigue exponent, C is the fatigue strength and N is the number of cycles. The linear damage accumulation is calculated by Palmgren - Miner rule [3, 4]:

$$D = 1 = \sum_i D_i = \sum_i \frac{n_i}{N_i}\,, \tag{2}$$

where D is the total damage, D_i is the damage caused by excitation with amplitude σ_i, N_i represents the number of cycles with amplitude σ_i required for total damage and n_i is the real number of cycles.

2.2 Damage Accumulation Correction Rule

Damage accumulation rule used for correcting linear damage accumulation and based on the structural non-linearity, is proposed as Eq. (2):

$$D_n = \sum_i D_i \cdot R^{n_i} = 1\,, \tag{3}$$

where R represents the constant correction-factor and n the rate of non-linearity which can be the experimentally identified from Eq.(4) presented in the next subsection.

2.3 Structural Non-linearity Rate Estimation

Experimental investigation, presented later in Chapter 4, is used for identifying of the non-linearity of the dynamical systems from measured frequency response functions (FRFs).
In order to estimate the rate of the non-linearity, experimentally obtained FRFs at different excitation levels need to be obtained. Rate of the non-linearity estimation was based on two assumptions. A FRF with relative low excitation level is assumed linear, while the changes in FRFs at relative hight excitation levels are assumed due to structure's non-linearity.
This research proposed calculation of the rate of non-linearity n as the root mean square error in the logarithmic scale:

$$n = \sqrt{\frac{\sum_{j=1}^{N}(\log_{10}(|\mathrm{FRF}_l|_j) - \log_{10}(|\mathrm{FRF}_n|_j))^2}{N}}\,. \tag{4}$$

FRF_l and FRF_n represent the linear FRF and non-linear FRF, respectively. The index j represents the points on the frequency axis while N represents the number of points. The logarithmic scale is used as the changes in FRFs are logarithmic, also the identification of the non-linearity is in the logarithmic scale.

3 THE NUMERICAL MODELLING

The motivation for this investigation was a real industrial vibration fatigue case of a thermal shield plate attached with rivets to the supporting structure. The rivets were braking due to vibration fatigue. Figure 1 shows a simplified numerical model which correspond with the real

case and consist of the steel plate and the aluminium supporting structure, attached by three rivets. The numerical model is built from 73 518 elements and 115 700 nodes. The tetrahedral (supporting structure), hexagonal (rivets) and triangle (plate) elements are used to build the discrete dynamic model. Experimental validation of the numerical model is presented in Section 4.

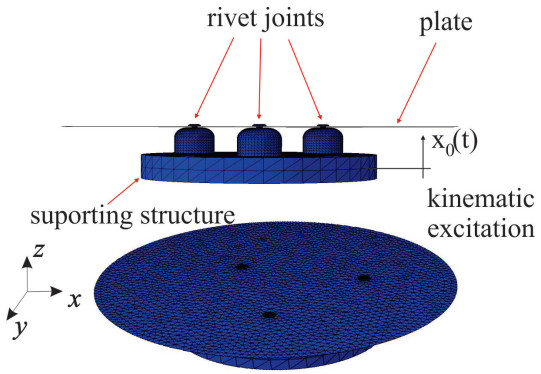


Figure 1: Dynamic - Numerical Model

With a validated numerical model the linear damage accumulation estimation requires the following steps: The first step is to obtain the stress frequency response function (SFRF) which is used with the excitation profile to obtain the stress response. The second step is to estimate the fatigue life-time in the frequency domain. The third step is the damage accumulation calculation. At different excitation levels, different fatigue life-times and different damage accumulations are obtained.

3.1 Stress Frequency Response and Stress Response Estimation

The numerical fatigue life-time estimation is based on the stress response prediction of the constrained structure similar to the real structure. The modal model, stress and displacement responses, required for the stress response prediction of the constrained structure, are obtained from modal analysis of the unconstrained structure. The unconstrained structure is modified by kinematic excitation like in real case and experimental research and also model is added by material parameters, damping and load parameters. The extended structural modification using response function (SMURF) method, presented by Česnik $et.\,al.$ [17] was used to predict a SFRF and stress response of the constrained structure using the modal model of the unconstrained structure in case of kinematic excitation. According to [17] equilibrium equations for a viscously damped MDOF force excited dynamic structure:

$$[\mathbf{M}]\{\ddot{\mathbf{x}}\} + [\mathbf{C}]\{\dot{\mathbf{x}}\} + [\mathbf{K}]\{\mathbf{x}\} = \{\mathbf{f}\}\,, \tag{5}$$

where **M**, **C** and **K** are mass, damping and stiffness matrices, respectively. **x** and **f** represent the vector of total displacements and excitation force vector, respectively. The solution to the Eq. (5) is given as:

$$\{\mathbf{x}\} = [{}^{\mathbf{c}}\mathbf{H}(\omega)]\{\mathbf{f}\}\ , \tag{6}$$

where ω represents frequency and ${}^{\mathbf{c}}\mathbf{H}(\omega)$ represents the constrained structure's receptance matrix calculated by using the modal model of unconstrained structure. With several transformations of Eq.(6) [17], response of the unconstrained point is:

$$\mathbf{x_u} = ({}^{\mathbf{u}}\mathbf{H_{uc}}\,{}^{\mathbf{u}}\mathbf{H_{cc}^{-1}})\,\mathbf{x_0} + ({}^{\mathbf{u}}\mathbf{H_{uu}} - {}^{\mathbf{u}}\mathbf{H_{uc}}\,{}^{\mathbf{u}}\mathbf{H_{cc}^{-1}}\,{}^{\mathbf{u}}\mathbf{H_{uc}})\,\mathbf{f_u}\,, \tag{7}$$

where $\mathbf{x_0}$ and $\mathbf{f_u}$ are base displacement and applied force, respectively. $\mathbf{x_0}$ is shown in Figure 1 and $\mathbf{f_u} = 0$ in this research. For fatigue life - time estimation stress response was predicted as:

$$\sigma = ({}^{\mathbf{u}}_{\sigma}\mathbf{H_c}\,{}^{\mathbf{u}}\mathbf{H_{cc}^{-1}})\,\mathbf{x_0}\,. \tag{8}$$

More details about extended SMURF method issues were presented in reference paper [17].

3.2 Fatigue Life - Time Estimation in Frequency Domain

Estimated stress response was used for fatigue life time estimation using the frequency domain methods. Mršnik et al.[18] compared different frequency-domain counting methods and it turned out that the Tovo-Benasciutti method [19, 20] gave the best estimation in the majority of experiments hence it is used in this research. Instead of the time-until-failure the damage intensity or damage per unit time ($\overline{D}$) is used here:

$$\overline{D} = \nu_p\, C^{-1} \int_0^{\infty} s^k\, p_a(s)\mathrm{ds}\,, \tag{9}$$

where ν_p is expected peak occurrence frequency, calculated from the random process defined by the power spectral density, C and k are material parameters and $p_a(s)$ is the cycle amplitude probability density function of the random process [18]. Fatigue life-times T are calculated from damage intensity as:

$$T = \frac{1}{\overline{D}}\,. \tag{10}$$

3.3 Linear Damage Accumulation Calculation

With regards to Eq.(2) and estimated fatigue life-times (Eq. 10), damage accumulation equation can be rewritten as:

$$D = 1 = \sum_{i=1} D_i = \sum_{i=1} \frac{t_i}{T_i}\,, \tag{11}$$

where t_i and T_i represent time during the structure excited and fatigue life-time for the i-th excitation level, respectively.

Initially, the linear numerical model was virtually excited for 30 minutes with random acceleration excitation with 5 g amplitude in the frequency range from 10 to 2000 Hz. The fatigue life-time is estimated by numerical procedure presented in Sections 3.1 and 3.2 and damage accumulation is calculated according to Eq.(11). For the numerical model procedure is repeated at higher excitation levels (6 g, 7 g,...), 30 min at each level, until cumulative damage reached 100 percent. The failure of the linear numerical model occurs after 15.83 min at the 12g excitation level.

Table 1. Damage Accumulation for the Linear Numerical Model

Excitation level (i) [g]	T_i[min]	t_i[min]	D[%]	$Acc.D$[%]
5	1819.98	30	1.6	1.6
6	916.87	30	3.3	4.9
7	513.5	30	5.8	10.7
8	310.8	30	9.7	20.4
9	199.58	30	15	35.4
10	134.28	30	22.3	57.7
11	93.83	30	32	89.7
12	67.65	15.83	10.3	100

Table 1 represents the numerical results. Excitation levels, fatigue life-times T_i, excitation times t_i, damage accumulation at each level D[%] and accumulated damage $Acc.D$[%] are presented in the first, second, third, fourth and fifth column, respectively.

4 Experimental Research

Experimental setup is shown in Figure 2. It is used for numerical model validation and updating (Section 3), estimation of the model non-linearity and identification of the experimental (real-model) fatigue life-time which is compared with numerical results. The following subsections deal with parts of the experimental research in details.

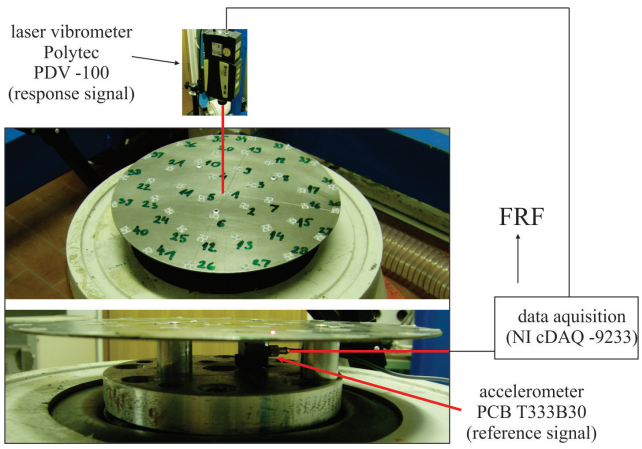


Figure 2: Electro-Dynamic Shaker and the Experimental Setup

4.1 Model Updating

Operational modal analysis was used for experimental validation of the numerical model with relative low excitation level where the structure was assumed as linear. Experimental validation was performed by estimating FRFs at 41 response points on the steel plate, see Figure 2. Reference signal was measured on the aluminium supporting structure with an accelerometer (Figure 2). The numerical model was updated according to the experimentally obtained natural frequencies and mode shapes.

4.2 Estimation of the Non-linearity

As it was explained in Section 2 estimated FRFs were used for estimation of the model's non-linearity rates for different excitation levels, see Eq.(4). For the FRF estimation, the response was measured at the center of the attached steel plate and the reference signal was measured at the controlled shaker fixation head, see Figure 2.

4.3 Accelerated Fatigue Test

Accelerated fatigue tests were performed with standard electro-dynamical shaker equipment. The vibration profile was controlled by vibration controller LDS Dactron, power amplifier LDS PA1000L and personal computer. The hardware and software with a control loop were used to generate the excitation according to given constant broad-band power spectral density in the range from 10 to 2000 Hz. At the same time, the measured signals were also discretized by DAQ module and saved for later analysis. The sampling frequency was 10000Hz.

4.4 Identification of the Fatigue Life

Experimental tests are also used for identification of the experimental fatigue life-times. The natural frequency close to 680 Hz has been chosen for tracking in the experimental fatigue life-times identification. A several research [8, 9, 10, 11] concerned with changing of the natural frequencies related to fatigue damage propagation and this is sensitive matter. According to mentioned research, 10 percentage decrease of the natural frequency was assumed as a crack appearance.

4.5 Corrected Damage Accumulation Rule

The corrected linear damage accumulation concept, presented in Section 2, was used on the two samples which slightly differ due to uncertainty in assembling and cause differences in the non-linearity of the samples. Each sample was excited for 1 min at 1g excitation level to obtain the linear FRF and then followed at excitation levels at 5 g, 6 g, 7 g, 8 g,..., until failure (each level was applied for a maximum of 30 minutes). Figure 3 present numerically simulated vibration fatigue damage accumulations, linear and corrected linear. The linear damage accumulation for each excitation level was divided into thirty (one minute long) parts to calculate the corrected linear damage accumulation D_n, according to the Eq.(3):

$$D_n = \sum_j D_j \cdot R^{n_j} = 1\,, \tag{12}$$

where index j presents number of steps (one minute represents one step for the all excitation levels) and D_i presents the linear damage accumulation for particular step (the damage accumulation for whole period (for all excitation levels) is divided that damage accumulation for each step is calculated). The rate of non-linearity n_i is calculated by Eq.(4). The constant correction-factor R is calculated as a result of the minimizing of the least-squares error between numerical and experimental results for both samples together:

$$E(R) = \sum_j^m [T_{ex_j} - T_{nu_j}]^2\,, \tag{13}$$

$$\frac{\partial E}{\partial R} = 0\,, \tag{14}$$

where T_{ex}, T_{nu} and m represent experimentally identified, numerically (corrected linear) estimated fatigue life-time and number of tested samples, respectively. The constant correction factor calculated according to the Eq.(13) for both samples is $R = 180$. Comparison of the results is shown in Table 2. The last column in Table 2 presents error for the each sample. Figure 3 shows damage accumulation curves for correction factor calculated due to minimizing of the common error.

Table 2. Comparison of results

Sample	Numerical (corrected - linear) [min], T_{nu}	Experimental [min], T_{ex}	Error [%]
1	80.8	82	1.46
2	87.6	93	5.8

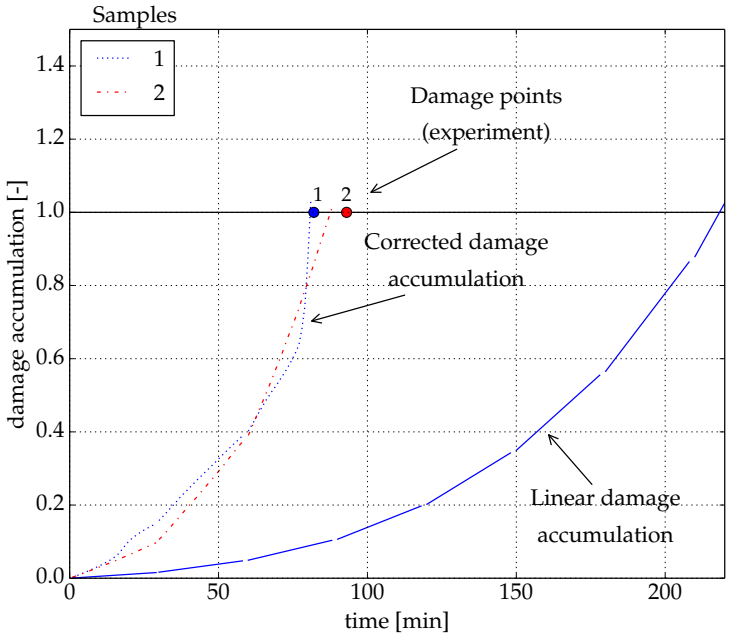


Figure 3: Linear and Non-linear Damage Accumulation (R=180)

In the linear damage accumulation the damage occurs at 12 g excitation level which is significantly higher then at the experiment (Figure 3).

5 DISCUSSIONS AND CONCLUSIONS

In order to make lighter structures, an appropriate damage accumulation prediction is one of the most important issues. This research proposes a methodology for enhancing the numerically obtained linear damage accumulation prediction with the experimentally identified structure's non-linearity. The rate of the structures' non-linearity is experimentally identified from the frequency response functions at different excitation levels. This research proposes a simple procedure for quantifying the structures' non-linearity and its implementation in updating the numerical linear damage accumulation estimation. Using this procedure it is possible to predict

the vibration fatigue life-time and damage accumulation for different models based on a linear numerical model and the experimentally identified non-linearity. This technique can be used for structural optimization based on vibration fatigue life-time as an objective parameter.

REFERENCES

[1] J. Schijve, *Fatigue of Structures and Materials*, Delft University of Technology, Faculty of Aerospace Engineering, The Netherlands, 2009

[2] A. Wöhler, *Über die Festigkeitsversuche mit Eisen und Stahl, Zeitschrift für Bauwesen* 20, 73-106, 1870

[3] A. Palmgren, *Lebensdauer von Kugellagern*, Zeitschrift des Vereins Deutscher Ingenieure 68, 339-341, 1924

[4] M. Miner, *Cumulative damage in fatigue*, Journal of Applied Mechanics - Transactions of the ASME 12, A159-A164, 1945

[5] S. Marco, W. Starkey, *A concept of fatigue damage*, Transactions of the ASME 76, 627-32, 1954

[6] A. Aid, A. Amrouche, B. Bouiadjra, M. Benguediab, G. Mesmacque, *Fatigue life prediction under variable loading based on a new damage model*, International Materials and Design 32, 183-191, 2011

[7] P. Huffman, S. Beckman, *A non-linear damage accumulation fatigue model for predicting strain life at variable amplitude loadings based on constant amplitude fatigue data*, International Journal of Fatigue 48, 165-169, 2013

[8] D. Shang, M. Barkey, Y. Wang, T. C. Lim, *Effect of fatigue damage on the dynamic response frequency of spot-welded joints*, International Journal of Fatigue 25, 311-316, 2003

[9] D. Shang, *Measurement of fatigue damage based on the natural frequency for spot-welded joints*, Materials and Design 30, 1008-1013, 2009

[10] V. Dattoma, N. Giannoccaro, A. Messina and R. Nobile, *Prediction of residual fatigue life of aluminium foam through natural frequencies and damping shift*, Fatigue and Fracture of Engineering Materials and Structures 32, 7, 601-616, 2009

[11] M. Česnik, J. Slavič, M. Boltežar, *Uninterrupted and accelerated vibrational fatigue testing with simultaneous monitoring of the natural frequency and damping*, Journal of Sound and Vibration 331, 5370-5382, 2012

[12] M. Česnik, *Strukturna dinamika pri vibracijskem utrujanju*; PhD Thesis, University of Ljubljana, Slovenia, 1998

[13] S. Suresh, *Fatigue of Materials*; Cambridge University Press, Cambridge, United Kingdom, 1998

[14] Y. Lee, J. Pan, R. B. Hathaway, M. Barkey, *Fatigue Testing and Analysis*; Theory and Practice, Elsevier, Oxford, 2005

[15] O. Basquin, *The exponential law of endurance tests*, Proceedings of American Society of Testing Materials, 10, 625-630, 1910

[16] N. Maia, J. Silva, *Theoretical and Experimental Modal Analysis*, Instituto Superior Technico, Portugal 1997

[17] M. Česnik, J. Slavič, P. Čermelj, M. Boltežar, *Frequency-based structural modification for the case of base excitation*, Journal of Sound and Vibration, 332, 5029-5039, 2013

[18] M. Mršnik, J. Slavič and M. Boltežar, *Frequency-domain methods for a vibration-fatigue-life estimation - Application to real data*, International Journal of Fatigue, 47, 8-17, 2013

[19] R. Tovo, *Cycle distribution and fatigue damage under broad-band random loading*, International Journal of Fatigue, 24, 1137-1147, 2002

[20] D. Benasciutti and R. Tovo, *Spectral methods for lifetime prediction under wide-band stationary random processes*, International Journal of Fatigue 27, 867-877, 2005.

11th International Conference on Engineering Vibration
Ljubljana, Slovenia, 7–10 September 2015

EQUIVALENT MATERIAL MODELLING OF SANDWICH BEAM ASSEMBLIES: PROPAGATING AND EVANESCENT WAVE CONSIDERATIONS

Sophie de Rijk *[1], Eugene Nijman[1]

[1]Virtual Vehicle Research Center, Inffeldgasse 21/A, 8010 Graz, Austria
sophie.derijk@v2c2.at, eugene.nijman@v2c2.at

Keywords: Sandwich, Equivalent Material, Timoshenko, Boundary Conditions, Evanescent Solution, Damping.

Abstract. *An approach to modelling sandwich structures in bending with a homogenised equivalent material is presented. The dispersion of the layered system is brought to a Timoshenko behaviour, and an equivalent damping coefficient is derived. The equivalent model can then be implemented in finite element (FE) models by means of commonly used shell elements with transverse shear stiffness. A critical review of the limitations of such an equivalent material is made, specifically in relation to the evanescent parts of the dispersion, which are of importance in assembled structures. A benchmark case with specific boundary conditions is presented to demonstrate the strengths and weaknesses of the approach.*

1 INTRODUCTION

In an effort to build more fuel-efficient vehicles, high stiffness to mass ratio solutions for vehicle structures are being researched and used in the automobile, train and aerospace industries alike. In this context, sandwich constructions have very promising characteristics as they present high bending stiffness for very low mass. Such structures however show a variety of types of behaviours over the range of frequencies in which they are excited during operation. Calculating their response by representing all their layers in FE requires large computing power and time. For design and modelling purposes, specifically in FE, representing the multi-layered system with an equivalent single-layered material would make computing costs significantly lower and allow for much more flexibility during the development phase of vehicles. Since the aim is to set-up a methodology easily employable using commercial FE packages, making an equivalent material using Timoshenko beam theory would be a convenient choice as it can be implemented easily using shell elements. In this paper we first present a brief overview of existing methodologies for modelling sandwich structures with equivalent beams, including damping and shear modelling in laminates. Subsequently, an example case is presented and the issues and shortcomings of the approach are highlighted.

2 STATE OF THE ART IN SANDWICH BEAMS AND PLATES DYNAMICS

Many publications can be found on vibrations of sandwich beams and plates. Over the past few decades, researchers have strived to describe the vibrations in bending of sandwich structures using theories with complexities ranging from classic plate theory (Euler beam), first order shear (Mindlin for plates, Timoshenko for beams) to higher order theories. Several reviews concerning previous work on vibrations of laminates and sandwich structures already exist. We redirect the reader to, for instance, the review of Mallikarjuna and Kant [1] or that of Denli and Sun [2]. This section limits itself to giving some examples of typical approaches that can be found in the literature. For general orthotropic laminates, Yang, Norris and Stavsky [3] developed general equations of motion, assuming plane stress in each layer and first order shear theory for the global displacements of the plate. They then also simplify to classic plate theory by ignoring transverse shear and rotary inertia terms. The stress-strain relations of the laminate are obtained by integration of the properties of each layer over the cross section. Yu and Cleghorn [4] calculate the eigenfrequencies of simply supported symmetric sandwich plates by constructing the stiffness and mass matrices of the system following in turn the classic plate theory, the Mindlin plate theory and Reddy's third order plate theory. The stress-strain relations are calculated analogously to [3]. Lok and Cheng [5] obtain the various stiffness terms for a Mindlin plate from static stiffness calculations of a unit element of the sandwich structure and then calculate their eigenfrequencies assuming simply supported boundary conditions. Another approach, presented for instance by Mead [6], Zhou and Li [7], and Banerjee et al. [8], is to consider separately the motion of the face sheets and core, using different assumptions for each layer and then coupling the layers in one plate. Publications by Gaudenzi and Carbonaro [9] and Kant and Swaminathan [10] are examples of higher order theory applications. Backström [11] bases his work on the description of the behaviour of a sandwich beam described by Nilsson and Nilsson [12] to define frequency-dependent stiffness terms for either an equivalent Euler or Timoshenko beam.

2.1 Damping

When modelling a sandwich structure as a single material, the various loss factors of each layer need to be merged into a single equivalent loss factor. An often adopted assumption in the literature is that only shearing in the core is dissipative since it typically has higher damping but relatively low elastic modulus, see [6]. Sadasiva, Rao and Nakra [13] consider the core to be dissipative both in in-plane elongation and transverse shear motion and calculate a system loss factor as the ratio between the imaginary and real parts of the complex stiffness for simply supported beams. Maheri, Adams and Hugon [14] treat the case of a simply supported plate, considering damping for the in-plane elongation, in-plane shear and transverse shear motion. The in-plane stresses in the core and transverse shear in the face sheets are however neglected. Modal damping capacities are then obtained by solving the eigenvalue problem. Cremer, Heckel and Petersson [15] present a more generalised methodology to compute system loss factors of layered systems by defining it as the ratio of dissipated energy over potential strain energy per cycle.

2.2 Transverse shear stress distribution and correction factors

In the formulations given by the first order shear theory as well as the one given by Nilsson and Nilsson [12], the shear term D_s implies uniform shear stress distribution over the cross section. This is however inaccurate as the shear stiffness varies over the layers and a no-shear condition is required at the top and bottom surfaces of the beam. To account for this, a shear correction factor κ_s must be applied to D_s. In the case of beams with rectangular cross section and homogeneous material, the default reference shear correction factor applied in most FE packages (for example ABAQUS or NASTRAN) for shell elements is $\kappa_s = 0.833$ given by Reissner [16], assuming a parabolic stress distribution. Several authors have also addressed the issue of defining such a correction factor for laminates, see for example [17], [18], [19] and [20]. The shear correction factor is calculated such that the shear strain energy from the uniform stress/strain distribution and the actual stress/strain distributions are the same. The difference in the approach between the various authors lies in the assumptions on the actual stress distribution.

3 FROM NILSSON SANDWICH BEAM TO TIMOSHENKO EQUIVALENT BEAM

For the work presented in this paper, the reference theory for the motion of a sandwich beam is taken from Nilsson and Nilsson [12]. This theory considers the total bending of the layup, the transverse shearing of the core and the individual bending of the face sheets about their own mid plane as well as global transverse and rotary inertias. The governing equations are then derived using the hamiltonian approach:

$$-D_s\left(\frac{\partial^2 W}{\partial x^2}-\frac{\partial \psi}{\partial x}\right)+2D_f\left(\frac{\partial^4 W}{\partial x^4}-\frac{\partial^3 \psi}{\partial x^3}\right)+\mu\frac{\partial^2 W}{\partial t^2}=0 \tag{1}$$

$$-D_{tot}\frac{\partial^2 \psi}{\partial x^2}+2D_f\left(\frac{\partial^3 W}{\partial x^3}-\frac{\partial^2 \psi}{\partial x^2}\right)-D_s\left(\frac{\partial W}{\partial x}-\psi\right)+I_\rho\frac{\partial^2 \psi}{\partial t^2}=0 \tag{2}$$

where W the transverse displacement and ψ the rotation angle of the cross sections. From Eqs. (1) and (2) and considering a general solution of the form $W = e^{i(\omega t-\kappa x)}$, a 6^{th} order dispersion equation is obtained:

$$2D_f\kappa^6+\left(D_s-2\frac{D_f}{D_{tot}}I_\rho\omega^2\right)\kappa^4-\left(\mu+2\frac{D_f}{D_{tot}}\mu+\frac{I_\rho D_s}{D_{tot}}\right)\kappa^2\omega^2-\frac{\mu D_s}{D_{tot}}\omega^2+\frac{I_\rho\mu}{D_{tot}}\omega^4=0 \tag{3}$$

where D_f is the individual bending stiffness of the face sheets, D_s the shear stiffness, D_{tot} the total bending stiffness, I_ρ the rotary inertia and μ the mass per unit length. The shear stiffness is considered to be simply that of the core, neglecting the contribution of the face sheets. We also point out here that in the original paper, no shear correction factor is considered. From Eq. (3) we obtain three distinct wave numbers. In the undamped case, the first wavenumber κ_1, is strictly real and represents the propagating part of the solution going from pure bending at low frequency to shearing in the mid-frequency range, then over to individual bending of the face sheets about their own mid plane in the high frequency range. The second wavenumber κ_2, takes purely imaginary values in the lower frequency range and real values past a given limit frequency. Below the limit frequency, the second wavenumber represents a slowly decaying evanescent solution. Above the limit frequency, the solution is propagating. The third wavenumber κ_3, is purely imaginary and is a very local exponential solution with a short decay. The various solutions of the dispersion relation (3) are shown in Figure 1.

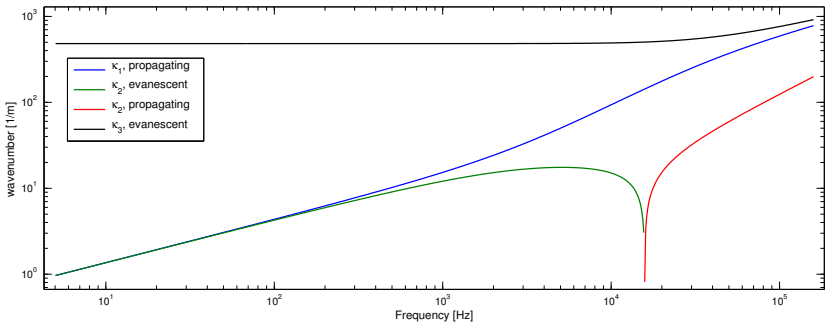


Figure 1: Solutions to the dispersion relation following Nilsson and Nilsson [12] for a 15 mm thick aluminium sandwich beam with 1 mm face sheets

As mentioned in the introduction, we will model sandwich beams with an equivalent Timoshenko beam for which the governing equations are:

$$-D_{st}\left(\frac{\partial^2 W}{\partial x^2}-\frac{\partial \psi}{\partial x}\right)+\mu_t\frac{\partial^2 W}{\partial t^2}=0 \tag{4}$$

$$-D_{bt}\frac{\partial^2 \psi}{\partial x^2}-D_{st}\left(\frac{\partial W}{\partial x}-\psi\right)+I_{\rho t}\frac{\partial^2 \psi}{\partial t^2}=0 \tag{5}$$

From which we obtain the following 4^{th} order dispersion equation:

$$D_{st}\kappa^4-\left(\mu_t+I_{\rho t}\frac{D_{st}}{D_{bt}}\right)\kappa^2\omega^2-\mu_t\frac{D_{st}}{D_{bt}}\omega^2+\frac{I_{\rho t}\mu_t}{D_{bt}}\omega^4=0 \tag{6}$$

where μ_t is the mass per unit length, $I_{\rho t}$ the rotary inertia, D_{st} is the transverse shear stiffness and D_{bt} the bending stiffness.

We can then define an equivalent material by choosing an elastic modulus, shear modulus, density and total thickness such that $D_{bt}=D_{tot}$, $D_{st}=D_s$, $I_{\rho t}=I_\rho$ and $\mu_t=\mu$. We draw attention to the fact that, while all previous authors agree on matching the bending and shear stiffness and density, most authors define the thickness of the equivalent material (H_t) to be either the total thickness of the sandwich layup, or that of the core alone. We choose to match

the rotary inertia instead, requiring the thickness of the equivalent material to be different from the total thickness of the layup:

$$\begin{cases} \mu_t = \mu \\ I_{\rho t} = I_\rho \end{cases} \implies H_t = \sqrt{\frac{12 I_\rho}{\mu}}\,,\ \rho_t = \frac{\mu}{H_t} \tag{7}$$

This choice is driven by the fact that, while the rotary inertia is typically too small to influence the propagating part of the solution κ_1 of the sandwich and Timoshenko beams, the κ_2 part of the solution is sensitive to the accuracy of I_ρ. As shown in Figure 2, if I_ρ is not exactly matched (but the total thickness H_{tot} is), the transition frequency between evanescent and propagating solutions of κ_2 changes as well as the propagating κ_2, compared to the sandwich dispersion.

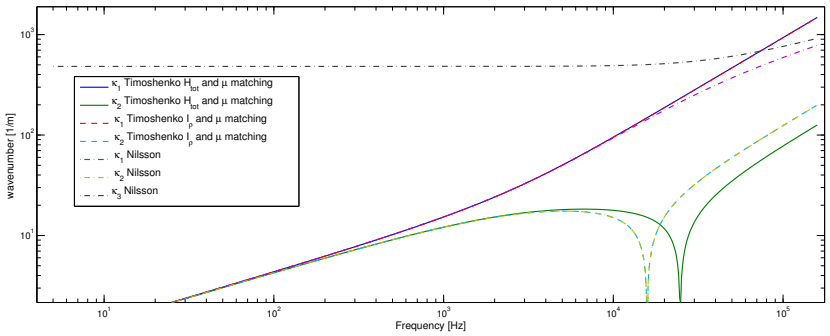


Figure 2: Dispersion solutions for a 15 mm aluminium honeycomb sandwich beam with 1 mm facesheets compared to equivalent Timoshenko solutions either matching H_{tot} and μ or I_ρ and μ

3.1 Equivalent loss factor

When using shell elements in FE, one typically sets the damping with a single loss factor such that $E_t = E_t^* (1 + i\,\eta_{tot})$ and $G_t = G_t^* (1 + i\,\eta_{tot})$, where E_t^* and G_t^* are the undamped moduli. We therefore need to define a single equivalent loss factor from the various loss factors of the face sheets and the core. We follow the approach given in [15] where the total loss factor η_{tot} is calculated as the ratio between dissipated energy and potential strain energy:

$$\eta_{tot} = \frac{E_{diss}}{2\pi E_{pot}} \tag{8}$$

We then consider the dissipative parts of the motion to be the elongation in the face sheets due to bending and the transverse shearing in the core:

$$E_{diss} = E_{dissL} + E_{dissS} = 2\pi\eta_f E_f^* h_f \left|\frac{d\epsilon_L}{dx}\right|^2 + \pi\eta_c G_c^* H_c |\gamma|^2 \tag{9}$$

where h_f the thickness of the face sheets, H_c the thickness of the core and ϵ_L the longitudinal displacement of the face sheets due to bending, which can be expressed in function of the rotation of the cross section ψ: $\epsilon_L = \frac{H_c + h_f}{2}\psi$. γ is the shear angle given by: $\frac{\partial W}{\partial x} - \psi$. The strain potential energy is considered, as given in [12], to be the sum of the total bending energy, the individual face sheet bending energy of the face sheets and the transverse shear energy:

$$E_{pot} = \frac{1}{2} D_{tot} \left|\frac{d\psi}{dx}\right|^2 + D_f \left|\frac{d\gamma}{dx}\right|^2 + \frac{1}{2} D_s |\gamma|^2 \tag{10}$$

Using the governing equations of the Nilsson sandwich beam, we can express γ in function of ψ. Considering the general solution of the form $\psi = e^{i(\omega t - \kappa x)}$, deriving by x is equivalent to multiplying by the wavenumber κ (we consider the propagating κ_1):

$$\frac{\partial \psi}{\partial x} \Longrightarrow \kappa \; ; \; \gamma \Longrightarrow \frac{D_{tot}}{\mu\omega^2}\kappa^4 + \frac{I_\rho}{\mu}\kappa^2 - 1 \; ; \; \frac{d\gamma}{dx} \Longrightarrow \frac{D_{tot}}{\mu\omega^2}\kappa^5 + \frac{I_\rho}{\mu}\kappa^3 - \kappa \tag{11}$$

The total equivalent loss factor is then:

$$\eta_{tot} = \frac{\frac{1}{2}\eta_f E_f^* h_f \left(h_f + H_c\right)^2 \kappa^2 + \eta_c G_c^* H_c \left(\frac{D_{tot}}{\mu\omega^2}\kappa^4 + \frac{I_\rho}{\mu}\kappa^2 - 1\right)^2}{D_{tot}\kappa^2 + 2D_f\left(\frac{D_{tot}}{\mu\omega^2}\kappa^5 + \frac{I_\rho}{\mu}\kappa^3 - \kappa\right) + D_s\left(\frac{D_{tot}}{\mu\omega^2}\kappa^4 + \frac{I_\rho}{\mu}\kappa^2 - 1\right)^2} \tag{12}$$

3.2 Slider-clamped beam numerical example

In the following, we calculate the response of a sandwich beam and its Timoshenko counterpart using the analytical formulations given in Section 3. All computations are implemented in MATLAB. For this numerical example, we choose to model a beam which is loaded by a unit force at $x = 0$ where a slider condition is assumed, so transverse motion W is allowed and is clamped at $x = L = 600$ mm. The boundary conditions set for both beam theories are listed in Table 1.

Nilsson	Timoshenko
$F(0) = 1$	$F(0) = 1$
$\psi(0) = 0$	$\psi(0) = 0$
$\frac{\partial W(0)}{\partial x} = 0$	
$W(L) = 0$	$W(L) = 0$
$\psi(L) = 0$	$\psi(L) = 0$
$\frac{\partial W(L)}{\partial x} = 0$	

Table 1: Considered boundary conditions

The sandwich beam modelled is composed of 1 mm thick aluminium face sheets (E_f = 70 GPa, G_f = 0, ρ_f = 2730 $\frac{kg}{m^3}$, η_f = 0.01) and a 13 mm aluminium honeycomb core (E_c = 0.166 MPa, G_c = 209 MPa, ρ_c = 40 $\frac{kg}{m^3}$, η_c = 0.1). Following Nilsson [12], the bending stiffness is set as that of the whole laminate, the shear stiffness to be given solely by the core with no shear correction factor. The rotary inertia and density per unit length are also kept identical. The damping of the equivalent material is defined in two different ways. The first, which is only possible if we are computing the response analytically, consists in setting separately the loss factor of the face sheets (on the bending terms) and of the core (in the shear terms), identically to the sandwich formulation. It therefore represents a best case scenario. The second is defined following Eq. (12) as a unique equivalent loss factor. Figure 3 shows the input mobility and dispersion solutions of the sandwich with its Timoshenko counterpart. Figure 4 then shows the force and moment transfer mobilities obtained in this case. While Figure 3 reflects the accuracy of the global response of the equivalent material, Figure 4 is meant to show how the boundary conditions are respected by the equivalent material.

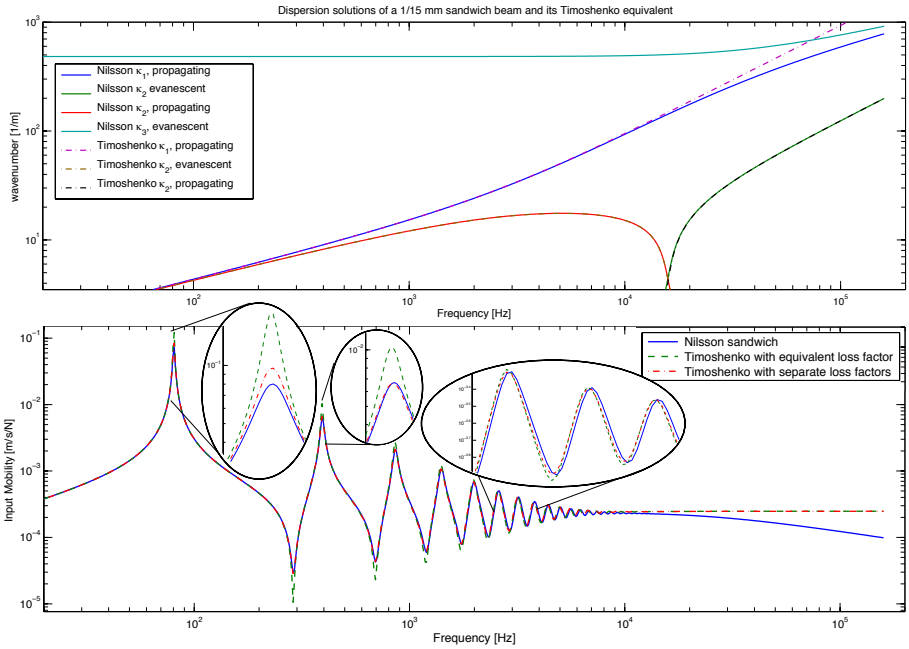


Figure 3: Dispersion and input mobility for a 15 mm sandwich beam and its equivalent Timoshenko beam, with damping defined by separate loss factors or by equivalent loss factor

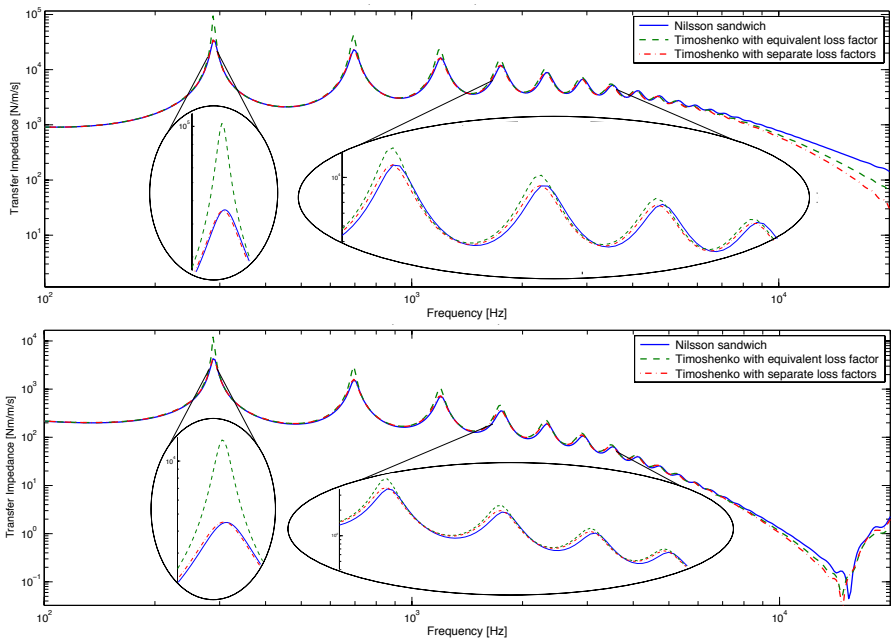


Figure 4: Force (top) and Moment (bottom) transfer impedance between x=0 and x=L for a 15 mm sandwich beam and its equivalent Timoshenko beam, with damping defined by separate loss factors or by equivalent loss factor

Firstly we notice from Figures 3 and 4 alike that the equivalent material with the damping defined with separate loss factors follows very accurately the behaviour of the sandwich beam up to about $f \simeq 3$ kHz (with the exception of the first peak value). Further on, a slight shift in the frequencies can be noticed (about 35 Hz shift at 3 kHz). The peak values however remain very close to the sandwich values (within 0.2 dB). At about $f \simeq 6$ kHz the response given by the equivalent material starts to diverge clearly from the reference sandwich. Looking at the response of the equivalent material with the unique global loss factor, we notice that it clearly underestimates the damping, but its accuracy improves as the frequency increases. The equivalent global loss factor is defined using only the propagating part κ_1 of the dispersion solution. At low frequencies however, the wavenumber of the evanescent κ_2 is of the same order of magnitude as that of the propagating solution κ_1. This implies that the evanescent field affects the total displacement (and therefore dissipated energy) with similar wavelengths as the propagating solution. As the frequency increases, the wavenumber of the propagating solution increases, which means it increasingly dominates the total integrated dissipated energy, while the evanescent solution serves more as a local scaling. This is visible in both Figures 3 and 4, where as frequency increases, the Timoshenko beam with the total equivalent loss factor starts to converge to the solution of its counterpart with the damping defined by parts. This observation highlights the importance of the evanescent field at lower frequencies and should therefore not be ignored. The influence of inaccurate damping is all the more striking in the force and moment transfer impedances. Another issue concerns the representation of shear stiffness. In the (common) case of thin face sheets, the assumption that the shear stiffness is only given by the core is reasonable. However, setting a shear correction factor of 1 is, in such cases, also inaccurate. The shear stress distribution in the laminate doesn't merely depend on the shear stiffness terms but also on the in-plane stiffnesses of the layers [17][18][19][20]. As the face sheets have high in-plane stiffness, their presence modifies the shear stress distribution. For the laminate considered here, the shear stiffness of the face sheets if of $h_f G_f = 2.63 \cdot 10^7$, that of the core is of $H_c G_c = 2.72 \cdot 10^6$, if one calculates the total shear stiffness following the approach of Madabhusi-Raman and Davalos [20] neglecting cross-plane (plate) effects, the total shear stiffness of the laminate becomes $D_s = 3.16 \cdot 10^6$. In this case, the difference in stiffness is of an acceptable 16%, but it clearly indicates that the face sheets do have an influence on the total shear stiffness. In order to be as generic as possible and cover a wide range of laminates from thinner to thicker face sheets, our methodology should include the face sheets in the computation of the shear stiffness. Simply adding up the stiffnesses is however clearly not an option, the actual stress distributions needs to be considered via shear correction factors. If a fully generic approach is considered in which one would include the face sheet shear stiffness, an added complication then comes when considering damping. As shearing is then considered over both the face sheets and core, the energy dissipated in each part needs to be quantified separately. This requires defining multiple shear correction factors for the laminate, one for the face sheets, one for the core:

$$E_{diss} = E_{dissL} + E_{dissS} = 2\pi\eta_f E_f^* h_f \left|\frac{d\epsilon_L}{dx}\right|^2 + \pi\left(2\kappa_{sf}\eta_f G_f^* h_f + \kappa_{sc}\eta_c G_c^* H_c\right)|\gamma|^2 \qquad (13)$$

where κ_{sf} and κ_{sc} are the shear correction factors in the face sheets and the core. These two shear correction factors can be obtained following the methodology given by Vlachoutsis [19] such that:

$$\kappa_s \sum_{i=1}^{3} G_i h_i = \sum_{i=1}^{3} \kappa_{si} G_i h_i \qquad (14)$$

were G_i, h_i and κ_{si} are the shear modulus, the thickness and the shear correction factor of each layer respectively.

4 CONCLUSIONS

In this paper, the approach to building an equivalent Timoshenko beam for representing a sandwich laminate based on current knowledge is presented. The final aim is to accelerate FE calculations of sandwich structures using shell elements with equivalent material properties. Then, on the basis of a practical example, some of the challenges that need to be tackled with ongoing research to make a reliable and generically applicable equivalent model are highlighted. The main issue arising from this example is the proper definition of an equivalent loss factor to be applied to the equivalent material. It has been shown here that the latter depends not only on the propagating part of the solution, which is commonly considered by modelling simply supported structures (purely sinusoidal solution), but also the evanescent field, especially at lower frequencies. The necessity to compute the shear stiffness considering both the face sheets and the core as well as separate shear correction factors is also pointed out.

5 ACKNOWLEDGEMENTS

The research work of Sophie de Rijk has been funded by the European Commission within the Marie Curie program through the EID eLiQuiD project (GA 316422). The authors acknowledge the financial support of the COMET K2 - Competence Centres for Excellent Technologies Programme of the Austrian Federal Ministry for Transport, Innovation and Technology (BMVIT), the Austrian Federal Ministry of Science, Research and Economy (BMWFW), the Austrian Research Promotion Agency (FFG), the Province of Styria and the Styrian Business Promotion Agency (SFG). We also acknowledge the support of the COST action TU1105.

REFERENCES

[1] Mallikarjuna and T. Kant, A critical review and some results of recently developed refined theories of of fiber-reinforced laminated composites and sandwiches. *Composite Structures*, **23**, 293–312, 1993.

[2] H. Denli and J. Sun, Structural-acoustic optimisation of composite sandwich structures: A review. *The Shock and Vibration Digest*, **39** (3), 189–200, 2007.

[3] P. Yang, C. Norris and Y. Stavsky, Elastic wave propagation in heterogeneous plates. *International Journal of Solids and Structures*, **2**, 665–684, 1966.

[4] S. Yu and W. Cleghorn, Free flexural vibration analysis of symmetric honeycomb panels. *Journal of Sound and Vibration*, **284**, 189–204, 2005.

[5] T.-S. Lok and Q.-H. Cheng, Free and forced vibration of simply supported, orthotropic sandwich panel. *Computers and Structures*, **79**, 301–312, 2001.

[6] D. Mead, A comparison of some equations for the flexural vibration of damped sandwich beams. *Journal of Sound and Vibration*, **83** (3), 363–377, 1982.

[7] H. Zhou and G. Li, Free vibration analysis of sandwich plates with laminated faces using spline finite point method. *Computers and Structures*, **59** (2), 257–263, 1996.

[8] J. Banerjee, C. Cheung, R. Morishima, M. Perera and J. Njuguna, Free vibration of a three-layered sandwich beam using the dynamic stiffness method and experiment. *International Journal of Solids and Structures*, **44**, 7543–7563, 2007.

[9] P. Gaudenzi and R. Carbonaro, An evaluation of higher-order effects on the eigenfrequencies of composite structures. *Composite Structures*, **47**, 821–825, 1999.

[10] T. Kant and K. Swaminathan, Analytical solutions for free vibration of laminated composite and sandwich plates based on a higher-order refined theory. *Composite Structures*, **53**, 73–85, 2001.

[11] D. Backström, *Vibration of sandwich beams*. Doctoral Thesis, KTH Stockholm, Sweden, 2006.

[12] E. Nilsson and A. Nilsson, Prediction and measurement of some dynamic properties of sandwich structures with honeycomb and foam cores. *Journal of Sound and Vibration*, **251** (3), 409–430, 2002.

[13] Y. Sadasiva Rao and B. Nakra, Vibrations of unsymmetrical sandwich beams and plates with viscoelastic cores. *Journal of Sound and Vibration*, **34** (3), 309–326, 1974.

[14] M. Maheri, R. Adams and J. Hugon, Vibration damping in sandwich panels. *Journal of Material Science*, **43**, 6604–6618, 2008.

[15] L. Cremer, M. Heckl, B. Petersson, *Structure-borne sound: Structural vibrations and sound radiation at audio frequencies*, 3rd edition. Spiringer, Berlin Heidelberg, Germany, 2005.

[16] E. Reissner, The effect of transverse shear deformation on the bending of elastic plates. *Journal of Applied Mechanics*, **12** (2), A69–A77, 1945.

[17] J. Whitney, Shear correction factors for orthotropic laminates under static load. *Journal of Applied Mechanics*, **40**, 302–303, 1973.

[18] C. Bert, Simplified analysis of static shear factors for beams of nonhomogeneous cross section. *Journal of Composite Materials*, **7**, 525–529, 1973.

[19] S. Vlachoutsis, Shear correction factors for plates and shells. *International Journal for Numerical Methods in Engineering*, **33**, 1537–1552, 1992.

[20] P. Madabhusi-Raman and J. Davalos, Static shear correction factor for laminated rectangular beams. *Composites: Part B*, **27B**, 285–293, 1996.

11th International Conference on Engineering Vibration
Ljubljana, Slovenia, 7–10 September 2015

AN INVERSE METHODOLOGY FOR LOW-FREQUENCY TRANSMISSION LOSS CHARACTERIZATION OF A LIGHTWEIGHT PANEL IN A SMALL REVERBERANT TRANSMISSION SUITE

V. D'Ortona*[1], E. Nijman[1]

[1]Virtual Vehicle Research Center, Inffeldgasse 21/A, 8010, Graz, Austria
vittorio.dortona@v2c2.at, eugene.nijman@v2c2.at

Keywords: Small Reverberant Chambers, Transmission Loss, Indirect Mobility Characterization, Patch Transfer Functions.

Abstract. *A new procedure for the low frequency Transmission Loss (TL) characterization of panels, by means of a small reverberant transmission suite is discussed. Moreover, in the case of lightweight panels the measurements are affected by a strong vibro-acoustic coupling between the sample tested and the fluid in the cabin, resulting in an unreliable TL prediction below the Schroeder's frequency. This paper proposes a novel methodology to retrieve the structural interface mobility matrix of lightweight panels, unaffected by the fluid coupling, using the Patch transfer Function (PTF) sub-structuring method. The retrieved mobility matrix allows then for reliable and standard-like TL predictions in different environments. This new approach has been numerically validated by a simple reference case of a homogeneous Aluminium plate coupled to a small cabin with simply supported boundary condition. The results show a very good matching between the known reference mobility and the estimated one. The limitations of this new procedure, possible applications and further studies are also discussed.*

1 INTRODUCTION

In order to investigate and predict Noise, Vibration and Harshness (NVH) properties of lightweight components, small reverberant chambers are being more and more implemented in the automotive, railway and aerospace fields. Compared to the standards (chambers of $80\ m^3$), the dimensions of these chambers allow for building own designed testrig, resulting to be practical and fast tools for testing and evaluating the vibro-acoustic behavior of lightweight panels of common use in the transport industry.

On the other hands, small reverberant chambers have a wide frequency region in which the field cannot be considered diffuse. The Schroeder's frequency is high, and below it a strong vibro-acousting coupling between the sample and the cabin might be present. The achieved noise reduction properties are then affected by the test rig in which they are measured and cannot be considered as representative for the tested panel's behavior. The lack of diffusivity is a common issue for small cabins and it does not allow for reliable Transmission Loss (TL) investigations in the low frequency region. A test campaign performed by the author on a sandwich panel with honeycomb core [1] enlightens this problem by comparing the noise reduction properties measured in a small reverberant chamber, designed at KU Leuven and named PMA Soundbox, with the TL measured in a standard facility.

In order to investigate the diffusivity problem, analytical and numerical models have been employed to show the influence of different parameters in the sound reduction index at low frequencies [2, 3]. Teresa Bravo and Stephen J. Elliot [4] try to address the problem from an experimental point of view by proposing the use of an array of loudspeaker, driven by partially uncorrelated signal in the near field of the partition, in order to reproduce a diffuse sound pressure field impining on the tested surface. Although there exist a lot of experimental and theoretical work on the variability of measurements at low frequencies, no effective solution has been found to address this problem. It still represents a big issue about obtaining a complete characterization of the noise reduction properties of lightweight structures and generating trustworthy numerical models to predict their behavior in practical applications.

Here a fast and new indirect procedure to retrieve the mobility matrix of structural components in the fully vibro-acustic coupled frequency region is introduced, independently from the environment in which it is tested. The methodology allow for the determination of the panel's mobility by using the PTF (Patch Transfer Function approach) and involving (i)direct measurements of the Sound Pressure Level on the inner surface of a sample tested in a small cabin, (ii)good knowledge of the acoustic characteristics of the test rig. The aim is to develop a hybrid numerical-experimental procedure in order to get, from a not standard test rig such as a small reverberant cabin, a reliable prediction of the standard noise and vibration properties of lightweight panels.

The present paper is structured as follow: an overview of the PTF method and its applications is given in the first section, then the proposed methodology is explained in detail and validated with a numerical reference case. In the last section, conclusions and an overview on possible future works are listed.

2 PATCH TRANSFER FUNCTIONS APPROACH

The PTF method has been initially developed with the goal to be a useful alternative tool to reduce the computational cost when solving coupled multi-system problems, while keeping a good accuracy in the results. Introduced by Ouisse et al. [6], it has been applied for acoustic coupling problems by Pavic [7], for a plate-cavity system by Aucejo et al. [8] and for transmis-

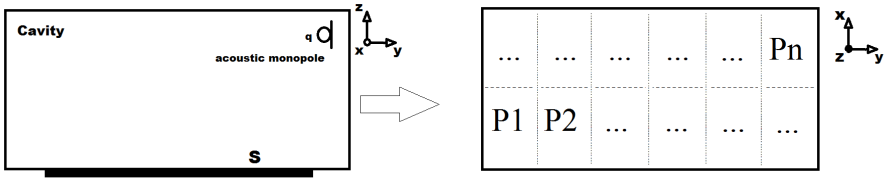
sion loss calculation of a multi-layer system by Chazot and Guyader [9]. A hybrid prediction scheme has been proposed and validate by Jan Rejlek et al. [10] to extend the PTF approach to vibro-acoustic systems containing numerically characterized fluid domains and experimentally characterized structural parts. Recently Veronesi et al. [11] implemented it to develop a novel experimental method for the characterization of poro-elastic materials.

3 METHODOLOGY

The PTF approach is modular, allowing for different procedures (numerical, experimental, analytical solution) to be used in order to assess impedance relation of each sub-system. The presented methodology takes advantage of this feature in order to develop an indirect procedure to characterize the mobility of a panel coupled to a small cabin excited by a set of acoustic sources. The first step is to divide the entire system in two subsystems coupled on an coupling surface, and then apply the the theorem formulated by Bobrovnitskii [5]. If one of the sub-systems hosts sound sources while the other is passive, the global sound field can be represented by the superposition of two simpler field components: the field produced by the running sources with the coupling surface fully blocked (blocked pressure field), and the one due to the velocity, at the coupling surface of the coupled system, when the internal sources are switched off. Applying this principle at the panel inner surface, i.e. the coupling surface, it is possible to retrieve its mobility. What is required is the knowledge of the following three quantities: the global pressure field , the blocked pressure field and the surface impedance of the fully blocked coupling surface.

3.1 Governing equations

Let us consider a simple fully coupled vibro-acoustic system (Figure 1.a)consisting in a thin flat plate and a small cavity excited by a monopole source. For practical reasons the coupling surface is considered to match the interface of the two sub-system, i.e. the panel's inner surface.



(a) (b)

Figure 1: Vibro-acoustic system: cavity, vibrating surface and acoustic monopole (a) - Division of the vibrating surface in N patches (b).

The PTF aproach consists in subdividing the coupling surface S in N elementary surfaces ΔS_i(Figure 1.b), also referred to as patches. On each patch the dynamic quantities are averaged and considered to assume a constant value. For the i-th patch, the averaged pressure and velocity are given by:

$$\overline{P}_i = \frac{1}{\Delta S_i} \int_{\Delta S_i} P_i(x,y)\, dS \tag{1}$$

$$\overline{V}_i = \frac{1}{\Delta S_i} \int_{\Delta S_i} V_i(x,y)\, dS \tag{2}$$

For the subsystem cavity, the transfer functions between the j-th excited patch and the i-th receiving one can be written in terms of blocked impedance as follow:

$$Z_{ij} = \frac{\overline{P}_i}{\overline{V}_j}|_{\overline{V}_{k\neq j}=0} \tag{3}$$

For the subsystem plate the transfer functions between the j-th excited patch and the i-th receiving one can be written in terms of mobility as follow:

$$Y_{ij} = \frac{\overline{V}_i}{\overline{P}_j}|_{\overline{P}_{k\neq j}=0} \tag{4}$$

Z_{ij} represents the averaged pressure $\overline{P}_j$ of the i-th patch when a unit velocity is imposed on the j-th patch while keeping all the others patches blocked, i.e. $\overline{V}_k = 0$ for $k = 1, .., N$ and $k \neq j$.

Y_{ij} represents the averaged velocity $\overline{V}_i$ of the i-th patch when a unit pressure is imposed on the j-th patch while keeping all the others patches free, i.e. $\overline{P}_k = 0$ for $k = 1, ..., N$ and $k \neq j$.

Applying Eqs. 3 and 4 to all the patches, the impedance and mobility matrix $\underline{Z}$ and $\underline{Y}$ can be built. They are symmetric square matrix with dimensions NxN .

Considering the acoustic sub-domain (indicated by the superscript 1), the total pressure on the i-th patch of the coupling surface, can be expressed as:

$$P_1^i = P_b^i + Z_{blocked}^{ij} V^j \tag{5}$$

P_b^i is the averaged blocked pressure on the i-th patch due to the running source and keeping the coupling surface fully blocked.

V_j is the velocity, at the coupling surface of the coupled system, when the internal sources are switched off.

Writing Eq. 1 for each patch, the vectors $\bar{P}_1$ and $\bar{V}_1$ can be built. They are vectors of dimensions Nx1 containing respectively the averaged pressures and velocities on every single patch. Eq. 1 can be than rewritten as follow:

$$\bar{P}_1 = \bar{P}_b + \bar{Z}_{blocked}\bar{V}_1 \tag{6}$$

Because of the continuity conditions between the two sub-systems, the pressures and velocities acting on the coupling surface have to be the same:

$$\bar{P}_1 = \bar{P}_2 = \bar{P}_{interface} \tag{7}$$

$$\bar{V}_1 = \bar{V}_2 = \bar{V}_{interface} \tag{8}$$

Considering that $\bar{P}_2$ and $\bar{V}_2$ are related by mean of the panel's mobility as follow:

$$\bar{V}_2 = \underline{Y}_{panel}\bar{P}_2 \tag{9}$$

Eq. 9 can be used together with the coupling conditions 7 and 8 in Eq. 6, and changing the sign of $\bar{V}_2$ when moving from sub-system 2 to subsystem 1, we obtain:

$$\bar{P}_S = \bar{P}_b - \underline{Z}_{blocked}\underline{Y}_{panel}\bar{P}_S \tag{10}$$

With some algebra Eq. 10 can be written as:

$$(\underline{I} + \underline{Z}_{blocked}\underline{Y}_{panel})\bar{P}_S = \bar{P}_b \tag{11}$$

The aim is to indirectly retrieve the mobility matrix $\underline{Y}_{panel}$ by using Eq. 11. For this purpose a matrix equation needs to be built. This goal can be reached by using a set of at least N acoustic loads. For the i-th acoustic excitation a vector equation like Eq. 11 can be written:

$$(\underline{I} + \underline{Z}_{blocked}\underline{Y}_{panel})\bar{P}_S^i = \bar{P}_b^i \tag{12}$$

Writing Eq. 12 for each acoustic load, and considering that the matrices $\underline{Z}_{blocked}$ and $\underline{Y}_{surface}$ are constant, being characteristics of the system and independent from the acoustic load, a set of N equations can be built and grouped in a matrix form as follow:

$$(\underline{I} + \underline{Z}_{blocked}\underline{Y}_{panel})\underline{P}_S = \underline{P}_b \tag{13}$$

where $\underline{P}_S = \left[\begin{array}{ccccc} \bar{P}_S^1 & .. & \bar{P}_S^i & .. & \bar{P}_S^N \end{array} \right]$ and $\underline{P}_b = \left[\begin{array}{ccccc} \bar{P}_b^1 & .. & \bar{P}_b^i & .. & \bar{P}_b^N \end{array} \right]$.
Eq. 13 can be solved for $\underline{Y}_{panel}$, obtaining:

$$\underline{Y}_{panel} = \underline{Z}_{blocked}^{-1}(\underline{P}_b\underline{P}_S^{-1} - \underline{I}) \tag{14}$$

Care has to be taken in the choice of the acoustic loads set. As shown in Eq. 14 the matrix $\underline{P}_S$ has to be inverted, so the N acoustic excitations have to be such that a set of N independent pressure fields will be generated on the coupling surface.

The quantities $\underline{Z}_{cavity}$ and $\underline{P}_b$ are only related to the testing room and the complete knowledge of its properties (like for an in situ designed small reverberant chamber or for simple regular geometries) allows for calculating them via FEM/BEM or analytically. $\underline{P}_S$ takes in account the global coupled response of the vibro-acoustic system and it can be experimentally achieved by mean of a set of microphones placed close by the inner surface of the tested panel.

4 NUMERICAL EXAMPLE

The proposed approach is presented here by means of a numerical example and the acquired mobility matrix compared with a reference one. As a vibro-acoustic system, a small rectangular cavity coupled to an homogeneous aluminum plate is considered (Figure 1). The plate is $5mm$ thick and its dimensions on the xy plane are $1.5m$ and $0.3m$ along x and y directions respectively. The panel surface is also considered as coupling surface, it covers entirely one wall of the cavity, which dimensions are then $1.5m$, $0.3m$ and $0.4m$ along x, y and z. Simply supported boundary conditions are imposed on each edge of the plate. The frequency range investigated goes from $0Hz$ to $250Hz$.

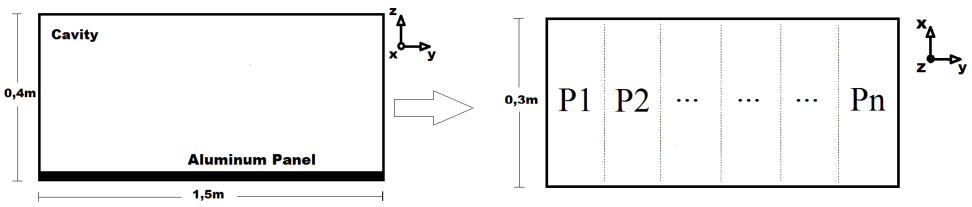


Figure 2: Rectangular cavity and Aluminum plate's size.

The material properties of the two subsystems are shown in Table 1.

Material	Density (Kg/m^3)	Phase speed (m/s)	Young's modulus (N/m)
Air	1,21	340	—
Aluminum	2770	—	$72 * 10^9$
Material	Poisson's ratio (ν)	Damping ratio(ξ)	Absorption coefficient (α)
Air	—	—	0,005
Aluminum	0,33	0,001	—

Table 1: Material properties used for modeling the fluid inside the acoustic sub-domain and the Aluminum plate.

In order to choose an optimal configuration for the number of patches to be used and for the typology of the subdivision in patches for the structural sub-system, a modal analysis has been performed in advance. Table 2 shows acoustical and structural eigenfrequencies together with the associated number of half-wave along x and y , for the plate, and x , y and z for the cavity.

Subsystem	Order	Eigenfrequency [Hz]	Type
Cavity	1	0	(0,0,0)
	2	113	(1,0,0)
	3	227	(2,0,0)
Panel	1	141	(1,1)
	2	157	(2,1)
	3	184	(3,1)
	4	222	(4,1)

Table 2: The natural frequencies and semi-wave number of the related eigenmodes of each uncoupled system.

In the frequency range of interest the panel has only mode shapes having one semi-wave along y , while the maximum number of semi-wave along x is four. The panel has been then divided in one row of 8 patches along x in order to have at least two patches for semi-waves in the whole frequency range analyzed. Is it important to underline that only one row of patches along y has been used because of the pressure will change predominantly along x resulting, in the analyzed frequency region, quite constant along y instead . Having another row of patches would translate in adding more load cases and creating bigger matrices, increasing the computational cost and decreasing the quality of the mobility matrix prediction. Indeed, at a fixed coordinate x, the pressure on the two patches along y would be almost the same, generating in the matrix $\underline{P}_S$ linearly dependent rows which will give singularity problems.

4.1 Reference Mobility Matrix

The reference mobility matrix of the Aluminum plate has been calculated by mean of FEM analysis. A finite element model of the in vacuum plate with simply supported boundary conditions has been generated and 8 analysis have been performed. The i-th run consists in a frequency response analysis of the plate under a uniform unit pressure load acting on the i-th patch. At the i-th unit pressure load, the averaged velocity of the j-th patch corresponds to

the component $Y^{ij}_{reference}$ of the reference mobility matrix, so, for each run, the structural frequency response has been averaged on each patch in terms of structural velocities allowing for the determination of the 8x8 $\underline{Y}^{reference}_{panel}$ matrix.

4.2 Blocked Impedance

The rectangular shape of the acoustic sub-system allows for the use of an analytical model, based on modal superposition, in order to determine the blocked impedance matrix $\underline{Z}_{blocked}$ on the coupling surface. In the acoustic sub-domain, the steady-state acoustic pressure perturbation field $p(r)$ is governed by the Helmotz equation [12]:

$$\nabla^2 p(\mathbf{r}) + k^2 p(\mathbf{r}) = 0 \quad \forall \mathbf{r} \epsilon \Omega_a \tag{15}$$

where k the acoustic wave number and c the speed of sound.

For a rectangular rigid cavity of dimensions Lx , Ly and Lz , the eigenmodes of the Helmotz equation can be written as follow:

$$\phi_i(\mathbf{r}) = \zeta_i cos\left(\frac{m_x(i)\pi x}{Lx}\right) cos\left(\frac{m_y(i)\pi y}{Ly}\right) cos\left(\frac{m_z(i)\pi z}{Lz}\right) \tag{16}$$

$$\zeta_i = \sqrt{2^s},\ s = sign(m_x(i)) + sign(m_y(i)) + sign(m_z(i)) \tag{17}$$

The Eigenfrequencies are:

$$\omega_i = \pi c \sqrt{\left(\frac{m_x(i)}{Lx}\right)^2 \left(\frac{m_y(i)}{Ly}\right)^2 \left(\frac{m_z(i)}{Lz}\right)^2} \quad m_x, m_y, m_z = 0, 1, 2... \tag{18}$$

with the integers $m(i)$ chosen to give a monotonous increase of ω_i with i increasing, $i = 1, 2...$ The patch-to-patch impedance between two patches of size $\triangle x$, $\triangle y$ and $\triangle x'$, $\triangle y'$ centered at $\mathbf{r}$ and $\mathbf{r}'$, respectively, is given by Pavic [7] as:

$$Z_{blocked}(\mathbf{r}, \mathbf{r}') = i\omega\rho c^2 \triangle x \triangle y \frac{\phi_i(\mathbf{r})\phi_i(\mathbf{r}')}{\omega_i^2 - \omega^2 + 2i\varepsilon\omega} sinc\left(\frac{m_{x,i}\triangle x}{2Lx}\right) sinc\left(\frac{m_{y,i}\triangle y}{2Ly}\right) sinc\left(\frac{m_{x,i}\triangle x'}{2Lx}\right) sinc\left(\frac{m_{y,i}\triangle y'}{2Ly}\right) \tag{19}$$

where ε represents the equivalent damping due to a small wall absorption coefficient $\alpha \ll 1$, and it can be expressed as:

$$\varepsilon = \alpha c \frac{1}{Lx} + \frac{1}{Ly} + \frac{1}{2Lz} \tag{20}$$

The amplitude of a wave propagating with a speed c of is assumed to be reduced by α when traveling across the cavity length. Eq. 20 is based on the simplification that in the z direction the damping is only half of the values in the other directions. That is because along z one surface is used for the coupling, this surface is then blocked per definition and therefore rigid without any damping.

4.3 Results

In the last step, a set of $M > N$ different acoustic loads has been chosen and applied to (i)the FE model of the coupled vibro-acoustic system in order to retrieve $\underline{P}_S$, (ii)the FE model of the sole acoustic sub-system having the coupling surface blocked in order to retrieve $\underline{P}_b$.

The reason why the number of acoustic loads is bigger than the number of patches, i.e. the minimum number of loads to solve the set of equations, is related to the necessity to get N independent pressures vectors $\bar{P}_S^i$. How to obtain this goal is not known a priori, so $M > N$ load cases have been used with a a random choice of the monopoles' positions and a pseudo-inverse matrix $\underline{P}_S^{-1}$ has been calculated. A methodology to understand a priori how would be a set of exactly N load cases able to generate N independent pressure field $\bar{P}_S^i$ is under investigation.

Using Eq. 14 the mobility matrix $\underline{Y}_{panel}$ has been calculated and compared with the reference one $\underline{Y}_{panel}^{reference}$.

Figure 3 shows a comparison between the components (4,4) of the above mentioned matrices.

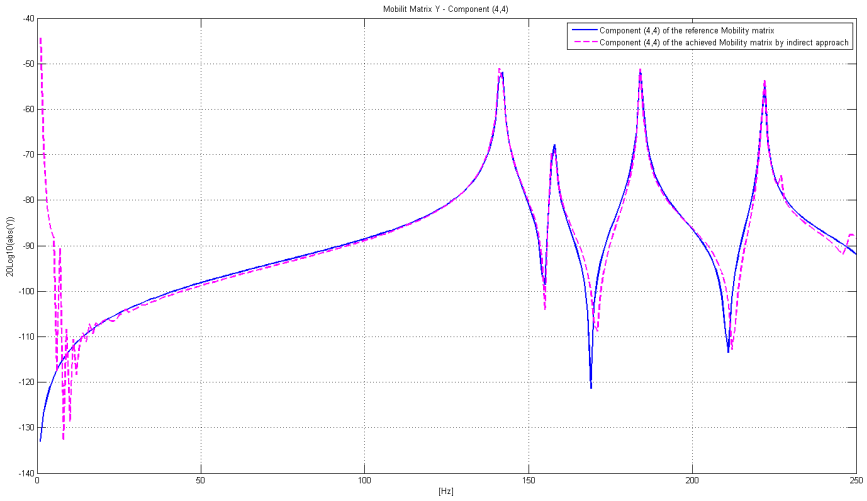


Figure 3: Comparison between the component (4,4) of the reference Mobility matrix (blue curve) and the achieved one by mean of an indirect approach (dashed magenta curve).

Is it possible to notice how the two curves matches really well in the frequency range of interest. A small shifting of the anti-resonant peaks can be observed; it is related to the averaging process of the velocity over the patches.

5 CONCLUSIONS

The proposed procedure has shown the capability to accurately estimate the mobility matrix of a homogeneous Aluminum plate by mean of an indirect approach. The procedure has only been validated numerically, but the possibility to experimentally apply this method to a small cabin reverberant chamber is quite appealing since (i)a coupled Sound Pressure Field can be achieved by acoustic measurements with a set of microphones placed inside the cavity, (ii)thanks to the deep knowledge about shape and acoustic properties of the test rig, it is pos-

sible to estimate the blocked impedance and blocked pressure matrices by mean of numerical simulations involving FE method.

The next step will be to validated the proposed approach by a set of experiments made on an Aluminum homogeneous plate coupled to a small rectangular cabin located at ViF's (Virtual Vehicles) laboratory in Graz.

Moreover, other three possible scenarios about future research works are now possible:

- To investigate the capability of scaling the acquired Mobility and predict the noise reduction properties of a standard sample in a standard facility.
- To investigate the feasibility of performing sensitivity studies in order to: (i)understand the influence of the test rig to the acoustic properties of the tested sample, (ii)correct the measurements to achieve a trustworthy experimental prediction of the noise reduction properties, i.e. to achieve standard like results unaffected by the test environment.
- To extend the presented method to the study of noise reduction properties of multilayer systems.

About the last point listed above, it is worth to mention that, for studying noise reduction properties of multilayer structures, methodologies based on sub-structuring the global system are quite often used [9, 13, 14, 15]. Given a certain incident sound pressure field, the transmitted one is achieved going step by step through every single layer; so the knowledge of their characteristic impedance and/or mobility properties is crucial and not easy to get by a direct experimental procedure. A numerical approach is often used, so the possibility to experimentally apply the here introduced procedure is of great interest in order to tackle this issue in a faster, and easier to realize, way.

6 ACKNOWLEDGEMENTS

The research work of Vittorio D'Ortona has been funded by the European Commission within the ITN Marie Curie Action project eLiQuiD under the 7th Framework Programme (EC grant agreement no. 316422). The authors acknowledge the financial support of the COMET K2 - Competence Centres for Excellent Technologies Programme of the Austrian Federal Ministry for Transport, Innovation and Technology (BMVIT), the Austrian Federal Ministry of Science, Research and Economy (BMWFW), the Austrian Research Promotion Agency (FFG), the Province of Styria and the Styrian Business Promotion Agency (SFG). Finally, the authors gratefully acknowledge the support of COST action TU1105.

REFERENCES

[1] V. D'Ortona, M. Vivolo, B. Pluymers, D. Vandepitte and W. Desmet, Experimental identification of noise reduction properties of honeycomb panels using a small cabin. In Proceedings of *Transport Research Arena 2014*, TRA 2014, Paris, France, 2014.

[2] T. Kihlman, On the meaning of the sound reduc tion index at low frequencies. *Acustica*, **18**, 11-20, 1967.

[3] W. Kropp, A. Pietrzyk, T. Kihlman, Sound radiation into a rectangular room. Applications to airborne sound transmission in buildings. *Acta Acustica*, **2**, 379-392, 1994.

[4] T. Bravo and S. J. Elliott, A Simulation Analysis of Low Frequency Sound transmission Measurements. In Proceedings of *International Congress on Acoustic 2004*, ICA 2004, Kyoto, Japan, 2004.

[5] Y. I. Bobrovnitskii Y, A theorem on the representation of the field of forced vibrations of a composite elastic system. *Acoustical Physics*, **47**, 507-510, 2001.

[6] M. Ouisse, L. Maxit, C. Cacciolati and J. Guyader, Patch transfer functions as a tool to couple linear acoustic problems. *Journal of Vibration and Acoustics*, **127**, 458-466, 2005

[7] G. Pavic, Air-borne sound source characterization by patch impedance coupling approach. *Journal of Sound and Vibration*, **329(23)**, 4907-4921, 2010.

[8] M. Aucejo, L. Maxit, N. Totaro and J. Guyader, Convergence acceleration using the residual shape technique when solving structure-acoustic coupling with the patch transfer functions method.

[9] J. Chazot and J.and Guyader, Prediction of transmission loss of double panels with a patch-mobility method. *Journal of the Acoustical Society of American*, **121**, 267-278, 2007. *Computers & Structures*, **88(11-12)**, 728-736, 2010.

[10] J. Rejlek, G. Veronesi, C. Albert, E.Nijman, A Combined Computational-Experimental Approach for Modelling of Coupled Vibro-Acoustic Problems. In Proceedings of *Society of Automotive Engineers 2013 Noise and Vibration Conference and Exhibition*, SAE 2013 Noise and Vibration Conference and Exhibition, Grand Rapids, Michigan, USA, 2013.

[11] G. Veronesi, C. Albert, E.Nijman, J. Rejlek, Patch Transfer Function Approach for Analysis of Coupled Vibro-Acoustic Problems Involving Porous Materials. In Proceedings of *Society of Automotive Engineers 2014 Noise and Vibration Conference and Exhibition*, SAE 2014 Noise and Vibration Conference and Exhibition, Graz, Austria, 2014.

[12] F. Fahy F, *Sound and Structural Vibration: Radiation, Transmission and Response*. Academic Press, ISBN 0122476719, 2000. *Journal of Sound and Vibration*, **233(4)**, 669-705, 2000.

[13] M. Villot and al., Predicting the acoustical radiation of finite size multi-layered structures by applying spatial windowing on infinite structures. *Journal of sound and vibration*, **245(3)**, 433-455, 2001.

[14] M. Villot and al., Using spatial windowing to take the finite size of plane structure into account in sound transmission. In Proceedings of *International Conference on Emerging Technologies of Noise and Vibration Analysis and Control 2005*, NOVEM 2005, Saint Raphael, France 2005.

[15] H. Nelisse, T. Onsay, N. Atalla ,Structure borne insertion loss of sound package components. In Proceedings of *Society of Automotive Engineers 2003 Noise & Vibration Conference and Exhibition Technical Papers*, SAE 2003 Noise & Vibration Conference and Exhibition Technical Papers, Traverse City (MI), 2003.

International Conference on Engineering Vibration
Ljubljana, Slovenia, 7-10 September 2015

THE FINITE ELEMENT ASSESSMENT OF STRUCTURE PROPERTIES FOR A L7E CLASS VEHICLE UNDER THE BENDING, TORSION STATIC AND CRASH LOADS

R. P. Jedrzejczyk*[1], T. Jost[2]

[1]Virtual Vehicle Research Center
RomanPawel.Jedrzejczyk@v2c2.at

[2] Virtual Vehicle Research Center
Thomas.Jost@v2c2.at

Keywords: Finite Element Analysis, Implicit, Explicit, Electric Vehicle, Crash Simulation, Electric Batteries, Nonlinear Analysis, Crash Scenarios, Inflammation.

Abstract. *This document researches the analysis of L7e class quadricylce vehicle structure and its influence on the critical parts of alternative powertrain system – safety of electric batteries. The strength of vehicle structure for the static bending and torsion loads is reported. For the numerical calculations state of the art nonlinear finite element software is used and the virtual layout of industry proven static mechanical tests are depicted. Furthermore, the effect of vehicle structure interactions on the battery cells during the dynamic crash simulations for various crash scenarios is examined. Those crash scenarios, like front, rear and side crash with rigid barriers, are newly proposed basing on the passenger car normative for vehicle safety. The results obtained by both, implicit and explicit finite element method are shown the needs for structural parts improvements for the vehicle of L7e class. The assessment criteria for the undergone deformations of battery cells under the crash loads are reported.*

1 INTRODUCTION

The future mobility at urban areas will increase a number of the lightweight alternative powered vehicles [1-2]. The automakers will migrate strongly in order to reduce the gas emission into the hybrid and electrification powertrain technology. The very small alternative powered city vehicles group will arise as a proposition for the mobility at city centres. Currently dominating trend represents the L7e vehicle class with the electric driven powertrain [3]. Many car manufacturers, as well as, the research centres consider some intermediate solutions for such vehicles based on the traditional powered vehicle, but replacing the powertrain unit for the alternative one – conversion approach design [4]. Regarding the traffic safety at the urban zones across Europe new higher restrictions for the speed limits to 30 km/h will be introduced [5, 6]. The lack of the legislative safety standards for the L7e vehicle class encourages some attempts (mainly done by the European New Car Assessment Programme – EuroNCAP) to bring up the attention of the occupant safety for such vehicles [7-8].
The lightweight alternative powered quadricycle vehicles seem to predestine to fulfil a new niche of small city centres vehicles [9]. Those vehicles due to their simple but lightweight design offer high ratio of travel distance range versus their mass. However, the current safety level of such vehicles is questionable [8]. Main issue is the poor occupant safety. Other interesting question remains the potentially inflammation risk of the lithium-ion batteries usage as electric power source during the crash and post-crash situations [10]. This paper covers the crash analysis of complete vehicle and the vehicle structure assessment by the explicit and implicit Finite Element Analysis (FEA) [11-12] using the LS-DYNA R7.1 software, respectively. The attention was made to verify the crashworthiness and toughness of vehicle structure, as well, as, its influence on the safety of electric batteries.

2 FEA ASSESSMENT UNDER THE STATIC AND CRASH LOADS

The vehicle structure toughness for the bending and torsion loads reflects the correctness of design [17]. In this particular case the aim was to obtain the value of strength and stiffness of the vehicle structure. Those numbers will be used in the vehicle concept modernisation phase realized as future work by the optimisation processes. Similar significance is related to the crash simulations. However, the main focus was laid on the electric batteries deformations and vehicle structure distortion. The vehicle model for the goals of the Finite Element (FE) analysis was based on electric driven quadricycle, called eQuad [4]. The vehicle was adapted by Virtual Vehicle to the full electric powertrain specification with lithium-ion batteries as power source. As the effect of conversion approach design the original tubular space-frame structure of eQuad was modified for the packaging purpose of electric powertrain components. On the Figure 1 is presented the vehicle after the conversion process.



Figure 1: eQuad converted by the Virtual Vehicle from the traditional combustion driven vehicle into the electrical driven vehicle.

2.1 Computer Aided Design Model

In order to perform FE analysis it was necessary to obtain the CAD geometry of vehicle. At the CAD model preparation phase were made the assumptions related to the reference points (like chassis fix points, wheels) of the vehicle. The position of all components were measured, controlled and stabilized with the respect to the reference points. The thickness and the main dimensions of the vehicle components were measured and verified too. The details level of the whole CAD model was maintained on the high level, acceptable for the geometry and packaging aspects, as well as, for the FEA aspects. From the justifiable reasons the bill-of-material was not able to obtain. The materials of components were assumed basing on the Virtual Vehicle experience and the literature [13] comparing the typical materials applications at automotive industry applications. Based on the current modelling technique some of the components were modelled with the reduced level of details. Only those details, which have the direct influence on the FEA results, were modelled. On the contact surfaces, geometries of structural elements and load bearing parts were laid high attention. The CAD model after the import and requested treatment of parts for the aims of Finite Element Method (FEM) is shown on the Figure 2.

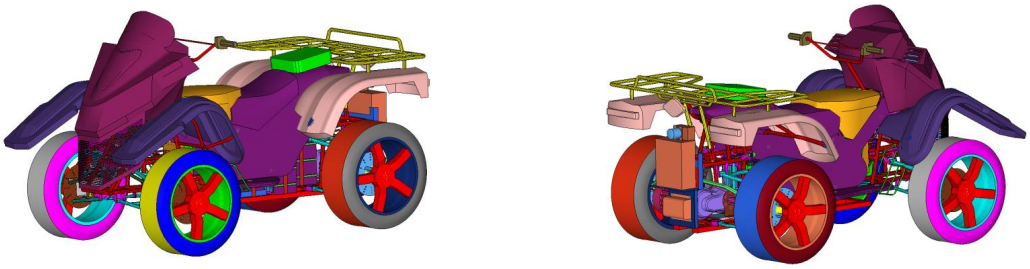


Figure 2: CAD model of the eQuad after imported and rearrangement into Pre-Processing software

The vehicle rear-end, as well as, front-end were modelled with high level of accuracy to assure correctness of FE simulations. Exact geometry was required to reproduce the contact areas of modelled parts and its energy absorption process. Figure 3 shows the parts of electric powertrain system, which were reproduced with the adequate precision. For the FE model from the Figure 2 the differential coupled to the electric motor was prepared too.

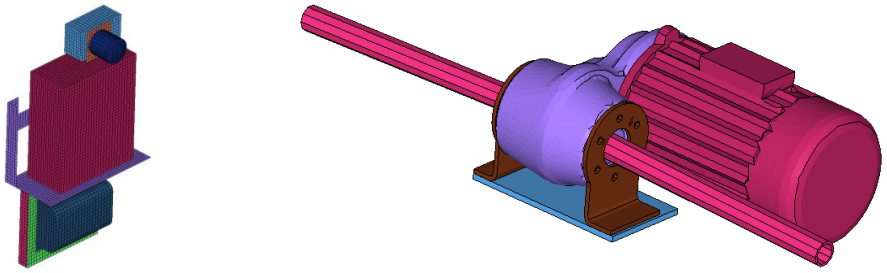


Figure 3: Electric powertrain system components: left – FE model of the veicle rear-end electric parts, right – FE model of the differential and electric motor

In this case the work was concentrated on the external housing parts. Both parts were modelled first at CAD environment and then at FE Pre-Processor by the tetra elements mesh as rigid bodies with corresponded physical mass. Therefore this drivetrain system was modelled with high level of accuracy for the external housing. In this way it is possible to

capture the eventual contacts of parts during the simulation. On the Figure 3 is shown the differential coupled to the electric motor with other parts of this powertrain system. The electric motor, as well as, the differential can be easy identified. Those parts were selected and reproduced in order to catch and depict the load bearing parts, as well as, fundamental equipments of drivetrain system.
During the CAD and FE models preparation phase the electric batteries were modelled too. For the conversion process mentioned before, the batteries from the company called the European Batteries Ltd were used. Unfortunately, due to the unexpected problems (bankruptcy) the information from the company side regarding to the technical specifications was not available [14]. Despite this, the effort was made to model the batteries with the high level of accuracy basing on the battery technical documentation, as well as, on the Virtual Vehicle technical expertise [24]. Fundamental objective was to represents in accepted way the presence and global behaviour of the battery packs.

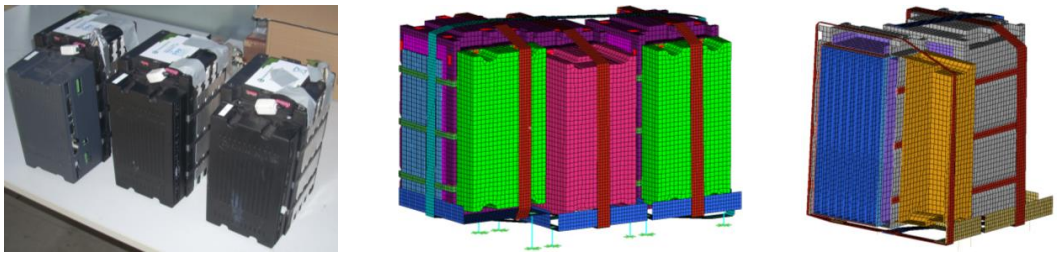


Figure 4: Battery packs of the eQuad, left – before final montage at vehicle, centre and right – FE model with the visible retain belts and supporting plates

The battery packs, which contain the batteries, are presented on the Figure 4. Each of the battery pack contains eight lithium-ion prismatic cells. The Battery Management System (BMS) master unit with a power unit and two BMS repeater units were joined additionally to the battery packs. The CAD and FE models were prepared as hollow structure in order to reproduce real behaviour of battery packs. Moreover, the attention was done to take into account the retaining belts made of woven fabric, which serve to hold in position the battery cells and battery packs. Farther, the battery packs housing and additional BMS parts were treated by the increasing the material distribution – amount the thickness of the parts walls to model a present of electronic components.

2.2 Materials and material models used in the simulations

For both type of implicit and explicit FEM simulations various material models were used. The complete FE model of eQuad contains of materials like: steel and aluminium, as well as, plastics, rubber and foam. As was mentioned in previous section due to the lack of detailed materials specifications the materials were assigned basing on the company experience and literature. From this reason the main material as steel S235 with the yielding stress point at 235MPa and the rupture stress at 370MPa with the total elongation more than 26% for the tubular space-frame was selected. Moreover other kinds of steel like spring steel with yielding stress at 420MPa and steel with the yielding stress at 270MPa for the suspension parts, as well as, the aluminium alloy with the yielding stress at 170MPa were chosen. To capture correctly the nonlinear behaviour of analyzed parts the nonlinear material models were applied [15]. All the metallic material models were optioned to consider strain rate behaviour of those materials. Most of metallic parts were modelled by the *MAT024/*MAT_PIECEWISE_LINEAR_PLASTICITY. This material model requires

providing the plastic part of the true engineering stress-strain curve for a modelled material. The *MAT024 was applied to simulate the parts made of polycarbonate-ABS (PC-ABS) too. Instead the material type *MAT081/*MAT_PLASTICITY_WITH_DAMAGE was selected for parts made of glass fibre reinforced polypropylene (PP-GF). Furthermore the material model *MAT083/*MAT_FU_CHANG_FOAM, which is suitable for foam materials, was used to model the parts made of expanded polypropylene (EPP) foam. The material model *MAT003/*MAT_ELASTIC for the linear behaved parts and *MAT020/*MAT_RIGID for the rigid parts of drivetrain were adopted.

2.3 Static loads simulations – bending and torsion

At the automotive industry there are few indicators, which represent the quality level of the engineering work done for the vehicle structure design. Those indicators usually are the value of the forces and momentums obtained from the static and dynamic mechanical tests. There are mainly two types of static load test for the vehicle body, which the automakers use to highlight improvement versus the previous vehicle generation or competitors, mainly: bending and torsion. The static bending test (sometimes called as H-point test) is based on the four-point bending (4PB) or rare three-point bending (3PB) test [17]. As was mentioned before the value of bending strength will be used in the future modernisation work as input data.

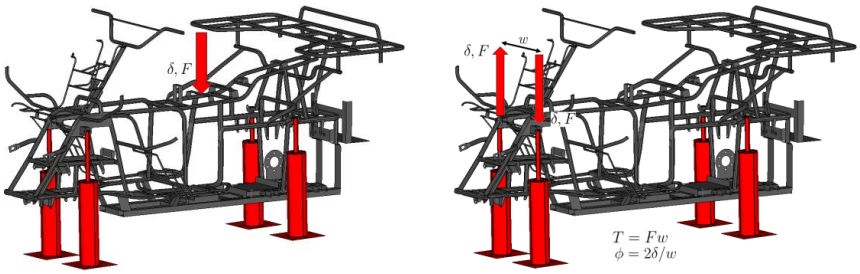


Figure 5: Static load case tests schema of the eQuad structure: left- three-point bending, right – torsion

On the Figure 5 is shown the schema of the 3PB test of the eQuad frame which corresponds to the tests seen in automotive industry [18-19]. The load is introduced into the structure by the load cell modelled by three dimensional solid finite elements as a stiffer cylinder. The preparation of the FE model was based on the indications reported at [16, 20-21]. For whole model the medium finite element length was ca. 6mm. Close to the stress concentration locations the density of FE mesh was increased to avoid the singularity. In order to maintain the quality criteria [21] the elements were controlled. The fully integrated shell elements were used. The rectangle mesh was mainly maintained, but the triangle elements due the geometry complicated shapes were applied too. The FE simulation was performed at implicit nonlinear mode [12, 16]. For the FEA the Boundary Conditions (BC) were not in accordance to the industrial practice [17-19]. Normally, the load in the form of a static force (usually as the multiplication of the acceleration of $2g$ for the max. 80% of the vehicle curb mass) at the location of passenger seats is applied to the vehicle structure. The analysis was performed in other way, mainly, the aim of the FE simulation was to obtain the point in which the small permanent deformations occur. Steady-state linear displacement as the load was applied. The force and the local displacement at the selected points on the vertical axis correspond to the line of acting load were registered. The value of bending stiffness and strength of eQuad tubular space-frame is presented on Figure 6. The bending strength corresponds to the point in

which the small permanent deformations on the vehicle body start to occur. The term "small permanent deformations" is different for each vehicle manufacturer. In this case the small permanent deformations mean that, on the structure occur the plastic deformations equal to or just little more than the yield strength R_{02}.

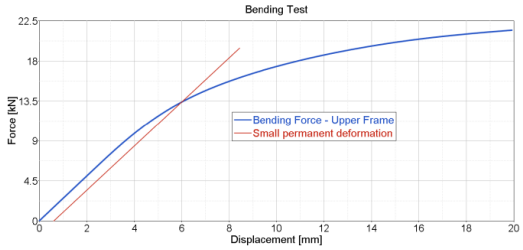


Figure 6: Bending FE implicit simulation results: determination of bending strength

The bending strength value is obtained by the cross point defined by the red line (small permanent deformations) and the blue curve. This moment is presented on the Figure 6. Based on this approach the bending stiffness is a part of the blue curve from the origin of the graph and goes till to the bending strength. The maximal bending force corresponding to the bending strength has the value of 13.5kN.

The torsion test is based on the concept, that there is a pair of the forces, which acting on the column strut mounting points on one axle (usually front axle), whereby the column strut mounting points on the second axle are constrained. The schema of the torsion test is presented on the Figure 5. It is worth to notice, that the values of torsion strength will be used in future modernisation studies as input data. The FE model was based on the previous model used for the bending test. The only differences are in the BC modelling. The FE torsion model has the linear steady-state displacement applied on the front column strut mounting points and the constrained displacements on the rear column strut mounting points. By the using of the load cell modelled as the solid elements cylinders placed at the locations of the acting displacement load, the forces registration for the corresponding nodal displacements was done. The same concept of small permanent deformation for the torsion strength determination as in the bending test case was applied. As any real validation torsion test was not performed, one additional test for further investigation of torsion strength with the obverse BC was done. At this step the linear steady-state displacement was applied on the rear column strut mounting points and the front column strut mounting points were constrained. On the Figure 7 are shown the results of both simulations. To obtain the torsion strength the cross point of two lines, a blue, which represents the value from FEA and a red, which represents "small permanent deformations" was defined. On each graph the line from the origin to the torsion strength means the torsion stiffness. Using the concept of "small permanent deformations" the result of torsion strength for the load on the front axle is 3.6kNm and for the load on the rear axle is 3.12kNm. The difference is provoked by the diverse spans of column strut mounting points for the front and rear axle. Additionally, during the results observation was noticed that, the development of plastic zones near the column strut mounting points happen earlier than on the structure of eQuad tubular space-frame. Basing on this fact farther investigation was made. Namely, the column strut mounting elements on the front axle (for the rear axle was not possible to perform this attempt due to the structural member, on which the strut and frame are connected) were removed and substituted by the *CONSTRAINED_NODAL_RIGID_BODY [16]. The aim of this action was to control, if it is any additional residual of torsion strength in the analyzed tubular space-frame. On the

Figure 8 are depicted the result for the front and rear torsion test, respectively. The expected increase of the torsion strength in both cases is observed. The torsion strength for the case with the load on the front axle and without the column strut mounting elements is 5.4kNm, which is 1.5 times higher than the value obtained from the complete torsion model. In the case of rear axle the value obtained from the reduced model is 4.2kNm, which is 1.35 times higher than in the case of complete torsion model. The torsion stiffness is equal, as it was mentioned for the bending simulation, a part of the blue curve from the origin of the graph and till to the torsion strength.

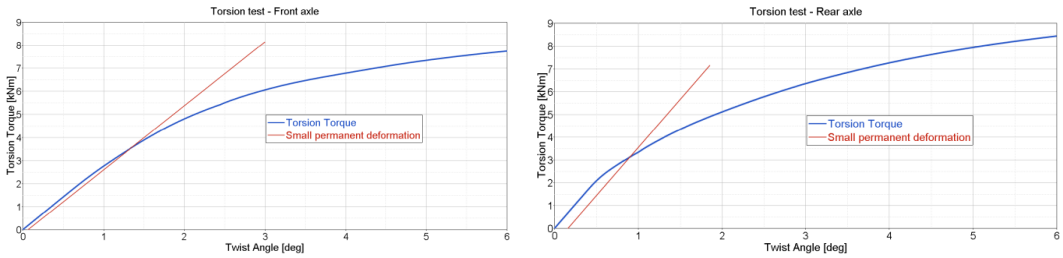


Figure 7: Torsion FE implicit simulation results: left – determination of torsion strength for front axle, right – determination of torsion strength for rear axle

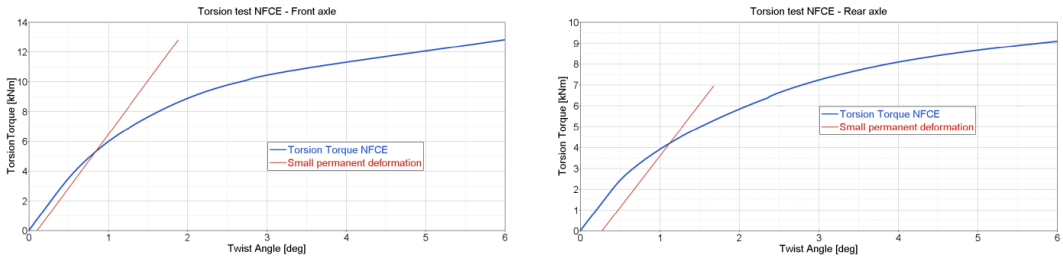


Figure 8: Torsion FE implicit simulation results: left – determination of torsion strength for front axle – no front connecting elements, right – determination of torsion strength for rear axle – no front connecting elements

2.4 Crash simulations

Main focus, beside the FE implicit simulations of static torsion and bending loads, was laid on the behaviour of battery packs during the crash simulations. As it was reported in [22] potentially hazard due to the penetration of battery cells by the foreign objects can be developed into the short circuits (internal or/and external) and then as consequences provokes the inflammation. When such developing inflammation process was happened, it is hard to arrest because of high exothermic chemical reactions at the burning of battery cells materials [23]. To avoid this phenomenon to happen, on the design stage it is require performing the crash analysis in order to capture possible contact zones and eventual perforations (punctures) on the battery cells. The preparation model phase for the FE crash analysis required some specified actions [21] related to the geometry, as well as, for the modelling concepts. On joining technique, contact definitions and the mounting elements of electric battery packs were paid high attention. The most parts were modelled as the shell elements. Only a few parts, like electric engine housing, differential housing, passenger seat, rear wheels mounting knuckle, steering handle and wheel rim hub were prepared as the solid elements. The electrical batteries, as a critical component regarding to the inflammable risk, need to be simulated and analyzed in the proper way. The focus was laid on the prismatic cells, which

were made with 1mm thickness of aluminium. The plastic parts of the battery pack were prepared with the corresponding to the each components thickness. Additionally, the mass ratio was controlled and the mass distribution by the keyword *ELEMENT_MASS_PART_SET in the 70% for the cells and 30% for the rest was applied. This approach is based on the Virtual Vehicle expertise of the electric batteries modelling for crash [24] and it was done to depict the presence of battery cells inside materials.

Crash Scenario	Target Speed [m/s]	Vehicle Frame Deformation	Battery Packs Behaviour	Battery Cells		
				Deformations	Eff. Plastic Strain [-]	Energy Absorption [kNmm]
RW Front	10	frontal part - high	medium rfm	small spots, lca (vehicle frame &each-other)	at contact spots max≈ 0.15	at local spots max≈ 0.04
RW Rear	10	rear part - high	high rfm	large spots, lca (differential &each-other)	at contact spots max≈ 0.2	at local spots max≈ 0.03
RW Side	8.3	rear part - small	high rfm	very small spots, lca (each-other)	at contact spots max≈ 0.06	at local spots max≈ 0.009
RW Half Side	8.3	rear part - small	high rfm	very small spots, lca (each-other)	at contact spots max≈ 0.07	at local spots max≈ 0.008
RP Front	10	frontal part - high	medium rfm	small spots, lca (vehicle frame &each-other)	at contact spots max≈ 0.13	at local spots max≈ 0.009
RP Rear	10	rear part - high	high rfm	large spots, lca (differential &each-other)	at contact spots max≈ 0.18	at local spots max≈ 0.021
RP Offset Front	10	frontal part - medium	medium rfm	very small spots, lca (each-other)	at contact spots max≈ 0.08	at local spots max≈ 0.009
RP Offset Rear	10	rear part - high	medium rfm	medium spots, lca (differential &each-other)	at contact spots max≈ 0.16	at local spots max≈ 0.005
RP Side	7.2	central part - medium	medium rfm	very small spots, lca (each-other)	at contact spots max≈ 0.07	at local spots max≈ 0.008

Where: RW – Rigid Wall, RP – Rigid Pole, rfm – relative free motions, lca – local contacts areas

Table 1: FE crash simulations results for the various simulation scenarios of the eQuad assessment process

The total vehicle mass was 425kg and the mass of all battery packs was 36kg, whereby the drive mass of 80kg as smeared mass near the driver seat position was included.
The behaviour of quadricycle vehicle (quad) during the rollover was investigated numerical using multi body simulation by Richardson *et al.* [25]. In this work was analyzed the critical behaviour of such vehicles, the factors, which provoke it and the possible solutions in order to obtain the increase of occupant safety level. At European region there are two protocols for the L7e vehicle class [26-27] provided by EuroNCAP, which suggest the methodology of crash test for the front and side collision scenarios, respectively. In both test protocols is necessary to use the deformable crash barrier, static or moveable, respectively. To simplify crash scenarios the layout of proposed tests was based on the rigid wall and pole as an obstacle. This approach allow to concern more on the structural aspects of investigated vehicle. The crash scenarios used in this paper for the FE simulations were developed basing on the test protocols of National Highway Traffic Safety Administration, USA [28-29]. However, only the main idea of the barrier form and suggestion of the tests realization were taken into account. To assess the vehicle structure behaviour and its influence on the batteries during the crash nine different crash scenarios divided into two groups of rigid barriers: wall and pole were prepared. The two layout examples (namely rigid wall front and rigid pole side) of those crash scenarios are reported on the Figure 9. The idea was to check the performance of the structure under the dynamic crash loads and to find the hot spots in its behaviour. The main criterion was to assure the safety of battery packs and the cells. First level of this criterion was the question, if there is any interaction from the vehicle structure on the battery packs. With the positive answer on this question was necessary to check, what provokes this interaction (e.g. relative free motions of battery packs) and how big is the effect of this interaction on the batteries (deformation zone, effective plastic strain, level of absorbed energy). This information is reported in the Table 1. From those data can be found that, the most severe cases are the frontal and rear for both, central and offset of central line, with rigid wall and pole crash scenarios. Other scenarios have minor effect on the battery safety due to the relative free motions of battery pack during the crash. Nevertheless, this minor effect should be to avoid. The relative free movements of battery packs are not permitted from vehicle dynamics point of view, as well as, could provoke under some special conditions (e.g. attrition) additional problems related to the short-circuits due to the contacts of cables.

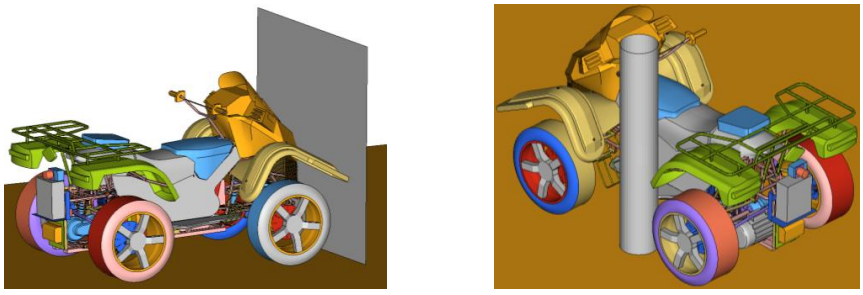


Figure 9: FE crash simulation layout: left – rigid wall front crash, right – rigid pole side crash

On the Figure 10 are shown exemplary results of FE crash simulation for the worst case reported at the Table 1. Those results show the areas where the deformation is very high and in the case of battery cells, where the contacts with the structural parts of examined vehicle were happened. Such deformations are not admissible and should be avoided. Those areas can be suspected to localize possible dangerous of inflammation by the deformation or even foreign-object penetration.

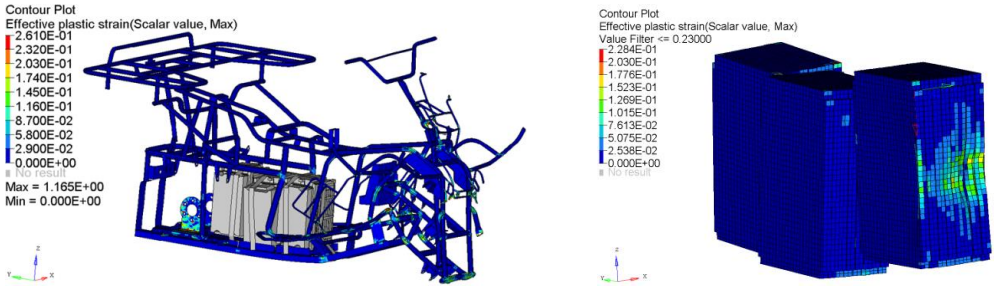


Figure 10: FE simulation results: left – effective plastic strain on the frame structure for rigid wall front crash, right – effective plastic strain on the battery cells for rigid wall rear crash

3 CONCLUSIONS

The assessment process of vehicle structure by the FE static implicit and dynamic explicit calculation was conducted and the simple tubular space-frame was revealed some weaknesses. In the case of static implicit bending and torsion simulations the weak parts of analyzed structure were shown. Removing those parts from the FE model the improvement of both, strength and stiffness was observed. In order to increase the stiffness in mentioned areas the redesign of corresponded parts is required. For static loads the design of analyzed tubular space-frame was verified as acceptable. However at some areas, which were founded during the FEA calculations, the necessity of improvements was stabilized. The obtained from FEA values of stiffness and strength will be applied as input data in the future modernisation work performing by optimisation processes.

In the case of dynamic crash explicit simulations the influence of vehicle structure on battery safety was presented. Poor protection of battery packs due to their insufficient anchorage to the vehicle frame was highlighted. In the result the battery packs have possibility to perform the relative free motions and to contact with the elements of vehicle structure and its equipments. During the crash simulations was noticed high deformation of tubular space-frame elements. These parts distortions are clear regarding the fact, that the frame was not designed for the crash loads. Using the results obtained from the both static and dynamic calculations it is obvious, that in order to improve the properties of vehicle frame and safety the modernisation work needs to be done. The optimisation process chain would be one of possible method to perform such modernisation work. All observed phenomena will be taken into account in the frame of future modernisation work as the input data and indications.

ACKNOWLEGEMENT

Authors would like to express the acknowledgements of the financial support for EU and the project GRESIMO of FP7 Marie Sklodowska-Curie Action. Moreover, authors extend the acknowledgement for the necessary support of Virtual Vehicle Competence Center and the Austrian Research Promotion Agency (FFG).

REFERENCES

[1] W. Lerner, *The Future of Urban Mobility. Towards networked, multimodal cities of 2050*. Artur D Little, 2011.

[2] M. Sattig, *The Future of Sustainable Mobility. Leading E-Mobility into a New Era*. BMW Group, 2011.
[3] C. C. Chin Ryan, *Reinventing the Automobile: Personal Urban Mobility for the 21st Century*. MIT Media Lab. 2011 MIT Europe Conference Innovation in a Networked World: Technology, People and Places
[4] Internet source, availability on 20.04.2015: http://www.v2c2.at/en/research/ee-and-software/projects/equad/
[5] Internet source, availability on 20.04.2015: http://www.tz.de/auto/ratgeber/urteil-tempolimit-wochentage-gelten-auch-feiertagen-zr-3205574.html
[6] Internet source, availability on 20.04.2015: http://en.30kmh.eu/
[7] Internet source, availability on 20.04.2015: http://www.ksta.de/service/-quad-fahren-birgt-hohes-todesrisiko,16126596,24784912.html
[8] Internet source, availability on 20.04.2015: http://www.euroncap.com/en/vehicle-safety/safety-campaigns/2014-quadricycles-tests/
[9] L. Cheah, J. Heywood, R. Kirchain, *The Energy Impact of U.S. Passenger Vehicle Fuel Economy Standards*. Sustainable Systems and Technology (ISSST), IEEE Conference Publications, 2010
[10] R. Justen, R. Schöneburg, *Crash Safety of Hybrid- and Battery Electric Vehicles*. Mercedes Car Group, Daimler AG, 2011
[11] K. Bathe, *Finite-elemente-methoden*. Springer, Heidelberg, 2002
[12] L. Nasdala, *FEM-Formelsammlung Statik und Dynamik*. 3.Auflage. Springer Vieweg, 2015
[13] Roloff / Matek, *Bauteilkatalog, Maschinen- und Antriebselemente, Erzeugnisse und Hersteller nach eCl@ss*. Vieweg + Teubner, 2009
[14] Internet source, availability on 20.04.2015: http://www.europeanbatteries.com/
[15] *LS-DYNA Keyword User's Manual. Volume II: Material Models*. LS-DYNA R7.1, LSTC 2014
[16] *LS-DYNA Keyword User's Manual. Volume I.* LS-DYNA R7.1, LSTC 2014
[17] D. E. Malen, *Fundamentals of Automobile Body Structure Design.* SAE International, 2011
[18] J. Helsen, L. Cremers, P. Mas, P. Sas, *Global static and dynamic car body stiffness based on a single experimental modal analysis test*. Proceedings of ISMA2010 including USD2010
[19] H. Singh, *NanoSteel Intensive Body-in-White. Light-weighting assessment of nano-structured sheet steel for vehicle structural components*. Final Report. EDAG, NanoSteel, 2013
[20] *LS-DYNA Theory Manual*. LSTC, 2014
[21] R. Moncur, S. Chandra, G. Jensen, S. Bala, *F1 PACE CAR: CRASH ANALYSIS, Crash Analysis Using LS-DYNA.* LSTC, 2010
[22] *Safety of Lithium-ion batteries*. European Association for Advanced Rechargeable Batteries, RECHARGE aisbl, 2013

[23] S. M. Summer, *Flammability Assessment of Lithium-Ion and Lithium-Ion Polymer Battery Cells Designed for Aircraft Power Usage*. Final Report. U.S. Department of Transportation, Federal Aviation Administration, 2010

[24] A. Thaler, D. Watzenig, *Automotive Battery Technology*. *Automotive Engineering: Simulation and Validation Methods*. Springer, 2014

[25] S. Richardson, T. Orton, A. Sandvik, C. Jones, N. Josevski, W. P. Pok, *Simulation of Quad Bike (ATV) Rollovers using PC-Crash to Evaluate Alternative Safety Systems*. 23rd International Technical Conference on the Enhanced Safety of Vehicles (Seoul, South Korea), 2013

[26] *L7e Full Width Frontal Testing Protocol*. European New Car Assessment Programme (Euro NCAP), 2014

[27] *L7e Side Impact Testing Protocol*. European New Car Assessment Programme (Euro NCAP), 2014

[28] *FMVSS 208*, Federal Motor Vehicle Safety Standards and Regulations, National Highway Traffic Safety Administration, USA

[29] *FMVSS 214*, Federal Motor Vehicle Safety Standards and Regulations, National Highway Traffic Safety Administration, USA

11th International Conference on Engineering Vibration
Ljubljana, Slovenia, 7–10 September 2015

A SAMPLING CRITERION FOR ACOUSTIC RADIATION PROBLEMS: PRACTICAL APPLICATIONS

Giorgio Veronesi*, Eugène J. M. Nijman

Virtual Vehicle Research Center, Inffeldgasse 21/A, 8010, Graz, Austria
{giorgio.veronesi,eugene.nijman}@v2c2.at

Keywords: Sampling criterion, Discretisation, Vibro-acoustics, Radiation, Patch, PTF.

Abstract. *When dealing with sound radiation problems, the radiating surface is discretised into elemental areas also referred to as patches. It can be shown that the discretisation of the structure according to the acoustical Nyquist criterion rather than the structural one will still result in a accurate estimate of the radiated power provided the complex valued vibration field is averaged over each patch. This is due to the fact that the averaging process, on one hand, reduces the structural velocity and simultaneously, determines an increased radiation efficiency. In this paper the theoretical background is briefly reviewed and experimental and numerical examples are given.*

1 INTRODUCTION

The sound radiation of vibrating structures is typically investigated by subdividing the radiating surfaces into finite-sized elemental areas, in which the surface vibrations are considered uniform over the element area. The size of these elemental areas, here also referred to as patches, has to be chosen. If the vibration field is sampled according to the acoustic Nyquist sampling criterion, taking into account the acoustic wavelength only, then spatial aliasing will occur if the structural wavelength is shorter than the acoustic wavelength. Difficulties will thus occurs below coincidence which is the frequency range addressed in this paper. This problem has been investigated by Holland et al. [1, 2] and later by Veronesi et al. [3, 4]. In the latter work the above mentioned area-averaged sampling scheme has been analysed for a simply supported baffled plate radiating into semi-infinite fluid. The authors have shown that an aliasing mechanism is established resulting in an oscillating wavelength which is, on average, constant and equal to 2.3 times the patch dimensions. Below the structural Nyquist frequency the patch-wave wavenumber follows the one of the actual structure. Analytical closed form expressions have been derived for the frequency band averaged velocities and structural wavelengths resulting from the sampling. By means of the derived expressions, it has been shown that, above the structural Nyquist frequency, the reduction of the phase averaged velocity of the discretised surface is associated with an increased radiation efficiency in the valid frequency range. The two trends are equal and opposite, so that the acoustic power radiated by the patch-plate is roughly equivalent to the one of the actual plate, provided that the patch size is carefully chosen. If one allows for a relatively small error in the power estimation coarser patches can be chosen and consequently a substantial reduction of the experimental investigation time can be achieved. Based on power considerations a sampling criterion has been derived and an analytical expression is given for the patch size as a function of the admissible error.

In the first part of this article the theory is briefly presented, showing that a patch discretised system can, in an average sense, be represented by an equivalent, frequency independent, structural wavelength equal to roughly 2.3 times the patch size. Moreover, an analytical model for the description of the averaged radiated sound power of a simply supported plate discretised into patches is shown. The above mentioned sampling criterion is applied on a test case in order to sample the field quantities for the application of the Patch Transfer Function (PTF) Approach. The advantage in the application of the proposed sampling criterion is that it allows for the identification of a trade-off between the patch dimensions, measurement effort and accuracy in the sound power assessment. Finally, a comparison in terms of mean square pressure and sound pressure levels is presented for direct measurements on a real system and estimations based on the PTF coupling procedure.

2 THEORY

2.1 Area averaged wavelength

The analysis of a one-dimensional plane propagating wave and its corresponding patch discretisation shows that the area averaging results in a propagating wave characterised by a lower amplitude and longer wavelength compared to the actual vibration field [3].

In case of a two-dimension propagating wave the spatial patch averaging creates a propagating wave, here referred as *patch-wave*, in a direction which is not necessarily corresponding with the one of the original field, depending whether the Nyquist structural criterion is satisfied or not in one or both $x-$ and $y-$projections. The patch wavelength λ_p is not, as usual, proportional with some power of the frequency but instead constantly oscillating between $\sqrt{2}d$ and

infinity. The minimum value occurs each time the projection of the structural half-waves on the x- and y-axis exactly fit an odd-integer times into the patch size d, whereas singularities occur each time the patch size corresponds with even-integer multiples of the wavelength projections of the original field. Close to the singularities the patch wavelength tends to infinity. Due to the oscillatory character of the patch wavelength it is meaningful to define a constant average value which is representative for broad band applications characterised by the superposition of many plane waves propagating in different directions with different wavelengths, as would be the case for broad band excited finite rectangular plates. Straightforward numerical integration of the oscillating wavelength over frequency bands, however, turns out problematic due to the singularities. Since the singularities correspond with zero patch velocity, and thus with zero power radiation, this problem is solved by averaging the velocity weighted patch wavelength. The weighting renders the integrand well-behaved posing no significant stability problems. The resulting frequency and propagation direction averaged wavelength of the patch-wave is equal to 2.3 times the patch size $\lambda_p = 2.3d$, therefore the patch wave can be described by a constant wavenumber defined as

$$k_p = 2\pi/2.3d. \tag{1}$$

2.2 Mean square velocity

The mean square normal velocity response of a point force excited isotropic thin plate averaged over frequency bands and over all possible excitation positions is given by Cremer et al. [5]

$$\overline{\langle\langle v(x,y)^2\rangle\rangle}\Big|_{\triangle\omega} = \frac{F_{\triangle}^2 k_s^2}{8S\overline{m}^2\omega^2\eta}, \tag{2}$$

where $\overline{m}$ is the mass per unit area, η the loss factor and k_s the structural wavenumber of the plate in bending, ω the angular frequency and S the surface of the plate.

The patch-plate mean square velocity is given by [3]

$$\overline{\left\langle\langle v\rangle^2\right\rangle}_{\Delta\omega} = \begin{cases} \frac{F_{\triangle}^2 k_s^2}{8S\overline{m}^2\omega^2\eta}, & \text{for } \omega \leq \omega_{Ns} \\ \frac{69F_{\triangle}^2 N_p^2}{\eta\pi^2\overline{m}^2\omega^2 k_s^2 S^3}, & \text{for } \omega > \omega_{Ns}, \end{cases} \tag{3}$$

respectively below and above the structural Nyquist limit $\omega_{N,s} = (\pi/d)^2\sqrt{D/m}$. N_p is the total number of patches in which the plate is discretised. The area-averaging process determines a reduced velocity compared to the actual structure once the structural Nyquist criterion is disobeyed.

2.3 Modal averaged radiation efficiency

A modal average radiation efficiency over frequency bands for the case of simply supported isotropic plates has been presented by Leppington et al. [6]. The radiation efficiency is averaged assuming k_s as a continuous functions in the wavenumber space. A normalised structural wavenumber is defined as

$$\mu_s = \frac{k_s}{k_0}. \tag{4}$$

For patch-plate, at frequencies for which the structural Nyquist criterion is disobeyed, the averaged wavenumber is given by Eq. (1). The patch-plate coincidence frequency will occurs at

$\omega_{cp} = \omega_{N,0} = 2\pi c_0/2.3d$. Therefore for the patch-plate

$$\mu_p = \begin{cases} \frac{k_s}{k_0}, & \text{for } \omega \leq \omega_{Ns} \\ \frac{k_p}{k_0}, & \text{for } \omega > \omega_{Ns}. \end{cases} \tag{5}$$

The radiation efficiency proposed in [6] will also be used for the patch-plate, as suggested in [3]. Because of the larger wavelength, the area discretised structure shows an increased radiation efficiency as compared to the actual one.

2.4 Sampling criterion and radiated sound power

The sampling criterion presented in [3] has been derived for a simply supported plate radiating into a semi infinite space. It is given by

$$d_\epsilon = 1.143\lambda_c 10^{|\epsilon|/5}, \tag{6}$$

where d_ϵ is the patch dimension, λ_c is the plate coincidence frequency and ϵ [dB] is a given maximum allowable error in the power assessment. If $\epsilon = 0$ Eq. (6) is equivalent to the structural Nyquist sampling criterion. It is useful to observe the sound power of the patch-structure and the actual structure. The acoustic power radiated by a simply supported plate based on the mean square velocity $\overline{v^2}$ and modal averaged radiation efficiency $\overline{\sigma}$ is given by

$$W = \rho_0 c_0 S \overline{v^2} \overline{\sigma}, \tag{7}$$

where ρ_0 and c_0 are the density and the speed of sound in air. It is interesting to analyse the ratio between the sound power radiated by the patch-plate and the actual plate, W_p/W, in order to assess the valid frequency range and the precision in the power estimation imposed by the discretisation. For $\omega < \omega_{Ns}$ the function W_p/W is unity since the patch-plate and the actual plate show the same mean square velocity and average radiation efficiency. Therefore, it is convenient to focus on the frequency range between ω_{Ns} and ω_{N0}. Thus, by combining Eqs. (2), (3), (7) and the expression for the modal average radiation efficiency the function W_p/W is given by

$$\frac{W_p}{W} = \frac{256\overline{C^2}}{\pi^2 d^4 k_s^4} \frac{\mu_s\sqrt{\mu_s^2-1}}{\mu_p\sqrt{\mu_p^2-1}} \frac{ln\left(\frac{\mu_p+1}{\mu_p-1}\right) + \frac{2\mu_p}{\mu_p^2-1}}{ln\left(\frac{\mu_s+1}{\mu_s-1}\right) + \frac{2\mu_s}{\mu_s^2-1}}. \tag{8}$$

For $\omega_{N,s} < \omega < \omega_{N,0}$ Eq. (8) can be simplified in

$$\frac{W_p}{W}(\omega) = \frac{256\overline{C^2}}{\pi^2 k_p d} \frac{1}{-2d\sqrt[4]{\frac{\overline{m}}{D}}} \frac{\frac{d}{c_0}\omega - 2k_p d}{\sqrt{\omega}\left[(k_p d)^2 - \left(\frac{d}{c_0}\omega\right)^2\right]^{3/2}}. \tag{9}$$

By inserting Eq. (6) in Eq. (9) and by plotting W_p/W as a function of ω, it is possible to assess the frequency limit $\omega_{lim,\epsilon}$ for which the patch-plate gives the same radiated power of the actual plate within $\pm\epsilon$ dB error, see Figure 1. This procedure allows to reduce the number of patches and therefore the experimental effort. Moreover, the valid frequency range is extended compared to the structural Nyquist criterion $\omega_{N,s}$. Above the structural Nyquist frequency, the reduction of the phase-averaged velocity of the patch-plate is associated with an increased radiation efficiency in the valid frequency range. The two trends are equal and opposite, so that the acoustic power radiated by the patch-plate is roughly equivalent to the one of the actual plate, provided that the patch size is carefully chosen.

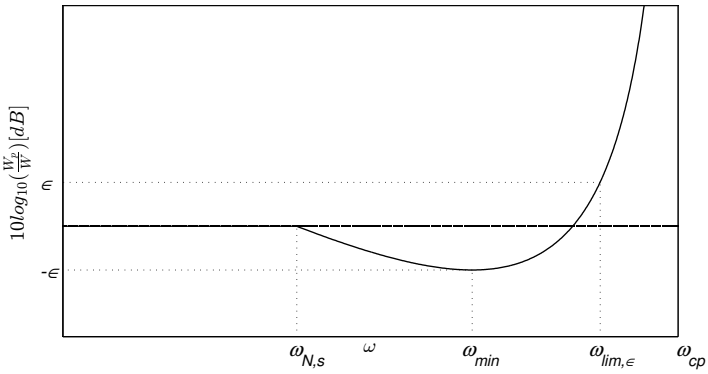


Figure 1: Power ratio, Eq. (9), as a function of the angular frequency below patch-plate coincidence ω_{cp}.

3 PATCH TRANSFER FUNCTION APPROACH

The discretisation rule addressed in this article can be applied to the Patch Transfer Function Approach. The objective is the analysis of radiation problems. The PTF allows for the assessment of the Sound Pressure Level (SPL) at a given position in an acoustic field. The PTF approach is a sub-structuring method presented by Ouisse et al. [7]. The principle consists in the sub-division of the vibro-acoustic domain into sub-domains and coupling them via interface patch impedance matrix relations. Each interface is subdivided into N elementary areas of dimensions d^2 called patches. The sub-structuring allows one to characterise each sub-domain independently by means of the most efficient calculation scheme available. In order to couple the sub-domains a set of area-averaged transfer function called Patch Transfer Functions (PTFs) must be computed. These transfer functions are based on averaged dynamic field quantities on the patches (mean sound pressure and normal velocity). Once the PTFs are known the coupling procedure consists of the application of the superposition principle. The patch values can be obtained by averaging or integrating over measured or simulated quantities over a patch area.

The patch transfer function between an excited patch j and a receiving patch i defined on the sub-system m can be expressed in terms of impedance and mobility by:

$$Z_{ij}^m = \left.\frac{\bar{p}_i^m}{\bar{v}_j^m}\right|_{\bar{v}_{k\neq j}^m=0}, \qquad (10) \qquad\qquad Y_{ij}^m = \left.\frac{\bar{v}_i^m}{\bar{p}_j^m}\right|_{\bar{p}_{k\neq j}^m=0}, \qquad (11)$$

respectively, where $\bar{p_j^m}$ and $\bar{v_j^m}$ are the averaged pressure and velocity for the j-th (i-th) patch of the m-th sub-system.

Let us consider the coupled system in Figure 2 where a thin plate excited by a point force F is coupled to an acoustic rigid cavity. Let $\boldsymbol{Y^S}$ denote the elastic plate mobility and $\boldsymbol{Z_1^C}$ the cavity surface impedance. The pressures loads vector $\boldsymbol{p^F}$ is given by the product between the magnitude of the excitation F and the vector $\boldsymbol{y}$ containing the transfer functions from the excitation point to each patch on the structural side at the coupling interface. The mobility and impedance relations at the coupling interface between the structural and the acoustic domains may be written as

$$\boldsymbol{v_1^S} = \boldsymbol{Y^S}\left(\boldsymbol{p_1^S} + \boldsymbol{p^F}\right), \qquad (12)$$

$$\boldsymbol{p_1^C} = \boldsymbol{Z_1^C}\boldsymbol{v_1^C}. \qquad (13)$$

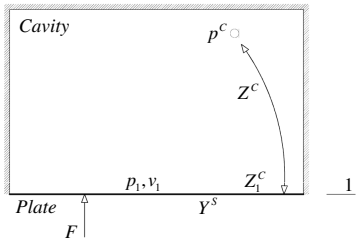


Figure 2: A coupled vibro-acousic problem: a structure coupled to a fluid layer.

$\boldsymbol{Y^S p^F = v_1^S}$ is the plate response to the force in vacuo ($\boldsymbol{p_1^S = 0}$). The continuity conditions for the coupled case are

$$\begin{aligned} \boldsymbol{p_1 = p_1^S = p_1^C}, \\ \boldsymbol{v_1 = v_1^S = v_1^C}. \end{aligned} \tag{14}$$

Combining Eq. (13) and (14) yields

$$\boldsymbol{p_1 = Z_1^C v_1}. \tag{15}$$

The mobility relation Eq. (12) yields

$$\boldsymbol{v_1 = Y^S \left(p_1 + p^F\right) = Y^S \left(Z_1^C v_1 + p^F\right)}, \tag{16}$$

which results in

$$\boldsymbol{\left(I - Y^S Z_1^C\right) v_1 = Y^S p^F}. \tag{17}$$

The pressure p^C at receiving point is given by

$$p^C = \boldsymbol{(z^C)^T v_1}, \tag{18}$$

where $\boldsymbol{(z^C)^T}$ is the transpose of the vector of the acoustic transfer functions between the patches on the interface 1 and the receiving position in the cavity.

4 EXPERIMENTS

The PTF coupling procedure has been applied on a test case and the proposed sampling criterion has been used for the choice of the patch dimensions. The set-up consist of a aluminium plate of dimensions 1.7 m $\times$ 0.8 m $\times$ 0.005 m constrained along the edges by a rigid frame. The plate radiates into a parallelepipedic rigid acoustic cavity of dimensions 1.7 m $\times$ 0.8 m $\times$ 1 m. A sketch of the test set-up is presented in Figure 3. The plate has been excited in a point ($x = 0.950$ m, $y = 0.450$ m, $z = 0$ m) by a impact hammer and the sound pressure has been measured in 10 positions inside the acoustic cavity by means of 1/4 inch sound pressure microphones. The coordinates of the receiver microphones are specified in Table 1. The sound power W is determined based on the mean square pressure $\overline{p_{rms}^2}$ averaged over space and time [8]. The experimental determination of the mean square sound pressure has been compared to the one determined by means of the Patch Transfer Function (PTF) Approach applied on the coupled plate-cavity system as shown by Rejlek et al. [9]. The PTF Approach has been applied in order to predict the sound pressure at the same 10 microphone positions used in the experiment. The structural Nyquist sampling criterion with a patch dimension of $d = 0.16$ m would

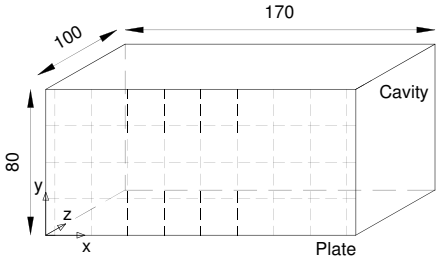


Figure 3: A metal plate coupled to a rigid acoustic cavity (dimensions in cm).

mic	1	2	3	4	5	6	7	8	9	10
x [m]	0.775	0.230	1.450	1.320	1.160	0.585	0.615	0.350	1.470	0.860
y [m]	0.655	0.190	0.345	0.235	0.580	0.370	0.575	0.395	0.375	0.455
z [m]	0.345	0.70	0.490	0.775	0.175	0.455	0.725	0.760	0.400	0.545

Table 1: Positions of the sound pressure microphones.

results in a frequency limit of 300 Hz and in a total number of 50 patches. In order to reduce the measurement effort Eq. (6) can be applied. In this case an error of ± 0.5 dB is accepted in the acoustic power estimation, the patch dimension can be increased of the 25% resulting in $d = 0.2$ m and, as a consequence, the total amount of patches reduces to 32. Simultaneously, the valid frequency range is extended till 500 Hz.

5 RESULTS AND DISCUSSION

In Figure 4 the analytical power ratio determined by means of Eq. (9) is presented. Even

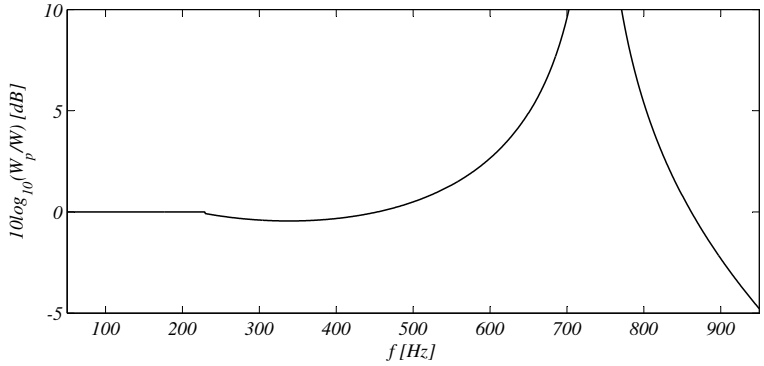


Figure 4: Analytically determined patch to plate power ratio, Eq. (9).

if the plate used in the experiment has different boundary conditions compared to simply supported edges, the analytical model gives an indication concerning the expected trend for the PTF prediction compared to a direct measurement in terms of SPL or mean square pressure. For f <230 Hz the power ratio is one since the structural Nyquist criterion is met, see Figure 4. The PTF is expected to match the direct measurement up to 230 Hz and to underestimate the power with less than 0.5 dB for 230 Hz $< f <$ 450 Hz. At frequencies between 450 Hz and 850 Hz an overestimation is expected due to the fact that the patch-plate reaches the coincidence condition. The patch-plate coincidence, or the acoustic Nyquist sampling criterion, is reached

at 750 Hz and at higher frequencies the power emitted by the patch-plate diverges from the one of the actual plate. Here, the patch discretisation does not satisfy the acoustic Nyquist sampling criterion and therefore the PTF approach is not valid.

In Figure 5 the narrow band measured mean square sound pressure is compared to the one determined by means of the PTF Approach. The discretisation indeed allows for an accurate

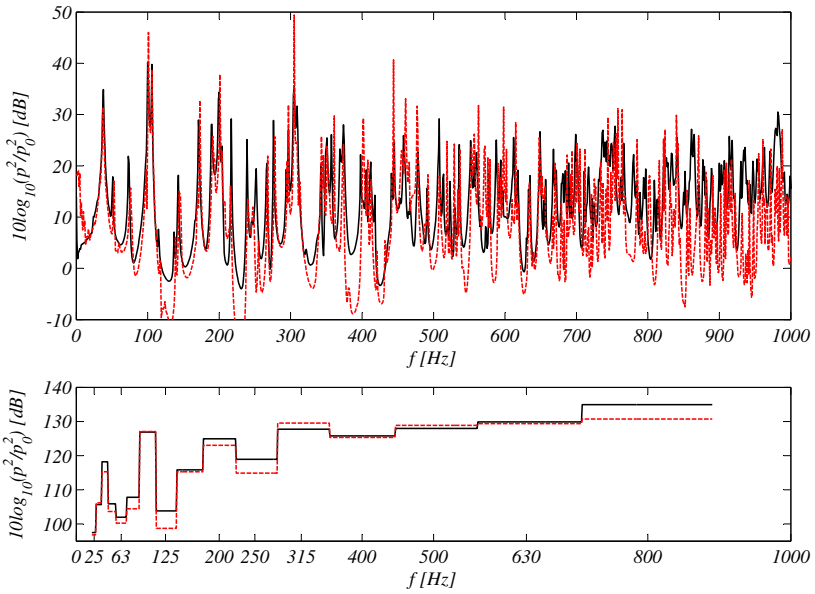


Figure 5: Comparison between the experimentally determined mean square pressure (solid line) and the one assessed by means of the PTF Approach (dotted line). Top narrow band, bottom third octave bands.

estimation of the mean square sound pressure up to 230 Hz. Up to this frequency the discretisation is able to well describes the mode shapes of the structure. As expected, there is an underestimation of the mean square pressure in the frequency band between 230 Hz and 280 Hz. The PTF assessed mean square sound pressure is overestimated for 400 Hz $< f <$ 500 Hz. In the frequency range between 500 Hz and 700 Hz the PTF determined pressure does not show a clear patch-plate coincidence and the values are fluctuating around the direct measurement line. At higher frequencies the PTF computed pressure diverges from the measurement line since the proposed sampling criterion is not satisfied. This is confirmed by the third octave band plot, see Figure 5. The proposed sampling criterion is derived based on frequency band averaged velocity and radiation efficiency assuming that each frequency band contains at least five natural frequencies. Below 200 Hz this assumption is not satisfied and indeed the PTF underestimate the actual mean square pressure up to 5 dB. The underestimation in the narrow band plot between 230 Hz and 280 Hz is also visible in the third octave bands plot at 250 Hz. For the third octave bands between 315 Hz and 630 Hz the difference between the PTF and the measured mean square pressure is less or equal to $\pm$ 1 dB. At higher frequencies the sampling criterion is not valid and therefore the PTF estimation diverges from the measured pressure. Although the sound power estimation is accurate, within $\pm$ 1 dB for the third octave bands between 315 Hz and 630 Hz, the sound field variables (local sound pressure and particle velocity) may show significantly deviations respect to the actual values. This is due to the fact that, when the structural Nyquist criterion is not satisfied, the patch-plate cannot reproduce the actual mode

shapes of the plate thus realising different directivity patterns. This assumption can be easily check by observing the comparison PTF prediction-direct measurement at different locations. From the analytical considerations an underestimation of the SPL is expected in the frequency range between 230 Hz and 450 Hz. Moreover, an overestimation is expected for 450 Hz $< f <$ 850 Hz where the patch-plate reaches the coincidence frequency region. In Figure 6 the PTF reconstruction at microphone position 8 is compared with a direct measurement. The PTF allows

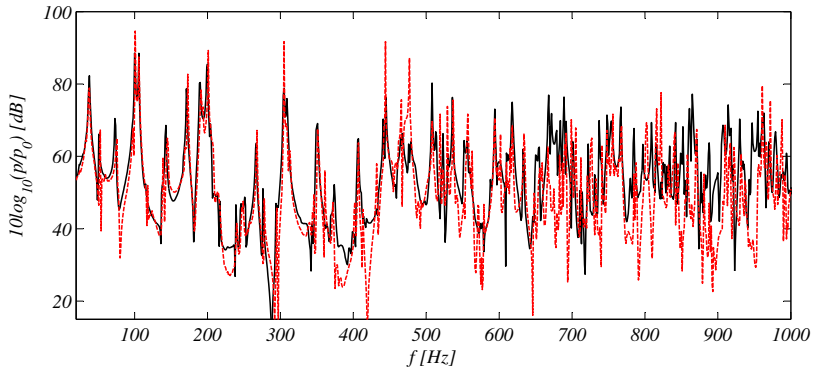


Figure 6: SPL at position 8, PTF (dotted line) compared to the direct measurement (solid line).

for a reliable estimation of the cavity SPL up to 300 Hz. In this frequency range the structural Nyquist criterion is satisfied and the mode shapes of the structure are captured well. For 450 Hz $< f <$ 650 Hz the PTF line approximates the direct measurement and at higher frequencies it diverges. In this spatial location the PTF shows an excellent approximation of the actual SPL. In Figure 7 the PTF reconstruction at microphone position 2 is compared with a direct measurement. The PTF prediction matches with the measurement up to 200 Hz. At higher frequencies

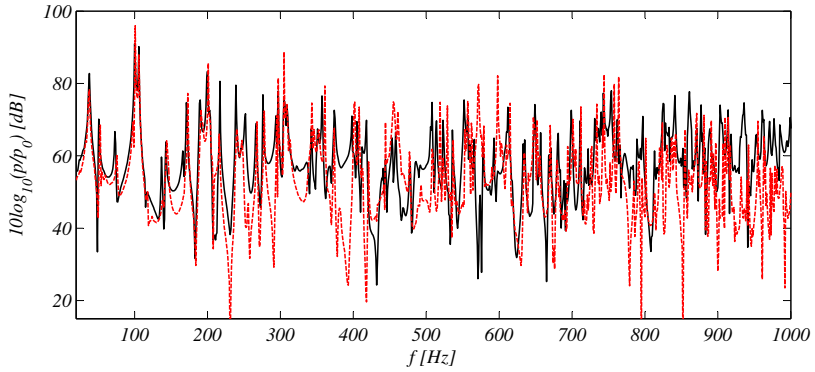


Figure 7: SPL at position 2, PTF (dotted line) compared to the direct measurement (solid line).

high fluctuations in the PTF prediction can be observed. Above the 700 Hz limit the PTF pressure diverges from the measured one. The PTF response in this microphone position is more influenced by the directivity pattern of the patch-plate compared to the response at position 8.

6 CONCLUSIONS

In this paper a sampling criterion for acoustic radiation problems has been investigated and applied on a test case. A weakly coupled vibro-acoustic problem has been solved by means

of the Patch Transfer Function (PTF) Approach and the proposed sampling criterion has been used in order to discretise the radiating surface. Finally, the calculated sound pressure has been compared with direct measurements in terms of SPL at two receivers positions in the cavity and in terms of mean square pressure. The coupling method and the sampling criterion give an accurate estimation in terms of sound power in the valid frequency range. The same accuracy cannot be systematically reached in terms of local sound pressure and particle velocity since the discretised structure may produce different directivity pattern compared to the actual one.

ACKNOWLEDGEMENTS

The research work of Giorgio Veronesi has been funded by the European Commission within the ITN Marie Curie Action project GRESIMO under the 7th Framework Programme (EC grant agreement no. 290050). The authors acknowledge the financial support of the COMET K2 - Competence Centres for Excellent Technologies Programme of the Austrian Federal Ministry for Transport, Innovation and Technology (BMVIT), the Austrian Federal Ministry of Science, Research and Economy (BMWFW), the Austrian Research Promotion Agency (FFG), the Province of Styria and the Styrian Business Promotion Agency (SFG). Finally, the authors gratefully acknowledges the support of COST action TU1105.

REFERENCES

[1] K. R. Holland and F. J. Fahy. A guide to the exploitation of vibroacoustic reciprocity in noise control technology. *ISVR Technical Report No 264*, 1997.

[2] K. R. Holland and F. J. Fahy. An investigation into spatial sampling criteria for use in vibroacoustic reciprocity. *ISVR Technical Report No 265*, 1997.

[3] G. Veronesi and E. J. M. Nijman. On the sampling criterion for structural radiation into fluid. *submitted in Journal of Sound and Vibration*.

[4] G. Veronesi. *A novel PTF-based experimental characterisation for poroelastic liners: method and sampling criterion*. PhD thesis, Università di Ferrara, Facoltà di Ingegneria, 2015.

[5] L. Cremer, M. Heckl, and B.A.T. Petersson. *Structure-Borne Sound: Structural Vibrations and Sound Radiation at Audio Frequencies*. Springer, 2005.

[6] F. G. Leppington, E. G. Broadbent, F.R.S., and K. H. Heron. The radiation efficiency of rectangular panels. *Proceedings of the Royal Society of London A*, 382:245–271, 1982.

[7] M. Ouisse, L. Maxit, C. Cacciolati, and J. Guyader. Patch transfer functions as a tool to couple linear acoustic problems. *Journal of Vibration and Acoustics*, 127:458,466, 2005.

[8] F. T. Agerkvist and F. Jacobsen. Sound power determination in reverberation rooms at low frequencies. *Journal of Sound and Vibration*, 166:179–190, 1993.

[9] J. Rejlek, G. Veronesi, C. Albert, E. Nijman, and A. Bocquillet. A combined computational-experimental approach for modelling of coupled vibro-acoustic problems. *SAE Technical Paper 2013-01-1997*, 2013.

11th International Conference on Engineering Vibration
Ljubljana, Slovenia, 7–10 September 2015

DETERMINING VIBRATION SOURCES IN SOLID MEDIA USING TIME REVERSAL TECHNIQUE

Amr Abboud*, Eugene Nijman

Virtual Vehicle Research Center, Inffeldgasse 21/A, 8010, Graz, Austria
{amr.abboud, eugene.nijman}@v2c2.at

Keywords: Time Reversal, transfer function, Wave back propagation, reciprocal media.

Abstract. *The identification of the noise source and its transfer path becomes more demanding in several fields of industry; that calls for a robust technique, which can guide to identify the noise source. The propagation of elastic waves is time reversible in a linear non-attenuative medium. This property can be used to rebuild the original response signal on the excitation point by means of recorded response signals at receiving points. This technique is called the time reversal mirror, which is based upon the feature of symmetry of the acoustic wave equation in some media, where the standard wave equation only contains even order derivatives. In this paper, the problem of determining the different source locations and their mutual importance using the time reversal technique is considered for some simple engineering structures. The responses of the structures to two forces of unknown magnitude and location are recorded in several receiver positions, reversed in time and sent back through the system. The resulting waves converge back at the points where they were originally emitted, a process referred to as 'focalisation'. Analytical models are built to support this theory, followed by experimental validation. The influence of parameters such as the number of transceivers, the structural complexity and the type of input signals were investigated. Particular interest was given to the effect of multiple inputs and the relation between the focalisation response and the original input power.*

1 INTRODUCTION

This report summarizes the results obtained from the work that was carried out at Virtual Vehicle Research Centre, within the framework of the GRESIMO project, under the topic 'Acoustics Time Reversal'. The work is conducted in order to understand the concept of acoustic time reversal, and its applications in noise and vibration.
The Acoustic Time reversal technique (ATRt) has been developed during the 80s of the last century in order to focus ultrasonic transient waves in complex media [1]. The technique is applied in an ultrasonic range in different fields such as a non-destructive testing, medical therapy and imaging, underwater acoustic communication, and sound field reconstruction. However, very few studies have been made about applying an audible range Acoustic Time Reversal (ATR) in solid media to identify the excitation sources. Vigours and Guyader have succeeded to localise a single vibration source in complex structure [8].
This study aims to show the possibilities of employing (ATRt) to solve noise and vibration issues in dynamic structures by localising multiple vibration sources and assessing their mutual importance. Analytical simulations were carried out on 2D structures in order to obtain a preliminary validation of the robustness of ATR to determine the initial sources. To validate the simulation results and investigate the application of ATRt far from the ideal conditions, a lab experiment consisting of a bounded thin plate excited by impact sources at different locations has been carried out.
The outline of this report is described as follows: section 2 describes the theory behind the ATRt method in time and frequency domains. In section 3, the simulation results are presented and discussed. In section 4, the validity of the simulation result through the comparison with the experimental results is shown. Conclusions are presented in section 5.

2 Acoustic Time Reversal (ATR)

In a typical time-reversal technique, the excitation response signals are recorded by a group of transducers, which function as both receivers and transmitters. The process is divided into two stages; in the first one, called the forward propagation, the receivers record the direct wave propagation from the source, and the reflected ones from the boundary. In a second stage, called the time reversal back-propagation stage, the recorded signals at the receivers are reversed in time, and re-broadcasted into the medium. The retro-focusing is automatically taking place at the excitation point. The acoustic time-reversal technique is based upon the reciprocity property of wave propagation in the system; giving symmetry to the wave's propagation equation . Therefore, this process -strictly speaking- is valid in a linear non-attenuative medium where the symmetry property is valid. However, in many practical cases of attenuative media, the time reversal process still holds, with decreased efficiency [6].
Consider a completely linear and time-invariant system, the wave propagation through a homogenized medium or a multiple-scattering medium may be described as a linear system with different impulse responses. If a source, located at r_0, sends a Dirac pulse $\delta(t)$ to the j^{th} transducer located at r_j, it will record the impulse response $h(r_0, r_j, t)$ that corresponds, to Green's function G(r_j , t| r_0, 0). Moreover, due to reciprocity, $h(r_0, r_j, t)$ is also the impulse response describing the propagation of a pulse from the j^{th} transducer to the source [13][1]. The reversed response which is sent back from the transceiver to the initial source is equal to $h(r_0, r_j, T-t)$, Where T : is the time delay which is used to insure causality in the process. Thus, the time-reversed response signal at the source is equal to the convolution product [1]

$$\Psi(\overrightarrow{r_0}, t) = h(r_0, r_j, t) \otimes h(r_0, r_j, T-t). \tag{1}$$

Whatever the impulse response $h(r_0, r_j, t)$, the convolution $h(r_0, r_j, t) \otimes h(r_0, r_j, T-t)$ is maximum at the time t = 0. This maximum is always positive and is equal to $\int h^2(r_0, r_j, t)$ dt [1] , i.e. the energy of the signal h_j(t). This is the classical procedure which is performed in time domain. If an N-element array is employed in the process, the time-reversed signal recreated on the source is written as a sum

$$\Psi(\overrightarrow{r_0}, t) = \sum_{j=1}^{j=N} h(r_0, r_j, t) \otimes h_j(r_0, r_j, T-t). \tag{2}$$

The directivity pattern of the reconstructed response at the source point can be calculated using the so called 'spatial correlator approach' as referred in [1], which is based on calculating the propagation impulse response $\overline{h(r_0, r_j, T-t)}$ from receiving points with regards to an observation point r_1 different from the source location r_0 (which has a propagation impulse response $h(r_0, r_j, t)$) , at time t = 0 the signal created in r_1 at time t = 0 is written

$$\Psi(r_1, 0) = \sum_{j=1}^{j=N} h(r_1, r_j, t) \otimes \overline{h(r_0, r_j, T-t)} dt \tag{3}$$

This expression can be used to define the directivity pattern of the time reversed waves around the source.

In bounded systems, the reflecting boundaries redirect one part of the incident wave towards the receivers, thus the reversal quality is increased, but this gain depends crucially on the duration of the recording process of data at the reception points. In contrast to bounded systems, data leave and never reflect back in open (infinite) systems. Consequently, only a limited part of the information can be captured by the receivers. Thus, a limited reversal and focusing quality is obtained [1]. Therefore, in order to compensate for the lack of boundaries; the excitation point must be completely surrounded by an array of receivers under the conditions matching with Huygens principle [6].

In a linear, time invariant, and deterministic systems, the impulse response (time domain characterization of the system) is equivalent to the transfer function (frequency domain characterization), and the time reversal process of the response signal is equivalent to phase complex conjugate of the transfer function components [11]. Therefore the time reversal process in frequency domain is equivalent to the product of the transfer function H(r_i,r_0,ω) by its complex conjugate.

$$H(r_i, r_0, \omega).H^*(r_i, r_0, \omega) = \mid H(r_i, r_0, \omega) \mid^2 \tag{4}$$

This product cancels out the phase of each component in frequency response as the reversed response signal is propagating backward to time zero. Certainly, with an N-element array, the time-reversed signal recreated on the source is written as a sum of the product

$$\sum_{i=1}^{i=N} H(r_i, r_0, \omega).H^*(r_i, r_0, \omega) = \sum_{i=1}^{i=N} \mid H(r_i, r_0, \omega) \mid^2 \tag{5}$$

The process of source localisation by means of the time reversal process in the frequency domain is performed through a product of the transfer function complex conjugate $H^*(r_i, r_0, \omega)$ by the system transfer function matrix. This product is a matching filter process [1][12], which results in a focalisation at the initial source points. In order to obtain the results in the time domain, Inverse Fourier Transform (IFFT algorithm) is performed on the output results. The ATR

procedure in this work has been carried out in the frequency domain. The excitation process is conducted through impulsive (hammer) forces that can be approximated as a Dirac function in the time domain.

3 Numerical Results

Analytical simulations were carried out on a simply supported plate using the available closed form solution [13]. The plate has a dimension (1.6 $\times$ 0.8 [m]) and following material properties:

- Density ρ = 7800 kg/m^3
- Young's modulus E = 2.1e11 Pa
- Thickness h = 0.001 m
- damping loss factor η= 0.005

The retro-focusing process was carried out for the case of two point-forces. The response was calculated at different receiving points, and used in the Acoustic Time Reversal Process (ATRP). To evaluate the focusing pattern and the directivity at the source points, the response to the time reversed field (back propagating) was evaluated on the entire plate surface at time t=0 . For that reason, the structure area was discretized into 162 equally distributed points. The results are shown in Figure (1). This simulation provides an initial idea regarding the applicability and the robustness of the ATRP not only in localising the initial sources but also with regard to the ability of ATR to access the mutual importance of the two forces.
The plate was initially excited by two equal forces, which were applied for a very short duration δt having a flat spectrum along a frequency range [0,1000]Hz. Frequency responses were calculated in that frequency range by seven receivers randomly distributed on the control surface. The frequency step was chosen to be equal to 0.2 Hz, corresponding to a time window of 5 seconds. Such a window is chosen in order to insure that the significant part of the transient response would be captured by all receivers. The spatial focalisation results are presented in Figure (1). The responses focus exactly at the initial source points. In the same figure, a gradient field ∇V of spatial parameter x and y is displayed as a field of arrows pointing to the source's points.

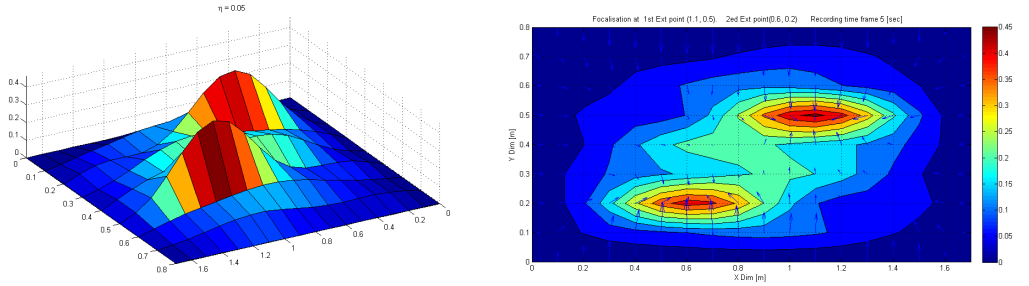


Figure 1: The spatial response of the back-propagating signal at time zero

As expected the ATR performs well with regards to the localisation process even for two input sources. But unfortunately ATR turns out less accurate when it concerns the reconstruction of the mutual importance of the two forces.

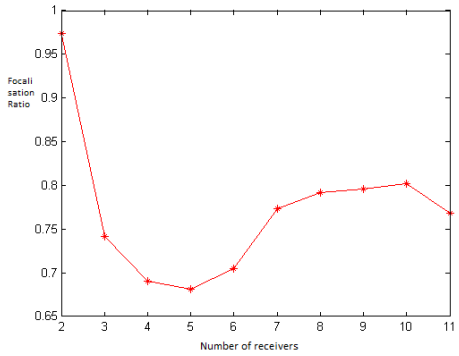


Figure 2: The effect of the number of receivers on the focalisation response ratio,The X-axis is the number of receivers. The Y-axis is focalisation response ratio from the two source

Figure (2) illustrates the relation between the focalisation ratio at two initial source points and the number of receivers. It's clearly indicating that the ratio is not unique, but depends on the number and the position of the receivers. An explanation of this feature maybe found in the so-called time reversal acoustic sink (TRAS) concept. The TRAS was introduced by Fink [9] in 2000 in order to correct for the fact that the time reversal field could fully converge the initial source points if a sink was introduced at time t=0. In other words, the author suggested that not only the field should be reversed but also the source. Although Fink introduced this concept to achieve a focalisation resolution better than $\lambda/2$ (The sink introduce near field), the same concept may also explain the failure to yield the correct amplitude ratio in the case of multi point excitation.

4 Lab experiment

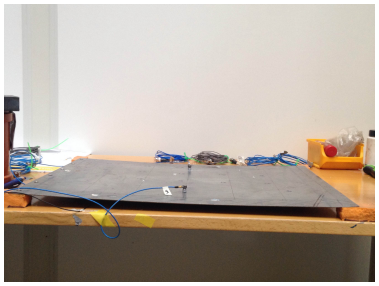


Figure 3: The tested plate

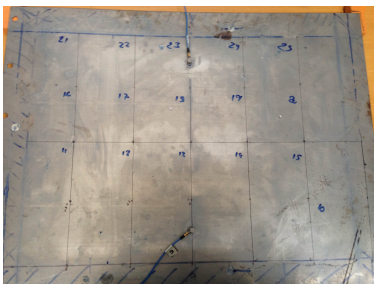


Figure 4: The tested plate with the accelerometers

The experiments were carried out on an isotropic steel plate, with dimensions 65×45 cm and thickness of 1 mm. During the measurement an impact hammer and four accelerometers were used to characterise the system properties in the frequency domain, and to record the

response from the initial source. The plate surface was divided into 24 patches; the distance between the centre points of the patches was 10 cm. The frequency characteristic of the system was evaluated by measuring the frequency response from the centre point of each patch to all receivers in frequency range [0∼1 kHz] with 4096 frequency lines. The 4 seconds recording time were sufficient to capture the significant part of the transient impulse response. After characterising the system, the plate was excited by two impulsive forces at two deterministic points. During the reconstruction step of the ATRP; the recorded response fields were reversed in time by taking the complex conjugate of the frequency response, and then re-fed into the system by multiplying the reversed velocity response by the system transfer function matrix $[A_{m*n}]$. The resultant time reversal field is depicted in figure (5).

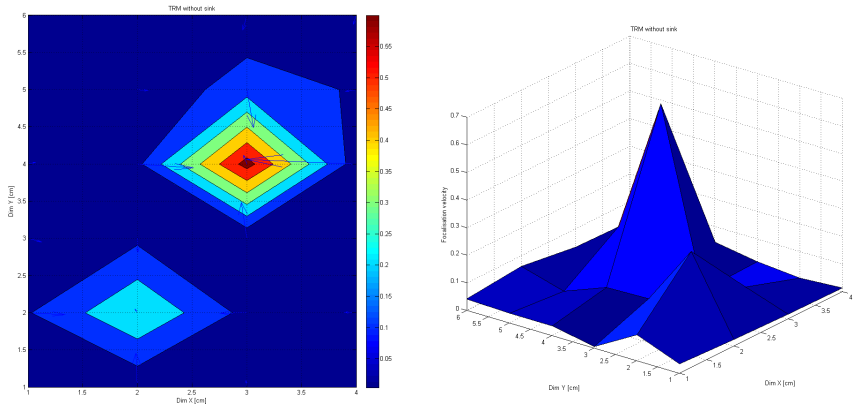


Figure 5: The space localisation of the initial excitation points at time zero.

As can be seen from figure (5) The focalisation ratio is approximately equal to 3. However, by redistributing the receivers at equal distance from each initial source, the focalisation ratio turns out to become 1. See figure (6)

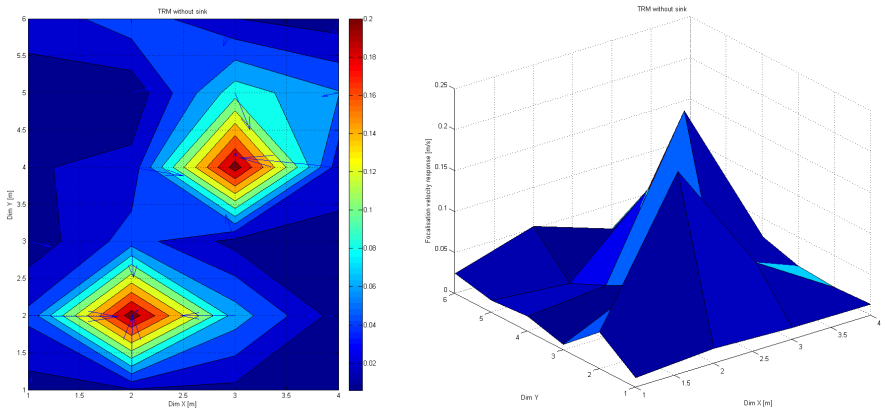


Figure 6: The space localisation of the initial excitation points at time zero, after redistributing the receivers around the sources.

In other words, the focalisation ratio is clearly depending on the receiver position, as opposed to the source localization which is correctly obtained, irrespective of the receivers locations.

5 CONCLUSIONS

Time reversal method for acoustic guided waves was examined as a tool for determining different source locations and their mutual importance. This examination was performed analytically on a 2D model, and experimentally on a lab set-up. The results from both procedures were essentially matched, showing the ability of the standard time reversal method to localise multiple sources. The reconstruction of the mutual importance of different sources, however, turned out to depend on receiver point locations and their number. In the future, the issue about the receiver positions and their effect on determining the input power relations for multi point excitation cases are going to be further studied in order to investigate the possibility to use the time reversal as a tool to rank the source and not only to locate them. Furthermore, the acoustic sink and its relation to the focalisation process of multiple sources in an audible frequency range is also going to be examined experimentally in solid structures.

6 Acknowledgements

The research work of Amr Abboud has been funded by the European Commission within the ITN Marie Curie Action project GRESIMO under the 7th Framework Programme (EC grant agreement no. 290050). The authors acknowledge the financial support of the COMET K2 - Competence Centres for Excellent Technologies Programme of the Austrian Federal Ministry for Transport, Innovation and Technology (BMVIT), the Austrian Federal Ministry of Science, Research and Economy (BMWFW), the Austrian Research Promotion Agency (FFG), the Province of Styria and the Styrian Business Promotion Agency (SFG), and gratefully acknowledges the support of COST action TU1105. Finally, the author would like to give a special thank to Yasser Elnemer (Virtual Vehicle) for useful discussions great help and friendly comments on both numerical work and experiment.

REFERENCES

[1] Fink, Mathias, and Claire Prada. "Acoustic time-reversal mirrors." Inverse problems 17.1 (2001): R1.

[2] Fink, Mathias, et al. "Time-reversed acoustics." Reports on progress in Physics 63.12 (2000): 1933.

[3] Fink, Mathias. "Time reversal of ultrasonic fields. I. Basic principles." Ultrasonics, Ferroelectrics, and Frequency Control, IEEE Transactions on 39.5 (1992): 555-566.

[4] Wu, Francois, Jean-Louis Thomas, and Mathias Fink. "Time reversal of ultrasonic fields. Il. Experimental results." Ultrasonics, Ferroelectrics, and Frequency Control, IEEE Transactions on 39.5 (1992): 567-578.

[5] Cassereau, Didier, and Mathias Fink. "Time-reversal of ultrasonic fields. III. Theory of the closed time-reversal cavity." Ultrasonics, Ferroelectrics, and Frequency Control, IEEE Transactions on 39.5 (1992): 579-592.

[6] Griffa, M., et al. ”Investigation of the robustness of time reversal acoustics in solid media through the reconstruction of temporally symmetric sources.” Journal of Physics D: Applied Physics 41.8 (2008): 085415.

[7] lvarez, Nicols Prez, et al. ”Frequency Domain Time Reversal in Acoustic Cavities.”.

[8] Vigoureux, Dorian, and Jean-Louis Guyader. ”A simplified time reversal method used to localize vibrations sources in a complex structure.” Applied Acoustics 73.5 (2012): 491-496.

[9] de Rosny, Julien, and Mathias Fink. ”Overcoming the diffraction limit in wave physics using a time-reversal mirror and a novel acoustic sink.” Physical review letters 89.12 (2002): 124301.

[10] Bavu, Eric, et al. ”Subwavelength sound focusing using a time-reversal acoustic sink.” Acta Acustica United with Acustica 93.5 (2007): 706-715.

[11] Wolfgang Kropp *Active noise control lecture notes* 2003: Chalmers University of Technology, Gothenburg, Sweden.

[12] Lyons, Richard G. Understanding digital signal processing. Pearson Education, 2010.

[13] Cremer, L., M. Heckl, and B. A. T. Petersson. ”Structure-borne sound.” Physics Today 28 (1975): 81.

[14] Abboud.A , Novak.A *Technical Acoustic one project B*. Chalmers University of Technology, Gothenburg, Sweden, 2011.

International Conference on Engineering Vibration
Ljubljana, Slovenia, 7-10 September 2015

SIMULTANEOUS OPTIMIZATION OF COMPOSITE STRUCTURES WITH SHUNTED PIEZOCERAMICS

Rogério Salloum*[1], Oliver Heuss[1], Dirk Mayer[1]

[1] Fraunhofer Institute for Structural Durability and System Reliability LBF
Bartningstraße 47, 64289 Darmstadt, Germany
rogerio.salloum@lbf.fraunhofer.de

Keywords: piezoelectric shunt damping, semi-active control, negative capacitance, smart structures, numerical optimization, composite materials, functional integration

Abstract. *Vibrations in modern machines such as cars, airplanes and bridges constitute a real issue that can cause undesirable noise, damages and even catastrophic failures. In order to reduce this harmful effect, passive vibration attenuation measures have been extensively used, but can no longer cope with the increasing complexity of engineering systems. In this sense, novel smart structures have been created to efficiently suppress vibration without notable adverse effects. In this work, a novel approach to deal with the application of shunted piezoceramics in lightweight composite structures for vibration attenuation is proposed. It is based on the simultaneous optimization of different sub-systems of the smart structure, i.e. host structure, transducers and electronics, so that a set of technical requirements can be met. Instead of being considered as an add-on solution, the shunted piezoceramics are regarded as additional design variables. In this sense, passive structural mass is substituted by active material in an intelligent way, which can potentially reduce overall weight and at the same time improve the dynamic response of the smart structure. Initially, numerical and experimental analyses are carried out using a scale model of a control arm. It consists of a cantilever carbon fiber beam with "I"-shaped cross-section, controlled by the use of piezoceramics. Vibration attenuation is achieved through an RL-shunt circuit connected in series with a negative capacitance, which is built through a synthetic circuit based on an operational amplifier. The classical sequential approach is first introduced, in which the piezoceramics are applied onto the surface of the beam. Then, it is compared to the novel approach, in which the beam, now with integrated piezoceramics, is fully optimized taking into account its geometry, the stacking sequence, the transducer dimensions and the shunt circuit components. Thanks to the simultaneous approach, not only the mechanical requirements of the structure, such as mass, global stiffness and dynamic behavior can be respected, but also the electrical characteristics of the shunt circuit.*

Power-transformer noise (MS13)

International Conference on Engineering Vibration
Ljubljana, Slovenia, 7-10 September 2015

THE INFLUENCE OF MAGNETIC ANISOTROPY ON MAGNETOSTRICTION FORCES AND VIBRATION IN POWER TRANSFORMERS

Pawel Witczak*, Krzysztof Majer

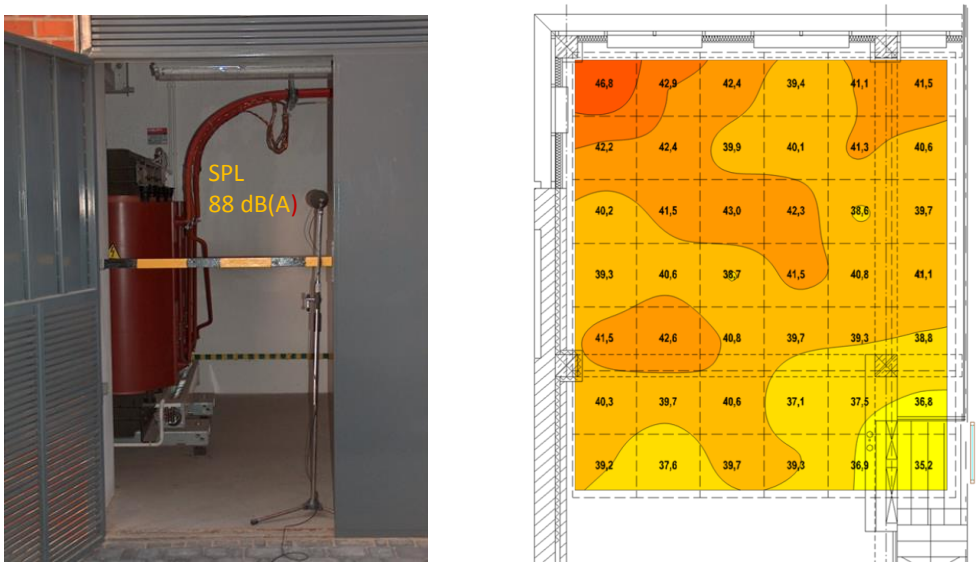
Institute of Mechatronics and Information Systems, The Lodz University of Technology, Poland
pawel.witczak@p.lodz.pl
krzysztof.majer@p.lodz.pl

Keywords: Power transformer, Vibration, Magnetostriction, Stress, Forces, Finite elements.

Abstract. *The paper analyses the no-load vibration of there-phase, three-limb distribution transformer caused by magnetostriction phenomena. The electromagnetic models use 2D finite elements representation combined with the time-stepping approach and consider the different structure of core joints – with and without overlapping, with isotropic or orthotropic nonlinear magnetic properties. Magnetostriction forces are calculated on the basis of the Becker-Döring two-constant elongation equation integrated over volumes of interest. The mechanical model is also built within the finite elements 3D technology with orthotropic properties of homogenised equivalent materials of transformer core and windings. Exemplary results of calculations are confronted with measurements.*

1 INTRODUCTION

The consumption of electric energy is growing all the time. It causes that distribution transformers are located closer and closer to their users. Large office or residential buildings are often equipped with the unit having the power of few MVA, which is dry type due to safety requirements. The transformer vibration together with the accompanying noise may substantially disturb the environment travelling along and across the walls, ceilings or ventilation ducts of the building. The example of such unwanted effects is presented in Figure 1.



a. *b.*

Figure 1. Exemplary acoustic disruption in office building [14]
a. view of transformer compartment at ground floor with two dry type units of power 1.6 MVA each
b. map of SPL(A) in room directly above – SPL_{max}=46.8 dB(A).

The problem of transformer noise is not new – it was analyzed fifty years ago and even earlier. Two fundamental physical effects – magnetostriction strains in the core and Lorentz forces in windings, are responsible for the deformation of transformer parts. Both are volumetric in nature and their mathematical description is well known [1-4]. It is also known that many design and technological details of transformer construction and manufacturing quality like the overlaping scheme [5-6], the level of core compression [7][9] or the winding stiffness [8] influence much on resultant vibration. The continued pressures to lower manufacturing costs are also not conducive to the vibration reduction.

The finite elements (FE) technology is nowadays the basic tool during the design process. There are many commercial and in-house systems enabling electromagnetic and mechanical calculations of 2D/3D non-linear fields, some of them are able to combine these two in one electromechanical problem. However, it should be remembered that topology of numerical meshes is rather different in both domains and also the available interfacing possibilities concern the Lorentz and surface magnetostatic forces only.

The aim of this paper is to present the outlook of the calculation approach to the vibration of the assembled core of the small, three-phase transformer caused by the magnetostriction

deformations. A special attention is paid to the detailed analysis of the differences introduced by the magnetic non-linear and anisotropic properties of the core lamination.

2 MAGNETIC FIELD ANALYSIS IN TRANSFORMER

The steady electromagnetic state is of interest here, but due to the magnetic nonlinearity the full transients must be calculated. It is assumed that investigated transformer is supplied with symmetric sinusoidal network at no-load having delta-connected primary windings. The outlook of considered device together with its 2D FE model is shown below. There is no electric current in the secondary windings, so, they are not included in the model.

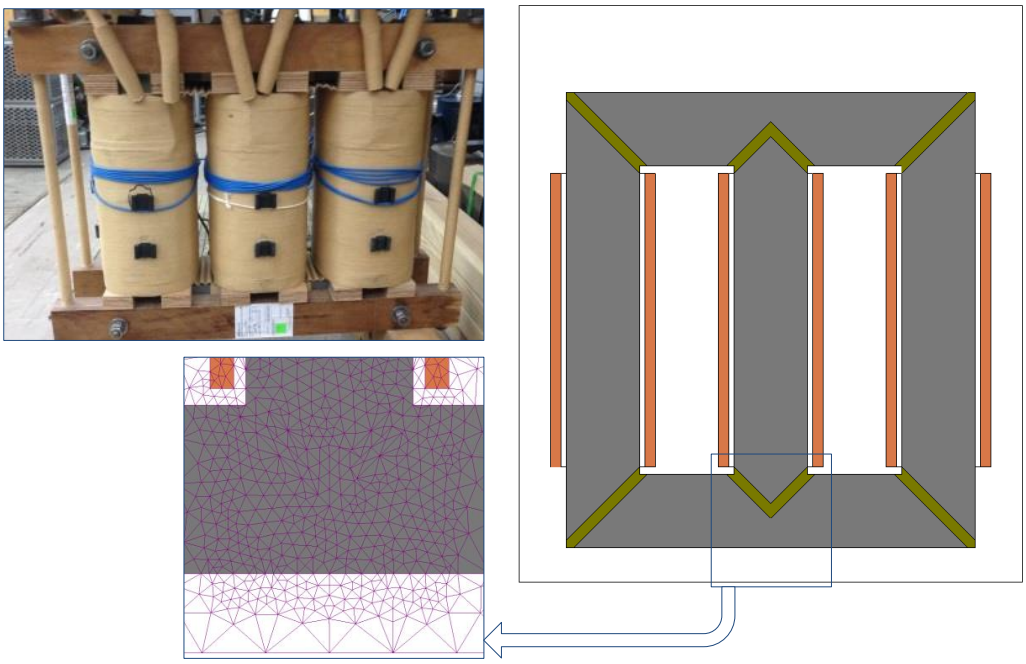


Figure 2. Photo of analysed transformer and its finite elements model.

As it will be explained later on, the calculations of magnetostriction phenomena require a quite accurate estimation of the flux density field which is a spatial derivative of the magnetic vector potential. Therefore, the density of the mesh is rather high and also the third order approximation for the solution field is used. The ferromagnetic area of the core consists of two materials: limbs and yokes where magnetic properties were modelled by isotropic or orthotropic flux density B versus magnetic field H curve(s) and overlapping zones characterised by the artificial, homogenised isotropic material. The way how it was obtained is presented elsewhere [11], resulting three B(H) curves are displayed in Figure 2. The time-stepping calculations were applied for the first 35 periods of supplying voltage with 80 samples per period. Three models were analysed – all assumed null conductivity of core materials:

I. yokes and limbs have nonlinear, isotropic B(H) measured along the rolling direction, overlapping areas have nonlinear, isotropic B(H) obtained during homogenization;

II. yokes and limbs have nonlinear, orthotropic B(H) measured along and transverse to the rolling direction, overlapping areas have nonlinear, isotropic B(H) obtained during homogenization;

III. yokes and limbs have nonlinear, orthotropic B(H) measured along and transverse to the rolling direction, overlapping areas are excluded from the model.

The exemplary magnetic fields obtained at the time step when the magnetic flux in one limb is negligible are shown in Figure 2 together with a plot of phase currents in Model II at the ending time period of the analysis.

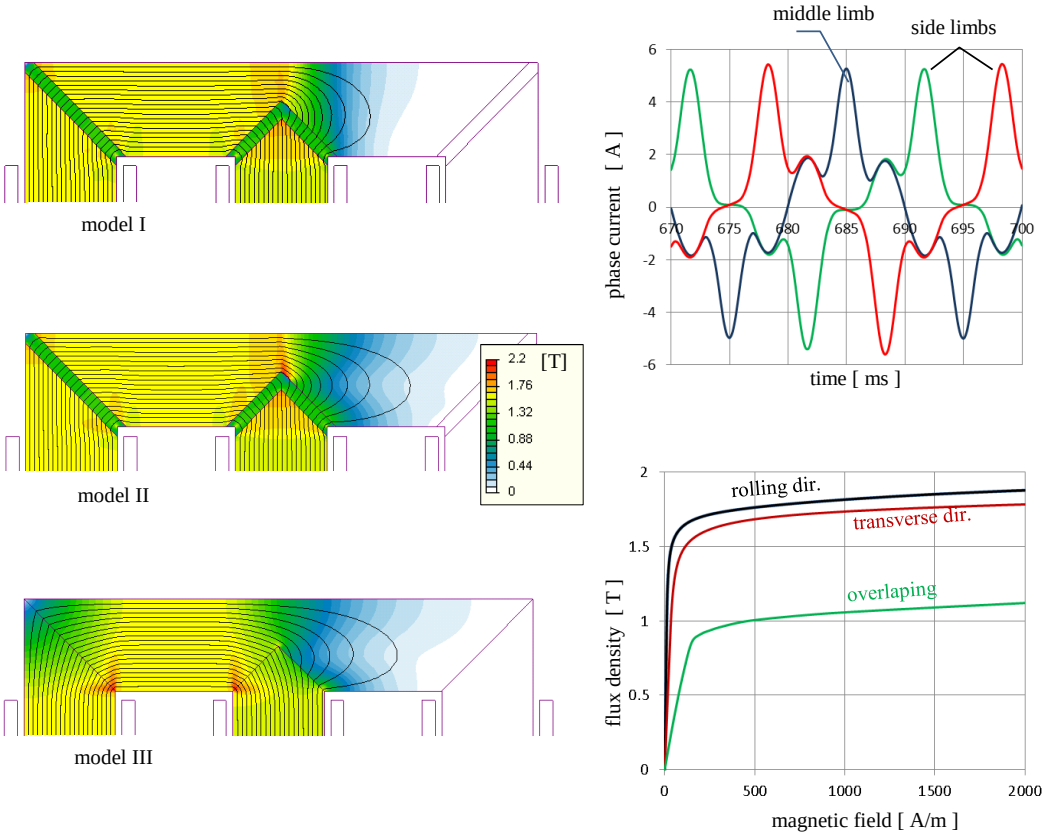


Figure 3. Instantaneous magnetic flux on background of flux density modulus – colour map is the same for all models, accompanied with calculated no-load phase currents in Model II and magnetization curves of materials used in analysis.

The accuracy of computations can be estimated comparing the steady state magnitudes of two main integral quantities – the mean flux density in the limb and the phase current, with measured values.

Magnitudes of integral quantities	Model I	Model II	Model III	Measured
Mean flux density in limb, [T]	1.78	1.76	1.79	1.75
Phase current, [A]	5.2	5.3	3.8	5.9

Table 1. Calculations versus measurements for investigated transformer.

Observing the field plots we see how the model geometry and material structure influences the space distribution of the flux density vector. The areas where the flux density vector changes its magnitude and position against the frame of reference are the most important because in these places the volumetric forces are present. It results from the general relationship linking the k-th component of the volume force density f_k with the stress tensor σ_{jk}

$$f_k = \frac{\partial}{\partial x_j}\sigma_{kj} \tag{1}$$

where the stress element σ_{jk} caused by magnetostriction is usually approximated after measurements by the second power polynomial against the flux density value.

3 CALCULATION OF MAGNETOSTRICTION STRESS AND FORCES

The magnetostrictive elongation/compression $\lambda(\{\alpha\},\{\beta\})$ is described by the Becker-Döring equation [1]

$$\begin{aligned}\lambda(\{\alpha\},\{\beta\}) = \frac{3}{2}\lambda_{100}\left(\alpha_1^2\beta_1^2 + \alpha_2^2\beta_2^2 + \alpha_3^2\beta_3^2 - \frac{1}{3}\right) + \\ +3\lambda_{111}(\alpha_1\alpha_2\beta_1\beta_2 + \alpha_2\alpha_3\beta_2\beta_3 + \alpha_3\alpha_1\beta_3\beta_1)\end{aligned} \tag{2}$$

describing deformation of the cubic iron crystallite in direction given by the set of cosines $\{\beta\}$ when the magnetic field is applied along line defined by directional cosines $\{\alpha\}$. The coordinates are tied to crystallite edges. Assuming the ideal Goss (edge) texture of lamination sheets in transformer core and constraining the position of the flux density vector in the sheet plane only it is possible to derive from (1) the expression defining two modes of magnetostrictive strain. Details of these manipulations are presented in [11]. For the component formed by the sum of $\alpha_j^2\beta_j^2$ we have

$$\left[\varepsilon_{jk}\right]_\gamma = \frac{3}{2}\lambda_\gamma\left(\cos^2\alpha - \frac{1}{3}\right)\begin{bmatrix}-0.5 & 0 & 0\\ 0 & -0.5 & 0\\ 0 & 0 & 1\end{bmatrix} \tag{3}$$

and for the second one

$$\left[\varepsilon_{jk}\right]_\varepsilon = \frac{3}{4}\lambda_\varepsilon\begin{bmatrix}(\cos^2\alpha - 1) & 0 & 0\\ 0 & (1-\cos^2\alpha) & \sin 2\alpha\\ 0 & \sin 2\alpha & 0\end{bmatrix} \tag{4}$$

Equations (3)(4) are defined in sheet oriented frame of reference, in order as follows: normal to plane, transverse to rolling direction, along rolling direction. The angle α is measured about the normal to the plane against the rolling direction. The material data λ_γ, λ_ε are obtained from measurements on samples cut and magnetized along ($\lambda_\parallel$,α=0) and perpendicular ($\lambda_\perp$,α=π/2) to the rolling direction. Following the restriction imposed on the magnetic flux the strain cannot be calculated inside the overlapping area where the magnetic field is three-dimensional. Therefore, instead of force densities the global forces acting on chosen volumes must be calculated. Figure 4 shows the placement and size of volumes of interest in and close to the upper yoke. The bottom yoke has an identical pattern of volumes being mirrored against the plane of transformer symmetry. The shape of these volumes comes from following rules: all volumes are cuboidal with sides parallel or perpendicular to the rolling direction, the size of the each volume is the smallest possible enclosing area where the flux lines are not parallel each other. The instantaneous force component F_k operating in a given volume V_m is obtained from the integral equivalent of the differential definition (1)

$$F_k = \oiint_{S(V_m)} 2G\left(\left[\varepsilon_{kj}\right]_\gamma + \left[\varepsilon_{kj}\right]_\varepsilon\right) n_j \, dS \tag{5}$$

where G is the shear modulus converting the strain into stress without volumetric change.

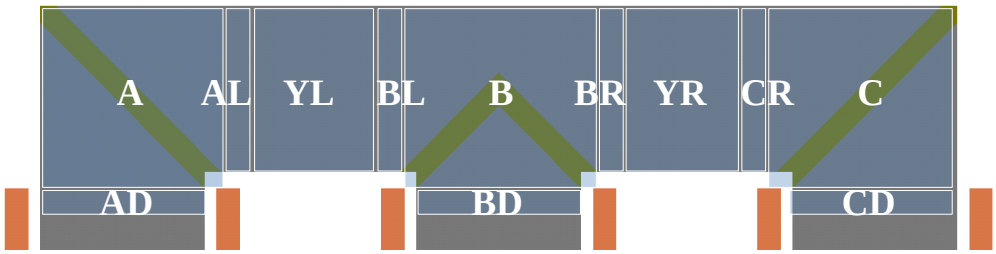


Figure 4. Volumes for force calculations in upper yoke.

The transformer core has no external input of momentum of magnetostriction origin – hanging freely the core cannot move or rotate as rigid body. Therefore, the stress components along core boundaries must be equal to zero. In other words, stress discontinuities on the core periphery resulting from (5) are equivalent to surface forces, which enforce the above requirement. Due to rather rough subdivision of the core, all surfaces of volumes parallel to the local rolling direction must have null stress, both normal and tangent.

The stress components coming from two modes of possible strain (3)(4) have completely different properties on surfaces perpendicular to the rolling direction **rd**. The mode γ is able to produce here the normal stress only and the mode ε is responsible for the tangent stress on these surfaces. The normal stress σ is always present if the flux density modulus is greater than zero and flux density vector acts not in magnetically the worst direction (α=55 deg). The shear stress τ appears when the direction of the flux density vector deviates by any angle α from the rolling direction, as it is illustrated in Figure 5.

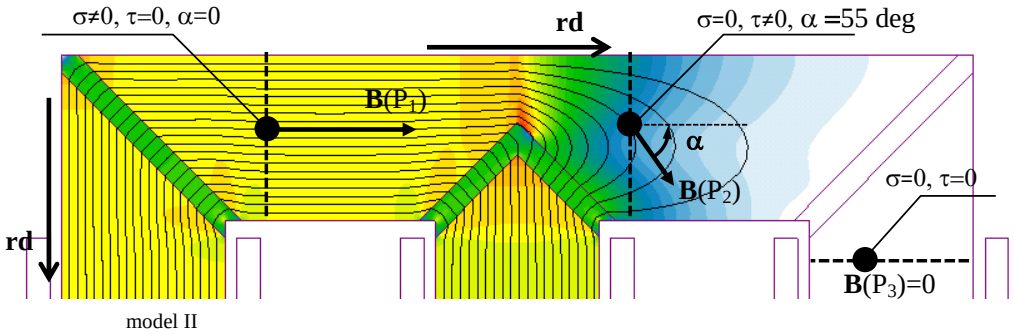


Figure 5. Explanation of occurrence of magnetostriction tensor components.

The variability in time is also very different for these modes. We may compare the surface forces contributing the integral (5) for two cases: analysing the joints alone e.g. A and B and together with their nearest neighbourhood i.e. (A+AD+AL) and (B+BD+BL+BR). In the first case the shear stress influences the resulting force but when the integral is calculated for a slightly larger volume the tangent stress on the integration surface disappears. Exemplary results obtained at λ_γ= - 0.7 μm/m, λ_ε=8 μm/m are displayed in Figure 6.

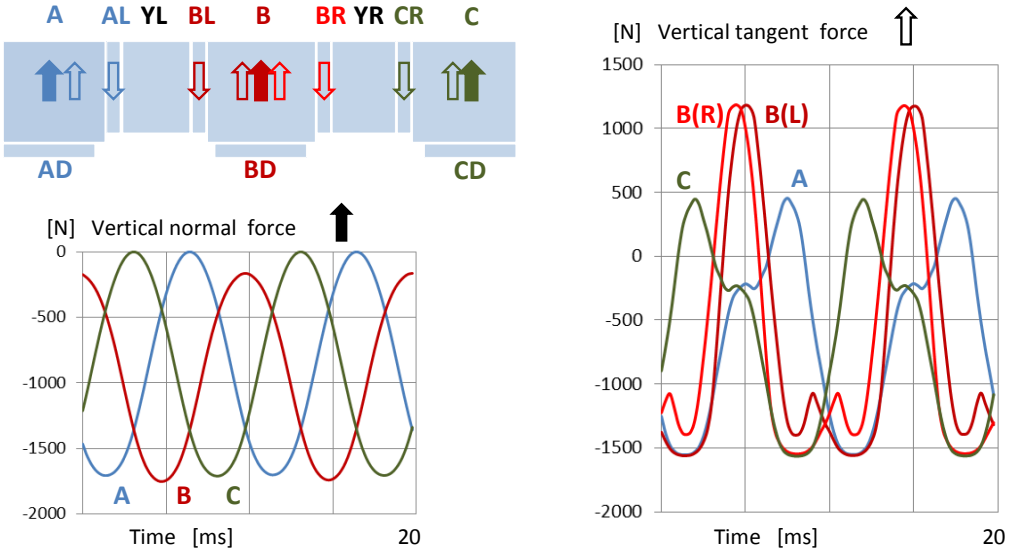


Figure 6. Time distribution of surface forces acting in vertical direction on joints A, B, C in upper transformer yoke of the Model II.

We see that normal forces acting in vertical direction on the each joint are, after removal of the DC part, almost sinusoidal with the doubled network frequency. Their tangent counterparts have also the same fundamental frequency but simultaneously they are significantly distorted with the components having not only odd but also even orders. The similar conclusions result from the analysis of horizontal forces. Again, the normal forces are almost monoharmonic and tangent forces possess the rich frequency spectrum. Another important property of the time shape of resultant forces arises from the transformer asymmetry – the T-joint has two surfaces where the horizontal forces appear and side joints each have one. It gives entirely different profiles of hodographs of resultant forces present in side and T-joint. Magnetic flux in given yoke part is in-phase with the flux in one of side limbs but the flux in the middle limb is symmetrically shifted in phase with fluxes in two parts of the yoke. This gives the oscillating profile of the position of the force vector in side joints and the rotational shape when the middle joint is considered. The Figure 7 shows details of it where one may observe that AC components in the T-joint are somewhat smaller than in the side counterpart.

The influence of magnetic anisotropy of core sheets manifests itself in the shape of flux lines close to core joints. It causes that transverse component of the flux density next to side joints in the isotropic model is more evident than in the anisotropic case. Observing the middle joint we see that under isotropic properties we have easier conditions for the turn of magnetic flux, when ampere-turns distribution forces one of limbs to have no flux inside. It also

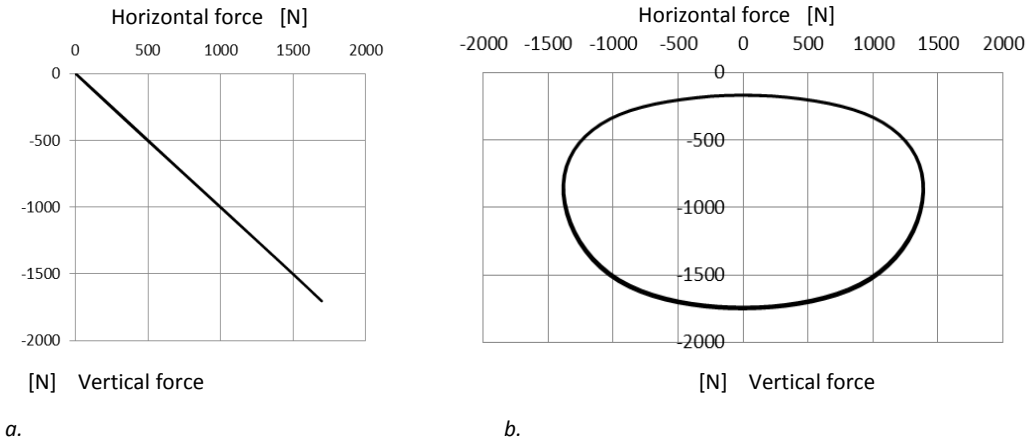


Figure 7. Hodographs of normal forces acting in side joint A (a.) and T-joint (b.) of the Model II.

means that gradient of flux density magnitude for anisotropic Model II must be smaller here than in isotropic Model I. We observe it in Figure 3 having the reduced penetration range of the yoke by magnetic flux for the isotropic case. All these differences affect only the shear stress and forces resulting therefrom, the normal forces remain unchanged because the mean flux density in the limb is almost the same in both cases, see Table 1.

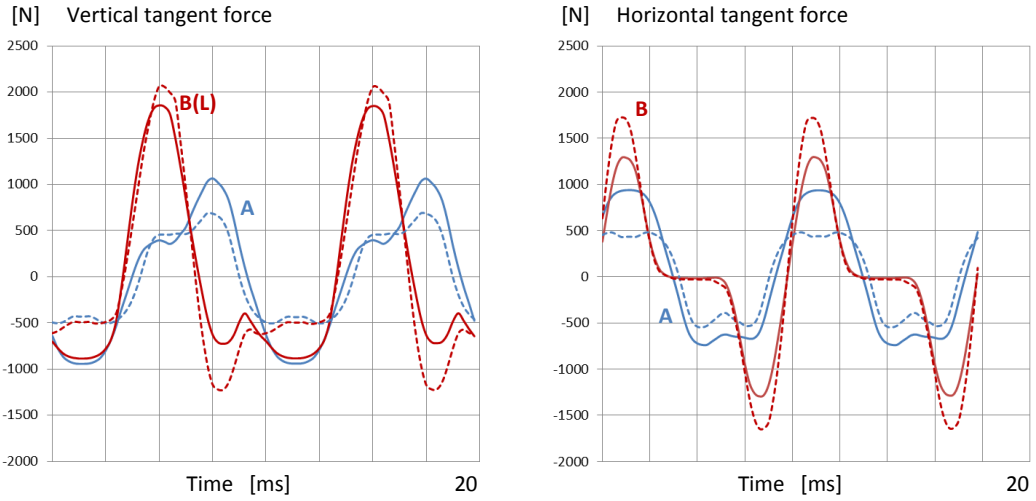


Figure 8. Influence of magnetic anisotropy on time distribution of tangent forces (AC component only), Model I – dashed line, Model II – full line.

4 VIBRATION ANALYSIS OF TRANSFORMER

The complex structure of the transformer construction requires the usage of numerical model. Apart from some minor changes in geometry, two basic simplifications were applied replacing the real material structure of the core and windings by the artificial materials obtained through the homogenization process. A small section of considered transformer part was modelled exactly and solved for pre-defined loads and constraints. Taking the averaging integrals [13] it was possible to get the data for layered elements in the final FE model.

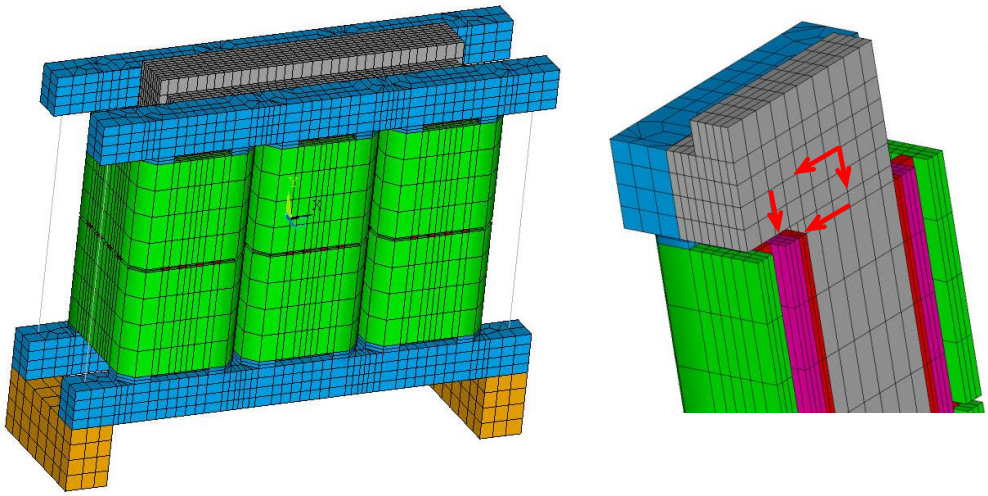


Figure 9. Overall and section views of finite elements model used in vibration calculations arrows are anchored in sets of nodes of the force application.

The wooden supports visible in the above picture were used during measurements, so, they were also included in theoretical model. The forces calculated for Model II by the algorithm presented in previous sections were Fourier transformed and inserted into mechanical model in form of one complex force at the centerline of the each volume. This force was scattered afterwards over all nodes of the FE mesh on this line. The instantaneous deformation of the transformer model obtained for the 100 Hz component of the force spectrum is shown in Figure 10 together with calculated and measured rms values of the vertical displacement on the upper surface of the yoke.

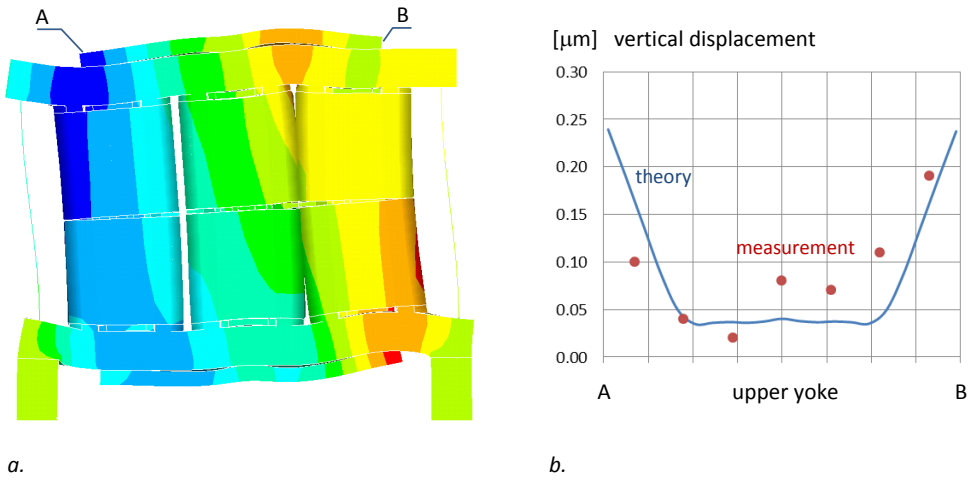


Figure 10. Operational deflection shape for 100 Hz set of forces
a. instantaneous model deformation with map of vertical displacement,
b. distribution of rms values of vertical displacement along upper yoke surface.

Due to bending deformations of yokes and limbs the gravity center of the transformer is not all the time in the same point. Therefore, the global inertial force must appear and it causes the rigid body rocking if the stiffness of supporting blocks is not identical. These displacements add to side limbs movements but with different phase to the each one. This is probably the origin of the non-symmetric displacement distribution measured along the yoke.

5 CONCLUSIONS

The method of vibration analysis described in this paper may be applied to any three-phase transformer. Results obtained are quite satisfactory, nevertheless, the number of subdivisions in space should be increased. This entails the need of deeper insight into the structure of theoretical model of overlapping, both in electromagnetic and mechanical domains. When large transformers are considered having, say, five or six steps in the each overlap, the Model III will be probably the best approximation.

REFERENCES

[1] R. Becker, W. Döring, *Ferromagnetism*. Springer, 1939.

[2] E. W. Lee, Magnetostriction and Magnetomechanical Effects, *Rep. Prog. Phys.* 18**,** 1955, pp.184-229.

[3] H. H. Woodson, J. R. Melcher, *Electromechanical Dynamics, Part 1*, J. Wiley, 1968.

[4] E.de Tremouillet du Lacheisserie, *Theory of Magnetostriction*, CSGE, New York 1988

[5] M. Elleuch, M. Poloujadoff, New transformer model including core joints air gaps and lamination anisotropy, *IEEE Trans. Magn*., 1998,34, pp.3701-3711.

[6] E. Napieralska-Juszczak, J-Ph. Lecointe, H. Nabil, K.Komeza, J. K. Sykulski, Computational and Experimental Verification of the Equivalent Permeability of the Step-lap Joints of Transformer Cores, *Computation in Electromagnetism, CEM 2008,* pp.38-39

[7] P. Klimczyk, Novel Techniques for Characterisation and Control of Magnetostriction in G.O.S.S., PhD Thesis, Cardiff University, 2012

[8] L. Lukic , M. Djapic , D. Lukic , A. Petrovic, Aspects of Design of Power Transformers for Noise Reduction, *Int. Conf. Noise and Vibration*, Nis 2012, pp.255-262

[9] R. Girgis, J. Anger, D. Chu, Sound of Silence - Designing and producing silent transformers, *ABB Review*, 2/2008

[10] W. Kubiak, P. Witczak, Vibration Analysis of Small Power Transformer, *COMPEL*, 2010, 29, pp.1116-1125

[11] P. Witczak, Magnetostriction Force Spectrum in Power Transformer, *Int. Conf. on Electric Machines*, Berlin, 2014, pp.2240-2245

[12] K. Majer, *Analysis of Vibration and Noise in Converter Transformers (in Polish)*, Lodz University of Technology, ZN 1178, 2013

[13] S. W. Tsai, H. W. Hahn, *Introduction to Composite Materials*, TECHNOMIC Publishing, 1980

[14] W. Kubiak, P. Witczak, *Origin of excessive noise in office building*, Expertise, Lodz University of Technology, 2010

International Conference on Engineering Vibration
Ljubljana, Slovenia, 7-10 September 2015

A COMPARISON BETWEEN NUMERICAL AND EXPERIMENTAL MODAL PARAMETERS OF TRANSFORMER CORE

M. Pirnat*[1], P. Tarman[2], M. Nastran[3]

[1]Kolektor ETRA d.o.o.
miha.pirnat@kolektor.com

[2]Kolektor ETRA d.o.o.
peter.tarman@kolektor.com

[3]Kolektor ETRA d.o.o.
miha.nastran@kolektor.com

Keywords: Transformer Core, Laminated Structure, Modal Analysis, Numerical Model.

Abstract. *A comparison between numerical and experimental modal parameters is shown for three different full-size transformer cores from a regular production process. Furthermore, the measurement setup for experimental modal analysis of the cores is presented and the numerical model used is outlined. On average the results show a discrepancy of approximately 17% between numerical and measured natural frequencies. This is considered to be a good result given the size and complexity of transformer cores.*

1 INTRODUCTION

Power transformer noise may contribute to health problems and discontent in surrounding population and is therefore undesirable. This fact is translated into demand for increasingly quieter transformers. In order to produce such low-noise transformers one of manufacturer's key actions is to identify excitation mechanisms and modal parameters of structures involved before the actual manufacturing process. The validated numerical models of appropriate structures allow just that.

Transformer noise is typically analysed and measured in load and no-load mode of operation. In the case of no-load conditions the main source of transformer noise is laminated core, which is excited due to magnetostriction in grain-orientated electrical steel and magnetic forces between lamina [1, 2]. Magnetostriction is a nonlinear phenomenon, which manifests as deformations of electrical steel under changing magnetic flux [3]. The magnetic flux is typically changing with 50 Hz. However, due to nonlinear nature of magnetostriction the core is excited also with higher harmonics. Therefore it is important to control transformer core modal parameters in order to avoid resonances as much as possible [4]. A number of papers can be found regarding numerical modelling of transformer cores. However, only small amount of experimental data is available [5, 6].

In this paper a comparison is shown between numerical and measured modal parameters for three full-size transformer cores from regular production process. The measured modal parameters are obtained using experimental modal analysis (EMA). A software named TrafoS is used for prediction of transformer core modal parameters. The software was developed in cooperation with University of Ljubljana at Laboratory for Dynamics of Machines and Structures (LADISK) which is a part of Faculty of Mechanical Engineering.

The article is organized as follows. The first section presents the software for prediction of transformer core modal parameters. In the second section a measurement setup used for experimental modal analysis of transformer core is presented. In the third section results for three different transformer cores are presented and compared. In the last section conclusions are given.

2 NUMERICAL MODELLING

Numerical model of transformer core implemented in TrafoS is based on results from [7]. Transformer core exhibits considerably lower stiffness in stacking direction than in other directions. A large portion of stiffness in stacking direction is due to friction between laminas due to core clamping forces. In order to model friction between laminations of transformer core a two stage procedure is used.

In the first stage (Figure 1a) every lamina is modelled with shell elements and connected to its neighbouring lamina via spring element with nonlinear stiffness. By loading the model with known clamping forces a pressure distribution is obtained on the surfaces of laminas.

In the second stage (Figure 1b) the nonlinear spring elements are replaced with beam elements and their shear modulus value is dictated by the pressure distribution obtained in the first stage. This way additional stiffness representing interlaminar friction is implemented into numerical model.

Once the two stage procedure is complete a modal analysis can be performed using the usual implicit methods.

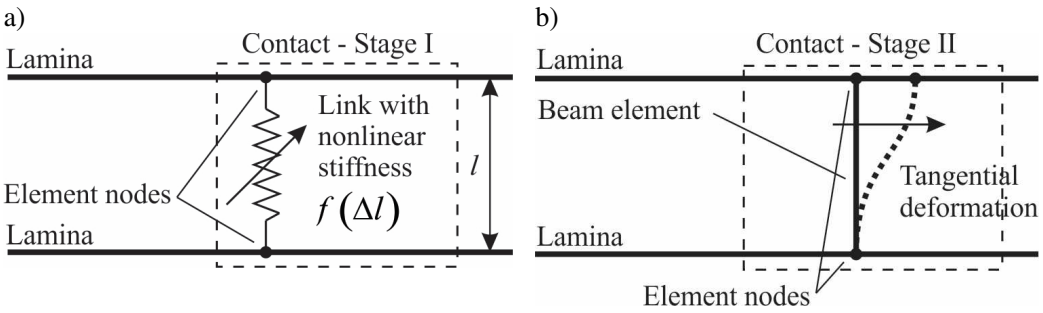


Figure 1: Modelling of interlaminar friction: a) first stage, b) second stage.

2.1 Input parameters for TrafoS application

TrafoS has a graphical user interface (GUI) to numerical model parameters. Parameters for specific transformer core are input via different tables as shown in Figure 2. In Figure 3 a finished model is shown which can be used for modal analysis.

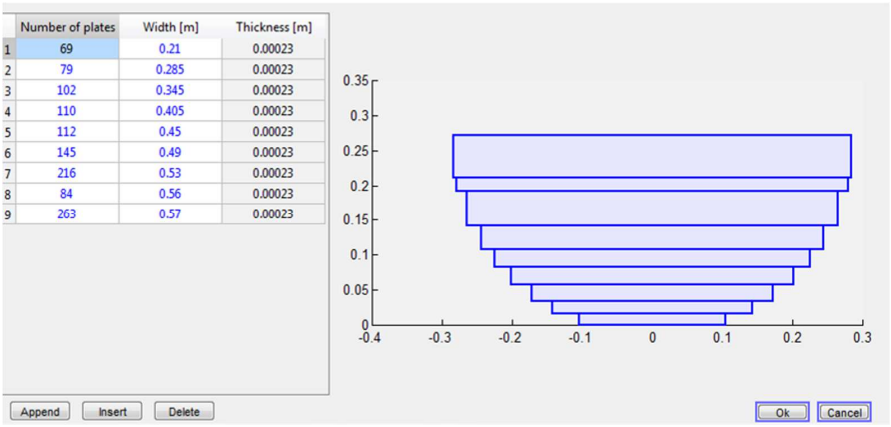


Figure 2: Example of parameter definition in TrafoS.

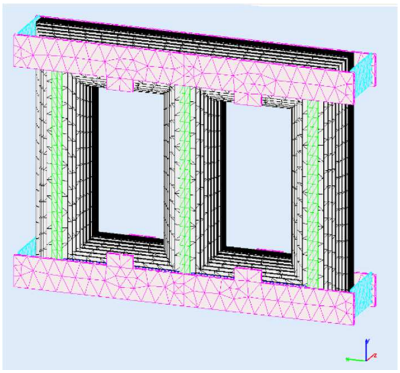


Figure 3: Numerical model of transformer core.

3 TRANSFORMER CORE EMA

Transformer core modal parameters were identified using experimental modal analysis (EMA) with measurement setup as shown in Figure 4. The core was excited using an impact hammer and response was captured with a 3-axis accelerometer. The excitation point was fixed and accelerometer was roved. Number of measurement points varies from 180 to 240, depending on the core size.

Data was acquired using National Instruments hardware and software, however, modal parameter identification was performed in OpenModal [8] software still under development and yet to be released as open source.

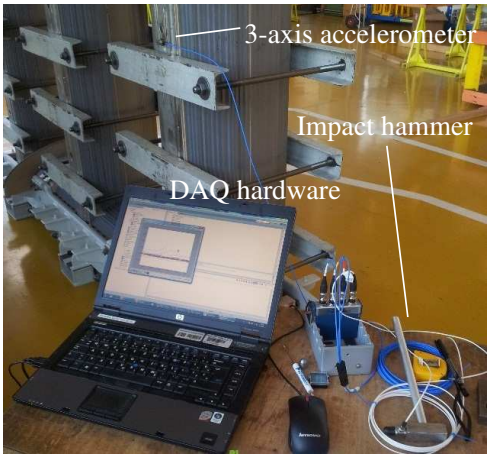


Figure 4: Measurement setup for experimental modal analysis.

4 COMPARISON OF MODAL PARAMETERS

In this section modal parameters are presented for three transformer cores of different sizes and compared to numerical results. Core dimensions are defined in Figure 5 and specified in Table 1.

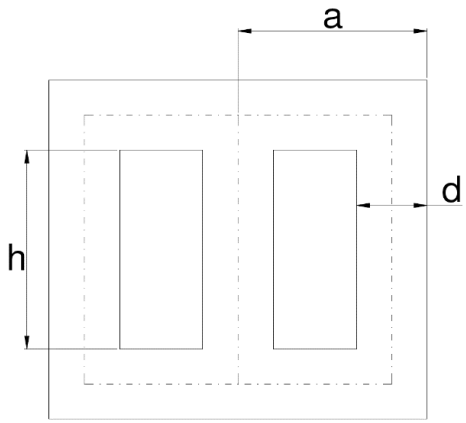


Figure 5: Transformer core dimension definition.

Core	h [mm]	a [mm]	d [mm]	Mass [kg]
A	1530	1170	538	16835
B	1360	980	560	15857
C	1470	1280	584	20188

Table 1: Dimensions of investigated transformer cores.

Core mode shapes identified in the frequency range of up to 85 Hz are shown in Table 2. Mode shapes in this frequency range are relatively simple and can be easily identified and compared, which facilitates the purpose of this paper.

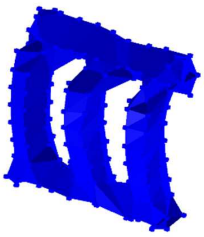
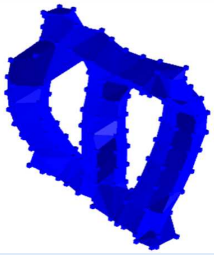
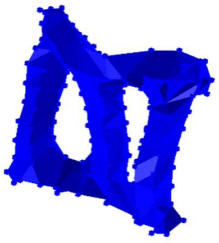
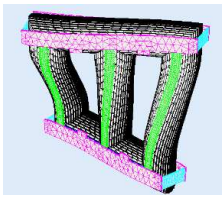
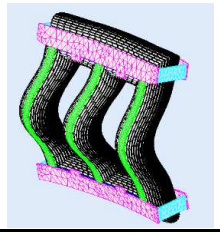
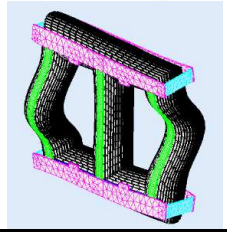
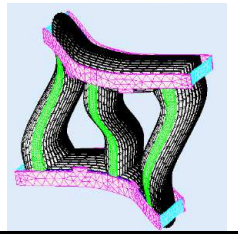
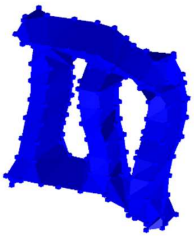
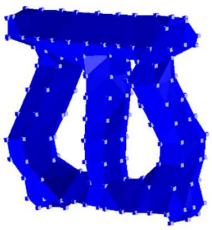
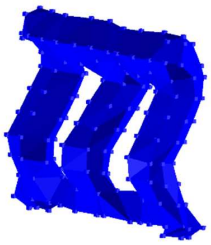
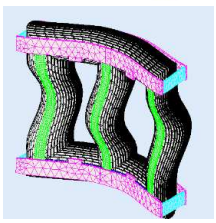
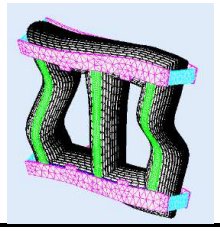
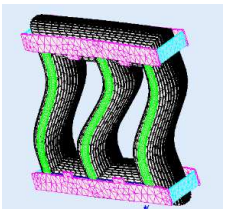
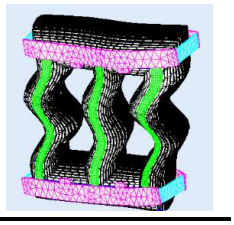
Mode	1	2	3	4
Exp.				
Num.				
Mode	**5**	**6**	**7**	**8**
Exp.				
Num.				

Table 2: Numerical and experimental mode shapes.

A comparison between measured and calculated modal parameters is shown in Tables 3-5, where f_{exp} is measured natural frequency, f_{num} is calculated natural frequency and e is error defined as:

$$e = \frac{|f_{num} - f_{exp}|}{f_{exp}} * 100\% \quad (1)$$

From Tables 3-5 can be observed that the average error for the calculated natural frequencies is approximately 17%, which is considered to be a good prediction of the numerical model bearing in mind size and complexity of the cores. Furthermore, the numerical model is still being improved in order to obtain more accurate results in the future.

Due to different sizes and clamping arrangements some mode shapes could not be identified for all the cores, this indicates that clamping of the core is important and can change modal parameters.

	Core A natural frequencies		
Mode shape	f_{exp} [Hz]	f_{num} [Hz]	e [%]
1	25.2	20.4	18.9
2	33.8	37.3	10.4
3	35.5	41.5	17.0
4	42.6	49.6	16.4
5	52.5	60.7	15.7
6	61.6	68.7	11.6
7	62.5	52.3	16.3
8	77.6	94.8	22.1
		Average:	16.0

Table 3: Comparison of measured and calculated natural frequencies for core A.

	Core B natural frequencies		
Mode shape	f_{exp} [Hz]	f_{num} [Hz]	e [%]
1	24.3	17.3	28.8
2	31.8	34.6	8.8
3	36.3	38.6	6.3
4	/	/	/
5	/	/	/
6	58.2	66.6	14.4
7	54.5	47.5	12.8
8	71.1	85.9	20.8
		Average:	15.3

Table 4: Comparison of measured and calculated natural frequencies for core B.

	Core C natural frequencies		
Mode shape	f_{exp} [Hz]	f_{num} [Hz]	e [%]
1	/	/	/
2	32.1	40.9	27.4
3	/	/	/
4	43.7	50.5	15.7
5	57.5	64.4	12.0
6	60.5	76.0	25.6
7	52.5	58.1	10.7
8	84.7	108.4	28.0
		Average:	19.9

Table 5: Comparison of measured and calculated natural frequencies for core C.

5 CONCLUSIONS

A comparison of the numerical and experimental modal parameters was shown for three full-size transformer cores, where first eight mode shapes and corresponding natural frequencies were used. The cores were analysed using EMA.

The approach used in numerical modelling of transformer core was briefly described as it is based on previous work.

Results of comparison show a discrepancy of approximately 17% between measurements and numerical model. This is considered to be a good result given the size and complexity of the transformer cores. However, the numerical model used in predictions is still under development in order to further improve accuracy.

REFERENCES

[1] B. Weiser and H. Pfützner, Relevance of magnetostriction and forces for the generation of audiable noise of transformer cores. *IEEE Transactions on Magnetics*, **36**, 3759-3777, 2000.

[2] A.J. Moses, P.I. Anderson, T. Phophongviwat and S. Tabrizi, Contribution of magnetostriction to transformer noise. *Universities Power Engineering Conference*, UPEC, Cardiff, England, 1-5, 2010.

[3] M. Javorski, J. Slavič and M. Boltežar, Frequency Characteristics of Magnetostriction in Electrical Steel Related to the Structural Vibrations, *IEEE Transactions on Magnetics*, **48**, 4727-4734, 2012.

[4] R.S. Girgis, M.S. Bernesjö, S. Thomas, J. Anger, D. Chu and H.R. Moore, Development of ultra-low-noise transformer technology, *IEEE Transactions on Power Delivery*, **26**, 228-234, 2011.

[5] R. Haettel, M. Kavasoglu, A. Daneryd and C. Ploetner, Prediction of transformer core noise, In: *Proceedings of the COMSOL Conference 2010*, Cambridge.

[6] W. Kubiak and P. Witczak, Vibration analysis of small power transformer, *COMPEL - The international journal for computation and mathematics in electrical and electronic engineering*, **29**, 1116-1124, 2010.

[7] M. Pirnat, G. Čepon and M. Boltežar, Introduction of the linear contact model in the dynamic model of laminated structure dynamics: An experimental and numerical identification, *Mechanism and Machine Theory*, **64**, 144-154, 2013.

[8] OpenModal webpage: www.openmodal.com

[1]International Conference on Engineering Vibration
Ljubljana, Slovenia, 7-10 September 2015

MEASUREMENT AND ANALYSIS OF NOISE AND VIBRATION OF 800-KV CONVERTER TRANSFORMERS

J. Pan*[1], Y. X. Wang[2], X.H. Du[2], Q.S. Tang[1], H. Huang,[1] C. M. Pei[3]

[1] *Department of Instrument Science and Engineering, Zhejiang University, 310027, China*
jpan@zju.edu.au, 2401972734@qq.com, hhai@zju.edu.cn

[2] *School of Mechanical and Chemical Engineering, The University of Western Australia, WA 6009, Australia*
20859125@student.uwa.edu.au; xuhao.du@research.uwa.edu.au

[3] *China Electrical Power Research Institute, Wuhan, 430074, China* peichunming@epri.sgcc.com.cn

Keywords: Ultrahigh voltage converter transformers, vibration, noise, field measurement

Abstract. While ultrahigh voltage (UHV) converter transformers provide economic advantages for long-distance power transmission, they also pose serious environmental noise issues. This paper summarises the results of a systematic field test of the vibration and noise of a number of converter transformer units at the Jing Hua UHV converter station in China. This experimental study not only offers an assessment of emitted noise from transformers with the same ratings and loadings but from different manufacturers compared to the existing standards for transformer noise, but also allows an analysis of the characteristics of the noise and vibration that are specific to converter transformers.

* Correspondence author: jpan@zju.edu.au

1 INTRODUCTION

The long-distance transmission of high-voltage direct current (HVDC) has the advantages of low electrical losses and good compatibility with electricity generated by renewable resources. However, since power stations and consumers both utilise electricity with alternating current (AC), conversions from AC to DC at the power generation end and from DC to AC at the distribution end are required. Figure 1 presents a schematic diagram showing the main components (converters and converter transformers) for HVDC transmission. Because of the stepped behaviour of DC to AC inversion, the phase currents sent through the converter transformers (CT) at the receiving end consist of a sequence of step functions in a cycle. For example, if the inverted current involves a sequence of n step functions per cycle, then strong harmonic components can be found at $nk \pm 1$ times the operating frequency, where $k = 1, 2, 3...$. In this case, the CT suffers not only from the electromagnetic excitations that occur in general power transformers, but also from higher frequency excitations due to the stepped behaviour of the phase current. As a result, noise from CTs may have an additional environmental impact.

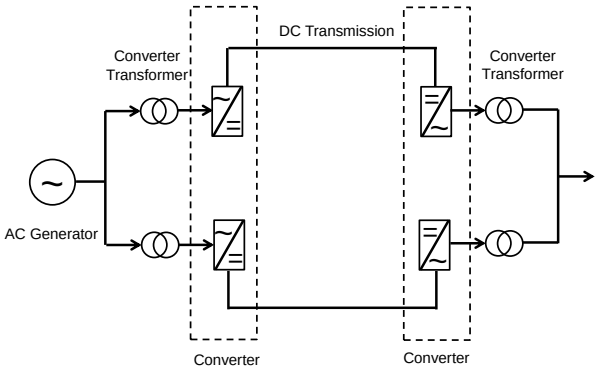


Figure 1: Schematic diagram showing the major components for HVDC transmission.

To understand the noise features of a CT, field measurements of the vibration and noise of a CT were conducted at the Jing Hua UHV converter station in China. Figure 2(a) shows an overview of the station, which has a bipolar configuration to handle ±800-kV DC current. The CT for each pole consists of four stages to accommodate four equal voltage gaps from zero to ±800 kV. Each stage has three single-phase transformers. Figure 2(b) shows a photo of a spare single-phase transformer. All the transformers are installed in acoustical enclosures for noise control purposes.



(a) (b)

Figure 2: (a) An overview of the Jing Hua UHV converter station. (b) A photo of a typical single-phase transformer at the station.

The purposes of these measurements are to (1) determine the vibration and noise characteristics of the CTs, (2) compare the noise and vibration levels of different single-phase transformers under similar operating conditions, and (3) evaluate the relationships between CT vibration and its radiated noise within an enclosure. The sound and vibration of twelve single-phase transformers at the second pole of the station (located at the far side in Figure 2(a)) are measured in order to assess the variation in the sound and vibration levels. The distributed vibrations of two specific transformers (Pole I, 800 kV, and phase C, and Pole II, 800 kV, and phase C) are used to extract the spatial vibration features of the transformers.

2 CHARACTERISTICS OF CT VIBRATION AND NOISE

The spatially averaged acceleration levels measured on the surfaces of the polar I 800 C transformer and the polar II 800 C transformer are shown in Figure 3. A total of 368 measurement points were selected on the three side walls of the polar I 800 Phase C transformer, and 344 measurement points were selected on the polar II 800 C transformer. The vibration spectrum of the CTs is characterised by the impulsive features of the input current. Because the electromagnetic excitation of the transformer is approximately proportional to the phase current squared and the phase voltage squared, the quadratic contribution of their frequency components at 50 Hz and at $50\times(nk\pm1)$ Hz implies significant excitation at 100 Hz, $100\times(n\pm1)$ Hz , and $100\times(2n\pm1)$ Hz , *etc*. The cross-term contribution of the components also gives rise to large excitations. The contribution to the excitation of the transformer vibration by the frequency components of the current is illustrated in Figure 4, where a sequence of step functions ($n=12$) are used to approximate the sinusoidal waveforms of the current.

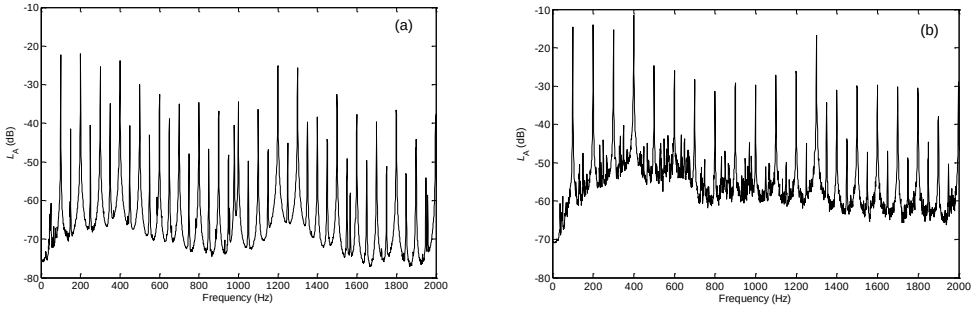


Figure 3: Spatially averaged acceleration levels measured on the surfaces of (a) the polar I 800 C transformer and (b) the polar II 800 C transformer (reference value for the acceleration level: 9.8 m/s^2).

Other harmonics of the 100 Hz components and the odd harmonics of the 50 Hz components (in Figure 3(a)) may be explained by the mechanisms involved in the transformer's magnetostrictive excitation, *e.g.*, hysteresis of the core material and DC current bias [1]. The vibration of the transformer tank structure is also dependent on the frequency response function of the transformer structure, consisting of the core, winding, cooling oil, transformer tank, and the coupling between them [2]. Therefore, a large acceleration level at a specific frequency of excitation may be attributed to the significant excitation and/or the resonance response of the transformer structure.

Although handling the same voltage gap and phase, the vibration levels of the polar I 800 C transformer and the polar II 800 C transformer are different, owing to their different structures and excitation mechanisms. The main differences are summarised as follows:

(1) The polar II 800 C transformer has a significantly higher background noise (15 dB higher, at around 400 Hz) compared to that of the polar I 800 C transformer, indicating larger broadband electromagnetic excitation mechanisms in the core and winding structure of this transformer; and

(2) The overall vibration level of the polar II 800 C transformer (−5 dB) is around 8 dB higher than that of the polar I 800 C transformer (−13 dB).

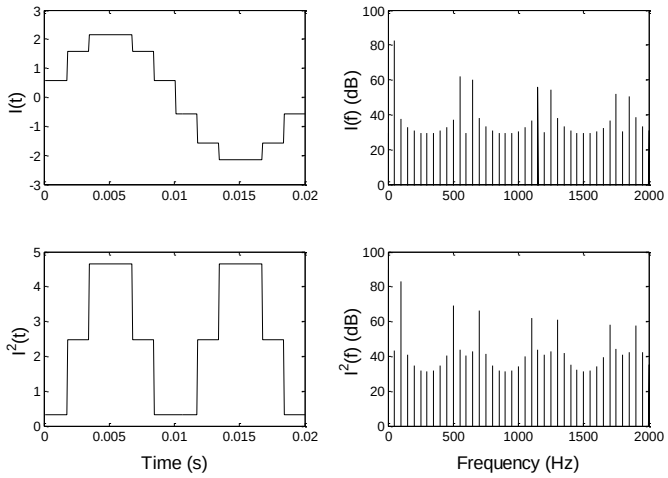


Figure 4: The current and its quadratic term in the time and frequency domains, indicating the frequency components of the electromagnetic excitation of the transformer's structural vibration.

Figure 5 shows a diagram of a typical CT in an acoustical enclosure. The spatially averaged sound pressure (Figure 6) at several locations in the enclosure (ten locations in the enclosure for the polar I 800 C transformer and nineteen locations in the enclosure for the polar II 800 C transformer) were measured in order to examine the relationship between the transformer's structural vibration and its radiated sound pressure.

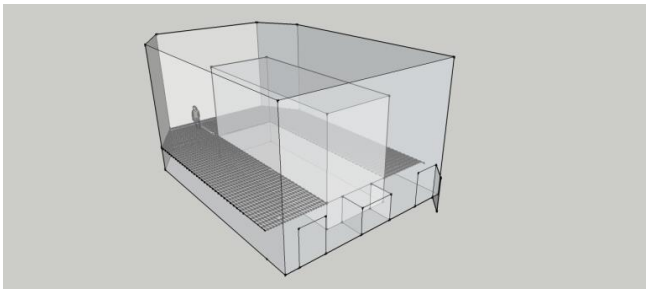


Figure 5: Diagram of a single-phase transformer within an acoustical enclosure.

The general proportional relationship between the sound pressure and its corresponding transformer vibration indicates that different designs of the transformer's mechanical and electrical–magnetic structure may result in different electromagnetic excitations and structural frequency response functions. Furthermore, a general trend of correlation exists between the

total sound energy in the enclosure and the vibration energy in the transformer tank at the frequencies (100 Hz and its harmonics) where major peaks in the transformer structural vibration spectrum are found. Figure 7 shows the ratios of the total sound energy in the enclosure:

$$E_R = \frac{< P_R^2 > V_R}{\rho_o c_o^2}, \tag{1}$$

and vibration energy in the transformer tank:

$$E_s = M_s < V_S^2 >, \tag{2}$$

where $< P_R^2 >$ and $< V_S^2 >$ are, respectively, the spatially averaged sound pressure and velocity; V_R is the volume of the enclosure; and M_S is the overall mass of the transformer tank.

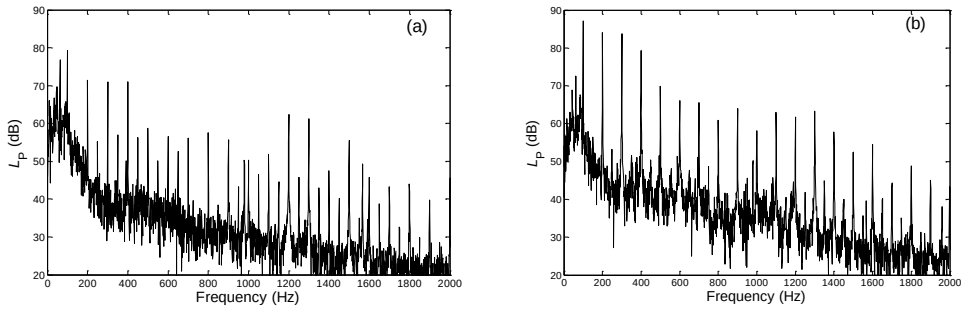


Figure 6: Spatially averaged sound pressure levels measured in the enclosures of (a) the polar I 800 C transformer and (b) the polar II 800 C transformer (reference value for the sound pressure level: 2×10^{-5} Pa)

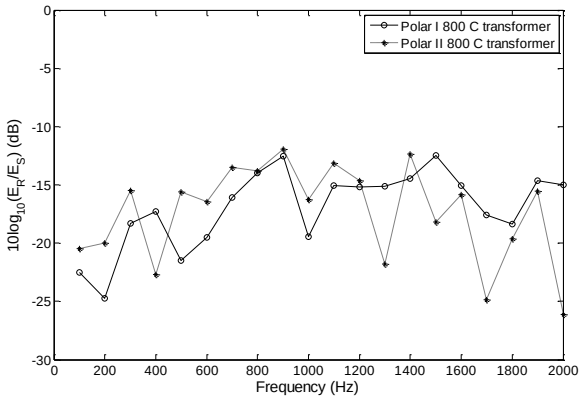


Figure 7: Ratios of sound energy in the enclosure and vibration energy in the transformer tank.

It is interesting to observe that the ratio of the total sound energy in the enclosure and the vibration energy in the transformer tank are around -18 dB within an approximately 15 dB fluctuation. It suggests a topic for future research in identifying the mechanisms that determine the average ratio and fluctuation.

3 VARIATION IN TRANSFORMER SOUND AND VIBRATION

In addition to the detailed measurements of the vibration of the polar I 800 C transformer and the polar II 800 C transformer, the sound and vibration of a total of twelve single-phase transformers at Pole II were measured for a study of the variation of sound and vibration be-

tween different transformers. The sound and vibration of three transformers at Pole I (800 A, B, and C) were also measured. In this study, only three measurement points were selected to describe the average vibration of each transformer. The locations were carefully selected, providing the vibration of the transformer (1) between the enhancement ribs, (2) on the top of the rib, and (3) on the side of the rib. More details about the wall structures of the Pole II transformers are shown in Figure 8.

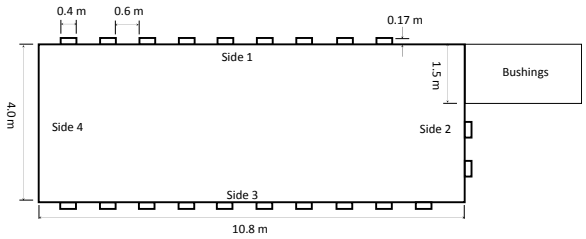


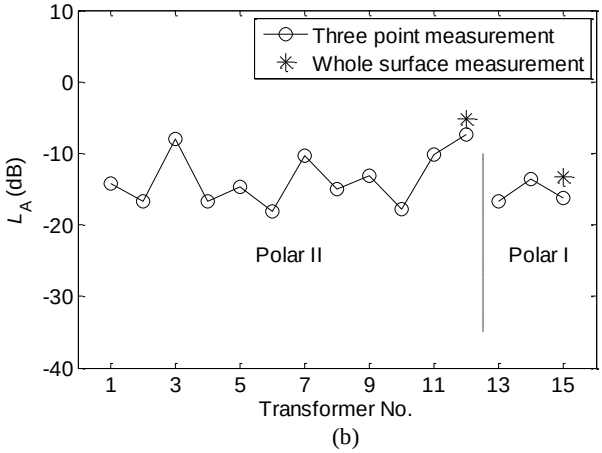
Figure 8: Distribution of the U-shaped ribs on the surface of the polar II 800 C transformer.

For all the transformers tested, these three locations are at approximately the same points on the front walls (Side 1 in Figure 8). A photo of the accelerometer locations is shown in Figure 9(a). During the measurements of all the transformers, the applied voltages and loadings were approximately unchanged.

As shown in Figure 9(b), the variation in the overall vibration level of the twelve transformers at Pole II is around 10 dB, while that of the three transformers of Pole I is around 5 dB. The comparison of the vibration levels found by the three-point measurement and by the whole-surface measurement indicates that the measurements from the three selected locations on the transformer structure provide a reasonable measurement of the vibration level of the transformer structure.



(a)



(b)

Figure 9: (a) Accelerometer locations on the transformer tank. (b) Variation of the overall vibration level of the single-phase transformers at Pole I and Pole II.

The variation of the spatially averaged sound pressure levels between different transformer enclosures is shown in Figure 10. The result from the single-point measurement was obtained simultaneously with that from the vibration measurement of the whole transformer surface. The variation of the sound pressure generally follows the same trend as that of the transformer's structural vibration.

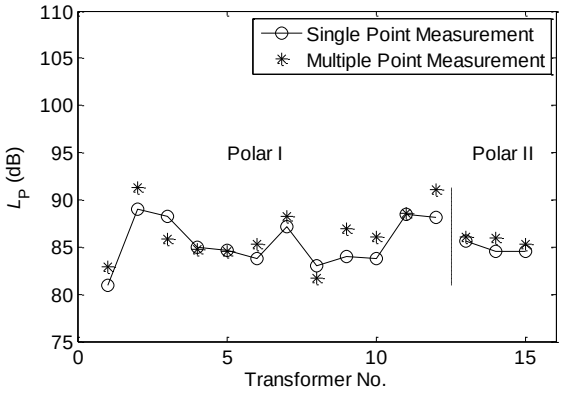
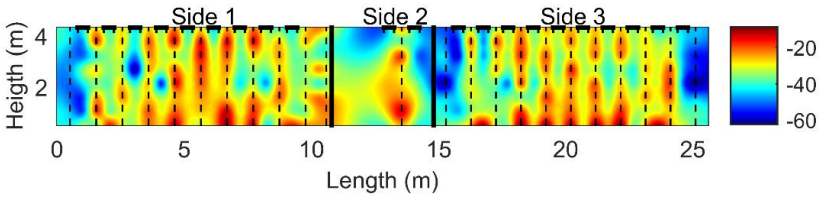


Figure 10: Variation of the overall sound pressure level in the enclosures of the single-phase transformers at Pole I and Pole II.

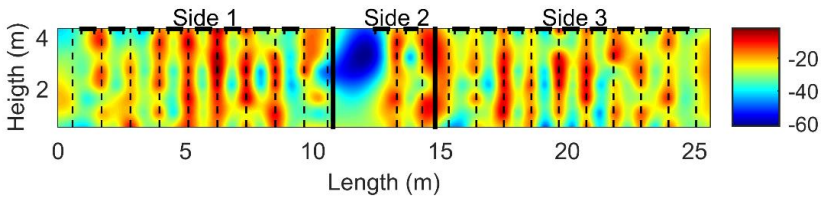
4 SPATIAL CHARACTERSICS OF THE TRANSFORMER VIBRATION

The vibration of the transformer tank is the major source of transformer noise. The distributed vibration on the transformer tank was measured for a future examination of the sound power and directionality. The side walls of the UHV CT tank are enforced by periodically located and U-shaped ribs, as shown in Figure 9(a). At 100 Hz, the vibration level at the area between the ribs is larger than that at the ribs (see Figure 11). Such a periodic distribution of the vibration is observed in both transformers.

At 300 Hz, the vibration tends to be greater at the upper part of the transformer tank (see Figure 12). Such a periodic distribution of the vibration is also observed in both transformers.

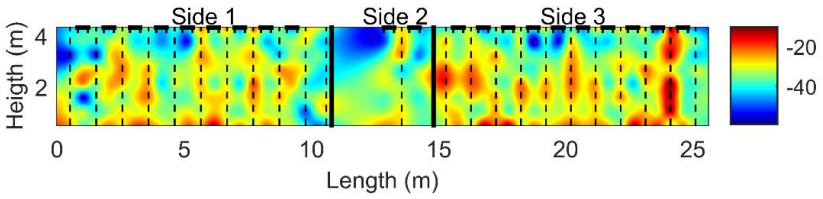


(a)

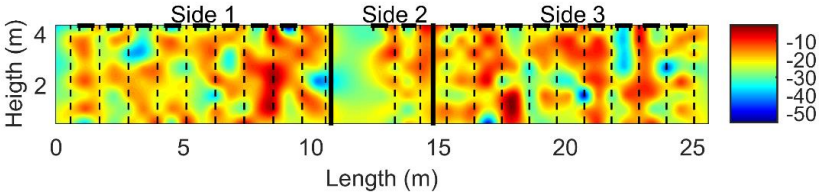


(b)

Figure 11: Vibration distribution on the surface of (a) the polar II transformer and (b) the polar I transformer at 100 Hz.



(a)



(b)

Figure 12: Vibration distribution on the surface of (a) the polar II transformer and (b) the polar I transformer at 300 Hz.

5 DISCUSSION AND CONCLUSIONS

The overall acceleration levels of the polar I transformer and the polar II transformer are, respectively, −13 dB and −5 dB (with reference to 9.8 m/s^2). The amplitudes of the frequency components of the vibration are dominated by 100 Hz and its harmonics. The higher peak values occur in the 100 Hz to 400 Hz and the 1000 Hz to 1400 Hz ranges, determined by a sequence of step functions in the phase current due to the DC-to-AC conversion, the magneto-strictive effect, hysteresis, and structural characteristics. The overall sound pressure levels in the enclosures of the transformers are 90 dB and 85 dB, respectively. The spectrum distribution of the sound pressure is approximately proportional to that of the structural velocity, and the ratio of the energy in the enclosure to that in the transformer structure fluctuates around -18 dB within a range of approximately 15 dB.

A clear periodic pattern of the transformer's structural vibration was identified at 100 Hz, as a result of the periodically distributed ribs on the transformer surface. This indicates the possible control of structural vibration and sound radiation through an optimal design of the periodic configuration of the transformer tank.

REFERENCES

[1] J. He, Z. Yu, R. Zeng, and B. Zhang, Vibration and audible noise characteristics of AC transformer caused by HVDC system under monopole operation, *IEEE Transactions on Power Delivery*, **27**, 4, 1835–1842, 2012.

[2] Y. Wang and J. Pan, Comparison of mechanically and electrically excited vibration frequency responses of a small distribution transformer, *IEEE Transactions on Power Delivery*, DOI 10.1109/TPWRD.2014.2383390, 2015.

International Conference on Engineering Vibration
Ljubljana, Slovenia, 7-10 September 2015

SPATIAL DISTRIBUTION OF MAGNETOSTRICTION, DISPLACEMENTS AND NOISE GENERATION OF MODEL TRANSFORMER CORES

Georgi Shilyashki*[1], Helmut Pfützner[1], Peter Hamberger[2], Martin Aigner[2], Anton Kenov[1], Ivo Matkovic[1]

[1]Inst. EMCE, TU Wien, Vienna, Austria
shilyashki@tuwien.ac.at

[2]Transformers Linz, Siemens AG Österreich, Linz, Austria

Keywords: Transformer Cores, Magnetostriction, Displacements, Vibrations, Audible Noise

Abstract. *Recently, the relevance of audible noise of power transformers tends to increase due to the growing environmental awareness. For sound assessment, two standardised methods reveal the global noise of the whole system, as resulting from the interaction of core, windings, oil and tank. But for a deeper understanding of noise generation, it would be advantageous to investigate also the individual roles of the single above components in closer ways. This paper summarizes attempts to study the first component, i.e. the soft magnetic core, by means of model cores. For the first time, we analyzed local distributions of all three strain, displacement and audible noise, keeping in mind that these quantities depend on many parameters like material, stacking, clamping, induction, rotational magnetization, or additional DC-bias, in complex ways. In-plane strain proved to be dominated by magnetostriction (MS), with maximum intensities in corners and T-joints. The interpretation of in-plane displacements proves to be complicated by the unknown resting point of the whole system. However, the results reflect contributions of both MS and magneto-static forces (MF). Out-of plane displacements proved to be dominated by effects of MF, in particular at overlaps of corners and T-joints, due to imperfect clamping. Regional measurements of audible noise were performed in the near-field mode by means of automatic scanning by microphone over free core regions within a noise-isolating scanning chamber. As to be expected, the results showed strongly inhomogeneous distributions with maxima at T-joints and corners. As a conclusion, model core results have very restricted relevance for full sized cores in quantitative ways. But they favour an understanding for crucial mechanisms and for core regions that play dominating roles.*

1 INTRODUCTION

Recently, the relevance of audible noise of power transformers tends to increase due to growing environmental awareness. Nowadays, transformers are located closer to the urban areas. Thus noise reduction may be more relevant than loss reduction. For the assessment of audible noise of industrial transformers, two standardized methods are generally used, i.e. Sound Pressure Measurement and Sound Intensity Measurement [1, 2]. Both reveal the *global* noise of the whole system as resulting from the interaction of core, windings, oil and tank. However, it is evident that a deeper understanding of noise generation needs separate investigations of the roles of the single above components in closer ways.

This paper summarizes studies on the first component, i.e. the core. Apart from the windings, the core can be assumed as a primary source of audible noise [3]. It is well known, that the latter originates from both magnetostriction and magneto-static forces. However, a clear distinction between them is an almost impossible task, since both interact, apart from exhibiting the same spectral components. We assume that a split would need very specific experimental and/or analytical modellings.

As it is well known, the core's audible noise generation is a complex process depending on many parameters like material, stacking, clamping, induction, rotational magnetization, additional DC-bias, etc. Concerning the material, it is known, that compared to non-oriented SiFe, that of grain-oriented (GO) SiFe is lower, due to weaker magnetostriction (MS) as a result of a highly ordered texture. Even better performance can be expected from laser scribed materials (e.g. [4]). The core clamping influences local strains of both MS and magneto-static forces, as closer discussed in [3]. Also rotational magnetization has a very significant impact on MS, causing increases up to a factor of 10, compared to mere alternating magnetization (AM; see [5]). Finally, additional DC-bias, caused e.g. by geomagnetically induced currents, leads to general increases of local strains, especially in regions of mere AM, audible noise being distinctly enhanced (e.g. [6]).

As already mentioned, most authors consider audible noise for the entirety of a transformer [1,2,7]. Only few ones concentrate on the magnetic core by numerical calculations, in particular of local distributions of core surface displacements, e.g. using FEM techniques [8]. In our own studies, we performed various experimental analyses on different 1-phase and 3-phase model cores. The latter prove to be very effective for basic studies on mechanisms of loss generation. On the other hand, studies on vibrations or even noise are problematical a priori, in particular due to the well known relevance of eigen-values [8, 9]. However, keeping the latter in mind, experiences show that experimental modelling may yield basic conclusions, in particular if local investigations are performed in compartive ways.

The main target of the current paper is to summarize experiences from regional measurements on magnetostriction, displacements and audible noise. A second aim is to discuss basic problems of such measurements, as well as restrictions of practical relevance.

2 LOCAL DISTRIBUTIONS OF STRAIN

As it is well known, measurements of magnetostriction (MS) are being performed in routine ways for all types of laminated soft magnetic magnetic materials as being applied for transformer cores. A material sample is magnetized in a so-called single sheet tester (SST) or

rotational single sheet tester (RSST), and MS-caused strains are detected by means of strain gauges (e.g. [5, 10]), or also by interferometers (e.g. [11, 12]). The results proved to be affected by many impact factors, as summarized in [5].

In a rather surprising way, literature does not report any study of regional in-situ measurements, as performed directly on transformer cores, neither on core surfaces nor in the core interior. A possible reason may be that such measurements are highly problematical, as revealed by our own attempts of investigations. First, let us report results, then discuss the problems of measurement.

In a series of studies, we arranged strain gauges on the surface – and partly also within the stack – of model transformer cores. Considering the large grain size of modern core steel, we use about 50 mm long sensors for averaging. Figure 1 shows typical results for a square 3-phase model transformer core with outer dimensions of 750 mm and a stacking height of 57 mm. The core was stacked from three packages of different width and height: main package P1 (width 150 mm, height 30 mm), outer package P2 (110 mm, 11 mm) and peripheral package P3 (100 mm, 8 mm). It was built up from of highly grain oriented (HGO) material of type 0.85-23DR.

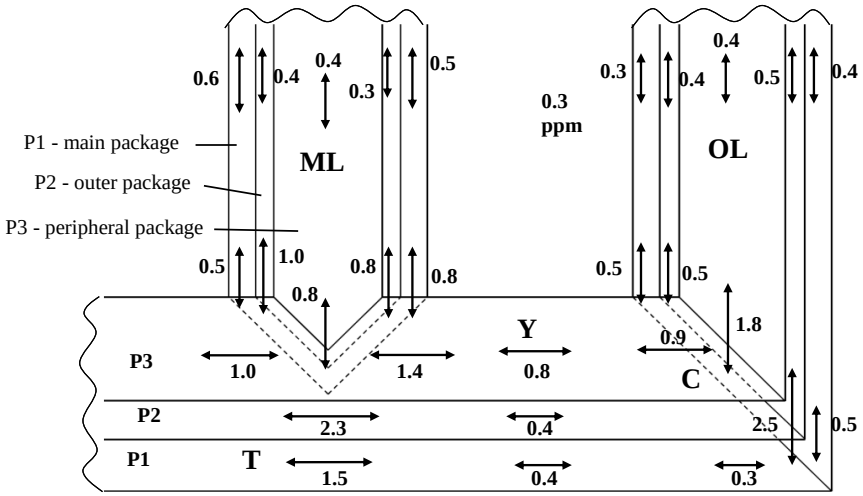


Figure 1: Local distribution of the distribution of peak-to-peak strain ε_{RD} in RD in a 3-phase, 3-package model transformer core, stacked from highly grain oriented material, for B_{NOM} = 1.7 T. All values are given in ppm. They are length-coded by double arrows in logarithmic scale.

Figure 1 includes results of measured strain values ε_{RD} (in ppm) in RD for the state of locally balanced clamping in all core regions (see below). Local values show strong variations as resulting from errors of measurement, but also from many impact sources like inhomogeneous induction, interactions of the three core packages, and others. However, the regional *mean* values in Table 1 reflect almost even strain distribution in the outer limb, the middle limb and the yoke with an order of ε_{RD} = 0.5 ppm. This value is in the range of catalogue values of magnetostriction for HGO materials. Higher values (approaching 1 ppm) at the end of the middle limb can be interpreted by regionally increased flux distortions. The latter cause increased harmonics of MS, leading to increases of the corresponding peak-to-peak values. But – much more important – they also cause higher harmonics that have high impact on audible noise, the human ear being highly sensitive to them.

region	OL	ML	Y	C	T
	outer limb	middle limb	yoke	corner	T-joint
averaged strain	0.4 ppm	0.6 ppm	0.5 ppm	1.2 ppm	1.4 ppm

Table 1: Regional mean values of measured peak-to-peak strain ε_{RD}.

Even higher values, above 1 ppm, were detected in the corner regions, indicating effects of partly saturated overlaps of laminations. Highest values arise in T-joint regions as a result of rotational magnetization, as discussed in detail in [5]. The highest MS-value of 2.3 ppm is detected straight below the V-element of the T-joint area. This coincides with maximum values of power losses. The area of V-element represents a kind of "worst spot", strongest rotational magnetization being linked with local saturations of overlaps, as well as with strong magnetostatic forces between the individual laminations [3]. Here, it should be noted that model cores built up from lower grade material showed distinctly higher strain values, up to 5 ppm, as reported in [5].

Above, it was mentioned that the results of Figure 1 represent a case of balanced mechanical clamping. The latter proves to be a crucial problem of model cores where some access to the core surface is demanded. Experience shows that too weak clamping favours magnetostatic forces (MF) as a reason of chaotic nature of both vibrations and local strain values. On the other hand, very strong clamping yields torsion of laminations with extreme strain values in locations of high mechanical compression. To attain "balanced" conditions, a medium state of clamping was adjusted that promises representative results. Anyhow, the tendencies according to Table 1 are compatible with physical expectations. This indicates that model core studies on magnetostriction have practical relevance, if interpreted in careful ways.

3 LOCAL DISTRIBUTION OF DISPLACEMENT

For straight-forward procedures, it offers itself to integrate over locally determined strain values ε (caused by MS and/or MF) in order to estimate the corresponding displacements δ of core surface positions. In literature, studies of local distributions tend to be restricted to singular points. For example [13] discusses one point on the middle limb and one at the yoke of a 3-phase transformer package modelled by FEM, finding maximum displacement values of about 5 µm. As well, [14,15] report FEM results in comparison with measurements at three positions, detecting values up to about 0.2 µm and 0.4 µm, respectively, however for extremely small 1-phase cores. In own experiments [3], we found for similar 1-phase arrangements, off-plane displacements δ_{ND} in normal direction (ND; perpendicular to the plane of magnetization) up to about 0.3 µm and in-plane values δ_{RD} in rolling direction of similar order.

In order to get closer to practical conditions, we focussed our more recent work on 3-phase model cores that are built up from three packages, as also described further up for strain. For displacement measurements, we applied acceleration piezo-electric sensors (B&K 4326) connected to a charge amplifier (B&K 2635). The signal acquisition and processing was performed in Labview. For the evaluation of δ, only the even harmonics (100 Hz, 200 Hz …1000 Hz) were considered.

Figure 2 shows results for a square 3-package core of 500 mm size assembled from GO material C130-30. Contrary to the case of MS-measurements, where additional balancing clamping in all core regions was performed, here the clamping was restricted to existing manufacture clamping, for access to surface positions.

Off-plane displacements δ_{ND} were measured at about 40 local positions. The corresponding results in Figure 2 show strongly inhomogeneous distributions. However, clear tendencies are indicated by regional values of Table 2. Lowest values round 1 µm were measured in the yoke, followed by about doubled ones in the limbs, the middle limb showing higher values than the outer one. As expected, the highest values were detected in the corners with about 4 µm, and in the T-joint region with about 6 µm. Close from the V-element of the T-joint we found a maximum value as high as 13.7 µm.

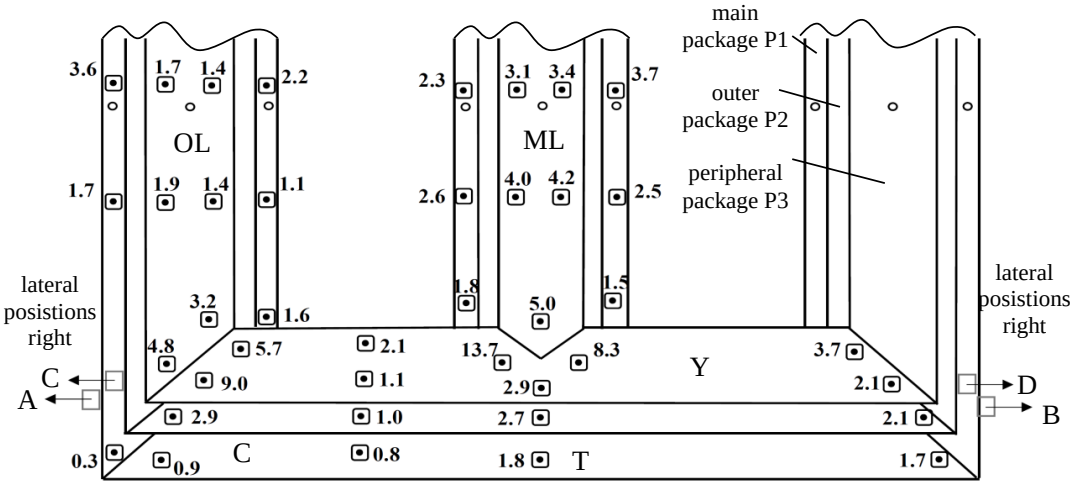


Figure 2: Regional displacement distributions in a 3-phase, 3-package model transformer core, stacked from GO material C130-30 for B_{NOM} = 1.7 T. All values are given in µm. The squares with dot mark positions of off-plane measurements. The blank squares mark four selected positions of in-plane measurements direction (lateral), A and B at the edges of the package P1, C and D of P2.

Concerning the individual packages, lowest values were registered in the main package P1, higher ones in P2 and highest in the peripheral package P3. One of the several possible reasons is the fact that the main package exhibits best clamping, also through the mass of the packages P2 and P3, the core being studied not in upright but in horizontal position.

region	OL outer limb	ML middle limb	Y yoke	C corner	T T-joint
averaged displacement in ND	2 µm	2.9 µm	1.3 µm	3.9 µm	5.7 µm

Table 2: Regional mean values of measured peak-to-peak displacement values δ_{ND} in the off-plane normal direction.

As an interpretation, the detected very high orders of off-plane displacement cannot be explained by mere magnetostriction, due to the low height of stacking. It is evident, that the dominant mechanism is given by magneto-static forces. In particular, in overlap regions of the corners and T-joints, strong forces arise between lamination ends, as a simple interpretation. We assume that the results do not have quantitative relevance for well clamped transformers. However, qualitative relevance is given with respect to differences for the individual regions, in particular for cases of deteriorated mechanical stabilization of a core, in connection to damaging or aging.

Besides the off-plane displacements, in-plane values δ_{RD} in rolling direction (RD) were measured at about 30 positions. Typically, they showed intensities of the order of 1 µm with irregular variations. Effective interpretations prove to be complicated through the problematic of lacking resting point. A priori, one could expect that a transformer core exhibits a permanent, centrally located point which can serve as a reference REF for displacements as registered at other locations. But this is not the case. Attempts of localisation indicate that REF may arise in any core region and change as a result of minor modifications of the system. This disfavours analyses of displacement. The alternative would be to put the focus on vibrations, however, with the disadvantage that physical interpretations become even more difficult. That is, the relationship to basic mechanisms like magnetostriction or forces is mantled even more.

To meet the problem of unknown point REF, we evaluated over-all displacement *differences* for core main axes, based on paired detection points, as illustrated in Figure 2 for the entirety of the yoke. For the main package P1, we evaluated displacements at the lateral positions A and B. The signals from the left side A and from the right side B were triggered at the flux of the middle limb. The effective over-all change of yoke length was calculated as the difference between the measured displacements according to

$$\delta_{BA}(t) = \delta_B(t) - \delta_A(t) \; . \qquad (1)$$

Figure 3a shows corresponding time-traces for P1. Both packages show well pronounced 100 Hz components of dynamic displacements. The two individual signals $\delta_B(t)$ and $\delta_A(t)$ exhibit strongly non-sinusoidal responses. $\delta_B(t)$ exhibits much stronger amplitude which yields the conclusion that REF is located in the left core half. In a rather surprising way, $\delta_{BA}(t)$ proves to be almost sinusoidal. This would mean that the periodical shrinking of the yoke – as resulting from magnetostriction and forces – has sinusoidal character, in approximation. The peak-to-peak intensity results close to 4 µm, a quite high value, even if we consider a strong contribution of rotational magnetization in the T-joint. On the other hand, the investigated core is not built up from HGO steel which means that magnetostriction tends to be high.

Figure 3b shows corresponding signals for the yokes outer package P2. Here, the amplitudes of the strongly distorted displacements $\delta_D(t)$ and $\delta_C(t)$ are more balanced. This would indicate a more central position of the packages individual point REF – a vague way of interpretation that should be put for discussion. The difference $\delta_{DC}(t)$ deviates from a sinus, showing indication of positive saturation. The intensity results as being close to 2 µm.

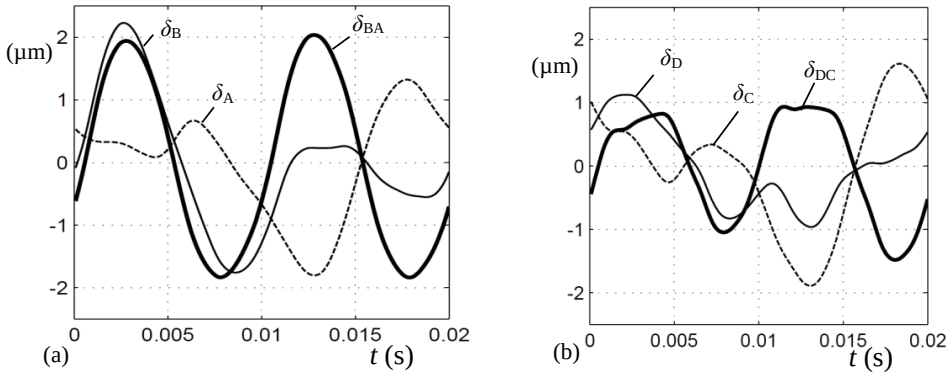


Figure 3: In plane displacements, measured by acceleration sensors in lateral positions of the left and the right side of the yoke for B_{NOM} = 1.7 T. The difference signals between right core side and left core side are given in bold. (a) Main package P1 (positions A and B. (b) Outer package P2 (positions C and D).

As a major conclusion, it seems to be rather impossible to apply model cores for a quantitative assessment of displacements as to be expected for full sized transformers. Main reasons are the restricted stacking height in combination with imperfect clamping. Off-plane displacements tend to reflect mere effects of magneto-static forces. On the other hand, laterally detected in-plane displacements can be assumed to reflect the total of contributions from magnetostriction and magnetostatic forces (at overlaps). While quantative conclusions are most problematic, qualitatively, the results of displacement show similar tendences with regional differences of measured strain values. That is, the relevance of different core regions is indicated in approximate ways. Further experiments should be performed with larger stacking height and more effective clamping, specifically designed for access of sensors to selected core surface positions.

4 LOCAL DISTRIBUTIONS OF NOISE GENERATION

Attempts to detect local distributions of noise generation were performed in a specifically adapted scanning chamber. As sketched in Figure 4, it shows cubic geometry of about 1.5 m inner dimensions and is equipped with a 3D computer-controlled scanning head with 10 µm spatial resolution. An extra insulation was provided for reducing contributions of noise coming from the windings. The local sound intensity (in undefined near-field mode) was measured, using a microphone B&K 4165 and a measuring amplifier B&K 2606. The microphone was mechanically attached to the scanning head. Partly, it was equipped with a shell for improved directional response. According to Figure 5a, the measurements were performed at nine equidistant locations 1...9 along the entire middle part of the whole yoke, at two different heights to the surface, d = 20 mm and d = 50 mm. The test procedure was controlled in a fully automatic way, by specific Labview software. At each single location, the acoustic signal was captured for about 3 s, for nominal magnetization of B_{NOM} = 1.7 T. The signal evaluation and the calculation of the corresponding local power levels were performed in Matlab.

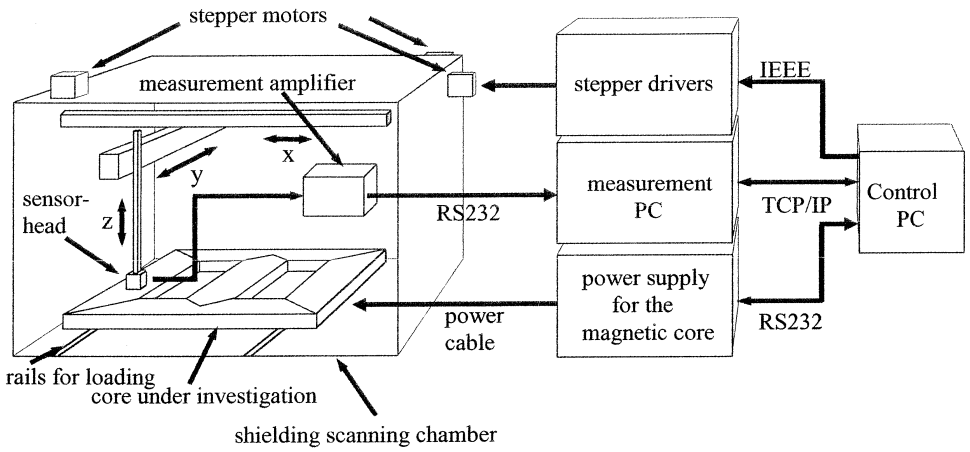
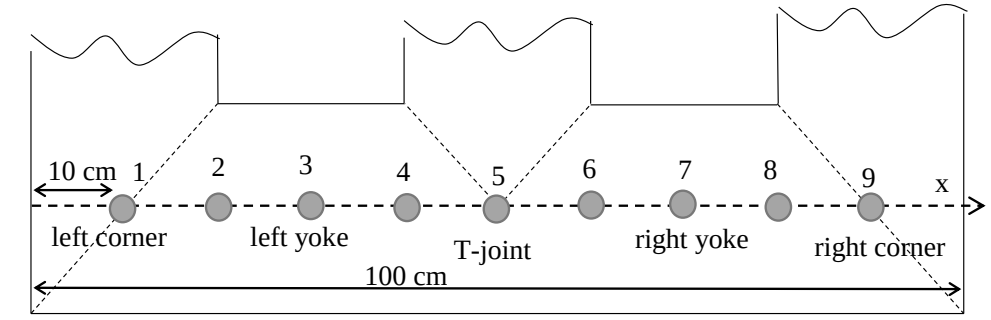


Figure 4: Test chamber for acoustic near-field analyses by automatical scanning.

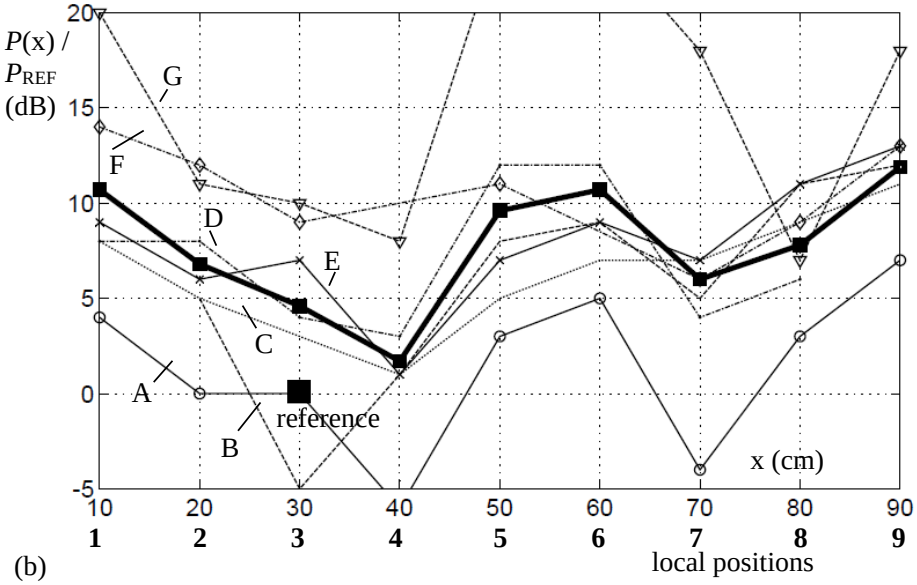
Figure 5b shows test results for a 3-phase 1 m x 1 m model transformer core package, stacked from HGO material with a stacking height of 16 mm. The data of the graph of results indicates a quite vague tendency of maximum noise intensities at the T-joint region and at the corners, the differences to the yoke regions being approximately 10 dB. However, local dif-

ferences of the same order proved to result from smallest modifications of clamping, depending also from the arrangement of shell and changes of detection distance. Distinct effects resulted from smallest modifications of the position of the magnetic core, as to be expected from changed eigen-frequencies.

As to be expected a priori, a model core will never reflect the noise generation of a full size core. However, the so far results indicate that carefully performed, regional near field measurements may give informations on consequences of modified core designs. For example, we expect qualitative informations on tendencies of different joint designs in dependence from the nominal induction. At present, we start measurements at model core of normal stacking height, aiming for more defined conditions of emission. Possibly, near the near field measurements may also prove effective as a diagnostic tool with respect of defects of stacking.



(a)



(b)

Figure 5: Acoustic measurements, performed at the surface of a transformer core package, stacked from highly grain oriented material for B_{NOM} = 1.7 T. All measured sound pressure levels are related to the sound pressure, measured in the left yoke (location 3) for case A. The eight individual curves concern the following conditions of measurement (d the distnce between sensor and lamination surface):

A – no clamping, with shell, d = 2 cm
B – no clamping, no shell, d = 2 cm
C – no clamping, no shell, d = 5 cm
D – with clamping, no shell, d = 2 cm
E – no clamping, with shell, d = 5 cm
F – with clamping, with shell, d = 5 cm
G – with clamping, with shell, d = 2 cm
H – over-all average (thick curve)

5 CONCLUSIONS

The current paper presents experiences from the application of transformer model cores in the context of audible noise. Many studies demonstrated that models are a helpful tool for the assessment of phenomena of energy loss, provided that specific model core effects are kept in mind. In particular, the latter concern the problem of scaling down, and up, respectively. As well, low stacking height, poor clamping, enhanced stray fields are further characteristics that restrict the validity of model cores. An alternative would be the application of numerical modelling like FEM. However, it has several drawbacks as well. For example, they concern difficulties to consider interactions of non-linearity, anisotropy, hysteresis and eddy currents, as well as the strong impact of joint designs.

Starting out from high experience with model cores for loss assessment, it was clear a priori that the field of audible noise would be much more complex and problematical. And indeed, the relevance of model core studies proves to be strongly restricted for three investigated quantities. The tests concerned regional distributions of magnetostiction, displacements and acoustic noise generation for different 3-phase transformer core geometries and different types of materials. As a whole, all cores show strongly inhomogeneous distributions of all three investigated characteristics. However, some spatial tendencies could be outlined in a general way: The T-joints exhibited maximum intensities of all three quantities, which confirms a significant role of rotational magnetization. Both 1-phase cores and 3-phase cores showed maxima at corners. It indicates an impact of saturated joint regions, but has also to be related to vibrations that are caused by magneto-static forces, due to imperfect clamping.

In more detail, regional strain measurements prove to be effective on model cores. It is likely that conclusions on full size cores are possible. The results confirm strong effects of rotational magnetization on magnetostriction. They also reveal the important role of clamping which should be balanced, keeping the total of core areas in a “relaxed” state to avoid local hyper-maxima of strain in mechanically compressed sub-regions.

Measurements of displacement in off-plane direction would need full stacking height in order to be of practical relevance. This should be considered in future experiments. The interpretation of in-plane displacement measurements is complicated by the fact that an investigated core lacks a symmetrically localised resting point. However, conclusions on integral-effects of magnetostrictive strains seem to be feasible.

Finally, regional tests on the generation of audible noise prove to be the most difficult task, the results of measurement being affected by smallest modifications of the involved system. However, the here reported near field measurements may offer a diagnostic tool for the identification of core defaults in comparative ways. It proved to be advantageous to use computerized scanning due to the fact that defined test procedures are repeatable under constant environmental conditions.

ACKNOWLEDGEMENT

This work was supported by the Austrian Research Promotion Agency FFG under Project 834159.

REFERENCES

[1] R. Girgis, K. Garner, M. Bernesjö, and J. Anger Measuring no-load noise and load noise of power transformers using the Sound Pressure and Sound Intensity methods - part I: outdoors measurements, *IEEE Pow.Eng.Soc. Gen.Meet., 1-8,* 2008.

[2] R. Girgis, K. Garner, M. Bernesjö, J. Anger, and D. Chu, Measuring no-load noise and load noise of power transformers using the Sound Pressure and Sound Intensity methods - part II: indoors measurements, *IEEE Pow.Eng.Soc. Gen.Meet., 1-8,* 2008.

[3] B. Weiser, H. Pfützner, and J. Anger, Relevance of magnetostriction and forces for generation of audible noise of transformer cores. *IEEE Trans.Magn.* **36**, 3759 - 3777, 2000.

[4] L.Lahn, C.Wang, A.Allwardt, T.Belgrand and J.Blaszkowski. Improved transformer noise behaviour by optimized laser domain refinement at Thyssen Krupp Electrical Steel. *IEEE Trans.Magn.* **48**, 1453-1456, 2012.

[5] G. Shilyashki, H. Pfützner, J. Anger, K. Gramm, G. Hofbauer, V. Galabov, and E. Mulasalihovic, Magnetostriction of transformer core steel considering rotational magnetization. *IEEE Trans.Magn.* **50**, 840015, 2014.

[6] Y. Li, Y. Gao, L. Li, D. Zhang and F. Han, Effects of DC magnetic bias on the magnetic and sound fields of transformer. *Energ. Pow. Eng.* **5**, 1097-1100, 2013.

[7] A. Petrovic, L. Lukic, M. Kolarevic, D. Lukic, Noise measurements of the power transformers. *Proc. 4 Int. Conf. Noise and Vibr.*,263-267, 2012.

[8] R. Haettel, M. Kavasoglu, A. Daneryd, and C. Ploetner, Prediction of transformer core noise. *COMSOL Conf. Cambridge Proc.* 2014.

[9] R.S.Gigis, M.S.Bernesjö, S.Thomas, J.Anger, D.Chu, H.R.Moore. Development of ultra-low-noise transformer technology. *IEEE Trans.Pow.Deliv.* **26**, 228-234, 2011.

[10] M. Yamagashira, D. Wakabayashi, and M. Enokizono, Vector Magnetic Properties and 2-D magnetostriction of various electrical steel sheets under rotating flux condition. *IEEE Trans.Magn.* **50**, 6100404, 2014.

[11] A. Hasenzagl, H. Pfützner, A. Saito and Y. Okazaki, Status of the Vienna hexagonal single sheet tester. *Proc. 5th Int. WS 2D Magn.Probl*., 33-42, 1997.

[12] S.G. Ghalamestani, T. Hilgert, L. Vandevelde, J. Dirckx and J. A.A.Melkebeek, Magnetostriction measurement by using dual Heterodyne Laser Interferometers. *IEEE Trans.Magn.*, **46**, 505-5ß8, 2010.

[13] L.Zhu, Q.Yang and R.Yan, Numerical analysis of vibration due to magnetostriction of three phase transformer core. *Proc. 6th Int.Conf. Elmagn. Field Probl.Applic.*, 1-4, 2012.

[14] S.G. Ghalamestani, L. Vandevelde, and J.A.A.Melkebeek, Identification of transformer core vibrations and the effect of third harmonic in the electricity grid. *Int. J.El.Comp.Energ. Commun. Eng.* **8**, 881-884, 2014.

[15] S.G.Ghalamestani, L.Vandevelde, J.J.J. Dirckx, P.Guillaume, and J.A.A. Melkebeek, Magnetostrictive deformation of a transformer:A comparison between calculation and measurement. *Int.J.Appl.El.Mech.* **44**, 295-299, 2014.

International Conference on Engineering Vibration
Ljubljana, Slovenia, 7-10 September 2015

NUMERICAL MACC-MODELING OF LOCAL PEAK-TO-PEAK MAGNETOSTRICTION DISTRIBUTION IN A 3-PHASE TRANSFORMER CORE PACKAGE

Georgi Shilyashki*[1], Helmut Pfützner[1], Peter Hamberger[2], Martin Aigner[2], Erich Gerstbauer[1], Gerald Trenner[1]

[1]Inst. EMCE, University of Technology Vienna, Austria
shilyashki@tuwien.ac.at
[2]Transformers Linz, Siemens AG Österreich, Linz, Austria

Keywords: Transformer Cores, Magnetostriction, Numerical Modeling, Flux Distribution

Abstract. *For the estimation of regional distributions of magnetostriction (MS) in transformer cores, the current paper proposes a novel methodology. It is based on a four-step procedure that is summarized in the following: (i) Local induction values of the transformer core are calculated by a novel Multidirectional Nonlinear Equivalence Circuit Calculation (MACC) method. The method considers the multi-directional non-linearity and anisotropy of the material. Local induction values in a large number of flux paths can be determined not only in rolling direction (RD), but also in transvers direction (TD) in order to simulate rotational magnetization and also in diagonal direction (DD) in order to consider the effects of the overlaps. (ii) A look-up table is established for MS-values for the given type of material for different magnetization conditions. The values are obtained from catalogue data or measured e.g. by means of Single Sheet Tester or Rotational Single Sheet Tester. (iii) The corresponding MS-values are assigned to each investigated flux path, taking into account the peak induction in RD and TD. This yields a 2D map of magnetostriction (3D maps being possible as well). (iv) Numerical integration is performed for individual directions, e.g. for the axis of the yoke, in order to estimate the global displacements of the core. The method was tested for a 3-phase transformer core package stacked from GO material C130-30 with outer dimensions of 1200 mm. Minimum values below 1 ppm resulted for the limbs. As to be expected, maximal values up to the order of 10 ppm resulted in the T-joint due to rotational magnetization. The results are in rough agreement with experimental data of model cores.*

1 INTRODUCTION

In the recent years, due to high environmental awareness, the importance of audible noise of power transformers has become very significant for both industry and research, worldwide. It is well known that the audible noise, originating from power transformers can be separated into two main parts: the load noise, and the no-load noise. While the load noise comes mainly from the windings and from the cooling system of the power transformer, the second, more important part [1], the no-load noise is generated by magnetostatic forces and magnetostriction (MS). Regional MS measurements within a transformer core [2, 3] is very difficult, on one hand due to the fact that a clear distinction between MS and magnetostatic forces is not possible, since both have the same spectral components. On the other hand, the local strain values depend strongly on the state of the clamping. A slight change in the clamping may cause a significant change in the local strain values. However, for a very well-clamped core, it can be assumed that the main source of core noise is given by strain resulting from magnetostriction [2].

Since determination of regional MS values in real transformer cores proves to be a very difficult task, depending on many parameters, the determination tends to be restricted to measurements on Epstein strips [4] or on single sheet specimens [3, 5]. The samples are magnetized under exactly defined alternating or rotational magnetization patterns, simulating the magnetization conditions in different core regions, and the MS is measured by means of strain gauges or interferometry methods. All performed measurements show that the intensity of MS depends on type of the core materials. The highest values are detected for non-oriented materials, much lower ones for grain oriented and especially for highly grain oriented materials, due to the higher ordered texture. The measurements shows also that for a given material type, the magnitude of MS increased in a non-linear way with increased induction. Another factor that has a great impact on magnetostriction is the type of magnetization, alternating or rotational magnetization (RM). The strength of RM, defined by the axis ratio, according to

$$a = B_{TD}/B_{RD} \approx B_{TD}/B_{NOM}\,, \tag{1}$$

has a great impact on magnetostriction [3]. Under RM, related to AM, the peak-to-peak MS increases in a distinct way with a, especially for HGO-materials. In [3] it was also shown that the locus and the angular velocity of $\boldsymbol{B}(t)$ have only an insignificant impact on the intensity of MS, apart from effects on harmonics. Summarizing, for a given type of a material, we can assume that the peak-to-peak MS in RD λ_{RD} is a mere function of the maximal induction intensity in RD B_{RD} and the axis ratio a.

Based on the latter, we propose a novel methodology for evaluation of the regional peak-to-peak magnetostriction values in transformer cores. The basic idea is the following: For a given nominal induction, we determine numerically the local induction distribution not only in RD but also in TD and based on the regional calculated values we assign the corresponding peak-to-peak MS values, obtained from catalogue data or measured e.g. by means of SST (Single Sheet Tester) or RSST (rotational SST).

2 METHODOLGIES

2.1 Calculation of the local induction values

The here used method was tested for a 3-phase, 3-limb transformer core package stacked from grain oriented material C130-30 with outer dimensions of 1200 mm and stacking height of 100 mm (compare Figure 1). We assume for the overlap regions a multi-step lap construction.

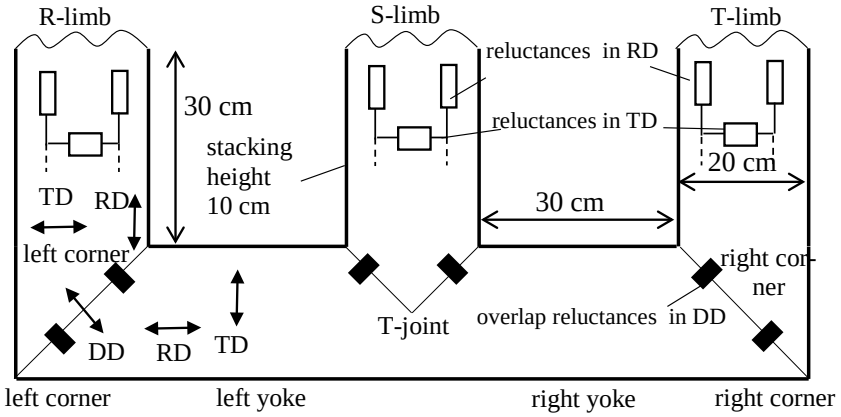


Figure 1: Investigated 3-phase, 3-limb transformer core package, stacked from GO-material C130-30 after [6]. A few of the reluctances in RD, TD and DD are symbolically depicted.

Local induction values B of the transformer core are calculated by a novel Multidirectional Nonlinear Magnetic Equivalence Circuit Calculation (MACC) method [6,7]. The basic advantage of the method is the consideration of the multi-directional non-linearities and the material anisotropy. The model takes also into account the impact of the overlaps of corners and T-joints. In the case of the given 3-phase transformer core, the model consider 47 sub regions located in the lower core half (the upper half shows symmetry). Each sub-region is modeled by a reluctance value, assuming homogeneity in the small sub area. Overall, for the given core package, 47 reluctances are given, 27 in rolling direction (RD), 14 in transverse direction (TD) and six ones in diagonal direction (DD). Using the duality principle, an equivalent electrical circuit is established.

As inputs parameters, the MACC-software uses the nominal induction value B_{NOM}, the non-linear permeability values μ_{RD} and μ_{TD} of the material in RD, and in TD, respectively as well as the corresponding non-linear dependency of the overlap reluctances from the induction $R_{DD} = f(B_{DD})$. The necessary data for the permeability and the overlap reluctances was taken from [8 (Figure 2a,b)] and [6 (Figure 3c)].

The calculation of the local induction values is performed using the MACC-software developed in Matlab. The basic idea of the software is to vary all considered local induction values as long until they all agree to the corresponding local permeability values [6]. The simulation is performed for 360 instants within one period of magnetization. The maximal local induction values B_{RD} in the period are calculated for each local sub region. For the calculation of the axis ratios a, the maximal induction values B_{TD} in TD are divided by the nominal induction according to Eq. (1).

2.2 Establishment of a look-up table with magnetostriction data

As mentioned in the introduction, a look-up table with the MS values λ can be established using catalogue values for the investigated type of material. However, catalogue data, especially for MS under rotational magnetization, is very restricted. Here, the look-up table was filled with data, that was extrapolated from measurements reported in [3]. The measurements were performed by means of a Rotational Single Sheet Tester under exactly defined magnetization patterns. According to Figure 2, λ_{RD} increases in a strong non-linear way for both, increased induction (Figure 2a) and increased axis ratio (Figure 2b).

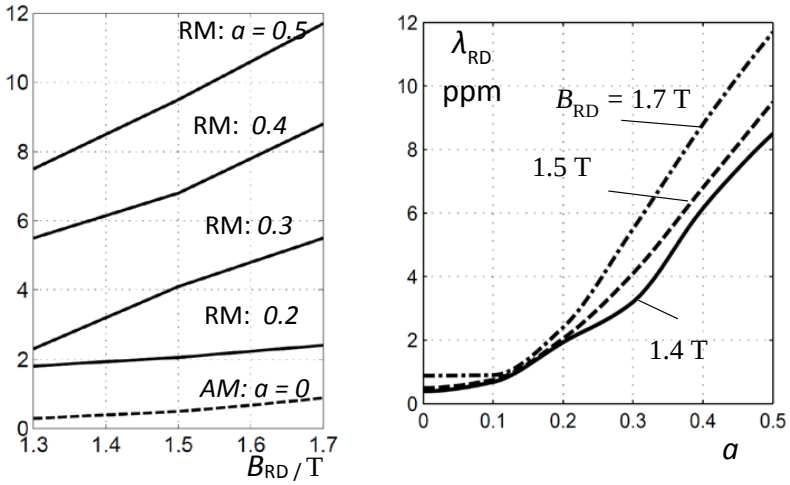


Figure 2: Magnetostriction data, measured by means of rotational single sheet tester after [3]. The data is used for the establishment of the look-up table. (a) λ_{RD} as a function of the induction B_{RD} in RD for different axis ratios a. The data was extrapolated from [3, Figure 5 and Figure 12a]. (b) $\lambda_{,RD}$ as a function of the axis ratio for different peak inductions B_{RD}. The data was extrapolated from [3, Figure 5 and Figure 12a].

As mentioned, the basic idea of the current publication is to evaluate numerically the maximal values of the local inductions B_{RD} in RD, and the corresponding axis ratios a, which result from Eq. (1) According to Figure 2, if the two parameters B_{RD} and a are known, the corresponding peak-to-peak MS value is assigned automatically.

3 LOCAL DISTRIBUTION OF MAXIMAL LOCAL INDUCTION AND MAXIMAL AXIS RATIO OF ROTATIONAL MAGNETIZATION

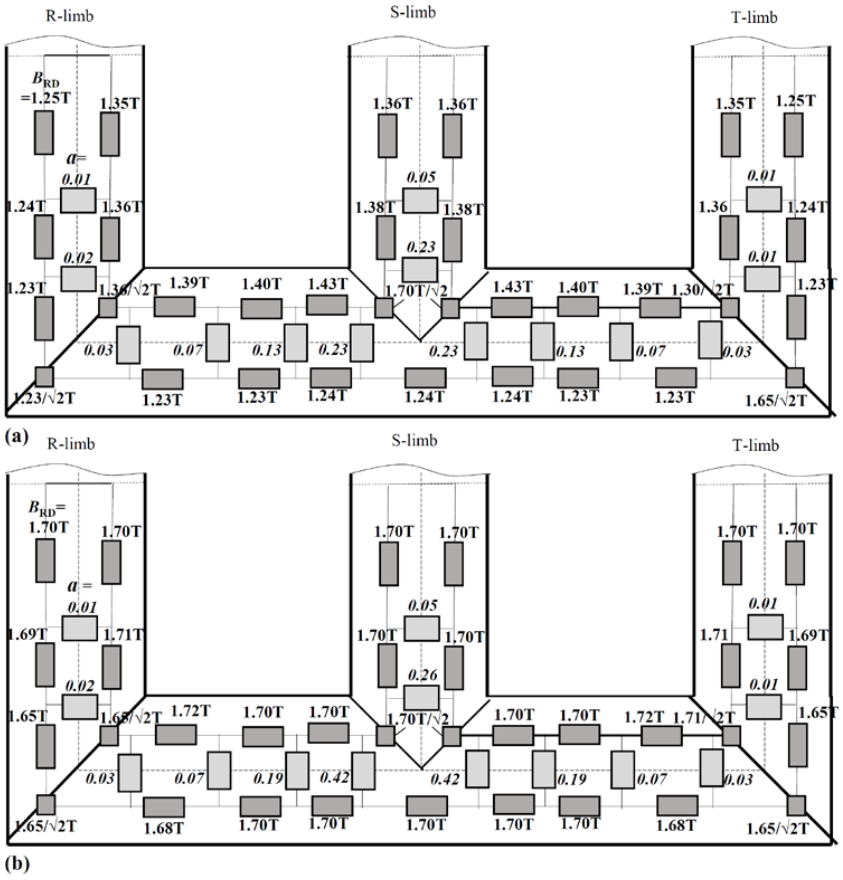


Figure 3: Maximal local induction values B in rolling direction and maximal local axis ratios a in *italic* for
(a) B_{NOM} = 1.3 T and
(b) B_{NOM} = 1.7 T.

A detailed flux distribution analysis of a 3-phase, 3-limb transformer core for important instants of time and also the corresponding rotational magnetization patterns were presented in [8]. Since the current paper is restricted to the evaluation of the regional peak-to-peak magnetostriction, as explained in introduction, only the maximal induction values B in RD along the inner and outer path and the axis ratios a, resulting from the interaction between the two paths are of interest. Figure 3 shows the local values B and the local values a for B_{NOM} = 1.3 T and 1.7 T.

For the case of B_{NOM} = 1.3 T, the calculation yields an uneven distribution of local inductions in the outer limbs. Due to the shorter path length, the induction along the inner path is even higher than B_{NOM} and are about 10% higher than the corresponding inductions of the outer path. The non-linear overlap reluctances of the corners cannot balance the effect of the shorter path length, since the corner induction values are very low for B < 1.4 T (compare [6, Figure 3c]). The inhomogeneity of the flux distribution is even stronger in the yoke where the differences of B between the inner and the outer path show increases up to about 15%.

The strong anisotropy of the GO material and the impact of T-joint reluctances cause a very complex flux distribution in T-joint area in connection with a strong rotational magnetization. Figure 3a shows that the axis ratio a increases from 0.03 shortly after the corner area, up to 0.23 in T-joint, supported by the non-linear permeability of the transverse direction (compare [8, Figure 2b]).

In contrast to the case of B_{NOM} = 1.3 T, for B_{NOM} = 1.7 T the maximal induction distribution along the inner and the outer path is evenly distributed in all core regions and equals the nominal induction. The effect of the shorter inner path length is effectively compensated by the non-linear overlap reluctances of the corners that are high for B > 1.3 T. The balancing effect for 1.7 T is much stronger, due to the strong non-linear dependence $R_{DD}(B_{DD})$. The rotational magnetization with axis ratio up to a = 0.42 is significantly higher than the corresponding RM for B_{NOM} = 1.3 T.

4 LOCAL DISTRIBUTION OF PEAK-TO-PEAK MAGNETOSTRICTION

Proved by previously performed measurements, the model assumes that the peak-to-peak magnetostriction λ_{RD} depends only on maximal local value of the induction in rolling direction and the axis ratios of rotational magnetization. For the evaluation of λ_{RD}, we assume that RM is restricted only to lamination centers, representing areas where the inner and outer flux paths interact between each other. It means that the values of λ_{RD}, illustrated at the edges of the transformer core, are a mere function of B_{RD} in the corresponding region, assuming a = 0. On the other side, for the assignment of MS-values to the elements in the lamination centers, not only an axis ratio a, but also the corresponding value B_{RD} is needed. For that purpose, for each element in TD, we take the mean induction value from the four surrounding elements in rolling direction.

Figure 4a shows a strong uneven regional distribution of the resulting MS values λ_{RD} in the outer limb and in the yoke for B_{NOM} = 1.3 T. The values from the regions close to the window side are roughly twice as large as that from the periphery, while the corresponding induction values differ only in the range between 10% and 15% (compare Figure 3a). The reason is the strong nonlinearity of the function $\lambda_{RD}(B_{RD})$ (Figure 2 a).

In the T-joint region, as expected, λ_{RD} increases distinctly due to the strong rotational magnetization with a = 0.23. λ_{RD} is about 2 ppm, which is about seven times higher than the values in the middle part of the limb, where we observe mere alternating magnetization. Another interesting effect was observed in the T-joint. Despite of the identical axis ratio (a = 0.23), the local λ_{RD} value in the T-joint at the side of middle limb is higher than λ_{RD} at the side of the yoke due to the higher local inductions of the surrounding elements in RD. The higher axis ratio at the side of the yoke is among others a result of the nonlinear permeability function $\mu_{RD}(B_{RD})$, having a maximum close to 1.2 T.

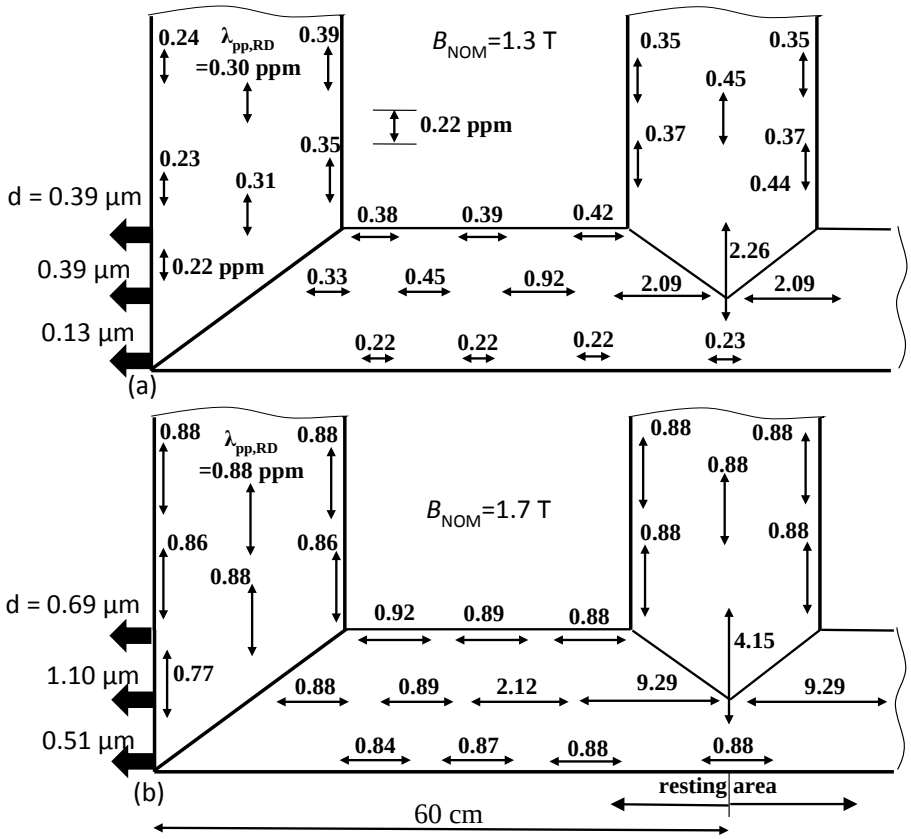


Figure 4: Regional distribution of peak-to-peak magnetostriction λ_{RD} in ppm for the rolling direction. Due to symmetry the corresponding values in the T-limb are not illustrated. The increases of λ_{RD}, related to the lowest value (λ_{RD} = 0.22 ppm) are given through the lengths of the double arrows in logarithmical scale. The maximal global peak-to-peak displacements *d* are given as well for
(a) B_{NOM} = 1.3 T and
(b) B_{NOM} = 1.7 T.

In contrast to 1.3T, for B_{NOM} =1.7 T, in correlation to the even distribution of the local induction values B_{RD} (Figure 3b), Figure 4b shows much more homogeneous distribution of the local MS-values with $\lambda_{pp,RD} \approx 0.9$ ppm for almost all core regions, except the T-joint. The reason is the much stronger balancing effect of the overlap reluctances of the corners, providing homogeneous flux distribution and in particular also the approaching saturation.

However, the even MS-distribution should be considered very carefully. It should be stressed that, one can expect for 1.7 T enhanced distortion of the time-course of local induction values, since for B_{NOM} = 1.3 T, the distribution is strongly inhomogeneous. It means that the inhomogeneous state is passed during the cycle of magnetization. In terms of magnetostriction, higher harmonics have to be expected, having a great impact on the audible noise [10], considering the physiological characteristics of the human ear.

Due to the strong RM, the highest values, as for the case of B_{NOM} = 1.3 T are observed in T-joint with λ_{RD} approaching the order of 10 ppm. However, while for B_{NOM} = 1.3 T the rela-

tive increase of MS is about seven, for 1.7 T it is even higher than ten. This is due to the fact, that for 1.7 T we observe much stronger RM with $a = 0.42$ compared to 0.23 for 1.3 T.

For the calculation of the maximal global peak-to-peak displacement d, the corresponding lengths in the yoke were considered. A rough numerical integration was performed for three individual axes of the yoke: inner, middle and peripheral direction (compare Figure 4). However, for the evaluation of d of the inner and middle axis, the peak-to-peak MS in TD of the middle and outer limb were also needed. They were derived from the corresponding peak-to-peak values, using the rough relation $\lambda_{TD} = 0.7\ \lambda_{RD}$ (from [9]).

The results in Figure 4 are based on the assumption of a resting area in the T-joint. They show, that the global displacements d for $B_{NOM} = 1.7$ T are much higher than the corresponding ones for $B_{NOM} = 1.3$ T. Furthermore, the middle axis, especially for 1.7 T, is much stronger affected, due to the very high magnetostriction in T-joint.

Measurements performed at ten local positions at a surface of 3-phase, 3-package model transformer core, stacked from grain oriented material C130-30 showed simillar trends (compare Figure 5) especially for the T-joint region and the outer and peripheral package of the yoke. However, the values for the main and outer package of the corner, 2.2 ppm and 1.6 ppm respectively, are clearly higher than the corresponding values calculated by the model (Figure 4b, $\lambda_{RD} \approx 0.9$ ppm). These differences can be explained by the following:

- As mentioned in the introduction, by measurements direct in transformer cores not only the magnetostriction, but also the magneto-static forces are captured, which tend to be strong, especially in the overlap regions.
- Local strain values depend strongly on the clamping [3]. A slight change in the clamping-state may lead to a strong change of local strain values.
- A real transformer core represents a 3-dimensional magnetization system [11] with a very special flux distribution that cannot be considered by the model. The local strain values are influenced by the complex interaction of the different width packages.

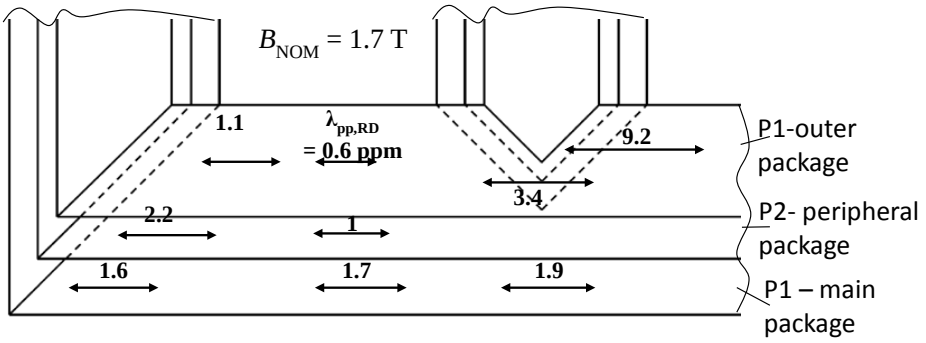


Figure 5: Regional strain distribution measured by mean of strain gauges at ten local position of 3-phase, 3-package transformer core, stacked from GO-material C130-30. Peak-to-peak magnetostriction values $\lambda_{pp,RD}$ in RD are illustrated for $B_{NOM} = 1.7$ T.

Summarizing, the presented numerical MACC-model for estimation of the local distribution of the peak-to-peak allows variation of material characteristics and core geometries in simplest and fast way, enabling effective tests of different types of cores, and providing reliable results in terms of local flux and magnetostriction distributions. However, due to above mentioned reasons, the model cannot replace corresponding measurements, that are very complicated as well.

5 CONCLUSIONS

The current work presents an application of a novel MACC-model for numerically calculation of the local peak-to-peak magnetostriction values in a 3-phase, 3-limb transformer core. The local MS-values are calculated for about 50 locations of the core, considering the nonlinearity of the permeability in RD and TD, as well as the impact of the overlap reluctances. Based on previous performed measurements, it was assumed that the peak-to-peak MS depends only on the maximal local induction value in RD and the maximal axis ratio of RM, neglecting the impact of locus and the angular velocity of $\boldsymbol{B}(t)$. The results show that while for B_{NOM} = 1.3T, the MS-values close to the core window are almost twice as high as the corresponding values in the periphery, for B_{NOM} = 1.7 T the MS-distribution tends to be homogeneous, due to both approaching saturation and the balancing effect of the overlap reluctances. The only exception is the T-joint region where extremely high MS values are predicted in the range of 10 ppm for B_{NOM} = 1.7 T. The numerically calculated values correlate well with performed measurements. However, the model cannot replace corresponding measurements in a real transformer core, due to existing magnetostatic forces, differences of clamping, as well as complex interactions between packages of different width.

ACKNOWLEDGEMENT:
This work was supported by the Austrian Research Promotion Agency FFG under Project 834159.

REFERENCES

[1] B. Weiser, H. Pfützner, and J. Anger, Relevance of magnetostriction and forces for generation of audible noise of transformer cores. *IEEE Trans.Magn.* **36-5**, 3759 - 3777, 2000.

[2] G. Shilyashki, H. Pfützner, F. Hofbauer, D. Sabic, V. Galabov, Magnetostriction distribution in a model transformer core. *J.El.Eng.* **61-7s**, 130-132, 2010.

[3] G. Shilyashki, H. Pfützner, J. Anger, K. Gramm, G. Hofbauer, V. Galabov, and E. Mulasalihovic, Magnetostriction of transformer core steel considering rotational magnetization. *IEEE Trans.Magn.* **50-1**, 840015, 2014.

[4] S. Somkun, A. Moses, P. Anderson, and P. Klimczyk, Magnetostriction anisotropy and rotational magnetostriction of a nonoriented electrical steel. *IEEE Trans.Magn.* **46-2**, 302-305, 2010.

[5] M. Yamagashira, D. Wakabayashi, and M. Enokizono, Vectro Magnetic Properties and 2-D magnetostriction of various electrical steel sheets under rotating flux condition. *IEEE Trans.Magn.* **50-4**, 6100404, 2014.

[6] H. Pfützner, G. Shilyashki, G. Trenner, E. Gerstbauer, Multi-directionally non-linear magnetic equivalence circuit calculation (MACC) of rotational magnetization intensity in transformer cores. *IJAEM*, submitted 2015.

[7] H. Pfützner, Proccedure for the calculation of 3-dimensional induction distribution (in German), AT patent, pending, reg. 2014.

[8] G. Shilyashki, H. Pfützner, E. Gerstbauer, G. Trenner, P. Hamberger, M. Aigner. MACC-simulation of local distributions of rotational magnetization patterns in a transformer core package, *IEEE Trans. Magn.*, submitted 2015.

[9] G. Shilyashki, *Magnetostriction of model transformer cores*. TU-Wien, PhD-Thesis, 2013.

[10] A. Moses, Measurement of magentostriction and vibrations with regard to transformer noise. *IEEE Trans.Magn.*, **10**-**2**, 154-156, 1974.

[11] H. Pfützner, G. Shilyashki, P. Hamberger, M. Aigner, F. Hofbauer, M. Palkovits, G. Trenner, E. Gerstbauer, I. Matkovic, V. Galabov, Automatic 3-D building factor analyses of a grain-oriented model transformer core. *IEEE Trans. Magn*. **50**-**4**, 8400604, 2014.

11th International Conference on Engineering Vibration
Ljubljana, Slovenia, 7–10 September 2015

DEVELOPMENT OF NUMERICAL MODEL FOR COMPUTATION OF POWER TRANSFORMER NOISE

Gregor Čepon*[1], Miha Nastran[2], Janko Slavič[1], Miha Boltežar[1]

[1]University of Ljubljana, Faculty of Mechanical Engineering, Aškerčeva 6, 1000 Ljubljana Slovenia
gregor.cepon, janko.slavic, miha.boltezar@fs.uni-lj.si
[2]KOLEKTOR Etra d.o.o., Šlandrova ulica 10, 1000 Ljubljana, Slovenia
Miha.Nastran@kolektor.com

Keywords: Noise, Power transformer, Magnetostriction, Lorentz forces

Abstract. *The prediction and the reduction of power-transformer noise are of increasing interest for the electrical power industry. In this paper the recently developed calculation scheme for numerical prediction of vibroacoustic properties of an oil-insulated power transformer is presented. Finite-element and boundary-element methods have been effectively applied to predict multi-physical nature of the power-transformer noise. The numerical model is capable of predicting the load and no-load noise, the electromagnetic field, the mechanical displacement field, as well as the acoustic pressure field. It is based on newly developed experiments, made in connection with original methods for modeling the magnetostriction and the dynamics of laminated structures. Finally the numerical model is implemented in the form of engineering software that enables geometrical, functional and technological optimization analyses.*

1 INTRODUCTION

For a long time, the energy efficiency of power transformers was by far the most important criteria when developing new products. However, in recent years this has changed as power transformers are frequently being located close to urban areas. For this reason, the sound emissions have to fulfill strict, low-noise standards. Therefore, the prediction and the reduction of power-transformer noise are of increasing interest for the electrical power industry. The manufacturing process for a power transformer lasts for several months, and only when the transformer is completely assembled can the noise level can be measured. Furthermore, any design changes at the manufacturing stage are demanding and, as a result, can be very expensive. This means that the manufacturer is at significant risk of not achieving the noise requirements and, therefore, can be subject to financial penalties. From the perspective of noise reduction it is essential to identify the sources of the noise and the way in which it is transmitted through the system. A simplified picture reveals that the magnetic field is generated by the coils [1] that are exposed to electromagnetic forces. Then, due to the alternating magnetic field, the core is exposed to the magnetostrictive effect [2], which leads to increased levels of vibration. These vibrations are transmitted via the cooling oil onto the transformer housing, which then radiates the vibrations in the form of acoustic noise to the environment. The transformer noise comes mainly from the following sources [1]: (1) the no-load noise caused by the magnetostrictive strain of the core laminations; (2) the load noise caused by the Lorentz forces resulting from the interaction between the stray magnetic field of the current-carrying coil conductors; and (3) the noise produced by the fans and the oil pumps. Since experiment-based investigations of the noise emitted by the core and the coil are lengthy and costly processes, there is an urgent need for an appropriate numerical simulation tool. Recently, the finite-element method (FEM) and the boundary-element method (BEM) have been effectively applied to model the sound field of an oil-insulated power transformer [3]. Using these methods it is possible to model the multiphysical nature of the power-transformer noise and the effects of different design parameters on this noise. Taking into account the research efforts in this field, here we present a detailed numerical model of a power transformer. The model is capable of predicting the load and the no-load noise, the electromagnetic field, the mechanical displacement field, as well as the acoustic pressure field. The basis of the model is our own experiments, made in connection with original methods for modeling the magnetostriction [4] and the dynamics of a laminated structure [5]. The developed numerical model is implemented in the form of engineering software that enables geometrical, functional and technological optimization analyses.

2 DEVELOPED NUMERICAL MODEL

In accordance with presented research efforts in the field of power transformer vibrio-acoustics the primary goal was to develop an integrated numerical model of power transformer that enables numerical simulations of vibrations and acoustic fields. Complexity of coupled magneto-structural-acoustic problems demands development of improved and more effective algorithms for solving multiphysical problems. All these research findings and developed numerical models are implemented in the form of computer software which enables simulations of noise and vibration for typical types of power transformers. The structure of numerical model is presented in Figure 1 and it consists of six modulus. The Core modulus is capable of predicting core vibrations due to the magnetostriction. The NN and VN coil modulus are used to simulate low and high voltage coil vibrations. The Tank modulus simulates the core and coil vibrations that are transmitted via cooling oil to the transformer housing. The Sound modulus predicts the

acoustic noise radiated to the environment due to the tank vibrations. The modulus 3D View is used for graphical representation and simulation of results.

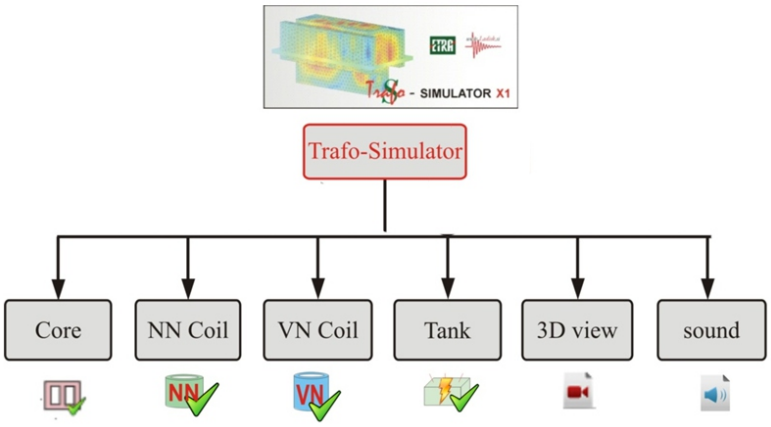


Figure 1: The structure of numerical model

2.1 CORE MODEL

In order to reduce the eddy currents and, consequently, any overheating, the magnetic core is usually made of a large number of thin electrical sheets. The magnetostriction of electrical steel is a phenomenon accompanying the magnetization process and presents a problem in terms of vibrations. It results in small deformations, where the change in the dimensions is independent of the magnetic flux direction and occurs with double the line frequency.
In order to predict the dynamic response of such structures it is necessary to develop a structural model of the laminated core, including an effective and reliable model of the contact, with friction between the metal sheets (Figure 2). Laminated structures are usually substantially more flexible than the equivalent homogeneous structures. They exhibit orthotropic behaviour and high levels of internal damping [1] due to interlaminar friction forces. A simple linear friction

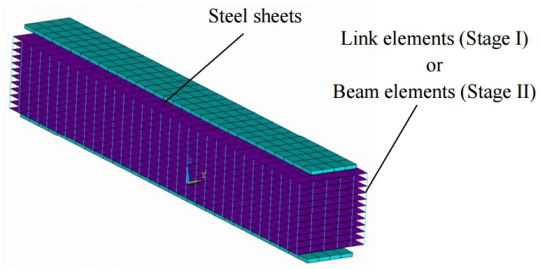


Figure 2: Finite-element model of a laminated stack

contact law was used to model the interactions between the steel sheets (Figure 3), which allowed the use of implicit methods in the framework of linear structural dynamics. The contact description is based on newly developed two-stage contact formulation [5]. In the first stage the

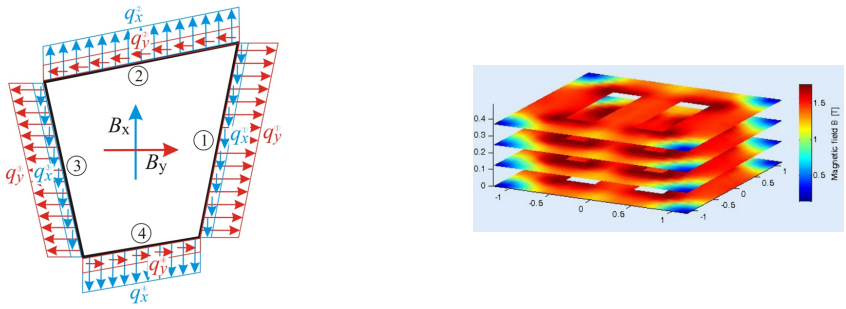
lamina surface pressure distribution is computed using static analyses. In order to correctly predict the distribution of the surface pressure the nonlinear contact stiffness has to be experimentally identified for a given height of the stack. In the second stage the link elements are replaced with beam elements (Figure 3b) because of their shear capability. A linear relation is assumed between the computed surface pressure and the beam shear modulus where the slope is defined by the stiffness contact parameter G_f. Sliding in the contact is represented by a beam tangential deformation characterized via a beam shear modulus; therefore, no actual sliding occurs in the numerical model. The identification of the contact parameters relies on the experimentally identified modal parameters [5]. The structural model of magnetic core enables the integration



a) b)

Figure 3: Modeling of the contact; a) Contact stage I, b) Contact stage II.

with the newly developed model of magnetostriction as it is presented in [4]. This integration is not straightforward, as different numerical methods are used in order to solve the magnetic and structural problems. The phenomenon of magnetostriction is modeled by introducing the so-



a) b)

Figure 4: Model of magnetostriction; a) Magnetostrictive in-plane nodal forces on a single finite element, b) Core magnetic field.

called magnetostrictive forces (Figure 4a). The magnetostriction model takes account of each harmonics of the magnetostriction separately. The following power approximation was found to accurately characterize the amplitude of harmonics [4]:

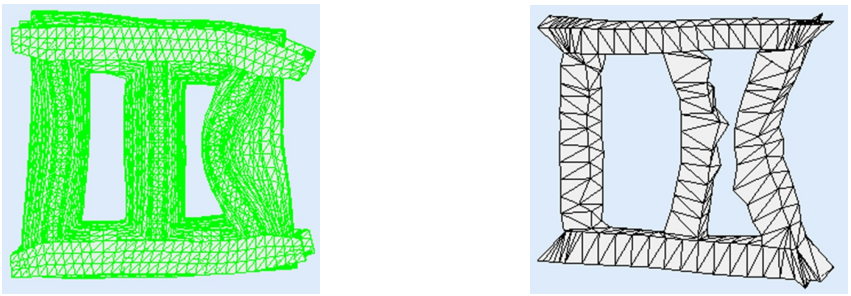
$$\varepsilon = k_B^i B^n, \tag{1}$$

where B is the amplitude of the magnetic flux density (Figure 4b) in given direction. Variable k_B^i presents the magnetostriction coefficient and n is the power of the approximation. Both parameters are identified for given harmonics based on single-axis magnetostriction measurement

as it is presented in [2]. The distributed forces due to the magnetostriction on arbitrary defined finite element can be computed as:

$$\left\{ \begin{array}{c} q_x \\ q_y \end{array} \right\} = h\,E\,k_B \left[\begin{array}{cc} 1 & -\nu \\ -\nu & 1 \end{array} \right] \left[\begin{array}{cc} 1 & -\nu_B \\ -\nu_B & 1 \end{array} \right] \left\{ \begin{array}{c} B_x^n \\ B_y^n \end{array} \right\}, \tag{2}$$

where ν is the Poisson's ratio, E is the elastic modulus and h is the thickness of the metal sheet.



a) b)

Figure 5: Response of the core to the magnetostriction at 300Hz; a) Numerical model b) Measurement

Ratio between the strain in the direction perpendicular to the magnetisation and the strain in the magnetisation direction is denoted as ν_B.

By using the proposed method it is possible to calculate the vibration of the core by considering the different modes, the complex forces exciting a three-phase transformer, and finally the response of the core due to the magnetostriction at fundamental harmonics (100Hz) and higher harmonics.

In Figure 5 the core response at 300Hz for the power transformer with rated power of 20MVA is presented. Good agreement between numerically and experimentally obtained operational deflection shape is observed. In Figure 6 the average amplitude of response at fundamental and higher harmonics is also presented. Numerical model together with experimentally obtained magnetostriction properties gives good prediction of response for first four harmonics which have the biggest influence on the no-load power transformer noise.

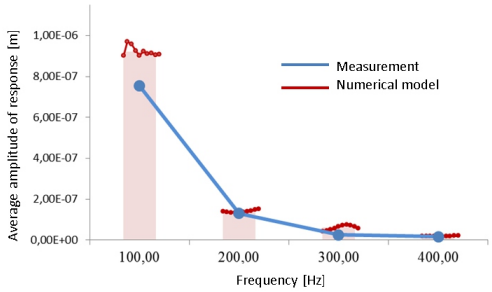
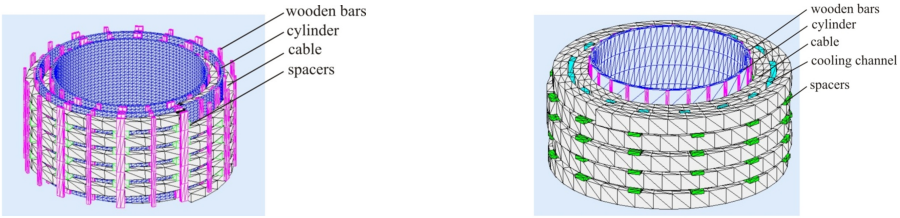


Figure 6: Displacement response of core

2.2 COIL MODEL

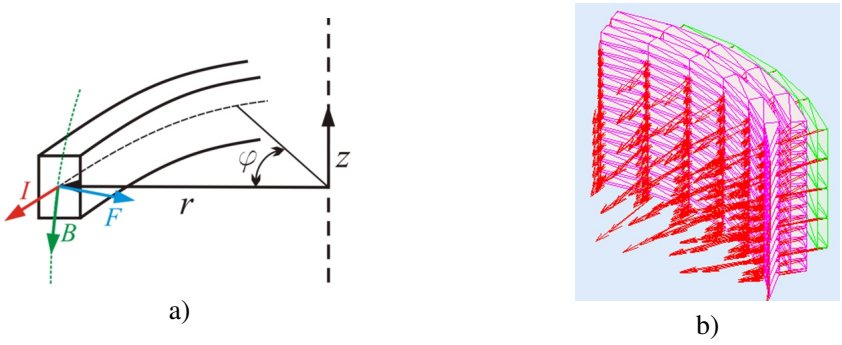
The load-based noise is generated by magnetic forces between coil windings that cause the vibration of entire coil. The windings of power transformers are constructed using several winding technologies, e.g., helix-like layer windings (for LV winding) and spiral-like coil windings (for HV winding), as shown in Figure 7. The developed structural model is based on Finite element method and accounts for different cable geometry together with contact formulation between cable and wooden parts (spacers, bars, cylinder, etc.) The Lorentz forces that acts due



a) b)

Figure 7: Coil model; a) Low voltage coil, b) High voltage coil

to the interaction between the transformers stray magnetic field and the current-carrying winding loops are presented in Figure 8. The interaction of these magnetic forces with mechanical structures causes vibrations. As the vibrations of the coil are difficult to measure at rated power



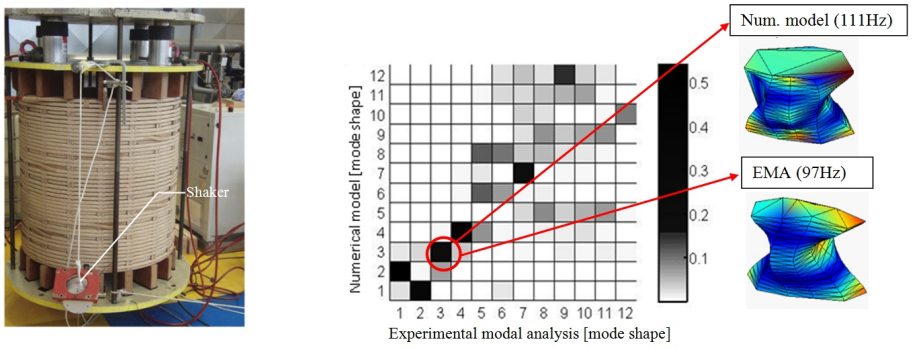
a) b)

Figure 8: Electromagnetic forces; a) Forces acting on current carrying conductor, b) Applied forces on HV coil

only the validation of the structural model was preformed. The experimental setup is presented in Figure 9a and the corresponding MAC analysis is presented in Figure 9b. It is evident that especially for lower frequencies the agreement between numerically and experimentally obtained mode shapes is acceptable.

2.3 Tank vibrations and the radiated sound field

The vibrations generated by the magnetic core and the coil are transmitted through the oil onto the external walls of the transformer tank. This represents a typical problem of the interaction between a flexible structure and a stationary fluid. Such an interaction is complex and



a) b)

Figure 9: Validation of coil structural model; a) Experimental setup for EMA, b) MAC analysis.

influences the dynamic response of the whole system as well as the transmission of vibrations through the core and the coils to the tank of the power transformer (Figure 10). Due to its mass and damping properties, the impact of the surrounding fluid is more pronounced on the dynamic response of the whole system. In the second step of the developed calculation scheme,

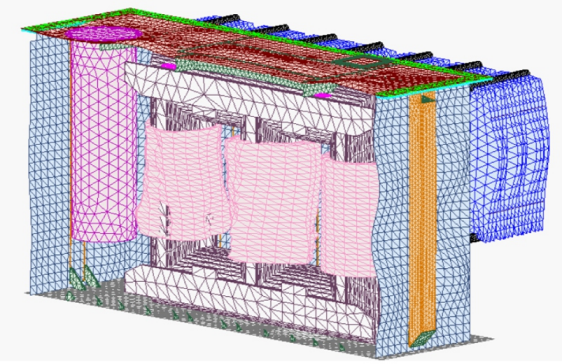
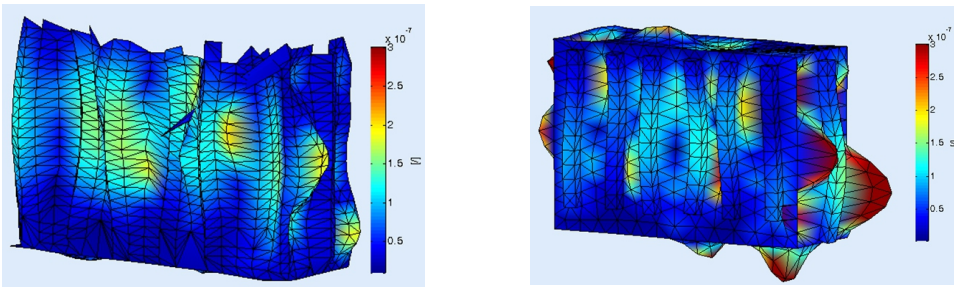


Figure 10: Model of tank including core and coil excitation

the previously calculated core- and winding-surface displacement are taken as the mechanical excitation in a 3D acoustic-mechanical FEM of the complete oil-filled tank. Furthermore, in the oil-filled tank model, the 120 phase shift between the three windings is taken into account. The vibrations from the core and the coils are transmitted via the insulation oil to the transformer tank. The surrounding oil is discretized by acoustic finite elements. The thin wall of the tank acts as an acoustic membrane, which causes an amplification and modification of the pressure waves, and especially in the case of resonance, an increased emission of noise. The tank should be designed in such a way as to avoid any unnecessary noise increase due to resonance. In Figure 11 the numerically and experimentally obtained tank vibrations due to the core excitation at fundamental harmonics (100Hz) are presented. The amplitude of vibrations as well as the response shape are in good agreement. In the final step, the previously calculated vibrations of the tank surface are applied as the mechanical excitation in the final acoustic simulation to calculate the radiated transformer noise. For the computation of the free-field sound radiation,



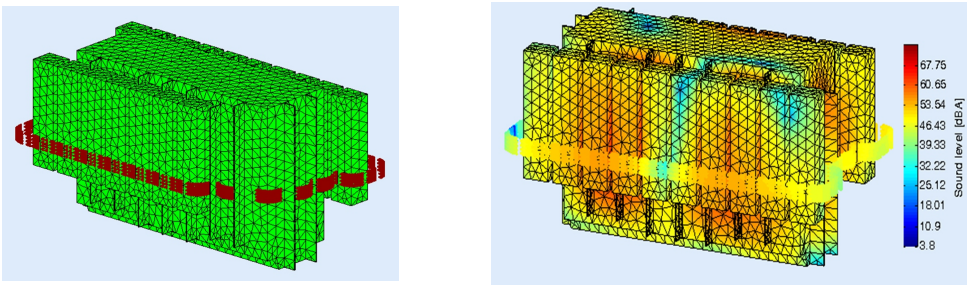
a) b)

Figure 11: Tank vibrations due to the core excitation at fundamental harmonics (100Hz); a) Measured operational deflection shape, b) Numerically obtained operational deflection shape.

the complete structure of the tank was discretized using boundary elements (Figure 12a). As the air surrounding the transformer has a negligible effect on the vibrations of the tank, a BEM is well suited for predicting the radiation of noise based on surface displacement field. For time-harmonic acoustic waves in a homogeneous isotropic acoustic medium E, acoustic pressure p is governed by the Helmholtz equation:

$$\Delta^2 p(x) + k^2 p(x) = -j\rho_0 \omega q, \qquad x \in E, \tag{3}$$

where q represents the distribution of external acoustic sources. In order to compute sound field the BEM method is applied and the final code is implemented and optimized for speed in FORTRAN language. Along with surface mesh the surrounding external points are proposed at the location where standard noise measurement is preformed and serves as reference of power transformer noise level. Thus, numerical model can predict mean sound pressure of no-load noise caused by core vibrations as well as load noise caused by the coil vibrations. Here only the validation procedure for no-load noise is presented however the procedure is similar for load noise. In the first stage the proposed procedure to compute sound pressure was validated

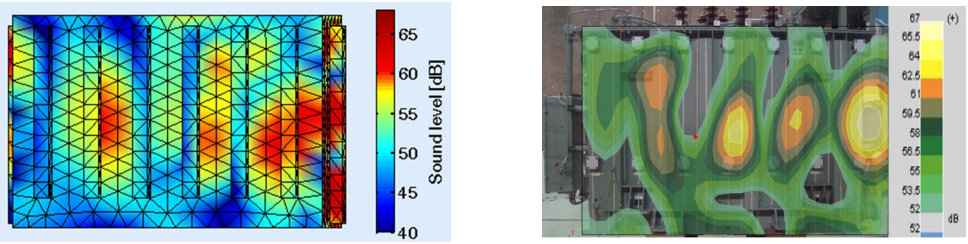


a) b)

Figure 12: Application of BEM to determine no-load noise; a) Surface discretization using boundary elements, b) Sound pressure field .

by measuring sound field by means of acoustic holography. The comparison of sound field pressure at 100Hz is presented in Figure 13. From the presented results it can be observed that

proposed procedure provides good prediction of acoustic levels as well as location of sound sources. Finally the overall sound pressure L_{pA} obtained by measurement is compared by results



a) b)

Figure 13: Sound pressure on the tank external walls at 100Hz; a) Acoustic holography, b) Prediction of numerical model.

obtained with numerical model (Figure 14). Good agreement is observed, moreover the highest levels of sound are in both cases identified at 300Hz. Although the fundamental harmonic of excitation is at 100Hz, due to the A-weighting of the sound level the highest contribution to the cumulative sound is at 300Hz.

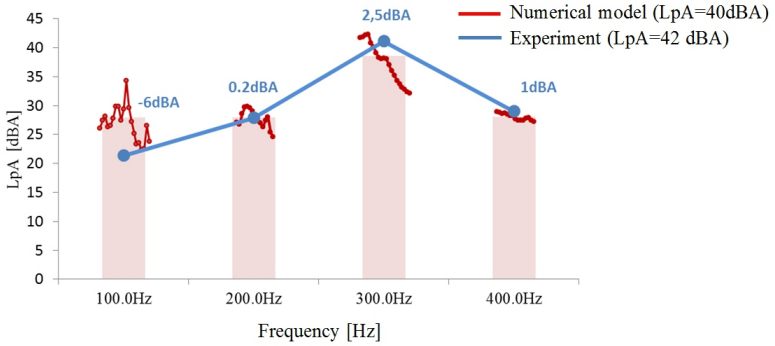


Figure 14: Overall sound pressure L_{pA}

3 CONCLUSIONS

In this paper a new numerical scheme is presented for the precise and efficient computer modeling of the load and no-load noise of the power transformers. From the perspective of noise generation, the main sources of noise are identified. Virtual design and the verification of power transformers will replace the time-consuming and very costly experimental testing. The presented computer simulations have been proven to be a useful tool for the prediction, investigation and reduction of power-transformer noise.

REFERENCES

[1] Rausch, M., Kaltenbacher, M.,Landes, H., Lerch, R. , Anger, J. , Gerth, J. ,Boss, P., Combination of finite and boundary element methods in investigation and prediction of load-controlled noise of power transformers, *Journal of Sound and Vibration* 2 (2001) 323–338.

[2] Javorski, M., Slavič, J., Boltežar, M., Frequency Characteristics of Magnetostriction in Electrical Steel Related to the Structural Vibrations, *IEEE Transactions on Magnetics* 48 (2012) 4727–4734.

[3] Ertl, M., Landes, H., Investigation of load noise generation of large power transformer by means of coupled 3D FEM analysis , *The International Journal for Computation and Mathematics in Electrical and Electronic Engineering* 26 (2001) 788–799.

[4] Javorski, M., Čepon, G., Slavič, J., Boltežar, M., A Generalized Magnetostrictive-Forces Approach to the Computation of the Magnetostriction-Induced Vibration of Laminated Steel Structures, *IEEE Transactions on Magnetics* 49 (2013) 5446–5453.

[5] Pirnat, M., Čepon, G., Boltežar, M., M., Introduction of the linear contact model in the dynamic model of laminated structure dynamics: an experimental and numerical identification, *Mech. mach. theor* 464 (2013) 144–154.

International Conference on Engineering Vibration
Ljubljana, Slovenia, 7-10 September 2015

ACOUSTIC FIELD INSIDE THE OIL-FILLED TRANSFORMER TANK MODEL AND ITS INFLUENCE ON THE OVERALL NOISE RADIATION

Michal Kozupa*[1], Grzegorz Kmita[1], Karolina Kolber[2]

[1] ABB Corporate Research, 13A Starowislna Str., 31-038 Cracow, Poland
{michal.kozupa, grzegorz.kmita}@pl.abb.com

[2] AGH University of Science and Technology, Faculty of Mechanical Engineering and Robotics, 30 Mickiewicz Ave., 30-059 Cracow, Poland
kkolber@agh.edu.pl

Keywords: Transformer noise, hydroacoustics, hydrophone, structure born noise, numerical analysis.

Abstract. *Vibration energy created in the active part of the oil-filled transformers is transferred to the tank walls, mainly through the fluid-structure interactions between insulating oil and structural parts as well as through mechanical couplings themselves. The question of how much vibration energy is transferred through oil and how much through mechanical connection remains unanswered. The paper describes the results of research on the propagation of acoustic waves inside the tank filled with transformer oil, in which a model transformer core was used as the source. Acoustic pressure inside the oil cavity was measured using a hydrophone, and the sound pressure level was then compared to the results of numerical prediction. The obtained good correlation allowed to describe the vibration pattern of the tank wall and to evaluate the propagation paths in the model.*

1 INTRODUCTION

The noise emitted by power transformer can be separated into two parts: caused by the magnetization of the core and by electromagnetic forces created by the magnetic field of the load current in the windings. In oil-filled transformers, vibration energy generated in active part is transferred onto the tank walls mainly in two ways: fluid and mechanical couplings. The question of how much vibration energy is transferred through oil and how much through mechanical connection is still lacking the answer.

The phenomenon of wave propagation inside oil-filled transformer tank can be mainly found in papers describing the propagation of partial discharge (PD) acoustic waves in power transformers [1-3]. Usually, the investigations are based on the finite element method (FEM) simulations or measurements on the transformer tank alone, therefore the authors of this publication performed especially interesting measurements inside the tank, in oil environment with hydrophone.

When the noise radiation from a large transformer is characterised both theoretically and experimentally, it can be shown, that the transformer radiation field can be described by the component of 100 Hz and its few first harmonic frequencies [4]. The phenomenon of acoustic wave propagation is very well described including acceleration measurements on tank wall, sound intensity measurements and correlation of both to predict far-field noise radiation. There are developed techniques for predicting noise generated by the power transformer [5,6]. In numerical modelling, solid-fluid interface is considered with mechanical stress of oil on the surfaces inside the winding. The study on influence of adding oil to the system showed changes in the resonance frequencies of the winding and its influence on the total noise radiation of the transformer [7].

This paper describes study on acoustic waves propagation inside the model transformer tank filled with transformer oil. The tank had reflective surfaces on the walls and the model magnetic core (active part) was used as the source of acoustic waves in this experimental setup. The aim for recognition the acoustic wave propagation in oil is to have clearer view on the vibroacoustic energy flow in such complicated system like the oil-filled transformer.

2 SOUND PRESSURE MEASUREMENTS IN OIL

2.1 Test setup

Measurement have been performed in free-field conditions in anechoic chamber with reflective plane at the floor. Tank model with dimensions of 860x460x550 mm filled with transformer oil was placed in middle of the anechoic chamber and a small magnetic core was used as source of harmonic vibrations. The core was placed inside the tank on a 3 mm thin vibro-isolating rubbercork mat at the bottom of the tank. Acoustic field measurements inside oil were performed with the use of a small, high-sensitivity transducer for making absolute sound measurements over the frequency range 0.1Hz to 180 kHz with a receiving sensitivity of −211 dB re 1V/μPa). The cavity of the oil volume was discretized by four heights W1 to W4 each having the matrix of 7 on 15 what eventually gave 26 to 105 measurement points, depending on the core presence in the measurement layer. The magnetic core supplied with 50 Hz voltage, placed on the middle of the bottom of the tank was acting as the harmonic sound and vibration source (Figure 1).

Acoustic pressure in air around the transformer tank was measured at 8 points using 8 microphones at one time.

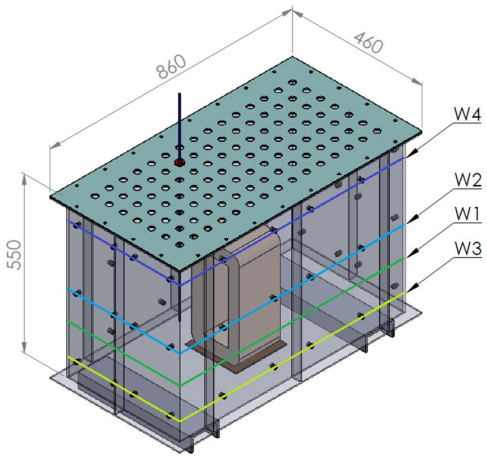


Figure 1: Geometry of the investigated transformer tank with core as a source, acoustic pressure inside the tank was measured at 4 heights, all heights are submerged in oil: W1 – ½ height of the core, W2 – ½ height of the tank, W3 – close to the bottom, W4 – above the core.

2.2 Results

Below, results of sound pressure level inside oil are cumulated in acoustic maps. Results show averaged level of sound pressure over the 10 Hz to 2000 Hz bandwidth and for harmonic frequencies 100 – 400Hz. The reference pressure value in oil was assumed 1µPa.

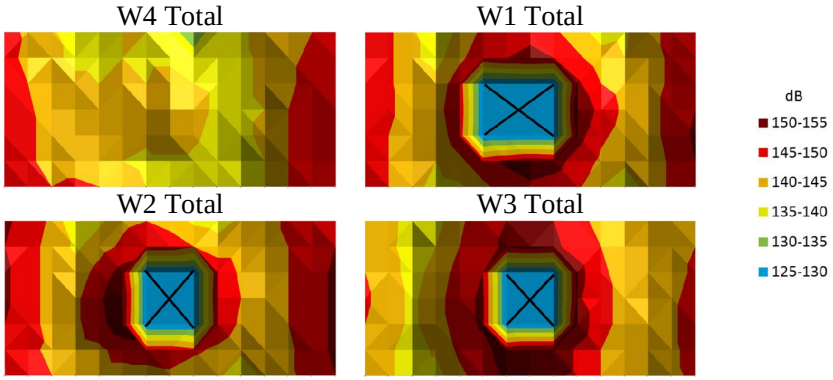


Figure 2: Total sound pressure level inside the tank filled with oil for 4 cross-sections in 10-2000 Hz bandwidth.

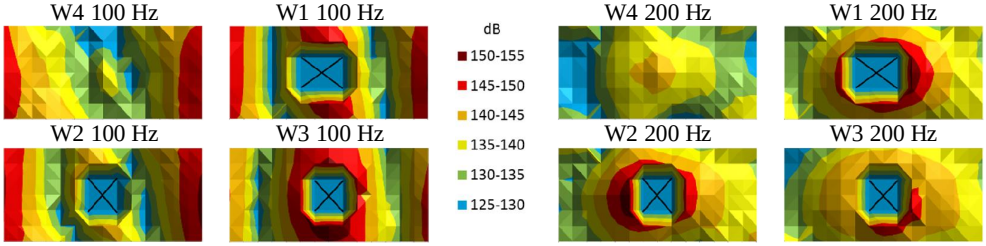


Figure 3: Sound pressure level inside the tank filled with oil for 100 Hz and 200 Hz at 4 cross-sections.

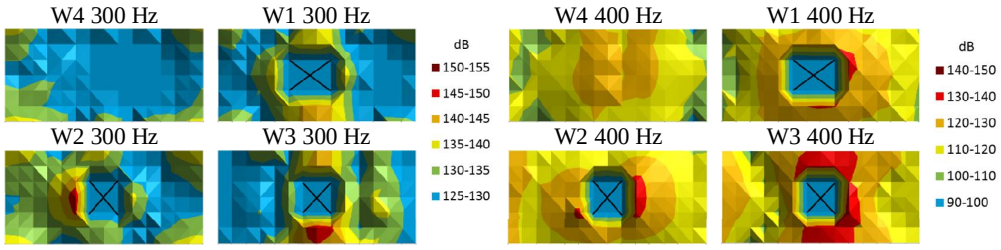


Figure 4: Sound pressure level inside the tank filled with oil for 300 Hz and 400 Hz at 4 cross-sections.

One can observe that for overall value in 10 – 2000 Hz bandwidth (Figure 3) acoustic energy is cumulated around the source (magnetic core), especially at W2, half height of the tank. Additional sound pressure increase is observed at the tank walls, but only short ones.

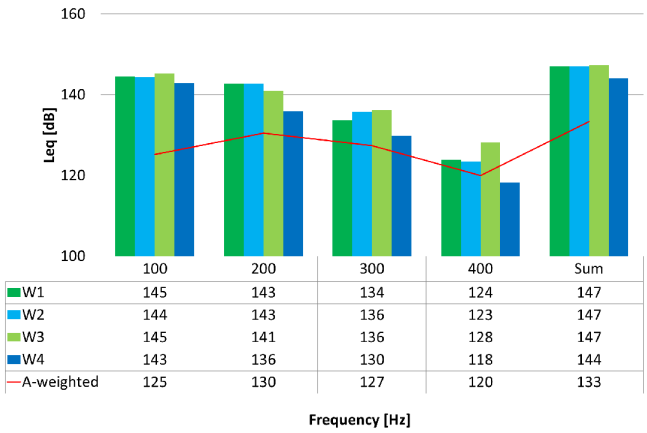
At 100 Hz frequency (Figure 4) results of sound pressure level show that in W2 height with the distance form source the level decreases, reaching again high levels close to the short tank walls. This increased pressure is most probably caused by the tank wall vibrations what will be further investigated in the paper after introduction of simulation results.

On Figure 5, where sound pressure levels at 200 Hz frequency are shown it can be seen that the highest pressure occurs around vibrating core. None of the results shows increase in sound pressure close to the tank walls as it was for 100 Hz frequency. In general, for the 200 Hz frequency, the closer to the vibration object the higher the sound pressure level. The reason for this is probably fact that there is viscous damping effect when acoustic wave is propagating in oil and reduce sound pressure with the distance from the core, though having very limited influence on the tank wall vibrations.

Results for 300 Hz frequency are summarized on Figure 6. One can see that for this particular frequency the levels are much lower, but there is phenomenon that was not visible in previous frequencies, that there are increased levels at the corners of the tank.

Figure 7 shows results obtained for 400 Hz and are presented in a different scale (90-150 dB) so the level maps are better visible and understood. Similar to 200 Hz the highest levels of sound pressure are visible around the core source but more evenly distributed in the oil volume. No influence of the tank wall vibrations is visible in the oil behaviour.

Below, Figure 8 summarizes averaged sound pressure levels at each measured height for particular frequency and summarized for the entire frequency bandwidth. One can see that the Leq (equivalent level) value is equal for W1 W2 and W3, W4 due to the biggest distance from the core is smaller. When looking at dominant frequencies in the spectrum 100 Hz frequency is the dominant and 200 Hz as the second, with level decreasing in higher frequencies. After applying A-weighting scale one can see, that 200 Hz becomes most significant in the frequency spectrum.



	100	200	300	400	Sum
W1	145	143	134	124	147
W2	144	143	136	123	147
W3	145	141	136	128	147
W4	143	136	130	118	144
A-weighted	125	130	127	120	133

Figure 5: The frequency spectrum and Leq values averaged for all measurement points in all four heights and spectrum corrected according to the A-weighting curve.

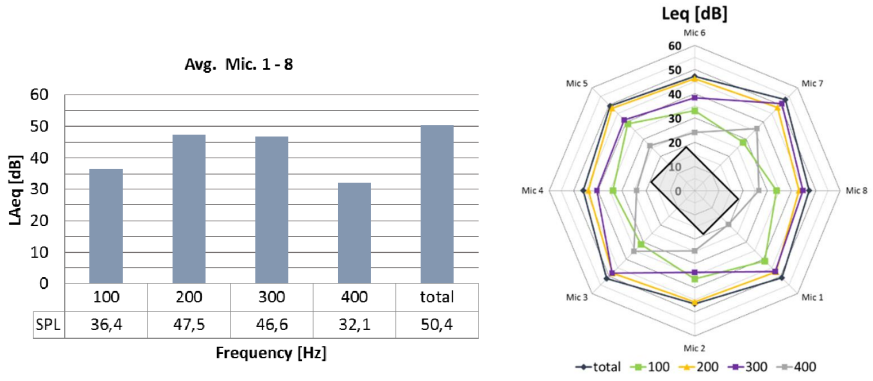
3 NOISE PROPAGATION IN AIR

To complement acoustic energy propagation of the oil-structure-air path, noise propagation around the tank model have been performed.

3.1 Measurement setup

Measurements of acoustic pressure in air around the transformer tank were made at 8 points using eight ½-inch microphones spaced at the distance of 30 cm from the tank walls (see fig. 11) at the half height of the tank. Diagrams present the averaged results for five series of measurements.

3.2 Results – SPL in air



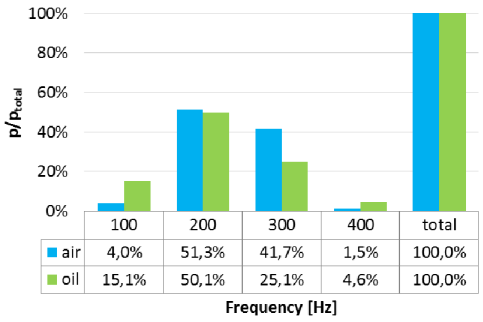
	100	200	300	400	total
SPL	36,4	47,5	46,6	32,1	50,4

Figure 6: Averaged level of sound spectrum and directivity in dominant frequencies

The dominant influence on total SPL in the air have components of 200 Hz and 300 Hz. The average SPL for 100 Hz is more than 10 dB lower than for 200 Hz and 300 Hz.

4 OIL TO AIR ACOUSTIC COMPARISON

To get the idea of acoustic wave propagation through three different media: oil, steel and air and try to estimate what is the impedance difference influence, the comparison of acoustic pressures inside and outside the tank was set. Below, the percentage values of pressure in particular harmonic frequencies are shown where the reference for both is the total value. It is well visible, that for 200 Hz frequency the acoustic energy propagation is on similar levels in oil and air while for 300 Hz the acoustic pressure outside the tank is amplified in comparison to the acoustic energy measured in oil. One of the possible explanation to this is the modal behaviour of the tank model structure. As can be seen in the numerical simulations at 200 Hz frequency the vibration pattern for the long side of the tank model is (2,2) mode. It is known that the even-even (eg. (2,2); (4,2); (4,4); …) modes radiate less energy in comparison to even-odd (eg. (1,2); (1,4); (2,3); …) and odd-odd (eg. (1,1); (1,3); (3,3); …) modes. At 300 Hz frequency vibration mode on the tank wall is (2,3) and even though the average acoustic pressure in oil is less than for 200 Hz we can observe better sound radiation from the tank wall and eventually higher sound pressure level in the air surrounding the tank.



	100	200	300	400	total
air	4,0%	51,3%	41,7%	1,5%	100,0%
oil	15,1%	50,1%	25,1%	4,6%	100,0%

Figure 7: Percentage values of acoustic pressure for particular harmonic in reference to total value.

5 NUMERICAL MODEL

5.1 Model description

Both structural and acoustic numerical simulations of the complete model have been performed in Abaqus software environment. The model consisted of three main parts: the core, which gives the mechanical excitation to the system, amplitude equal in all frequencies, oil coupled with the core and the tank, modelled with acoustic mesh and the tank model. The material parameters taken for calculations are the following, for steel material: density = 7850 kg/m3, Young's Modulus = 210 GPa, for mineral oil: density = 870 kg/m3, Bulk Modulus = 1,9 GPa. It is assumed that the mass of the core is equal to 28,8 kg. The model was excited with concentrated force of magnitude 10 N at the core cross-section in the vertical direction and fixed at the profiles.

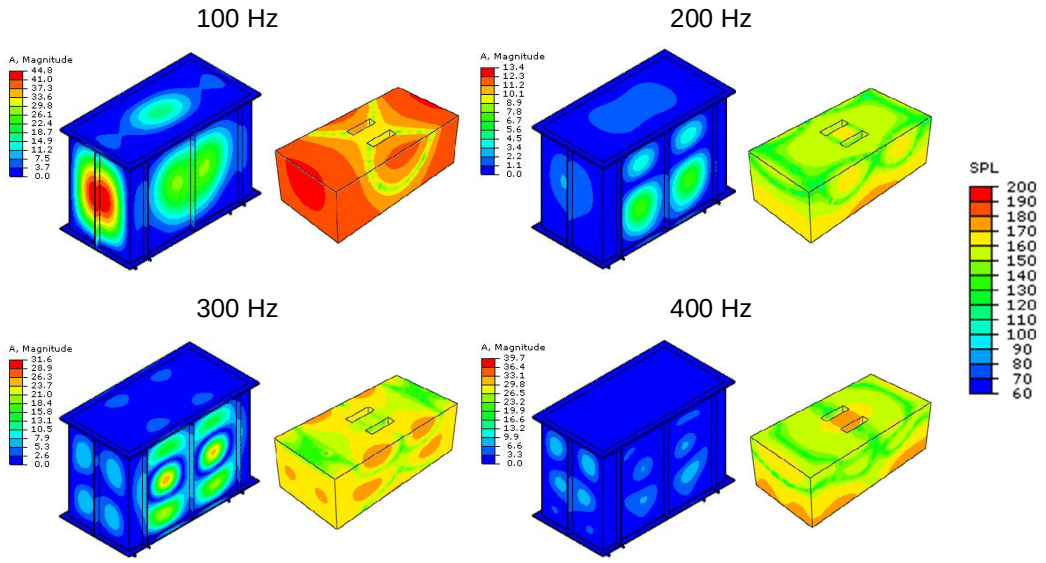


Figure 8: Vibration acceleration on the transformer tank and sound pressure level inside transformer tank filled with oil – FEM simulation results for harmonic frequencies.

The simulations results are qualitatively consistent with measurement results, the quantitative convergence would be hard to achieve due to specific frequency spectrum of the core source and in fact it would not bring additionally significant information.

The similarities that can be observed when comparison to the real measurements are the following:

- the increase of SPL was observed near to the core, the tank walls and the bottom
- the maximum value of the vibrations occurred at the shorter tank wall at 100 Hz as well in simulation as in measurements.
- also at 100 Hz were obtain the maximum values of the SPL in oil
- for the frequencies of 200, 300 and 400 Hz high vibration values and high SPL values were calculated near to the bottom of the tank.

All above bring the conclusion that the phenomena representation in the numerical model is close to the real state and future modeling of higher cavities and sizes can be based on the work done.

6 SUMMARY

The paper describes propagation of the vibration energy created in the active part of the oil-filled transformers and its transfer through the fluid-structure interactions in insulating oil and mechanical couplings to the tank walls. It has been investigated how much vibration energy is transferred through oil on the tank and eventually radiated as acoustic pressure. Acoustic pressure inside the oil cavity was measured and compared to the results of numerical prediction. The obtained good correlation allowed to describe the vibration pattern of the tank wall and to evaluate the propagation paths in the model.

REFERENCES

[1] D. Wotzka, T. Boczar and D. Zmarzly, *Analysis of Acoustic Wave Propagation in a Power Transformer Model*, Acta Physica Polonica A, Vol. 116 (3), 2009

[2] A. O. Akumu, F. Adachi, N. Kawaguchi, R. Ozaki, H. Ihori, M. Fujii, K. Arii, *A 3-D numerical simulation of partial discharge acoustic wave propagation in a model transformer*. IEEE Int. Symp. on Electrical Insulation, Boston (MA, USA), 2002.

[3] A.O. Akumu, N. Kawaguchi, R. Ozaki, H. Ihori, M. Fujii, K. Arii, *A study of partial discharge acoustic signal propagation in a model transformer,* IEEE Int. Symp. on Electrical Insulating Materials, 2001.

[4] R.S. Ming, J. Pan, M. P. Norton, S. Wende, H. Huang, *The sound-field characterisation of a power transformer,* Applied Acoustics 56 (1999) 257-272.

[5] M. Ertl, S. Voss, *The role of load harmonics in audible noise of electrical transformers,* Journal of Sound and Vibration, 333 (2014), 2253-2270.

[6] M. Rausch, M. Kaltenbacher, H. Landes And R. Lerch, J. Anger And J. Gerth, P. Boss, *Combination of finite and boundary element methods in investigation and prediction of load-controlled noise of power transformers*, Journal of Sound and Vibration (2002), 250 (2), 323-338.

[7] M. Kavasoglu, Load Controlled Noise of Power Transformers: 3D Modelling of Interior and Exterior Sound Pressure Field, Master Thesis, Royal Institute of Technology, Stockholm, 2010.

International Conference on Engineering Vibration
Ljubljana, Slovenia, 7-10 September 2015

VIBROACOUSTIC BEHAVIOR OF 120 MVA POWER TRANSFORMER

Michal Kozupa*[1], Michal Swiatkowski [2], Grzegorz Kmita[1]

[1] ABB Corporate Research, 13A Starowislna Str., 31-038 Cracow, Poland
{michal.kozupa, grzegorz.kmita}@pl.abb.com

2 ABB Sp. z o.o., 67/93 Aleksandrowska St., 91-205 Lodz, Poland
michal.swiatkowski@pl.abb.com

Keywords: Transformer noise, structure born sound, laser vibrometry, sound intensity scan, harmonic noise

Abstract. *The origin of the power transformer noise takes place in the active part itself, where electromagnetic phenomena are responsible for conversion of energy into mechanical vibration. The mechanical vibrations are then transferred to the surroundings which are, in the case of power transformers, oil cavity and tank. Eventually, the noise is radiated from the tank walls and also from the auxiliary equipment such as radiators, connection boxes etc. These elements, especially radiators, can have a significant influence on the noise radiation and in consequence sound power that is then calculated. This paper presents the results of detailed study on noise and vibration behaviour of a 120 MVA power transformer, which was investigated using sound intensity probe(s) and a laser vibrometer. The results of this study bring general conclusions, which can be transferred to a wider range of transformers and provide insight to the transformer noise from the perspective of vibration.*

1 INTRODUCTION

The continual expansion of urban areas is increasingly bringing people and electricity infrastructure into close proximity. The sound of electrical apparatus such as transformers must be kept under control to provide acceptable levels for residential areas. The noise in the transformer is a component of several sources of vibration and noise, namely core, windings, magnetic shield, etc. The vibrations are transferred by construction elements and the oil volume to the tank and emitted to the surroundings. The individual transformer parts generate the vibrations which can be classified by their own specific dominant frequency, which strictly depends on the network frequency, in which they work. In most of the world markets transformers are working in a 50 Hz voltage network, the notable exceptions are North and Central America, with the biggest markets in the USA and Canada, where 60 Hz is the network frequency. The primary source of noise in transformers, for the load conditions, are the windings and magnetic shields having a dominant vibration frequency of double the network frequency, which is 100 Hz or 120 Hz respectively. The secondary (still important) source of noise, occurs while the transformer works in no-load conditions, is the magnetic core which vibrates, depending on its size and geometrical properties, with a dominant frequency of 300 Hz (50 Hz network) and 360 Hz (60 Hz network).

This paper will show detailed investigations on sound and vibration behaviour of transformer manufactured for the 60 Hz network market. Commonly during standard tests on the transformer only the sound power level is calculated, either by sound pressure or sound intensity measurements, as described in the relevant standard [1]. Sound radiation from the structures is the so called “structure born sound”, knowing the vibration velocity one can estimate the sound power that is radiated [2]. Up to now some investigations have been performed to correlate vibration velocity measurements, sound radiation efficiency and sound pressure level or calculated sound power [3-5].

2 VIBRATION AND ACOUSTIC BEHAVIOUR OF TRANSFORMER

2.1 Vibration measurements method

The scanning Laser Doppler Vibrometry (LDV) technique was used to identify vibration velocities of the transformer tank. The LDV technique is based on the frequency change between the emitted and reflected laser beam, utilizing Doppler effect and due to the very high frequency of the laser light (~400 THz) the accuracy of measurement is extremely high. The LDV measurement is contactless and therefore the tested part is not influenced during the measurement, also of importance is that this allows the performance of a safe measurement session on a transformer that is energised with high voltage during the test. Eventually, the device can be measured directly during its operation, either at the test facility or onsite and the vibration pattern information is much more reliable. When measuring vibration with standard accelerometers one must not only take into account the load situation of the transformer, but it is also the time required to collect the high resolution of the vibration patterns. LDV technique allows a unique density of measurement points and eventually analysis of deflection shapes of the tank in all details.

2.2 Vibration deflection shapes results

Measurements were performed on the Low Voltage (LV) side of the power transformer, the longer tank wall. At high powers of transformer, such as the 120 MVA in this case, heat dissipating radiators are almost always necessary and are often placed on the tank itself. During the

measurement session the radiators have been removed to provide the laser spot access to the tank wall and 780 points have been distributed across the tank, stiffeners and connection box.

The measured frequency band was 0 – 1600 Hz and for results discussion the value of vibration velocity, normal to tank surface direction, both in linear and dB scale was taken for results presentation. Thanks to the reference signal measurements and their correlation to all 780 measurement points the phase plot could be also plotted.

Figure 1 shows vibration velocity results measured on tank surfaces averaged for the total frequency band (0 – 1600 Hz) and for particular, dominant frequencies: 120 Hz and 240 Hz. The vibration pattern in linear scale for the total frequency band shows increased amplitudes at three tank sections, however it can be seen that the stiffeners fulfil the function having small amplitudes and help the tank wall construction to reduce its noise radiation. The same results, but post processed in dB scale which is better to interpret sound radiation, show quite even vibration distribution on the tank. Results for the 120 Hz frequency are very similar to the one averaged for whole measured spectrum, vibrations at this 120 Hz frequency dominate in the spectrum and have the biggest contribution in the vibration behaviour. The vibration pattern at 240 Hz is somewhat peculiar due to the concentration of vibrations in two middle sections on the tank, the stiffeners again fulfil the purpose and block further vibration propagation. In the dB scale one can assume that the two sections will have significant influence on noise radiation.

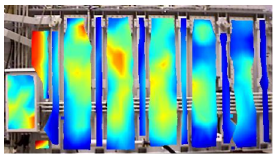
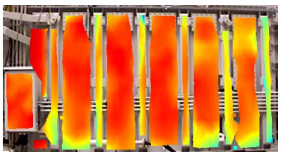
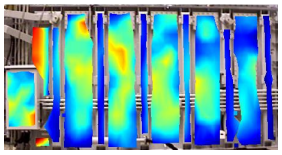
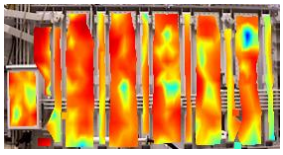
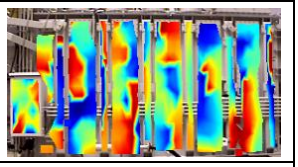
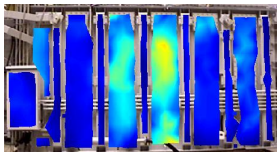
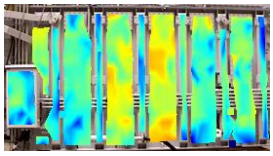
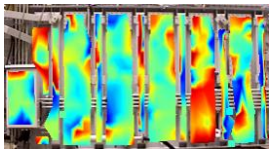
Frequency	Vibration velocity m/s	Vibration velocity dB, (re 0,1 μm/s)	Phase (-180 ÷ 180 deg.)
Total (0 – 1600 Hz)			
120 Hz			
240 Hz			

Figure 1: Normal direction vibration velocity in linear and logarithmic scale.

2.3 Sound intensity scan

Sound intensity describes the rate of energy flow through a unit area, in the SI system of units the unit area is 1 m^2 and hence the units for sound intensity are Watts per square meter. Sound intensity also gives a measure of direction as there will be energy flow in some directions but not in others. Therefore sound intensity is a vector quantity, as it has both magnitude and direction, in comparison to the pressure level where only magnitude is measured. Additionally sound intensity results are more resistant to the background noise and when we position the probe accurate it will only show the noise coming from the transformer direction. A sound intensity scan is a very efficient sound source localization method. When a sound intensity scan is performed a grid is set up to define a surface. Sound intensity measurements normal to the

surface are made from a number of equally spaced points on the surface, the same measurements can then be used to calculate the sound power over the grid. A matrix of intensity levels – one value for each point is achieved and lines of equal intensity can be drawn by interpolating and joining up points of equal intensity. These are sometimes called iso-intensity lines and they can be drawn either at single frequencies or for an overall level.

2.4 Sound pressure and intensity grid summary

Sound measurements have been performed according to standard [1] which says that when transformer is higher than 2,5 m the record must be made at two heights (1/3 and 2/3 of the transformer height) and at the distance of 0,3 m. The microphone positions around transformer can be seen in Figure 2, where the presented results are points 14 to 22, which are equally spaced and not more than 1 m apart.

Figure 2 summarizes sound pressure and sound intensity results for the total frequency spectrum available for the intensity probe spacer, which is 32 Hz to 1,6 kHz, one third octave band: 125 Hz and 250 Hz, both containing in their bandwidth the first dominant frequency of 120 Hz and second 240 Hz. All results are plotted for the long side of the transformer at the low voltage (LV) side. Looking at the total sound pressure level, one can say that the noise radiation is reasonably evenly distributed with lower levels at point 15 (1/3 h) and 21 (1/3 h). When comparing to vibration images the most right part of the transformer tank has lower vibration amplitude. The sound intensity scan results illustrate even more the differences, with the less intensity level at point 21 (1/3 h), although having positive direction coming from the tank. Sound intensity figure for the first dominant frequency of 120 Hz which is included in the 1/3 octave band of 125 Hz (the centre frequency) shows minimum value at the point 19 (2/3 h). When referring to the vibration image there can be seen large amplitudes of the vibrations but when looking at the phase plot, second and third panel from the right site have opposite phase shifts and this can lead to a situation where the pressure waves are negatively interfering. The second dominant frequency of 240 Hz, embedded in the 250 Hz (1/3 oct.) centre frequency of octave band, have the most varied intensity and pressure images. The situation of very close proximity of high and low amplitude is between point 17 and 18, both at 1/3 height. As commented in the deflection shape results, both middle panels have high vibration amplitudes giving high noise radiation, the parameter that causes the reduced pressure and intensity in the close distance is again the phase pattern of the vibrating tank.

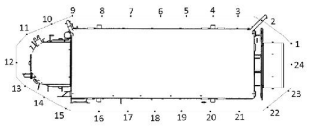
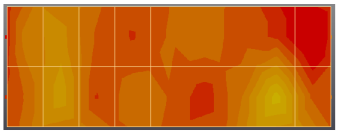
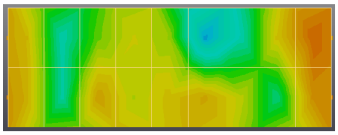
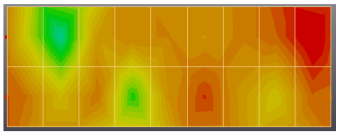
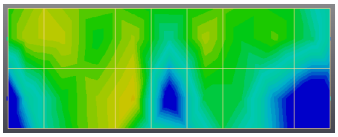
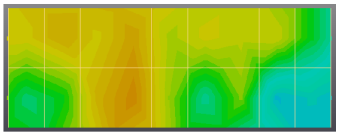
	Sound intensity level, dB(A)	Sound pressure level, dB(A)
Measurement points	14|15|16|17|18|19|20|21|22	14|15|16|17|18|19|20|21|22
Total (32 – 1600 Hz)		
125 Hz (1/3 oct.)		
250 Hz (1/3 oct.)		

Figure 2: Total spectrum sound intensity and pressure level A weighted.

3 VIBRATION TO NOISE CORRELATION

When analysing acoustic images and vibration patterns of the transformer the correlations and conclusions need to be carefully drawn with a good knowledge of what is the conversion of the vibration to noise energy. Figure 3 shows a diagram describing main steps of conversion of the structure vibration to noise level. The acoustic power which is radiated by the structure can be calculated knowing its surface dimensions, radiation efficiency and vibration velocity. The decibel scale transfer is done according to the acoustic power level formula and as the transformer noise is measured in units of A-weighted sound pressure level, the vibration velocity is also in A-weighting.

Main steps of conversion of the structure vibration to noise level:

- The acoustic power which is radiated by the structure can be calculated knowing its surface dimensions, radiation efficiency and vibration velocity
- The decibel scale transfer is done according to the acoustic power level formula
- Transformer noise is measured in units of A-weighted sound pressure level, the vibration velocity is also in A-weighting

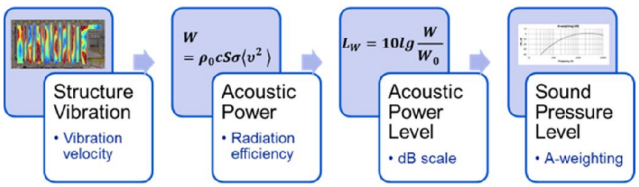


Figure 3: Vibration to noise energy conversion chain.

3.1 Result discussion

The above calculations help to estimate the expected noise radiation of the transformer which is summarized in the Figure 4, where sound pressure (Lp) and sound intensity levels (Li) are listed together with vibration velocity level (Lv) of transformer tank wall. The decibel scale for sound pressure and intensity is with the standard reference levels of 20 μPa and 1 pW/m^2 respectively, while for vibration level it was set to have similar amplitudes to pressure and intensity levels and it is set at 0,1 μm/s. The frequency spectrum is presented in the one third octave-band with center frequency form 100 Hz to 1 kHz.

It can be clearly seen that for the dominant frequencies of 120 Hz and 240 Hz covered by the 1/3 octave-band of 125 Hz and 250 Hz respectively the levels of pressure and intensity match with the vibration velocity of the complete transformer. Obviously in all octave band's sound intensity level (Li) is lower in comparison to pressure level (Lp), due to the physics of both measurement techniques. During intensity measurements only the sound coming from the normal direction (the tank wall) is measured, while in pressure method sound is measured omni-directional. The vibration levels are well matched at the dominant frequencies and still for the third harmonic of 360 Hz (400 Hz band) it shows good correlation to noise and indicates well the spectrum image. At other than dominant frequencies: 100 Hz, 160 Hz, 200 Hz the levels of noise and vibration are not so consistent, the reason may be the fact that vibration amplitudes are much lower, though underestimated, there might be other vibration sources that emit noise and were not measured with the laser vibrometer and the vibration pattern has a higher radiation efficiency.

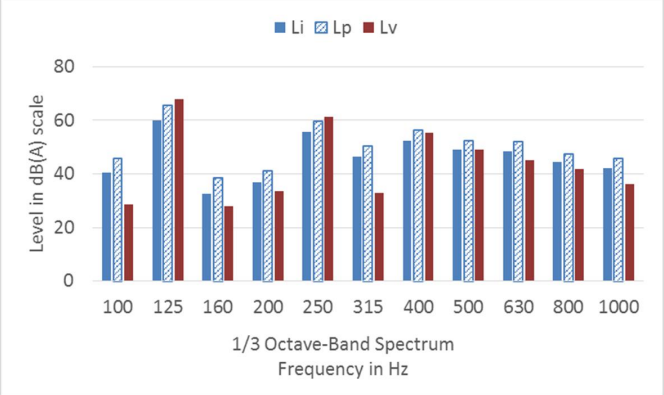


Figure 4: Frequency spectrum of transformer noise: Li – sound intensity level (re 1 pW/m2), Lp – sound pressure level (re 20 μPa) and transformer vibrations: Lv – vibration velocity level in dB scale (re 0,1 μm/s).

Estimating sound spectrum of the transformer by its vibration velocity levels works sufficiently for the determination of the dominant frequency, first two harmonics 120 Hz and 240 Hz are in close by the levels of SPL and vibrations.

4 CONCLUSIONS

This paper presents a detailed investigation of noise radiation and vibration behavior of a power transformer that is designed to work in 60 Hz net and tested with such voltage frequency. Usually when performing routine tests on the transformer, sound power level is calculated from pressure or intensity measurements. A study has been carried out to investigate the possibility of utilizing vibration measurement results, performed by the scanning laser vibrometer, and to correlate this with noise measurements. Vibration patterns of the transformer tank

wall, while operating in on load conditions, showed detailed information and along with the phase plots there is good basis for noise radiation origin and radiation. Moreover comparison of dB scaled vibration velocities to pressure or intensity levels are sufficiently matched so as to be used for noise spectrum investigation when sound measurements are not possible.

REFERENCES

[1] IEC 60076-10:2001: Power transformers – Part 10: Determination of sound levels

[2] Fahy F. *Sound and Structural vibrations. Second Edition*, Academic Press, Oxford, 2007.

[3] M. Kozupa and K. Kolber, Radiation efficiency as a crucial parameter in transformer noise evaluation, FORUM ACUSTICUM 2014, Krakow, Poland, 2014

[4] K. Kolber, A. Snakowska, M. Kozupa, The Effect of Plate Discretization on Accuracy of the Sound Radiation Efficiency Measurements, *Journal. Archives of Acoustics* vol. 39, page 511-518, 2014

[5] M.Kozupa, G.Kmita, Investigation on noise radiation to structure vibration correlation in vibroacoustic of transformer, *Vibroengineering PROCEDIA*, 3; 160-164, 2014

International Conference on Engineering Vibration
Ljubljana, Slovenia, 7-10 September 2015

THE BEHAVIOUR OF VIBRATION AND NEAR- AND FAR-FIELD NOISE OF ULTRAHIGH VOLTAGE (1000 KV) POWER TRANSFORMERS – A FIELD TEST INVESTIGATION

C.M. Pei,[1] Y.X. Wang,[3] X.H. Du,[3] Q.S. Tang,[2] H. Huang,[2] J.W. Du[2], J. Pan[*2]

[1] *China Electrical Power Research Institute, Wuhan, 430074, China* peichunming@epri.sgcc.com.cn

[2] *Department of Instrument Science and Engineering, Zhejiang University, 310027, China*
b111120131@smail.nju.edu.cn, hhai@zju.edu.cn, jwduzju@163.com, jpan@zju.edu.au

[3] *School of Mechanical and Chemical Engineering, The University of Western Australia, WA 6009, Australia*

20859125@student.uwa.edu.au, xuhao.du@research.uwa.edu.au

Keywords: UHV transformer, field measurement, transformer vibration, near-field and far-field noise

Abstract. *An extensive field test was undertaken to measure the vibration and near- and far-field noise of an ultrahigh voltage (UHV) power transformer unit at the Anji UHV power station in China. Unlike conventional power transformers, the UHV power transformer unit consists of three closely located transformer tanks. Each tank encloses one of the three-phase windings of the unit. As a result, the near- and far-field low-frequency noises radiated from the tanks are affected by interference from the radiated sound fields from individual vibrating tanks. This paper presents the properties of the transformer vibration and noise and proposes further investigations into several fundamental questions regarding transformer vibration and sound radiation, which may be useful for the estimation and control of noise from UHV transformers.*

[*] Correspondence author: jpan@zju.edu.au

1 INTRODUCTION

Accompanying the development of ultrahigh voltage (UHV) technology in recent years was a challenge in assessing and controlling environmental noise from 1000-kV transformers. Many field tests have been conducted to determine the radiated sound power from power transformers with a maximum voltage below 500 kV [1–3]. There have only been a few works on the noise and vibration characteristics of 1000-kV transformers. Zhou *et al.* conducted a field measurement of the sound power of three single-phase transformers comprising a UHV transformer unit under normal (2 kMW) and overload (2.5 kMW) conditions [4]. They found that the noise of a UHV transformer is mainly concentrated in the low-frequency range of 100–200 Hz. The near-field (1 m from the surface of a transformer) sound pressure varies from 66 dB(A) to 80 dB(A), owing to the significant influence of noise from cooling fans. The sound power level of one of the transformers, found via the sound intensity method, was 102.7 dB(A) at normal load conditions and 105.9 dB(A) at overload conditions. They also compared the sound power levels from the three transformers and found that the variation between them was less than 1 dB. The spatial distribution of the sound pressure level showed that sound pressure decays at 1 dB/m within 10 m from the transformer surfaces and stays between 68 and 65 dB within the range of 10 m to 25 m from the transformers.

Because the transformer's noise and vibration level are generally proportional to its MVA rating [5], UHV transformers rated at 1000 kV and 12,000 MVA may generate a greater environmental noise. On the other hand, dealing with the noise issues generated by UHV transformers also provides an opportunity to revisit some fundamental problems in the field measurement of transformer sound power and in the characteristics of transformer noise and vibration. UHV transformers also have different configurations to other power transformers. In particular, each UHV transformer consists of three single-phase transformers located side-by-side and separated by fire-protection walls.

The purpose of this paper is to present several observations from an extensive field measurement of the noise and vibration of a UHV transformer at the Anji UHV power station in China. The discussion of these observations raises some important questions that may motivate a systematic study of transformer vibration and noise.

2 DESECRIPTION OF FIELD MEASUREMENT

The UHV transformer used for the field measurements is located in the Anji UHV power station, including three single-phase transformers, as indicated by the arrow in Figure 1(a). A front view of the three single-phase transformers is shown in Figure 1(b). The dimensions of one of the single-phase transformers are presented in Figure 2, where the cooling fans are located at the front, rear, and left sides of the transformer. The cylindrical-shaped structure on the front of the transformer represents the insulation pole for the transformer input.

To obtain the distributed vibration on the transformer surface, multiple accelerometers were used to measure the vibration of all four sides of the phase-B transformer, and the front sides of the phase-A and phase-C transformers. The acceleration at each location was measured simultaneously with a reference accelerometer located on the bottom left of the cylindrically shaped structure, such that the distributed phase of the surface vibration was also available.

Vibration was also measured at the top and supporting ground of the transformer and on the case of the cooling fans, in order to identify any other surfaces, other than the transformer body, which may have a significant contribution to the sound radiation from the transformers.

It is also worth noting that the transformer tank structure is reinforced by periodically located ribs as shown in Figure 3. Such a periodical transformer structure may have a significant influence on the characteristics of transformer tank vibration and sound radiation.

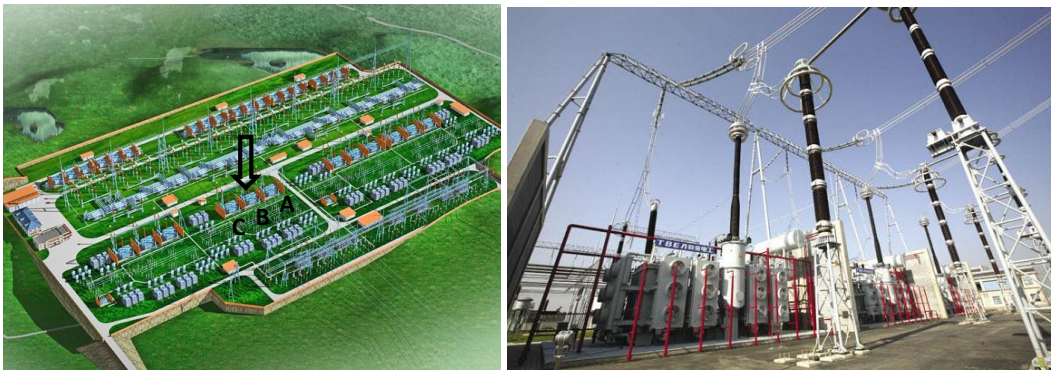


Figure 1: (a) An overview of Anji UHV power station and (b) a front view of the three single-phase transformers of the #2 UHV transformer unit.

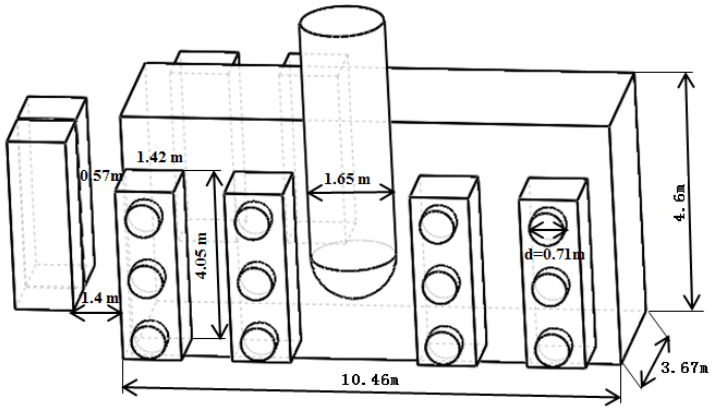


Figure 2: Approximate dimensions of the single-phase transformer.

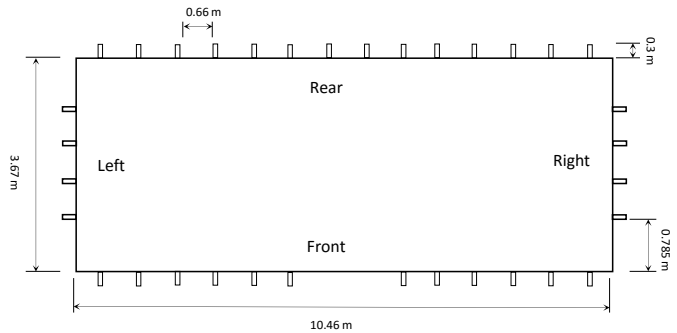


Figure 3: Illustration of the periodically ribbed transformer tank structure.

In addition to the measurement of sound pressure and sound intensity for the estimation of the near-field sound power of the transformer, the distributed near- and far-field sound pressures were also measured simultaneously with reference to the reference acceleration. The measurement area (30 m × 69 m) of the sound pressure is sketched in Figure 4. The microphones are all 1.5 m above the ground. In the *y* direction were 31 rows of measurement points, located 1 m apart. There were 17 groups of measurement points in each row. Each group consisted of six measurement microphones located 0.5 m apart. The distance between the groups was 1.125 m. The distance between the first row in the *y* direction and the surface of the cooling fan was 2.25 m.

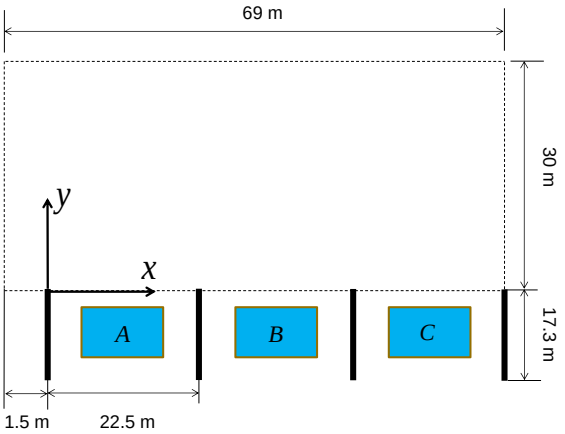
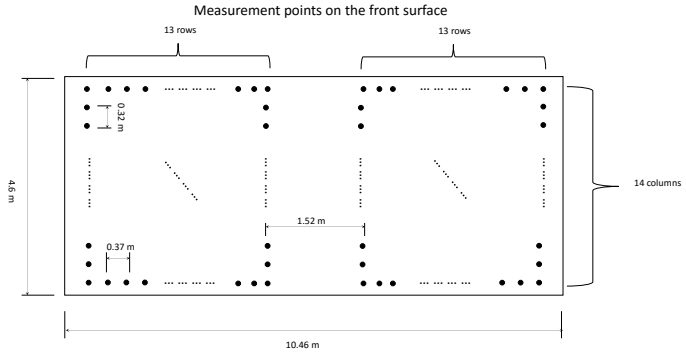
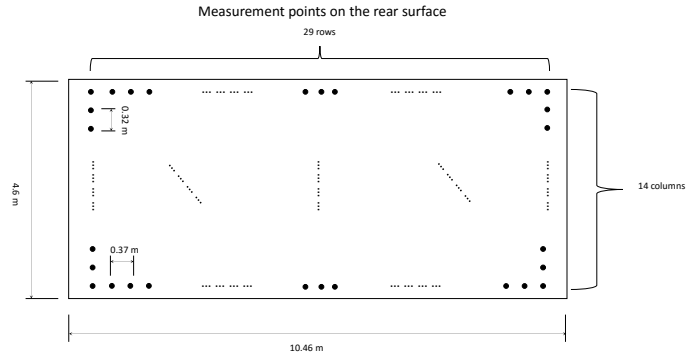


Figure 4: Schematics of the measurement area for radiated sound pressure from the UHV transformer.

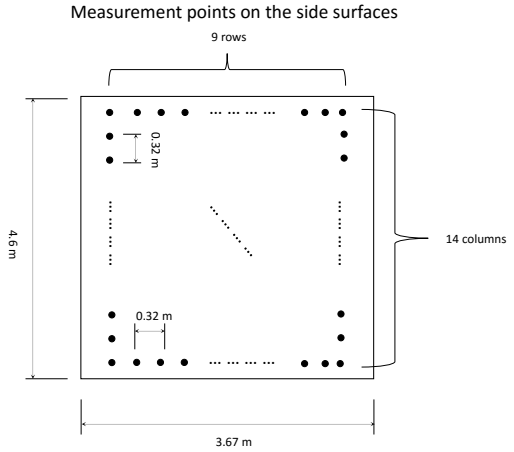
The transformer loading was monitored throughout the measurements. All the field measurements were made when the transformers were operated at under a normal loading condition of 2 kMW. The measurement points on the tank of the phase-B transformer are shown in Figure 5.



(a)



(b)



(c)

Figure 5: Measurement points on the (a) front, (b) rear, and (c) side surfaces.

3 VIBRATION OF THE UHV TRANSFORMER

The spatially averaged acceleration spectra over the front surfaces of the three single-phase transformers are presented in Figure 5. These three transformers have similar frequency spectra and the maximum variation in the overall structural acceleration level is 2 dB. Figure 6 shows that the average vibration on the front surfaces of the transformer tanks is dominated by components at 100 Hz, 200 Hz, and 300 Hz, with the maximum value at 300 Hz.

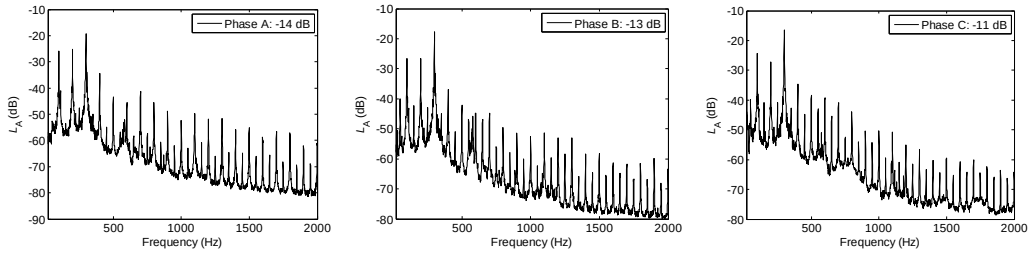


Figure 6: Spatially averaged acceleration levels of the three single-phase transformers.

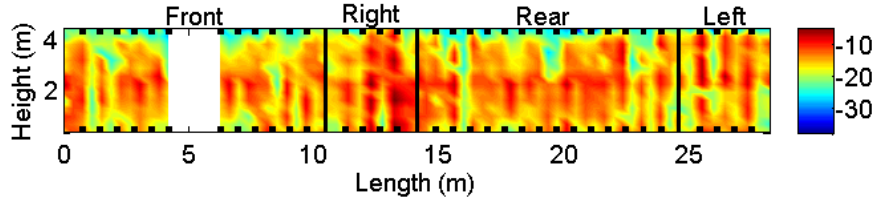
The maximum vibration component at 300 Hz is one of the major vibration features of the Anji UHV transformers, indicating that the majority of the vibration energy of the transformer tank is in the low-frequency range of 100–300 Hz, and that the peak energy is located 300 Hz.

A comparison of the phase differences between the vibrations at similar locations on the three single-phase transformers (Table 1) demonstrates that the vibrations of the three transformers have significantly differences in phase. Further analysis of the transformer's structural vibration is required to explain the distributed phase of the tank vibration.

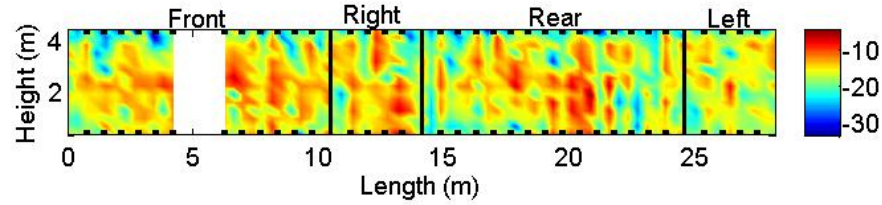
Table 1: Phase differences between the vibrations at similar locations on the three single-phase transformers.

Phase Difference	100 Hz	200Hz	300Hz
$\phi_A - \phi_B$	306^o	80^o	178^o
$\phi_C - \phi_B$	125^o	-95^o	137^o

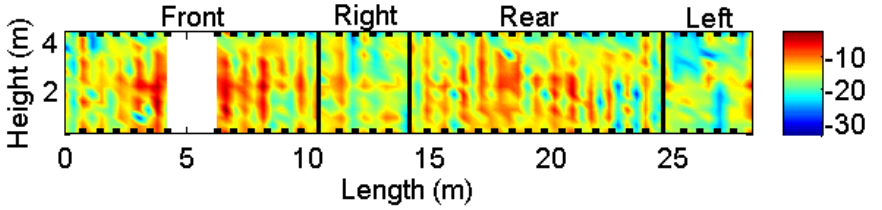
Figure 7 shows the distributions of acceleration levels of the four side walls of the phase-B transformer. A clear vibration pattern corresponding to the periodically located ribs (as shown in Figure 3) can be observed at 100 Hz, 200 Hz, and 300 Hz.



(a)



(b)



(c)

Figure 7: Distributions of the acceleration levels of the phase-B transformer tank at (a) 100 Hz, (b) 200 Hz, and (c) 300 Hz.

4 SOUND PRESSURE AND ITS SPATIAL DISTRIBUTION

The A-weighted sound pressure spectra, averaged over the sound pressures measured in three different rows ($y = 0$ m , $y = 15$ m , and $y = 30$ m) are shown in Figure 8. These results are consistent with the characteristics of the transformer vibration, and they demonstrate that the A-weighted sound field radiated from the UHV transformer is dominated by the first three frequency components at 100 Hz, 200 Hz, and 300 Hz. These results add an additional 300 Hz component to the 100 Hz and 200 Hz components dominating the sound pressure, as reported by Zhou *et al*. [4].

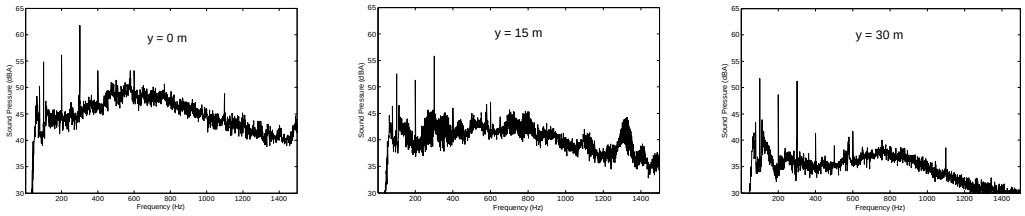


Figure 8: Spatially averaged sound pressure spectra at near, middle and far field locations of the transformers.

The spatial distributions of the sound pressure field at 100 Hz, 200 Hz, and 300 Hz are illustrated in Figure 9. In the measurement area, the sound pressure at 100 Hz decays slightly with distance. Areas of increased and decreased sound pressure can be observed, caused by the interference of the radiated sound from the three single-phase transformers. These interference patterns should be further analysed in order to relate them to the distributed vibration of the transformers.

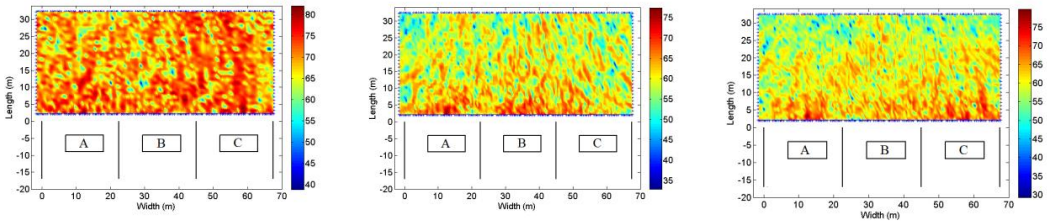


Figure 9: Spatial distributions of the sound pressure field radiated by the UHV transformers at (a) 100 Hz, (b) 200 Hz, and (c) 300 Hz.

To observe the features of the decay of the radiated sound field (at 100 Hz, 200 Hz, and 300 Hz) from the UHV transformers, the sound pressure levels averaged over each row of the measured pressure are presented in Figure 10 as a function of the distance from the surface of the transformers. The decay rates of the sound pressure increase with frequency. The fluctuations in the decay curves may be attributed to interference between the radiated sound from the sources and their mirror images due to ground reflection.

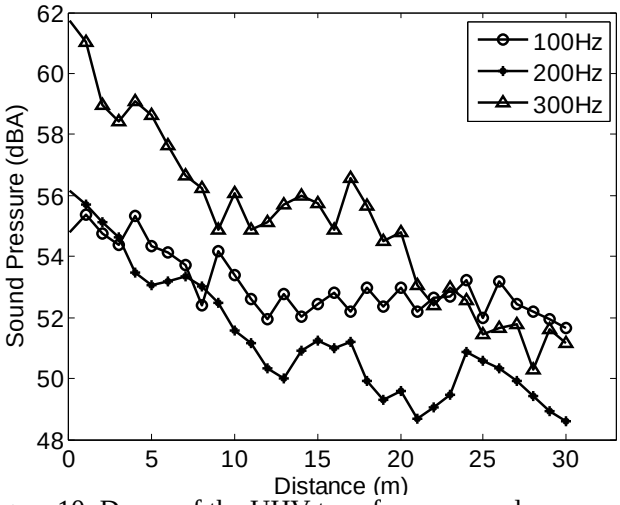


Figure 10: Decay of the UHV transformer sound pressure with distance.

5 SOUND POWER BY THREE METHODS

Based on the AS/NZS and ISO standards, the sound power from the phase-B UHV transformer was determined by sound intensity [5], sound pressure [5], and vibration [6] methods. Figure 11 shows the sound power spectra and overall sound power levels of the transformer found by the three methods. The spectra found by the sound intensity method are presented in terms of the 1/3-octave-band sound power. It is worth noting that all the methods are capable of capturing the frequency characteristics of the transformer noise source. However, significant differences occur between the measured overall sound power levels found by the different methods.

Girgis *et al*. compared the sound pressure levels measured by the sound pressure and sound intensity methods [2,3,4]. Similar to most measurement configurations, their measurements were taken at discrete positions on the contours of two different heights and with a fixed distance around the transformer. Their comparisons concluded that the sound intensity method is the more accurate and consistent method of measuring the "true" noise level of a transformer. The accuracy of the sound pressure method is limited by ambient noise (including background noise, cooling fan noise, and noise from other transformers), reflected sound (due to the fire protection walls), and reactive near-field sound close to the transformer being tested. Typically, the difference between the measured sound pressure and sound intensity levels at the same location is used to determine if a correction for pressure measurement is required. The "true" sound pressure level is interpreted as that which could be used to determine the spatially averaged free-field sound intensity. Multiplying it by the total surface area (which encloses the transformer and includes the measurement contours) yields the radiated sound power.

Sound power and directivity are the key features of a sound source for accurate determination of the radiated sound field. Indeed, exact experimental determination requires the measurement of the far-field sound pressure or the near-field sound intensity on the entire surface enclosing the noise source. However, such a measurement configuration is not practical for field transformers. Further work is required to re-examine the basis for the measurement of the pressure and intensity on the contours and possible differences between the "true"

sound pressure measured at the contours and what is suitable for accurate estimation of the sound power.

On the other hand, the measurement of transformer vibration promises a reliable and accurate determination of the source characteristics of the transformers, because the distributed vibrational velocity of the transformer and the radiation environment are all required for this determination. However, the current vibration method for determining the radiated sound power requires the radiation efficiency of the transformer structure. Simply using a unity value to approximate the radiation efficiency may result in considerable error in sound power estimation. Some effort has been made to calculate the radiated sound power using the sound radiation model of the vibration transformer [1]. Future work will extend this method to estimate the sound power from UHV transformers.

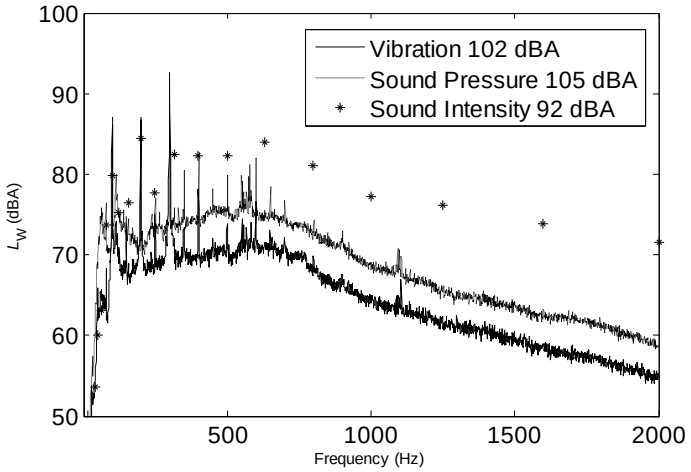


Figure 11: Sound power from the phase-B transformer measured by the sound pressure, sound intensity, and vibration methods.

6 CONCLUSIONS

This paper presented the results of an extensive field measurement of the sound and vibration of three single-phase transformers within a UHV transformer unit at the Anji UHV power station in China. The key observations are summarized as follows:

(1) The acceleration level of the UHV transformer structure is dominated by three low-frequency components at 100 Hz, 200 Hz, and 300 Hz. The 300 Hz component has the maximum amplitude around 10 dB greater than those at 100 Hz and 200 Hz.

(2) The distributed vibration on the transformer surface shows clear periodic patterns in the frequencies of the dominating vibration. This distribution is clearly related to the periodic ribbed structure of the transformer tank.

(3) The vibrations of the three single-phase transformers exhibit clear phase differences. Such phase differences between the distributed vibrations of the transformers should also contribute to the interference in the radiated sound field.

(4) The spatially averaged sound pressure spectra in the near-, middle-, and far-fields of the transformer confirm that the radiated transformer noise is also dominated by the three frequency components at 100 Hz, 200 Hz, and 300 Hz.

(5) The decay rates of the spatially averaged sound pressures at 100 Hz, 200 Hz, and 300 Hz are increase with frequency. The distributions of the sound field at these frequencies also fluctuate with the distance from the transformers, because of the interference between the direct and reflected sound of the transformer vibration.

(6) The distributed sound pressure levels at 100 Hz, 200 Hz, and 300 Hz also exhibit interference patterns, which can be attributed to the superposition of the radiated sound field by the three single-phase transformers.

(7) The sound powers determined by the sound pressure, sound intensity, and vibration methods are capable of capturing the frequency characteristics of the transformer noise. However, the significant differences between the overall levels of the sound power determined by the three methods motivate a revisiting of the challenging question of how to accurately and efficiently determine the radiated power and radiation directivity of UHV transformers.

REFERENCES

[1] R. S. Ming, J. Pan, M. P. Norton, S. Wende, H. Huang, The sound-field characterisation of a power transformer, *Applied Acoustics*, **56**, 257–272 (1999).

[2] R. S. Girgis, M. Bernesjö, Appropriate test conditions proposed for industry standards of measuring transformer noise, DOI: 10.1109/PES.2010.5590027, 2010 IEEE Power and Energy Society General Meeting.

[3] R. S. Girgis, K. Garner, M. Bernesjö, J. Anger, Measuring no-load and load noise of power transformers using the sound pressure and sound intensity methods—Part - I: Outdoors measurements, 2008 IEEE Power and Energy Society General Meeting—Conversion and Delivery of Electrical Energy in the 21st Century, Pittsburgh, PA.

[4] R. S. Girgis, K. Garner, M. Bernesjö, J. Anger, D. Chu, Measuring no-load and load noise of power transformers using the sound pressure and sound intensity Methods—Part - II: Indoors measurements, , 2008 IEEE Power and Energy Society General Meeting—Conversion and Delivery of Electrical Energy in the 21st Century, Pittsburgh, PA.

[5] B. Zhou, C. Pei, Y. Ni, J. Zhang, Noise measurement and analysis of UHV AC station, *Journal of Noise and Vibration Control*, S1, 245–249, 2012.

[6] AS/NZS 60076.10:2009 Power transformers – Determination of sound levels (IEC 60076-10, Ed. 1 (2001) MOD).

[7] ISO 7849-1987: Acoustics - Estimation of airborne noise emitted by machinery using vibration measurement, 1987.

ACKNOWLEDGEMENTS

The financial support from the State Grid Corporation of China and the China Electric Power Research Institute is gratefully acknowledged. We would also like to thank Y. Ni, B. Zhang, R. Huang, and H. G. Liu from the China Electric Power Research Institute for their assistance in field measurement, and L. Song and X. F. Dong from the Anji UHV power station for their on-site support and safety training.

The dynamics of an axially moving continuum (MS14)

International Conference on Engineering Vibration
Ljubljana, Slovenia, 7-10 September 2015

MODELLING THE BELT – ENVELOPE INTERACTIONS DURING THE POSTAL MAIL CONVEYING BY A SORTING MACHINE

L. Manin*[1], S. Braun[1], D. Hugues[2]

[1] LaMCoS, Université de Lyon, CNRS, INSA Lyon, F69100, Villeurbanne, France
lionel.manin@insa-lyon.fr

[2] Solystic S.A, 25600 Bourg lès Valence, France
damien.hugues@solystic.com

Keywords: Mail sorting machine, belts, envelope, conveying, simulation.

Abstract. *The purpose of this study is to predict the trajectory of an envelope when conveyed between two flat belts in a mail sorting machine, as it is often the case in postal centers. Each of the envelopes sides is in contact with one belt. The friction coefficient can vary between the two sides, e.g. for the cases of a postcard or a plastic windowed envelope. The two belts are supposed to travel horizontally with the same velocities, but in real world small velocity differences can occur. Also, some deviation from the horizontality of the belts can be observed. These phenomena can lead to unexpected situations where the relative position of the envelope to the belt changes during transportation. The work focuses on the belt-envelope mechanical interactions in order to predict the envelope position during its conveying. A 2D model is developed which considers the dynamic equilibrium of the envelope and simulates the transient behavior at different locations in the sorting machine. In the dynamic friction model, the contact surfaces between the envelopes sides and the belts have to be determined at each time step. The belt/envelope friction forces are applied at the centers of these contact surfaces One side of the envelope is considered stuck (in adhesion) to the belt while the other is considered slipping. The position of the envelope center of gravity and the angle with the horizontal axis are calculated.. For evaluation of the proposed dynamic model, several cases of operation are simulated. The results obtained are consistent with observations made on a real sorting machine. The influence of multiple driving parameters are highlighted: the plastic window location on the envelope, the friction coefficient and the speed difference between belts.*

1 INTRODUCTION

The research presented in this paper is based on the mechanics of mail conveying in sorting machines as used in postal sorting centres. The general concept of these machines is illustrated in Figure 1. A lot of different technologies are used in such systems: automatic address scanning and recognition, coding printer, etc. For robust machine operation, the correct conveying of the letters has to be ensured, which is equivalent to sustaining a stable position of the envelopes with respect to the belts that transport them. To give an idea, the machine can handle up to 53,000 mail pieces/hour depending on the length of the pieces processed.

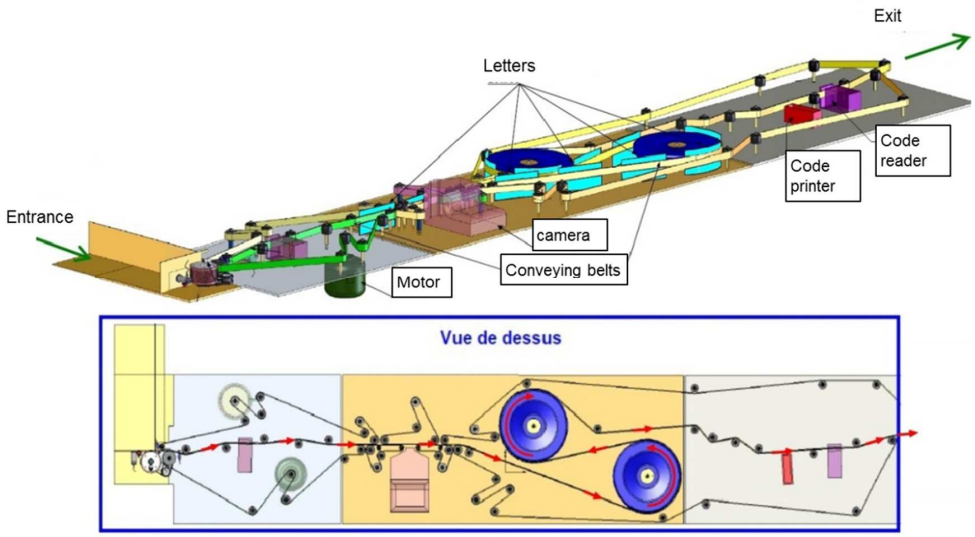


Figure 1: schematic representation of a mail conveying machine

In the scope of this research, a simulation tool is developed that predicts the trajectory of a letter being conveyed between two flat belts and crossing several direction switches (Fig. 2) where the envelope/belt contact surface is reduced (Fig. 4a & 5).



(a) (b)

Figure 2: (a) Envelope conveying, (b) Envelope passing through a direction switch.

2 MODEL PRESENTATION

The proposed dynamic model is two-dimensional. The envelope and the front and back side belts are considered as vertical planes as illustrated in figure 3. The belts have constant and independent velocities and can be inclined with respect to the horizontal axis. The aim is to determine the envelope position in function of time. The dynamic equilibrium of the envelope is written at the mass centre G. The forces considered are the weight of the envelope and the friction forces of the belts onto the envelope sides. The contact surfaces have to be determined at each time step of the simulation process. The proposed method is presented in the next paragraphs.

2.1 Parameter definition

The envelope is defined by: its height h_p and width l_p, its mass m_p and inertia I_p, the position of the plastic window if any and its size (h_f* l_f), the mass centre coordinates (x_G, y_G), the left bottom corner coordinates (x_{0p}, y_{0p}), the initial angle with respect to the horizontal axis θ_p. The belts are defined each by the coordinates of the two lower corner points and the width (Fig. 3). From these geometry input parameters, the angles between the belts and the horizontal axis is deduced.

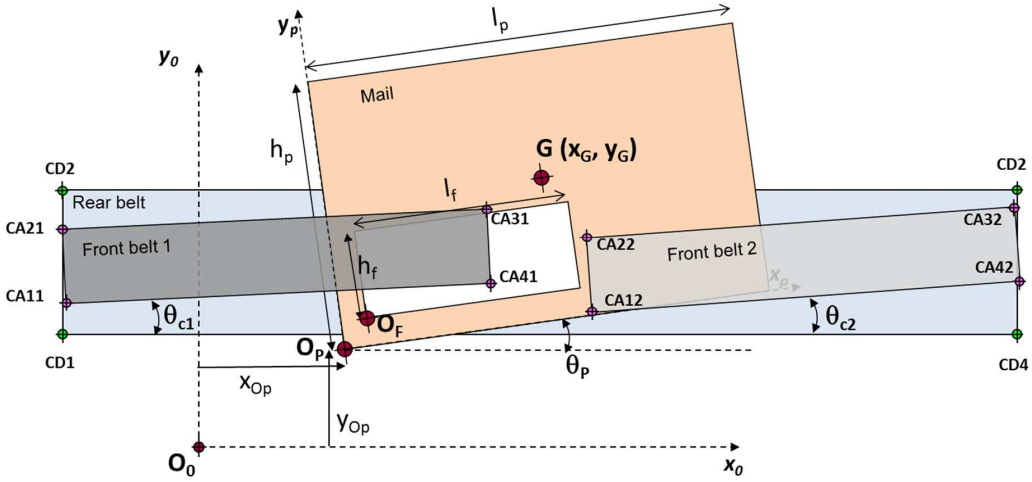
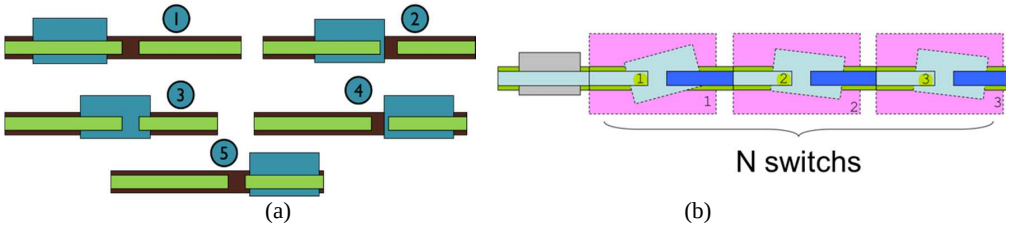


Figure 3: Definition of the geometry for the belts and the conveyed mail envelope, general case including a sorting switch



(a) (b)

Figure 4: Contact cases between belts and envelope when travelling through a direction switch, conveying with several direction switches

When the envelope is travelling through a direction switch (Fig. 2) the contact surface with the front belt(s) more complicated to determine than the contact surface with the backside belt.

This is due to the front belt being divided into two neighbouring belts, introduction a discontinuity. As the envelope passes this discontinuity, five contact cases can occur as shown in Figure 4. These cases are implicitly taken into account with our parameter definition. A standard mail sorting machine contains several successive direction switches which can be represented by the scheme in Figure 4b. In that case, multiple front belts are considered as on the machine.

2.2 Forces acting on the envelope

Theoretically the front and rear belts have the same velocities. However, a small difference can exist which are estimated at around 5%. We have made several assumptions when setting up the model: the envelope is adhering to the slowest belt (rear or front) and is sliding with respect to the faster belt(s). To give an example: if the rear belt is slower than the two front belts (Fig. 5) then the envelope is subjected only to the friction forces applied by the front belts. As a consequence of these assumptions, the envelope minimum traveling velocity is equal to that of the slowest belt.

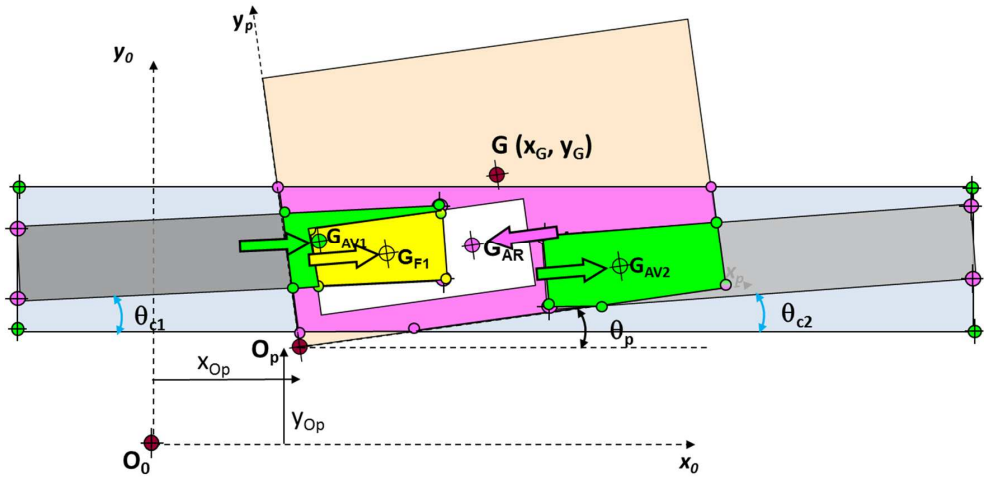


Figure 5: Contact surfaces and friction forces between belts and envelope.

The minimum contact pressure that prevents the envelope from falling freely can be estimated from Eq. (1), where S_{p_total} is the total contact surface with the envelope paper, S_f the contact surface with the plastic window, and the friction coefficients f_p and f_f (belt/envelope, plastic window/envelope). If Eq. (1) is satisfied, the envelope does not fall.

$$p.\left(S_{p_total}.f_p + S_f.f_f\right) \geq m_p.g \tag{1}$$

The friction forces are calculated for each contact surface S_i using the belt/envelope contact pressure p (supposed constant and uniform), the angles of the belts θ_{cj}, the friction coefficients f_i and the velocities of the belts (Eq. 2&3). In Eq. (3) the terms inside the parenthesis are considered only if the Eq. (1) is not satisfied.

$$F_{x,i} = sign\left(V_{front_j} - V_{rear}\right).f_i.p.S_i.\cos\theta_{cj} \tag{2}$$

$$F_{y,i} = sign\left(V_{front_j} - V_{rear}\right).f_i.p.S_i.\sin\theta_{cj} \tag{3}$$

As already mentioned, a key point is the determination of the different contact surfaces S_i and their mass centers G_i where the friction forces are applied. This is developed in the next paragraph.

The envelope is subjected to its proper weight and to the friction forces applied by the front and rear belts. The dynamic equilibrium of the envelope in the vertical plane can be written with

- the sum of external forces equalling the mass of the belt times its acceleration and
- the sum of the moment of the external forces calculated at point *G* equalling the envelope inertia times the angular acceleration.

The vector of the external forces applied to the envelope is given in Eq. (4), where the subscript p denotes the friction forces on the envelope paper, the subscript f denotes the friction forces on the envelope plastic window. The moment of the friction forces expressed at point *G* is given in Eq. (5). The coordinates of each contact surface centre G_i are (x_{Si} , y_{Si}). Finally, the equations of motion of the envelope are given in Eq. (6).

$$F_{ext} = \begin{pmatrix} \sum_i F_{x,i} \\ \sum_i F_{y,i} \quad (+)\ (m_p.g + f_f.p.S_f + f_p.p.S_{p_total}) \end{pmatrix} \quad (4)$$

$$\mathrm{M}_{ext}(G) = \left(\sum_i \left(F_{x,i}.(y_G - y_{Si}) + F_{y,i}.(x_{Si} - x_G) \right) + \sum_j \left(F_{x,j}.(y_G - y_{Sj}) + F_{y,j}.(x_{Sj} - x_G) \right) \right) \quad (5)$$

$$\begin{bmatrix} m_p \frac{d^2 x_G}{dt^2} \\ m_p \frac{d^2 y_G}{dt^2} \\ I_p \frac{d^2 \theta_G}{dt^2} \end{bmatrix} = \begin{bmatrix} F_{ext,x} \\ F_{ext,y} \\ \mathrm{M}_{ext}(G) \end{bmatrix} \quad \text{where } I_p = \frac{m_p}{12}(l_p^2 + h_p^2) \quad (6)$$

An Euler iterative numerical scheme is used to solve Eq. (6), as detailed in Eq. (7 & 8). One should note that at each time step the contact surfaces and their centre coordinates change and have to be re-calculated.

$$\ddot{x_n} = \begin{bmatrix} \frac{d^2 x_G}{dt^2} \\ \frac{d^2 y_G}{dt^2} \\ \frac{d^2 \theta_p}{dt^2} \end{bmatrix} = \begin{bmatrix} F_{ext,x}/m_p \\ F_{ext,y}/m_p \\ \mathrm{M}_{ext}(G)/I_p \end{bmatrix} = F_{ext_n} \rightarrow \dot{x} = \begin{bmatrix} \frac{dx_G}{dt} \\ \frac{dy_G}{dt} \\ \frac{d\theta_p}{dt} \end{bmatrix} \rightarrow x = \begin{bmatrix} x_G \\ y_G \\ \theta_p \end{bmatrix} \quad (7)$$

$$\dot{x}_{n+1} = \dot{x}_n + dt.F_{ext_n} \quad and \quad x_{n+1} = x_n + dt.\dot{x}_n \quad (8)$$

Some initial conditions are considered depending on the running conditions simulated:

$$x_0 = \begin{bmatrix} x_{G_0} \\ y_{G_0} \\ \theta_{p_0} \end{bmatrix}, \qquad \dot{x}_0 = \begin{bmatrix} V_{rear} \\ 0 \\ 0 \end{bmatrix}, \qquad \ddot{x_0} = \begin{bmatrix} 0 \\ 0 \\ 0 \end{bmatrix}, F_{ext_0} = \begin{bmatrix} 0 \\ 0 \\ 0 \end{bmatrix} \quad (9)$$

2.3 Calculation of the contact surfaces

The contact surfaces S_i are represented by polygons P_i (Fig. 5). They are the intersections between the belts and the two sides of the envelope with one side including a plastic window. all these parts are polygons that are defined by the coordinates of their four corners. The proposed method relies on getting the intersection polygons and the coordinates of their points in order to determine the contact surfaces and their mass centers (Fig. 6).

In literature, this problem is known as polygon clipping, often found in computer graphics. Several algorithms have been proposed for the calculation of the intersection area between polygons. Implementations of the Sutherland – Hodgman [1] algorithm are provided under MATLAB (see 'polybool' function from the 'Mapping Toolbox'). In addition, there are several libraries for polygon clipping which are written in C but can be used under Matlab after a conversion as MEX files (Matlab Executable), e.g. 'Angus clipping library' [2], 'General Polygon Clipper library' [3]. Details and comparisons can be found in literature [4 - 11]. It appears that the free 'Angus clipping library' (based on Vatti's clipping algorithm) is the most reliable and it validates all of our test case.. Once the intersection polygons are determined, the surface areas and mass centres are calculated using the 'polyarea' and 'centroid' functions of Matlab.

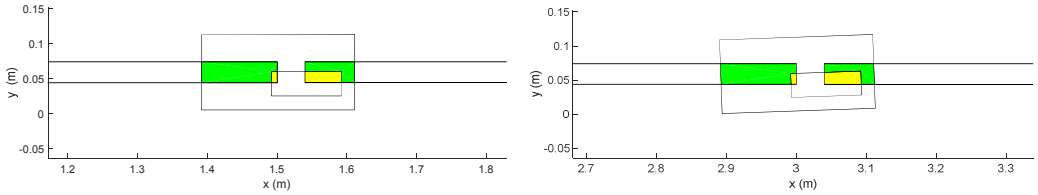


Figure 6: Contact surfaces between the front belts and the envelope paper and plastic window.

2.4 Input data

The data defining the system are gathered in an Excel file which is read by the simulation program under the MATLAB environment. An example is given in Table 1.

Front belts	X1	Y1	X4	Y4	width [m]	v [m/s]	Rear belts	X1	Y1	X4	Y4	width [m]	v[m/s]
1	0,5	4,40E-02	1,5	4,40E-02	3,00E-02	4	1	0,5	4,40E-02	5	4,40E-02	3,00E-02	3,99
2	1,54	4,40E-02	3	4,40E-02	3,00E-02	4							
3	3,04	4,40E-02	4,5	4,40E-02	3,00E-02	4							

Parameter	Value	Description
mp	0,02	mail mass[kg]
lp	0,219	mail width [m]
hp	0,108	mail heigth [m]
xop	1	[m], lower left corner
yop	5,00E-03	[m], lower left corner
thetap0	0	[°], initial angle
Xf	0,1	[m],window position
Yf	0,02	[m],window position
lf	0,1	[m],window length
hf	0,035	[m],window heigth
g	9,81	[m/sec^2], gravity
fp	0,4	friction coefficient belt/paper
ff	0,41	friction coefficient belt/window
dt	0,001	time step
p	60	[Pa] contact pressure

Table 1: Input data file.

From these input data, the system can represented graphically as shown in Figure 7.

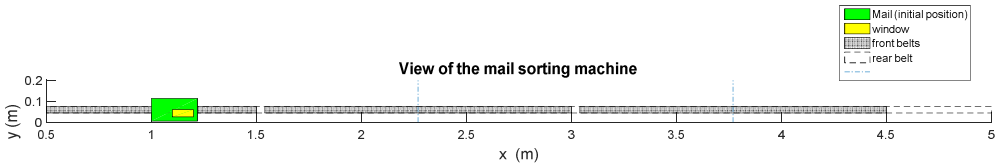
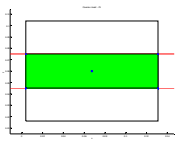
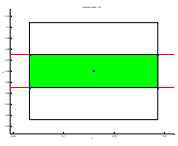
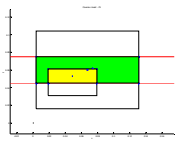
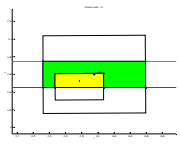


Figure 7: Representation of the mail sorting machine.

3 RESULTS

3.1 Test cases

In order to validate the model developed, some simulation test cases have been considered. They are based on real observations made on a mail sorting machine, and also on some intuition on how the envelope position will evolve under different running conditions. The test cases are presented in Figure 8. All tests were done for two different types of envelope: onewithout and one with a plastic window. The envelope is adhering to the rear belt and the rear belt is slower than the front belt. o direction switch isconsidered. When the inertia center of the envelope is centered with the belts, no rotation is observed for the envelope without window (Fig. 8-1b), but a slight rotation is observed for the envelope with a window (Fig. 8-1d). This is due to the difference of friction coefficients between the paper (f_p) and the plastic (f_f) with the belt. With $f_f > f_p$, the consequence is the generation of an anticlockwise moment that initiates the envelope rotation.

	Initial state	*Final State*	*Initial state*	*Final State*
1				

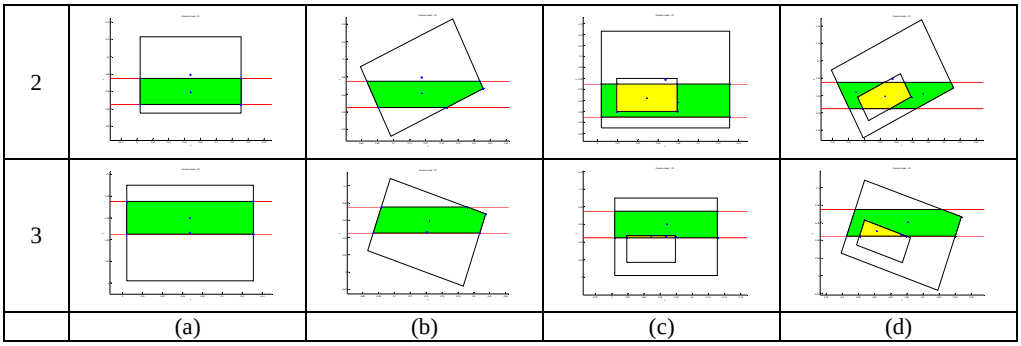


Figure 8: Simulation test cases, (1) inertia centre centred with the belts, (2) inertia centre above belt centre, (3) inertia centre below belt centre, adhesion to the rear belt $V_{front} > Vr_{ear}$.

The influence of the envelope inertia centre position with respect to the belt is highlighted with the simulation cases 2 and 3. A rotation is generated by the unbalance of the friction force moments. This phenomena is amplified when the envelope has a plastic window. The final states obtained for the several test cases correspond to those that were expected and confirm the viability of the model.

Figure 9 shows the vertical position of the inertia centre y_G and the rotation angle θ_p versus the conveying length. When the envelope is passing through a direction switch, there are three phases where the contact surfaces are reduced (Fig. 4a) and there is a risk of falling if the vertical friction forces are smaller than the envelope weight, as illustrated in Figure 9. Several running conditions can be simulated, we only present here some results to show the capability of the model.

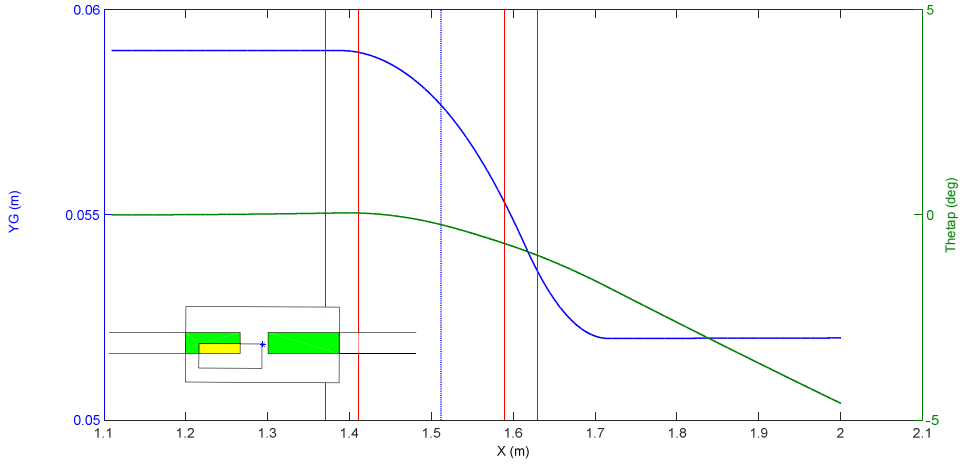


Figure 9: Envelope vertical position and angle θ_p while passing through a direction switch

3.2 Simulation of a conveying

Several generic cases of mail conveying are considered (Fig. 10). The graphical interface enables the visualization of the successive positions taken by the envelope. Some alerts have been

implemented in the code so that when the envelope reaches a position which is no more realistic, the simulation is stopped. For example, if the lower point of the envelope has a negative vertical coordinate, or the rotation angle is larger than 30° then the simulation is stopped.

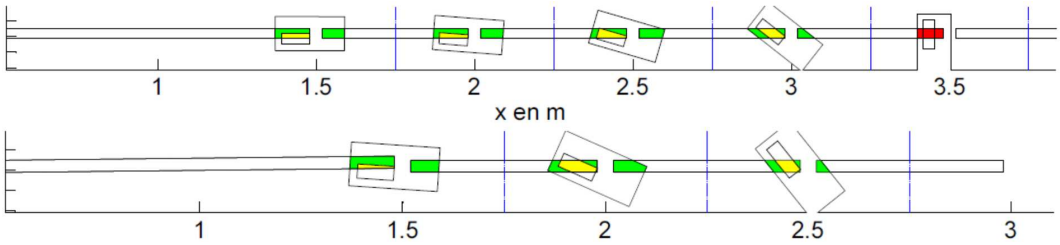


Figure 10: Snap shots of the envelope while being conveyed.

4 CONCLUSIONS

The work described in this paper deals with the simulation of the mail conveying in a postal sorting machine. It is based on an industrial demand and therefore corresponds to real issues encountered in such machines. The intention was to develop a simple simulation model in order to predict the envelope trajectory in the mail sorting machine under different operating conditions. The model developed considers simple and windowed envelopes. Some assumptions were made in order to simplify the analysis and the dynamic equilibrium. The forces considered are the envelope's weight and the friction forces applied by the front and rear belts between which the envelope is maintained. The data definition permits the simulation of machines with several direction switches. These switches happen to be the most critical situations in the conveying process. The proposed model is very flexible, as the dimensions of the envelope can be changed as well as all the other parameters describing the geometry of the conveying path. The core of the model relies on the calculation of the contact surfaces between the envelope sides and the belts for each simulation time step. This is based on the theory of polygon clipping that permits the computation of intersection surfaces. Evaluation of several test cases showed that the results obtained by simulation are consistent with real world observations.

REFERENCES

[1] http://rosettacode.org/wiki/Sutherland-Hodgman_polygon_clipping.

[2] http://www.angusj.com/delphi/clipper.php.

[3] http://www.cs.man.ac.uk/~toby/alan/software/.

[4] http://rogue-modron.blogspot.de/2011/04/polygon-clipping-wrapper-benchmark.html.

[5] http://www.mathworks.de/matlabcentral/fileexchange/36241-polygon-clipping-and-offsetting.

[6] Max K. Agoston. Computer Graphics and Geometric Modeling – Implementations and Algorithms. Springer, 2010.

[7] Emmett. Polygon clipping and o_setting. http://www.mathworks.fr/matlabcentral/fileexchange/36241-polygon-clipping-and-offsetting.

[8] Kai Hormann G unther Greiner. E_cient clipping of arboitrary polygons. ACM New York, 1998.

[9] MATHWORKS. Supported and compatible compilers { release 2012b. http://www.mathworks.fr/support/compilers/R2012b/win64.html.

[10] Lucanus J. Simonson. Industrial strength polygon clipping : A novel algorithm with applications in vlsi cad. http://119.93.223.179/ScienceDirect/Computer-Aided%20Design/Computer-Aided%20Design%20Volume%202010/Computer-Aided%20Design%20Volume%202010%20Issue%20-%20(12)/sdarticle_012.pdf, 2010.

[11] Bala R. Vatti. A generic solution to polygon clipping. ACM New York, 1992.

11th International Conference on Engineering Vibration
Ljubljana, Slovenia, 7–10 September 2015

EXPERIMENTAL ANALYSIS OF NONLINEAR RESPONSE IN SIMPLY SUPPORTED BEAM SUBJECTED TO PARAMETRIC EXCITATION

Naoto Araumi*[1], Hiroshi Yabuno*[2]

[1]University of Tsukuba
s1520744@u.tsukuba.ac.jp

[2]University of Tsukuba
yabuno@esys.tsukuba.ac.jp

Keywords: Nonlinear dynamics, Parametric excitation, Parametric resonance, Method of multiple scales.

Abstract. *Recently, parametric resonances become positively utilized in MEMS devices such as mechanical filters, energy harvesters, and so on, due to the characteristic resonance mechanism and the large response amplitude. The presentation is to show the basic nonlinear investigations for the parametric resonance using a macro simply supported beam. The nonlinear characteristics of the frequency response curve are theoretically and experimentally investigated under the parametric resonance produced in the axial harmonic excitation. First, according to the conventional way, taking into account the nonlinearity of curvature of beams and using Hamilton' s principle, the equation of motion of the beam in the lateral direction is derived. Employing the method of multiple scales, the equations which show the modulation of the amplitude and phase of the parametric resonance are obtained. The stability and bifurcations of the response amplitude are investigated considering the nonline arities of the systems. The theoretically obtained frequency response was partially agreement with the experimental one in the third order analysis, but they have a big difference in the global point of view. Hence, there is a saddle-node bifurcation in the experimental frequency response curve. It is clarified that the fifth-order analysis is needed to theoretical analysis. Accordingly, we perform the nonlinear analysis in the accuracy of fifth order and compare the theoretical frequency response curve with experimental one.*

International Conference on Engineering Vibration
Ljubljana, Slovenia, 7-10 September 2015

THE NATURAL FREQUENCIES OF AN AXIALLY MOVING BEAM SUPPORTED BY AN INTERMEDIATE SPRING

F. Kostekci*[1], A. K. Banik[2]

[1]Department of Mechanical Engineering Hitit University Corum Turkey
feridkostekci@hitit.edu.tr

[2]Department of Civil Engineering NIT Durgapur-713209, WB, India
akbanik@gmail.com

Keywords: Natural Frequency, Axially Moving Beam, Intermediate Spring, Method of Multiple Time Scales, Perturbation Methods.

Abstract. *This paper evaluates the natural frequencies of an axially moving beam having an intermediate simple support resting on a spring for pinned and clamped ends. The intermediate support of the Euler-Bernoulli beam means that there is one simple support on spring-foundation in-span. The beam travels under an applied tensional force. The differential equations of motion and boundary conditions are obtained using Hamilton's Principle and solved using a perturbation technique namely the Multiple Scales Method. The natural frequencies are obtained numerically for various combinations of flexural rigidities, intermediate support locations and spring constants under various end conditions. Natural frequency-mean axial speed curves showing the effects of variations of mean axial speed and location constant of the intermediate support on the natural frequencies of the beam are depicted. The first three transverse mode shapes of the axially moving beam were given. The variation of the natural frequencies with the increase in the mean moving velocity occurs as follows: While the mean translating velocity increases, the natural frequencies decrease.*

1 INTRODUCTION

Traveling materials [1-4] such as magnetic tapes drives, band saw, power transmission belts, robot arms, serpentine belts and aerial cable tramways are industrial examples classified as axially moving stringlike or beamlike structures. Some engineering applications that have flexible medium such as printing machines, fiber textiles machines, oil pipelines facilities are the other most common examples of these types of structures. In paper [5], it has been stated that wire and sheet metal straightening systems can be considered as axially moving continua. Poor quality and failure related to vibrations of moving materials must be eliminated to have good designs.

Many structural elements can be modelled as simple continua such as beams, plates, and shells. The dynamic response analysis of these elements has been one of the research interests and many researchers have examined both experimentally and theoretically. In many situations, continuous flexible systems are composed of various components such as mass, spring, mass-spring, non-ideal ends at various locations [6-20].

Moving structures are formulated mathematically as either a traveling beam or string. A vast literature exists for the vibrations of axially translating materials. By employing the Galerkin's method [21-24], the method of perturbation [25, 26], Green's function [27], finite element [28, 29], the vibration of moving beam has been examined in corresponding references. Axially transporting beams based on Timoshenko beam model, Rayleigh model, Shear model and Euler-Bernoulli beam model were considered, modes, natural frequencies and critical speeds were derived and calculated for beams under various end conditions and the effects of variations in axial speed, inertial moment and shear moment on natural frequencies were depicted in [30]. With modal analysis approach and Green's function method, linear solutions for the transverse vibrations of axially translating strings and beams were obtained and the related critical speeds are found in Ref. [27]. In Ref. [10], the nonlinear vibrations of a beam-spring-mass system were investigated and it was pointed out that the nonlinearity due to mid-line stretching has a great effect on frequency-response and force-response. The nonlinear free and forced dynamics of a travelling beam were investigated through a combination of harmonic balance and perturbation techniques and the near-resonance responses of the beam were also studied out using the non-linear complex normal modes [4]. A theoretical examination on transverse vibrations of a simply supported axially moving beam was conducted and infinite mode approximate solutions were presented by employing the method of multiple scales [31]. The numerical results of linear vibration problems of axially moving beams has been depicted to show the effects of variations in bending rigidity, mean moving speed and the location of intermediate support on natural frequencies in Ref. [5].

In this research we intend to deal with linear vibrations of an axially moving beam under various end conditions with an intermediate supporting spring via a perturbation technique namely multiple scales. The beam travels under an applied tensional force. The differential equations of motion and boundary conditions are obtained using Hamilton's Principle and solved. The natural frequencies are founded numerically for several flexural rigidities, intermediate support locations and transporting velocities.

2 THE MATHEMATICAL MODEL

For the axially moving beam depicted schematically in Figure 1, the equations of motion can be obtained following a derivation similar to that of reference [32] using Hamilton's Principle. Here, w_1^*, w_2^* and u_1^* and u_2^* are respectively the transverse and longitudinal displacements, v^* is the harmonic axial traveling speed fluctuating slightly, t^* denotes time and P is the applied axial tension, where the variables with asterisk denote dimensional ones. Properties of the

beam include the beam length L, the cross-section area A, the cross-sectional moment of inertia I, the mass density ρ and the Young's modulus E. A translational spring is used with a simple support as simply supporting foundation. k is the translational stiffness of the spring.

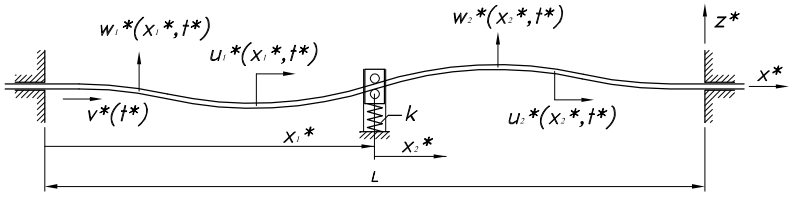


Figure 1: Nomenclature for a moving beam having one intermediate simple support on spring.

The beam, under an applied tension force P, is moving axially at a slightly varying harmonic velocity v^*. After writing the kinetic and potential energies of the system, the Lagrangian for the axially moving beam can be formulized as

$$\begin{aligned}
\pounds = \frac{1}{2}\Big(&\int_{x_0^*}^{x_1^*}\rho A\big((\dot{w}_1^* + w_1^{*\prime}v^*)^2 + (v^* + \dot{u}_1^* + u_1^{*\prime}v^*)^2\big)^2 dx^* \\
&+ \int_{x_1^*}^{x_2^*}\rho A\big((\dot{w}_2^* + w_2^{*\prime}v^*)^2 + (v^* + \dot{u}_2^* + u_2^{*\prime}v^*)^2\big)^2 dx^*\Big) \\
-\frac{1}{2}\Big(&\int_{x_0^*}^{x_1^*} EA(u_1^{*\prime} + \frac{1}{2}w_1^{*\prime})^2 dx^* + \int_{x_0^*}^{x_1^*} EIw_1^{*\prime\prime 2} dx^* + \int_{x_0^*}^{x_1^*} P(u_1^{*\prime} + \frac{1}{2}w_1^{*\prime 2})^2 dx^* \\
+&\int_{x_1^*}^{x_2^*} EA(u_2^{*\prime} + \frac{1}{2}w_2^{*\prime})^2 dx^* + \int_{x_1^*}^{x_2^*} EIw_2^{*\prime\prime 2} dx^* + \int_{x_1^*}^{x_2^*} P(u_2^{*\prime} + \frac{1}{2}w_2^{*\prime 2})^2 dx^* + \frac{1}{2}k\, w_1^{*2}(x_1^*)\Big)
\end{aligned} \tag{1}$$

where u_1^* and u_2^* are the left and the right side axial displacements of the beam respectively, and w_1^* and w_2^* are the left and the right side transverse displacements of the beam respectively. Here, ($\dot{}$) denotes differentiation with respect to time (t*) and ($'$) denotes differentiation with respect to the spatial variable (x*). The values of the spatial variable at the boundaries namely x_0^* and x_2^* should be written as 0 and L respectively. It is assumed that the beam has immovable boundaries at the outer ends. The equations of motion are derived through the Hamilton's Principle:

$$\begin{aligned}
&-\rho A(\ddot{w}_1^* + 2\dot{w}_1^{*\prime}v^* + w_1^{*\prime}v^* + w_1^{*\prime\prime}v^{*2}) + EA\big((u_1^{*\prime} + \frac{1}{2}w_1^{*\prime 2})'\, w_1^{*\prime} + (u_1^{*\prime} + \frac{1}{2}w_1^{*\prime 2})\, w_1^{*\prime\prime}\big) - EIw_1^{*iv} + Pw_1^{*\prime\prime} = 0 \\
&-\rho A(\ddot{w}_2^* + 2\dot{w}_2^{*\prime}v^* + w_2^{*\prime}v^* + w_2^{*\prime\prime}v^{*2}) + EA\big((u_2^{*\prime} + \frac{1}{2}w_2^{*\prime 2})'\, w_2^{*\prime} + (u_2^{*\prime} + \frac{1}{2}w_2^{*\prime 2})\, w_2^{*\prime\prime}\big) - EIw_2^{*iv} + Pw_2^{*\prime\prime} = 0
\end{aligned} \tag{2}$$

$$\begin{aligned}
&-\rho A(\dot{v}^* + \ddot{u}_1^* + 2v^*\dot{u}_1^{*\prime} + \dot{v}^*u_1^{*\prime} + v^{*2}u_1^{*\prime\prime}) + EA(u_1^* + \frac{1}{2}w_1^{*\prime 2}) + P' = 0 \\
&-\rho A(\dot{v}^* + \ddot{u}_2^* + 2v^*\dot{u}_2^{*\prime} + \dot{v}^*u_2^{*\prime} + v^{*2}u_2^{*\prime\prime}) + EA(u_2^* + \frac{1}{2}w_2^{*\prime 2}) + P' = 0
\end{aligned} \tag{3}$$

We will examine the problem in a non-dimensional formulation so the following non-dimensional variables and parameters introduced in Refs. [5, 33] are employed.

$$\begin{aligned}
&w_1 = w_1^*/L;\ w_2 = w_2^*/L;\ u_1 = u_1^*/L;\ u_2 = u_2^*/L;\ x_0 = x_0^*/L;\ x_1 = x_1^*/L;\ x_2 = x_2^*/L \\
&v = v^*/\sqrt{P/\rho A};\ t = \gamma t^*;\ v_b^2 = EA/P;\ \bar{v}_f^2 = EI/PL^2;\ \gamma = (1/L)\sqrt{P/\rho A}
\end{aligned} \tag{4}$$

In addition to those given in Eq. 4, the following dimensionless pan-wise variable, which represents dimensionless location constant of the intermediate support and may take a value bigger than 0 and smaller than 1, is introduced: $x_1 = \eta$. Dimensionless parameter v_b presents the longitudinal rigidity parameter, and $\bar{v}_f$ denotes the flexural rigidity parameter. Substituting Eq. 4 into Eq. 2-Eq. 3, performing required operations and adding damping term ($\bar{\mu}$) yield the dimensionless equations of motion and relevant non-dimensional boundary conditions.

$$\begin{aligned}
&\ddot{w}_1 + 2\dot{w}_1' v + w_1' \dot{v} + w_1''(v^2 - 1) + \bar{v}_f^2 w_1^{iv} + \bar{\mu}(\dot{w}_1 + v\, w_1') = v_b^2 (1/2)\left(\int_0^{\eta} w_1'^{\,2}\, dx + \int_{\eta}^{1} w_2'^{\,2}\, dx\right) w_1'' \\
&\ddot{w}_2 + 2\dot{w}_2' v + w_2' \dot{v} + w_2''(v^2 - 1) + \bar{v}_f^2 w_2^{iv} + \bar{\mu}(\dot{w}_2 + v\, w_2') = v_b^2 (1/2)\left(\int_0^{\eta} w_1'^{\,2}\, dx + \int_{\eta}^{1} w_2'^{\,2}\, dx\right) w_2''
\end{aligned} \tag{5}$$

$$\begin{aligned}
&w_1(0,t) = 0;\ w_1'(0,t) = 0;\ w_2(1,t) = 0;\ w_2'(1,t) = 0;\ w_1(\eta,t) = w_2(\eta,t);\ w_1'(\eta,t) = w_2'(\eta,t) \\
&w_1''(\eta,t) = w_2''(\eta,t);\ w_1'''(\eta,t) - w_2'''(\eta,t) = \alpha_k\, w_1(\eta,t)
\end{aligned} \tag{6}$$

where the following abbreviations are introduced.

$$\alpha_k = \frac{k}{EI/L^3} \tag{7}$$

3 METHOD OF MULTIPLE SCALES

A perturbation method namely the method of multiple scales will be employed here as to a method of solution which was used in [34]. This method known as direct perturbation method will be applied directly to the partial differential equation. In higher-order schemes and for finite mode truncations, the method yields better approximation to the real problem [35].

The axial transport velocity varying about an arbitrary constant value, v_0, with a small amplitude fluctuation frequency is given as below

$$v(t) = \mathrm{v}_0 + \varepsilon\, \mathrm{v}_1 \sin(\Omega\, t) \tag{8}$$

where ε denotes a small variation of the velocity. The terms w_1 and w_2 representing displacements in Eq. 5 may be supposed in the following form: $w_1 = \sqrt{\varepsilon} y_1$, $w_2 = \sqrt{\varepsilon} y_2$. Also, viscous damping term $\varepsilon\mu$ is in ε order: $\bar{\mu} = \varepsilon\mu$. The order of the flexural rigidity parameter is as flowing: $\bar{v}_f^2 = \varepsilon^0 v_f^2$ .The displacement functions $y(x,t,\varepsilon)$ can be expressed in series forms as the following

$$\begin{aligned}
y_1(x,t,\varepsilon) &= y_{11}(x,T_0,T_1) + \varepsilon\, y_{12}(x,T_0,T_2) + \ldots \\
y_2(x,t,\varepsilon) &= y_{21}(x,T_0,T_1) + \varepsilon\, y_{22}(x,T_0,T_2) + \ldots
\end{aligned} \tag{9}$$

where $T_0 = t$, is the usual fast-time scale and $T_1 = t\varepsilon$ is the slow-time scales. The time derivatives are as the followings: $d/dt = \varepsilon^0 D_0 + \varepsilon^1 D_1 + \ldots$, $d^2/dt^2 = \varepsilon^0 D_0{}^2 + 2\varepsilon^1 D_0 D_1 + \ldots$ where $D_0 = \partial/\partial T_i$. Substituting the above expansions into Eqs. 5, expanding outcomes and retaining terms up to $O(\varepsilon^0)$, result in the following equation of motion.

$$\begin{aligned}
&D_0{}^2 y_{11} + 2v_0 D_0 y_{11}' + v_f^2 y_{11}^{iv} + (v_0^2 - 1) y_{11}'' = 0 \\
&D_0{}^2 y_{21} + 2v_0 D_0 y_{21}' + v_f^2 y_{21}^{iv} + (v_0^2 - 1) y_{21}'' = 0
\end{aligned} \tag{10}$$

3.1 Linear Problem

The exact solution to Eqs. 13 is fully presented in Reference [10] and is used here. In the same way, the displacement function for the two sides of the beam can be expanded as below:

$$\begin{aligned} y_{11}(x,T_0,T_1;\varepsilon) &= A(T_1)e^{i\omega T_0}Y_1(x) + \overline{A}(T_1)e^{-i\omega T_0}\overline{Y}_1(x) \\ y_{21}(x,T_0,T_1;\varepsilon) &= A(T_1)e^{i\omega T_0}Y_2(x) + \overline{A}(T_1)e^{-i\omega T_0}\overline{Y}_2(x) \end{aligned} \tag{11}$$

where ω represents the natural frequency, A and $\overline{A}$ are complex amplitudes and their conjugates, respectively. By means of substituting Eqs. 11 into Eqs. 10, zero-order (ε^0) equations are obtained for two sides of the beam as the followings:

$$\begin{aligned} v_f^2 Y_1^{iv} + (v_0^2 - 1)Y_1'' + 2i\omega v_0 Y_1' - \omega^2 Y_1 = 0 \\ v_f^2 Y_2^{iv} + (v_0^2 - 1)Y_2'' + 2i\omega v_0 Y_2' - \omega^2 Y_2 = 0 \end{aligned} \tag{12}$$

The non-dimensional boundary conditions are as the following.

$$\begin{aligned} &Y_1(0,t) = 0;\ Y_1'(0,t) = 0;\ Y_2(1,t) = 0;\ Y_2'(1,t) = 0;\ Y_1(\eta,t) = Y_2(\eta,t) \\ &Y_1'(\eta,t) = Y_2'(\eta,t);\ Y_1''(\eta,t) = Y_2''(\eta,t);\ Y_1'''(\eta,t) - Y_2'''(\eta,t) = \alpha_k Y_1(\eta,t) \end{aligned} \tag{13}$$

The general solutions of the ordinary differentials in Eqs. 17 can be written in the form, with

$$\begin{aligned} Y_1 &= c_1 e^{i\beta_1 x} + c_2 e^{i\beta_2 x} + c_3 e^{i\beta_3 x} + c_4 e^{i\beta_4 x} \\ Y_2 &= c_5 e^{i\beta_5 x} + c_6 e^{i\beta_6 x} + c_7 e^{i\beta_7 x} + c_8 e^{i\beta_8 x} \end{aligned} \tag{14}$$

where eight integration constants c_1 - c_4 and c_5 - c_8 are used. These constants must be evaluated via the boundary conditions. By substituting the functions given with Eqs. 14 into Eqs. 12, we find the dispersion relation:

$$v_f^2\beta^4 + (1 - v_0^2)\beta^2 + 2\omega v_0\beta - \omega^2 = 0 \tag{15}$$

It is clear that there must be the following relationships among the eigenvalues: $\beta_1 = \beta_5$, $\beta_2 = \beta_6$, $\beta_3 = \beta_7$, $\beta_3 = \beta_8$. We can numerically evaluate natural frequencies according to the scheme of reference literature [25]. Using the boundary conditions given with Eq. 13 the matrix of the coefficients can be written. In order to have a non-triviality condition, the determinant of the matrix of the coefficients has to be zero.

4 NUMERICAL EVALUATIONS

This section is concerned in working with the numerical examples of linear formulas founded in the preceding sections. The mechanical properties of the beam with rectangular form used for numerical investigations are listed in Table 1.

Table 1 Mechanical properties of the system

Beam's material density, kg/m^3	ρ =7860
Width of the cross section area, mm	b=80
Young's modulus of the beam, N/m^2	E = 211 10^9
Axial tension stress in beam, kg/mm^2	0.03
Length of the beam, m	L=1.50

Numerical values of the applied tension force P, the flexural rigidity parameter v_f and α_k based upon the mechanical properties given in Table 1 are calculated for a number of the height (h) of the cross section and seen in Table 2. Natural frequency-mean axial speed curves showing the effects of variations of mean axial speed and location constant of the intermediate support on the natural frequencies of the beam will be depicted and be discussed at first in this section.

Table 2 Numerical values of the height (h) of the cross section, the tension force P, the flexural rigidity parameter v_f and α_k spring-dependent coefficient.

h, mm	P, N/m^2	v_f	α_k
2	47.09	0.32591	1387.51
4	94.18	0.65181	346.88
6	141.26	0.97772	154.17
8	188.35	1.30363	86.72

Figure 2 depicts the first three mode shapes of the axially moving beam under the following geometrical conditions and with the following physical properties: the bending rigidity constant $v_f = 0.651$, the location of the intermediate support $\eta = 0.2$, axial speed $v_0 = 2.80$, the spring-dependent value $\alpha_k = 346.88$

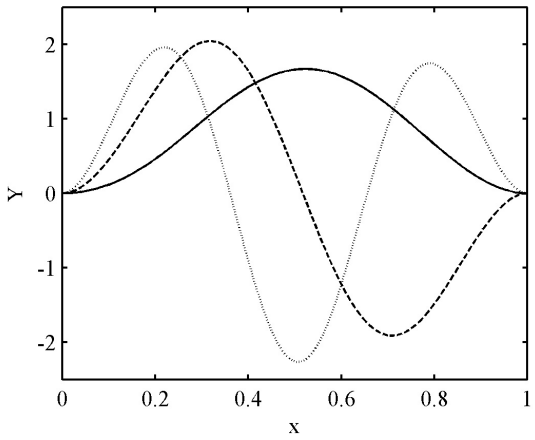


Figure 2: The first three mode shapes of the cantilever beam moving axially: First mode (—), second (– –), third (…).

Natural frequency-mean axial speed curves in Figure 3 and Figure 4 illustrate the variation of the first, second and the third natural frequencies with mean moving velocity for the four cases of the location intermediate support, $\eta = 0.1, 0.2, 0.3$ and 0.4, of the simply supported beams and beams with clamped ends respectively for the flexural stiffness constant ($v_f = 0.32591$). The variation of the natural frequencies with the increase in the mean moving velocity occurs as follows: While the mean translating velocity increases, the natural frequencies decrease. This condition is characteristic of axially moving systems. It can be noticed from the figure that locating the intermediate support towards the middle of the beam increases in natural frequency

of the first mode for the same transporting velocity. This conclusion is not valid for both the second natural frequency and the third.

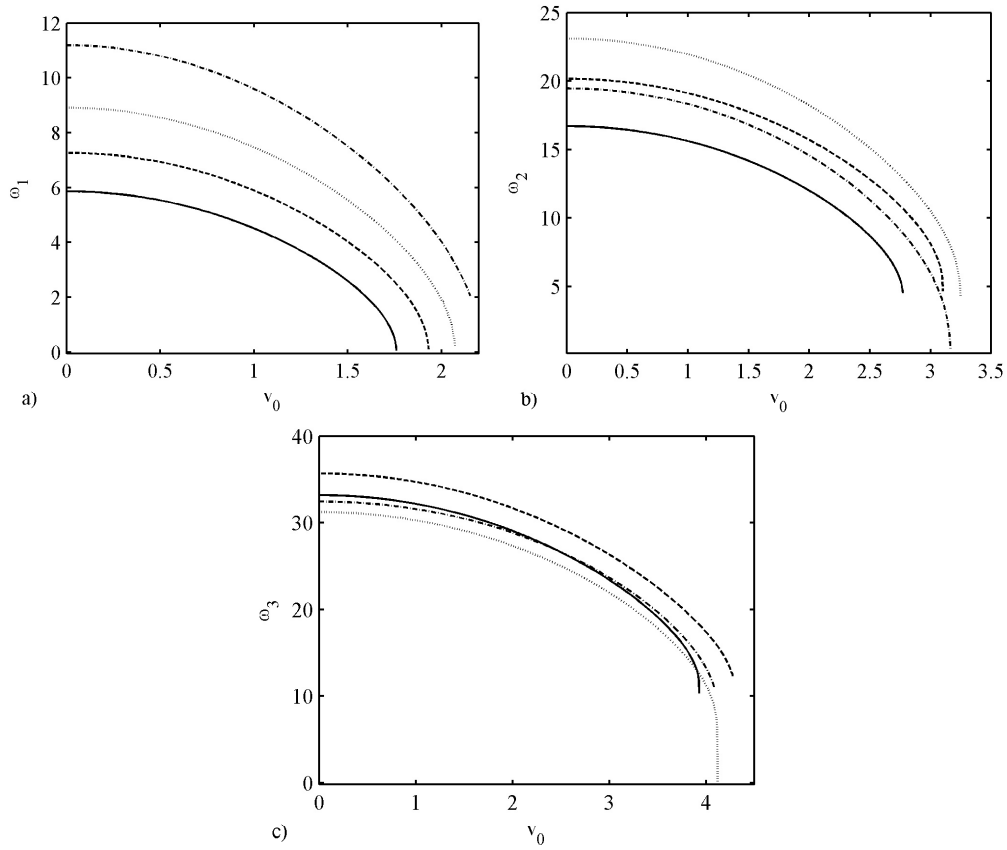
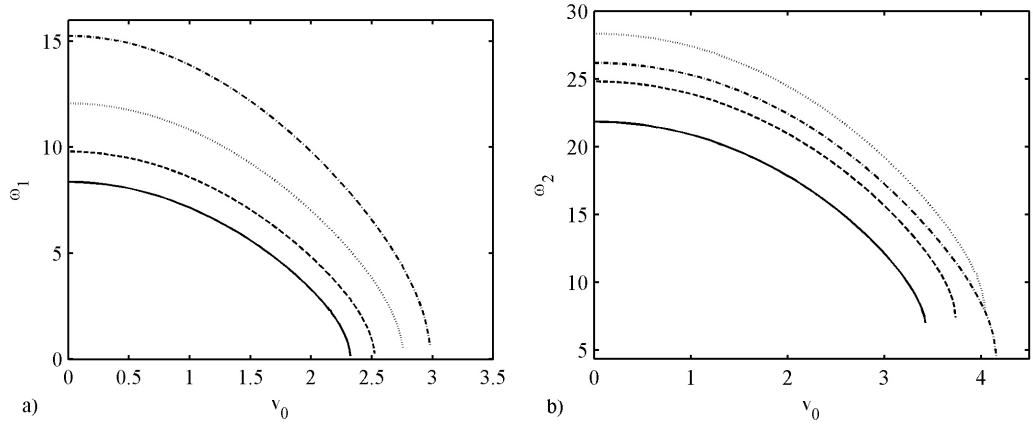


Figure 3: Natural frequency variations of the simply supported beams moving axially versus transport velocities for four different locations $\eta = 0.10$ (—), $\eta = 0.20$ (− −), $\eta = 0.30$ (…) and $\eta = 0.40$ (-.) of the intermediate support: the first mode (a), the second mode (b) and the third mode (c)



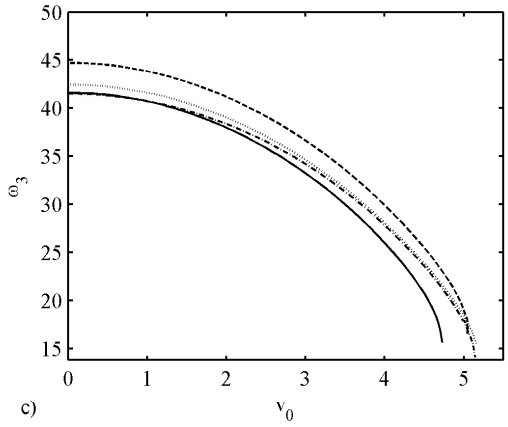


Figure 4: Natural frequency variations of beams moving axially versus transport velocities with clamped ends for four different locations $\eta = 0.10$ (—), $\eta = 0.20$ (– –), $\eta = 0.30$ (…) and $\eta = 0.40$ (-.) of the intermediate support: the first mode (a), the second mode (b) and the third mode (c)

5 CONCLUSIONS

- The variation of the natural frequencies with the increase in the mean moving velocity occurs as follows: While the mean transporting velocity increases, the natural frequencies decrease.
- It is found out that the beam with clamped-clamped boundary condition has higher natural frequency value than simply supported one.

REFERENCES

[1] K.Y. Sze, S.H. Chen, J.L. Huang, The Incremental Harmonic Balance Method for Nonlinear Vibration of Axially Moving Beams. *Journal of Sound and Vibration*, **281**, 611-626, 2005.
[2] L.H. Chen, W. Zhang, F.H. Yang, Nonlinear Dynamics of Higher-Dimensional System for an Axially Accelerating Viscoelastic Beam with In-Plane and Out-Of-Plane Vibrations. *Journal of Sound and Vibration*, **329**, 5321-5345, 2010.
[3] M.H. Ghayesh, S. Balar, Non-linear Parametric Vibration and Stability Analysis for Two Dynamic Models of Axially Moving Timoshenko Beams. *Applied Mathematical Modelling*, **34**, 2850-2859, 2010.
[4] G. Chakraborty, A.K. Mallik, H. Hatwal, Non-Linear Vibration of a Travelling Beam. *International Journal of Non-Linear Mechanics*, **34**, 655-670, 1999.
[5] F. Köstekci, Effects of Flexural Stiffness, Axial Velocity and Internal Support Locations on Translating Beam's Natural Frequencies. *Applied Mechanics and Materials*, **532**, 316-319, 2014.
[6] M. Gürgöze, A Note on the Vibrations of Restrained Beams and Rods with Point Masses. *Journal o f Sound and Vibration*, **96**, 461-468, 1984.
[7] J.-S. Wu, T.-L. Lin, Free Vibration Analysis of a Uniform Cantilever Beam with Point Masses by an Analytical-and-Numerical-Combined Method. *Journal of Sound and Vibration*, **136**, 201-213, 1990.

[8] M.N. Hamdan, B.A. Jubran, Free and Forced Vibrations of a Restrained Uniform Beam Carrying an Intermediate Lumped Mass and a Rotary Inertia. *Journal of Sound and Vibration*, **W**, 203-216, 1991.
[9] M.P. Paidoussis, C. Semler, Nonlinear Dynamics of a Fluid-Conveying Cantilevered Pipe with an Intermediate Spring Support. *Journal o f Fluids and Structures*, **7**, 269-298, 1993.
[10] M. Pakdemirli, A.H. Nayfeh, Nonlinear Vibrations of a Beam-Spring-Mass System. *Journal of Vibration and Acoustics*, **116**, 433-439, 1994.
[11] J.S. Wu, H.M. Chou, Free Vibration Analysis of a Cantilever Beam Carrying Any Number of Elastically Mounted Point Masses with the Analytical-and-Numerical-Combined Method. *Journal of Sound and Vibration*, **213**, 317-332, 1998.
[12] J.S. Wu, D.W. Chen, Dynamic Analysis of a Uniform Cantilever Beam Carrying a Number Of Elastically Mounted Point Masses with Dampers. *Journal of Sound and Vibration*, **229**, 549-578, 2000.
[13] A.H. Nayfeh, D.T. Mook, Nonlinear Oscillations, Wiley, 2008.
[14] M.H. Ghayesh, M.P. Païdoussis, Three-dimensional dynamics of a cantilevered pipe conveying fluid, additionally supported by an intermediate spring array. *International Journal of Non-Linear Mechanics*, **45**, 507-524, 2010.
[15] M.H. Ghayesh, F. Alijani, M.A. Darabi, An Analytical Solution for Nonlinear Dynamics of a Viscoelastic Beam-Heavy Mass System. *Journal of Mechanical Science and Technology*, **25**, 1915-1923, 2011.
[16] M.H. Ghayesh, M.P. Païdoussis, Y. Modarres-Sadeghi, Three-dimensional dynamics of a fluid-conveying cantilevered pipe fitted with an additional spring-support and an end-mass. *Journal of Sound and Vibration*, **330**, 2869-2899, 2011.
[17] M.H. Ghayesh, S. Kazemirad, M.A. Darabi, P. Woo, Thermo-Mechanical Nonlinear Vibration Analysis of a Spring-Mass-Beam System. *Arch Appl Mech*, **82**, 317–331, 2012.
[18] M.A. Darabi, S. Kazemirad, M.H. Ghayesh, Free Vibrations of Beam–Mass–Spring Systems: Analytical Analysis with Numerical Confirmation. *Acta Mech. Sin.*, **28**, 468–481, 2012.
[19] M.H. Ghayesh, M. Amabili, Nonlinear Vibrations and Stability of an Axially Moving Timoshenko Beam with an Intermediate Spring Support. *Mechanism and Machine Theory*, **67**, 1-16, 2013.
[20] E. Özkaya, M. Pakdemirli, H.R. Öz, Non-Liner Vibrations of a Beam–Mass System Under Different Boundary Conditions. *Journal of Sound and Vibration*, **199**, 679-696, 1997.
[21] F. Pellicano, V. F., Nonlinear Dynamics and Bifurcations of an Axially Moving Beam. *Journal of Vibration and Acoustics*, **122/21**, 2000.
[22] C.D. Mote Jr, A Study of Band Saw Vibrations. *Journal of the Franklin Institute*, **279**, 430-444, 1965.
[23] S.-J. Hwang, N.C. Perkins, Supercritical Stability of an Axially Moving Beam Part I: Model and Equilibrium Analysis. *Journal of Sound and Vibration*, **154**, 381-396, 1992.
[24] S.-J. Hwang, N.C. Perkins, Supercritical Stability of an Axially Moving Beam Part II: Vibration and Stability Analyses. *Journal of Sound and Vibration*, **154**, 397-409, 1992.
[25] H.R. Öz, M. Pakdemirli, Vibrations of an Axially Moving Beam with Time-Dependent Velocity. *Journal of Sound and Vibration*, **227**, 239-257, 1999.
[26] H.R. ÖZ, On the Vibrations of an Axially Travelling Beam on Fixed Supports with Variable Velocity. *Journal of Sound and Vibration*, **239**, 556-564, 2001.
[27] J.A. Wickert, C.D. Mote, Jr., Classical Vibration Analysis of Axially Moving Continua. *ASME Journal of Applied Mechanics*, 738–744, 1990.
[28] M. Stylianou, B. Tabarrok, Finite Element Analysis of an Axially Moving Beam, Part I: Time Integration. *Journal o f Sound and Vibration*, **178**, 433-453, 1994.

[29] T.R. Sreeram, N.T. Sivaneri, Fe-Analysis of a Moving Beam Using Lagrangian Multiplier Method. *Int. J. Solids Structures*, **35**, 3675-3694, 1998.
[30] Y.-Q. Tang, L.-Q. Chen, X.-D. Yang, Natural Frequencies, Modes and Critical Speeds of Axially Moving Timoshenko Beams with Different Boundary Conditions. *International Journal of Mechanical Sciences*, **50**, 1448-1458, 2008.
[31] M. Pakdemirli, H.R. Öz, Infinite mode analysis and truncation to resonant modes of axially accelerated beam vibrations. *Journal of Sound and Vibration*, **311**, 1052-1074, 2008.
[32] J.A. Wickert, Non-Linear Vibration of a Traveling Tensioned Beam. *International Journal of Non-Linear Mechanics*, **27**, 503-517, 1992.
[33] S.M. Bağdatli, E. Özkaya, H.R. Öz, Dynamics of Axially Accelerating Beams with an Intermediate Support. *Journal of Vibration and Acoustics*, **133**, 031013, 2011.
[34] A.H. Nayfeh, Introduction to Perturbation Techniques, Wiley, 1993.
[35] H.R. Öz, M. Pakdemirli, H. Boyacı, Non-Linear Vibrations and Stability of an Axially Moving Beam with Time-Dependent Velocity. *International Journal of Non-Linear Mechanics*, **36**, 107-115, 2001.

11th International Conference on Engineering Vibration
Ljubljana, Slovenia, 7–10 September 2015

ROTATIONAL RESPONSE AND SLIP PREDICTION OF SERPENTINE BELT DRIVES UNSING ABSOLUTE NODAL COORDINATE FORMULATION

Gregor Čepon*[1], Miha Boltežar[1]

[1]University of Ljubljana, Faculty of Mechanical Engineering, Slovenia
gregor.cepon, miha.boltezar@fs.uni-lj.si

Keywords: Dynamics, Belt Drive, Absolute Nodal Coordinate Formulation, Slip, Radial Compliance

Abstract. *In the past decade the applicability of belt-drives has been extended significantly due to their increased reliability. A serpentine belt drives are widely used to power all front accessories of the engine in modern vehicles. Although belt drives are much quieter compared to gear drives they can exhibit complex dynamics behavior; therefore it is very important to predict the dynamic response of such systems using validated numerical models. In this study the dynamic response and slip behavior of V-ribbed belt drive is investigated. The relation between belt-drive parameters and the speed loss is predicted using numerical model based on absolute nodal coordinate formulation. Moreover, the belt pulley contact forces were formulated as a linear complementarity problem, which enabled the incorporation of the discontinuous Coulomb friction law.*

1 INTRODUCTION

Belt drives are commonly used to transmit power in many engineering applications, such as automotive engines, industrial machines, etc. V-ribbed, belt-drive systems have become increasingly important to the automotive industry since their introduction in the late 1970s. Because of their simple installation and low maintenance, together with an ability to absorb shocks, they are frequently used instead of chain or geared transmission systems. Usually, V-ribbed belts in automotive engines drive multiple accessory pulleys, leading to compactness, smaller pulley diameters and longer belt life. However, these belt-drives can exhibit complex dynamic behaviors such as transverse vibrations of the belt spans, tension fluctuations, sliding of the belt over the pulley, etc. This can lead to fatigue of the belt, sliding wear and unexpected angular speed loss between the driver and the driven pulleys. All this phenomena impact belts life as well as the acoustic comfort. It is, therefore, very important to find an effective and validated approach for predicting the dynamic response of such belt-drives.
To ensure stable working conditions the dynamic response of such systems has been studied extensively. The review of the literature [1] identifies two well-defined groups of studies. The first group deals with the transverse belt-span response [2–4] and the second group with rotational response of the pulleys in the belt-drive [5–7] . Leamy and Wasfy [8, 9] proposed a general, dynamic finite-element model of a belt drive system including detailed frictional contact. Most recently, Čepon and Boltežar [10] presented a belt-drive model using absolute nodal coordinate formulation (ANCF) with a detailed contact formulation between the belt and the pulley.
Experimental studies of the contact between a grooved pulley and a V or V-ribbed belt are presented in [11] and [13]. In [13] the authors identified the contact parameters that are suitable for incorporation into the planar, multibody, belt-drive model that is presented in [10] and [12]. In this paper the dynamic response and slip behavior of V-ribbed belt drive is investigated. The relation between belt-drive parameters and the speed loss is predicted using numerical model based on absolute nodal coordinate formulation as it is presented in [10]. The two-pulley belt drive configuration is proposed in order to numerically and experimentally predict the angular speed loss at different belt-drive operational conditions. It is demonstrated that angular speed loss between the driven and driver pulley has a significant effect on the power-transmission efficiency.

2 NUMERICAL BELT DRIVE MODEL

The numerical belt-drive model is based on multibody system dynamics together with the absolute nodal coordinate system (ANCF) [14]. An ANCF is proposed that can be used in large rotation and deformation analyses of flexible bodies that undergo arbitrary displacements. The belt is modeled as a collection of two-dimensional beam elements that are based on the element originally proposed by Berzeri and Shabana [15]. Here, a viscoelastic belt material that obeys the Kelvin model is proposed, with the constitution relation:

$$\sigma_l(x,t) = E\,\varepsilon_l(x,t) + c\frac{\partial \varepsilon_l(x,t)}{\partial t}, \tag{1}$$

where σ_l is the axial distributed stress, E is Young's modulus, c is the viscoelastic damping factor and ε_l is the Lagrangian strain:

$$\varepsilon_l = \frac{1}{2}\left(\mathbf{r}'^{\mathrm{T}}\mathbf{r}' - 1\right), \qquad \mathbf{r}' = \frac{\mathrm{d}\mathbf{r}}{\mathrm{d}x}, \qquad \mathbf{r} = \mathbf{S}(x)\,\mathbf{e}^j. \tag{2}$$

The system of equations of motion, including all the beam elements and the constraint equations describing the connectivity constraints, can be written as:

$$\begin{bmatrix} \mathbf{M}_B & \mathbf{C}_{eB}^{\mathrm{T}} \\ \mathbf{C}_{eB} & \mathbf{0} \end{bmatrix} \begin{Bmatrix} \ddot{\mathbf{e}} \\ \boldsymbol{\lambda}_B \end{Bmatrix} = \begin{bmatrix} \mathbf{Q}_{eB} \\ \mathbf{Q}_{dB} \end{bmatrix}, \tag{3}$$

where $\mathbf{M}_B$ is the constant mass matrix of the belt, $\mathbf{C}_{eB}$ is the Jacobian of the constraint equations and $\boldsymbol{\lambda}_B$ is the vector of Lagrange multipliers. The vector $\mathbf{Q}_{eB}$ is the generalized force vector that includes external forces, $\mathbf{Q}_f$ is the generalized force vector due to the stiffness and damping forces, and $\mathbf{e}$ includes the accelerations of generalized coordinates of all the belt elements.

In a belt-drive, the belt is constrained to move over the surface of the pulley. The contact is considered to be between the belt element j and the pulley k, as shown in Figure 1a. The distances, relative velocities and changes of the relative velocities are determined by means of the relative kinematics. In the tangential contact direction we use the representation of Coulomb's friction

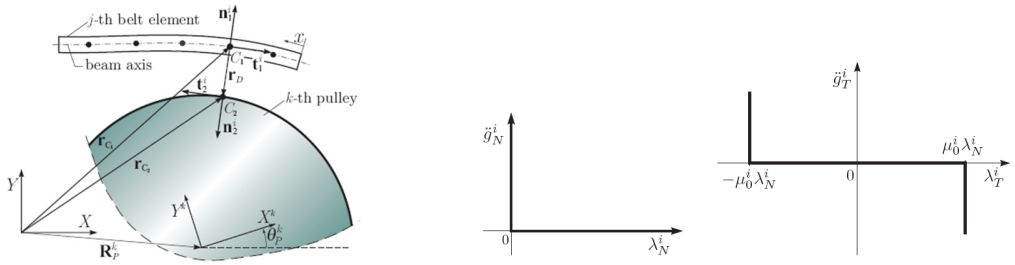


Figure 1: Belt-pulley contact formulation; a) Contact kinematics, b) Contact law in normal and tangential direction

law (Figure 1b) on the acceleration level:

$$\left.\begin{array}{lrcl} \text{sticking:} & |\lambda_T^i| < \mu_0\, F_N^i & \Longrightarrow & |\ddot{g}_T^i| = 0 \\ \text{sliding:} & |\lambda_T^i| = \mu_0\, F_N^i & \Longrightarrow & |\ddot{g}_T^i| > 0 \end{array}\right\}, \quad i \in I_H, \tag{4}$$

The normal distance can be written as:

$$g_N^i = {\mathbf{n}_2^i}^{\mathrm{T}} \mathbf{r}_D, \tag{5}$$

where $\mathbf{r}_D^i = \mathbf{r}_{C_2} - \mathbf{r}_{C_1}$ is the distance vector and $\mathbf{n}_2^i$ is the normal of the contact. The relative accelerations of the contact points can be expressed as [16]:

$$\ddot{g}_N^i = {\mathbf{W}_N^i}^{\mathrm{T}} \ddot{\mathbf{q}}^{jk} + w_N^i, \qquad \ddot{g}_T^i = {\mathbf{W}_T^i}^{\mathrm{T}} \ddot{\mathbf{q}}^{jk} + w_T^i, \tag{6}$$

where

$$\mathbf{W}_N^i = \begin{Bmatrix} -\mathbf{S}(x_{C_1})^{\mathrm{T}} \\ \mathbf{I} \\ \mathbf{u}_{C_2}^{\mathrm{T}} \mathbf{A}_\theta(\theta_P^k)^{\mathrm{T}} \end{Bmatrix} \mathbf{n}_2^i, \qquad \mathbf{W}_T^i = \begin{Bmatrix} -\mathbf{S}(x_{C_1})^{\mathrm{T}} \\ \mathbf{I} \\ \mathbf{u}_{C_2}^{\mathrm{T}} \mathbf{A}_\theta(\theta_P^k)^{\mathrm{T}} \end{Bmatrix} \mathbf{t}_2^i, \tag{7}$$

$$w_N^i = {\mathbf{n}_2^i}^{\mathrm{T}} \left(-\mathbf{A}(\theta_P^k)(\dot{\theta}_P^k)^2 \mathbf{u}_{C_2} + \mathbf{A}_\theta(\theta_P^k)\dot{\theta}_P^k \dot{\mathbf{u}}_{C_2} \right) + \dot{\mathbf{n}}_2^{i\,\mathrm{T}} \left(\dot{\mathbf{R}}_P^k + \mathbf{A}_\theta(\theta_P^k)\dot{\theta}_P^k \mathbf{u}_{C_2} - \mathbf{S}(x_{C_1})\dot{\mathbf{e}} \right), \tag{8}$$

$$w_T^i = {\mathbf{t}_2^i}^{\mathrm{T}} \left(-\mathbf{A}(\theta_P^k)(\dot{\theta}_P^k)^2 \mathbf{u}_{C_2} + \mathbf{A}_\theta(\theta_P^k)\dot{\theta}_P^k \dot{\mathbf{u}}_{C_2} \right) + \dot{\mathbf{t}}_2^{i\,\mathrm{T}} \left(\dot{\mathbf{R}}_P^k + \mathbf{A}_\theta(\theta_P^k)\dot{\theta}_P^k \mathbf{u}_{C_2} - \mathbf{S}(x_{C_1})\dot{\mathbf{e}} \right). \tag{9}$$

The matrix $\mathbf{A}$ is the transformation matrix, $\mathbf{A}_\theta$ is the partial derivative of the transformation matrix $\mathbf{A}$ with respect to θ and $\mathbf{q}^{jk} = \{\mathbf{e}_B^j,\, \mathbf{q}_P^k\}^{\mathrm{T}}$ is the vector of j-th belt element and the k-th pulley coordinates.
Both the normal reaction force F_N and the tangential friction force F_T are generated when the belt element contacts the pulley surface. In order to model contact forces the contact laws that are valid during the continuous contacts and sticking as well as for the transition to sliding and sticking and vice versa have to be applied. The equation of motion of the belt-drive including the contact forces can be written in the form:

$$\ddot{\mathbf{q}}_r = \mathbf{H}_F \left(\mathbf{W}_N \boldsymbol{\lambda}_N + \mathbf{W}_T \boldsymbol{\lambda}_T\right) + \mathbf{h}, \tag{10}$$

The contact normal and tangential forces are written as Lagrange multipliers $\boldsymbol{\lambda}_N$ and $\boldsymbol{\lambda}_T$. Finally, the contact problem can be formulated in the form of a linear complementarity problem and solved using an iterative Lemke algorithm. As it is reported in [10] this formulation leads to an accurate prediction of the belt-pulley contact forces when non-steady belt-drive operational conditions are considered. In this special case the normally used approximate Coulomb friction law may give an erroneous prediction of the contact forces. In Figure 2 a typical distribution of the normal and tangential contact forces are presented for two-pulley belt-drive during nonsteady operation.

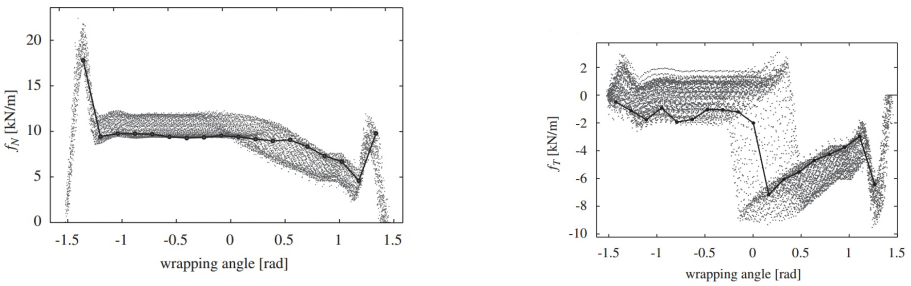


Figure 2: Non-steady belt-driver pulley contact forces; a) Normal contact force per unit length, b) Tangential contact force per unit length.

3 PREDICTION OF ANGULAR SPEED LOSS

3.1 Two pulley belt-drive experimental setup

The validation of the belt-drive model was done using a two-pulley belt-drive, as shown in Figure 3. A V-ribbed belt with five ribs and a K-rib section (5PK) was used. The material properties and contact parameters of the belt are given in [12] and [13] and presented in Table 1. To verify the numerical model the numerical results were compared with the experimentally obtained results. The driver pulley was rotated by DC motor and the torque on the driven pulley was achieved by a piston hydraulic pump. The angular velocity of driven and driver pulley was measured with HAIDENHAIN ERN1325 2048 precise optical encoders. The initial tension of the belt spans was set by changing the mid-distance of the pulleys. The torque on the driver and the driven shaft was measured with strain gages.

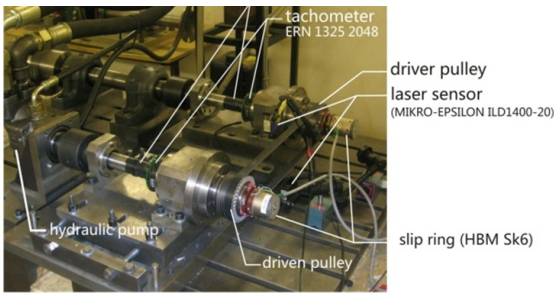


Figure 3: Belt-pulley contact formulation.

Parameter	Value
Radius of pulley	$0.05\,\mathrm{m}$
Belt length	$1.2\,\mathrm{m}$
Pulley mass moment of inertia	$0.013\,\mathrm{kgm}^2$
Span length	$0.045\,\mathrm{m}$
Belt mass	$0.096\,\mathrm{kg/m}$
Axial stiffness	$30400\,\mathrm{N/rib}$
Viscoelastic damping factor	$4.1\,\mathrm{Ns/rib}$
Bending stiffness	$5.2 \cdot 10^{-3}\,\mathrm{N/m}^2$
Damping coefficient of contact model	$300\,/\mathrm{m}$
Number of elements in belt model	48

Table 1: Belt drive parameters

3.2 Numerical model and identification of friction coefficient

The numerical two-pulley belt-drive model is presented in Figure 4 and the belt-drive parameters are given in Table 1. The discretization of the belt involved using 48 beam elements. Three

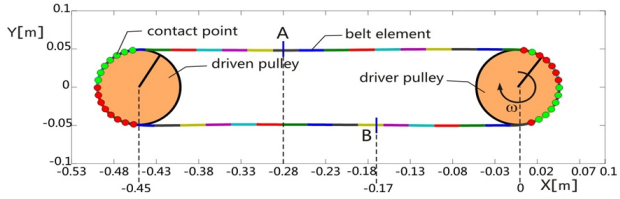


Figure 4: Numerical belt-drive model

contact points were proposed in the contact between one beam element and the pulley. As the beam elements have equal length the contact points are equally spaced along the length of the belt. Thus, the periodic excitation due to the discretization is incorporated into the numerical model. This can be avoided by randomly changing the length of the beam elements, which also has effects on the location of the contact points. The random length of the beam elements was computed using following equation:

$$L^i_{rand} = \frac{L_j}{n_e}\left(1 + 0.12 \cdot \mathrm{rand}\right), \qquad \sum_{i=1}^{n_e} L^i_{\mathrm{rand}} - L_J \leq 1 \cdot 10^{-4}\,\mathrm{m} \tag{11}$$

where L_J is the length of the belt, L^i_{rand} is the i-th length of the beam segment and "rand" is the random function that generates random numbers in the interval [-1,1].
In order to simulate belt-drive dynamics response the friction coefficient must be identified. The torque transmission between the pulley and the flat or V-ribbed belts is mainly governed by the friction. By assuming that the belt is sliding against the pulley and that the friction is fully developed along the groove, we can write the Euler-Eytelwein equation for the tension ratio:

$$\frac{T_t}{T_s} = e^{\mu\beta}. \tag{12}$$

The variables T_t and T_s are the tensions in the tight and slack belt spans and β represents the contact arc between the belt and the pulley. From the tensions in both belt spans the friction

coefficient can be obtained as:

$$\mu = \frac{1}{\beta} \ln \left(\frac{T_d}{T_j} \right), \tag{13}$$

where μ is the global friction coefficient, including the influence of the belt material as well as the belt and pulley-rib profiles. The test setup for measuring friction consists of a specially developed test rig, as shown in Figure 5. In order to measure the tension in the belt spans two

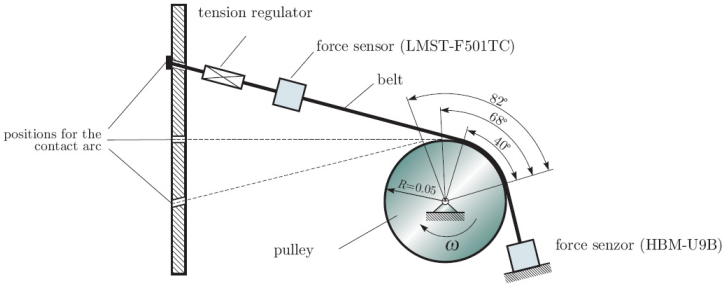


Figure 5: Experimental setup for measuring the friction coefficient.

load transducers were used. A total of three arcs of contact were studied ($\beta_1 = 40\,^{\circ}$, $\beta_2 = 68\,^{\circ}$, $\beta_3 = 82\,^{\circ}$).

For each contact arc, the tests were performed with eight different initial tensions T_0 and five pulley rotational velocities ω. Using this procedure we can identify the influence of the relative tangential velocity and the normal contact force on the friction coefficient. The average values of the friction coefficients are presented in Figure 6. Clearly, the friction coefficient de-

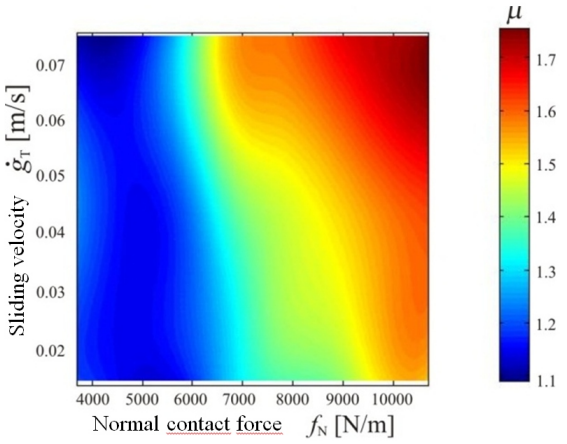


Figure 6: Friction coefficient versus the normal contact force and the relative tangential velocity

pends on the normal contact force and the relative tangential velocity. If the dependence of the friction coefficient on the normal contact force was expected, the observed strong influence of the relative tangential velocity on the friction coefficient is somehow surprising. The measured friction characteristics is finally incorporated into developed numerical model. During numerical integration for each contact point the normal contact force and relative tangential velocity is evaluated and friction coefficient is deduced from friction plane given in Figure 6

3.3 Angular Speed Loss

The angular speed loss between the driver and the driven pulley has a significant effect on the efficiency of the power-transmission. Therefore, an accurate prediction of angular speed loss is of great importance, especially in the automotive industry. There are three contributions to consider when dealing with angular speed loss [11]:

- the creep along belt,
- the radial compliance,
- the shear deflection.

Creep represents the belt stretching in the slip contact region between the belt and the pulley. Radial compliance represents the radial deformation as the rubber layer is subjected to a radial load when it is pressed against the pulley (Figure 7a). For this reason the radius at the entry and exit regions of the belt-pulley contact are not equal, which then affects the angular speed loss. The shear deflection along the belt is caused by the frictional forces that are transferred from the belt-pulley contact though the rubber to the cord layer (Figure 7b). Usually, the analytical

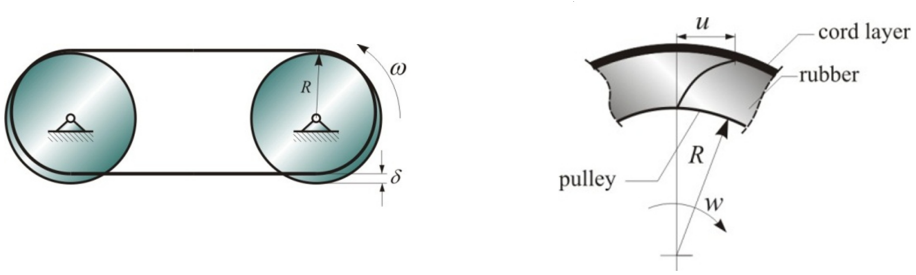


Figure 7: Angular speed loss; a) Radial compliance, b) Shear deflection of the rubber layer.

equation that estimates the angular speed loss is given as [10]:

$$\Delta\omega = \left(1 - \frac{2T_0R - M + 2R\,k}{2T_0R + M + 2R\,k}\right) \tag{14}$$

where T_0 is the initial tension, R is the radius of the pulley, M is the torque on the pulley, k is the stiffness of the belt and ω_1 is the angular velocity of the driver pulley. Eq. 14 only accounts for the creep theory and neglects all the other phenomena that impact on the angular speed loss. However, in our numerical model, along with creep, the radial compliance is also taken into account.

In Figure 8 the computed angular speed losses with the analytical equation (Eq. 14) and the developed numerical model are compared with the experimentally obtained angular speed losses. The measured speed losses are much higher than those predicted by the analytical model or our numerical model. The grey region in Figure 8a presents the difference between the results obtained with the numerical model of the belt-drive and the experimentally obtained results. This difference is due to the tangential deformation of the belt-rubber layer, which is not accounted for in the numerical belt-drive model. It can be seen that the effect of the shear deformation becomes significant at higher torque values. The blue region presents the difference between the

numerical model and the analytical model. This difference is the effect of the radial compliance, which is not accounted for in the analytical solution. In our numerical model this radial deformation is taken into account through the elastic component of the penalty contact force. From

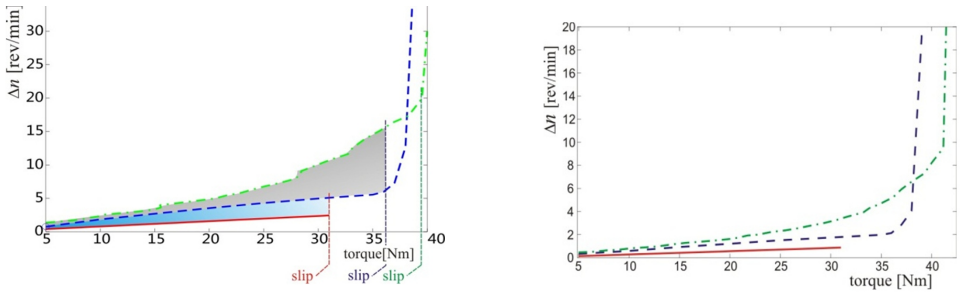


Figure 8: Angular speed loss between the driver and driven pulley

the comparisons presented in Figure 8 it is evident that the analytical model gives the poorest prediction of the angular speed loss. Moreover, the point of belt slippage is not correctly determined. However, our numerical model gives more reliable predictions of the angular speed loss, especially at low torques. In addition, the numerical model can quite accurately predict the point of the belt slippage. This accurate prediction is the result of a well-identified friction coefficient and the rigidity of the belt bending [12]. At high values of torque, which occur near the slippage point, the axial force in the slack span results mainly due to the bending of the belt span. The belt bending stiffness forces the belt to bulk outwards, which generates additional axial forces in the belt. This acts as a tensioner, which supplies the minimal axial force in the slack span.

4 CONCLUSIONS

In this paper a belt-drive model using the absolute nodal coordinate formulation is presented and belt slip is predicted. The continuous contacts in the normal direction and the possible sticking contacts in the tangential direction of the contact were formulated as the linear complementarity problem. The discontinuous Coulomb friction law was applied in order to model the frictional forces. A two-pulley experimental setup was proposed. Good agreement between the experimental and numerically obtained results was found. It was also shown that the numerical belt-drive model gives a reliable prediction of the angular-speed loss, especially at low torques. Moreover, it accurately predicts the point of belt slippage.

REFERENCES

[1] S. Abrate, Vibrations of belts and belt drives, *Mechanism and Machine Theory* 27 (1992) 645–659.

[2] A. Pramila, J. Laukkanen, M. Pautamo, Vibration of axially moving material using the FEM, *The American Society of Mechanical Engineers (Paper)* (1983) 83-DET-96.

[3] F. Pellicano, G. Catellani, A. Fregolent, Parametric instability of belts: theory and experiments, *Computers and Structures* 82 (2004) 81–91.

[4] G. Čepon, M. Boltežar, Computing the dynamic response of an axially moving continuum, *Journal of Sound and Vibration* 300 (2007) 316–329.

[5] S.J. Hwang, N.C. Perkins, A.G. Ulsoy, R.J. Meckstroth, Rotational Response and Slip Prediction of Serpentine Belt Drive Systems, *Journal of Vibration and Acoustics* 116 (1994) 71–78.

[6] T.C. Kraver, G.W. Fan, J.J. Shah, Complex Modal Analysis of a Flat Belt Pulley System With Belt Damping and Coulomb-Damped Tensioner, *Journal of Mechanical Design* 118 (1996) 306–311.

[7] T. Iwatsubo, K. Hasegawa, S. Arii, K. Shiohata, The formulation and dynamic analysis of a multiple belt system,

[8] M.J. Leamy, T.M. Wasfy, Transient and Steady-State Dynamic Finite Element Modeling of Belt-Drives, *Journal of Dynamic Systems, Measurement, and Control* 124 (2002) 575–581

[9] T.M. Wasfy, M.J. Leamy, Effect of bending stiffness on the dynamic and steady-state responses of belt-drives, *ASME 2002 Design Engineering Technical Conferences*, 2002

[10] G. Čepon, M. Boltežar, Dynamics of a Belt-Drive System using a Linear Complementarity Problem for the Belt-Pulley Contact Description, *Journal of Sound and Vibration*, 319 (2009) 1019–1035.

[11] G. Gerbert, Belt Slip-A Unified Approach, *Journal of Mechanical Design* 118 (1996) 432–438.

[12] G. Čepon, L. Manin, M. Boltežar, Introduction of damping into the flexible multibody belt-drive model: A numerical and experimental investigation, *Journal of Sound and Vibration*, 324 (2009) 283–296.

[13] G. Čepon, L. Manin, M. Boltežar, Experimental identification of the contact parameters between a V-ribbed bel and pulley, *Mechanism and Machine Theory*, 45 (2009) 1424–1433.

[14] A.A. Shabana, *Dynamics of Multibody Systems*, Third Edition, Cambridge University Press, 2005.

[15] M. Berzeri, A.A. Shabana, Development of simple models for the elastic forces in the absolute nodal co-ordinate formulation, *Journal of Sound and Vibration* 235 (2000), 539–565.

[16] F. Pfeiffer, C. Glocker, *Multibody dynamics with unilateral contacts*, John Wiley & Sons. Inc., 1996.

Engineering solutions for damping vibrations (MS15)

International Conference on Engineering Vibration
Ljubljana, Slovenia, 7-10 September 2015

TUNED MASS DUMPER USE FOR STRUCTURAL IMPROVEMENT BEHAVIUOR IN SOME REPRESENTATIVE ITALIAN CONSTRUCTIONS

N. Longarini*[1], M. Zucca[2], G. Silvestro[3]

[1] MSc Engineer, Milan, Italy
nicola.longarini@polimi.it

[2]MSc Engineer, Cagliari, Italy
marco.zucca@polimi.it

[3]MSc Engineer, Melfi, Italy
giuseppe.silvestro@aol.it

Keywords: vibration control, TMD, tall building, chimney, seismic and wind structural improvements

Abstract. *The paper discusses the Tuned Mass Dumper (TMD) use in some representative Italian constructions having a symbolic architectural value. In particular, the paper presents the TMD use for a new tall building in Milan, two footbridges (having each other different structures) and historical chimneys (hit by a strong earthquake in 2012) located in Lombardia region. By the TMDs, these constructions improve their structural behaviours, either in the Ultimate Limit State (ULS), either in the Serviceability Limit State (SLS). Therefore, by the TMDs, the structural performances improve under the seismic and wind actions with a greater comfort, in daily use, for the occupants. For each cases the structural analysis (by finite elements model, FEM) without TMD, the related TMD's parameters optimization and a subsequent structural analysis with TMD (emphasizing the improvements) are illustrated. Finally, for each TMDs, a design hypothesis are showed pointing out the installation procedure and the relatives costs.*

1 INTRODUCTION

Some TMD solutions to mitigate the effects of lateral loads and to control the vibrations are analysed for some representative Italian constructions: in a new slender tall building case to increase the comfort for the occupants mitigating the accelerations due to the wind (for ULS and SLS), in two new footbridges to control the vibrancy under the pedestrian and crowd loads and in historical chimneys to improve the seismic behaviour reducing the stress effects at the base and the top displacement (for Life Safety Limit State LSLS). In the chimneys case, the TMD is called Tuned Mass Control System (TMcS).

2 NEW SLENDER TALL BUILDING CASE

To improve the structural behavior under wind loads in tall buildings a TMD installation could be a valid solution, especially if it isn't possible to modify the geometrical proportions changing the symbolic shape or increase the geometrical slenderness (λ) [1]. Some tall buildings have $\lambda > 5 \div 7$, presenting dynamic effects specially due to the wind actions. To reduce the dangerous dynamic effects, the passive TMD could be considered for SLS. In the following, a 220m height tall building with 74m x 28m rectangular section (λ=7.85) is presented. It's afflicted by vortex shedding effects. The structure is characterized by: two lateral cores in high strength reinforced concrete (HSC, C70/85) located about 50m mutual distance, beams and columns in HSC, and 0.25m post tense concrete slab deck. In the wind analysis, for a return period (T_R) T_R=50 years, directional wind velocity (v) come from 16 different directions (Figure) is taken in account. The X longitudinal building axis (along the 74m length side) is directed like the 0°-180° wind direction and the Y transversal building axis (along the 28m length side) is directed like the 90°-270° wind direction. By the wind tunnel tests and the application of the High Frequency Force Balance (HFFB) [1], [2], [3] procedure, the base shear (V), the base moment (M) and the top acceleration (α_{max}) is evaluated for all the wind directions. The main frequencies (f), estimated by 2D Finite Elements Model (FEM), are f_1=0.14Hz, f_2=0.15Hz and f_3=0.26 Hz.

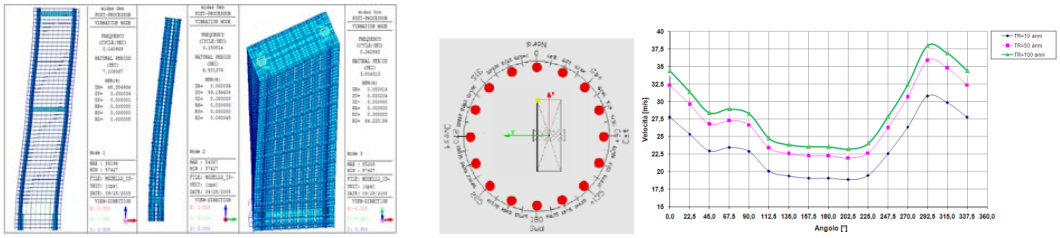


Figure 1: FEM and main vibration modes (on the right); direction wind velocity (on the left)

A results in terms of V, obtained by the Italian CNR code and HFFB procedure, are shown in the Table 1. To not exceed the TMD's limit installation (specially due an excessive mass [1]) by the HFFB, the V, M and α_{max} are evaluated considering a total damping coefficient (ξ) value in the range ξ=1÷4% (ξ considers the summation of the SLS concrete damping, ξ_s=1%, and the TMD damping, ξ_{tmd} = 3%).

For the SLS comfort building conditions, by the TMD, the α_{max} has to be minor than the limit acceleration (α_{lim}) suggested in literature [3] for tall buildings using for office (in T_R=10 years case, α_{lim} = 0.25 m/s^2). In order to consider acceptable the HFFB results for different ξ values, a comparison in terms of acceleration between wind time history analysis (TH) and HFFB application is carried out. The results, for TH and HFFB, are shown in the Table 2.

	wind direction	by CNR [kN]	by HFFB [kN]
0°-180°	along-w	12211	10816
	across -w	10079	33863
90°-270°	along-w	31881	33597
	across -w	13322	15499
292.5°	along-w	---	27955
	across -w	---	46052

Table 1. base shear V comparison.

	TH [m/s^2]	HFFB [m/s^2]
ξ=1%	0.45	0.47
ξ=4%	0.25	0.24

Table 2. α_{max} in TH and HFFB analysis T_R=10 years case.

Moreover, in the TH's FEM, the TMD located at the top floor is implemented by a nodal mass linked to the center of gravity of the top last floor by general links (represented a spring and dashpot in parallel to reproduce a TMD or LTMD). The links' characteristics come out from [4], [5].

Another damping solution to control the vibration is the viscous damper (VD) solutions positioned in the first 20 cores (from the base), limiting the invasiveness in terms of commercial surfaces occupancy; nevertheless the oblique positioning limits the inner layout. By VD, the acceleration decreases from 0.40m/s^2 to 0.32m/s^2 in the time histories analysis.

3 FOOTBRIDGES CASE

3.1 Assumptions

For two different footbridges (in the following called FA and FB) a vibrancy analysis is carried out considering the pedestrian load and in the overcrowding situation. For the analysis FEM is implemented and the eigenvalue analysis are conducted.

For the vibrancy analysis under pedestrian load, some methods, summarized in Table 3, could be considered. Applying the forces described in Table 3 by time varying functions, the effects of the pedestrian load are evaluated in terms of acceleration (in the following the methods applied are Bachmann, BS5400 and Allen-Murray); moreover a comparison between the evaluated accelerations and the limit acceleration (a_{lim}), indicated in (1) for the BS-5400, the ONT83 and in the ISO 10137/200, are carried out.

methods	function	note	see Table
Bachmann	$F_p(t) = G + \sum_{i=1}^{n} G \cdot \alpha_i \cdot sen(2\pi_i f_p t - \phi_i)$	G=800 N α_i is i-harmonic coefficient f_p is the "activity" frequency ϕ_i is the the i-harmonic phase respect the first harmonic	4
BS5400	$F_p(t) = A \cdot \sin(2\pi f_v t)$	A=180 N; velocity v is constant $v = 0.9 \cdot f_v$ (f_v is the vertical frequency)	---
Allen-Murray	$F_p(t) = P(1 + \sum \alpha_i \cdot \cos 2\pi \cdot i \cdot f \cdot t)$	P = 700 N f is the walking frequency α_i is the dynamic coefficient of the i-harmonic	5
AIJ	$F_p(t) = 11,78 \cdot sen(78.5)$ $F_p(t) = 70,69 \cdot sen(78.5)$	walking 0.3 kgf·sec applied for 0.04s running 1.8 kgf·sec applied for 0.04s	---

Table 3: methods for pedestrian load evaluation.

activity	activity rate [Hz]		Fourier coefficient and phase lag					design [person/m^2]
			α_1	α_2	ϕ_1	α_3	ϕ_3	
walking	vertical	2.0	0.4	0.1	$\pi/2$	0.1	$\pi/2$	≅1
		2.4	0.5					
	forward	2.0	0.2	0.1				
			α_1/α_2=0.1					
	lateral	2.0	α_1/α_2=0.1	α_3/α_2=0.1				

Table 4:coefficients for Bachman method.

harmonic (i)	frequency range (i*f)	dynamic load factor (α_i)
1	1.6 to 2.2	0.5
2	3.2 to 4.4	0.2
3	4.8 to 6.6	0.1
4	6.4 to 8.8	0.05

Table 5:coefficients for Allen Murray method.

The a_{lim} value are obtained by the following relations.

$$a_{lim-BS5400} = 0.5 \cdot (f)^{0.5};\ a_{lim-ONT83} = 0.25 \cdot (f)^{0.78};\ a_{lim-ISO10137} = 60 \cdot \sqrt{2} \cdot 0.005 \quad (1)$$

The structural behaviour under crowd load is studied in terms of frequency, evaluating the vertical and horizontal vibration mode shapes and comparing the frequency values to the acceptable ranges proposed in the Setra [6] and in the most important structural international

codes. In fact, it's possible to associate the risk of structural resonance (R) to the footbridge's frequency (f). For the vertical frequency, SETRA proposes an high R value for f= 1.7÷2.1 Hz, a medium R for f=0.9÷1.7 Hz and f=2.1÷2.6 Hz, a low R for f=2.6÷5.0 Hz and very low R for f=0÷0.9 Hz and f > 5 Hz. Other limits to be considered are: EC2 (1.6÷2.4 Hz), EC 5 (0÷5 Hz), BS5400 (0÷5 Hz), Japan AIJ (1.5÷2.3 Hz), ISO/DIS Standard 10137 (1.7÷2.3 Hz), CEB 209 Bulletin (1.65÷2.35 Hz), Bachman (1.6÷2.4 Hz).

For the horizontal frequency, SETRA proposes an high R value for f = 0.5÷1.1 Hz, a medium R for f=0.3÷0.5 Hz and f=1.1÷1.3 Hz, a low R for f = 1.3÷2.5 Hz and very low R for f=0÷0.3 Hz and f > 2.5 Hz. Moreover, EC1 suggests to evaluate the vertical and horizontal footbridge frequencies limiting to indicate acceptable ranges, precisely: for the vertical frequency the range is 1÷3 Hz, for the horizontal frequency the range is 0.5÷1.5 Hz.

For the vibrancy analysis in the SLS, others practical methods could be used, in particular the Reither-Mesiter-Lenzen (RML) [7] or the Arcelormittal (AR) [8]. By RML and AR it's possible to estimate if the deck vibrancy is acceptable for the occupants in the SLS classifying the structural behaviour by acceptable ranges defined by a correlation between the frequency deck and the maximum vertical displacements. The analysis by the RML method is specifically valid for floor deck vibrancy study, however it is here conduced to evaluate the structural behaviour in a potential overcrowding situation in footbridge case.

Knowing the FA and FB behaviours under the pedestrian and overcrowd loads, if the acceptable limits (in terms of acceleration or acceptable vibrancy range) are not respected TMD solutions are studied. The damper characteristics are evaluated by the Den Hartog [9] formulations (2). Estimating the ratio (μ) between the TMD mass (m) and the mass of the main structure involved in the mode shape to hit (m_i), the optimal damping ratio (ξ_{opt}) and optimal frequency ratio (f_{opt}) are evaluated by the following relations.

$$\mu = \frac{m_{tmd}}{m_i};\ \xi_{opt} = \sqrt{\frac{3\mu}{8(1+\mu)^3}};\ f_{opt} = \frac{f_i}{1+\mu} \tag{2}$$

3.2 FA footbridge

The first footbridge (in the following FA) connects two buildings renovated for EXPO 2015; it presents a S355 steel structures and its architectural design presents a Vierendeel configurations (30m total length, 5.10m width, 4m roof level height). The footbridge has two levels: the walkway level and the roof level. The footbridge could be classified III class by the SETRA; for a III class the crowd load is defined by the 0.5 pedestrian/m^2 density.

In the structural analysis carried out by FEM, the FA is implemented by beam elements and the lower and upper decks (in integrated trapezoidal sheet with a 4 cm concrete thickness layer) are implemented by plate elements. The footbridge is supported by n.°4 general links; they connect the n.°4 extremity nodes (n.°2 for each sides) of the lower deck to fixed nodes positioned at a distance equal to the supports height (in vertical direction from the deck). In particular: on the left footbridge side, the supports are fixed and multi-directional; on the right side, the supports are movable along the longitudinal footbridge axis and multi-directional.

Therefore, from the geometrical characteristics of the chosen supports, it's possible calculate the translational and rotational stiffness (UNI EN 1337-3-2005). The dead and live loads are applied with the seismic action (considered in according to the Italian Code (NTC 2008) by the elastic site spectrum with the ductility structure factor q = 2). To evaluate the seismic effects (LSLS) the eigenvalue analysis is carried out, calculating the vibration mode shapes and the related mass involved, obtained the values shown in Table 6 and Figure 2.

mode	frequency [Hz]	mass [%]	main direction [/]
1	2.16	79.85	Z global, vertical
5	6.22	32.79	Y global, horizontal
7	7.40	77.42	X global, horizontal

Table 6:FA main vibration modes.

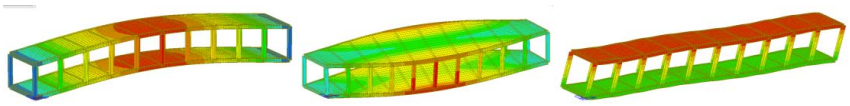


Figure 2: FA footbridge; 1-5-7 vibration mode shapes.

For FA, the analysis under the pedestrian load is carried out by the Bachman, BS5400 and Allen-Murray methods. In the Bachman case, the time history force is applied along the central nodes of the longitudinal axis (in the nodes having a 0.65 m mutual distance). Besides, in BS5400 and Allen Murray cases, the time history forces is applied in the node with the maximum vertical displacement (under the dead and life loads); the BS5400 and Allen-Murray [10] forces applied in the FEM are showed in the next Figure 3.

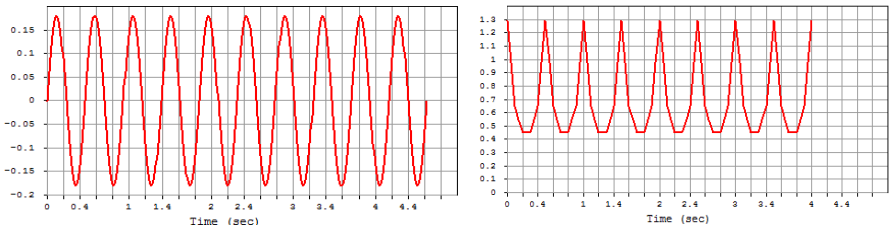


Figure 3: (left) Time History force for BS5400 and (right) Allen Murray

Applied the force time histories, the accelerations (a_{max}) are evaluated and compared to the limit value (a_{lim}). By Bachman, all of the verifies are satisfied: $a_{max} = 0.25$ m/s^2 is minor than $a_{lim\text{-}BS5400} = 0.73$ m/s^2, $a_{lim\text{-}ONT83} = 0.49$m/s^2 and $a_{lim\text{-}ISO1037} = 0.42$ m/s^2. Equally, FA is verified by BS5400 ($a_{max} = 0.021$ m/s^2) and by Allen Murray ($a_{max} = 0.032$m/s^2). In BS5400 and Alley Murray, the acceleration time histories are showed in the next Figure 4.

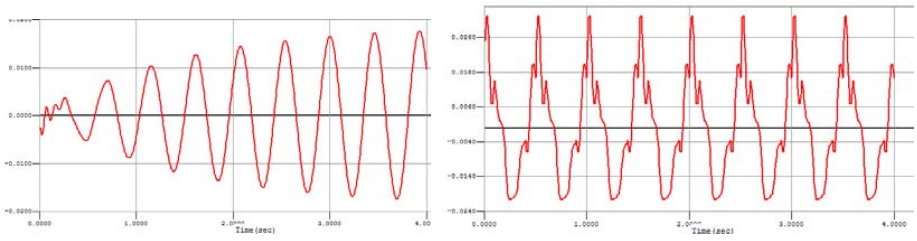


Figure 4:acceleration for BS5400 (left) and Allen-Murray (right) methods

About the vibrancy – under the crowd load - the RML and AR methods is applied. For RML, dynamic nodal loads (descripted in [7]) are applied on mesh the nodes having a mutual distance of 0.70 m. The only walkway level frequency is considered. The maximum dis-

placement (δ_{max}) is δ_{max} = 0.93 mm and the first walkway deck frequency is T_f =1.08 Hz, so the footbridge has a very perceptible oscillating move without TMD.

A different result is obtained by the AR (for 1% structural damping) combining T_f = 1.08 Hz and the modal mass (m) of the floor involved (m =42949 kg, equal to 69% of the 62246 kg total mass). The OS-$_{RMS\ 90}$ value is 0.6 included in the recommended range (0.2÷0.8) for the class C floor retail [8]. To improve the vibrancy behavior of the walkway deck a TMD are studied and optimized. By the TMD (m_{tmd} = 6.4 kN, K_{tmd} = 28.33 kN/m, c_{tmd}= 0.68 kNs/m, optimum ratio of frequencies α_{opt} = 0.97 and optimal equivalent viscous damping ratio ξ = 8.02%), implemented like a nodal mass linked to the walkway deck by a spring and linear dashpot, the maximum displacement decreases to 0.725 mm (the frequency is slightly reduced to f_1 = 1.04 Hz) so the footbridge improves to a lightly perceptible oscillating move [7]. It's important to underline, considering only the walkway, by SETRA classification the f_1 = 1.04 Hz is in the medium R range, but considering all of the footbridge structure the f_1 = 2.16 Hz is in the high R range.

3.3 FB footbridge

The second footbridge analyzed is called FB. Having 67.6 m length and 7.08 m width, it's characterized by a steel deck and static conceptual scheme showed in the next Figure 5.

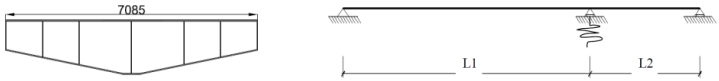


Figure 5: footbridge section and structural conceptual design (L1 = 45.9 m , L2 = 21.7m)

The FB connects two urban areas in a Italian city and it's part of an important urban requalification. It's classified like III class SETRA footbridge. Two FEM are implemented to analyse the FB: a beam model and a plate model with 2D elements. Comparing the vibration modes by eigenvalue analysis carried out in both FEMs, the results are practically the same in terms of vibration mode shapes and stress effects. To decrease the first vibration mode to improve the FB vibrancy behaviour a TMD solution is implemented. The TMD could be installed inside of the deck (close the maximum vertical displacement zone). TMD is implements like mentioned in FA case.

The TMD has to works for the vertical mode shapes because, from the FEM analysis: the first frequency is f_1 = 2.11 Hz (in vertical direction) and the mass involved is the 47.30% of the total mass; besided, the second frequency is f_2= 6.66 Hz (horizontal direction) and the mass involved is the 71.21% of the total mass.

By SETRA, the f_1 is in the high R frequency range for vertical direction shape. So the TMD studied is characterized by a mass of 1.25% mass involved in the first mode (m_{tmd} = 18.2kN), a stiffens K_{tmd} = 312 kN/m a damping coefficient c_{tmd} = 3.61 kNs/m, an optimum ratio of frequencies α_{opt} = 0.98 and an optimal equivalent viscous damping ratio ξ = 7.56%. By RML method, implementing the TMD in the FEM, the δ_{max} = 1.2 mm (associate to f_1 = 2.11 Hz) decreases to δ_{max} = 0.3 mm (associated to f_1= 0.61Hz), so the vibrancy is reduced to a lower lightly perceptible state [7].

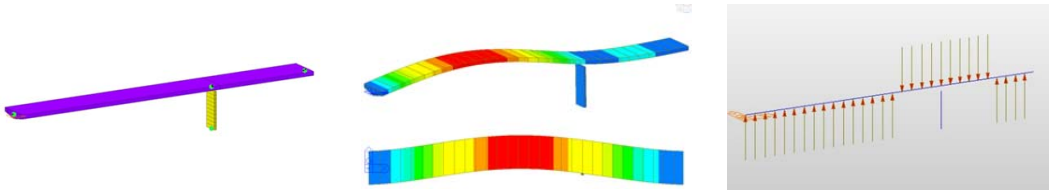


Figure 6: (left) FEM; (center) I and II vibration mode shapes; (left) SETRA vertical crowd load application

Evaluating the structural behaviour under the crowd load it's possible to follow the SETRA indications. The load is applied in the direction of the deformations and the value for the vertical direction (Figure 6), is defined in the following relation (3) where: d is the kN/m^2 due to the crowd – for dense traffic and III class d = 0.5 pedestrian/m^2 , ξ is a no dimensional damping ratio, n is the number of people on the footbridge deck.

Applying the SETRA described load, in the FEM with the TMD implemented, the acceleration decreases to 0.23 m/s^2, a value included in the more comfortable range for the III class acceleration in vertical direction.

$$Q = d \cdot (280N) \cdot \cos(2\pi f_v t) \cdot 10.8 \cdot (\xi/n)^{0.5} \cdot \psi \qquad (3)$$

4 HISTORICAL CHIMNEYS CASE

The structural improvements due to a TMcS installation in two historical chimneys is here discussed. The masonry chimneys are part of the same plants, but they have different structures. The first one (CA) having 50m height and it's characterized by two cylindrical skins connected themselves by n.°8 meridians and n.°11 parallels. The inner skin is tapered up to the top and all the structural parts having 0.27m thickness; the second one (CB) having the same height and configuration of CA but it presents only the outer skin at the last 10m (from 40m to 50m). CA and CB appears very similar but they have different vibration mode shapes and the seismic improvement by TMcS could be different.

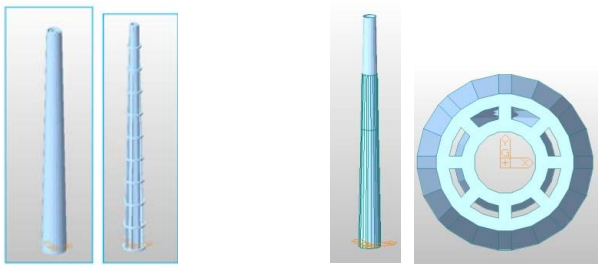


Figure 7: (left) CA's FEM with meridians and parallels system –(right) CB's FEM and tapered double skins).

In the FEMs, modulus of elasticity (E) and the ultimate compression strength value ($f_{dc,rid}$) - deduced by flat jacks tests- of the masonry are E=12185MPa and $f_{dc,rid}$ = 3.55MPa (decreased from evaluated 4.96MPa by coefficients c_1=1.2 and c_2=0.86 [13]. For CA and CB, a first FEM is implemented by using beam elements and a perfect join base boundary condition; dead load is applied combined to the seismic action implemented by the seven spectrum-compatible accelerograms. In the FEM (where the ductility factor q chosen is q = 2) an eigenvalue analysis is carried out to identify the main vibrational mode shapes with the related mass involved. Applying the seismic load, base shear (V), base bending moment (M) and top displacement (η) are evaluated for CA and CB.

Without the TMcS, CA shows V_A = 451 kN, M_A = 8120 kNm and η_A = 0.04 m with an eccentricity (e) e_A = 1.92; without TMcS, CB shows V_B = 196 kN, M_B= 5120 kNm and η_B = 0.033 m with e_B = 1.91 m.

By the eigenvalue analysis, in CA the first and second vibration modes (T_1 and T_2) are T_{1A} = T_{2A} = 1.08 s and the related masses (m_1 and m_2) are m_{1A} = m_{2A} = 0.56% of the total CA's mass; in CB, T_{1B} = T_{2B} = 0.82 s and the related masses (m_1 and m_2) are m_{1B} = m_{2B} = 0.85% of the total CB's mass. For CA and CB, the best TMcS characteristics [11-12] are calculate starting from a ratio ($\mu = m_{TMcS}/m_{str}$) between the TMcS mass (m_{TMcS}) and the main structure mass (m_{str}) to define: the optimal coefficient of frequencies (α_{opt}), the optimal equivalent viscous damping ratio (ξ_{opt}) for the TMcS, the TMcS horizontal stiffness (k_{TMcS}) and the TMcS horizontal damping coefficient of each viscous damper (C_{TMcS}), [13].

For the α_{opt}, ξ_{opt} and the k_{TMcS} evaluation, μ value has to be optimized normally varying in the 1.0%÷5% percentage range [13]. By the predicted seven spectrum-compatible accelerograms, varying the μ value, in the stresses effects time histories the μ value minimized V, M and η is found out. For CA, implementing in the FEM the TMcS at 45 m height, the better improvements are obtained by μ = 0.032 (with m_{TMcS} = 75.71 kN, k_{TMcS} = 143.68 kN/m and C_{TMcS} = 7.53kNs/m) and so the stresses effects (V_A ,M_A and η_A) under the seismic action decreases like shown in the Table 7 (in terms of ΔV, ΔM and $\Delta\eta$ percentage).

For CB, the TMcS is implemented in two positions: at h = 45 m (in one skin part) and at h = 40 m (at the end of the double skins part), Figure 7.

If the TMcs is at h = 45 m, the best μ is a very low value μ_{1skin}= 0.007 (with m_{TMcS} = 15.8 kN, k_{TMcS} = 90.55 kN/m and C_{TMcS} = 1.39 kNs/m); if the TMcS is at 40 m height, the best μ increases to μ_{2skin} = 0.0125 (with m_{TMcS} = 33.9 kN, k_{TMcS} = 189.48 kN/m and C_{TMcS} = 4.17 kNs/m). For different μ values, V and M at the base of CB vary like showed in Figure 9. Choosing an average value μ = 0.01 the improvements in Table 7 are obtained. In every cases, for CA and CB, the TMcS' mass acceleration is always minor then the limit value a_{lim} = 1g. To confirm the improvements a new 3D FEM is implemented with the masonry characterized by a non-linear behavior and with a possible TMcS structural configuration [13], (Figure 10).

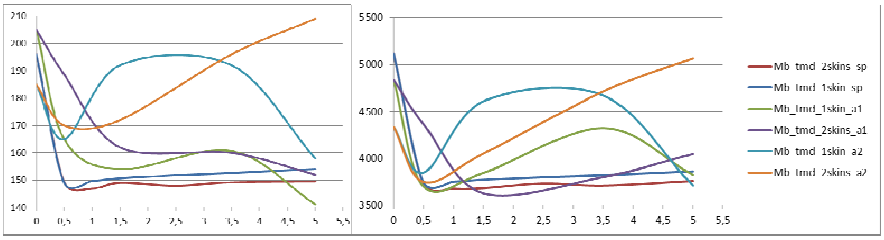


Figure 8: V and M with different μ , for seismic spectrum (sp) and 2 accelerogram (a1 and a2)application.

	μ [%]	TMcS installation [m]	ΔV [%]	ΔM [%]	$\Delta\eta$ [%]
CA	3.2	45	32	43	28
CB	1.0	45	24	27	22
CB	1.0	40	25	28	25

Table 7: seismic improvements for CA and CB, with TMcS .

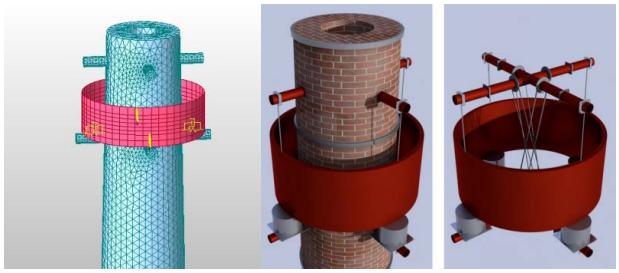


Figure 9: 3D FEM and 3D possible structural solution (for CB)

5 CONCLUSIONS

In the paper, the mitigation of the dynamic effects by TMD in symbolic constructions are discussed. For each cases the dynamic effects to mitigate are explained and some different solutions are calculated and proposed with related possible TMD installations..

REFERENCES

[1] Longarini N, Crespi P, Analisi al vento dei nuovi alti edifici di Milano. *IX Convegno Nazionale Ingegneria del Vento, Spoleto (Italy),* June 30-July 03, 2010

[2] Y.Zhou, A.Kareem, *Aerodynamic loads on tall buildings: an interactive database*. ASCE-2002

[3] Nicholas J.Cook, *The designer's guide to wind loading of building structures*. Part 2.: Static structures.

[4] .Abe,Y. Fujino, *Dynamic characterization of multiple tuned mass dampers and some design formulas,* Earthquake Eng. Struct. Dyn. 23:8 , 813–835

[5] Ahmed A. Farghaly, Mahmoud S. Ahmed, *Optimum Design of TMD System for Tall Buildings*, ISRN Civil Engineering Vol. 2012 Article ID 716469, 13; 2012

[6] Setra, *Footbridges*: *Assessment of vibrational behavior of footbridges under pedestrian loading*, 2006

[7] Bungale, Taranath, *Steel, Concrete and composite design of tall buildings*, McGrow Hill, NY, 1998

[8] Feldman, Heinemeyer, Volling, *Design Guide for floor vibrations,* ArcelorMittall, 1996

[9] J.P. Den Hartog, *Mechanical Vibrations,* 4th Edition Ed .Dover Publication, NY, 1956

[10] Allen D., Murray T., *Design criterion for vibrations due to walking*, AISC Engineering Joirnal, Fourth Quarter,pages 117-129;1993

[11] C. Li, W.An, *Optimum properties of multiple tuned muss dumper for reduction of translational and torsional response of structures subjected to ground acceleration*, Engineering Structures 28(4): pages 472-492.

[12] Z.T.Rakicevivc, A. Bogdanovic, D. Jurukovski, P. Nawrotzki, *Effectivness of tuned mass damper in the reduction of the seismic response of the structure*, Bulletin of Earthquake Engineering Vol 10, Issue 3, pp 1049-1073, June 2012

[13] Longarini N, Zucca M., *A chimney's seismic assessment by a tuned mass damper*, Engineering Structures 79(2014): pages 290–296, 2014

International Conference on Engineering Vibration
Ljubljana, Slovenia, 7-10 September 2015

STIFFNESS AND LOSS FACTOR OF UNBONDED, MULTI-STRAND BEAMS UNDER FLEXURAL DEFORMATION

Haval K. Asker*, Jem A. Rongong and Charles E. Lord

The University of Sheffield, Department of Mechanical Engineering

hkaasker2@sheffield.ac.uk

Keywords: unbonded beam, multi-strand, loss factor, energy dissipation, three point bend.

Abstract. *Beam-like structures constructed from many long strands that are constrained rather than bonded together can provide high levels of structural damping through friction between individual strands. This paper describes experimental and numerical studies carried out on square-section metal beams that are aimed at improving understanding of the relationship between construction and performance. The beams used in this study are constructed from lengths of square-section, key steel. The bundle of strands is held together at various compression loads with pre-calibrated clamps. Flexural behaviour of an assembled beam is simulated using standard finite element analysis and simple Coulomb friction at the interfaces. The validity of the assumptions used in the models is confirmed by comparison with three point bend tests on a regular nine strand construction at several different clamp loads. Subsequent numerical studies are used to investigate the effects of increasing the number of strands whilst the overall cross-section of the bundle remains unchanged. It is found that overall stiffness drops and loss factor increases when more strands are used. Interestingly, the energy dissipated by each beam construction is almost the same.*

1 INTRODUCTION

Vibration control using dry metal friction mechanisms may has considerable concerns about understanding, explaining and optimising these systems which may need more study as systems involving such behaviour can provide useful damping levels over a large range of operating temperatures. This mechanism in this study depends on dissipating energy through the dry friction occurring between the mating contact surfaces inside the beam-like system.

One of the earliest researches that used the dry friction mechanism to control vibration can be the work of Goodman and Klumpp [1] in the 50's of the last century which is based on utilizing the interfacial frictional contact effect to reduce the resonant stresses in the turbine blades experimentally and then developed a general equation for the energy dissipation per cycle in a coulomb friction type in the interface region for two beams in contact having an external distributed pressure to keep the mating surfaces in contact under steady-state cyclic loading.

The Coulomb friction cause a nonlinear behaviour to the vibrational systems as the frictional force always resists the motion in a way opposite to the motion direction. Basically, in any hysteretic damping system the stiffness may be presented as a complex stiffness which is a combination of the stiffness k and the damping coefficient ηk, imaginary part,[2] [3]. Coulomb friction may introduce in a form of an equivalent viscous damping which can linearize and simplify the Coulomb mathematical formulation. This assumption used in the work of Pratt and Williams [4] when they were counting for the number of sticks per cycle for two bodies in contact.

This study adopts the loss factor as an indicator for the level of the damping that exists in a system. This is expressed as the ratio between the energy dissipated per cycle to the maximum strain energy stored in that system. Generally, there are direct methods and approximate methods for finding the loss factor. For example the free decay method and the half power method would be considered approximate methods as other parameters need to be calculated to find the estimated value of the loss factor. Alternatively, calculation of energy dissipation and stored strain energy would be a direct method [5]. To dissipate energy in a multi-strand beam, a proper clamping mechanism should be provided to keep contacted beams together [6].

The simulation of experiments by finite element software can provide the potential of extending the experimental study by introducing and investigating more parameters and building more models with less cost. Chen & Deng [7] found that a finite element model was able to simulate slip damping observed in the previous experimental studies of Goodman and Klumpp [1] and Metherell and Diller [8]. As finite element packages have become more reliable and able to provide similar boundary conditions to that of the experiments, the frictional damping behaviour of multi-layer beams have commence [9] [10]. This has included direct comparison of hysteresis [11].

Specific area, the ratio of surface area to the mass, is a significant factor affecting loss factor values as it can affect the total strain energy. Zhou et al [12] considered specific area when analysing the damping developed by carbon nanotubes. They found that the larger the specific area the higher the loss factor values were.

This paper presents a study of multi-strand beams where the total cross-section of the unit remains the same but the number of strands varies. This means that the specific area is varied.

2 EXPERIMENTAL STUDY

Quasi-static tests were conducted on multi-strand beams arrangements. The term quasi-static is used to describe a test in which changes in the applied loading occur over time periods well below system natural frequencies. This means that the system can be analysed as several static states and the change in the force or displacement will not affect the dynamic characteristics of the system.

The aim of the experiment was to investigate the effect of sliding interfaces on the loss factor of a bundle of beams. These beams were held together by clamps. A hydraulic test machine was used to provide bending loads on the beams with the applied displacement being perpendicular to the neutral axes of the beams.

2.1 Methodology

Three point bend tests were conducted on the multi-strand beams in order to understand parameters affecting stiffness and loss factor of the system. The beam arrangement had nine beams as depicted in Figure 1 with span distance of 250 mm between the support rollers of the bending clamp as shown in Figure 2. The cross-section for individual strands was 4×4 mm^2. The parameters that were altered were the clamping force and the applied deformation.

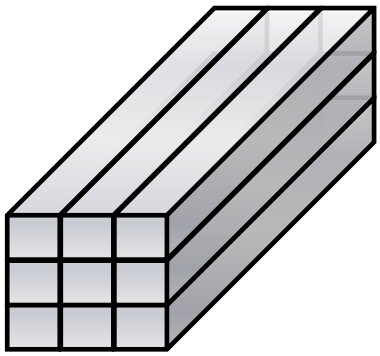


Figure 1: Nine beam arrangement.

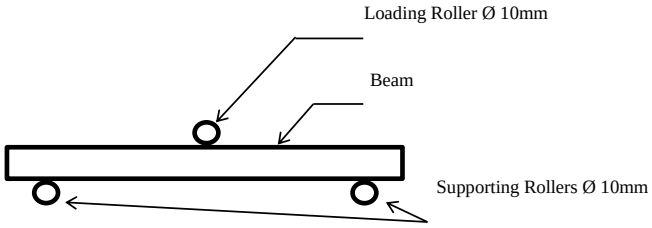


Figure 2: Layout of the three point bend test.

The quasi-static displacement applied was in the form of a compressive sinusoidal load with a frequency of 1 Hz. The loading was applied in four stages (1 mm, 1.7 mm, 2.5 mm and 1 mm) in each test with 15 cycles for each load stage. Three different levels of clamping force (used to hold the strands together) were selected.

2.2 Applied displacement calculations

The applied displacement values were chosen to obtain the maximum possible applied displacement whilst avoiding plastic deformation of the strands. For a simply supported beam, the displacement can be obtained from,

$$\delta = \frac{Fl^3}{48E_eI_e}. \quad (1)$$

where F is the maximum applied force at the centre, l is the span distance, E_e is the effective modulus of elasticity and I_e is the effective second moment of area.

In order to solve Eq. (1), I_e and F are required. In this work the beams were assumed to be unbonded which means that each beam had its individual neutral axis and bent separately. The effective second moment of area therefore could not be solved directly using the parallel axis theorem. Instead, the minimum effective stiffness was estimated by considering the condition when the friction is zero. The stands act in parallel giving,

$$I_e = \sum_1^N I_0 \, , \quad (2)$$

where N is the number of individual beams and

$$I_o = \frac{bh^3}{12} \, . \quad (3)$$

The effective second moment of area for the nine strand beam with an overall cross-section size of 4 mm × 4 mm was equal to 192 mm^4. This value was verified by building a numerical model and applying a displacement. The results from this model indicated an effective second moment of area of 189.6 mm^4.

The maximum applied force (F) can be calculated by the use of Euler-Bernoulli bending theory for the whole system of the beams Eq. (4).

$$F = \frac{4 \ \sigma_y \ I_{effe}}{l \ y} \, . \quad (4)$$

where, σ_y is the yield stress 650 MPa, l is the beam length and y is the distance to the neutral axis. Then the maximum applied displacement can be predicted using Eq. (1) and it was equal to 3.1 mm. To ensure that the beam system will behave in the elastic region it had been decided to use 80% of the maximum displacement that the beams could hold which was 2.5 mm. the four loading stages had been chosen to investigate most of the loading regions and reaching the maximum elastic limit and returning back to the initial loading stage which will give an indication if permanent damage happen in the beams.

2.3 The clamping force and its calibrations

Clamping rollers are used in the experiment to hold the beam arrangement together and to apply the clamping force at the same time. Two sets of clamping rollers are used in each side of the beam arrangement in order to clamp the assembly horizontally and vertically. The clamping rollers are located about 20 mm far from the supporting rollers of the Table Top hydraulic test machine toward the inside direction. Figure 6 depict the nine beam arrangement clamped by two sets of clamping rollers at each side.

Three different clamping force values were used in the experiment to investigate the effect of these forces on the damping behaviour of the multi-strand beam as the clamping force is directly affecting the frictional forces between the mating surfaces. The range of the clamping force was decided to be between 100 N and 250 N. The clamp effect applied as a torque on the screws that hold clamping rollers on the beams. It was required to convert the applied

torque to an equivalent clamping force the present the applied force from the clamp rollers on the multi-strand beam.

A test rig had been used to convert the torque values (ozf.in) into force values (N) through the use of the load cell of the type Loadstar sensor 222 N capacity MFD-050-050. Basically, the torque applied on the clamp roller screws will transfer as a force acting on the load cell as depicted in Figure 3 then; the load cell will measure the amount of the applied force on the clamp by specific software on the PC. These force values were considered equivalent to the applied torque on the load cell clamp. The tests have been repeated five times for the purpose of repeatability as shown in Figure 4. Figure 5 shows the equivalent force values for the applied torque wrench.

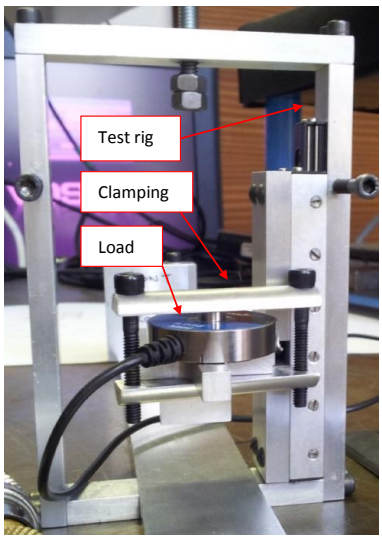


Figure 3: Torque values conversion test.

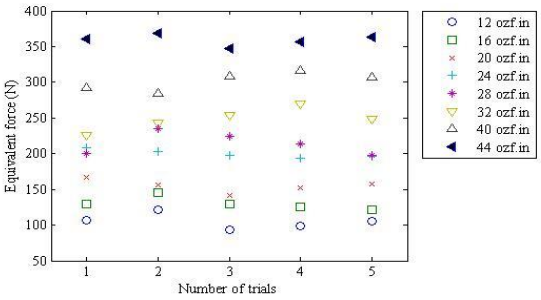


Figure 4: Torque values conversion trials.

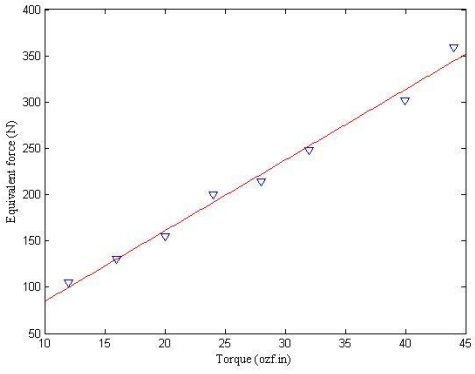


Figure 5: Equivalent clamping force values (N).

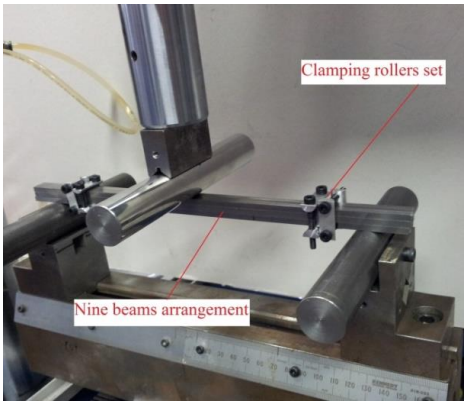


Figure 6: Nine beam arrangement and clamping rollers position.

3 NUMERICAL STUDY

Finite element models had been built to simulate four multi-strand beams. These systems had the same over all cross-section size which was 12×12 mm^2 however each system had different number of beams as well as different individual beam cross-section sizes. The individual beam cross-section size was 6×6 mm^2, 4×4 mm^2, 3×3 mm^2 and 2×2 mm^2 for the multi-strand beam with four beams, nine beams, sixteen beams and thirty six beams respectively as depicted in Figure 7. The coefficient of friction between the beams was assumed to be 0.2. The types of elements that are used to build the finite element model are; 20-Node brick element, 3-D 8-node surface-surface contact (CONTA174) and 3-D target segment (TARGE170). The contact between the beams follows the augmented.

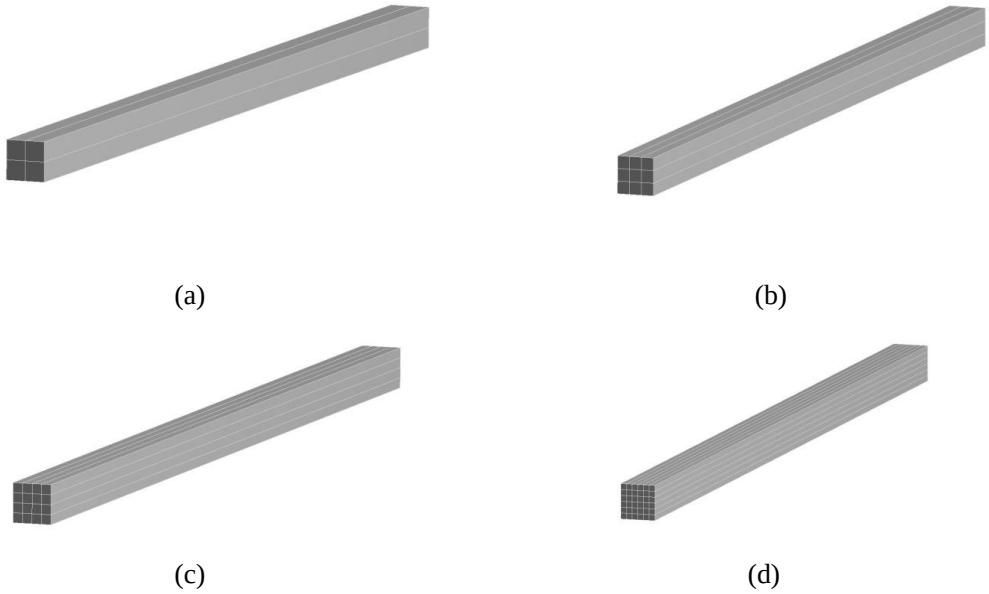


Figure 7: Multi-strand beam with (a) four beams. (b) nine beams. (c) sixteen beams. (d) thirty six beams.

4 VALIDATION STUDY

The nine beam arrangement finite element (FE) model was selected for comparison with the experimentally obtained data as this model has the same parameters and the same number of beams as shown in Figure 8. The clamping force was simulated with equivalent distributed pressure along both the outer upper and outer lower surfaces for the nine beam arrangement and the same experimental boundary conditions have been applied to the FE model to ensure best simulation for the three point bend experimental test. The FE model that chosen to validate the experiment has overall cross-section size of 12×12 mm^2 and each individual strand had a cross-section of 4×4 mm^2 and a span distance of 250.

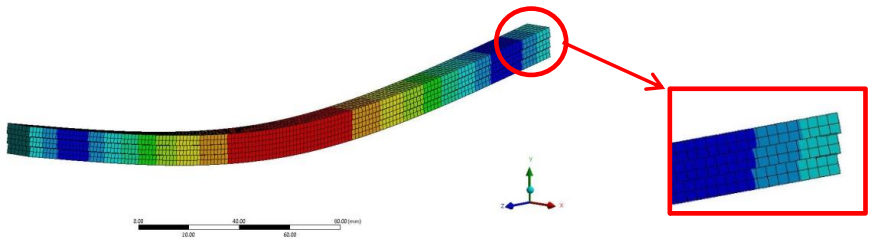


Figure 8: FE model for the nine beam arrangement during bending.

Hysteresis loops (force-displacement curves) were used for the comparison as they provide information on both stiffness and energy dissipation. Figure 9 shows a comparison between the experimental and numerical hysteresis loops for sinusoidal loading of 1mm, frequency of 1 Hz and three sets of clamping forces 100 N, 190 N and 250 N. Figures 10 and 11 show equivalent curves for 1.7 mm and 2.5 mm displacement respectively.

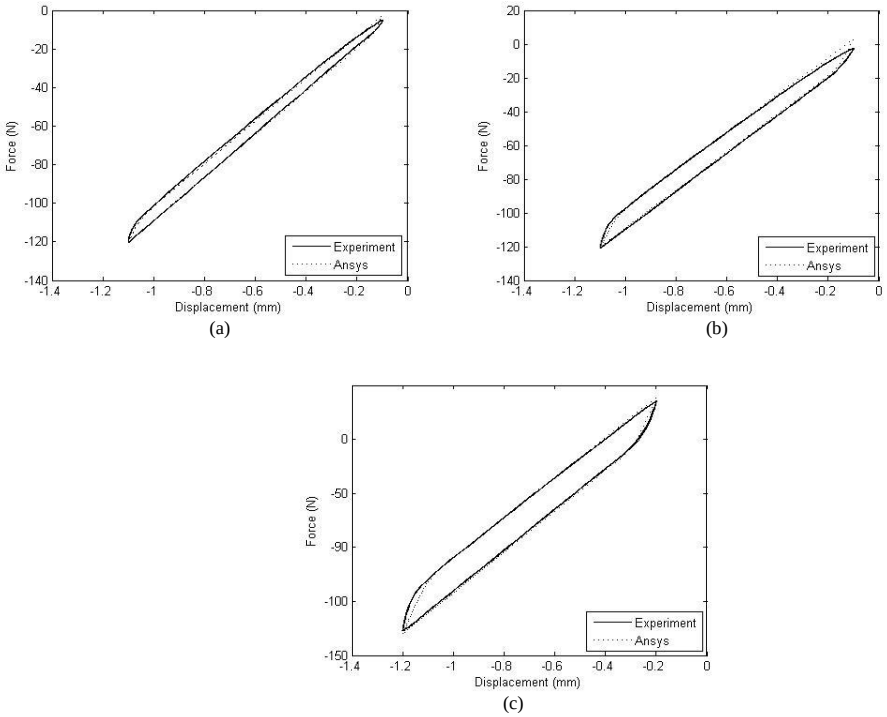


Figure 9: Comparing experimental and numerical hysteresis loops for a sinusoidal load of 1mm and a clamping force of (a) 100 N, E 190GPa, μ 0.2. (b) 190 N, E 192GPa, μ 0.2. (c) 250 N, E 188GPa, μ 0.2.

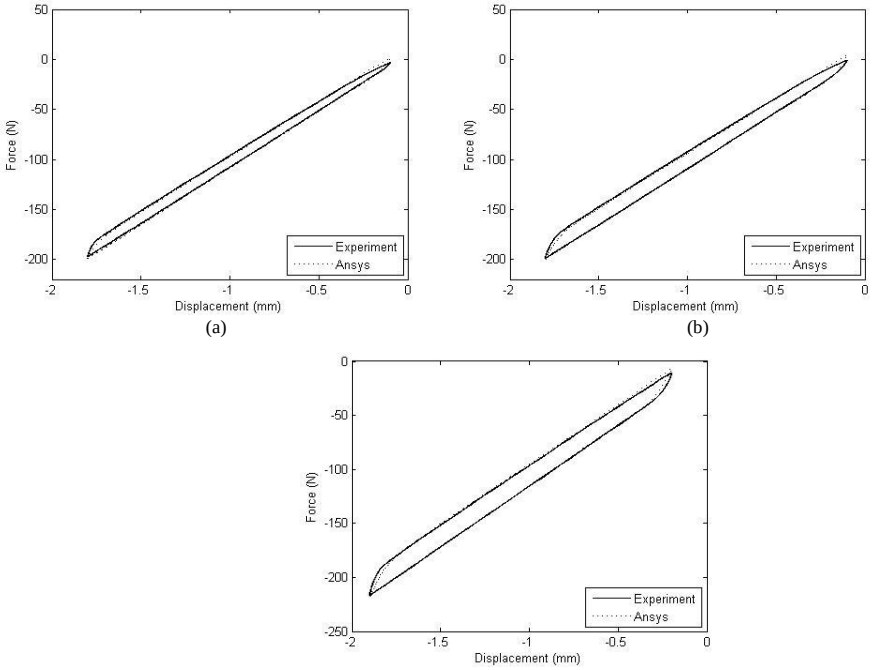


Figure 10: Comparing experimental and numerical hysteresis loops for a sinusoidal load of 1.7 mm and a clamping force of (a) 100 N, E 192GPa, μ 0.3. (b) 190 N, E 190GPa, μ 0.25. (c) 250 N, E 192GPa, μ 0.25.

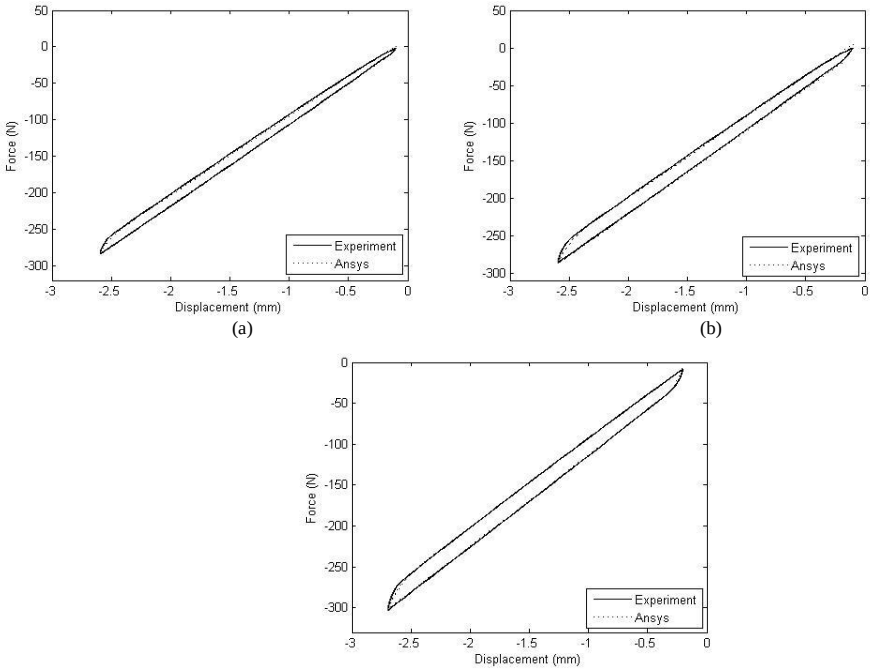


Figure 11: Comparing experimental and numerical hysteresis loops for a sinusoidal load of 2.5 mm and a clamping force of (a) 100 N, E 188GPa, μ 0.3. (b) 190 N, E 188GPa, μ 0.3. (c) 250 N, E 188GPa, μ 0.25.

Figures 9, 10 and 11 show a good agreement between the experimental and numerical hysteresis loops results. The hysteric behaviour agrees well with the dry friction hysteresis loop behaviour reported by Zhou and Ghosh [13]. Maximum energy dissipation is obtained when the sinusoidal displacement is 1 mm and the clamping displacement in its maximum value as can be seen in Figure 9 through Figure 11. For these reasons theses boundary conditions will be applied to the FE models in the case study.

These results verify that the FE model can adequately represent the experiment performed.

5 CASE STUDY

Four FE models were built with four, nine, sixteen and thirty six strands respectively as shown in Figure 7. Note that all the FE models had the same overall cross-section. The coefficient of friction is assumed to be 0.2 in the simulation. The number of elements and nodes for each model are listed in Table 1. Figure 12, 8, 13 and 14 depict the flexural behaviour for the FE models with four, nine, sixteen and thirty six beams. A three point bend configuration is adopted for the simulation and a sinusoidal displacement has been applied to beam-like structure at the middle and supports have been added where these supports are prevented from moving in the vertical direction (loading direction).

No of beams	Cross-section	Span distance (mm)	No of nodes	No of elements
4	4mm × 4mm	250	34688	13200
9	4mm × 4mm	250	41796	20496
16	4mm × 4mm	250	75840	43648
36	4mm × 4mm	250	70272	47664

Table 1: Numeric information of the FE models.

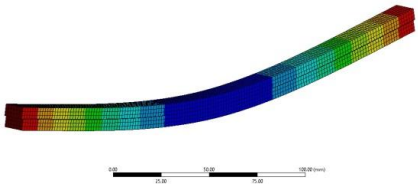


Figure 12: Four beam flexure bending.

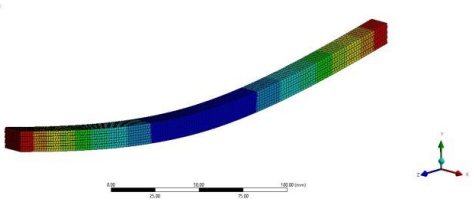


Figure 13: Sixteen beam flexure bending.

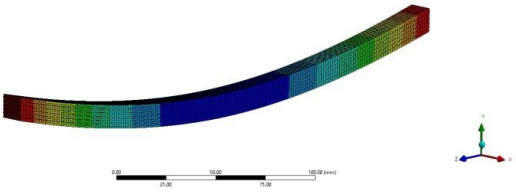


Figure 14: Thirty six beam flexure bending.

The average effective stiffness was estimated from a polynomial fit to the average force-displacement behaviour and the dissipated energy was measured by numerical integration of the force-displacement curve minus the stiffness effect. The loss factor will be calculated depending on the

hysteresis loops results by considering the area of the energy dissipated and the area of the total energy [14] Eq. (5).

$$\eta = \frac{dW}{\pi U_{tot}} . \quad (5)$$

where, η is the loss factor, dW is the energy loss per cycle, U_{tot} is the total strain energy.

In a linear force-displacement relationship, Eq. (6) would be used to evaluate the loss factor as it will consider only one side of the force-displacement curve to calculate the maximum energy dissipated however for a non-linear system, total energy dissipation will be required to be calculated.

$$\eta = \frac{dW}{2\pi U_{max}} . \quad (6)$$

6 RESULTS AND DISCUSSION

Figure 17 show a comparison of the force-displacement curve (hysteresis loops) between the four types of multi-strand beams. It can be concluded from this figure that the more beams contained in the system the less force needed to bend the system with maintaining the overall cross-section size of the system with no change however the individual beam cross-section sizes inside each system are changed. This case is true when the contact status between the mating beams is frictional or frictionless as there will be beam sliding case and each row of beams have their separate neutral axis. In addition, Figure 17 presents the area of the energy dissipated during the loading-unloading cycles for each case.

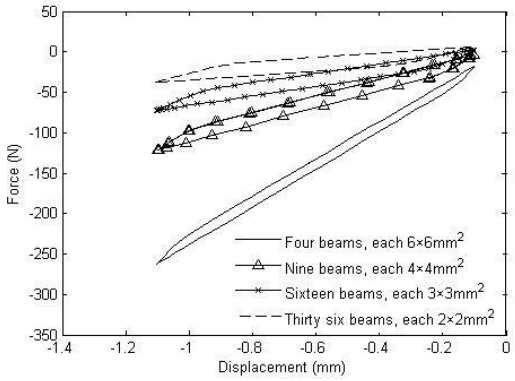


Figure 17: Force-displacement curves for the four multi-strand beams.

Figure 18 is a displacement-damper force curve and it is depict the energy dissipated in the beam-like structure for the four case studies (four beams, nine beams, sixteen beams and thirty six beams) and its clear that all the four systems shows similar levels for the energy dissipation during the loading-unloading cycles.

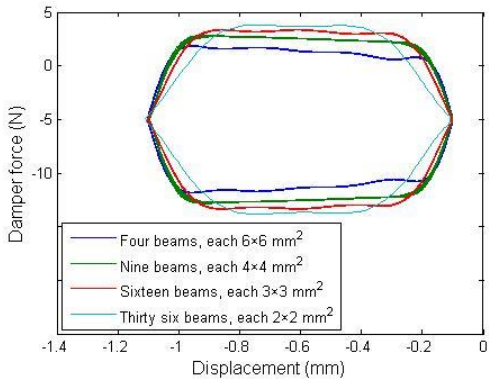


Figure 18: Damper force-displacement curves for the four multi-strand beams.

The facts above may be interesting when inspecting Eq. (5). The energy dissipation is per cycle is approximately the same for all the four multi-strand beams while the total energy per cycle is decreased with increasing the number of beams in the systems which means that the stiffness affected be the number of beams inside the system even when all the four systems have the same overall cross-section sizes.

Figure 19 comparing the loss factor values for the multi-strand beam with four, nine, sixteen and thirty six beams. It is clear from this figure that the system with greater number of beams can produce higher values of the loss factor with dissipating the same amount of energy in all the four systems.

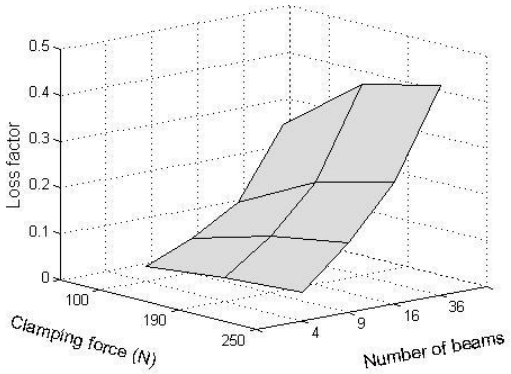


Figure 19: Loss factor values for the all the four multi-strand beams with different clamping force.

7 CONCLUSIONS

This work clearly shows that for a multi-strand beam, the total energy dissipated per cycle remains more-or-less the same, no matter how many strands are used. A larger number of strands results in a more flexible structure. This reduction in stiffness means that the loss factor increases when increasing the number of beams in the system.

REFERENCES

[1] L. E. Goodman and J. H. Klumpp, "Analysis of slip damping with reference to turbine blade vibration," *J. Appl. Mech.*, vol. Vol 23, pp. 421–429, 1956.

[2] B. Lazan, *Damping of materials and members in structural mechanics.* Pergamon Press Inc., 1968.

[3] D. J. Inman, *Engineering vibration*, Third edit. Pearson, 2007.

[4] T. K. Pratt and R. Williams, "Non-linear analysis of stick/slip motion," *J. Sound Vib.*, vol. 74, no. 4, pp. 531–542, Feb. 1981.

[5] M. Carfagni, E. Lenzi, and M. Pierini, "The loss factor as a measure of mechanical damping," in *16th International Modal Analysis Conference*, 1998, pp. 580–584.

[6] Y. K. Ponomarev, "Control of Damping for Multi-layer Vibration Insulators with Dry Friction on Contact Surfaces," *Int. J. Eng. Technol.*, vol. 6, no. 5, pp. 2225–2228, 2014.

[7] W. Chen and X. Deng, "Structural damping caused by micro-slip along frictional interfaces," *Int. J. Mech. Sci.*, vol. 47, no. 8, pp. 1191–1211, Aug. 2005.

[8] A. F. Metherell and S. V Diller, "Instantaneous energy dissipation rate in a lap joint — uniform clamping pressure," *ASME J. Appl. Mech.*, vol. 35, pp. 123–128, 1968.

[9] H. M. Sedighi, K. H. Shirazi, and K. Naderan-Tahan, "Stick-slip analysis in vibrating two-layer beams with frictional interface," *Lat. Am. J. Solids Struct.*, vol. 10, pp. 1025–1042, 2013.

[10] H. M. Sedighi, K. H. Shirazi, and K. Naderan-Tahan, "Stick-slip vibrations of layered structures undergoing large deflection and dry friction at the interface," *J. Vib. Acoust.*, vol. 135, no. 6, p. 061006, Jun. 2013.

[11] Y.-J. Yum, "Frictional behavior of automotive leaf spring," in *in Proceedings of the 4th Korea-Russia International Symposium on Science and Technology, Ulsan, South Korea*, 2000, vol. 3, pp. 5–10.

[12] X. Zhou, E. Shin, K. W. Wang, and C. E. Bakis, "Interfacial damping characteristics of carbon nanotube-based composites," *Compos. Sci. Technol.*, vol. 64, no. 15, pp. 2425–2437, Nov. 2004.

[13] N. Zhou and T. K. Ghosh, "On-line measurement of fabric-bending behaviour: background, need and potential solutions," *Int. J. Cloth. Sci. Technol.*, vol. 10, no. 2, pp. 143–156, 1998.

[14] K. Chandrasekhar, J. A. Rongong, and E. J. Cross, "Frequency and amplitude dependent behaviour of tangled metal wire dampers," *Proc. ISMA2014 Incl. USD2014*, pp. 559–572, 2014.

International Conference on Engineering Vibration
Ljubljana, Slovenia, 7-10 September 2015

NONLINEAR DYNAMIC ABSORBER TO REDUCE VIBRATION IN HAND-HELD IMPACT MACHINES

Hans Lindell*[1], Viktor Berbyuk[2], Mattias Josefsson[2], Snævar Leó Grétarsson[2],

[1]Swerea IVF
Box 104, SE-431 22 Mölndal, Sweden
hans.lindell@swerea.se

[2]Department of Applied Mechanics
Chalmers University of Technology
SE-412 96 Göteborg, Sweden
viktor.berbyuk@chalmers.se, matjos@student.chalmers.se, snvar@student.chalmers.se

Keywords: Nonlinear tuned vibration absorber, Tuned vibration damper, Impact machine, Optimisation.

Abstract. *Hand-held impact machines have been used since the early 20th century. Up to day still a little has been changed in their fundamental design. Despite them being robust and efficient, vibration, noise, dust and poor ergonomics cause a large number of injuries to the operators, especially in the stone industry. In this paper, vibration dynamics of a pneumatic hand-held impact machine (HHIM) equipped with a nonlinear tuned vibration absorber (NLTVA) is in focus. The considered HHIM has the same parameters as the existing conventional one with respect to piston weight, impact energy and operating frequency. The paper presents the mathematical and computational models of vibration dynamics of the HHIM with NLTVA as well as the experimental set-up developed for model validation. The advantage of using a nonlinear spring is shown and how the effective vibration reduction frequency of the NLTVA can be made to follow the excitation frequency and thereby in principal achieving the same conditions as is the case for tuned pendulum absorbers for torsional vibrations where the resonance frequency follows the engine order. Using the verified and validated computational model, the sensitivity analysis of vibration dynamics has been performed in a broad set of feasible operational scenarios with respect to structural parameters of the HHIM equipped with NLTVA. Sensitivity analysis results have formed the base for optimisation of the parameters of NLTVA. It was shown by simulations as well as it was proved by experiment that the vibration of the HHIM equipped with NLTVA can be reduced significantly in a broader range of operating frequencies compared to the vibration of the same machine equipped with linear tuned vibration absorber. The results obtained confirm the possibility to design a user friendly low vibration impact machine efficiently operating in a broad frequency range. Optimised NLTVA combined with vibration isolation has shown to significantly reduce the vibration on the operator.*

1 INTRODUCTION

Vibration exposure from hand-held impact machines (HHIM) such as rock drills, rammers and breakers with a reciprocating action is a major cause for injuries to the workers in the industry. In order to improve the work environment in the stone industry, a project was started with the objectives to redesign the tools to achieve low vibration as well as improved ergonomics, dust removal and reduced noise while maintaining productivity [1]. Redesign of current hand-held pneumatic impact machines can reduce the vibration level and thereby reduce injuries to workers. Hand-arm vibration injury, often called Hand-Arm Vibration Syndrome (HAVS), is one of the most common reasons for work related injuries among this group of workers in the industry.

Although impact machines have been used since the early 20th century, little has been changed in their fundamental design to date. Despite them being robust and efficient, vibration, noise, dust and poor ergonomics cause a large number of injuries to the operators. Previous work has been done to reduce vibrations from these machines, some of which have been patented [2, 3]. One approach is to use traditional linear tuned vibration absorbers (TVA) invented in 1909 by Frahm and described by Den Hartog [4]. However, this technology is to a large extent limited in practical use on this application since it is only effective in a narrow frequency range. At higher frequencies, the TVA will instead increase the vibration and at lower frequencies will the effect rapidly decrease.

A thorough analysis of the dynamics of the HHIM together with an implementation of a TVA in the handle of the machine in combination with a vibration isolated handle is described in [5]. More general aspects of the NLTVA are analysed in [6] which show how different parameters influence the stability of the overall system.

However, by introducing nonlinear spring characteristic of the auxiliary mass, the effective frequency range can be greatly increased and thereby can the technology be effectively implemented to this kind of machines [7]. As a result, a new generation of impact machines is developed by approaching the redesign from a user perspective, and starting adhering to strict conditions of low vibration, noise and dust as well as sound ergonomics.

The objective of this study has therefore been to develop a user friendly low vibration impact machine using NLTVA together with integrated vibration isolation. A HHIM with a NLTVA combined with vibration isolation has shown to significantly reduce the vibration on the operator from 20 m/s^2_{haw} to 2.7 m/s^2_{haw} [1].

2 ENGINEERING MODEL OF HHIM

The pneumatic HHIM in question consists of the following machine functional components (MFCs): the housing of mass m_h, the main mass m_m, the piston of mass m_{pist} moving in the cylinder, the NLTVA with auxiliary mass m_a, the chisel, and the handle. The detailed engineering model of the HHIM is depicted in Figure 1. It is assumed that the MFCs are under the action of the external loads modelled by the exciting force F_e applied to the main mass and the internal loads modelled by the forces exerted by springs and dampers. The effective mass of the hand-arm system is quite small and is neglected in this study. The following additional notations are in use: k_m, k_a, k_h, k_p are the stiffness between main mass and ground, main mass and auxiliary mass, main mass and housing, and the hand-arm stiffness representing the operator, respectively; c_m, c_a, c_h, c_p are the damping between main mass and ground, main mass and auxiliary mass, main mass and housing, and the hand-arm damping representing the operator, respectively; a and F_0 are the half gap length and the spring preload, respectively, characterising the TVA nonlinearity.

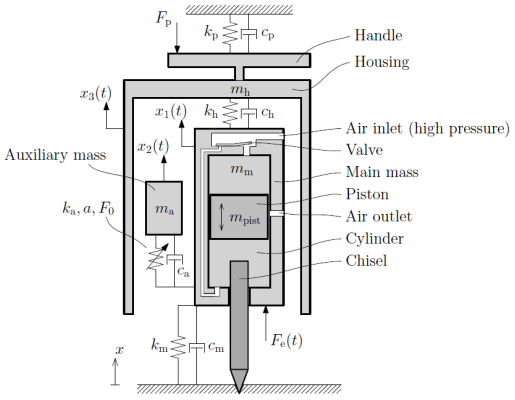


Figure 1: Engineering model of the HHIM.

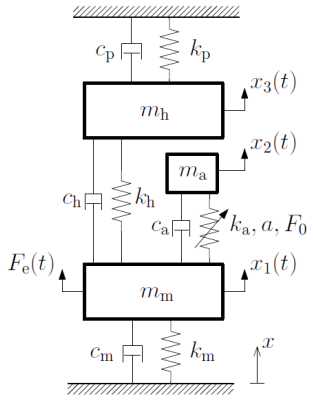


Figure 2: Sketch of the HHIM as 3-DoF vibrating system.

Parameter values used in the modelling are introduced in Table 1, except for k_a, a, F_0 which are subject to optimisation. All values, except the three masses and k_h, have been estimated. For example, hand-arm stiffness k_p was taken from [8, 9] and hand-arm damping c_p was taken from [9]. Auxiliary damping c_a is kept as low as possible in the HHIM for maximum performance of the NLTVA. It is therefore given a low value in the model. It has been noted that all parameters pertinent to the coupling between main mass and housing as well as the couplings to ground have a minor influence on system response for excitations near nominal operating frequency since that is well above the first two resonance frequencies of the system [10]. Amplitude of the exciting force F_e in a HHIM prototype has previously been measured to be 351 N at an operating frequency of 26.1 Hz [10], which is utilised in this model. It was also concluded that a sinusoidal force is a good approximation, and its amplitude is assumed to increase quadratic with operating frequency since the displacement of the piston is constant.

	Masses [kg]			Stiffness coefficients [kN/m]			Viscous damping coefficients [Ns/m]			
Parameter	m_m	m_a	m_h	k_m	k_h	k_p	c_m	c_a	c_h	c_p
Nominal value	2.7	1	3.1	500	14000	1000	100	1	20	60

Table 1: Model parameters.

3 MATHEMATICAL AND COMPUTATIONALTIONAL MODELS

With described engineering model, the HHIM is considered as a vibrating system with three degrees of freedom, the sketch of which is depicted in Figure 2. By introducing generalized coordinates x_1, x_2, x_3 the equations of motion of the system can be written as follows

$$m_m\ddot{x}_1 + (c_m + c_h)\dot{x}_1 - c_h\dot{x}_3 + (k_m + k_h)x_1 - k_h x_3 = F_e(t) + F_k(\mathbf{x}) + F_c(\mathbf{x},\dot{\mathbf{x}}) - m_m g \quad (1)$$

$$m_a\ddot{x}_2 = -F_k(\mathbf{x}) - F_c(\mathbf{x},\dot{\mathbf{x}}) - m_a g \quad (2)$$

$$m_h\ddot{x}_3 - c_h\dot{x}_1 + (c_h + c_p)\dot{x}_3 - k_h x_1 + (k_h + k_p)x_3 = -m_h g \quad (3)$$

Here in Eqs. (1-3), $\mathbf{x} = [x_1, x_2, x_3]^T$, $\dot{\mathbf{x}} = [\dot{x}_1, \dot{x}_2, \dot{x}_3]^T$ are the vectors of generalized coordinates and velocities, respectively. $F_k(\mathbf{x})$ and $F_c(\mathbf{x},\dot{\mathbf{x}})$ are nonlinear spring force and damping force exerted by the NLTVA and applied to the main mass. g is acceleration due to gravity.

Different expressions for $F_k(\mathbf{x})$ and $F_c(\mathbf{x},\dot{\mathbf{x}})$ can be chosen and thus different concepts of the TVA can be studied. The following representations for these forces are proposed

$$F_k(\mathbf{x}) = \begin{cases} F_0 + k_\mathrm{a}(x_2 - x_1 - a) & \text{if } x_2 - x_1 > a \\ -F_0 - k_\mathrm{a}(-x_2 + x_1 - a) & \text{if } x_2 - x_1 < -a \\ 0 & \text{else} \end{cases} \tag{4}$$

$$F_c(\mathbf{x},\dot{\mathbf{x}}) = c_\mathrm{a}(\dot{x}_2 - \dot{x}_1) \tag{5}$$

Here in the expressions (4) and (5), the parameters a, F_0, k_a, and c_a are the half gap length, the spring preload, the stiffness between main mass and auxiliary mass and the damping between main mass and auxiliary mass of the NLTVA.

The following direct dynamics problem for the HHIM is formulated.

Problem A. Let the engineering model of the HHIM, the exciting force applied to the main mass $F_\mathrm{e}(t)$, $t \in [0, t_\mathrm{f}]$ and the internal loads modelled by the forces exerted by springs and dampers of the NLTVA $F_k(\mathbf{x})$ and $F_c(\mathbf{x},\dot{\mathbf{x}})$ be given. It is required to determine the vectors of generalized coordinates $\mathbf{x} = [x_1, x_2, x_3]^\mathrm{T}$ and generalized velocities $\dot{\mathbf{x}} = [\dot{x}_1, \dot{x}_2, \dot{x}_3]^\mathrm{T}$ of the steady-state performance of the HHIM that satisfy the equations of motion Eqs. (1-3) and arbitrary prescribed initial conditions $\mathbf{x}(0) = \mathbf{x}_0$, $\dot{\mathbf{x}}(0) = \dot{\mathbf{x}}_0$. Note that the final state of the machine as well as the final time instant are not prescribed, i.e. the components of the vectors $\mathbf{x}(t_\mathrm{f}), \dot{\mathbf{x}}(t_\mathrm{f})$ and the final time instant t_f are free. All structural parameters of the machine including parameters of the NLTVA are assumed to be given.

In order to solve *Problem A*, a computational model of the HHIM in question has been developed and implemented in MATLAB©. The core of the computational model is the numerical algorithm of the solution of the initial value problem for Eqs. (1-3) based on MATLAB function *ode45* with the value of both the relative and absolute error tolerances equal to 10^{-8}.

4 MODEL VERIFICATION AND VALIDATION

4.1 Model verification

To ensure correctness and accuracy of numerical solutions obtained from the computational model, a verification of the model is done by comparing its results with reference results.

Firstly, the modelled system was configured as a linear system by setting both the gap a and preload F_0 in Eq. (4) to zero. Perfect correlation was seen between the numerical solution and the analytical solution of the same system, with respect to displacements, velocities, accelerations and phase angles. Secondly, simulations were run for the unforced undamped auxiliary system, i.e. the auxiliary mass restricted by the nonlinear spring described by Eq. (4), initiated from a spring compression b. Since that system is not dissipative, the auxiliary mass should oscillate with the same amplitude indefinitely. The said system was simulation for 20 seconds for several different configurations of the parameters k_a, a, F_0 and b. The undamped resonance frequency has been derived analytically in [10] and is given by

$$f_\mathrm{res} = \sqrt{\frac{k_\mathrm{a}}{m_\mathrm{a}}}\left[2\pi - 4\arcsin\left(\frac{F_0}{F_0 + k_\mathrm{a} b}\right) + 4a\sqrt{\frac{k_\mathrm{a}}{k_\mathrm{a} b^2 + 2F_0 b}}\right]^{-1} \tag{6}$$

4.2 Model validation

Validations of the computational models have been made in two experimental set-ups, a dedicated test rig [11] and in a pneumatic HHIM prototype. In the test rig, all relevant parameters could be controlled and measured and most important, the excitation frequency could be

varied from stand still up to 18 Hz. The test rig employed the TVA nonlinearity created by a gap but no preload in this test. In the HHIM prototype on the other hand, all parameter were close to a real HHIM although the exciting force frequency could not be varied easily and parameters as the stiffness to ground, damping and exciting force needed to be estimated or measured indirectly.

Validation in test rig

In the test rig, the force is generated from an electric motor to a pneumatic piston connected to a force transducer that is attached to the main mass, Figure 3. The force can be varied to frequency by the motor speed and to amplitude by restricting the air openings in the pneumatic cylinder or changing the stroke length. Displacement of the main and auxiliary mass is measured by laser displacement sensors. In the experiments, the force is increasing linearly with a peak of 45 N at the frequency 18 Hz. The set-up of the system is chosen so that the main mass has a resonance frequency at 2 Hz and the auxiliary mass is tuned to give the lowest vibration of the main mass at 9 Hz.

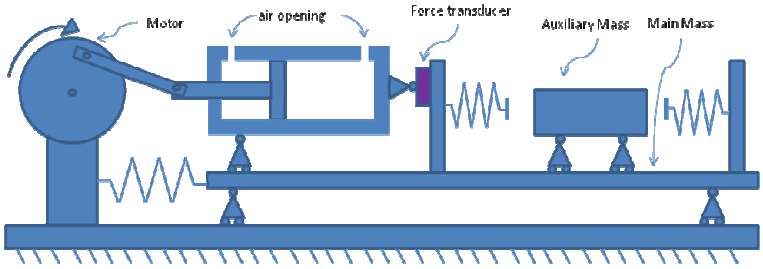


Figure 3: Test rig.

The results from the experiments compared to the simulations are shown in Figure 4. It is clearly seen that there is a substantial reduction in vibration amplitude of the main mass when the NLTVA is active in a broad frequency range. The deviations are mainly believed to be due to that the experimental exciting force is not purely sinusoidal but has a substantial degree of harmonic content. There are also uncertainties in the spring force for the auxiliary mass since it was compressed partly beyond its specifications. The exciting force in the simulation model was purely sinusoidal.

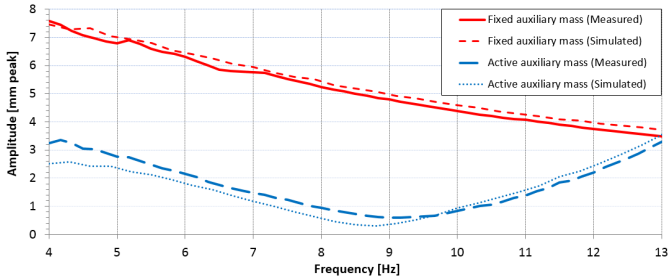


Figure 4: Experimental and simulated results of main mass vibration for active and inactive auxiliary mass.

Validation using the prototype

Since the working frequency and the amplitude of the exciting force in the prototype cannot be varied, gap length a was varied to see if the model would predict the changes in reality. To be able to measure the motion of the auxiliary mass, the housing was removed during

measurements and simulations. Since the operating frequency varied slightly between measurements, the frequency from each measurement was used as the excitation frequency in respective simulation. The gap lengths used were 3.2, 6.1 and 9.7 mm and corresponding measured operating frequencies were 26.5, 25.8 and 25.4 Hz, respectively. The simulated and measured root mean square (RMS) displacements for different gap lengths are compared in Figure 5. RMS response of the experimental data was calculated after applying a 5th order high-pass Butterworth filter with a cutoff frequency of 6.5 Hz. The comparison shows very similar results, especially when taking into account that many of the parameters in the prototype cannot be measured very accurately. The model predicts the change in vibration level of both the auxiliary and main mass well.

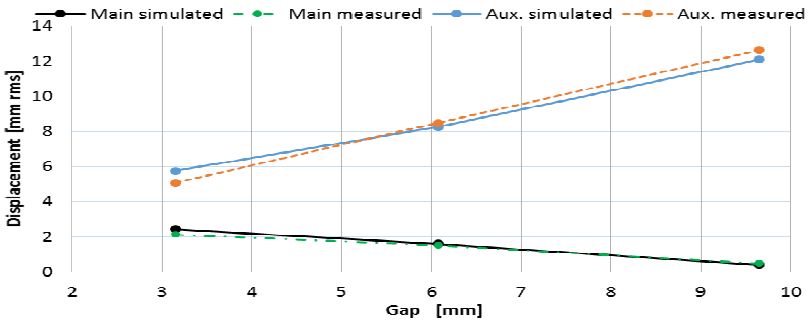


Figure 5: Experimental and simulation results for the prototype when the gap length is varied.

5 SENSITIVITY ANALYSIS AND OPTIMISATION

To investigate how the three NLTVA parameters k_a, a and F_0 that are subject to optimisation affects the vibration suppression, each parameter was varied around its nominal value. The results from varying single parameters separately can be seen in Figure 6.

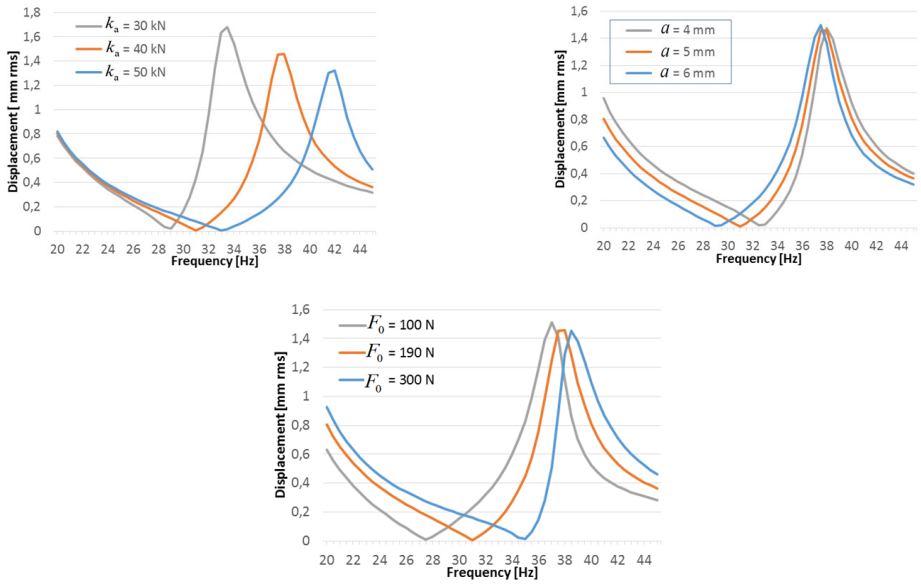


Figure 6: Vibration of the handle for different values of the NLTVA parameters. Only one parameter is varied at a time while other parameters are kept at their nominal values; k_a = 40 kN/m, a = 5 mm, F_0 = 190 N.

Figure 6 clearly shows that any of the NLTVA parameters can be adjusted to change the frequency that has maximum suppression, i.e. the tuned frequency. When the stiffness k_a is increased, the tuned frequency moves upwards and vice versa if the stiffness is lowered. The unwanted resonance above the tuned frequency is also moved considerably upwards in frequency when the stiffness is increased, and vice versa when the stiffness is decreased. The resonance is however not affected significantly when the gap length a and preload F_0 are changed. This suggests that an optimal result would be a high stiffness k_a to move the unwanted resonance to a higher frequency, combined with a lowered preload F_0 and/or an increased gap length a to keep the minimum, i.e. the tuned frequency, around 28 Hz.

The following optimisation problem is formulated in order to optimise the proposed NLTVA in the considered HHIM:

$$\left(k_a, a, F_0\right)_{\text{optim}} = \underset{k_a, a, F_0}{\operatorname{argmin}}\ L\left(k_a, a, F_0\right) \tag{7}$$

Here in Eq. (7), L is the objective function and k_a, a and F_0 are the NLTVA parameters subject to optimisation. The objective function is defined as the area under a weighted response curve in a frequency range that spans ±15 % of the nominal operating frequency, 28 Hz, to account for variations.

$$L(k_a, a, F_0) = \int_{23.8\ \text{Hz}}^{32.2\ \text{Hz}} \dot{x}_{3,\text{RMS}}(f, k_a, a, F) \cdot W(f)\ \mathrm{d}f \tag{8}$$

In Eq. (8), $\dot{x}_{3,\text{RMS}}$ is the velocity RMS response at the handles, computed by the numerical model, and $W(f)$ is a weighting function that provides priority of minimisation at the nominal operating frequency, 28 Hz, but still lets the response at the frequency bounds 23.8 Hz and 32.2 Hz be accounted for. The weighting function is a normal distribution centred at the nominal frequency with a standard deviation of 2.83 Hz. Choosing this standard deviation makes the weighting function being three times as large at the nominal frequency as at the frequency bounds. In the optimisation routine, the frequency range of interest, $f \in \left[23.8,\ 32.2\right]$ Hz, is discretised into 15 points such that the density of points is proportional to the weighting function $W(f)$. The objective function is computed by summing the velocity RMS responses evaluated at the discrete frequencies. The minimisation problem in Eq. (7) is solved in MATLAB with *lsqnonlin*, a nonlinear least squares solver implementing the trust-region-reflective method. During optimisation, all parameters are restricted by a lower bound of zero and upper bounds which are 500 kN/m for stiffness k_a, 40 mm for gap a and 500 N for preload F_0. To increase the chance of reaching the global optimum sought in Eq. (7), multiple starts are run, each with an initial guess randomised uniformly within the parameter bounds.

Optimisation results

The optimisation has been run using over 250 randomised starts. About half of the optimisation runs resulted in parameters that gave very low objective function. The parameters that gave the lowest found objective function value were k_a = 164.23 kN, a = 10.21 mm and F_0 = 98.2 N. The parameters are as expected considering the findings of the sensitivity study. The stiffness is very high, which places the unwanted resonance frequency far above the operating frequency, and the increased gap length a moves the tuned frequency down to 28 Hz. Figure 7 compares the response of the handle between using the optimised NLTVA and the traditional linear TVA. The suppression band with the optimised NLTVA is much wider than with the linear TVA, clearly demonstrating the advantage of using a NLTVA.

It is thus shown that there is a substantial advantage in using a nonlinear spring characteristic instead of the traditional linear spring for the auxiliary mass in order to achieve a broader useful frequency range and thereby a more robust system. The core reason for the improve-

ment can be explained to a large extent by that the phase of the auxiliary mass remains close to 180° in relation to the exciting force over a very broad frequency range, Figure 8 and Figure 9. The counterphase of the auxiliary mass is maintained because the resonance frequency of the auxiliary system to a large extent follows the increasing excitation frequency, Figure 10. The reason for this in turn is that the displacement amplitude of the auxiliary mass increases with higher excitation frequencies, which is also seen in Figure 10, and, since the auxiliary spring characteristic from the optimised k_a , a and F_0 is nonlinear stiffening, the resonance frequency of the auxiliary system will then increase.

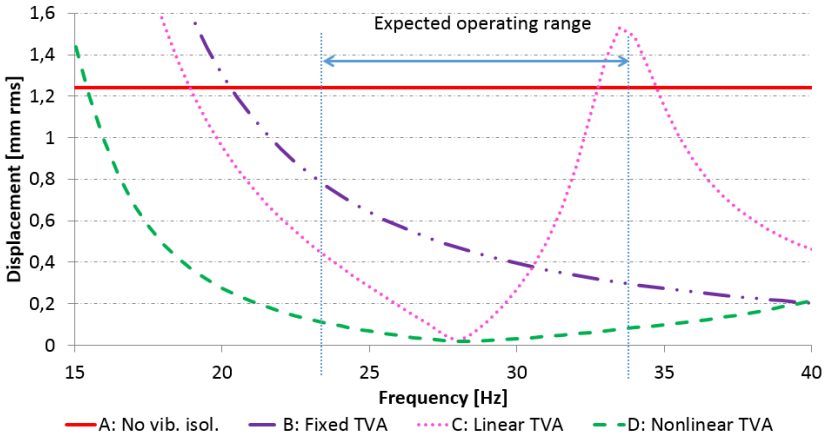


Figure 7: Vibration of the handle. Comparison between using the optimised NLTVA, the LTVA tuned to 28 Hz, deactivated TVA (vibration isolation only) as well as no means of vibration reduction at all.

In Figure 8 and the close-up in Figure 9, the phase and amplitude are compared between using a linear and a nonlinear TVA that are both optimised to reduce vibrations in the area around 28 Hz of the system.

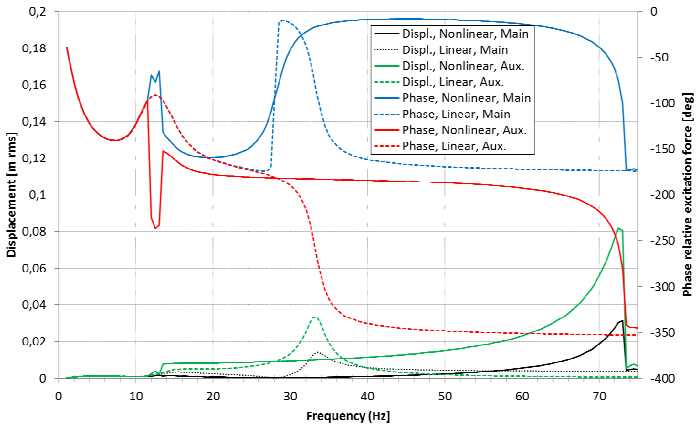


Figure 8: Phase and displacement for NLTVA and LTVA.

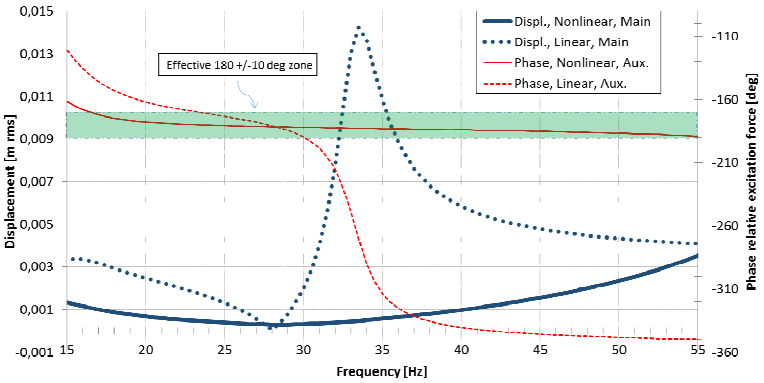


Figure 9: Phase and displacement for NLTVA and LTVA, close-up.

What can be seen from these figures is that the linear auxiliary mass is only in counterphase to the excitation up to about 30 Hz. Just above 30 Hz, there is a phase shift and a severe amplification of the vibration. In the nonlinear system on the other hand, the auxiliary mass maintains the counterphase and reduces vibration even up to about 60 Hz. The resonance introduced by adding the TVA to the system is considerably far above and on a safe distance from the tuned frequency in the nonlinear case, making the effectiveness of the NLTVA very insensitive to varying excitation frequency.

In Figure 10, it is shown how the resonance frequency of the auxiliary mass is increasing with increased excitation frequency. The analytical resonance frequency is given by Eq. (6) and is a system where the exciting force is increasing quadratic with increased frequency. This condition is valid for most mechanical systems which vibrations are mass controlled and where there is a constant displacement of moving components over the operating frequency.

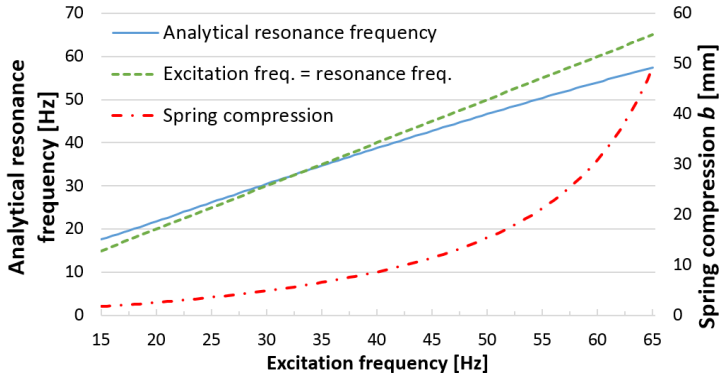


Figure 10: Analytical resonance frequency and spring compression versus excitation frequency.

The relation that the resonance frequency is increasing with excitation frequency can also be found in the closely related "sister" technology with tuned pendulum torsion absorbers [4]. The tuned pendulums are used to create torque on a shaft to reduce torsional vibrations, e.g. in the shaft from a combustion engine. In the tuned pendulum system, the resonance frequency is proportional to the rotating speed which means that the resonance frequency will follow the engine order and thereby have an effective vibration reduction throughout the whole speed range.

6 CONCLUSIONS

A 3-DoF computational model for a pneumatic HHIM utilising a NLTVA in combination with vibration isolation was developed and implemented in MATLAB. The numerically modelled HHIM is excited by a harmonic force exerted by a piston reciprocating with constant amplitude. The model was verified against analytical results and validated against experimental data from a dedicated test rig as well as from a HHIM prototype.

Sensitivity analysis and optimisation of the three NLTVA parameters; stiffness, gap and spring preload, have performed based on the numerical model. The obtained results showed that, for the considered HHIM, the optimised NLTVA is superior to a linear TVA tuned to the same frequency, especially in terms of its insensitivity to variations in operating frequency. In combination with vibration isolation, the optimised NLTVA can significantly and reliably reduce vibration on the operator in a broad range of operating frequencies.

ACKNOWLEDGEMENTS

This project was funded by AFA Insurance, AP Sten, Benders and Emmaboda Granit. A special thanks to Bert Andersson, TM Verkstad for manufacturing prototypes.

REFERENCES

[1] H. Lindell, Redesign of hand-held impact machines to reduce hand-arm vibration, *Canadian Acoustics*, **39**, 80-81, 2011.

[2] F. Moessnang, US Patent US7712548B2.

[3] S. Henriksson, O. Ostensson, US Patent US20080073095A1.

[4] J. P. Den Hartog, *Mechanical Vibrations*. Dower Publication, New York, 1985.

[5] E. V. Golysheva, V. I. Babitsky, A. M. Veprik. Vibration protection for an operator of a hand-held percussion machine. *Journal of Sound and Vibration*, **274**, 351-367, 2004.

[6] T. Detroux, G. Habib, L. Massett, G. Kerschen. Performance, robustness and sensitivity analysis of the nonlinear tuned vibration absorber. *Mechanical Systems and Signal Processing*, **60-61**, 799-809, 2015.

[7] H. Lindell, Patent WO 2014/095936 A1.

[8] F. A. Mussa-Ivaldi, N. Hogan, E. Bizzi. Neural, mechanical, and geometric factors subserving arm posture in humans. *The Journal of Neuroscience*, **5**, 2732-2743, 1985.

[9] T. Tsuji et al. Human hand impedance characteristics during maintained posture. *Biological Cybernetics*, **72**, 475-485, 1995.

[10] M. Josefsson, S. L. Grétarsson. "Optimisation of a non-linear tuned vibration absorber in a hand-held impact machine". Master's thesis. Chalmers University of Technology, 2015.

[11] A. Nilsson, T. Östgårdh "Verifiering av matematisk modell för vibrationsdämpare". Bachelor's thesis. Chalmers University of Technology, 2014.

11th International Conference on Engineering Vibration
Ljubljana, Slovenia, 7–10 September 2015

EHRLICH-ABERTH ITERATION FOR VIBRATIONAL SYSTEMS

Peter Benner[1], **Jonas Denißen***[1]

[1] Max Planck Institute for Dynamics of Complex Technical Systems,
Sandtorstrasse 1,
39106 Magdeburg,
{benner,denissen}@mpi-magdeburg.mpg.de

Keywords: Ehrlich-Aberth iteration, vibrational system, quadratic eigenproblem, discrete viscous damper, low rank.

Abstract. *We consider the computation of the eigenvalues of the quadratic eigenproblem (QEP)*

$$Q(\lambda)x = (M\lambda^2 + C\lambda + K)x = 0, \tag{1}$$

where the coefficient matrices $M, C, K \in \mathbb{R}^{n\times n}$ are known as mass, damping and stiffness matrix. They are positive definite and (M, K) is regular. The damping matrix is the sum of internal damping C_{int} and external damping C_{ext} of rank $r \ll n$, hence $C = C_{\text{int}} + C_{\text{ext}}$. Internal damping is an essential property and it can guarantee characteristics such as passivity and stability of the problem. The most popular models are Rayleigh or proportional critical damping.

Computing the eigenvalues of (1) *is viewed as a root-finding problem on $q(\lambda) := \det Q(\lambda)$ by an Ehrlich-Aberth iteration (EAI), which is a Newton-like method to find all eigenvalues simultaneously. By including internal damping of the aforementioned form, we extend an idea of Taslaman [10] that is designed to work with low rank matrices. The flop count of the Newton-like update in the EAI is then of order $\mathcal{O}(r^2n + r^3)$. Starting points are crucial to the performance of EAI and can be given by the eigenvalues of the quadratic eigenproblem neglecting external damping or by further insight into the problem.*

Matrix polynomials of the form (1) *appear in the analysis of vibrating structures with discrete viscous dampers. For example, a special structure arises when optimizing the positions i_j of the discrete dampers. The external damping $C_{\text{ext}} = \nu \sum_{j=1}^{r} e_{i_j} e_{i_j}^T$ is varied due to the discrete positioning and viscosity ν, but the internal damping C_{int} remains constant. Numerical experiments illustrate that similar external damper configurations yield similar eigenvalues, and hence good starting points for EAI.*

1 INTRODUCTION

We analyze and investigate the eigenvalues of a QEP (1) which appears in vibrating structures. Here, we focus on a QEP with a special structure of the damping matrix C, which is given as the sum of internal damping C_{int} and external damping C_{ext},

$$C = C_{\text{int}} + C_{\text{ext}}, \tag{2}$$

where C_{ext} has low rank, i.e., $r := \operatorname{rank}(C_{\text{ext}}) \ll n$. In the following, we consider as internal damping the so called critical damping

$$\gamma C_{\text{crit}} = 2\gamma M^{1/2}\sqrt{M^{-1/2}KM^{-1/2}}M^{1/2} \tag{3}$$

with some proportionality's parameter $0 < \gamma < 1$.

In absence of the external damping C_{ext}, the QEP (1) has a lot of nice properties. Especially, the QEP can be simultaneously diagonalized. For that purpose let Φ be a matrix that simultaneously diagonalizes M and K, i.e.,

$$\begin{aligned} \Phi^T M\Phi &= I \qquad \text{and} \\ \Phi^T K\Phi &= \Omega^2 = \operatorname{diag}(\omega_1^2, \ldots, \omega_n^2). \end{aligned}$$

Since the internal damping is given as critical damping (3), we see that Φ diagonalizes the internal damping, too, i.e.,

$$\Phi^T C_{\text{crit}}\Phi = 2\gamma\Omega.$$

Hence, when external damping is absent, i.e., $C_{\text{ext}} = 0$, solving (1) is not harder than finding a transformation Φ by solving the generalized eigenproblem (GEP)

$$K\varphi_i = \omega_i^2 M\varphi_i, \tag{4}$$

for $i = 1, \ldots, n$. Then Φ is defined as $\Phi = [\varphi_1, \ldots, \varphi_n]$, and the eigenvalues for critical damping are

$$\lambda_i^{\text{crit}} = \left(-\gamma \pm \sqrt{\gamma^2 - 1}\right)\omega_i \tag{5}$$

for $i = 1, \ldots, n$.

Our goal is to design an algorithm that computes the eigenvalues of the QEP by taking the external damping into account but not to increase the complexity significantly.

2 EHRLICH-ABERTH ITERATION

Let $q(x)$ be a polynomial of degree $2n$. The Ehrlich-Aberth iteration [1, 4] determines the roots $\lambda_1, \lambda_2, \ldots, \lambda_{2n}$ of q, i.e., $q(\lambda_k) = 0$ for $k = 1, \ldots, 2n$, simultaneously and iteratively. Let $\lambda_1^{(i)}, \ldots, \lambda_{2n}^{(i)} \in \mathbb{C}$ be the current approximations of the zeros of $q(x)$. The Ehrlich-Aberth iteration takes the form

$$\lambda_k^{(i+1)} = \lambda_k^{(i)} - \frac{\frac{q(\lambda_k^{(i)})}{q'(\lambda_k^{(i)})}}{1 - \frac{q(\lambda_k^{(i)})}{q'(\lambda_k^{(i)})}\left(\sum_{j<k}\frac{1}{\lambda_k^{(i)} - \lambda_j^{(i+1)}} + \sum_{j>k}\frac{1}{\lambda_k^{(i)} - \lambda_j^{(i)}}\right)} \qquad \text{for } k = 1, \ldots, 2n, \tag{6}$$

where each new approximation $\lambda_j^{(i+1)}$ is used as soon as it is computed, i.e., in a Gauß-Seidel fashion. While Bini and Noferini used the Ehrlich-Aberth iteration for finding the eigenvalues of regular matrix polynomials [2], Taslaman used it for QEPs with external low rank damping but without internal damping [10]. As for any iterative algorithm, a stopping criteria is needed. Bini and Noferini suggested to stop updating when the condition number of $Q(\lambda_i)$ is sufficiently large or when the associated backward error is sufficiently small. The first criterion can only be used if the approximated eigenvalues are semi-simple. Let us first repeat the steps that are needed for external low rank damping as in [10]. Let $Q(\lambda)$ be a second order matrix polynomial, the Ehrlich-Aberth iteration is then applied to the equation $\det Q(\lambda) = q(\lambda) = 0$. The evaluation of $q(\lambda)/q'(\lambda)$ is the crucial part of the update, by using Jacobi's formula

$$\frac{\mathrm{d}}{\mathrm{d}\lambda} \det Q(\lambda) = \operatorname{trace}\left(Q(\lambda)^{-1}Q'(\lambda)\right) \det Q(\lambda),$$

Bini and Noferini [2] showed

$$\frac{q'(\lambda)}{q(\lambda)} = \operatorname{trace}\left(Q(\lambda)^{-1}Q'(\lambda)\right). \tag{7}$$

If no structure is exploited, each update costs $\mathcal{O}(n^3)$ flops. We derive in the following a formula for $\operatorname{trace}\left(Q(\lambda)^{-1}Q'(\lambda)\right)$ such that the essential step in the Ehrlich-Aberth iteration, i.e., the computation of $\frac{q(\lambda)}{q'(\lambda)}$ can be computed in $\mathcal{O}(r^2n + r^3)$. The following deduction exploits the low rank of the external damping as in [10] and finally, it is summarized in Algorithm 1. After diagonalization, i.e., after applying Φ and its transpose, $Q(\lambda)$ and $Q'(\lambda)$ are given as

$$\begin{aligned} Q(\lambda) &= \lambda^2 I_n + \lambda\left[D + \hat{S}\hat{S}^T\right] + \Omega^2, \\ Q'(\lambda) &= 2\lambda I_n + \left[D + \hat{S}\hat{S}^T\right], \end{aligned}$$

where $I_n, D, \Omega^2 \in \mathbb{R}^{n\times n}$ are diagonal matrices and D represents critical damping, i.e., $D = 2\gamma\Omega$ and $\hat{S} \in \mathbb{R}^{n\times r}$ such that $\hat{S}\hat{S}^T = \Phi^T C_{\text{ext}}\Phi$. To compute the trace, first we use the Sherman-Morrison-Woodbury formula in order to compute the inverse $Q(\lambda)^{-1}$ cheaply:

$$Q(\lambda)^{-1} = \left(A + \lambda\hat{S}I_r\hat{S}^T\right)^{-1} = A^{-1} - \lambda A^{-1}\hat{S}\left(I_r + \lambda\hat{S}^T A^{-1}\hat{S}\right)^{-1}\hat{S}^T A^{-1}, \tag{8}$$

where $A = \lambda^2 I_n + \lambda D + \Omega^2$. Since A is diagonal, its inverse is given as the reciprocal of the diagonal matrix, i.e., $A^{-1} = \operatorname{diag}\left(\frac{1}{a_{11}}, \ldots, \frac{1}{a_{nn}}\right)$. Hence,

$$\begin{aligned} Q(\lambda)^{-1}Q'(\lambda) &= 2\lambda A^{-1} + A^{-1}(D + \hat{S}\hat{S}^T) - 2\lambda^2 A^{-1}\hat{S}\left(I_r + \lambda\hat{S}^T A^{-1}\hat{S}\right)^{-1}\hat{S}^T A^{-1} \\ &\quad -\lambda A^{-1}\hat{S}\left(I_r + \lambda\hat{S}^T A^{-1}\hat{S}\right)^{-1}\hat{S}^T A^{-1}(D + \hat{S}\hat{S}^T) \end{aligned}$$

and with $B = A^{-1}\hat{S}$, $B^T = \hat{S}^T A^{-1}$ and $C = \hat{S}^T B$

$$\begin{aligned} Q(\lambda)^{-1}Q'(\lambda) &= 2\lambda A^{-1} + A^{-1}(D + \hat{S}\hat{S}^T) - 2\lambda^2 B\left(I_r + \lambda C\right)^{-1} B^T \\ &\quad -\lambda B\left(I_r + \lambda C\right)^{-1} B^T(D + \hat{S}\hat{S}^T). \end{aligned}$$

For readability, let us in the following abbreviate the trace of a matrix A by $\mathrm{tr}(A)$. We apply the properties of the trace, especially its linearity and invariance under cyclic permutations, i.e., $\mathrm{tr}(ABC) = \mathrm{tr}(BCA) = \mathrm{tr}(CAB)$,

$$\begin{aligned}\mathrm{tr}\left(Q(\lambda)^{-1}Q'(\lambda)\right) &= 2\lambda\,\mathrm{tr}\left(A^{-1}\right) + \mathrm{tr}\left(A^{-1}D\right) + \mathrm{tr}\left(C\right) - 2\lambda^2\,\mathrm{tr}\left(\left(I_r + \lambda C\right)^{-1}B^TB\right)\\ &- \lambda\,\mathrm{tr}\left(\left(I_r + \lambda C\right)^{-1}B^TDB\right) - \lambda\,\mathrm{tr}\left(\left(I_r + C\right)^{-1}C^TC\right).\end{aligned}$$

Therefore, we end up with Algorithm 1 for the computation of $\mathrm{tr}(Q(\lambda)^{-1}Q'(\lambda))$. The total flop count is dominated by step 3 and the linear system solves in steps 5-7. The computation of the matrix C can be done in $\mathcal{O}(r^2n)$ flops since B and $\hat{S}$ are of size $n \times r$ and solving an $r \times r$ linear system can be done in $\mathcal{O}(r^3)$ flops. Hence, the total flop count of the Algorithm 1 is of order $\mathcal{O}(r^2n + r^3)$.

Algorithm 1 Computes $\mathrm{trace}(Q(\lambda)^{-1}Q'(\lambda))$, where $Q(\lambda) = \lambda^2 I_n + \lambda\left[D + \hat{S}\hat{S}^T\right] + \Omega^2$

Require: $D, \Omega^2 \in \mathbb{R}^{n\times n}$ are diagonal matrices, $\hat{S} \in \mathbb{R}^{n\times r}$ and λ
Ensure: $\mathrm{trace}(Q(\lambda)^{-1}Q'(\lambda))$
1: $A := \lambda^2 I_n + \lambda D + \Omega^2$
2: $B := A^{-1}\hat{S}$
3: $C := \hat{S}^TB$
4: $E := I_r + \lambda C$
5: $F := E^{-1}(B^TB)$
6: $G := E^{-1}(B^TDB)$
7: $H := E^{-1}(C^TC)$
8: Return $2\lambda\,\mathrm{tr}\left(A^{-1}\right) + \mathrm{tr}\left(A^{-1}D\right) + \mathrm{tr}\left(C\right) - 2\lambda^2\,\mathrm{tr}\left(F\right) - \lambda\,\mathrm{tr}\left(G\right) - \lambda\,\mathrm{tr}\left(H\right)$.

We modify the algorithm by Taslaman [10] by including internal damping in Algorithm 2. Step 3 in Algorithm 2 locks the starting points $\lambda^{(0)}$ if they are eigenvalues of the QEP (1). For the optimization problem described in Section 4, we do not need the eigenvectors x of the QEP (1). Hence, we exclude the eigenvector computation in Algorithm 2. It can be done by inverse iteration as proposed in [2, 10].

Algorithm 2 Computes all eigenvalues of (1) with internal damping

Require: $M, C_{\mathrm{int}}, C_{\mathrm{ext}}, K$, starting points $\lambda^{(0)}$
Ensure: $\lambda_i, i = 1, \ldots, 2n$
1: Compute $S \in \mathbb{R}^{n\times r}$ such that $C_{\mathrm{ext}} = SS^T$.
2: Compute $\Phi \in \mathbb{R}^{n\times n}$ such that

$$\Phi^T\left(M\lambda^2 + \left[C_{\mathrm{int}} + SS^T\right]\lambda + K\right)\Phi = I_n\lambda^2 + \left[D + \hat{S}\hat{S}^T\right]\lambda + \Omega^2, \tag{9}$$

where $I_n, D, \Omega^2 \in \mathbb{R}^{n\times n}$ are diagonal matrices.
3: Lock starting points $\lambda^{(0)}$ that are eigenvalues of (1).
4: Compute the eigenvalues λ_i of (9) by the Ehrlich-Aberth iteration (6).

3 VIBRATIONAL SYSTEMS

QEPs appear in vibrational systems, where the structural behavior is described by a finite element discretization and the displacements of the nodes are given by the solution to a system

of ordinary differential equations of the form

$$\left(M\frac{\mathrm{d}^2}{\mathrm{d}t^2} + C_{\text{int}}\frac{\mathrm{d}}{\mathrm{d}t} + K\right)x(t) = 0. \tag{10}$$

The damping model depends in general on the application. In equation (10), critical damping is considered as internal damping. By adding a viscous damper to a structure, it prevents movement in a certain direction. Modeling a viscous damper by finite elements yields a positive semidefinite rank one term in the damping matrix C_{ext}. Viscous dampers are costly and therefore, it is desired to have as few additional viscous dampers as possible. If the structure has r viscous dampers, then the corresponding external damping matrix C_{ext} has rank r, and the system of ordinary differential equations is extended to

$$\left(M\frac{\mathrm{d}^2}{\mathrm{d}t^2} + [C_{\text{int}} + C_{\text{ext}}]\frac{\mathrm{d}}{\mathrm{d}t} + K\right)x(t) = 0. \tag{11}$$

The general solution to a vibrational system has the form

$$x(t) = Xe^{Jt}c, \tag{12}$$

where (X, J) is a Jordan pair [5, 7] and $c \in \mathbb{C}^{2n}$ is a vector of arbitrary constants. A Jordan pair consist of the Jordan matrix J of size $2n \times 2n$ that contains the eigenvalues and their multiplicities such that $J = \operatorname{diag}(J_1, \ldots, J_t)$, where each $J_i \in \mathbb{C}^{m_i \times m_i}$ is a Jordan block and $\sum_{i=1}^{t} m_i = 2n$. The matrix $X = [x_1, \ldots, x_{2n}]$ is of size $n \times 2n$ and contains the corresponding Jordan chains x_i for $i = 1, \ldots, 2n$. The vector of constants c can be determined by a given initial conditions $x(0) = x_0$ and $\dot{x}(0) = \dot{x}_0$ for the vibrational systems. Of course, one obtains in general different solutions $x(t)$ for different external dampers, i.e., C_{ext} changes in equation (11).

For the vibrational system (10) the solution is given due to the transformation matrix Φ which diagonalizes the matrices M, C_{int} and K. Hence, the eigenvalues of the Jordan matrix J are given in equation (5) for critical damping. The Jordan chains x_i for $i = 1, \ldots, 2n$ are given as the eigenvectors of the GEP in equation (4) if all eigenvalues are semi simple.

4 NUMERICAL RESULTS

We consider in the following the spectral abscissa [3, 6, 9] and the damping ratio [8, 9] in order to judge the quality of the external damper positions i_j for $j = 1, \ldots, r$. The spectral abscissa μ is the asymptotic rate of the system. It is defined as $\mu = \max\{\operatorname{Re}\lambda_i : i = 1, \ldots, t\}$, where t is the number of different Jordan blocks. If $\mu < 0$, then the system is asymptotically stable. The energy of a solution $x(t)$ is defined as

$$E(t) = \frac{1}{2}\langle \dot{x}(t), M\dot{x}(t)\rangle + \frac{1}{2}\langle x(t), Kx(t)\rangle,$$

where $\langle\cdot,\cdot\rangle$ denotes the Euclidian inner product. The spectral abscissa gives the (asymptotic) behavior such that the energy of the system vanishes, see [3], i.e.,

$$\mu = \min\left\{w : \exists\kappa \text{ s.t. } E(t) \le \kappa E(0)e^{2wt}, \forall t > 0\right\}.$$

As the inequality $E(t) \le \kappa E(0)e^{2wt}$ indicates, the energy decays in general faster than at the asymptotic rate. P. Freitas and P. Lancaster [6] give conditions on how to construct a damping

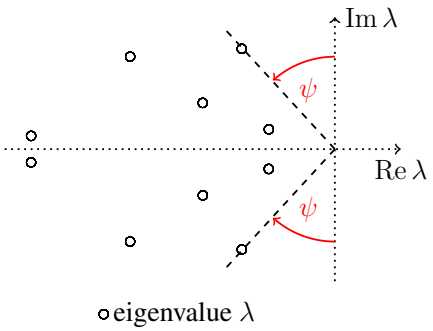


Figure 1: Damping ratio $\zeta = \sin\psi$.

matrix such that this inequality is tight for all times and all initial conditions. Actually, the QEP has then a single eigenvalue with multiplicity $2n$. In our setting, this idea cannot be employed due to the structure of the damping matrix (2). Hence, we optimize the damping positions such that the system's energy decays (asymptotically) as fast as possible, i.e., our first optimization criterion is

$$\min_{i_1,\ldots,i_r} \mu(i_1,\ldots,i_r), \tag{13}$$

where i_j with $1 \leq j \leq r$ is the index of damper j w.r.t. all possible damper positions, which are enumerated as $1,\ldots,N$.

Now, we come to the second optimization criterion. Let us first introduce the damping ratio for complex eigenvalues. It is a measure how fast the system decays after a displacement and it is defined as $\zeta = -\max\left\{\frac{\operatorname{Re}\lambda_i}{|\lambda_i|} : i = 1,\ldots,t\right\}$. A large damping ratio results not only in a fast decay of its mode in a few periods but it also guarantees small amplitudes for harmonically excited system, i.e., the system behaves well w.r.t. perturbations [9]. The damping ratio is shown exemplarily in Figure 1. The second optimization criterion is to find the largest damping ratio w.r.t. external damping positions, i.e.,

$$\max_{i_1,\ldots,i_r} \zeta(i_1,\ldots,i_r). \tag{14}$$

An example of a vibrational system is an n-mass oscillator with n masses $m_1,\ldots,m_n$ and $n+1$ springs with stiffnesses being equal to $k_1,\ldots,k_{n+1}$ which is shown in Figure 2. The mass matrix is diagonal, $M = \operatorname{diag}(m_1, m_2, \ldots, m_n)$, and the stiffness matrix K is given by a tridiagonal matrix,

$$K = \begin{pmatrix} k_1+k_2 & -k_2 & & & \\ -k_2 & k_2+k_3 & -k_3 & & \\ & \ddots & \ddots & \ddots & \\ & & -k_{n-1} & k_{n-1}+k_n & -k_n \\ & & & -k_n & k_n+k_{n+1} \end{pmatrix}.$$

The internal damping C_{int} is given as critical damping (3) with the proportional parameter $\gamma = 0.025$.

We address the question to which mass an external discrete damper should be attached to w.r.t. the two optimization criteria defined above. Hence, the number of damper positions coincides with the system dimension, i.e., $N = n$. We compare the average number of Ehrlich-Aberth

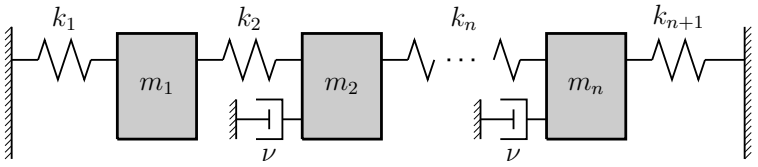


Figure 2: Multiple mass oscillator with two external discrete dampers with viscosity ν.

iterations based on various strategies for starting points of EAI. Therefore, we generate various test sets by varying the system dimension $n = 100, 250, 500, 1000, 1500, 2000, 3000, 4000$. One has to face the combinatorial explosion of damper configurations, i.e., $\binom{N}{r}$ different damper combinations exist. E.g. for $n = 500$ and $r = 5$, more than $2.5 \cdot 10^{11}$ combinations exist, hence we restrict ourself only to a small subset of them. We randomly generate 100 damper configuration such that r external dampers are attached to r distinct masses, i.e., $i_1, \ldots, i_r \in \{1, \ldots, n\}$. We consider the cases of five and ten discrete external dampers with viscosities $\nu = 10^{-1}, 10^1, 10^3$.

To judge the quality of the starting points, we consider the average number of Ehrlich-Aberth iteration (6) until an eigenvalue is found. The number of Ehrlich-Aberth iterations is directly connected to the running time of the Algorithm 2. The stopping criterion for the Ehrlich-Aberth iteration is chosen as $|\lambda_k^{(i)} - \lambda_k^{(i+1)}| < \epsilon |\lambda_k^{(i)}|$, where ϵ is chosen initially as machine precision and relaxed after 50 iterations as proposed in [10].

system dimension	**Viscosity** $\nu = 0.1$		**Viscosity** $\nu = 10$		**Viscosity** $\nu = 1000$	
n	**absent**	**similar**	**absent**	**similar**	**absent**	**similar**
100	3.0183	**2.9776**	7.1852	**6.6998**	6.8425	**6.7186**
250	**2.9215**	2.9499	6.2649	**5.9907**	**6.2972**	6.6759
500	**2.9105**	2.9291	5.5882	**5.2398**	**6.0597**	6.5541
1000	**2.9069**	2.9233	5.0644	**4.5787**	**5.9370**	6.4795
1500	**2.8752**	2.9255	4.7688	**4.2940**	**5.8414**	6.4688
2000	**2.8685**	2.8940	4.5368	**4.1478**	**5.8261**	6.3905
3000	**2.8716**	2.8974	4.2004	**3.9910**	**5.7970**	6.3922
4000	**2.8577**	2.8855	4.0469	**3.8880**	**5.7544**	6.3684

Table 1: Average number of EAI updates for five external dampers, i.e., $r = 5$.

The results for the average number of Ehrlich-Aberth iteration updates are shown in the Tables 1 and 2 for five and ten external dampers. It can be noted that the average number of iterations for a fixed viscosity decreases w.r.t. the system dimension. For small system dimensions the number of updates decreases significantly, e.g. $\nu = 10$ and $n = 100, 250$. Here, we call the strategy for choosing starting points for EAI *absent*, if the eigenvalues of the vibrational problem (10) are used as starting points, i.e., external damping is absent, $C_{\text{ext}} = 0$. This strategy was proposed in [10]. We tested various other strategies to characterize a *similar* damper configuration. The best suited strategy was to sort the damper positions w.r.t. the masses $m_1, \ldots, m_n$ and computing the $\|\cdot\|_2$-norm between the current and the previously computed damper configurations. We then use the eigenvalues of the previous damper configuration which minimizes the $\|\cdot\|_2$-norm as starting points for EAI. This is a heuristic approach and of course examples can be constructed where other choices of starting points might be better suited. The

lower average number of updates in the Table 1 and 2 w.r.t. the two strategies are plotted in bold.

For sufficiently small viscosities, the eigenvalues of the vibrational problems (10) and (11) are very similar. Hence, the strategy *absent* is suited very well (except for a relatively small system dimension $n = 100, 250$) as it can be seen in the second and third column of the Tables 1 and 2 for the viscosity $\nu = 0.1$. For moderate viscosities, i.e., with a magnitude of one or two, the strategy *similar* is better suited than *absent* regardless of the chosen system dimension. The average number of Ehrlich-Aberth iterations were improved from 4.6% to 23% which may be crucial for a large number of vibrational problem solves due to the combinatorial explosion of damper configurations. As the viscosity is increased, the strategy *absent* was again superior to *similar*.

Using any previously computed damper configuration as starting points for EAI, was always worse than the strategy *similar*, hence, it is expected that for an increased number of damper configurations, the strategy *similar* will have even less updates.

system dimension	**Viscosity** $\nu = 0.1$		**Viscosity** $\nu = 10$		**Viscosity** $\nu = 1000$	
n	**absent**	**similar**	**absent**	**similar**	**absent**	**similar**
100	3.7762	**3.0036**	9.2433	**7.5173**	9.1721	**8.0468**
250	3.0731	**2.9921**	7.9465	**6.7040**	**7.4781**	7.6672
500	**2.9784**	2.9860	7.1177	**6.1486**	**6.7842**	7.4331
1000	**2.9567**	2.9803	6.2862	**5.3707**	**6.3899**	7.2603
1500	**2.9560**	2.9790	5.7722	**4.9563**	**6.2635**	7.1673
2000	**2.9490**	2.9681	5.4226	**4.6475**	**6.2201**	7.1609
3000	**2.9483**	2.9773	5.1631	**4.4300**	**6.1597**	7.1103
4000	**2.9304**	2.9585	4.9907	**4.2527**	**6.0993**	7.0679

Table 2: Average number of EAI updates for ten external dampers, i.e., $r = 10$.

It cannot be guaranteed that the starting points defined by the eigenvalues when external damping is absent are any good, in fact it has even be argued that they might be arbitrarily bad due to Ackermann's formula for pole placement [10]. The same argument holds here, when internal damping is included, as well. But nevertheless, we have shown by numerical examples that the starting point for the Ehrlich-Aberth iteration can be improved by choosing the eigenvalues of a previously solved QEP as starting points of EAI for moderate viscosities. Moderate viscosities are often the most important in engineering applications.

5 OUTLOOK

In this paper, we considered proportional critical damping as internal damping, but of course the eigenvalue computation by the Ehrlich-Aberth iteration can easily be extended to any internal damping that is simultaneously diagonalized by Φ, i.e., C_{int} satisfies the orthogonality relation

$$\varphi_i^T C_{\text{int}} \varphi_j = 0, \qquad i \neq j. \tag{15}$$

It means that the ideas presented here, can also be employed e.g. for Rayleigh damping, which is also known as classical damping where $C_{\text{int}} = \alpha M + \beta K$ for any $\alpha, \beta \geq 0$.

Furthermore, a discrete damper can be built with viscosities in some given range, i.e., $\nu \in (0, \nu_{\max})$. In a second step, we would like to not only find the best position where a discrete damper should be attached to but also find its best viscosity. Therefore, we consider the viscosity

ν as a parameter of the vibrational system (11), i.e., $C_{\text{ext}} = C_{\text{ext}}(\nu)$ and then the solution depends not only on the external dampers but on the viscosity as well, i.e., $x(t) = x(t;\nu) = X(\nu)e^{J(\nu)t}c(\nu)$. Here, we can consider two different cases, first of all, that all viscous dampers have the same viscosity ν and secondly, viscous dampers with different viscosities. In [10], a class of problems, the so called homotopy methods, has been identified where the starting points can be given by the eigenvalues corresponding to a given parameter. The optimization problems damping ratio and spectral abscissa can be viewed as homotopy methods by solving a parameter dependent eigenproblem by a sequence of eigenproblems where the parameter is the viscosity of the external viscous dampers. Hence, one solves the QEP (1) for increasing viscosities, i.e., $\nu_0 < \nu_1 < \nu_2 < \dots$

In the optimization procedure, we would like to combine the results for the initial starting points for EAI as presented in this paper depending on the magnitude of ν_0.

ACKNOWLEDGEMENTS

We thank Leo Taslaman for helpful discussions and for sharing his MATLAB® codes.

REFERENCES

[1] O. Aberth. Iteration methods for finding all zeros of a polynomial simultaneously. *Math. Comp.*, 27:339–344, 1973.

[2] D. A. Bini and V. Noferini. Solving polynomial eigenvalue problems by means of the Ehrlich-Aberth method. *Linear Algebra Appl.*, 439(4):1130–1149, 2013.

[3] S. J. Cox. Designing for optimal energy absorption, 1: Lumped parameter systems. *J. Vib. Acoust.*, 120:339–345, 1998.

[4] L. W. Ehrlich. A Modified Newton Method for Polynomials. *Commun. ACM*, 10(2):107–108, February 1967.

[5] I. Gohberg, P. Lancaster, and L. Rodman. *Matrix Polynomials*. Classics in Applied Mathematics. Society for Industrial and Applied Mathematics, 2009.

[6] P. Lancaster and P. Freitas. On the optimal value of the spectral abscissa for a system of linear oscillators. *SIAM J. Matrix Anal. Appl.*, 21(1):195–208, 1999.

[7] P. Lancaster and M. Tismenetsky. *The Theory of Matrices: With Applications*. Computer Science and Scientific Computing Series. Academic Press, 1985.

[8] P. C. Müller and M. Gürgöze. Optimale Dämpfungsstärke eines viskosen Dämpfers bei einem mehrläufigen Schwingungssystem. *Z. Angew. Math. Mech.*, 71:60–63, 1991.

[9] P. C. Müller and W. Schiehlen. *Lineare Schwingungen*. Akademische Verlagsgesellschaft Wiesbaden, 1976.

[10] L. Taslaman. An algorithm for quadratic eigenproblems with low rank damping. *SIAM J. Matrix Anal. Appl.*, 36(1):251–272, 2015.

International Conference on Engineering Vibration
Ljubljana, Slovenia, 7-10 September 2015

STRUCTURAL OPTIMIZATION OF A MATERIAL EXHIBITING NEGATIVE STIFFNESS

Zuzana Dimitrovová*[1], Jan Heczko[2], Helder C. Rodrigues[3]

[1]Departamento de Engenharia Civil, Faculdade de Ciências e Tecnologia, Universidade Nova de Lisboa and IDMEC, Instituto Superior Técnico, Universidade de Lisboa, Lisboa, Portugal
zdim@fct.unl.pt

[2]European Centre of Excellence, NTIS, University of West Bohemia, Pilsen, Czech Republic
jan.heczko@gmail.com

[3]IDMEC, Instituto Superior Técnico, Universidade de Lisboa, Lisboa, Portugal
hcr@tecnico.ulisboa.pt

Keywords: Material Models and Fitting, Negative Stiffness, Extreme Damping, Structural Optimization.

Abstract. *In this paper a material realization of a structure exhibiting negative stiffness is presented. The structure is formed by polyethylene foam sheets that are used as a base material and the negative stiffness feature is provided by an inherent bistable element introduced with the help of curved cuts. The present material realization is intent to be optimized in order to supply improved passive damping performance in conformity with the literature, where it is demonstrated that extreme damping can be achieved in materials incorporating negative stiffness inclusions. It is shown that even for the initial guess, the damping of the structure is much superior than the one of the base material. Structural optimization can be performed numerically by the finite element method combined with some metaheuristic optimization algorithm. As design variables geometrical characteristics of the additional cuts and material density are considered. The objective function involves strain delay as a measure of the damping performance. As a necessary step, a reliable finite element model must be available. This paper shows material models testing and fitting of the material parameters according to the experimental examination. The difficulty is attributed to strong orthotropy and to the fact that during the displacement controlled test several regions of the structure are severely stretched or compressed and therefore the material model must be highly non-linear and cover correctly very large range of strains.*

1 INTRODUCTION

Significant progress in material processing has stimulated interest in material design optimization. New materials realizations can be tailored by optimization techniques to achieve optimal responses to given solicitations. It has already been proven that extreme damping can be attained in materials incorporating negative stiffness inclusions. Nevertheless, material realization in this regard is still a challenging task.

A typical representation of a negative stiffness mechanism is formed by two inclined springs/bars allowing for snap-though. Based on this feature and in continuation with previous works, Structure with inherent bistable elements (SIBE) periodically distributed is suggested to be made of polyethylene sheets with additional semi-circular cuts. Therefore, as a Base material (BM), polyethylene of low density (20-50kg/m^3) is used in form of plates made of two thinner sheets glued together, giving the total thickness of around 2 cm.

SIBE is unstable and therefore can only be examined under displacement control test. In preliminary testing it was shown [1] that SIBE provides the expected behaviour. The damping performance can be measured by the strain delay (imposed displacement) with respect to the generated stress (total force). It was shown that even the initial guess of SIBE without any optimization achieves damping characteristics much superior than the ones of the BM [2]. By techniques of structural optimization the global loss factor can be further improved and maximized. Several geometrical parameters describing the position and size of the additional cuts can be taken as design variables. As an additional parameter the material density can be introduced. The optimization can be accomplished within a finite element model and, at the same time, with the help of a simple discrete mechanism. The procedure of obtaining the discrete mechanism is described in [1] and it is reviewed at the end of this paper. The main advantage of this representation is that the mechanism dynamic behaviour characteristics can be solved analytically. Then the optimization can be easily accomplished.

For the structural optimization, based on the finite element analysis, an adequate material model accounting for orthotropy induced by the polyethylene bubbles direction, for high compressibility and stretching occurring close to the cuts and sharp corners, and for material viscoelasticity must be available. Several specimens of BM with different sizes and densities were tested experimentally under unilateral tension, compression, cyclic and relaxation tests using a universal testing machine. Distribution of the Lagrangian strain tensor was extracted with the help of digital image correlation and tracking and transformed to the left or right Cauchy-Green strain tensors. Material parameters of several hyperelastic models were adjusted by fitting modules, created in Matlab. Statistical treatment and design of experiments was used to identify significant factors and interactions among the size, shape and arrangement of the additional cuts, as well as the density of the BM. Allowable ranges of these factors define the design space and then the global loss factor can be maximized by some metaheuristic algorithm.

The paper is organized in the following way. In Section 2 resume of the most important experimental results is given, in Section 3 material fitting is presented and the global loss factors is extracted. In Section 4 the discrete model is described and the paper is concluded in Section 5.

2 EXPERIMENTAL EXAMINATION

Some characteristics of the BM and SIBE specimens of low density of 20kg/m^3 are presented in Table 1. These specimens were tested on a universal testing machine (model 5566, Instron Corporation Canton, USA) with a load cell of 10 kN. The cross-head velocity was in

the range of 3 to 9 mm/min. At the time of these tests the digital image correlation and tracking equipment was not available.

	Width [mm]	Thickness [mm]	Length [mm]	Uniaxial Test
T01L	37.45	22.78	125	Tension (9mm/min)
T02T	39.92	22.38		
C01L	21.9	38.26	24.46	Compression (3mm/min)
C02T	21.93	38.63	24.45	
C03T	22.1	38.69	24.89	
C04L	25.14	39.1	24.97	
TS01	174	21.39	154	Tension (4mm/min)
TS02	174	21.39	154	Tension (9mm/min)

Table 1: Specimens characteristics.

Regarding the legend used in Table 1: first "T" means traction and "C" denotes compression. "01" and similar is the sample number. BM specimens have additional designation: "L" means that the stiffer direction was the longitudinal one, i.e. coincident with the direction of the applied force, and "T" that it was the transversal one. "S" in used for SIBE samples.

In Figure 1 resume of some results on BM is presented. It is seen that by separating the tension and compression tests, there is e non-smooth passage between positive and negative stresses which complicates the material fitting.

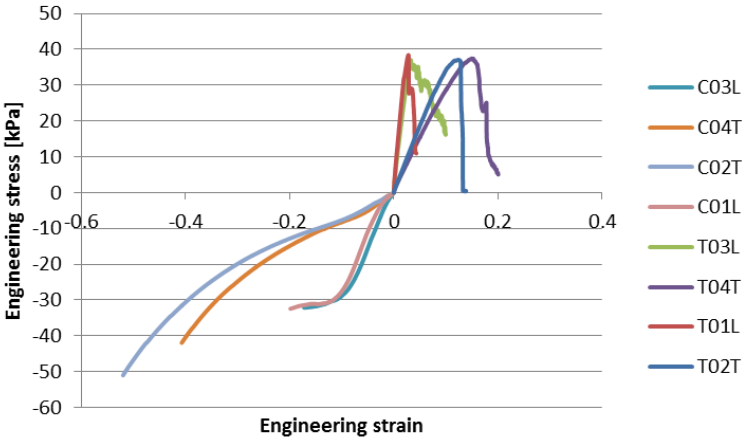


Figure 1: Resume of some results on BM.

Figure 2 presents an evolution of the tension test on SIBE. Figures 3 and 4 relate the imposed displacement with the total force. It is seen that the negative stiffness region is well-formed. In Figure 3 captions "-1" and "-2" stand for the number of the test performed on the same specimen TS02. Specimen TS01 was left until the failure. In addition, cyclic tests were performed on the specimen TS02. The objective of the cyclic tests was to show that in displacement controlled regime the specimen can operate solely over the negative stiffness branch. These results are presented in Figure 4.

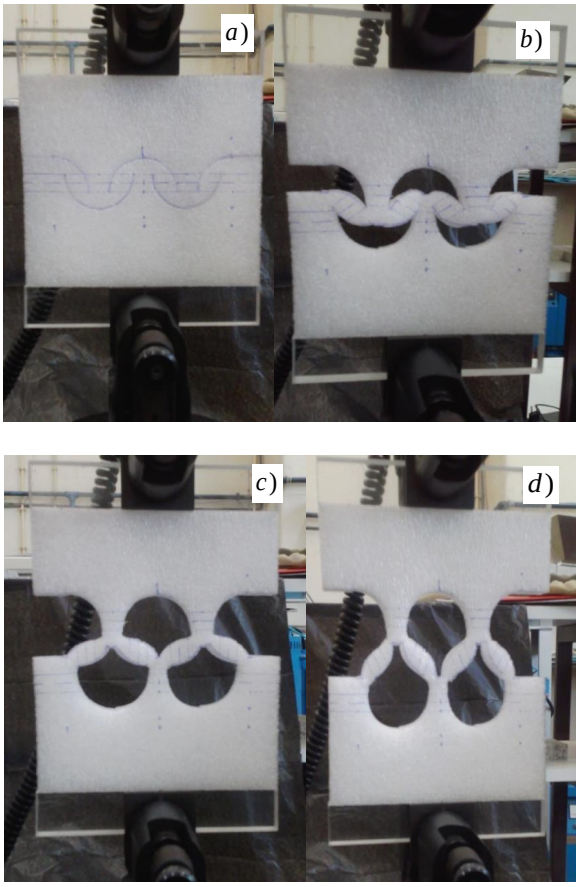


Figure 2: Tension test on the bistable material: (a) initial position, (b) beginning of the negative stiffness, (c) new beginning of the positive stiffness, (d) initiation of failure.

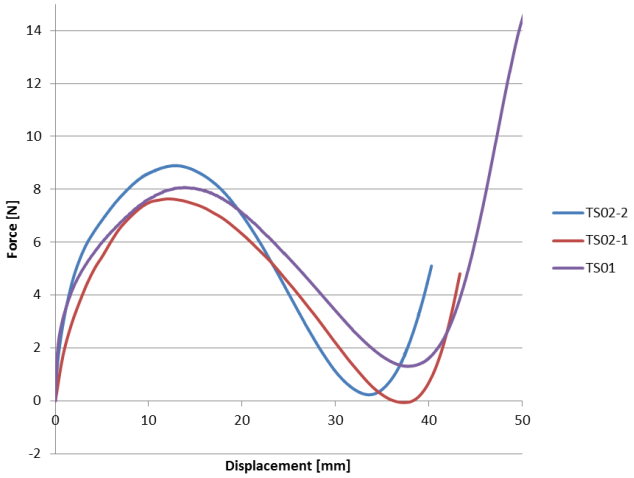


Figure 3: Tension tests on SIBE.

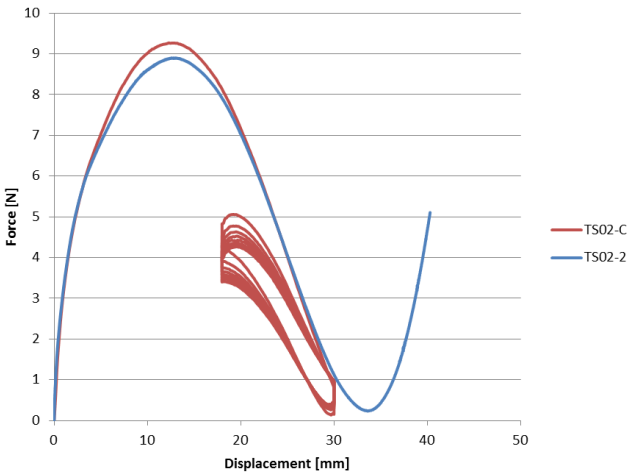


Figure 4: Tension and cyclic tests on SIBE.

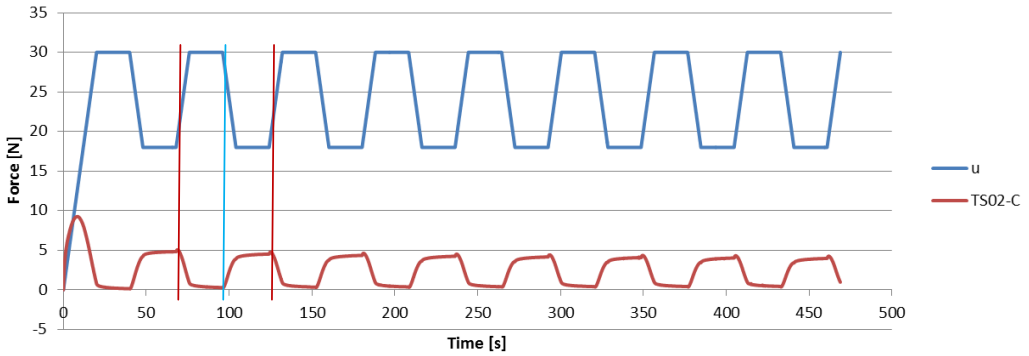


Figure 5: Damping estimation.

In Figure 5 the procedure for calculating the strain delay is briefly shown. Imposed displacement on SIBE (in mm) is compared with the registered force as a function of time. From the time delay $\tan\delta_{SIBE} = -0.32$ can be estimated. The same procedure, when applied on BM, gives $\tan\delta_{BM} = 0.07$, which demonstrates a significant improvement of SIBE versus BM.

3 MATERIAL FITTING

The experiments showed in previous section were described in terms of engineering (nominal) stress tensor and engineering strain. Therefore, the material models should be fitted in this form and not in terms of the true Cauchy stress. Several attempts summarized in [1] were performed on non-linear elastic materials in software ANSYS. Better results were, however, obtained on hyperelastic models, because of their numerical stability, as "infinite" compression is allowed without reverting the element volume to a negative value. There are few models that account for orthotropy, but acceptable results were obtained on isotropic highly compressible model specifically derived for compressible forms, i.e. the Ogden-Storakers model, with orthotropy simulated by additional constraints. The strain energy density with a suitable volumetric function is given by:

$$W=\sum_{k=1}^{n}2\frac{\mu_k}{\alpha_k^2}\left[\lambda_1^{\alpha_k}+\lambda_2^{\alpha_k}+\lambda_3^{\alpha_k}-3+\frac{1}{\beta_k}\left(J^{-\alpha_k\beta_k}-1\right)\right] \tag{1}$$

where α_k, β_k and μ_k are material constants, λ_i are principal stretches defined as square roots of eigenvalues of the Left Cauchy-Green strain tensor $\mathbf{B}=\mathbf{F}\cdot\mathbf{F}^T$, $\mathbf{F}$ is the deformation gradient and $J=\det(\mathbf{F})$. For the uniaxial tests, $\lambda_2=\lambda_3$ and the longitudinal Cauchy stress is given by

$$\sigma_{11}=2\left(\lambda_1\lambda_2^2\right)^{-1}\sum_{k=1}^{n}\frac{\mu_k}{\alpha_k}\left[\lambda_1^{\alpha_k}-\left(\lambda_1\lambda_2^2\right)^{-\alpha_k\beta_k}\right] \tag{2}$$

where the relation between λ_1 and λ_2 is obtained from the nullity of transversal stresses

$$0=\sum_{k=1}^{n}\frac{\mu_k}{\alpha_k}\left[\lambda_2^{\alpha_k}-\left(\lambda_1\lambda_2^2\right)^{-\alpha_k\beta_k}\right] \tag{3}$$

For *n*=1 this relation can be explicitly written as

$$\lambda_2=\lambda_1^{-\frac{\beta}{1+2\beta}} \tag{4}$$

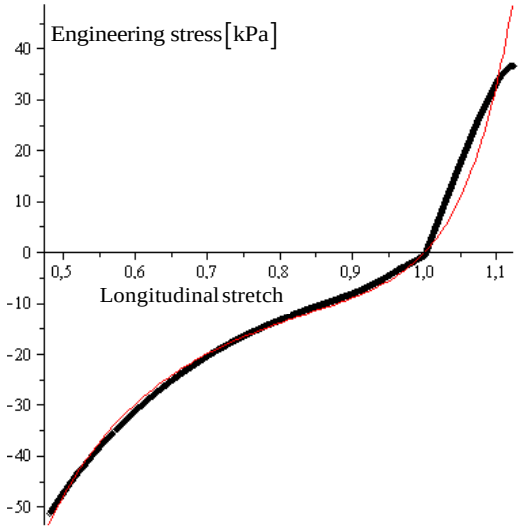


Figure 6: Fitting of the Ogden-Storakes model: black dots – experimental results, thin red line – analytical material curve.

For some experimental tests very good fitting could be obtained by MATLAB modulus, as shown in Figure 6. The analytical material curve is obtained for $\alpha=17.9$, $\beta=0.11$ and $\mu=70\text{kPa}$. It is seen that the agreement is excellent especially in compression. Discrepancy in tension is caused by the discontinuity in slope of the experimental curve, originated by the fact that experiments in tension and compression were performed separately. Numerical results with the additional constraint are in good correlation with the experiment, as shown in Figure 7. For higher *n*, relation between stretches must be solved from a non-linear equation and due to a high number of material parameters, other optimization methods should be used.

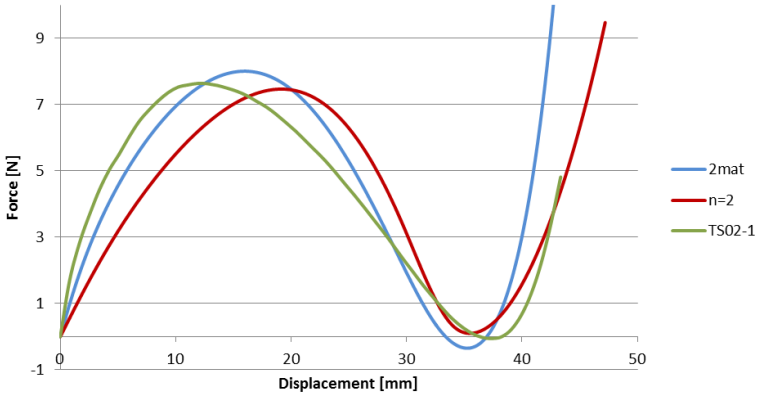


Figure 7: Results of finite element analysis: 2mat in blue stands for the fitted material with additional constraint, n=2 stands for the fitted material without the additional constraint.

4 DISCRETE MODEL

The discrete model can be formed by linear springs that geometrically represent SIBE as shown in Figure 8.

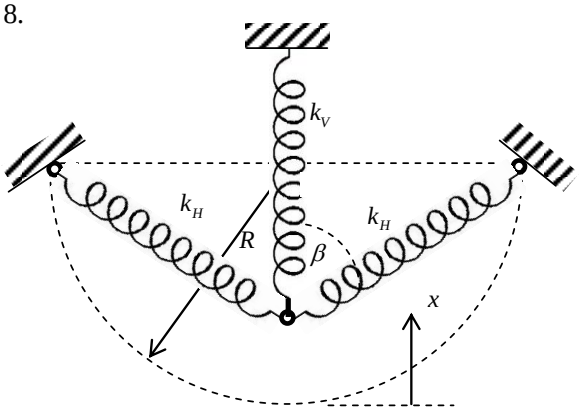


Figure 8: The discrete model.

Springs stiffnesses, k_V and k_H, can be optimized by implementation of the difference of the four fundamental conditions that express the position and value of the zero stiffness and can thus be represented analytically on the discrete model. In accordance with the experimental tests, it is assumed that the undeformed springs have their free extremities at the position $x = 0$. Other geometrical details are related to the semi-circular cuts in the structure. The non-linear force representing the system in Figure 8 can be written as:

$$F_V = k_V x - 2\cos\beta N = k_V x - 2\frac{R-x}{\sqrt{R^2+(R-x)^2}} k_H \left(\sqrt{R^2+(R-x)^2} - R\sqrt{2}\right) = \\ k_V R\xi - 2(1-\xi)k_H R\left(1-\frac{1}{\sqrt{1-\xi+\xi^2/2}}\right) \tag{5}$$

where $\xi = x/R$ and N stands for the elastic force developed in the inclined springs. The objective is to tailor force-displacement curve of this model to be reasonably proximate to the physical model. The parameter connected to the specimen geometry, R, is equal to 25 mm. Consequently, there are only two variables, springs stiffnesses, and four essential conditions to fulfil. Optimal parameters, $k_V = 0.18\text{N/mm}$ and $k_H = 1\text{N/mm}$ can be obtained by a parametric optimization. As already stated, the discrete model can be easily analyzed. Stationary points are determined by:

$$\xi_1 = 1 - \frac{1}{k_V + 2k_H}\sqrt{-\left(k_V + 2k_H\right)^2 + 2\sqrt[3]{k_H^2\left(k_V + 2k_H\right)^4}} \tag{6}$$

$$\xi_2 = 1 + \frac{1}{k_V + 2k_H}\sqrt{-\left(k_V + 2k_H\right)^2 + 2\sqrt[3]{k_H^2\left(k_V + 2k_H\right)^4}} \tag{7}$$

Under the assumption that

$$8k_H\left(k_V + 2k_H\right)^2 \geq \left(k_V + 2k_H\right)^3 \tag{8}$$

The global performance of the discrete model is represented in Figure 8.

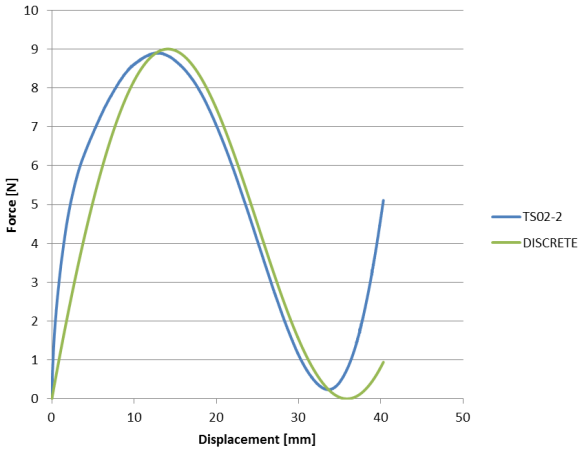


Figure 8: The discrete model performance versus the experiment.

It is seen that the fitted results looks quite good, nevertheless, the initial slope is very different from the tested specimen. It is seen, that a compressive force must be present, to secure the unstable horizontal position of the lateral springs, which is probably the effect of the testing machine. More tests and more details about the material behaviours must be gathered and analysed before the structural optimization can be started.

5 CONCLUSIONS

In this paper a material realization of a structure exhibiting negative stiffness, the structure with inherent bistable elements (SIBE), is presented. The present material realization can be optimized in order to supply extreme passive damping performance in conformity with the literature. It was shown that even for the initial guess, the damping of SIBE is much superior to the one of the base material (BM) formed by polyethylene foam sheets. Structural optimization can be performed numerically by the finite element method combined with some me-

taheuristic optimization algorithm. As design variables geometrical characteristics and material density of SIBE can be considered. The objective function involves strain delay as a measure of the damping performance. As a necessary step, a reliable finite element model must be available. This paper showed several attempts of reaching the suitable material model and procedures for material parameters fitting. The difficulty is attributed to strong orthotropy and to the fact that during the displacement controlled test several regions of the structure are severely stretched or compressed and therefore the material model must be highly non-linear and cover correctly very large range of strains. Nevertheless, acceptable correspondence with the finite element model and the discrete model has already been established.

ACKNOWLEDGEMENTS

This work was supported by the Fundação para a Ciência e a Tecnologia (FCT), Portugal, both directly in the form of a project PTDC/EME-PME/67658/2006 and through IDMEC, under LAETA, project UID/EMS/50022/2013.

REFERENCES

[1] J. Heczko, Z. Dimitrovová, H.C. Rodrigues, Negative stiffness materials for vibration damping: a material realization of a nonlinear bistable element, *International Journal of Innovations in Materials Science and Engineering*, **1** (2), 75-81, 2014.

[2] J. Heczko, Z. Dimitrovová, H.C. Rodrigues, "Optimization of a material with a negative stiffness provided by an inherent bistable element", *4th International Conference on Engineering Optimization* (EngOpt 2014), A. Araujo (Ed.), CRC Press, Lisbon, Portugal, 2014 (ISBN: 978-1-138-02725-1)

Full Field Measurements for Advanced Structural Dynamics (MS18)

11th International Conference on Engineering Vibration
Ljubljana, Slovenia, 7–10 September 2015

COMPARATIVE STUDIES ON FULL FIELD FRFS ESTIMATION FROM COMPETING OPTICAL INSTRUMENTS

Alessandro Zanarini[1,2]

[1]University of Bologna, DIN - Industrial Engineering Dept., Italy
a.zanarini@unibo.it

[2]Vienna University of Technology, Institute of Mechanics & Mechatronics, Austria
alessandro.zanarini@tuwien.ac.at

Keywords: Full field vibration measurements, Frequency Response Functions, Optical metrology, SLDV, Hi-Speed DIC, Dynamic ESPI.

Abstract. *Advanced optical measurement systems are nowadays at disposal for complex dynamic and modal tests on lightweight structures, each with its own advantages, drawbacks and preferred usage domains, in order to obtain highly spatially defined vibration patterns for many applications in vibration engineering and product development.*

This work aims at comparing the potential of three completely different technologies on a common target and test rig. SLDV, dynamic ESPI and hi-speed DIC are here deployed in a unique test on the estimation of FRFs with high spatial accuracy from a thin plate, which exhibits a broad band dynamics and high modal density in the common frequency domain where the techniques can find an operative intersection. The comparison of estimated FRFs and related quality features is detailed with notes on acquisition and processing techniques, in order to draw conclusions on the full field measurement approach and the specific gear.

Assessing the successful Full Field FRF estimation stage turns to be the basic step in developing further analyses, like experimental full field modal analysis for enhanced reliability in modeshapes estimation, numerical model tuning and risk assessment in complex structures.

1 INTRODUCTION

First qualitative and not competitive in terms of time-to-result, like the silver alloyed holography at a particular frequency of interest, from their beginning full field measurements were showing the other side of the structural dynamics: a highly detailed spatial domain against the lumped sensor placement, with surface deflection shapes rapidly changing from frequency to frequency, functions of the complex superposition of the eigensolutions in non-conventional patterns, giving relevant information on where to better locate the lumped vibration sensors or strain-gauges. With the recent development of the digital processing of optical measurement results it appears possible to have access to reliable full field quantitative data. Also other technologies are approaching the subject of increasing the spatial resolution: automated scanning schemes or distributed sensor grids try to enhance more traditional procedures.

A non-native full field instrumentation like the Scanning Laser Doppler Vibrometer (SLDV) has expanded the technique of contact-less point measurement in time/frequency domains to a fine grid of locations, thus extending the concept of the velocity sensors to a detailed acquisition, also adding no mass to the specimen. Thus SLDV is nowadays the reference when the need of spatially detailed FRF measurements for NVH tools is demanded, because SLDV has kept the same peculiarities of previous technologies and proven procedures, just adding more dofs at a reasonable cost. Native full field technologies, those based on an imaging sensor that acquires information synchronously at every dof, approach the measurement from the point of the acknowledged quality obtainable in the spatial domain, especially in terms of consistency of the deflection field in the neighbouring dofs[1]. Electronic Speckle Pattern Interferometry (ESPI) gives nowadays [2, 3, 4] an extremely accurate displacement field at the frequency of interest (up to several kHz, more depending on the excitability of the component); but having populated data in a broad frequency band was prohibitive, due to time-consuming stepped sine excitation/acquisition, not completely automated. Digital Image Correlation (DIC), with high-speed cameras, has good detail in the time resolved displacement maps, but can be more limited in the frequency domain, due to the specifications of the cameras, which, though, are seeing rapid electronics improvements. The extraction of the correlated fields is still very time demanding. Whether ESPI or DIC is used, broad frequency band *receptance* FRFs can be successfully extracted also from native full field technologies[4, 5], keeping in mind that they might be less sensitive at higher frequency than mobility FRFs.

Native Full Field FRFs can be the strong link between advanced experimental analysis and numerical modelling, adding highly consistent and detailed fields to proven NVH approaches and fatigue life, reliability or integrity predictions, giving an alternative to the SLDV technology, with broad opportunities of successful application[6, 7].

Extensive and comparative research work has been carried out by the author at Vienna University of Technology, Austria, with the project TEFFMA[1] to assess advantages and drawbacks of today full field measurement techniques on a common experimental set-up, where Full Field FRFs have to be extracted in a broad frequency range.

In this paper an overview of accurate & high resolution impedance model for *receptance* FRFs is described and discussed in detail with extensive pointwise comparison on SLDV, Hi-Speed DIC and dynamic ESPI, showing the high quality of experimental models nowadays obtainable, for a clear benefit of all the product development process.

[1] A. Zanarini, Experienced researcher in the project TEFFMA - Towards Experimental Full Field Modal Analysis, financed by the Marie Curie FP7-PEOPLE-IEF-2011 PIEF-GA-2011-298543 grant

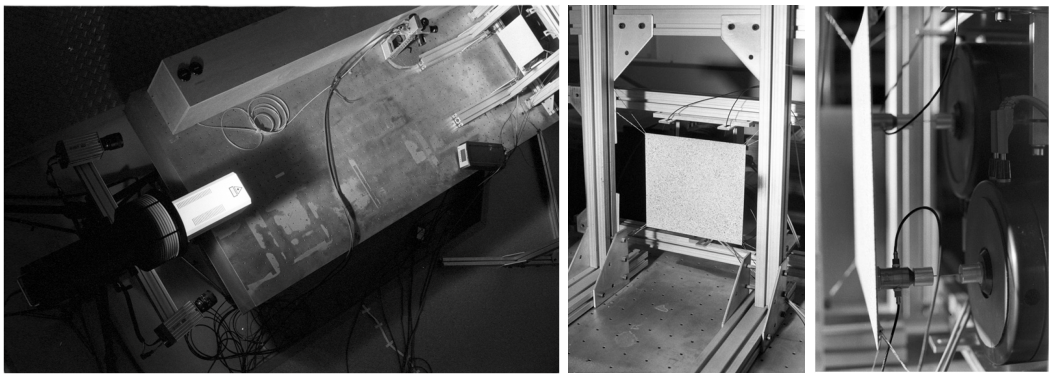


Figure 1: The experimental set-up for vibration measurements by means of optical equipment

2 DIRECT EXPERIMENTAL CHARACTERISATION BY MEANS OF FRFS

In this paper will be used the declination known as *receptance* matrix [8], as spectral relation $\mathbf{d}(x, y, j\omega)$ between displacements and forces, describing the dynamic behaviour of a *many*-degree-of-freedom system, with potentially multi-input excitation, here by two shakers.

Even if rooted to the practice of single sensor tests or of measurements with a very coarse grid, the *coherence function* is here used as index of quality of the FRF estimation. A cause of low *coherence function* which can be appreciated with increased spatial sampling, beyond the not correlated sources, is limited motion against force in the areas (as on nodal lines) where the *coherence function* is evaluated, which means that it is related to the dynamics of the component and not to any measurement chain error. Instead, due to its formulation, the *coherence function* does not take into account the consistency of the measurements with the neighbouring result, leading to the judgement of very highly coherent (with the excitation force) displacements even when the grid is scattered by relevant uncertainty around a mean, and more physical, shape.

2.1 Full Field FRFs adding higher spatial resolution

Full field technologies can expand the analyses in the spatial domain, a region whose potentialities have not been sufficiently explored. But this transition needs strong efforts in the direction of refining the technologies and the analysis approaches, when not to re-think some known procedures. The same milestones achieved by traditional NVH environment have to be delivered, or the permeation of native full field technologies in NVH practice will face contrasts. On the other side, adding high spatial resolution in dynamic models by means of accurate FRFs will be a valuable addition to the state-of-the-art of the design of complex systems and will surely lead to the exploration of new FRF-based quantities derived from enhanced displacement fields, such as surface rotations, strains[4, 9] & stresses and failure point distributions[5, 10].

2.2 Sensor placement in a wide frequency band

When broad band frequency excitation is expected, the selection of locations where to place the sensors becomes increasingly important, due to the superposition of the eigenshapes and their nodal lines, being these latter the cause of the diminishing of the signal-to-noise ration and the *coherence function* as previously said. Normally this selection might be refined by means of a numerical model, but this needs to be updated on the test, causing time and costs increase.

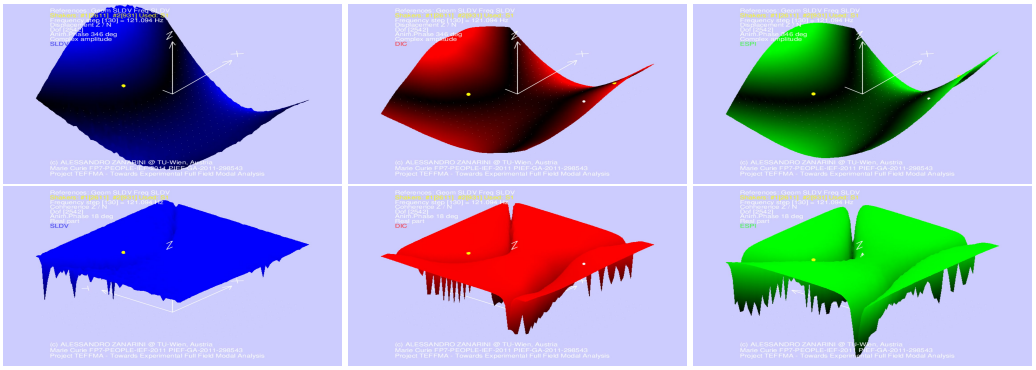


Figure 2: FRF & Coherence function maps at 121Hz from SLDV, DIC and ESPI, excitation from shaker 1

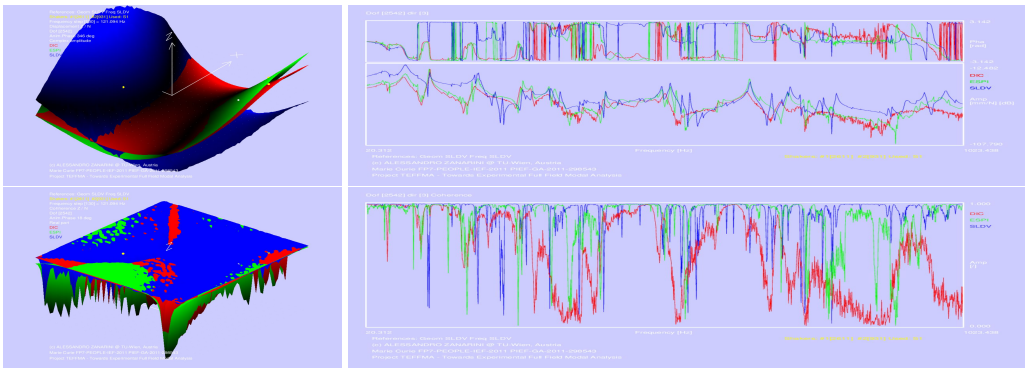


Figure 3: Comparison of FRF & Coherence maps at 121Hz, of single functions at dof 2542 in the whole frequency domain from SLDV, DIC and ESPI, excitation from shaker 1

Since full field technologies are mostly optical, they are also not invasive with added mass and cabling. The finer spatial grid increases the mapping ability of the sensing unit. Native full field sensors deliver more consistent fields of data, with more continuity in the field maps due to the synchronous acquisition of all the viewed field: this is of uttermost relevance when dealing with real boundaries and couplings, inhomogeneous materials, like compounds or structured layers, to discriminate if unexpected local behaviour was originated by a component or a measurement issue.

3 FULL FIELD FRFS RESEARCH IN TEFFMA PROJECT

The fundamental research project funded by the European Commission and carried out by Dr. Alessandro Zanarini at the Vienna University of Technology aims at making a comparison between the state-of-the-art in native full field technologies and the SLDV as reference, to understand at which point of their development these experimental procedures can provide NVH applications with enhanced peculiarities. In the well equipped laboratory of the TU-Wien it was possible to build a complex set-up for the comparison of the qualities of the different technologies available in acquiring Full Field FRFs. This paper wants to highlight the results obtained on *receptance* map estimation and, further, on coherence function maps, on a pointwise comparative approach focused on results at the same physical location on the test specimen.

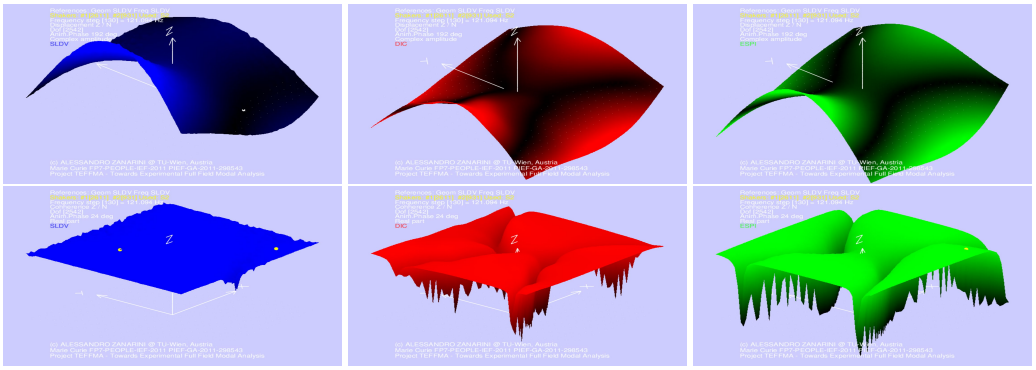


Figure 4: FRF & Coherence function maps at 121Hz from SLDV, DIC and ESPI, excitation from shaker 2

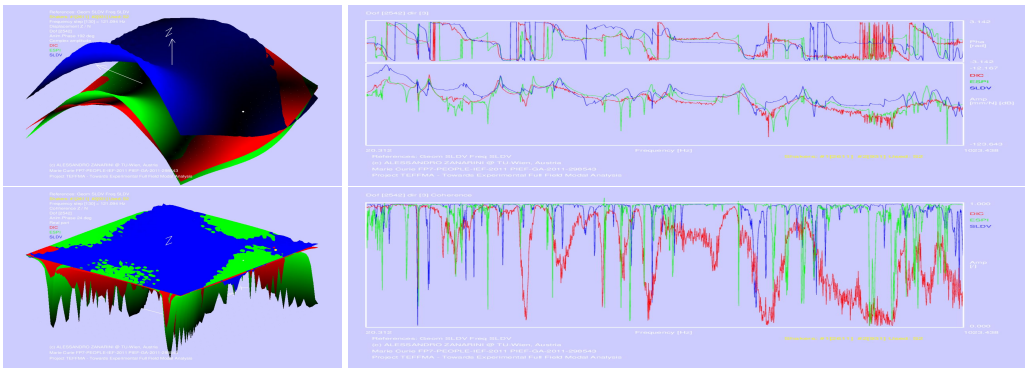


Figure 5: Comparison of FRF & Coherence maps at 121Hz, of single functions at dof 2542 in the whole frequency domain from SLDV, DIC and ESPI, excitation from shaker 2

3.1 Brief summary of the technological equipment

The laboratory facility at TU-Wien has a dedicated room with seismic floor and air-cushion anti-vibration optical table. A Polytec PSV 300 (from 2003) is at disposal, with 1D (out-of-plane) scanning head OFV-056. Due to its peculiarities of being the junction instrument between the traditional NVH measurement technologies and the growing pure full field apparel, SLDV is taken as reference. As pure full field equipment there is the Dantec Ettemeyer Q-500 Hi-Res (a prototype dated back to 2004), the laser speckle pattern interferometer for 3D dynamic measurements in stroboscopic monochromatic light, and the Dantecdynamics Q-450 for 3D dynamic measurements by means of image correlation and hi-speed cameras (Nanosense Mk III, 4 GB of memory - 1040 fps at 1280 x 1024 pixels maximal resolution) in white light (from 2008). It completes the equipment an LMS-Scadas Mobile SCM05 16 channels acquisition unit, with its dedicated LMS Test.Lab software, B&K shakers and force cells, amplifiers and dedicated waveform generators.

3.2 Experimental set-up description

The experimental set-up was designed in order to let all the three measurement technologies focus on the same dynamic behaviour, as this was populated by high modal density inside the frequency range of interest. An aluminium rectangular thin plate (250x236x1.5mm) was tight-

ened by wires fixed to a solid frame on the air-spring optical table (see Figure 1) to restrain excessive rigid body movement. The surface of the plate was sprayed with a random noise pattern paint layer to full-fill the requirements of DIC. The excitation was given by electrodynamic shakers positioned on the back side of the plate, to full-fill the stepped-sine acquisition procedure for dynamic ESPI measurements. SLDV works with both impact testing or electrodynamic shaker excitation, so a common set-up was possible. LMS Test.Lab drove the excitation in SLDV and DIC measurements, while ESPI system used an external sine waveform generator, synchronised with the phase-shifting procedures. To be able to calculate the *receptance* FRFs, force signal was sampled at the shaker-plate interface by means of force cells. Great attention was paid to understand the limits & requirements of all these technologies in order to find a common intersection of measurements conditions: there resulted a promising compromise. The linearity assumption was forced, after some comparative test with varying input power, to be able to compare measurements done at three different source power levels; while SLDV and dynamic ESPI delivered matching results in whole range, Hi-Speed DIC sensed a slightly different dynamics at higher frequencies, due to the much higher input force level and related non-linearities.

4 A POINTWISE COMPARATIVE APPROACH

In [4] the FRF datasets saw an earlier comparison, but limited to a promising qualitative investigation of the operational shapes and single FRFs, without the ability to make a pointwise comparison and follow precisely how the competing technologies approached the same test.

The need of finding a common reference for all the three techniques comes from the observation on practical issues. Albeit these optical technologies offer a highly defined description of the geometry under investigation, further alignment, scaling and rotation need to be considered. SLDV had arbitrary scaling factor and origin, plus a cushion distortion due to the lens through which the specimen is seen and the scanning grid is designed. DIC, even if precisely calibrated for the vibration measurements, gave a rotated and slightly perspective distorted grid, later restricted for the correlation evaluations. ESPI was the only with native rectangular grid of data. But then a more tough problem arose: do they acquire data from the exactly same location of the sample? Unfortunately, even with the best accuracy, there was a slight error on location assessment and size of the measured surface. This means that no pointwise comparison could be made without pre-processing and matching of the datasets.

The proposed procedure starts with the identification of two common reference points on each dataset, then proceeds to scale, rotate and align the grids to a common coordinate system. Instead of marking the accessible surface of the plate, not to ruin the stochastic pattern sprayed for best DIC measurements, the shakers' locations were sought by means of FRFs analysis. Later, once the three grids were in the wanted position and properly scaled, the common portion of the measured area had to be extracted, based on discrete geometry considerations. This has brought to three different reference grids against which making the pointwise comparison of the other two techniques, by means of spatial interpolation of the datasets. Differences in frequency sampling were coped with interpolation in frequency domain, once a reference frequency axis was chosen.

4.1 Full field *receptance* and coherence function map processing

In TEFFMA project all the combinations of geometrical and frequency references were explored, but not here presented for the limitation of space, raising the overall quality of the

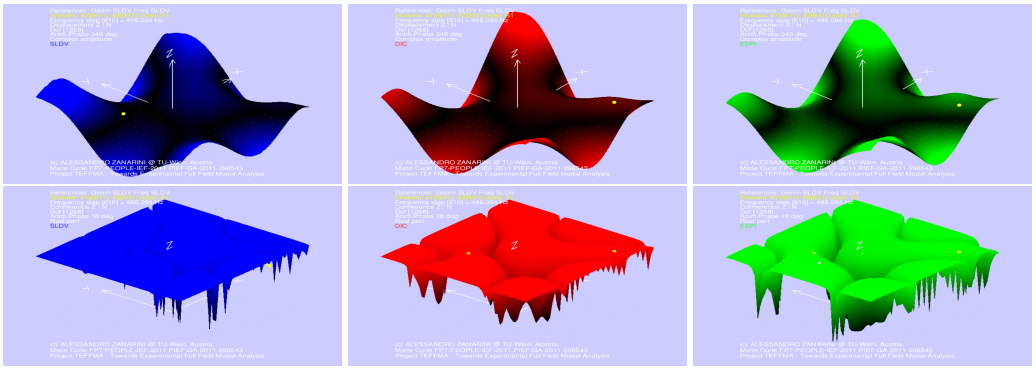


Figure 6: FRF & Coherence function maps at 496Hz from SLDV, DIC and ESPI, excitation from shaker 1

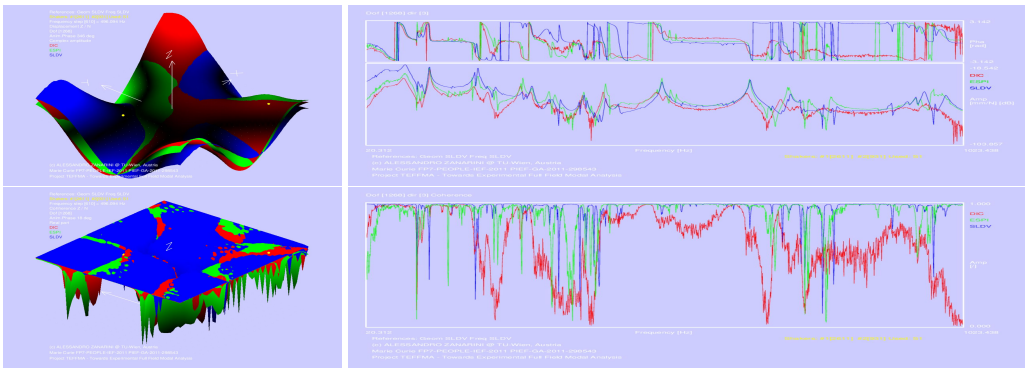


Figure 7: Comparison of FRF & Coherence maps at 496Hz, of single functions at dof 1268 in the whole frequency domain from SLDV, DIC and ESPI, excitation from shaker 1

experimental results to the new reference level awaited from full field measurements since the early activities of the author [3]. In this paper are presented pointwise comparisons of the out-of-plane results obtained from all the three technologies (SLDV head was 1D limited). The restricted geometry grid of reference for all the three technologies is here that of SLDV (57 x 51 dofs), due to scattering of the data on the measured maps; the frequency axis is limited in the range [20.312 - 1023.438] Hz with spectral spacing of 0.78125 Hz, native of SLDV; all this not to add even more error to the SLDV datasets with interpolation, but down-sampling the DIC and ESPI measurements.

SLDV is not a native full-field technology: it requires perfect steady-state conditions during the time consuming high resolution scans (also a few days). Room heating problems were faced in the tests, the non-synchronous measurements showed unexpected spatial inconsistency, like lost phase correlation or time delay, leading to mistaken bands / behaviours on the measurements. Other causes could be overheating and clock errors in the electronics of the whole system, due to the continuous work, but it was not possible to find a better solution. The quality of the measured surface, even if the system gave optimal feedback, was sometime unexpectedly poor, but the worst unusable *receptance* maps were instead omitted.

The acquisition of the time domain dynamic signals was very fast by DIC, with strong power by the shakers, and the off-line work was heavy: half an hour was required to download the time series from the cameras, about 3 days to evaluate the displacement fields in the time domain,

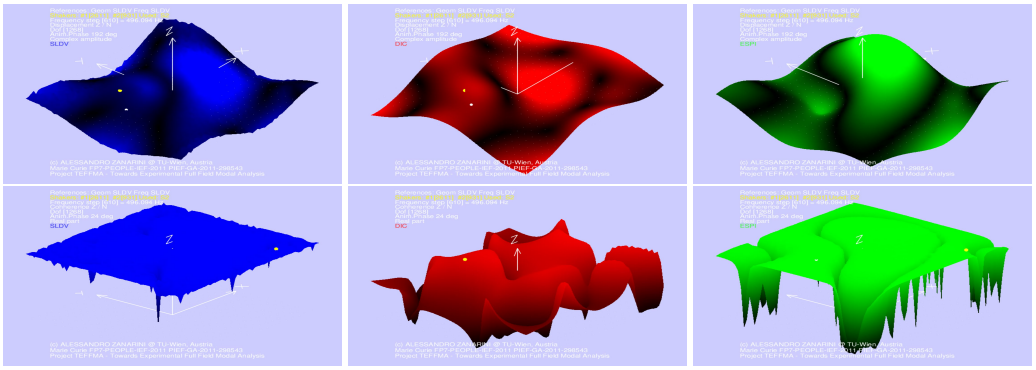


Figure 8: FRF & Coherence function maps at 496Hz from SLDV, DIC and ESPI, excitation from shaker 2

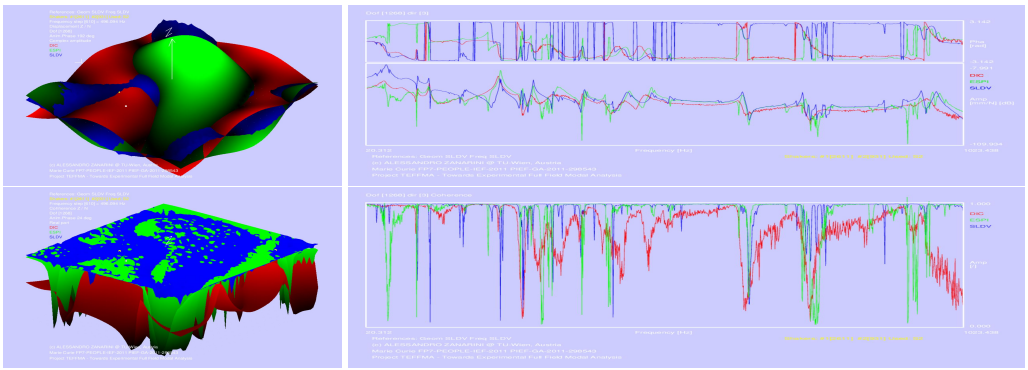


Figure 9: Comparison of FRF & Coherence maps at 496Hz, of single functions at dof 1268 in the whole frequency domain from SLDV, DIC and ESPI, excitation from shaker 2

and 2 days for frequency domain processing.

Each frequency step of interest in ESPI measurements needed about 2 minutes to acquire and evaluate the complex-valued displacement maps. To assure the best quality of the resolvable fringe systems, with such a sensitive system as ESPI that works in the sub-micron range, a very low input force was calibrated at each narrow frequency interval to obtain the best signal-to-noise ratio and avoid unresolvable areas in the fringe maps, coming from excessive displacement. The deflection shapes showed high quality fields induced by both shakers, deserving further investigations on the relevance of the input location[7].

The quality reached in the processed measurements (more than 1 week on a dual Xeon X5670 and 192GB RAM machine, by means of a custom software written in C-language and extending proven routines[11, 8, 12]) is promising for all the potential elaborations in frequency domain [9, 10, 7]. The structural dynamics retained seems again to play a relevant role in determining the distributions of critical locations inside the area and reflect that high modal density searched for at the time of the design of the experiment.

In Figures 2,4,6,8 are proposed the results obtained with the processing of all the techniques: the *receptance* maps are shown alone at matching frequencies and with two locations of the excitation, together with corresponding *coherence function* map; in all these figures first are shown the SLDV results in blue, followed by DIC in red and ESPI in green tones. The *coherence function* maps show the high quality of measurement and processing obtained with Hi-speed DIC

technology in almost the frequency range, starting to rival the more traditional SLDV technology. On the other side, dynamic ESPI *receptance* results outperform SLDV and DIC in terms of surface consistency and frequency accuracy in the whole range, coupled with excellent *coherence function* maps. Especially regarding DIC and ESPI, a finer treatment of the spikes in the FRF was obtained, highlighted by the broad range in the amplitude of the single FRF maps and by the uniformity of the *coherence function* at the maxima of the *receptance* shape, where, instead, SLDV showed some limits (ruining the surface quality & *coherence function* maps); it can be seen that the *coherence function* is not sensible enough to the scattering on SLDV *receptance* maps that leaves some trouble for further processing[7]; on the omitted frequency lines, SLDV showed unacceptable surfaces, while, apparently, on the single dof-base the measurements were optimal in terms of amplification gain and coherence results, probably giving the resonances an unsteady-state behaviour.

In Figures 3,5,7,9 can be seen the superposition of *receptance* and *coherence function* maps on the left, while on the right side there are the FRFs obtained with all the three technologies at the same (with the best precision of the pointwise approach) geometry location and shaker excitation. It can again be seen a relevant drop of accuracy (by means of the *coherence function*) of DIC measurements above 3/4 of the frequency range of interest, while dynamic ESPI still delivers consistent results at much higher frequencies, due to its sensibility to much lower displacements and proper tuning of the excitation to optimise the measurement quality. It must be also remarked how the high modal density retained in this experiment plays a relevant role on the output *coherence functions*, since the nodal lines are fast moving in the frequency range and crossing many times the points of interest.

5 CONCLUSIONS

This paper has highlighted the importance that full field measurements can have in advanced design procedures, in particular showing the potential benefits that may come from a widespread usage of Full Field FRFs and accurate spatial refinement. In this paper the first pointwise comparison from growing full field measurements (SLDV, Hi-Speed DIC and dynamic ESPI) have been shown, with promising quality on the same advanced experimental set-up. The pure full field (Hi-Speed DIC & dynamic ESPI) measurement techniques showed to take advantage of the spatial resolution and consistency for a detailed evaluation of experimental *receptance* surfaces. This was the first step of a quantitative pointwise comparison in TEFFMA project to assess the potentiality of today image-based sensing techniques in approaching traditional NVH analysis and deliver the promised advanced spatial sampling. The path towards experimental Full Field NVH is paved with intriguing advancements.

Acknowledgements

This activity is part of the Project TEFFMA - Towards Experimental Full Field Modal Analysis, funded by the European Commission at the Technische Universitaet Wien, through the Marie Curie FP7-PEOPLE-IEF-2011 PIEF-GA-2011-298543 grant, for which the Research Executive Agency is greatly acknowledged. This work is intended to be part of the spreading of the results thereof. Vienna University of Technology, in the person of Prof. Wassermann and his staff, are kindly acknowledged for hosting the TEFFMA project of the author at the *Schwingungs- und Strukturanalyse* / Optical Vibration Measurement Laboratory. Dantecdynamics GmbH (Ulm, Germany) is also acknowledged for the precious technical support given for DIC and ESPI equipment used in the project.

REFERENCES

[1] Zanarini, A., 2005. *Dynamic behaviour carachterization of a brake disc by means of electronic speckle pattern interferometry measurements*. In Proceedings of the IDETC/CIE ASME International Design Engineering Technical Conferences & Computers and Information in Engineering Conference, Long Beach, California, USA, September 24-28, ASME, pp. 1–8. Paper DETC2005-84630.

[2] Van der Auweraer. H. et al., 2001. *Industrial applications of pulsed-laser ESPI vibration analysis*. In Proc. of the XIX IMAC, Kissimmee, FL, USA, SEM.

[3] Zanarini, A., 2007. *Full field ESPI measurements on a plate: challenging experimental modal analysis*. In Proceedings of the XXV IMAC, Orlando (FL) USA, Feb 19-22,, SEM. Paper s34p04.

[4] Zanarini, A., 2014. *On the estimation of frequency response functions, dynamic rotational degrees of freedom and strain maps from different full field optical techniques*. In Proceedings of the ISMA2014 International Conference on Noise and Vibration Engineering, Leuven, Belgium, September 15-17, KU Leuven, pp. 1–15. paper ID676.

[5] Zanarini, A., 2014. *Dynamic strain & stresses for enhanced reliability: from full field optical measurements to simulations*. In Proceedings of the ICAIM2014 International Conference on Applications for Image based Measurements, Leipzig, Germany, June 24-25, Dantecdynamics, pp. 1–18. ISBN 978-3-00-045317-5.

[6] Zanarini, A., 2014. *On the role of spatial resolution in advanced vibration measurements for operational modal analysis and model updating*. In Proceedings of the ISMA2014 International Conference on Noise and Vibration Engineering, Leuven, Belgium, September 15-17, KU Leuven, pp. 1–15. paper ID676.

[7] Zanarini, A., 2015. *Model updating from full field optical experimental datasets*. In Proceedings of the ICoEV2015 International Conference on Engineering Vibration, Ljubljana, Slovenia, September 7-10, IFToMM, pp. 1–10. ID196.

[8] Heylen, W., Lammens, S., and Sas, P., 1998. *Modal Analysis Theory and Testing*. Katholieke Universiteit Leuven, Leuven (Belgium). ISBN 90-73802-61-X.

[9] Zanarini, A., 2015. *Accurate FRFs estimation of derivative quantities from different full field measuring technologies*. In Proceedings of the ICoEV2015 International Conference on Engineering Vibration, Ljubljana, Slovenia, September 7-10, IFToMM, pp. 1–10. ID192.

[10] Zanarini, A., 2015. *Full field experimental modelling in spectral approaches to fatigue predictions*. In Proceedings of the ICoEV2015 International Conference on Engineering Vibration, Ljubljana, Slovenia, September 7-10, IFToMM, pp. 1–10. ID193.

[11] Press, W. H., Teukolsky, S. A., Vetterling, W. T., and Flannery, B. P., 1992. *Numerical Recipes in C: The Art of Scientific Computing*, 2^{nd} ed. Cambridge Univ. Press, England.

[12] Bendat, J., and Piersol, A., 2000. *Random data: analysis and measurement procedures*, 3^{rd} ed. John Wiley & Sons Inc.

11th International Conference on Engineering Vibration
Ljubljana, Slovenia, 7–10 September 2015

ACCURATE FRF ESTIMATION OF DERIVATIVE QUANTITIES FROM DIFFERENT FULL FIELD MEASURING TECHNOLOGIES

Alessandro Zanarini[1,2]

[1]University of Bologna, DIN - Industrial Engineering Dept., Italy
a.zanarini@unibo.it

[2]Vienna University of Technology, Institute of Mechanics & Mechatronics, Austria
alessandro.zanarini@tuwien.ac.at

Keywords: Full field vibration measurements, Frequency Response Functions, Optical metrology, dynamic rotational degrees of freedom, dynamic strain maps.

Abstract. *Full field measurement technologies can not estimate only spatially detailed displacement fields, but can exploit the consistency of the results by means of differentiation operators to obtain rotational degrees of freedom and superficial strain distributions. Both extracted results can be used as advanced benchmarks for numerical models, advanced finite element formulation and fatigue analysis, as well as experimental and hybrid models in sub-structuring frameworks.*

Approaching the task with the aid of superior quality receptance maps, this work implements proper differentiation operators and signal processing techniques to calculate and to compare rotational dofs and dynamic strains from three different full field technologies: SLDV, Hi-Speed DIC and dynamic ESPI. A thin plate dynamics is benchmarked as light-weight structure with broad band dynamics and high modal density in a unique comparative set-up. The extraction of dynamic rotational dof & strain distribution features is discussed, benchmarked and compared in detail.

1 INTRODUCTION

Advanced reliability predictions are strongly related to the accuracy with which the physical quantities of interest are obtainable in a complex environment such as the structural dynamics. Reliability can be declined as the capacity to accurately predict component behaviours in a wide frequency range, as well as estimate its life cycle or assure the manufacturing quality to meet specific dynamic targets. Many times the rotational dofs are disregarded for complexity or burden of their measurement, while are recognized as relevant[1, 2] for the successful build of a reliable dynamic model for complex structures. In the model updating of FE models references about rotational dofs might be very useful to tune the element formulation, especially with anisotropic and layered materials. Also, it is common practice, when dealing with structural dynamics, to assess dynamic strains by means of lumped strain measurements and finite element models: few strain gauges are placed on the structure and the numerical model is paired with the measurements to simulate the distribution of strains, eventually of stresses with constitutive parameters of the material. But more than a question may arise: where should we locate the gauges? is the finite element model reliable? are we doing a complete pairing of test with the numerical model, or just a qualitative one? can we do better to enhance the estimation of the whole dynamic behaviour, and finally the structural reliability prediction[3] of the components?

2 NOMENCLATURE

$\mathbf{d}(x, y, j\omega)$ receptance map
$\mathbf{r}(x, y, j\omega)$ rotational impedance model map
$\boldsymbol{\varepsilon}(x, y, j\omega)$ strain tensor impedance model map

3 DYNAMIC EXPERIMENTAL ROTATION & STRAIN DISTRIBUTIONS

Pure full field experimental techniques like ESPI and DIC become particularly suited for the evaluation of the rotational and strain field in dynamic events, since they deliver consistent displacement maps as fields with superior continuity, as highlighted already in the analyses of *receptange* maps[4, 5]. This high consistency of data fields is particularly appreciated in all the numerical derivative evaluations of rotational dofs and strain FRFs.

If the full field sensor reference system is parallel to a flat surface to be measured, thanks to the high spatial resolution available, at each frequency the dynamic rotations of a locally tangent plane can be calculated by means of a robust differential operator on the receptance map $\mathbf{d}(x, y, j\omega)$ along *x & y* directions:

$$\mathbf{r}(x, y, j\omega)_x = \frac{\partial \mathbf{d}(x, y, j\omega)}{\partial y}, \mathbf{r}(x, y, j\omega)_y = -\frac{\partial \mathbf{d}(x, y, j\omega)}{\partial x} \tag{1}$$

Whereas strain tensor impedance model components $\varepsilon(x, y, j\omega)_{ik}$ can be calculated with accuracy, e.g. from plane stress assumption in strain theory, by means of the successive derivations of the receptance map $\mathbf{d}(x, y, j\omega)$ along *q* directions:

$$\varepsilon(x, y, j\omega)_{ik} = \frac{1}{2}\left(\frac{\partial \mathbf{d}(x, y, j\omega)_i}{\partial q_k} + \frac{\partial \mathbf{d}(x, y, j\omega)_k}{\partial q_i}\right) \tag{2}$$

In the plane stress scenario, the in-plane displacements give their contribution to the tensor

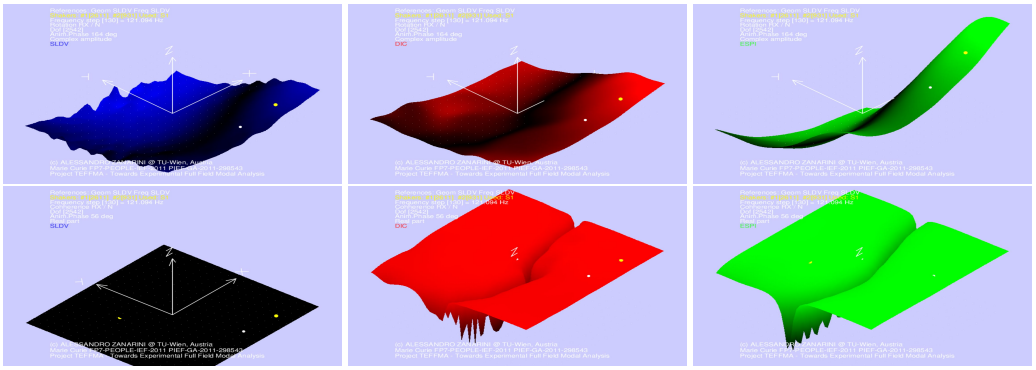


Figure 1: Rotational RX FRF & Coherence function maps at 121Hz from SLDV, DIC and ESPI, excitation from shaker 1

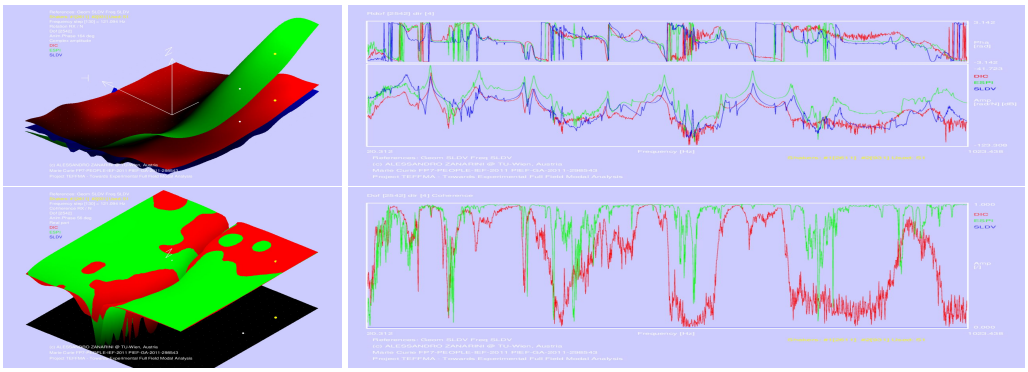


Figure 2: Comparison of rotational RX FRF & Coherence maps at 121Hz, of single functions at dof 2542 in the whole frequency domain from SLDV, DIC and ESPI, excitation from shaker 1

components as:

$$\begin{aligned} \varepsilon(x,y,j\omega)_{xx} &= \frac{\partial \mathbf{d}(x,y,j\omega)_x}{\partial x},\ \varepsilon(x,y,j\omega)_{yy} = \frac{\partial \mathbf{d}(x,y,j\omega)_y}{\partial y}, \\ \gamma(x,y,j\omega)_{xy} &= \gamma(x,y,j\omega)_{yx} = \frac{\partial \mathbf{d}(x,y,j\omega)_x}{\partial y} + \frac{\partial \mathbf{d}(x,y,j\omega)_y}{\partial x} \end{aligned} \tag{3}$$

while from the out-of-plane displacements bending-related in-plane strain results:

$$\begin{aligned} \varepsilon(x,y,j\omega)_{xx_b} &= -\frac{s}{2}\frac{\partial^2 \mathbf{d}(x,y,j\omega)_z}{\partial x^2},\ \varepsilon(x,y,j\omega)_{yy_b} = -\frac{s}{2}\frac{\partial^2 \mathbf{d}(x,y,j\omega)_z}{\partial y^2}, \\ \gamma(x,y,j\omega)_{xy_b} &= \gamma(x,y,j\omega)_{yx_b} = -s\frac{\partial^2 \mathbf{d}(x,y,j\omega)_z}{\partial x \partial y} \end{aligned} \tag{4}$$

where *s* is the thickness of the bending surface. The principal strains can be then easily evaluated at each frequency line, together with their principal directions.

3.1 Beyond strain gauges

The dynamic $\boldsymbol{\varepsilon}(x,y,j\omega)$- tensor model can be used to assess the actual strains due to a peculiar known input, without the need of a finite element model, just from experimental results.

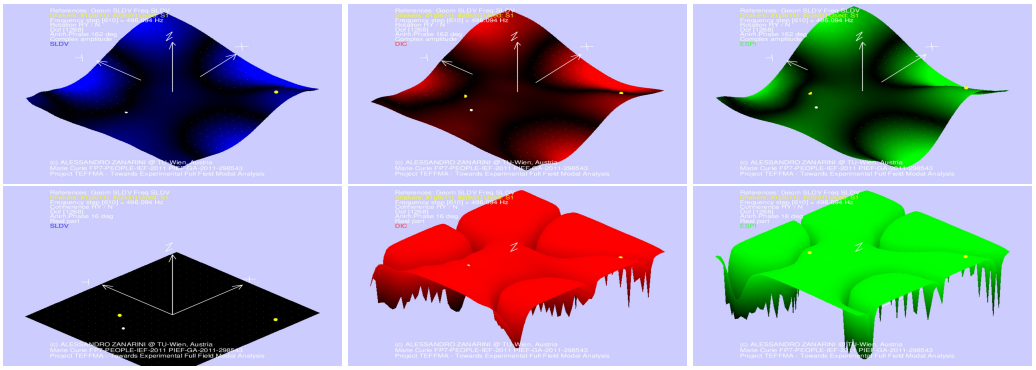


Figure 3: Rotational RY FRF & Coherence function maps at 496Hz from SLDV, DIC and ESPI, excitation from shaker 1

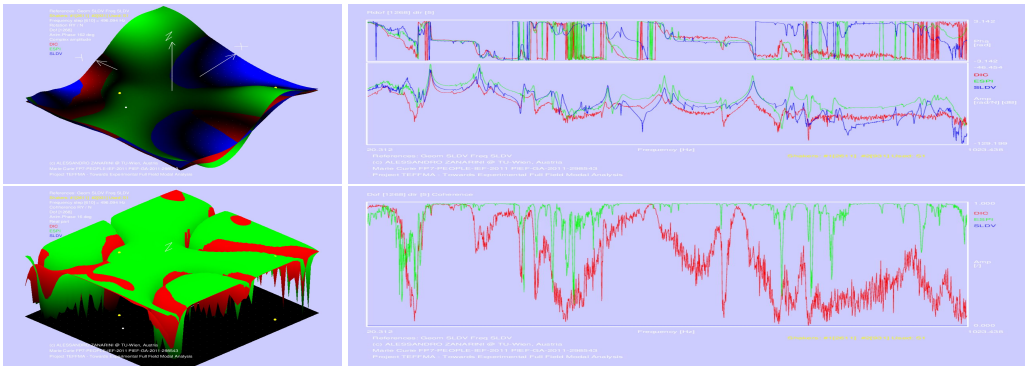


Figure 4: Comparison of rotational RY FRF & Coherence maps at 496Hz, of single functions at dof 1268 in the whole frequency domain from SLDV, DIC and ESPI, excitation from shaker 1

It is in fact sufficient to known different inputs to obtain the related dynamic strains on the whole measured surface, just as a multiplication of the impedance matrix by the known input in frequency domain or convolution to time domain. This advantage opens promising investigations on the dynamic characterisation of the component junctions and failure locations in broad frequency band dynamic events. Also, full field optical technologies deliver measurements independently of the material type: this latter can be also a structured or anisotropic material, ranging from metallic to rubbery, to fabrics or to organic compounds, which might be hard to numerically model. This is not commonly achieved with conventional instruments, like the widespread strain gauges, which may face some problems, like effective sensor placement, spatial averaging, mass burden and lumped measurements. Multi-modal behaviour of the structure under dynamic loading in service increases the strain-gage location assessment uncertainty. Attention must be paid on the fact that strain gauges, in order to enhance their sensitivity, may find a better location when not placed on the same positions where displacement/velocity/acceleration sensors are installed (remember the use of brittle lacquer coatings showing the most densely cracked areas in foregoing failure tests), this meaning at least two different tests for structural dynamics and strain measurements, and can not certainly achieve a fine spatial resolution on the whole surface. High spatial resolution in full field optical measurements brings also a reduction of sensor area-averaging effect and set-up complexity, as can be found instead with strain rosettes or other more conventional instruments. For these latter,

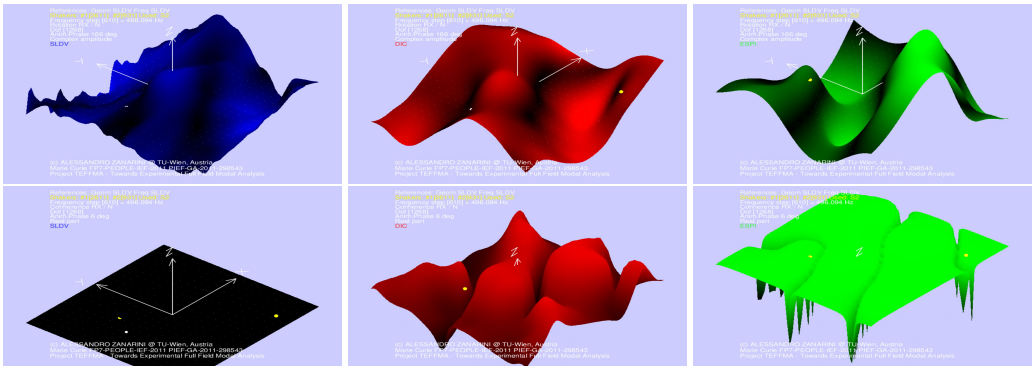


Figure 5: Rotational RX FRF & Coherence function maps at 496Hz from SLDV, DIC and ESPI, excitation from shaker 2

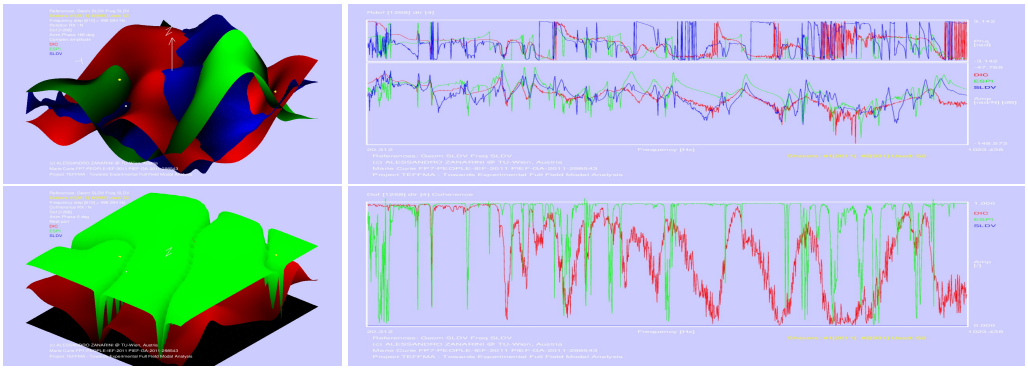


Figure 6: Comparison of rotational RX FRF & Coherence maps at 496Hz, of single functions at dof 1268 in the whole frequency domain from SLDV, DIC and ESPI, excitation from shaker 2

the analysis across the whole domain must then be completed by means of detailed numerical models, calibrated on the few points measured. Obtaining receptance maps and dynamic strain tensor impedance model from pure full field technologies has a great relevance to shrink test steps & costs and to gain better accuracy, due to no assumption required by any numerical model nor having sensor placement issues.

4 FULL FIELD FRFS RESEARCH IN TEFFMA PROJECT

The TEFFMA[1] fundamental research project funded by the European Commission at the TU-Wien aims at making a comparison between the state-of-the-art in native full field technologies and the SLDV as reference, to understand at which point of their development these experimental procedures can provide NVH applications with enhanced peculiarities. In the well equipped laboratory of the TU-Wien it was possible to build a complex set-up[4, 5] for the comparison of the qualities of the different technologies available in acquiring Full Field FRFs. This paper wants to highlight the results obtained on *rotational dof FRF* estimation and related *coherence function maps*, and, further, on *dynamic strain FRFs*, by means of a pointwise comparative approach focused on results at the same physical location on the test specimen.

[1] A. Zanarini, Experienced researcher in the project TEFFMA - Towards Experimental Full Field Modal Analysis, financed by the Marie Curie FP7-PEOPLE-IEF-2011 PIEF-GA-2011-298543 grant

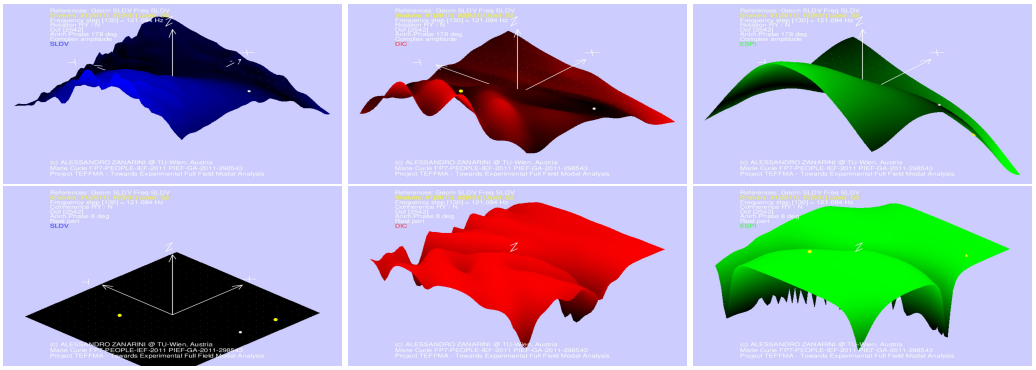


Figure 7: Rotational RY FRF & Coherence function maps at 121Hz from SLDV, DIC and ESPI, excitation from shaker 2

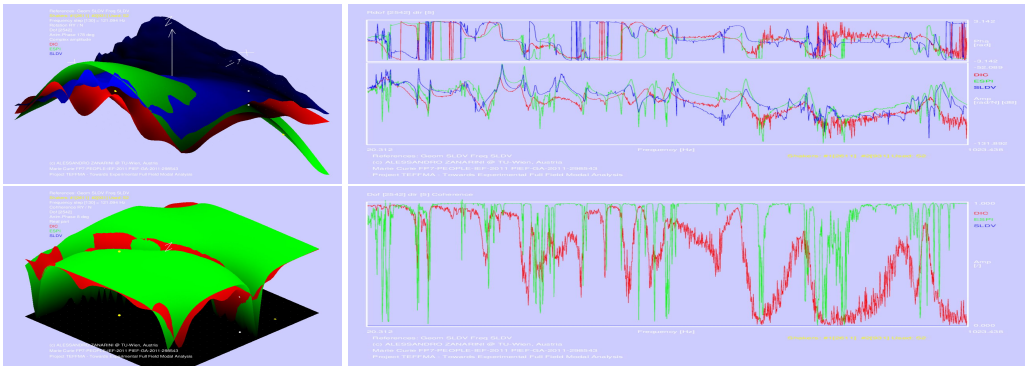


Figure 8: Comparison of rotational RY FRF & Coherence maps at 121Hz, of single functions at dof 2542 in the whole frequency domain from SLDV, DIC and ESPI, excitation from shaker 2

5 A POINTWISE COMPARATIVE APPROACH

In [4] the FRF datasets saw an earlier comparison, but limited to a promising qualitative investigation of the operational shapes and single FRFs, without the ability to make a pointwise comparison and follow precisely how the competing technologies approached the same test.

The need of finding a common reference for all the three techniques comes from the observation on practical issues. Albeit these optical technologies offer a highly defined description of the geometry under investigation, further alignment, scaling and rotation need to be considered. SLDV had arbitrary scaling factor and origin, plus a cushion distortion due to the lens through which the specimen is seen and the scanning grid is designed. DIC, even if precisely calibrated for the vibration measurements, gave a rotated and slightly perspective distorted grid, later restricted for the correlation evaluations. ESPI was the only with native rectangular grid of data. But then a more tough problem arose: do they acquire data from the exactly same location of the sample? Unfortunately, even with the best accuracy, there was a slight error on location assessment and size of the measured surface. This means that no pointwise comparison could be made without pre-processing and matching of the datasets.

The proposed procedure starts with the identification of two common reference points on each dataset, then proceeds to scale, rotate and align the grids to a common coordinate system. Instead of marking the accessible surface of the plate, not to ruin the stochastic pattern sprayed

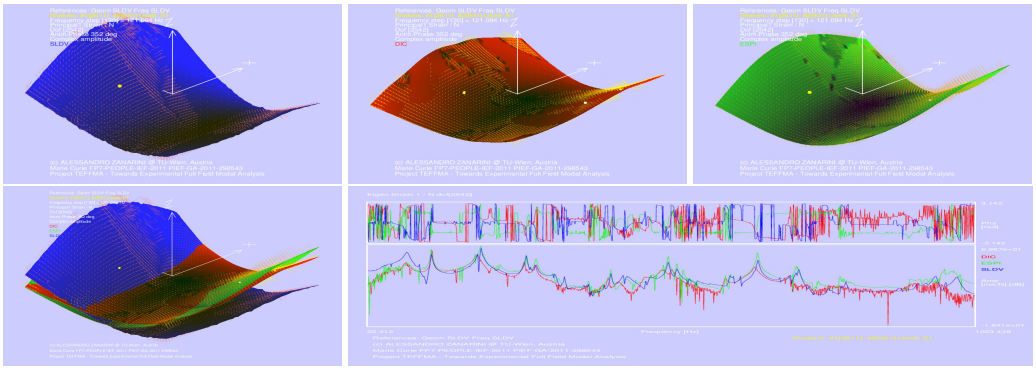


Figure 9: Comparison of Principal Strain 1 FRF maps at 121Hz, of single functions at dof 2542 in the whole frequency domain from SLDV, DIC and ESPI, excitation from shaker 1

for best DIC measurements, the shakers' locations were sought by means of FRFs analysis. Later, once the three grids were in the wanted position and properly scaled, the common portion of the measured area had to be extracted, based on discrete geometry considerations. This has brought to three different reference grids against which making the pointwise comparison of the other two techniques, by means of spatial interpolation of the datasets. Differences in frequency sampling were coped with interpolation in frequency domain, once a reference frequency axis was chosen.

5.1 Full field *rotational impedance* and *coherence function* map processing

The extended details on the receptance maps acquisition can be found in [5]. The basic features of the datasets here analysed are the restricted geometry grid (57 x 51 dofs) of reference for all the three technologies from that of SLDV and the frequency axis in the range [20.312 - 1023.438] Hz, with the SLDV native spectral spacing of 0.78125 Hz. The quality reached in the processed measurements (more than 1 week on a dual Xeon X5670 and 192GB RAM machine, by means of a custom software written in C-language and extending proven routines [7, 8, 9]) is promising for all the potential elaborations in frequency domain [5, 10]. The structural dynamics retained seems again to play a relevant role in determining the distributions of critical locations inside the area and reflect that high modal density searched for in the experiment.

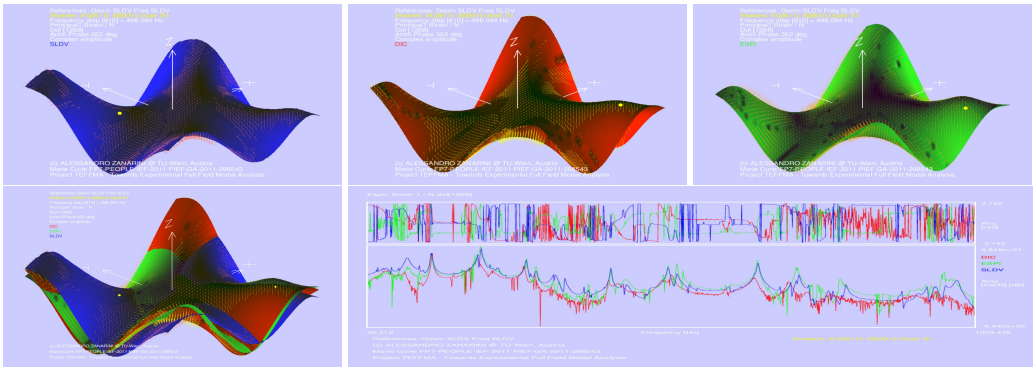


Figure 10: Comparison of Principal Strain 1 FRF maps at 496Hz, of single functions at dof 1268 in the whole frequency domain from SLDV, DIC and ESPI, excitation from shaker 1

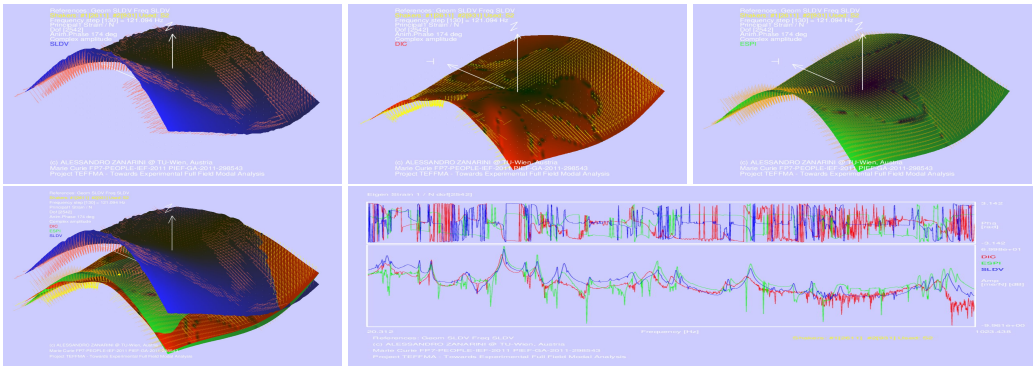


Figure 11: Comparison of Principal Strain 1 FRF maps at 121Hz, of single functions at dof 2542 in the whole frequency domain from SLDV, DIC and ESPI, excitation from shaker 2

In [4, 5] it was already pointed out how the performances of SLDV were affected by unexpected scattering of the data on the *receptance* maps, when not a total destruction of a clear pattern. The poor spatial continuity of SLDV data, on purpose not overtaken with smoothing or smearing post-processing to make a fair comparison with the other techniques, strongly affects the quality of any derived quantity, such as rotation and dynamic strain. No coherence function for SLDV rotational dofs is available, since the equipment released the *mobility FRFs* only. Native full field technologies gave instead much higher continuity of the field, especially for ESPI at higher frequencies, where, instead, DIC lost coherence. The unevenness of DIC maps at some low frequency is indeed amplified in the derivative process.

In Figures 1,3,5,7 are shown results from the processing of all the techniques data: the *rotational impedance* maps are shown alone at matching frequencies, together with corresponding *coherence function* map; in Figures 2,4,6,8, where all the three *rotational impedance* and *coherence function* maps are superimposed, are also added single corresponding functions at two locations (with the best precision of the pointwise approach); in all these figures first are shown the SLDV results in blue, followed by DIC in red and ESPI in green tones. Both shakers were highlighted.

The *coherence function* maps show the good quality of processing obtainable from Hi-speed DIC technology in only a part of the frequency range, amplifying the wide drops already seen in [4, 5]. On the other side, dynamic ESPI *rotational impedance* results outperform by far SLDV and DIC in terms of surface consistency and frequency accuracy in the whole range, coupled with excellent *coherence function* maps.

Dynamic ESPI still delivers consistent results at much higher frequencies, due to its sensibility to much lower displacements and proper tuning of the single sine excitation to optimise the measurement quality. It must be also remarked how the high modal density is retained in the derivative quantities, in terms of amplitude peaks and quite matching phases.

5.2 Full field impedance models for *dynamic strains*

From the high quality *receptance* maps evaluated, as with *rotational dofs*, can come the derivation (by means of the custom software) of the *dynamic strain tensor models* and (not here predicted) fatigue life estimations[10] that prove the advantages of having such complex measurement instrumentation as that needed for Full Field FRF measurements. In Figures 9-12 are shown the *first principal strains* in the *impedance model*, with amplitude that colours

(from dark to bright) the *receptance* shape, and related fields of eigenvectors (as small arrows) diagonalising the strain tensor impedance model at each dof. In all these figures first are shown the SLDV results in blue, followed by DIC in red and ESPI in green tones. Both shakers were considered. The second principal strains, very close in amplitude, proved to be rightly calculated as orthogonal to the first ones, but here not depicted for editing reasons. DIC & ESPI results were down-sampled in the frequency domain to match SLDV frequency axis.

In Figures 9-12 are also shown the single point first principal strain FRFs at the highlighted dof, denoting its complex-valued nature in an experimental impedance base modelling. While the complex amplitude retains the high modal density of the *receptance* maps, the phasing appears contaminated by increasing errors, spreading in the second derivation of the data fields. No coherence functions were evaluated to simply limit the computational costs, but could be also extracted as for every measured quantity from DIC & ESPI.

In the whole model there are thousands of principal strain FRF, to be free of measurement location for an advanced dynamic strain evaluation. Again it is important to remark that what obtained is a direct experimental impedance model, with all its advantages previously explained.

By comparing the quality of the *receptance* shapes in [5] to the evaluated dynamic principal strain field models in Figures 9-12 it is possible to appreciate, as with rotational dofs evaluations, the beneficial effects of field consistency that native full field technologies can exploit in derivative operations.

6 CONCLUSIONS

This paper has highlighted the importance that native full field measurements can have in deriving advanced features, here rotations and strains, for complex design procedures, in particular showing the relevant advantage of consistent data fields when numerically processed. The pure full field contactless measurement techniques (Hi-Speed DIC & dynamic ESPI) showed to take great advantage of the spatial resolution and continuity for a detailed derivation of experimental *receptance* surfaces. This was the first step of a quantitative pointwise comparison in TEFFMA project to assess the potentiality of today image-based sensing techniques in advancing traditional NVH analysis with new experimental based quantities, which might be at disposal to enhance model calibration, hybrid applications or direct experimental predictions.

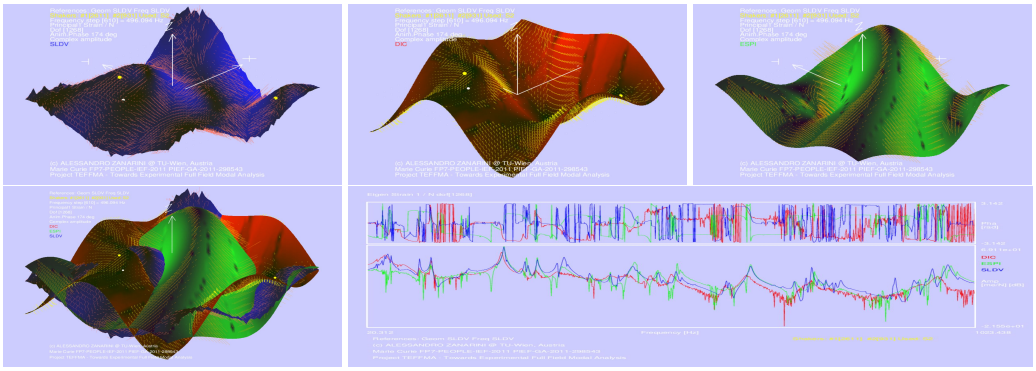


Figure 12: Comparison of Principal Strain 1 FRF maps at 496Hz, of single functions at dof 1268 in the whole frequency domain from SLDV, DIC and ESPI, excitation from shaker 2

Acknowledgements

This activity is part of the Project TEFFMA - Towards Experimental Full Field Modal Analysis, funded by the European Commission at the Technische Universitaet Wien, through the Marie Curie FP7-PEOPLE-IEF-2011 PIEF-GA-2011-298543 grant, for which the Research Executive Agency is greatly acknowledged. This work is intended to be part of the spreading of the results thereof. Vienna University of Technology, in the person of Prof. Wassermann and his staff, are kindly acknowledged for hosting the TEFFMA project of the author at the *Schwingungs- und Strukturanalyse* / Optical Vibration Measurement Laboratory. Dantecdynamics GmbH (Ulm, Germany) is also acknowledged for the precious technical support given for DIC and ESPI equipment used in the project.

REFERENCES

[1] Liu, W., and Ewins, D., 1999. *The Importance Assessment of RDOF in FRF Coupling Analysis*. In Proceedings of the IMAC 17th Conference,Fissimmee, Florida,1999. Fissimmee, Florida.

[2] Research network, 1998. Quattro brite-euram project no: Be 97-4184. Tech. rep., Eurpean Commision Research Framework Programs.

[3] Zanarini, A., 2008. *Fatigue life assessment by means of full Field ESPI vibration measurements*. In Proceedings of the ISMA2008 Conference, September 15-17, Leuven (Belgium), P. Sas, ed., KUL, pp. 1–15. Paper 326.

[4] Zanarini, A., 2014. *On the estimation of frequency response functions, dynamic rotational degrees of freedom and strain maps from different full field optical techniques*. In Proceedings of the ISMA2014 International Conference on Noise and Vibration Engineering, Leuven, Belgium, September 15-17, KU Leuven, pp. 1–15. paper ID676.

[5] Zanarini, A., 2015. *Comparative studies on full field FRFs estimation from competing optical instruments*. In Proceedings of the ICoEV2015 International Conference on Engineering Vibration, Ljubljana, Slovenia, September 7-10, IFToMM, pp. 1–10. ID191.

[6] Zanarini, A., 2007. *Full field ESPI measurements on a plate: challenging experimental modal analysis*. In Proceedings of the XXV IMAC, Orlando (FL) USA, Feb 19-22,, SEM. Paper s34p04.

[7] Press, W. H., Teukolsky, S. A., Vetterling, W. T., and Flannery, B. P., 1992. *Numerical Recipes in C: The Art of Scientific Computing*, 2^{nd} ed. Cambridge Univ. Press, England.

[8] Heylen, W., Lammens, S., and Sas, P., 1998. *Modal Analysis Theory and Testing*. Katholieke Universiteit Leuven, Leuven (Belgium). ISBN 90-73802-61-X.

[9] Bendat, J., and Piersol, A., 2000. *Random data: analysis and measurement procedures*, 3^{rd} ed. John Wiley & Sons Inc.

[10] Zanarini, A., 2015. *Full field experimental modelling in spectral approaches to fatigue predictions*. In Proceedings of the ICoEV2015 International Conference on Engineering Vibration, Ljubljana, Slovenia, September 7-10, IFToMM, pp. 1–10. ID193.

11th International Conference on Engineering Vibration
Ljubljana, Slovenia, 7–10 September 2015

MODEL UPDATING FROM FULL FIELD OPTICAL EXPERIMENTAL DATASETS

Alessandro Zanarini[1,2]

[1]University of Bologna, DIN - Industrial Engineering Dept., Italy
a.zanarini@unibo.it

[2]Vienna University of Technology, Institute of Mechanics & Mechatronics, Austria
alessandro.zanarini@tuwien.ac.at

Keywords: Full field vibration measurements, Frequency Response Functions, Optical metrology, model updating, modeshapes.

Abstract. *Are optical measurements and high spatial dense datasets effective in advanced model updating of lightweight structures with complex structural dynamics? The generally accepted reference in measuring vibration patterns with high spatial definition might be the Laser Doppler Velocimetry, with it's scanning variances, but also with the noise shown in the raw signal of some experiments, which poses issues in proficiently exploiting the added data in a fruitful model updating procedure. Instead, native full field measuring technologies like Hi-Speed DIC and dynamic ESPI have shown recently intrinsic smoother data fields due to their image-based nature and evaluation algorithms, promising benefits on model optimisations.*

In this paper, in the framework of established procedures for model updating of dynamically excited structures, a comparison is made by means of all the cited challenging technologies on the same broad band vibration measurement problem, with different spatial resolution and quality of the measured patterns.

Model updating results are compared between scanning and native full field technologies, with comments and details on the test rig, on the advantages and drawbacks of the approaches.

1 INTRODUCTION

Optical measurements are a breakthrough for hi-resolution spatial description of a deforming surface, either statically or dynamically. Optical full field measurements deliver displacement maps composed of many degrees of freedom (dofs), instead of one single channel as traditional transducers. Plus, the calculated fields might be also 3D, meaning that it is like having thousand of three-axial sensors precisely located on the surface under investigation, but without the mass loading they would bring. The advantage for light weight structure measurements in mechanical and aeronautical applications is straightforward. They also open the path to a consistent experimental evaluation of dynamic strains and rotational dofs[1, 2], both relevant for enhanced updating process of complex models, and substructuring frameworks. On the opposite side, nowadays the optical measurements have the drawback of having too many dofs to handle, compared to the quantity for which traditional approaches [3, 4] and, later, commercial software were developed: it is easy to deal with 10-50k dofs instead of few mono-axial channels, with clear impact on the whole identification & optimisation process, which might require advanced featuring techniques to exploit the data redundancy [5]. Image-based technologies are pushed by the recent advances in electronic components, from image capturing sensors, to computing engines, to hi-speed embedded RAM and solid state storage, together with a general rebate of the experimental equipment costs.

While not completely mature, full field technologies are tempting in EMA and model updating to add the spatial sampling needed in increasingly more application. Besides, it is not completely proved the advantage of having more data, when these might be extended source of variance in the estimations, due to the measurement process quality. The purpose of the activities here reported is clearly to assess the impact of high spatial accuracy on the identification and model updating process by means of an extended comparison of today full field optical technologies, with a focus on SLDV, Hi-Speed DIC and Dynamic ESPI. All the measurement techniques have been challenged on the same structural dynamic problem, a simple plate with high modal density [1, 6], to make it possible the first precise comparison of the obtainable outputs. The results obtained are reported below and commented in detail.

2 EXPERIMENTAL MODAL ANALYSIS FROM FULL FIELD OPTICAL MEASUREMENTS

The fundamental research project TEFFMA[1], funded by the European Commission at the Vienna University of Technology, aims at making a comparison between the state-of-the-art in native full field technologies (Hi-Speed DIC & Dynamic ESPI) and the SLDV as reference, to understand at which point of their development these experimental procedures can provide NVH applications with enhanced peculiarities. In the well equipped laboratory of the TU-Wien it was possible to build a complex set-up for the comparison of the qualities of the different technologies available in acquiring Full Field FRFs.

The experimental set-up was that widely described in [7, 1, 8, 6] for the works of TEFFMA project, from which the *receptance* FRF datasets from two shaker excitations were taken. No extra smoothing was applied to the data, neither in space domain nor in frequency domain, to obtain a fair comparison of the three optical technologies. For all the identifications, the same parameters were kept in the Least Squares Frequency Domain (LSFD) modal extractor of the commercial software FEMtools 3.8 [9], which was able to deal with the relevant dimensions of

[1] A. Zanarini, Experienced researcher in the project TEFFMA - Towards Experimental Full Field Modal Analysis, financed by the Marie Curie FP7-PEOPLE-IEF-2011 PIEF-GA-2011-298543 grant



Figure 1: Stabilisation chart, AutoMAC matrix and FRF synthesis from EMA on SLDV dataset

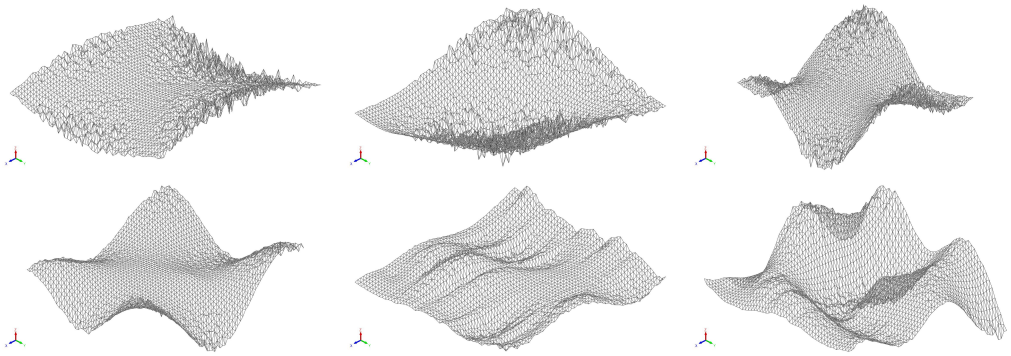


Figure 2: Modeshapes from EMA on SLDV dataset (126.2, 246.2, 301.3, 517.2, 724.9 and 978.1 Hz)

all the datasets in reasonable time, except for ESPI at native frequency resolution.

2.1 Extracting the modal base from SLDV

The SLDV dataset was taken in its native spatial (2907 dofs) and frequency (0.78125 Hz) resolution, only reduced [6] to the common measured area among all the three optical gears. Though, it appeared to have relevant scattering on the FRF maps, with potential repercussion on the quality of modal base identification steps.

In Figure 1 are briefly reported the steps of the modal identification from the SLDV dataset, with stabilisation diagram highlighting the FRF sum function and the CMIF, with the AutoMAC matrix emphasising potential similarities among the eigenshapes, and with the driving point FRF at shaker S1 checking the FRF synthesis with the identified modal base. While the AutoMAC matrix appears cleaner than that from the other optical technologies, it does not take into account the bad continuity of the eigenmode surfaces, as depicted in Figure 2, where the shapes appear heavily scattered by noise; on the fifth shape appear also some bands, as unexpectedly encountered during FRF acquisition [1, 6].

2.2 Extracting the modal base from Hi-Speed DIC

Also DIC dataset was taken in its native spatial (11988 dofs) and frequency resolution (0.5 Hz), only reduced [6] to the common measured area among all the three optical gears. It must

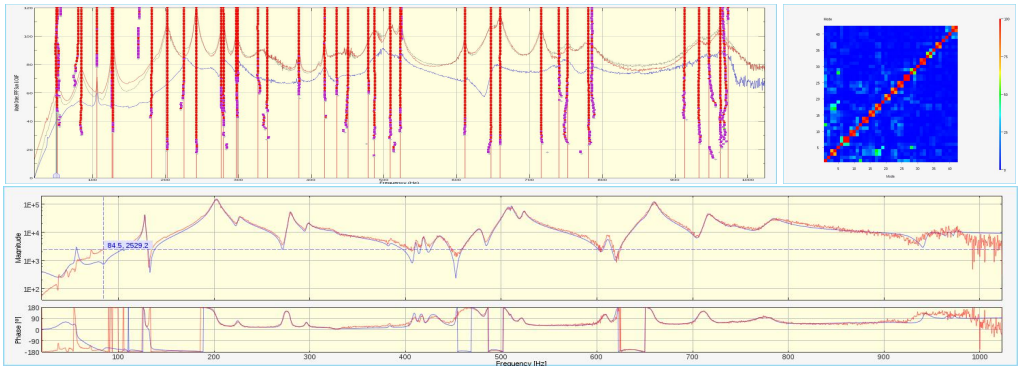


Figure 3: Stabilisation chart, AutoMAC matrix and FRF synthesis from EMA on DIC dataset

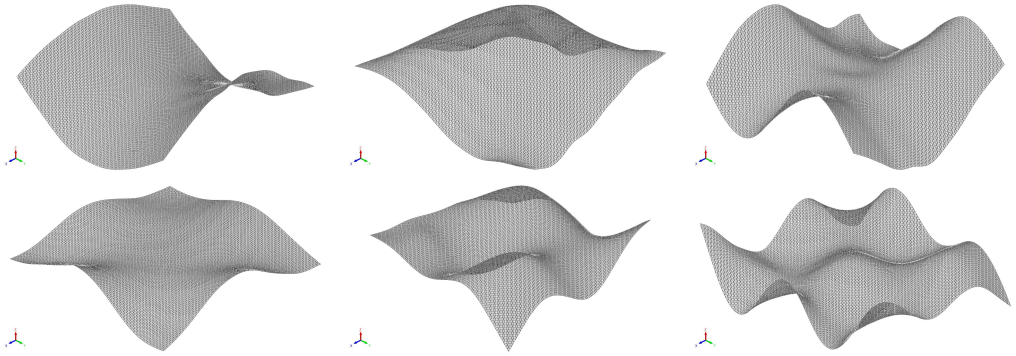


Figure 4: Modeshapes from EMA on DIC dataset (126.6, 242.3, 299.5, 508.2, 716.1 and 973.2 Hz)

be pointed out that some local artefacts in spatial domain were recorded on low frequency FRF maps[1, 6, 2]: some traces might be expected on the eigenshapes.

While the AutoMAC matrix of Figure 3 highlights higher similarity among low frequency eigenshapes, again it does not confirm the much better continuity, compared to that of SLDV, of the shapes in Figure 4; still, some trace of the artefacts can be noticed on the first and third eigenmode deployment. Many complex-valued pairs of double modes where identified. Also, the driving point FRF synthesised appears better described by the modal base extracted, whereas the structural dynamics at higher frequencies in the range appears less clear, starting from the stabilisation diagram, due to the minor sensitivity of native *receptance* FRF of DIC againts *mobility* FRF of SLDV. The discrepancy in the eigenfrequencies is linked to the much higher excitation force during the test, to let DIC acquire the displacements, but underlining non-linearities especially at higher frequencies, thus sensing a slightly softer structural dynamics.

2.3 Extracting the modal base from Dynamic ESPI

The ESPI dataset was instead taken in its native spatial resolution (49042 dofs), only reduced [6] to the common measured area among all the three optical gears, but down-sampled in the frequency domain to a spectral distance of 0.5 Hz by means of interpolation. Also, ESPI datasets were obtained with prototype instruments that, while surprisingly accurate in spatial domain, could be sometime disappointing on the frequency domain, especially at lower spectral lines.

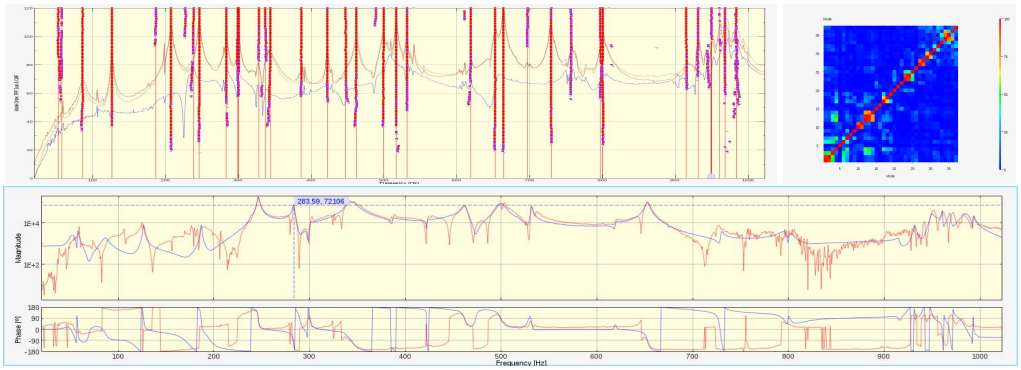


Figure 5: Stabilisation chart, AutoMAC matrix and FRF synthesis from EMA on ESPI dataset

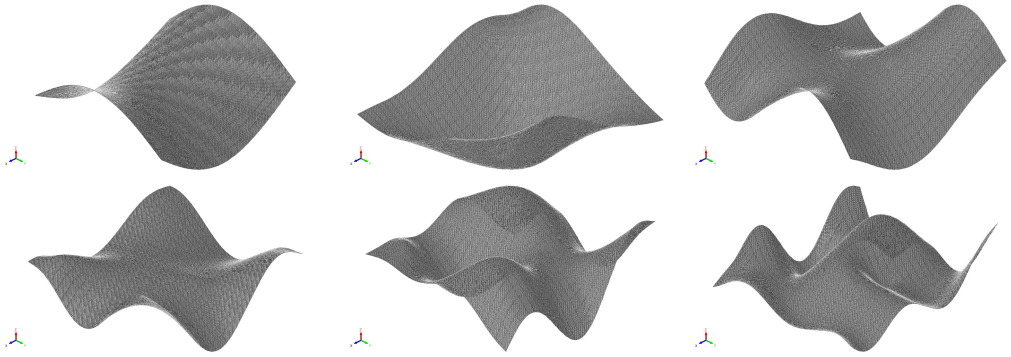


Figure 6: Modeshapes from EMA on ESPI dataset (126.2, 246.5, 301.2, 517.0, 724.8 and 982.9 Hz)

This, again, might arise potential repercussions on the quality of modal base identification steps.

The stabilisation diagram of Figure 5 is enriched with more information at higher frequency than that from DIC, comparable with Figure 1. Also the eigenfrequencies are extremely close to those of SLDV datasets, confirming the linearity checks between the two experiments. Instead, the synthesis of the driving point FRF shows flows in the phase subdiagram, especially at lower frequency. Again, the AutoMAC does not put enough in evidence the quality of the shapes in Figure 6 in terms of continuity or smoothness of the fields, which have no artefact nor distortions, and are so accurate to highlight the shakers' impedance head locations.

Even more than in DIC identification, complex-valued pairs of double modes where identified. As noted in [8], the higher, and much more reliable, spatial sampling helps in the selection of the most physical shapes, leaving micro unevenness for the badly identified modes.

3 BRIEF DESCRIPTION OF THE FE MODEL ADOPTED

The numerical model of the test case had to reproduce not only the thin aluminium plate, but also the restraining wires at the plate corners, the shaker impedance head influences and light restrains, as sketched in Figure 7. This advanced FE model (compared to that in [8]) highlights that asymmetry found in the displacement maps of the extensive full field measurement tests, showing nodal lines close to the location of the shaker inputs. It must be taken into account that the plate is not completely fixed, but is in a quasi-free-free conditions, since the wires were

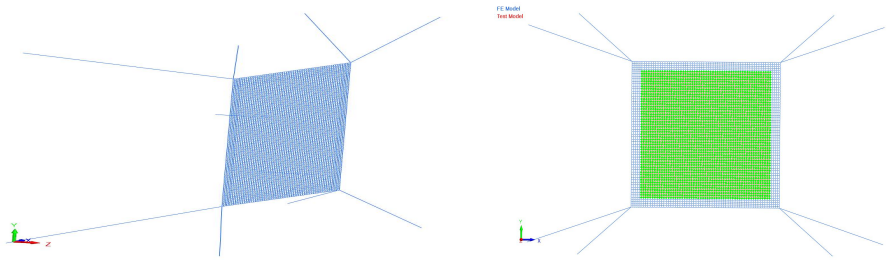


Figure 7: FE model grid and node point pairs with test measurements

used as a high-pass filter with threshold at 20Hz (due to the limit of dynamic ESPI technology on very small displacements, which otherwise are masked by rigid body motion). The model was written by means of the script language of the FEMtools 3.8.1 software[9], which served also as solver and model updating driver.

3.1 Details of the numerical model

The aluminium plate itself, with dimensions as 250x236x1.5 mm, is modelled with thin shell isotropic elements; the inner grid of Figure 7 matches exactly that of the measurements to have the proper comparison of all the test results, which were taken on only a portion of the surface, with SLDV geometry as reference. The out-of-plane displacements are of interest in the comparison with tests in the updating procedure. Structural damping is added in the model.

3.1.1 Constraints

At each corner two different metallic rope assemblies were used to restrain the rigid body modes. There follows that 8 potentially different spring elements were added to the FE model, with higher stiffness for the 4 short wires. Also structural damping was modelled in these restraints. All the end points of the wires were then grounded by means of boundary conditions on their 3 dofs. The dynamic solution of the model searches for eigenmodes from 5 Hz up to 25% more than the upper frequency limit of the experimental data, thus 1250 Hz. In this way a mixture of rigid-body and elastic modes can be found at lower frequencies up to 90 Hz.

3.1.2 Complex-valued data

Since the EMA identified shapes were complex-valued, complex-valued Lanczos algorithm with eigenvector maximum normalization was used, as well as for the normalised test shapes; this solution gave the more consistent results in terms of final MAC value of the paired shapes.

3.1.3 Optimization strategy

The attention was focused on the out-of-plane displacements only. The parameters of the updating were the density, the plate thickness and Young modulus, together with stiffness properties of the 8 springs, for a total of 11 variables. Double modes could be considered (also due to the complex-valued solution) and only modes above 0.6 MAC value could be coupled. As minimizing target, eigenshape distance on most active dofs was taken as responses: there resulted many responses, in the range of 10^5, depending on the adopted thresholds and test shape measurement quality. The standard Bayesian sensitivity[10] driven optimisation approach was

M	Hz	SLDV	Hz	MAC	M	Hz	DIC	Hz	MAC	M	Hz	ESPI	Hz	MAC
6	99.62	3	106.90	87.3	5	117.72	4	126.61	86.7	5	123.37	6	127.02	97.5
8	122.56	4	126.17	66.4	8	117.72	5	127.70	88.6	8	123.37	5	126.25	97.6
10	214.52	6	208.19	72.7	10	207.49	7	202.32	91.9	9	215.08	8	198.50	95.7
12	252.00	7	246.24	70.8	13	274.64	11	279.56	89.7	10	215.08	9	207.81	93.5
14	295.47	8	282.77	79.2	15	274.64	10	276.58	77.6	11	253.49	10	226.40	84.9
29	658.36	21	665.03	68.9	27	506.13	22	522.35	77.8	13	287.48	13	283.60	91.5

Table 1: Best pairs of modeshapes from model and test SLDV, DIC and ESPI datasets

adopted in FEMtools[9], but also the pseudo-inverse solution was tested, due to the non-optimal convergence to the best compromise. Non linear optimisation was here not approached.

4 MODEL UPDATING WITH FULL FIELD EXPERIMENTAL MODAL BASE

It must be pointed out that for the model updating stage were used three EMA sets (from SLDV, DIC, ESPI), but all restrained to the reference grid of the SLDV technology (57x51 nodes), due to the scattering seen in SLDV maps [6]. DIC and ESPI were reduced before running the EMA, thus are not the reduced version of the dataset previously shown in Figures 4 and 6. Exactly the same FE model was used at the starting point of the updating sequence. While already close to the measured test specimen, the model was updated by all the three datasets without finding a clear convergence, but only testing parameter values close to the starting ones: the results are here shown, but further work is necessary to improve the model optimisation stage.

4.1 Comparison of the FE model versus SLDV modal base

Despite its reference technology position in the instrument market, the SLDV technology, here tested without extra smoothing on the data, proved to be the worst of the three non-contacting optical technologies, as can be seen in Table 1 and Figure 8, where the best mode pairs resulting from the model updating are proposed. In Figure 9 the eigenmodes of the FEA model against those of test are sketched. The question might arise, if the scattering of SLDV data was a strong penalty in the usage of the EMA results, as the matching modes shown the lowest MAC values.

4.2 Comparison of the FE model versus DIC modal base

In Figure 10 are show the results of the model refinement by means of DIC dataset, sketching higher correlation from MAC values in Table 1 and Figure 8 than that of SLDV, but for a reduced frequency range (here just the first six best matching pairs were presented, but it stops at 647

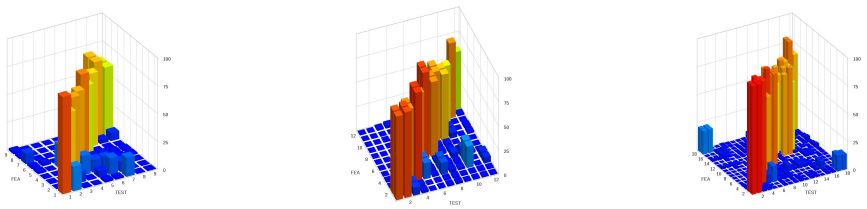


Figure 8: Modal Assurance criterion matrices of FEA vs TEST modeshapes from SLDV, DIC and ESPI datasets

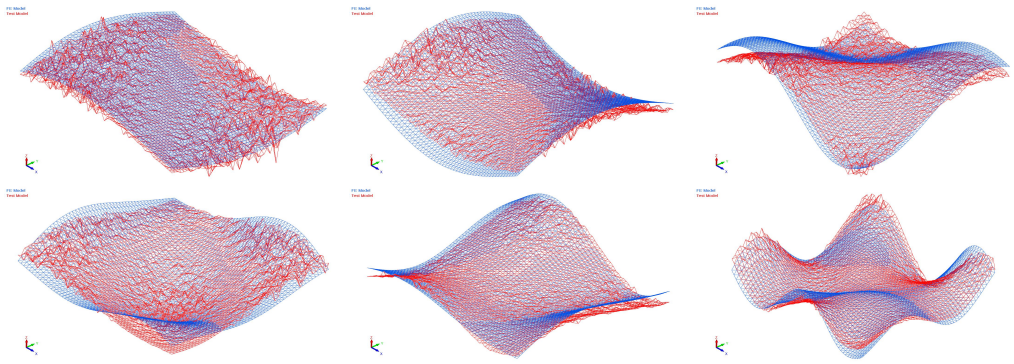


Figure 9: Best FEA vs TEST modeshape pairs from SLDV dataset (MAC values at pairs 1: 87.3, 2: 66.4, 3: 72.7, 4: 70.8, 5: 79.2, 8: 68.9)

Hz with MAC 0.601). Probably the artefacts of the lower frequency modes counter plays for achieving the best correlation.

4.3 Comparison of the FE model versus ESPI modal base

The matching of the model with ESPI modal base is remarkably better, here shown in Table 1 and Figures 8, 11 just till 284 Hz, but extendible to 763 Hz with MAC 0.805, and waving values in between. It appears that the high continuity of the ESPI shapes gives a strong contribution in refining the comparison with the numerical model.

5 CONCLUSIONS

The research work of the author from the early steps in [11] has brought to relevance the quality of native full field technologies in sensing accurate displacements in broad band structural dynamics. It appears now possible to run proficiently EMA with increased spatial sampling thanks to the emerging full field optical techniques and augmented computing power, even with more accuracy and ease than that obtained in the past [12], when virtual datasets had to be managed to cope with the huge calculations of ESPI modal analysis, or with advanced reduction schemes [5].

The analyses made in this work have highlighted also potential weaknesses of today proto-

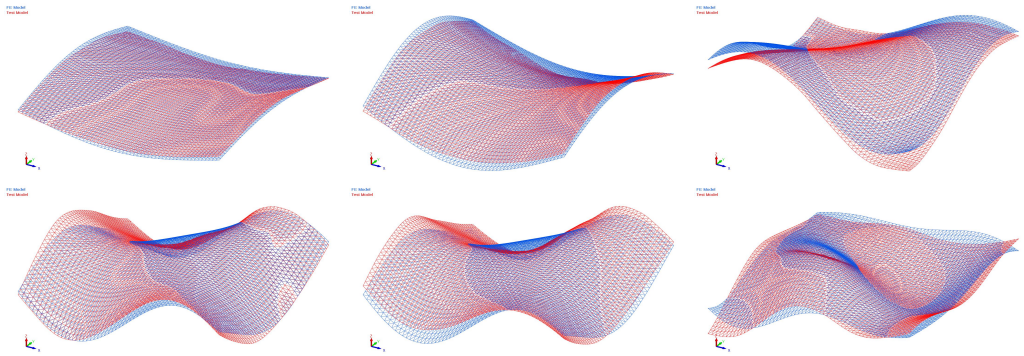


Figure 10: Best FEA vs TEST modeshape pairs from DIC dataset (MAC values at pairs 1: 86.7, 2:88.6, 4: 91.9, 6: 89.7, 7: 77.6, 11: 77.8)

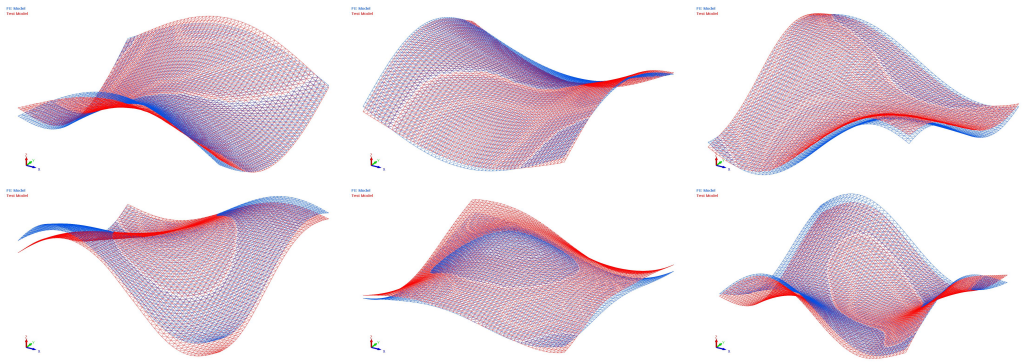


Figure 11: best FEA vs TEST modeshape pairs from ESPI dataset (MAC values at pairs 1: 97.5, 2: 97.6, 3: 95.7, 4: 93.5, 5: 84.9, 7: 91.5)

type gears: further refinements of all the three optical technologies will sure enhance the level of contact-less vibration measurements. While not yet mature as the SLDV, Hi-Speed DIC and Dynamic ESPI have shown in this paper to properly add the awaited quality on the eigenshapes for driving a full modal identification and use proficiently the obtained modal base to make enhanced comparisons with numerical models, for all the applications that well assessed NVH procedures [4, 3] can investigate.

Acknowledgements

This activity is part of the Project TEFFMA - Towards Experimental Full Field Modal Analysis, funded by the European Commission at the Technische Universitaet Wien, through the Marie Curie FP7-PEOPLE-IEF-2011 PIEF-GA-2011-298543 grant, for which the Research Executive Agency is greatly acknowledged. This work is intended to be part of the spreading of the results thereof. Vienna University of Technology, in the person of Prof. Wassermann and his staff, are kindly acknowledged for hosting the TEFFMA project of the author at the *Schwingungs- und Strukturanalyse* / Optical Vibration Measurement Laboratory. Dantecdynamics GmbH (Ulm, Germany) is also acknowledged for the precious technical support given for DIC and ESPI equipment used in the project.

REFERENCES

[1] Zanarini, A., 2014. *On the estimation of frequency response functions, dynamic rotational degrees of freedom and strain maps from different full field optical techniques*. In Proceedings of the ISMA2014 International Conference on Noise and Vibration Engineering, Leuven, Belgium, September 15-17, KU Leuven, pp. 1–15. paper ID676.

[2] Zanarini, A., 2015. *Accurate FRFs estimation of derivative quantities from different full field measuring technologies*. In Proceedings of the ICoEV2015 International Conference on Engineering Vibration, Ljubljana, Slovenia, September 7-10, IFToMM, pp. 1–10. ID192.

[3] Heylen, W., Lammens, S., and Sas, P., 1998. *Modal Analysis Theory and Testing*. Katholieke Universiteit Leuven, Leuven (Belgium). ISBN 90-73802-61-X.

[4] Ewins, D. J., 2000. *Modal Testing - theory, practice and application*, 2^{nd} ed. Research Studies Press Ltd., Baldock, Hertfordshire, England. ISBN 978-0-86380-218-8.

[5] Wang, W., Mottershead, J., and Siebert, T., 2011. "Frequency response functions of shape features from full-field vibration measurements using digital image correlation". *MSSP,* **28**, pp. 333–347. Elsevier Science Ltd.

[6] Zanarini, A., 2015. *Comparative studies on full field FRFs estimation from competing optical instruments*. In Proceedings of the ICoEV2015 International Conference on Engineering Vibration, Ljubljana, Slovenia, September 7-10, IFToMM, pp. 1–10. ID191.

[7] Zanarini, A., 2014. *Dynamic strain & stresses for enhanced reliability: from full field optical measurements to simulations*. In Proceedings of the ICAIM2014 International Conference on Applications for Image based Measurements, Leipzig, Germany, June 24-25, Dantecdynamics, pp. 1–18. ISBN 978-3-00-045317-5.

[8] Zanarini, A., 2014. *On the role of spatial resolution in advanced vibration measurements for operational modal analysis and model updating*. In Proceedings of the ISMA2014 International Conference on Noise and Vibration Engineering, Leuven, Belgium, September 15-17, KU Leuven, pp. 1–15. paper ID676.

[9] Dynamic Design Solutions, 2015. Femtoos 3.8.1 software. http://www.femtools.com.

[10] Mottershead, J., Link, M., and Friswell, M. I., 2011. "The sensitivity method in finite element model updating: A tutorial". *MSSP,* **25(7)**, pp. 2275–2296. Elsevier Science Ltd.

[11] Zanarini, A., 2007. *Full field ESPI measurements on a plate: challenging experimental modal analysis*. In Proceedings of the XXV IMAC, Orlando (FL) USA, Feb 19-22,, SEM. Paper s34p04.

[12] Van der Auweraer, H., Steinbichler, H., Haberstok, C., Freymann, R., and Storer, D., 2000. *Integration of pulsed-laser ESPI with spatial domain modal analysis: results from the salome project*. In Proc. of the 4th International Conference on Vibration Measurements by Laser Techniques: Advances and Applications, Vol. 4072, SPIE.

11th International Conference on Engineering Vibration
Ljubljana, Slovenia, 7–10 September 2015

DETERMINING SUBPIXEL FULL-FIELD DISPLACEMENTS FROM VIDEOS BY USING OPTICAL FLOW

Jaka Javh[1], **Janko Slavič***[1], **Miha Boltežar**[1]

[1]University of Ljubljana, Faculty of Mechanical Engineering, Ljubljana, Slovenia
jaka.javh@fs.uni-lj.si, janko.slavic@fs.uni-lj.si, miha.boltezar@fs.uni-lj.si

Keywords: optical flow, full-field contactless displacement measurement, subpixel resolution, photogrammetry, harmonic displacements

Abstract. *This research looks at the possibilities for full-field, contactless, displacement measurements based on high-speed video analyses. The displacements are determined by monitoring the colour-intensity changes of a subset with respect to a reference image using a gradient method. The focus of this research is small (subpixel) harmonic displacements. The aperture problem is solved by using colour information (RGB). The resolution potential and the effect of noise are explored theoretically. These theoretical findings help to determine the appropriate areas for calculation and thrust. Different colour patterns are tested in a synthetic simulation to check the resolution, the effect of noise and the processing time. The identified displacement can be much smaller than one pixel. The reconstruction is demonstrated at a displacement amplitude of 0.005 pixel. The simulations also demonstrate a strong robustness to noise. The reconstruction of displacements with an amplitude of less than one pixel is still possible, even at high 0 dB noise. Compared to digital image correlation, the processing time of the proposed method is hundreds of times shorter, when processing the same amount of data.*

1 Introduction

Full-field optical techniques are increasingly being used in structural engineering as a means of measuring displacement. Recently, computer vision has found a use in vibration analysis [1][2], and another study showed that sound can be reconstructed from the vibrations captured by the camera [3].

The most common image processing technique to determine a displacement in structural engineering is called digital image correlation (DIC) [4]. DIC is based on calculating the correlation between sequential images. It determines the displacements in an image by calculating the locations of highest correlation [4]. The highest correlation location is determined by an iterative process that checks selected subsets in the area. This usually involves the Newton-Raphson method [5]. A good initial guess is required in order to achieve the appropriate convergence [5]. The DIC technique is well established in engineering, because it provides good results and a high (subpixel) displacement resolution [6]; however it lacks simplicity, resulting in a long processing time [7]. More accurate DIC methods, using more robust correlation criteria [5], higher-order shape functions and higher-order interpolation schemes, are even more demanding [8].

A vibration analysis is usually performed in the frequency domain [9]. In image processing a high frame rate and a wide time span are required for a good frequency resolution and high frequencies. Long image sequences at a high picture resolution result in large quantities of data (several gigabytes of raw data), which needs to be processed in a reasonable time. To limit the amount of processing, DIC normally uses smaller subset sizes and is performed only at selected points on the image, resulting in a reduced spatial resolution.

Compared to DIC, gradient-based optical flow approaches [12] such as the Lucas-Kanade method [10] and the Horn-Schunck method [11] are fast and often used in real-time operations [13]. Gradient-based optical flow methods are based on the optical flow equation [11], and hence on the colour gradient determining the velocity from the difference in the pixel intensity between sequential images [14]. The optical flow equation is an undetermined system and can only provide information about the velocity in the direction of the colour gradient (aperture problem [15]). This is usually solved with information from the surrounding pixels using smoothness constraints [11], or with multiple constraints such as RGB colours [16].

This study proposes a gradient-based optical flow method that is optimised for small harmonic displacements. The proposed method analyses colour-intensity values in the frequency domain to determine the displacements in the direction of the separate colour gradients. Two-dimensional results are obtained by combining the complex amplitudes of the RGB colours.

The text is organized as follows: Section 2 covers the basics of the gradient-based optical flow approach. Section 3 derives a linear relation between the colour and the displacement from the optical flow and uses this relation to determine the displacement

amplitudes in the direction of the colour gradient. Section 4 combines information from the RGB colours to reconstruct the displacement amplitudes in two dimensions. Section 5 discusses the maximum resolution potential. The different colour patterns are tested in Section 6 and the effect of noise is tested in Section 7.

2 Optical flow in the direction of the colour field gradient

A gray image is a 2D matrix of $m \times n$ pixels containing colour-intensity values. The discrete 2D matrix can be interpreted as a 2D function of the intensity values over the camera is projection coordinates x and y and is denoted as $I(x, y)$. The colour field is a feature of the object's surface. When the object moves, the colour field in the camera's projection x, y shifts, thereby changing the pixel intensities (Figure 1). The object moves with time; therefore, the intensity values are time dependent $I(x, y, t)$. Optical flow assumes that there is brightness conservation [14]. Furthermore, the colour-intensity of a point $(x_j,\, y_k)$ on the object that moved to $(x_j + \mathrm{d}x,\, y_k + \mathrm{d}y)$ is assumed to be constant:

$$I(x_j, y_k, t) = I(x_j + \mathrm{d}x, y_k + \mathrm{d}y, t + \mathrm{d}t) \tag{1}$$

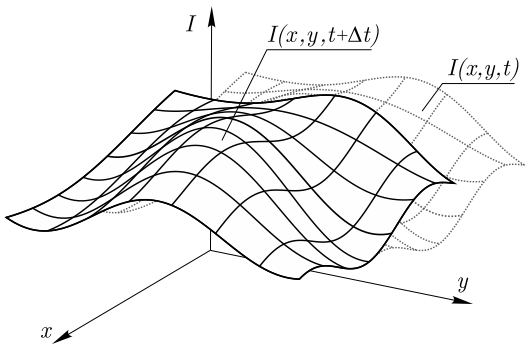


Figure 1: An example of a colour-intensity field as it shifts

Most optical flow methods approximate the image-intensity function with a Taylor series as:

$$\begin{aligned} I(x_j + \mathrm{d}x, y_k + \mathrm{d}y, t + \mathrm{d}t) &= I(x_j, y_k, t) + \frac{\partial I}{\partial x}\Delta x \\ &+ \frac{\partial I}{\partial y}\Delta y + \frac{\partial I}{\partial t}\Delta t + ..., \end{aligned} \tag{2}$$

where $\partial I/\partial x$, $\partial I/\partial y$ are the derivatives in their individual directions $x,\ y$, and $\partial I/\partial t$ is the derivative of time. For a small deformation and short time intervals the higher-order

terms in Eq. (2) can be neglected. Taking into account the optical flow condition (1), Eq. (2) takes a new form as the optical flow equation [10][11]:

$$\frac{\partial I}{\partial x}\Delta x + \frac{\partial I}{\partial y}\Delta y + \frac{\partial I}{\partial t}\Delta t = 0 \tag{3}$$

For a discrete problem $\partial I/\partial t\,\Delta t$ is interpreted as the change in the intensity at a pixel between sequential pictures:

$$\frac{\partial I}{\partial t}\Delta t = I(x_j, y_k, t + \Delta t) - I(x_j, y_k, t) \tag{4}$$

Eq. (3) can now be written as:

$$\frac{\partial I}{\partial x}\,\Delta x + \frac{\partial I}{\partial y}\,\Delta y = I(x_j, y_k, t) - I(x_j, y_k, t + \Delta t) \tag{5}$$

Since the object's colour field I is known, the gradients $\partial I/\partial x$ and $\partial I/\partial y$ can be determined. The resulting Eq. (5) has two unknowns, Δx, Δy, and therefore cannot be solved (aperture problem). Eq. (5) offers the results of the displacements in the direction of the colour gradient, only. Consequently, Eq. (5) is rewritten here in the direction of the gradient:

$$\mid \nabla I \mid \; \Delta s = I(x_j, y_k, t) - I(x_j, y_k, t + \Delta t) \tag{6}$$

$\mid \nabla I \mid$ is the known scalar value of the colour gradient and is calculated from the partial derivatives of the first image:

$$\mid \nabla I \mid = \sqrt{\frac{\partial I}{\partial x}^2 + \frac{\partial I}{\partial y}^2} \tag{7}$$

Δs is the unknown scalar value of the displacement in the direction of the colour gradient.

Figure 2 shows the relation written in Eq. (6) when a small displacement of the object produces a colour field shift. A point on the object carrying the colour field moves from point 1 to point 1' and the colour-intensity in the camera pixel (x_j, y_k) changes from point 1 to point 2.

Normally, the video would be analysed frame by frame, determining the gradient $\mid \nabla I \mid$ and the intensity $I(x, y, t)$ of the first image and deducing the displacement Δs to the following intensity $I(x, y, t + \Delta t)$ using Eq. (6). This step would then be repeated for every subsequent pair of images.

For the harmonic analysis, the displacements measured with optical flow would then be transformed to the frequency domain.

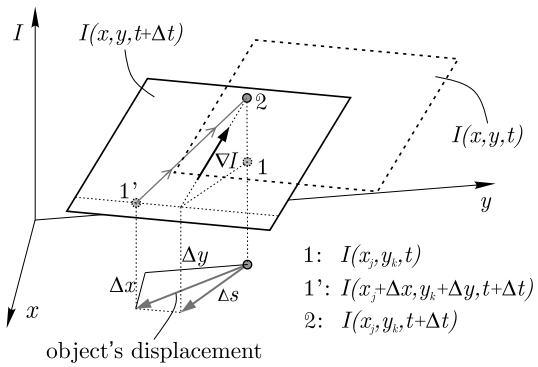


Figure 2: Displacement of the colour field and the intensity change at the selected pixel (x_j, y_k)

3 Optical flow in the frequency domain

This section introduces an alternative approach that relates the colour-intensity to the frequency domain displacement directly.

For small (subpixel) harmonic displacements that stay within an area of an approximately constant colour gradient, the displacement s can be observed in terms of the initial (reference) image, by monitoring the pixel intensity between the first image $I_0(x, y)$ and subsequent respective sequential images $I(x, y, t)$:

$$\mid \nabla I_0 \mid \; s(x_j, y_k, t) = I_0(x_j, y_k) - I(x_j, y_k, t), \tag{8}$$

where ∇I_0 is the colour gradient of the reference image and $s(x_j, y_k, t)$ is the displacement between the reference and the current image.

The partial derivatives $\partial I/\partial x$, $\partial I/\partial y$, required to determine the gradient (7), are calculated numerically for every pixel based on the surrounding pixels using a gradient filter (Sobel operator [17], Prewit operator [18]). Eq. (8) provides a linear relation between the displacement and the intensity level. The change in the intensity of a selected pixel is proportional to the displacement s and the colour gradient $\mid \nabla I_0 \mid$ in that pixel. This linear relation is a necessary condition for a direct transition to the frequency domain via the Fourier transform of Eq. (8). As the colour gradient $\mid \nabla I_0 \mid$ is constant over time, the Discrete Fourier transform $\mathcal{F}\{\}$ on the left-hand side of Eq. (8) is:

$$\begin{aligned} \mathcal{F}\{\mid \nabla I_0 \mid \cdot s(x_j, y_k, t)\} &= \mid \nabla I_0 \mid \cdot \mathcal{F}\{s(x_j, y_k, t)\} \\ &= \mid \nabla I_0 \mid \cdot S(x_j, y_k, f), \end{aligned} \tag{9}$$

where S is the complex amplitude of the displacements in the direction of the colour gradient. Fourier transforming the right-hand side of Eq. (8) gives:

$$\mathcal{F}\{I_0(x_j, y_k) - I(x_j, y_k, t)\} = A_0 - A(x_j, y_k, f), \tag{10}$$

where A is the complex amplitude of the intensity. The static term A_0 will be neglected as we are not interested in it. The amplitude of the displacements in the direction of the colour gradient for any pixel (x_j, y_k) in the $m \times n$ image matrix is obtained as:

$$S(x_j, y_k, f) = -\frac{A(x_j, y_k, f)}{\mid \nabla I_0 \mid} \tag{11}$$

4 Using colours to determine the displacement in x and y directions

Section 3 introduced the aperture problem, which states that the displacement can only be determined in the direction of the colour gradient. The problem will be solved by using information from two colours.

Separate colours have individual colour fields (e.g. $I_R(x, y, t)$ - red, $I_G(x, y, t)$ - green, $I_B(x, y, t)$ - blue). As the object moves, the colour field shifts, inducing colour-intensity changes for each colour respectively. To reconstruct the displacements in x and y axis at least two colours with different gradient directions are required, see Figure 3. Each colour gives a complex amplitude of the displacements in the direction of its colour gradient (11):

$$S_R = -\frac{R}{\mid \nabla I_R \mid} \tag{12}$$

$$S_G = -\frac{G}{\mid \nabla I_G \mid} \tag{13}$$

$$S_B = -\frac{B}{\mid \nabla I_B \mid}, \tag{14}$$

where R, G, B are the complex colour amplitudes and ΔI_R, ΔI_G, ΔI_B are the gradients of the red, green and blue colours, respectively.

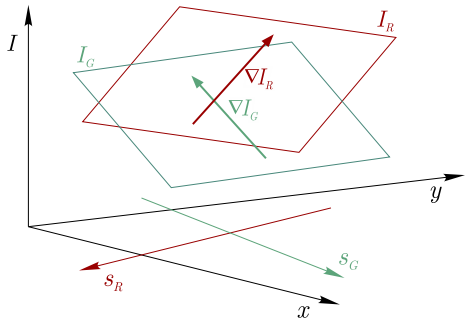


Figure 3: Two colours with diverging colour gradients

Figure 4 shows the real displacement amplitudes $\Re(S_R)$, $\Re(S_G)$ attained from the red and green colours in the directions of the separate colour gradients s_R, s_G. The real

amplitudes $\Re(X)$, $\Re(Y)$ in the x and y directions are reconstructed, respectively, by combining the real parts from the two colours ($\Re(S_R)$ and $\Re(S_G)$ when using the red and green colours). This is carried out geometrically (see Figure 4):

$$\Re(X) = \frac{\Re(S_G)\ \sin(\varphi_R) - \Re(S_R)\ \sin(\varphi_G)}{\sin(\varphi_R)\ \cos(\varphi_G) - \sin(\varphi_G)\ \cos(\varphi_R)} \tag{15}$$

$$\Re(Y) = \frac{\Re(S_R)\ \cos(\varphi_G) - \Re(S_G)\ \cos(\varphi_R)}{\sin(\varphi_R)\ \cos(\varphi_G) - \sin(\varphi_G)\ \cos(\varphi_R)} \tag{16}$$

The sine and cosine values are determined from the reference image using the partial derivatives and the gradient for every colour separately:

$$\sin(\varphi_R) = \frac{\frac{\partial I}{\partial x}}{|\ \nabla I_R\ |} \tag{17}$$

$$\cos(\varphi_R) = \frac{\frac{\partial I}{\partial y}}{|\ \nabla I_R\ |} \tag{18}$$

The imaginary values are obtained in the same way, but by using imaginary colour amplitudes.

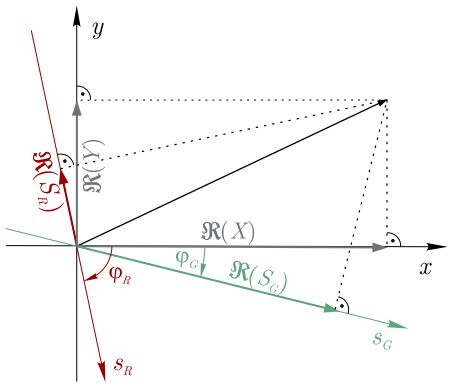


Figure 4: Real amplitude reconstruction from the amplitudes in the directions of the individual colours

5 Theoretical displacement resolution potential

Structure vibrations usually exhibit small displacements, which can be barely visible, if at all. A good displacement resolution is therefore required. This section takes a closer look at the achievable pixel-displacement resolution of the suggested method.

When filming with an 8-bit colour depth camera, a line with the values 0 (gray-scale black) on the left and 255 (gray-scale white) on the right, passing over a single pixel,

will produce a steady increase in the intensity values in this pixel from 0 to 255 over all 255 intensities, giving a $1/255$ or ≈ 0.004 pixel-displacement resolution. This concept is shown in Figure 5. The resolution potential when observing one pixel is therefore a function of the intensity depth in bits n:

$$\Delta x_{\min} = \frac{1}{(2^n - 1)} \tag{19}$$

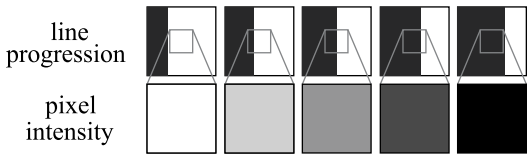


Figure 5: The upper fields show the progression of the colour line over the pixel, the lower fields show the registered colour-intensity in the pixel

However, the potential is even greater when observing a larger subset with a size of $d \times d$ pixels. When the line moves over the observed subset the individual pixels change their values independently. Since the line is moving from left to right, the values in pixels can only increase. From left to right the line crosses d pixels. During the crossing $(2^n - 1)\, d^2$ states are encountered, or $(2^n - 1)\, d$ states over a one-pixel move. For a $n = 3$ bit depth and a subset size of $d = 3$ this produces 9 states registered during a one-pixel move, see Figure 6. These states can be accounted by calculating the sum of the subset. The resolution potential when observing a subset is therefore:

$$\Delta x_{\min} = \frac{1}{(2^n - 1)\, d} \tag{20}$$

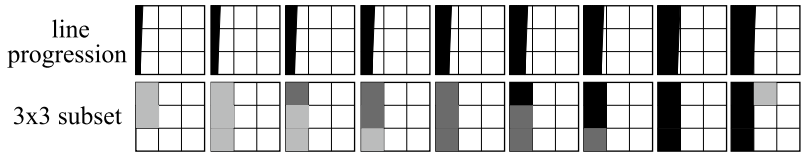


Figure 6: All 9 states present on a 3×3 subset during a one-pixel progression of the line at an angle for a 3-bit gray-scale image

Eq. (20) holds even if the line is not perfectly sharp, as long as the subset covers the whole intensity range and the states do not increase simultaneously. The values will not increase simultaneously if the line does not cross absolutely perpendicularly or if there is a small amount of noise causing some pixels to jump values earlier than others (which will be discussed later).

An average camera measures 8-bit intensity levels. Filming a whole range of intensities (0 to 255) and observing a subset with a size of $d = 5$ gives a theoretical resolution of up to 0.0008 pixel. However, caution needs to be taken with respect to these predictions. The states do not necessarily increase completely linearly, two or more states may be triggered at the same time, see Figure 7.

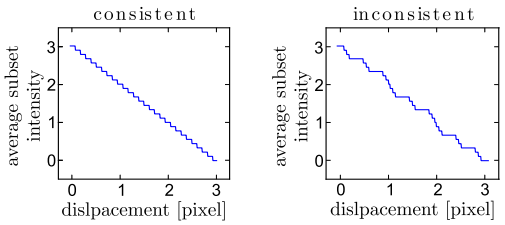


Figure 7: Relatively linear relation between the displacement and the average subset colour-intensity (left) and the possible inconsistencies (right)

Observing a larger subset has the added benefit of decreasing the effect of the noise. The noise decreases with the sample size [19]:

$$\sigma_{avg} = \sigma\sqrt{\frac{1}{N}}, \tag{21}$$

where σ is the standard deviation of the signal noise and N is the number of samples. In the present case N is the number of pixels in the subset:

$$N = d^2 \tag{22}$$

6 Synthetic experiment

The method works with a random colour texture, but gives better results when filming contrasting colours with diverging colour gradients. The following is a synthetic experiment on three patterns: A) a random texture, B) a colour-gradient pattern and C) a colour-lines pattern.

Pattern A (Figure 8) is a section taken from an image of a painting; pattern B consists of linear gradients for every colour in a different direction (Figure 9); and pattern C is a pattern of red and green colour lines, where the lines of the different colours run perpendicular (Figure 10). The colour intensities of pattern B and C range from 64 to 192, which is half of the 8-bit range.

Every pixel was assigned a displacement based on a harmonic in the x direction with an angular frequency ω, a second harmonic in the y direction with an angular frequency $2\,\omega$ and a third harmonic in the x direction with an angular frequency $3\,\omega$.

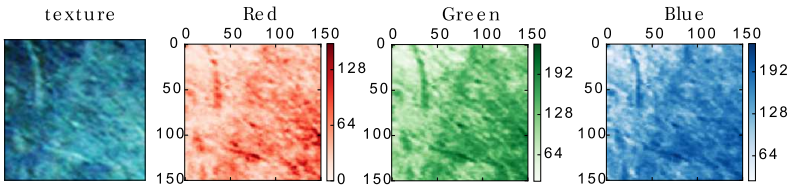


Figure 8: Pattern A; a random texture

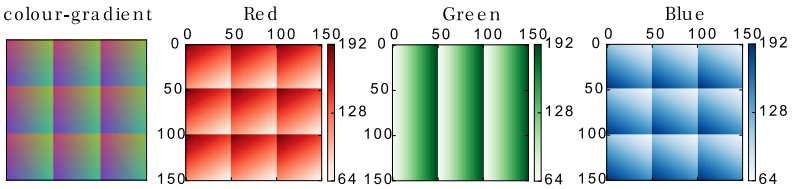


Figure 9: Pattern B; a colour-gradient pattern

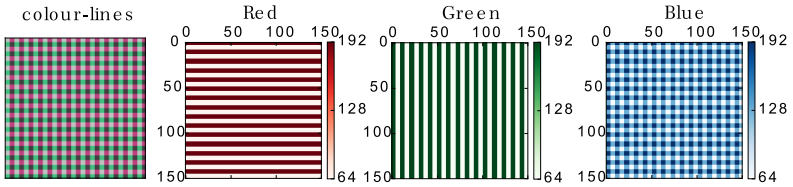


Figure 10: Pattern C; a colour-lines pattern

Each harmonic was simulated using a different phase:

$$\begin{aligned}\Delta x &= 0.5\left(\frac{y}{m}+(\frac{x}{m}-0.5)^2\right)\sin(\omega\,t+0.13)\\ &\quad +1.2\left(0.3-\frac{y}{n}+(\frac{x}{n}-0.5)^3\right)\sin(3\,\omega\,t+1.1) \qquad (23)\\ \Delta y &= 0.3\left((\frac{x}{m}-0.5)^2+(\frac{y}{n}-0.5)^2\right)\\ &\quad \sin(2\,\omega\,t-0.07), \qquad (24)\end{aligned}$$

where $m \times n$ is the size of the images in pixels. The image sizes are 150×150. The patterns were distorted according to the displacements (23,24) using a bilinear interpolation [20] for every time interval. A sequence of 30 images was generated, covering the period of the first harmonic. The amplitudes of the displacements are different for every pixel, and are listed in Figure 11 in the first column. They form mode shapes [9].

The displacement amplitudes were reconstructed from the simulated sequence by calculating the displacement amplitudes of all three colour pairs $(X,Y)_{RG}$, $(X,Y)_{GB}$

and $(X,Y)_{BR}$. The average amplitudes were used as the result. The sizes of the subsets for the random texture and the colour-gradient pattern were one pixel and the size of the subset for the colour-lines pattern was the width of a single colour square, which is $d = 5$ pixels. The undeformed image was taken as the reference image I_0. The reconstructed absolute displacement amplitudes of the pixels are compared to the true simulated values for all three harmonics and can be seen in Figure 11.

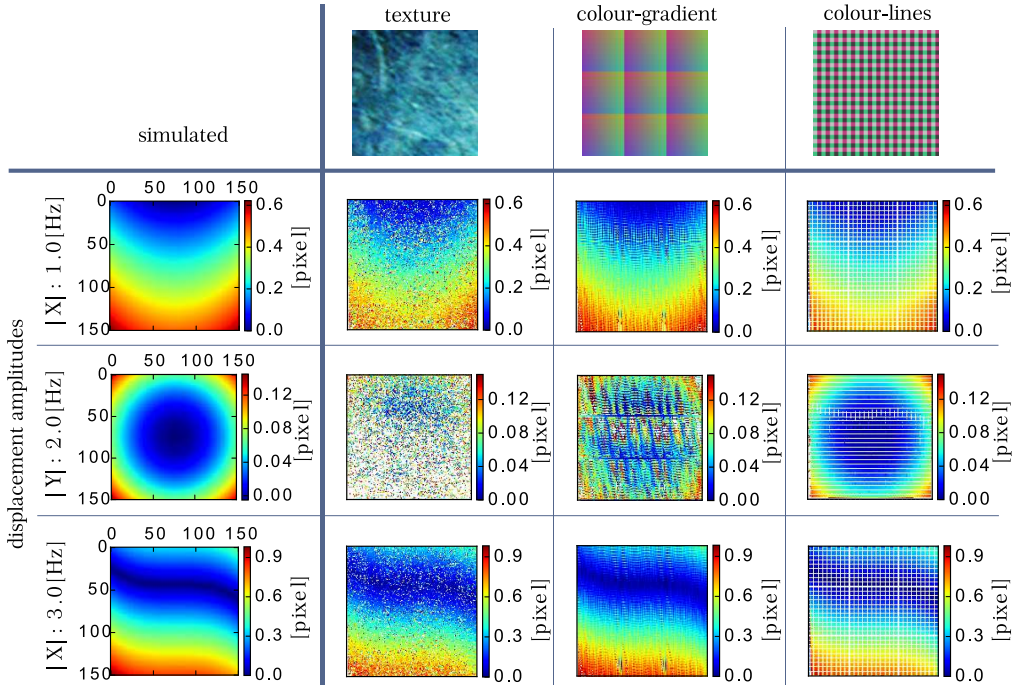


Figure 11: Simulation amplitude results compared to the true simulated values

The white areas are where the values were cropped for exceeding the scale, due to inappropriate criteria for the reconstruction. The criteria for the appropriate reconstruction are diverging colour-gradient directions (Section 4), sufficient gradient (Section 5) and gradient linearity (Section 2), with an emphasis on the first two. These criteria can be checked in the initial image and the errors can then be predicted.

Pattern A is problematic, because only local pixels satisfy all the criteria. This gradient is the least linear amongst all three patterns and the reconstruction is the poorest.

Pattern B has linear colour gradients and produces a good reconstruction when the displacements are sufficient, as in the first and third harmonics, but fails, due to a small colour gradient, when the displacements are smaller than in the second harmonic.

Pattern C produces the best results, even at small displacements, because the colour lines produce the steepest gradient. The reconstruction is not possible at the middle of the colour lines, because the gradient there is zero.

The method was realized in the Python 3.4 environment. Processing the pattern C image sequence on a laptop with an intel i7-4510U processor took approximately 0.7 seconds, 60% of which was taken up by the calculations concerning the reference-image. The reference image calculations barely increase when processing long image sequences.

7 Influence of noise

Gradient-based optical flow is known to be sensitive to noise. This is mainly due to the gradient being calculated on noisy images. The proposed method uses the gradient of a reference image. The reference image I_0 is best obtained by averaging the pixel intensities over time, thereby generating an average-value image that is less affected by the noise.

The synthetic experiment from Section 6 is repeated here with uniform noise added to the sequence of images. Tests were performed using different noise amplitudes: 0.5, 2.5, 5, 10, 25, 50 and 64 intensity levels. Figure 12 shows some of the results. Pattern A performed similarly to pattern B, and is excluded from the subsequent text for better clarity. Pattern B is much more sensitive to noise than pattern C, which achieves a decent reconstruction of the more evident mode shapes up to a noise amplitude of 64, which is equal to a $SNR = 0$ dB. This noise robustness is in part due to observing a larger subset but mostly due to the high contrast of the colours present at the edges of the colour lines.

8 Resolution test

To test the achievable resolution, an image sequence with even smaller displacement amplitudes was simulated. The pixel displacements were assigned as:

$$\Delta x = 0.06 \left((\frac{x}{m} - 0.5)^2 - (\frac{y}{n} - 0.5)^2 \right) \sin(\omega\, t - 0.61) \tag{25}$$

The resolution potential using pattern C with values from 64 to 192 (128 colour range) is approximately 0.0078, when observing a single pixel (19), and approximately 0.0016, when observing a $d = 5$ subset (20). The maximum simulated amplitude using Eq. (25) to determine the displacements is 0.015 pixel, which is twice that of the expected single-pixel resolution.

The colour-lines pattern that was used has absolutely perpendicular lines and Eq. (20) does not apply to it. Eq. (20) does, however, apply in the case of the noise. The sequence was therefore also generated with small noise, the amplitude of which was 0.5. The results using the displacements from Eq. (25) and using the same displacement, but $1/3$ the amplitude, are compared in Figure 13.

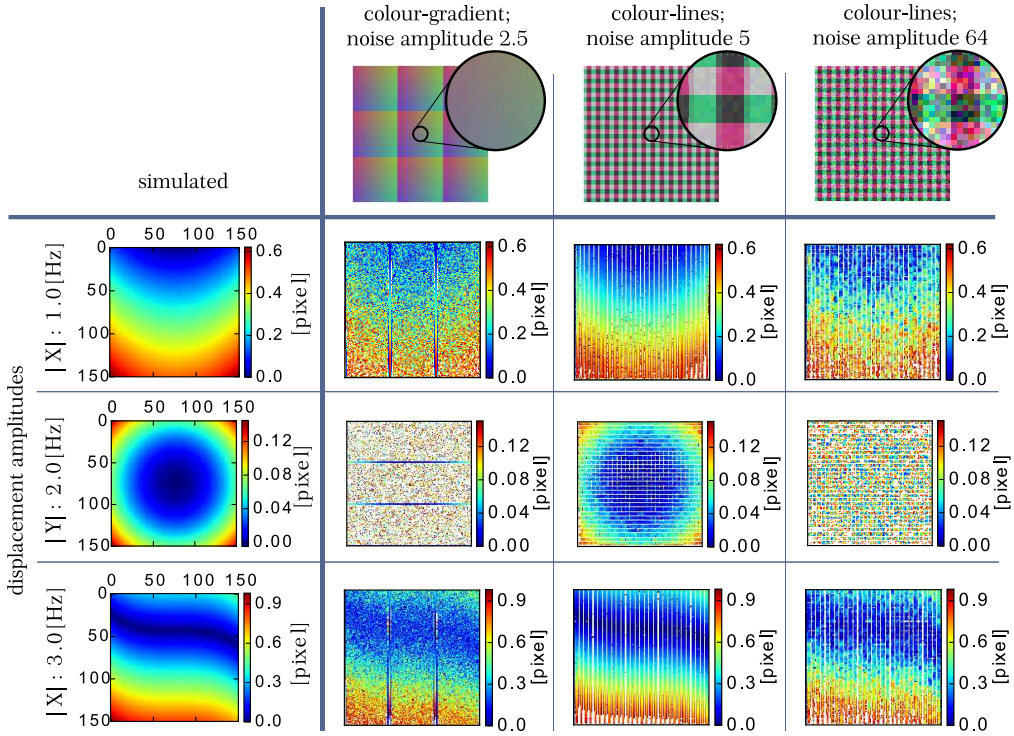


Figure 12: Simulation amplitude results for different noise-amplitude levels

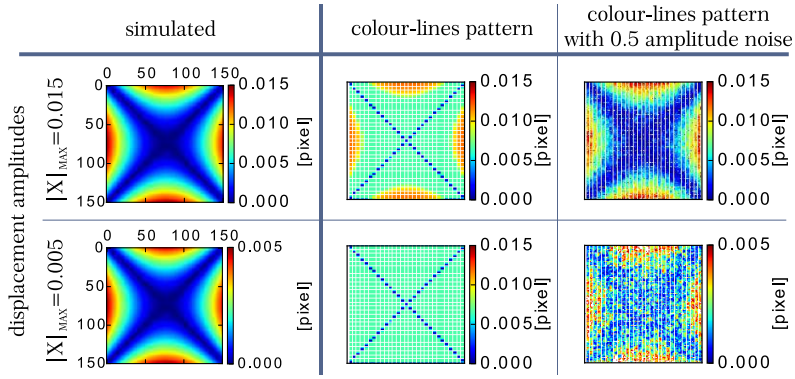


Figure 13: Smallest reconstructible displacements with and without noise

The reconstruction is still possible in spite of the small displacements. The added noise demonstrates the higher resolution potential when using a larger subset size and

reconstructs a recognisable mode shape, even for the smallest displacements.

9 Conclusion

The goal of this research was an algorithm optimised for measuring small harmonic vibrations in videos. Frequently, approaches use the DIC method to determine the displacements and perform a further frequency analysis on this data. The proposed method uses optical flow, with the assumption of smaller harmonic displacements. All the sequential images are now compared to a reference image, giving a linear relation between the colour and the displacement. This is reflected in short processing times, which are hundreds of times faster than those of the DIC method, when processing the same amount of data. There is no longer a need to reduce the number of analysed points, as is common with the DIC method, enabling true full-field measurements on average processors. The research on the achievable resolution suggests a matching resolution to that of DIC. The resolution is dependent on the colour depth, the size of the observed area and the image pattern. Findings suggest subpixel displacement resolutions of hundredths, to less than thousandths, of a pixel, given the appropriate conditions. The simulations confirm these findings. Local averaging, an appropriate pattern and a good reference image, provide good robustness to noise.

REFERENCES

[1] Helfrick, M. N., Niezrecki, C., Avitabile, P., & Schmidt, T. 3D digital image correlation methods for full-field vibration measurement. *Mechanical Systems and Signal Processing,* (2011), 25(3), 917-927.

[2] Wang, W. J. E., Siebert, T., & Pipino, A. Frequency response functions of shape features from full-field vibration measurements using digital image correlation. *Mechanical systems and signal processing,* (2012), 28, 333-347.

[3] Davis, A., Rubinstein, M., Wadhwa, N., Mysore, G. J., Durand, F., & Freeman, W. T. The visual microphone: passive recovery of sound from video. *ACM Transactions on Graphics* (TOG), (2014), 33(4): 79.

[4] Peters, W. H., & Ranson, W. F. Digital imaging techniques in experimental stress analysis. *Optical Engineering*, (1982), 21(3): 213427.

[5] Pan, B., Qian, K., Xie, H., & Asundi, A. Two-dimensional digital image correlation for in-plane displacement and strain measurement: a review. *Measurement science and technology*, (2009), 20(6): 062001.

[6] Xavier, J., Sousa, A. M., Morais, J. J., Filipe, V. M., & Vaz, M. Measuring displacement fields by cross-correlation and a differential technique: experimental validation. *Optical Engineering*, (2012), 51(4): 043602.

[7] Pan, B. Accurate, fast, and robust digital image correlation. *Sensing & Measurement*, (2013), 20(6): 062001.

[8] Langerholc, M., Slavič, J., & Boltežar, M. Absolute nodal coordinates in digital image correlation. *Experimental Mechanics*, (2013), 53(5), 807-818.

[9] Maia, N. M. M., & Silva, J. M. M. (ed.). *Theoretical and experimental modal analysis.* Taunton: Research Studies Press, (1997).

[10] Lucas, B.D., & Kanade, T. An iterative image registration technique with an application to stereo vision. In: *IJCAI*. (1981), 674-679.

[11] Horn, B. K., & Schunck, B. G. Determining optical flow. In: *1981 Technical Symposium East. International Society for Optics and Photonics*, (1981), 319-331.

[12] Barron, J. L., Fleet, D. J., & Beauchemin, S. S. Performance of optical flow techniques. *International journal of computer vision*, (1994), 12(1), 43-77.

[13] Liu, H., Hong, T. H., Herman, M., Camus, T., & Chellappa, R. Accuracy vs efficiency trade-offs in optical flow algorithms. *Computer vision and image understanding*, (1998), 72(3), 271-286.

[14] Fennema, C. L., & Thompson, W. B., Velocity determination in scenes containing several moving objects. *Computer graphics and image processing* (1979), 9(4), 301-315.

[15] Hildreth, E. (1983). *The measurement of visual motion*. PhD thesis, MIT.

[16] Ohta, N. Optical flow detection by color images. In: *Proc. Tenth International Conference on Pattern Recognition, Singapore, September 1989*, (1989), 801?805.

[17] Sobel, I., & Feldman, G. A 3x3 isotropic gradient operator for image processing. *a talk at the Stanford Artificial Project in*, (1968), 271-272.

[18] Prewitt, J. MS. Object enhancement and extraction. *Picture processing and Psychopictorics*, (1970), 10(1), 15-19.

[19] Bendat, J. S., & Piersol, A. G. *Random data: analysis and measurement procedures*. John Wiley & Sons, (2011).

[20] Gonzales, R. C., & Woods, R. E. *Digital Image Processing, 2-nd Edition*. Upper Saddle River, NJ: Prentice Hall, (2002).

Non-smooth Dynamical Systems (MS19)

11th International Conference on Engineering Vibration
Ljubljana, Slovenia, 7–10 September 2015

HIDDEN DYNAMICS OF DRY-FRICTION OSCILLATORS

Mike R. Jeffrey

University of Bristol
mike.jeffrey@bristol.ac.uk

Keywords: nonsmooth, switching, dynamics, sliding, sticking, discontinuity, singularity, bifurcation

Abstract.

The theory of nonsmooth dynamics describes how discontinuities in dynamical laws, such as those caused by friction, impacts, shape buckling, or mechanical relays, affect the deterministic and otherwise smooth behaviour of a mechanical system. In the geometric theory of dynamics, a system 'flows' through a phase space, sometimes encountering limit sets, bifurcations, or chaos. The phase space of a nonsmooth flow is also permeated by switching thresholds. The flow can kink as it crosses the threshold, but it can also stick to the threshold, corresponding to frictional sticking, and resulting phenomena like stick-slip oscillations have been a fruitful area of study for mechanical modeling. The interaction of multiple objects undergoing coupled stick-slip oscillations have not been studied from the same point of view, however, because, perhaps surprisingly, the continuous time dynamical methods for multiple sticking events were derived only recently.

We summarize those methods here, including the extension of Filippov's methods to multiple switches, and the introduction of hidden dynamics inside a discontinuity. We show the implications these have for a series of coupled dry friction oscillators, giving insight into complex self-sustained oscillations. We derive the basic mechanisms of entry and exit from single or multiple sticking modes (i.e. sticking of multiple oscillators), which include both deterministic and determinacy-breaking exit points. Both of these kinds of exit point can cluster in higher dimensional systems, and both lead to complexity of behaviour in the form of robust, repeatable, but unpredictable behaviour. The study of exit points reveals how large scale unpredictability, with no obvious global structure, nevertheless has local origins in the form of local sensitivity to initial conditions at exit point singularities.

1 Introduction

One might not expect that much remains to be learned about the elementary mechanics underlying dry friction oscillators, especially when assuming the simplest Coulomb-type (step function) contact force. In this paper we begin showing how advances in the mathematical theory of nonsmooth dynamics alter our view of how complex mechanical phenomena emerge from simple underlying geometry, and highlight some of the techniques that can be used to study them.

The systems we will consider relate a set of displacements $\mathbf{x} = (x_1, x_2, ..., x_n)$, and their time derivatives, by a relation of the general form

$$\ddot{\mathbf{x}} = \mathbf{f}(\mathbf{x}, \dot{\mathbf{x}}; \boldsymbol{\lambda}) \ . \tag{1}$$

A vector of parameters $\boldsymbol{\lambda} = (\lambda_1, \lambda_2, ..., \lambda_m)$ will typically represent contact forces which obey

$$\lambda_i \in \begin{cases} \text{sign}\,(h_i(\mathbf{x})) & \text{if} \quad h_i(\mathbf{x}) \neq 0 \ , \\ [-1, +1] & \text{if} \quad h_i(\mathbf{x}) = 0 \ , \end{cases} \tag{2}$$

for $i = 1, 2, ...m$, in terms of smooth scalar functions h_1, h_2, ... h_m. On each surface $h_i(\mathbf{x}) = 0$, if there exists a solution to the inclusion (1)-(2) such that $\dot{h}_i(\mathbf{x}) = 0$, then the system has trajectories that *stick to* (or in the dynamics system parlence 'slide along') the surface $h_i = 0$ for some interval of time. Likewise if $\dot{h}_i(\mathbf{x}) = 0$ on $h_i(\mathbf{x}) = 0$ can be solved for a subset of $i \in \{1, 2, ..., m\}$, trajectories exist that stick to the intersection of the surfaces $h_i = 0$. The general principles of how to determine the existence and dynamics of sticking modes can be found in [8], but for the mechanical oscillator they are particularly simple.

In the following we shall consider one, two, and then multiple oscillators, coupled via springs and dampers, situated on a surface moving with constant speed and subject to Coulomb dry friction. The functions h_i will become the slipping speed of the i^{th} oscillator relative to the surface, positive and negative h_i denoting right and leftward motion, respectively. We will look at the mechanics by which oscillators are released from stick ($h_i = 0$) to slip ($h_i \neq 0$), observed as singularities in the phase space of $\mathbf{x}$ and $\dot{\mathbf{x}}$, and show how this leads to either *deterministic* or *determinacy-breaking* exits from sticking. We then discuss the way clusters of exit events tend to appear, creating a likelihood that multiple oscillators will exit simultaneously, or in close succession, from stick to slip. The effect of this geometry on large numbers of oscillators is then studied in numerical experiments, revealing short term unpredictability against a background of long term self-organisation, which reveals itself in the statistics of stick-slip cascades.

2 Slip and Stick for a single oscillator

We begin with the simple dry friction oscillator, reviewing certain basic insights that we shall extend to many oscillators below. A block rests on a surface that moves with constant speed v. The block is attached to a fixed apparatus by a spring with stiffness κ and extension z, and by a dashpot with damping coefficient ρ. The block's mass can be scaled out of the equations, resulting in

$$\ddot{z} + \rho\dot{z} + \kappa z + \mu\left(\dot{z} - v\right) = 0 \ , \tag{3}$$

where $\mu(\dot{z} - v)$ is a function describing the coefficient of friction between the block and the surface, satisfying

$$\mu(u) \in \tilde{\mu} \begin{cases} \text{sign}(u) & \text{if} \quad u \neq 0 \ , \\ [-1, +1] & \text{if} \quad u = 0 \ . \end{cases} \tag{4}$$

The constant $\tilde{\mu}$ denotes the coefficient of kinetic friction. We can form a first order ordinary differential equation by letting $\dot{z} = y + v$, where y is the block's velocity relative to the moving surface. This and similar systems have been extensively studied from analytical, numerical, and experimental viewpoints, see e.g. [4, 7, 12, 13], especially with regard to periodic or chaotic dynamics when a periodic forcing is added to (3).

The block's motion is illustrated in phase space in fig. 1, as a primer for the more complicated situations to follow. The block switches its direction of slip as $\dot{z} - v$ passes through zero, but only if the spring force $(-\kappa z)$ is great enough that $(\rho v + \kappa z)^2 > \tilde{\mu}^2$, otherwise the block and the surface stick together, seen as the trajectory traveling along $\dot{z} = v$ in fig. 1. During the sticking phase we can find the resistance force provided by considering μ to be a variable in (3), and finding its value by solving

$$\ddot{z} + \rho\dot{z} + \kappa z + \mu = 0\ , \quad \dot{z} = v\ , \quad \ddot{z} = 0 \qquad \Rightarrow \qquad \mu = -\rho v - \kappa z\ . \tag{5}$$

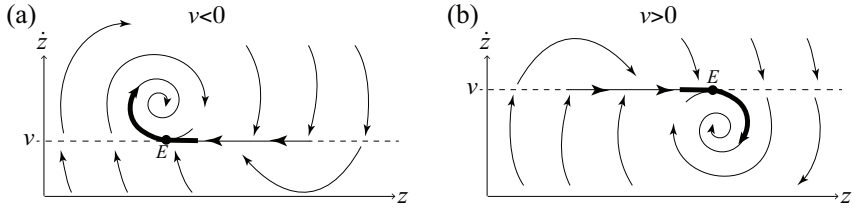


Figure 1: The phase space of the dry friction oscillator for $v < 0$ and $v > 0$. Slipping motion to the right or left correspond to relative speeds $\dot{z} > v$ or $\dot{z} < v$ respectively. Crossing between slip directions takes place where the line $\dot{z} = v$ is dashed, while sticking occurs between the two points where the flows fold towards or away from the line. A fold where the flow curves away creates an exit point (marked E), where the oscillator goes from stick to right slip in (i) or from stick to left slip in (ii), and the exiting trajectory is shown as a bold curve.

The boundary between the two cases (slip-slip transition or slip-stick transition) is delimited by folds in the slipping flow at $z = (\mp\tilde{\mu} - \rho v)/\kappa$, where the flow is quadratically tangent to the discontinuity. Whether the flow turns towards or away from the discontinuity surface at these points is determined by the curvature term $\dddot{z} = -\rho\ddot{z} - \kappa\dot{z} = -\kappa v$, which implies that the flow curves upwards at both folds if $v < 0$ (downwards if $v > 0$ but we mainly consider the former here). Places where the flow curves away from the discontinuity create *exit points* from sticking (the point E in the figure), and will take on increasing importance in what we consider below.

In systems of multiple oscillators studied in the next two sections, it is possible for exit points like those in fig. 1(i-ii) to form on both sides of the discontinuity simultaneously. This causes an ambiguity in which side of the discontinuity a trajectory will exit from sticking. The general ambiguity has been much studied in the last two decades (see [3] and references therein), but seems not to arise easily in low dimensional mechanical systems. Below we shall see that ambiguous exits play a more significant role as more oscillators are added.

3 Slip and Stick for a pair of oscillators

Consider now a pair of blocks each independently of the form (3) (labelled by subscripts 1 and 2), and coupled by an additional spring with stiffness κ_{12}. We have

$$\begin{aligned} \ddot{z}_1 + \rho_1\dot{z}_1 + \kappa_1 z_1 + \kappa_{12}(z_1 - z_2) + \mu_1\,(y_1 - v) = 0\ , \\ \ddot{z}_2 + \rho_2\dot{z}_2 + \kappa_2 z_2 + \kappa_{12}(z_2 - z_1) + \mu_2\,(y_2 - v) = 0\ . \end{aligned} \tag{6}$$

Again v is the speed of the surface on which the blocks rest. Such systems have been much studied for their periodic or chaotic dynamics under periodic forcing, see e.g. [1], but, as for the single oscillator, we are more interested in local properties and omit any external forcing. The coupled system dynamics occupies the phase space of $(z_1, z_2, \dot{z}_1, \dot{z}_2)$, with discontinuity at the two surfaces $z_1 = v$ and $z_2 = v$, where the two blocks switch between left and right slip.

Consider the discontinuity surface $y_1 = v$ first. Sticking occurs for displacements z_1, z_2, satisfying $(\rho_1 v + \kappa_1 z_1 + \kappa_{12}(z_2 - z_1))^2 < \tilde{\mu}_1^2$, and elsewhere on $y_1 = v$ the first block flips between left and right slip without sticking. The two cases are separated, as in section 2, by folds of the slipping flows, which occur on planes $(\kappa_1 - \kappa_{12})z_1 + \kappa_{12} z_2 = \mp\tilde{\mu}_1 - \rho_1 v$. Whether the flow turns towards or away from the discontinuity is determined by the curvature term $\dddot{z}_1 = (\kappa_{12} - \kappa_1)v - \kappa_{12}\dot{z}_2$, whose sign is dependent on the velocity $\dot{z}_2$ of the second block, and on the relative sizes of κ_1 and κ_{12}. Clearly the quantity $\dddot{z}_1$ itself can vanish, creating a cusp or higher order tangency between the flow and the discontinuity, see e.g. [5, 14].

We can perform similar analysis for the second block to find that, on the discontinuity surface $y_2 = v$, sticking occurs where $(\rho_2 v + \kappa_2 z_1 - \kappa_{12}(z_2 - z_1))^2 < \tilde{\mu}_2^2$, folds occur on planes $(\kappa_2 - \kappa_{12})z_2 + \kappa_{12} z_1 = \mp\tilde{\mu}_2 - \rho_2 v$, where the curvature term $\dddot{z}_2 = (\kappa_{12} - \kappa_2)v - \kappa_{12}\dot{z}_1$ decides the existence of exit points.

Sticking of both blocks occurs where both sticking conditions hold, on a region taking the form of a parallelogram in the (z_1, z_2) space on $\dot{z}_1 = \dot{z}_2 = v$ (bottom-left in fig. 2),

$$\begin{array}{l} -\tilde{\mu}_1 < \rho_1 v + (\kappa_1 - \kappa_{12},\ \kappa_{12}) \cdot (z_1,\ z_2) < +\tilde{\mu}_1 \ , \\ -\tilde{\mu}_2 < \rho_2 v + (\kappa_{12},\ \kappa_2 - \kappa_{12}) \cdot (z_1,\ z_2) < +\tilde{\mu}_2 \ . \end{array} \tag{7}$$

The edges of this region are the two fold planes. As a trajectory leaves the parallelogram (7) at one of these edges, one of the blocks begins to slip, and may be closely followed by the second block beginning to slip. Figure 2(a) depicts a bold trajectory where block 1 and then block 2 slip in close succession.

Our greater interest now resides in the corners of the parallelogram, where exit points coincide when both blocks may exit from sticking contact simultaneously. These are two-fold singularities of the kind described in [10], where there is a fold both of the first and second oscillator's flow. Solving both of the fold conditions to find the corner gives the isolated points

$$\begin{pmatrix} z_1 \\ z_2 \end{pmatrix} = -\tfrac{\rho_1 v \pm \tilde{\mu}_1}{K} \begin{pmatrix} \kappa_{12} - \kappa_1 \\ \kappa_{12} \end{pmatrix} - \tfrac{\rho_2 v \pm \tilde{\mu}_2}{K} \begin{pmatrix} \kappa_{12} \\ \kappa_{12} - \kappa_2 \end{pmatrix} \ , \tag{8}$$

writing $K = \kappa_1\kappa_2 - \kappa_{12}(\kappa_1 + \kappa_2)$. The different combinations of $\pm\tilde{\mu}_1$ and $\pm\tilde{\mu}_2$ give four such points. The curvature in the $\dot{z}_1$ and $\dot{z}_2$ directions takes the same value at each point, namely

$$\dddot{z}_1 = -\kappa_1 v \ , \qquad \dddot{z}_2 = -\kappa_2 v \ , \tag{9}$$

meaning for $v < 0$ the flow curves always in the position direction with respect to the $\dot{z}_1$ and $\dot{z}_2$ directions, and thus towards the discontinuity from below, and away from it from above. Hence the point given by $\{+\tilde{\mu}_1, +\tilde{\mu}_2\}$ is a double exit point, where both blocks are carried away from sticking by the flow, and therefore both begin slipping simultaneously. The points given by $\{+\tilde{\mu}_1, -\tilde{\mu}_2\}$ and $\{-\tilde{\mu}_1, +\tilde{\mu}_2\}$ are illustrated in fig. 2 (b) and (c) respectively. The dynamics in each scenario are described in the caption, and reveal that only (b) forms an exit point, in which both blocks simultaneously cease sticking.

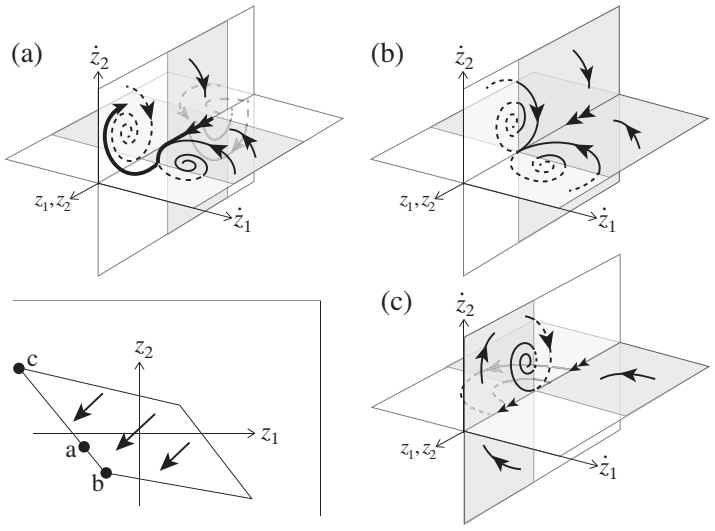


Figure 2: A representation of dynamics in the four dimensional phase space of $(z_1, z_2, \dot{z}_1, \dot{z}_2)$, showing the discontinuity surfaces $\dot{z}_1 = v$ and $\dot{z}_2 = v$, on which sticking occurs in the shaded regions. Illustrating: (a) a typical case, showing the flow on the discontinuity surfaces when sticking occurs (dotted curves show the'virtual' flow, indicating the flow off the surfaces where there is no sticking); (b) a visible two-fold forms a double exit point, a boundary where both oscillators cease sticking, and since the exit takes place into a region where there is no sticking the flow is well-determined; (c) a two-fold of mixed visibility has a well-defined trajectory emanating from it, but the flow in the (z_1, z_2) plane reveals it is not an exit point as the flow cannot enter the point (c) along the intersection. This is a sketch generated from simulations for constants $\rho_1 = \rho_2 = 0.1$, $\kappa_1 = 1.1$, $\kappa_2 = 1.6$, $\kappa_{12} = 0.5$, $\tilde{\mu}_1 = \tilde{\mu}_2 = 1$, $v = -1$. The different points are shown in (z_1, z_2) space (bottom-left) as the corners of the sticking parallelogram (7), whose edges are the fold sets, and on which the flow during sticking obeys $(\dot{z}_1, \dot{z}_2) = (v, v)$.

4 Slip and Stick for multiple oscillators

We now generalize the above system to any number of oscillators, constrained to move along a line, but to avoid being overly prescriptive, we allow them to be coupled by an arbitrary arrangement of springs. The system we shall study here extends (3) and (6) to n blocks by writing

$$\ddot{z}_i + M^{\rho}_{ij}\dot{z}_j + M^{\kappa}_{ij}z_j + \mu_i\left(y_i - v\right) = 0\ , \qquad i = 1, ..., n, \tag{10}$$

where M^{ρ} and M^{κ} are $n \times n$ square matrices, and we sum over the index $j = 1, ..., n$. The matrix of damping coefficients M^{ρ} is diagonal, the matrix of spring stiffness coefficients M^{κ} has a diagonal part (of individual springs) and an antisymmetric part (of spring couplings).

Systems of multiple coupled oscillators similar to this have again been much studied, but the continuous time approaches used for the low dimensional systems as above have tended to be surpassed by discrete methods. Such models are now a huge topic of network complexity science, building on earthquake models such as [2], and typically modelled as discrete time algorithmic models (where 'stick' and 'slip' are discrete modes). In the light of the continuous time dynamics above, and exit points in particular, we shall now re-consider what the continuous time dynamical theory implies for the behaviour of a high dimensional system.

In section 2 the system had two fold points which bounded the sticking dynamics. In section 3 the system had four lines of folds which intersected in pairs (bottom-left in fig. 2), near which there is an increased chance of one exit (one block beginning to slip) being followed by another (the second block beginning to slip). As more oscillators are introduced, say a total of

n oscillators, we obtain $2n$ folds. If r oscillators are sticking, the dynamics occupies a $2n-r$ dimensional phase space, upon which k folds may intersect where $n+k \leq 2n-r$, and there will be up to 2^k such points. Thus there exist up to 2^k points where up to $k \leq n$ of $r \leq k$ sticking oscillators may begin slipping simultaneously, nearby by which cascades of up to 2^k oscillators may be seen beginning to slip, one after another in rapid succession.

Obviously, displaying simulations of systems of multiple oscillators in phase space will be of limited use, and already in section 3 we have been able to give only schematic representations of the phase space dynamics for two blocks. From that analysis, however, the central feature of interest is the codimension of the motion, equivalent to the number of intersecting discontinuity surfaces upon which sticking motion occurs, or, in physical terms, simply the number of blocks sticking at a given time. We label this the *sticking codimension* n_{stick}. Exit points are then easily observed as incremental decreases in the sticking codimension. If clusters of exit points occur as expected, they will be seen as cascades of decreasing sticking codimension n_{stick}.

The following plots are taken from a simulation of the system (10) with $v=-0.2$, with all $\tilde{\mu}_i = 1$, and with initial conditions $z_i = -0.7$, $\dot{z}_i = -0.4$, for all oscillators. The damping constants are taken as random values in the range $M^{\rho}_{ij} \in [\rho, 2\rho]$ with $\rho = 3.5$, the spring constants as random values in the range $M^{\kappa}_{ij} \in [0,\kappa]$ with $\kappa = 0.2$. These various details have little impact on the qualitative outcomes of the simulations, the key parameters which provide the behaviour below being v, ρ, and κ.

Figure 3(i) shows the sticking codimension for a system of 20 oscillators. Four oscillators stick almost immediately, followed by a succession of exit points through which all slip at around $t \approx 24$, and after a short return to sticking all oscillators eventually slip. The behaviour becomes more interesting as we increase the dimension. For 100 oscillators, in fig. 3(ii), numerous cascades of exit points, and countering returns to stick, occur over a time period of around 100 or so increments (but after $t \gtrsim 150$ all oscillators are eventually found to slip). For 200 oscillators, in fig. 3(iii), these complex stick-slip transitions become self-sustaining, with cascades of exit points and collapse back to sticking mediating each other over long times.

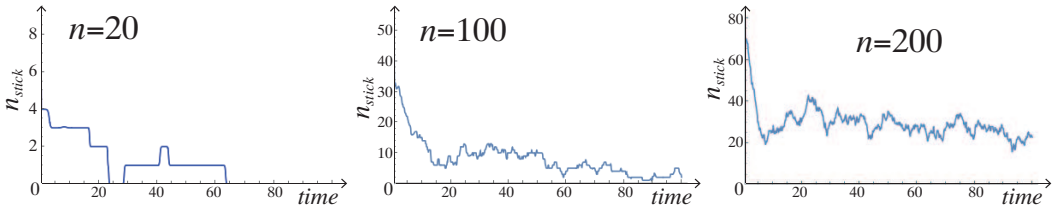


Figure 3: Plots of the sticking codimension n_{stick} for systems of n oscillators, as described in the text.

We shall look closer into this long-term behaviour below. First, as discussed in section 3, a system becomes very sensitive around exit points and should be sensitive to modeling assumptions. In fig. 4 we investigate the system's robustness, first to perturbations of the switching model and then to perturbations of the mechanical constants. An important simplification we have made in the simulations here is to approximate each sign function $\mu_i(u)$ by a sigmoid $\mu(u) = \phi(u/\epsilon)$, in fact we take $\phi \equiv \tanh$ and $\epsilon = 0.03$, and this permits us to simulate using a standard ODE package (in this case the Mathematica routine NDSolve). The precise choice of sigmoid does not matter typically (see e.g. [9, 11]), but as noted in [6] can create novel behaviours near exit points. In fig. 4(i)-(ii) each switching function $\mu_i(u)$ is replaced by a sigmoid

$\mu(u) = \tanh(u/r_i\epsilon)$, each with a different stiffness $r_i\epsilon$ where the r_i's are a random numbers between 0 and 1. The result of four such simulations for 20 and 200 oscillators are shown. As expected if exit points with sensitivity to initial conditions are involved, the short-time dynamics is sensitive to these small changes in the modeling stiffness. The long time behaviour, however, is largely unaffected, even exhibiting similar large scale structures in the sustained oscillations of 200 oscillators. That is, we observe short-term sensitivity but long-term robustness, despite the complexity of the long-term dynamics. In fig. 4(iii)-(iv) we probe the robustness of

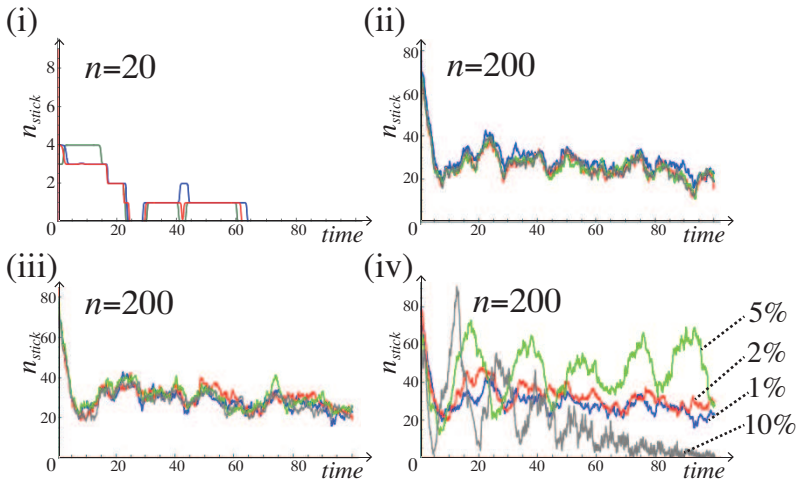


Figure 4: Plots of the sticking codimension n_{stick} for systems of n oscillators, simulated: (i-ii) for four random perturbations of the stiffness parameter $r_i\epsilon$ with $r_i \in [0, 1]$; (iii) for four different random sets of perturbations of the mechanical constants up to 1% of κ and ρ, (iv) for random sets of perturbations of the mechanical constants up to 1%, 2%, 5%, 10%, of κ and ρ. [Colour online]

the physical system rather than the simulation itself. We return to modeling each switch as $\mu(u) = \tanh(u/\epsilon)$, but vary the damping and spring stiffness constants (the components of M^ρ and M^κ), by adding random values on the order of 1% in (iii), for three different sets of random perturbations, and of orders 1%, 2%, 5%, 10%, in (iv). For small perturbations in (iii) the results are similar to before, namely that short-time behaviour is sensitive and unpredictable, but long-term behaviour is robust and large-scale structures are preserved. In fig. 4(iv) we demonstrate that sufficiently large changes in the constants do yield a different system, with perturbations on the order of a few percent or more giving a very distinct system with large (period ~ 20) oscillations at 5%, and total collapse such that all oscillators are slipping at 10%.

To conclude let us explore this long-term dynamics a little further. Again we fix all $r_i = 1$ with $\epsilon = 0.03$ for the simulation. Now we shall perform simulations on a system of 200 oscillators, with different random matrices of damping and spring constants M^ρ and M^κ (these are randomly chosen, and not small perturbations of each other as in fig. 4(iii)). We simulate these for a significantly longer period of time, and observe in most cases (as in the three shown) that the complex stick-slip cascades persist over time in a self-sustaining manner, though occasional instances of constants can be found that collapse to $n_{stick} = 0$. The plots of sticking codimension for three sample cases are shown in fig. 5(i).

With so many oscillators and such long timescales, further insight is provided by considering the statistics of these self-sustaining stick slip events. We plot in fig. 5(ii) the size of cascades

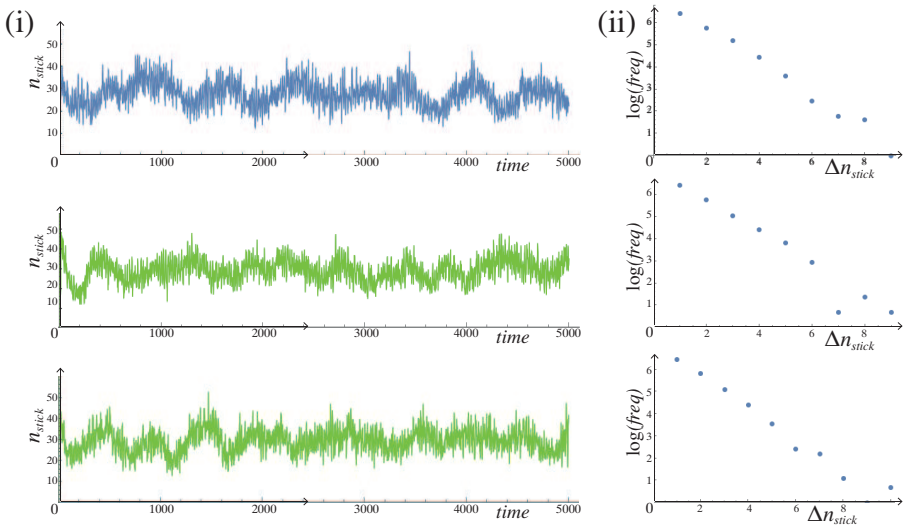


Figure 5: Plots of the sticking codimension n_{stick} for systems of 200 oscillators for three different sets of spring and damping coefficients in (i), and the frequency of stick-slip cascades of size Δn_{stick} in (ii) shows a logarithmic pattern for each system in (i).

Δn_{stick} (defined as the number of successive time increments in which the sticking codimension decreases), against the frequency of events of each size, showing that the frequency f of cascades of size Δn_{stick} fits a relation $f \propto e^{-\gamma \Delta n_{stick}}$ with $\gamma \approx 0.74$.

5 Hidden dynamics

What precisely goes on inside the sticking mode requires analysis beyond the standard Filippov/Utkin theory of sliding modes [5, 15], and must be determined by revealing the *hidden dynamics* [9], obtained by singular perturbation technique of performing a 'blow up' of the discontinuities. This also justifies the use of the sigmoid function in the simulations below, the stiffness parameters $r_i\epsilon$ playing the role of time scalings that give fast contraction (the fast element of the hidden dynamics) onto any sticking modes, see e.g. [11, 6].

The blow up analysis is performed as follows, and we express it in a general form. We relabel the different component vector fields in (1) by writing $\mathbf{f}^{\lambda_1 ... \lambda_m}(\mathbf{x}) = \mathbf{f}(\mathbf{x}; (\lambda_1, ..., \lambda_m))$, so that the piecewise-smooth system becomes

$$\dot{\mathbf{x}} = \left\{ \mathbf{f}^{\lambda_1 ... \lambda_m}(\mathbf{x}) \text{ where } \lambda_i = \text{sign}\left(h_i(\mathbf{x})\right) \right\} . \tag{11}$$

and then combine these in a *convex canopy* of values [8]

$$\mathbf{f} = \sum_{i_1, i_2, ... i_m = \pm} \lambda_1^{(i_1)} \lambda_2^{(i_2)} ... \lambda_m^{(i_m)} \mathbf{f}^{i_1 i_2 ... i_m} , \qquad \lambda_j^{(\pm)} \equiv (1 \pm \lambda_j)/2 . \tag{12}$$

If all oscillators are slipping then all h_j are nonzero, and all λ_j's take values ± 1. If some oscillators $j = 1, ..., r$ are sticking, we take coordinates $x_j = h_j$ for $j = 1, ..., r$, write $\mathbf{f}$ as $(f_1, ..., f_n)$, and form the blow up system by writing

$$\left\{ \begin{array}{rcl} (\lambda_1', ..., \lambda_r') & = & (f_1(\mathbf{x}; \boldsymbol{\lambda}) \quad , ..., f_r(\mathbf{x}; \boldsymbol{\lambda})) \ , \\ (\dot{x}_{r+1}, ..., \dot{x}_n) & = & (f_{r+1}(\mathbf{x}; \boldsymbol{\lambda}), ..., f_n(\mathbf{x}; \boldsymbol{\lambda})) \ . \end{array} \right. \tag{13}$$

The prime on the lefthand side denotes a fast dummy timescale, instantaneous on the timescale of the original system. This facilitates either the transition from one slipping direction to another, or, if equilibria of the fast subsystem exist, the λ_j's collapse in fast time to values λ_j^s given by

$$\begin{cases} (0,...,0) &= (f_1(\mathbf{x};\boldsymbol{\lambda}^s) \quad ,...,f_r(\mathbf{x};\boldsymbol{\lambda}^s)) \ , \\ (\dot{x}_{r+1},...,\dot{x}_n) &= (f_{r+1}(\mathbf{x};\boldsymbol{\lambda}^s),...,f_n(\mathbf{x};\boldsymbol{\lambda}^s)) \ , \end{cases} \tag{14}$$

where $\boldsymbol{\lambda}^s = (\lambda_1^s,...,\lambda_r^s,\lambda_{r+1},...,\lambda_n)$, and these correspond precisely to the usual notion of sticking modes deriving from [5].

In fig. 6 we illustrate the blow up system (13) applied to the two oscillator system in section 3. Panel (a) shows the typical situation inside the sticking parallelogram, when (z_1,z_2) take values such that a unique sticking mode exists, observed in the blow up as an equilibrium in the blow up dynamics on (μ_1,μ_2). As (z_1,z_2) vary outside the parallelogram shown in fig. 2, this equilibrium leaves the box $(\mu_1,\mu_2)\in[-1,+1]\times[-1,+1]$ depicted.

As an example of more novel hidden dynamics, in (6) let us replace the functions μ_1 and μ_2 by $\mu_1-\mu_2(1-\mu_1^2)$ and $\mu_2-\mu_1(1-\mu_2^2)$ respectively. During slip, when $\mu_{1,2}=\pm1$, the additional nonlinear μ_i terms vanish, changing nothing in the original Coulomb friction problem. But in the sticking mode when $\mu_{1,2}\in[-1,+1]$ these new terms are non-vanishing, and signify a more complicated static friction interaction. These particular terms are chosen arbitrarily to demonstrate interesting dynamics, in practice their precise form would depend on refinements to the contact laws that we lack space to investigate here. The scenario shown in (b) illustrates an example where three solutions of (14) exist, giving three sticking modes, though only two are stable. Which of these the system attains depends on the entry trajectory, and can only be determined by full consideration of the system (13), not from the existence of sticking modes alone. Exit points will occur where either of the two stable equilibria leave the depicted region.

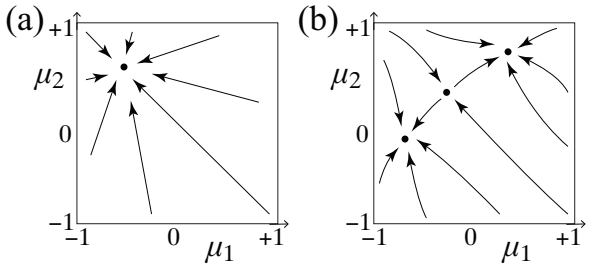


Figure 6: Two examples of hidden dynamics for the two oscillator system, showing: (a) attraction to a unique sticking solution, and (b) attraction to either of two possible sticking solutions (solutions of (14)).

6 Closing remarks

We have demonstrated a few key elements of recent piecewise-smooth dynamical systems theory that provide new insights into basic mechanisms lying behind complex dynamics in dry friction oscillators. This includes some surprises, particularly pertaining to self-sustaining stick-slip cascades, showing a regular logarithmic relation in the frequency of cascades of given size, and showing short-term unpredictability but long-term robustness to perturbation. Ongoing work will investigate further how the local geometry of exit points, shown here to underly

global dynamical patterns, lead to the statistics and criticality thresholds observed, and begin applying these ideas to more specific large dimensional oscillator systems.

REFERENCES

[1] J. Awrejcewicz, L. Dzyubak, and C. Grebogi. Estimation of chaotic and regular (stick-slip and slip-slip) oscillations exhibited by coupled oscillators with dry friction. *Nonlinear Dynamics*, 42:383–394, 2005.

[2] R. Burridge and L. Knopoff. Model and theoretical seismicity. *Bull. Seism. Soc. Am.*, 57:341–371, 1967.

[3] A. Colombo and M. R. Jeffrey. The two-fold singularity: leading order dynamics in n-dimensions. *Physica D*, 265:1–10, 2013.

[4] B. Feeny and F.C. Moon. Chaos in a forced dry-friction oscillator: Experiments and numerical modelling. *J. Sound Vib.*, 170(3):303–323, 1994.

[5] A. F. Filippov. *Differential Equations with Discontinuous Righthand Sides*. Kluwer Academic Publ. Dortrecht, 1988.

[6] N. Guglielmi and E. Hairer. Classification of hidden dynamics in discontinuous dynamical systems. *SIADS, in press*, 2015.

[7] N. Hinrichs, M. Oestreich, and K. Popp. On the modelling of friction oscillators. *J. Sound Vib.*, 216(3):435–459, 1998.

[8] M. R. Jeffrey. Dynamics at a switching intersection: hierarchy, isonomy, and multiple-sliding. *SIADS*, 13(3):1082–1105, 2014.

[9] M. R. Jeffrey. Hidden dynamics in models of discontinuity and switching. *Physica D*, 273-274:34–45, 2014.

[10] M. R. Jeffrey. Determinacy-breaking exit from sliding along switching intersections in piecewise-smooth flows. *submitted*, 2015.

[11] M. R. Jeffrey. The mathematical description of friction between solid bodies. *Nonlinear Dynamics, in press*, 2015.

[12] P. Kowalczyk and P.T. Piiroinen. Two-parameter sliding bifurcations of periodic solutions in a dry-friction oscillator. *Physica D: Nonlinear Phenomena*, 237(8):1053 – 1073, 2008.

[13] S. W. Shaw. On the dynamics response of a system with dry friction. *J. Sound Vib.*, 108(2):305–325, 1986.

[14] M. A. Teixeira. Generic bifurcation of sliding vector fields. *J. Math. Anal. Appl.*, 176:436–457, 1993.

[15] V. I. Utkin. Variable structure systems with sliding modes. *IEEE Trans. Automat. Contr.*, 22, 1977.

11th International Conference on Engineering Vibration
Ljubljana, Slovenia, 7–10 September 2015

MODELLING THE NON-SMOOTH DYNAMICS OF WINDSCREEN WIPERS

G. Lancioni*[1], S. Lenci[1], G. Cocchi[1], U. Galvanetto[2]

[1]Dipartimento di Ingegneria Civile, Edile e Architettura, Universitá Politecnica delle Marche,
Via Brecce Bianche 1, 60131 Ancona, Italy
g.lancioni@univpm.it, lenci@univpm.it, g.cocchi@univpm.it

[2]Dipartimento di Ingegneria Industriale, Universitá di Padova,
Via Venezia 1, 35131 Padova, Italy
ugo.galvanetto@unipd.it

Keywords: Wiper blade motion, friction-induced oscillation, non-smooth dynamics, squeal noise, chattering.

Abstract. *This paper anticipates some results of the work [1], addressed to explore the dynamics of a mass-spring-damper system on a moving frictional surface, reproducing the motion of a windshield wiper blade. Since the contact between the system and the surface is governed by Stribeck's friction law, and impacts of the system on the surface are modelled by Poisson's impact law, the resulting dynamics is non-smooth. The model is numerically implemented in an event-driven code, and simulations are performed with the aim of reproducing and investigating the undesired squeal and chattering vibrations typically observed in the wiping motion of windscreen wipers.*

1 INTRODUCTION

A simplified model consisting of a mass-spring-damper system on a moving frictional surface is proposed to reproduce the motion of a wiper blade on a windshield (see Fig. 1). The model is similar to the frictional impact oscillator proposed and studied in [2] and numerically investigated in [3], but, to be more realistic, it is enriched in two parts: the Stribeck's friction law [4] is assumed to properly describe the contact of a wiper rubber blade on a wet glass windscreen, and a varying rotational stiffness is considered to account for the contact of the wiper lip with the shoulder of the wiper head. The impacts of the system on the surface are modelled by the Poisson's impact law [5]. The Stribeck's friction law and the Poisson's impact law govern the transitions between three different regimes of motion, i.e., slip or stick, when the system is in contact with the surface, and free-flight, when it is detached from the surface, and they make the resulting dynamics non-smooth.

The model is numerically implemented in an event-driven code, and simulations are performed which reproduce the main vibrations typically observed in the wiping motion of windscreen wipers, that is the squeal and the chattering noises. The squeal noise is a friction-induced slip or stick-slip oscillation [6, 7, 8], which occurs at frequency of 500-1000 Hz, when the windshield glass is wet. It can be induced in the model by the large negative gradient of the Stribeck curve in the static-to-hydrodynamic transition phase [9]. Since the transition regime happens at low slip velocities (around 0.1 m/s), vibrations are observed before and after the wiper reversal.

Chattering or beep noise is a low frequency oscillation (< 100 Hz) mainly due to geometrical reasons, i.e., the inappropriate bent configuration often assumed by the wiper blade with respect to the normal to the glass surface [10, 11], measured by the so-called attack angle (the angle between the symmetry axis of the blade cross-section and the normal to the glass surface). This vibration happens usually when the wiping motion has the direction pointed by the blade projection on the surface.

In the present paper, first the basic equations of the model are recalled, then the results of some numerical simulations are presented, which highlight the ability of the model in capturing the above mentioned vibrations. Finally, some practical indications are proposed to reduce the undesired vibrations.

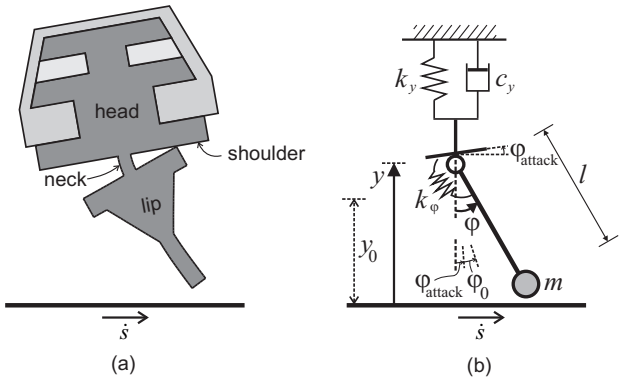


Figure 1: (a) Windscreen wiper blade section; (b) geometrical scheme of the model.

2 THE MODEL

In the following, the model is briefly described and the basic equations of its dynamics are recalled. We refer to [1, 3] for a detailed model description. The wiper blade cross-section of Fig 1(a) is modelled by the system of Fig. 1(b), consisting of a pendulum of length l, constrained by a moving surface (with velocity $\dot{s}$). The vertical spring and dashpot represent the action of the wiper arm which opposes lifting. The bar is supposed to be rigid and the whole flexibility of the blade lip is concentrated in the rotational spring of elastic coefficient k_φ.

To account for the different stiffness registered when the lip is in contact with the shoulder of the wiper head, and when it is not, we assume $k_\varphi = k_m$ when $|\varphi - \varphi_{attack}| \leq \tilde{\varphi}$, and $k_\varphi = k_M$ when $|\varphi - \varphi_{attack}| > \tilde{\varphi}$, with $\tilde{\varphi}$ the angle at which the lip touches the shoulder. The natural unstressed configurations of the linear and rotational springs are y_0 and φ_0, respectively. The angle φ_{attack} is the so-called attack angle, and it represents the inclination of the wiper head. The mass m accounts also for the rotational inertia of the blade. The frictional contact between the mass m and the moving surface is governed by the Stribeck law, which assumes that the friction coefficient μ depends on the relative velocity $\dot{g}_T$ according to the curve of Fig. 2, taken from [9]. Notice that the curve is characterized by three regimes: an initial boundary regime with large values of μ, a transition zone where the curve decreases attaining large negative slopes, and a final hydrodynamic regime with small values of μ.

The kinematics of the system is described by the tilt angle φ of the bar, and the vertical position y of the hinge, which are collected in the vector $\mathbf{u} = [\varphi, y]^T$.

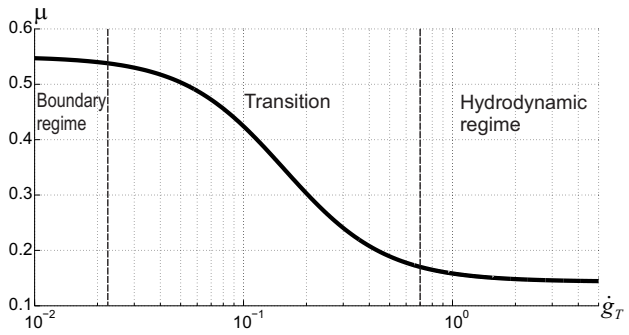


Figure 2: Stribeck curve.

2.1 Time-varying Dynamics

The system dynamics is divided in three different regimes, which are free-flight, slip and stick, each characterized by a different number of degree of freedom (dofs). Each regime is characterized by different motion equations, conditions for the regime persistence, and appropriate laws of transition to the other regimes.

In free-flight regime, the mass m is detached from the moving surface, and the motion is governed by a two-dof equation of the form

$$\mathbf{M}(\mathbf{u})\ddot{\mathbf{u}} + \mathbf{h}(\mathbf{u}, \dot{\mathbf{u}}) = \mathbf{0}. \tag{1}$$

Free-flight occurs as long as $g_N = y - l\cos\varphi > 0$. When $g_N = 0$ and $\dot{g}_N < 0$, m experiences an impact, which is described by the Poisson's impact law [5]. A sequence of bounces (of

decreasing amplitude) leads to lied regimes: the motion continues in slip mode if $|\Lambda_T| = \mu\Lambda_N$, with Λ_T and Λ_N the tangential and normal forces, respectively, or in stick mode if $\dot{g}_T = 0$.

The slip motion is described by a one-dof problem

$$a_0(\varphi)\ddot{\varphi} + a_1(\varphi)\dot{\varphi}^2 + a_2(\varphi,\dot{\varphi})\dot{\varphi} + a_3(\varphi,\dot{\varphi}) = 0, \tag{2}$$

where the unique independent variable is φ, since y depends on φ through the relation $y = l\cos\varphi$, and a_i, $i = 0,\ 1,\ 2,\ 3$ are coefficients defined in [1]. The normal reactive force is

$$\lambda_N = m(\ddot{y} + l\ddot{\varphi}\sin\varphi + l\dot{\varphi}^2\cos\varphi) + c_v\dot{y} + k_v(y - y_0), \tag{3}$$

and, according to the Coulomb's law, the tangential reactive force is $\lambda_T = -\mathrm{sign}(\dot{g}_T)\mu\lambda_N$. Slip occurs if $\dot{g}_T \neq 0$ and $\lambda_N > 0$. The motion moves from slip to stick when $\dot{g}_T = 0$, and from slip to free-flight when $\lambda_N = 0$. In stick motion, the angle φ is determined (zero dof)

$$\varphi(t) = \arcsin[\,\sin\hat{\varphi} + \frac{1}{l}\int_{\hat{t}}^{t}\dot{s}(\tau)d\tau\,], \tag{4}$$

with $\hat{\varphi}$ the angle and $\hat{t}$ the time at the beginning of the stick regime. Sticking occurs as far as $|\lambda_T| < \mu\lambda_N$ and $\lambda_N > 0$. When $|\lambda_T| = \mu\lambda_N$ we have a transition to slip, and when $\lambda_N = 0$ we have a transition to free-flight.

2.2 Stability in slip mode

Stable equilibrium in slip model is desired in the motion of a windscreen wiper. Indeed, noises are produced when equilibrium is lost and unwanted oscillating motions appear. Accordingly, it is important to analyze the stability of the equilibrium configuration in slip regime.

In the phase space $(\varphi,\dot{\varphi})$, let $(\bar{\varphi},0)$ be an equilibrium point (from (2), $\bar{\varphi}$ is solution of $a_3(\varphi,0) = 0$), and let $\mathbf{J}(\bar{\varphi},0)$ be the Jacobian matrix of equation (2) evaluated at an equilibrium point. Equilibrium is stable if the real part of the eigenvalues of $\mathbf{J}$ is negative. This condition is satisfied if a certain function $\chi(\bar{\varphi}, d\mu/d\dot{g}_T)$, which depends on the configuration $\bar{\varphi}$ and on the so-called speed characteristic $d\mu/d\dot{g}_T$, is positive. The analytical expression of χ is given in [1]. The stability condition $\chi > 0$ is not satisfied if sufficiently large negative speed characteristics are reached. In the case of the Stribeck curve of Fig. 2, large negative speed characteristics are reached in the transition phase, and the resulting loss of stability brings to self-excited oscillations. These vibrations characterize the so-called squeal noise [9, 12], which typically manifests just before and after the wiper inversion of motion, when $\dot{g}_T$ attains small values.

If we assign all the problem parameters (values given in Sect. 3), with the exception of $\dot{s}$, the stability function χ can be expressed in term of $\dot{s}$ $(= -\dot{g}_T)$, and its graph is plotted in Fig. 3. The function χ attains negative values for velocities which belong to the instability range $\Delta\dot{s}$, and correspond to the friction speed characteristics of the transition region of Fig. 2.

3 NUMERICAL RESULTS

A careful study aimed at identifying the problem parameters has been done in [1], which cannot be proposed in the present paper for conciseness reasons. We just report the values used in the simulations, which are referred to the unit length of the wiper arm: $l = 6.9$ mm, $m = 2.3 \cdot 10^{-3}$ Kg, $k_M = 1.19$ Nm, and $k_m = 0.19$ Nm, $k_y = 5000$ N/m, $y_0 = 0.4l$, $\varphi_0 = 0$, $\varphi_{attack} = 0$, $c_y = 40$ Ns/m, $\dot{s} = 0.5\sin(\pi t)$ m/s.

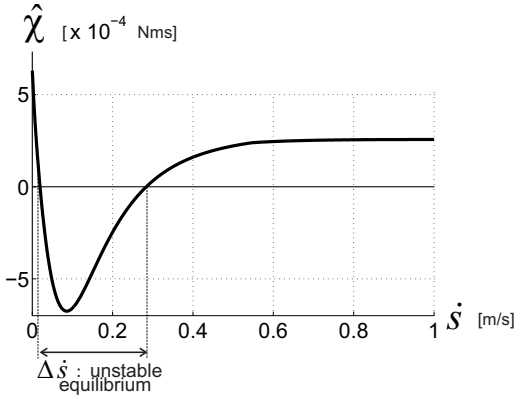


Figure 3: Stability function $\hat{\chi}$ for the Stribeck law (Fig. 2).

3.1 Squeal and chattering noises

Within each period of the belt motion, the dynamics observed is characterized by stick and slip phases. The horizontal motion $x_1 = l\sin\varphi$ of m is plotted in Fig. 4 for a period of 2 seconds, and stick and slip motion regimes are distinguished using different colors. The motion is mainly in slip regime, and only at reversal of the belt velocity, m experiences stick. Stick-slip fast-oscillations are observed before and after the belt velocity reversals (see the enlargements in Fig. 4), which are the manifestation of the so-called squeal noise. These vibrations are only induced by friction. They are due to the negative friction speed characteristics of the Stribeck curve in the transition phase, which produces instability of the slip equilibrium solution. Indeed the squeal noises totally disappear if a constant friction coefficient is assumed (Coulomb's law). The frequency of the squeal vibrations is about 500 Hz.

The extent and intensity of the oscillations is considerably influenced by the problem parameters, in particular by the springs coefficients and the springs unstressed configurations. If we assume $y_0/l = 0.65$, corresponding to a small pushing action of the wiper arm, then oscillations occur for the whole period, as shown in Fig. 5 (a).

If we suppose that the wiper blade suffers permanent plastic deformations which compromise its natural vertical configuration, and we set $\varphi_0 = 0.1$ Rad, oscillations take place for half a period (Fig. 5 (b)). Since $\varphi_0 > 0$, vibrations occur when $\dot{s} < 0$. Indeed, in this situation, the moving belt forces the pendulum to assume negative values of φ, while, on the contrary, the rotational spring forces toward the natural configuration of positive values of φ, and this two opposite actions produce fast-oscillations.

If larger values of φ_0 are considered, then chattering is observed, where the oscillating motion combines stick slip and free-flight regimes. In Fig. 6, the vertical motions of m, i.e., $x_2(t) = y - l\cos\varphi$, is plotted for $\varphi_0 = 0.3$ rad. The mass m undergoes bounces occurring periodically with a frequency of about 100 Hz. Within each fast period, after few bounces (see Fig. 6(b,c)), the lied motion is recovered, and m first slides and then it again exhibits stick motion, dragged by the surface.

An in depth parametric analysis has been carried out in [1], which has furnished useful indications on how to reduce the undesired vibrations in windscreen wipers.

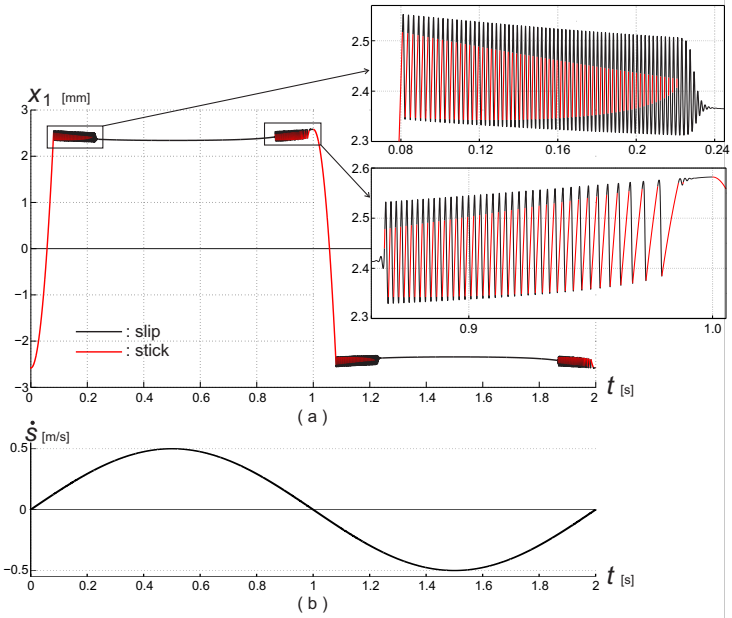


Figure 4: (a) Horizontal oscillation $x_1(t)$ of mass m in a period. (b) Belt velocity $\dot{s}$.

4 CONCLUSIONS

A mass-spring-damper system in contact with a moving frictional surface has been proposed to reproduce the motion of a windscreen wiper blade. Despite the model is quite simple, being characterized by few parameters, it exhibits an intricate dynamics, which is time-varying, since it accounts for three different regimes of motion with different degrees of freedom, it is non-smooth, since the transition from one regime to the other is governed by non-smooth relations (Stribeck's friction law and Poisson's impact law governing the contact between the system and the moving surface), and it is geometrically non-linear, since the system undergoes large displacements.

The resulting dynamical problem has been solved numerically by means of a code based on an event-driven scheme, and numerical tests have been conducted to give an insight into the causes of the undesired squeal and chattering noises. The squeal noises observed in the numerical tests manifest as stick-slip oscillations occurring before and after the reversal of the surface motion, and, in agreement with the analytical stability results given in Sect. 2.2, they are friction-induced oscillations, caused by the negative speed characteristic of the static-to-hydrodynamic transition phase.

Low frequency chattering oscillations are observed when the blade inclination with respect to the normal to the glass surface is sufficiently large. Such a sloped configuration, usually due to geometrical misalignment or to permanent plastic deformations of the rubber, produces quite complex oscillations combining stick, slip and free-flight regimes of motion.

In conclusion, the model can be a useful tool to explore the different vibrations encountered in the motion of windscreen wipers, and the resulting numerical simulations can be used to properly set the design parameters to reduce undesired noises.

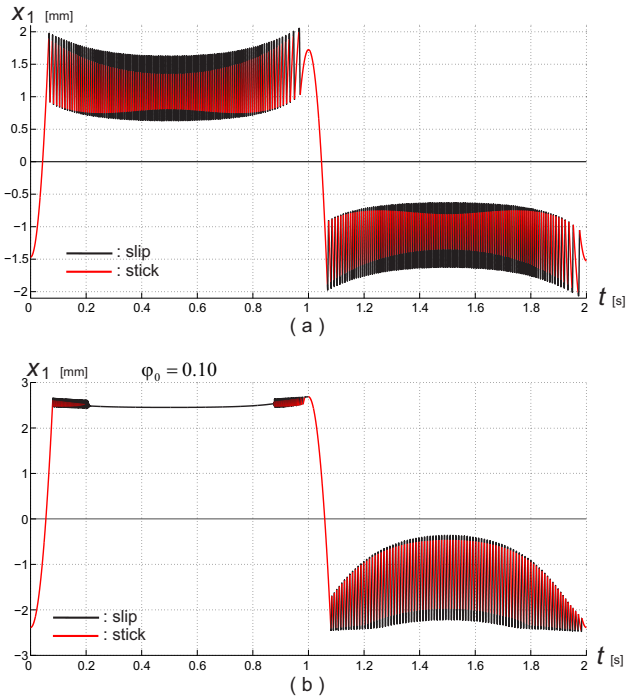


Figure 5: Horizontal oscillation $x_1(t)$ for (a) $y_0/l = 0.65$, (b) $\varphi_0 = 0.1$ Rad.

REFERENCES

[1] G. Lancioni, S. Lenci, U. Galvanetto, Dynamics of windscreen wiper blades: squeal noise, reversal noise and chattering, preprint, 2015.

[2] R.I. Leine, B. Brogliato, H. Nijmeijer, Periodic motion and bifurcations induced by the Painlevé paradox, *Eur. J. Mech. A/Solids*, **21**, 869-896, 2002.

[3] G. Lancioni, S. Lenci, U. Galvanetto, Non-linear dynamics of a mechanical system with a frictional unilateral constraint, *Int. J. Non-Linear Mech.*, **44**, 658674, 2009.

[4] A. Koenen, A. Sanon, , ribological and vibroacoustic behavior of a contact between rubber and glass (application to wiper blade), *Tribology International*, **40**, 1484-1491, 2007.

[5] F. Pfeiffer, C. Glocker, *Multibody dynamics with unilateral contacts*. John Wiley & Sons, Inc., 1996

[6] G.Sheng, *Friction-induced vibrations and sound; Principles and applications*, CRC,Taylor and Francis, 2008.

[7] R.A. Ibrahim, Friction-induced vibration, chatter, squeal, and chaospart II: Mechanics of contact and friction, *Appl. Mech. Rev.* **47**(7), 209-226, 1994.

[8] R.A. Ibrahim, Friction-induced vibration, chatter, squeal, and chaospart II: Dynamics and modeling, *Appl. Mech. Rev.* **47**(7), 227-253, 1994.

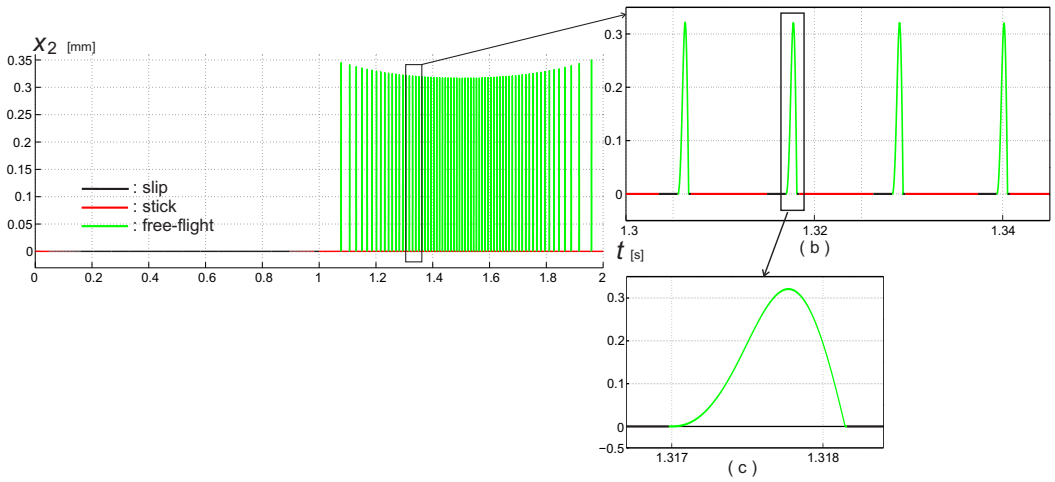


Figure 6: Vertical oscillation $x_2(t)$ of m for $\varphi_0 = 0.3$ Rad.

[9] J. Le Rouzic, A. Le Bot, J. Perret-Liaudet, M. Guibert, A. Rusanov, L. Douminge, F. Bretagnol, D. Mazuyer, Friction-Induced Vibration by Stribecks Law: Application to Wiper Blade Squeal Noise, *Tribol. Lett.*, **49**, 563-572, 2013.

[10] I.M. Awang, A.R. AbuBakar, B.A. Ghani, R.A. Rahman, and M.Z.M. Zain, Complex eigenvalue Analysis of Windscreen Wiper Chatter Noise and its Suppression by Structural Modifications, *Int. J. Vehicle Structures & Systems*, **1**(1-3), 24-29, 2009.

[11] C.R. Chevennement, T. Dreher, P. Alliot, E. Aubry, J.P. Lainé, L. Jézéquel, Flexible Wiper System Dynamic Instabilities: Modelling and Experimental Validation, *Experimental Mechanics*, **47**, 201210, 2007.

[12] S. Goto, H. Takahashi, T. Oya, Clarification of the mechanism of wiper blade rubber squeal noise generation, *JSAE Review*, **22**, 57-62, 2001.

11th International Conference on Engineering Vibration
Ljubljana, Slovenia, 7–10 September 2015

STICK-SLIP CHAOTIC MOTIONS OF AN ARCHETYPAL SELF-EXCITED SD OSCILLATOR WITH DRY FRICTION

Zhixin Li*[1], Qingjie Cao[1]

[1]School of Astronautics, Harbin Institute of Technology, Harbin 150001 P. R. China

Lzxin1234@163.com, Qingjiecao@hotmail.com

Keywords: Self-exited SD oscillator, Melnikov method, Homoclinic orbit, Stick-slip chaos.

Abstract. *In this paper, we propose an archetypal self-excited smooth and discontinuous (SD) oscillator driven by moving belt friction, which is constructed with the SD oscillator and the classical moving belt. The moving belt friction is modeled as the Coulomb type for the proposed self-exited SD oscillator. The analytical expressions of homoclinic orbits of the unperturbed SD oscillator are derived by using a special coordinate transformation without any pronominal truncation to retain the natural characteristics, which allows us to utilize the Melnikov method to get the chaotic thresholds of the self-excited SD oscillator in the presence of the damping and external excitation. Numerical simulations are carried out to demonstrate the multiple stick-slip dynamics of the proposed system, which show the efficiency of the prediction for stick-slip chaos of the perturbed self-excited system. The results presented here in this paper show the complicated dynamics of the multiple stick-slip motions, coexistence of asymmetric stick-slip solutions for the self-excited oscillator.*

1 INTRODUCTION

Dry friction appears at the physical interface between two surfaces in contact which plays an important role in many mechanical systems such as transmissions, brakes and wheels, etc.[1], It is a source of self-excited oscillations, as known as stick-slip oscillations. This oscillations exist in a wide of engineering systems, e.g. like door hinges, drill strings, chattering machine tools and other systems. The study of stick-slip motion is currently an active research area and various theoretical and experimental investigations have been carried out on the stick-slip motion for many years [2–4]. Recently, Li,*et al.*[5] investigated the stick-slip periodic solution of a single degree of freedom oscillator with dry friction under the assumption of kinetic friction being the Coulomb friction. Fang and Xu [6] studied the stick-slip motions of a vibration-driven system with Coulomb friction on a horizontal plane in view of sliding bifurcation.

Up to now there are many papers devoted to investigations of the chaotic motion of mechanical systems with friction. Shi and Zou [7] proposed a extended Melnikov approach for non-smooth dynamical systems to study the appearance of transversal homoclinic orbits and chaos. Recently, Tsobgni-Fozap, *et al.* [8] discussed the synchronization of stick-slip chaos motion in two mutually coupled dynamical systems based on the Lyapunov stability theory. However, only few results are on analytical prediction of stick-slip chaos. Awrejcewicz [9, 10] investigated the chaos prediction in non-smooth systems by using the derived Melnikov approach to derive one homoclinic chaos threshold, but, the prediction might be incomplete, which had not taken into another homoclinic orbit allowed to get a additional analytical criterion for chaos occurrence.

In this paper, an oscillating mass block-belt system investigated is based upon the SD(Smooth and Discontinuous) oscillator proposed by Cao *et al.* [11–13], which allows one to study the transition from smooth to discontinuous dynamics. The nonlinearity associated with the oscillator is with reference to its geometric configuration. The nonlinearity can be classified as smooth or discontinuous depending on the value of a non-dimensional parameter termed as smoothness parameter α.

The motivation of this paper is to propose a novel self-excited SD oscillator with dry friction, which can be regarded as the SD oscillator moving the belt with dry friction vibrating horizontally. Another motivation of this paper is to make a stick-slip chaos prediction of the self-excited SD oscillator by employing the Melnikov method. By introducing a special coordinate transformation, the analytical expression of the homoclinic orbits for the unperturbed SD oscillator can be directly derived and utilized in Melnikov' procedure to investigate the chaotic threshold. The analysis is based on the stick-slip chaos prediction and numerical validation for this system which can exhibit rich stick-slip dynamical behavior.

2 The governing equation

The system analysed in this paper is composed by a block of mass M, supported by a moving belt, connected to a fixed support by a inclined linear spring of stiffness coefficient K, which is capable of resisting both tension and compression, as shown in Fig.1. The contact surface between the mass and belt is rough so that the belt exerts a friction force on the mass. The mass vibrates under the influence of dry friction F_S modeled as Coulomb friction existing in the contact zone created by the mass 's surface and the outer belt's surfaces that moves with a constant velocity V_0. We assume a non-deformable moving belt being under action of normal force from total force of the gravity $N = Mg$ and spring force in the contact zone, and the mass is secured to move in the horizontal direction without leaving the belt. The position of the mass

over the belt is represented by X.

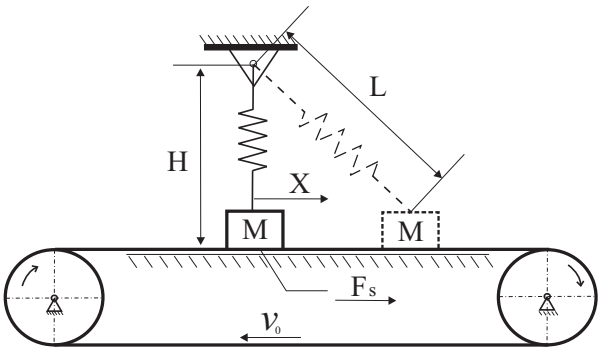


Figure 1: The mechanical model of the self-excited SD oscillator moving on the belt.

The one-degree of freedom sick-slip oscillations are governed by the following second-order differential equation

$$M\ddot{X} + KX\Big(1 - \frac{L}{\sqrt{X^2 + H^2}}\Big) + F_S = 0, \tag{1}$$

where L is the original length of the spring, H is the distance between fixed point and belt, and the friction force F_S is given as

$$F_S = \mu F_N sgn(\dot{X} - V_0), \tag{2}$$

where μ is the friction coefficient of contacting surfaces and assumed to be constant in this friction model, $F_N = Mg - KH\Big(1 - \frac{L}{\sqrt{X^2 + H^2}}\Big)$ is the total force of the gravity of the mass and vertical component of the spring force to be assumed that $F_N > 0$, $\dot{X} - V_0$ is the relative velocity of mass and belt.

3 The perturbed dynamics

Now suppose system (1) has been perturbed by a viscous damping of coefficient C and an external harmonic excitation of amplitude F and frequency Ω. The equation of motion can be written as

$$M\ddot{X}+C\dot{X}+KX\Big(1-\frac{L}{\sqrt{X^2+H^2}}\Big)+\mu\Big[Mg-KH\Big(1-\frac{L}{\sqrt{X^2+H^2}}\Big)\Big]sgn(\dot{X}-V_0) = F\cos\Omega t. \tag{3}$$

Then, the non-dimensional equation of motion for this system is obtained by letting $x = X/L$, $c = C/(M\omega_0)$, $\omega_0^2 = K/M$, $\alpha = H/L$, $g_1 = g/(L\omega_0^2)$, $v_0 = V_0/(L\omega_0)$, $f = F/(KL)$, $\omega = \Omega/\omega_0$, $\tau = \omega_0 t$ as following

$$\ddot{x} + c\dot{x} + x\Big(1 - \frac{1}{\sqrt{x^2 + \alpha^2}}\Big) + \mu\Big[g_1 - \alpha\Big(1 - \frac{1}{\sqrt{x^2 + \alpha^2}}\Big)\Big]sgn(\dot{x} - v_0) = f\cos\omega\tau, \tag{4}$$

where the $(\cdot)$ denotes the differentiation with respect to the non-dimensional time τ.

The Eq.(4) can be written as two first order differential equations

$$\begin{cases} \dot{x} = y \\ \dot{y} = -cy - x\Big(1 - \dfrac{1}{\sqrt{x^2+\alpha^2}}\Big) - \mu\Big[g_1 - \alpha\Big(1 - \dfrac{1}{\sqrt{x^2+\alpha^2}}\Big)\Big] sgn(y - v_0) + f\cos\omega_f\tau, \end{cases} \tag{5}$$

The scale transformations may be introduced as follows:

$$c \to \varepsilon c, \mu \to \varepsilon\mu, f \to \varepsilon f.$$

The Eq.(5) can be rewritten in the following form with the perturbation

$$\begin{cases} \dot{x} = \dfrac{\partial \mathscr{H}}{\partial y} + \varepsilon q_1, \\ \dot{y} = -\dfrac{\partial \mathscr{H}}{\partial x} + \varepsilon q_2, \end{cases} \tag{6}$$

where the Hamiltonian function is of the form

$$\mathscr{H}(x,y) = \frac{1}{2}y^2 + \frac{1}{2}x^2 - \sqrt{x^2+\alpha^2} + \alpha, \tag{7}$$

and

$$q_1 = 0, q_2 = -cy - \mu\Big[g_1 - \alpha\Big(1 - \frac{1}{\sqrt{x^2+\alpha^2}}\Big)\Big] sgn(y - v_0) + f\cos\omega_f\tau.$$

For $\varepsilon = 0$ there are three critical points for $0 < \alpha < 1$: two centres at $(\pm\sqrt{1-\alpha^2}, 0)$ and a hyperbolic saddle at the origin connected to itself by a pair of symmetric homoclinic orbits $\Gamma_{1,2} = (x_{1,2}, y_{1,2})$ satisfying the following equation

$$\frac{1}{2}y_{1,2}^2 + \frac{1}{2}x_{1,2}^2 - \sqrt{x_{1,2}^2+\alpha^2} + \alpha = 0, \tag{8}$$

and the homoclinic orbits of Eq.(8) are shown in Fig.(2) with red lines.

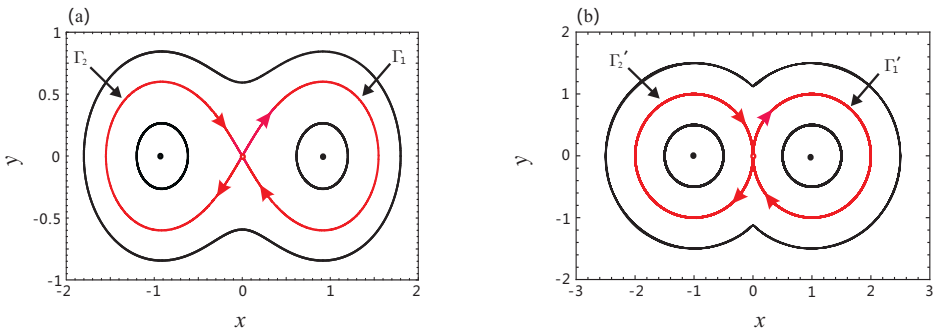


Figure 2: Homoclinic orbits $\Gamma_{1,2}$ in system (6) for $\varepsilon = 0$. (a) $0 < \alpha < 1$, (b) α=0.

3.1 The analytical solutions

It is noted that the Hamiltonian function $\mathscr{H}(x, y)$ includes an irrational term, which is not readily analysed by the conventional methods directly. In this section, we introduced a series of coordinate transformation [15, 16],

$$\begin{cases} x = \sqrt{2B}\cos\theta, \\ y = \sqrt{2B}\sin\theta, (B \geqslant 0), \end{cases} \tag{9}$$

After some calculations and transformations, the homoclinic orbits $\Gamma_{1,2}$ of Eq.(8) satisfy

$$\begin{aligned} x_{1,2} &= 2\sqrt{\cos^2\theta - \alpha}\cos\theta, \\ y_{1,2} &= 2\sqrt{\cos^2\theta - \alpha}\sin\theta, \end{aligned} \tag{10}$$

where θ satisfies

$$-2\theta - \frac{\sqrt{\alpha}}{2\sqrt{1-\alpha}}\ln\frac{\sqrt{1-\alpha}\cos\theta + \sqrt{\alpha}\sin\theta}{\sqrt{1-\alpha}\cos\theta - \sqrt{\alpha}\sin\theta} = \tau, \tag{11}$$

and $-\dfrac{\pi}{2} \leqslant \theta \leqslant \dfrac{\pi}{2}$ for Γ_1 (Γ_1'), $\dfrac{\pi}{2} \leqslant \theta \leqslant \dfrac{3\pi}{2}$ for $\Gamma_2(\Gamma_2')$.

3.2 The perturbed chaotic threshold

In this section, we will focus our attention on the prediction of stick-slip chaotic motion of this nonsmooth system by using the Melnikov method [17, 18].

The Melnikov function of our system is given by

$$M_{1,2}(\tau_0) = \int_{-\infty}^{\infty} y_{1,2}[q_0(\tau+\tau_0)]G[q_0(\tau+\tau_0), \tau]\mathrm{d}\tau, \tag{12}$$

where $q_0(x(\tau), y(\tau))$ is defined by Eq. (10), and

$$G(x(\tau), y(\tau), \tau) = f\cos\omega_f\tau - cy - \mu sgn(y - v_0)\Big[g_1 - \alpha\Big(1 - \frac{1}{\sqrt{x^2+\alpha^2}}\Big)\Big].$$

After some transformations we obtain the Melnikov function for the homoclinic orbit Γ_1 as

$$\begin{aligned} M_1(\tau_0) = &- f\sin\omega_f\tau_0\varphi_1 + Z_1 \\ &+ \begin{cases} 4\mu(g_1-\alpha)(Q_1Q_2 - P_1P_2) + 4\mu\alpha\ln\dfrac{Q_1+Q_2}{P_1+P_2} & \text{for} \quad v_0 \leqslant 1-\alpha, \\ 0 & \text{for} \quad v_0 > 1-\alpha. \end{cases} \end{aligned} \tag{13}$$

where

$$\begin{aligned} Q_1 &= \sqrt{\frac{1+\alpha}{2} + \frac{1}{2}\sqrt{(1-\alpha)^2 - v_0^2}}, \qquad Q_2 = \sqrt{\frac{1+\alpha}{2} + \frac{1}{2}\sqrt{(1-\alpha)^2 - v_0^2} - \alpha}, \\ P_1 &= \sqrt{\frac{1+\alpha}{2} - \frac{1}{2}\sqrt{(1-\alpha)^2 - v_0^2}}, \qquad P_2 = \sqrt{\frac{1+\alpha}{2} - \frac{1}{2}\sqrt{(1-\alpha)^2 - v_0^2} - \alpha}. \end{aligned} \tag{14}$$

Then, the Melnikov's criterion of chaos for Γ_1 is given by

$$f|\varphi_1| > \begin{cases} \left| Z_1 + 4\mu(g_1-\alpha)(Q_1Q_2 - P_1P_2) + 4\mu\alpha \ln \dfrac{Q_1+Q_2}{P_1+P_2} \right| & \text{for} \quad v_0 \leqslant 1-\alpha, \\ |Z_1| & \text{for} \quad v_0 > 1-\alpha. \end{cases} \tag{15}$$

The Melnikov function defined by Eq.(12) for the homoclinic orbit Γ_2 can also be obtained

$$\begin{aligned} M_2(\tau_0) = &- f\sin\omega_f\tau_0\varphi_2 + Z_1 \\ &- \begin{cases} 4\mu(g_1-\alpha)(Q_1Q_2 - P_1P_2) + 4\mu\alpha \ln \dfrac{Q_1+Q_2}{P_1+P_2} & \text{for} \quad v_0 \leqslant 1-\alpha, \\ 0 & \text{for} \quad v_0 > 1-\alpha. \end{cases} \end{aligned} \tag{16}$$

Then, the Melnikov's criterion of chaos for Γ_2 is given by

$$f|\varphi_2| > \begin{cases} \left| Z_1 - 4\mu(g_1-\alpha)(Q_1Q_2 - P_1P_2) - 4\mu\alpha \ln \dfrac{Q_1+Q_2}{P_1+P_2} \right| & \text{for} \quad v_0 \leqslant 1-\alpha, \\ |Z_1| & \text{for} \quad v_0 > 1-\alpha. \end{cases} \tag{17}$$

Fig.3 shows the thresholds curves C_1 (C_1') and C_2 (C_2') of chaos for the system (5) in the (f, v_0) plane obtained from the relations (15) and (17) respectively for $g_1 = 2$, $\mu = 0.1$, $\omega_f = 1.08$. Above these curves, marked by grey, chaos can appear, because near the curves, the stable and unstable manifolds intersect transversally.

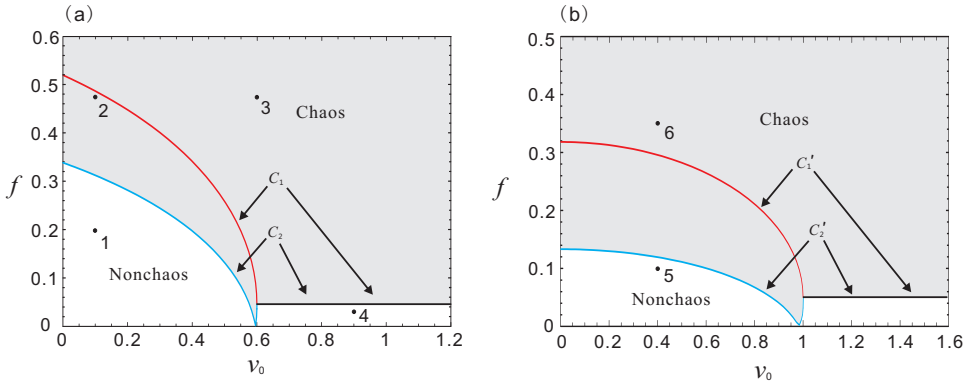


Figure 3: Chaotic boundaries for system (5) in the (f, v_0) plane.(a) α=0.4, (b) α=0.

3.3 Numerical simulation

In order to verify the analytical conditions (17) and (15) of the chaotic motion occurrence, some numerical simulations are given for different values of f and v_0 in system (5). For comparison with the analytical results, we choose several simulated points 1, 2, 3 and 4 in Fig.3(a). For the corresponding points 1, 2, 3 and 4, the phase portraits and Poincaré sections are shown

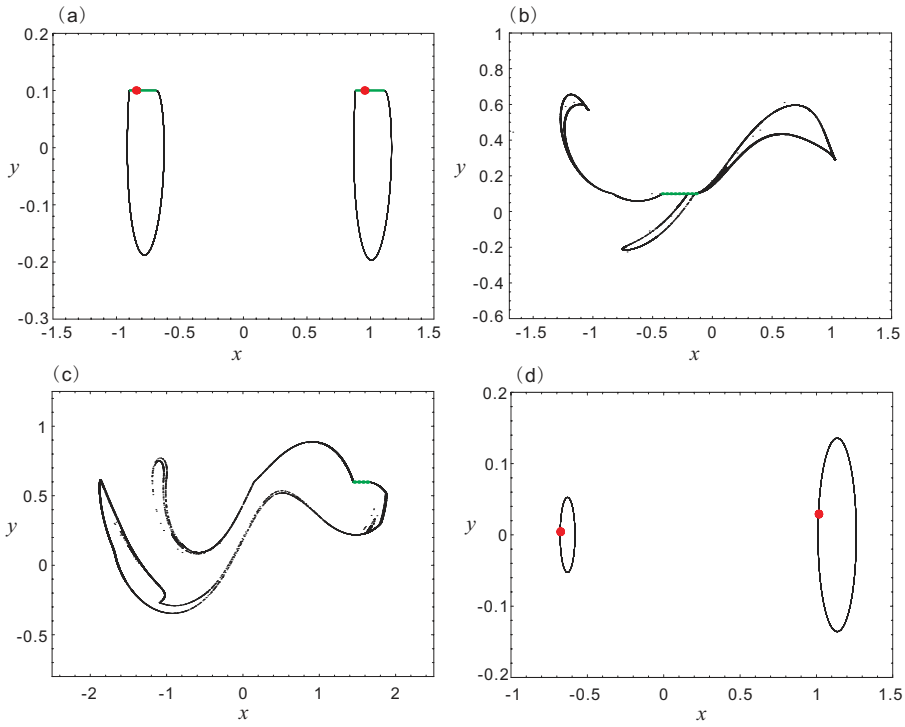


Figure 4: The periodic motion and chaotic attractors of system (5) for $\alpha = 0.4$ in (a)-(d) for the corresponding points 1, 2, 3 and 4 in Fig.3.(a) respectively. (a) Coexisting stick-slip period-1 solutions for $f = 0.2, v_0 = 0.1$, (b) the chaotic attractor for $f = 0.474, v_0 = 0.1$ with the largest Lyapunov exponent 0.0825, (c) the chaotic attractor for $f = 0.474, v_0 = 0.6$ with the largest Lyapunov exponent 0.0452, (d) coexisting period-1 solutions for $f = 0.03, v_0 = 0.9$.

in Figs.4(a)-4(d) differently. It is noted that in all the following phase portraits, the cusps correspond to a sign change of the relative velocity, as well as the short horizontal parts (marked with green lines) in phase portraits correspond to the sticking during the motions.

On one hand, when $v_0 = 0.1$ and $f = 0.2$ (i.e.point 1 in Fig.3(a)), a pair of asymmetric stick-slip period 1 solutions coexist with different initial conditions (x_0, y_0)=(-1,0)(left) and (x_0, y_0)=(1,0)(right), as shown in Fig.4(a). With an increase of amplitude f, the regular motions vanish and the stick-slip chaotic motion follows when $f = 0.474$ (i.e.point 2 in Fig.3(a)), the corresponding chaotic attractor is depicted in Fig.4(b), which confirms the necessity of taking into two homoclinic orbits allowed to get two analytical criterions for chaos occurrence. On the other hand, when $f = 0.474$, and v_0 increases from $v_0 = 0.1$ to v_0=0.6 (i.e.point 3 in Fig.3(a)), the stick-slip chaotic motion occurs yet, as shown in Fig.4(c). Similarly, when $f = 0.03$ and $v_0 = 0.9$ (i.e.point 4 in Fig.3(a)) for two different initial conditions $(x_0, y_0) = (-0.3, 0)$ (left) and $(x_0, y_0) = (1, 0)$ (right), two coexisting asymmetric period-1 solutions are shown in Fig.4(d).

Fig. 5 also shows the coexisting periodic solutions and a chaotic attractor of system (5) for $\alpha = 0$ in (a)-(b) for the corresponding points 5 and 6 in Fig.3(b) respectively. When $v_0 = 0.4$ and $f = 0.1$ (i.e.point 5 in Fig.3(b)), a pair of asymmetric stick-slip period-1 solutions coexist with different initial conditions (x_0, y_0)=(-1,0)(left) and (x_0, y_0)=(1,0)(right), as depicted in Fig.

5(a). The stick-slip chaotic motion follows when f increases to $f = 0.351$ (i.e.point 6 in Fig.3(b)), the corresponding chaotic attractor is depicted in Fig.5(b).

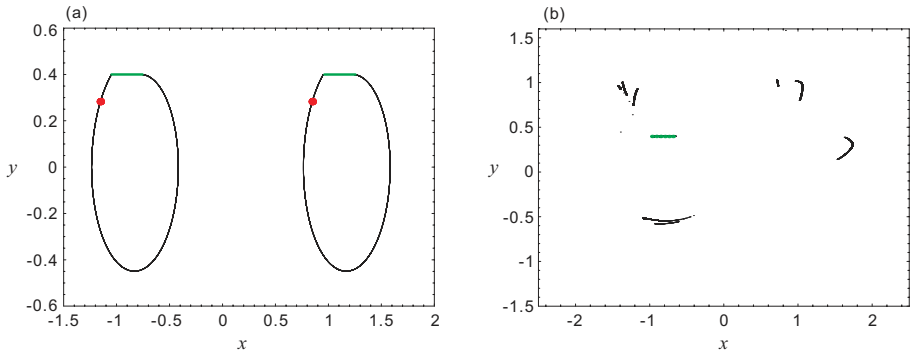


Figure 5: The periodic motion and chaotic attractors of system (5) $\alpha = 0$ in (a)-(b) for the corresponding points 5 and 6 in Fig.3(b) respectively. (a) Coexisting stick-slip period-1 solutions for $f = 0.1, v_0 = 0.4$, (b) chaotic attractor for $f = 0.351, v_0 = 0.4$ with the largest Lyapunov exponent 0.0112.

4 Summary and Conclusion

In this paper, we have proposed a novel self-excited SD oscillator driven by moving belt friction based upon the SD oscillator and classical moving belt. The mathematical model of the belt-driven system has been investigated where the friction characteristic is modeled as the Coulomb friction. Analytical expressions of homoclinic orbits for the unperturbed SD oscillator are obtained by introducing a serie of transformations, which avoids the approximation caused by the conventional Taylor's expansion. Application of the Melnikov approach to the perturbed self-excited SD oscillator has made it to predict the stick-slip chaotic boundaries. The efficiency of the criterions for chaotic motion obtained in this paper is verified via some numerical simulations in the system.

References

[1] J.P. den Hartog, Forced vibration with combined Colomb and viscous Damping. *Transactions of the American Society of Mechanical Engineering*. **53**, 107-115, 1931.

[2] A. K. Banerjee, Influence of kinetic friction of the critical velocity of stick-slip motion. *Wear*, **12**(2), 107-116, 1968.

[3] K. Popp, P. Stelter, Stick-slip vibrations and chaos. *Philosophical Transactions: Physical Sciences and Engineering*, **332**(1624), 89-105, 1990.

[4] B. Armstrong-Helouvry, Stick-slip and control in low-speed motion. *IEEE Transacts on Automatic Control*, **38**(10), 1483-1496, 1993.

[5] Q. H. Li, Y. M. Chen, Z. Y. Qin, Existence of stick-slip periodic solutions in a dry friction oscillator. *Chin. Phys. Lett.*, **28**(3), 030502, 2011.

[6] H. B. Fang, J. Xu, Stick-slip effect in a vibration-driven system with dry friction: sliding bifurcations and optimization. *Journal of applied mechanics, ASME*, **81**(5), 051001, 2014.

[7] L. S. Shi, Y. K. Zou, T. K*ü*pper, Melnikov method and detection of chaos for non-smooth systems. *Acta Mathematicae Applicatae Sinica, English Series,* **29**(4), 881-896, 2013

[8] D. C. Tsobgni-Fozap, A. Kenfack-Jiotsa, G. I. Koumene-Taffo and T. C. Kofané, Effect of coupling, synchronization of chaos and stick-slip motion in two mutually coupled dynamical systems. *Nonlinear Dyn.*, **78**, 1157-1177, 2014.

[9] J. Awrejcewicz, M.M. Holicke, Analytical prediction of stick-slip chaos in a double self-excited Duffing-type oscillator. *Mathematical Problems in Engineering*, **2006**, 1-79, 2006.

[10] J. Awrejcewicz, M.M. Holicke, Melnikov's method and stick-slip chaotic oscillations in very weakly forced mechanical systems. *Int.J.Bifur.Chaos*, **9**(3), 505-518, 1999.

[11] Q. J. Cao, M. Wiercigroch, E. E. Pavlovskaia, J. M. T. Thompson, C. Grebogi, Archetypal oscillator for smooth and discontinuous dynamics. *Phys Rev. E.*, **74**, 046218, 2006.

[12] Q. J. Cao, M. Wiercigroch, E. E. Pavlovskaia, C. Grebogi, J. M. T. Thompson, The limit case response of the archetypal oscillator for smooth and discontinuous dynamics. *Int. J. Nonlin. Mech.*, **43,** 462-473, 2008.

[13] Q. J. Cao, M. Wiercigroch, E. E. Pavlovskaia, J. M. T. Thompson, C. Grebogi, Piecewise linear approach to an archetypal oscillator for smooth and discontinuous dynamics. *Phil. Trans. R. Soc. A*, **366**(1865), 635-652, 2008.

[14] A. F. Filippov, *Differential equations with discontinuous right-hand sides*. Kluwer Acadamic, Dordrecht, 1988.

[15] W. Q. Yu, F. Q. Chen, Global bifurcations of a simply supported rectangular metallic plate subjected to a transverse harmonic excitation. *Nonlinear Dyn.*, **59**, 129-141, 2010.

[16] R. L. Tian, X. W. Yang, Q. J. Cao, Q. L. Wu, Bifurcations and chaotic threshold for a nonlinear system with an irrational restoring force. *Chin. Phys. B*, **21**(2), 020503, 2010.

[17] J. Guckenheimer, P. Holmes, *Nonlinear oscillations, dynamical systems, and bifurcations of vector fileds*. New York, Springer, 1997.

[18] V. K. Melnikov, On the stability of the center for time periodic perturbations. *Trans. Moscow Math. Society*, **12**, 1-57, 1963.

11th International Conference on Engineering Vibration
Ljubljana, Slovenia, 7–10 September 2015

MULTIPLE BUCKLING AND HIGH CO-DIMENSION ANALYSIS OF A NOVEL SMOOTH AND DISCONTINUOUS OSCILLATOR

Qingjie Cao*[1], Yanwei Han[1], Marian Wiercigroch[2]

[1]Centre for Nonlinear Dynamics, Harbin Institute of Technology, School of Astronautics
No.92, Xidazhi Street, Harbin 150001 China.
Email. qingjiecao@hotmail.com; hanyanweihyw@163.com

[2]Centre for Applied Dynamics Research, Department of Engineering, Fraser Noble Building, Kings College, University of Aberdeen, Aberdeen AB24 3UE, Scotland,UK
m.wiercigroch@abdn.ac.uk

Keywords: Smooth and discontinuous (SD) oscillator; multiple buckling; irrational nonlinearity; co-dimension bifurcation, high order quasi zero stiffness

Abstract. *In this paper, we propose a nonlinear smooth and discontinuous (SD) oscillator which is composed of a lumped mass and three titled springs. Even the springs are linear, the oscillator behaves strongly nonlinear due to the geometrical configuration admitting multiple well dynamics leading to multiple bucklings and high codimension with multiple parameters. we will formulate the dimensionless mathematical model using Langrange method to derive the complex multiple bucklings and multiple well dynamics with transition as the parameters changing over the parameter space. The codimension four bifurcation phenomena with three parameters are presented by employing the unfolding theory. Meanwhile, we will propose the engineering applications in vibration isolation by providing an opportunity to construct a series of high order quasi-zero stiffness system.*

1 INTRODUCTION

An oscillator is a system that works on the principles of oscillation with a periodic fluctuation between the states based on energy exchange, which plays an critical important role in modern physics and engineering, [1, 2]. The simple oscillator or a harmonic oscillator is an abstracted system from variety of engineering, electronic and modern physics systems. The typical example of these systems is the mass-spring oscillator which consists of a lumped mass connected with a spring vibrating around its equilibrium position undergoing a sinusoidal with a constant amplitude A depended on the initial position x_0 and the initial velocity $\dot{x}_0$ and a constant frequency ω (which does not depend on the amplitude) determined by the size of m and k and a constant amplitude, [3]. It is known that the frequency and the amplitude of the damped vibration can be reduced and decayed, respectively, depending on the ratio of damping, while the frequency and the amplitude of the steady state vibration of the driven system (excited by both damping and external harmonic forcing) depends upon the frequency and amplitude of the excitation subjected to the system.

It is critical important that the frequency of the vibrating system could not be always the same constant, such as the simple pendulum, which indicates that the harmonic oscillator is insufficient to meet the requirements in engineering and physics. There are three kinds of motions of a simple pendulum of angular vibration, rotating and the separatrix. The isochronism discovered Galileo valid states that the pendulum swings is the same as the harmonic oscillator, that is the period is independent of the amplitude θ_0, which is only valid for a small-angle approximation, seen in [4]. In 1674, Huygens discovered the periodicity of large swings, [5], which deviates from the law of isochronism, which was one of the earliest records of nonlinear vibration [6].

Even the concept of nonlinear vibrations was known and there had been mathematical analysis of nonlinear oscillators in [7] and [8] before Duffing's book [9], in which his famous equation is given, Duffing was the one to tackle the problem of a nonlinear oscillator in a systematic way starting with the linear oscillator, and examining the effects of quadratic and cubic stiffness nonlinearities. He emphasised the differences between the linear and the nonlinear oscillators for both free and forced vibration, also considering the effects of damping.

Ueda [10, 11] firstly noticed the chaos at the end of 1961 in his doctoral thesis research on force Duffing oscillator with only cubic nonlinearity. Moon and Holmes [12] showed the double-well Duffing oscillator and provided a simplest model for the forced vibration of a cantilever beam in the nonuniform field of two permanent magnets. van der Pol [**?**] provided an example of an oscillator with nonlinear damping which originated in the modeling of an electrical circuit with a triode valve. Lorenz [14] presented an analysis of a coupled set of three quadratic ordinary differential equations representing three modes of the Oberbeck-Bouqssinesq equations for fluid convection in a two-dimension layer hearted from below. Chen [15] and Lu [16] proposed a generalized Lorenz systems family, i.e. Chen oscillator and Lu oscillator, which the strange attractors are observed from a physical electronic chaotic circuit with a single nonlinear resistor.

The harmonic oscillator has been extensively applied in engineering and quantum mechanics [17, 18, 19]. Recently, a smooth and discontinuous oscillator (SD oscillator) [20, 21, 22] comprising mass and oblique springs with double stability has been proposed to study transition from smooth to discontinuous dynamics. This SD oscillator was found to exhibit abundant nonlinear dynamics using theoretical [23, 24, 25], numerical [26, 27] and experimental [28] approaches. The restoring force of the SD oscillator is a single irrational nonlinearity having

one switch point for the snap-through buckling at which a transition from single well to double well dynamics occurs. This switch point is a degenerate singular point having codimension two bifurcation, which has been investigated. Later, a generalized SD (GSD) oscillator [29] with triple stability has been presented to investigate the transitions between the triple wells for two snap-through bucklings phenomena. The GSD system can be regarded as a rigid coupling of two separate SD oscillators vibrating horizontally. This archetypal has multiple dynamics, codimension three of high order degenerated singularity and also the transitions between the multiple well, [30] which imply the multiple stability or from the mechanics point of view multiple snap-through bucklings [31].

The main objective of this paper is to design a archetypal novel nonlinear oscillator with smooth and discontinuous dynamics and quadruple stability properties by making the best use of the properties of SD and the related SD oscillator [32, 33, 34, 35, 36]. It is expected that the spectacular behaviour of multiple stability and multiple snap-through bucklings in the proposed oscillator will stimulate more research interest in this area, further development of new methodology, and broaden applications in engineering. Due to its geometrical configuration, this nonlinear system can also behave the archetypal characteristic of negative stiffness [37, 38, 39], which can be used for the design of nonlinear isolator with both linear and cubic quasi-zero-stiffness (QZS) characteristic [40, 41, 42]. Finally, we will formulate the dimensionless mathematical model using Langrange method to derive the the complex multiple bucklings and multiple well dynamics with transition as the parameters changing over the parameter space. The codimension four bifurcation phenomena with three parameters are presented by employing the unfolding theory, [43, 44].

2 Unperturbed Dynamics

In this section, we propose a nonlinear oscillator, shown in Fig 1(a) composed of a lumped mass and three titled springs. Even the springs are linear, the oscillator behaves strongly nonlinear due to the geometrical configuration.

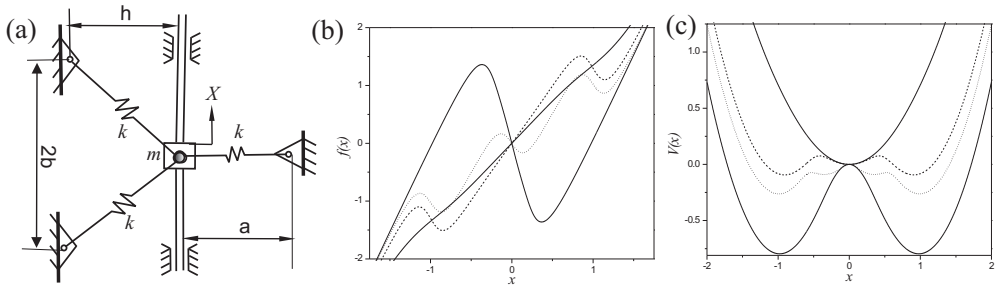


Figure 1: (a) An oscillator with a lumped mass m and three titled springs of stiffness k with equilibrium length L; Restoring forces in (b) and the corresponding potentials (c): the bold $\alpha = \beta = 1.0, \gamma = 0.7$; the thin $\alpha = \beta = \gamma = 0.2$; the dashed for $\alpha = \beta = 0.2, \gamma = 1.0$ and the dotted for $\alpha = \beta = 0.1, \gamma = 0.57$, respectively.

Dimensionless equations for the oscillators can be obtained using Langrange equation by

letting $x = X/L, \alpha = a/L, \beta = b/L$ and $\gamma = h/L$ assuming $\omega_0^2 = k/m = 1$ as the followings.

$$\ddot{x}+(x-\beta)\left(1-\frac{1}{\sqrt{(x-\beta)^2+\gamma^2}}\right)+x\left(1-\frac{1}{\sqrt{x^2+\alpha^2}}\right)+(x+\beta)\left(1-\frac{1}{\sqrt{(x+\beta)^2+\gamma^2}}\right)=0 \tag{1}$$

which can be smooth for both $\alpha \neq 0$ and $\gamma \neq 0$ and discontinuous $\alpha = 0$ or $\gamma = 0$.

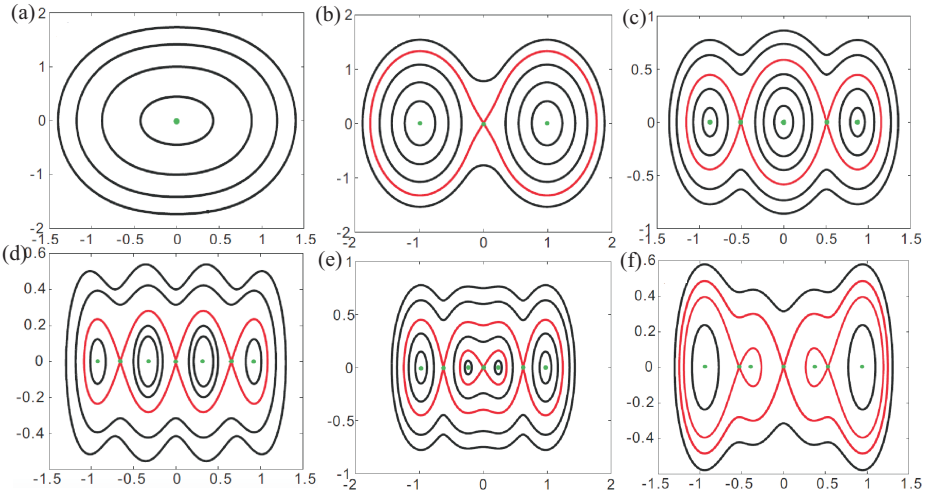


Figure 2: Unperturbed Phase portraits: (a), (b) and (c) the single well, double well and triple well dynamics, respectively; while (d), (e) and (f) for special types of quadruple well dynamics.

For convenient, the nonlinear restoring force is written as

$$F(x) = 3x - \frac{(x-\beta)}{\sqrt{(x-\beta)^2+\gamma^2}} - \frac{x}{\sqrt{x^2+\alpha^2}} - \frac{x+\beta}{\sqrt{(x+\beta)^2+\gamma^2}} = 0, \tag{2}$$

which consists of three terms irrational restoring force applied to the lumped mass provided by the springs in Fig.1(a), the selected graphs of which are plotted in Fig.1(b) with the detailed information in the caption.

Fig.1(b) plots the resisting force of the the system with different value of parameters. While the Hamiltonian of the system can be obtained by letting $\dot{x} = y$.

$$H(x,y) = \frac{1}{2}y^2 + V(x) = \frac{1}{2}y^2 + \frac{3}{2}x^2 - \sqrt{(x-\beta)^2+\gamma^2} - \sqrt{x^2+\alpha^2} - \sqrt{(x+\beta)^2+\gamma^2}, \tag{3}$$

where $V(x)$ is the potential of the system, the graphs of which corresponding to the restoring forces are plotted in Fig.1(c), the detailed information can be seen in the corresponding caption, showing the transition among the multiple well dynamics.

With the help of Hamiltonian (3), the unperturbed dynamics can be obtained and classified, part of typical phase portraits are plotted in Fig.3. Fig.3(a), (b) and (c) corresponding to the single well, double well and triple well dynamics; while Fig.3(d), (e) and (f) are the typical type of quadruple well dynamics.

3 Multiple Bucklings

In this section, we will focuss our attention on the a nonlinear multiple buckling behaviour of the oscillator.

Generally speaking the buckling occurs at the balanced potential energy stored in the springs and the work done by the external load which can be given in a dimensionless form by

$$\bar{U}(x,\alpha,\beta,p) = \frac{3}{2}x^2 + \sqrt{(x-\beta)^2+\gamma^2} + \sqrt{x^2+\alpha^2} + \sqrt{(x+\beta)^2+\gamma^2} - px, \qquad (4)$$

where x and p are the displacement and the dimensionless load respectively.

The static equilibrium position are characterized by the vanishing of the first variation of the total potential which leading to the equilibrium equation

$$p = (x+\beta)\left(1 - \frac{1}{\sqrt{(x+\beta)^2+\gamma^2}}\right) + x\left(1 - \frac{1}{\sqrt{x^2+\alpha^2}}\right) + (x-\beta)\left(1 - \frac{1}{\sqrt{(x-\beta)^2+\gamma^2}}\right). \quad (5)$$

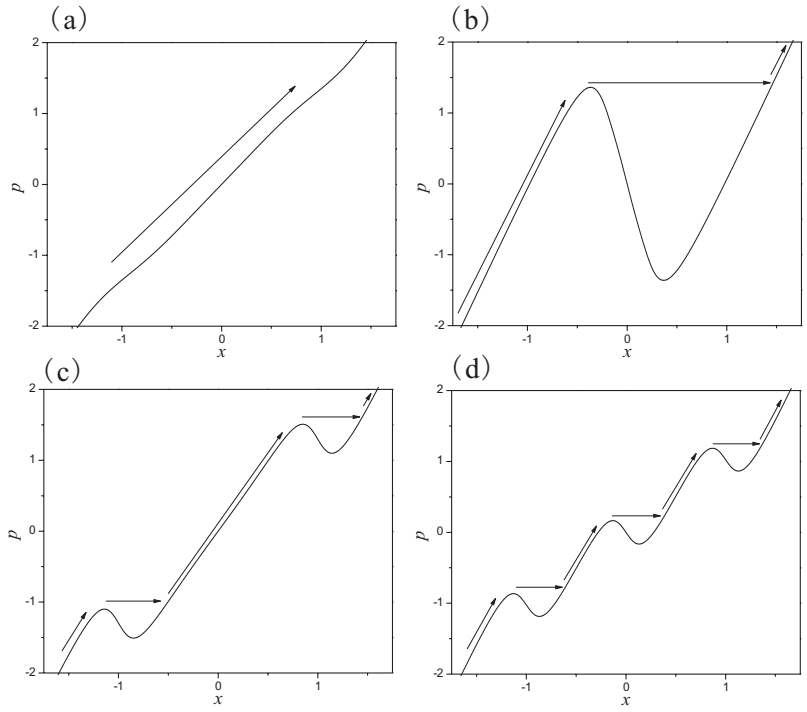


Figure 3: multiple bucklings: (a) non-buckling or single well dynamics for $\alpha = \beta = 1.0, \gamma = 0.7$; (b) single-buckling for $\alpha = \beta = \gamma = 0.2$; (c) double-buckling for $\alpha = \beta = 0.2, \gamma = 1.0$ and (d) triple-buckling for $\alpha = \beta = 0.1, \gamma = 0.57$, respectively.

Fig.3 shows that the system exhibits no-buckling behaviour, single buckling, double bucklings and triple buckling behaviour, respectively, depending on the valule of the system parameters.

4 High co-dimension bifurcations with multiple parameters

In this section, we reveal the High co-dimension bifurcations with multiple parameters of the oscillator.

System (1) can be approximated by expanding the resisting force in to a Taylor series up to the seventh term in the neighborhood of $x = 0$ as, which satisfies the finite determinacy conditions, see [43]:

$$\ddot{x} + C_1 x + C_3 x^3 + C_5 x^5 + C_7 x^7 = 0, \tag{6}$$

where

$$C_1 = f_x(0) = \Upsilon(\alpha, \beta, \gamma),$$
$$C_3 = \frac{1}{3!} f_{xxx}(0) = \Phi(\alpha, \beta, \gamma),$$
$$C_5 = \frac{1}{5!} f_{xxxxx}(0) = \Psi(\alpha, \beta, \gamma),$$
$$C_7 = \frac{1}{7!} f_{xxxxxxx}(0) = \Omega(\alpha, \beta, \gamma).$$

The high order catastrophe point $P(\alpha_0, \beta_0, \gamma_0)$ of System (6) can be obtained by letting $C_1(\alpha, \beta, \gamma) = C_3(\alpha, \beta, \gamma) = C_5(\alpha, \beta, \gamma) = 0$. It can also been proved that the non-vanishing of $C_7(\alpha, \beta, \gamma)$, that is, $C_7(\alpha, \beta, \gamma) \neq 0$. In this case, System (6) can be re-written in the following form.

$$\ddot{x} + \lambda x + \mu x^3 + \nu x^5 + x^7 = 0, \tag{7}$$

which is a norm form of codimension four with three parameters λ, μ and ν coreesponding the system parameters α, β and γ in terms of $\lambda = \Lambda, \mu = \Delta$ and $\nu = \Gamma$.

The universal unfolding of this norm (7) can be obtained by introducing a nonlinear damping in the following form.

5 High order quasi-zero stiffness isolation

In this section, we demonstrate the efficiency of high order quasi-zero stiffness isolations in engineering application.

Without loss of generality we still use the model shown in Fig.1a (if needed a vertical spring can be added in to the system), the dimensionless equation of motion can be made dimensionless form system (1) assuming the vertical spring is removed .

The high order quasi zero stiffness could be achieved by playing with the springs in the mechanical model in Fig.1a.

5.1 Quasi-zero stiffness isolator

If the right pair of springs are removed from the system and the position parameter $\alpha = 1$, that is the spring is at neither tension and compression stage. The equation could be written in the form.

$$\ddot{x} + x\left(1 - \frac{1}{\sqrt{x^2 + 1}}\right) = 0, \tag{8}$$

which is the quasi-zero stiffness isolator with $f(0) = f_x(0) = 0$ and $f_{xxx}(0) \neq 0$. The details can be seen in [26].

5.2 Cubic Quasi-zero stiffness isolator

If the left side springs is removed from the system and the position parameter $\beta_0 = 4\sqrt{5}/25$ and $\gamma_0 = 8\sqrt{5}/25$, in this case the equation could be written in the form.

$$\ddot{x} + (x+\beta_0)\left(1 - \frac{1}{\sqrt{(x+\beta_0)^2+\gamma_0^2}}\right) + +(x-\beta_0)\left(1 - \frac{1}{\sqrt{(x-\beta_0)^2+\gamma_0^2}}\right) = 0, \quad (9)$$

which is the cubic quasi-zero stiffness isolator with $f(0) = f_x(0) = 0 = f_{xxx}(0 = 0$ and $f_{xxxxx}(0) \neq 0$. The details can be seen in [29, 30].

5.3 Quintic quasi-zero stiffness isolator

In the same way, the geometry parameter $(\alpha_0, \beta_0, \gamma_0)$ can be obtained (at least theoretically) by letting $f(0) = f_x(0) = 0 = f_{xxx}(0) = f_{xxxxx}(0) = 0$ the equation of motion can be formulated in the following form.

$$\begin{aligned}\ddot{x} + (x+\beta_0)\left(1 - \frac{1}{\sqrt{(x+\beta_0)^2+\gamma_0^2}}\right) + (x-\beta_0)\left(1 - \frac{1}{\sqrt{(x-\beta_0)^2+\gamma_0^2}}\right) \\ +x\left(1 - \frac{1}{\sqrt{x^2+\alpha_0^2}}\right) = 0,\end{aligned} \quad (10)$$

which is the quintic quasi-zero stiffness isolator with $f(0) = f_x(0) = 0 = f_{xxx}(0 = 0$ and $f_{xxxxx}(0) \neq 0$ and $f_{xxxxxxx}(0) \neq 0$, which implies $\alpha = \alpha_0$, $\beta = \beta_0$ and $\gamma = \gamma_0$ by letting

$$\begin{cases} \Upsilon(\alpha, \beta, \gamma) = 0, \\ \Phi(\alpha, \beta, \gamma) = 0, \\ \Psi(\alpha, \beta, \gamma) = 0. \end{cases} \quad (11)$$

6 Conclusions and discussions

In this paper, we have proposed a nonlinear smooth and discontinuous (SD) oscillator which is composed of a lumped mass and three titled springs. Even the springs are linear, the oscillator behaves strongly nonlinear due to the geometrical configuration admitting multiple well dynamics leading to multiple bucklings and high codimension with multiple parameters. Langrange methods is employed to formulate the dimensionless mathematical to derive the the complex multiple bucklings and multiple well dynamics with transition as the parameters changing over the parameter space. The codimension four bifurcation phenomena has also been demonstrated with three parameters are presented by employing the unfolding theory, which is still remains an open problem. At the end of this paper, we have presented the engineering applications in vibration isolation by providing an opportunity to construct a series of high order quasi-zero stiffness system with quasi zero, cubic quasi zero and the quintic quasi zero stiffness.

Acknowledgements

The first two authors acknowledge the financial support from the National Natural Science Foundation of China (Grant No. 11372082) and the National Basic Research Program of China (Grant No. 2015CB057405).

REFERENCES

[1] Serway, R. A., Jewett, J. W. [2003] Physics for Scientists and Engineers (with PhysicsNOW and InfoTrac), Brooks Cole, ISBN 10: 0534408427.

[2] Tipler, P. [1998] Physics for Scientists and Engineers: Vol. 1 (4th ed.). W. H. Freeman.

[3] Wylie, C. R. [1975] Advanced Engineering Mathematics (4th ed.). McGraw-Hill.

[4] Nelson, R., Olsson, M. G.[1986]. "The pendulum: Rich physics from a simple system". *Am. J. Phys.* 54 (2): pp. 112-121.

[5] Matthews, M. R. [2000]. Time for science education. Springer.

[6] Carvalhaes, C. G., Suppes, P. [2008], "Approximations for the period of the simple pendulum based on the arithmetic-geometric mean", *Am. J. Phys.* 76 (12): 1150-1154.

[7] Helmholtz, H.L.F. [1895] On the Sensations of Tone as a Physiological Basis for the Theory of Music, App. XII, Theory of combinatorial tones, 411-413, translated by Ellis, A.J., 3rd edn, Longmans Green and Co., Reprinted by Dover publications, New York.

[8] [1894] Strutt,J.W., Rayleigh B. The Theory of Sound, Vol I, 77, 2nd edn, Constable and Co. Ltd., Reprinted by Dover publications, New York.

[9] Duffing, G. [1918] Erzwungene Schwingungen bei veranderlicher Eigenfrequenz und ihre technische Bedeutung, Series: Sammlung Vieweg, No 41/42. Vieweg & Sohn, Braunschweig.

[10] Ueda Y. [1980] "Explosion of strange attractors exhibited by Duffing's equation," *Nonlin. Dyn. Annals of the New York Academy of Sciences* **357**, 167-434.

[11] Ueda Y. [2001] The Road to Chaos-II, Aerial Press, Santa Cruz.

[12] Guckenheimer, J. & Holmes, P. [1983] Nonlinear Oscillations, Dynamical Systems, and Bifurcations of Vector Fields, Springer-Verlag, New York.

[13] Van der Pol, B.[1927] "Forced oscillations in a circuit with nonlinear resistance (receptance with reactive trive)," *Londdon, Edinburgh and Dublin Phil. Mag.* **3**, 65-80.

[14] Lorenz, E. N. [1963] "Deterministic non-periodic flow," *J. Atmos. Sci.* **20**, 130-141.

[15] Chen, G. R. & Ueta, T. [1999] "Yet another chaotic attractor," *Int. J. Bifurcation and Chaos* **9**, 1465-1466.

[16] Lu J. & Chen, G. [2002] "A new chaotic attractor coined," *Int. J. Bifurcation and Chaos* **12**, 659-661.

[17] Griffiths, David J. [2004] Introduction to Quantum Mechanics (2nd ed.). Prentice Hall. ISBN 0-13-805326-X.

[18] Liboff, Richard L. [2002] Introductory Quantum Mechanics. Addison Wesley. ISBN 0-8053-8714-5.

[19] Rashid, Muneer A. [2006] "Transition amplitude for time-dependent linear harmonic oscillator with Linear time-dependent terms added to the Hamiltonian" (PDF-MICROSOFT POWERPOINT). M.A. Rashid Center for Advanced Mathematics and Physics. National Center for Physics. Retrieved 2010.

[20] Cao, Q. J., Wiercigroch, M., Pavlovskaia, E. E., Thompson, J. M. T. & Grobogi, C. [2006] "Archetypal oscillator for smooth and discontinuous dynamics," *Phys. Rev. E*, **74**, 046218-046222.

[21] Cao, Q. J., Wiercigroch, M., Pavlovskaia, E. E., Thompson, J. M. T. & Grobogi, C. [2008a] "Piecewise linear approach to an archetypal oscillator for smooth and discontinuous dynamics," *Phil. Trans. R. Soc. A* **366**, 635-652.

[22] Cao, Q. J., Wiercigroch, M., Pavlovskaia, E. E., Thompson, J. M. T. & Grobogi, C. [2008] "The limit case response of the archetypal oscillator for smooth and discontinuous dynamics," *Int. J. Nonlin. Mech.*, **43**, 462-473.

[23] Araki, A., Asai, T. & Kimura, K. [2013] "Nonlinear vibration isolator with adjustable restoring force," *J. Sound Vibr.* **332**, 6063-6077.

[24] Tian, R. L., Cao, Q. J. & Yang, S. P. [2010] "The co-dimension-two bifurcation for the recent proposed SD oscillator," *Nonlin. Dyn.* **59**, 19-27.

[25] Li, Z. X., Cao, Q. J., Wiercigroch, M. & Leger, A. [2013] "Analysis of the periodic solutions of a smooth and discontinuous oscillator," *Acta Mech. Sin.* **29**, 575-582.

[26] Hao, Z. F., Cao, Q. J. & Wiercigroch, M. [2014] "A novel dynamical model for GVT nonlinear supporting system with stable-quasi-zero-stiffness," *J. Theor. Appl. Mech.* **52**, 199-213.

[27] Lu, Z. Q., Bramman, M. J. & Yang, T. J. [2013] "An investigation of a two-stage nonlinear vibration isolation system," *J. Sound Vibr.* **332**, 1456-1464.

[28] Chen, E. L., Cao, Q. J., Feng, M. & Tian, R. L. [2012] "The preliminary investigation on design and experimental research of nonlinear characheristics of SD oscillator," *Chin. J. Theory Mech.* **44**, 584-590.

[29] Han, Y. W., Cao, Q. J., Chen, Y. S. & Wiercigroch M. [2012] "A novel mass-spring based smooth and discontinuous oscillator withstrongly irrational nonlinearities," *Sci. China-Phys Mech Astron.* **55**, 1832-1843.

[30] Cao, Q. J., Han, Y. W. Liang T. W., Wiercigroch, M. & Piskarev S. "Multiple buckling and codimension-three bufurcaiton phenonmena of a nonlinear oscillator," *Int. J. Bifurcation and Chaos* **24**, 1430005.

[31] Han, Y. W., Cao, Q. J., Chen, Y. S. & Wiercigroch M. [2014] "Chaotic thresholds for the piecewise linear discontinuous system with multiple well potentials," *Int. J. Nonlin. Mech.* (In press, DOI: 10.1016/j.ijnonlinmec.2014.09.007).

[32] Cao, Q. J., Xiong Y. P., & Wiercigroch, M. [2011] " Resonances of the SD oscillator due to the discontinuous phase," *J. Appl. Analy. Comp.* **1**, 183-191.

[33] Cao, Q. J., Wang, D., Chen Y. S. & Wiercigroch, M. [2012] "Irrational elliptic functions and the analytical solution of SD oscillator," *J. Theor. Appl. Mech.* **50**, 701-7015.

[34] Cao, Q. J., Xiong Y. P. & Wiercigroch, M. [2013] "A novel model of dipteran flight mechanism," *Int. J. Dyn. Control.* **1**, 1-11.

[35] Cao, Q. J., Han, N. & Tian, R. L. [2011] "A rotating pendulum linked by an oblique spring," *Chin. Phys. Lett.* **28**, 060502.

[36] Han, N., Cao, Q. J., & Wiercigroch, M. [2013] "Estimation of chaotic thresholds for the rocently proplsed rotating pendulum," *Int. J. Bifurcation and Chaos* **23**, 1350074

[37] Peng, Z. K., Meng, G., Lang, Z., Zhang, W. & Chu, F. [2012] "Study of the effects of cubic nonlinear damping on vibration isolations using harmonic balance method," *Int. J. Nonlin. Mech.* **47**, 1073-1080.

[38] Sun, J. Y., Huang, X. C. & Liu, X. T. [2013] "Study on the force transmissibility of vibration isolators with geometric nonlinear damping," *Nonlin. Dyn.* **74**, 1103-1112.

[39] Xu, D. L. , Yu, Q. P. & Zhou, J. X. [2013] "Theoretical and experimental analyses of a nonlinear magnetic vibration isolator with quasi-zero-stiffness characteristic, *J. Sound Vibr.* **332**, 3377-3389.

[40] Molyneux, W. G. [1957] "Supports for vibration isolator," ARC/CP-322. *Aeronautical Research Council Current Paper*, Great Britain.

[41] Carrella, A., Brennan, M. J., Kovacic, I. & Waters, T. P. [2009] "On the force transmissibility of a vibration isolator with quasi-zero-stiffness," *J. Sound Vibr.* **332**, 707-717.

[42] Yang, J. Xiong, Y. P. & Xing, J. T. [2013] "Dynamics and power flow behaviour of a nonlinear vibration isolation system with a negative stiffness mechanism," *J. Sound Vibr.* **332**, 167-183.

[43] Golubitsky, M., Schaeffer, D. [1985] Singularities and groups in bifurcations theory, I, Springer-Verlag, New York.

[44] Nayfeh A. H. and Sanchez N. E. [1989] "given the bifurcations in forced softening Duffing oscillator," *Int. J. Nonlin. Mech.* **24**, 483-497.

Posters

International Conference on Engineering Vibration
Ljubljana, Slovenia, 7-10 September 2015

THERMAL BUCKLING OF FUNCTIONALLY GRADED PANELS BASED ON PHYSICAL NEUTRAL SURFACE

Seok-in Bae[1], Ji-Hwan Kim[2]*

[1]Department of Mechanical and Aerospace Engineering, Seoul National University Gwanak-ro 1, Gwanak-gu, Seoul, 151-744, Republic of Korea
care13@snu.ac.kr

[2]Department of Mechanical and Aerospace Engineering, Seoul National University Gwanak-ro 1, Gwanak-gu, Seoul, 151-744, Republic of Korea
jwhkim@snu.ac.kr

Keywords: Functionally Graded Plates, Neutral Surface Position, Thermal Buckling Analysis.

Abstract. *Present study deals with the thermal buckling behavior of Functionally Graded (FG) plates with the gradually changed material properties from one surface to the other. Generally, the model is developed as microscopically inhomogeneous composites using a mixture of two different materials such as a metal and a ceramic. Due to the asymmetry of material properties in the thickness direction, neutral surface concept is used as a reference plane. In this regards, various research works already have been performed using the neutral surface concept. In this work, thermal buckling of FG plate model with temperature dependent material properties is analyzed using finite element method. In the numerical analysis, the buckling behaviors under temperature rises in the thickness direction are investigated. The results reveal that the neutral surface position of the model is a very important factor for the behavior of Functionally Graded Materials.*

1 INTRODUCTION

Functionally Graded Materials (FGMs) are a class of advanced composite material with a continuous variation of material properties from one surface to the other. Especially, the materials mitigate the stress concentration found in conventional composite. Conventionally, FGMs are made up of ceramic and light metal. And then, a ceramic has high compressive strength and heat resistance with low fracture toughness, while, a metal exhibits better mechanical strength but cannot withstand high thermal environment. Therefore, FGMs can withstand high-temperature while maintain the role for structural integrity. These advantages of FGMs have increased the popularity in engineering applications such as aerospace, nuclear reactors and automotive engineering. Especially, the structural models are developed for general use in extremely high temperature environments. Furthermore, neutral surface has been used as a reference plane for static equilibrium instead of the middle surface of the structures due to the asymmetry of the material properties of FGMs in the thickness direction. [1, 2] Zhang and Zhou[3] employed the classical plate theory to derive the governing equations of motion for the plate model based on the neutral surface. And then, the bending, buckling and free vibration behaviors of FGM model are also analyzed. Bodaghi and Saidi[4] studied the buckling of Functionally Graded(FG) plates resting on elastic foundation under nonlinearly varying in-plane loads using the concept. Prakash et al.[5] employed the first-order shear deformation theory of plate to investigate the influence of neutral surface position on the stability behavior of FG plates model. Zhang[6] proposed the modeling and analysis of FGM rectangular plates based on physical neutral surface and higher order shear deformation theory.

In this work, thermal buckling of FG plate model with temperature dependent material properties is investigated using finite element method. In the numerical analysis, the thermal buckling behavior under uniform, non-linear temperature rise in the thickness direction are investigated. Additionally, the results present the change of critical temperature due to the effect of temperature fields and volume fractions.

2 FORMULATION

2.1 Physical neutral surface

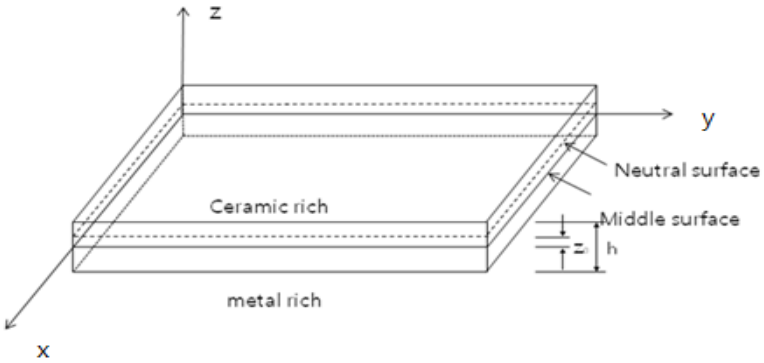


Figure 1 : Neutral surface and Mid-plane of FGMs.

Fig.1 shows a structural model with middle surface and neutral surface, and numerous research works have been performed using the middle surface to consider FGM models, while material properties in the thickness direction is asymmetric. In this study, neutral surface is

chosen as a reference plane of deformation. In order to determine the location of the neutral surface under the thermal environments for the panel, the first moment with respect to elasticity modulus equals to zero as [3]

$$\int_{-\frac{h}{2}}^{\frac{h}{2}} E(z,T)(z-z_0(T))dz = 0 \tag{1}$$

Thus, the position of neutral surface $z_0(T)$ can be obtained as

$$z_0(T) = \frac{\int_{-\frac{h}{2}}^{\frac{h}{2}} E(z,T)zdz}{\int_{-\frac{h}{2}}^{\frac{h}{2}} E(z,T)dz} \tag{2}$$

2.2 Modeling

A mixture of ceramic and metal is selected as a model, and the mixing ratio is varying continuously and smoothly in the thickness direction.

Then the volume fraction is defined as

$$V_c(z) = \left(\frac{z}{h}+\frac{1}{2}\right)^k \quad (0 \le k < \infty), \quad V_c(z)+V_m(z) = 1 \tag{3}$$

where V_c, superscript *k*, subscripts *c* and *m* represent the volume fraction of ceramic, the volume fraction index, ceramic and metal, respectively.

Further, the temperature dependent material properties *P* can be written as

$$P(T) = P_0\left(\frac{P_{-1}}{T}+1+P_1T+P_2T^2+P_3T^3\right) \tag{4}$$

where *T* stands for the temperature, and P_0, P_{-1}, P_1, P_2 and P_3 are constants in the cubic fit of the material properties.

Using the rule of mixture for material properties:

$$\begin{aligned} P_{\text{eff}}(z,T) &= P_m(T)V_m(z)+P_c(T)V_c(z) \\ &= P_m(T)+(P_c(T)-P_m(T))\left(\frac{z}{h}+\frac{1}{2}\right)^k \end{aligned} \tag{5}$$

Then, Young's modulus of the material is

$$E(z,T) = E_m(T)+(E_c(T)-E_m(T))\left(\frac{z}{h}+\frac{1}{2}\right)^k \tag{6}$$

3 GOVERNING EQUATIONS

3.1 Displacement fields and constitutive equations

Considering a FGM plate of length a, width b and thickness h with the use of neutral surface as a reference plane. Based on the first-order shear deformation theory of plate, and introduce the physical neutral surface z_0, then the displacements are

$$\begin{aligned} u(x,y,z,t) &= u_0(x,y,t) + (z-z_0)\phi_x(x,y,t) \\ v(x,y,z,t) &= v_0(x,y,t) + (z-z_0)\phi_y(x,y,t) \\ w(x,y,t) &= w_0(x,y,t) \end{aligned} \tag{7}$$

where u, v and w are the displacements in the x, y and z direction, while ϕ_x and ϕ_y are the rotations of the normal in the xz and yz planes, respectively. In addition, the subscript '0' is a value at the physical neutral surface.

The constitutive equations can be obtained defined as

$$\begin{Bmatrix} N \\ M \end{Bmatrix} = \begin{bmatrix} A & B \\ B & D \end{bmatrix} \begin{Bmatrix} \varepsilon_0 \\ \kappa \end{Bmatrix} - \begin{Bmatrix} N_{\Delta T} \\ M_{\Delta T} \end{Bmatrix} \tag{8}$$

$$Q_s = A_s \gamma_0 \ , \ A_s = k_p \int_{-h/2}^{h/2} \frac{E(z)}{2(1+\nu)} \begin{bmatrix} 1 & 0 \\ 0 & 1 \end{bmatrix} dz \tag{9}$$

where N, M, Q_s and A_s denote the in-plane force resultant, the moment resultant , the transverse shear force resultant vectors and transverse shear stiffness, respectively. Further, k_p denote the transverse shear correction coefficient for FGM due to the variation of Poisson's though the thickness as

$$k_p = \frac{5}{6 - (\nu_m V_m + \nu_c V_c)} \tag{10}$$

while A, B and D stand for the in-plane, in-plane bending coupling stiffness and bending stiffness matrices as

$$(A, B, D) = \int_{-h/2}^{h/2} E(1, (z-z_0), (z-z_0)^2) dz \tag{11}$$

Further, $N_{\Delta T}$ and $M_{\Delta T}$ are the thermal in-plane force resultant and the thermal moment resultant vectors as

$$\left(N_{\Delta T}, M_{\Delta T}\right) = \int_{-h/2}^{h/2} (1, (z-z_0)) E \begin{pmatrix} \alpha(z) \\ \alpha(z) \\ 0 \end{pmatrix} \Delta T(z) dz \tag{12}$$

where the elastic coefficient matrix is

$$E = \frac{E(z)}{1-\nu^2}\begin{bmatrix} 1 & \nu & 0 \\ \nu & 1 & 0 \\ 0 & 0 & \frac{1-\nu}{2} \end{bmatrix} \tag{13}$$

3.2 Thermal bucking behavior

In this work, uniform temperature rise case and heat transfer in the FGMs model are considered. And then, the critical temperature can be obtained by solving the standard eigen-value problem

$$[K^e + \lambda K^t]q^D = 0 \tag{14}$$

where, λ and q^D are the eigenvalue and the eigenvector, respectively. In addition, K^e is the global bending stiffness matrix which is obtained by assembling the A, B and D matrix and K^t is the global thermal stiffness matrix in terms of $N_{\Delta T}, M_{\Delta T}$.

Therefore, the lowest eigenvalue of λ, the critical temperature T_{cr} is given by

$$T_{cr} = T_{ref} + \Delta T_{cr} = T_{ref} + \lambda \Delta T \tag{15}$$

4 NUMERICAL RESULTS & DISCUSSION

4.1 Code Verification

To compare the neutral surface shift, Figure 2 shows the results with the previous data. The constituents materials are Alumina (Al_2O_3) and Aluminium (Al). The Young's modulus of Alumina, Aluminum and Poisson's ratio are E_c = 380 GPa , E_m = 70 GPa and 0.3, respectively. The non-dimensional shift (z_o / h) of neutral surface is calculated based on Eq.(2). Figure shows the effect of volume index variation according to the position of neutral surface, and the results are good agreement with the previous data in Ref.[5].

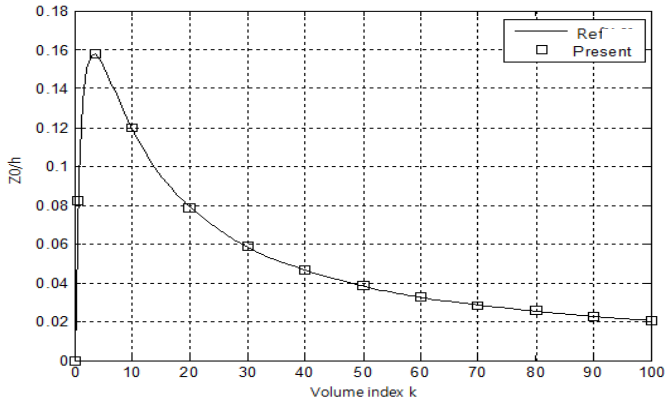


Figure 2 : Neutral surface shift from mid-surface.

4.2 Thermal buckling analysis

In this section, the thermal buckling behaviors of FGM model are analyzed for fully simply supported rectangular plates. Elasticity modulus, coefficient of thermal expansion and thermal conductivity for constituent materials are listed in Table 1.

	Property			
	E(GPa)	α (1/K)	k(W/mK)	γ
Al	70	23E-6	204	0.3
Al_2O_3	380	7.4 E-6	10.4	0.3

Table 1 : Material properties of Al/Al_2O_3.

Fig. 3 compares the effect of neutral surface(NS) on the thermal buckling behavior under uniform (U) and nonlinear(N) temperature rises. It shows that the buckling temperature decreases by using neutral surface as the reference plane. It is concluded that the buckling temperature decreases by the increase of the volume index, and decreases by the increase of the thickness ratios. Also, the buckling temperature considering heat transfer is higher than the case for uniform temperature rises.

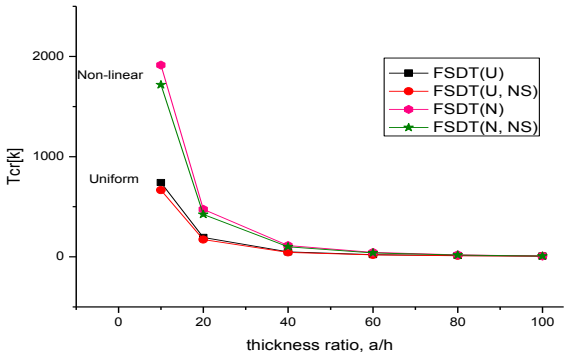


Figure 3 : Comparison of thermal buckling temperature(k=1).

5 CONCLUSIONS AND FUTURE WORK

In this study, thermal buckling analysis is performed for the Functionally Graded Material models. Based on the first-order shear deformation theory of plate, concept of neutral surface is applied to derive the governing equations. To verify the results of the works, the results in the present analysis are compared with the previous data for the case without thermal effects. Also, parametric studies have been performed under uniform and heat conduction conditions to examine the influences of volume index, thickness ratio and neutral surface positions. It can be shown that the buckling temperature increases as volume fraction index k is decreased. Additionally, the buckling temperature decreases when the thickness ratio increases. Moreo-

ver, buckling temperature is decreased with the neutral surface as the reference plane, and the result is due to the stiffness matrix becomes weaker than using mid-surface.

REFERENCES

[1] T. Morimoto, Y. Tanigawa and R. Kawamura, Thermal buckling of functionally graded rectangular plates subjected to partial heating. *International Journal of Mechanical Science*, **48**, 926-937, 2006.

[2] S. Abrate, Functionally graded plates behave like homogeneous plates. *Composites Part B*, **39**, 151–158, 2008.

[3] D. Zhang and Y. Zhou, A theoretical analysis of FGM thin plates based on physical neutral surface. *Computer and Material Science*, **44**, 716-720, 2008.

[4] M. Bodaghi and AR. Saidi, Stability analysis of functionally graded rectangular plates under nonlinearly varying in-plane loading resting on elastic foundation. Archieves Applied Mechanics, **81**, 765–780, 2011.

[5] T. Prakash, M. Singha and M. Ganapathi, Influence of neutral surface position on the nonlinear stability behavior of functionally graded plates. Computational Mechanics, **43**, 341–350, 2009.

[6] D. Zhang, Modeling and analysis of FGM rectangular plates based on physical neutral surface and higher order shear deformation theory. *International Journal of Mechanical Science*, **68**, 92-104, 2013.

International Conference on Engineering Vibration
Ljubljana, Slovenia, 7-10 September 2015

MODAL PROPERTIES AND SIMULATION OF SELF-SUPPORTING SANDWICH FACADE PANELS

Pavel Hisem*[1], Jarmil Vlach[2]

[1]VÚTS, a. s.
pavel.hisem@vuts.cz

[2]VÚTS, a. s.
jarmil.vlach@vuts.cz

Keywords: Facade panel, sandwich, polyurethane based adhesive, modal properties, simulation, experiment.

Abstract. *Exterior design of buildings is important part of civil engineering. There many requirements and restrictions to facades, which must be satisfied. It was demonstrated, that it is very important to use sandwich panels as noise barriers, heat insulation and because of its other makings such as low weight and quite high stiffness. Especially low weight directly influences good manipulation, transport and installation process. This article is aimed to modal properties and simulation of self-supporting sandwich exterior panels, which are manufactured and certified in accordance with EN standards. Facade consist of aluminum facing reinforced by low density honeycomb core which is bond by polyurethane (PU) based adhesive. It is necessary to investigate mechanical properties like natural frequencies of structures and its relationship to the temperature. There are many possibilities how to predict elastic features in the main directions of anisotropy. However studying of mechanical properties for steady modulus of elasticity is well known, to describe the influence of vibrations is more complicated. It is known that properties investigated at equilibrium state of strain may give different values of natural frequencies. If the adhesive is near to its glass transition temperature or its melting point, natural frequencies depend more on dynamic strain values. As first we bring mechanical properties and mechanical model of composite panels at different temperatures and directions of anisotropy, then we carry a natural frequencies which we obtained by the experimental. We were also interested to the properties of connecting joints and its influence to the modal properties of facade. Finally there is comparison of results which we obtained from FE analysis, analytical solution and experiments.*

1 INTRODUCTION

Light structures like honeycomb sandwich panels become very popular at civil engineering. They can be used just for its good design, as heat insulation or noise barrier. It is also used because of its outstanding mechanical makings which is good balance of weight to stiffness. The example of self-supporting sandwich honeycomb panel shows Figure 1.

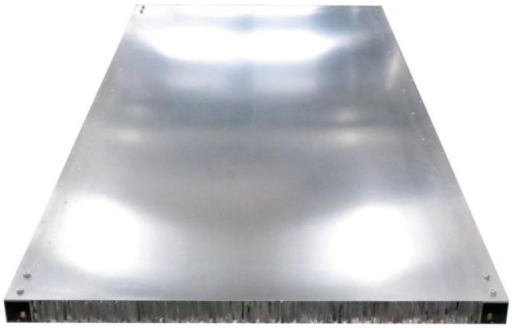


Figure 1: Honeycomb sandwich facade panel reinforced with beam inserts.

The structure usually consists from two thin facing layers which are fixed by adhesive to the reinforcing honeycomb core. We should point that there are many requirements and restrictions that must be satisfied to make the structures reliable and safe. This article is focused to honeycomb structures, which are certified in accordance with EN standards [1]. In this case the adhesive is (PU) Neopur 2238 was used. We investigated modal properties under different temperature.

2 THEORY

There are few ways, how to calculate natural frequencies of panels. In this article we show method, which is based on 1st order deformation plate theory [2]. Meaning of some used symbols and signs is pointed in Table 1.

Symbol	Meaning
φ_x	Rotation angle
w_o	Bending displacement
t	Time
ω	Angular velocity
ρ_o	Panel average density
a	Length
m	Frequency constant
I_{xy}	Rotatory inertia term
B_m	Linear constant
C_m	Linear constant
D_{11}	Bending stiffness factor
F_{55}	Shear stiffness factor
k_{55}	Correction factor

Table 1: Sandwich panel features.

Eqns. (1) and (2) are governing equations for free flexural vibrating process.

$$k_{55}.F_{55}.\left(\frac{\partial\varphi_x}{\partial x}+\frac{\partial^2 w_o}{\partial x^2}\right)=\rho_s.\frac{\partial^2 w_o}{\partial t^2} \qquad (1)$$

$$D_{11}.\frac{\partial^2\varphi_x}{\partial x^2}-k_{55}.F_{55}.\left(\varphi_x+\frac{\partial w_o}{\partial x}\right)=I_{xy}.\frac{\partial^2\varphi_x}{\partial t^2} \qquad (2)$$

Eqns. (3) and (4) give relationship between rotation, displacement and frequency of panel.

$$\varphi_x=B_m.e^{i\omega t}\,cos\frac{m\pi x}{a} \qquad (3)$$

$$w_o=C_m.e^{i\omega t}\,sin\frac{m\pi x}{a} \qquad (4)$$

Eqns. (1-4) give set of 2 equations for linear constants B_m and C_m [2],

$$F_{55}.\frac{m\pi}{a}.B_m+\left(F_{55}.\frac{m^2\pi^2}{a^2}-\rho_s.\omega^2\right).C_m=0 \qquad (6)$$

$$\left(D_{11}.\frac{m^2\pi^2}{a^2}+F_{55}\ -I_{xy}.\omega^2\right).B_m+F_{55}.\frac{m\pi}{a}.C_m=0 \qquad (7)$$

where parameters ρ_s and I_{xy} can be calculated with Eq. 8 and Eq. 9.

$$\rho_s=\rho_o.h \qquad (8)$$

$$I_{xy}=\rho_o.\frac{h^3}{12} \qquad (9)$$

Bending and shear stiffness factors are given by Eqns. (10-11).

$$D_{11}=\frac{1}{2}.\frac{E_f}{1-\mu^2}.h_f.h_c.(h_f+h_c) \qquad (10)$$

$$F_{11}=h_f.G_{zx,c} \qquad (11)$$

Solving a determinant of linear equations, we obtain two natural frequencies.

$$\begin{bmatrix} F_{55}.\frac{mx}{a} & F_{55}.\frac{m^2x^2}{a^2}-\rho_s.\omega^2 \\ D_{11}.\frac{m^2x^2}{a^2}+F_{55}\ -I_{xy}.\omega^2 & F_{55}.\frac{mx}{a} \end{bmatrix}\begin{bmatrix}B_m\\C_m\end{bmatrix}=\begin{bmatrix}0\\0\end{bmatrix} \qquad (12)$$

Analytic solution of set of Eqns. (1-4) can be obtained by using Eqns. (13) and (14).

$$\omega_m^2=\frac{1}{2\rho_s I_{xy}}\left[F_{55}.\left(\frac{m^2\pi^2}{a^2}.I_{xy}+\rho_s\right)+D_{11}.\frac{m^2x^2}{a^2}.\rho_s\pm\sqrt{\Delta}\right] \qquad (13)$$

$$\Delta=\left[F_{55}.\left(\frac{m^2\pi^2}{a^2}.I_{xy}+\rho_s\right)+D_{11}.\frac{m^2x^2}{a^2}.\rho_s\right]^2-4.F_{55}.D_{11}.\frac{m^4x^4}{a^4}.\rho_s.I_{xy} \qquad (14)$$

3 PANEL SPECIFICATION

Example of tested panel with its dimensions shows Figure 2. More technical details with facing properties are pointed in Tables (2-3). Material and geometric features of honeycomb core show Tables (4-5) and Figure 3.

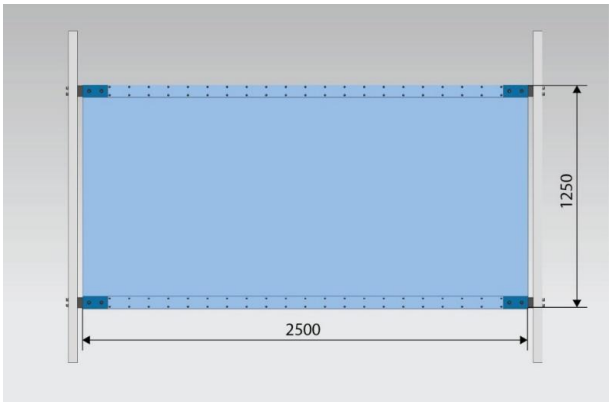


Figure 2: Example of bonded facade panel.

Panel mk.	Panel thickness h [mm]	Core height h_c [mm]	Length [mm]	Width [mm]
D14 2-70-2	74	70	2500	1250

Table 2: Sandwich panel features.

Material	Length [mm]	Width [mm] x [mm]	Thickness h_f [mm]	Density [kg.m^{-3}]	Modulus of elasticity E_f/G_f [MPa]
EN AW 6082	2500	1250	2	2.86	70228/27010

Table 3: Facing layer properties.

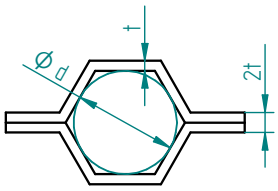


Figure 3: Honeycomb cell unit.

Material	Core density ρ [kg.m^{-3}]	Core parameter d [mm]	Thickness t [mm]
Al 99.5	27.3	14	0.066

Table 4: Honeycomb reinforcement properties.

Feature	21°C	40°C	80°C
$E_{x,c}$ [MPa]	0.029335	0.029253	0.02917
$E_{y,c}$ [MPa]	0.26397	0.26323	0.26249
$E_{z,c}$ [MPa]	363.988	301.988	176.862
$G_{xy,c}$ [MPa]	247.5	247.268	247.037
$G_{yz,c}$ [MPa]	119.966	106.411	61.015
$G_{zx,c}$ [MPa]	53.454	48.643	27.187
$\upsilon_{xy,c}$ [-]	0.3333	0.3333	0.3333
$\upsilon_{yz,c}$ [-]	0.000048492	0.000048402	0.000048311
$\upsilon_{zx,c}$ [-]	0.14	0.14	0.14

Table 5: Sandwich core panel features.

Material	Length [mm]	Height x Width [mm] x [mm]	Thickness [mm]	Weight [kg.m^{-1}]	Modulus of elasticity E_{rfb}/G_{rfb} [MPa]
EN AW 6082	2500	70 x 70	4	2.86	70000/26923

Table 6: Reinforcing beam insert parameters.

Material	Modulus of elasticity E_{con}/G_{con} [MPa]	Length [mm]	Height x Width [mm] x [mm]
EN AW 6082	70000/26923	80	62 x 62

Table 7: Connecting part features.

4 EXPERIMENTS

At first, we measured temperature dependence of shear dynamic modulus in two main directions of anisotropy. Honeycomb core dynamic properties are noted in Table 5. Those experiments were practised in heat chamber. Scheme of experiment shows Figure 4.

As the next step we measured natural free flexural vibration frequencies of simply supported sandwich panel in longitudinal direction at the temperature range 21 °C to 40 °C. Results of experiments show Table 9. DMA analysis was used to analyse dynamic response of signals in both experiments [3][4][5]. Governing equation for material response, which is a function of time, temperature and angular velocity shows Eq. 15. Results of all are carried carry in bending.

$$H(\omega,t,T)=\frac{X(\omega,t,T)}{F(\omega,t,T)} \qquad (15)$$

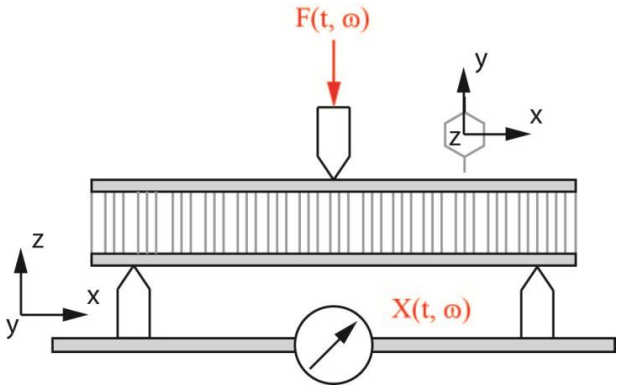


Figure 4: Scheme dynamic test in heat chamber.

5 FEM MODEL AND CALCULATION OF NATURAL FREQUENCIES

The aim of our work was comparison of calculated values of natural frequencies to a model. Real facade panels and its connection to a structure show Figure 5. There were simulated 3 different types of panels. First simulation and analytical solution deals with panels, which are simply reinforced just by a light honeycomb core. In second simulation, we study free flexural vibrations of facade, which is reinforced with aluminium alloy beam profiles along the longitudinal direction. Third simulation shows flexural vibrations of panel, which is fixed at frame in 4 points. Scheme of fully fixed part shows Figure 6. Names of its parts are denoted at Table 8.

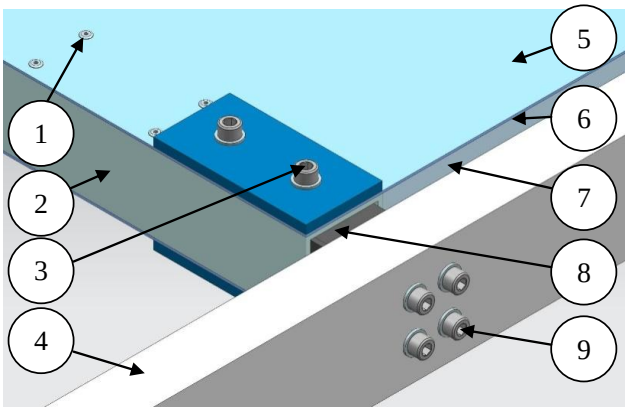


Figure 5: Scheme of structure fixed to rigid frame.

Symbol No.	Meaning
1	Rivet
2	Reinforcing profile
3	Bolt
4	Frame
5	Facing sheet
6	Adhesive
7	Honeycomb core
8	Connecting part
9	Frame connecting bolt

Table 8: Sandwich panel features.

FE model with the orientation of material anisotropy and its directions shows Figure 6.

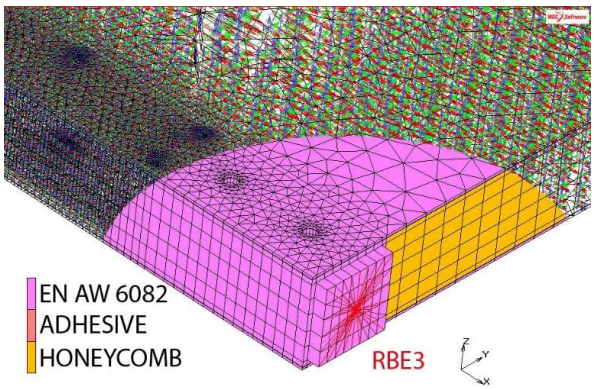


Figure 6: FEM model with fixing boundary condition.

Analytical solution of non-reinforced panel was calculated in accordance with Eqns. (1-14). In this case we considered value of k_{55}=1. FE model and FEA results come from MSC.MARC 2012. Boundary condition which represents bolt connection to a rigid frame is represented as RBE3 (Rigid Body Elements).

6 RESULTS

Experimental results of non reinforced honeycomb sandwich panel shows Table 9. Table 10 notes analytic solution and prediction of natural frequencies. In Table 11 we can read results of FEM analysis.

Type	21 °C	40 °C
Non reinforced panel	43.48	44.16
Reinforced panel	45.44	45.15

Table 9: Natural frequencies obtained from experiment.

Type	21 °C	40 °C	80 °C
Non reinforced panel	40.72	40.44	38.21

Table 10: Natural frequencies calculated with analytic solution.

Type	21 °C	40 °C	80 °C
Non reinforced panel	42.51	42.22	40.02
Reinforced panel	42.99	44.17	41.91
Reinforced panel connected to a rigid frame	64.23	63.98	62.47

Table 11: Natural frequencies calculated with MSC.MARC.

7 CONCLUSIONS

- Analysis shows that dynamic shear modulus of bond structure depends on temperature.
- However the value of dynamic modulus is temperature dependent, natural frequency is not influenced too much. It depends mainly on core density and stiffness of facing layers.
- Natural frequencies obtained by using FEM analysis and analytical solution match together with the maximum value of absolute error lower than 5 %.
- Simulation and experiment show, that used reinforcing beams don't influence value of natural frequency generally.
- FEM Simulation shows that natural frequency of beam reinforced panel is nearly 51 % higher than simply supported one.

REFERENCES

[1] EN 14509. *Self-supporting skin metal faced insulating panels*. Brussels: Europian committee for standardization, 2013.

[2] Berthelot J. M.; *Composite materials, Mechanical behavior and structural analysis.* New York, Springer, 1999.

[3] Miláček S.; *Modální analýza mechanických kmitů*, Vydavatelství ČVUT: 2001.

[4] Meissner, B.; Zilvar, V. *Fyzika polymerů, Struktura a vlastnosti polymerních materiálů*, 1st ed.; SNTL: Praha, 1987.

[5] McKelvey, J. M. *Polymer processing*. 1st ed. New York: John Wiley & Sons Inc., 1962. ISBN 0471584436.

International Conference on Engineering Vibration
Ljubljana, Slovenia, 7-10 September 2015

INTERACTING ACOUSTIC WAVES WITH STATIONARY STRATIFIED MEDIUM COMPRISING A LAYER OF BUBBLY LIQUID

Damir A. Gubaidullin*[1,2], Anatolii A. Nikiforov[1,2]

[1]Institute of Mechanics and Engineering, Kazan Science Center,
Russian Academy of Sciences, Kazan, Russia
[2]Kazan (Volga Region) Federal University, Kazan, Russia
damirgubaidullin@gmail.com, anikiforov1@yandex.ru

Keywords: Acoustic Waves, Bubbly Liquid, Attenuation Coefficient, Phase Velocity.

Abstract. *The dynamics of acoustic waves in stationary stratified medium comprising a layer of liquid with polydisperse gas bubbles is theoretically studied. The proposed method to calculate pressure pulse propagation in a multilayer medium uses a fast Fourier transform algorithm. An illustration of the method is given for an acoustic waves propagation problem: a piezoelectric transducer generated a pulse of pressure that propagated through water, transmitted through three-layer medium (plastic, bubbly liquid, plastic), and reached the hydrophone in water. Thus the acoustic signal did not propagate only through the bubbly liquid but through five media: water, plastic, bubbly liquid, plastic, and water again. Each layer of the stratified medium has a finite thickness; the amplitude of the acoustic signal is small. For calculations of the interaction acoustic waves with a layer of polydisperse bubbly liquid the dispersion relation (i.e. the function of the complex wave number on the frequency) is presented. The results show that the special dispersive and dissipative properties of the layer with bubble liquid can significantly affect the dynamics of the acoustic signal in a multilayer medium, depending on the central frequency of the signal. Dispersion behavior is distinctly observed when the center frequency of the acoustic signal is in the same frequency range as the peak of the attenuation coefficient of the bubbly liquid, this leads to a strong signal attenuation and distortion. The present calculations show good agreement with the available experiments.*

1 INTRODUCTION

It is well known that even an insignificant (on volume or mass) number of bubbles in a liquid strongly affects the acoustic properties of the liquid. The fundamentals of mechanics and thermal physics of bubble liquids and the most essential results on studying the wave processes in such media are presented in [1, 2]. The conditions under which the carrying-liquid compressibility manifests itself for the problems of acoustics of bubble liquids are established in [3]. The results of experimental investigations of bubble-gel samples are given in [4]. In [5, 6], the propagation of weak harmonic perturbations in two-fraction mixes of a liquid with polydisperse bubbles of gas of different composition was investigated. We study pressure-pulse propagation in a polydisperse bubble medium on the basis of [6]. The dependence of the complex wave number on the vibration frequency according to [6] provided that the disperse phase consists only of bubbles of one gas; i.e., the volume content of the second-fraction bubbles is zero and has the form

$$\left(\frac{K_*}{\omega}\right)^2 = \frac{1}{C_f^2} + \frac{3\alpha_{20}\alpha_{10}\rho_{10}\langle Q\rangle}{3\gamma_2 p_{10} - \langle QS\rangle} \tag{1}$$

$$C_f = C_1/\alpha_{10},\ \ Q = 1 - 3(\gamma_2 - 1)(y\cdot\coth(y) - 1)/y^2,\ \ y = \sqrt{i\omega a^2/\kappa_2},$$

$$S = i\omega a^2 h_a \rho_{10}/(1 + h_a t_a),\ \ h_a = -i\omega + 4\nu_1/a^2,\ \ \ t_a = a/(C_1(\alpha_{20})^{\beta}),$$

$$\langle Q\rangle = \frac{1}{\rho_2}\int_{a_{min}}^{a_{max}} N(a)g_0(a)Q da,\ \ \langle QS\rangle = \frac{1}{\rho_2}\int_{a_{min}}^{a_{max}} N(a)g_0(a)QS da,$$

$$\rho_2 = \int_{a_{min}}^{a_{max}} N(a)g_0(a)da,\ \ \ g_0(a) = \frac{4}{3}\pi a^3\rho_{20},$$

where ρ_{10}° and p_{10} are the true density and pressure of unperturbed liquid, C_1 is the sound speed in liquid, ν_1 is the kinematic viscosity of liquid, ρ_{20} is the true density of gas in bubbles, γ_2 is the adiabatic exponent of gas in bubbles, $N(a)$ is the distribution function over bubble sizes a, κ_2 is the thermal diffusivity of gas, and c_{p2} is the specific heat capacity of gas in bubbles at constant pressure.

2 RESULTS

Further, we calculated the dynamics of the pulse perturbation of the pressure in liquid containing the multilayer barrier and compared the results with the experiment. In [4], a sample consisting of two polycarbonate layers and the layer containing industrial gel with polydisperse bubbles was investigated experimentally.

The scheme of the experiment is shown in Figure 1. The sample is placed in a vessel with water between an acoustic-signal source (the piezoelectric converter) and a hydrophone. On the basis of the analysis of the parameters of sound waves transmitted through a sample, the data on its properties are found. The function of the distribution of bubbles over sizes was determined as

$$N(a) = \frac{n_t}{\sqrt{2\pi}\varepsilon} \exp\left\{ - \frac{\left[\ln\left(a / a_0\right)\right]^2}{2\varepsilon^2} \right\}, \quad a_{min} \le a \le a_{max}.$$

Where $a_0 = 0.08$ mm, $\varepsilon = 0.05$ is the distribution parameters [4]. For approximating the initial pulse from the experiment, the pressure pulse perturbation is set with the help of the imaginary part of the Morlet wavelet with the splash frequency $\nu_B = \omega_B / 2\pi = 0.25$ MHz:

$$p'(0,t) = \mathrm{Im}\left\{ \exp\left[- i 2\pi \nu_B (t - \tau) \right] \exp\left[\frac{-(t-\tau)^2}{2\delta^2} \right] \right\}. \tag{2}$$

The parameters $\tau = 20\,\mu$s and $\delta = 3\,\mu$s determine the splash location and width, respectively.

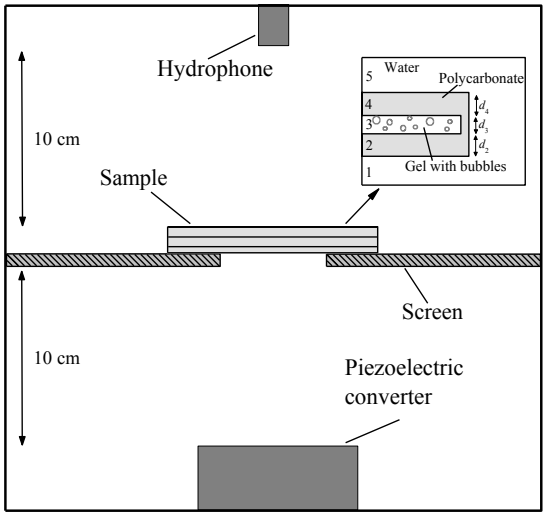


Figure 1. Scheme of installation for acoustic diagnostics from expermental data [4]

According to [7], the result of transmission of a plane monochromatic wave $\sim \exp\left[i(Kx - \omega t)\right]$ through a multilayer sample is a plane wave $\sim W \exp\left[i(Kx - \omega t)\right]$, where W is the wave-transmission coefficient, which is determined through the layer impedances Z_i and the input layer-boundary impedances Z_i^{in}:

$$W = \frac{Z_4^{in} + Z_4}{Z_4^{in} + Z_5} e^{iK_4 d_4} \frac{Z_3^{in} + Z_3}{Z_3^{in} + Z_4} e^{iK_3 d_3} \frac{Z_2^{in} + Z_2}{Z_2^{in} + Z_3} e^{iK_2 d_2} \frac{2Z_1}{Z_1 + Z_2}. \tag{3}$$

$$Z_j = \rho_j \frac{\omega}{K_j}, \quad Z_j^{in} = \rho_j \frac{Z_{j-1}^{in} - iZ_j \mathrm{tg}\left(K_j d_j\right)}{Z_j - iZ_{j-1}^{in} \mathrm{tg}\left(K_j d_j\right)} Z_j, \quad Z_1^{in} = Z_1.$$

Here, d_j and K_j are, respectively, the thickness and wavenumber of the *j*-th layer (for the liquid layer with bubble inclusions $d_3 = h$, $K_3 = K_*$).

Using the subroutine of the fast Fourier transform (FFT), we calculate the evolution of pressure pulse (2). With the help of the inverse Fourier transform, we determined the complex amplitudes of the harmonic components of initial pressure pulse (2) at $x = 0$. Then, using equation (3), we determine the amplitudes of harmonic components of the pulse transmitted through a multilayer sample to the hydrophone (at $x = \sum d_j$). The variation of pressure as a function of time in a new position is calculated with the help of the direct Fourier transform.

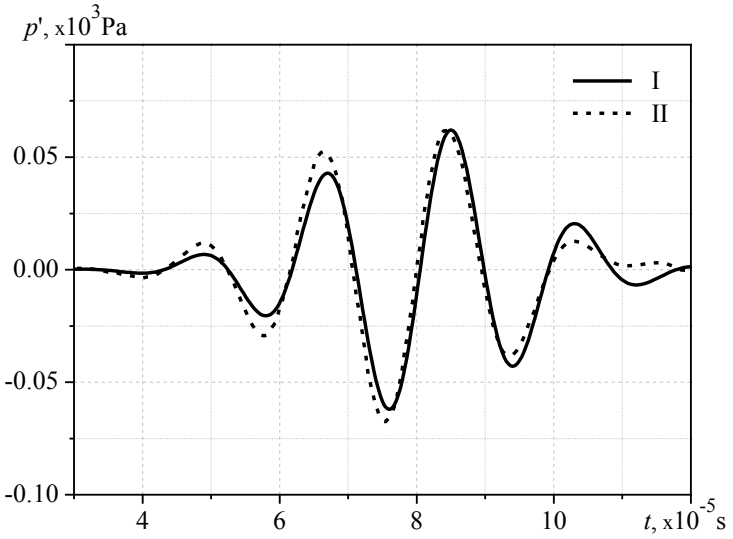


Figure 2. Pulse perturbation of pressure with the central frequency of 0.05MHz in purified water (I is the calculation, and II is the experimental data [4])

The results of calculation of evolution of the pressure pulse perturbation were compared with the experimental results [4]. The data in Figure 2 and Figure 4 for the initial signal show that function (2) describes well the initial acoustic signal written in the experiment [4]. The number of harmonics in the subroutine FFT was selected from the condition of the pulse motion in purified water (when there is no dispersion or dissipation) without distortion.

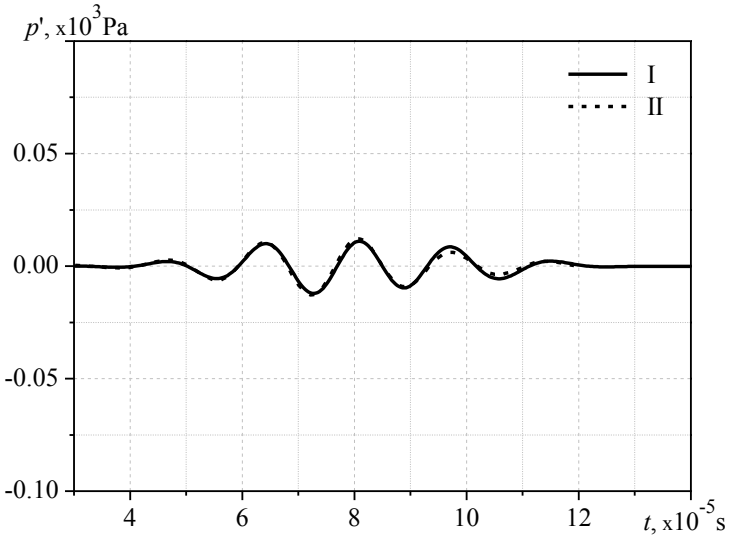


Figure 3. Pulse perturbation of pressure with the central frequency of 0.05MHz in water containing a multilayered sample (I is the calculation, and II is the experimental data [4])

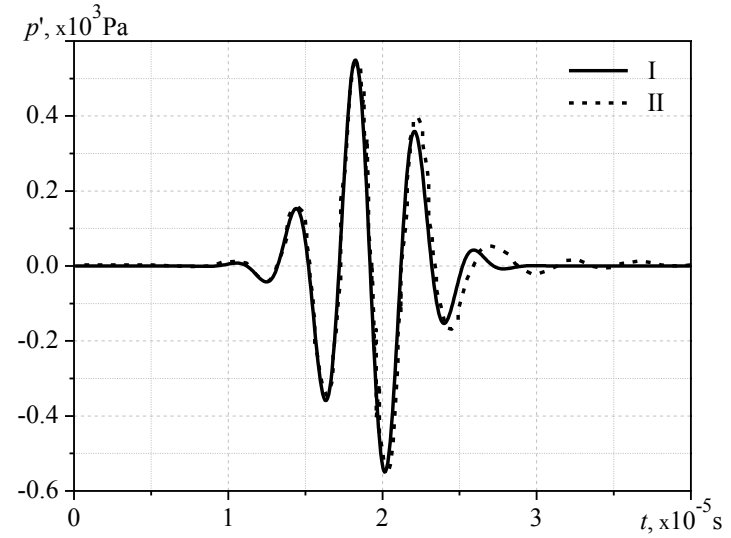


Figure 4. Pulse perturbation of pressure with the central frequency of 0.25MHz in purified water (I is the calculation, and II is the experimental data [4])

The experimental results [4] shown in Figure 3 and Figure 5 are obtained at the following bubble-layer parameters: $h = 2$ mm, $\alpha_{20} = 0.0015$, $a_0 = 0.08$ mm, and correspond to the average distance $l = a_0 / \alpha_{20}^{1/3} = 0.7$ mm between bubbles. In this case, the wavelength under consideration on a pure liquid is $L = 2\pi C_1 / \omega = 15$ mm. The continuum model under consideration for a bubble liquid is valid for $L >> l$ and $h >> l$. Although the second

condition is not completely fulfilled, the theoretical curve of the dependence of the pressure at the hydrophone on the reduced time agrees well with the experiment.

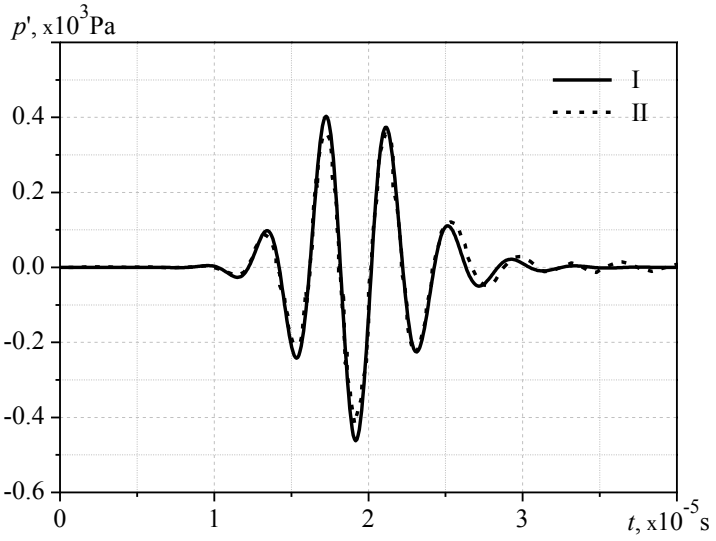


Figure 5. Pulse perturbation of pressure with the central frequency of 0.25MHz in water containing a multilayered sample (I is the calculation, and II is the experimental data [4])

Thus, the theory under consideration can be used confidently for calculation of the distortion of the acoustic signal in the diagnostics of multilayer samples with bubble inclusions.

3 CONCLUSIONS

- A theoretical method for calculating of the distortion of the acoustic signal when interacting with a multi-layer object is developed. The calculations on the interaction of pulse pressure perturbations of small amplitude with a multilayered sample containing a layer of polydispersed bubbly liquid is performed, comparison with experimental data is executed.
- It is shown, that the special dispersion and dissipative properties of the layer of bubble in liquid can significantly affect the dynamics of the acoustic signal in a multilayer medium, depending on the fundamental frequency of the signal.
- It is shown, that using the obtained method can be carried out verification of theoretical models of the dynamics of multiphase media on the basis of experimental data. It is found, that the developed theory can confidently be used to calculate the distortion of the acoustic signal when it interacts with multilayer sample containing a layer of bubble liquid.

ACKNOWLEDGMENTS

The study was performed by a grant from the Russian Science Foundation (project No. 15-11-10016).

REFERENCES

[1] R. I. Nigmatulin, *Dynamics of Multiphase Media*, Hemisphere, New York, 1991.

[2] V. E. Nakoryakov, B. G. Pokusaev and I. R. Shreiber, *Wave Propagation in Gas-Liquid Media*, CRC Press, New York, 1993.

[3] R. I. Nigmatulin, V. Sh. Shagapov and N. K. Vakhitova, Influence of compressibility of carrying phase on wave propagation in bubbly liquids, *USSR Academy of Sciences Doklady*, **304**, 1077–1081, 1989.

[4] V. Leroy, A. Strybulevych, J. H. Page and M. G. Scanlon, Sound velocity and attenuation in bubbly gels measured by transmission experiments, *Journal of the Acoustical Society of America*, **123**, 1931–1940, 2008.

[5] R. I. Nigmatulin, D. A. Gubaidullin, Yu. V. Fedorov, Sound waves in two-fractional polydisperse bubble liquids, *Doklady Physics*, **57**, 451–454, 2012.

[6] R. I. Nigmatulin, D. A. Gubaidullin, Yu. V. Fedorov, Acoustic waves of different geometry in polydisperse bubble liquids: Theory and experiment, *Doklady Physics*, **58**, 261–265, 2013.

[7] L. M. Brekhovskikh, *Waves in layered media*, Academic Press, New York, 1980.

International Conference on Engineering Vibration
Ljubljana, Slovenia, 7-10 September 2015

DMA ANALYSIS AND VISCOELASTIC MODEL OF POLYURETHANE BASED ADHESIVE UNDER VARIOUS CONDITIONS

Pavel Kavan*[1], Jarmil Vlach[2]

[1]VÚTS, a. s.
pavel.kavan@vuts.cz

[2]VÚTS, a. s.
jarmil.vlach@vuts.cz

Keywords: Polyurethane adhesive, temperature, water absorbtion, DMA analysis, loss factor, rheological properties.

Abstract. *Research of polyurethane based adhesives is very important because it belongs to group of the most popular polymers. It is well known that it is used in mechanical, civil, marine and aircraft engineering because of its outstanding properties and diverse mechanical properties. Bonded structures are also very popular because it`s low weight and good design. Using of adhesive cause, that little amount or any bolts and rivets are usually needed to connect parts of sets and subsets together. It makes all processes, such as installation, faster and less complicated. This article aims to polyurethane adhesive NEOPUR 2238, which is used in civil engineering. It's also known that mechanical properties of final product strongly depend on temperature and humidity. In case of large bonded surface structures this may cause failures, dangerous or other bad acoustic effects. We measured it`s features under various physical conditions and we especially focused to the material damping and viscoelastic makings. We studied temperature dependence of loss factor, storage and loss modulus. They were performed two basic types of experiments. First we bring results of compress tests of cylinder shaped specimens. The other experiments deal with the dynamic shear properties of thin bonded layer. All samples were tested at 4 different temperatures in frequency range from 0.01 to 10 Hz within 3 load amplitudes. DMA analysis method was used to study this phenomenon. Measured signals and data size were filtered, reduced and analysed by using direct Fourier transformation. Kelvin's rheological model and it's compliance to the material behavior is discussed.*

1 INTRODUCTION

This article is about testing polyurethane based plastic adhesive under various conditions in two different configurations. It is known that using adhesives is popular for bonded façade panels which example shows Fig. 1.



Figure 1: Example of bonded facade panel.

This work deals with tests of the polyurethane based adhesive Neopur 2238. It is well known that polyurethane based adhesives mechanical properties usually depend on temperature and humidity. We investigated it`s property changes at 4 different temperatures under the same preload and 3 different load amplitudes. Sample load was derived from safety standards for civil engineering [1]. We investigated material changes of static and dynamic stiffness and it`s damping properties. To determinate this we used DMA analysis, which is the robust method usually used for description viscoelastic material makings [3][4].

2 THEORY

One can say that Kelvin`s rheological model is one of the most popular models, which can be used for modelling of polymer based material properties. It is given by spring, which represents elastic mechanical property and damper which causes damping and viscosity. Physical model of shear stress preloaded sample is given by the Eq. (1)

$$\tau_o + G.\gamma(t) + \eta.\frac{d\gamma(t)}{dt} = \tau(t) \qquad (1)$$

, where γ means shear strain, τ_o is preload stress, η means kinematic viscosity and G is shear modulus. In case of simply tension or press experiment material stress response to the harmonic signal Eq. (2) can be given by Eq. (3).

$$\varepsilon(t) = \varepsilon_o + \varepsilon_A.sin(\omega.t) \qquad (2)$$

$$\sigma(t) = \sigma_o + \sigma'(\omega).sin(\omega.t) + \sigma''(\omega).cos(\omega.t) \quad (3)$$

Storage and loss modulus is given by Eq. 4, 5.

$$\sigma'(\omega) = \varepsilon_A.E'(\omega).sin(\omega.t) \quad (4)$$

$$\sigma''(\omega) = \varepsilon_A.E''(\omega).sin(\omega.t) \quad (5)$$

In case of stress equivalency of experiments and same area tested sample, we can write

$$\sigma_o = \frac{F_o}{A} \; or \; \sigma_o = E_o.\varepsilon_o \quad (6)$$

Relationship between dynamic, storage and loss modulus is given by Eqs. (7), (8), (9) and (10).

$$|E^*| = \sqrt{[E'(\omega)]^2 + [E''(\omega)]^2} \quad (7)$$

$$|E^*| = \frac{\sigma_A}{\varepsilon_A} \quad (8)$$

$$E'(\omega) = |E^*|.cos\,\delta \quad (9)$$

$$E''(\omega) = |E^*|.sin\,\delta \quad (10)$$

Loss factor describes Eq. (11).

$$tan\,\delta = \frac{E''(\omega)}{E'(\omega)} \quad (11)$$

3 SPECIMENS

Shape of specimens, which were used during the compress and shear experiments shows Fig. 2. Geometric features are pointed in Tab. 1.

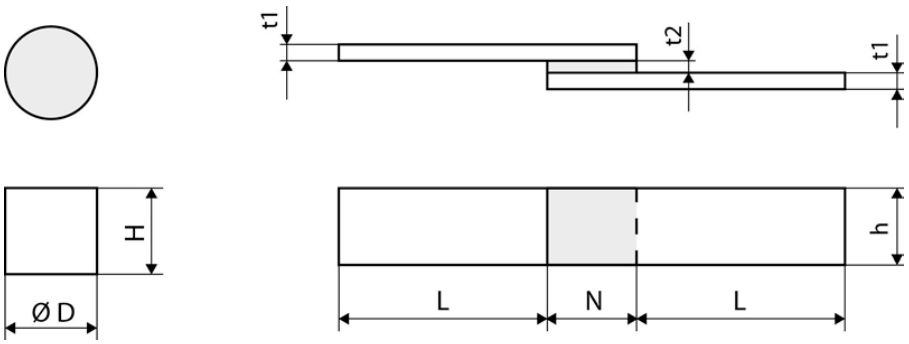


Figure 2: Specimens, type A – left, type B – right.

Dimension	Value
t1	1.6 mm
t2	0.2 mm
L	80 mm
N	12 mm
h	15 mm
H	15 mm
D	15 mm
A	177 mm^2

Table 1: Specimens properties

4 EXPERIMENTS

They were performed two basic types of experiments. In experiment type-A, cylinder shaped specimens were tested dynamically in pressing. Experiment type-B deals with the shear properties of thin bonded layer under the same conditions as type-A. Both tests were performed on the representative group of 10 specimens. All samples had the same test area, which was 177 mm^2. It shows Fig. 2. , the area has light grey colour. They were initially pre-loaded by force 50 N and tested in frequency range from 0.01 to 10 Hz within 3 different force amplitudes 15, 25 and 35 N. Measured signals and data size were filtered, reduced and analysed using direct Fourier transformation. Example of experiment shows Fig. 3. The example measured signal shows Fig. 4. Tests were practiced at the conditioned chamber with the test machine Instron Electropulse E3000.

Moisture absorption test was inspired by standards [1] and [2]. Test requires a chamber with constant temperature and humidity.

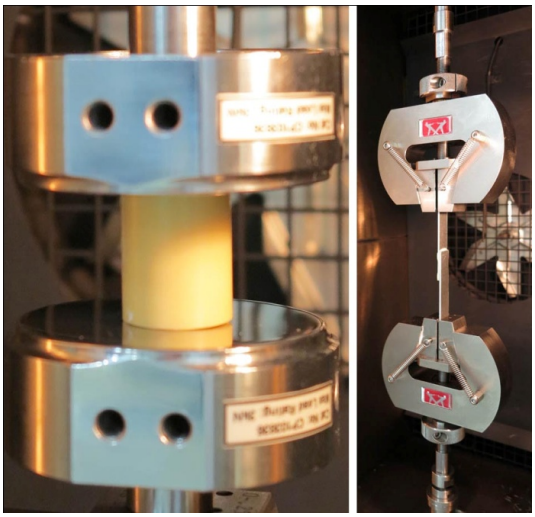


Figure 3: Experiments, type A – left, type B – right.

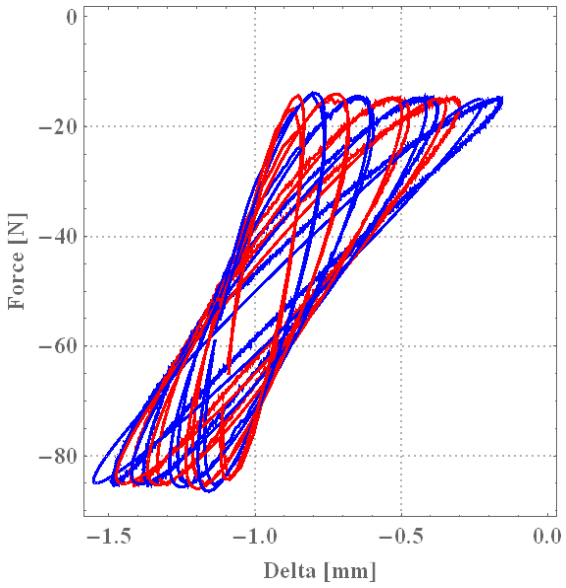


Figure 4: Experiment-A (40 °C), experimental data vs. model.

Steady state modulus at temperature	Value [MPa]
E_o (0 °C)	18.91
E_o (20 °C)	18.87
E_o (40 °C)	4.97
E_o (80 °C)	4.36
G_o (0 °C)	5.41
G_o (20 °C)	5.39
G_o (40 °C)	1.12
G_o (80 °C)	1.07

Table 2: Compress and shear steady state modulus at different temperatures.

5 RESULTS

5.1 Experiment - A

Results of elastic properties, which were obtained from compress dynamic tests of cylinder shaped specimens show Fig. 5, 6 and 7.

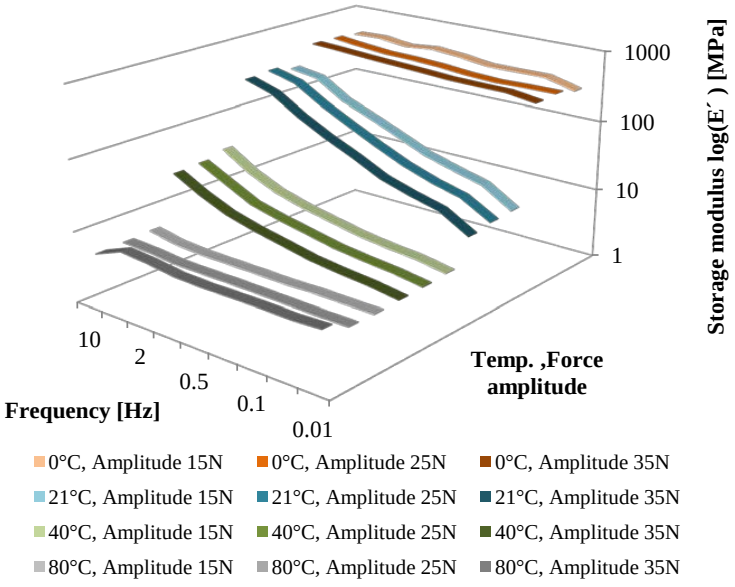


Figure 5: Experiment-A, storage modulus under various conditions.

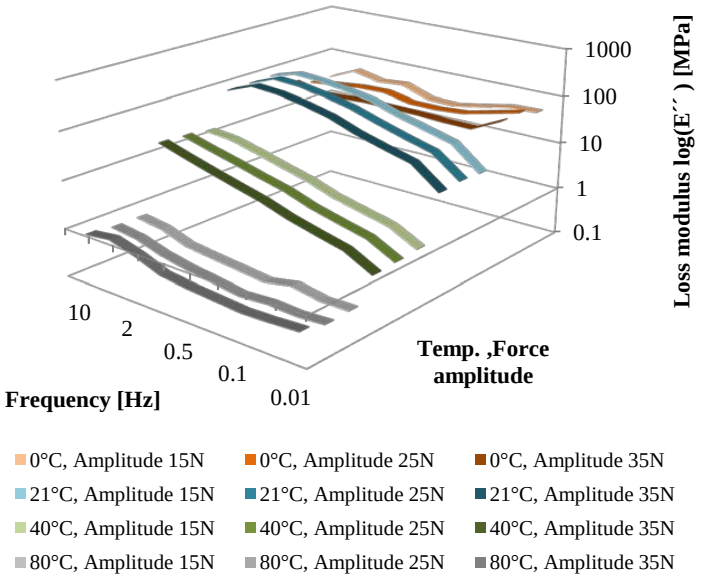


Figure 6: Experiment-A, loss modulus under various conditions.

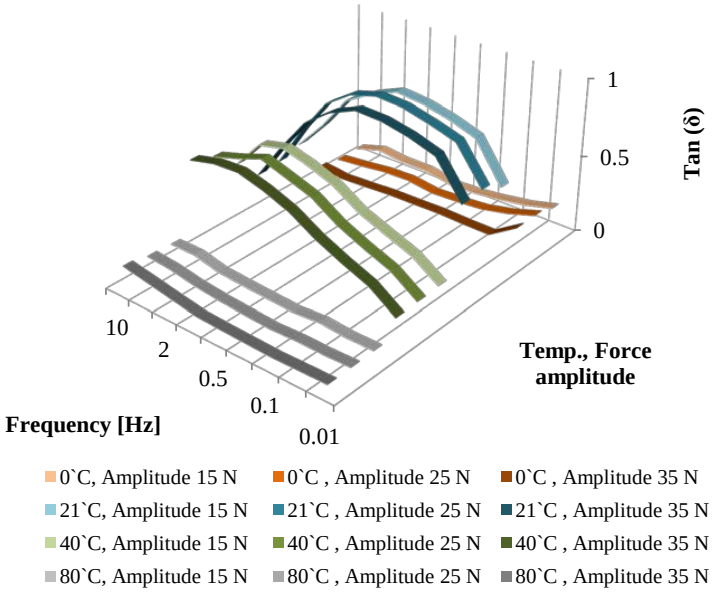


Figure 7: Experiment-A, loss factor under various conditions.

5.2 Experiment - B

Results of elastic properties, which determined from shear tests of bonded specimens show Fig. 8, 9 and 10.

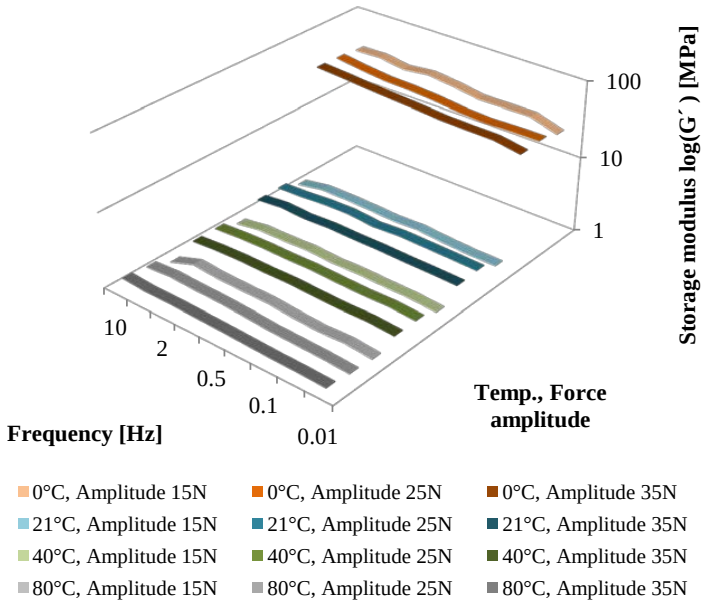


Figure 8: Experiment-B, shear storage modulus under various conditions.

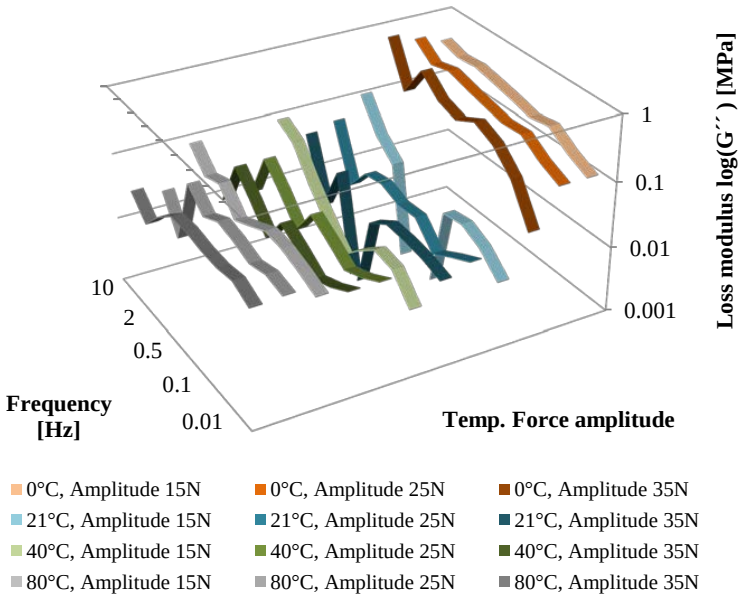


Figure 9: Experiment-B, shear loss modulus under various conditions.

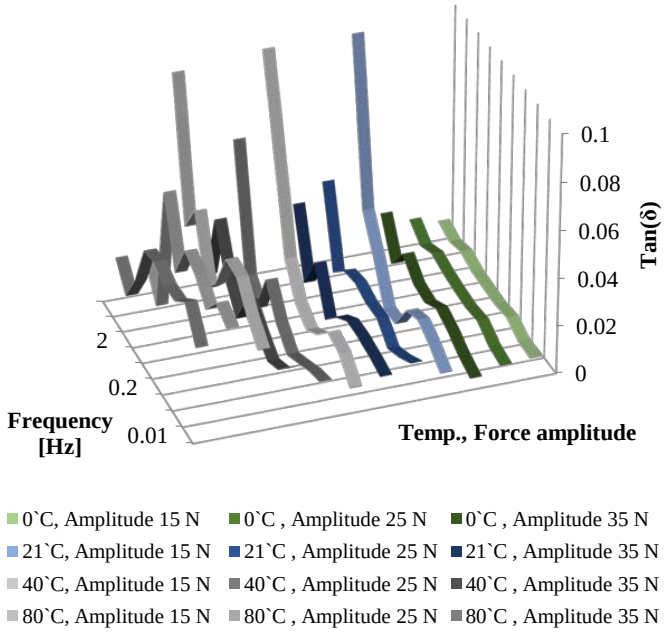


Figure 10: Experiment-B, shear loss factor under various conditions.

6 CONCLUSIONS

- The experiments show that material properties strongly depend on the temperature.
- Experiment type-A shows smooth and expectable evolution of mechanical properties. Value of storage modulus falls in the direction of rising temperature. Those properties are typical for amorphous polymers such as polycarbonate [3].
- Experiment type-B differs to type-A pretty much. However the trend of descending value of both moduli is the same, it changes in one huge step.
- We did not find any influence of moister absorbtion to the mechanical properties. We found that material is nearly hydrophobic. During the experiments any sample failure was obtained.
- Experiments also shows that value of compress and shear equilibrium modulus (Tab. 2) differ from storage modulus which shows Fig. 5 and Fig. 8.
- We can see that Kelvin`s model satisfy our tests and the match is good. It shows Fig. 4. Our results will be used for other following tests and FEM models of bonded structures.

REFERENCES

[1] EN 1990. *Basis of structural design*. Brussels: Europian committee for standardization, 2002.

[2] EN 14509. *Self-supporting skin metal faced insulating panels*. Brussels: Europian committee for standardization, 2013.

[3] Meissner, B.; Zilvar, V. *Fyzika polymerů, Struktura a vlastnosti polymerních materiálů*, 1st ed.; SNTL: Praha, 1987.

[4] McKelvey, J. M. *Polymer processing*. 1st ed. New York: John Wiley & Sons Inc., 1962. ISBN 0471584436.

International Conference on Engineering Vibration
Ljubljana, Slovenia, 7-10 September 2015

LAMB WAVE GENERATION USING LASER ABLATION

Naoki Hosoya*[1], Ryosuke Umino[2], Atsushi Kanda[3], Itsuro Kajiwara[4], Atsushi Yoshinaga[2]

[1]Department of Engineering Science and Mechanics, Shibaura Institute of Technology
hosoya@sic.shibaura-it.ac.jp

[2]Division of Mechanical Engineering, Shibaura Institute of Technology
{md14009, md15093} @shibaura-it.ac.jp

[3]Aeronautical Technology Directorate, Japan Aerospace Exploration Agency
kanda@chofu.jaxa.jp

[4]Division of Human Mechanical Systems and Design, Hokkaido University
ikajiwara@eng.hokudai.ac.jp

Keywords: Laser Ablation, Lamb Wave, Shock Wave, Non-Contact Laser Excitation

Abstract. *This paper proposes a method of Lamb wave generation using laser ablation for a non-contact damage detection. Conventional inspections of aircraft structures integrity with wide area, such as hammering tests and visual checks, are difficult to detect the damages of the aircraft structures precisely and quickly, because these inspections are based on empirical and subjective approaches. In past years, Lamb waves that were generated by contact-type sensors such as piezoelectric zirconate titanate devices were studied for detecting the damages. Since the contact-type sensors have to be attached to the aircraft structures at site, they cannot be used for conducting cost-effective and time-efficient damage detection. In this paper, Lamb waves that contain a broadband frequency element more than several hundred kHz are generated by non-contact impulse excitation using laser ablation. Laser ablation is widely used for vibration test in high frequency range, laser peening, propulsion of micro-aircraft, bolt loosening diagnosis, etc. In addition, scanning laser Doppler vibrometer is used to measure Lamb waves. Therefore, we establish a non-contact damage detection based on Lamb waves using laser ablation for acting the input, and laser Doppler vibrometer for measuring the output.*

1 INTRODUCTION

Lamb waves can propagate over long distances due to their small attenuation [1-5]. Conventionally Lamb waves with a single frequency are generated using a contact device such as a piezoelectric zirconate titanate (PZT) actuator [6-9]. Because Lamb waves generated via a non-contact device may quickly realize large-area damage detection on a huge object such as an aircraft, laser ultrasonic generation of Lamb waves using a non-contact device has been investigated [10-11].

An ultrasonic laser employs thermoelastic waves generated by a localized sudden temperature rise induced by pulse laser radiation on the target structure. However, laser-thermoelastically generated Lamb waves have small amplitudes of several hundred picometers. Consequently, numerous measurements (more than several hundred) are required to improve the signal-to-noise (SN) ratio, hindering practical applications to detect damage over large areas.

Although this method has been applied to some structures, it is still being researched as the type and degree of detectable damage have yet to be elucidated. If non-contact Lamb waves can be generated with an amplitude on the same level as conventional contact device–generated Lamb waves using pulse lasers, then the SN ratio will be improved, reducing the number of required measurements. This should decrease the time necessary to detect damage on a large object.

The laser ablation (LA) produces a high-temperature, high-density plasma plume (comprised of atoms, electrons, and ions) from a solid surface due to irradiation with a high-power pulse laser beam on a solid surface. The momentum (impulse) of the generated plasma from the solid acts as an excitation to the irradiated object by the laser beam. LA has a broad range of applications, including machining [12], propulsion [13], vibration testing [14-16], detection of loose bolts [17], and acoustic testing [18]. In vibration testing [14-16], LA containing components in the high-frequency region of several tens of kHz was applied as an ideal impulse excitation to a target structure. The impulse excitation generated using LA realized Lamb waves with large amplitudes over a broad range of frequencies. One advantage over conventional methods is that LA does not require contact.

The present paper discusses Lamb wave generation using LA and investigates the applicability of the proposed method. In this series of experiments, a laser beam was focused using a flat convex lens to elevate the laser fluence above the threshold for LA, which is 10^{12} to 10^{14} W/m^2 [19], and irradiated onto the LA generation point of the target structure.

2 LA EXCITAITON

Figure 1 shows the principle of how LA-generated impulse excitation acts on the target structure. A laser beam is irradiated on the solid surface. When the laser fluence reaches the LA threshold of 10^{12} to 10^{14} W/m^2 [19], the surface temperature of the solid increases rapidly to impart atoms, molecules, and their ions explosively, forming a plasma plume with a high temperature and high density. When mass Δm is imparted from the solid surface at velocity v, the momentum is given by Δmv, which acts as the impulse. Because the plasma plume is radially emitted in relation to the tangent plane of the solid surface where the laser beam is irradiated, the direction of the impulse is in the normal direction to the tangent plane of the solid surface. This impulse is the excitation force to the structure [14-16].

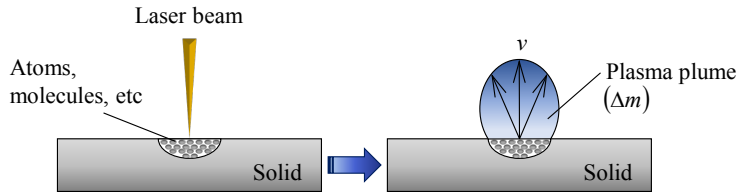


Figure 1: Principle of impulse excitation force generated by LA.

3 LAMB WAVE GENERATION

A non-contact Lamb wave generation system was constructed using LA.

3.1 LA-generated Lamb waves

Figure 2 shows the Lamb wave generation system using LA. The beam from a Nd: YAG pulse laser (Continuum, surelite III-10: wavelength, 1064 nm; beam diameter, 9.5 mm; pulse width, 5 ns; maximum output power, 1 J; beam divergence angle, 0.5 mrad) was focused on the excitation point of the target structure using a flat convex lens (focal length, 100 mm) to induce LA.

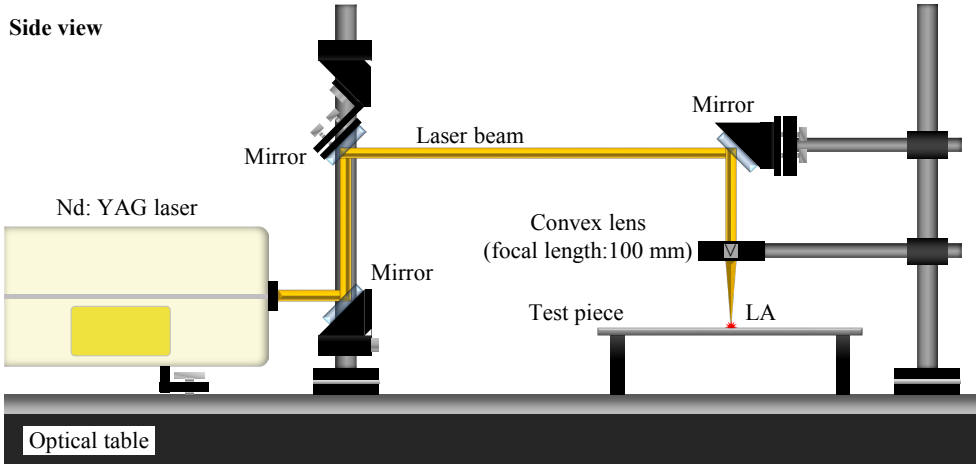


Figure 2: Non-contact laser excitation using LA.

3.2 Lamb wave measurements

Figure 3 shows the measurement system and measurement points on the test piece. The LA was induced by focusing the laser beam on the excitation point of the test piece using a flat convex lens to induce LA. The test piece was a 2-mm thick square duralumin plate (400 mm × 400 mm). The measurement region was a 100 mm × 100 mm square area, which was 50 mm away from the LA excitation point. The measurements were performed by a scanning laser Doppler vibrometer (LDV) (Polytec, PSV-500: He-Ne laser; measurement velocity, 0-20

m/s; sampling MAX, 5.12 MHz) over a length of 100 mm with a spacing of 2 mm per scan, totaling 2601 points (51 × 51). The sampling frequency, the number of sampling points, band-pass filter frequency range, and the number of measurements were 2.56 MHz, 2048, 0 to 400 kHz, and 10 times, respectively. The velocities measured by the LDV were integrated and measured as the displacement.

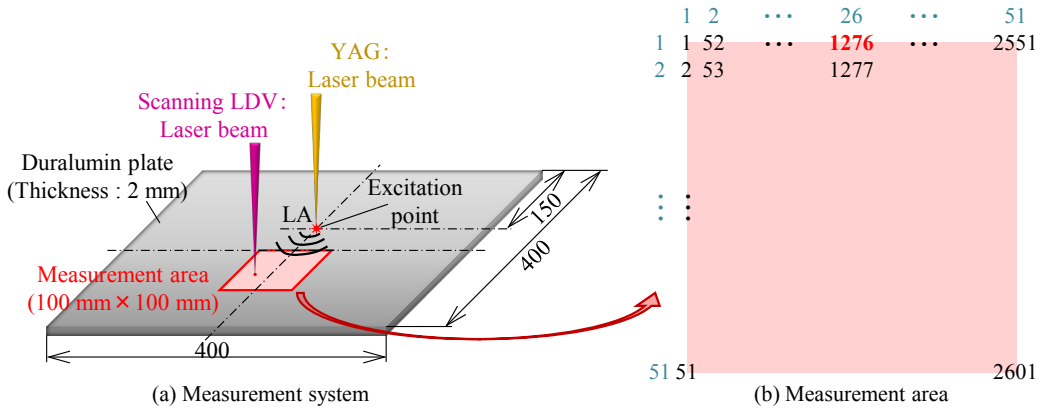


Figure 3: Lamb wave measurement system generated by LA.

3.3 Lamb wave propagation

Figure 4 shows the time response waveform of the Lamb waves measured at the measurement point closest to the excitation point (No. 1276) within the measurement area shown in Figure 3. Figure 5 shows the propagation of the Lamb waves at (a) 0 μs, (b) 80 μs, (c) 100 μs, and (d) 300 μs. The results around 150 μs in Figure 4, and Figure 7 (discussed later) indicate that the propagation velocities of the Lamb waves are several km/s. Additionally, the Lamb waves are velocity-dispersive containing a broad range of frequencies. Moreover, the pulse around 170 μs in Figure 4, has a propagation velocity of about 378 m/s based on the analysis shown in Figure 7 (discussed later). This means that a shock wave is generated by LA propagating on the test piece [18]. Figure 4 (at 170 μs and later) and Figure 5 (d) show that the Lamb waves are reflected at the boundaries and superimposed with the direct waves.

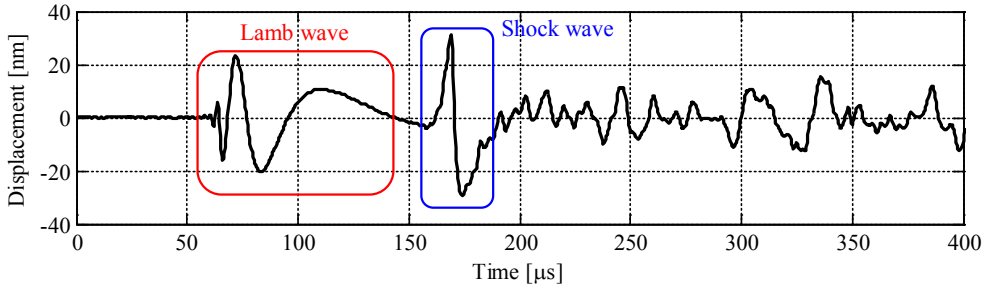


Figure 4: Time response of Lamb waves generated by LA.

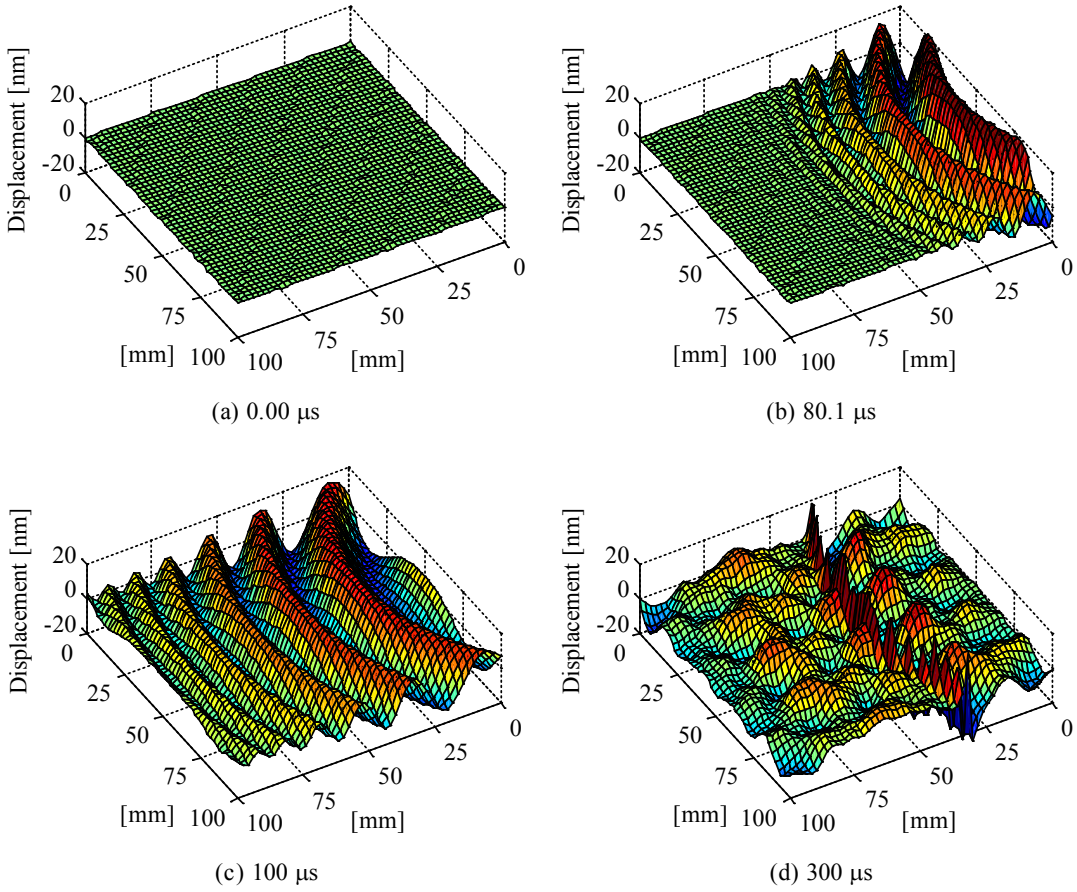


Figure 5: Lamb wave propagation generated by LA.

3.4 Lamb wave velocity in each frequency band

Figure 6 schematically shows the analysis procedure used to calculate the propagation velocities of the LA-generated Lamb waves. The displacements in the entire measurement area were lined up chronologically in terms of the measurement time and sliced at any cross-section, yielding cross-sectional images over time on the horizontal axis and distance on the vertical axis. These cross-sectional images visualize the propagation paths of the Lamb waves, and the slope of this straight line yields the propagation velocity. In the present paper, the slicing was performed at the center of the measurement area (No. 1276) to generate a cross-sectional image. Additionally, the wave propagation velocities were calculated for each 50-kHz section up to the upper frequency of the measurement filter at 400 kHz.

Figure 7 shows the cross-sectional images of the Lamb waves generated by LA at the following bands: (a) original and (b) 100 to 150 kHz. Figure 7 (a) indicates that the slope of the LA-generated Lamb waves gradually changes, confirming that the LA-generated Lamb waves contain a broad range of frequencies and have velocity dispersive characteristics. Figures 7

(b) indicates that the wave propagation velocities are larger for higher frequency bands. Furthermore, the fact that the slope of the path is constant means that the propagation velocities of the desired frequency bands are calculated correctly. Figure 7 indicates that large amplitude waves of about 220 μs to 480 μs are propagated. The calculated velocity of this propagation is approximately 378 m/s, which suggests that this is a displacement path due to the LA-generated shock waves propagated on the surface of the target structure.

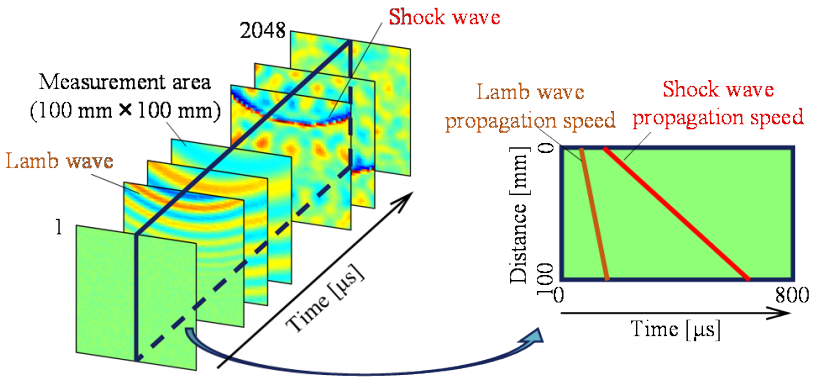


Figure 6: Calculation flow of the Lamb waves propagation speed.

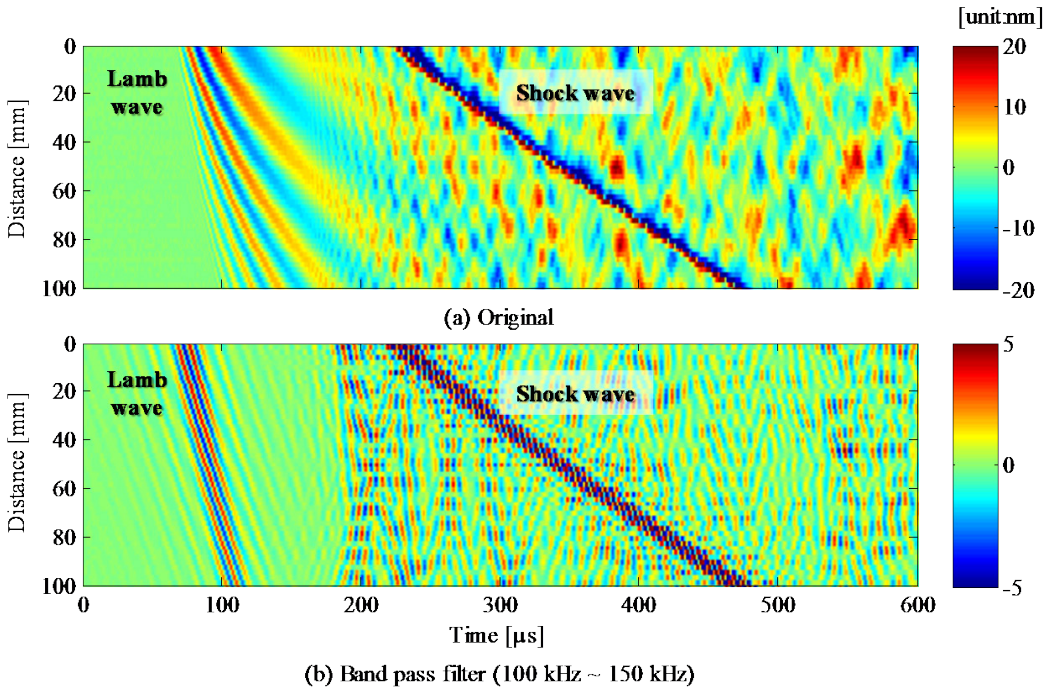


Figure 7: Lamb wave propagation velocity for traction-free duralumin plate.

4 CONCLUSIONS

This study aims to realize a non-contact damage detection system for large objects such as an aircraft. Irradiating the target surface with a high-power Nd: YAG pulse laser induces LA and generates Lamb waves. Then the resulting responses are measured by a scanning LDV. The effectiveness of the LA-generated Lamb waves using the proposed system is demonstrated.

The LA-generated Lamb waves have amplitudes several hundred times larger than those generated by conventional laser ultrasonic Lamb waves, improving the SN ratio. The improved SN ratio reduces the required number of measurements, resulting in a shorter measurement time. Thus, the proposed method can be applied to detect damage on a large area of a large structure.

ACKNOWLEDGMENTS

This study was supported by a Grant-in-Aid for Challenging Exploratory Research [26630080] from the Japan Society for the Promotion of Science.

REFERENCES

[1] G. Kulkarni and M. Mira, Simulation of time reversibility of Lamb wave in symmetric composite laminate. *International Journal of Mechanical Sciences*, **54**, 277-286, 2012.

[2] N. Bourasseau, E. Moulin, C. Delebarre, and P. Bonniau, Radome health monitoring with Lamb waves: Experimental approach. *NDT&E International*, **33**, 393-400, 2000.

[3] Y. Lu, L. Ye, Z. Su, and C. Yang, Quantitative assessment of through-thickness crack size based on Lamb wave scattering in aluminium plates. *NDT&E International*, **41**, 59-68, 2008.

[4] Z. Chang and A. Mal, Scattering of Lamb waves from a rivet hole with edge cracks. *Mechanics of Materials*, **31**, 197-204, 1999.

[5] L.D. Marchi, A. Perelli, A. Marzani, A signal processing approach to exploit chirp excitation in Lamb wave defect detection and localization procedures. *Mechanical Systems and Signal Processing*, **39**, 20-31, 2013.

[6] Z. Su, L. Ye, and Y. Lu, Guided Lamb waves for identification of damage in composite structure: A review. *Journal of Sound and Vibration*, **295**, 753-780, 2006.

[7] S. Park, C. Lee, and H. Sohn, Reference-free crack detection using transfer impedances. *Journal of Sound and Vibration*, **329**, 2337-2348, 2010.

[8] M.K. Kim, E.J. Kim, Y.K. An, H.W. Park, and H. Sohn, Reference-free impedance-based crack detection in plates. *Journal of Sound and Vibration*, **330**, 5949-5962, 2011.

[9] D. Cernadas, C. Trillo, A.F. Doval, O. Lopez, C. Lopez, B.V. Dorrio, J.L. Fernandez, and M. Perez-Amor, Non-destructive testing of plates based on the visualisation of Lamb waves by double-pulsed TV holography. *Mechanical Systems and Signal Processing*, **20**, 1338-1349, 2006.

[10] D. Clorennec, C. Prada, D. Royer, and T.W. Murray, Laser impulse generation and interferometer detection of zero group velocity Lamb mode resonance. *Applied Physics Letters*, **89**, 024101, 2006.

[11] J-R. Lee, H-J. Shin, C.C. Chia, D. Dhital, D-J. Yoon, and Y-H. Huh, Long distance laser ultrasonic propagation imaging system for damage visualization. *Optics and Lasers in Engineering*, **49**, 1361-1371, 2011.

[12] M. Kamata, M. Obara, R.R. Gattass, L.R. Cerami, and E. Mazur. Optical vibration sensor fabricated by femtosecond laser micromachining. *Applied Physics Letters*, **87**, 051106, 2005.

[13] T. Yabe, C. Phipps, M. Yamaguchi, R. Nakagawa, K. Aoki, H. Mine, Y. Ogata, C. Baasandash, M. Nakagawa, E. Fujiwara, K. Yoshida, A. Nishiguchi, and I. Kajiwara, Microairplane propelled by laser driven exotic target. *Applied Physics Letters*, **80**, 4318 ,2002.

[14] I. Kajiwara and N. Hosoya, Vibration testing based on impulse response excited by laser ablation. *Journal of Sound and Vibration*, **330**, 5045-5057, 2011.

[15] N. Hosoya, I. Kajiwara, and T. Hosokawa, Vibration testing based on impulse response excited by pulsed-laser ablation: Measurement of frequency response function with detection-free input. *Journal of Sound and Vibration*, **331**, 1355-1365, 2012.

[16] N. Hosoya, I. Kajiwara, and K. Umenai, Dynamic characterizations of underwater structures using non-contact vibration test based on nanosecond laser ablation in water: investigation of cavitation bubbles by visualizing shockwaves using the Schlieren method. *Journal of Vibration and Control*, ***, ****-****, 2015. (in press)

[17] F. Huda, I. Kajiwara, N. Hosoya, and S Kawamura, Bolt loosening analysis and diagnosis by non-contact laser excitation vibration tests. *Mechanical Systems and Signal Processing*, **40**, 589-604, 2013.

[18] N. Hosoya, I. Kajiwara, T. Inoue, and K. Umenai, Non-contact acoustic tests based on nanosecond laser ablation: Generation of a pulse sound source with a small amplitud *Journal of sound vibration*, **333**, 4254-4264, 2014.

[19] L. Torrisi, A. Borrielli, and D. Margarone, Study on the ablation threshold induced by pulse lasers at different wave lengths, *Nuclear Instruments and Methods in Physics Research B*, **255**, 373-379, 2007.

International Conference on Engineering Vibration
Ljubljana, Slovenia, 7-10 September 2015

ELASTIC WAVE PROPAGATION IN PLANE ROD SYSTEM

Alexandr O. Shimanovsky

Belarusian State University of Transport, Gomel, 246653, Belarus
tm.belsut@gmail.com

Keywords: Wave Propagation, Timoshenko Equation, Laplace Transform, Transmission coefficient, Reflection Coefficient.

Abstract. *Problem of stresses and strains waves propagation in the rod system is solved using the Laplace transform by time. Longitudinal movements are described by the classical wave equation, transverse movements – by Timoshenko equation. It is demonstrated that Timoshenko equations can be equivalently represented relatively to the cross sections rotation and shear angles. In this case the deflection function is obtained by coordinate integration of the angles sum. Thus the dynamical model of the beam can be considered as a combination of two waveguides with relative load, reflecting their interactions. The structure of forces and movements representation is found out. It allows to determine the values of the reflection and refraction coefficients at passing through the rod system node quickly. There was performed the calculation of wave passing through the sample plane node. This node is the connection of four rods of different cross-sections with perpendicular axes. It is shown that the consistent application to several nodes of the derived formulas for refraction and reflection coefficients allows to execute full rod system calculation. In this case, the equations for the kinematic characteristics and internal force factors representations do not depend on the parameters of the system as a whole. They are the multiplication of the corresponding to the traversed nodes coefficients. Thus the calculation can be performed locally, without taking into account all structure characteristics. The suggested method allows to reduce the computation time significantly in comparison with existing numerical methods.*

1 INTRODUCTION

When solving series of engineering problems there is a necessity of stresses and deformations investigation for waves propagation along rods and rod systems. For example, in [1] there were analyzed the oscillations of a high-rise building exited by its base motion during earthquakes. In the book [2] considerable attention is paid to calculations of dust shake off in the industrial electrostatic precipitators. The usage of numerical methods for the considered problems solution requires significant time and other resources. So, the most actual solving methods are the analytical ones.

The analysis of the longitudinal waves propagation along the stepped rods is well studied [3, 4], but there is only a small amount of investigations devoted to systems including at the same time longitudinal waves propagation and rods bending. In [5] the propagation of waves in the cross-bar systems are investigated and bending is described by the Euler-Bernoulli equation adjusted for rotational inertia of cross-sections. The authors of this study point out the presence of discrepancies between theoretical calculations and experimental data at the analysis of wave propagation through the junction of four rods with the same cross-section. Authors of [6] note, that especially for higher frequencies, Timoshenko's theory gives more reliable results than Euler-Bernoulli's theory, systems of beams, like frames, under arbitrary dynamic excitations should be analyzed on the basis of this refined theory.

The main methods of wave propagation investigation by the Timoshenko beam method are the usage of Fourier and Laplace transforms [1, 7]. For cases of oscillations of rods and rod systems caused by the impact, the Laplace transform by time is more convenient to use. This can be explained by the short time of the impact impulse. So the expansion of Laplace transform parameter in a power series can be used for calculations [2].

Thus, the main purpose of the present work is to develop a calculating algorithm for wave propagation through nodes of a system unit which bending is described by Timoshenko equation, and the propagation of longitudinal waves is described by the classical equation for the one-dimensional model.

2 WAVE PROPAGATION ALONG THE STEPPED ROD

To define the structure of the forces and movements equations there is a need to analyze the process of longitudinal elastic wave propagation along the stepped rod consisted of two parts: a finite length section and semi-infinite length section (Figure 1).

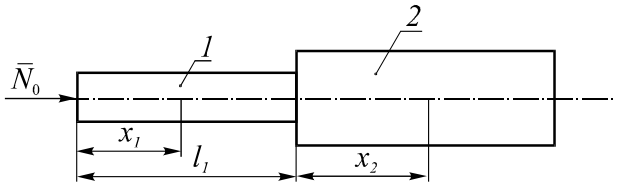


Figure 1: Scheme of rod with finite length section and semi-infinite length section.

Equations of longitudinal rods motion in the classical formulation are of the following form:

$$E_i F_i \frac{\partial^2 u_i}{\partial x_i^2} = \rho_i F_i \frac{\partial^2 u_i}{\partial t^2}; \quad i = 1,2 \tag{1}$$

where E_i, F_i, ρ_i – modulus of elasticity, cross-sectional areas, densities of rods materials;

x_i, u_i – coordinates and longitudinal displacements of rods points;

t – time.

Initial conditions for the case of rod non-deformed state before force application are the following:

$$u_i(x_i;0)=0;\ \frac{\partial u_i}{\partial t}(x_i;0)=0. \tag{2}$$

After Laplace transform in time application to (1), new form is obtained:

$$E_iF_i\tilde{U}_i''=\rho_iF_is^2\tilde{U}_i, \tag{3}$$

where s – Laplace transform parameter;

$\tilde{U}_i$ – displacement image.

Primes here and below denote the differentiation with respect to the coordinate.

The solution of the linear differential equation (3) is the function

$$\tilde{U}_i=A_ie^{\frac{s}{c_i}x_i}+Be^{-\frac{s}{c_i}x_i};\ c_i=\sqrt{\frac{E_i}{\rho_i}}, \tag{4}$$

where c_i – velocity of the wave front.

To define constants A_i, B_i it is necessary to consider boundary conditions:

$$\tilde{N}_1(0)=E_1F_1\tilde{U}_1'(0)=-\tilde{N}_0; \tag{5}$$

$$\tilde{N}_1(l)=E_1F_1\tilde{U}_1'(l_1)=E_2F_2\tilde{U}_2'(0)=\tilde{N}_2(0); \tag{6}$$

$$\tilde{U}_1(l_1)=\tilde{U}_2(0); \tag{7}$$

$$\tilde{U}_2(l_2)=(0), \tag{8}$$

where $\tilde{N}_0$ – an image of the longitudinal force attached to the rod end.

The second rod is of semi- infinite length, so the value of l_2 is big, and $A_2 = 0$. The equation for the image points movement of the second semi-infinite rod is:

$$\tilde{U}_2=B_2e^{-\frac{s}{c_2}x_2}; \tag{9}$$

Conditions (5-7) now allow to write the linear equations system to determine A_1, B_1, B_2:

$$\begin{cases} E_1F_1\dfrac{s}{c_1}(A_1-B_1)=-\tilde{N}_0; \\ E_1F_1\dfrac{s}{c_1}(A_1e^{\frac{s}{c_1}l_1}-B_1e^{-\frac{s}{c_1}l_1})=E_2F_2\dfrac{s}{c_2}(-B_2); \\ A_1e^{\frac{s}{c_1}l_1}+B_1e^{-\frac{s}{c_1}l_1}=B_2 \end{cases} \tag{10}$$

After system solution and considering in equation (4) the formulas for $\tilde{U}_1$ and $\tilde{U}_2$ are obtained:

$$\tilde{U}_1 = \frac{\tilde{N}_0}{\rho_1 F_1 c_1 s} \cdot \frac{(1+\mu)e^{-\frac{s}{c_1}x_1} - (\mu-1)e^{\frac{s}{c_1}(x_1-2l_1)}}{(1+\mu)+(\mu-1)e^{-2\frac{s}{c_1}l_1}}; \tag{11}$$

$$\tilde{U}_2 = \frac{\tilde{N}_0}{\rho_1 F_1 c_1 s} \cdot \frac{2e^{-\frac{s}{c_1}l_1 - \frac{s}{c_2}x_2}}{(1+\mu)+(\mu-1)e^{-2\frac{s}{c_1}l_1)}}, \tag{12}$$

where $$\mu = \frac{E_2 F_2 c_1}{E_1 F_1 c_2}.$$

After expanding the reciprocal to denominator value in a series in powers $e^{-2\frac{s}{c_1}l_1}$ we got

$$\frac{1}{(1+\mu)+(\mu-1)e^{-2\frac{s}{c_1}l_1}} = \frac{1}{1+\mu}\left(1+\sum_{n=1}^{\infty}\left(\frac{1-\mu}{1+\mu}e^{-2\frac{s}{c_1}l_1}\right)^n\right) \tag{13}$$

Substituting (13) in (11) and (12), we obtain:

$$\tilde{U}_1 = \frac{\tilde{N}_0}{\rho_1 F_1 c_1 s}\left\{e^{-\frac{s}{c_1}x_1} + \sum_{n=1}^{\infty}\left[\left(\frac{1-\mu}{1+\mu}\right)^n e^{\frac{s}{c_1}x_1 - 2n\frac{s}{c_1}l_1}\right] + \right.$$
$$\left. + \frac{1-\mu}{1+\mu}e^{\frac{s}{c_1}x_1 - 2\frac{s}{c_1}l_1} + \frac{1-\mu}{1+\mu}\sum_{n=1}^{\infty}\left[\left(\frac{1-\mu}{1+\mu}\right)^n e^{\frac{s}{c_1}x_1 - 2\frac{s}{c_1}l_1 - 2n\frac{s}{c_1}l_1}\right]\right\}; \tag{14}$$

$$\tilde{U}_2 = \frac{\tilde{N}_0}{\rho_1 F_1 c_1 s} \cdot \frac{2}{1+\mu}\left\{e^{-\frac{s}{c_1}l_1 - \frac{s}{c_2}x_2} + \sum_{n=1}^{\infty}\left[\left(\frac{1-\mu}{1+\mu}\right)^n e^{-\frac{s}{c_1}l_1 - \frac{s}{c_2}x_2 - 2n\frac{s}{c_1}l_1}\right]\right\}. \tag{15}$$

The following originals correspond to the received images:

$$u_1(x_1;t) = \frac{1}{\rho_1 F_1 c_1}\left\{\int_0^{t-\frac{x_1}{c_1}} N_0(\tau)d\tau + \sum_{n=1}^{\infty}\left(\frac{1-\mu}{1+\mu}\right)^n \int_0^{t-\frac{x_1}{c_1}-2n\frac{l_1}{c_1}} N_0(\tau)d\tau + \right.$$
$$\left. + \frac{1-\mu}{1+\mu}\int_0^{t-\frac{2l_1-x_1}{c_1}} N_0(\tau)d\tau + \sum_{n=1}^{\infty}\left[\left(\frac{1-\mu}{1+\mu}\right)^{n+1} \int_0^{t-\frac{2l_1-x_1}{c_1}-2n\frac{l_1}{c_1}} N_0(\tau)d\tau\right]\right\} \tag{16}$$

$$u_2(x_2;t) = \frac{1}{\rho_1 F_1 c_1} \cdot \frac{2}{1+\mu}\left\{\int_0^{t-\frac{x_1}{c_1}-\frac{x_2}{c_2}} N_0(\tau)d\tau + \sum_{n=1}^{\infty}\left[\left(\frac{1-\mu}{1+\mu}\right)^n \int_0^{t-\frac{l_1}{c_1}-\frac{x_2}{c_2}-2n\frac{l_1}{c_1}} N_0(\tau)d\tau\right]\right\} \tag{17}$$

Similarly, expressions for the longitudinal forces N_1 and N_2 considering (5) and (6) take the following form:

$$N_1(x_1;t) = -\left\{ N_0(t-\frac{x_1}{c_1}) + \sum_{n=1}^{\infty}\left[\left(\frac{1-\mu}{1+\mu}\right)^n N_0(t-\frac{x_1}{c_1}-\frac{2nl_1}{c_1})\right] + \right.$$
$$\left. + \frac{\mu-1}{\mu+1} N_0(t-\frac{2l_1-x_1}{c_1}) + \frac{\mu-1}{\mu+1}\sum_{n=1}^{\infty}\left[(\frac{1-\mu}{1+\mu})^n N_0(t-\frac{2l_1-x_1}{c_1}-\frac{2nl_1}{c_1})\right]\right\}; \quad (18)$$

$$N_2(x_2;t) = -\frac{2\mu}{1+\mu}\left\{ N_0\left(t-\frac{l_1}{c_1}-\frac{x_2}{c_2}\right) + \sum_{n=1}^{\infty}\left[\left(\frac{1-\mu}{1+\mu}\right)^n N_0\left(t-\frac{l_1}{c_1}-\frac{x_2}{c_2}-\frac{2nl_1}{c_1}\right)\right]\right\} \quad (19)$$

Function arguments for the applied force in the equations (18) and (19), and also upper integration limits in (16) and (17) are the equations of $(t - t_0)$ type, where t_0 – time for wave front to pass the distance from the point of force application to a cross-section requiring the displacement and inner strength determination.

The first terms in all four equations are the result of direct (without reflections) propagation of the deformation wave from the force application point to the considered cross-section. They correspond to the first terms of the numerator and denominator in the formulas (11, 12).

The second terms of the expressions (16–19) show the result of the deformation wave propagation $2n$ times reflected from the end of the first rod in the x coordinate direction. They correspond to the first terms of the numerator and the second terms of the denominator in the equations (11, 12).

The third terms of the expressions (16, 18) are the result of the first wave reflection from the neighboring rods. In the formula (11) the second term of the numerator and the first term of the denominator result in the presence of such member.

The last terms in the equations (16, 18) are the result of the deformation wave propagation 2n times reflected from the end of the first rod in the direction of x coordinate decrease. They correspond to the second terms of the numerator and denominator in the formula (11).

Then we calculate the values for waves reflection and waves transmission coefficients. They characterize the ratio between the parameters of the corresponding waves after and before the node.

Thus, the coefficient of waves transmission k_t is determined by the ratio of the first terms in the formulas (17) and (16). On the other hand, this parameter can be calculated directly from the expressions (11, 12) as the ratio of the coefficients near $e^{-\frac{s}{c_1}l_1-\frac{s}{c_2}x_2}$ and near $e^{-\frac{s}{c_1}x_1}$ in the equations for $\tilde{U}_2$ and $\tilde{U}_1$ respectively.

The waves reflection coefficient k_r is determined by the ratio of the third and the first terms in the formula (16) or by the ratio of coefficient near $e^{-2\frac{s}{c_1}l_1+\frac{s}{c_1}x_1}$ and coefficient near $e^{-\frac{s}{c_1}x_1}$ in the equation (11). Thus we get:

$$k_t = \frac{2}{1+\mu}; \quad k_r = \frac{1-\mu}{1+\mu}. \quad (20)$$

The obtained results coincide with the same values calculated by another method in [4].

Using k_t and k_r values, we can create the $N_1 = N_1(x_1; t)$ and $N_2 = N_2(x_2; t)$ dependences on the base of only $N_0 = N_0(t)$ function.

3 DETERMINATION OF TIMOSHENKO BEAM REACTION ON THE SHORT-TERM FORCE APPLICATION

Based on Timoshenko model [8] the system of equations for rod oscillations can be presented in an equivalent manner with respect to the shear angle γ and the rotation angle of cross-sections ψ:

$$\begin{cases} \dfrac{GF}{k}\gamma'' - \rho F\ddot{\gamma} - \rho F\ddot{\psi} = 0; \\ EI\psi'' - \rho I\ddot{\psi} + \dfrac{GF}{k}\gamma = 0. \end{cases} \quad (21)$$

where G – shear modulus, Pa.

I, k – moment of inertia, and the coefficient of cross-sectional shape [8].

Then function of the beam axis deflection can be determined from the equation

$$y' = \psi + \gamma. \quad (22)$$

The system (21) allows to consider a dynamic model of the beam as a couple of two waveguides described by the first two terms from each of the system equations. The last terms in the equations reflect the interaction of these waveguides. We assumed that the waveguides operate independently. Then the image by Laplace

$$\tilde{\gamma}'' - \lambda_1^2\tilde{\gamma} = 0; \;\; \tilde{\psi}'' - \lambda_2^2\tilde{\psi} = 0, \quad (23)$$

where $$\lambda_1 = \frac{s}{c_s}, \;\; \lambda_2 = \frac{s}{c_r},$$

c_s, c_r – velocity of the shear and rotation wave.

Solution of the system (23) is

$$\tilde{\gamma} = A_1 e^{\lambda_1 x} + B_1 e^{-\lambda_1 x}, \quad (24)$$

$$\tilde{\psi} = A_2 e^{\lambda_2 x} + B_2 e^{-\lambda_2 x}, \quad (25)$$

Expression (24) describes the simple shear model (for $\psi = 0$). Our carried out earlier investigations [9] showed that the acceleration calculated on the base of this model are very similar to the obtained by Timoshenko model based on the exact solution. These data, as well as a comparison with the experimental results, allowed to make a conclusion about the possibility of shear model applying to the calculation of the acceleration in the bars under the impact loading.

4 PROPAGATION OF DEFORMATION WAVES THROUGH THE ROD SYSTEM NODES

4.1 Differential equations solution for the crossed bars motion

Flat bar system can be calculated for the case of impact, if you know how the waves refract and reflect in a typical rod node. We restrict ourselves with the case when the rods are perpendicular to each other (Figure 2). The material was assumed as linear elastic with small deformations.

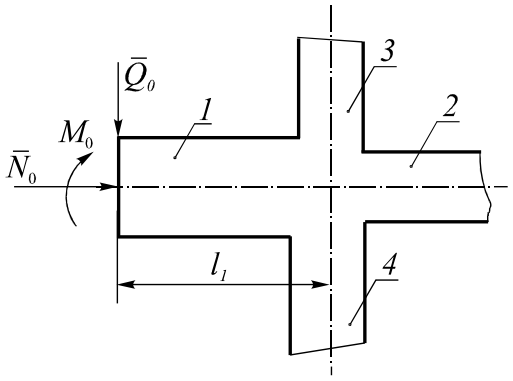


Figure 2: Typical node.

Interacting rods movement can be described by differential equations:

$$\left.\begin{aligned} &\rho_i F_i \ddot{u}_i - E_i F_i u_i'' = 0; \\ &\rho_i F_i \ddot{\gamma}_i - \frac{G_i F_i}{k_i}\gamma_i'' + \rho_i F_i \ddot{\psi}_i = 0; \\ &\rho_i I_i \ddot{\psi}_i - E_i I_i \psi_i'' - \frac{G_i F_i}{k_i}\gamma_i = 0, \end{aligned}\right\} \quad i = 1, 2, 3, 4, \tag{26}$$

where u_i, γ_i, ψ_i – longitudinal displacements, angles of displacements and rotation of the cross-sections for the i-th rod;

ρ_i, E_i, G_i – density and elasticity modulus of the i-th rod;

F_i, I_i, k_i – area, moment of inertia, coefficient of cross-section shape for the i-th rod;

Dots denote differentiation with respect to time t, dashes denote differentiation with respect to longitudinal coordinate z.

Lateral displacements of rods axes points can be defined from the equations:

$$y_i' = \gamma_i + \psi_i . \tag{27}$$

Then the Laplace transform by variable t is applied to system (26). If the initial conditions are equal to zero we get the equations in images:

$$\left.\begin{aligned} &\tilde{u}_i'' - \lambda_{0i}^2 \tilde{u}_i = 0; \\ &\tilde{\gamma}_i'' - \frac{s^2}{c_{1i}^2}(\tilde{\gamma}_i + \tilde{\psi}_i) = 0; \\ &\tilde{\psi}_i'' - \frac{s^2}{c_{0i}^2}\psi_i' + \frac{1}{\mu_i^2 r_i^2}\tilde{\lambda}_i = 0, \end{aligned}\right\} . \tag{28}$$

where $\lambda_{0i} = \dfrac{s}{c_{0i}}$; $c_{0i}^2 = \dfrac{E_i}{\rho_i}$; $c_{1i}^2 = \dfrac{G_i}{\rho_i k_i}$; $\mu_i^2 = \dfrac{E_i k_i}{G_i}$; $r_i^2 = \dfrac{I_i}{F_i}$.

Solution of system (28) with taking into account (27) can be written in the form:

$$\tilde{u}_i = A_i e^{\lambda_{0i} z} + B_i e^{-\lambda_{0i} z}.$$

$$\tilde{\gamma}_i = C_{1i} e^{\lambda_{1i} z} + C_{2i} e^{-\lambda_{1i} z} + D_{1i} e^{\lambda_{2i} z} + D_{2i} e^{-\lambda_{2i} z};.$$

$$\tilde{\psi}_i = \left(\frac{\lambda_{1i}^2 c_{1i}^2}{s^2} - 1 \right) \left(C_{1i} e^{\lambda_{1i} z} + C_{2i} e^{-\lambda_{1i} z} \right) + \left(\frac{\lambda_{2i}^2 C_{1i}^2}{s^2} - 1 \right) \left(D_{1i} e^{\lambda_{2i} z} + D_{2i} e^{-\lambda_{2i} z} \right). \tag{29}$$

$$\tilde{y}_i = \frac{c_{1i}^2}{s^2} \left[\lambda_{1i} \left(C_{1i} e^{\lambda_{1i} z} - C_{2i} e^{-\lambda_{1i} z} \right) + \left(D_{1i} e^{\lambda_{2i} z} - D_{2i} e^{-\lambda_{2i} z} \right) \right].$$

where $$\lambda_{1i,2i} = \frac{s}{c_{0i}} \sqrt{\frac{1+\mu_i^2}{2} \pm \sqrt{\left(\frac{1-\mu_i^2}{2} \right)^2 - \frac{c_{0i}^2}{r_i^2 s^2}}}.$$

The total number of constants in required solution is equal to twenty four. Due to the semi-infinity of three rods in the node the constants A_{1i}, C_{1i}, C_{1i} are equal to zero at $i = 2,3,4$. To determine remaining constants it is necessary to consider boundary conditions.

Conditions of dynamic equilibrium:

$$E_1 F_1 \tilde{u}_1'(0) = -\tilde{N}_0; \;\; \tilde{N}_1(l_1) = \tilde{N}_2(0) + \tilde{Q}_3(0) - \tilde{Q}_4(0);$$

$$\frac{G_1 F_1}{k_1} \tilde{\gamma}_1(0) = -\tilde{Q}_0; \;\; \tilde{Q}_1(l_1) = \tilde{Q}_2(0) + \tilde{N}_3(0) - \tilde{N}_4(0); \tag{30}$$

$$E_1 I_1 \tilde{\psi}_1'(0) = -\tilde{M}_0; \;\; \tilde{M}_1(l_1) = \tilde{M}_2(0) + \tilde{M}_3(0) - \tilde{M}_4(0);$$

Conditions of joint movement:

$$\tilde{u}_1(l_1) = \tilde{u}_2(0) = \tilde{y}_3(0) = \tilde{y}_4(0);$$

$$\tilde{y}_1(l_1) = \tilde{y}_2(0) = \tilde{u}_3(0) = \tilde{u}_4(0); \tag{31}$$

$$\tilde{\psi}_1(l_1) = \tilde{\psi}_2(0) = \tilde{\psi}_3(0) = \tilde{\psi}_4(0).$$

After substituting the expressions for displacements and angles (29), a system of fifteen algebraic equations is obtained. In general, the solution process for the system is very time-consuming, but the resulting analytical expressions give the important information about the influence of all rods parameters on the waves transmission through the node. Moreover, as it was noted above, to calculate a single deformation wave transmission it is enough to take into account only the first terms of the numerator and denominator (without considering the exponential factor). We have received expressions of these coefficients with the help of MATHEMATICA software. Here they are not presented because of their bulkiness.

4.2 Waves refraction at a number of rod system nodes

The consistent application of the gotten expressions to several nodes makes it possible to carry out the complete calculation for rod system. Procedure for the internal forces calculation can be considered by the example system shown in Figure 3. The initial data corresponds to the real design of the industrial precipitator electrode: $F_{1\text{-}5}$ = 10,64cm^2; F_6 = 16 cm^2, $I_{1\text{-}5}$ = 4167 cm^4, I_6 = 85,3 cm^4, E = 210 GPa, G = 80 GPa, ρ = 7950 kg/m^3, $k_{1\text{-}5}$ = 1,66, k_6 = 1,2, l_0 = 0,64 m.

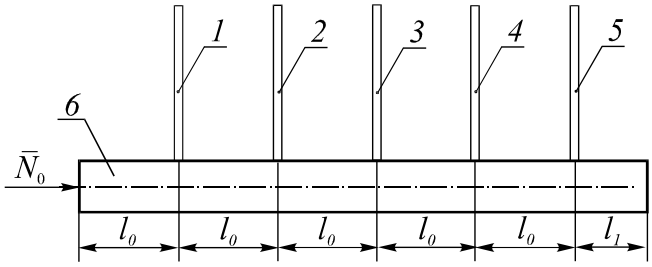


Figure 3: Precipitator scheme.

To determine the law of internal longitudinal force change N in the area of the beam 6 between the bars 1 and 2 the expression for the transmission coefficient (in the images) is used. Then the formula for image N_1 takes the form of:

$$\tilde{N}_1 = k(s)\tilde{N}_0. \tag{32}$$

To define force N in the area of the beam 6 between the bars 2 and 3 the image N_1 is assumed as the initial image. Then

$$\tilde{N}_2 = k(s)\tilde{N}_1 = k^2(s)\tilde{N}_0. \tag{33}$$

Similarly, we obtain:

$$\tilde{N}_i = k^n(s)\tilde{N}_0. \tag{34}$$

Thus, the obtained expressions don't depend on the parameters of the system as a whole. They are only a function of the traversed nodes characteristics (the ratio $2l_0/c_0$ is more than 160 μs, so the reflected waves could be neglected). Based on the transform results the plot for $N_n(t)$ was created for the case when $N_0(t)$ is a sine half-wave of 160 μs length (Figure 4).

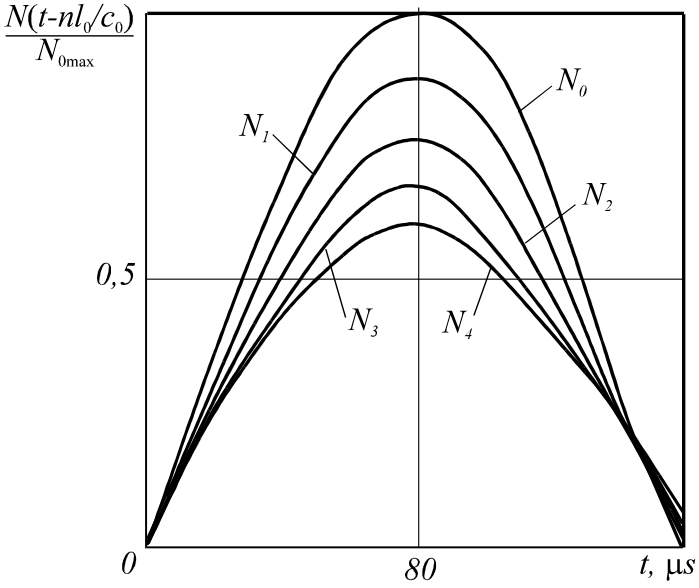


Figure 4: Longitudinal forces at the rod system points.

5 CONCLUSIONS

- Consistent application to several nodes of the derived formulas for refraction and reflection coefficients allows to execute full rod system calculation. In this case, the equations for the kinematic characteristics and internal force factors representations do not depend on the parameters of the system as a whole. They are the multiplication of the corresponding to the traversed nodes coefficients. Thus the calculation can be performed locally, without taking into account all structure characteristics.
- This maintains high reliability of the results and significantly reduces the computation time compared with other existing techniques.

REFERENCES

[1] M. Ebrahimian, M. I. Todorovska, Wave propagation in a timoshenko beam building model. *Journal of Engineering Mechanics*, **140**, No. 5, 1-10, 2014.

[2] V. B. Mescheryakov, *Statics, dynamics and stability of thin-walled rods considering shear deformations*. Construction Institutes Association, Moscow, 2014 (in Russian).

[3] K. F. Graff, *Wave motion in elastic solids*. Dover Publications, New York, 1991.

[4] V. K. Manzhosov, V. V. Slepukhin, *Modeling of longitudinal impact in rod systems with inhomogeneous structure*, Ul'yanovsk State Technical University, Ul'yanovsk, 2011 (in Russian).

[5] V. I. Erofeev, I. D. Konyuhova, V. M. Rodyushkin, Wave propagation in cruciform rod systems. *Applied Mechanics and Technical Physics*, No. 2, 153–156, 1987 (in Russian).

[6] H. Antes, M. Schanz, S. Alvermann, Dynamic analyses of plane frames by integral equations for bars and Timoshenko beams. Journal of Sound and Vibration, **276**, No. 3–5, 807–836, 2004.

[7] Y.-C. Su, C.-C. Ma, Theoretical analysis of transient waves in a simply-supported Timoshenko beam by ray and normal mode methods. *International Journal of Solids and Structures*, **48**, No. 3–4, 535–552, 2011.

[8] W. Weaver, Jr., S. P. Timoshenko, D. H. Young, *Vibration Problems in Engineering*. John Wiley & Sons, New York, 1990.

[9] V. B. Mescheryakov, A. O. Shimanovsky, V. I. Isaev, Approximate models to determine the reaction of the beam in the short-term concentrated force, *Research on the mechanics of structures and materials*, 71-76, 1990 (in Russian).

International Conference on Engineering Vibration
Ljubljana, Slovenia, 7-10 September 2015

SIMULATION OF LIQUID OSCILLATIONS IN ROAD TANK AT ITS BRAKING

Maryna G. Kuzniatsova, Alexandr O. Shimanovsky*

Belarusian State University of Transport, Gomel, 246653, Belarus
tm.belsut@gmail.com

Keywords: Liquid Sloshing, Road Tank, Hydrodynamic Pressure, Non-Newtonian Liquids, Energy Dissipation, Modal Analysis.

Abstract. *The results of computer simulation of liquid cargo oscillations in the road tank are presented. The models created in the ANSYS-CFX software considered liquid-structure interaction. It was performed the comparison of maximal hydrodynamic pressures in the reservoir and liquid cargo energy dissipation per one oscillation cycle for Newtonian and non-Newtonian liquids. The obtained results demonstrated that the maximal values of hydrodynamic pressures take place at first 0.2–0.3 seconds after braking starting. These values are directly proportional to liquid densities both for Newtonian and non-Newtonian liquids. The analysis results for 50-70% filling levels of the reservoir have shown that the values of liquid energy dissipation for liquids with the identical density are 2-2.9 times more for the Bingham-Shwedov model and 30 % less for the model of Ostwald de Waele in comparison with the Newtonian model. Thus, the fulfilled analysis demonstrated that liquid energy dissipation values for Newtonian liquids can be applied to the non-Newtonian liquids movements with constant correction coefficients.*

1 INTRODUCTION

Road tanks reservoirs have to be of sufficient capacity and required strength, as well as to ensure the safety of the transported liquid cargo. In cases of road accidents not safe conditions for people life and health and environmental pollution can appear. Creation of new tanks designs is associated with the analysis of the dynamics of systems including liquid with a free surface interacting with the movable body. Such an analysis is a complex mathematical problem even for Newtonian fluids.

Usually problems of the tanks dynamics are based on the analysis of fluid mechanics as a continuous medium as described, for example, in papers [1–5]. However, road transport carries a wide variety of non-Newtonian liquids but the peculiarities of their oscillations in transport reservoir have not been studied yet. The purpose of the paper is to compare the features of Newtonian and non-Newtonian liquid cargo sloshing in road tank reservoir at its braking.

2 EQUATIONS FOR LIQUID CARGO MOVEMENT

Pressures of liquid cargo in road tanks don't reach the considerable values, so all analyzed liquids were considered incompressible. At vehicle movement along the road its vertical oscillations always appear and they become a constant source of eddies. Besides, at such transitional movement modes as emergency braking or acceleration, there is a hydroimpact acting the tank wall and top or damping devices. Therefore, all simulations of liquid cargo sloshing at non-stationary movement modes of tanks were carried out taking into account the presence of turbulence. This fact causes a need of turbulent stresses considering in liquid cargo movement equations. To calculate these stresses it is necessary to enable a relation between the pulsation and averaged rate in a turbulent flow [6]:

$$\begin{cases} \dfrac{\partial \overline{u}}{\partial t}+\overline{u}\dfrac{\partial \overline{u}}{\partial x}+\overline{v}\dfrac{\partial \overline{u}}{\partial y}+\overline{w}\dfrac{\partial \overline{u}}{\partial z}=F_x+\dfrac{1}{\rho}\left[-\dfrac{\partial \overline{p}}{\partial x}+\dfrac{\partial}{\partial x}\left(\overline{\tau}_{xx}-\rho\overline{u'u'}\right)+\dfrac{\partial}{\partial y}\left(\overline{\tau}_{xy}-\rho\overline{v'u'}\right)+\dfrac{\partial}{\partial z}\left(\overline{\tau}_{xz}-\rho\overline{w'u'}\right)\right]; \\ \dfrac{\partial \overline{v}}{\partial t}+\overline{u}\dfrac{\partial \overline{v}}{\partial x}+\overline{v}\dfrac{\partial \overline{v}}{\partial y}+\overline{w}\dfrac{\partial \overline{v}}{\partial z}=F_y+\dfrac{1}{\rho}\left[-\dfrac{\partial \overline{p}}{\partial y}+\dfrac{\partial}{\partial x}\left(\overline{\tau}_{yx}-\rho\overline{u'v'}\right)+\dfrac{\partial}{\partial y}\left(\overline{\tau}_{yy}-\rho\overline{v'v'}\right)+\dfrac{\partial}{\partial z}\left(\overline{\tau}_{yz}-\rho\overline{w'v'}\right)\right]; \\ \dfrac{\partial \overline{w}}{\partial t}+\overline{u}\dfrac{\partial \overline{w}}{\partial x}+\overline{v}\dfrac{\partial \overline{w}}{\partial y}+\overline{w}\dfrac{\partial \overline{w}}{\partial z}=F_z+\dfrac{1}{\rho}\left[-\dfrac{\partial \overline{p}}{\partial z}+\dfrac{\partial}{\partial x}\left(\overline{\tau}_{zx}-\rho\overline{u'w'}\right)+\dfrac{\partial}{\partial y}\left(\overline{\tau}_{zy}-\rho\overline{v'w'}\right)+\dfrac{\partial}{\partial z}\left(\overline{\tau}_{zz}-\rho\overline{w'w'}\right)\right]; \\ \dfrac{\partial \overline{u}}{\partial x}+\dfrac{\partial \overline{v}}{\partial y}+\dfrac{\partial \overline{w}}{\partial z}=0; \\ \dfrac{\partial u'}{\partial x}+\dfrac{\partial v'}{\partial y}+\dfrac{\partial w'}{\partial z}=0, \end{cases} \quad (1)$$

where $\overline{u}, \overline{v}, \overline{w}$ – projections of the liquid particles averaged rate on x, y, z axes respectively, m/s^2;

t – time, s;

u', v', w' – projections of the liquid particles pulse rate on x, y, z axes respectively, m/s^2;

F_x, F_y, F_z – projections of external volume (mass) forces, N/m^3;

ρ – liquid cargo density, kg/m^3;

$\overline{\tau}_{ij}$ – averaged stress tensor components, Pa.

The analysis in [7] shows that for the solution of our problem the κ-ε turbulence model [8, 9] is more preferable to use. It involves solving of two additional equations for the turbulent kinetic energy κ and turbulence energy dissipation rate ε for each finite element of liquid at each time step [8, 9]:

$$\frac{\partial(\rho\kappa)}{\partial t}+\frac{\partial(\rho\overline{v}_j\kappa)}{\partial x_j}=\frac{\partial}{\partial x_j}\left[(\mu+\frac{\mu_t}{\sigma_\kappa})\frac{\partial\kappa}{\partial x_j}\right]-\rho\overline{v_i'v_j'}\frac{\partial\overline{v}_i}{\partial x_j}-\rho\varepsilon; \tag{2}$$

$$\frac{\partial(\rho\varepsilon)}{\partial t}+\frac{\partial(\rho\overline{v}_j\varepsilon)}{\partial x_j}=\frac{\partial}{\partial x_j}\left[(\mu+\frac{\mu_t}{\sigma_\varepsilon})\frac{\partial\varepsilon}{\partial x_j}\right]+\frac{\varepsilon}{\kappa}\left[C_{\varepsilon1}\left(-\rho\overline{v_i'v_j'}\frac{\partial\overline{v}_i}{\partial x_j}\right)-C_{\varepsilon2}\rho\varepsilon\right], \tag{3}$$

where κ – specific (per unit mass) liquid turbulent kinetic energy, m^2/s^2;

$$\kappa=\frac{\overline{v_j'v_j'}}{2}; \tag{4}$$

$\overline{v}$ – averaged velocity, m/s;
μ – dynamic viscosity of a liquid, Pa·s;
μ_t – turbulence eddy viscosity, Pa·s:

$$\mu_t=C_\mu\rho\frac{\kappa^2}{\varepsilon} \tag{5}$$

ε – specific (per unit mass) dissipation rate of liquid turbulent kinetic energy, m^2/s^3;
σ_ε, σ_κ, C_μ, $C_{\varepsilon1}$, $C_{\varepsilon2}$ – some dimensionless empirical constants.

Earlier investigations on road tanks dynamics were associated with analysis of Newtonian liquids sloshing, for example in [10]. Shear stresses of such liquids is directly proportional to the relative velocity of their layers and depend on the type of liquid [7]:

$$\tau=\mu\frac{d\vec{v}}{d\vec{n}}=\mu\dot{\gamma} \tag{6}$$

where $\vec{v}$ – full velocity vector, m/s;
$\vec{n}$ – unit vector in the perpendicular to the liquid flow direction;
$\dot{\gamma}$ – shear rate, s^{-1}.

For non-Newtonian fluids the $\tau-\dot{\gamma}$ dependence is not directly proportional and the dynamic viscosity is not constant. For oil solutions and polymer melts, suspensions, paints, honey, molasses etc. the $\tau-\dot{\gamma}$ dependence is nonlinear. To describe movement of such liquids during their modeling the power law of Ostwald de Waele [7] is used. It gives the following equation for the dynamic viscosity coefficient

$$\mu=K(\lambda\dot{\gamma})^{n_L-1}, \tag{7}$$

where K – consistent liquid viscosity (flow density ratio), Pa s;
n_L – indicator of liquid behavior (for pseudoplastic liquids $n_L<1$, for Newtonian $n_L=1$, for dilatant $n_L>1$);
λ – time constant, s.

Flow of Bingham (Bingham-Shvedov) liquids (muds, oil paints, etc.). starts at some initial shear stress which exceeds the yield stress. The τ-$\dot{\gamma}$ relationship is the following [11]

$$\tau-\tau_0=\mu_\rho\dot{\gamma},\ \ \tau>\tau_0 \tag{8}$$

where μ_ρ – plastic viscosity of non-Newtonian liquids (shear factor) Pa·s;
τ_0 – initial shear stress (for Newtonian liquids $\tau_0=0$), Па; for example, for pure concrete mixtures the shear stress is close to 2 Pa.

Analytical solution of equations (1) has not been received yet for the problems of the liquid flows for random initial and boundary conditions, so their analysis is usually done using numerical methods. We've used ANSYS CFX software as a tool for solving the above-mentioned equations.

3 SIMULATIONS OF LIQUID CARGO SLOSHING IN THE MOVING TANK

The process of numerical solution obtaining in ANSYS CFX consists of several stages. The first stage includes the transformation of the system of partial differential equations describing the process of liquid flow to a discrete system of algebraic equations. The object of research is divided into separate volumes with 4–8 nodes, each of them has its own system of equations: basic equations, describing liquid sloshing process, and support equations, including initial and boundary conditions. Formation of the coefficients matrices and their subsequent solutions are being carried out by algebraic multigrid method means [12, 13]. Then it is performed a joint numerical solution of equations at each time step with the linearization of nonlinear terms [14]. At each time step an iterative solution is done. Then, on the basis of the numerical solutions for each grid node the approximate numerical solution for the whole object is obtained.

The performed analysis [15] showed that for simulations of liquid sloshing in road reservoirs of 2–12 m^3 volume with internal baffles and without them it is advisable to use a finite element mesh with 50000–200000 finite elements. At simulations the internal volume of road tank reservoir was divided into two liquid fractions: liquid cargo and air. The interface of the two liquid phases in reservoir was determined by the method of Harlow cells and markers method [16], which is also known as the finite volume method, or VOF.

Most part of the liquid sloshing investigations described in literature deal with flows in pipes (generally constant cross-section) or with the "input" and "output" defined boundaries of liquid flow. The peculiarities of our created models for simulations in the software package ANSYS is the presence of an enclosed space for liquid sloshing and two phase flow. Also, a certain difficulty is to consider the presence of an internal perforated baffle because a multiply connected region between the reservoir, baffle and liquid cargo appears. Uniting the total volume of liquid in one domain allowed us to solve this problem. Boundary conditions were set on the surfaces of the partitions such as walls for the tank. The presented results were obtained on the base of the described features of liquid sloshing simulations.

4 2-D MODELING OF LIQUID SLOSHING IN ROAD TANKS

To improve methods of finite element modeling there were performed two-dimensional simulations for liquid sloshing in a road reservoir with rectangular longitudinal cross-section of 1.5 m height and 4 m length. The created models from 6,000 to 30,000 finite elements.

It was assumed that initially the liquid is at a relative rest, and its free surface is flat. As a kinematic boundary condition the adhesion condition was used. The time step was taken equal to 0.001-0.01. Simulations were performed for road tank braking with 0,6g acceleration.

To analyze the influence of tank filling level on liquid energy dissipation values there were carried out simulations for water sloshing (at 20°C) in the reservoir filled by 50–90 % (Figure 1). The results showed that at 80% filling the values of water energy dissipation are minimal but at the same time oscillations of liquid center of mass are insignificant, so they don't influence the tank dynamics significantly. If the liquid cargo fills reservoir by 50–60%, the oscillations of liquid center of mass have large amplitudes and liquid energy dissipation has a local minimum. Similar results are obtained for tanks with internal baffles. Therefore, in further simulations the filling level of the reservoir was assumed to be 60% as the most adverse.

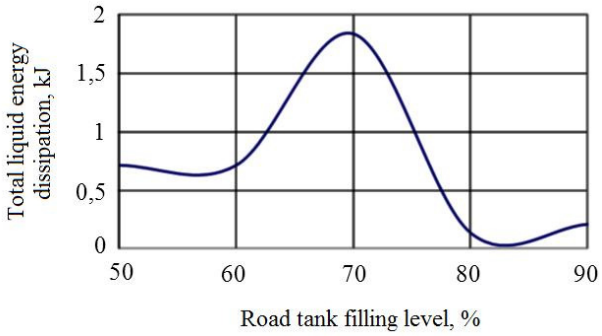
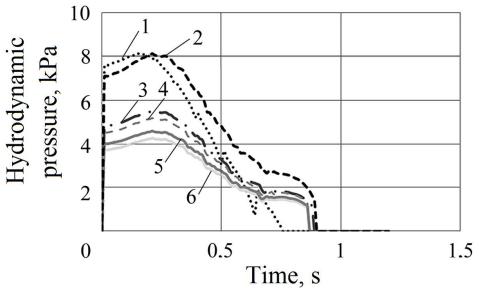


Figure 1: The dependence of total water energy dissipation for the first oscillation cycle on tank filling level.

To analyze the influence of liquid cargo density and viscosity on hydrodynamic loading of the reservoir there were performed simulations for liquids with different physical properties sloshing in tank without baffles. The results demonstrated that the hydrodynamic pressure of liquid cargo particles on reservoir shells is almost directly proportional to liquid density (Figure 2). The coefficients of pressures-densities proportionalities for different liquids compared with water are given in Table 1. The analysis of further computations showed that the dependencies of Newtonian and non-Newtonian liquids hydrodynamic pressures are almost the same both for tanks with and without partitions. At the same time liquid viscosity insignificantly effects the values of pressures in the reservoir.



1 – nitric acid; 2 – treacle; 3 – xylol; 4 – sunflower oil; 5 – kerosene; 6 – gasoline

Figure 2: The dependence of total water energy dissipation for the first oscillation cycle on tank filling level.

Type of liquid cargo	Liquid cargo density		Maximal values of hydrodynamic pressures	
	kg/m^3	relative to water density	kPa	relative to water pressure
Nitric acid	1512.6	1.51	8.29	1.46
Gasoline	734.5	0.74	4.20	0.74
Water	998.2	1.00	5.69	1.00
Kerosene	815.0	0.82	4.63	0.81
Xylol	980.0	0.98	5.41	0.95
Treacle	1440.0	1.40	8.02	1.41
Sunflower oil	920.0	0.92	5.25	0.92

Table 1: Comparison of liquids density and pressure values with the corresponding values for water.

However, two-dimensional models allow to obtain only an approximate estimate of the features in the liquid cargo sloshing in road tanks. For a more complete and complex analysis three-dimensional models should be analyzed.

5 SIMULATIONS OF NON NEWTONIAN LIQUIDS SLOSHING IN ROAD TANK RESERVOIRS

The three-dimensional simulations for non-Newtonian liquids were carried out for cylindrical road tank reservoirs of 2 m diameter and 4 m length with internal perforated baffle and without it.

The results for water (Newtonian liquid, $\rho = 997$ kg/m^3), concrete mixture (Bingham liquid $\rho = 2000$ kg/m^3) and heavy oil (de Waele model $n_L = 1{,}5$; $\rho = 967$ kg/m^3) in the reservoir without baffles demonstrated that Bingham liquid position in the tank over time is slightly different from water position. The water (Newtonian model) and heavy oil (de Waele model) oscillations occurs at a higher rate compared with Bingham liquid due to the higher density of the latter.

In order to analyze the influence of liquids rheological properties on their sloshing in the tank with baffles, on the hydrodynamic pressures values and liquid energy dissipation, the analysis of cargo braking with 0.6g acceleration was performed. Liquid cargo for all simulations had the same density of 967 kg/m^3 and the viscosity at the initial time $\mu_0 = 0{,}1$ Pa·s. The finite element model of the reservoir with perforated baffle (7 holes of 20 cm diameter) is presented at Figure 3.

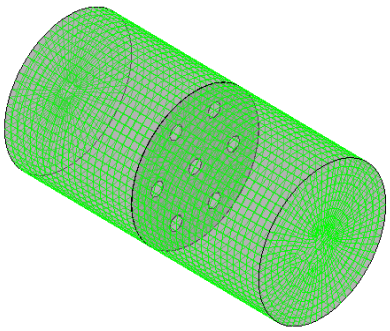


Figure 3: Finite element model of the reservoir with perforated baffle.

Liquid cargo free surface position at several time steps and the hydrodynamic pressures distribution in the reservoir are shown in Figures 4 and 5. Figure 4 demonstrates that the leakage of liquids at the end wall and the gap from the inner cylindrical surface has minor differences for analyzed models. Figure 5 shows that the maximal values of the hydrodynamic pressure in the reservoir correspond to the Newtonian model and are equal to 1.14 MPa. So, they are 2.9% higher than the values obtained for the non-Newtonian models. The difference in hydrodynamic pressure values for the two non-Newtonian models is less than 0.3%.

The computational results showed that the total energy dissipation of the liquid cargo ($\rho = 967$ kg/m^3) is the maximal for the Bingham model and it is twice more compared with the values obtained for other models. At the same time the results for de Waele and Newtonian models are less than 10% different for one cycle of liquid oscillations (Figure 6).

To analyze the influence of reservoir filling level on the total energy dissipation of liquids with different densities there were performed several simulations. They were carried out for liquid cargo sloshing in the partially filled reservoir with one transverse perforated baffle con-

taining holes of 20 cm diameter. The computations were made for water (Newtonian liquid), concrete mixture (Bingham liquid) and heavy oil (de Waele liquid; $n_L = 1,5$).

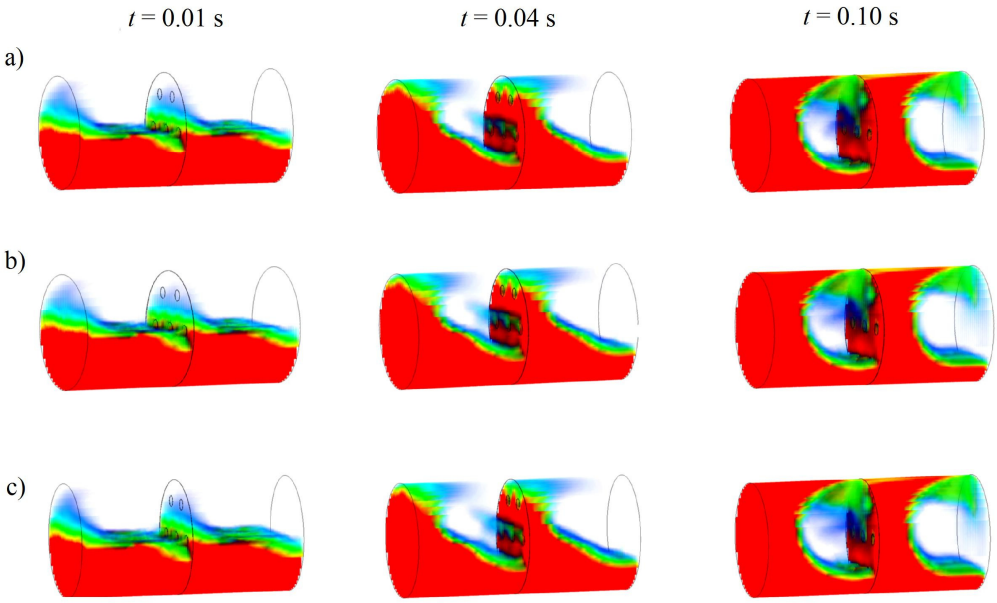


Figure 4: Liquid cargo ($\rho = 967$ kg/m^3) free surface position for models of a) de Waele, b) Bingham, c) Newton.

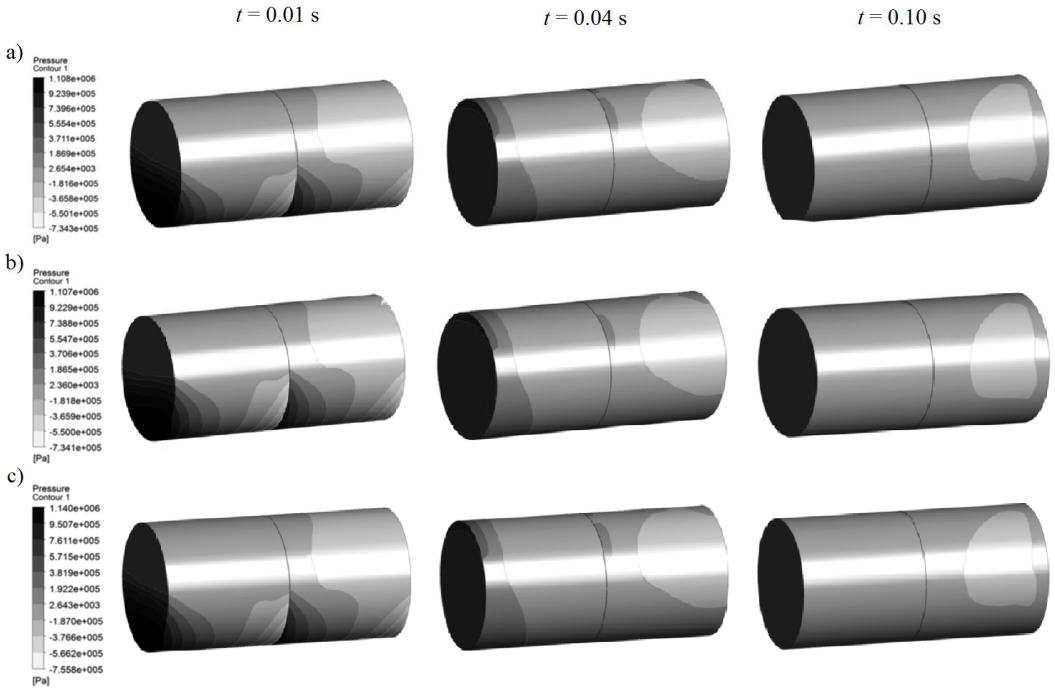
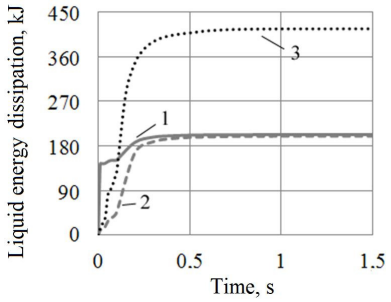


Figure 5: Distribution of liquid cargo ($\rho = 967$ kg/m^3) pressures in the reservoir for models of a) de Waele, b) Bingham, c) Newton.



1 – Newtonian model; 2 – de Waele model; 3 – Bingham model

Figure 6: Liquid cargo (ρ = 967 kg/m^3) energy dissipation for models of Newton, de Waele and Bingham.

Computational results for 60% filling level demonstrated that pressures in the most loaded point of the tank (interaction area between the end wall bottom and shell of the reservoir) change by the same laws for all liquids (Figure 7). These laws are similar for other areas of tank shell either.

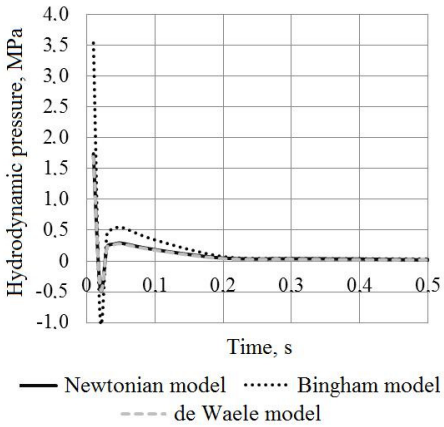
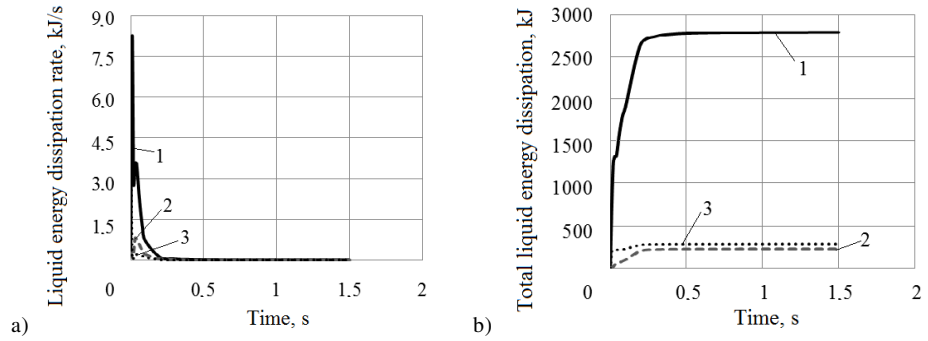


Figure 7: The pressure-time dependence for the most loaded area of tank shell.

Results of simulations (Figure 8) show that the highest liquid energy dissipation rate at the beginning of 60 %-filled road tank braking corresponds to Newtonian liquid. After the start of braking (at t = 0,01 s) it decreases sharply at first and then it gradually decreases. The results for non-Newtonian liquids are characterized by a gradual increase and then decrease of the energy dissipation rate.

Performed simulations have shown that 50-60% tank filling level is the most adverse for water and oil because of slow liquid oscillations damping, whereas for the concrete mixture the worst filling level is 50 % (Figure 9). The difference in total liquid energy dissipation for analyzed liquids is 20-35% for the first cycle oscillations and can be explained by different liquid cargo viscosities.

Thus, the investigations have shown that the computational results for Newtonian liquids sloshing can be applied to non-Newtonian liquids. The maximal values of hydrodynamic pressures in the reservoir after the start of braking (for the first 0.2-0.3 seconds), for different liquids are approximately proportional to their densities. The values of total energy dissipation for Bingham liquid (concrete mixture) is 5 times more than for Newtonian one (water). The values for de Waele liquid (heavy oil) energy dissipation are 70 % of Newtonian (water).



1 – Bingham liquid (concrete mixture); 2 – de Waele liquid (heavy oil); 3 – Newtonian liquid (water)

Figure 8: The dependence of liquid energy dissipation rate (a) and total liquid energy dissipation (b) on time for 60 % tank filling level.

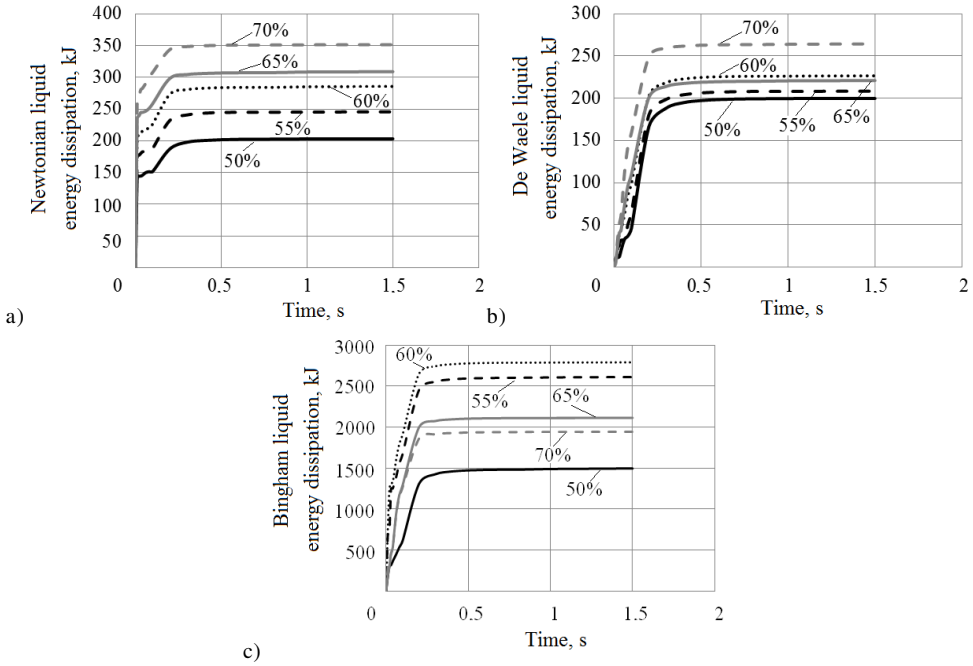


Figure 9: Summarized liquid energy dissipation for a) Newtonian liquid (water) b) de Waele liquid (heavy oil) and c) Bingham liquid (concrete mixture) at their sloshing in road tank reservoir with transverse perforated baffle with 20 cm diameter holes.

6 CONCLUSIONS

- The results of the simulations for non-Newtonian liquids sloshing in road tanks reservoirs with internal baffles and without them showed that the maximal values of hydrodynamic pressures in the reservoir after the start of braking (for the first 0.2-0.3 seconds), for different liquids are approximately proportional to their densities.
- The results of liquid (ρ = 967 kg/m^3) energy dissipation calculations in 50–70 %-filled reservoirs for Newtonian and non-Newtonian models demonstrated that total energy dissipation value for de Waele model is in average 30% less than for Newtonian model. The corresponding values for Bingham model are 2-2,9 times more compared to a Newtonian model.

- The investigations have shown that the computational results for Newtonian liquids sloshing can be applied to non-Newtonian liquids with correction coefficients, for example, 5 to concrete mixtures and 0.7 for heavy oil total energy dissipation.

REFERENCES

[1] S. M. Hasheminejad, M. Aghabeigi, Sloshing characteristics in half-full horizontal elliptical tanks with vertical baffles. *Applied Mathematical Modelling*, **1**, No 36, 57–71, 2012.

[2] T. Kandasamy, S. Rakheja, A. K. W. Ahmed, An analysis of baffles designs for limiting fluid slosh in partly filled tank trucks. *The Open Transportation Journal*, **4**, 23–32, 2010.

[3] K. Modaressi-Tehrani, S. Rakheja, I. Stiharu, Three-dimensional analysis of transient slosh within a partly-filled tank equipped with baffles. *Vehicle System Dynamics*, **45**, No 6, 525–548, 2007.

[4] B. Molin, Experimental and numerical study of the sloshing motion in a rectangular tank with a perforated screen. *Journal of Fluids and Structures*, **43**, 462–480, 2013.

[5] G. Yan, *Liquid slosh and its influence on braking and roll responses of partly filled tank vehicles*. Concordia University, Montreal, Quebec, 2008.

[6] D. A. Anderson, J. C. Tannehill, R. H. Pletcher, *Computational fluid mechanics and heat transfer*, McGraw-Hill, New York, 1984.

[7] Z. P. Shulman, *Convective heat transfer of rheologically complex liquids*. Energy, Moscow, 1975 (in Russian).

[8] Yu. V. Lapin, Statistical Theory of Turbulence (Past and Present – a Brief Outline of Ideas). *Scientific and Technical News*, No 2, 7–20, 2004 (in Russian).

[9] M. A. Scherbakov, A. A. Yun, B. A. Krylov, Comparative analysis of turbulence models using a scientific code «Fastest-3D» and the commercial package ANSYS CFX". *Vestnik MAI*, **16**, N 5, 2–12, 2010 (in Russian).

[10] M. S. Visotskij, Yu. M. Pleskachevskii, A. O. Shimanovsky, *Dynamics of automobile and railroad tanks*. Belavtotractorostroenie, Minsk, 2006 (in Russian).

[11] W. L. Wilkinson, *Non-Newtonian fluids: Fluid mechanics, mixing and heat transfer*. Pergamon Press, London, 1960.

[12] M. A. Olshanskii, *Lectures and exercises on multigrid methods*. MSU, Moscow, 2003 (in Russian).

[13] K. Stueben, *Algebraic multigrid (AMG): An introduction with applications.* GMD, St. Augustin, Germany, 1999.

[14] A. F. Sikovskii, *Computational methods of thermal physics*. Novosibirsk State University press, Novosibirsk, 2013 (in Russian).

[15] A. Shimanovsky, M. Kuzniatsova, A. Sapietová, Modeling of Newtonian and non-Newtonian liquid sloshing in road tanks while braking, *Applied Mechanics and Materials*, **611**, 137–144, 2014.

[16] F. H. Harlow, J. E. Welch, Numerical study of large amplitude free surface motion. *Physics of Fluids*, **9**, No 5, 842–851, 1966.

International Conference on Engineering Vibration
Ljubljana, Slovenia, 7-10 September 2015

OVERVIEW OF THE SOURCE AND ADDITIONAL FACTORS WHICH INFLUENCE THE POWER TRANSFORMER NOISE

A. Hackl*[1], P. Hamberger[2], M. Aigner[2]

[1] Siemens AG Österreich - Transformers Linz
Kraußstraße 7 - 4020 Linz
alexander.hackl@siemes.com

[2] Siemens AG Österreich - Transformers Linz
Kraußstraße 7 - 4020 Linz
{peter.hamberger, martin.aigner}@ siemes.com

Keywords: power transformer, noise, vibration, acoustics.

Abstract. *Core and winding vibrations are the main noise sources of power transformers. The basic physical effects of magnetostriction in core sheets and Lorentz forces on the conductors are well known, but for the noise emission the total coupled system is relevant. It starts with the non-linear and anisotropic sheet material, where thousands of them are stacked to a core and ends at the texture of the tank surface which radiates the noise. In this paper we give an overview of the relevant effects starting from the noise sources to the emitting surface, based on measurements and simulations. As a result, the laminated core structure has a wide resonance width, the different phase angles of the excitation in the limbs caused a directed radiation, the oil connects all mechanical vibrations of the active part directly to the tank and the tank structure distributes the vibration energy over the surface.*

1 INTRODUCTION

From the noise perspective, a power transformer is a huge liquid filled box with a low frequency vibration source. Even this simple description contains one parameter of the noise generation, the fluid-structure interaction, the source of the strong coupling of the each part of the transformer, which raise the complexity of the measurements and analyse. Figure 1 shows the main parts of a transformer, the core surrounded by the windings held together with a clamping frame and the tank filled with oil.

The core and the winding are the main noise sources with different physical origins. The alternating magnetic flux density in the core causes magnetostriction in the sheets and magnetic forces in the gaps and corner joints, called no-load noise. Additional to these nonlinear effects the electrical steel is optimized for a high permeability in rolling direction therefore causing lower permeability in transverse direction. This intrinsic anisotropic material behaviour is overlaid by additional effects, as the inhomogeneous pressure distribution of the clamping frame or different shapes of the sheets and the core geometry itself which influence the resonance behaviour.

On the other hand, the stray flux and the current in the conductor generate Lorentz-forces which result in vibrations of the winding, called load noise. The vibrations are transferred via the clamping frame and the oil to the tank wall which is the noise radiation surface.

The basic physical effects are well known, but each part of the transformer, such as the core lamination, the winding assembly and the fluid coupling, add phonemes which are still part of investigations. Measurements on the final transformer are not possible, because all parts sealed in the closed tank. Simulations are also a challenge, because the core material is anisotropic and non-linear and a winding model must capture an element size ranging from millimeters to meters.

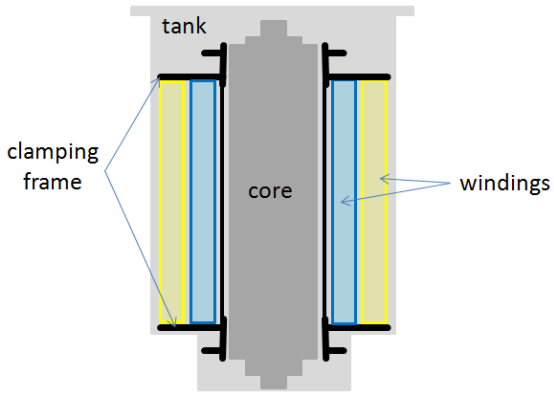


Figure 1: Schematic of a transformer.

2 CORE

A transformer core is a bulk of electrical steel sheets which are kept together with a pressing assembly.

Today's core material for power transformers is mainly grain oriented electrical steel. As a basis silicon steel with a certain polycrystalline structure is used. By certain techniques the crystal structure can be oriented in a certain direction, afterwards the surfaces is treated with a special coating. All these techniques allow to improve the certain magnetic properties such as

a high permeability and a small hysteresis compared to conventional carbon steel. Of course these measures have also a direct influence on the magnetostrictive behaviour and as results on the radiated noise level. The magnetic mechanic properties of single sheets and laminations are still under investigation [1, 2]

A power transformer core has thousand of sheets and the weight goes from 10 t to more over 40 t, so measurements on real sized cores are a challenging task. On the other hand the principal acoustic properties can also be studied on small cores. So we decide to produce a 3 limb core with a wooden pressing assembly, shown in Figure 2 (left side). With the 10 turns of the windings and a frequency converter we reach inductions up to 1.7 T and frequencies up to 500 Hz. The active part is placed in an oil filled tank which is shown in Figure 2 on the right side.



Figure 2: Schematic of an experimental core with a limp diameter of 200 mm (left) and the transformer tank (right).

The geometry and the boundary conditions of an object define the eigen-frequencies. In most of the cases a prediction is a challenging task, because the boundary conditions, here the pressure distribution and the interaction of the stacked sheets, are unknown. Moreover, the excitation frequency is very precise and little shifts of a specific eigen-frequency can have a big influence on the noise level [3]. The measured resonant characteristic gives us an overview and explains some physical effects.

To measure the eigen-frequencies an impact hammer Kistler Typ 9724A2000 and a laser vibrometer Polytec PSV-400-H4 is used.

The characteristics of the three limbs are similar and the mean values are shown in Figure 3. Up to 400 eigen-frequencies were found. Above 400 Hz the left hand pictures show a mixture of damped eigen-frequencies. To investigate the influence of the oil, the core was immersed into oil. It can be shown, that the eigen-frequencies below 200 Hz are shifted dramatically based on the inter-laminar oil, which changes the coupling between sheets.

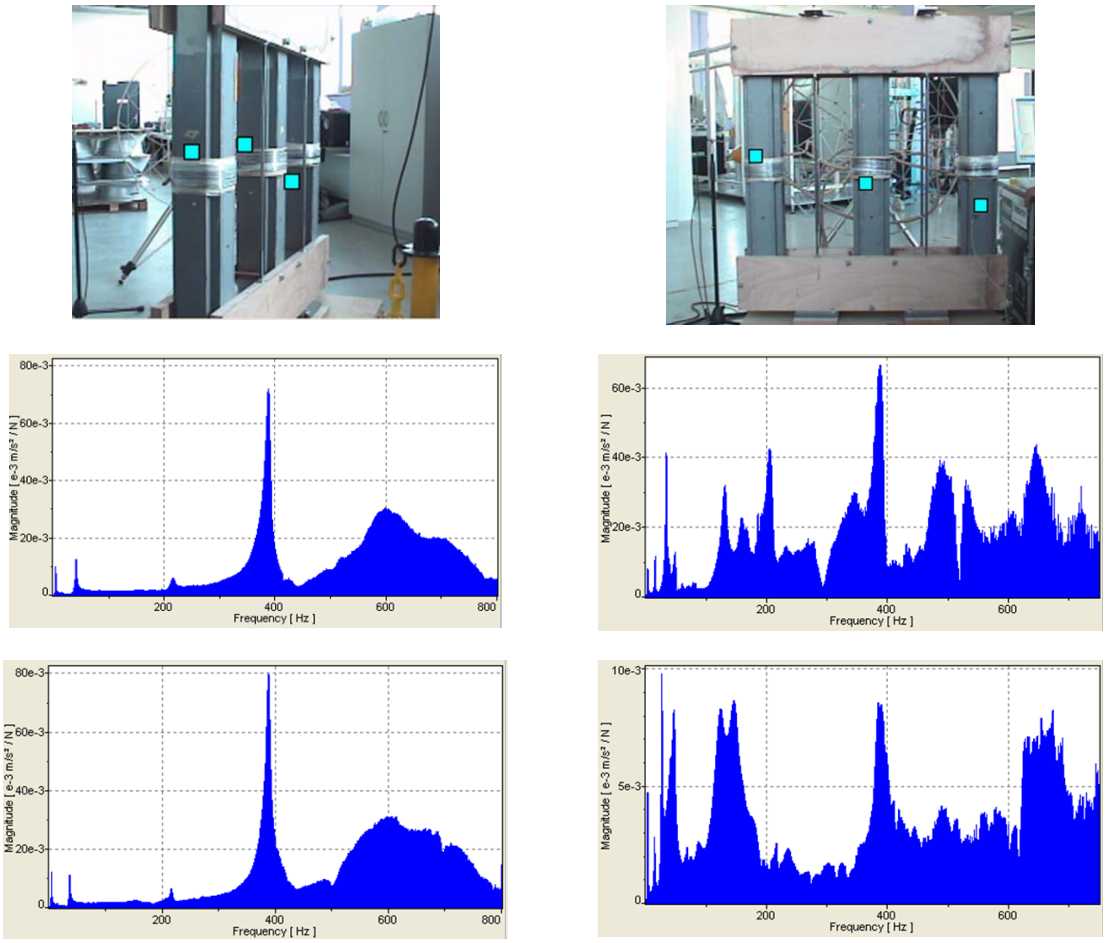


Figure 3: (top) Position of the measurement point.
(mid) Response spectra of the dry core.
(bottom) Response spectra of the oil immersed core.

After a sound pressure measurement the source of the peak near 400 Hz was identified as vibration of the tie rods which are assembled between the limbs (Figure 4).

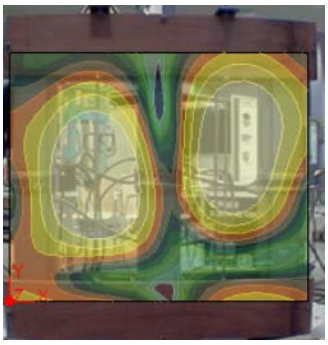


Figure 4: Sound pressure distribution at a vibration frequency of 368

In contrast to the core, which is comparable to a real transformer, the windings consist only of 10 turns each which are wounded around the core and are far away to be a good approximation of a real winding, where the Lorentz-forces has a big influence on the noise level. Further investigations will focus on this part of noise source.

3 OIL COUPLING

The thermal losses of the active part are transferred to the cooling equipment, like radiators via the transformer oil, so the noise sources are totally immersed in a fluid. The mass lower the measured in air eigen-frequencies and increase the damping, but the phase shift of each limb in combination with the strong coupling result in a non symmetric emission of the noise. A 2D FEM simulation of three “breathing” cylinders surrounded with oil and a phase shift of 120° illustrate the effect, shown in Figure 5.

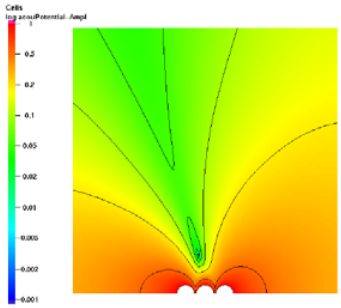


Figure 5: 2D acoustic potential of three “breathing” cylinders surrounded of oil with a phase shift of 120°

4 TANK

The tank of a power transformer must carry the active part, the cooling oil and is designed to withstand a vacuum, resulting in a tank surface with many vertical or horizontal stiffeners. The areas between the stiffeners are the main noise source and the vibration pattern influences the radiation factor. The oil inside of the tank induces a strong coupling of the active part and the tank wall, but also a coupling of the tank sides, so each local modification on one surface influences the overall behaviour. On the other side a global change, as a warm up, results in different vibration patterns and influence the radiated noise. Figure 6 shows the effect of a warm-up on the sound pressure level.

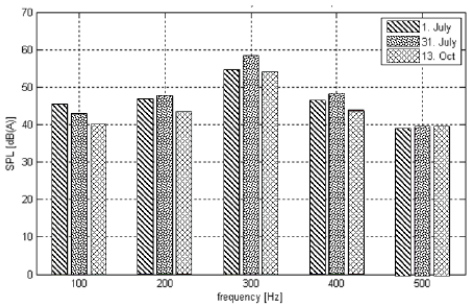


Figure 6: Sound pressure level after different warm-up and cooling-down phases.

The vibration pattern is manly composed by a few resonant modes near the excitation frequency. The result of the combinations depends on the phase between the involved modes and this phase shift depends on the boundary conditions, as on the temperature of the oil [3].

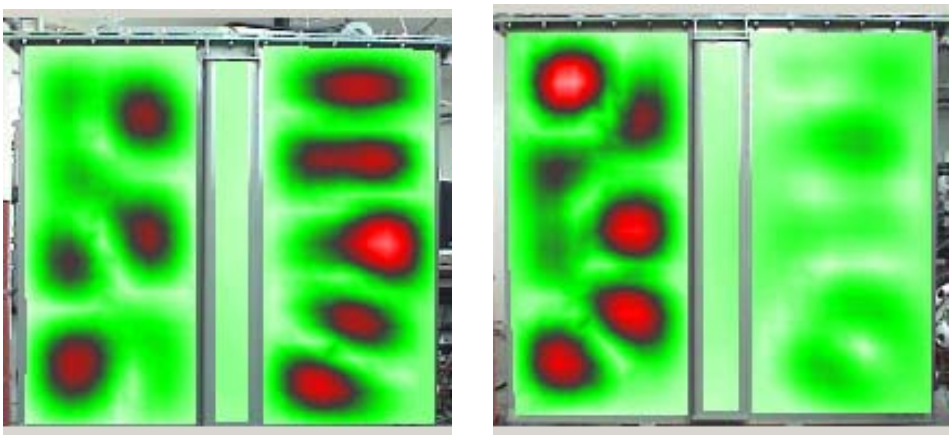


Figure 7: Measurement of the vibration patter before and after a warm up

5 CONCLUSIONS

- The laminate core structure shows damped eigen-frequencies which are shifted, based on the inter-laminar oil. More investigations must be done to identify the components and investigate their influence on the radiate noise.
- The phase shift and the coupling of the noise source result in asymmetric radiation pattern.
- The oil inside the tank entails a strong coupling of the tank walls, so local changes in the stiffness or global changes, such as warm ups, have a strong influence on the vibration pattern.

REFERENCES

[1] G. Shilyashki et al., *A Tangential Induction Sensor for 3D-Analyses of Peripheral*. IEEE Transactions on Magnetics, 2014.

[2] H. Pfützner et al.,, *Automatic 3-Dimensional Building Factor Analyses of a Grain Oriented Model Transformer Core*. IEEE Transactions on Magnetics, 2014

[3] A. Hackl and P. Hamberger, Investigation of Surface Velocity Pattern of Power Transformers Tanks, ICEM, 2010.

Index of authors

Abbadi Zouhir, 1318
Abboud Amr, 1384
Acikmese Behcet, 1155
Acri Antonio, 383
Aguiar Romulo, 1164
Aigner Martin, 1421, 1431, 1702
Almeida Alan, 1036
Alonso Gustavo, 17
Alvarez Gilberto, 499
Americo Cunha Jr, 1173
Andrew Ian, 571
Araumi Naoto, 1487
Asadi Saeed, 553
Ashish Srivastava, 591
Asker Haval, 1518
Asnaashari Erfan, 571
Atsushi Kanda, 1674
Atsushi Yoshinaga, 1674
Azevedo João Luiz, 326

Böswald Marc, 393
Bae Seok-In, 1643
Baginski Pawel, 509
Baldanzini Niccolo, 1331
Balthazar José Manoel, 621, 1026, 1036, 1046
Banaszek Slawomir, 509
Banik A. K., 1488
Barboza Rafael Rangel, 925
Bartl Andreas, 1235
Battiato Giuseppe, 131
Bekdaş Gebrail, 852, 860, 878
Belotti Roberto, 1192
Benasciutti Denis, 743
Benner Peter, 1540
Berbyuk Viktor, 28, 152, 553, 1530
Bernardini Davide, 1046
Berruti Teresa, 131
Bertini Leonardo, 217
Bestle Pascal, 1068
Bianchin Rafael, 1036
Bissembayev Kuatbay, 38
Bitar Diala, 681
Boduroğlu M. Hasan, 868
Boltežar Miha, 144, 185, 278, 298, 403, 783, 1265, 1332, 1441, 1498, 1589
Borges Flavia, 318
Borozan Ion, 611
Boström Anders, 152
Boucher Matthew, 1297
Bouhaddi Noureddine, 681
Boyaci Aydin, 469
Brasil Reyolando M.L.R.F, 1036
Bratuš Vitoslav, 403
Braun Stefan, 1477
Brumat Matija, 278
Brzeski Piotr, 1118
Byrtus Miroslav, 529

Candreva Stefano, 611
Cao Chun-feng, 336
Cao Qingjie, 704, 1623, 1632
Cao Yanmei, 966
Castello Daniel, 48, 318, 1212
Castro Helio de, 1202
Chasalevris Athanasios, 445, 457, 578
Chate Andris, 288
Chatzisavvas Ioannis, 469
Chen Xiaoxin, 325
Claeys Claus, 1306
Cocchi Giammichele, 1615
Cooper Samson, 308
Cornelis Bram, 763
Corradi Roberto, 383
Cosco Francesco, 611
Čepon Gregor, 1441, 1498

D'Ambrogio Walter, 1225
D'Ortona Vittorio, 1352
da Silva José Guilherme Santos, 925, 935, 945
Dal Abdurrahim, 519
David Sergio A., 621
De Simone Marco Claudio , 843
Debona Gilvan Lunz, 935
Debruyne Stijn, 1218
Deckers Elke, 1306
DelliCarri Arnlado, 308
Demidov Ivan, 71
Denißen Jonas, 1540
Desmet Wim, 119, 1297, 1306
Desvard Ludovic, 651
DiMaio Dario, 308
Dimitrovová Zuzana, 994, 1549
Dmitriev Sergey, 71
Douville Marc-André, 809
Du X. H, 1412
Du X.H., 1466

Eberhard Peter, 1068, 1069
Ehrlich Christian, 226
Elbhbah Keri, 571
Ellermann Katrin, 163
Elliott Robert, 691

Fabbrocino Giovanni, 432
Faraj Rami, 916
Faventi Roberto, 651
Faverjon Béatrice, 809
Felix Jorge L.P., 1036
Ferfecki Petr, 563
Ferguson Neil, 539
Fidlin Alexander, 1079, 1099
Fiedler Bernd, 99
Firrone Christian, 131
Fischer Cyril, 662
Forghani S. Mohsen, 1184
Forster Ian, 1129
Fregolent Annalisa, 1225

Gagliardini Laurent, 1318
Galvanetto Ugo, 1615
Gargaro Danilo, 432
Gaspar Cássio Marques Rodrigues, 945
Gaudin Arnaud, 1318
Gaul Lothar, 226
Gautier François, 1318
Gekeler Simon, 591
Gerlach Erik, 99
Gerstbauer Erich, 1431
Glück Oskar, 591

Godoy Diego, 48
Goedecker Holger, 1088
Goh B.H.T., 320
Gomar Adrien, 651
Gonçalves Paulo, 690
Gonçalves Paulo B., 268, 1005, 1015
Gonca Vladimirs, 631
Gong S.W., 320
Govers Yves, 393
Grétarsson Snaevar Leó, 1530
Graebner Nils, 1088
Green J.S., 691
Gruber Fabian M., 1245, 1255
Gubaidullin Damir, 79, 1658
Guida Domenico, 843
Gupta Sayan, 61

Hacioglu Yuksel, 897
Hack A.l, 1702
Hahn Wlofgang, 571
Hajžman Michal, 529
Hamberger Peter, 1421, 1431, 1702
Han Ning, 704
Han Yanwei, 1632
Hanss Michael, 1068
Hebler Anne, 393
Heczko Jan, 1549
Hernandez Diego, 48
Herold Sven, 187
Heuss Oliver, 1392
Hisem Pavel, 1650
Holnicki-Szulc Jan, 916
Hopper Hugh, 651
Huang H., 1412, 1466
Huang Hung-Tsai, 173
Hugues Damien, 1477
Hussein Mohammed, 974
Husung Isabel, 99

Ihi Rafael, 326
Ihrle Sebastian, 1069
Irfan Muhammad, 28
Irvine Tom, 725, 792
Iskakov Zharilkassin, 38
Itsuro Kajiwara, 1674
Ivanov Kirill, 71

Janeliukstis Rims, 288
Jaquet-Richardet Georges, 809
Javh Jaka, 1589
Jedrzejczyk Roman Pawel, 1362
Jehle Georg, 1079
Jeličić Goran, 393
Jeong Kyeong-Hoon, 348
Jhung Myung-Jo, 348
Jiménez Homero, 499
Johansson Anders, 1275
Johansson Håkan, 28, 553
Jones Adrian, 691
Josefsson Mattias, 1530
Jost Thomas, 1362

Köstekci F., 1488
Kacem Najib, 681
Kaipio Jari, 1212
Kapelke Simon, 794
Kapitaniak Tomasz, 1118
Karaçay Tuncay, 519
Kavan Pavel, 1665
Kenov Anton, 1421
Khoo B.C., 320
Kim Ji-Hwan, 1643
Kim Jinseong, 908
Kim Jong-Wook, 348
Kireenkov Alexey, 819
Klanner Michael, 163
Klaseboer E., 320
Kmita Grzegorz, 1451, 1459
Knez Luka, 298
Kolber Karolina, 1451
Koutsovasilis Panagiotis, 469
Kovalovs Andrejs, 288
Kozánek Jan, 563
Kozik Krzysztof, 373
Koziol Piotr, 985
Kozupa Michal, 1451, 1459
Králik Juraj, 197, 207
Kranjc Tadej, 1265
Kremer Eugen, 358
Kumar Pankaj, 61
Kuzniatsov Maryna G, 1692

Lancioni Giovanni, 1615
Larsen Curtis, 792
Latalski Jaroslaw, 489
Lee Ming-Gong, 173
Lenci Stefano, 680, 1015, 1056, 1615
Li Zhixin, 1623
Li Zi-Cai, 173
Lihua Xu, 109
Lindell Hans, 1530
Linderholt Andreas, 1275
Longarini Nicola, 1508
Lord Charles, 1518

M. Luis Fernando Paullo, 268
Müller Dominic, 422
Magalhaes Leonardo P., 621
Magluta Carlos, 318
Majer Krzysztof, 1394
Mall Phillip, 1099
Manin Lionel, 1477
Manoach Emil, 1057
Massenhove Korneel Van, 1218
Matkovic Ivo, 1421
Mayer Dirk, 1392
Mayet Johannes, 1235
Mazlan Ahmad Zhafran Ahmad, 592
McKay Andrew, 802
Medina Juan Camilo Rivera, 48
Meier Jürg, 422
Melz Tobias, 187
Mezenin Anton, 71
Mike Jeffrey, 1605
Mlakar Tomaž, 403
Modak S.V., 234
Morais Vinicius Calazans, 925
Mršnik Matjaž, 783
Mueller-Hirsch Wolfgang, 187
Mundo Domenico, 119, 611, 1287
Murachev Andrey, 71

Náprstek Jiří, 662
Naoki Hosoya, 1674
Narayanan S, 61, 714
Nastran Miha, 1404, 1441
Nateghi Alireza, 1306
Neri Paolo, 217
Neubert Michael, 1145
Neuhaus Jan, 1109
Nigdeli Sinan Melih, 852, 860, 868, 878
Nijman E. J. M., 1374
Nijman Eugene, 383, 1342, 1352, 1384
Nikiforov Anatolii, 1658

Offner Guenter, 383
Ohl S.W., 320
Orlando Diego, 1015
Ostermeyer Georg-Peter, 1145
Ozer Hasan Omur, 886, 897

Padmanabhan C, 714
Palermo Antonio, 119
Palomba Ilaria, 1192
Pan J., 1412, 1466
Paullo Munoz Luis Fernando, 690
Pavlovskaia Ekaterina, 346, 1118
Pehlivanturk Can, 1155
Pei C. M., 1466
Pei M., 1412

Perlikowski Przemyslaw, 1118
Pesaresi Luca, 691
Pezerat Charles, 1318
Pfützner Helmut, 1421, 1431
Piccirillo Vinícius, 1046
Pierini Marco, 1331
Pinto Fernando Castro, 48
Pinto Hernandez William, 318
Pinto William, 48
Pioldi Fabio, 412, 641
Pirnat Miha, 1404
Pluymers Bert, 1297, 1306
Polukoshko Svetlana, 631
Postnikov Andrey, 346
Pradhan Sharad, 234
Prado Zenón J. G. N. Del, 1005
Proso Uroš, 1332
Pumhoessel Thomas, 601
Putelat Thibaut, 802

Rainieri Carlo, 432
Reckmann Hanno, 1145
Rega Giuseppe, 680, 1015, 1046
Repetto Maria Pia, 753
Rezende Andrei, 1202
Richiedei Dario, 89, 1192
Rijk Sophie de, 1342
Ripin Zaidi Mohd, 592
Ritto Thiago G., 1164
Ritto Tiago G., 1184
Rivola Alessandro, 763
Rixen Daniel J., 1235, 1245, 1255
Rizzi Egidio, 412, 641
Rocha Rodrigo T., 1036
Rodrigues Helder, 1549
Roitman Ney, 318
Rongong Jem, 1518
Rovšček Domen, 403
Rucevskis Sandris, 288
Rusinek Rafal, 373, 672
Rustighi Emiliano, 539
Rutzmoser Johannes B., 1245, 1255
Ruzziconi Laura, 1056
Ryosuke Umino, 1674

Sala Ramses, 1331
Salles Loic, 691
Salloum Rogério , 1392
Salvi Jonathan, 412, 641
Sampaio Rubens, 1164, 1173
Santhosh B, 714
Santus Ciro, 217
Sanz-Andres Angel, 17
Sattler Henrique A. R., 1005
Sayin Alaattin, 886
Scheel Maren, 1275
Schmidt André, 226
Schulte Frank, 1109
Schweizer Bernhard, 469
Schwingshackl Christoph W., 691
Schwochow Jan, 393
Sedlar Damir, 359
Seemann Wolfgang, 794
Sextro Walter, 1109
Shamsah Sami Ibn, 479
Sharma Anuj, 187
Shilyashki Georgi, 1421, 1431
Shimanovsk Alexandr O, 1682, 1692
Shin Gangsig, 908
Shoja Siavash, 152
Shor Roman, 1155
Shweiki Shadi, 119
Silva Andréa, 268, 690
Silva Frederico M. A., 1005
Silveira Marcos, 1026
Silveira Ricardo, 268, 690
Silvestro Giuseppe, 1508
Sinha Jyoti, 479, 571
Skrinjar Luka, 185
Slavič Janko, 144, 185, 278, 298, 403, 783, 1265, 1332, 1441, 1589
Smolík Luboš, 529
Sogabe Masamichi, 956
Soize Christian, 1173
Sokolov Sergei, 827
Sorribes-Palmer Felix, 17
Sousa Rafael V., 621
Steinbuch Rolf, 591
Steinwolf Alexander, 763
Swiatkowski Michal, 1459
Szmit Zofia, 489
Szymanski Marcin, 373

Tanabe Makoto, 956
Tanabe Yasuko, 956
Tanaka Yudai, 1025
Tang Q.S, 1412
Tang Q.S., 1466
Tarman Peter, 1404
Tehrani Maryam Ghandchi, 974, 1026
Tergeist Mathias, 1145
Tkachenko Liudmila, 79
Tomac Ivan, 359
Toso Alessandro, 119
Tournour Michel, 1287
Trenner Gerald, 1431
Trevisan Lucas R., 621
Trevisani Alberto, 89, 1192
Treviso Alessandra, 1287
Troncossi Marco, 763
Turel Aleš, 144
Tusset Angelo, 1046
Tyminski Natalia, 1202

Utz von Wagner, 1088

Vázquez Benjamín, 499
Vaisberg Leonid, 71
Valentim Carlos A., 621
van Oort Eric , 1155
Vandepitte Dirk, 1218
Veronesi Giorgio, 1374
Vlach Jarmil, 1650, 1665

Wahl Philipp, 1069
Wakui Hajime, 956
Wang Fuxing, 966
Wang Y. X., 1412
Wang Y.X, 1466
Wang Ying, 966
Warminska Anna, 1057
Warminski Jerzy, 373, 489, 1057
Wesolowski Miroslaw, 288
Wiercigroch Marian, 346, 672
Wimmel Thomas Secall, 422
Witczak Pawel, 1394
Wolfsteiner Peter, 733
Woodhouse Jim, 802

Xiang Yi-qiang, 336

Yabuno Hiroshi, 325, 1025, 1487
Yagiz Nurkan, 897
Yamashita Kiyotaka, 325
Yin Chi, 109
Younis Mohammad, 1056
Yu Kun-Ming, 173
Yushan Gu, 109

Zakaria Azrul Abidin, 539
Zanarini Alessandro, 773, 1559, 1569, 1579
Zapomel Jaroslav, 563
Zaripov Rinat, 79
Ziegler Pascal, 1069
Zimmermann Klaus, 99
Zucca Marco, 1508
Zywica Grzegorz, 509
Lozina Željan, 359

Proceedings of ICoEV 2015
International Conference on Engineering Vibration

Editors:
Miha Boltežar, Janko Slavič, Marian Wiercigroch

Pages:
1713

Publisher:
University of Ljubljana,
Faculty for Mechanical Engineering

URL address: www.icoev.org

Ljubljana, 2015
ISBN 978-961-6536-97-4

ISBN 978-961-6536-97-4

